



MONASH University

The structure and function of G protein-coupled receptors

Patrick M. Sexton
BSc. Hons, PhD

A thesis submitted for the degree of *Doctor of Science* at
Monash University in 2021

Copyright notice

© The author 2021.

All published work has been reproduced without alteration. Copyright of the published work has been assigned to the publisher as required for publication. This work is reproduced here for the purpose of examination of the award of the DSc degree and as a collection of the works for this purpose. Reproduction of any material within this thesis requires permission of the relevant copyright owner.

Abstract

Membrane proteins are the principal gatekeepers for control of cellular response, with G protein-coupled receptors (GPCRs) the largest family of cell surface proteins. These proteins participate in virtually all physiological responses, are ubiquitously important for pathophysiological control, and are a major target for drug discovery. While these receptors are highly successful drug targets (>30% of current drugs), lack of clinical efficacy remains an important reason for candidate drug failure. This has highlighted gaps in our understanding of the function of GPCRs, and of the limitations of the classic approach to drug discovery that targets the natural ligand-binding site. My research has been at the forefront of elucidating molecular understanding of, and quantifying novel modes of drug action at, GPCRs, specifically allosteric, bitopic and biased ligands. This provides unprecedented opportunity for fine-tuning of drug response. My research has crossed boundaries of chemistry, biochemistry, endocrinology, pharmacology and structural biology with particular relevance for concepts of the pharmacology of biased agonists and allosteric modulators of GPCRs, and the structure and function of GPCRs with a particular emphasis on the class B subfamily.


Declaration

This thesis is submitted for consideration of the award of the Higher Degree “Doctor of Science”. It is an amalgamation of selected research published since 2008, the year that marked 20 years since the award of my last degree. Work submitted to ACS Pharmacol Transl Sci during my term as Editor-in-Chief was independently handled by Assoc. Editors and I was completely blinded to the review process, in line with ACS journals policy.

Statement on jointly authored research

For all listed papers, I played a major role in the conceptualisation, design, supervision of research performed, interpretation of data, and in the final editing of manuscripts. In many cases, I also had a major role in the writing of the published work. For all manuscripts, I am either the sole corresponding author or a joint corresponding author (denoted by “*”). In recent years, my laboratory has been co- managed by Denise Wootten, and consequently there are multiple papers included where Denise is a co-senior (corresponding) author. In all these cases, whether Denise or I are last listed, we equally contributed to the research described. A list of the papers submitted for consideration is compiled below. In other cases, the published work was part of collaborations between my group and other laboratories.

A number of papers formed components of the Thesis submission of students for their PhD. These include the following papers: [2,4-6,34,36], Cassandra Koole; [17,20], Marlies Hager (not enrolled through Monash); [19,22], Thomas Coudrat; [24,25,31], Emma dal Maso; [26], Saifei Lei (not enrolled through Monash); [27], Chris Draper-Joyce; [30], Madeleine Fletcher; [33], Rulue Chang (not enrolled through Monash). Citations are from Google Scholar

Signature: 

Print Name: Patrick Sexton

Date: August 5th 2021

Acknowledgements

First and foremost, I would like to thank my wife, Jennifer, for her unwavering support during my research career that was regularly a dominating feature of our life. This work would not have been possible without her (long suffering) tolerance and generosity.

As everyone who works in medical research understands, we achieve the largest gains through collaboration. I have been extremely fortunate to work with many excellent and brilliant scientists at all levels of their careers. The work encapsulated in this thesis is a testament to everyone who has been involved in the research. I may be the thread that links this tapestry of shared knowledge, but it would not have been possible without everyone who has collaborated with me on this journey.

While it would be tedious to list everyone, there are some critical individuals who have been instrumental to my research and career. First and foremost, Arthur Christopoulos, my close friend and long-term colleague. Our joint success over the years is a great example of human synergy, amplifying the scope, breadth and impact well beyond what we would have otherwise achieved. The second key person is Denise Wootten. Denise embodies the qualities of brilliance, generosity and leadership. She continues to challenge me (in a good way) and it has been a pleasure to share leadership of our research team with Denise over the last decade. Both Denise and Arthur have shaped the direction and scope of my research and the impact of the body of work described in this thesis belongs equally to these amazing people.

I would also like to give a shout out to Jack Martin, who helped to shape my early years as a scientist, and Bill Charman who has guided and supported me and my team since we joined MIPS in 2009.

Apologies to everyone else involved in this research journey, who deserved to be explicitly named, your contributions are not lessened by this.

Finally, research costs money and I would like to acknowledge the many different funding bodies that have contributed to enabling my research. Critically important among these have been the National Health and Medical Research Council of Australia and the Australian Research Council. However, our team has been generously supported by international funding bodies such as the Wellcome Trust and the National Institutes of Health, as well as the many industry partners for both academic and commercially focused research. Among these, I would like to particularly thank friends and colleagues at Servier in France who have been amazing supporters of our research over many years.

Summary of the development of the work

In the last decade, we have become increasingly aware that our understanding of how both natural ligands and drugs act at GPCRs is incomplete. Historically these receptors were viewed principally as on-off switches, and this evolved to a more nuanced view akin to a dimer switch analogy where there was a linear relationship between the ability of drugs to bind and activate the receptor and the level of cellular response. We now understand that GPCR control of cellular function is much more complex, and that they can activate different spectra of signaling response depending on the specific receptor type, and also the activating ligand. If we view the cell as a full symphonic orchestra, then the GPCR could be viewed as a specialised orchestra, from a string quartet through to an almost complete ensemble of instruments. This represents the degree of potential signaling that an individual GPCR may initiate. In the orchestratic setting both the score and the conductor's interpretation will influence the extent and timing of how different instruments within the available orchestra are used. In the same way, we now recognise that individual ligands act more as conductors distinctly regulating the ensemble and timing of instruments used within each GPCR suborchestra. This allows highly selective control of cellular signaling. In the context of drug discovery, it provides scope for more efficacious drugs, and/or drugs with improved safety by selectively activating on-target beneficial effects to the exclusion of on-target side effects. The ability to exploit such complex drug behaviour requires a quantitative framework that can be applied to evaluate structure-activity relationships linked to optimal signaling, an understanding of the basis of efficacy and structural understanding of the active state of receptors, particularly those where the transducer (signaling partner) is in complex with the receptor. The enclosed body of research encompasses key contributions that have been made under my direction, often collaboratively with other laboratories both within Australia and internationally, which have helped to advance the field in these key areas. The work can be broadly viewed under 3 major heading; (i) pharmacology of biased agonists and allosteric modulators, (ii) structure-function analysis of receptors and how this relates to pharmacological behaviour of ligands, and (iii) structure determination. While the work spans multiple classes of GPCRs, my laboratory has had a particular focus on class B1 GPCRs that respond to peptide hormones that play critical roles in regulation of major physiological responses including metabolism, bone turnover and calcium regulation, cardiovascular/lymphatic development and response, immune response and integrative central nervous system responses [see reviews; 37,38-41].

Pharmacology of biased agonists and allosteric molecules

My laboratory has been at the forefront of novel research into the molecular nature of efficacy and the quantification and understanding of biased agonism and allosteric modulation of class B1 GPCRs. This has included extensive work identifying and quantifying allosteric modulation of this receptor family by both proteins, such as receptor activity-modifying proteins (RAMPs) [1], and other GPCRs [8], and small molecules [2-4,6,8,10,11] that included the demonstration of the ability of allosteric ligands to rescue loss of function polymorphic variants of receptors [4,11], and augmentation of otherwise low potency metabolites of endogenous GPCR agonists [7]. Major reviews in this area include [36,38,39,41].

My laboratory has also been at the forefront of the identification and quantification of biased agonism, particularly at class B1 GPCRs [2,9,10,13,14,16,17,20,23,24,26,30], including demonstration of widespread signalling bias for both approved drugs and investigational tools of the clinically important glucagon-like peptide-1 receptor (GLP-1R). This body of work also included major contributions to advancement in our understanding of G protein efficacy; illustrating that ligand-induced differences in efficacy extended beyond distinct ligand-

dependent receptor conformations (that altered recruitment of G proteins), to propagation of conformational changes to the transducer G protein. These changes altered guanine nucleotide turnover, G protein-receptor residency and the rate of activation of downstream signaling pathways [16]. In addition to broadening our understanding of partial agonism, the work had implications for mechanisms underlying biased agonism. Major reviews in this area include [39,41,43].

Structure-function analysis of class B1 GPCRs

My laboratory has played a field-leading role in the study of relationships between receptor structure and function through extensive mutagenesis of class B1 GPCRs and broad analysis of the functional significance of mutation enabled by detailed quantitative assessment of multi-pathways signaling and distinct ligands [5,6,9,11,13-15,21,23,25,26,31,32,33-35]. This work has started to unravel how subdomains of the receptor differentially contribute to propagation of acute, G protein-dependent signaling, and to convergent pathways that require recruitment of alternate transducers, such as arrestin proteins. It has also allowed deep understanding of the relationship between receptor residues that contact the agonist ligand versus those that are involved in conformational propagation of the signal.

GPCR structure

While I have played a substantial role in work describing novel inactive structures of the muscarinic receptor subfamily [12], and the adenosine A1 receptor [18], the biggest impact that my laboratory's research has had on the field is in the determination of active-state GPCRs by cryo-electron microscopy (cryo-EM) [21,23,27-29,31,33-35,42,44].

Despite the critical importance of active GPCRs to understanding endogenous ligand and drug signaling, until 2017 the only structure of a GPCR in complex with both an agonist and its canonical transducer, G protein heterotrimer, was the 2011 paper of Kobilka & colleagues (Rasmussen et al, Nature 2011) of the β 2-adrenoceptor:Gs complex. This was solved by x-ray crystallography and included the critical development of a tool to stabilise the G protein heterotrimer (nanobody (Nb) 35). This work was a major contributor to the award of the 2012 Nobel Prize to Brian Kobilka. While there had been tremendous effort in the community to derive additional GPCR:G protein heterotrimer structures by crystallography, this has been unsuccessful, albeit that a limited number of complexes with transducer mimetic nanobodies or mini-G proteins were solved.

Developments in cryo-EM, recognized by the 2017 Nobel Prize in Chemistry, have enabled high-resolution structure determination, but its application to GPCRs was limited by the small particle size of active GPCR complexes. My laboratory was the first to demonstrate that cryo-EM could be applied to GPCR structure determination (a collaboration with laboratories in Stanford, USA (Kobilka/Skiniotis) and the Max Planck Institute, Germany (Khoshouei/Danev)) [21]. This was applied to the calcitonin receptor, a class B1 GPCR, enabling the first insights into the activation of this class of receptors. Moreover, we demonstrated that (unlike most receptors solved by crystallography) it could be applied to minimally engineered receptors. This was the first receptor to be solved in complex with a heteromeric G protein since the Kobilka 2011 publication. While this initial structure was of moderate resolution (4.1Å), my laboratory is now routinely applying cryo-EM to determine structures of higher resolutions (3.3-3.6 Å for papers published over 12 months ago [23,27,28,33], and now most under 3 Å and many under 2.5 Å, e.g. [34,35]). Of note, these resolutions are for the entire complex, including regions of high mobility and low resolution; within the receptor core, ligand binding site and G protein interface, there is higher resolution. We also pioneered the use of dominant negative mutations in the G α protein

subunit to increase the stability of the α - $\beta\gamma$ heterotrimer when complexed to the receptor [23,27-29,33-35]. This has enabled formation, purification and determination of novel complexes not possible with just Nb35. This facilitated the determination of a novel structure of the GLP-1 receptor bound to a biased agonist that provided unique structural insight into the structural basis of biased agonism [23]. The approach was also successful for determination of one of the first non-Gs structures [27], and the very recent structure of the first heterodimeric GPCR complex, the CGRP receptor that is a major target for treatment of migraine [28]. This work has helped to revolutionize GPCR structure determination and my laboratory continues to innovate in this space.

Candidate significance statement

The work from my laboratory has played a key role in understanding of the concepts of allostery and biased agonism at class B GPCRs, including demonstration that both clinical and tool agonists of the GLP-1R exhibit biased agonism, with potential implications for observed differential efficacy in patients, along with the design of next generation therapeutics that extend the clinical application of GLP-1R agonists to obesity and neurodegenerative disease. We are international leaders in quantitative analysis of bias and allostery and more recently in unravelling the mechanistic basis for these pharmacological parameters. This has included work published in *Cell* on the nature of efficacy that demonstrated that different agonists of an individual receptor not only distinctly alter receptor conformation, but that this extended to the conformation of the transducer protein in ternary complex with agonist and receptor. This modified the turnover of G proteins and thus the measured efficacy of ligands. This altered the prevailing view that the distinct ligand-receptor conformations only altered the affinity (and thus recruitment) of the G protein to the receptor. The mechanistic work has also included numerous structure function analyses where the effect of receptor mutations has been examined across multiple pathways and multiple ligands, where application of our quantitative analytical methods has allowed interpretation of the relative effect of mutations on affinity and efficacy, for each pathway and ligand. This was fundamental to our ability to map how different regions of the receptors contribute to ligand affinity and to pathway specific efficacies (and thus biased agonism). This has been encapsulated in a substantive body of work published in journals including *Cell*, *PNAS*, *Biochem Pharmacol*, *JBC*, *Mol Pharmacol* and *ACS Pharmacol Transl Sci*. More recently, my laboratory has worked towards providing a molecular understanding of the control of receptor activation by different natural and synthetic agonists. To do this, we needed to be able to determine structures of active-state receptors bound to both agonists and transducer proteins, particularly heterotrimeric G proteins. When embarking on this, there was only a single GPCR structure that had been solved, the β 2-adrenoceptor:Gs complex. This had been achieved using x-ray crystallography and had not been replicated for other receptors. This required both modification of the receptor, and development of a new tool to stabilize the complex. We were particularly interested in trying to work with near native receptors (modified only at the far N- or C- terminus with affinity tags for purification, which could also be cleaved if required), as we believed that receptor dynamics could play an integral role in their function. With advice from the Kobilka laboratory, we were eventually able to form and purify stable complexes, but these did not form crystals. Cryo-EM was a rapidly evolving methodology at this time but GPCRs were considered too small to be amenable to cryo-EM. By collaborating with the Danev laboratory in Germany who had developed the Volta phase plate technology to enhance image contrast, we were able to solve the first GPCR to near atomic resolution by cryo-EM (*Nature* 2017) that was also the first active-state class B GPCR solved, the first to GPCR solved that had not been modified, and the second ever agonist:GPCR:G protein complex to be determined. This profoundly changed the structural approach to GPCR determination, with cryo-EM now the pre-eminent method being applied.

My laboratory, working with Rado Danev and his team, including Maryam Khoshouei, has remained at the forefront of the use of cryo-EM to understand GPCR structure, including the development new biochemistry (dominant negative G proteins) that has enabled the solution of complexes not stable with only Nb35 stabilisation, and application to other (non-Gs) families of G protein, and included structures of the GLP-1R with a biased agonist (Nature 2018), the CGRP receptor (a heterodimer of a GPCR and a single pass transmembrane protein, RAMP1; Nature 2018), and the adenosine A1R in complex with a Gi protein (Nature 2018). Since this time, working with our collaborators, we have now solved >80 structures, many published in the last 12 months and many unpublished, brought the routine resolution of GPCR structures to 2.5 angstrom and below (and thus our structures are among the highest resolution GPCR structures by any method), and very recently demonstrated that (well behaved) GPCRs can be solved by cryo-EM at sub 2 angstrom resolution (unpublished; something many experts did not think would be possible with cryo-EM), and used analytical methods to extract information on GPCR dynamics from the cryo-EM particle stacks that has been critical for understanding selectivity and function of multiple receptors and ligands. However, the key advance from my laboratory is not in GPCR structure *per se* but in our ability to integrate this information with detailed molecular pharmacology and analytical pharmacological analysis of GPCRs and ligands to evolve our understanding of how agonists differentially modulate GPCR function.

Original research [Pages 13 – 834]

- 1) M Morfis, N Tilakaratne, SGB Furness, G Christopoulos, TD Werry, A Christopoulos and **PM Sexton**. Receptor activity modifying proteins differentially modulate the G protein-coupling efficiency of amylin receptors. *Endocrinology* **149**: 5423-5431, 2008. [Pages 14 – 22] Citations 118.
- 2) Koole C, Wootten D, Simms J, Valant C, Sridhar R, Woodman OL, Miller LJ, Summers RJ, Christopoulos A, **Sexton PM**. Allosteric ligands of the glucagon-like peptide 1 receptor (GLP-1R) differentially modulate endogenous and exogenous peptide responses in a pathway-selective manner; implications for drug screening. *Mol Pharmacol* **78**: 456-465, 2010. [Pages 23 – 39] Citations 191.
- 3) Wootten D, Simms J, Koole C, Woodman OL, Summers RJ, Christopoulos A, **Sexton PM**. Modulation of the glucagon-like peptide-1 receptor signalling by naturally occurring and synthetic flavonoids. *J Pharmacol Exp Therap* **336**: 540-550, 2011. [Pages 40 – 50] Citations 81.
- 4) Koole C, Wootten D, Simms J, Valant C, Miller LJ, Christopoulos A, **Sexton PM**. Polymorphism and ligand dependent changes in human glucagon-like peptide-1 receptor (GLP-1R) function: allosteric rescue of loss of function mutation. *Mol Pharmacol* **80**: 486-497, 2011. [Pages 51 – 64] Citations 80.
- 5) Koole C, Wootten D, Simms J, Miller LJ, Christopoulos A, **Sexton PM**. The second extracellular loop of the human glucagon-like peptide-1 receptor (GLP-1R) has a critical role in GLP-1 peptide binding and receptor activation. *J Biol Chem* **287**: 3642-3648, 2012. [Pages 65 – 82] Citations 90.
- 6) Koole C, Wootten D, Simms J, Savage EE, Miller LJ, Christopoulos A, **Sexton PM**. The second extracellular loop of the human glucagon-like peptide-1 receptor (GLP-1R) differentially regulates orthosteric but not allosteric agonist binding and function. *J Biol Chem* **287**: 3659-3673, 2012. [Pages 83 – 98] Citations 36.
- 7) Wootten D, Savage EE, Valant C, May LT, Sloop KW, Ficorilli J, Showalter AD, Willard FS, Christopoulos A, **Sexton PM**. Allosteric modulation of endogenous metabolites as an avenue for drug discovery. *Mol Pharmacol* **82**: 281-290, 2012. [Pages 99 – 117] Citations 76.
- 8) Harikumar KG, Wootten D, Pinon DI, Koole C, Ball AM, Furness SGB, Graham B, Dong M, Christopoulos A, Miller LJ*, **Sexton PM***. Glucagon-like peptide-1 receptor dimerisation differentially regulates agonist signalling but does not affect small molecule allostery. *Proc Natl Acad Sci* **109**: 18607-18612, 2012. [Pages 118 – 123] Citations 61.
- 9) Wootten D, Simms J, Miller LJ, Christopoulos, A and **Sexton PM**. Polar transmembrane interactions drive formation of ligand-specific and signal pathway-biased Family B GPCR conformations. *Proc Natl Acad Sci USA* **110**: 5211-5216, 2013. [Pages 124 – 141] Citations 161.

- 10) Wootten D, Savage EE, Willard FS, Bueno AB, Sloop KW, Christopoulos A, **Sexton PM**. Differential activation and modulation of the glucagon-like peptide-1 receptor by small molecule ligands. *Mol Pharmacol* **83**: 822-834, 2013. [Pages 142 – 171] Citations 87.
- 11) Koole C, Wootten D, Simms J, Miller LJ, Christopoulos A, **Sexton PM**. Differential impact of amino acid substitutions on critical residues of the human glucagon-like peptide-1 receptor (GLP-1R) involved in peptide activity and small molecule allostery. *J Pharmacol Exp Therap* **353**: 52-63, 2015. [Pages 172 – 183] Citations 16.
- 12) Thal DM, Sun B, Feng D, Nawaratne V, Leach K, Felder CC, Bures MG, Evans DA, Weis WI, Bachhawat P, Kobilka TS, **Sexton PM***, Kobilka BK*, Christopoulos A*. Crystal structures of the M₁ and M₄ muscarinic acetylcholine receptors and insights into their allosteric modulation. *Nature* **531**: 335-340, 2016. [Pages 184 – 201] Citations 221.
- 13) Wootten D, Reynolds CA, Koole C, Smith KJ, Mobarec JC, Simms J, Quon T, Coudrat T, Furness SGB, Miller LJ, Christopoulos A, **Sexton PM**. A hydrogen-bonded polar network in the core of the glucagon-like peptide-1 receptor is a fulcrum for biased agonism: Lessons from Class B crystal structures. *Mol Pharmacol* **89**: 335-347, 2016. [Pages 202 – 214] Citations 55.
- 14) Wootten D, Reynolds CA, Smith KJ, Mobarec JC, Koole C, Savage EE, Pabreja K, Simms J, Sridhar R, Furness SGB, Liu M, Thompson PE, Miller LJ, Christopoulos A, **Sexton PM**. The GLP-1 receptor extracellular surface is a molecular trigger for biased agonism. *Cell* **165**: 1632-1643, 2016. [Pages 215 – 227] Citations 103.
- 15) Wootten D, Reynolds CA, Smith KJ, Mobarec JC, Furness SGB, Miller LJ, Christopoulos A, **Sexton PM**. Key interactions by conserved polar amino acids located at the transmembrane helical boundaries in Class B GPCRs modulate activation, effector specificity and biased signalling of the glucagon-like peptide-1 receptor. *Biochem Pharmacol* **118**: 68-87, 2016. [Pages 228 – 247] Citations 32.
- 16) Furness SGB, Liang Y-L, Nowell CJ, Halls ML, Wookey PJ, Dal Maso E, Inoue A, Christopoulos A, Wootten D, **Sexton PM**. Ligand-dependent modulation of G protein conformation alters drug efficacy. *Cell* **167**: 739-749, 2016. [Pages 248 – 270] Citations 93.
- 17) Hager MV, Johnson LM, Wootten D*, **Sexton PM***, Gellman SH*. β -Arrestin-biased agonists of the GLP-1 receptor from β -amino acid residue incorporation into GLP-1 analogues. *J Am Chem Soc* **138**: 14970-14979, 2016. [Pages 271 – 280] Citations 63.
- 18) Glukhova A, Thal DM, Nguyen AT, Vecchio EA, Jörg M, Scammells PJ, May LT, **Sexton PM*** and Christopoulos A*. Structure of the adenosine A₁ receptor reveals the basis for subtype selectivity. *Cell* **168**: 867-877, 2017. [Pages 281 – 305] Citations 178.
- 19) Coudrat T, Christopoulos A, **Sexton PM***, Wootten D*. Structural features embedded in G protein-coupled receptor co-crystal structures are key to their success in virtual screening. *PLoS One* **12**: e0174719. doi: 10.1371/journal.pone.0174719. [Pages 306 – 334] Citations 9.
- 20) Hager MV, Clydesdale L, Gellman SH*, **Sexton PM***, Wootten D*. Characterization of signal bias at the GLP-1 receptor induced by backbone modification of GLP-1. *Biochem Pharmacol* **136**: 99-108, 2017. [Pages 335 – 357] Citations 44.
- 21) Liang Y-L, Khoshouei M, Radjainia M, Zhang Y, Glukhova A, Tarrasch J, Thal DM, Furness SGB, Christopoulos G, Coudrat T, Danev R, Baumeister W, Miller LJ, Christopoulos A, Kobilka BK, Wootten D*, Skiniotis G*, **Sexton PM***. Phase-plate cryo-EM structure of a class B GPCR-G protein complex. *Nature* **546**: 118-123, 2017. [Pages 358 – 375] Citations 358.
- 22) Coudrat T, Simms J, Christopoulos A, Wootten D*, **Sexton PM***. Improving virtual screening of G protein-coupled receptors via ligand-directed modeling. *PLoS Comp Biol* **13**: e1005819, 2017. doi: 10.1371/journal.pcbi.1005819. [Pages 376 – 415] Citations 9.
- 23) Liang Y-L, Khoshouei M, Glukhova A, Furness SGB, Zhao P, Clydesdale L, Koole C, Troung TT, Thal DM, Lei S, Radjainia M, Danev R, Baumeister W, Wang M-W, Miller LJ, Christopoulos A, **Sexton PM***, Wootten D*. Phase-plate cryo-EM structure of a biased agonist-bound human GLP-1 receptor-Gs complex. *Nature* **555**: 121-125, 2018. [Pages 416 – 435] Citations 203.
- 24) Dal Maso E, Just R, Hick C, Christopoulos A, **Sexton PM***, Wootten D*, Furness SGB*. Characterisation of signalling and regulation of common calcitonin receptor splice variants and polymorphisms. *Biochem Pharmacol* **148**: 111-129, 2018. [Pages 436 – 454] Citations 12.
- 25) Dal Maso E, Zhu Y, Pham V, Reynolds CA, Deganutti G, Hick CA, Yang D, Christopoulos A, Hay DL, Wang M-W, **Sexton PM***, Furness SGB*, Wootten D*. Extracellular loops 2 and 3 of the calcitonin receptor selectively modify agonist binding and efficacy. *Biochem Pharmacol* **150**: 214-244, 2018. [Pages 455 – 485] Citations 18.

- 26) Lei S, Clydesdale L, Dai A, Cai X, Feng Y, Yang D, Liang Y-L, Koole C, Zhao P, Coudrat T, Christopoulos A, Wang M-W*, Wootten D*, **Sexton PM***. Two distinct domains of the glucagon-like peptide-1 receptor control peptide-mediated biased agonism. *J Biol Chem* **293**: 9370-9387, 2018. [Pages 486 – 504] Citations 29.
- 27) Draper-Joyce CJ, Khoshouei M, Thal D, Liang Y-L, Nguyen ATN, Furness SGB, Venugopal H, Baltos J, Plitzko JM, Danev R, Baumeister W, May LT, Wootten D, **Sexton PM***, Glukhova A*, Christopoulos A*. Structure of the adenosine-bound human adenosine A1 receptor-Gi complex. *Nature* **558**: 559-563, 2018. [Pages 505 – 525] Citations 194.
- 28) Liang Y-L, Khoshouei M, Deganutti G, Glukhova A, Koole C, Peat TS, Radjainia M, Plitzko JM, Baumeister W, Miller LJ, Hay DL, Christopoulos A, Reynolds CA, Wootten D, **Sexton PM***. Cryo-EM structure of the active, Gs-protein complexed, human CGRP receptor. *Nature* **561**: 492-497, 2018. [Pages 526 – 549] Citations 131.
- 29) Liang Y-L, Zhao P, Draper-Joyce CJ, Baltos J, Glukhova A, Troung TT, May LT, Christopoulos A, Wootten D*, **Sexton PM***, Furness SGB*. Dominant negative G proteins enhance formation and purification of agonist-GPCR-G protein complexes for structure determination. *ACS Pharmacol Transl Sci* **1**: 12-20, 2018. [Pages 550 – 558] Citations 35.
- 30) Fletcher MM, Halls ML, Zhao P, Clydesdale L, Christopoulos A, **Sexton PM***, Wootten D*. Glucagon-like peptide-1 receptor internalisation controls spatiotemporal signalling mediated by biased agonists. *Biochem Pharmacol* **156**: 406-419, 2018. [Pages 559 – 572] Citations 29.
- 31) Dal Maso E, Glukhova A, Zhu Y, Garcia-Nafria J, Tate CG, Atanasio S, Reynolds CA, Ramirez-Aportela E, Carazo J-M, Hick CA, Furness SGB, Hay DL, Liang Y-L, Miller LJ, Christopoulos A, Wang M-W, Wootten D*, **Sexton PM***. The molecular control of calcitonin receptor (CTR) signaling. *ACS Pharmacol Transl Sci* **2**: 31-51, 2019. [Pages 573 – 593] Citations 24.
- 32) Pham V, Dal Maso E, Reynolds CA, Deganutti G, Atanasio S, Hick CA, Yang D, Christopoulos A, Hay DL, Furness SGB, Wang M-W, Wootten D*, **Sexton PM***. Deconvoluting the molecular control of binding and signalling at the Amylin 3 receptor: RAMP3 alters signal propagation through extracellular loops of the calcitonin receptor. *ACS Pharmacol Transl Sci* **2**: 183-197, 2019. [Pages 594 – 608] Citations 7.
- 33) Chang R, Zhang X, Qiao A, Dai A, Belousoff MJ, Tan Q, Shao L, Zhong L, Lin G, Liang Y-L, Ma L, Han S, Yang D, Danev R, Wang M-W*, Wootten D*, Wu B*, **Sexton PM***. Cryo-electron microscopy structure of the glucagon receptor with a dual-agonist peptide. *J Biol Chem* **295**: 9313-9325, 2020. [Pages 609 – 629] Citations 9.
- 34) Dong M, Deganutti G, Piper SJ, Liang Y-L, Khoshouei M, Belousoff MJ, Harikumar KG, Reynolds CA, Glukhova A, Furness SGB, Christopoulos A, Danev R, Wootten D*, **Sexton PM***, Miller LJ*. Structure and dynamics of the active, Gs-coupled, human secretin receptor. *Nat Commun* **11**: 4137, 2020 [Pages 630 – 673] Citations 13.
- 35) Liang Y-L, Belousoff MJ, Fletcher MM, Zhang X, Khoshouei M, Deganutti G, Koole C, Furness SGB, Miller LJ, Hay DL, Christopoulos A, Reynolds CA, Danev R, Wootten D*, **Sexton PM***. Structure and dynamics of adrenomedullin receptors AM₁ and AM₂ reveal key mechanisms in the control of receptor phenotype by receptor activity-modifying proteins. *ACS Pharmacol Transl Sci* **3**: 263-284, 2020. [Pages 674 – 709] Citations 28.

Reviews [Pages 710-834]

- 36) Valant C, Lane JR, **Sexton PM***, Christopoulos A*. The best of both worlds? Biotopic orthosteric/allosteric ligands of G protein-coupled receptors. *Ann. Rev. Pharmacol. Toxicol.* **52**:153-78, 2012. [Pages 711 – 736] Citations 148.
- 37) Koole C, Pabreja K, Savage EE, Wootten D, Furness SGB, Miller LJ, Christopoulos A, **Sexton PM**. Recent advances in understanding GLP-1 receptor function. *Biochem Soc Trans* **41**: 172-179, 2013. [Pages 737 – 744] Citations 69.
- 38) Wootten D, Christopoulos A, **Sexton PM**. Emerging paradigms in GPCR allostery: implications for drug discovery. *Nature Rev Drug Discov* **12**: 630-644, 2013. [Pages 745 – 759] Citations 376.
- 39) Koole C, Savage EE, Christopoulos A, Miller LJ, **Sexton PM***, Wootten D*. Signal bias, allostery and polymorphic variation at the GLP-1R: Implications for drug discovery. *Mol Endocrinol* **27**: 1234-1244, 2013. [Pages 760 – 770] Citations 42.
- 40) **Sexton PM***, Wootten D*. Structural biology: meet the B family. *Nature* **499**:417-418, 2013. [Pages 771 – 772] Citations 8.

- 41) Wootten D*, Miller LJ, Koole C, Christopoulos A, **Sexton PM***. Allostery and Biased Agonism at Class B G Protein-Coupled Receptors. *Chem Rev* **117**: 111-138, 2017. [**Pages 773 – 800**] Citations 66.
- 42) Thal DM*, Vuckovic Z, Draper-Joyce CJ, Liang Y-L, Glukhova A, Christopoulos A, **Sexton PM***. Recent advances in the determination of G Protein-coupled receptor structures. *Curr Opin Struct Biol* **51**: 28-34, 2018. [**Pages 801 – 807**] Citations 47.
- 43) Wootten D*, Christopoulos A, Marti-Solano M, Babu MM, **Sexton PM***. Mechanisms of signalling and biased agonism in G-protein-coupled receptors. *Nature Rev Mol Cell Biol* **19**: 638-653, 2018. [**Pages 808 – 823**] Citations 220.
- 44) Glukhova A*, Draper-Joyce CJ, Sunahara RK, Christopoulos A, Wootten D, **Sexton PM***. Rules of engagement: GPCRs and G proteins. *ACS Pharmacol Transl Sci* **1**: 73-83, 2018. [**Pages 824 – 834**] Citations 59.

ORIGINAL RESEARCH

Receptor Activity-Modifying Proteins Differentially Modulate the G Protein-Coupling Efficiency of Amylin Receptors

Maria Morfis, Nanda Tilakaratne, Sebastian G. B. Furness, George Christopoulos, Tim D. Werry, Arthur Christopoulos, and Patrick M. Sexton

Drug Discovery Biology Laboratory (M.M., N.T., S.G.B.F., G.C., T.D.W., A.C., P.M.S.), Monash Institute of Pharmaceutical Sciences, and Department of Pharmacology, Monash University, Clayton, Victoria 3800, Australia and Howard Florey Institute and Department of Pharmacology (M.M.), The University of Melbourne, Victoria 3010, Australia

Receptor activity-modifying proteins (RAMPs) 1, 2, and 3 are prototypic G protein-coupled receptor accessory proteins that can alter not only receptor trafficking but also receptor phenotype. Specific RAMP interaction with the calcitonin receptor (CTR) generates novel and distinct receptors for the peptide amylin; however, the role of RAMPs in receptor signaling is not understood. The current study demonstrates that RAMP interaction with the CTR in COS-7 or HEK-293 cells leads to selective modulation of signaling pathways activated by the receptor complex. There was a 20- to 30-fold induction in amylin potency at CTR/RAMP1 (AMY₁) and CTR/RAMP3 (AMY₃) receptors, compared with CTR alone, for formation of the second-messenger

cAMP that parallels an increase in amylin binding affinity. In contrast, only 2- to 5-fold induction of amylin potency was seen for mobilization of intracellular Ca⁺⁺ or activation of ERK1/2. In addition, in COS-7 cells, the increase in amylin potency for Ca⁺⁺ mobilization was 2-fold greater for AMY₃ receptors, compared with AMY₁ receptors and this paralleled the relative capacity of overexpression of G_{αq} proteins to augment induction of high affinity [¹²⁵I]-amylin binding. These data demonstrate that RAMP-complexed receptors have a different signaling profile to CTRs expressed in the absence of RAMPs, and this is likely due to direct effects of the RAMP on G protein-coupling efficiency. (*Endocrinology* 149: 5423–5431, 2008)

G PROTEIN-COUPLED RECEPTORS (GPCRs) are the largest family of cell surface receptors; they play roles in virtually every physiological system and are implicated in most major diseases. Recently increasing attention has focused on the role of accessory proteins in the modulation of GPCR function (1–3). Receptor activity-modifying proteins (RAMPs) are prototypical accessory proteins that interact with specific receptors to alter their function including, in a receptor-dependent manner, cell surface expression, binding phenotype, internalization, and recycling (4, 5). The most characterized partners for RAMP interaction are the calcitonin (CT) and calcitonin receptor-like receptors that, with RAMPs, yield receptors for calcitonin family peptides, including CT, amylin, calcitonin gene-related peptide (CGRP), and adrenomedullin.

Amylin, a 37-amino acid peptide, is cosecreted with insulin from the pancreatic β -cells after food intake and has a range of effects on a number of different tissues to modulate nutritional status. It is a potent inhibitor of vagally mediated gastric emptying and has additional effects including reduced appetite,

reduced postprandial glucagon secretion, and the inhibition of insulin-stimulated glycogen production in skeletal muscle (6, 7). The stable amylin analog, pramlintide, has recently received Food and Drug Administration approval for adjunct treatment of type 2 diabetes (7). Amylin is related to the other CT peptide family members and shares a number of actions with the other peptides, particularly CT (4). Nonetheless, CT has a distinct set of physiological actions, most notably to regulate blood calcium levels by inhibiting osteoclast mediated bone resorption and stimulating renal calcium clearance. It is commonly used for the therapeutic treatment of hypercalcemic conditions, including Paget's disease and osteoporosis (8).

Amylin receptors are generated from the CT receptor (CTR) gene product when coexpressed with RAMPs (9). RAMPs constitute a unique family of type I transmembrane proteins, comprising RAMP1, RAMP2, and RAMP3. Each RAMP possesses a large extracellular N-terminal domain, a single transmembrane α -helix and a small intracellular C-terminal domain. Although RAMPs share a common basic structure, including four conserved cysteines in the N terminus, they share only a relatively low (~30%) amino acid sequence identity. Originally discovered by McLatchie *et al.* (10) during attempts to clone the receptor for CGRP, RAMPs were shown to chaperone the calcitonin receptor-like receptor (CL-R) to the cell surface to form high-affinity CGRP and adrenomedullin receptor receptors. Unlike CL-R, CTR when expressed alone, traffics to the cell surface and functions as a high-affinity receptor for CT peptides. However, when coexpressed with RAMP1, RAMP2, or RAMP3, the CTR/RAMP complexes generate pharmacologically distinct amylin receptors, AMY₁, AMY₂, and AMY₃, respectively (4). Hence, RAMPs can act as a pharmacological

First Published Online July 3, 2008

Abbreviations: AMY, Amylin receptor; CGRP, calcitonin gene-related peptide; CL-R, calcitonin receptor-like receptor; CT, calcitonin; CTR, calcitonin receptor; FBS, fetal bovine serum; GPCR, G protein-coupled receptor; HA, hemagglutinin; HBSS, Hanks' buffered saline solution; hCT, human calcitonin; HEK-293, human embryonic kidney-293; PI, phosphoinositol; PKA, phosphokinase A; PKC, phosphokinase C; PLC, phospholipase C; RAMP, receptor activity modifying protein; rAmy, rat amylin.

Endocrinology is published monthly by The Endocrine Society (<http://www.endo-society.org>), the foremost professional society serving the endocrine community.

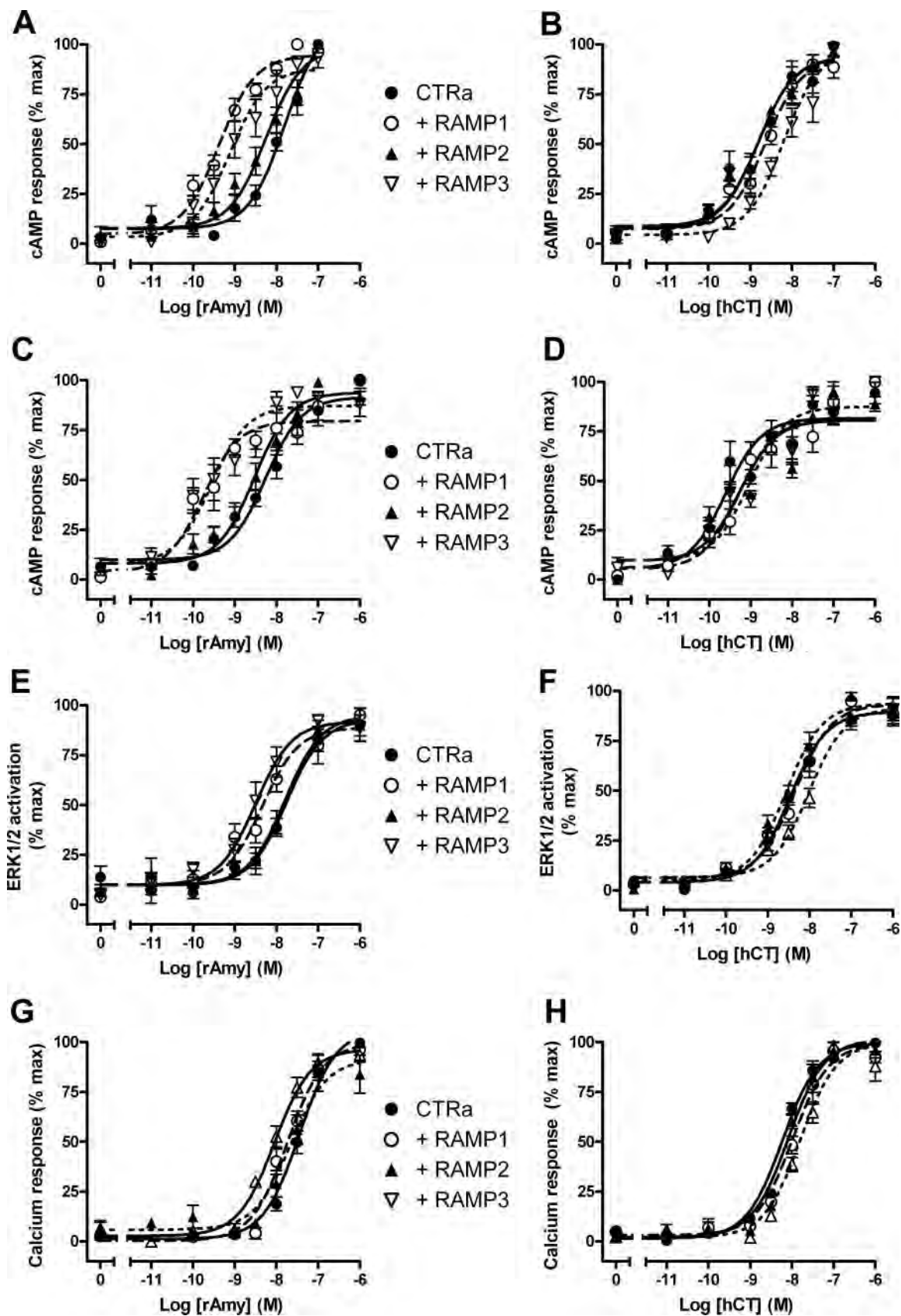


FIG. 1. Measurement of rAmy- or hCT-induced signaling activation via the CTa receptor in the absence or presence of RAMPs. COS7 cells were cotransfected with CTRa and either RAMP1 (open circles), RAMP2 (filled triangles), RAMP3 (open inverted triangles), or pcDNA control (filled circle)

switch for these two GPCRs, providing a sophisticated and novel mechanism for modulating receptor phenotype.

To date, there have been only limited studies looking at the potential role of RAMPs in modulation of CL-R or CTR signaling. Coexpression of RAMPs with the predominant receptor isoform CTRa had no effect on the magnitude of cAMP accumulation or phosphatidylinositol (PI) hydrolysis in COS-7 cells (11). Despite that early study, it is clear that the ability of RAMP2 to form functional amylin receptors is dependent on cellular background and on receptor isoform. For instance, CTRa expressed with RAMP2 generated an amylin receptor in CHO-P cells but only very weakly induced an amylin response in COS-7 cells (12). Furthermore, RAMP2 coexpressed with the CTRb isoform (differing to CTRa by a 16-aa insert in the first intracellular loop) was able to induce amylin receptors in COS7 cells (12), whereas the CTRa isoform effectively cannot. Interestingly, there is no significant difference in peptide binding between the two receptor isoforms, yet the presence of this loop does impair G protein coupling and signaling in a cell-specific manner (13, 14). Differences in the ability or availability of particular G proteins to interact with specific RAMP receptor heterodimers may account for the alterations in pharmacological phenotype and cell type specificity. This theory is supported by evidence that overexpression of $G_{\alpha s}$ proteins can modify the formation of functional RAMP/CTRa complexes in COS-7 cells (15).

The current study demonstrates that RAMP interaction with the CTRa leads to selective modulation of signaling pathways activated by the receptor complex. There was a marked induction in amylin potency at AMY_1 and AMY_3 receptors for formation of the second messenger cAMP that parallels the increase in amylin binding affinity. In contrast, only very weak induction of amylin potency was seen for mobilization of intracellular Ca^{2+} or activation of ERK 1/2. In addition, subtle differences in the effect of RAMP1 *vs.* RAMP3 were observed that were also seen in the relative capacity of overexpression of G_{α} proteins to augment induction of high-affinity amylin binding. These data demonstrate that RAMP-complexed receptors have a different signaling profile to CTRs expressed in the absence of RAMPs, and this is likely due to direct effects of the RAMP on G protein-coupling efficiencies.

Materials and Methods

Materials

Human calcitonin (hCT) and rat amylin (rAmy) were purchased from Auspep (Parkville, Victoria, Australia). Rat amylin is used in preference to human amylin due to the amyloidogenic property of human amylin. CGRP_{8–37} was from Bachem (Bubendorf, Switzerland). AC187 was a gift from Dr. Andrew Young (Amylin Pharmaceuticals Inc., La Jolla, CA). BSA, isobutyl methylxanthine, and poly-L-lysine were from Sigma (St. Louis, MO). Amplified luminescent proximity homogenous assay-screen cAMP kits were purchased from PerkinElmer (Boston, MA). ERK Surefire assay kits were a kind gift from TGR Bioscience (Adelaide, Australia). Fluo-4 label was purchased from Molecular Probes (Invitrogen, Carlsbad, CA). DMEM and HEPES were from Invitrogen; fetal bovine serum (FBS) was from TRACE Biosciences (Sydney, Australia). Cell culture plasticware was from

Nunc (Roskilde, Denmark), and Metafectene was from Biontex supplied by Scientifix (Melbourne, Australia). ^{125}I rat amylin was prepared using Bolton-Hunter reagent; 2000 Ci/mmol from Amersham (Buckinghamshire, UK), and purified by reverse-phase HPLC as described previously (16). ^{125}I -labeled goat antimouse IgG was obtained from PerkinElmer. The inhibitors H-89, U-73122, PD98059, U0126, wortmannin, and staurosporine were purchased from BIOMOL International (Plymouth Meeting, PA). Tyrphostin AG1478, R6-31–8220, and ET-18-OCH₃ were purchased from Calbiochem (La Jolla, CA). Pertussis toxin and forskolin were purchased from Sigma-Aldrich (St. Louis, MO).

cDNA constructs

The preparation of cDNA with a double-hemagglutinin (HA) epitope tag at the N terminus of human CTRa receptor (leucine⁴⁴⁷ variant) has been described previously (17). Human RAMP1, RAMP2, and RAMP3 cDNA constructs were a gift from Dr. Steven Foord (GlaxoSmithKline, Stevenage, UK) (10). cDNA for $G_{\alpha s}$ (short), $G_{\alpha i2}$, $G_{\alpha oA}$, and $G_{\alpha q}$ were from the UMR cDNA resource center (www.cdna.org). All constructs had been subcloned into the pcDNA3.1 mammalian expression vector (Invitrogen).

Cell culture and transfection

Green monkey kidney COS-7 cells were maintained in DMEM supplemented with 5% FBS and maintained at 37 °C in a humidified atmosphere of 5% CO₂. Human embryonic kidney-293 (HEK-293) cells were maintained in DMEM supplemented with 10% FBS and maintained at 37 °C in a humidified atmosphere of 5% CO₂. For competition binding assays, cells were seeded in 48 (1 cm²)-well plates at a density of about 125,000 cells/well. The following day, when cells were 90–100% confluent, they were transfected using 0.75 μ l/cm² of Metafectene with 50 ng and 75 ng/cm² of CTRa and RAMP cDNA, respectively, as previously described (18). For analysis of the effect of overexpression of G_{α} protein on RAMP-induced amylin binding, cells were seeded into 24-well plates to achieve a final density of about 250,000 cells/well. Cells were incubated under growth conditions for a further 36 h before being used in radioligand binding assay. For the functional assays, cells were seeded in 75-cm² flasks and grown overnight to about 90% confluence. HEK-293 cells were grown for 36 h to 90% confluence. Each flask of COS-7 cells was transfected with 3.2 μ g of CTRa and 4.6 μ g of RAMPs or pcDNA3-1 cDNA using 30 μ l of metafectene per flask. Each flask of HEK-293 cells was transfected with 3.75 μ g of CTRa and 5.7 μ g of RAMP or pcDNA3-1 cDNA using 60 μ l of metafectene per flask. Cells were incubated and recovered in growth media as described above. Cells were harvested 16 h after transfection and seeded for use in cAMP, ERK1/2 phosphorylation, and Ca^{2+} mobilization assays or for antibody binding experiments. The 96-well plates seeded with HEK-293 cells were poly-D-lysine treated before use. Allowing 16 h incubation for cells to adhere, cells were subsequently serum starved for a further 24 h before use in the functional assays.

Measurement of cAMP

Intracellular cAMP levels were determined using the AlphaScreen cAMP kit (PerkinElmer Life Sciences). On the day of assay, cells were harvested and assayed as previously described (18). Each assay point was performed in triplicate, and the quantity of cAMP generated was calculated from the raw data using a cAMP standard curve. For antagonist experiments, antagonist peptides were coadministered with agonist ligands as previously described (18).

Radioligand binding

Cells transfected in 48-well plates and incubated for approximately 36 h were assayed for ^{125}I -rat amylin binding. Cells were incubated in binding buffer [DMEM with 0.3% (wt/vol) BSA] containing approximately 120 pM ^{125}I -rat amylin in the absence (total binding) or presence

and cells were assayed 64 h afterward. The *left-hand panels* represent dose responses to rAmy stimulation and the *right-hand panels* to hCT stimulation. A and B, Agonist-mediated cAMP accumulation, measured after 30 min stimulation with rAmy or hCT, respectively. C and D, cAMP accumulation after 5 min stimulation. E and F, Graphed changes in ERK1/2 phosphorylation after agonist stimulation for 5 min; the time point of peak response determined from time-course assays (data not shown). Graphs (G and H) show the Fluo4-measured intracellular Ca^{2+} release. Data are presented as mean \pm SEM, $n = 4–9$.

of increasing concentrations of unlabeled peptide (10^{-11} to 10^{-6} M). Cells were incubated for 1 h at 37°C before being washed with 250 μ l PBS and then solubilized with 250 μ l of 0.5 M NaOH. The cell lysate was collected and counted in a Packard γ -counter (75% efficiency) to determine bound radioactivity. Experiments were performed in duplicate ($n = 4$). To assess the effect of overexpression of G_{α} proteins on induction of AMY receptor phenotype, cells were plated into 24-well plates and transfected with CTRa (100 ng) and one of the four ($G_{\alpha s}$, $G_{\alpha i2}$, $G_{\alpha oA}$, $G_{\alpha q}$) G_{α} subtypes (150 ng) together with either pcDNA3.1 empty vector or one of RAMP1, RAMP2, or RAMP3 (100 ng). Whole cells were assayed for 125 I-rat amylin binding 48 h after transfection by incubating transfected cells with radioligand (80 pM) in the absence (total binding) or presence of 10^{-6} M unlabeled rAmy (nonspecific binding). Experiments were performed in triplicate ($n = 3$ –5).

Measurement of cell surface expression of HA-CTR by antibody binding

Cell surface expression of HA-tagged CTRa receptor was determined as previously described (18) about 48 h after transfection using mouse anti-HA (12CA5) antibody and 125 I-labeled goat antimouse IgG secondary.

Calcium mobilization assay

Transfected cells were seeded in poly-L-lysine-coated 96-well plates at a density of 50,000 cells/well, incubated overnight, and serum starved for a further 24 h. Cells were washed three times with a modified Hanks' buffered saline solution [HBSS; containing (in millimoles): NaCl 150; KCl 2.6; $MgCl_2$ 1.18; D-glucose 10; HEPES 10; $CaCl_2$ 2.2; probenecid 2, and 0.5% (wt/vol) BSA]. In light-diminished conditions, 100 μ l of wash solution were added containing the cell-permeant Ca^{2+} fluorophore, Fluo-4/AM (10 μ M), and incubated for 1 h at 37°C. The fluorophore solution was aspirated from the wells, and cells were washed twice and then incubated for 30 min in modified HBSS at 37°C. The assay plate was transferred to a FlexStation (Molecular Devices, Palo Alto, CA), which performed the robotic addition of ligands ($10 \times$ stocks in modified HBSS). Receptor-mediated changes in intracellular Ca^{2+} concentration were immediately recorded by the FlexStation using an excitation wavelength of 485 nm and emission wavelength of 520 nm. Data were collected for each well every 1.52 sec for a total of 135 sec.

ERK phosphorylation assay

Transfected cells were seeded in 96-well plates at a density of 50,000 cells/well and incubated for 16 h before being serum starved overnight. On the day of assay, cells were pretreated with buffer or inhibitors (at the concentrations specified) and then stimulated with agonist at 37°C. Concentrations of inhibitors used in this study were determined previously (19, 20), by inhibitor concentration response curves, or sourced from the literature. Inhibitors were dissolved in dimethylsulfoxide, and the final concentration of solvent in the assay was less than 1% and this did not affect the assay. Time-course results demonstrated a peak response at 5 min

for all receptor complexes after agonist stimulation; this time point was subsequently used in concentration-response studies. ERK1/2 phosphorylation was measured using the AlphaScreen-based ERK SureFire assay kit as previously described (19). Data are expressed as fold change from basal (control treated cells). For antagonist experiments, agonist and antagonist peptides were coadministered to the wells.

Data analysis

Competition binding data and cAMP, ERK1/2 phosphorylation, and Ca^{2+} mobilization concentration-response data were analyzed via non-linear regression using PRISM version 4.3 (GraphPad Software, San Diego, CA). In all instances, data shown are the mean \pm SE. Comparisons between data were performed by one-way ANOVA; *post hoc* testing was via either Dunnett's test for comparisons with control or Tukey-Kramer's test for multiple comparisons. Statistical analysis was performed within the Prism 4.3 environment. Unless otherwise stated, values of $P < 0.05$ were taken as significant. Potency data are presented as negative log molar (p) as errors are log normally distributed.

Results and Discussion

The CTRa functionally couples to multiple effector pathways including the proximal second messengers, cAMP and Ca^{2+} , and the more distal effector, phosphorylated-ERK1/2 (8, 13, 14). We therefore examined the ability of RAMPs to induce amylin receptors that are linked to these pathways.

We first compared the relative ability of amylin, acting via RAMP/CTR complexes, to induce cAMP accumulation and stimulate ERK1/2 phosphorylation. CTRa was coexpressed in COS-7 cells with RAMP1, RAMP2, RAMP3, or vector control plasmid, and induction of cAMP accumulation or ERK1/2 phosphorylation was assessed in parallel. In agreement with previous findings in this cellular background, RAMP1 and RAMP3 induced a marked increase in amylin potency for cAMP production (27- and 21-fold, respectively), compared with CTRa receptor and vector, whereas RAMP2 had only a weak effect (Fig. 1A and Table 1) (9, 12). Responses to hCT were not affected by RAMP1 or RAMP2 but decreased (~ 3 -fold) with RAMP3, presumably due to reduction in free CTRa availability (18) (Fig. 1B). In contrast to cAMP production, the potency of amylin in stimulating ERK1/2 phosphorylation in CTRa/RAMP coexpressing cells was much smaller (3.8- and 4.7-fold potency increase for RAMP1 and RAMP3, respectively) (Fig. 1E and Table 1).

TABLE 1. Agonist potency estimates in COS-7 cells

	cAMP (30 min)	Δ Change	cAMP (5 min)	Δ Change	ERK1/2 (5 min)	Δ Change	Ca^{2+}	Δ Change
rAmy								
CTRa + pcDNA3	7.80 \pm 0.11 (5)		8.26 \pm 0.11 (5)		7.76 \pm 0.11 (7)		7.44 \pm 0.06 (9)	
CTRa + RAMP1	9.23 \pm 0.07 (6) ^a	27	9.76 \pm 0.15 (5) ^a	31	8.34 \pm 0.13 (8) ^a	3.8	7.73 \pm 0.07 (9) ^a	2.0
CTRa + RAMP2	8.25 \pm 0.10 (6) ^{a,b}	2.8	8.53 \pm 0.09 (5) ^b	1.8	7.83 \pm 0.10 (8) ^b	1.2	7.66 \pm 0.14 (4)	0.7
CTRa + RAMP3	9.12 \pm 0.13 (6) ^a	21	9.57 \pm 0.14 (5) ^a	20	8.43 \pm 0.11 (8) ^a	4.7	8.04 \pm 0.08 (9) ^{a,c}	4.0
hCT								
CTRa + pcDNA3	8.80 \pm 0.12 (5)		9.61 \pm 0.16 (4)		8.47 \pm 0.09 (8)		8.23 \pm 0.04 (9)	
CTRa + RAMP1	8.64 \pm 0.11 (6)		9.28 \pm 0.16 (4)		8.35 \pm 0.07 (8)		7.98 \pm 0.09 (4)	
CTRa + RAMP2	8.82 \pm 0.09 (6)		9.27 \pm 0.18 (4)		8.56 \pm 0.07 (8)		8.08 \pm 0.08 (4)	
CTRa + RAMP3	8.20 \pm 0.09 (6) ^a		9.03 \pm 0.13 (4)		8.02 \pm 0.08 (8) ^a		7.80 \pm 0.08 (4) ^a	

Shown are the pEC_{50} values for peptide-induced cAMP production (for both 30 and 5 min agonist stimulation), ERK1/2 activation, and intracellular Ca^{2+} mobilization. Data are presented as mean \pm SEM. The number of individual experiments analyzed is shown in parentheses. Fold Δ , Fold change in amylin potency when comparing potency for CTRa/RAMP1 complexes with CTRa + pcDNA3.

^a Significantly different from CTRa control.

^b Significantly different from CTRa/RAMP1 and CTRa/RAMP3.

^c Significantly different from CTRa/RAMP1 and CTRa/RAMP2. One-way ANOVA with Tukey-Kramer multiple comparisons *post hoc* test ($P < 0.05$).

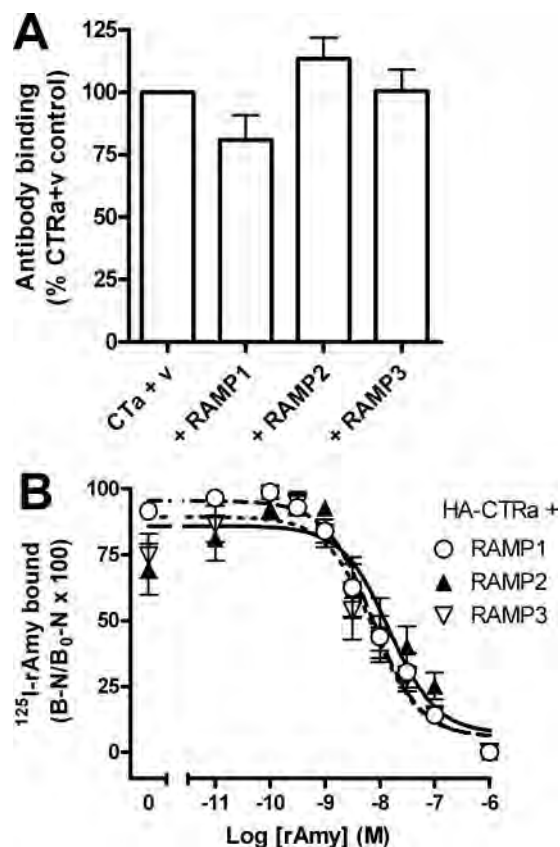


FIG. 2. Competition binding and cell surface receptor labeling for HA-CTra receptor in the absence or presence of RAMPs. **A**, Cell surface expression of CTRa protein. COS-7 cells are transiently transfected with CTRa and pcDNA3 empty vector (v) or CTRa and RAMP1, RAMP2, or RAMP3, measured by binding anti-HA antibody to the 2 × HA-N-terminal-tagged CTRa followed by detection with incubation of a 125 I-labeled goat antimouse IgG secondary antibody. Data are expressed as a percentage of the binding of 125 I-IgG antibody to cells expressing the CTRa protein alone. Data are mean \pm SEM from eight independent experiments. **B**, Peptide competition binding for 125 I-rAmy binding to CTRa and RAMP1, RAMP2, or RAMP3. Data were mean \pm SEM of four separate experiments with duplicate repeats. **B**, 125 I-rAmy. B_0 , Total binding in the absence of cold peptide; N , nonspecific binding (measured in the presence of 10^{-6} M peptide).

Given the marked divergence in potency between the two signaling pathways we sought to establish whether the small increase in Amylase potency for ERK activation was via the same

receptor mediating the larger cAMP response. Therefore, we performed concentration-response analysis of amylin-induced ERK1/2 phosphorylation in the presence of CGRP₈₋₃₇, a selective antagonist that is able to differentiate between CTRa and AMY receptors due to substantial differences between the affinities of this antagonist for these receptor subtypes (18). CGRP₈₋₃₇ caused a rightward shift of the amylin dose-response curve at AMY₁ (CTRa + RAMP1) and AMY₃ (CTRa + RAMP3) receptors but not at CTRa (alone), whereas the nonselective antagonist AC187 right-shifted both hCT and amylin responses at each of the receptor complexes. The values of the negative logarithms of the antagonist equilibrium dissociation constant for the antagonist CGRP₈₋₃₇ at the AMY₁ and AMY₃ receptors were 6.8 ± 0.2 and 6.4 ± 0.4 , respectively, and this is equivalent to those reported previously for cAMP accumulation (18). Thus, whereas the change is small, the increase in amylin potency observed in ERK1/2 activation is via the RAMP/CTR complexes. Direct stimulation of adenylate cyclase with forskolin was ineffective at activating ERK1/2 (data not shown), suggesting that ERK activation in this system could not be stimulated by cAMP alone and must result from coupling to alternative pathways. Taken together, the above results raise the possibility that the coupling efficiencies of AMY₁ and AMY₃ receptors for different G protein subtypes differs from that of the CTRa.

We subsequently investigated the ability of CTRa and AMY receptors to couple to $G_{\alpha q}$ by measuring the downstream release of intracellular Ca^{2+} . Analogous to cAMP responses, hCT-induced intracellular Ca^{2+} mobilization was mostly unaffected by coexpression of RAMPs, with only a small decrease in potency seen with coexpression of RAMP3 (Fig. 1H). CTRa coexpression with RAMP1 or RAMP3 led to a weak increase in amylin potency for Ca^{2+} mobilization of 2- and 4-fold, respectively (Fig. 1G). Together with the data from ERK1/2 activation (Fig. 1E and Table 1), this suggests that the relative coupling of AMY receptors is much stronger to $G_{\alpha s}$ than to the alternative pathways investigated.

This large difference in coupling efficiency across the three effector pathways measured was not observed at the CTRa in the absence of RAMPs; when CTRa was expressed alone, the agonist potencies in the cAMP, ERK1/2, and Ca^{2+} mobilization were similar for both rAmy and for hCT (Table 1). When comparing the potency of amylin across the CTRa/RAMP com-

TABLE 2. Agonist potency estimates in HEK-293 transfected cells

	cAMP (30 min)	Δ Change	ERK1/2 (5 min)	Δ Change	Ca^{2+}	Δ Change
rAmy						
CTRa + pcDNA3	8.28 \pm 0.23 (4)		7.53 \pm 0.16 (4)		7.51 \pm 0.14 (4) ^a	
CTRa + RAMP1	9.69 \pm 0.28 (4) ^a	25.4	7.78 \pm 0.10 (4)	1.8	8.22 \pm 0.09 (4) ^a	4.0
CTRa + RAMP2	9.08 \pm 0.31 (4)	6.2	7.57 \pm 0.13 (4)	1.1	7.44 \pm 0.11 (4) ^b	0.7
CTRa + RAMP3	9.92 \pm 0.13 (4) ^a	42.9	8.09 \pm 0.12 (4) ^a	3.6	8.23 \pm 0.02 (4) ^a	4.1
hCT						
CTRa + pcDNA3	9.79 \pm 0.13 (4)		7.89 \pm 0.03 (4)		8.07 \pm 0.27 (4)	
CTRa + RAMP1	9.88 \pm 0.12 (4)		8.12 \pm 0.18 (4)		7.65 \pm 0.09 (4)	
CTRa + RAMP2	9.70 \pm 0.25 (4)		8.09 \pm 0.10 (4)		8.11 \pm 0.05 (4)	
CTRa + RAMP3	8.78 \pm 0.06 (4) ^a		7.83 \pm 0.06 (4)		7.73 \pm 0.17 (4)	

Shown below are the pEC_{50} values for peptide-induced cAMP production, ERK1/2 activation, and intracellular Ca^{2+} mobilization. Data are presented as mean \pm SEM. The number of individual experiments analyzed is shown in parentheses. Fold Δ , Fold change in amylin potency when comparing potency for CTRa/RAMP1 complexes with CTRa + pcDNA3.

^a Significantly different from CTRa control.

^b Significantly different from CTRa/RAMP1 and CTRa/RAMP3. One-way ANOVA with Tukey-Kramer multiple comparisons *post hoc* test ($P < 0.05$).

plexes, we also found that amylin was more potent on AMY_3 than AMY_1 receptors for Ca^{2+} mobilization (Table 1), which is the reverse of that observed in cAMP accumulation in the COS-7 cell background.

To eliminate the possibility that the changes in amylin potency observed were due to differences in receptor expression, we measured cell surface receptor expression in parallel to the functional assays by immunodetection using antibodies against the HA tag on the N terminus of the CTRa. The presence of RAMPs did not significantly alter the amount of CTRa expressed on the cell surface (Fig. 2A). As a further control, we used unlabeled rAmy to competitively inhibit ^{125}I rAmy binding to cells coexpressing CTRa and RAMPs. The data illustrate

that rAmy has approximately equal affinity for AMY_1 , AMY_2 , and AMY_3 receptors (Fig. 2B) with pIC_{50} values of 8.13 ± 0.10 , 7.83 ± 0.17 , and 8.13 ± 0.12 , respectively, although the level of induced binding was less with RAMP2; this is in agreement with previously published data in this cellular background (12, 21).

The cAMP, ERK1/2, and Ca^{2+} functional responses assessed in this study were measured over different time scales. The cAMP assay is an accumulation assay in which receptors are exposed to the agonist for 30 min before quantifying the amount of cAMP produced. In comparison, ERK1/2 phosphorylation is measured 5 min after agonist stimulation, whereas the Ca^{2+} mobilization is measured as peak response that occurs seconds after ligand exposure. For both ERK1/2

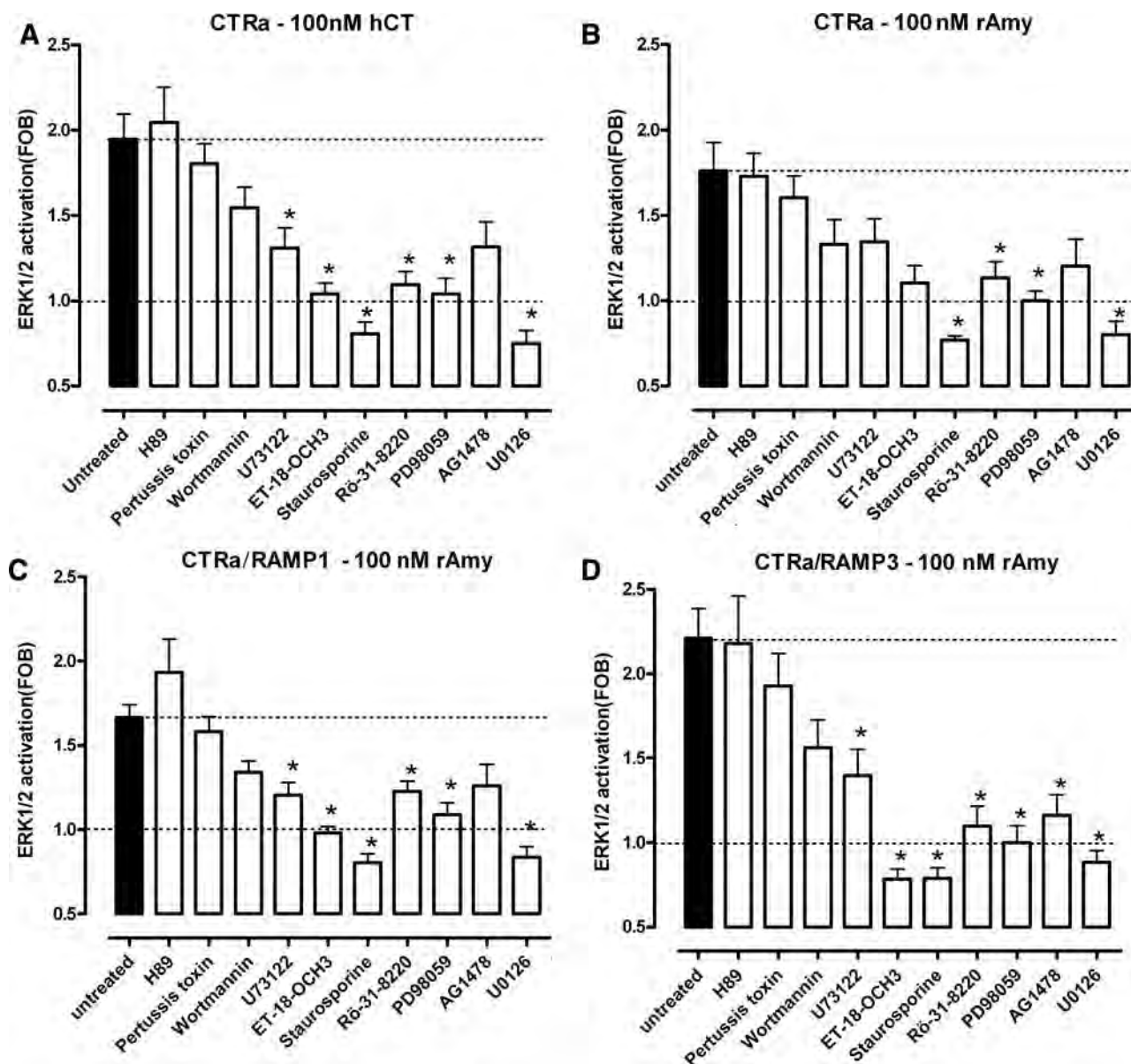


FIG. 3. Pharmacological inhibitor-based analysis of signaling components involved in activation of ERK1/2. Shown is peak (5 min) ERK1/2 phosphorylation in COS7 cells expressing CTRa and pcDNA3-1 (A and B), RAMP1 (C), or RAMP3 (D) after stimulation with 100 nM rAmy (A, C, and D) or hCT (B). Before stimulation with agonists, cells were preincubated with either buffer (untreated) or one of the following inhibitors; H-89 (10 μ M, 1 h), pertussis toxin (100 ng/ml, 18 h), wortmannin (100 nM, 30 min), U73122 (10 μ M, 30 min), ET-18-OCH₃ (100 μ M, 30 min), staurosporine (1 μ M, 30 min), Rö-31-8220 (10 μ M, 30 min), PD98059 (20 μ M, 30 min), Tyrphostin AG1478 (100 nM, 30 min), or U0126 (10 μ M, 30 min). Data are mean \pm SEM, $n = 3-4$. *, Significantly different from vector control group; one-way ANOVA with Dunnett's *post hoc* test.

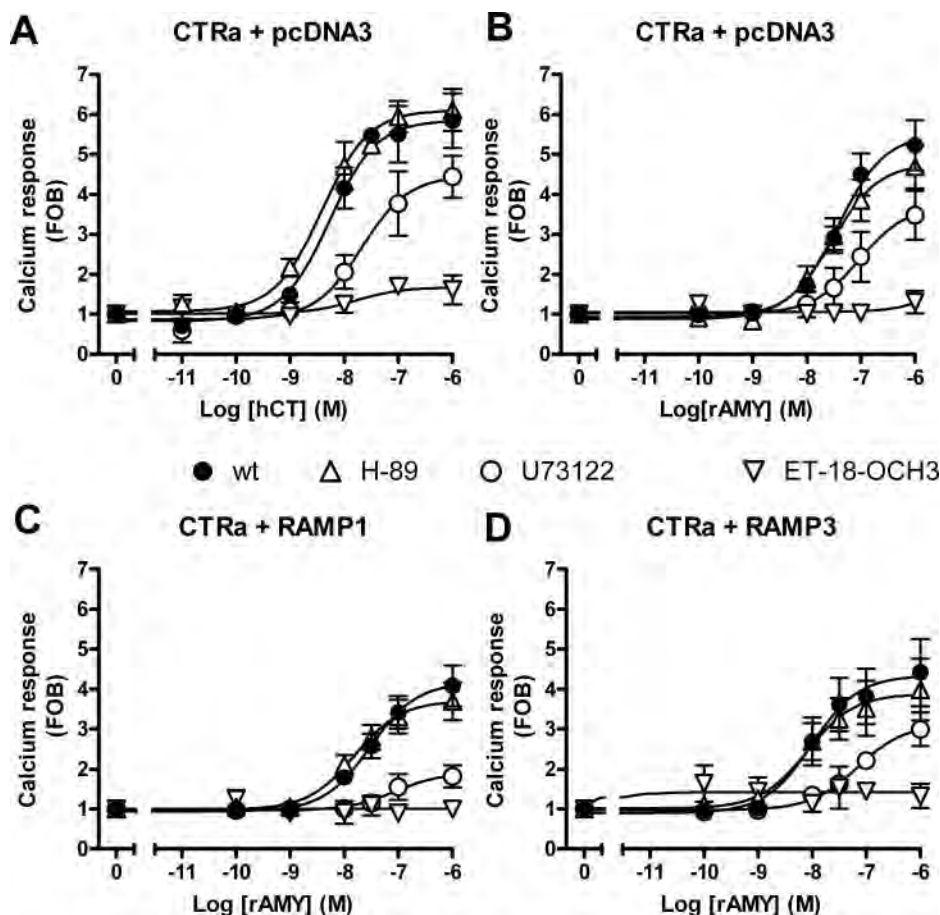
and Ca^{2+} assays, the ligand has not had sufficient time to equilibrate in the system before the measurement of downstream signaling and this may cause difficulties in comparing results of these assays with the cAMP assay, in which equilibrium can be reached. To ensure that the differences we observed were caused by RAMPs and not by a nonequilibrium effect, we repeated the cAMP accumulation assay, measuring cAMP production after only 5 min agonist treatment, equivalent to the agonist stimulation time of the ERK1/2 activation assay. The results demonstrate that the strong induction of amylin phenotype at the CTRa in the presence of RAMP1 and RAMP3 is maintained, with a 31- and 20-fold enhancement of potency, respectively, compared with CTRa alone (Fig. 1C). Interestingly, the $p\text{EC}_{50}$ values for the 5-min cAMP assay are all consistently 2- to 6-fold greater than the 30-min assay, which is probably due to the nonequilibrated status of the system (Table 1). The data confirm that the greater induction of amylin phenotype seen in the cAMP assays, compared with the ERK1/2 phosphorylation and Ca^{2+} mobilization assays is not due to the assay conditions.

We subsequently extended these studies to examine signaling via CT and AMY receptors in an alternate cell background, HEK-293 cells. As seen for COS-7 cells, a strong induction of amylin-mediated cAMP signaling was observed with AMY_1 and AMY_3 receptors (25- and 43-fold, respectively; Table 2), but only weak induction of signaling was seen in ERK1/2 activation and Ca^{2+} mobilization assays (1.8- to 4.1-fold; Table 2). Interestingly, although AMY recep-

tor-mediated ERK and Ca^{2+} signaling was relatively weak, there was greater fold induction seen in the Ca^{2+} vs. the ERK assay; this is the reverse of the pattern observed in COS-7 cells (Table 2 vs. Table 1). This suggests that some cell background-dependent modulation of signaling occurs. These data also suggest that the results demonstrated in COS-7 cells may be more generally relevant. Additional support for the differential coupling of CT and AMY receptors can be found in early studies on endogenously expressed amylin receptors in α -TSH thyrotroph cells. The α -TSH cell line has an AMY_{1a} -like receptor, having similar affinity for CGRP and amylin, in addition to an endogenous CTR. In this cell line, both cAMP and intracellular calcium mobilization were measured; however, amylin evoked responses only via the cAMP pathway (22), consistent with relatively weak coupling to calcium mobilization.

We next performed ERK1/2 phosphorylation and intracellular Ca^{2+} mobilization assays in the presence of selective signaling inhibitors to interrogate the pathway of activation for differing RAMP/receptor complexes. The use of inhibitors of protein kinase A (PKA) (H89; 10 μM , 1 h) and $G_{\alpha i/o}$ proteins (pertussis toxin; 100 ng/ml, 18 h) established that stimulation of ERK1/2 phosphorylation was independent of activation of PKA or $G_{\alpha i/o}$ proteins, the former being consistent with lack of forskolin-mediated activation of ERK1/2 in the COS-7 cells. Inhibition of both PI 3-kinase (wortmannin; 100 nM, 30 min) and PI-phospholipase C (PLC) (U73122; 10 μM , 30 min) led to partial inhibition of response, as did inhibition of the epidermal growth factor receptor tyrosine

FIG. 4. rAmy-induced Ca^{2+} mobilization is differentially modulated by PLC inhibition in CTRa/RAMP1 vs. CTRa/RAMP3 expressing COS-7 cells. Ca^{2+} mobilization in response to increasing concentrations of hCT (A) or rAmy (B–D) in COS-7 cells transiently transfected with CTRa together with pcDNA3-1 (A and B), RAMP1 (C), or RAMP3 (D). Cells were pretreated with buffer (filled circles) or inhibitors for the times indicated before agonist stimulation in the continued presence of inhibitor. The inhibitors used were: H-89 (open triangles, PKA inhibitor; 10 μM , 1 h); U73122 (open circles, PLC inhibitor; 10 μM , 30 min); ET-18-OCH₃ (open inverted triangles, PLC, PI 3-kinase, PKC inhibitor; 100 μM , 30 min). Data are mean \pm SEM, $n = 3$. FOB, Fold over basal. Maximum response (E_{max}) values (FOB) for the AMY_1 receptor in the absence and presence of U73122 were 4.17 ± 0.27 , $n = 5$, and 1.91 ± 0.19 , $n = 3$, respectively. E_{max} values for the AMY_3 receptor in the absence and presence of U73122 were 4.34 ± 0.40 , $n = 5$, and 3.12 ± 0.20 , $n = 3$, respectively. The effect of U73122 was significantly greater for the AMY_1 receptor, compared with the AMY_3 receptor or CTRa alone, $P < 0.05$; one-way ANOVA followed by Bonferroni's multiple comparison test.



kinase (AG1478; 100 nM, 30 min), indicating that each of these pathways could contribute to the ERK response. Inhibition of protein kinase C (PKC; staurosporine; 1 μ M, 30 min; R318220; 10 μ M, 30 min) led to the abolition of signaling, as did inhibition of MAPK kinase (U0126; 10 μ M, 30 min; PD98059; 20 μ M, 30 min), indicating that there is convergence on PKC and eventually MAPK kinase for activation. ET-18-OCH₃, which can inhibit PI-PLC, PI 3-kinase, and Raf (100 μ M, 30 min) also abolished signaling. However, there was no significant difference in the relative contribution of the different signaling pathways to ERK activation between the CTRa alone or the AMY₁ or AMY₃ receptor complexes (Fig. 3). The inability to detect pathway differences in the activation of ERK is likely to be due, at least in part, to the strong background phenotype of the CTRa alone in the RAMP cotrans-

fect cells coupled with only a weak induction of amylin phenotype for signaling to this pathway.

For Ca²⁺ mobilization, the PKA inhibitor H89 had no effect on responses to either hCT or amylin, whereas the broad-spectrum inhibitor ET-18-OCH₃ completely abolished signaling at each of the receptors (Fig. 4). In contrast, there were receptor-specific differences in the capacity of the PI-PLC inhibitor U73122 to inhibit responses. There was strong inhibition of signaling via the AMY₁ receptor complex (~72%), compared with weak inhibition for the CTRa alone or the AMY₃ receptor complex (30–40% inhibition).

The above signaling data implied that the different RAMP/CTR complexes were causing differential modulation of the ability of the receptor to interact with specific G proteins. To test this more empirically, we examined the

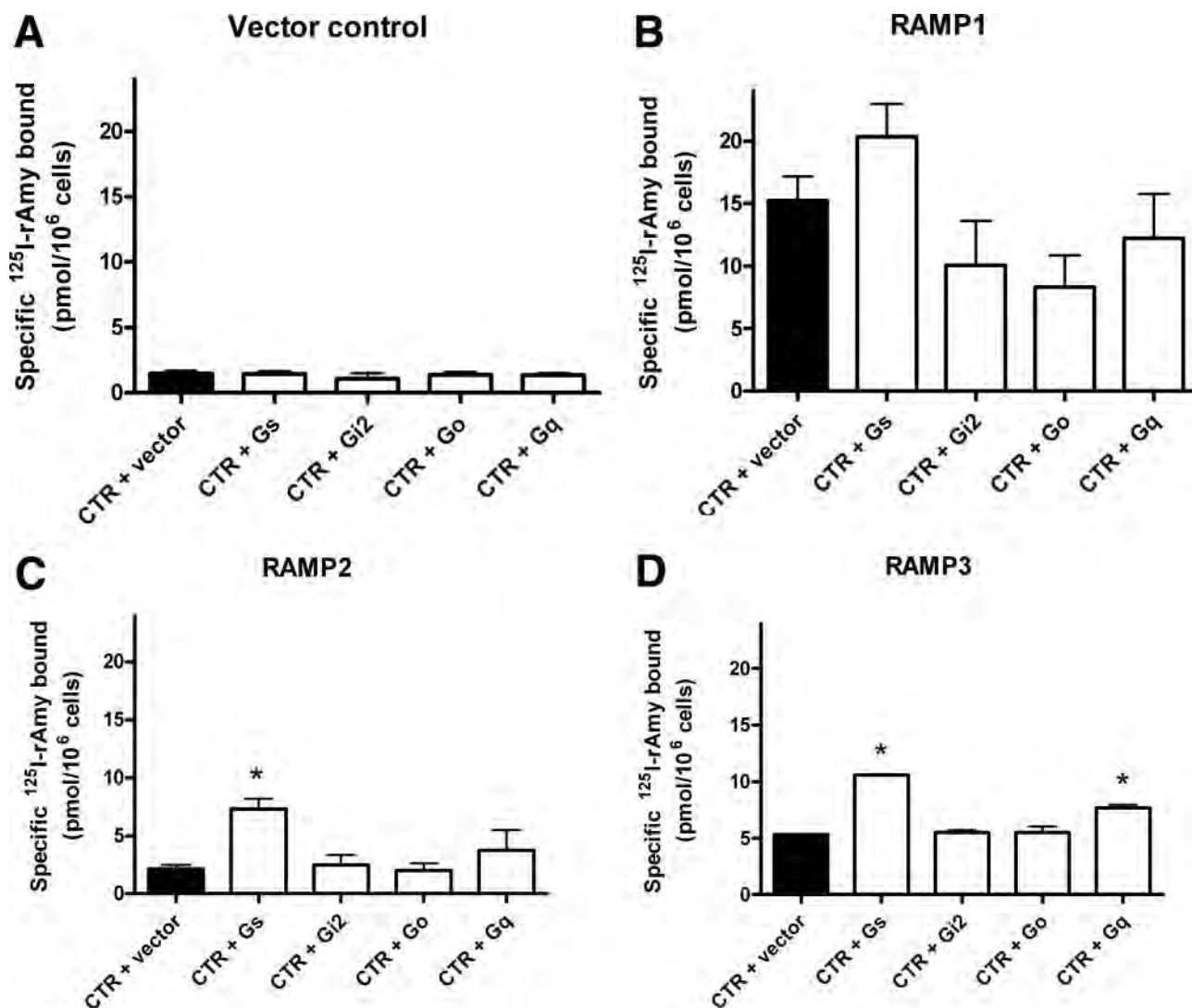


FIG. 5. Overexpression of G α subunits differentially modulates induction of amylin receptor phenotypes by RAMPs. ¹²⁵I-rAmy binding to COS-7 cells cotransfected with CTRa (100 ng) and one of the four (G α _s, G α _{i2}, G α _{oA}, G α _q) G α subtypes (150 ng) together with either pcDNA3.1 empty vector (A), RAMP1 (B), RAMP2 (C), or RAMP3 (D) DNA (150 ng). Whole cells were assayed for ¹²⁵I-rAmy binding 48 h after transfection by incubating transfected cells with radioligand (80 pM/well) in the absence (total binding) or presence of 10⁻⁶ M unlabeled rAmy (nonspecific binding). Specific binding was determined by subtracting nonspecific from total binding. Data are mean \pm SEM, n = 3–5. *, Significantly different from vector control group; one-way ANOVA with Dunnett's *post hoc* test.

effect of over expression of different $G\alpha$ protein subunits (G_s , G_{12} , G_{oA} , G_q) on the ability of individual RAMPs to induce high affinity ^{125}I -rAmy binding. As previously reported in this cell background, RAMP1 and RAMP3 potently induced ^{125}I -rAmy binding, with the greatest effect seen with RAMP1, whereas RAMP2 generated only a low level of induced binding (Fig. 5). None of the $G\alpha$ subunits modulated the binding to the CTRa expressed alone (Fig. 5A). Similarly, whereas there were trends for G_s to increase and G_o to decrease RAMP1-induced binding, neither of these was significant (Fig. 5B). In contrast, there was a large increase in RAMP2-induced binding in the presence of G_s but not other $G\alpha$ proteins (Fig. 5C), whereas both G_s and G_q led to increased ^{125}I -rAmy binding with RAMP3 (Fig. 5D). Thus, these data support the proposition that individual RAMPs may each lead to a different profile of signaling from the CTR expressed alone.

Structurally, the three RAMPs have only a very short intracellular C-terminal tail of about 10 amino acids (10). Evidence for a direct role of this domain in the signaling specificity of RAMP receptor complexes arises from chimeras of RAMP1 and RAMP2 in which the potency of CGRP, a high-affinity ligand of RAMP1-complexed CTR but not RAMP2-complexed CTR, to stimulate cAMP production was contextual on the C-terminal domain present; CGRP had increased potency when the RAMP1 C terminus was present, despite an overt binding phenotype that was primarily influenced by the N-terminal domain present (23). Further evidence for involvement of the C terminus in G protein interaction arose from studies on C terminally truncated RAMPs; deletion of the last eight amino acids led to a marked loss in the capacity of RAMPs to induce high-affinity amylin receptors from CTRa receptors. This loss could be, at least partially, recovered by the overexpression of G_{as} protein, indicating that the RAMPs were contributing directly to the ability of the receptor complexes to interact with G proteins (15). Intriguingly and consistent with the current study, truncation of the C terminus differentially affected individual RAMPs, and there were also differences in the sensitivity of the truncated RAMP/CTR complexes to recovery by G_{as} overexpression.

In conclusion, this study demonstrates that RAMPs can differentially modulate the coupling efficiency of CTRa to various G proteins. This expands the repertoire of actions that RAMPs have in modulating GPCR function, and likely extends beyond the CTR investigated in the current work. This form of fine manipulation of receptor signaling provides new opportunities for development of novel therapeutic agents targeting RAMP complexed receptors.

Acknowledgments

Received December 17, 2007. Accepted June 26, 2008.

Address all correspondence and requests for reprints to: Professor Patrick M. Sexton, Department of Pharmacology, Building 13E, Monash University, Wellington Road, Clayton, Victoria 3800, Australia. E-mail: patrick.sexton@med.monash.edu.au.

This work was supported by Grants 299810 and 436781 from the National Health and Medical Research Council (NHMRC) of Australia (to P.M.S. and A.C.). P.M.S. is a principal research fellow of the NHMRC. A.C. is a senior research fellow of the NHMRC. M.M. is a NHMRC Peter Doherty postgraduate scholar.

Current address for T.D.W.: Biochemical Pharmacology, Psychiatry Discovery Technology Group, GlaxoSmithKline, Harlow, Essex CM19 5AW, United Kingdom.

Disclosure Statement: M.M., N.T., S.G.B.F., G.C., T.D.W., and A.C. have nothing to declare. P.M.S. is an ad hoc consultant for Merck & Co. P.M.S. has received lecture fees from Bristol Myers Squibb.

References

- Bockaert J, Fagni L, Dumuis A, Marin P 2004 GPCR interacting proteins (GIP). *Pharmacol Ther* 103:203–221
- Sato M, Blumer JB, Simon V, Lanier SM 2006 Accessory proteins for G proteins: partners in signaling. *Annu Rev Pharmacol Toxicol* 46:151–187
- Tilakaratne N, Sexton PM 2005 G Protein-coupled receptor-protein interactions: basis for new concepts on receptor structure and function. *Clin Exp Pharmacol Physiol* 32:979–987
- Poyner DR, Sexton PM, Marshall I, Smith DM, Quirion R, Born W, Muff R, Fischer JA, Foord SM 2002 International Union of Pharmacology. XXXII. The mammalian calcitonin gene-related peptides, adrenomedullin, amylin, and calcitonin receptors. *Pharmacol Rev* 54:233–246
- Hay DL, Poyner DR, Sexton PM 2006 GPCR modulation by RAMPs. *Pharmacol Ther* 109:173–197
- Young A 2005 Amylin, physiology and pharmacology. In *Advances in pharmacology*. Vol 52. San Diego: Academic Press; 360
- Want LL, Ratner RE 2006 Pramlintide: a new tool in diabetes management. *Curr Diab Rep* 6:344–349
- Sexton PM, Findlay DM, Martin TJ 1999 Calcitonin. *Curr Med Chem* 6:1067–1093
- Christopoulos G, Perry KJ, Morris M, Tilakaratne N, Gao Y, Fraser NJ, Main MJ, Foord SM, Sexton PM 1999 Multiple amylin receptors arise from receptor activity-modifying protein interaction with the calcitonin receptor gene product. *Mol Pharmacol* 56:235–242
- McLatchie LM, Fraser NJ, Main MJ, Wise A, Brown J, Thompson N, Solari R, Lee MG, Foord SM 1998 RAMPs regulate the transport and ligand specificity of the calcitonin-receptor-like receptor. *Nature* 393:333–339
- Christopoulos A, Christopoulos G, Morris M, Udawela M, Laburthe M, Couvineau A, Kuwasako K, Tilakaratne N, Sexton PM 2003 Novel receptor partners and function of receptor activity-modifying proteins. *J Biol Chem* 278:3293–3297
- Tilakaratne N, Christopoulos G, Zumpfe ET, Foord SM, Sexton PM 2000 Amylin receptor phenotypes derived from human calcitonin receptor/RAMP coexpression exhibit pharmacological differences dependent on receptor isoform and host cell environment. *J Pharmacol Exp Ther* 294:61–72
- Moore EE, Kuestner RE, Stroop SD, Grant FJ, Matthews SL, Brady CL, Sexton PM, Findlay DM 1995 Functionally different isoforms of the human calcitonin receptor result from alternative splicing of the gene transcript. *Mol Endocrinol* 9:959–968
- Raggatt LJ, Evdokiou A, Findlay DM 2000 Sustained activation of Erk1/2 MAPK and cell growth suppression by the insert-negative, but not the insert-positive isoform of the human calcitonin receptor. *J Endocrinol* 167:93–105
- Udawela M, Christopoulos G, Morris M, Christopoulos A, Ye S, Tilakaratne N, Sexton PM 2006 A critical role for the short intracellular C terminus in receptor activity-modifying protein function. *Mol Pharmacol* 70:1750–1760
- Bhogal R, Smith DM, Bloom SR 1992 Investigation and characterization of binding sites for islet amyloid polypeptide in rat membranes. *Endocrinology* 130:906–913
- Pham V, Wade JD, Purdue BW, Sexton PM 2004 Spatial proximity between a photolabile residue in position 19 of salmon calcitonin and the amino terminus of the human calcitonin receptor. *J Biol Chem* 279:6720–6729
- Hay DL, Christopoulos G, Christopoulos A, Poyner DR, Sexton PM 2005 Pharmacological discrimination of calcitonin receptor: receptor activity-modifying protein complexes. *Mol Pharmacol* 67:1655–1665
- Van der Westhuizen ET, Werry TD, Sexton PM, Summers RJ 2007 The relaxin family peptide receptor 3 (RXFP3) activates ERK1/2 through a PKC dependent mechanism. *Mol Pharmacol* 71:1618–1629
- Werry TD, Gregory KJ, Sexton PM, Christopoulos A 2005 Characterization of serotonin 5HT_{2C} receptor signaling to extracellular-signal regulated kinases 1 and 2. *J Neurochem* 93:1603–1615
- Zumpfe ET, Tilakaratne N, Fraser NJ, Christopoulos G, Foord SM, Sexton PM 2000 Multiple ramp domains are required for generation of amylin receptor phenotype from the calcitonin receptor gene product. *Biochem Biophys Res Commun* 267:368–372
- Perry KJ, Quiza M, Myers DE, Christopoulos G, Sexton PM 1997 Characterization of amylin and calcitonin receptor binding in the mouse α -TSH thyrotroph cell line. *Endocrinology* 138:3486–3496
- Udawela M, Christopoulos G, Tilakaratne N, Christopoulos A, Albiston A, Sexton PM 2006 Distinct receptor activity-modifying protein domains differentially modulate interaction with calcitonin receptors. *Mol Pharmacol* 69:1984–1989

Allosteric Ligands of the Glucagon-Like Peptide 1 Receptor (GLP-1R) Differentially Modulate Endogenous and Exogenous Peptide Responses in a Pathway-Selective Manner: Implications for Drug Screening^S

Cassandra Koole, Denise Wootten, John Simms, Celine Valant, Rohan Sridhar, Owen L. Woodman, Laurence J. Miller, Roger J. Summers, Arthur Christopoulos, and Patrick M. Sexton

Drug Discovery Biology Laboratory, Monash Institute of Pharmaceutical Sciences and Department of Pharmacology, Monash University, Parkville, Victoria, Australia (C.K., D.W., C.V., A.C., R.J.S., R.S., J.S., P.M.S.); Department of Molecular Pharmacology and Experimental Therapeutics, Mayo Clinic, Scottsdale, Arizona (L.J.M.); and School of Medical Sciences, RMIT University, Bundoora, Victoria, Australia (O.L.W.).

Received April 16, 2010; accepted June 14, 2010

ABSTRACT

The glucagon-like peptide-1 (GLP-1) receptor is a key regulator of insulin secretion and a major therapeutic target for treatment of diabetes. However, GLP-1 receptor function is complex, with multiple endogenous peptides that can interact with the receptor, including full-length (1–37) and truncated (7–37) forms of GLP-1 that can each exist in an amidated form and the related peptide oxyntomodulin. We have investigated two GLP-1 receptor allosteric modulators, Novo Nordisk compound 2 (6,7-dichloro-2-methylsulfonyl-3-*tert*-butylaminoquinoxaline) and quercetin, and their ability to modify binding and signaling (cAMP formation, intracellular Ca²⁺ mobilization, and extracellular signal-regulated kinase 1/2 phosphorylation) of each of the naturally occurring endogenous peptide agonists, as well as the clinically used peptide mimetic exendin-4. We identified and quantified stimulus bias across multiple endogenous peptides, with response profiles for truncated GLP-1 peptides distinct

from those of either the full-length GLP-1 peptides or oxyntomodulin, the first demonstration of such behavior at the GLP-1 receptor. Compound 2 selectively augmented cAMP signaling but did so in a peptide-agonist dependent manner having greatest effect on oxyntomodulin, weaker effect on truncated GLP-1 peptides, and negligible effect on other peptide responses; these effects were principally driven by parallel changes in peptide agonist affinity. In contrast, quercetin selectively modulated calcium signaling but with effects only on truncated GLP-1 peptides or exendin and not oxyntomodulin or full-length peptides. These data have significant implications for how GLP-1 receptor targeted drugs are screened and developed, whereas the allosterically driven, agonist-selective, stimulus bias highlights the potential for distinct clinical efficacy depending on the properties of individual drugs.

This work was funded in part by the National Health and Medical Research Council (NHMRC) of Australia [Program Grant 519461]; and by an NHMRC of Australia Principal Research Fellowship (to P.M.S.) and a Senior Research Fellowship (to A.C.).

C.K., D.W. and J.S. contributed equally to this work.

Article, publication date, and citation information can be found at <http://molpharm.aspetjournals.org>.
doi:10.1124/mol.110.065664.

^S The online version of this article (available at <http://molpharm.aspetjournals.org>) contains supplemental material.

Introduction

Type II (non-insulin-dependent) diabetes mellitus (DM) is a major disease of the Western world with many complications, including renal failure and vascular conditions leading to heart attack and stroke (Wild et al., 2004). Type II DM is characterized by a decrease in peripheral tissue response to insulin in association with impaired β cell function, which results in an increase in fasting glycemia (DeFronzo, 1992). Although antihyperglycemic drugs such as metformins, sulfonylureas, or thiazolidinediones may be prescribed to pro-

ABBREVIATIONS: DM, diabetes mellitus; GLP-1R, glucagon-like peptide 1 receptor; GPCR, G protein-coupled receptor; DPP-IV, dipeptidyl peptidase IV; DMEM, Dulbecco's modified Eagle's medium; FBS, fetal bovine serum; ERK1/2, extracellular signal-regulated kinases 1 and 2; BCA, bicinchoninic acid; CHO, Chinese hamster ovary; BSA, bovine serum albumin; LY2033298, 3-amino-5-chloro-6-methoxy-4-methyl-thieno(2,3-*b*)pyridine-2-carboxylic acid cyclopropylamide; compound 2, (6,7-dichloro-2-methylsulfonyl-3-*tert*-butylaminoquinoxaline); GLP-1, glucagon-like peptide 1.

mote insulin secretion or enhance insulin sensitivity (Mitri and Hamdy, 2009), these drugs do not target all of the symptoms of type II DM. In recent years, drugs that enhance the activity of the glucagon-like peptide 1 receptor (GLP-1R) have been of particular interest to the pharmaceutical industry, in that activation of this receptor addresses most of the manifestations of the condition.

The GLP-1R is a family B peptide hormone G protein-coupled receptor (GPCR) primarily expressed in pancreatic β cells and responds to at least four distinct endogenous GLP-1 variants as well as to the related peptide oxyntomodulin and exogenous mimetic peptides such as exendin-4. The four secreted forms of GLP-1 include a full-length peptide GLP-1(1–37) and a truncated form GLP-1(7–37), each of which also has an amidated counterpart: GLP-1(1–36)NH₂ and GLP-1(7–36)NH₂, respectively (Estall and Drucker, 2006; Baggio and Drucker, 2007). Although levels of GLP-1 are reduced in patients with type II DM, the receptor retains insulinotropic properties (Toft-Nielsen et al., 2001). However, the promise of this receptor as a target in the development of type II DM is hindered by the rapid degradation of endogenous peptides by dipeptidyl peptidase IV (DPPIV) in vivo (Deacon et al., 1995a; Kieffer et al., 1995). This has in part been overcome by the development of DPPIV-resistant GLP-1 mimetics such as exendin-4 (Göke et al., 1993; Edwards et al., 2001) and liraglutide (Knudsen et al., 2000; Elbrønd et al., 2002) as well as DPPIV inhibitors that prolong the plasma half-life of endogenous GLP-1R peptides (Deacon et al., 1995b). Although these have therapeutic potential (indeed, exendin-4 is currently used clinically), they require frequent intravenous or subcutaneous administration, reducing compliance. In addition, exendin-4 has also been associated with significant adverse side effects in some patients, including pancreatitis (Olansky, 2010), of which the mechanistic basis is unknown. These difficulties have therefore driven the search for the development of small molecule orally active drugs that augment GLP-1R signaling.

Allosteric ligands bind to GPCRs at sites distinct from the orthosteric (endogenous agonist) binding site and can modulate binding and/or signaling pathways of the receptor, as well as potentially acting as agonists themselves. Allosteric modulation has recently gained much traction as a means to overcome the limitations of many orthosterically targeted ligands, because it has the ability to provide novel receptor specificity and selectively control receptor function (Christopoulos and Kenakin, 2002). Little is known about allosteric modulation of the GLP-1R, and few small nonpeptide ligands acting allosterically at the GLP-1R have been reported. A number of small-molecule agonists have recently been identified by Novo-Nordisk; the most potent of these, compound 2, increases the affinity of GLP-1(7–36)NH₂ and also displays intrinsic efficacy in cAMP accumulation assays (Knudsen et al., 2007). There is also a preliminary report that the naturally occurring flavonol quercetin may modulate GLP-1R-mediated calcium (Ca²⁺) signaling by GLP-1(7–36)NH₂ (Schann et al., 2009) and evidence that the substituted cyclobutane Boc5 may also act as an agonist of the receptor (Chen et al., 2007).

A major development in GPCR research is the recognition that different ligands can engender unique receptor conformations, giving rise to distinct signaling profiles. This concept of “ligand-induced stimulus bias” is particularly relevant to receptor systems that have multiple endogenous ligands and is fur-

ther complicated when allosteric ligands are considered. Although allosteric drugs acting at the GLP-1R offer great promise as therapeutics, the consequences of allosteric modulation of the GLP-1R and whether such ligands promote or modify stimulus bias at the receptor have not been fully explored. Furthermore, the natural complexity of the GLP-1R system, encompassing numerous endogenous peptide agonists, provides potential for small-molecule compounds to differentially modulate individual peptide responses, a behavior termed “probe dependence” (Kenakin, 2008). Consequently, we investigated the signaling and binding properties of these putative allosteric modulators in association with the physiologically relevant endogenous agonists of the GLP-1R, as well as the clinically used mimetic exendin-4. We demonstrate, for the first time, that compound 2 and quercetin each have distinct pharmacological profiles, exhibiting selective modulation of specific peptide agonists and engendering stimulus bias at the GLP-1R. These data have significant implications for how GLP-1 receptor targeted drugs are screened and developed, whereas the allosterically driven, agonist-selective, stimulus bias highlights the potential for distinct clinical efficacy depending on the properties of individual drugs.

Materials and Methods

Materials. Dulbecco's modified Eagle's medium (DMEM) and Fluo-4 acetoxymethyl ester were purchased from Invitrogen (Carlsbad, CA). Fetal bovine serum (FBS) was purchased from Thermo Fisher Scientific (Melbourne, VIC, Australia). AlphaScreen reagents, ¹²⁵I-exendin(9–39), 96-well UniFilter GF/C filter plates, 384-well ProxiPlates and MicroScint 40 scintillant were purchased from PerkinElmer Life and Analytical Sciences (Waltham, MA). SureFire extracellular signal-regulated kinases 1 and 2 (ERK1/2) reagents were obtained from TGR Biosciences (Adelaide, SA, Australia). The bicinchoninic acid (BCA) protein assay kit was purchased from Thermo Fisher Scientific. Compound 2 was generated, according to a method published previously (Teng et al., 2007), to a purity of >95%, and compound integrity was confirmed by NMR. GLP-1 and GLP-1 peptide analogs were purchased from American Peptide (Sunnyvale, CA). All other reagents were purchased from Sigma-Aldrich (St. Louis, MO) or BDH Merck (Melbourne, VIC, Australia) and were of an analytical grade.

Cell Culture. FlpIn Chinese hamster ovary (CHO) cells stably transfected with human GLP-1R (FlpInCHO-huGLP-1R) were generated using Gateway technology (Invitrogen) as described previously (May et al., 2007a). These cells expressed the human GLP-1R at a density of 123,500 ± 1368 receptors/cell. Cells were maintained in DMEM supplemented with 10% heat-inactivated FBS and were incubated in a humidified environment at 37°C in 5% CO₂. Untransfected CHO-FlpIn cells were used to control for receptor-independent effects. Additional control experiments were performed using COS-7 cells expressing the human CTa calcitonin receptor (Morris et al., 2008).

Radioligand Binding Assay. Membrane preparations of FlpInCHO-huGLP-1R were prepared as described previously (Avlani et al., 2004). Protein concentration was determined using the BCA protein assay kit (Thermo Fisher Scientific) according to the manufacturer's instructions, with bovine serum albumin (BSA) as standard. Competition binding assays were performed in 96-well plates using 20 µg of membrane expressing GLP-1R. Membranes were incubated in HEPES buffer [1 mM HEPES, 10 mM MgCl₂, 100 mM NaCl, and 1% (w/v) BSA, pH 7.4] containing 0.5 nM ¹²⁵I-exendin(9–39) and increasing concentration of unlabeled ligand for 1 h. For interaction studies, competition of ¹²⁵I-exendin(9–39) binding by each orthosteric agonist was performed in the presence of increasing concentrations of either compound 2 or quercetin. For all experi-

ments, nonspecific binding was defined by 1 μ M GLP-1(7–36)NH₂. Incubation was terminated by rapid filtration through Whatman (Clifton, NJ) GF/C filters (presoaked in 0.03% (v/v) polyethylenimine for a min of 2 h) using a 96-well harvester (Tomtec, Hamden, CT). Filters were washed three times with 0.9% NaCl (w/v) and 0.3% BSA (w/v) and allowed to dry before addition of 30 μ l of scintillant and determination of radioactivity by scintillation counting.

cAMP Accumulation Assay. FlnCHO-huGLP-1R cells were seeded at a density of 5×10^4 cells/well into 96-well culture plates and incubated overnight at 37°C in 5% CO₂. Growth media was replaced with stimulation buffer [phenol-free DMEM containing 0.1% (w/v) BSA and 1 mM 3-isobutyl-1-methylxanthine] and incubated for a further 1 h at 37°C in 5% CO₂. Cells were stimulated with increasing concentrations of peptide ligand alone, allosteric ligand alone, or simultaneously with increasing concentrations of allosteric ligand and peptide, and incubated for 30 min at 37°C in 5% CO₂. Selected additional experiments were also performed 5 and 10 min after ligand stimulation to account for the potential for kinetic differences between different signaling assays to contribute to apparent stimulus bias. The reaction was terminated by rapid removal of the ligand-containing buffer and addition of 50 μ l of ice-cold 100% ethanol. After ethanol evaporation, 75 μ l of lysis buffer [0.1% (w/v) BSA, 0.3% (v/v) Tween 20, and 5 mM HEPES, pH 7.4] was added, and 10 μ l of lysate was transferred to a 384-well ProxiPlate (PerkinElmer Life and Analytical Sciences). Five microliters of acceptor bead mix (1.0% AlphaScreen cAMP acceptor beads diluted in lysis buffer) and 15 μ l of donor bead mix [0.3% AlphaScreen cAMP donor beads, 0.025% AlphaScreen cAMP biotinylated cAMP (133 units/ μ l) diluted in lysis buffer, and preincubated for a minimum of 30 min] were added in reduced lighting conditions. Plates were incubated at room temperature overnight before measurement of the fluorescence using a Fusion-Alpha plate reader (PerkinElmer Life and Analytical Sciences) with standard AlphaScreen settings. All values were converted to concentration of cAMP using a cAMP standard curve performed in parallel.

ERK1/2 Phosphorylation Assay. FlnCHO-huGLP-1R cells were seeded at a density of 5×10^4 cells/well into 96-well culture plates, and receptor-mediated ERK1/2 phosphorylation was determined by using the AlphaScreen ERK SureFire protocol as described previously (May et al., 2007a). Initial ERK1/2 phosphorylation time course experiments were performed over 1 h to determine the time at which ERK1/2 phosphorylation was maximal after stimulation by agonists. Cells were stimulated with peptide ligand and/or simultaneously with increasing concentrations of allosteric ligand for the time required to generate a maximal ERK1/2 phosphorylation response (10 min). Data were normalized to the maximal 3% FBS response, determined at 7 min (peak FBS response).

Intracellular Ca²⁺ Mobilization Assay. FlnCHO-huGLP-1R cells were seeded at a density of 5×10^4 cells/well into 96-well culture plates, and receptor-mediated intracellular Ca²⁺ mobilization was determined as described previously (Werry et al., 2005). Because of their autofluorescence at high concentrations, increasing concentrations of allosteric modulators were added 30 min before addition of peptide agonist in the FlexStation (Molecular Devices, Palo Alto, CA) to establish a basal fluorescence signal. Fluorescence was determined immediately after peptide addition, with an excitation wavelength set to 485 nm and an emission wavelength set to 520 nm, and readings were taken every 1.36 s for 120 s. Peak magnitude was calculated using five-point smoothing, followed by correction against basal fluorescence. The peak value was used to create concentration-response curves. Data were normalized to the maximal response elicited by 100 μ M ATP.

Data Analysis. All data obtained were analyzed in Prism 5.02 (GraphPad Software Inc., San Diego, CA). Concentration response signaling data were analyzed using a three-parameter logistic equation as described previously (May et al., 2007a).

$$Y = \text{Bottom} + \frac{(\text{Top} - \text{Bottom})}{1 + 10^{(\log \text{EC}_{50} - \log [A])}} \quad (1)$$

where Bottom represents the y value in the absence of ligand(s), Top represents the maximal stimulation in the presence of ligand/s, $[A]$ is the molar concentration of ligand, and EC₅₀ represents the molar concentration of ligand required to generate a response halfway between Top and Bottom. Likewise, this equation was used in inhibition binding, replacing EC₅₀ with IC₅₀. In this case, Bottom defines the specific binding of the radioligand that is equivalent to nonspecific ligand binding, whereas Top defines radioligand binding in the absence of a competing ligand. In a similar manner, the IC₅₀ value represents the molar concentration of ligand required to generate a response halfway between Top and Bottom.

Allosteric modulator inhibition binding data were subsequently analyzed according to an allosteric ternary complex model (May et al., 2007a) to determine ligand cooperativity. In this case, nondepletion of ligands was assumed (Avlani et al., 2008):

$$Y = \frac{B_{\max} \times [A]}{[A] + K_{\text{App}}} + \text{NS} \quad (2)$$

where

$$K_{\text{App}} = \frac{K_A \times K_B}{\alpha \times [B] + K_B} \times \frac{1 + [I]/K_I + [B]/K_B + (\alpha' \times [I] \times [B])}{K_I \times K_B} \quad (3)$$

and where Y represents radioligand binding, B_{\max} denotes maximal binding site density, and NS denotes the fraction of nonspecific binding. $[A]$ and K_A denote the concentration of radioligand and equilibrium dissociation constant for the radioligand, respectively. $[B]$ and K_B denote the concentration of allosteric ligand and equilibrium dissociation constant for the allosteric ligand, respectively. $[I]$ and K_I denote the concentration of peptide agonist used in competition with the radioligand and the equilibrium dissociation constant for the peptide agonist, respectively. α and α' represent cooperativity factors, which are measures of the magnitude and direction of the allosteric interaction between the modulator and the radioligand, or the peptide agonist, respectively. Values of $\alpha > 1$ are indicative of a modulator-mediated increase in binding activity, whereas values of α between 0 and 1 are indicative of a modulator-mediated decrease in binding affinity.

cAMP interaction data were also analyzed with an operational model of allosterism:

$$Y = \text{Basal} + \frac{(E_{\max} - \text{Basal}) \times (([A] \times (K_B + \alpha\beta \times [B]) + \tau[B] \times [B] \times \text{EC}_{50})^n)}{(([A] \times (K_B + \alpha\beta \times [B]) + \tau[B] \times [B] \times \text{EC}_{50})^n) \times (\text{EC}_{50})^n \times (K_B + [B])^n} \quad (4)$$

where E_{\max} is the maximal possible response of the system (not the agonist), basal is the basal level of response in the absence of agonist, K_B denotes the functional equilibrium dissociation constant of the agonist (B), τ is an index of the coupling efficiency (or efficacy) of the agonist and is defined as the total concentration of receptors divided by the concentration of agonist-receptor complex that yields half the maximum system response (E_{\max}), and n is the slope of the transducer function that links occupancy to response. $\alpha\beta$ is the combined affinity-efficacy parameter that measures the magnitude and direction of the functional interaction between the modulator and peptide agonist.

To quantify signaling bias, which may be manifested either as selective affinity (K_A) and/or efficacy (τ) of an agonist for a given pathway, agonist concentration-response curves data were analyzed with an operational model (Gregory et al., 2010), but modified to directly estimate the ratio of τ/K_A , in a manner similar to that described by Figueroa et al. (2009), for each pathway:

$$\frac{E_{\max} \times (\tau/K_A)^n \times [B]^n}{[B]^n \times (\tau/K_A)^n + (1 + [B]/K_B)^n} \quad (5)$$

where all other parameters are as defined for eq. 4.

All estimated parameters are expressed as logarithms (mean \pm S.E.M.); where relevant, statistical analysis was performed by one-way analysis of variance and Dunnett's post test using GraphPad Prism 5.02, and statistical significance was accepted at $p < 0.05$.

Results

Compound 2 and Quercetin Selectively Modulate the Binding Affinity of Antagonists and Agonists of the GLP-1R. To establish the ability of the putative small molecule GLP-1R modulators, compound 2 and quercetin, to modify peptide binding affinity, equilibrium binding studies were performed between each of these modulators and the radiolabeled orthosteric antagonist ^{125}I -exendin(9–39). Analysis of the data using an allosteric ternary complex model revealed negative cooperativity between compound 2 and the antagonist, with the level of inhibition reaching a limit consistent with the predicted allosteric mode of inhibition (Table 1, Fig. 1B). Quercetin also displayed weak negative cooperativity with ^{125}I -exendin(9–39) (Table 1, Fig. 1B). Affinity estimates (pK_B) for compound 2 and quercetin were 7.58 ± 0.22 and 6.79 ± 0.41 , respectively.

To establish the ability of compound 2 to modulate orthosteric agonist affinity, competition binding studies were performed with GLP-1(7–36) NH_2 , GLP-1(7–37), GLP-1(1–36) NH_2 , GLP-1(1–37), oxyntomodulin, or exendin-4 in the absence or presence of increasing concentrations of compound 2 (Fig. 2, Table 1, Supplemental Fig. S1) or quercetin (Supplemental Fig. S2,

Table 1). These assays demonstrated that compound 2 displays probe dependence (Leach et al., 2007), whereby the cooperativity between the orthosteric and allosteric binding sites is dependent on the orthosteric ligand present in the system. Compound 2 caused a concentration-dependent increase in the affinity of GLP-1(7–36) NH_2 (Fig. 2A, Table 1) and GLP-1(7–37) (Supplemental Fig. S1A, Table 1). Compound 2 also displayed robust positive cooperativity for oxyntomodulin to a greater extent than either GLP-1(7–36) NH_2 or GLP-1(7–37) (Fig. 2D, Table 1). In contrast, compound 2 minimally altered the binding of GLP-1(1–36) NH_2 , GLP-1(1–37) and exendin-4, therefore displaying neutral cooperativity with these agonists (Fig. 2, B and C, Supplemental Fig. S1B, Table 1). No significant modulation in affinity of any peptide agonist was observed in interaction binding studies with quercetin (Supplemental Fig. S2, Table 1).

Compound 2 but Not Quercetin Selectively Augments cAMP Responses in an Agonist-Specific Manner at the GLP-1R. The GLP-1R preferentially couples to the $\text{G}\alpha_s$ pathway, activating adenylate cyclase and augmenting intracellular levels of cAMP, which in turn play a direct role in the secretion of insulin (Drucker et al., 1987). Compound 2 stimulated a robust increase in cAMP production displaying low potency partial agonism in the absence of an orthosteric ligand (Fig. 3E, Table 2). In contrast, quercetin did not act as an agonist at the GLP-1R for cAMP (Supplemental Fig. S3G),

TABLE 1

Differential effects of putative allosteric modulators used in this study on binding properties of peptide agonists of the human GLP-1R

Data were fit with a one-site competition plus allosteric modulator model as defined in eqs. 2 and 3 or by a three-parameter logistic model to yield binding parameters. pK_i is the negative logarithm of the estimated affinity of the peptide agonist for the receptor. pK_B is the negative logarithm of the estimated affinity of the allosteric compounds. $\text{Log}\alpha$ is the logarithm of the cooperativity factor governing the allosteric interaction between the peptide ligand and modulator. Antilogarithms are shown in parentheses. All values are mean \pm S.E.M. from three to six independent experiments performed in duplicate.

	pK_i or pK_B	$\text{Log}\alpha$	
		Compound 2	Quercetin
GLP-1(7–36) NH_2	9.38 ± 0.07	0.74 ± 0.13 (5.49)	N.D.
GLP-1(1–36) NH_2	6.47 ± 0.09	0.05 ± 0.09 (1.12)	N.D.
Exendin-4	9.63 ± 0.06	0.15 ± 0.18 (1.41)	N.D.
Oxyntomodulin	7.53 ± 0.11	1.11 ± 0.22 (12.88)	N.D.
GLP-1(7–37)	9.09 ± 0.04	0.47 ± 0.12 (2.95)	N.D.
GLP-1(1–37)	6.43 ± 0.26	0.10 ± 0.14 (1.26)	N.D.
^{125}I -Exendin(9–39)		-0.37 ± 0.04 (0.43)	-0.11 ± 0.02 (0.78)
Compound 2	7.58 ± 0.22		
Quercetin	6.79 ± 0.41		

N.D., data unable to be experimentally defined or with incomplete curves.

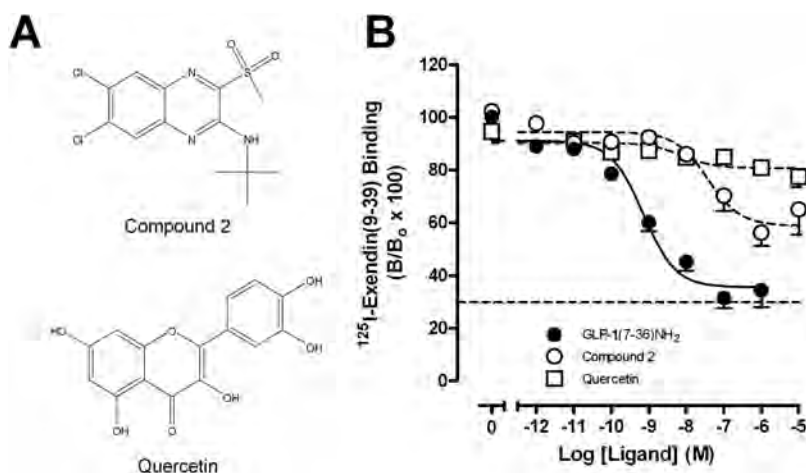


Fig. 1. Structure and binding interactions elicited by allosteric modulators of the human GLP-1R. A, structures of the human GLP-1R small-molecule allosteric modulators used in this study. B, characterization of the inhibition binding profiles of compound 2 and quercetin at the human GLP-1R in relation to the endogenous peptide agonist GLP-1(7–36) NH_2 using ^{125}I -exendin(9–39) as the radioligand and membranes prepared from FlpInCHO cells stably expressing the human GLP-1R. Data are normalized to total binding and are analyzed with an allosteric modulator titration curve as defined in eqs. 2 and 3, assuming non-depletion (compound 2 and quercetin) or a competitive inhibition model [GLP-1(7–36) NH_2]. All values are mean \pm S.E.M. of 6 to 12 independent experiments conducted in duplicate. Nonspecific binding, measured in the presence of 10^{-6} M exendin-4, ranged from 25 to 30% of total binding (dotted line in B). B, bound radioligand; B_0 , binding in the absence of peptide ligand (total binding).

whereas no response was seen in untransfected CHO-FlpIn cells for any of the ligands studied.

To investigate the potential for allosteric effects on peptide agonist-mediated cAMP signaling, interaction studies between the small molecule modulators and peptide ligands were performed. Coaddition of each of the peptides with compound 2 resulted in an observed elevation in cAMP at low concentrations of peptide agonist as a result of the intrinsic efficacy of compound 2 (Fig. 3). Analysis of the interaction between compound 2 and each of the peptides with the allosteric operational model revealed combined affinity-efficacy ($\alpha\beta$) estimates (Table 2) that were consistent with the affinity cooperativity estimates from the binding studies (Table 1), suggesting that effects of compound 2 on peptide-mediated cAMP responses were driven principally by changes in affinity. Thus, where peptides exhibited neutral cooperativity with compound 2 in binding, as seen for exendin-4, GLP-1(1–36)NH₂, and GLP-1(1–37), the $\alpha\beta$ estimates for compound 2 were not significantly different from 1 (Fig. 3, B and C, Supplemental Fig. S4B, Table 2), whereas oxyntomodulin displayed greatest combined cooperativity with compound 2 (Fig. 3D, Table 2), and GLP-1(7–36)NH₂ and GLP-1(7–37) only modest cooperativity (Fig. 3A, Supplemental Fig. S4A, Table 2). For the latter two peptides, this level of cooperativity was insufficient to elicit a significant change in potency, consistent with simulation of the interaction, based on the affinity cooperativity estimate, which predicts a log unit shift of only 0.06 in potency at 10 μ M compound 2 (Supplemental

Fig. S5). Additional experiments after either 5 or 10 min of agonist stimulation revealed equivalent profiles of compound 2 interaction (data not shown).

Quercetin did not influence the production of cAMP for any of the peptides used in this study (Supplemental Fig. S3). This is consistent with the binding data, where the presence of quercetin did not alter the binding profile of any peptide (Supplemental Fig. S2).

Quercetin but Not Compound 2 Selectively Modifies Intracellular Ca²⁺ Responses via the GLP-1R in an Agonist-Specific Manner. Given that allosteric ligands can bind simultaneously with orthosteric ligands and promote unique changes in receptor conformation, the resulting conformations may engender “stimulus-bias” across different signaling pathways in the same cellular background (Urban et al., 2007). In addition to G α_s coupling, the GLP-1R couples to G α_q proteins, resulting in mobilization of intracellular Ca²⁺ (Hällbrink et al., 2001). To investigate whether compound 2 or quercetin could impose stimulus bias on the actions of the orthosteric peptide agonists, we performed functional interaction assays for mobilization of intracellular Ca²⁺. Neither compound 2 nor quercetin displayed any intrinsic efficacy for the GLP-1R in this pathway (Supplemental Fig. S6E, Fig. 4E). To assess the roles of these allosteric modulators, concentration-response curves were established for the peptide ligands in the presence and absence of increasing concentrations of compound 2 or quercetin. In contrast to the cAMP data, quercetin caused biphasic changes in

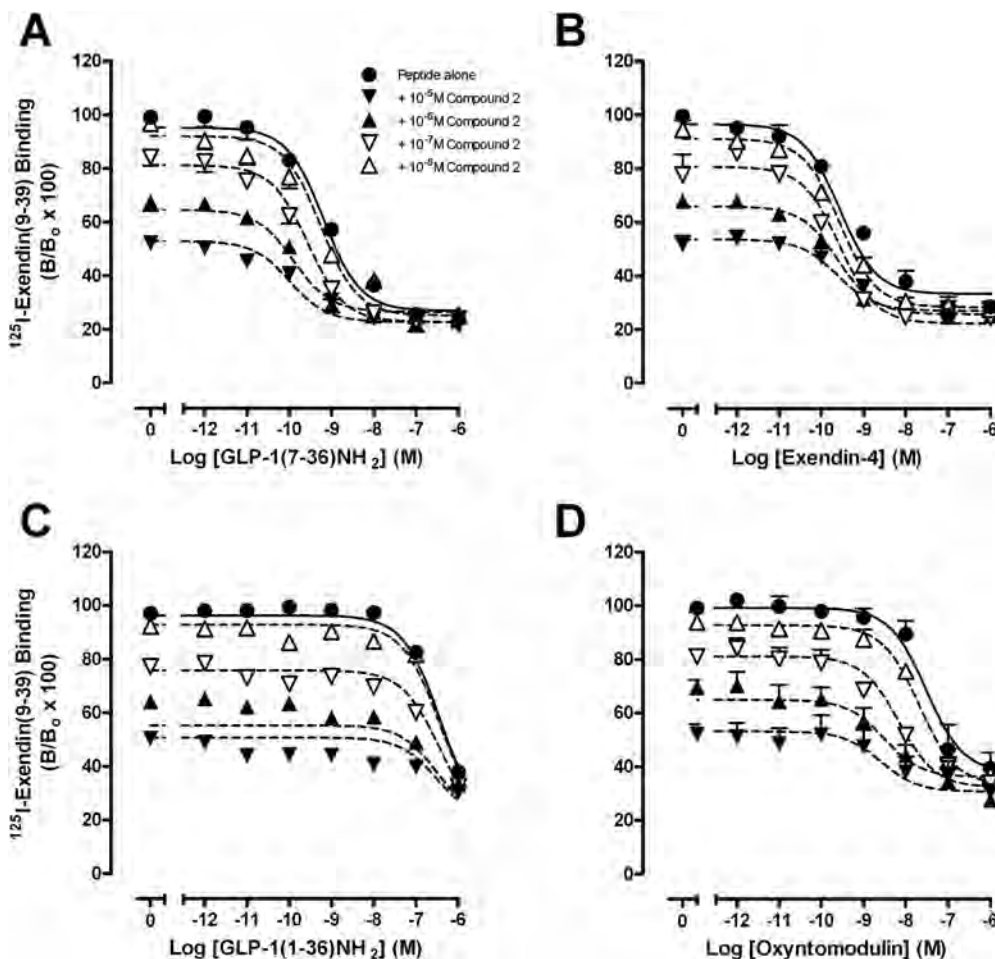


Fig. 2. Characterization of the inhibition binding of varying concentrations of compound 2 in the presence of GLP-1(7–36)NH₂ (A), exendin-4 (B), GLP-1(1–36)NH₂ (C), or oxyntomodulin using membranes prepared from FlpInCHO cells stably expressing the human GLP-1R (D). Data are normalized to total radioligand binding and are analyzed with a one-site competition plus allosteric modulator curve as defined in eqs. 2 and 3, assuming nondepletion. All values are mean \pm S.E.M. of four to six independent experiments conducted in duplicate. Nonspecific binding, measured in the presence of 10^{–6} M exendin-4, ranged from 25 to 30% of total binding. B, bound radioligand; B₀, binding in the absence of peptide ligand (total binding).

peptide agonist potency and efficacy for GLP-1(7–36)NH₂, GLP-1(7–37), and exendin-4 (Fig. 4, A–C). Weak inhibition of peptide efficacy was observed between 10 nM and 1 μ M quercetin, whereas augmentation of peptide efficacy was observed between 30 and 50 μ M quercetin. However, no significant modulation of efficacy was observed for oxyntomodulin, which itself is only a partial agonist for this signaling pathway (Fig. 4D). In contrast to quercetin, compound 2 had no effect on peptide agonist-mediated Ca²⁺ responses (Supplemental Fig. S6). Loss of Ca²⁺ signal with the addition of 10 μ M compound 2 was observed with all peptides studied; however, there was also a parallel reduction in the observed ATP response, indicating that this effect was an experimental artifact at this concentration of compound 2. In contrast, all ATP responses in the presence of increasing concentrations of quercetin remained robust and consistent, as did calcitonin-mediated Ca²⁺ signaling in CTa receptor expressing COS-7 cells, consistent with quercetin's effects on high-affinity agonists being mediated at the level of the GLP-1 receptor. Neither GLP-1(1–36)NH₂ nor GLP-1(1–37) displayed any agonism in this signaling pathway at the tested concentration range (1 pM–1 μ M) in either the absence or presence of compound 2 or quercetin (Supplemental Fig. S6E, Fig. 4E).

Neither Compound 2 nor Quercetin Modulates Agonist-Mediated ERK1/2 Phosphorylation via the GLP-1R. ERK1/2 phosphorylation is often used as a general

marker of convergent activation of multiple pathways, including G protein-independent signaling such as arrestin scaffolding (Lee et al., 2008). Although we observed that both compound 2 and quercetin could engender stimulus bias for a subset of peptides, we failed to observe any modulation of agonist responses in ERK1/2 phosphorylation in the presence of compound 2 or quercetin (Fig. 5, Supplemental Fig. S7). However, compound 2 displayed weak partial agonism for phosphorylation of ERK1/2 with a pEC₅₀ of 5.76 ± 0.06 and a maximum of 51% of the GLP-1(7–36)NH₂ response (Fig. 5G). In contrast, quercetin displayed no intrinsic agonism in any pathway tested.

Discussion

Despite the increasing prevalence of “biologicals” (high molecular weight natural or modified peptides/proteins) for the clinical treatment of disease, low molecular weight, orally active compounds are still pursued as the idealized therapeutic drug. Such drugs have traditionally been developed to mimic the properties of the natural ligand of the receptor by targeting the orthosteric binding site. Although this approach has been broadly successful for many GPCRs, including adrenergic receptors and histamine receptors (Black, 1989), there are many cases in which it has been problematic. Consequently, there has been increasing interest in the development of allosteric and/or bitopic drugs as a way of targeting these receptors (Valant et al.,

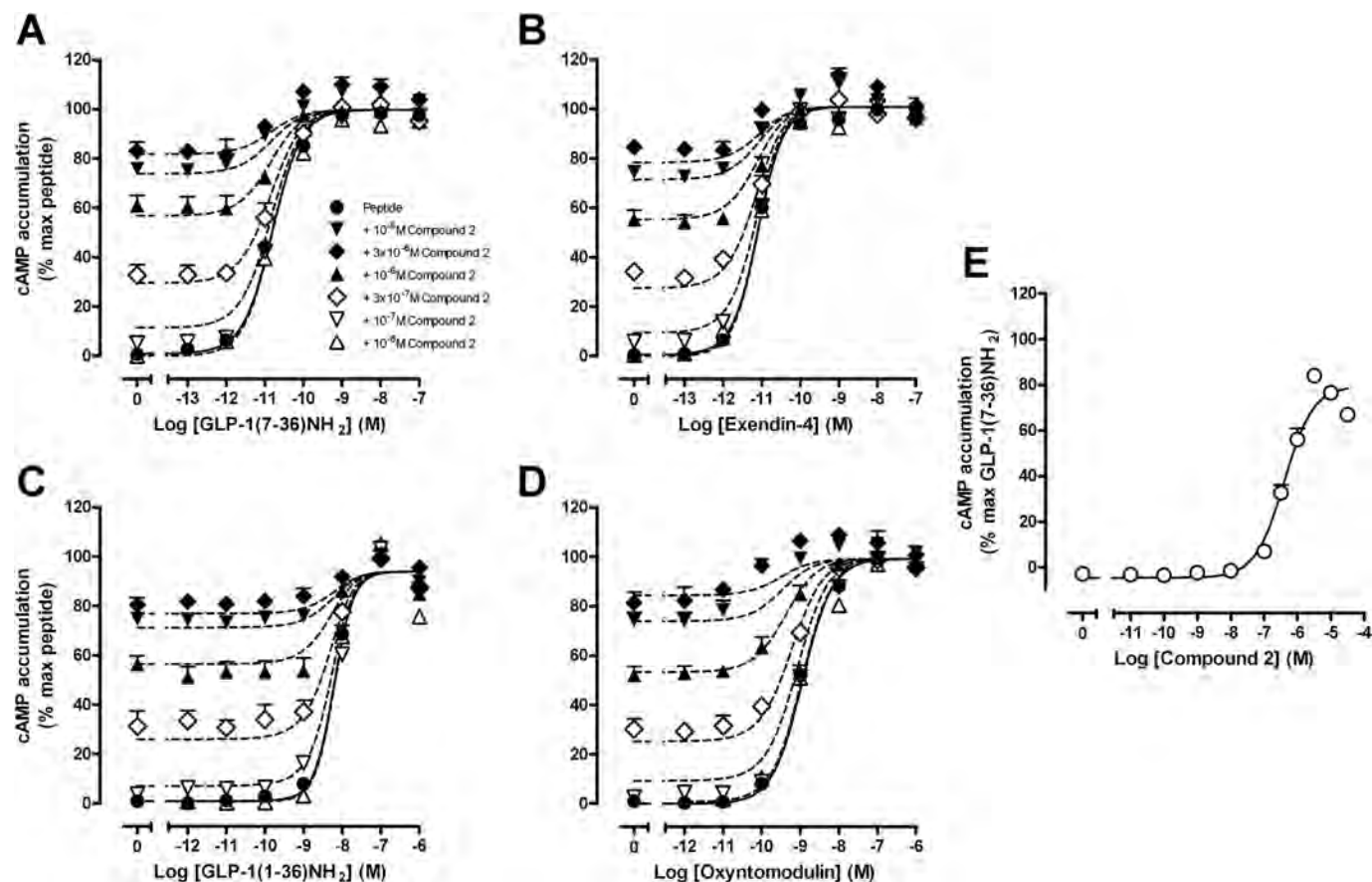


Fig. 3. Characterization of the interaction between compound 2 and GLP-1(7–36)NH₂ (A), exendin-4 (B), GLP-1(1–36)NH₂ (C), or oxyntomodulin (D) in a cAMP accumulation assay using FlpInCHO cells stably expressing the human GLP-1R. E, compound 2 alone. Data are normalized to maximal peptide response and analyzed with an operational model of allosterism as defined in eq. 4. All values are mean \pm S.E.M. of three to eight independent experiments conducted in duplicate.

2009). However, allosteric interactions are often complex, with the potential for modulation of affinity and efficacy, independently or concomitantly, as well as potential for the allosteric ligand to exhibit its own intrinsic efficacy; efficacy modulation and intrinsic efficacy may also be manifested in a pathway-dependent manner (May et al., 2007b). Furthermore, the na-

TABLE 2

Differential effects of compound 2 on peptide agonists of the human GLP-1R in cAMP accumulation in FlpInCHO cells stably expressing the human GLP-1R

Data were analyzed with an operational model of allosterism as defined in eq. 4. pEC_{50} values represent the negative logarithm of the concentration of agonist that produces half the maximal response. E_{max} represents the maximal response normalized to that of GLP-1(7–36)NH₂. $Log\alpha\beta$ values represent the logarithm of the product of binding (α) and activation (β) cooperativity factors between compound 2 and the peptide agonists. Antilogarithms are shown in parentheses. All values are mean \pm S.E.M. of three to six independent experiments, conducted in duplicate. Data were analyzed with one-way analysis of variance and Dunnett's post test.

	pEC_{50}	E_{max}	$Log\alpha\beta$ (Compound 2)
GLP-1(7–36)NH ₂	10.81 \pm 0.03	100	0.69 \pm 0.17 (4.90)*
GLP-1(1–36)NH ₂	8.21 \pm 0.03	96 \pm 2	0.19 \pm 0.19 (1.55)
Exendin-4	11.09 \pm 0.03	99 \pm 5	0.37 \pm 0.16 (2.34)
Oxyntomodulin	8.95 \pm 0.03	96 \pm 4	1.40 \pm 0.19 (25.12)*
GLP-1(7–37)	10.84 \pm 0.04	98 \pm 3	0.81 \pm 0.19 (6.46)*
GLP-1(1–37)	7.86 \pm 0.02	97 \pm 1	0.06 \pm 0.19 (1.15)
Compound 2	6.40 \pm 0.07	83 \pm 2	
Quercetin	N.D.	N.D.	

N.D., data unable to be experimentally defined or with incomplete curves.

* Statistically significant at $P < 0.05$.

ture of the allosteric interaction is probe-dependent (May et al., 2007b). In many physiological systems, this behavior is largely irrelevant, because there is principally one endogenous ligand for the receptor. However, there are numerous examples in which individual receptors can respond physiologically or pathophysiologically to multiple endogenous ligands, including the melanocortin receptors α -melanocyte stimulating hormone, adrenocorticotropin, agouti-related peptide (Tao, 2010), the parathyroid hormone receptor 1 (Gardella and Jüppner, 2000), and GLP-1Rs. In this study, we have demonstrated that allosteric modulation of the GLP-1R is complex, with pathway-dependent modulation of receptor response that is reliant upon both the peptide ligand and the allosteric modulator. Furthermore, it highlights the fact that distinct peptide ligands can exhibit stimulus bias at the GLP-1R and that allosteric modulators can impose further bias on this activity. Although some caution should be applied when interpreting data from a transfected cell background rather than a native GLP-1R-expressing cell line, collectively, these data stress the need for broad elucidation of mechanism of action when developing allosteric compounds.

The GLP-1R is pleiotropically coupled, eliciting signals via diverse pathways, including, prominently, the formation of cAMP (Baggio and Drucker, 2007). The signaling downstream of GLP-1R activation leading to the release of insulin is well studied and is critically dependent upon the activation

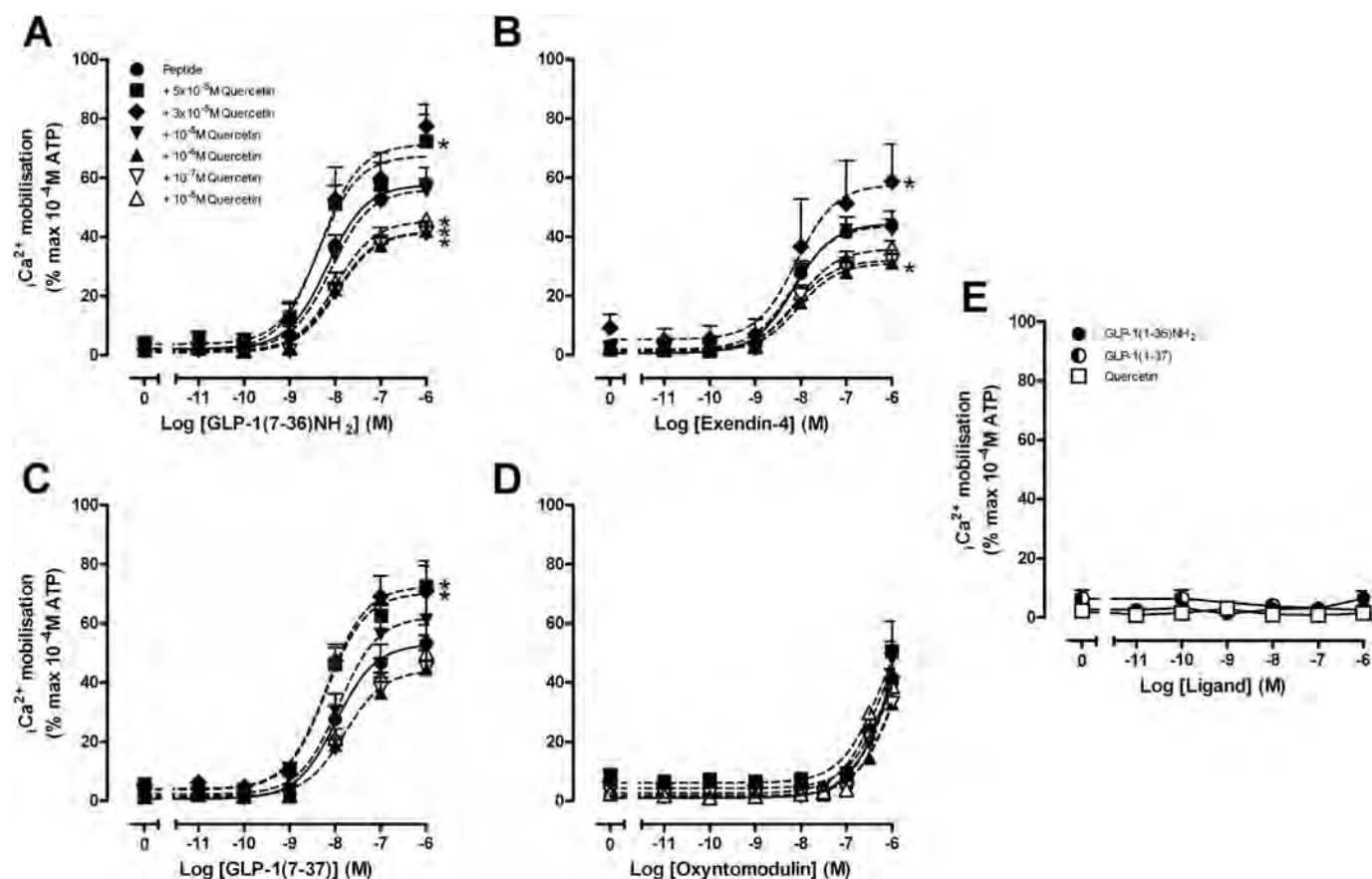


Fig. 4. Characterization of the interaction between quercetin and GLP-1(7–36)NH₂ (A), exendin-4 (B), GLP-1(7–37) (C), or oxyntomodulin in an intracellular Ca²⁺ mobilization assay using FlpInCHO cells stably expressing the human GLP-1R (D). E, GLP-1(1–36)NH₂, GLP-1(1–37), or quercetin alone. Data are normalized to the maximal response elicited by 100 μ M ATP and analyzed with a three-parameter logistic curve as defined in eq. 1. All values are mean \pm S.E.M. of four to eight independent experiments conducted in duplicate. Statistical significance of changes in E_{max} in the presence of quercetin in comparison to the E_{max} of the peptide alone were determined by one-way analysis of variance and Dunnett's post test and are indicated with an asterisk (*, $p < 0.05$).

of G_{α_s} and formation of cAMP with subsequent effects via protein kinase A and exchange protein directly activated by cAMP, including direct inhibition of K_{ATP} channels, cell depolarization, and influx of extracellular Ca^{2+} (Baggio and Drucker, 2007). Nonetheless, there is also a role for mobilization of intracellular Ca^{2+} in augmentation of response (Baggio and Drucker, 2007), which is also manifested with G_{α_q} -coupled receptors such as the muscarinic M3 acetylcholine receptor (Gautam et al., 2008). Sustained effects on gene transcription and the preservation of β -cell mass involve multiple signaling pathways, both cAMP-dependent and -independent; the latter include activation of mitogen-activated protein kinases such as ERK1/2. However, for many therapeutically important effects, including the modulation of appetite, the underlying GLP-1R-mediated signaling is not yet fully elucidated. Nonetheless, it is clear that the physiological response is a composite of the interplay between the various signaling pathways activated by individual ligands.

Evaluation of signaling across three pathways (cAMP production, elevation of intracellular Ca^{2+} , and ERK1/2 phosphorylation) demonstrated, as expected, that all of the peptide agonists coupled the receptor most strongly to G_{α_s} -mediated cAMP production. Each of the high-affinity agonists, GLP-1(7–36)NH₂, GLP-1(7–37), and exendin-4 exhibited a similar profile of activation (Table 3), consistent with other functional and physiological studies with these peptides (Göke et al., 1993; Baggio and Drucker, 2007). In contrast, GLP-1(1–36)NH₂, GLP-1(1–37), and oxyntomodulin exhibited significant bias relative to GLP-1(7–36)NH₂. Oxyntomodulin exhibited less preference for cAMP relative to ERK1/2, but similar preference for cAMP relative to Ca^{2+} , indicating that physiological responses to oxyntomodulin via the GLP-1R could differ from those elicited by GLP-1(7–36)NH₂ (Table 3). Oxyntomodulin, like GLP-

1(7–36)NH₂ and GLP-1(7–37), is elevated postprandially, reaches higher plasma levels than those of GLP-1(1–36)NH₂ and GLP-1(1–37), and can reach very high levels in some conditions, including celiac disease in children (Le Quellec et al., 1998). However, it is generally thought to play only a limited role therapeutically because of its lower affinity for the GLP-1R. Although oxyntomodulin can bind to both the glucagon and GLP-1R, most of its physiological responses seem to be mediated via the GLP-1R, as demonstrated in GLP-1R-knockout mice (Estall and Drucker, 2006). Oxyntomodulin, however, has a physiological profile distinct from that of GLP-1(7–36)NH₂ (Druce and Bloom, 2006; Maida et al., 2008), which is not fully consistent with a purely affinity-driven reduction in signaling but is consistent with the observations of stimulus bias in this study.

The flavonol quercetin lacked intrinsic activity but selectively modulated intracellular Ca^{2+} responses for the high-affinity agonists GLP-1(7–36)NH₂, GLP-1(7–37), and exendin-4, causing weak inhibition at low concentrations and significant augmentation of response at concentrations above 10 μ M, but had no effect on oxyntomodulin response. Thus, quercetin imparts stimulus bias with respect to Ca^{2+} signaling, but in a peptide-agonist dependent manner, which is consistent with a receptor-dependent mode of action. The selective bias for the high-affinity peptides is consistent with the overlap in signaling pathway activation profile exhibited by the peptides, which suggests that these peptides induce similar receptor conformations.

In contrast, analysis of the actions of compound 2 revealed intriguing differences in behavior of peptide agonists and also in modulation of peptide agonist function. Compound 2 displayed intrinsic efficacy for cAMP accumulation and ERK1/2 phosphorylation; while more efficacious

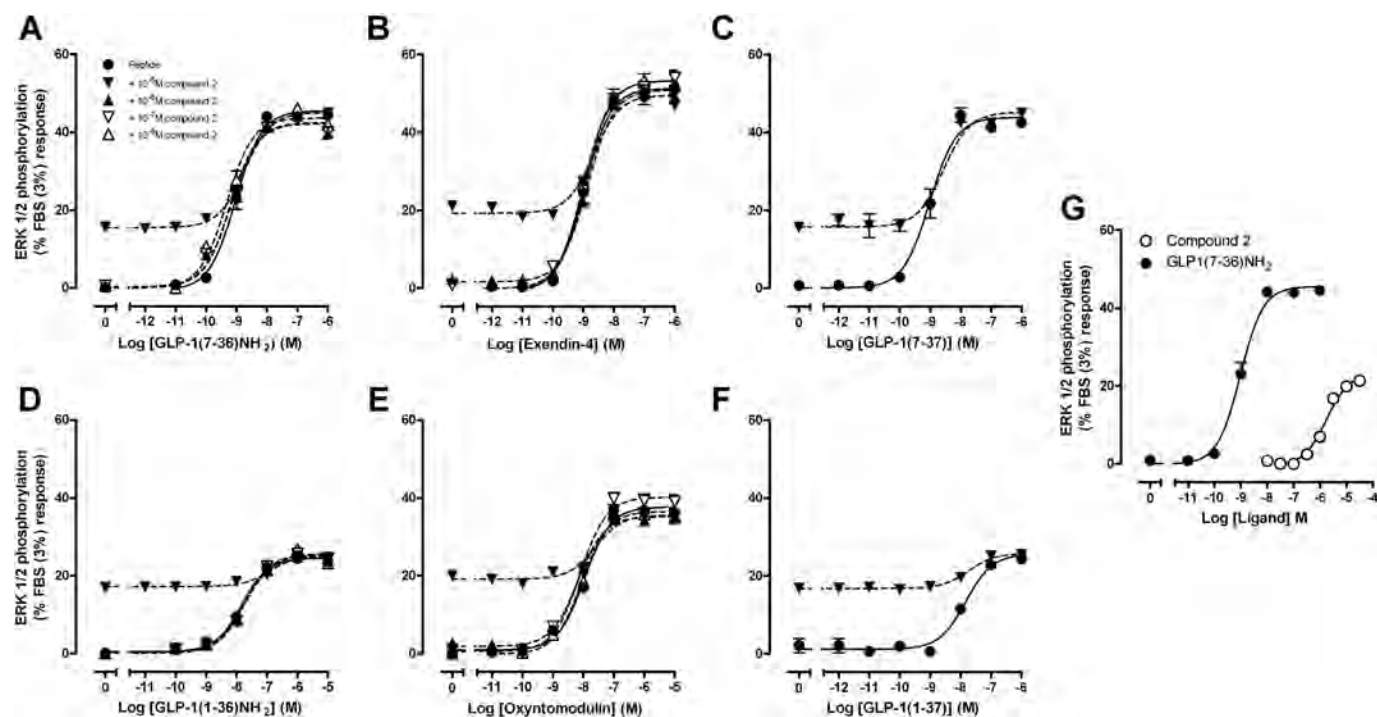


Fig. 5. Characterization of the interaction between compound 2 and GLP-1(7–36)NH₂ (A), exendin-4 (B), GLP-1(7–37) (C), GLP-1(1–36)NH₂ (D), oxyntomodulin (E), or GLP-1(1–37) (F) in an ERK 1/2 phosphorylation assay using FlpInCHO cells stably expressing the human GLP-1R. G, compound 2 alone. Data are normalized to maximal peptide response and analyzed with a three-parameter logistic curve as defined in eq. 1. All values are mean \pm S.E.M. of three independent experiments conducted in duplicate.

in the former, it demonstrated less bias between these pathways than the peptide agonists of the receptor (Table 3). A formal assessment of relative signaling via mobilization of intracellular Ca^{2+} was not possible because of the nonspecific loss of response seen at higher compound 2 concentrations in the CHO cell background. Such distinction in receptor activation by compound 2 versus peptide agonists is not surprising, because it engages the receptor via different interactions and could be expected to engender unique conformation(s). This type of behavior has recently been observed at the M4 muscarinic acetylcholine receptor, where the allosteric agonist 3-amino-5-chloro-6-methoxy-4-methyl-thieno(2,3-*b*)pyridine-2-carboxylic acid cyclopropylamide (LY2033298) activates the receptor by conformational shifts that are partially distinct from those used by orthosteric agonists (Nawaratne et al., 2010).

In binding assays, compound 2 displayed significant probe dependence for modulation of affinity, negative cooperativity with the antagonist radioligand ^{125}I -exendin(9–39), strong positive cooperativity with oxyntomodulin, weaker positive cooperativity with GLP-1(7–36) NH_2 and GLP-1(7–37), and essentially neutral cooperativity with exendin-4 and full-length GLP-1 peptides. The differential modulation of affinity for peptide agonists versus antagonists is not necessarily surprising because compound 2 is an allosteric agonist and thus would be expected to favor binding to activated states of the receptor (Hall, 2000). However, the profile for modulation of peptide agonists reveals unanticipated effects that could translate into unexpected responses in preclinical and/or clinical evaluation of drug efficacy. In this regard, there were a number of important findings: the first was a markedly greater modulation of oxyntomodulin affinity relative to that for GLP-1(7–36) NH_2 and GLP-1(7–37), which manifested in the cAMP assay as significant augmentation of oxyntomodulin potency but minimal augmentation of truncated GLP-1 peptide signaling; this response could be expected to allow drugs with this type of profile to elicit actions via oxyntomodulin that would not normally be seen with circulating levels of the peptide [40–60 pM physiologically and >500 pM in some pathophysiological states (Le Quellec et al., 1998)]. A second important observation was that GLP-1(7–

36) NH_2 and GLP-1(7–37) had a distinct interaction with compound 2 from that of exendin-4. As discussed above, exendin-4 and the truncated forms of GLP-1 are considered functionally equivalent; however, the positive cooperativity between compound 2 and truncated GLP-1 peptides versus neutral cooperativity with exendin-4 implies that the conformational state(s) adopted by exendin-4 is indeed different from that induced/occupied by GLP-1(7–36) NH_2 and GLP-1(7–37); this may lead to divergence in signaling outcomes between the endogenous peptides, and exendin-4 may be detected if more broad analysis of signaling and/or receptor regulation is undertaken. Such differences in receptor interaction could underlie unexpected side effect profiles in susceptible populations.

Like quercetin, compound 2 modulated peptide signaling from only one of the three pathways assayed in the current study. Although quercetin modulated GLP-1R-mediated intracellular Ca^{2+} , compound 2 modulated GLP-1R-mediated cAMP, suggesting that both modulators engender distinct forms of stimulus bias. Although efficacy cooperativity may be influenced by the propensity of an allosteric ligand to activate an individual pathway (Hall, 2000), simulation of compound 2 modulation of response based on affinity cooperativity, in the absence of intrinsic efficacy, predicts that there should be increased potency for each pathway, at least for oxyntomodulin. The absence of this effect indicates that compound 2 is generating true stimulus bias toward production of cAMP relative to the other pathways measured. Because allosteric interactions are due to conformational changes in the receptor as a result of co-occupancy of two ligands and conformational differences are the driver for biased signaling, broad understanding of receptor signaling is critical to understanding the success/failure of allosteric drugs during clinical development. It also highlights the importance of determining the function of putative allosteric modulators in both binding and signaling assays, and that discrimination of allosteric properties of small molecules depends on screening in multiple pathways, regardless of coupling strength. Likewise, for endogenous receptor systems that involve the interplay of multiple natural ligands, probe dependence of allosteric drugs is a major factor that needs

TABLE 3

Efficacy of agonists of the GLP-1R in FlpInCHO cells stably expressing the human GLP-1R

τ is an index of the coupling efficiency (or efficacy) of the agonist and is defined as the total concentration of receptors divided by the concentration of agonist-receptor complex that yields half the maximum system response (E_{max}). K_A is the affinity of the agonist. Ratios were determined using eq. 5. $\text{Log}[\tau/K_A]_{\text{normalized}}$ is expressed relative to the $\text{Log}[\tau/K_A]$ values for GLP-1(7–36) NH_2 and is a measure of the relative strength of coupling of each individual agonist for an individual pathway relative to that of the control agonist. $\text{Log}[\text{stimulus bias}]$ is the ratio of the efficacy of each agonist for the two pathways relative to the values for GLP-1(7–36) NH_2 and is a measure of the degree of stimulus bias exhibited by individual agonists across the pathways, relative to that of the control agonist. Data are mean \pm S.E.M. of three to eight individual experiments.

	GLP-1(7–36) NH_2	GLP-1(7–37)	Exendin-4	GLP-1(1–36) NH_2	Oxyntomodulin	Compound 2
$\text{Log}[\tau/K_A]$						
cAMP	10.93 \pm 0.03	10.89 \pm 0.05	11.16 \pm 0.03	8.29 \pm 0.03	9.05 \pm 0.03	6.36 \pm 0.04
ERK1/2	9.09 \pm 0.05	9.09 \pm 0.06	9.02 \pm 0.03	7.87 \pm 0.12	8.05 \pm 0.08	5.78 \pm 0.11
Ca^{2+}	8.27 \pm 0.32	7.93 \pm 0.49	8.06 \pm 0.51	N.D.	5.75 \pm 0.47	N.D.
$\text{Log}[\tau/K_A]_{\text{normalized}}$						
cAMP	0	0.04 \pm 0.05	–0.23 \pm 0.04	2.64 \pm 0.04	1.88 \pm 0.04	4.57 \pm 0.05
ERK1/2	0	0.00 \pm 0.08	0.07 \pm 0.06	1.22 \pm 0.13	1.04 \pm 0.09	3.31 \pm 0.12
Ca^{2+}	0	0.34 \pm 0.59	0.21 \pm 0.60	N.D.	2.52 \pm 0.57	N.D.
$\text{Log}[\text{stimulus bias}]^a$						
cAMP/ERK1/2	0	0.04 \pm 0.28	–0.30 \pm 0.25	1.42 \pm 0.36*	0.84 \pm 0.31*	1.26 \pm 0.35*
cAMP/ Ca^{2+}	0	–0.30 \pm 0.59	–0.44 \pm 0.60	N.D.	–0.64 \pm 0.57	N.D.
ERK1/2/ Ca^{2+}	0	–0.34 \pm 0.59	–0.14 \pm 0.60	N.D.	–1.48 \pm 0.58*	N.D.

N.D., not determined because of insufficient response.

^a $\text{Log}[\text{stimulus bias}]$ data were assessed for difference from “0” [null hypothesis, no bias relative to GLP-1(7–36) NH_2] through calculation of confidence intervals.

* Values that do not include “0” within the 95% confidence interval.

consideration during discovery and development; indeed, this could also extend to otherwise inert metabolic products of the ligands.

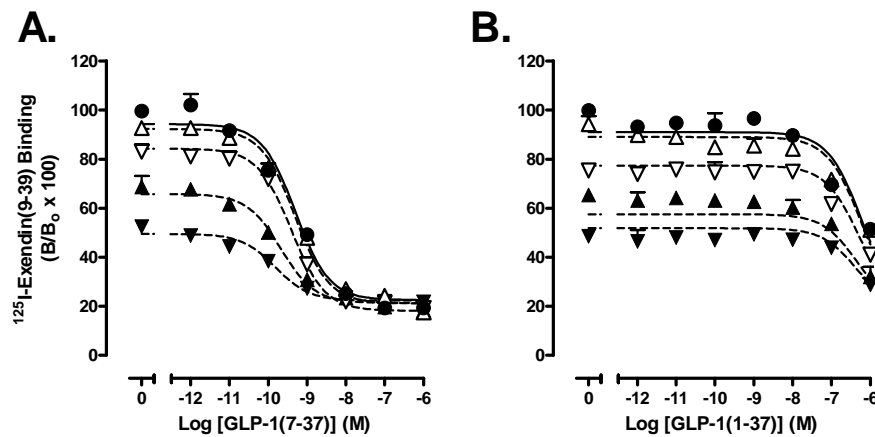
References

- Avlani V, May LT, Sexton PM, and Christopoulos A (2004) Application of a kinetic model to the apparently complex behavior of negative and positive allosteric modulators of muscarinic acetylcholine receptors. *J Pharmacol Exp Ther* **308**: 1062–1072.
- Avlani VA, McLoughlin DJ, Sexton PM, and Christopoulos A (2008) The impact of orthosteric radioligand depletion on the quantification of allosteric modulator interactions. *J Pharmacol Exp Ther* **325**:927–934.
- Baggio LL and Drucker DJ (2007) Biology of incretins: GLP-1 and GIP. *Gastroenterology* **132**:2131–2157.
- Black J (1989) Drugs from emasculated hormones: the principle of syntopic antagonism. *Science* **245**:486–493.
- Chen D, Liao J, Li N, Zhou C, Liu Q, Wang G, Zhang R, Zhang S, Lin L, Chen K, et al. (2007) A nonpeptidic agonist of glucagon-like peptide 1 receptors with efficacy in diabetic db/db mice. *Proc Natl Acad Sci USA* **104**:943–948.
- Christopoulos A and Kenakin T (2002) G protein-coupled receptor allostery and complexing. *Pharmacol Rev* **54**:323–374.
- Deacon CF, Johnsen AH, and Holst JJ (1995a) Degradation of glucagon-like peptide-1 by human plasma in vitro yields an N-terminally truncated peptide that is a major endogenous metabolite in vivo. *J Clin Endocrinol Metab* **80**:952–957.
- Deacon CF, Nauck MA, Toft-Nielsen M, Pridal L, Willms B, and Holst JJ (1995b) Both subcutaneously and intravenously administered glucagon-like peptide I are rapidly degraded from the NH₂-terminus in type II diabetic patients and in healthy subjects. *Diabetes* **44**:1126–1131.
- DeFronzo RA (1992) Pathogenesis of type 2 (non-insulin dependent) diabetes mellitus: a balanced overview. *Diabetologia* **35**:389–397.
- Druce MR and Bloom SR (2006) Oxyntomodulin: a novel potential treatment for obesity. *Treat Endocrinol* **5**:265–272.
- Drucker DJ, Philippe J, Mojsov S, Chick WL, and Habener JF (1987) Glucagon-like peptide I stimulates insulin gene expression and increases cyclic AMP levels in a rat islet cell line. *Proc Natl Acad Sci USA* **84**:3434–3438.
- Edwards CM, Stanley SA, Davis R, Brynes AE, Frost GS, Seal LJ, Ghatei MA, and Bloom SR (2001) Exendin-4 reduces fasting and postprandial glucose and decreases energy intake in healthy volunteers. *Am J Physiol Endocrinol Metab* **281**:E155–E161.
- Elbrønd B, Jakobsen G, Larsen S, Agersø H, Jensen LB, Rolan P, Sturis J, Hatorp V, and Zdravkovic M (2002) Pharmacokinetics, pharmacodynamics, safety, and tolerability of a single-dose of NN2211, a long-acting glucagon-like peptide 1 derivative, in healthy male subjects. *Diabetes Care* **25**:1398–1404.
- Estall JL and Drucker DJ (2006) Glucagon and glucagon-like peptide receptors as drug targets. *Curr Pharm Des* **12**:1731–1750.
- Figuerola KW, Griffin MT, and Ehlerl FJ (2009) Selectivity of agonists for the active state of M1 to M4 muscarinic receptor subtypes. *J Pharmacol Exp Ther* **328**:331–342.
- Gardella TJ and Jüppner H (2000) Interaction of PTH and PTHrP with their receptors. *Rev Endocr Metab Disord* **1**:317–329.
- Gautam D, Jeon J, Li JH, Han SJ, Hamdan FF, Cui Y, Lu H, Deng C, Gavrilova O, and Wess J (2008) Metabolic roles of the M3 muscarinic acetylcholine receptor studied with M3 receptor mutant mice: a review. *J Recept Signal Transduct Res* **28**:93–108.
- Göke R, Fehmman HC, Linn T, Schmidt H, Krause M, Eng J, and Göke B (1993) Exendin-4 is a high potency agonist and truncated exendin-(9–39)-amide an antagonist at the glucagon-like peptide 1-(7–36)-amide receptor of insulin-secreting beta-cells. *J Biol Chem* **268**:19650–19655.
- Gregory KJ, Hall NE, Tobin AB, Sexton PM, and Christopoulos A (2010) Identification of orthosteric and allosteric site mutations in M2 muscarinic acetylcholine receptors that contribute to ligand-selective signaling bias. *J Biol Chem* **285**:7459–7474.
- Hall DA (2000) Modeling the functional effects of allosteric modulators at pharmacological receptors: an extension of the two-state model of receptor activation. *Mol Pharmacol* **58**:1412–1423.
- Hällbrink M, Holmqvist T, Olsson M, Ostenson CG, Efendic S, and Langel U (2001) Different domains in the third intracellular loop of the GLP-1 receptor are responsible for Alpha(s) and Galpha(i)/Galpha(o) activation. *Biochim Biophys Acta* **1546**:79–86.
- Kenakin T (2008) Functional selectivity in GPCR modulator screening. *Comb Chem High Throughput Screen* **11**:337–343.
- Kieffer TJ, McIntosh CH, and Pederson RA (1995) Degradation of glucose-dependent insulinotropic polypeptide and truncated glucagon-like peptide 1 in vitro and in vivo by dipeptidyl peptidase IV. *Endocrinology* **136**:3585–3596.
- Knudsen LB, Kiel D, Teng M, Behrens C, Bhumralkar D, Kodra JT, Holst JJ, Jeppesen CB, Johnson MD, de Jong JC, et al. (2007) Small-molecule agonists for the glucagon-like peptide 1 receptor. *Proc Natl Acad Sci USA* **104**:937–942.
- Knudsen LB, Nielsen PF, Huusfeldt PO, Johansen NL, Madsen K, Pedersen FZ, Thøgersen H, Wilken M, and Agersø H (2000) Potent derivatives of glucagon-like peptide-1 with pharmacokinetic properties suitable for once daily administration. *J Med Chem* **43**:1664–1669.
- Le Quellec A, Clapié M, Callamand P, Lehmann M, Kervran A, Bataille D, and Rieu D (1998) Circulating oxyntomodulin-like immunoreactivity in healthy children and children with celiac disease. *J Pediatr Gastroenterol Nutr* **27**:513–518.
- Leach K, Sexton PM, and Christopoulos A (2007) Allosteric GPCR modulators: taking advantage of permissive receptor pharmacology. *Trends Pharmacol Sci* **28**:382–389.
- Lee MH, El-Shewy HM, Luttrell DK, and Luttrell LM (2008) Role of beta-arrestin-mediated desensitization and signaling in the control of angiotensin AT1a receptor-stimulated transcription. *J Biol Chem* **283**:2088–2097.
- Maida A, Lovshin JA, Baggio LL, and Drucker DJ (2008) The glucagon-like peptide-1 receptor agonist oxyntomodulin enhances beta-cell function but does not inhibit gastric emptying in mice. *Endocrinology* **149**:5670–5678.
- May LT, Avlani VA, Langmead CJ, Herdon HJ, Wood MD, Sexton PM, and Christopoulos A (2007a) Structure-function studies of allosteric agonism at M2 muscarinic acetylcholine receptors. *Mol Pharmacol* **72**:463–476.
- May LT, Leach K, Sexton PM, and Christopoulos A (2007b) Allosteric modulation of G protein-coupled receptors. *Annu Rev Pharmacol Toxicol* **47**:1–51.
- Mitri J and Hamdy O (2009) Diabetes medications and body weight. *Expert Opin Drug Saf* **8**:573–584.
- Morfis M, Tilakaratne N, Furness SG, Christopoulos G, Werry TD, Christopoulos A, and Sexton PM (2008) Receptor activity-modifying proteins differentially modulate the G protein-coupling efficiency of amylin receptors. *Endocrinology* **149**: 5423–5431.
- Nawaratne V, Leach K, Felder CC, Sexton PM, and Christopoulos A (2010) Structural determinants of allosteric agonism and modulation at the M4 muscarinic acetylcholine receptor: identification of ligand-specific and global activation mechanisms. *J Biol Chem* **285**:19012–19021.
- Olansky L (2010) Do incretin-based therapies cause acute pancreatitis? *J Diabetes Sci Technol* **4**:228–229.
- Schann S, Mayer S, Frauli M, Franchet C, and Neuville P (2009) Sounds of silence: innovative approach for identification of novel GPCR-modulator chemical entities. 238th American Chemical Society National Meeting; 16–20 August 2009; Washington DC. pp MEDI-432.
- Tao YX (2010) The melanocortin-4 receptor: physiology, pharmacology, and pathophysiology. *Endocr Rev* doi:10.1210/er.2009-0037.
- Teng M, Johnson MD, Thomas C, Kiel D, Lakis JN, Kercher T, Aytes S, Kostrowicki J, Bhumralkar D, Truesdale L, et al. (2007) Small molecule ago-allosteric modulators of the human glucagon-like peptide-1 (hGLP-1) receptor. *Bioorg Med Chem Lett* **17**:5472–5478.
- Toft-Nielsen MB, Damholt MB, Madsbad S, Hilsted LM, Hughes TE, Michelsen BK, and Holst JJ (2001) Determinants of the impaired secretion of glucagon-like peptide-1 in type 2 diabetic patients. *J Clin Endocrinol Metab* **86**:3717–3723.
- Urban JD, Clarke WP, von Zastrow M, Nichols DE, Kobilka B, Weinstein H, Javitch JA, Roth BL, Christopoulos A, Sexton PM, et al. (2007) Functional selectivity and classical concepts of quantitative pharmacology. *J Pharmacol Exp Ther* **320**:1–13.
- Valant C, Sexton PM, and Christopoulos A (2009) Orthosteric/allosteric bitopic ligands: going hybrid at GPCRs. *Mol Interv* **9**:125–135.
- Werry TD, Gregory KJ, Sexton PM, and Christopoulos A (2005) Characterization of serotonin 5-HT_{2C} receptor signaling to extracellular signal-regulated kinases 1 and 2. *J Neurochem* **93**:1603–1615.
- Wild S, Roglic G, Green A, Sicree R, and King H (2004) Global prevalence of diabetes: estimates for the year 2000 and projections for 2030. *Diabetes Care* **27**:1047–1053.

Address correspondence to: Prof. Patrick M. Sexton, Drug Discovery Biology Laboratory, Monash Institute of Pharmaceutical Sciences, Monash University, 381 Royal Parade, Parkville, Victoria 3052, Australia. E-mail: patrick.sexton@med.monash.edu.au

1) Koole et al, *Allosteric ligands of the glucagon-like peptide 1 receptor (GLP-1R) differentially modulate endogenous and exogenous peptide responses in a pathway selective manner; implications for drug screening. Molecular Pharmacology #65664*

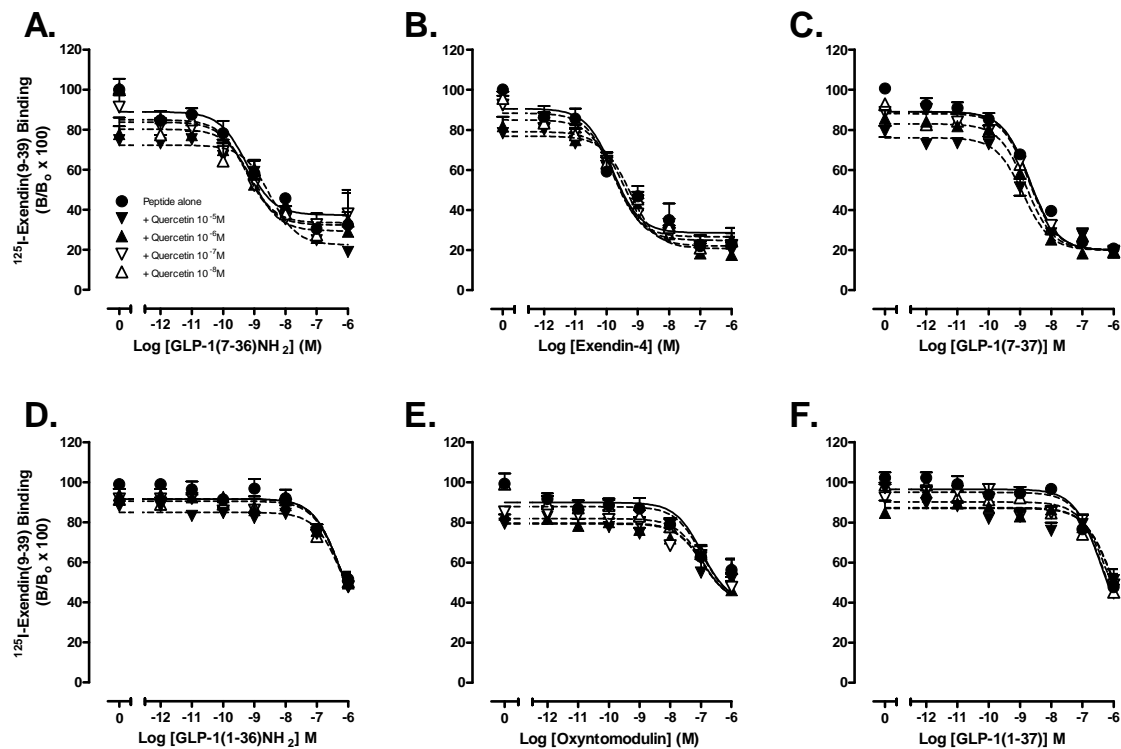
SI Figure S1.



Supplementary Figure S1. Characterisation of the inhibition binding of varying concentrations of compound 2 in the presence of (A) GLP-1(1-36) NH_2 or (B) GLP-1(1-37) using membranes prepared from FlpInCHO cells stably expressing the human GLP-1R. Data are normalised to total radio-ligand binding and analyzed with a one-site competition plus allosteric modulator curve as defined in (Equation 2) and (Equation 3), assuming non-depletion. All values are mean \pm S.E.M. of three independent experiments, conducted in duplicate. Non-specific binding, measured in the presence of 10^{-6}M exendin-4, ranged from 25-30% of total binding. B, bound radioligand; B_0 , binding in the absence of peptide ligand (total binding).

2) Koole et al, *Allosteric ligands of the glucagon-like peptide 1 receptor (GLP-1R) differentially modulate endogenous and exogenous peptide responses in a pathway selective manner; implications for drug screening. Molecular Pharmacology #65664*

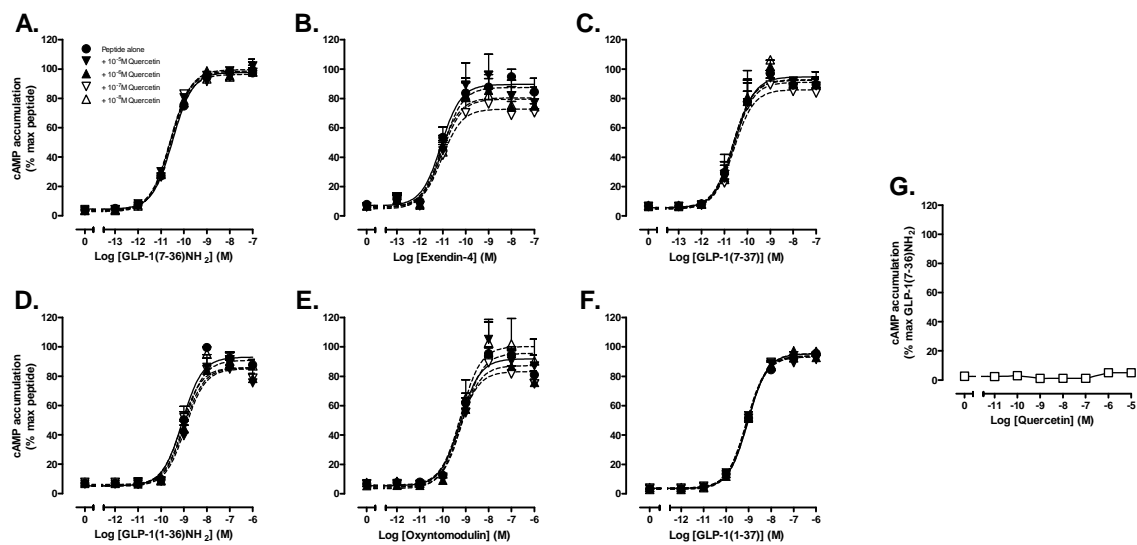
SI Figure S2.



Supplementary Figure S2. Characterisation of the inhibition binding of varying concentrations of quercetin in the presence of (A) GLP-1(7-36)NH₂, (B) exendin-4, (C) GLP-1(7-37) (D) GLP-1(1-36)NH₂, (E) oxyntomodulin or (F) GLP-1(1-37) using membranes prepared from FlpInCHO cells stably expressing the human GLP-1R. Data are normalised to total radio-ligand binding and analyzed with a one-site competition plus allosteric modulator curve as defined in (Equation 2) and (Equation 3), assuming non-depletion. All values are mean ± S.E.M. of three independent experiments, conducted in duplicate. . Non-specific binding, measured in the presence of 10⁻⁶M exendin-4, ranged from 25-30% of total binding. B, bound radioligand; B₀, binding in the absence of peptide ligand (total binding).

3) Koole et al, *Allosteric ligands of the glucagon-like peptide 1 receptor (GLP-1R) differentially modulate endogenous and exogenous peptide responses in a pathway selective manner; implications for drug screening. Molecular Pharmacology #65664*

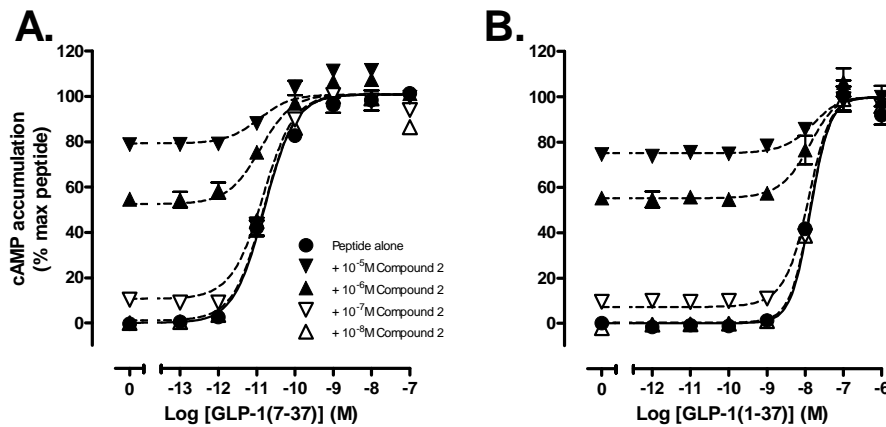
SI Figure S3.



Supplementary Figure S3. Characterisation of the interaction between compound 2 and (A) GLP-1(7-37) or (B) GLP-1(1-37) in a cAMP accumulation assay using FlpInCHO cells stably expressing the human GLP-1R. Data are normalised to maximal peptide response and are analyzed with a three-parameter logistic curve as defined in (Equation 1). All values are mean \pm S.E.M. of three independent experiments, conducted in duplicate.

4) Koole et al, *Allosteric ligands of the glucagon-like peptide 1 receptor (GLP-1R) differentially modulate endogenous and exogenous peptide responses in a pathway selective manner; implications for drug screening. Molecular Pharmacology* #65664

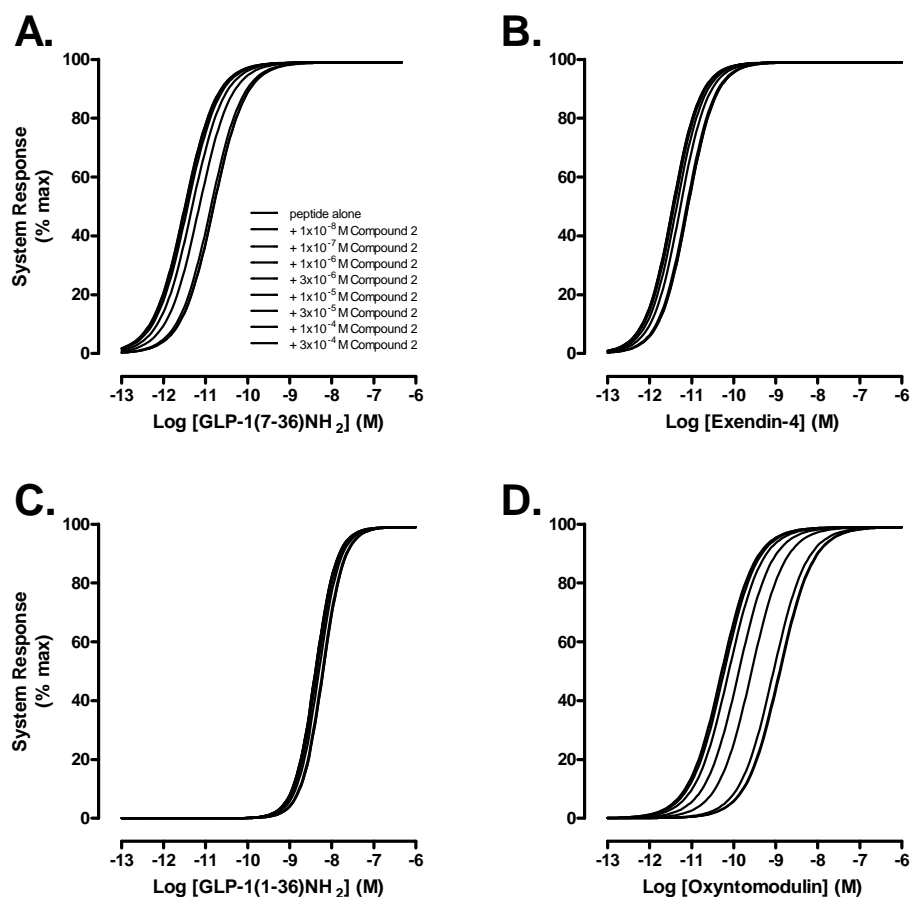
SI Figure S4.



Supplementary Figure S4. Characterisation of the interaction between quercetin and (A) GLP-1(7-36)NH₂, (B) exendin-4, (C) GLP-1(7-37), (D) GLP-1(1-36)NH₂, (E) oxyntomodulin, or (F) GLP-1(1-37) in a cAMP accumulation assay using FlpInCHO cells stably expressing the human GLP-1R. (G) quercetin alone. Data are normalised to maximal peptide response and are analyzed with a three-parameter logistic curve as defined in (Equation 1). All values are mean \pm S.E.M. of three to four independent experiments, conducted in duplicate.

5) Koole et al, *Allosteric ligands of the glucagon-like peptide 1 receptor (GLP-1R) differentially modulate endogenous and exogenous peptide responses in a pathway selective manner; implications for drug screening*. **Molecular Pharmacology #65664**

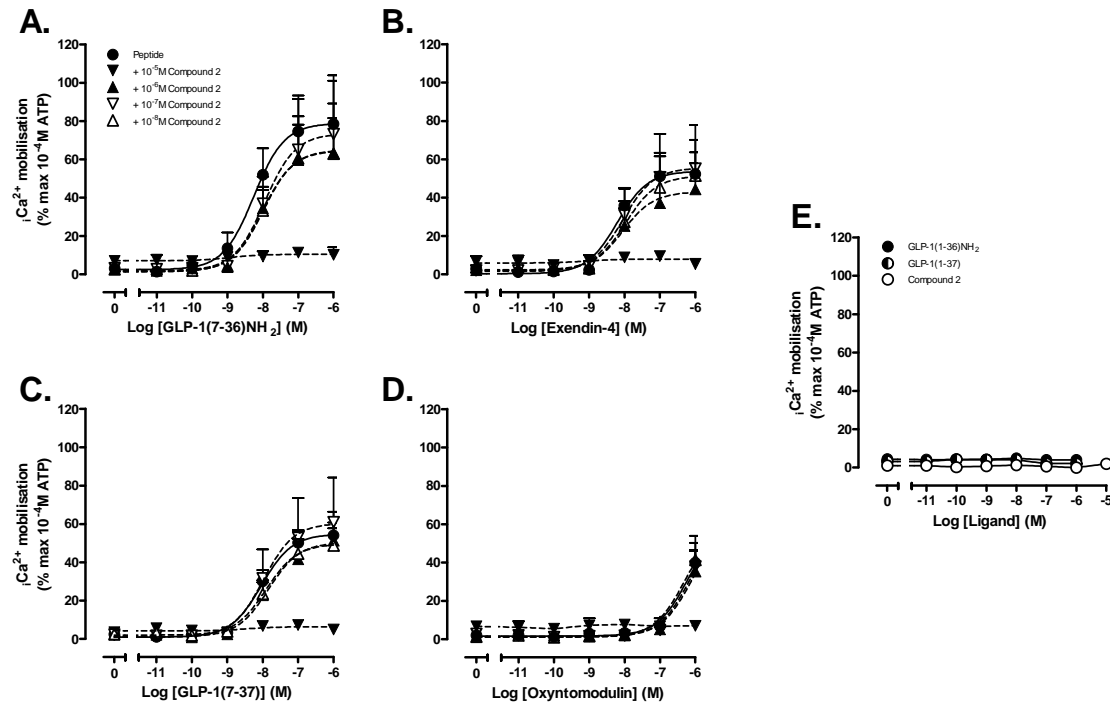
SI Figure S5.



Supplementary Figure S5. Predicted functional interaction curves between compound 2 and peptide agonists, in the absence of intrinsic efficacy, based on the Log α values obtained from compound 2 binding interaction studies (Table 1).

6) Koole et al, *Allosteric ligands of the glucagon-like peptide 1 receptor (GLP-1R) differentially modulate endogenous and exogenous peptide responses in a pathway selective manner; implications for drug screening. Molecular Pharmacology #65664*

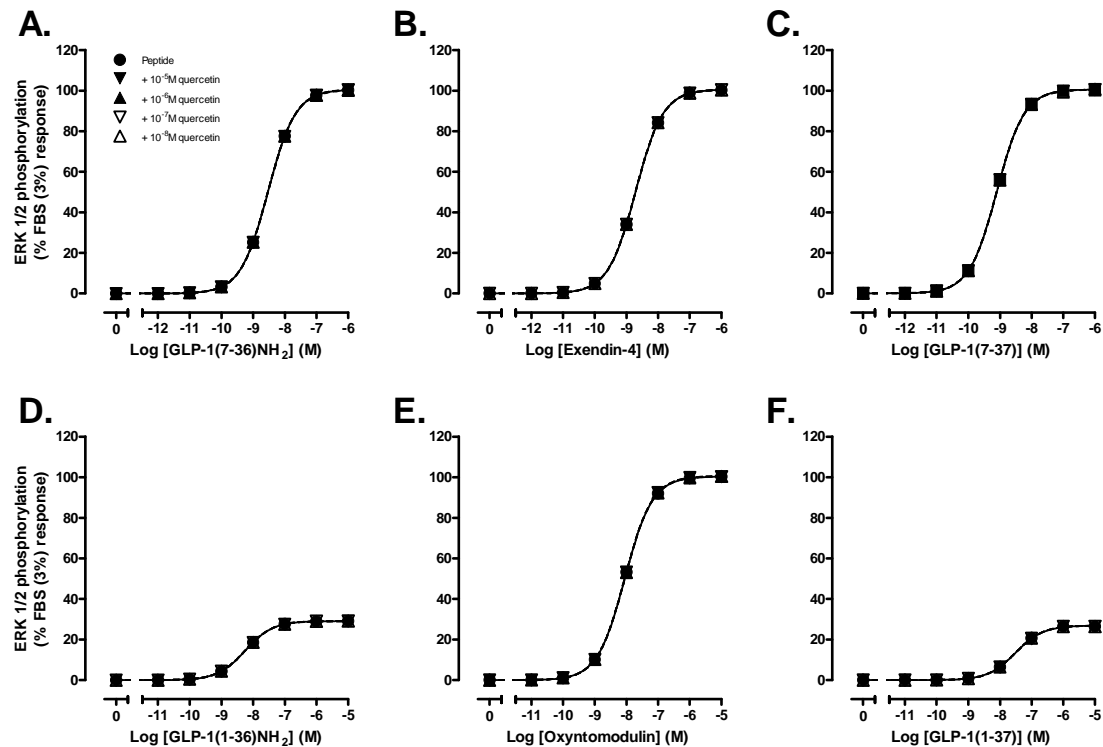
SI Figure S6.



Supplementary Figure S6. Characterisation of the interaction between compound 2 and (A) GLP-1(7-36)NH₂, (B) exendin-4, (C) GLP-1(7-37), or (D) oxyntomodulin in an intracellular Ca^{2+} mobilisation assay using FlpInCHO cells stably expressing the human GLP-1R. (E) GLP-1(1-36)NH₂, GLP-1(1-37) or compound 2 alone. Data are normalised to maximal response generated by 100 μM ATP and are analyzed with a three-parameter logistic curve as defined in (Equation 1). All values are mean \pm S.E.M. of three independent experiments, conducted in duplicate.

7) Koole et al, *Allosteric ligands of the glucagon-like peptide 1 receptor (GLP-1R) differentially modulate endogenous and exogenous peptide responses in a pathway selective manner; implications for drug screening. Molecular Pharmacology* #65664

SI Figure S7.



Supplementary Figure S7. Characterisation of the interaction between quercetin and (A) GLP-1(7-36)NH₂, (B) exendin-4, (C) GLP-1(7-37) (D) GLP-1(1-36)NH₂, (E) oxyntomodulin or (F) GLP-1(1-37) in an ERK1/2 phosphorylation assay using FlpInCHO cells stably expressing the human GLP-1R. Data are normalised to maximal peptide response and are analyzed with a three-parameter logistic curve as defined in (Equation 1). All values are mean \pm S.E.M. of three independent experiments, conducted in duplicate.

Modulation of the Glucagon-Like Peptide-1 Receptor Signaling by Naturally Occurring and Synthetic Flavonoids

Denise Wootten, John Simms, Cassandra Koole, Owen L. Woodman, Roger J. Summers, Arthur Christopoulos, and Patrick M. Sexton

Drug Discovery Biology Laboratory, Monash Institute of Pharmaceutical Sciences and Department of Pharmacology, Monash University, Parkville, Victoria, Australia (D.W., J.S., C.K., R.J.S., A.C., P.M.S.); and School of Medical Sciences and Health Innovations Research Institute, Royal Melbourne Institute of Technology University, Bundoora, Victoria, Australia (O.L.W.)

Received October 18, 2010; accepted November 10, 2010

ABSTRACT

The glucagon-like peptide 1 receptor (GLP-1R) is a promising target for the treatment of type II diabetes mellitus because of its role in metabolic homeostasis. In recent years, difficulties with peptide therapies have driven the search for small-molecule compounds to modulate the activity of this receptor. We recently identified quercetin, a naturally occurring flavonoid, as a probe-dependent, pathway-selective allosteric modulator of GLP-1R-mediated signaling. Using Chinese hamster ovary cells expressing the human GLP-1R, we have now extended this work to identify the structural requirements of flavonoids to modify GLP-1R binding and signaling (cAMP formation and intracellular Ca^{2+} mobilization) of each of the GLP-1R endogenous agonists, as well as the clinically used exogenous peptide mimetic exendin-4. This study identified a chemical series of hydroxyl flavonols with the ability to selectively augment

calcium (Ca^{2+}) signaling in a peptide agonist-specific manner, with effects only on truncated GLP-1 peptides [GLP-1(7–36) NH_2 and GLP-1(7–37)] and exendin-4, but not on oxyntomodulin or full-length GLP-1 peptides [GLP-1(1–36) NH_2 and GLP-1(1–37)]. In addition, the 3-hydroxyl group on the flavone backbone (i.e., a flavonol) was essential for this activity, however insufficient on its own, to produce the allosteric effects. In contrast to hydroxyl flavonols, catechin had no effect on peptide-mediated Ca^{2+} signaling but negatively modulated peptide-mediated cAMP formation in a probe-dependent manner. These data represent a detailed examination of the action of different flavonoids on peptide agonists at the GLP-1R and may aid in the development of future small molecule compounds targeted at this receptor.

Introduction

Glucagon-like peptide-1 (GLP-1) is an endogenous incretin hormone released by L cells of the intestine in response to nutrient intake that stimulates insulin secretion (Drucker and Nauck, 2006). GLP-1 has attracted interest from the pharmaceutical industry in recent years as a treatment for type II diabetes and its accompanying obesity, because it has multiple antidiabetic actions. For example, GLP-1 stimulates insulin and suppresses glucagon secretion, inhibits gastric emptying, and reduces appetite and food intake, therefore aiding weight loss (Drucker and Nauck, 2006). In addition,

GLP-1 increases pancreatic β -cell mass by inducing neogenesis, proliferation, and antiapoptosis of the β -cells (Vahl and D'Alessio, 2004). However, the therapeutic potential of GLP-1 is limited because of its rapid degradation in the plasma by dipeptidyl peptidase-IV and its relatively narrow therapeutic window associated with nausea at high doses (Larsen et al., 2001; Vilsboll et al., 2003). Clinical studies revealed that replacement therapies with metabolically stable GLP-1 mimetics, or treatment with dipeptidyl peptidase-IV inhibitors, can improve the management of hyperglycemia for some patients. Both exenatide (Byetta; Amylin Pharmaceuticals, Inc., San Diego, CA) and liraglutide (Victoza; Novo Nordisk A/S, Bagsværd, Denmark) have been approved by the U.S. Food and Drug Administration for the treatment of type II diabetes (Kolterman et al., 2003; Drucker et al., 2010). However, as peptide analogs of GLP-1, these require administration by intravenous or subcutaneous injection and have been associated with significant adverse side effects, including pan-

This work was funded in part by the National Health and Medical Research Council of Australia (NHMRC) [Program Grant 519461] (to P.M.S., A.C., and R.J.S.); a Principal Research Fellowship of the NHMRC (to P.M.S.); and a Senior Research Fellowship of the NHMRC (to A.C.).

Article, publication date, and citation information can be found at <http://jpet.aspetjournals.org>.

doi:10.1124/jpet.110.176362.

ABBREVIATIONS: GLP-1, glucagon-like peptide-1; GPCR, G protein-coupled receptor; GLP-1R, glucagon-like peptide-1 receptor; ERK, extracellular signal-regulated kinase; DMEM, Dulbecco's modified Eagle's medium; BSA, bovine serum albumin; SAR, structure-activity relationship.

creatitis (Olansky, 2010). Therefore, orally active small-molecule agonists or modulators that augment signaling via the GLP-1 receptor are highly desirable.

GLP-1 is a member of the glucagon peptide superfamily and exerts its effects by binding to the GLP-1R, a family B G protein-coupled receptor (GPCR). The GLP-1R is primarily expressed in pancreatic β -cells and is principally coupled to G_{α_s} , thereby mediating its effects through generation of cAMP, causing cell depolarization and increased cytosolic calcium (Ca^{2+}) concentration, ultimately resulting in augmentation of insulin secretion (Drucker et al., 1987; Holz et al., 1993; Wheeler et al., 1993). Although insulin release downstream of GLP-1R activation is known to be critically dependent upon the formation of cAMP, there is also a role for mobilization of intracellular Ca^{2+} and activation of mitogen-activated protein kinases such as extracellular signal-regulated kinase 1 and 2 (ERK1/2) in augmentation of insulin response (Baggio and Drucker, 2007). Furthermore, for many therapeutically relevant effects of GLP-1R activation, including the modulation of appetite, the underlying GLP-1R-mediated signaling is not fully understood, but physiological responses are known to be a composite of multiple signaling pathways.

The GLP-1R system is further complicated because the receptor is activated by multiple endogenous ligands, including four variants of GLP-1 and the related peptide oxyntomodulin, and can also be activated by exogenous mimetics such as exendin-4. The four active secreted forms of GLP-1 include a full-length peptide, GLP-1(1–37), and a truncated form, GLP-1(7–37), each of which has an amidated counterpart: GLP-1(1–36)NH₂ and GLP-1(7–36)NH₂. In the past, the search for nonpeptide small-molecule agonists for any

family B GPCR has been largely unsuccessful. Recently, however, a number of small-molecule compounds have been identified that are able to activate the GLP-1R. These include a series of substituted quinoxalines, the most potent of which is compound 2 (Knudsen et al., 2007; Teng et al., 2007), a series of pyrimidines (Sloop et al., 2010), and a cyclobutane derivative (Chen et al., 2007).

We have also reported that quercetin can modulate GLP-1R activation in both a pathway and ligand-specific manner (Koole et al., 2010). Quercetin selectively modulated Ca^{2+} signaling for the high-affinity agonists GLP-1(7–37), GLP-1(7–36)NH₂, and exendin-4 but not oxyntomodulin; however, it had no effect on any of the peptide ligands in cAMP accumulation or ERK1/2 phosphorylation assays. In separate studies, experiments in streptozotocin-induced diabetic rats showed significantly lower plasma glucose levels, urine output, and urine glucose content when these animals are treated with an appropriate amount of quercetin compared with control diabetic rats (Vessal et al., 2003; Shetty et al., 2004), suggesting that quercetin may have potential in the management of type II diabetes, effects that may be mediated in part, via modulation of the GLP-1R. Quercetin is a flavonol, a subgroup of the flavonoids that are found in a wide variety of plants and plant derivatives and are widely consumed in the human diet (Hertog and Hollman, 1996). In this study, we investigated the structure/activity relationship of various flavonoids (flavones, flavonols, isoflavones, and catechins; Fig. 1) in the allosteric modulation of GLP-1R signaling and identify a potential structural scaffold that may be useful in development of small-molecule modulators for future drug discovery programs.

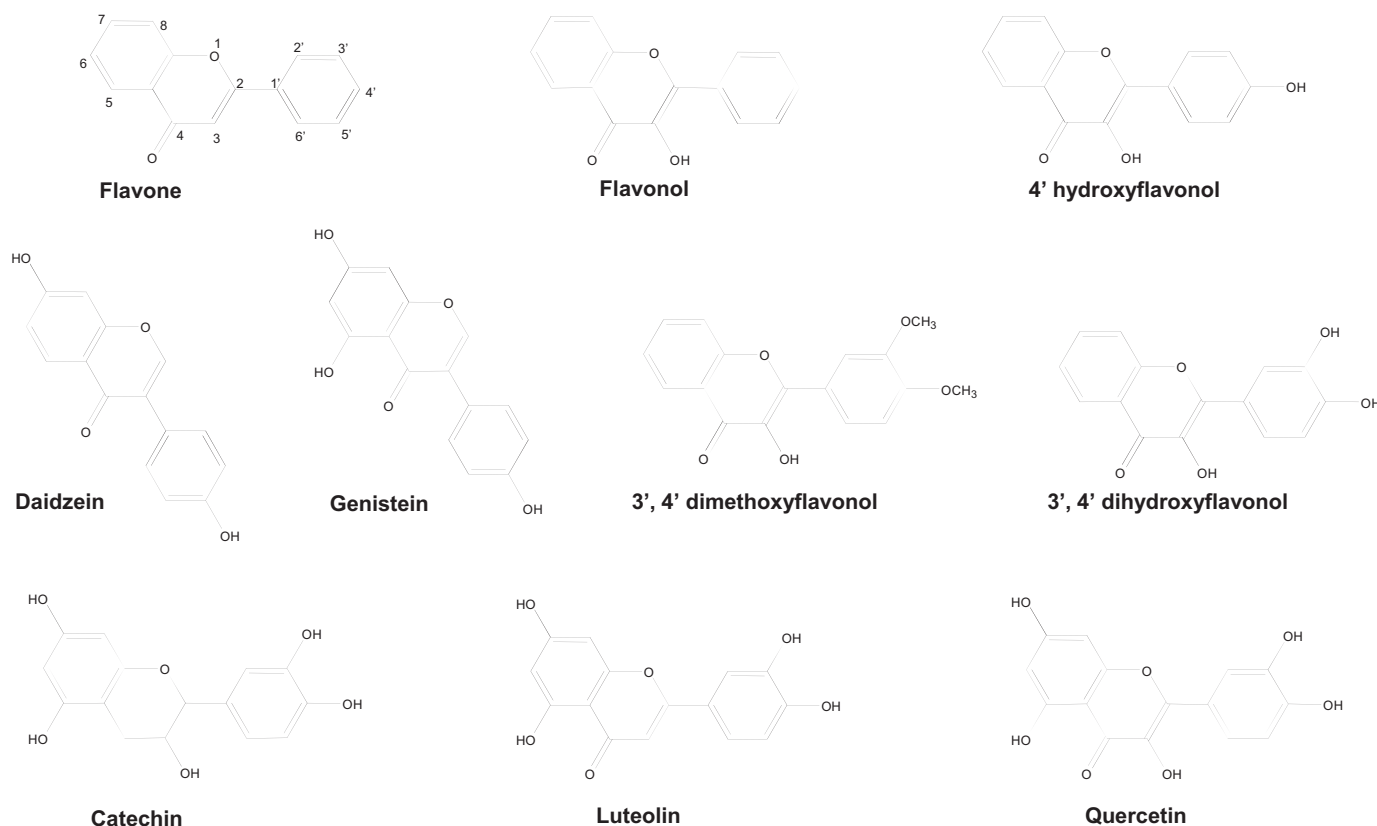


Fig. 1. Structures of flavonoids used in this study. The numbers on the ring positions of the 2-phenylchrome-4-one scaffold are labeled on the flavone structure.

Materials and Methods

Materials. Dulbecco's modified Eagle's medium (DMEM) and Fluo-4 acetoxymethyl ester were purchased from Invitrogen (Carlsbad, CA). Fetal bovine serum was purchased from Thermo Fisher Scientific (Melbourne, VIC, Australia). AlphaScreen reagents, ^{125}I -exendin(9–39), 96-well UniFilter GF/C filter plates, 384-well Proxiplates and Microscint 40 scintillant were purchased from PerkinElmer Life and Analytical Sciences (Waltham, MA). The bicinchoninic acid protein assay kit was purchased from Thermo Fisher Scientific (Rockford, IL). GLP-1 and GLP-1 peptide analogs were purchased from American Peptide (Sunnyvale, CA). All other reagents were purchased from Sigma-Aldrich (St. Louis, MO) or BDH Merck (Melbourne, VIC, Australia) and were of an analytical grade.

Cell Culture. FlpIn Chinese hamster ovary cells stably transfected with human GLP-1R (FlpInCHO-huGLP-1R) and FlpIn 3T3 cells stably expressing the calcitonin receptor Leu polymorphism were generated using Gateway technology (Invitrogen) as described previously (May et al., 2007a). Cells were maintained in DMEM supplemented with 10% heat-inactivated fetal bovine serum and incubated in a humidified environment at 37°C in 5% CO_2 .

Radioligand Binding Assays. Membrane preparations of FlpInCHO-huGLP-1R were prepared as described previously (Avlani et al., 2004). Protein concentration was determined using the bicinchoninic acid protein assay kit (Thermo Fisher Scientific) following the manufacturer's instructions, with bovine serum albumin (BSA) as standard. Competition binding assays were performed in 96-well plates using 20 μg of membrane expressing GLP-1R. Membranes were incubated in HEPES buffer [1 mM HEPES, 10 mM MgCl_2 , 100 mM NaCl, and 1% (w/v) BSA, pH 7.4] containing 0.5 nM ^{125}I -exendin(9–39) and increasing concentrations of unlabeled ligand for 1 h. For interaction studies, competition of ^{125}I -exendin(9–39) binding by each orthosteric agonist was performed in the presence of increasing concentrations of each flavonoid. For all experiments, nonspecific binding was defined by 1 μM exendin(9–39). Incubation was terminated by rapid filtration through Whatman GF/C filters [presoaked in 0.03% (v/v) polyethylenimine for a min of 2 h] using a 96-well harvester (Tomtec, Hamden, CT). Filters were washed three times with 0.9% (w/v) NaCl and 0.3% (w/v) BSA and were allowed to dry before addition of 30 μl of scintillant and determination of radioactivity by scintillation counting.

cAMP Accumulation Assay. FlpInCHO-huGLP-1R cells were seeded at a density of 5×10^4 cells/well into 96-well culture plates and incubated overnight at 37°C in 5% CO_2 . Growth media were replaced with stimulation buffer [phenol-free DMEM containing 0.1% (w/v) BSA and 1 mM 3-Isobutyl-1-methylxanthine] and incubated for a further 1 h at 37°C in 5% CO_2 . Cells were stimulated with peptide ligand and/or flavonoid and incubated for 30 min at 37°C in 5% CO_2 . The reaction was terminated by rapid removal of the buffer and addition of 50 μl of ice-cold 100% ethanol. After ethanol evaporation, 75 μl of lysis buffer [0.1% (w/v) BSA, 0.3% (v/v) Tween 20 and 5 mM HEPES, pH 7.4] was added and 10 μl of lysate was transferred to a 384-well ProxiPlate. Five microliters of acceptor bead mix (1.0% AlphaScreen cAMP acceptor beads diluted in lysis buffer) and 15 μl of donor bead mix [(0.3% AlphaScreen cAMP donor beads and 0.025% AlphaScreen cAMP biotinylated cAMP (133 units/ μl)] diluted in lysis buffer, and preincubated for a minimum of 30 min) were added in reduced lighting conditions. Plates were incubated at room temperature overnight before measurement of the fluorescence using a Fusion- α plate reader (PerkinElmer Life and Analytical Sciences) with standard AlphaScreen settings. All values were converted to concentration of cAMP using a cAMP standard curve performed in parallel and normalized to maximal peptide response.

Intracellular Ca^{2+} Mobilization Assay. FlpInCHO-huGLP-1R cells were seeded at a density of 5×10^4 cells/well into 96-well culture plates, and receptor-mediated intracellular Ca^{2+} mobilization was determined as described previously (Werry et al., 2005).

Because of their autofluorescence at high concentrations, each flavonoid was added 30 min before addition of peptide agonist in the FlexStation (Molecular Devices, Sunnyvale, CA). Fluorescence was determined immediately after peptide addition, with an excitation wavelength set to 485 nm and an emission wavelength set to 520 nm, and readings taken every 1.36 s for 120 s. Peak magnitude was calculated using five-point smoothing, followed by correction against basal fluorescence. The peak value was used to create concentration-response curves. Data were normalized to the maximal response elicited by the peptide.

Data Analysis. All data obtained were analyzed in Prism (ver. 5.0.2; GraphPad Software Inc., San Diego, CA). Concentration response binding and signaling data were fitted with a three-parameter logistic equation as described previously (May et al., 2007a), assuming a slope of 1:

$$E = \text{basal} + \frac{(E_{\text{max}} - \text{basal})}{1 + 10^{(\text{LogEC}_{50} - \text{Log}[A])}} \quad (1)$$

where E is response, E_{max} and basal are the top and bottom asymptotes of the curve, respectively, $\text{Log}[A]$ is the logarithm of the agonist concentration, and LogEC_{50} is the logarithm of the agonist concentration that gives a response halfway between E_{max} and basal. Likewise, this equation was used in inhibition binding, instead replacing EC_{50} with IC_{50} . In this case, basal defines the specific binding of the radioligand that is equivalent to nonspecific ligand binding, whereas E_{max} defines radioligand binding in the absence of a competing ligand. In a similar manner, the IC_{50} value represents the molar concentration of A required to generate a response halfway between E_{max} and basal.

In addition to fitting the three-parameter logistic equation, Ca^{2+} interaction data were fitted to the following to an operational model of allosterism and agonism (Leach et al., 2007; Aurelio et al., 2009) to derive functional estimates of modulator affinity and cooperativity:

$$E = \text{Basal} + \frac{(E_{\text{max}} - \text{Basal})(\tau_A[A](K_B + \alpha\beta[B]) + \tau_B[B]K_A)^n}{([A]K_B + K_AK_B + K_A[B] + \alpha[A][B])^n + (\tau_A[A](K_B + \alpha\beta[B]) + \tau_B[B]K_A)^n} \quad (2)$$

where E_{max} is the maximum attainable system response for the pathway under investigation, $[A]$ and $[B]$ are the concentrations of orthosteric agonist and allosteric modulator/agonist, respectively, K_B is the dissociation constant of the allosteric modulator, n is a transducer slope factor linking occupancy to response, α is the cooperativity factor governing allosteric effects of the modulator on orthosteric agonist binding affinity, β is the factor governing allosteric effects on signaling efficacy, and τ_A and τ_B are operational measure of the ligands' respective signaling efficacies that incorporate receptor expression levels and efficiency of stimulus-response coupling (Leach et al., 2007; Aurelio et al., 2009). In all cases, the value of α was fixed to 1 because binding studies revealed neutral cooperativity between the orthosteric peptides and each of the flavonoids. All analytical data are expressed in logarithms as mean \pm S.E.M. and, where relevant, statistical analysis was performed by one-way analysis of variance and Dunnett's post test using Prism 5.0.2, and statistical significance accepted at $p < 0.05$.

Results

Hydroxyl Flavonols Selectively Augment Intracellular Ca^{2+} Signaling via the GLP-1R. The GLP-1R is promiscuous, in that it has been shown to couple to multiple G proteins, activating multiple signaling pathways (Montrose-Rafizadeh et al., 1999; Bavec et al., 2003; Koole et al., 2010). Although the GLP-1R is known to preferentially couple to G_{α_s} , it can also couple to G_{α_q} proteins, resulting in mobili-

zation of intracellular Ca^{2+} . In a previous study, we showed that quercetin could impart stimulus bias with respect to Ca^{2+} signaling but in a peptide-specific manner. Here we investigated the ability of a range of flavonoid compounds (Fig. 1) to modulate GLP-1R-mediated Ca^{2+} signaling. All of the flavonoid compounds in this study lacked intrinsic efficacy because no change was observed in the basal Ca^{2+} signaling in the presence of these compounds alone (data not shown). However, concentration response curves, established for the peptide ligands in the absence and presence of 30 μM concentrations of each flavonoid suggested a structure-activity relationship (SAR) for allosteric effects of selective flavonoids on peptide-mediated Ca^{2+} signaling (Fig. 2). In agreement with our previous study (Koole et al., 2010), augmentation of GLP-1(7–36) NH_2 , GLP1(7–37), or exendin-4 peptide efficacy and potency was observed at this concentration of quercetin; however, no significant change was ob-

served for oxyntomodulin (Figs. 2 and 3, Table 1). In addition, 3',4'-dihydroxyflavonol displayed positive modulation of Ca^{2+} responses (to a lesser, but significant degree) induced by GLP-1(7–36) NH_2 , GLP-1(7–37), or exendin-4, with an observed increase in both maximal effect and potency of the agonist responses (Figs. 2 and 3, Table 1). This flavonol also displayed probe dependence, with no observed changes in oxyntomodulin-induced Ca^{2+} signaling. A general trend for modulation of Ca^{2+} responses can also be observed by hydroxyl flavonols, in that 4'-hydroxyflavonol increased the E_{max} and potency of the high-affinity peptide agonists but not oxyntomodulin; however, only the change in potency of GLP-1(7–36) NH_2 reached statistical significance ($p < 0.05\%$) (Figs. 2 and 3, Table 1). In contrast, compounds that do not belong to the hydroxyl flavonol class of flavonoids did not alter the responses of any peptide agonist in this signaling pathway (Figs. 2 and 3, Table 1).

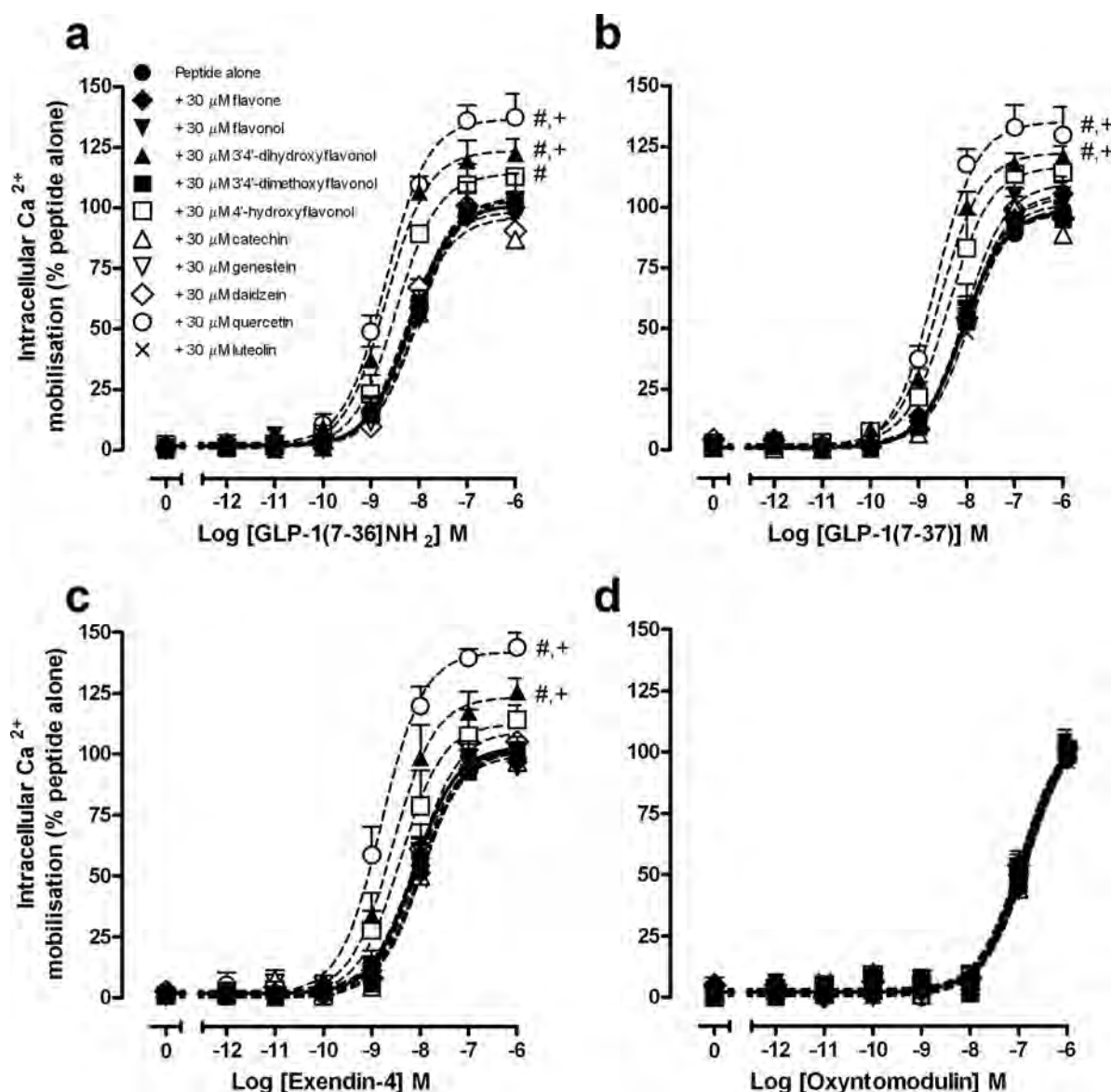


Fig. 2. Characterization of the interaction between 30 μM concentrations of each flavonoid and GLP-1(7–36) NH_2 (a), GLP-1(7–37) (b), exendin-4 (c), and oxyntomodulin (d) in an intracellular Ca^{2+} mobilization assay using FlpInCHO cells stably expressing the human GLP-1R. Data are normalized to the maximal response elicited by peptide alone and analyzed with a three-parameter logistic curve as defined in eq. 1. All values are mean \pm S.E.M. of four independent experiments performed in duplicate. Statistical significance of changes in E_{max} (+) and EC_{50} (#) in the presence of flavonoid in comparison with those of the peptide alone were determined by one-way analysis of variance and Dunnett's post test ($p < 0.05$).

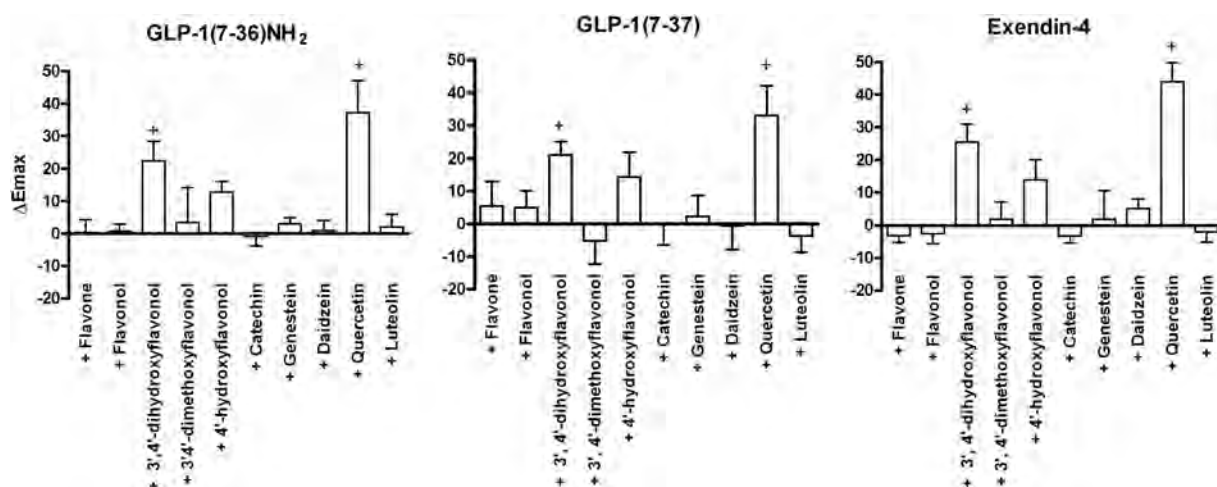


Fig. 3. Comparison of the E_{\max} values of peptide agonists in an intracellular Ca^{2+} mobilization assay in the presence of 30 μM different flavonoid compounds. Bars represent the difference in E_{\max} value from that of peptide alone. All values are mean \pm S.E.M. of four independent experiments performed in duplicate. +, data statistically different from peptide alone ($p < 0.05$) as measured by one-way analysis of variance followed by a Dunnett's post test.

TABLE 1

Differential effects of flavonoids on peptide agonists of the human GLP-1R in calcium mobilization in FlpInCHO cells stably expressing the human GLP-1R

Data were analyzed using eq. 1. pEC_{50} value represent the negative logarithm of the concentration of agonist that produces half the maximal response. E_{\max} represents the maximal response normalized to that of peptide alone. All values are mean \pm S.E.M. of four independent experiments. Data were analyzed with one-way analysis of variance and Dunnett's post test.

30 μM Flavonoid Compound	Orthosteric Peptide Ligand							
	GLP-1(7-36) NH_2		GLP-1(7-37)		Exendin-4		Oxyntomodulin	
	pEC_{50}	E_{\max}	pEC_{50}	E_{\max}	pEC_{50}	E_{\max}	pEC_{50}	E_{\max}
Peptide alone (no flavonoid)	8.19 ± 0.06	100 ± 3	8.07 ± 0.06	100 ± 2	8.19 ± 0.05	100 ± 5	6.89 ± 0.07	100 ± 6
Flavone	8.15 ± 0.06	100 ± 4	7.99 ± 0.06	105 ± 7	8.03 ± 0.08	97 ± 2	6.90 ± 0.13	97 ± 5
Flavonol	8.02 ± 0.08	101 ± 2	8.04 ± 0.05	105 ± 5	8.09 ± 0.13	97 ± 3	6.81 ± 0.11	99 ± 6
4'-Hydroxyflavonol	$8.47 \pm 0.08^*$	112 ± 4	8.37 ± 0.11	114 ± 8	8.41 ± 0.12	113 ± 6	6.88 ± 0.10	101 ± 6
3',4'-Dihydroxyflavonol	$8.68 \pm 0.07^*$	$122 \pm 6^*$	$8.55 \pm 0.06^*$	$121 \pm 4^*$	$8.57 \pm 0.10^*$	$125 \pm 6^*$	6.95 ± 0.14	99 ± 6
3',4'-Dimethoxyflavonol	8.13 ± 0.11	103 ± 11	8.05 ± 0.07	94 ± 7	8.03 ± 0.08	101 ± 5	6.91 ± 0.10	100 ± 5
Quercetin	$8.72 \pm 0.07^*$	$137 \pm 10^*$	$8.65 \pm 0.09^*$	$132 \pm 9^*$	$8.81 \pm 0.09^*$	$143 \pm 6^*$	6.84 ± 0.08	100 ± 2
Luteolin	8.18 ± 0.06	102 ± 4	7.97 ± 0.05	96 ± 5	7.96 ± 0.08	98 ± 3	6.90 ± 0.09	96 ± 6
Daidzein	8.27 ± 0.09	101 ± 4	8.06 ± 0.10	99 ± 9	8.08 ± 0.06	105 ± 3	6.95 ± 0.12	102 ± 7
Genistein	8.06 ± 0.05	103 ± 2	8.01 ± 0.06	102 ± 6	8.16 ± 0.09	101 ± 9	6.84 ± 0.09	98 ± 1
Catechin	8.20 ± 0.07	101 ± 3	8.11 ± 0.09	100 ± 4	7.97 ± 0.08	97 ± 2	6.84 ± 0.10	102 ± 7

* $P < 0.05$, statistically significant from peptide alone.

In agreement with previous findings (Koole et al., 2010), neither GLP-1(1-36) NH_2 nor GLP-1(1-37) displayed any agonism in Ca^{2+} signaling pathway in either the absence or presence of any of the tested flavonoids (data not shown). Control experiments showed that all ATP responses in the presence of 30 μM any flavonoid tested remained robust and constant. In addition, Ca^{2+} signaling mediated by calcitonin in calcitonin receptor Leu polymorphism (another family B GPCR)-expressing FlpIn 3T3 cells was unaltered by these flavonoids (data not shown). This, in addition to the probe dependence displayed by the hydroxyl flavonol compounds, is consistent with these compounds' mediating their effects specifically at the GLP-1R.

To further investigate the interaction between the hydroxyl flavonols (4'-hydroxyflavonol, 3',4'-dihydroxyflavonol, and quercetin) and the high-affinity peptide agonists, interaction studies between a range of concentrations (1–50 μM) of these modulators and each of the peptides were performed (Fig. 4). Analysis of the data using an allosteric operational model revealed pK_b estimates of the flavonols, in addition to cooperativity (β) estimates, the rank order of cooperativity

being quercetin > 3',4'-dihydroxyflavonol > 4'-hydroxyflavonol for all three peptides [GLP-1(7-36) NH_2 , GLP-1(7-37), and exendin-4] (Table 2).

Hydroxyl Flavonols and Catechin Selectively Impart Stimulus Bias at the GLP-1R. Ligands acting allosterically at a given GPCR have the potential to promote unique receptor conformations that may engender stimulus bias across different signaling pathways. Functional interaction assays for cAMP accumulation between each flavonoid and the orthosteric peptide agonists revealed that hydroxyl flavonols displayed "stimulus bias" in that they did not alter cAMP signaling of any peptide agonist at the GLP-1R despite modulating high-affinity agonists in intracellular Ca^{2+} mobilization assays (Fig. 5, Table 3). In addition, catechin displayed signaling bias in a peptide-specific manner. In Ca^{2+} mobilization assays, catechin had no effect on agonist-mediated signaling; however, cAMP accumulation assays in the presence and absence of 30 μM catechin revealed catechin as a negative modulator of both GLP-1(7-36) NH_2 and GLP-1(1-36) NH_2 in this signaling pathway, with significant

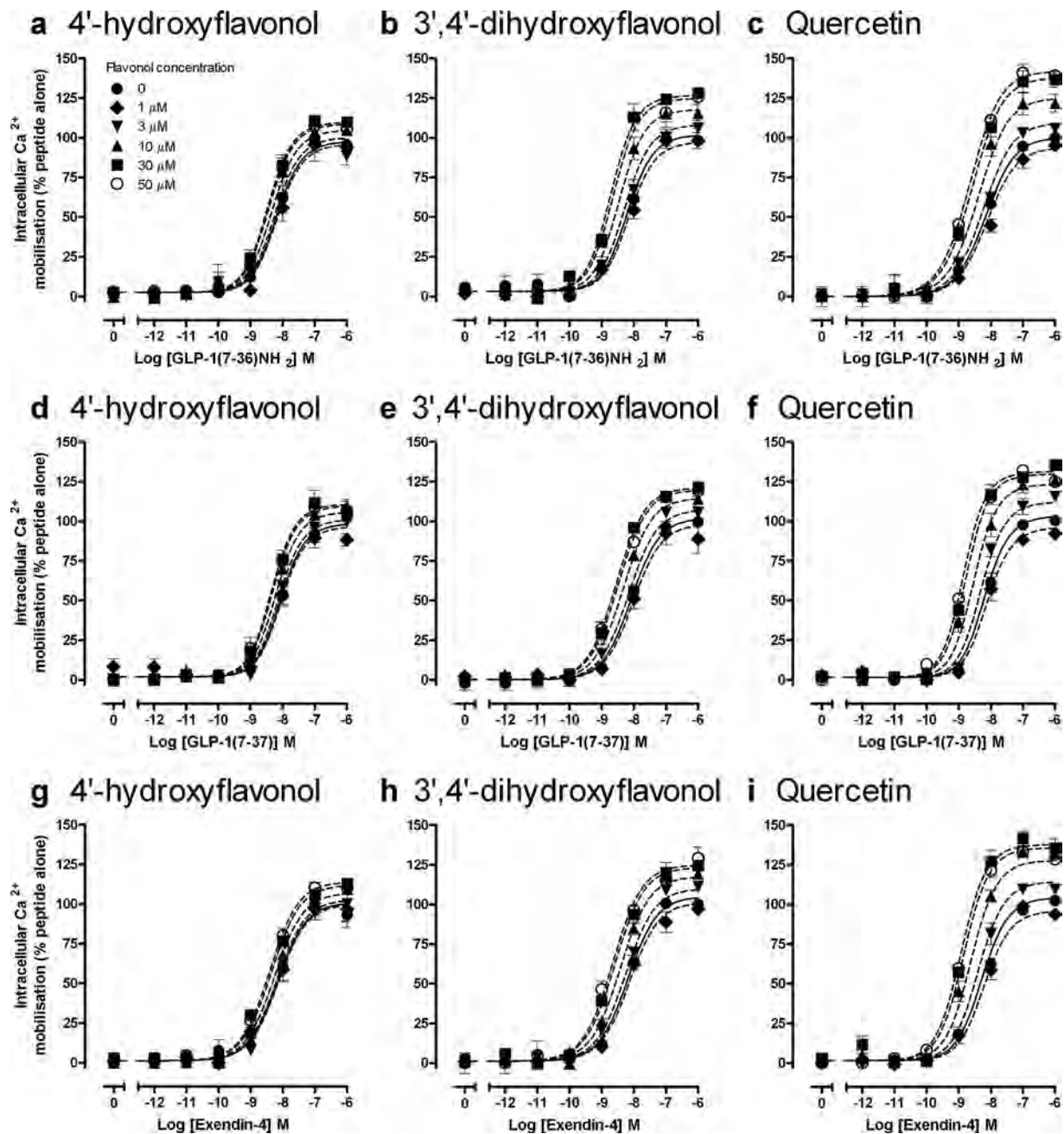


Fig. 4. Characterization of the interaction between a range of concentrations (1–50 μM) of flavonols [4'-hydroxyflavonol (a, d, g), 3',4'-dihydroxyflavonol (b, e, h), and quercetin (c, f, i)] and GLP-1(7–36) NH_2 (a–c), GLP-1(7–37) (d–f), and exendin-4 (g–i) in an intracellular Ca^{2+} mobilization assay using FlpInCHO cells stably expressing the human GLP-1R. Data are normalized to the maximal response elicited by peptide alone and analyzed with an allosteric operational model as defined in eq. 2. All data are mean \pm S.E.M. of three independent experiments performed in duplicate.

TABLE 2

Allosteric operational model parameters for the functional allosteric interaction between flavonols and peptide ligands of the GLP-1R

All values are mean \pm S.E.M. of three independent experiments analyzed according to eq. 2. pK_b is the negative logarithm of the estimated affinity of the flavonol compounds. This value was derived from the interaction data of GLP-1(7–36) NH_2 . Consistent values were obtained from GLP-1(7–37) and exendin-4 analyses. Estimated $\text{Log}\beta$ is the logarithm of the factor governing the allosteric effects on activation between flavonols and the peptide agonists. Antilogarithms are shown in parentheses (β).

Flavonol	pK_b	Estimated $\text{Log}\beta$		
		GLP-1(7–36) NH_2	GLP-1(7–37)	Exendin-4
4'-Hydroxyflavonol	4.7 ± 0.2	0.40 ± 0.10 (2.5)	0.39 ± 0.09 (2.5)	0.49 ± 0.16 (3.1)
3',4'-Dihydroxyflavonol	4.5 ± 0.1	0.79 ± 0.12 (6.2)	0.75 ± 0.09 (5.6)	0.80 ± 0.10 (6.3)
Quercetin	4.4 ± 0.2	0.99 ± 0.13 (9.8)	0.98 ± 0.09 (9.6)	1.04 ± 0.10 (10.9)

reductions in the observed maximal response (Fig. 5, Table 3). Furthermore, the potency of the cAMP response produced by GLP-1(7–37) was also significantly reduced (8-fold) in the

presence of catechin, whereas cAMP responses to GLP-1(1–37), exendin-4, and oxyntomodulin were unaltered (Fig. 5, Table 3). All other flavonoids studied showed no modulation

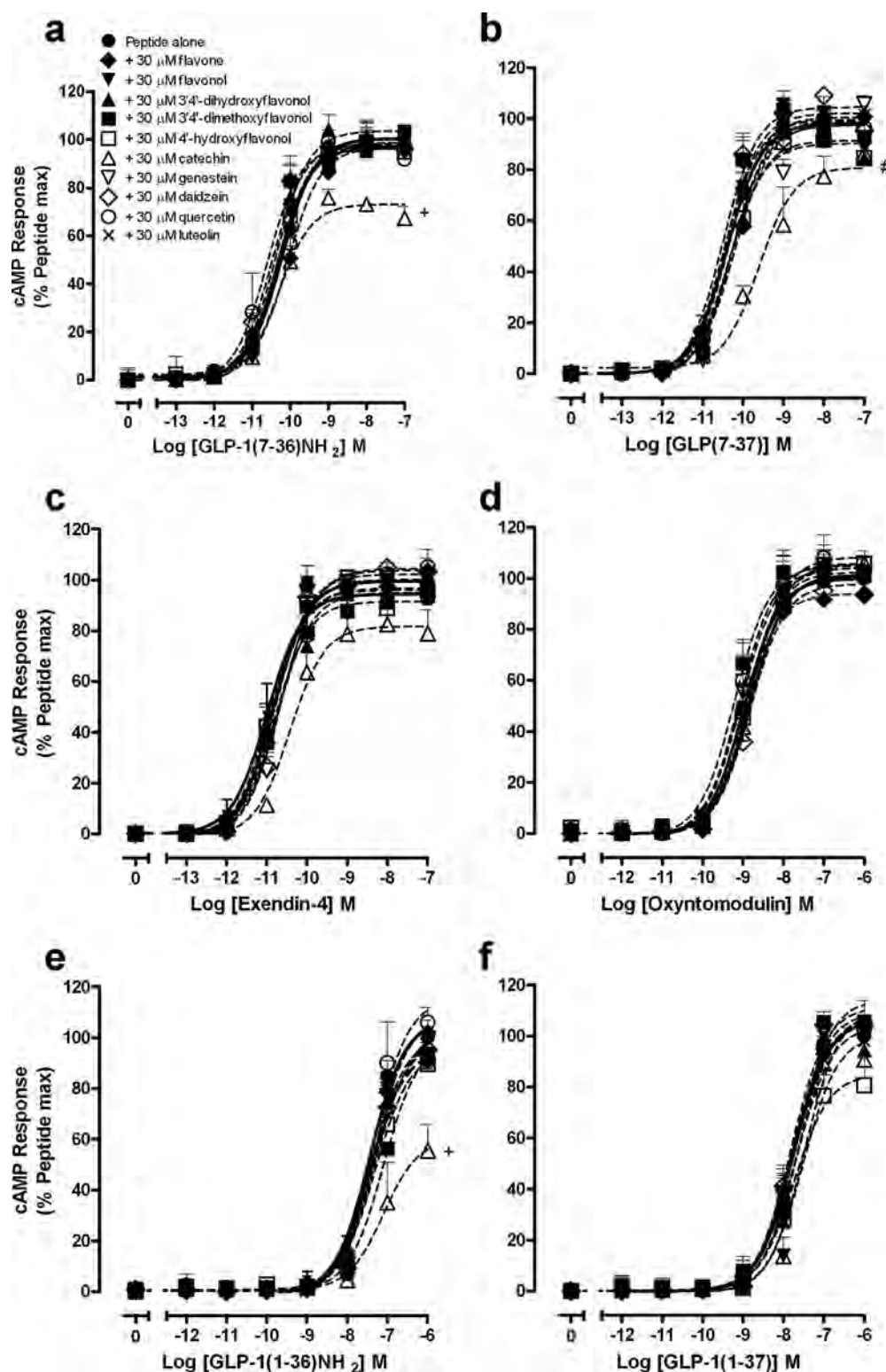


Fig. 5. Characterization of the interaction between 30 μ M concentrations of flavonoid compounds and GLP-1(7–36) NH_2 (a), GLP-1(7–37) (b), exendin-4 (c), oxyntomodulin (d), GLP-1(1–36) NH_2 (e), and GLP-1(1–37) (f) in a cAMP accumulation assay using FlpInCHO cells stably expressing the human GLP-1R. Data are normalized to maximal peptide response. All data are mean \pm S.E.M. of four independent experiments performed in duplicate. Statistical significance of changes in E_{max} (+) and EC_{50} (#) in the presence of flavonoid in comparison with those of the peptide alone were determined by one-way analysis of variance and Dunnett's post test ($p < 0.05$).

of GLP-1R peptide ligands in cAMP accumulation assays (Fig. 5, Table 3).

Flavonoids Selectively Modulate the Binding Affinity of Antagonists and Agonists of the GLP-1R. Equilibrium binding studies were performed between each of the flavonoids and a radiolabeled orthosteric GLP-1R antagonist [^{125}I -exendin(9–39)] to establish the ability of flavonoids to modify peptide binding affinity. All the flavonoids revealed

weak negative cooperativity with the antagonist, the greatest degree of inhibition being observed in hydroxyl flavonols (4'-hydroxyflavonol, 3',4'-dihydroxyflavonol, and quercetin) (Fig. 6).

To establish the ability of the different flavonoids to modulate orthosteric agonist affinity, competition binding studies were performed with GLP-1(7–36) NH_2 , GLP1(7–37), GLP-1(1–36) NH_2 , GLP-1(1–37), oxyntomodulin, or exendin-4 in

* $P < 0.05$, statistically significant from peptide alone.

We reported recently that the flavonol quercetin lacked intrinsic efficacy but selectively modulated intracellular Ca^{2+} responses in a probe-dependent manner. At concentrations above 1 μM , quercetin augmented signaling of the high-affinity agonists GLP-1(7-36)/NH_2 , GLP-1(7-37) , and exendin-4 but had no effect on oxyntomodulin signaling (Koole et al., 2010). Quercetin also engenders “stimulus bias” at the level of the GLP-1R , in that no modulation of cAMP signaling was observed. To systematically explore the SAR of quercetin as a modulator of GLP-1R signaling, a selection of flavonoid compounds were analyzed based on the flavone (2-phenylchromen-4-one) backbone (Fig. 1). In addition, two isoflavones containing a 3-phenylchromen-4-one backbone were examined. Important structural features of flavonoids were identified in this study that distinguishes those that have the ability to modulate GLP-1R -mediated signaling from those that are inactive. A series of hydroxyl flavonols displayed no intrinsic efficacy, but all modulated Ca^{2+} signaling in a probe-dependent manner. The greater the number of hydroxyl substituents contained in these flavonol compounds, the more pronounced the observed modulator ability. A structure-activity series can therefore be assigned to these compounds; quercetin, which contains hydroxyl groups at positions 3, 5, 7, 3', and 4' (see Fig. 1), displayed the largest degree of modulation, which is evident by its larger cooperativity factor ($\beta = 9.6\text{--}10.9$ depending on the orthosteric peptide). 3',4'-Dihydroxyflavonol with hydroxyl groups at positions 3, 3', and 4' showed a smaller degree of modulation

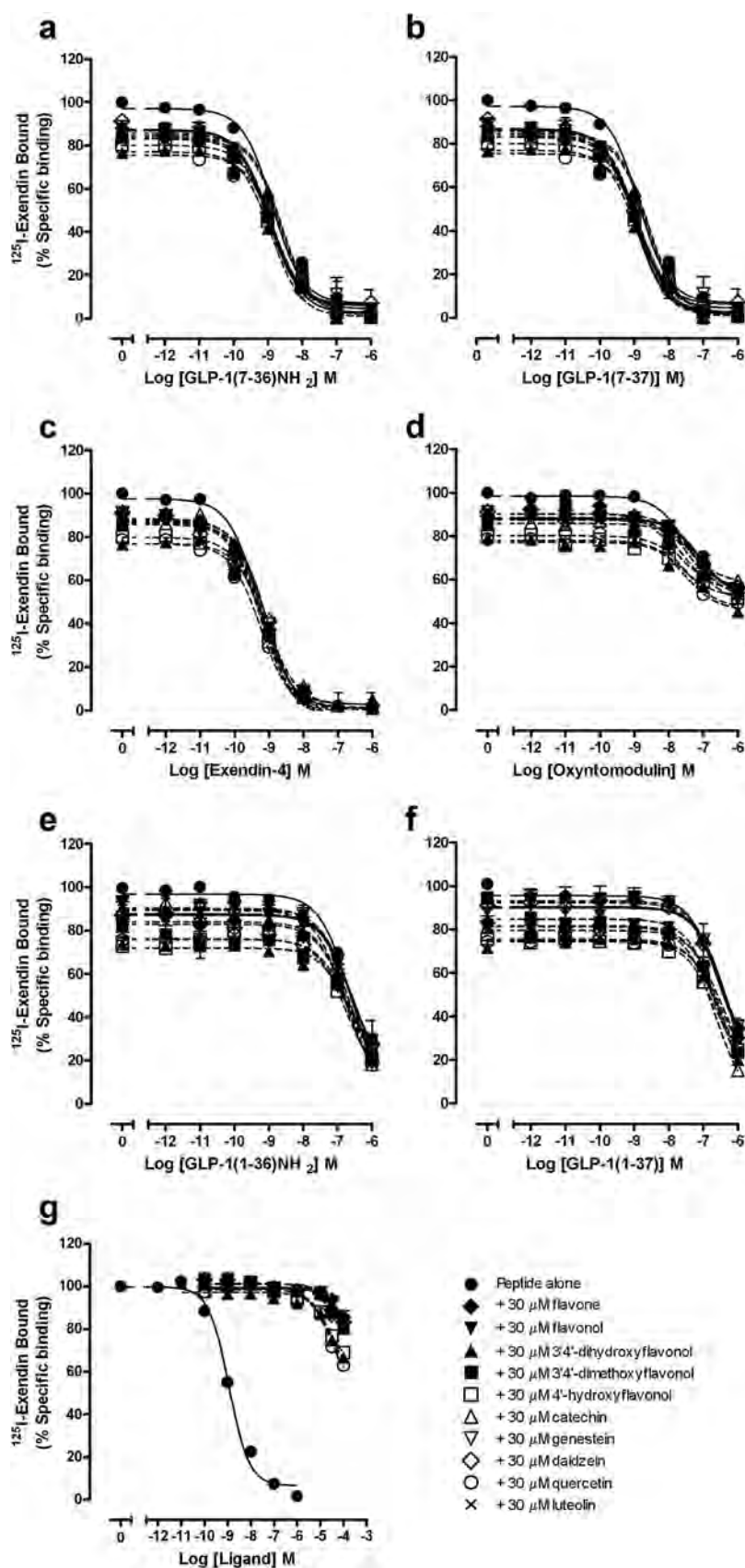


Fig. 6. Characterization of the inhibition of ^{125}I -exendin(9–39) binding by peptide agonists and/or flavonoids using membranes prepared from FlpInCHO cells stably expressing the human GLP-1R: GLP-1(7–36) NH_2 (a), GLP-1(7–37) (b), exendin-4 (c), oxyntomodulin (d), GLP-1(1–36) NH_2 (e), and GLP-1(1–37) (f) in the presence of 30 μM flavonoid compound. g, inhibition of flavonoid compounds alone. The peptide-alone curve represents inhibition binding by GLP-1(7–36) NH_2 . Data are presented as percentage specific binding, with nonspecific binding measured in the presence of 1 μM exendin(9–39). All values are mean \pm S.E.M. of four independent experiments performed in duplicate.

than quercetin ($\beta = 5.6\text{--}6.3$) but greater than that by 4'-hydroxyflavonol ($\beta = 2.5\text{--}3.1$) with hydroxyl groups at only positions 3 and 3'. It is noteworthy that replacement of the

hydroxyl groups at positions 3' and 4' by the more bulky methoxy groups (3',4'-dimethoxyflavonol) removed the ability of the compound to modulate Ca^{2+} signaling. The pres-

ence of just the flavonol backbone (hydroxyl at position 3) was also inactive. However, the hydroxyl group at position 3 of the 2-phenylchromen-4-one scaffold was essential but not sufficient on its own for modulation of Ca^{2+} responses by the high-affinity peptide ligands. The flavone luteolin is structurally very similar to quercetin, lacking only the hydroxyl group at position 3. Consequently, luteolin did not modulate Ca^{2+} signaling of any of the peptide ligands (Figs. 2 and 3) indicating that this hydroxyl group is essential for the allosteric actions of hydroxyl flavonoids. This is also supported by the lack of activity observed for the isoflavones daidzein and genistein, which lack the 3-hydroxyl group because of the presence of the bulky hydroxyphenyl group at this position.

The hydroxyl flavonols tested all imparted stimulus bias; no modulation in peptide-mediated cAMP signaling was observed. The flavonoid catechin also displayed pathway-selective modulation. However, in contrast to hydroxyl flavonols, analysis of the actions of catechin revealed no modulation in Ca^{2+} signaling but interesting differences in the modulation of peptide agonist function for cAMP accumulation. Catechin contains a slightly different scaffold (a chromene backbone) compared with all the other tested compounds, lacking the carbonyl group at position 4 (Fig. 1). This introduces flexibility into the phenolic structure; however, it contains all the same hydroxyl groups as quercetin. The introduction of flexibility into the backbone removes the ability of the flavonoid to modulate peptide-mediated Ca^{2+} signaling, but imparts an inhibition in the ability of some, but not all, orthosteric peptides to generate cAMP; the efficacy was significantly reduced for the endogenous ligands GLP-1(1–36) NH_2 and GLP-1(7–36) NH_2 , whereas the potency (but not the efficacy) was reduced for GLP-1(7–37), with no significant changes in GLP-1(1–37), oxyntomodulin or exendin-4 signaling. Exendin-4 and the truncated forms of GLP-1 are thought to be functionally equivalent because they have similar pharmacology; however, negative cooperativity between catechin and the truncated GLP-1 peptides versus neutral cooperativity with exendin-4 implies that the conformational states adopted by the truncated GLP-1 peptides and exendin-4 are different. Likewise, using the Novo Nordisk allosteric modulator compound 2, positive binding cooperativity was observed between compound 2 and truncated forms of GLP-1 but neutral cooperativity for exendin-4 (Koole et al., 2010). The subtle differences in the inhibition of cAMP signaling of GLP-1(7–36) NH_2 and GLP-1(7–37) in the presence of catechin also suggest that these two truncated versions of GLP-1 may produce different receptor conformational states.

Taken together, the results described above suggest that the difference in the backbone between hydroxyl flavonols and catechin is sufficient to engender unique receptor conformations that can either augment Ca^{2+} signaling or inhibit cAMP signaling of endogenous/exogenous ligands. In binding assays, hydroxyl flavonols and catechin both displayed weak inhibition of the radioligand but displayed neutral cooperativity with the peptide agonists. This implies that the observed allosteric pathway-selective cooperativity (positive for hydroxyl flavonols, negative for catechin) is purely driven by changes in orthosteric efficacy. The lack of effects of the flavonoids in competition binding assays suggests that they are acting at an allosteric site to produce these effects.

The GLP-1R is pleiotropically coupled, and it is clear that the physiological response leading to insulin secretion is a

composite of activation of multiple signaling pathways by multiple ligands (Baggio and Drucker, 2007). Because the underlying GLP-1R-mediated signaling to target many of the therapeutically important effects is not fully understood, further work is required to identify the optimal combination of signaling outputs and pathway bias to target for treatment of type II diabetes. Thus, it is becoming increasingly important for screening efforts to focus on multiple signaling outputs, regardless of coupling strength, rather than focusing on a single endpoint, because the ultimate clinical efficacy may be determined by an optimal combination of collateral efficacies. In addition, for receptors such as the GLP-1R that involve the interplay between multiple endogenous ligands, probe dependence of allosteric drugs is a major consideration. The truncated forms of GLP-1 are considered the predominant ligands for the GLP-1R, oxyntomodulin and the full-length GLP-1 forms playing a minor role in comparison. However, when studying allosteric interactions, it is important to study the effects on all endogenous ligands because there is the potential for allosteric effects on weak endogenous agonists that may potentiate the activity of these ligands to physiologically relevant levels, effects that may be beneficial or contribute to unwanted or adverse side effects.

Flavonoid compounds are naturally occurring, and the fact that their structural backbone can engender receptor conformations that either augment Ca^{2+} signaling or inhibit cAMP signaling may aid in developing compounds with favorable pharmacological properties for the treatment of disease conditions. The lack of effect observed on the calcitonin receptor Leu polymorphism and ATP responses in Ca^{2+} signaling assays, in addition to the probe dependence observed for GLP-1R agonists, are consistent with the idea that these compounds act at the GLP-1R. However, at the high concentrations used in this study, flavonoids are reported to exert multiple pharmacological effects, in addition to those that may be beneficial to treatment type II diabetes. Some of these are discussed extensively in Middleton et al., 2000. As a consequence of this lack of specificity, flavonoids are unlikely to provide a good starting structure for development of selective allosteric ligands; however, the flavonol scaffold may provide a useful tool for studying GLP-1R modulation, in addition to providing proof of concept for the use of SAR to probe allosteric interactions at this receptor.

In conclusion, we have shown that naturally occurring and synthetic flavonoids can differentially traffic stimuli imparted to the GLP-1R by multiple but not all endogenous agonists. An SAR approach revealed crucial roles of the 3-hydroxyl group and multiple substituent hydroxyl groups of the phenyl ring for positive allosteric modulator activity. Additional phenyl groups at positions 5 and 7 of the chromen-4-one ring further enhance the positive modulator activity. These data represent a detailed examination of the role of naturally occurring compounds on peptide agonists at the GLP-1R, and may aid drug discovery efforts in the development of viable therapeutics for the management of type II diabetes.

Authorship Contributions

Participated in research design: Wootten, Simms, Woodman, and Sexton.

Conducted experiments: Wootten.

Contributed new reagents or analytical tools: Woodman.

Performed data analysis: Wootten.

Wrote or contributed to the writing of the manuscript: Wootten, Simms, Koole, Woodman, Summers, Christopoulos, and Sexton.

References

- Aurelio L, Valant C, Flynn BL, Sexton PM, Christopoulos A, and Scammells PJ (2009) Allosteric modulators of the adenosine A1 receptor: synthesis and pharmacological evaluation of 4-substituted 2-amino-3-benzoylthiophenes. *J Med Chem* **52**:4543–4547.
- Avlani V, May LT, Sexton PM, and Christopoulos A (2004) Application of a kinetic model to the apparently complex behavior of negative and positive allosteric modulators of muscarinic acetylcholine receptors. *J Pharmacol Exp Ther* **308**:1062–1072.
- Baggio LL and Drucker DJ (2007) Biology of incretins: GLP-1 and GIP. *Gastroenterology* **132**:2131–2157.
- Bavec A, Hällbrink M, Langel U, and Zorko M (2003) Different role of intracellular loops of glucagon-like peptide-1 receptor in G-protein coupling. *Regul Pept* **111**:137–144.
- Chen D, Liao J, Li N, Zhou C, Liu Q, Wang G, Zhang R, Zhang S, Lin L, Chen K, et al. (2007) A nonpeptidic agonist of glucagon-like peptide 1 receptors with efficacy in diabetic db/db mice. *Proc Natl Acad Sci USA* **104**:943–948.
- Drucker DJ, Dritselis A, and Kirkpatrick P (2010) Liraglutide. *Nat Rev Drug Discov* **9**:267–268.
- Drucker DJ and Nauck MA (2006) The incretin system: glucagon-like peptide-1 receptor agonists and dipeptidyl peptidase-4 inhibitors in type 2 diabetes. *Lancet* **368**:1696–1705.
- Drucker DJ, Philippe J, Mojsov S, Chick WL, and Habener JF (1987) Glucagon-like peptide I stimulates insulin gene expression and increases cyclic AMP levels in a rat islet cell line. *Proc Natl Acad Sci USA* **84**:3434–3438.
- Hertog MG and Hollman PC (1996) Potential health effects of the dietary flavonol quercetin. *Eur J Clin Nutr* **50**:63–71.
- Holz GG 4th, Kühtreiber WM, and Habener JF (1993) Pancreatic beta-cells are rendered glucose-competent by the insulinotropic hormone glucagon-like peptide-1(7–37). *Nature* **361**:362–365.
- Knudsen LB, Kiel D, Teng M, Behrens C, Bhumralkar D, Kodra JT, Holst JJ, Jeppesen CB, Johnson MD, de Jong JC, et al. (2007) Small-molecule agonists for the glucagon-like peptide 1 receptor. *Proc Natl Acad Sci USA* **104**:937–942.
- Kolterman OG, Buse JB, Fineman MS, Gaines E, Heintz S, Bicsak TA, Taylor K, Kim D, Aisporna M, Wang Y, et al. (2003) Synthetic exendin-4 (exenatide) significantly reduces postprandial and fasting plasma glucose in subjects with type 2 diabetes. *J Clin Endocrinol Metab* **88**:3082–3089.
- Koole C, Wootten D, Simms J, Valant C, Sridhar R, Woodman OL, Miller LJ, Summers RJ, Christopoulos A, and Sexton PM (2010) Allosteric ligands of the glucagon-like peptide 1 receptor (GLP-1R) differentially modulate endogenous and exogenous peptide responses in a pathway-selective manner: implications for drug screening. *Mol Pharmacol* **78**:456–465.
- Larsen J, Hylleberg B, Ng K, and Damsbo P (2001) Glucagon-like peptide-1 infusion must be maintained for 24 h/day to obtain acceptable glycemia in type 2 diabetic patients who are poorly controlled on sulphonylurea treatment. *Diabetes Care* **24**:1416–1421.
- Leach K, Sexton PM, and Christopoulos A (2007) Allosteric GPCR modulators: taking advantage of permissive receptor pharmacology. *Trends Pharmacol Sci* **28**:382–389.
- May LT, Avlani VA, Langmead CJ, Herdon HJ, Wood MD, Sexton PM, and Christopoulos A (2007a) Structure-function studies of allosteric agonism at M2 muscarinic acetylcholine receptors. *Mol Pharmacol* **72**:463–476.
- May LT, Leach K, Sexton PM, and Christopoulos A (2007b) Allosteric modulation of G protein-coupled receptors. *Annu Rev Pharmacol Toxicol* **47**:1–51.
- Middleton E, Jr., Kandaswami C, and Theoharides TC (2000) The effects of plant flavonoids on mammalian cells: implications for inflammation, heart disease, and cancer. *Pharmacol Rev* **52**:673–751.
- Montrose-Rafizadeh C, Avdonin P, Garant MJ, Rodgers BD, Kole S, Yang H, Levine MA, Schwindinger W, and Bernier M (1999) Pancreatic glucagon-like peptide-1 receptor couples to multiple G proteins and activates mitogen-activated protein kinase pathways in Chinese hamster ovary cells. *Endocrinology* **140**:1132–1140.
- Olansky L (2010) Q: Do incretin drugs for type 2 diabetes increase the risk of acute pancreatitis? *Cleve Clin J Med* **77**:503–505.
- Shetty AK, Rashmi R, Rajan MGR, Sambaiah K, and Salimath PV (2004) Antidiabetic influence of quercetin in streptozotocin-induced diabetic rats *Nutr Res* **24**:373–381.
- Sloop KW, Willard FS, Brenner MB, Ficorilli J, Valasek K, Showalter AD, Farb TB, Cao JX, Cox AL, Michael MD, et al. (2010) Novel small molecule glucagon-like peptide-1 receptor agonist stimulates insulin secretion in rodents and from human islets. *Diabetes* **59**:3099–3107.
- Teng M, Johnson MD, Thomas C, Kiel D, Lakis JN, Kercher T, Aytes S, Kostrowicki J, Bhumralkar D, Truesdale L, et al. (2007) Small molecule ago-allosteric modulators of the human glucagon-like peptide-1 (hGLP-1) receptor. *Bioorg Med Chem Lett* **17**:5472–5478.
- Vahl TP and D'Alessio DA (2004) Gut peptides in the treatment of diabetes mellitus. *Expert Opin Investig Drugs* **13**:177–188.
- Vessal M, Hemmati M, and Vasei M (2003) Antidiabetic effects of quercetin in streptozotocin-induced diabetic rats. *Comp Biochem Physiol C Toxicol Pharmacol* **135C**:357–364.
- Viltsbøll T, Agersø H, Krarup T, and Holst JJ (2003) Similar elimination rates of glucagon-like peptide-1 in obese type 2 diabetic patients and healthy subjects. *J Clin Endocrinol Metab* **88**:220–224.
- Werry TD, Gregory KJ, Sexton PM, and Christopoulos A (2005) Characterization of serotonin 5-HT_{2C} receptor signaling to extracellular signal-regulated kinases 1 and 2. *J Neurochem* **93**:1603–1615.
- Wheeler MB, Lu M, Dillon JS, Leng XH, Chen C, and Boyd AE 3rd (1993) Functional expression of the rat glucagon-like peptide-I receptor, evidence for coupling to both adenylyl cyclase and phospholipase-C. *Endocrinology* **133**:57–62.

Address correspondence to: Prof. Patrick M. Sexton, Drug Discovery Biology Laboratory, Monash Institute of Pharmaceutical Sciences, Monash University, 381 Royal Parade, Parkville, Victoria 3052, Australia. E-mail: patrick.sexton@med.monash.edu.au

Polymorphism and Ligand Dependent Changes in Human Glucagon-Like Peptide-1 Receptor (GLP-1R) Function: Allosteric Rescue of Loss of Function Mutation^[S]

Cassandra Koole, Denise Wootten, John Simms, Celine Valant, Laurence J. Miller, Arthur Christopoulos, and Patrick M. Sexton

Drug Discovery Biology, Monash Institute of Pharmaceutical Sciences and Department of Pharmacology, Monash University, Parkville, Victoria, Australia (C.K., D.W., J.S., C.V., A.C., and P.M.S.); and Department of Molecular Pharmacology and Experimental Therapeutics, Mayo Clinic, Scottsdale, Arizona (L.J.M.)

Received April 11, 2011; accepted May 26, 2011

ABSTRACT

The glucagon-like peptide-1 receptor (GLP-1R) is a key physiological regulator of insulin secretion and a major therapeutic target for the treatment of type II diabetes. However, regulation of GLP-1R function is complex with multiple endogenous peptides that interact with the receptor, including full-length (1–37) and truncated (7–37) forms of GLP-1 that can exist in an amidated form (GLP-1(1–36)NH₂ and GLP-1(7–36)NH₂) and the related peptide oxyntomodulin. In addition, the GLP-1R possesses exogenous agonists, including exendin-4, and the allosteric modulator, compound 2 (6,7-dichloro-2-methylsulfonyl-3-*tert*-butylaminoquinoxaline). The complexity of this ligand-receptor system is further increased by the presence of several single nucleotide polymorphisms (SNPs) that are distributed across the receptor. We have investigated 10 GLP-1R SNPs, which were characterized in three physiologically rele-

vant signaling pathways (cAMP accumulation, extracellular signal-regulated kinase 1/2 phosphorylation, and intracellular Ca²⁺ mobilization); ligand binding and cell surface receptor expression were also determined. We demonstrate both ligand- and pathway-specific effects for multiple SNPs, with the most dramatic effect observed for the Met¹⁴⁹ receptor variant. At the Met¹⁴⁹ variant, there was selective loss of peptide-induced responses across all pathways examined, but preservation of response to the small molecule compound 2. In contrast, at the Cys³³³ variant, peptide responses were preserved but there was attenuated response to compound 2. Strikingly, the loss of peptide function at the Met¹⁴⁹ receptor variant could be allosterically rescued by compound 2, providing proof-of-principle evidence that allosteric drugs could be used to treat patients with this loss of function variant.

Introduction

The glucagon-like peptide-1 receptor (GLP-1R) is a key target in the development of treatments for type II diabetes mellitus, with actions including glucose-dependent increases in insulin synthesis and release; decreases in β -cell apoptosis, body mass, and gastric emptying; and a decrease in peripheral resistance to insulin that address fundamental symptoms associated with the condition (DeFronzo, 1992;

Drucker, 2006). The GLP-1R is a family B peptide hormone G protein-coupled receptor primarily expressed in pancreatic β -cells that responds to at least four distinct endogenous GLP-1 variants: two full-length GLP-1 peptides [GLP-1(1–36)NH₂ and GLP-1(1–37)] and two truncated and more prominent circulating forms [GLP-1(7–36)NH₂ and GLP-1(7–37)] (Baggio and Drucker, 2007). In addition, the related endogenous peptide oxyntomodulin and exogenous mimetic peptide exendin-4 act at the GLP-1R to increase the biosynthesis and secretion of insulin, decrease β -cell apoptosis and decrease gastric emptying in a similar manner to the endogenous GLP-1 peptides (Jarrousse et al., 1984; Jarrousse et al., 1985; Göke et al., 1993). Although levels of GLP-1 are reduced in patients with type II diabetes mellitus, the retention of its insulinotropic properties at the GLP-1R make it one of the most promising ligand-receptor systems to target in the development of treatments for type II diabetes (Nauck et al.,

This work was funded in part by the National Health and Medical Research Council (NHMRC) of Australia [Grants 519461, 1002180]; and by an NHMRC Australian Principal Research Fellowship (to P.M.S.) and a Senior Research Fellowship (to A.C.).

Article, publication date, and citation information can be found at <http://molpharm.aspetjournals.org>.
doi:10.1124/mol.111.072884.

[S] The online version of this article (available at <http://molpharm.aspetjournals.org>) contains supplemental material.

ABBREVIATIONS: GLP-1R, glucagon-like peptide-1 receptor; SNP, single nucleotide polymorphism; DMEM, Dulbecco's modified Eagle's medium; ERK, extracellular signal-regulated kinase; FBS, Fetal bovine serum; CHO, Chinese hamster ovary; BSA, bovine serum albumin; compound 2, 6,7-dichloro-2-methylsulfonyl-3-*tert*-butylaminoquinoxaline.

1993; Toft-Nielsen et al., 2001). Recent medical developments to target this system include the GLP-1 mimetic liraglutide (Knudsen et al., 2000; Elbrønd et al., 2002) and dipeptidyl peptidase IV inhibitors that prolong the plasma half-life of endogenous GLP-1R peptides (Deacon et al., 1995a,b). The latter compounds fail to achieve the weight loss seen with peptide therapeutics, whereas the peptides have significant potential for reduced patient compliance due to the requirement for subcutaneous administration. To overcome this, small orally active drugs that can augment GLP-1R signaling are continually being pursued. One example, compound 2 (6,7-dichloro-2-methylsulfonyl-3-*tert*-butylaminoquinoxaline; Novo Nordisk A/S, Bagsværd, Denmark), allosterically enhances peptide binding affinity and subsequently influences insulin secretion (Knudsen et al., 2007; Koole et al., 2010) and provides an exemplar for understanding allosteric modulation of the receptor. However, developing allosteric therapeutics for a pleiotropically coupled receptor with multiple endogenous ligands poses a significant challenge (Koole et al., 2010). In addition, the presence of naturally occurring nonsynonymous single nucleotide polymorphisms (SNPs), add a further element of complexity in the development of these drugs for therapeutic application. The presence of SNPs may be linked to the rate of onset of disease or effectiveness of receptor targeted treatments. Although SNPs have been characterized in great detail for many G protein-coupled receptors, there is limited knowledge on the effects of SNPs at the GLP-1R. Several GLP-1R SNPs have been assessed previously in vitro, although not explored in a wide range of functional outputs (Beinborn et al., 2005; Fortin et al., 2010) and at least one has been reported to have a loose association with type II diabetes mellitus (Tokuyama et al., 2004). A better understanding of the role of these polymorphisms in receptor function is therefore required, not only to gain an insight into the effects they have on receptor function but also to understand their possible association with the onset of disease or effectiveness of drug therapies.

In this study, we found ligand- and pathway-dependent alteration in signaling via select polymorphisms of the GLP-1R. Furthermore, we demonstrate that the major loss of GLP-1R function to peptide agonists at the Met¹⁴⁹ polymorphic receptor variant can be restored via allosteric modulation of the receptor, providing potential therapeutic paths to the treatment of diabetic patients carrying this SNP.

Materials and Methods

Materials. Dulbecco's modified Eagle's medium (DMEM), hygromycin-B, and Fluo-4 acetoxymethyl ester were purchased from Invitrogen (Carlsbad, CA). Fetal bovine serum (FBS) was purchased from Thermo Fisher Scientific (Melbourne, VIC, Australia). The QuikChange site-directed mutagenesis kit was purchased from Stratagene (La Jolla, CA). AlphaScreen reagents, Bolton-Hunter reagent (¹²⁵I), and 384-well ProxiPlates were purchased from PerkinElmer Life and Analytical Sciences (Waltham, MA). SureFire extracellular signal-regulated kinases 1 and 2 (ERK1/2) reagents were generously provided by TGR Biosciences (Adelaide, SA, Australia). SigmaFast *o*-phenylenediamine dihydrochloride tablets and antibodies were purchased from Sigma-Aldrich (St. Louis, MO). Compound 2 was generated according to a method published previously (Teng et al., 2007), to a purity of >95%, and compound integrity was confirmed by NMR. GLP-1 and GLP-1 peptide analogs were purchased from American Peptide Co., Inc. (Sunnyvale, CA). All other reagents were purchased from Sigma-Aldrich (St. Louis, MO) or BDH Merck (Melbourne, VIC, Australia) and were of an analytical grade.

Receptor Mutagenesis. Natural variants of the human GLP-1R with supporting nucleotide sequences reported to exist in the population were identified using the SwissProt database (<http://www.uniprot.org/uniprot/P43220>) and in a previous clinical report (Tokuyama et al., 2004) (Table 1; Fig. 1A). Each of these variants were introduced into a double c-myc-labeled wild-type human GLP-1R in the pEF5/FRT/V5-DEST destination vector (Invitrogen) using oligonucleotides for site-directed mutagenesis from GeneWorks (Hindmarsh, SA, Australia) (Supplemental Table 1) and the QuikChange site-directed mutagenesis kit (Stratagene). The integrity of the subsequent receptor clones were confirmed by cycle sequencing as described previously (May et al., 2007). In this study, the wild-type

TABLE 1
Human GLP-1R single nucleotide polymorphisms

Single nucleotide polymorphisms were generated for this study based on those identified in the Swissprot database (www.uniprot.org/uniprot/P43220) in association with those identified to exist in a cohort of normal and diabetic subjects in Tokuyama et al., 2004. Frequency data is reported from the Swissprot database.

Residue	Amino Acid	Nucleotide Substitution	Frequency of Nucleotide Substitution		NCBI Identification Number	Reference in Addition to SwissProt
			Homozygous	Heterozygous		
7	Pro	CCG	0.60	0.29	rs10305420	Tokuyama et al., 2004
	Leu	CTG	0.11			
20	Arg	AGG	0.99	0.01	rs10305421	
	Lys	AAG	Unknown			
44	Arg	CGC	0.99	0.01	rs2295006	Tokuyama et al., 2004
	His	CAC	Unknown			
131	Arg	CGA	0.92	0.08	rs3765467	Tokuyama et al., 2004
	Gln	CAA	Unknown			
149	Thr	ACG	Unknown	Unknown	112198	Tokuyama et al., 2004
	Met	ATG	Unknown			
168	Gly	GGC	0.76	0.2	rs6923761	
	Ser	AGC	0.04			
260	Phe	TTC or TTT	0.31 ^a	0.56	rs1042044	Tokuyama et al., 2004
	Leu	TTA	0.13			
316	Ala	GCC	0.98	0.02	rs10305492	
	Thr	ACC	Unknown			
333	Ser	TCC	0.99	0.01	rs10305493	
	Cys	TGC	Unknown			
421	Arg	CGG	0.99	0.01	rs10305510	
	Gln	CAG	Unknown			

^a No global information for TTT nucleotide variant.

GLP-1R was defined as the form of the receptor comprised of the following residues at the sites of polymorphic variation: Pro⁷, Arg²⁰, Arg⁴⁴, Arg¹³¹, Thr¹⁴⁹, Gly¹⁶⁸, Phe²⁶⁰, Ala³¹⁶, Ser³³³, and Arg⁴²¹.

Transfections and Cell Culture. Wild-type and polymorphic human GLP-1R were isogenically integrated into FlpIn-Chinese hamster ovary (FlpInCHO) cells (Invitrogen) and selection of receptor-expressing cells accomplished by treatment with 600 μ g/ml hygromycin B as described previously (May et al., 2007). Transfected and parental FlpInCHO cells were maintained in DMEM supplemented with 10% heat-inactivated FBS and incubated in a humidified environment at 37°C in 5% CO₂.

Radioligand Binding Assay. FlpInCHO wild-type and polymorphic human GLP-1R cells were seeded at a density of 3×10^4 cells/well into 96-well culture plates and incubated overnight at 37°C in 5% CO₂. Growth media was replaced with binding buffer [DMEM containing 25 mM HEPES and 0.1% (w/v) BSA] containing 0.5 nM

¹²⁵I-exendin(9–39) (K_i for the wild-type receptor, 12.5 nM) and increasing concentrations of unlabeled ligand. Cells were then incubated overnight at 4°C, followed by three washes in ice-cold 1× PBS to remove unbound radioligand. Cells were then solubilized in 0.1 M NaOH, and radioactivity determined by γ -counting. For interaction studies, competition of ¹²⁵I-exendin(9–39) binding by each orthosteric agonist was performed in the presence of 3 μ M compound 2, added simultaneously. For all experiments, nonspecific binding was defined by 1 μ M exendin(9–39).

cAMP Accumulation Assay. FlpInCHO wild-type and polymorphic human GLP-1R cells were seeded at a density of 3×10^4 cells/well into 96-well culture plates and incubated overnight at 37°C in 5% CO₂, and cAMP detection carried out as described previously (Koole et al., 2010). For interaction studies, increasing concentrations of peptide ligand and 3 μ M compound 2 were added simultaneously, and cAMP accumulation measured after 30 min of cell

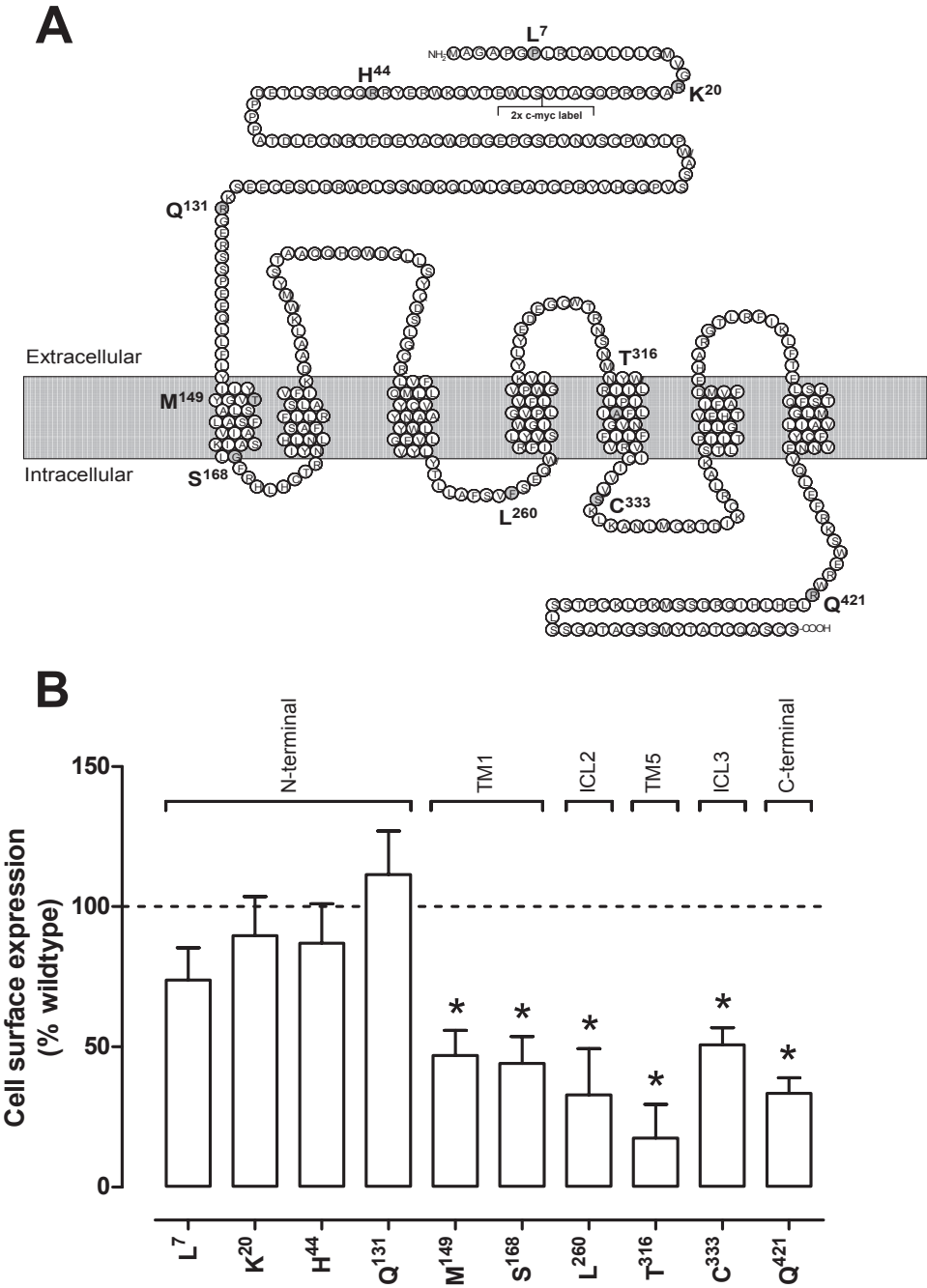


Fig. 1. A, schematic diagram of the human GLP-1R; location of residues subject to polymorphic variance is highlighted in gray, B, cell surface expression profiles of the human GLP-1R polymorphisms stably transfected into FlpInCHO cells as determined through antibody detection of the N-terminal *c-myc* epitope label. Statistical significance of changes in total cell surface expression compared with wild-type human GLP-1R expression (100%) were determined by one-way analysis of variance and Dunnett's post-test and are indicated with an asterisk (*, $p < 0.05$). All data are mean \pm S.E.M. of five to seven independent experiments conducted in triplicate. TM, transmembrane; ICL, intracellular loop.

stimulation. All values were converted to concentration of cAMP using a cAMP standard curve performed in parallel, and data were subsequently normalized to the response of 100 nM forskolin.

ERK1/2 Phosphorylation Assay. FlnCHO wild-type and polymorphic human GLP-1R cells were seeded at a density of 3×10^4 cells/well into 96-well culture plates and incubated overnight at 37°C in 5% CO₂. Receptor-mediated ERK1/2 phosphorylation was determined by using the AlphaScreen ERK1/2 SureFire protocol as described previously (May et al., 2007). Initial ERK1/2 phosphorylation time-course experiments were performed over 1 h to determine the time at which ERK1/2 phosphorylation was maximal after stimulation by agonists. Subsequent experiments were then performed at the time required to generate a maximal ERK1/2 phosphorylation response (7 min). For interaction studies, increasing concentrations of peptide ligand and 3 μM compound 2 were added simultaneously, and ERK1/2 phosphorylation was measured after 7 min of cell stimulation. Data were normalized to the maximal response elicited by 10% FBS, determined at 7 min (peak FBS response).

Intracellular Ca²⁺ Mobilization Assay. FlnCHO wild-type and polymorphic human GLP-1R cells were seeded at a density of 3×10^4 cells/well into 96-well culture plates and incubated overnight at 37°C in 5% CO₂, and receptor-mediated intracellular Ca²⁺ mobilization determined as described previously (Werry et al., 2005). Fluorescence was determined immediately after peptide addition, with an excitation wavelength set to 485 nm and an emission wavelength set to 520 nm, and readings taken every 1.36 s for 120 s. For interaction studies, 3 μM compound 2 was added 30 min before peptide addition because of autofluorescence. Subsequent fluorescence was then determined immediately after peptide addition with the conditions detailed above. Peak magnitude was calculated using five-point smoothing, followed by correction against basal fluorescence. The peak value was used to create concentration-response curves. Data were normalized to the maximal response elicited by 100 μM ATP.

Cell Surface Receptor Expression. FlnCHO wild-type and polymorphic human GLP-1R cells, with receptor DNA previously N-terminally labeled with a double c-myc epitope label, were seeded at a density of 25×10^4 cells/well into 24-well culture plates and incubated overnight at 37°C in 5% CO₂, washed three times in 1× PBS and fixed with 3.7% paraformaldehyde at 4°C for 15 min. To determine the effects of compound 2 on cell surface receptor expression, adherent cells were treated for 4 or 18 h with 3 μM compound 2 and subsequently fixed as described above. Cell surface receptor detection was performed using a mouse monoclonal (9E10) primary antibody (1:2000) to detect the c-myc tag, and a mouse-raised IgG horseradish peroxidase-linked secondary antibody (1:2000), both diluted in blocking solution [1× PBS containing 2% (w/v) BSA and 0.05% (w/v) Tween 20]. Peroxidase activity was then measured using SigmaFast o-phenylenediamine dihydrochloride tablets (Sigma) according to the manufacturer's instructions, and fluorescence detected at an emission wavelength of 492 nm. Data were normalized to the basal fluorescence detected in FlnCHO parental cells.

Data Analysis. All data were analyzed in Prism 5.02 (GraphPad Software Inc., San Diego, CA). Concentration response signaling data were analyzed using a three-parameter logistic equation as described previously (May et al., 2007):

$$Y = \text{Bottom} + \frac{(\text{Top} - \text{Bottom})}{1 + 10^{(\log EC_{50} - \log[A])}} \quad (1)$$

where Bottom represents the Y value in the absence of ligand(s), Top represents the maximal stimulation in the presence of ligand/s, [A] is the molar concentration of ligand, and EC₅₀ represents the molar concentration of ligand required to generate a response halfway between Top and Bottom. Likewise, this equation was used in the analysis of inhibition binding data, replacing EC₅₀ with IC₅₀. In this case, Bottom defines the specific binding of the radioligand that is equivalent to nonspecific ligand binding, whereas Top defines radio-

ligand binding in the absence of a competing ligand, and the IC₅₀ value represents the molar concentration of ligand required to generate a response halfway between Top and Bottom.

Statistics. Changes in peptide affinity, efficacy, potency, and cell surface expression of polymorphic variants compared with wild-type control were statistically analyzed with one-way analysis of variance and Dunnett's post test, and significance was accepted at $p < 0.05$. Differential modulation of oxyntomodulin potency by the allosteric ligand compound 2 at each of the polymorphic variants was assessed in comparison with an oxyntomodulin control using a paired t test, and statistical significance was accepted at $p < 0.05$.

Results

Cell Surface Expression of Human GLP-1R Polymorphic Variants. Each of the human GLP-1R polymorphisms was isogenically integrated into FlnCHO host cells (Invitrogen) by recombination, allowing comparison of relative cell surface expression without complication from variation in gene transcription. In this study we observed an interesting trend in the cell surface expression profiles of the GLP-1R polymorphisms as assessed by antibody labeling of the N-terminally incorporated c-myc tag (Fig. 1B). Although the polymorphisms occurring in the N-terminal domain of the receptor seemed to have cell surface expression similar to that of the wild-type human GLP-1R, most other polymorphic variants distributed across the receptor had reduced cell surface expression, with greatest effect seen for the Thr³¹⁶ variant.

The Human GLP-1R Met¹⁴⁹ Polymorphic Variant Displays a Reduction in Orthosteric Agonist Affinity. To establish the binding profiles at each of the reported human GLP-1R polymorphisms, we performed equilibrium binding studies with the orthosteric GLP-1R agonists or the allosteric agonist compound 2, in competition with the radio-labeled orthosteric antagonist ¹²⁵I-exendin(9–39). There was no significant influence of the polymorphisms on orthosteric agonist potency for inhibition of the radiolabel, except for the Met¹⁴⁹ receptor variant, which had reductions in the affinities of GLP-1(7–36)NH₂, exendin-4, oxyntomodulin (Fig. 2; Table 2), and GLP-1(7–37) (data not shown)¹. It is noteworthy that the extent of apparent affinity reduction differed between agonists, with a 251-fold shift for GLP-1(7–36)NH₂ and oxyntomodulin (Table 2) but only a 32-fold shift for exendin-4 (Table 2). Minimal effects were observed on GLP-1(1–36)NH₂, compound 2 (Fig. 2), and GLP-1(1–37) (data not shown)² binding within the concentration range measured, suggesting the affinity of these agonists is not greatly affected in any of the human GLP-1R variants compared with wild-type.

The Human GLP-1R Met¹⁴⁹ Polymorphic Variant Displays Reduced Orthosteric but Not Allosteric Agonist Potency in cAMP Accumulation. The cAMP accumulation profile of all orthosterically binding peptides at each of the GLP-1R polymorphic variants was similar to that of wild-type human GLP-1R, with the exception of the Met¹⁴⁹ polymorphism, where each peptide exhibited reduced potency, with observed decreases in potency of 158-fold for

¹ The response to GLP1(7–36)NH₂ and GLP-1(7–37) are effectively equivalent; therefore, only a limited analysis was performed for the GLP-1(7–37) peptide with data limited to one or two experiments only.

² The response to GLP1(1–36)NH₂ and GLP-1(1–37) are effectively equivalent, therefore, only a limited analysis was performed for the GLP-1(1–37) peptide with data limited to one or two experiments only.

GLP-1(7–36)NH₂, 200-fold for exendin-4, and >500-fold for oxyntomodulin (Fig. 3; Table 3). Full concentration-response relationships for the lower potency agonists GLP-1(1–36)NH₂, GLP-1(1–37), oxyntomodulin, and compound 2 could not be determined; however, the effect appeared more profound for oxyntomodulin relative to the truncated GLP-1 peptides and exendin-4 (Fig. 3). In contrast, the potency and efficacy of the allosteric agonist compound 2 at the Met¹⁴⁹ polymorphic variant, was similar to that observed with the Thr¹⁴⁹ variant, with pEC₅₀ values of 5.5 ± 0.1 and 5.5 ± 0.1, respectively (*n* = 4) (Fig. 3; Table 3). However, at the Cys³³³ polymorphism, where orthosteric peptide profiles were equivalent to those of wild-type, compound 2 displayed a reduced cAMP response (Fig. 3; Table 3).

Human GLP-1R Polymorphisms Have Variable Intracellular Ca²⁺ Mobilization Responses. In accord with previous studies (Koole et al., 2010), no Ca²⁺ response was seen for full-length GLP-1 peptides or compound 2 at the wild-type receptor, and this was true also for each of the polymorphic receptor variants (Fig. 4). In the case of oxyntomodulin, only a weak response was observed, and this was submaximal at 1 μM, even at the wild-type receptor. The weak response made interpretation of the effect of polymorphic variation difficult; however, a reduced response at 1 μM was seen for the Met¹⁴⁹ and Thr³¹⁶ variants (Fig. 4; Table 4).

No significant alteration in the potency of GLP-1(7–36)NH₂, GLP-1(7–37), or exendin-4 peptides was observed; however, marked reduction in peptide efficacy was found for selected receptor variants (Fig. 4; Table 4). For each of the higher affinity peptides, there was reduced efficacy at the Gln¹³¹, Met¹⁴⁹, Ser¹⁶⁸, Thr³¹⁶, and Gln⁴²¹ variants, the greatest reduction in efficacy being seen at the Met¹⁴⁹ variant, which exhibited no measurable agonist-induced response (Fig. 4; Table 4). In addition, for exendin-4 only, there were reductions in efficacy at the Cys³³³ and Lys²⁰ variants; for Lys²⁰, this occurred despite wild-type levels of cell surface

receptor expression. In systems with low receptor reserve, changes in receptor density can affect observed efficacy and potency. In many instances, there was evidence of reduced cell surface receptor expression, as assessed by antibody binding to the c-myc epitope (Fig. 1B), that probably contributed to the observed decrease in efficacy, because there is little reserve for coupling to this pathway. Intriguingly, the Leu²⁶⁰ variant had essentially wild-type response to the peptides, despite significantly reduced cell surface receptor expression, suggesting that the Leu²⁶⁰ substitution may actually favor coupling via Gα_q.

Effect of Receptor Polymorphisms on ERK1/2 Phosphorylation. Agonist-induced ERK1/2 phosphorylation was determined at 7 min for each of the human GLP-1R polymor-

TABLE 2
Effects of naturally occurring human GLP-1R polymorphisms on agonist binding
Data were analyzed using a three-parameter logistic equation as defined in eq. 1. pIC₅₀ values represent the negative logarithm of the concentration of agonist that inhibits binding of half the total concentration of radiolabeled antagonist [¹²⁵I]-exendin(9–39). Data are normalized to maximum [¹²⁵I]-exendin(9–39) binding of each individual data set, with nonspecific binding measured in the presence of 1 μM exendin(9–39). All values are mean ± S.E.M. of three to four independent experiments, conducted in duplicate. Data were analyzed with one-way analysis of variance and Dunnett's post test.

	pIC ₅₀		
	GLP-1(7–36)NH ₂	Exendin-4	Oxyntomodulin
Wild type	8.9 ± 0.1	9.4 ± 0.1	7.9 ± 0.1
Leu ⁷	8.9 ± 0.2	9.5 ± 0.1	8.2 ± 0.1
Lys ²⁰	8.8 ± 0.1	9.6 ± 0.1	7.9 ± 0.2
His ⁴⁴	8.9 ± 0.1	9.5 ± 0.1	7.9 ± 0.1
Gln ¹³¹	8.8 ± 0.1	9.3 ± 0.1	7.9 ± 0.1
Met ¹⁴⁹	6.5 ± 0.2*	7.9 ± 0.2*	5.5 ± 0.2*
Ser ¹⁶⁸	9.3 ± 0.1	9.5 ± 0.1	8.2 ± 0.1
Leu ²⁶⁰	9.2 ± 0.2	9.4 ± 0.2	7.9 ± 0.1
Thr ³¹⁶	9.5 ± 0.2	9.7 ± 0.2	8.4 ± 0.2
Cys ³³³	9.0 ± 0.1	9.6 ± 0.1	8.0 ± 0.1
Gln ⁴²¹	9.1 ± 0.2	9.6 ± 0.2	8.1 ± 0.2

* Statistically significant at *p* < 0.05.

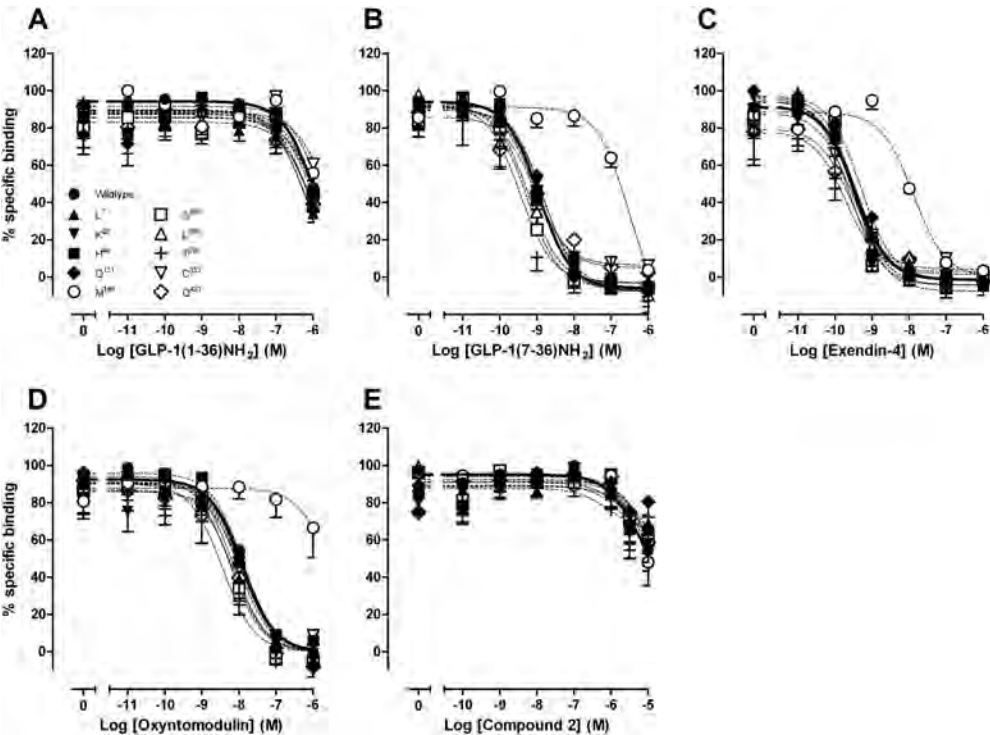


Fig. 2. Characterization of the binding of GLP-1(1–36)NH₂ (A), GLP-1(7–36)NH₂ (B), exendin-4 (C), oxyntomodulin (D), and compound 2 (E) in competition with the radiolabeled antagonist [¹²⁵I]-exendin(9–39) in whole FlpInCHO cells stably expressing each of the human GLP-1R polymorphisms or the wild-type GLP-1R. Data are normalized to the maximum [¹²⁵I]-exendin(9–39) binding of each individual data set, with nonspecific binding measured in the presence of 1 μM exendin(9–39). Data are analyzed with a three-parameter logistic equation as defined in eq. 1. All values are mean ± S.E.M. of three to four independent experiments conducted in duplicate.

phic variants. Most receptor variants exhibited ERK1/2 responses similar to those of peptide agonists or compound 2 at the wild-type GLP-1R with the exception of the Met¹⁴⁹ variant (Fig. 5, Table 5). There was a decrease in the potency and/or efficacy of all orthosteric peptides with the Met¹⁴⁹ polymorphic variant, but this was not as pronounced as in the other pathways, suggesting alteration to signal bias of the receptor. The allosteric ligand compound 2 retained its weak agonism at this variant, sharing an ERK1/2 phosphorylation profile similar to that of compound 2 at the wild-type human GLP-1R (Fig. 5; Table 5).

Effect of Receptor Polymorphisms on the Allosteric Modulation of the cAMP Response to Oxyntomodulin by Compound 2. We have demonstrated previously that compound 2 positively modulates binding affinity and, as a

result cAMP potency, of the endogenous peptide agonists oxyntomodulin and, to a lesser extent, GLP-1(7–36)NH₂ and GLP-1(7–37) (Koole et al., 2010). Oxyntomodulin was the most robustly enhanced peptide and was used to explore whether allosteric regulation of the peptide response was retained at the polymorphic receptor variants. Compound 2 significantly enhanced the oxyntomodulin response at the wild-type receptor, Lys²⁰, and His⁴⁴ receptor variants (Table 6). At the Cys³³³ variant, which had attenuated cAMP agonism to compound 2, the allosteric modulator failed to enhance the oxyntomodulin response. It is noteworthy that despite retaining cAMP agonism upon activation with compound 2, the oxyntomodulin response at the Leu⁷ and Thr³¹⁶ variants was not significantly modified by compound 2, and although there was a trend toward enhancement with the Gln¹³¹, Ser¹⁶⁸,

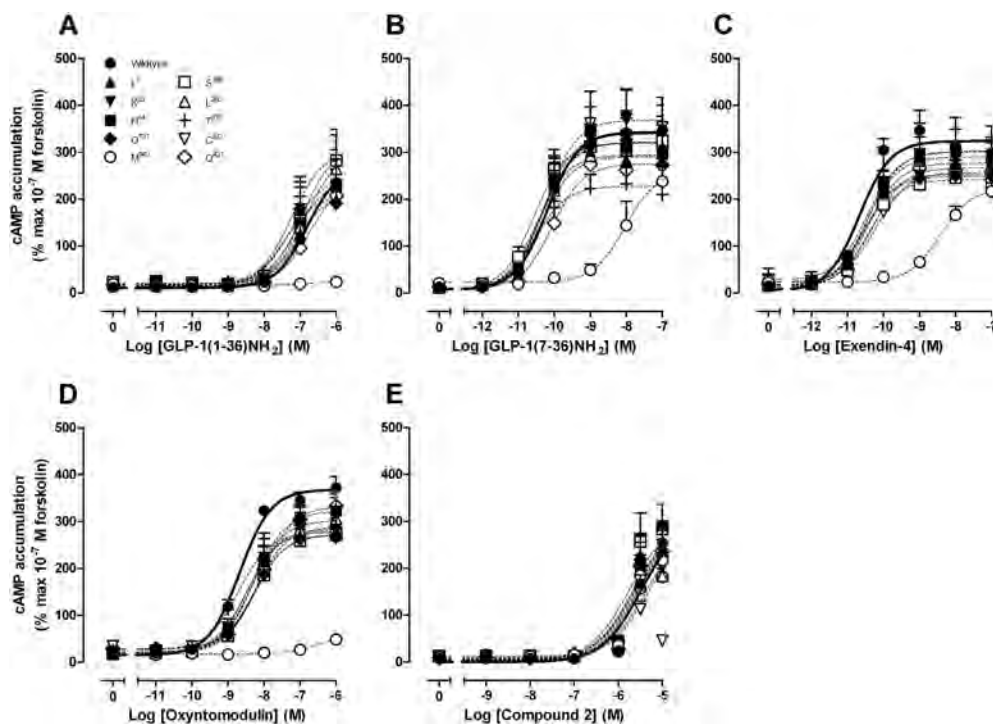


Fig. 3. Characterization of cAMP accumulation in the presence of GLP-1(1–36)NH₂ (A), GLP-1(7–36)NH₂ (B), exendin-4 (C), oxyntomodulin (D), and compound 2 (E) in FlpInCHO cells stably expressing each of the human GLP-1R polymorphisms or the wild-type GLP-1R. Data are normalized to the response elicited by 100 nM forskolin and analyzed with a three-parameter logistic equation as defined in eq. 1. All values are mean \pm S.E.M. of 4 to 12 experiments conducted in duplicate.

TABLE 3

Effects of naturally occurring human GLP-1R polymorphisms on agonist signaling via cAMP

Data were analyzed using a three-parameter logistic equation as defined in eq. 1. pEC₅₀ values represent the negative logarithm of the concentration of agonist that produces half the maximal response. E_{max} represents the maximal response normalized to the response elicited by that of 100 nM forskolin. All values are mean \pm S.E.M. of four to ten independent experiments, conducted in duplicate. Data were analyzed with one-way analysis of variance and Dunnett's post test.

	cAMP Accumulation									
	pEC ₅₀					E _{max}				
	GLP-1 (1–36)NH ₂	GLP-1 (7–36)NH ₂	Exendin-4	Oxyntomodulin	Compound 2 ^a	GLP-1 (1–36)NH ₂	GLP-1 (7–36)NH ₂	Exendin-4	Oxyntomodulin	Compound 2 ^b
Wild type	6.8 \pm 0.2	10.2 \pm 0.2	10.7 \pm 0.1	8.7 \pm 0.1	5.5 \pm 0.1	270 \pm 36	343 \pm 21	299 \pm 9	368 \pm 9	254 \pm 44
Leu ⁷	7.1 \pm 0.2	10.5 \pm 0.2	10.4 \pm 0.2	8.5 \pm 0.1	5.6 \pm 0.1	217 \pm 18	294 \pm 18	277 \pm 14	283 \pm 13*	242 \pm 50
Lys ²⁰	7.3 \pm 0.2	10.3 \pm 0.2	10.6 \pm 0.2	8.5 \pm 0.2	5.6 \pm 0.1	244 \pm 26	339 \pm 19	249 \pm 12	279 \pm 18*	200 \pm 26
His ⁴⁴	7.1 \pm 0.2	10.4 \pm 0.2	10.4 \pm 0.2	8.3 \pm 0.1	5.7 \pm 0.1	244 \pm 27	321 \pm 18	302 \pm 16	322 \pm 17	291 \pm 46
Gln ¹³¹	7.4 \pm 0.3	10.4 \pm 0.2	10.6 \pm 0.2	8.3 \pm 0.2	5.6 \pm 0.1	209 \pm 31	322 \pm 21	253 \pm 15	271 \pm 14*	225 \pm 35
Met ¹⁴⁹	N.D.	8.0 \pm 0.3*	8.4 \pm 0.1*	N.D.	5.5 \pm 0.1	N.D.	N.D.	223 \pm 13	N.D.	217 \pm 24
Ser ¹⁶⁸	6.9 \pm 0.2	10.5 \pm 0.2	10.4 \pm 0.2	8.3 \pm 0.2	5.8 \pm 0.1	314 \pm 33	320 \pm 17	242 \pm 11	273 \pm 14*	283 \pm 13
Leu ²⁶⁰	6.9 \pm 0.2	10.4 \pm 0.3	10.5 \pm 0.2	8.4 \pm 0.1	5.3 \pm 0.1	297 \pm 28	291 \pm 21	290 \pm 13	302 \pm 12	184 \pm 30
Thr ³¹⁶	7.2 \pm 0.2	10.5 \pm 0.3	10.5 \pm 0.4	8.7 \pm 0.3	5.3 \pm 0.1	304 \pm 33	228 \pm 16*	301 \pm 30	277 \pm 22*	182 \pm 18
Cys ³³³	6.9 \pm 0.2	10.2 \pm 0.3	10.2 \pm 0.2	8.2 \pm 0.2	N.D.	259 \pm 24	331 \pm 26	257 \pm 12	288 \pm 16	46 \pm 8*
Gln ⁴²¹	6.7 \pm 0.2	10.1 \pm 0.2	10.3 \pm 0.2	8.1 \pm 0.1	5.6 \pm 0.1	242 \pm 23	275 \pm 15	267 \pm 13	332 \pm 15	236 \pm 45

N.D., data unable to be experimentally defined or with incomplete curves.

^a For estimation of pEC₅₀ values, E_{max} was set to \leq 300% of the 100 nM forskolin response.

^b Compound 2 response at 10^{–5} M.

* Statistically significant at $p < 0.05$.

Leu²⁶⁰, and Gln⁴²¹ variants, this was attenuated relative to the wild-type receptor.

Allosteric Rescue of GLP-1R Function at the Met¹⁴⁹ Polymorphic Variant. Compound 2 exhibits differential modulation of individual peptide agonists at the “wild-type” GLP-1R, a behavior termed “probe dependence” (Keov et al., 2011), with greatest modulation of the oxyntomodulin response relative to that of the more potent peptides, GLP-1(7–36)NH₂, GLP-1(7–37), and exendin-4 and indeed has minimal effect on exendin-4-mediated cAMP responses (Koole et al., 2010). Remarkably, compound 2 rescued the binding and

cAMP signal of most peptide agonists at the Met¹⁴⁹ receptor variant (excluding full-length GLP-1 peptides) (Figs. 6 and 7; Tables 7 and 8), with binding affinity and potency of truncated GLP-1 and exendin-4 recovered to within 8-fold of the wild-type receptor (Figs. 6 and 7; Tables 7 and 8). Because agonist functional potency is a composite of efficacy and affinity, this parameter can be influenced by receptor expression and receptor reserve. Consequently, we assessed the role of compound 2 on cell surface expression of the Met¹⁴⁹ variant of the receptor. Compound 2 had no significant effect on the level of cell surface expression of Met¹⁴⁹ over the time

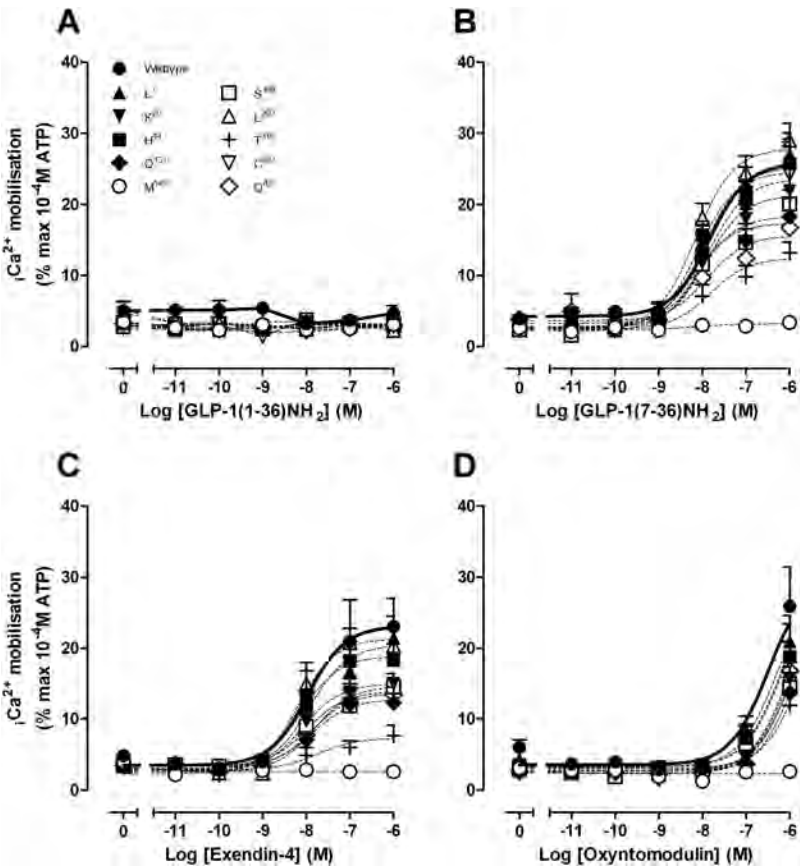


Fig. 4. Characterization of intracellular Ca²⁺ mobilization in the presence of GLP-1(1–36)NH₂ (A), GLP-1(7–36)NH₂ (B), exendin-4 (C), and oxyntomodulin (D) in FlpInCHO cells stably expressing each of the human GLP-1R polymorphisms or the wild-type GLP-1R. Data are normalized to the maximal response elicited by 100 μM ATP and analyzed with a three-parameter logistic equation as defined in eq. 1. All values are mean ± S.E.M. of five to nine experiments conducted in duplicate.

TABLE 4
Effects of naturally occurring human GLP-1R polymorphisms on agonist signaling via intracellular Ca²⁺ mobilization
Data were analyzed using a three-parameter logistic equation as defined in eq. 1. pEC₅₀ values represent the negative logarithm of the concentration of agonist that produces half the maximal response. E_{max} represents the maximal response normalized to the response elicited by that of 10^{−4} M ATP. All values are mean ± S.E.M. of 5 to 10 independent experiments, conducted in duplicate. Data were analyzed with one-way analysis of variance and Dunnett’s post test.

	Intracellular Ca ²⁺ Mobilization					
	pEC ₅₀			E _{max}		
	GLP-1(7–36)NH ₂	Exendin-4	Oxyntomodulin	GLP-1(7–36)NH ₂	Exendin-4	Oxyntomodulin ^a
Wild type	7.8 ± 0.2	8.0 ± 0.3	N.D.	25.8 ± 1.5	23.1 ± 2.5	25.9 ± 5.5
Leu ⁷	8.0 ± 0.2	7.9 ± 0.2	N.D.	25.2 ± 1.4	20.4 ± 1.4	21.0 ± 2.5
Lys ²⁰	7.9 ± 0.2	8.1 ± 0.1	N.D.	21.3 ± 1.4	15.0 ± 0.7*	15.7 ± 1.6
His ⁴⁴	8.1 ± 0.2	8.1 ± 0.2	N.D.	24.5 ± 1.4	18.9 ± 1.3	18.8 ± 2.1
Gln ¹³¹	8.2 ± 0.2	7.9 ± 0.3	N.D.	17.3 ± 1.4*	12.8 ± 1.1*	13.7 ± 1.5
Met ¹⁴⁹	N.D.	N.D.	N.D.	N.D.	N.D.	2.6 ± 0.4*
Ser ¹⁶⁸	8.1 ± 0.2	8.0 ± 0.2	N.D.	18.3 ± 1.0*	13.9 ± 0.8*	14.4 ± 0.9
Leu ²⁶⁰	8.2 ± 0.1	8.2 ± 0.1	N.D.	27.8 ± 1.2	21.3 ± 1.0	19.0 ± 1.9
Thr ³¹⁶	7.8 ± 0.2	7.7 ± 0.5	N.D.	12.4 ± 1.0*	7.3 ± 0.9*	11.9 ± 1.9*
Cys ³³³	7.8 ± 0.3	7.8 ± 0.2	N.D.	23.6 ± 2.4	14.6 ± 1.1*	15.0 ± 2.4
Gln ⁴²¹	7.9 ± 0.3	7.9 ± 0.3	N.D.	15.6 ± 1.7*	13.6 ± 1.3*	16.8 ± 7.8

N.D., data unable to be experimentally defined or with incomplete curves.
* Statistically significant at *p* < 0.05.
^a Response at 10^{−6} M oxyntomodulin.

scale of the assay (data not shown). We also performed interaction studies between compound 2 and GLP-1(7–36)NH₂, oxyntomodulin, or exendin-4 for ERK1/2 phosphorylation and intracellular Ca²⁺ mobilization, but no modulation of these responses was observed at this receptor variant (data not shown). This indicates that compound 2 retains the pathway-specific modulation of response that we had previously observed at the wild-type human GLP-1R (Koole et al., 2010). No modulation of GLP-1(1–36)NH₂ at the Met¹⁴⁹ variant was observed (not shown).

Discussion

There is a paucity of information examining either the prevalence or influence of GLP-1R polymorphisms in, and on,

susceptibility to diseases such as type II diabetes and obesity. Indeed, only a single study identified the Met¹⁴⁹ polymorphism in a patient with type II diabetes (Tokuyama et al., 2004), and study of other polymorphisms in vitro has been very limited (Beinborn et al., 2005; Fortin et al., 2010). Greater understanding of the potential pharmacological impact of GLP-1R polymorphisms is thus required to drive clinical research in this area. In this study, we have identified major pharmacological differences in the signaling profile or allosteric modulation of multiple human GLP-1R polymorphic variants and, importantly, that the loss of function associated with the most detrimental substitution, Met¹⁴⁹, can be allosterically rescued with a small molecule modulator.

The GLP-1R is pleiotropically coupled to signaling path-

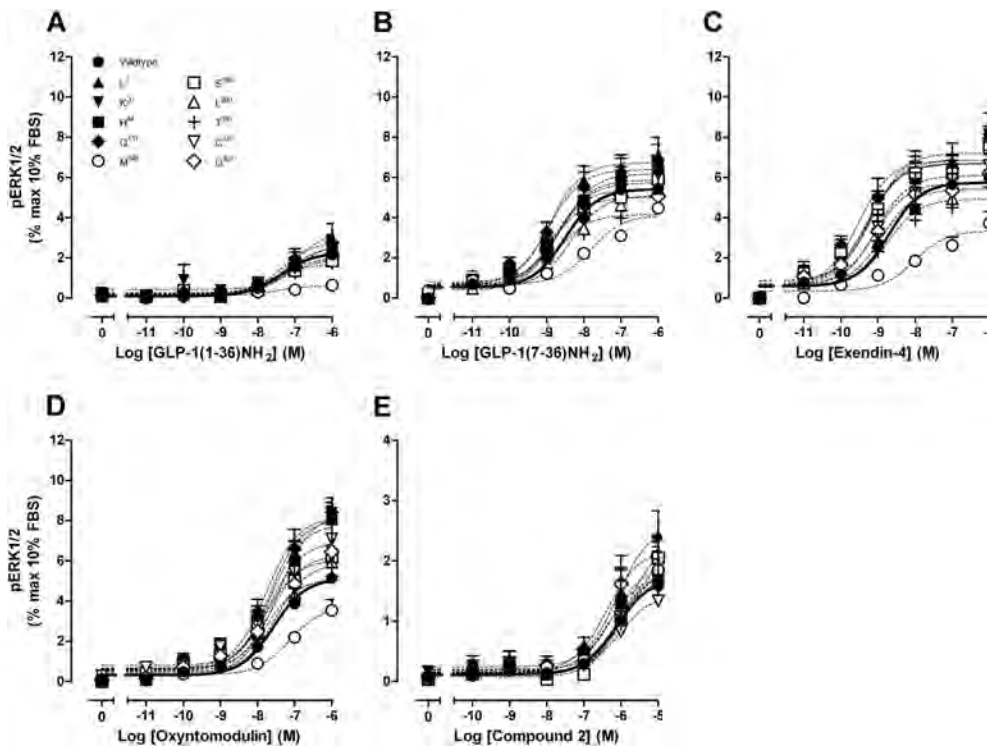


Fig. 5. Characterization of ERK1/2 phosphorylation in the presence of GLP-1(1–36)NH₂ (A), GLP-1(7–36)NH₂ (B), exendin-4 (C), oxyntomodulin (D), and compound 2 (E), in FlpInCHO cells stably expressing each of the human GLP-1R polymorphisms or the wild-type GLP-1R. Data are normalized to the maximal response elicited by 10% FBS and analyzed with a three-parameter logistic equation as defined in eq. 1. All values are mean \pm S.E.M. of four to five independent experiments conducted in duplicate.

TABLE 5

Effects of naturally occurring human GLP-1R polymorphisms on agonist signaling via ERK1/2 phosphorylation

Data were analyzed using a three-parameter logistic equation as defined in eq. 1. pEC₅₀ values represent the negative logarithm of the concentration of agonist that produces half the maximal response. E_{max} represents the maximal response normalized to the response elicited by that of 10% FBS. All values are mean \pm S.E.M. of four to five independent experiments, conducted in duplicate. Data were analyzed with one-way analysis of variance and Dunnett's post test.

	ERK1/2 Phosphorylation									
	pEC ₅₀					E _{max}				
	GLP-1 (1–36)NH ₂	GLP-1 (7–36)NH ₂	Exendin-4	Oxyntomodulin	Compound 2	GLP-1 (1–36)NH ₂	GLP-1 (7–36)NH ₂	Exendin-4	Oxyntomodulin	Compound 2
Wild type	7.4 \pm 0.4	8.5 \pm 0.3	8.7 \pm 0.2	7.6 \pm 0.1	6.1 \pm 0.3	2.3 \pm 0.4	5.4 \pm 0.4	6.6 \pm 0.4	6.4 \pm 0.3	1.7 \pm 0.3
Leu ⁷	7.1 \pm 0.2	8.8 \pm 0.2	9.2 \pm 0.2	7.7 \pm 0.1	6.1 \pm 0.2	3.3 \pm 0.4	7.1 \pm 0.4	7.2 \pm 0.4	8.1 \pm 0.3	2.6 \pm 0.3
Lys ²⁰	6.9 \pm 0.3	8.7 \pm 0.1	9.3 \pm 0.2	7.4 \pm 0.1	5.9 \pm 0.2	2.8 \pm 0.5	5.7 \pm 0.2	6.9 \pm 0.4	8.4 \pm 0.4	1.9 \pm 0.2
His ⁴⁴	7.2 \pm 0.2	8.6 \pm 0.2	9.3 \pm 0.2	7.6 \pm 0.2	6.3 \pm 0.3	2.6 \pm 0.3	6.2 \pm 0.3	6.7 \pm 0.4	7.8 \pm 0.6	1.8 \pm 0.2
Gln ¹³¹	7.3 \pm 0.2	8.9 \pm 0.2	9.5 \pm 0.2	7.8 \pm 0.2	6.2 \pm 0.3	2.8 \pm 0.2	6.4 \pm 0.3	6.9 \pm 0.4	8.2 \pm 0.5	1.9 \pm 0.3
Met ¹⁴⁹	N.D.	7.8 \pm 0.3	8.0 \pm 0.2	7.1 \pm 0.2	5.9 \pm 0.3	0.6 \pm 0.1	4.1 \pm 0.5	3.4 \pm 0.3*	3.7 \pm 0.3*	2.0 \pm 0.4
Ser ¹⁶⁸	7.3 \pm 0.2	8.8 \pm 0.2	9.3 \pm 0.3	7.8 \pm 0.1	5.9 \pm 0.2	2.0 \pm 0.2	5.4 \pm 0.3	6.7 \pm 0.5	6.1 \pm 0.3	2.3 \pm 0.3
Leu ²⁶⁰	7.3 \pm 0.4	8.4 \pm 0.4	8.9 \pm 0.4	7.5 \pm 0.3	6.0 \pm 0.3	2.2 \pm 0.3	5.1 \pm 0.6	5.4 \pm 0.7	5.9 \pm 0.7	1.9 \pm 0.3
Thr ³¹⁶	7.3 \pm 0.4	8.8 \pm 0.3	8.8 \pm 0.3	7.8 \pm 0.3	6.0 \pm 0.3	2.0 \pm 0.3	4.2 \pm 0.4	4.9 \pm 0.5	5.1 \pm 0.6	1.8 \pm 0.3
Cys ³³³	7.7 \pm 0.2	8.7 \pm 0.2	9.1 \pm 0.3	7.7 \pm 0.2	6.0 \pm 0.2	1.7 \pm 0.2	5.9 \pm 0.4	6.1 \pm 0.5	7.0 \pm 0.5	1.4 \pm 0.2
Gln ⁴²¹	7.2 \pm 0.4	8.9 \pm 0.3	9.1 \pm 0.2	7.7 \pm 0.4	6.1 \pm 0.3	2.3 \pm 0.4	5.0 \pm 0.5	5.7 \pm 0.4	6.3 \pm 0.9	2.9 \pm 0.4

N.D., data unable to be experimentally defined or with incomplete curves.

* Statistically significant at $p < 0.05$.

ways, and the physiological response to peptides represents a convergence of all pathways activated. In this study, we chose three well characterized second messenger pathways, each linked to physiological outcomes from the receptor, to assess the functional impact of the GLP-1R polymorphisms. Both cAMP production and intracellular Ca²⁺ mobilization are critical to the incretin response (Baggio and Drucker, 2007), whereas ERK1/2 signaling is involved in pancreatic β-cell growth and survival (Klinger et al., 2008; Quoyer et al., 2010). Furthermore, the GLP-1R can respond to multiple endogenous peptides, as well as mimetics such as exendin-4 that are used clinically (Göke et al., 1993), requiring detailed assessment to infer the impact of polymorphic receptor variance clinically. Our analysis has revealed major new findings on the pharmacology of GLP-1R polymorphisms that have implications both physiologically and for development of therapeutic interventions for treatment of patients carrying these receptor variants.

All polymorphic receptors were well expressed at the cell surface although total expression was reduced with individual variants, relative to “wild-type” receptor. The greatest effect was observed with the Thr³¹⁶ substitution, located at the second extracellular loop/transmembrane 5 interface. The majority of the polymorphic variants had minimal impact on receptor interaction with agonists and consequent signaling. However, with respect to intracellular Ca²⁺ mobilization, the loss in Ca²⁺ signaling was largely paralleled by a decrease in cell surface receptor expression, particularly for the Thr³¹⁶ variant, which exhibited the lowest level of cell surface expression and a weak Ca²⁺ response to each of the agonists. For this variant, there was also a parallel loss in efficacy of the low-potency peptide agonist oxyntomodulin. In the current study, receptor constructs were isogenically integrated into the host cell genome and thus the loss of cell surface receptor expression is probably linked to changes in protein stability or trafficking. Although the prevalence of the Thr³¹⁶ polymorphism is relatively rare (Table 1), homozygote expression in people could potentially lead to impaired GLP-1 responses.

The greatest impact on Ca²⁺ signaling occurred with the

TABLE 6
Differential modulation of oxyntomodulin at naturally occurring human GLP-1R polymorphisms in cAMP accumulation
Data were analyzed using a three-parameter logistic equation as defined in eq. 1. pEC₅₀ values represent the negative logarithm of the concentration of agonist that produces half the maximal response. All data are normalized to the response elicited by that of 10^{−7}M forskolin, and are mean ± S.E.M. of three to five independent experiments, conducted in duplicate.

	pEC50	
	Oxyntomodulin	+ 3 μM Compound 2
Wild type	8.7 ± 0.1	10.2 ± 0.7*
Leu ⁷	8.7 ± 0.1	9.1 ± 0.7
Lys ²⁰	8.6 ± 0.2	9.5 ± 0.5*
His ⁴⁴	8.4 ± 0.1	10.2 ± 1.2*
Gln ¹³¹	8.7 ± 0.1	9.2 ± 0.4
Met ¹⁴⁹	N.D.	7.7 ± 1.5*
Ser ¹⁶⁸	8.9 ± 0.1	9.4 ± 0.4
Leu ²⁶⁰	8.6 ± 0.2	9.2 ± 0.5
Thr ³¹⁶	8.6 ± 0.1	8.7 ± 0.6
Cys ³³³	8.2 ± 0.1	8.3 ± 0.2
Gln ⁴²¹	8.4 ± 0.1	9.1 ± 0.6

N.D., data unable to be experimentally defined or with incomplete curves.
* Statistically significant, *P* < 0.05 compared with oxyntomodulin control, paired *t* test.

Met¹⁴⁹ variant where responses to all peptides were effectively abolished. There was also greater impact of polymorphic variation on exendin-4 Ca²⁺ signaling relative to the GLP-1(7–36)NH₂ peptide. In particular, there was significant attenuation of exendin-4 signaling with the Lys²⁰ and Cys³³³ variants that had no effect on GLP-1(7–36)NH₂ response. Although the mechanistic basis for this is unclear, it nonetheless provides additional evidence for a differential mode of receptor activation by exendin-4, relative to the GLP-1 peptides, that is not affinity driven. It is interesting to note that one of these variants, Cys³³³, also displayed selectively reduced cAMP signaling by compound 2.

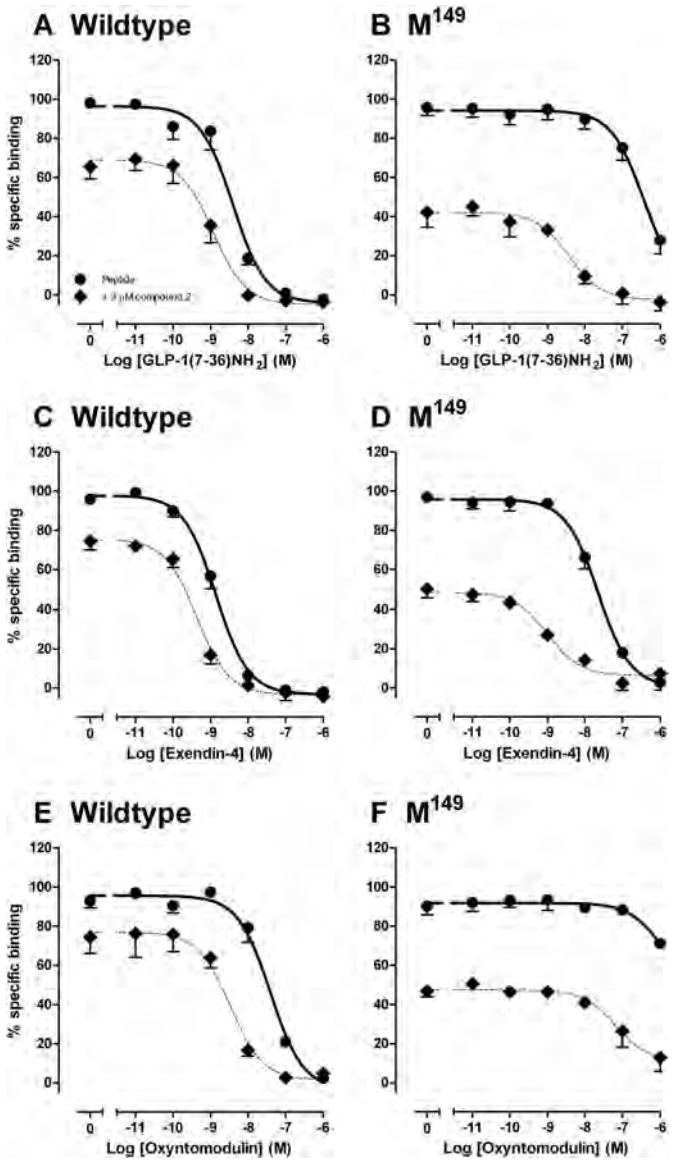


Fig. 6. Characterization of the binding of GLP-1(7–36)NH₂ (A and B), exendin-4 (C and D), and oxyntomodulin (E and F) in whole FlpInCHO cells stably expressing the human GLP-1R wild-type (A, C, and E) or human GLP-1R Met¹⁴⁹ variant (B, D, and F) in the presence (●) or absence (○) of 3 μM compound 2 and in competition with the radiolabeled antagonist ¹²⁵I-exendin(9–39). Data are normalized to the maximum ¹²⁵I-exendin(9–39) binding of each individual data set, with nonspecific binding measured in the presence of 1 μM exendin(9–39). Data are analyzed with a three-parameter logistic equation as defined in eq. 1. All values are mean ± S.E.M. of three to four independent experiments conducted in duplicate.

Assessment of ligand binding revealed minimal effect of GLP-1R polymorphic variants on potency, with the exception of the Met¹⁴⁹ variant. It is noteworthy that the loss of peptide potency at this variant was limited to GLP-1(7–36)NH₂/GLP-1(7–37), exendin-4, and oxyntomodulin, with no observed effect on the antagonist exendin(9–39) [Beinborn et al., 2005; pIC₅₀ values of 8.0 and 8.1, *n* = 1 for the wild-type and Met¹⁴⁹ variant, respectively (data not shown)], full-length GLP-1 peptides, or compound 2 binding. These data are consistent with the critical involvement of amino acid 149 in activation transition of the receptor by peptide agonists, with the higher relative affinity of the truncated GLP-1 peptides, exendin-4, and oxyntomodulin linked to their ability to interact/induce an activated state of the receptor.

Consistent with previous data, the most detrimental of all polymorphisms that we studied was the Met¹⁴⁹ polymorphic

variant (Beinborn et al., 2005). This variant has previously been associated with a case of type II diabetes (Tokuyama et al., 2004) and a loss of binding affinity and cAMP potency in the presence of GLP-1(7–36)NH₂ and exendin-4 only (Beinborn et al., 2005). By performing similar binding and cAMP accumulation assays in the presence of all peptide agonists of the GLP-1R, we observed that the effect of the Met¹⁴⁹ polymorphic variant is ligand-dependent, with a greater effect on oxyntomodulin (251-fold decrease in binding affinity, >500-fold decrease in cAMP potency) relative to GLP-1(7–36)NH₂ (decreases of 251- and 158-fold in binding affinity and cAMP potency, respectively) or exendin-4 (decreases of 32- and 200-fold in binding affinity and cAMP potency, respectively). We also found that effects on signaling at this polymorphic variant are pathway-dependent, in that the loss of function was more pronounced in cAMP accumulation and Ca²⁺ mobilization than ERK1/2 phosphorylation. Intriguingly, both the binding and signaling responses to compound 2 were unaltered, providing supporting evidence for a distinct molecular mechanism for receptor activation from that of orthosteric-acting peptide agonists. In parallel, and perhaps most importantly, compound 2 retained its ability to modulate peptide-mediated binding and cAMP responses at the Met¹⁴⁹ polymorphic variant, indicating that there is potential for developing therapeutics to treat patients possessing polymorphic receptor variants that are refractory to peptide-mimetic therapy. The data from the Met¹⁴⁹ polymorphic variant is also informative, suggesting that the principal allosteric

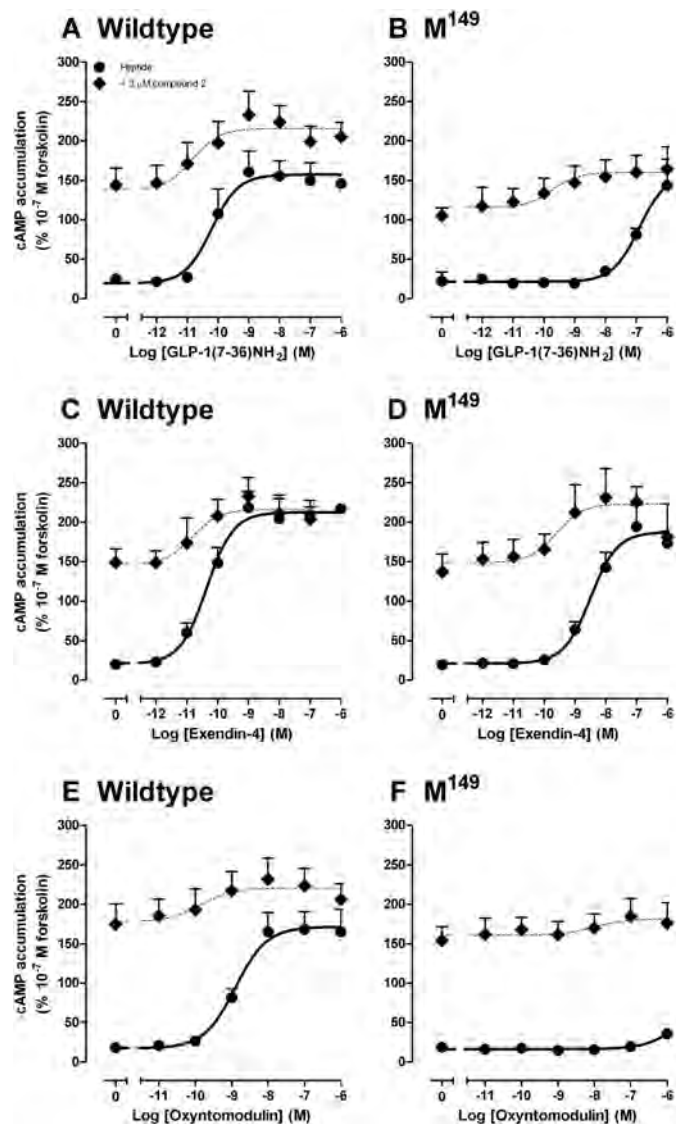


Fig. 7. Characterization of cAMP accumulation generated by GLP-1(7–36)NH₂ (A and B), exendin-4 (C and D), and oxyntomodulin (E and F) in FlpInCHO cells stably expressing the human GLP-1R wild-type (A, C, and E) or human GLP-1R Met¹⁴⁹ variant (B, D, and F) in the presence (◆) or absence (●) of 3 μM compound 2. Data are normalized to the response elicited by 100 nM forskolin and analyzed with a three-parameter logistic equation as defined in eq. 1. All values are mean ± S.E.M. of three to five independent experiments conducted in duplicate.

TABLE 7

Differential modulation of agonist binding at the human GLP-1R Met¹⁴⁹ receptor variant by compound 2

Data were analyzed using a three-parameter logistic equation as defined in eq. 1. pIC₅₀ values represent the negative logarithm of the concentration of agonist that inhibits binding of half the total concentration of radiolabeled antagonist, [¹²⁵I]-exendin(9–39). All data are normalized to the maximum [¹²⁵I]-exendin(9–39) binding in each individual data set, with non-specific binding measured in the presence of 1 μM exendin(9–39). All values are mean ± S.E.M. of three to four independent experiments, conducted in duplicate.

	pIC ₅₀			
	Wild Type		Met ¹⁴⁹	
	Peptide	+ 3 μM Compound 2	Peptide	+ 3 μM Compound 2
GLP-1(7–36)NH ₂	8.4 ± 0.1	8.9 ± 0.1*	6.4 ± 0.2	8.4 ± 0.2*
Exendin-4	8.9 ± 0.1	9.4 ± 0.1	7.6 ± 0.1	9.0 ± 0.2*
Oxyntomodulin	7.4 ± 0.1	8.5 ± 0.2*	6.0 ± 1.0	7.2 ± 0.3

* Statistically significant, *P* < 0.05 compared with peptide control, paired *t* test.

TABLE 8

Differential modulation of agonist peptides at the human GLP-1R Met¹⁴⁹ receptor variant by compound 2 in cAMP accumulation

Data were analyzed using a three-parameter logistic equation as defined in eq. 1. pEC₅₀ values represent the negative logarithm of the concentration of agonist that produces half the maximal response. All data are normalized to the response elicited by 10^{−7} M forskolin and are mean ± S.E.M. of three to five independent experiments, conducted in duplicate.

	pEC ₅₀			
	Wild Type		Met ¹⁴⁹	
	Peptide	+ 3 μM Compound 2	Peptide	+ 3 μM Compound 2
GLP-1(7–36)NH ₂	10.2 ± 0.3	10.8 ± 0.6	7.0 ± 0.2	9.7 ± 0.8*
Exendin-4	10.4 ± 0.2	10.8 ± 0.6	8.5 ± 0.2	9.6 ± 0.7†
Oxyntomodulin	8.9 ± 0.2	9.8 ± 1.0†	N.D.	N.D.

N.D., data unable to be experimentally defined or with incomplete curves.

* Statistically significant, *P* < 0.05 compared with peptide control, paired *t* test.

† *P* = 0.05 compared with peptide control, paired *t* test.

effect of compound 2 is to lower the energy barrier for activation transition, in particular with respect to the receptor conformation(s) linked to $G\alpha_s$ coupling. At the “wild-type” receptor, GLP-1(7–36)NH₂, GLP-1(7–37), and exendin-4 are all highly potent and efficacious peptide ligands, and addition of compound 2 has a limited effect on receptor binding and signaling output because the receptor is already in a highly active state. The weaker agonist, oxyntomodulin, which has a lower response in the system, however, was positively modulated to a greater extent by compound 2. At the Met¹⁴⁹ variant, our results suggest that there is a higher barrier to establish an active state transition as engaged by the peptide agonists. The addition of compound 2, which modifies the receptor in a manner that is insensitive to the Met¹⁴⁹ substitution, lowers the barrier to allow the recovery of the response, so that an active conformation can more readily be achieved. As also previously noted by Beinborn et al. (2005), the Met¹⁴⁹ polymorphic variant does not alter antagonist [exendin(9–39)] binding to the receptor. This is consistent with the involvement of residue 149 in an activation transition rather than directly disrupting peptide binding interactions.

The recovery of GLP-1(7–36)NH₂ and exendin-4 potency at the Met¹⁴⁹ polymorphic variant in cAMP accumulation to within 8-fold of the GLP-1R wild-type range provides an excellent example of the potential to rescue detrimental receptor polymorphisms with the application of allosteric ligands. Nonetheless, broad assessment of the impact of different GLP-1R polymorphisms on the allosteric potentiation of oxyntomodulin cAMP response indicated that multiple receptor variants had attenuated responses. Not surprisingly, the C³³³ variant had minimal allosteric response because this substitution also led to attenuation of cAMP signaling by compound 2, suggesting that it interferes with the ability of compound 2 to promote a $G\alpha_s$ -interacting conformation of the receptor; previous work has demonstrated a correlation between allosteric potentiation and the ability of compounds to promote an active state of the receptor (Leach et al., 2010; Keov et al., 2011). Intriguingly, the Leu⁷, Gln¹³¹, Ser¹⁶⁸, Leu²⁶⁰, Thr³¹⁶, and Gln⁴²¹ also exhibited attenuated allosteric enhancement of oxyntomodulin cAMP signaling in the presence of compound 2. The mechanistic basis for the loss of effect is unclear, but it highlights the potential complexity of the allosteric interaction between peptides and small molecule ligands. Although this effect is likely to be chemotype-dependent, it nonetheless highlights the need for careful consideration in clinical trial design where potential allosteric drugs are being assessed. In the case of the GLP-1R, at least one of the variants with loss of oxyntomodulin modulation, Leu⁷, is reported in the SwissProt database to occur in 40% of assessed populations in either homozygous or heterozygous form.

In conclusion, we have demonstrated important pharmacological effects arising from polymorphisms of the GLP-1R. For the Met¹⁴⁹ variant, this is likely to be clinically relevant, albeit for a small percentage of patients. Importantly, we have demonstrated that loss of function arising from polymorphisms such as the Met¹⁴⁹ substitution can be rescued by allosteric modulation of the receptor, with small molecule compounds providing scope for therapeutic intervention for patients whose disease is linked to such polymorphic variation.

Acknowledgments

We thank Prof. Roger Summers for helpful discussions on this work and Drs. Ron Osmond and Michael Crouch of TGR BioSciences (Hindmarsh, SA, Australia), who generously provided the SureFire ERK1/2 reagents.

Authorship Contributions

Participated in research design: Koole, Wootten, Simms, Christopoulos, and Sexton.

Conducted experiments: Koole.

Contributed new reagents or analytical tools: Valant.

Performed data analysis: Koole.

Wrote or contributed to writing of the manuscript: Koole, Wootten, Simms, Miller, Christopoulos, Sexton.

References

- Baggio LL and Drucker DJ (2007) Biology of incretins: GLP-1 and GIP. *Gastroenterology* **132**:2131–2157.
- Beinborn M, Worrall CI, McBride EW, and Kopin AS (2005) A human glucagon-like peptide-1 receptor polymorphism results in reduced agonist responsiveness. *Regul Pept* **130**:1–6.
- Deacon CF, Johnsen AH, and Holst JJ (1995a) Degradation of glucagon-like peptide-1 by human plasma in vitro yields an N-terminally truncated peptide that is a major endogenous metabolite in vivo. *J Clin Endocrinol Metab* **80**:952–957.
- Deacon CF, Nauck MA, Toft-Nielsen M, Pridal L, Willms B, and Holst JJ (1995b) Both subcutaneously and intravenously administered glucagon-like peptide I are rapidly degraded from the NH₂-terminus in type II diabetic patients and in healthy subjects. *Diabetes* **44**:1126–1131.
- DeFronzo RA (1992) Pathogenesis of type 2 (non-insulin dependent) diabetes mellitus: a balanced overview. *Diabetologia* **35**:389–397.
- Drucker DJ (2006) The biology of incretin hormones. *Cell Metab* **3**:153–165.
- Elbrønd B, Jakobsen G, Larsen S, Agersø H, Jensen LB, Rolan P, Sturis J, Hatorp V, and Zdravkovic M (2002) Pharmacokinetics, pharmacodynamics, safety, and tolerability of a single-dose of NN2211, a long-acting glucagon-like peptide 1 derivative, in healthy male subjects. *Diabetes Care* **25**:1398–1404.
- Fortin JP, Schroeder JC, Zhu Y, Beinborn M, and Kopin AS (2010) Pharmacological characterization of human incretin receptor missense variants. *J Pharmacol Exp Ther* **332**:274–280.
- Göke R, Fehmann HC, Linn T, Schmidt H, Krause M, Eng J, and Göke B (1993) Exendin-4 is a high potency agonist and truncated exendin(9–39)-amide an antagonist at the glucagon-like peptide 1 (7–36)-amide receptor of insulin-secreting beta-cells. *J Biol Chem* **268**:19650–19655.
- Jarrousse C, Audoussert-Puech MP, Dubrasquet M, Niel H, Martinez J, and Bataille D (1985) Oxyntomodulin (glucagon-37) and its C-terminal octapeptide inhibit gastric acid secretion. *FEBS Lett* **188**:81–84.
- Jarrousse C, Bataille D, and Jeanrenaud B (1984) A pure enteroglucagon, oxyntomodulin (glucagon 37), stimulates insulin release in perfused rat pancreas. *Endocrinology* **115**:102–105.
- Keov P, Sexton PM, and Christopoulos A (2011) Allosteric modulation of G protein-coupled receptors: a pharmacological perspective. *Neuropharmacology* **60**:24–35.
- Klinger S, Poussin C, Debril MB, Dolci W, Halban PA, and Thorens B (2008) Increasing GLP-1-induced beta-cell proliferation by silencing the negative regulators of signaling cAMP response element modulator-alpha and DUSP14. *Diabetes* **57**:584–593.
- Knudsen LB, Kiel D, Teng M, Behrens C, Bhumralkar D, Kodra JT, Holst JJ, Jeppesen CB, Johnson MD, de Jong JC, et al. (2007) Small-molecule agonists for the glucagon-like peptide 1 receptor. *Proc Natl Acad Sci USA* **104**:937–942.
- Knudsen LB, Nielsen PF, Huusfeldt PO, Johansen NL, Madsen K, Pedersen FZ, Thøgersen H, Wilken M, and Agersø H (2000) Potent derivatives of glucagon-like peptide-1 with pharmacokinetic properties suitable for once daily administration. *J Med Chem* **43**:1664–1669.
- Koole C, Wootten D, Simms J, Valant C, Sridhar R, Woodman OL, Miller LJ, Summers RJ, Christopoulos A, and Sexton PM (2010) Allosteric ligands of the glucagon-like peptide 1 receptor (GLP-1R) differentially modulate endogenous and exogenous peptide responses in a pathway-selective manner: implications for drug screening. *Mol Pharmacol* **78**:456–465.
- Leach K, Loiacono RE, Felder CC, McKinzie DL, Mogg A, Shaw DB, Sexton PM, and Christopoulos A (2010) Molecular mechanisms of action and in vivo validation of an M4 muscarinic acetylcholine receptor allosteric modulator with potential antipsychotic properties. *Neuropsychopharmacology* **35**:855–869.
- May LT, Avlani VA, Langmead CJ, Herdon HJ, Wood MD, Sexton PM, and Christopoulos A (2007) Structure-function studies of allosteric agonism at M2 muscarinic acetylcholine receptors. *Mol Pharmacol* **72**:463–476.
- Nauck MA, Klein N, Orskov C, Holst JJ, Willms B, and Creutzfeldt W (1993) Normalization of fasting hyperglycaemia by exogenous glucagon-like peptide 1 (7–36 amide) in type 2 (non-insulin-dependent) diabetic patients. *Diabetologia* **36**:741–744.
- Quoyer J, Longuet C, Broca C, Linck N, Costes S, Varin E, Bockaert J, Bertrand G, and Dalle S (2010) GLP-1 mediates anti-apoptotic effect by phosphorylating Bad through a beta-arrestin 1-mediated ERK1/2 activation in pancreatic beta-cells. *J Biol Chem* **285**:1989–2002.
- Teng M, Johnson MD, Thomas C, Kiel D, Lakis JN, Kercher T, Aytes S, Kostrowicki J, Bhumralkar D, Truesdale L, et al. (2007) Small molecule ago-allosteric modu-

- lators of the human glucagon-like peptide-1 (hGLP-1) receptor. *Bioorg Med Chem Lett* **17**:5472–5478.
- Toft-Nielsen MB, Damholt MB, Madsbad S, Hilsted LM, Hughes TE, Michelsen BK, and Holst JJ (2001) Determinants of the impaired secretion of glucagon-like peptide-1 in type 2 diabetic patients. *J Clin Endocrinol Metab* **86**:3717–3723.
- Tokuyama Y, Matsui K, Egashira T, Nozaki O, Ishizuka T, and Kanatsuka A (2004) Five missense mutations in glucagon-like peptide 1 receptor gene in Japanese population. *Diabetes Res Clin Pract* **66**:63–69.

Werry TD, Gregory KJ, Sexton PM, and Christopoulos A (2005) Characterization of serotonin 5-HT_{2C} receptor signaling to extracellular signal-regulated kinases 1 and 2. *J Neurochem* **93**:1603–1615.

Address correspondence to: Prof. Patrick M. Sexton, Drug Discovery Biology, Monash Institute of Pharmaceutical Sciences, Monash University, 381 Royal Parade, Parkville, Victoria 3052, Australia. E-mail: patrick.sexton@monash.edu

Correction to “Polymorphism and Ligand Dependent Changes in Human Glucagon-Like Peptide-1 Receptor (GLP-1R) Function: Allosteric Rescue of Loss of Function Mutation”

In the above article [Koole C, Wootten D, Simms J, Valant C, Miller LJ, Christopoulos A, and Sexton PM (2011) *Mol Pharmacol* **80**:486–497], acknowledgment of funding from the National Institutes of Health National Institute of Diabetes and Digestive and Kidney Diseases [Grant DK46577] was omitted.

The authors regret this error and apologize for any confusion and inconvenience it may have caused.

Koole et al., *Polymorphism and ligand dependent changes in human glucagon-like peptide-1 receptor (GLP-1R) function: allosteric rescue of loss of function mutation*. **Molecular Pharmacology**

SI Table S1. Summary of the oligonucleotides used in this study. Oligonucleotides were designed for use with the QuikChange site-directed mutagenesis kit (Stratagene) to generate polymorphisms into the human GLP-1R. Bold italicized characters denote nucleotides at which the mutations were introduced.

Polymorphism	Oligonucleotide orientation	Oligonucleotide sequence (5'-3')
L ⁷	forward	GCCCCCGGCC T GCTGCGCCTTG
	reverse	CAAGGCGCAGCAGGCCGGGGGC
K ²⁰	forward	GATGGTGGGCAAGGCCGGCCCC
	reverse	GGGGCCGGCC T TGCCCAACCATC
H ⁴⁴	forward	GAGAATACCGACACCAAGTGCCAGCG
	reverse	CGCTGGCACTGG T GTCGGTATTCTC
Q ¹³¹	forward	GAGGAGTCCAAGCAGGGGGAGAGAAGC
	reverse	GCTTCTCTCCCC T GCTTGGAATCCTC
M ¹⁴⁹	forward	CTACATCATCTACATGGTGGGCTACGCAC
	reverse	GTGCGTAGCCCACCATGTAGATGATGTAG
S ¹⁶⁸	forward	GCGATCCTCCTCAGCTTCAGACACC
	reverse	GGTGTCTGAAGC T GAGGAGGATCGC
L ²⁶⁰	forward	CTGGCCTTCTCGGTCC T GTCTGAGCAATGGATC
	reverse	GATCCATTGCTCAGACAGGACCGAGAAGGCCAG
T ³¹⁶	forward	CTGCCCATTCTCTTTACCATTTGGGGTGAAC
	reverse	GTTCACCCCAATGG T AAAGAGAATGGGCAG
C ³³³	forward	CTGCATCGTGGTATGCAAACTGAAGGCC
	reverse	GGCCTTCAGTTTGCAACACGATGCAG
Q ⁴²¹	forward	GGGAGCGCTGGCAGCTTGAGCACTTG
	reverse	CAAGTGCTCAAGC T GCCAGCGCTCCC

Signal Transduction:
Second Extracellular Loop of Human
Glucagon-like Peptide-1 Receptor
(GLP-1R) Has a Critical Role in GLP-1
Peptide Binding and Receptor Activation



Cassandra Koole, Denise Wootten, John
Simms, Laurence J. Miller, Arthur
Christopoulos and Patrick M. Sexton
J. Biol. Chem. 2012, 287:3642-3658.
doi: 10.1074/jbc.M111.309328 originally published online December 6, 2011

Access the most updated version of this article at doi: [10.1074/jbc.M111.309328](https://doi.org/10.1074/jbc.M111.309328)

Find articles, minireviews, Reflections and Classics on similar topics on the [JBC Affinity Sites](https://www.jbc.org/).

Alerts:

- [When this article is cited](#)
- [When a correction for this article is posted](#)

[Click here](#) to choose from all of JBC's e-mail alerts

Supplemental material:

<http://www.jbc.org/content/suppl/2011/12/06/M111.309328.DC1.html>

This article cites 80 references, 49 of which can be accessed free at
<http://www.jbc.org/content/287/6/3642.full.html#ref-list-1>

Second Extracellular Loop of Human Glucagon-like Peptide-1 Receptor (GLP-1R) Has a Critical Role in GLP-1 Peptide Binding and Receptor Activation^{*[S]}

Received for publication, September 30, 2011, and in revised form, November 29, 2011. Published, JBC Papers in Press, December 6, 2011, DOI 10.1074/jbc.M111.309328

Cassandra Koole[‡], Denise Wootten[‡], John Simms[‡], Laurence J. Miller[§], Arthur Christopoulos^{‡1}, and Patrick M. Sexton^{‡2}

From the [‡]Drug Discovery Biology, Monash Institute of Pharmaceutical Sciences and Department of Pharmacology, Monash University, Parkville, Victoria 3052, Australia and the [§]Department of Molecular Pharmacology and Experimental Therapeutics, Mayo Clinic, Scottsdale, Arizona 85259

Background: The ECL2 of family B GPCRs has been suggested to contribute to biological activity.

Results: Mutation of most ECL2 residues to alanine results in changes in binding and/or efficacy of GLP-1 peptide agonists.

Conclusion: The ECL2 of the GLP-1R is critical for GLP-1 peptide-mediated receptor activation and selective signaling.

Significance: This work reveals broad significance for ECL2 in maintaining receptor conformations driving selective signaling.

The glucagon-like peptide-1 receptor (GLP-1R) is a therapeutically important family B G protein-coupled receptor (GPCR) that is pleiotropically coupled to multiple signaling effectors and, with actions including regulation of insulin biosynthesis and secretion, is one of the key targets in the management of type II diabetes mellitus. However, there is limited understanding of the role of the receptor core in orthosteric ligand binding and biological activity. To assess involvement of the extracellular loop (ECL) 2 in ligand-receptor interactions and receptor activation, we performed alanine scanning mutagenesis of loop residues and assessed the impact on receptor expression and GLP-1(1–36)-NH₂ or GLP-1(7–36)-NH₂ binding and activation of three physiologically relevant signaling pathways as follows: cAMP formation, intracellular Ca²⁺ (Ca²⁺_i) mobilization, and phosphorylation of extracellular signal-regulated kinases 1 and 2 (pERK1/2). Although antagonist peptide binding was unaltered, almost all mutations affected GLP-1 peptide agonist binding and/or coupling efficacy, indicating an important role in receptor activation. However, mutation of several residues displayed distinct pathway responses with respect to wild type receptor, including Arg-299 and Tyr-305, where mutation significantly enhanced both GLP-1(1–36)-NH₂- and GLP-1(7–36)-NH₂-mediated signaling bias for pERK1/2. In addition, mutation of Cys-296, Trp-297, Asn-300, Asn-302, and Leu-307 significantly increased GLP-1(7–36)-NH₂-mediated signaling bias toward pERK1/2. Of all mutants studied, only mutation of Trp-306 to alanine abolished all biological activity. These data suggest a critical role of ECL2 of the GLP-1R in the activation

transition(s) of the receptor and the importance of this region in the determination of both GLP-1 peptide- and pathway-specific effects.

GPCRs³ are the largest family of transmembrane (TM)-spanning proteins, accounting for ~1% of the human genome, and are the leading target of marketed therapeutics (1, 2). Family B peptide hormone receptors are a small subfamily of GPCRs that include receptors for secretin, calcitonin, vasoactive intestinal polypeptide, pituitary adenylate cyclase-activating polypeptide, corticotrophin-releasing factor, parathyroid hormone, gastric inhibitory polypeptide, glucagon, and glucagon-like peptides (GLPs). Each receptor possesses a characteristically large and sequence-divergent extracellular N-terminal domain; however, there is conservation of key residues, including three disulfide bonds within this domain, that aids in stability and confers similarities in secondary structure (3, 4). The widely accepted peptide-receptor binding model for family B GPCRs is the two domain model, whereby the α -helical C terminus of the endogenous ligand interacts with the N-terminal domain of the receptor, and the N terminus of the peptide interacts with the core domain of the receptor, which includes both the extracellular loops and TM bundle (5–7). Generically, the N-terminal domain of the receptor is primarily responsible for ligand recognition and specificity, whereas the core of the receptor has a major influence in signaling specificity and transmission (8). Indeed, there is evidence through generation of both chimeric receptors and peptides to suggest that this is true for many family B receptors (9–16). However, there is also evidence that ligand recognition and affinity determination can rely on interaction with the receptor core (14, 17–24); this is particularly evident with the glucagon receptor, where changes in the N terminus of the glucagon peptide significantly alter its binding affinity at the glucagon receptor (17, 25, 26). In addition, sub-

^{*} This work was supported in part by the National Health and Medical Research Council of Australia Project Grant 1002180 and Program Grant 519461 and by National Health and Medical Research Council Principal Research Fellowship (to P. M. S.) and a Senior Research Fellowship (to A. C.).

[S] This article contains supplemental Table S1 and Fig. S1.

¹ Senior Research Fellow of the National Health and Medical Research Council.

² Principal Research Fellow of the National Health and Medical Research Council. To whom correspondence should be addressed: Drug Discovery Biology, Monash Institute of Pharmaceutical Sciences, Monash University, 381 Royal Parade, Parkville, Victoria 3052, Australia. Tel.: 3-9903-9069; Fax: 3-9903-9581; E-mail: Patrick.Sexton@monash.edu.

³ The abbreviations used are: GPCR, G protein-coupled receptor; ECL, extracellular loop; GLP-1R, glucagon-like peptide 1 receptor; Ca²⁺_i, intracellular calcium; TM, transmembrane.

stitution of many N-terminal residues of the GLP-1, vasoactive intestinal polypeptide, and secretin peptides for alanine significantly reduce binding affinity at the GLP-1R, VPAC receptors, and secretin receptor, respectively (21, 23, 24), illustrating that effective ligand recognition, binding, and subsequent biological activity require the entire length of peptide and involve multiple domains within the receptor.

Although crystal and NMR structures have been resolved for the isolated N terminus of several ligand-bound family B GPCRs, including the gastric inhibitory polypeptide receptor (27), corticotrophin-releasing factor receptors (28–30), parathyroid hormone 1 receptor (31), and GLP-1 R (32, 33), only limited mutagenesis and photoaffinity labeling data are available to aid in understanding the role of core domain residues. Nevertheless, the data available highlight the significance of the receptor core region in both peptide binding and receptor activation (34, 35), including residues within the putative ECL2 of the GLP-1R (36, 37), secretin receptor (18), corticotrophin-releasing factor receptors (38, 39), and parathyroid hormone receptors (16), suggesting this potentially forms a significant site of interaction for the N-terminal amino acids of the peptide ligands and/or plays an important role in stabilizing active state conformations in the presence of ligand.

Like most GPCRs, family B receptors are promiscuously coupled, including pathway coupling that leads to cAMP signaling, Ca^{2+} mobilization, and pERK1/2, each of which is linked to important physiological functions of the receptors (40–42). The relative activation of these signaling pathways may therefore be important for optimal development of therapeutics. Nonetheless, our mechanistic understanding of how family B receptors activate these distinct pathways is limited.

In this study, we explore the influence of individual ECL2 residues on human GLP-1R function. The GLP-1R is an important target in the development of therapeutics for type II diabetes mellitus, with actions including glucose-dependent increases in insulin biosynthesis and secretion, increasing β -cell mass, and decreasing body mass, all effects that address major symptoms of type II diabetes mellitus (43). Despite its therapeutic promise, relatively limited data are available on the contribution of domains in the receptor core on ligand binding and receptor activation. We have performed systematic substitution of each residue of ECL2 of the human GLP-1R by alanine and assessed the effects across a series of pharmacological outputs, which demonstrated critical residues for receptor activation that vary in an agonist peptide- or pathway-specific manner.

EXPERIMENTAL PROCEDURES

Materials—Dulbecco's modified Eagle's medium (DMEM), hygromycin-B, and Fluo-4 acetoxymethyl ester were purchased from Invitrogen. Fetal bovine serum (FBS) was purchased from Thermo Fisher Scientific (Melbourne, Victoria, Australia). The QuikChangeTM site-directed mutagenesis kit was purchased from Stratagene (La Jolla, CA). AlphaScreenTM reagents, Bolton-Hunter reagent (¹²⁵I), and 384-well ProxiPlates were purchased from PerkinElmer Life Sciences. SureFireTM ERK1/2 reagents were generously supplied by TGR Biosciences (Adelaide, South Australia, Australia). SigmaFast o-phenylene-

diamine dihydrochloride tablets and antibodies were purchased from Sigma. GLP-1 peptides were purchased from American Peptide (Sunnyvale, CA). All other reagents were purchased from Sigma or Merck and were of an analytical grade.

Receptor Mutagenesis—To study the influence of specific amino acids of ECL2 on receptor function, the desired mutations were introduced to an N-terminally double c-Myc-labeled wild type human GLP-1R in the pEF5/FRT/V5-DEST destination vector (Invitrogen); this receptor had equivalent pharmacology to the untagged human GLP-1R (data not shown). Mutagenesis was carried out using oligonucleotides for site-directed mutagenesis from GeneWorks (Hindmarsh, South Australia, Australia) (supplemental Table S1) and the QuikChangeTM site-directed mutagenesis kit (Stratagene). Sequences of receptor clones were confirmed by cycle sequencing as described previously (44). Mutated residues and their conservation across human family B peptide hormone receptors are illustrated in Fig. 1.

Transfections and Cell Culture—Wild type and mutant human GLP-1R were isogenically integrated into FlpIn-Chinese hamster ovary (FlpInCHO) cells (Invitrogen) and selection of receptor-expressing cells accomplished by treatment with 600 $\mu\text{g ml}^{-1}$ hygromycin-B as described previously (44). Transfected and parental FlpInCHO cells were maintained in DMEM supplemented with 10% heat-inactivated FBS and incubated in a humidified environment at 37 °C in 5% CO_2 .

Radioligand Binding Assay—FlpInCHO wild type and mutant human GLP-1R cells were seeded at a density of 3×10^4 cells/well into 96-well culture plates and incubated overnight at 37 °C in 5% CO_2 , and radioligand binding was carried out as described previously (45). For each cell line in all experiments, total binding was defined by 0.5 nM [¹²⁵I]-exendin(9–39) alone, and nonspecific binding was defined by 1 μM exendin(9–39). For analysis, data are normalized to the B_0 value for each individual experiment.

cAMP Accumulation Assay—FlpInCHO wild type and mutant human GLP-1R cells were seeded at a density of 3×10^4 cells/well into 96-well culture plates and incubated overnight at 37 °C in 5% CO_2 , and cAMP detection was carried out as described previously (46). All values were converted to concentration of cAMP using a cAMP standard curve performed in parallel, and data were subsequently normalized to the response of 100 μM forskolin in each cell line.

pERK1/2 Assay—FlpInCHO wild type and mutant human GLP-1R cells were seeded at a density of 3×10^4 cells/well into 96-well culture plates and incubated overnight at 37 °C in 5% CO_2 . Receptor-mediated pERK1/2 was determined using the AlphaScreenTM ERK1/2 SureFireTM protocol as described previously (44). Initial pERK1/2 time course experiments were performed over 1 h to determine the time at which agonist-mediated pERK1/2 was maximal. Subsequent experiments were then performed at the time required to generate a maximal pERK1/2 response (6 min). Data were normalized to the maximal response elicited by 10% FBS in each cell line, determined at 6 min (peak FBS response).

Ca^{2+} Mobilization Assay—FlpInCHO wild type and mutant human GLP-1R cells were seeded at a density of 3×10^4 cells/

GLP-1R ECL2 Is Critical for Receptor Activation

well into 96-well culture plates and incubated overnight at 37 °C in 5% CO₂, and receptor-mediated Ca²⁺_i mobilization was determined as described previously (47). Fluorescence was determined immediately after peptide addition, with an excitation wavelength set to 485 nm and an emission wavelength set to 520 nm, and readings were taken every 1.36 s for 120 s. Peak magnitude was calculated using five-point smoothing, followed by correction against basal fluorescence. The peak value was used to create concentration-response curves. Data were normalized to the maximal response elicited by 100 μM ATP.

Cell Surface Receptor Expression—FlpInCHO wild type and mutant human GLP-1R cells, with receptor DNA previously incorporated with an N-terminal double c-Myc epitope label, were seeded at a density of 25 × 10⁴ cells/well into 24-well culture plates and incubated overnight at 37 °C in 5% CO₂, washed three times in 1 × PBS, and fixed with 3.7% paraformaldehyde at 4 °C for 15 min. Cell surface receptor detection was then performed as described previously (45). Data were normalized to the basal fluorescence detected in FlpInCHO parental cells. Specific ¹²⁵I-exendin(9–39) binding at each receptor mutant, as identification of functional receptors at the cell surface, was also determined (corrected for nonspecific binding using 1 μM exendin(9–39)).

Data Analysis—All data were analyzed using Prism 5.04 (GraphPad Software Inc., San Diego). For all analyses the data are unweighted, and each *y* value (mean of replicates for each individual experiment) is considered an individual point. Concentration response signaling data were analyzed using a three-parameter logistic equation as described previously (44) and as shown in Equation 1,

$$Y = \text{Bottom} + \frac{(\text{Top} - \text{Bottom})}{1 + 10^{(\log EC_{50} - \log[A])}} \quad (\text{Eq. 1})$$

where Bottom represents the *y* value in the absence of ligand(s); Top represents the maximal stimulation in the presence of ligand(s); [A] is the molar concentration of ligand, and EC₅₀ represents the molar concentration of ligand required to generate a response halfway between Top and Bottom. Similarly, Equation 1 was used in the analysis of inhibition binding data, instead replacing EC₅₀ with IC₅₀. In this case, Bottom defines the specific binding of the radioligand that is equivalent to non-specific ligand binding, whereas Top defines radioligand binding in the absence of a competing ligand, and the IC₅₀ value represents the molar concentration of ligand required to generate a response halfway between Top and Bottom. IC₅₀ values obtained were then corrected for radioligand occupancy as described previously (48) using the radioligand affinity (*K*_i) experimentally determined for each mutant.

To quantify efficacy in the system, all data were fitted with an operational model of agonism (49) as shown in Equation 2,

$$Y = \text{Bottom} + \frac{E_m - \text{Bottom}}{1 + ((10^{\log K_A}) + (10^{\log[A]})) / (10^{\log \tau + \log[A]})} \quad (\text{Eq. 2})$$

where Bottom represents the *y* value in the absence of ligand(s); *E_m* represents the maximal stimulation of the system; *K_A* is the

agonist-receptor dissociation constant, in molar concentration; [A] is the molar concentration of ligand, and *τ* is the operational measure of efficacy in the system, which incorporates signaling efficacy and receptor density. Constraints for this model were determined by fitting the operational model for a partial agonist to each of the peptides at the wild type receptor, with the most efficacious peptide fitted with Equation 3,

$$Y = \text{Bottom} + \frac{E_m - \text{Bottom}}{1 + 10^{(\log EC_{50} - \log[A])}} \quad (\text{Eq. 3})$$

and the less efficacious peptides were fitted with Equation 2, to obtain a value for the system maximum (*E_m*) at the wild type receptor. This value was then globally constrained in the operational model (Equation 2) when applied at each of the mutant receptors. All estimated *τ* values were then corrected to cell surface expression (*τ_c*) as determined by specific ¹²⁵I-exendin(9–39) binding, and errors were propagated from both *τ* and cell surface expression. Changes in *τ_c* with respect to wild type for each mutant were used to generate correlation plots, which were subsequently fitted with linear regression and outliers established at greater than three standard deviations from regression.

To quantify signaling bias, peptide agonist concentration-response curves were analyzed with nonlinear regression using an operational model of agonism (50), but modified to directly estimate the ratio of *τ_c/K_A*, in a manner similar to that described by Figueroa *et al.* (51). For each pathway, as shown in Equation 4,

$$Y = \frac{E_{\max} \times (\tau_c/K_A)^n \times [A]^n}{[A]^n \times (\tau_c/K_A)^n + (1 + [A]/K_A)^n} \quad (\text{Eq. 4})$$

the parameters are as defined for Equation 2. All estimated *τ_c/K_A* ratios included propagation of error for both *τ_c* and *K_A*. Changes in *τ_c/K_A* ratios with respect to wild type of each mutant were used to quantitate bias between signaling pathways. Accordingly, bias factors included propagation of error from *τ_c/K_A* ratios of each pathway.

Data were also normalized to maximal agonist response at the wild type receptor in each signaling pathway, fitted with a three-parameter logistic equation, and equimolar concentrations of agonists in each pathway plotted against one other. In this way, the bias of any given agonist for one pathway over another can be visualized (50). In all cases, individual data sets were unweighted during the analyses.

Statistics—Changes in peptide affinity, potency, efficacy, and cell surface expression of ECL2 mutants in comparison with wild type control were statistically analyzed with one-way analysis of variance and Dunnett's post test, and significance was accepted at *p* < 0.05.

RESULTS

Cell Surface Expression of Human GLP-1R ECL2 Alanine Mutants

Wild type c-Myc human GLP-1R and each of the human GLP-1R ECL2 alanine mutants (Fig. 1A) were isogenically integrated into FlpInCHO host cells by recombination, allowing the

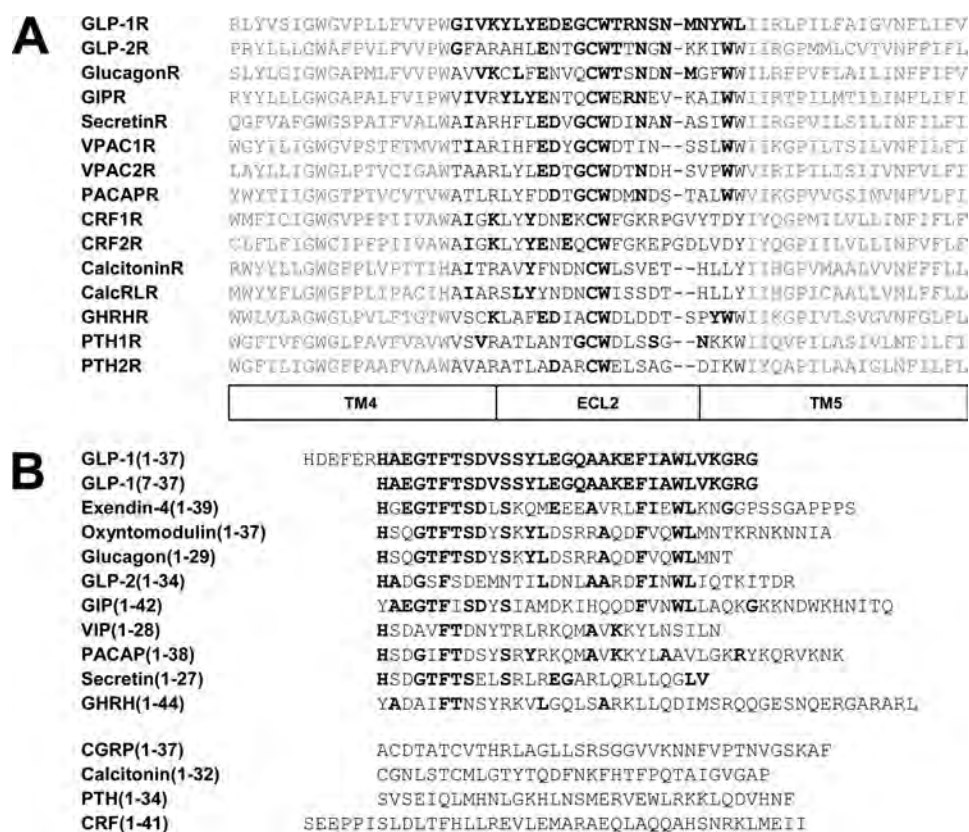


FIGURE 1. **Amino acid sequence alignments.** A, alignments of putative ECL2 of human family B GPCRs, with absolute conservation of residues with respect to human GLP-1R, are highlighted in **boldface**, and putative TM/ECL2 boundaries are indicated; B, human family B peptides, with absolute conservation of residues with respect to human GLP-1 peptide, are highlighted in **boldface**.

comparison of cell surface expression by antibody detection of the N-terminal double c-Myc epitope label without complications arising from variations in gene transcription. In this study, we observed total abolishment of cell surface receptor expression of the W306A mutant (Fig. 2A and Table 1). Significant increases in cell surface receptor antibody labeling were observed for the N300A and M303A mutants, although decreases were observed for D293A, C296A, W297A, S301A, N304A, Y305A, and L307A. No other mutant deviated significantly in cell surface receptor antibody labeling in comparison with wild type, although there were occasional trends for increases or decreases. In most cases, the changes in cell surface expression identified through antibody detection of the epitope label were consistent with the pattern of specific binding of 125 I-exendin(9–39) at each of the mutant receptors in comparison with wild type receptor, although generically the 125 I-exendin(9–39) binding trended lower for the mutants relative to the wild type, when compared with receptor antibody labeling (Fig. 2B and Table 1). Notable exceptions to this were E294A and T298A that demonstrated increased 125 I-exendin(9–39) binding but wild type levels of receptor antibody labeling and Y305A that displayed wild type levels of 125 I-exendin(9–39) binding and reduced antibody labeling. At each of these receptor mutants, the affinity of exendin(9–39) (determined through homologous competition binding) was not significantly different from the wild type receptor (Table 1). As exendin(9–39) affinity was unaltered at all mutant receptors, reductions in 125 I-exendin(9–39) binding but not antibody

labeling may suggest a subpopulation of receptors for which the ligand binding domain of the receptor is misfolded, leading to loss of functional receptors at the cell surface. In these cases, however, antibody detection of the inserted epitope tag does not discriminate between different conformational states of the ligand binding domain and therefore has most likely detected all populations of receptor at the cell surface. The mechanism underlying high 125 I-exendin(9–39) in the absence of changes to antibody labeling is less clear but may be due to altered conformation of the c-Myc epitope or an increase in the relative proportion of receptors in an inactive state.

Select Mutants of the Human GLP-1R ECL2 Influence GLP-1(7–36)-NH₂ Binding Affinity but Not Exendin(9–39) Affinity

To establish the binding profiles of each of the human GLP-1R ECL2 alanine mutants, equilibrium binding studies were performed with the endogenous peptide agonists GLP-1(1–36)-NH₂ and GLP-1(7–36)-NH₂ in competition with the radiolabeled orthosteric antagonist, 125 I-exendin(9–39). There was no significant deviation in antagonist exendin(9–39) affinity at any of the mutated ECL2 residues, with the exception of the W306A mutant, where no value could be defined as it was undetectable at the cell surface (Table 1).

Full inhibition curves for the GLP-1(1–36)-NH₂ peptide could not be established over the concentration range tested; at the highest concentration assayed (1 μ M), the level of binding inhibition for most of the mutants was not significantly different from wild type receptor (Fig. 3, A and B). However, no clear

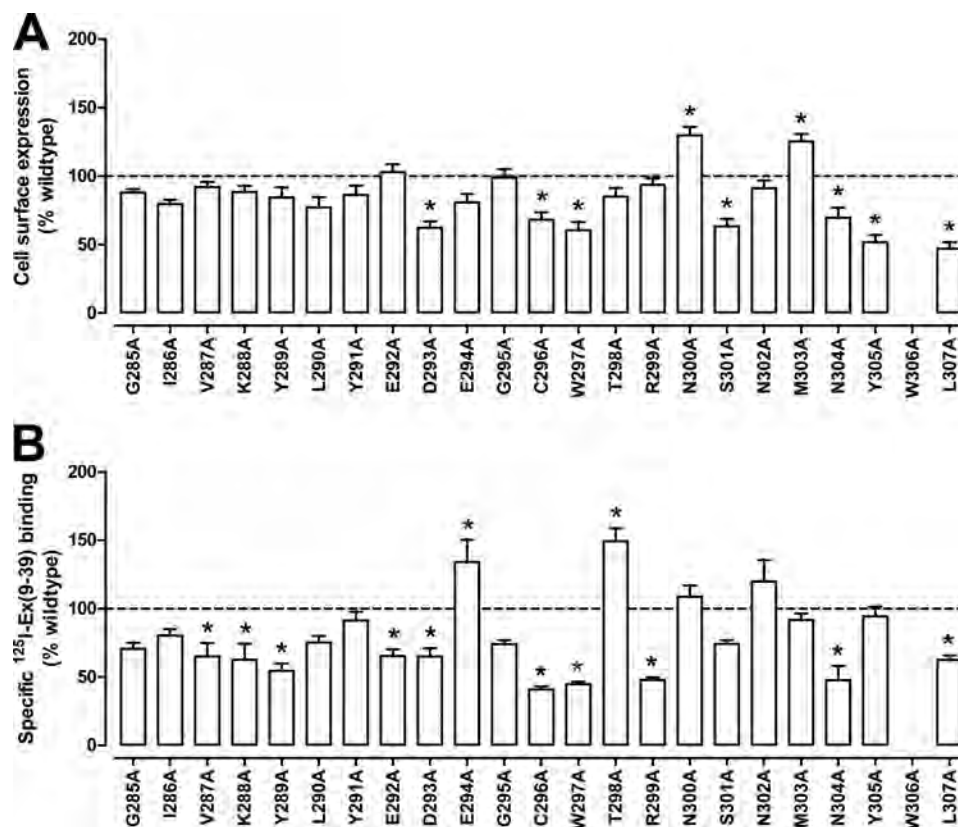


FIGURE 2. Cell surface expression profiles of human GLP-1R ECL2 alanine mutants. Cell surface expression profiles of each of the human GLP-1R ECL2 alanine mutants are compared with wild type stably transfected into FlpInCHO cells as determined through antibody detection of the N-terminal c-Myc epitope label (A) and by specific ¹²⁵I-exendin(9–39) binding (B). Statistical significance of changes in total cell surface expression in comparison with wild type human GLP-1R expression (100%) was determined by one-way analysis of variance and Dunnett's post-test and are indicated with an asterisk (*, $p < 0.05$). All data are means \pm S.E. of seven to nine or three to four independent experiments conducted in duplicate for antibody detection and specific ¹²⁵I-exendin(9–39) binding, respectively.

effect on binding was observed for C296A, W297A, R299A, and Y305A (Fig. 3, A and B). This was likely a result of the poor radioligand binding window for these mutants arising from the low specific ¹²⁵I-exendin(9–39) binding (Table 1).

There were no significant changes in affinity of GLP-1(7–36)-NH₂ in comparison with the wild type control for G285A, I286A, V287A, Y289A, L290A, Y291A, E294A, G295A, T298A, S301A, and N304A (Table 1). Decreases in binding affinity of GLP-1(7–36)-NH₂ in comparison with wild type were observed for K288A, E292A, D293A, R299A, N300A, N302A, M303A, Y305A, and L307A mutants, as highlighted by gray shading in Table 1 (Fig. 3, C and D, and Table 1).

Effect of Human GLP-1R ECL2 Alanine Mutations on Peptide-mediated cAMP Accumulation

Binding Affinity-modified Mutants—There was no measurable GLP-1(1–36)-NH₂-mediated cAMP response at the K288A, E292A, C296A, W297A or N300A mutants, and significant depression in E_{\max} was observed at the D293A, R299A, N302A, M303A, Y305A, and L307A mutants (Fig. 4A and Table 2). Application of the operational model indicated that each of these mutant receptors had a significantly reduced coupling efficiency for cAMP, after correction for functional cell surface receptor levels (Fig. 4, A and E, and Table 2). Throughout the results, the operational measure of efficacy (τ_e) is used as the principal measure of changes in efficacy for each pathway, as

this accounts for both alterations in coupling efficiency and cell surface receptor expression (50).

All mutants displaying significantly decreased GLP-1(7–36)-NH₂ binding affinity (K288A, E292A, D293A, C296A, W297A, R299A, N300A, N302A, M303A, Y305A, and L307A) also exhibited reduced potency for cAMP in response to this peptide, although this was not significant for the M303A mutant (Fig. 4B and Table 2). Assessment of the effect on efficacy indicated that all mutants also had diminished coupling efficiency in addition to decreased affinity, although this effect was minimal for D293A, C296A, and Y305A, where statistical significance was not reached (Fig. 4, B and F, and Table 2). Not surprisingly, cells expressing the W306A mutant did not respond to peptide stimulation (Table 2).

Mutants with Unaltered Binding Affinity—For mutants that were not affected at the level of peptide agonist binding, potency was mostly unaltered with two exceptions as follows: the V287A mutant, where decreased potency of GLP-1(7–36)-NH₂ was observed, and the T298A mutant that had increased potency of GLP-1(7–36)-NH₂ (Fig. 4D and Table 2). For the latter, the increased potency was paralleled by higher expression of functional cell surface receptors (Fig. 1B) but was accompanied by reduced efficacy (Fig. 4F and Table 2). Interestingly, the loss of potency at the V287A mutant occurred in the absence of significant changes in efficacy, for either the

TABLE 1**Effects of human GLP-1R ECL2 alanine mutants on peptide ligand binding and cell surface expression**

Binding data were analyzed using a three-parameter logistic equation as defined in Equation 1 to obtain pIC_{50} values. pIC_{50} values were then corrected for radioligand occupancy using the radioligand dissociation constant for each mutant, allowing determination of ligand affinity (K_d). Data are normalized to maximum ^{125}I -exendin(9–39) binding in the absence of ligand, with nonspecific binding measured in the presence of $1 \mu M$ exendin(9–39). For specific ^{125}I -exendin(9–39) binding, data are expressed as a maximum of specific ^{125}I -exendin(9–39) binding at the wild type human GLP-1R. Cell surface expression was determined through antibody detection of the N-terminal c-Myc epitope label, with data expressed as a maximum of wild type human GLP-1R expression. All values are expressed as means \pm S.E. of three to four (binding) or seven to nine (cell surface expression) independent experiments, conducted in duplicate. Data were analyzed with one-way analysis of variance and Dunnett's post test. Gray shading highlights residues affecting peptide agonist binding affinity. ND means data were unable to be experimentally defined.

	Binding (pK_d)**		Cell surface expression (% wildtype)	Specific ^{125}I -exendin(9–39) binding (% wildtype)
	GLP-1(7–36)NH ₂	Exendin(9–39)		
Wildtype	8.7 \pm 0.1	7.7 \pm 0.1	100 \pm 6	100 \pm 2
G285A	9.1 \pm 0.1	7.7 \pm 0.1	88 \pm 3	70 \pm 4
I286A	8.8 \pm 0.1	7.7 \pm 0.2	79 \pm 3	80 \pm 5
V287A	8.5 \pm 0.1	7.7 \pm 0.1	92 \pm 4	65 \pm 10*
K288A	6.6 \pm 0.3*	8.0 \pm 0.1	88 \pm 5	62 \pm 12*
Y289A	8.9 \pm 0.1	7.6 \pm 0.2	84 \pm 7	55 \pm 5*
L290A	8.3 \pm 0.1	7.7 \pm 0.1	77 \pm 7	75 \pm 5
Y291A	8.3 \pm 0.1	7.8 \pm 0.1	86 \pm 7	91 \pm 7
E292A	6.7 \pm 0.2*	7.7 \pm 0.1	103 \pm 6	65 \pm 5*
D293A	7.3 \pm 0.1*	7.9 \pm 0.1	62 \pm 5*	65 \pm 6*
E294A	8.8 \pm 0.1	8.0 \pm 0.1	81 \pm 6	134 \pm 16*
G295A	8.7 \pm 0.1	7.7 \pm 0.1	99 \pm 6	74 \pm 3
C296A	7.6 \pm 0.4*	7.6 \pm 0.2	68 \pm 5*	41 \pm 2*
W297A	6.9 \pm 0.5*	7.9 \pm 0.2	60 \pm 6*	45 \pm 2*
T298A	9.1 \pm 0.1	8.1 \pm 0.1	85 \pm 6	149 \pm 10*
R299A	7.2 \pm 0.4*	7.4 \pm 0.2	94 \pm 5	48 \pm 2*
N300A	6.6 \pm 0.2*	7.9 \pm 0.1	130 \pm 6*	109 \pm 8
S301A	8.8 \pm 0.1	8.1 \pm 0.1	63 \pm 5*	74 \pm 3
N302A	7.3 \pm 0.1*	8.0 \pm 0.1	91 \pm 6	120 \pm 16
M303A	8.1 \pm 0.1*	8.1 \pm 0.1	125 \pm 5*	92 \pm 5
N304A	8.4 \pm 0.3	7.5 \pm 0.2	70 \pm 7*	48 \pm 10*
Y305A†	6.8 \pm 0.2*	7.7 \pm 0.1	52 \pm 5*	94 \pm 7
W306A†	N.D.	N.D.	N.D.	N.D.
L307A	7.6 \pm 0.2*	8.0 \pm 0.1	47 \pm 5*	63 \pm 3*

* Data are statistically significant at $p < 0.05$, one-way analysis of variance, and Dunnett's post test in comparison with wild type response.

** R^2 values for the curve fits were all >0.5 , except for GLP-1(7–36)-NH₂ at the W297A ($R^2 = 0.42$) and R299A ($R^2 = 0.46$) mutants.

† GLP-1(1–36)-NH₂ binding profile deviates from wild type, but the pIC_{50} value for this ligand was unable to be determined in the concentration range tested.

full-length or truncated peptide. Overall, similar effects on efficacy were observed for GLP-1(1–36)-NH₂ and GLP-1(7–36)-NH₂ across the ECL2 mutants (Fig. 4, *E* and *F*, and Table 2). G285A, I286A, V287A, and Y289A, located at the top of TM4/proximal ECL2, had minimal effects on the efficacy of both peptides. Similarly, there was little effect on cAMP efficacy with the G295A mutant. All other mutants displayed loss of efficacy for both peptides, although the effect was not always significant for both peptides. For example, there was a greater effect on GLP-1(1–36)-NH₂ efficacy with the L290A mutant and a greater effect on GLP-1(7–36)-NH₂ efficacy for the E294A, T298A, and S301A mutants. For both peptides, the greatest decrease in efficacy was seen with the N304A mutant (Table 2).

Effect of Human GLP-1R ECL2 Alanine Mutations on Peptide-mediated pERK1/2

Binding Affinity-modified Mutants—Peptide-induced pERK1/2 was determined at 6 min for each of the human GLP-1R ECL2

alanine mutants. Consistent with cAMP accumulation, there were no statistically significant differences in GLP-1(1–36)-NH₂ potency at these mutant receptors, although no measurable response was seen for either N300A or W306A (Fig. 5A and Table 3). In general, there was less impact of the ECL2 mutants on GLP-1(1–36)-NH₂-mediated pERK1/2 signaling relative to effects on cAMP response. Whereas the K288A, E292A, C296A, W297A, and N300A all lacked measurable cAMP responses in the presence of GLP-1(1–36)-NH₂, only the N300A mutant also failed to yield a pERK1/2 signal (Tables 2 and 3). Operational modeling of the effect of mutation on peptide efficacy failed to identify any significant changes for these mutants, although most trended toward lower efficacy (Fig. 5, A and E, and Table 3). The exception to this was R299A that trended higher in efficacy for pERK1/2 (Table 3).

As with the GLP-1(1–36)-NH₂ responses, there was generally less impact of ECL2 mutation on GLP-1(7–36)-NH₂-mediated pERK1/2 responses relative to the cAMP response (Fig. 5B and Tables 2 and 3). Potency was largely unaffected with only the K288A mutant exhibiting significantly lower potency, although there was a trend toward lower potency with some of the other affinity altered mutants, including E292A and C296A (Fig. 5, B and E, and Table 3). The greatest effects on GLP-1(7–36)-NH₂ efficacy were seen with E292A and N300A, the former being significantly lower (Fig. 5F and Table 3). K288A, D293A, W297A, N302A, Y305A, and L307A also trended toward lower efficacy. In contrast, C296A, R299A, and M303A displayed higher efficacy than the wild type receptor, although these effects did not reach significance. Interestingly, the effect on coupling efficiency of GLP-1(1–36)-NH₂ and GLP-1(7–36)-NH₂ was opposite for C296A and M303A suggesting that there are ligand-dependent effects imparted by these mutations (Table 3). Intriguingly, the R299A mutant displayed consistent effects for the two peptides but distinct effects in cAMP (decreased efficacy) versus pERK1/2 signaling (increased efficacy), suggesting a pathway selective role for this residue (Tables 2 and 3).

Mutants with Unaltered Binding Affinity—Overall, there was only limited impact of ECL2 mutants on the pERK1/2 responses for mutant receptors that had unaltered agonist binding affinity, and indeed, none of the effects achieved statistical significance for either GLP-1(1–36)-NH₂ or GLP-1(7–36)-NH₂ (Fig. 5, C and D, and Table 3). Nonetheless, there was further distinction in the pattern of pERK1/2 efficacy changes relative to Ca^{2+}_i and cAMP signaling in that efficacy tended to increase for many of the mutants, including G285A, I286A, V287A, Y289A, G295A, and T298A in comparison with wild type (Fig. 5, C–F, and Table 3). The L290A and Y291A mutants tended to have decreased efficacy for the GLP-1(7–36)-NH₂ peptide but had little effect on GLP-1(1–36)-NH₂ responses. In contrast, N304A had an apparent increase in efficacy for GLP-1(1–36)-NH₂ but unaltered GLP-1(7–36)-NH₂ response (Table 3).

Effect of Human GLP-1R ECL2 Alanine Mutations on Peptide-mediated Ca^{2+}_i Mobilization

Binding Affinity-modified Mutants—Consistent with previous data (46), there was no Ca^{2+}_i response with full-length

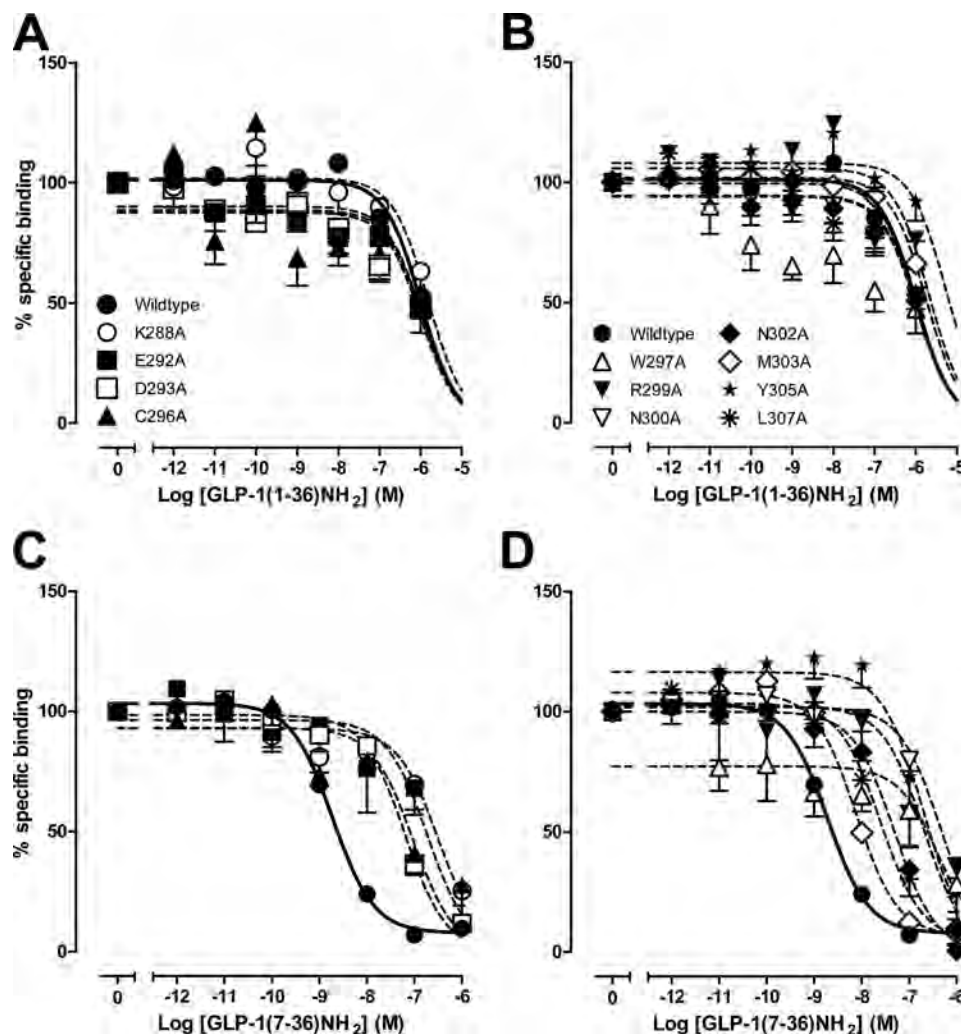


FIGURE 3. **Agonist binding profiles of human GLP-1R ECL2 alanine mutants.** Characterization of the binding of GLP-1(1–36)-NH₂ (A and B) and GLP-1(7–36)-NH₂ (C and D) in competition with the radiolabeled antagonist, ¹²⁵I-exendin(9–39), in whole FlpInCHO cells stably expressing the wild type human GLP-1R or each of the human GLP-1R ECL2 alanine mutants. Data are normalized to maximum ¹²⁵I-exendin(9–39) binding, with nonspecific binding measured in the presence of 1 μ M exendin(9–39) and analyzed with a three-parameter logistic equation as defined in Equation 1. All values are means \pm S.E. of three to four independent experiments, conducted in duplicate.

GLP-1 at either the wild type receptor or any of the alanine mutants (data not shown).

Mutants that displayed reduced GLP-1(7–36)-NH₂ binding affinity (K288A, E292A, D293A, C296A, W297A, R299A, N300A, N302A, M303A, Y305A, and L307A) displayed either significantly reduced Ca²⁺_i signaling or complete loss of signaling (Fig. 6A and Table 4). Notably, receptors with abolished Ca²⁺_i signaling (K288A, E292A, C296A, W297A, and N300A) were those that had the weakest ability to couple to the cAMP pathway, with the exception of C296A (Table 2). In addition, these mutants also had weak coupling to the pERK1/2 pathway, with the exception of C296A and W297A (Table 3). Dramatic reductions in GLP-1(7–36)-NH₂ efficacy were observed at the remaining affinity-affected mutant receptors D293A, R299A, N302A, M303A, Y305A, and L307A (Fig. 6, A and C, and Table 4). These decreases in ability to couple to the Ca²⁺_i pathway were mostly reflected in cAMP responses, although the extent of reductions in efficacy was in some cases inconsistent; D293A and Y305A were the most affected mutants in Ca²⁺_i but the least

affected in cAMP coupling in the presence of GLP-1(7–36)-NH₂ (Tables 2 and 4). Generically, the decreases in Ca²⁺_i coupling were also reflected in pERK1/2 pathway coupling, with the exception of R299A and M303A (Tables 3 and 4).

Mutants with Unaltered Binding Affinity—All mutants had reduced GLP-1(7–36)-NH₂ efficacy relative to the wild type receptor, although the effect was not significant for G285A, I286A, V287A, L290A, G295A, and S301A that were among the least affected with respect to cAMP response (Fig. 6, B and C, and Table 4). For nonbinding affected mutants, the greatest effect on efficacy was observed with the N304A mutant, again consistent with the magnitude of effect on cAMP signaling (Tables 2 and 4).

Effect of Human GLP-1R ECL2 Alanine Mutations on Peptide-mediated Signal Bias

As noted previously (46), GLP-1(1–36)-NH₂ exhibits distinct signal bias to that evoked by GLP-1(7–36)-NH₂. GLP-1(7–36)-NH₂ is strongly biased toward cAMP formation relative to either pERK1/2 or Ca²⁺_i mobilization (supplemental Fig. S1, B and C). In

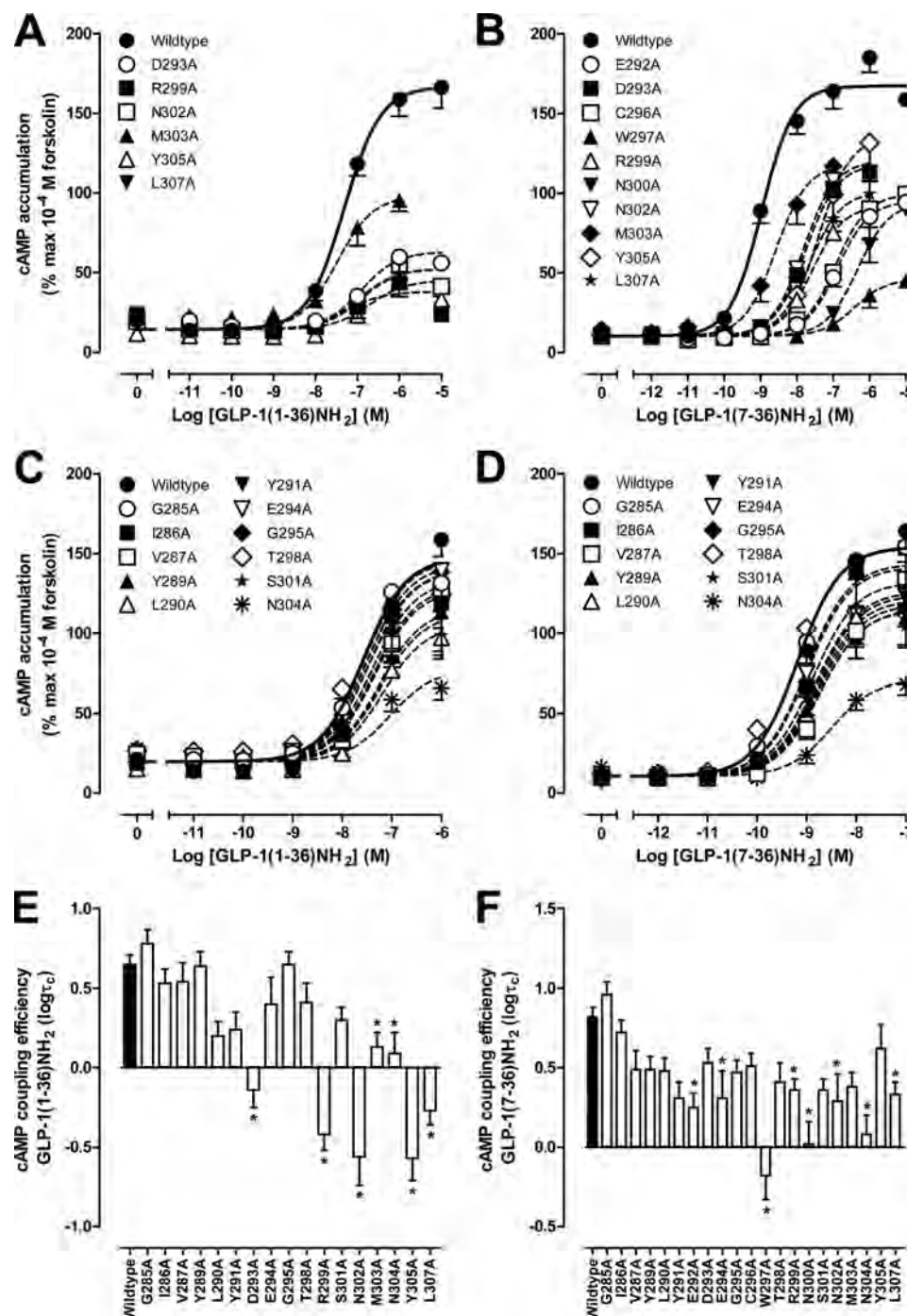


FIGURE 4. **cAMP accumulation profiles of human GLP-1R ECL2 alanine mutants.** Characterization of cAMP accumulation in the presence of GLP-1(1-36)-NH₂ (A and C) and GLP-1(7-36)-NH₂ (B and D) in FlpInCHO cells stably expressing the wild type human GLP-1R or each of the human GLP-1R ECL2 alanine mutants that effect peptide binding affinity (A and B) or has no significant effect on peptide binding affinity (C and D) is shown. Data are normalized to the response elicited by 100 μ M forskolin and analyzed with an operational model of agonism as defined in Equation 2. All values are means \pm S.E. of four to seven independent experiments, conducted in duplicate. Visual representation of cAMP pathway coupling efficacy ($\log \tau_c$) in the presence of GLP-1(1-36)-NH₂ (E) and GLP-1(7-36)-NH₂ (F) is shown. Statistical significance of changes in coupling efficacy in comparison with wild type human GLP-1R was determined by one-way analysis of variance and Dunnett's post-test and is indicated with an asterisk (*, $p < 0.05$). All values are $\log \tau_c \pm$ S.E. of four to seven independent experiments, conducted in duplicate.

contrast, GLP-1(1-36)-NH₂ has equivalent preference for cAMP and pERK1/2 (supplemental Fig. S1A). GLP-1(7-36)-NH₂, however, has only weak bias for the pERK1/2 pathway relative to Ca²⁺_i mobilization (supplemental Fig. S1D). As the GLP-1(1-36)-NH₂ peptide did not elicit a Ca²⁺_i response, relative bias against this pathway could not be

determined. Nonetheless, the absence of response is indicative of bias toward cAMP and pERK1/2.

Bias plots provide a convenient visual representation of relative pathway response that is independent of absolute potency (50), although bias factors are a quantitative measure of changes to pathway bias, relative to the wild type receptor (50).

TABLE 2

Effects of human GLP-1R ECL2 alanine mutants on peptide agonist signaling via cAMP

Data were analyzed using a three-parameter logistic equation as defined in Equation 1. pEC_{50} values represent the negative logarithm of the concentration of agonist that produces half the maximal response. E_{max} represents the maximal response normalized to that elicited by 100 μM forskolin. All mutants were analyzed with an operational model of agonism (Equation 2) to determine $\log\tau$ values. All $\log\tau$ values were then corrected to specific [^{125}I]-exendin(9–39) binding ($\log\tau_c$). Values are expressed as mean \pm S.E. of four to seven independent experiments, conducted in duplicate. Data were analyzed with one-way analysis of variance and Dunnett's post test. Gray shading highlights residues affecting peptide agonist binding affinity. ND means data were unable to be experimentally defined. R^2 values for the global curve fits were 0.88 for GLP-1(7–36)-NH₂ and 0.92 for GLP-1(1–36)-NH₂, respectively.

	cAMP accumulation					
	GLP-1(1–36)NH ₂			GLP-1(7–36)NH ₂		
	pEC_{50}	E_{max}	$\log\tau_c$ (τ_c)	pEC_{50}	E_{max}	$\log\tau_c$ (τ_c)
Wildtype	7.3 \pm 0.1	166.7 \pm 5.3	0.65 \pm 0.06 (4.47)	9.0 \pm 0.1	167.4 \pm 4.6	0.82 \pm 0.06 (6.61)
G285A	7.7 \pm 0.2	139.1 \pm 9.7*	0.78 \pm 0.09 (6.03)	9.1 \pm 0.1	155.2 \pm 4.9	0.96 \pm 0.08 (9.12)
I286A	7.6 \pm 0.2	127.7 \pm 9.2*	0.53 \pm 0.09 (3.39)	8.8 \pm 0.2	156.8 \pm 10.2	0.72 \pm 0.08 (5.25)
V287A	7.2 \pm 0.2	134.4 \pm 10.4*	0.54 \pm 0.12 (3.47)	8.4 \pm 0.1*	137.3 \pm 7.0*	0.49 \pm 0.12 (3.09)
K288A	N.D.	N.D.	N.D.	N.D.	N.D.	N.D.
Y289A	7.6 \pm 0.3	119.3 \pm 12.9*	0.64 \pm 0.09 (4.37)	8.9 \pm 0.2	110.9 \pm 6.9*	0.49 \pm 0.08 (3.09)
L290A	7.3 \pm 0.1	102.6 \pm 5.1*	0.20 \pm 0.09 (1.58)	8.7 \pm 0.1	134.1 \pm 7.1*	0.48 \pm 0.08 (3.02)
Y291A	7.2 \pm 0.1	119.3 \pm 6.8*	0.24 \pm 0.11 (1.74)	8.6 \pm 0.1	126.9 \pm 5.9*	0.31 \pm 0.10 (2.04)
E292A	N.D.	N.D.	N.D.	6.9 \pm 0.1*	94.9 \pm 5.4*	0.25 \pm 0.09 (1.78)*
D293A	6.8 \pm 0.3	64.1 \pm 6.7*	-0.14 \pm 0.11 (0.72)*	7.8 \pm 0.1*	118.0 \pm 3.8*	0.53 \pm 0.09 (3.39)
E294A	7.4 \pm 0.1	144.3 \pm 7.3	0.40 \pm 0.17 (2.51)	9.1 \pm 0.1	122.5 \pm 4.5*	0.31 \pm 0.17 (2.04)*
G295A	7.4 \pm 0.1	145.7 \pm 5.1	0.65 \pm 0.08 (4.47)	9.1 \pm 0.0	113.6 \pm 1.9*	0.47 \pm 0.08 (2.95)
C296A	N.D.	N.D.	N.D.	6.9 \pm 0.0*	99.4 \pm 2.7*	0.51 \pm 0.08 (3.24)
W297A	N.D.	N.D.	N.D.	6.5 \pm 0.1*	45.4 \pm 3.6*	-0.18 \pm 0.15 (0.66)*
T298A	7.8 \pm 0.1	126.9 \pm 5.3*	0.41 \pm 0.12 (2.57)	9.7 \pm 0.1*	116.2 \pm 5.3*	0.41 \pm 0.12 (2.57)
R299A	7.2 \pm 0.5	15.6 \pm 2.8*	-0.42 \pm 0.10 (0.38)*	7.6 \pm 0.1*	92.4 \pm 4.1*	0.36 \pm 0.07 (2.29)*
N300A	N.D.	N.D.	N.D.	6.3 \pm 0.1*	94.5 \pm 6.1*	0.02 \pm 0.14 (1.05)*
S301A	7.5 \pm 0.2	102.9 \pm 6.5*	0.30 \pm 0.08 (2.00)	9.0 \pm 0.2	105.9 \pm 6.5*	0.36 \pm 0.07 (2.29)
N302A	7.0 \pm 0.3	52.4 \pm 5.4*	-0.56 \pm 0.18 (0.28)*	7.8 \pm 0.1*	120.3 \pm 5.9*	0.29 \pm 0.17 (1.95)*
M303A	7.3 \pm 0.2	100.3 \pm 6.4*	0.13 \pm 0.09 (1.35)*	8.5 \pm 0.2	119.1 \pm 7.5*	0.38 \pm 0.09 (2.40)
N304A	7.4 \pm 0.3	69.5 \pm 6.0*	0.09 \pm 0.13 (1.23)*	8.5 \pm 0.2	71.2 \pm 4.8*	0.08 \pm 0.12 (1.20)*
Y305A	6.9 \pm 0.2	44.9 \pm 3.5*	-0.57 \pm 0.14 (0.27)*	7.4 \pm 0.2*	136.0 \pm 11.8*	0.62 \pm 0.15 (4.17)
W306A	N.D.	N.D.	N.D.	N.D.	N.D.	N.D.
L307A	7.0 \pm 0.2	52.4 \pm 3.9*	-0.27 \pm 0.09 (0.54)*	7.6 \pm 0.1*	101.0 \pm 4.9*	0.33 \pm 0.08 (2.14)*

* Data were statistically significant at $p < 0.05$, one-way analysis of variance and Dunnett's post test in comparison with the wild type response.

Comparison of all mutants in this manner indicates that most ECL2 mutants engender at least subtle changes to receptor bias, although residues Gly-285 and Ile-286 at the top of TM4 are exceptions to this (supplemental Fig. S1). The G285A mutation is interesting in that it engenders efficacy improvements for cAMP and pERK1/2 responses and was minimally altered with respect to Ca²⁺_i signaling. The mutants with the most dramatic effects on relative signal bias were also those that were altered in binding affinity of GLP-1(7–36)-NH₂, with the exception of N304A, which consistently had a large differential effect across pathways, and the T298A mutant that was among those mutants with greatest effect on pERK1/2/cAMP for GLP-1(1–36)-NH₂ and for Ca²⁺_i/pERK1/2 for GLP-1(7–36)-NH₂ (supplemental Fig. S1, A and D), although the effect of these mutants was not significant in bias factor calculations (Table 5). Bias of cAMP or pERK1/2 relative to Ca²⁺_i was only moderately affected by most mutants (supplemental Fig. S1, C and D); the principal effect for Ca²⁺_i/cAMP for GLP-1(7–36)-NH₂ was a loss of efficacy for cAMP production rather than alteration to bias *per se*, and this is reflected in the generally small changes to bias factors for these pathways (Table 5). This is probably not

surprising as Ca²⁺_i is the weakest coupled pathway at the wild type receptor, as discussed above. The greatest effects on bias were seen with specific mutants on pERK1/2/cAMP profiles (supplemental Fig. S1, A and B; Table 5). This was evident as preservation of pERK1/2 response with near abolition of cAMP response for R299A, N302A, N304A, and Y305A for GLP-1(1–36)-NH₂ and a complete reversal of bias for GLP-1(7–36)-NH₂ such that pERK1/2 was favored over cAMP for N300A, W297A, C296A, and R299A. There was no clear bias for E292A, N302A, N304A, and L307A, indicating loss of the cAMP bias seen with the wild type receptor.

The effect of mutations to both increase and decrease efficacy of ERK1/2 activation likely reflects the divergent pathways that link receptor activation to pERK1/2, including both G protein-independent (52–55) and G protein-dependent mechanisms (56). It is interesting to note that the most profound differential effects on signaling occur with mutation to residues distal to, or including, the conserved Cys-296/Trp-297 motif. This segment of ECL2 is also the most important with respect to binding of small molecule ligands into the TM region of family A GPCRs (57–61).

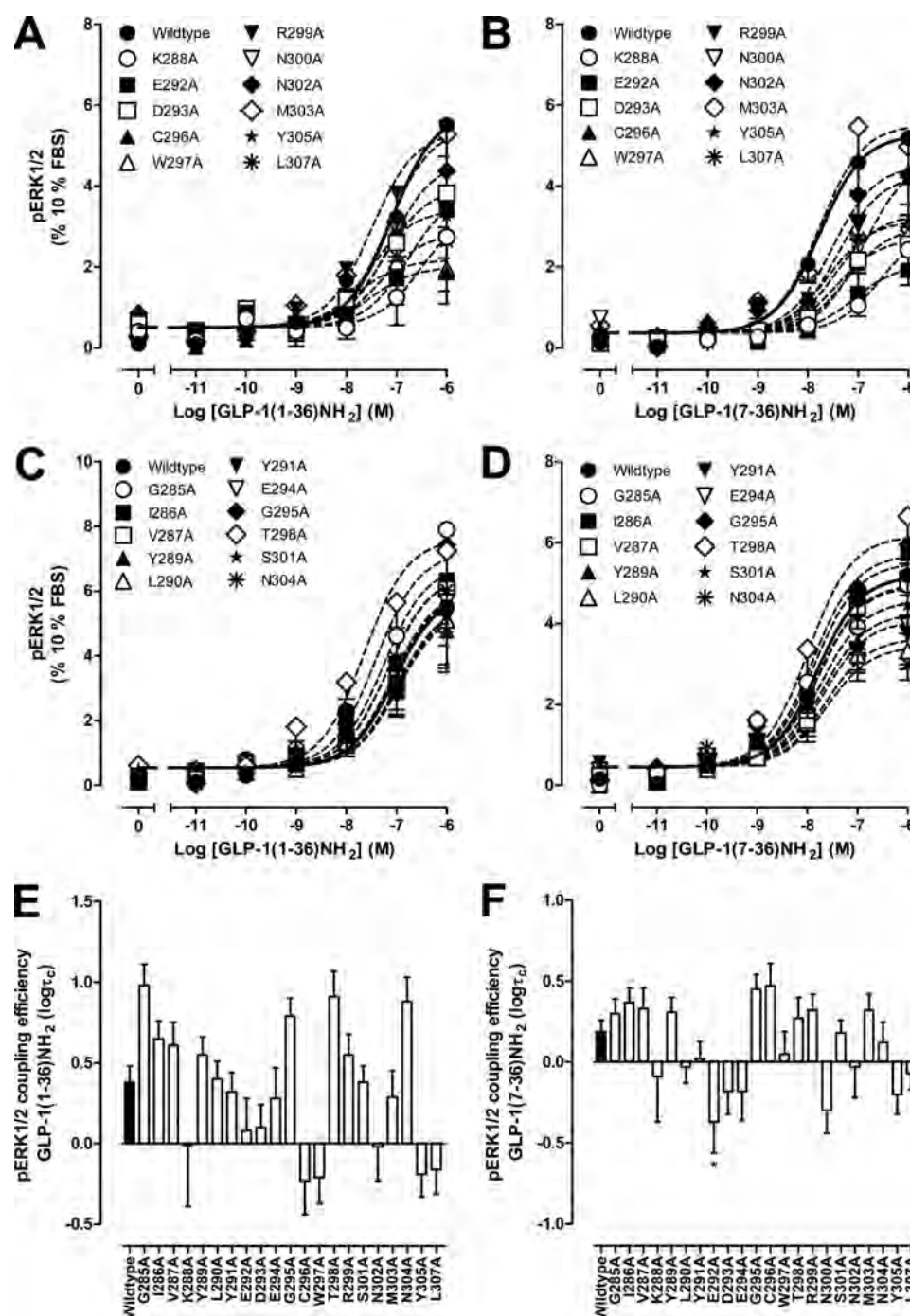


FIGURE 5. **pERK1/2 profiles of human GLP-1R ECL2 alanine mutants.** Characterization of pERK1/2 in the presence of GLP-1(1–36)-NH₂ (A and C) and GLP-1(7–36)-NH₂ (B and D) in FlpInCHO cells stably expressing the wild type human GLP-1R or each of the human GLP-1R ECL2 alanine mutants that effect peptide binding affinity (A and B) or has no significant effect on peptide binding affinity (C and D) is shown. Data are normalized to the maximal response elicited by 10% FBS and analyzed with an operational model of agonism as defined in Equation 2. All values are means \pm S.E. of five to seven independent experiments, conducted in duplicate. Visual representation of ERK1/2 coupling efficacy ($\log\tau_c$) in the presence of GLP-1(1–36)-NH₂ (E) and GLP-1(7–36)-NH₂ (F). Statistical significance of changes in coupling efficacy in comparison with wild type human GLP-1R was determined by one-way analysis of variance and Dunnett's post-test and is indicated with an asterisk (*, $p < 0.05$). All values are $\log\tau_c \pm$ S.E. five to seven independent experiments, conducted in duplicate.

DISCUSSION

It is widely accepted that the ECLs of family A GPCRs, particularly ECL2, are an important component for receptor function, with roles that include facilitating ligand binding, receptor trafficking, communication of ligand signal, and/or stabilization of an active ligand-receptor complex. Indeed, there is a plethora of evidence for many of these features (62–66), including the activation of rhodopsin relying on the displacement of the β -hairpin forming ECL2 via TM movement to allow ligand binding (67), the design of antibodies against ECL2 of several GPCRs that initiate a functional response (68, 69), and the substitution of several domains in the ECL2 of the human gonadotropin-releasing hormone receptor converting the activity of an antagonist to an agonist (70).

It is widely accepted that the ECLs of family A GPCRs, particularly ECL2, are an important component for receptor function, with roles that include facilitating ligand binding, receptor trafficking, communication of ligand signal, and/or stabilization of an active ligand-receptor complex. Indeed, there is a plethora of evidence for many of these features (62–66), including the activation of rhodopsin relying on the displacement of the β -hairpin forming ECL2 via TM movement to allow ligand binding (67), the design of antibodies against ECL2 of several GPCRs that initiate a functional response (68, 69), and the substitution of several domains in the ECL2 of the human gonadotropin-releasing hormone receptor converting the activity of an antagonist to an agonist (70).

GLP-1R ECL2 Is Critical for Receptor Activation

TABLE 3

Effects of human GLP-1R ECL2 alanine mutants on peptide agonist signaling via pERK1/2

Data were analyzed using a three-parameter logistic equation as defined in Equation 1. pEC_{50} values represent the negative logarithm of the concentration of agonist that produces half the maximal response. E_{max} represents the maximal response normalized to that elicited by 10% FBS. All mutants were analyzed with an operational model of agonism (Equation 2) to determine $\log\tau$ values. All $\log\tau$ values were then corrected to specific ^{125}I -exendin(9–39) binding ($\log\tau_c$). Values are expressed as means \pm S.E. of five to seven independent experiments, conducted in duplicate. Data were analyzed with one-way analysis of variance and Dunnett's post test. R^2 values for the global curve fits were 0.68 for GLP-1(7–36)-NH₂ and 0.57 for GLP-1(1–36)-NH₂, respectively. Gray shading highlights residues effecting peptide agonist binding affinity. ND means data were unable to be experimentally defined.

	pERK1/2					
	GLP-1(1–36)NH ₂			GLP-1(7–36)NH ₂		
	pEC_{50}	E_{max}	$\log\tau_c$ (τ_c)	pEC_{50}	E_{max}	$\log\tau_c$ (τ_c)
Wildtype	7.2 \pm 0.2	5.7 \pm 0.5	0.38 \pm 0.10 (2.40)	7.8 \pm 0.2	5.3 \pm 0.4	0.19 \pm 0.07 (1.55)
G285A	7.1 \pm 0.1	8.3 \pm 0.6	0.98 \pm 0.13 (9.55)	8.1 \pm 0.2	4.6 \pm 0.4	0.30 \pm 0.09 (2.00)
I286A	7.2 \pm 0.2	6.5 \pm 0.8	0.65 \pm 0.11 (4.47)	7.8 \pm 0.2	5.7 \pm 0.4	0.37 \pm 0.09 (2.34)
V287A	6.9 \pm 0.2	6.8 \pm 0.7	0.61 \pm 0.14 (4.07)	7.6 \pm 0.3	5.3 \pm 0.6	0.33 \pm 0.13 (2.14)
K288A	6.6 \pm 0.6	3.3 \pm 1.1	−0.01 \pm 0.38 (0.98)	6.7 \pm 0.3*	2.9 \pm 0.5*	−0.09 \pm 0.28 (0.81)
Y289A	7.3 \pm 0.4	4.9 \pm 0.8	0.55 \pm 0.11 (3.55)	7.4 \pm 0.3	5.0 \pm 0.6	0.31 \pm 0.09 (2.04)
L290A	7.0 \pm 0.2	5.5 \pm 0.6	0.40 \pm 0.11 (2.51)	7.9 \pm 0.3	3.4 \pm 0.4*	−0.03 \pm 0.10 (0.93)
Y291A	6.9 \pm 0.3	5.7 \pm 1.0	0.32 \pm 0.12 (2.09)	7.8 \pm 0.3	4.1 \pm 0.4	0.02 \pm 0.11 (1.05)
E292A	6.7 \pm 0.3	3.9 \pm 0.7	0.08 \pm 0.20 (1.20)	7.2 \pm 0.2	2.0 \pm 0.2*	−0.37 \pm 0.19 (0.43)*
D293A	7.2 \pm 0.3	4.0 \pm 0.5	0.10 \pm 0.14 (1.26)	7.5 \pm 0.3	2.7 \pm 0.3*	−0.18 \pm 0.14 (0.66)
E294A	7.1 \pm 0.2	6.0 \pm 0.5	0.28 \pm 0.19 (1.91)	7.8 \pm 0.2	4.0 \pm 0.3	−0.18 \pm 0.18 (0.66)
G295A	6.9 \pm 0.2	8.1 \pm 0.9	0.79 \pm 0.11 (6.17)	7.8 \pm 0.2	5.9 \pm 0.5	0.45 \pm 0.09 (2.82)
C296A	7.8 \pm 0.4	2.0 \pm 0.4*	−0.23 \pm 0.21 (0.59)	6.9 \pm 0.3	4.7 \pm 0.7	0.47 \pm 0.14 (2.95)
W297A	7.9 \pm 0.5	2.2 \pm 0.4*	−0.21 \pm 0.16 (0.62)	7.3 \pm 0.4	3.0 \pm 0.5*	0.05 \pm 0.14 (1.12)
T298A	7.8 \pm 0.2	6.9 \pm 0.5	0.91 \pm 0.16 (8.13)	8.0 \pm 0.2	6.1 \pm 0.5	0.27 \pm 0.13 (1.86)
R299A	7.5 \pm 0.3	5.4 \pm 0.8	0.55 \pm 0.13 (3.55)	7.5 \pm 0.2	4.2 \pm 0.4	0.32 \pm 0.10 (2.09)
N300A	N.D.	N.D.	N.D.	7.6 \pm 0.3	3.1 \pm 0.4*	−0.30 \pm 0.14 (0.50)
S301A	7.3 \pm 0.2	4.8 \pm 0.5	0.38 \pm 0.10 (2.40)	7.8 \pm 0.2	4.5 \pm 0.4	0.18 \pm 0.08 (1.51)
N302A	7.0 \pm 0.3	5.4 \pm 1.0	−0.02 \pm 0.21 (0.95)	7.5 \pm 0.3	4.5 \pm 0.5	−0.03 \pm 0.19 (0.93)
M303A	7.2 \pm 0.3	5.5 \pm 0.8	0.29 \pm 0.16 (1.95)	7.8 \pm 0.2	5.5 \pm 0.4	0.32 \pm 0.10 (2.09)
N304A	7.5 \pm 0.2	5.8 \pm 0.5	0.88 \pm 0.15 (7.59)	7.9 \pm 0.3	3.2 \pm 0.4*	0.12 \pm 0.13 (1.32)
Y305A	7.5 \pm 0.2	3.4 \pm 0.3	−0.19 \pm 0.14 (0.65)	7.5 \pm 0.3	3.3 \pm 0.3*	−0.20 \pm 0.12 (0.63)
W306A	N.D.	N.D.	N.D.	N.D.	N.D.	N.D.
L307A	7.4 \pm 0.2	2.8 \pm 0.2*	−0.16 \pm 0.15 (0.69)	7.6 \pm 0.2	3.1 \pm 0.3*	−0.07 \pm 0.10 (0.85)

* Data were statistically significant at $p < 0.05$, one-way analysis of variance, and Dunnett's post test in comparison with wild type response.

In this study we have used alanine scanning of ECL2 and adjacent residues to probe the function of this domain of the human GLP-1R. Virtually all mutations impacted on receptor function, in particular on ligand efficacy, although the nature and extent of effect varied considerably depending on the pathway, the ligand, and the mutation. Collectively, the data are indicative of a critical role for the GLP-1R ECL2 in the activation transition of the receptor. A global role for this domain in activation transition is supported by analysis of efficacy changes to mutants across the different pathways (Fig. 7). Although there are exceptions (discussed below), there was generally a good correlation between the magnitude of efficacy change for the different pathways for individual mutants, although the direction of change in the case of pERK1/2 was not always in the same direction as the other two pathways (that were almost uniformly negative) (Fig. 7). The correlations suggest that the mutations alter the ensemble of conformations formed/sam-

pled by the receptor in response to agonists; for a subset of mutants there is greater propensity to form conformations linked to activation of pERK1/2, but this is gained at the expense of conformations linked to either cAMP formation or Ca²⁺_i mobilization. The almost uniform loss of Ca²⁺_i efficacy with individual mutations suggests that there is a high energy barrier for formation of conformations allowing coupling to this pathway, and this is consistent with the inability of GLP-1(1–36)-NH₂ to activate this pathway.

The recent solution of the crystal structure of the agonist-bound β_2 -adrenergic receptor in complex with G α_s (71) has provided novel insight into the structural changes in the receptor that accompany activation transition. This receptor undergoes two major rearrangements on its intracellular face as follows: an outward displacement of TM6 by ~ 14 Å and an α -helical extension of TM5. These changes open up the receptor for interaction with the G protein. In the activated structure,

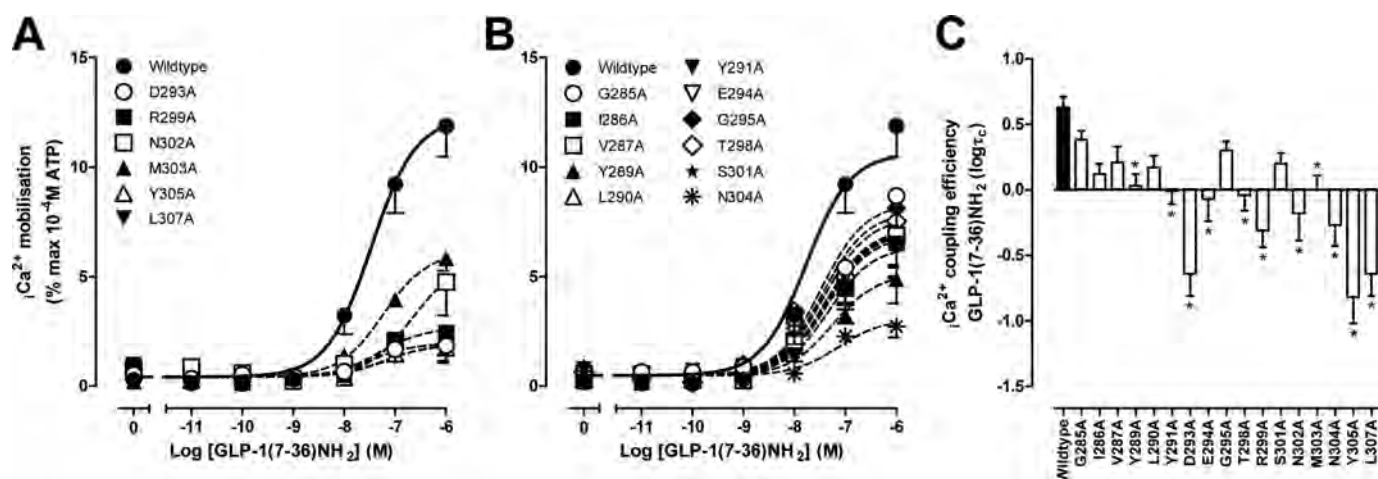


FIGURE 6. Ca^{2+} mobilization profiles of human GLP-1R ECL2 alanine mutants. Characterization of Ca^{2+} mobilization in the presence of GLP-1(7–36)-NH₂ in FlpInCHO cells stably expressing the wild type human GLP-1R or each of the human GLP-1R ECL2 alanine mutants that effect peptide binding affinity (A) or has no significant effect on peptide binding affinity (B) is shown. Data are normalized to the maximal response elicited by 100 μ M ATP and analyzed with an operational model of agonism as defined in Equation 2. All values are means \pm S.E. of three to five independent experiments, conducted in duplicate. Visual representation of Ca^{2+} coupling efficacy ($\log\tau_c$) in the presence of GLP-1(7–36)-NH₂ (C) is shown. Statistical significance of changes in coupling efficacy in comparison with wild type human GLP-1R was determined by one-way analysis of variance and Dunnett's post-test and is indicated with an asterisk (*, $p < 0.05$). All values are $\log\tau_c \pm$ S.E. of three to five independent experiments, conducted in duplicate.

the $\alpha 5$ helix of $G\alpha_s$ forms a network of polar interactions with TM5, and therefore, the transmission of conformational change to TM5 is likely to be very important for at least $G\alpha_s$ interactions. Our data are indicative of ECL2 playing a critical role in the activation transition of the GLP-1R, potentially via effects on the conformation of TM5. Consistent with this, there was generally greater impact of mutation to residues that were distal to the conserved Cys (Cys-296) that resides near the top of TM5.

For all mutants expressed at the cell surface, binding of the antagonist peptide exendin(9–39) was unaltered, and binding affinity changes were restricted to the high affinity agonist peptide GLP-1(7–36)-NH₂ for a subset of mutants. The interpretation of binding affinity changes for agonist peptides can be difficult. Although agonists enable the transition of the receptor to facilitate G protein binding, the ternary complex of the receptor with the G protein (or indeed with other regulatory proteins) provides thermodynamically reciprocal (allosteric) regulation of agonist binding (72). This has been empirically demonstrated for GPCRs using purified proteins, and for the β_2 -adrenoreceptor, it has been demonstrated that the full conformational alteration to the receptor requires both agonist and G protein to be bound (73, 74). As such, major effects on receptor-G protein interactions will manifest as selective loss of high affinity agonist binding, such as those observed in this study, and distinguishing direct effects on peptide binding from indirect effects is problematic.

The most dramatic effects on receptor function were seen with those mutants that also had reduced affinity for GLP-1(7–36)-NH₂. For the mutants with greatest loss of apparent affinity, K288A, E292A, C296A, W297A, and N300A, there was a corresponding major loss of receptor function, although the loss of affinity alone was insufficient to account for the extent of functional loss. For the GLP-1(7–36)-NH₂ peptide, these mutations led to abolition of the Ca^{2+} response and marked decrease in potency for cAMP formation. For most mutants,

there was also a parallel loss in cAMP efficacy, and the exception to this was C296A, where efficacy was preserved (Tables 1–4). For GLP-1(1–36)-NH₂ there was total loss of response in cAMP formation. The effect on pERK1/2 was more complex. Lys-288, Cys-296, and Trp-297 are each very highly conserved across the B subfamily of peptide hormone GPCRs and this may indicate a structural role for these residues (Fig. 1A). This is supported by the loss of functional cell surface receptors seen with alanine mutants of these residues (Table 1 and Fig. 2). For Cys-296, a structural role is clearly evident with this amino acid forming a disulfide bond with Cys-226 at the top of TM3; this structural motif is highly conserved across the superfamily of GPCRs and is evident in solved crystal structures for family A GPCRs (57–61, 75, 76). In the rat GLP-1R, double mutation of Cys-226 and Cys-296 to alanine restored the loss of GLP-1(7–36)-NH₂ binding affinity and cAMP signaling seen with individual mutation of these residues, indicating that the disulfide link itself is not required for efficient activation of the receptor (77).

Recent photoaffinity cross-linking work has demonstrated that Leu-20 of GLP-1(7–36)-NH₂ is proximal to Trp-297 of the receptor, with subsequent molecular modeling indicating that it could form a direct interaction that may contribute to the loss of function observed with mutation of this residue (36). Interestingly, Leu-20 is distal to the segment of the GLP-1 peptide (and indeed other related peptide hormones) that is linked to agonistic activity. Dipeptidyl peptidase IV cleavage of the two N-terminal residues markedly attenuates the activity of GLP-1(7–36)-NH₂, and truncation by six amino acids is sufficient to abolish agonist activity (78). In this study binding affinity of the antagonist peptide exendin(9–39) was unaltered by any of the mutations, and thus it seems unlikely that the extent of loss of function seen with the W297A is due to loss of a direct interaction. It has been speculated that low binding affinity for GLP-1(7–36)-NH₂ for the isolated N-terminal extracellular domain of the GLP-1R is due to decreased capacity of GLP-1(7–36)-

TABLE 4

Effects of human GLP-1R ECL2 alanine mutants on peptide agonist signaling via Ca^{2+} mobilization

Data were analyzed using a three-parameter logistic equation as defined in Equation 1. pEC_{50} values represent the negative logarithm of the concentration of agonist that produces half the maximal response. E_{max} represents the maximal response normalized to that elicited by 100 μM ATP. All mutants were analyzed with an operational model of agonism (Equation 2) to determine $\log\tau$ values. All $\log\tau$ values were then corrected to specific ^{125}I -exendin(9–39) binding ($\log\tau_c$). Values are expressed as means \pm S.E. of three to five independent experiments, conducted in duplicate. Data were analyzed with one-way analysis of variance and Dunnett's post test. The R^2 value for the global curve fit was 0.79. Gray shading highlights residues effecting peptide agonist binding affinity. ND means data were unable to be experimentally defined.

	Ca^{2+} mobilization		
	GLP-1(7–36)NH_2		
	pEC_{50}	E_{max}	$\log\tau_c$ (τ_c)
Wildtype	7.5 ± 0.1	12.2 ± 0.8	0.63 ± 0.08 (4.27)
G285A	7.3 ± 0.2	$8.7 \pm 0.9^*$	0.38 ± 0.07 (2.40)
I286A	8.0 ± 0.3	$5.9 \pm 0.6^*$	0.12 ± 0.08 (1.32)
V287A	7.3 ± 0.2	$7.0 \pm 0.7^*$	0.21 ± 0.12 (1.62)
K288A	N.D.	N.D.	N.D.
Y289A	7.4 ± 0.3	$4.8 \pm 0.6^*$	0.03 ± 0.09 (1.07)*
L290A	7.5 ± 0.2	$6.8 \pm 0.7^*$	0.17 ± 0.09 (1.48)
Y291A	7.2 ± 0.2	$6.7 \pm 0.7^*$	-0.01 ± 0.10 (0.98)*
E292A	N.D.	N.D.	N.D.
D293A	7.5 ± 0.4	$2.0 \pm 0.3^*$	-0.64 ± 0.17 (0.23)*
E294A	7.6 ± 0.3	$6.6 \pm 0.8^*$	-0.07 ± 0.17 (0.85)*
G295A	7.3 ± 0.2	$8.3 \pm 0.7^*$	0.30 ± 0.07 (2.00)
C296A	N.D.	N.D.	N.D.
W297A	N.D.	N.D.	N.D.
T298A	7.8 ± 0.1	$7.0 \pm 0.4^*$	-0.04 ± 0.12 (0.91)*
R299A	7.3 ± 0.5	$2.7 \pm 0.6^*$	-0.31 ± 0.13 (0.49)*
N300A	N.D.	N.D.	N.D.
S301A	7.6 ± 0.2	$6.7 \pm 0.5^*$	0.20 ± 0.08 (1.58)
N302A	6.6 ± 0.4	$5.9 \pm 1.4^*$	-0.18 ± 0.21 (0.66)*
M303A	7.2 ± 0.1	$6.1 \pm 0.4^*$	0.00 ± 0.11 (1.00)*
N304A	7.3 ± 0.3	$2.9 \pm 0.4^*$	-0.27 ± 0.16 (0.54)*
Y305A	7.2 ± 0.4	$1.7 \pm 0.3^*$	-0.82 ± 0.20 (0.15)*
W306A	N.D.	N.D.	N.D.
L307A	7.0 ± 0.4	$2.4 \pm 0.5^*$	-0.64 ± 0.17 (0.23)*

* Data were statistically significant at $p < 0.05$, one-way analysis of variance, and Dunnett's post test in comparison with wild type response.

NH_2 to form an extended α -helix in the absence of the receptor core (79). It is possible that one role of Trp-297 is to help stabilize peptide secondary structure. Nonetheless, Trp-297 is completely conserved across all B family members suggesting that it is structurally important.

Mutation of Lys-288 to alanine in the rat GLP-1R leads to a similar decrease in GLP-1(7–36)- NH_2 affinity to that observed in this study, and although a cAMP response via the rat GLP-1R is detectable, there is a marked decrease in potency. At the equivalent position in other family B receptors, this amino acid is highly conserved with an invariant basic residue (Arg or Lys) present (Fig. 1A). Al-Sabah and Donnelly (37) have speculated that Lys-288 likely resides at the border between TM4 and ECL2 and that a basic residue in this position is potentially required for important interactions with neighboring TM residues. Nonetheless, such basic amino acids may also reside at the hydrophobic face of TM helices and undergo what is termed "snorkeling," where the side chain is oriented parallel to

TABLE 5

Effects of human GLP-1R ECL2 alanine mutants on peptide agonist-mediated signaling bias

Data were analyzed using an operational model of agonism as defined in Equation 4 to estimate $\log\tau_c/K_A$ ratios. Changes in $\log\tau_c/K_A$ ratios with respect to wild type were used to quantitate bias between signaling pathways. Values are expressed as means \pm S.E. of three to seven independent experiments, conducted in duplicate. Data were analyzed with one-way analysis of variance and Dunnett's post test. Gray shading highlights residues effecting peptide agonist binding affinity. ND means were data unable to be experimentally defined.

	Bias Factors			
	GLP-1(1–36)NH_2		GLP-1(7–36)NH_2	
	cAMP-ERK	cAMP-ERK	cAMP-Ca^{2+}	ERK-Ca^{2+}
Wildtype	0.00 ± 0.22	0.00 ± 0.19	0.00 ± 0.17	0.00 ± 0.21
G285A	-0.39 ± 0.23	0.02 ± 0.19	0.42 ± 0.23	0.40 ± 0.22
I286A	$-0.34 \pm 0.27^*$	-0.19 ± 0.22	0.41 ± 0.19	0.59 ± 0.22
V287A	-0.44 ± 0.24	-0.29 ± 0.24	0.15 ± 0.25	0.44 ± 0.29
K288A	N.D.	N.D.	N.D.	N.D.
Y289A	0.03 ± 0.25	-0.33 ± 0.21	0.19 ± 0.38	0.52 ± 0.34
L290A	-0.45 ± 0.32	-0.43 ± 0.35	-0.07 ± 0.29	0.35 ± 0.40
Y291A	-0.38 ± 0.30	-0.60 ± 0.30	0.06 ± 0.29	0.65 ± 0.33
E292A	N.D.	$-1.36 \pm 0.41^*$	N.D.	N.D.
D293A	-1.17 ± 0.35	-0.90 ± 0.33	-0.45 ± 0.60	0.45 ± 0.68
E294A	-0.22 ± 0.26	-0.03 ± 0.30	0.22 ± 0.27	0.25 ± 0.34
G295A	-0.50 ± 0.23	-0.55 ± 0.25	0.05 ± 0.20	0.80 ± 0.25
C296A	N.D.	$-1.51 \pm 0.19^*$	N.D.	N.D.
W297A	N.D.	$-2.52 \pm 0.38^*$	N.D.	N.D.
T298A	-0.79 ± 0.23	-0.54 ± 0.22	0.25 ± 0.18	0.80 ± 0.20
R299A	$-1.53 \pm 0.43^*$	$-1.36 \pm 0.21^*$	-0.72 ± 0.43	0.64 ± 0.46
N300A	N.D.	$-2.64 \pm 0.29^*$	N.D.	N.D.
S301A	-0.36 ± 0.22	-0.52 ± 0.27	-0.21 ± 0.23	0.31 ± 0.30
N302A	-1.17 ± 0.33	$-1.13 \pm 0.24^*$	-0.11 ± 0.22	1.02 ± 0.30
M303A	-0.45 ± 0.25	-0.77 ± 0.27	0.05 ± 0.24	0.82 ± 0.30
N304A	-1.07 ± 0.23	-0.89 ± 0.33	-0.02 ± 0.55	0.67 ± 0.48
Y305A	$-1.76 \pm 0.48^*$	$-1.32 \pm 0.19^*$	-0.47 ± 0.63	0.85 ± 0.64
W306A	N.D.	N.D.	N.D.	N.D.
L307A	-1.15 ± 0.47	$-1.25 \pm 0.31^*$	-0.32 ± 0.56	0.93 ± 0.61

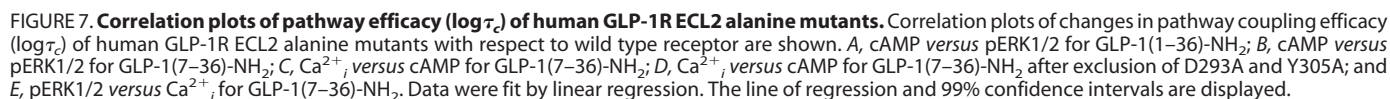
* Data were statistically significant at $p < 0.05$, one-way analysis of variance, and Dunnett's post test in comparison with wild type response.

the membrane helix leading to stabilization of the top of the TM helix (80), and this may be important in receptor function.

Glu-292 and Asn-300 are partially conserved across B family receptors, being homologous with more closely related members of the family (Fig. 1A). These receptors also have the greatest degree of homology with the N-terminal sequences of their activating peptides (Fig. 1B), and this may suggest more direct importance for interaction between the receptors and peptides. Although among the most deleterious of mutations for all pathways, their effect on relative efficacy across pathways is consistent with most other ECL2 mutations (Fig. 7). Nonetheless, the N300A mutant, like C296A and W297A, reversed GLP-1(7–36)- NH_2 -mediated signal bias between pERK1/2 and cAMP formation (supplemental Fig. S1B).

Of all the mutants studied, only W306A was not expressed at the cell surface, indicating that the mutation leads to misfolding of the receptor. Curiously, double mutation of Tyr-305 and Trp-306 to alanine in the rat GLP-1R resulted in a population of receptors that were cell surface-expressed and responded to peptide agonists, albeit with marked effects on potency (77), suggesting that either interspecies differences in receptor sequence provide for greater stability of rat receptor structure or that the additional mutation compensated for some of the detrimental interactions arising from individual mutation of Trp-306.

All of the other mutations that altered the affinity of GLP-1(7–36)- NH_2 , D293A, R299A, N302A, M303A, Y305A, and



These data are indicative of a novel and important role for ECL2 in conferring the distinct conformations that underlie pathway selective signaling. Whether this occurs purely through effects on the conformation of TM5 or whether additional interactions of ECL2 residues with other loop regions are involved is unclear.

The two GLP-1 peptides used in this study differ only by a six-amino acid extension to the GLP-1(7–36)-NH₂ sequence. Not surprisingly, most mutations had similar effects on responses to both peptides. Nonetheless, GLP-1(1–36)-NH₂ exhibits distinct signal bias to that demonstrated by GLP-1(7–36)-NH₂, indicating that it produces a different ensemble of receptor conformations to that of the truncated peptide. Consistent with the effects of the different peptides in altering receptor bias, C296A, R299A, N302A, N304A, and Y305A had differential effects on the truncated and full-length GLP-1 peptides. Differential effects were also seen with the G285A mutant. Both peptides displayed increased efficacy at this mutant receptor; however, greater improvement in pERK1/2 efficacy was seen for GLP-1(1–36)-NH₂ relative to GLP-1(7–36)-NH₂. Alanine at this position may thus provide some conformational restriction that allows the lower affinity full-length peptide to more readily activate the pERK1/2 pathway compared with the wild type receptor.

In conclusion, we have demonstrated a critical role for ECL2 in activation of the GLP-1R. However, the precise molecular mechanisms driving these effects remain elusive in the absence of high resolution structural information for family B GPCRs. Our data point to a major role for ECL2 in activation transition and that changes to structure in this receptor region can alter pathway bias of the receptor that can be manifested in a ligand-specific manner.

REFERENCES

- Harmar, A. J., Hills, R. A., Rosser, E. M., Jones, M., Buneman, O. P., Dunbar, D. R., Greenhill, S. D., Hale, V. A., Sharman, J. L., Bonner, T. I., Caterall, W. A., Davenport, A. P., Delagrange, P., Dollery, C. T., Foord, S. M., Gutman, G. A., Laudet, V., Neubig, R. R., Ohlstein, E. H., Olsen, R. W., Peters, J., Pin, J. P., Ruffolo, R. R., Searls, D. B., Wright, M. W., and Spedding, M. (2009) IUPHAR-DB. The IUPHAR database of G protein-coupled receptors and ion channels. *Nucleic Acids Res.* **37**, D680–D685
- Overington, J. P., Al-Lazikani, B., and Hopkins, A. L. (2006) How many drug targets are there? *Nat. Rev. Drug Discov.* **5**, 993–996
- Bazarsuren, A., Grauschof, U., Wozny, M., Reusch, D., Hoffmann, E., Schaefer, W., Panzner, S., and Rudolph, R. (2002) *In vitro* folding, functional characterization, and disulfide pattern of the extracellular domain of human GLP-1 receptor. *Biophys. Chem.* **96**, 305–318
- Grauschof, U., Lilie, H., Honold, K., Wozny, M., Reusch, D., Esswein, A., Schäfer, W., Rücknagel, K. P., and Rudolph, R. (2000) The N-terminal fragment of human parathyroid hormone receptor 1 constitutes a hormone binding domain and reveals a distinct disulfide pattern. *Biochemistry* **39**, 8878–8887
- Bisello, A., Adams, A. E., Mierke, D. F., Pellegrini, M., Rosenblatt, M., Suva, L. J., and Chorev, M. (1998) Parathyroid hormone-receptor interactions identified directly by photocross-linking and molecular modeling studies. *J. Biol. Chem.* **273**, 22498–22505
- Dong, M., Li, Z., Pinon, D. I., Lybrand, T. P., and Miller, L. J. (2004) Spatial approximation between the amino terminus of a peptide agonist and the top of the sixth transmembrane segment of the secretin receptor. *J. Biol. Chem.* **279**, 2894–2903
- Dong, M., Pinon, D. I., Cox, R. F., and Miller, L. J. (2004) Molecular approximation between a residue in the amino-terminal region of calcitonin and the third extracellular loop of the class B G protein-coupled calcitonin receptor. *J. Biol. Chem.* **279**, 31177–31182
- Hoare, S. R. (2005) Mechanisms of peptide and nonpeptide ligand binding to Class B G-protein-coupled receptors. *Drug Discov. Today* **10**, 417–427
- Bergwitz, C., Gardella, T. J., Flannery, M. R., Potts, J. T., Jr., Kronenberg, H. M., Goldring, S. R., and Jüppner, H. (1996) Full activation of chimeric receptors by hybrids between parathyroid hormone and calcitonin. Evidence for a common pattern of ligand-receptor interaction. *J. Biol. Chem.* **271**, 26469–26472
- Graziano, M. P., Hey, P. J., and Strader, C. D. (1996) The amino-terminal domain of the glucagon-like peptide-1 receptor is a critical determinant of subtype specificity. *Receptors Channels* **4**, 9–17
- Holtmann, M. H., Hadac, E. M., and Miller, L. J. (1995) Critical contributions of amino-terminal extracellular domains in agonist binding and activation of secretin and vasoactive intestinal polypeptide receptors. Studies of chimeric receptors. *J. Biol. Chem.* **270**, 14394–14398
- Wilmen, A., Göke, B., and Göke, R. (1996) The isolated N-terminal extracellular domain of the glucagon-like peptide-1 (GLP)-1 receptor has intrinsic binding activity. *FEBS Lett.* **398**, 43–47
- Wilmen, A., Van Eyll, B., Göke, B., and Göke, R. (1997) Five out of six tryptophan residues in the N-terminal extracellular domain of the rat GLP-1 receptor are essential for its ability to bind GLP-1. *Peptides* **18**, 301–305
- Gelling, R. W., Wheeler, M. B., Xue, J., Gyomai, S., Nian, C., Pederson, R. A., and McIntosh, C. H. (1997) Localization of the domains involved in ligand binding and activation of the glucose-dependent insulinotropic polypeptide receptor. *Endocrinology* **138**, 2640–2643
- Castro, M., Nikolaev, V. O., Palm, D., Lohse, M. J., and Vilardaga, J. P. (2005) Turn-on switch in parathyroid hormone receptor by a two-step parathyroid hormone binding mechanism. *Proc. Natl. Acad. Sci. U.S.A.* **102**, 16084–16089
- Bergwitz, C., Jusseaume, S. A., Luck, M. D., Jüppner, H., and Gardella, T. J. (1997) Residues in the membrane-spanning and extracellular loop regions of the parathyroid hormone (PTH)-2 receptor determine signaling selectivity for PTH and PTH-related peptide. *J. Biol. Chem.* **272**, 28861–28868
- Hjorth, S. A., Adelhorst, K., Pedersen, B. B., Kirk, O., and Schwartz, T. W. (1994) Glucagon and glucagon-like peptide 1. Selective receptor recognition via distinct peptide epitopes. *J. Biol. Chem.* **269**, 30121–30124
- Holtmann, M. H., Ganguli, S., Hadac, E. M., Dolu, V., and Miller, L. J. (1996) Multiple extracellular loop domains contribute critical determinants for agonist binding and activation of the secretin receptor. *J. Biol. Chem.* **271**, 14944–14949
- Buggy, J. J., Livingston, J. N., Rabin, D. U., and Yoo-Warren, H. (1995) Glucagon-glucagon-like peptide I receptor chimeras reveal domains that determine specificity of glucagon binding. *J. Biol. Chem.* **270**, 7474–7478
- Xiao, Q., Jeng, W., and Wheeler, M. B. (2000) Characterization of glucagon-like peptide-1 receptor-binding determinants. *J. Mol. Endocrinol.* **25**, 321–335
- Adelhorst, K., Hedegaard, B. B., Knudsen, L. B., and Kirk, O. (1994) Structure-activity studies of glucagon-like peptide-1. *J. Biol. Chem.* **269**, 6275–6278
- Mojsov, S. (1992) Structural requirements for biological activity of glucagon-like peptide-I. *Int. J. Pept. Protein Res.* **40**, 333–343
- Nicole, P., Lins, L., Rouyer-Fessard, C., Drouot, C., Fulcrand, P., Thomas, A., Couvineau, A., Martinez, J., Brasseur, R., and Laburthe, M. (2000) Identification of key residues for interaction of vasoactive intestinal peptide with human VPAC1 and VPAC2 receptors and development of a highly selective VPAC1 receptor agonist. Alanine scanning and molecular modeling of the peptide. *J. Biol. Chem.* **275**, 24003–24012
- Dong, M., Le, A., Te, J. A., Pinon, D. I., Bordner, A. J., and Miller, L. J. (2011) Importance of each residue within secretin for receptor binding and biological activity. *Biochemistry* **50**, 2983–2993
- Runge, S., Wulff, B. S., Madsen, K., Bräuner-Osborne, H., and Knudsen, L. B. (2003) Different domains of the glucagon and glucagon-like peptide-1 receptors provide the critical determinants of ligand selectivity. *Br. J. Pharmacol.* **138**, 787–794
- Runge, S., Gram, C., Brauner-Osborne, H., Madsen, K., Knudsen, L. B., and Wulff, B. S. (2003) Three distinct epitopes on the extracellular face of the glucagon receptor determine specificity for the glucagon amino terminus. *J. Biol. Chem.* **278**, 28005–28010
- Parthier, C., Kleinschmidt, M., Neumann, P., Rudolph, R., Manhart, S., Schlenzig, D., Fanghänel, J., Rahfeld, J. U., Demuth, H. U., and Stubbs, M. T. (2007) Crystal structure of the incretin-bound extracellular domain of a G protein-coupled receptor. *Proc. Natl. Acad. Sci. U.S.A.* **104**, 13942–13947

28. Grace, C. R., Perrin, M. H., DiGruccio, M. R., Miller, C. L., Rivier, J. E., Vale, W. W., and Riek, R. (2004) NMR structure and peptide hormone-binding site of the first extracellular domain of a type B1 G protein-coupled receptor. *Proc. Natl. Acad. Sci. U.S.A.* **101**, 12836–12841
29. Grace, C. R., Perrin, M. H., Gulyas, J., DiGruccio, M. R., Cante, J. P., Rivier, J. E., Vale, W. W., and Riek, R. (2007) Structure of the N-terminal domain of a type B1 G protein-coupled receptor in complex with a peptide ligand. *Proc. Natl. Acad. Sci. U.S.A.* **104**, 4858–4863
30. Pioszak, A. A., Parker, N. R., Suino-Powell, K., and Xu, H. E. (2008) Molecular recognition of corticotropin-releasing factor by its G-protein-coupled receptor CRFR1. *J. Biol. Chem.* **283**, 32900–32912
31. Pioszak, A. A., and Xu, H. E. (2008) Molecular recognition of parathyroid hormone by its G protein-coupled receptor. *Proc. Natl. Acad. Sci. U.S.A.* **105**, 5034–5039
32. Runge, S., Thøgersen, H., Madsen, K., Lau, J., and Rudolph, R. (2008) Crystal structure of the ligand-bound glucagon-like peptide-1 receptor extracellular domain. *J. Biol. Chem.* **283**, 11340–11347
33. Underwood, C. R., Garibay, P., Knudsen, L. B., Hastrup, S., Peters, G. H., Rudolph, R., and Reedtz-Runge, S. (2010) Crystal structure of glucagon-like peptide-1 in complex with the extracellular domain of the glucagon-like peptide-1 receptor. *J. Biol. Chem.* **285**, 723–730
34. López de Maturana, R., and Donnelly, D. (2002) The glucagon-like peptide-1 receptor binding site for the N-terminus of GLP-1 requires polarity at Asp-198 rather than negative charge. *FEBS Lett.* **530**, 244–248
35. López de Maturana, R., Treece-Birch, J., Abidi, F., Findlay, J. B., and Donnelly, D. (2004) Met-204 and Tyr-205 are together important for binding GLP-1 receptor agonists but not their N-terminally truncated analogues. *Protein Pept. Lett.* **11**, 15–22
36. Miller, L. J., Chen, Q., Lam, P. C., Pinon, D. I., Sexton, P. M., Abagyan, R., and Dong, M. (2011) Refinement of glucagon-like peptide 1 docking to its intact receptor using mid-region photolabile probes and molecular modeling. *J. Biol. Chem.* **286**, 15895–15907
37. Al-Sabah, S., and Donnelly, D. (2003) The positive charge at Lys-288 of the glucagon-like peptide-1 (GLP-1) receptor is important for binding the N-terminus of peptide agonists. *FEBS Lett.* **553**, 342–346
38. Assil-Kishawi, I., and Abou-Samra, A. B. (2002) Sauvagine cross-links to the second extracellular loop of the corticotropin-releasing factor type 1 receptor. *J. Biol. Chem.* **277**, 32558–32561
39. Liaw, C. W., Grigoriadis, D. E., Lovenberg, T. W., De Souza, E. B., and Maki, R. A. (1997) Localization of ligand-binding domains of human corticotropin-releasing factor receptor. A chimeric receptor approach. *Mol. Endocrinol.* **11**, 980–985
40. Baggio, L. L., and Drucker, D. J. (2007) Biology of incretins. GLP-1 and GIP. *Gastroenterology* **132**, 2131–2157
41. Quoyer, J., Longuet, C., Broca, C., Linck, N., Costes, S., Varin, E., Bockaert, J., Bertrand, G., and Dalle, S. (2010) GLP-1 mediates antiapoptotic effect by phosphorylating Bad through a β -arrestin 1-mediated ERK1/2 activation in pancreatic beta-cells. *J. Biol. Chem.* **285**, 1989–2002
42. Klinger, S., Poussin, C., Debril, M. B., Dolci, W., Halban, P. A., and Thorens, B. (2008) Increasing GLP-1-induced beta-cell proliferation by silencing the negative regulators of signaling cAMP-response element modulator- α and DUSP14. *Diabetes* **57**, 584–593
43. Drucker, D. J., and Nauck, M. A. (2006) The incretin system. Glucagon-like peptide-1 receptor agonists and dipeptidyl peptidase-4 inhibitors in type 2 diabetes. *Lancet* **368**, 1696–1705
44. May, L. T., Avlani, V. A., Langmead, C. J., Herdon, H. J., Wood, M. D., Sexton, P. M., and Christopoulos, A. (2007) Structure-function studies of allosteric agonism at M2 muscarinic acetylcholine receptors. *Mol. Pharmacol.* **72**, 463–476
45. Koole, C., Wootten, D., Simms, J., Valant, C., Miller, L. J., Christopoulos, A., and Sexton, P. M. (2011) Polymorphism and ligand-dependent changes in human glucagon-like peptide-1 receptor (GLP-1R) function: allosteric rescue of loss of function mutation. *Mol. Pharmacol.* **80**, 486–497
46. Koole, C., Wootten, D., Simms, J., Valant, C., Sridhar, R., Woodman, O. L., Miller, L. J., Summers, R. J., Christopoulos, A., and Sexton, P. M. (2010) Allosteric ligands of the glucagon-like peptide 1 receptor (GLP-1R) differentially modulate endogenous and exogenous peptide responses in a pathway-selective manner: implications for drug screening. *Mol. Pharmacol.* **78**, 456–465
47. Werry, T. D., Gregory, K. J., Sexton, P. M., and Christopoulos, A. (2005) Characterization of serotonin 5-HT_{2C} receptor signaling to extracellular signal-regulated kinases 1 and 2. *J. Neurochem.* **93**, 1603–1615
48. Cheng, Y., and Prusoff, W. H. (1973) Relationship between the inhibition constant (K_i) and the concentration of inhibitor which causes 50% inhibition (I_{50}) of an enzymatic reaction. *Biochem. Pharmacol.* **22**, 3099–3108
49. Black, J. W., and Leff, P. (1983) Operational models of pharmacological agonism. *Proc. R. Soc. Lond. B Biol. Sci.* **220**, 141–162
50. Gregory, K. J., Hall, N. E., Tobin, A. B., Sexton, P. M., and Christopoulos, A. (2010) Identification of orthosteric and allosteric site mutations in M2 muscarinic acetylcholine receptors that contribute to ligand-selective signaling bias. *J. Biol. Chem.* **285**, 7459–7474
51. Figueroa, K. W., Griffin, M. T., and Ehler, F. J. (2009) Selectivity of agonists for the active state of M1 to M4 muscarinic receptor subtypes. *J. Pharmacol. Exp. Ther.* **328**, 331–342
52. Luttrell, L. M., Ferguson, S. S., Daaka, Y., Miller, W. E., Maudsley, S., Della Rocca, G. J., Lin, F., Kawakatsu, H., Owada, K., Luttrell, D. K., Caron, M. G., and Lefkowitz, R. J. (1999) β -Arrestin-dependent formation of β 2-adrenergic receptor-Src protein kinase complexes. *Science* **283**, 655–661
53. DeFea, K. A., Zalevsky, J., Thoma, M. S., Déry, O., Mullins, R. D., and Bunnett, N. W. (2000) β -Arrestin-dependent endocytosis of proteinase-activated receptor 2 is required for intracellular targeting of activated ERK1/2. *J. Cell Biol.* **148**, 1267–1281
54. Luttrell, L. M., Roudabush, F. L., Choy, E. W., Miller, W. E., Field, M. E., Pierce, K. L., and Lefkowitz, R. J. (2001) Activation and targeting of extracellular signal-regulated kinases by β -arrestin scaffolds. *Proc. Natl. Acad. Sci. U.S.A.* **98**, 2449–2454
55. Shenoy, S. K., Drake, M. T., Nelson, C. D., Houtz, D. A., Xiao, K., Mada-bushi, S., Reiter, E., Premont, R. T., Lichtarge, O., and Lefkowitz, R. J. (2006) β -Arrestin-dependent, G protein-independent ERK1/2 activation by the β 2-adrenergic receptor. *J. Biol. Chem.* **281**, 1261–1273
56. Pearson, G., Robinson, F., Beers Gibson, T., Xu, B. E., Karandikar, M., Berman, K., and Cobb, M. H. (2001) Mitogen-activated protein (MAP) kinase pathways. Regulation and physiological functions. *Endocr. Rev.* **22**, 153–183
57. Warne, T., Serrano-Vega, M. J., Baker, J. G., Moukhametzianov, R., Edwards, P. C., Henderson, R., Leslie, A. G., Tate, C. G., and Schertler, G. F. (2008) Structure of a β 1-adrenergic G-protein-coupled receptor. *Nature* **454**, 486–491
58. Palczewski, K., Kumasaka, T., Hori, T., Behnke, C. A., Motoshima, H., Fox, B. A., Le Trong, I., Teller, D. C., Okada, T., Stenkamp, R. E., Yamamoto, M., and Miyano, M. (2000) Crystal structure of rhodopsin. A G protein-coupled receptor. *Science* **289**, 739–745
59. Cherezov, V., Rosenbaum, D. M., Hanson, M. A., Rasmussen, S. G., Thian, F. S., Kobilka, T. S., Choi, H. J., Kuhn, P., Weis, W. I., Kobilka, B. K., and Stevens, R. C. (2007) High resolution crystal structure of an engineered human β 2-adrenergic G protein-coupled receptor. *Science* **318**, 1258–1265
60. Chien, E. Y., Liu, W., Zhao, Q., Katritch, V., Han, G. W., Hanson, M. A., Shi, L., Newman, A. H., Javitch, J. A., Cherezov, V., and Stevens, R. C. (2010) Structure of the human dopamine D3 receptor in complex with a D2/D3 selective antagonist. *Science* **330**, 1091–1095
61. Jaakola, V. P., Griffith, M. T., Hanson, M. A., Cherezov, V., Chien, E. Y., Lane, J., Jizerman, A. P., and Stevens, R. C. (2008) The 2.6 Å crystal structure of a human A2A adenosine receptor bound to an antagonist. *Science* **322**, 1211–1217
62. Ahn, K. H., Bertalovitz, A. C., Mierke, D. F., and Kendall, D. A. (2009) Dual role of the second extracellular loop of the cannabinoid receptor 1. Ligand binding and receptor localization. *Mol. Pharmacol.* **76**, 833–842
63. Avlani, V. A., Gregory, K. J., Morton, C. J., Parker, M. W., Sexton, P. M., and Christopoulos, A. (2007) Critical role for the second extracellular loop in the binding of both orthosteric and allosteric G protein-coupled receptor ligands. *J. Biol. Chem.* **282**, 25677–25686
64. Conner, M., Hawtin, S. R., Simms, J., Wootten, D., Lawson, Z., Conner, A. C., Parslow, R. A., and Wheatley, M. (2007) Systematic analysis of the entire second extracellular loop of the V(1a) vasopressin receptor. Key

- residues, conserved throughout a G-protein-coupled receptor family, identified. *J. Biol. Chem.* **282**, 17405–17412
65. Scarselli, M., Li, B., Kim, S. K., and Wess, J. (2007) Multiple residues in the second extracellular loop are critical for M3 muscarinic acetylcholine receptor activation. *J. Biol. Chem.* **282**, 7385–7396
66. Shi, L., and Javitch, J. A. (2004) The second extracellular loop of the dopamine D2 receptor lines the binding-site crevice. *Proc. Natl. Acad. Sci. U.S.A.* **101**, 440–445
67. Ahuja, S., Hornak, V., Yan, E. C., Syrett, N., Goncalves, J. A., Hirshfeld, A., Ziliox, M., Sakmar, T. P., Sheves, M., Reeves, P. J., Smith, S. O., and Eilers, M. (2009) Helix movement is coupled to displacement of the second extracellular loop in rhodopsin activation. *Nat. Struct. Mol. Biol.* **16**, 168–175
68. abu Alla, S., Qwitterer, U., Grigoriev, S., Maidhof, A., Haasemann, M., Jarnagin, K., and Müller-Esterl, W. (1996) Extracellular domains of the bradykinin B2 receptor involved in ligand binding and agonist sensing defined by anti-peptide antibodies. *J. Biol. Chem.* **271**, 1748–1755
69. Lebesgue, D., Wallukat, G., Mijares, A., Granier, C., Argibay, J., and Hoebeke, J. (1998) An agonist-like monoclonal antibody against the human β 2-adrenoceptor. *Eur. J. Pharmacol.* **348**, 123–133
70. Ott, T. R., Troskie, B. E., Roeske, R. W., Illing, N., Flanagan, C. A., and Millar, R. P. (2002) Two mutations in extracellular loop 2 of the human GnRH receptor convert an antagonist to an agonist. *Mol. Endocrinol.* **16**, 1079–1088
71. Rasmussen, S. G., Devree, B. T., Zou, Y., Kruse, A. C., Chung, K. Y., Kobilka, T. S., Thian, F. S., Chae, P. S., Pardon, E., Calinski, D., Mathiesen, J. M., Shah, S. T., Lyons, J. A., Caffrey, M., Gellman, S. H., Steyaert, J., Skiniotis, G., Weis, W. I., Sunahara, R. K., and Kobilka, B. K. (2011) Crystal structure of the β 2 adrenergic receptor-Gs protein complex. *Nature* **477**, 549–555
72. Christopoulos, A., and Kenakin, T. (2002) G protein-coupled receptor allostery and complexing. *Pharmacol. Rev.* **54**, 323–374
73. Rosenbaum, D. M., Zhang, C., Lyons, J. A., Holl, R., Aragao, D., Arlow, D. H., Rasmussen, S. G., Choi, H. J., Devree, B. T., Sunahara, R. K., Chae, P. S., Gellman, S. H., Dror, R. O., Shaw, D. E., Weis, W. I., Caffrey, M., Gmeiner, P., and Kobilka, B. K. (2011) Structure and function of an irreversible agonist- β (2) adrenoceptor complex. *Nature* **469**, 236–240
74. Rasmussen, S. G., Choi, H. J., Fung, J. J., Pardon, E., Casarosa, P., Chae, P. S., Devree, B. T., Rosenbaum, D. M., Thian, F. S., Kobilka, T. S., Schnapp, A., Konetzki, I., Sunahara, R. K., Gellman, S. H., Pautsch, A., Steyaert, J., Weis, W. I., and Kobilka, B. K. (2011) Structure of a nanobody-stabilized active state of the β (2) adrenoceptor. *Nature* **469**, 175–180
75. Shimamura, T., Shiroishi, M., Weyand, S., Tsujimoto, H., Winter, G., Katritch, V., Abagyan, R., Cherezov, V., Liu, W., Han, G. W., Kobayashi, T., Stevens, R. C., and Iwata, S. (2011) Structure of the human histamine H1 receptor complex with doxepin. *Nature* **475**, 65–70
76. Wu, B., Chien, E. Y., Mol, C. D., Fenalti, G., Liu, W., Katritch, V., Abagyan, R., Brooun, A., Wells, P., Bi, F. C., Hamel, D. J., Kuhn, P., Handel, T. M., Cherezov, V., and Stevens, R. C. (2010) Structures of the CXCR4 chemokine GPCR with small molecule and cyclic peptide antagonists. *Science* **330**, 1066–1071
77. Mann, R. J., Al-Sabah, S., de Maturana, R. L., Sinfield, J. K., and Donnelly, D. (2010) Functional coupling of Cys-226 and Cys-296 in the glucagon-like peptide-1 (GLP-1) receptor indicates a disulfide bond that is close to the activation pocket. *Peptides* **31**, 2289–2293
78. Montrose-Rafizadeh, C., Yang, H., Rodgers, B. D., Beday, A., Pritchette, L. A., and Eng, J. (1997) High potency antagonists of the pancreatic glucagon-like peptide-1 receptor. *J. Biol. Chem.* **272**, 21201–21206
79. Mann, R. J., Nasr, N. E., Sinfield, J. K., Paci, E., and Donnelly, D. (2010) The major determinant of exendin-4/glucagon-like peptide 1 differential affinity at the rat glucagon-like peptide 1 receptor N-terminal domain is a hydrogen bond from SER-32 of exendin-4. *Br. J. Pharmacol.* **160**, 1973–1984
80. Segrest, J. P., De Loof, H., Dohlman, J. G., Brouillette, C. G., and Anantharamaiah, G. M. (1990) Amphipathic helix motif. Classes and properties. *Proteins* **8**, 103–117

Signal Transduction:
Second Extracellular Loop of Human
Glucagon-like Peptide-1 Receptor
(GLP-1R) Differentially Regulates
Orthosteric but Not Allosteric Agonist
Binding and Function



Cassandra Koole, Denise Wootten, John
Simms, Emilia E. Savage, Laurence J. Miller,
Arthur Christopoulos and Patrick M. Sexton
J. Biol. Chem. 2012, 287:3659-3673.
doi: 10.1074/jbc.M111.309369 originally published online December 6, 2011

Access the most updated version of this article at doi: [10.1074/jbc.M111.309369](https://doi.org/10.1074/jbc.M111.309369)

Find articles, minireviews, Reflections and Classics on similar topics on the [JBC Affinity Sites](https://www.jbc.org/).

Alerts:

- [When this article is cited](#)
- [When a correction for this article is posted](#)

[Click here](#) to choose from all of JBC's e-mail alerts

Supplemental material:

<http://www.jbc.org/content/suppl/2011/12/06/M111.309369.DC1.html>

This article cites 37 references, 18 of which can be accessed free at
<http://www.jbc.org/content/287/6/3659.full.html#ref-list-1>

Second Extracellular Loop of Human Glucagon-like Peptide-1 Receptor (GLP-1R) Differentially Regulates Orthosteric but Not Allosteric Agonist Binding and Function^{*[5]}

Received for publication, September 30, 2011, and in revised form, November 29, 2011 Published, JBC Papers in Press, December 6, 2011, DOI 10.1074/jbc.M111.309369

Cassandra Koole[‡], Denise Wootten[‡], John Simms[‡], Emilia E. Savage[‡], Laurence J. Miller[§], Arthur Christopoulos^{‡1}, and Patrick M. Sexton^{‡2}

From the [‡]Drug Discovery Biology, Monash Institute of Pharmaceutical Sciences and Department of Pharmacology, Monash University, Parkville, Victoria 3052, Australia and the [§]Department of Molecular Pharmacology and Experimental Therapeutics, Mayo Clinic, Scottsdale, Arizona 85259

Background: The ECL2 of the GLP-1R is critical for GLP-1 peptide-mediated selective signaling.

Results: Mutation of most ECL2 residues to alanine results in changes in binding and/or efficacy of oxyntomodulin and exendin-4 but not allosteric agonists.

Conclusion: ECL2 of the GLP-1R has ligand-specific as well as general effects on peptide agonist-mediated receptor activation.

Significance: This work provides insight into control of family B GPCR activation transition.

The glucagon-like peptide-1 receptor (GLP-1R) is a prototypical family B G protein-coupled receptor that exhibits physiologically important pleiotropic coupling and ligand-dependent signal bias. In our accompanying article (Koole, C., Wootten, D., Simms, J., Miller, L. J., Christopoulos, A., and Sexton, P. M. (2012) *J. Biol. Chem.* 287, 3642–3658), we demonstrate, through alanine-scanning mutagenesis, a key role for extracellular loop (ECL) 2 of the receptor in propagating activation transition mediated by GLP-1 peptides that occurs in a peptide- and pathway-dependent manner for cAMP formation, intracellular (Ca^{2+}_i) mobilization, and phosphorylation of extracellular signal-regulated kinases 1 and 2 (pERK1/2). In this study, we examine the effect of ECL2 mutations on the binding and signaling of the peptide mimetics, exendin-4 and oxyntomodulin, as well as small molecule allosteric agonist 6,7-dichloro-2-methylsulfonyl-3-*tert*-butylaminoquinoline (compound 2). Lys-288, Cys-296, Trp-297, and Asn-300 were globally important for peptide signaling and also had critical roles in governing signal bias of the receptor. Peptide-specific effects on relative efficacy and signal bias were most commonly observed for residues 301–305, although R299A mutation also caused significantly different effects for individual peptides. Met-303 was more important for exendin-4 and oxyntomodulin action than those of GLP-1 peptides. Globally, ECL2 mutation was more detrimental to exendin-4-mediated Ca^{2+}_i release than GLP-1(7–36)- NH_2 , providing additional evidence for subtle differences in receptor activation by these two peptides. Unlike peptide activation of

the GLP-1R, ECL2 mutations had only limited impact on compound 2 mediated cAMP and pERK responses, consistent with this ligand having a distinct mechanism for receptor activation. These data suggest a critical role of ECL2 of the GLP-1R in the activation transition of the receptor by peptide agonists.

The family B GPCR,³ GLP-1R, is an important target for the treatment of type II diabetes mellitus, and it has multiple endogenous ligands, including four forms of GLP-1, plus the related peptide oxyntomodulin (1, 2). Therapeutically, the mimetic peptide exendin-4 and metabolically stabilized forms of GLP-1 have recently been approved for treatment of type II diabetes mellitus (3, 4), although an oxyntomodulin derivative is also in clinical trials. In addition, there are a number of small molecule agonists/modulators that can augment responses via the GLP-1R (5–8), including the Novo Nordisk compound 2 (6). Exendin-4 is believed to closely mimic the actions of GLP-1(7–36)- NH_2 at the receptor, but oxyntomodulin and the small molecule ligand, compound 2, display biased signaling relative to the truncated GLP-1 peptides (5, 6, 9). The molecular basis for these distinct actions is not known. Nonetheless, there is accumulating evidence that ECLs, in particular ECL2, may be important for peptide-mediated activation of family B GPCRs (10–17).

In our accompanying article (18), we demonstrate that individual amino acids within ECL2 play a critical role in the activation transition linking GLP-1 peptide binding to intracellular signaling (18) and that it is intimately linked to conformational control of signal bias initiated by peptide binding. However, peptide-specific differences in the effect of ECL2 mutations were also observed between GLP-1(1–36)- NH_2 and GLP-1(7–36)- NH_2 consistent with the ability of ECL2 to contribute to peptide-selective signal bias.

^{*} This work was supported in part by National Health and Medical Research Council of Australia Project Grant 1002180 and Program Grant 519461 and by a National Health and Medical Research Council Principal Research Fellowship (to P. M. S.) and a Senior Research Fellowship (to A. C.).

[5] This article contains supplemental Figs. S1–S3.

¹ Senior Research Fellow of the National Health and Medical Research Council.

² Principal Research Fellow of the National Health and Medical Research Council. To whom correspondence should be addressed: Drug Discovery Biology, Monash Institute of Pharmaceutical Sciences, Monash University, 381 Royal Parade, Parkville, Victoria 3052, Australia. Tel.: 3-9903-9069; Fax: 3-9903-9581; E-mail: patrick.sexton@monash.edu.

³ The abbreviations used are: GPCR, G protein-coupled receptor; compound 2, 6,7-dichloro-2-methylsulfonyl-3-*tert*-butylaminoquinoline; GLP-1R, glucagon-like peptide 1 receptor; Ca^{2+}_i , intracellular calcium.

In this study, we have further explored the function of ECL2 and adjacent domains of the human GLP-1R through pharmacological characterization of the alanine-scanning mutants of ECL2 in the presence of the exogenous GLP-1 peptide mimetic exendin-4, the endogenous peptide agonist oxyntomodulin, or the allosteric agonist compound 2. We demonstrate that select ECL2 residues are critically involved in oxyntomodulin and exendin-4 binding and receptor activity, while also showing that ECL2 has little influence on compound 2 binding and activity, consistent with small molecule agonists having a distinct mode of action.

EXPERIMENTAL PROCEDURES

Materials—Compound 2 was generated in our laboratory, according to the method published previously (19), to a purity of >95%, and compound integrity was confirmed by NMR. Exendin-4 and oxyntomodulin were purchased from American Peptide (Sunnyvale, CA). All other reagents were obtained from suppliers as described in the accompanying article (18).

Methods—Receptor mutagenesis, cell transfection and cell culture, measurement of cell surface expression by antibody labeling of the c-Myc epitope, radioligand binding assays, cAMP accumulation, pERK1/2, and Ca^{2+}_i mobilization assays were each performed as described in our accompanying article (18). For pertussis toxin pretreatment experiments, cells were cultured in FBS-free DMEM containing 100 ng ml⁻¹ pertussis toxin and incubated overnight at 37 °C in 5% CO₂. Data for these experiments were normalized to the maximal response elicited by peptide alone. All other data normalization was performed as described in our accompanying article (18).

Data analysis for determination of IC₅₀, EC₅₀, and operational measures of efficacy was performed as described in our accompanying article (18).

Statistics—Changes in ligand affinity, potency, efficacy, and cell surface expression of ECL2 mutants in comparison with wild type control were statistically analyzed with one-way analysis of variance and Dunnett's post test, and significance was accepted at $p < 0.05$.

RESULTS

Cell Surface Expression of Human GLP-1R ECL2 Alanine Mutants—As reported in our accompanying article (18), cell surface expression determined through detection of the N-terminal double c-Myc epitope label was reduced for mutant receptors D293A, C296A, W297A, S301A, N304A, Y305A, and L307A, and it increased for N300A and M303A, although no significant changes were observed for the remaining mutants (Table 1). In most cases, specific binding of ¹²⁵I-exendin(9–39) followed the same trend as antibody labeling. The exceptions to this were E294A and T298A that had increased specific ¹²⁵I-exendin(9–39) binding in comparison with wild type control, but decreased or unchanged cell surface antibody labeling, and R299A that had decreased specific ¹²⁵I-exendin(9–39) binding but unaltered cell surface antibody labeling. The W306A mutant, however, was not expressed at all at the cell surface and will not be described further.

Select Mutants of the Human GLP-1R ECL2 Influence Exendin-4 and Oxyntomodulin Binding Affinity but Not Exendin(9–39) Affinity—Affinity of exendin-4 and oxyntomodulin at each of the mutants was assessed by competition for

TABLE 1

Effects of human GLP-1R ECL2 alanine mutants on peptide ligand binding and cell surface expression

Binding data were analyzed using a three-parameter logistic equation as defined in Equation 1 of the accompanying article. pIC₅₀ values were then corrected for radioligand occupancy using the radioligand dissociation constant for each mutant, allowing determination of ligand affinity (K_i). All values are expressed as means ± S.E. of three to four independent experiments, conducted in duplicate. Data were analyzed with one-way analysis of variance and Dunnett's post test. R^2 values for curve fits were all >0.5. Gray shading highlights residues effecting peptide agonist binding affinity. ND indicates data unable to be experimentally defined.

	Binding (pK _i)	
	Exendin-4	Oxyntomodulin
Wildtype	9.4 ± 0.1	7.7 ± 0.1
G285A	9.4 ± 0.1	7.9 ± 0.1
I286A	9.4 ± 0.1	7.7 ± 0.2
V287A	9.2 ± 0.1	7.4 ± 0.1
K288A	7.5 ± 0.1*	6.7 ± 0.2*
Y289A	9.4 ± 0.3	7.9 ± 0.2
L290A	9.2 ± 0.1	7.4 ± 0.3
Y291A	9.0 ± 0.1	7.4 ± 0.2
E292A	7.6 ± 0.2*	6.5 ± 0.4*
D293A	8.3 ± 0.2*	6.9 ± 0.2
E294A	9.5 ± 0.1	7.7 ± 0.1
G295A	9.4 ± 0.2	8.0 ± 0.2
C296A	7.6 ± 0.2*	N.D.
W297A	7.6 ± 0.2*	N.D.
T298A	9.6 ± 0.1	8.2 ± 0.1
R299A	7.9 ± 0.3*	N.D.
N300A	7.6 ± 0.1*	6.7 ± 0.3*
S301A	9.4 ± 0.1	7.8 ± 0.1
N302A	8.2 ± 0.1*	6.6 ± 0.3*
M303A	8.7 ± 0.1*	7.0 ± 0.1
N304A	9.1 ± 0.2	7.3 ± 0.2
Y305A	7.7 ± 0.1*	N.D.
W306A	N.D.	N.D.
L307A	8.6 ± 0.1*	7.1 ± 0.3

* Data are statistically significant at $p < 0.05$, one-way analysis of variance, and Dunnett's post test in comparison with wild type response.

¹²⁵I-exendin(9–39) binding under equilibrium conditions (Table 1). There were no significant changes in binding affinity of exendin-4 or oxyntomodulin in comparison with the wild type control for receptor mutants G285A, I286A, V287A, Y289A, L290A, Y291A, E294A, G295A, T298A, S301A, and N304A, although decreases in affinity for both ligands were observed for receptor mutants K288A, E292A, D293A, C296A, W297A, R299A, N300A, N302A, M303A, Y305A, and L307A,

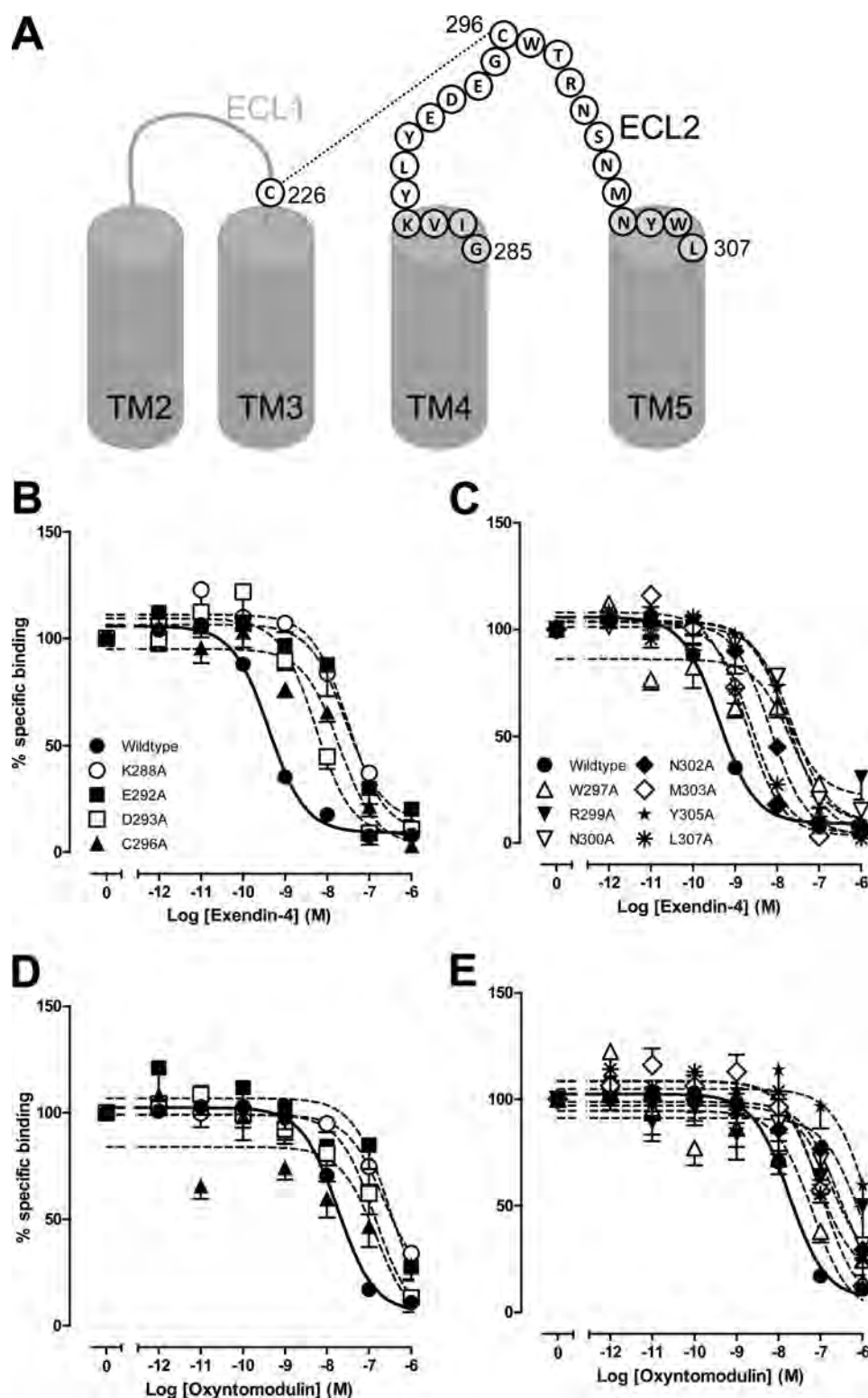


FIGURE 1. Agonist binding profiles of human GLP-1R ECL2 alanine mutants. *A*, schematic representation of the human GLP-1R ECL2, with disulfide interactions indicated (—) and boundaries indicated in gray shading. Characterization of the binding of exendin-4 (*B* and *C*) and oxyntomodulin (*D* and *E*) in competition with the radiolabeled antagonist, [125 I]-exendin(9–39), in whole FlpInCHO cells stably expressing the wild type human GLP-1R or each of the human GLP-1R ECL2 alanine mutants that effect peptide binding affinity or the wild type GLP-1R. Data are normalized to maximum [125 I]-exendin(9–39) binding, with nonspecific binding measured in the presence of 1 μ M exendin(9–39) and analyzed with a three-parameter logistic equation as defined in Equation 1 of the accompanying article. All values are means \pm S.E. of three to four independent experiments, conducted in duplicate.

as highlighted in gray in Table 1 (Fig. 1, *B–E*, and Table 1). This shading is maintained throughout all tables as an indication of mutants affected in binding affinity. Curves could not be accu-

rately fitted for C296A and W297A in the presence of oxyntomodulin, most likely a result of the narrow window of signal generated by the significant decrease in specific [125 I]-

TABLE 2

Effects of human GLP-1R ECL2 alanine mutants on peptide agonist signaling via cAMP

Data were analyzed using a three-parameter logistic equation as defined in Equation 1 of the accompanying article. pEC_{50} values represent the negative logarithm of the concentration of agonist that produces half the maximal response. E_{max} represents the maximal response normalized to that elicited by 100 μ M forskolin. All mutants were analyzed with an operational model of agonism (Equation 2 of the accompanying article) to determine $\log\tau$ values. All $\log\tau$ values were then corrected to specific 125 I-exendin(9–39) binding ($\log\tau_c$). Values are expressed as means \pm S.E. of three to seven independent experiments, conducted in duplicate. Data were analyzed with one-way analysis of variance and Dunnett's post test. R^2 values for the global curve fits were 0.87 for exendin-4 and 0.91 for oxyntomodulin, respectively. Gray shading highlights residues effecting peptide agonist binding affinity. ND indicates data unable to be experimentally defined.

	cAMP accumulation					
	Exendin-4			Oxyntomodulin		
	pEC_{50}	E_{max}	$\log\tau_c$ (τ_c)	pEC_{50}	E_{max}	$\log\tau_c$ (τ_c)
Wildtype	10.4 \pm 0.1	177.6 \pm 5.4	1.03 \pm 0.09 (10.72)	7.9 \pm 0.1	154.8 \pm 5.5	0.83 \pm 0.07 (6.76)
G285A	10.3 \pm 0.2	145.6 \pm 8.0*	0.82 \pm 0.09 (6.61)	7.9 \pm 0.1	145.1 \pm 5.9	0.90 \pm 0.08 (7.94)
I286A	10.3 \pm 0.2	167.8 \pm 9.3	0.98 \pm 0.11 (9.55)	7.7 \pm 0.2	167.0 \pm 14.0	0.93 \pm 0.09 (8.51)
V287A	10.2 \pm 0.1	132.3 \pm 5.2*	0.66 \pm 0.12 (4.57)	7.3 \pm 0.1	132.3 \pm 5.2	0.52 \pm 0.12 (3.31)
K288A	N.D.	N.D.	N.D.	N.D.	N.D.	N.D.
Y289A	10.4 \pm 0.3	114.0 \pm 8.8*	0.58 \pm 0.09 (3.80)*	7.7 \pm 0.2	118.1 \pm 9.6*	0.61 \pm 0.08 (4.07)
L290A	10.1 \pm 0.2	138.0 \pm 7.6*	0.63 \pm 0.09 (4.27)	7.3 \pm 0.1	150.4 \pm 6.4	0.58 \pm 0.09 (3.80)
Y291A	9.9 \pm 0.2	139.4 \pm 8.9*	0.50 \pm 0.10 (3.16)*	7.2 \pm 0.1	145.6 \pm 4.9	0.40 \pm 0.09 (2.51)
E292A	8.3 \pm 0.1*	122.4 \pm 5.2*	0.49 \pm 0.09 (3.09)*	6.5 \pm 0.3*	30.1 \pm 3.3*	-0.61 \pm 0.17 (0.25)*
D293A	9.3 \pm 0.2*	118.1 \pm 6.5*	0.44 \pm 0.10 (2.75)*	6.5 \pm 0.1*	71.3 \pm 4.6*	0.05 \pm 0.10 (1.12)*
E294A	10.1 \pm 0.1	141.7 \pm 3.1*	0.42 \pm 0.18 (2.63)*	7.6 \pm 0.1	135.7 \pm 7.1	0.38 \pm 0.17 (2.40)
G295A	10.2 \pm 0.1	149.5 \pm 5.4*	0.80 \pm 0.09 (6.31)	8.0 \pm 0.1	150.3 \pm 6.5	0.97 \pm 0.09 (9.33)
C296A	8.4 \pm 0.1*	122.5 \pm 3.6*	0.69 \pm 0.08 (4.90)	6.4 \pm 0.2*	42.6 \pm 3.9*	-0.15 \pm 0.12 (0.71)*
W297A	7.7 \pm 0.2*	65.8 \pm 5.1*	0.03 \pm 0.11 (1.07)*	N.D.	N.D.	N.D.
T298A	10.6 \pm 0.2	133.4 \pm 6.1*	0.48 \pm 0.13 (3.02)*	8.0 \pm 0.1	141.9 \pm 6.8	0.62 \pm 0.13 (4.17)
R299A	9.8 \pm 0.2	106.3 \pm 6.5*	0.44 \pm 0.06 (2.75)*	6.9 \pm 0.1*	78.9 \pm 4.7*	0.28 \pm 0.06 (1.91)*
N300A	7.9 \pm 0.1*	143.1 \pm 5.9*	0.53 \pm 0.15 (3.39)*	6.6 \pm 0.3*	33.7 \pm 3.4*	-0.76 \pm 0.14 (0.17)*
S301A	10.3 \pm 0.2	99.4 \pm 5.7*	0.27 \pm 0.08 (1.86)*	7.8 \pm 0.2	101.5 \pm 8.0*	0.37 \pm 0.07 (2.34)
N302A	9.6 \pm 0.1*	119.3 \pm 5.4*	0.19 \pm 0.17 (1.55)*	6.9 \pm 0.1*	95.3 \pm 4.2*	0.08 \pm 0.17 (1.20)*
M303A	10.2 \pm 0.1	107.9 \pm 3.0*	0.18 \pm 0.08 (1.51)*	7.4 \pm 0.1	128.8 \pm 8.2*	0.69 \pm 0.13 (4.90)
N304A	10.1 \pm 0.2	73.8 \pm 3.4*	0.17 \pm 0.13 (1.48)*	7.4 \pm 0.2	75.8 \pm 6.4*	0.19 \pm 0.12 (1.55)*
Y305A	9.2 \pm 0.2*	136.1 \pm 9.5*	0.50 \pm 0.12 (3.16)*	6.6 \pm 0.1*	69.7 \pm 4.5*	-0.13 \pm 0.10 (0.74)*
W306A	N.D.	N.D.	N.D.	N.D.	N.D.	N.D.
L307A	9.6 \pm 0.2*	103.6 \pm 7.2*	0.29 \pm 0.08 (1.95)*	6.9 \pm 0.1*	74.5 \pm 4.6*	0.10 \pm 0.07 (1.26)*

* Data are statistically significant at $p < 0.05$, one-way analysis of variance, and Dunnett's post test in comparison with the wild type response.

exendin(9–39) binding (Table 1 of Ref. 18). In addition, binding affinity could not be determined for oxyntomodulin at mutant receptors R299A and Y305A due to incomplete curves, although reductions in binding affinity were apparent (Fig. 1). Notably, although the extent of affinity reduction of exendin-4 and oxyntomodulin was generally similar, differential effects of mutation were observed for the K288A, E292A, and N300A mutants with decreases in binding affinity of 79-, 63-, and 63-fold, respectively, for exendin-4, but only 10-, 16-, and 10-fold, respectively, for oxyntomodulin (Table 1).

Effect of Human GLP-1R ECL2 Alanine Mutations on Peptide-mediated cAMP Accumulation—The effect of mutation on ligand-induced cAMP formation was assessed via determination of potency and efficacy; the latter was estimated using an operational model corrected for receptor expression (τ_c , Table 2). Although both peptides were full agonists, exendin-4 had higher efficacy than oxyntomodulin in this system ($\log\tau_c$ 1.03 \pm 0.09 and 0.83 \pm 0.07, respectively). With the exception of the M303A mutant, all mutants with reduced peptide agonist binding displayed reduced potency and efficacy, although the exendin-4 potency shift for R299A did not reach significance (Fig. 2,

A, B, E, and F, and Table 2). The greatest effects on cAMP formation, for both peptides, were seen with the K288A and W297A mutants, with signaling essentially abolished at K288A and complete loss of oxyntomodulin signaling and marked attenuation of exendin-4 potency and efficacy at W297A (Fig. 2, A, B, E, and F, and Table 2). Similar reductions in responses elicited by both peptides were seen for the D293A, R299A, N302A, Y305A, and L307A mutants. In contrast, E292A, C296A, and N300A showed greater relative loss of exendin-4 potency, compared with that of oxyntomodulin with fold decreases in potency of 126, 100, and 316, respectively, for exendin-4 and 25, 32, and 20, respectively, for oxyntomodulin. This differential effect on potency was paralleled by greater decreases in binding affinity of exendin-4 for E292A and N300A, although the magnitude of effect on C296A affinity for oxyntomodulin could not be accurately determined (see above). Interestingly, at these mutants there was a correspondingly greater reduction in efficacy for oxyntomodulin relative to exendin-4, illustrating distinction in the impact of these residues on oxyntomodulin and exendin-4 function (Fig. 2, A and B, and Table 2).

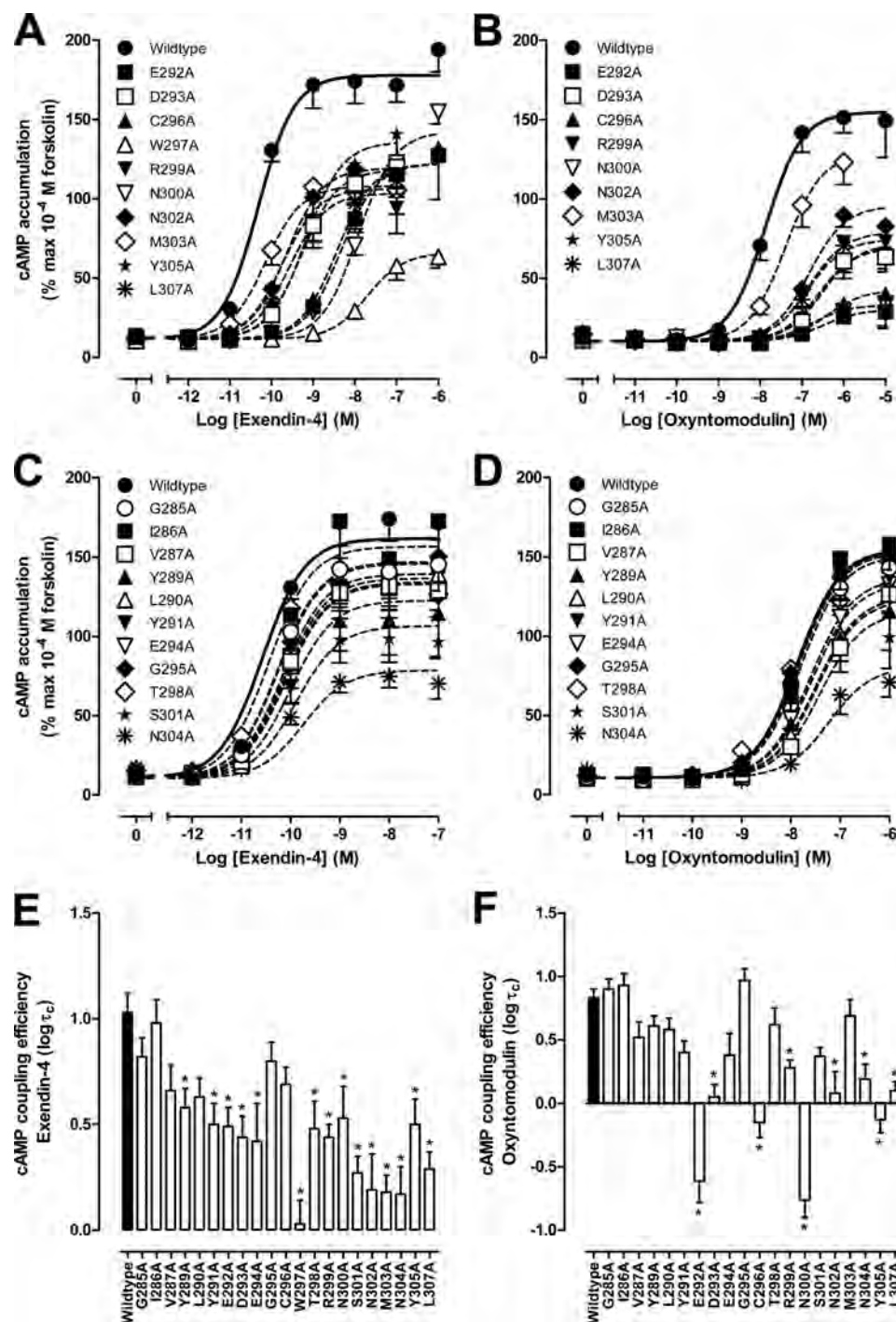


FIGURE 2. cAMP accumulation profiles of human GLP-1R ECL2 alanine mutants. Characterization of cAMP accumulation in the presence of exendin-4 (A and C) and oxyntomodulin (B and D) in FlpInCHO cells stably expressing the wild type human GLP-1R or each of the human GLP-1R ECL2 alanine mutants that effect peptide binding affinity (A and B) or have no significant effect on peptide binding affinity (C and D). Data are normalized to the response elicited by 100 μ M forskolin and analyzed with an operational model of agonism as defined in Equation 2 of the accompanying article. All values are means \pm S.E. of three to seven independent experiments, conducted in duplicate. Visual representation of cAMP pathway coupling efficacy ($\log \tau_c$) in the presence of exendin-4 (E) and oxyntomodulin (F) is shown. Statistical significance of changes in coupling efficacy in comparison with wild type human GLP-1R was determined by one-way analysis of variance and Dunnett's post test, and values are indicated with an asterisk (*, $p < 0.05$). All values are $\log \tau_c \pm$ S.E. of three to seven independent experiments, conducted in duplicate.

For those mutants that did not affect peptide binding, the effect on cAMP signaling was similar for both peptides. None of the mutants significantly altered potency of the peptides, although efficacy was also unaltered for the G285A, I286A, and G295A mutants (Fig. 2, C–F, and Table

2). All other mutants exhibited modest decreases in efficacy for the two peptides, although the effects did not always reach significance. The greatest effects on efficacy were seen with the S301A and N304A mutants (Fig. 2, E and F, and Table 2).

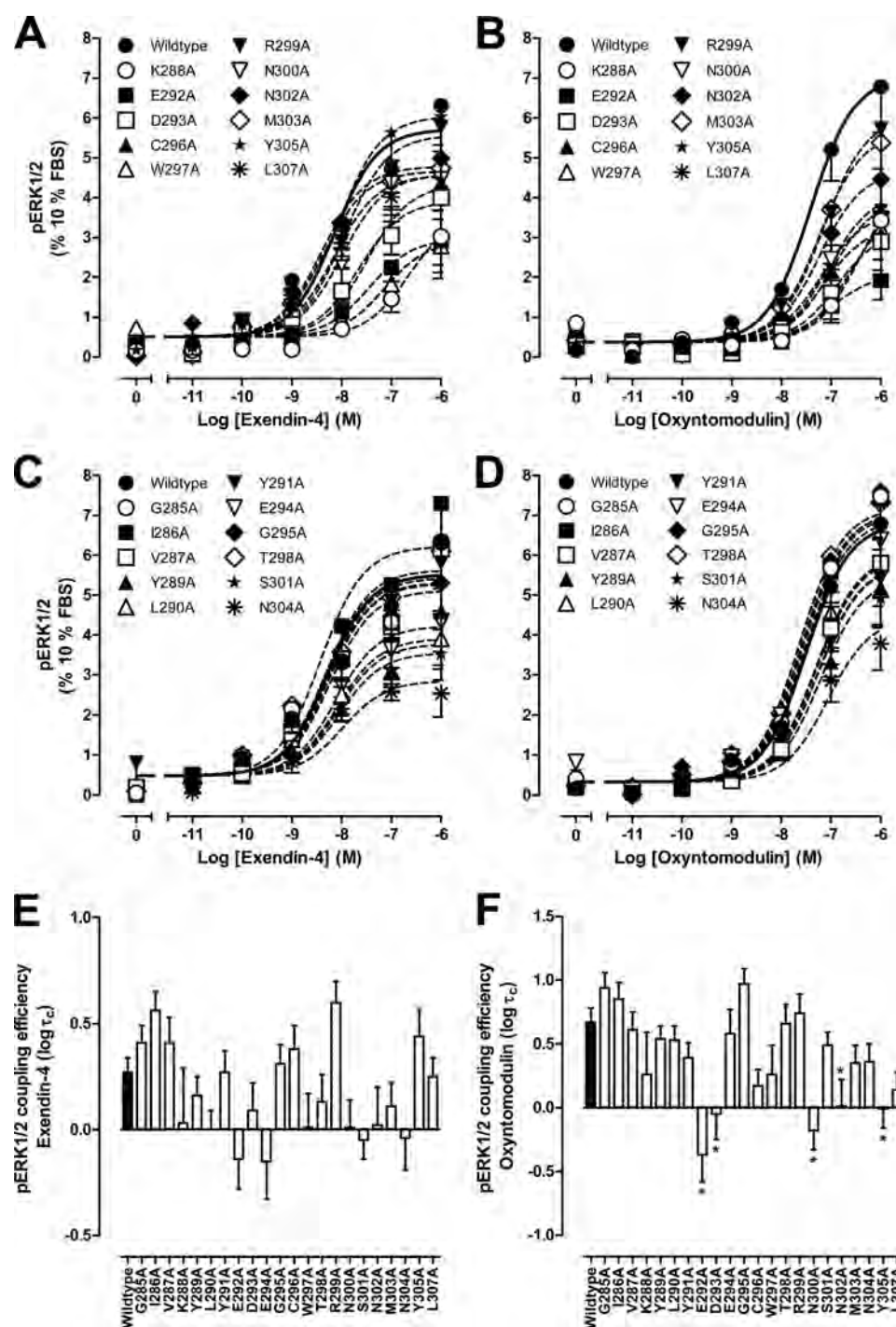


FIGURE 3. **pERK1/2 profiles of human GLP-1R ECL2 alanine mutants.** Characterization of pERK1/2 in the presence of exendin-4 (A and C) and oxyntomodulin (B and D) in FlpInCHO cells stably expressing the wild type human GLP-1R or each of the human GLP-1R ECL2 alanine mutants that effect peptide binding affinity (A and B) or have no significant effect on peptide binding affinity (C and D). Data are normalized to the maximal response elicited by 10% FBS and analyzed with an operational model of agonism as defined in Equation 2 of the accompanying article. All values are means \pm S.E. of five to seven independent experiments, conducted in duplicate. Visual representation of pERK1/2 coupling efficacy (log τ_c) in the presence of exendin-4 (E) and oxyntomodulin (F) is shown. Statistical significance of changes in coupling efficacy in comparison with wild type human GLP-1R was determined by one-way analysis of variance and Dunnett's post test, and values are indicated with an asterisk (*, $p < 0.05$). All values are log $\tau_c \pm$ S.E. of five to seven independent experiments, conducted in duplicate.

Effect of Human GLP-1R ECL2 Alanine Mutations on Peptide-mediated pERK1/2—Peptide-induced pERK1/2 was determined at 6 min for each of the human GLP-1R ECL2 alanine mutants. As noted in our accompanying article (18) for GLP-1(7–36)-NH₂, ECL2 mutations globally had a lower impact on

pERK1/2 relative to cAMP formation. There was also a generally greater impact on oxyntomodulin-induced signaling relative to that of exendin-4 (Fig. 3, A, B, E, and F, and Table 3). Only K288A had any effect on peptide potency, with decreased exendin-4 potency and a trend toward decreased

TABLE 3

Effects of human GLP-1R ECL2 alanine mutants on peptide agonist signaling via pERK1/2

Data were analyzed using a three-parameter logistic equation as defined in Equation 1 of the accompanying article. pEC_{50} values represent the negative logarithm of the concentration of agonist that produces half the maximal response. E_{max} represents the maximal response normalized to that elicited by 10% FBS. All mutants were analyzed with an operational model of agonism (Equation 2 of the accompanying article) to determine $\log\tau$ values. All $\log\tau$ values were then corrected to specific ^{125}I -exendin(9–39) binding ($\log\tau_c$). Values are expressed as means \pm S.E. of five to seven independent experiments, conducted in duplicate. Data were analyzed with one-way analysis of variance and Dunnett's post test. R^2 values for the global curve fits were 0.67 for exendin-4 and 0.66 for oxyntomodulin, respectively. Gray shading highlights residues affecting peptide agonist binding affinity. ND indicates data unable to be experimentally defined.

	pERK1/2					
	Exendin-4			Oxyntomodulin		
	pEC_{50}	E_{max}	$\log\tau_c$ (τ_c)	pEC_{50}	E_{max}	$\log\tau_c$ (τ_c)
Wildtype	8.1 \pm 0.2	5.7 \pm 0.5	0.27 \pm 0.07 (1.86)	7.4 \pm 0.2	7.0 \pm 0.6	0.67 \pm 0.11 (4.68)
G285A	8.2 \pm 0.2	5.5 \pm 0.5	0.41 \pm 0.08 (2.57)	7.4 \pm 0.1	7.8 \pm 0.5	0.94 \pm 0.12 (8.71)
I286A	8.3 \pm 0.2	6.5 \pm 0.5	0.56 \pm 0.09 (3.63)	7.4 \pm 0.1	7.7 \pm 0.7	0.85 \pm 0.13 (7.08)
V287A	8.2 \pm 0.2	5.4 \pm 0.4	0.41 \pm 0.12 (2.57)	7.3 \pm 0.2	6.1 \pm 0.6	0.61 \pm 0.14 (4.07)
K288A	6.8 \pm 0.3*	3.4 \pm 0.6*	0.03 \pm 0.26 (1.07)	6.4 \pm 0.5	4.6 \pm 1.5	0.26 \pm 0.33 (1.82)
Y289A	7.9 \pm 0.2	4.1 \pm 0.4	0.16 \pm 0.09 (1.45)	7.2 \pm 0.2	5.4 \pm 0.5	0.54 \pm 0.10 (3.47)
L290A	8.6 \pm 0.3	3.5 \pm 0.3*	0.00 \pm 0.09 (1.00)	7.5 \pm 0.2	5.5 \pm 0.5	0.53 \pm 0.11 (3.39)
Y291A	8.1 \pm 0.3	5.6 \pm 0.6	0.27 \pm 0.10 (1.86)	7.3 \pm 0.2	5.6 \pm 0.6	0.39 \pm 0.12 (2.45)
E292A	7.6 \pm 0.3	2.9 \pm 0.3*	-0.14 \pm 0.14 (0.72)	7.1 \pm 0.3	2.1 \pm 0.3*	-0.37 \pm 0.21 (0.43)*
D293A	7.7 \pm 0.3	3.9 \pm 0.4*	0.09 \pm 0.13 (1.23)	7.0 \pm 0.3	3.2 \pm 0.5*	-0.05 \pm 0.20 (0.89)*
E294A	8.3 \pm 0.3	4.1 \pm 0.4	-0.15 \pm 0.18 (0.71)	7.6 \pm 0.3	6.7 \pm 0.3	0.58 \pm 0.19 (3.80)
G295A	8.4 \pm 0.3	4.9 \pm 0.4	0.31 \pm 0.09 (2.04)	7.4 \pm 0.2	7.9 \pm 0.8	0.97 \pm 0.12 (9.33)
C296A	7.4 \pm 0.3	4.4 \pm 0.5	0.38 \pm 0.11 (2.40)	7.2 \pm 0.3	3.3 \pm 0.5*	0.17 \pm 0.13 (1.48)
W297A	7.1 \pm 0.4	2.9 \pm 0.5*	0.01 \pm 0.16 (1.02)	6.6 \pm 0.6	3.9 \pm 1.3*	0.26 \pm 0.23 (1.82)
T298A	8.4 \pm 0.3	5.4 \pm 0.5	0.13 \pm 0.13 (1.35)	7.5 \pm 0.2	7.6 \pm 0.8	0.66 \pm 0.15 (4.57)
R299A	8.0 \pm 0.2	5.6 \pm 0.5	0.60 \pm 0.10 (3.98)	7.2 \pm 0.2	6.0 \pm 0.6	0.74 \pm 0.15 (5.50)
N300A	8.0 \pm 0.3	4.6 \pm 0.4	0.01 \pm 0.13 (1.02)	7.2 \pm 0.5	3.6 \pm 0.8*	-0.18 \pm 0.15 (0.66)*
S301A	8.4 \pm 0.2	3.3 \pm 0.2*	-0.05 \pm 0.09 (0.89)	7.5 \pm 0.2	5.3 \pm 0.5	0.49 \pm 0.10 (3.09)
N302A	8.4 \pm 0.3	4.8 \pm 0.5	0.02 \pm 0.18 (1.05)	7.2 \pm 0.2	4.7 \pm 0.5	0.01 \pm 0.21 (1.02)*
M303A	8.5 \pm 0.3	4.6 \pm 0.4	0.11 \pm 0.11 (1.29)	7.3 \pm 0.2	5.6 \pm 0.5	0.35 \pm 0.14 (2.24)
N304A	8.6 \pm 0.2	2.6 \pm 0.2*	-0.04 \pm 0.15 (0.91)	7.4 \pm 0.2	3.9 \pm 0.4*	0.36 \pm 0.14 (2.29)
Y305A	8.1 \pm 0.2	6.0 \pm 0.4	0.44 \pm 0.13 (2.75)	7.1 \pm 0.2	4.1 \pm 0.4*	-0.01 \pm 0.15 (0.98)*
W306A	N.D.	N.D.	N.D.	N.D.	N.D.	N.D.
L307A	8.2 \pm 0.2	4.6 \pm 0.4	0.25 \pm 0.09 (1.78)	7.0 \pm 0.2	4.0 \pm 0.4*	0.14 \pm 0.14 (1.38)

* Data are statistically significant at $p < 0.05$, one-way analysis of variance, and Dunnett's post test in comparison with wild type response.

potency for oxyntomodulin (Table 3). Of the other mutants that displayed reduced exendin-4 binding affinity, none had statistically significant effects on efficacy. For oxyntomodulin, significant loss of efficacy was observed for the E292A, D293A, N300A, N302A, and Y305A mutants. Whereas similar trends for lower efficacy were seen for exendin-4 at most of these mutants, Y305A efficacy was increased (Fig. 3, A, B, E, and F, and Table 3). No significant effects on efficacy were seen for either peptide or for the mutants that did not modulate peptide binding affinity (Fig. 3, C–F, and Table 3).

Effect of Human GLP-1R ECL2 Alanine Mutations on Peptide-mediated Ca^{2+}_i Mobilization—Of the three signaling pathways studied, Ca^{2+}_i mobilization is the least well coupled and is also the one most affected by ECL2 mutations (Table 4). For the mutations that reduced exendin-4 binding affinity (K288A, E292A, D293A, C296A, W297A, R299A, N300A, Y305A, and L307A), there was effectively complete loss of exen-

din-4-mediated signaling and only weak responses for N302A and M303A, with marked reduction in efficacy, but no significant change in potency (Fig. 4A and Table 4). For mutants that did not alter exendin-4 affinity, reduced efficacy was also observed, with the exceptions being G285A, G295A, T298A, and S301A (Fig. 4, B and C, and Table 4).

As observed previously (5, 9), oxyntomodulin has very weak coupling to Ca^{2+}_i mobilization, and full concentration-response curves could not be established over the concentration range assessed. Comparison of responses at the highest concentration used (1 μ M) revealed reduced responses for each of the mutants that decreased oxyntomodulin affinity (K288A, E292A, D293A, C296A, W297A, R299A, N300A, N302A, M303A, Y305A, and L307A) (Fig. 4D). Reduced responses were also observed for T298A and N304A. Of note, no significant change in response was observed for E294A, despite a significantly reduced exendin-4 response (Fig. 4, B and D).

TABLE 4**Effects of human GLP-1R ECL2 alanine mutants on peptide agonist signaling via Ca^{2+} mobilization**

Data were analyzed using a three-parameter logistic equation as defined in Equation 1 of the accompanying article. pEC_{50} values represent the negative logarithm of the concentration of agonist that produces half the maximal response. E_{max} represents the maximal response normalized to that elicited by $100 \mu\text{M}$ ATP. All mutants were analyzed with an operational model of agonism (Equation 2 of the accompanying article) to determine $\log\tau$ values. All $\log\tau$ values were then corrected to specific ^{125}I -exendin(9–39) binding ($\log\tau_c$). Values are expressed as means \pm S.E. of four to five independent experiments, conducted in duplicate. Data were analyzed with one-way analysis of variance and Dunnett's post test. The R^2 value for the global curve fit was 0.85. Gray shading highlights residues effecting peptide agonist binding affinity. ND indicates data unable to be experimentally defined.

	iCa ²⁺ mobilization		
	Exendin-4		
	pEC_{50}	E_{max}	$\log\tau_c (\tau_c)$
Wildtype	7.8 ± 0.1	12.4 ± 0.6	$0.70 \pm 0.07 (5.01)$
G285A	7.9 ± 0.2	$8.1 \pm 0.5^*$	$0.42 \pm 0.07 (2.63)$
I286A	7.9 ± 0.2	$4.8 \pm 0.4^*$	$-0.08 \pm 0.08 (0.83)^*$
V287A	7.8 ± 0.2	$4.0 \pm 0.4^*$	$-0.15 \pm 0.12 (0.71)^*$
K288A	N.D.	N.D.	N.D.
Y289A	7.1 ± 0.2	$3.8 \pm 0.5^*$	$-0.24 \pm 0.09 (0.58)^*$
L290A	7.6 ± 0.4	$3.6 \pm 0.6^*$	$-0.29 \pm 0.09 (0.51)^*$
Y291A	7.3 ± 0.3	$4.2 \pm 0.5^*$	$-0.35 \pm 0.10 (0.45)^*$
E292A	N.D.	N.D.	N.D.
D293A	N.D.	N.D.	N.D.
E294A	7.6 ± 0.3	$5.3 \pm 0.6^*$	$-0.29 \pm 0.17 (0.51)^*$
G295A	7.6 ± 0.1	$9.0 \pm 0.4^*$	$0.42 \pm 0.07 (2.63)$
C296A	N.D.	N.D.	N.D.
W297A	N.D.	N.D.	N.D.
T298A	7.6 ± 0.1	$9.8 \pm 0.5^*$	$0.21 \pm 0.12 (1.62)$
R299A	N.D.	N.D.	N.D.
N300A	N.D.	N.D.	N.D.
S301A	7.9 ± 0.2	$6.9 \pm 0.5^*$	$0.25 \pm 0.06 (1.78)$
N302A	7.0 ± 0.3	$2.5 \pm 0.4^*$	$-0.74 \pm 0.21 (0.18)^*$
M303A	7.7 ± 0.2	$4.0 \pm 0.3^*$	$-0.33 \pm 0.09 (0.47)^*$
N304A	7.0 ± 0.4	$3.9 \pm 0.8^*$	$-0.19 \pm 0.13 (0.65)^*$
Y305A	N.D.	N.D.	N.D.
W306A	N.D.	N.D.	N.D.
L307A	N.D.	N.D.	N.D.

* Data are statistically significant at $p < 0.05$, one-way analysis of variance, and Dunnett's post test in comparison with wild type response.

Effect of Human GLP-1R ECL2 Alanine Mutations on the Function of the GLP-1R Allosteric Agonist, Compound 2—In addition to analyzing the effects of human GLP-1R ECL2 on peptide agonist binding and function, we also analyzed the effect of these mutants on binding and function of the GLP-1R allosteric agonist, compound 2 (Fig. 5 and Table 5) (5, 6). Compound 2 is a weak allosteric inhibitor of ^{125}I -exendin(9–39) binding (5). Mutation of ECL2 had no effect on compound 2 inhibition of the radioligand relative to the wild type receptor, although for mutants with low specific ^{125}I -exendin(9–39) binding (see Table 1 of Ref. 18), the effect of the mutations on compound 2-mediated inhibition of binding could not be robustly determined (data not shown).

Compound 2 is a low potency but high efficacy partial agonist for GLP-1R-mediated increases in cAMP formation and a weak partial agonist for receptor-mediated pERK1/2 (5). The maximal concentration of compound 2 used in this study was $10 \mu\text{M}$, which approaches the solubility limit of the compound.

Although previous studies suggest that this concentration elicits a near maximal cAMP response (5, 9), the upper plateau of the concentration-response curve was not fully defined in this study, preventing application of the operational model fitting to the data and determination of efficacy-related effects independent of receptor expression. Analysis of the effect of mutations on cAMP formation revealed limited impact on compound 2-mediated signaling with no change to potency and only small decreases in maximal response (Fig. 5, A and B, and Table 5). The decreases observed in maximal response were paralleled by decreases in functional cell surface receptor expression (18), suggesting that this likely underlies loss of signaling rather than a direct effect on receptor activation by compound 2. There was no significant alteration to potency or maximal response to compound 2-mediated pERK1/2 for any of the ECL2 mutants (Fig. 5, C and D, and Table 5).

Human GLP-1R ECL2 Is Critical for Peptide-mediated Activation Transition of GLP-1R—Overall, there was a strong correlation of the effect of the mutations on changes to efficacy for peptide-mediated cAMP and pERK1/2, albeit that the changes were not necessarily in the same direction, and this was particularly true for oxyntomodulin responses (Fig. 6). A lower degree of correlation was seen between the effect of mutation on exendin-4 between either cAMP or pERK1/2 and Ca^{2+} (Fig. 6, B and C), although this is likely related, at least in part, to the large number of mutants without a measurable Ca^{2+} response to this peptide. Globally, this is consistent with a key role for ECL2 in the generation of the ensemble of receptor conformations linked to signaling responses. The relative preservation, or even increase, in pERK1/2 response upon ECL2 mutation relative to the other signaling pathways suggests that the ensemble of conformations mediating pERK1/2 are quite distinct from those linked to cAMP formation and Ca^{2+} mobilization. Nonetheless, although the data are consistent with a major role of ECL2 in conformational propagation, there were clear examples where individual mutation had pathway-selective effects on efficacy. For oxyntomodulin, there was a very tight correlation between the effect of most mutations on pERK1/2 and cAMP efficacy. The exceptions to this were the R299A and M303A mutants (Fig. 6D), indicating differential effects on oxyntomodulin-mediated signaling. For the M303A mutation this manifests as a minimal loss of cAMP signaling compared with pERK1/2, although for the R299A mutation there was a relatively greater loss of cAMP signaling. For exendin-4, there was proportionally greater loss of cAMP efficacy relative to pERK1/2 efficacy for M303A, L307A, and W297A, although L290A exhibited relatively preserved cAMP efficacy relative to the loss of pERK1/2 signaling. The outliers for exendin-4 and oxyntomodulin were mostly distinct from those observed with the GLP-1 peptides (18), although R299A, L290A, and W297A were also among those residues that exhibited noncorrelative effects across different pathways. For the GLP-1 peptides, N304A also displayed pathway- and peptide-dependent effects on efficacy, although this residue displayed mostly consistent effects across pathways for exendin-4 and oxyntomodulin. Thus, although ECL2 is globally important for receptor activation, individual residues likely contribute to secondary structure that is important for peptide-specific receptor activation.

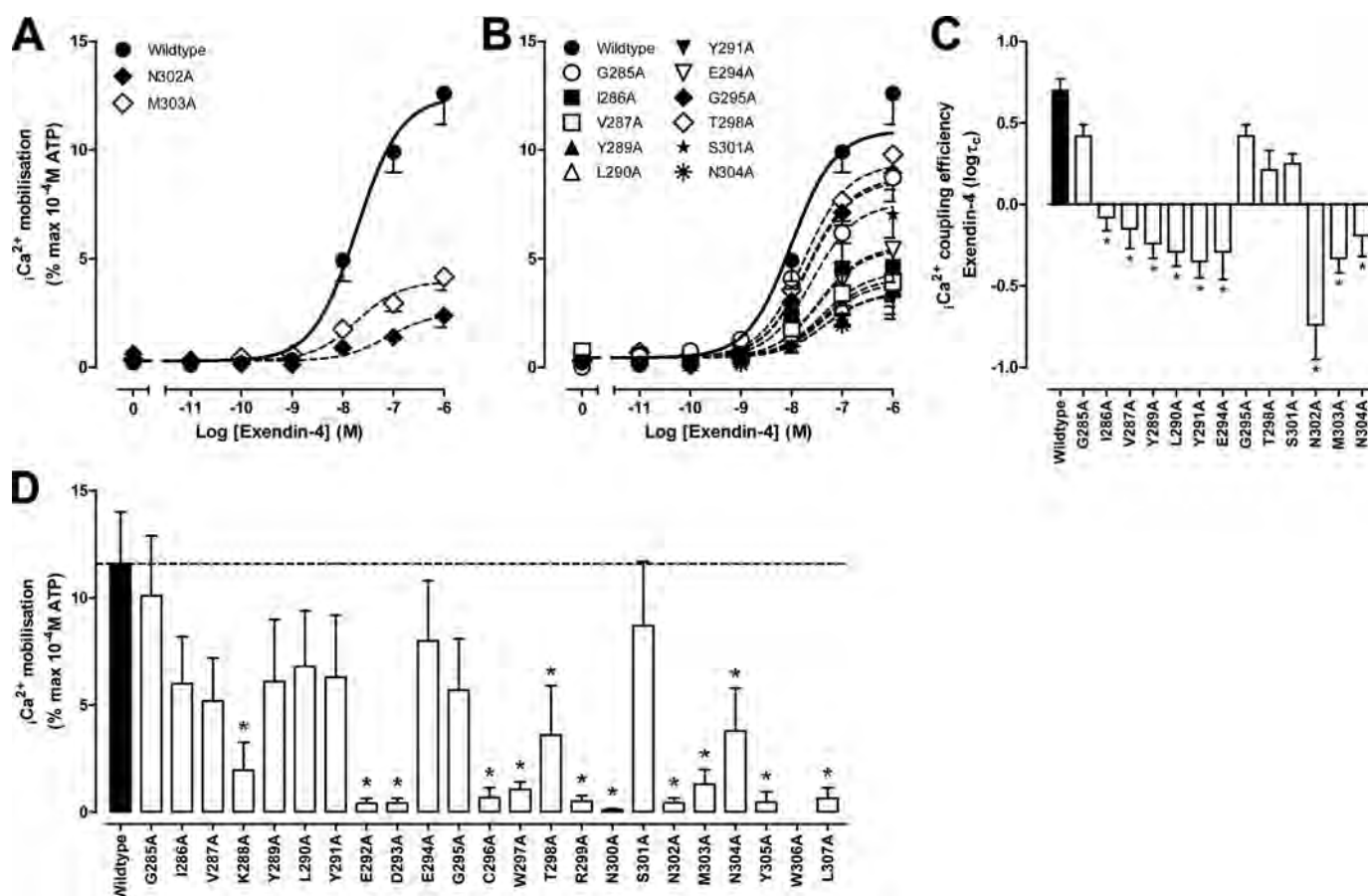


FIGURE 4. Ca^{2+} mobilization profiles of human GLP-1R ECL2 alanine mutants. Characterization of Ca^{2+} mobilization in the presence of exendin-4 (A and B) in FlpInCHO cells stably expressing the wild type human GLP-1R or each of the human GLP-1R ECL2 alanine mutants that effect peptide binding affinity (A) or have no significant effect on peptide binding affinity (B) is shown. Data are normalized to the maximal response elicited by 100 μ M ATP and analyzed with an operational model of agonism as defined in Equation 2 of the accompanying article. All values are means \pm S.E. of four to five independent experiments, conducted in duplicate. Visual representation of Ca^{2+} coupling efficacy (log τ_c) in the presence of exendin-4 (C) is shown. Statistical significance of changes in coupling efficacy in comparison with wild type human GLP-1R was determined by one-way analysis of variance and Dunnett's post test, and values are indicated with an asterisk (*, $p < 0.05$). All values are log $\tau_c \pm$ S.E. error of four to five independent experiments, conducted in duplicate. Data presented in D are levels of Ca^{2+} mobilization in the presence of 1 μ M oxyntomodulin and are normalized to the maximal response elicited by 100 μ M ATP. Statistical significance of changes in response in comparison with wild type human GLP-1R was determined by one-way analysis of variance and Dunnett's post-test, and values are indicated with an asterisk (*, $p < 0.05$). All values are means \pm S.E. of three to five independent experiments, conducted in duplicate.

Effect of Human GLP-1R ECL2 Alanine Mutations on Peptide-mediated Signal Bias—Bias plots provide a useful tool for comparing relative bias of peptides across two pathways independent of absolute potency (20). Visualization of signaling in this manner revealed strong relative bias of exendin-4 for cAMP formation relative to pERK1/2, with weaker relative bias for pERK1/2 over Ca^{2+} mobilization (supplemental Fig. S1, A–C). In contrast, oxyntomodulin was only weakly biased toward cAMP signaling relative to pERK1/2 (supplemental Fig. S1D) but was poorly coupled to Ca^{2+} mobilization. Whereas most mutations had minimal effect on bias (although distinct effects on efficacy could be distinguished), a number of mutations appeared to be critically important for maintaining pathway bias, albeit in a peptide-dependent manner (Table 6 and supplemental Fig. S1). Asn-300 appeared to play a critical role in maintaining pathway bias of exendin-4, oxyntomodulin, and GLP-1(7–36)-NH₂ (18) toward cAMP formation over pERK1/2 and likely has a similar influence on GLP-1(1–36)-NH₂, where cAMP formation was completely abrogated (18). For all three peptides, there was a complete reversal of bias with this mutant for these two pathways (supplemental Fig. S1, A and D) (18).

Trp-297 was similarly important for exendin-4 and GLP-1(7–36)-NH₂ (18) and a prerequisite for cAMP signaling at the weaker agonist peptides. Arg-299, Asn-302, and Cys-296 were important for maintaining oxyntomodulin and GLP-1(7–36)-NH₂ (18) bias for cAMP over pERK1/2 but were less critical for exendin-4-mediated bias (Table 6 and supplemental Fig. S1). Mutation of Arg-299 and Tyr-305 to alanine also promoted bias toward pERK1/2 for GLP-1(1–36)-NH₂ (18). The N304A mutation, however, was associated with a preferential loss of cAMP signaling over pERK1/2 for GLP-1(7–36)-NH₂ and GLP-1(1–36)-NH₂ (18) and to a lesser extent exendin-4, with limited impact on oxyntomodulin.

DISCUSSION

There is increasing evidence that the ECL2 of family A GPCRs plays a critical role in activation transition of GPCRs as well as being an important region for allosteric modulation of receptors (14, 20–26). In this study, we have used alanine scanning of residues of ECL2 and adjacent amino acids to examine the role of these residues in binding and signaling mediated by peptide and nonpeptide ligands of the GLP-1R, a family B

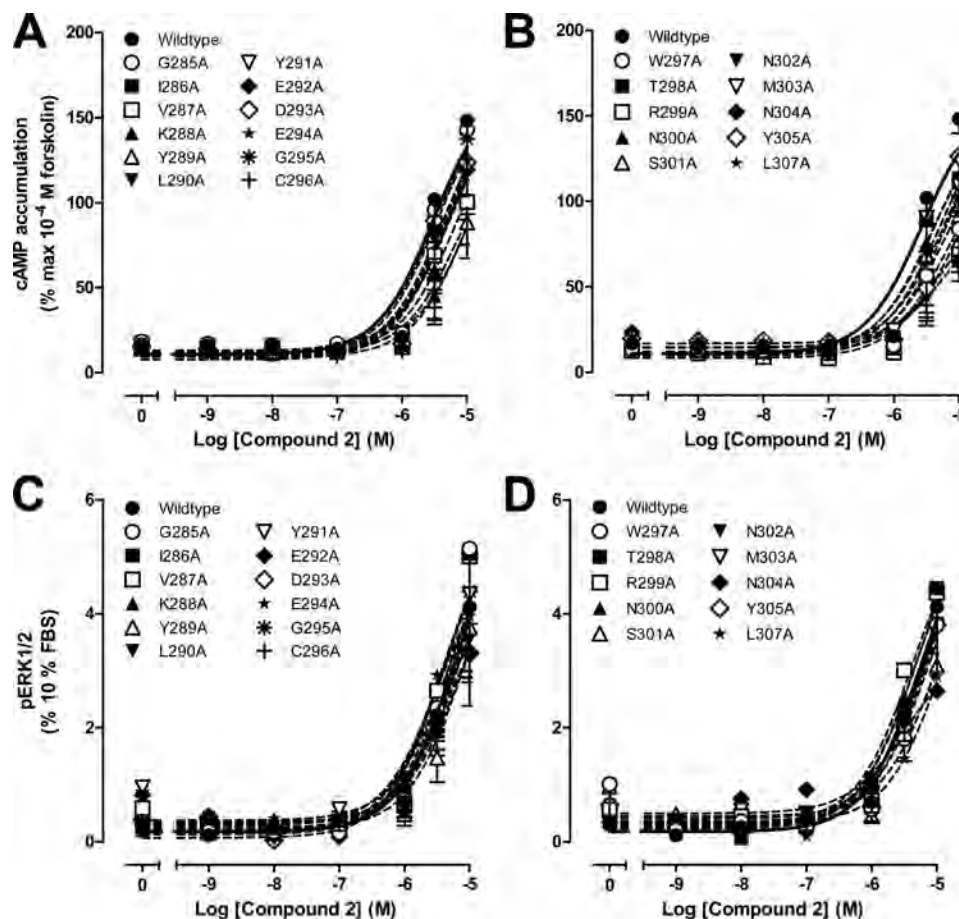


FIGURE 5. **Compound 2-mediated cAMP accumulation and pERK1/2 profiles of human GLP-1R ECL2 alanine mutants.** Characterization of cAMP accumulation (A and B) and pERK1/2 (C and D) in the presence of compound 2 in FlpInCHO cells stably expressing the wild type human GLP-1R or each of the human GLP-1R ECL2 alanine mutants is shown. cAMP accumulation data are normalized to the response elicited by 100 μ M forskolin, and pERK1/2 data are normalized to the maximal response elicited by 10% FBS, and all data are analyzed with a three-parameter logistic equation as defined in Equation 1 of the accompanying article. All values are means \pm S.E. of four to seven independent experiments, conducted in duplicate.

GPCR. Exendin-4 is a high affinity GLP-1 peptide mimetic currently approved for clinical treatment of type II diabetics (3, 27, 28), although oxyntomodulin is a naturally occurring GLP-1R peptide ligand with intermediate potency between full-length and truncated GLP-1 peptides (1, 29). In accord with observations for GLP-1 peptides in our accompanying article (18), ECL2 was critically important for activation transition of the GLP-1R by exendin-4 and oxyntomodulin, albeit with distinctions in the involvement of individual residues. In contrast, activation of the receptor by the small molecule agonist, compound 2, was relatively unaffected by ECL2 mutations, with most effects tracking with loss in cell surface receptor expression. As such, ECL2 appeared to play only a limited role in compound 2-mediated receptor activation.

As also noted for GLP-1 peptides (18), residues that were highly conserved across family B peptide hormone receptors (Lys-288, Asp-293, Cys-296, Trp-297, and Trp-306) were among those most critical for receptor function, demonstrating marked loss in agonist peptide binding and marked attenuation of peptide-mediated signaling. W306A was not expressed at the cell surface and consequently could not be examined further. Of the others, K288A was the most deleterious, and this likely relates to a critical structural role for this residue for peptide-mediated actions. We have previously speculated that this may

be involved in stabilization of the top of TM4 by “snorkeling” (18), which may be required for correct orientation of ECL2 for peptide-mediated receptor activation. Nonetheless, this was not critical to compound 2-mediated receptor activation, indicating that this ligand activates the receptor in a unique manner as discussed below. Although Cys-296 and Trp-297 are highly conserved and likely to be structurally important for the entire B receptor subfamily (see Fig. 1A of Ref. 18), they also appear to contribute to signal bias of high affinity peptide agonists of the GLP-1R (supplemental Fig. S1). Cys-296 is predicted to form a disulfide bridge with Cys-226 at the top of TM3 in a similar manner to family A GPCRs (30), providing conformational restriction on the movement of ECL2. Residues distal to this amino acid likely contribute to propagation of conformational rearrangement of TM5 that has been shown to undergo translational movements on the intracellular face of the receptor for agonist-occupied G protein-coupled β_2 -adrenoreceptor (31–33), and this is likely important in receptor activation. Consistent with this, residues distal to Cys-296 generally had a greater impact on receptor signaling.

Comparison of Effect of Human GLP-1R ECL2 Alanine Mutations on Peptide Binding and Function, Exendin-4 Versus Oxyntomodulin—For mutants at which binding affinity could robustly be estimated for both peptides, most mutants had comparable effects on affinity. The exceptions were C296A,

TABLE 5

Effects of human GLP-1R ECL2 alanine mutants on the allosteric agonist compound 2

Data were analyzed using a three-parameter logistic equation as defined in Equation 1 of the accompanying article. pEC_{50} values represent the negative logarithm of the concentration of agonist that produces half the maximal response. $E_{100\mu M}$ in the data represents the response elicited at 10 μM compound 2, normalized to the response elicited by 100 μM forskolin (cAMP) or 10% FBS (pERK1/2). Values are expressed as means \pm S.E. of four to seven independent experiments, conducted in duplicate. Data were analyzed with one-way analysis of variance and Dunnett's post test. Gray shading highlights residues effecting peptide agonist binding affinity. ND indicate data unable to be experimentally defined.

	Binding (pIC_{50})	Compound 2			
		cAMP accumulation		pERK1/2	
		pEC_{50}	$E_{100\mu M}$	pEC_{50}	$E_{100\mu M}$
Wildtype	N.D.	N.D.	148.2 \pm 8.4	N.D.	4.1 \pm 0.8
G285A	N.D.	N.D.	142.7 \pm 29.5	N.D.	5.1 \pm 1.1
I286A	N.D.	N.D.	121.7 \pm 24.1	N.D.	5.1 \pm 1.1
V287A	N.D.	N.D.	100.6 \pm 10.6	N.D.	5.0 \pm 1.1
K288A	N.D.	N.D.	89.1 \pm 13.5	N.D.	4.2 \pm 0.8
Y289A	N.D.	N.D.	88.3 \pm 20.9	N.D.	3.8 \pm 0.8
L290A	N.D.	N.D.	119.3 \pm 14.3	N.D.	3.6 \pm 0.7
Y291A	N.D.	N.D.	144.9 \pm 25.5	N.D.	4.3 \pm 1.1
E292A	N.D.	N.D.	119.5 \pm 7.0	N.D.	3.3 \pm 0.5
D293A	N.D.	N.D.	123.8 \pm 20.1	N.D.	3.3 \pm 0.9
E294A	N.D.	N.D.	124.9 \pm 12.3	N.D.	4.0 \pm 1.0
G295A	N.D.	N.D.	137.7 \pm 18.0	N.D.	4.4 \pm 0.8
C296A	N.D.†	N.D.	93.2 \pm 18.2	N.D.	3.8 \pm 0.9
W297A	N.D.†	N.D.	83.8 \pm 16.0	N.D.	3.8 \pm 0.9
T298A	N.D.	N.D.	113.3 \pm 19.9	N.D.	4.5 \pm 0.9
R299A	N.D.†	N.D.	69.0 \pm 10.4*	N.D.	4.4 \pm 1.1
N300A	N.D.	N.D.	111.2 \pm 8.1	N.D.	4.4 \pm 1.3
S301A	N.D.	N.D.	91.8 \pm 14.9	N.D.	3.1 \pm 0.7
N302A	N.D.	N.D.	100.2 \pm 8.9	N.D.	3.8 \pm 0.9
M303A	N.D.	N.D.	108.7 \pm 12.4	N.D.	3.8 \pm 0.8
N304A	N.D.	N.D.	64.2 \pm 10.9*	N.D.	2.6 \pm 0.7
Y305A	N.D.†	N.D.	126.5 \pm 32.0	N.D.	3.8 \pm 0.9
W306A	N.D.†	N.D.†	N.D.	N.D.†	N.D.
L307A	N.D.	N.D.	84.9 \pm 16.6	N.D.	2.9 \pm 0.8

* Data are statistically significant at $p < 0.05$, one-way analysis of variance, and Dunnett's post test in comparison with wild type response.

† Profiles deviate from wild type, but pIC_{50} and/or pEC_{50} values for this ligand were unable to be determined in concentration range tested.

W297A, R299A, and Y305A, where affinity estimates could not be determined for oxyntomodulin due to incomplete or poorly defined curves, and K288A, E292A, and N300A, where there was greater loss of exendin-4 affinity relative to that of oxyntomodulin. Each of these was among the most profoundly affected mutants for exendin-4 affinity and may, at least in part, reflect differences in affinity of the two peptides for active *versus* inactive states of the receptor, as discussed below.

Although the effect of ECL2 mutation on peptide-mediated cAMP formation was generally similar for exendin-4 and oxyntomodulin, three mutations, E292A, C296A, and N300A, had differential effects for the two peptides. In each case, there was a greater effect on exendin-4 potency that paralleled the differential effect on binding affinity between the peptides. At each of these mutants, however, oxyntomodulin efficacy was reduced to a greater extent than the equivalent mutation on exendin-4 response, with respect to wild type. Nonetheless, the changes to cAMP signaling likely reflect a mechanistically similar effect across the two peptides. For these three mutants, the oxyntomodulin potency and estimates of affinity are equivalent. Operationally, loss of efficacy is manifested as a collapse of the

potency toward the affinity value of peptides with subsequent diminution of maximal response. Where changes in agonist peptide affinity occur, this may be due to decreased ability to form the active, high affinity ARG ternary complex, wherein the measured affinity collapses to the affinity for the inactive state receptor (34). Although there may be direct effects of the mutations on ligand contact and affinity, the data are principally consistent with decreased ability to form G protein-complexed receptors.

In contrast, the M303A mutant had distinct effects on the efficacy of exendin-4 and oxyntomodulin in the absence of altered potency with selective loss of exendin-4 efficacy. As described above, this mutant was also an outlier in the correlation analyses of cAMP *versus* pERK1/2 signaling for both peptides (supplemental Fig. S1). Thus Met-303 appears to play a distinct role for cAMP formation (and by inference G_{α_s} coupling) for these peptides with GLP-1(7–36)-NH₂ exhibiting an intermediate profile (supplemental Fig. S2) (9).

Although operational measures of oxyntomodulin efficacy for Ca²⁺_i mobilization could not be determined due to the weak response, comparison of the maximal effect of oxyntomodulin at 1 μM with the responses to exendin-4 revealed apparent differences in the effect of mutation on Ca²⁺_i signaling for the two peptides, with preservation of oxyntomodulin responses for L290A, Y291A, and E294A, and significant loss of exendin-4 signaling. For these mutants, there was no significant decrease in [¹²⁵I]-exendin(9–39) binding (see Table 1 of Ref. 18) suggesting that there was a similar level of functional cell surface receptors. Ca²⁺_i responses to GLP-1(7–36)-NH₂ were also decreased at these four mutants, suggesting that there are differences in how oxyntomodulin, and the high affinity peptides modulate Ca²⁺_i signaling.

Comparison of Effect of Human GLP-1R ECL2 Alanine Mutations on Peptide Function, Exendin-4 Versus GLP-1(7–36)-NH₂—Exendin-4 and GLP-1(7–36)-NH₂ are generally considered to interact with and activate the receptor in an equivalent manner, and indeed, the efficacy of these two peptides for the three pathways studied was very similar (Tables 2–4 of this paper and Ref. 18). This was also generally reflected in the effect of mutation on the function of the two peptides. Nonetheless, some subtle differences in responses were observed (supplemental Fig. S2). In the assay of cAMP formation, all except two of the mutants had effectively equivalent magnitude of potency alteration (<0.5 log unit difference); the exceptions were R299A and L307A that exhibited greater loss in potency for GLP-1(7–36)-NH₂ compared with exendin-4. The effect on efficacy of the two peptides was also similar; however, residues after Cys-296 had greater loss of exendin-4 efficacy relative to GLP-1(7–36)-NH₂, with the exception of N300A that had the opposite effect. This suggests that translation of exendin-4 signaling to G_{α_s} coupling is more reliant on structural conservation of the distal segment of ECL2.

There was also a strong correlation between the effect of mutants on exendin-4 and GLP-1(7–36)-NH₂ efficacy for pERK1/2. Nonetheless, the N300A mutant appeared to discriminate between the two peptides, and indeed this was true for oxyntomodulin and GLP-1(1–36)-NH₂ (see Table 3 of Ref. 18), with a rank order for loss of efficacy of GLP-1(1–

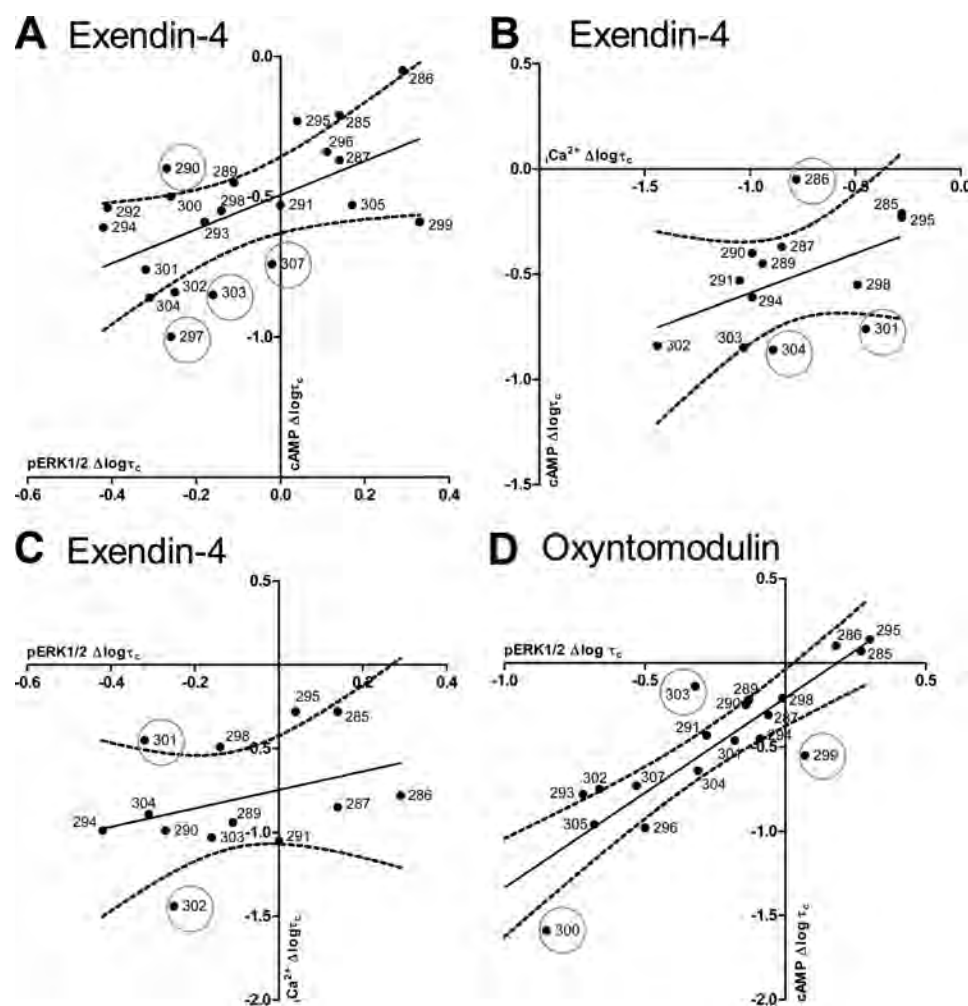


FIGURE 6. **Correlation plots of pathway efficacy ($\log\tau_c$) of human GLP-1R ECL2 alanine mutants.** Correlation plots of changes in pathway coupling efficacy ($\log\tau_c$) of human GLP-1R ECL2 alanine mutants with respect to wild type receptor are shown. A, pERK1/2 versus cAMP for exendin-4; B, Ca^{2+} versus cAMP for exendin-4; C, pERK1/2 versus Ca^{2+} for exendin-4; and D, pERK1/2 versus cAMP for oxyntomodulin. Data were fit by linear regression. The line of regression and 99% confidence intervals (—) are displayed.

36)-NH₂ > oxyntomodulin > GLP-1(7–36)-NH₂ > exendin-4. As described above, the Asn-300 residue is also linked to signal bias of peptides between cAMP and pERK1/2 for exendin-4, GLP-1(7–36)-NH₂, and oxyntomodulin and suggests that it makes critical intra-receptor interactions that underlie this effect.

Although the efficacy for exendin-4 and GLP-1(7–36)-NH₂ was similar at the wild type receptor in Ca^{2+} signaling ($\log\tau_c$ 0.70 ± 0.07 and 0.63 ± 0.08 (18), respectively), there was greater relative loss of exendin-4 Ca^{2+} signaling with mutation of ECL2. This was manifest as virtual abolishment of exendin-4-mediated responses for E293A, R299A, Y305A, and L307A, although reduced but measurable responses were observed with GLP-1(7–36)-NH₂ (18). This differential effect on Ca^{2+} may be due to differences in the mechanism of receptor coupling to Ca^{2+} signaling for the two peptides; exendin-4 signaling was relatively insensitive to pertussis toxin pretreatment (reduced $28.7 \pm 8.3\%$), whereas the GLP-1(7–36)-NH₂ response was attenuated by $37.0 \pm 7.1\%$ (supplemental Fig. S3) indicating that $G_{\alpha_{i/o}}$ proteins play a greater role in GLP-1(7–36)-NH₂ signaling linked to Ca^{2+} mobilization. Although not

conclusive, the $G_{\alpha_{i/o}}$ response may be less dependent upon conformational propagation through ECL2.

Generically, the inability to couple to Ca^{2+} in the cases of K288A, E292A, D293A, C296A, W297A, R299A, Y305A, and L307A in the presence of exendin-4 was also reflected in severe impairment to couple to the cAMP pathway, suggesting that these residues are perhaps not important in pathway selectivity between cAMP and Ca^{2+} . However, receptor mutants C296A, R299A, and Y305A all demonstrated increased ability to couple to pERK1/2 despite no detectable signaling through the Ca^{2+} pathway, suggesting some involvement in pathway selectivity at these residues. Additionally, although N302A and M303A had some ability to couple to the Ca^{2+} pathway when activated by exendin-4, it was noted that these were two of the most severely impaired mutant receptors in cAMP coupling but also only had small reductions in pERK1/2 coupling, which may indicate importance in pathway selectivity at these residues. These results suggest that ECL2 has a greater influence on Ca^{2+} activation by exendin-4 than other signaling pathways.

Collectively, the data suggest that exendin-4 and GLP-1(7–36)-NH₂ likely activate the receptor via subtly different mech-

TABLE 6**Effects of human GLP-1R ECL2 alanine mutants on exendin-4- and oxyntomodulin-mediated signaling bias**

Data were analyzed using an operational model of agonism as defined in Equation 4 of the accompanying article to estimate $\log\tau_c/K_A$ ratios. Changes in $\log\tau_c/K_A$ ratios with respect to wild type were used to quantitate bias between signaling pathways. Values are expressed as means \pm S.E. of three to seven independent experiments, conducted in duplicate. Data were analyzed with one-way analysis of variance and Dunnett's post test. Gray shading highlights residues effecting peptide agonist binding affinity. ND indicates data unable to be experimentally defined.

	Bias factors			
	Oxyntomodulin		Exendin-4	
	cAMP-ERK	cAMP-Ca ²⁺	cAMP-ERK	ERK-Ca ²⁺
Wildtype	0.00 \pm 0.23	0.00 \pm 0.19	0.00 \pm 0.21	0.00 \pm 0.20
G285A	-0.12 \pm 0.23	0.18 \pm 0.25	-0.30 \pm 0.30	0.49 \pm 0.27
I286A	-0.19 \pm 0.23	0.58 \pm 0.28	-0.21 \pm 0.26	0.78 \pm 0.29
V287A	-0.36 \pm 0.27	0.45 \pm 0.35	-0.35 \pm 0.31	0.81 \pm 0.35
K288A	N.D.	N.D.	N.D.	N.D.
Y289A	0.00 \pm 0.29	0.37 \pm 0.20	-0.09 \pm 0.32	0.47 \pm 0.31
L290A	-0.48 \pm 0.27	0.53 \pm 0.37	-0.44 \pm 0.42	0.97 \pm 0.48
Y291A	-0.20 \pm 0.27	0.25 \pm 0.23	-0.53 \pm 0.29	0.78 \pm 0.24
E292A	-1.22 \pm 0.65	N.D.	-1.25 \pm 0.38*	N.D.
D293A	-0.79 \pm 0.39	N.D.	-0.67 \pm 0.30	N.D.
E294A	-0.42 \pm 0.25	0.22 \pm 0.25	-0.35 \pm 0.38	0.56 \pm 0.33
G295A	0.03 \pm 0.25	-0.07 \pm 0.21	-0.49 \pm 0.31	0.42 \pm 0.29
C296A	-1.44 \pm 0.40*	N.D.	-1.38 \pm 0.26*	N.D.
W297A	N.D.	N.D.	-1.87 \pm 0.43*	N.D.
T298A	-0.20 \pm 0.24	-0.12 \pm 0.19	-0.58 \pm 0.25	0.46 \pm 0.25
R299A	-0.98 \pm 0.20	N.D.	-0.70 \pm 0.23	N.D.
N300A	-1.36 \pm 0.44*	N.D.	-2.33 \pm 0.24*	N.D.
S301A	-0.28 \pm 0.23	-0.32 \pm 0.23	-1.12 \pm 0.28	0.39 \pm 0.39
N302A	-0.86 \pm 0.22	0.68 \pm 0.52	-0.71 \pm 0.37	1.80 \pm 0.55*
M303A	-0.24 \pm 0.18	0.39 \pm 0.35	-0.59 \pm 0.34	0.98 \pm 0.39
N304A	-0.18 \pm 0.33	-0.15 \pm 0.21	-0.56 \pm 0.23	0.42 \pm 0.23
Y305A	-1.00 \pm 0.27	N.D.	-1.30 \pm 0.25*	N.D.
W306A	N.D.	N.D.	N.D.	N.D.
L307A	-0.63 \pm 0.26	N.D.	-0.97 \pm 0.33	N.D.

* Data are statistically significant at $p < 0.05$, one-way analysis of variance, and Dunnett's post test in comparison with wild type response.

anisms, and this may have implications for their use as therapeutic agents. Indeed, the evidence for different mechanisms of activity is also seen with mutation of Lys-288 at the rat GLP-1R, with significantly greater decreases in binding affinity of GLP-1(7–36)-NH₂ than exendin-4 (13). Furthermore, the affinity of GLP-1(7–36)-NH₂ is highly sensitive to N-terminal truncation, whereas exendin-4 is not; exendin-4 can be truncated by up to eight residues without significant loss of binding affinity for the GLP-1R (35). In addition, despite identical homology in the N-terminal seven residues, GLP-1(9–36)-NH₂ is a partial ago-

nist, although exendin(3–39) is an antagonist (35). Although this is most likely a composite of both N- and C-terminal peptide interactions with the receptor, these differences in GLP-1 and exendin-4 binding and function are supportive of differential mechanisms of activation at the GLP-1R (36–38).

Distinct Receptor Activation Mechanisms for Peptide and Small Molecule Agonists—In contrast to the dramatic effects on peptide-mediated binding and signaling, mutation of ECL2 residues had limited impact on activation of the receptor by the small molecule agonist compound 2. In the cases where there

was a reduction in cAMP E_{\max} , there was a parallel loss in functional receptors at the cell surface that may account for the effect of these mutations. Likewise, there was little effect on signal bias for compound 2 across the mutants, with observed alterations paralleling loss of cAMP signaling that accompanied lower functional cell surface receptor expression (supplemental Fig. S1E). A similar distinction in effect on peptide *versus* small molecule activation of the receptor was seen for the inactivating polymorphic variant Met-149, which selectively attenuated GLP-1(7–36)-NH₂ and exendin-4, but not compound 2 signaling (9). At this variant, compound 2 could also allosterically rescue peptide activation of the receptor (9). Collectively, these data provide evidence for distinct modes of receptor activation for peptide and nonpeptide agonists, with peptide-mediated activation of the receptor critically involving conformational propagation through ECL2, although compound 2-mediated activation appears to principally occur independently of this.

The conformational transition leading to interaction with signaling effectors in response to agonist occupation of the receptor is thought to involve reorganization of hydrogen bonding networks within the transmembrane domain of the receptors leading to marked changes in the intracellular face of the receptor (31–33). How agonists bind to the receptor to mediate these effects is still mostly unclear. In this study, we have provided evidence for a critical role of the ECL2 of the GLP-1R in propagating this conformational change upon peptide binding, and also for directing signaling bias at this receptor. The data also suggest that individual peptides differentially influence ECL2 to mediate their effects, although the small molecule agonist, compound 2, has a distinct mechanism for receptor activation.

REFERENCES

- Fehmann, H. C., Jiang, J., Schweinfurth, J., Wheeler, M. B., Boyd, A. E., 3rd, and Göke, B. (1994) Stable expression of the rat GLP-I receptor in CHO cells. Activation and binding characteristics utilizing GLP-I(7–36)-amide, oxyntomodulin, exendin-4, and exendin(9–39). *Peptides* **15**, 453–456
- Baggio, L. L., and Drucker, D. J. (2007) Biology of incretins. GLP-1 and GIP. *Gastroenterology* **132**, 2131–2157
- Furman, B. L. (2010) The development of Byetta (exenatide) from the venom of the Gila monster as an antidiabetic agent. *Toxicol.*, in press
- Drucker, D. J., Dritselis, A., and Kirkpatrick, P. (2010) Liraglutide. *Nat. Rev. Drug Discov.* **9**, 267–268
- Koole, C., Wootten, D., Simms, J., Valant, C., Sridhar, R., Woodman, O. L., Miller, L. J., Summers, R. J., Christopoulos, A., and Sexton, P. M. (2010) Allosteric ligands of the glucagon-like peptide 1 receptor (GLP-1R) differentially modulate endogenous and exogenous peptide responses in a pathway-selective manner. Implications for drug screening. *Mol. Pharmacol.* **78**, 456–465
- Knudsen, L. B., Kiel, D., Teng, M., Behrens, C., Bhumralkar, D., Kodra, J. T., Holst, J. J., Jeppesen, C. B., Johnson, M. D., de Jong, J. C., Jorgensen, A. S., Kercher, T., Kostrowicki, J., Madsen, P., Olesen, P. H., Petersen, J. S., Poulsen, F., Sidelmann, U. G., Sturis, J., Truesdale, L., May, J., and Lau, J. (2007) Small molecule agonists for the glucagon-like peptide 1 receptor. *Proc. Natl. Acad. Sci. U.S.A.* **104**, 937–942
- Irwin, N., Flatt, P. R., Patterson, S., and Green, B. D. (2010) Insulin-releasing and metabolic effects of small molecule GLP-1 receptor agonist 6,7-dichloro-2-methylsulfonyl-3-*N*-tert-butylaminoquinoline. *Eur. J. Pharmacol.* **628**, 268–273
- Sloop, K. W., Willard, F. S., Brenner, M. B., Ficorilli, J., Valasek, K., Showalter, A. D., Farb, T. B., Cao, J. X., Cox, A. L., Michael, M. D., Gutierrez Sanfeliciano, S. M., Tebbe, M. J., and Coghlan, M. J. (2010) Novel small molecule glucagon-like peptide-1 receptor agonist stimulates insulin secretion in rodents and from human islets. *Diabetes* **59**, 3099–3107
- Koole, C., Wootten, D., Simms, J., Valant, C., Miller, L. J., Christopoulos, A., and Sexton, P. M. (2011) Polymorphism and ligand-dependent changes in human glucagon-like peptide-1 receptor (GLP-1R) function. Allosteric rescue of loss of function mutation. *Mol. Pharmacol.* **80**, 486–497
- Hoare, S. R. (2005) Mechanisms of peptide and nonpeptide ligand binding to Class B G-protein-coupled receptors. *Drug Discov. Today* **10**, 417–427
- Coopman, K., Wallis, R., Robb, G., Brown, A. J., Wilkinson, G. F., Timms, D., and Willars, G. B. (2011) Residues within the transmembrane domain of the glucagon-like peptide-1 receptor involved in ligand binding and receptor activation. Modeling the ligand-bound receptor. *Mol. Endocrinol.* **25**, 1804–1818
- Miller, L. J., Chen, Q., Lam, P. C., Pinon, D. I., Sexton, P. M., Abagyan, R., and Dong, M. (2011) Refinement of glucagon-like peptide 1 docking to its intact receptor using mid-region photolabile probes and molecular modeling. *J. Biol. Chem.* **286**, 15895–15907
- Al-Sabah, S., and Donnelly, D. (2003) The positive charge at Lys-288 of the glucagon-like peptide-1 (GLP-1) receptor is important for binding the N terminus of peptide agonists. *FEBS Lett.* **553**, 342–346
- Holtmann, M. H., Ganguli, S., Hadac, E. M., Dolu, V., and Miller, L. J. (1996) Multiple extracellular loop domains contribute critical determinants for agonist binding and activation of the secretin receptor. *J. Biol. Chem.* **271**, 14944–14949
- Assil-Kishawi, I., and Abou-Samra, A. B. (2002) Sauvagine cross-links to the second extracellular loop of the corticotropin-releasing factor type 1 receptor. *J. Biol. Chem.* **277**, 32558–32561
- Liaw, C. W., Grigoriadis, D. E., Lovenberg, T. W., De Souza, E. B., and Maki, R. A. (1997) Localization of ligand-binding domains of human corticotropin-releasing factor receptor. A chimeric receptor approach. *Mol. Endocrinol.* **11**, 980–985
- Bergwitz, C., Jusseaume, S. A., Luck, M. D., Jüppner, H., and Gardella, T. J. (1997) Residues in the membrane-spanning and extracellular loop regions of the parathyroid hormone (PTH)-2 receptor determine signaling selectivity for PTH and PTH-related peptide. *J. Biol. Chem.* **272**, 28861–28868
- Koole, C., Wootten, D., Simms, J., Miller, L. J., Christopoulos, A., and Sexton, P. M. (2012) Second extracellular loop of human glucagon-like peptide-1 receptor (GLP-1R) has a critical role in GLP-1 peptide binding and receptor activation. *J. Biol. Chem.* **287**, 3642–3658
- Teng, M., Johnson, M. D., Thomas, C., Kiel, D., Lakis, J. N., Kercher, T., Aytes, S., Kostrowicki, J., Bhumralkar, D., Truesdale, L., May, J., Sidelmann, U., Kodra, J. T., Jorgensen, A. S., Olesen, P. H., de Jong, J. C., Madsen, P., Behrens, C., Pettersson, L., Knudsen, L. B., Holst, J. J., and Lau, J. (2007) Small molecule ago-allosteric modulators of the human glucagon-like peptide-1 (hGLP-1) receptor. *Bioorg. Med. Chem. Lett.* **17**, 5472–5478
- Gregory, K. J., Hall, N. E., Tobin, A. B., Sexton, P. M., and Christopoulos, A. (2010) Identification of orthosteric and allosteric site mutations in M2 muscarinic acetylcholine receptors that contribute to ligand-selective signaling bias. *J. Biol. Chem.* **285**, 7459–7474
- Avlani, V. A., Gregory, K. J., Morton, C. J., Parker, M. W., Sexton, P. M., and Christopoulos, A. (2007) Critical role for the second extracellular loop in the binding of both orthosteric and allosteric G protein-coupled receptor ligands. *J. Biol. Chem.* **282**, 25677–25686
- Conner, M., Hawtin, S. R., Simms, J., Wootten, D., Lawson, Z., Conner, A. C., Parslow, R. A., and Wheatley, M. (2007) Systematic analysis of the entire second extracellular loop of the V(1a) vasopressin receptor. Key residues, conserved throughout a G-protein-coupled receptor family, identified. *J. Biol. Chem.* **282**, 17405–17412
- Ahn, K. H., Bertalovitz, A. C., Mierke, D. F., and Kendall, D. A. (2009) Dual role of the second extracellular loop of the cannabinoid receptor 1. Ligand binding and receptor localization. *Mol. Pharmacol.* **76**, 833–842
- Scarselli, M., Li, B., Kim, S. K., and Wess, J. (2007) Multiple residues in the second extracellular loop are critical for M3 muscarinic acetylcholine receptor activation. *J. Biol. Chem.* **282**, 7385–7396
- Hawtin, S. R., Simms, J., Conner, M., Lawson, Z., Parslow, R. A., Trim, J., Sheppard, A., and Wheatley, M. (2006) Charged extracellular residues, conserved throughout a G-protein-coupled receptor family, are required

- for ligand binding, receptor activation, and cell-surface expression. *J. Biol. Chem.* **281**, 38478–38488
26. Ott, T. R., Troskie, B. E., Roeske, R. W., Illing, N., Flanagan, C. A., and Millar, R. P. (2002) Two mutations in extracellular loop 2 of the human GnRH receptor convert an antagonist to an agonist. *Mol. Endocrinol.* **16**, 1079–1088
27. Kolterman, O. G., Kim, D. D., Shen, L., Ruggles, J. A., Nielsen, L. L., Fine-man, M. S., and Baron, A. D. (2005) Pharmacokinetics, pharmacodynamics, and safety of exenatide in patients with type 2 diabetes mellitus. *Am. J. Health Syst. Pharm.* **62**, 173–181
28. Göke, R., Fehmann, H. C., Linn, T., Schmidt, H., Krause, M., Eng, J., and Göke, B. (1993) Exendin-4 is a high potency agonist and truncated exendin-(9–39)-amide an antagonist at the glucagon-like peptide 1-(7–36)-amide receptor of insulin-secreting beta-cells. *J. Biol. Chem.* **268**, 19650–19655
29. Schmidtler, J., Dehne, K., Allescher, H. D., Schusdziarra, V., Classen, M., Holst, J. J., Polack, A., and Schepp, W. (1994) Rat parietal cell receptors for GLP-1-(7–36) amide. Northern blot, cross-linking, and radioligand binding. *Am. J. Physiol.* **267**, G423–G432
30. Mann, R. J., Al-Sabah, S., de Maturana, R. L., Sinfield, J. K., and Donnelly, D. (2010) Functional coupling of Cys-226 and Cys-296 in the glucagon-like peptide-1 (GLP-1) receptor indicates a disulfide bond that is close to the activation pocket. *Peptides* **31**, 2289–2293
31. Rasmussen, S. G., Choi, H. J., Fung, J. J., Pardon, E., Casarosa, P., Chae, P. S., Devree, B. T., Rosenbaum, D. M., Thian, F. S., Kobilka, T. S., Schnapp, A., Konetzki, I., Sunahara, R. K., Gellman, S. H., Pautsch, A., Steyaert, J., Weis, W. I., and Kobilka, B. K. (2011) Structure of a nanobody-stabilized active state of the $\beta(2)$ adrenoceptor. *Nature* **469**, 175–180
32. Rasmussen, S. G., Devree, B. T., Zou, Y., Kruse, A. C., Chung, K. Y., Kobilka, T. S., Thian, F. S., Chae, P. S., Pardon, E., Calinski, D., Mathiesen, J. M., Shah, S. T., Lyons, J. A., Caffrey, M., Gellman, S. H., Steyaert, J., Skiniotis, G., Weis, W. I., Sunahara, R. K., and Kobilka, B. K. (2011) Crystal structure of the $\beta(2)$ adrenergic receptor-Gs protein complex. *Nature* **477**, 549–555
33. Rosenbaum, D. M., Zhang, C., Lyons, J. A., Holl, R., Aragao, D., Arlow, D. H., Rasmussen, S. G., Choi, H. J., Devree, B. T., Sunahara, R. K., Chae, P. S., Gellman, S. H., Dror, R. O., Shaw, D. E., Weis, W. I., Caffrey, M., Gmeiner, P., and Kobilka, B. K. (2011) Structure and function of an irreversible agonist- $\beta(2)$ adrenoceptor complex. *Nature* **469**, 236–240
34. Kobilka, B. K., and Deupi, X. (2007) Conformational complexity of G-protein-coupled receptors. *Trends Pharmacol. Sci.* **28**, 397–406
35. Montrose-Rafizadeh, C., Yang, H., Rodgers, B. D., Beday, A., Pritchette, L. A., and Eng, J. (1997) High potency antagonists of the pancreatic glucagon-like peptide-1 receptor. *J. Biol. Chem.* **272**, 21201–21206
36. Al-Sabah, S., and Donnelly, D. (2003) A model for receptor-peptide binding at the glucagon-like peptide-1 (GLP-1) receptor through the analysis of truncated ligands and receptors. *Br. J. Pharmacol.* **140**, 339–346
37. Al-Sabah, S., and Donnelly, D. (2004) The primary ligand-binding interaction at the GLP-1 receptor is via the putative helix of the peptide agonists. *Protein Pept. Lett.* **11**, 9–14
38. Mann, R., Nasr, N., Hadden, D., Sinfield, J., Abidi, F., Al-Sabah, S., de Maturana, R. L., Treece-Birch, J., Willshaw, A., and Donnelly, D. (2007) Peptide binding at the GLP-1 receptor. *Biochem. Soc. Trans.* **35**, 713–716

Allosteric Modulation of Endogenous Metabolites as an Avenue for Drug Discovery[§]

Denise Wootten, Emilia E. Savage, Celine Valant, Lauren T. May, Kyle W. Sloop, James Ficorilli, Aaron D. Showalter, Francis S. Willard, Arthur Christopoulos, and Patrick M. Sexton

Drug Discovery Biology, Monash Institute of Pharmaceutical Sciences and Department of Pharmacology, Monash University, Parkville, Victoria, Australia (D.W., E.E.S., C.V., L.T.M., A.C., P.M.S.); and Endocrine Discovery (K.W.S., J.F., A.D.S.) and Translational Science and Technologies (F.S.W.), Lilly Research Laboratories, Eli Lilly and Company, Indianapolis, Indiana

Received April 13, 2012; accepted May 10, 2012

ABSTRACT

G protein-coupled receptors (GPCRs) are the largest family of cell surface receptors and a key drug target class. Recently, allosteric drugs that can cobind with and modulate the activity of the endogenous ligand(s) for the receptor have become a major focus of the pharmaceutical and biotechnology industry for the development of novel GPCR therapeutic agents. This class of drugs has distinct properties compared with drugs targeting the endogenous (orthosteric) ligand-binding site that include the ability to sculpt cellular signaling and to respond differently in the presence of discrete orthosteric ligands, a behavior termed “probe dependence.” Here, using cell signaling assays combined with ex vivo and in vivo studies of insulin secretion, we demonstrate that allosteric ligands can cause marked potentiation of previously “inert” metabolic products of

neurotransmitters and peptide hormones, a novel consequence of the phenomenon of probe dependence. Indeed, at the muscarinic M₂ receptor and glucagon-like peptide 1 (GLP-1) receptor, allosteric potentiation of the metabolites, choline and GLP-1(9–36)NH₂, respectively, was ~100-fold and up to 200-fold greater than that seen with the physiological signaling molecules acetylcholine and GLP-1(7–36)NH₂. Modulation of GLP-1(9–36)NH₂ was also demonstrated in ex vivo and in vivo assays of insulin secretion. This work opens up new avenues for allosteric drug discovery by directly targeting modulation of metabolites, but it also identifies a behavior that could contribute to unexpected clinical outcomes if interaction of allosteric drugs with metabolites is not part of their preclinical assessment.

Introduction

G protein-coupled receptors (GPCRs) are the largest superfamily of cell surface proteins and play crucial roles in virtually every physiological process. Their widespread abundance and ability to couple to a variety of signaling and

effector systems make them extremely attractive targets for drug development (Christopoulos, 2002). GPCR agonist drug discovery efforts have traditionally focused on either increasing the endogenous orthosteric agonist concentration by inhibiting its breakdown or targeting the orthosteric binding site of the receptor with surrogate agonists. However, in recent years there has been a significant increase in the identification of small molecules that target topographically distinct allosteric sites on GPCRs (May et al., 2007b). Binding of allosteric ligands can elicit a conformational change in the receptor while still allowing the orthosteric ligand to bind, thus modulating the pharmacological properties (affinity and/or efficacy) of the orthosteric ligand, in addition to

This work was supported by the National Health and Medical Research Council of Australia [Project Grants 1002180, 519461] and the Australian Research Council [Discovery Grant 110100687].

D.W. and E.E.S. contributed equally to this work.

Article, publication date, and citation information can be found at <http://molpharm.aspetjournals.org>.

<http://dx.doi.org/10.1124/mol.112.079319>.

[§] The online version of this article (available at <http://molpharm.aspetjournals.org>) contains supplemental material.

ABBREVIATIONS: GPCR, G protein-coupled receptor; GLP-1, glucagon-like peptide 1; GLP-1R, glucagon-like peptide 1 receptor; LUF6000, *N*-(3,4-dichlorophenyl)-2-cyclohexyl-1*H*-imidazo[4,5-*c*]quinolin-4-amine; A₃-AR, adenosine receptor subtype 3; M₂ mAChR, muscarinic acetylcholine receptor, subtype 2; A₁-AR, adenosine receptor subtype 1; ERK1/2, extracellular signal-regulated kinase 1 and 2; DMEM, Dulbecco's modified Eagle's medium; FBS, fetal bovine serum; LY2033298, 3-amino-5-chloro-*N*-cyclopropyl-6-methoxy-4-methyl-thieno[2,3-*b*]pyridine-2-carboxamide; Compound 2, 6,7-dichloro-2-methylsulfonyl-3-*tert*-butylaminoquinoxaline; BETP, (4-(3-benzoyloxyphenyl)-2-ethylsulfinyl-6-(trifluoromethyl)pyrimidine; VCP171, (2-amino-4-(3-(trifluoromethyl)phenyl)thiophen-3-yl)(phenyl)methanone; CHO, Chinese hamster ovary; ACh, acetylcholine; Ch, choline; PD81723, (2-amino-4,5-dimethyl-3-thienyl)(3-(trifluoromethyl)phenyl)-methanone; GTPγS, guanosine 5'-O-(3-thio)triphosphate; IVGTT, intravenous glucose tolerance test; pERK1/2, extracellular signal-related kinase 1 and 2 phosphorylation; DM, diabetes mellitus.

potentially activating the receptor in the absence of orthosteric ligand. Allosteric drugs have substantial potential as therapeutic agents, because they can provide novel receptor selectivity, in addition to offering the possibility of “fine tuning” existing physiological responses while maintaining the spatial and temporal characteristics of innate endogenous signaling (Christopoulos and Kenakin, 2002).

One characteristic of allostery is the phenomenon of “probe dependence,” whereby the extent and direction of an allosteric interaction varies with the nature of the orthosteric ligand occupying the receptor (Kenakin, 2005). Furthermore, biased signaling leading to pathway-selective allosteric modulation can also result (Leach et al., 2007). These concepts are particularly relevant to receptor systems that have multiple endogenous ligands, such as the glucagon-like peptide-1 receptor (GLP-1R) system (Baggio and Drucker, 2007), because probe dependence can lead to different endogenous agonists of the same GPCR being allosterically modulated in strikingly different ways (Koole et al., 2010). However, a hitherto-unappreciated extension of this phenomenon is the possibility that endogenous metabolites of GPCR agonists, which may normally be minimally active in their own right, can also be influenced by allosteric modulators. Indeed, a recent study reported that the allosteric compound *N*-(3,4-dichlorophenyl)-2-cyclohexyl-1*H*-imidazo[4,5-*c*]quinolin-4-amine (LUF6000) can enhance signaling by inosine (the metabolite of adenosine) at the adenosine A₃ receptor (A₃-AR) (Gao et al., 2011). Although drug discovery programs focusing on developing small molecule allosteric drugs invariably screen for compounds that modulate responses mediated by the predominant orthosteric receptor agonist, it is currently not routine to incorporate similar studies on endogenous metabolites. However augmentation of metabolite signaling could offer a new therapeutic avenue for development of novel drugs, especially in systems in which the endogenous ligand is rapidly degraded to its (ostensibly) inactive metabolite (Fig. 1).

In this study, we investigated the potential to allosterically modulate the activity of the predominant, inactive metabolite of the physiological ligand at three different GPCRs for which small molecule allosteric modulators have been described: the GLP-1R (Knudsen et al., 2007; Koole et al., 2010; Sloop et al., 2010), the M₂ muscarinic acetylcholine receptor (M₂ mAChR) (Valant et al., 2012), and the adenosine A₁ receptor (A₁-AR) (Bruns and Fergus, 1990) (Supplemental Fig. 1). In each instance, we find a significant degree of allosteric potentiation of the endogenous metabolite by the allosteric modulator. Moreover, for the GLP-1R, we also provide evidence of the allosteric modulator engendering biased signaling in terms of enhancing cAMP signaling mediated by the metabolite, while having little effect on extracellular signal-regulated kinases 1 and 2 (ERK1/2) phosphorylation or intracellular Ca²⁺ mobilization. Ex vivo studies using static cultures of rat pancreatic islets, as well as in vivo experiments also revealed that allosteric modulation of the GLP-1 metabolite resulted in glucose-dependent insulin secretion. To our knowledge, this is the first study to explore the potential to allosterically modulate endogenous metabolites of multiple GPCR ligands at their respective receptors. The outcomes could have significant implications in development and screening of novel therapeutic agents in drug discovery programs.

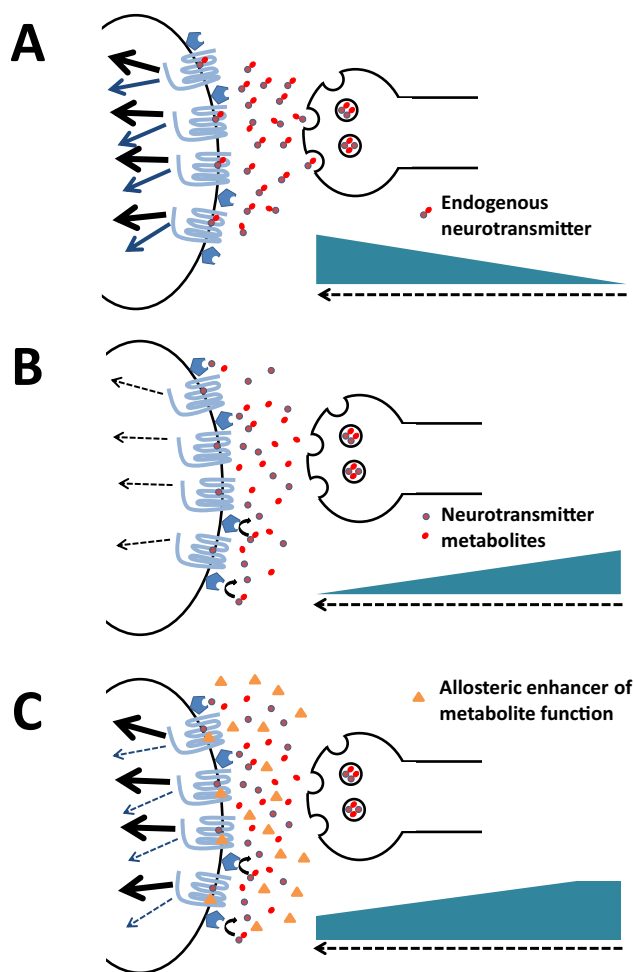


Fig. 1. Allosteric enhancement of metabolite activity as a novel mechanism of drug action. A, schematic illustration of neurotransmitter release and activation of postsynaptic receptors to elicit physiological signaling. B, the neurotransmitter is rapidly degraded by metabolizing enzymes, leading to decay of neurotransmitter signaling. C, an allosteric enhancer of metabolite activity (orange triangles) binds with the metabolite engendering and/or enhancing signaling to extend the activation of the receptor. A similar process can be envisaged for rapidly metabolized hormones or paracrine regulators.

Materials and Methods

Materials

Dulbecco's modified Eagle's medium (DMEM), hygromycin B, and Fluo-4 acetoxymethyl ester were purchased from Invitrogen (Carlsbad, CA). Fetal bovine serum (FBS) was purchased from Thermo Fisher Scientific (Melbourne, VIC, Australia). AlphaScreen reagents, ¹²⁵I-labeled Bolton-Hunter reagent, and 384-well ProxiPlates were purchased from PerkinElmer Life and Analytical Sciences (Waltham, MA). SureFire ERK1/2 reagents were generously provided by TGR BioSciences (Adelaide, SA, Australia). 6,7-Dichloro-2-methylsulfonyl-3-*tert*-butylaminoquinoxaline (compound 2) was generated according to a method published previously (Teng et al., 2007) to a purity of >95%, and compound integrity was confirmed by NMR. (4-(3-Benzoyloxyphenyl)-2-ethylsulfinyl-6-(trifluoromethyl)pyrimidine (BETP) and 3-amino-5-chloro-*N*-cyclopropyl-6-methoxy-4-methyl-thieno[2,3-*b*]pyridine-2-carboxamide (LY2033298) were provided by Eli Lilly and GLP-1 peptides were purchased from American Peptide (Sunnyvale, CA). All other reagents were purchased from Sigma-Aldrich (St. Louis, MO) or BDH Merck (Melbourne, VIC, Australia) and were of an analytical grade.

Transfections and Cell Culture

GLP-1R, M₂ mAChR, and A₁-AR were isogenically integrated into FlpIn-Chinese hamster ovary (FlpInCHO) cells (Invitrogen), and selection of receptor-expressing cells was accomplished by treatment with 600 µg/ml hygromycin B as described previously. Transfected and parental FlpInCHO cells were maintained in DMEM supplemented with 10% heat-inactivated FBS and incubated in a humidified environment at 37°C in 5% CO₂. For all whole-cell assays, cells were seeded at a density of 3×10^4 cells/well into 96-well culture plates and incubated overnight at 37°C in 5% CO₂ before assaying.

Radioligand Binding Assay

GLP-1R Experiments. Growth medium was replaced with binding buffer [DMEM containing 25 mM HEPES and 0.1% (w/v) bovine serum albumin] containing 0.5 nM [¹²⁵I]-exendin(9–39) and increasing concentrations of unlabeled peptide in the presence and absence of increasing concentrations of allosteric ligand. Cells were incubated overnight at 4°C, followed by three washes in ice-cold phosphate-buffered saline to remove unbound radioligand. Then 0.1 M NaOH was added, and radioactivity was determined by gamma counting. For GLP-1R experiments, nonspecific binding was defined by 1 µM exendin(9–39).

M₂ mAChR Experiments. M₂ mAChR FlpInCHO membrane homogenates (5–20 µg) were incubated in a 500-µl total volume of assay buffer containing [³H]N-methylscopolamine (0.5 nM) with a range of concentrations of choline in the absence and presence of LY2033298 (1 and 10 µM) at 30°C for 90 min. All assays were performed in the presence of guanosine-5'-(β-γ-imino)triphosphate. For all experiments, nonspecific binding was defined by 10 µM atropine, and the effects of vehicle were also determined. Incubation was terminated by rapid filtration through Whatman GF/B filters using a cell harvester (Brandell Inc., Gaithersburg, MD). Filters were washed three times with 3-ml aliquots of ice-cold 0.9% NaCl buffer and dried before the addition of 4 ml of scintillation mixture (Ultima-Gold; PerkinElmer Life and Analytical Sciences). Vials were then left to stand until the filters became uniformly translucent before radioactivity was determined in disintegrations per minute using scintillation counting.

cAMP Assays

cAMP accumulation assays were performed using the AlphaScreen SureFire kit as described previously (Koole et al., 2010). Cells were stimulated with peptide ligand and/or allosteric ligand and incubated for 30 min at 37°C in 5% CO₂. cAMP accumulation was measured after 30 min of cell stimulation. All values were converted to concentration of cAMP, and data were subsequently normalized to the maximum response elicited by GLP-1(7–36)NH₂.

ERK1/2 Phosphorylation Assay

Receptor-mediated ERK1/2 phosphorylation was determined by using the AlphaScreen ERK1/2 SureFire protocol as described previously (May et al., 2007a). Initial ERK1/2 phosphorylation time course experiments were performed over 1 h to determine the time at which ERK1/2 phosphorylation was maximal after stimulation by agonists. For GLP-1R, all responses peaked at 7 min; for M₂ mAChR, ACh, and Ch, responses peaked at 5 min, and for LY2033298, responses peaked at 8 min. For A₁-AR, adenosine and inosine peaked at 5 min, and (2-amino-4,5-dimethyl-3-thienyl)(3-(trifluoromethyl)phenyl)-methanone (PD81723) and (2-amino-4-(3-(trifluoromethyl)phenyl)thiophen-3-yl)(phenyl)methanone (VCP171) peaked at 7 min. Subsequent concentration-response curves were constructed at the peak time point for each receptor/ligand combination.

Intracellular Ca²⁺ Mobilization Assay

Intracellular Ca²⁺ mobilization was determined as described previously (Werry et al., 2005). Fluorescence was determined immediately after drug addition, with an excitation wavelength set to 485

nm and an emission wavelength set to 520 nm, and readings were taken every 1.36 s for 120 s. Concentration-response curves were constructed from the peak response, calculated using five-point smoothing, followed by correction against basal fluorescence.

[³⁵S]GTPγS Binding Assay

[³⁵S]GTPγS binding was determined as described previously (Valant et al., 2012). M₂ mAChR FlpInCHO cell membranes (5–25 µg) were equilibrated in a 500-µl total volume of assay buffer containing 10 µM guanosine 5'-diphosphate and a range of concentrations of ligands (ACh or Ch) in the absence or presence of LY2033298 (0.1–10 µM) at 30°C for 60 min. After this time, 50 µl of [³⁵S]GTPγS (1 nM) was added, and incubation continued for 30 min at 30°C. Incubation was terminated by rapid filtration through Whatman GF/B filters using a cell harvester (Brandell, Gaithersburg, MD). Filters were washed three times with 3-ml aliquots of ice-cold 0.9% NaCl buffer and dried before the addition of 4 ml of scintillation mixture (Ultima-Gold). Vials were then left to stand until the filters became uniformly translucent before radioactivity was determined in disintegrations per minute using scintillation counting.

Ex Vivo Pancreatic Islet Assays and In Vivo IVGTT Studies

Animals were maintained in accordance with the Institutional Animal Use and Care Committee of Eli Lilly and Company and the National Institutes of Health *Guide for the Care and Use of Laboratory Animals* (Institute of Laboratory Animal Resources, 1996).

Ex Vivo Pancreatic Islet Assays

The procedures for isolating islets and performing the insulin secretion assays were described previously (Sloop et al., 2010). Islets were isolated from pancreases of male Sprague-Dawley rats using Hanks' balanced salt solution buffer (Sigma-Aldrich) containing 2% bovine serum albumin (Applichem, Boca Raton, FL) and 1 mg/ml collagenase (Sigma-Aldrich). Islets were purified using Histopaque (Histopaque-1077-Histopaque-11991 mixture; Sigma-Aldrich) gradients and cultured overnight in RPMI-1640 medium containing 10% FBS, 100 U/ml penicillin, and 100 µg/ml streptomycin (Invitrogen). For the insulin secretion assays, islets were cultured at 37°C for 90 min in Earle's balanced salt solution (Invitrogen) containing the indicated concentrations of glucose and treatment conditions. Insulin that was released into the medium was measured using homogeneous time-resolved fluorescence technology (Cisbio Bioassays, Bedford, MA).

In Vivo IVGTT Studies

Male Wistar rats were purchased from Harlan (Indianapolis, IN) and maintained on a 12-h light/dark cycle at 21°C. For the studies, rats were fasted overnight and anesthetized the next morning with 60 mg/kg Nembutal (Lundbeck, Deerfield, IL). Catheters were then surgically inserted into the jugular vein and carotid artery for compound and/or peptide infusions and blood collection, respectively. For animal treatment, BETP was solubilized in a dosing solution containing 10% ethanol-Solutol, 20% polyethylene glycol 400, and 70% phosphate-buffered saline, pH 7.4, and infused intravenously alone or in combination with GLP-1(9–36)-NH₂ (Bachem California, Torrance, CA) formulated in saline containing 0.1% albumin. Blood was collected to determine glucose, insulin, and total GLP-1 levels after administration of an intravenous glucose bolus of 0.5 g/kg. Plasma levels of glucose were measured using a Hitachi 912 clinical chemistry analyzer (Roche, Indianapolis, IN), and insulin and total GLP-1 levels were determined using electrochemiluminescence assays for each (Meso Scale, Gaithersburg, MD).

Data Analysis

All data obtained were analyzed in GraphPad Prism 5.0.2 (GraphPad Software Inc., San Diego, CA). Radioligand inhibition binding data were fitted to a one-site inhibition mass action curve. Where

possible, in whole-cell ligand interaction studies, data were fitted to the following two forms of an operational model of allosterism and agonism (Leach et al., 2007; Aurelio et al., 2009) to derive functional estimates of modulator affinity and cooperativity.

$E =$

$$\frac{E_m(\tau_A[A](K_B + \alpha\beta[B]) + \tau_B[B]K_A)^n}{([A]K_B + K_A K_B + [B]K_A + \alpha[A][B])^n + (\tau_A[A](K_B + \alpha\beta[B]) + \tau_B[B]K_A)^n} \quad (1)$$

$$E = \frac{E_m(\tau_A[A](K_B + \alpha\beta[B]) + \tau_B[B]EC_{50})^n}{EC_{50}^n(K_B + [B])^n + (\tau_A[A](K_B + \alpha\beta[B]) + \tau_B[B]EC_{50})^n} \quad (2)$$

where E_m is the maximum attainable system response for the pathway under investigation, $[A]$ and $[B]$ are the concentrations of orthosteric agonist and allosteric modulator/agonist, respectively, K_B is the dissociation constant of the allosteric modulator, EC_{50} is the concentration of orthosteric (full) agonist yielding 50% of the response between minimal and maximal receptor activation in the absence of allosteric ligand, n is a transducer slope factor linking occupancy to response, α is the binding cooperativity factor, β is an empirical scaling factor describing the allosteric effect of the modulator on orthosteric agonist signaling efficacy, respectively, and τ_A and τ_B are operational measure of the ligands' respective signaling efficacies that incorporate receptor expression levels and efficiency of stimulus-response coupling. Equation 1 was used in interaction studies performed between allosteric ligand and a partial agonist, whereas eq. 2 was used when the modulator was interacted with full agonists, depending on the pathway investigated. This is so because eq. 2 is only valid in cases where the orthosteric agonist has high efficacy ($\tau \gg 1$) such that K_A is $\gg [A]$. For all other data, concentration-response curves were fitted with a three-parameter logistic equation.

Results

Allosteric Modulation of GPCR Agonist Metabolites Is Potentially a Widespread Phenomenon. To validate our hypothesis that metabolites of endogenous ligands can be

allosterically modulated at the GPCR of the parental ligand, we performed an initial screen using a representative allosteric ligand for three different model systems: the M_2 mAChR, the A_1 -AR, and the GLP-1R. In a recent study, we characterized LY2033298 as an allosteric modulator of the M_2 mAChR (Valant et al., 2012). PD81723 is a well accepted allosteric modulator of the A_1 -AR (Bruns and Fergus, 1990), and we have also recently identified a series of low-molecular-weight pyrimidine-based compounds that activate the GLP-1R allosterically, the most potent representative being BETP (designated compound B in Sloop et al., 2010). These three ligands (Supplemental Fig. 1D) were selected as representative modulators for each receptor, respectively. Both the M_2 mAChR and the A_1 -AR are predominantly coupled to $G\alpha_i$ proteins, whereas the GLP-1R is primarily coupled to $G\alpha_s$. Therefore, in the initial screen ERK1/2 phosphorylation was assessed for both the M_2 mAChR and the A_1 -AR, whereas cAMP accumulation assays were performed for the GLP-1R. All data were analyzed using an operational model of allosterism to derive global cooperativity estimates [$\alpha\beta$, a composite cooperativity factor quantifying allosteric modulation of the orthosteric ligand affinity (α) and efficacy (β)] (Table 1).

The cognate agonist for the M_2 mAChR, ACh, is rapidly converted to its inactive metabolites, Ch, and acetate, in the synaptic cleft by acetylcholinesterase (Birks and Macintosh, 1957) (Supplemental Fig. 1A). In this study, Ch exhibited greater than 1000-fold lower potency in ERK1/2 phosphorylation compared with the parent agonist ACh (Fig. 2, A and B). However, LY2033298 strongly potentiated the ERK1/2 response of Ch to a greater extent (112-fold) than that of ACh itself (Fig. 2, A and B; Table 1). In addition, assessment using a more proximal assay of M_2 mAChR activation (GTP γ S binding) revealed LY2033298 potentiated the response to both ACh and Ch, but this effect was much greater for the metabolite (Supplemental Fig. 2;

TABLE 1

Allosteric parameters determining the cooperativity for the interaction between the allosteric modulators and agonist/metabolite at the three different GPCRs, using various signal outputs

Data were analyzed with an operational model of allosterism as defined under *Materials and Methods*. $\text{Log}\alpha\beta$ values represent the composite cooperativity between the allosteric modulator and the orthosteric ligand. Antilogarithms are shown in parentheses. $\text{p}K_B$ values (the negative logarithm of the affinity) for the allosteric ligands derived from application of the operational model of allosterism were 5.01 ± 0.23 for BETP, 5.14 ± 0.16 for Compound 2, and 4.58 ± 0.32 for PD81723. For LY2033298, the $\text{p}K_B$ was fixed to the equilibrium dissociation constant (4.74) previously determined in radioligand binding assays (Valant et al., 2012). $\alpha\beta$ is the cooperativity factor that defines the fold change in receptor signaling by the allosteric modulator.

Allosteric Ligand and Signaling Pathway	$\text{Log } \alpha\beta (\alpha\beta)$					
	Orthosteric Ligand			Orthosteric Metabolite		
	GLP-1(7–36)NH ₂	ACh	Adenosine	GLP-1(9–36)NH ₂	Ch	Inosine
GLP-1R						
BETP						
cAMP	0.18 ± 0.15 (1.5)			N.D. ^a		
pERK1/2	-0.97 ± 0.39 (0.1)			-0.01 ± 0.11 (1.0)		
Ca ²⁺	N.D. ^a			N.D.		
Compound 2						
cAMP	0.36 ± 0.14 (2.3)			2.63 ± 0.43 (426)		
pERK1/2	-0.27 ± 0.26 (0.53)			0.25 ± 0.31 (1.8)		
Ca ²⁺	N.D.			N.D.		
M_2 mAChR						
LY2033298						
pERK1/2		0.31 ± 0.07 (2.0)			2.35 ± 0.16 (224)	
GTP γ S		1.20 ± 0.08 (16)			1.85 ± 0.10 (71)	
A_1 -AR						
PD81723						
pERK1/2			1.31 ± 0.12 (20)			1.08 ± 0.12 (12)

N.D., data were not able to be experimentally defined.

^a Cooperativity factors could not be defined, but positive allosteric modulation was observed.

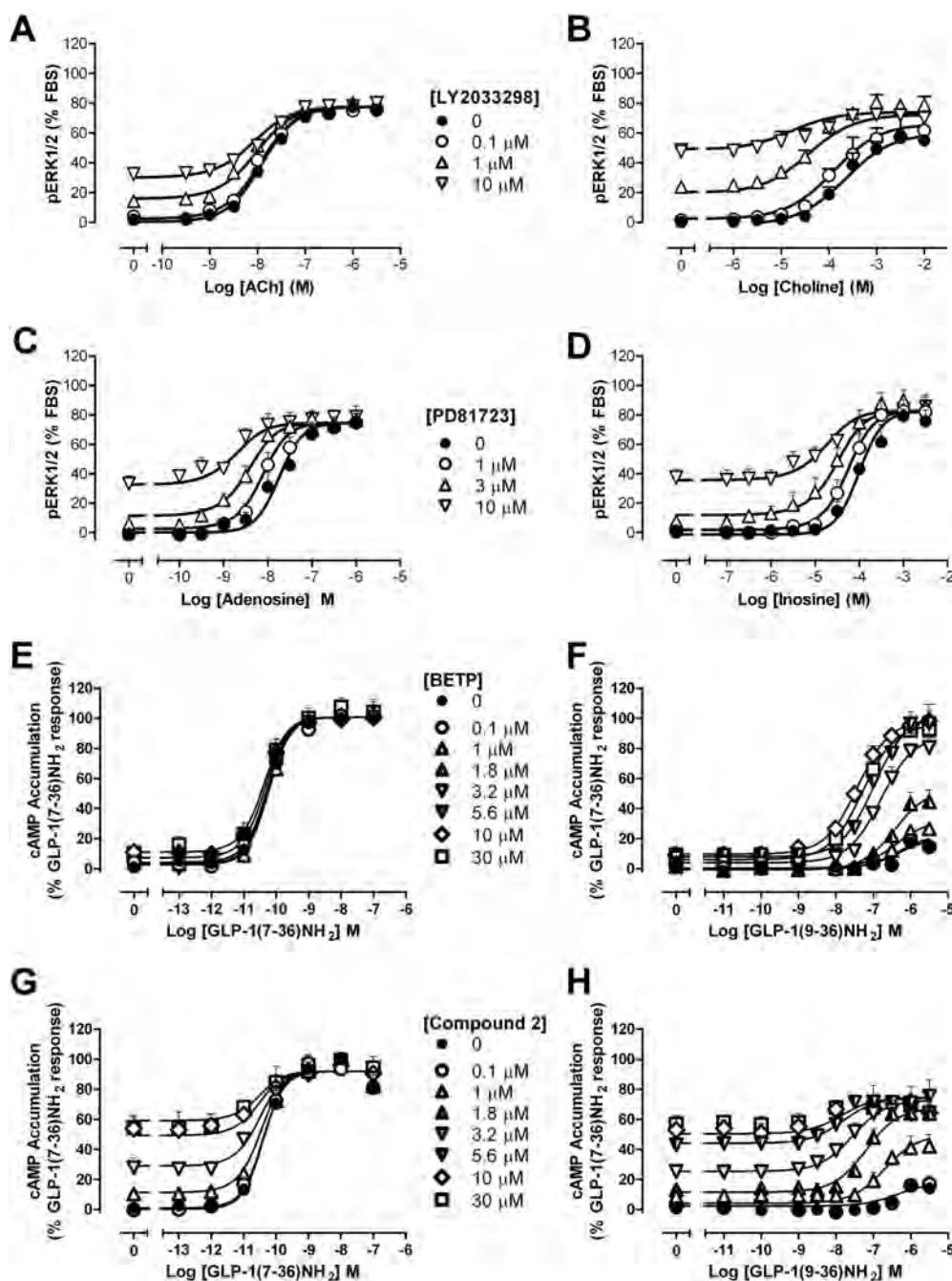


Fig. 2. Small-molecule ligands of three different GPCRs display a high degree of positive allosteric modulation of the metabolite of the cognate ligand in intact cells. Interaction studies were performed in ERK1/2 phosphorylation assays between LY2033298 and ACh (A) or Ch (B) in FlpInCHO cells stably expressing the human M_2 mAChR. Interaction studies between PD81723 and adenosine (C) or inosine (D) were performed in ERK phosphorylation assays in FlpInCHO cells expressing the A_1 -AR. cAMP accumulation interaction studies were performed between BETP and GLP-1(7-36)NH₂ (E) or GLP-1(9-36)NH₂ (F) or between compound 2 and GLP-1(7-36)NH₂ (G) or GLP-1(9-36)NH₂ (H) in FlpInCHO cells stably expressing the human GLP-1R. All values are means \pm S.E.M. of three to six independent experiments performed in duplicate.

Table 1). Competition binding assays revealed weak positive modulation of Ch affinity (13-fold) (Supplemental Fig. 3), indicating that potentiation of Ch in functional assays is principally via efficacy modulation. In our earlier study, we showed that LY2033298 also displayed positive cooperativity with ACh in binding affinity (16-fold) indicating that there is no efficacy modulation by LY2033298 with the parent agonist (Valant et al., 2012). Similarly to ACh, adenosine is also rapidly metabolized (by adenosine deaminase) to inosine (Plagemann et al., 1985) (Supplemental Fig. 1B); inosine displayed greater than 1000-fold lower potency at the A_1 -AR in ERK1/2 phosphorylation compared with its parent ligand, adenosine. In addition, this response was significantly potentiated by the allosteric modulator, PD81723 (Fig. 2, C and D); although in this

instance the degree of potentiation was no greater than that observed with adenosine (Table 1). At the GLP-1R, BETP displayed very weak partial agonism in cAMP accumulation (Fig. 2, E and F) but had no effect on cAMP responses mediated by GLP-1(7-36)NH₂ in interaction assays (Fig. 2E). In the absence of allosteric modulation, the metabolite GLP-1(9-36)NH₂ only exhibited very weak partial agonism for cAMP, with 1000-fold lower potency and only approximately 15% of the maximal signal compared with GLP-1(7-36)NH₂ (Fig. 2F). However, this weak response was strongly potentiated in a concentration-dependent manner by BETP (Fig. 2F). Cooperativity estimates could not be derived for this data set because the operational model of allosterism could not adequately describe the data. Regardless, there is a strikingly strong positive

allosteric effect with both an increase in potency (pEC_{50} shift from 6.4 ± 0.08 to 7.5 ± 0.07) and maximal agonist effect (E_{max} shift from 15 ± 3 to $99 \pm 4\%$) of GLP-1(9–36)NH₂-mediated response (Fig. 2F). For all ligands studied, no response was seen in untransfected cells. Collectively these data identify a novel consequence of allosteric drug action, specifically, the augmentation of metabolite signaling that in two of the three cases studied (the M₂ mAChR and GLP-1R) cannot be predicted from assessment of the parent ligand.

Activation of the GLP-1R by the Major Metabolite of GLP-1(7–36)NH₂ [GLP-1(9–36)NH₂] Is Augmented by Structurally Distinct Small Molecule Allosteric Ligands in a Pathway Selective Manner. To further explore this phenomenon, we performed additional studies using the GLP-1R as a model system. In addition to BETP, we characterized the quinoxaline-based Novo Nordisk compound 2 (Supplemental Fig. 1D) for its ability to modulate the metabolite in cAMP accumulation assays. In a previous study, we showed that compound 2 has a limited ability to augment the actions of GLP-1 or its endogenous peptide variants at the GLP-1R in cAMP signaling, despite showing direct allosteric agonism in its own right (Koole et al., 2010) (Fig. 2G). However, similar to that observed with BETP (Fig. 2, E and F), there was a large potentiation of GLP-1(9–36)NH₂-mediated cAMP signaling (Fig. 2H). Derivation of global cooperativity estimates ($\alpha\beta$) revealed a greater than 400-fold potentiation of the metabolite response and an ~180-fold greater magnitude of positive cooperativity between compound 2 and GLP-1(9–36)NH₂ compared with that for GLP-1(7–36)NH₂ (Table 1). Both compound 2 and BETP exhibited almost neutral cooperativity with GLP-1(7–36)NH₂ and GLP-1(9–36)NH₂ peptides in whole-cell competition binding assays (Supplemental Fig. 4), indicating that the allosteric effects of these compounds on GLP-1(9–36)NH₂-mediated cAMP signaling are principally driven by changes in orthosteric agonist efficacy.

Despite the critical role of GLP-1R-mediated cAMP production in insulin secretion, there is also a role for other signaling components/pathways such as β -arrestin signaling, mobilization of intracellular Ca²⁺, and activation of mitogen-activated kinases such as ERK1/2 in the augmentation of the insulin response and β -cell survival (Baggio and Drucker, 2007; Sonoda et al., 2008). We therefore extended the study to explore allosteric effects of BETP and compound 2 on GLP-1(9–36)NH₂ in ERK1/2 phosphorylation and Ca²⁺ mobilization (Fig. 3) and compared the effects with the parent peptide. In agreement with our previous findings, GLP-1(7–36)NH₂ displayed robust agonism in ERK phosphorylation and Ca²⁺ mobilization (Fig. 3, A, C, E, and G). Of significance, GLP-1(9–36)NH₂ also displayed agonism in pERK1/2 in a concentration-dependent manner, but only a very weak Ca²⁺ response was observed (at 3 μ M peptide). In interaction studies, BETP exhibited negative cooperativity with GLP-1(7–36)NH₂ in ERK phosphorylation but an augmentation in Ca²⁺ signaling at the highest concentration tested (30 μ M), with a small increase in pEC_{50} and E_{max} (Fig. 3, A and C; Table 1). In contrast, GLP-1(9–36)NH₂ displayed neutral cooperativity with BETP in ERK1/2 phosphorylation (Fig. 3B), and there was also no apparent change in Ca²⁺ response mediated by GLP-1(9–36)NH₂ in the presence of 30 μ M BETP (the small change in response can be attributed to

agonism from BETP alone) (Fig. 3D). Compound 2 displayed neutral cooperativity in both ERK1/2 phosphorylation and intracellular Ca²⁺ mobilization when interacted with either GLP-1(7–36)NH₂ or GLP-1(9–36)NH₂ (Fig. 3, E–H; Table 1). Taken together, these results suggest that allosteric modulation can engender functional selectivity in the actions of both the metabolite and the parent ligand when acting at the GLP-1R. However, the differential modulation between the metabolite and the cognate ligand on the different signaling pathways highlights a novel use of allosteric ligands to engender pathway-selective modulation of response of the metabolite, even if no modulation is observed from the cognate agonist of the system.

Allosteric Modulation of the Metabolite GLP-1(9–36)NH₂ via the GLP-1R Results in Glucose-Dependent Insulin Secretion Ex Vivo in Rat Islets and In Vivo. Activation of the GLP-1R by GLP-1 only increases insulin secretion in conditions of elevated glucose (Göke et al., 1993; Sloop et al., 2010). To evaluate the ability of the metabolite to activate glucose-dependent insulin secretion, pancreatic islets isolated from Sprague-Dawley rats were used. In a previous study, we showed that GLP-1(7–36)NH₂ had insulinotropic activity in islet experiments using high-glucose conditions, and BETP also caused a robust concentration-dependent increase in insulin secretion (Sloop et al., 2010). Here we show that in high glucose conditions, GLP-1(9–36)NH₂ does not induce insulin secretion at concentrations of up to 10 μ M (Fig. 4; Supplemental Fig. 5A). However, in the presence of 1 μ M BETP (which only minimally increases insulin levels by itself), a dose-dependent increase in GLP-1(9–36)NH₂-mediated insulin-secretion was observed, with a pEC_{50} of 7.4 ± 0.3 (EC_{50} 38 nM) and a maximal response achieved at 100 nM (Fig. 4A). Maximum insulin levels in islet cultures treated with the combination of BETP and 1 μ M metabolite were similar to those induced by 100 nM GLP-1(7–36)NH₂ (Supplemental Fig. 5A).

To explore the in vivo insulinotropic effects, glucose-stimulated insulin secretion was measured in compound-treated male Wistar rats undergoing an IVGTT. Similar to our previous study (Sloop et al., 2010), GLP-1(7–36)NH₂ displayed insulin secretagogue activity during the 20-min time course; however, compared with vehicle, animals dosed with 150 nmol/kg GLP-1(9–36)NH₂ had lower levels of plasma insulin than those treated with GLP-1(7–36)NH₂ (Fig. 4B). BETP had no insulinotropic activity at the dose administered (Fig. 4B). However, coadministration of GLP-1(9–36)NH₂ and BETP elicited an elevation in plasma insulin similar to that of animals dosed with GLP-1(7–36)NH₂, although insulin levels remained elevated over the 20-min time period for GLP-1(7–36)NH₂, whereas in the animals dosed with BETP and GLP-1(9–36)NH₂ plasma insulin levels dropped to the level of vehicle after 10 min (Fig. 4B). Determination of total GLP-1 levels throughout the time course showed that GLP-1(9–36)NH₂ was cleared from the plasma within this same 10-min time period and, in addition, revealed that BETP did not alter the pharmacokinetics of GLP-1(9–36)NH₂ (Supplemental Fig. 6). In addition, plasma insulin levels remained elevated [similar to GLP-1(7–36)NH₂] when animals were administered with higher doses of GLP-1(9–36)NH₂ (400 nmol/kg) in the presence of BETP (10 mg/kg) (Supplemental Fig. 5B). Taken together, the ex vivo and in vitro studies support a model whereby BETP allosterically potentiates

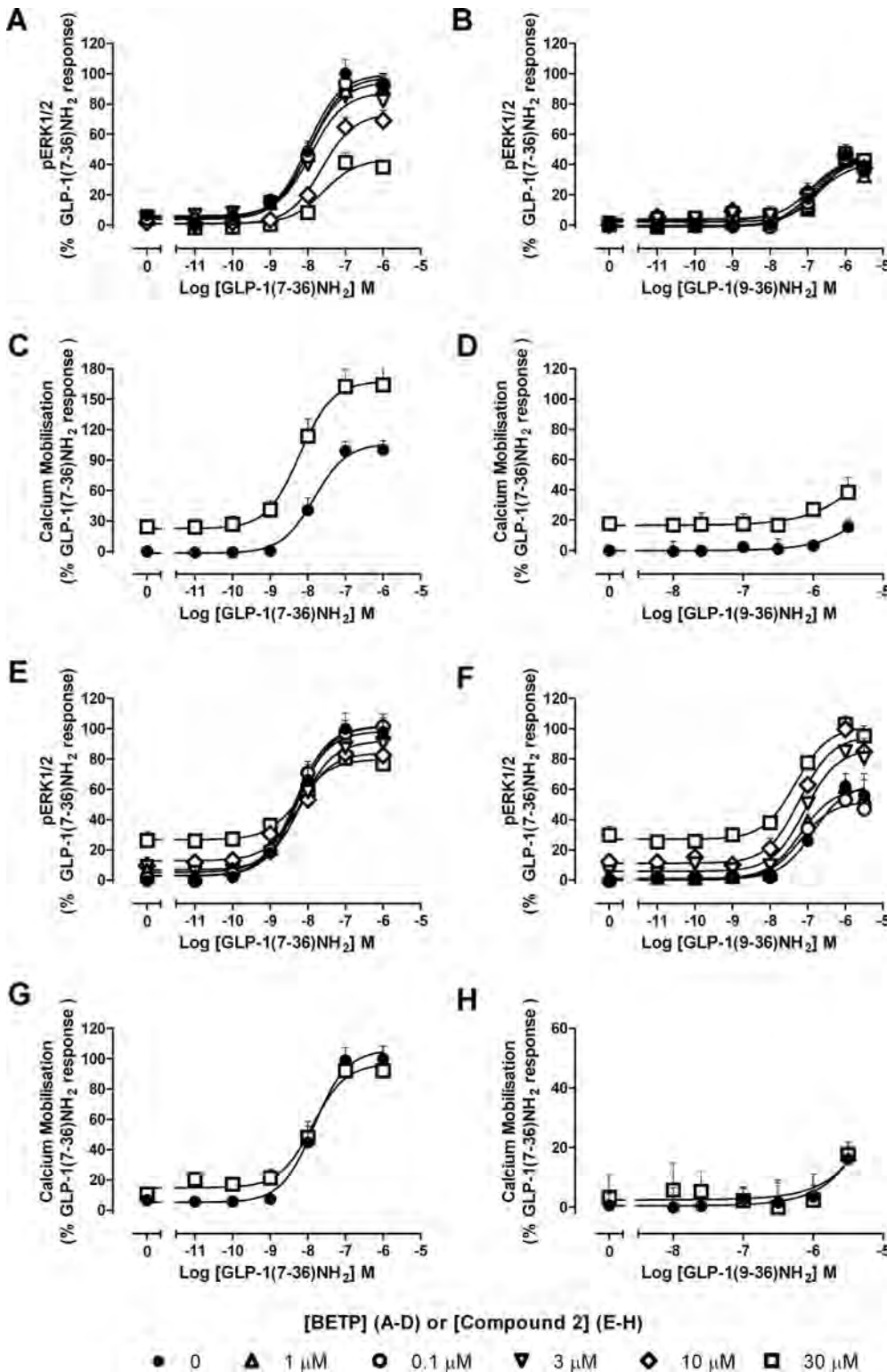


Fig. 3. Differing degrees of allosteric modulation of GLP-1(7-36)NH₂ and GLP-1(9-36)NH₂ by BETP or compound 2 at the GLP-1R in ERK1/2 phosphorylation and intracellular calcium mobilization in intact cells. Interaction studies between BETP (A-D) and GLP-1(7-36)NH₂ (A and C) or GLP-1(9-36)NH₂ (B and D) in ERK1/2 phosphorylation (A and B) or intracellular calcium mobilization (C and D), respectively. Interaction studies between compound 2 (E-H) and GLP-1(7-36)NH₂ (E and G) or GLP-1(9-36)NH₂ (F and H) in ERK1/2 phosphorylation (E and F) or intracellular calcium mobilization (G and H), respectively. All values are means \pm S.E.M. of three to four independent experiments performed in duplicate.

GLP-1(9-36)NH₂-mediated cAMP signaling resulting in insulin release. The ability of BETP to specifically augment GLP-1(9-36)NH₂-mediated cAMP signaling in GLP-1R-expressing cells, in combination with the ability to modulate glucose-dependent insulin secretion, provides compelling proof of concept that allosteric potentiation of metabolites is a viable approach for the development of GLP-1R-based therapeutics.

Discussion

In this study, we demonstrate the ability of allosteric ligands to modulate signaling mediated by an inactive metabolite of the primary endogenous ligand. To determine the generality of this hypothesis, three receptors (the GLP-1R, M₂ mAChR, and the A₁-AR) from two different subclasses of GPCRs were selected, each of which is a thera-

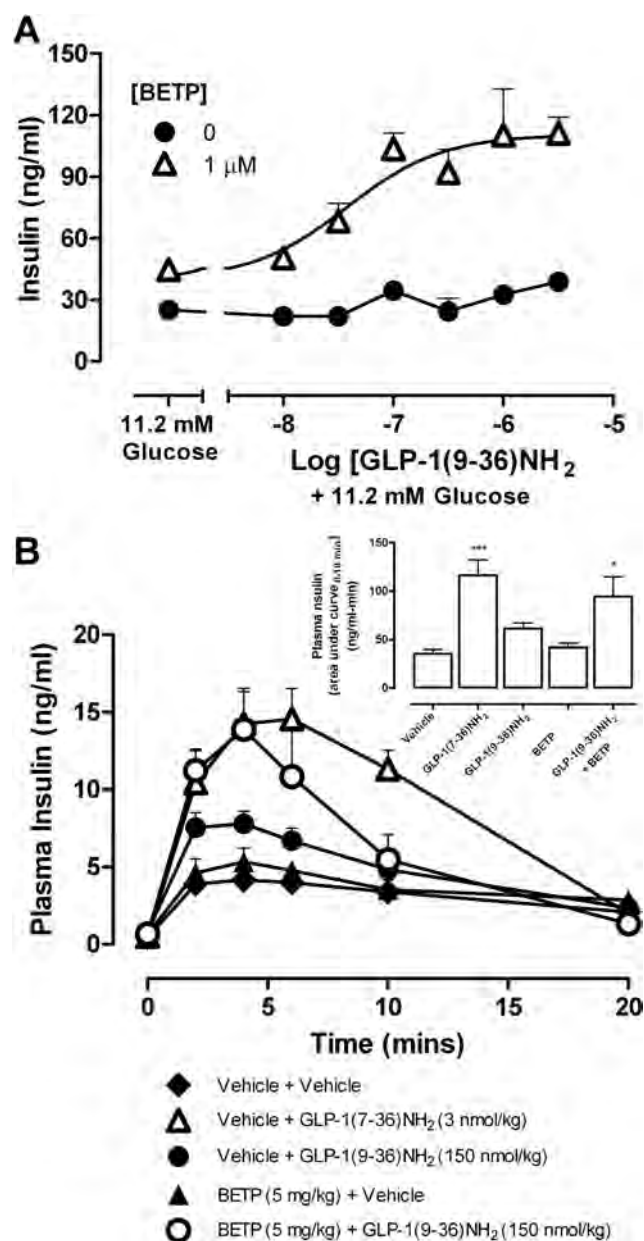


Fig. 4. Ex vivo and in vivo studies reveal allosteric modulation of the GLP-1 metabolite at the GLP-1R leads to insulin secretion. **A**, insulin concentrations from cultures of Sprague-Dawley rat islets incubated in medium containing high glucose (11.2 mM) and BETP with increasing concentrations of GLP-1(9-36)NH₂. Islet treatments were performed for 90 min. **B**, time course of plasma insulin concentrations in fasted, anesthetized animals treated with either vehicle, GLP-1(7-36)NH₂ (3 nmol/kg), GLP-1(9-36)NH₂ (150 nmol/kg), BETP (5 mg/kg), or coadministration of BETP and GLP-1(9-36)NH₂, immediately before intravenous administration of a glucose bolus (0.5 g/kg). Inset, AUC_{0-10 min} of the insulin secretion for the various treatment groups. All results are expressed as mean \pm S.E.M. of five experiments. *, $p < 0.05$ as determined using a one-way analysis of variance followed by Dunnett's comparison to vehicle group.

peutic target and also has identified allosteric modulators. The GLP-1R is a family B GPCR and is a promising target in the development of treatments for type 2 diabetes mellitus (DM). Both the M₂ mAChR and A₁-AR are prototypical family A GPCRs, with separate mechanisms of activation compared with family B GPCRs, and are therapeutic targets for treatment of Alzheimer's disease/asthma and neuropathic pain, respectively.

For all three receptors, the potency of the metabolite alone at the selected signaling pathway (ERK1/2 phosphorylation for G α_i -coupled M₂ mAChR and A₁-AR and cAMP for G α_s -coupled GLP-1R) was markedly lower than that of the cognate agonist (greater than 1000-fold). However, in each case, an allosteric ligand markedly potentiated signaling by the metabolite. In two of the cases (the GLP-1R and M₂ mAChR), the allosteric effect on the metabolite was much more pronounced than the effect on the parent ligand. Taken together, these findings highlight the virtually untapped potential for metabolic products of GPCR endogenous agonists to recruit signaling pathways that would otherwise remain quiescent after inactivation of the parent agonist. The ability to activate responses from convergent and divergent signaling cascades could therefore have the potential to generate a more tuneable response from the metabolite than that of the parent compound.

The ability of each of these allosteric ligands to promote strong potentiation on the actions of the respective metabolite may be therapeutically relevant. Choline levels in the brain have been reported to range between 10 and 15 μ M, depending on the species (Tucek, 1985). Choline affinity for the M₂ mAChR is low (in the millimolar range); however, both affinity (>10 -fold) and potency (>200 -fold) can be enhanced by the allosteric ligand LY2033298. This result suggests that it is very likely that allosteric potentiation of these responses may be possible in a physiological setting. Likewise, resting inosine levels in the brain and the heart can reach concentrations as high as 10 μ M and at least 30-fold higher in ischemic conditions (Bäckström et al., 2003). Evidence for modulation of inosine at the A₁-AR (in addition to previous evidence for modulation at the A₃-AR (Gao et al., 2011) provides additional proof that targeting metabolites is viable. Furthermore, circulating GLP-1(9-36)NH₂ concentrations are >10 -fold higher than that of GLP-1(7-36)NH₂ (Göke et al., 1993). However, this metabolite exhibits a ~ 1000 -fold lower binding affinity for the GLP-1R and equally low efficacy and potency for cAMP accumulation. This observation indicates that at least 100-fold potentiation of the metabolite response would be required for a therapeutically beneficial effect. The in vitro experiments show that compound 2 can produce this degree of potentiation (>250 -fold), consistent with modulation of metabolites as a therapeutically relevant approach.

ACh and adenosine both act at several subtypes of the mAChR and adenosine receptor, respectively. Therefore, it is plausible that the metabolites investigated in this study could also have effects at these other subtypes. Certainly this is true for inosine, for which allosteric potentiation of cAMP signaling at the A₃-AR has been reported (Gao et al., 2011). One advantage of allosteric ligands is their ability to provide selectivity, and, therefore, use of a selective modulator should, in theory, only modulate the metabolite at the subtype where the allosteric ligand binds.

As an extension of our initial screen, the GLP-1R was used as a model system to further explore the phenomenon. The GLP-1R has actions that address key symptoms associated with DM, including glucose-dependent increases in insulin synthesis and release, decreases in β -cell apoptosis, body mass, and gastric emptying (Vahl and D'Alessio, 2004; Drucker and Nauck, 2006). GLP-1 is principally released from intestinal L cells in its amidated form [GLP-1(7-

36)NH₂] in response to meal ingestion, resulting in insulin release (Drucker, 2006). It is very rapidly degraded by dipeptidyl peptidase IV (within 1–2 min) to GLP-1(9–36)NH₂, with only ~10% reaching the systemic circulation and even lower levels reaching the pancreatic β cells (Deacon et al., 1995). The metabolite is thus the major circulating form of GLP-1; however, it does not stimulate insulin secretion (Deacon et al., 1995; Tomas and Habener, 2010), presumably due to the lack of GLP-1R-mediated increases in cAMP, which is thought to be a major contributor to insulin secretion.

A novel treatment for type 2 DM, therefore, would be to potentiate the actions of GLP-1(9–36)NH₂ mediated through cAMP to elicit insulin secretion. Our results show that this is indeed possible, with two structurally distinct allosteric ligands, BETP and compound 2, able to strongly potentiate cAMP signaling in heterologous cell systems. A key finding in our study was the demonstration that one of these compounds, BETP, could also strongly potentiate the ability of the GLP-1 metabolite to promote insulin secretion in both ex vivo and in vivo rat models. Relatively high concentrations of GLP-1(9–36)NH₂ were required to elicit an insulin response (even in the presence of BETP) in the isolated islets (30 nM and above) compared with circulating levels of GLP-1(9–36)NH₂ in normal physiology (approximately 100 pM). However, it is not uncommon to require much larger doses of hormones in ex vivo experiments compared with in vivo, for example, the EC₅₀ for GLP-1(7–36)NH₂ stimulation of islet culture insulin release is 1 to 10 nM (Göke et al., 1993; Sloop et al., 2010; Tomas et al., 2010), only ~10-fold lower than the augmented metabolite response. As the metabolite circulates at >10-fold higher concentrations than the parental peptide, these data suggest that regulation of physiological levels of GLP-1(9–36)NH₂ may be possible, even with compounds that have not been optimized for allosteric activity. Further exploration of this phenomenon in vivo at physiological levels of metabolite is currently limited because of the poor pharmacokinetic properties of the allosteric ligands available. However, in vivo effects on insulin secretion and blood glucose elicited by GLP-1(9–36)NH₂ are modulated by BETP, albeit with pharmacological dosing with the metabolite. This result provides the proof of concept that modulation of metabolites is possible for physiologically relevant endpoints. It is likely that specific screening programs to identify modulators optimized for potentiation of metabolites are required to conclusively show that allosteric modulation of metabolites can occur in an endogenous system.

To date, the level of modulation seen with the metabolites for existing compounds is purely serendipitous, however, the ability to develop allosteric ligands that induce very strong potentiation certainly exists. Screening programs using the endogenous ligand ACh identified an M₄ mAChR allosteric ligand that enhanced the response mediated by ACh 780-fold (Leach et al., 2010). Likewise, benzylquinolone carboxylic acid, an M₁ mAChR allosteric ligand, can potentiate the actions of ACh by up to 10,000-fold (Canals et al., 2012). Thus, there is clear precedent for the ability to develop compounds that will be effective even where metabolite activity is only 1/1000th that of the parent ligand (assuming that the metabolite levels do not reach levels higher than those of the parent). Thus, these data provide compelling evidence for proof of concept that allosteric modulation of metabolites

could lead to physiologically relevant responses that are therapeutically beneficial.

At present, for the therapeutically relevant effects of GLP-1R activation, the underlying signaling is not fully understood, but it is clear that physiological responses are a composite of multiple pathways. In our in vitro assays, we showed that allosteric ligands can engender functional selectivity in the actions of the metabolite when acting at the GLP-1R whereby cAMP signaling was strongly potentiated but no change was observed in ERK phosphorylation or Ca²⁺ mobilization. Together with the islet experiments and in vivo studies, this suggests that modulation of cAMP without altering pERK1/2 and calcium signaling is sufficient to promote insulin secretion. Nonetheless, the ideal signaling profiles for other therapeutically relevant effects of GLP-1R activation, such as β -cell survival, still remain to be determined. As more information becomes available, a more detailed understanding of the required combination of collateral efficacies required to therapeutically target different disease states will become apparent. Therefore, information characterizing functional selectivity of all classes of ligands and behavior will become increasingly important in drug discovery programs.

Probe dependence of allosteric drugs has multiple implications in drug discovery and the ability to modulate the action of normally inactive endogenous metabolites could be exploited to develop novel therapeutic agents. In addition, metabolites are often further metabolized, offering additional scope for drug discovery. However, in some cases, modulation of metabolites could also contribute to unwanted or unanticipated side effects of drugs. This study thus highlights the need to understand allosteric effects on all ligands, including metabolites normally considered to be inactive as part of the profile of modulator action. This concept is also relevant for other non-GPCR drug targets, such as ligand-gated ion channels. As a further layer of complexity, the breakdown product of one ligand could activate a different receptor with desirable properties, offering the potential to develop allosteric ligands with properties for modulating that specific receptor target. The findings of pronounced potentiation (in some cases) compared with the endogenous agonist has substantial, previously unrecognized, implications for therapeutic development of small molecule modulators.

Authorship Contributions

Participated in research design: Wootten, Sloop, Willard, Christopoulos, and Sexton.

Conducted experiments: Wootten, Savage, Valant, May, Ficorilli, and Showalter.

Contributed new reagents or analytic tools: Sloop and Willard.

Performed data analysis: Wootten, Savage, Valant, May, Sloop, Willard, Christopoulos, and Sexton.

Wrote or contributed to the writing of the manuscript: Wootten, Sloop, Christopoulos, and Sexton.

References

- Aurelio L, Valant C, Flynn BL, Sexton PM, Christopoulos A, and Scammells PJ (2009) Allosteric modulators of the adenosine A1 receptor: synthesis and pharmacological evaluation of 4-substituted 2-amino-3-benzoylthiophenes. *J Med Chem* 52:4543–4547.
- Bäckström T, Gojny M, Lockowandt U, Liska J, and Franco-Cereceda A (2003) Cardiac outflow of amino acids and purines during myocardial ischemia and reperfusion. *J Appl Physiol* 94:1122–1128.
- Baggio LL and Drucker DJ (2007) Biology of incretins: GLP-1 and GIP. *Gastroenterology* 132:2131–2157.

- Birks RI and Macintosh FC (1957) Acetylcholine metabolism at nerve-endings. *Br Med Bull* **13**:157–161.
- Bruns RF and Fergus JH (1990) Allosteric enhancement of adenosine A1 receptor binding and function by 2-amino-3-benzoylthiophenes. *Mol Pharmacol* **38**:939–949.
- Canals M, Lane JR, Wen A, Scammells PJ, Sexton PM, and Christopoulos A (2012) A Monod-Wyman-Changeux mechanism can explain G protein-coupled receptor (GPCR) allosteric modulation. *J Biol Chem* **287**:650–659.
- Christopoulos A (2002) Allosteric binding sites on cell-surface receptors: novel targets for drug discovery. *Nat Rev Drug Discov* **1**:198–210.
- Christopoulos A and Kenakin T (2002) G protein-coupled receptor allostereism and complexing. *Pharmacol Rev* **54**:323–374.
- Deacon CF, Johnsen AH, and Holst JJ (1995) Degradation of glucagon-like peptide-1 by human plasma in vitro yields an N-terminally truncated peptide that is a major endogenous metabolite in vivo. *J Clin Endocrinol Metab* **80**:952–957.
- Drucker DJ (2006) The biology of incretin hormones. *Cell Metab* **3**:153–165.
- Drucker DJ and Nauck MA (2006) The incretin system: glucagon-like peptide-1 receptor agonists and dipeptidyl peptidase-4 inhibitors in type 2 diabetes. *Lancet* **368**:1696–1705.
- Gao ZG, Verzijl D, Zweemer A, Ye K, Göblyös A, Ijzerman AP, and Jacobson KA (2011) Functionally biased modulation of A₃ adenosine receptor agonist efficacy and potency by imidazoquinolinamine allosteric enhancers. *Biochem Pharmacol* **82**:658–668.
- Göke R, Wagner B, Fehmann HC, and Göke B (1993) Glucose-dependency of the insulin stimulatory effect of glucagon-like peptide-1 7–36 amide on the rat pancreas. *Res Exp Med (Berl)* **193**:97–103.
- Institute of Laboratory Animal Resources (1996) *Guide for the Care and Use of Laboratory Animals*, 7th ed, Institute of Laboratory Animal Resources, Commission on Life Sciences, National Research Council, Washington, DC.
- Kenakin T (2005) New concepts in drug discovery: collateral efficacy and permissive antagonism. *Nat Rev Drug Discov* **4**:919–927.
- Knudsen LB, Kiel D, Teng M, Behrens C, Bhummalkar D, Kodra JT, Holst JJ, Jeppesen CB, Johnson MD, de Jong JC, et al. (2007) Small-molecule agonists for the glucagon-like peptide 1 receptor. *Proc Natl Acad Sci USA* **104**:937–942.
- Koole C, Wootten D, Simms J, Valant C, Sridhar R, Woodman OL, Miller LJ, Summers RJ, Christopoulos A, and Sexton PM (2010) Allosteric ligands of the glucagon-like peptide 1 receptor (GLP-1R) differentially modulate endogenous and exogenous peptide responses in a pathway-selective manner: implications for drug screening. *Mol Pharmacol* **78**:456–465.
- Leach K, Loiacono RE, Felder CC, McKinzie DL, Mogg A, Shaw DB, Sexton PM, and Christopoulos A (2010) Molecular mechanisms of action and in vivo validation of an M4 muscarinic acetylcholine receptor allosteric modulator with potential antipsychotic properties. *Neuropsychopharmacology* **35**:855–869.
- Leach K, Sexton PM, and Christopoulos A (2007) Allosteric GPCR modulators: taking advantage of permissive receptor pharmacology. *Trends Pharmacol Sci* **28**:382–389.
- May LT, Avlani VA, Langmead CJ, Herdon HJ, Wood MD, Sexton PM, and Christopoulos A (2007a) Structure-function studies of allosteric agonism at M2 muscarinic acetylcholine receptors. *Mol Pharmacol* **72**:463–476.
- May LT, Leach K, Sexton PM, and Christopoulos A (2007b) Allosteric modulation of G protein-coupled receptors. *Annu Rev Pharmacol Toxicol* **47**:1–51.
- Plagemann PG, Wohlhueter RM, and Kraupp M (1985) Adenosine uptake, transport, and metabolism in human erythrocytes. *J Cell Physiol* **125**:330–336.
- Sloop KW, Willard FS, Brenner MB, Ficorilli J, Valasek K, Showalter AD, Farb TB, Cao JX, Cox AL, Michael MD, et al. (2010) Novel small molecule glucagon-like peptide-1 receptor agonist stimulates insulin secretion in rodents and from human islets. *Diabetes* **59**:3099–3107.
- Sonoda N, Imamura T, Yoshizaki T, Babendure JL, Lu JC, and Olefsky JM (2008) β -Arrestin-1 mediates glucagon-like peptide-1 signaling to insulin secretion in cultured pancreatic beta cells. *Proc Natl Acad Sci USA* **105**:6614–6619.
- Teng M, Johnson MD, Thomas C, Kiel D, Lakis JN, Kercher T, Aytes S, Kostrowicki J, Bhummalkar D, Truesdale L, et al. (2007) Small molecule ago-allosteric modulators of the human glucagon-like peptide-1 (hGLP-1) receptor. *Bioorg Med Chem Lett* **17**:5472–5478.
- Tomas E and Habener JF (2010) Insulin-like actions of glucagon-like peptide-1: a dual receptor hypothesis. *Trends Endocrinol Metab* **21**:59–67.
- Tomas E, Stanojevic V, and Habener JF (2010) GLP-1 (9–36) amide metabolite suppression of glucose production in isolated mouse hepatocytes. *Horm Metab Res* **42**:657–662.
- Tucek S (1985) Regulation of acetylcholine synthesis in the brain. *J Neurochem* **44**:11–24.
- Vahl TP and D'Alessio DA (2004) Gut peptides in the treatment of diabetes mellitus. *Expert Opin Investig Drugs* **13**:177–188.
- Valant C, Felder CC, Sexton PM, and Christopoulos A (2012) Probe dependence in the allosteric modulation of a G protein-coupled receptor: implications for detection and validation of allosteric ligand effects. *Mol Pharmacol* **81**:41–52.
- Werry TD, Gregory KJ, Sexton PM, and Christopoulos A (2005) Characterization of serotonin 5-HT_{2C} receptor signaling to extracellular signal-regulated kinases 1 and 2. *J Neurochem* **93**:1603–1615.

Address correspondence to: Prof. Patrick M. Sexton, Drug Discovery Biology, Monash Institute of Pharmaceutical Sciences, Monash University, 381 Royal Parade, Parkville, Victoria 3052, Australia. E-mail: patrick.sexton@monash.edu

Supplementary Information

Article Title

Allosteric modulation of endogenous metabolites as an avenue for drug discovery

Authors

Wootten D, Savage EE, Valant C, May LT, Sloop KW, Ficorilli J, Showalter AD, Willard FS, Christopoulos A, Sexton PM

Journal Title

Molecular Pharmacology

Supplemental Fig. 1. Metabolic breakdown of endogenous ligands to their metabolites and structures of the allosteric ligands used in this study. (A) Acetylcholine is metabolised by acetylcholinesterases to choline and acetate. (B) Adenosine is metabolised by adenosine deaminase to inosine. (C) The peptide GLP-1(7-36)NH₂ is degraded by dipeptidyl peptidase IV to the inert metabolite GLP-1(9-36)NH₂ (the primary amino acid sequences are shown). (D) Structures of the four allosteric ligands used in this study.

Supplemental Fig. 2. The allosteric agonist LY2033298 displays positive allosteric modulation of the metabolite choline in GTP γ S binding in membranes expressing M2 mAChR. Interaction studies between LY2033298 and ACh (A) or Ch (B) GTP γ S binding assays. All values are mean \pm SEM of three independent experiments performed in duplicate.

Supplemental Fig. 3. The allosteric agonist LY2033298 shows weak positive allosteric modulation of the metabolite choline in competition binding assays in membranes expressing M2 mAChR. Interaction studies between LY2033298 and Ch in a competition radioligand binding assay using the radioligand [³H]NMS. Curves were fitted using a one site modulator plus allosteric ligand model. The log α for NMS was fitted to 0.5 as determined in Valant *et al* 2012. All values are mean \pm SEM of three independent experiments performed in duplicate.

Supplemental Fig. 4. Small molecule ligands of the GLP-1R do not modulate binding affinity of the GLP-1(7-36)NH₂ or its metabolite GLP-1R(9-36)NH₂ in competition binding experiments in intact cells expressing human GLP-1R. Effects of increasing concentrations of

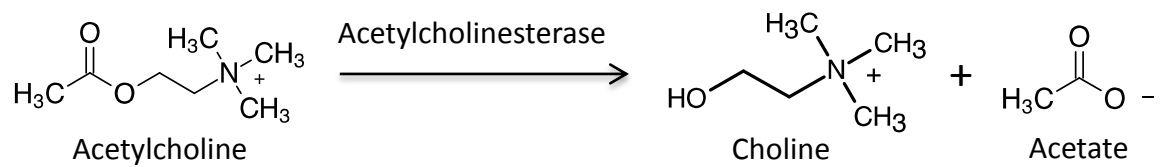
either Compound 2 (A and B) or BETP (C and D) on the inhibition of 125 I-exendin(9-39) binding by GLP-1(7-36)NH₂ (A and C) or GLP-1(9-36)NH₂ (B and D). Data are normalised to specific radioligand binding. Nonspecific binding was determined by inhibition of 125 I-exendin(9-39) by 1 μ M exendin(9-39). All values are mean \pm SEM of four independent experiments performed in duplicate.

Supplemental Fig. 5. Ex vivo and in vivo studies reveal allosteric modulation of the GLP-1 metabolite at the GLP-1R leads to insulin secretion. (A) Insulin concentrations from cultures of SD rat islets incubated in media containing low glucose (2.8mM), high glucose (11.2 mM), GLP-1(7-36)NH₂ (100 nM), BETP (1 μ M) and GLP-1(9-36)NH₂ (1 and 10 μ M) in the presence and absence of BETP (1 μ M). Islet treatments were performed for 90 min. (B) Timecourse of plasma insulin concentrations in fasted, anaesthetised animals treated with either vehicle, GLP-1(7-36)NH₂ (3 nmol/kg), GLP-1(9-36)NH₂ (400 nmol/kg), BETP (10 mg/kg) or co-administration of BETP and GLP-1(9-36)NH₂, immediately prior to intravenous administration of a glucose bolus (0.5 g/kg). Inset, AUC_{0-20min} of the insulin secretion for the various treatment groups. All results are expressed as mean \pm SEM of five experiments, (* = $p < 0.05$ as determined using a one way anova followed by Dunnett's comparison to vehicle group).

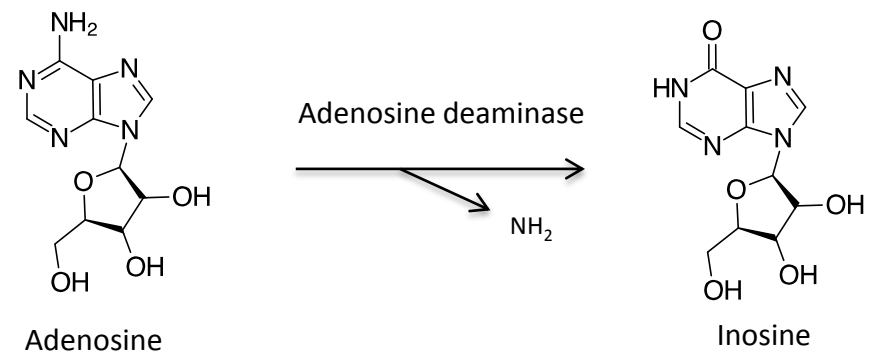
Supplemental Fig. 6. In vivo studies reveal BETP does not alter the pharmacokinetics of GLP-1(9-36)NH₂. Time course of total plasma GLP-1 levels in fasted anaesthetized animals treated with either vehicle, GLP-1(7-36)NH₂ (3 nmol/kg), GLP-1(9-36)NH₂ (150 nmol/kg), BETP (5 mg/kg) or GLP-1(9-36)NH₂ (150 nmol/kg) in the presence of BETP (5 mg/kg) immediately prior to intravenous administration of a glucose bolus (0.5 g/kg). Inset. Same data set with smaller y axis. Results are expressed as mean \pm SEM of six experiments (* = $p < 0.05$ as determined using a one way anova followed by Dunnett's comparison to vehicle group).

Supplementary Figure 1.

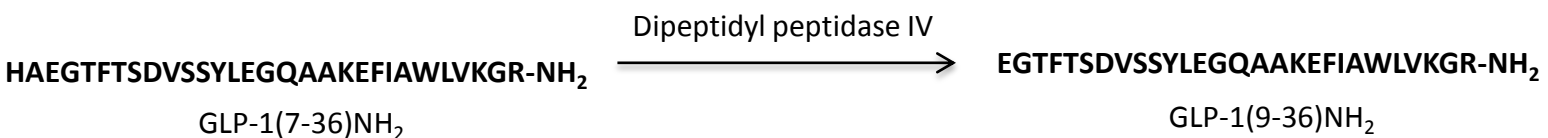
A



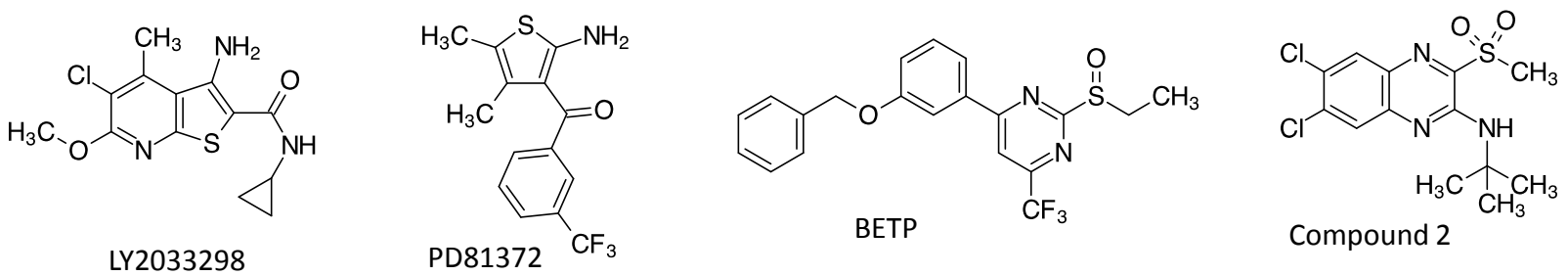
B



C

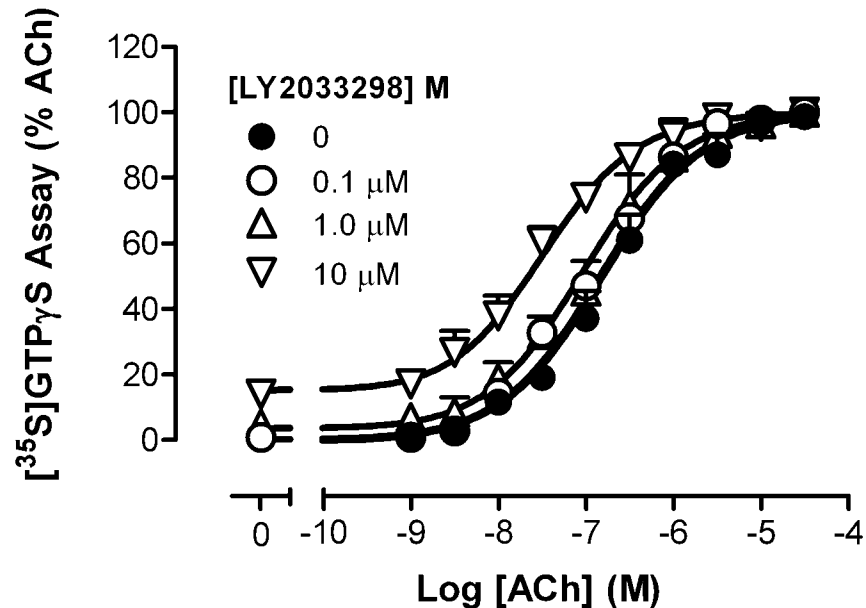


D

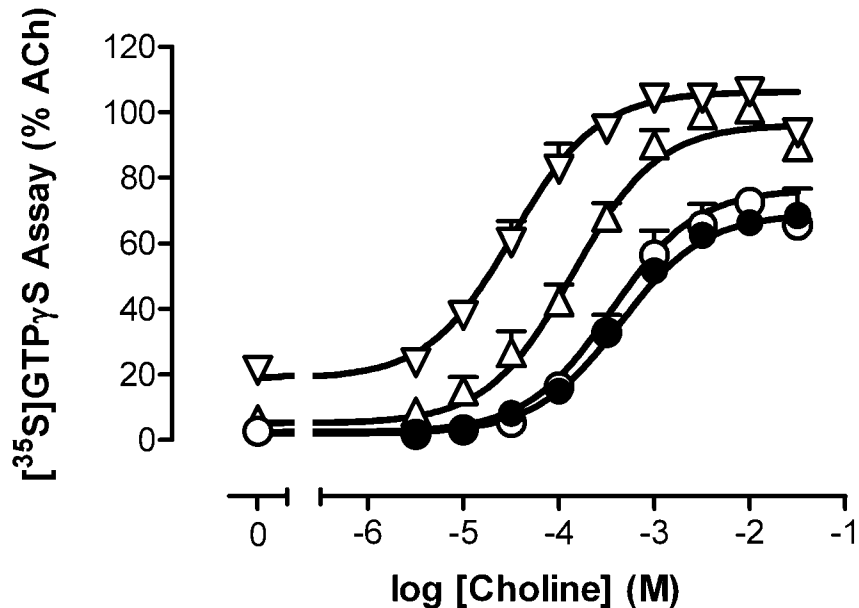


Supplemental Fig. 2

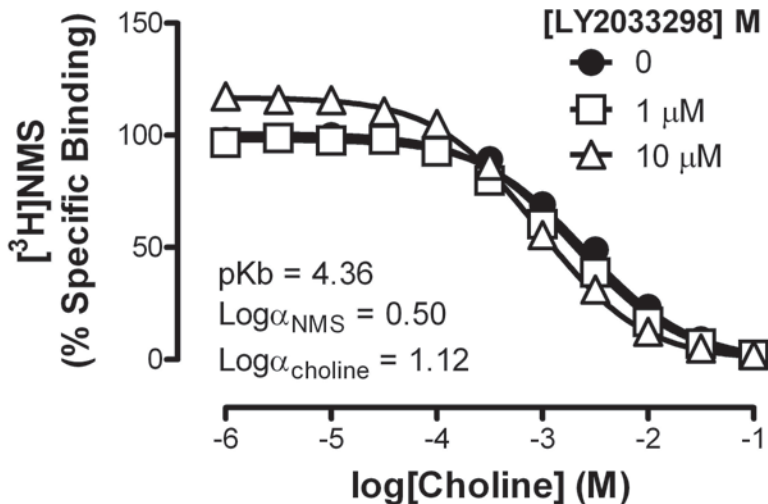
A.



B.

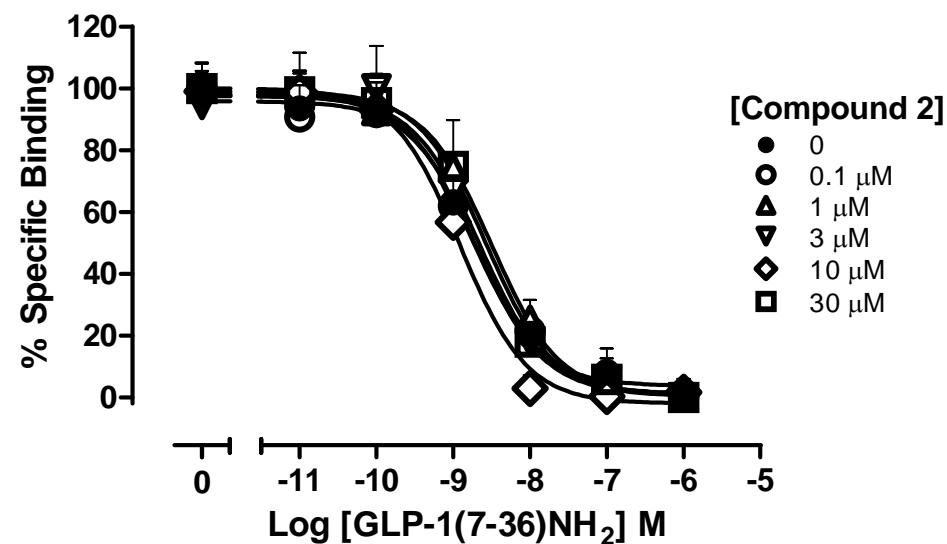


Supplemental Fig. 3

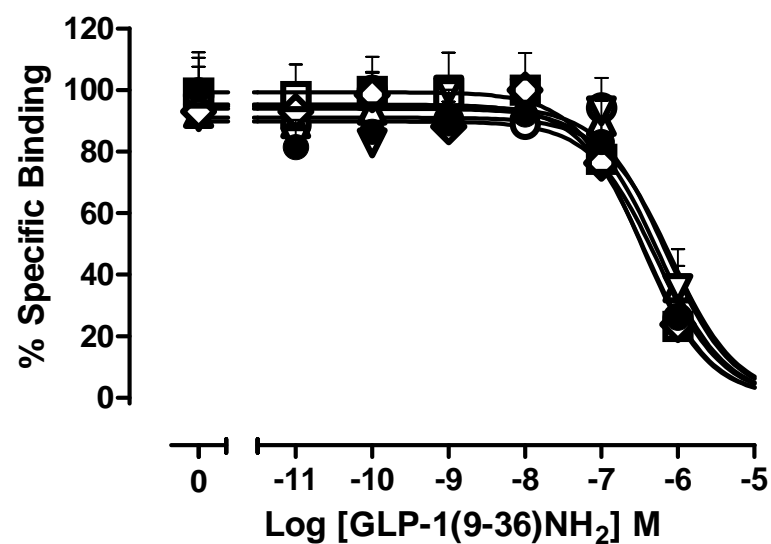


Supplemental Figure 4.

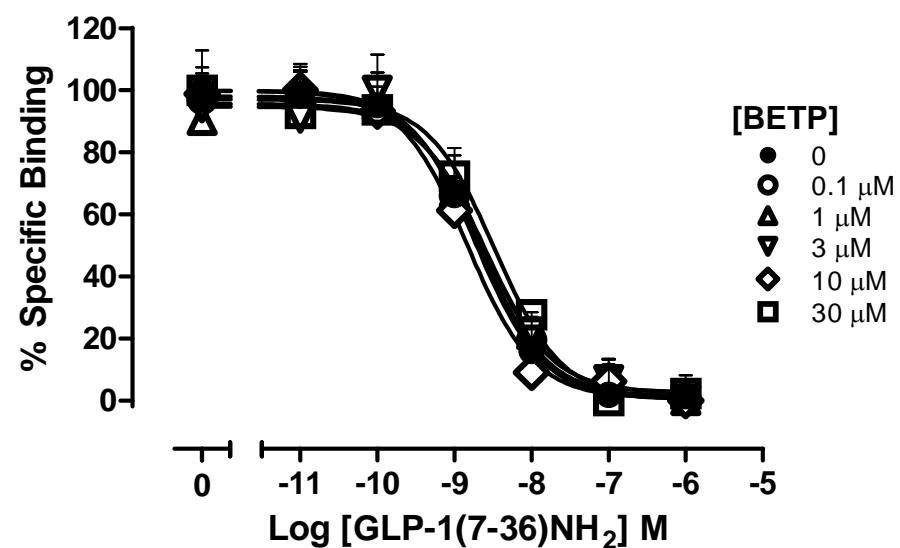
A.



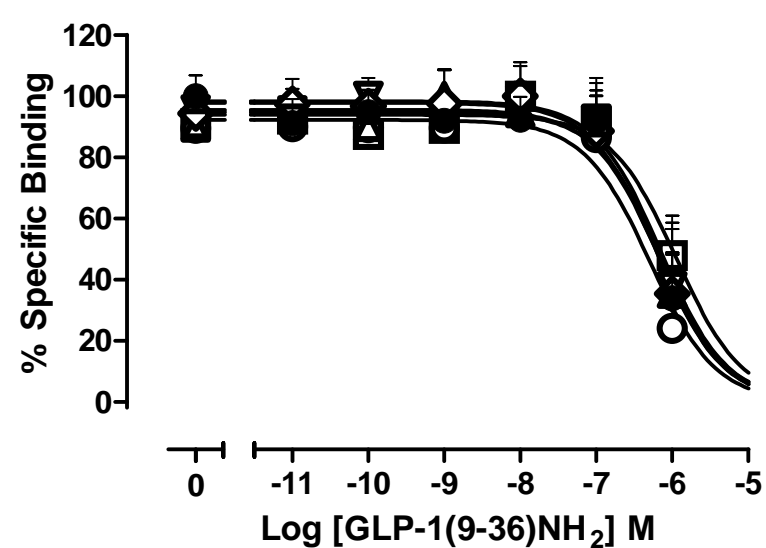
B.



C.

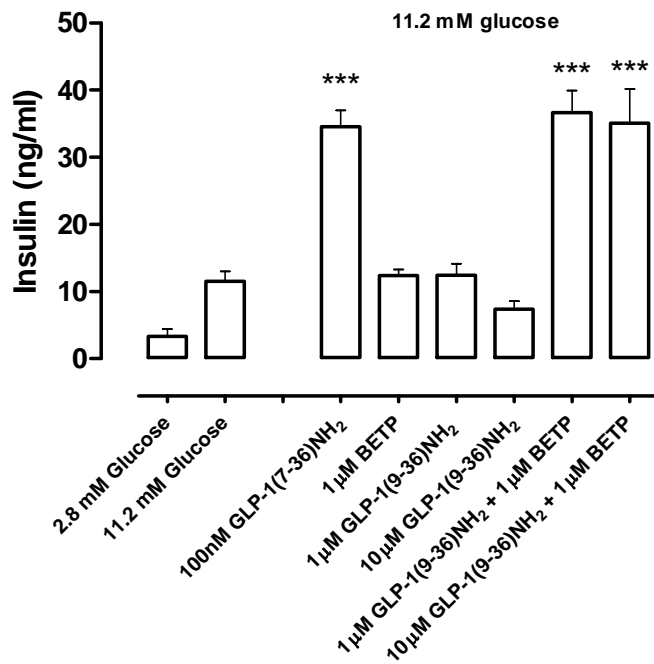


D.

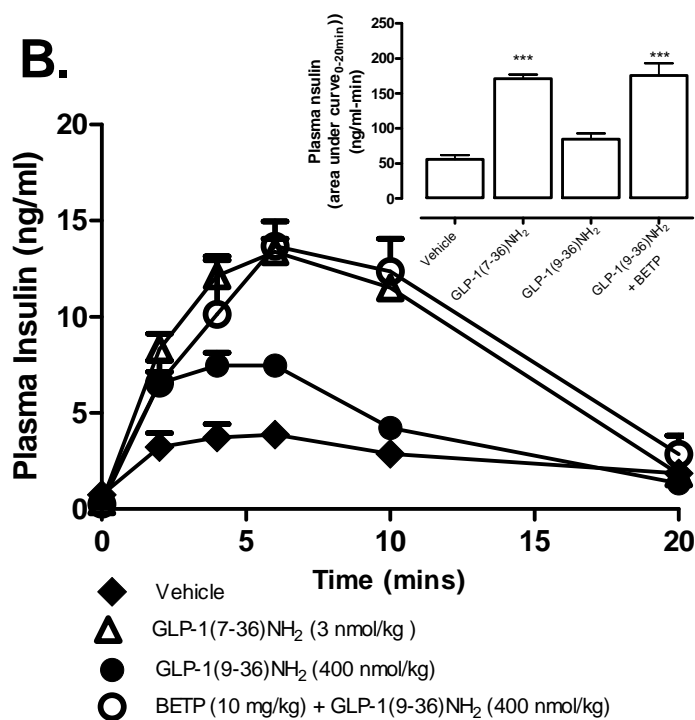


Supplemental Figure 5.

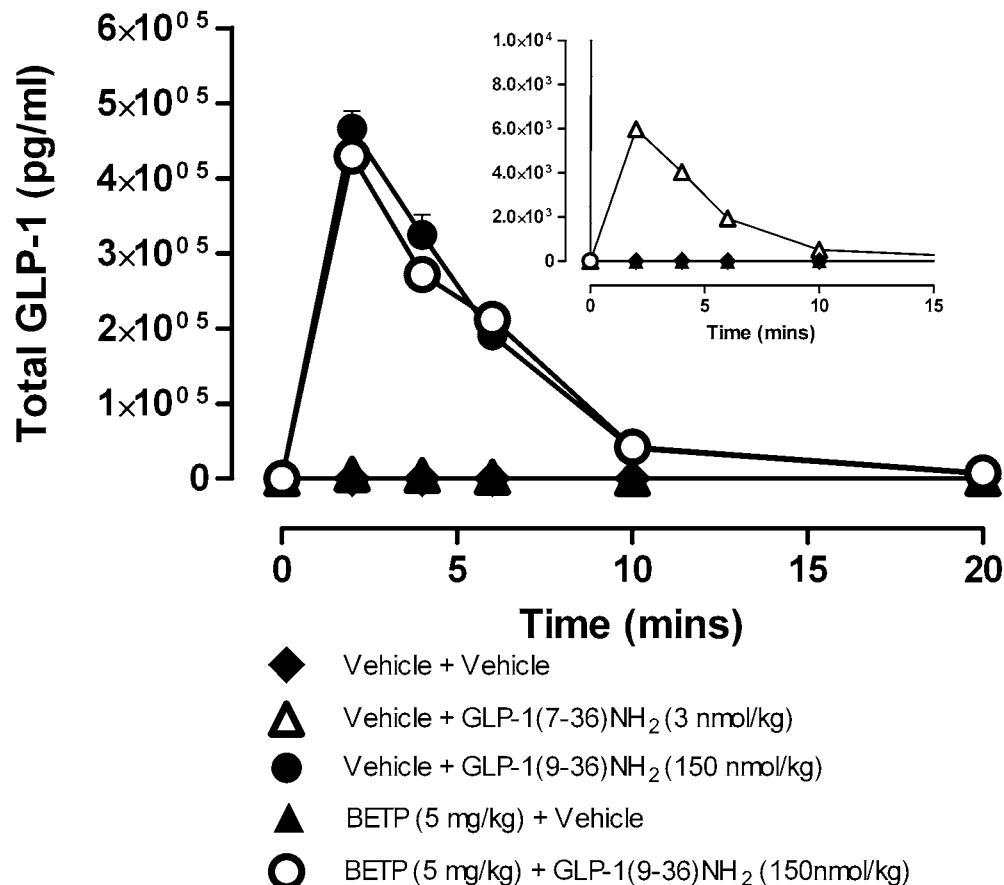
A.



B.



Supplementary Fig. 6



Glucagon-like peptide-1 receptor dimerization differentially regulates agonist signaling but does not affect small molecule allostery

Kaleeckal G. Harikumar^{a,1}, Denise Wootten^{b,1}, Delia I. Pinon^a, Cassandra Koole^b, Alicja M. Ball^a, Sebastian G. B. Furness^b, Bim Graham^c, Maoqing Dong^a, Arthur Christopoulos^b, Laurence J. Miller^{a,2}, and Patrick M. Sexton^{b,2}

^aDepartment of Molecular Pharmacology and Experimental Therapeutics, Mayo Clinic, Scottsdale, AZ 85259; and ^bDrug Discovery Biology, Monash Institute of Pharmaceutical Sciences and Department of Pharmacology, and ^cMedicinal Chemistry, Monash Institute of Pharmaceutical Sciences, Monash University, Parkville, VIC 3052, Australia

Edited* by Brian K. Kobilka, Stanford University School of Medicine, Stanford, CA, and approved September 24, 2012 (received for review March 28, 2012)

The glucagon-like peptide-1 receptor (GLP-1R) is a family B G protein-coupled receptor and an important drug target for the treatment of type II diabetes, with activation of pancreatic GLP-1Rs eliciting glucose-dependent insulin secretion. Currently, approved therapeutics acting at this receptor are peptide based, and there is substantial interest in small molecule modulators for the GLP-1R. Using a variety of resonance energy transfer techniques, we demonstrate that the GLP-1R forms homodimers and that transmembrane helix 4 (TM4) provides the primary dimerization interface. We show that disruption of dimerization using a TM4 peptide, a minigene construct encoding TM4, or by mutation of TM4, eliminates G protein-dependent high-affinity binding to GLP-1(7-36)NH₂ but has selective effects on receptor signaling. There was <10-fold decrease in potency in cAMP accumulation or ERK1/2 phosphorylation assays but marked loss of intracellular calcium mobilization by peptide agonists. In contrast, there was near-complete abrogation of the cAMP response to an allosteric agonist, compound 2, but preservation of ERK phosphorylation. Collectively, this indicates that GLP-1R dimerization is important for control of signal bias. Furthermore, we reveal that two small molecule ligands are unaltered in their ability to allosterically modulate signaling from peptide ligands, demonstrating that these modulators act *in cis* within a single receptor protomer, and this has important implications for small molecule drug design.

allosteric modulation | biased signaling | G protein-coupled receptors | family B GPCRs

G protein-coupled receptors (GPCRs) are the largest superfamily of cell surface proteins and play crucial roles in virtually every physiological process. Their widespread abundance, yet selective distribution, and ability to couple to a variety of signaling and effector systems make them extremely attractive targets for drug development (1). Recently, there has been increasing interest in the stoichiometry of receptors involved in GPCR signaling complexes and how this may impact on receptor function and drug discovery (2–4).

With the exception of family C GPCRs, where obligate dimerization can occur (4), the role of oligomerization in GPCR function has remained controversial (2–8), and this has been the subject of a number of recent reviews (9–11). Although there is an increasing body of evidence supporting dimerization of GPCRs as a widespread feature of GPCR biology, including numerous studies on family A GPCRs, whether these are stable, transient, constitutive, or ligand dependent, and how they impact on receptor function and drug discovery are less clear, and general rules for oligomeric behavior are not evident (9–16). Even where effects on signaling are studied, these are generally linked to a single pathway and the role of dimerization in the control of receptor engagement and preference for distinct intracellular signaling intermediates (i.e., signal bias) is virtually unstudied.

For family B GPCRs, which encompass many therapeutically important peptide receptors, including those for glucagon, glucagon-like peptides 1 and 2 (GLP-1, GLP-2), parathyroid hormone, and calcitonin, there is consistent evidence for homodimerization

(17–25). There is also emerging evidence for functionally significant heterodimerization (25–27). Furthermore, although there is an emerging theme in which dimerization contributes to high-affinity peptide binding and cAMP signaling (17, 18), how dimerization contributes more globally to receptor signaling and whether it plays a role in ligand-directed stimulus bias are unknown.

There is parallel interest in the development of allosteric drugs targeting otherwise intractable GPCRs to enable enhanced selectivity, fine control of receptor function, and/or maintenance of spatial and temporal elements of endogenous (orthosteric) signaling (1, 28). However, little is known on whether such drugs act through cooccupancy of a single receptor protomer (*in cis*), or asymmetrically across dimers (*in trans*), with most drug development assumptive on an *in cis* mechanism of action. Allosteric drugs are likely to be required for targeting of family B GPCRs, given the diffuse orthosteric pharmacophore of their peptide agonists (29) and the difficulty in mimicking this with small molecule compounds. Understanding how such molecules bind and modulate receptor function is crucial for successful optimization of such drugs.

In this study, we demonstrate functionally important homodimerization of the GLP-1 receptor (GLP-1R) that occurs through an interface along transmembrane segment 4 (TM4) and that this dimerization is critical for selective coupling of the receptor to physiologically relevant signaling pathways. Furthermore, dimerization is important for the signal bias of the receptor and discriminates between peptide and nonpeptide-mediated receptor activation, but is not required for small molecule allosteric modulation of the receptor, indicating that rational design of allosteric therapeutics is possible within a single receptor protomer model.

Results

GLP-1 Receptor Forms Functionally Important Homodimers. A number of complementary biochemical, biophysical, and pharmacological approaches were used to demonstrate the oligomeric nature of GLP-1R interactions and the impact on ligand–receptor interactions. As previously observed with other family B GPCRs (17, 18, 25), analysis of receptor–receptor interaction in live cells using a combination of static and saturation bioluminescence resonance energy transfer (BRET) analyses revealed constitutive, specific homooligomerization of the GLP-1R (Fig. 1*A* and *B*). No specific BRET signal was seen with coexpression of the BRET donor GLP-1R-Rluc and the family A cholecystokinin 2 GPCR (CCK2R), or between GLP-1R-YFP and soluble Rluc protein,

Author contributions: K.G.H., D.W., M.D., A.C., L.J.M., and P.M.S. designed research; K.G.H., D.W., D.I.P., C.K., A.M.B., S.G.B.F., B.G., and M.D. performed research; B.G. contributed new reagents/analytic tools; K.G.H., D.W., C.K., A.C., L.J.M., and P.M.S. analyzed data; and K.G.H., D.W., S.G.B.F., A.C., L.J.M., and P.M.S. wrote the paper.

The authors declare no conflict of interest.

*This Direct Submission article had a prearranged editor.

¹K.G.H. and D.W. contributed equally to this work.

²To whom correspondence may be addressed. E-mail: miller@mayo.edu or patrick.sexton@monash.edu.

This article contains supporting information online at www.pnas.org/lookup/suppl/doi:10.1073/pnas.1205227109/-DCSupplemental.

although a strong BRET signal was observed for the CCK2R homodimer (Fig. S1 A and B), demonstrating specificity of the GLP-1R homooligomeric interaction. This interaction was also not significantly altered by saturating concentrations of either peptide [GLP-1(7-36)NH₂, exendin-4, oxyntomodulin] or non-peptide (6,7-dichloro-2-methylsulfonyl-3-*tert*-butylaminoquinoline, compound 2) (30) agonists of the receptor (Fig. S1C). We also used a combination of bimolecular-fluorescence complementation and BRET to probe whether evidence for higher order oligomers of the GLP-1R could be established. However, coexpression of GLP-1R-Rluc with both the GLP-1R-YN and GLP-1R-YC constructs failed to yield a significant BRET signal (Fig. S1E), despite the generation of functional YFP from the fluorescence complementation established at the level of the dimeric receptor complex (Fig. S1D). All GLP-1R fusion constructs had equivalent binding and cAMP signaling to the wild-type receptor (Fig. S2, Table S1). These data indicate that the GLP-1R dimer is the major oligomeric form of the receptor. Negative cooperativity of peptide binding to the secretin family B GPCR has been described (31), and this was also observed in dissociation kinetic studies of the GLP-1R (Fig. S3A), confirming the oligomeric nature of the GLP-1R.

As seen with the related calcitonin and secretin family B GPCRs (17, 18), disruption of the TM4 interface by either GLP-1R TM4 peptides or by mutation of the hydrophobic face of TM4 (L256A, V259A, or G252A, L256A, V259A; Fig. S4) abolished the BRET signal (Fig. 1A and B), consistent with TM4 constituting the principal dimer interface for GLP-1Rs as well as other family B GPCRs (17, 18, 31). Disruption of GLP-1R dimerization either by coinubation of GLP-1R BRET constructs with GLP-1R TM4 (Fig. 1C) or mutation of TM4 (Fig. 1D), led to a ~10-fold decrease in GLP-1(7-36)NH₂ potency to form cAMP, indicating that dimerization is important for efficient coupling of the receptor to the Gs/AC/cAMP signaling cascade. The decrease in potency at

the mutant receptors was not due to changes in cell surface expression because whole-cell binding measurements revealed that expression of these mutant receptors was not significantly different from the wild-type receptor. Analysis of GLP-1(7-36)NH₂ peptide inhibition binding, in GLP-1R-expressing Cos-1 membranes, revealed a complex pattern of binding that was best fit with a three-site mass action model (Fig. 1E, Table 1). Disruption of dimerization via the TM4 mutants led to complete loss of the very-high-affinity state (K_1) and marked reduction in the proportion of high-affinity (K_2) sites (Table 1, Fig. 1F, Fig. S5A), and a similar effect is observed with coinubation of the wild-type receptor with the TM4 peptide (Fig. S5B). This effect was mimicked by incubation of membranes with the nonhydrolyzable GTP analog, GppNHP (Fig. 1E, Table 1), suggesting that the principal effect of dimerization is to maintain a high-affinity G protein-complexed state. Coinubation of GLP-1R TM mutant membranes with GppNHP had minimal additional effect on agonist peptide binding (Table 1, Fig. 1F), whereas the negative cooperativity observed in dissociation kinetic studies (Fig. S3A) was abolished in the G252A, L256A, V259A GLP-1R mutant (Fig. S3B).

Dimerization Plays Distinct Roles in GLP-1R Peptide and Small Molecule Agonist Signaling.

To date, investigation of the role of homodimerization on family B receptor signaling has been confined to examination of cAMP formation (17, 18). Family B receptors, however, are pleiotropically coupled, with multiple signaling pathways important for receptor function (32). In addition to cAMP formation, both phosphorylation of ERK and mobilization of intracellular calcium are physiologically important in GLP-1-mediated control of pancreatic β -cell function (33). We have used the dimer-disrupting triple mutant (GLP-1R G252A, L256A, V259A) to probe the extent to which dimerization contributes to GLP-1R signaling across these three pathways. A similar (<10-fold) decrease in GLP-1(7-36)NH₂ potency was observed

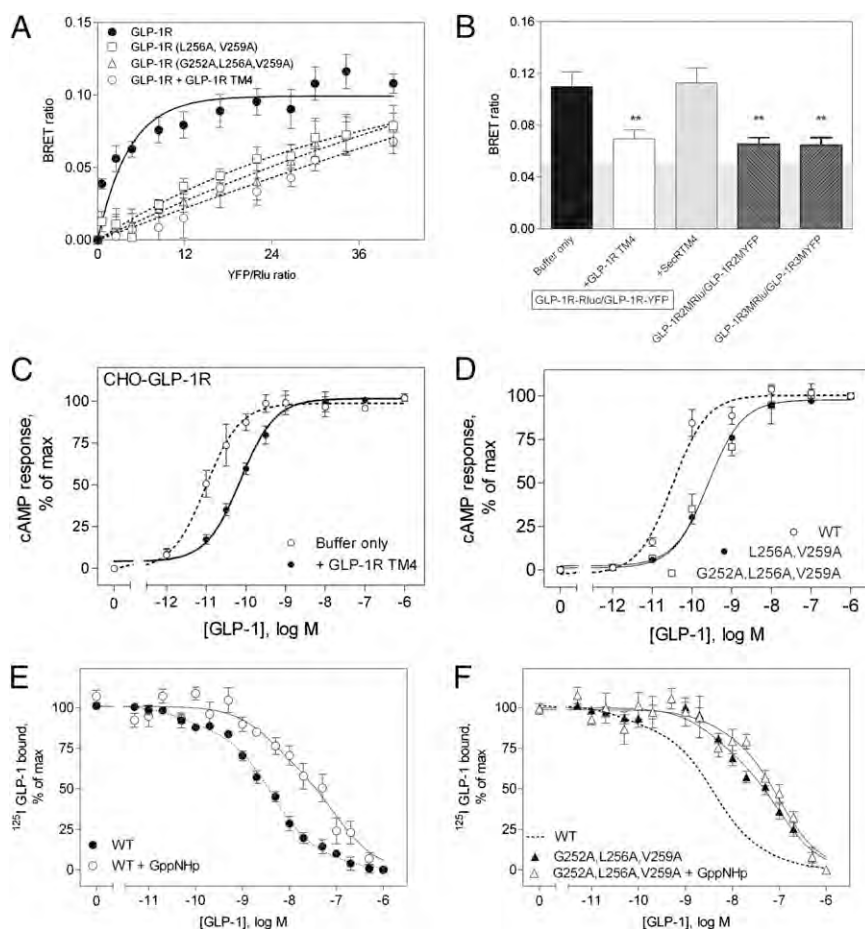


Fig. 1. Dimerization of the GLP-1R is important for high-affinity agonist binding and receptor coupling to cAMP production. Saturation (A) and static (B) BRET data from transient coexpression, in Cos-1 cells, of Rluc- and YFP-tagged GLP-1R constructs of wild-type, in the presence or absence of TM4 peptides from the GLP-1R or from the secretin receptor, or dimer disrupting mutants of TM4. In the presence of the GLP-1R TM4 peptide or when TM4 double/triple mutants were present, the static BRET ratio was reduced and was not significantly different from background signal. (C) GLP-1(7-36)NH₂ stimulated cAMP responses in CHO cells stably expressing the GLP-1R in the presence or absence of the GLP-1 receptor TM4 segment peptide. (D) GLP-1(7-36)NH₂ stimulated cAMP responses in Cos-1 cells transiently expressing either the wild-type or L256A, V259A, or G252A, L256A, V259A TM4 mutant GLP-1Rs. The cell surface expression of the G252A, L256A, V259A mutant was $112 \pm 10\%$ of the wild-type receptor. (E) Inhibition of ¹²⁵I-GLP-1(7-36)NH₂ binding, to membranes from Cos-1 cells transiently transfected with the wild-type GLP-1R, by unlabeled GLP-1(7-36)NH₂ in the presence or absence of 10 μ M GppNHP. (F) Inhibition of ¹²⁵I-GLP-1(7-36)NH₂ by unlabeled GLP-1(7-36)NH₂ in the presence or absence of 10 μ M GppNHP, to membranes from Cos-1 cells transiently transfected with the G252A, L256A, V259A mutant GLP-1R. For reference, the curve for the WT receptor is shown with a dashed line. Values are means \pm SEM of data from four to five independent experiments performed in duplicate.

Table 1. Disruption of GLP-1R dimerization attenuates high-affinity GLP-1 binding

Receptor construct	K_1	K_2	K_3
Binding affinity (pIC ₅₀)*	10.29 ± 0.60	8.40 ± 0.13	6.99 ± 0.12
Fraction			
–GppNHp			
GLP-1R	0.14 ± 0.06	0.76 ± 0.08	0.10
GLP-1R(L256A, V259A)	0.00 ± 0.04	0.46 ± 0.08	0.54
GLP-1R(G252A, L256A, V259A)	0.00 ± 0.03	0.31 ± 0.08	0.69
+GppNHp			
GLP-1R	0.00 ± 0.05	0.38 ± 0.09	0.62
GLP-1R(G252A, L256A, V259A)	0.00 ± 0.06	0.14 ± 0.10	0.86

Binding data were analyzed with a three-site logistic fit and presented as –logM estimates.

*Binding affinity parameters were shared across the data set.

in cAMP accumulation and ERK phosphorylation assays (Fig. 2*A* and *B*), with no change in the time course for pERK (Fig. S6). However, there was almost complete abrogation of the intracellular calcium response (Fig. 2*C*), demonstrating distinct consequences of dimerization across pathways. Oxyntomodulin is an endogenous agonist of the GLP-1R that exhibits signal bias relative to that of GLP-1 peptides for at least cAMP versus pERK (34), whereas exendin-4 is clinically used as a GLP-1 mimetic (35). Disruption of dimerization had similar effect on the responses to all three peptides (Fig. 2*D* and *E*, Fig. S7), with loss of calcium signaling maintained even at 10^{–5} M. In contrast, there was marked loss of cAMP signaling by the small molecule agonist, compound 2, but only a relatively small reduction in pERK signaling (Fig. 2*G* and *H*), the latter likely because of decreased affinity of that compound (Fig. 3). Equivalent effects were seen in CHO-FlpIn cells transfected with the mutant receptors (Fig. S8), demonstrating that the effects were independent of cellular background. To further confirm that the differential effects on signaling were due to disruption of dimerization, we have also used a minigene encoding TMs 3 and 4 of the GLP-1R, with TM3 required to enable correct orientation of the TM4 segment. Transfection of this construct into CHO-FlpIn cells stably expressing the GLP-1R yielded qualitatively similar results to the mutant receptor (Fig. S9), although the magnitude of effect for all three pathways was dependent on transfection efficiency. Collectively, these data indicate distinct modes of receptor activation for peptide versus small molecule agonists of the GLP-1R. The differential effects on signaling pathways is unlikely to be due to simply changing coupling efficiency across the board, because the relative potency of ligands for pERK and calcium signaling are similar at the wild-type receptor, with dramatically larger effects of disrupting dimerization on calcium mobilization.

Allosteric Modulation of the GLP-1R Occurs Within a Single Receptor Protomer. Currently, very little is known with respect to how allosteric modulators exert their cooperativity, including whether this requires dimerization of receptors or is due to coincident binding to a single monomeric unit. As demonstrated previously (34), compound 2 displays weak positive cooperativity with GLP-1(7–36)NH₂ and strong positive cooperativity with oxyntomodulin (Fig. 3*A* and *C*, Fig. S10, and Table 2). This cooperativity was not significantly altered by the dimer-disrupting mutant, despite the loss of agonism seen with compound 2 (Fig. 3*B* and *D*, Fig. S10, and Table 2). An equivalent preservation of allosteric cooperativity was seen with the structurally distinct modulator, 4-(3-benzyloxy-phenyl)-2-ethyl-sulfinyl-6-(trifluoromethyl)pyrimidine (BETP) (Fig. 3*E* and *F*). To confirm that this cooperativity was not probe dependent, we also examined the allosteric modulation of the GLP-1 metabolite, GLP-1(9–36)NH₂ (Fig. S11) (36). These data demonstrate that the allosteric modulation of the GLP-1R occurs within a single monomeric unit and does not require dimerization of the receptor.

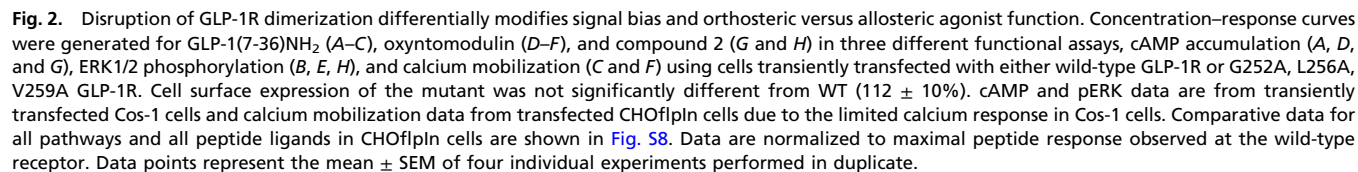
Discussion

The occurrence and significance of dimerization remains controversial outside of family C GPCRs, where there is evidence for obligate oligomerization. For family B receptors, there is consistent evidence for homooligomerization, together with the potential for functionally important heterooligomerization (18–23, 25–27). Within this theme, there is an emerging paradigm of behavior in which homodimerization of receptors occurs via a TM4/TM4 interface and that this interaction is required for optimal function of the receptor, generation of high-affinity agonist binding, and signaling via formation of cAMP (17, 18, 31); this paradigm is true also for the GLP-1R.

A major finding of the current study is that disruption to the dimer interface had differential impact on signaling engaged by the GLP-1R, with attenuation of cAMP formation and phosphorylation of ERK, but almost complete abrogation of the intracellular calcium mobilization response. Although differential effects on the signal pathways could be due to different strength of stimulus coupling, these results cannot be interpreted as simply a consequence of strength of stimulus coupling as pERK1/2 (in addition to intracellular calcium mobilization) is also less well coupled than cAMP and this pathway is only minimally (less so than cAMP) affected by disruption of dimerization. This suggests that fine control of GLP-1R signaling, and the ability to engage with its full range of signaling intermediates is linked to the ability of the receptor to form dimers. As receptor-mediated intracellular calcium mobilization is less well coupled than Gs-mediated cAMP formation, it may require both receptor dimerization and occupancy of both receptor protomers within the dimer to elicit the response, providing a mechanism through which receptors and ligands achieve the conformational complexes associated with signal bias of the receptor. However, this is not the case for coupling to ERK1/2 phosphorylation. The GLP-1R has been shown to signal downstream of coupling to Gs, Gi/o, and Gq proteins as well as β-arrestins (33, 37), with at least part of the intracellular calcium signal being Gi dependent (38) and at least part of the pERK response dependent on β-arrestin (37). It is likely that the disruption to dimerization seen in the current study differentially alters the coupling efficiency of the receptor to these different effectors. Furthermore, it provides a potential mechanistic basis through which changes to G protein-coupling preferences occur at higher concentrations of agonist.

A second major finding of the current study was the distinct contribution of dimerization to orthosteric versus allosteric activation of cAMP signaling through the GLP-1R, with effective abrogation of cAMP response (>30-fold) to compound 2, whereas there was only limited (<8-fold) loss of peptide-mediated cAMP formation. This implies that compound 2 has limited capacity to activate Gs protein via monomeric GLP-1R and that the allosteric agonist has a distinct mode of receptor activation to the peptide agonists. This further supports a role for dimerization in controlling signal bias (rather than a phenomenon related to strength of coupling) as disruption of dimerization has a stronger effect on cAMP formation than on phosphorylation of ERK, despite greater relative efficacy for compound 2 in formation of cAMP. A differential mode of receptor activation by compound 2 is consistent with findings of distinct effects of receptor polymorphism (T149M) or mutation (ECL2 mutants) on peptide versus allosteric agonist activation of the receptor, where the allosteric agonism is preserved at receptors with impaired peptide response (38, 39). Furthermore, it demonstrates that dimerization can contribute to ligand-directed signal bias.

A third significant finding of the current study was that allosteric modulation of orthosteric peptide binding and signaling was maintained after disruption of the dimer, despite loss of allosteric agonism, demonstrating that the allosteric modulation was occurring *in cis* within a single protomer. The use of two chemically distinct modulators, compound 2 from NovoNordisk (30) and BETP from Eli Lilly (40), confirmed that this is likely to be a generalized feature of allosteric modulation of the GLP-1R. Understanding how allosteric drugs alter the function of orthosteric ligands is important for drug development, particularly for



It is unclear whether the TM4 peptide or the TM4 mutation fully abrogates dimerization or changes the interaction from stable to transient, such that a BRET signal is not observed. Nonetheless, it is clear that stable dimerization is required for critical elements of GLP-1R function. The content of monomeric

In conclusion, our work provides mechanistic insight into the role of the oligomeric status of the GLP-1R for biased agonism and allosteric modulation of the receptor, and this has important implications for drug discovery and development at the therapeutically attractive B family of GPCRs.

GLP-1R Constructs. Human GLP-1R constructs tagged with *Renilla* luciferase (RLU) or yellow fluorescent protein (YFP) inserted in frame at the carboxyl terminus of the mature protein were prepared, as described previously (26). GLP-1R alanine-replacement mutants were generated using the QuikChange site-directed mutagenesis kit (Stratagene), replacing residues 252, 256, and 259 within the predicted lipid-exposed face of TM4 separately and in combination. Additional GLP-1R constructs were prepared by inserting amino-terminal or carboxyl-terminal portions of YFP, representing residues 1–158 (YN) or residues 159–238 (YC) just before the TGA stop codon. The sequences of all receptor constructs were verified by direct DNA sequencing. All constructs had equivalent binding affinity and potency in cAMP accumulation assays (Table S1, Fig. S2).

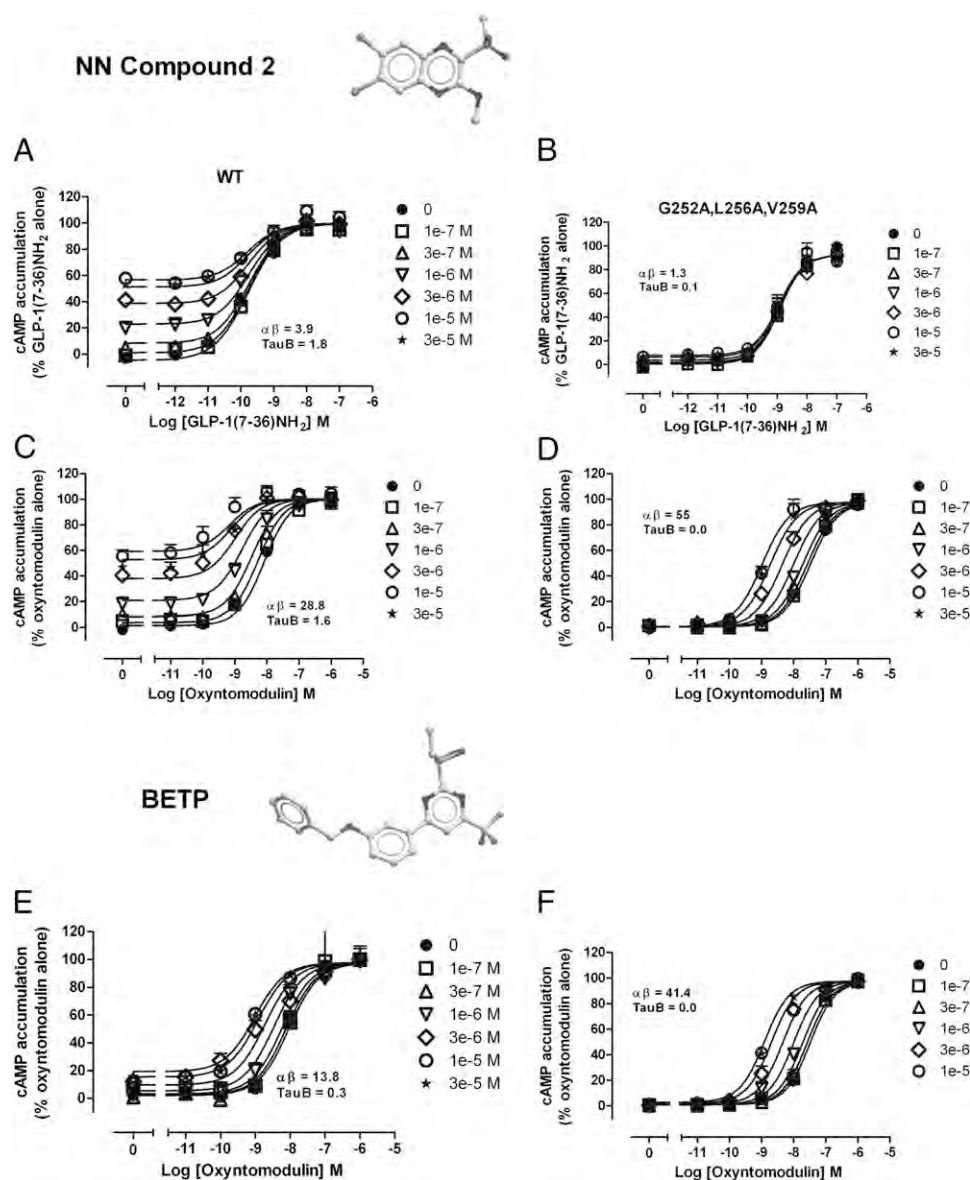


Fig. 3. Allosteric modulation of the GLP-1R occurs within a single receptor protomer. Concentration-response curves were generated for GLP-1(7-36)NH₂ (A, C, and E) and oxyntomodulin (B, D, and F) in the presence and absence of increasing concentrations of compound 2 (A–D) or BETP (E and F) in cAMP accumulation assays using Cos-1 cells expressing wild-type GLP-1R (Left) or G252A, L256A, V259A GLP-1R (Right). Data are normalized to maximal peptide response, are fitted with an operational model of allosterism, and are representative of the mean ± SEM of four independent experiments performed in duplicate.

Transfections and Cell Culture. Cos-1, CHO, or FlpInCHO cells used for transient transfections were maintained in DMEM supplemented with 5% (vol/vol) heat-inactivated FBS and incubated in a humidified environment at 37 °C in 5% (vol/vol) CO₂. GLP-1R receptor constructs were transiently transfected using either the DEAE-dextran method as previously described or

metafectene (Invitrogen) following the manufacturer's protocol. CHO cells stably expressing the human GLP-1 receptor (CHO-GLP-1R) were propagated in Ham's F-12 medium supplemented with 5% (vol/vol) FBS (46). For all whole-cell assays, cells were seeded into 96-well culture plates 24 h after transfection at a density of 15,000–20,000 cells/well for Cos-1 cells or 30,000

Table 2. Allosteric parameters for WT and G252A, L256A, V259A GLP-1Rs

Interacting ligands	GLP-1R wild type		GLP-1R(G252A, L256A, V259A)	
	pK _B	Logαβ (αβ)	pK _B	Logαβ (αβ)
Compound 2	5.56 ± 0.13		4.71 ± 0.21	
GLP-1(7-36)NH ₂		0.59 ± 0.11 (3.9)		0.13 ± 0.15 (1.3)
Oxyntomodulin		1.46 ± 0.15 (29)		1.74 ± 0.12 (55)
BETP	5.20 ± 0.20		4.78 ± 0.15	
Oxyntomodulin		1.14 ± 0.14 (14)		1.62 ± 0.11 (42)

Quantitative parameters for the allosteric interaction of compound 2 or BETP with GLP-1(7-36)NH₂ or oxyntomodulin. cAMP data were analyzed with an operational model of allosterism as defined in *Methods*. pK_B values represent the negative logarithm of the affinity for the allosteric ligands derived from application of the operational model of allosterism. Logαβ values represent the composite cooperativity between the allosteric modulator and the orthosteric ligand. Antilogarithms are shown in parentheses.

cells/well for CHOFlpIn cells and incubated overnight at 37 °C in 5% (vol/vol) CO₂ before assaying. The level of cell surface-expressed mutant and wild-type receptors was not significantly different. For robustness, experiments were performed in multiple cellular backgrounds, with a subset of control experiments performed in both the American and Australian laboratories. All signaling assays performed in Cos-1 cells transiently expressing the wild-type or mutant receptors were repeated in transiently transfected CHOFlpIn cells (Fig. S8).

BRET Studies. BRET studies were performed on receptor-expressing Cos-1 cells as previously described (18).

Bimolecular Fluorescence Complementation. Bimolecular fluorescence complementation assays were carried out in HEK293 cells expressing YN- and YC-tagged receptor constructs, as described previously (19).

cAMP Assays. cAMP accumulation assays were carried out using the AlphaScreen kit or the LANCE assay as previously described (18, 34).

Radioligand Binding Assays. Receptor binding assays were carried out either using intact Cos-1 cells expressing the tagged receptor or isolated receptor-bearing membranes, as described previously (25, 34).

ERK1/2 Phosphorylation Assay. Receptor-mediated ERK1/2 phosphorylation was determined by using the AlphaScreen ERK1/2 SureFire protocol as described previously (34).

Intracellular Ca²⁺ Mobilization Assay. Intracellular Ca²⁺ mobilization was determined as described previously (34).

Data Analysis. All data obtained were analyzed in GraphPad Prism 5.0.3 (GraphPad Software). Radioligand inhibition binding data were fitted to a three-site inhibition mass action curve. In whole-cell ligand interaction studies, data were fitted to an operational model of allosterism and agonism to derive functional estimates of modulator affinity and cooperativity. For all other data, concentration–response curves were fitted with a three-parameter logistic equation.

For more detailed methods, see *SI Methods*.

ACKNOWLEDGMENTS. We thank Mary-Lou Augustine for her excellent technical assistance and Drs. Kyle Sloop and Francis Willard for supplying BETP. P.M.S. is a Principal Research Fellow and A.C. is a Senior Research Fellow of the National Health and Medical Research Council of Australia (NHMRC). This work was funded in part by NHMRC Project Grant 1002180, NHMRC Program Grant 519461, and National Institutes of Health Grant DK46577.

- Christopoulos A (2002) Allosteric binding sites on cell-surface receptors: Novel targets for drug discovery. *Nat Rev Drug Discov* 1(3):198–210.
- Casadó V, et al. (2009) GPCR homomers and heteromers: A better choice as targets for drug development than GPCR monomers? *Pharmacol Ther* 124(2):248–257.
- Milligan G (2009) G protein-coupled receptor hetero-dimerization: Contribution to pharmacology and function. *Br J Pharmacol* 158(1):5–14.
- Kniazeff J, Prézeau L, Rondard P, Pin JP, Goudet C (2011) Dimers and beyond: The functional puzzles of class C GPCRs. *Pharmacol Ther* 130(1):9–25.
- Bayburt TH, Leitz AJ, Xie G, Oprian DD, Sligar SG (2007) Transducin activation by nanoscale lipid bilayers containing one and two rhodopsins. *J Biol Chem* 282(20):14875–14881.
- Whorton MR, et al. (2007) A monomeric G protein-coupled receptor isolated in a high-density lipoprotein particle efficiently activates its G protein. *Proc Natl Acad Sci USA* 104(18):7682–7687.
- Han Y, Moreira IS, Urizar E, Weinstein H, Javitch JA (2009) Allosteric communication between protomers of dopamine class A GPCR dimers modulates activation. *Nat Chem Biol* 5(9):688–695.
- Albizu L, et al. (2010) Time-resolved FRET between GPCR ligands reveals oligomers in native tissues. *Nat Chem Biol* 6(8):587–594.
- Pin JP, et al. (2007) International Union of Basic and Clinical Pharmacology. LXVII. Recommendations for the recognition and nomenclature of G protein-coupled receptor heteromultimers. *Pharmacol Rev* 59(1):5–13.
- Ferré S, et al. (2009) Building a new conceptual framework for receptor heteromers. *Nat Chem Biol* 5(3):131–134.
- Khelashvili G, et al. (2010) GPCR-OKB: The G protein coupled receptor oligomer knowledge base. *Bioinformatics* 26(14):1804–1805.
- Herr JA, et al. (2010) Formation and dissociation of M1 muscarinic receptor dimers seen by total internal reflection fluorescence imaging of single molecules. *Proc Natl Acad Sci USA* 107(6):2693–2698.
- Lambert NA (2010) GPCR dimers fall apart. *Sci Signal* 3(115):pe12.
- Fonseca JM, Lambert NA (2009) Instability of a class A G protein-coupled receptor oligomer interface. *Mol Pharmacol* 75(6):1296–1299.
- Kasai RS, et al. (2011) Full characterization of GPCR monomer-dimer dynamic equilibrium by single molecule imaging. *J Cell Biol* 192(3):463–480.
- Fung JJ, et al. (2009) Ligand-regulated oligomerization of beta(2)-adrenoceptors in a model lipid bilayer. *EMBO J* 28(21):3315–3328.
- Harikumar KG, Ball AM, Sexton PM, Miller LJ (2010) Importance of lipid-exposed residues in transmembrane segment four for family B calcitonin receptor homodimerization. *Regul Pept* 164(2–3):113–119.
- Harikumar KG, Pinon DI, Miller LJ (2007) Transmembrane segment IV contributes a functionally important interface for oligomerization of the Class II G protein-coupled secretin receptor. *J Biol Chem* 282(42):30363–30372.
- Harikumar KG, Happs RM, Miller LJ (2008) Dimerization in the absence of higher-order oligomerization of the G protein-coupled secretin receptor. *Biochim Biophys Acta* 1778(11):2555–2563.
- Héroux M, Hogue M, Lemieux S, Bouvier M (2007) Functional calcitonin gene-related peptide receptors are formed by the asymmetric assembly of a calcitonin receptor-like receptor homo-oligomer and a monomer of receptor activity-modifying protein-1. *J Biol Chem* 282(43):31610–31620.
- Kraetke O, et al. (2005) Dimerization of corticotropin-releasing factor receptor type 1 is not coupled to ligand binding. *J Recept Signal Transduct Res* 25(4–6):251–276.
- Langer I, Gaspard N, Robberecht P (2006) Pharmacological properties of Chinese hamster ovary cells coexpressing two vasoactive intestinal peptide receptors (hVPAC1 and hVPAC2). *Br J Pharmacol* 148(8):1051–1059.
- Pioszak AA, Harikumar KG, Parker NR, Miller LJ, Xu HE (2010) Dimeric arrangement of the parathyroid hormone receptor and a structural mechanism for ligand-induced dissociation. *J Biol Chem* 285(16):12435–12444.
- Seck T, Baron R, Horne WC (2003) The alternatively spliced deltae13 transcript of the rabbit calcitonin receptor dimerizes with the C1a isoform and inhibits its surface expression. *J Biol Chem* 278(25):23085–23093.
- Harikumar KG, Morfis MM, Lisenbee CS, Sexton PM, Miller LJ (2006) Constitutive formation of oligomeric complexes between family B G protein-coupled vasoactive intestinal polypeptide and secretin receptors. *Mol Pharmacol* 69(1):363–373.
- Harikumar KG, Morfis MM, Sexton PM, Miller LJ (2008) Pattern of intra-family hetero-oligomerization involving the G-protein-coupled secretin receptor. *J Mol Neurosci* 36(1–3):279–285.
- Schelshorn D, et al. (2012) Lateral allosterism in the glucagon receptor family: Glucagon-like peptide 1 induces G-protein-coupled receptor heteromer formation. *Mol Pharmacol* 81(3):309–318.
- May LT, Leach K, Sexton PM, Christopoulos A (2007) Allosteric modulation of G protein-coupled receptors. *Annu Rev Pharmacol Toxicol* 47:1–51.
- Hoare SR (2007) Allosteric modulators of class B G-protein-coupled receptors. *Curr Neuropharmacol* 5(3):168–179.
- Knudsen LB, et al. (2007) Small-molecule agonists for the glucagon-like peptide 1 receptor. *Proc Natl Acad Sci USA* 104(3):937–942.
- Gao F, et al. (2009) Functional importance of a structurally distinct homodimeric complex of the family B G protein-coupled secretin receptor. *Mol Pharmacol* 76(2):264–274.
- Alexander SPH, Mathie A, Peters JA (2011) Guide to Receptors and Channels (GRAC), 5th Ed. *Br J Pharmacol* 164(Suppl 1):S1–S324.
- Baggio LL, Drucker DJ (2007) Biology of incretins: GLP-1 and GIP. *Gastroenterology* 132(6):2131–2157.
- Koole C, et al. (2010) Allosteric ligands of the glucagon-like peptide 1 receptor (GLP-1R) differentially modulate endogenous and exogenous peptide responses in a pathway-selective manner: Implications for drug screening. *Mol Pharmacol* 78(3):456–465.
- Lovshin JA, Drucker DJ (2009) Incretin-based therapies for type 2 diabetes mellitus. *Nat Rev Endocrinol* 5(5):262–269.
- Wooten D, et al. (2012) Allosteric modulation of endogenous metabolites as an avenue for drug discovery. *Mol Pharmacol* 82(2):281–290.
- Sonoda N, et al. (2008) Beta-Arrestin-1 mediates glucagon-like peptide-1 signaling to insulin secretion in cultured pancreatic beta cells. *Proc Natl Acad Sci USA* 105(18):6614–6619.
- Koole C, et al. (2012) Second extracellular loop of human glucagon-like peptide-1 receptor (GLP-1R) differentially regulates orthosteric but not allosteric agonist binding and function. *J Biol Chem* 287(6):3659–3673.
- Koole C, et al. (2011) Polymorphism and ligand dependent changes in human glucagon-like peptide-1 receptor (GLP-1R) function: Allosteric rescue of loss of function mutation. *Mol Pharmacol* 80(3):486–497.
- Sloop KW, et al. (2010) Novel small molecule glucagon-like peptide-1 receptor agonist stimulates insulin secretion in rodents and from human islets. *Diabetes* 59(12):3099–3107.
- Guo W, et al. (2008) Dopamine D2 receptors form higher order oligomers at physiological expression levels. *EMBO J* 27(17):2293–2304.
- Guo W, Shi L, Filizola M, Weinstein H, Javitch JA (2005) Crosstalk in G protein-coupled receptors: Changes at the transmembrane homodimer interface determine activation. *Proc Natl Acad Sci USA* 102(48):17495–17500.
- Guo W, Shi L, Javitch JA (2003) The fourth transmembrane segment forms the interface of the dopamine D2 receptor homodimer. *J Biol Chem* 278(7):4385–4388.
- Ziegler N, Bätz J, Zabel U, Lohse MJ, Hoffmann C (2011) FRET-based sensors for the human M1-, M3-, and M5-acetylcholine receptors. *Bioorg Med Chem* 19(3):1048–1054.
- Ambrosio M, Lohse MJ (2012) Nonequilibrium activation of a G-protein-coupled receptor. *Mol Pharmacol* 81(6):770–777.
- Dong M, Gao F, Pinon DI, Miller LJ (2008) Insights into the structural basis of endogenous agonist activation of family B G protein-coupled receptors. *Mol Endocrinol* 22(6):1489–1499.

Polar transmembrane interactions drive formation of ligand-specific and signal pathway-biased family B G protein-coupled receptor conformations

Denise Wootten^{a,1,2}, John Simms^{a,1}, Laurence J. Miller^b, Arthur Christopoulos^a, and Patrick M. Sexton^{a,2}

^aDrug Discovery Biology, Monash Institute of Pharmaceutical Sciences, and Department of Pharmacology, Monash University, Parkville, VIC 3052, Australia; and ^bDepartment of Molecular Pharmacology and Experimental Therapeutics, Mayo Clinic, Scottsdale, AZ 85259

Edited* by Brian K. Kobilka, Stanford University School of Medicine, Stanford, CA, and approved February 15, 2013 (received for review December 10, 2012)

Recently, the concept of ligand-directed signaling—the ability of different ligands of an individual receptor to promote distinct patterns of cellular response—has gained much traction in the field of drug discovery, with the potential to sculpt biological response to favor therapeutically beneficial signaling pathways over those leading to harmful effects. However, there is limited understanding of the mechanistic basis underlying biased signaling. The glucagon-like peptide-1 receptor is a major target for treatment of type-2 diabetes and is subject to ligand-directed signaling. Here, we demonstrate the importance of polar transmembrane residues conserved within family B G protein-coupled receptors, not only for protein folding and expression, but also in controlling activation transition, ligand-biased, and pathway-biased signaling. Distinct clusters of polar residues were important for receptor activation and signal preference, globally changing the profile of receptor response to distinct peptide ligands, including endogenous ligands glucagon-like peptide-1, oxyntomodulin, and the clinically used mimetic exendin-4.

G protein-coupled receptors (GPCRs) are the largest group of cell-surface proteins and mediate signal transduction across cell membranes by recognizing a wide range of extracellular stimuli (1). They signal through heterotrimeric G proteins, as well as various G protein-independent mechanisms (2). These receptors exist in a dynamic equilibrium between different conformational states and activation occurs through a number of intermediate conformations (3, 4). This equilibrium is not only controlled by the binding of specific receptor ligands and effector proteins but is also supplemented by clusters of residues within the receptor that act to stabilize subsets of receptor conformations (5).

Polar transmembrane (TM) residues are rarely found within the core of the membrane bilayer because their insertion in a hydrophobic environment is energetically unfavorable (6). Therefore, most polar residues in TM helices are buried within the interior of the protein, often lining internal water-filled cavities and forming hydrogen-bond interactions with buried water molecules and other polar residues (7, 8). Consequently, they play essential roles in the function of α -helical membrane proteins by mediating and stabilizing their helical interactions (9), in addition to playing key roles in transmission of signals across membranes through forming interactions with ligands and establishing interaction networks required for protein conformational changes (10).

A number of highly conserved polar residues are present in the family A subclass of GPCRs, and there is a wealth of information confirming their functional role. In these receptors, key conformational changes associated with activation occur through local changes in structural constraints that involve reorganization of hydrogen bonds between the polar residues and buried waters (11–14). Recent studies also revealed that distinct ligands interacting at the same receptor can stabilize different subsets of conformational states at the expense of others, which in turn can lead to the engagement of different intracellular effectors (15–17). It is these phenomena that can provide the mechanistic basis for biased agonism.

Family B GPCRs are an important class of physiological and therapeutic targets that are pleiotropically coupled, and there is

evidence of ligand-directed stimulus bias for both natural and synthetic ligands of these receptors (18–20). The glucagon-like peptide-1 receptor (GLP-1R) is a prototypical member of this family that is activated by a range of endogenous and exogenous peptides that are used for the treatment of type-2 diabetes, and these ligands can elicit stimulus bias (18). These attributes make the GLP-1R an ideal candidate to study the molecular basis of receptor activation that may lead to both pathway-biased and ligand-dependent signaling occurring in family B GPCRs.

Although family B GPCRs do not share the conserved polar residues that are essential for family A GPCR function, they possess their own unique set of highly conserved intramembranous polar residues that have the potential to serve an role analogous to those in family A. Using the GLP-1R as a model, we have combined mutagenesis with molecular modeling to assess the role of these conserved polar residues (Fig. S1). This study demonstrates the importance of these residues for protein folding and expression, peptide binding, and in controlling activation transition, ligand-biased and pathway-biased signaling.

Results

Universal Numbering System for Residues in Family B GPCRs. Residues were numbered using a system similar to the nomenclature used for family A GPCRs (21). The most conserved residue in each family B GPCR TM domain (Fig. S1) was assigned the locant of .50, and this number is preceded by the TM number. Each residue is numbered according to its relative position to the residue at .50 in each helix and its absolute residue number is shown in superscript.

Conserved Polar Residues May Form Functionally Important Hydrogen Bonding Networks. To aid in understanding of mutational data, a model was generated of the GLP-1R TM bundle (Fig. S1). Predicted interactions formed by conserved polar side chains are listed in Table S1. Inspection of the model revealed two extensive hydrogen-bond networks formed between polar residues in TMs 2, 3, 6, and 7 and buried waters (Fig. S1). Three small polar residues, S1.50¹⁵⁵, S2.56¹⁸⁶, and S7.47³⁹², reside outside of these networks and are predicted to facilitate packing between individual TMs.

Experimental Analysis of GLP-1R Constructs. WT and mutant GLP-1Rs were isogenically integrated into FlpIn-Chinese hamster ovary (FlpInCHO) cells by recombination. Antibody detection of the N-terminal c-myc epitope and whole-cell binding using [¹²⁵I]

Author contributions: D.W., J.S., L.J.M., A.C., and P.M.S. designed research; D.W. and J.S. performed research; D.W. and J.S. analyzed data; and D.W., J.S., L.J.M., A.C., and P.M.S. wrote the paper.

The authors declare no conflict of interest.

*This Direct Submission article had a prearranged editor.

¹D.W. and J.S. contributed equally to this work.

²To whom correspondence may be addressed. E-mail: denise.wootten@monash.edu or patrick.sexton@monash.edu.

This article contains supporting information online at www.pnas.org/lookup/suppl/doi:10.1073/pnas.1221585110/-DCSupplemental.

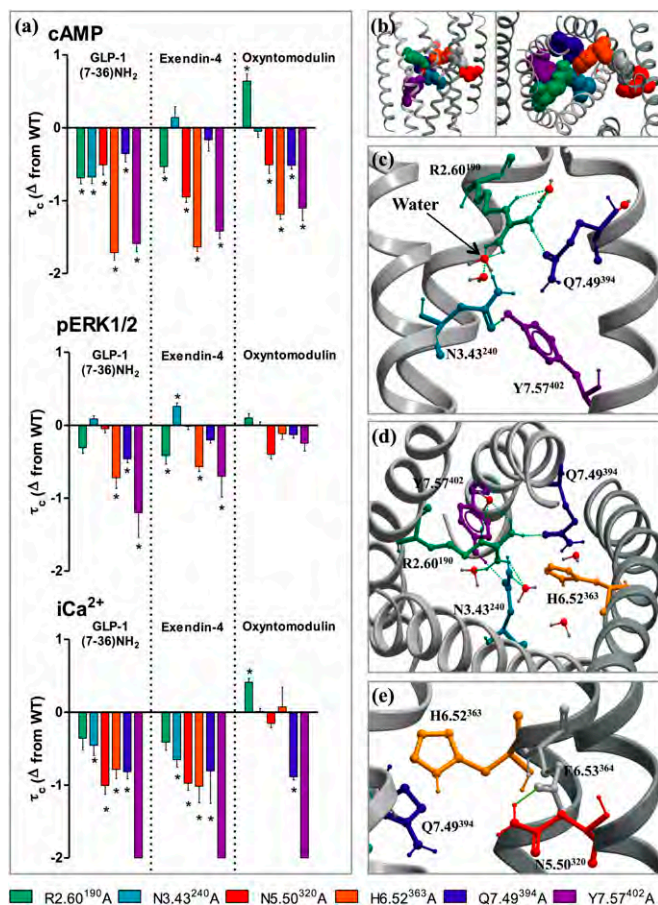


Fig. 1. Ligand-dependent and pathway-dependent effects upon mutation of residues composing the predicted central interaction network. (A) Differences in the coupling efficiency ($\log\tau_c$) of GLP-1, exendin-4, and oxyntomodulin to three signaling pathways [cAMP (Top), pERK1/2 (Middle), and iCa²⁺ mobilization (Bottom)] at individual mutants compared with the WT receptor. Statistical significance of changes in coupling efficacy in comparison with WT was determined by one-way analysis of variance and Dunnett's posttest, and values are indicated with an asterisk (* $P < 0.05$). All values are $\log\tau_c \pm$ SEM of four to six independent experiments, conducted in duplicate. (B) The model of the TM domain of the GLP-1R from the side (Left) and top (Right) highlighting the location of each of the six residues mutated. (C) Interactions in the model between R2.60¹⁹⁰, N3.43²⁴⁰, Q7.49³⁹⁴, and Y7.57⁴⁰². (D) View of the TM domain from the top showing the location of H6.52³⁵³ in relation to R2.60¹⁹⁰, N3.43²⁴⁰, Q7.49³⁹⁴, and Y7.57⁴⁰². (E) N5.50³²⁰ forms an interaction with E6.53³⁶⁴, located next to H6.52³⁵³ in the GLP-1R model.

favors a different mechanism of activation because the double mutation had little effect in pERK1/2 signaling and no greater effect than Q7.49³⁹⁴A alone on coupling to cAMP and iCa²⁺.

Calculation of bias factors between signaling pathways showed that relative to WT, R2.60¹⁹⁰A was significantly biased toward iCa²⁺ mobilization when activated by exendin-4, R2.60¹⁹⁰ and N3.43²⁴⁰ are biased toward pERK1/2 when activated by GLP-1 (and N3.43²⁴⁰ for oxyntomodulin), and significant bias was observed for Q7.49³⁹⁴A toward cAMP and pERK1/2 relative to iCa²⁺ for all ligands (Fig. S6 and Table S3). At H6.52³⁵³A, GLP-1 was significantly biased toward iCa²⁺ mobilization and to some extent pERK1/2 over cAMP, whereas oxyntomodulin and exendin-4 were biased toward pERK1/2. All three ligands were heavily biased toward pERK1/2 at N5.50³²⁰A, but little bias was observed at Y7.57A⁴⁰² (Fig. S6 and Table S3). Collectively, these data suggest that residues forming this central interaction network are crucial for fine-tuning ligand and pathway-specific receptor responses.

Characterization of Mutants in a Hydrogen Bonding Network Near the Cytoplasmic Face. The predicted cytoplasmic-face hydrogen-bond network involved the amino acid side chains of H2.50¹⁸⁰ (TM2), E3.50²⁴⁷ (TM3), and T6.42³⁵³ (TM6). Ala substitution resulted in receptors that were very poorly expressed ($18 \pm 1\%$, $18 \pm 4\%$, and $30 \pm 2\%$ of WT for H2.50¹⁸⁰A, E3.50²⁴⁷A, and T6.42³⁵³A, respectively) (Fig. 2, Fig. S2, and Table 1). [¹²⁵I]exendin (9–39) binding at these mutants was not detectable, so agonist affinity could not be calculated. Weak or no signaling was detectable for these receptors in any measured pathway with any of the three agonists. Mutation of all three residues together resulted in a complete loss of receptor expression and no detectable function (Fig. 2 and Fig. S4).

Because H2.50¹⁸⁰ was protonated in the GLP-1R model, this side chain is predicted to form a hydrogen bond with N7.61⁴⁰⁶ in TM7 (Fig. S7). N7.61 is absolutely conserved in family B GPCRs; however, no dramatic alterations in signaling were observed for N7.61⁴⁰⁶A, although subtle changes to receptor bias occurred for all ligands, with a selective increase in iCa²⁺ signaling, no change in cAMP, and a small reduction in pERK1/2, albeit none of these changes reached statistical significance (Figs. S4 and S6 and Tables S2 and S3).

Conserved Small Polar Residues Fine-Tune Activation Transition, Resulting in Controlled Activation of Different Intracellular Signaling Pathways. The three remaining conserved polar TM residues are all serines in the GLP-1R, two of which are small residues in all family B GPCRs (1.50 and 2.56) (Fig. S2). Mutation of S2.56¹⁸⁶ and S7.47³⁹² had no effect on the cell-surface expression but S1.50¹⁵⁵A expression was significantly impaired (Fig. S2). S2.56¹⁸⁶A and S7.47³⁹²A did not alter the affinity for any agonist, whereas S1.50¹⁵⁵A displayed small reductions in affinity for GLP-1 and exendin-4 but not oxyntomodulin (Fig. S2 and Table 1).

Interestingly, all three mutants had global effects on stimulus bias regardless of the activating ligand. S1.50¹⁵⁵A had reduced coupling efficiency for cAMP and iCa²⁺ mobilization (where no response was detectable) yet enhanced efficacy for pERK1/2. In contrast, S2.56¹⁸⁶A and S7.47³⁹²A showed efficacy similar to WT for cAMP, reduced efficacy for pERK1/2, and an enhanced

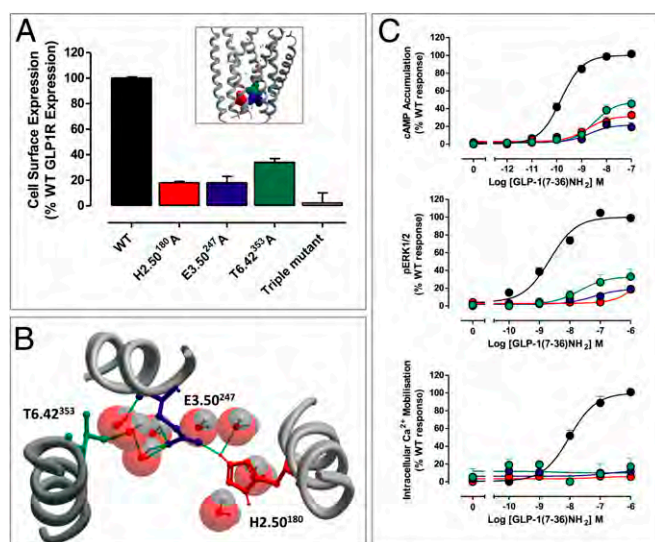


Fig. 2. Effects on mutation of residues located in the hydrogen-bonding network located at the cytoplasmic face. (A) Cell-surface expression relative to the WT receptor (by antibody detection of the N-terminal cMyc epitope tag) of H2.50¹⁸⁰A, E3.50²⁴⁷A, T6.42³⁵³A, and the triple mutant (H2.50¹⁸⁰A/E3.50²⁴⁷A/T6.42³⁵³A). (B) Interactions formed between H2.50¹⁸⁰A, E3.50²⁴⁷A, T6.42³⁵³A, and waters in the GLP-1R model. (C) Dose-response curves generated in response to GLP-1 in cAMP accumulation (Top), pERK1/2 (Middle), and iCa²⁺ mobilization (Bottom) assays.

ability to mobilize $i\text{Ca}^{2+}$ (Fig. 3, Fig. S5, and Table S2). The changes in global bias induced by these mutations can be clearly seen in bias plots (Fig. 3) that provide a visual representation of relative pathway response. Calculation of bias factors confirmed S1.50¹⁵⁵A was prejudiced toward pERK1/2 relative to cAMP and $i\text{Ca}^{2+}$, whereas S2.46¹⁸⁶A and S7.47³⁹²A exhibited bias toward $i\text{Ca}^{2+}$ signaling relative to cAMP and pERK1/2, although these bias factors did not reach statistical significance for all ligands (Table S3).

Discussion

Polar residues in membrane proteins are under evolutionary pressure for conservation and hence maintain common functions with essential roles in stability, activation, and interhelical association through the formation of hydrogen bonds (8). Based on our GLP-1R model, two main hydrogen-bond networks involving conserved polar side chains located between TMs 2, 3, 6, and 7 and waters are evident. Six conserved residues lie within a centrally located network including R2.60¹⁹⁰, N3.43²⁴⁰, N5.50³²⁰, H6.52³⁶³, Q7.49³⁹⁴, and Y7.57⁴⁰². Mutations in this central core often [although not in all cases (e.g., N3.43²⁴⁰A)] had similar effects on cAMP and $i\text{Ca}^{2+}$ mobilization, but effects on pERK1/2 signaling were less pronounced. This suggests that fine control of GLP-1R signaling is linked to changes in interactions formed by these buried polar residues. In addition, although in

the majority of cases activation by GLP-1 and exendin-4 was similar for the six different mutations across three signaling pathways, oxyntomodulin had a strikingly different pattern of behavior, and only the mutation of Y7.57⁴⁰² (and to some extent Q7.49³⁹⁴) had a trend consistent with that of the other two peptides. Therefore, oxyntomodulin's interaction with the GLP-1R and/or the precise mechanism by which it activates the receptor is different from that of the other peptides. This is in agreement with previous studies on bias at the WT receptor (18). In addition, Ala mutations to residues in extracellular loop 2 differentially altered ligand interactions and functional responses for oxyntomodulin compared with GLP-1 and exendin-4 (22).

R2.60¹⁹⁰A significantly lowered the affinity and efficacy of GLP-1 and exendin-4. In other receptors belonging to the family B subclass [vasoactive intestinal polypeptide type-1 and type-2 receptors (VPAC1R and VPAC2R) and secretin receptor (SecR)] the equivalent residue has been argued to interact with an Asp at position 3 of the agonist ligand (23, 24). GLP-1 and exendin-4 both contain an equivalent Glu at position 3 and therefore R2.60¹⁹⁰ could serve a similar role. Interestingly oxyntomodulin contains a Gln at position 3 and the affinity of this peptide was unaltered at R2.60¹⁹⁰A, supporting a differential mode of binding. However, the antagonist exendin (9–39) does not contain the first eight amino acids, and yet its binding was also reduced, albeit to a lesser extent.

Although less common, there were also significant differences in effect of mutation between pathways activated by GLP-1 and exendin-4 (Fig. 1 and Fig. S6). This indicates there are differing mechanisms of receptor activation for these two ligands. Thus, all three of the related peptides activate the receptor via subtly different mechanisms, which is particularly relevant because GLP-1 and oxyntomodulin both act endogenously and exendin-4 is used clinically to mimic the physiological functions of GLP-1.

All GPCRs are able to activate common G proteins, suggesting a conserved mechanism for G protein activation. For transition from inactive to active conformations, family A GPCRs undergo a global rearrangement of the helix bundle that shifts the cytoplasmic end of TM6 (and to a smaller extent TM5) away from the receptor core by a rotation in TM6, aided by a bend in the helix caused by a highly conserved proline (P6.50) (25–27). Early studies performed using Zn^{2+} binding suggest similar helical movements of TM6 occur in the $\beta_2\text{AR}$ (a well characterized family A GPCR) and the parathyroid hormone (PTH) receptor (a family B GPCR) and, like family A GPCRs, family B receptors contain a highly conserved proline in TM6 that is important for coupling to G proteins (28–30). These large global changes are nonetheless mediated by small conformational changes within or near the receptor binding pocket that are propagated through the receptor core (26, 31). From this study, we propose that binding of different peptides to the GLP-1R results in differential (perhaps even minor) changes around the binding pocket that are linked either directly through binding or indirectly via other interactions to a hydrogen-bond network involving the conserved residues R2.60¹⁹⁰, N3.43²⁴⁰, Q7.49³⁹⁴, structural waters and other non-conserved residues. This is likely to be an early event in receptor activation because the different ligands had different effects between mutations and across signaling pathways and no mutant displayed the same profile in all pathways for the same ligand or for all ligands in the same pathway. A role for these three conserved residues (2.60, 3.43, and 7.49) was also proposed for the early stages of activation of the VPAC1R (32).

Although the magnitude of effect upon mutation varied, the effects on function observed upon mutation of N5.50³²⁰, H6.52³⁶³, and Y7.57⁴⁰² were more consistent between pathways and ligands and thus may assist the formation of larger-scale conformational changes within TMs 5 and 6, transmitting conformational movements from the early stages of activation that lead to coupling of effectors at the cytoplasmic face. Potentially, these residues may play roles in activation analogous to W6.48 (H6.52³⁶³), Y5.58 (N5.50³²⁰), and Y7.53 (Y7.57⁴⁰²) in family A GPCRs (25).

H6.52³⁶³A resulted in a marked reduction in affinity of all ligands and all functional responses, independent of the

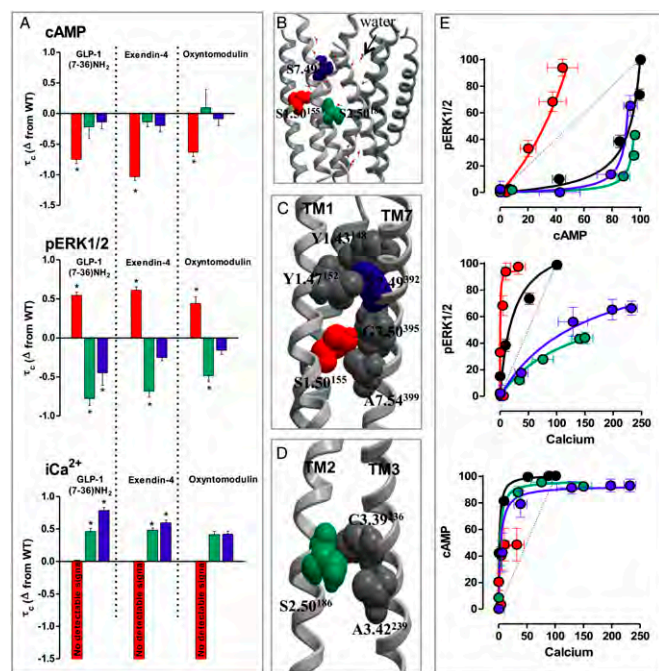


Fig. 3. Stimulus bias effects upon mutation of small polar residues in TMs 1, 2, and 7. (A) The coupling efficiency relative to WT ($\Delta\log\tau$) of GLP-1, exendin-4, and oxyntomodulin to three signaling pathways [cAMP (Top), pERK1/2 (Middle), and $i\text{Ca}^{2+}$ mobilization (Bottom)] at S1.50¹⁵⁵A, S2.56¹⁸⁶A, and S7.47³⁹²A. Statistical significance was determined by one-way analysis of variance and Dunnett's posttest (* $P < 0.05$). (B) The relative location of S1.50¹⁵⁵, S2.56¹⁸⁶, and S7.47³⁹² in the GLP-1R model. (C) Predicted packing interactions between TMs 1 and 7 formed by S1.50¹⁵⁵ and S7.47³⁹². (D) Predicted packing interactions formed by S2.50¹⁸⁶ between TMs 2 and 3. (E) Bias plots of WT, S1.50¹⁵⁵A, S2.56¹⁸⁶A, and S7.47³⁹²A for cAMP vs. pERK1/2 (Top), pERK1/2 vs. $i\text{Ca}^{2+}$ mobilization (Middle) and cAMP vs. $i\text{Ca}^{2+}$ mobilization (Bottom) for GLP-1. Data for each pathway are normalized to the maximal response elicited by peptide at the WT GLP-1R and analyzed with a three-parameter logistic equation as defined in Eq. S1, with 150 points defining the curve. A similar bias was observed when cells expressing receptors were stimulated with exendin-4 and oxyntomodulin as evidenced by bias factor calculations (Fig. S6 and Table S3).

decreased affinity (with the exception of oxyntomodulin-induced pERK1/2 and $i\text{Ca}^{2+}$). In water pockets, histidines can be readily protonated and deprotonated depending on the local environment (33). In the model, H6.52³⁶³ is only singly protonated, so it is uncharged, but changes in the protonation state owing to the exchange of bulk waters could arise owing to an opening up of the bundle upon peptide binding. If this does occur, TM6 would rotate away from TM2 and TM3 because of the proximity of the positively charged R2.60¹⁹⁰, consistent with helical movements that occur in family A GPCRs (26, 34).

N5.50³²⁰A reduced affinity of GLP-1 and exendin-4 and their ability to activate both cAMP and $i\text{Ca}^{2+}$ mobilization; however, there was no change in coupling to pERK1/2. There was a similar effect on oxyntomodulin affinity and coupling to cAMP; however, in this case pERK1/2 and $i\text{Ca}^{2+}$ mobilization were unaltered. Our model suggests an interaction of N5.50³²⁰ with E6.53³⁶⁴, located next to H6.52³⁶³, that is also crucial in activation of the GLP-1R leading to cAMP signaling. Mechanistically this is interesting, because a rotation in TM6 upon activation would result in a movement of TM5 that would be aided by the proposed interaction between N5.50³²⁰ with E6.53³⁶⁴, opening up the helical bundle at the cytoplasmic face (Fig. S7). Mutation of N5.50³²⁰ seems to alter the ensemble of conformations that the GLP-1R can sample (or the frequency with which they sample subsets of populations) in response to agonists such that there is a greater propensity to form conformations linked to pERK1/2 than to cAMP and $i\text{Ca}^{2+}$. Therefore, N5.50³²⁰ may mediate receptor transitions thorough aiding movement of TM5 to open up the bundle allowing G-protein coupling but is less important for transitions enabling G-protein-independent signaling (pERK1/2).

Y7.57⁴⁰²A had a global impact on receptor function regardless of the activating ligand. Y7.57⁴⁰² forms part of a conserved VXXXXY motif that may be the family B equivalent of the NPXXY motif, playing a role similar to Y7.53 in family A GPCRs (27). Y7.57⁴⁰² in the GLP-1R forms hydrophobic packing contacts through its bulky aromatic ring and a hydrogen bond interaction with N3.43²⁴⁰A and also waters through its polar moiety. These interactions are likely to be broken upon receptor activation and may aid transmission of signal from the hydrogen-bond network in the core of the protein to the cytoplasmic face, stabilizing conformations that allow effectors to bind.

In addition to a role in aiding conformational rearrangements R2.60¹⁹⁰, H6.52³⁶³, and Y7.57⁴⁰² are also required for efficient cell-surface expression. The reduction in cell-surface-expressed receptors for R2.60¹⁹⁰A, H6.52³⁶³A, and Y7.57⁴⁰²A indicates that these mutations either disrupt trafficking/insertion of the receptor into the bilayer and/or disrupt the stability of the helical bundle. R2.60¹⁹⁰ could perform both of these roles. In our model, His6.52³⁶³ resides in close proximity to R2.60¹⁹⁰ and forms π stacking interactions with F6.56³⁶⁷ and F7.45³⁹⁰, polar interactions with T7.46³⁹¹ in TM7, and hydrophobic packing with L6.49³⁶⁰ and L6.48³⁵⁹, whereas Y7.57⁴⁰² packs between two phenylalanine residues in TM2. These packing interactions are likely to provide structural integrity (Fig. S7). Although we have proposed that effects on signaling following mutation of these residues may be due to their involvement in a central interaction network, these effects could also arise due to indirect effects on folding and structural integrity via other mechanisms.

The predicted bottom hydrogen-bond network involves H2.50¹⁸⁰A, E3.50²⁴⁷, T6.42³⁵³, and multiple waters. Mutation of these residues individually resulted in heavily impaired cell-surface expression and subsequently impaired functional responses to all ligands in all pathways. One proposal is that H2.50¹⁸⁰ and E3.50²⁴⁷ play a role in family B GPCRs similar to the highly conserved D(E)RY motif in family A GPCRs. Family A GPCRs also have a proposed lock between TMs 3 and 6 that stabilize these receptors in their inactive conformation (35, 36). The extended network in our model revealed water-connected hydrogen-bond interactions between E3.50²⁴⁷ and T6.42³⁵³ that may play a similar role, locking the receptor in an inactive conformation. Often in family A GPCRs, mutation of either the D(E)RY motif or the interacting

residues in TM6 (E6.30 and T6.34) results in constitutive activity (36). However, sometimes this manifests as a reduction in cell-surface expression, due to a destabilization of the receptor structure and/or constitutive internalization (36). The inability to detect binding in crude membrane fractions and whole cells upon mutation of these residues supports a crucial role of this bottom network for receptor folding and stability. It is also interesting to note that mutation of both H2.50 and T6.42 in the PTH and SecR receptors and of H2.50 in the VPAC1R leads to constitutive activation, supporting the evolutionarily conserved role of these residues in ground-state stabilization (37–40).

In addition to large polar and charged amino acids, mutation to three small polar residues promotes receptor conformations that altered the equilibrium between the different signaling cascades; however, these mutants had global impacts on signaling regardless of the activating ligand. Relative to WT, S1.50¹⁵⁵A displayed significant bias toward pERK1/2 over calcium and cAMP, whereas S2.50¹⁸⁶A and S7.47³⁹²A were biased toward $i\text{Ca}^{2+}$ (Fig. 3). Small weakly polar residues (Ser, Thr, and Cys) within the TM domains of membrane proteins are key determinants in helix–helix interactions (41). In our model, S1.50¹⁵⁵ packs up against two small residues in TM7 (G7.50³⁹⁵ and A7.54³⁹⁹), aiding close packing of TMs1 and 7, and S2.50¹⁸⁶ in TM2 packs with C3.39²³⁶ in TM3, allowing tight packing of these helices. S2.50¹⁸⁶ is also in close proximity to A3.42²³⁹, and an interaction with this residue may occur on conformational transition (Fig. 3). It is not clear whether Ala mutation results in more tightly packed helices or creates space in the structure, but clearly subtle changes in these regions have very selective effects on the conformational landscape that the receptor can explore. Interestingly, S7.47³⁹² in TM7 does not cause tight packing but instead borders a solvated pocket, forming a direct interaction with Y1.48¹⁴⁸ in TM1 and through water contact with D2.68¹⁹⁸ (Table S1). This Asp has been highlighted as a potential contact for peptides and when mutated significantly alters GLP-1R function (42). Ala mutation of S7.47³⁹² did not alter affinity of any ligand, but its ability to selectively enhance signaling to $i\text{Ca}^{2+}$ but not pERK1/2 or cAMP indicated that disruption of these interactions significantly lowers the energy barrier, allowing the receptor to mobilize $i\text{Ca}^{2+}$. In addition, N7.61⁴⁰⁶A also resulted in an increase in $i\text{Ca}^{2+}$ for all ligands, although the pathway selectivity was not as pronounced as those mentioned above. Nonetheless, these effects were similar to those of S2.56¹⁸⁶ and S7.47³⁹² (also located in TMs 2 and 7). Taken together, these residues seem to optimally pack TM helices to allow fine-tuning of receptor response to different intracellular effectors.

Collectively, this study indicates that conserved polar residues within the TM domain of the GLP-1R are essential for structural integrity and activation transition, including signaling preferences and ligand-directed stimulus bias. This likely involves reordering of interaction networks between polar side chains and buried waters, providing a mechanism through which receptors and ligands achieve conformational complexes associated with signaling bias. The high degree of conservation of these residues suggests that they may play a similar role in signaling of other family B GPCRs.

Materials and Methods

Receptor Mutagenesis and Cell Culture. Thirteen conserved polar residues located in the TM domain that are predicted to be buried within the core of the GLP-1R were selected for mutagenesis (Fig. S1). This was achieved using the QuikChange site-directed mutagenesis kit (Stratagene), and stable cell lines were generated using gateway technology (Invitrogen).

Expression, Binding, and Functional Assays. Cell-surface expression, radioligand binding (22), cAMP accumulation, pERK1/2, and $i\text{Ca}^{2+}$ mobilization assays (18) were performed as previously described.

Molecular Modeling. All atom canonical alpha helices for each TM region of the GLP-1R were generated using TINKER (43, 44). Each helix was fitted to the equivalent helix in bovine rhodopsin (1GZM) using lipid facing residue

information extracted from the Trans-Membrane helix-LIPid web server. For those helices containing proline residues helices were picked from the pool of helical turns to minimize polar residue exposure to the lipid environment. A coarse-grain representation of the helical bundle was generated according to the MARTINI force field before insertion into a palmitoyl oleoyl phosphatidylcholine bilayer (45). The system was simulated for 1 μ s with snapshots taken every 10 ns, then transformed from coarse-grain to all-atom representation using PULCHRA and OPUS_ROTATE and scored using OPUS_PSP. The best scoring bundle was subjected to 5e8 steps in a replica exchange Monte Carlo simulation as implemented in hippo using default values. Water positions were predicted using DOWSER.

Data Analysis. All data were analyzed using Prism 5.04 (GraphPad Software Inc.) as previously described (46).

For more details on experimental methods and data analysis, see *SI Materials and Methods*.

ACKNOWLEDGMENTS. This work was funded by National Health and Medical Research Council (NHMRC) Project Grant 1002180, NHMRC Program Grant 519461, Australian Research Council Discovery Project DP0985210, and a Victorian Life Sciences Computation Initiative (VLSCI) Grant (VR0024) on its Peak Computing Facility at the University of Melbourne, an initiative of the Victorian Government, Australia.

- Pierce KL, Premont RT, Lefkowitz RJ (2002) Seven-transmembrane receptors. *Nat Rev Mol Cell Biol* 3(9):639–650.
- Shenoy SK, Lefkowitz RJ (2005) Seven-transmembrane receptor signaling through beta-arrestin. *Sci STKE* 2005(308):cm10.
- Hofmann KP, et al. (2009) A G protein-coupled receptor at work: The rhodopsin model. *Trends Biochem Sci* 34(11):540–552.
- Swaminath G, et al. (2004) Sequential binding of agonists to the beta2 adrenoceptor. Kinetic evidence for intermediate conformational states. *J Biol Chem* 279(1):686–691.
- Unal H, Karnik SS (2012) Domain coupling in GPCRs: The engine for induced conformational changes. *Trends Pharmacol Sci* 33(2):79–88.
- White SH, Wimley WC (1999) Membrane protein folding and stability: physical principles. *Annu Rev Biophys Biomol Struct* 28:319–365.
- Isom DG, Cannon BR, Castañeda CA, Robinson A, García-Moreno B (2008) High tolerance for ionizable residues in the hydrophobic interior of proteins. *Proc Natl Acad Sci USA* 105(46):17784–17788.
- Illergård K, Kauko A, Elofsson A (2011) Why are polar residues within the membrane core evolutionary conserved? *Proteins* 79(1):79–91.
- Zhou FX, Cocco MJ, Russ WP, Brunger AT, Engelman DM (2000) Interhelical hydrogen bonding drives strong interactions in membrane proteins. *Nat Struct Biol* 7(2):154–160.
- Curran AR, Engelman DM (2003) Sequence motifs, polar interactions and conformational changes in helical membrane proteins. *Curr Opin Struct Biol* 13(4):412–417.
- Angel TE, Chance MR, Palczewski K (2009) Conserved waters mediate structural and functional activation of family A (rhodopsin-like) G protein-coupled receptors. *Proc Natl Acad Sci USA* 106(21):8555–8560.
- Angel TE, Gupta S, Jastrzebska B, Palczewski K, Chance MR (2009) Structural waters define a functional channel mediating activation of the GPCR, rhodopsin. *Proc Natl Acad Sci USA* 106(34):14367–14372.
- Deupi X, et al. (2012) Stabilized G protein binding site in the structure of constitutively active metarhodopsin-II. *Proc Natl Acad Sci USA* 109(1):119–124.
- Patel AB, et al. (2005) Changes in interhelical hydrogen bonding upon rhodopsin activation. *J Mol Biol* 347(4):803–812.
- Mary S, et al. (2012) Ligands and signaling proteins govern the conformational landscape explored by a G protein-coupled receptor. *Proc Natl Acad Sci USA* 109(21):8304–8309.
- Rahmeh R, et al. (2012) Structural insights into biased G protein-coupled receptor signaling revealed by fluorescence spectroscopy. *Proc Natl Acad Sci USA* 109(17):6733–6738.
- Liu JJ, Horst R, Katritch V, Stevens RC, Wüthrich K (2012) Biased signaling pathways in β 2-adrenergic receptor characterized by 19F-NMR. *Science* 335(6072):1106–1110.
- Koole C, et al. (2010) Allosteric ligands of the glucagon-like peptide 1 receptor (GLP-1R) differentially modulate endogenous and exogenous peptide responses in a pathway-selective manner: implications for drug screening. *Mol Pharmacol* 78(3):456–465.
- Spengler D, et al. (1993) Differential signal transduction by five splice variants of the PACAP receptor. *Nature* 365(6442):170–175.
- Gesty-Palmer D, et al. (2009) A beta-arrestin-biased agonist of the parathyroid hormone receptor (PTH1R) promotes bone formation independent of G protein activation. *Sci Transl Med* 1(1):1ra1.
- Ballesteros JA, Weinstein H (1995) Integrated methods for the construction of three-dimensional models and computational probing of structure-function relations in G protein-coupled receptors. *Methods Neurosci Receptor Mol Biol* 25:366–428.
- Koole C, et al. (2012) Second extracellular loop of human glucagon-like peptide-1 receptor (GLP-1R) differentially regulates orthosteric but not allosteric agonist binding and function. *J Biol Chem* 287(6):3659–3673.
- Langer I, Robberecht P (2007) Molecular mechanisms involved in vasoactive intestinal peptide receptor activation and regulation: Current knowledge, similarities to and differences from the A family of G-protein-coupled receptors. *Biochem Soc Trans* 35(Pt 4):724–728.
- Di Paolo EDNP, et al. (1998) Contribution of the second transmembrane helix of the secretin receptor to the positioning of secretin. *FEBS Lett* 424(3):207–210.
- Rosenbaum DM, Rasmussen SG, Kobilka BK (2009) The structure and function of G-protein-coupled receptors. *Nature* 459(7245):356–363.
- Rasmussen SG, et al. (2011) Crystal structure of the β 2 adrenergic receptor-Gs protein complex. *Nature* 477(7366):549–555.
- Standfuss J, et al. (2011) The structural basis of agonist-induced activation in constitutively active rhodopsin. *Nature* 471(7340):656–660.
- Sheikh SP, et al. (1999) Similar structures and shared switch mechanisms of the beta2-adrenoceptor and the parathyroid hormone receptor. Zn(II) bridges between helices III and VI block activation. *J Biol Chem* 274(24):17033–17041.
- Conner AC, et al. (2005) A key role for transmembrane prolines in calcitonin receptor-like receptor agonist binding and signalling: Implications for family B G-protein-coupled receptors. *Mol Pharmacol* 67(1):20–31.
- Bailey RJ, Hay DL (2007) Agonist-dependent consequences of proline to alanine substitution in the transmembrane helices of the calcitonin receptor. *Br J Pharmacol* 151(5):678–687.
- Warne T, Edwards PC, Leslie AG, Tate CG (2012) Crystal structures of a stabilized β 1-adrenoceptor bound to the biased agonists bucindolol and carvedilol. *Structure* 20(5):841–849.
- Chugunov AO, et al. (2010) Evidence that interaction between conserved residues in transmembrane helices 2, 3, and 7 are crucial for human VPAC1 receptor activation. *Mol Pharmacol* 78(3):394–401.
- Li S, Hong M (2011) Protonation, tautomerization, and rotameric structure of histidine: a comprehensive study by magic-angle-spinning solid-state NMR. *J Am Chem Soc* 133(5):1534–1544.
- Scheerer P, et al. (2008) Crystal structure of opsin in its G-protein-interacting conformation. *Nature* 455(7212):497–502.
- Palczewski K, et al. (2000) Crystal structure of rhodopsin: A G protein-coupled receptor. *Science* 289(5480):739–745.
- Rovati GE, Capra V, Neubig RR (2007) The highly conserved DRY motif of class A G protein-coupled receptors: Beyond the ground state. *Mol Pharmacol* 71(4):959–964.
- Schipani E, Kruse K, Jüppner H (1995) A constitutively active mutant PTH-PTHrP receptor in Jansen-type metaphyseal chondrodysplasia. *Science* 268(5207):98–100.
- Schipani E, et al. (1996) Constitutively activated receptors for parathyroid hormone and parathyroid hormone-related peptide in Jansen's metaphyseal chondrodysplasia. *N Engl J Med* 335(10):708–714.
- Gaudin P, Maoret JJ, Couvineau A, Rouyer-Fessard C, Laburthe M (1998) Constitutive activation of the human vasoactive intestinal peptide 1 receptor, a member of the new class II family of G protein-coupled receptors. *J Biol Chem* 273(9):4990–4996.
- Ganguli SC, et al. (1998) Protean effects of a natural peptide agonist of the G protein-coupled secretin receptor demonstrated by receptor mutagenesis. *J Pharmacol Exp Ther* 286(2):593–598.
- Liu W, Eilers M, Patel AB, Smith SO (2004) Helix packing moments reveal diversity and conservation in membrane protein structure. *J Mol Biol* 337(3):713–729.
- López de Maturana RDD, Donnelly D (2002) The glucagon-like peptide-1 receptor binding site for the N-terminus of GLP-1 requires polarity at Asp198 rather than negative charge. *FEBS Lett* 530(1–3):244–248.
- Ulmschneider MB, Ulmschneider JP (2008) Membrane adsorption, folding, insertion and translocation of synthetic trans-membrane peptides. *Mol Membr Biol* 25(3):245–257.
- Ulmschneider JP, Jorgensen WL (2004) Polypeptide folding using Monte Carlo sampling, concerted rotation, and continuum solvation. *J Am Chem Soc* 126(6):1849–1857.
- Marrink SJ, Risselada HJ, Yefimov S, Tieleman DP, de Vries AH (2007) The MARTINI force field: Coarse grained model for biomolecular simulations. *J Phys Chem B* 111(27):7812–7824.
- Koole C, et al. (2012) Second extracellular loop of human glucagon-like peptide-1 receptor (GLP-1R) has a critical role in GLP-1 peptide binding and receptor activation. *J Biol Chem* 287(6):3642–3658.

Supporting Information

Wootten et al. 10.1073/pnas.1221585110

SI Materials and Methods

DMEM, hygromycin-B, and Fluo-4 acetoxymethyl ester were purchased from Invitrogen. FBS was purchased from Thermo Fisher Scientific. The QuikChange site-directed mutagenesis kit was purchased from Stratagene. AlphaScreen reagents, Bolton-Hunter reagent [125 I], and 384-well ProxiPlates were purchased from PerkinElmer Life and Analytical Sciences. SureFire ERK1/2 reagents were generously supplied by TGR Biosciences. SigmaFast *o*-phenylenediamine dihydrochloride tablets and antibodies were purchased from Sigma-Aldrich. GLP-1 peptides were purchased from American Peptide. All other reagents were purchased from Sigma-Aldrich or BDH Merck and were of an analytical grade.

Identification of Family B G Protein-Coupled Receptor Conserved Polar Residues Selected for Mutagenesis. A CLUSTALW profile alignment (using the Blossum matrix) was created against the 15 human secretin-like family B G protein-coupled receptors (GPCRs) transmembrane (TM) domains (TM boundaries were predicted using a combination of TMHMM, HMMTOP, and Zpred (part of TopCons) web servers (1). Thirteen conserved polar residues located in the TM domain that are predicted to be buried within the core of the GLP-1R were selected for mutagenesis (Fig. 1A). Conserved polar residues predicted to reside at the boundary of TMs or interact with lipids were excluded from this study.

Receptor Mutagenesis. To study the influence of polar TM amino acids on receptor function, the desired mutations were introduced to an N-terminally double c-myc labeled WT human glucagon-like peptide-1 receptor (GLP-1R) in the pEF5/FRT/V5-DEST destination vector (Invitrogen); this receptor had pharmacology equivalent to the untagged human GLP-1R. Mutagenesis was carried out using oligonucleotides for site-directed mutagenesis purchased from GeneWorks and the QuikChange site-directed mutagenesis kit (Stratagene) and confirmed by automated sequencing. Mutated residues and their conservation across human family B peptide hormone receptors are illustrated in Fig. 1.

Transfections and Cell Culture. WT and mutant human GLP-1R were isogenically integrated into FLPIn-Chinese hamster ovary (FLPInCHO) cells (Invitrogen) and selection of receptor-expressing cells accomplished by treatment with 600 μ g/mL hygromycin-B. Transfected and parental FLPInCHO cells were maintained in DMEM supplemented with 10% (vol/vol) heat-inactivated FBS and incubated in a humidified environment at 37 °C in 5% CO₂.

Radioligand Binding Assay. Whole cells. FLPInCHO WT and mutant human GLP-1R cells were seeded at a density of 3×10^4 cells per well into 96-well culture plates and incubated overnight at 37 °C in 5% CO₂, and radioligand binding was carried out as previously described (2). For each cell line in all experiments, total binding was defined by 0.5 nM [125 I]exendin (9–39) alone, and nonspecific binding was determined in the presence of 1 μ M exendin (9–39). For analysis, data are normalized to the specific binding for each individual experiment.

Crude membranes. Membrane preparations were prepared as described previously (3). Protein concentration was determined using the BCA protein assay kit (Thermo Scientific) following the manufacturer's instructions, with BSA as standard. Competition binding assays were performed in 96-well plates using 20 μ g of membrane expressing WT or mutant GLP-1Rs. Membranes were

incubated in Hepes buffer (1 mM Hepes, MgCl₂, NaCl, and BSA, pH 7.4) containing 0.5 nM [125 I]exendin (9–39) and increasing concentration of unlabeled ligand for 1 h. For all experiments nonspecific binding was defined by 1 μ M GLP-1 (7–36) amide and/or 1 μ M exendin (9–39). Incubation was terminated by rapid filtration through Whatman GF/C filters [presoaked in 0.03% (vol/vol) polyethylenimine for a minimum of 2 h) using a 96-well Tomtec Harvester. Filters were washed three times with 0.9% NaCl (wt/vol) and 0.3% BSA (wt/vol) and allowed to dry before addition of 30 μ L of scintillant and determination of radioactivity by scintillation counting.

cAMP Accumulation Assay. FLPInCHO WT and mutant human GLP-1R cells were seeded at a density of 3×10^4 cells per well into 96-well culture plates and incubated overnight at 37 °C in 5% CO₂, and cAMP detection was carried out as previously described (3). All values were converted to concentration of cAMP using a cAMP standard curve performed in parallel, and data were subsequently normalized to the response of 100 μ M forskolin in each cell line.

Phosphorylation of extracellular regulated kinases 1/2 Assay. FLPInCHO WT and mutant human GLP-1R cells were seeded at a density of 3×10^4 cells per well into 96-well culture plates and incubated overnight at 37 °C in 5% CO₂. Receptor-mediated phosphorylation of extracellular regulated kinases 1/2 (pERK1/2) was determined using the AlphaScreen pERK1/2 SureFire protocol as previously described (3). Initial pERK1/2 time course experiments were performed over 1 h to determine the time at which agonist-mediated pERK1/2 was maximal. Subsequent experiments were then performed at the time required to generate a maximal pERK1/2 response (6 min). Data were normalized to the maximal response elicited by 10% (vol/vol) FBS in each cell line, determined at 6 min (peak FBS response).

iCa²⁺ Mobilization Assay. FLPInCHO WT and mutant human GLP-1R cells were seeded at a density of 3×10^4 cells per well into 96-well culture plates and incubated overnight at 37 °C in 5% CO₂, and receptor-mediated iCa²⁺ mobilization was determined as previously described (3). Fluorescence was determined immediately after peptide addition, with an excitation wavelength set to 485 nm and an emission wavelength set to 520 nm, and readings were taken every 1.36 s for 120 s. Peak magnitude was calculated using five-point smoothing, followed by correction against basal fluorescence. The peak value was used to create concentration-response curves. Data were normalized to the maximal response elicited by 100 μ M ATP.

Cell-Surface Receptor Expression. FLPInCHO WT and mutant human GLP-1R cells, with receptor DNA previously incorporated with an N-terminal double c-myc epitope label, were seeded at a density of 25×10^4 cells per well into 24-well culture plates and incubated overnight at 37 °C in 5% CO₂, washed three times in 1 \times PBS, and fixed with 3.7% (vol/vol) paraformaldehyde at 4 °C for 15 min. Cell-surface receptor detection was then performed as previously described (2). Data were normalized to the basal fluorescence detected in FLPInCHO parental cells. Specific [125 I]exendin (9–39) binding at each receptor mutant, as identification of functional receptors at the cell surface, was also determined [corrected for nonspecific binding using 1 μ M exendin (9–39)].

Molecular Modeling. TM regions were predicted using a combination of TMHMM, HMMTOP, and Zpred (part of TopCons

(1)) web servers for 81 family B GPCRs and a multiple sequence alignment was annotated with these predicted starts and ends of the helices, after which a consensus approach by visual inspection was used to annotate the alignment before deciding the absolute positions of the TM domain. All atom canonical alpha helices for each TM region of the GLP-1R were generated using TINKER (4, 5). For those TM regions that contained proline residues a further set of helices were generated such that the backbone torsions (phi and psi) were set to -57 to 47 , 57 to 70 , -71 to 18 for those residues one turn before the proline residue, to represent alpha, pi, or 310 helix deformations, respectively. Omega was set to 180 . Each helix was fitted to the equivalent helix in bovine rhodopsin (1GZM) using lipid facing residue information extracted from the Trans-Membrane helix-LIPid web server, for those helices containing proline residues helices were picked from the pool of helical turns to minimize polar residue exposure to the lipid environment. A coarse-grain representation of the helical bundle was generated according to the MARTINI force field before insertion into a palmitoyl oleoyl phosphatidylcholine bilayer containing 512 lipid molecular and 8,000 water beads (6). The system was simulated for 1 μ s with snapshots taken every 10 ns. Each bundle snapshots were transformed from coarse-grain to all-atom representation using a combination of PULCHRA and OPUS_ROTATE. The bundles were scored using OPUS_PSP. The best scoring bundle was subjected to 5e8 steps in a replica exchange Monte Carlo simulation as implemented in hippo using default values. Water positions were predicted using DOWSER.

Data Analysis. All data were analyzed using Prism 5.04 (GraphPad Software Inc.). For all analyses the data are unweighted and each y value (mean of replicates for each individual experiment) is considered an individual point. Concentration response signaling data were analyzed using a three-parameter logistic equation as previously described:

$$Y = Bottom + \frac{(Top - Bottom)}{1 + 10^{(LogEC_{50} - \log[A])}}, \quad [S1]$$

where *Bottom* represents the y value in the absence of ligand(s), *Top* represents the maximal stimulation in the presence of ligand(s), $[A]$ is the molar concentration of ligand, and EC_{50} represents the molar concentration of ligand required to generate a response halfway between *Top* and *Bottom*. Similarly, this equation was used in the analysis of inhibition binding data, instead replacing EC_{50} with IC_{50} . In this case, *Bottom* defines the specific binding of the radioligand that is equivalent to nonspecific ligand binding, whereas *Top* defines radioligand binding in the absence of a competing ligand, and the IC_{50} value represents the molar concentration of ligand required to generate a response halfway between *Top* and *Bottom*. IC_{50} values obtained were then corrected for radioligand occupancy as previously described using the radioligand affinity (K_i) experimentally determined for each mutant.

To quantify efficacy in the system, all data were fitted with an operational model of agonism:

$$Y = Bottom + \frac{E_m - Bottom}{1 + ((10^{\log K_A}) + (10^{\log [A]})) / (10^{(\log \tau + \log [A])})}, \quad [S2]$$

where *Bottom* represents the y value in the absence of ligand(s), E_m represents the maximal stimulation of the system, K_A is the agonist-receptor dissociation constant, in molar concentration, $[A]$ is the molar concentration of ligand, and τ is the operational measure of efficacy in the system, which incorporates signaling efficacy and receptor density. Constraints for this model were determined by fitting the operational model for a partial agonist to each of the peptides at the WT receptor, with the most efficacious peptide fitted with

$$Y = Bottom + \frac{E_m - Bottom}{1 + 10^{(LogEC_{50} - \log[A])}}, \quad [S3]$$

and the less efficacious peptides fitted with Eq. S2, to obtain a value for the system maximum (E_m). This value was then globally constrained in the operational model (Eq. S2). All estimated τ values were then corrected to cell-surface expression (τ_c) as determined by cell-surface ELISA and errors propagated from both τ and cell-surface expression.

To quantify signaling bias, peptide agonist concentration-response curves were analyzed with nonlinear regression using an operational model of agonism but modified to directly estimate the ratio of τ_c/K_A , in a manner similar to that described by Figueroa et al. (7). For each pathway,

$$Y = \frac{E_{max} \times (\tau_c/K_A)^n \times [A]^n}{[A]^n \times (\tau_c/K_A)^n + (1 + [A]/K_A)^n}, \quad [S4]$$

where parameters are as defined for Eq. S2. All estimated τ_c/K_A ratios included propagation of error for both τ_c and K_A . Changes in τ_c/K_A ratios with respect to WT of each mutant were used to quantitate bias between signaling pathways. Accordingly, bias factors included propagation of error from τ_c/K_A ratios of each pathway.

Data were also normalized to maximal agonist response at the WT receptor in each signaling pathway, fitted with a three-parameter logistic equation, and equimolar concentrations of agonists in each pathway were plotted against one other. In this way, the bias of any given agonist for one pathway over another can be visualized. In all cases, individual data sets were unweighted during the analyses.

Statistics. Changes in peptide affinity, potency, efficacy, and cell-surface expression and bias of each mutant receptor in comparison with the WT control were statistically analyzed with one-way analysis of variance and Dunnett's posttest, and significance was accepted at $P < 0.05$.

- Bernsel A, Viklund H, Hennerdal A, Elofsson A (2009) TOPCONS: Consensus prediction of membrane protein topology. *Nucleic Acids Res* 37(Web Server issue):W465-8.
- Koole C, et al. (2012) Second extracellular loop of human glucagon-like peptide-1 receptor (GLP-1R) differentially regulates orthosteric but not allosteric agonist binding and function. *J Biol Chem* 287(6):3659-3673.
- Koole C, et al. (2010) Allosteric ligands of the glucagon-like peptide 1 receptor (GLP-1R) differentially modulate endogenous and exogenous peptide responses in a pathway-selective manner: Implications for drug screening. *Mol Pharmacol* 78(3):456-465.

- Ulmschneider JP, Jorgensen WL (2004) Polypeptide folding using Monte Carlo sampling, concerted rotation, and continuum solvation. *J Am Chem Soc* 126(6):1849-1857.
- Marrink SJ, Risselada HJ, Yefimov S, Tieleman DP, de Vries AH (2007) The MARTINI force field: Coarse grained model for biomolecular simulations. *J Phys Chem B* 111(27):7812-7824.
- Koole C, et al. (2012) Second extracellular loop of human glucagon-like peptide-1 receptor (GLP-1R) has a critical role in GLP-1 peptide binding and receptor activation. *J Biol Chem* 287(6):3642-3658.
- Figueroa KW, et al. (2009) Selectivity of agonists for the active state of M1 to M4 muscarinic receptor subtypes. *J. Pharmacol. Exp. Ther.* 328:331-342.

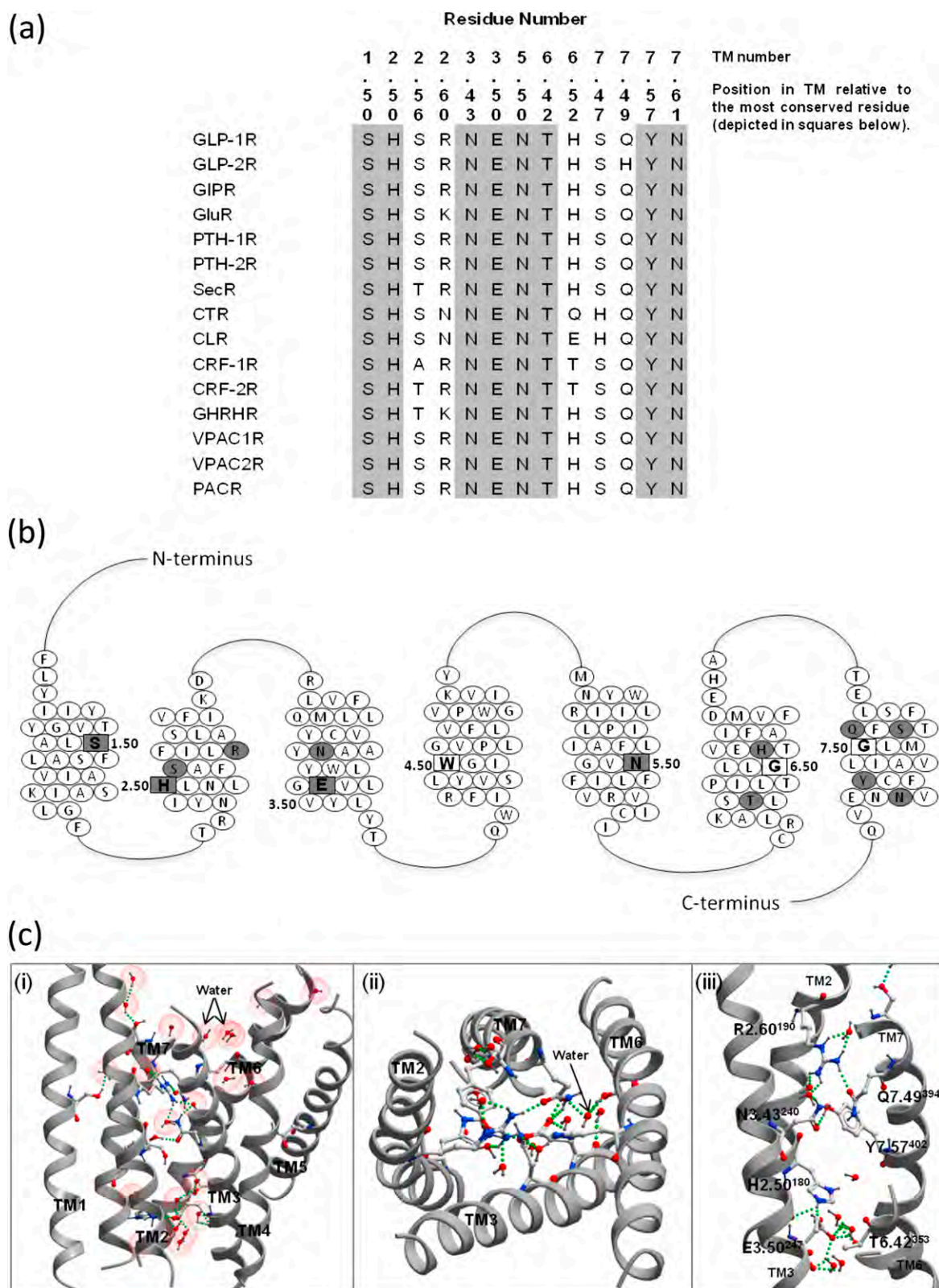


Fig. S1. Conservation and relative location of polar residues mutated in this study. (A) Conserved polar residues in the human family B GPCRs (the secretin-like subclass). Residues absolutely conserved are highlighted in gray. These residues shown are conserved as polar across all mammalian species of receptor cloned to date. CLR, calcitonin-like receptor; CRF1, corticotropin-releasing factor receptor 1; CRF2, corticotropin-releasing factor receptor 2; CTR, calcitonin receptor; GHRHR, growth hormone-releasing hormone receptor; GIP, gastric inhibitory polypeptide receptor; GLP-1R, glucagon-like peptide-1 receptor; GLP-2R, GLP-2 receptor; GluR, glucagon receptor; PACR, pituitary adenylate cyclase activating polypeptide 1 receptor; PTH-1R, parathyroid hormone receptor 1; PTH-2R, PTH receptor 2; SecR, secretin receptor; VPAC1R, vasointestinal polypeptide type-1 receptor; VPAC2R, vasointestinal polypeptide type-2 receptor. The

Legend continued on following page

numbers along the top indicate the position of the residue in the receptor using our proposed numbering system (*Results*). (B) Schematic representation of the TM domain of the human GLP-1R. The most conserved residue in each helix is highlighted as a square with a bold letter and represents residue 0.50 for that helix. Residues mutated in the present study are shown in gray. All of these residues are conserved as polar in family B (secretin-like) GPCRs. (C) Three-dimensional model of the TM bundle of GLP-1R showing conserved polar residues and structural waters. (i) TMs 1–7 of the GLP-1R highlighting the positions of all side chains mutated as part of this study. Hydrogen-bond networks between these conserved polar residues and structural waters are shown as green spheres. (ii and iii) TMs 2, 3, 6, and 7 of the GLP-1R bundle viewed from the top (ii) and the side (iii) showing the two main hydrogen-bonding networks identified in the model. TMs 1, 4, and 5 have been removed for clarity.

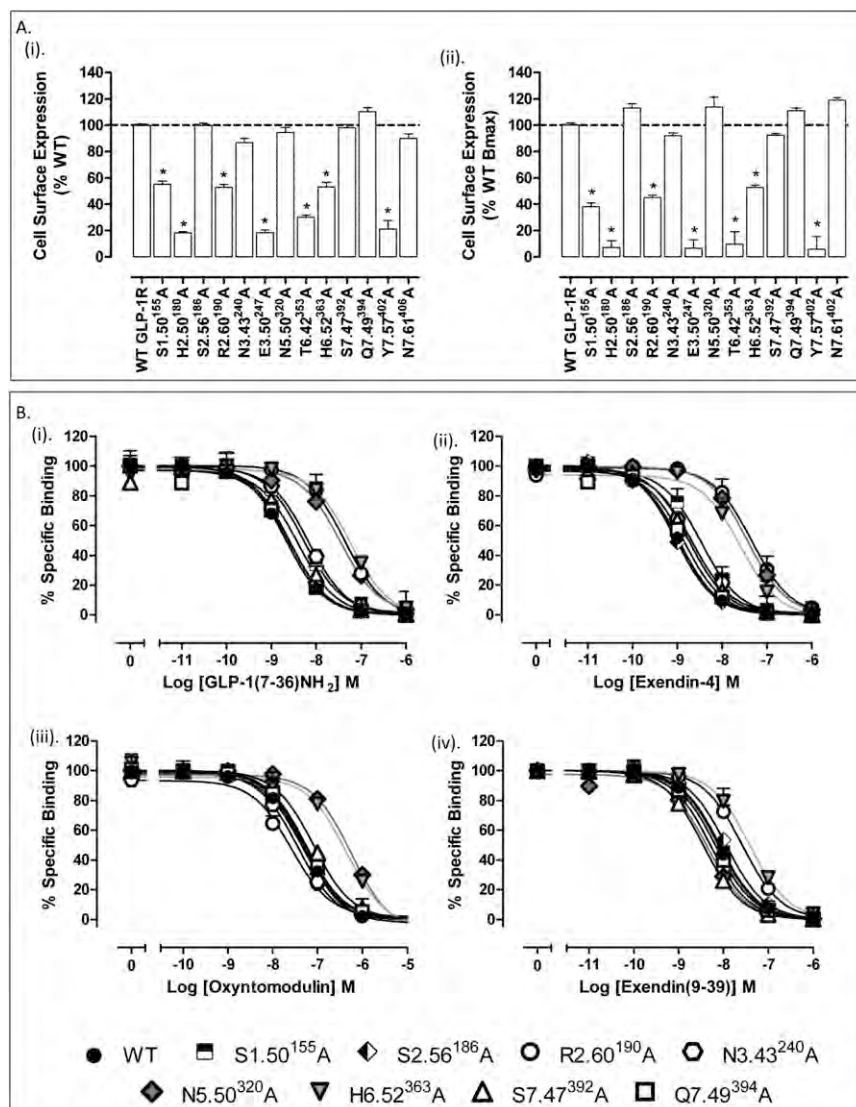


Fig. S2. Cell-surface expression and binding profiles of GLP-1R polar TM Ala mutants. (A) Cell-surface expression profiles of each of the GLP-1R polar TM mutants, compared with WT stably transfected into FlpInCHO cells as determined through antibody detection of the N-terminal c-Myc epitope label (i) and by specific [¹²⁵I]exendin (9–39) binding (ii). Statistical significance of changes in total cell-surface expression in comparison with WT expression (100%) was determined by one-way analysis of variance and Dunnett's posttest and are indicated with an asterisk (**P* < 0.05). (B) Characterization of the binding of (i) GLP-1, (ii) exendin-4, (iii) oxyntomodulin, and (iv) exendin (9–39) in competition with the radiolabeled antagonist, [¹²⁵I]exendin (9–39), in whole FlpInCHO cells stably expressing WT or mutant receptors. Data are normalized to maximum [¹²⁵I]exendin (9–39) binding, with nonspecific binding measured in the presence of 1 μM exendin (9–39). Data are analyzed with a three-parameter logistic equation as defined in Eq. S1. All values are means ± SEM of four to six independent experiments, conducted in duplicate.

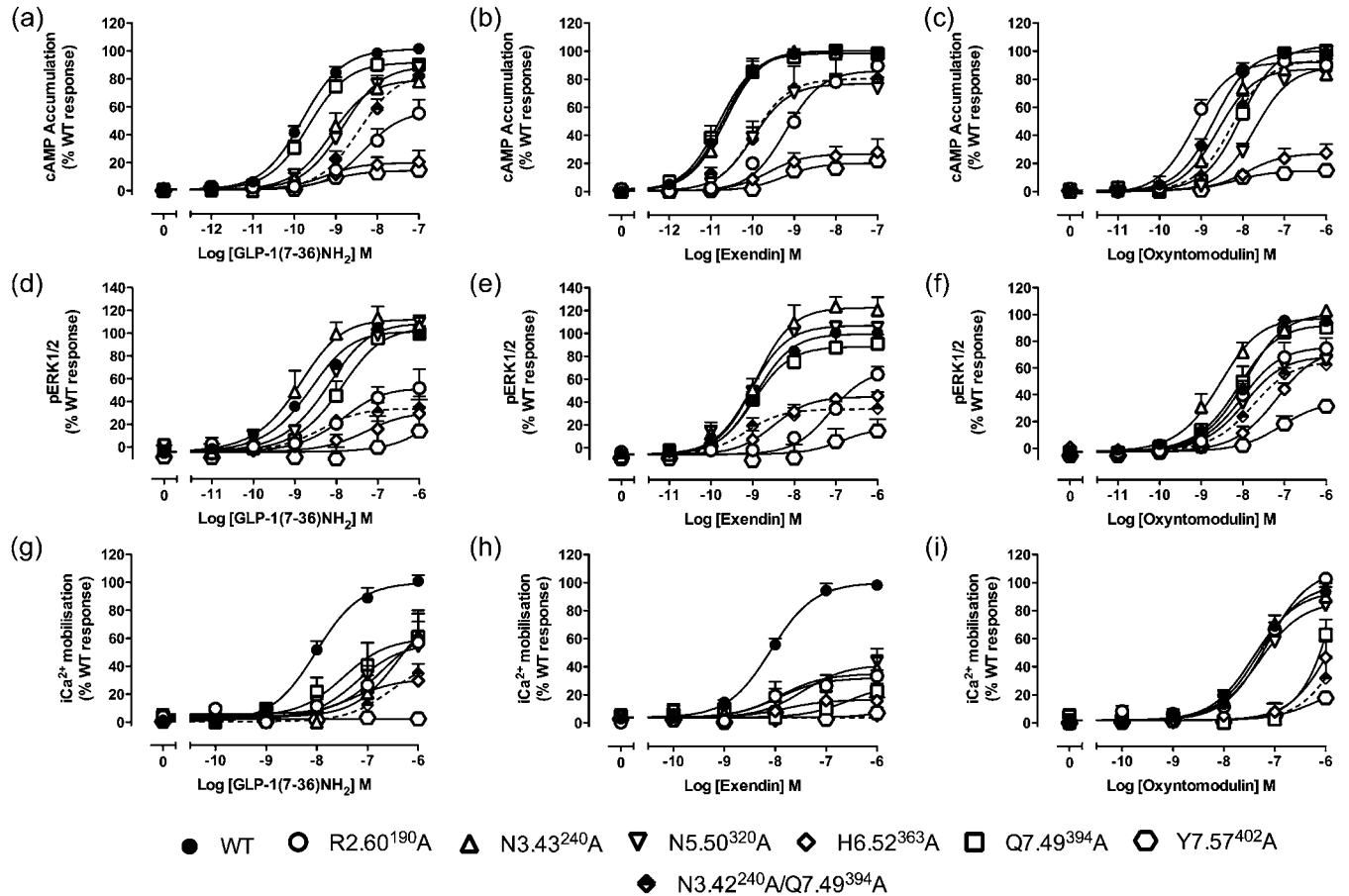




Fig. S7. Three-dimensional model of the TM bundle of GLP-1R showing interactions of polar residues with waters and other residues not mutated as part of this study and proposed mechanism of TM5 movements upon receptor activation. (A) TMs 2, 3, and 7 of the GLP-1R highlighting water-mediated hydrogen-bond interactions formed by R2.60¹⁹⁰, N3.43²⁴⁰, Q7.47³⁹⁴, and Y7.57⁴⁰² and other residues. (B) Packing interactions formed by H6.52³⁶³ (orange). (C) Aromatic packing interactions formed between Y7.57⁴⁰² (purple) and two phenylalanine residues in TM2. (D) Interactions between the cytoplasmic hydrogen-bond network and waters. (E) Proposed mechanism of TM5 movements upon receptor activation mediated by an interaction between N5.50³²⁰ and E6.53³⁶⁴. In the inactive receptor model (*Upper*), N5.50³²⁰A in TM5 interacts with E6.53³⁶⁴ in TM6. Assuming movements in the GLP-1R analogous to those observed in family A GPCRs, upon activation by ligand, TM6 movement provides the driving force for activation. The interaction between the glutamic acid in TM6 and the Asn in TM5 aids movements of TM5 with TM6 opening up a pocket on the intracellular face for G protein binding (*Lower*). Upon mutation to Ala, TM6 may still move but TM5 does not as readily move owing to a loss of this interaction.

Table S1. Interactions between mutated residues and surrounding residues/waters in the GLP-1R model

Residue	Directly interacts with	Interactions with waters	Water-mediated interactions
S1.50 ¹⁵⁵	A7.54 ³⁹⁹ (H), [G7.50 ³⁹⁵ (H)]	W13	S7.47 ³⁹²
H2.50 ¹⁸⁰	E3.50 ²⁴⁷ (E), N7.61 ⁴⁰⁶ (E)		
S2.56 ¹⁸⁶	C3.39 ²³⁶ (H), [A3.42 ²³⁹ (H)]	W9	
R2.60 ¹⁹⁰	C3.39 ²³⁶ (H), N3.43 ²⁴⁰ (E), T7.46 ³⁹¹ (E), Q7.49 ³⁹⁴ (E)	W3, W5, W9	C3.39 ²³⁶ , N3.43 ²⁴⁰ , T7.46 ³⁹¹ , Y7.57 ⁴⁰²
N3.43 ²⁴⁰	R2.60 ¹⁹⁰ (E), Q7.49 ³⁹⁴ (E), Y7.57 ⁴⁰² (E)	W5	R2.60 ¹⁹⁰
E3.50 ²⁴⁷	H2.50 ¹⁸⁰ (E)	W4, W6, W7, W12, W15	T6.42 ³⁵³ , W18
N5.50 ³²⁰	Y3.44 ²⁴¹ (A), E6.53 ³⁶⁴ (E)		
T6.42 ³⁵³		W6, W15	E3.50 ²⁴⁷
H6.52 ³⁶³	V3.40 ²³⁷ (H), L6.48 ³⁵⁹ (H), F6.56 ³⁶⁷ (H), F7.45 ³⁹⁰ (H), Q7.49 ³⁹⁴ (A)	W8	
S7.47 ³⁹²	Y1.47 ¹⁵² (E)	W2	Y1.47 ¹⁵² , D2.68 ¹⁹⁸
Q7.49 ³⁹⁴	R2.60 ¹⁹⁰ (E), N3.43 ²⁴⁰ (E), H6.52 ³⁶³ (A)		
Y7.57 ⁴⁰²	F2.54 ¹⁸⁴ (A), F2.57 ¹⁸⁷ (A), N3.43 ²⁴⁰ (E), W3.46 ²⁴³ (A)	W9	R2.60 ¹⁹⁰ , C3.39 ²³⁶
N7.61 ⁴⁰⁶	H2.50 ¹⁸⁰ (E)	W16	

Based on the generated GLP-1R model (which contained 21 buried water molecules), the interactions of each of the mutated residues with other amino acids and waters are presented. This includes electrostatic interactions (e.g., hydrogen bonds and charge attraction) (E), aromatic π interactions (A), and hydrophobic interactions (Van der Waals forces) (H). Residues in brackets reside very close in the model but do not directly interact.

Mutant and WT GLP-1Rs were stably expressed in CHO/Pln cells and dose-response curves were generated for each construct in each pathway for the three agonists. All data were analyzed with an operational model of agonism (Eq. S2) to determine log_r values. All log_r values were corrected to cell-surface expression data from the ELISA (log_r). Values are expressed as mean ± SEM of four to six independent experiments, conducted in duplicate. Data were analyzed with one-way analysis of variance and Dunnett's posttest (**P* < 0.05). ND, data were unable to be experimentally defined.

$\Delta \log R_n$ relative to WT

Data were analyzed using an operational model of agonism as defined in Eq. S4 to estimate $\log \tau_c/K_A$ ratios, where τ_c is an index of signaling efficacy of the receptor for a given pathway and K_A is the equilibrium dissociation constant of the agonist. Changes in $\log \tau_c/K_A$ ratios with respect to WT ($\Delta \log \text{Rn} [(\log \tau_c/K_A)_{\text{mutant}} - (\log \tau_c/K_A)_{\text{WT}}]$) were calculated to provide a measure of the degree of stimulus bias exhibited by mutant receptors across the three pathways relative to that of the control receptor (WT). Values are expressed as means \pm SEM of four to six independent experiments, conducted in duplicate. Data were analyzed with one-way analysis of variance and Dunnett's posttest ($*P < 0.05$). ND, data were unable to be experimentally defined.

Differential Activation and Modulation of the Glucagon-Like Peptide-1 Receptor by Small Molecule Ligands[§]

Denise Wootten, Emilia E. Savage, Francis S. Willard, Ana B. Bueno, Kyle W. Sloop, Arthur Christopoulos, and Patrick M. Sexton

Drug Discovery Biology, Monash Institute of Pharmaceutical Sciences and Department of Pharmacology, Monash University, Parkville, Victoria, Australia (D.W., E.E.S., A.C., P.M.S.); Endocrine Discovery (K.W.S.) and Translational Science and Technologies (F.S.W.), Lilly Research Laboratories, Eli Lilly and Company, Indianapolis, Indiana; Centro de Investigación Lilly, Eli Lilly and Company, Alcobendas, Spain (A.B.B.)

Received December 17, 2012; accepted January 24, 2013

ABSTRACT

The glucagon-like peptide-1 receptor (GLP-1R) is a major therapeutic target for the treatment of type 2 diabetes due to its role in glucose homeostasis. Despite the availability of peptide-based GLP-1R drugs for treatment of this disease, there is great interest in developing small molecules that can be administered orally. The GLP-1R system is complex, with multiple endogenous and clinically used peptide ligands that exhibit different signaling biases at this receptor. This study revealed that small molecule ligands acting at this receptor are differentially biased to peptide ligands and also from each other with respect to the signaling pathways that they activate. Furthermore, allosteric small molecule ligands were also able to induce bias in signaling mediated by orthosteric ligands. This was dependent on both the orthosteric and allosteric

ligand as no two allosteric-orthosteric ligand pairs could induce the same signaling profile. We highlight the need to profile compounds across multiple signaling pathways and in combination with multiple orthosteric ligands in systems such as the GLP-1R where more than one endogenous ligand exists. In the context of pleiotropic coupling of receptors and the interplay of multiple pathways leading to physiologic responses, profiling of small molecules in this manner may lead to a better understanding of the physiologic consequences of biased signaling at this receptor. This could enable the design and development of improved therapeutics that have the ability to fine-tune receptor signaling, leading to beneficial therapeutic outcomes while reducing side effect profiles.

Introduction

Type 2 diabetes mellitus and its associated obesity are predominantly characterized by a decrease in peripheral tissue response to insulin in association with impaired pancreatic β -cell function that results in an increase in fasting glycemia (DeFronzo, 1992). The incretin hormone, glucagon-like peptide-1 (GLP-1) has well established effects on pancreatic β -cell insulin secretion and, despite a reduction in secreted levels of this hormone in diabetic patients, it retains its potent insulinotropic activity. This action combined with a number of other important effects, including reduction in glucagon secretion, delayed gastric emptying, induction of satiety, and increasing pancreatic β -cell mass, have attracted

significant interest in GLP-1 and related analogs for the treatment of type 2 diabetes mellitus (Drucker and Nauck, 2006).

GLP-1 exerts its effects by binding to the GLP-1 receptor (GLP-1R), which belongs to the family B subclass of the G protein-coupled receptor (GPCR) superfamily. In recent years, it has become clear that individual GPCRs can exist in multiple receptor conformations and can elicit numerous functional responses, both G protein- and non-G protein-mediated. This has led to the discovery that different ligands can stabilize distinct subsets of receptor conformations that can “traffic” stimulus to diverse functional outputs with varying prominence, a concept referred to as biased agonism (also known as functional selectivity, stimulus bias or ligand-directed signaling) (Kenakin, 2011). The GLP-1R is predominantly expressed in pancreatic β -cells and mediates its effects through coupling primarily to G_{α_s} , resulting in an increase in cAMP, cell depolarization and an increase in

This work was funded by National Health and Medical Research Council project [Grants 1002180 and 519461].
dx.doi.org/10.1124/mol.112.084525.

[§] This article has supplemental material available at molpharm.aspetjournals.org.

ABBREVIATIONS: β -Arr, beta arrestin; BETP, 4-(3-benzyloxyphenyl)-2-ethylsulfanyl-6-(trifluoromethyl)pyrimidine; Boc5, 1,3-bis [[4-(tert-butoxy-carbonylamino)benzoyl]amino]-2,4-bis[3-methoxy-4-(thiophene-2-carboxyloxy)-phenyl]cyclobutane-1,3-dicarboxylic acid; BRET, bioluminescence resonance energy transfer; BSA, bovine serum albumin; CHO, Chinese hamster ovary; Compound 2, 6,7-dichloro-2-methylsulfonyl-3-tert-butylaminoquinoline; ERK1/2, extracellular signal-related kinases 1 and 2; FBS, fetal bovine serum; Forskolin, (3R,4aR,5S,6S,6aS,10S,10aR,10bS)-6,10,10b-trihydroxy-3,4a,7,7,10a-pentamethyl-1-oxo-3-vinyldodecahydro-1H-benzo[f]chromen-5-yl acetate; GLP-1, glucagon-like peptide; GLP-1R, glucagon-like peptide-1 receptor; GPCR, G protein-coupled receptor; iCa^{2+} , intracellular calcium; TT15, (2S)-2-[[[(8S)-7-benzoyl-3-[4-[(3,4-dichlorophenyl)methoxy]phenyl]-2-oxo-1,6,8,9-tetrahydropyrido[4,3-g][1,4]benzoxazine-8-carbonyl]amino]-3-[4-(4-cyanophenyl)phenyl]propanoic acid.

cytosolic calcium that ultimately promotes insulin secretion (Drucker et al., 1987; Holz et al., 1993). Although cAMP formation is a critical component of GLP-1R-mediated signaling required for insulin secretion, there are also roles of other signaling pathways in augmentation of insulin responses. In addition to cAMP formation, activated GLP-1Rs can promote epidermal growth factor receptor transactivation (Buteau et al., 2003), phosphatidylinositol 3 kinase activity, insulin receptor substrate-2 signaling (Park et al., 2006), extracellular signal-regulated kinase 1 and 2 (ERK1/2) activity (Montrose-Rafizadeh et al., 1999), mobilization of intracellular calcium (iCa^{2+}) (Baggio and Drucker, 2007), as well as nuclear translocation of protein kinase C to mediate β -cell proliferation and differentiation and promote insulin gene transcription (Buteau et al., 2003). Recent studies also support an essential role of β -arrestins in downstream GLP-1R-mediated insulin secretion (Sonoda et al., 2008; Quoyer et al., 2010). Although some of these pathways have been linked to therapeutically relevant outputs, such as insulin secretion and β -cell survival, the underlying GLP-1R-mediated signaling required for therapeutically beneficial effects, such as delaying gastric emptying and inducing satiety, are not fully understood.

Currently, approved therapeutics acting at the GLP-1R are peptide-based; however, there is substantial interest in development of small molecule drugs. In recent years, an increasing number of reports have shown discovery of structurally diverse small molecule agonists of the GLP-1R (Willard et al., 2012a). These include (but are not limited to) a series of quinoxalines, the best characterized being Compound 2 (6,7-dichloro-2-methylsulfonyl-3-tert-butylaminoquinoxaline), a series of pyrimidines, the best characterized being BETP (4-(3-benzoyloxyphenyl)-2-ethylsulfinyl-6-(trifluoromethyl)pyrimidine), substituted cyclobutanes such as Boc5 (1,3-bis[[4-(tert-butoxy-carbonylamino)benzoyl]amino]-2,4-bis[3-methoxy-4-(thiophene-2-carbonyloxy)-phenyl]cyclobutane-1,3-dicarboxylic acid), and a series of compounds reported in patents by Transtech Pharma. In addition to displaying agonism in their own right, small molecule compounds that bind allosterically to the GLP-1R have the potential to modulate the function of endogenous hormones, allowing fine control of receptor function and/or spatial and temporal elements of endogenous orthosteric peptide signaling. There are many orthosteric peptide agonists of the GLP-1R, including multiple endogenous ligands, as well as several peptides that are used therapeutically or are in clinical trials (Baggio and Drucker, 2007). All peptide agonists studied to date preferentially activate cAMP over ERK1/2 and iCa^{2+} mobilization in vitro (Koole et al., 2010). However, the relative degree of bias is variable between ligands, with truncated GLP-1 peptides and exendin-4 having greater bias toward cAMP than full-length GLP-1 peptides and oxyntomodulin (Koole et al., 2010). In addition, allosteric ligands can differentially alter the signaling profile mediated by these endogenous peptides and can therefore induce biased signaling in a peptide-specific manner.

While most of the small molecules developed to date are not drug-like compounds, they may represent pharmacophores that can be further optimized for clinical evaluation. They also provide us with a range of useful research tools that can be used to help understand the mechanism by which these small

molecules bind and exert their physiologic effects. In this study, we used an analytical approach, investigating the signaling of the GLP-1R across multiple signaling pathways to assess and quantify stimulus bias for a range of low molecular weight ligands (both peptide and nonpeptide). The ability of these small ligands to act allosterically to modulate the responses and bias of distinct orthosteric peptide ligands was also assessed.

Materials and Methods

Materials. Small molecule GLP-1 ligands BETP (Sloop et al., 2010), Compound 2 (Knudsen et al., 2007), Boc5 (Chen et al., 2007), [(2S)-2-[[[(8S)-7-benzoyl-3-[4-[(3,4-dichlorophenyl)methoxy]phenyl]-2-oxo-1,6,8,9-tetrahydropyrido[4,3-g][1,4]benzoxazine-8-carbonyl]amino]-3-[4-(4-cyanophenyl)phenyl]propanoic acid] (TT15) (Rao, 2009), and BMS21 (Mapelli et al., 2009) were synthesized according to literature and standard methods (see Supplemental Data, experimental procedure for more details). GLP-1(7–36) NH_2 , GLP-1(1–36) NH_2 , exendin-4, and oxyntomodulin were purchased from American Peptide Company (Sunnyvale, CA). Dulbecco's modified Eagle's medium and Fluo-4 AM were purchased from Invitrogen (Carlsbad, CA). Fetal bovine serum (FBS) was purchased from Thermo Electron Corporation (Melbourne, VIC, Australia). AlphaScreen reagents, 96-well UniFilter GF/C filter plates, 384-well Proxiplates, and Microscint 40 scintillant were purchased from PerkinElmer Life and Analytical Sciences (Waltham, MA). SureFire ERK1/2 reagents were obtained from TGR Biosciences (Adelaide, SA, Australia). All other reagents were purchased from Sigma-Aldrich (St. Louis, MO) or BDH Merck (Melbourne, VIC, Australia) and were of an analytical grade.

Transfections and Cell Culture. Human GLP-1Rs were isogenically integrated into Flp-In-Chinese hamster ovary (Flp-In-CHO) cells (Invitrogen) and selection of receptor-expressing cells accomplished by treatment with 600 μ g/ml hygromycin-B as previously described (May et al., 2007). Transfected and parental Flp-In-CHO cells were maintained in Dulbecco's modified Eagle's medium supplemented with 10% heat-inactivated FBS and incubated in a humidified environment at 37°C in 5% CO_2 .

Radioligand Binding Assay. Flp-In-CHO GLP-1R cells were seeded at a density of 3×10^4 cells/well into 96-well culture plates and incubated overnight at 37°C in 5% CO_2 , and radioligand binding carried out as previously described (Koole et al., 2011). For each cell line in all experiments, total binding was defined by 0.5 nM [^{125}I]-exendin(9–39) alone, and nonspecific binding was defined by 1 μ M exendin(9–39). For analysis, data are normalized to the specific binding for each individual experiment.

cAMP Accumulation Assay. Flp-In-CHO wild-type and mutant human GLP-1R cells were seeded at a density of 3×10^4 cells/well into 96-well culture plates and incubated overnight at 37°C in 5% CO_2 , and cAMP detection carried out using the PerkinElmer AlphaScreen kit, as previously described (Koole et al., 2010). All values were converted to concentration of cAMP using a cAMP standard curve performed in parallel, and data were subsequently normalized to the response of 100 μ M forskolin.

pERK1/2 Assay. Flp-In-CHO GLP-1R cells were seeded at a density of 3×10^4 cells/well into 96-well culture plates and incubated overnight at 37°C in 5% CO_2 . Receptor-mediated pERK1/2 was determined using the AlphaScreen ERK1/2 SureFire protocol as previously described (May et al., 2007). Initial pERK1/2 time course experiments were performed over 1 hour to determine the time at which agonist-mediated pERK1/2 was maximal. Subsequent experiments were then performed at the time required to generate a maximal pERK1/2 response (7 minutes). Data were normalized to the maximal response elicited by 10% FBS determined at 6 minutes (peak FBS response).

Intracellular Ca^{2+} Mobilization Assay. Flp-In-CHO GLP-1R cells were seeded at a density of 3×10^4 cells/well into 96-well culture

plates and incubated overnight at 37°C in 5% CO₂, and receptor-mediated iCa²⁺ mobilization determined as previously described (Werry et al., 2005). Fluorescence was determined immediately after ligand addition, with an excitation wavelength set to 485 nm and an emission wavelength set to 520 nm, and readings taken every 1.36 seconds for 120 seconds. Peak magnitude was calculated using five-point smoothing, followed by correction against basal fluorescence. The peak value was used to create concentration-response curves. Data were normalized to the maximal response elicited by 100 μM ATP.

β-Arrestin Recruitment Assays. Flp-In-CHO cell lines stably expressing GLP-1 receptor-Rluc8 and either β-arrestin (β-Arr)1- or β-Arr2-Venus were generated using gateway technology as previously described (Willard et al., 2012b). Cells were seeded in 96-well white culture plates at a density of 40,000 cells/well and cultured for 24 hours. Cells were rinsed once with Hanks' balanced salt solution to remove traces of phenol red and incubated in fresh Hanks' balanced salt solution for a further 15 minutes. The Rluc substrate coelenterazine-h was added to reach a final concentration of 5 μM. After a 5-minute incubation, the corresponding agonist was added and bioluminescence resonance energy transfer (BRET) readings were collected using a LumiSTAR Omega instrument (BMG Labtech, Ortenberg, Germany) that allows sequential integration of signals detected in the 465–505- and 515–555-nm windows using filters with the appropriate band pass. The BRET signal was calculated by subtracting the ratio of 515–555-nm emission over 465–505-nm emission for a vehicle-treated cell sample from the same ratio for the ligand-treated cell sample. In this calculation, the vehicle-treated cell sample represents background, and results are expressed as ligand-induced BRET. This eliminates the requirement for measuring a donor-only control sample. Initial time course experiments were performed over 20 minutes to determine the time at which β-Arr1 and β-Arr2 recruitment was maximal for each ligand in the absence and presence of BETP. Coaddition of ligands was performed for interaction assays and BRET signals were collected at this peak time point.

Data Analysis. Data were analyzed using Prism 5.03 (GraphPad, La Jolla, CA) using the three-parameter logistic equation or an operation model of allosteric agonism.

Allosteric modulator-inhibition binding data were fitted to the following allosteric-ternary complex model. In this case, nondepletion of ligands was assumed (Avlani et al., 2008):

$$Y = \frac{B_{\max} \times [A]}{[A] + K_{APP}} + NS \quad (1)$$

where

$$K_{APP} = \frac{K_A \times K_B}{\alpha \times [B] + K_B} \times \frac{1 + [I]/K_I + [B]/K_B + (\alpha' \times [I] \times [B])}{K_I \times K_B} \quad (2)$$

where Y represents radioligand binding, B_{\max} denotes maximal binding site density, and NS denotes the fraction of nonspecific binding. $[A]$ and K_{APP} denote the concentration of radioligand and equilibrium dissociation constant for the radioligand, respectively. $[B]$ and K_B denote the concentration of allosteric ligand and equilibrium dissociation constant for the allosteric ligand, respectively. $[I]$ and K_I denote the concentration of peptide agonist used in competition with the radioligand and the equilibrium dissociation constant for the peptide agonist, respectively. α and α' represent cooperativity factors, which are defined as the allosteric interaction of the modulator with the radioligand, and modulator with the peptide agonist, respectively. Values of α or $\alpha' > 1$ are indicative of an allosteric-mediated increase in binding activity, while values of $0 < \alpha$ or $\alpha' < 1$ are indicative of an allosteric-mediated decrease in binding affinity.

To compare agonist profiles and quantify stimulus bias (functional selectivity) between the different ligands, agonist concentration-response curves were fitted to the following form of the operational

model of agonism ((Black and Leff, 1983; Koole et al., 2010; Evans et al., 2011),

$$Y = basal + \frac{(E_m - basal) \left(\frac{\tau}{K_A} \right)^n [A]^n}{[A]^n \left(\frac{\tau}{K_A} \right)^n + \left(1 + \frac{[A]}{K_A} \right)^n} \quad (3)$$

where E_m is the maximal possible response of the system; $basal$ is the basal level of response; K_A denotes the equilibrium dissociation constant of the agonist (A); τ is an index of the signaling efficacy of the agonist and is defined as R_T/K_E , where R_T is the total number of receptors and K_E is the coupling efficiency of each agonist-occupied receptor; and n is the slope of the transducer function that links occupancy to response. The analysis assumes that the maximal system responsiveness (E_m) and the transduction machinery used for a given cellular pathway are the same for all agonists, such that the E_m and transducer slope (n) are shared between agonists. The ratio, τ/K_A (determined as a logarithm, i.e., $\log(\tau/K_A)$) is referred to herein as the “transduction coefficient” (Kenakin et al., 2012), as this composite parameter is sufficient to describe agonism and bias for a given pathway, i.e., stimulus-biased agonism can result from either a selective affinity (K_A^{-1}) of an agonist for a given receptor state(s) and/or a differential coupling efficacy (τ) toward certain pathways. To cancel the impact of cell-dependent effects on the observed agonism at each pathway, the $\log(\tau/K_A)$ values were then normalized to that determined for the endogenous agonist, GLP-1(7–36)NH₂, at each pathway to yield a “normalized transduction coefficient,” $\Delta\log(\tau/K_A)$, i.e., $\Delta\log(\tau/K_A) = \log(\tau/K_A)_{\text{test}} - \log(\tau/K_A)_{\text{GLP-1(7-36)NH}_2}$. Finally, to determine the actual bias of each agonist for different signaling pathways, the $\Delta\log(\tau/K_A)$ values were evaluated statistically between the pathways. The ligand bias of an agonist for one pathway, $j1$, over another, $j2$, is given as

$$Bias = 10^{\Delta\log\left(\frac{\tau}{K_A}\right)_{j1-j2}} \quad (4)$$

where

$$\Delta\log\left(\frac{\tau}{K_A}\right)_{j1-j2} = \log(bias) = \Delta\log\left(\frac{\tau}{K_A}\right)_{j1} - \Delta\log\left(\frac{\tau}{K_A}\right)_{j2} \quad (5)$$

A lack of functional selectivity will thus result in bias values not substantially different from the value of 1 between pathways and, hence, $\log(bias)$ values not significantly different from zero. To account for the propagation of error associated with the determination of composite parameters, the following equation was used.

$$Pooled\ SE = \sqrt{(SE2)^1 + (SE2)^2} \quad (6)$$

In cell-signaling ligand interaction studies, data were fitted to the following two forms of an operational model of allosterism and agonism to derive functional estimates of modulator affinity and cooperativity (Leach et al., 2007; Aurelio et al., 2009)

$$E = \frac{E_m(\tau_A[A](K_B + \alpha\beta[B]) + \tau_B[B]EC_{50})^n}{EC_{50}^n(K_B + [B])^n + (\tau_A[A](K_B + \alpha\beta[B]) + \tau_B[B]EC_{50})^n} \quad (7)$$

$$E = \frac{E_m(\tau_A[A](K_B + \alpha\beta[B]) + \tau_B[B]K_A)^n}{([A]K_B + K_AK_B + [B]K_A + \alpha[A][B])^n + (\tau_A[A](K_B + \alpha\beta[B]) + \tau_B[B]K_A)^n} \quad (8)$$

where E_m is the maximum attainable system response for the pathway under investigation, $[A]$ and $[B]$ are the concentrations of orthosteric agonist and allosteric modulator/agonist, respectively, K_B is the dissociation constant of the allosteric modulator, EC_{50} is the concentration of orthosteric (full) agonist yielding 50% of the response between minimal and maximal receptor activation in the absence of

allosteric ligand, n is a transducer slope factor linking occupancy to response, α is the binding cooperativity factor, β is an empirical scaling factor describing the allosteric effect of the modulator on orthosteric agonist signaling efficacy, respectively, and τ_A and τ_B are operational measures of the ligands' respective signaling efficacies that incorporate receptor expression levels and efficiency of stimulus-response coupling. Equation 4 was used in interaction studies performed between allosteric ligand (BETP) and a full agonist (in cAMP and pERK1/2 assays), while eq. 5 was used when the BETP was interacted with a partial agonist (in iCa^{2+} , β -Arr1, and β -Arr2 assays). This is so because eq. 4 is only valid in cases where the orthosteric agonist has high efficacy ($\tau \gg 1$) such that K_A is $\gg [A]$.

Statistics. All data are represented as mean \pm S.E.M. and were compared using analysis of variance followed by Dunnett's test. Repeated measures analysis of variance was used to assess the statistical significance between time courses. The null hypothesis was rejected at $P < 0.05$.

Results

Small Molecules Ligands and Peptides Differentially Couple the GLP-1R to Cellular Effectors. The ability of a GPCR to couple to multiple intracellular signaling components is a requirement for stimulus bias. Like most GPCRs, the GLP-1R couples to different classes of heterotrimeric G proteins, including G_{α_s} , G_{α_q} , and G_{α_i} , as

well as various other signaling and regulatory proteins such as the β -Arrs. In this study, the selective GLP-1R small molecules, BETP (Sloop et al., 2010), Compound 2 (Knudsen et al., 2007), TT15 (Rao, 2009), Boc5 (Chen et al., 2007), and a modified GLP-1 analog (BMS21) (Mapelli et al., 2009) (Fig. 1) were assessed for their ability to activate various intracellular signaling pathways. These included cAMP (as a surrogate of canonical G_{α_s} coupling), iCa^{2+} mobilization (as a measure of G_{α_q} , and to some extent G_{α_i} coupling), pERK1/2 [as a downstream measure of various convergent pathways (G protein and non-G protein-mediated)], and recruitment of the regulatory proteins β -Arr1 and β -Arr2.

GLP-1(7–36)NH₂ can activate all five of these signaling/regulatory pathways in the Flp-In-CHO GLP-1R cell line selected for this study; however, none of the small molecules or the 11-mer peptide (BMS21) tested were able to fully mimic the actions of the native peptide ligand (Fig. 2; Table 1). BMS21 had a much lower potency than GLP-1(7–36)NH₂; however, this ligand displayed higher efficacy for cAMP signaling with an increased E_{\max} (Fig. 2; Table 1). Interestingly, this small peptide displayed a similar potency in pERK1/2 and iCa^{2+} -mobilization assays as in the cAMP assay; however, in these instances the observed E_{\max} was dramatically lower than that of GLP-1(7–36)NH₂. In addition, BMS21

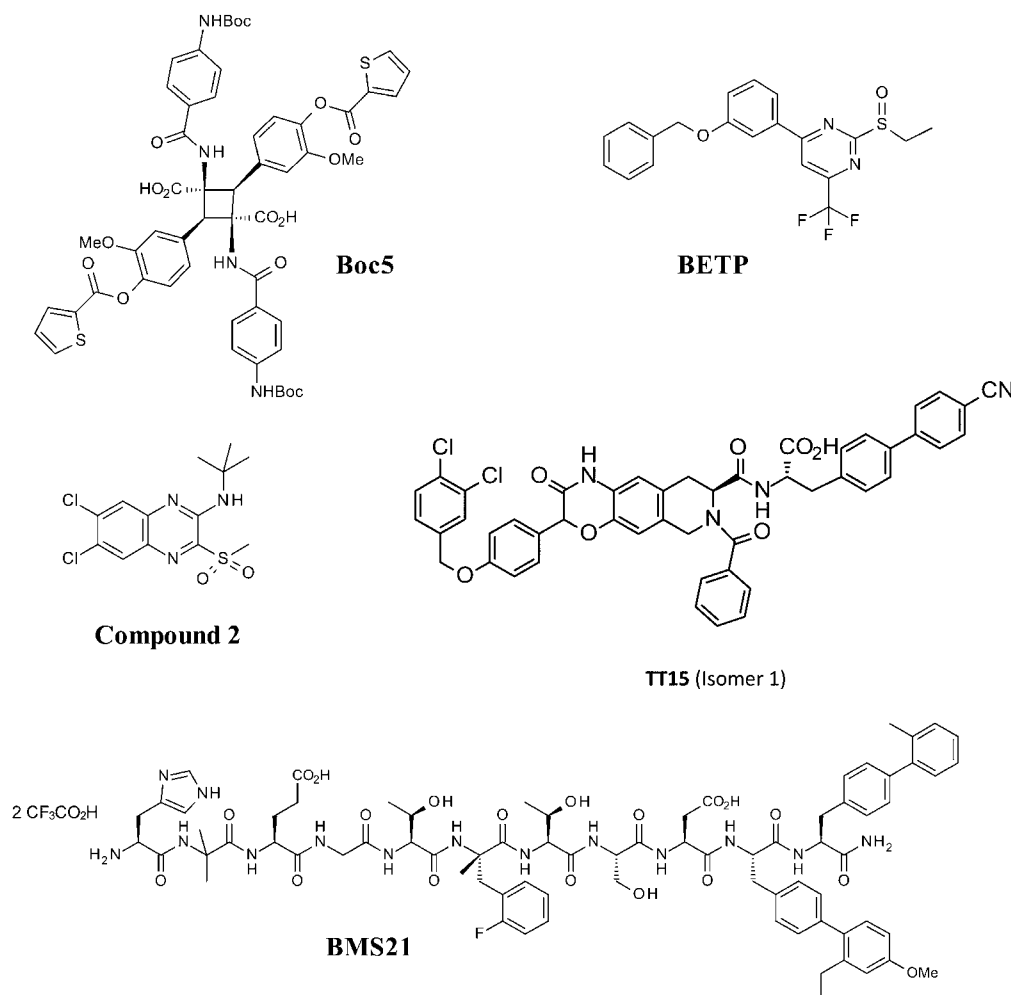


Fig. 1. Small molecule ligand structures. Structures of small molecule ligands used in this study.

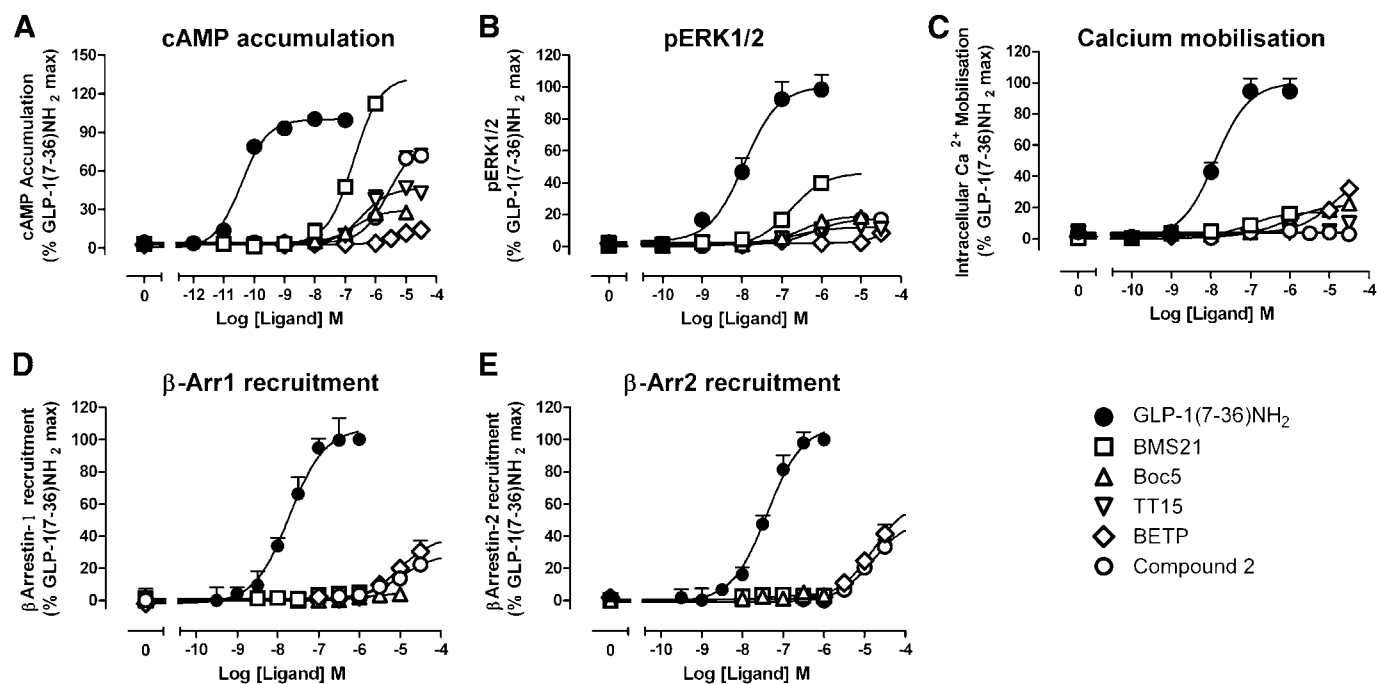


Fig. 2. Signaling profiles of GLP-1R ligands. Dose response curves for cAMP accumulation (A), pERK1/2 (B), iCa^{2+} mobilization (C), β -Arr1 recruitment (D), and β -Arr2 (E) recruitment for GLP-1(7–36)NH₂, BMS21, Boc5, TT15, BETP, and Compound 2. Data are normalized to the response elicited by GLP-1(7–36)NH₂ and analyzed using a three-parameter logistic equation. All values are means \pm S.E.M. of three to four independent experiments conducted in duplicate.

was unable to recruit β -Arrest within the tested concentration range (Fig. 2; Table 1) suggesting that although this peptide is similar to the N-terminal portion of the native ligand, this in itself is insufficient to mimic the functions of full length GLP-1(7–36)NH₂.

In agreement with previous studies, the nonpeptidic compound Boc5 was able to increase cAMP with a lower potency and efficacy than GLP-1(7–36)NH₂ and BMS21 (Fig. 2A; Table 1). Boc5 also had similar efficacy in pERK1/2 and iCa^{2+} -mobilization assays. No β -Arr recruitment could be

detected for this ligand. TT15 displayed a similar potency but a marginally higher E_{max} for cAMP signaling compared with Boc5; however, it displayed a weaker pERK1/2 response and no iCa^{2+} mobilization was detectable (Fig. 2; Table 1). Unfortunately, this ligand nonspecifically interfered with BRET assay for β -Arr recruitment and therefore characterization of TT15 for β -Arr recruitment could not be performed. Compound 2 and BETP are low potency agonists for cAMP accumulation with BETP displaying weak partial agonism and Compound 2 strong partial agonism. Both compounds

TABLE 1

Differential effects of peptide/small molecule agonists of the human GLP-1R in cAMP accumulation, iCa^{2+} mobilization, pERK1/2, and β -arrestin1 and β -arrestin2 recruitment in Flp-In-CHO cells stably expressing the human GLP-1R

pEC₅₀ values are the negative logarithm of the concentration of agonist that produces half the maximal response. E_{max} represents the maximal response normalized to that of GLP-1(7–36)NH₂. All values are mean \pm S.E.M. of three to five independent experiments conducted in duplicate.

Signaling Pathway		Ligand					
		GLP-1(7–36)NH ₂	BMS21	Boc5	TT15	BETP	Compound 2
cAMP	pEC ₅₀	10.4 \pm 0.1	6.7 \pm 0.6	6.7 \pm 0.2	6.5 \pm 0.2	5.2 \pm 0.2	5.6 \pm 0.1
	E_{max}	100 \pm 2	132 \pm 6	30 \pm 2	46 \pm 3	17 \pm 2	81 \pm 4
pERK1/2	pEC ₅₀	7.9 \pm 0.1	6.8 \pm 0.1	6.5 \pm 0.1	6.7 \pm 0.3	NR	6.2 \pm 0.1
	E_{max}	100 \pm 5	46 \pm 2	19 \pm 1	12 \pm 1	NR	18 \pm 1
iCa^{2+}	pEC ₅₀	7.9 \pm 0.1	7.0 \pm 0.3	6.0 \pm 0.3	NR	5 \pm 0.3	NR
	E_{max}	100 \pm 5	17 \pm 3	22 \pm 2	NR	42 \pm 10	NR
β -Arr1	pEC ₅₀	7.7 \pm 0.1	NR	NR	ND	5.0 \pm 0.2	5.0 \pm 0.2
	E_{max}	100 \pm 6	NR	NR	ND	40 \pm 7	30 \pm 5
β -Arr2	pEC ₅₀	7.4 \pm 0.1	NR	NR	ND	5.0 \pm 0.3	4.8 \pm 0.2
	E_{max}	100 \pm 5	NR	NR	ND	63 \pm 15	51 \pm 0.2

β -Arr, beta arrestin; BETP, 4-(3-benzyloxyphenyl)-2-ethylsulfinyl-6-(trifluoromethyl)pyrimidine; Boc5, 1,3-bis[[4-(tert-butoxy-carbonylamino)benzoyl]amino]-2,4-bis[3-methoxy-4-(thiophene-2-carbonyloxy)-phenyl]cyclobutane-1,3-dicarboxylic acid; Compound 2, 6,7-dichloro-2-methylsulfonyl-3-tert-butylaminoquinoxaline; ERK1/2, extracellular signal-related kinases 1 and 2; iCa^{2+} , intracellular calcium; ND, not detected; NR, no response; TT15, (2S)-2-[[[(8S)-7-benzoyl-3-[4-[(3,4-dichlorophenyl)methoxy]phenyl]-2-oxo-1,6,8,9-tetrahydropyrido[4,3-g][1,4]benzoxazine-8-carbonyl]amino]-3-[4-(4-cyanophenyl)phenyl]propanoic acid.

also displayed weak partial agonism in pERK1/2; however, in the case of BETP this was barely detectable within the concentration range assessed. Compound 2 displayed no detectable $i\text{Ca}^{2+}$ response; however, BETP was an agonist for this pathway with an EC_{50} similar to that observed for its cAMP response, and with an E_{max} of $42 \pm 10\%$ of that of GLP-1(7–36) NH_2 . However, both ligands were weak agonists for β -Arr1 and β -Arr2 recruitment with E_{max} estimates of 30–40% of the response of GLP-1(7–36) NH_2 (Fig. 2; Table 1).

These effects on ligand bias can be readily observed in bias plots, which display the response observed to equimolar concentrations of ligand for one pathway relative to another (Fig. 3). More importantly, this relative bias can be quantified by calculation of bias factors to compare relative bias to the reference ligand, in this case the primary endogenous ligand GLP-1(7–36) NH_2 (Table 2). It is apparent for all of the small molecule ligands that the GLP-1R shows less preference for coupling to cAMP over other pathways in comparison with activation by GLP-1(7–36) NH_2 . However some ligands heavily change the relative bias. The most dramatic changes in bias are observed with activation by BETP, whereby signaling is biased toward $i\text{Ca}^{2+}$ mobilization and β -Arr1 and β -Arr2 recruitment over cAMP and pERK1/2 compared with the reference agonist (Fig. 3, B–E, H, and J; Table 2). However, little change in the relative bias between $i\text{Ca}^{2+}$ and arrestin recruitment was observed (Fig. 3F; Table 2). In contrast BMS21 biases the receptor toward pERK1/2 and

cAMP over arrestin recruitment and $i\text{Ca}^{2+}$ mobilization relative to GLP-1(7–36) NH_2 (Fig. 3, C–E; Table 2). In addition, compared with GLP-1(7–36) NH_2 , compound 2 biases the receptor conformations toward β -Arr1 and β -Arr2 recruitment relative to $i\text{Ca}^{2+}$ (where no response was observed) and cAMP (Fig. 3, F and G; Table 2).

BETP and Compound 2 Selectively Modulate the Affinity of Agonists at the GLP-1R. In agreement with our previous study, Compound 2 displayed probe dependence in that it caused a concentration-dependent increase in affinity of oxyntomodulin, but not of GLP-1(7–36) NH_2 , exendin-4, or GLP-1(1–36) NH_2 . BETP also displayed the same probe dependence with potentiation of oxyntomodulin affinity and no effect on the other three peptides (Supplemental Fig. 2). The other small molecules did not alter the competition binding profile of ^{125}I -exendin(9–39) in the presence of any peptide ligand tested (Supplemental Fig. 1).

BETP and Compound 2 Differentially Alter Peptide-Mediated GLP-1R Signaling Bias. Analysis of the interaction between BETP and orthosteric peptide ligands with the allosteric operational model revealed BETP differentially modulated GLP-1R agonist intrinsic efficacy in a ligand and pathway-dependent manner. (Figs. 4–7; Table 3). Combined affinity-efficacy ($\alpha\beta$) estimates for cAMP were consistent with affinity cooperativity estimates from the binding studies (Fig. 4; Supplemental Fig. 2; Table 3). Thus, exendin-4, GLP-1(7–36) NH_2 , and GLP-1(1–36) NH_2 displayed neutral cooperativity for both binding and cAMP accumulation,

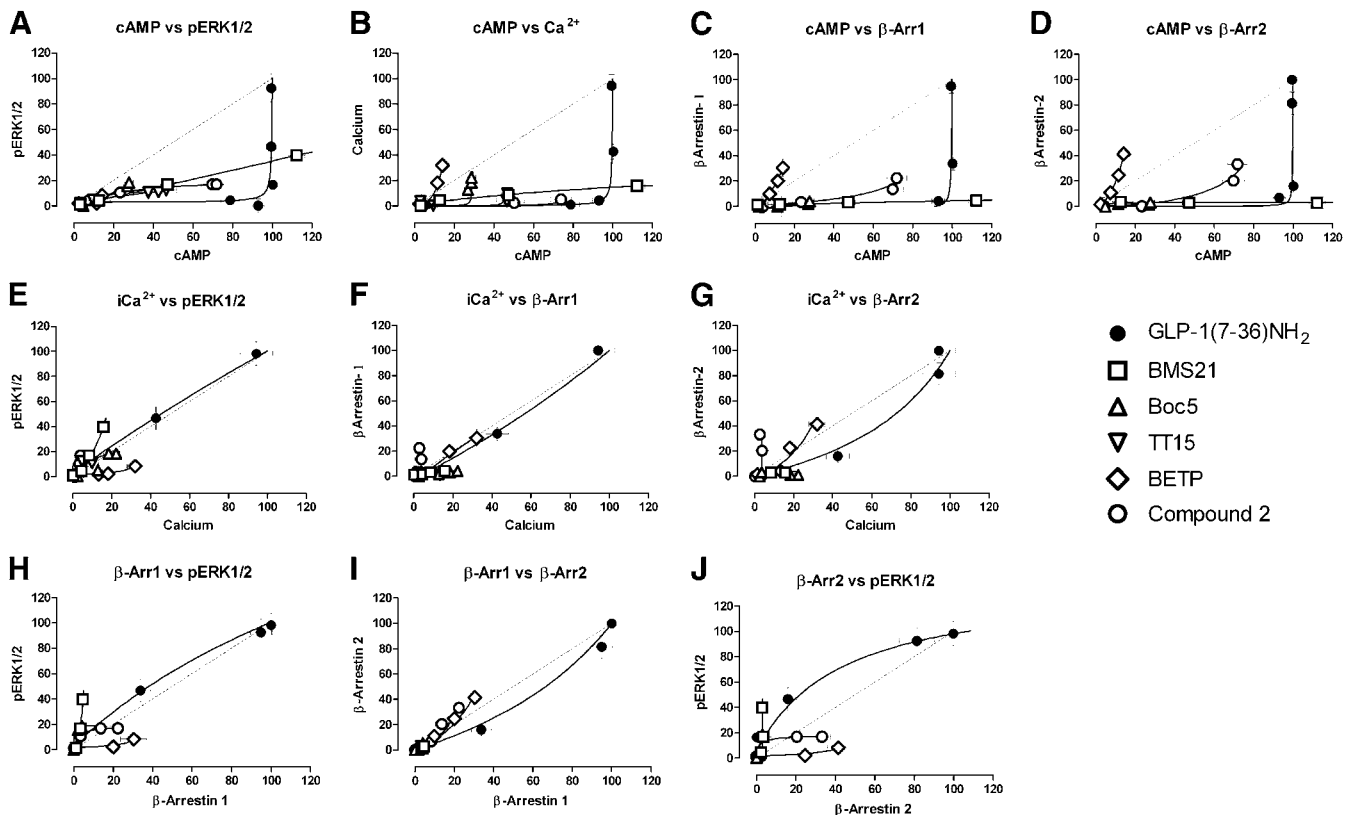


Fig. 3. Synthetic ligands display stimulus bias relative to the endogenous ligand GLP-1(7–36) NH_2 . Bias plots of cAMP versus pERK1/2 (A), cAMP versus $i\text{Ca}^{2+}$ mobilization (B), cAMP versus β -Arr1 (C), cAMP versus β -Arr2 (D), $i\text{Ca}^{2+}$ versus pERK1/2 (E), $i\text{Ca}^{2+}$ versus β -Arr1 (F), $i\text{Ca}^{2+}$ versus β -Arr2 (G), β -Arr1 versus pERK1/2 (H), β -Arr1 versus β -Arr2 (I), and β -Arr2 versus pERK1/2 (J). Data for each ligand in each pathway are normalized to the maximal response elicited by GLP-1(7–36) NH_2 , and analyzed with a three-parameter logistic equation with 150 points defining the curve.

TABLE 2

Stimulus bias exhibited by ligands relative to the reference agonist GLP-1(7–36)NH₂

Data were analyzed using an operational model of agonism as defined in eq. 4 to estimate log τ_e/K_A ratios. Changes in log τ_e/K_A ratios were calculated to provide a measure of the degree of stimulus bias exhibited between different signaling pathways relative to that of the reference agonist (GLP-1(7–36)NH₂). Values are expressed as means \pm S.E.M. of three to five independent experiments conducted in duplicate. Data were analyzed with one-way analysis of variance and Dunnett's post test.

Pathway 1: Pathway 2		Ligand					
		GLP-1(7–36)NH ₂	BMS21	Boc5	TT15	BETP	Compound 2
pERK1/2:	cAMP	0 \pm 0.11 (1)	0.83 \pm 0.34 (6.7)	1.77 \pm 0.49* (59)	1.45 \pm 0.55 (28)	1.09 \pm 0.60 (12)	1.05 \pm 0.43 (11)
	iCa ²⁺	0 \pm 0.10 (1)	0.28 \pm 0.36 (1.9)	-0.22 \pm 0.56 (0.6)	ND	-1.23 \pm 0.44 (0.06)	ND
	β -Arr1	0 \pm 0.09 (1)	ND	ND	ND	-1.39 \pm 0.46 (0.04)*	0.22 \pm 0.46 (1.7)
	β -Arr2	0 \pm 0.11 (1)	ND	ND	ND	-1.97 \pm 0.46 (0.01)*	-0.08 \pm 0.44 (0.83)
iCa:	cAMP	0 \pm 0.14 (1)	0.60 \pm 0.37 (3.9)	0.52 \pm 0.28 (3.3)	ND	1.74 \pm 0.42 (55)*	ND
	pERK1/2	0 \pm 0.10 (1)	-0.28 \pm 0.36 (0.53)	0.22 \pm 0.56 (1.6)	ND	1.23 \pm 0.44 (20)	ND
	β -Arr1	0 \pm 0.08 (1)	ND	ND	ND	-0.16 \pm 0.16 (0.70)	ND
	β -Arr2	0 \pm 0.14 (1)	ND	ND	ND	-1.22 \pm 0.16 (0.06)*	ND
β -Arr1:	cAMP	0 \pm 0.09 (1)	ND	ND	ND	2.38 \pm 0.43 (239)*	1.73 \pm 0.22 (54)*
	pERK1/2	0 \pm 0.09 (1)	ND	ND	ND	1.39 \pm 0.46 (24)*	-0.22 \pm 0.46 (0.61)
	iCa ²⁺	0 \pm 0.08 (1)	ND	ND	ND	0.16 \pm 0.16 (1.43)	ND
	β -Arr2	0 \pm 0.10 (1)	ND	ND	ND	-0.58 \pm 0.19 (0.26)	-0.3 \pm 0.24 (0.50)
β -Arr2:	cAMP	0 \pm 0.11 (1)	ND	ND	ND	2.96 \pm 0.43 (918)*	2.03 \pm 0.17 (108)*
	pERK1/2	0 \pm 0.11 (1)	ND	ND	ND	1.97 \pm 0.46 (93)*	0.08 \pm 0.44 (1.2)
	iCa ²⁺	0 \pm 0.16 (1)	ND	ND	ND	1.22 \pm 0.16 (17)*	ND
	β -Arr1	0 \pm 0.10 (1)	ND	ND	ND	0.58 \pm 0.19 (3.8)	0.3 \pm 0.24 (2.0)

β -Arr, beta arrestin; BETP, 4-(3-benzoyloxyphenyl)-2-ethylsulfinyl-6-(trifluoromethyl)pyrimidine; Boc5, 1,3-bis [[4-(tert-butoxy-carbonylamino)benzoyl]amino]-2,4-bis [3-methoxy-4-(thiophene-2-carboxyloxy)-phenyl]cyclobutane-1,3-dicarboxylic acid; Compound 2, 6,7-dichloro-2-methylsulfonyl-3-tert-butylaminoquinoline; ERK1/2, extracellular signal-related kinases 1 and 2; iCa²⁺, intracellular calcium; ND, not defined; TT15, (2S)-2-[(8S)-7-benzoyl-3-[4-[(3,4-dichlorophenyl)methoxy]phenyl]-2-oxo-1,6,8,9-tetrahydropyrido[4,3-g][1,4]benzoxazine-8-carbonyl]amino]-3-[4-(4-cyanophenyl)phenyl]propanoic acid.

* $P < 0.05$.

whereas BETP potentiated oxyntomodulin affinity and cAMP responses (Fig. 4; Supplemental Fig. 2). In contrast, BETP showed significant negative cooperativity with exendin-4, GLP-1(7–36)NH₂, and GLP-1(1–36)NH₂ for coupling to pERK1/2 and neutral/weak negative cooperativity with oxyntomodulin for this pathway. In iCa²⁺-mobilization assays, BETP displayed positive cooperativity with exendin-4 and to a lesser extent GLP-1(7–36)NH₂; however, neutral cooperativity with oxyntomodulin was observed (Fig. 6). Assessment of β -Arr recruitment revealed neutral cooperativity between BETP and exendin-4 for both β -Arr1 and β -Arr2 and neutral cooperativity for GLP-1(7–36)NH₂ in recruiting β -Arr1 (Fig. 7; Table 3). However, weak potentiation of β -Arr2 and of both β -Arr1 and β -Arr2 recruitment was observed for GLP-1(7–36)NH₂ and oxyntomodulin, respectively, in the presence of BETP (Fig. 7; Table 3). These data indicate that BETP can engender stimulus bias at the level of the signaling pathway in a ligand-dependent manner.

Functional interaction assays for cAMP accumulation and iCa²⁺ mobilization between each peptide ligand and Compound 2 confirmed previous findings (Koole et al., 2010); Compound 2 potentiated oxyntomodulin-induced cAMP responses but not intracellular calcium mobilization (Supplemental Figs. 3 and 4). In contrast, neutral cooperativity was observed between Compound 2 and the other three peptides in both pathways. Interaction assays for the pERK1/2 experiments included higher concentrations of Compound 2 than previously published, which revealed significant negative cooperativity of Compound 2 on exendin-4-mediated pERK1/2 responses (Supplemental Fig. 5). A similar trend was observed for both the full-length and truncated GLP-1 peptides (and to a lesser extent oxyntomodulin), although this negative cooperativity did not reach statistical significance. In contrast, Compound 2 displayed positive cooperativity with exendin-4, GLP-1(7–36)NH₂, and oxyntomodulin for recruitment of both β -Arr1 and β -Arr2. The estimated cooperativity

factors ($\alpha\beta$) revealed that this potentiation was greater for GLP-1(7–36)NH₂ and oxyntomodulin than that of exendin-4 (Fig. 8). Like BETP, Compound 2 can also generate stimulus bias in a probe-dependent manner; however, it is important to note that these two allosteric ligands engender significantly different signaling profiles that only manifest when multiple signaling pathways are explored.

GLP-1(1–36)NH₂ did not display agonism in either iCa²⁺-mobilization assays or in recruitment of β -Arrs either in the presence or absence of either BETP or Compound 2.

In contrast to BETP and Compound 2, the small molecules TT15, Boc5, and the BMS21 peptide did not modulate any signaling pathway mediated by any of the GLP-1 peptide agonists (Supplemental Figs. 6–8). These compounds at high concentrations (particularly evident with BMS21) have characteristics consistent with a competitive mode of action with GLP-1- and GLP-1-related peptide agonists, which suggests these small ligands may share at least a partially overlapping binding site with the orthosteric pocket.

BETP and Compound 2 Can Potentiate Responses to BMS21, TT15, and Boc5. Consistent with the evidence above indicating at least a partial overlap in binding interactions formed by TT15 and BMS21 with orthosteric ligands, these two ligands when tested for interaction with each other in a cAMP assay displayed behavior consistent with a competitive interaction (Supplemental Fig. 9). In addition, BETP and Compound 2 strongly potentiated cAMP responses mediated by both TT15 and the small peptide, BMS21 (Fig. 9; Table 4). Interestingly, BETP also potentiated Boc5-mediated cAMP responses (Fig. 9; Table 4); however, only weak modulation was observed using Compound 2 (Fig. 9; Table 4). This is particularly interesting as Boc5, when interacted in a cAMP assay with either TT15 or BMS, had a profile consistent with competitive behavior between the two ligands (Supplemental Fig. 9). This indicates that although both ligands may bind in a site partially overlapping

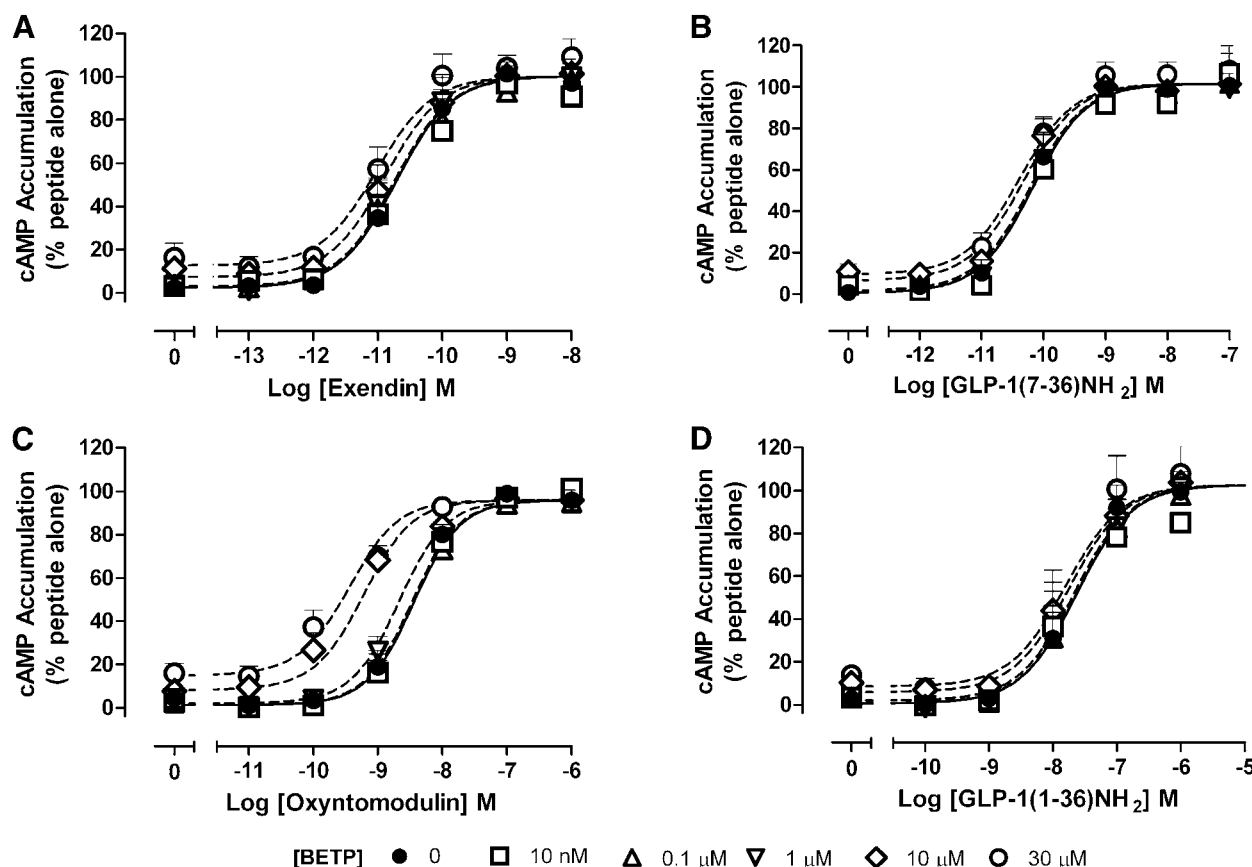


Fig. 4. BETP displays positive allosteric effects on GLP-1R-mediated cAMP accumulation in an agonist-dependent manner. Concentration response curves were generated for exendin-4 (A), GLP-1(7–36)NH₂ (B), oxyntomodulin (C), or GLP-1(1–36)NH₂ (D) in the absence and presence of increasing concentrations of BETP in Flp-In-CHO cells stably expressing the human GLP-1R. The curves represent the best global fit of an operational model of allosterism (eq. 4). All values are mean \pm S.E.M. of three to four independent experiments performed in duplicate. Panel C reproduced from Willard et al. (2012b).

the orthosteric site, the cooperativity between the site of Compound 2 binding and Boc5 is different from that of TT15 and BMS21. In addition, the differential degrees of cooperativity induced by the two structurally distinct modulators, BETP and Compound 2, indicate that these two compounds interact differentially with the GLP-1R.

Discussion

The GLP-1R is a major therapeutic target for the treatment of type 2 diabetes, however, despite the success of natural or modified GLP-1R-binding peptides for clinical treatment, low molecular weight, orally active compounds are still pursued as the preferred therapeutic approach. Traditionally, these types of molecules were designed to mimic the properties of the natural ligand by targeting the orthosteric site and this approach has been successful for many GPCR targets (Black, 1989). However, there are many cases where this has been unsuccessful, in particular for non-family A GPCRs.

Orthosteric peptide ligands for family B GPCRs bind predominantly to the large N-terminal domain prior to initiating receptor activation (Hoare, 2005). This is mechanistically different from many family A GPCRs, whose ligands primarily make contact within the transmembrane domain. Due to the size of peptide ligands and their mechanism of receptor activation, the discovery of surrogate small molecule

agonists that mimic these actions has been difficult. However, several groups have recently reported small molecule non-peptide and smaller peptide fragments that act as GLP-1R agonists or positive allosteric modulators. In this study we have revealed significant signaling bias induced by these compounds when compared with the predominant endogenous peptide, indicating that small ligands may not be able to fully mimic the actions of larger peptide hormones. In addition, we show that allosteric modulation is complex, with pathway-dependent modulation of receptor response that is determined by the combination of orthosteric ligand and allosteric ligand used. This emphasizes the need for broad elucidation of mechanism of action when developing allosteric compounds.

Activation by peptide ligands predominantly couples the GLP-1R to G α_s -proteins, leading to an increase in cAMP. This is the best studied pathway of the GLP-1R and is crucial for enhancing glucose-dependent insulin secretion (Baggio and Drucker, 2007). However, like many GPCRs, the GLP-1R elicits signals via diverse pathways, including iCa²⁺ mobilization and pERK1/2, in addition to coupling to regulatory proteins such as β -Arres that can activate other effectors (Montrose-Rafizadeh et al., 1999; Sonoda et al., 2008). Each of these pathways has been linked to physiologic effects of GLP-1. iCa²⁺ mobilization can significantly modulate the magnitude of insulin secretion, and β -Arr1 also has a role in insulin

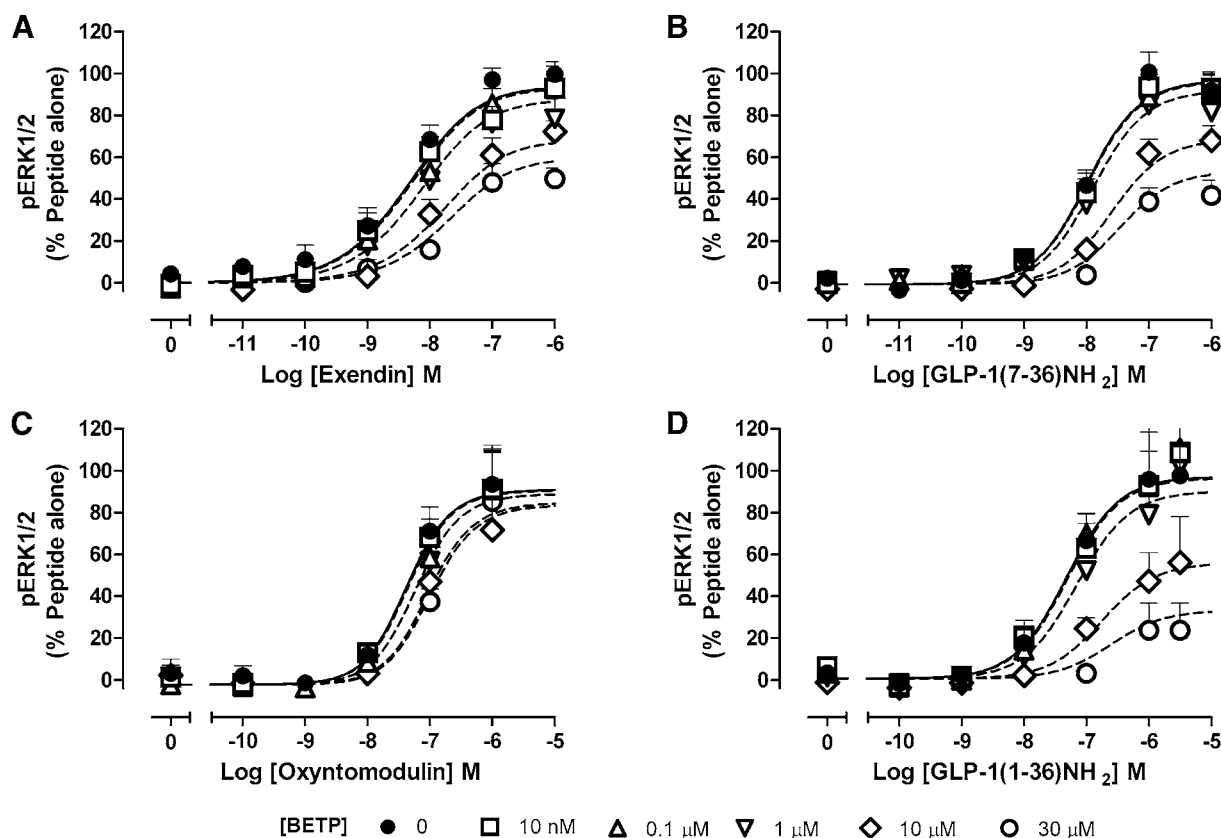


Fig. 5. BETP displays negative allosteric effects on GLP-1R-mediated pERK1/2 by peptide ligands. Concentration response curves were generated for exendin-4 (A), GLP-1(7-36)NH₂ (B), oxyntomodulin (C) or GLP-1(1-36)NH₂ (D) in the absence and presence of increasing concentrations of BETP in Flp-In-CHO cells stably expressing the human GLP-1R. The curves represent the best global fit of an operational model of allosterism (eq. 5). All values are mean \pm S.E.M. of three to four independent experiments performed in duplicate. Panel C reproduced from Willard et al. (2012b).

secretion, although the molecular mechanism of this regulation is poorly understood. Sustained effects on gene transcription and the preservation of β -cell mass involve multiple signaling pathways; both cAMP-dependent and -independent; the latter include activation of mitogen-activated kinases, such as ERK1/2. It is clear that the physiological response downstream of GLP-1R activation is a composite of the interplay of various signaling pathways, but even for those that have been identified, the extent and magnitude to which these effectors contribute to the physiological signaling profile

and the ideal combination of these that lead to a therapeutically beneficial output has yet to be established.

Evaluation of signaling across five pathways (cAMP, pERK1/2, iCa²⁺ mobilization, β -Arr1, and β -Arr2 recruitment) demonstrated that, in comparison with the reference ligand [GLP-1(7-36)NH₂], all of the small ligands, with the exception of BETP, coupled most strongly to cAMP production. In addition, for BMS21, TT15, and Boc5, the relative order of efficacy for the five pathways was similar to GLP-1(7-36)NH₂ (Fig. 1; Table 1). Despite this, each of the

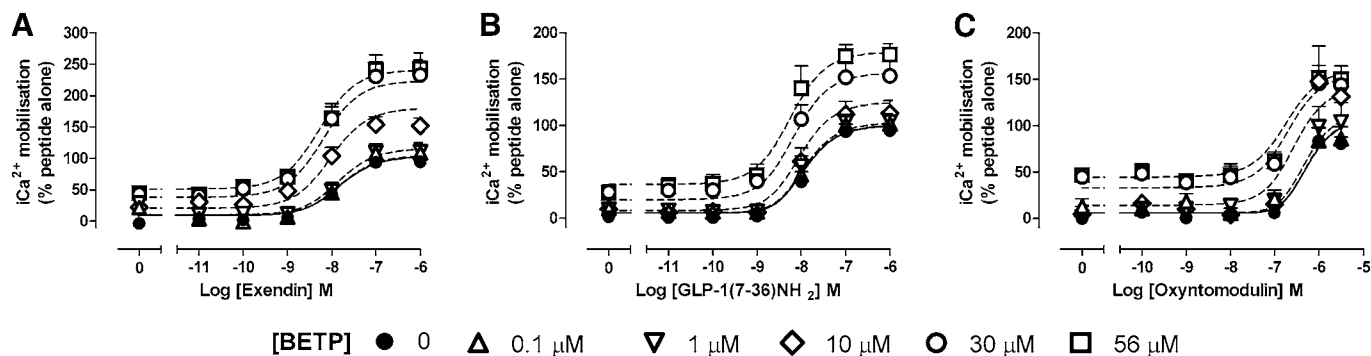


Fig. 6. BETP positively modulates GLP-1R-mediated iCa²⁺ mobilization by peptide ligands. Concentration response curves were generated for exendin-4 (A), GLP-1(7-36)NH₂ (B) or oxyntomodulin (C) in the absence and presence of increasing concentrations of BETP in Flp-In-CHO cells stably expressing the human GLP-1R. The curves represent the best global fit of an operational model of allosterism (eq. 5). All values are mean \pm S.E.M. of three to four independent experiments performed in duplicate. Panel C reproduced from Willard et al. (2012b).

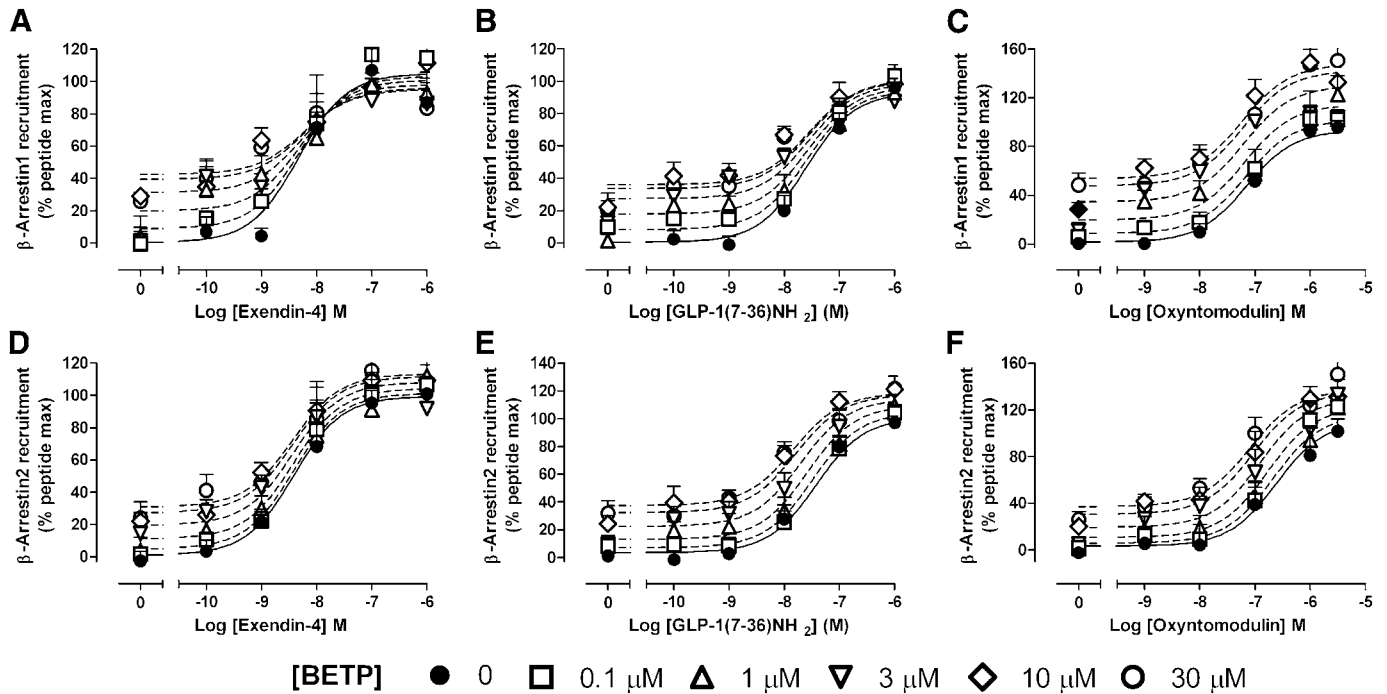


Fig. 7. BETP does not significantly alter GLP-1R-mediated recruitment of β -arrestins by peptide ligands. Concentration response curves were generated for exendin-4 (A and D), GLP-1(7–36)NH₂ (B and E), or oxyntomodulin (C and F) in the absence and presence of increasing concentrations of BETP for β -Arr1 (A–C) and β -Arr2 (D–F) recruitment. The curves represent the best global fit of an operational model of allostery (eq. 5). All values are mean \pm S.E.M. of four to five independent experiments performed in duplicate. Panel C reproduced from Willard et al. (2012b).

ligands showed elements of signal bias, with all three having less preference for cAMP relative to pERK1/2, but no significant change when comparing the preference between all other pathways (Table 2). However, Compound 2 displayed significant signal bias with less preference for cAMP signaling relative to iCa²⁺ mobilization, β -Arr1, or β -Arr2. Interestingly BETP displayed a very different profile to GLP-1(7–36)NH₂, as this compound heavily biased GLP-1R signaling to β -Arr1, β -Arr2, and iCa²⁺ mobilization relative to cAMP and pERK1/2. The response was also biased toward β -Arr1 recruitment and iCa²⁺ mobilization over β -Arr2 (Table 2). The ability of individual ligands to differentially activate the GLP-1R to produce distinct functional profiles may provide a unique

opportunity in drug development, with the potential to sculpt receptor signaling to target physiologically important responses and exclude those that do not provide beneficial outputs.

This concept also extends to allosteric modulation of orthosteric ligand responses. In addition to small molecules displaying differential intrinsic efficacy profiles, if they bind allosterically, they can also differentially modulate peptide (both endogenous and exogenous) responses in a pathway-specific manner. Therefore, determining the modulatory profile of small molecule ligands in numerous functional outputs and using multiple orthosteric ligands is important, especially when the endogenous systems involve the interplay

TABLE 3

Functional cooperativity estimates for the interaction between BETP or Compound 2 and GLP-1R peptide ligands

Data derived from analysis of interaction concentration-response curves with an operational model of allostery as defined in eqs. 4 and 5. pKb values are the negative logarithms for the functional affinity of the allosteric ligands; log $\alpha\beta$ represents the composite cooperativity between the allosteric ligand and the orthosteric peptide ligand. Antilogarithms are shown in parentheses. Values represent the mean \pm S.E.M. of four to six independent experiments performed in duplicate. Data were analyzed with one-way analysis of variance and Dunnett's post test.

Pathway	Allosteric Ligand	pKb	Log $\alpha\beta$ ($\alpha\beta$)			
			Exendin-4	GLP-1(7–36)NH ₂	Oxyntomodulin	GLP-1(1–36)NH ₂
cAMP	BETP	5.01 \pm 0.04	0.45 \pm 0.20 (2.8)	0.31 \pm 0.18 (2.0)	1.21 \pm 0.17 (16)*	0.20 \pm 0.12 (1.6)
	Cpd2	5.43 \pm 0.29	0.24 \pm 0.30 (1.7)	0.22 \pm 0.28 (1.7)	1.48 \pm 0.27 (29)*	0.31 \pm 0.17 (2.0)
pERK1/2	BETP	5.46 \pm 0.29	–0.90 \pm 0.21 (0.13)*	–1.03 \pm 0.23 (0.09)*	–0.44 \pm 0.19 (0.36)	–1.85 \pm 0.88 (0.01)
	Cpd2	5.29 \pm 0.19	–0.77 \pm 0.21 (5.9)	–0.48 \pm 0.17 (0.33)	–0.21 \pm 0.13 (0.62)	–0.44 \pm 0.20 (0.36)
iCa ²⁺	BETP	4.83 \pm 0.16	1.0 \pm 0.26 (10)*	0.58 \pm 0.19 (3.8)	0.23 \pm 0.11 (1.7)	NR
	Cpd2	5.58 \pm 0.38	0.28 \pm 0.15 (1.9)	–0.20 \pm 0.15 (0.63)	0.14 \pm 0.16 (1.4)	NR
β -Arr1	BETP	5.42 \pm 0.17	–0.05 \pm 0.04 (0.89)	–0.01 \pm 0.02 (1.0)	0.40 \pm 0.17 (2.5)	NR
	Cpd2	5.27 \pm 0.18	0.72 \pm 0.18 (5.2)*	1.07 \pm 0.19 (12)*	1.05 \pm 0.14 (11)*	NR
β -Arr2	BETP	5.38 \pm 0.16	0.18 \pm 0.26 (1.5)	0.67 \pm 0.18 (4.7)	0.54 \pm 0.19 (3.5)	NR
	Cpd2	5.30 \pm 0.19	0.69 \pm 0.20 (4.9)*	1.06 \pm 0.13 (11)*	0.99 \pm 0.19 (10)*	NR

β -Arr, beta arrestin; BETP, 4-(3-benzoyloxyphenyl)-2-ethylsulfinyl-6-(trifluoromethyl)pyrimidine; Compound 2, 6,7-dichloro-2-methylsulfonyl-3-tert-butylaminoquinoline; iCa²⁺, intracellular calcium; NR, no response; pKb, negative logarithms for the functional affinity of the allosteric ligands.

* $P < 0.05$.

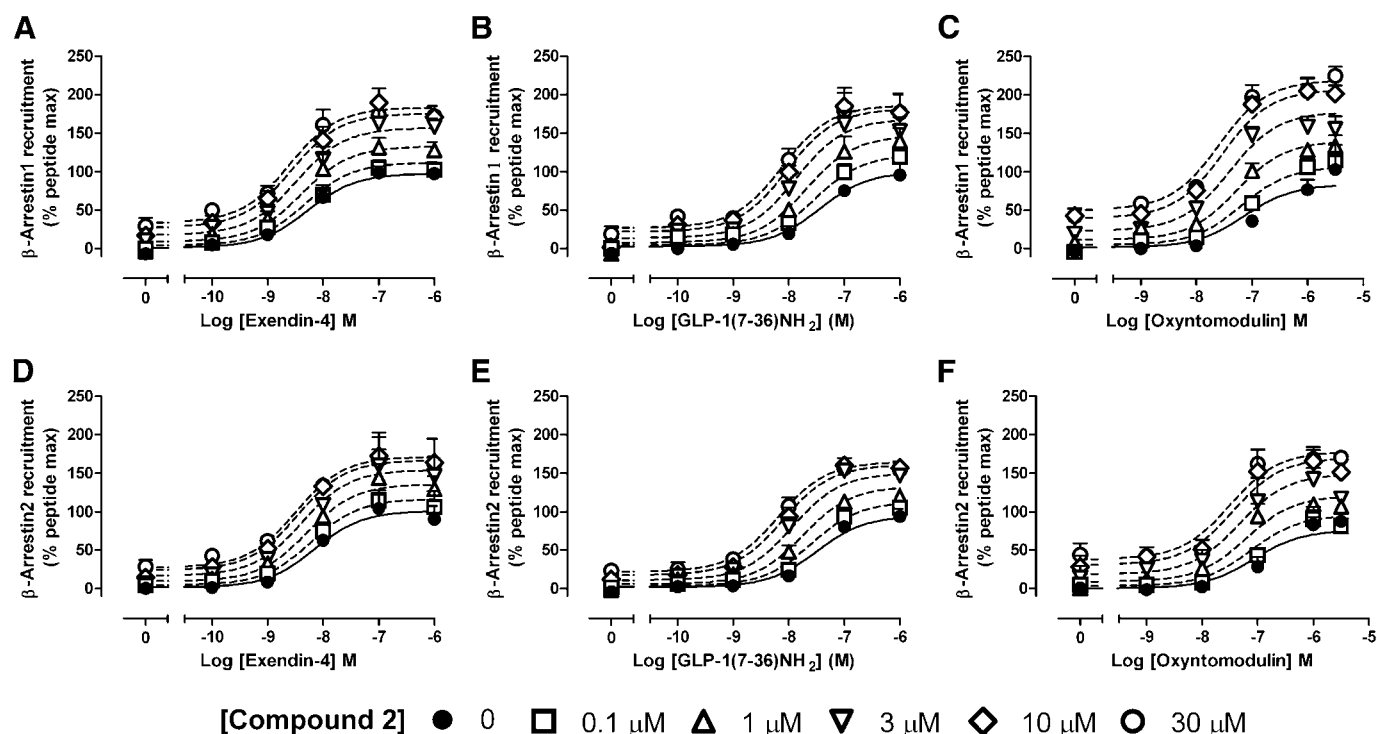


Fig. 8. Compound 2 potentiates GLP-1R-mediated recruitment of β -arrestins by peptide ligands. Concentration response curves were generated for exendin-4 (A and D), GLP-1(7–36)NH₂ (B and E) or oxyntomodulin (C and F) in the absence and presence of increasing concentrations of Compound 2 for β -Arr1 (A–C) and β -Arr2 (D–F) recruitment. The curves represent the best global fit of an operational model of allosterism (eq. 5). All values are mean \pm S.E.M. of four to five independent experiments performed in duplicate.

of many natural ligands and several signaling pathways to elicit physiological consequences. Compound 2 engendered significant bias in the response mediated by oxyntomodulin with selective enhancement of cAMP, β -Arr1, and β Arr2; however, for GLP-1(7–36)NH₂, only β -Arr responses were enhanced. BETP also engendered significant stimulus bias in a probe-dependent manner, with selective enhancement of oxyntomodulin-mediated cAMP responses and to a smaller extent β -Arr-1 and -2, but only iCa²⁺ mobilization and β -Arr2 responses were weakly enhanced when GLP-1(7–36)NH₂ was co-bound, while a strong negative effect on pERK1/2 was observed. When considering the clinically used exendin-4, the bias was again different; in this case only iCa²⁺ mobilization was significantly enhanced, with negative cooperativity seen for pERK1/2. This revealed that GLP-1R conformations induced by the cobinding of an allosteric modulator and orthosteric ligand can vastly alter the combined signaling profile of the receptor such that no two combinations of allosteric-orthosteric ligand pair were able to produce the same profile of behavior. From these studies, it is unclear whether Compound 2 and BETP share a common binding pocket, and further elucidation to identify their binding site(s) will be required. However, even if they do occupy the same pocket, the specific interactions formed between these compounds and the receptor is clearly different as they induce very distinct bias in their efficacy and modulatory properties.

This type of behavior, where ligands can alter one pathway while having very different effect on another pathway and differential probe-dependent effects at both acute and regulatory signaling pathways, may provide a therapeutic advantage by allowing fine-tuning of receptor response. However, this

also presents a significant challenge, as currently it is not clear what will be the key pathway/combination of pathways that need to be manipulated to provide an ideal therapeutic response. Understanding the activity profiles of small ligands may be key for drug discovery programs. These types of compounds, which display differential efficacy and modulatory profiles, provide us with tools that could potentially be used in an *in vivo/ex vivo* setting to explore the physiological consequences of biased signaling. Further research is required to fully understand these concepts and ascertain the preferred signaling profile for new and better therapeutics.

The final part of this study identified that Compound 2 and BETP were able to strongly modulate cAMP responses of BMS21 and TT15 at the GLP-1R. Boc5 could also be potentiated but to a lesser extent. Data from our interaction assays also suggest that these compounds behave in a competitive manner with peptide ligands and each other. BMS21 was designed to mimic the N-terminal region of GLP-1, which is proposed to bind to the top of the transmembrane bundle and extracellular loop regions of the receptor. It is also possible that TT15 may bind in a similar region. Boc5 has also been proposed to bind in the extracellular regions of the receptor; however, its binding site may be distinct from that of BMS and TT15 as weaker cooperativity was observed with BETP and Compound 2. These observations could also represent an opportunity to aid in drug optimization. For example, ligands like BMS21, TT15, and Boc5 are less biased agonists than Compound 2 and BETP, and if mimicking the actions of GLP-1(7–36)NH₂ rather than altering the bias of the natural hormone was identified as the best therapeutic

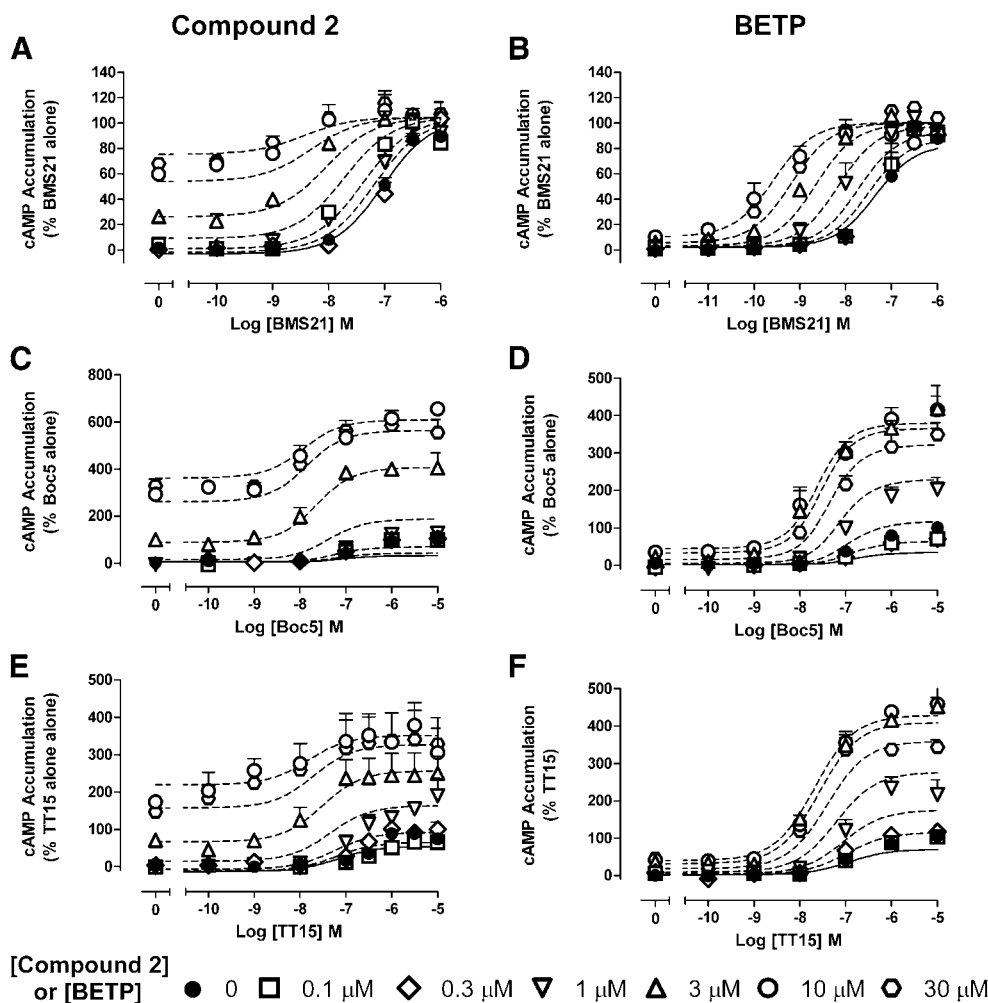


Fig. 9. Compound 2 and BETP potentiate GLP-1R-mediated cAMP accumulation by BMS21, Boc5 and TT15. Concentration response curves were generated for BMS21 (A and B), Boc5 (C and D), or TT15 (E and F) in the absence and presence of increasing concentrations of either Compound 2 (A, C, and E) or BETP (B, D, and F) in Flp-In-CHO cells stably expressing the human GLP-1R. The curves represent the best global fit of an operational model of allosterism (eq. 5). All values are mean \pm S.E.M. of three independent experiments performed in duplicate.

approach, then elucidation of the binding sites for these ligands could aid in development of higher affinity drug-like molecules that bind to the same binding pocket. Alternatively, all small ligands identified to date display weak affinity for the GLP-1R that could arguably be due to the limited number of contacts they can form with the receptor (compared with

peptide ligands). The ability of one small molecule to enhance the signaling induced by another (and vice versa) may indicate some therapeutic potential for small molecule therapies to be used in combination.

In conclusion, we have demonstrated that small molecule ligands induce biased signaling at the GLP-1R and also bias in the signaling profile of orthosteric ligands. Further work is required to delineate the extent to which such bias exists in a native cellular environment and the in vivo consequences. In recent years, the pace of identifying small molecule GLP-1R ligands has increased and this should aid in the types of studies that may lead to the discovery and development of compounds with the potential to sculpt therapeutics that show greater selectivity and improved therapeutic outcomes.

TABLE 4

Functional cooperativity estimates for the interaction between BETP or Compound 2 and Boc5, TT15, or BMS21

Data derived from analysis of interaction dose-response curves with an operational model of allosterism as defined in eq. 4. Log $\alpha\beta$ represents the composite cooperativity between the allosteric ligand and the orthosteric peptide ligand. Antilogarithms are shown in parentheses. Values represent the mean \pm S.E.M. of four to six independent experiments performed in duplicate. Data were analyzed with one-way analysis of variance and Dunnett's post test.

	Log $\alpha\beta$ ($\alpha\beta$)	
	Compound 2	BETP
Boc5	0.84 \pm 0.39 (6.9)*	1.28 \pm 0.44 (19)*
TT15	1.89 \pm 0.41 (78)*	1.66 \pm 0.28 (46)*
BMS21	2.09 \pm 0.35 (123)*	2.75 \pm 0.22 (562)*

BETP, 4-(3-benzyloxyphenyl)-2-ethylsulfanyl-6-(trifluoromethyl)pyrimidine; Boc5, 1,3-bis [[4-(tert-butoxy-carbonylamino)benzoyl]amino]-2,4-bis[3-methoxy-4-(thiophene-2-carboxyloxy)-phenyl]cyclobutane-1,3-dicarboxylic acid; Compound 2, 6,7-dichloro-2-methylsulfonfyl-3-tert-butylaminoquinoxaline; TT15, (2S)-2-[(8S)-7-benzoyl-3-[4-[(3,4-dichlorophenyl)methoxy]phenyl]-2-oxo-1,6,8,9-tetrahydropyrido[4,3-g][1,4]benzoxazine-8-carbonyl]amino]-3-[4-(4-cyanophenyl)phenyl]propanoic acid.

* $P < 0.05$.

Acknowledgments

The authors thank Dan Kohlman, Mark Tebbe, Mike Coghlan, and Jorge Alsina-Fernandez for technical assistance and support.

Authorship Contributions

Participated in research design: Wootten, Willard, Sloop, Christopoulos, Sexton.

Conducted experiments: Wootten, Savage.

Contributed new reagents or analytic tools: Willard, Bueno, Sloop.

Performed data analysis: Wootten, Savage.

Wrote or contributed to the writing of the manuscript: Wootten, Willard, Bueno, Sloop, Christopoulos, Sexton.

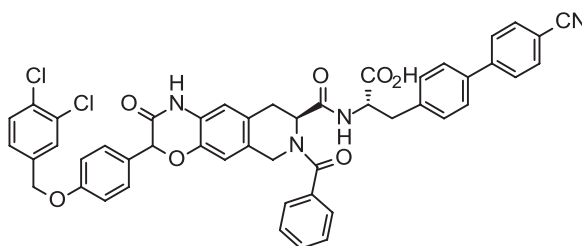
References

- Aurelio L, Valant C, Flynn BL, Sexton PM, Christopoulos A, and Scammells PJ (2009) Allosteric modulators of the adenosine A1 receptor: synthesis and pharmacological evaluation of 4-substituted 2-amino-3-benzoylthiophenes. *J Med Chem* **52**:4543–4547.
- Avlani VA, McLoughlin DJ, Sexton PM, and Christopoulos A (2008) The impact of orthosteric radioligand depletion on the quantification of allosteric modulator interactions. *J Pharmacol Exp Ther* **325**:927–934.
- Baggio LL and Drucker DJ (2007) Biology of incretins: GLP-1 and GIP. *Gastroenterology* **132**:2131–2157.
- Black JW and Leff P (1983) Operational models of pharmacological agonism. *Proc R Soc Lond B Biol Sci* **220**:141–162.
- Black J (1989) Drugs from emasculated hormones: the principle of syntopic antagonism. *Science* **245**:486–493.
- Buteau J, Foisy S, Joly E, and Prentki M (2003) Glucagon-like peptide 1 induces pancreatic beta-cell proliferation via transactivation of the epidermal growth factor receptor. *Diabetes* **52**:124–132.
- Chen D, Liao J, Li N, Zhou C, Liu Q, Wang G, Zhang R, Zhang S, Lin L, and Chen K et al. (2007) A nonpeptidic agonist of glucagon-like peptide 1 receptors with efficacy in diabetic db/db mice. *Proc Natl Acad Sci USA* **104**:943–948.
- DeFronzo RA (1992) Pathogenesis of type 2 (non-insulin dependent) diabetes mellitus: a balanced overview. *Diabetologia* **35**:389–397.
- Drucker DJ and Nauck MA (2006) The incretin system: glucagon-like peptide-1 receptor agonists and dipeptidyl peptidase-4 inhibitors in type 2 diabetes. *Lancet* **368**:1696–1705.
- Drucker DJ, Philippe J, Mojsov S, Chick WL, and Habener JF (1987) Glucagon-like peptide I stimulates insulin gene expression and increases cyclic AMP levels in a rat islet cell line. *Proc Natl Acad Sci USA* **84**:3434–3438.
- Evans BA, Broxton N, Merlin J, Sato M, Hutchinson DS, Christopoulos A, and Summers RJ (2011) Quantification of functional selectivity at the human $\alpha(1A)$ -adrenoceptor. *Mol Pharmacol* **79**:298–307.
- Hoare SR (2005) Mechanisms of peptide and nonpeptide ligand binding to Class B G-protein-coupled receptors. *Drug Discov Today* **10**:417–427.
- Holz GG, 4th, Kühtreiber WM, and Habener JF (1993) Pancreatic beta-cells are rendered glucose-competent by the insulinotropic hormone glucagon-like peptide-1 (7–37). *Nature* **361**:362–365.
- Kenakin T (2011) Functional selectivity and biased receptor signaling. *J Pharmacol Exp Ther* **336**:296–302.
- Kenakin T, Watson C, Muniz-Medina V, Christopoulos A, and Novick S (2012) A simple method for quantifying functional selectivity and agonist bias. *ACS Chem Neurosci* **3**:193–203.
- Knudsen LB, Kiel D, Teng M, Behrens C, Bhumralkar D, Kodra JT, Holst JJ, Jeppesen CB, Johnson MD, and de Jong JC et al. (2007) Small-molecule agonists for the glucagon-like peptide 1 receptor. *Proc Natl Acad Sci USA* **104**:937–942.
- Koole C, Wootten D, Simms J, Valant C, Sridhar R, Woodman OL, Miller LJ, Summers RJ, Christopoulos A, and Sexton PM (2010) Allosteric ligands of the glucagon-like peptide 1 receptor (GLP-1R) differentially modulate endogenous and exogenous peptide responses in a pathway-selective manner: implications for drug screening. *Mol Pharmacol* **78**:456–465.
- Koole C, Wootten D, Simms J, Valant C, Miller LJ, Christopoulos A, and Sexton PM (2011) Polymorphism and ligand dependent changes in human glucagon-like peptide-1 receptor (GLP-1R) function: allosteric rescue of loss of function mutation. *Mol Pharmacol* **80**:486–497.
- Leach K, Sexton PM, and Christopoulos A (2007) Allosteric GPCR modulators: taking advantage of permissive receptor pharmacology. *Trends Pharmacol Sci* **28**:382–389.
- Mapelli C, Natarajan SI, Meyer JP, Bastos MM, Bernatowicz MS, Lee VG, Pluscec J, Rieckinger DJ, Sieber-McMaster ES, and Constantine KL et al. (2009) Eleven amino acid glucagon-like peptide-1 receptor agonists with antidiabetic activity. *J Med Chem* **52**:7788–7799.
- May LT, Avlani VA, Langmead CJ, Herdon HJ, Wood MD, Sexton PM, and Christopoulos A (2007) Structure-function studies of allosteric agonism at M2 muscarinic acetylcholine receptors. *Mol Pharmacol* **72**:463–476.
- Montrose-Rafizadeh C, Avdonin P, Garant MJ, Rodgers BD, Kole S, Yang H, Levine MA, Schwindinger W, and Bernier M (1999) Pancreatic glucagon-like peptide-1 receptor couples to multiple G proteins and activates mitogen-activated protein kinase pathways in Chinese hamster ovary cells. *Endocrinology* **140**:1132–1140.
- Park S, Dong X, Fisher TL, Dunn S, Omer AK, Weir G, and White MF (2006) Exendin-4 uses Irs2 signaling to mediate pancreatic beta cell growth and function. *J Biol Chem* **281**:1159–1168.
- Quoyer J, Longuet C, Broca C, Linck N, Costes S, Varin E, Bockaert J, Bertrand G, and Dalle S (2010) GLP-1 mediates antiapoptotic effect by phosphorylating Bad through a beta-arrestin 1-mediated ERK1/2 activation in pancreatic beta-cells. *J Biol Chem* **285**:1989–2002.
- Rao M (2009) inventor, TransTech Pharma Inc., assignee. Ligands for the GLP-1 receptor and methods for discovery thereof. International patent application E, PCT/US2009/039905. 2009 Oct 15.
- Sloop KW, Willard FS, Brenner MB, Ficorilli J, Valasek K, Showalter AD, Farb TB, Cao JX, Cox AL, and Michael MD et al. (2010) Novel small molecule glucagon-like peptide-1 receptor agonist stimulates insulin secretion in rodents and from human islets. *Diabetes* **59**:3099–3107.
- Sonoda N, Imamura T, Yoshizaki T, Babendure JL, Lu JC, and Olefsky JM (2008) Beta-Arrestin-1 mediates glucagon-like peptide-1 signaling to insulin secretion in cultured pancreatic beta cells. *Proc Natl Acad Sci USA* **105**:6614–6619.
- Werry TD, Gregory KJ, Sexton PM, and Christopoulos A (2005) Characterization of serotonin 5-HT_{2C} receptor signaling to extracellular signal-regulated kinases 1 and 2. *J Neurochem* **93**:1603–1615.
- Willard FS, Bueno AB, and Sloop KW (2012a) Small molecule drug discovery at the glucagon-like peptide-1 receptor. *Exp Diabetes Res* **2012**:709893.
- Willard FS, Wootten D, Showalter AD, Savage EE, Ficorilli J, Farb TB, Bokvist K, Alsina-Fernandez J, Furness SGB, Christopoulos A, Sexton PM, and Sloop KW (2012b) Small molecule allosteric modulation of the glucagon-like peptide-1 receptor enhances the insulinotropic effect of oxyntomodulin. *Mol Pharmacol* **82**:1066–1073.

Address correspondence to: Dr. Patrick M. Sexton, Drug Discovery Biology, Monash Institute of Pharmaceutical Sciences, Monash University, 381 Royal Parade, Parkville, Victoria 3052, Australia. E-mail: patrick.sexton@monash.edu

Correction to “Differential Activation and Modulation of the Glucagon-Like Peptide-1 Receptor by Small Molecular Ligands”

In the above article [Wootten, D, Savage EE, Willard FS, Bueno AB, Sloop KW, Christopoulos A, and Sexton PM (2013) *Mol Pharmacol* **83**:822–834], the structure drawing of TT15 in Fig. 1 is wrong. The structure should be as represented below. The name of the compound in the abbreviations on pages 822 and 823 and in Tables 1, 2, and 4 is also incorrect; it should be TT15, (2*S*)-2-[[[(8*S*)-7-benzoyl-3-[4-[(3,4-dichlorophenyl)methoxy]phenyl]-2-oxo-1,6,8,9-tetrahydropyrido[4,3-*g*][1,4]benzoxazine-8-carbonyl]amino]-3-[4-(4-cyanophenyl)phenyl]propanoic acid (IUPAC name), as indicated in the supplemental material. Intermediate 5 of the synthesis of TT15 (see supplemental material) corresponds to “intermediate A” in Mjalli, A. M. M. US Patent 7, 727, 983 B2 “Oxadiazanthracene compounds for the treatment of diabetes,” Granted patent, Editor, TransTech Pharma.



TT15 (Isomer 1)

The HTML and PDF versions of the article have been corrected.

The authors regret this error and any inconvenience it may have caused.

Differential activation and modulation of the glucagon-like peptide-1 receptor by small molecule ligands

Wootten D, Savage EE, Willard FS, Bueno AB, Sloop KW, Christopoulos A, Sexton PM

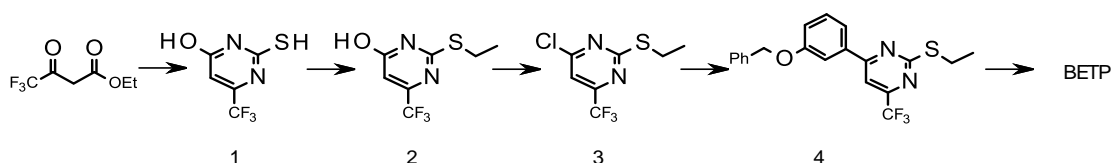
Molecular Pharmacology

Supplemental Information

Experimental procedure.

General synthesis. All chemicals were reagent grade and used as purchased. Flash chromatography was performed in Biotage Radial Compression system or flash chromatography using Merck silica gel 60 mesh. Eluents are indicated for each compound. ^1H NMR and ^{13}C NMR spectra were recorded in δ units relative to deuterated solvent as an internal reference using a Varian 400 MHz NMR or a Bruker 300 MHz NMR instrument. Signal multiplicities are represented by s (singlet), d (doublet), t (triplet), q (quartet), bs (broad singlet), and m (multiplet). HPLC/MS was used for the determination of reaction conversion on a series 1100 liquid chromatography/mass selective detector LC/MSD (Agilent, Waldbronn, Germany) driven by ChemStation software (Rev. A10.02, Agilent Technologies). LC/UV analysis was carried out at low or high pH. Conditions for low pH: Column: Gemini C18 3 μm (2 x 50 mm); UV: 214 and 300; eluent: A: 0.1% H₂O-formic acid pH 2.7, B: acetonitrile-formic acid 0.1%; flow: 1 ml/min; T: 50°C; gradient: from 5 to 100% B in 7 min. Conditions for high pH: Column: Xbridge C18 3.5 μm (2.1 x 50 mm); UV: 214 and 300; eluent: A: 10mM ammonium bicarbonate pH 9, B: acetonitrile; flow: 1 ml/min; T: 50°C; gradient: from 10 to 100% B in 7 min.

BETP synthesis



2-Mercapto-6-trifluoromethyl-pyrimidin-4-ol (1) A solution of ethyl 4,4,4-trifluoro-3-oxobutanoate (100 g, 543.14 mmol) and thiourea (100 g, 131.0 mmol) was suspended in 1.2 L of methanol. Sodium methoxide (68 g, 126.0 mmol) was added in portions over a 5 minute period (the temperature rose from 23°C to 44°C during addition). The mixture was refluxed overnight. The cooled solution was concentrated to ~1/3 volume, transferred to a separatory funnel, acidified to pH 2 with 12N HCl, and extracted with *t*-butylmethylether (2 x 2 L). The organic layers were washed with water and brine, dried (MgSO₄), filtered, and the filtrate evaporated to provide 2-mercapto-6-trifluoromethyl-pyrimidin-4-ol (79 g, 74% yield). LCMS *m/z* 197 [M+1]; ¹H NMR (400 MHz, DMSO-d₆) δ-6.38 (s, 1H); ¹⁹F NMR (376 MHz, DMSO-d₆) δ -68.1 (s, CF₃).

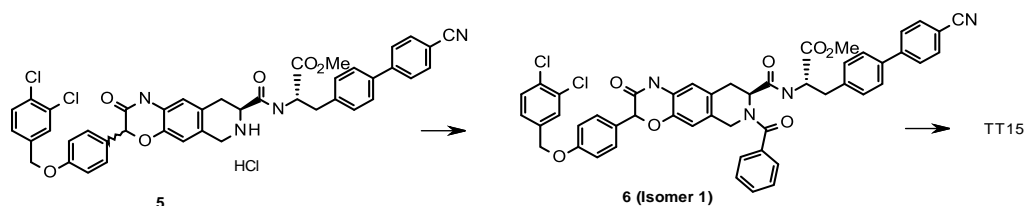
2-Ethylsulfanyl-6-trifluoromethyl-pyrimidin-4-ol (2) A solution of 2-mercapto-6-trifluoromethyl-pyrimidin-4-ol (79 g, 402.75 mmol) was dissolved in 800 mL of DMSO and treated with potassium carbonate (56 g, 405.19 mmol), followed by iodoethane (62 g, 397.52 mmol) in portions over a five minute period. The temperature gently rose from ambient to 38°C after addition. After stirring overnight at room temperature, the mixture was poured into water (4 L), the pH adjusted to ~2 with 12 N HCl and extracted with ethyl acetate (2 x 2 L). The organic extracts were washed with water and brine, dried (MgSO₄), filtered, and the filtrate evaporated to provide 2-ethylsulfanyl-6-trifluoromethyl-pyrimidin-4-ol (88.6 g, 98% yield) as an off white solid. LCMS *m/z* 223 [M-1]; ¹H NMR (400 MHz, DMSO-d₆) δ-13.27 (bs, 1H), 6.55 (s, 1H), 3.08 (q, *J* = 7.4 Hz, 2H), 1.26 (t, *J* = 7.4 Hz, 3H); ¹⁹F NMR (376 MHz, DMSO-d₆) δ-70.5 (s, CF₃).

4-Chloro-2-ethylsulfanyl-6-trifluoromethyl-pyrimidine (3) A slurry of 2-ethylsulfanyl-6-trifluoromethyl-pyrimidin-4-ol (88.6 g, 395.17 mmol) was combined with phosphoryl chloride (500 mL, 538.0 mmol), treated with dimethylformamide (2 mL, 25.87 mmol), and gently refluxed for 2 hours. The phosphoryl chloride was evaporated off, and the residue slowly poured in vigorously stirred water (1 L) at room temperature over a 20 minute period. After stirring 2 hours, the mixture was transferred to a separatory funnel and extracted with ethyl acetate (2 x 750 mL). The organic layers were washed with water, saturated sodium bicarbonate and brine, dried (MgSO₄), filtered, and the filtrate evaporated to provide

4-chloro-2-ethylsulfanyl-6-trifluoromethyl-pyrimidine (74 g, 77% yield) as an oily yellow solid. ^1H NMR (400 MHz, DMSO- d_6) δ -7.94 (s, 1H), 3.08 (q, $J = 7.4$ Hz, 2H), 1.26 (t, $J = 7.4$ Hz, 3H); ^{19}F NMR (376 MHz, DMSO- d_6) δ -68.0 (s, CF_3).

4-(3-Benzyloxy-phenyl)-2-ethylsulfanyl-6-trifluoromethyl-pyrimidine (4) To a solution of 3-benzyloxyphenylboronic acid (25 g, 109.62 mmol) and 4-chloro-2-ethylsulfanyl-6-trifluoromethyl-pyrimidine (15 g, 61.82 mmol) was added 1,4-dioxane (600 mL) and water (120 mL). Sodium carbonate (14 g, 132.09 mmol) was then added and the mixture was degassed via nitrogen flow through a glass gas dispersion tube for 20 min. The reaction was stirred overnight at 80 °C. The cooled mixture was diluted with water (1.5 L) and extracted with ethyl acetate (2 x 1 L). The black organic layers were washed with water and brine, dried (MgSO_4), filtered, and the filtrate evaporated. The crude was purified by chromatography on silica gel eluting with hexanes followed by 20% dichloromethane in hexanes to afford 4-(3-benzyloxy-phenyl)-2-ethylsulfanyl-6-trifluoromethyl-pyrimidine (12.5 g, 52% yield) as a colorless oil. LCMS m/z 391 [$\text{M}+1$]; ^1H NMR (400 MHz, DMSO- d_6) δ -8.22 (s, 1H), 7.90-7.88 (m, 2H), 7.50-7.24 (m, 7H), 5.20 (s, 2H), 3.20 (q, $J = 7.0$ Hz, 2H), 1.36 (t, $J = 7.0$ Hz, 3H); ^{19}F NMR (376 MHz, DMSO- d_6) δ -68.3 (s, CF_3).

4-(3-Benzyloxyphenyl)-2-[ethylsulfinyl]-6-(trifluoromethyl)pyrimidine (BETP) A solution of 4-(3-benzyloxy-phenyl)-2-ethylsulfanyl-6-trifluoromethyl-pyrimidine (9.5 g, 20.93 mmol) was dissolved in methanol (400 mL) and poured into water (80 mL) under nitrogen. Potassium monopersulfate (7.4 g, 12.04 mmol) was added and the mixture was stirred overnight at room temperature. The mixture was concentrated to $\sim 1/3$ volume, diluted with water, and extracted with ethyl acetate (2 x 200 mL). The organic layers were dried (MgSO_4), filtered, and the filtrate evaporated. The crude material was purified by flash chromatography on silica gel eluting with 1:2 ethyl acetate/hexane to provide racemic 4-(3-benzyloxyphenyl)-2-[ethylsulfinyl]-6-(trifluoromethyl)pyrimidine (7 g, 82% yield) as a white solid. LCMS m/z 407 [$\text{M}+1$]; ^1H NMR (400 MHz, DMSO- d_6) δ -8.69 (s, 1H), 7.98 (m, 2H), 7.53-7.29 (m, 7H), 5.21 (s, 2H), 3.28 (m, 1H), 3.17 (m, 1H), 1.13 (m, 3H); ^{19}F NMR (376 MHz, DMSO- d_6) δ -68.1 (s, CF_3); ^{13}C NMR (300 MHz, DMSO- d_6) δ 173.2, 166.5, 158.5, 155.9 (c, $J = 36$ Hz), 136.2, 134.9, 130.0, 127.9, 127.4, 127.3, 120.1, 119.0, 113.6, 113.4 (c, $J = 2$ Hz), 69.1, 46.0, 5.3; CF_3 not detected due to low signal to noise.

TT15 synthesis

Methyl (2S)-2-[[[(8S)-7-benzoyl-3-[4-[(3,4-dichlorophenyl)methoxy]phenyl]-2-oxo-1,6,8,9-tetrahydropyrido[4,3-g][1,4]benzoxazine-8-carbonyl]amino]-3-[4-(4-cyanophenyl)phenyl]propanoate (6). Compound **5** corresponds to Intermediate A described in Rao, 2009 and was synthesized according to this procedure. Compound **5** (4.2 g, 5.26 mmol) was dissolved in dichloromethane (85 mL), triethylamine (2.24 mL, 15.7 mmol) was added under nitrogen and the solution was cooled to 0°C. Benzoyl chloride (0.88 g, 6.31 mmol) was slowly added and the reaction was allowed to warm to room temperature for 4h. Water was added (100 mL) and the reaction mixture was stirred vigorously. Layers were separated and the organic layer was washed with brine, dried (Na₂SO₄), filtered and concentrated. The crude material was purified by flash chromatography eluting with ethyl acetate/hexane (from 0:100 to 80:20) to provide 4g of a mixture of diastereoisomers. Chiral separation of diastereomers (chiral HPLC conditions: 8x31 cm Chiralcel OD, 20 µm; eluent: 90/10 MeOH/acetonitrile; flow: 400 ml/min) provided 3.1g of compound **6** (isomer 1) in 94% purity.

(2S)-2-[[[(8S)-7-benzoyl-3-[4-[(3,4-dichlorophenyl)methoxy]phenyl]-2-oxo-1,6,8,9-tetrahydropyrido[4,3-g][1,4]benzoxazine-8-carbonyl]amino]-3-[4-(4-cyanophenyl)phenyl]propanoic acid (TT15). Compound **6** (3.8 g, 3.6 mmol) was dissolved in tetrahydrofuran (200 mL) and lithium hydroxide (21.5 g, 35.6 mmol) was added. The mixture was stirred at room temperature overnight. 1N hydrochloric acid was added to pH 2 and the mixture was concentrated. The crude material was purified by reverse phase chromatography to provide 1.2 g of **TT15** as a white solid in 95% purity. LCMS m/z 851 [M+1]; ¹H NMR (300 MHz, DMSO-d₆, 100°C) δ 7.76 and 7.68 (AA'BB' system, 4H), 7.59 (m, 1H), 7.53 and 7.12 (AA'BB' system, 4H), 7.42-7.27 (m, 10H), 6.92 (m, 2H), 6.77 (s, 1H), 6.58 (bs, 1H), 6.56 (s, 1H), 5.10 (bs, 2H), 5.02 (s, 2H), 4.28 (m, 1H), 4.13 (m, 1H), 3.17-

2.95 (m, 4H); ^{13}C NMR (300 MHz, DMSO- d_6 , 100°C) δ 171.6, 170.1, 168.2, 164.3, 157.9, 144.2, 140.6, 138.7, 137.7, 135.7, 135.4, 131.9 (2C), 130.8, 130.0, 129.4, 128.9, 128.7, 128.4, 128.2, 127.8, 127.0, 126.9, 126.6, 126.3, 126.1, 125.8, 125.5, 118.1, 114.7, 114.6, 113.3, 109.3, 77.2, 67.7, 53.8 (2C), 40.4, 36.2, 29.0.

Boc-5, **Compound 2** and **BMS21** were synthesized according to the methods described in the literature (Chen *et al*, 2007; Teng *et al*, 2007; Mapelli *et al*, 2009). The structures of all new compounds were consistent with their ^1H and mass spectra, and were $\geq 95\%$ pure as measured by HPLC.

- Chen D, Liao J, Li N, Zhou C, Liu Q, Wang G, Zhang R, Zhang S, Lin L, Chen K, Xie X, Nan F, Young AA and Wang MW (2007) A nonpeptidic agonist of glucagon-like peptide 1 receptors with efficacy in diabetic db/db mice. *Proc Natl Acad Sci U S A* **104**(3):943-948.
- Mapelli C, Natarajan SI, Meyer JP, Bastos MM, Bernatowicz MS, Lee VG, Pluscec J, Riexinger DJ, Sieber-McMaster ES, Constantine KL, Smith-Monroy CA, Golla R, Ma Z, Longhi DA, Shi D, Xin L, Taylor JR, Koplowitz B, Chi CL, Khanna A, Robinson GW, Seethala R, Antal-Zimanyi IA, Stoffel RH, Han S, Whaley JM, Huang CS, Krupinski J and Ewing WR (2009) Eleven amino acid glucagon-like peptide-1 receptor agonists with antidiabetic activity. *J Med Chem* **52**(23):7788-7799.
- Rao M (2009) PCT/US2009/039905 "Ligands for the Glp-1 Receptor and methods for discovery thereof", I.P. Application, Editor, TransTech Pharma.
- Teng M, Johnson MD, Thomas C, Kiel D, Lakis JN, Kercher T, Aytes S, Kostrowicki J, Bhumralkar D, Truesdale L, May J, Sidelman U, Kodra JT, Jørgensen AS, Olesen PH, de Jong JC, Madsen P, Behrens C, Pettersson I, Knudsen LB, Holst JJ, Lau J (2007) Small molecule ago-allosteric modulators of the human glucagon like peptide-1 (hGLP-1) receptor. *Bioorg Med Chem Lett* **17** (19) 5472–5478.

Figure legends

Supplementary figure 1. Competition binding assays.

Characterisation of the binding of (A) TT15, (B) BMS21 (D) Boc5, (E) BETP and (F) Compound 2 in competition with the radiolabeled antagonist, ^{125}I -exendin(9–39), in whole FlpInCHO cells stably expressing the human GLP-1R. On all graphs competition binding between the control ligand GLP-1(7-36) NH_2 and the radioligand are also shown. Data are normalized to maximum ^{125}I -exendin(9–39) binding, with nonspecific binding measured in the presence of 1 μM exendin(9–39). Data are analysed with a three-parameter logistic equation. All values are means \pm S.E.M of three to four independent experiments, conducted in duplicate.

Supplementary figure 2. BETP and Compound 2 selectively potentiate the affinity of oxyntomodulin.

Inhibition binding curves of (A, E) exendin-4, (B, F) GLP-1(7-36) NH_2 , (C, G) Oxyntomodulin and (D, H) GLP-1(1-36) NH_2 in the absence and presence of increasing concentrations of either Compound 2 (A-D) or BETP (E-H). Data are normalised to max ^{125}I -exendin(9-39) binding and are analysed with a one-site competition plus allosteric modulator curve as defined in equations 1 and 2. All values are means \pm S.E.M of three to four independent experiments, conducted in duplicate.

Supplementary figure 3. Compound 2 displays positive allosteric effects on GLP-1R-mediated cAMP accumulation in an agonist-dependent manner.

Concentration response curves were generated for (A) exendin-4, (B) GLP-1(7-36) NH_2 , (C) oxyntomodulin or (D) GLP-1(1-36) NH_2 in the absence and presence of increasing concentrations of Compound 2 in FlpInCHO cells stably expressing the human GLP-1R. The curves represent the best global fit of an operational model of allosterism (equation 4). All values are mean \pm SEM of three to four independent experiments performed in duplicate.

Supplementary figure 4. Compound 2 does not alter GLP-1R-mediated iCa^{2+} mobilisation by peptide ligands.

Concentration response curves were generated for (A) exendin-4, (B) GLP-1(7-36) NH_2 or (C) Oxyntomodulin in the absence and presence of increasing concentrations of Compound 2 in FlpInCHO cells stably expressing the human GLP-1R. The curves represent the best global fit of an operational model of allosterism (equation 4). All values are mean \pm SEM of three to four independent experiments performed in duplicate.

Supplementary figure 5. Compound 2 displays negative allosteric effects on GLP-1R-mediated pERK1/2 by peptide ligands .

Concentration response curves were generated for (A) exendin-4, (B) GLP-1(7-36) NH_2 , (C) Oxyntomodulin or (D) GLP-1(1-36) NH_2 in the absence and presence of increasing concentrations of Compound 2 in FlpInCHO cells stably expressing the human GLP-1R. The curves represent the best global fit of an operational model of allosterism (equation 5). All values are mean \pm SEM of three to four independent experiments performed in duplicate.

Supplementary figure 6. BMS21 does not modulate peptide-mediated GLP-1R signalling.

Concentration response curves were generated for exendin-4 (A, E, I), GLP-1(7-36)NH₂ (B, F, J), Oxyntomodulin (C, G, K) or GLP-1(1-36)NH₂ (D, H, L) in the absence and presence of increasing concentrations of BMS21 for cAMP accumulation (A-D), pERK1/2 (E-H) and iCa²⁺ mobilisation (I-L) in FlpInCHO cells stably expressing the human GLP-1R. Data are analysed with a three-parameter logistic equation. All values are means \pm S.E.M of three independent experiments, conducted in duplicate.

Supplementary figure 7. Boc5 displays behaviour consistent with competitive interaction with peptides in GLP-1R-mediated signalling.

Concentration response curves were generated for exendin-4 (A, E, I), GLP-1(7-36)NH₂ (B, F, J), Oxyntomodulin (C, G, K) or GLP-1(1-36)NH₂ (D, H, L) in the absence and presence of increasing concentrations of Boc5 for cAMP accumulation (A-D), pERK1/2 (E-H) and iCa²⁺ mobilisation (I-L) in FlpInCHO cells stably expressing the human GLP-1R. Data are analysed with a three-parameter logistic equation. All values are means \pm S.E.M of three independent experiments, conducted in duplicate.

Supplementary figure 8. TT15 displays behaviour consistent with competitive interaction with peptides in GLP-1R-mediated signalling.

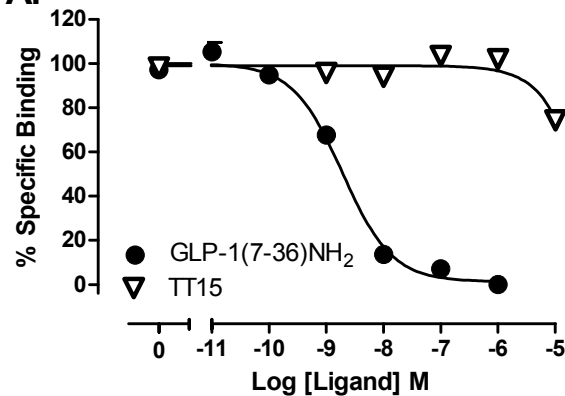
Concentration response curves were generated for exendin-4 (A, E, I), GLP-1(7-36)NH₂ (B, F, J), Oxyntomodulin (C, G, K) or GLP-1(1-36)NH₂ (D, H, L) in the absence and presence of increasing concentrations of TT15 for cAMP accumulation (A-D), pERK1/2 (E-H) and iCa²⁺ mobilisation (I-L) in FlpInCHO cells stably expressing the human GLP-1R. Data are analysed with a three-parameter logistic equation. All values are means \pm S.E.M of three independent experiments, conducted in duplicate.

Supplementary figure 9. BMS21, Boc5 and TT15 display behaviour consistent with competitive interaction when interacted together in GLP-1R-mediated cAMP signalling.

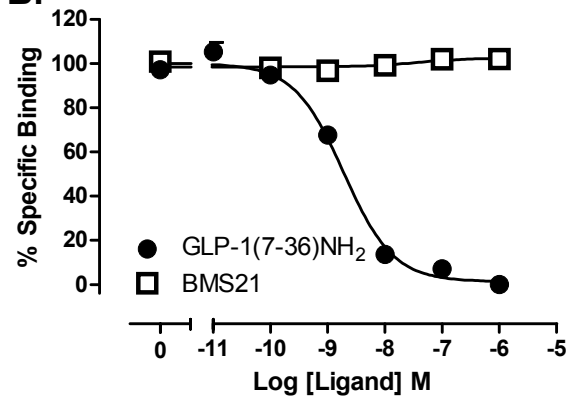
Concentration response curves were generated for Boc5 (A, B) and TT15 (C) in the absence and presence of increasing concentrations of either TT15 (A) or BMS21 (B-C) in FlpInCHO cells stably expressing the human GLP-1R. Data are analysed with a three-parameter logistic equation. All values are means \pm S.E.M of three independent experiments, conducted in duplicate.

Supplementary figure 1

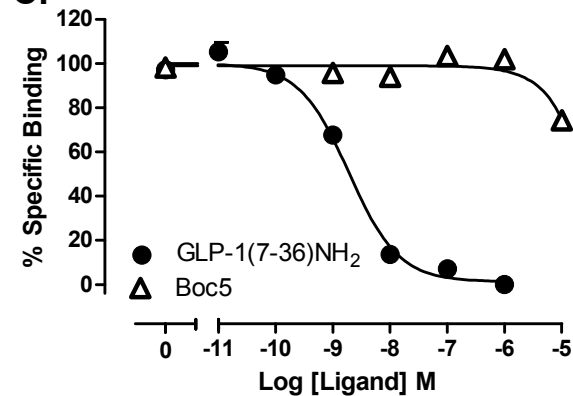
A.



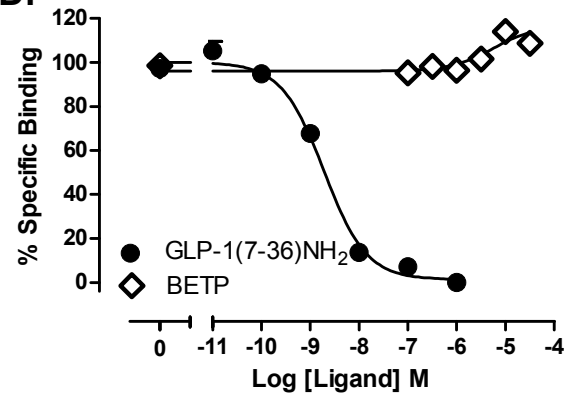
B.



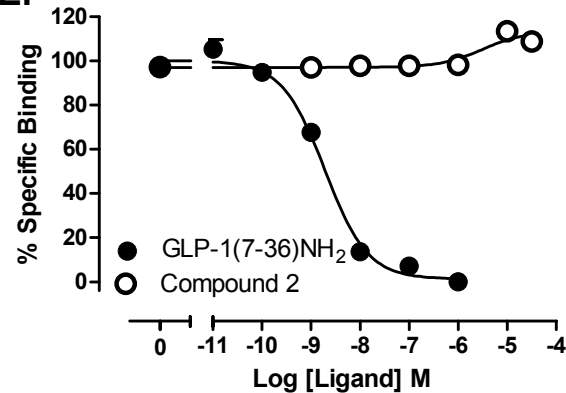
C.



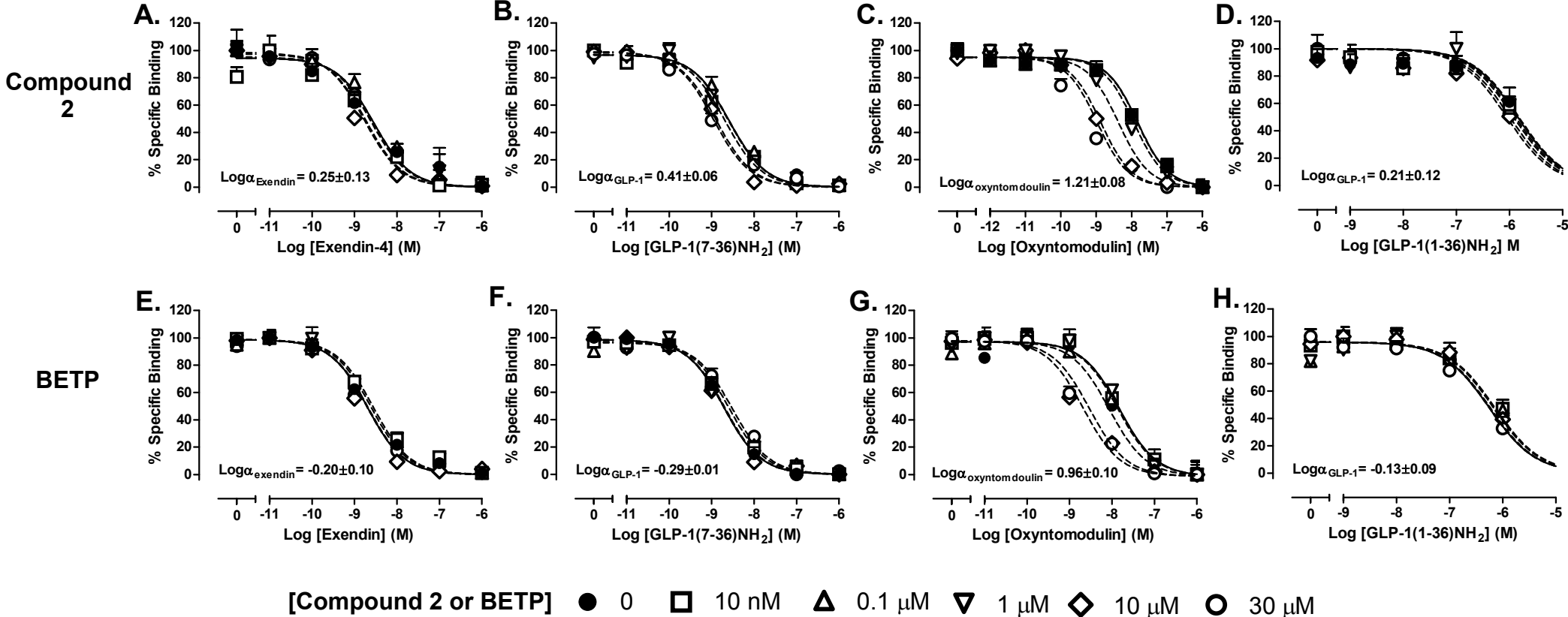
D.



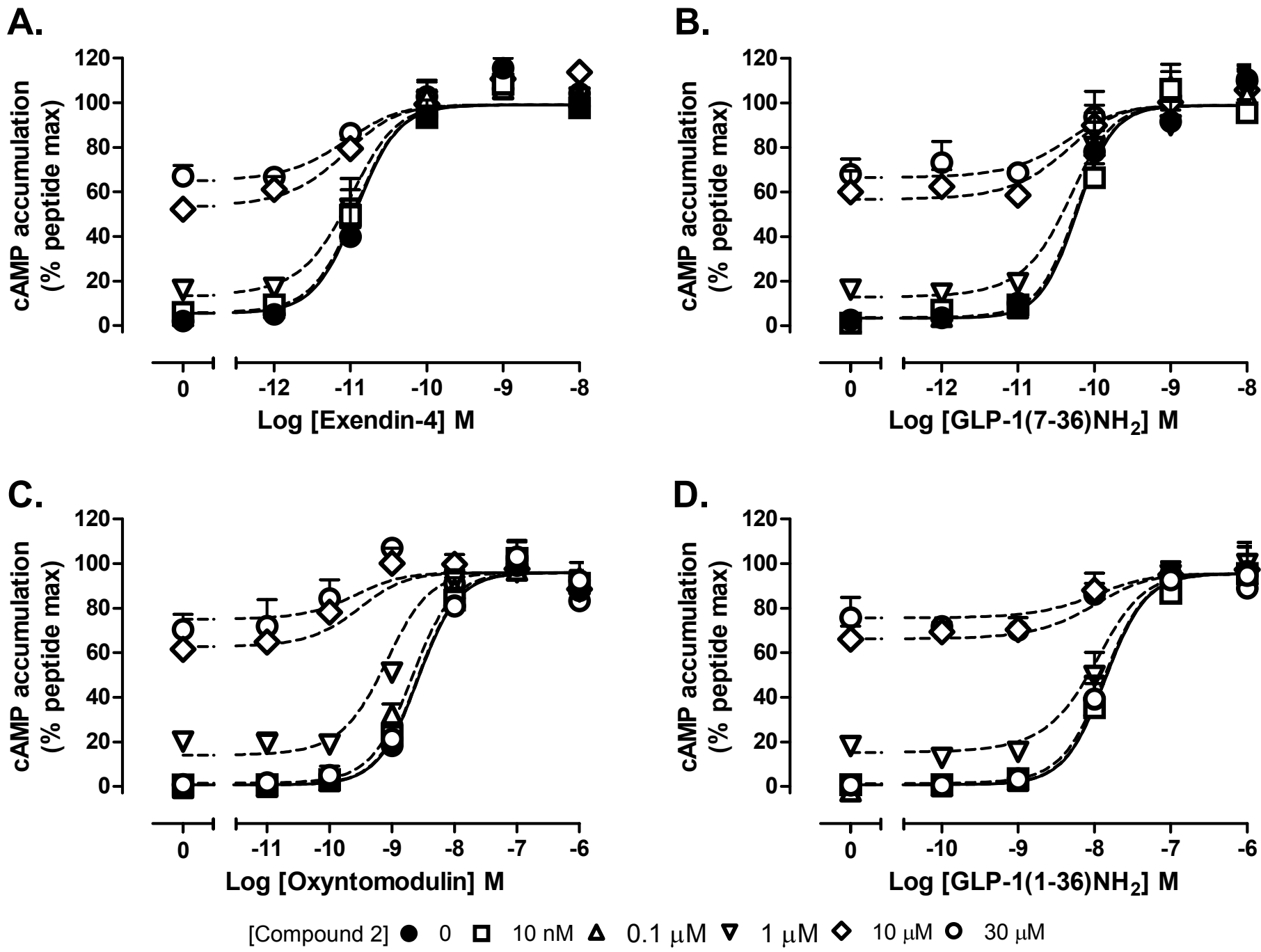
E.



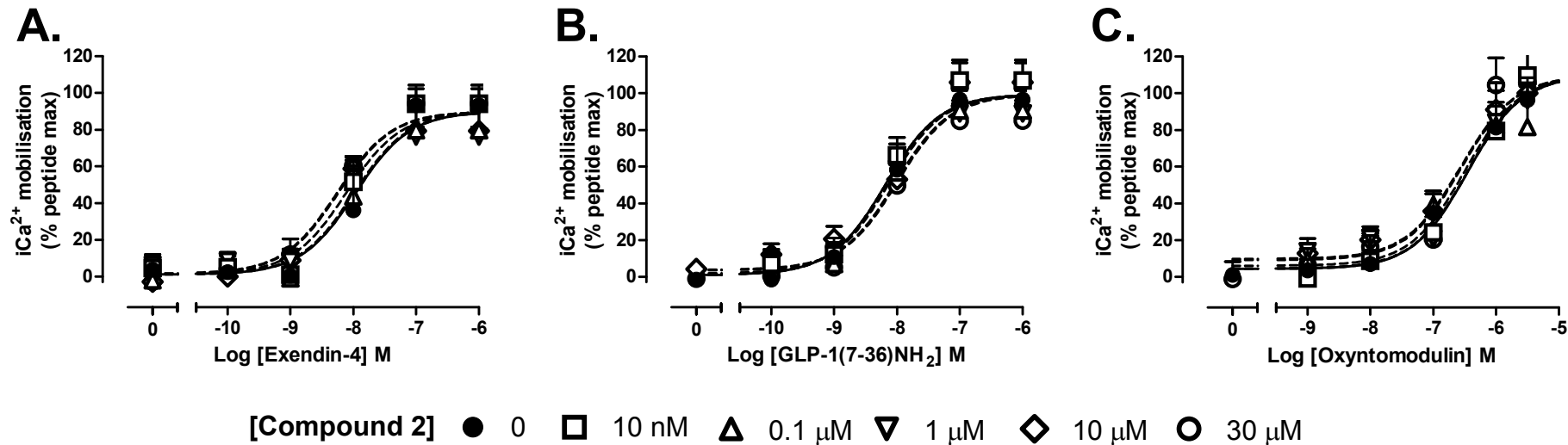
Supplementary figure 2



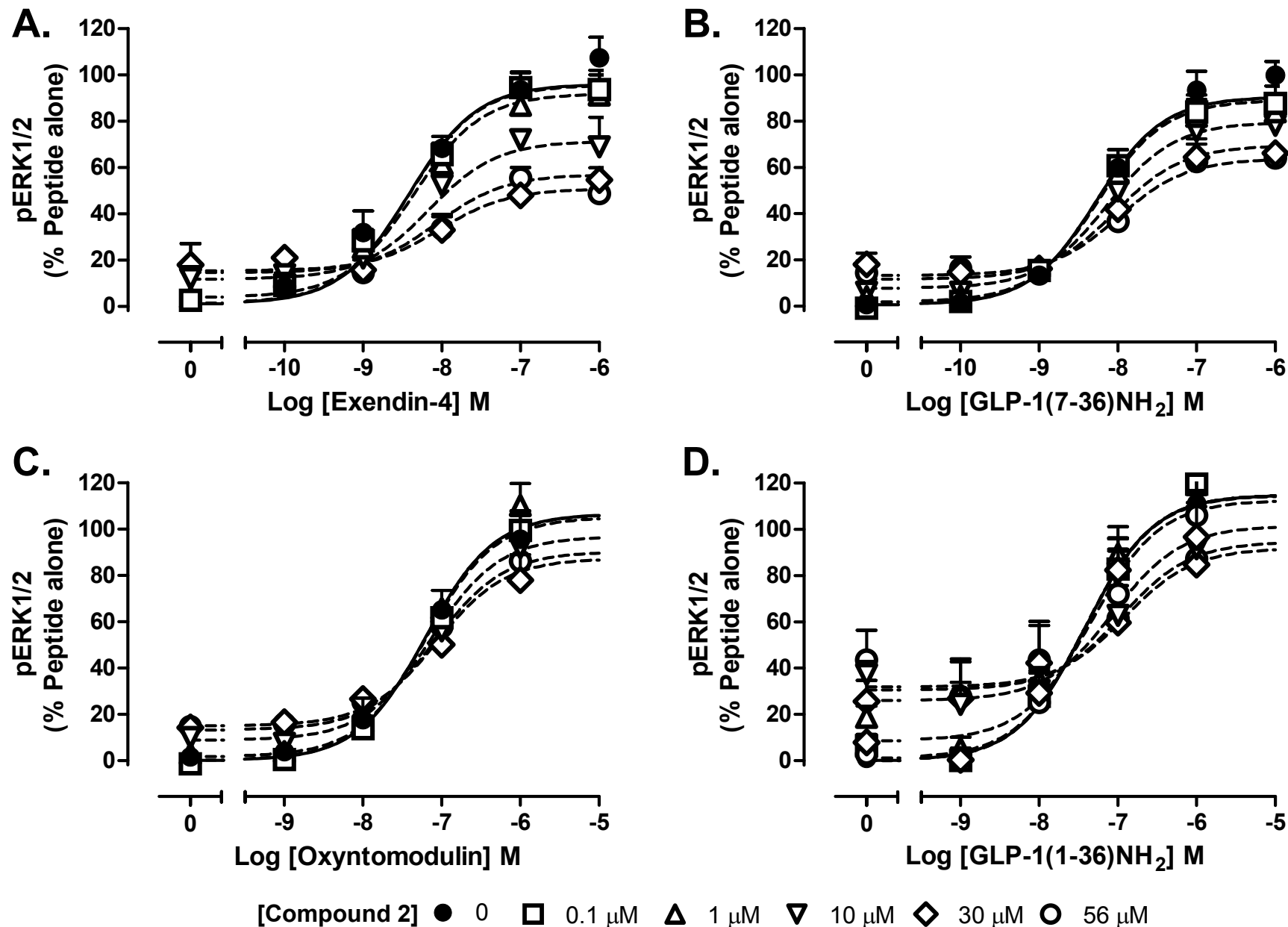
Supplementary figure 3



Supplementary figure 4

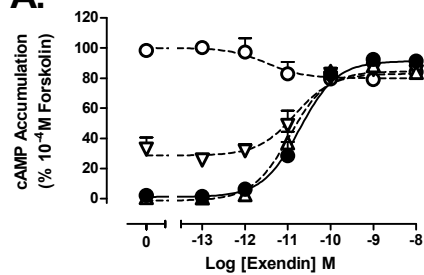


Supplementary figure 5

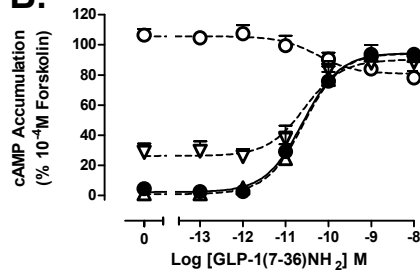


Supplementary figure 6

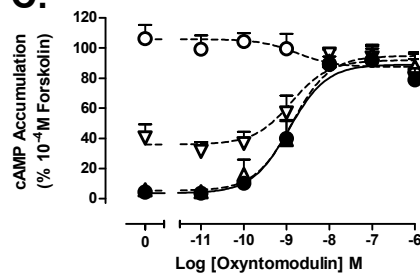
A.



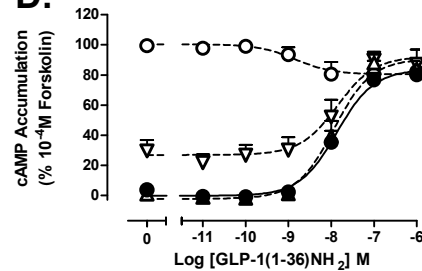
B.



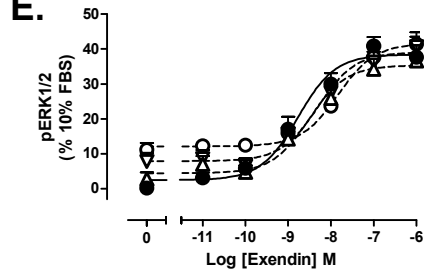
C.



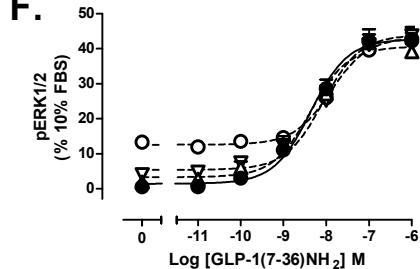
D.



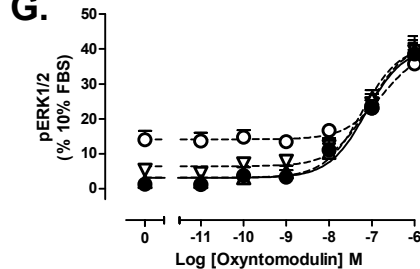
E.



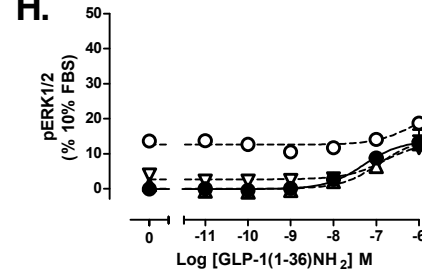
F.



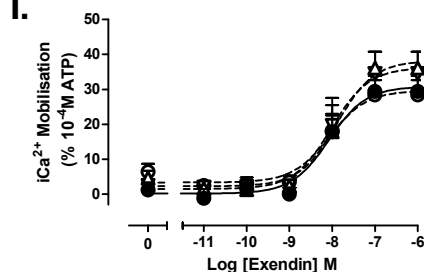
G.



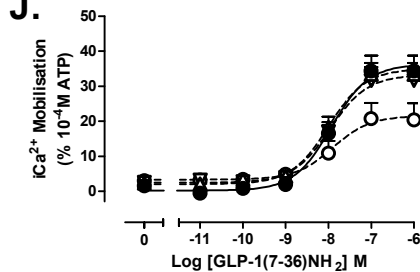
H.



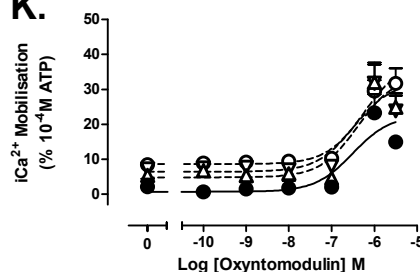
I.



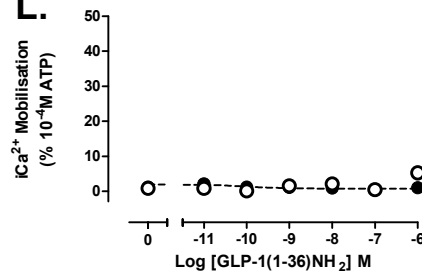
J.



K.



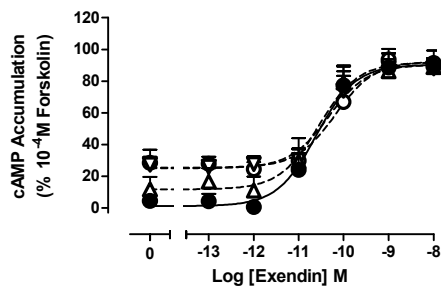
L.



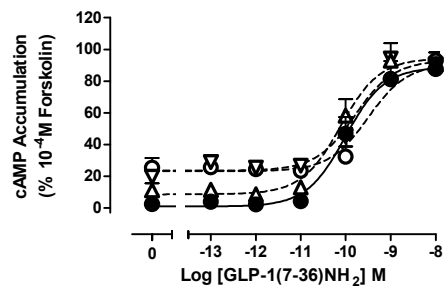
[BMS21] ● 0 ▲ 10 nM ▼ 0.1 μ M ○ 1 μ M

Supplementary figure 7

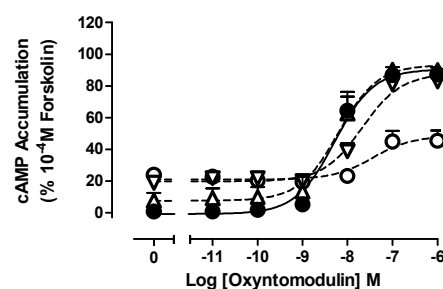
A.



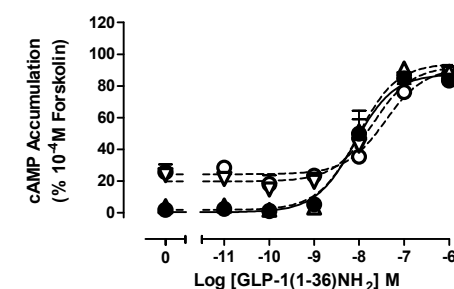
B.



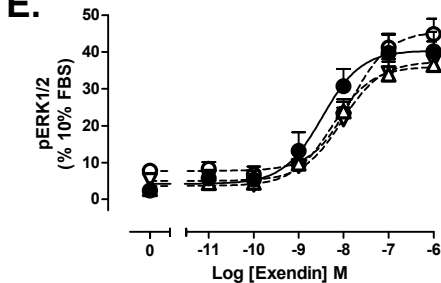
C.



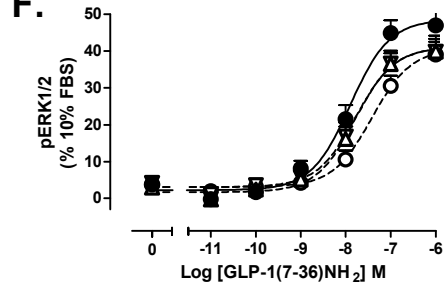
D.



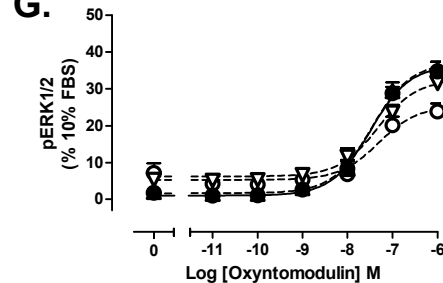
E.



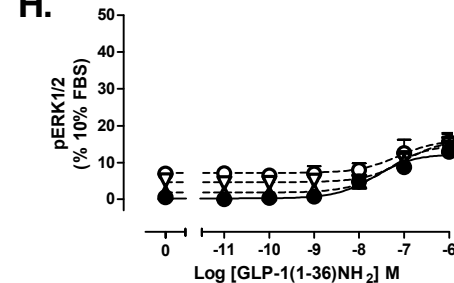
F.



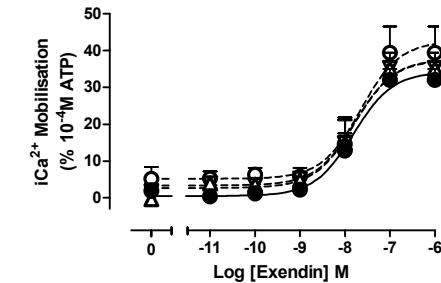
G.



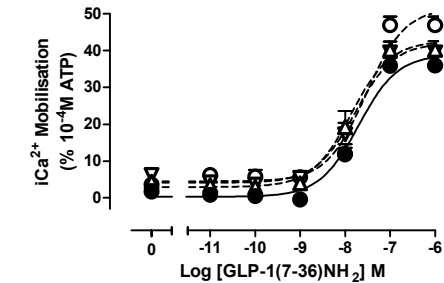
H.



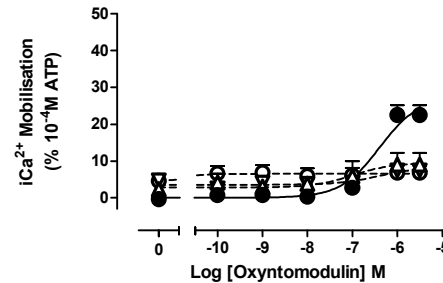
I.



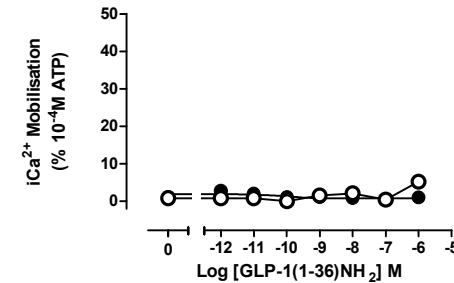
J.



K.



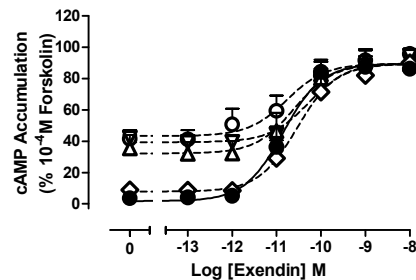
L.



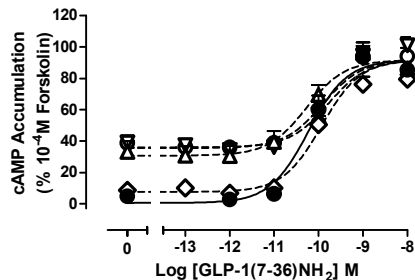
[Boc5] ● 0 ▲ 0.1 μ M ▼ 1 μ M ○ 10 μ M

Supplementary figure 8

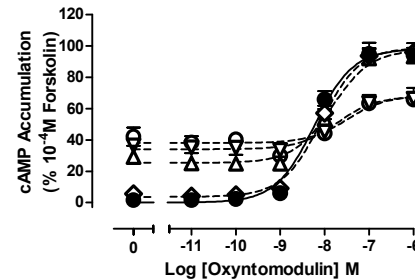
A.



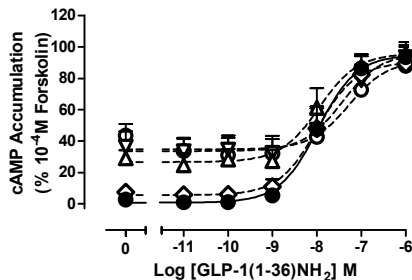
B.



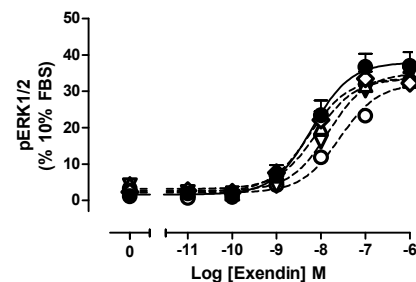
C.



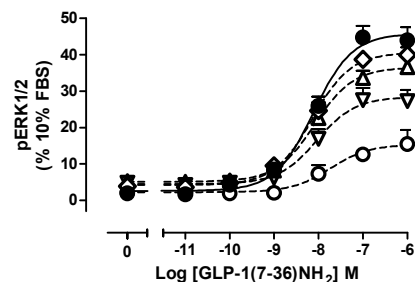
D.



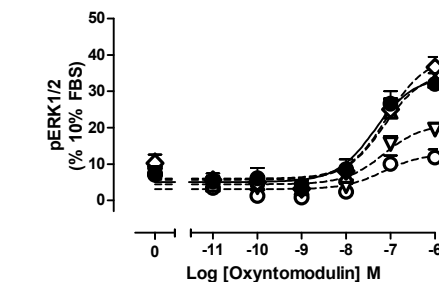
E.



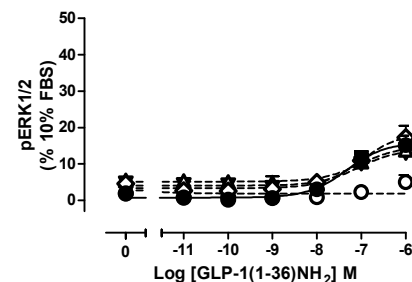
F.



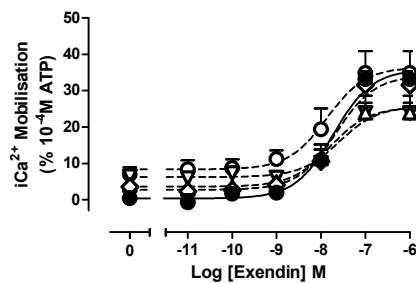
G.



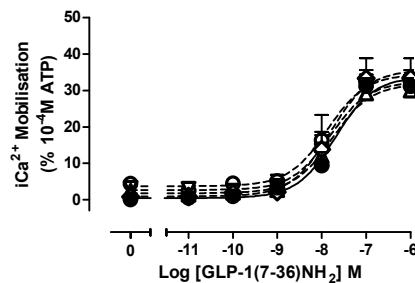
H.



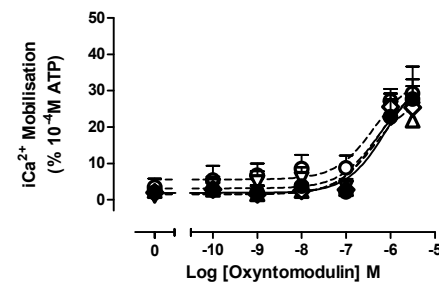
I.



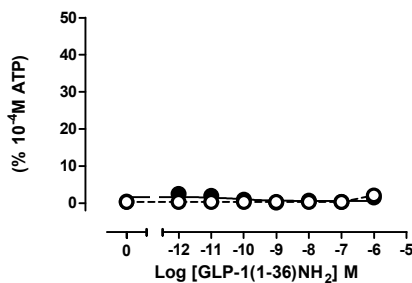
J.



K.



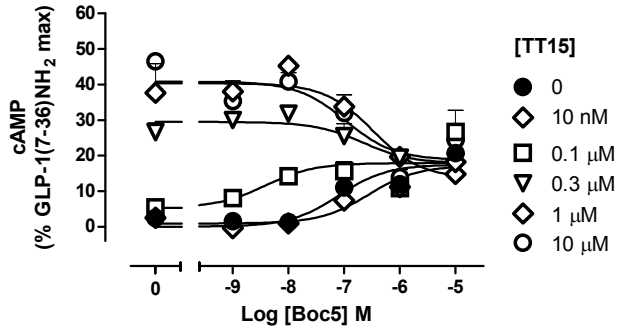
L.



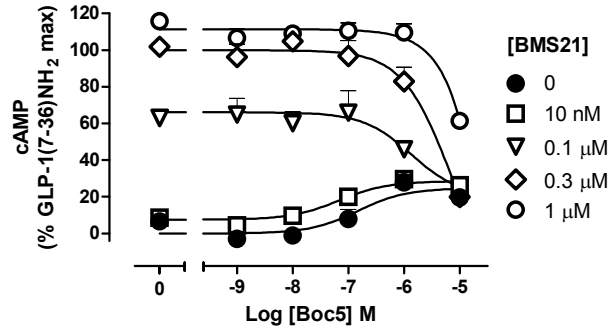
[TT15] ● 0 ◇ 0.1 μ M ▲ 1 μ M ▼ 10 μ M ○ 30 μ M

Supplementary figure 9

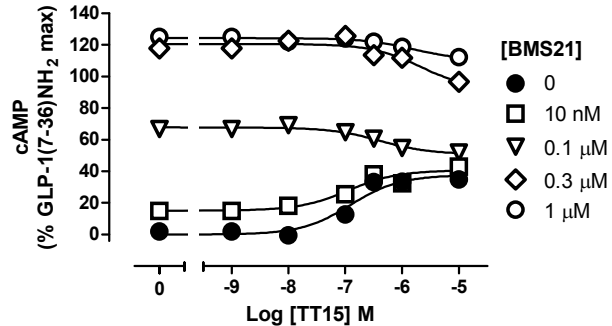
A.



B.



C.



Differential Impact of Amino Acid Substitutions on Critical Residues of the Human Glucagon-Like Peptide-1 Receptor Involved in Peptide Activity and Small-Molecule Allostery[§]

Cassandra Koole, Denise Wootten, John Simms,¹ Laurence J. Miller, Arthur Christopoulos, and Patrick M. Sexton

Drug Discovery Biology Laboratory, Monash Institute of Pharmaceutical Sciences and Department of Pharmacology, Monash University, Parkville, Victoria, Australia (C.K., D.W., J.S., A.C., P.M.S.); and Department of Molecular Pharmacology and Experimental Therapeutics, Mayo Clinic, Scottsdale, Arizona (L.J.M.)

Received October 20, 2014; accepted January 26, 2015

ABSTRACT

The glucagon-like peptide-1 receptor (GLP-1R) is a class B G protein-coupled receptor that has a critical role in the regulation of glucose homeostasis, principally through the regulation of insulin secretion. The receptor system is highly complex, able to be activated by both endogenous [GLP-1(1–36)NH₂, GLP-1(1–37), GLP-1(7–36)NH₂, GLP-1(7–37), oxyntomodulin], and exogenous (exendin-4) peptides in addition to small-molecule allosteric agonists (compound 2 [6,7-dichloro-2-methylsulfonyl-3-*tert*-butylaminoquinoxaline], BETP [4-(3-benzyloxy)phenyl]-2-ethylsulfinyl-6-(trifluoromethyl)pyrimidine]). Furthermore, the GLP-1R is subject to single-nucleotide polymorphic variance, resulting in amino acid changes in the receptor protein. In this study, we investigated two polymorphic variants previously reported to impact peptide-mediated receptor activity (M149) and small-molecule allostery (C333). These residues were mutated to a series of alternate

amino acids, and their functionality was monitored across physiologically significant signaling pathways, including cAMP, extracellular signal-regulated kinase 1 and 2 phosphorylation, and intracellular Ca²⁺ mobilization, in addition to peptide binding and cell-surface expression. We observed that residue 149 is highly sensitive to mutation, with almost all peptide responses significantly attenuated at mutated receptors. However, most reductions in activity were able to be restored by the small-molecule allosteric agonist compound 2. Conversely, mutation of residue 333 had little impact on peptide-mediated receptor activation, but this activity could not be modulated by compound 2 to the same extent as that observed at the wild-type receptor. These results provide insight into the importance of residues 149 and 333 in peptide function and highlight the complexities of allosteric modulation within this receptor system.

Introduction

The glucagon-like peptide 1 receptor (GLP-1R) is a class B peptide hormone G protein-coupled receptor (GPCR) with physiologically important actions, including increases in insulin biosynthesis and secretion from pancreatic β -cells and decreases in β -cell apoptosis, gastric emptying, and peripheral tissue resistance to insulin. For these reasons, the GLP-1R is one of the key targets in the development of therapeutics for type 2 diabetes mellitus (DM). However, with increasing interest in establishing novel, long-acting and orally available therapeutics that eliminate or at least significantly reduce detrimental side

effects, the pharmacologic complexities of targeting this receptor system are becoming evident.

The most well documented consequence of GLP-1R activation is enhanced cAMP production, which, along with cell membrane depolarization and the influx of Ca²⁺, is critical in the biosynthesis and exocytosis of insulin from pancreatic β -cells (Fehmann and Habener, 1992; Lu et al., 1993). However, the GLP-1R can couple via other G protein-dependent mechanisms, including G α_i , G α_o , and G $\alpha_{q/11}$ (Montrose-Rafizadeh et al., 1999; Hallbrink et al., 2001), as well as via β -arrestin recruitment and signaling (Jorgensen et al., 2005, 2007; Sonoda et al., 2008). Furthermore, with the ability to be activated by multiple endogenous agonists [GLP-1(1–36)NH₂, GLP-1(1–37), GLP-1(7–36)NH₂, GLP-1(7–37) and oxyntomodulin] as well as the exogenous peptide agonist exendin-4 (exenatide, Byetta; Astra-Zeneca, Wilmington, DE) that is currently used as a type 2 diabetic treatment and allosteric ligands such as compound 2 [6,7-dichloro-2-methylsulfonyl-3-*tert*-butylaminoquinoxaline], the phenomenon of biased agonism can be clearly observed at this receptor (Kenakin, 1995, 2011; Koole et al., 2010, 2012a,b).

This work was funded by National Health and Medical Research Council of Australia (NHMRC) project [Grant 1061044, 1065410] and program [Grant 1055134] grants. P.M.S. and A.C. are Principal Research Fellows of the NHMRC.

¹Current affiliation: Department of Pharmacology, Aston University, Birmingham, United Kingdom.

dx.doi.org/10.1124/jpet.114.220913.

[§] This article has supplemental material available at jpet.aspetjournals.org.

ABBREVIATIONS: BETP, 4-(3-benzyloxy)phenyl]-2-ethylsulfinyl-6-(trifluoromethyl)pyrimidine; CHO, Chinese hamster ovary; compound 2, 6,7-dichloro-2-methylsulfonyl-3-*tert*-butylaminoquinoxaline; CRF, corticotropin-releasing factor; DM, diabetes mellitus; FBS, fetal bovine serum; GLP-1R, glucagon-like peptide-1 receptor; GPCR, G protein-coupled receptor; ICL, intracellular loop; pERK1/2, phosphorylated extracellular signal regulated kinase 1 and 2; SNP, single nucleotide polymorphism; TM, transmembrane.

Adding to the complexity of this receptor system, recent pharmacologic analysis of GLP-1R single nucleotide polymorphisms (SNPs) (Beinborn et al., 2005; Fortin et al., 2010; Koole et al., 2011) identified two variants that significantly influence receptor function: M149 [transmembrane domain (TM) 1], which attenuates endogenous and exogenous peptide-mediated receptor function (Beinborn et al., 2005; Koole et al., 2011), and C333 [intracellular loop (ICL) 3], which reduces the allosteric agonism of the GLP-1R small-molecule compound 2, as well as significantly impacting its modulatory profile (Koole et al., 2011). Although population analysis of these receptor variants suggests a low heterozygous frequency and unknown homozygous frequency, for at least the M149 variant, there has been a direct implication in the onset of type 2 DM (Tokuyama et al., 2004). Moreover, the significant loss of peptide function at this receptor variant would also suggest that subjects administered peptide mimetics, such as exendin-4, would experience limited effectiveness in management of the condition (Koole et al., 2011).

In the absence of high-resolution crystal structures of the GLP-1R in its entirety, and, in fact, any class B GPCR as a whole entity, the structural role of these residues and their influence on the mechanistic function of the receptor are largely unclear. However, with the emergence of two class B TM crystal structures (Hollenstein et al., 2013; Siu et al., 2013) and a plethora of mutagenesis (Lopez de Maturana and Donnelly, 2002; Lopez de Maturana et al., 2004; Coopman et al., 2011; Koole et al., 2012a,b; Wootten et al., 2013) and photoaffinity labeling data (Al-Sabah and Donnelly, 2003; Dong et al., 2004, 2007, 2011; Chen et al., 2009, 2010; Miller et al., 2011; Coin et al., 2013), structurally and functionally important components of the GLP-1R can begin to be predicted and complementary molecular models can be further refined. In this study, we have created a series of mutations at two GLP-1R residues subject to polymorphic variance (amino acids 149 and 333; Fig. 1) at which receptor function is significantly affected, to examine more broadly their involvement in receptor structure and function. We observed that mutation of residue 149, at which Thr most frequently occurs, is poorly tolerated in the context of peptide-mediated receptor activation but not that of the allosteric agonist compound 2. In addition, mutants of this residue with significantly reduced peptide activity were able to have at least partial restoration of function through compound 2-mediated allosteric modulation of the receptor. Conversely, at residue 333, at which Ser most frequently occurs, receptor mutants exerted little influence on peptide function in any detected output; however, modulation of oxyntomodulin-induced cAMP formation by compound 2 was significantly attenuated despite compound 2 retaining agonism. Together, these results not only enhance our understanding of the role of SNPs in receptor activity but also facilitate the refinement of models in understanding the complex molecular mechanisms involved in GLP-1R activity.

Materials and Methods

Dulbecco's modified Eagle's medium, hygromycin-B, and Fluo-4 acetoxymethyl ester were purchased from Invitrogen (Carlsbad, CA). Fetal bovine serum (FBS) was purchased from Thermo Fisher Scientific (Melbourne, VIC, Australia). The QuikChange site-directed mutagenesis kit was purchased from Stratagene (La Jolla, CA). AlphaScreen reagents, Bolton-Hunter reagent ($[^{125}\text{I}]$), and 384-well ProxiPlates were

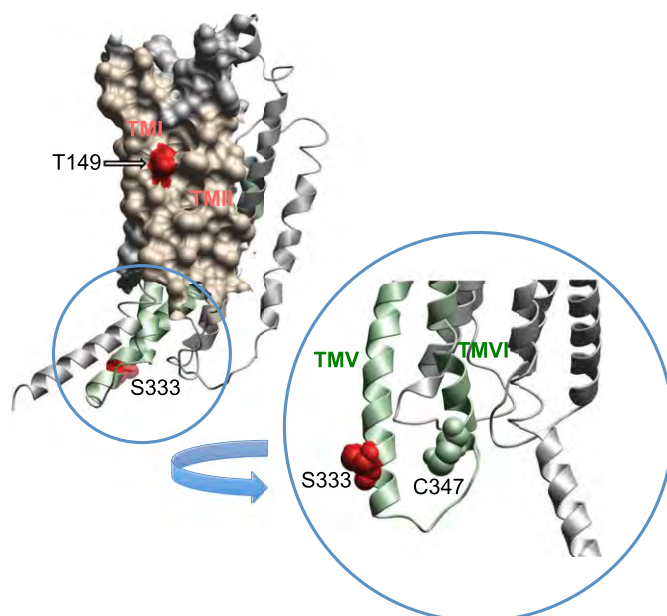


Fig. 1. Homology model of the GLP-1R based on the glucagon receptor structure. The positions of residues 149 and 333 are illustrated in red. The surface map of TM1 and TM2 helices is colored beige. TM5 and TM6 are depicted in green (ribbon structure). Inset: Magnification of ICL3 illustrating the position of residue 333 and C347 that is involved in covalent interaction with compound 2.

purchased from PerkinElmer Life and Analytical Sciences (Waltham, MA). SureFire ERK1/2 reagents were generously supplied by TGR Biosciences (Adelaide, SA, Australia). SigmaFast *O*-phenylenediamine dihydrochloride tablets and antibodies were purchased from Sigma-Aldrich (St. Louis, MO). Compound 2 was generated according to a method published previously (Teng et al., 2007) to a purity of >95%, and compound integrity was confirmed by NMR. GLP-1 and GLP-1 peptide analogs were purchased from American Peptide (Sunnyvale, CA). All other reagents were purchased from Sigma-Aldrich or BDH Merck (Melbourne, VIC, Australia) and were of an analytical grade.

Receptor Mutagenesis. SNPs of the GLP-1R with pharmacologic profiles deviating from wild-type, as determined from our previous study (Koole et al., 2011), were mutated to a selection of amino acids. Mutations were introduced to an N-terminally double c-myc labeled wild-type human GLP-1R in the pEF5/FRT/V5-DEST destination vector (Invitrogen); this receptor had equivalent pharmacology to the untagged human GLP-1R (data not shown). Mutagenesis was carried out using oligonucleotides for site-directed mutagenesis from GeneWorks (Hindmarsh, SA, Australia) (Supplemental Table S1) and the QuikChange site-directed mutagenesis kit (Stratagene). Sequences of receptor clones were confirmed by cycle sequencing as previously described (May et al., 2007). In this study, wild-type GLP-1R is composed of T149 and S333.

Transfections and Cell Culture. Wild-type and mutant human GLP-1R were isogenically integrated into FlpIn-Chinese hamster ovary (FlpInCHO) cells (Invitrogen), and selection of receptor-expressing cells was accomplished by treatment with $600 \mu\text{g ml}^{-1}$ hygromycin-B as previously described (May et al., 2007). Transfected and parental FlpInCHO cells were maintained in Dulbecco's modified Eagle's medium supplemented with 10% heat-inactivated FBS and incubated in a humidified environment at 37°C in 5% CO_2 .

Radioligand Binding Assay. FlpInCHO wild-type and mutant human GLP-1R cells were seeded at a density of 3×10^4 cells/well into 96-well culture plates and incubated overnight at 37°C in 5% CO_2 , and radioligand binding was carried out at 4°C as previously described (Koole et al., 2011). For each cell line in all experiments, total binding was defined by 0.5 nM $[^{125}\text{I}]$ exendin(9–39) alone, and nonspecific binding was defined by 1 μM exendin(9–39). For analysis, data are normalized to the B_0 value for each individual experiment. Of note, the

condition of assay for radioligand binding and functional experiments are different and as such cannot be directly compared.

cAMP Accumulation Assay. FlpInCHO wild-type and mutant human GLP-1R cells were seeded at a density of 3×10^4 cells/well into 96-well culture plates and incubated overnight at 37°C in 5% CO₂, and cAMP detection carried out as previously described (Koole et al., 2010). For interaction studies, increasing concentrations of peptide and 3 μM compound 2 were added simultaneously, and cAMP accumulation measured after 30 minutes of cell stimulation. All values were converted to concentration of cAMP using a cAMP standard curve performed in parallel, and data were subsequently normalized to the response of 100 μM forskolin in each cell line. Agonist stimulation and interaction studies were performed as two different series of experiments and on different cell passages.

Phosphorylated Extracellular Signal-Regulated Kinase 1 and 2 Assay. FlpInCHO wild-type and mutant human GLP-1R cells were seeded at a density of 3×10^4 cells/well into 96-well culture plates and incubated overnight at 37°C in 5% CO₂. Receptor-mediated phosphorylated extracellular signal-regulated kinase 1 and 2 (pERK1/2) was determined using the AlphaScreen ERK1/2 SureFire protocol as previously described (May et al., 2007). Initial pERK1/2 time course experiments were performed over 1 hour to determine the time at which agonist-mediated pERK1/2 was maximal. Subsequent experiments were then performed at the time required to generate a maximal pERK1/2 response (6 minutes). Data were normalized to the maximal response elicited by 10% FBS in each cell line, determined at 6 minutes (peak FBS response).

iCa²⁺ Mobilization Assay. FlpInCHO wild-type and mutant human GLP-1R cells were seeded at a density of 3×10^4 cells/well into 96-well culture plates and incubated overnight at 37°C in 5% CO₂, and receptor-mediated iCa²⁺ mobilization was determined as previously described (Werry et al., 2005). Fluorescence was determined immediately after peptide addition, with an excitation wavelength set to 485 nm and an emission wavelength set to 520 nm; readings were taken every 1.36 seconds for 120 seconds. Peak magnitude was calculated using five-point smoothing, followed by correction against basal fluorescence. The peak value was used to create concentration-response curves. Data were normalized to the maximal response elicited by 100 μM ATP.

Cell-Surface Receptor Expression. FlpInCHO wild-type and mutant human GLP-1R cells, with receptor DNA previously incorporated

with an N-terminal double c-myc epitope label, were seeded at a density of 25×10^4 cells/well into 24-well culture plates and incubated overnight at 37°C in 5% CO₂, washed three times in 1× PBS, and fixed with 3.7% paraformaldehyde at 4°C for 15 minutes. Cell-surface receptor detection was then performed as previously described (Koole et al., 2011). Data were normalized to the basal fluorescence detected in FlpInCHO parental cells. Specific [¹²⁵I]exendin(9–39) binding at each receptor mutant, as identification of functional receptors at the cell surface, was also determined [corrected for nonspecific binding using 1 μM exendin(9–39)].

Data Analysis. All data were analyzed using Prism 5.04 (Graph-Pad Software Inc., San Diego, CA). For all analyses, the data were unweighted, and each y value (mean of replicates for each individual experiment) was considered an individual point. Concentration-response signaling data were analyzed using a three-parameter logistic equation (eq. 1) as previously described (May et al., 2007):

$$E = \text{Bottom} + \frac{(\text{Top} - \text{Bottom})[A]}{[A] + [EC_{50}]} \quad (1)$$

where *bottom* represents the *E* value in the absence of ligand(s), *top* represents the maximal stimulation in the presence of ligand(s), *[A]* is the molar concentration of ligand, and *EC*₅₀ represents the molar concentration of ligand required to generate a response halfway between *top* and *bottom*. Similarly, this equation was used in the analysis of inhibition binding data, replacing *EC*₅₀ with *IC*₅₀. In this case, *bottom* defines the specific binding of the radioligand that is equivalent to nonspecific ligand binding, whereas *top* defines radioligand binding in the absence of a competing ligand, and the *IC*₅₀ value represents the molar concentration of ligand required to generate a response halfway between *top* and *bottom*. *IC*₅₀ values obtained were then corrected for radioligand occupancy as previously described (Cheng and Prusoff, 1973) using the radioligand affinity (*K*_i) experimentally determined for each mutant.

To quantify efficacy in the system, all data were fitted with an operational model of agonism shown in eq. 2 (Black and Leff, 1983):

$$E = \text{Bottom} + \frac{(\text{Top} - \text{Bottom})\tau[A]}{\tau[A] + [A] + K_A} \quad (2)$$

where *top* represents the maximal stimulation in the system; *K*_A is the agonist-receptor dissociation constant, in molar concentration; *τ* is the

TABLE 1

Effects of human GLP-1R 149 or 333 mutation on peptide ligand binding and cell surface expression

Binding data were analyzed using a three-parameter logistic equation as defined in eq. 1 to obtain p*IC*₅₀ values. p*IC*₅₀ values were then corrected for radioligand occupancy using the radioligand dissociation constant for each mutant, allowing determination of ligand affinity (*K*_i). Data were normalized to maximum [¹²⁵I]exendin(9–39) binding in the absence of ligand, with nonspecific binding measured in the presence of 1 μM exendin(9–39). For specific [¹²⁵I]exendin(9–39) binding, data are expressed as a maximum of specific [¹²⁵I]exendin(9–39) binding at the wild-type human GLP-1R. Cell surface expression was determined through antibody detection of the N-terminal c-myc epitope label, with data expressed as a maximum of wild-type human GLP-1R expression. All values are expressed as mean ± S.E.M. of three to four independent experiments, conducted in duplicate. Data were analyzed with one-way analysis of variance and Dunnett's post-test.

	Binding (p <i>K</i> _i)				Cell-Surface Expression	Specific [¹²⁵ I]Exendin(9–39) Binding
	GLP-1(7–36)NH ₂	Exendin-4	Oxyntomodulin	Exendin(9–39) ^a		
						% <i>Wild-type</i>
Wild-type (T ¹⁴⁹ , S ³³³)	9.1 ± 0.1	9.7 ± 0.1	8.1 ± 0.1	8.0 ± 0.0	100 ± 6	100 ± 14
M ^{149b}	6.5 ± 0.2*	7.9 ± 0.2*	5.5 ± 0.2*	NA	47 ± 9*	NA
A ¹⁴⁹	6.8 ± 0.1*	7.8 ± 0.1*	6.2 ± 0.1*	8.0 ± 0.0	110 ± 7	113 ± 30
C ¹⁴⁹	7.6 ± 0.1*	8.4 ± 0.1*	6.9 ± 0.1*	8.0 ± 0.0	156 ± 6*	218 ± 29**
F ¹⁴⁹	6.4 ± 0.1*	7.5 ± 0.1*	5.6 ± 0.1*	8.0 ± 0.0	94 ± 6	90 ± 23
I ¹⁴⁹	6.8 ± 0.1*	7.8 ± 0.1*	6.0 ± 0.2*	8.0 ± 0.0	99 ± 5	154 ± 20
S ¹⁴⁹	8.3 ± 0.1*	9.4 ± 0.0	7.6 ± 0.1*	8.0 ± 0.0	88 ± 7	125 ± 24
V ¹⁴⁹	6.7 ± 0.1*	7.8 ± 0.1*	6.2 ± 0.1*	8.0 ± 0.0	72 ± 4*	139 ± 26
Y ¹⁴⁹	6.8 ± 0.1*	7.5 ± 0.1*	6.0 ± 0.1*	8.0 ± 0.0	53 ± 5*	87 ± 15
C ^{333b}	9.0 ± 0.1	9.6 ± 0.1	8.0 ± 0.1	NA	51 ± 6*	NA
A ³³³	9.1 ± 0.1	9.6 ± 0.1	8.0 ± 0.1	8.0 ± 0.0	122 ± 9	124 ± 15
V ³³³	9.2 ± 0.1	9.8 ± 0.1	8.4 ± 0.1	8.0 ± 0.0	86 ± 5	101 ± 26

NA, data not experimentally determined in Koole et al., 2011.

^aEquivalent at one significant figure.

^bData obtained from Koole et al., 2011. Reported values for binding are p*IC*₅₀.

*Statistically significant at *P* < 0.05, one-way analysis of variance and Dunnett's post-test in comparison with wild-type control; ***P* = 0.11.

estimated measure of efficacy in the system, which incorporates both signaling efficacy and receptor density; and all other parameters are as defined for eq. 1. Constraints for this model were determined by fitting the most efficacious peptide with the eq. 3:

$$E = Bottom + \frac{(E_m - Bottom)[A]}{[A] + [EC_{50}]} \quad (3)$$

The value obtained for the system maximum (E_m) was then globally constrained as the parameter, *top*, in the operational model (eq. 2) when applied at each mutant receptor. All estimated τ values were then corrected to cell surface expression (τ_c) as determined by percent specific [125 I]exendin(9–39) binding and errors propagated from both τ and cell surface expression relative to wild-type receptor. Of note, differences in functional K_A values derived from fitting the operational model may arise from the presence of noninterconverting states that are unique to ligand-receptor-effector complexes (Leff et al., 1997; Holst et al., 2001; Zheng et al., 2008; McPherson et al., 2010; Strachan et al., 2010; Nijmeijer et al., 2012), and this is observed for peptide agonists at the wild-type GLP-1R (Supplemental Table S2).

Statistics. Changes in peptide affinity, potency, efficacy, and cell-surface expression of human GLP-1R mutants in comparison with wild-type human GLP-1R control were statistically analyzed with one-way analysis of variance and Dunnett's post-test, and significance was accepted at $P < 0.05$.

Results

Mutation of Residue 149 or 333 Has Minimal Impact on Functional Human GLP-1R Expression at the Cell Surface. Wild-type N-terminally c-myc-tagged human GLP-1R or receptors incorporating the mutations of residues 149 or 333

were isogenically introduced into FlpInCHO host cells by recombination, and cell surface expression was determined through antibody detection of the c-myc epitope label (Table 1). In this study, mutation of residue 333 to either Ala or Val caused little deviation in cell surface expression in comparison with the wild-type human GLP-1R. In contrast, mutation of residue 149 to Val or Tyr significantly reduced receptor cell surface expression, whereas mutation of residue 149 to Cys significantly increased cell surface expression in comparison with wild-type control. No significant change in specific [125 I]exendin(9–39) binding was observed, although the C149 mutant trended toward increased binding ($P = 0.11$) consistent with the cell surface expression as monitored by c-myc antibody binding (Table 1). In addition, there was no significant difference in the level of receptor expression as determined by [125 I]exendin(9–39) binding. Wild-type receptor expression was 1.87 ± 0.33 million receptors/cell, and the mean level of expression across all mutants was 1.55 ± 0.32 million receptors/cell (data not shown).

Mutation of Residue 149 but Not 333 of the Human GLP-1R Significantly Affects Peptide Agonist Binding Affinity but Not Antagonist Exendin(9–39) Binding Affinity. Binding affinity of orthosteric GLP-1R peptide ligands at each of the mutant receptors was determined through equilibrium binding in the presence of the radiolabeled antagonist, [125 I]exendin(9–39) (Fig. 2; Table 1). Homologous competition identified no significant changes in antagonist exendin(9–39) binding affinity at any mutant receptor (Table 1). Consistent with results previously published (Koole et al., 2012a), complete inhibition curves were unable to be determined in the presence of GLP-1(1–36)NH₂ at any receptor mutant; given the

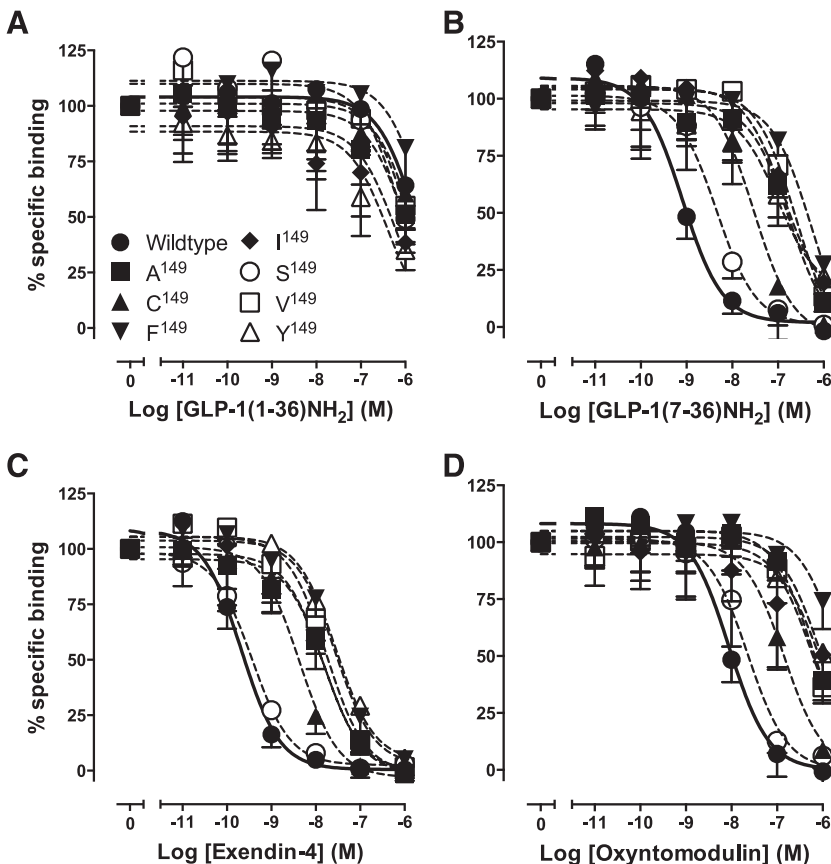


Fig. 2. Characterization of the binding of GLP-1(1–36)NH₂ (A), GLP-1(7–36)NH₂ (B), exendin-4 (C), and oxyntomodulin (D) in competition with the radiolabeled antagonist, [125 I]exendin(9–39), in whole FlpInCHO cells stably expressing wild-type human GLP-1R or each of the human GLP-1R mutants at the 149 receptor residue. Data are normalized to maximum [125 I]exendin(9–39) binding, with nonspecific binding measured in the presence of 1 μ M exendin(9–39), and analyzed with a three-parameter logistic equation as defined in eq. 1. $X = 0$ corresponds to conditions in which no ligand was added. All values are means \pm S.E.M. of three independent experiments, conducted in duplicate.

small window for competition within the concentration range tested, any deviations in binding affinity of this peptide at receptor mutants in comparison with wild-type control were difficult to interpret (Fig. 2A). For the remaining agonist peptides, no significant changes in binding affinity were observed for either Ala or Val substitutions at residue 333, whereas decreases in the binding affinity of GLP-1(7–36)NH₂, exendin-4, and oxyntomodulin were observed at all residue 149 receptor mutants (Fig. 2, B–D; Table 1). However, the extent of affinity reduction was variable, depending on both the residue substituted as well as the peptide present, with an overall greater effect of mutation on the affinity of GLP-1(7–36)NH₂ than exendin-4 or oxyntomodulin (Table 1). This is clearly evident at mutant receptors A149 and V149, with reductions of 79-fold for exendin-4 and oxyntomodulin at both mutants but 200- and 251-fold, respectively, for GLP-1(7–36)NH₂. Similarly, mutation of residue 149 to Phe resulted in decreases in binding affinity of 158-, 316-, and 501-fold for exendin-4, oxyntomodulin, and GLP-1(7–36)NH₂, respectively. Perhaps not surprisingly, mutation of residue 149 to Ser, which has properties of greatest similarity to that of the most frequently occurring residue, Thr, had the least effect on peptide binding affinity, albeit most reductions still reached statistical significance.

Most Mutations of Residue 149 but Not 333 of the Human GLP-1R Significantly Decrease Peptide-Mediated cAMP Accumulation. Whereas the GLP-1R is recognized as a pleiotropically coupled receptor, it is most well characterized for its role in enhancing adenylate cyclase activity and promoting the formation of cAMP, which is directly linked to the secretion of insulin (Baggio and Drucker, 2007). Consequently,

we assessed the ability of each mutant receptor to augment cAMP accumulation in the presence of each peptide agonist (Fig. 3; Table 2). Consistent with effects on binding affinity, no significant effect of mutation of residue 333 on peptide potency in cAMP accumulation was observed (Table 2). Taking into account cell-surface receptor expression and pathway coupling efficiency, application of the operational model to yield the operational measure of efficacy (τ_e) illustrated a general trend for decreased peptide-mediated cAMP coupling at both Ala and Val mutants of residue 333, although this trend did not reach statistical significance. In contrast, decreases in peptide potency in cAMP were observed for all mutant receptors of residue 149 (Fig. 3; Table 2). In agreement with binding data, peptide-mediated cAMP was least affected at S149 with respect to wild-type (T149), and this was also reflected by no significant differences in coupling efficacy (τ_e) when the operational model was applied (Table 2). However, there were trends for decreases in coupling efficacy in the presence of GLP-1(7–36)NH₂ and oxyntomodulin but increases in the presence of GLP-1(1–36)NH₂ and exendin-4, suggesting that the additional methyl group of Thr may contribute to discrimination of orthosteric peptide signaling profiles. Mutation of residue 149 to Cys resulted in decreased peptide potency but reached statistical significance only for oxyntomodulin. Analysis with the operational model revealed no significant deviations in pathway coupling efficacy (τ_e) at C149 in the presence of any peptide, although there was a trend toward decreases for all peptides in comparison with the wild-type (T149) receptor. Significant reductions in peptide-mediated cAMP were noted with mutation of T149 to Ala, Phe, Ile, Val, and Tyr, with only weak

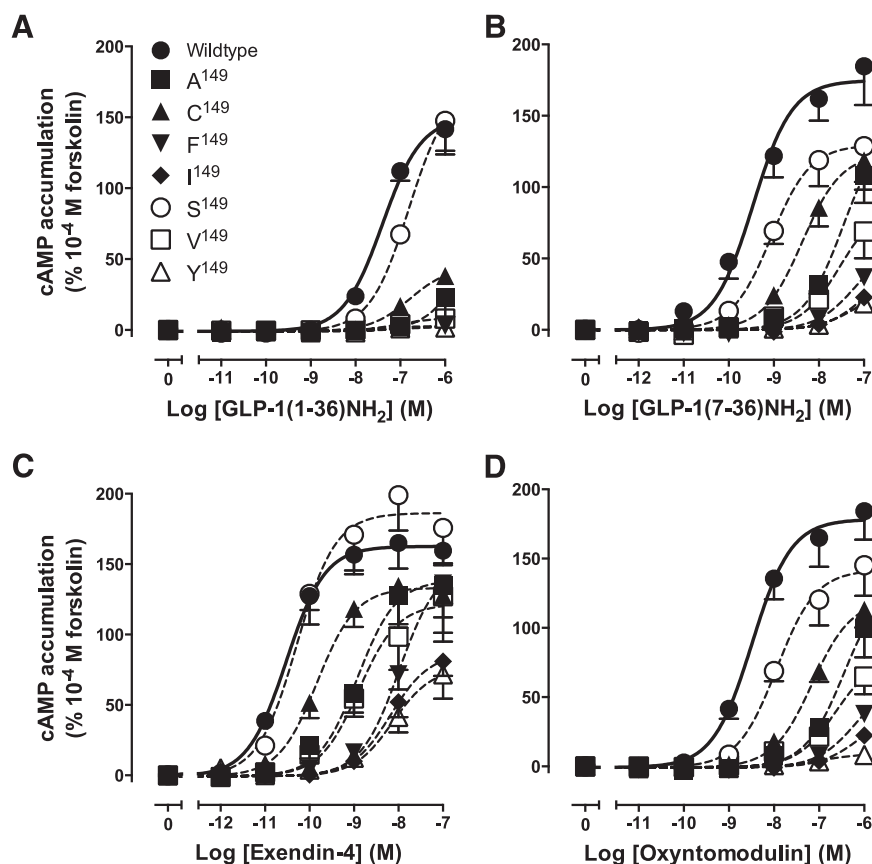


Fig. 3. Characterization of cAMP accumulation in the presence of GLP-1(1–36)NH₂ (A), GLP-1(7–36)NH₂ (B), exendin-4 (C), and oxyntomodulin (D) in FlpInCHO cells stably expressing the wild-type human GLP-1R or each of the human GLP-1R mutants at the 149 receptor residue. Data are normalized to the response elicited by 100 μ M forskolin and analyzed with an operational model of agonism as defined in eq. 2. $X = 0$ corresponds to conditions in which no ligand was added. All values are means \pm S.E.M. of four to five independent experiments, conducted in duplicate.

responses detected and potency values unable to be determined for GLP-1(1–36)NH₂, GLP-1(7–36)NH₂, and oxyntomodulin. Despite the inability to determine peptide potency values at these mutants, the rank order of reduction in peptide-mediated cAMP was consistent for all peptides: Ala > Val > Phe > Ile > Tyr (Fig. 3).

Most Mutations of Residue 149 but Not 333 of the Human GLP-1R Abolish iCa²⁺ Mobilization. Consistent with work presented previously (Koole et al., 2010), iCa²⁺ was weakly coupled to GLP-1R activation in F1phCHO cells, with no notable response for GLP-1(1–36)NH₂ at either the wild-type (T149, S333) or any receptor mutant (data not shown). Similarly, complete concentration-response curves in the presence of oxyntomodulin could not be established over the concentration range tested in this study. Comparison of responses at the highest peptide concentration tested (1 μM) revealed that mutation of residue 333 caused small increases in oxyntomodulin-mediated iCa²⁺ mobilization; however, these increases were not statistically significant (Table 3). Increases in *E*_{max} were also observed in GLP-1(7–36)NH₂- and exendin-4-mediated iCa²⁺ mobilization responses at both 333 mutants, despite little deviation in peptide potency. Although this increase in *E*_{max} reached statistical significance for GLP-1(7–36)NH₂, these data did not translate into significantly enhanced pathway coupling efficacy (τ_c) as determined through operational modeling (Table 3). Almost all substitutions at residue 149 had a significant impact on peptide-mediated iCa²⁺ mobilization (Fig. 4). The exception was S149, which displayed similar activity to that of the wild-type (T149) GLP-1R in the presence of all measurable peptide responses, reflected in the coupling efficacy (Fig. 4; Table 3). Interestingly, C149 showed no significant changes in peptide potency for either GLP-1(7–36)NH₂ or exendin-4, but it showed significant attenuation of maximal response for exendin-4 and oxyntomodulin (the latter a measure of response at 1 μM) and was also reflected in the estimated coupling efficacy (τ_c) whereby although both GLP-1(7–36)NH₂ and exendin-4 had reduced efficiency in the Ca²⁺ pathway, only exendin-4 reached statistical significance, indicating possible ligand specific effects of this residue on peptide activity (Table 3).

Most Mutations of Residue 149 but Not 333 of the Human GLP-1R Significantly Decrease Peptide-Mediated pERK1/2. Peptide-mediated pERK1/2 was measured at 6 minutes for each receptor mutant, the time at which maximal stimulation of pERK1/2 occurred at the wild-type GLP-1R (data not shown). For mutants with measurable peptide-mediated pERK1/2 responses, there was no significant alteration of peptide potency (Fig. 5; Table 4). This finding is consistent with what we have previously seen at GLP-1R mutants, indicating that receptor mutation generically has a lesser impact on coupling to ERK1/2 signaling (Koole et al., 2011). In accord with iCa²⁺ mobilization data, no significant alterations in peptide potency were noted at either mutant of residue 333, yet both mutants displayed notable increases in *E*_{max} that were in turn reflected in an increase in pathway coupling efficacy. However, these increases did not reach statistical significance for any peptides (Table 4). Receptor mutants F149, I149, V149, and Y149 profoundly affected pERK1/2 signaling, with little to no detectable responses for both GLP-1 peptides and significant effects on maximal responses for exendin-4 and oxyntomodulin (Fig. 5; Table 4). However, in most cases operational modeling revealed no statistically significant changes in coupling efficiency

TABLE 2
Effects of human GLP-1R 149 or 333 mutation on agonist signaling via cAMP

Data were analyzed using a three-parameter logistic equation as defined in eq. 1. pEC₅₀ values represent the negative logarithm of the concentration of agonist that produces half the maximal response. *E*_{max} represents the maximal response normalized to that elicited by 100 μM forskolin. All mutants were analyzed with an operational model of agonism (eq. 2) to determine logτ values. All logτ values were then corrected to specific [¹²⁵I]exendin(9–39) binding (logτ_c). Values are expressed as mean ± S.E.M. of four to five independent experiments, conducted in duplicate. Data were analyzed with one-way analysis of variance and Dunnett's post-test.

	cAMP Accumulation														
	GLP-1(1–36)NH ₂			GLP-1(7–36)NH ₂			Exendin-4			Oxyntomodulin			Compound 2		
	pEC ₅₀	<i>E</i> _{max}	Logτ _c (τ _c)	pEC ₅₀	<i>E</i> _{max}	Logτ _c (τ _c)	pEC ₅₀	<i>E</i> _{max}	Logτ _c (τ _c)	pEC ₅₀	<i>E</i> _{max}	Logτ _c (τ _c)	pEC ₅₀	<i>E</i> _{max}	Logτ _c (τ _c)
Wild-type	7.4 ± 0.1	149.7 ± 7.8	0.53 ± 0.16 (3.36)	9.4 ± 0.2	175.7 ± 10.1	0.94 ± 0.22 (8.63)	10.5 ± 0.1	162.5 ± 5.4	0.70 ± 0.19 (5.05)	8.5 ± 0.1	178.3 ± 8.8	1.03 ± 0.24 (10.74)	6.0 ± 0.2	115.4 ± 9.2	0.18 ± 0.17 (1.51)
M ¹⁴⁹	ND	ND	NA	8.0 ± 0.3*	ND	NA	8.4 ± 0.1*	223 ± 13	NA	ND	ND	NA	5.5 ± 0.1	217 ± 24	NA
A ¹⁴⁹	ND	ND	ND	ND	ND	ND	8.9 ± 0.2*	139.1 ± 11.0	0.34 ± 0.33 (2.20)	ND	ND	ND	5.7 ± 0.4	70.2 ± 10.4*	−0.27 ± 0.32 (0.53)
C ¹⁴⁹	6.8 ± 0.2	44.7 ± 4.9	−0.86 ± 0.32 (0.14)	8.4 ± 0.2	123.5 ± 10.2	−0.10 ± 0.31 (0.79)	9.8 ± 0.2	133.3 ± 10.0	0.00 ± 0.30 (1.00)	7.1 ± 0.1*	120.6 ± 7.0*	−0.13 ± 0.31 (0.74)	5.7 ± 0.3	81.7 ± 9.9	−0.46 ± 0.30 (0.35)
F ¹⁴⁹	ND	ND	ND	ND	ND	ND	8.0 ± 0.1*	150.6 ± 9.5	0.57 ± 0.33 (3.75)	ND	ND	ND	5.9 ± 0.3	82.9 ± 9.6	−0.06 ± 0.25 (0.87)
I ¹⁴⁹	ND	ND	ND	ND	ND	ND	8.2 ± 0.1*	86.6 ± 6.6*	−0.28 ± 0.26 (0.52)	ND	ND	ND	6.1 ± 0.3	83.7 ± 7.8	−0.29 ± 0.22 (0.51)
S ¹⁴⁹	6.8 ± 0.1	170.1 ± 9.5	0.74 ± 0.34 (5.52)	9.1 ± 0.2	129.5 ± 9.4	0.20 ± 0.25 (1.57)	10.3 ± 0.2	186.0 ± 12.4	1.23 ± 0.50 (17.02)	7.9 ± 0.2	141.7 ± 9.1	0.33 ± 0.26 (2.13)	5.9 ± 0.2	80.8 ± 9.9	−0.23 ± 0.25 (0.59)
V ¹⁴⁹	ND	ND	ND	ND	ND	ND	8.9 ± 0.3*	122.1 ± 13.0	0.08 ± 0.29 (1.21)	ND	ND	ND	6.0 ± 0.4	105.9 ± 12.3	−0.05 ± 0.27 (0.90)
Y ¹⁴⁹	ND	ND	ND	ND	ND	ND	8.1 ± 0.2*	77.5 ± 10.5*	−0.13 ± 0.22 (0.74)	ND	ND	ND	5.8 ± 0.3	41.6 ± 4.9*	−0.46 ± 0.19 (0.34)
C ^{333a}	6.9 ± 0.2	259 ± 24	NA	10.2 ± 0.3	331 ± 26	NA	10.2 ± 0.2	257 ± 12	NA	8.2 ± 0.2	288 ± 16	NA	ND	46 ± 8 ^{a,b}	NA
A ³³³	7.4 ± 0.1	142.9 ± 9.7	0.35 ± 0.17 (2.25)	9.5 ± 0.1	166.7 ± 8.6	0.68 ± 0.19 (4.82)	10.5 ± 0.2	168.2 ± 11.7	0.71 ± 0.21 (5.15)	8.4 ± 0.2	162.7 ± 9.4	0.61 ± 0.19 (4.09)	5.8 ± 0.2	142.7 ± 13.0	0.36 ± 0.19 (2.29)
V ³³³	7.2 ± 0.1	112.1 ± 8.7	0.13 ± 0.27 (1.36)	9.5 ± 0.2	120.8 ± 8.2	0.21 ± 0.27 (1.63)	10.5 ± 0.2	132.4 ± 7.1	0.33 ± 0.27 (2.13)	8.6 ± 0.2	97.5 ± 7.2*	0.00 ± 0.27 (1.00)	5.9 ± 0.2	100.9 ± 9.6	0.05 ± 0.28 (1.12)

NA, data not experimentally determined in Koole et al., 2011; ND, data not able to be experimentally defined or with incomplete curves.

^aData obtained from Koole et al., 2011. Reported *E*_{max} values are normalized to 100 nM forskolin.

^bCompound 2 response at 10^{−5} M.

*Statistically significant at *P* < 0.05, one-way analysis of variance and Dunnett's post-test in comparison with wild-type control.

TABLE 3

Effects of human GLP-1R 149 or 333 mutation on agonist signaling via Ca^{2+} mobilization

Data were analyzed using a three-parameter logistic equation as defined in eq. 1. pEC_{50} values represent the negative logarithm of the concentration of agonist that produces half the maximal response. E_{max} represents the maximal response normalized to that elicited by 100 μM ATP. All mutants were analyzed with an operational model of agonism (eq. 2) to determine $\log\tau$ values. All $\log\tau$ values were then corrected to specific [^{125}I]exendin(9–39) binding ($\log\tau_c$). Values are expressed as mean \pm S.E.M. of five to seven independent experiments, conducted in duplicate. Data were analyzed with one-way analysis of variance and Dunnett's post-test.

	Ca^{2+} Mobilization						
	GLP-1(7–36) NH_2			Exendin-4			Oxyntomodulin
	pEC_{50}	E_{max}	$\log\tau_c$ (τ_c)	pEC_{50}	E_{max}	$\log\tau_c$ (τ_c)	E_{max}^a
Wild-type	7.6 ± 0.2	14.3 ± 1.3	0.08 ± 0.16 (1.20)	7.3 ± 0.2	17.3 ± 1.5	0.29 ± 0.16 (1.95)	10.8 ± 1.8
M ^{149b}	ND	ND	NA	ND	ND	NA	$2.6 \pm 0.4^*$
A ¹⁴⁹	ND	ND	ND	ND	ND	ND	ND
C ¹⁴⁹	7.2 ± 0.1	11.9 ± 0.8	-0.42 ± 0.3 (0.38)	7.5 ± 0.3	$6.1 \pm 0.8^*$	-0.86 ± 0.31 (0.14)*	$3.1 \pm 2.6^*$
F ¹⁴⁹	ND	ND	ND	ND	ND	ND	ND
I ¹⁴⁹	ND	ND	ND	ND	ND	ND	ND
S ¹⁴⁹	7.1 ± 0.2	17.9 ± 2.2	0.23 ± 0.26 (1.70)	7.1 ± 0.2	15.5 ± 1.7	0.05 ± 0.26 (1.12)	5.2 ± 2.4
V ¹⁴⁹	ND	ND	ND	ND	ND	ND	ND
Y ¹⁴⁹	ND	ND	ND	ND	ND	ND	ND
C ^{333b}	7.8 ± 0.3	23.6 ± 2.4	NA	7.8 ± 0.2	$14.6 \pm 1.1^*$	NA	15.0 ± 2.4
A ³³³	7.8 ± 0.2	$19.1 \pm 1.4^*$	0.35 ± 0.17 (2.24)	7.4 ± 0.2	19.3 ± 1.7	0.36 ± 0.18 (2.29)	13.3 ± 2.3
V ³³³	7.8 ± 0.2	17.4 ± 1.6	0.30 ± 0.27 (2.00)	7.6 ± 0.2	18.7 ± 1.7	0.40 ± 0.27 (2.51)	15.9 ± 3.2

NA, data not experimentally determined in Koole et al., 2011; ND, data unable to be experimentally defined or with incomplete curves.

^aResponse at 1 μM oxyntomodulin.

^bData obtained from Koole et al., 2011. Reported E_{max} values are normalized to 100 μM ATP.

*Statistically significant at $P < 0.05$, one-way analysis of variance and Dunnett's post-test in comparison with wild-type control.

(τ_c) at these mutants. Mutation of 149 to either Ala or Cys significantly impacted the E_{max} of both GLP-1(7–36) NH_2 and oxyntomodulin, but it had little effect on exendin-4. However, application of the operational model revealed that although all peptides had reduced coupling efficacy (τ_c) at these mutants, none reached statistical significance. As predicted, there was little deviation in peptide responses at the S149 mutant.

Effect of Residue 149 or 333 of the Human GLP-1R on the Signaling Profile of the Allosteric Agonist Compound 2. Previously, we demonstrated that despite a loss of peptide agonist binding and signaling at the naturally occurring M149 receptor variant, the agonist profile of the small-molecule GLP-1R allosteric ligand compound 2 was

retained (Koole et al., 2011). In the present study, mutation of residue 333 did not significantly affect the potency of compound 2 in either cAMP or pERK1/2 signaling profiles (Tables 2 and 4). Despite significant reductions observed at the polymorphic variant C333, A333 and V333 did not display any significant effects on compound 2 agonism. Mutation of 149 did not significantly affect the potency of compound 2 in either cAMP accumulation or pERK1/2 outputs (Tables 2 and 4). Coupling efficacy in pERK1/2 increased for A149, F149, S149, and Y149, although these increases were not statistically significant (Table 4). Consistent with previous studies, no measurable agonism was observed for compound 2 in Ca^{2+} mobilization at either the wild-type or any of the mutant receptors (data not shown).

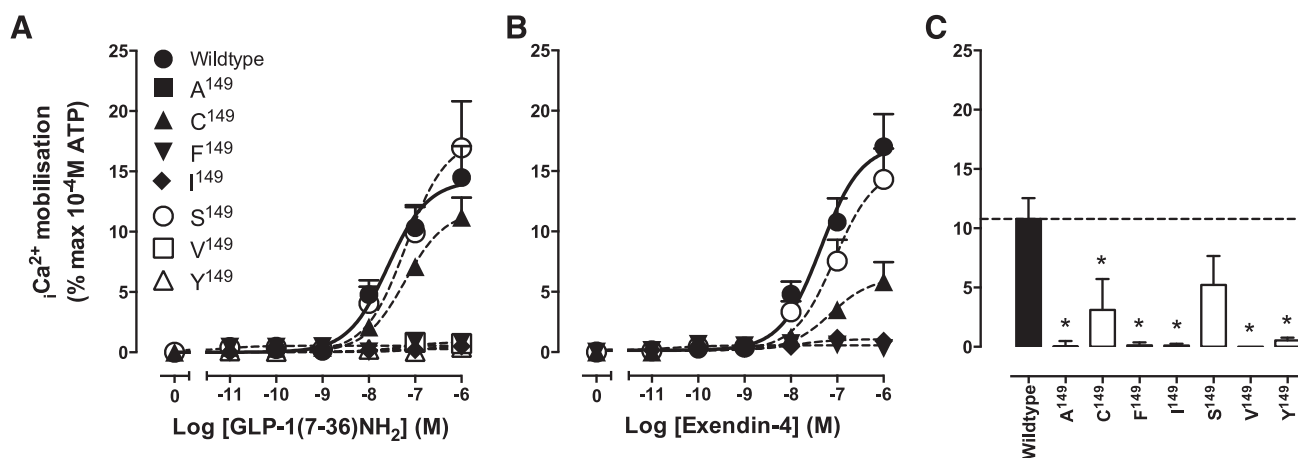


Fig. 4. Characterization of Ca^{2+} mobilization in the presence of GLP-1(7–36) NH_2 (A), exendin-4 (B), and oxyntomodulin (C) in FlpInCHO cells stably expressing the wild-type human GLP-1R or each of the human GLP-1R mutants at the 149 receptor residue. Data are normalized to the response elicited by 100 μM ATP and analyzed with an operational model of agonism as defined in eq. 2 (A and B). $X = 0$ corresponds to conditions in which no ligand was added. Data presented in (C) are levels of Ca^{2+} mobilization in the presence of 1 μM oxyntomodulin and are normalized to the maximal response elicited by 100 μM ATP. Statistical significance of changes in response in comparison with wild-type human GLP-1R were determined by one-way analysis of variance and Dunnett's post-test and are indicated with an asterisk (* $P < 0.05$). All values are mean \pm S.E.M. of five to seven independent experiments, conducted in duplicate.

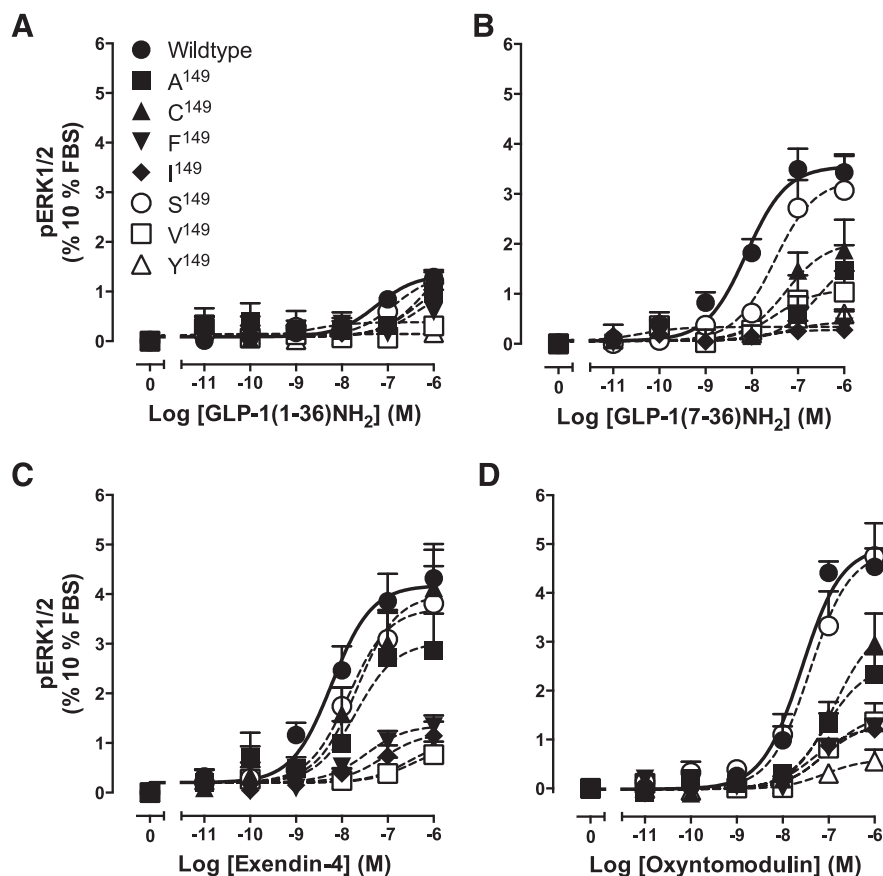


Fig. 5. Characterization of pERK1/2 in the presence of GLP-1(1–36)NH₂ (A), GLP-1(7–36)NH₂ (B), exendin-4 (C), and oxyntomodulin (D) in FlpInCHO cells stably expressing the wild-type human GLP-1R or each of the human GLP-1R 149 mutants. Data are normalized to the maximal response elicited by 10% FBS and analyzed with an operational model of agonism as defined in eq. 2. $X = 0$ corresponds to conditions in which no ligand was added. All values are mean \pm S.E.M. of four to six independent experiments, conducted in duplicate.

Effect of Residue 149 or 333 of the Human GLP-1R on the Modulatory Profile of Compound 2. We have previously shown that the loss of agonist peptide binding and cAMP signaling at the naturally occurring M149 receptor variant could be partially rescued in the presence of compound 2 (Koole et al., 2011). In addition, the C333 receptor variant was not modulated by compound 2 to the extent observed at the wild-type GLP-1R (S333) (Koole et al., 2011). In the present study, we therefore examined the role of compound 2 in modulating peptide-induced cAMP responses of residue 149 and 333 mutants. Similar to previous observations, significant positive modulation of oxyntomodulin-mediated cAMP occurred with the addition of compound 2 at the wild-type GLP-1R, but no significant effects were seen on GLP-1(1–36)NH₂, GLP-1(7–36)NH₂, or exendin-4 (Table 5; Supplemental Figs. S1–S4; Koole et al., 2010). Although no modulation of these last peptides was observed at either 333 mutants, compound 2 also failed to modulate significantly the oxyntomodulin responses at A333 and V333 (Table 5; Supplemental Fig. S4). Similar to wild-type GLP-1R, mutation of residue 149 to Ser had little effect on the modulatory profile of compound 2, with a substantial enhancement of oxyntomodulin potency but no significant effect on other peptides (Table 5; Supplemental Figs. S1–S4). At all other substitutions of residue 149, significant compound 2-mediated augmentation of oxyntomodulin potency was observed; however, the extent of modulation was somewhat variable among mutants; the greatest detectable recovery of potency was observed at the A149 mutant, whereas only modest recovery was seen at the F149 mutant (100- and 16-fold enhancement of oxyntomodulin potency, respectively) (Table 5;

Supplemental Fig. S4). As seen with the M149 receptor variant (Koole et al., 2011), in addition to modulation of oxyntomodulin, compound 2 positively modulated most other peptide responses of 149 mutant receptors (Table 5; Supplemental Fig. S1–S3). In several cases (F149, I149, V149, Y149), compound 2 restored the function of undetectable or undefined cAMP responses (Table 5; Supplemental Fig. S1–S4). This was particularly evident for Y149, with no detectable cAMP response for low-potency agonists GLP-1(1–36)NH₂ and oxyntomodulin but recovery of a detectable peptide response in the presence of compound 2. Despite positively modulating most peptide responses at 149 mutants, the extent of modulation by compound 2 was not consistent across all mutants. Clear examples are A149, for which compound 2 modulated GLP-1(7–36)NH₂ and oxyntomodulin potency to a greater extent than GLP-1(1–36)NH₂ and exendin-4 (changes of 63-, 100-, 6-, and 6-fold, respectively), whereas at F149, exendin-4 potency was modulated to a greater extent than oxyntomodulin (changes of 200- and 16-fold, respectively) (Table 5). Interestingly, compound 2 modulated both GLP-1(7–36)NH₂ and oxyntomodulin at C149, but it had little influence on GLP-1(1–36)NH₂ and exendin-4 (changes of 8-, 32-, 1-, and 3-fold, respectively) (Table 5). These subtle changes in modulation profiles suggest an important role of residue 149 in directing probe-dependent effects on cooperativity.

Discussion

Class B GPCRs are important regulators for a number of physiologic processes. Consequently, they have become valuable therapeutic targets for multiple disorders including neurodegenerative

TABLE 4

Effects of human GLP-1R 149 or 333 mutation on agonist signaling via pERK1/2

Data were analyzed using a three-parameter logistic equation as defined in eq. 1. pEC₅₀ values represent the negative logarithm of the concentration of agonist that produces half the maximal response. E_{\max} represents the maximal response normalized to that elicited by 10% fetal bovine serum. All mutants were analyzed with an operational model of agonism (eq. 2) to determine log τ values. All log τ values were then corrected to specific [¹²⁵I]exendin (9–39) binding (log τ_c). Values are expressed as mean \pm S.E.M. of four to six independent experiments, conducted in duplicate. Data were analyzed with one-way analysis of variance and Dunnett's post-test.

	pERK1/2														
	GLP-1(1–36)NH ₂			GLP-1(7–36)NH ₂			Exendin-4			Oxyntomodulin			Compound 2		
	pEC ₅₀	E_{\max}	Log τ_c (τ_c)	pEC ₅₀	E_{\max}	Log τ_c (τ_c)	pEC ₅₀	E_{\max}	Log τ_c (τ_c)	pEC ₅₀	E_{\max}	Log τ_c (τ_c)	pEC ₅₀	E_{\max}	Log τ_c (τ_c)
Wild-type	7.3 \pm 0.2	1.3 \pm 0.1	−0.72 \pm 0.16 (0.19)	8.0 \pm 0.2	3.6 \pm 0.2	−0.10 \pm 0.15 (0.79)	8.1 \pm 0.2	4.2 \pm 0.3	0.02 \pm 0.16 (1.05)	7.6 \pm 0.1	5.0 \pm 0.2	0.21 \pm 0.16 (1.62)	5.9 \pm 0.2	0.45 \pm 0.1	−1.21 \pm 0.19 (0.06)
M ^{149a}	ND	0.6 \pm 0.1	NA	7.8 \pm 0.3	4.1 \pm 0.5	NA	8.0 \pm 0.2	3.4 \pm 0.3*	NA	7.1 \pm 0.2	3.7 \pm 0.3*	NA	5.9 \pm 0.3	2.0 \pm 0.4	NA
A ¹⁴⁹	ND	ND	ND	6.9 \pm 0.4	1.7 \pm 0.4*	−0.58 \pm 0.41 (0.26)	7.6 \pm 0.4	3.0 \pm 0.5	−0.30 \pm 0.32 (0.50)	7.0 \pm 0.2	2.6 \pm 0.2*	−0.38 \pm 0.32 (0.42)	4.7 \pm 0.7	0.99 \pm 0.7	−0.95 \pm 0.38 (0.11)
C ¹⁴⁹	6.4 \pm 0.5	1.6 \pm 0.6	−0.90 \pm 0.43 (0.13)	7.3 \pm 0.4	2.0 \pm 0.4*	−0.82 \pm 0.31 (0.15)	7.7 \pm 0.3	4.0 \pm 0.4	−0.36 \pm 0.31 (0.44)	6.9 \pm 0.2	3.3 \pm 0.4*	−0.48 \pm 0.31 (0.33)	5.6 \pm 0.4	0.33 \pm 0.1	−1.67 \pm 0.38 (0.02)
P ¹⁴⁹	ND	ND	ND	ND	ND	ND	7.7 \pm 0.2	1.3 \pm 0.1*	−0.71 \pm 0.32 (0.19)	7.1 \pm 0.2	1.3 \pm 0.1*	−0.64 \pm 0.28 (0.23)	4.8 \pm 0.4	0.87 \pm 0.4	−0.78 \pm 0.45 (0.17)
I ¹⁴⁹	ND	ND	ND	ND	ND	ND	7.6 \pm 0.3	1.1 \pm 0.2*	−1.02 \pm 0.39 (0.10)	7.3 \pm 0.2	1.3 \pm 0.1*	−0.91 \pm 0.26 (0.12)	5.2 \pm 0.4	0.71 \pm 0.2	−1.21 \pm 0.26 (0.06)
S ¹⁴⁹	6.8 \pm 0.4	1.4 \pm 0.3	−0.82 \pm 0.26 (0.15)	7.5 \pm 0.2	3.3 \pm 0.4	−0.27 \pm 0.25 (0.54)	7.9 \pm 0.2	3.7 \pm 0.3	−0.19 \pm 0.26 (0.65)	7.3 \pm 0.2	4.9 \pm 0.5	0.09 \pm 0.25 (1.23)	5.2 \pm 0.4	0.79 \pm 0.2	−1.04 \pm 0.29 (0.09)
V ¹⁴⁹	ND	ND	ND	7.5 \pm 0.6	1.1 \pm 0.3*	−0.97 \pm 0.34 (0.11)	7.2 \pm 0.8	0.8 \pm 0.4*	−1.12 \pm 0.95 (0.08)	7.1 \pm 0.3	1.5 \pm 0.3*	−0.77 \pm 0.31 (0.17)	5.5 \pm 0.6	0.29 \pm 0.1	−1.50 \pm 0.42 (0.03)
Y ¹⁴⁹	ND	ND	ND	ND	ND	ND	6.7 \pm 0.6	1.0 \pm 0.3*	−0.85 \pm 0.67 (0.14)	7.0 \pm 0.5	0.6 \pm 0.2*	−1.02 \pm 0.36 (0.10)*	4.8 \pm 0.8	0.49 \pm 0.4	−1.15 \pm 0.41 (0.07)
C ^{333a}	7.7 \pm 0.2	1.7 \pm 0.2	NA	8.7 \pm 0.2	5.9 \pm 0.4	NA	9.1 \pm 0.3	6.1 \pm 0.5	NA	7.7 \pm 0.2	7.0 \pm 0.5	NA	6.0 \pm 0.2	1.4 \pm 0.2	NA
A ³³³	7.0 \pm 0.2	1.7 \pm 0.2	−0.66 \pm 0.17 (0.22)	7.8 \pm 0.2	6.1 \pm 0.6*	0.40 \pm 0.18 (2.51)	8.0 \pm 0.3	6.7 \pm 0.8*	0.60 \pm 0.21 (3.98)	7.5 \pm 0.2	7.5 \pm 0.7*	1.07 \pm 0.36 (11.75)	6.2 \pm 0.3	0.70 \pm 0.1	−1.10 \pm 0.17 (0.08)
V ³³³	7.0 \pm 0.2	1.4 \pm 0.2	−0.70 \pm 0.28 (0.20)	7.8 \pm 0.1	4.1 \pm 0.2	0.02 \pm 0.27 (1.05)	8.0 \pm 0.1	4.7 \pm 0.3	0.13 \pm 0.27 (1.35)	7.6 \pm 0.2	6.3 \pm 0.5	0.57 \pm 0.28 (3.72)	5.9 \pm 0.4	1.11 \pm 0.2	−0.79 \pm 0.27 (0.16)

NA, data not experimentally determined in Koole et al., 2011; ND, data unable to be experimentally defined or with incomplete curves.

^aData obtained from Koole et al., 2011. Reported E_{\max} values are normalized to 10% fetal bovine serum.

*Statistically significant at $P < 0.05$, one-way analysis of variance and Dunnett's post-test in comparison with wild-type control.

and inflammatory conditions (vasoactive intestinal peptide and pituitary adenylate cyclase-activating peptide receptors) (Abad et al., 2006; Breneman, 2007), bowel disorders (GLP-2 receptors) (Hornby and Moore, 2011), chronic stress [corticotropin releasing factor (CRF) receptors] (Gilligan and Li, 2004), bone-related disorders (calcitonin and parathyroid hormone receptors) (Mulder et al., 2006), and type 2 DM (glucagon, amylin, and GLP-1Rs) (Estall and Drucker, 2006; Brubaker, 2007; Adeghate and Kalasz, 2011). Many of these GPCRs exhibit single-nucleotide polymorphic variance, with the variant proteins linked to development of multiple diseases, and there is additional potential to impact the effectiveness of treatments targeted to that receptor (Hager et al., 1995; Taboulet et al., 1998; Schipani et al., 1999; Sadee et al., 2001; Siyani et al., 2001; Tang and Insel, 2005).

The naturally occurring GLP-1R variant, M149, markedly reduces peptide-mediated functional responses in vitro, suggesting that this would engender a pathophysiological phenotype. In accord, possession of this variant has been associated with poor glycemic control (Tokuyama et al., 2004). The mechanistic basis behind this loss of function receptor variant is largely unclear because of the paucity of structural information within this class of GPCRs. Consequently, we have substituted amino acids with different physicochemical properties to examine critically the functional profile of the 149, as well as the 333 polymorphic variant of the human GLP-1R to further elucidate the potential contribution of these residues to receptor structure and function.

We have also shown, in a previous study, that an SNP of the human GLP-1R that results in the conversion of Ser to Cys at amino acid residue 333 attenuated both the allosteric agonism as well as the modulatory properties of the Novo Nordisk small molecule, compound 2 (Koole et al., 2011). This effect was observed in the absence of any significant effects on peptide binding affinity or function as measured through cAMP accumulation, pERK1/2, and Ca^{2+} mobilization outputs. In the current study, mutation of residue 333 to either Ala or Val did not significantly impact on peptide binding affinity or functional activity. Homology modeling of the GLP-1R using the glucagon receptor structure as a template places residue 333 in ICL3, close to the TM5/ICL3 boundary (Fig. 1) (Siu et al., 2013). There is significant evidence to suggest that ICL3 is a major interaction interface for G proteins (Bavenc et al., 2003), and this is illustrated in multiple mutagenesis studies (Heller et al., 1996; Takhar et al., 1996; Mathi et al., 1997; Salapatek et al., 1999), as well as in studies where G protein activation can be achieved with ICL3-corresponding peptides (Hallbrink et al., 2001). This work suggests an involvement of residues V327, I328 (Mathi et al., 1997), V331 (Mathi et al., 1997; Salapatek et al., 1999), I332, A333 (Salapatek et al., 1999), K334 (Takhar et al., 1996; Mathi et al., 1997; Salapatek et al., 1999), and R348 (Heller et al., 1996) in allowing effective G protein coupling to the GLP-1R. Notably, these mutagenesis data have been obtained using the rat GLP-1R. The human, mouse, and rat GLP-1Rs share almost identical amino acid sequence in ICL3, suggesting that conservation of this region is important in the G protein coupling profile of the receptor across species. However, although S333 is conserved in both the human and mouse GLP-1R proteins, this residue is an Ala in the rat GLP-1R, consistent with our current data that indicate that this is not a critical residue in peptide-mediated G protein coupling. These data may suggest that S333 lies outside the domain of critical importance in receptor–G protein interaction. In agreement,

TABLE 5

Differential modulation of agonist peptides at human GLP-1R 149 or 333 mutants by compound 2 in cAMP accumulation

Data were analyzed using a three-parameter logistic equation as defined in eq. 1. pEC_{50} values represent the negative logarithm of the concentration of agonist that produces half the maximal response. All data are normalized to the response elicited by 100 μ M forskolin and then normalized to the response elicited by 1 μ M peptide [GLP-1(1–36)NH₂, oxyntomodulin] or 100 nM peptide [GLP-1(7–36)NH₂, exendin-4] at each mutant. Values are expressed as mean \pm S.E.M. of four to nine independent experiments, conducted in duplicate.

	cAMP Accumulation (pEC_{50})							
	GLP-1(1–36)NH ₂	+3 μ M Compound 2	GLP-1(7–36)NH ₂	+3 μ M Compound 2	Exendin-4	+3 μ M Compound 2	Oxyntomodulin	+3 μ M Compound 2
Wild-type	7.8 \pm 0.1	7.5 \pm 0.4	10.6 \pm 0.1	10.9 \pm 0.5	11.1 \pm 0.1	10.8 \pm 0.8	9.5 \pm 0.1	10.4 \pm 0.8*
M ^{149a}	ND	ND	7.0 \pm 0.2	9.7 \pm 0.8*	8.5 \pm 0.2	9.6 \pm 0.7*	ND	7.7 \pm 1.5*
A ¹⁴⁹	7.0 \pm 0.1	7.8 \pm 0.8*	8.7 \pm 0.1	10.5 \pm 0.2*	9.9 \pm 0.1	10.7 \pm 0.4*	7.6 \pm 0.1	9.6 \pm 0.2*
C ¹⁴⁹	7.2 \pm 0.1	7.1 \pm 0.7	9.3 \pm 0.1	10.2 \pm 0.5	10.6 \pm 0.2	11.0 \pm 0.9	8.0 \pm 0.1	9.5 \pm 0.8*
F ¹⁴⁹	ND	7.2 \pm 1.4	ND	10.0 \pm 0.2	8.8 \pm 0.1	11.1 \pm 0.5*	7.3 \pm 0.2	8.5 \pm 0.7*
I ¹⁴⁹	ND	ND	ND	8.9 \pm 0.5	8.8 \pm 0.0	9.9 \pm 0.6*	ND	7.7 \pm 3.1
S ¹⁴⁹	7.4 \pm 0.1	7.4 \pm 0.5	10.4 \pm 0.2	10.9 \pm 0.8	11.0 \pm 0.1	11.3 \pm 0.5	9.0 \pm 0.1	10.0 \pm 0.4*
V ¹⁴⁹	ND	7.3 \pm 1.6	8.5 \pm 0.0	ND	9.8 \pm 0.1	9.8 \pm 0.4	7.3 \pm 0.1	8.7 \pm 0.5*
Y ¹⁴⁹	ND	7.4 \pm 0.7	ND	10.0 \pm 0.3	8.7 \pm 0.1	10.8 \pm 0.2*	ND	8.3 \pm 0.5
C ^{333a}	NA	NA	NA	NA	NA	NA	8.2 \pm 0.1	8.3 \pm 0.2
A ³³³	7.6 \pm 0.1	7.5 \pm 0.8	10.5 \pm 0.2	10.3 \pm 0.5	11.2 \pm 0.1	11.2 \pm 0.5	9.4 \pm 0.1	9.6 \pm 0.4
V ³³³	8.0 \pm 0.1	7.8 \pm 0.8	10.6 \pm 0.1	10.7 \pm 0.5	11.1 \pm 0.1	11.6 \pm 0.4	9.5 \pm 0.1	10.0 \pm 0.5

NA, data not experimentally determined in Koole et al., 2011; ND, data unable to be experimentally defined or with incomplete curves.

^aData obtained from Koole et al., 2011. Reported values are normalized to 100 nM forskolin.

*Statistically significant at $P \leq 0.05$, compared with respective peptide control, paired t test.

Mathi et al. (1997) proposed that the N-terminal region of ICL3 is a helical projection of TM5 with S333 facing away from the G protein binding pocket, and this is supported by the glucagon receptor and CRF1 receptor crystal structures and in our homology model (Fig. 1) (Hollenstein et al., 2013; Siu et al., 2013).

Despite little deviation in peptide function at the 333 residue in either the case of the polymorphic variant (C333; Koole et al., 2011) or the mutations introduced in this study (A333, V333), all these substitutions impact the cooperativity between compound 2 and oxyntomodulin, with no significant modulation of oxyntomodulin-mediated cAMP formation at C333 (Koole et al., 2011) and only weak positive modulation at the A333 and V333 mutants. However, unlike the C333 mutant, which shows compromised compound 2-induced cAMP production in comparison with the wild-type GLP-1R (Koole et al., 2011), no significant change in cAMP production was observed at either the A333 or the V333 mutants. Whereas the mechanistic basis of these observations is unclear, the evidence suggests that the potentially distinct receptor conformations stabilized by compound 2 drive agonism versus cooperativity.

Recently, it was revealed that compound 2 acts via covalent modification of the GLP-1R at C347 (located at the juxtaposition of ICL3/TM6; Fig. 1), in a mechanism similar to that of the modulator BETP [4-(3-benzyloxy)phenyl]-2-ethylsulfinyl-6-(trifluoromethyl)pyrimidine] (Nolte et al., 2014). Mutation of C347 to Ala resulted in loss of compound 2 agonism, in addition to loss of the positive allosteric modulator activity in the presence of GLP-1(9–36)NH₂, whereas peptide-mediated signaling was unaltered. It is possible that mutation of residue 333 impacts the neighboring interactions required for compound 2 to attach covalently and/or induce conformations that favor sampling of receptor active states. Furthermore, the greater loss of compound 2 activity seen with the C333 mutant (Koole et al., 2011) may arise, at least in part, through alternate cross-linking through this site.

Unlike residue 333, most mutations of residue 149 resulted in significant attenuation of peptide binding and functional activity. The loss of binding affinity tracked through most functional

assay systems assessed, manifesting as an attenuation of functional efficacy. Not surprisingly, mutation of 149 to Ser, which has similar chemical properties to that of the most frequently occurring residue, Thr, was relatively well tolerated and had the least influence on peptide binding and function in comparison with the other mutants. Nonetheless, a significant reduction in affinity was observed with most peptides, with variable effects on signaling that suggest that even minor modification at the 149 position impact on receptor function.

Removal of the hydroxyl functional group from T149, with maintenance of chain length, by mutation to Val significantly reduced peptide binding affinity and cAMP and iCa^{2+} responses. Similarly, replacement of the hydroxyl group with a thiol group by means of mutation to Cys significantly reduced peptide binding affinity, which generally corresponded with decreases in cAMP and iCa^{2+} outputs, albeit not always to significance. Interestingly, peptide-mediated pERK1/2 coupling efficacy (τ_c) at both V149 and C149 was not significantly altered.

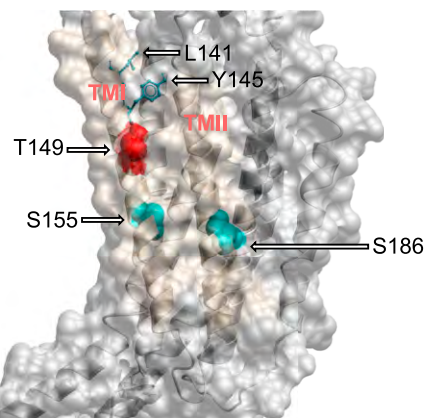


Fig. 6. Homology model of the GLP-1R illustrating the location of T149 (red, cpb representation) in relation to L141 and Y145, which are reported to be in close proximity to GLP-1 peptide residues 16 and 12, respectively (Chen et al., 2010; Miller et al., 2011; blue ball and stick representation), and S155 (TM1) and S186, (TM2), which are involved in peptide-mediated signal bias (Wootten et al., 2013).

This result is consistent with distinct mechanisms of conformational transition driving pERK1/2 versus cAMP/Ca²⁺ signaling (Koole et al., 2011, 2012a; Wootten et al., 2013).

All other assessed mutations of residue 149 were poorly tolerated by the GLP-1R. Similar to the naturally occurring polymorphism M149, these residues are considerably more hydrophobic and bulky than the wild-type Thr; consistent with M149, they have large detrimental effects, which is perhaps not surprising given the recent structural information emerging for the GLP-1R. Recently, Miller and colleagues used photoaffinity labeling that detected close proximity between residues 16 and 12 of the GLP-1 peptide with residues 141 and 145 of the GLP-1R, respectively (Chen et al., 2010; Miller et al., 2011). Given that these residues precede, and would neighbor residue 149 in an α -helical tertiary structure, it indicates that 149 is near the endogenous peptide binding pocket. Although not necessarily a ligand interaction point itself, as suggested by homology assessment with CRF1 and glucagon receptor TM structures (Fig. 6) (Hollenstein et al., 2013; Siu et al., 2013), it may provide essential conformational restraints involving other TMs. This hypothesis is supported by recent alanine mutagenesis data of conserved polar residues in TM1 and TM2, where mutation of S155 (TM1) and S186 (TM2) differentially changed peptide-mediated signal bias at the receptor (Wootten et al., 2013). These residues are predicted to be involved in tight packing interactions with TM7 and TM3, respectively (Fig. 6), and the data are consistent with a proximal role of residue 149 in the activation transition of the receptor following peptide binding.

Despite significant attenuation of peptide binding and function at almost all mutants of 149, the ability of compound 2 to signal via the receptor was, in most cases, minimally affected. Similar to our previous work showing that compound 2 was able to partially restore the binding affinity and cAMP response of M149, in this study, we observed that compound 2 was able to modulate almost all peptide responses when measured in cAMP. The most striking data observed here included the restoration of functional responses at the F149 and Y149 mutants that had severely abrogated cAMP signaling, demonstrating that compound 2 is able to lower the energy required for activation at receptor mutants that either have no detectable cAMP or very weakly stimulate a cAMP response. Given that antagonist binding was unaffected at any of these receptor mutants, this finding provides evidence for our previous hypothesis that residue 149 is involved in activation transition instead of direct disruption to peptide binding interactions (Koole et al., 2011).

Collectively, these results provide us with insight into domains that are essential for receptor function, as well as the role that allosteric ligands play in receptor modulation.

Acknowledgments

The authors thank Dr. Michael Crouch (TGR Biosciences) for the generous donation of the Surefire ERK reagents.

Authorship Contributions

Participated in research design: Koole, Wootten, Simms, Sexton.

Conducted experiments: Koole.

Performed data analysis: Koole.

Wrote or contributed to the writing of the manuscript: Koole, Wootten, Simms, Miller, Christopoulos, Sexton.

References

- Abad C, Gomariz RP, and Waschek JA (2006) Neuropeptide mimetics and antagonists in the treatment of inflammatory disease: focus on VIP and PACAP. *Curr Top Med Chem* 6:151–163.
- Adeghate E and Kalász H (2011) Amylin analogues in the treatment of diabetes mellitus: medicinal chemistry and structural basis of its function. *Open Med Chem J* 5 (Suppl 2):78–81.
- Al-Sabah S and Donnelly D (2003) The positive charge at Lys-288 of the glucagon-like peptide-1 (GLP-1) receptor is important for binding the N-terminus of peptide agonists. *FEBS Lett* 553:342–346.
- Baggio LL and Drucker DJ (2007) Biology of incretins: GLP-1 and GIP. *Gastroenterology* 132:2131–2157.
- Bavec A, Hallbrink M, Langel U, and Zorko M (2003) Different role of intracellular loops of glucagon-like peptide-1 receptor in G-protein coupling. *Regul Pept* 111: 137–144.
- Beinborn M, Worrall CI, McBride EW, and Kopin AS (2005) A human glucagon-like peptide-1 receptor polymorphism results in reduced agonist responsiveness. *Regul Pept* 130:1–6.
- Black JW and Leff P (1983) Operational models of pharmacological agonism. *Proc R Soc Lond B Biol Sci* 220:141–162.
- Brenneman DE (2007) Neuroprotection: a comparative view of vasoactive intestinal peptide and pituitary adenylate cyclase-activating polypeptide. *Peptides* 28: 1720–1726.
- Brubaker PL (2007) Incretin-based therapies: mimetics versus protease inhibitors. *Trends Endocrinol Metab* 18:240–245.
- Chen Q, Pinon DI, Miller LJ, and Dong M (2009) Molecular basis of glucagon-like peptide 1 docking to its intact receptor studied with carboxyl-terminal photolabile probes. *J Biol Chem* 284:34135–34144.
- Chen Q, Pinon DI, Miller LJ, and Dong M (2010) Spatial approximations between residues 6 and 12 in the amino-terminal region of glucagon-like peptide 1 and its receptor: a region critical for biological activity. *J Biol Chem* 285:24508–24518.
- Cheng Y and Prusoff WH (1973) Relationship between the inhibition constant (K_i) and the concentration of inhibitor which causes 50 per cent inhibition (I₅₀) of an enzymatic reaction. *Biochem Pharmacol* 22:3099–3108.
- Coin I, Katritch V, Sun T, Xiang Z, Siu FY, Beyermann M, Stevens RC, and Wang L (2013) Genetically encoded chemical probes in cells reveal the binding path of urocortin-I to CRF class B GPCR. *Cell* 155:1258–1269.
- Coopman K, Wallis R, Robb G, Brown AJ, Wilkinson GF, Timms D, and Willars GB (2011) Residues within the transmembrane domain of the glucagon-like peptide-1 receptor involved in ligand binding and receptor activation: modelling the ligand-bound receptor. *Mol Endocrinol* 25:1804–1818.
- Dong M, Lam PC, Gao F, Hosohata K, Pinon DI, Sexton PM, Abagyan R, and Miller LJ (2007) Molecular approximations between residues 21 and 23 of secretin and its receptor: development of a model for peptide docking with the amino terminus of the secretin receptor. *Mol Pharmacol* 72:280–290.
- Dong M, Lam PC, Pinon DI, Hosohata K, Orry A, Sexton PM, Abagyan R, and Miller LJ (2011) Molecular basis of secretin docking to its intact receptor using multiple photolabile probes distributed throughout the pharmacophore. *J Biol Chem* 286: 23888–23899.
- Dong M, Li Z, Pinon DI, Lybrand TP, and Miller LJ (2004) Spatial approximation between the amino terminus of a peptide agonist and the top of the sixth transmembrane segment of the secretin receptor. *J Biol Chem* 279:2894–2903.
- Estall JL and Drucker DJ (2006) Glucagon and glucagon-like peptide receptors as drug targets. *Curr Pharm Des* 12:1731–1750.
- Fehmann HC and Habener JF (1992) Insulinotropic hormone glucagon-like peptide-I (7–37) stimulation of proinsulin gene expression and proinsulin biosynthesis in insulinoma beta TC-1 cells. *Endocrinology* 130:159–166.
- Fortin JP, Schroeder JC, Zhu Y, Beinborn M, and Kopin AS (2010) Pharmacological characterization of human incretin receptor missense variants. *J Pharmacol Exp Ther* 332:274–280.
- Gilligan PJ and Li YW (2004) Corticotropin-releasing factor antagonists: recent advances and exciting prospects for the treatment of human diseases. *Curr Opin Drug Discov Devel* 7:487–497.
- Hager J, Hansen L, Vaisse C, Vionnet N, Philippi A, Poller W, Velho G, Carcassi C, Contu L, Julier C, et al. (1995) A missense mutation in the glucagon receptor gene is associated with non-insulin-dependent diabetes mellitus. *Nat Genet* 9:299–304.
- Hallbrink M, Holmqvist T, Olsson M, Ostenson CG, Efendic S, and Langel U (2001) Different domains in the third intracellular loop of the GLP-1 receptor are responsible for Galpha(s) and Galpha(i)/Galpha(o) activation. *Biochim Biophys Acta* 1546:79–86.
- Heller RS, Kieffer TJ, and Habener JF (1996) Point mutations in the first and third intracellular loops of the glucagon-like peptide-1 receptor alter intracellular signaling. *Biochem Biophys Res Commun* 223:624–632.
- Hollenstein K, Kean J, Bortolato A, Cheng RK, Doré AS, Jazayeri A, Cooke RM, Weir M, and Marshall FH (2013) Structure of class B GPCR corticotropin-releasing factor receptor 1. *Nature* 499:438–443.
- Holst B, Hastrup H, Raffetseder U, Martini L, and Schwartz TW (2001) Two active molecular phenotypes of the tachykinin NK1 receptor revealed by G-protein fusions and mutagenesis. *J Biol Chem* 276:19793–19799.
- Hornby PJ and Moore BA (2011) The therapeutic potential of targeting the glucagon-like peptide-2 receptor in gastrointestinal disease. *Expert Opin Ther Targets* 15: 637–646.
- Jorgensen R, Kubale V, Vrecl M, Schwartz TW, and Elling CE (2007) Oxyntomodulin differentially affects glucagon-like peptide-1 receptor beta-arrestin recruitment and signaling through Galpha(s). *J Pharmacol Exp Ther* 322:148–154.
- Jorgensen R, Martini L, Schwartz TW, and Elling CE (2005) Characterization of glucagon-like peptide-1 receptor beta-arrestin 2 interaction: a high-affinity receptor phenotype. *Mol Endocrinol* 19:812–823.
- Kenakin T (1995) Agonist-receptor efficacy. II. Agonist trafficking of receptor signals. *Trends Pharmacol Sci* 16:232–238.

- Kenakin T (2011) Functional selectivity and biased receptor signaling. *J Pharmacol Exp Ther* **336**:296–302.
- Koole C, Wootten D, Simms J, Miller LJ, Christopoulos A, and Sexton PM (2012a) Second extracellular loop of human glucagon-like peptide-1 receptor (GLP-1R) has a critical role in GLP-1 peptide binding and receptor activation. *J Biol Chem* **287**:3642–3658.
- Koole C, Wootten D, Simms J, Savage EE, Miller LJ, Christopoulos A, and Sexton PM (2012b) Second extracellular loop of human glucagon-like peptide-1 receptor (GLP-1R) differentially regulates orthosteric but not allosteric agonist binding and function. *J Biol Chem* **287**:3659–3673.
- Koole C, Wootten D, Simms J, Valant C, Miller LJ, Christopoulos A, and Sexton PM (2011) Polymorphism and ligand dependent changes in human glucagon-like peptide-1 receptor (GLP-1R) function: allosteric rescue of loss of function mutation. *Mol Pharmacol* **80**:486–497.
- Koole C, Wootten D, Simms J, Valant C, Sridhar R, Woodman OL, Miller LJ, Summers RJ, Christopoulos A, and Sexton PM (2010) Allosteric ligands of the glucagon-like peptide 1 receptor (GLP-1R) differentially modulate endogenous and exogenous peptide responses in a pathway-selective manner: implications for drug screening. *Mol Pharmacol* **78**:456–465.
- Leff P, Scaramellini C, Law C, and McKechnie K (1997) A three-state receptor model of agonist action. *Trends Pharmacol Sci* **18**:355–362.
- López de Maturana R and Donnelly D (2002) The glucagon-like peptide-1 receptor binding site for the N-terminus of GLP-1 requires polarity at Asp198 rather than negative charge. *FEBS Lett* **530**:244–248.
- López de Maturana R, Treece-Birch J, Abidi F, Findlay JB, and Donnelly D (2004) Met-204 and Tyr-205 are together important for binding GLP-1 receptor agonists but not their N-terminally truncated analogues. *Protein Pept Lett* **11**:15–22.
- Lu M, Wheeler MB, Leng XH, and Boyd AE, 3rd (1993) The role of the free cytosolic calcium level in beta-cell signal transduction by gastric inhibitory polypeptide and glucagon-like peptide I(7-37). *Endocrinology* **132**:94–100.
- Mathi SK, Chan Y, Li X, and Wheeler MB (1997) Scanning of the glucagon-like peptide-1 receptor localizes G protein-activating determinants primarily to the N terminus of the third intracellular loop. *Mol Endocrinol* **11**:424–432.
- May LT, Avlani VA, Langmead CJ, Herdon HJ, Wood MD, Sexton PM, and Christopoulos A (2007) Structure-function studies of allosteric agonism at M2 muscarinic acetylcholine receptors. *Mol Pharmacol* **72**:463–476.
- McPherson J, Rivero G, Baptist M, Llorente J, Al-Sabah S, Krasel C, Dewey WL, Bailey CP, Rosethorne EM, Charlton SJ, et al. (2010) μ -Opioid receptors: correlation of agonist efficacy for signalling with ability to activate internalization. *Mol Pharmacol* **78**:756–766.
- Miller LJ, Chen Q, Lam PC, Pinon DI, Sexton PM, Abagyan R, and Dong M (2011) Refinement of glucagon-like peptide 1 docking to its intact receptor using mid-region photolabile probes and molecular modeling. *J Biol Chem* **286**:15895–15907.
- Montrose-Rafizadeh C, Avdonin P, Garant MJ, Rodgers BD, Kole S, Yang H, Levine MA, Schwindinger W, and Bernier M (1999) Pancreatic glucagon-like peptide-1 receptor couples to multiple G proteins and activates mitogen-activated protein kinase pathways in Chinese hamster ovary cells. *Endocrinology* **140**:1132–1140.
- Mulder JE, Kolatkar NS, and LeBoff MS (2006) Drug insight: Existing and emerging therapies for osteoporosis. *Nat Clin Pract Endocrinol Metab* **2**:670–680.
- Nijmeijer S, Vischer HF, Rosethorne EM, Charlton SJ, and Leurs R (2012) Analysis of multiple histamine H_4 receptor compound classes uncovers $G_{\alpha i}$ protein- and β -arrestin2-biased ligands. *Mol Pharmacol* **82**:1174–1182.
- Nolte WM, Fortin JP, Stevens BD, Aspnes GE, Griffith DA, Hoth LR, Ruggeri RB, Mathiowetz AM, Limberakis C, Hepworth D, et al. (2014) A potentiator of orthosteric ligand activity at GLP-1R acts via covalent modification. *Nat Chem Biol* **10**:629–631.
- Sadee W, Hoeg E, Lucas J, and Wang D (2001) Genetic variations in human G protein-coupled receptors: implications for drug therapy. *AAPS PharmSci* **3**:E22.
- Salapatek AM, MacDonald PE, Gaisano HY, and Wheeler MB (1999) Mutations to the third cytoplasmic domain of the glucagon-like peptide 1 (GLP-1) receptor can functionally uncouple GLP-1-stimulated insulin secretion in HIT-T15 cells. *Mol Endocrinol* **13**:1305–1317.
- Schipani E, Langman C, Hunzelman J, Le Merrer M, Loke KY, Dillon MJ, Silve C, and Jüppner H (1999) A novel parathyroid hormone (PTH)/PTH-related peptide receptor mutation in Jansen's metaphyseal chondrodysplasia. *J Clin Endocrinol Metab* **84**:3052–3057.
- Siani A, Iacone R, Russo O, Barba G, Russo P, Cappuccio FP, Galletti F, and Strazzullo P (2001) Gly40Ser polymorphism of the glucagon receptor gene is associated with central adiposity in men. *Obes Res* **9**:722–726.
- Siu FY, He M, de Graaf C, Han GW, Yang D, Zhang Z, Zhou C, Xu Q, Wacker D, Joseph JS, et al. (2013) Structure of the human glucagon class B G-protein-coupled receptor. *Nature* **499**:444–449.
- Sonoda N, Imamura T, Yoshizaki T, Babendure JL, Lu JC, and Olefsky JM (2008) Beta-arrestin-1 mediates glucagon-like peptide-1 signaling to insulin secretion in cultured pancreatic beta cells. *Proc Natl Acad Sci USA* **105**:6614–6619.
- Strachan RT, Sciaky N, Cronan MR, Kroeze WK, and Roth BL (2010) Genetic deletion of p90 ribosomal S6 kinase 2 alters patterns of 5-hydroxytryptamine 2A serotonin receptor functional selectivity. *Mol Pharmacol* **77**:327–338.
- Taboulet J, Frenkian M, Frendo JL, Feingold N, Jullienne A, and de Vernejoul MC (1998) Calcitonin receptor polymorphism is associated with a decreased fracture risk in post-menopausal women. *Hum Mol Genet* **7**:2129–2133.
- Takhar S, Gyomai S, Su RC, Mathi SK, Li X, and Wheeler MB (1996) The third cytoplasmic domain of the GLP-1[7-36 amide] receptor is required for coupling to the adenylyl cyclase system. *Endocrinology* **137**:2175–2178.
- Tang CM and Insel PA (2005) Genetic variation in G-protein-coupled receptors—consequences for G-protein-coupled receptors as drug targets. *Expert Opin Ther Targets* **9**:1247–1265.
- Teng M, Johnson MD, Thomas C, Kiel D, Lakis JN, Kercher T, Aytes S, Kostrowicki J, Bhumralkar D, Truesdale L, et al. (2007) Small molecule ago-allosteric modulators of the human glucagon-like peptide-1 (hGLP-1) receptor. *Bioorg Med Chem Lett* **17**:5472–5478.
- Tokuyama Y, Matsui K, Egashira T, Nozaki O, Ishizuka T, and Kanatsuka A (2004) Five missense mutations in glucagon-like peptide 1 receptor gene in Japanese population. *Diabetes Res Clin Pract* **66**:63–69.
- Werry TD, Gregory KJ, Sexton PM, and Christopoulos A (2005) Characterization of serotonin 5-HT_{2C} receptor signaling to extracellular signal-regulated kinases 1 and 2. *J Neurochem* **93**:1603–1615.
- Wootten D, Simms J, Miller LJ, Christopoulos A, and Sexton PM (2013) Polar transmembrane interactions drive formation of ligand-specific and signal pathway-biased family B G protein-coupled receptor conformations. *Proc Natl Acad Sci USA* **110**:5211–5216.
- Zheng H, Chu J, Qiu Y, Loh HH, and Law PY (2008) Agonist-selective signaling is determined by the receptor location within the membrane domains. *Proc Natl Acad Sci USA* **105**:9421–9426.

Address correspondence to: Prof. Patrick M. Sexton, Drug Discovery Biology Laboratory, Monash Institute of Pharmaceutical Sciences, Monash University, 381 Royal Parade, Parkville, VIC 3052, Australia. E-mail: Patrick.Sexton@monash.edu

Crystal structures of the M1 and M4 muscarinic acetylcholine receptors

David M. Thal^{1*}, Bingfa Sun^{2*}, Dan Feng², Vindhya Nawaratne¹, Katie Leach¹, Christian C. Felder³, Mark G. Bures⁴, David A. Evans⁵, William I. Weis^{6,7}, Priti Bachhawat², Tong Sun Kobilka², Patrick M. Sexton¹, Brian K. Kobilka^{2,6} & Arthur Christopoulos¹

Muscarinic M1–M5 acetylcholine receptors are G-protein-coupled receptors that regulate many vital functions of the central and peripheral nervous systems. In particular, the M1 and M4 receptor subtypes have emerged as attractive drug targets for treatments of neurological disorders, such as Alzheimer's disease and schizophrenia, but the high conservation of the acetylcholine-binding pocket has spurred current research into targeting allosteric sites on these receptors. Here we report the crystal structures of the M1 and M4 muscarinic receptors bound to the inverse agonist, tiotropium. Comparison of these structures with each other, as well as with the previously reported M2 and M3 receptor structures, reveals differences in the orthosteric and allosteric binding sites that contribute to a role in drug selectivity at this important receptor family. We also report identification of a cluster of residues that form a network linking the orthosteric and allosteric sites of the M4 receptor, which provides new insight into how allosteric modulation may be transmitted between the two spatially distinct domains.

The M1–M5 muscarinic acetylcholine receptors constitute an important family of class A G-protein-coupled receptor (GPCRs) activated by the neurotransmitter, acetylcholine¹. Both the M1 and M4 receptors have been associated with learning, memory, and cognition^{2,3} and have emerged as attractive targets for the treatment of various central nervous system disorders, including Alzheimer's disease, schizophrenia, and drug addiction^{4–6}. However, the orthosteric acetylcholine-binding site is highly conserved, and the clinical translation of compounds targeting these receptor subtypes has remained largely unsuccessful owing to adverse side effects from off-target activity at peripheral M2 and M3 receptor subtypes^{7–9}. Encouragingly, muscarinic receptors possess spatially distinct allosteric binding sites that offer greater potential for selective receptor targeting^{10–12}, and the M1 and M4 receptors are prime examples where highly selective positive allosteric modulators (PAMs) with central nervous system activity and preclinical efficacy have been identified^{4,13–17}.

So far, however, the structural basis of drug action at these receptor types has been largely restricted to mutational analyses^{18–21}, with the only reported muscarinic receptor crystal structures being of the M2 and M3 subtypes^{22,23}. Thus, to better understand the molecular basis for orthosteric and allosteric drug interactions with the M1 and M4 receptors, we sought to obtain high-resolution X-ray crystal structures of both subtypes. To gain additional insight into potential mechanisms of allosteric modulation, we complemented our findings with active-state homology modelling to rationalize the effects of targeted mutations on the interaction between a well-characterized PAM and acetylcholine at the M4 receptor.

Crystallization of the M1 and M4 receptors

To determine the structures of the M1 and M4 muscarinic receptors, we used protein engineering and lipidic cubic phase methodology^{24,25}. Both receptors were crystallized in the presence of the high-affinity and clinically used inverse agonist, tiotropium (Spiriva), to stabilize

the inactive state. Intracellular loop 3 (ICL3) of the M1 receptor was replaced with a T4 lysozyme fusion protein, and in the case of the M4 receptor a minimal T4 lysozyme (mT4L)²⁶ fusion was used to aid crystallization (Extended Data Fig. 1). It was also necessary to remove the first 21 residues of the amino (N) terminus from the M4 receptor to improve diffraction. The M1 receptor was also crystallized with the N2Q and N12Q mutations to remove glycosylation sites, and, unintentionally, an N110Q^{3,37} mutation. Importantly, the binding affinities of [³H]QNB (M1 receptor), [³H]NMS (M4 receptor), acetylcholine, or tiotropium were not significantly different at either fusion construct compared with the wild-type receptor, suggesting that the alterations did not perturb the orthosteric site; the M1 N110Q^{3,37} mutation also had no significant effect on receptor functionality in the absence of T4 lysozyme (Supplementary Table 1). The M1 and M4 structures were subsequently determined to a resolution of 2.7 Å and 2.6 Å, respectively (Extended Data Table 1).

Comparison of muscarinic receptor structures

Overall, the structures of the M1 and M4 receptors are similar to the previously solved inactive M2 and M3 receptors^{22,23}, with similar positioning of the seven-transmembrane (TM1–7) bundle and root mean squared deviations of 0.6–0.9 Å (Fig. 1a). Subtle differences between the receptors are observed on the extracellular and intracellular sides (Fig. 1b, c) corresponding to regions that are least conserved across the muscarinic subtypes (Extended Data Fig. 2). For example, the M2 receptor differs from the other receptors in the tilt and position of TM1 and TM7 (Fig. 1a, b). Notably, the M1 receptor was co-crystallized with a Flag peptide co-bound on the intracellular side, which makes extensive contacts with TM6 and ICL3 (Extended Data Fig. 3a, b), and probably contributes to observed differences in TM5, TM6, and a variable linkage between TM7–helix8 (Extended Data Fig. 3c). The M1–N110Q^{3,37} mutation has little effect on the M1 structure other than creating a slight bulge in TM4 due to the loss of a hydrogen bond with

¹Drug Discovery Biology and Department of Pharmacology, Monash Institute of Pharmaceutical Sciences, Monash University, Parkville, 3052, Victoria, Australia. ²ConformetRx, 3070 Kenneth Street, Santa Clara, California 95054, USA. ³Neuroscience, Eli Lilly, Indianapolis, Indiana 46285, USA. ⁴Computational Chemistry and Chemoinformatics, Eli Lilly, Indianapolis, Indiana 46285, USA. ⁵Computational Chemistry and Chemoinformatics, Eli Lilly, Sunninghill Road, Windlesham GU20 6PH, UK. ⁶Department of Molecular and Cellular Physiology, Stanford University School of Medicine, Stanford, California 94305, USA. ⁷Department of Structural Biology, Stanford University School of Medicine, Stanford, California 94305, USA.

*These authors contributed equally to this work.

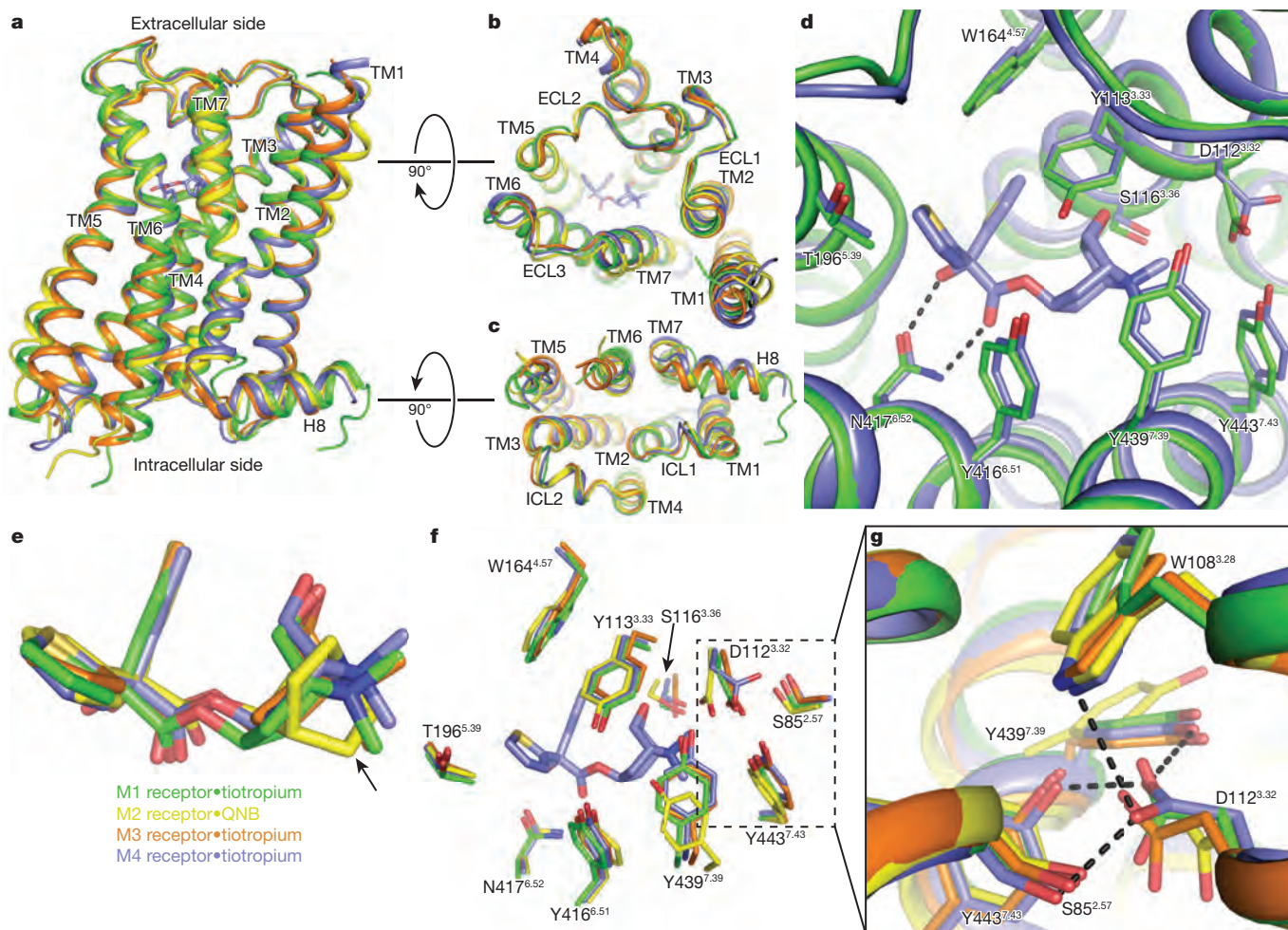


Figure 1 | Structural comparison of the M1–M4 receptors. **a**, The overall view of the muscarinic structures is shown as cartoons aligned to the M3 receptor, with the M1 coloured in green, M2 in yellow (PDB accession number 3UON), M3 (PDB accession number 4U15, chain A) in orange, and M4 (chain A) in blue. Root mean squared deviations for the alignment (excluding T4L fusions) of M1, M2, and M4 versus the M3 receptor are 0.86 Å, 0.81 Å, and 0.62 Å, respectively. The ligand, tiotropium, for the M4 receptor is shown as sticks and coloured according to element: carbon, light blue; oxygen, red; nitrogen, dark blue; sulfur, yellow. **b**, **c**, Comparison of the views from **(b)** the extracellular side

and **(c)** the intracellular side. **d**, M1 and M4 residues involved in tiotropium binding are shown as sticks (several residues are omitted for clarity). The black dashed line indicates a bidentate hydrogen bond between N^{6.52} and tiotropium. **e**, Superposition of tiotropium from the M1, M3, and M4 structures and QNB from the M2 structure. The arrow indicates the main structural difference between tiotropium and QNB. **f**, Comparison of the orthosteric binding site of the M1–M4 receptors with orthosteric site residues shown as sticks. **g**, The rotameric change of D112^{3.32} is stabilized by a network of hydrogen bonds.

S^{4.53} (Extended Data Fig. 3d). More interestingly, the M4 receptor was crystallized with an intact ionic lock (Extended Data Fig. 3e) a feature uncommonly seen in other GPCRs and not present in the other muscarinic structures. It is important to note that the observed differences in the intra- and extracellular sides of the receptor occur in regions that are solvent accessible or are involved in crystal packing interactions, which could contribute to the observed perturbations between subtypes; however, none of the crystal packing interactions grossly affect the structure or the core of the receptor.

Like the inactive M3 receptor, the M1 and M4 receptors were crystallized in complex with the inverse agonist, tiotropium, and this binding site is buried deep within the transmembrane core (Fig. 1d). The binding pose of tiotropium and surrounding residues between these three structures is nearly identical (Fig. 1d–f), which is not surprising given the near absolute conservation of residues lining the orthosteric site in the muscarinic family (Extended Data Fig. 2). However, this high degree of sequence conservation does not preclude the possibility of differences in tertiary structure with respect to the orthosteric site. Indeed, one surprising difference is a change in the rotamer of D112^{3.32} of the M4 receptor (Fig. 1 f, g); a residue that is conserved throughout

the biogenic amine GPCRs and serves as the counter ion for positively charged neurotransmitters²⁷. This rotameric change points D112^{3.32} away from tiotropium and is accompanied by slight movements of Y439^{7.39} and Y443^{7.43}, allowing them to form a network of hydrogen bond interactions between D112^{3.32} and S85^{2.57}, W108^{3.28}, Y439^{7.39}, and Y443^{7.43}, which is distinct from the M1, M2, and M3 muscarinic receptor structures (Fig. 1g).

Further comparison of the M1, M3, and M4 tiotropium-bound structures with the M2 receptor, which was crystallized with the structurally similar inverse agonist, QNB, also revealed considerable differences around residues D^{3.32}, Y^{7.39}, and Y^{7.43}. These three residues surround the amine group, which is slightly more bulky for QNB than tiotropium (Fig. 1e–g). Indeed, previous mutagenesis studies²⁸ on the M1 receptor revealed ligand-specific changes in binding affinities of NMS and QNB upon mutation of Y^{7.39} and Y^{7.43} to alanine. For the ligand NMS, which has a structurally similar tropane ring to tiotropium, a 25- and 48-fold loss of binding affinity was observed for the Y^{7.39} and Y^{7.43} mutations, respectively, whereas little effect was observed for QNB. This suggests a potential role for these two residues in stabilizing different inactive-state conformations with QNB potentially making compensatory

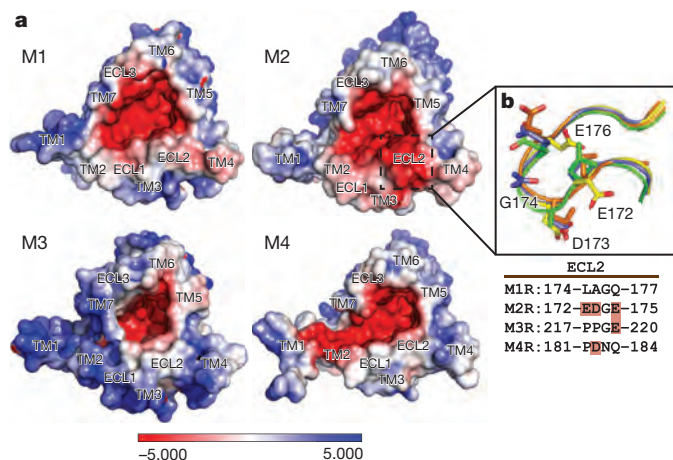


Figure 3 | Electrostatic and surface properties of the different muscarinic receptor structures. **a**, Electrostatic potentials ($+5kT/e$ in blue and $-5kT/e$ per electron in red) mapped on the surfaces of the M1–M4 receptor structures calculated at pH 7.0 using the programs PDB2PQR^{43,44} and APBS⁴⁵. **b**, Residues in ECL2 that make up the EDGE sequence at the M2 receptor and the corresponding regions at the other subtypes are shown as sticks. Negatively charged residues in the sequence alignment are coloured red.

On the basis of the recent structure of the active M2 receptor bound to the LY2033298 congener, LY2119620 (refs 35, 37, 38), it is likely that such PAMs bind to an essentially pre-formed closed state of the extracellular vestibule. As such, residues whose mutation might alter the cooperativity between acetylcholine and LY2033298 fall into three general categories: (1) those that make tighter contacts with the ligands in the closed state than the open state; (2) those that are immobilized by the binding of either ligand, such that the entropic cost is paid by the first binding event; (3) non-ligand-contact residues that alter the free energy of activation of the receptor and thus the open to closed transition. We chose to focus on residues within and between the extracellular vestibule and orthosteric sites, which are likely to reflect the first two categories; mutagenesis of non-contact residues that govern the free energy of receptor transitions are beyond the scope of the current work.

Because prior mutagenesis studies suggested a role for aromatic residues in receptor interaction with LY2033298, we generated alanine mutations of selected aromatic residues near the top of the receptor and applied an allosteric ternary complex model to the data (Methods) to determine the effect of each mutation on the affinity of acetylcholine (K_A) or LY2033298 (K_B) for the free receptor and the magnitude of positive cooperativity (α) between the two ligands. We also chose to investigate selected (non-aromatic) residues that line the proximal and distal ends of ECL2, given the important role this region plays in the binding of modulators to the extracellular vestibule^{18,39–41}. The results of these experiments are summarized in Supplementary Tables 2–4 and include prior mutagenesis results from our laboratory for the same set of ligands. To rationalize our findings, we used the recent active state M2 receptor structure as a template to generate a homology model of the M4 receptor bound to acetylcholine and LY2033298, and compared this with our inactive state crystal structure (Fig. 4 and Extended Data Fig. 6).

The most dramatic effect on the affinity of the PAM was noted upon mutation of W435^{7.35} at the top of TM7, with a complete loss in LY2033298 binding, similar to our previous observations²¹ upon alanine substitution of F186^{ECL2} (Fig. 5, Extended Data Fig. 7 and Supplementary Tables 3 and 4). Alanine mutations of residues Y113^{3.33}, Y416^{6.51}, and Y439^{7.39}, which form the roof of the orthosteric site, led to significant decreases in cooperativity. A slight increase in modulator affinity and significant decrease in cooperativity was also noted with mutation of Y89^{2.61}, together with our prior identification of residues W108^{3.28} and L109^{3.29} as likely contributors to the PAM binding

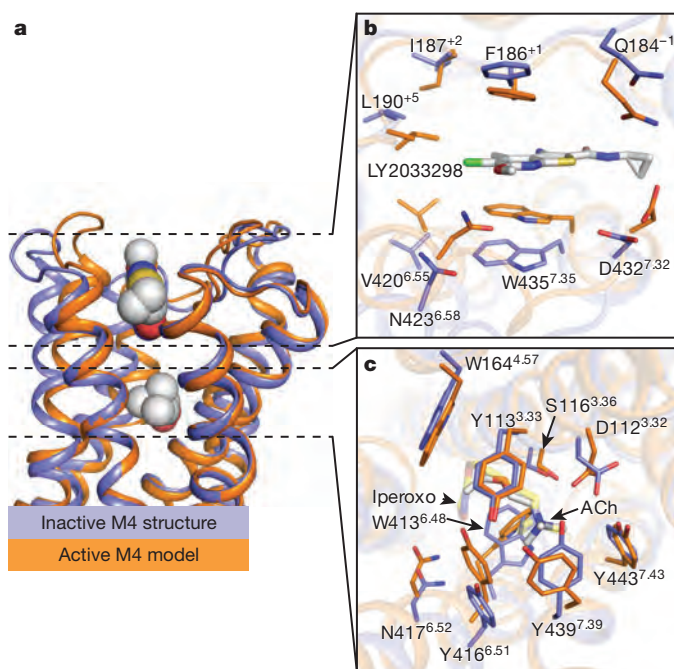


Figure 4 | Model of an active M4 receptor bound to acetylcholine and LY2033298. **a**, Comparison of the M4•tiotropium receptor structure (blue) versus an active-state model (orange) bound to acetylcholine and LY2033298 on the basis of the active M2•iperoxoxo•LY2119620 structure (PDB accession number 4MQT) as viewed from the membrane. The active M4 model was aligned to the M4•tiotropium structure (chain A, excluding T4L) with a root mean squared deviation of 0.9 Å. **b**, **c**, Cross-sectional views of the (b) allosteric site and (c) orthosteric site as viewed from the extracellular side with a 90° rotation relative to the membrane from **a**. Residues surrounding each site are shown as sticks (several removed for clarity). Acetylcholine and LY2033298 are shown as (a) spheres or (b, c) sticks and coloured according to element: carbon, cyan; oxygen, red; nitrogen, blue; sulfur, yellow; chlorine, green. Acetylcholine is in the *trans* conformation and aligns in a similar pose to iperoxoxo (c, transparent yellow sticks).

pocket²⁰. Comparison of our inactive state structure to the active state model now provides a mechanistic rationale for our findings, specifically a contraction of the extracellular vestibule that results predominantly in an inward movement of N423^{6.58}, F186^{ECL2}, and W435^{7.35} allowing π -stacking interactions to occur with the modulator in the active state (Fig. 4b). For the acetylcholine-binding pocket, there is a contraction of the pocket mediated by an inward movement of the top of TM6 to accommodate the large difference in size between acetylcholine and tiotropium resulting in significant movement of residues Y416^{6.51}, N417^{6.52}, W413^{6.48}, and Y439^{7.39} (Fig. 4c). Additionally, D112^{3.32} is reoriented to interact with the choline head-group of acetylcholine, and is no longer stabilized by the same hydrogen bond network that is seen in the inactive state (Fig. 1g).

Importantly, mapping of the amino-acid residues that significantly affect the cooperativity between acetylcholine and LY2033298 upon mutation also identified, for the first time, a network that appears to link the allosteric and orthosteric sites, involving the interface between TMs 2, 3, 6, and 7, and extending along the top of ECL2 (Fig. 5; orange coloured residues); this network is consistent with views of allosteric modulation that propose a preferred energetic link between orthosteric and allosteric sites⁴² but, to our knowledge, has never been directly mapped before in a GPCR. Interestingly, a comparison of the side-chain locations between the inactive M4 structure and active M4 model for residues in the allosteric network reveals that the majority of residues at the TM2/3/7 interface that contribute to cooperativity are not predicted to undergo appreciable movement between states, whereas comparison of residues further away from the interface (F186^{ECL2}, Y416^{6.51},

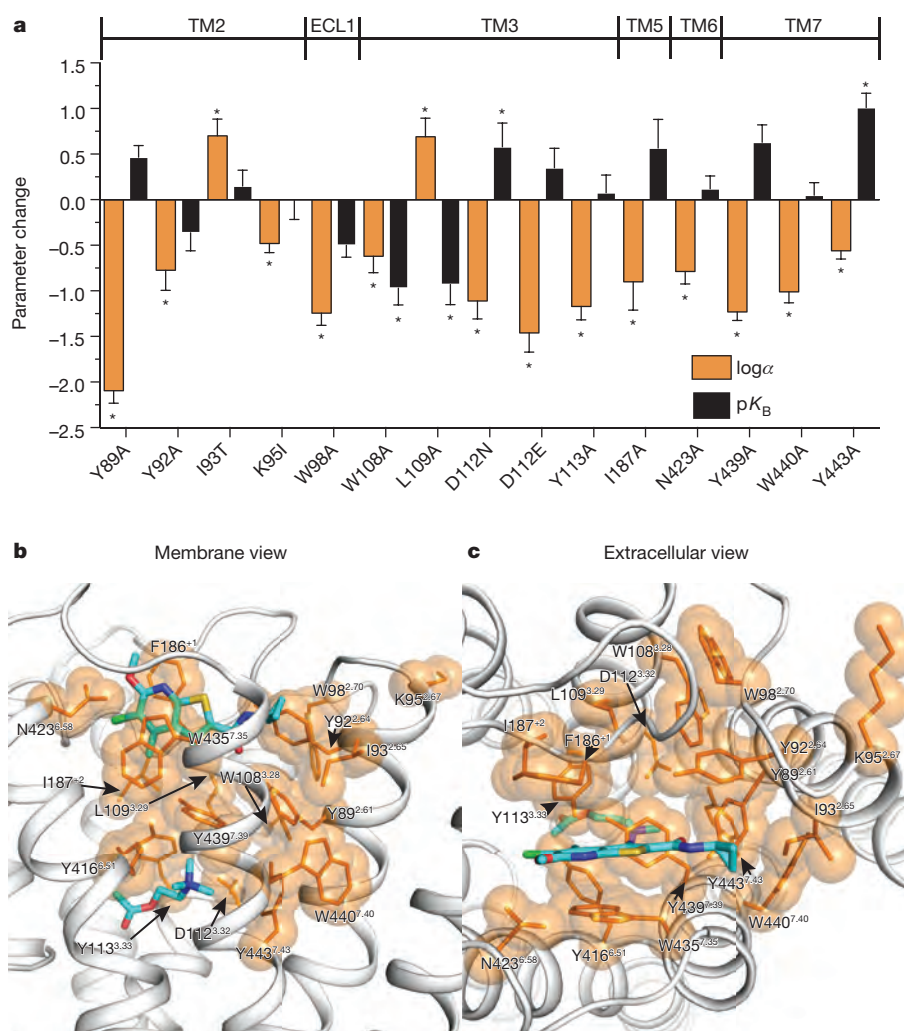


Figure 5 | A cooperativity network at the M4 receptor. a, Changes in either LY2033298 binding affinity (Δ pK_B, coloured black) or cooperativity (Δ log α , coloured orange) relative to wild-type M4 are shown for each mutation. Data represent the mean \pm s.e.m. from at least three experiments performed in duplicate. Statistical differences between pharmacological parameters at wild-type versus mutant M4 receptors are indicated by asterisks and were determined by one-way analysis of variance with Dunnett's post hoc test, where $P < 0.01$ (Supplementary

Table 3) or $P < 0.05$ (for previously determined mutations; Supplementary Table 4) were considered statistically significant. Cooperativity and binding values for F186⁺¹ and W435^{7.35} were not determined owing to a lack of LY2033298 binding (see Supplementary Tables 2–4). **b**, **c**, Residues from **a** were mapped onto the M4 active-state model and coloured as orange sticks with translucent spheres with views from **(b)** the membrane and **(c)** the extracellular side. LY2033298 and acetylcholine are shown as sticks and coloured the same as in Fig. 4.

N423^{6.58}, and W435^{7.35}) are predicted to move significantly between the two states (Extended Data Fig. 8). The TM2/3/7 interface, which forms part of the hydrophobic core of the receptor, may act as a hinge mediating conformational rearrangements in the extracellular vestibule between the inactive (open extracellular vestibule) and active (closed extracellular vestibule) states of the receptor. Disruption of this hinge by mutagenesis alters the packing interactions within the interface and might change the energetic barrier between the open and closed conformations of the receptor leading to either an increase or decrease in PAM cooperativity. Thus, binding of a PAM to the allosteric site might stabilize the conformation of the allosteric network residues that are otherwise found in a more dynamic state. Presumably, structures of the inactive state and active M4 model described here represent the lowest energy conformations, as they were obtained using crystallography, or are based on the X-ray structures of the active M2 receptor³⁵ (Extended Data Fig. 8).

Another noteworthy feature of LY2033298 is that it is selective towards the M4 receptor versus the M1 receptor when tested against acetylcholine¹⁵. This difference in selectivity could arise either through differential binding affinities of LY2033298 or through a difference in the cooperativity between LY2033298 and acetylcholine between the two subtypes (Extended Data Fig. 9).

Conclusions

Muscarinic receptors remain important drug targets, and designing molecules to selectively target the orthosteric binding site has proved challenging, as highlighted by the lack of prominent differences between the receptor subtypes. Alongside the previously determined M2 and M3 structures, the M1 and M4 structures presented here now offer a near complete view of the inactive state of this important sub-family of GPCRs. Excitingly, comparison of these structures clearly reveals a divergence in residues lining the allosteric site, highlighting the importance of this region for designing selective drugs. Moreover, our enriched structure–function analysis of the M4 receptor indicates that it is possible to combine crystal structure and mutagenesis data to uncover new insights into GPCR allosteric modulation, and our results point to the TM2/3/7 interface as a network for further studies on the mechanistic basis of allostery at class A GPCRs. Together with the recent solution of the inactive M2 and M3 receptors, as well as the active and PAM-bound M2 receptor, our study has contributed to an emerging picture of mechanisms of allostery at a therapeutically important receptor family that may facilitate the design of novel agents targeting a variety of CNS disorders while avoiding peripheral off-target effects.

Online Content Methods, along with any additional Extended Data display items and Source Data, are available in the online version of the paper; references unique to these sections appear only in the online paper.

Received 1 June 2015; accepted 29 January 2016.

Published online 9 March 2016.

- Wess, J., Eglén, R. M. & Gautam, D. Muscarinic acetylcholine receptors: mutant mice provide new insights for drug development. *Nature Rev. Drug Discov.* **6**, 721–733 (2007).
- Hasselmo, M. E. The role of acetylcholine in learning and memory. *Curr. Opin. Neurobiol.* **16**, 710–715 (2006).
- Hasselmo, M. E. & Giocomo, L. M. Cholinergic modulation of cortical function. *J. Mol. Neurosci.* **30**, 133–135 (2006).
- Kruse, A. C. *et al.* Muscarinic acetylcholine receptors: novel opportunities for drug development. *Nature Rev. Drug Discov.* **13**, 549–560 (2014).
- Kruse, A. C., Hu, J., Kobilka, B. K. & Wess, J. Muscarinic acetylcholine receptor X-ray structures: potential implications for drug development. *Curr. Opin. Pharmacol.* **16**, 24–30 (2014).
- Foster, D. J., Jones, C. K. & Conn, P. J. Emerging approaches for treatment of schizophrenia: modulation of cholinergic signaling. *Discov. Med.* **14**, 413–420 (2012).
- Shekhar, A. *et al.* Selective muscarinic receptor agonist xanomeline as a novel treatment approach for schizophrenia. *Am. J. Psychiatry* **165**, 1033–1039 (2008).
- Bodick, N. C. *et al.* Effects of xanomeline, a selective muscarinic receptor agonist, on cognitive function and behavioral symptoms in Alzheimer disease. *Arch. Neurol.* **54**, 465–473 (1997).
- Heinrich, J. N. *et al.* Pharmacological comparison of muscarinic ligands: historical versus more recent muscarinic M1-preferring receptor agonists. *Eur. J. Pharmacol.* **605**, 53–56 (2009).
- Conn, P. J., Christopoulos, A. & Lindsley, C. W. Allosteric modulators of GPCRs: a novel approach for the treatment of CNS disorders. *Nature Rev. Drug Discov.* **8**, 41–54 (2009).
- Digby, G. J., Shirey, J. K. & Conn, P. J. Allosteric activators of muscarinic receptors as novel approaches for treatment of CNS disorders. *Mol. Biosyst.* **6**, 1345–1354 (2010).
- Keov, P., Sexton, P. M. & Christopoulos, A. Allosteric modulation of G protein-coupled receptors: a pharmacological perspective. *Neuropharmacology* **60**, 24–35 (2011).
- Suratman, S. *et al.* Impact of species variability and ‘probe-dependence’ on the detection and *in vivo* validation of allosteric modulation at the M4 muscarinic acetylcholine receptor. *Br. J. Pharmacol.* **162**, 1659–1670 (2011).
- Leach, K. *et al.* Molecular mechanisms of action and *in vivo* validation of an M4 muscarinic acetylcholine receptor allosteric modulator with potential antipsychotic properties. *Neuropsychopharmacology* **35**, 855–869 (2010).
- Chan, W. Y. *et al.* Allosteric modulation of the muscarinic M4 receptor as an approach to treating schizophrenia. *Proc. Natl Acad. Sci. USA* **105**, 10978–10983 (2008).
- Shirey, J. K. *et al.* A selective allosteric potentiator of the M1 muscarinic acetylcholine receptor increases activity of medial prefrontal cortical neurons and restores impairments in reversal learning. *J. Neurosci.* **29**, 14271–14286 (2009).
- Ma, L. *et al.* Selective activation of the M1 muscarinic acetylcholine receptor achieved by allosteric potentiation. *Proc. Natl Acad. Sci. USA* **106**, 15950–15955 (2009).
- Abdul-Ridha, A. *et al.* Molecular determinants of allosteric modulation at the M1 muscarinic acetylcholine receptor. *J. Biol. Chem.* **289**, 6067–6079 (2014).
- Abdul-Ridha, A. *et al.* Mechanistic insights into allosteric structure-function relationships at the M1 muscarinic acetylcholine receptor. *J. Biol. Chem.* **289**, 33701–33711 (2014).
- Leach, K., Davey, A. E., Felder, C. C., Sexton, P. M. & Christopoulos, A. The role of transmembrane domain 3 in the actions of orthosteric, allosteric, and atypical agonists of the M4 muscarinic acetylcholine receptor. *Mol. Pharmacol.* **79**, 855–865 (2011).
- Nawaratne, V., Leach, K., Felder, C. C., Sexton, P. M. & Christopoulos, A. Structural determinants of allosteric agonism and modulation at the M4 muscarinic acetylcholine receptor: identification of ligand-specific and global activation mechanisms. *J. Biol. Chem.* **285**, 19012–19021 (2010).
- Kruse, A. C. *et al.* Structure and dynamics of the M3 muscarinic acetylcholine receptor. *Nature* **482**, 552–556 (2012).
- Haga, K. *et al.* Structure of the human M2 muscarinic acetylcholine receptor bound to an antagonist. *Nature* **482**, 547–551 (2012).
- Caffrey, M. & Cherezov, V. Crystallizing membrane proteins using lipidic mesophases. *Nature Protocols* **4**, 706–731 (2009).
- Chun, E. *et al.* Fusion partner toolbox for the stabilization and crystallization of G protein-coupled receptors. *Structure* **20**, 967–976 (2012).
- Thorsen, T. S., Matt, R., Weis, W. I. & Kobilka, B. K. Modified T4 lysozyme fusion proteins facilitate G protein-coupled receptor crystallogenesis. *Structure* **22**, 1657–1664 (2014).
- van Rhee, A. M. & Jacobson, K. A. Molecular architecture of G protein-coupled receptors. *Drug Dev. Res.* **37**, 1–38 (1996).
- Lu, Z.-L., Saldanha, J. W. & Hulme, E. C. Transmembrane domains 4 and 7 of the M1 muscarinic acetylcholine receptor are critical for ligand binding and the receptor activation switch. *J. Biol. Chem.* **276**, 34098–34104 (2001).
- Caulfield, M. P. & Birdsall, N. J. M. International Union of Pharmacology. XVII. Classification of muscarinic acetylcholine receptors. *Pharmacol. Rev.* **50**, 279–290 (1998).
- Goodwin, J. A., Hulme, E. C., Langmead, C. J. & Tehan, B. G. Roof and floor of the muscarinic binding pocket: variations in the binding modes of orthosteric ligands. *Mol. Pharmacol.* **72**, 1484–1496 (2007).
- Gregory, K. J., Sexton, P. M. & Christopoulos, A. Allosteric modulation of muscarinic acetylcholine receptors. *Curr. Neuropharmacol.* **5**, 157–167 (2007).
- Stockton, J. M., Birdsall, N. J., Burgen, A. S. & Hulme, E. C. Modification of the binding properties of muscarinic receptors by gallamine. *Mol. Pharmacol.* **23**, 551–557 (1983).
- Gnagay, A. L., Seidenberg, M. & Ellis, J. Site-directed mutagenesis reveals two epitopes involved in the subtype selectivity of the allosteric interactions of gallamine at muscarinic acetylcholine receptors. *Mol. Pharmacol.* **56**, 1245–1253 (1999).
- Tautermann, C. S. *et al.* Molecular basis for the long duration of action and kinetic selectivity of tiotropium for the muscarinic M3 receptor. *J. Med. Chem.* **56**, 8746–8756 (2013).
- Kruse, A. C. *et al.* Activation and allosteric modulation of a muscarinic acetylcholine receptor. *Nature* **504**, 101–106 (2013).
- Conn, P. J., Jones, C. K. & Lindsley, C. W. Subtype-selective allosteric modulators of muscarinic receptors for the treatment of CNS disorders. *Trends Pharmacol. Sci.* **30**, 148–155 (2009).
- Schober, D. A., Croy, C. H., Xiao, H., Christopoulos, A. & Felder, C. C. Development of a radioligand, [³H]LY2119620, to probe the human M₂ and M₄ muscarinic receptor allosteric binding sites. *Mol. Pharmacol.* **86**, 116–123 (2014).
- Croy, C. H. *et al.* Characterization of the novel positive allosteric modulator, LY2119620, at the muscarinic M₂ and M₄ receptors. *Mol. Pharmacol.* **86**, 106–115 (2014).
- Khouri, E., Clément, S. & Laporte, S. A. Allosteric and biased G protein-coupled receptor signaling regulation: potentials for new therapeutics. *Front. Endocrinol.* **5**, 68 (2014).
- Scarselli, M., Li, B., Kim, S. K. & Wess, J. Multiple residues in the second extracellular loop are critical for M₃ muscarinic acetylcholine receptor activation. *J. Biol. Chem.* **282**, 7385–7396 (2007).
- Avlani, V. A. *et al.* Critical role for the second extracellular loop in the binding of both orthosteric and allosteric G protein-coupled receptor ligands. *J. Biol. Chem.* **282**, 25677–25686 (2007).
- Lockless, S. W. & Ranganathan, R. Evolutionarily conserved pathways of energetic connectivity in protein families. *Science* **286**, 295–299 (1999).
- Dolinsky, T. J., Nielsen, J. E., McCammon, J. A. & Baker, N. A. PDB2PQR: an automated pipeline for the setup of Poisson-Boltzmann electrostatics calculations. *Nucleic Acids Res.* **32**, W665–W667 (2004).
- Dolinsky, T. J. *et al.* PDB2PQR: expanding and upgrading automated preparation of biomolecular structures for molecular simulations. *Nucleic Acids Res.* **35**, W522–W525 (2007).
- Baker, N. A., Sept, D., Joseph, S., Holst, M. J. & McCammon, J. A. Electrostatics of nanosystems: application to microtubules and the ribosome. *Proc. Natl Acad. Sci. USA* **98**, 10037–10041 (2001).

Supplementary Information is available in the online version of the paper.

Acknowledgements We thank L. Lopez for generating initial M4 homology models. This work was funded by Program Grant APP1055134 of the National Health and Medical Research Council (NHMRC) of Australia (A.C., P.M.S.). Portions of this work were supported by a Lilly Research Award Program grant. W.I.W. and B.K.K. were supported by the Mathers Foundation. A.C. is a Senior Principal, and P.M.S. a Principal, Research Fellow of the NHMRC. GM/CA @ APS has been funded in whole or in part with federal funds from the National Cancer Institute (Y1-CO-1020) and the National Institute of General Medical Science (Y1-GM-1104). Use of the Advanced Photon Source was supported by the US Department of Energy, Basic Energy Sciences, Office of Science, under contract number W-31-109-ENG-38.

Author Contributions D.M.T. performed cloning, protein expression, purification, crystallization, data collection, structure refinement, and radioligand binding assays on the M4 receptor. D.F. purified and crystallized the M1 receptor. B.S. performed data collection and structure refinement on the M1 receptor. K.L., V.N., and D.M.T. performed mutagenesis and radioligand binding studies that examined the effects of amino-acid substitutions on ligand pharmacology. C.C.F., M.G.B., and D.E. provided the pirenzepine IFD and active-state M4 homology model. P.B. generated the active-state model of the M1 receptor. T.S.K. supervised the M1 muscarinic receptor production and purification. W.I.W. supervised structure refinement. B.K.K., P.M.S., and A.C. provided overall project supervision. D.M.T. and A.C. wrote the manuscript.

Author Information Atomic coordinates and structure factors for the M1 and M4 receptors, respectively, have been deposited in the Protein Data Bank (PDB) under accession numbers 5CXV and 5DSG. Reprints and permissions information is available at www.nature.com/reprints. The authors declare competing financial interests: details are available in the online version of the paper. Readers are welcome to comment on the online version of the paper. Correspondence and requests for materials should be addressed to P.M.S. (patrick.sexton@monash.edu), B.K.K. (kobilka@stanford.edu) or A.C. (arthur.christopoulos@monash.edu).

METHODS

No statistical methods were used to predetermine sample size. The experiments were not randomized. The investigators were not blinded to allocation during experiments and outcome assessment.

M1 and M4 receptor expression and purification. The human M4 muscarinic receptor gene (<http://www.cdna.org>) was cloned into a modified pFastBac1 vector to give a receptor containing an N-terminal Flag epitope tag and a carboxy (C)-terminal 8× histidine tag. Residues 226–389 of ICL3 were removed and replaced by a minimal Cys-free T4 lysozyme fusion protein²⁶. The human M1 muscarinic receptor gene was also cloned into the modified pFastBac1 vector, and residues 219–354 of ICL3 were removed and replaced by a Cys-free T4 lysozyme fusion protein. Both fusion proteins were expressed using the Bac-to-Bac Baculovirus Expression System (Invitrogen) in Sf9 cells. Cells were infected at a density of 4.0×10^6 to 5.0×10^6 cells per millilitre, treated with 10 μ M atropine, and harvested at 60 h. Receptor was solubilized and purified in the presence of tiotropium as previously described for the M3 (ref. 22) receptor using Ni-NTA chromatography, Flag affinity chromatography, and size-exclusion chromatography. The N terminus of the M4 receptor was removed by cleavage with HRV 3C protease at a concentration of 2% (w/w) during concentration of the receptor before size-exclusion chromatography (~2 h at 4 °C). After size-exclusion chromatography, purified receptor was concentrated to 85 absorbance units (~50 mg ml⁻¹) and flash frozen in small aliquots using liquid nitrogen.

Pharmacology of crystallization constructs. Sf9 cells expressing wild-type M4 or M4-mT4L receptor, as described above, were pelleted and washed with PBS three times for 1 h each to remove any bound atropine. Cells were resuspended in binding buffer (10 mM HEPES pH 7.5, 100 mM NaCl, and 10 mM MgCl₂) and flash frozen with liquid nitrogen. Saturation binding assays were performed using approximately 20,000 cells per well with 9 different concentrations of [³H]NMS in a total volume of 0.5 ml for 3 h at 37 °C. Competition binding assays with acetylcholine and tiotropium were performed in the presence of a fixed concentration of [³H]NMS over 10 different concentrations of ligand for 3 h at 37 °C. Non-specific binding was measured in the presence of 10 μ M atropine, and reactions were harvested by rapid filtration through GF/B filters. Data were analysed using Prism 6.0d. Similar methods were applied for binding assays using wild type M1 and M1-T4L, except that [³H]QNB was used as the radioligand.

Crystallization. Purified M1-T4L•tiotropium and M4-mT4L•tiotropium were crystallized using lipid cubic phase technology. Each receptor was reconstituted by mixing the protein solution into 10:1 (w/w) monoolein:cholesterol (Sigma) in 1:1.5 parts w/w protein:lipid ratio using the two-syringe method²⁴. For the M1 receptor, samples of 50 nl (20–40 nl for M4) were spotted onto 96-well glass plates and overlaid with 800 nl (600 nl for M4) of precipitant solution for each well using a Gryphon LCP (Art Robbins Instruments). Glass plates were then sealed using a glass cover film and incubated at 20 °C. Initial crystals for the M1 receptor formed after 24 h in conditions containing 33% PEG 300, 100 mM sodium acetate, and 100 mM Bis-Tris Propane (pH 8.0). For the M4 receptor, initial crystals formed after 24 h in conditions containing 25–40% PEG 300, 50–100 mM EDTA (pH 8.0), and 100 mM MES (pH 5.5–6.5). M1 and M4 crystals were harvested using mesh grid loops (MiTeGen) and stored in liquid nitrogen before use.

Data collection, processing, and structure determination. X-ray diffraction data were collected at the Advanced Photon Source at Argonne National Laboratories at GM/CA beamline 23ID-D. Crystals were located by initial rastering using an 80 μ m by 30 μ m beam with fivefold attenuation and 1 s exposure. Regions that contained strong diffraction were then sub-rastered using a 10 μ m collimated beam with fivefold attenuation. Data were then collected with the 10 μ m beam using no attenuation with 1–2 s exposures and 1 degree oscillations. To prevent radiation damage, data were collected in wedges of 3–10° before moving onto either a different site on the same crystal or a new crystal. Diffraction data were processed using HKL2000 (M1 receptor) or XDS⁴⁶ (M4 receptor) and statistics are summarized in Extended Data Table 1. Both structures were solved by molecular replacement using Phaser⁴⁷. For the M1 receptor, the inactive M3 structure²² (PDB accession number 4DAJ) was split into its receptor and T4L components and used as corresponding search models. The refinement was performed using Refmac5 (ref. 48) with manual building in Coot⁴⁹. For the M4 receptor, the inactive M2 structure²³ (PDB accession number 3UON) and the inactive M3-mT4L²⁶ (PDB accession number 4U15) were used as search models for the receptor and mT4L fusion domains, respectively. The resulting model was completed by iterative refinement in Phenix⁵⁰ and manual building with Coot⁴⁹. MolProbity⁵¹ was used for structure validation, and figures were prepared using PyMol⁵². Final refinement statistics are reported in Extended Data Table 1.

Induced fit docking of pirenzepine. The inactive state structures of M1, M2, M3 (PDB 4U15, chain B), and M4 (chain A) receptors were processed by the protein preparation wizard of the Schrodinger 2014-2 suite⁵³, after deleting the lysozyme insertion region. Missing side chains were added by Prime and hydrogens refined

by minimization with the OPLS2.1 force field. Binding grids were defined using the default settings in Glide, centring the grid on the crystallized orthosteric ligand in each case. The PEG ligand in the extracellular vestibule of M3 and M4 receptors was deleted before grid generation. The ligand, pirenzepine, was treated with ligprep software to generate initial protonated 3D structures. Compound structures were docked using the induced fit docking protocol with default settings, which involves the use of the OPLS_2005 force field to refine residues around poses docked by Glide SP, followed by redocking into the generated receptor conformations, also with Glide SP. The poses with the lowest induced fit score were selected. This scoring function takes into account an estimate of the protein conformational penalty along with a protein–ligand interaction docking score.

Molecular modelling of active M4 receptor. A homology model of a human active-state M4 receptor was constructed using the Prime program implemented in Maestro version 2014.1 from Schrodinger. The crystal structure of the M2 receptor with an orthosteric and allosteric agonist bound (PDB accession number 4MQT) was used as a template to build the M4 model. The M2–M4 sequence alignment generated by Prime needed no adjustment owing to the overall significant sequence homology between the two isoforms. The initial M4 receptor model was built with the allosteric ligand (LY2119620) present in the M2 crystal structure bound in the M4 allosteric site and with iperoxo bound in the orthosteric site (as also present in the M2 structure). The binding mode of LY2119620 in M4 was used as a guide to manually dock LY2033298 into the M4 allosteric binding site. In addition, iperoxo from the M4 model was manually modified into acetylcholine (ACh). The M4-ACh-LY2033298 complex was then subjected to 500 steps of energy minimization (MacroModel implemented in Maestro 2014.1 from Schrödinger⁵³) to optimize key interactions in the binding sites. The resulting model of ACh and LY2033298 bound to M4 was used in subsequent modelling studies described in this paper.

Molecular modelling of active M1 receptor. The active state of the M1 receptor was modelled on the basis of the active state structure of M2 bound to iperoxo (PDB accession number 4MQT), using the automated protein structure homology modelling web server Swiss-Model^{54,55}. The nanobody structure was removed and the resulting coordinates were used as a template to model the M1 primary sequence without intracellular loop 3 residues (residues 213–240). The model was built using Promod-II, minimized by steepest descent energy minimization using a GROMOS96 force field and the quality was assessed by the QMEAN scoring function. ACh and LY2033298 were docked in the M1 homology model using Swiss-Dock⁵⁶, using steric and chemical considerations such as shape, charge complementarity, and keeping the protein structure constant. The top-scoring clusters were evaluated manually on the basis of chemical and steric considerations to pick the favourable pose. Owing to static docking, the top four ACh poses did not affect the docking results for LY2033298. For ACh, the selected pose is in the trans conformation similar to the M4•ACh•LY2033298 model. Finally, the structures with the ligand were energy minimized using Chimera with standard Steepest Descent and Conjugate Gradient steps.

Receptor mutagenesis and generation of cell lines. DNA encoding the human M4 mAChR with a triple HA²⁰ or cmv²¹ tag at its N terminus was subjected to QuikChange site-directed mutagenesis (Stratagene) to generate M4 mAChR sequences with the desired amino-acid substitutions. DNA constructs in pEF5/frt/V5 (Invitrogen) were stably expressed in Flp-In-CHO cells (Invitrogen), which were maintained in high-glucose Dulbecco's modified Eagle's medium containing 10% FBS, 16 mM HEPES, and 400 μ g ml⁻¹ hygromycin B. Mycoplasma testing was performed regularly on cell lines using the MycoAlertTM kit (Lonza); cell lines were mycoplasma-free before experiments were conducted.

Radioligand binding assays. Cell membranes were prepared as described previously^{14,57}. [³H]QNB affinity (K_A) at the M4 WT receptor and mutants was determined by saturation binding assays, performed by incubating varying concentrations of [³H]QNB with 10–100 μ g of membranes at 37 °C for 1 h, in a final volume of 0.5–1 ml binding buffer (20 mM HEPES, 100 mM NaCl, and 10 mM MgCl₂ at pH 7.4).

Radioligand inhibition binding assays were performed by co-incubating 10–100 μ g of membranes with a K_A concentration of [³H]QNB (determined in saturation assays, Supplementary Table 2) and varying concentrations of the non-radiolabelled test compound in 0.5–1 ml binding buffer in the presence of the guanine nucleotide, GppNHp (100 μ M), which was used to promote receptor/G-protein uncoupling. These experiments determined the concentration of ACh that inhibited 20% [³H]QNB binding, defined as the 20% inhibitory concentration (IC₂₀), which was used in subsequent interaction studies between [³H]QNB, ACh, and LY2033298. These experiments were performed by co-incubating 10–100 μ g of membranes, an IC₂₀ concentration of ACh, and a K_A concentration of [³H]QNB with increasing concentrations of LY2033298 in binding buffer containing GppNHp (100 μ M). The reaction was left to reach equilibrium for 3 h at 37 °C. For all experiments, non-specific binding was defined in the presence of

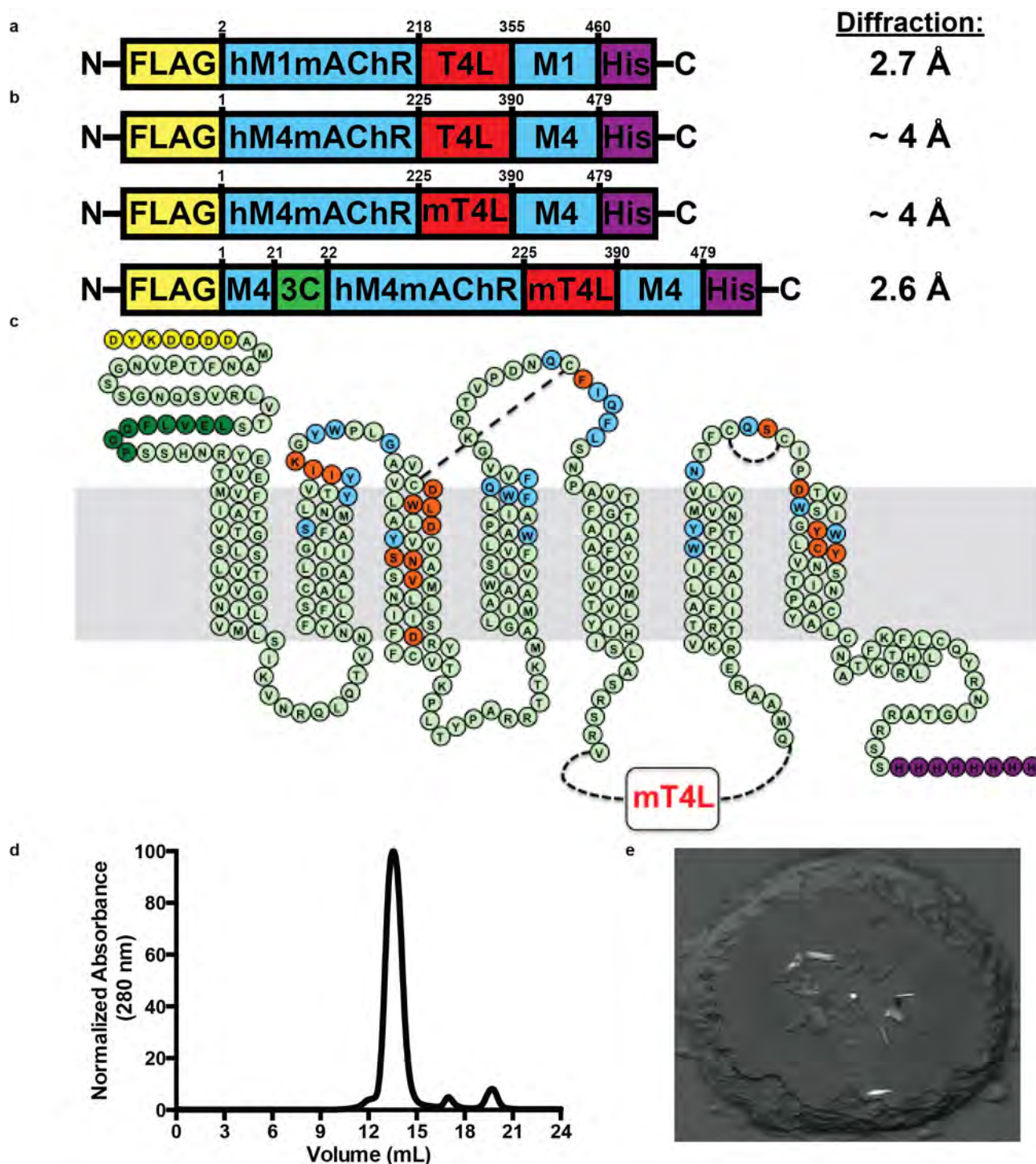
10 μ M atropine, total binding was determined in the absence of the test ligand, and vehicle effects were determined with 0.1% dimethylsulfoxide (DMSO). The assays were terminated by vacuum filtration through GF-B glass fibre filters, which were washed three times with ice-cold 0.9% NaCl. [3 H]QNB radioactivity was measured using a Packard 1600 TR liquid scintillation beta counter. Owing to a lack [3 H]QNB binding, affinity data for W164A^{4,57} were determined from functional pERK1/2 experiments performed as previously described^{20,21}.

Data analysis. Data were analysed using Prism (GraphPad). For radioligand saturation binding, non-specific and total binding data were analysed as described previously⁵⁸. Inhibition binding curves between [3 H]QNB and ACh were fitted to a one-site binding model⁵⁸. Interaction experiments between [3 H]QNB, ACh, and LY2033298 were fitted to the following allosteric ternary complex model^{20,21,59}:

$$Y = \frac{B_{\max} [A]}{[A] + \left(\frac{K_A K_B}{\alpha' [B] + K_B} \right) \left(1 + \frac{[I]}{K_I} + \frac{[B]}{K_B} + \frac{\alpha [I][B]}{K_I K_B} \right)}$$

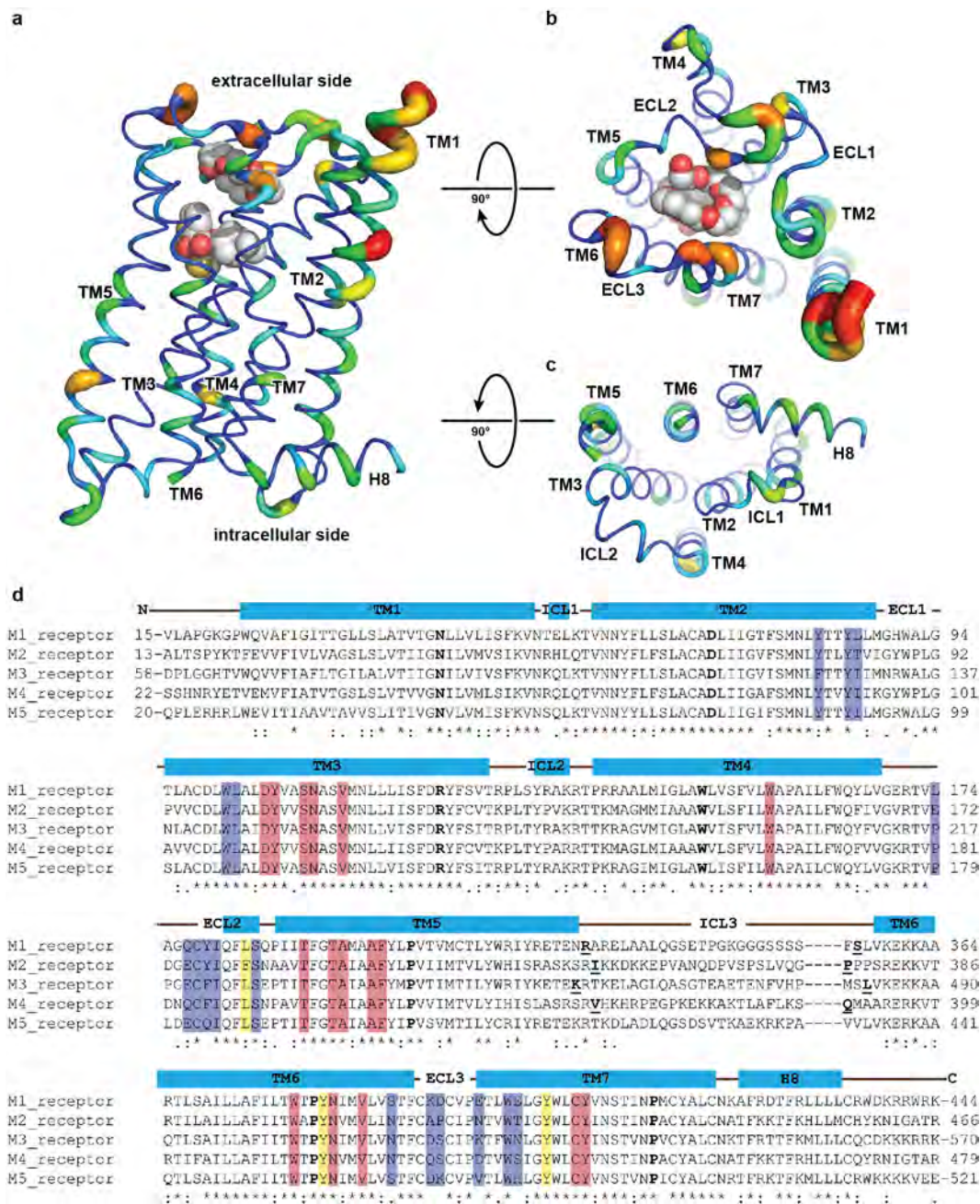
where Y is the specific radioligand binding, B_{\max} is the total number of receptors, [A], [B], and [I] are the concentrations of radioligand, allosteric modulator, and unlabelled orthosteric ligand, respectively, K_A , K_B , and K_I are the equilibrium dissociation constants of the radioligand, allosteric modulator, and unlabelled orthosteric ligand, respectively, and α' and α are the cooperativity factors between allosteric modulator and the radioligand or unlabelled orthosteric ligand, respectively. The value of α' was taken as 1 when the binding of [3 H]QNB changed by less than 10% at 10^{-5} M LY2033298 relative to zero LY2033298, and was fixed as such for all analyses. Otherwise, the value of α' was determined using a global fit to the allosteric ternary complex model. Statistical differences between pharmacological parameters at wild-type versus mutant M4 receptors were determined by one-way analysis of variance with Dunnett's post hoc test, where $P < 0.01$ was considered statistically significant.

46. Kabsch, W. XDS. *Acta Crystallogr. D* **66**, 125–132 (2010).
47. McCoy, A. J. *et al.* Phaser crystallographic software. *J. Appl. Crystallogr.* **40**, 658–674 (2007).
48. Skubák, P., Murshudov, G. N. & Pannu, N. S. Direct incorporation of experimental phase information in model refinement. *Acta Crystallogr. D* **60**, 2196–2201 (2004).
49. Emsley, P., Lohkamp, B., Scott, W. G. & Cowtan, K. Features and development of Coot. *Acta Crystallogr. D* **66**, 486–501 (2010).
50. Adams, P. D. *et al.* PHENIX: a comprehensive Python-based system for macromolecular structure solution. *Acta Crystallogr. D* **66**, 213–221 (2010).
51. Chen, V. B. *et al.* MolProbity: all-atom structure validation for macromolecular crystallography. *Acta Crystallogr. D* **66**, 12–21 (2010).
52. Schrödinger, L. The PyMOL Molecular Graphics System, version 1.7.0.3 (2010).
53. Schrödinger release 2014-2: Maestro, version 9.7 (2014).
54. Guex, N., Peitsch, M. C. & Schwede, T. Automated comparative protein structure modeling with SWISS-MODEL and Swiss-PdbViewer: a historical perspective. *Electrophoresis* **30** (Suppl. 1), S162–S173 (2009).
55. Arnold, K., Bordoli, L., Kopp, J. & Schwede, T. The SWISS-MODEL workspace: a web-based environment for protein structure homology modelling. *Bioinformatics* **22**, 195–201 (2006).
56. Grosdidier, A., Zoete, V. & Michielin, O. SwissDock, a protein-small molecule docking web service based on EADock DSS. *Nucleic Acids Res.* **39**, W270–W277 (2011).
57. Nawaratne, V. *et al.* New insights into the function of M4 muscarinic acetylcholine receptors gained using a novel allosteric modulator and a DREADD (designer receptor exclusively activated by a designer drug). *Mol. Pharmacol.* **74**, 1119–1131 (2008).
58. Motulsky, H. & Christopoulos, A. *Fitting Models to Biological Data Using Linear and Nonlinear Regression: A Practical Guide to Curve Fitting* (Oxford Univ. Press, 2004).
59. Ehlert, F. J. Estimation of the affinities of allosteric ligands using radioligand binding and pharmacological null methods. *Mol. Pharmacol.* **33**, 187–194 (1988).
60. Celniker, G. *et al.* ConSurf: using evolutionary data to raise testable hypotheses about protein function. *Isr. J. Chem.* **53**, 199–206 (2013).
61. Ashkenazy, H., Erez, E., Martz, E., Pupko, T. & Ben-Tal, N. ConSurf 2010: calculating evolutionary conservation in sequence and structure of proteins and nucleic acids. *Nucleic Acids Res.* **38**, W529–W533 (2010).
62. Landau, M. *et al.* ConSurf 2005: the projection of evolutionary conservation scores of residues on protein structures. *Nucleic Acids Res.* **33**, W299–W302 (2005).
63. Glaser, F. *et al.* ConSurf: identification of functional regions in proteins by surface-mapping of phylogenetic information. *Bioinformatics* **19**, 163–164 (2003).
64. Larkin, M. A. *et al.* Clustal W and Clustal X version 2.0. *Bioinformatics* **23**, 2947–2948 (2007).
65. Molecular Operating Environment (MOE) (Chemical Computing Group, 2015).
66. Karplus, P. A. & Diederichs, K. Linking crystallographic model and data quality. *Science* **336**, 1030–1033 (2012).



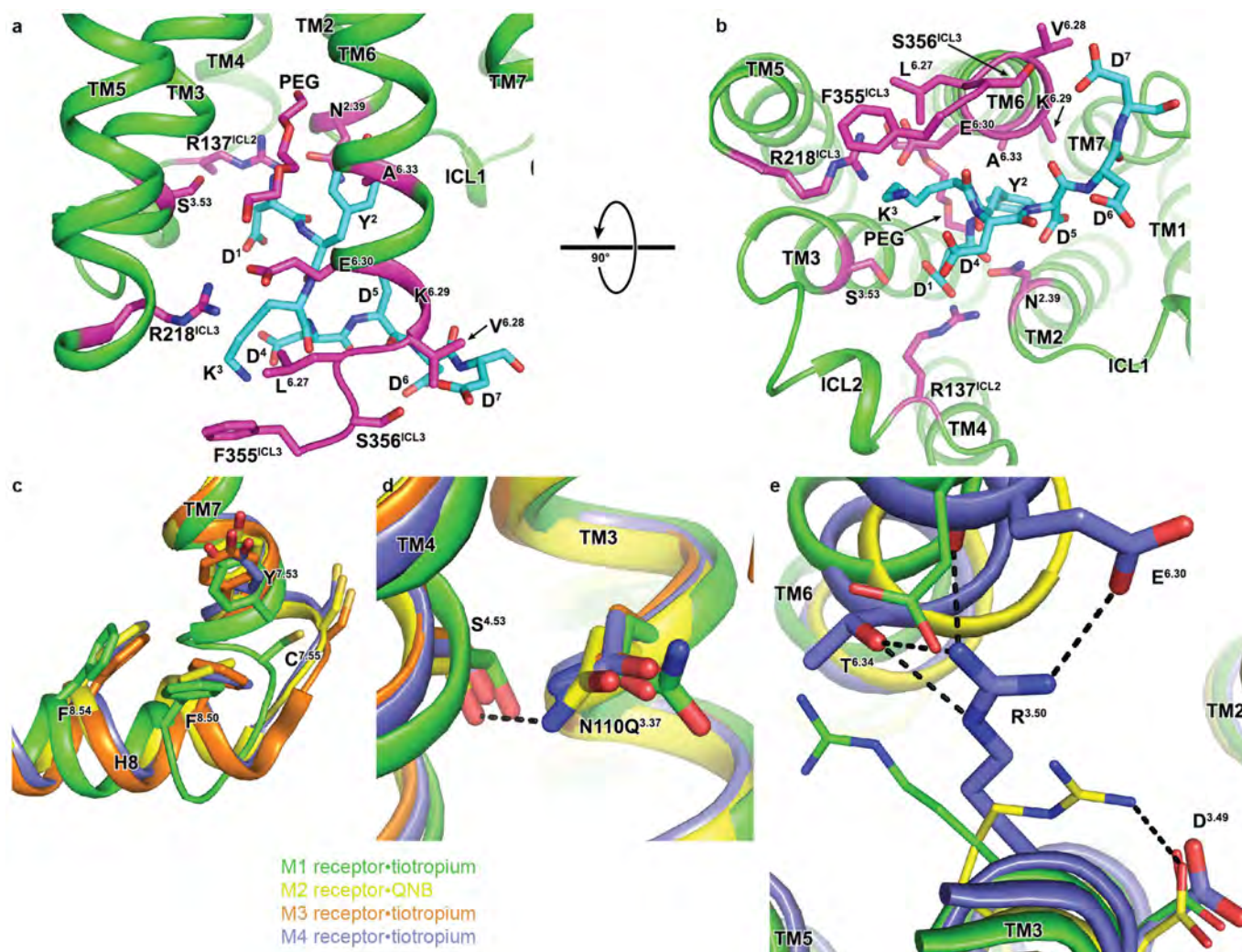
Extended Data Figure 1 | Crystallization construct design, purification and crystallization. **a, b,** Crystallization constructs used for the **(a)** M1 receptor and **(b)** M4 receptor. All constructs contain an N-terminal Flag epitope (yellow), C-terminal histidine tag (purple), and a T4L lysozyme fusion protein (red). For the M4 receptor, initial constructs diffracted out to 4 Å; however, the diffraction data appeared to suffer from a lattice translocation disorder and were unsolvable. The final crystallization construct contained a shortened N terminus with an HRV 3C cleavage

site, shown in dark green, and a minimal T4 lysozyme fusion (mT4L)²⁶, shown in red. **c,** Snake-plot diagram of the best diffracting M4 mAChR construct coloured according to **a**. Residues coloured blue are single-point mutations from this study, and residues coloured orange are previously studied mutations^{20,21}. **d,** Size-exclusion chromatography trace of purified monodispersed M4-mT4L bound to tiotropium. **e,** Crystals of M4-mT4L obtained in lipidic cubic phase and observed under circularly polarized light.



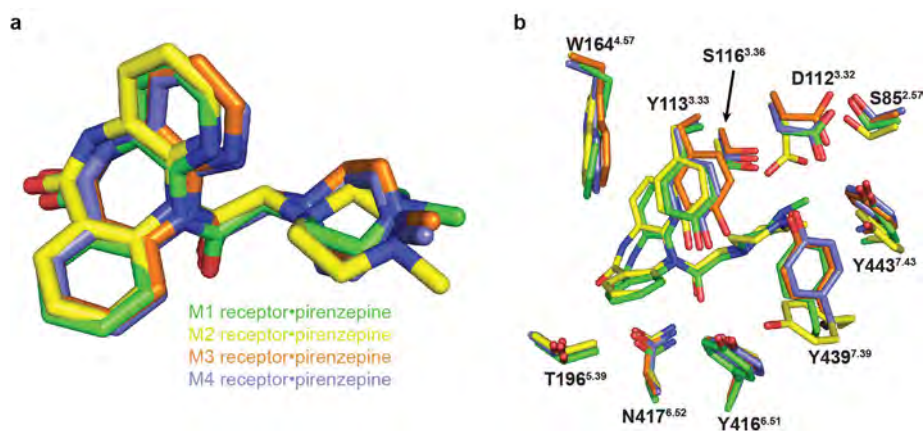
Extended Data Figure 2 | Sequence conservation across the muscarinic receptor subfamily. **a–c**, The sequence alignment of the human M1–M5 receptors **(d)** was determined on the ConSurf server to calculate amino-acid conservation scores^{60,61}. Conservation scores for each residue were mapped^{62,63} onto the M4 structure and coloured as a gradient from blue (highly conserved) to red (least conserved) with views from the **(b)** extracellular and **(c)** intracellular sides. The radius of the cartoon increases as the residues at each position become more poorly conserved. Tiotropium and PEG 300 from the M4 structure are shown as spheres and coloured with carbon in white, oxygen in red, nitrogen in blue, and sulfur

in yellow. **d**, Amino-acid sequences of the human M1–M5 receptors were aligned using the ClustalW2 server⁶⁴. Alpha helical regions are shown as blue boxes as determined by the consensus of the M1–M4 structures. The most conserved residue in each TM (X.50) is in bold lettering. Regions of the N terminus, C terminus, and ICL3 regions are removed for space and clarity. Insertion points of the T4 lysozyme fusion proteins between TM5 and TM6 are underlined with bold lettering. Residues from the orthosteric binding-site are highlighted in red and allosteric binding-site residues in blue. Residues that contribute to both sites are coloured in yellow.



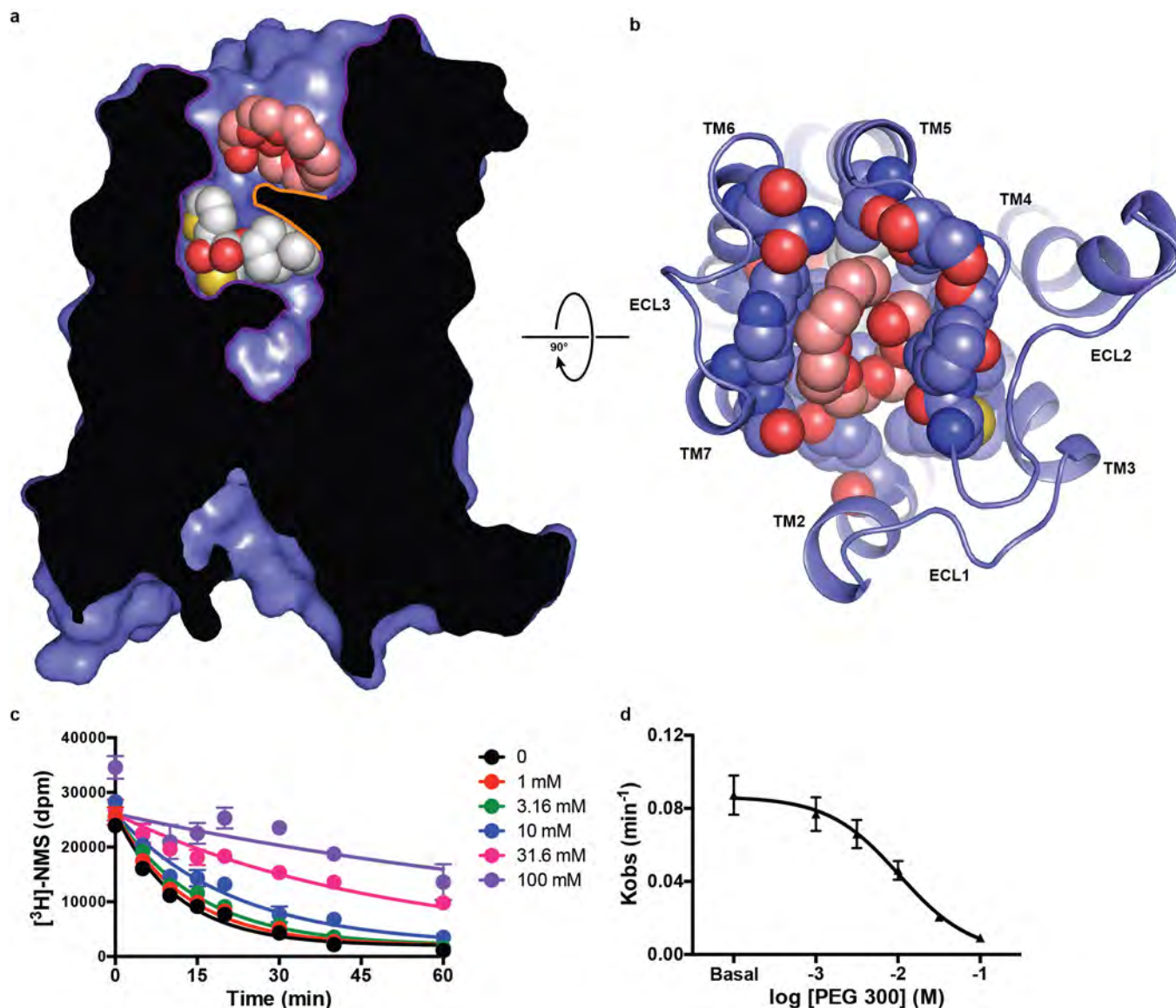
Extended Data Figure 3 | Distinct structural features for the M1 and M4 receptors. The receptors shown are aligned and coloured as in Fig. 1. **a, b**, The M1 receptor was crystallized with the Flag peptide (DYKDDDD; coloured cyan sticks) co-bound on the cytoplasmic surface. Residues of the M1 receptor within 4 Å of the Flag peptide are shown as magenta coloured sticks with views from the (a) membrane and (b) cytoplasmic side. **c**, The

linkage between TM7 and helix 8 of the M1 receptor undergoes a bend starting with a change in rotamer of residue Y^{7.53}, which may be a result of perturbations in TM6 due to the Flag peptide. **d**, The M1-N110Q^{3.37} mutation causes a slight bulge in TM4 due to the loss of a hydrogen bond with S^{4.53}. **e**, Chain B of the M4 receptor has an intact ionic lock with R^{3.50} forming hydrogen bonds with T^{6.34} and E^{6.30}.



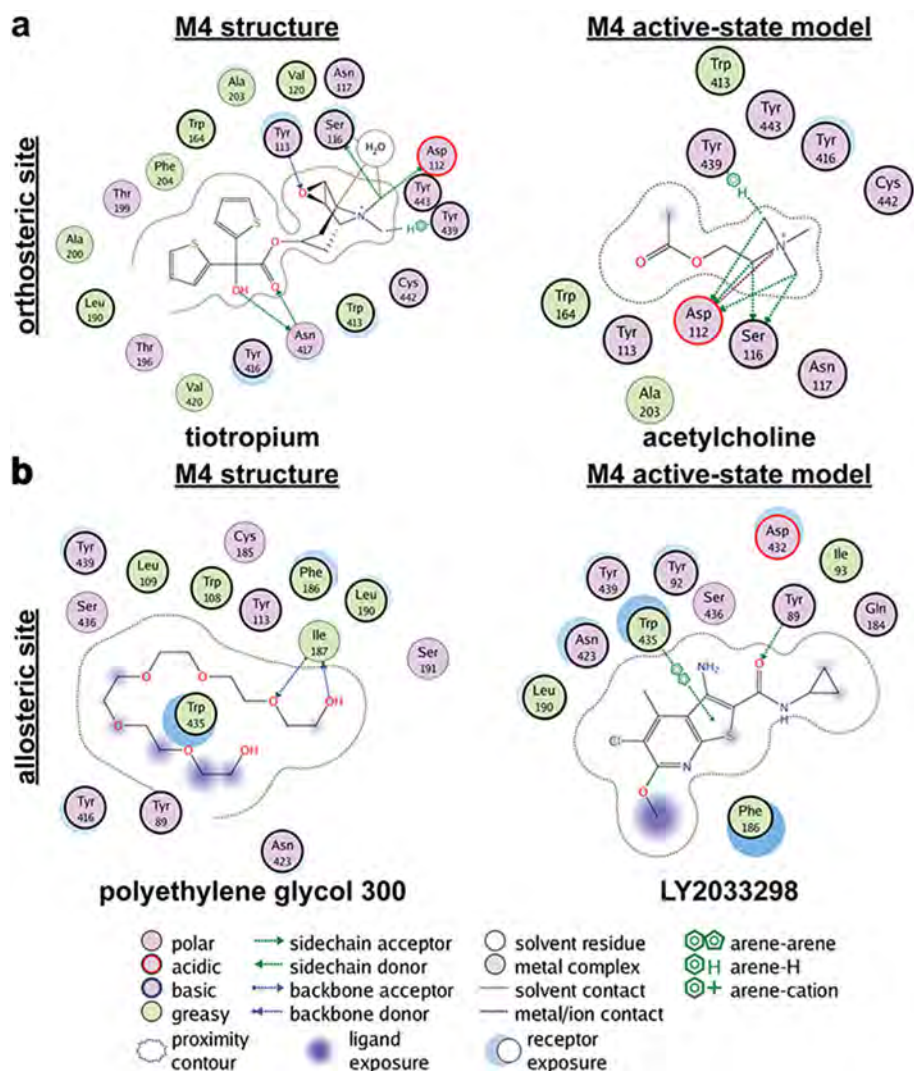
Extended Data Figure 4 | Induced fit docking of pirenzepine into the M1–M4 structures. The receptors shown are aligned and coloured as in Fig. 1. **a**, Superposition of the poses of pirenzepine from the IFD

experiments. **b**, Comparison of the pirenzepine poses for the M1 and M4 receptor with residues that contribute to the orthosteric site of the M1–M4 receptors (several residues omitted for clarity).



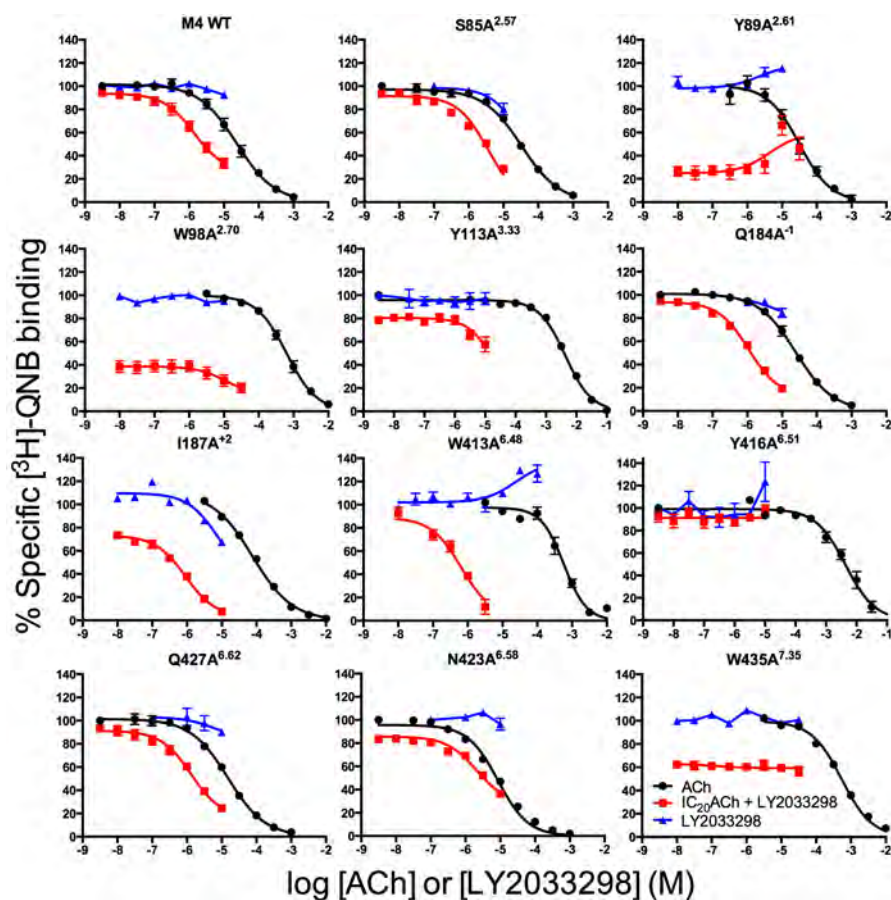
Extended Data Figure 5 | PEG 300 occupies the allosteric binding site of the inactive M4 receptor. **a**, The cross section of the solvent accessible surface area of the M4 receptor is coloured blue. Tiotropium and PEG 300 are shown as spheres with respective carbons coloured white and peach. The aromatic cage of covering tiotropium is highlighted in orange **b**, View from the extracellular side with residues that contact PEG 300 shown as spheres. **c**, Dissociation kinetics of [^3H]NMS in the presence

of PEG 300. [^3H]NMS was incubated with M4-mT4L membranes at 37 °C for 3 h, followed by addition of 10 μM atropine \pm PEG 300 at the indicated concentrations and time points. Representative data from three experiments, performed in duplicate, fitted to a one-phase exponential decay are shown. **d**, PEG 300 has an apparent binding affinity for the NMS-occupied receptor of approximately 10 mM ($\log(\text{IC}_{50}) = -1.95 \pm 0.02$).



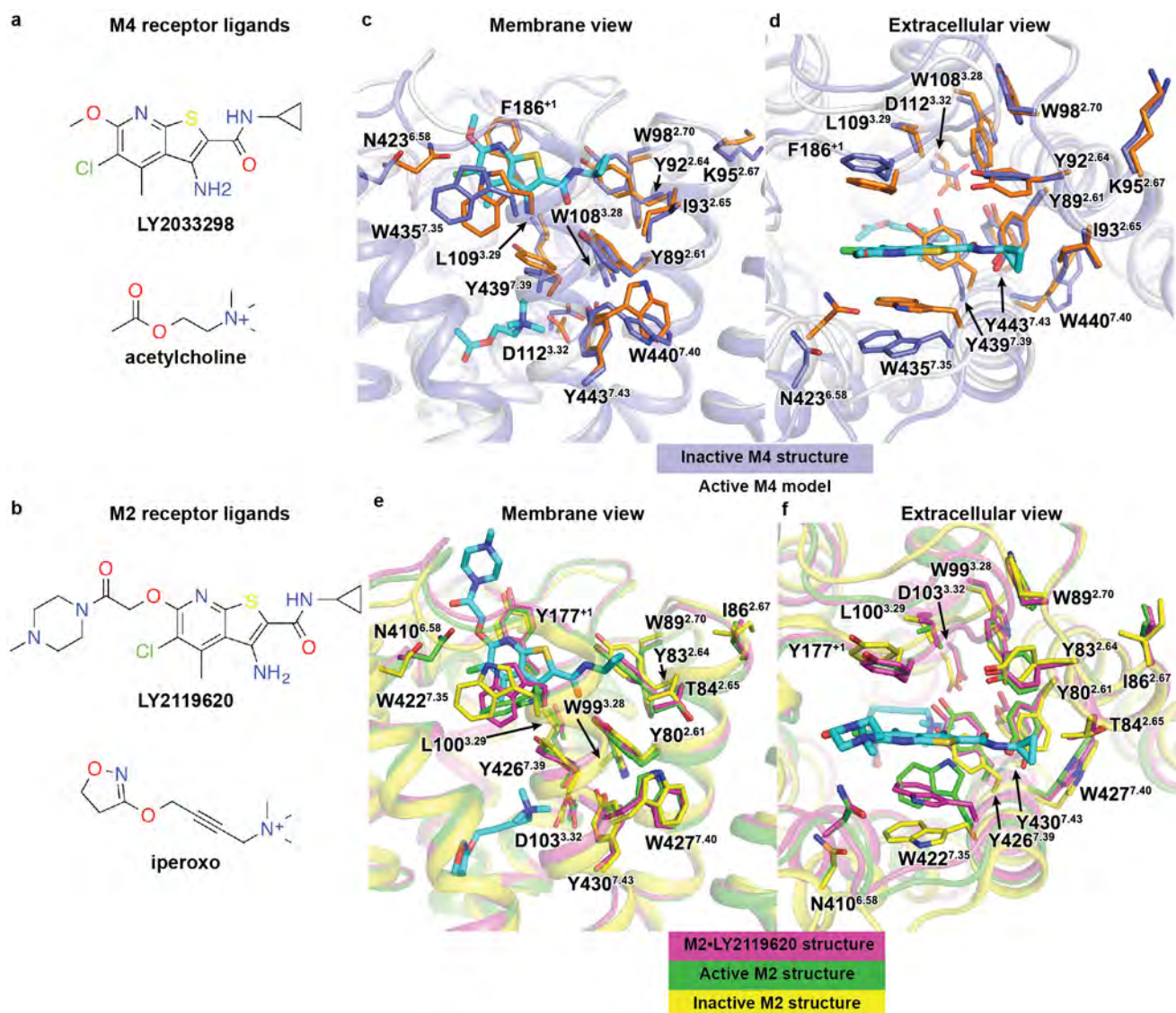
Extended Data Figure 6 | Ligand interaction diagrams for the M4 receptor. a, b, The molecular interactions between the (a) orthosteric and (b) allosteric binding sites are shown by the program

MOE⁶⁵ for the inactive (M4•tiotropium structure) and active states (M4•acetylcholine•LY2033298 model). Residues with a bold outline were selected in this study or others^{20,21} as single-point mutations.



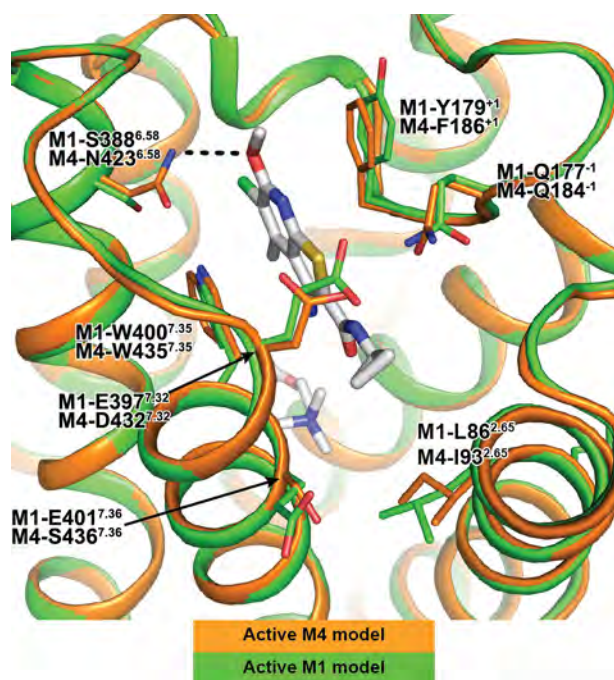
Extended Data Figure 7 | Identification of key residues that govern LY2033298 affinity and binding cooperativity with ACh at the M4 receptor. Competition between a fixed concentration of [^3H]QNB and increasing concentrations of ACh (black circles), LY2033298 (blue triangles), or LY2033298 in the presence of an IC_{20} concentration of ACh (red squares) are shown. The curves drawn through the points

represent the best global fit of an extended ternary complex model. For data sets where the binding of [^3H]QNB changed by less than 10% at 10^{-5} M LY2033298 relative to zero LY2033298, the value of α' was fixed to 1 (connecting line shown). Data points represent the mean \pm s.e.m. of at least three experiments performed in triplicate.



Extended Data Figure 8 | Comparison of cooperativity network residues between the inactive and active-states. a, b, Chemical structures of (a) the M4 ligands used in this study and (b) the M2 ligands from the active-state crystal structures (PDB accession number 4MQT and 4MQS). c–f, Mapping of the allosteric network onto the (c, d) inactive M4

structure (blue residues), M4 active-state model (orange residues) and (e, f) the inactive (yellow residues) and active-state M2 structures (magenta and green residues) with views from the (c, e) membrane or (d, f) extracellular surface. Ligands are coloured according to element: carbon, cyan; oxygen, red; nitrogen, blue; sulfur, yellow; chlorine, green.



Extended Data Figure 9 | LY2033298 binding to active-state M1 and M4 models. Comparison of active-state M1 (green) and M4 (orange) models bound to LY2033298 and acetylcholine, with acetylcholine and LY2033298 shown as sticks and coloured according to element: carbon, white; oxygen, red; nitrogen, blue; sulfur, yellow; chlorine, green. Several residues surrounding LY2033298 are shown as sticks and coloured according to receptor. M4-N423^{6.58} is predicted to undergo significant movement between the inactive and active states to form a hydrogen bond with the methoxy group of LY2033298. In the M1 receptor this residue is a serine (S388^{6.58}) and is unable to form a similar hydrogen bond. However, mutation of N423^{6.58} to alanine at the M4 receptor results in no loss of LY2033298 affinity, but does result in a sixfold loss in cooperativity between acetylcholine and LY2033298 (Supplementary Table 3). This is suggestive of selectivity being derived through cooperativity as a possible mechanism between the M1 and M4 receptors. Additional determinants for M1 and M4 selectivity could also arise through differences in residues on TMs 2 and 7, which contribute to (I93^{2.65}) or sit proximal to (D432^{7.32} and S436^{7.36}) the allosteric network.

Extended Data Table 1 | Data collection and refinement statistics

Data collection*	M1-T4L•tiotropium	M4mT4L•tiotropium
Beamline	GM/CA 23-ID-D	GM/CA 23-ID-D
Number of crystals	8	64
Space group	P 2 ₁ 2 ₁ 2 ₁	P 1 2 ₁ 1
Cell dimensions		
<i>a</i> , <i>b</i> , <i>c</i> (Å)	58.0, 72.2, 175.7	48.5, 172.0, 60.7
α , β , γ (°)	90, 90, 90	90, 94.4, 90
Resolution (Å)	30.00–2.70 (2.80– 2.70)	28.99–2.60 (2.69– 2.60)
R _{merge} (%)	15.5 (83.6)	21.3 (94.7)
<I/σI>	8.7 (1.9)	8.2 (1.5)
CC _{1/2} (%)	N.D. [†]	99.0 (54.5)
Completeness	97.1 (98.2)	99.7 (97.9)
Multiplicity	4.3 (4.2)	13.1 (4.9)
Refinement		
Resolution (Å)	30.00–2.70	28.53–2.60
No. of reflections working / test set	19,223 / 1,011	30,299 / 2,146
R _{work} /R _{free} (%)	22.8 / 27.5	22.7 / 24.0
No. of atoms (Chain A / Chain B)		
Protein	3439	3058 / 3115
Ligands	210	176 / 167
Average B-factors (Chain A / Chain B; Å ²)	73.6	74.0 / 70.5
Receptor	62.5	63.9 / 64.6
T4 lysozyme	64.4	99.5 / 85.3
Tiotropium	66.5	47.4 / 47.9
Allosteric site PEG 300	—	74.9 / 81.6
Waters	58.1	53.7 / 46.7
Other ligands	74.8	80.8 / 78.4
RMS deviation from ideality		
Bond length (Å)	0.009	0.002
Bond angles (°)	1.39	0.61
Ramachandran statistics [‡]		
Favored regions (%)	96.2	99.2
Allowed regions (%)	3.6	0.8
Outliers (%)	0.2	0.0

*Highest shell statistics in parenthesis.

[†]N.D., Not determined, because the structure was solved before CC_{1/2} values were introduced⁶⁶.[‡]As calculated by Molprobity.

A Hydrogen-Bonded Polar Network in the Core of the Glucagon-Like Peptide-1 Receptor Is a Fulcrum for Biased Agonism: Lessons from Class B Crystal Structures[§]

Denise Wootten, Christopher A. Reynolds, Cassandra Koole,¹ Kevin J. Smith, Juan C. Mobarec, John Simms, Tezz Quon, Thomas Coudrat, Sebastian G. B. Furness, Laurence J. Miller, Arthur Christopoulos, and Patrick M. Sexton

Monash Institute of Pharmaceutical Sciences and Department of Pharmacology, Monash University, Parkville, Victoria, Australia (D.W., C.K., T.Q., T.C., S.G.B.F., A.C., P.M.S.); School of Biological Sciences, University of Essex, Wivenhoe Park, Colchester, UK (C.A.R., K.J.S., J.C.M.); School of Life and Health Sciences, Aston University, Birmingham, UK (J.S.); and Department of Molecular Pharmacology and Experimental Therapeutics, Mayo Clinic, Scottsdale, AZ (L.J.M.)

Received August 4, 2015; accepted December 17, 2015

ABSTRACT

The glucagon-like peptide 1 (GLP-1) receptor is a class B G protein-coupled receptor (GPCR) that is a key target for treatments for type II diabetes and obesity. This receptor, like other class B GPCRs, displays biased agonism, though the physiologic significance of this is yet to be elucidated. Previous work has implicated R2.60¹⁹⁰, N3.43²⁴⁰, Q7.49³⁹⁴, and H6.52³⁶³ as key residues involved in peptide-mediated biased agonism, with R2.60¹⁹⁰, N3.43²⁴⁰, and Q7.49³⁹⁴ predicted to form a polar interaction network. In this study, we used novel insight gained from recent crystal structures of the transmembrane domains of the glucagon and corticotropin releasing factor 1 (CRF1) receptors to develop improved models of the GLP-1 receptor that predict additional key molecular interactions with these amino acids. We have introduced E6.53³⁶⁴A, N3.43²⁴⁰Q, Q7.49³⁹⁴N,

and N3.43²⁴⁰Q/Q7.49³⁹⁴N mutations to probe the role of predicted H-bonding and charge-charge interactions in driving cAMP, calcium, or extracellular signal-regulated kinase (ERK) signaling. A polar interaction between E6.53³⁶⁴ and R2.60¹⁹⁰ was predicted to be important for GLP-1- and extendin-4-, but not oxyntomodulin-mediated cAMP formation and also ERK1/2 phosphorylation. In contrast, Q7.49³⁹⁴, but not R2.60¹⁹⁰/E6.53³⁶⁴ was critical for calcium mobilization for all three peptides. Mutation of N3.43²⁴⁰ and Q7.49³⁹⁴ had differential effects on individual peptides, providing evidence for molecular differences in activation transition. Collectively, this work expands our understanding of peptide-mediated signaling from the GLP-1 receptor and the key role that the central polar network plays in these events.

Introduction

Glucagon-like peptide 1 (GLP-1), a key incretin hormone controlling insulin secretion in response to meal ingestion, has a broad range of actions potentially beneficial for treatment of type II diabetes and obesity. These include promotion of

insulin synthesis and release, decreased glucagon production, preservation of pancreatic β -cell mass, decreased appetite and gastric emptying, and preservation and promotion of cardiac function [reviewed in Baggio and Drucker (2007); Koole et al. (2013); Pabreja et al. (2014)]. GLP-1 acts via the GLP-1 receptor, a class B peptide hormone G protein-coupled receptor (GPCR). This class includes receptors for many important peptides, including parathyroid hormone, secretin, calcitonin, amylin, vasoactive intestinal polypeptide, corticotropin-releasing hormone (CRF), gastric inhibitory peptide, glucagon, as well as the glucagon-like peptides (Hollenstein et al., 2014). As such, understanding how these peptides bind to and activate their cognate receptors is critical to understanding their action and to unlocking the therapeutic potential of targeting this receptor class.

The revolution in membrane protein crystallography and GPCR structural biology has generated novel insight into our understanding of the structural basis for receptor activation, including the importance of structural waters and polar

This work was supported by National Health and Medical Research Council of Australia (NHMRC) project grants [1061044] and [1065410], and NHMRC program grant [1055134]; Biotechnology and Biological Sciences Research Council of the United Kingdom project grant [BB/M006883/1]; and Medical Research Council (UK) grant [G1001812]. P.M.S. and A.C. are NHMRC Principal Research Fellows. D.W. is a NHMRC Career Development Fellow. C.K. is a NHMRC C.J. Martin Postdoctoral Fellow. T.C. is the recipient of a Victorian Life Sciences Computation Initiative (VLSCI) scholarship. The computational studies were supported by resource allocation scheme grant no. VR0024 of the VLSCI on its Peak Computing Facility at the University of Melbourne.

¹Current affiliation: Laboratory of Chemical Biology and Signal Transduction, The Rockefeller University, New York, NY.
dx.doi.org/10.1124/mol.115.101246.

[§] This article has supplemental material available at molpharm.aspetjournals.org.

ABBREVIATIONS: CHO, Chinese hamster ovary; CRF, corticotropin releasing factor; ECL, extracellular loop; ECD, extracellular domain; ERK, extracellular signal-regulated kinase; FBS, fetal bovine serum; GLP-1, glucagon-like peptide-1; GPCR, G protein-coupled receptor; Ca^{2+} , intracellular Ca^{2+} ; MD, molecular dynamics; pERK1/2, phosphorylated extracellular signal-regulated kinase 1 and 2; POPC, 1-palmitoyl-2-oleoyl-sn-glycero-3-phosphocholine; TM, transmembrane helix.

hydrogen bond networks for propagation of the conformational rearrangements required for receptor activation and coupling of the receptor to effector proteins (Caltabiano et al., 2013; Katritch et al., 2014). Many of these key networks are conserved within subfamilies of class A GPCRs (Venkatakrishnan et al., 2013). It is also increasingly recognized that individual ligands acting at the same GPCR can elicit distinct profiles of signaling and regulation, a phenomenon termed biased agonism (Shonberg et al., 2014). At a molecular level this occurs through the distinct interactions that individual ligands make with their target receptor and the potential for these interactions to stabilize distinct conformational ensembles that in turn favor differential interaction with effector proteins (Shonberg et al., 2014). How these distinct interactions drive conformational propagation is still poorly understood, but it may involve selective recruitment of structurally important interaction networks.

Less is understood about the activation of class B peptide GPCRs as they do not contain the key conserved amino acids that are signatures of class A receptors and critical for their function. Nonetheless, class B GPCRs have their own unique set of conserved, intramembranous, polar residues that are likely comparable to those in class A. Prototypical of this receptor class is the GLP-1 receptor that displays pleiotropic coupling and both peptide- and nonpeptidic-biased agonism (Jorgensen et al., 2007; Coopman et al., 2010; Koole et al., 2010; Cheong et al., 2012; Willard et al., 2012; Wootten et al., 2013a; Weston et al., 2014). Recently, the role of the conserved intramembranous polar residues in this receptor was probed by alanine scanning mutagenesis, which revealed clusters of amino acids important for a range of functions, including protein expression and the control of activation transition for both general signal pathway bias and ligand-directed biased signaling (Wootten et al., 2013b). A key network for differential effects on peptide-mediated signaling for GLP-1, exendin-4, and oxyntomodulin was identified and shown to involve R2.60¹⁹⁰, N3.43²⁴⁰, H6.52³⁶³, and Q7.49³⁹⁴ [Wootten et al. (2013a); numbering scheme: amino acid numbers are shown in superscript]. Using an early model of the GLP-1 receptor, it was predicted that the R2.60¹⁹⁰ coordinated interactions with Asn and Gln and that these interactions were differentially important for signaling via the individual peptides. Nonetheless, double mutation of Asn3.43²⁴⁰ and Gln7.49³⁹⁴ did not fully recapitulate the phenotype of the Arg2.60¹⁹⁰ mutation (Wootten et al., 2013b), suggesting that the model was insufficient to fully explain the differential effects on signaling.

Recently, transmembrane crystal structures of the glucagon and corticotropin-releasing factor 1 (CRF1) receptors were solved (Hollenstein et al., 2013; Siu et al., 2013). These revealed that the class B GPCRs have distinct arrangements of the transmembrane bundle compared with class A GPCRs, leading to a large, solvent exposed, V-shaped extracellular-facing cavity that is likely critical for peptide-mediated receptor activation. These distinctions contribute to the historic difficulty in modeling class B receptors. The new structural data revealed that our original GLP-1 receptor model used to interpret data on polar residue mutants was inaccurate, although the predicted interactions between R^{2.60}, N3.43²⁴⁰, and Q7.49³⁹⁴ were maintained.

To gain further insight into the role of the predicted network, we have generated new GLP-1 receptor models on the basis of available crystal structures and performed additional mutagenesis to probe the nature and importance of

this network for peptide-mediated activation of key signaling pathways.

Materials and Methods

Materials. Dulbecco's modified Eagle's medium, hygromycin B, and Fluo-4 acetoxymethyl ester were purchased from Invitrogen (Carlsbad, CA). Fetal bovine serum (FBS) was purchased from Thermo Fisher Scientific (Melbourne, Australia). The QuikChange site-directed mutagenesis kit was purchased from Stratagene (La Jolla, CA). AlphaScreen reagents, Bolton-Hunter reagent [¹²⁵I], and 384-well ProxiPlates were purchased from PerkinElmer Life and Analytical Sciences (Waltham, MA). SureFire phosphorylated extracellular signal-regulated kinase 1 and 2 (pERK1/2) reagents were generously supplied by TGR Biosciences (Adelaide, Australia). Sigma-Fast *o*-phenylenediamine dihydrochloride tablets and antibodies were purchased from Sigma-Aldrich (St. Louis, MO). GLP-1 peptides were purchased from American Peptide (Sunnyvale, CA). All other reagents were purchased from Sigma-Aldrich or BDH Merck (Melbourne, Australia) and were of an analytical grade.

Receptor Mutagenesis. The desired mutations were introduced to an N-terminally double c-myc-labeled wild-type human GLP-1 receptor (GLP-1 receptor) in the pEF5/FRT/V5-DEST destination vector (Invitrogen/ThermoFisher Scientific, Waltham, MA); this receptor is pharmacology equivalent to the untagged human GLP-1 receptor (data not shown). Mutagenesis was carried out using oligonucleotides for site-directed mutagenesis purchased from GeneWorks (Thebarton, SA, Australia) and the QuikChange site-directed mutagenesis kit (Stratagene, La Jolla, CA), and confirmed by automated sequencing.

Transfections and Cell Culture. Wild-type and mutant human GLP-1 receptor were isogenically integrated into FlpIn-Chinese hamster ovary (FlpIn-CHO) cells (Invitrogen), and selection of receptor-expressing cells accomplished by treatment with 600 μ g/ml of hygromycin B. Transfected and parental FlpIn-CHO cells were maintained in Dulbecco's modified Eagle's medium supplemented with 10% (v/v) heat-inactivated FBS and incubated in a humidified environment at 37°C in 5% CO₂. Whenever a new series of mutant receptors is generated and used for generation of stable cell lines, the cells used for the specific set of transfections are used to generate a new wild-type receptor control, to account for any drift in cell background with change of passage. Experiments on mutant receptors are run in parallel with these controls. Where data from wild-types from different series of experiments was equivalent, these data were pooled.

Radioligand Binding Assay. FlpIn-CHO wild-type and mutant human GLP-1 receptor cells were seeded at a density of 3×10^4 cells per well into 96-well culture plates and incubated overnight at 37°C in 5% CO₂, and radioligand binding carried out as previously described (Koole et al., 2011). For each cell line in all experiments, total binding was defined by ~ 0.05 nM [¹²⁵I]exendin(9–39) alone, and nonspecific binding was determined in the presence of 1 μ M exendin(9–39). For analysis, data are normalized to the specific binding for each individual experiment.

cAMP Accumulation Assay. FlpIn-CHO wild-type and mutant human GLP-1 receptor cells were seeded at a density of 3×10^4 cells per well into 96-well culture plates and incubated overnight at 37°C in 5% CO₂, and cAMP detection was carried out as previously described (Koole et al., 2010). All values were converted to concentration of cAMP using a cAMP standard curve performed in parallel, and data were subsequently normalized to the response of 100 μ M forskolin in each cell line.

pERK1/2 Assay. FlpIn-CHO wild-type and mutant human GLP-1 receptor cells were seeded at a density of 3×10^4 cells per well into 96-well culture plates and incubated overnight at 37°C in 5% CO₂. Receptor-mediated pERK1/2 was determined using the AlphaScreen pERK1/2 SureFire protocol as previously described (Koole et al., 2010). Initial pERK1/2 time-course experiments were performed over

1 hour to determine the time at which agonist-mediated pERK1/2 was maximal. Subsequent experiments were then performed at the time required to generate a maximal pERK1/2 response (6 minutes). Data were normalized to the maximal response elicited by 10% (v/v) FBS in each cell line, determined at 6 minutes (peak FBS response).

Intracellular Ca^{2+} Mobilization Assay. Fln-CHO wild-type and mutant human GLP-1 receptor cells were seeded at a density of 3×10^4 cells per well into 96-well culture plates and incubated overnight at 37°C in 5% CO_2 , and receptor-mediated intracellular Ca^{2+} (Ca^{2+}) mobilization was determined as previously described (Koole et al., 2010). Fluorescence was determined immediately after peptide addition, with an excitation wavelength set to 485 nm and an emission wavelength set to 520 nm, and readings were taken every 1.36 seconds for 120 seconds. Peak magnitude was calculated using five-point smoothing, followed by correction against basal fluorescence. The peak value was used to create concentration-response curves. Data were normalized to the maximal response elicited by 100 μM ATP, and to the wild-type receptor responses.

Cell-Surface Receptor Expression. Fln-CHO wild-type and mutant human GLP-1 receptor cells, with receptor DNA previously incorporated with an N-terminal double c-myc epitope label, were seeded at a density of 25×10^4 cells per well into 24-well culture plates and incubated overnight at 37°C in 5% CO_2 , washed three times in $1 \times$ phosphate buffered saline, and fixed with 3.7% (v/v) paraformaldehyde at 4°C for 15 minutes. Cell-surface receptor detection was then performed as previously described (Koole et al., 2011). Data were normalized to the basal fluorescence detected in Fln-CHO parental cells. Specific [^{125}I]exendin(9–39) binding at each receptor mutant, as identification of functional receptors at the cell surface, was also determined [corrected for nonspecific binding using 1 μM exendin(9–39)].

Data Analysis. All data were analyzed using Prism 6.0 (Graph-Pad Software Inc., San Diego, CA). For all analyses the data were unweighted and each y value (mean of replicates for each individual experiment) was considered an individual point. Concentration response signaling data were analyzed using a three-parameter logistic equation as previously described (May et al., 2007):

$$Y = \text{Bottom} + \frac{(\text{Top} - \text{Bottom})}{1 + 10^{(\text{LogEC}_{50} - \log[A])}} \quad (1)$$

where *Bottom* represents the y value in the absence of ligand(s), *Top* represents the maximal stimulation in the presence of ligand(s), $[A]$ is the molar concentration of ligand, and EC_{50} represents the molar concentration of ligand required to generate a response halfway between *Top* and *Bottom*. Similarly, this equation was used in the analysis of inhibition binding data, with IC_{50} replacing EC_{50} . In that case, *Bottom* defines the specific binding of the radioligand that is equivalent to

nonspecific ligand binding, whereas *Top* defines radioligand binding in the absence of a competing ligand, and the IC_{50} value represents the molar concentration of ligand required to generate an effect halfway between *Top* and *Bottom*.

To quantify efficacy in the system, all data were fitted with an operational model of agonism (Black and Leff, 1983):

$$Y = \text{Bottom} + \frac{E_m - \text{Bottom}}{1 + ((10^{\log K_A}) + (10^{\log[A]})) / (10^{(\log \tau + \log[A])})} \quad (2)$$

where E_m represents the maximal stimulation in the system; K_A is the agonist-receptor functional dissociation constant, in molar concentration, that is dependent on the receptor-effector complex driving signaling for an individual pathway (Kenakin et al., 2012; Kenakin and Christopoulos, 2013); τ is the estimated measure of efficacy in the system, which incorporates both signaling efficacy and receptor density; and all other parameters are as defined for eq. (1). Constraints for this model were determined by fitting the most efficacious peptide with the following equation:

$$Y = \text{Bottom} + \frac{E_m - \text{Bottom}}{1 + 10^{(\text{LogEC}_{50} - \log[A])}} \quad (3)$$

The value obtained for the system maximum (E_m) was then globally constrained in the operational model (eq. 2) when applied at each mutant receptor. All estimated τ values were then corrected to cell-surface expression (τ_c); B_{max} from homologous competition (eq. 4) of [^{125}I]exendin(9–39) binding by unlabeled exendin(9–39) where B_{max} is the maximum binding of ligand to receptors, $[Hot]$ is the concentration of [^{125}I]exendin(9–39) in nM, $[Cold]$ is the concentration of unlabeled exendin(9–39) in nM, and K_d is the equilibrium dissociation constant of the ligand in nM, with *Bottom* as defined in eq. (1). Errors were propagated from both τ and cell-surface expression relative to wild-type receptor.

$$Y = \frac{B_{\text{max}} \times [Hot]}{[Hot] + [Cold] + K_d} + \text{Bottom} \quad (4)$$

Statistics. Changes in peptide affinity, potency, efficacy, and cell-surface expression of human GLP-1 receptor mutants in comparison with wild-type human GLP-1 receptor control were statistically analyzed with one-way analysis of variance and Dunnett's post-test, and significance accepted at $p < 0.05$.

Molecular Modeling. The apo GLP-1R model of the transmembrane (TM) domain [Supplemental Data File 1 (.pdb)] was generated from the glucagon X-ray crystal structure (Siu et al., 2013) using the homology modeling and minimization facilities of Protein Local Optimization Program (PLOP) (Jacobson et al., 2004). The full GLP-1-bound GLP-1R used additional templates, namely the X-ray structure of the

TABLE 1

Major constraints used in Modeler

GLP-1R Position (A)	GLP-1 Position (B)	Origin for GLP-1R – GLP-1 Constraint	Constraint ^a (Å)	Reference
ECD; E133; C _γ	A24; C _β	Bpa ²⁴ GLP-1 photoaffinity crosslink.	$r_{AB} \leq 9.0$	Chen et al. 2009 ^c
TM1; L141; C _{δ1}	V16; C _{γ1}	Bpa ¹⁶ GLP-1 photoaffinity crosslink.	$r_{AB} \leq 9.0$	Miller et al. (2011)
TM1; Y145; C _ε	F12; C _γ	Bpa ¹² GLP-1 photoaffinity crosslink.	$r_{AB} \leq 6.0$	Chen et al. (2010)
ECL2; W297; C _{η2}	L20; C _γ	Bpa ²⁰ GLP-1 photoaffinity crosslink.	$r_{AB} \leq 9.0$	Miller et al. (2011)
TM2; K197; N _ε	E9; O _{e2}	Reciprocal mutagenesis of residues between VIP and VIP-R-1/VIP-R-2 resulting in gain of function ^b	$r_{AB} \leq 4.0$	Solano et al. (2001); Vertongen et al. (2001)
ECL3; R380; N _{η2}	D15; O _{e2}	Reciprocal mutagenesis of residues between GLP-1 and GLP-1R resulting in gain of function.	$r_{AB} \leq 4.0$	Moon et al. (2015)

^aThese distance constraints were estimated from preliminary models that used tyrosine to represent Bpa, since the O_η of the tyrosine is topologically equivalent to the reactive carbon atom of Bpa; a 6-Å constraint was used between the O_η and a suitable point on the target residue.

^bThese residues are conserved between GLP-1R and VPAC-2R. The restraint gives similar results for E⁹ with K197 and/or R190; if the constraint is used with both residues it can be relaxed to $r_{AB} \leq 5.0$ Å or $r_{AB} \leq 6.0$ Å.

^cThe potential constraint between O_{e1} of E125 and C_α of G³⁵ reported by Chen et al. (2009) (21.5 Å) was not used as the distance in the ECD X-ray structure; this is possibly a constraint to another molecule within an oligomeric array.

extracellular domain (ECD) with GLP-1(10-35) bound (Underwood et al., 2010), the CRF1-R X-ray structure (used to model extracellular loop (ECL)1, which is missing in the glucagon structure) (Hollenstein et al., 2013) and the nuclear magnetic resonance (NMR) structure of a conformationally constrained GLP-1(7-17) analog (Hoang et al., 2015) docked to a GLP-1R model (preprimed to bind GLP-1 using Modeler; Eswar et al., 2007) using GLIDE (v6.9) SP peptide and the OPLS 3.0 force field (Friesner et al., 2004; Tubert-Brohman et al., 2013). A $20 \times 20 \times 20\text{-}\text{\AA}^3$ inner docking box and a $44 \times 44 \times 44\text{-}\text{\AA}^3$ outer docking box centered at the opening of the TM bundle was used; the peptide backbone was held rigid during the docking. GLP-1(7-17) NH_2 generated

from model 7 from the NMR ensemble (.pdb code 2N0I) using PLOP gave the highest scoring docked pose. Because this analog had similar activity to GLP-1(7-36) NH_2 and was conformationally constrained (Hoang et al., 2015), it provided the best currently available model for the conformation of GLP-1. In addition, the X-ray structure of the C-terminal peptide of the G protein alpha subunit (R373-L394) in complex with the intracellular part and TM5 and TM6 of the β_2 -adrenergic receptor from the X-ray structure of the receptor/G protein complex (Rasmussen et al., 2011) (mutated to its GLP-1R equivalent using Modeler) was used as an additional template to facilitate generation of an active model. The success of the comparative modeling required a

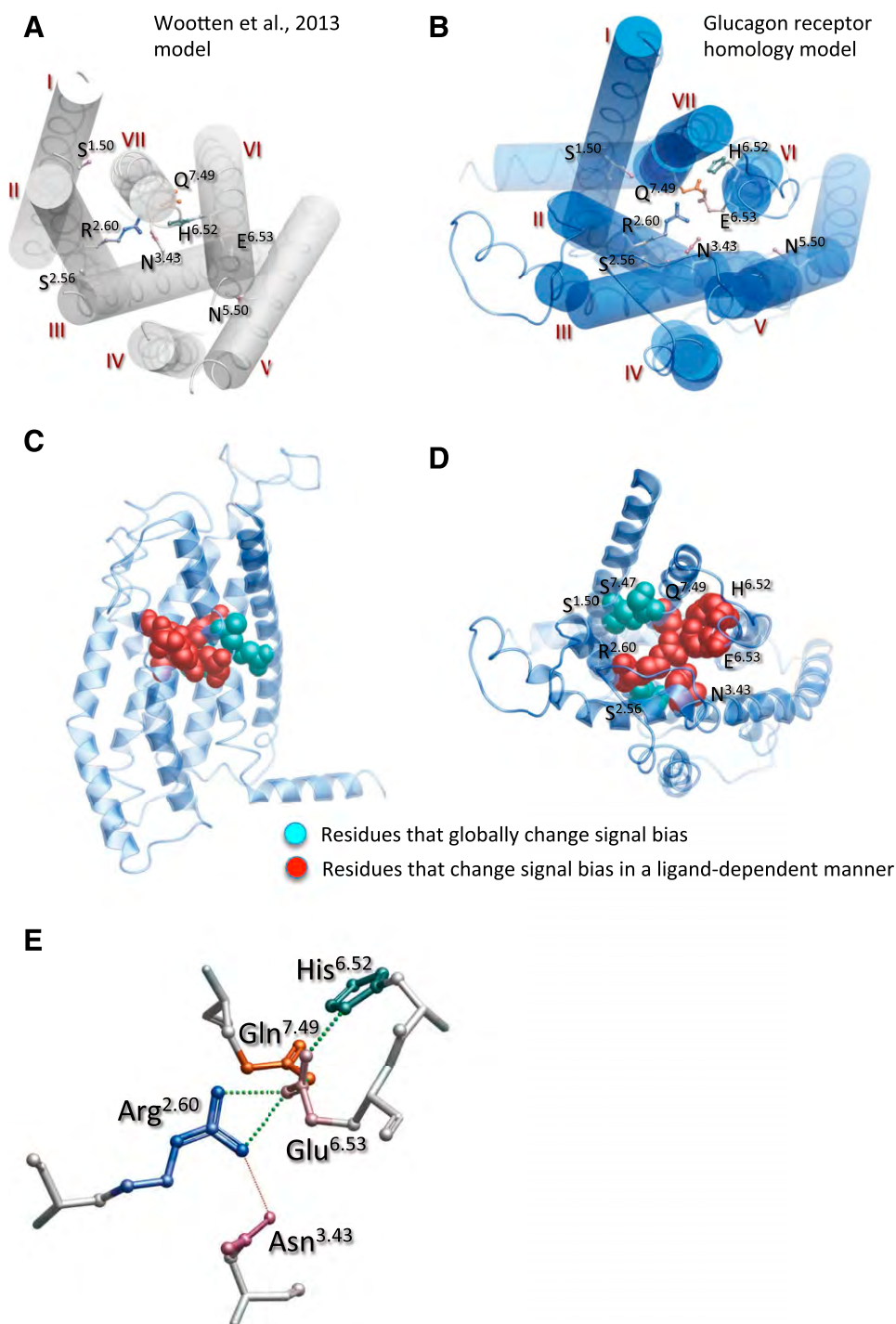


Fig. 1. Comparison of original (A) (Wootten et al., 2013b) and new apo homology model of the human GLP-1 receptor (B–E). R2.60¹⁹⁰, N3.43²⁴⁰, H6.52³⁶³, E6.53³⁶⁴, and Q7.49³⁹⁴ comprise key residues involved in peptide-mediated signaling bias. (A, B) Top down views of the transmembrane bundle and positioning of key amino acids (as x-stick, colored by amino acid side chain). The major differences include opening of the extracellular vestibule, clockwise rotation of TM6, and intracellular offset of TM5 by two helical turns. (C, D) Homology model illustrating the relative positions of R2.60¹⁹⁰, N3.43²⁴⁰, H6.52³⁶³, E6.53³⁶⁴, and Q7.49³⁹⁴ residues involved in peptide-mediated signaling bias (depicted with red space fill) and S.150¹⁵⁵, S2.56¹⁸⁶, S7.47³⁹² (blue space fill) small polar residues involved in intramembraneous packing and globally involved in receptor-dependent signal bias. These residues sit in a fulcrum position at the convergence of the helices, with the residues involved in ligand-dependent signal bias located within the core of the receptor. (C) View from the transmembrane face of the receptor. (D) View from the extracellular space. (E) The central polar network depicted as x-stick (colored by amino acid side chain), illustrating predicted H-bonding within the network (colored dotted lines; sphere size is proportional to predicted strength of interaction).

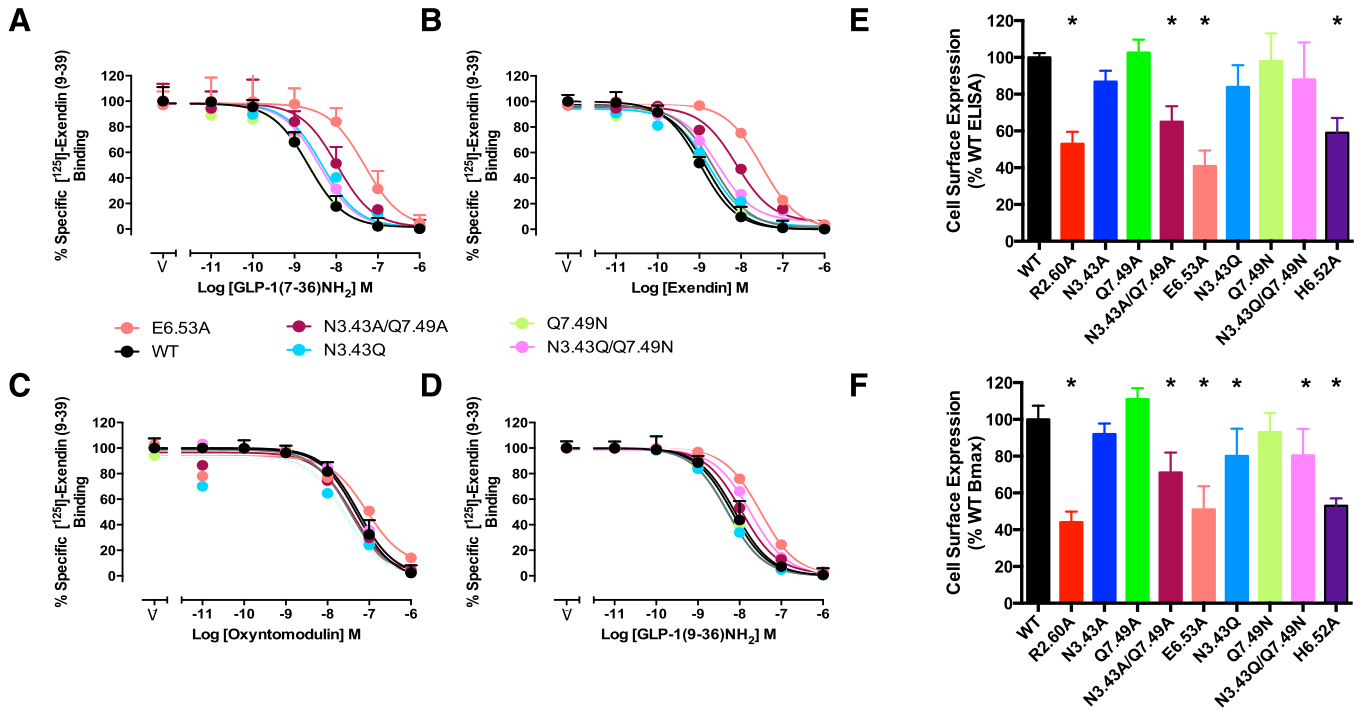


Fig. 2. Effect of mutation of the central polar network on peptide binding and cell-surface receptor expression. (A–D) Inhibition of $[^{125}\text{I}]$ exendin(9-39) binding by agonist and antagonist peptides at the wild-type and new mutant receptors. For clarity, only data from new mutants, or those not quantified previously, are displayed. (E) Cell-surface expression of mutant receptors (normalized to that of the wild-type receptor) as measured by anti-c-myc antibody binding to the N-terminal c-myc epitope in an enzyme-linked immunosorbent assay. (F) Cell-surface expression of mutant receptors (normalized to that of the wild-type receptor) determined as B_{max} from homologous competition of $[^{125}\text{I}]$ exendin(9-39) binding by unlabeled exendin(9-39). Data are displayed as mean \pm S.E.M. of four to seven independent experiments, conducted in duplicate. *Significantly different from wild-type receptor at $P < 0.05$, ANOVA with Dunnett's post-test. V, vehicle. Data for expression of the previously published R2.60¹⁹⁰A, N3.43²⁴⁰A, Q7.49³⁹⁴A, and H6.52³⁶³ receptor mutants (Wootten et al., 2013b) are included for comparison.

reasonable structural overlap between the TM region and the ECD region, and for this reason GLP-1(7-36)NH₂ was structurally aligned to GLP-1(10-35) of the ECD complex using VMD (Humphrey et al., 1996) to generate an ECD complex containing GLP-1(7-35). These templates were linked by a global alignment, which was used by Modeler to generate a full GLP-1R model with GLP-1(7-36)NH₂ bound. Modeler used 4 *p*-benzoylphenylalanine (Bpa) photoaffinity crosslinking-derived distance constraints between GLP-1 and GLP-1R (Chen et al., 2009, 2010; Miller et al., 2011) and two sets of constraints derived from reciprocal mutagenesis experiments that resulted in gain of function

(Solano et al., 2001; Vertongen et al., 2001; Moon et al., 2015), as shown in Table 1; the effect of these constraints was to provide additional information on the peptide-receptor interaction in the region between the TM and ECD templates. These reciprocal mutagenesis results were essentially the only mutagenesis results used in the generation of the model. Two thousand models were generated by Modeler and the model with the best (lowest) discrete optimized protein energy score was selected. This model was subjected to further refinement of ECL1 using a template derived from the CRF1-R structure and the additional constraints given in (Supplemental Table 1; the final model selected had

TABLE 2

Effects of human GLP-1 receptor mutation on peptide ligand binding and cell-surface expression

Binding data were analyzed using a three-parameter logistic equation as defined in eq. (1) to obtain pIC_{50} values. Data were normalized to maximum $[^{125}\text{I}]$ exendin(9-39) binding in the absence of ligand, with nonspecific binding measured in the presence of 1- μM exendin(9-39). Cell-surface expression (B_{max}) was determined through homologous competition binding with $[^{125}\text{I}]$ exendin(9-39), and data are expressed as a maximum of specific $[^{125}\text{I}]$ exendin(9-39) binding at the wild-type human GLP-1R. All values are expressed as mean \pm S.E.M. of three to seven independent experiments, conducted in duplicate. Data were analyzed with one-way analysis of variance and Dunnett's post-test.

	Binding (pIC ₅₀)				Cell-Surface Expression ELISA (% Wild-Type)	Cell-Surface Expression (B_{max}) (% Wild-Type)
	GLP-1 (7-36)NH ₂	Exendin-4	Oxyntomodulin	Exendin(9-39)		
Wild-Type ^a	8.7 \pm 0.1	9.0 \pm 0.0	7.3 \pm 0.1	8.1 \pm 0.1	100 \pm 1	100 \pm 3
R2.60 ¹⁹⁰ A ^a	7.4 \pm 0.1*	7.3 \pm 0.1*	7.6 \pm 0.2	7.6 \pm 0.1*	53 \pm 3*	44 \pm 2*
N3.43 ²⁴⁰ A ^a	8.2 \pm 0.1*	8.7 \pm 0.1	7.4 \pm 0.1	8.3 \pm 0.1	86 \pm 3	92 \pm 2
Q7.49 ³⁹⁴ A ^a	8.6 \pm 0.1	8.8 \pm 0.1	7.3 \pm 0.2	8.2 \pm 0.1	103 \pm 3	111 \pm 2
N3.43 ²⁴⁰ A/Q7.49 ³⁹⁴ A	8.0 \pm 0.1*	8.1 \pm 0.1*	7.4 \pm 0.1	8.0 \pm 0.1	65 \pm 4*	71 \pm 4*
N3.43 ²⁴⁰ Q	8.3 \pm 0.1	8.8 \pm 0.1	7.6 \pm 0.1	8.3 \pm 0.1	84 \pm 6	80 \pm 7*
Q7.49 ³⁹⁴ N	8.7 \pm 0.1	8.8 \pm 0.1	7.4 \pm 0.1	8.2 \pm 0.1	98 \pm 7	93 \pm 5
N3.43 ²⁴⁰ Q/Q7.49 ³⁹⁴ N	8.4 \pm 0.1	8.6 \pm 0.1*	7.3 \pm 0.0	7.7 \pm 0.1*	88 \pm 10	80 \pm 7*
E6.53 ³⁶⁴ A	7.3 \pm 0.1*	7.5 \pm 0.1*	7.1 \pm 0.2	7.5 \pm 0.1*	41 \pm 4*	51 \pm 6*
H6.52 ³⁶³ A ^a	7.3 \pm 0.1*	7.5 \pm 0.1*	6.5 \pm 0.1*	7.4 \pm 0.1*	59 \pm 4*	53 \pm 2*

*Statistically significant at $p < 0.05$, one-way analysis of variance and Dunnett's post-test in comparison with wild-type control. For easy comparison between effects of different ligands and mutants, these are also highlighted in bold.

^aData obtained from Wootten et al. (2013a).

the best discrete optimized energy score from 5000 models. The structures are available from ftp://ftp.essex.ac.uk/pub/oyster/Wootten_GLP-1R_2015/ [username: ftp, password: anonymous; (Supplemental Data File 2 (.pdb)]. Molecular dynamics (MD) simulations were carried out using fully hydrated models in a 1-palmitoyl, 2-oleoyl-sn-glycero-3-phosphocholine (POPC) bilayer using the Acellera ACEMD (Harvey et al., 2009), with parameters taken from the AMBER 14SB force field (Hornak et al., 2006) and the lipid 14 force field (Walker et al., 2014); the apo model for MD was generated by removing the ligand and running for 240 nanoseconds.

Hydration of the glucagon receptor transmembrane domain crystal structure was predicted using the Sample Flood algorithm within the ICM package (Molsoft, San Diego, CA).

Results

In this research, we generated a homology model of the apo form of the GLP-1 receptor transmembrane domain on the basis of the inactive glucagon receptor TM crystal structure. Although marked distinction in the upper regions of the

receptor occurred relative to our previously reported model (Wootten et al., 2013b), the key interaction network coordinated by R2.60¹⁹⁰, predicted in initial modeling, was maintained (Fig. 1, B and E). Nonetheless, there were substantial differences in the position of TM6 with a rotation and an outward translocation of the extracellular end of the helix that contributes to the opening of the extracellular face of the receptor, and also in the positioning of TM5 that is translocated two helical turns toward the intracellular face of the receptor (Fig. 1, A and B). This latter difference positions N5.50³²⁰ much deeper into the membrane. The rotation of TM6 moves H6.52³⁶³ away from the core of the transmembrane domain bundle and E6.53³⁶⁴ into the core (Fig. 1, A, B, E). Collectively, the new modeling predicts that key residues involved in receptor-mediated signaling bias, both those involved in peptide-mediated bias and those involved globally in altering signaling bias for all peptides (Wootten et al., 2013b), are co-located in the mid-region of the helical bundle

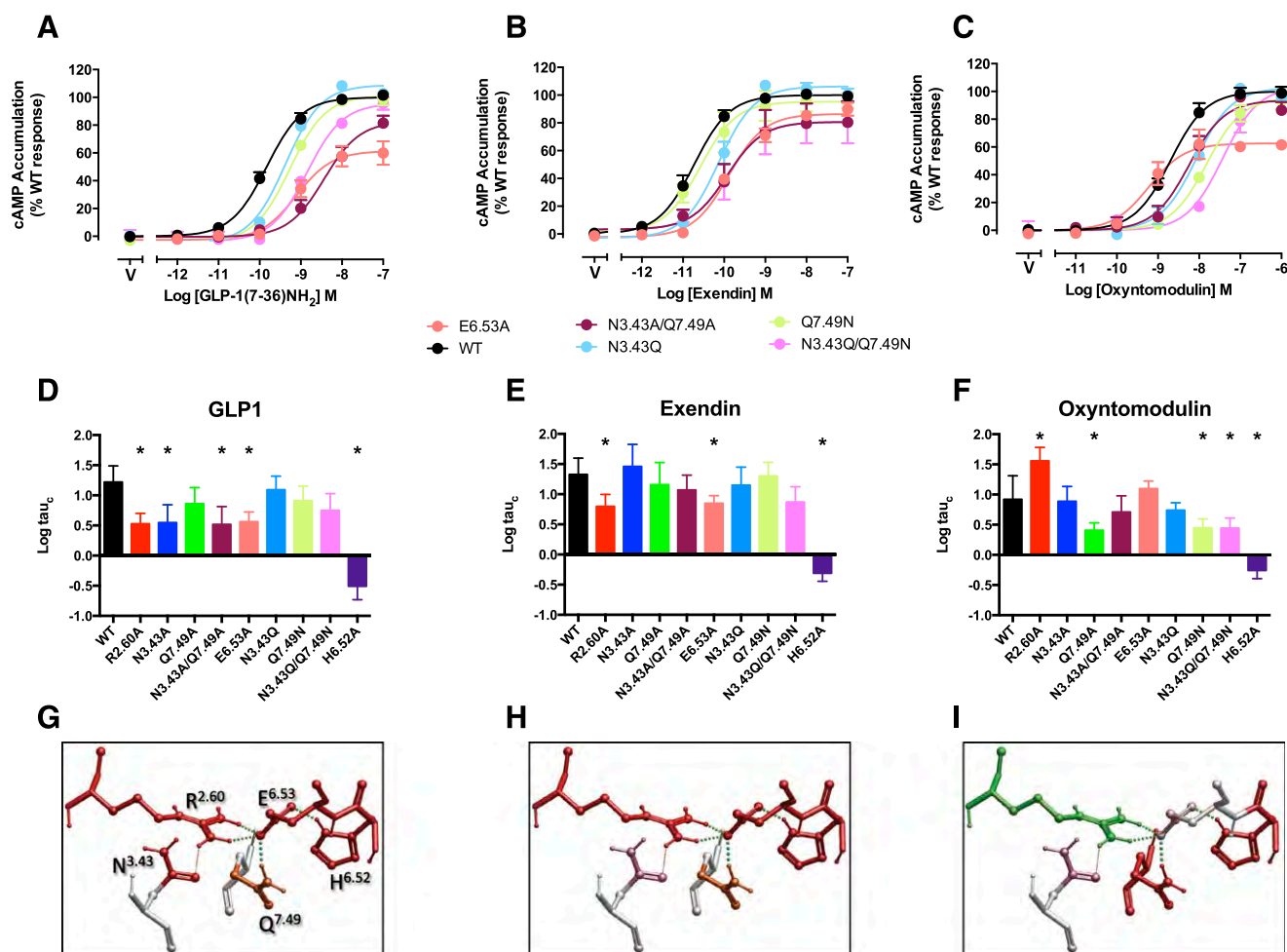


Fig. 3. Effect of mutation of the central polar network on peptide-mediated cAMP production. Upper panels (A–C) illustrate concentration-response curves for each of the peptides at the wild-type and mutant receptors with data fitted to the operational model. For clarity, only data from new mutants, or those not quantified previously, are displayed. Middle panels (D–F) illustrate affinity-independent measures of efficacy (Log tau) determined by operational modeling of the data, corrected for receptor B_{max} at the cell surface: (A, D) GLP-1-mediated responses, (B, E) exendin-4-mediated responses, (C, F) oxyntomodulin-mediated responses. Data are displayed as mean \pm S.E.M. of four to six independent experiments, conducted in duplicate. *Significantly different from wild-type receptor at $P < 0.05$, analysis of variance with Dunnett's post-test. V, vehicle. Data for expression of the previously published R2.60¹⁹⁰A, N3.43²⁴⁰A, Q7.49³⁹⁴A, and H6.52³⁶³ receptor mutants (Wootten et al., 2013b) is included for comparison. (G–I) Molecular models (x-stick format) illustrating the predicted central interaction network and their impact on peptide-mediated cAMP formation: (G) GLP-1, (H) exendin-4, (I) oxyntomodulin. Amino acids negatively impacted by mutation are colored red, those positively impacted in green, while those unaffected are colored by side-chain as in Fig. 1E. Predicted H-bonds are displayed as dotted lines.

TABLE 3

Effects of human GLP-1 receptor mutation on agonist signaling

All mutants were analyzed with an operational model of agonism (eq. 2) to determine $\log r$ values. All $\log r$ values were then corrected to B_{max} values determined from homologous competition binding between [125 I]exendin(9-39) and unlabeled exendin(9-39) ($\log r_c$). Values are expressed as mean \pm S.E.M. of four to six independent experiments, conducted in duplicate. Data were analyzed with one-way analysis of variance and Dunnett's post-test.

	cAMP Accumulation ($\log r_c$)			pERK1/2 ($\log r_c$)			iCa^{2+} Mobilization ($\log r_c$)		
	GLP-1 (7-36)NH ₂	Exendin-4	Oxynto- modulin	GLP-1 (7-36)NH ₂	Exendin-4	Oxynto- modulin	GLP-1 (7-36)NH ₂	Exendin-4	Oxynto-modulin
Wild-type	1.22 \pm 0.11	1.33 \pm 0.11	0.92 \pm 0.16	-0.08 \pm 0.03	-0.09 \pm 0.03	-0.07 \pm 0.03	-0.30 \pm 0.00	-0.31 \pm 0.03	-0.31 \pm 0.02
R2.60 ¹⁹⁰ A ^a	0.53 \pm 0.07*	0.80 \pm 0.08*	1.56 \pm 0.09*	-0.39 \pm 0.08*	0.51 \pm 0.12*	0.03 \pm 0.07	-0.66 \pm 0.16	-0.72 \pm 0.11	0.11 \pm 0.05*
N3.43 ²⁴⁰ A ^a	0.55 \pm 0.12*	1.46 \pm 0.15	0.89 \pm 0.10	0.01 \pm 0.04	0.19 \pm 0.05*	0.04 \pm 0.02	-0.76 \pm 0.16	-0.96 \pm 0.10*	-0.29 \pm 0.04
Q7.49 ³⁹⁴ A ^a	0.86 \pm 0.11	1.16 \pm 0.15	0.41 \pm 0.05*	-0.54 \pm 0.05*	-0.29 \pm 0.05	-0.20 \pm 0.01	-1.12 \pm 0.13*	-1.13 \pm 0.34*	N.D.
N3.43 ²⁴⁰ A/Q7.49 ³⁹⁴ A	0.52 \pm 0.12*	1.07 \pm 0.11	0.71 \pm 0.12	-0.56 \pm 0.04*	-0.43 \pm 0.07*	-0.09 \pm 0.03	-1.11 \pm 0.19*	N.D.	N.D.
N3.43 ²⁴⁰ Q	1.09 \pm 0.13	1.15 \pm 0.17	0.74 \pm 0.07	-0.09 \pm 0.04	-0.05 \pm 0.03	-0.27 \pm 0.04	-0.80 \pm 0.05*	-0.71 \pm 0.10	N.D.
Q7.49 ³⁹⁴ N	0.91 \pm 0.14	1.30 \pm 0.13	0.45 \pm 0.09*	-0.09 \pm 0.04	-0.05 \pm 0.03	-0.10 \pm 0.03	-0.70 \pm 0.04	-0.67 \pm 0.03	-0.59 \pm 0.07*
N3.43 ²⁴⁰ Q/Q7.49 ³⁹⁴ N	0.75 \pm 0.16	0.87 \pm 0.15	0.44 \pm 0.10*	-0.06 \pm 0.04	-0.00 \pm 0.03	-0.44 \pm 0.06*	-1.15 \pm 0.10*	-1.00 \pm 0.14*	N.D.
E6.53 ³⁶⁴ A	0.56 \pm 0.07*	0.85 \pm 0.06*	1.10 \pm 0.06	-0.35 \pm 0.08	-0.37 \pm 0.09	-0.11 \pm 0.07	-0.38 \pm 0.13	-0.68 \pm 0.04	0.04 \pm 0.05
H6.52 ³⁶³ A ^a	-0.51 \pm 0.11*	-0.31 \pm 0.06*	-0.26 \pm 0.06*	-0.81 \pm 0.15*	-0.67 \pm 0.07*	-0.19 \pm 0.08	-1.09 \pm 0.13*	-1.33 \pm 0.22*	-0.23 \pm 0.27

N.D., no data.

*Statistically significant at $p < 0.05$, one-way analysis of variance and Dunnett's post-test in comparison with wild-type control. For easy comparison between effects of different ligands and mutants, these are also highlighted in bold.^aData obtained from Wootten et al. (2013a).

(Fig. 1C). This places them at the convergence of the open extracellular vestibule in a key fulcrum position for propagation of conformational rearrangements (Fig. 1, C–E). Residues involved in peptide-mediated bias faced principally toward the core of the bundle, whereas the small polar serines implicated in global changes to signal bias exhibited a more peripheral localization (Fig. 1, C and D).

Predicted Interaction Networks

In the revised model, R2.60¹⁹⁰ is predicted to form H-bond interactions with E6.53³⁶⁴ and to a lesser extent N3.43²⁴⁰. E6.53³⁶⁴ is also predicted to form H-bond interactions with both H6.52³⁶³ and Q7.49³⁹⁴, suggesting that the central core network likely forms interdependent interactions (Fig. 1E); these interactions can also be seen in MD simulations (Supplemental Movie 1), and the stability of the interactions mapped from the MD trajectories (Supplemental Fig. 1).

To gain further insight into the nature of these interactions and their role in controlling peptide-dependent signaling, we generated an additional series of mutations that comprised E6.53³⁶⁴A, N3.43²⁴⁰Q, Q7.49³⁹⁴N, and the double mutant N3.43²⁴⁰Q/Q7.49³⁹⁴N. These mutants were designed to test the importance of the interaction between E6.53³⁶⁴ and R2.60¹⁹⁰, and the hydrogen bonding patterns arising from N3.43²⁴⁰ and Q7.49³⁹⁴. The mutants were analyzed for effect on peptide binding and receptor activation of canonical signaling pathways (cAMP accumulation, pERK1/2, and iCa^{2+} mobilization). Functional data were analyzed using the operational model (Black and Leff, 1983) to calculate effects on efficacy independent of those on affinity. Quantitative data were also generated for the N3.43²⁴⁰A/Q7.49³⁹⁴A double mutant that was qualitatively reported previously (Wootten et al., 2013b).

Effect of Mutation on Receptor Expression and Agonist Peptide Binding. Consistent with the previous observation of decreased cell-surface expression and affinity for GLP-1, exendin-4, and exendin(9-39) for R2.60¹⁹⁰A (Wootten et al., 2013b), the E6.53³⁶⁴A mutant also decreased cell-surface expression and the affinity of these peptides, but not that of oxyntomodulin (Fig. 2, Table 2). Cell-surface receptor expression was not significantly affected by Q7.49³⁹⁴N, and only a small decrease ($\sim 20\%$) in B_{max} was seen with the N3.43²⁴⁰Q or N3.43²⁴⁰Q/Q7.49³⁹⁴N mutants (Fig. 2, E and F). Oxyntomodulin affinity was not altered by any of these mutants (Fig. 2C, Table 2). Neither the Q7.49³⁹⁴N nor the N3.43²⁴⁰Q mutants significantly altered affinity for any of the peptides, whereas the N3.43²⁴⁰Q/Q7.49³⁹⁴N double mutant significantly decreased exendin-4 and exendin(9-39) affinity but not that of GLP-1 (Fig. 2, A–D; Table 2).

Effect of Mutation on cAMP Production. Only the E6.53³⁶⁴A mutant significantly attenuated cAMP signaling by exendin-4 and this is consistent with the loss of signaling seen previously with the R2.60¹⁹⁰ mutant (Fig. 3, E and H; Table 3).

The E6.53³⁶⁴A mutation also reduced GLP-1 efficacy, but this peptide was more broadly affected by mutation of other amino acids in the network (Fig. 3, A, D, G; Table 3). As previously reported, N3.43²⁴⁰A significantly attenuated signaling (Wootten et al., 2013b), and the N3.43²⁴⁰A/Q7.49³⁹⁴A double mutant yielded a similar level of impairment (Fig. 2, A and D). Interestingly, the N3.43²⁴⁰Q mutant had very little effect. Likewise, there was no significant loss of signaling with the N3.43²⁴⁰Q/Q7.49³⁹⁴N double mutant (Fig. 3 A and D).

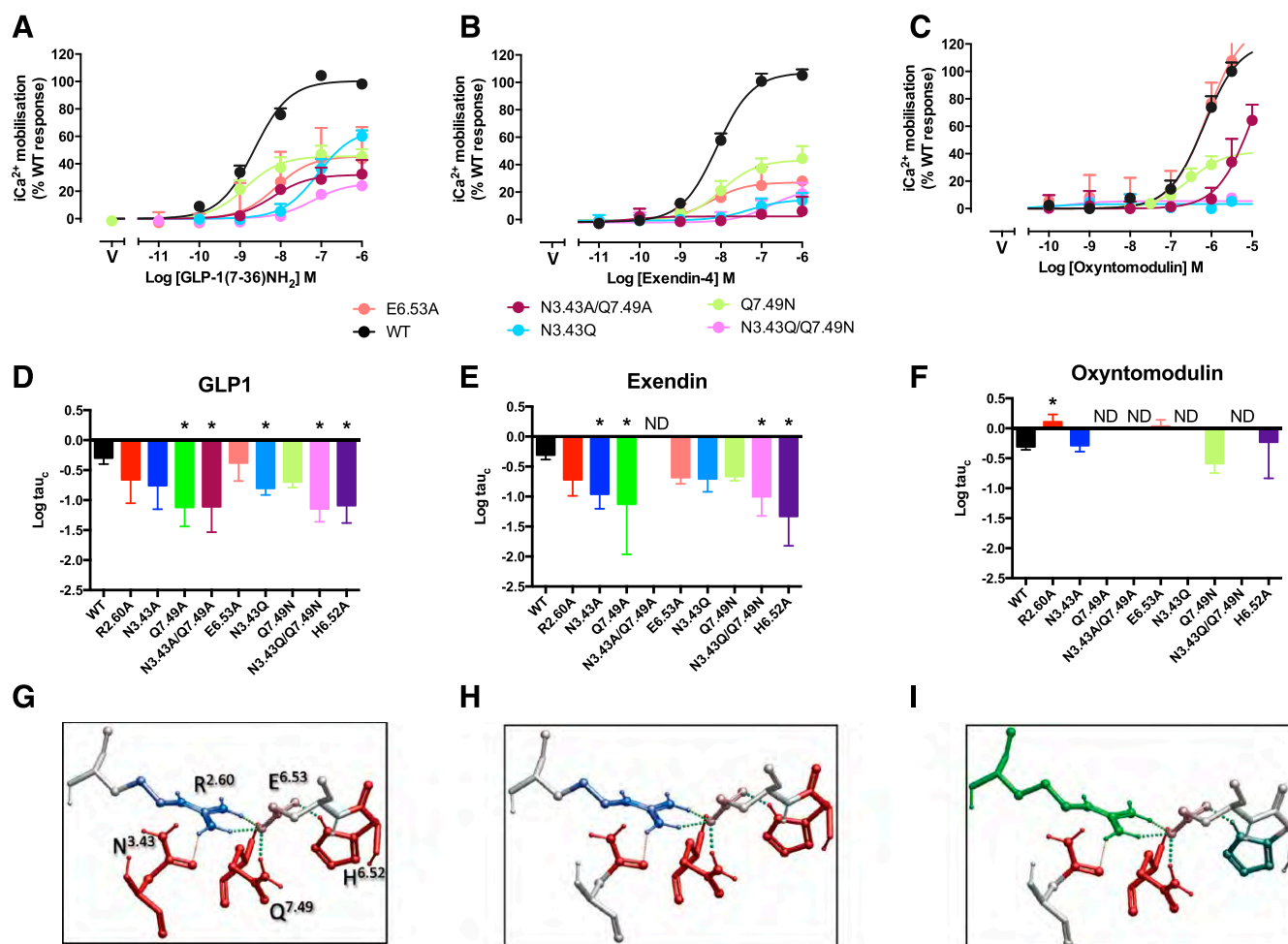


Fig. 4. Effect of mutation of the central polar network on peptide-mediated iCa^{2+} mobilization. Upper panels (A–C) illustrate concentration-response curves for each of the peptides at the wild-type and mutant receptors with data fitted to the operational model. For clarity, only data from new mutants, or those previously not quantified, are displayed. Middle panels (D–F) illustrate affinity-independent measures of efficacy (Log τ_c) determined by operational modeling of the data, corrected for receptor B_{max} at the cell surface: (A, D) GLP-1-mediated responses, (B, E) exendin-4-mediated responses, (C, F) oxyntomodulin-mediated responses. Data are displayed as mean \pm S.E.M. of four to six independent experiments, conducted in duplicate. *Significantly different from wild-type receptor at $P < 0.05$, ANOVA with Dunnett's post-test. N.D., no response detected. V, vehicle. Data for expression of the previously published R2.60¹⁹⁰A, N3.43²⁴⁰A, Q7.49³⁹⁴A, and H6.52³⁶³ receptor mutants (Wootten et al., 2013b) is included for comparison. (G–I) Molecular models (x-stick format) illustrating the predicted central interaction network and their impact on peptide-mediated intracellular calcium mobilization: (G) GLP-1, (H) exendin-4, (I) oxyntomodulin. Amino acids negatively impacted by mutation are colored red, those positively impacted in green, and those unaffected are colored by side-chain as in Fig. 1E. Predicted H-bonds are displayed as dotted lines.

Whereas mutational analysis provides increasing evidence for differences in the mechanism of receptor activation by GLP-1 and exendin-4, oxyntomodulin exhibits biased signaling for canonical pathways even at the wild-type receptor (Koole et al., 2010; Willard et al., 2012), and this is reflected in the effect of mutations on oxyntomodulin-mediated signaling. In contrast to GLP-1 and exendin-4, neither the E6.53³⁶⁴A nor the R2.60¹⁹⁰A (Wootten et al., 2013b) mutant impaired oxyntomodulin-mediated cAMP formation (Fig. 3, C, F, I; Table 3); indeed, the R2.60¹⁹⁰A mutant augmented signaling. Interestingly, the most critical residues in this network were Q7.49³⁹⁴ and H6.52³⁶³. Both the Q7.49³⁹⁴N and the previously published Q7.49³⁹⁴A attenuated signaling. Also of note, the N3.43²⁴⁰Q/Q7.49³⁹⁴N mutant was more detrimental than the N3.43²⁴⁰A/Q7.49³⁹⁴A mutant.

H6.52³⁶³ is critical for cAMP production by all three peptides (Wootten et al., 2013b; Fig. 3; Table 3), and this may be a common component of all signaling to this pathway, albeit that the mechanism driving changes to the residue may be different for individual peptides.

Effect of Mutation on Calcium Mobilization. The network required for calcium mobilization was distinct from that for cAMP generation for each of the peptides. For both GLP-1 (Fig. 4, A, D, G) and exendin-4 (Fig. 4, B, E, H), Q7.49³⁹⁴ and H6.52³⁶³ are critical for this signaling (Wootten et al., 2013b; Table 3). R2.60¹⁹⁰ and E6.53³⁶⁴ were not required, as mutation to alanine did not significantly alter efficacy (Fig. 4, D, E; Table 3); thus, unlike cAMP signaling, the predicted interaction between these residues is not required for iCa^{2+} mobilization. In addition, for both GLP-1 and exendin-4, N3.43²⁴⁰ also appeared to play a limited role in efficacy. For exendin-4, the N3.43²⁴⁰A mutation was detrimental (Wootten et al., 2013b; Fig. 4E; Table 3), whereas the N3.43²⁴⁰Q displayed significantly different efficacy in response to GLP-1 (Fig. 4D; Table 3). Nonetheless, a similar trend to decrease efficacy was observed for the nonsignificant mutations of this amino acid for the two peptides. Interestingly, for oxyntomodulin, although Q7.49³⁹⁴ was also critical for calcium signaling (Fig. 4, C, F, I; Table 3), H6.52³⁶³ was not required. Instead,

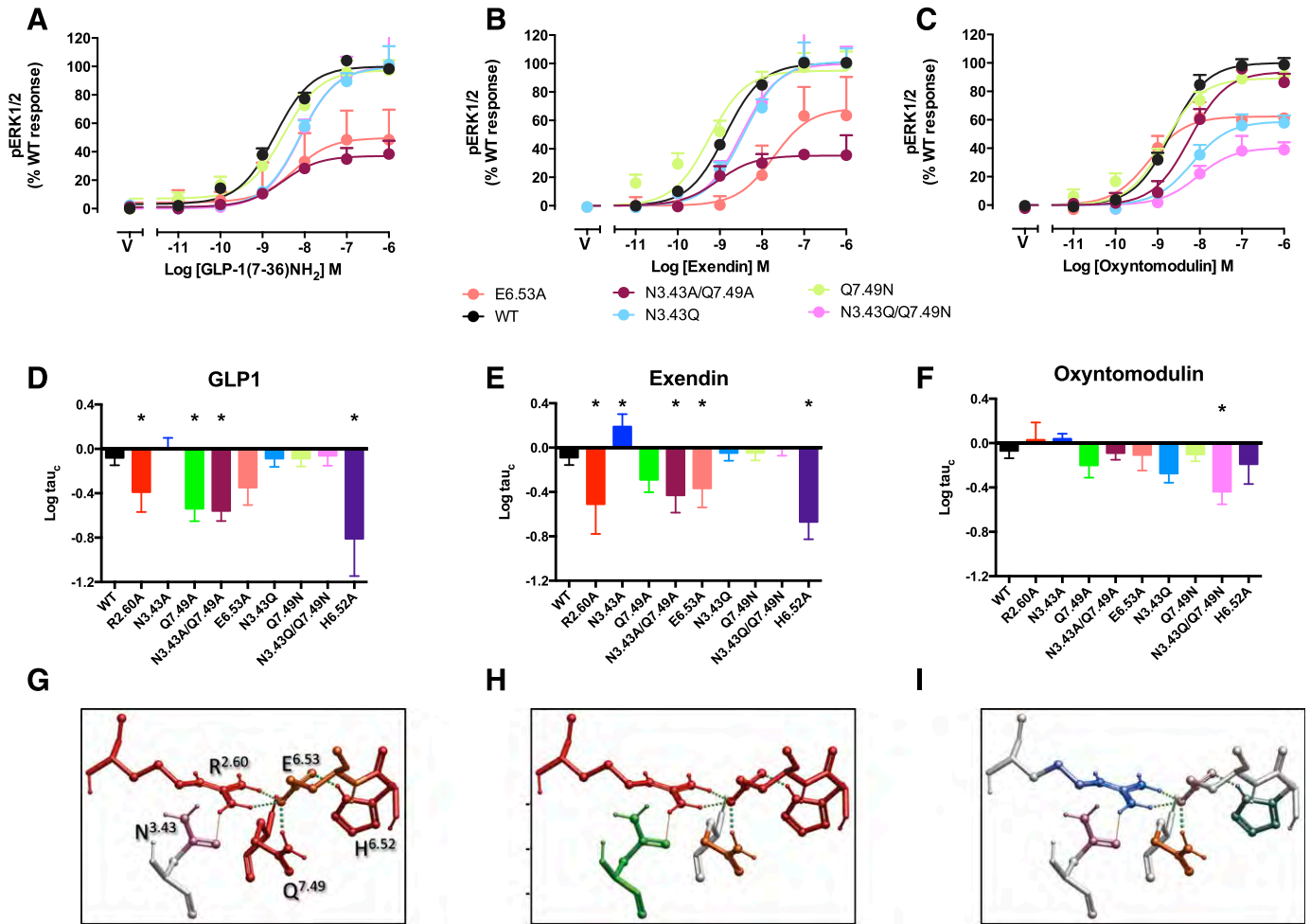


Fig. 5. Effect of mutation of the central polar network on peptide-mediated ERK phosphorylation. Upper panels (A–C) illustrate concentration-response curves for each of the peptides at the wild-type and mutant receptors with data fitted to the operational model. For clarity, only data from new mutants, or those previously not quantified, are displayed. Middle panels (D–F) illustrate affinity-independent measures of efficacy (Log tau) determined by operational modeling of the data, corrected for receptor B_{max} at the cell surface: (A, D) GLP-1-mediated responses, (B, E) exendin-4-mediated responses, (C, F) oxyntomodulin-mediated responses. Data are displayed as mean \pm S.E.M. of four to six independent experiments, conducted in duplicate. *Significantly different from wild-type receptor at $P < 0.05$, ANOVA with Dunnett's post-test. V, vehicle. Data for expression of the previously published R2.60¹⁹⁰A, N3.43²⁴⁰A, Q7.49³⁹⁴A, and H6.52³⁶³ receptor mutants (Wootten et al., 2013b) is included for comparison. (G–I) Molecular models (x-stick format) illustrating the predicted central interaction network and their impact on peptide-mediated ERK phosphorylation: (G) GLP-1, (H) exendin-4, (I) oxyntomodulin. Amino acids negatively impacted by mutation are colored red, those positively impacted in green, while those unaffected are colored by side-chain as in Fig. 1E. Predicted H-bonds are displayed as dotted lines.

both R2.60¹⁹⁰A and E6.53³⁶⁴A enhanced signaling, although this latter effect did not reach significance (Fig. 4, F; Table 3; Wootten et al., 2013b). In the wild-type receptor, R2.60¹⁹⁰ and E6.53³⁶⁴ may retard the efficiency of oxyntomodulin-mediated signaling by limiting the conformational sampling available to Q7.49³⁹⁴ (Fig. 4I). Although the N3.43²⁴⁰A mutation did not have a significant effect on oxyntomodulin signaling, N3.43²⁴⁰Q caused marked attenuation of signaling (Fig. 4F; Table 3).

Effect of Mutation on ERK1/2 Phosphorylation. The pattern of effect of mutation on peptide-mediated pERK1/2 was similar for GLP-1 (Fig. 5, A, D, G) and exendin-4 (Fig. 5, B, E, H), although subtle differences were observed. Both R2.60¹⁹⁰ and E6.53³⁶⁴ appeared to be important, albeit that the E6.53³⁶⁴A mutant effect did not reach significance for GLP-1 (Fig. 5, D and E; Table 3; Wootten et al., 2013b). Neither N3.43²⁴⁰Q, Q7.49³⁹⁴N, nor the N3.43²⁴⁰Q/Q7.49³⁹⁴N double mutant had any effect on efficacy; however, as described previously (Wootten et al., 2013b), N3.43²⁴⁰A either increased efficacy (exendin-4) or had no effect (GLP-1), and the

Q7.49³⁹⁴A mutant decreased efficacy mediated by GLP-1, but this effect was not significant for exendin-4, although it followed the same trend (Fig. 5, D and E; Table 3; Wootten et al., 2013b). In both cases, the N3.43²⁴⁰A/Q7.49³⁹⁴A mutant was detrimental, whereas H6.52³⁶³A was the most unfavorable of the mutations in this network (Fig. 5, D and E; Table 3). In contrast, oxyntomodulin was minimally affected by any of the mutations, a limited decrease in efficacy with the N3.43²⁴⁰Q/Q7.49³⁹⁴N double mutant being the only significant effect (Fig. 5, C, F, I; Table 3).

Discussion

Class B peptide hormone receptors are critical for normal physiology and are significant targets for potential treatment of major disease, including diabetes and obesity. As such, understanding how peptides interact with and activate these receptors is fundamentally important. The recent solution of structures of the transmembrane domain of the glucagon and

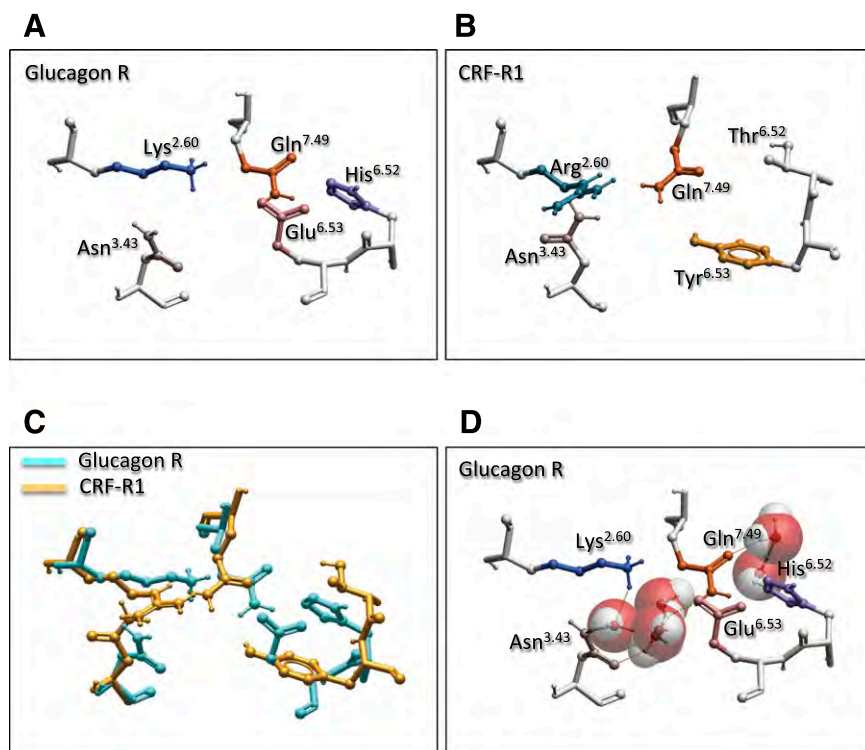


Fig. 6. Comparison of the central polar network in the inactive (inverse-agonist bound) structures of the glucagon receptor (x-stick with polar hydrogens displayed) (A, C, D) and the inverse-agonist bound CRF1 receptor (B, C), illustrating that, despite divergence in amino acid sequence, the positionally equivalent residues have a similar orientation. (D) Hydration of the glucagon receptor structure predicts potential water-mediated H-bond interactions within the network. Waters are illustrated in CPK file format: red, oxygen; off-white, hydrogen.

CRF1 receptors has provided novel insight into the nature of the core region of the receptor that is responsible for the allosteric transition that occurs upon peptide binding to enable effector coupling. In the inactive state, these receptors present a very open extracellular face that is likely to be hydrated (Hollenstein et al., 2013, 2014; Siu et al., 2013), suggesting that a key component of the binding and activation process may involve bulk displacement of water and/or the reordering of hydrogen bond networks; the latter is consistent with the current understanding of receptor activation for class A receptors (Zhou et al., 2000; Curran and Engelman, 2003; Angel et al., 2009; Illergard et al., 2011).

We previously reported the identification of a key network of amino acids in the GLP-1 receptor comprising R2.60¹⁹⁰, N3.43²⁴⁰, and Q7.49³⁹⁴ that, when mutated, differentially altered the signaling of the peptide agonists GLP-1, exendin-4, and oxyntomodulin (Wootten et al., 2013b). In the current study we have used the recent structural information on class B GPCRs to re-evaluate our understanding of this network. Key differences in the original and revised GLP-1 receptor models included the relative positions of E6.53³⁶⁴ and H6.52³⁶³, within this network, and N5.50³²⁰, which, although important for signaling, was not predicted to directly interact with the network in the revised model. Interestingly, this led to clustering of key residues in a fulcrum position at the convergence of the extracellular ends of the TM helices (Fig. 1, C and D). The nature of the revised interaction network thus formed was further explored via mutation of E6.53³⁶⁴, which has been predicted to interact with R2.60¹⁹⁰, along with conservative changes to N3.43²⁴⁰ and Q7.49³⁹, extending or reducing the side chain length, respectively, in a manner that probed the probable importance of hydrogen bonding.

Comparison of the equivalent amino acid side chains in the glucagon and CRF1 structures revealed conservation in relative orientation of side chains (Fig. 6, A–C), even though quite

distinct residues occurred in TM6 of the CRF1 receptor, namely Tyr at 6.53 and Thr at 6.52. In the glucagon receptor, maintenance of this network may be partially coordinated by water-mediated H-bonding (Fig. 6D). Thus, this network is likely to be highly constrained in the inactive state of the receptor. Indeed, in the glucagon receptor, the position of K2.60 (equivalent to R2.60 in the GLP-1 and CRF1 receptors) is restricted by H-bonding to S7.46, which in turn interacts with Y1.47, suggesting that one component of activation may include release of these constraints on amino acid 2.60, allowing a reordering of the network. In the GLP-1 receptor homology model, a similar interaction is predicted between T7.46³⁹¹ and R2.60¹⁹⁰/E6.53³⁶⁴ (Fig. 7A). Nonetheless, T7.46³⁹¹A had limited effect on GLP-1 affinity and cAMP formation (Coopman et al., 2011), suggesting that other interactions predominate, at least for activation of this pathway. In the current study, we have modeled a GLP-1 bound form of the full-length receptor that incorporates known distance constraints from published cross-linking studies (Fig. 7B), and this model is generally consistent with that for the modeled peptide-bound glucagon receptor, where the peptide forms an extended helix and the N-terminus of the peptide binds within the open cavity of the TM bundle (Siu et al., 2013; Yang et al., 2015). In our model, the GLP-1 peptide is predicted to bind deep within the TM bundle and is associated with disruption of the central H-bond network (Fig. 7A versus Fig. 7B).

As previously noted, the GLP-1 receptor exhibits peptide-dependent biased agonism across the canonical signaling pathways of cAMP formation, calcium mobilization, and ERK phosphorylation and this is most notable for oxyntomodulin, which is biased toward pERK1/2 at the wild-type receptor (Koole et al., 2010; Wootten et al., 2013a; Willard et al., 2012). Whereas GLP-1 and exendin-4 have similar biases for these pathways at the wild-type receptor, there is increasing evidence from mutational studies that these

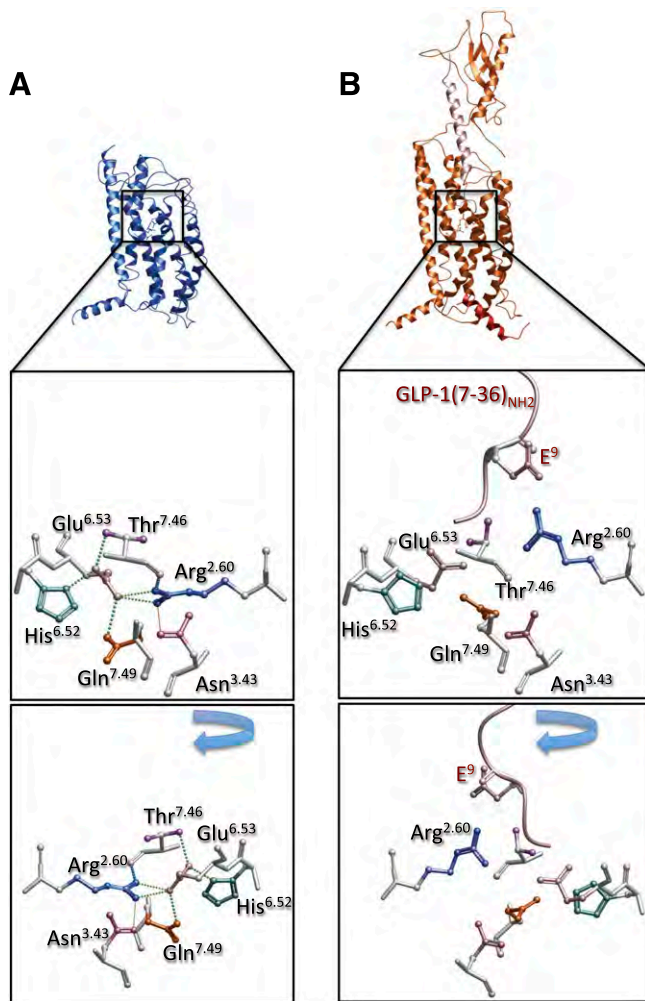


Fig. 7. Human GLP-1 receptor homology models. (A) Apo, transmembrane domain, model (blue backbone), with middle and bottom (180-degree rotation from the middle panel) panels, illustrating the central polar interaction network (x-stick, colored by amino acid side chain) and predicted H-bond interactions (colored dotted lines). (B) Full-length receptor model (orange backbone), bound to GLP-1(7-36)NH₂ (pink), and C-terminal G protein peptide (red); middle and bottom (180-degree rotation from the middle panel) panels illustrate the central polar interaction network (x-stick, colored by amino acid side chain) and predicted disruption of the inactive network interactions. In this model, a direct interaction is predicted between peptide E⁹ and receptor R2.60¹⁹⁰.

peptides have distinct modes of receptor activation (Koole et al., 2012a and b, Wootten et al., 2013b), and this is also supported by differences in peptide-mediated activation of G protein chimeras in yeast (Weston et al., 2014). The current study provides additional evidence for how these peptides use the central polar network to drive activation of the receptor. The use of operational, analytical modeling of functional responses enables the separation of mutational effects on affinity from those on efficacy and allows the impact of mutation on different signaling endpoints to be measured.

Potential Mechanisms Driving Pathway Specific Signaling. For GLP-1 and exendin-4, the principal driver for cAMP generation is the interaction between R2.60¹⁹⁰ and E6.53³⁶⁴ that likely leads to conformational rearrangement of TM6. It is possible that this is initiated by release of H-bond interactions with upstream polar residues that are observed in the inactive glucagon receptor. In the case of GLP-1, optimal

efficiency for this interaction is predicted to involve coordination of the position of R2.60¹⁹⁰ through hydrogen bonding with N3.43²⁴⁰ that may favor interaction with peptide side-chain residues, in particular between R2.60¹⁹⁰ and Glu at residue 3 [amino acid 9, where His⁷ is the first residue of GLP-1(7-36)NH₂] of the GLP-1 (Fig. 7B) and exendin-4 peptides. This constraint can also be maintained by Gln substitution of 3.43, potentially by allowing more efficient hydrogen bonding to occur. In contrast, oxyntomodulin-mediated cAMP formation is driven via Q7.49³⁹⁴ and H6.52³⁶³ and could potentially involve formation of a hydrogen bond between these two amino acids, when the interaction between R2.60¹⁹⁰ and E6.53³⁶⁴ is not fully disrupted (Fig. 3I). H6.52³⁶³ is a critical residue for all peptide-mediated cAMP formation through rearrangement of the side chain on activation, speculatively through either loss of interaction with E6.53³⁶⁴, via either disruption of the E6.53³⁶⁴/R2.60¹⁹⁰ interaction (GLP-1, exendin-4), or via formation of a novel interaction with Q7.49³⁹⁴ (oxyntomodulin).

In contrast to the requirements for cAMP formation, peptide-mediated calcium mobilization does not require alteration of the interaction between R2.60¹⁹⁰ and E6.53³⁶⁴ (Fig. 4, G–I). The common, critical residue for calcium mobilization by all peptides is Q7.49³⁹⁴. For GLP-1 and exendin-4, H6.52³⁶³ is also critical. This amino acid potentially forms interactions with Q7.49³⁹⁴ that constrain conformational sampling required for efficacy. The selective effects of other mutations may support the importance of conformational flexibility of Q7.49³⁹⁴ for calcium signaling, albeit in a peptide-selective manner. E6.53³⁶⁴ is predicted to H-bond directly with Q7.49³⁹⁴, constraining its mobility. For oxyntomodulin, which does not appear to activate the receptor in a manner that modifies interactions of R2.60¹⁹⁰, the H-bond interaction between R2.60¹⁹⁰ and E6.53³⁶⁴ potentially constrains the interaction between E6.53³⁶⁴ and Q7.49³⁹⁴, leading to reduced efficiency of signaling such that the R2.60¹⁹⁰A mutation increases efficacy. As noted for cAMP, subtle differences in mechanism of receptor activation also occur for GLP-1 and exendin-4 and this is also seen for calcium signaling where the magnitude of effect for mutation of N3.43²⁴⁰ to Ala or Gln differs for the two peptides. We speculate that N3.43²⁴⁰ can also interact with R2.60¹⁹⁰ and that this may in turn alter interactions with Q7.49³⁹⁴ indirectly via events coordinated through E6.53³⁶⁴ (Fig. 4, G and H).

While cAMP production and calcium mobilization are predominantly G protein-mediated, the transient phosphorylation of ERK1/2 is the result of convergent signaling of both G protein-dependent and independent effectors (Montrose-Rafizadeh et al., 1999; Baggio and Drucker, 2006). As seen with cAMP accumulation, the interaction between R2.60¹⁹⁰ and E6.53³⁶⁴ (Fig. 5, G and H) appeared to be required for efficient GLP-1- and exendin-4-mediated pERK1/2, although the magnitude of effect tended to be greater for the cAMP response. Likewise, H6.52³⁶³ was also critical for the response of these peptides, and this may be indicative of a significant contribution of G proteins to ERK1/2 signaling. N3.43²⁴⁰ and Q7.49³⁹⁴ played distinct roles for GLP-1 and exendin-4 but only in the context of nonconservative mutation and may imply a differential role of these residues in coordination with R2.60¹⁹⁰ and/or E6.53³⁶⁴ for the two peptides.

In contrast to the effect of mutation on GLP-1- and exendin-4-mediated pERK1/2, there was very little effect of any of the

mutants on oxyntomodulin-mediated signaling (Fig. 5F), with only the N3.43²⁴⁰Q/Q7.49³⁹⁴N double mutant significantly attenuating the response. This is consistent with the strong bias seen with oxyntomodulin for pERK1/2 versus cAMP or Ca^{2+} signaling (Koole et al., 2010; Willard et al., 2012; Wootten et al., 2013a). It may also imply distinction in the extent of engagement with different effectors. Thus the central network exemplified in the current study may be critical for G protein-mediated signaling but play a lesser role in non-G protein-dependent signaling. Furthermore, in addition to emphasizing major differences in receptor activation by oxyntomodulin compared with GLP-1 and exendin-4, the current work provides additional evidence of differences in the mechanism of activation transition elicited by GLP-1 and exendin-4. Recent work using chimeric G proteins in yeast indicates that exendin-4, as well as oxyntomodulin, may be biased toward Gi over Gs compared with GLP-1 (Weston et al., 2014), and arrestin recruitment studies also support distinct bias between GLP-1 and exendin-4 (Wootten et al., 2013a).

The conservation of key residues in the network and its fulcrum position in the structure of class B GPCRs suggests that it is likely to play a critical role in signaling for this subfamily. However, the distinctions in the data for different ligands of the GLP-1 receptor indicate that the specific mechanism of receptor activation is likely to be different for individual receptor ligand combinations. There are supporting data from studies of other class B receptors of the critical role of this network in receptor activation, with interaction of R2.60¹⁸⁸, N3.43²²⁹, and Q7.49³⁸⁰ predicted from mutagenesis and modeling studies of the VPAC1 receptor (Solano et al., 2001; Chugunov et al., 2010; Langer, 2012). Intriguingly, R2.60¹⁸⁸ is predicted to interact via a salt-bridge with D³ of vasoactive intestinal peptide, with this interaction contributing to receptor activation (Langer, 2012); the equivalent amino acid in GLP-1 and exendin-4 is Glu, whereas it is a Gln in oxyntomodulin. Modeling of GLP-1 peptide docking to the full-length receptor is consistent with formation of a direct, salt-bridge interaction between peptide Glu⁹ and R2.60¹⁹⁰ (Fig. 7B). It is interesting to speculate that lack of an acidic residue at the third amino acid of oxyntomodulin may underlie the lack of engagement of the R2.60¹⁹⁰/E6.53³⁶⁴ interaction in receptor activation.

Collectively, this work expands our understanding of peptide-mediated signaling from the GLP-1 receptor and the key role that the central polar network plays in these events. The ever-increasing availability of high-resolution structural data provides better understanding of the atomic events that are likely to drive receptor activation, though the dynamic nature of activation transition and the distinct ability of individual ligands to affect this process means that we will still require multiple approaches to derive an accurate understanding of these dynamics.

Authorship Contributions

Participated in research design: Wootten, Sexton.

Conducted experiments: Wootten, Reynolds, Smith, Mobarec, Quon, Simms, Coudrat.

Performed data analysis: Wootten, Koole, Mobarec, Sexton, Christopoulos.

Wrote or contributed to the writing of the manuscript: Wootten, Koole, Reynolds, Furness, Miller, Christopoulos, Sexton.

References

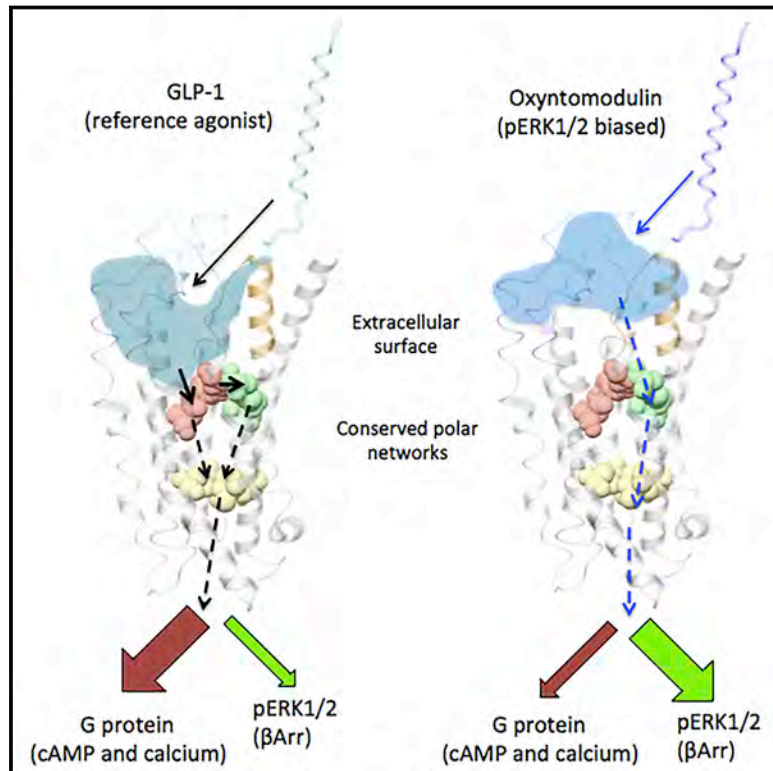
- Angel TE, Chance MR, and Palczewski K (2009) Conserved waters mediate structural and functional activation of family A (rhodopsin-like) G protein-coupled receptors. *Proc Natl Acad Sci USA* **106**:8555–8560.
- Baggio LL and Drucker DJ (2006) Therapeutic approaches to preserve islet mass in type 2 diabetes. *Annu Rev Med* **57**:265–281.
- Baggio LL and Drucker DJ (2007) Biology of incretins: GLP-1 and GIP. *Gastroenterology* **132**:2131–2157.
- Black JW and Leff P (1983) Operational models of pharmacological agonism. *Proc R Soc Lond B Biol Sci* **220**:141–162.
- Caltabiano G, Gonzalez A, Cordomi A, Campillo M, and Pardo L (2013) The role of hydrophobic amino acids in the structure and function of the rhodopsin family of G protein-coupled receptors. *Methods Enzymol* **520**:99–115.
- Chen Q, Pinon DI, Miller LJ, and Dong M (2009) Molecular basis of glucagon-like peptide 1 docking to its intact receptor studied with carboxyl-terminal photolabile probes. *J Biol Chem* **284**:34135–34144.
- Chen Q, Pinon DI, Miller LJ, and Dong M (2010) Spatial approximations between residues 6 and 12 in the amino-terminal region of glucagon-like peptide 1 and its receptor: a region critical for biological activity. *J Biol Chem* **285**:24508–24518.
- Cheong YH, Kim MK, Son MH, and Kaang BK (2012) Two small molecule agonists of glucagon-like peptide-1 receptor modulate the receptor activation response differently. *Biochem Biophys Res Commun* **417**:558–563.
- Chugunov AO, Simms J, Poyner DR, Dehouck Y, Rooman M, Gilis D, and Langer I (2010) Evidence that interaction between conserved residues in transmembrane helices 2, 3, and 7 are crucial for human VPAC1 receptor activation. *Mol Pharmacol* **78**:394–401.
- Coopman K, Huang Y, Johnston N, Bradley SJ, Wilkinson GF, and Willars GB (2010) Comparative effects of the endogenous agonist glucagon-like peptide-1 (GLP-1)-(7-36) amide and the small-molecule ago-allosteric agent “compound 2” at the GLP-1 receptor. *J Pharmacol Exp Ther* **334**:795–808.
- Coopman K, Wallis R, Robb G, Brown AJH, Wilkinson GF, Timms D, and Willars GB (2011) Residues within the transmembrane domain of the glucagon-like peptide-1 receptor involved in ligand binding and receptor activation: modelling the ligand-bound receptor. *Mol Endocrinol* **25**:1804–1818.
- Curran AR and Engelman DM (2003) Sequence motifs, polar interactions and conformational changes in helical membrane proteins. *Curr Opin Struct Biol* **13**:412–417.
- Dickson CJ, Madej BD, Skjevik AA, Betz RM, Teigen K, Gould IR, and Walker RC (2014) Lipid 14: The Amber Lipid Force Field. *J Chem Theory Comput* **10**:865–879.
- Eswar N, Webb B, Marti-Renom MS, Madhusudham MS, Eramian D, Shen MY, Pieper U, and Sali A (2007) Comparative protein structure modeling with MODELLER. *Curr Protoc Protein Sci* 2:Unit 2.9.
- Friesner RA, Banks JL, Murphy RB, Halgren TA, Klicic JJ, Mainz DT, Repasky MP, Knoll EH, Shelley M, and Perry JK et al. (2004) Glide: a new approach for rapid, accurate docking and scoring. 1. Method and assessment of docking accuracy. *J Med Chem* **47**:1739–1749.
- Harvey MJ, Giupponi G, and Fabritius GD (2009) ACEMD: Accelerating biomolecular dynamics in the microsecond time scale. *J Chem Theory Comput* **5**:1632–1639.
- Hoang HN, Song K, Hill TA, Derksen DR, Edmonds DJ, Kok WM, Limberakis C, Liras S, Loria PM, and Mascitti V et al. (2015) Short hydrophobic peptides with cyclic constraints are potent glucagon-like peptide-1 receptor (GLP-1R) agonists. *J Med Chem* **58**:4080–4085.
- Hollenstein K, de Graaf C, Bortolato A, Wang MW, Marshall FH, and Stevens RC (2014) Insights into the structure of class B GPCRs. *Trends Pharmacol Sci* **35**:12–22.
- Hollenstein K, Kean J, Bortolato A, Cheng RK, Doré AS, Jazayeri A, Cooke RM, Weir M, and Marshall FH (2013) Structure of class B GPCR corticotropin-releasing factor receptor 1. *Nature* **499**:438–443.
- Hornak V, Abel R, Okur A, Strockbine B, Roitberg A, and Simmerling C (2006) Comparison of multiple Amber force fields and development of improved protein backbone parameters. *Proteins* **65**:712–725.
- Humphrey W, Dalke A, and Schulten K (1996) VMD: Visual molecular dynamics. *J Mol Graph* **14**:33–38.
- Illergård K, Kauko A, and Elofsson A (2011) Why are polar residues within the membrane core evolutionary conserved? *Proteins* **79**:79–91.
- Jacobson MP, Pincus DL, Rapp CS, Day TJ, Honig B, Shaw DE, and Friesner RA (2004) A hierarchical approach to all-atom protein loop prediction. *Proteins* **55**:351–367.
- Jorgensen R, Kubale V, Vreel M, Schwartz TW, and Elling CE (2007) Oxyntomodulin differentially affects glucagon-like peptide-1 receptor β -arrestin recruitment and signaling through Galphas. *J Pharmacol Exp Ther* **322**:148–154.
- Katritch V, Fenalti G, Abola EE, Roth BL, Cherezov V, and Stevens RC (2014) Allosteric sodium in class A GPCR signaling. *Trends Biochem Sci* **39**:233–244.
- Kenakin T and Christopoulos A (2013) Signalling bias in new drug discovery: detection, quantification and therapeutic impact. *Nat Rev Drug Discov* **12**:205–216.
- Kenakin T, Watson C, Muniz-Medina V, Christopoulos A, and Novick S (2012) A simple method for quantifying functional selectivity and agonist bias. *ACS Chem Neurosci* **3**:193–203.
- Koole C, Pabreja K, Savage EE, Wootten D, Furness SG, Miller LJ, Christopoulos A, and Sexton PM (2013) Recent advances in understanding GLP-1R (glucagon-like peptide-1 receptor) function. *Biochem Soc Trans* **41**:172–179.
- Koole C, Wootten D, Simms J, Valant C, Sridhar R, Woodman OL, Miller LJ, Summers RJ, Christopoulos A, and Sexton PM (2010) Allosteric ligands of the glucagon-like peptide 1 receptor (GLP-1R) differentially modulate endogenous and exogenous peptide responses in a pathway-selective manner: implications for drug screening. *Mol Pharmacol* **78**:456–465.
- Koole C, Wootten D, Simms J, Valant C, Miller LJ, Christopoulos A, and Sexton PM (2011) Polymorphism and ligand dependent changes in human glucagon-like peptide-1 receptor (GLP-1R) function: allosteric rescue of loss of function mutation. *Mol Pharmacol* **80**:486–497.

- Koole C, Wootten D, Simms J, Miller LJ, Christopoulos A, and Sexton PM (2012a) Second extracellular loop of human glucagon-like peptide-1 receptor (GLP-1R) has a critical role in GLP-1 peptide binding and receptor activation. *J Biol Chem* **287**:3642–3658.
- Koole C, Wootten D, Simms J, Savage EE, Miller LJ, Christopoulos A, and Sexton PM (2012b) Second extracellular loop of human glucagon-like peptide-1 receptor (GLP-1R) differentially regulates orthosteric but not allosteric agonist binding and function. *J Biol Chem* **287**:3659–3673.
- Langer I (2012) Conformational switches in the VPAC(1) receptor. *Br J Pharmacol* **166**:79–84.
- May LT, Avlani VA, Langmead CJ, Herdon HJ, Wood MD, Sexton PM, and Christopoulos A (2007) Structure-function studies of allosteric agonism at M2 muscarinic acetylcholine receptors. *Mol Pharmacol* **72**:463–476.
- Miller LJ, Chen Q, Lam PC, Pinon DI, Sexton PM, Abagyan R, and Dong M (2011) Refinement of glucagon-like peptide 1 docking to its intact receptor using mid-region photolabile probes and molecular modeling. *J Biol Chem* **286**:15895–15907.
- Montrose-Rafizadeh C, Avdonin P, Garant MJ, Rodgers BD, Kole S, Yang H, Levine MA, Schwindinger W, and Bernier M (1999) Pancreatic glucagon-like peptide-1 receptor couples to multiple G proteins and activates mitogen-activated protein kinase pathways in Chinese hamster ovary cells. *Endocrinology* **140**:1132–1140.
- Moon MJ, Lee YN, Park S, Reyes-Alcaraz A, Hwang JI, Millar RP, Choe H, and Seong JY (2015) Ligand binding pocket formed by evolutionarily conserved residues in the glucagon-like peptide-1 (GLP-1) receptor core domain. *J Biol Chem* **290**:5696–5706.
- Pabreja K, Mohd MA, Koole C, Wootten D, and Furness SG (2014) Molecular mechanisms underlying physiological and receptor pleiotropic effects mediated by GLP-1R activation. *Brit J Pharmacol* **171**:1114–1128.
- Rasmussen SGF, DeVree BT, Zou Y, Kruse AC, Chung KY, Kobilka TS, Thian FS, Chae PS, Pardon E, and Calinski D et al. (2011) Crystal structure of the β_2 adrenergic receptor-Gs protein complex. *Nature* **477**:549–555.
- Shonberg J, Lopez L, Scammells PJ, Christopoulos A, Capuano B, and Lane JR (2014) Biased agonism at G protein-coupled receptors: the promise and the challenges—a medicinal chemistry perspective. *Med Res Rev* **34**:1286–1330.
- Siu FY, He M, de Graaf C, Han GW, Yang D, Zhang Z, Zhou C, Xu Q, Wacker D, and Joseph JS et al. (2013) Structure of the human glucagon class B G-protein-coupled receptor. *Nature* **499**:444–449.
- Solano RM, Langer I, Perret J, Vertongen P, Juarranz MG, Robberecht P, and Waelbroeck M (2001) Two basic residues of the h-VPAC1 receptor second transmembrane helix are essential for ligand binding and signal transduction. *J Biol Chem* **276**:1084–1088.
- Tubert-Brohman I, Sherman W, Repasky M, and Beuming T (2013) Improved docking of polypeptides with Glide. *J Chem Inf Model* **53**:1689–1699.
- Underwood CR, Garibay P, Knudsen LB, Hastrup S, Peters GH, Rudolph R, and Reedtz-Runge S (2010) Crystal structure of glucagon-like peptide-1 in complex with the extracellular domain of the glucagon-like peptide-1 receptor. *J Biol Chem* **285**:723–730.
- Venkatakrishnan AJ, Deupi X, Lebon G, Tate CG, Schertler GF, and Babu MM (2013) Molecular signatures of G-protein-coupled receptors. *Nature* **494**:185–194.
- Vertongen P, Solano RM, Perret J, Langer I, Robberecht P, and Waelbroeck M (2001) Mutational analysis of the human vasoactive intestinal peptide receptor subtype VPAC(2): role of basic residues in the second transmembrane helix. *Br J Pharmacol* **133**:1249–1254.
- Weston C, Poyner D, Patel V, Dowell S, and Ladds G (2014) Investigating G protein signalling bias at the glucagon-like peptide-1 receptor in yeast. *Br J Pharmacol* **171**:3651–3665.
- Willard FS, Wootten D, Showalter AD, Savage EE, Ficorilli J, Farb TB, Bokvist K, Alsina-Fernandez J, Furness SG, and Christopoulos A et al. (2012) Small molecule allosteric modulation of the glucagon-like Peptide-1 receptor enhances the insulinotropic effect of oxyntomodulin. *Mol Pharmacol* **82**:1066–1073.
- Wootten D, Savage EE, Willard FS, Bueno AB, Sloop KW, Christopoulos A, and Sexton PM (2013a) Differential activation and modulation of the glucagon-like peptide-1 receptor by small molecule ligands. *Mol Pharmacol* **83**:822–834.
- Wootten D, Simms J, Miller LJ, Christopoulos A, and Sexton PM (2013b) Polar transmembrane interactions drive formation of ligand-specific and signal pathway-biased family B G protein-coupled receptor conformations. *Proc Natl Acad Sci USA* **110**:5211–5216.
- Yang L, Yang D, de Graaf C, Moeller A, West GM, Dharmarajan V, Wang C, Siu FY, Song G, and Reedtz-Runge S et al. (2015) Conformational states of the full-length glucagon receptor. *Nat Commun* **6**:7859 10.1038/ncomms8859.
- Zhou FX, Cocco MJ, Russ WP, Brunger AT, and Engelman DM (2000) Interhelical hydrogen bonding drives strong interactions in membrane proteins. *Nat Struct Biol* **7**:154–160.

Address correspondence to: Dr. Denise Wootten or Dr. Patrick Sexton, Drug Discovery Biology, Monash Institute of Pharmaceutical Sciences, Monash University, 381 Royal Parade, Parkville, Victoria 3052, Australia. E-mail: denise.wootten@monash.edu or patrick.sexton@monash.edu

The Extracellular Surface of the GLP-1 Receptor Is a Molecular Trigger for Biased Agonism

Graphical Abstract



Authors

Denise Wootten, Christopher A. Reynolds, Kevin J. Smith, ..., Laurence J. Miller, Arthur Christopoulos, Patrick M. Sexton

Correspondence

denise.wootten@monash.edu (D.W.),
patrick.sexton@monash.edu (P.M.S.)

In Brief

Understanding how different ligands engage and activate signaling pathways downstream of the GLP-1 receptor, a key type II diabetes target, suggests strategies for shaping signaling outcomes to favor physiologically beneficial effects.

Highlights

- Effect of mutation on affinity and efficacy of biased ligands mapped onto 3D models
- Biased agonists form distinct interactions with the GLP-1R extracellular surface
- Engagement of unique elements of the extracellular surface promotes biased agonism
- Insights into class B GPCR activation/biased agonism can aid rational drug design



The Extracellular Surface of the GLP-1 Receptor Is a Molecular Trigger for Biased Agonism

Denise Wootten,^{1,*} Christopher A. Reynolds,³ Kevin J. Smith,³ Juan C. Mobarec,³ Cassandra Koole,^{1,4} Emilia E. Savage,¹ Kavita Pabreja,¹ John Simms,⁵ Rohan Sridhar,¹ Sebastian G.B. Furness,¹ Mengjie Liu,² Philip E. Thompson,² Laurence J. Miller,⁶ Arthur Christopoulos,¹ and Patrick M. Sexton^{1,*}

¹Drug Discovery Biology

²Medicinal Chemistry

Monash Institute of Pharmaceutical Sciences, Monash University, Parkville, Victoria 3052, Australia

³School of Biological Sciences, University of Essex, Colchester CO4 3SQ, UK

⁴Laboratory of Chemical Biology and Signal Transduction, The Rockefeller University, 1230 York Avenue, New York, NY 10065, USA

⁵School of Life and Health Sciences, Aston University, Birmingham B4 7ET, UK

⁶Department of Molecular Pharmacology and Experimental Therapeutics, Mayo Clinic, Scottsdale, AZ 85259, USA

*Correspondence: denise.wootten@monash.edu (D.W.), patrick.sexton@monash.edu (P.M.S.)

<http://dx.doi.org/10.1016/j.cell.2016.05.023>

SUMMARY

Ligand-directed signal bias offers opportunities for sculpting molecular events, with the promise of better, safer therapeutics. Critical to the exploitation of signal bias is an understanding of the molecular events coupling ligand binding to intracellular signaling. Activation of class B G protein-coupled receptors is driven by interaction of the peptide N terminus with the receptor core. To understand how this drives signaling, we have used advanced analytical methods that enable separation of effects on pathway-specific signaling from those that modify agonist affinity and mapped the functional consequence of receptor modification onto three-dimensional models of a receptor-ligand complex. This yields molecular insights into the initiation of receptor activation and the mechanistic basis for biased agonism. Our data reveal that peptide agonists can engage different elements of the receptor extracellular face to achieve effector coupling and biased signaling providing a foundation for rational design of biased agonists.

INTRODUCTION

G protein-coupled receptors (GPCRs) are critical for the transmission of extracellular signals across the cell membrane to initiate intracellular responses (Fredriksson et al., 2003) and are the leading targets of currently marketed therapeutics (Overington et al., 2006). It is therefore vital to understand molecular interactions that govern ligand binding and how these interactions initiate intracellular signaling. Key advances in GPCR structural biology have greatly enhanced our knowledge of ligand interaction with GPCRs and yielded insight into receptor activation (reviewed in Katritch et al., 2013). However, to date, full-length structures have only been solved for a subset of class A GPCRs, mostly in complex with small-molecule ligands and in single

inactive conformations. In contrast, there is limited information addressing the molecular details by which peptide binding at class B GPCRs couples to effector activation.

Class B peptide hormone receptors are a subfamily of GPCRs that are major targets for the treatment of chronic disease, including type 2 diabetes, obesity, and dis-regulated bone metabolism (Couvineau and Laburthe, 2012). They include receptors that bind calcitonin, calcitonin gene-related peptide, vasoactive intestinal polypeptide, pituitary adenylate cyclase-activating polypeptide, corticotropin releasing factor (CRF), gastric inhibitory polypeptide, parathyroid hormone, glucagon, and glucagon-like peptides (GLP-1 and GLP-2). Class B GPCRs share the basic seven transmembrane (TM) topology common to all GPCRs but also possess a large N terminus that forms the major binding site for selective recognition of peptide ligands (Couvineau and Laburthe, 2012). Despite sequence divergence in this region between different receptors, this extracellular domain (ECD) contains key conserved residues, including three disulphide bonds that aid in stability and confer structural similarities between receptors.

Structural data for class B receptors are limited to partial domains, including several NMR and crystal structures of peptide-bound N-terminal domains (reviewed in Pal et al., 2012) and, more recently, two inactive structures of the isolated TM core of the CRF1 receptor (CRF1R) and the glucagon receptor (GCGR) (Hollenstein et al., 2013; Siu et al., 2013). This structural data, along with structure-activity studies, support the proposed two-domain model for peptide binding to class B GPCRs, with the α -helical C terminus binding to the receptor N-terminal ECD and the peptide N terminus interacting with the extracellular face of the TM bundle (this includes the top of the TMs and the extracellular loops [ECLs]) (Pal et al., 2012). However, there is very limited information available to define these N-terminal peptide interactions with the extracellular face of the receptor core and even less to indicate how this engagement drives receptor activation. Photoaffinity and mutagenesis data highlight the significance of the core domain in both peptide binding and receptor activation, including residues within the three ECLs and their juxtamembrane regions of class B GPCRs (Barwell et al., 2011; Bergwitz et al., 1997). These studies suggest

that the extracellular face of the TM bundle forms a significant site of receptor interaction and/or plays an important role in stabilizing active receptor conformations in the presence of agonists, allowing for activation of intracellular signaling.

The GLP-1R couples to multiple effectors, and *in vivo* data support this as important for normal physiology in both glucose and energy homeostasis (Baggio and Drucker, 2007). The GLP-1R is an important target for treatment of type 2 diabetes mellitus, and there are multiple endogenous peptides that activate this receptor. These include four forms of GLP-1 and the related peptide oxyntomodulin (Baggio and Drucker, 2007). In addition, there are clinically approved peptides for treatment of type 2 diabetes, including exendin-4 and metabolically stabilized forms of GLP-1 (Reid, 2013). N-terminally truncated forms of these peptides are antagonists, for example exendin-4(9-39). In previous studies, we identified exendin-4 and oxyntomodulin as biased agonists relative to GLP-1 (GLP-1(7-36)NH₂) (Koole et al., 2010; Wootten et al., 2013a). The phenomenon of biased agonism describes the ability of different ligands acting at the same receptor to promote distinct cellular responses (Kenakin and Christopoulos, 2013). Intriguingly, a biased GLP-1R peptide agonist, P5, that maintains G protein signaling, while exhibiting attenuated β -arrestin recruitment, induced adiposity and was more effective at correcting hyperglycaemia in diabetic animals than exendin-4, despite having markedly lower insulinotropic properties (Zhang et al., 2015). This highlights the potential utility of biased agonists as novel GLP-1R therapeutics.

Biased agonism is currently of great interest for drug discovery, with the potential to sculpt cellular responses to favor therapeutically beneficial signaling pathways over those leading to harmful effects. However, the mechanistic basis underlying biased signaling needs to be understood if this is to be exploited for rational drug design. Pleiotropic coupling of the GLP-1R leads to cAMP production, Ca²⁺ mobilization, and phosphorylation of ERK1/2 (pERK1/2) (Koole et al., 2010), each of which are physiologically important (Baggio and Drucker, 2007). The contribution of these signaling pathways and the extent to which one is activated relative to another is therefore important for optimal development of therapeutics. Existing data demonstrate that biased signaling does indeed occur at the GLP-1R; however, the mechanistic basis for this is unknown (Koole et al., 2010; Wootten et al., 2013a).

Using a combination of alanine-scanning mutagenesis, followed by pharmacological quantification of the effects of mutation on peptide agonist affinity and three distinct signaling pathways, we have identified critical regions within the extracellular face of the receptor core both for peptide agonist affinity and for driving receptor coupling to distinct signaling pathways, extending our initial work on ECL2 (Koole et al., 2012). We used a GLP-1R model in conjunction with experimental data to generate comparative heatmaps of the contribution of the extracellular surface to agonist affinity and signaling efficacy. These revealed distinct elements of the extracellular face of the GLP-1R that are engaged to activate individual signaling pathways in a ligand-dependent manner. Collectively, the work allows us to yield novel molecular insights into the initiation of receptor activation and the mecha-

nistic basis for biased agonism at this important class B GPCR. This provides a framework to enable future design of agonists with tailored signal bias for this receptor.

RESULTS

To understand the functional interface at the GLP-1R extracellular surface, we completed alanine-scanning mutagenesis of the ECLs and adjacent TM residues, coupled with analysis of ligand affinity and signaling for three key pathways that are involved in GLP-1R function and rely on different effector engagement (Figure S1). We assessed three peptides (GLP-1, oxyntomodulin, and exendin-4) with highly conserved N-terminal sequences that display biased agonism (Figure S2). This biased agonism can be observed in both the recombinant cells used in this mutagenesis study and natively expressing insulinoma cells that display key features of β islets, where both exendin-4 and oxyntomodulin were biased away from GLP-1 in promotion of cellular proliferation and reducing apoptosis, compared to cAMP signaling (Figure S2). In addition to measurements of agonist binding affinity, the effects on signaling efficacy for each of the pathways were quantified using an operational model of agonism (Black and Leff, 1983). This enables comparison of effects of mutations across the different signaling pathways and reveals how individual peptide ligands interact with the receptor surface to elicit signaling. To understand the importance of residues in ligand binding and function, we developed a full-length, GLP-1-bound, GLP-1R model (Active model S1) (Wootten et al., 2016). Residues located within the ECL/TM boundaries of the N-terminal ECD are numbered based on their location in the protein sequence. Residues that are located within the TM bundle also contain, in superscript, the class B numbering described in Wootten et al. (2013b).

The predicted ECL1 and adjacent TM boundary comprises 23 residues from L201 to S223, ECL2, 23 residues from G285 to L307 and ECL3, 16 residues from D372 to E387. The results for the pharmacology of ECL2 mutants have been published previously (Koole et al., 2012) and are discussed here, along with novel data on ECL1 and ECL3, in context of the 3D surface map developed for the receptor.

All mutant receptors, with the exception of W306A, were expressed at the cell surface, and most were expressed at levels equivalent to wild-type (Table S1) (Koole et al., 2012). Of the ECL1 and ECL3 mutants, only three exhibited a change in antagonist binding: H374A, an effect specific to exendin-4 (9–39); K383A, which had global effects on peptide binding; and F381A, which had selective effects dependent on the peptide (Table S1). Given that only limited mutations grossly altered cell-surface expression and antagonist affinity, altered effects on receptor function (affinity and efficacy) for most engineered mutations are likely a result of loss of direct interactions with ligands (affinity) or of altering (either directly or indirectly) interactions between receptor side chains and disruptions to hydrogen bonding networks that are crucial for the receptor to explore its conformational landscape, thereby indicating residues that are important in the mechanism of signal propagation.

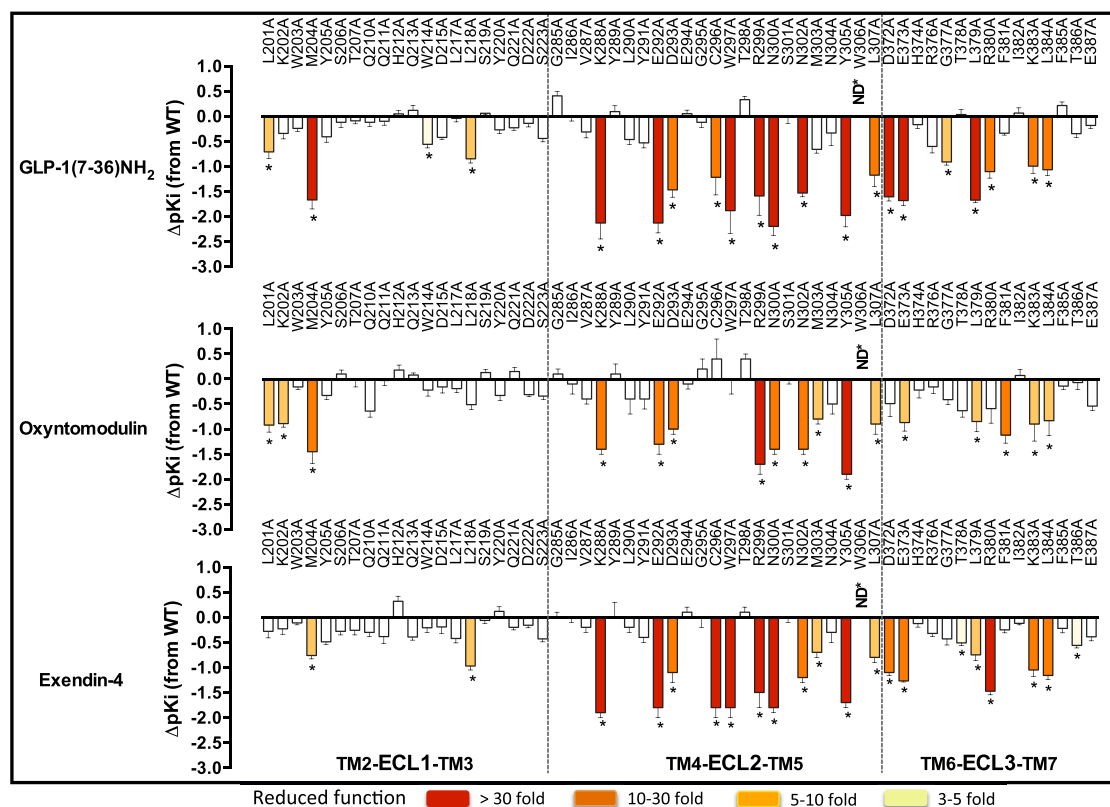


Figure 1. Agonist Affinity Profiles of GLP-1R ECL Alanine Mutants Reveal the Importance of Individual Residues for Peptide Affinity

pKi values for each peptide were derived from radioligand inhibition-binding experiments. Bars represent differences in calculated affinity (pKi) values for each mutant relative to the wild-type receptor for GLP-1 (top), oxyntomodulin (middle), and exendin-4 (bottom). Statistical significance of changes in affinity in comparison with wild-type was determined by one-way analysis of variance and Dunnett's post-test, and values are indicated with an asterisk (* $p < 0.05$). Data that are statistically significant are colored based on the extent of effect. All values are \pm SEM of four to six independent experiments, conducted in duplicate.

Involvement of the Extracellular Surface in Agonist Peptide-Binding Affinity

Effects of mutations on agonist affinity were established by heterologous competition with the antagonist radioligand (125 I-exendin-4 (9–39)) (Table S1) (Koole et al., 2012). The affinity measures for each mutant were compared to the wild-type to determine the relative importance of each individual residue in peptide agonist affinity (Figure 1). These were mapped onto the 3D model to provide a comparative heatmap of the contribution of the extracellular surface to agonist affinity (Figure 2, Active model S1).

Overall, there was a high degree of overlap in the impact of alanine mutation on binding of GLP-1, exendin-4, and oxyntomodulin. In 3D space, there is a continuum of residues from K288, E292, D293, R299, N300 within the proximal part of ECL2 that link to TM6/ECL3 membrane-proximal residues D372, E373 and L379, K383, L384 in ECL3 that are globally important for binding affinity, along with most residues in the distal segment of ECL2 (Table S1, Figures 1 and 2, Active model S1).

In addition, M204 at the TM2/ECL1 boundary lines the peptide-binding groove in our model and is important for the affinity of all peptides. There is an additional network of residues deeper

in the protein (C296, W297, R380) that are important for GLP-1 and exendin-4 affinity but have little role in oxyntomodulin binding (Table S1, Figures 1 and 2, Active model S1). L218 within ECL1 is also important for the affinity of GLP-1 and exendin-4 but not oxyntomodulin. Additionally, L201 lies deeper in the peptide groove of the protein and is important for GLP-1 and oxyntomodulin affinity but not exendin-4 (Table S1, Figures 1 and 2, Active model S1). Only a limited number of residues were selectively important for affinity of individual peptides: W214 (ECL1) and G377 (ECL3) for GLP-1; K202 (ECL1) and F381 (ECL3) for oxyntomodulin; and T378 and T386 (both in ECL3) for exendin-4.

Of all the residues important for peptide affinity, most are likely to have indirect effects on peptide binding. Alterations to agonist affinity can be achieved by the mutation either altering the conformation of residues that directly interact with the peptide within the binding pocket or altering the shape of the binding pocket such that the peptide cannot bind in the same manner. The only ECL side chains that our modeling predicted to interact directly with GLP-1 are L201, W297, R299, N300, and R380 (Figure S3). This includes three residues that, when mutated, have differential effects on peptide affinity. Although all are important for GLP-1 affinity, alanine mutation of L201 had little effect on exendin-4 affinity, and mutation of W297 and R380 had no effect on

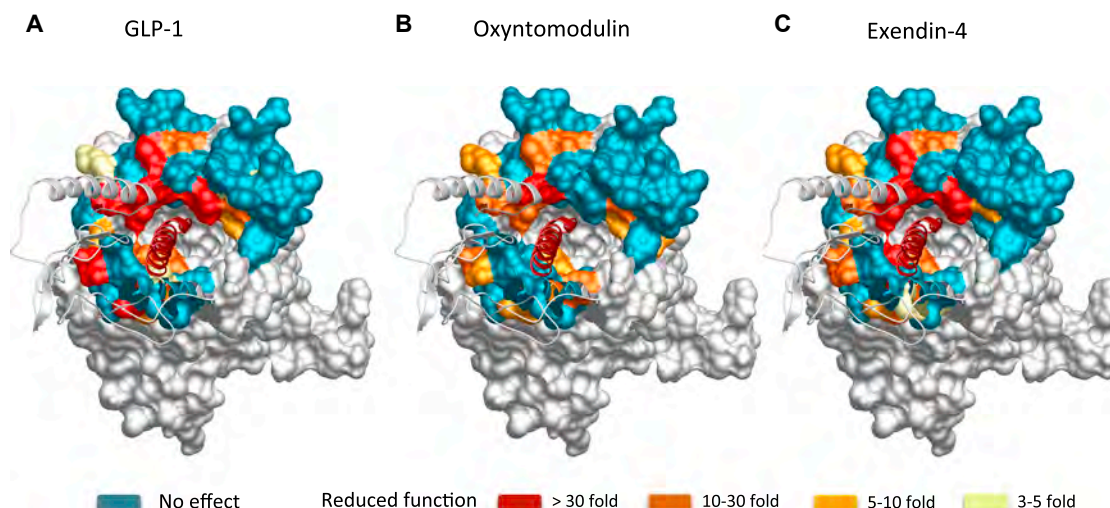


Figure 2. Heatmap 3D Representation of the GLP-1R Extracellular Face Based on Affinity-Binding Data

Molecular model of the GLP-1R-GLP-1 complex showing the extracellular surface of the TM bundle. Residues that altered affinity of GLP-1 (A), oxyntomodulin (B), and exendin-4 (C) when mutated are highlighted. Teal indicates residues that were assessed and did not alter affinity; yellow (3- to 5-fold), pale orange (5- to 10-fold), orange (10- to 30-fold), and red (>30-fold) are residues that statistically altered affinity.

oxyntomodulin affinity (Figures 1 and 2, Table S1). This is particularly interesting, as the residues in the GLP-1 peptide that are predicted to interact with these side chains are absolutely conserved in the N terminus of the three peptide ligands (Figure S3). This implies that differential interactions of the C terminus of the peptides with the N-terminal ECD may differentially orient the N terminus of these peptides in the binding groove such that they form distinct interactions with the bundle.

Involvement of the Extracellular Surface in Ligand Efficacy

Agonist potency is a composite of efficacy and affinity and cannot be used to distinguish pathway-specific effects of mutations. In contrast, in the operational model, the efficacy term “ τ ” relates receptor occupancy to magnitude of response for an individual pathway and is independent of ligand affinity, although not receptor expression levels. However, τ values can be normalized to experimentally determined levels of cell-surface expression to provide a measure of pathway activation (τ_c) that is independent of both affinity and cell-surface expression levels (Kenakin and Christopoulos, 2013). Concentration response curves for each of the peptides for cAMP formation, pERK1/2, and Ca^{2+} mobilization were established for wild-type and each receptor mutation to determine EC_{50} and E_{max} and τ_c values for each pathway for all mutants (Tables S2, S3, and S4). As with affinity, τ_c estimates for each mutant receptor were compared to the wild-type to determine the relative importance of each residue for efficacy in each pathway (Figures 3, 4, and 5). These were mapped onto the 3D model to provide a comparative heatmap of the contribution of the extracellular surface to efficacy for individual pathways (Figure 6, Active model S1). Overall, there was a significant correlation between residues identified as important for peptide affinity, cAMP formation, and Ca^{2+} mobilization. Generally, there was less correlation between agonist af-

finity and pERK1/2 efficacy with a distinct pattern of residues in 3D space being important for transmitting efficacy down this pathway (Figures 6 and 7).

Involvement of the Extracellular Surface in Peptide-Mediated cAMP Formation

Consistent with binding studies, there was a high degree of overlap in the impact of alanine mutation on cAMP-mediated signaling by GLP-1, exendin-4, and oxyntomodulin (Figures 3 and 6; Tables S1 and S2). These residues were concentrated mainly within ECL2 and the more buried, membrane-proximal regions of ECL1 and ECL3 that included residues deep within the binding groove important for affinity of these peptides (Figures 3 and 6A–6C, Active model S1). However, when mutated, these residues had a smaller effect on cAMP efficacy than they did on affinity (Figures 1, 2, 3, and 6A–6C). An additional residue, Y205, proximal to the binding groove at the TM2/ECL1 boundary was important for cAMP efficacy by all three peptides. Furthermore, two residues within the peptide binding groove (W297 and R380) that were important for GLP-1 and exendin-4, but not oxyntomodulin, affinity were required for all three peptides to activate this signaling pathway. Here the effect of mutation was larger for oxyntomodulin (no appreciable cAMP response) (Figures 2, 3, and 6; Table S2) (Koole et al., 2012). GLP-1 and exendin-4 also engage a large proportion of ECL2 and ECL3 with only minor contributions from ECL1 for transmission of efficacy to the cAMP pathway (Figures 3, 6A, and 6C). In contrast, a large proportion of all three loops contributed to cAMP signaling via the peptide oxyntomodulin, with more involvement of ECL1 but less involvement of ECL2 compared with GLP-1 and exendin-4 (Figures 3 and 6B). The heatmaps indicate that the lower-affinity ligand oxyntomodulin engages regions (albeit not necessarily the same residues) in the extracellular surface similar to those of GLP-1 and exendin-4 upon binding to the receptor

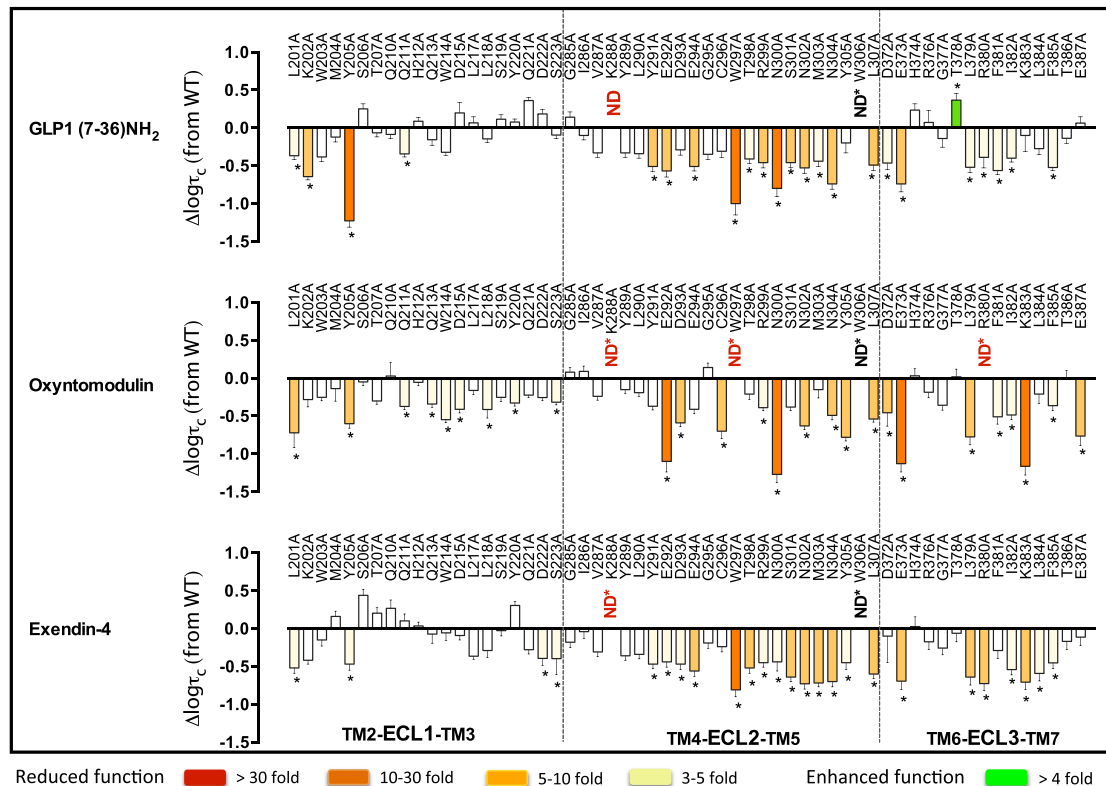


Figure 3. Peptide-Dependent Effects of ECL Mutations on cAMP Efficacy

Differences in the coupling efficiency ($\log \tau_c$) for cAMP formation of ECL mutations, compared to the wild-type receptor, by GLP-1 (top), oxyntomodulin (middle), and exendin-4 (bottom). Statistical significance of changes in coupling efficacy was determined by one-way analysis of variance and Dunnett's post-test, and values are indicated with an asterisk (* $p < 0.05$ compared with wild-type). Data that are statistically significant are colored based on the direction and extent of effect. All values are $\log \tau_c \pm \text{SEM}$ of four to six independent experiments, conducted in duplicate.

but requires distinct regions of this surface to promote conformational transitions leading to formation of cAMP (Figures 2 and 6, Active model S1).

Despite the critical importance of ECL2 and the membrane-proximal region of ECL3 for all three peptides to couple to cAMP, the relative contribution of each individual residue within this region varied considerably between oxyntomodulin and the other two peptides (Figure 7). This included a number of residues within ECL2 (Y291, E294, T298, S301, and M303) that were required for GLP-1- and exendin-4-mediated cAMP accumulation but not for oxyntomodulin and two residues, C296 in ECL2 and E387 in ECL3, that had the reverse profile. In addition, there were a number of residues that had global effects across all three peptides but with different magnitudes in the extent of effect (Figures 3, 6, and 7; Table S2). Only a very limited number of residues were selectively important for cAMP efficacy between GLP-1 and exendin-4. K202 (ECL1) was selective for GLP-1 only, and Q211 (ECL1), D372, and I382 (ECL3) affected both GLP-1 and oxyntomodulin but not exendin-4. D222 (ECL1) and L384 (ECL3) were selective for exendin-4 only, whereas mutation of S223 (ECL1), D293, Y305 (ECL2), and K383 (ECL3) altered cAMP signaling by both exendin-4 and oxyntomodulin but not GLP-1 (Figures 3, 6, and 7; Table S2).

Involvement of the Extracellular Surface in Peptide-Mediated Intracellular Calcium Mobilization

Due to the low efficacy of oxyntomodulin for promoting Ca²⁺ mobilization, this pathway was only assessed for GLP-1 and exendin-4 (Figures 4, 6D, and 6E, Active model S1). Consistent with binding and cAMP data, a continuum of residues in 3D space within ECL2 (K288, E292, D293, C296, W297, R299, N300) linking the membrane-proximal residues in ECL3 (D372, E373, L379, R380, K383), along with most residues in the distal segment of ECL2, were required for both ligands to promote Ca²⁺ mobilization. However, mutation of these residues had a larger impact on exendin-4 than on GLP-1, with more mutant receptors unable to produce a detectable exendin-4-mediated Ca²⁺ response (Figures 4, 6D, and 6E). In addition, residues within the TM2/ECL1 membrane-proximal region (L201, K202, M204, Y205, T207) were globally important for both peptides. There were also additional residues within the TM4/ECL2 (I286, V287, Y289, L290, Y291) and the ECL3/TM7 (L384, T386) membrane-proximal portions of ECL2 and ECL3, respectively, that were important for exendin-4-mediated signaling to this pathway, but with little role for GLP-1 coupling (Figures 4, 6D, and 6E). These residues extend within 3D space from the continuum of residues that are globally important.

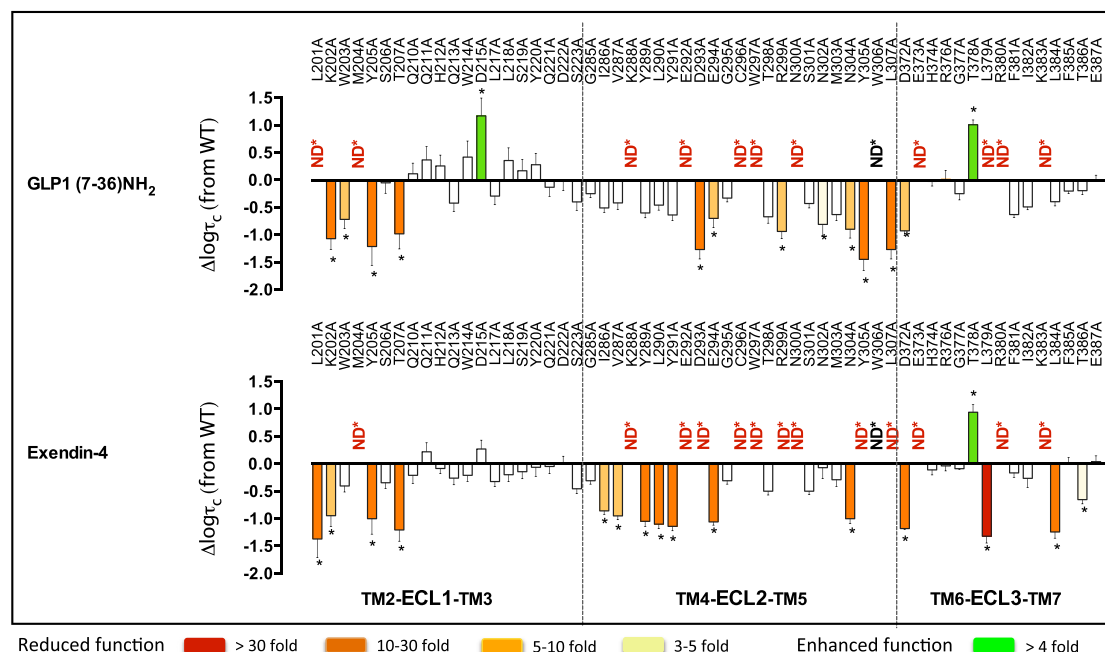


Figure 4. Peptide-Dependent Effects of ECL Mutations on Efficacy for Ca^{2+} Mobilization

Differences in the coupling efficiency ($\log \tau_c$) for Ca^{2+} mobilization of ECL mutations, compared to the wild-type receptor, by GLP-1 (top) and exendin-4 (bottom). Statistical significance of changes in coupling efficacy was determined by one-way analysis of variance and Dunnett's post-test, and values are indicated with an asterisk (* $p < 0.05$ compared with wild-type). Data that are statistically significant are colored based on the extent of effect. All values are $\log \tau_c \pm \text{SEM}$ of four to six independent experiments, conducted in duplicate.

Interestingly, mutation of two residues (D215 in ECL1 and T378 in ECL3) lying outside of the predicted peptide-binding groove enhances the ability of GLP-1 to promote Ca^{2+} mobilization, and one of these residues (T378) also had the same effect for exendin-4 (Figures 4 and 6).

Involvement of the Extracellular Surface in Peptide-Mediated pERK1/2

Mapping mutational effects for coupling to pERK1/2 onto the 3D model revealed a strikingly distinct pattern in regions of the GLP-1R extracellular face that were involved in coupling to this pathway, in comparison to those important for affinity, cAMP, and Ca^{2+} mobilization. Whereas these latter aspects of receptor function required a large area of the protein's extracellular surface for transmission of signal, residues important for pERK1/2 were localized mainly to membrane-proximal residues of ECL3 (Figures 5 and 6F–6H, Active model S1) with very little involvement (at least for GLP-1 and exendin-4) of ECL2 (the most critical domain for all other assessed aspects of receptor function). Only one residue throughout the entire extracellular surface, Y205 in ECL1, was globally important for coupling all three peptides to cAMP, iCa^{2+} , and pERK1/2 (Figures 3, 4, 5, 6, and 7).

Despite all three peptides utilizing ECL3 for coupling receptor activation to pERK1/2, the importance of individual residues within this loop varied between the ligands. D372, T378 and R380, and T386 were globally important for signaling by all three peptides, but for T378 and R380, the effect of mutation varied. Interestingly, T378A increased the efficacy for GLP-1 and exen-

din-4 but had the opposite effect on oxyntomodulin, reducing its efficacy. The reverse effect was observed for R380A, where oxyntomodulin efficacy was increased and GLP-1 and exendin-4 efficacies were both impaired (Figures 5, 6F–6H, and 7). This implies that these residues may be important for conformational switching of the receptor, altering the ensemble of conformations that allow for coupling to this pathway. In addition, within this loop, E373 was required for both GLP-1 and exendin-4 but played little role in the ability of oxyntomodulin to activate this pathway. Furthermore, mutation of R376, L379, F381, and I382 significantly altered signaling by GLP-1, with a similar trend displayed by exendin-4 but little role in oxyntomodulin-mediated pERK1/2 (Figure 5).

Although, compared to GLP-1, exendin-4 utilized a larger proportion of the extracellular surface for coupling the GLP-1R to iCa^{2+} mobilization, mutational effects on pERK1/2 were even more confined to ECL3 than those for GLP-1. Intriguingly, despite requiring a very large portion of ECL2 for intracellular Ca^{2+} mobilization, this domain played no role in coupling exendin-4 binding to pERK1/2. ECL2 played a limited role for GLP-1 coupling to this pathway with E292 and N300 being important. These residues were also important for oxyntomodulin coupling to pERK1/2 along with D293, N302, and Y305 (Figures 5, 6F, and 6G).

Additional residues selectively important for pERK1/2 by individual peptides included M204 and Q213 (ECL1) for GLP-1; L201 (ECL1) and F385 (ECL3) for oxyntomodulin; and W203 (ECL1) for exendin-4.

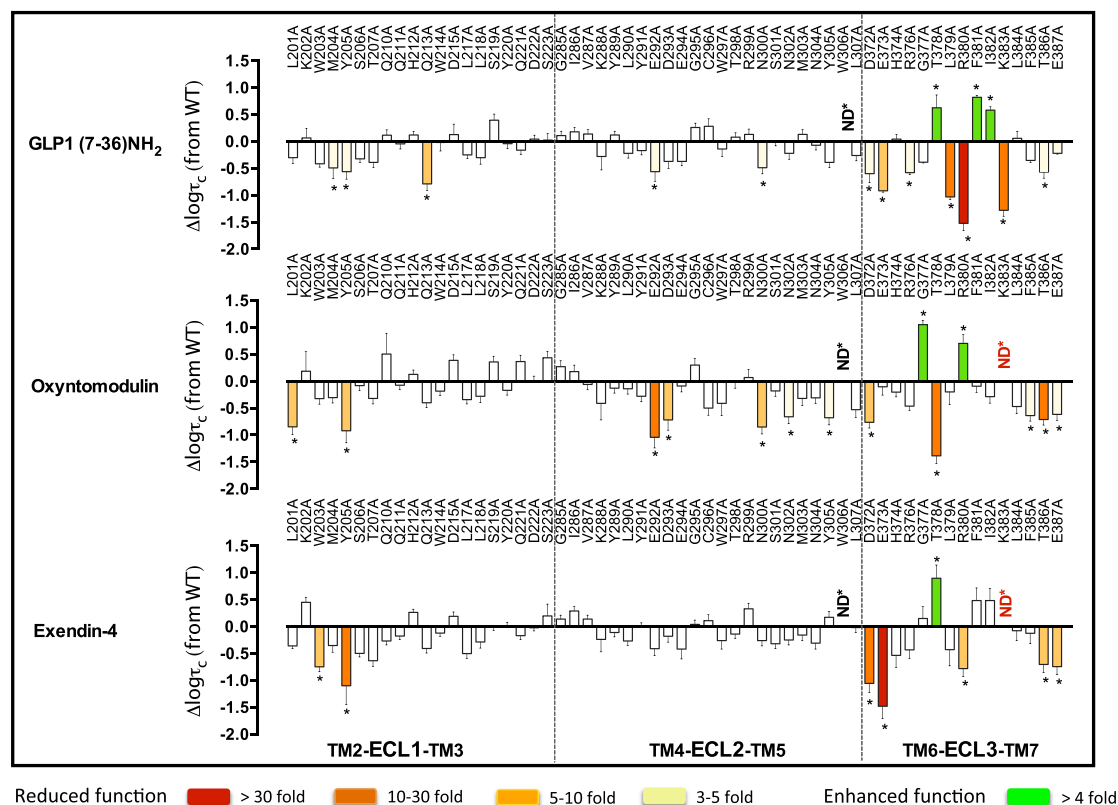


Figure 5. Peptide-Dependent Effects of ECL Mutations on pERK1/2 Efficacy

Differences in the coupling efficiency ($\log \tau_c$) to pERK1/2 of ECL mutations, compared to the wild-type receptor, by GLP-1 (top), oxyntomodulin (middle), and exendin-4 (bottom). Statistical significance of changes in coupling efficacy was determined by one-way analysis of variance and Dunnett's post-test, and values are indicated with an asterisk (* $p < 0.05$ compared with wild-type). Data that are statistically significant are colored based on the direction and extent of effect. All values are $\log \tau_c \pm \text{SEM}$ of four to six independent experiments, conducted in duplicate.

DISCUSSION

Ligands binding to GPCRs modify the conformational landscape and thus stabilize a subset of conformational ensembles, providing the basis for both differential efficacy and biased agonism. There is limited information linking the dynamic events of receptor activation to engagement of specific effector proteins, and this is particularly true for class B GPCRs. The current study explores the molecular determinants for ligand affinity and engagement of signaling. Specifically, we highlight crucial surface residues within a class B GPCR that link initial peptide agonist interactions to distinct intracellular signaling pathways and biased agonism.

Peptide interactions with the extracellular surface and TM domains of class B GPCRs promote conformational transitions required to allow the binding of signaling effectors at the intracellular surface of these receptors. The ability of receptor mutants to affect signaling at only a single pathway highlights that different elements of the extracellular face are required for coupling to different effectors. In addition, differential effects on signaling by the three peptide agonists following mutation of individual residues supports the notion that the extracellular face of the receptor is important for initiating a switch in the

conformational landscape that the receptor explores, with different ligands capable of promoting/stabilizing alternative subsets of ensembles that lead to biased agonism.

Importance of the ECL Regions of the GLP-1R for Peptide Binding

Large portions of ECL2, ECL3 and the juxtamembrane positions of TM2/ECL1, ECL2/TM5 and TM6/ECL3 were important for molecular recognition of all peptide agonists but not for binding of the N-terminally truncated antagonist exendin-4(9–39). Despite the separation in sequence of these residues, they are all located together in 3D space. In addition, there is a network of residues provided by all three loops lining the cavity entrance in the TM bundle, and these residues are important for GLP-1 affinity, extending the peptide-binding groove from the N-terminal ECD into the TM domain cavity. These residues include L201, M204 (TM2/ECL1), E294, W297, T298, R299, N300, Y305 (ECL2), R380, L384 (ECL3) (Figure S4). Interestingly, most of these residues appear to have indirect effects on agonist affinity as only five of these residues interact directly with GLP-1 in our model (L201, W297, R299, N300 and R380) (Figure S3).

The peptide-binding groove in the molecular model extends from the ECLs down into the TM bundle, forming a deep cavity

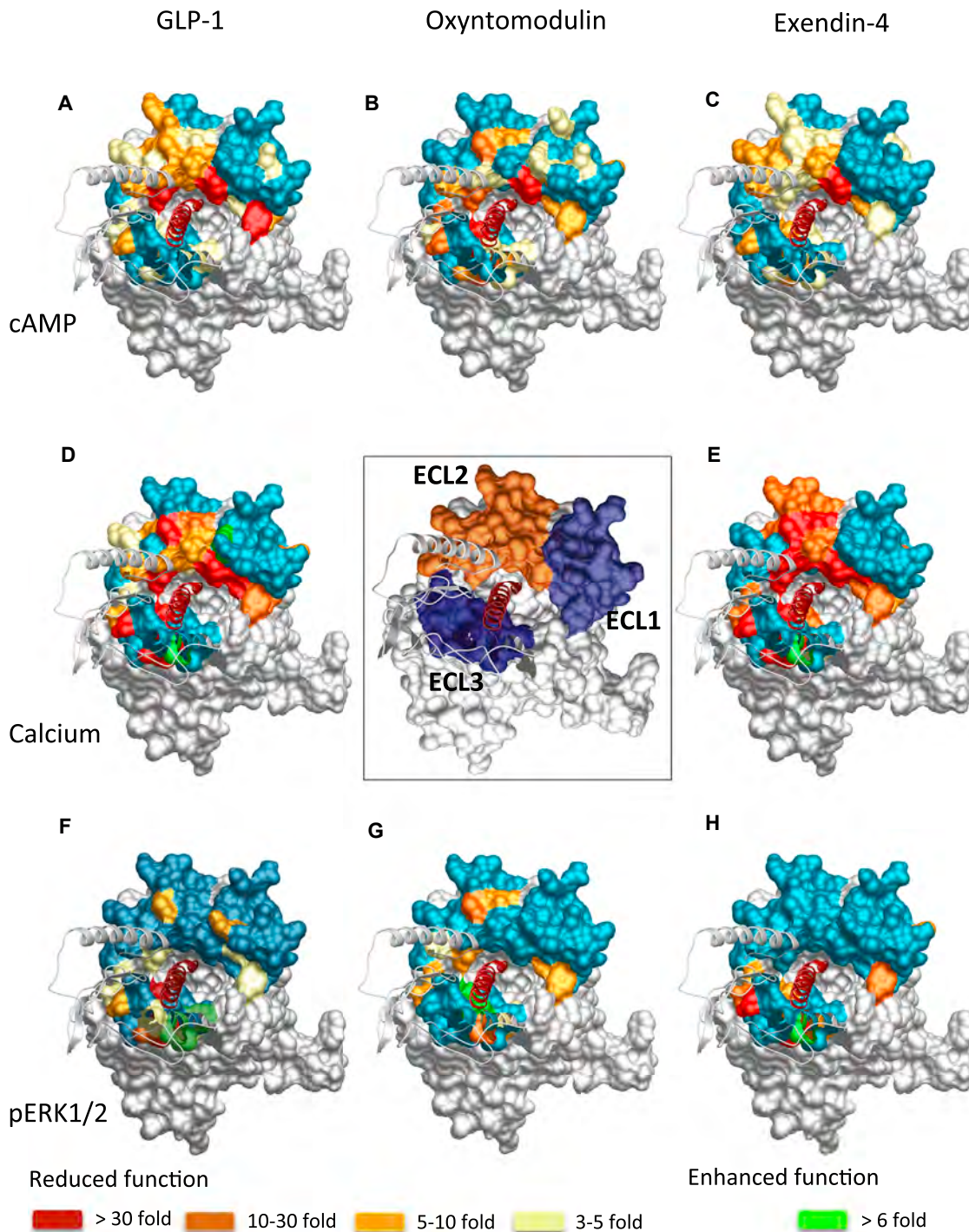


Figure 6. Heatmap 3D Representation of the GLP-1R Extracellular Face Based on Efficacy Data from Three Different Signaling Assays

Molecular model of the GLP-1R-GLP-1 complex showing the extracellular surface of the TM bundle. All residues assessed in this study are shown in the center box; the locations of residues in ECL1, ECL2, and ECL3 are highlighted in purple, orange, and blue, respectively. Residues that when mutated altered efficacy are highlighted in (A)–(H). (A–C) cAMP efficacy of GLP-1 (A), oxyntomodulin (B), and exendin-4 (C); (D and E) Ca^{2+} efficacy of GLP-1 (D) and exendin-4 (E); (F–H) pERK1/2 efficacy of GLP-1 (F), oxyntomodulin (G), and pERK1/2 (H). Teal indicates residues that were assessed and did not alter efficacy; yellow (3- to 5-fold), pale orange (5- to 10-fold), orange (10- to 30-fold), and red (>30-fold) are residues that statistically altered efficacy. The 3D heatmaps can be found in Active model S1 (Data S1).

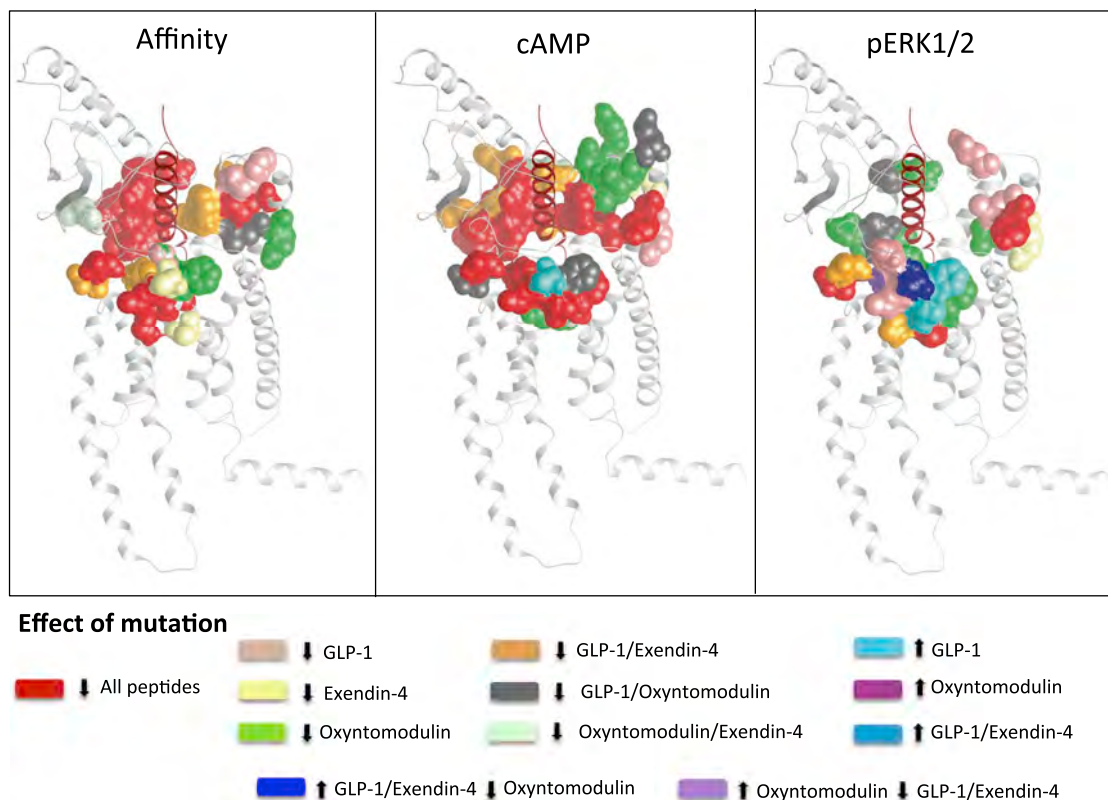


Figure 7. 3D Model Illustrating GLP-1R ECL Loop Residues that Are Globally or Selectively Important for GLP-1, Oxyntomodulin, and Exendin-4

Based on statistical significance ($p < 0.05$) of effect when mutated to alanine, experimentally observed effects on peptide affinity and efficacy can be mapped onto the molecular model to clearly highlight similarities and differences between the three peptide agonists. Residues highlighted in red reduce function (affinity [A] or efficacy [B and C]) of all three peptides, those in pink selectively reduce GLP-1 only, those in yellow selectively reduce exendin-4 only, and those in green selectively reduce oxyntomodulin only. A large number of residues are important for both GLP-1 and exendin but not oxyntomodulin, and these are highlighted in orange. Other colors represent either enhanced function (GLP-1 only/oxyntomodulin only or GLP-1 and exendin) or existence of opposite effects when mutated on oxyntomodulin compared to GLP-1 and exendin-4.

lined by residues in all TMs except TM4 (Figure S4). In addition to the identified residues within the ECLs, published information on the requirement of other residues within this proposed cavity for GLP-1 affinity support our molecular model wherein GLP-1 enters into this cavity upon binding, with its N terminus residing deep within the helical bundle in the final ligand-docked model (Figures S3, S4, S5, and S6, Active model S1). Four of the residues that reside at the bottom of this pocket (R190^{2,60}, N240^{3,43}, E364^{6,53}, and Q394^{7,49}) form part of a hydrogen bond network in the inactive, unliganded receptor and are important for the binding and function of GLP-1 and exendin-4, though these residues also have roles in the biased agonism of these peptides (Wootten et al., 2013b, 2016). K197^{2,67} sits below L201 and W297 in 3D space and is important for GLP-1 binding and activation (Coopman et al., 2010). R310^{5,40} resides below N300 and also displays reduced potency in cAMP when mutated to alanine. Our model is also consistent with recent extensive studies on the GCGR (Siu et al., 2013) and CRF1R (Coin et al., 2013).

Despite the conservation of N-terminal sequence across all three peptides, oxyntomodulin appears to engage with the

GLP-1R in a manner that is significantly different from that of exendin-4 and GLP-1. Although this ligand also requires large portions of ECL2 and, although to a lesser degree, the residues L201 and L384 deep in the extracellular surface of the protein, it does not require some key residues lining the entry to the cavity, including C296/W297 in ECL2 and R380 in ECL3, that are crucial for affinity of the other two peptides. The deeper membrane-proximal residues of ECL2 and ECL3 are also less important, and other residues such as L218 in ECL1 play no role in the affinity of oxyntomodulin, and this implies that oxyntomodulin, which has a lower affinity than GLP-1 and exendin-4, may not bind in the same manner as the other two peptides. This is supported by previous data that show only a limited role of residues at the bottom of the binding cavity (R190^{2,60}, N240^{3,43}, E364^{6,53}, and Q394^{7,49}) in oxyntomodulin affinity or cAMP formation (Wootten et al., 2013b, 2016). Indeed, a key predicted interaction in the GLP-1-GLP-1R model occurs between E⁹ (position 3) of the peptide and R190^{2,60} of the receptor. However, oxyntomodulin contains a Q at this position that would not be expected to form a salt bridge with R190^{2,60}. Modified GLP-1 and oxyntomodulin peptides where the residue at position 3 is swapped

converts the behavior of these two peptides such that R190^{2,60} is required for cAMP production by the modified oxyntomodulin but not for the modified GLP-1 (Figure S3). This provides strong evidence validating the positioning of the N-terminal segment of GLP-1 in our molecular model, and extended molecular dynamics (MD) simulation indicates that this interaction is stable (Figures S5E–S5H).

Although the extreme N terminus of GLP-1 is predicted to interact in the deep cavity within the TM bundle, MD simulations where the peptide N terminus is placed in a superficial position in a model of the open inactive receptor predict that the peptide ligand initially makes interactions with the extracellular surface of the GLP-1R prior to movement of the peptide deeper into the cavity driven by E⁹ (Figure S5). In the open conformation, ECLs 2 and 3 reside further apart in 3D space (Figures S5A–S5D), suggesting that there is also a reorganization of the ECLs in response to peptide binding with ECL2 and ECL3 moving closer together in 3D space in the activated, ligand-occupied receptor (Figures S5E–S5H). Mapping of mutational data (affinity and efficacy) onto this surface formed by ECL2 and ECL3 reveals a continuous surface illustrating that this 3D surface is critical for stabilization of peptide binding and for activation of downstream effectors (Figures 6 and 7, Active model S1). Taken together with the extensive crosslinking/cysteine-trapping studies on other class B GPCRs (Coin et al., 2013; Dong et al., 2012), this supports a role for both interactions of peptide ligands with the extracellular loops and deeper interactions within the TM bundle, which are both important for peptide binding, leading to propagation of signaling in class B GPCRs.

Importance of the ECL Regions of the GLP-1R for Efficacy

Overall, there was a very high correlation between residues important for peptide affinity and those linked to efficacy for cAMP formation and Ca²⁺ mobilization (Figures 2, 6, and 7). This is perhaps not surprising as both cAMP and Ca²⁺ mobilization are predominantly G protein-mediated pathways (Figure S1), and the ternary complex of the agonist-occupied receptor and effector (e.g., G protein) provides thermodynamically reciprocal regulation of agonist binding (De Lean et al., 1980). As such, the heatmaps of mutant effects on agonist affinity are a composite of direct effects on binding and those allosterically imposed via the effects of effector coupling, in particular, G protein coupling. For GLP-1 and exendin-4, unlike effects on affinity, almost the entire region of ECL2 is required for transmission of signal. Moreover, the contribution of individual residues varies between the different functional measures and the two ligands. Exendin-4 and GLP-1 display a similar efficacy for coupling to cAMP; however, exendin-4 is less efficient than GLP-1 at coupling to Ca²⁺ mobilization (Figure S2). Interestingly, the Ca²⁺ response mediated by exendin-4 is more sensitive to mutations within ECL2, ECL3, and TM2 membrane-proximal regions of ECL1 than that mediated by GLP-1, perhaps suggesting that subtle differences in the interactions formed by these ligands account for the small distinctions in signaling bias that are observed experimentally. These subtle differences in bias and the effect of mutations may be reflective of the nature of effector coupling that drives stimulation of individual signaling

pathways. This is observed in inhibitor studies where relatively subtle differences were observed between GLP-1 and exendin-4, most notably in the relative contribution of G_{βγ} subunits to pERK1/2 and iCa²⁺ signaling (Figure S1).

In addition to distinctions in the pattern of residues required for oxyntomodulin affinity compared to GLP-1 and exendin-4, there are also significant differences in the pattern of residues important for coupling the receptor to cAMP. Like the other two peptides, oxyntomodulin utilizes ECL2 and membrane-proximal regions of ECL3 for its function, and there is also evidence for the involvement of deeper residues in ECL2 and ECL3 that were not required for its affinity. However, in contrast to GLP-1 and exendin-4, there is a large involvement of residues in ECL1 and no requirement for residues in the proximal region of ECL2. Oxyntomodulin displays a very distinct signaling profile to GLP-1 (Figure S2), and collectively, the affinity and cAMP data support the notion that oxyntomodulin does not interact in the same manner, requiring a much larger portion of the extracellular surface to engender conformational transitions linking peptide interactions to signaling inside the cell. Furthermore, in contrast to GLP-1 and exendin-4, a component of the oxyntomodulin-mediated cAMP production is dependent on G_{βγ} subunits, suggesting perhaps that a different subset of adenylate cyclases are activated to generate this cAMP response.

In addition to the network of interconnected residues along the extracellular surface of the receptor, a number of more distal residues were also identified to contribute to signaling efficacy. Studies of the GCGR have suggested that interactions between the receptor ECD and ECLs can occur and that these can influence conformational transitions required for signaling (Koth et al., 2012). It is likely that similar interactions also occur for the GLP-1R, and these may account for the observed effects of some residues distal to the interconnected networks. Extended MD simulation of the full-length receptor is consistent with the potential for such interactions to occur (Movies S1 and S2).

Interactions Determining Activation of Distinct Signaling Pathways and Promotion of Biased Signaling

Regardless of the ligand, ECL3 is essential for coupling the peptide-receptor interaction to pERK1/2, whereas ECL2 is critical for coupling of these interactions to cAMP and Ca²⁺. Using inhibitors to disrupt various G protein- and β-arrestin-mediated signaling pathways revealed that whereas cAMP and Ca²⁺ mobilization are predominantly driven by G protein-mediated signaling, pERK1/2 is a composite of both G protein- and β-arrestin-driven events, with approximately 30%–60% (depending on the peptide) of the signal attributed to this latter mechanism (Figure S1). As the signaling events leading to pERK1/2 are partially independent of G proteins, this may explain why there is a very distinct region of the receptor required for signaling to this pathway in comparison to Ca²⁺ and cAMP signaling, which are predominantly G protein mediated.

In addition to heatmapping, the data from this study can also be mapped onto models depicting global importance of residues across sets of ligands or importance of residues for individual ligands. In this way, it is easy to visually observe distinct regions of

the receptor that can achieve biased agonism. In Figure 7, which summarizes the three measures of function with data for all three peptides, the differential importance of regions in the extracellular face for oxyntomodulin compared to GLP-1 and exendin-4 can be clearly observed. Oxyntomodulin is a highly biased ligand compared to GLP-1 (and exendin-4), with bias toward both pERK1/2 signaling and regulatory protein recruitment (including β -arrestins) (Figure S2), biases that may be linked given the greater contribution of β -arrestins to the pERK1/2 response of oxyntomodulin relative to the other two peptides (Figure S1). Therefore, it is not surprising that quite a different pattern of residues are required for transmission of signal for this peptide. Compared to GLP-1, exendin-4 only has very minor bias in its signaling profile for the pathways assessed in the current study, and therefore it is not necessarily surprising that the residues important at the extracellular face for each of these peptides to signal to various pathways are similar, even if (as the heatmapping suggests) the extent to which each of these residues contributes may be different.

Combining this study with previously published quantitative information of residues that also contribute to conformational changes associated with activation provides additional context to how these surface interactions link with intramembranous networks to differentially control signaling (Figure S6). This type of information allows us to begin to understand how initial peptide interactions at the extracellular surface engage with distinct networks of intramembranous residues to link extracellular binding to engagement of intracellular effectors.

Mapping mutational effects on efficacy onto molecular models may also provide a basis for rational design of biased peptide agonists. If the required cellular efficacy for translation to therapeutic success is known, then this provides an ability to design peptides that exploit signaling bias therapeutically. This hypothesis can be tested to some extent using the metabolite of GLP-1, GLP-1(9-36)NH₂. Whereas this ligand lacks the first two amino acids of GLP-1, including the N-terminal His⁷ that is critical for affinity and activation of cAMP (Adelhorst et al., 1994), it retains mid-regions of the peptide that, in our molecular model, interact with ECL3. Although unable to activate the cAMP pathway, the metabolite can still promote pERK1/2 (Figure S7). This suggests that peptides that maintain interactions with ECL3 while altering/removing interactions deeper in the bundle and perhaps with ECL2 could bias ligands toward pERK1/2; however, it remains to be seen whether ECL3 is a common activation domain for this subclass of receptors to promote coupling to β -arrestin-mediated signaling pathways such as pERK1/2.

Biased agonism is likely to be a crucial element of the function of class B GPCRs, as many of them can be activated by multiple endogenous ligands and their receptors are capable of activating multiple intracellular signaling pathways. Therefore, understanding the molecular determinants linking ligand interactions to activation of distinct signaling pathways, in addition to the physiological benefit of activating individual pathways, could have significant ramifications for future drug development and may provide the potential to rationally design future drug therapies, and this is highlighted by the *in vivo* actions of the biased GLP-1 agonist, P5 (Zhang et al., 2015).

EXPERIMENTAL PROCEDURES

Molecular Biology

We used Quikchange (Stratagene) to introduce mutations into the GLP-1R cloned into the pEF5/Frt/V5-Dest vector.

Cell Culture

Stable FlpIn CHO cell lines were generated using Gateway technology. For all assays, cells were seeded in 96-well plates at a density of 30,000 cells per well.

Radioligand-Binding Assays

Whole-cell competition radioligand binding was performed using [¹²⁵I]-exendin-4(9–39) as the tracer ligand and competing with increasing concentrations of unlabeled peptide ligands as described previously (Koole et al., 2010).

Cell-Surface Expression

Cell-surface expression was detected either by using a cell-surface ELISA to detect a double c-Myc epitope label incorporated with the N-terminal region of the GLP-1R constructs or by calculation of the B_{max} in the radioligand-binding experiments (Koole et al., 2012; Wootten et al., 2016).

Signaling Assays

For cAMP assays, cells were stimulated for 30 min in the presence of the phosphodiesterase inhibitor IBMX and then lysed. For pERK1/2, cells were stimulated for 6 min (the peak of the response) before lysis. Detection of cAMP and pERK1/2 in the lysates was performed using Alphascreen technology as previously described (Koole et al., 2010). Ca²⁺ mobilization was detected using a Fluo-4-AM dye immediately after ligand addition with an excitation wavelength of 485 nm and an emission wavelength of 520 nm with values derived from the peak response.

Data Analysis

Concentration response data were analyzed using a three-parameter logistic equation to determine affinity, EC₅₀, and E_{max} values. Efficacy was calculated by applying the operational model of agonism:

$$Y = \text{Bottom} + \frac{E_m - \text{Bottom}}{1 + ((10^{\log K_A}) + (10^{\log [A]})) / (10^{(\log \tau + \log [A])})}$$

where *Bottom* represents the *y* value in the absence of ligand, *E_m* is maximal system stimulation, *K_A* is the agonist-receptor dissociation constant, [*A*] is the ligand concentration, and τ is the operational measure of efficacy in the system, which incorporates signaling efficacy and receptor density. Derived τ values were corrected to cell-surface expression (τ_c) measured by ELISA, and errors were propagated from both τ and cell-surface expression.

Molecular Modeling

Energy-based conformational modeling of the GLP-1R complex with GLP-1 was performed with Modeler 9.15, and peptide docking and energy optimization were guided by published experimental data (Tables S5 and S6), as previously described (Wootten et al., 2016).

Detailed procedures and analysis are reported in the Supplemental Experimental Procedures.

SUPPLEMENTAL INFORMATION

Supplemental Information includes Supplemental Experimental Procedures, seven figures, six tables, one data file, and two movies and can be found with this article online at <http://dx.doi.org/10.1016/j.cell.2016.05.023>.

AUTHOR CONTRIBUTIONS

Conceptualization, D.W., J.S., P.M.S.; Methodology, D.W., C.A.R., K.J.S., J.C.M., M.L., P.E.T., P.M.S.; Software, C.A.R., K.J.S., J.C.M.; Formal Analysis, D.W., C.K., A.C., P.M.S.; Investigation, D.W., C.A.R., K.J.S., J.C.M., C.K., E.E.S., K.P., M.L., J.S., R.S.; Writing – Original Draft, D.W., C.A.R., L.J.M., A.C., P.M.S.; Writing – Review and Editing, C.K., S.G.B.F.; Visualization,

D.W., P.M.S.; Supervision, D.W., C.A.R., P.E.T., P.M.S.; Project Administration, D.W., P.M.S.; Funding Acquisition, D.W., C.A.R., A.C., P.M.S.

ACKNOWLEDGMENTS

This work was supported by National Health and Medical Research Council of Australia (NHMRC) project grants (1061044 and 1065410) and NHMRC program grant (1055134); Biotechnology and Biological Sciences Research Council of the United Kingdom project grant (BB/M006883/1); and Medical Research Council (UK) Research Leader Fellowship (G1001812) (C.A.R.). D.W. is a NHMRC Career Development Fellow. P.M.S. is a NHMRC Principal Research Fellow, and A.C. is a NHMRC Senior Principal Research Fellow. C.K. is a NHMRC CJ Martin Postdoctoral Fellow.

Received: December 1, 2015

Revised: February 16, 2016

Accepted: May 3, 2016

Published: June 16, 2016

REFERENCES

- Adelhorst, K., Hedegaard, B.B., Knudsen, L.B., and Kirk, O. (1994). Structure-activity studies of glucagon-like peptide-1. *J. Biol. Chem.* 269, 6275–6278.
- Baggio, L.L., and Drucker, D.J. (2007). Biology of incretins: GLP-1 and GIP. *Gastroenterology* 132, 2131–2157.
- Barwell, J., Conner, A., and Poyner, D.R. (2011). Extracellular loops 1 and 3 and their associated transmembrane regions of the calcitonin receptor-like receptor are needed for CGRP receptor function. *Biochim. Biophys. Acta* 1813, 1906–1916.
- Bergwitz, C., Jusseaume, S.A., Luck, M.D., Jüppner, H., and Gardella, T.J. (1997). Residues in the membrane-spanning and extracellular loop regions of the parathyroid hormone (PTH)-2 receptor determine signaling selectivity for PTH and PTH-related peptide. *J. Biol. Chem.* 272, 28861–28868.
- Black, J.W., and Leff, P. (1983). Operational models of pharmacological agonism. *Proc. R. Soc. Lond. B Biol. Sci.* 220, 141–162.
- Coin, I., Katritch, V., Sun, T., Xiang, Z., Siu, F.Y., Beyermann, M., Stevens, R.C., and Wang, L. (2013). Genetically encoded chemical probes in cells reveal the binding path of urocortin-I to CRF class B GPCR. *Cell* 155, 1258–1269.
- Coopman, K., Huang, Y., Johnston, N., Bradley, S.J., Wilkinson, G.F., and Willars, G.B. (2010). Comparative effects of the endogenous agonist glucagon-like peptide-1 (GLP-1)-(7-36) amide and the small-molecule ago-allosteric agent “compound 2” at the GLP-1 receptor. *J. Pharmacol. Exp. Ther.* 334, 795–808.
- Couvineau, A., and Laburthe, M. (2012). The family B1 GPCR: structural aspects and interaction with accessory proteins. *Curr. Drug Targets* 13, 103–115.
- De Lean, A., Stadel, J.M., and Lefkowitz, R.J. (1980). A ternary complex model explains the agonist-specific binding properties of the adenylate cyclase-coupled beta-adrenergic receptor. *J. Biol. Chem.* 255, 7108–7117.
- Dong, M., Xu, X., Ball, A.M., Makhoul, J.A., Lam, P.C., Pinon, D.I., Orry, A., Sexton, P.M., Abagyan, R., and Miller, L.J. (2012). Mapping spatial approximations between the amino terminus of secretin and each of the extracellular loops of its receptor using cysteine trapping. *FASEB J.* 26, 5092–5105.
- Fredriksson, R., Lagerström, M.C., Lundin, L.G., and Schiöth, H.B. (2003). The G-protein-coupled receptors in the human genome form five main families. Phylogenetic analysis, paralogon groups, and fingerprints. *Mol. Pharmacol.* 63, 1256–1272.
- Hollenstein, K., Kean, J., Bortolato, A., Cheng, R.K., Doré, A.S., Jazayeri, A., Cooke, R.M., Weir, M., and Marshall, F.H. (2013). Structure of class B GPCR corticotropin-releasing factor receptor 1. *Nature* 499, 438–443.
- Katritch, V., Cherezov, V., and Stevens, R.C. (2013). Structure-function of the G protein-coupled receptor superfamily. *Annu. Rev. Pharmacol. Toxicol.* 53, 531–556.
- Kenakin, T., and Christopoulos, A. (2013). Signalling bias in new drug discovery: detection, quantification and therapeutic impact. *Nat. Rev. Drug Discov.* 12, 205–216.
- Koole, C., Wootten, D., Simms, J., Valant, C., Sridhar, R., Woodman, O.L., Miller, L.J., Summers, R.J., Christopoulos, A., and Sexton, P.M. (2010). Allosteric ligands of the glucagon-like peptide 1 receptor (GLP-1R) differentially modulate endogenous and exogenous peptide responses in a pathway-selective manner: implications for drug screening. *Mol. Pharmacol.* 78, 456–465.
- Koole, C., Wootten, D., Simms, J., Miller, L.J., Christopoulos, A., and Sexton, P.M. (2012). Second extracellular loop of human glucagon-like peptide-1 receptor (GLP-1R) has a critical role in GLP-1 peptide binding and receptor activation. *J. Biol. Chem.* 287, 3642–3658.
- Koth, C.M., Murray, J.M., Mukund, S., Madjidi, A., Minn, A., Clarke, H.J., Wong, T., Chiang, V., Luis, E., Estevez, A., et al. (2012). Molecular basis for negative regulation of the glucagon receptor. *Proc. Natl. Acad. Sci. USA* 109, 14393–14398.
- Overington, J.P., Al-Lazikani, B., and Hopkins, A.L. (2006). How many drug targets are there? *Nat. Rev. Drug Discov.* 5, 993–996.
- Pal, K., Melcher, K., and Xu, H.E. (2012). Structure and mechanism for recognition of peptide hormones by class B G-protein-coupled receptors. *Acta Pharmacol. Sin.* 33, 300–311.
- Reid, T.S. (2013). Practical use of glucagon-like peptide-1 receptor agonist therapy in primary care. *Clin. Diabetes* 31, 148–157.
- Siu, F.Y., He, M., de Graaf, C., Han, G.W., Yang, D., Zhang, Z., Zhou, C., Xu, Q., Wacker, D., Joseph, J.S., et al. (2013). Structure of the human glucagon class B G-protein-coupled receptor. *Nature* 499, 444–449.
- Wootten, D., Savage, E.E., Willard, F.S., Bueno, A.B., Sloop, K.W., Christopoulos, A., and Sexton, P.M. (2013a). Differential activation and modulation of the glucagon-like peptide-1 receptor by small molecule ligands. *Mol. Pharmacol.* 83, 822–834.
- Wootten, D., Simms, J., Miller, L.J., Christopoulos, A., and Sexton, P.M. (2013b). Polar transmembrane interactions drive formation of ligand-specific and signal pathway-biased family B G protein-coupled receptor conformations. *Proc. Natl. Acad. Sci. USA* 110, 5211–5216.
- Wootten, D., Reynolds, C.A., Koole, C., Smith, K.J., Mobarec, J.C., Simms, J., Quon, T., Coudrat, T., Furness, S.G.B., Miller, L.J., et al. (2016). A hydrogen-bonded polar network in the core of the glucagon-like peptide-1 receptor is a fulcrum for biased agonism: Lessons from class B crystal structures. *Mol. Pharmacol.* 89, 335–347.
- Zhang, H., Sturchler, E., Zhu, J., Nieto, A., Cistrone, P.A., Xie, J., He, L., Yea, K., Jones, T., Turn, R., et al. (2015). Autocrine selection of a GLP-1R G-protein biased agonist with potent antidiabetic effects. *Nat. Commun.* 6, 8918.



Key interactions by conserved polar amino acids located at the transmembrane helical boundaries in Class B GPCRs modulate activation, effector specificity and biased signalling in the glucagon-like peptide-1 receptor



Denise Wootten^{a,*}, Christopher A. Reynolds^b, Kevin J. Smith^b, Juan C. Mobarec^b, Sebastian G.B. Furness^a, Laurence J. Miller^c, Arthur Christopoulos^a, Patrick M. Sexton^{a,*}

^a Drug Discovery Biology, Monash Institute of Pharmaceutical Sciences and Department of Pharmacology, Monash University, Parkville, Victoria 3052, Australia

^b School of Biological Sciences, University of Essex, Wivenhoe Park, Colchester CO4 3SQ, UK

^c Department of Molecular Pharmacology and Experimental Therapeutics, Mayo Clinic, Scottsdale, AZ 85259, USA

ARTICLE INFO

Article history:

Received 22 June 2016

Accepted 15 August 2016

Available online 26 August 2016

Keywords:

Glucagon-like peptide-1 receptor

Biased agonism

G protein-coupled receptor

Cell signaling

ABSTRACT

Class B GPCRs can activate multiple signalling effectors with the potential to exhibit biased agonism in response to ligand stimulation. Previously, we highlighted key TM domain polar amino acids that were crucial for the function of the GLP-1 receptor, a key therapeutic target for diabetes and obesity. Using a combination of mutagenesis, pharmacological characterisation, mathematical and computational molecular modelling, this study identifies additional highly conserved polar residues located towards the TM helical boundaries of Class B GPCRs that are important for GLP-1 receptor stability and/or controlling signalling specificity and biased agonism. This includes (i) three positively charged residues (R3.30²²⁷, K4.64²⁸⁸, R5.40³¹⁰) located at the extracellular boundaries of TMs 3, 4 and 5 that are predicted in molecular models to stabilise extracellular loop 2, a crucial domain for ligand affinity and receptor activation; (ii) a predicted hydrogen bond network between residues located in TMs 2 (R2.46¹⁷⁶), 6 (R6.37³⁴⁸) and 7 (N7.61⁴⁰⁶ and E7.63⁴⁰⁸) at the cytoplasmic face of the receptor that is important for stabilising the inactive receptor and directing signalling specificity, (iii) residues at the bottom of TM 5 (R5.56³²⁶) and TM6 (K6.35³⁴⁶ and K6.40³⁵¹) that are crucial for receptor activation and downstream signalling; (iv) residues predicted to be involved in stabilisation of TM4 (N2.52¹⁸² and Y3.52²⁵⁰) that also influence cell signalling. Collectively, this work expands our understanding of peptide-mediated signalling by the GLP-1 receptor.

© 2016 The Authors. Published by Elsevier Inc. This is an open access article under the CC BY license (<http://creativecommons.org/licenses/by/4.0/>).

1. Introduction

GPCRs mediate signal transduction across cell membranes in response to a wide range of extracellular stimuli [43]. Understand-

Abbreviations: cAMP, 3',5'-cyclic adenosine monophosphate; CHO, Chinese hamster ovary; CRF1R, corticotrophin releasing factor receptor-1; DMEM, Dulbecco's modified Eagle medium; FBS, fetal bovine serum; GCGR, glucagon receptor; GLP-1, glucagon-like peptide-1; GPCR, G protein-coupled receptor; Ca^{2+} , intracellular calcium; pERK, extracellular signal-regulated kinase 1 and 2 phosphorylation; PBS, phosphate buffered saline; TM, transmembrane helix.

* Corresponding authors at: Drug Discovery Biology, Monash Institute of Pharmaceutical Sciences, Monash University, 381 Royal Parade, Parkville, Victoria 3052, Australia.

E-mail addresses: denise.wootten@monash.edu (D. Wootten), patrick.sexton@monash.edu (P.M. Sexton).

<http://dx.doi.org/10.1016/j.bcp.2016.08.015>

0006-2952/© 2016 The Authors. Published by Elsevier Inc.

This is an open access article under the CC BY license (<http://creativecommons.org/licenses/by/4.0/>).

ing how these receptors function at the molecular level requires knowledge of how agonist binding is converted to receptor activation and consequently stimulation of downstream signalling cascades that can be both G protein-dependent and G protein-independent [37]. GPCRs are dynamic proteins that can explore multiple conformational states and with the advances in GPCR structural biology, new insights into the structural basis of GPCR activation have revealed the importance of inter-connected networks of residues for conformational transitions that allow agonist bound receptors to activate intracellular signalling cascades [29,40].

Sequence alignments of related membrane proteins suggest that polar residues are under evolutionary pressure for conservation and hence maintain common structural and functional roles [25,26]. In support of this, there are a number of highly conserved

polar residues present in Class A GPCRs that participate in key interactions associated with their activation [4,5,42]. Class B GPCRs typically contain more conserved polar residues in their transmembrane (TM) bundle than Class A GPCRs, which may be reflective of the diversity of receptors/ligands found within the Class A subfamily, however, it may also reflect the mode by which Class B ligands bind and activate their receptors. Peptide ligands associate primarily with the large extracellular N-terminal domain of Class B GPCRs, but also need to interact with the TM bundle to promote receptor activation [6,47,48,41]. Previously, we revealed the importance of networks of conserved polar residues located in the TM bundle of Class B GPCRs for controlling receptor activation and downstream signalling of the glucagon-like peptide-1 receptor (GLP-1R) [64,66,68]. This receptor plays an essential role in nutrient regulated insulin release, and has emerged as a major target for therapeutic treatment of type 2 diabetes and obesity. The GLP-1R is pleiotropically coupled to multiple signalling pathways with evidence for biased agonism by the physiological ligand oxyntomodulin, clinically used peptide mimetics and synthetic non-peptide ligands, relative to the cognate agonist GLP-1 [33,65,67]. In our previous studies, we identified conserved buried polar residues were not only important in receptor activation, but that some of these residues were also important for biased agonism at this receptor. The breakthrough crystal structures of the inactive TM domain of two Class B GPCRs (the glucagon receptor (GCGR) and the corticotrophin releasing factor receptor-1 (CRF1R)) that were subsequently published, largely supported the predictions and conclusions from the molecular modelling in these studies, highlighting that these conserved residues may form conserved hydrogen bond networks that are important for activation transition of all members of this class of GPCRs [22,49].

The high resolution TM domain structures have provided better structural templates for Class B GPCR modelling and enabled the generation of a homology model of the inactive state of the GLP-1R TM bundle [64,68]. In addition to the hydrogen bond networks predicted in our previous model, the new model identified another network of residues in the inactive GLP-1R. This was formed between conserved Class B polar residues located within TMs 2, 6 and 7 at the intracellular face of the receptor and was also evident in the crystal structures of the GCGR and the CRF1R [22,49]. In addition to participation in hydrogen bond networks, polar side chains located within the TM bundle of GPCRs can have other important functions. These include the formation of interactions with ligands or effectors and their ability to snorkel out towards phospholipid head groups, thereby stabilising TM helices within the bilayer [51]. These functions of polar TM residues are often (although not always) limited to residues that reside either towards the extracellular or intracellular TM boundaries. While our earlier studies on the GLP-1R focused on conserved polar residues that our original model predicted to reside in water-mediated hydrogen bond interaction networks, or in the central region of the TM bundle forming helical packing interactions, this current study explores the roles of the remaining conserved Class B GPCR TM polar residues, which are predicted to reside close to the TM boundaries (Fig. 1). This set of residues includes the amino acids located within the additional hydrogen bond network at the intracellular face of Class B GPCRs. We have assessed the role of these residues on GLP-1R function using a combination of mutagenesis, molecular modelling and pharmacological characterisation of multiple ligands for affinity and activation of three signalling endpoints. This identified residues important for ligand affinity, receptor folding and those contributing to biased agonism, expanding the current understanding of the functional role of highly conserved polar residues within Class B GPCRs.

2. Materials and methods

2.1. Materials

Dulbecco's modified Eagle's medium (DMEM), hygromycin-B and Fluo-4 acetoxymethyl (AM) ester were purchased from Invitrogen (Carlsbad, CA, USA). Foetal bovine serum (FBS) was purchased from Thermo Fisher Scientific (Melbourne, VIC, Australia). The QuikChange™ site-directed mutagenesis kit was purchased from Stratagene (La Jolla, CA, USA). AlphaScreen™ reagents, Bolton-Hunter reagent [¹²⁵I] and 384-well ProxiPlates were purchased from PerkinElmer Life and Analytical Sciences (Waltham, MA, USA). SureFire™ ERK1/2 reagents were generously supplied by TGR Biosciences (Adelaide, SA, Australia). SigmaFast o-phenylenediamine dihydrochloride (OPD) tablets and antibodies were purchased from Sigma-Aldrich (St. Louis, MO, USA). GLP-1 peptides were purchased from Mimotopes (Clayton, VIC, Australia). All other reagents were purchased from Sigma-Aldrich (St. Louis, MO, USA) or BDH Merck (Melbourne, VIC, Australia) and were of an analytical grade.

2.2. Residue numbering

Throughout, residues were numbered using the numbering system described previously [66], whereby the most conserved residue in each Class B GPCR TM domain was assigned 0.50 with this number preceded by the TM number. Each residue is numbered according to its relative position to the residue at 0.50 in each helix and its absolute residue number is shown in superscript. The relative positions of the residues assessed in this study are shown in Fig. 1B–D.

2.3. Receptor mutagenesis

To study the influence of polar TM amino acids on receptor function, the desired mutations were introduced to an N-terminally double c-myc labelled wildtype human GLP-1R in the pEF5/FRT/V5-DEST destination vector (Invitrogen); this receptor had equivalent pharmacology to the untagged human GLP-1R. Mutagenesis was carried out using oligonucleotides for site-directed mutagenesis purchased from GeneWorks (Hindmarsh, SA, Australia) and the QuikChange™ site-directed mutagenesis kit (Stratagene). Sequences of receptor clones were confirmed by automated sequencing at the Australian Genome Research Facility. Mutated residues and their conservation across human Class B peptide hormone receptors are illustrated in Fig. 1.

2.4. Transfections and cell culture

Wildtype and mutant human GLP-1R were isogenically integrated into FlpIn-Chinese hamster ovary (FlpInCHO) cells (Invitrogen) and selection of receptor-expressing cells was achieved through treatment with 600 µg ml⁻¹ hygromycin-B. Transfected and parental FlpInCHO cells were maintained in DMEM supplemented with 10% heat-inactivated FBS and incubated in a humidified environment at 37 °C in 5% CO₂. For all experiments cells passages 8–20 were used.

2.4.1. Radioligand binding assay

FlpInCHO wildtype and mutant human GLP-1R cells were seeded at a density of 3×10^4 cells/well into 96-well culture plates and incubated overnight at 37 °C in 5% CO₂, and radioligand binding carried out as previously described [32]. Briefly, binding assays were performed on whole cells incubated overnight at 4 °C with 0.05 nM [¹²⁵I]-exendin-4(9–39) tracer and increasing concentrations

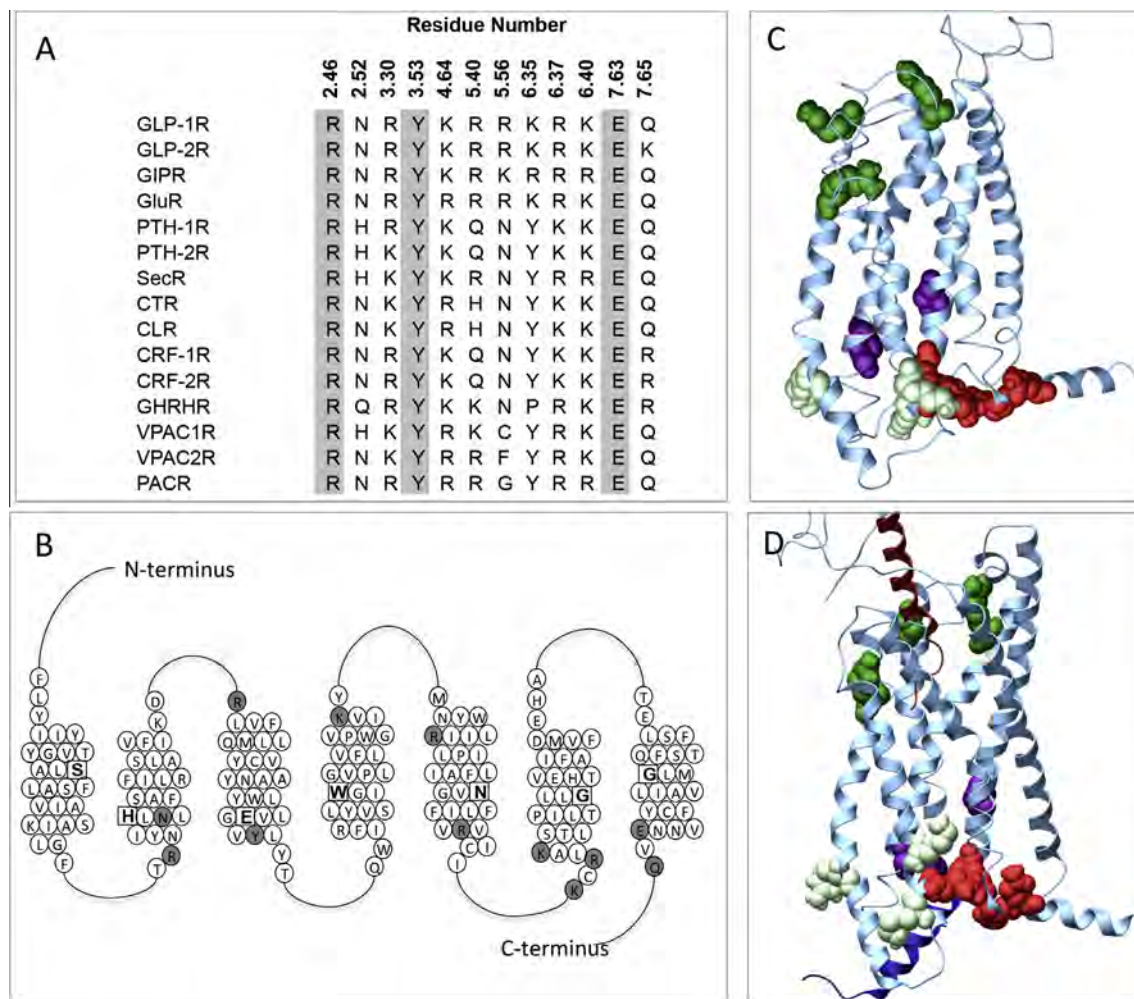


Fig. 1. Conservation and location of polar residues mutated in this study. (A) Conservation of polar residues mutated in this study across the human Class B GPCRs (the secretin-like subclass). Residues absolutely conserved are highlighted in grey. These residues shown are conserved as polar (with the exception of 5.56 and 6.35 where one receptor subtype is not) across all mammalian species of receptor cloned to date. GLP-1R; glucagon-like peptide-1 receptor; GLP-2R; GLP-2 receptor; GIPR, gastric inhibitory polypeptide receptor; GluR, glucagon receptor; PTH-1R, parathyroid hormone receptor 1; PTH-2R, PTH receptor 2; SecR, secretin receptor; CTR, calcitonin receptor; CLR, calcitonin-like receptor; CRF1, corticotropin-releasing factor receptor 1; CRF2, corticotropin-releasing factor receptor 2; GHRHR, GH-releasing hormone receptor; VPAC1R, vasoactive intestinal polypeptide type-1 receptor; VPAC2R, vasoactive intestinal polypeptide type-2 receptor; PACR, pituitary adenylate cyclase activating polypeptide 1 receptor. (B) Schematic representation of the TM domain of the human GLP-1R. The most conserved residue in each helix is highlighted as a square with a bold letter and represent residue 0.50 for that helix. Residues mutated in the present study are shown in grey. (C) Three-dimensional molecular homology model of the inactive TM bundle of the GLP-1R. (D) Three-dimensional molecular model of the TM bundle of the active full length model of the GLP-1R. The bound GLP-1 peptide is shown dipping into the bundle (dark red helix) and the $G_{\alpha s}$ peptide fragment bound at the intracellular face is shown in dark blue. In (C) and (D), side chains mutated in this study are highlighted in space fill with dark green indicating positively charged residues located towards the extracellular face of the bundle and interact with ECL2; pale green, positively charged residues located towards the intracellular face that may interact with lipid headgroups; red, residues in TMs 2, 6 and 7 that form a hydrogen bond network in the apo receptor; purple, residues in TMs 2 and 3 that stabilise interactions with TM4. (For interpretation of the references to colour in this figure legend, the reader is referred to the web version of this article.)

of unlabelled peptide. Cells were washed, solubilised in 0.1 M NaOH and radioactivity determined by γ -counting. For each cell line in all experiments, total binding was defined by 0.05 nM 125 I-exendin-4(9–39) alone, and nonspecific binding was defined by co-incubation with 1 μ M exendin-4(9–39). For analysis, data are normalised to the specific binding for each individual experiment.

2.5. cAMP accumulation assay

FlpInCHO wildtype and mutant human GLP-1R cells were seeded at a density of 3×10^4 cells/well into 96-well culture plates and incubated overnight at 37 °C in 5% CO₂. cAMP assays were carried out as previously described [33]. Briefly, cells were incubated with increasing concentrations of peptide ligands for 30 min at 37 °C in the presence of IBMX. Cells were lysed and cAMP levels

were detected using a cAMP AlphaScreen™ detection kit (PerkinElmer). All values were converted to concentration of cAMP using a cAMP standard curve performed in parallel, and data were subsequently normalised to the response of 100 μ M forskolin in each cell line.

2.6. pERK1/2 assay

FlpInCHO wildtype and mutant human GLP-1R cells were seeded at a density of 3×10^4 cells/well into 96-well culture plates and incubated overnight at 37 °C in 5% CO₂. Ligand-mediated pERK1/2 was determined using the AlphaScreen™ ERK1/2 SureFire™ protocol as previously described [39]. Briefly, cells were serum starved for 6 h prior to assay. Initial pERK1/2 time course experiments were performed over 1 h in the presence of either vehicle or 1 μ M peptide to determine the time at which agonist-mediated

pERK1/2 was maximal. pERK1/2 was detected using the AlphaScreen™ ERK1/2 SureFire™ kit. Subsequent experiments were then performed with increasing concentrations of peptides at the time required to generate a maximal pERK1/2 response using 1 μ M peptide. The kinetics of pERK1/2 response for each mutant receptor was similar to WT, peaking at 6 min. Data were normalised to the maximal response elicited by 10% FBS in each cell line, determined at 6 min (peak FBS response).

2.7. Ca^{2+} mobilisation assay

FlpInCHO wildtype and mutant human GLP-1R cells were seeded at a density of 3×10^4 cells/well into 96-well culture plates and incubated overnight at 37 °C in 5% CO_2 , and receptor-mediated Ca^{2+} mobilisation determined as previously described [61]. Briefly, cells were incubated for 1 h with the cell-permeant Ca^{2+} fluorophore, Fluo-4/AM (10 μ M) in the presence of 2 mM probenecid prior to determining peptide-mediated changes in fluorescence in a Molecular Devices FlexStation (Molecular Devices, Palo Alto, CA, USA). Fluorescence was determined immediately after peptide addition, with an excitation wavelength set to 485 nm and an emission wavelength set to 520 nm, and readings taken every 1.36 s for 120 s. Peak magnitude was calculated using five-point smoothing, followed by correction against basal fluorescence. The kinetics for ligand-mediated Ca^{2+} were not altered by any of the mutations. The peak value was used to create concentration–response curves. Data were normalised to the maximal response elicited by 100 μ M ATP.

2.8. Cell surface receptor expression

FlpInCHO wildtype and mutant human GLP-1R cells, with receptor DNA previously incorporated with an N-terminal double c-myc epitope label, were seeded at a density of 25×10^4 cells/well into 24-well culture plates and incubated overnight at 37 °C in 5% CO_2 , washed three times in $1 \times$ PBS and fixed with 3.7% paraformaldehyde (PFA) at 4 °C for 15 min. Cell surface receptor detection was then performed using a cell surface ELISA protocol to detect the cMyc epitope tag located at the extracellular N-terminus of the receptor, as previously described [32]. Data were normalised to the basal fluorescence detected in FlpInCHO parental cells. Specific ^{125}I -exendin-4(9–39) binding at each receptor mutant, as identification of functional receptors at the cell surface, was also determined (corrected for nonspecific binding using 1 μ M exendin-4(9–39)) as described in [65].

2.9. Molecular modelling

Two GLP-1R models were used to aid interpretation of mutational data; the methods for generation of these models have been described previously [64]. Briefly, the molecular models were constructed in three stages. An NMR structural ensemble of a short, conformationally constrained GLP-1 agonist (equivalent to GLP-1(7–18), pdb code 2NOI [21], was docked into a preliminary TM comparative model of GLP-1R, which was based on the glucagon X-ray crystal structure (PDB code 4L6R, (Sui et al., 2013)), using Glide (v6.9) SP peptide and the OPLS force field [56]. The conformationally constrained peptide was mutated to GLP-1 using PLOP [27]. GLP-1(7–18) was structurally aligned with GLP-1(10–35) co-crystallised with the ECD (PDB code 3IOL [58]), using VMD [24]. Duplicated residues were selectively removed from the complex, thus creating two overlapping templates that were key to combining the TM and ECD domains. These templates and the relevant portions of the X-ray structure of the β_2 -adrenergic receptor: G protein complex [45] were used to generate 2000 full length active GLP-1R (R27–R421) models containing the GLP-1(7–36)-

NH_2 peptide and the C-terminal peptide of the G protein (Gs) (R374–L394) using the comparative modelling programme Modeller 9.16 [16]; the modelling was carried out in the presence of a set of distance constraints as described in [64]. These structures are available from ftp://ftp.essex.ac.uk/pub/oyster/Wootten_JBC_2016/ (username ftp, password anonymous).

2.10. Molecular dynamics simulations

The GLP-1R model was inserted into a hydrated equilibrated palmitoylcholine phosphatidylcholine (POPC) bilayer using the CHARMM-GUI interface [28]. Potassium and chloride ions were added to neutralise the system at an ionic strength of approximately 150 mM. Lipid14 (for POPC), AMBER99SP (for the protein) and TIP3P water model parameters were added using ambertools [7]. The simulations were carried out using ACEMD [19] on a purpose-built metrocube GPU workstation. The system was energy minimised, heated from 0 K to 300 K in the NVT ensemble for 160 ps then simulated in the NPT ensemble, with 10 kcal mol $^{-1}$ Å $^{-2}$ positional harmonic restraints applied to the protein heavy atoms, which were progressively reduced to 0 over the course of 15 ns. Bond lengths to hydrogen atoms were constrained using M-SHAKE [34]. Production simulations were performed in the NPT ensemble at 300 K and 1 atm, using a Langevin thermostat for temperature coupling and a Berendsen barostat for pressure coupling. Non-bonded interactions were cutoff at 10.0 Å, and long-range electrostatic interactions were computed using the particle mesh Ewald method (PME) with dimensions of $86 \times 86 \times 142$ using a spacing of 1.00 Å. The unconstrained simulation was run for 500 ns. Quantitative analysis of the trajectory was conducted in VMD.

2.11. Data analysis

All data were analysed using Prism 6 (GraphPad Software Inc., San Diego, CA, USA). For all analyses the data are unweighted and each y value (mean of replicates for each individual experiment) is considered an individual point. To calculate IC_{50} , EC_{50} and E_{max} values, concentration response signalling data were analysed as previously described [30] using a three-parameter logistic equation. IC_{50} values obtained from binding studies were then corrected for radioligand occupancy as previously described using the radioligand affinity (K_i) experimentally determined for each mutant.

To quantify efficacy in the system, all data were fitted with an operational model of agonism to calculate estimated τ values. τ is the operational measure of efficacy in the system, which incorporates signalling efficacy and receptor density. This model has been extensively described previously [30,66,64]. All estimated τ values were then corrected to cell surface expression (τ_c) as determined by cell surface ELISA and errors propagated from both τ and cell surface expression.

Signalling bias was also quantified as previously described by analysis of concentration–response curves with nonlinear regression using an operational model of agonism, but modified to directly estimate the ratio of τ_c/K_A [30,66,64]. All estimated τ_c/K_A ratios included propagation of error for both τ_c and K_A . Changes in τ_c/K_A ratios with respect to wildtype of each mutant were used to quantitate bias between signalling pathways. Accordingly, bias factors included propagation of error from τ_c/K_A ratios of each pathway.

2.12. Statistics

Changes in peptide affinity, potency, efficacy, cell surface expression and bias of each mutant receptor in comparison to

the wildtype control were statistically analysed with one-way analysis of variance and Dunnett's post test, and significance was accepted at $p < 0.05$.

3. Results

Sequence alignments of the human Class B receptor subtypes reveal 22 conserved polar residues that are predicted to reside either in the TM bundle or at the membrane interface (10 of which are absolutely conserved as the same residue). An additional 2 residues are also very highly conserved in this subfamily (with the exception of 1 receptor subtype for loci 6.35 and 3 receptor subtypes for 5.56). We have previously reported the effects of mutation of 13 of these residues in the GLP-1R [64,66]. In this study we have probed the function of the remaining residues (Fig. 1A). All of these are located at TM helical boundaries/interfaces with loops, with the exception of Q7.65⁴¹⁰ that is located intracellularly within the predicted helix 8 (H8) at the bottom of TM7 (Fig. 1B–D). Each residue was individually mutated to Ala, verified by DNA sequencing and analysed for the effect of mutation on receptor function.

Wildtype and mutant human GLP-1Rs were isogenically integrated into FlpInCHO host cells by recombination that allows for direct comparison of cell surface expression as there should not be variations that arise due to differences in gene transcription. Cell surface expression was assessed by both antibody detection of the N-terminal double c-myc epitope label using ELISA and whole cell binding using [¹²⁵I]-exendin-4(9–39) (Table 1). A number of mutations resulted in significantly altered cell surface expression relative to the wildtype receptor, with consistent expression changes observed using both methods. Whole cell equilibrium competition binding studies were used to assess orthosteric peptide ligand affinities for the wildtype and each of the mutant GLP-1Rs (Table 1). These were performed with the endogenous agonists GLP-1(7–36)NH₂ (GLP-1) and oxyntomodulin, in addition to the exogenous agonist exendin-4 and an antagonist exendin-4(9–39), all in competition with the radiolabelled ligand [¹²⁵I]-exendin-4(9–39). This revealed a number of mutations that globally altered peptide affinity and those that had selective effects of peptide affinity (Table 1).

Activation/strength of coupling to three cellular signalling cascades (cAMP production, ERK1/2 phosphorylation (pERK1/2) and intracellular calcium mobilisation (Ca^{2+})) was evaluated through the generation of concentration–response curves for all receptors

with each peptide agonist (Figs. 2–4). In most cases, mutations that resulted in changes in cell surface expression and/or affinity also produced significant changes on EC₅₀ and/or E_{max} values (Table 2). A direct measure of efficacy via calculation of Log τ_c values allows for direct comparison of receptor activation of individual intracellular signalling pathways at the different receptor mutants compared to the wildtype receptor, independently of their ligand affinity and cell surface expression. These were determined by analysing all concentration–response curves using an operational model of agonism to determine relative signalling efficacy estimates (log τ values) that were corrected to different receptor expression levels by normalisation to what they would be if the mutant receptor were expressed at the same level as the wildtype (log τ_c values, Table 3). Cell surface expression data obtained from antibody binding were used for this correction instead of the Bmax from ligand binding studies, as one mutant showed no detectable radioligand binding, however correction with Bmax yielded similar efficacy values (data not shown). In addition, functional affinities (LogK_A) that describe the affinity of the receptor when coupled to a given signalling pathway were also derived from the operational analysis (Table 4). The assessment of multiple signalling pathways also provided the ability to measure the signal bias of mutant receptors relative to the wildtype to obtain a quantitative measure of the relative bias between two pathways (Table 5, Fig. 5).

To aid in interpretation of the experimental data, we used our two published GLP-1R models [64]; an inactive apo model of the TM bundle only and a GLP-1R:GLP-1:G_{αs} complex that was generated using multiple structural templates (Fig. 1C–D). The combined results from expression, affinity and efficacy data (derived from the concentration–response curves) are presented in detail in the context of the predicted locations of mutated residues within these molecular models, clustering those located close in 3D space.

3.1. Three conserved positively charged residues located at the extracellular ends of TM helices 3, 4 and 5 are essential for high affinity agonist binding and conformational transitions linked to pleiotropic effector coupling through stabilisation of ECL2

Three highly conserved positively charged residues, R3.30²²⁷, K4.64²⁸⁸ and R5.40³¹⁰, located close to the extracellular surface of the GLP-1R are predicted to form direct interactions with residues in ECL2 in the apo and peptide bound models (Fig. 6). R3.30²²⁷ is predicted to interact within the proximal region of

Table 1
Effects of mutation on GLP-1R peptide ligand affinities and cell surface expression. Mutant and WT GLP-1Rs were stably expressed in ChoFlpIn cells and agonist affinities determined by equilibrium competition binding using [¹²⁵I]-exendin-4(9–39). Ligand affinities were determined using a three-parameter logistic equation and values are expressed as mean \pm S.E.M of four to six independent experiments, conducted in duplicate. Cell surface expression was measured by ELISA against the c-myc epitope and by saturation binding, both normalised to the wildtype receptor. All data are expressed as mean \pm S.E.M of four to six independent experiments, conducted in duplicate. Differences in affinity or expression were analysed with one-way analysis of variance (compared to the wildtype receptor) and Dunnett's post test ($p < 0.05$). ND means data were unable to be experimentally defined.

Receptor construct	Ligand binding affinity (pKi)				Cell surface expression	
	GLP-1(7–36)NH ₂	Oxyntomodulin	Exendin-4	Exendin-4(9–39)	ELISA	Bmax
Wildtype	8.67 \pm 0.05	7.26 \pm 0.04	8.87 \pm 0.04	8.11 \pm 0.04	100 \pm 1	100 \pm 2
R2.46 ¹⁷⁶ A	8.40 \pm 0.07	7.28 \pm 0.08	8.61 \pm 0.11	8.17 \pm 0.08	66 \pm 2*	72 \pm 1*
N2.52 ¹⁸² A	ND	ND	ND	ND	39 \pm 5*	ND
R3.30 ²²⁷ A	7.41 \pm 0.08*	6.69 \pm 0.12*	7.60 \pm 0.09*	8.52 \pm 0.08*	95 \pm 4	83 \pm 2
Y3.53 ²⁵⁰ A	8.49 \pm 0.09	6.99 \pm 0.24	8.68 \pm 0.23	7.94 \pm 0.06	82 \pm 8	97 \pm 4
K4.64 ²⁸⁸ A	6.90 \pm 0.08*	6.29 \pm 0.07*	7.39 \pm 0.05*	8.16 \pm 0.05	107 \pm 3	116 \pm 2
R5.40 ³¹⁰ A	7.45 \pm 0.12*	6.11 \pm 0.08*	7.99 \pm 0.11*	7.87 \pm 0.14	40 \pm 8*	23 \pm 3*
R5.56 ³²⁶ A	8.51 \pm 0.09	7.22 \pm 0.06	8.59 \pm 0.07	8.09 \pm 0.08	112 \pm 10	141 \pm 3*
K6.35 ³⁴⁶ A	9.20 \pm 0.07*	7.68 \pm 0.05	9.34 \pm 0.06*	8.37 \pm 0.04	175 \pm 13*	159 \pm 5*
R6.37 ³⁴⁸ A	8.38 \pm 0.08	7.21 \pm 0.08	8.80 \pm 0.08	7.98 \pm 0.08	57 \pm 4*	60 \pm 1*
K6.40 ³⁵¹ A	8.39 \pm 0.07	7.25 \pm 0.14	8.92 \pm 0.06	7.76 \pm 0.08*	81 \pm 3	76 \pm 2
E7.63 ⁴⁰⁸ A	8.62 \pm 0.12	7.34 \pm 0.09	8.29 \pm 0.11*	8.12 \pm 0.07	59 \pm 5*	45 \pm 4*
Q7.65 ⁴¹⁰ A	8.72 \pm 0.09	7.22 \pm 0.05	9.08 \pm 0.09	8.39 \pm 0.06	71 \pm 5*	78 \pm 7

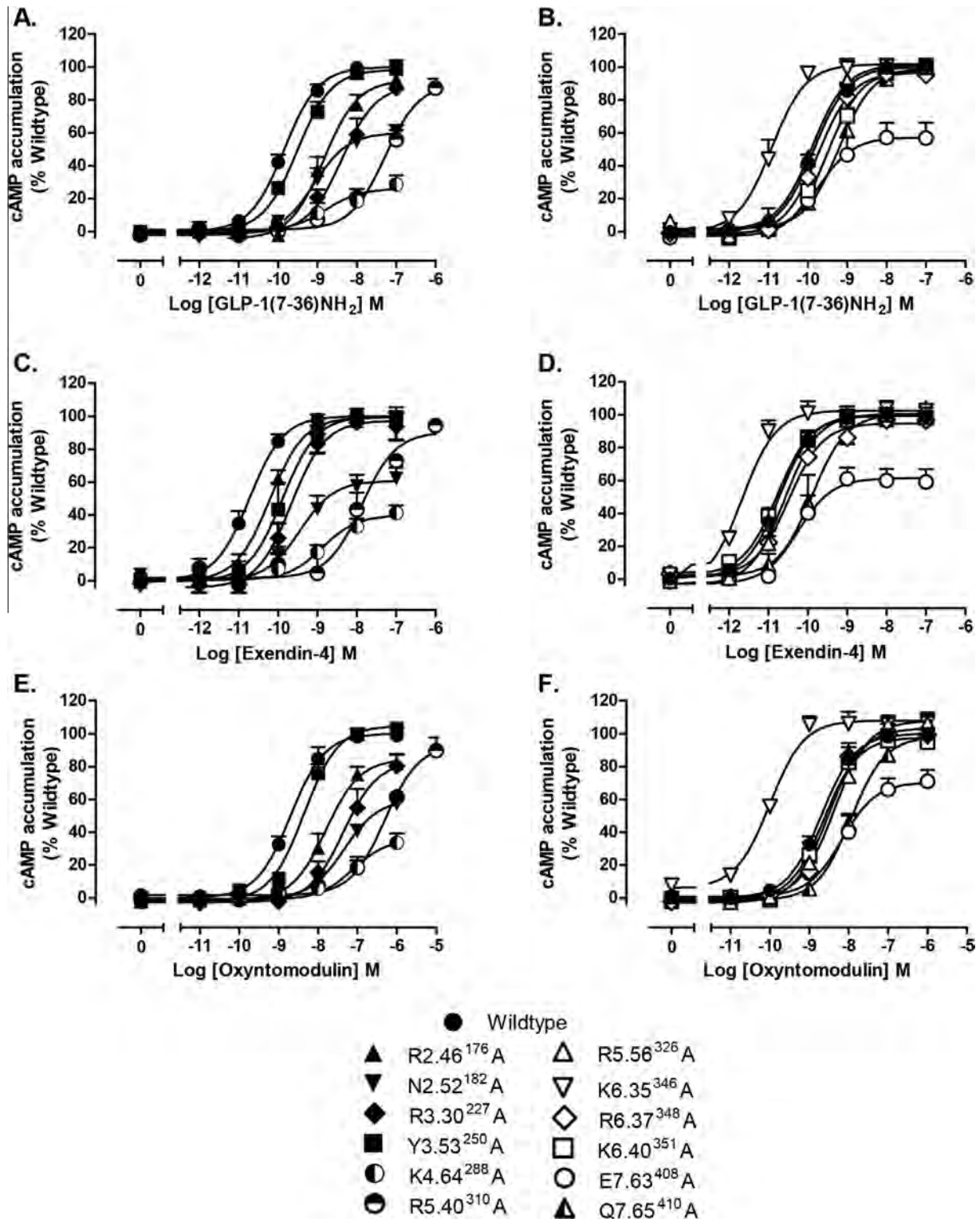


Fig. 2. cAMP concentration–response curves for polar TM boundary Ala mutants. Concentration–response curves for cAMP accumulation of wildtype and mutant receptors stimulated by GLP-1 (A, B), exendin-4 (C, D) or oxyntomodulin (E, F) in CHOFlpIn cells stably expressing wildtype or mutant receptors. Data are normalised to the response elicited by the wildtype receptor and analysed with an operational model agonism. All values are mean \pm S.E.M of four to six independent experiments, conducted in duplicate.

ECL2 near to the top of TM4 in both the apo model and the GLP-1 bound model (Fig. 6). K4.64²⁸⁸ forms interactions at the opposite end of ECL2, close to the top of TM5 in the apo receptor and forms multiple interactions with ECL2 in the GLP-1 peptide bound model.

In both inactive and active models, R5.40³¹⁰ resides close to N300 that is also predicted to form a direct interaction with GLP-1. R5.40³¹⁰ also resides close to His⁷ of GLP-1 in the active model where it may form a direct interaction (Fig. 6). MD simulations per-

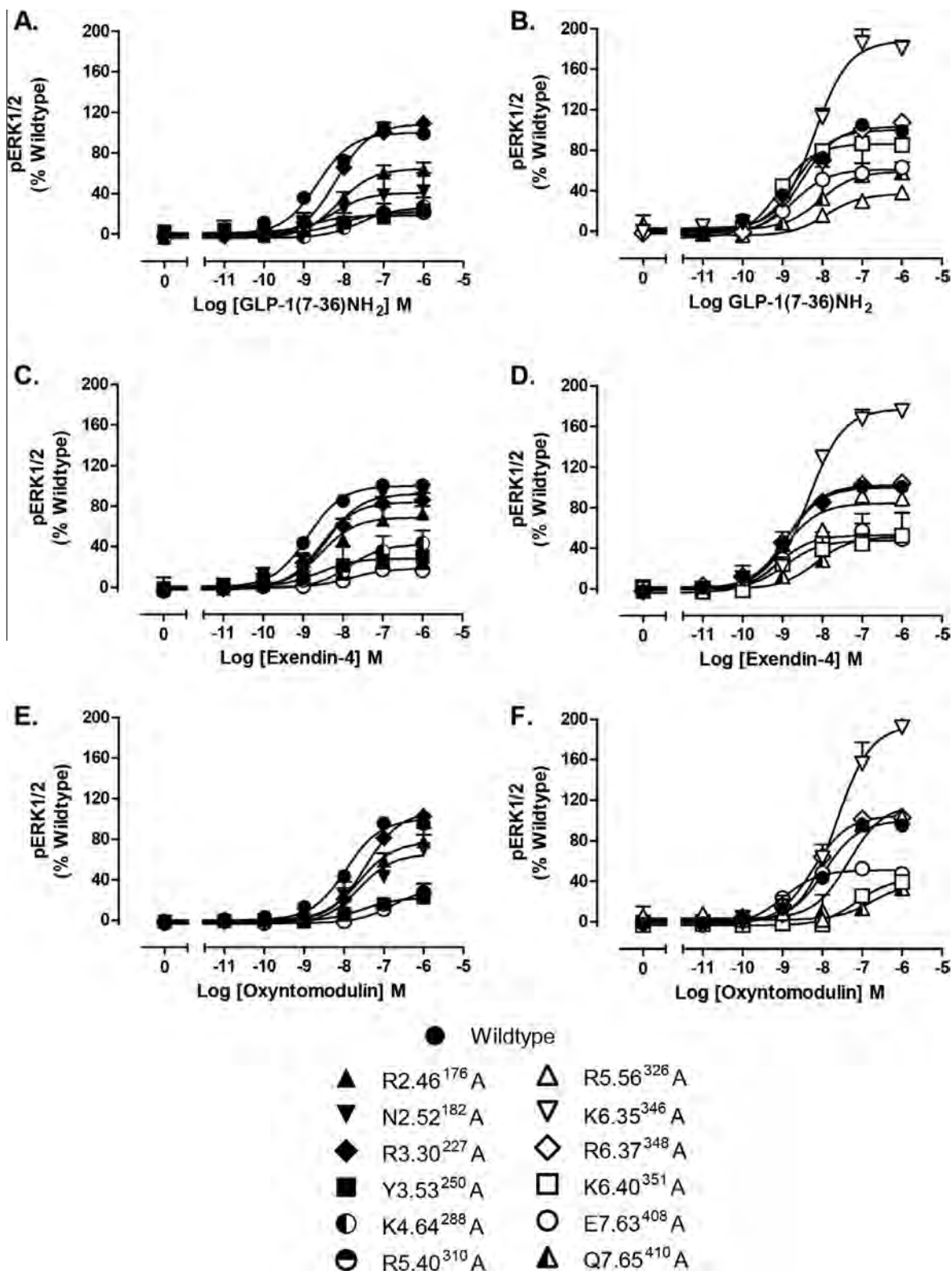


Fig. 3. pERK1/2 concentration–response curves for polar TM boundary Ala mutants. Concentration–response curves of pERK of wildtype and mutant receptors stimulated by GLP-1 (A, B), exendin-4 (C, D) or oxyntomodulin (E, F) in CHOFlpIn cells stably expressing wildtype or mutant receptors. Data are normalised to the response elicited by the wildtype and analysed with an operational model agonism. All values are mean \pm S.E.M of four to six independent experiments, conducted in duplicate.

formed on this static GLP-1 bound active model revealed that R5.40³¹⁰ forms transient hydrogen bond interactions with both N300 in ECL2 and His⁷ of GLP-1 in the first 360 ns of the MD sim-

ulation, however both of these interactions are lost towards the end of the simulation with R5.40³¹⁰ forming a direct interaction with E6.53³⁶⁴ in TM6 (Fig. 7).

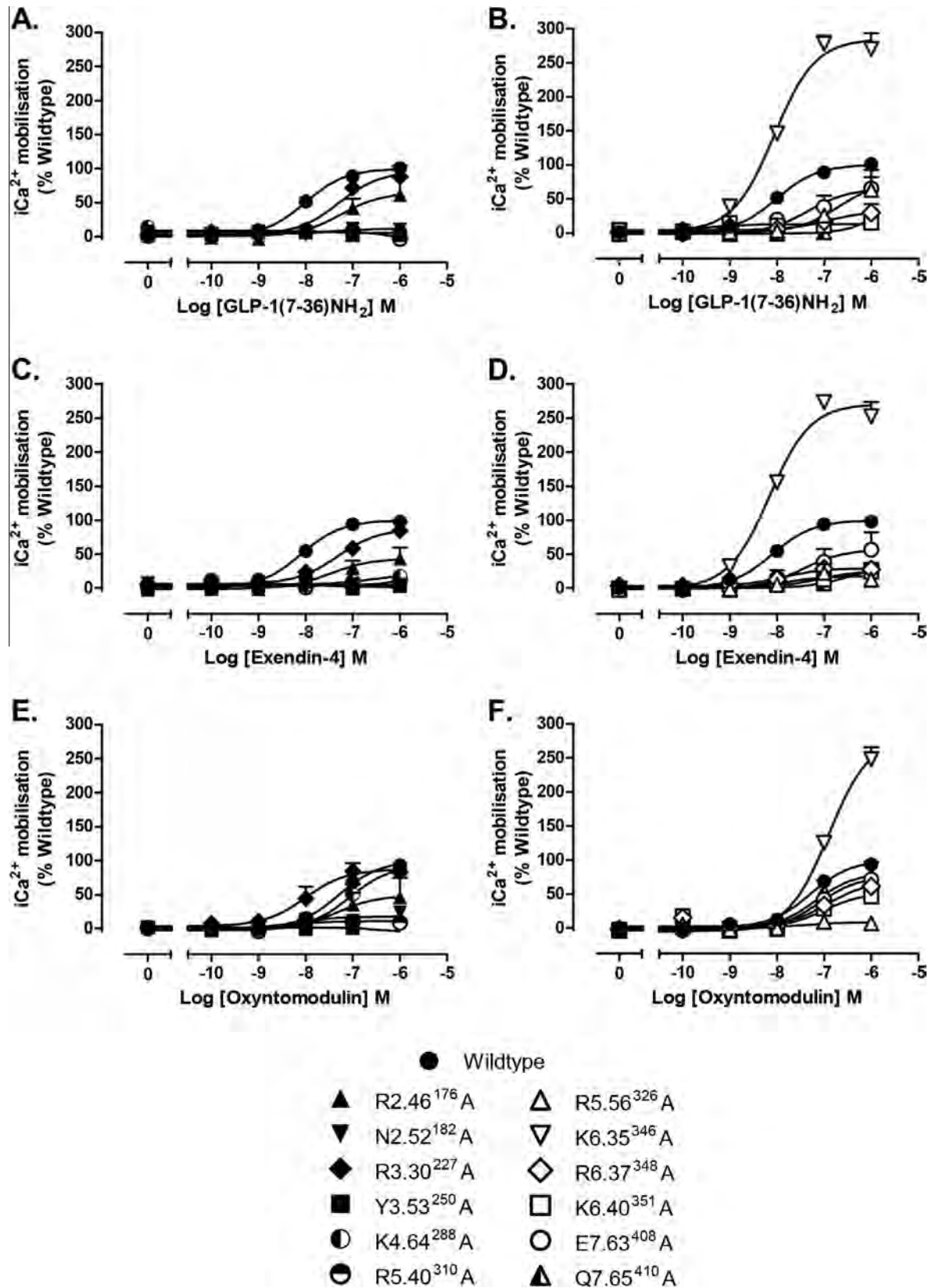


Fig. 4. iCa^{2+} mobilisation concentration–response curves for polar TM boundary Ala mutants. Concentration–response curves of iCa^{2+} mobilisation of wildtype and mutant receptors stimulated by GLP-1 (A, B), exendin-4 (C, D) or oxyntomodulin (E, F) in CHO/Pln cells stably expressing wildtype or mutant receptors. Data are normalised to the response elicited by the wildtype and analysed with an operational model agonism. All values are mean \pm S.E.M of four to six independent experiments, conducted in duplicate.

Table 2

Effects of mutation on GLP-1R peptide concentration response in cAMP, pERK1/2 and Ca^{2+} mobilisation. Mutant and WT GLP-1Rs were stably expressed in CHOFlpIn cells and concentration–response curves were generated in each pathway for the three agonists. pEC_{50} and E_{max} values were determined using a three-parameter logistic equation and values are expressed as mean \pm S.E.M. of four to six independent experiments, conducted in duplicate. Differences in pEC_{50} or E_{max} were analysed with one-way analysis of variance (compared to the wildtype receptor) and Dunnett's post test ($p < 0.05$). ND means data were unable to be experimentally defined.

Signalling pathway	Receptor construct	GLP-1		Oxyntomodulin		Exendin-4	
		pEC_{50}	E_{max} (% WT)	pEC_{50}	E_{max} (% WT)	pEC_{50}	E_{max} (% WT)
cAMP	Wildtype	9.84 ± 0.06	100 ± 2	8.70 ± 0.08	100 ± 3	10.7 ± 0.08	100 ± 2
	R2.46 ¹⁷⁶ A	$8.84 \pm 0.09^*$	92 ± 4	$7.80 \pm 0.10^*$	$85 \pm 4^*$	$10.2 \pm 0.09^*$	99 ± 3
	N2.52 ¹⁸² A	$9.09 \pm 0.12^*$	$60 \pm 3^*$	$7.37 \pm 0.14^*$	$60 \pm 4^*$	$9.49 \pm 0.19^*$	$61 \pm 4^*$
	R3.30 ²²⁷ A	$8.38 \pm 0.12^*$	89 ± 5	$7.35 \pm 0.15^*$	$83 \pm 6^*$	$9.70 \pm 0.12^*$	97 ± 1
	Y3.53 ²⁵⁰ A	9.51 ± 0.08	98 ± 3	8.35 ± 0.06	105 ± 3	$9.89 \pm 0.13^*$	100 ± 4
	K4.64 ²⁸⁸ A	$8.78 \pm 0.38^*$	$26 \pm 4^*$	$7.12 \pm 0.23^*$	$36 \pm 5^*$	$8.87 \pm 0.17^*$	$40 \pm 3^*$
	R5.40 ³¹⁰ A	$7.28 \pm 0.09^*$	89 ± 4	$6.30 \pm 0.08^*$	93 ± 4	$7.88 \pm 0.19^*$	90 ± 7
	R5.56 ³²⁶ A	9.90 ± 0.06	101 ± 2	8.37 ± 0.07	108 ± 3	10.6 ± 0.09	100 ± 4
	K6.35 ³⁴⁶ A	$10.9 \pm 0.11^*$	102 ± 3	$10.0 \pm 0.08^*$	108 ± 2	$11.6 \pm 0.13^*$	103 ± 3
	R6.37 ³⁴⁸ A	9.74 ± 0.09	97 ± 3	8.52 ± 0.09	103 ± 3	10.5 ± 0.16	95 ± 4
	K6.40 ³⁵¹ A	9.50 ± 0.14	98 ± 5	8.63 ± 0.07	98 ± 3	10.8 ± 0.08	99 ± 2
	E7.63 ⁴⁰⁸ A	9.70 ± 0.24	$57 \pm 5^*$	$8.17 \pm 0.16^*$	$70 \pm 4^*$	10.3 ± 0.20	$61 \pm 4^*$
	Q7.65 ⁴¹⁰ A	$9.21 \pm 0.13^*$	100 ± 5	$7.94 \pm 0.06^*$	98 ± 2	$9.89 \pm 0.15^*$	100 ± 5
pERK1/2	Wildtype	8.65 ± 0.07	100 ± 2	7.95 ± 0.05	100 ± 2	8.88 ± 0.04	100 ± 1
	R2.46 ¹⁷⁶ A	8.14 ± 0.12	$64 \pm 3^*$	7.61 ± 0.14	77 ± 5	8.54 ± 0.25	$69 \pm 6^*$
	N2.52 ¹⁸² A	8.30 ± 0.51	$41 \pm 8^*$	7.63 ± 0.36	$66 \pm 11^*$	8.41 ± 0.13	92 ± 4
	R3.30 ²²⁷ A	8.20 ± 0.10	109 ± 4	7.46 ± 0.07	107 ± 3	8.57 ± 0.12	84 ± 4
	Y3.53 ²⁵⁰ A	8.80 ± 0.91	$18 \pm 5^*$	7.53 ± 0.21	$22 \pm 2^*$	8.58 ± 0.98	$28 \pm 9^*$
	K4.64 ²⁸⁸ A	7.61 ± 0.25	$26 \pm 3^*$	7.54 ± 0.22	$21 \pm 3^*$	7.85 ± 0.13	$42 \pm 2^*$
	R5.40 ³¹⁰ A	8.03 ± 0.48	$22 \pm 4^*$	$6.81 \pm 0.25^*$	$32 \pm 5^*$	7.80 ± 0.63	$18 \pm 5^*$
	R5.56 ³²⁶ A	7.91 ± 0.07	$37 \pm 1^*$	7.34 ± 0.20	116 ± 4	8.95 ± 0.13	84 ± 4
	K6.35 ³⁴⁶ A	8.20 ± 0.07	$188 \pm 5^*$	7.66 ± 0.10	$194 \pm 9^*$	8.34 ± 0.07	$177 \pm 5^*$
	R6.37 ³⁴⁸ A	8.51 ± 0.08	103 ± 3	8.25 ± 0.09	105 ± 4	8.89 ± 0.11	102 ± 4
	K6.40 ³⁵¹ A	9.08 ± 0.08	86 ± 3	7.14 ± 0.11	$43 \pm 3^*$	8.92 ± 0.24	$47 \pm 4^*$
	E7.63 ⁴⁰⁸ A	8.71 ± 0.24	$61 \pm 5^*$	$8.99 \pm 0.11^*$	$51 \pm 2^*$	9.14 ± 0.17	$53 \pm 3^*$
	Q7.65 ⁴¹⁰ A	8.07 ± 0.43	$59 \pm 10^*$	$6.74 \pm 0.59^*$	$39 \pm 14^*$	8.16 ± 0.49	$51 \pm 10^{*PII}$
Ca^{2+}	Wildtype	8.01 ± 0.09	100 ± 4	7.29 ± 0.11	100 ± 6	8.10 ± 0.06	100 ± 3
	R2.46 ¹⁷⁶ A	7.25 ± 0.38	$65 \pm 12^*$	7.36 ± 0.56	$49 \pm 14^*$	7.48 ± 0.38	$44 \pm 8^*$
	N2.52 ¹⁸² A	ND	ND	ND	ND	ND	ND
	R3.30 ²²⁷ A	7.30 ± 0.20	96 ± 9	8.01 ± 0.22	87 ± 8	7.33 ± 0.19	87 ± 8
	Y3.53 ²⁵⁰ A	ND	ND	ND	ND	ND	ND
	K4.64 ²⁸⁸ A	ND	ND	7.06 ± 0.15	94 ± 8	ND	ND
	R5.40 ³¹⁰ A	ND	ND	ND	ND	ND	ND
	R5.56 ³²⁶ A	6.69 ± 0.27	76 ± 13	ND	ND	7.84 ± 0.64	$18 \pm 5^*$
	K6.35 ³⁴⁶ A	8.06 ± 0.07	$285 \pm 8^*$	6.90 ± 0.06	$281 \pm 10^*$	8.16 ± 0.07	$271 \pm 8^*$
	R6.37 ³⁴⁸ A	6.90 ± 0.48	33 ± 8	6.92 ± 0.19	69 ± 9	7.86 ± 0.32	$30 \pm 3^*$
	K6.40 ³⁵¹ A	ND	ND	7.01 ± 0.27	$53 \pm 11^*$	7.10 ± 0.60	$26 \pm 8^*$
	E7.63 ⁴⁰⁸ A	7.34 ± 0.41	$65 \pm 13^*$	7.11 ± 0.12	77 ± 5	7.46 ± 0.49	$57 \pm 12^*$
	Q7.65 ⁴¹⁰ A	ND	ND [*]	7.18 ± 0.29	82 ± 13	$6.47 \pm 0.58^*$	$34 \pm 15^*$

Mutation of R5.40³¹⁰ (R5.40³¹⁰A) resulted in a receptor that was very poorly expressed at the cell surface (<40% of wildtype), whereas R3.30²²⁷A and K4.64²⁸⁸A were expressed at a similar level to the wildtype receptor (Table 1). All three mutant receptors displayed a marked loss in affinity for peptide agonists (Fig. 6, Table 1). This was greater for GLP-1 and exendin-4 at R3.30²²⁷A (18–19-fold) and K4.64²⁸⁸A (59- and 30-fold, respectively), compared to oxyntomodulin where a 4- and 9-fold loss of affinity was observed, respectively. R5.40³¹⁰A displayed a similar reduction in affinity for all three agonists (8–17-fold). The binding of the antagonist, exendin-4(9–39), was not altered at K4.64²⁸⁸A or R5.40³¹⁰A compared to wildtype, whereas a small, yet significant increase in affinity was measured for R3.30²²⁷A (Table 1).

After correction for changes in expression, R3.30²²⁷A showed similar efficacy for generation of cAMP production and pERK1/2 relative to wildtype for the three peptides (Fig. 6, Table 3). However, there was a small, yet significant increase in efficacy for Ca^{2+} for oxyntomodulin that was not observed with the other two peptide agonists. For R5.40³¹⁰A, a small reduction in cAMP efficacy was observed for GLP-1 and exendin-4, but not oxyntomodulin. In addition, pERK1/2 efficacy was also slightly reduced for exendin-4 and GLP-1 (3–5-fold), but not for oxyntomodulin (Fig. 6, Table 3). In contrast, no detectable Ca^{2+} was evident for

any peptide at R5.40³¹⁰A. K4.64²⁸⁸A impaired cAMP efficacy for all three peptides, but this was greater for GLP-1 and exendin-4 (42–50-fold) compared to oxyntomodulin (18-fold). In addition, there was no detectable calcium response with GLP-1 and exendin-4, although the oxyntomodulin efficacy for this pathway was unaltered. In contrast, all three ligands displayed a similar reduction in pERK1/2 efficacy (7–14-fold) (Fig. 6, Table 3).

Calculation of bias factors revealed that R5.40³¹⁰ did not significantly alter the ability of the receptor to sample between distinct conformations for activation of pERK1/2 and cAMP. Bias could not be calculated relative to Ca^{2+} , as there was no detectable response for this pathway (Fig. 5, Table 5). K4.64²⁸⁸A biased the receptor towards Ca^{2+} over cAMP and pERK1/2 when activated by oxyntomodulin and for exendin-4 towards pERK1/2 relative to cAMP (Fig. 5, Table 5). R3.30²²⁷ significantly biased GLP-1 towards Ca^{2+} over cAMP, with a similar trend for oxyntomodulin and exendin-4 (Fig. 5, Table 5). This trend may not have been predicted from efficacy values alone as, unlike the majority of mutants assessed in this study, the functional K_A values predicted from operational modelling were also altered differentially in the distinct pathways (Table 4). The functional K_A linked to cAMP accumulation tracked with the loss of affinity, however in Ca^{2+} , little reduction in the functional K_A was observed compared to the wildtype receptor.

Table 3

Effects of mutation on GLP-1R coupling efficiency to downstream effectors, cAMP, pERK1/2 and iCa^{2+} mobilisation. Mutant and WT GLP-1Rs were stably expressed in CHOFlpIn cells and concentration–response curves were generated for each construct in each pathway for the three agonists. All data were analysed with an operational model of agonism to determine $\log \tau$ values that define efficacy. All $\log \tau$ values were corrected to cell surface expression data from the ELISA ($\log \tau_c$). Values are expressed as mean \pm S.E.M of four to six independent experiments, conducted in duplicate. Data were analysed with one-way analysis of variance and Dunnett's post test ($p < 0.05$). ND means data were unable to be experimentally defined.

Receptor construct	Log Tau _c								
	cAMP			pERK1/2			iCa^{2+}		
	GLP-1	Oxyntomodulin	Exendin-4	GLP-1	Oxyntomodulin	Exendin-4	GLP-1	Oxyntomodulin	Exendin-4
Wildtype	1.22 \pm 0.09 (17)	0.92 \pm 0.16 (8.4)	1.33 \pm 0.15 (21)	−0.08 \pm 0.03 (0.83)	−0.07 \pm 0.03 (0.84)	−0.09 \pm 0.03 (0.81)	−0.30 \pm 0.04 (0.50)	−0.31 \pm 0.02 (0.49)	−0.31 \pm 0.03 (0.49)
R2.46 ¹⁷⁶ A	0.72 \pm 0.21 (5.3)	0.49 \pm 0.11 (3.1)	1.07 \pm 0.07 (12)	−0.29 \pm 0.05 (0.52)	−0.09 \pm 0.06 (0.80)	−0.28 \pm 0.05 (0.52)	−0.58 \pm 0.12 (0.26)	−0.40 \pm 0.08 (0.40)	−0.62 \pm 0.13 (0.24)
N2.52 ¹⁸² A	0.55 \pm 0.07 (3.5)*	0.48 \pm 0.07 (3.1)	0.55 \pm 0.05 (3.6)*	−0.39 \pm 0.09 (0.41)	0.01 \pm 0.09 (1.03)	0.20 \pm 0.05 (1.58)	ND	ND	ND
R3.30 ²²⁷ A	0.86 \pm 0.17 (7.2)	0.53 \pm 0.12 (3.3)	1.22 \pm 0.10 (17)	0.02 \pm 0.04 (1.05)	0.09 \pm 0.06 (1.23)	−0.22 \pm 0.05 (0.61)	−0.29 \pm 0.07 (0.52)	0.08 \pm 0.04 (1.20)*	−0.34 \pm 0.06 (0.46)
Y3.53 ²⁵⁰ A	1.13 \pm 0.29 (13)	0.93 \pm 0.40 (8.5)	0.99 \pm 0.20 (10)	−1.23 \pm 0.15 (0.06)*	−1.12 \pm 0.16 (0.08)*	−1.16 \pm 0.12 (0.07)*	ND	ND	ND
K4.64 ²⁸⁸ A	−0.47 \pm 0.08 (0.34)*	−0.32 \pm 0.08 (0.48)*	−0.28 \pm 0.05 (0.5)*	−1.11 \pm 0.14 (0.08)*	−1.22 \pm 0.16 (0.06)*	−0.96 \pm 0.09 (0.11)*	ND	−0.40 \pm 0.05 (0.39)	ND
R5.40 ³¹⁰ A	0.67 \pm 0.09 (4.7)*	0.76 \pm 0.06 (5.8)	0.75 \pm 0.06 (5.6)*	−0.55 \pm 0.15 (0.28)	−0.27 \pm 0.29 (0.54)	−0.85 \pm 0.21 (0.14)*	ND	ND	ND
R5.56 ³²⁶ A	1.18 \pm 0.10 (15)	0.91 \pm 0.14 (8.0)	1.12 \pm 0.13 (13)	−1.01 \pm 0.10 (0.10)*	−0.07 \pm 0.08 (0.85)	−0.44 \pm 0.06 (0.36)*	−1.06 \pm 0.17 (0.09)*	ND	−1.09 \pm 0.27 (0.08)*
K6.35 ³⁴⁶ A	1.99 \pm 0.10 (98)*	1.81 \pm 0.24 (66)*	1.93 \pm 0.37 (85)*	0.57 \pm 0.09 (3.72)*	0.35 \pm 0.06 (2.21)	0.68 \pm 0.09 (4.74)*	0.50 \pm 0.20 (3.2)*	0.32 \pm 0.09 (2.1)*	1.12 \pm 0.21 (13)*
R6.37 ³⁴⁸ A	1.36 \pm 0.19 (16)	1.37 \pm 0.35 (23)	1.19 \pm 0.12 (16)	0.12 \pm 0.04 (1.32)	0.20 \pm 0.06 (1.59)	0.13 \pm 0.05 (1.33)	−0.94 \pm 0.21 (0.11)*	−0.16 \pm 0.08 (0.69)	−0.86 \pm 0.04 (0.14)*
K6.40 ³⁵¹ A	1.34 \pm 0.10 (22)	0.95 \pm 0.17 (9.0)	1.38 \pm 0.19 (24)	−0.15 \pm 0.04 (0.71)	−0.82 \pm 0.16 (0.15)*	−0.69 \pm 0.08 (0.20)*	ND	−0.47 \pm 0.11 (0.34)	−1.02 \pm 0.22 (0.10)*
E7.63 ⁴⁰⁸ A	0.44 \pm 0.06 (2.8)*	0.58 \pm 0.07 (3.8)	0.50 \pm 0.05 (3.2)*	−0.19 \pm 0.05 (0.64)	−0.28 \pm 0.07 (0.52)	−0.38 \pm 0.05 (0.42)	−0.23 \pm 0.13 (0.59)	−0.07 \pm 0.06 (0.85)*	−0.33 \pm 0.10 (0.47)
Q7.65 ⁴¹⁰ A	0.97 \pm 0.10 (9.3)	0.67 \pm 0.07 (4.7)	0.96 \pm 0.11 (9.2)	−0.47 \pm 0.07 (0.40)	−0.70 \pm 0.19 (0.20)*	−0.58 \pm 0.09 (0.26)*	ND	−0.22 \pm 0.05 (0.60)	−1.19 \pm 0.17 (0.07)*

Table 4

Effects of mutation on the function K_A derived from operational fitting to cAMP, pERK1/2 and iCa^{2+} mobilisation data. Mutant and WT GLP-1Rs were stably expressed in CHOFlpIn cells and concentration–response curves were generated for each construct in each pathway for the three agonists. All data were analysed with an operational model of agonism (Eq. 2) to determine $\log K_A$ (functional affinity) values. Values are expressed as mean \pm S.E.M of four to six independent experiments, conducted in duplicate. ND means data were unable to be experimentally defined.

Receptor construct	−Log K_A								
	cAMP			pERK1/2			iCa^{2+}		
	GLP-1	Oxyntomodulin	Exendin-4	GLP-1	Oxyntomodulin	Exendin-4	GLP-1	Oxyntomodulin	Exendin-4
Wildtype	8.35 \pm 0.10	7.44 \pm 0.09	9.24 \pm 0.10	7.84 \pm 0.11	7.46 \pm 0.08	8.31 \pm 0.07	7.32 \pm 0.14	7.23 \pm 0.34	7.46 \pm 0.05
R2.46 ¹⁷⁶ A	8.08 \pm 0.22	7.01 \pm 0.10	8.95 \pm 0.36	7.75 \pm 0.14	7.39 \pm 0.13	8.12 \pm 0.09	7.26 \pm 0.13	7.38 \pm 0.04	7.39 \pm 0.12
N2.52 ¹⁸² A	8.50 \pm 0.09	7.13 \pm 0.13	9.16 \pm 0.18	7.91 \pm 0.13	7.40 \pm 0.12	8.21 \pm 0.12	ND	ND	ND
R3.30 ²²⁷ A	7.50 \pm 0.27	6.69 \pm 0.22	8.13 \pm 0.10	6.81 \pm 0.06	6.81 \pm 0.13	7.31 \pm 0.05	6.79 \pm 0.21	7.81 \pm 0.24	6.82 \pm 0.13
Y3.53 ²⁵⁰ A	8.24 \pm 0.10	7.23 \pm 0.22	9.37 \pm 0.10	7.70 \pm 0.11	7.11 \pm 0.08	8.11 \pm 0.19	ND	ND	ND
K4.64 ²⁸⁸ A	6.91 \pm 0.32	6.29 \pm 0.06	8.16 \pm 0.23	7.13 \pm 0.40	7.30 \pm 0.38	7.01 \pm 0.12	ND	6.90 \pm 0.17	ND
R5.40 ³¹⁰ A	7.52 \pm 0.35	6.07 \pm 0.41	7.79 \pm 0.30	7.91 \pm 0.15	6.35 \pm 0.35	7.53 \pm 0.31	ND	ND	ND
R5.56 ³²⁶ A	8.61 \pm 0.13	7.56 \pm 0.17	9.22 \pm 0.13	7.83 \pm 0.11	7.10 \pm 0.28	8.33 \pm 0.41	7.26 \pm 0.17	ND	7.10 \pm 0.19
K6.35 ³⁴⁶ A	9.18 \pm 0.19	7.64 \pm 0.07	9.91 \pm 0.11	8.32 \pm 0.04	7.68 \pm 0.03	8.21 \pm 0.07	7.91 \pm 0.15	7.27 \pm 0.16	7.78 \pm 0.08
R6.37 ³⁴⁸ A	8.53 \pm 0.21	7.43 \pm 0.08	9.37 \pm 0.10	7.73 \pm 0.12	7.39 \pm 0.17	8.35 \pm 0.30	7.50 \pm 0.14	7.01 \pm 0.10	7.08 \pm 0.09
K6.40 ³⁵¹ A	8.14 \pm 0.23	7.48 \pm 0.10	9.31 \pm 0.09	7.80 \pm 0.15	7.51 \pm 0.19	8.12 \pm 0.19	ND	7.40 \pm 0.10	7.15 \pm 0.21
E7.63 ⁴⁰⁸ A	8.87 \pm 0.18	7.11 \pm 0.11	8.89 \pm 0.18	7.81 \pm 0.09	7.02 \pm 0.19	8.35 \pm 0.27	7.16 \pm 0.21	6.91 \pm 0.23	7.01 \pm 0.09
Q7.65 ⁴¹⁰ A	8.01 \pm 0.31	6.99 \pm 0.33	9.41 \pm 0.11	7.70 \pm 0.18	7.33 \pm 0.23	8.35 \pm 0.27	ND	7.25 \pm 0.15	7.10 \pm 0.30

3.2. Three conserved positively charged residues residing near the intracellular ends of TMs 5 and 6 contribute to conformational transitions upon receptor activation

R5.56³²⁶ and K6.35³⁴⁶ reside towards the intracellular side of TMs 5 and 6, respectively. In the inactive apo model, both of these residues are predicted to hydrogen bond to regions in ICL2 that may be required to stabilise ground state receptor interactions. Interestingly, alanine mutation of either of these residues increased cell surface expression (Fig. 8, Table 1). For K6.35³⁴⁶A, this was detectable by both antibody labelling (175% of wildtype) and whole cell binding (159% of wildtype). While increased expression was detect-

able at R5.56³²⁶A using antibody labelling (112% wildtype), there was significantly enhanced expression when calculating B_{max} values from radioligand binding (141% of wildtype) (Table 1).

In our active, peptide bound molecular model R5.56³²⁶ and K6.35³⁴⁶ are predicted to undergo a reorientation compared to the apo model, with both residues pointing away from the bundle (Fig. 8). An additional charged residue, K6.40³⁵¹ in TM6 is also located in an outward orientation relative to the bundle that is in a distinct orientation in the active model relative to the apo (Fig. 8).

While mutation of R5.56³²⁶ to alanine did not alter affinity of either of the peptide agonists or the antagonist exendin-4(9–39), K6.35³⁴⁶A and K6.40³⁵¹A both had small, yet significant selective

Table 5

Effects of GLP-1R mutation on signal pathway bias. Data were analysed using an operational model of agonism to estimate $\log \tau_c/K_A$ ratios. Changes in $\log \tau_c/K_A$ ratios with respect to WT were calculated to provide a measure of the degree of stimulus bias exhibited by mutant receptors across the three pathways relative to that of the control receptor (WT). Values are expressed as mean \pm S.E.M of four to six independent experiments, conducted in duplicate. Data were analysed with one-way analysis of variance and Dunnett's post test ($p < 0.05$). ND indicates data unable to be experimentally defined.

	AlogRn relative to WT								
	pERK1/2-cAMP			ERK- Ca^{2+}			Ca^{2+} -cAMP		
	GLP-1	Oxyntomodulin	Exendin-4	GLP-1	Oxyntomodulin	Exendin-4	GLP-1	Oxyntomodulin	Exendin-4
Wildtype	0.00 \pm 0.12 (1.0)	0.00 \pm 0.07 (1.0)	0.00 \pm 0.09 (1.0)	0.00 \pm 0.11 (1.0)	0.00 \pm 0.10 (1.0)	0.00 \pm 0.10 (1.0)	0.00 \pm 0.13 (1.0)	0.00 \pm 0.15 (1.0)	0.00 \pm 0.09 (1.0)
R2.46 ¹⁷⁶ A	0.29 \pm 0.15 (1.9)	0.70 \pm 0.15 (5.0)	0.37 \pm 0.16 (2.3)	0.29 \pm 0.29 (1.9)	-0.24 \pm 0.33 (0.57)	0.57 \pm 0.31 (3.7)	0.57 \pm 0.32 (3.7)	0.52 \pm 0.33 (3.3)	-0.21 \pm 0.31 (0.62)
N2.52 ¹⁸² A	0.31 \pm 0.32 (2.0)	0.86 \pm 0.21 (7.2)	0.99 \pm 0.20 (9.8)*	ND	ND	ND	ND	ND	ND
R3.30 ²²⁷ A	0.52 \pm 0.24 (3.3)	0.97 \pm 0.12 (9.3)	0.25 \pm 0.17 (1.8)	0.26 \pm 0.17 (1.8)	-1.06 \pm 0.15 (0.09)*	0.24 \pm 0.18 (1.7)	0.86 \pm 0.26 (7.2)*	0.81 \pm 0.17 (6.4)	0.52 \pm 0.14 (3.3)
Y3.53 ²⁵⁰ A	-0.94 \pm 0.39 (0.11)	-1.13 \pm 0.36 (0.07)*	-0.44 \pm 0.30 (0.36)	ND	ND	ND	ND	ND	ND
K4.64 ²⁸⁸ A	0.69 \pm 0.32 (4.9)	0.68 \pm 0.37 (4.8)	1.17 \pm 0.12 (15)*	ND	-0.80 \pm 0.28 (0.16)	ND	ND	1.17 \pm 0.32 (15)*	ND
R5.40 ³¹⁰ A	1.04 \pm 0.41 (11)	0.65 \pm 0.33 (4.5)	0.96 \pm 0.49 (9.1)	ND	ND	ND	ND	ND	ND
R5.56 ³²⁶ A	-1.03 \pm 0.23 (0.09)*	0.49 \pm 0.16 (3.1)	-0.02 \pm 0.17 (0.95)	-0.19 \pm 0.35 (0.64)	ND	0.67 \pm 0.57 (4.7)	-0.83 \pm 0.18 (0.15)*	ND	-0.50 \pm 0.35 (0.32)
K6.35 ³⁴⁶ A	-0.51 \pm 0.26 (0.31)	-0.65 \pm 0.26 (0.22)	-0.38 \pm 0.11 (0.42)	-0.56 \pm 0.23 (0.34)	0.08 \pm 0.24 (1.2)	-0.82 \pm 0.07 (0.15)	-0.66 \pm 0.13 (0.22)	-1.54 \pm 0.11 (0.03)*	0.37 \pm 0.10 (2.3)
R6.37 ³⁴⁸ A	-0.16 \pm 0.16 (0.69)	0.49 \pm 0.13 (3.1)	0.49 \pm 0.14 (3.1)	1.38 \pm 0.36 (24)*	0.61 \pm 0.24 (4.1)	0.84 \pm 0.09 (6.9)	-1.40 \pm 0.25 (0.04)*	-0.11 \pm 0.23 (0.79)	-0.25 \pm 0.29 (0.56)
K6.40 ³⁵¹ A	-0.19 \pm 0.21 (0.65)	-1.18 \pm 0.28 (0.07)*	-0.51 \pm 0.24 (0.30)	ND	-1.07 \pm 0.18 (0.09)*	0.10 \pm 0.24 (1.3)	ND	-0.24 \pm 0.29 (0.57)	-1.08 \pm 0.21 (0.08)*
E7.63 ⁴⁰⁸ A	0.80 \pm 0.27 (6.3)	0.36 \pm 0.21 (2.3)	0.64 \pm 0.22 (4.4)	0.15 \pm 0.33 (1.4)	-0.54 \pm 0.27 (0.29)	-0.30 \pm 0.29 (0.50)	0.90 \pm 0.15 (8.0)*	0.70 \pm 0.24 (5.0)	0.88 \pm 0.29 (7.7)
Q7.65 ⁴¹⁰ A	-0.37 \pm 0.10 (0.43)	-0.48 \pm 0.44 (0.33)	-0.10 \pm 0.25 (0.79)	ND	-1.07 \pm 0.48 (0.08)*	0.90 \pm 0.54 (7.9)	ND	0.47 \pm 0.18 (3.0)	-1.24 \pm 0.52 (0.06)*

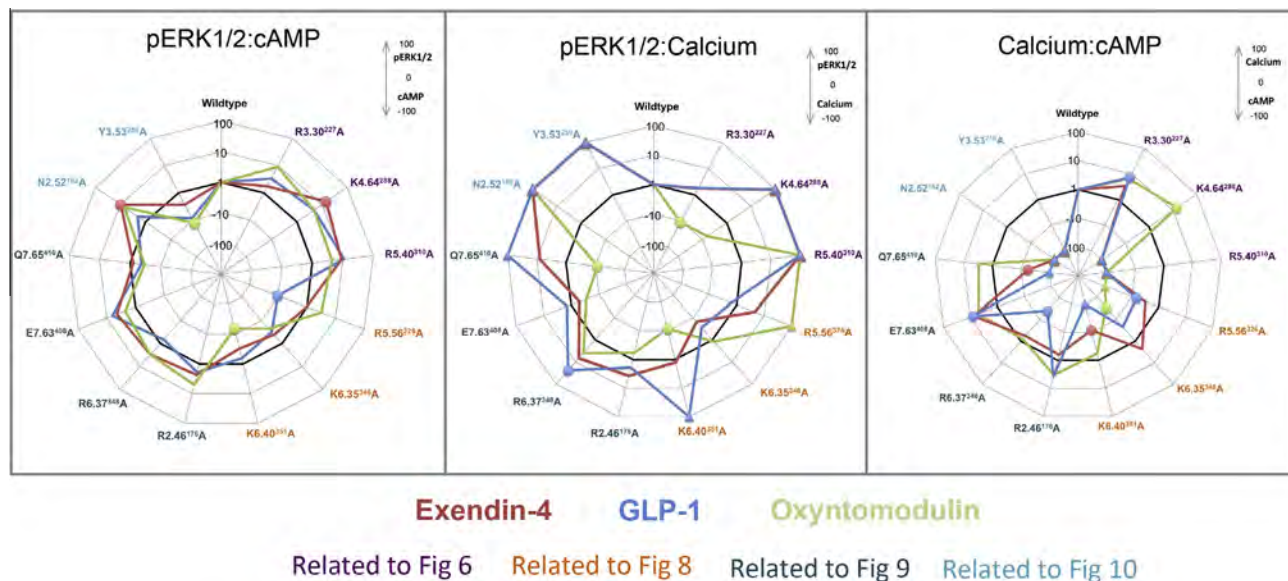


Fig. 5. Effect of mutations on agonist bias of GLP-1R signalling pathways. Radial plots of agonist bias factors ($\Delta\Delta\tau_c/K_A$, the ratio of the transduction coefficient for one pathway vs another, each normalised to the values determined for the wildtype receptor) derived from an operational model of agonism (see “Section 2”) plotted for each receptor variant. Values greater than 1 denote bias towards pathway 1, and values less than 1 denote bias towards pathway 2 relative to signalling at the wildtype receptor. Left, pERK1/2 (pathway 1) vs cAMP (pathway 2); middle, pERK1/2 (pathway 1) vs Ca^{2+} mobilisation (pathway 2); right, Ca^{2+} mobilisation (pathway 1) vs cAMP (pathway 2). All plots show the bias factors for the mutant receptors relative to the wildtype receptor for GLP-1 (blue), exendin-4 (salmon) and oxyntomodulin (green). Data points plotted as circles indicate statistically significant bias relative to the wildtype receptor (WT highlighted by the black reference line), whereas data plotted as triangles (at a value of -100 or 100) indicate that no significant signal could be detected for a particular pathway and therefore a bias factor could not be calculated. These values at -100 indicate no signalling in pathway 1 (therefore implied bias towards pathway 2), whereas +100 indicates no signalling in pathway 2 (therefore implied bias towards pathway 1). The residues are highlighted in the colour relevant to the clustering (and relevant figure) in which they are discussed in the results section.

effects on ligand affinity (Table 1). K6.35³⁴⁶A selectively enhanced GLP-1 and exendin-4 affinity, with oxyntomodulin displaying a similar trend, however no effect was observed on the affinity of

the antagonist. In contrast, K6.40³⁵¹A did not alter the affinity of the peptide agonists, but showed reduced affinity for exendin-4 (9–39) compared to the wildtype receptor (Table 1).

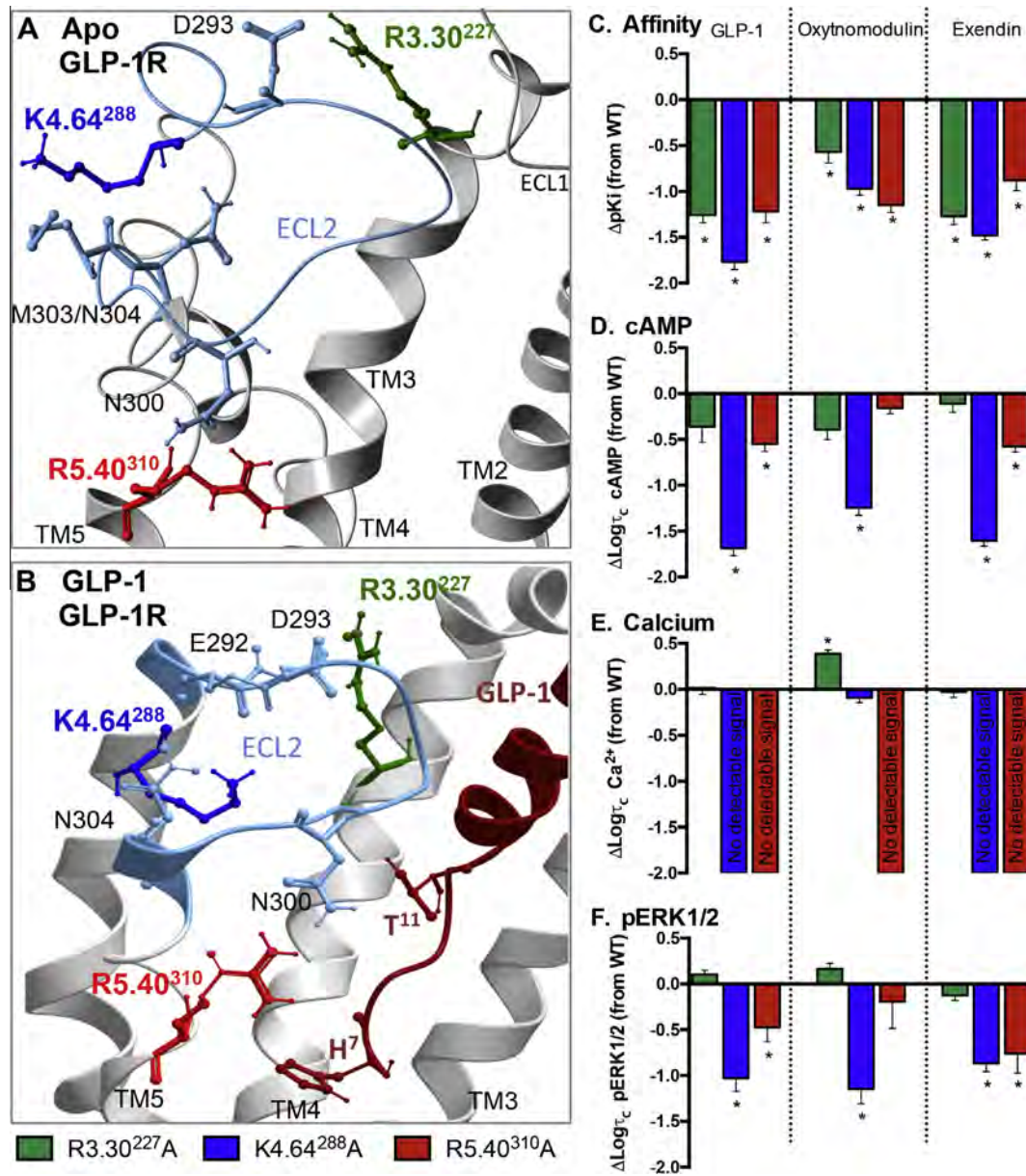


Fig. 6. Mutation of positively charged residues predicted to interact with ECL2 impairs agonist affinity and alters receptor signalling in a pathway dependent manner. (A) Tops of TMs 2, 3, 4 and 5 of the apo GLP-1R TM bundle highlighting interactions between charged residues R3.30²²⁷, K4.64²⁸⁸, R5.40³¹⁰ and residues located within ECL2 (R3.30²²⁷-D293, K4.64²⁸⁸-N304, R5.40³¹⁰-N300). (B) TMs 2, 3, 4 and 5 of the GLP-1 docked activated GLP-1R TM bundle highlighting interactions between charged residues R3.30²²⁷, K4.64²⁸⁸, R5.40³¹⁰ and residues located within ECL2 (R3.30²²⁷-D293, K4.64²⁸⁸-E292/N304, R5.40³¹⁰-N300). Also shown is the GLP-1 peptide (dark red) with T¹¹ that interacts directly with N300 located within ECL2. H⁷ of GLP-1 is also highlighted residing close to R5.40³¹⁰. (C) Differences in equilibrium binding affinity (pKi) of mutant receptors relative to wildtype for GLP-1, oxyntomodulin and exendin-4. (D–F) Differences in the coupling efficiency (log τ_c) of GLP-1, exendin-4 and oxyntomodulin to three signalling pathways (cAMP production (D), pERK1/2 (E) and Ca^{2+} mobilisation (F)) at individual mutants compared to the wildtype receptor. These log τ_c were calculated from concentration–response curves presented in Figs. 2–4, and corrected for cell surface expression as measured by antibody labelling recorded in Table 1. Statistical significance of changes in affinity or coupling efficacy in comparison with wildtype were determined by one-way analysis of variance and Dunnett's post test, and values are indicated with an asterisk (*, $p < 0.05$). All values are \pm S.E.M of four to six independent experiments, conducted in duplicate.

K6.35³⁴⁶A enhanced the efficacy of all three agonists for the three signalling pathways, although this did not reach statistical significance for oxyntomodulin in pERK1/2 (Fig. 8, Table 3). While GLP-1 and oxyntomodulin displayed a similar fold increase in efficacy for calcium signalling (5–6-fold), there was a larger enhancement for exendin-4 at this mutant (26-fold) (Fig. 8, Table 2).

Neither R5.56³²⁶A nor K6.40³⁵¹A altered cAMP efficacy of any ligand, but both had ligand-selective negative effects on pERK1/2. R5.56³²⁶A reduced the efficacy of GLP-1 (8-fold) and to a lesser extent exendin-4, with no effect on oxyntomodulin. In contrast, K6.40³⁵¹A reduced the efficacy of oxyntomodulin and exendin-4,

with no effect on GLP-1. R5.56³²⁶A and K6.40³⁵¹A also heavily impaired Ca^{2+} when activated by GLP-1 and exendin-4, whereas oxyntomodulin-mediated Ca^{2+} was impaired only at R5.56³²⁶A (Fig. 8, Table 3).

The ability of these mutations to selectively alter efficacy of distinct pathways and/or ligands resulted in different bias profiles of these mutant receptors relative to the wildtype (Table 5, Fig. 5). K6.35³⁴⁶A altered the coupling preference induced by oxyntomodulin, such that the receptor was even more strongly biased towards cAMP relative to Ca^{2+} than wildtype, with a similar trend also seen for GLP-1 (Table 5, Fig. 5). R5.56³²⁶A biased GLP-1 signalling

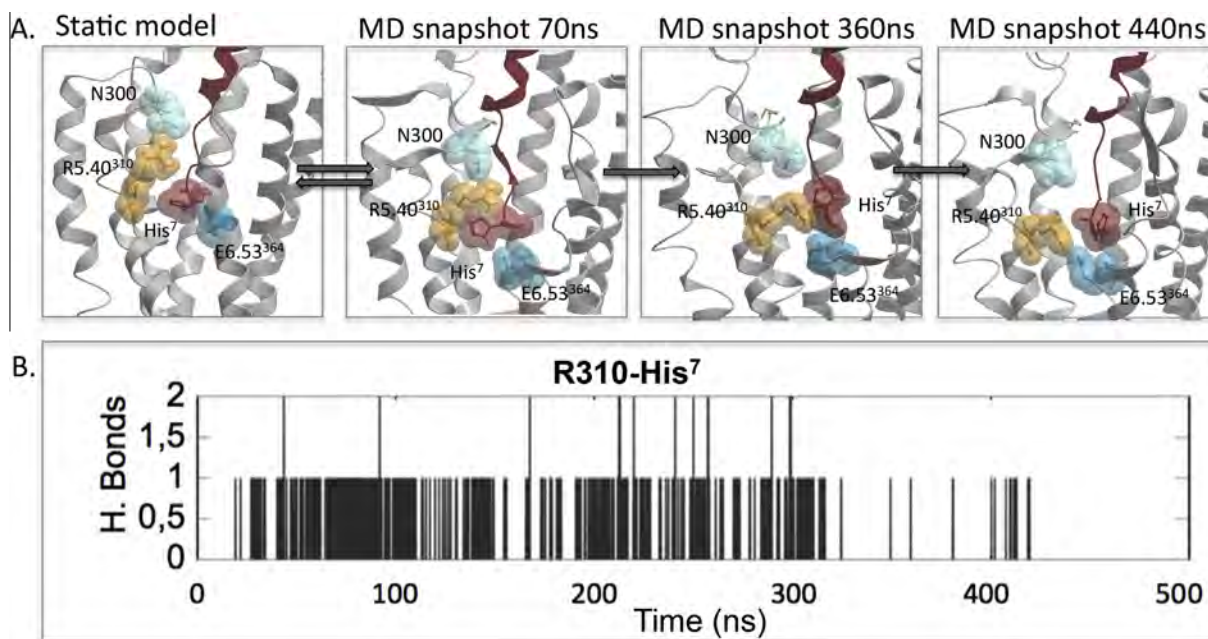


Fig. 7. R5.40³¹⁰ forms transient interactions with His⁷ of GLP-1. Molecular dynamics simulation was performed for a total of 500 ns commencing with the final model of the GLP-1 bound GLP-1R. (A) Interactions are identified between R5.40³¹⁰ and both N300 and His⁷ throughout the first half of the simulation. However towards the end of the simulation the interactions with both N300 and His⁷ are lost and R5.40³¹⁰ forms a stable interaction with E6.53³⁶⁴. (B) Hydrogen bonds formed between R5.40³¹⁰-His⁷ during the 500 ns simulation. Hydrogen bonds were defined with the donor-acceptor distance < 3.0 Å and an angle cutoff of 20°.

towards cAMP relative to iCa^{2+} and pERK1/2. Oxyntomodulin did not signal to iCa^{2+} at this mutant and therefore may be biased towards pERK1/2 and cAMP over iCa^{2+} (Fig. 5, Table 5). Exendin-4 showed no significant change from wildtype at R5.56³²⁶A. K6.40³⁵¹A was biased away from iCa^{2+} towards both cAMP and pERK1/2 when activated by GLP-1. Exendin-4 signaling also showed a significant bias for cAMP relative to iCa^{2+} . In contrast, oxyntomodulin biased the signaling away from pERK1/2 relative to cAMP and iCa^{2+} at this receptor in comparison to the wildtype (Fig. 5, Table 5).

3.3. A hydrogen bond network at the intracellular face stabilises the apo-GLP-1R and plays a role in controlling conformational transitions linked to biased signalling

Molecular modelling of the GLP-1R revealed a network of residues residing at the intracellular face of the receptor involving residues in TM2 (R2.46¹⁷⁶), TM6 (R6.37³⁴⁸) and TM7 (N7.61⁴⁰⁶ and E7.63⁴⁰⁸). These are predicted to form an extensive hydrogen bond network in the ground state apo model (Fig. 9) that is disrupted in the active state model. We have previously reported the effects of alanine mutation of N7.61⁴⁰⁶ that demonstrated little effect on receptor expression, ligand binding, cAMP formation or iCa^{2+} ([66], Fig. 9). However, there were small, yet significant reductions in the ability of this mutant to promote pERK1/2 when activated by GLP-1 and oxyntomodulin, but not exendin-4 (Fig. 9).

Mutation of R2.46¹⁷⁶, R6.37³⁴⁸ or E7.63⁴⁰⁸ to alanine each resulted in a significant loss of cell surface expression (Fig. 9, Table 1). Interestingly, each mutation reduced this expression to a similar extent (57–66% of wildtype), supporting the role of these residues in a combined network. Despite this, relatively subtle effects were observed on other aspects of receptor function. All three mutants maintained the ability to bind the three agonists and the antagonist, albeit that a small yet significant reduction (4-fold) in exendin-4 affinity was observed for E7.63⁴⁰⁸A (Table 1). In addition, subtle changes to receptor bias occurred that did not always affect all three peptide ligands equally (Fig. 9, Tables 3

and 5). E7.63⁴⁰⁸A reduced cAMP signalling by all peptides, although this did not reach significance for oxyntomodulin (Fig. 9, Table 3). This resulted in E7.63⁴⁰⁸A being biased towards iCa^{2+} relative to cAMP for all ligands, but this only reached significance for GLP-1 (Fig. 5, Table 5). R6.37³⁴⁸A selectively altered effector signalling, reducing iCa^{2+} for GLP-1 and exendin-4, but not oxyntomodulin (Fig. 9, Table 3). This resulted in a statistically significant switch in the receptor bias when activated by GLP-1, such that it more readily activated effector coupling linked to pERK1/2 and cAMP compared to iCa^{2+} (Table 5, Fig. 5). R2.46¹⁷⁶A had no significant effect on efficacy relative to wildtype.

3.4. A conserved polar residue in H8 is selectively important for GLP-1 mediated signalling, with little impact on exendin-4 and oxyntomodulin

Q7.65⁴¹⁰A was assessed as part of this study as it is highly conserved in class B GPCRs, but it is not located with the TM bundle, rather at the start of the predicted helix 8 (H8) at the bottom of TM7. In our apo model Q7.65⁴¹⁰ is predicted to form a direct hydrogen bond with the backbone of TM7 (F7.59⁴⁰⁴) and with the side chain of N7.62⁴⁰⁷ and therefore may stabilise the hinge region between TM7 and H8 (Fig. 9). In the active model the interaction with the backbone of TM7 is maintained, but the interaction with N7.62⁴⁰⁷ is lost due to a reorientation of the bottom of TM7 upon activation where N7.62⁴⁰⁷ then resides close to the G_{ss} fragment (Fig. 9). While mutation of Q7.65⁴¹⁰ slightly reduced cell surface expression, it had selective effects on GLP-1R efficacy, with no significant effect on affinity of any ligand (Table 1). GLP-1 and exendin-4 mediated cAMP formation and pERK1/2 were also unaffected, however no iCa^{2+} could be detected when activated by GLP-1 and there was also reduced exendin-4 efficacy for this pathway (Fig. 9, Tables 1 and 3). This resulted in a significant bias of this mutant receptor relative to the wildtype towards cAMP formation compared to iCa^{2+} for exendin-4, and implies a similar bias for GLP-1 (Fig. 5, Table 5). For oxyntomodulin a different profile was observed; this ligand displayed reduced efficacy for pERK1/2 with

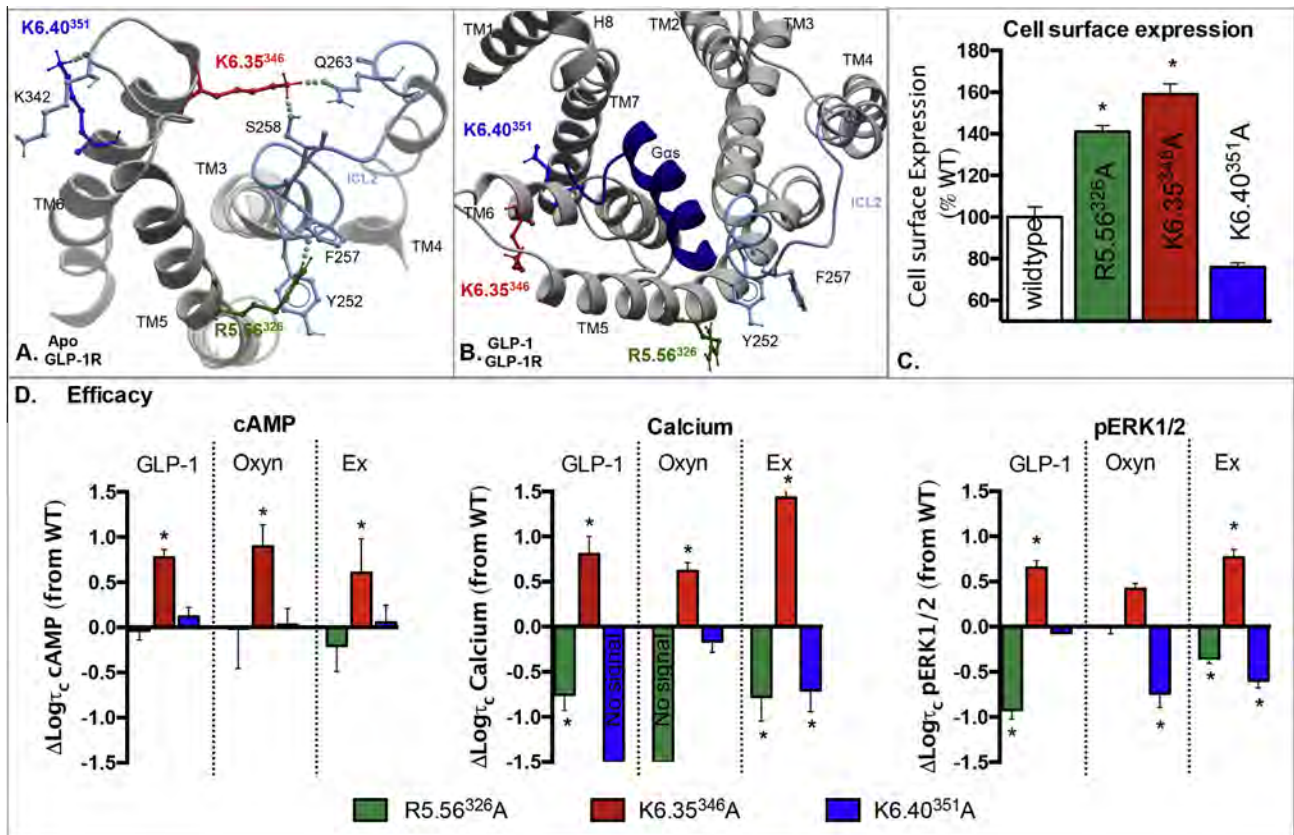


Fig. 8. Mutation of positively charged residues predicted to interact with ICL2 and/or the lipid bilayer alters cell surface expression and receptor signalling in a pathway dependent manner. (A) TMs 3, 4, 5 and 6 of the apo GLP-1R TM bundle as viewed from the cytoplasmic face, highlighting interactions between charged residues R5.56³²⁶ and K6.35³⁴⁶ with residues in ICL2. K6.40³⁵¹ is also shown where it points away from the bundle, interacting with the backbone of ICL3 and potentially interacting with lipid head groups. (B) The activated GLP-1R TM bundle as viewed from the intracellular face with a G_s peptide fragment docked at the cytoplasmic face. The lipid facing location of R5.56³²⁶, K6.35³⁴⁶ and K6.40³⁵¹ are highlighted. Of particular note, interactions of K6.35³⁴⁶ with ICL2 are broken to accommodate opening up of the TM bundle and G protein interaction. R5.56³²⁶ interactions with the backbone of ICL2 are also broken although R5.56³²⁶ maintains within H bond proximity to Y252. (C) Cell surface expression of mutations R5.56³²⁶A, K6.35³⁴⁶A and K6.40³⁵¹A relative to the wildtype receptor as assessed by antibody binding to the N-terminal c-myc epitope tag. (D) Differences in the coupling efficiency (log_{τ_c}) of GLP-1, oxyntomodulin and exendin-4 to three signalling pathways (cAMP production (left), Ca^{2+} mobilisation (middle), and pERK1/2 (right)) for R5.56³²⁶A, K6.35³⁴⁶A and K6.40³⁵¹A compared to the wildtype receptor. These log_{τ_c} were calculated from concentration–response curves presented in Figs. 2–4, and corrected for cell surface expression as measured by antibody labelling recorded in Table 1. Statistical significance of changes in cell surface expression or coupling efficacy in comparison with wildtype were determined by one-way analysis of variance and Dunnett's post test, and values are indicated with an asterisk (*, $p < 0.05$). All values are \pm S.E. M of four to six independent experiments, conducted in duplicate.

no effect on Ca^{2+} or cAMP resulting in a significant bias of Q7.65⁴¹⁰A towards Ca^{2+} relative to pERK1/2 compared to the wildtype receptor (Figs. 5 and 9, Tables 3 and 5).

3.5. N2.52¹⁸² and Y3.53²⁵⁰ stabilise interactions between TMs 2, 3 and 4 important for GLP-1R stability and controlling conformational transitions linked to specific activation of individual signalling pathways

N2.52¹⁸² and Y3.53²⁵⁰ located in TMs 2 and 3, respectively, are predicted to form interactions with residues V4.46²⁷⁰ (and potentially W4.50²⁷⁴) and the backbone of Y4.45²⁶⁹, respectively, in the apo receptor, all located in TM4. Our GLP-1 bound active receptor model suggests a reordering of TM2 relative to TM3 and TM4 upon receptor activation resulting in formation of new interactions by the side chain of N2.52¹⁸². In the active state, while this residue remains close to TM4, it also interacts with Y2.48¹⁷⁸ in TM2 and W3.46²⁴³ in TM3 (Fig. 10).

While the TM3–TM4 interaction does not appear to be important for receptor stability (as mutation of Y3.53²⁵⁰ had no effect on receptor expression), the interaction of N2.52¹⁸² in TM2 with TM4 residues may be important for receptor integrity as its mutation to alanine heavily impaired cell surface expression (39% of

wildtype through antibody detection) (Table 1, Fig. 10). Due to this heavily impaired expression, radioligand binding could not be detected and therefore ligand affinities could not be assessed (Table 1). Following correction for the loss in cell surface expression, pERK1/2 efficacy was not significantly altered at this mutation, however cAMP production was impaired for GLP-1 and exendin-4 (5–6-fold) and no Ca^{2+} could be detected for any of the three peptides (Fig. 10, Tables 2 and 3). N2.52¹⁸²A significantly enhanced the coupling preference to pERK1/2 relative to cAMP for exendin-4 only, although a similar trend was observed with oxyntomodulin (Fig. 5, Table 5). The inability to detect an Ca^{2+} signal for N2.52¹⁸²A indicates that this receptor is likely biased towards cAMP and pERK1/2 relative to Ca^{2+} for all ligands (Fig. 5, Table 5).

While mutation of Y3.53²⁵⁰ had little effect on receptor expression, agonist affinity or cAMP formation, pERK1/2 was impaired (around 10-fold) and there was no detectable Ca^{2+} when activated by all three agonist peptides (Fig. 10, Tables 1–3). Despite this, only oxyntomodulin displayed significantly altered bias with bias towards cAMP production relative to pERK1/2, but as there was no detectable Ca^{2+} response for any peptide, it could be speculated that this mutation may also alter the bias of the GLP-1R away from Ca^{2+} , towards cAMP and pERK1/2 for all peptide agonists (Fig. 5, Table 5).

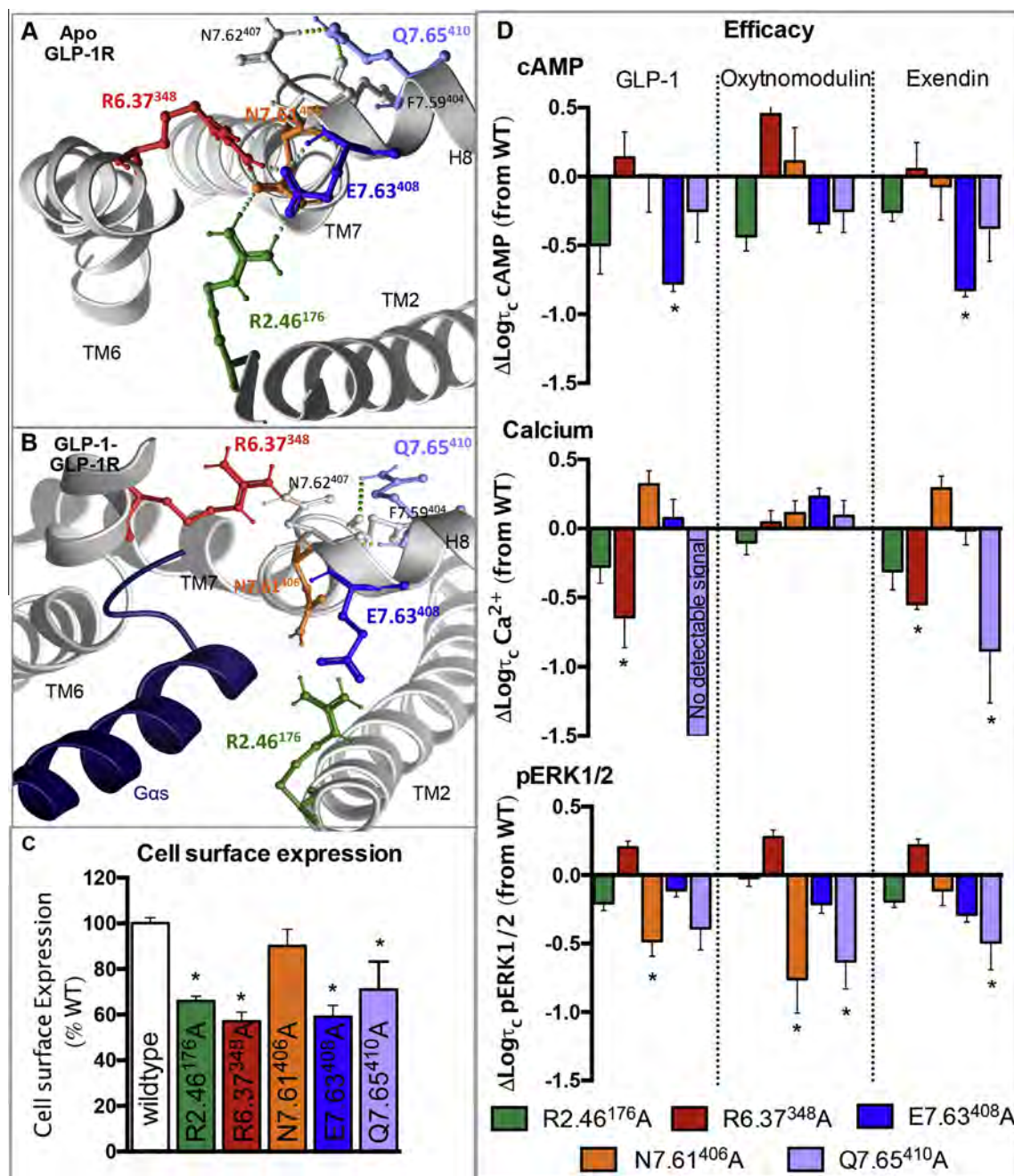


Fig. 9. Effects on mutation of residues located in the hydrogen bonding network located between TMs 2, 6 and 7 at the cytoplasmic face. (A) TMs 2, 6, 7 and helix 8 (H8) of the apo GLP-1R TM bundle as viewed from the cytoplasmic face, highlighting an extensive hydrogen bond network between R2.46¹⁷⁶, R6.37³⁴⁸, N7.61⁴⁰⁶ and E7.63⁴⁰⁸. Q7.65⁴¹⁰ at the start of H8 is also shown where it forms hydrogen bonds with the side chain of N7.61⁴⁰⁷ and the backbone of TM7 at F7.59⁴⁰⁴. (B) TMs 2, 6, 7 and H8 of the GLP-1 docked GLP-1R TM bundle as viewed from the cytoplasmic face with the G_{as} peptide fragment indicating the extensive hydrogen bond network between R2.46¹⁷⁶, R6.37³⁴⁸, N7.61⁴⁰⁶ and E7.63⁴⁰⁸ is broken in the activated receptor. Q7.65⁴¹⁰ at the start of H8 is also shown where it still maintains a backbone interaction with F7.59⁴⁰⁴. (C) Cell surface expression of mutations R2.46¹⁷⁶A, R6.37³⁴⁸A, N7.61⁴⁰⁶A, E7.63⁴⁰⁸A and Q7.65⁴¹⁰A relative to the wildtype receptor (as assessed by antibody binding to the N-terminal c-myc epitope tag). (D) Differences in the coupling efficiency (log τ_c) of GLP-1, exendin-4 and oxyntomodulin to three signalling pathways (cAMP production (top), Ca^{2+} mobilisation (middle), and pERK1/2 (bottom)) for R2.46¹⁷⁶A, R6.37³⁴⁸A, N7.61⁴⁰⁶A, E7.63⁴⁰⁸A and Q7.65⁴¹⁰A compared to the wildtype receptor. These log τ_c were calculated from concentration–response curves presented in Figs. 2–4, and corrected for cell surface expression as measured by antibody labelling recorded in Table 1. Statistical significance of changes in cell surface expression or coupling efficacy in comparison with wildtype were determined by one-way analysis of variance and Dunnett's post test, and values are indicated with an asterisk (*, $p < 0.05$). All values are \pm S.E.M of four to six independent experiments, conducted in duplicate.

4. Discussion

Class B GPCRs are activated through interaction of the N-terminal region of their peptide agonists with the TM bundle of the receptor [47,48,6,41]. ECL2 plays an important role in this activation process [23,30,63] and mutations within this domain in the GLP-1R result in impaired cAMP production and Ca^{2+} with less

dramatic effects on pERK1/2 [30,31,65]. In addition, these mutations within ECL2 altered the efficacy of the pERK1/2 biased agonist oxyntomodulin differentially to GLP-1 and exendin-4 highlighting a key role of this domain in biased agonism. Here, we reveal ligand-dependent roles in peptide affinity and activation of the GLP-1R of three highly conserved positively charged residues (R3.30²²⁷, K4.64²⁸⁸ and R5.40³¹⁰) that have previously been implicated in

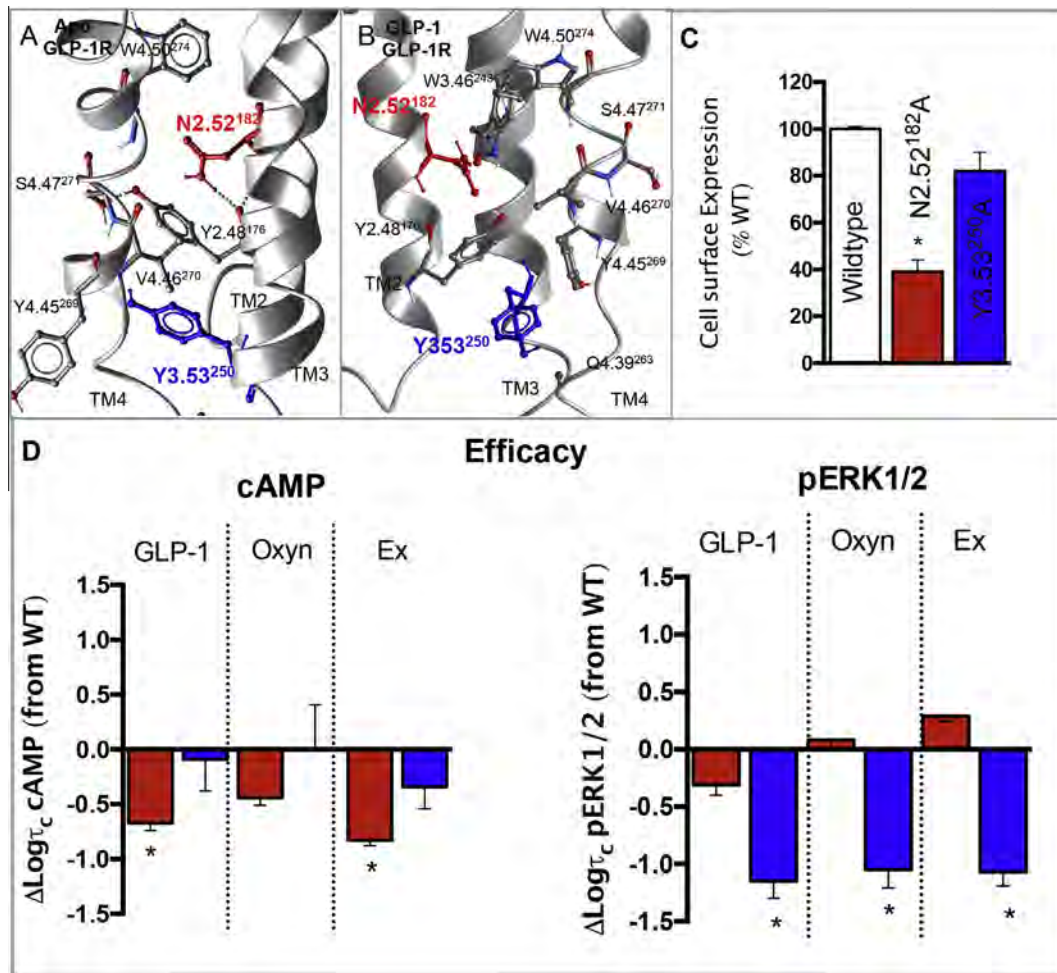


Fig. 10. Effects on mutation of residues located TMs 2 and 3 that are predicted to interact with TM4. TMs 2, 3 and 4 of the apo GLP-1R TM bundle (A) and the activated GLP-1: GLP-1:G_{αs} peptide fragment (B) highlighting N2.52¹⁸² (red) and Y3.53²⁵⁰ (blue) and interacting residues within TM4 and TM3 (in the active model). (C) Cell surface expression of mutations N2.52¹⁸²A and Y3.53²⁵⁰A relative to the wildtype receptor (as assessed by antibody binding to the N-terminal c-myc epitope tag). (D) Differences in the coupling efficiency (log_{τ_c}) of GLP-1, exendin-4 and oxyntomodulin to cAMP production (left) and pERK1/2 (right) for N2.52¹⁸²A and Y3.53²⁵⁰A compared to the wildtype receptor. These log_{τ_c} were calculated from concentration–response curves presented in Figs. 2–4, and corrected for cell surface expression presented in (C). There was no detectable signalling for either mutant in calcium mobilisation for any of the three peptides. Statistical significance of changes in cell surface expression or coupling efficacy in comparison with wildtype were determined by one-way analysis of variance and Dunnett's post test, and values are indicated with an asterisk (*, *p* < 0.05). All values are ±S.E. *M* of four to six independent experiments, conducted in duplicate. (For interpretation of the references to colour in this figure legend, the reader is referred to the web version of this article.)

GLP-1-mediated function (Table 6), and are predicted in our current molecular models to form stabilising interactions with ECL2. The conservation of positively charged residues at positions 3.30 and 4.64 in all Class B GPCRs and the negative effect on receptor function that is observed following mutation in multiple Class B GPCRs (Table 6) implies there may be a common role in stabilisation of ECL2 by these residues for this class of receptors. The distinct effects of mutation of R3.30²²⁷ and K4.64²⁸⁸ on affinity and efficacy of GLP-1 and exendin-4 relative to oxyntomodulin are particularly interesting as oxyntomodulin is a biased agonist relative to GLP-1 and exendin-4. These observations were more prominent for K4.64²⁸⁸ and mutation of the proposed interacting residues in ECL2 (E292A and N304A) also resulted in similar ligand-dependent changes [30,31]. These data support a role for K4.64²⁸⁸ in controlling activation transition leading to biased agonism by influencing the conformation of ECL2 and its interaction with distinct agonists. A recent study also predicted a similar interaction of K4.64²⁸⁸ with ECL2, further supporting this theory [15]. Interestingly, for the calcitonin-like receptor (CLR) where a receptor activity modifying protein (RAMP) is required for function, mutation of R4.64 altered adrenomedullin function at CLR-RAMP2 or CLR-RAMP3 complexes,

but not CGRP function at CLR-RAMP1 [60,63]. This suggests that in Class B receptor-RAMP complexes, stabilisation of ECL2 by R/K4.64 may have distinct functional consequences, in addition to controlling biased agonism of ligands acting at the same receptor.

R5.40³¹⁰, also conserved as a positive charge in many Class B GPCRs, interacts with ECL2 in our modelling, residing close to N300 that is predicted to form a direct interaction with GLP-1 (Fig. 6). R5.40³¹⁰ and N300 are both required for high affinity binding of GLP-1, exendin-4 and oxyntomodulin, with mutations of each having similar effects on affinity and both affecting efficacy of all three peptide agonists [30,31], therefore their proposed interaction may be important for peptide recognition. A polar residue at 5.40 is also required for function in other Class B GPCRs, particularly those in the glucagon subfamily (Table 6). In contrast to this proposed interaction of R5.40³¹⁰ with N300, a recently published study predicted a direct interaction of R5.40³¹⁰ with His⁷ of GLP-1 [15]. Although absent in our static active state model, these side chains are in close proximity and in MD simulations (500 ns), R5.40³¹⁰ forms transient interactions with His⁷ of GLP-1 (Fig. 7). Interestingly, for the GLP-1R, R5.40³¹⁰ also plays a role in controlling biased agonism, with distinct negative effects upon mutation

Table 6

Published information for Class B GPCRs following mutation of the conserved polar residues assessed in this study. h, human; o, opossum; r, rat. GLP-1(R); glucagon-like peptide-1 (receptor); CLR, calcitonin-like receptor; RAMP, receptor activity modifying protein; CGRP, calcitonin gene related peptide; SecR, secretin receptor; PTH-(R), parathyroid hormone (receptor); GCGR, glucagon receptor; VPAC-(R), vasoactive intestinal polypeptide (receptor); GIP(R), glucose-dependent insulinotropic peptide (receptor). CRE; cAMP response element.

Position (Class B Wootten numbering)	Mutant	Receptor	Effect compared with WT	Reference
2.46	R2.46A	hGLP-1R	Decreased GLP-1 mediated cAMP potency	[38]
	R2.46A	rGCGR	No detectable cell surface expression	[52]
	R2.46A	hCLR-RAMP 1	Reduced CGRP mediated cAMP potency.	[59]
2.52	R2.46A	SecR	Decreased secretin mediated calcium potency but not cAMP potency	[17]
	N2.52A	hCLR-RAMP1	No effect on CGRP affinity or cAMP production	[59]
	H2.52A	oPTH-1R	No effect on PTH-1 cAMP production.	[57]
3.30	R3.30A	rGLP-1R	Reduced GLP-1 mediated cAMP production	[69]
	R3.30A	hGCGR	Reduced expression and glucagon affinity	[15]
	R3.30A	rSecR	Reduced secretin-mediated cAMP production	[14]
	K3.30A	hCLR-RAMP1	No effect on CGRP mediated cAMP production	[59]
	K3.30A	hCLR-RAMP2	Reduced adrenomedullin cAMP production	[60]
3.53	K3.30A	hCLR-RAMP3	Reduced adrenomedullin cAMP production	[60]
	Y3.53A	hVPAC1R	Reduced VIP mediated cAMP production	[55]
	K4.64A	rGLP-1R	Reduced GLP-1 affinity	[1]
4.64	K4.64A	hGLP-1R	Reduced expression, GLP-1 affinity and cAMP efficacy	[15]
	K4.64L	hGCGR	Reduced glucagon affinity	[15]
	R4.64A	oPTH-1R	No effect on PTH mediated cAMP	[57]
	R4.64A	rSecR	Decreased secretin mediated cAMP potency.	[14]
	R4.64A	hCLR-RAMP1	Reduced CGRP mediated cAMP pEC ₅₀ .	[59]
	R4.64A	hCLR-RAMP2	Reduced adrenomedullin mediated cAMP production	[60]
	R4.64A	hCLR-RAMP3	Reduced adrenomedullin mediated cAMP production	[60]
	R5.40A	hGLP-1R	Reduced expression, GLP-1 affinity and GLP-1 mediated cAMP potency.	[12]
5.40	R5.40A	hGLP-1R	Reduced expression, GLP-1 affinity and cAMP efficacy.	[15]
	R5.40A	hGCGR	Reduced expression and glucagon affinity	[15]
	R5.40A	hGIPR	Reduced GIP mediated cAMP production.	[71]
	H5.40A	hCLR-RAMP1	Reduced CGRP-mediated cAMP pEC ₅₀	[59]
	N5.56A	hCLR-RAMP1	No effect on CGRP cAMP mediated production	[59]
6.35	Y6.35A	hVPAC1R	No effect on VIP mediated cAMP	[13]
	K6.37A	hCLR-RAMP1	No effect on CGRP mediated cAMP production	[10]
	R6.37A	hVPAC1R	No effect on VIP mediated cAMP production	[13]
6.37/6.40	R6.37A	hSecR	No effect on secretin mediated cAMP production	[8]
	R6.37G	rGLP-1R	Decreased GLP-1 affinity	[20]
	R6.37A	rGLP-1R	No effect on GLP-1 mediated cAMP production	[54]
	R6.37A	rGCGR	Enhanced glucagon mediated CRE reporter activity (potency and Emax)	[52]
	R6.37A	hVPAC2R	Reduced VIP mediated cAMP potency	[35]
	K6.37A	hCRF-1R	Increased CRF mediated cAMP potency (Gs), reduced pERK1/2 (Gi)	[44]
	R6.37A/K6.40A	hSecR	Reduced secretin mediated cAMP and calcium, no effect on affinity or receptor expression	[17]
	R6.40A	hCLR-RAMP1	5-fold reduction in CGRP affinity, 30-fold reduction in CGRP mediated cAMP production	[10]
6.40	R6.40A	hVPAC1R	Reduced VIP mediated IP ₃ production, no effect on cAMP	[36]
	K6.40A	rGLP-1R	No effect on GLP-1 mediated cAMP production	[54]
	R6.40A	hVPAC2R	Reduced VIP mediated cAMP potency	[35]
	K6.40A	hCRF-1R	Increased urocortin mediated cAMP (Gs), reduced IP ₃ (Gq)	[44]
7.61	N7.61A	hGLP-1R	No effect on expression, affinity, cAMP or calcium mobilisation, but reduced GLP-1 and oxyntomodulin mediated pERK1/2 (not exendin-4)	[66]
	N7.61A	rGCGR	Enhanced potency in glucagon mediated CRE reporter activity assay	[52]
7.63	E7.63A	hCLR-RAMP1	Reduced CGRP-mediated cAMP potency	[59]
	E7.63A	rGCGR	Enhanced basal activity and enhanced potency in glucagon mediated CRE reporter activity assay	[52]
	E7.63 K	oPTH-1R	No effect on PTH mediated cAMP	[57]
	E7.63A	hVPAC1R	Decreased VIP mediated cAMP production	[13]

for GLP-1 and exendin-4 relative to the biased ligand oxyntomodulin. Interestingly, towards the end of our 500 ns MD simulation on the GLP-1:GLP-1R model, transient interactions of R5.40³¹⁰ with His⁷ of GLP-1 and with N300 in ECL2 are lost and R5.40³¹⁰, as well

as His⁷ of GLP-1 form stable interactions with E6.53³⁶⁴ (Fig. 6); part of a key, central, hydrogen bond network that is critical for controlling GLP-1R biased agonism [64–66]. The mutational effect of R5.40³¹⁰ on GLP-1 and exendin-4 mediated signalling relative to

oxyntomodulin is consistent with mutational studies on residues residing in this central hydrogen bond network [64,65]; and suggests distinct functional requirements of R5.40³¹⁰, in combination with the central hydrogen bond network for controlling peptide-mediated GLP-1R activation leading to biased agonism. These MD simulations with GLP-1 also suggest R5.40³¹⁰ and N300 are key residues in guiding the N-terminus of these peptide agonists into the TM cavity for receptor activation (Fig. 7).

We have also previously reported on a key hydrogen bond network located at the cytoplasmic side of the TM bundle, between TMs 2, 3 and 6 that is essential for receptor integrity and for global activation of the GLP-1R [64,66]. The current study reveals the importance of an additional hydrogen bond network, also at the intracellular face, formed by residues in TM2 (R2.46¹⁷⁶), TM6 (R6.37³⁴⁸) and TM7 (N7.61⁴⁰⁸ and E7.63⁴⁰⁸) that is evident in the crystal structures of the GCGR and CRF₁R [22,49]. Differences in our apo models vs GLP-1 peptide bound models suggest a reorganisation of these intracellular networks involving a disruption of crucial contacts between TMs 3 and 6, and TMs 2 and 7 result in the TM bundle opening at the intracellular face, allowing for effector coupling. Mutation of these residues in both networks (with the exception of N7.61⁴⁰⁸) significantly reduced cell surface expression highlighting a role for both networks in receptor stability ([66], Fig. 9). The role of these networks are also consistent with experimental data from other Class B GPCRs where mutation of residues either induced constitutive cAMP activity, enhanced potency for cAMP production or result in poor receptor expression at the cell surface, observations that are all consistent with destabilisation of the inactive state [59], (Table 6). These combined data across Class B GPCRs, in addition to the conservation of these interactions in the two solved inactive state Class B GPCR TM crystal structures support a common role for hydrogen bond networks at the cytoplasmic face in stabilisation of the apo receptor [22,49].

Residues within the newly reported TM2-6-7 network in the GLP-1R also have independent roles for signal transduction after being released from their ground state constraints. While we did not identify a role for R2.46¹⁷⁶ in transmission of efficacy, it may play a minor role, as observed in a mutational study at the rat GLP-1R (Table 6). In contrast, we revealed distinct roles for R6.37³⁴⁸ and E7.63⁴⁰⁸ in directing signalling specificity. Consistent with other Class B GPCRs (Table 6), E7.63⁴⁰⁸ selectively couples the GLP-1R to cAMP (G_{α_s}). In contrast, R6.37³⁴⁸ plays a role in coupling the GLP-1R to iCa^{2+} that is non- G_{α_s} -mediated [65], but only when the receptor was activated by GLP-1 and exendin-4. Along with R6.37³⁴⁸, K6.40³⁵¹ forms part of a basic-X-X-basic motif (BxxB) that is highly conserved in both Class A and B GPCRs, but the effects of mutation are variable depending on the receptor being studied. Evidence suggest residues in this motif play only minor roles in G_{α_s} /cAMP efficacy for Class B GPCRs, but are more important for IP₃/calcium mobilisation (Table 6). This is consistent with this current study on the GLP-1R, where mutation of both basic residues had little effect on cAMP production by any peptide, but reduced the efficacy of GLP-1 and exendin-4 for iCa^{2+} . However, there was no alteration in oxyntomodulin efficacy, consistent with distinct receptor conformational propagation achieved by the ligand that exposes distinct side chains for effector interaction. Therefore, the BxxB motif may have distinct roles in controlling receptor conformation and effector coupling between ligands acting at the same receptor. The observed effects of mutation of R6.37³⁴⁸, K6.40³⁵¹ and E7.63⁴⁰⁸ for signalling specificity could arise due to direct contacts with effector proteins or indirectly through forming interactions (either within the receptor or with lipids) that stabilise active receptor conformations required for coupling to distinct pathways. Indeed, R6.37³⁴⁸ and E7.63⁴⁰⁸ are in the vicinity of G_{α_s} in the GLP-1 bound molecular model and therefore relatively small differences in conformational rearrangement upon binding

of distinct agonists could subtly alter interactions with effector proteins giving rise to the observed changes in signal bias.

Lys and Arg residues found near the polar/a-polar interfaces can hydrogen bond to phosphate head groups and esterified oxygens of the lipid backbone, anchoring TMs in the bilayer in the optimal orientation in the membrane for receptor function [51]. From our GLP-1R models, three residues R5.56³²⁶, K6.35³⁴⁶ and K6.40³⁵¹ may play such a role as our active state model places these residues pointing out towards lipid. The reorientation of these three side chains between the two models suggests that these residues may be important for controlling TM movements during activation transition. Mutation of R5.56³²⁶ and K6.35³⁴⁶ also increased cell surface expression, an effect that is often associated with stabilisation of the ground state conformation. Indeed, Ala mutation of an equivalent residue, Y6.35, in the CRF₁R TM domain crystal structure was used to increase the thermostability of the inactive receptor protein and to aid in crystallisation [22]. R5.56³²⁶A also selectively impaired pERK1/2 by GLP-1 and exendin-4 and heavily impaired iCa^{2+} by all ligands, consistent with stabilisation of an inactive receptor. In contrast, K6.35³⁴⁶A enhanced affinity and signalling efficacy by all ligands to all three pathways. This residue is only positively charged in the glucagon subfamily of Class B GPCRs (being a polar Tyr in most others (Fig. 1)), and therefore may play a different role in this glucagon subclass compared to the other Class B members.

TM4 is the most peripherally located TM and forms the interface for GLP-1R homodimerisation in Class B GPCRs that is important for GLP-1R signalling [18]. N2.52¹⁸² and Y3.53²⁵⁰ pack up against TM4 and play global roles in GLP-1R activation by peptide agonists, with both residues being crucial for iCa^{2+} mobilisation, but selectively involved in cAMP (N2.52¹⁸²) or pERK signalling (Y3.53²⁵⁰), effects that may arise due to stabilisation of the important dimerisation interface. Consistent with this, mutation of either residue had the largest impact on calcium signalling, which parallels with the greater loss of calcium signalling relative to cAMP and pERK1/2 following mutation of the TM4 dimerisation interface within the GLP-1R [18]. Molecular modelling also predicts a reordering of TM2 relative to TM3 and TM4 that may stabilise residues within TM3 in the activated receptor, a key domain for signal transduction that may also contribute to the altered signalling at these mutant receptors compared to the wildtype.

Collectively, this work expands our understanding of how peptides activate the GLP-1R receptor to promote signalling, highlighting additional key conserved Class B GPCR polar side chains within the TM domain beyond those already reported. There is now a large body of evidence from multiple Class B GPCRs that shed light on how these complex receptors are activated with conserved polar residues playing a crucial role in this process (Table 6 [68,66,64,65,59,9]). Despite their distinct mode of ligand interaction relative to Class A GPCRs, there are some parallels in how these two classes of receptors are activated. There is now substantial evidence that ECL2 plays a major role in the binding and activation of both classes of receptors [30,63,11,62]. However, conformational differences within ECL2 have been identified, even within the Class A subfamily [62], suggesting different networks of interactions are involved in stabilisation of this important domain. In addition, despite different conserved amino acids in the two subclasses, polar interactions are crucial for signal propagation, facilitating conformational TM rearrangements through the reorganisation of hydrogen bond networks in Class A and Class B GPCRs [2,3,42,66,64,9,59]. For Class A GPCRs, there is substantial evidence that this results in a large-scale conformational transition of TM6 relative to TM3 that requires the disruption of key polar networks at the intracellular face [46,45]. Limited evidence supports a similar movement of TM6 relative to TM3 in Class B GPCRs [50]. This study, taken together with our previous studies [66,64], suggest

that breaking of key polar networks at the intracellular face of Class B GPCRs (TM2-TM3-TM6 and TM2-TM6-TM7), like Class A GPCRs, are crucial in this subfamily of receptors to facilitate movements within TM6 allowing for effector interaction.

Additionally, there is an increasing body of evidence from mutational studies supporting distinct modes of receptor activation by biased peptides at the GLP-1R, with this study providing additional evidence for the role of polar interaction networks in influencing how these differences may be achieved. There is also evidence that the ability of individual ligands to influence polar interactions within Class A GPCRs contributes to biased agonism [53,70]. While our mutagenesis studies combined with GLP-1R models can be used to facilitate understanding of mechanisms for activation of Class B GPCRs and propagation of biased signalling, additional and more complex structural and biophysical analysis of this receptor, (or any Class B GPCR) are required to gain an in depth understanding of the large scale conformational movements that allow these very complex receptor-ligand systems to transmit signals from the ligand binding pocket at the extracellular face to cytoplasmic signalling molecules.

Author contributions

Participated in research design: Wootten, Sexton.

Conducted experiments: Wootten, Reynolds, Smith, Mobarec.

Performed data analysis: Wootten, Sexton, Mobarec, Christopoulos.

Wrote or contributed to writing of the manuscript: Wootten, Sexton, Reynolds, Furness, Miller, Christopoulos.

Conflict of interest statement

The authors have no conflicts of interest to declare.

Acknowledgements

This work was supported by National Health and Medical Research Council of Australia (NHMRC) project grants [1061044] and [1065410], and NHMRC program grant [1055134]; Biotechnology and Biological Sciences Research Council of the United Kingdom project grant [BB/M006883/1]; and Medical Research Council (UK) grant [G1001812].

P.M.S. is a NHMRC Principal Research Fellow.

A.C. is a NHMRC Senior Principal Research Fellow.

D.W. is a NHMRC Career Development Fellow.

The computational studies were supported by resource allocation scheme grant no. VR0024 of the VLSCI on its Peak Computing Facility at the University of Melbourne.

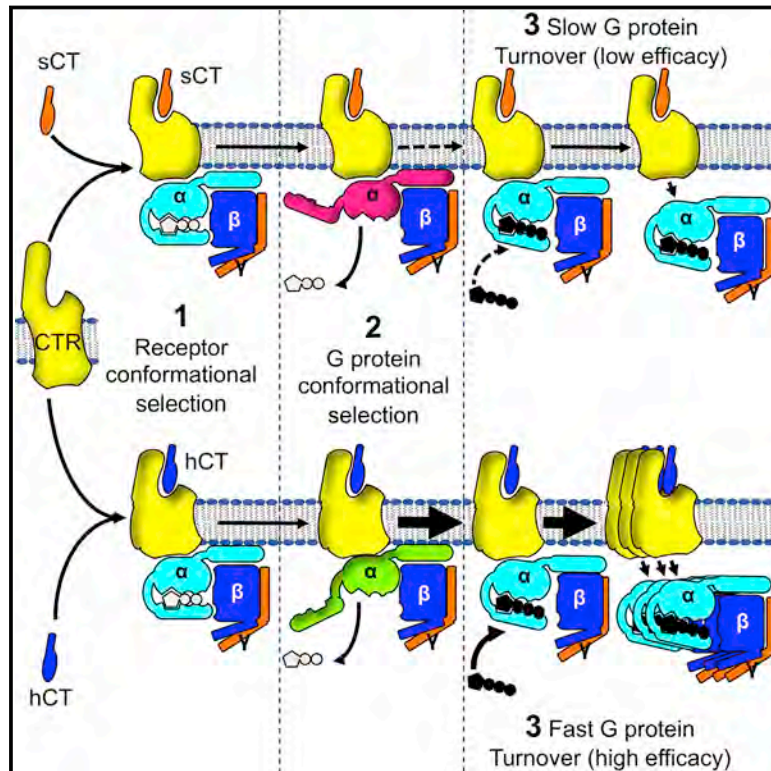
References

- [1] S. Al-Sabah, D. Donnelly, The positive charge at Lys-288 of the glucagon-like peptide-1 (GLP-1) receptor is important for binding the N-terminus of peptide agonists, *FEBS Lett.* 553 (3) (2003) 342–346.
- [2] T.E. Angel, M.R. Chance, K. Palczewski, Conserved waters mediate structural and functional activation of family A (rhodopsin-like) G protein-coupled receptors, *Proc. Natl. Acad. Sci. U.S.A.* 106 (21) (2009) 8555–8560.
- [3] T.E. Angel, S. Gupta, B. Jastrzebska, K. Palczewski, M.R. Chance, Structural waters define a functional channel mediating activation of the GPCR, rhodopsin, *Proc. Natl. Acad. Sci. U.S.A.* 106 (34) (2009) 14367–14372.
- [4] J.A. Ballesteros, A.D. Jensen, G. Liapakis, S.G. Rasmussen, L. Shi, U. Gether, J.A. Javitch, Activation of the beta 2-adrenergic receptor involves disruption of an ionic lock between the cytoplasmic ends of transmembrane segments 3 and 6, *J. Biol. Chem.* 276 (31) (2001) 29171–29177.
- [5] L.S. Barak, L. Menard, S.S. Ferguson, A.M. Colapietro, M.G. Caron, The conserved seven-transmembrane sequence NP(X)₂Y of the G-protein-coupled receptor superfamily regulates multiple properties of the beta 2-adrenergic receptor, *Biochemistry* 34 (47) (1995) 15407–15414.
- [6] C. Bergwitz, T.J. Gardella, M.R. Flannery, J.T. Potts, H.M. Kronenberg, S.R. Goldring, H. Jüppner, Full activation of chimeric receptors by hybrids between parathyroid hormone and calcitonin. Evidence for a common pattern of ligand-receptor interaction, *J. Biol. Chem.* 271 (43) (1996) 26469–26472.
- [7] D.A. Case, J.T. Berryman, R.M. Betz, D.S. Cerutti, T.E. Cheatham, T.A. Darden, R.E. Duke, T.J. Giese, H. Gohlke, A.W. Goetz, N. Homeyer, S. Izadi, P. Janowski, J. Kaus, A. Kovalenko, T.S. Lee, S. LeGrand, P. Li, T. Luchko, R. Luo, B. Madej, K.M. Merz, G. Monard, P. Needham, H. Nguyen, H.T. Nguyen, I. Omelyan, A. Onufriev, D.R. Roe, A. Roitberg, R. Salomon-Ferrer, C.L. Simmerling, W. Smith, J. Swails, R. C. Walker, J. Wang, R.M. Wolf, X. Wu, D.M. York, P.A. Kollman, AMBER 2015, University of California, San Francisco, 2015.
- [8] K.Y. Chan, R.T. Pang, B.K. Chow, Functional segregation of the highly conserved basic motifs within the third endolope of the human secretin receptor, *Endocrinology* 142 (9) (2001) 3926–3934.
- [9] A.O. Chungunov, J. Simms, D.R. Poyner, Y. Dehouck, M. Roman, D. Gills, I. Langer, Evidence that interaction between conserved residues in transmembrane helices 2, 3 and 7 are crucial for human VPAC1 receptor activation, *Mol. Pharmacol.* 78 (3) (2010) 394–401.
- [10] A.C. Conner, J. Simms, M.T. Conner, D.L. Wootten, M. Wheatley, D.R. Poyner, Diverse functional motifs within the three extracellular loops of the CGRP(1) receptor, *Biochemistry* 45 (2006) 12976–12985.
- [11] M. Conner, S.R. Hawtin, J. Simms, D. Wootten, Z. Lawson, A.C. Conner, R.A. Parslow, M. Wheatley, Systematic analysis of the entire second extracellular loop of the V(1a) vasopressin receptor: key residues, conserved throughout a G-protein-coupled receptor family, identified, *J. Biol. Chem.* 282 (24) (2007) 17405–17412.
- [12] K. Coopman, R. Wallis, G. Robb, A.J. Brown, G.F. Wilkinson, D. Timms, G.B. Willars, Residues within the transmembrane domain of the glucagon-like peptide-1 receptor involved in ligand binding and receptor activation: modelling the ligand-bound receptor, *Mol. Endocrinol.* 25 (10) (2011) 1804–1818.
- [13] A. Couvineau, J.J. Lacapere, Y.V. Tan, C. Rouyer-Fessard, P. Nicole, M. Laburthe, Identification of cytoplasmic domains of hVPAC1 receptor required for activation of adenyllyl cyclase. Crucial role of two charged amino acids strictly conserved in class II G protein-coupled receptors, *J. Biol. Chem.* 278 (27) (2003) 24759–24766.
- [14] E. Di Paolo, J.P. Vilardaga, H. Petry, N. Moguilevsky, A. Bollen, P. Robberecht, M. Waelbroeck, Role of charged amino acids conserved in the vasoactive intestinal polypeptide/secretin family of receptors on the secretin receptor functionality, *Peptides* 20 (10) (1999) 1187–1193.
- [15] R.L. Dods, D. Donnelly, The peptide agonist-binding site of the glucagon-like peptide-1 (GLP-1) receptor based on site-directed mutagenesis and knowledge-based modelling, *Biosci. Rep.* 36 (1) (2015) e00285.
- [16] N. Eswar, B. Webb, M.S. Marti-Renom, D.E. Madhusudham, M.Y. Shen, U. Pieper, A. Sali, Comparative protein structure modeling with MODELLER, *Curr. Protoc. Bioinf.* (2007) 2.9.1–2.9.31.
- [17] G.L. Garcia, M. Dong, L.J. Miller, Differential determinants for coupling of distinct G proteins with the class B secretin receptor, *Am. J. Physiol. Cell Physiol.* 302 (8) (2012) C1202–C1212.
- [18] K.G. Hari Kumar, D. Wootten, D.I. Pinon, C. Koole, A.M. Ball, S.G. Furness, B. Graham, M. Dong, A. Christopoulos, L.J. Miller, P.M. Sexton, Glucagon-like peptide-1 receptor dimerization differentially regulates agonist signaling but does not affect small molecule allostery, *Proc. Natl. Acad. Sci. U.S.A.* 109 (45) (2012) 18607–18612.
- [19] M.J. Harvey, G. Giupponi, G. De Fabritiis, ACEDMD: accelerating biomolecular dynamics in the microsecond time scale, *J. Chem. Theory Comput.* 5 (2009) 1632–1639.
- [20] R.S. Heller, T.J. Kieffer, J.L. Habener, Point mutations in the first and third intracellular loops of the glucagon-like peptide-1 receptor alter intracellular signaling, *Biochem. Biophys. Res. Commun.* 223 (1996) 624–632.
- [21] H.N. Hoang, K. Song, T.A. Hill, D.R. Derksen, D.J. Edmonds, W.M. Kok, C. Limberakis, S. Liras, P.M. Loria, V. Mascitti, A.M. Mathiowetz, J.M. Mitchell, D. W. Piotrowski, D.A. Price, R.V. Stanton, J.Y. Suen, J.M. Withka, D.A. Griffith, D.P. Fairlie, short hydrophobic peptides with cyclic constraints are potent glucagon-like peptide-1 receptor (GLP-1R) agonists, *J. Med. Chem.* 58 (2015) 4080–4085.
- [22] K. Hollenstein, J. Kean, A. Bortolato, R.K. Cheng, A.S. Dore, A. Jazayeri, R.M. Cooke, M. Weir, F.H. Marshall, Structure of class B GPCR corticotropin-releasing factor receptor 1, *Nature* 499 (7459) (2013) 438–443.
- [23] M.H. Holtmann, S. Ganguli, E.M. Hadac, V. Dolu, L.J. Miller, Multiple extracellular loop domains contribute critical determinants for agonist binding and activation of the secretin receptor, *J. Biol. Chem.* 271 (25) (1996) 14944–14949.
- [24] W. Humphrey, A. Dalke, K. Schulten, VMD: visual molecular dynamics, *J. Mol. Graph.* 14 (1996) 33–38.
- [25] K. Illergard, A. Kauko, A. Elofsson, Why are polar residues within the membrane core evolutionary conserved? *Proteins* 79 (1) (2011) 79–91.
- [26] D.G. Isom, B.R. Cannon, C.A. Castaneda, A. Robinson, B. Garcia-Moreno, High tolerance for ionizable residues in the hydrophobic interior of proteins, *Proc. Natl. Acad. Sci. U.S.A.* 105 (46) (2008) 17784–17788.
- [27] M.P. Jacobson, D.L. Pincus, C.S. Rapp, T.J. Day, B. Honig, D.E. Shaw, R.A. Friesner, A hierarchical approach to all-atom protein loop prediction, *Proteins* 55 (2004) 351–367.
- [28] S. Jo, T. Kim, V.G. Iyer, W. Im, CHARMM-GUI: a web-based graphical user interface for CHARMM, *J. Comput. Chem.* 29 (2008) 1859–1865.

- [29] B. Kobilka, The structural basis of G-protein-coupled receptor signaling (Nobel Lecture), *Angew. Chem.* 52 (25) (2013) 6380–6388.
- [30] C. Koole, D. Wootten, J. Simms, L.J. Miller, A. Christopoulos, P.M. Sexton, Second extracellular loop of human glucagon-like peptide-1 receptor (GLP-1R) has a critical role in GLP-1 peptide binding and receptor activation, *J. Biol. Chem.* 287 (6) (2012) 3642–3658.
- [31] C. Koole, D. Wootten, J. Simms, E.E. Savage, L.J. Miller, A. Christopoulos, P.M. Sexton, Second extracellular loop of human glucagon-like peptide-1 receptor (GLP-1R) differentially regulates orthosteric but not allosteric agonist binding and function, *J. Biol. Chem.* 287 (6) (2012) 3659–3673.
- [32] C. Koole, D. Wootten, J. Simms, C. Valant, L.J. Miller, A. Christopoulos, P.M. Sexton, Polymorphism and ligand dependent changes in human glucagon-like peptide-1 receptor (GLP-1R) function: allosteric rescue of loss of function mutation, *Mol. Pharmacol.* 80 (3) (2011) 486–497.
- [33] C. Koole, D. Wootten, J. Simms, C. Valant, R. Sridhar, O.L. Woodman, L.J. Miller, R.J. Summers, A. Christopoulos, P.M. Sexton, Allosteric ligands of the glucagon-like peptide 1 receptor (GLP-1R) differentially modulate endogenous and exogenous peptide responses in a pathway-selective manner: implications for drug screening, *Mol. Pharmacol.* 78 (3) (2010) 456–465.
- [34] V. Kräutler, W.F. van Gunsteren, P.H. Hünenberger, A fast SHAKE algorithm to solve distance constraint equations for small molecules in molecular dynamics simulations, *J. Comput. Chem.* 22 (2001) 501–508.
- [35] I. Langer, C. Langlet, P. Robberecht, Effect of inactivating mutations on phosphorylation and internalization of the human VPAC2 receptor, *J. Mol. Endocrinol.* 34 (2005) 405–414.
- [36] I. Langer, P. Robberecht, Mutations in the carboxy-terminus of the third intracellular loop of the human recombinant VPAC1 receptor impair VIP-stimulated $[Ca^{2+}]_i$ increase but not adenylate cyclase stimulation, *Cell Signal.* 17 (1) (2005) 17–24.
- [37] R.J. Lefkowitz, S.K. Shenoy, Transduction of receptor signals by beta-arrestins, *Science* 308 (5721) (2005) 512–517.
- [38] S.K. Mathi, Y. Chan, X. Li, M.B. Wheeler, Scanning of the glucagon-like peptide-1 receptor localizes G protein-activating determinants primarily to the N terminus of the third intracellular loop, *Mol. Endocrinol.* 11 (4) (1997) 424–432.
- [39] L.T. May, V.A. Avlani, C.J. Langmead, H.J. Herdon, M.D. Wood, P.M. Sexton, A. Christopoulos, Structure-function studies of allosteric agonism at M2 muscarinic acetylcholine receptors, *Mol. Pharmacol.* 72 (2) (2007) 463–476.
- [40] R. Nygaard, Y. Zou, R.O. Dror, T.J. Mildorf, D.H. Arlow, A. Manglik, A.C. Pan, C.W. Liu, J.J. Fung, M.P. Bokoch, F.S. Thian, T.S. Kobilka, D.E. Shaw, L. Mueller, R.S. Prosser, B.K. Kobilka, The dynamic process of beta(2)-adrenergic receptor activation, *Cell* 152 (3) (2013) 532–542.
- [41] K. Pal, K. Melcher, H.E. Xu, Structure and mechanism for recognition of peptide hormones by Class B G-protein-coupled receptors, *Acta Pharmacol. Sin.* 33 (3) (2012) 300–311.
- [42] A.B. Patel, E. Crocker, P.J. Reeves, E.V. Getmanova, M. Eilers, H.G. Khorana, S.O. Smith, Changes in interhelical hydrogen bonding upon rhodopsin activation, *J. Mol. Biol.* 347 (4) (2005) 803–812.
- [43] K.L. Pierce, R.T. Premont, R.J. Lefkowitz, Seven-transmembrane receptors, *Nat. Rev. Mol. Cell Biol.* 3 (9) (2002) 639–650.
- [44] A. Punj, J. Chen, M. Delidakis, J. Tang, G. Liapakis, H. Lehnert, M.A. Levine, D.K. Grammatopoulos, Mapping structural determinants within third intracellular loop that direct signaling specificity of type 1 corticotropin-releasing hormone receptor, *J. Biol. Chem.* 287 (12) (2012) 8974–8985.
- [45] S.G.F. Rasmussen, B.T. DeVree, Y.Z. Zou, A.C. Kruse, K.Y. Chung, T.S. Kobilka, F.S. Thian, P.S. Chae, E. Pardon, D. Calinski, J.M. Mathiesen, S.T.A. Shah, J.A. Lyons, M. Caffrey, S.H. Gellman, J. Steyaert, G. Skiniotis, W.I. Weis, R.K. Sunahara, B.K. Kobilka, Crystal structure of the beta(2) adrenergic receptor-Gs protein complex, *Nature* 477 (2011). 549–U311.
- [46] D.M. Rosenbaum, S.G. Rasmussen, B.K. Kobilka, The structure and function of G-protein-coupled receptors, *Nature* 459 (7245) (2009) 356–363.
- [47] S. Runge, C. Gram, H. Brauner-Osborne, K. Madsen, L.B. Knudsen, D.S. Wulff, Three distinct epitopes in the extracellular face of the glucagon receptor determine specificity for the glucagon amino terminus, *J. Biol. Chem.* 278 (30) (2003) 28005–28010.
- [48] S. Runge, D.S. Wulff, K. Madsen, H. Brauner-Osborne, L.B. Knudsen, Different domains of the glucagon and glucagon-like peptide-1 receptors provide the critical determinants of ligand selectivity, *Br. J. Pharmacol.* 138 (5) (2003) 787–794.
- [49] F.Y. Siu, M. He, C. de Graaf, G.W. Han, D. Yang, Z. Zhang, C. Zhou, Q. Xu, D. Wacker, J.S. Joseph, W. Liu, J. Lau, V. Cherezov, V. Katritch, M.W. Wang, R.C. Stevens, Structure of the human glucagon class B G-protein-coupled receptor, *Nature* 499 (7459) (2013) 444–449.
- [50] S.P. Sheikh et al., Similar structures and shared switch mechanisms of the beta2-adrenoceptor and the parathyroid hormone receptor. Zn(II) bridges between helices III and VI block activation, *J. Biol. Chem.* 274 (24) (1999) 17033–17041.
- [51] E. Strandberg, S. Morein, D.T. Rijkers, R.M. Liskamp, P.C. van der Wel, J.A. Killian, Lipid dependence of membrane anchoring properties and snorkeling behavior of aromatic and charged residues in transmembrane peptides, *Biochemistry* 41 (23) (2002) 7190–7198.
- [52] N. Strudwick, N. Bhogal, N.A. Evans, F.E. Blaney, J.B. Findlay, Evidence to support a spectrum of active states for the glucagon receptor, *Biochem. Soc. Trans.* 32 (Pt 6) (2004) 1037–1039.
- [53] G. Swaminath, X. Deupi, T.W. Lee, W. Zhu, F.S. Thian, T.S. Kobilka, B. Kobilka, Probing the beta2 adrenoceptor binding site with catechol reveals differences in binding and activation by agonists and partial agonists, *J. Biol. Chem.* 280 (23) (2005) 22165–22171.
- [54] S. Takhar, S. Gyomai, R.C. Su, S.K. Mathi, X. Li, M.B. Wheeler, The third cytoplasmic domain of the GLP-1[7-36]amide receptor is required for coupling to the adenylate cyclase system, *Endocrinology* 137 (1996) 2175–2178.
- [55] J.W. Tams, S.M. Knudsen, J. Fahrenkrug, Characterisation of a G protein coupling “YL” motif of the human VPAC1 receptor, equivalent to the first two amino acids in the “FRY” motif of the rhodopsin family, *J. Mol. Neurosci.* 17 (2001) 325–330.
- [56] I. Tubert-Brohman, W. Sherman, M. Repasky, T. Beuming, Improved docking of polypeptides with Glide, *J. Chem. Inf. Model.* 53 (2013) 1689–1699.
- [57] P.R. Turner, S. Mefford, T. Bambino, R.A. Nissenson, Transmembrane residues together with the amino terminus limit the response of the parathyroid hormone (PTH) 2 receptor to PTH-related peptide, *J. Biol. Chem.* 273 (1998) 3830–3837.
- [58] C.R. Underwood, P. Garibay, L.B. Knudsen, S. Hastrup, G.H. Peters, R. Rudolph, S. Reedtz-Runge, Crystal structure of glucagon-like peptide-1 in complex with the extracellular domain of the glucagon-like peptide-1 receptor, *J. Biol. Chem.* 285 (2010) 723–730.
- [59] S. Vohra, B. Taddese, A.C. Conner, D.R. Poyner, D.L. Hay, J. Barwell, P.J. Reeves, G.J. Upton, C.A. Reynolds, Similarity between class A and class B G-protein-coupled receptors exemplified through calcitonin gene-related peptide receptor modelling and mutagenesis studies, *J. R. Soc. Interface* 10 (79) (2013) 20120846.
- [60] H.A. Watkins, M. Chakravarthy, R.S. Abhayawardana, J.J. Gingell, M. Garelja, M. Pardamwar, J.M. McElhinney, A. Lathbridge, A. Constantine, P.W. Harris, T.Y. Yuen, M.A. Brimble, J. Barwell, D.R. Poyner, M.J. Woolley, A.C. Conner, A.A. Pioszak, C.A. Reynolds, D.L. Hay, Receptor activity-modifying proteins 2 and 3 generate adrenomedullin receptor subtypes with distinct molecular properties, *J. Biol. Chem.* 291 (22) (2016) 11657–11675.
- [61] T.D. Werry, K.J. Gregory, P.M. Sexton, A. Christopoulos, Characterization of serotonin 5-HT2C receptor signaling to extracellular signal-regulated kinases 1 and 2, *J. Neurochem.* 93 (6) (2005) 1603–1615.
- [62] M. Wheatley, D. Wootten, M.T. Conner, J. Simms, R. Kendrick, R.T. Logan, D.R. Poyner, J. Barwell, Lifting the lid on GPCRs: the role of extracellular loops, *Br. J. Pharmacol.* 165 (6) (2012) 1688–1703.
- [63] M.J. Woolley, H.A. Watkins, B. Taddese, Z.G. Karakullukcu, J. Barwell, K.J. Smith, D.L. Hay, D.R. Poyner, C.A. Reynolds, A.C. Conner, The role of ECL2 in CGRP receptor activation: a combined modelling and experimental approach, *J. R. Soc. Interface* 10 (88) (2013) 20130589.
- [64] D. Wootten, C. Reynolds, K.J. Smith, J.C. Mobarec, C. Koole, E.E. Savage, K. Pabreja, J. Simms, R. Sridhar, S.G.B. Furness, M. Liu, P.E. Thompson, L.J. Miller, A. Christopoulos, P.M. Sexton, The GLP-1 receptor extracellular surface is a molecular trigger for biased agonism, *Cell* 165 (7) (2016) 1632–1643.
- [65] D. Wootten, L.J. Miller, C. Koole, A. Christopoulos, P.M. Sexton, Allosteric and biased agonism at Class B G protein-coupled receptors, *Chem. Rev.* (2016). in press.
- [66] D. Wootten, J. Simms, L.J. Miller, A. Christopoulos, P.M. Sexton, Polar transmembrane interactions drive formation of ligand-specific and signal pathway-biased family B G protein-coupled receptor conformations, *Proc. Natl. Acad. Sci. U.S.A.* 110 (13) (2013) 5211–5216.
- [67] D. Wootten, E.E. Savage, F.S. Willard, A.B. Bueno, K.W. Sloop, A. Christopoulos, P.M. Sexton, Differential activation and modulation of the glucagon-like peptide-1 receptor by small molecule ligands, *Mol. Pharmacol.* 83 (4) (2013) 822–834.
- [68] D. Wootten, C.A. Reynolds, C. Koole, K.J. Smith, J.C. Mobarec, J. Simms, T. Quon, T. Coudrat, S.G. Furness, L.J. Miller, A. Christopoulos, P.M. Sexton, A hydrogen-bonded polar network in the core of the glucagon-like peptide-1 receptor is a fulcrum for biased agonism: lessons from class B crystal structures, *Mol. Pharmacol.* 89 (3) (2016) 335–347.
- [69] Q. Xiao, W. Jeng, M.B. Wheeler, Characterization of glucagon-like peptide-1 receptor-binding determinants, *J. Mol. Endocrinol.* 25 (3) (2000) 321–335.
- [70] X. Yao, C. Parnot, X. Deupi, V.R. Ratnala, G. Swaminath, D. Farrens, B. Kobilka, Coupling ligand structure to specific conformational switches in the beta2-adrenoceptor, *Nat. Chem. Biol.* 2 (8) (2006) 417–422.
- [71] T. Yaqub, I.R. Tikhonova, J. Lattig, R. Magnan, M. Laval, C. Escricu, C. Boulegue, C. Hewage, D. Fourmy, Identification of determinants of glucose dependent insulinotropic polypeptide receptor that interact with N-terminal biologically active region of the natural ligand, *Mol. Pharmacol.* 77 (2010) 547–558.

Ligand-Dependent Modulation of G Protein Conformation Alters Drug Efficacy

Graphical Abstract



Authors

Sebastian George Barton Furness,
Yi-Lynn Liang, Cameron James Nowell, ...,
Arthur Christopoulos, Denise Wootten,
Patrick Michael Sexton

Correspondence

sebastian.furness@monash.edu
(S.G.B.F.),
patrick.sexton@monash.edu (P.M.S.)

In Brief

Ligand binding to a G protein-coupled receptor not only affects the receptor conformation, but also modulates the bound G protein to shape downstream signaling.

Highlights

- Ligands stabilize distinct calcitonin receptor conformations
- Distinct ligand-promoted receptor complexes stabilize specific effector conformations
- Differential effector conformation contributes to ligand efficacy



Ligand-Dependent Modulation of G Protein Conformation Alters Drug Efficacy

Sebastian George Barton Furness,^{1,*} Yi-Lynn Liang,¹ Cameron James Nowell,¹ Michelle Louise Halls,¹ Peter John Wookey,² Emma Dal Maso,¹ Asuka Inoue,^{3,4} Arthur Christopoulos,¹ Denise Wootten,¹ and Patrick Michael Sexton^{1,5,*}

¹Drug Discovery Biology, Monash Institute of Pharmaceutical Sciences and Department of Pharmacology, Monash University, Parkville, 3052 VIC, Australia

²Department of Medicine, Austin Health, University of Melbourne, Austin Campus, Heidelberg, VIC 3084, Australia

³Graduate School of Pharmaceutical Sciences, Tohoku University, 6-3, Aoba, Aramaki, Aoba-ku, Sendai 980-0065, Japan

⁴Japan Science and Technology Agency (JST), Precursory Research for Embryonic Sciences and Technology (PRESTO), 4-1-8 Honcho, Kawaguchi, Saitama 332-0012, Japan

⁵Lead Contact

*Correspondence: sebastian.furness@monash.edu (S.G.B.F.), patrick.sexton@monash.edu (P.M.S.)

<http://dx.doi.org/10.1016/j.cell.2016.09.021>

SUMMARY

G protein-coupled receptor (GPCR) signaling, mediated by hetero-trimeric G proteins, can be differentially controlled by agonists. At a molecular level, this is thought to occur principally via stabilization of distinct receptor conformations by individual ligands. These distinct conformations control subsequent recruitment of transducer and effector proteins. Here, we report that ligand efficacy at the calcitonin GPCR (CTR) is also correlated with ligand-dependent alterations to G protein conformation. We observe ligand-dependent differences in the sensitivity of the G protein ternary complex to disruption by GTP, due to conformational differences in the receptor-bound G protein hetero-trimer. This results in divergent agonist-dependent receptor-residency times for the hetero-trimeric G protein and different accumulation rates for downstream second messengers. This study demonstrates that factors influencing efficacy extend beyond receptor conformation(s) and expands understanding of the molecular basis for how G proteins control/influence efficacy. This has important implications for the mechanisms that underlie ligand-mediated biased agonism.

INTRODUCTION

G protein-coupled receptors (GPCRs) are the largest family of cell-surface receptors, sensing a diverse array of stimuli from the extracellular environment and transmitting these signals to evoke cellular responses. This fundamental function is encapsulated by the concept of efficacy, which relates receptor occupancy by an agonist to the magnitude of the cellular response (Kenakin, 2002). The existence of ligands displaying different efficacies and, in particular, ligands displaying preferential signaling to different effectors has led to a model in which

GPCRs can adopt multiple active states (Kenakin, 2002; Kim et al., 2013). Such ligand-directed signaling bias (biased agonism) is now an important focus in drug discovery (Kenakin and Christopoulos, 2013), but there are limited data addressing the mechanisms by which such differential efficacy occurs.

GPCRs are highly dynamic proteins that rapidly sample a range of both active and inactive conformations (Deupi and Kobilka, 2010). Activation of GPCRs occurs due to changes in the proportion of time the receptor spends in one or more active states upon agonist binding. This is due to a relative decrease in the energy state of the active receptor in the receptor:agonist complex (Deupi and Kobilka, 2010). The principal driver for differential efficacy is thought to be distinct receptor conformations stabilized by different ligands. For example, ligands with distinct efficacies show divergent sampling of conformational space for the β_2 -adrenoceptor (ADRB2) (Nygaard et al., 2013), the ghrelin (GHSR) (Mary et al., 2012), serotonin (HTR2B) (Wacker et al., 2013), and the glucagon-like peptide 1 (GLP1R) receptors (Wootten et al., 2013). These divergent active conformations are thought to have different affinities for their cognate G protein hetero-trimer, providing a mechanism by which agonists could achieve differential receptor activation.

Early work by Seifert et al. (1999, 2001), however, provided the first hint that the ligand-receptor complex may also distinctly affect G protein conformations, and this has been supported by G protein fluorescence resonance energy transfer (FRET) in the presence of partial versus full agonists (Nikolaev et al., 2006). Additionally, recent work by Goricanec et al. (2016) has shown that the $G\alpha$ subunit itself is highly dynamic, sampling a number of conformations in both GDP-bound and nucleotide-free states. Nonetheless, these data on differences in receptor:G protein complexes have principally been interpreted as differences in G protein recruitment to the receptor due to distinct ligand-receptor conformations. At the most basic level, the role of the GPCR is as a guanine nucleotide exchange factor (GEF), responsible for stimulating the exchange of GDP for GTP at the $G\alpha$ subunit of hetero-trimeric G proteins resulting in their activation. By extension therefore, the formation of an agonist:receptor complex potentiates the receptor's GEF activity; thus, the agonist is a positive allosteric modulator of the GPCRs GEF

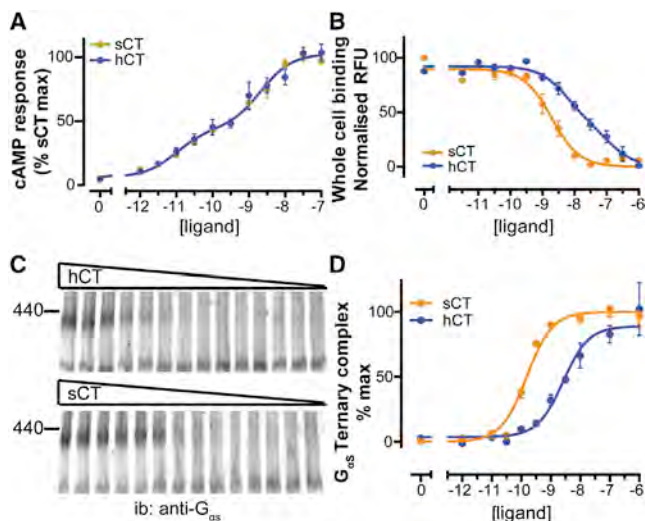


Figure 1. Functional Characterization of the Relative Efficacy of CTR Agonists and Identification of the receptor:agonist:Gs Affinity State

(A) cAMP accumulation assay in COS-7 cells stably expressing CTR with cells stimulated for 30 min in the presence of IBMX with the indicated concentrations of hCT or sCT. Both agonist response curves are best described by a biphasic curve (F test, $p < 0.0001$) with a common fit (F test, $p = 0.979$, $n = 8$, each n in triplicate with different drug dilutions on different days, data are mean \pm SEM) with log EC_{50} values of -11.00 ± 0.18 and -8.67 ± 0.12 .

(B) Whole-cell competition ligand binding in which cells were incubated overnight at 4°C with 10 nM sCT8-32:AF568 (antagonist, affinity defined by saturation binding; Figure S1B) in the presence of the indicated concentrations of cold competing agonist. sCT competition is best described by a single-site fit with a log K_i of -9.10 ± 0.07 ; hCT competition fits to a two-site model (F test, $p = 0.0007$) with log K_i values of -7.30 ± 0.31 and -8.64 ± 0.26 ($n = 6$, each n in triplicate with different drug dilutions on different days, data are mean \pm SEM). (C and D) Plasma-membrane preparations from COS-7 cells expressing CTR were treated with various concentrations of agonists prior to solubilization in Lauryl Maltose Neopentyl Glycol (MNG)/Cholesterol Hemisuccinate (CHS) and separation on a 6%–11% clear native page and transfer. The ternary complex was identified by probing for mobility shift in $G_{\alpha s}$ with a representative blot (from $n = 4$, each n with different plasma-membrane preparations and different drug dilutions on different days) shown in (C) and quantified densitometry (Fiji) shown in (D) (data are mean \pm SEM). Estimated log EC_{50} values for ternary complex formation are -8.58 ± 0.13 for hCT and -9.80 ± 0.08 for sCT (F test, p value for different EC_{50} of <0.0001).

See also Figure S1.

activity. As such, we posit that efficacy differences must translate into differential GEF activity of the GPCR. This could be due to differences in GPCR affinity for G protein but potentially also due to agonist-dependent conformational differences in G proteins, resulting in changes to nucleotide exchange rate.

The human calcitonin receptor (CTR) is the most ancient of class B GPCRs (Fredriksson et al., 2003; Nag et al., 2007). It is widely expressed in adults and during development and has complex roles in bone metabolism, brain function, cell cycle, and cancer (Clarke et al., 2015; Davey and Findlay, 2013; Venkatanarayan et al., 2015; Yamaguchi et al., 2015), including an anti-apoptotic role in osteoclasts (Selander et al., 1996) and thymic lymphomas (Venkatanarayan et al., 2015). CTR is a clinical target for the treatment of multiple diseases including Paget's disease, osteoporosis, and hypercalcemia of malignancy, with both hu-

man and salmon calcitonins (hCT and sCT, respectively) used clinically. These two peptides display distinct potency/efficacy for guanine nucleotide-binding protein G(s) subunit alpha isoforms short ($G_{\alpha s}$)-mediated cyclic AMP (cAMP) production, in a cell-dependent manner (Andreassen et al., 2014; Hilton et al., 2000; Kuestner et al., 1994). We sought to understand the mechanistic basis of the differential efficacy displayed by hCT and sCT at the CTR. Here, we demonstrate that variations in cellular efficacy are correlated with agonist-dependent, conformational differences promoted in G proteins. This current work extends the concept of conformational selection at the level of the agonist: receptor complex to one that includes conformational selection at the level of the agonist:receptor:G protein complex.

RESULTS

CTR Ligands Have Distinct Potencies for G Protein Recruitment

The CTR is most strongly coupled to the stimulatory G alpha subunit, $G_{\alpha s}$, upstream of adenylate-cyclase-mediated cAMP production. To define the cellular efficacy of hCT and sCT, we performed cAMP accumulation and ligand binding assays (Figures 1A, 1B, and S1A–S1E). Consistent with previous publications (Andreassen et al., 2014; Hilton et al., 2000), in cAMP accumulation assays (Figure 1A) the concentration response curves to both ligands were not significantly different, with similar EC_{50} and E_{\max} values. We performed competition binding on whole cells and isolated plasma membranes to determine the affinity constants for both ligands (Figures 1B and S1A–S1E). sCT had high affinity for the receptor that could be defined by a single binding constant. In contrast, hCT had lower affinity with two discernible affinity states, both of which are lower than that of sCT. Similar to certain chemokine GPCRs (Di Salvo et al., 2000), and, in contrast to GPCRs for small molecules such as biogenic amines and acetylcholine (Brodde et al., 1982; Kellar et al., 1985), we found that the distribution of CTR affinity states was unaffected by the non-hydrolysable GTP analog GppNhp (Figures S1D and S1E), suggesting that binding of G protein to the CTR is not a major driver of conformational selection for this receptor, unlike recent data for the β_2 adrenergic receptor (DeVree et al., 2016).

The observed affinity represents a composite of all the interchangeable affinity states of the receptor at equilibrium (Liu et al., 2012; Nygaard et al., 2013). To define the particular affinity state(s) associated with the ternary complex containing native $G_{\alpha s}$, we explicitly identified this complex using native PAGE (Wittig et al., 2006, 2007) (Figures 1C, 1D, S2, and 2B). This allowed us to directly establish concentration-response curves for agonist promoted recruitment of $G_{\alpha s}$ protein (Figures 1C and 1D). Similar to measures of ligand affinity (Figure 1B), sCT had an ~ 10 -fold greater potency over hCT for promotion of $G_{\alpha s}$ recruitment (Figure 1D). This suggests that the equivalent efficacy of the ligands in cAMP accumulation (Figure 1A) was not purely driven by efficiency of G protein recruitment (Figures 1A versus 1D). To better understand the nature of the agonist: receptor:G protein (ternary) complex, the relative stoichiometry of receptor and G protein was defined by using Fab fragments to induce discrete mobility shifts (Figures 2A–2C). The presence of a single shift in mobility of the ternary complex with increasing

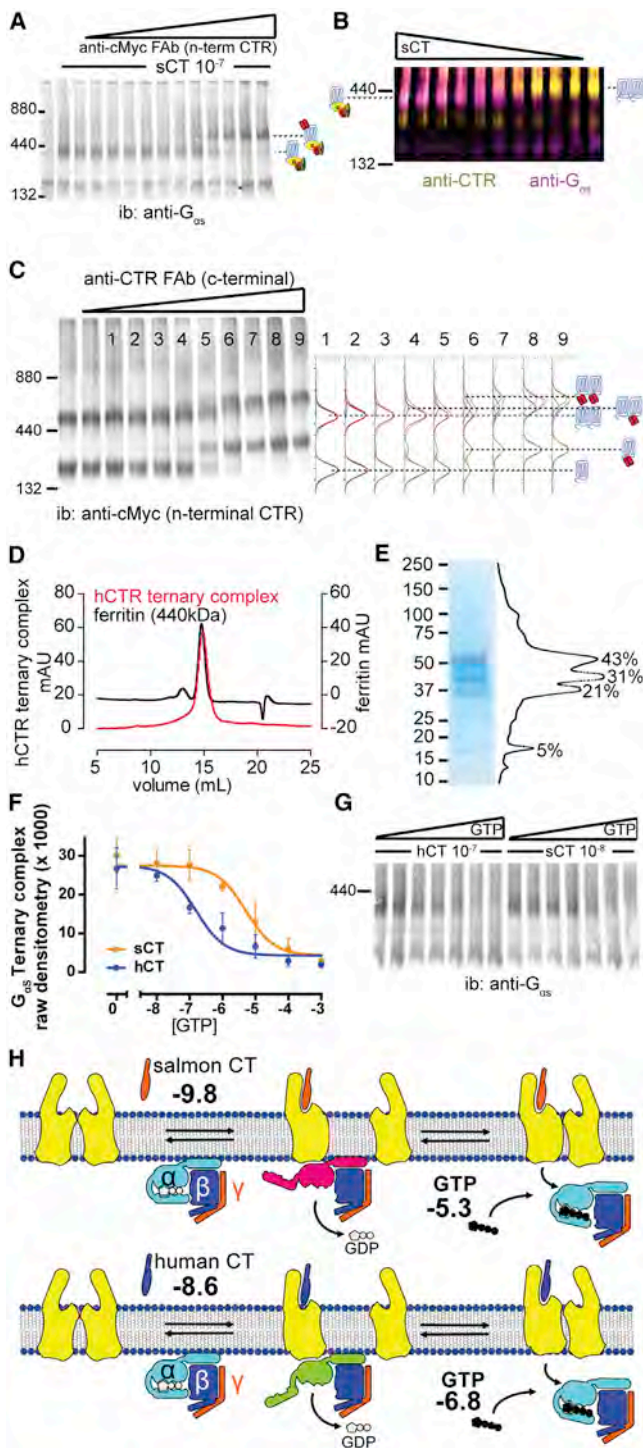


Figure 2. CTR Activates G α s in *cis* and the GTP Affinity of the Ternary Complex Is Agonist Dependent

All *n* numbers for all experiments were performed with different (plasma) membrane preparations on different days.

(A) A representative mobility shift assay (*n* = 3) using an Fab directed against the N-terminal epitope tag of CTR shows that the ternary complex contains only one CTR protomer, which is shown in cartoon with CTR in blue.

concentrations of Fab against the receptor indicated a monomeric receptor in the G protein-bound complex (Figure 2A). In contrast, in the absence of agonist, the two different receptor bands undergo either single or double Fab-induced mobility shifts, suggesting both monomeric and dimeric receptor species (Figure 2C). Taken together with the loss of dimeric receptor with increasing G protein interaction (Figure 2B), this indicated that the ligand-responsive receptor species is dimeric, but, upon G protein binding, the dimeric interface weakens and G protein activation occurs in *cis* (Figure 2A and compare with Figure S2). This is consistent with a proposed model for β 1 adrenergic receptor activation where the dimer interface partially overlaps the G protein-binding interface (Huang et al., 2013) and is depicted in the cartoon in Figure 2H. The apparent mobility observed for the ternary complex by native PAGE was lower than predicted from the molecular weight of the individual components. As an additional confirmation, the same relative mobility (~440 kDa) and stoichiometry (1:1:1 [molecular weight divided by intensity]) of the ternary complex was observed when expressed and purified from insect cells (Figures 2D and 2E).

CT Ligands Promote Distinct G Protein Conformations Linked to Guanine Nucleotide Exchange and Signaling

To understand how G_{αs} activation might differ between hCT and sCT, we defined the transduction mechanism of the

(B) A representative two-color blot (*n* = 4) of ligand-dependent transition of CTR (yellow) and G_{αs} (magenta) to the ternary complex indicating the mobility of CTR increases as it transitions to the ternary complex, consistent with a transition from the dimeric complex (Figure S2).

(C) Plasma-membrane preparations from COS-7 cells expressing CTR were incubated with increasing amounts of anti-CTR C-terminal Fab (1H10, IgG_{2a}) during solubilization in digitonin at 6 g/g for 50 min at 4°C, separation on a 4%–13.5% blue native page and transfer. Solubilization in digitonin followed by blue native PAGE preserves the 1H10 Fab interaction with CTR but results in relatively poor solubilization of CTR. The shift in CTR mobility was identified using anti-cMyc (9E10, IgG₁) followed by an isotype-specific secondary; the quantified densitometry was fitted to Gaussian distributions indicating a single shift in the lower-molecular-weight complex and two shifts in the higher molecular weight complex (*n* = 3).

(D and E) (D) A representative size exclusion chromatography trace comparing the relative mobility of insect cell-expressed and purified sCT/CTR/G_{αs}/G_{βγ} ternary complex with that of a known standard, ferritin, with the purified material shown on a Coomassie-stained gel in (E) and quantified by densitometry supportive of a 1:1:1:1 stoichiometry (representative of more than five experiments).

(F) Extensively washed plasma-membrane preparations from COS-7 cells stably expressing CTR were treated with various concentrations of GTP in the presence of (saturating) equi-occupant concentrations of agonist prior to solubilization and separation on a 6%–11% native page and transfer.

(G) The ternary complex was identified by probing for mobility shift in G_{αs} with a representative blot (from *n* = 3) shown in (G) and quantified densitometry shown in (F) (data are mean ± SEM). Estimated log EC₅₀ values for GTP-dependent disruption of ternary complexes are -6.84 ± 0.16 for hCT and -5.32 ± 0.19 for sCT (F test, *p* value for different EC₅₀ for GTP sensitivity <0.0001). Maximum recruitment of G_{αs} did not differ between ligands (F test, *p* value for different maximum = 0.42).

(H) A cartoon depiction of the differences in receptor:G protein coupling in the presence of salmon and human calcitonin. sCT has higher affinity for the ternary complex, but the resulting ternary complex has a lower sensitivity to GTP, causing lower efficacy (shown in bold are the log EC₅₀ values for each step). See also Figure S2.

receptor:agonist: $G_{\alpha S}$ ternary complex. Using equi-occupant ligand concentrations, with respect to $G_{\alpha S}$ recruitment (Figures 1C and 1D), we determined the susceptibility of the different ternary complexes, containing native G-protein, gamma subunit (G_{γ}): $G_{\alpha S}$: G-protein, beta subunit (G_{β}), to GTP by native-PAGE (Figures 2F and 2G). Both ligands were analyzed on the same gel, which revealed that, although there was no difference in the amount of G protein recruited (Figure 2G, E_{max} not significantly different), the hCT-occupied complex was disrupted by GTP at ~ 10 -fold lower GTP concentration than for sCT-occupied complexes (Figures 2F and 2G). Thermodynamically, binding of GTP to disrupt the ternary complex must be the same if the target (G protein) conformation is the same. As this differs for the two ligand-occupied complexes upon equivalent levels of G protein recruitment, it is indicative of a ligand-specific conformational difference in the recruited G protein. To test this model, we used bioluminescent resonance energy transfer (BRET) to measure rearrangement between G_{γ} , N-terminally labeled with Venus (G_{γ} :Venus), and $G_{\alpha S}$ with Rluc8 inserted at position 72 ($G_{\alpha S}^{72}$:Rluc8) (Figure 3A). $G_{\alpha S}^{72}$:Rluc8 coupled to both CTR and adenylate cyclase with sCT or hCT potencies similar to wild-type $G_{\alpha S}$, when transfected into cells genetically engineered to lack $G_{\alpha S}$ (HEK293A $\Delta G_{\alpha S}$, see STAR Methods; Schrage et al., 2015; and Figure S3A) and responded to agonist stimulation in COS7 cells in live-cell BRET experiments (Figure S3C).

We performed BRET assays on washed membrane preparations in which the nucleotide concentration could be controlled. At high agonist concentrations (100 nM), we observed a rapid and sustained increase in BRET ratio (Figure 3B) with a greater magnitude apparent in the presence of sCT, consistent with a different conformational rearrangement of the G protein in the presence of sCT versus hCT. The release of G protein (and consequent rearrangement of the G_z and G_{γ} subunits) from agonist-receptor complex requires binding of GTP to the receptor-bound nucleotide-free G protein. The addition of 300 μ M GTP caused a rapid decrease in BRET signal. This decrease in BRET could be reversed by addition of high concentrations of agonist (Figures 3C and S3B). We interpreted these ratio changes as a conformational shift from the apo to the nucleotide-bound form of the $G_{\gamma 2}$:Venus: $G_{\alpha S}^{72}$:Rluc8: $G_{\beta 1}$ hetero-trimer, consistent with previous reports of subunit rearrangement (Bünemann et al., 2003; Galés et al., 2006). Supporting this model of subunit rearrangement, subsequent agonist addition led to a BRET increase above that of vehicle (Figures 3C and S3B). The rate of change in BRET signal following addition of 100 nM ligand was significantly faster ($p < 0.0001$) for sCT compared to hCT (Figure 3D), which we believe to be driven principally by the rate of agonist binding. In contrast, at approximate EC_{50} concentrations, the rate of change in BRET was significantly faster for hCT compared to sCT ($p = 0.0007$) (Figure 3E). These data are inconsistent with a model in which increased efficacy is merely driven by increased transducer (i.e., G protein) affinity.

To further evaluate the differences in agonist-induced changes to G protein BRET, concentration-dependent time-course assays were performed (Figure S3D), and normalized area under curve (AUC) was used to plot concentration response curves (Figure 3F). The potency for driving conformational rearrangement was lower for hCT compared with sCT (Figure 3F),

consistent with the lower potency of hCT to induce ternary complex formation by native PAGE (Figures 1C and 1D). The maxima of the agonist concentration response curves were also significantly different by AUC ($p < 0.0001$ Figure 3F) with hCT showing a lower maximum, supportive of different G protein hetero-trimer conformation in the agonist:receptor:G protein complex. The saturable and significant difference in the E_{max} for this signal is consistent with different receptor-bound G protein states for these agonists (see time courses in Figure S3D). This finding is in contrast to previous reports that activation of the same hetero-trimeric G protein complex by different receptors results in similar rearrangements (Galés et al., 2006). While the assay design should ensure full occupancy of the agonist receptor complex by G protein at saturating concentrations of ligand (e.g., Figure 2B), we directly tested whether there is an agonist-dependent difference in receptor-bound G protein conformation using in-gel FRET by native PAGE. HEK293A $\Delta G_{\alpha S}$ stably expressing CTR were transiently transfected with two different G protein FRET pairs using myristoylation-positive $G_{\alpha S}$, with the fluorescent protein inserted at position 72 and N-terminally tagged $G_{\gamma 2}$ ($^{Myr+}G_{\alpha S}^{72}$ -mCherry: $G_{\gamma 2}$ -Venus or $^{Myr+}G_{\alpha S}^{72}$ -Venus: $G_{\gamma 2}$ -mCherry) and used to prepare washed membranes. Using saturating ligand concentrations, the in-gel fluorescence of the receptor-bound G protein hetero-trimer (arrows, Figure 3H) was directly quantitated. Consistent with the native PAGE experiments in Figure 2, equivalent levels of G protein were recruited to the hCT- and sCT-induced complexes as determined by direct excitation of the acceptor ($G_{\alpha S}$ -mCherry [circles] or $G_{\gamma 2}$ -mCherry [squares]; Figure 3I). In contrast, a small and significant difference in FRET between the $G_{\alpha S}$ and $G_{\gamma 2}$ was observed between the agonist:receptor:G protein complexes with the hCT-bound complex exhibiting a lower FRET signal than the equivalent sCT-occupied complex (Figure 3J). This provides corroborating evidence of a difference in conformational rearrangement of the hetero-trimeric G protein in the sCT- versus hCT-occupied complexes.

To accommodate these data, the agonist-dependent receptor-bound G protein state needs to be more sensitive to GTP concentration for the more efficacious agonist, hCT, allowing for faster G protein turnover and more effective activation of adenylate cyclase. In a cellular context, GTP is present in the 200- to 400- μ M range; we therefore performed BRET on extensively washed membranes containing G_{γ} :Venus/ $G_{\alpha S}^{72}$:Rluc8 pair with the addition of GTP prior to agonist stimulation (Figures 3G and S3E). We observed a significant reduction in EC_{50} for ligand-induced BRET for hCT in the presence of GTP, but not for sCT. This is consistent with a greater sensitivity of the hCT ternary complex to GTP in native PAGE (Figures 2F and 2G). Collectively, these data support that the hCT-occupied ternary complex has a different receptor-bound G protein conformation that is more sensitive to disruption by GTP.

To correlate the differences in GTP sensitivity from native PAGE (Figures 2F and 2G) and G protein BRET (Figure 3G) with the apparent conformational differences by BRET (e.g., Figure 3F) and in-gel FRET by Native PAGE (Figure 3J), we measured the rate of association of GTP to $G_{\alpha S}$ in pre-formed ternary complex. HEK293A $\Delta G_{\alpha S}$ stably expressing CTR were transiently transfected with $^{Myr+}G_{\alpha S}^{72}$ -mCherry and used to

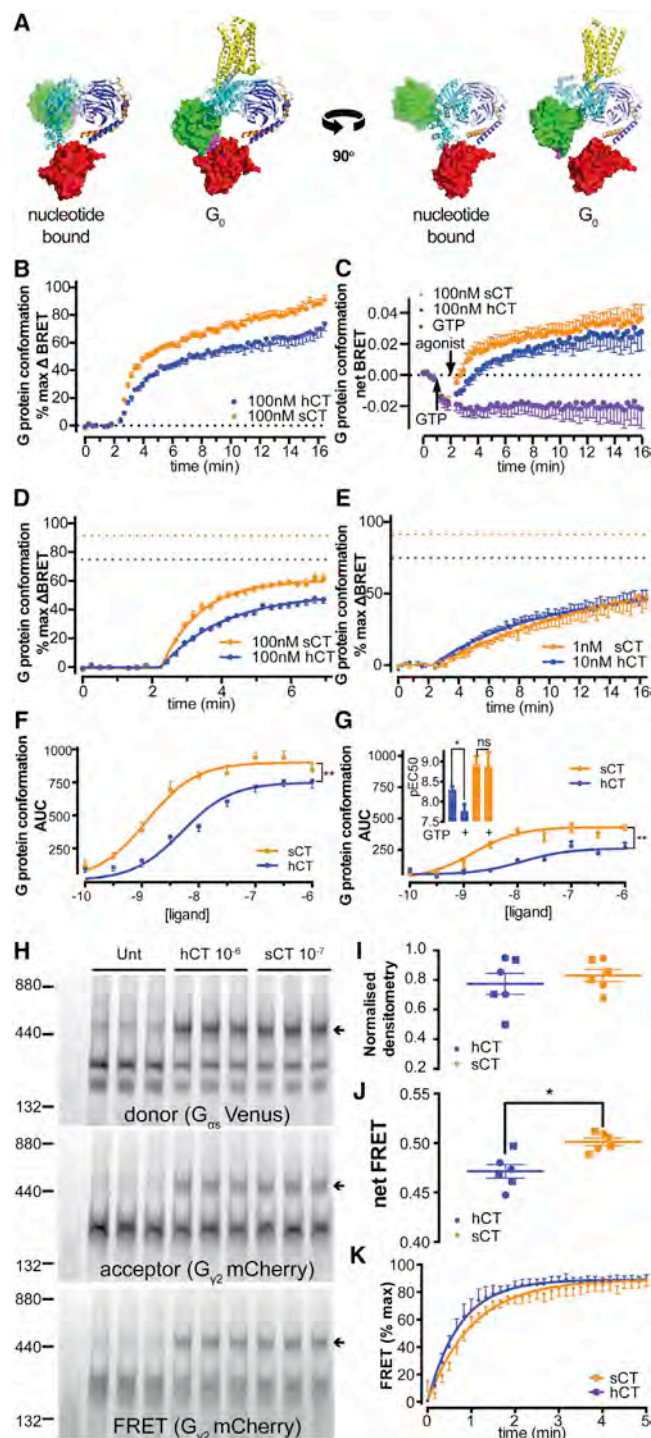


Figure 3. Agonist Promoted Changes in Heterotrimeric G Protein Conformation

(A) A cartoon illustrating the change in relative position of the BRET donor and acceptor was generated in PyMOL using PDB structures for the β_2 adrenergic receptor (yellow) in complex with $G_{\alpha s}$ (cyan) β_1 (blue) γ_2 (orange) (PDB: 3SN6), GDP-bound conformation of $G_{\alpha s}$ (cyan) (PDB: 1AZT), Rluc8 (green) (PDB: 2SPSD), and eYFP (red) (PDB: 3V3D); residues 156–171 of the Rluc8 cap are colored magenta to highlight the rotation and translation Rluc8 must undergo to accommodate the opening of $G_{\alpha s}$.

prepare washed membranes. These were pre-incubated with saturating concentrations of either hCT or sCT before mixing with 30 nM of ATTO488- γ -(6-Aminoethyl)-GTP and the rate of association measured by FRET transfer between GTP and $G_{\alpha s}$. The fitted rate was significantly faster in the presence of hCT (Figure 3K).

In (B)–(G), each n was conducted with different plasma-membrane preparations from independent transfections and different drug dilutions on different days.

(B and C) COS-7 cells stably expressing CTR were transfected with $G_{\alpha 2}$: Venus/ $G_{\alpha 2}$:Rluc8/ $G_{\beta 1}$ 16 hr before preparation of extensively washed, crude membranes. Membranes were equilibrated and baseline BRET measured for 1 min prior to addition of vehicle or 300 μ M GTP and measured for another 45 s prior to addition of ligand (baseline BRET indicated by black dotted line). (B) Time course for ligand-induced change in BRET at 100 nM (n = 9, data are mean \pm SEM). (C) Time course for ligand-induced change in BRET at 100 nM after the addition of 300 μ M GTP (n = 4, data are mean \pm SEM).

(D and E) Rate of change in BRET signal fitted to an exponential curve (the maximum sCT- and hCT-induced BRET signal is shown by orange and blue dotted lines, respectively), (D) 100 nM, p < 0.0001 for faster Δ BRET in the presence of sCT, and (E) 1 nM sCT c.f. 10 nM hCT, with hCT showing faster Δ BRET p = 0.0007.

(F and G) Normalized AUC for the indicated ligand concentrations is plotted as a concentration response curve. (F) The log EC_{50} values for ligand-induced changes in BRET are -8.30 ± 0.08 for hCT and -8.94 ± 0.08 for sCT (n = 9, F test, p value for different EC_{50} for ligand-induced change in BRET < 0.0001) with AUC top of 744 ± 24 for hCT and 900 ± 22 for sCT (n = 9 F test, *p value for different top for ligand-induced change in BRET < 0.0001, data are presented as mean \pm SEM). (G) Log EC_{50} values for ligand-induced change in BRET in the presence of 300 μ M GTP are -7.77 ± 0.17 for hCT and -8.87 ± 0.18 for sCT (n = 4, F test, p value for different EC_{50} for ligand-induced change in BRET = 0.0001), with an AUC top of 304 ± 19 for hCT and 472 ± 21 for sCT (n = 4, F test, *p value for different top for ligand-induced change in BRET < 0.0001, data are mean \pm SEM). GTP-induced change in p EC_{50} is shown in inset with a significant decrease for hCT (n = 4–9, t test, p value for different p EC_{50} in the absence of GTP = 0.0069) but no change for sCT (n = 4–9, t test, p value for different p EC_{50} in the absence of GTP = 0.68).

(H–J) Extensively washed plasma-membrane preparations from HEK293A $\Delta G_{\alpha s}$ cells (stably expressing CTR and transiently transfected with $G_{\alpha 2}$: Venus/ $G_{\alpha 2}$:mCherry/ $G_{\beta 1}$ (circles) OR $G_{\alpha 2}$:mCherry/ $G_{\alpha 2}$:Venus/ $G_{\beta 1}$ (squares) 36 hr before preparation) were either untreated or treated with (saturating) equi-occupant concentrations of hCT (1 μ M) or sCT (100 nM) prior to solubilization and separation on a 6%–11% native page. The ternary complex was identified by direct in-gel fluorescence, and data are presented as individual determinations \pm SEM with FRET swap shown in circles and squares and representative gel (from n = 6, each n conducted with triplicate lanes with different plasma-membrane preparations from independent transfections and different drug dilutions on different days) shown in (H). Quantified densitometry of the acceptor only channel is shown in (I), with no difference in densitometry between hCT- and sCT-induced G protein recruitment (n = 6, t test, *p value for different densitometry = 0.51). (J) Calculated net-FRET from quantified densitometry; 0.471 ± 0.007 for hCT and 0.501 ± 0.004 for sCT (n = 6, t test, *p value for different FRET = 0.0036).

(K) HEK293A $\Delta G_{\alpha s}$ cells stably expressing CTR were transiently transfected with $G_{\alpha 2}$:mCherry/ $G_{\alpha 2}$:mCherry/ $G_{\beta 1}$ 16 hr before preparation of extensively washed crude membranes. Membranes were pre-equilibrated with 1 μ M of either hCT or sCT before the association of fluorescently labeled GTP (ATTO-488- γ -(6-Aminoethyl)-GTP) was measured by FRET. (K) Time course for increase in FRET signal upon mixing of membranes with 30 nM labeled GTP as mean \pm SEM; the observed k for hCT is $1.35 \pm 0.08 \text{ min}^{-1}$ ($t_{1/2} \sim 0.51 \text{ min}$) and for sCT is $0.97 \pm 0.05 \text{ min}^{-1}$ ($t_{1/2} \sim 0.71 \text{ min}$) (n = 6, two independent transfections, six independent drug dilutions, F test, p value for different k < 0.0001).

See also Figure S3.

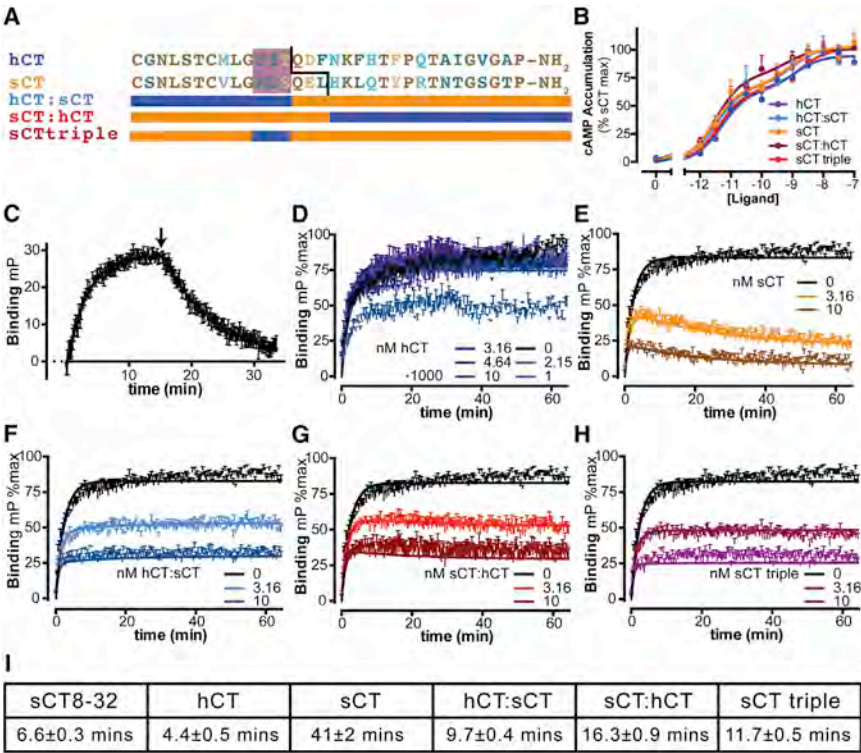


Figure 4. Agonist Structural Determinants of Dissociation Rates

(A) Alignment of hCT and sCT; identical residues shown in brown, conserved in light brown, weakly conserved in light cyan and non-conserved in dark cyan. Cartoon illustrating the chimeric peptides used in this study is shown underneath.

(B) cAMP accumulation assay in COS-7 cells stably expressing CTR with cells stimulated for 30 min in the presence of IBMX with the indicated concentrations of hCT, sCT, and chimeric peptides. All agonist response curves are biphasic (F test, p better than 0.03 for all curves) and are best described by a common fit (F test, $p = 0.762$, $n = 3$, each n conducted in triplicate with different drug dilutions on different days, data are mean \pm SEM) with shared log EC_{50} values of -11.4 ± 0.13 and -8.85 ± 0.23 .

(C) Homogeneous association and dissociation of sCT8-32:AF568 by fluorescence polarization on membranes from COS-7 cells stably expressing CTR, $K_{on} = 1.91 \pm 0.19 \times 10^7 \text{ M}^{-1} \text{ min}^{-1}$ and $K_{off} = 0.1043 \pm 0.005 \text{ min}^{-1}$ ($n = 9$, each n conducted with different plasma-membrane preparations and different drug dilutions on different days, $K_d = 5.3 \text{ nM}$, consistent with equilibrium binding; **Figures S1B** and **S1C**) corresponding to a $t_{1/2}$ of 6.6 min.

(D–H) Homogenous kinetic competition between sCT-8-23:AF568 and indicated ligands by fluo-

rescence polarization on membranes from COS-7 cells stably expressing CTR (hCT $n = 8$, all other peptides $n = 6$, data are mean \pm SEM, each n conducted with different plasma-membrane preparations and different drug dilutions on different days).
(I) Calculated $t_{1/2}$ values for all ligands.

To exclude the possibility that these differences in apparent efficacy and G protein conformation were the result of kinetic effects due to the slow dissociation rate of sCT, chimeric peptides (Hilton et al., 2000), as shown in **Figure 4A**, were generated and tested. In cAMP accumulation assays, these chimeric peptides displayed concentration response curves that overlaid with those of the parental peptides (**Figure 4B**). Association and dissociation rates were determined using kinetic competition against a fluorescently labeled antagonist (**Figure 4C**). As expected, wild-type sCT had a very slow off rate (Andreassen et al., 2014; Hilton et al., 2000), with a $T_{1/2}$ of $>40 \text{ min}$, whereas all chimeric peptides displayed significantly faster off rate kinetics (**Figures 4D–4I**), demonstrating that observed potencies in the cAMP assay are not correlated with peptide binding kinetics. The potency of ligands to cause changes in G protein conformation was then assessed by BRET assays, as described above (**Figures 5A–5C**). The hCT:sCT chimera, containing the amino terminal 13 amino acids of hCT and the last 19 amino acids of sCT, induced a maximal change in BRET (G protein conformational rearrangement) that was similar to that induced by hCT but significantly different from that induced by sCT. In contrast, the EC_{50} was similar to that of sCT (**Figure 5D**). These data are consistent with the peptide amino terminus driving receptor activation, while the affinity for the complex is driven by interactions of the peptide C terminus with the receptor extracellular domain (Wooten et al., 2016). Similarly, the sCT(1-16):hCT(17-32) chimera, elicited a maximal change in

BRET equivalent to that of sCT, and significantly different to that of hCT, while the EC_{50} of the response was intermediate between that of sCT and hCT (**Figure 5E**). Finally the sCT triple chimera, containing three amino acids from the central portion of hCT, promoted a conformational rearrangement yielding a potency and maximal effect similar to those of sCT (**Figure 5F**) in spite of its significantly faster off rate (c.f. **Figures 4E** with **4H**). Collectively, these data demonstrate that cellular efficacy results from a complex interplay between G protein recruitment affinity and the subsequent G protein conformation in the ternary complex, and that this is independent of ligand dissociation rates.

CT Ligands Differentially Stabilize Receptor-G Protein Complexes at the Cell Surface

To accommodate the equivalent cellular potency of the lower-affinity agonist, hCT, with the higher-affinity agonist sCT, and taking into account the difference in GTP binding, we reasoned that the turnover of G protein at the hCT-bound receptor would be faster than that at the sCT-bound receptor. We therefore imaged fluorescent G protein mobility at the apical surface by total internal reflection (TIRF) microscopy as depicted schematically in **Figure S4**. Using a fluorescently tagged sCT analog, we established that the mobility of agonist-bound CTR is limited (data not shown) at the timescale of tens-to-hundreds of milliseconds (at 20°C). We observed two distinct, mutually exclusive, distributions of fluorescently tagged G proteins (both $G_{\alpha s}$ and $G_{\gamma 2}$), either rapidly mobile G proteins with latency in the

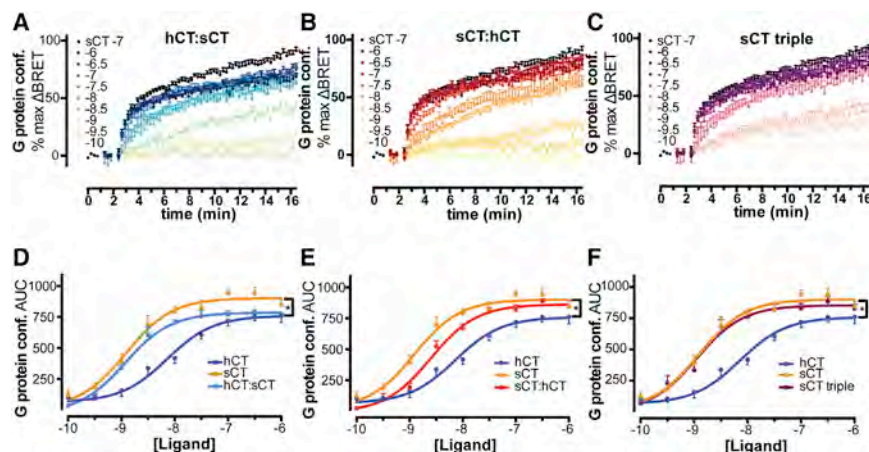


Figure 5. Agonist Structural Determinants of Differential Effects on Heterotrimeric G Protein Conformation

(A–C) Full kinetic responses, using washed, crude membranes, at all concentrations tested of hCT:sCT chimera (A), sCT:hCT (B), and sCT triple mutant (C) (all data are $n = 4$, each n conducted in triplicate with different plasma-membrane preparations from independent transfections and different drug dilutions on different days and are shown as mean \pm SEM; sCT maximum response curve is in black).

(D–F) The normalized AUC for the indicated ligand concentrations is plotted as a concentration response curve and shown as mean \pm SEM (D) the log EC_{50} for hCT:sCT-induced changes in BRET is -8.89 ± 0.05 ($n = 4$, F test, p value for different EC_{50} c.f. hCT < 0.001 and sCT = 0.667) with AUC top of 785 ± 15 ($n = 4$, F test, p value for different top c.f. hCT = 0.187 and sCT = 0.0006).

(E) The log EC_{50} for sCT:hCT-induced changes in BRET is -8.95 ± 0.05 ($n = 4$, F test, p value for different EC_{50} c.f. hCT = 0.0111 and sCT = 0.0007) with AUC top of 864 ± 18 ($n = 4$, F test, p value for different top c.f. hCT = 0.0008 and sCT = 0.288).

(F) The log EC_{50} for sCT triple-induced changes in BRET is -8.95 ± 0.06 ($n = 4$, F test, p value for different EC_{50} c.f. hCT < 0.0001 and sCT = 0.856) with AUC top of 854 ± 20 ($n = 4$, F test, p value for different top c.f. hCT = 0.0019 and sCT = 0.166).

evanescent field on the tens of millisecond timescale or those that remained essentially immobile over timescales in the minutes (at 20°C). Cells transiently overexpressing $G_{\gamma 2}$ Venus and native $G_{\alpha s}$ and exhibiting rapid G protein mobility (Movie S1) were imaged. The latency of individual $G_{\gamma 2}$ Venus events in the evanescent field was extracted prior to and after stimulation with saturating concentrations of agonist and fitted to an exponential decay curve. Both ligands increased the half-life of $G_{\gamma 2}$ Venus at the plasma membrane, with a significantly longer ($p = 0.005$) half-life in the presence of sCT (24.1 ± 1.2 versus 20.8 ± 1.1 ms for hCT and 17.9 ± 0.5 ms for unstimulated at 20°C , $n = 3$, Figure 6A). This is consistent with proportionately faster G protein turnover in response to hCT versus sCT. To confirm this, we also visualized the $G_{\alpha s}$ subunit; the biological activity of $G_{\alpha s}^{72}$ mCherry was confirmed by transient transfection into cells genetically engineered to lack $G_{\alpha s}$ (see STAR Methods; Schrage et al., 2015; and Figure S5A). Cells transiently overexpressing $G_{\gamma 2}:G_{\alpha s}^{72}$ mCherry: $G_{\beta 1}$ and exhibiting rapid G protein mobility (Movie S2) were imaged. Only sCT produced a significant increase in the latency of individual $G_{\alpha s}^{72}$ mCherry events in the evanescent field over vehicle ($p < 0.0001$) (Figure 6A and representative 3D histograms from a small subset of data in Figure 6B). This slower G protein mobility suggests slower GTP turnover and therefore that the GTP binding step is rate limiting when sCT is bound at the receptor. These data are consistent with native PAGE, in which hCT shows greater GTP sensitivity (Figures 2F and 2G), and the GTP induced change in G protein BRET EC_{50} for hCT and not sCT (Figures 3F and 3G). Importantly, they further support a model in which hCT promotes a receptor-bound G protein conformation that is less open than the sCT conformation. This results in faster GTP binding and more rapid G protein turnover (Figure 6C), potentially allowing more rapid signaling.

CT Ligands Display Differential cAMP Production Rates in Live Cells

To test the latter prediction, we used a cAMP biosensor to measure the rates at which cAMP accumulates in response to these

ligands. At saturating concentrations, we saw no difference in the rate or magnitude of cAMP accumulation (Figure 7A, $p = 0.215$), but at 10 pM we observed a significantly faster ($p = 0.018$) accumulation of cAMP in response to hCT compared with sCT (Figure 7B). This was confirmed in a cell line that endogenously expresses CTR (Figures 7C and 7D) and supports our model (Figure 6C) in which the hCT-occupied CTR is capable of promoting more G protein activation per time compared with the sCT-occupied receptor.

DISCUSSION

Differential efficacy at GPCRs has already been exploited clinically with the use of partial agonists, for example, at adrenergic and opioid receptors (Cowan, 2003; Lipworth and Grove, 1997). In spite of this, and the emergence of biased agonism as another means to tailor the clinical efficacy of drugs, there are few data that address the underlying molecular basis of differential efficacy. There is now a broad appreciation that different ligands acting at a single GPCR can alter the sampling of the conformational landscape explored by the GPCR (Deupi and Kobilka, 2010; Kim et al., 2013; Mary et al., 2012; Nygaard et al., 2013; Wacker et al., 2013; Wootton et al., 2013). In general, it is thought that the consequence of ligand-dependent conformational selection is to alter the affinity of the receptor for particular transducers and thus alter signaling efficacy and/or bias. Although distinct G protein conformations linked to individual receptor complexes have been alluded to (Seifert et al., 1999, 2001), collectively, our work provides evidence of ligand-dependent ternary complexes controlling guanine nucleotide exchange, via promotion of distinct changes in G protein conformation. We were able to show that binding of the high-affinity ligand, sCT, results in a ternary complex that has a lower tendency to dissociate in the presence of GTP. This is analogous to the concept that a G protein that has disproportionately high affinity for a GPCR can act in a physiologically and/or clinically relevant, “dominant-negative” fashion (Berlot, 2002; Grishina and Berlot,

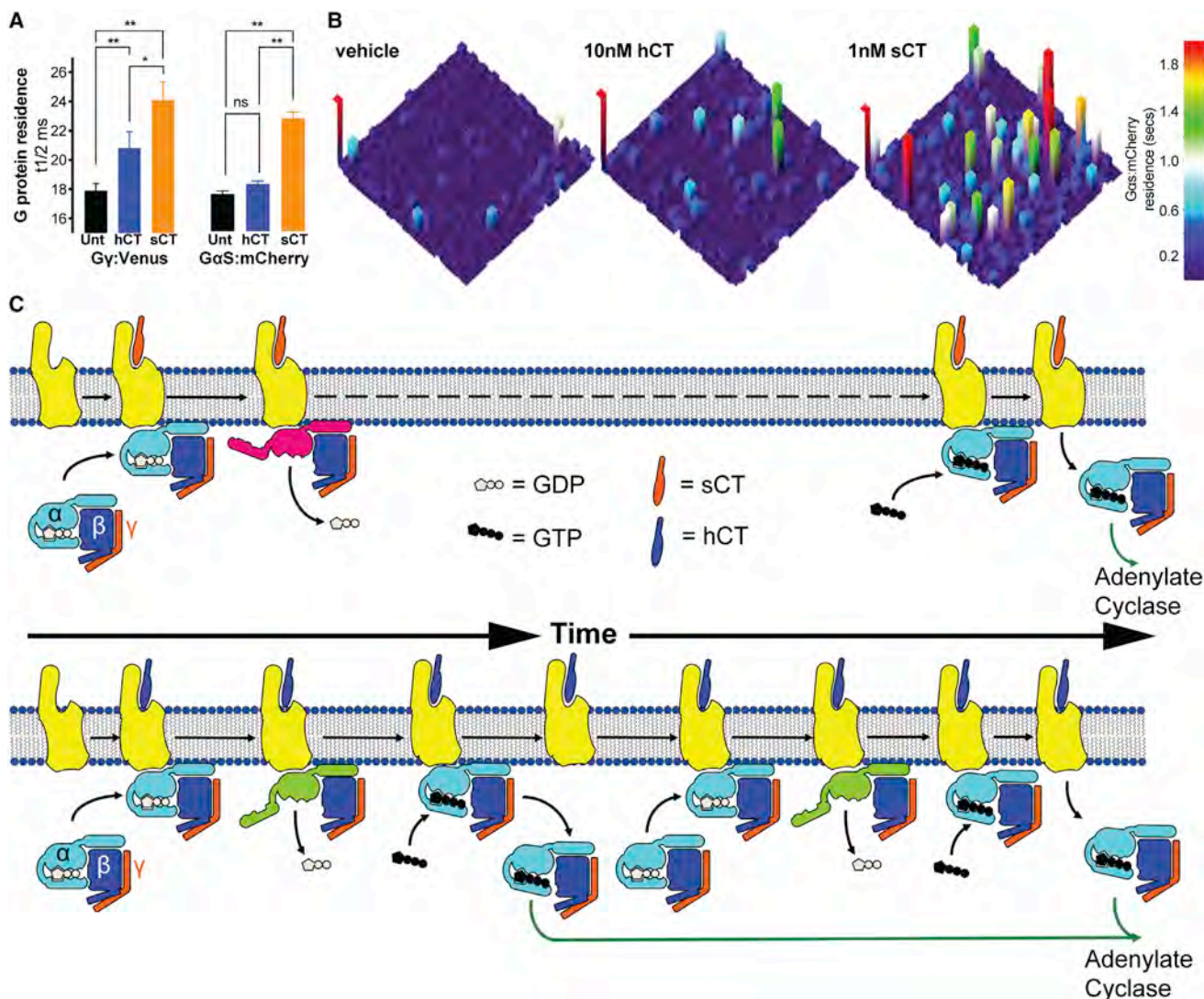


Figure 6. Agonist-Promoted G Protein Residency in Live Cells

(A) COS-7 cells stably expressing CTR were transfected with either G_{γ2}:Venus or G_{γ2}/G_{αs}⁷²:mCherry/G_{β1} 16 hr before assay. Ligand-induced changes in G_{γ2} or G_{αs}⁷²:mCherry residence were measured on live cells under TIRF at 33 or 40 frames/second with the addition of equi-occupant concentrations of sCT (1 nM) and hCT (10 nM) after 2 min of baseline data collection at 20°C. For G_{γ2}:Venus residency three independent experiments were performed with three to five different cell areas imaged with at least 3,000 spots of two or more frames per ligand per experiment (total of 11 cells per ligand). Spot sizes were not significantly different between hCT- and sCT-treated cells. For G_{αs}⁷²:mCherry residency, four independent experiments were performed with three different cell areas imaged with at least 3,000 spots of two or more frames per ligand per experiment (total of 12 cells per ligand). G protein latency in the TIRF field was fitted to an exponential decay curve and derived half-lives plotted (mean ± SEM p value for difference between unstimulated and ligand-induced decay rate of G_{γ2}:Venus <0.0001 (**), and for difference between sCT and hCT = 0.0046 (*), one-way ANOVA (n = 3, unstimulated k = 38.3 ± 1.1, hCT k = 33.0 ± 1.9 and sCT k = 28.5 ± 0.6), p value for difference between unstimulated sCT decay rate of G_{αs}⁷²:mCherry < 0.0001 (**), no significant difference between unstimulated and hCT (ns), one-way ANOVA (n = 4, unstimulated k = 39.2 ± 0.5, hCT k = 38.3 ± 0.5 and sCT k = 30.7 ± 0.6).

(B) The residence time of 625 representative spots (of >10,000 of two or more frames) was plotted in 2D with the length of residence plotted in the z dimension (as shown on scale).

(C) Cartoon indicating the relative efficacy of sCT (orange) compared with hCT (blue) in which the rate-limiting step for agonist-induced G protein activation is GTP association to the receptor-bound G protein complex. The rate at which this occurs is faster in the presence of hCT allowing for quantitatively more G protein and adenylate cyclase activation per unit time in spite of lower receptor occupancy.

See also Figure S4 and Movies S1 and S2.

2000; Iiri et al., 1994, 1999). We therefore argue that, as different ligands acting at the same receptor engender differences in the sampling of conformational space by the receptor, this differential sampling extends to the heterotrimeric G protein bound in the

ternary complex. Distinct, ligand-dependent conformations of transducer proteins has recently been proposed for arrestins and may control secondary signaling from these key scaffolding proteins (Lee et al., 2016; Nuber et al., 2016). Since the prime,

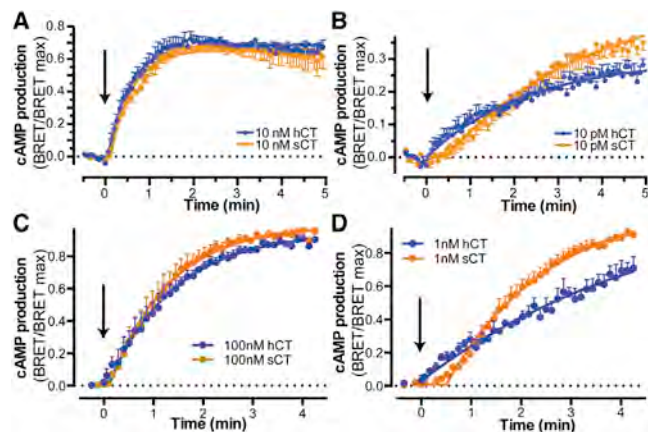


Figure 7. Agonist-Promoted Rates of cAMP Accumulation in Live Cells

(A and B) Rate of increase of intracellular cAMP as measured by a BRET cAMP sensor (CAMYEL) in COS-7 cells transiently transfected with CTR. cAMP formation data were fitted using an exponential one phase model with the rate of production in response to 10 pM hCT being significantly faster than 10 pM sCT (B) (F test, $p = 0.018$), whereas no statistical difference in formation rate was seen at 10 nM (A) (F test, $p = 0.215$, $n = 4$, each n conducted in triplicate from independent transfections and different drug dilutions on different days; data are mean \pm SEM).

(C and D) Rate of increase of intracellular cAMP as measured by a BRET cAMP sensor (CAMYEL) in CHO-K1 cells expressing endogenous CTR. cAMP formation data were fitted using an exponential one phase model with the onset of production in response to 1 nM hCT being significantly faster than 1 nM sCT (D) (F test, $p < 0.0001$), whereas no statistical difference in formation rate was seen at 100 nM (C) (F test, $p = 0.0687$, $n = 3$, each n conducted in triplicate on separate days with separate drug dilutions; data are mean \pm SEM).

See also Figure S5.

orthodox, role of a ligand-bound GPCR is to accelerate the rate of nucleotide exchange at G_{α} , we would argue that there is a fine balance between the affinity that the ligand-bound receptor has for its cognate G protein and its ability to release this G protein once nucleotide exchange has occurred. Indeed, for GPCRs that possess more than one endogenous agonist, this could provide another means by which their different physiological effects are engendered. Moreover, it provides an additional mechanism through which biased agonism, at the level of the G protein, can occur. Our work thus extends the understanding of the molecular basis of G protein-dependent efficacy.

STAR★METHODS

Detailed methods are provided in the online version of this paper and include the following:

- **KEY RESOURCES TABLE**
- **CONTACT FOR REAGENT AND RESOURCE SHARING**
- **EXPERIMENTAL MODEL AND SUBJECT DETAILS**
 - Cell Lines
- **METHOD DETAILS**
 - Fluorescently labeled peptides
 - Cell Culture

- CTR and G protein expression and purification from insect cells
- cAMP accumulation assay
- Competition fluorescent binding assay
- Kinetic ligand binding
- Membrane preparations
- Native PAGE
- G protein BRET
- GTP association
- G protein residency
- Modeling G protein rearrangement
- BRET CAMYEL assay

● QUANTIFICATION AND STATISTICAL ANALYSIS

- cAMP accumulation assay analysis
- Ligand binding analysis
- Analysis of Native PAGE
- G protein BRET analysis
- GTP association analysis
- G protein residency analysis

● DATA AND SOFTWARE AVAILABILITY

- TIRF residency script
- In gel FRET quantitation script

SUPPLEMENTAL INFORMATION

Supplemental Information includes five figures and two movies and can be found with this article online at <http://dx.doi.org/10.1016/j.cell.2016.09.021>.

A video abstract is available at <http://dx.doi.org/10.1016/j.cell.2016.09.021#mmc3>.

AUTHOR CONTRIBUTIONS

Conceptualization, S.G.B.F. and P.M.S.; Methodology, S.G.B.F.; Software, C.J.N.; Formal Analysis, S.G.B.F. and C.J.N.; Investigation, S.G.B.F., L.L., M.L.H., D.W., and E.D.M.; Resources, P.J.W.; Writing – Original Draft, S.G.B.F.; Writing – Review & Editing, P.J.W., C.J.N., D.W., A.C., and P.M.S.; Visualization, S.G.B.F. and P.M.S.; Supervision, P.M.S. and S.G.B.F.; Funding Acquisition, P.M.S. and A.C.

ACKNOWLEDGMENTS

This work was funded by National Health and Medical Research Council (NHMRC) Project Grant APP1061044 and NHMRC Program Grant APP1055134. P.M.S. is an NHMRC Principal Research Fellow and A.C. an NHMRC Senior Principal Research Fellow. M.L.H. is a NHMRC RD Wright Fellow (1061687). D.W. is an NHMRC Career Development Fellow. A.I. was funded by JST, PRESTO. We thank N.A. Lambert for the constructs encoding $G_{\alpha s}^{T2}$:RLuc8 and $G_{\alpha s}^{T2}$:mCherry and for critiquing the manuscript. We thank B.K. Kobilka for the construct encoding Nb35 and for advice on expression and purification of the CTR ternary complex from insect cells. We thank P. Zhao and J.R. Lane for discussions. We also thank J.B. Furness and M.L. Whitelaw for critiquing the manuscript.

Received: June 14, 2016

Revised: July 28, 2016

Accepted: September 8, 2016

Published: October 6, 2016

REFERENCES

Andreassen, K.V., Hjuler, S.T., Furness, S.G., Sexton, P.M., Christopoulos, A., Nosjean, O., Karsdal, M.A., and Henriksen, K. (2014). Prolonged calcitonin

- receptor signaling by salmon, but not human calcitonin, reveals ligand bias. *PLoS ONE* 9, e92042.
- Berlot, C.H. (2002). A highly effective dominant negative α s construct containing mutations that affect distinct functions inhibits multiple Gs-coupled receptor signaling pathways. *J. Biol. Chem.* 277, 21080–21085.
- Brodde, O.E., Hardung, A., Ebel, H., and Bock, K.D. (1982). GTP regulates binding of agonists to α 2-adrenergic receptors in human platelets. *Arch. Int. Pharmacodyn. Ther.* 258, 193–207.
- Bünemann, M., Frank, M., and Lohse, M.J. (2003). Gi protein activation in intact cells involves subunit rearrangement rather than dissociation. *Proc. Natl. Acad. Sci. USA* 100, 16077–16082.
- Clarke, M.V., Russell, P.K., Findlay, D.M., Sastra, S., Anderson, P.H., Skinner, J.P., Atkins, G.J., Zajac, J.D., and Davey, R.A. (2015). A role for the calcitonin receptor to limit bone loss during lactation in female mice by inhibiting osteocytic osteolysis. *Endocrinology* 156, 3203–3214.
- Cowan, A. (2003). Buprenorphine: New pharmacological aspects. *Int. J. Clin. Pract. Suppl.*, 3–8, discussion, 23–24.
- Davey, R.A., and Findlay, D.M. (2013). Calcitonin: Physiology or fantasy? *J. Bone Miner. Res.* 28, 973–979.
- Deupi, X., and Kobilka, B.K. (2010). Energy landscapes as a tool to integrate GPCR structure, dynamics, and function. *Physiology (Bethesda)* 25, 293–303.
- DeVree, B.T., Mahoney, J.P., Vélez-Ruiz, G.A., Rasmussen, S.G.F., Kuszak, A.J., Edwald, E., Fung, J.J., Manglik, A., Masureel, M., Du, Y., et al. (2016). Allosteric coupling from G protein to the agonist-binding pocket in GPCRs. *Nature* 535, 182–186.
- Di Salvo, J., Koch, G.E., Johnson, K.E., Blake, A.D., Daugherty, B.L., DeMartino, J.A., Sirotina-Meisher, A., Liu, Y., Springer, M.S., Cascieri, M.A., and Sullivan, K.A. (2000). The CXCR4 agonist ligand stromal derived factor-1 maintains high affinity for receptors in both Galpha(i)-coupled and uncoupled states. *Eur. J. Pharmacol.* 409, 143–154.
- Fredriksson, R., Lagerström, M.C., Lundin, L.-G., and Schiöth, H.B. (2003). The G-protein-coupled receptors in the human genome form five main families. Phylogenetic analysis, paralogon groups, and fingerprints. *Mol. Pharmacol.* 63, 1256–1272.
- Galés, C., Van Durm, J.J.J., Schaak, S., Pontier, S., Percherancier, Y., Audet, M., Paris, H., and Bouvier, M. (2006). Probing the activation-promoted structural rearrangements in preassembled receptor-G protein complexes. *Nat. Struct. Mol. Biol.* 13, 778–786.
- Goricanec, D., Stehle, R., Egloff, P., Grigoriu, S., Plückthun, A., Wagner, G., and Hagn, F. (2016). Conformational dynamics of a G-protein α subunit is tightly regulated by nucleotide binding. *Proc. Natl. Acad. Sci. USA* 113, E3629–E3638.
- Grishina, G., and Berlot, C.H. (2000). A surface-exposed region of G(salpa) in which substitutions decrease receptor-mediated activation and increase receptor affinity. *Mol. Pharmacol.* 57, 1081–1092.
- Hilton, J.M., Dowton, M., Houssami, S., and Sexton, P.M. (2000). Identification of key components in the irreversibility of salmon calcitonin binding to calcitonin receptors. *J. Endocrinol.* 166, 213–226.
- Hobbs, S., Jitrapakdee, S., and Wallace, J.C. (1998). Development of a bicistronic vector driven by the human polypeptide chain elongation factor 1 α promoter for creation of stable mammalian cell lines that express very high levels of recombinant proteins. *Biochem. Biophys. Res. Commun.* 252, 368–372.
- Huang, J., Chen, S., Zhang, J.J., and Huang, X.-Y. (2013). Crystal structure of oligomeric β 1-adrenergic G protein-coupled receptors in ligand-free basal state. *Nat. Struct. Mol. Biol.* 20, 419–425.
- Iiri, T., Herzmark, P., Nakamoto, J.M., van Dop, C., and Bourne, H.R. (1994). Rapid GDP release from Gs α in patients with gain and loss of endocrine function. *Nature* 371, 164–168.
- Iiri, T., Bell, S.M., Baranski, T.J., Fujita, T., and Bourne, H.R. (1999). A Gsalpa mutant designed to inhibit receptor signaling through Gs. *Proc. Natl. Acad. Sci. USA* 96, 499–504.
- Jiang, L.I., Collins, J., Davis, R., Lin, K.-M., DeCamp, D., Roach, T., Hsueh, R., Rebres, R.A., Ross, E.M., Taussig, R., et al. (2007). Use of a cAMP BRET sensor to characterize a novel regulation of cAMP by the sphingosine 1-phosphate/G13 pathway. *J. Biol. Chem.* 282, 10576–10584.
- Kellar, K.J., Martino, A.M., Hall, D.P., Jr., Schwartz, R.D., and Taylor, R.L. (1985). High-affinity binding of [3 H]acetylcholine to muscarinic cholinergic receptors. *J. Neurosci.* 5, 1577–1582.
- Kenakin, T. (2002). Drug efficacy at G protein-coupled receptors. *Annu. Rev. Pharmacol. Toxicol.* 42, 349–379.
- Kenakin, T., and Christopoulos, A. (2013). Signalling bias in new drug discovery: Detection, quantification and therapeutic impact. *Nat. Rev. Drug Discov.* 12, 205–216.
- Kim, T.H., Chung, K.Y., Manglik, A., Hansen, A.L., Dror, R.O., Mildorf, T.J., Shaw, D.E., Kobilka, B.K., and Prosser, R.S. (2013). The role of ligands on the equilibria between functional states of a G protein-coupled receptor. *J. Am. Chem. Soc.* 135, 9465–9474.
- Kuestner, R.E., Elrod, R.D., Grant, F.J., Hagen, F.S., Kuijper, J.L., Matthews, S.L., O'Hara, P.J., Sheppard, P.O., Stroop, S.D., Thompson, D.L., et al. (1994). Cloning and characterization of an abundant subtype of the human calcitonin receptor. *Mol. Pharmacol.* 46, 246–255.
- Lee, M.-H., Appleton, K.M., Strungs, E.G., Kwon, J.Y., Morinelli, T.A., Peterson, Y.K., Laporte, S.A., and Luttrell, L.M. (2016). The conformational signature of β -arrestin2 predicts its trafficking and signalling functions. *Nature* 531, 665–668.
- Lipworth, B.J., and Grove, A. (1997). Evaluation of partial beta-adrenoceptor agonist activity. *Br. J. Clin. Pharmacol.* 43, 9–14.
- Liu, J.J., Horst, R., Katritch, V., Stevens, R.C., and Wüthrich, K. (2012). Biased signaling pathways in β 2-adrenergic receptor characterized by 19F-NMR. *Science* 335, 1106–1110.
- Mary, S., Damian, M., Louet, M., Floquet, N., Fehrentz, J.-A., Marie, J., Martinez, J., and Banères, J.-L. (2012). Ligands and signaling proteins govern the conformational landscape explored by a G protein-coupled receptor. *Proc. Natl. Acad. Sci. USA* 109, 8304–8309.
- Motulsky, H.J., and Mahan, L.C. (1984). The kinetics of competitive radioligand binding predicted by the law of mass action. *Mol. Pharmacol.* 25, 1–9.
- Nag, K., Kato, A., Sultana, N., Ogoshi, M., Takei, Y., and Hirose, S. (2007). Fish calcitonin receptor has novel features. *Gen. Comp. Endocrinol.* 154, 48–58.
- Nikolaev, V.O., Hoffmann, C., Bünemann, M., Lohse, M.J., and Vilardaga, J.-P. (2006). Molecular basis of partial agonism at the neurotransmitter α 2A-adrenergic receptor and Gi-protein heterotrimer. *J. Biol. Chem.* 281, 24506–24511.
- Nuber, S., Zabel, U., Lorenz, K., Nuber, A., Milligan, G., Tobin, A.B., Lohse, M.J., and Hoffmann, C. (2016). β -Arrestin biosensors reveal a rapid, receptor-dependent activation/deactivation cycle. *Nature* 531, 661–664.
- Nygaard, R., Zou, Y., Dror, R.O., Mildorf, T.J., Arlow, D.H., Manglik, A., Pan, A.C., Liu, C.W., Fung, J.J., Bokoch, M.P., et al. (2013). The dynamic process of β (2)-adrenergic receptor activation. *Cell* 152, 532–542.
- Schindelin, J., Arganda-Carreras, I., Frise, E., Kaynig, V., Longair, M., Pietzsch, T., Preibisch, S., Rueden, C., Saalfeld, S., Schmid, B., et al. (2012). Fiji: An open-source platform for biological-image analysis. *Nat. Methods* 9, 676–682.
- Schrage, R., Schmitz, A.-L., Gaffal, E., Annala, S., Kehraus, S., Wenzel, D., Bülesbach, K.M., Bald, T., Inoue, A., Shinjo, Y., et al. (2015). The experimental power of FR900359 to study Gq-regulated biological processes. *Nat. Commun.* 6, 10156.
- Seifert, R., Gether, U., Wenzel-Seifert, K., and Kobilka, B.K. (1999). Effects of guanine, inosine, and xanthine nucleotides on β (2)-adrenergic receptor/G(s) interactions: Evidence for multiple receptor conformations. *Mol. Pharmacol.* 56, 348–358.
- Seifert, R., Wenzel-Seifert, K., Gether, U., and Kobilka, B.K. (2001). Functional differences between full and partial agonists: Evidence for ligand-specific receptor conformations. *J. Pharmacol. Exp. Ther.* 297, 1218–1226.

- Selander, K.S., Härkönen, P.L., Valve, E., Mönkkönen, J., Hannuniemi, R., and Väänänen, H.K. (1996). Calcitonin promotes osteoclast survival in vitro. *Mol. Cell. Endocrinol.* **122**, 119–129.
- Venkatarayanan, A., Raulji, P., Norton, W., Chakravarti, D., Coarfa, C., Su, X., Sandur, S.K., Ramirez, M.S., Lee, J., Kingsley, C.V., et al. (2015). IAPP-driven metabolic reprogramming induces regression of p53-deficient tumours in vivo. *Nature* **517**, 626–630.
- Verziji, D., Storelli, S., Scholten, D.J., Bosch, L., Reinhart, T.A., Streblow, D.N., Tensen, C.P., Fitzsimons, C.P., Zaman, G.J.R., Pease, J.E., et al. (2008). Noncompetitive antagonism and inverse agonism as mechanism of action of nonpeptidergic antagonists at primate and rodent CXCR3 chemokine receptors. *J. Pharmacol. Exp. Ther.* **325**, 544–555.
- Wacker, D., Wang, C., Katritch, V., Han, G.W., Huang, X.-P., Vardy, E., McCorvy, J.D., Jiang, Y., Chu, M., Siu, F.Y., et al. (2013). Structural features for functional selectivity at serotonin receptors. *Science* **340**, 615–619.
- Wittig, I., Braun, H.-P., and Schägger, H. (2006). Blue native PAGE. *Nat. Protoc.* **1**, 418–428.
- Wittig, I., Karas, M., and Schägger, H. (2007). High resolution clear native electrophoresis for in-gel functional assays and fluorescence studies of membrane protein complexes. *Mol. Cell. Proteomics* **6**, 1215–1225.
- Wookey, P.J., McLean, C.A., Hwang, P., Furness, S.G.B., Nguyen, S., Kourakis, A., Hare, D.L., and Rosenfeld, J.V. (2012). The expression of calcitonin receptor detected in malignant cells of the brain tumour glioblastoma multiforme and functional properties in the cell line A172. *Histopathology* **60**, 895–910.
- Wootten, D., Simms, J., Miller, L.J., Christopoulos, A., and Sexton, P.M. (2013). Polar transmembrane interactions drive formation of ligand-specific and signal pathway-biased family B G protein-coupled receptor conformations. *Proc. Natl. Acad. Sci. USA* **110**, 5211–5216.
- Wootten, D., Miller, L.J., Koole, C., Christopoulos, A., and Sexton, P.M. (2016). Allosteric and biased agonism at class B G protein-coupled receptors. *Chem. Rev.* Published online April 4, 2016. <http://dx.doi.org/10.1021/acs.chemrev.6b00049>.
- Yamaguchi, M., Watanabe, Y., Ohtani, T., Uezumi, A., Mikami, N., Nakamura, M., Sato, T., Ikawa, M., Hoshino, M., Tsuchida, K., et al. (2015). Calcitonin receptor signaling inhibits muscle stem cells from escaping the quiescent state and the niche. *Cell Rep.* **13**, 302–314.

STAR★METHODS

KEY RESOURCES TABLE

REAGENT or RESOURCE	SOURCE	IDENTIFIER
Antibodies		
Mouse monoclonal IgG ₁ anti-cMyc epitope	ATCC	MYC 19E10.2 [9E10] (ATCC CRL1729)
Mouse monoclonal IgG _{2a} anti-CTR	Wellcome Receptor Antibodies	1H10
Rabbit polyclonal anti-G _{zs} SC383	Santa-Cruz	SC383; RRID: AB_631539
Goat anti-mouse AF647	ThermoFisher	A-21235; RRID: AB_2535804
Goat anti-rabbit AF532	ThermoFisher	A-11009; RRID: AB_2534076
Goat anti-mouse IgG ₁ AF568	ThermoFisher	A-21124; RRID: AB_2535766
Goat anti-mouse IgG _{2a} AF633	ThermoFisher	A-21136; RRID: AB_2535775
Chemicals, Peptides, and Recombinant Proteins		
sCT8-32 VLGLKSQELHKLQTYPRNTGSGTP-NH ₂	Mimotopes	sCT8-32
sCT8-32 (R11,R18,K14) VLGRLSKELHRLQTYPRNTGSGTP-NH ₂	Mimotopes	sCT8-32 (R11,R18,K14)
AF568: sCT8-32 (R11,R18,K14) VLGRLSK(AF568) ELHRLQTYPRNTGSGTP-NH ₂	This paper	AF568: sCT8-32 (R11,R18,K14)
sCT CSNLSTCVLGLKSQELHKLQTYPRNTGSGTP-NH ₂ 1-7 disulphide bond	Mimotopes	sCT
sCT (R11,R18,K14) CSNLSTCVLGRLSKELHRLQTYPRNTGSGTP-NH ₂ 1-7 disulphide bond	Mimotopes	sCT (R11,R18,K14)
AF647: sCT (R11,R18,K14) CSNLSTCVLGRLSKELHRLQTYPRNTGSGTP-NH ₂ 1-7 disulphide bond	This paper	AF647: sCT (R11,R18,K14)
hCT CGNLSTCMLGTYTQDFNKFHTFPQTAIGVGAP-NH ₂ 1-7 disulphide bond	Mimotopes	hCT
hCT:sCT CGNLSTCMLGTYTQELHKLQTYPRNTGSGTP-NH ₂ 1-7 disulphide bond	Mimotopes	hCT:sCT
sCT:hCT CSNLSTCVLGLKSQELNKFHTFPQTAIGVGAP-NH ₂ 1-7 disulphide bond	Mimotopes	sCT:hCT
sCTtriple CSNLSTCVLGTYTQELHKLQTYPRNTGSGTP-NH ₂ 1-7 disulphide bond	Mimotopes	sCTtriple
Lauryl Maltose Neopentyl Glycol (2,2-didecylpropane-1,3-bis-β-D-maltopyranoside)	Anatrace	MNG or NG310
Cholesteryl Hemisuccinate	Anatrace	CHS or CH210
γ-(6-Aminohexyl)-GTP - ATTO-488	Jena Biosciences	NU-834-488
Experimental Models: Cell Lines		
COS-7	N/A	N/A
COS-7 cMychCTRaLeu	This paper	COS-7 CTR
HEK293A del G _{zs} /G _{off}	Asoka Inoue (to be published elsewhere)	HEK293A del G _{zs}
HEK293A del G _{zs} /G _{off} cMychCTRaLeu	This paper	HEK293A del G _{zs} / CTR
Recombinant DNA		
Human Gβ ₁ pcDNA3.1+	http://cdna.org/home.php?cat=0	#GNB0100000
Human Gγ ₂ pcDNA3.1+	http://cdna.org/home.php?cat=0	#GNG0200000
Human G _{zs} long pcDNA3.1+	http://cdna.org/home.php?cat=0	#GNA0SL0000
cMychCTRaLeu in pEF-IRESpuro6	This paper	cMychCTRaLeu
G _{γ2} :Venus pcDNA3.1+	This paper	G _{γ2} :Venus
G _{γ2} :mCherry pcDNA3.1	This paper	G _{γ2} :mCherry

(Continued on next page)

Continued

REAGENT or RESOURCE	SOURCE	IDENTIFIER
G _{as} ⁷² :Rluc8 pcDNA3.1	The laboratory of Nevin Lambert	G _{as} ⁷² :Rluc8
G _{as} ⁷² :mCherry pcDNA3.1	The laboratory of Nevin Lambert	G _{as} ⁷² :mCherry
G _{as} ⁷² :Venus pcDNA3.1	The laboratory of Nevin Lambert	G _{as} ⁷² :Venus
Myr+G _{as} ⁷² :mCherry pcDNA3.1	This paper	Myr+G _{as} ⁷² :mCherry
Myr+G _{as} ⁷² :Venus pcDNA3.1	The laboratory of Nevin Lambert	Myr+G _{as} ⁷² :Venus
Software and Algorithms		
TIRF residency script	This paper	https://figshare.com/articles/TIRF_Residency_script_Cell_Furness2016_ijm/3798480
Ingel densitometry script	This paper	https://figshare.com/articles/Ingel_FRET_densitometry_script/3798522

CONTACT FOR REAGENT AND RESOURCE SHARING

Patrick M. Sexton can be reached through postal mail (Monash Institute of Pharmaceutical Sciences, Monash University, Parkville, 3052 Victoria, Australia) or via email (patrick.sexton@monash.edu).

EXPERIMENTAL MODEL AND SUBJECT DETAILS**Cell Lines****COS-7 cells (ATCC CRL-1651)**

A COS-7 cell line stably transfected with pEF-IRESpuo6 (adapted from (Hobbs et al., 1998)) expression vector containing cMyc tagged hCTRaLeu (Andreassen et al., 2014) was generated as follows: A polyclonal population was selected (2μg/mL puromycin) and FACS sorted using 9E10 (anti-cMyc, produced in-house) and goat anti-mouse AF647 secondary (Life technologies). A corresponding control cell line was generated in parallel. Cell surface receptor expression was determined to be $1.2 \pm 0.7 \times 10^5$ sites per cell, by whole cell saturation binding. Cells were maintained in DMEM (Life-technologies) with 2μg/mL puromycin (Invivogen) and 5% FBS.

HEK293A with CRISPR deletion of GNAS (G_{as}) and GNAL (G_{o1t}) were generated by CRISPR in the same manner as GNAQ/GNA11 disruption in Schrage et al., 2015 (Schrage et al., 2015) and successful introduction of null mutations was confirmed by DNA sequencing, western blot and functional assays. This cell line is referred to as HEK293A delG_{as} (E.T. van der Westhuizen, W. Stallaert, A.-M. Schönege, B. Plouffe, M. Hogue, A.I., S. Ishida, J. Aoki, and M. Bouvier, unpublished data). These were maintained in DMEM supplemented with 5% FBS.

A HEK293A delG_{as} cell line stably transfected with pEF-IRESpuo6 (adapted from (Hobbs et al., 1998)) expression vector containing cMyc tagged hCTRaLeu (Andreassen et al., 2014) was generated as follows: A polyclonal population was selected (10μg/mL puromycin) and receptor expression confirmed by flow cytometry and activity confirmed using a cAMP accumulation assay with transient transfection of wild-type G_{as}.

METHOD DETAILS**Fluorescently labeled peptides**

K11R, Q14K, K18R substituted versions of sCT and sCT8-32 were purchased from Mimotopes. sCT8-32 was labeled with a 3-fold molar excess of AF568 succinimide NHS ester (Life technologies) at pH 8.3 and free dye removed using a 3 kDa molecular weight cut off centrifugal concentrator (Amicon). Labeled peptide was separated from unlabelled peptide by reverse phase HPLC and buffer exchanged into PBS before storing at -80°C . sCT was labeled with a 3-fold molar excess of AF647 succinimide NHS ester (Life technologies) at pH 8.3 and free dye removed using a 3 kDa molecular weight cut off centrifugal concentrator (Amicon). The degree of labeling was assessed using a Nanodrop (Thermo Scientific) and confirmed to be 1:1. The peptide ligands were then tested for receptor binding by flow cytometry and confocal microscopy and agonist activity confirmed in a cAMP accumulation assay.

Cell Culture

Transient transfections for live cell BRET, cAMP assays in HEK293A and preparation of membranes for membrane BRET assay were performed with PEI (Verzijl et al., 2008). Linear PEI (m.w. 25000, Polysciences) was prepared in advance at 1mg/mL in sterile 150mM NaCl and the pH adjusted to 7.0. DNA was diluted to 0.02μg/μL in sterile 150mM NaCl and PEI diluted to 0.12μg/μL in sterile 150mM NaCl for a 1:6 ratio. These dilutions were immediately mixed and incubated for 10 min at room temperature before being added drop-wise to the adherent cells in fresh media. DNA was added proportional to the area of cells being transfected at a concentration of

0.066 $\mu\text{g}/\text{cm}^2$. Transient transfections for live cell imaging were performed according to manufacturers instructions using Lipofectamine-2000 (Life technologies).

CTR and G protein expression and purification from insect cells

The human calcitonin receptor (hCTR) was cloned into pFastBac1 vector to give a receptor containing an N-terminal Flag epitope and a C-terminal 8x histidine tag. hCTR, human $G_{\alpha s}$ short, His₆-bovine $G_{\beta 1}$ and $G_{\gamma 2}$ were expressed in HighFive insect cells grown in ESF 921 serum free media (Expression Systems). Culture were grown to a density of 4 million cells per ml and then infected with 3 virus' each containing the gene for hCTR, human $G_{\alpha s}$ short and dual vector of His₆-bovine $G_{\beta 1}$ and $G_{\gamma 2}$. Cultures were grown at 27°C and harvested by centrifugation 48 hr post infection.

Cells were suspended in 20mM HEPES (pH 7.4), 50mM NaCl, 2mM MgCl_2 supplemented with cOmplete Protease Inhibitor Cocktail tablets (Roche) 1 μM salmon calcitonin, nanobody 35 (10 $\mu\text{g}/\text{mL}$) and Apyrase (25mU/mL, NEB). The complex was solubilised by 0.5% (w/v) MNG (NG-310, Anatrace) supplemented with 0.03% (w/v) cholesteryl hemisuccinate for 1 hr at 4°C. Insoluble material was removed by centrifugation and the solubilised complex were immobilised by batch binding to M1 Flag affinity resin. The resin was packed into a glass column and washed with 20mM HEPES (pH 7.4), 100mM NaCl, 2mM MgCl_2 , 3mM CaCl_2 , 100nM salmon calcitonin, 0.01% (w/v) MNG and 0.006% (w/v) cholesteryl hemisuccinate before bound material was eluted in buffer containing 5mM EDTA and 0.1mg/mL FLAG peptide. The complex was then concentrated using a Amicon Ultra Centrifugal Filters (MWCO 100 kDa) and subjected to size exclusion chromatography on a Superose 6 10/300 Increase column (GE Healthcare) in a buffer of 20mM HEPES (pH 7.4), 100mM NaCl, 2mM MgCl_2 , 100nM salmon calcitonin or 100nM human calcitonin, 0.01% (w/v) MNG and 0.006% (w/v) cholesterol hemisuccinate.

cAMP accumulation assay

cAMP assays were performed as follows: complete media was replaced with phenol red free DMEM with 1mM IBMX (3-isobutyl-1-methylxanthine) and 0.1% BSA and incubated for 30 min. Cells were treated with ligands for 30 min prior to measurement of cAMP using a SureFire alphascreen cAMP kit (PerkinElmer) or Lance TR-FRET cAMP kit (PerkinElmer). All data were interpolated to actual cAMP concentration using an internal cAMP standard then normalized to the maximum forskolin or salmon calcitonin response.

Competition fluorescent binding assay

Cells were plated in 96 well black CulturPlate (Perkin Elmer) at 10,000 cells per well 8 hr prior to assay. Media was replaced with ice cold DMEM with 0.1% BSA and 10nM of antagonist sCT8-32:AF568 competed against either hCT or sCT on whole cells at 4°C overnight. Cells were washed 3 times quickly with ice-cold DMEM/0.1% BSA and sCT8-32:AF568 fluorescence measured in a Pherastar (BMG Labtech).

The equilibrium constant for sCT8-32:AF568 was determined using saturation binding on whole cells at 4°C overnight in phenol red free DMEM with 0.1% BSA with non-specific determined on control cells. Cells were washed 3 times quickly with ice-cold DMEM/0.1% BSA and sCT8-32:AF568 fluorescence measured in a Pherastar (BMG Labtech).

Membrane equilibrium competition fluorescent binding assays were performed with crude plasma membrane preparations (below). Binding to membranes was performed in a final volume of 200 μL in fluorescent ligand binding buffer (150 mM NaCl / 2.6 mM KCl / 1.18 mM MgCl_2 / 0.05% BSA / 1 mM DTT / 0.1 mM PMSF / 1:1000 protease inhibitor cocktail (P8340, Sigma) / 10 mM HEPES [pH 7.4]) in 96 well, black polypropylene round bottom plates (Corning) and measured homogeneously using fluorescence anisotropy in a Pherastar (BMG Labtech) after overnight incubation at 4°C.

Kinetic ligand binding

Membrane kinetic and kinetic competition fluorescent ligand binding assays were performed with crude plasma membrane preparations (below). Binding to membranes was performed in a final volume of 250 μL in fluorescent ligand binding buffer (150 mM NaCl / 2.6 mM KCl / 1.18 mM MgCl_2 / 0.05% BSA / 1 mM DTT / 0.1 mM PMSF / 1:1000 protease inhibitor cocktail (P8340, Sigma) / 10 mM HEPES [pH 7.4]) in 96 well, black polypropylene round bottom plates (Corning) and measured homogeneously using fluorescence anisotropy in a Pherastar (BMG Labtech) at 30°C with 4 measurements per well per minute. For all experiments crude plasma membrane was titrated to reduce maximum FP signal to ≤ 30 mP to minimize the effects of ligand depletion. For association: dissociation experiments baseline FP signal was measured with 10nM sCT8-32:AF568 followed by addition of membranes for association then 31.6 μM unlabelled sCT8-32 for dissociation. For kinetic competition baseline FP signal was measured with 10nM sCT8-32:AF568 and indicated concentrations of CTR agonists followed by addition of membranes and measurement for 60 min.

Membrane preparations

Crude membranes were prepared by harvesting cells (~1.5 g packed volume) into 17 ml membrane preparation buffer (20 mM BisTris [pH 7.4] / 50 mM NaCl / 1 mM MgCl_2 / 1:1000 P8340 (protease inhibitor cocktail, Sigma) / 1 mM DTT / 0.1 mM PMSF) followed by homogenization with a polytron homogenizer at 4°C. The homogenate was then centrifuged for 10 min at 700 g. The supernatant was centrifuged at 100,000 $\times g$ for 30 min at 4°C. The pellet was washed by re-suspension in 17mL membrane preparation buffer and re-centrifuged at 100,000 $\times g$ for 30 min at 4°C. The final pellet, containing cell membranes was resuspended in 800 μL membrane preparation buffer and stored at -80°C.

Crude plasma membranes were prepared by harvesting cells (~1.5 g packed volume) into 10 ml membrane preparation buffer followed by homogenization with a polytron homogenizer at 4°C. The homogenate was loaded onto a stepped sucrose gradient (40% / 10% / homogenate) and centrifuged at 100,000 × g for 2 hr 30 min at 4°C. The 40% / 10% interface (~1.5 mL) was collected and diluted to 17 ml with membrane preparation buffer followed by centrifugation at 100,000 × g for 30 min at 4°C. The final pellet, containing crude plasma membranes was resuspended in ~350 µL membrane preparation buffer and stored at –80°C.

Enriched plasma membranes were prepared by harvesting cells (~1.5 g packed volume) into 5 ml membrane preparation buffer followed by homogenization with a polytron homogenizer at 4°C. The homogenate was loaded onto a stepped sucrose gradient (40% / 35% / 22.5% / 10% / homogenate) and centrifuged at 100,000 × g for 2 hr 30 min at 4°C. The 22.5% / 10% interface (~1.5 mL) was collected and diluted to 17 ml with membrane preparation buffer followed by centrifugation at 100,000 × g for 30 min at 4°C. The final pellet, containing enriched plasma membranes was resuspended in ~250 µL membrane preparation buffer and stored at –80°C.

Native PAGE

In vitro transformation; either 20 µg (all COS-7/CTR experiments) or 40 µg (all HEK293A ΔG_{zs} / CTR experiments) of purified plasma membrane was added to 1 mL of plasma membrane preparation buffer containing the indicated concentrations of agonist and nucleotide, incubated for 30 min at 30°C before centrifugation at 20,000 × g at 4°C. Membrane pellets were then solubilised in 15 µL of plasma membrane preparation buffer containing either 2% digitonin (Serva) or 1% MNG (Affimatrix)/ 0.1% CHS (Affimatrix) and 10% glycerol for 10 min at 4°C. For antibody shift experiments FAbs (9E10, anti-cMyc (in-house) and 1H10, anti-CTR (Wellcome Receptor Antibodies (Wookey et al., 2012))) were added at this point and incubated at 4°C for 1 hr. Insoluble material was pelleted by centrifugation at 20,000 × g for 5 min at 4°C. The methods of Wittig et al. were adapted for blue native PAGE (Wittig et al., 2006) and high resolution clear native PAGE (Wittig et al., 2007). For blue native PAGE samples were then directly loaded. For high-resolution clear native PAGE ponceau S (Serva) was added to a final concentration of 0.1% w/v. High resolution native PAGE, 6%–11% and 4%–13.5% linear gradient gels were prepared using a BisTris / Tricine / 6-amino caproic acid buffering system. Electrophoresis was performed at 4°C at pH 7.4. For blue native PAGE the cathode buffer contained 0.02% Coomassie G-250; for high-resolution clear native PAGE there was 0.02% MNG/0.002% CHS (Affimatrix) in the cathode buffer.

For blue native PAGE transfers were performed using a BisTris / Tricine buffer at pH 7.4, whereas, a Tris / Acetate buffer at pH 8.6 for transfer from high-resolution clear native PAGE.

For in gel fluorescence and FRET measurements between G_{zs} and $G_{\gamma 2}$ HEK293A ΔG_{zs} cells stably expressing CTR were transfected with 1:1:1 ratios of $G_{\gamma 2}$:Venus / $Mry^+ G_{zs}^{72}$:mCherry / $G_{\beta 1}$ OR $G_{\gamma 2}$:mCherry / $Mry^+ G_{zs}^{72}$:Venus / $G_{\beta 1}$ 36 hr prior to harvesting and preparation of crude plasma membranes (above). In vitro transformation with agonists was performed as described above. Gels were immediately imaged post electrophoresis using a Typhoon multimode imager (GE Healthcare life sciences). The lane order was randomized between experiments to eliminate systematic errors that may be introduced while imaging. The donor (Venus) channel was imaged using the 488 laser and 520/40 emission filter, acceptor with the 532 laser and 610/30 emission filter while the FRET signal was captured using the 488 laser and 610/30 emission filter.

Immunoblotting was performed using anti-cMyc antibody (9E10 (IgG₁), in house), anti-CTR (1H10 (IgG_{2a}) Wellcome Receptor Antibodies), anti- G_{zs} SC383 (Santa-Cruz) primary antibodies and highly cross absorbed goat anti-mouse AF647, goat anti-rabbit AF532, goat anti-mouse IgG1 AF568 and goat anti-mouse IgG2a AF633 secondaries (Life-Technologies). Transfers were performed as described above, overnight at 4°C at 20V to low fluorescence PVDF membrane (BioRad). Transfers from blue native PAGE were first destained with methanol then rinsed with MQ H₂O. Transfers were stained with 0.2% Ponceau / 3% trichloroacetic acid in MQ H₂O and molecular weight standards marked with a pencil. Membranes were then destained with PBS/0.05% Tween20 and blocked for 1 hr with 5% BSA in PBS/0.05% Tween20. All primary antibodies were diluted to a final concentration of 1 µg/mL in PBS with 1% BSA, 0.05% Tween20 and 0.02% sodium azide. Membranes were incubated either overnight at 4°C or room temperature for 2 hr with primary antibody dilutions. Membranes were then washed 3 times for 5 min each in PBS/0.05% Tween20. All secondary antibodies were diluted to 1 µg/mL in PBS/0.05% Tween20. Membranes were incubated in secondary antibody mixtures for 90 min at room temperature. Membranes were then washed 3 times for 5 min each in PBS/0.05% Tween20 prior to imaging. All images were captured using a Typhoon multimode imager (GE Healthcare life sciences).

G protein BRET

Live cell BRET: COS-7 cells stably expressing CTR were transfected with 2:1:2 ratios of $G_{\gamma 2}$:Venus / G_{zs}^{72} :Rluc8 / $G_{\beta 1}$ 16 hr prior to assay. Media was replaced with DMEM/0.05% BSA and cells equilibrated for 30 min. 10 min prior to assay coelantrazine h was added to a final concentration of 5 mM. Baseline measurements were taken for 1 min prior to addition of vehicle or agonists and reading for a further 9 min. All assays were performed in a final volume of 200 µL and BRET measurements were made in a Pherastar.

BRET on crude membranes. COS-7 cells stably expressing CTR were transfected with 2:1:2 ratios of $G_{\gamma 2}$:Venus / G_{zs}^{72} :Rluc8 / $G_{\beta 1}$ 16 hr prior to harvesting and preparation of crude membranes (above). Membranes were added at 20 µg per well in a modified HBSS buffer consisting of HBSS with 10 mM HEPES (final pH 7.4) / 1 mM DTT / 0.1 mM PMSF / 1:1000 P8340 and 0.01% BSA at 37°C. Coelantrazine h (Nanolight) was added to a final concentration of 5 mM and baseline measurements taken for 1 min prior to the addition of vehicle or GTP. A further 1 min of measurements were taken, followed by addition of vehicle or agonist and reading for a further 15 min. All assays were performed in a final volume of 250 µL and measured in a Pherastar.

GTP association

HEK293A $\Delta G_{\alpha s}$ cells stably expressing CTR were transfected with 1:1:1 ratios of $G_{\gamma 2} / Mry+G_{\alpha s}^{72}:mCherry / G_{\beta 1}$ 16 hr prior to harvesting and preparation of crude membranes (above). 100 μ g of crude membrane was diluted to 50 μ L in membrane preparation buffer containing an additional 10mM $MgCl_2$, 500 μ M ATP, 1mM DTT, 1:1000 P8340 and 0.05% BSA and 1 μ M of either hCT or sCT prior to incubation at 30°C for 20 min. This was then allowed to cool to room temperature (25°C) for approximately 5 min. 50 μ L aliquots of membrane preparation buffer containing an additional 10mM $MgCl_2$, 500 μ M ATP, 1mM DTT, 1:1000 P8340 and 0.05% BSA and 60nM ATTO488- γ -(6-Aminohexyl)-GTP buffer were transferred to 96 well, black polypropylene round bottom plates (Corning) and allowed to equilibrate to 25°C in a Pheratar (BMG Labtech). Binding was initiated by addition of pre-equilibrated membranes and FRET measured homogeneously using a Pherastar (BMG Labtech) at 25°C with 6 measurements per well per minute.

G protein residency

COS-7 cells stably expressing CTR were plated onto fibronectin (Sigma) coated transwell inserts (Falcon) 24 hr prior to assay. 16 hr prior to assay cells were transiently transfected either with $G_{\gamma 2}:Venus$ OR 1:1:1 ratio of $G_{\gamma 2} / G_{\alpha s}^{72}:mCherry / G_{\beta 1}$. On the day of assay media was replaced with room temp (20°C) phenol red free DMEM with 0.05% BSA. The transwell insert was then removed and the PET membrane carefully removed with a scalpel blade. This was placed apical side down on a fluorodish (Precision World Instruments) and a custom manufactured, food grade stainless steel weight added to the periphery, all in room temp (20°C) phenol red free DMEM with 0.05% BSA. Apical cell regions were imaged with a Leica TIRF microscope with a 160x (Plan Apo), 1.47NA oil objective at 33 frames per second ($G_{\gamma 2}:Venus$) or 40 frames a second ($G_{\alpha s}^{72}:mCherry$). An image sequence of (typically) 2 min was captured prior to the addition of agonist followed by 2 – 5 min of image acquisition.

Modeling G protein rearrangement

The crystal structure of the β_2 adrenergic receptor in complex with $G_{\alpha s}\beta_1\gamma_2$ (PDB: 3SN6) was used as a template, the crystal structure of Rluc8 (PDB: 2SPSD) was positioned to align its N- and C-terminal amino acids with the unresolved loop of the $G_{\alpha s}$ chain where the genetic insertion was made and the crystal structure of eYFP (PDB: 3V3D) placed at the C- terminus of the $G_{\gamma 2}$ chain. The crystal structure of the GDP bound conformation of $G_{\alpha s}$ (PDB: 1AZT) was aligned to the ternary complex structure by RMSD minimization of the RAS-like domain of the ternary bound and GDP bound subunit; the ternary bound $G_0 G_{\alpha s}$ was thus replaced with inactive $G_{\alpha s}$ and Rluc8 (PDB: 2SPSD) was positioned to align its N- and C-terminal amino acids with the unresolved loop of the $G_{\alpha s}$ chain where the genetic insertion was made and the crystal structure of eYFP (PDB: 3V3D) placed at the C- terminus of the $G_{\gamma 2}$ chain. Amino acids 156-171 of Rluc8 are highlighted in magenta to show the rotation and translation of Rluc8 necessary to accommodate the open versus closed state of $G_{\alpha s}$.

BRET CAMYEL assay

COS-7 cells were simultaneously transfected using linear polyethyleneimine (Verzijl et al., 2008) 24 hr prior to assay. Cells (approximately 1.8×10^5) were mixed with 300 ng CTR DNA and 500 ng/well BRET cAMP biosensor DNA (CAMYEL (Jiang et al., 2007)) at a 1:6 DNA to PEI ratio, prior to seeding into 16 wells of a white opaque 96-well plate in 5% FBS (v/v) DMEM with penicillin/streptomycin.

Cells were washed with Hank's balanced salt solution (HBSS), and then equilibrated in HBSS with 0.1% (w/v) BSA at 37°C for 30 min prior to assay. RLuc luminescence and YFP fluorescence were measured using a Pherastar microplate reader (BMG LabTech) following addition of the RLuc substrate, coelenterazine h (Nanolight, 3 μ M, 30 min prior to read). The baseline BRET ratio was measured for 1 min. Following automated addition of vehicle, hCT or sCT, the stimulated BRET ratio was measured for 5 min, prior to the manual addition of a positive control cocktail (10 μ M forskolin, 100 μ M 3-isobutyl-1-methylxanthine [IBMX] and 100 nM prostaglandin E_1) to confirm sub-saturating stimulation by hCT and sCT (see Figures S5B and S5C). The change in BRET in response to the positive control cocktail was measured for 4 min. Measurements were made in duplicate, every 4 s.

Increases in cAMP were analyzed by determining the BRET signal as a ratio of the light emitted at 465-505 nm (RLuc) to the light emitted at 505-555 nm (YFP). For each well, the BRET data were expressed as the change in BRET signal relative to the average baseline and positive control responses in the first and last min of the time course, respectively ((BRET signal – average BRET baseline)/maximum BRET signal; BRET/BRET_{Max}). Data were fitted to a one-phase association curve using PRISM and an extra sum-of-squares F test applied to determine whether differences in association rate existed.

QUANTIFICATION AND STATISTICAL ANALYSIS

cAMP accumulation assay analysis

All data were interpolated to actual cAMP concentration by fitting and internal standard of known cAMP concentrations to a 3 parameter logistic curve in PRISM (Graphpad) and then normalized to the maximum forskolin or salmon calcitonin response. This data were analyzed using a biphasic, 4-parameter concentration response equation in PRISM (Graphpad) and an extra sum-of-squares F test applied to determine whether differences in E_{max} and EC_{50} existed.

Ligand binding analysis

The equilibrium constant for sCT8-32:AF568 was calculated using a one-site fit using PRISM (Graphpad) with non-specific binding determined by binding to parental (untransfected) cells.

Whole cell and membrane equilibrium competition binding was analyzed using a single phase or biphasic (chosen on the basis of an extra sum-of-squares F test comparison between models), 4-parameter competition equation in PRISM (Graphpad) with equilibrium constant of the probe determined by saturation binding (above) and an extra sum-of-squares F test applied to determine whether differences in K_i existed.

Kinetic parameters for sCT8-32:AF568 were calculated in PRISM (Graphpad) using an association then dissociation model to derive K_{on} and K_{off} from direct measurements of K_{obs} and K_{off} .

Kinetic competition parameters for all unlabelled ligands were calculated using the K_{on} and K_{off} calculated for sCT8-32:AF568 by fitting data from multiple concentrations of unlabelled competitor to a model of competitive binding kinetics using PRISM (Graphpad) (see (Motulsky and Mahan, 1984)).

Analysis of Native PAGE

For immunoblotting of native PAGE densitometry was performed using standard methods with the Fiji distribution of ImageJ (Schindelin et al., 2012) and data analyzed using a 3-parameter concentration response equation in PRISM (Graphpad) and an extra sum-of-squares F test applied to determine whether differences in EC_{50} existed.

For in gel fluorescence and FRET a script was written to average the densitometry from the 3 control lanes and subtract this average from the agonist lanes. The AUC for the receptor recruited G protein band was quantified for all ligand lanes in donor, acceptor and FRET channels. To allow comparison across experiments the lane with the largest acceptor AUC value (regardless of which ligand) was used to normalize the AUC for all lanes. This lane was also then used to normalize the remaining 2 channels. The net FRET was calculated as follows: $FRET / (donor + acceptor)$. An unpaired t test was used to determine whether differences in acceptor or FRET signal differed between ligand treatments.

G protein BRET analysis

For rate calculations data were fitted to a one-phase association curve in PRISM (Graphpad) and an extra sum-of-squares F test applied to determine whether differences in association rate existed. For EC_{50} and E_{max} determinations AUC was used to fit 3-parameter concentration response curves using PRISM (Graphpad) on individual experiments. The derived EC_{50} and E_{max} values were then used to perform paired t tests to determine whether differences existed and mean values used to generate curve fits shown in figures.

GTP association analysis

Rate data were fitted to a one-phase association curve in PRISM (Graphpad) and an extra sum-of-squares F test applied to determine whether differences in association rate existed.

G protein residency analysis

Residency times were measured using the Fiji distribution of ImageJ (Schindelin et al., 2012). A script was developed to apply the following analysis to all image sequences: A Gaussian blur (1 sigma) was applied to the time series. The centroid of the local spot maxima was detected using the Find maxima command (threshold varied between 50 and 250 depending on signal strength). Binary masks of single spots were created and dilated by 2 pixels to allow robust detection of subsequent spots in the time series. Overlapping dilated spots were then assessed for how many frames they were present. This process was repeated for all detected spots in a given time series. The number of spots occurring for each frame bin (bins from 1 to 100 frames) was counted for each image sequence. Spots occurring for a single frame only were discarded to eliminate sampling error. The sum of the remaining spots was used to convert the absolute number per bin to a percentage. Percentages from a particular experiment were averaged and the averages from all experiments used to derive an exponential decay curve to estimate residency time. Each experiment was performed on 3 separate days ($n = 3$), on each day at least 2 separate image sequences for an unstimulated, hCT and sCT stimulated cell was captured and only image sequences containing $> 3,000$ events of longer than 2 frames were used for analysis. For 3D residency plots the residency of 625 spots from representative image sequences were plotted as a 2D histograms.

DATA AND SOFTWARE AVAILABILITY

TIRF residency script

The custom script (<http://dx.doi.org/10.4225/03/57C81DC64E72B>) was written to measure the time a given spot was present in the TIRF field. This is achieved by extracting the individual spots as single binary points and then measuring how many frames each one is present for before the signal decreases to background.

In gel FRET quantitation script

The custom script (<http://dx.doi.org/10.4225/03/57C821AE2C2DDc>) was written to allow automated and unbiased background subtraction and quantitation of the fluorescence densitometry.

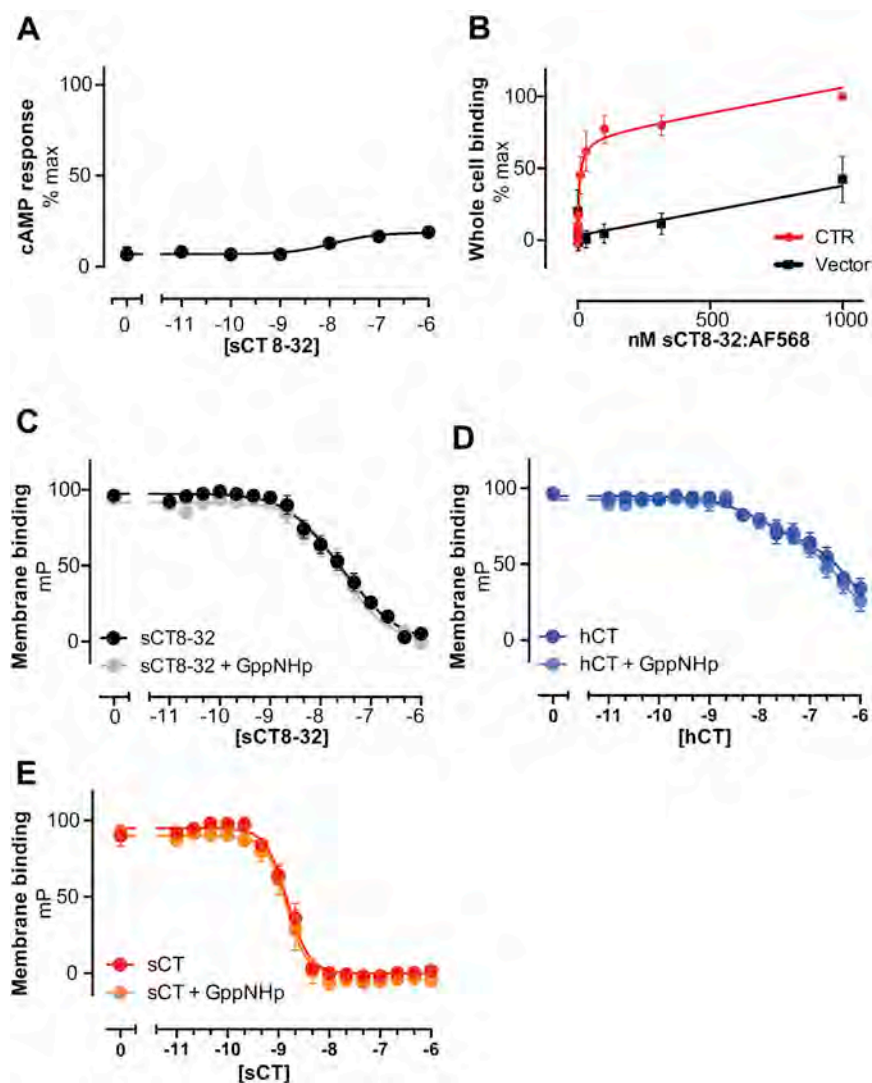


Figure S1. Functional Characterization of the Relative Efficacy of CTR Antagonist and Binding Affinities of Agonists, Related to Figure 1

(A) cAMP accumulation assay in COS-7 cells stably expressing CTR with cells stimulated for 30 min in the presence of IBMX with the indicated concentrations of sCT8-32 ($n = 4$, each n conducted in triplicate on separate days with separate drug dilutions and data are presented as mean \pm SEM). The cAMP response to sCT8-32 has an E_{\max} of $18\% \pm 2\%$ of the full agonist response with a $\log EC_{50}$ of -7.93 ± 0.43 .

(B) Whole cell saturation ligand binding in which cells were incubated overnight at 4°C with indicated concentrations of sCT8-32:AF568, $K_d = 7 \pm 2.9$ nM ($n = 5$, each n conducted in triplicate on separate days with separate drug dilutions and data are presented as mean \pm SEM).

(C–E) Fluorescence Polarization competition binding on purified plasma membrane incubated overnight at room temp in the presence or absence of 1 mM GppNHp and 10 nM sCT8-32:AF568 in the presence of the indicated concentrations of competing unlabeled sCT8-32 (C, antagonist), $\log K_i = -7.95 \pm 0.04$; hCT (D) $\log K_i = -8.48 \pm 0.34$ and -6.76 ± 0.32 ; and sCT (E) -9.22 ± 0.05 ($n = 4$, each n conducted in triplicate on separate days with separate membrane preparations, separate drug dilutions and data are presented as mean \pm SEM).

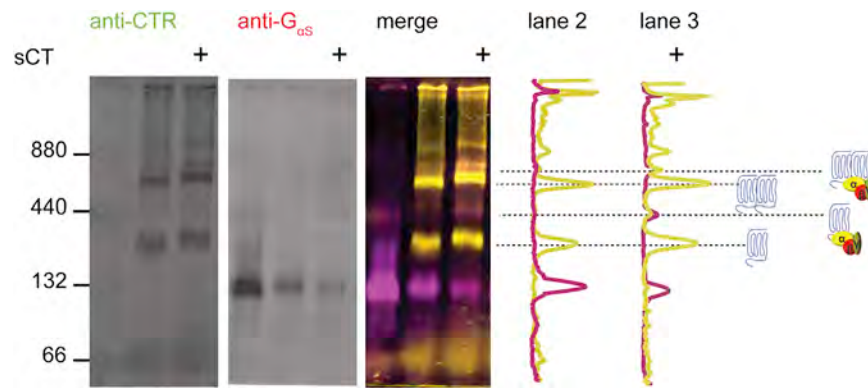


Figure S2. Additional Characterization of receptor:agonist: $G_{\alpha s}$ Ternary Complex Stoichiometry, Related to Figure 2

(A) Plasma membrane preparations from COS-7 cells expressing CTR were treated with 100nM sCT (+) prior to solubilization in digitonin at 6g/g followed by separation on a 4%–13.5% blue native PAGE and transfer. Solubilisation in digitonin followed by blue native PAGE preserves high and low mobility ternary complexes but results in relatively poor solubilization of CTR. The ternary complex was identified by probing for co-migration of CTR (green) and $G_{\alpha s}$ (red) with a representative blot ($n = 4$, each n conducted on separate days with separate membrane preparations) shown along with ratiometric densitometry indicating 2 ternary complex species composed of 2:1 and 1:1 CTR: $G_{\alpha s}$ stoichiometry.

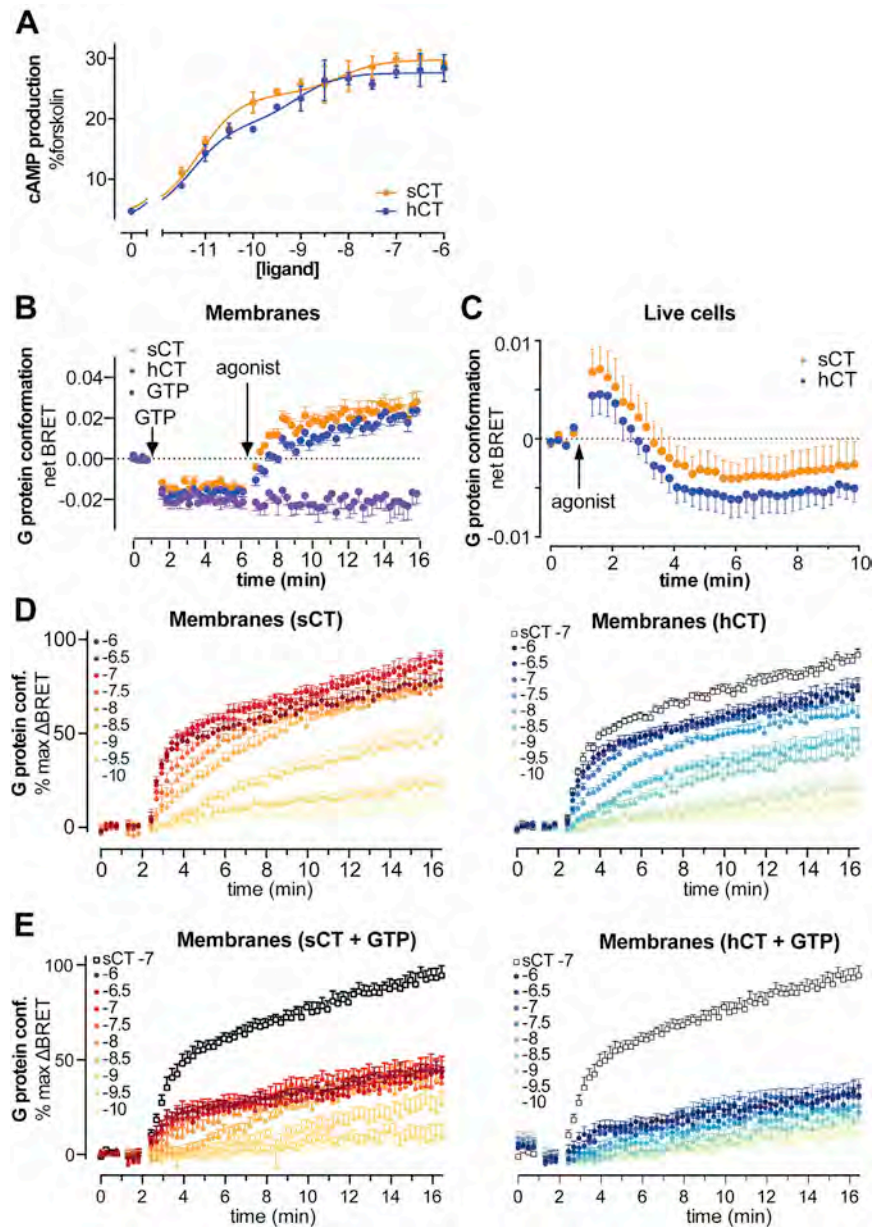


Figure S3. Agonist-Induced Changes in Heterotrimeric G Protein Conformation, Related to Figure 3

(A) Representative cAMP accumulation assay (conducted twice) in HEK293A ΔG_{zs} cells 20 hr after transient transfection with 1:1:1:1 CTR/ $G_{\gamma 2}$:Venus/ G_{zs}^{72} :Rluc8/ $G_{\beta 1}$ and stimulated for 30 min in the presence of IBMX with the indicated concentrations of sCT and hCT.

(B) COS-7 cells stably expressing CTR were transfected with $G_{\gamma 2}$:Venus/ G_{zs}^{72} :Rluc8/ $G_{\beta 1}$ 16 hr prior to preparation of extensively washed, crude membranes. Membranes were equilibrated and baseline BRET measured for 1 min prior to addition of vehicle or 300 μ M GTP. Time-course for ligand induced change in BRET at 100 nM with addition of 300 μ M GTP for 5 min before agonist addition ($n = 3$, each n conducted in triplicate on separate days with separate membrane preparations, separate drug dilutions and data are presented as mean \pm SEM).

(C) COS-7 cells stably expressing CTR were transfected with $G_{\gamma 2}$:Venus/ G_{zs}^{72} :Rluc8/ $G_{\beta 1}$ 16 hr prior to live cell BRET. Time-course for ligand induced change in BRET with 1 μ M agonist addition ($n = 5$, each n conducted in triplicate on separate days with separate drug dilutions and data are presented as mean \pm SEM).

(D) Curves showing full kinetic responses, using washed, crude membranes, at all concentrations tested of sCT (left), hCT (right, sCT maximum response curve in black, $n = 9$ each n conducted in triplicate on separate days with separate membrane preparations, separate drug dilutions and data are presented as mean \pm SEM).

(E) Curves showing full kinetic responses, using washed, crude membranes, at all concentrations tested of sCT (D, sCT maximum response curve (no GTP) in black) and hCT (E, hCT maximum response curve (no GTP) in black), in the presence of 300 μ M GTP ($n = 6$, each n conducted in triplicate on separate days with separate membrane preparations, separate drug dilutions and data are presented as mean \pm SEM).

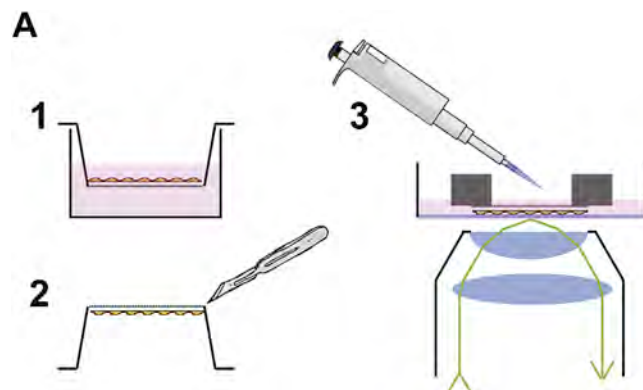


Figure S4. Scheme for TIRF on Apical Cell Surface, Related to Figure 6

Schematic for live cell total internal reflection fluorescence (TIRF) microscopy on the apical plasma membrane, (1) cells are grown on transwell inserts, just prior to assay the transwell membrane was cutout (2), placed upside down onto the imaging dish and weighed down at the periphery to allow TIRF imaging (3).

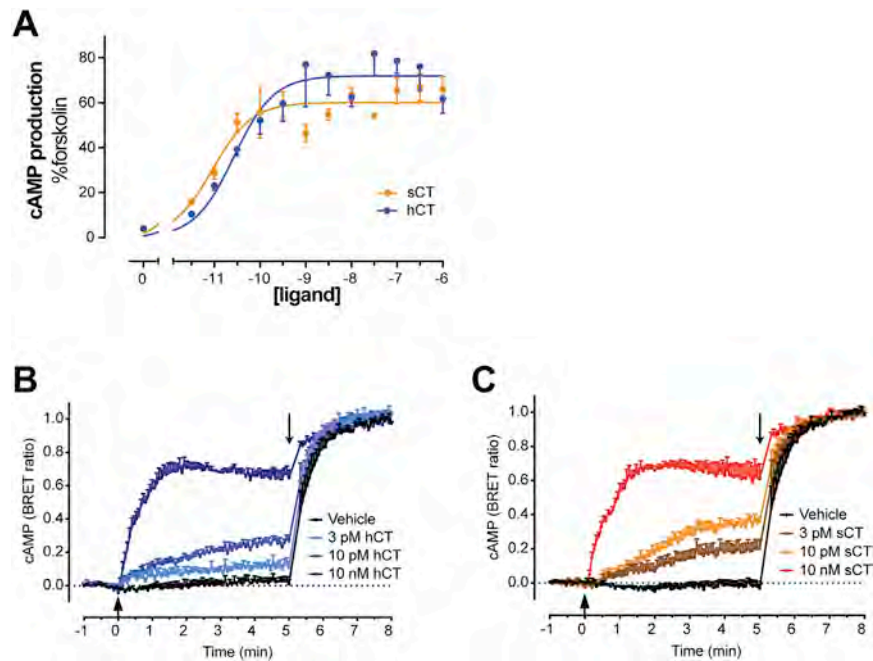


Figure S5. Agonist-Induced G Protein Residency and Activation in Live Cells, Related to Figures 6 and 7

(A) Representative cAMP accumulation assay (conducted twice) in HEK293A ΔG_{2S} cells 20 hr after transient transfection with 1:1:1:1 CTR/ $G_{\gamma 2}$:Venus/ G_{2S}^{72} :mCherry/ $G_{\beta 1}$ and stimulated for 30 min in the presence of IBMX with the indicated concentrations of sCT and hCT.

(B and C) Full time courses for rate of increase of intracellular cAMP as measured by a BRET cAMP sensor (CAMYEL) in COS-7 cells transiently transfected with CTR and stimulated with CTR agonists at time 0 then with a cocktail to assess total sensor capacity at 5 min (10 μ M forskolin, 100 μ M 3-isobutyl-1-methylxanthine [IBMX] and 100 nM prostaglandin E_1 , $n = 4$, $n = 4$, each n conducted in triplicate with different drug dilutions on different days, data are presented as mean \pm SEM).

β -Arrestin-Biased Agonists of the GLP-1 Receptor from β -Amino Acid Residue Incorporation into GLP-1 Analogues

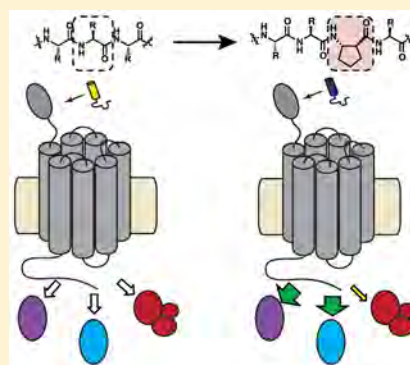
Marlies V. Hager,[†] Lisa M. Johnson,^{†,§} Denise Wootten,^{*,‡} Patrick M. Sexton,^{*,‡} and Samuel H. Gellman^{*,†}

[†]Department of Chemistry, University of Wisconsin, Madison, Wisconsin 53706 United States

[‡]Drug Discovery Biology, Monash Institute of Pharmaceutical Sciences and Department of Pharmacology, Monash University, Parkville, VIC 3052, Australia

Supporting Information

ABSTRACT: Activation of a G protein-coupled receptor (GPCR) causes recruitment of multiple intracellular proteins, each of which can activate distinct signaling pathways. This complexity has engendered interest in agonists that preferentially stimulate subsets among the natural signaling pathways (“biased agonists”). We have examined analogues of glucagon-like peptide-1 (GLP-1) containing β -amino acid residues in place of native α residues at selected sites and found that some analogues differ from GLP-1 in terms of their relative abilities to promote G protein activation (as monitored via cAMP production) versus β -arrestin recruitment (as monitored via BRET assays). The $\alpha \rightarrow \beta$ replacements generally cause modest declines in stimulation of cAMP production and β -arrestin recruitment, but for some replacement sets cAMP production is more strongly affected than is β -arrestin recruitment. The central portion of GLP-1 appears to be critical for achieving bias toward β -arrestin recruitment. These results suggest that backbone modification via $\alpha \rightarrow \beta$ residue replacement may be a versatile source of agonists with biased GLP-1R activation profiles.



■ INTRODUCTION

G protein-coupled receptors (GPCRs) play critical physiological roles by transmitting information encoded in extracellular molecules to the cytoplasm. Signal transduction requires interaction of an activated GPCR with intracellular partner proteins, which can include several G proteins (G_{α_s} , G_{α_i} , G_{α_q} , etc.), β -arrestin-1, and β -arrestin-2 (Figure 1A). Each of these effector proteins stimulates one or more signaling pathways. G_{α_s} , for example, leads to the production of the second messenger cAMP, G_{α_q} leads to mobilization of intracellular Ca^{2+} , and β -arrestins mediate receptor internalization and/or serve as scaffolds for G protein-independent signaling.^{1–3} GPCR structure is dynamic, and each effector protein is thought to bind to a unique receptor conformation.^{4,5} GPCR ligands that favor engagement of certain effector proteins over others, referred to as “conformationally selective” or “biased” agonists, are believed to favor a subset among the activated GPCR conformations (a hypothetical, idealized example of a β -arrestin-biased agonist is shown in Figure 1B; in contrast, the bias we report here stems from diminished activity in all channels relative to the native agonist, with greater diminution in some channels relative to others).^{6–8} Mechanistic understanding of ligand bias remains limited, despite extensive study.^{9–11} Little structural information is available for GPCR complexes of biased agonists,^{12,13} which hinders both rational design of agonists with pathway selectivity and molecular-level elucidation of the origins of bias.

The glucagon-like peptide-1 receptor (GLP-1R) is a member of the B subclass of GPCRs, which are activated by long polypeptide hormones. GLP-1R is primarily expressed in pancreatic β cells, which secrete insulin to regulate glucose concentration in the bloodstream. This receptor can be engaged by multiple endogenous peptides, including at least six forms of glucagon-like peptide-1. The full-length forms, GLP-1(1–36) NH_2 and GLP-1(1–37), are considered weak agonists or antagonists of GLP-1R.¹⁴ The mature forms, GLP-1(7–36) NH_2 and GLP-1(7–37), are potent agonists; these two forms display indistinguishable activity.^{14,15} After release into the bloodstream, the mature forms of GLP-1 are rapidly cleaved by dipeptidyl peptidase-4 (DPP-4), to generate GLP-1(9–36) NH_2 and GLP-1(9–37), which are low-affinity, low-efficacy agonists of GLP-1R-mediated signaling and can function as antagonists.¹⁴ In addition, the peptide hormones glucagon¹⁶ and oxyntomodulin^{16,17} (which is an eight-residue extension of glucagon) can activate GLP-1R (sequences shown in Figure 2).

Binding of the mature forms of GLP-1 (referred to below simply as “GLP-1”) to the GLP-1R is associated with diverse effects that are critical for human health, but the intracellular signaling networks initiated in this way have not yet been fully elucidated. GLP-1 binding to the GLP-1R activates G_{α_s} and

Received: August 9, 2016

Published: November 4, 2016

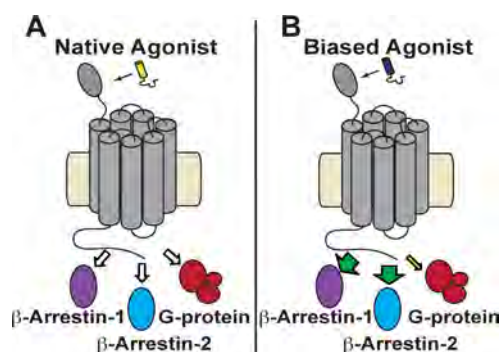


Figure 1. Schematic depicting the intracellular proteins, investigated in the current study, that are recruited to a GPCR upon stimulation with (A) the native receptor agonist or with (B) a β -arrestin-biased agonist. In (A), equally sized and colored arrows indicate equal recruitment of each potential partner protein upon stimulation with the native agonist, while in (B) larger green arrows pointing to β -arrestin-1 and β -arrestin-2 indicate a greater level of β -arrestin recruitment upon stimulation with a β -arrestin-biased agonist relative to the native agonist, and the smaller yellow arrow pointing to a G protein indicates a diminished level of G protein recruitment upon stimulation with a β -arrestin-biased agonist relative to the native agonist.

thereby induces a rise in intracellular cAMP, which leads to glucose-stimulated insulin secretion.¹⁸ GLP-1 binding recruits also β -arrestin-1 and β -arrestin-2 to the GLP-1R. Recruitment of β -arrestin-1 promotes β cell proliferation¹⁹ and protects these cells from apoptosis.^{20,21} The effects of GLP-1-induced β -arrestin-2 recruitment to the GLP-1R are not yet clear.²² GLP-1R ligands that manifest strong selectivity in terms of effector protein recruitment and activation would be valuable tools for elucidating the role(s) of individual effector proteins.

Synthetic peptide agonists of GLP-1R have been developed to treat type II diabetes by enhancing glucose-stimulated insulin secretion from pancreatic β cells, among other mechanisms. Exendin-4, for example, is a component of the venom of the Gila monster and functions as a potent agonist of this receptor.²³ Liraglutide is nearly identical in sequence to GLP-1(7–37) but bears a hexadecanoyl appendage on the side chain of Lys-26.²⁴ This appendage promotes binding to serum albumin, which protects liraglutide from DPP-4 cleavage and dramatically enhances lifetime in the bloodstream.²⁵

Variations in the α -amino acid sequences of GLP-1R agonists lead to differences in the relative and absolute abilities of these agonists to induce recruitment of intracellular effector proteins to the receptor and differences in the stimulation of downstream signaling events. Thus, for example, relative to mature GLP-1, both exendin-4 and oxyntomodulin show a bias toward recruitment of β -arrestin-1 and β -arrestin-2 relative to cAMP generation (which presumably reflects $G\alpha_s$ activation).²⁶

Zhang et al. recently reported discovery of an exendin-4 derivative that displays significant bias in favor of G protein activation, which leads to an altered in vivo efficacy profile relative to exendin-4.²⁷ Furthermore, allosteric GLP-1R ligands can influence the pattern of intracellular protein recruitment induced by a given peptide agonist.^{28,29} These observations are of great interest from the biomedical perspective, because it has been proposed that therapeutic benefits may be maximized (and deleterious side effects minimized) with drugs that exert specifically tailored activating effects on the GLP-1R (or other GPCRs).^{6,30,31} However, the origins of ligand-dependent variations in signaling outcome are not yet clear at the molecular level, and the rational design of agonists with predetermined bias profiles at a given GPCR is currently not possible.

Here we show that GLP-1 analogues containing β -amino acid residues can display substantial bias in terms of intracellular partner engagement by the GLP-1R. These findings are significant because nearly all known GLP-1 analogues are composed exclusively of α -amino acid residues, although a few examples with unnatural backbone components have been described.^{32–34} β residue incorporation is simple in the context of conventional solid-phase peptide synthesis, and the findings disclosed here suggest that evaluation of small sets of peptide hormone analogues containing $\alpha \rightarrow \beta$ replacements could be a generally productive strategy for discovery of molecules with mechanistic and perhaps ultimately therapeutic utility.

RESULTS

Peptide Design. We previously described a small set of GLP-1(7–36)-NH₂ analogues, including 1–4 (Figure 3), that contain $\alpha \rightarrow \beta$ replacements in the C-terminal region of the hormone and retain agonist activity at the GLP-1R.³⁵ The most heavily modified member of this set, 4, contains two $\alpha \rightarrow \text{Aib}$ (2-aminoisobutyric acid) substitutions as well as five $\alpha \rightarrow \beta$ substitutions. The β residue placement in this set conforms to an $\alpha\alpha\alpha\beta$ pattern. The ring constraint in the β residues employed in 1–4 is known to support adoption of an α -helix-like conformation by α/β -peptides;³⁶ a cocrystal structure of GLP-1 and the GLP-1R extracellular domain shows that the C-terminal portion of the hormone adopts an α -helical conformation in the bound state.³⁷

In the previous study we sought to maximize β residue content in order to minimize the susceptibility of our α/β -peptides to proteolytic degradation. Extension of the $\alpha\alpha\alpha\beta$ pattern evident in 3 to a sixth site (position 14), however, caused a substantial decline in agonist activity.³⁵ We therefore turned to $\alpha \rightarrow \text{Aib}$ replacements in the N-terminal portion to enhance protease resistance. GLP-1 is rapidly cleaved between Ala8 and Glu9 by dipeptidyl peptidase-4 (DPP-4), but this

	1	5	10	15	20	25	30	35
GLP-1 (1–37)	H	D	E	F	E	R	H	A
GLP-1 (1–36)NH ₂	H	D	E	F	E	R	H	A
GLP-1 (7–37)			H	A	E	G	T	F
GLP-1 (7–36)NH ₂			H	A	E	G	T	F
GLP-1 (9–37)				E	G	T	F	T
GLP-1 (9–36)NH ₂				E	G	T	F	T
Glucagon	H	S	Q	G	T	F	T	S
Oxyntomodulin	H	S	Q	G	T	F	T	S

Figure 2. Amino acid sequences of each endogenous form of GLP-1, as well as the sequences of related peptides glucagon and oxyntomodulin.

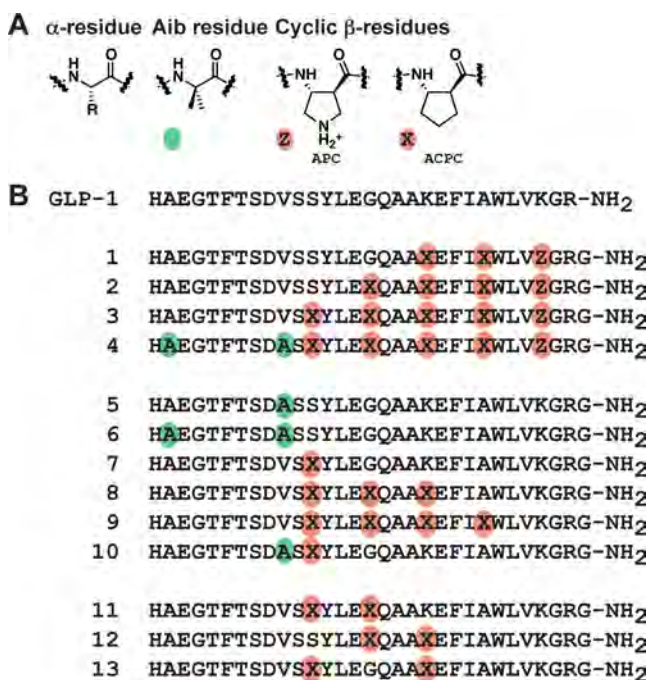


Figure 3. (A) α -Amino acid and β -amino acid residues. The colored circles used to indicate non-natural substitutions in sequences below are defined: green circles represent the α residue Aib, and orange circles represent ring-constrained β residues (X = ACPC, Z = APC). (B) GLP-1(7–36)NH₂ and α/β -peptide analogues 1–13 (based on GLP-1(7–37)NH₂). Each peptide has a free N-terminus and a primary amide at the C-terminus.

cleavage can be blocked with maintenance of agonist activity by replacing Ala8 with Aib.³⁸ Aib was therefore placed at position 8 in α/β -peptide 4. The other protease known to degrade GLP-1 in vivo is neprilysin,³⁹ which cleaves at many sites in the C-terminal and central regions of the hormone. We introduced Aib at position 16 in 4 to augment the protection from neprilysin expected from the five $\alpha \rightarrow \beta$ substitutions in 3.³⁵

Our initial studies of GLP-1R activation by α/β -peptides³⁵ focused on cAMP accumulation; the work described here expands this evaluation to include recruitment of β -arrestin-1 and β -arrestin-2, as well as a more sensitive alternative assay for cAMP production. In an effort to elucidate the origin of pathway selectivities detected among α/β -peptides 1–4, we expanded this collection to include 5–13 (Figure 3), analogues of GLP-1(7–37)NH₂ that contain different subsets among the $\alpha \rightarrow \beta$ and/or $\alpha \rightarrow$ Aib replacements found in 4. Although GLP-1(7–37)NH₂ does not occur naturally, this peptide is as

potent as the two mature forms of the hormone.⁴⁰ One of the natural mature forms, GLP-1(7–36)NH₂, serves as the reference agonist in these studies; we found that GLP-1(7–36)NH₂ and GLP-1(7–37)NH₂ behave identically in terms of stimulating cAMP production, β -arrestin-1 recruitment and β -arrestin-2 recruitment (Figure S1).

Evaluation of GLP-1R Activation Induced by α/β -Peptides 1–4. As a prelude to evaluating β -arrestin recruitment induced by α/β -peptide analogues of GLP-1, we reassessed cAMP production via a kinetic, GloSensor assay.^{41,42} In contrast to previous results for 1–4,³⁵ which were based on cAMP accumulation and quantification, cAMP generation potency as monitored by the GloSensor assay declines modestly with each additional $\alpha \rightarrow \beta$ replacement (Table 1; Figure 4A). However, the two assays are consistent in indicating that α/β -peptides 1–3 match GLP-1 in terms of maximum cAMP generation via the GLP-1R; the maximum activation by 4 is lower than that of GLP-1 or the other α/β -peptides according to the GloSensor assay.

Although the new assay for cAMP production indicates that α/β -peptide 4 has significantly lower potency and efficacy relative to GLP-1, previous studies demonstrated that 4 can control blood glucose in vivo, and that this effect is prolonged relative to glucose control achieved with GLP-1.³⁵ In addition, 4 and GLP-1 were indistinguishable as insulin secretagogues in experiments involving mouse pancreatic islets.³⁵ These functional similarities between GLP-1 and 4 may indicate that the resistance to proteolysis engendered by the nonproteinogenic residues in the α/β -peptide compensates for a diminished efficacy in activating the GLP-1R for cAMP production.

Recruitment of β -arrestin-1 and β -arrestin-2 to the GLP-1R induced by α/β -peptides 1–4 was evaluated via previously described bioluminescence resonance energy transfer (BRET) assays.¹⁶ Constructs for the GLP1R-RLuc8 and GFP²- β -arrestin-1 or GFP²- β -arrestin-2 (R393E, R395E) fusion proteins were transiently transfected into HEK293FT cells along with a construct for G protein-coupled receptor kinase 5 (GRK5). The (R393E, R395E) variant of β -arrestin-2 prevents loss of BRET signal due to GLP-1R internalization.¹⁶ Cotransfection with GRK5 has been shown to enhance the maximum BRET signal in this assay by promoting GLP-1R phosphorylation,^{16,22} which increases the affinity of both β -arrestins for the GLP-1R.

Increasing the number of β residues in the GLP-1 analogues, starting near the C-terminus (1 \rightarrow 2 \rightarrow 3), causes a progressive decline in the potency and/or maximum level of recruitment for each β -arrestin (Table 1, Figures 4B–C). The most dramatic changes are observed for α/β -peptide 4, which is

Table 1. Potency and Maximum Response Measured for GLP-1 and α/β -Peptides 1–4^a

	cAMP		β -arrestin-1		β -arrestin-2	
	pEC ₅₀ (M)	max response (% GLP-1)	pEC ₅₀ (M)	max response (% GLP-1)	pEC ₅₀ (M)	max response (% GLP-1)
GLP-1	−10.3 ± 0.1	100	−8.4 ± 0.2	100	−8.1 ± 0.3	100
α/β -peptide 1	−9.8 ± 0.1	101 ± 1	−8.0 ± 0.1	88 ± 6	−7.9 ± 0.1	78 ± 4
α/β -peptide 2	−9.4 ± 0.1	100 ± 2	−7.6 ± 0.1	87 ± 6	−7.7 ± 0.1	63 ± 3
α/β -peptide 3	−8.8 ± 0.1	97 ± 3	−7.8 ± 0.1	48 ± 4	−7.9 ± 0.1	47 ± 4
α/β -peptide 4	−8.2 ± 0.1	60 ± 5		6 ± 8		13 ± 4

^aValues are the mean ± SEM of ≥ 3 independent experiments, with duplicate measurements per experiment. Values represent G α_s activation, as measured by the luciferase-based GloSensor cAMP reporter assay, β -arrestin-1 recruitment, as measured using a β -arrestin-1 BRET assay and β -arrestin-2 recruitment, as measured using a β -arrestin-2 BRET assay. The β -arrestin-2 plasmid contained (R393E, R395E) mutations, which prevent receptor internalization.¹⁶ For 4, β -arrestin-1 and β -arrestin-2 maximum responses represent the maximal response at 1 μ M peptide.

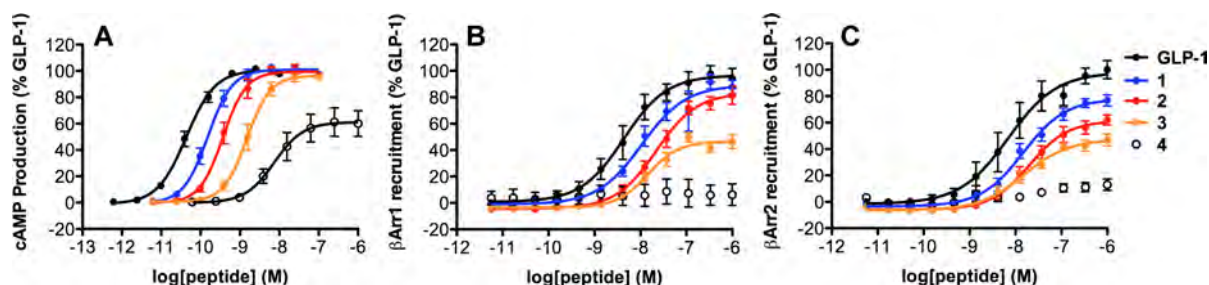


Figure 4. GLP-1R activation comparisons among GLP-1(7–36)NH₂ and α/β -peptides 1–4 (based on GLP-1(7–37)NH₂). Data points are the mean \pm SEM of ≥ 3 independent experiments, with duplicate measurements for each experiment. Concentration–response curves for peptide-induced activation of GLP-1R as manifested by (A) G_{α_s} activation, measured by the luciferase-based GloSensor cAMP reporter assay; (B) β -arrestin-1 recruitment, measured using a β -arrestin-1 BRET assay; (C) β -arrestin-2 recruitment, measured using a β -arrestin-2 BRET assay. The β -arrestin-2 plasmid contains (R393E, R395E) mutations, which prevent receptor internalization.¹⁶

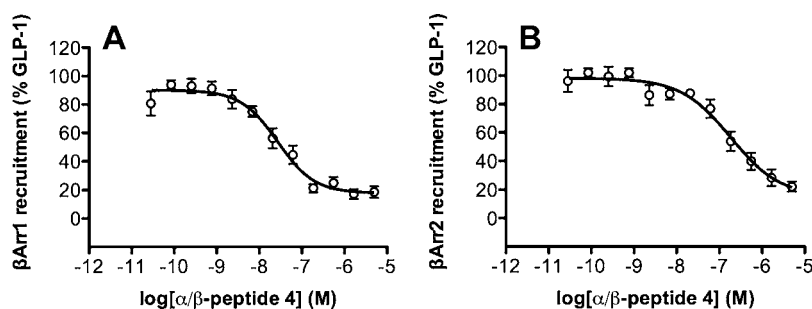


Figure 5. Competition between GLP-1(7–36)NH₂ and α/β -peptide 4 for binding to GLP-1R, as detected by BRET assays for recruitment of (A) β -arrestin-1 or (B) β -arrestin-2. Data points are the mean \pm SEM of ≥ 3 independent experiments, with duplicate measurements for each experiment. The concentration of GLP-1(7–36)NH₂ was held constant at 10 nM, and the concentration of 4 was varied. The β -arrestin-2 plasmid contains (R393E, R395E) mutations, which prevent receptor internalization.¹⁶

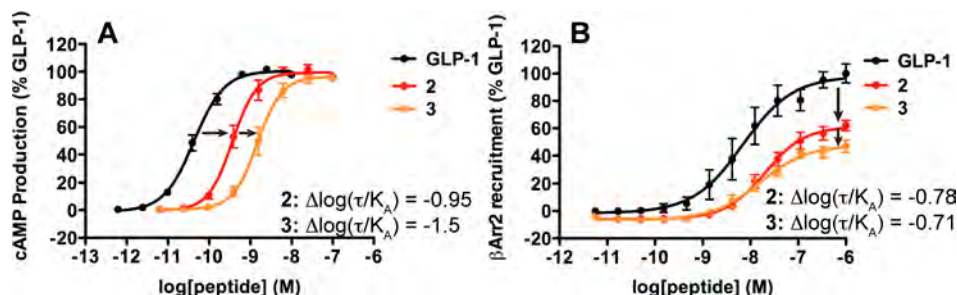


Figure 6. Illustration of the importance of using the operational model for detecting biased agonism. Concentration–response curves generated for GLP-1 and α/β -peptides 2 and 3 in (A) cAMP production and (B) β -arrestin-2 recruitment. The $\Delta\log(\tau/K_A)$ values calculated for α/β -peptide 2 relative to GLP-1 in each response demonstrate that the efficacy of α/β -peptide 2 is similar between cAMP production and β -arrestin-2 recruitment, despite the different changes in the concentration-dependent behavior of this peptide in the two responses. In contrast, the $\Delta\log(\tau/K_A)$ values calculated for α/β -peptide 3 relative to GLP-1 in each response demonstrate that the efficacy of α/β -peptide 3 is greater for β -arrestin-2 recruitment than for cAMP production.

barely active in these assays. α/β -Peptides 3 and 4 have the same five $\alpha \rightarrow \beta$ replacements, but 4 contains two Aib residues not found in 3.

Competition BRET assays, in which 4 was added to cells in the presence of 10 nM GLP-1, show that this α/β -peptide is fully competent to bind to the receptor under these conditions, because 4 serves as an antagonist of GLP-1-induced recruitment of either β -arrestin-1 ($pIC_{50} = -7.6 \pm 0.1$) or β -arrestin-2 ($pIC_{50} = -6.7 \pm 0.2$) (Figure 5).

Analysis of GLP-1R Activation Bias by α/β -Peptides 1–4. For a receptor such as GLP-1R that can activate multiple intracellular partner proteins, such as G proteins and β -arrestins, the availability of a new agonist leads to an important question: how do the relative efficacies of this new agonist

among the possible signaling pathways compare with the relative efficacies of a benchmark agonist? In other words, does the new agonist show a preference pattern among the available signaling pathways that differs from the preference pattern of the benchmark agonist? In the context of the present study, a specific example of this type of question is: “how does the relative efficacy of α/β -peptide 3 for inducing cAMP production (presumably via activation of G_{α_s}) vs recruiting β -arrestin-2 compare with the relative efficacy of the benchmark agonist GLP-1(7–36)NH₂ for these two processes?” If the balance of efficacy along these two signaling axes is substantially different for 3 relative to GLP-1(7–36)NH₂, then 3 is identified as a “biased agonist” of the GLP-1R.

We have used the operational model of Black and Leff^{43,44} to determine whether our α/β -peptide analogues display biased agonism relative to GLP-1(7–36)NH₂. This model describes the effect of an agonist on a receptor with two terms, (i) K_A , the dissociation constant that characterizes the agonist binding to the receptor conformation induced by association with a given effector protein (e.g., a G protein or a β -arrestin), and (ii) τ , the efficacy of the agonist, a term that accounts for the potency of agonist action on the receptor and assay-dependent factors, including the density of receptors and strength of receptor-effector coupling.⁴⁴ K_A and τ can be estimated from standard concentration–response data sets. The expression $\log(\tau/K_A)$, referred to as the “transduction coefficient,” is a measure of the strength of activation of a particular pathway by a specific agonist. The way a given α/β -peptide differs from benchmark agonist GLP-1(7–36)NH₂ in activating a particular pathway can be expressed as a difference in transduction coefficients, $\Delta\log(\tau/K_A)$. A “bias factor” for a given α/β -peptide relative to GLP-1(7–36)NH₂ can be defined based on comparing two specific outcomes of GLP-1R activation, e.g., cAMP generation vs β -arrestin-2 recruitment, by calculating $\Delta\log(\tau/K_A)$.

The importance of using the operational model for comparisons among responses involving different effector proteins is illustrated in Figure 6, which focuses on a subset of the data presented in Figure 4. Figure 6A shows that the effect on cAMP production of four or five $\alpha \rightarrow \beta$ replacements in GLP-1, to generate 2 or 3, is manifested as a rightward shift in the concentration–response curve. There is very little difference among the maxima in cAMP production for these three compounds. In contrast, Figure 6B shows that the effect on β -arrestin-2 recruitment of the same $\alpha \rightarrow \beta$ replacements is manifested primarily as a drop in the maximum recruitment extent. If one focuses on maximum response and pEC₅₀, the parameters provided in Table 1, it is not clear how to compare the impact of the $\alpha \rightarrow \beta$ replacements on cAMP production vs β -arrestin-2 recruitment. However, application of the operational model allows calculation of bias factors for 2 and 3 relative to GLP-1 in both assays, and comparison is now straightforward.

Estimation of the $\Delta\log(\tau/K_A)$ values reveals parallel losses of efficacy for recruitment of β -arrestin-1 and β -arrestin-2 and for cAMP signaling for α/β -peptides 1 and 2 relative to GLP-1(7–36)NH₂ (Table 2). For α/β -peptide 3, however, the loss

Table 2. Bias Factors ($\Delta\log(\tau/K_A)$) Calculated for GLP-1 and α/β -Peptides 1–3^a

	$\Delta\log(\tau/K_A)$	
	β -arrestin-1 vs cAMP	β -arrestin-2 vs cAMP
GLP-1	0	0
α/β -peptide 1	0.1 ± 0.2	0.1 ± 0.2
α/β -peptide 2	0.1 ± 0.2	0.2 ± 0.3
α/β -peptide 3	0.6 ± 0.2	0.8 ^b ± 0.2
α/β -peptide 4	ND	ND

^aBias factors ($\Delta\log(\tau/K_A)$) calculated in terms of β -arrestin-1 recruitment relative to cAMP production, and β -arrestin-2 recruitment relative to cAMP production. These bias factors were derived from experimental data as described in the text. Bias factors could not be calculated for α/β -peptide 4, because the β -arrestin recruitment assays showed no quantifiable activity for this molecule (Figure 2). ND: not determined. ^bStatistically significant difference from GLP-1 using one-way analysis of variance followed by Dunnett's test ($P < 0.05$).

of cAMP signaling is greater than the loss of β -arrestin-1 or –2 recruitment. Thus, 3 displays a bias for β -arrestin recruitment relative to GLP-1 although the calculated bias factor for 3 is statistically significant only for β -arrestin-2. The lack of statistical significance for β -arrestin-1 bias factor calculated for 3 may be due to a greater degree of scatter in the β -arrestin-1 BRET data for 1–4 relative to the β -arrestin-2 BRET data for these peptides. Bias factors could not be determined for 4 because no significant recruitment of β -arrestin-1 or –2 could be detected in our assays for this α/β -peptide within the concentration range examined.

Evaluation of Peptides 5–13. New analogues of GLP-1(7–37)NH₂ were prepared in an effort to determine whether a particular subset among the substitutions in α/β -peptides 3 and 4 relative to GLP-1 plays a dominant role in mediating biased agonism. α -Peptide analogues containing either the Val16 \rightarrow Aib replacement (5) or both Aib replacements (6) were very similar to one another and to GLP-1(7–36)NH₂ (Table 3, Figure 7). For the two β -arrestins, both 5 and 6 displayed small declines in maximum recruitment but little change in EC₅₀ relative to GLP-1. For cAMP production, both 5 and 6 were ~3-fold less potent than GLP-1 (EC₅₀), but both α -peptides were indistinguishable from GLP-1 in terms of maximum response. The similarities in activity among 5, 6, and GLP-1(7–36)NH₂ suggest that the previously described analogue³⁸ containing only Ala8 \rightarrow Aib should manifest an activity profile comparable to those of 5 and 6.

Analogue 7 contains a single $\alpha \rightarrow \beta$ replacement at position 18; introduction of a β residue at this position in the original series (2 \rightarrow 3) induced an increase in β -arrestin-1 and –2 recruitment bias relative to GLP-1 (Table 2). In contrast, $\alpha \rightarrow \beta$ replacement at position 18 alone causes only minimal (and comparable) changes to cAMP production and β -arrestin recruitment (Table 3, Figure 7). Introduction of additional β residues, at positions 22 and 26 (8 and 9), causes decreases in both β -arrestin recruitment and cAMP production relative to GLP-1 (Table 3, Figure 7). Analysis of these data using the operational model (Table 4) indicates that engagement of the GLP-1R by α/β -peptide 8 or 9 causes a preference for recruitment of β -arrestin-1 and –2 over production of cAMP, relative to engagement of the GLP-1R by GLP-1. Thus, α/β -peptides 8 and 9 are β -arrestin-biased agonists of the GLP-1R. α/β -Peptide 10, containing only the Val16 \rightarrow Aib and Ser18 \rightarrow β replacements, displays significant decreases in recruitment of β -arrestin-1 and –2, similar to those seen for 8 and 9; however, the cAMP response for 10 is stronger than that induced by 8 or 9, and application of the operational model indicates that α/β -peptide 10 does not show significant signal bias relative to GLP-1.

To define the $\alpha \rightarrow \beta$ replacement sites that are dominant in terms of the bias toward recruitment of β -arrestin-1 and –2 manifested by α/β -peptides 8 and 9, we prepared and evaluated 11–13 (Table 3, Figure 8). This α/β -peptide set contains each possible pair among the three β residues in 8. Analysis of the results with the operational model indicates that none among 11–13 displays significant signaling bias relative to GLP-1 (Table 4). Thus, it appears that the three $\alpha \rightarrow \beta$ replacements in 8 represent a minimum level of modification required to generate a β -arrestin-biased agonist for the GLP-1R.

DISCUSSION

α/β -Peptide 4 contains seven substitutions relative to GLP-1, which, collectively, lead to losses in this analogue's ability to

Table 3. Potency and Maximum Response Measured for GLP-1 and Peptides 5–13^a

	cAMP		β -arrestin-1		β -arrestin-2	
	pEC ₅₀ (M)	max response (% GLP-1)	pEC ₅₀ (M)	max response (% GLP-1)	pEC ₅₀ (M)	max response (% GLP-1)
GLP-1	-10.3 ± 0.1	100	-8.0 ± 0.1	100	-8.0 ± 0.1	100
α -peptide 5	-9.8 ± 0.2	101 ± 1	-8.2 ± 0.1	97 ± 2	-8.0 ± 0.1	83 ± 2
α -peptide 6	-9.8 ± 0.1	103 ± 3	-8.1 ± 0.1	86 ± 4	-7.9 ± 0.1	76 ± 4
α/β -peptide 7	-10.0 ± 0.1	99 ± 1	-7.9 ± 0.1	81 ± 5	-8.1 ± 0.1	84 ± 2
α/β -peptide 8	-9.0 ± 0.2	96 ± 1	-7.7 ± 0.2	43 ± 3	-8.0 ± 0.1	63 ± 5
α/β -peptide 9	-8.4 ± 0.2	97 ± 2	-7.5 ± 0.1	41 ± 4	-8.0 ± 0.1	59 ± 2
α/β -peptide 10	-9.6 ± 0.1	100 ± 1	-8.0 ± 0.1	30 ± 1	-8.0 ± 0.1	53 ± 5
α/β -peptide 11	-9.8 ± 0.1	102 ± 1	-8.0 ± 0.1	37 ± 1	-8.1 ± 0.1	52 ± 4
α/β -peptide 12	-10.0 ± 0.1	103 ± 1	-7.8 ± 0.1	85 ± 3	-8.0 ± 0.1	78 ± 3
α/β -peptide 13	-10.1 ± 0.1	104 ± 1	-7.8 ± 0.2	80 ± 3	-8.0 ± 0.1	74 ± 4

^aValues are the mean ± SEM of ≥3 independent experiments, with duplicate measurements for each experiment. Values represent G α_s activation, as measured by the luciferase-based GloSensor cAMP reporter assay, β -arrestin-1 recruitment, as measured using a β -arrestin-1 BRET assay and β -arrestin-2 recruitment, as measured using a β -arrestin-2 BRET assay. β -Arrestin-2 plasmid contained (R393E, R395E) mutations, which prevent receptor internalization.¹⁶

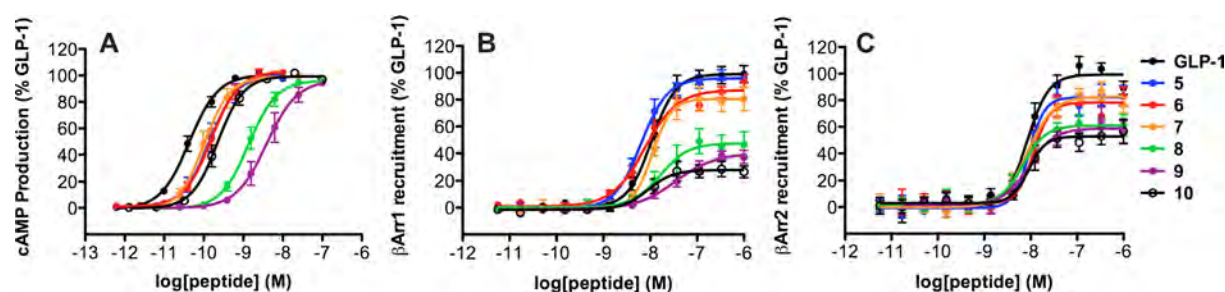


Figure 7. GLP-1R activation comparisons among GLP-1(7–36)NH₂ and α/β -peptides 5–10 (based on GLP-1(7–37)NH₂). Data points are the mean ± SEM of ≥3 independent experiments, with duplicate measurements for each experiment. Concentration–response curves for peptide-induced activation of GLP-1R as manifested by (A) G α_s activation, measured by the luciferase-based GloSensor cAMP reporter assay; (B) β -arrestin-1 recruitment, measured using a β -arrestin-1 BRET assay; (C) β -arrestin-2 recruitment, measured using a β -arrestin-2 BRET assay. The β -arrestin-2 plasmid contains (R393E, R395E) mutations, which prevent receptor internalization.¹⁶

Table 4. Bias Factors ($\Delta\Delta\log(\tau/K_A)$) Calculated for GLP-1 and Peptides 5–13^a

	$\Delta\Delta\log(\tau/K_A)$	
	β -arrestin-1 vs cAMP	β -arrestin-2 vs cAMP
GLP-1	0	0
α -peptide 5	0.2 ± 0.1	0.2 ± 0.1
α -peptide 6	0.2 ± 0.1	0.0 ± 0.1
α/β -peptide 7	0.2 ± 0.1	0.2 ± 0.1
α/β -peptide 8	0.6 ^b ± 0.2	1.2 ^b ± 0.1
α/β -peptide 9	0.9 ^b ± 0.2	1.6 ^b ± 0.1
α/β -peptide 10	0.0 ± 0.1	0.3 ± 0.1
α/β -peptide 11	0.1 ± 0.1	0.2 ± 0.1
α/β -peptide 12	-0.0 ± 0.1	0.1 ± 0.1
α/β -peptide 13	-0.3 ± 0.2	-0.1 ± 0.1

^aBias factors ($\Delta\Delta\log(\tau/K_A)$) calculated in terms of β -arrestin-1 recruitment relative to cAMP production, and β -arrestin-2 recruitment relative to cAMP production. These bias factors were derived from experimental data as described in the text. ^bStatistically significant difference from GLP-1 using one-way analysis of variance followed by Dunnett's test ($P < 0.05$).

stimulate cAMP production or induce β -arrestin recruitment, relative to GLP-1. Exploration of subsets among the $\alpha \rightarrow \beta$ and $\alpha \rightarrow$ Aib replacement sites of 4 reveals substitution patterns that have little effect on peptide efficacy in terms of either cAMP production or β -arrestin recruitment (5, 6, 12, and 13), substitution patterns that reduce peptide efficacy in each

signaling pathway (1, 2, 7, 10, and 11) and, most interestingly, substitution patterns that differentially affect cAMP production versus β -arrestin recruitment (3, 8, and 9).

Comparing 3, 8, and 9 indicates that $\alpha \rightarrow \beta$ replacements in the central region of GLP-1 are the most consequential in terms of engendering a bias toward β -arrestin recruitment relative to cAMP production. While the incorporation of an $\alpha \rightarrow \beta$ replacement at position 18 (2 \rightarrow 3) is necessary for the induction of selectivity for β -arrestin recruitment, neither the Ser18 $\rightarrow \beta$ substitution alone (7) nor double substitution at Ser18 and Gly22 (11) is sufficient to induce this selectivity. In addition, implementing only the two outer $\alpha \rightarrow \beta$ replacements in 8, at Ser18 and Lys26, to generate 13, does not induce pathway selectivity. These findings are significant because they suggest that G protein activation is more sensitive than is β -arrestin recruitment to changes in a relatively focused region near the middle of a GLP-1R agonist. In addition, our results suggest that this region of the peptide must contain a minimum density of $\alpha \rightarrow \beta$ replacements (e.g., all three $\alpha \rightarrow \beta$ replacements in 8) in order to induce a bias toward β -arrestin recruitment relative to G protein-mediated signaling.

The importance revealed here of the GLP-1 segment encompassing residues 18–26 in terms of G α_s activation by the GLP-1R, as manifested by cAMP production, can be related to the available structural information for the hormone-GPCR complex. A cocrystal structure of GLP-1(7–37) with the extracellular domain of GLP-1R³⁷ shows that direct contact begins at hormone residue Ala24 and extends toward the

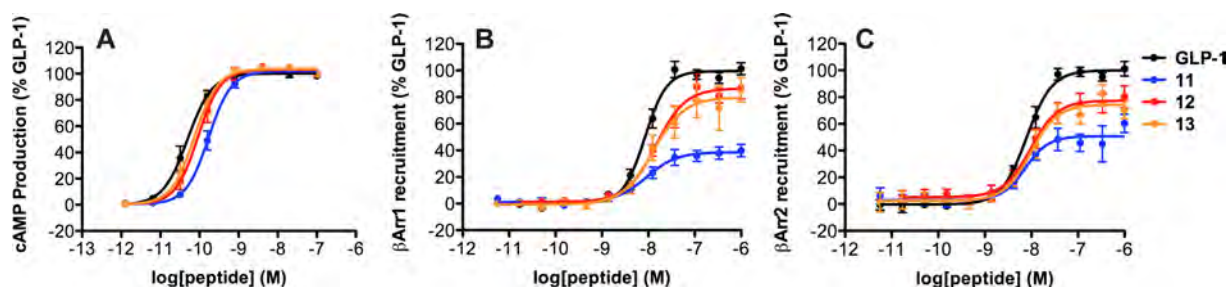


Figure 8. GLP-1R activation comparisons among GLP-1(7–36)NH₂ and α/β -peptides 11–13 (based on GLP-1(7–37)NH₂). Data points are the mean \pm SEM of ≥ 3 independent experiments, with duplicate measurements for each experiment. Concentration–response curves for peptide-induced activation of GLP-1R as manifested by (A) G α_s activation, measured by the luciferase-based GloSensor cAMP reporter assay; (B) β -arrestin-1 recruitment, measured using a β -arrestin-1 BRET assay; (C) β -arrestin-2 recruitment, measured using a β -arrestin-2 BRET assay. The β -arrestin-2 plasmid contains (R393E, R395E) mutations, which prevent receptor internalization.¹⁶

hormone C-terminus; thus, interactions of the 18–26 region of GLP-1 with the receptor must largely involve the membrane-embedded domain of the GLP-1R. Photoreactive labeling previously identified a direct interaction between position 20 of GLP-1 and Trp-297 in extracellular loop 2 (ECL2) of the GLP-1R.⁴⁵ Receptor mutation studies revealed that ECL2 plays an important role in GLP-1-induced signaling (cAMP production, Ca²⁺ mobilization and ERK phosphorylation).^{9,11} In addition, recent mutation studies involving ECL3 suggest that several residues in this loop are critical in mediating signaling induced by GLP-1, exendin-4 or oxyntomodulin.²⁶ The $\alpha \rightarrow \beta$ replacements made in the 18–26 region of GLP-1 to generate 8 may disrupt critical interactions between the ligand and the ECLs of the GLP-1R.

To begin to explore how β -arrestin-biased α/β -peptides might interact with the ECLs of the GLP-1R, we examined a recently reported model of the GLP-1 + GLP-1R complex, and highlighted the positions of GLP-1 that are modified in α/β -peptide 8 to generate Figure 9.⁴⁶ This image suggests that there

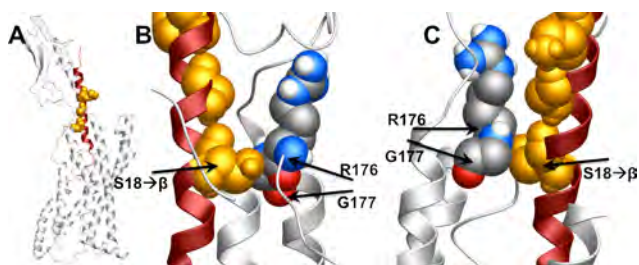


Figure 9. Images depicting a hypothetical interaction between the GLP-1R (gray) and α/β -peptide 8 (red), generated from an existing model of the GLP-1R complexed to GLP-1,⁴³ by highlighting in orange the residues in GLP-1 that are modified to β residues in 8. (A) Full view of the GLP-1R + GLP-1 model. (B, C) Close-up views of position 18 of GLP-1 (β residue in 8) in contact with R376 and G377 of ECL3 of GLP-1R. Images were generated using MolSoft ICM Browser software.

may be a close contact between the β residue at position 18 of 8 and residues within ECL3 that were previously found to be critical in mediating ERK1/2 phosphorylation induced by GLP-1, exendin-4 and oxyntomodulin via their interactions with the GLP-1R.²⁶ Oxyntomodulin is biased toward ERK1/2 phosphorylation over cAMP production relative to GLP-1, a selectivity that may arise from the bias of oxyntomodulin toward β -arrestin recruitment.²⁶ Based on this precedent, we speculate that the contacts we propose between the central

portion of 8 and ECL3 of the GLP-1R might contribute to the β -arrestin bias displayed by this α/β -peptide.

As noted above, 8 and related α/β -peptides have lower efficacy relative to GLP-1 in terms of cAMP production and β -arrestin recruitment, but the impact of $\alpha \rightarrow \beta$ substitution on cAMP production is larger than the impact on β -arrestin recruitment. The results of the computational modeling raise the possibility that interactions between centrally located β residues on these α/β -peptides and ECL3 on the receptor may explain why efficacy for β -arrestin recruitment suffers less from $\alpha \rightarrow \beta$ replacement than does efficacy for cAMP production.

CONCLUSIONS

We have shown that evaluation of a small family of peptide hormone derivatives containing $\alpha \rightarrow \beta$ replacements can lead to discovery of agonists with significant signaling bias relative to the native hormone, despite the decline in overall signaling efficacy among the α/β -peptides relative to GLP-1 itself. This type of backbone-modified peptide is readily accessible via conventional solid-phase synthesis but has received relatively little attention from the perspective of exploring new agonists for Class B GPCRs. Promising results have recently been reported for α/β analogues of parathyroid hormone(1–34)⁴⁷ and vasoactive intestinal peptide.⁴⁸ Collectively, these recent studies and the work reported here suggest that backbone-modified analogues of peptide hormones may prove to be a rich source of new agonists that can serve as tools for elucidating the physiological consequences of specific GPCR-initiated signaling pathways; these unusual peptides may ultimately lead to therapeutic advances.

Our finding that a central segment of GLP-1 appears to be more critical for G protein-mediated activity than for β -arrestin recruitment at the GLP-1R is of general significance from the perspective of new strategies for discovery of biased agonists of this medically important receptor. In addition, this finding is intriguing in the context of the recent report of a G protein-biased analogue of exendin-4.²⁷ Exendin-4 is a lizard-derived peptide that serves as a potent GLP-1R agonist and is approved for treatment of type 2 diabetes.²³ The new α -peptide was identified via screening of a massive biosynthetic library of exendin-4 variants differing in the N-terminal segment.²⁷ Thus, the bias induced by this combinatorially derived peptide arises from changes at the N-terminus of exendin-4, an observation that contrasts with and is complemented by our finding that β -arrestin bias can be achieved via modifications in the central segment of GLP-1.

■ EXPERIMENTAL METHODS

Peptide Synthesis and Purification. Peptides were prepared by microwave-assisted solid phase peptide synthesis³⁶ on ChemMatrix H-PAL amide resin based on Fmoc-protection of the main chain amino groups. Full details on peptide synthesis and purification can be found in the [Supporting Information](#).

cAMP Production Assays. cAMP signaling was assessed in HEK293-derived cells (GS-22A)³⁹ stably expressing the GloSensor cAMP reporter.⁴⁰ These cells were a gift from Prof. Thomas Gardella at Massachusetts General Hospital. Human GLP-1R was transiently transfected into these cells (10 μ g GLP-1R for 10 cm plate of cells) using FuGene HD transfection reagent (3:1 FuGene HD to GLP-1R). On the day of transfection, culture medium was replaced with antibiotic-free DMEM supplemented with 10% FBS, 4 mM L-glutamine, and 1 mM sodium pyruvate. GLP-1R and FuGene HD were combined in OptiMEM (1 mL), and this mixture was incubated for 15 min before being added to cells. Cells were exposed to transfection reagents for 24 h before being plated into opaque, clear-bottomed 96-well plates at 30 000 cells per well in antibiotic-free DMEM supplemented with 10% FBS, 4 mM L-glutamine, and 1 mM sodium pyruvate. The plate was incubated for 24 h. For cAMP concentration–response assays, cells were preincubated with D-PBS buffer containing D-luciferin (0.5 mM) until a stable background luminescence signal was achieved (30 min). Various doses of peptide were then added, and luminescence was measured for 30 min on a BioTek Synergy 2 plate reader. The maximal luminescence response (usually observed 16–20 min after peptide addition) was used to generate concentration–response curves.

Reported EC₅₀ and maximum response values are the average of ≥ 3 independent experiments. Each experiment involved ≥ 7 different concentrations of GLP-1 or analogue, with solutions prepared via serial dilution of a stock solution of each peptide (usually 1 μ M, which becomes 100 nM in the assay), with each resulting data point representing the average of two replicate wells. Changing pipet tips after each dilution was found to be critical for reproducible concentration–response curves. Both commercially obtained GLP-1 and GLP-1 we had prepared were tested in these assays, with identical results ([Figure S2](#)). GLP-1(7–36)NH₂ and GLP-1(7–37)NH₂ behaved identically in these assays ([Figure S1](#)).

Bioluminescence Resonance Energy Transfer Assays. Recruitment of β -arrestin-1 and β -arrestin-2 to the GLP-1R was assessed in HEK293FT cells, using a bioluminescence resonance energy transfer (BRET) assay based on a previous report.¹⁶ GLP-1R-Rluc8, GFP²- β -arrestin-1, or GFP²- β -arrestin-2(R393E, R395E), and GRK5 (which has previously been shown to enhance BRET signal in this assay²²) were transiently cotransfected using polyethylenimine (PEI). A 1:1 ratio of PEI/DNA was used, because cell viability was compromised at higher PEI/DNA ratios. On the day of transfection, culture medium was changed to DMEM with no supplements. DNA and PEI were combined in OptiMEM, and the mixture was incubated at room temperature for 20 min before being added to cells. After 6 h, DMEM supplemented with 20% FBS was added to the cells. After 24 h of transfection, cells were plated into opaque, white-bottomed 96-well plates and incubated for 24 h.

Prior to BRET experiments, cells were rinsed twice with PBS and then incubated with D-PBS for 1 h at 37 °C. Various concentrations of peptide were then added and incubated for 20 min at 37 °C. Rluc8 substrate DeepBlueC (60 μ M in EtOH) was then added and incubated for 20–40 min before BRET signal ($I_{515\text{nm}}/I_{410\text{nm}}$) was measured on a Tecan Infinite 200 or BioTek Synergy 2 plate reader. Incubation with DeepBlueC prior to signal detection reduced signal variability, which presumably arises in the absence of preincubation because of variability in time required for DeepBlueC to penetrate cells and become available for oxidation by Rluc8. The BRET signal for GLP-1 usually remained constant over this time, though sometimes the signal for GLP-1 and analogues decreased slightly (to similar extents) over the course of 1 h. In some experiments, we observed that the BRET signal for some α/β -peptides (7 and 10) to decrease slightly ($\sim 5\%$ decrease relative to GLP-1) over the course of an hour. Thus, the BRET signal

for each peptide was measured at the same time in replicate experiments.

Reported EC₅₀ and maximum response values are the average of ≥ 3 independent experiments. Each experiment consists of ≥ 7 different concentrations of GLP-1 or analogue, with solutions prepared via serial dilution of the stock solution of each peptide (usually 12 μ M, which becomes 1 μ M in the assay), with each resulting data point representing the average of two replicate wells.

For competition BRET assays, various concentrations of α/β -peptide 4 were added to cells, and a constant concentration of GLP-1 (130 nM, which becomes 10 nM in the assay) was added immediately after addition of α/β -peptide. All subsequent steps were performed as above.

Full details on molecular biology operations that were employed to access BRET fusion protein constructs and on BRET transfection ratio optimization can be found in the [Supporting Information](#).

Data Analysis. Data were processed using Microsoft Excel and GraphPad Prism 5 software. Concentration–response data for each experiment were normalized to the maximum signal observed for GLP-1(7–36)NH₂ for that experiment. The normalized data points from each independent experiment were averaged to determine the average concentration–response behavior for GLP-1 and each analogue as depicted in concentration–response curves. EC₅₀ and maximum response values were extracted from concentration–response data by fitting the concentration–response for each individual experiment to a sigmoidal dose–response model with variable slope, and then calculating the average and SEM for each individual experiment.

To quantify the efficacy of each peptide in the different pathways assayed, each concentration–response curve for each pathway (cAMP production, β -arrestin-1 recruitment, and β -arrestin-2 recruitment) was fitted to an operational model of agonism,^{43,44} as shown in [eq 1](#). In [eq 1](#), $[A]$ is the concentration of agonist and E is the response at each tested $[A]$ (i.e., the independent and dependent variables in the assay). As described in the main text, K_A is the dissociation constant that characterizes the agonist binding to the receptor conformation induced by association with a given effector protein. τ is the efficacy of the agonist, a term that accounts for the potency of agonist action on the receptor and assay-dependent factors, including the density of receptors and strength of receptor–effector coupling.

$$E = \frac{E_{\max} \tau [A]}{[A](1 + \tau) + K_A} \quad (1)$$

For each peptide, the efficacy in each signaling pathway was extracted as the $\log(\tau/K_A)$ (mean \pm SEM), and then compared to GLP-1 by subtracting the value of $\log(\tau/K_A)$ for GLP-1 from that of the peptide to yield $\Delta\log(\tau/K_A)$ for the peptide. The $\Delta\log(\tau/K_A)$ values obtained for the peptide relative to GLP-1 were compiled to determine the average \pm SEM $\Delta\log(\tau/K_A)$ for the peptide. The bias factor (differential efficacy of a peptide relative to GLP-1 in two separate pathways) for each peptide was determined by subtracting the $\Delta\log(\tau/K_A)$ in the arrestin pathway from the $\Delta\log(\tau/K_A)$ for that peptide in the cAMP pathway, yielding $\Delta\Delta\log(\tau/K_A)$ for each peptide. Error in each $\Delta\Delta\log(\tau/K_A)$ value was calculated by propagating the error in the $\log(\tau/K_A)$ (SEM obtained from averaging individual $\Delta\log(\tau/K_A)$ values) for the peptide and GLP-1 in each pathway (cAMP and either β -arrestin-1 recruitment or β -arrestin-2 recruitment).

To determine whether the $\Delta\Delta\log(\tau/K_A)$ for a given peptide was statistically significant, $\Delta\Delta\log(\tau/K_A)$ values were compared using one-way analysis of variance (ANOVA) followed by Dunnett's post test. $P < 0.05$ denotes statistical significance.

■ ASSOCIATED CONTENT

Supporting Information

The Supporting Information is available free of charge on the ACS Publications website at DOI: 10.1021/jacs.6b08323.

Additional figures and details for experimental protocols (PDF)

■ AUTHOR INFORMATION

Corresponding Authors

*E-mail: Denise.Wootten@monash.edu.

*E-mail: Patrick.Sexton@monash.edu.

*E-mail: gellman@chem.wisc.edu.

Present Address

[§]L.M.J.: Laboratory Medicine & Pathology, Mayo Memorial Building, 420 Delaware St., S.E., Minneapolis, MN 55455.

Notes

The authors declare the following competing financial interest(s): L.M.J. and S.H.G. are inventors on a patent application covering GLP-1 analogues described here; S.H.G. is a cofounder of Longevity Biotech, Inc., which is pursuing biomedical applications of α/β -peptides.

■ ACKNOWLEDGMENTS

This work was supported by the National Institute of General Medical Sciences (NIGMS) (GM056414, to S.H.G.) and the National Health and Medical Research Council of Australia (NHMRC) (project grants [1061044] and [1065410], and NHMRC program grant [1055134] to P.M.S. and D.W.); P.M.S. is a NHMRC Principal Research Fellow. D.W. is a NHMRC Career Development Fellow. M.V.H. and L.M.J. were supported in part by a Chemical Biology Interface Training Grant from NIGMS (T32 GM008505). Support for this research was provided by the University of Wisconsin—Madison, Office of the Vice Chancellor for Research and Graduate Education with funding from the Wisconsin Alumni Research Foundation. The authors gratefully acknowledge Prof. Thomas Gardella for sharing cells containing the GloSensor cAMP plasmid, Jakob Lerche Hansen and Rasmus Jorgensen for sharing GLP1R-Rluc8, GRK5, and GFP²- β -arrestin-2 plasmids, and Prof. Alan Attie and group members Dr. Mark Keller, Dr. Sushant Bhatnagar, Dr. Lindsay Wrighton, and Donnie Stapleton for technical expertise and helpful discussion.

■ REFERENCES

- (1) Pierce, K. L.; Premont, R. T.; Lefkowitz, R. J. *Nat. Rev. Mol. Cell Biol.* **2002**, *3*, 639–650.
- (2) Shenoy, S. K.; Lefkowitz, R. J. *Sci. STKE* **2005**, 308, cm10.
- (3) DeWire, S. M.; Ahn, S.; Lefkowitz, R. J.; Shenoy, S. K. *Annu. Rev. Physiol.* **2007**, *69*, 483–510.
- (4) Kenakin, T. *Trends Pharmacol. Sci.* **2003**, *24*, 346–354.
- (5) Kobilka, B. K.; Deupi, X. *Trends Pharmacol. Sci.* **2007**, *28*, 397–406.
- (6) Kenakin, T.; Christopoulos, A. *Nat. Rev. Drug Discovery* **2013**, *12*, 205–216.
- (7) Rajagopal, S.; Rajagopal, K.; Lefkowitz, R. J. *Nat. Rev. Drug Discovery* **2010**, *9*, 373–386.
- (8) Reiter, E.; Ahn, S.; Shukla, A. K.; Lefkowitz, R. J. *Annu. Rev. Pharmacol. Toxicol.* **2012**, *52*, 179–197.
- (9) Koole, C.; Wootten, D.; Simms, J.; Savage, E. E.; Miller, L. J.; Christopoulos, A.; Sexton, P. M. *J. Biol. Chem.* **2012**, *287*, 3659–3673.
- (10) Wootten, D.; Simms, J.; Miller, L. J.; Christopoulos, A.; Sexton, P. M. *Proc. Natl. Acad. Sci. U. S. A.* **2013**, *110*, 5211–5216.
- (11) Koole, C.; Wootten, D.; Simms, J.; Miller, L. J.; Christopoulos, A.; Sexton, P. M. *J. Biol. Chem.* **2012**, *287*, 3642–3658.
- (12) Warne, T.; Edwards, P. C.; Leslie, A. G.; Tate, C. G. *Structure* **2012**, *20*, 841–849.
- (13) Shukla, A. K.; Singh, G.; Ghosh, E. *Trends Biochem. Sci.* **2014**, *39*, 594–602.
- (14) Baggio, L. L.; Drucker, D. J. *Gastroenterology* **2007**, *132*, 2131–2157.
- (15) Hansen, L.; Deacon, C. D.; Orskov, C.; Holst, J. J. *Endocrinology* **1999**, *140*, 5356–5363.
- (16) Jorgensen, R.; Kubale, V.; Vrecl, M.; Schwartz, T. W.; Elling, C. E. *J. Pharmacol. Exp. Ther.* **2007**, *322*, 148–154.
- (17) Baggio, L. L.; Huang, Q.; Brown, T. J.; Drucker, D. J. *Gastroenterology* **2004**, *127*, 546–558.
- (18) Willard, F. S.; Sloop, K. W. *Exp. Diabetes Res.* **2012**, *2012*, 470851.
- (19) Talbot, J.; Joly, E.; Prentki, M.; Buteau, J. *Mol. Cell. Endocrinol.* **2012**, *364*, 65–70.
- (20) Quoyer, J.; Longuet, C.; Broca, C.; Linck, N.; Costes, S.; Varin, E.; Bockaert, J.; Bertrand, G.; Dalle, S. *J. Biol. Chem.* **2010**, *285*, 1989–2002.
- (21) Sonoda, N.; Imamura, T.; Yoshizaki, T.; Babendure, J. L.; Lu, J. C.; Olefsky, J. M. *Proc. Natl. Acad. Sci. U. S. A.* **2008**, *105*, 6614–6619.
- (22) Jorgensen, R.; Martini, L.; Schwartz, T. W.; Elling, C. E. *Mol. Endocrinol.* **2005**, *19*, 812–823.
- (23) Robles, G. I.; Singh-Franco, D. *Drug Des., Dev. Ther.* **2009**, *3*, 219–240.
- (24) Knudsen, S. M.; Nielsen, P. F.; Huusfeldt, P. O.; Johansen, N. L.; Madsen, K.; Pedersen, F. Z.; Thøgersen, H.; Wilken, M.; Agerso, H. *J. Med. Chem.* **2000**, *43*, 1664–1669.
- (25) Steensgaard, D. B.; Thomsen, J. K.; Olsen, H. B.; Knudsen, S. M. *Diabetes* **2008**, *51* (Suppl. 1), A164.
- (26) Wootten, D.; Reynolds, C. A.; Smith, K. J.; Mobarec, J. C.; Koole, C.; Savage, E. E.; Pabreja, K.; Simms, J.; Sridhar, R.; Furness, S. G. B.; Liu, M.; Thompson, P. E.; Miller, L. J.; Christopoulos, A.; Sexton, P. M. *Cell* **2016**, *165*, 1632–1643.
- (27) Zhang, H.; Sturchler, E.; Zhu, J.; Nieto, A.; Cistrone, P. A.; Xie, J.; He, L.; Yea, K.; Jones, T.; Turn, R.; Di Stefano, P. S.; Griffin, P. R.; Dawson, P. E.; McDonald, P. H.; Lerner, R. A. *Nat. Commun.* **2015**, *6*, 8918.
- (28) Wootten, D.; Savage, E. E.; Willard, F. S.; Bueno, A. B.; Sloop, K. W.; Christopoulos, A.; Sexton, P. M. *Mol. Pharmacol.* **2013**, *83*, 822–834.
- (29) Koole, C.; Wootten, D.; Simms, J.; Valant, C.; Sridhar, R.; Woodman, O. L.; Miller, L. J.; Summers, R. J.; Christopoulos, A.; Sexton, P. M. *Mol. Pharmacol.* **2010**, *78*, 456–465.
- (30) Appleton, K. M.; Luttrell, L. M. *J. Recept. Signal Transduction Res.* **2013**, *33*, 153–161.
- (31) Whalen, E. J.; Rajagopal, S.; Lefkowitz, R. J. *Trends Mol. Med.* **2011**, *17*, 126–139.
- (32) Denton, E. V.; Craig, C. J.; Pongratz, R. L.; Appelbaum, J. S.; Doerner, A. E.; Narayanan, A.; Shulman, G. I.; Cline, G. W.; Schepartz, A. *Org. Lett.* **2013**, *15*, 5318–5321.
- (33) Broichhagen, J.; Podewin, T.; Meyer-Berg, H.; von Ohlen, Y.; Johnston, N. R.; Jones, B. J.; Bloom, S. R.; Rutter, G. A.; Hoffmann-Roder, A.; Hodson, D. J.; Trauner, D. *Angew. Chem., Int. Ed.* **2015**, *54*, 15565–15569.
- (34) Bai, X.; Niu, Y.; Zhu, J.; Yang, A. Q.; Wu, Y. F.; Ye, X. S. *Bioorg. Med. Chem.* **2016**, *24*, 1163–1170.
- (35) Johnson, L. M.; Barrick, S.; Hager, M. V.; McFedries, A.; Homan, E. A.; Rabaglia, M. E.; Keller, M. P.; Attie, A. D.; Saghatelian, A.; Bisello, A.; Gellman, S. H. *J. Am. Chem. Soc.* **2014**, *136*, 12848–12851.
- (36) Horne, S. W.; Johnson, L. M.; Ketas, T. J.; Klasse, P. J.; Lu, M.; Moore, J. P.; Gellman, S. H. *Proc. Natl. Acad. Sci. U. S. A.* **2009**, *106*, 14751–14756.
- (37) Underwood, C. R.; Garibay, P.; Knudsen, L. B.; Hastrup, S.; Peters, G. H.; Rudolph, R.; Reedtz-Runge, S. *J. Biol. Chem.* **2010**, *285*, 723–730.
- (38) Deacon, C. F.; Madsen, K.; Wiberg, F. C.; Jacobsen, O.; Holst, J. *J. Diabetologia* **1998**, *41*, 271–278.
- (39) Hupe-Sodmann, K.; McGregor, G. P.; Bridenbaugh, R.; Goke, R.; Goke, B.; Thole, H.; Zimmermann, B.; Voigt, K. *Regul. Pept.* **1995**, *58*, 149–156.
- (40) Sarrauste de Menthier, C.; Chavanieu, A.; Grassy, G.; Dalle, S.; Salazar, G.; Kervran, A.; Pfeiffer, B.; Renard, P.; Delagrè, P.

Manechez, D.; Bakes, D.; Ktorza, A.; Calas, B. *Eur. J. Med. Chem.* **2004**, 39, 473–480.

(41) Carter, P. H.; Dean, T.; Bhayana, B.; Khatri, A.; Rajur, R.; Gardella, T. J. *Mol. Endocrinol.* **2015**, 29, 307–321.

(42) Binkowski, B. F.; Butler, B. L.; Stecha, P. F.; Eggers, C. T.; Otto, P.; Zimmerman, K.; Vidugiris, G.; Wood, M. G.; Encell, L. P.; Fan, F.; Wood, K. V. *ACS Chem. Biol.* **2011**, 6, 1193–1197.

(43) Black, J. W.; Leff, P. *Proc. R. Soc. London, Ser. B* **1983**, 220, 141.

(44) Kenakin, T.; Watson, C.; Muniz-Medina, V.; Christopoulos, A.; Novick, S. *ACS Chem. Neurosci.* **2012**, 3, 193–203.

(45) Miller, L. J.; Chen, Q.; Lam, P. C.; Pinon, D. I.; Sexton, P. M.; Abagyan, R.; Dong, M. *J. Biol. Chem.* **2011**, 286, 15895–15907.

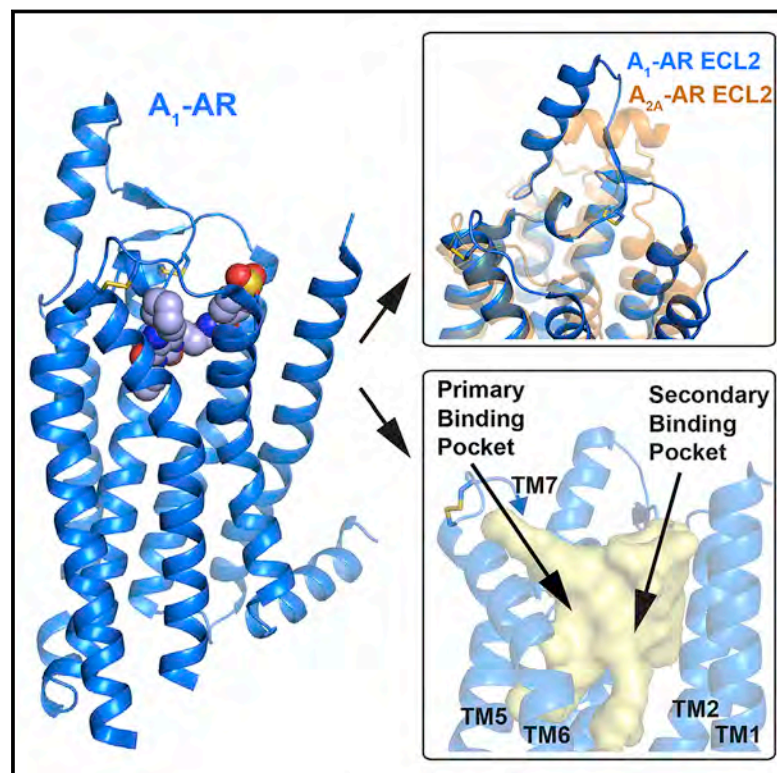
(46) Wootten, D.; Reynolds, C. A.; Koole, C.; Smith, K. J.; Mobarec, J. C.; Simms, J.; Quon, T.; Coudrat, T.; Furness, S. G. B.; Miller, L. J.; Christopoulos, A.; Sexton, P. M. *Mol. Pharmacol.* **2016**, 89, 335–347.

(47) Cheloha, R. W.; Maeda, A.; Dean, T.; Gardella, T. J.; Gellman, S. H. *Nat. Biotechnol.* **2014**, 32, 653–655.

(48) Olson, K. E.; Kosloski-Bilek, L. M.; Anderson, K. M.; Diggs, B. J.; Clark, B. E.; Gledhill, J. M., Jr.; Shandler, S. J.; Mosley, R. L.; Gendelman, H. E. *J. Neurosci.* **2015**, 35, 16463–16470.

Structure of the Adenosine A₁ Receptor Reveals the Basis for Subtype Selectivity

Graphical Abstract



Authors

Alisa Glukhova, David M. Thal, Anh T. Nguyen, ..., Lauren T. May, Patrick M. Sexton, Arthur Christopoulos

Correspondence

patrick.sexton@monash.edu (P.M.S.), arthur.christopoulos@monash.edu (A.C.)

In Brief

The structure of the adenosine receptor A₁ provides insights into the ways selectivity among adenosine receptor subtypes is achieved, opening avenues for design of subtype-specific drugs.

Highlights

- 3.2 Å resolution antagonist-bound structure of the adenosine A₁ receptor solved
- Major differences found in extracellular loop regions relative to the A_{2A} structure
- Drug selectivity is predominantly determined by binding site shape, not composition
- Unexpectedly wide A₁ receptor cavity reveals insights into allosteric drug actions



Structure of the Adenosine A₁ Receptor Reveals the Basis for Subtype Selectivity

Alisa Glukhova,^{1,3} David M. Thal,^{1,3} Anh T. Nguyen,¹ Elizabeth A. Vecchio,¹ Manuela Jörg,² Peter J. Scammells,² Lauren T. May,¹ Patrick M. Sexton,^{1,*} and Arthur Christopoulos^{1,4,*}

¹Drug Discovery Biology

²Medicinal Chemistry

Monash Institute of Pharmaceutical Sciences, Monash University, Parkville, Victoria 3052, Australia

³Co-first author

⁴Lead Contact

*Correspondence: patrick.sexton@monash.edu (P.M.S.), arthur.christopoulos@monash.edu (A.C.)

<http://dx.doi.org/10.1016/j.cell.2017.01.042>

SUMMARY

The adenosine A₁ receptor (A₁-AR) is a G-protein-coupled receptor that plays a vital role in cardiac, renal, and neuronal processes but remains poorly targeted by current drugs. We determined a 3.2 Å crystal structure of the A₁-AR bound to the selective covalent antagonist, DU172, and identified striking differences to the previously solved adenosine A_{2A} receptor (A_{2A}-AR) structure. Mutational and computational analysis of A₁-AR revealed a distinct conformation of the second extracellular loop and a wider extracellular cavity with a secondary binding pocket that can accommodate orthosteric and allosteric ligands. We propose that conformational differences in these regions, rather than amino-acid divergence, underlie drug selectivity between these adenosine receptor subtypes. Our findings provide a molecular basis for AR subtype selectivity with implications for understanding the mechanisms governing allosteric modulation of these receptors, allowing the design of more selective agents for the treatment of ischemia-reperfusion injury, renal pathologies, and neuropathic pain.

INTRODUCTION

The purine nucleoside, adenosine, is a vital cytoprotective molecule mediating effects through activation of four subtypes of Class A G-protein-coupled receptors (GPCRs), the A₁, A_{2A}, A_{2B}, and A₃ adenosine receptors (ARs) (Fredholm et al., 2011). Given the broad distribution of ARs in the central nervous system and the periphery, strategies for enhancing or inhibiting the activity of ARs have been pursued for potential treatments of disorders associated with cardiovascular function, blood flow, anxiety, dementia, Parkinson's disease, pain, respiration, sleep, inflammation, and immunity (Jacobson and Gao, 2006). Nonetheless, very few AR drug candidates have successfully progressed through clinical trials. One reason for this failure is the widespread distribution of ARs. If a drug candidate has insuffi-

cient selectivity for a given AR subtype, then the potential exists for off-target side-effects (Chen et al., 2013). Even when appropriate selectivity can be achieved, a second reason for drug candidate failures is that, like most GPCRs, ARs couple to multiple signaling pathways and can thus mediate both beneficial and undesirable effects, depending on the pathway.

In this regard, the A₁-AR is a key model for addressing these challenges. For instance, A₁-AR activation can reduce cardiac and renal ischemia reperfusion injury, atrial fibrillation, and neuropathic pain (Jacobson and Gao, 2006), whereas inhibition of A₁-ARs may prove useful for developing potassium sparing diuretics or cognition enhancers (Müller and Jacobson, 2011). However, clinical trials of A₁-AR selective agonists for ischemic heart disease have failed predominantly due to dose-limiting on-target bradycardia, atrioventricular block, and hypotension (Braunwald, 2011; Kloner et al., 2006; Mustafa et al., 2009), while the A₁-AR antagonist, rolofylline, developed as a diuretic for patients with acute heart failure and caused off-target stroke and on-target seizures (Massie et al., 2010; Teerlink et al., 2012).

Alternative paths are thus required for improving drug action at the A₁-AR. One approach is to selectively target allosteric sites, which are spatially distinct from the orthosteric site and can also promote conformational states that emphasize beneficial signaling while minimizing on-target adverse effects—a phenomenon referred to as “biased agonism” (Changeux and Christopoulos, 2016; Kenakin and Christopoulos, 2013). Indeed, the A₁-AR possesses at least one allosteric site (Bruns and Fergus, 1990) that has been exploited to promote biased agonism (Valant et al., 2014). However, despite mutational analyses implicating the extracellular regions of the A₁-AR in allosteric modulator action (Kennedy et al., 2014; Nguyen et al., 2016b; Peeters et al., 2012), the precise location of this site remains undetermined, as do mechanisms underlying A₁-AR allostery. A second major avenue for improving GPCR drug selectivity is to exploit recent breakthroughs in structural biology that may guide structure-based drug design (Jazayeri et al., 2015).

Despite these exciting developments, the only high-resolution information available for the ARs comes from structures of the A_{2A}-AR (Carpenter et al., 2016; Congreve et al., 2012; Doré et al., 2011; Hino et al., 2012; Jaakola et al., 2008; Lebon et al., 2015, 2011; Liu et al., 2012; Segala et al., 2016; Xu et al., 2011). Unfortunately, the low sequence identity between

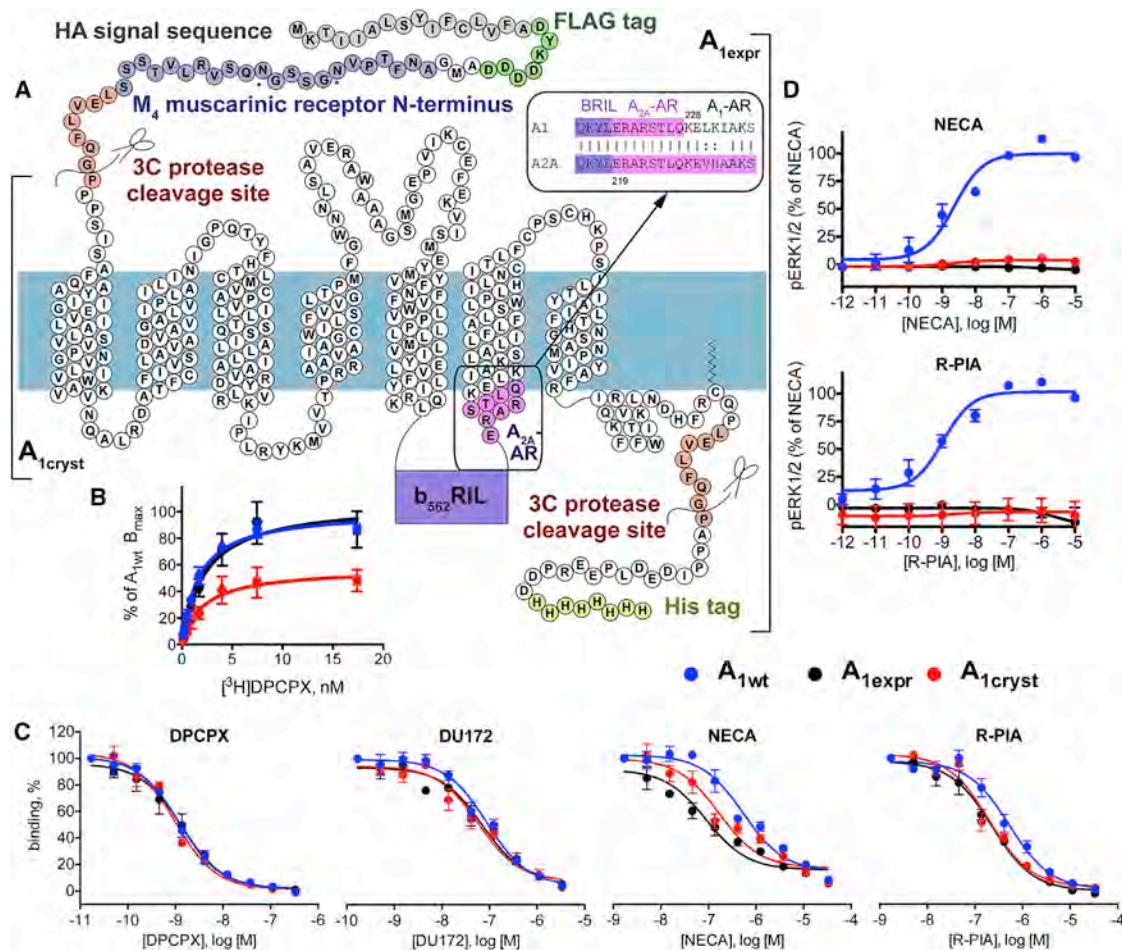


Figure 1. Design and Characterization of the Human A₁-AR Constructs

(A) A₁-AR_{expr} denotes the complete construct; A₁-AR_{cryst} denotes the construct truncated at the 3C protease cleavage site used for crystallization.

(B) [³H]DPCPX binding at A₁-AR_{expr}, A₁-AR_{cryst} and the wild-type, A₁-AR_{wt}.

(C) [³H]DPCPX competition with antagonists (DPCPX or DU172) and agonists (NECA or R-PIA) at A₁-AR_{expr}, A₁-AR_{cryst}, and A₁-AR_{wt}.

(D) Receptor-mediated ERK1/2 phosphorylation of the different A₁-AR constructs in the presence of the agonists NECA or R-PIA. Data points are the mean values ± SEM from three-four independent experiments performed in duplicate.

See also Tables S1 and S2.

A_{2A}- and A₁-ARs, especially in the extracellular loops, makes homology modeling of this region unreliable. In contrast, there exists a very high conservation of residues between the A₁- and A_{2A}-ARs in the orthosteric site, yet this fact is difficult to reconcile with the known array of subtype-selective agonists and antagonists that have been reported for these receptors.

Here, we present the high-resolution crystal structure of the A₁-AR in complex with a covalent antagonist, DU172 (originally published as ‘compound 23a’ in Beauglehole et al., 2000). Compared to the A_{2A}-AR, the A₁-AR possesses a more open binding site cavity that can accommodate orthosteric and allosteric ligands. We propose that spatial differences due to rearrangements of TMs 1, 2, 3, 7, ECL3, and a single amino acid substitution at position 270, rather than specific differences in residues lining the orthosteric binding pocket, underlie drug selectivity between A₁- and A_{2A}-ARs and offer an alternative template for AR structure-based drug design.

RESULTS

Optimization of A₁-AR Crystallization Constructs and Ligand Selection

To aid with A₁-AR expression, 22 amino acids of the human M₄ muscarinic acetylcholine receptor N terminus, containing 3 N-glycosylation sites, were inserted before the A₁-AR N terminus, followed by a 3C protease cleavage site (Figure 1A). To promote A₁-AR crystallization, a thermostable apocytochrome b₅₆₂RIL (BRIL) (Chun et al., 2012) was inserted into the third intracellular loop 3 (ICL3) between residues 211 and 220 (all numbering is relative to the unmodified human A₁-AR: “A₁-AR_{wt}”; the A₁-AR C terminus was truncated after amino acid 311 by inserting a 3C protease cleavage site, and a single A₁-AR N-glycosylated residue, N159, was mutated to alanine. For optimization of the BRIL insertion sites, we also substituted amino acids 220–228 of the A₁-AR with those of the A_{2A}-AR.

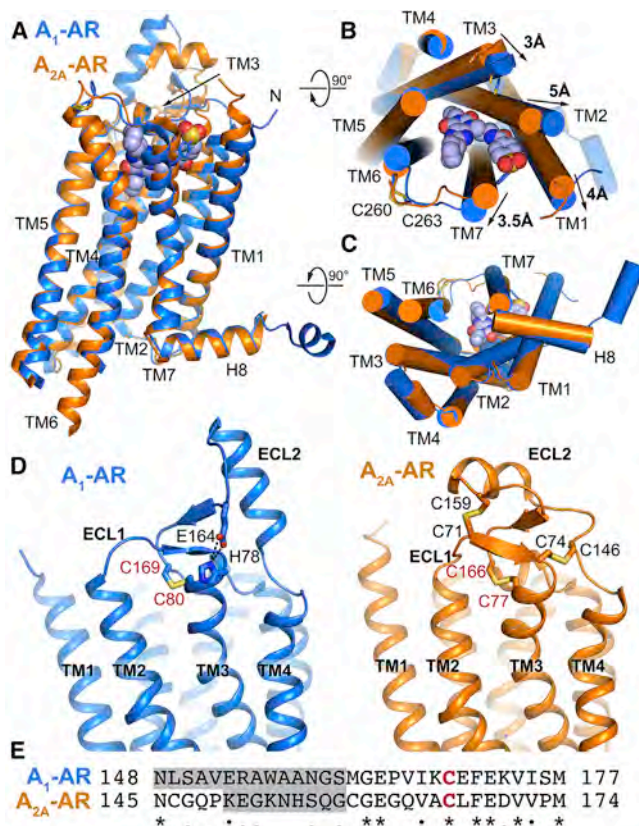


Figure 2. Overall View of the A₁-AR·DU172 Crystal Structure

(A–D) Aligned structures of the A₁-AR and A_{2A}-AR (PDB: 4EIY). (A) Side view. (B) Extracellular view (ECL2s are omitted for clarity). (C) Intracellular view. (D) Side-view of the ECL2 regions. The A₁-AR backbone is colored in marine and orange in the A_{2A}-AR. The C atoms of DU172 are shown in light blue spheres; N, O, and S atoms are colored in blue, red, and yellow, respectively. Hydrogen bonds are shown as dashed lines. ZM241385 is omitted from the A_{2A}-AR structure for clarity. BRIL and the A_{2A}-AR linker are omitted from the A₁-AR structure.

(E) Sequence alignment of ECL2 between A₁- and A_{2A}-ARs. In the alignment, the helical part of the ECL2s is highlighted in gray. Conserved cysteines between A₁-AR and A_{2A}-AR are labeled in red, non-conserved residues are labeled in black.

See also Table S3.

Importantly, unmodified A_{1wt}, “A_{1exp}” (before 3C cleavage), and “A_{1cryst}” (crystallized construct) showed no difference in binding affinities for the A₁-AR antagonist DPCPX or the irreversible antagonist DU172 (Figures 1B, 1C, S1, and Table S1), although A_{1cryst} displayed a lower B_{max}, most likely reflecting variability in the transient transfections used for these experiments. As noted previously with T4 lysozyme fusions of the A_{2A}-AR or β₂ adrenergic receptors (Jaakola et al., 2008; Rosenbaum et al., 2007), the engineered A₁-AR constructs exhibited higher affinity for agonists, in this instance, NECA and R-PIA (Figure 1C and Table S2). However, consistent with findings at the A_{2A}-AR (Liu et al., 2012), BRIL insertion into the A₁-AR ICL3 prevented G protein coupling, resulting in no functional response (Figure 1D).

Subsequently, we tested a variety of non- and subtype-selective AR agonists and antagonists for their ability to increase the

melting temperature (T_m) of the A₁-AR in a thermal stability assay (Figure S2) (Alexandrov et al., 2008). Among all the ligands tested, only highly selective A₁-AR antagonists substantially increased the stability of the A₁-AR construct used for crystallization. The covalent compounds, FSCPX and DU172, promoted the largest increase in thermal stability (~16°C), and due to the higher chemical stability of DU172 compared to FSCPX (Beauglehole et al., 2000), DU172 was used in all subsequent crystallization trials.

Overall Structural Organization of the A₁-AR·DU172 Complex

The A₁-AR·DU172 complex was crystallized in a lipid cubic phase. Data from 29 crystals were merged together, yielding a dataset at 3.2 Å resolution (Figures 2 and S3 and Table S3). The A₁-AR crystallized with two receptor copies per asymmetric unit in parallel orientations (Figure S3). Overall, electron density maps were of good quality with well-resolved amino acid side chains, with the exception of poor density around BRIL in chain A. Interestingly, we noted two types of receptor-receptor interfaces (Figure 3). The first was a non-crystallographic 2-fold symmetry interface (Figures 3A, 3B, S3A, and S3C) stabilized through contacts at the extracellular side of TM3 through a π-π interaction between two Y76^{3.21} residues in chains A and B, an interaction between two H78^{3.23} residues (superscript refers to Ballesteros-Weinstein numbering [Ballesteros and Weinstein, 1995]), and an unidentified molecule (a 12σ blob in the Fo-Fc map). A second, more extensive, interface between two adjacent A₁-AR molecules (Figures 3C, 3D, S3B, and S3C) occurs between crystallographic symmetry mates of chain A (between repeating units within a crystal), which buries a large hydrophobic area of TM4 and TM5 (860 Å²) with a number of residues, V137^{4.55}, F144^{4.62}, W146^{4.64}, Y182^{5.40}, F183^{5.41}, V187^{5.45}, and W188^{5.46}, forming hydrophobic contacts bringing both ECL2s in close proximity (Figure 3D). Interestingly, a recent mutagenesis study (Nguyen et al., 2016a) identified residues of the A₁AR ECL2 (N148, E153, S150, R154, and W156) to be key determinants in the signaling efficacy of the orthosteric agonist, NECA. Our structure now reveals that all of these residues are located in the A₁-AR ECL2 helical region, with R154 and S150 in particular (Figure 3D) forming contacts between ECL2 loops of two A₁AR monomers. This finding provides a possible structural explanation for why these residues are key to agonist efficacy, particularly in the context of an emerging view that ECL2 can contribute to the transition of GPCRs between different active states (Avlani et al., 2007; Bokoch et al., 2010). Collectively, and in light of another recent study suggesting that the A₁-AR could form homodimers capable of cooperative orthosteric ligand binding (Gracia et al., 2013), this interface is an attractive target for future investigation, but additional pharmacological experiments will be required to confirm that observed interaction is physiologically relevant rather than an artifact of crystallization.

Overall, the structure of the A₁-AR is typical of other Class A GPCRs crystallized in an inactive conformation (Figures 2A and 2C) with a partially formed “ionic lock” (Figure S4) that constrains GPCRs in an inactive state and may thus explain why the A₁-AR displays relatively low constitutive activity (Savinainen et al., 2003). There is little difference intracellularly, with the exception of a 2 Å outward shift of TM5 and TM6 at the BRIL insertion site

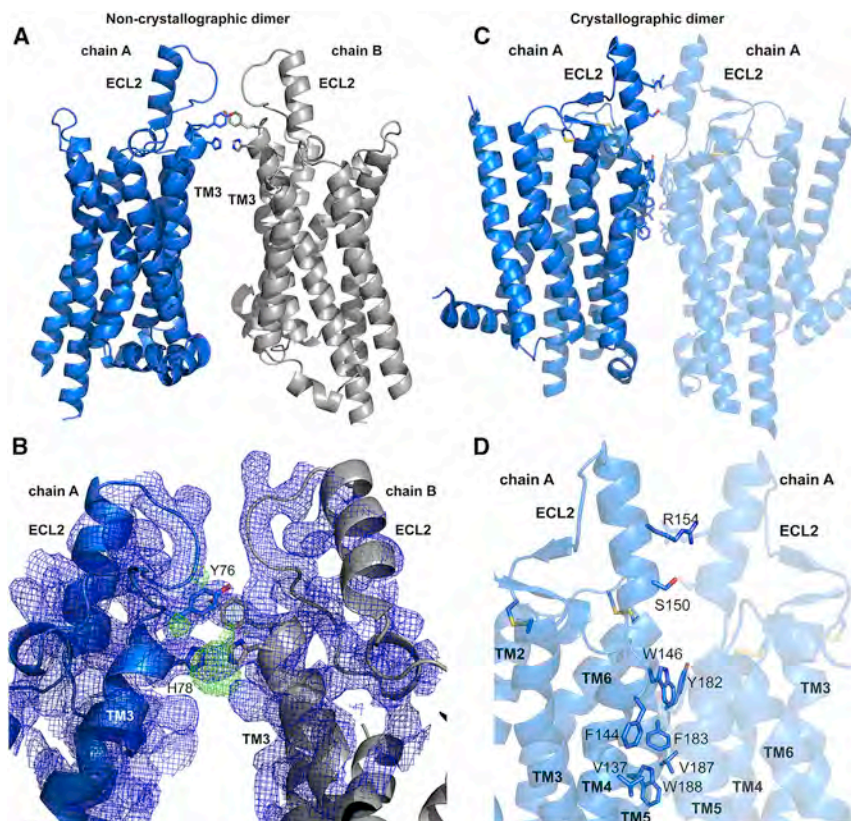


Figure 3. Contacts between Parallel A₁-AR Monomers within the Structure

(A and B) Contacts between two non-crystallographic copies of the A₁-AR within the same asymmetric unit. Blue mesh represents 2 m|Fo|-D|Fc| map contoured at 1 σ and green m|Fo|-D|Fc| map contoured at 3 σ (unidentified molecule). (C and D) Crystallographic contacts featuring extensive hydrophobic contacts between two A₁-AR monomers in parallel orientation. See also Figure S3.

due to crystal contacts (Figure 2C). However, the extracellular ends of the TM helices move considerably compared to the A_{2A}-AR (Figure 2B), with lateral movements of TMs 1, 2, 3, and 7. A highly conserved Class A GPCR disulphide bond (C80^{3.25} and C169) tethers ECL2 to TM3 (Figure 2D), and an additional disulphide, C260-C263 (Figure 2B), present in both A₁- and A_{2A}-ARs, “staples” ECL3. The compact arrangement of the TM bundle of the A_{2A}-AR might thus be the result of its unique disulphide bond, C74-C146, tethering the beginning of TM3 to the end of ECL2 (Figure 2D). Lack of this interaction in the A₁-AR allows for shifts in TMs 1, 2, and 3. TM7 also tilts toward TM6, possibly as a result of a shorter ECL3 in the A₁-AR due to the deletion of one amino acid.

The most striking difference between the A₁- and A_{2A}-ARs is the conformation of their ECL2s (Figure 2D). In both chains A and B of the A₁-AR, ECL2 is well resolved and adopts an identical orientation despite different crystallographic environments, indicating that the observed loop conformation is not a crystallographic artifact nor is it influenced by the location of the BRIL fusion (which is more than 10 Å away). Of note, ECL2 residues from N148 to S161 form a longer helix compared to the A_{2A}-AR (from K150 to G158) (Figure 2E), extending it away from the A₁-AR transmembrane regions and almost perpendicular to the plane of the membrane (Figure 2D). This conformation likely results from the absence of another A_{2A}-AR disulphide bond (between C71 and C159) in the A₁-AR, which tethers the A_{2A}-AR ECL2 helix to ECL1. Instead, it is partially compensated for by the presence of a salt bridge between E164 and H78^{3.24} on

TM3 in the A₁-AR, which stabilizes a short β sheet between amino acids 75–77 of ECL1 and 165–167 of ECL2 (Figure 2D). Interestingly, the helical part of ECL2 in previously solved β_1 and β_2 adrenergic receptors also adopts a conformation parallel to the plane of the membrane due to intra-loop disulphides. As such, the presence of extra disulphide bonds likely serves to restrict the mobility of ECL2 in β_1 , β_2 , and A_{2A} receptors, whereas this is not the case for the A₁-AR.

Ligand Interactions in the A₁-AR Orthosteric Site

The electron density for the covalent antagonist, DU172, allowed for its unambiguous placement within the binding site of the A₁-AR and identified Y271^{7.36} as the site of covalent attachment via a benzene-sulfonate linkage (Figure 4A and Figure S5). Key interactions with the ligand are formed via residues located on TMs 1, 3, 6, 7, and ECL2 (Figure 4C). Compared to the orientation of ZM241385 in A_{2A}-AR structures (Hino et al., 2012; Jaakola et al., 2008; Liu et al., 2012), the xanthine ring of DU172 is rotated by 135° (Figure 4B), positioning the propyl group above W247^{6.48}, a residue responsible for TM rearrangements during A_{2A}-AR agonist binding (Xu et al., 2011). Despite different orientations of the xanthine ring relative to the triazolo-triazine substructure of ZM241385, key interactions anchoring the ligand in the binding site are preserved, including a π -stacking interaction with F171 (F168 in A_{2A}-AR) and a bidentate hydrogen bond with N254^{6.55} (Figures 4B–4F and S5). However, the chemical nature of DU172 leads to formation of a different set of H bonds with residue N^{6.55}. In the A_{2A}-AR, N253^{6.55} contacts the oxygen of the furan ring and the amine substituent of the triazine ring of ZM241385; the corresponding N254^{6.55} in A₁-AR interacts with the 6-oxy group and N7 of the DU172 xanthine ring (Figure 4B). This H-bonding shift results in DU172 positioning deeper in the A₁-AR orthosteric site compared to ZM241385 in the A_{2A}-AR. DU172 is further stabilized by an H bond of the amide linker with Y12^{1.35}, which can explain why DU172-like FSCPX derivatives, in which the amide linker was exchanged to two methylenes, display lower affinity for the A₁-AR (Beauglehole et al., 2000). In addition, many A₁-AR residues interact with DU172 via hydrophobic interactions (Figure 4E and S5).

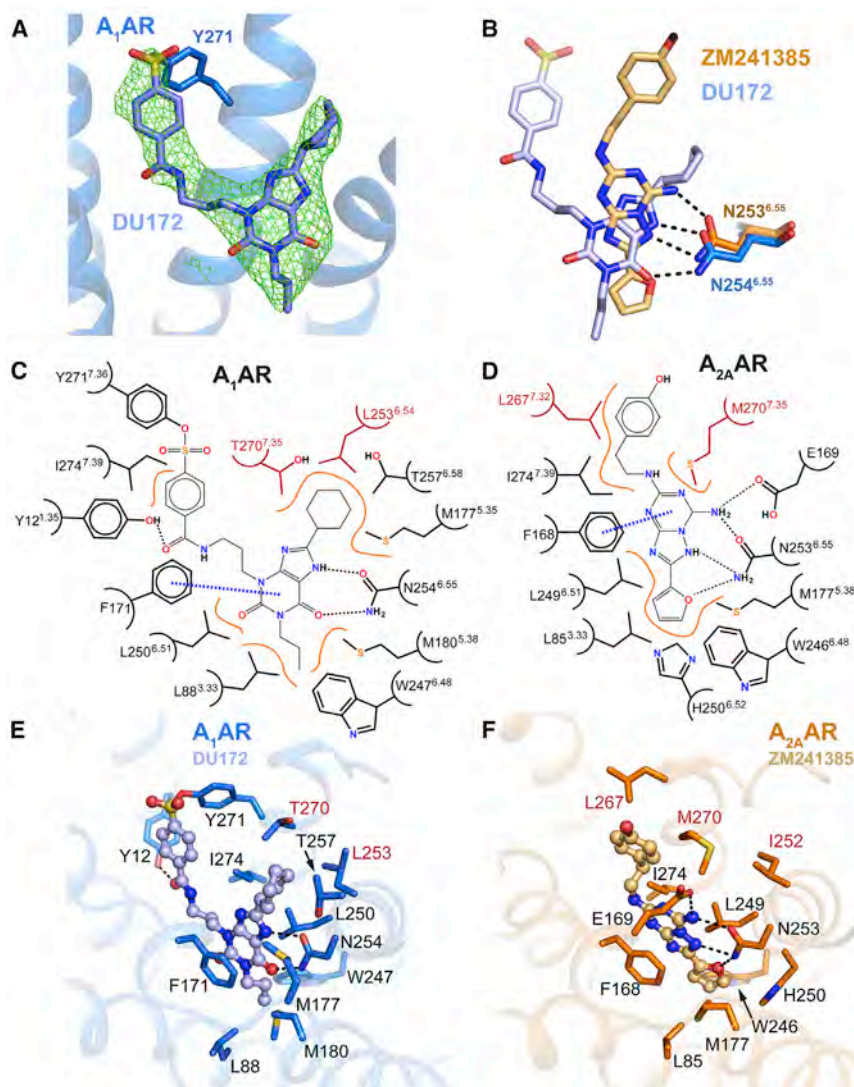


Figure 4. Comparison of Ligand-Binding Residues in the Crystal Structures of the A₁- and A_{2A}-ARs

(A) A 3 σ m[Fo]-D[Fc] omit map (green mesh) for DU172 covalently bound to Y271.

(B) Poses of DU172 (A₁-AR) and ZM241385 (A_{2A}-AR; PDB: 4E1Y) in their respective structures forming H-bonds with residue N^{6.55}.

(C–F) 2D diagrams of the receptor residues making contact with corresponding ligands (C and D) and structures (E and F) of the binding sites for A₁- (C and E) and A_{2A}- (D and F) ARs. Color scheme is the same as in Figure 2, with conserved residues between A₁- and A_{2A}-AR labeled in black and non-conserved in red. Binding site residues are shown as sticks; DU172 and ZM241385 are shown as stick-ball models. Black dashed lines represent H-bonds, blue dashed lines represent π -stacking interactions, orange freehand curves denote van der Waals contacts. See also Figure S5.

xanthine core of DU172 are accommodated laterally, engaging both sides of the wide binding cavity (Figures 5A and 5B).

In addition to the substantial effect of overall binding site topology on A₁-AR versus A_{2A}-AR selectivity, the hydrophobic pocket responsible for engaging the cyclohexane group of DU172 (and likely other cyclic groups found in the C8 position of A₁-AR selective antagonists) is inaccessible in the A_{2A}-AR due to a single amino acid difference in position 270^{7.35}. This residue acts as a “gatekeeper,” either allowing access to residues M177^{5.35}, L253^{6.54}, and T257^{6.57} in the A₁-AR, where amino acid 270 is a threonine, or limiting access in the A_{2A}-AR, where bulky methionine points into the

Basis for Subtype Selectivity between the A₁- and A_{2A}-ARs

Given the existence of numerous selective agonists and antagonists for the A₁- and A_{2A}-ARs, it was surprising to find most residues involved in DU172 binding to be conserved between the two receptors, with the exception of L253^{6.54} and T270^{7.35} (I252^{6.54} and M270^{7.35} in the A_{2A}-AR, respectively) (Figures 4C and 4D). Such high conservation suggests that mechanisms other than receptor-specific amino acids must be responsible for subtype selectivity. Indeed, the shapes of the binding pockets are very different. The A_{2A}-AR pocket is elongated and narrow compared to the very wide and open cavity of the A₁-AR, resulting from movements of TMs 1, 2, 3, 7, and ECL3 (Figures 5A–5E). In the structures of a non-thermostabilized A_{2A}-AR (Hino et al., 2012; Jaakola et al., 2008; Liu et al., 2012), ZM241385 adopts an extended conformation and binds perpendicularly to the plane of the membrane (Figures 5C and 5D). In contrast, the bulky substituents in the 3- and 8-positions of the

binding pocket (Figure 5E). This residue is also variable in the A₁-AR of different species, leading to significant effects on the affinity of A₁-AR ligands (Tucker et al., 1994). Therefore, to test the hypothesis that residue 270^{7.35} can contribute to subtype selectivity, we performed mutagenesis experiments that swapped the residues in this position between the A₁- and A_{2A}-ARs (Figures 5F and 5G). As predicted, T270M substitution into the A₁-AR significantly decreased the affinity of DPCPX (Figure 5H and Table S4), while the reverse substitution, M270T in the A_{2A}-AR, led to a significant increase in DPCPX affinity (Figure 5H and Table S4). As ZM241385 lacks substituents capable of engaging the aforementioned hydrophobic pocket of the A₁-AR, T270M substitution has little effect on the affinity of this ligand (Figure 5H and Table S4). However, since M270 is involved in coordinating ZM241385 in the A_{2A}-AR, M270T leads to a significant loss of affinity (Figure 5H and Table S4).

A further expansion of the A₁-AR binding site results from a 3.5 Å movement of ECL3 away from the orthosteric pocket

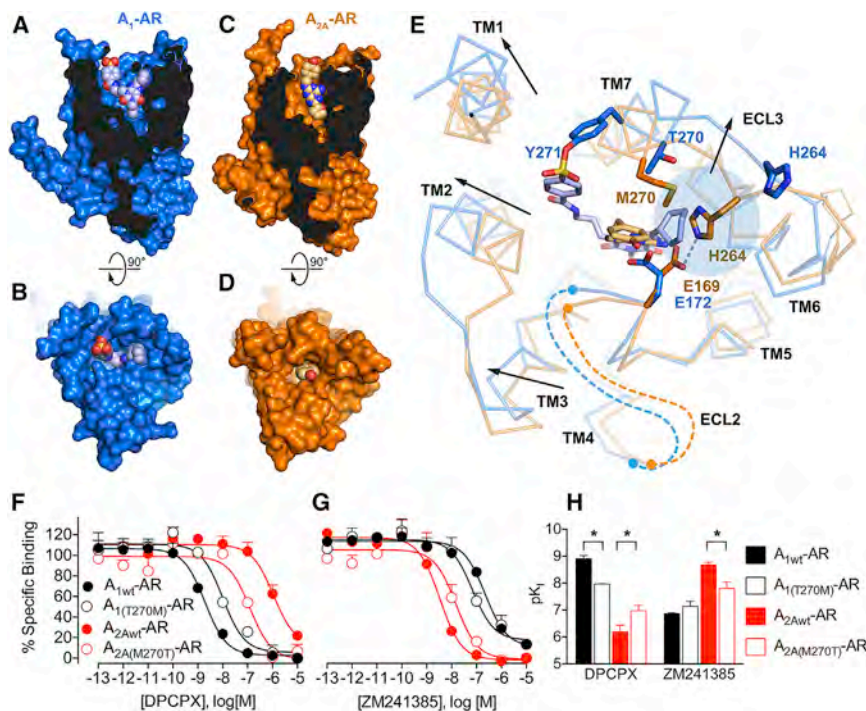


Figure 5. Binding Pockets of the A₁- and A_{2A}-ARs and Determinants of Subtype Selectivity

(A–D) Receptor surfaces are sliced to show the binding site cavity. DU172 and ZM241385 are shown as spheres.

(E) Displacement of the A₁-AR TMs relative to the A_{2A}-AR, leading to a wider binding site cavity. Receptor backbones are shown as ribbon; disulfide bonds are shown as lines, residues forming a salt bridge between ECL2 and ECL3 in the A_{2A}-AR; and the "gatekeeper" residue 270 are shown as sticks. Arrows indicate the directions of displacement of the TM extracellular ends. ECL2s are schematically shown as dashed lines for clarity. Blue shading indicates hydrophobic pocket shielded by "gatekeeper" residue 270.

(F–H) Radioligand competition binding of (F) DPCPX or (G) ZM241385 at the wild-type A₁- or A_{2A}-ARs relative to mutant receptors where the "gatekeeper" residue at position 270 was switched between the two subtypes. Data points are the mean values \pm SEM from three independent experiments performed in duplicate. (H) Effects of mutations on the affinity of the indicated ligand relative to the wild-type receptor, determined as negative logarithms of the dissociation constant.

* $p \leq 0.05$ (Unpaired t test comparing the indicated mutant construct to its respective wild-type). See also Table S4.

(Figure 5E). This leads to inability of the A₁-AR to form a salt bridge between ECL2 and ECL3 observed in most A_{2A}-AR structures (H264-E169). Interestingly, in most A_{2A}-AR crystal structures published to date (Congreve et al., 2012; Doré et al., 2011; Hino et al., 2012; Jaakola et al., 2008; Lebon et al., 2015, 2011; Liu et al., 2012; Segala et al., 2016), ECL3 brings H264 within the range for salt bridge formation with E169. The status of the H264-E169 interaction can also affect ligand residence time for the A_{2A}-AR, as compounds that stabilize it exhibit slower dissociation rates (Segala et al., 2016). The 8-cyclohexyl-1-propylxanthine moiety of DU172 is very similar to DPCPX, a compound with a short $t_{1/2}$ (May et al., 2005), and the broken bridge between H264 and E172 in our A₁-AR structure (Figure 5E) is a possible molecular mechanism that can explain such faster kinetics. Given that ligand residence time has emerged as a major consideration in modern drug discovery programs (Copeland et al., 2006; Guo et al., 2016a, 2016b; Segala et al., 2016), a molecular understanding of the basis of the phenomenon will play an important role in guiding future structure-based drug design programs.

In contrast to the key role of hydrophobic interactions in the pocket formed by residues M177^{5.35}, L253^{6.54}, and T257^{6.57} in the A₁-AR, high binding affinity for selective A_{2A}-AR ligands is mediated through the narrow entrance into its binding site (Figures 5C and 5D). Tight arrangement of the TM bundle, enforced by the extra disulfide bond (from C74 to C146) of the A_{2A}-AR, brings L267^{7.32}, important for receptor affinity (Lebon et al., 2015), within van der Waals distance from the phenyl ring of ZM241385 (Figures 4D and 4F) and other ligands with similar scaffolds (Segala et al., 2016). The 3.5 Å outward movement of

the extracellular part of TM7 that we observe in our A₁-AR structure (Figure 2B) would prevent this interaction. Thus, it is evident that the spatial differences in the A₁- and A_{2A}-AR orthosteric sites are the major determinants underlying the subtype selectivity of their respective compounds.

To confirm that the wide A₁-AR binding pocket was not an artifact of the covalent attachment by DU172 and to investigate whether other A₁-AR selective antagonists share this pocket, we performed additional experiments. First, we synthesized the novel, reversible sulfonic acid (MIPS2712) and *N*, *N*-dimethylsulfonamide (MIPS2719) analogs of DU172 (Figure S1), which exhibited even higher selectivity for the A₁- over the A_{2A}-AR compared to the irreversible DU172 (Figures S6A–S6C). Molecular docking of both compounds using ICM revealed similar modes of binding to DU172 in the A₁-AR structure, which cannot be accommodated by the narrow binding site of the A_{2A}-AR, as it prevents their xanthine cores from entering and interacting with N253^{6.55} or F171 (Figures S6D and S6E). Second, we investigated whether other, less bulky, A₁-AR selective antagonists shared the same binding pocket by performing additional computational docking (Figure 6 and Table S5). Most reversible A₁-AR antagonists, including DPCPX, PSB36, and the clinical agent rolophylline have a scaffold similar to DU172 (Figure S1). Our docking predicted a common binding site for all of these compounds (Figures 6A–C). Third, molecular dynamics simulations of DPCPX bound to the A₁-AR over a 104 ns timescale further confirmed stable conformations of both ligand and receptor, with no change or collapse of the wide binding cavity (Figures S6F–S6H). One exception from a xanthine-based selective A₁-AR scaffold is SLV320 (Figure S1). When docked into the

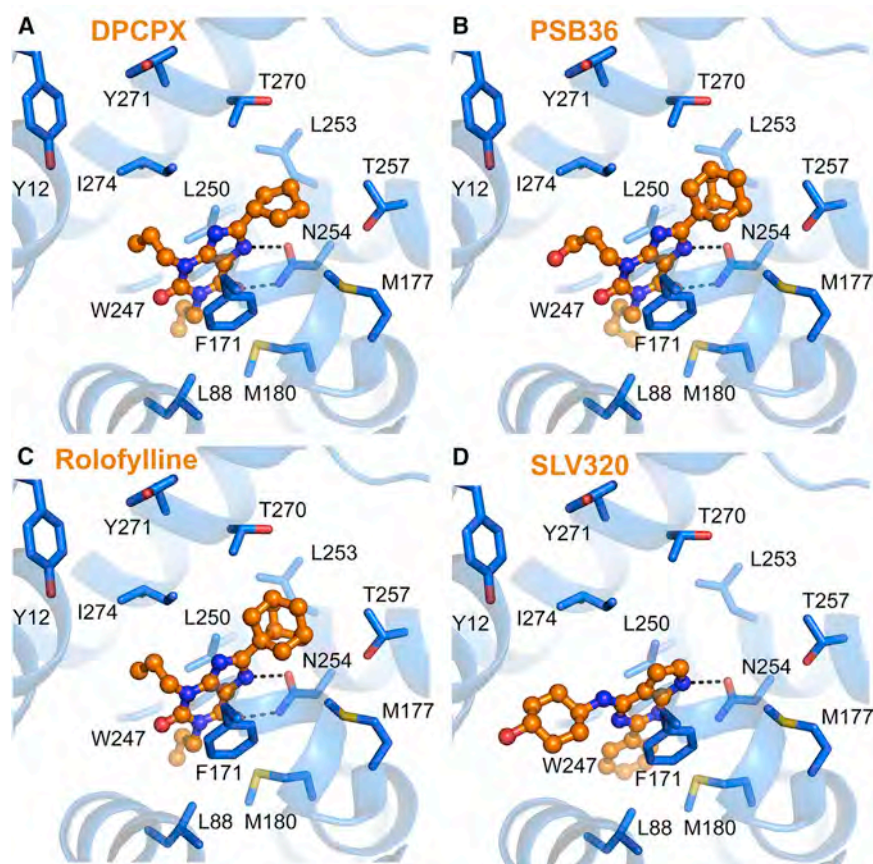


Figure 6. Lowest Energy Docking Conformations of Selective A₁-AR Antagonists

(A-C) DPCPX, PSB36, and rolofylline also engage the hydrophobic pocket made up by the side chains of M177^{5,35}, L253^{6,54}, T257^{6,57}, and T270^{7,35}.

(D) The aminocyclohexanol group of SLV320 is oriented toward a space occupied by the linker and irreversible moiety of DU172 in the crystal structure of the A₁-AR. All ligands are predicted to interact with L88^{3,34} and W247^{6,48} at the bottom of the binding site with alkane or aromatic substituents of the xanthine ring. Docked ligands are shown as orange stick-ball models with carbon atoms colored in orange; binding site residues as sticks with marine carbon atoms; N, O, and S atoms are colored in blue, red, and yellow, respectively. Dashed lines represent H-bonding to N254^{6,55}.

See also Table S5 and Figures S1 and S6.

A₁-AR, the pyrrolopyrimidine core assumes a topologically similar orientation to the xanthine cores of other compounds, which position the aminocyclohexanol group within van der Waals distance from V87^{3,32}, H278^{7,43}, and V62^{2,57}, and H-bonding distance from the carbonyl of V62^{2,57}. As such, instead of exploring the hydrophobic pocket near T270, like other selective A₁-AR antagonists, SLV320 engages the other side of the wide binding site of the A₁-AR (Figure 6D).

Location of a Secondary Pocket in the A₁-AR

The A₁-AR is the first GPCR for which synthetic small molecule positive allosteric modulators (PAMs) of orthosteric agonists were described (Bruns and Fergus, 1990). In contrast, far fewer reports have described A_{2A}-AR modulators (Göblyös and IJzerman, 2011; Guo et al., 2016b). These findings may be explained by the substantial differences when comparing the extracellular surfaces of the A₁-AR versus the A_{2A}-AR. Indeed, recent mutagenesis studies have suggested a role for ECL2 in the actions of A₁-AR allosteric modulators (Kennedy et al., 2014; Nguyen et al., 2016b; Peeters et al., 2012). Another intriguing property of many A₁-AR modulators, exemplified by VCP171 (Figure S1) and related derivatives, is the fact that they invariably act as PAMs of orthosteric agonists of the receptor, but as inhibitors of orthosteric antagonists at the same receptor (Bruns and Fergus, 1990; Bruns et al., 1990; Kourounakis et al., 2000; van der Klein et al., 1999). One possible explanation for this finding is

that modulators of this class bind to a spatially distinct allosteric site in the inactive state that promotes negative cooperativity with antagonists (thus acting as negative allosteric modulators, or NAMs), while stabilizing a different conformation in the active state that yields positive cooperativity with agonists—as has been observed, for instance, with the muscarinic acetylcholine GPCRs (Dror et al., 2013; Kruse et al., 2013). However, an alternative explanation is that A₁-AR modulators actually bind to the *orthosteric* site in the unoccupied (inactive) receptor, thus essentially acting as “competitive” antagonists, and adopt a second, allosteric, binding mode only when the receptor’s orthosteric site is occupied by an agonist in the active state.

Given that we established that the wide extracellular A₁-AR cavity is not an artifact of the covalent attachment by DU172, it is of note that part of this cavity is engaged in binding of the linker and the irreversible group of DU172. However, when less bulky prototypical reversible orthosteric antagonists, such as DPCPX, are docked into the A₁-AR, a significant part of the binding site is left un-accommodated, in contrast to the binding cavity of the A_{2A}-AR occupied by ZM241385 (Figures 7A and 7B). This un-accommodated secondary pocket may thus represent a putative allosteric binding site in the inactive-state A₁-AR or may contribute to the formation of such a site upon activation of the receptor. To investigate possible mechanisms underlying the behaviors of known A₁-AR allosteric ligands described above, we performed computational docking of VCP171 (Aurelio et al., 2009; Valant et al., 2014) and compound 13b (Ferguson et al., 2008) (Figures S1 and S7). Although both compounds inhibit the binding of the antagonist, [³H]DPCPX (Ferguson et al., 2008; Nguyen et al., 2016b), VCP171 is a PAM of agonist binding and function (Nguyen et al., 2016b), while compound 13b exerts highly potent inhibitory effects on both agonists and antagonists, despite being able to slow the dissociation of a radiolabeled

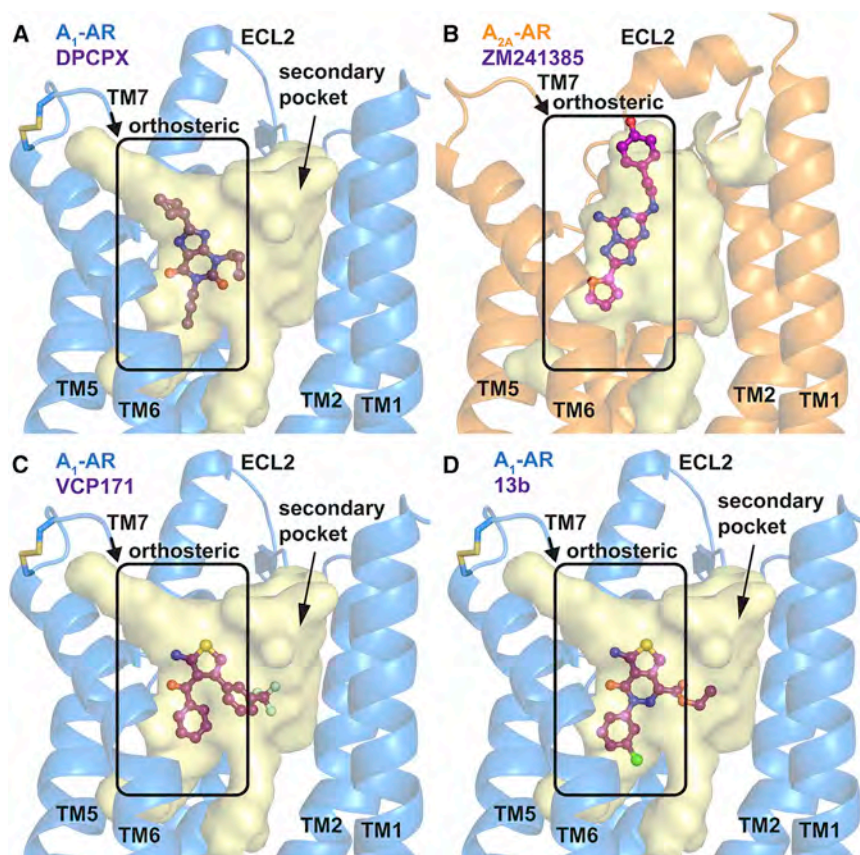


Figure 7. A Secondary Pocket in the Inactive A_1 -AR and Mode of Interaction of Previously Identified A_1 -AR Modulators

(A) DPCPX, docked into the A_1 -AR structure, leaves a significant part of the binding site unoccupied.

(B) The A_{2A} -AR binding pocket is more substantially occupied by ZM241385.

(C) VCP171, which is a PAM of A_1 -AR agonists but an inhibitor of A_1 -AR antagonists, preferentially docks into the orthosteric site of the inactive A_1 -AR.

(D) Compound 13b, which inhibits both agonists and antagonists at the A_1 -AR, also preferentially docks into the orthosteric binding site. The A_1 -AR receptor is shown in marine, A_{2A} -AR as orange, the binding pocket is shown as a yellow surface, and ligands are shown as stick-ball models with carbon atoms colored in purple and N, O, S, F, and Cl atoms colored in blue, red, yellow, cyan, and green, respectively. TM7 is omitted for clarity. See also Figure S7.

orthosteric agonist when tested at high concentrations (Ferguson et al., 2008); the latter is usually a hallmark of an allosteric interaction. Interestingly, we found that, in both instances, the ligands preferred to dock in the *orthosteric* site on the unoccupied A_1 -AR structure (Figures 7C and 7D) utilizing similar binding interactions as DU172 (Figure S7). Taken together, the finding that different types of A_1 -AR modulators prefer to occupy the orthosteric site in the inactive A_1 -AR can explain the long-standing conundrum of why such classes of “allosteric” ligand consistently behave as apparent competitive inhibitors of A_1 -AR antagonists such as DPCPX (Aurelio et al., 2009; Valant et al., 2014), which preferentially bind to the inactive state. This also suggests that, mechanistically, it may be the transition between the inactive to the active state in the agonist-occupied receptor that changes the conformation of both the orthosteric and secondary pocket to yield an “optimal” allosteric site that allows positive agonist modulation by ligands such as VCP171, although this remains speculative in the absence of an active A_1 -AR structure bound to agonist, PAM, or both.

DISCUSSION

The A_1 -AR remains a highly pursued therapeutic target (Fredholm et al., 2011; Jacobson and Gao, 2006), yet there are no selective, clinically approved, A_1 -AR agonists or antagonists currently available. Nonetheless, numerous attempts have been

made to develop selective ligands of this important GPCR, including structure-activity studies focusing on orthosteric ligands, allosteric modulators, and, more recently, hybrid “bitopic” molecules that concomitantly target both orthosteric and allosteric sites (Guo et al., 2016b). To date, however, it has not been possible to contextualize any of these advances at the molecular level. Our solution of the crystal structure of this receptor can now facilitate structure-based drug design of A_1 -AR therapeutics. Despite sharing general mechanisms of function with the Class A GPCR superfamily, our structure more importantly reveals surprising differences that can account for the molecular basis of AR subtype selectivity and sheds light on some long-standing questions regarding the actions of allosteric modulators.

The solution of multiple crystal structures of the A_{2A} -AR has yielded insights into mechanisms of receptor activation, ligand binding, and modulation by endogenous substances such as sodium ions (Doré et al., 2011; Hino et al., 2012; Jaakola et al., 2008; Lebon et al., 2011; Liu et al., 2012; Xu et al., 2011), in addition to facilitating structure-based drug design (Gutiérrez-de-Terán et al., 2017). Yet, it is well-established that even subtle differences between related GPCRs can have a profound effect on drug selectivity (Granier et al., 2012; Manglik et al., 2012; Thal et al., 2016), which is of particular relevance when trying to use previously solved GPCR structures to model or screen for new leads at other receptors. From a structural perspective, our A_1 -AR structure displays many of the key features associated with inactive-state GPCRs, including a well-resolved “ionic lock” that plays a vital role in maintaining the ground state of the receptor. From a pharmacological and chemical perspective, however, the most surprising feature is the divergence observed in the extracellular regions, particularly the differences in ECL2 orientation when comparing the A_1 - with the A_{2A} -AR. In

combination with the “gatekeeper” role of residue 270^{7,35} in these structures, the overall changes in the extracellular regions have a profound effect on the entrance and definition of the binding pocket between the two AR subtypes, thus providing a molecular mechanism for orthosteric ligand subtype selectivity.

The extracellular regions of various Class A GPCRs, including the A₁- and A₃-ARs, the muscarinic, adrenergic, and dopaminergic receptors, have also been implicated in the binding of synthetic small molecule allosteric modulators (Guo et al., 2016b; Kruse et al., 2013). To date, however, only the active-state structure of the M₂ muscarinic acetylcholine receptor bound to an agonist and a PAM has been solved (Kruse et al., 2013). The location of the allosteric site(s) for synthetic modulators at the A₁-AR remains unknown but has been inferred to involve the extracellular domains (Kennedy et al., 2014; Nguyen et al., 2016b; Peeters et al., 2012). Our atomic resolution of these regions now raises a number of interesting considerations. The first is the presence of a secondary pocket in the A₁-AR that is not observed in the A_{2A}-AR due to the more open arrangement of the extracellular domains of the former receptor. A second consideration, based on our modeling, is that ligands previously classed as “allosteric modulators” of the A₁-AR may actually prefer to interact with the orthosteric site in the unoccupied (inactive) receptor. This finding can explain the long-standing conundrum that most A₁-AR PAMs of orthosteric agonists actually behave as *inhibitors* of orthosteric antagonists (Bruns and Ferguson, 1990; Bruns et al., 1990; Kourounakis et al., 2000; van der Klein et al., 1999). Finally, albeit speculatively, we hypothesize that the TM regions of the A₃-AR, which are more homologous to the A₁-AR, can potentially adopt an “open” orientation like the A₁-AR, which may explain the fact that numerous A₃-AR allosteric modulators have also been identified relative to the paucity of allosteric ligands for A_{2A}-AR (Guo et al., 2016b).

Taken together, our findings provide important insights into a highly valued GPCR target. In addition to revealing the molecular basis of subtype selectivity, our structure can potentially explain the differential effects that A₁-AR allosteric ligands display against agonists versus antagonists and can even be used as an “anti-target” for screening of A_{2A}-AR selective antagonists currently in clinical development for Parkinson’s disease (Pinna, 2014) and cancer immunotherapy (Leone et al., 2015).

STAR★METHODS

Detailed methods are provided in the online version of this paper and include the following:

- KEY RESOURCES TABLE
- CONTACT FOR REAGENT AND RESOURCE SHARING
- METHODS DETAILS
 - Expression and purification
 - Crystallization
 - Data collection, processing & structure determination
 - Pharmacology
 - Thermal stability assays
 - Docking of A₁-AR antagonists and allosteric modulators
 - Molecular Dynamics (MD) Simulations

- Chemistry
- Statistical Analysis

● DATA AND SOFTWARE AVAILABILITY

SUPPLEMENTAL INFORMATION

Supplemental Information includes seven figures and five tables and can be found with this article online at <http://dx.doi.org/10.1016/j.cell.2017.01.042>.

AUTHOR CONTRIBUTIONS

A.G. performed cloning, protein expression, purification, crystallization, data collection, structure refinement, radioligand binding experiments, and docking studies. D.M.T. assisted with protein engineering, protein expression, crystallization, and structure refinement. L.T.M. performed radioligand binding experiments and supervised A.T.N. and E.A.V. A.T.N. performed cAMP assays, docking studies, and molecular dynamic simulations. E.A.V. generated membrane preparations. P.J.S. designed and supervised the chemical synthesis of the compounds. M.J. synthesized MIPS2712 and MIPS2719. P.M.S. and A.C. provided overall project supervision. A.G., D.M.T., and A.C. wrote the manuscript, with contributions from all authors.

ACKNOWLEDGMENTS

Data collection was undertaken at the MX2 beamline at the Australian synchrotron. This work was funded by the National Health and Medical Research Council of Australia (NHMRC) Program Grant APP1055134 and Project Grant APP1084246. A.T.N. is a recipient of an Australian Endeavour Scholarship and Fellowship. L.T.M. is a recipient of an Australian Research Council (ARC) Discovery Early Career Researcher Award (DECRA). A.C. is a Senior Principal Research Fellow, and P.M.S. is a Principal Research Fellow, of the NHMRC. E.A.V. holds an Australian Postgraduate Award and an Australian Cancer Therapeutics scholarship. We thank Prof. Brian Kobilka for helpful discussions.

Received: October 9, 2016
 Revised: December 15, 2016
 Accepted: January 30, 2017
 Published: February 23, 2017

REFERENCES

- Alexandrov, A.I., Mileni, M., Chien, E.Y.T., Hanson, M.A., and Stevens, R.C. (2008). Microscale fluorescent thermal stability assay for membrane proteins. *Structure* 16, 351–359.
- Aurelio, L., Valant, C., Flynn, B.L., Sexton, P.M., Christopoulos, A., and Scammells, P.J. (2009). Allosteric modulators of the adenosine A₁ receptor: synthesis and pharmacological evaluation of 4-substituted 2-amino-3-benzoylthiophenes. *J. Med. Chem.* 52, 4543–4547.
- Avlani, V.A., Gregory, K.J., Morton, C.J., Parker, M.W., Sexton, P.M., and Christopoulos, A. (2007). Critical role for the second extracellular loop in the binding of both orthosteric and allosteric G protein-coupled receptor ligands. *J. Biol. Chem.* 282, 25677–25686.
- Ballesteros, J.A., and Weinstein, H. (1995). Integrated methods for the construction of three-dimensional models and computational probing of structure-function relations in G protein-coupled receptors. *Methods Neurosci.* 25, 366–428.
- Baltos, J.-A., Gregory, K.J., White, P.J., Sexton, P.M., Christopoulos, A., and May, L.T. (2016). Quantification of adenosine A₁ receptor biased agonism: Implications for drug discovery. *Biochem. Pharmacol.* 99, 101–112.
- Beauglehole, A.R., Baker, S.P., and Scammells, P.J. (2000). Fluorosulfonyl-substituted xanthines as selective irreversible antagonists for the A₁-adenosine receptor. *J. Med. Chem.* 43, 4973–4980.
- Biasini, M., Bienert, S., Waterhouse, A., Arnold, K., Studer, G., Schmidt, T., Kiefer, F., Cassarino, T.G., Bertoni, M., Bordoli, L., and Schwede, T. (2014).

- SWISS-MODEL: modelling protein tertiary and quaternary structure using evolutionary information. *Nucleic Acids Res.* 42, W252–W258.
- Bokoch, M.P., Zou, Y., Rasmussen, S.G.F., Liu, C.W., Nygaard, R., Rosenbaum, D.M., Fung, J.J., Choi, H.-J., Thian, F.S., Kobilka, T.S., et al. (2010). Ligand-specific regulation of the extracellular surface of a G-protein-coupled receptor. *Nature* 463, 108–112.
- Braunwald, E. (2011). Clinical efforts to reduce myocardial infarct size—the next step. *J. Cardiovasc. Pharmacol. Ther.* 16, 349–353.
- Bruns, R.F., and Fergus, J.H. (1990). Allosteric enhancement of adenosine A₁ receptor binding and function by 2-amino-3-benzoylthiophenes. *Mol. Pharmacol.* 38, 939–949.
- Bruns, R.F., Fergus, J.H., Coughenour, L.L., Courtland, G.G., Pugsley, T.A., Dodd, J.H., and Tinney, F.J. (1990). Structure-activity relationships for enhancement of adenosine A₁ receptor binding by 2-amino-3-benzoylthiophenes. *Mol. Pharmacol.* 38, 950–958.
- Carpenter, B., Nehmé, R., Warne, T., Leslie, A.G.W., and Tate, C.G. (2016). Erratum: Structure of the adenosine A_{2A} receptor bound to an engineered G protein. *Nature* 538, 542.
- Changeux, J.-P., and Christopoulos, A. (2016). Allosteric Modulation as a Unifying Mechanism for Receptor Function and Regulation. *Cell* 166, 1084–1102.
- Chen, V.B., Arendall, W.B., 3rd, Headd, J.J., Keedy, D.A., Immormino, R.M., Kapral, G.J., Murray, L.W., Richardson, J.S., and Richardson, D.C. (2010). MolProbity: all-atom structure validation for macromolecular crystallography. *Acta Crystallogr. D Biol. Crystallogr.* 66, 12–21.
- Chen, J.-F., Eltzhig, H.K., and Fredholm, B.B. (2013). Adenosine receptors as drug targets—what are the challenges? *Nat. Rev. Drug Discov.* 12, 265–286.
- Chun, E., Thompson, A.A., Liu, W., Roth, C.B., Griffith, M.T., Katritch, V., Kunken, J., Xu, F., Cherezov, V., Hanson, M.A., and Stevens, R.C. (2012). Fusion partner toolchest for the stabilization and crystallization of G protein-coupled receptors. *Structure* 20, 967–976.
- Congreve, M., Andrews, S.P., Doré, A.S., Hollenstein, K., Hurrell, E., Langmead, C.J., Mason, J.S., Ng, I.W., Tehan, B., Zhukov, A., et al. (2012). Discovery of 1,2,4-triazine derivatives as adenosine A_{2A} antagonists using structure based drug design. *J. Med. Chem.* 55, 1898–1903.
- Copeland, R.A., Pompliano, D.L., and Meek, T.D. (2006). Drug-target residence time and its implications for lead optimization. *Nat. Rev. Drug Discov.* 5, 730–739.
- Doré, A.S., Robertson, N., Errey, J.C., Ng, I., Hollenstein, K., Tehan, B., Hurrell, E., Bennett, K., Congreve, M., Magnani, B., et al. (2011). Structure of the adenosine A_{2A} receptor in complex with ZM241385 and the xanthines XAC and caffeine. *Structure* 19, 1283–1293.
- Dror, R.O., Green, H.F., Valant, C., Borhani, D.W., Valcourt, J.R., Pan, A.C., Arlow, D.H., Canals, M., Lane, J.R., Rahmani, R., et al. (2013). Structural basis for modulation of a G-protein-coupled receptor by allosteric drugs. *Nature* 503, 295–299.
- Emsley, P., Lohkamp, B., Scott, W.G., and Cowtan, K. (2010). Features and development of Coot. *Acta Crystallogr. D Biol. Crystallogr.* 66, 486–501.
- Essmann, U., Perera, L., Berkowitz, M.L., Darden, T., Lee, H., and Pedersen, L.G. (1995). A smooth particle mesh Ewald method. *J. Chem. Phys.* 103, 8577–8593.
- Evans, P.R., and Murshudov, G.N. (2013). How good are my data and what is the resolution? *Acta Crystallogr. D Biol. Crystallogr.* 69, 1204–1214.
- Ferguson, G.N., Valant, C., Horne, J., Figler, H., Flynn, B.L., Linden, J., Chalmers, D.K., Sexton, P.M., Christopoulos, A., and Scammells, P.J. (2008). 2-aminothienopyridazines as novel adenosine A₁ receptor allosteric modulators and antagonists. *J. Med. Chem.* 51, 6165–6172.
- Foadi, J., Aller, P., Alguel, Y., Cameron, A., Axford, D., Owen, R.L., Armour, W., Waterman, D.G., Iwata, S., and Evans, G. (2013). Clustering procedures for the optimal selection of data sets from multiple crystals in macromolecular crystallography. *Acta Crystallogr. D Biol. Crystallogr.* 69, 1617–1632.
- Fredholm, B.B., IJzerman, A.P., Jacobson, K.A., Linden, J., and Müller, C.E. (2011). International Union of Basic and Clinical Pharmacology. LXXXI. Nomenclature and classification of adenosine receptors—an update. *Pharmacol. Rev.* 63, 1–34.
- Göblyös, A., and IJzerman, A.P. (2011). Allosteric modulation of adenosine receptors. *BBA - Biomembranes* 1808, 1309–1318.
- Gracia, E., Moreno, E., Cortés, A., Lluís, C., Mallol, J., McCormick, P.J., Canela, E.I., and Casadó, V. (2013). Homodimerization of adenosine A₁ receptors in brain cortex explains the biphasic effects of caffeine. *Neuropharmacology* 71, 56–69.
- Granier, S., Manglik, A., Kruse, A.C., Kobilka, T.S., Thian, F.S., Weis, W.I., and Kobilka, B.K. (2012). Structure of the δ -opioid receptor bound to naltrindole. *Nature* 485, 400–404.
- Guo, D., Pan, A.C., Dror, R.O., Mocking, T., Liu, R., Heitman, L.H., Shaw, D.E., and IJzerman, A.P. (2016a). Molecular Basis of Ligand Dissociation from the Adenosine A_{2A} Receptor. *Mol. Pharmacol.* 89, 485–491.
- Guo, D., Heitman, L.H., and IJzerman, A.P. (2016b). Kinetic Aspects of the Interaction between Ligand and G Protein-Coupled Receptor: The Case of the Adenosine Receptors. *Chem. Rev.* 117, 38–66.
- Gutiérrez-de-Terán, H., Sallander, J., and Sotelo, E. (2017). Structure-Based Rational Design of Adenosine Receptor Ligands. *Curr. Top. Med. Chem.* 17, 40–58.
- Hino, T., Arakawa, T., Iwanari, H., Yurugi-Kobayashi, T., Ikeda-Suno, C., Nakada-Nakura, Y., Kusano-Arai, O., Weyand, S., Shimamura, T., Nomura, N., et al. (2012). G-protein-coupled receptor inactivation by an allosteric inverse-agonist antibody. *Nature* 482, 237–240.
- Humphrey, W., Dalke, A., and Schulten, K. (1996). VMD: visual molecular dynamics. *J. Mol. Graph.* 14, 33–38, 27–28.
- Jaakola, V.-P., Griffith, M.T., Hanson, M.A., Cherezov, V., Chien, E.Y.T., Lane, J.R., IJzerman, A.P., and Stevens, R.C. (2008). The 2.6 angstrom crystal structure of a human A_{2A} adenosine receptor bound to an antagonist. *Science* 322, 1211–1217.
- Jacobson, K.A., and Gao, Z.-G. (2006). Adenosine receptors as therapeutic targets. *Nat. Rev. Drug Discov.* 5, 247–264.
- Jazayeri, A., Dias, J.M., and Marshall, F.H. (2015). From G Protein-coupled Receptor Structure Resolution to Rational Drug Design. *J. Biol. Chem.* 290, 19489–19495.
- Kabsch, W. (2010). XDS. *Acta Crystallogr. D Biol. Crystallogr.* 66, 125–132.
- Kenakin, T., and Christopoulos, A. (2013). Signalling bias in new drug discovery: detection, quantification and therapeutic impact. *Nat. Rev. Drug Discov.* 12, 205–216.
- Kennedy, D.P., McRobb, F.M., Leonhardt, S.A., Purdy, M., Figler, H., Marshall, M.A., Chordia, M., Figler, R., Linden, J., Abagyan, R., and Yeager, M. (2014). The second extracellular loop of the adenosine A₁ receptor mediates activity of allosteric enhancers. *Mol. Pharmacol.* 85, 301–309.
- Kloner, R.A., Forman, M.B., Gibbons, R.J., Ross, A.M., Alexander, R.W., and Stone, G.W. (2006). Impact of time to therapy and reperfusion modality on the efficacy of adenosine in acute myocardial infarction: the AMISTAD-2 trial. *Eur. Heart J.* 27, 2400–2405.
- Kourounakis, A.P., Van der Klein, P.A.M., and IJzerman, A.P. (2000). Elucidation of structure-activity relationships of 2-amino-3-benzoylthiophenes: Study of their allosteric enhancing vs. antagonistic activity on adenosine A₁ receptors. *Drug Dev. Res.* 49, 227–237.
- Kruse, A.C., Ring, A.M., Manglik, A., Hu, J., Hu, K., Eitel, K., Hübner, H., Pardon, E., Valant, C., Sexton, P.M., et al. (2013). Activation and allosteric modulation of a muscarinic acetylcholine receptor. *Nature* 504, 101–106.
- Lebon, G., Warne, T., Edwards, P.C., Bennett, K., Langmead, C.J., Leslie, A.G.W., and Tate, C.G. (2011). Agonist-bound adenosine A_{2A} receptor structures reveal common features of GPCR activation. *Nature* 474, 521–525.
- Lebon, G., Edwards, P.C., Leslie, A.G.W., and Tate, C.G. (2015). Molecular Determinants of CGS21680 Binding to the Human Adenosine A_{2A} Receptor. *Mol. Pharmacol.* 87, 907–915.

- Leone, R.D., Lo, Y.-C., and Powell, J.D. (2015). A2aR antagonists: Next generation checkpoint blockade for cancer immunotherapy. *Comput. Struct. Biotechnol. J.* 13, 265–272.
- Liu, W., Chun, E., Thompson, A.A., Chubukov, P., Xu, F., Katritch, V., Han, G.W., Roth, C.B., Heitman, L.H., IJzerman, A.P., et al. (2012). Structural basis for allosteric regulation of GPCRs by sodium ions. *Science* 337, 232–236.
- Mackerell, A.D., Jr., Feig, M., and Brooks, C.L., 3rd. (2004). Extending the treatment of backbone energetics in protein force fields: limitations of gas-phase quantum mechanics in reproducing protein conformational distributions in molecular dynamics simulations. *J. Comput. Chem.* 25, 1400–1415.
- Manglik, A., Kruse, A.C., Kobilka, T.S., Thian, F.S., Mathiesen, J.M., Sunahara, R.K., Pardo, L., Weis, W.I., Kobilka, B.K., and Granier, S. (2012). Crystal structure of the μ -opioid receptor bound to a morphinan antagonist. *Nature* 485, 321–326.
- Massie, B.M., O'Connor, C.M., Metra, M., Ponikowski, P., Teerlink, J.R., Cotter, G., Weatherley, B.D., Cleland, J.G.F., Givertz, M.M., Voors, A., et al.; PROTECT Investigators and Committees (2010). Rolofylline, an adenosine A₁-receptor antagonist, in acute heart failure. *N. Engl. J. Med.* 363, 1419–1428.
- May, L.T., Sexton, P.M., and Christopoulos, A. (2005). Effects of urea pretreatment on the binding properties of adenosine A₁ receptors. *Br. J. Pharmacol.* 146, 1119–1129.
- McCoy, A.J., Grosse-Kunstleve, R.W., Adams, P.D., Winn, M.D., Storoni, L.C., and Read, R.J. (2007). Phaser crystallographic software. *J. Appl. Cryst.* 40, 658–674.
- Motulsky, H., and Christopoulos, A. (2004). Fitting models to biological data using linear and nonlinear regression: a practical guide to curve fitting (New York: Oxford University Press).
- Müller, C.E., and Jacobson, K.A. (2011). Recent developments in adenosine receptor ligands and their potential as novel drugs. *BBA - Biomembranes* 1808, 1290–1308.
- Murshudov, G.N., Skubák, P., Lebedev, A.A., Pannu, N.S., Steiner, R.A., Nicholls, R.A., Winn, M.D., Long, F., and Vagin, A.A. (2011). REFMAC5 for the refinement of macromolecular crystal structures. *Acta Crystallogr. D Biol. Crystallogr.* 67, 355–367.
- Mustafa, S.J., Morrison, R.R., Teng, B., and Pelleg, A. (2009). Adenosine receptors and the heart: role in regulation of coronary blood flow and cardiac electrophysiology. *Handbook Exp. Pharmacol.* 193, 161–188.
- Neves, M.A.C., Totrov, M., and Abagyan, R. (2012). Docking and scoring with ICM: the benchmarking results and strategies for improvement. *J. Comput. Aided Mol. Des.* 26, 675–686.
- Nguyen, A.T., Baltos, J.-A., Thomas, T., Nguyen, T.D., Muñoz, L.L., Gregory, K.J., White, P.J., Sexton, P.M., Christopoulos, A., and May, L.T. (2016a). Extracellular loop 2 of the adenosine A₁ receptor has a key role in orthosteric ligand affinity and agonist efficacy. *Mol. Pharmacol.* 90, 703–714.
- Nguyen, A.T., Vecchio, E.A., Thomas, T., Nguyen, T.D., Aurelio, L., Scammells, P.J., White, P.J., Sexton, P.M., Gregory, K.J., May, L.T., and Christopoulos, A. (2016b). Role of the second extracellular loop of the adenosine A₁ receptor on allosteric modulator binding, signaling, and cooperativity. *Mol. Pharmacol.* 90, 715–725.
- Peeters, M.C., Wisse, L.E., Dinaj, A., Vrolijk, B., Vriend, G., and IJzerman, A.P. (2012). The role of the second and third extracellular loops of the adenosine A₁ receptor in activation and allosteric modulation. *Biochem. Pharmacol.* 84, 76–87.
- Phillips, J.C., Braun, R., Wang, W., Gumbart, J., Tajkhorshid, E., Villa, E., Chipot, C., Skeel, R.D., Kalé, L., and Schulten, K. (2005). Scalable molecular dynamics with NAMD. *J. Comput. Chem.* 26, 1781–1802.
- Pinna, A. (2014). Adenosine A_{2A} receptor antagonists in Parkinson's disease: progress in clinical trials from the newly approved istradefylline to drugs in early development and those already discontinued. *CNS Drugs* 28, 455–474.
- Rosenbaum, D.M., Cherezov, V., Hanson, M.A., Rasmussen, S.G.F., Thian, F.S., Kobilka, T.S., Choi, H.-J., Yao, X.-J., Weis, W.I., Stevens, R.C., and Kobilka, B.K. (2007). GPCR engineering yields high-resolution structural insights into beta2-adrenergic receptor function. *Science* 318, 1266–1273.
- Savinainen, J.R., Saario, S.M., Niemi, R., Järvinen, T., and Laitinen, J.T. (2003). An optimized approach to study endocannabinoid signaling: evidence against constitutive activity of rat brain adenosine A₁ and cannabinoid CB₁ receptors. *Br. J. Pharmacol.* 140, 1451–1459.
- Segala, E., Guo, D., Cheng, R.K.Y., Bortolato, A., Deflorian, F., Doré, A.S., Errey, J.C., Heitman, L.H., IJzerman, A.P., Marshall, F.H., and Cooke, R.M. (2016). Controlling the Dissociation of Ligands from the Adenosine A_{2A} Receptor through Modulation of Salt Bridge Strength. *J. Med. Chem.* 59, 6470–6479.
- Teerlink, J.R., Iragui, V.J., Mohr, J.P., Carson, P.E., Hauptman, P.J., Lovett, D.H., Miller, A.B., Piña, I.L., Thomson, S., Varosy, P.D., et al. (2012). The safety of an adenosine A₁-receptor antagonist, rolofylline, in patients with acute heart failure and renal impairment: findings from PROTECT. *Drug Saf.* 35, 233–244.
- Thal, D.M., Sun, B., Feng, D., Nawaratne, V., Leach, K., Felder, C.C., Bures, M.G., Evans, D.A., Weis, W.I., Bachhawat, P., et al. (2016). Crystal structures of the M1 and M4 muscarinic acetylcholine receptors. *Nature* 531, 335–340.
- Totrov, M., and Abagyan, R. (1997). Flexible protein-ligand docking by global energy optimization in internal coordinates. *Proteins (Suppl 1)*, 215–220.
- Tucker, A.L., Robeva, A.S., Taylor, H.E., Holeten, D., Bockner, M., Lynch, K.R., and Linden, J. (1994). A1 adenosine receptors. Two amino acids are responsible for species differences in ligand recognition. *J. Biol. Chem.* 269, 27900–27906.
- Valant, C., May, L.T., Aurelio, L., Chuo, C.H., White, P.J., Baltos, J.A., Sexton, P.M., Scammells, P.J., and Christopoulos, A. (2014). Separation of on-target efficacy from adverse effects through rational design of a bitopic adenosine receptor agonist. *Proc. Natl. Acad. Sci. USA* 111, 4614–4619.
- van der Klein, P.A.M., Kourounakis, A.P., and IJzerman, A.P. (1999). Allosteric modulation of the adenosine A₁ receptor. Synthesis and biological evaluation of novel 2-amino-3-benzoylthiophenes as allosteric enhancers of agonist binding. *J. Med. Chem.* 42, 3629–3635.
- Vanommeslaeghe, K., Hatcher, E., Acharya, C., Kundu, S., Zhong, S., Shim, J., Darian, E., Guvench, O., Lopes, P., Vorobyov, I., and Mackerell, A.D., Jr. (2010). CHARMM general force field: A force field for drug-like molecules compatible with the CHARMM all-atom additive biological force fields. *J. Comput. Chem.* 31, 671–690.
- Xu, F., Wu, H., Katritch, V., Han, G.W., Jacobson, K.A., Gao, Z.-G., Cherezov, V., and Stevens, R.C. (2011). Structure of an agonist-bound human A_{2A} adenosine receptor. *Science* 332, 322–327.

STAR★METHODS

KEY RESOURCES TABLE

REAGENT or RESOURCE	SOURCE	IDENTIFIER
Antibodies		
Mouse monoclonal M1 anti-FLAG (4E11)	ATCC	Cat#HB-9259; RRID: CVCL_J730
Bacterial and Virus Strains		
ESF921 Insect Cell Culture	Expression systems	96-001-01
BestBac 2.0 Δ v-cath/chiA Baculovirus Cotransfection	Expression systems	91-200
Chemicals, Peptides, and Recombinant Proteins		
n-dodecyl-beta-D-maltopyranoside (DDM)	Anatrace	Cat#D310
Cholesteryl hemisuccinate tris salt	Anatrace	Cat#CH210
Lauryl maltose neopentyl glycol	Anatrace	Cat#NG310
Cholesterol	Anatrace	Cat#CH200
1-Oleoyl-rac-glycerol	Hampton research	Cat#HR2-435
Iodacetamide	Sigma	Cat#I1149
Benzonase	Sigma	Cat#E1014
Phenylmethanesulfonyl fluoride	Sigma	Cat#P7626
Benzamidine Hydrochloride	Sigma	Cat#434760
Trypsin Inhibitor from chicken egg white	Sigma	Cat#T9253
Leupeptin	Purar chemicals	N/A
FLAG peptide	Purar chemicals	N/A
Ammonium fluoride	Sigma	Cat#338869
Polyethylenimine	Polysciences	Cat#23966
Polyethylene glycol 300	Hampton research	Cat#HR2-517
Chelating Sepharose Fast Flow	GE Healthcare	Cat#17-0575-02
N-[4-(7-diethylamino-4methyl-3-coumarinyl)phenyl]maleimide dye (CPM)	Sapphire Bioscience	Cat#CDX-D0042
Cyclopentyl-1, 3-Dipropylxanthine, 8-[Dipropyl-2, 3-3H(N)] ([3H]DPCPX)	PerkinElmer	NET974001MC
SLV 320	Tocris	Cat#3344
8-Cyclopentyl-1,3-dipropylxanthine (DPCPX)	Sigma	Cat#C101
5'-(N-Ethylcarboxamido)adenosine (NECA)	Sigma	Cat#E2387
(-)-N ⁶ -(2-Phenylisopropyl)adenosine (R-PIA)	Sigma	Cat#P4532
[3H]ZM 241385	American Radiolabeled Chemicals	Cat#ART 0884
ZM 241385	Sigma	Cat#Z0153
Hygromycin B	Roche	Cat#10843555001
Fetal bovine serum	Thermo Fisher	Cat# 10437-028 (Lot 1706567)
Rolipram	Sigma	Cat#R6520
Forskolin	Sigma	Cat#F6886
HEPES	ThermoFisher Scientific	Cat#11344041
Bovine Serum Albumin (BSA)	Sigma	Cat#A7906
Fugene HD Transfection Reagent	Promega	E2311
Critical Commercial Assays		
AlphaScreen SureFire p-ERK1/2 kit	PerkinElmer	Cat#TGRESB50K

(Continued on next page)

Continued

REAGENT or RESOURCE	SOURCE	IDENTIFIER
LANCE cAMP 384 kit	PerkinElmer	Cat#AD0264
Deposited Data		
A ₁ -AR●DU172	This paper	PDB: 5UEN
Experimental Models: Cell Lines		
Sf9 cells	Expression Systems	Cat#94-001F
FlpIn Chinese hamster ovary cells	ThermoFisher	Cat#R75807
Recombinant DNA		
Human A ₁ -AR gene	cdna.org	Cat#ADRA100000
Human A ₂ -AR gene	cdna.org	Cat#ADRA2A0000
pVL1392 vector	Expression Systems	Cat#91-030
pcDNA3.1 vector (+)	ThermoFisher	Cat#V79020
Sequence-Based Reagents		
A ₁ AR_N159A_forward mutagenesis primer	IDT	CCTGGGCAGCCGCCGAGCATGG
A ₁ cryst_forward mutagenesis primer	IDT	AGTGTGGTGGAAATCACCATGGGTCC TCCGCCCTCCATCTC
A ₁ cryst_reverse mutagenesis primer	IDT	CACCACACTTCTAGAATTACTGGAAG AGCACCTCCAGAGGC
A ₁ expr_forward mutagenesis primer	IDT	AGTGTGGTGGAAATCACCATGAAGAC GATCATCGCCCTGAGCTAC
A ₁ expr_reverse mutagenesis primer	IDT	CACCACACTTCTAGAATTAATGGTGATG GTGGTGATGATGGTGGTCATC
A ₁ -AR_T270M_forward mutagenesis primer	IDT	CAAGCCCAGCATCCTTATGTACATTGC CATCTTCC
A _{2A} -AR_M270T_forward mutagenesis primer	IDT	CTCTCTGGCTCACGTACCTGGCCATC
Software and Algorithms		
XDS	Kabsch, 2010	http://xds.mpimf-heidelberg.mpg.de
BLEND	Foadi et al., 2013	http://www.ccp4.ac.uk/html/blend.html
Aimless	Evans and Murshudov, 2013	http://www.ccp4.ac.uk/html/aimless.html
Phaser	McCoy et al., 2007	http://www.ccp4.ac.uk/html/phaser.html
SWISS-MODEL	Biasini et al., 2014	https://swissmodel.expasy.org
Refmac5	Murshudov et al., 2011	http://www.ccp4.ac.uk/html/refmac5.html
Coot	Emsley et al., 2010	https://www2.mrc-lmb.cam.ac.uk/personal/pemsley/coot/
Molprobit	Chen et al., 2010	http://molprobit.biochem.duke.edu
PyMOL Molecular Graphics System	Schrödinger	https://www.pymol.org
Prism v6.0	Graphpad Software	https://www.graphpad.com/scientific-software/prism/
ICM v3.8.0	Molsoft	http://www.molsoft.com
NAMD2.10	Phillips et al., 2005	http://www.ks.uiuc.edu/Research/namd/
CGenFF v3.0.1	Vanommeslaeghe et al., 2010	https://cgenff.paramchem.org
VMD v1.9.2	Humphrey et al., 1996	http://www.ks.uiuc.edu/Research/vmd/

CONTACT FOR REAGENT AND RESOURCE SHARING

Please contact Lead Contact Arthur Christopoulos (arthur.christopoulos@monash.edu) for reagents and resources generated in this study.

METHODS DETAILS

Expression and purification

Our initial construct for the A₁-AR expression, containing a HA signal sequence, N-terminal Flag tag, followed by a 3C protease cleavage site, and a C-terminal 8xHis tag expressed poorly. Thus, 22 amino acids of the M₄ muscarinic receptor, with 3 N-glycosylation sites, were added at the N terminus before a 3C-protease cleavage site, which increased receptor expression levels several fold. Generally, the addition of the M₄ N terminus increased the B_{max} in saturation binding experiments from 1.7-3 nmol/L to 19-27 nmol/L in Sf9 cells, as well as the actual protein yield in test purification experiments (from less than 70 µg/L to 200-400 µg/L of culture for different constructs). We inserted an additional 3C site at the C terminus, after amino acid 311, substituted ICL3 (amino 211-220) with b₅₆₂RIL (BRIL), and made an N159A substitution to promote crystallization. Though this construct yielded crystals, the diffraction quality was poor and we reasoned that optimization of the BRIL insertion site was required. Consequently, the first 8 amino acids of TM6, immediate to the C-terminal BRIL insertion site, were changed to corresponding residues of the A_{2A}-AR. The resulting construct was cloned into a pVL1392 vector, followed by expression in Sf9 cells using the Best-Bac Baculovirus expression system (Expression Systems). Cells were infected at 4x10⁶ cells/ml and harvested 62 hr later. Due to the presence of adenosine in the media, no ligand addition was necessary.

All purification steps were performed in the presence of 0.2 µM DU172. Insect cells were lysed by osmotic shock in the buffer containing 10 mM Tris pH 7.5, 1 mM EDTA, 1 mM MgCl₂, 1 mg/mL iodoacetamide with benzonase and protease inhibitors. Cell membranes were solubilized in solubilization buffer (30 mM HEPES pH 7.5, 1% dodecyl maltoside (DDM), 0.03% cholesterol hemisuccinate (CHS), 750 mM NaCl, 30% glycerol, 1 mM MgCl₂, 1 mg/mL iodoacetamide with benzonase and protease inhibitors) for 2 hr at 4°C, spun down from insoluble debris and batch-bound to Ni-chelating resin for 1.5 hr at 4°C. Ni resin was then loaded on a glass column and washed by gravity flow using Ni-wash buffer (30 mM HEPES pH 7.5, 0.1% DDM, 0.003% cholesterol, 750 mM NaCl, 30% glycerol and 5 mM imidazole). Receptor was eluted in the wash buffer with 250 mM imidazole, supplemented with 2 mM CaCl₂ and then loaded onto an anti-Flag M1 antibody column at a flow rate of 1 ml/min. Detergent was exchanged into 30 mM HEPES pH 7.5, 0.1% lauryl maltose neopentyl glycol (MNG), 0.01% CHS, 100 mM NaCl, 2 mM CaCl₂ over the course of 1 hr. The final wash was done using 10xCMC buffer (30 mM HEPES pH 7.5, 0.01% MNG, 0.001% CHS, 100 mM NaCl) supplemented with 2 mM CaCl₂, followed by elution into 10xCMC buffer with 10 mM EDTA and 0.2 mg/ml of FLAG peptide. Digest with 3C protease (1:7 w/w) was carried out overnight at 4°C in the presence of 22 µM DU172. Size-exclusion chromatography was performed using Superdex S200 Increase column in 10xCMC buffer. Monodispersed receptor fractions were pooled together, supplemented with 200 µM DU172 and concentrated to an A₂₈₀ of 84 and flash frozen in liquid N₂ in single-use aliquots.

Crystallization

A₁-AR was reconstituted into the lipid cubic phase by mixing it with a 10:1 monoolein:cholesterol (Hampton and Anatrache) mixture at 1:1.5 (w/w) ratio. Approximately 100 cycles of mixing were performed at 2 µl/sec using a Gryphon LCP mixing platform (Art Robbins Instruments). LCP crystallization was performed in siliconized 96-well plates overlaying 30 nL protein solution drops with 0.6 µl of well solution using the Gryphon LCP. Sealed glass plates were incubated at 20°C for 1-2 weeks. The best diffracting crystals grew in 100 mM HEPES pH 7.0-8.0, 28%-38% PEG 300 and 500-700 mM NH₄F. For data collection whole drops were harvested using mesh grid loops (Mitegen) and flash frozen in liquid N₂.

Data collection, processing & structure determination

Diffraction data were collected at the MX2 beamline on an ADSC Quantum detector at the Australian synchrotron. Rastering and data collection was done at 13 keV with unattenuated beam collimated to 20x70 µm, using 1 s exposure per 1° oscillation in 5-10° wedges from each crystal. Data from 51 crystals were processed with XDS (Kabsch, 2010), analyzed using BLEND (Foadi et al., 2013) and the best datasets from 29 crystals were scaled and merged using Aimless (Evans and Murshudov, 2013). Phaser (McCoy et al., 2007) was used to find an initial solution using an A₁-AR homology model built by SWISS-MODEL as a template using an A_{2A}-AR crystal structure (PDB: 4EIY) (Liu et al., 2012). Refinement was carried out in Refmac5 (Murshudov et al., 2011), and manual rebuilding was done using Coot (Emsley et al., 2010). Model validation was performed using Molprobity (Chen et al., 2010). All structure-related figures were prepared in PyMOL Molecular Graphics System, Version 1.7.2.1 (Schrödinger, LLC).

Pharmacology

Pharmacological characterization of the A₁-AR constructs was carried out in transiently transfected FlpIn Chinese hamster ovary (FlpIn CHO) cells. Constructs, A₁^{expr}-, A₁^{cryst}-, A₁(wt)-, A₁(T270M)-, A_{2A}(wt)- and A_{2A}(M270T)-AR were cloned into a pcDNA3.1 vector for transient transfection. A₁^{expr} contained the full sequence of the construct expressed in Sf9 insect cells for crystallization. A₁^{cryst} was truncated at 3C protease cleavage sites (with an added methionine at the N terminus) and was equivalent to the crystallized construct. Transient transfection with pcDNA3.1 was carried out in suspension before plating cells into 96-well plates using 100 ng of DNA and 600 ng of polyethylenimine per well. FlpIn CHO cells were maintained in DMEM media containing 10% FBS in a humidified incubator containing 5% CO₂ at 37°C for 36 hr, followed by 12 hr of serum starvation prior to assaying.

Radioligand saturation binding experiments were performed in binding buffer (10 mM HEPES pH 7.5, 145 mM NaCl, 5 mM KCl, 1 mM MgSO₄, 2 mM CaCl₂, 1.5 mM NaHCO₃, 10 mM D-glucose) on whole FlpIn CHO cells grown in 96-well Iso-plates. After removal

of cell media and a brief wash with binding buffer, cells were incubated in a final volume of 300 μ L with different concentrations of [3 H] DPCPX for 3 hr at 4°C. Radioligand was discarded, cells were washed twice with ice-cold phosphate buffer saline (PBS, 10 mM Na₂HPO₄; 1.8 mM KH₂PO₄; 137 mM NaCl; 2.7 mM KCl), and dissolved in 100 μ L Ultima Gold scintillation liquid (PerkinElmer) followed by β -counting. Concentrations of [3 H]DPCPX used in the assay were determined by β -counting using MicroBeta LumiJET counter (PerkinElmer). After subtraction of the nonspecific binding, measured in the presence of 1 μ M SLV320, from total, curves were fitted to the “One site-specific binding” equation in Prism 6.0 (GraphPad) yielding B_{max} and K_d values. To account for different transfection efficiencies, all data were normalized to B_{max} of the A_{1wt}. For radioligand competition binding experiments, cells were incubated with different concentrations of competing ligands (DPCPX, DU172, NECA and R-PIA) in the presence of approximately 2 nM [3 H]DPCPX (precise concentrations in each experiment were determined by β -counting) for 3 hr at 4°C, followed by the same treatment as in saturation binding. Additional competition binding experiments were also performed to assess the effects of rationally designed mutations on the affinity of the antagonists DPCPX and ZM241385. For these latter experiments, A_{1(wt)}⁻, A_{1(T270M)}⁻, A_{2A(wt)}⁻, A_{2A(M270T)}⁻AR constructs were transiently transfected into FlpIn CHO cells as described above, and competition binding was performed in a final volume of 100 μ L HEPES buffer (145 mM NaCl, 10 mM D-Glucose, 5 mM KCl, 1 mM MgSO₄, 10 mM HEPES, 1.3 mM CaCl₂, 15 mM NaHCO₃, pH 7.4) in the absence or presence of approximately 1 nM [3 H]DPCPX or 1 nM [3 H]ZM241385 (precise concentrations in each experiment were determined by β -counting) and a range of concentrations of the competing ligands DPCPX or ZM241385 at 37°C for 1 hr. Cells were then treated as outlined in saturation binding. In all cases, competition binding data were normalized to radioligand binding values in the absence of competitors. Competition curves were fitted to the one-site competition binding equation in Prism 6.0 (GraphPad Software, San Diego, CA) yielding logK_i values. One-way ANOVA (Dunnett’s post hoc) or an unpaired t test, as appropriate, was used to determine significance by comparing the logK_i value for each mutant receptor to the corresponding wild-type construct.

For functional ERK 1/2 phosphorylation assays, transiently transfected FlpIn CHO cells 12 hr post serum starvation were assayed as described previously (Baltos et al., 2016). Briefly, cells were incubated with increasing concentrations of agonists (NECA or R-PIA) in DMEM media for 5 min (peak response) in a humidified incubator containing 5% CO₂ at 37°C. Reaction was rapidly terminated by removal of media and addition of 100 μ L SureFire lysis buffer to each well followed by 10 min shaking at 20°C. For detection, lysate was mixed with activation buffer, reaction buffer, AlphaScreen acceptor beads and AlphaScreen donor beads (AlphaScreen SureFire ERK1/2 kit from PerkinElmer) at 80:20:120:1:1 (v/v/v/v/v) ratio in a 384-well Proxiplate. Plates were incubated in the dark at 37°C for 1.5 hr followed by measurement on an EnVision plate reader (PerkinElmer) using AlphaScreen settings. Data were baseline-corrected and normalized to the response of A_{1wt} caused by 10 μ M NECA.

For functional cAMP accumulation assays, the FlpIn CHO cells stably expressing the human A₁-AR and A_{2A}-AR were seeded into 96-well culture plates at a density of 2 × 10⁴ cells/well in DMEM containing 10% FBS, 600 μ g/mL hygromycin B and incubated in a humidified incubator at 37°C in 5% CO₂ overnight. The accumulation of cAMP was determined as described previously (Nguyen et al., 2016a). Briefly, media was replaced with stimulation buffer (140 mM NaCl, 5.4 mM KCl, 0.8 μ M MgSO₄, 0.2 mM Na₂HPO₄, 0.44 mM KH₂PO₄, 1.3 mM CaCl₂, 5.6 mM D-glucose, 5 mM HEPES, 0.1% bovine serum albumin (BSA), and 10 μ M rolipram, pH 7.45) and incubated at 37°C for 30 min. Cells were then exposed to antagonist (DU172, MIPS2712, MIPS2719) for 30 min. NECA concentration response curves were performed by the subsequent addition of increasing concentrations of NECA and 3 μ M forskolin (A₁-AR-FlpIn-CHO only) in a final volume of 100 μ L for 30 min at 37°C. The reactions were terminated by the addition of 50 μ L ice cold 100% ethanol. The lysis buffer (0.1% BSA, 0.3% tween-20, 5 mM HEPES, pH 7.45) was added to the cells after the complete evaporation of ethanol. Detection of cAMP was performed using LANCE cAMP 384 kits (PerkinElmer) following manufacture’s protocol and fluorescence was measured with an EnVision® plate reader (PerkinElmer). Agonist concentration-response curves were normalized to the response mediated by 3 μ M forskolin alone and buffer alone. All experiments were performed in duplicate.

For A₁-AR-FlpIn CHO cells, the G_{i/o} protein-mediated inhibition of cAMP accumulation was determined as described previously (Nguyen et al., 2016a). Briefly, media was replaced with 70 μ L stimulation buffer (140 mM NaCl, 5.4 mM KCl, 0.8 μ M MgSO₄, 0.2 mM Na₂HPO₄, 0.44 mM KH₂PO₄, 1.3 mM CaCl₂, 5.6 mM D-glucose, 5 mM HEPES, 0.1% bovine serum albumin (BSA), and 10 μ M rolipram, pH 7.45) and incubated at 37°C for 30 min. Cells were incubated with 10 μ L of increasing concentrations of each antagonist (DU172, MIPS2712, MIPS2719) for 30 min. Concentration response assays were performed by subsequent incubation of increasing concentration of NECA (10 μ L) and 3 μ M forskolin (10 μ L) for an additional 30 min at 37°C. The reactions were terminated by the addition of 50 μ L ice cold 100% ethanol. The lysis buffer (0.1% BSA, 0.3% tween-20, 5 mM HEPES, pH 7.45) was added to the cells after the complete evaporation of ethanol. Detection of cAMP was performed using LANCE cAMP 384 kits (PerkinElmer) following manufacture’s protocol and fluorescence was measured with an EnVision® plate reader (PerkinElmer). Agonist concentration-response curves were normalized to the response mediated by 3 μ M forskolin (0%) or buffer (100%) alone. All experiments were performed in duplicate.

For A_{2A}-AR-FlpIn CHO cells, the G_s protein-mediated stimulation of cAMP accumulation was determined as described below. After the removal of media, cells were incubated with 80 μ L stimulation buffer at 37°C for 30 min. Cells were then exposed to a 30 min incubation with increasing concentrations of each antagonist (10 μ L), follow by a further 30 min incubation with increasing concentrations of NECA (10 μ L). Termination of the reactions and detection of cAMP were performed as described above. Agonist concentration-response curves were normalized to the response mediated by 3 μ M forskolin (100%) or buffer (0%) alone. All experiments were performed in duplicate.

All data were analyzed using GraphPad Prism 6.0.

Functional interaction studies between NECA and multiple concentrations of each antagonist in the cAMP assays were fit to the following competitive model (Motulsky and Christopoulos, 2004):

$$\text{Response} = \text{Bottom} + \frac{(E_{\text{max}} - \text{bottom})}{1 + \left(\frac{10^{-\text{pEC}_{50}} \left[1 + \left(\frac{[B]}{10^{-\text{pA}_2}} \right)^S \right]}{[A]} \right)^{\text{HillSlope}}} \quad (\text{Equation 1})$$

Where pEC_{50} is the negative logarithm of the EC_{50} of NECA (A) in the absence of antagonist (B). HillSlope is the slope of the agonist curve, S is the Schild slope, pA_2 is the negative logarithm of the molar concentration of antagonist necessary to shift the agonist EC_{50} by a factor of two. The Schild slope parameter, S, was constrained to 1 and therefore the estimated pA_2 values for each antagonist are equal to the pK_B (negative logarithm of the antagonist equilibrium dissociation constant).

Thermal stability assays

The A_1 -AR construct used for crystallization studies was expressed and purified as described above. The thermal stability assay protocol was adapted from Alexandrov et al. (Alexandrov et al., 2008). Purified receptor (0.2 μg) in 15 μL volume was incubated with 10 or 100 μM compounds for 1 hr at 20°C in 10xCMC buffer in black PCR plates (Bio-Rad) under 4 μL of silicone oil (Sigma). Then, 5 μL of N-[4-(7-diethylamino-4-methyl-3-coumarinyl)phenyl]maleimide dye (CPM; Sapphire Bioscience) was added to a final concentration of 10 μM and incubated for additional 15 min at 20°C. After a brief spin, the plate was gradually heated from 20 to 80°C in 3° intervals using a PCR machine. Each temperature was held for 90 s followed by a rapid (30 s) fluorescence reading using an EnVision plate reader (PerkinElmer) with 380/470 nm excitation/emission filters. After subtraction of the internal CPM fluorescence, data points were fitted to Boltzmann sigmoidal equation in Prism 6.0 (GraphPad) and T_m was defined as the halfway of the transition.

Docking of A_1 -AR antagonists and allosteric modulators

Docking of selective A_1 -AR antagonists (DPCPX, PSB36, rolofylline, SLV320, MIPS2712 and MIPS2719) and allosteric modulators (VCP171 and compound 13b) was performed using ICM version 3.8.0 (Molsoft L.L.C., La Jolla, CA) (Neves et al., 2012). Docking was performed by global optimization of the flexible ligand in the receptor field (Totrov and Abagyan, 1997). DU172 and non-receptor molecules were removed from the structure. The binding pocket was defined around DU172 in the A_1 -AR crystal structure or around ZM241385 in the A_{2A} -AR crystal structure (PDB: 4EIY). Maps were generated in a 0.5 Å grid size within a 42.4 × 35.2 × 40.2 Å box for the A_1 -AR and a 36.0 × 45.0 × 41.1 Å box for the A_{2A} -AR, encompassing the binding site and the extracellular region of the receptor. To ensure sufficient Monte Carlo sampling, docking “thoroughness” was set to 30. Other parameters were set as defaults. The docking procedure was repeated 5 times for each ligand, and the docking pose with the lowest ICM score was chosen. Subsequent molecular dynamics simulation was performed for the DPCPX· A_1 -AR complex.

Molecular Dynamics (MD) Simulations

MD simulations of the DPCPX· A_1 -AR complex were carried out with the NAMD2.10 (Phillips et al., 2005) package using CHARMM TIP3P model for water, CHARMM27 (Mackerell et al., 2004) for protein, lipids and salt ions, and CHARMM General Force Field (CGenFF) version 3.0.1 for the ligand. Force field parameters for DPCPX were generated using CGenFF program version 1.0.0 (Vanommeslaeghe et al., 2010). The BRIL on ICL3 was removed and the chain termini at the 211 and 220 positions were capped with neutral groups (N terminus acetyl and C terminus *N*-methylamide). All histidines were protonated on the epsilon nitrogen. The simulation system contained the A_1 -AR receptor, DPCPX, a lipid bilayer containing ~220 palmitoyl oleoyl phosphatidyl chloride (POPC) molecules generated using the membrane plugin of the VMD software (version 1.9.2) (Humphrey et al., 1996), and ~15800 water molecules. Sodium and chloride ions were added to neutralize the system, with extra NaCl added to reach a final concentration of 150 mM. The initial dimension of the system was 97 Å × 98 Å × 97 Å.

During the MD simulations, a 2 fs time step was used and full electrostatic interactions were computed every 6 fs. The particle mesh Ewald (PME) (Essmann et al., 1995) method was used to evaluate long-range electrostatics. Van der Waals and short-range electrostatic interactions were cut off at 12 Å. Langevin dynamics were used as a thermostat to maintain the temperature at a constant 310 K with a damping coefficient of 5 ps^{-1} . The Langevin piston Nosé-Hoover method was used to maintain pressure at 1 atm, period 200 fs, decay 50 fs. The SHAKE algorithm was used to constrain all bonds to hydrogen atoms. Coordinates were written to the output trajectory file every 10 ps.

The simulation was initiated with a 10000-step minimization, followed by 10 ns equilibration of lipid tails while the receptor, ligand, lipid head groups, water, and ion molecules were fixed. The whole system was then subjected to a 10000-step minimization, followed by 10 ns of equilibration with 10 $\text{kcal mol}^{-1} \text{Å}^{-2}$ harmonic-position restraints applied to all heavy atoms of the receptor and the ligand. Subsequently, the final unconstrained MD simulations was run for 104 ns. VMD version 1.9.2 was used for the visualization and analysis of the system. Molecular images were generated using PYMOL (Schrödinger).

Chemistry

4-((3-(8-Cyclohexyl-2,6-dioxo-1-propyl-1,2,6,7-tetrahydro-3H-purin-3-yl)propyl)carbamoyl)benzenesulfonic acid (MIPS2712)

DU172 (10.0 mg, 19.3 μ mol) was dissolved in THF (1 ml) and a lithium hydroxide solution (0.25 M in water, 2 mL). The reaction mixture was stirred in a sealed microwave tube at room temperature for the duration of 16 hr. The reaction mixture was purified by preparative column chromatography. The title compound was obtained as a white solid (7 mg, 70%). ^1H NMR (400.13 MHz, CD_3OD) δ 8.00 – 7.81 (m, 4H), 4.25 (t, J = 6.7 Hz, 2H), 4.01 – 3.92 (m, 2H), 3.45 (t, J = 6.5 Hz, 2H), 2.77 (tt, J = 11.9, 3.5 Hz, 1H), 2.10 (p, J = 6.6 Hz, 2H), 1.99 – 1.91 (m, 2H), 1.88 – 1.79 (m, 2H), 1.78 – 1.63 (m, 3H), 1.56 (ddd, J = 24.7, 12.4, 3.0 Hz, 2H), 1.45 – 1.33 (m, 2H), 1.32 – 1.22 (m, 1H), 0.96 (t, J = 7.5 Hz, 3H); m/z MS (TOF ES $^+$) 517.9 $[\text{M}+\text{H}]^+$; LC-MS t_R : 3.12; HRMS - $\text{C}_{24}\text{H}_{32}\text{N}_5\text{O}_6\text{S}$ $[\text{M}+\text{H}]^+$ calcd 518.2073; found 518.2067.

N-(3-(8-Cyclohexyl-2,6-dioxo-1-propyl-1,2,6,7-tetrahydro-3H-purin-3-yl)propyl)-4-(N,N-dimethylsulfamoyl)benzamide (MIPS2719)

DU172 (10.0 mg, 19.3 μ mol) was dissolved in a dimethylamine solution (2 M in THF, 3 mL). The reaction mixture was stirred in a sealed microwave tube at room temperature for the duration of 4 days. Then, the volatile components were removed under reduced pressure and the residue was purified by preparative column chromatography. The title compound was obtained as a white solid (8 mg, 76%). ^1H NMR (400.13 MHz, CD_3OD) δ 8.08 – 8.03 (m, 2H), 7.91 – 7.86 (m, 2H), 4.24 (t, J = 6.8 Hz, 2H), 3.98 – 3.91 (m, 2H), 3.46 (t, J = 6.5 Hz, 2H), 2.74 (tt, J = 11.9, 3.5 Hz, 1H), 2.72 (s, 6H), 2.09 (p, J = 6.7 Hz, 2H), 1.97 – 1.90 (m, 2H), 1.84 – 1.76 (m, 2H), 1.75 – 1.60 (m, 3H), 1.54 (ddd, J = 24.7, 12.4, 3.0 Hz, 2H), 1.43 – 1.31 (m, 2H), 1.30 – 1.17 (m, 1H), 0.94 (t, J = 7.5 Hz, 3H); m/z MS (TOF ES $^+$) 544.9 $[\text{M}+\text{H}]^+$; LC-MS t_R : 3.28; HRMS - $\text{C}_{26}\text{H}_{37}\text{N}_6\text{O}_5\text{S}$ $[\text{M}+\text{H}]^+$ calcd 545.2546; found 545.2547.

Statistical Analysis

All measures of drug affinity or potency were estimated as negative logarithms. Statistical comparisons were performed in GraphPad Prism 6.0. using either an unpaired t test or a one way ANOVA, followed by a Dunnett's post-test, as indicated in the main text.

DATA AND SOFTWARE AVAILABILITY

The accession number for the coordinates and structures factors of the A1_DU172 complex reported in this paper is PDB: 5UEN.

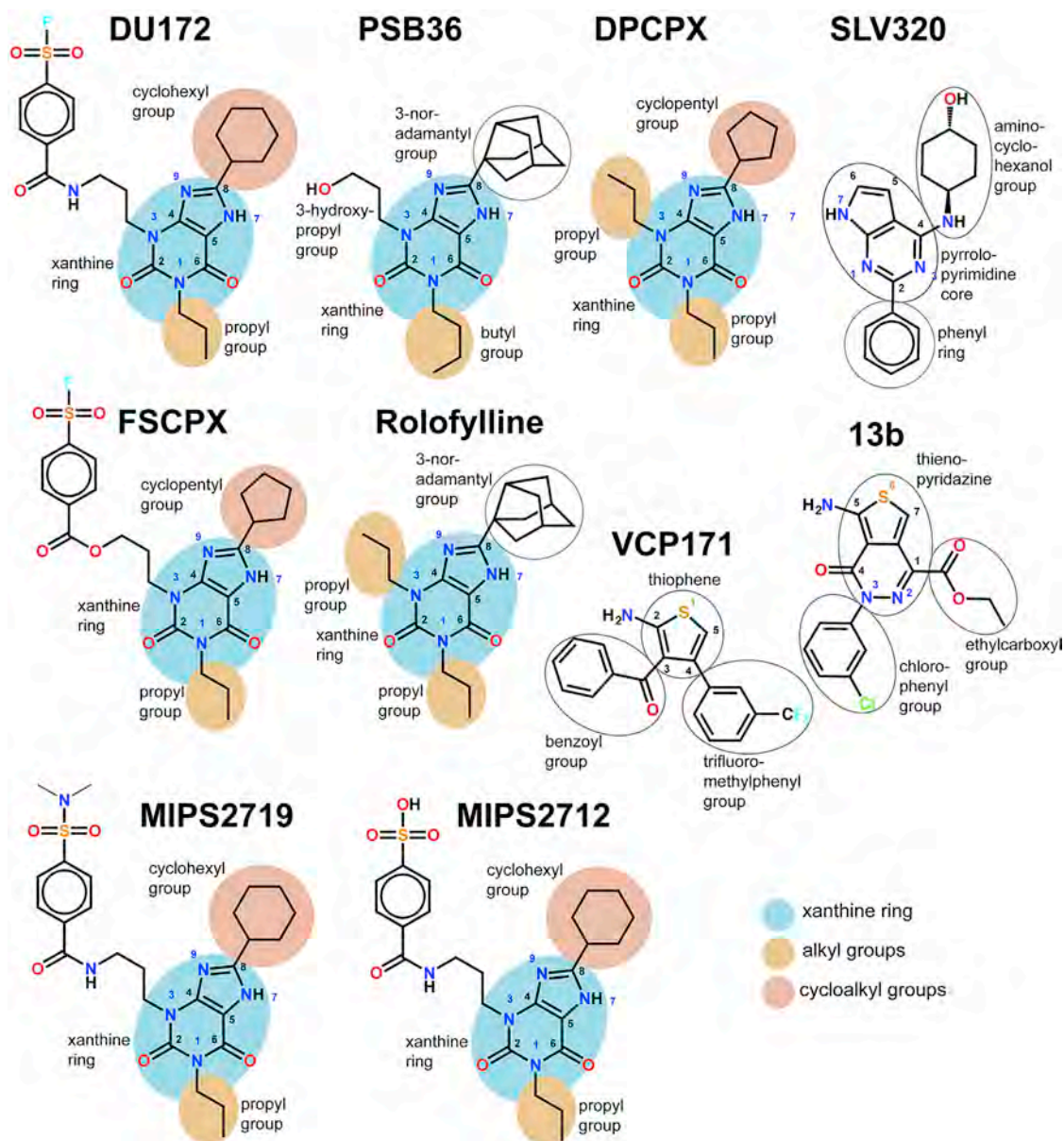


Figure S1. Selective A₁-AR Ligands Investigated in This Study, Related to Figures 1, 2, 3, 6, 7, S2, S6, and S7

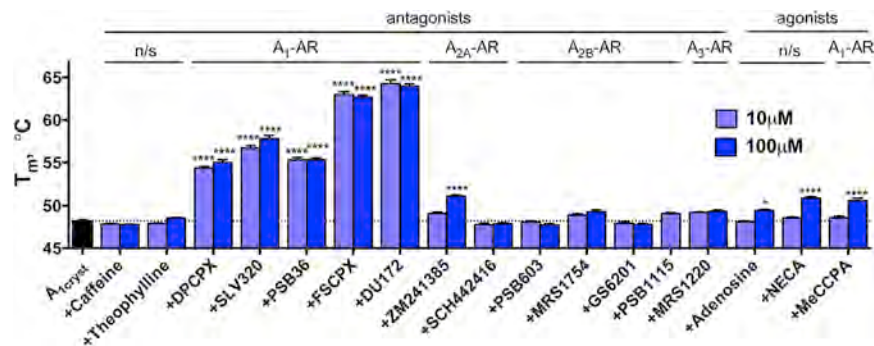


Figure S2. Melting Temperature (T_m) of the Crystallized A_1 -AR Construct A_{1cryst} in the Presence of Various AR Agonists and Antagonists, Related to Figure 2

Selective A_1 -AR antagonists resulted in greater thermostability compared to agonists, nonselective (n/s) antagonists, or subtype-selective antagonists of other ARs (A_1 , A_{2A} , A_{2B} , and A_3). The greatest increase in T_m was observed with the covalent antagonists, FSCPX or DU172. Data points are the mean \pm SEM from three independent experiments performed in duplicate. * $p \leq 0.05$, **** $p \leq 0.0001$ (One-way ANOVA, Dunnett's post test, compared to T_m of A_{1cryst} in the absence of drugs).

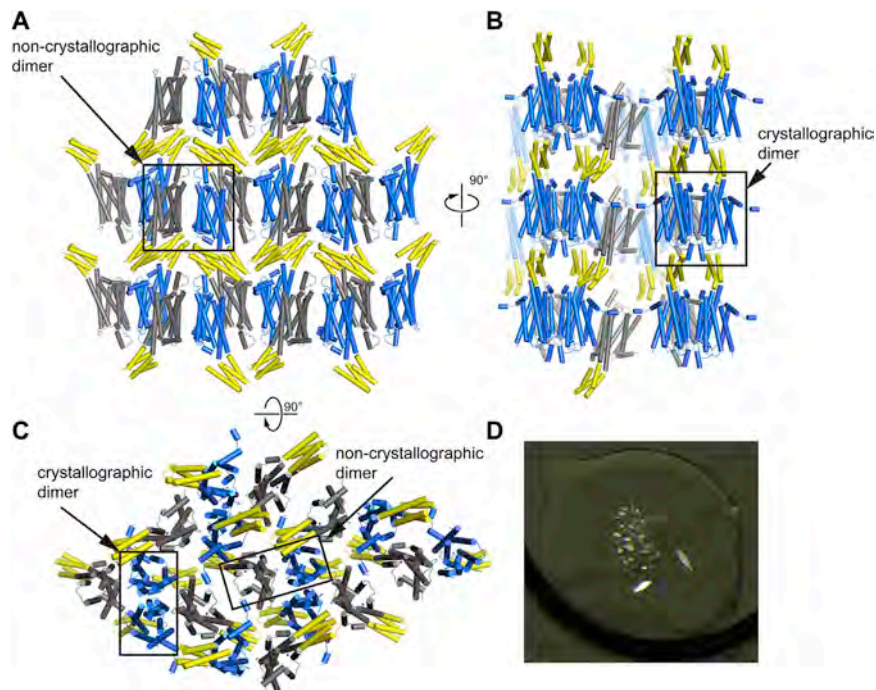


Figure S3. Crystals and Crystal Packing of the A₁-AR, Related to Figures 2 and 3

(A–C) Contacts within the A₁-AR crystals. (A and B) Receptor molecules are organized into layers intercalated with layers of BRIL packed into the solvent channels. (C) Packing within a single layer. Receptor is colored marine for chain A and gray for chain B, BRIL is shown in yellow. (D) Example of A₁-AR crystals in an LCP drop used for data collection.

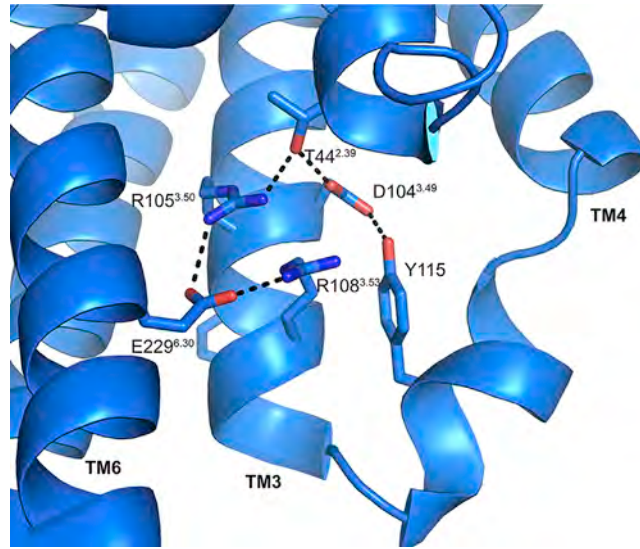


Figure S4. Conformation of “Ionic Lock” Residues in the A₁-AR Crystal Structure, Related to Figure 2

Similar to interactions observed in A_{2A}-AR (PDB: 4EIY), D104^{3.49} in the DRY motif forms H-bond (dashed line) interactions with T44^{2.39} and Y115 in the helical region of ICL2. However, a change in the rotamer conformation relative to the A_{2A}-AR, orients the side chain of E229^{6.30} in a position to form ionic interactions with R105^{3.50} (part of the DRY motif), and R108^{3.53}. In contrast to the ionic lock in rhodopsin, D104^{3.49} and R105^{3.50} in the A₁-AR are too far apart for salt bridge formation (4.5 Å). However, they interact via hydrogen bonding with T44^{2.39}.

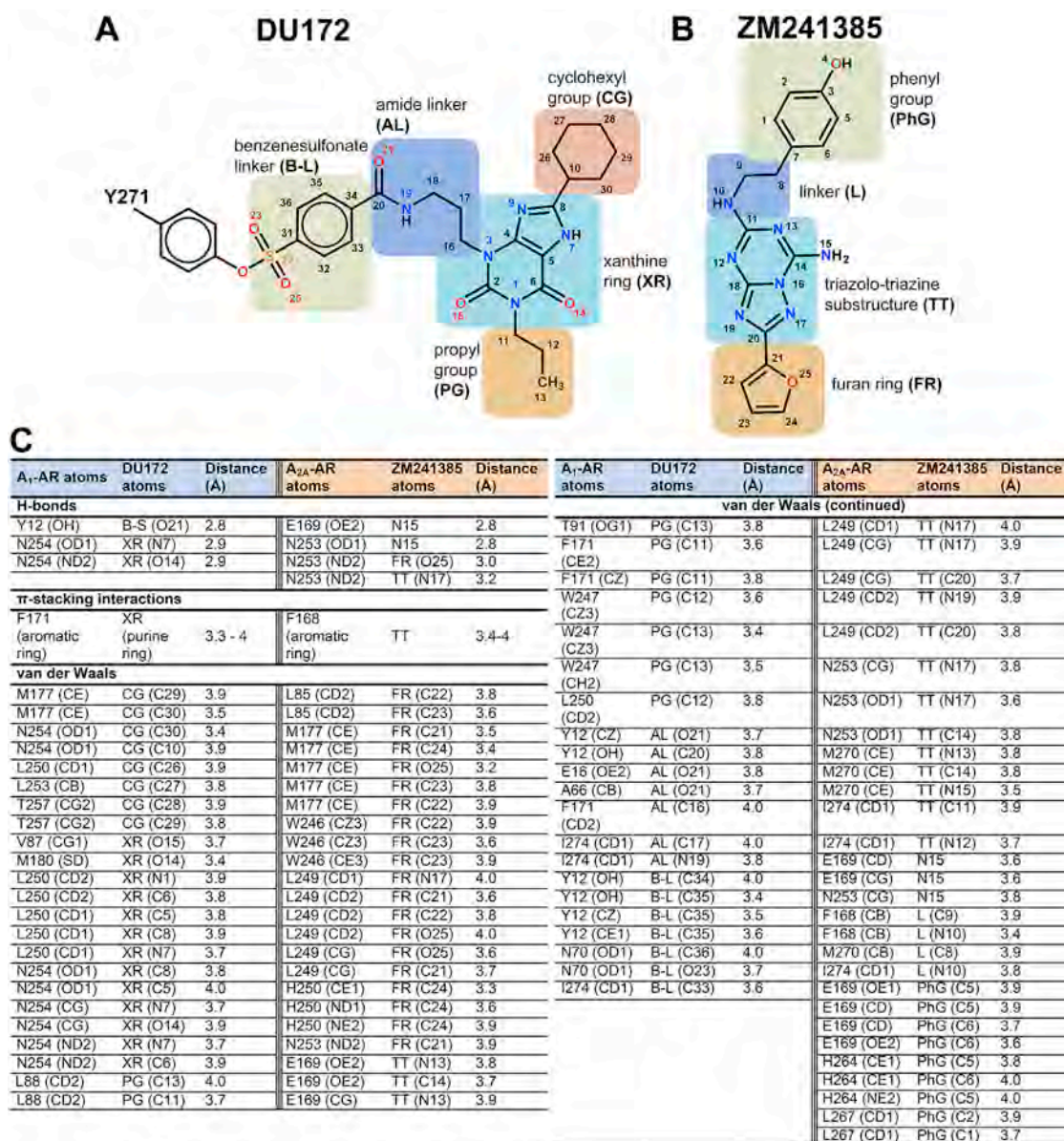


Figure S5. Noncovalent Contacts between Ligands and Receptors in the A₁-AR·DU172 and A_{2A}-AR·ZM241385 Complexes, Related to Figure 4

(A and B) Structures of DU172 and ZM241385. Atom labels and chemical groups are indicated.

(C) Contacts between receptor and ligand atoms within 4 Å from each other. AL, amide linker; B-L, benzenesulfonate linker; CG, cyclohexyl group; FR, furan ring; L, linker; PG, propyl group; PhG, phenyl group; TT, triazolo-triazine substructure; XR, xanthine ring.

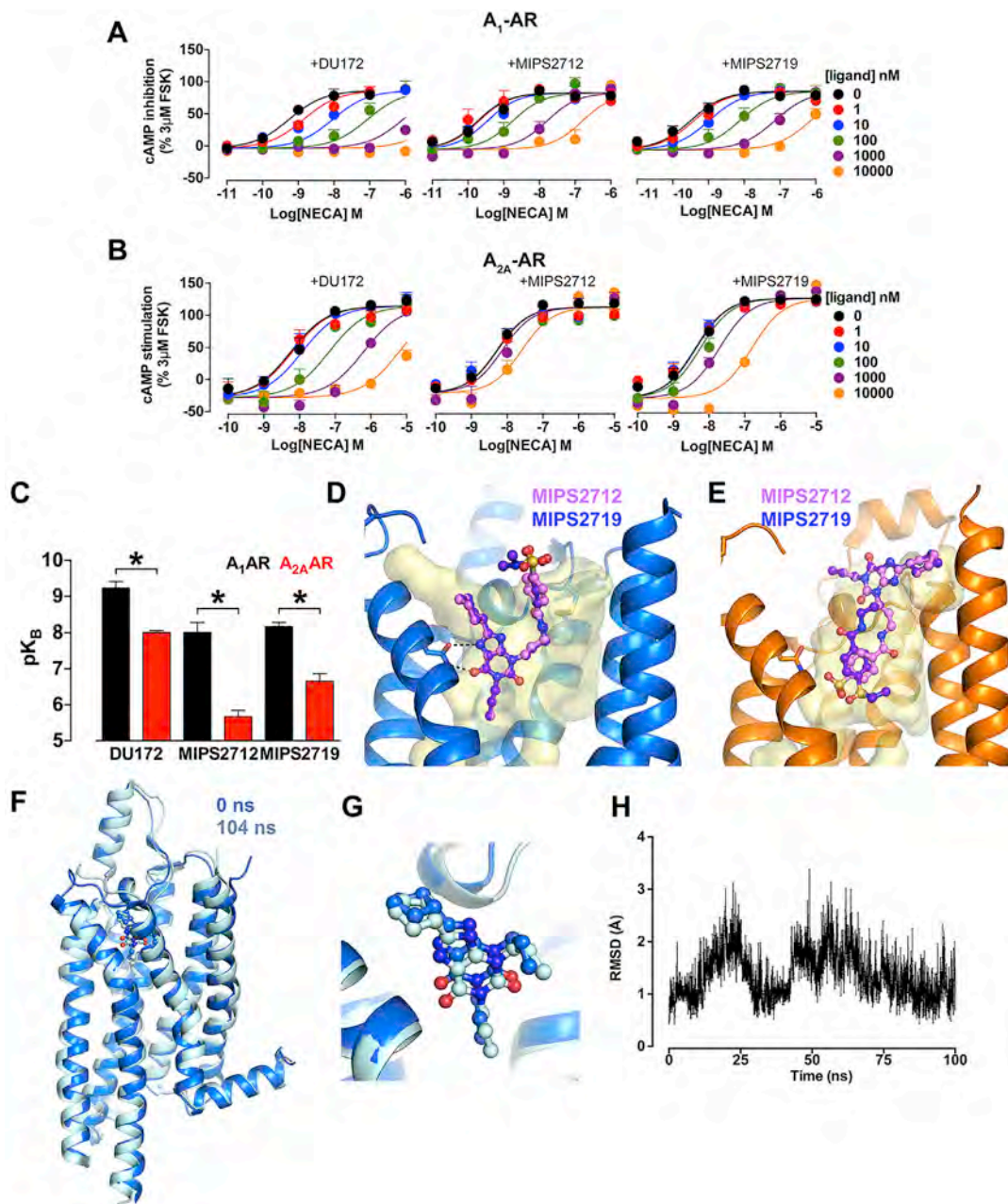


Figure S6. The Wide Binding Site Pocket Is Preserved in A_1 -AR Bound to Reversible Ligands, Related to Figures 6, 7, S1, and Table S5

(A and B) (A) Inhibition of forskolin-stimulated cAMP accumulation or (B) direct stimulation of cAMP accumulation by stably expressed (A) A_1 -AR or (B) A_{2A} -AR by NECA in the presence of different concentrations of DU172 or its reversible analogs (MIPS2712 or MIPS2719).

(C) Functional binding affinities for DU172, MIPS2712 and MIPS2719, determined by Gaddum/Schild analysis with the Schild slope constrained to 1. The estimated negative logarithms of the dissociation constants for each ligand were significantly different for the A_1 -AR and A_{2A} -AR (pK_B 9.2 ± 0.2 and 8.0 ± 0.1 , respectively, for DU172, 8.0 ± 0.3 and 5.7 ± 0.2 , respectively, for MIPS2712 and 8.2 ± 0.1 and 6.7 ± 0.2 , respectively, for MIPS2719). Data points are the mean values \pm SEM from three independent experiments performed in duplicate. * $p \leq 0.05$ (Unpaired t test comparing the indicated mutant construct to its respective wild-type).

(D and E) Lowest energy docking conformations for the A_1 -AR (D) and A_{2A} -AR (E) bound to MIPS2712 or MIPS2719. The A_1 -AR receptor is shown in marine, A_{2A} -AR as orange, the binding pocket is shown as a yellow surface. Docked ligands are shown as stick-ball models with carbon atoms colored in violet (MIPS2712) or purple blue (MIPS2719). Dashed lines represent H-bonding to N254^{6,55}. (F-H) Molecular dynamics simulation of DPCPX docked into the A_1 -AR structure.

(F) Overall view of the receptor at the beginning (0 ns) and the end (104 ns) of the simulation. RMSD = 1.12 Å.

(G) Changes in DPCPX position between the beginning (0 ns) and the end (104 ns) of the simulation.

(H) RMSD differences of DPCPX position during simulation. Receptor backbone and DPCPX carbon atoms are shown in marine at 0 ns, and as light cyan at 104 ns. N, O, S, atoms are colored in blue, red, yellow, respectively.

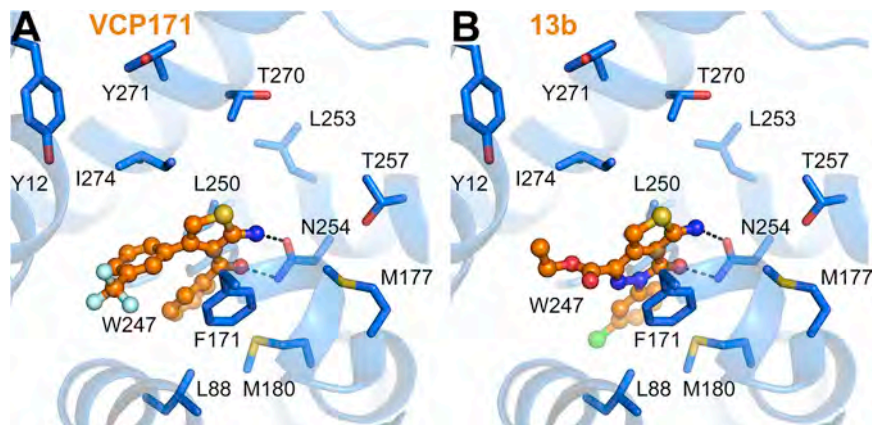


Figure S7. Lowest Energy Docking Conformations of A₁-AR Allosteric Modulators in the Inactive A₁-AR Structure, Related to Table S5 and Figures 7 and S1

(A and B) (A) VCP171 and (B) compound 13b. Docked ligands are shown as stick-ball models with carbon atoms colored in orange; binding site residues as sticks with marine carbon atoms; N, O, S, F, and Cl atoms are colored in blue, red, yellow, cyan, and green, respectively. Dashed lines represent H-bonding to N254^{6,55}.

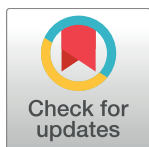
RESEARCH ARTICLE

Structural features embedded in G protein-coupled receptor co-crystal structures are key to their success in virtual screening

Thomas Coudrat, Arthur Christopoulos, Patrick Michael Sexton*, Denise Wootten*

Drug Discovery Biology, Monash Institute of Pharmaceutical Sciences and Department of Pharmacology, Monash University, Royal Parade, Parkville, Victoria, Australia

* denise.wootten@monash.edu (DW); patrick.sexton@monash.edu (PMS)



OPEN ACCESS

Citation: Coudrat T, Christopoulos A, Sexton PM, Wootten D (2017) Structural features embedded in G protein-coupled receptor co-crystal structures are key to their success in virtual screening. PLoS ONE 12(4): e0174719. <https://doi.org/10.1371/journal.pone.0174719>

Editor: Yogendra Kumar Mishra, Institute of Materials Science, GERMANY

Received: November 8, 2016

Accepted: March 14, 2017

Published: April 5, 2017

Copyright: © 2017 Coudrat et al. This is an open access article distributed under the terms of the [Creative Commons Attribution License](https://creativecommons.org/licenses/by/4.0/), which permits unrestricted use, distribution, and reproduction in any medium, provided the original author and source are credited.

Data Availability Statement: All relevant data are within the paper and its Supporting Information files.

Funding: This research was supported by the National Health and Medical Research Council of Australia (NHMRC), award numbers APP1055134 and APP106101044 to PMS and APP1089966 to DW, a NHMRC Career Development Fellow. This research was also supported by Melbourne Bioinformatics at the University of Melbourne, grant number VR0024 to PMS. PMS is a NHMRC

Abstract

Structure based drug discovery on GPCRs harness atomic detail X-ray binding pockets and large libraries of potential drug lead candidates in virtual screening (VS) to identify novel lead candidates. Relatively small conformational differences between such binding pockets can be critical to the success of VS. Retrospective VS on GPCR/ligand co-crystal structures revealed stark differences in the ability of different structures to identify known ligands, despite being co-crystallized with the same ligand. When using the OpenEye toolkit and the ICM modeling package, we identify criteria associated with the predictive power of binding pockets in VS that consists of a combination of ligand/receptor interaction pattern and predicted ligand/receptor interaction strength. These findings can guide the selection and refinement of GPCR binding pockets for use in SBDD programs and may also provide a potential framework for evaluating the ability of computational GPCR binding pocket refinement tools in improving the predictive power of binding pockets.

Introduction

G protein-coupled receptors (GPCRs) form the largest protein superfamily in mammalian genomes [1,2] and play a crucial role in physiological processes through mediating the cell's response to extracellular signals [3]. Among the members of this family are receptors for hormones, neurotransmitters, small peptides and even photons of light [4]. Their implication in various pathophysiology has made them attractive targets, with over 40% of currently marketed drugs targeting this family of proteins [5]. GPCRs can be selectively activated and inhibited via their extracellular face by endogenous agonists and inhibitors, respectively.

Dysregulation of this finely tuned machinery is a common cause of pathology that can be alleviated by intervention with synthetic ligands acting at GPCRs to recover normal function [6].

Design of novel small molecule chemical compounds that target a specific GPCR with high affinity and selectivity is challenging. Lead compounds have been identified in the past largely through high-throughput screens (HTS), where a physical assay is used to rank a large library of compounds to identify chemical scaffolds that can be optimized. Running an HTS on several million compounds is expensive, and in recent years there has been a growing interest in

Principal Research Fellow, and AC a NHMRC Senior Principal Research Fellow. The funders had no role in study design, data collection and analysis, decision to publish, or preparation of the manuscript.

Competing interests: The authors have declared that no competing interests exist.

computational methods that help focus the physical screen on a subset of molecules predicted to bind the target of interest. These can be divided into ligand-based drug discovery (LBDD) and structure-based drug discovery (SBDD) methods. LBDD methods link the physicochemical properties of known active molecules with their measured activity on the GPCR target, whereas SBDD methods can be readily applied to a new GPCR target for which there is limited ligand data. As they rely on the 3D structure of the target protein, SBDD methods offer better potential for identification of novel ligand scaffolds through virtual screening (VS).

SBDD requires detailed understanding of the molecular interactions between a ligand and its receptor. Ligand docking is a computationally cost-effective method that predicts the conformation of a ligand inside the binding pocket of the target protein, based on the physicochemical properties of both the ligand and the target. VS by docking ranks libraries of small molecules based on a docking score, which is followed by experimental validation of the top ranked virtual hits predicted to be enriched in active compounds [7]. VS has extensively and successfully been used on many soluble protein drug targets (e.g. enzymes) and more recently on GPCRs [8].

The increased success in recent years for GPCR SBDD is in part due to experimental breakthroughs in GPCR X-ray crystallography, opening up the GPCR structural landscape at the atomic level. Through the GPCR X-ray crystallography revolution, a total of 154 GPCR structures have been obtained, including 38 unique structures, providing atomic details on the arrangement of their seven transmembrane (7TM) helices [9]. Additionally, 73 unique ligand/receptor complexes provide critical information on ligand interaction patterns, including differences between agonists and inhibitors. Resolution of these crystal structures is a metric that is often used to evaluate the quality of the overall X-ray crystal structure with a higher resolution guiding greater accuracy of the position of atoms in the resulting model. Further assessment of fit between the experimental data, the electron density map, and the generated model of the co-crystal structure, can be performed on a residue per residue basis using real-space correlation coefficients (RSCCs).

The choice of GPCR structure for use in SBDD is critical for the outcome of the SBDD program. Indeed, even small conformational changes in a binding pocket, induced by the stabilizing ligand can have a marked effect on VS results as observed in studies where GPCR X-ray crystal structures stabilized by a ligand of a given pharmacology preferentially select new compounds with that same pharmacology (i.e. agonist vs inhibitor) [10,11]. In these cases, ligand/protein interaction fingerprints (IFPs) may be useful to shift the selectivity of a crystal structure in VS towards that of a different pharmacology, if the desired IFP is known [11]. This was exemplified in a recent case study using β -adrenoceptor crystal structures where the predicted IFP for a full agonist was successful at screening for agonists over antagonists in VS performed on crystal structures co-crystallized with either full agonists, partial agonists, antagonists or inverse agonists [11]. However, despite this success, the selected crystal structure still influenced the extent to which the IFP was able to shift the selectivity and the final enrichment values within these screens.

Furthermore, two co-crystal structures of the same GPCR bound by the same small molecule ligand do not always have identical binding pocket shapes and ligand/receptor interaction patterns [11,12]. This is most clearly exemplified when looking at the different orientations of ZM-241385 (ZM) in the adenosine A_{2A} receptor (AA2AR) binding pockets, that may arise due to different protein engineering methods, such as insertions and/or thermostabilizing mutations [13] or different crystallization conditions, for example, differences in pH [14]. These can lead to subtle distinctions in receptor side-chains and ligand conformation, in turn resulting in different IFPs in the co-crystal structure. There are now several GPCR structures available that are bound to the same ligand, offering an important view of the variability that can

occur between GPCR X-ray structures. These structures can be grouped based on their bound ligand (Table 1).

The increased accessibility of GPCR structures is paired with the availability of annotated databases of compounds that are known to be active on these GPCRs. Compound databases with linked GPCR activity such as ChEMBL [29], ZINC [30], PubChem [31], GLIDA [32], IUPHAR [33] are of crucial importance in the early stage of a SBDD program. The capacity of GPCR binding pockets to assign high docking scores to known active compounds is one of the metrics that evaluate these binding pockets before prospective VS. Furthermore, developing decoy libraries that have similar physicochemical properties to the known compounds, but are not validated ligands of a particular GPCR, allows the evaluation of GPCR binding pockets for their capacity to recover known ligands over decoys. The GPCR ligand library and GPCR decoys database (GLL/GDD) was generated to run such retrospective VS, where for each known ligand there is a set of 39 decoy ligands matching its physical properties [34].

Another important consideration for GPCR SBDD programs revolves around the validation of a GPCR structure that relies known ligands. Small molecules often have more than one chiral center, leading to multiple combinations of molecules with identical composition but different geometries or enantiomers. Chiral molecules are often not tested in biological assays as pure enantiomeric forms, but rather in a racemic mix containing all possible enantiomers. Hence when a compound's pharmacology is identified, the exact active enantiomer is often not known, and therefore the activity is attributed to the racemic mix. However, the enantiomeric state can have a drastic effect on activity, for example, between the identification of an active allosteric modulator and inactive compound at the muscarinic acetylcholine receptor 5 [35] or two different biased agonists at the β -2 adrenoceptor (B2AR) [36]. Properly recording and dealing with enantiomeric states is therefore an important consideration in GPCR SBDD programs.

In this study, we sought to establish criteria that could be used to guide the selection of a crystal structure for use in VS, when more than one structure is available. Seven GPCR/ligand co-structures, where there is more than one structure crystallized with the same ligand, were selected and evaluated using VS, ranking known ligands relative to decoys and known agonists relative to inhibitors. Using the Molsoft ICM modeling software [37] for docking, we report stark differences between the performance of GPCRs co-crystallized with the same ligand, for known ligand enrichment, as well as selectivity for agonists or inhibitors. Furthermore, using the ICM modeling software [37] and the OpenEye OEChem toolkit [38], we extracted structural and conformational information about each crystal structure and identified key criteria that can influence the predictive power of binding pockets. These include a combination of ligand/receptor interaction patterns and predicted interaction strength in the co-crystal X-ray structure used for screening. These findings can guide the selection and refinement of binding pockets for use in GPCR SBDD programs.

Methods

X-Ray co-crystal binding pocket selection and preparation

We selected seven GPCR co-crystal structures for which the bound ligand is reported in at least two GPCR co-crystal structures. The selected structures feature three agonist-bound and four inhibitor-bound GPCRs including AA2AR, β -1 adrenoceptor (B1AR), B2AR and δ -opioid receptor (DOR) [13±28], all class A GPCRs. Details regarding the resolution, protein engineering methods used for stabilization as well as mutated or missing residues are listed in Table 1. In this study, we investigated these ligand/receptor complexes and how small differences between co-crystal structures could influence VS performance. In structures where

Table 1. GPCR X-ray crystal structures co-crystallized with a common orthosteric ligand.

GPCR	PDB ID and chain(s) used	Orthosteric ligand name and abbreviation	Resolution (Å)	Ligand pharmacology	Other molecules	Insertion	Stabilization		References
							Missing side-chain(s)	Mutation(s)	
ADORA2A	4UG2 (A, B)	CGS-21680 (CGS)	2.60	selective agonist	dimer	-	chain A: R222, S223, chain B: E219, R220, R222, S223	L48A, A54L, T65A, Q89A	Lebon et al. 2015 [15]
	4UHR		2.60			-	L216, E219	L48A, A54L, T65A, Q89A	Lebon et al. 2015 [15]
	3EML	ZM-241,385 (ZM)	2.6	high-affinity subtype selective antagonist	-	T4L (ICL3)	-	-	Jaakola et al. 2008 [16]
	3PWH		3.3		-	-	-	A54L, T88A, R107A, K122A, L202A, L235A, V239A, S277A	Doré et al. 2011 [13]
	3VG9		2.70		antibody Fab 2838	-	-	N154Q	Hino et al. 2012 [17]
	3VGA		3.10		antibody Fab 2838	-	R220, R222	N154Q	Hino et al. 2012 [17]
ADRB1	4E1Y		1.8		-	BRIL (ICL3)	Q148, E161, R220, R293	M215W, H310I, R314L	Liu et al. 2012 [18]
	2Y00 (A, B)	Dobutamine (DOB)	2.50	agonist	dimer	-	-	R68S, M90V, C116L, Y227A, A282L, F327A, F338M, C358A	Warne et al. 2011 [14]
	2Y01 (A, B)		2.60		dimer	-	chain A: L83	R68S, M90V, C116L, Y227A, A282L, F327A, F338M, C358A	Warne et al. 2011 [14]
	2VT4 (B)	Cyanopindolol (CYP)	2.70	weak partial agonist	tetramer	-	-	R68S, M90V, C116L, Y227A, A282L, F327A, F338M, C358A	Warne et al. 2008 [19]
	2YCX (A)		3.25		dimer	-	-	R68S, M90V, C116L, Y227A, A282L, F327A, F338M, C358A	Moukhametzanov et al. 2011 [20]
	2YCY (A)		3.15		dimer	-	-	R68S, M90V, C116L, Y227A, A282L, F327A, F338M, C358A	Moukhametzanov et al. 2011 [20]
ADRB2	4BVN		2.10		-	-	-	R68S, M90V, C116L, I129V, Y227A, A282L, D322K, F327A, F338M, Y343L, C358A	Miller-Gallacher et al. 2014 [21]
	3P0G	BI-167107 (BI)	3.5	agonist	Camelid antibody fragment: nanobody Nb80	-	-	E27Q, N187E	Rasmussen, Choi, et al. 2011 [22]
	3SN6		3.2		Heterotrimeric Gs protein. Nanobody Nb35.	T4L (N-term)	R63, K97, T98, W99, F101, K149, R175, D192, F193, F194, T195, K267, H269, K270, L272, Q299, N301, L302, R304, E306, R333	M96T, M98T, N187E	Rasmussen, DeVree, et al. 2011 [23]
	4LDE		2.79		Nanobody Nb6B9	T4L (N-term)	K60, E62, K149, F223, Q224, Q231, K263, F264, K270	M96T, M98T, N187E, C265A	Ring et al. 2013 [24]
	2RH1	Carazotol (CAR)	2.40	inhibitor	-	T4L (ICL3)	D29	N187E	Cherezov et al. 2007 [25]
	4GBR		3.99		-	T4L (N-term)	-	M96T, M98T, N187E	Zou, Weis, and Koblika 2012 [26]
DOR	4EJ4	Naltrindole (NAL)	3.4	inhibitor	-	T4L (ICL3)	K79, V154, K155, R192, Q201, R241, S242, R244, K252, R291, R292, E323, N324, R327	M80L, R190Q, D290N (*)	Granier et al. 2012 [27]
	4N6H		1.8		-	BRIL (N-term)	R41, V154, L157, K166, R192, D193, K250, E251, K252, R254, K326, R330, Q331, R334, K335	P37S	Fenalti et al. 2014 [28]

For each structure, the name of the GPCR, the PDB ID accession number, the name of the bound orthosteric ligand and the resolution of the structure are listed. Further information relating to the components contributing to the stabilization of the structure are also included; these include details on the ligand pharmacology and selectivity, information about molecules used for receptor stabilization as well as notes about dimer state where relevant, insertion molecule (and position of the insertion), residues for which at least one heavy-atom side-chain is missing from the structure and mutations present in 7TM domain structure (residues in bold refer to residues in the binding pocket: combination of residues within 5 Å of bound ligands). References to each X-ray crystal structure are also provided. (*) residues different compared to the *human* DOR gene).

<https://doi.org/10.1371/journal.pone.0174719.t001>

crystal symmetry yielded oligomers, the representative monomer described for that X-ray structure was used (2VT4 (B chain), 2YCX (A chain) and 2YCY (A chain)). In cases where different IFPs were observed amongst monomers, each monomer was screened as a separate binding pocket, and the chain was used as a suffix: 4UG2-A and 4UG2-B, 2Y00-A and 2Y00-B, 2Y01-A and 2Y01-B.

Mutations introduced for crystallography and missing side-chains present within 5 Å radius of the bound ligand are critical to small molecule docking and in turn could affect comparisons of VS performance between GPCR co-crystals. These are shown in Table 1. In the case of AA2AR CGS-21680-bound (CGS) structures, all three binding pockets contain the same mutation, in which case comparison is valid. Among AA2AR ZM-bound binding pockets, 3PWH was crystallized making extensive use of thermostabilizing mutations. This includes only one mutation within 5 Å of ZM, T88A. In this case, no polar contact is made between threonine 88 and ZM in other pockets and its position deep inside the binding pocket makes it unlikely to influence docking experiments. Finally, missing side-chains in the B2AR BI-bound 3SN6 were added using the ICM software and were optimized in presence of BI. This optimization protocol was used on all B2AR BI-bound pockets.

GPCR models were prepared from the deposited PDB files as follows: (i) non-GPCR residues, and non-ligand molecules (including waters) were removed. (ii) GPCR residues were renumbered in cases where the numbering didn't match the gene numbering (4LDE and 4GBR) (iii) Ligand/receptor complex was converted to an ICM object that adds hydrogen atoms and missing side-chains and flips the asparagine, glutamine and histidine side-chains to improve molecular interactions. The conversion to an ICM object is a necessary step for energy calculations performed on the molecular model during docking. This optimization did not have a notable impact on VS performance in all cases tested (S1 Fig), but did have a significant impact on the conformation of the side-chains added by ICM when these were missing from their original X-ray structure. Therefore, it was applied on B2AR BI-bound pockets as described above. Waters are removed as X-ray structures with a range of resolution are compared, most with resolution too low to identify water positions. Although binding pocket waters are important for docking when their positions are known, this is rarely the case for GPCR X-ray structures, thus deleting waters from all binding pockets enables an even comparison on the binding pockets' VS performance.

Ligand libraries

Ligand libraries were selected from the GPCR ligand library and GPCR decoys database (GLL & GDD) [34]. The co-crystallized ligand of each GPCR complex used in this study were added to their corresponding GLLs, and the lists were manually inspected and errors removed. The ICM software was used to manage the GLL and GDD library, which were downloaded and processed in SDF format. These libraries, hereafter termed the original GLL/GDD, store a single 3D enantiomer to represent each ligand. We identified these libraries in many instances contained the wrong enantiomer for known ligands and therefore may also contain the wrong enantiomer for ligands where the enantiomeric state is unknown. We decided to sample and dock all enantiomeric forms for each ligand in the GLL/GDD. We thus used ICM to generate a new library, hereafter termed the racemic GLL/GDD, which involved converting the original GLL/GDD to 2D depiction and assigning racemic flags to the molecules containing at least one chiral center. By docking all enantiomeric states for each racemic mix, we ensure that the right enantiomer is evaluated. In some cases, this library processing generated doubles in the racemic GLL/GDD, as some molecules in the original GLL/GDD were present in more than one enantiomeric state. These molecules were counted only once in the VS analysis. We used

the racemic GLL/GDD to make observations and draw conclusions, but we also screened all binding pockets with the original GLL/GDD for comparison (S2 Fig).

Each known ligand library was clustered based on chemotype similarity and a maximum of 4 clusters (A, B, C and D) were selected to illustrate the chemotype variety of the library, while the cluster 'other' was populated with the remaining molecules. We opted to analyze known ligand diversity based on a set number of clusters instead of a set cutoff value in order to generate a manageable number of clusters for analysis. As resulting cutoffs vary amongst different libraries, these are only used to comment on chemotype preference within a library and are not intended to be used for comparison amongst libraries. Clusters containing the X-ray ligand were annotated with its three letter ligand name, and the center of each chemotype cluster is identified with an asterisk (S3, S4, S5 and S6 Figs). The center of each cluster was used to illustrate the chemotype of that cluster, and the chiral center composition of each chemotype was calculated (S1 Table).

Virtual screening setup

VS was performed using ICM version 3.7-3b. The docking box was defined by selecting all residues within 4 Å of the crystal ligand, which was subsequently removed from the model. Each ligand from the library was docked three times. VS parameters were left as default except for the following parameters that were modified to include all screened molecules: maximum number of hydrogen bond donor, set to 15; maximum ligand size, set to 1000 (calculated as 15 x number of heavy atoms); maximum number of hydrogen bond acceptor/donor, set to 20; maximum predicted logP value set to 15; minimum predicted logP value, set to -10. Additional parameters identified in the laboratory to improve VS outcome were modified, including ring sampling parameter set to 1, charge mode of ligand ionizable groups set to auto. The effort value influences the length of the docking simulation and was set to 5 throughout this study, unless stated otherwise. Finally, the racemic GLL/GDD was screened using the following parameters: database type set to 'mol 2D' and racemic sampling set to 'yes'. The latter performs a sampling of all enantiomers for that ligand, all of which are docked, and the best scoring enantiomer is returned as a result.

Virtual screening analysis

Docking of each ligand involves a conformational sampling performed by a biased probability Monte Carlo procedure [39]. Given the stochastic nature of this procedure, docking was repeated three times and the best scoring repeat was retained to represent that ligand in terms of conformation and docking score. VS results were visualized using receiver operating characteristic (ROC) curves, which show the percentage of true positives as a function of the percentage false positives recovered in the VS ranked ligand library. Two types of ROC curves were used to discriminate (i) known ligands against decoys, and (ii) agonists against inhibitors (or vice versa). Binding pockets were compared by their capacity to rank true positives higher relative to false positives, with an emphasis on early recovery. In order to compare ROC curves based on these parameters, the normalized square root area under the curve (NSQ_AUC) was calculated as described previously [40] using Eq 1.

$$NSQ_{AUC} = 100 * \frac{SQ_{AUC} - SQ_{AUC}_{random}}{SQ_{AUC}_{perfect} - SQ_{AUC}_{random}} \quad (1)$$

Its definition builds on the area under the curve (AUC) definition by putting emphasis on the early recovery, as well as normalizing the results between perfect recovery (NSQ_AUC = 100) and random recovery (NSQ_AUC = 0). Negative NSQ_AUC values

represent ROC curves that discriminate for false positives. In order to establish statistical significance in VS performance, we have also calculated the mean NSQ_AUC \pm standard error of the mean (S.E.M.) of the three docked library repeats. For more than two binding pocket comparisons, we performed a one-way ANOVA followed by a Tukey multiple comparison test (S2 and S6 Tables). For comparisons between two binding pockets, we performed an unpaired t-test with Welch's correction (S7 and S8 Tables).

An additional measure of VS performance was used to assess the known ligand enrichment within fractions of the ranked screened database (combined known ligands and decoys). In this study, enrichment factors (EFs) [41] were used to assess the early recovery of a binding pocket for each known ligand chemotype of the target receptor described above. Thus EF values were plotted for each chemotype at 2, 5 and 10% of the ranked screened database noted EF2, EF5 and EF10, respectively (S7, S8, S9, S10, S11, S12 and S13 Figs). Eq (2) describes the calculation of EF at a fraction of the ranked screened database x (i.e. 2, 5, or 10), where TP represents the total count of true positives of a specific chemotype and N , the total count of screened compounds in the database. TP_x represents the count of true positives of that chemotype within the fraction x of the screened database, and N_x represents the count of compounds within that fraction.

$$EF_x = \frac{TP_x/N_x}{TP/N} \quad (2)$$

All tasks described in the present section, namely the setup of VS experiments including preparation of target and libraries, execution on clusters, extraction of data and plotting of ROC curves with NSQ_AUC calculations as well as EF bargraphs were performed using the open source set of Python (www.python.org) scripts `toolbx_vs` (https://github.com/thomas-coudrat/toolbx_vs). This uses the following libraries: Matplotlib [42], Numpy [43] and scikit-learn [44].

Binding pocket analysis

Each group of GPCR/ligand complexes were first superimposed. Root mean square deviations (RMSDs) were calculated on heavy atoms. Two RMSD comparisons were performed: ligand RMSD and binding pocket RMSD. The ligand RMSD was calculated, without further superimposition, in order to capture their relative orientation but also their relative position within the binding pocket. The binding pocket was defined as the combination of residues within 5 Å of the bound ligand in all ligand/receptor complexes compared. The binding pocket RMSD was calculated on heavy atoms of matching residues.

Docking of the cognate ligand for each binding pocket was performed using the same docking parameters as described for the VS. The score and conformation of the best scoring docked pose out of the three repeats was selected. The score of this docked pose was extracted and the RMSD to the crystal ligand of that binding pocket calculated as described above.

ICM offers an interactive scoring function that outputs a predicted score for a ligand/receptor complex in-place, with no conformational sampling. ICM scoring contains energy terms, namely solvation electrostatics and internal forcefield strain energy change, which are calculated as a difference between the ligand free and bound state. In regular scoring of a ligand/receptor complex during a docking procedure, ICM samples the ligand conformation prior to docking and the lowest energy conformation is used as the reference free state for energy calculation. As no sampling is performed in ICM's interactive scoring, this score should not directly be compared to docking scores. In this study, ICM's interactive scoring on X-ray ligand/receptor complexes was used in order to evaluate their predicted interaction strength.

ICM's interactive scoring was subsequently evaluated on docked ligand/receptor complexes to enable comparisons of predicted interaction strength with X-ray ligand receptor complexes. ICM's interactive scoring is thus used as a quantitative evaluation of the ligand/receptor interaction.

IFPs describe the qualitative nature of interaction between a ligand and its binding pocket and have been identified as an effective method to post process docking poses of ligands in VS to identify those with a desired function (i.e. agonist vs antagonist)¹¹. In this study, we assess IFPs of co-crystal structures and compared these to their VS performance. IFPs were computed by calculating distances and orientation between sets of atoms to define the ligand/receptor interaction pattern. The interaction types considered in this study include hydrophobic contact, hydrogen bond donor and acceptor, weak hydrogen bond donor and acceptor, ionic interaction and aromatic contact. The exact parameters used to define these interactions were described previously [45]. IFPs were generated using `toolbox_pdb` (https://github.com/thomas-coudrat/toolbox_pdb), a set of Python scripts for manipulation and execution of tasks on protein structure ensembles. These scripts use the libraries Matplotlib [42], Numpy [43], SciPy [46], scikit-learn [44] and the IFP implementation uses OpenEye OEChem toolkit [38] version 2014.10.2. Considering the rules and cutoffs that define the presence of an interaction using `toolbox_pdb` may not be identical as those defined in ICM's forcefield, IFPs are used in this study as a tool to identify likely interactions rather than stating their absolute presence.

The resolution of X-ray crystal structures is an overall data quality metric for the model created from electron density (Table 1). Real-space correlation coefficient (RSCC) data were obtained for the binding pockets of all structures used in this study and plotted alongside B-factor values (S13, S14, S15, S16, S17, S18, S19 and S20 Figs). RSCC plots provide a residue per residue, as well as ligand, assessment of fit between the model and the electron density map that was used to generate it. A weak correlation, below a RSCC cutoff of 0.8, indicates a poor fit with electron density, which indicates either a lack of order in the modeled region, or errors in the model [47]. A problematic residue or ligand is further confirmed when low RSCC is correlated with high B-factor value. Of note, X-rays can cause radiation damage that would negatively affect the RSCC value of the damaged residue. Residues with potential for damage includes aspartic and glutamic acids, cysteines involved in disulfide bridges, methionines and tyrosines [48]. For this reason, in the current study, conclusions were not drawn based on low RSCC values associated to the aforementioned residues.

The software suite Phenix [49] was used to generate RSCC data that was plotted with in-house scripts. The Phenix utility was used to download the PDB data and convert reflection files to the MTZ format. A CIF file with the final geometry from file was downloaded for each non-protein and non-water molecule in the PDB file based on their 3-letter code, using the Phenix program `eLBOW`. Finally, Phenix was used to run the comprehensive validation, which computed the RSCC values that were later plotted with the scripts. R-free flags were missing from the reflection file for the following structures: 2VT4, 2Y00 and 2Y01. R-free data is not required for RSCC computation, hence the reflection files were edited with Phenix's reflection file editor. After loading the reflection file, amplitude or intensity array was added, but R-free array was not. The R-free flags were then generated and extended to full resolution range.

The docked pose of the cognate ligand from each complex was analyzed based on its ICM docking score. Computing the RMSD on heavy atoms without superimposition facilitated comparisons between the docked pose and the X-ray pose. Additionally, the ICM interactive score was calculated for each of the docked ligand/receptor complexes.

Results and discussion

GPCR ligand libraries

The GLL was generated by retrieving known ligand information from the PubChem database [31], which provides 2D and 3D models of molecules. For a molecule whose activity is known to be associated with a defined enantiomeric state, both the 2D and 3D models are of the enantiomeric state. However, for molecules where activity was defined from a racemic sample, PubChem's 2D data reflects this by not assigning the state of chiral centers, and by attributing an arbitrary enantiomeric state to the 3D molecule, which may in effect be an inactive substance. In this study, we addressed this by using the racemic GLL/GDD and sampling all enantiomeric states for each ligand that had chiral centers.

Although data analysis in this study focused on the results obtained using the racemic GLL/GDD, we did also screen the original GLL/GDD for comparison. All results were analyzed using the computed NSQ_AUC value of ROC curves from both known ligand against decoys and agonists against inhibitors VS (S2 Fig). Overall, the NSQ_AUC values obtained between racemic and original GLL/GDD were similar for all groups of binding pockets, although in many cases the racemic GLL/GDD performed slightly better than the original GLL/GDD. The naltrindole-bound (NAL) DOR binding pockets produced low NSQ_AUC scores for all VS run with both the racemic GLL/GDD and the original GLL/GDD, even after increasing the docking effort parameter from 5 to 10 (S2 and S21 Figs). This may be due in part to the complex chirality of NAL, which is shared amongst many DOR inhibitors.

AA2AR

Three AA2AR CGS-bound co-crystal structures that were elucidated in the same study contain identical thermostabilizing mutations and were solved at the same resolution (2.6 Å) (Table 1). One of these thermostabilizing mutations was present in the binding pocket, but as it was present in all structures, VS performance comparison between these structures was valid, providing an even comparison between the three pockets. All three CGS-bound AA2AR binding pockets showed good recovery of known agonists against decoys, but 4UHR outperformed the others with around 80% recovery (compared to 60%) within 10% of the screened decoys (Fig 1b and S8 Table). In terms of agonist versus inhibitor recovery, the three binding pockets also performed well with again 4UHR outperforming 4UG2-A and 4UG2-B (Fig 1c). This difference in agonist enrichment was attributed mostly to 4UHR being more selective for chemotype cluster A (CGS-like) in early recovery with EF2 values of 16.8, 17.7 and 26.6 for 4UG2-a, 4UG2-b and 4UHR, respectively (S7 Fig).

Visualization of CGS binding poses in 4UG2-A, 4UG2-B and 4UHR revealed a similar adenosine moiety conformation but differed slightly in the CGS interfaces with the loop region of the receptor (Fig 1a). These differences were identified with RMSD comparisons on the ligands, showing 4UHR were more distant than both 4UG2 chains (Fig 1d). The same is true for the binding pocket conformation (Fig 1e). These differences translate to small distinctions in the ligand/receptor interaction pattern in the 4UHR co-crystal relative to the 4UG2 chains (Fig 2). Despite 4UHR containing the least number of contacts between the three complexes, it bears essential contacts with the adenosine moiety of the CGS compound with ECL2 (E-168 and E-169), TM6 (L-249 and N-253) and TM7 (S-277 and H-278). Both 4UG2 A and B complexes also share these contacts, in addition to interactions specific to the CGS chemotype. As the vast majority of AA2AR agonists are based around the adenosine substructure (S1 Table), specific interaction patterns of both 4UG2 binding pockets with CGS moieties that are not part of the adenosine structure may impact on their overall recovery rate of known ligands

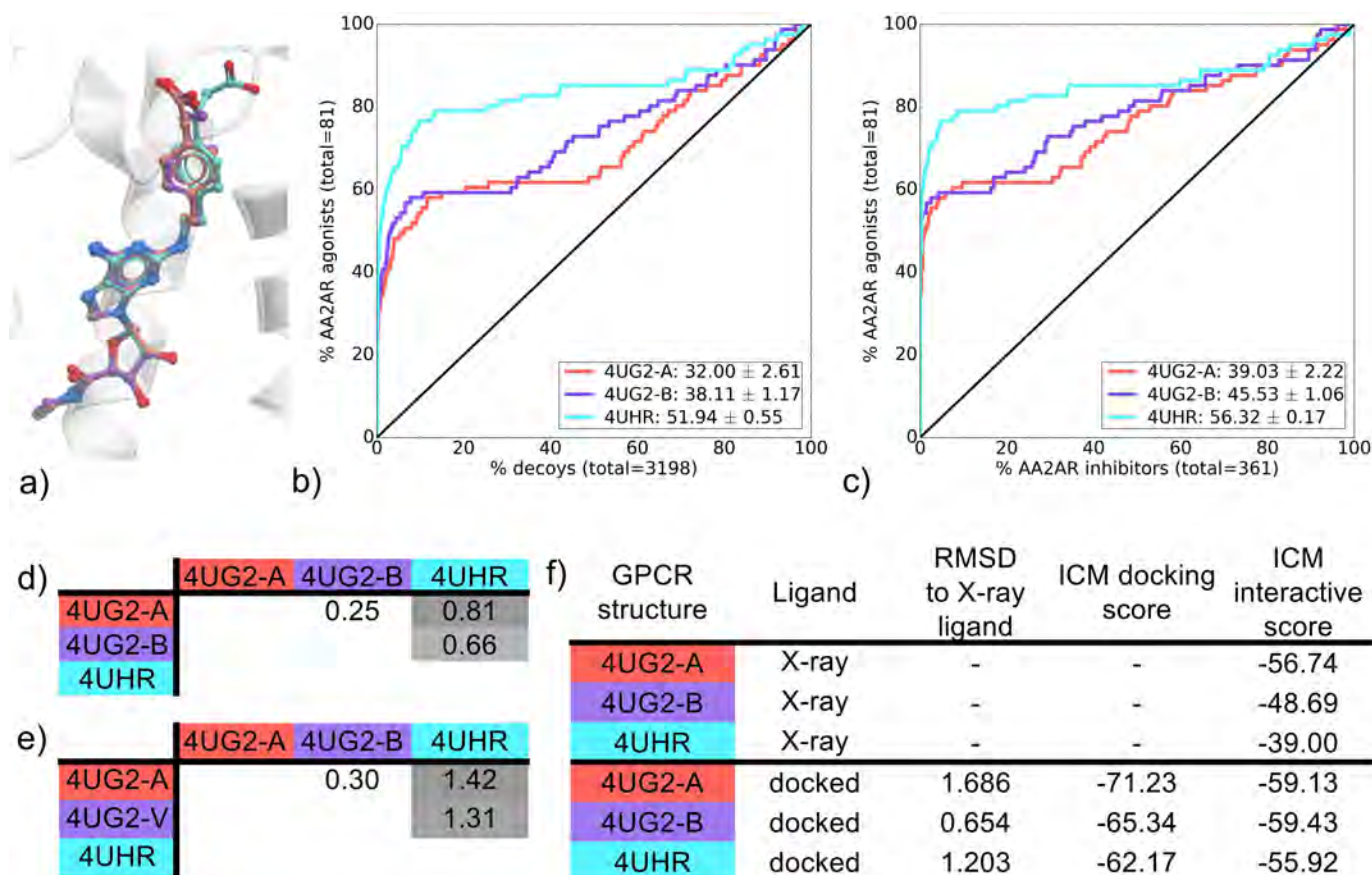


Fig 1. Comparison of AA2AR CGS-bound binding pockets (4UG2-A, 4UG2-B, 4UHR). (a) binding pose overlay, (b, c) binding pocket virtual screen results displayed as ROC curves of (b) AA2AR agonists against decoys and (c) AA2AR agonists against AA2AR inhibitors. The ROC curves are representations of the VS, picking the best scoring ligand after docking three independent times. A black line depicts the hypothetical random recovery of true positives. The rank of the docked co-crystal ligand relative to the percentage false positives is identified with a vertical dashed line. All vertical lines are drawn but some may not be visible as they are hidden by the main curve and/or the y-axis. The inset values are the mean NSQ_AUC \pm S.E.M. of three independent experiments. Statistical significance of binding pockets is reported in S2 Table. (d, e) Heavy atom RMSD comparison of X-ray structure with (d) bound ligands and (e) binding pocket residues. (f) Comparison of X-ray structures and docked poses: RMSD to X-ray ligand, ICM docking score of the docked ligand and ICM interactive scores.

<https://doi.org/10.1371/journal.pone.0174719.g001>

compared to 4UHR. This outcome doesn't preclude the use of 4UG2 X-rays structures, as indeed they have good NSQ_AUC values for both agonists vs decoys and agonists vs inhibitors. Indeed, the predicted interaction strength gives favorable scores for all three binding pockets studied. The high performance of all three CGS-bound binding pockets in recovering agonists over inhibitors may be influenced by presence of the adenosine moiety in almost all AA2AR agonists, creating a favorable conformation where adenosine can bind, thus scoring these higher than AA2AR inhibitors. Additionally, the thermostabilizing mutations present on all CGS-bound structures, may impact on AA2AR inhibitor docking. This finding for AA2AR is in agreement with a study by Kooistra and coworkers on the B2AR [11], where using the smallest subset of key IFPs to post process docking poses in rescoring, yielded the best VS outcome.

The five ZM-bound binding pockets compared were from crystal structures that used combinations of mutations, insertions and antibodies to stabilize the protein for crystallography. The resolution for these structures range from 1.8 Å for 4E1Y to 3.3 Å for 3PWH (Table 1).

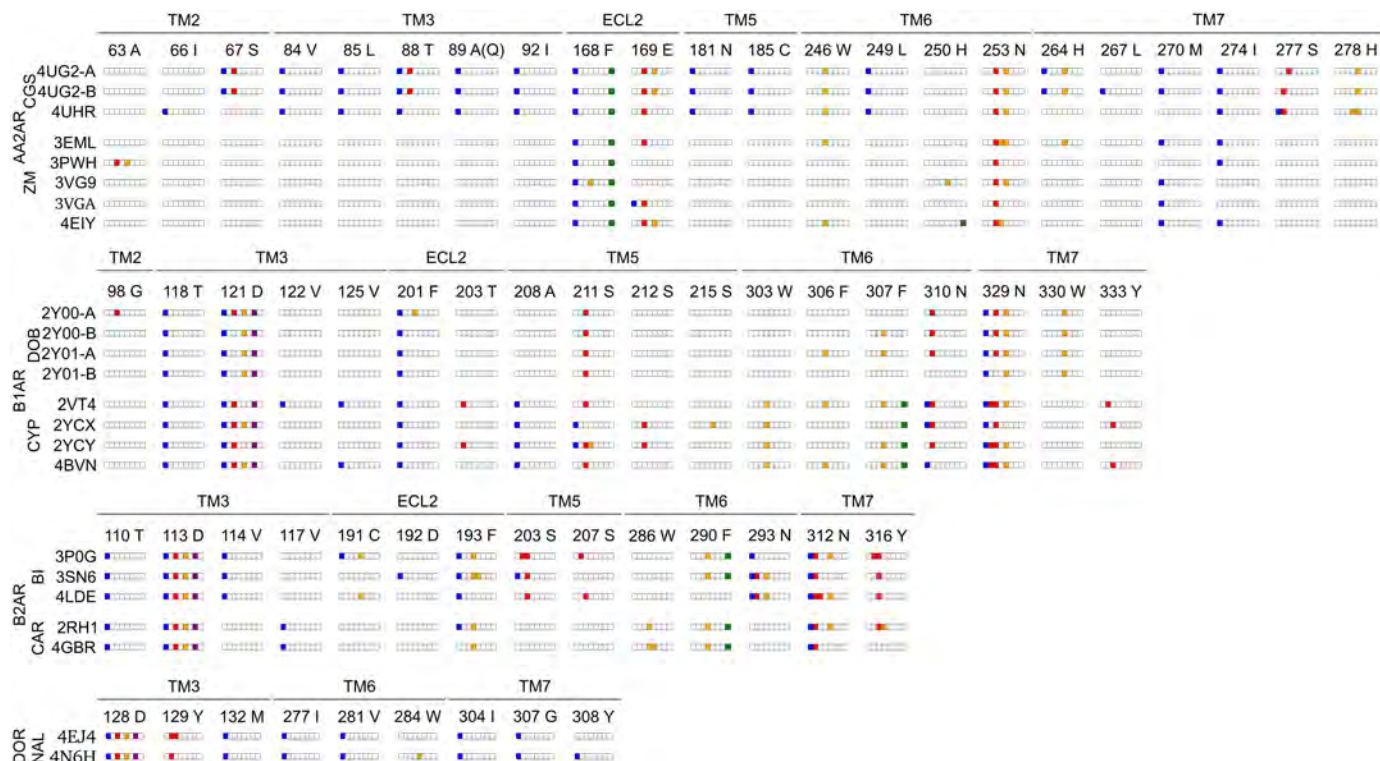


Fig 2. Structural interaction fingerprints for the seven groups of co-crystal X-ray structures. AA2AR CGS-bound and ZM-bound, B1AR DOB-bound and CYP-bound, B2AR BI-bound and CAR-bound, DOR NAL-bound. Interactions were determined using `toolbx_pdb` between the bound ligand and its receptor. Interaction types include hydrophobic (blue), hydrogen bond donor and acceptor (red), weak hydrogen-bond donor and acceptor (orange), ionic (purple) and aromatic (green). White denotes the absence of interaction. Residues forming the binding pocket are annotated by residue type, residue number and location in the 7TM domain. For AA2AR, residue 89 was mutated to A in CGS-bound binding pockets and was wild type (Q) in ZM-bound binding pockets. Co-crystal structure of the same GPCR but different co-crystal ligand (agonist/inhibitor) are aligned to highlight the differences in interaction pattern.

<https://doi.org/10.1371/journal.pone.0174719.g002>

Interestingly, poor cognate docking performance was reported for the lower resolution structures (3PWH and 3VGA) in a previous study [12]. In the current study, poor cognate docking performance was unique to ZM-bound AA2AR structures (Fig 3f) a result that corroborates the findings of Ciancetta and coworkers [12]. Specifically, a high RMSD of almost 9 Å for the cognate docked pose in 3VG9 arises as the ZM docked pose was flipped 180 degrees compared to the X-ray ligand. Interestingly, the docked pose in 3PWH, with a 3.2 Å observed difference from the X-ray ligand, does not adopt a unique conformation (as observed in the crystal structure), but instead is oriented in a similar fashion to the other AA2AR ZM-bound co-crystals (S8 Fig). Moreover, the pockets clustered into two groups when comparing inhibitor recovery vs decoys: 3VG9 and 3VGA were close to random, while the remaining three binding pockets 3EML, 3PWH and 4EIY showed inhibitor recovery (Fig 3b) with above 35% of known AA2AR inhibitors recovered at 10% of decoys. However, the 4EIY binding pocket, performed significantly better than the other two (S3 Table), reaching 40% inhibitor recovery within 10% of decoys and also recovered ZM earlier in the screen relative to 3EML and 3PWH that ZM within the top 20% of decoys recovered. Comparing EF5 values for inhibitor chemotypes, this difference in performance of the top three binding pockets comes from their capacity to recover non-ZM chemotypes while the other binding pockets could not. All three had similar EF5 values for chemotype B (ZM-like), but 4EIY was more versatile at recovering alternate chemotypes A and C (S9 Fig).

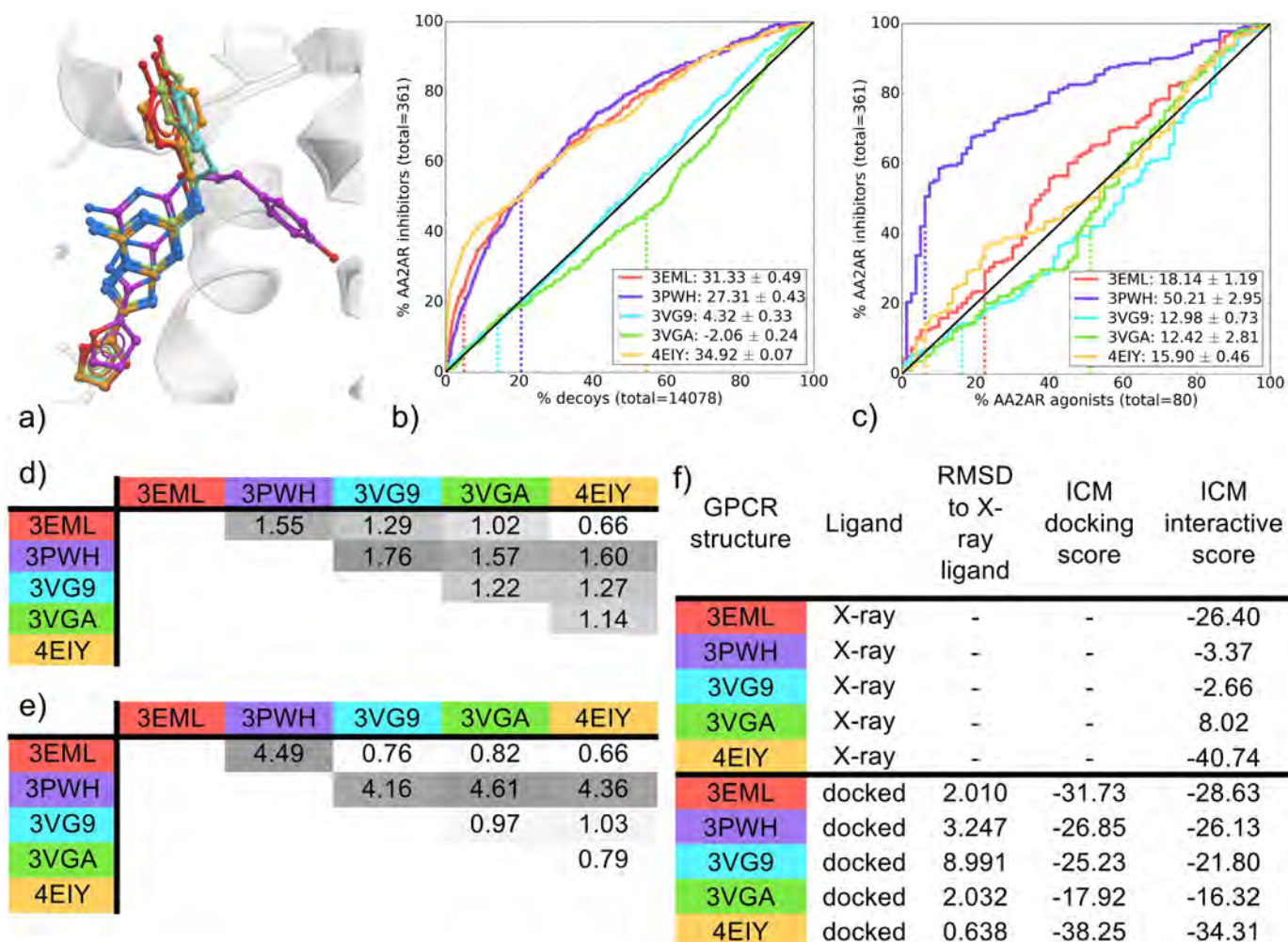


Fig 3. Comparison of AA2AR ZM-bound binding pockets (3EML, 3PWH, 3VG9, 3VGA and 4EIY). (a) Binding pose overlay. (b, c) Binding pocket virtual screen results displayed as ROC curves of (b) AA2AR inhibitors against decoys and (c) AA2AR inhibitors against AA2AR agonists. The ROC curves are representations of the VS, picking the best scoring ligand after docking three independent times. A black line depicts the hypothetical random recovery of true positives. The rank of the docked co-crystal ligand relative to the percentage false positives is identified with a vertical dashed line. All vertical lines are drawn but some may not be visible as they are hidden by the main curve and/or the y-axis. The inset values are the mean NSQ_AUC \pm S.E.M. of three independent experiments. Statistical significance of binding pockets is reported in S3 Table. (d, e) Heavy atom RMSD comparison of X-ray structure with (d) bound ligands and (e) binding pocket residues. (f) Comparison of X-ray structures and docked poses: RMSD to X-ray ligand, ICM docking score of the docked ligand and ICM interactive scores.

<https://doi.org/10.1371/journal.pone.0174719.g003>

Surprisingly, the binding pockets did not group in the same manner when comparing inhibitor/agonist recovery rates. Here, the 3PWH binding pocket was highly selective for AA2AR inhibitors over agonists, while the remaining binding pockets were close to random selectivity (however, 3EML and 4EIY were both better than 3VG9 and 3VGA) (Fig 3c). Interestingly, 3VG9 and 3VGA were solved using the same set of thermostabilizing mutations at two different resolutions of 2.7 Å and 3.1 Å, respectively, and exhibit a similar VS performance pattern. This resolution is close to 3EML (2.6 Å) and 3PWH (3.3 Å) that exhibit better VS performance indicating a limitation in the sole use of resolution for binding pocket selection for VS.

To summarize, the binding pockets 3EML, 3PWH and 4EIY showed the best VS performance. Within these best performers, 4EIY was the best at inhibitor recovery over decoys and 3PWH at inhibitor selectivity over agonist. Looking at the superimposed ZM-bound structures, all but one share a common conformation, with 3PWH being the exception (Fig 3a). All complexes share a common aromatic interaction with E-168 (ECL2) and a polar interaction with N-253 (TM6) (Fig 2). Analyzing similarities across complexes in more detail shows that 3EML and 4EIY are the closest in ligand conformation, while 3PWH unsurprisingly is the most distant (Fig 3d); with over 4 Å difference in RMSD with other binding pocket conformation (Fig 3e). Similarly to their high mean NSQ_AUCs in inhibitor vs decoys VS, 3EML and 4EIY also uniquely share a common set of polar contacts with E-169 (ECL2) and W-246 (TM6). 4EIY does have a better early recovery reflected in a higher mean NSQ_AUC value, due to its superior EF2 and EF5 performance for all chemotypes (S9 Fig) that could be linked to a different orientation of H-250 (TM6) that enables an additional aromatic interaction in 4EIY. Indeed, 4EIY was solved at a resolution of 1.8 Å that leads to a slightly improved fitting of side-chains, having notable impact on the VS outcome. The higher model quality of 4EIY, and to a lesser extent 3EML, can additionally be identified from the high RSCC values of their binding pocket residues (S15 Fig). In addition, interactive scoring ranks 3EML and 4EIY ligand/receptor complexes the highest with scores of -26.40 and -40.74, respectively (Fig 3f).

In this case, IFP comparisons on the starting co-crystal structures could not distinguish between high performing pockets (3EML and 4EIY) and poor pockets (3VG9 and 3VGA), but the interactive scoring betrayed a very poor fit for ZM within the 3VG9 and 3VGA binding pockets. This score might be negatively impacted by the repulsion component of the van der Waals potential as calculated by ICM²³ that is greatly influenced by small changes in inter-atomic distances. This would negatively impact the predicted interaction strength between two molecules, an influence that would not be picked-up by the IFP.

The 3PWH pocket, which was significantly superior in VS of AA2AR inhibitors against agonists (Fig 3c & S5 Table), contains a different ligand binding pose compared to all the other structures, with ZM's phenol moiety pointing towards TM2 interacting with the carboxyl group of A63 (Fig 3a). The 3PWH complex does not have all the polar contacts present in 3EML and 4EIY, and the RSCC plot of 3PWH indicates a poor fit of the ligand ZM with its electron density (S14b Fig). Despite this, the ligand's unique orientation and its effect on the binding pocket conformation seems to favor AA2AR inhibitors over agonists. Although cognate docking in the 3PWH binding pocket does not replicate the same unique X-ray binding pose (S8 Fig), the data suggest that screening for known inhibitors benefit from the unique binding pocket conformation stabilized by ZM, whereas agonists do not.

B1AR

The four dobutamine-bound (DOB) B1AR binding pockets extracted from two crystal structures, showed good early recovery of known inhibitors over decoys as well as selectivity of known inhibitors over agonists. The 2Y00-A binding pocket however had the best overall VS performance, showing significantly superior mean NSQ_AUC values for both agonists over decoys and agonists over inhibitors, compared to the other DOB-bound binding pockets (Fig 4b and 4c and S4 Table). The early recovery for 2Y00-A may be influenced in part by superior EF2, EF5 and EF10 values for chemotypes A (S10 Fig), which is over represented amongst B1AR agonists (S1 Table). The similar VS performance of B1AR DOB-bound binding pockets could be expected from a set of X-ray structures obtained from the same study where slightly different crystallization conditions were used.

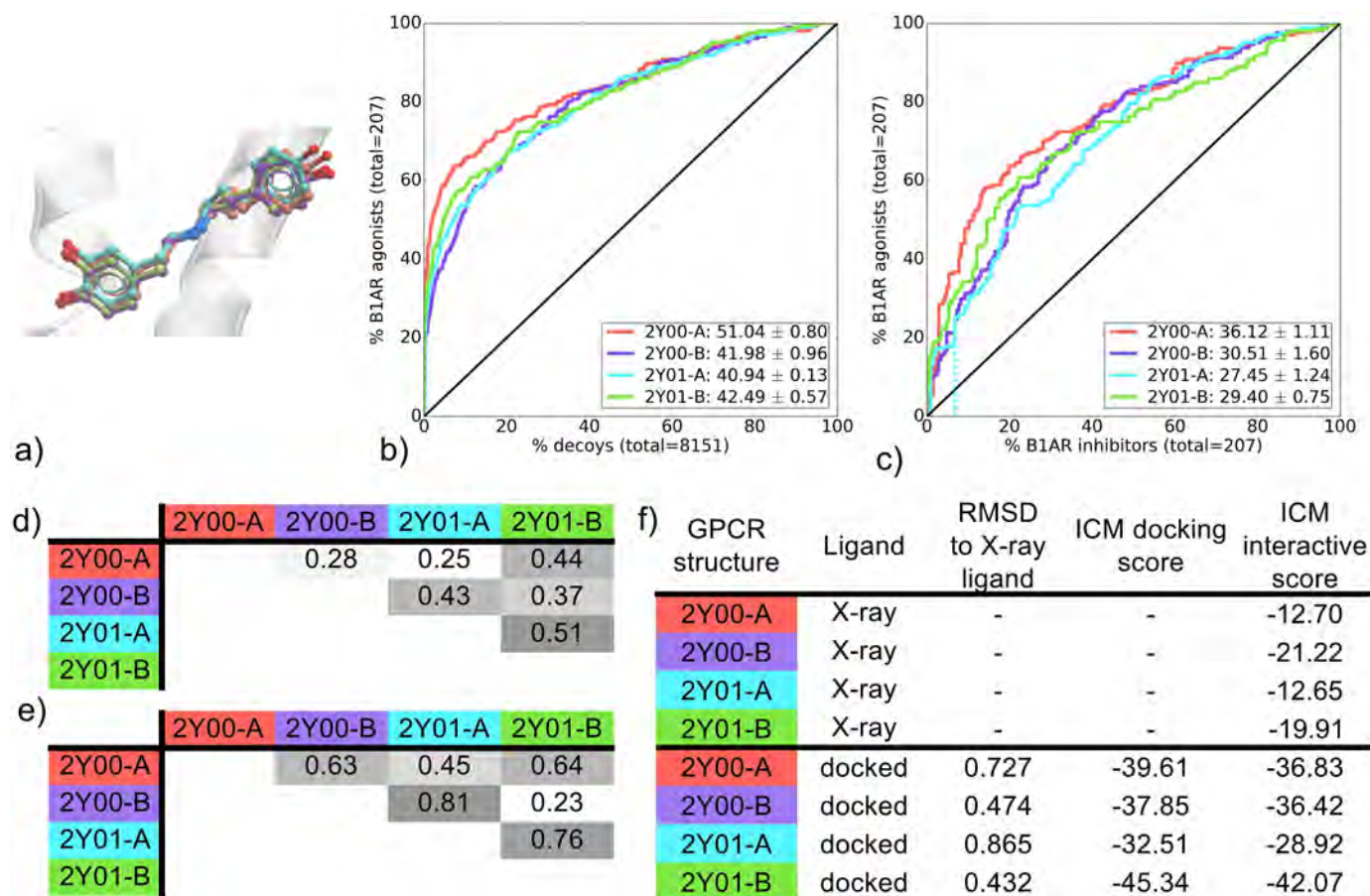


Fig 4. Comparison of B1AR DOB-bound binding pockets (2Y00-A, 2Y00-B, 2Y01-A and 2Y01-B). (a) Binding pose overlay. (b, c) Binding pocket virtual screen results displayed as ROC curves of (b) B1AR agonists against decoys and (c) B1AR agonists against B1AR inhibitors. The ROC curves are representations of the VS, picking the best scoring ligand after docking three independent times. A black line depicts the hypothetical random recovery of true positives. The rank of the docked co-crystal ligand relative to the percentage false positives is identified with a vertical dashed line. All vertical lines are drawn but some may not be visible as they are hidden by the main curve and/or the y-axis. The inset values are the mean NSQ_AUC ± S.E.M. of three independent experiments. Statistical significance of binding pockets is reported in S4 Table. (d, e) Heavy atom RMSD comparison of X-ray structure with (d) bound ligands and (e) binding pocket residues. (f) Comparison of X-ray structures and docked poses: RMSD to X-ray ligand, ICM docking score of the docked ligand and ICM interactive scores.

<https://doi.org/10.1371/journal.pone.0174719.g004>

Most complexes exhibit polar interactions in TM3 (D-121), TM5 (S-211) and TM7 (N-310, N-329, W-330). They also all share the ionic interaction with D-121 in TM3 that is conserved amongst aminergic GPCRs. However, 2Y00-A has a different interaction pattern with additional contacts to TM2 (G-98) and ECL2 (F-201) that may be responsible for its slightly better recovery of agonists over both decoys and inhibitors, relative to the other structures.

Cyanopindolol (CYP) was co-crystallized in four different B1AR binding pockets. All CYP-bound binding pockets performed similarly in recovery of known ligands vs decoys, as seen by mean NSQ_AUC values ranging from 41.49 to 49.66 (Fig 5b). In this case, statistical analysis points to 2VT4 as the highest performer (S5a Table). All CYP-bound binding pockets also showed selectivity for B1AR inhibitors over agonists and 2VT4 was again found to significantly outperform other binding pockets (Fig 5c and S5b Table). In both inhibitors vs. decoys and inhibitors vs. agonists, 4BVN was ranked second in mean NSQ_AUC value (Fig 5b and 5c).

Despite different resolutions (ranging from 2.10 Å to 3.25 Å), all B1AR CYP-bound structures share the same set of thermostabilizing mutations. All complexes have a common ligand/

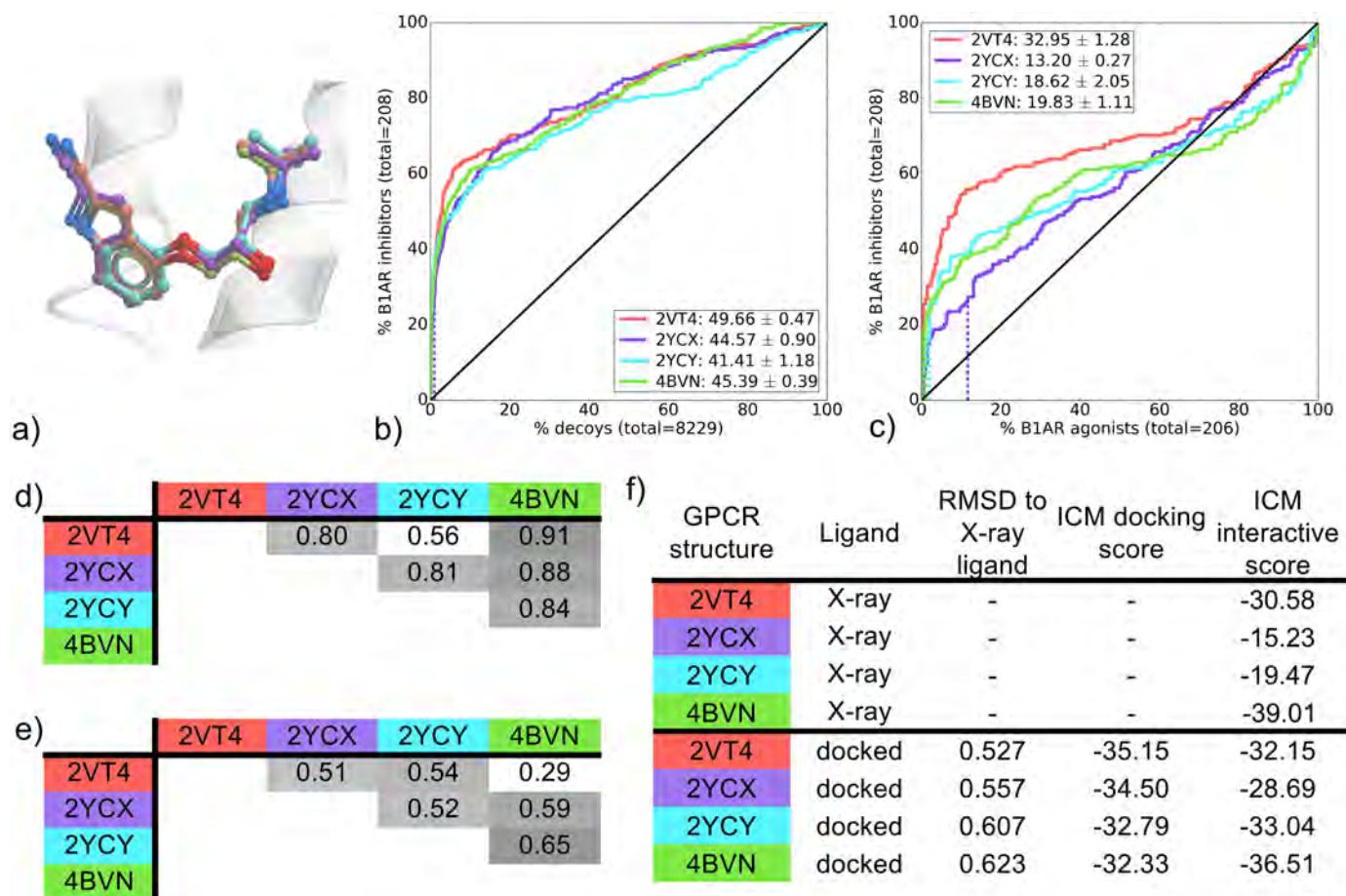


Fig 5. Comparison of B1AR CYP-bound binding pockets (2VT4, 2YCX, 2YCY and 4BVN). (a) Binding pose overlay. (b, c) Binding pocket virtual screen results displayed as ROC curves of (b) B1AR inhibitors against decoys and (c) B1AR inhibitors against B1AR agonists. The ROC curves are representations of the VS, picking the best scoring ligand after docking three independent times. A black line depicts the hypothetical random recovery of true positives. The rank of the docked co-crystal ligand relative to the percentage false positives is identified with a vertical dashed line. All vertical lines are drawn but some may not be visible as they are hidden by the main curve and/or the y-axis. The inset values are the mean NSQ_AUC ± S.E.M. of three independent experiments. Statistical significance of binding pockets is reported in S5 Table. (d, e) Heavy atom RMSD comparison of X-ray structure with (d) bound ligands and (e) binding pocket residues. (f) Comparison of X-ray structures and docked poses: RMSD to X-ray ligand, ICM docking score of the docked ligand and ICM interactive scores.

<https://doi.org/10.1371/journal.pone.0174719.g005>

receptor ionic and polar interaction with D-121, an aromatic interaction with F-307 and a polar interaction with N-329, beyond these, each complex contains a different combination of hydrophobic and polar contacts (Fig 2). When looking at the interactive scoring, the most favorable scores are predicted for 2VT4 and 4BVN with -30.58 and -39.01, respectively (Fig 5f). To summarize, 2VT4 showed a significantly superior VS performance with 4BVN also performing well in both retrospective screens. While an interaction pattern responsible for this result is difficult to identify, the interactive score does pick out the best binding pockets, which incidentally are the closest in conformation (Fig 5e).

B2AR

The BI-bound B2AR pockets were stabilized differently for crystallization using combinations of insertions, mutations and stabilizing molecules. The latest structure to be solved, 4LDE, has

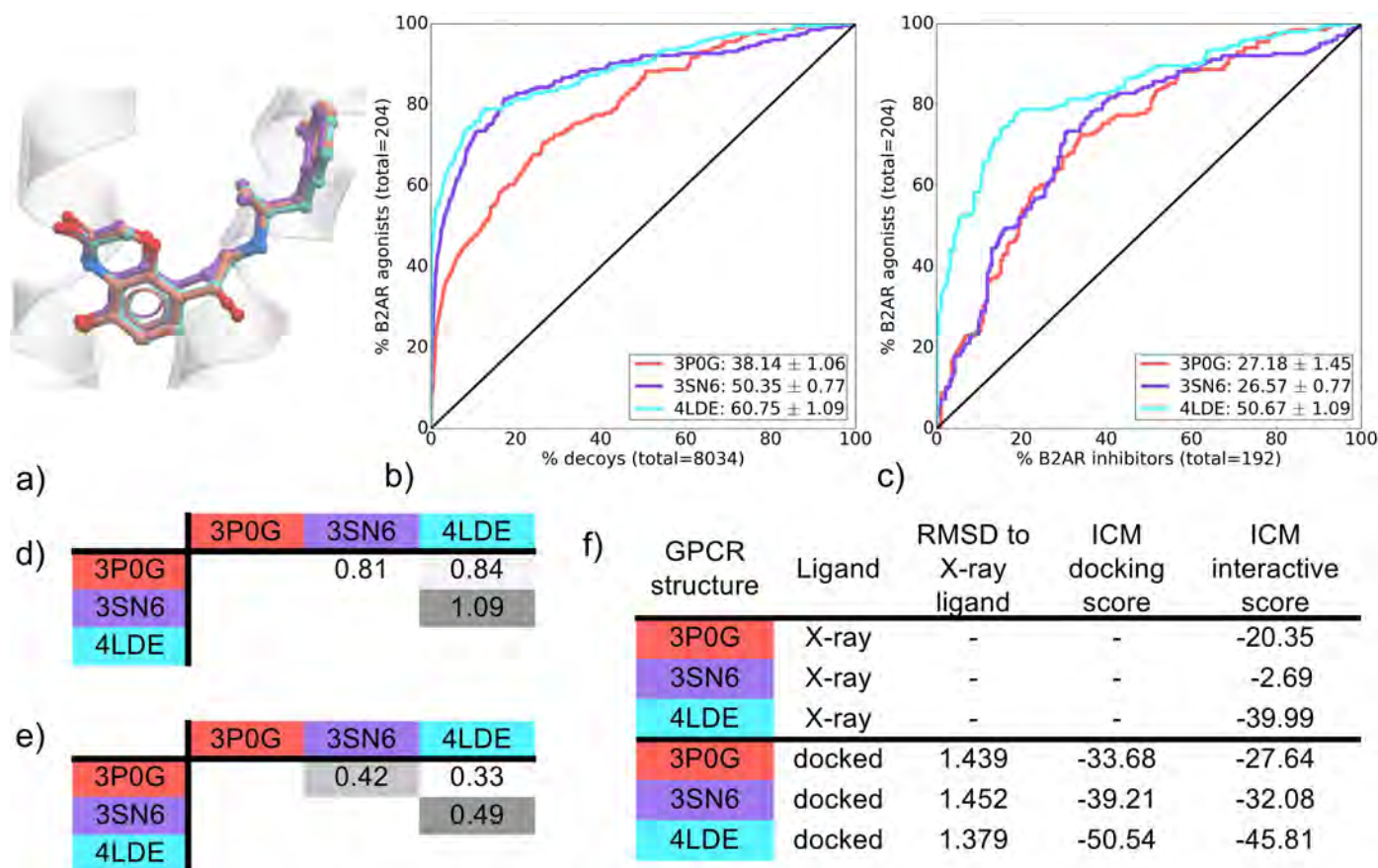


Fig 6. Comparison of B2AR BI-bound binding pockets (3P0G, 3SN6 and 4LDE). (a) Binding pose overlay. (b, c) Binding pocket virtual screen results displayed as ROC curves of (b) B2AR agonists against decoys and (c) B2AR agonists against B2AR inhibitors. The ROC curves are representations of the VS, picking the best scoring ligand after docking three independent times. A black line depicts the hypothetical random recovery of true positives. The rank of the docked co-crystal ligand relative to the percentage false positives is identified with a vertical dashed line. All vertical lines are drawn but some may not be visible as they are hidden by the main curve and/or the y-axis. The inset values are the mean NSQ_AUC ± S.E.M. of three independent experiments. Statistical significance of binding pockets is reported in S6 Table. (d, e) Heavy atom RMSD comparison of X-ray structure with (d) bound ligands and (e) binding pocket residues. (f) Comparison of X-ray structures and docked poses: RMSD to X-ray ligand, ICM docking score of the docked ligand and ICM interactive scores.

<https://doi.org/10.1371/journal.pone.0174719.g006>

the best resolution at 2.79 Å and also has very high RSCC values for its ligand and binding pocket residues (S18c Fig). The three binding pockets compared in this study had very different VS performance profiles. All three were able to distinguish known B2AR agonists from decoys with mean NSQ_AUC values ranging from 38.14 ± 1.06 (3P0G) to 60.75 ± 1.09 (4LDE). 4LDE and 3SN6 were particularly effective with their representative ROC curve showing a recovery of known agonists very early on, reaching around 70% and 60% recovery, respectively, of known agonists within 10% of decoys (Fig 6b). This early enrichment was associated with a superior early recovery of known ligands of chemotype A (S12 Fig), a different chemotype than that of the co-crystallized ligand (BI-167107) (BI) (S1 Table). When the three binding pockets were compared for their ability to distinguish B2AR agonists from inhibitors, the 4LDE binding pocket was significantly better than the other two with a mean NSQ_AUC value of 50.67 ± 1.09 (Fig 6c and S6 Table). In this case, the best VS performer corresponds to the best X-ray structure resolution. Additionally, this showcases another example where the best binding pocket for recovering known ligands against decoys also performs the best for agonist/inhibitor distinction.

Comparing the ligand/receptor interaction patterns, all three complexes share a common polar interaction network in TM3 (D-113), TM5 (S-203) and TM7 (N-312, Y-316) as well as the conserved ionic interaction D-113, for aminergic GPCRs (Fig 2). However, the top two VS performers 4LDE and 3SN6 are differentiated from 3P0G by the presence of three key interactions in both structures of BI with TM6 and TM7; polar interactions with N-293 (TM6) and for 4LDE, a double hydrogen bond interaction with N-312 (TM7). Combined, these additional contacts may contribute to increased recognition of known agonists over decoys and/or inhibitors. Interestingly, 4LDE is the only binding pocket without a ligand contact to F-290 in TM6. This provides additional space in the binding pocket that may be critical in allowing the larger agonists of chemotype A (S1 Table) to be greatly enriched at EF2 in 4LDE (S11 Fig).

Comparing the ICM interactive scores for each binding pocket, 4LDE is favored at -39.99, with 3SN6 and 3P0G both scored too low to be compared to one another (-2.69 and -20.35, respectively) (Fig 6f). The low RSCC value of the ligand BI in the binding pocket of 3SN6 may contribute to its very low score (S18b Fig). It should also be noted that missing side-chains were added to the binding pocket of 3SN6 followed by optimization prior to VS. Although the same optimization procedure was applied on all three BI-bound binding pockets, the addition of these key side-chains in ECL2 (F193, F194, T195) by the ICM software using its forcefield and scoring function may have contributed to improving the VS performance of 3SN6.

The binding pockets of 2RH1 and 4GBR are both carazolol-bound (CAR) B2AR X-ray structures that were solved with a resolution of 2.4 Å and 3.99 Å, respectively (Table 1). In both cases T4L insertion and thermostabilizing mutations were used to facilitate crystal formation; ICL3 T4L insertion and one mutation for 2RH1, N-term T4L insertion and three mutations for 4GBR. Although both binding pockets recovered inhibitors from decoys, 2RH1 significantly outperformed 4GBR (Fig 7b and S7 Table). This can be attributed to its versatility in identifying ligands of multiple chemotypes as it achieved superior EF2, EF5 and EF10 values for all three major chemotypes A, B (CAR-like) and C (S13 Fig). Both binding pockets were also compared for their recovery of B2AR inhibitors over agonists, where 2RH1 also outperformed 4GBR in overall mean NSQ_AUC score (Fig 7c).

Both CAR-bound B2AR X-ray structures are similar in binding pocket and bound ligand conformation (Fig 7d and 7e). This observation extends to the ligand/receptor interactions, as both complexes share a very similar pattern. One key difference is a set of polar contacts between ligand and Y-316 (TM7) only found in 2RH1 (Fig 2). The precise orientation of Y-316 in this structure provides an additional anchor point that may contribute to an improved VS performance for 2RH1. As has been the case for previous groups of binding pockets, the interactive score correlates with VS performance with 2RH1 scoring -40.70 compared to a poor score of -8.43 for 4GBR (Fig 7f).

DOR

Two DOR naltrindole-bound (NAL) binding pockets were compared. 4EJ4 is the *mouse* receptor whereas 4N6H is a *human* receptor, however there are only three amino acids that differ between the two species, all of which are located away from the binding pocket (Table 1). Known ligands for the *human* DOR were screened in this study on both binding pockets. The VS performance was poor for both DOR binding pockets (Fig 8b and 8c). While ROC curves for 4N6H were close to random in both inhibitors vs decoys and inhibitors vs agonists, they were significantly better than 4EJ4, which identified false positives at a higher rate than true positives (S8 Table). Only 15 known DOR inhibitors were screened in the DOR VS, and indeed none of these molecules were recovered at EF10 (data not shown). Increasing the docking effort parameter from 5 to 10 did not greatly improve these results (S21 Fig). The

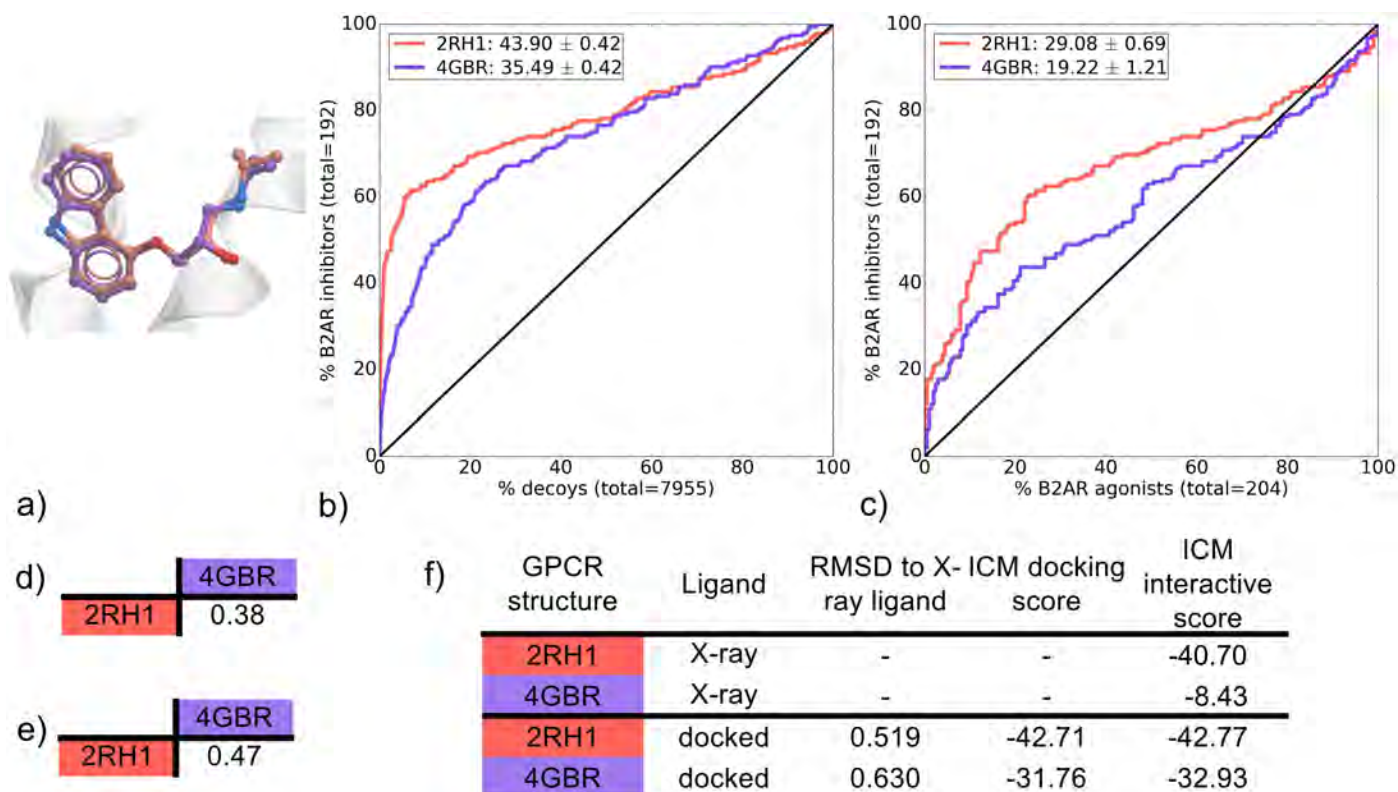


Fig 7. Comparison of B2AR CAR-bound binding pockets (2RH1 and 4GBR). (a) Binding pose overlay. (b, c) Binding pocket virtual screen results displayed as ROC curves of (b) B2AR inhibitors against decoys and (c) B2AR inhibitors against B2AR agonists. The ROC curves are representations of the VS, picking the best scoring ligand after docking three independent times. A black line depicts the hypothetical random recovery of true positives. The rank of the docked co-crystal ligand relative to the percentage false positives is identified with a vertical dashed line. All vertical lines are drawn but some may not be visible as they are hidden by the main curve and/or the y-axis. The inset values are the mean NSQ_AUC \pm S.E.M. of three independent experiments. Statistical significance of binding pockets is reported in S7 Table. (d, e) Heavy atom RMSD comparison of X-ray structure with (d) bound ligands and (e) binding pocket residues. (f) Comparison of X-ray structures and docked poses: RMSD to X-ray ligand, ICM docking score of the docked ligand and ICM interactive scores.

<https://doi.org/10.1371/journal.pone.0174719.g007>

NSQ_AUC values were slightly better when screened with the original GLL/GDD in comparison with the racemic GLL/GDD, but these still remained very poor (S2 Fig). These results make it difficult to draw conclusions on the overall VS performance of these binding pockets. Additionally, while waters are not taken into account in this study's docking procedure, their inclusion may positively affect the VS outcomes. Indeed it was shown previously that a κ -opioid receptor (KOR) model including key crystal waters displayed superior performance in VS [50]. Nevertheless, some relevant information can be drawn from these results. The two co-crystal ligand/receptor interaction patterns are very similar, with NAL forming hydrogen bonds with TM3's D-128 and Y-129 as well as an ionic interaction with D-128 in both complexes (Fig 2). However, the interactive scoring differs with a value of -16.46 for 4EJ4 compared to a much more favorable -29.77 for 4N6H (Fig 8f). This corresponds to the resolution of the respective structures, where 4EJ4 was solved at 3.4 Å and 4N6H was solved at a very high resolution of 1.8 Å. As in other examples, the best performing binding pocket corresponds to the one with the highest resolution as well as the highest ICM interactive scoring for the X-ray ligand.

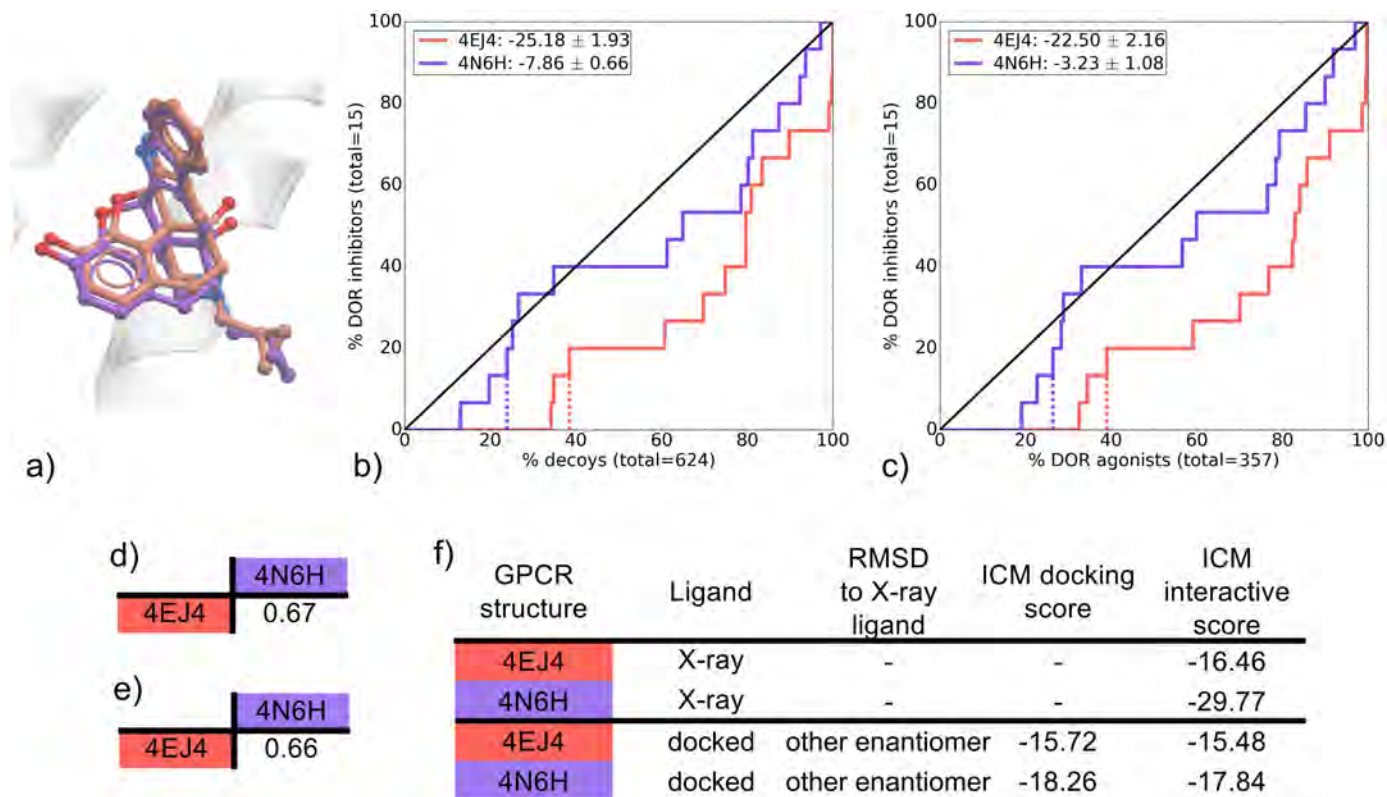


Fig 8. Comparison of DOR NAL-bound binding pockets (4EJ4 and 4N6H). (a) Binding pose overlay. (b, c) binding pocket virtual screens results displayed as ROC curves of (b) DOR inhibitors against decoys and (c) DOR inhibitors against DOR agonists. The ROC curves are representations of the VS, picking the best scoring ligand after docking three independent times. A black line depicts the hypothetical random recovery of true positives. The rank of the docked co-crystal ligand relative to the percentage false positives is identified with a vertical dashed line. All vertical lines are drawn but some may not be visible as they are hidden by the main curve and/or the y-axis. The inset values are the mean NSQ_AUC \pm S.E.M. of three independent experiments. Statistical significance of binding pockets is reported in S8 Table. (d, e) Heavy atom RMSD comparison of X-ray structure with (d) bound ligands and (e) binding pocket residues. (f) Comparison of X-ray structures and docked poses: RMSD to X-ray ligand, ICM docking score of the docked ligand and ICM interactive scores.

<https://doi.org/10.1371/journal.pone.0174719.g008>

Conclusions

This study and others highlight that GPCR structure(s) used at the start of a prospective VS will dictate the success of a SBDD program. We took advantage of the increasing number of GPCR X-ray crystal structures available to identify key criteria that may contribute to VS performance. By selecting a range of GPCR complexes bound to both agonists and inhibitors, we aimed to draw conclusions that are broadly applicable and may aid in selection of a structure for VS programs where multiple are available. VS performance of each GPCR binding pocket was evaluated by comparing recovery rates of known ligands against decoys, as well as agonists against inhibitors. While our study was performed with the use of a single docking software (icm), similar results in VS selectivity were observed by Kooistra and coworkers for the B1AR and B2AR [11] using a different docking software, highlighting that our findings will likely extend to the use of other docking software. The case study on the B1AR and B2AR identified that IFPs used to post process docking poses enhanced the retrieval of ligands in VS with select pharmacology (i.e. inhibitors vs agonists or vice versa). However, this method requires extensive knowledge of the desired IFP and, just as in the case of VS in the absence of IFP rescoring,

the crystal structure used in VS also affected the degree to which the selected IFP was able to influence the VS enrichment [11]. In this current study, the focus was on identification of criteria to guide the selection of a co-crystal structure template for use in VS when more than one is available to enhance the chances of a successful outcome.

In addition to the B1AR and B2AR, two additional class A GPCRs (AA2AR and DOR) were also investigated and larger libraries of known ligands and decoys were used for retrospective screens compared to those employed in the study by Kooistra and coworkers [11]. This enabled an in depth analysis of the VS outcomes that were visualized using ROC curve representations, where relative rank of ligands was based on their best out of three docking scores. Additionally, these three repeats allowed to calculate mean NSQ_AUC \pm S.E.M., which places emphasis on early recovery, and enables comparison of VS performance significance amongst binding pockets. Additionally, screening exhaustive known ligand libraries enabled assessment of the recovery of different known ligand chemotypes using EF barcharts. As numerous known ligands may be attributed the wrong enantiomeric state in the original GLL/GDD, the racemic GLL/GDD that generally had improved performance in VS were used.

Interestingly, we observed that oligomers identified within the same X-ray structure can perform differently in VS, however a greater difference in both performance and chemotype selectivity profile was seen in binding pockets obtained from different X-ray structures. Whereas a retrospective VS on known ligands and decoys across numerous binding pockets can be computationally costly, in the majority of cases, VS performance for agonists vs inhibitors followed the same trend exhibited by known ligands against decoys recovery (Fig 9). The selectivity task has the additional benefit of screening for the required pharmacology representing a thorough test on the viability of a binding pocket for prospective VS, while being much less computationally expensive compared with vs decoys. Known ligand libraries tested represented various different chemotypes for each GPCR target. In the current study the best VS performance was achieved from binding pockets that were versatile in recovering a wide range of known ligand chemotype.

GPCR X-ray structures are obtained through the use of a number of experimental and protein engineering methods that include thermostabilizing mutations, insertion of proteins within regions of the GPCR, deletion of flexible regions and stabilization by other molecules such as nanobodies. These modifications facilitate the crystallization of the receptors by stabilizing them in a single conformational state and enhancing crystal contacts. The current study does not point to a particular set of crystallization methods that correlate with their VS performance. The current de-facto metric used to evaluate an X-ray structure for VS, is its resolution and indeed, in most cases, a higher resolution was indicative of a better VS performance, presumably because a higher resolution enables a better fit of side-chains and ligand into the electron density, therefore producing a better model. This was complemented in some cases by the analysis of RSCC plots, which inform more specifically on the quality of the modeled binding pocket and bound ligand. Interestingly, the differential performance of binding pockets in VS was always dictated by extremely small differences in the relative position of atoms of the screened binding pocket model. Cases where lower resolution structures showed better VS performance than others of higher resolution prompts the need for additional metrics that may aid in identifying the best binding pocket to select for SBDD.

In this study, we undertook a quantitative analysis of all ligand/receptor interactions using the ICM scoring function used in the VS experiments. The ICM interactive scoring provides a value of the scoring function's interpreted interaction strength between ligand and receptor. We identified ICM interactive scores as an indicator of binding pocket VS performance. This is particularly true for ICM scores of -20 or better, as lower scores tend to be less meaningful. An additional tool complementing the ICM interactive score analysis was a detailed qualitative

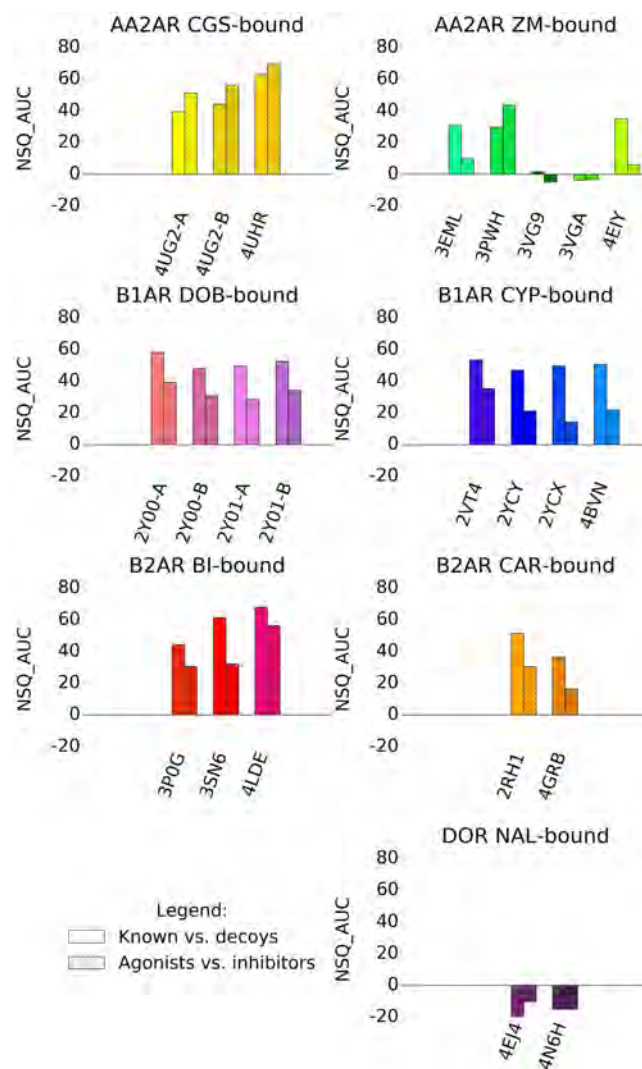


Fig 9. Comparison of VS performance on groups of binding pockets bound by the same ligand.

Compared are recovery of known ligands against decoys shown in plain, and recovery of agonists against inhibitors (or vice-versa) shown in hatched. NSQ_AUCs values emphasize early recovery of a ROC curve. These are normalized between perfect (NSQ_AUC = 100) and random (NSQ_AUC = 0) recovery. A negative NSQ_AUC value indicates a ROC curve below random.

<https://doi.org/10.1371/journal.pone.0174719.g009>

analysis of interaction patterns between the co-crystallized ligands and receptors. With these IFPs, we identified that the presence of specific hydrogen bond interactions in the starting structures was key to VS performance, at least for these class A GPCRs assessed, these interactions were present mostly on TM3, TM6, TM7 and for some GPCRs ECL2. Two interesting findings arise from the IFP analysis that was not captured by ICM interactive scoring. Firstly, an alternative binding pose, such as the one seen in AA2AR ZM-bound binding pockets can offer an effective binding pocket in VS, even if its ligand/receptor interaction is not favorably scored by ICM. Secondly, as seen in AA2AR CGS-bound binding pockets, an increased number of polar contacts between ligand and receptor may hinder the recovery of known ligands outside the chemotype of the ligand used for crystallization, as that ligand/receptor interaction is too specific to the chemotype of the co-crystallized ligand. Although this does not preclude

Table 2. GPCR X-ray structure features indicative of their relative VS performance.

GPCR	Co-crystal ligand	Resolution	Interaction strength	Interaction pattern	Ligand conformation	Binding pocket conformation
AA2AR	CGS	-	-	✓	✓	✓
AA2AR	ZM	-	✓	✓	✓	✓
B1AR	DOB	-	-	-	-	-
B1AR	CYP	-	✓	-	-	✓
B2AR	BI	✓	✓	✓	-	✓
B2AR	CAR	✓	✓	✓	-	-
DOR	NAL	✓	✓	✓	-	-

Interaction strength refers to the calculated ICM interactive scoring. Interaction pattern refers to the qualitative IFP scoring. Ligand and binding pocket conformation refer RMSD difference. No difference identified in the VS performance and features assessed between the different x-ray structures are denoted by "°" and an indication of an important feature for VS performance is denoted by "✓".

<https://doi.org/10.1371/journal.pone.0174719.t002>

the use of such a binding pocket for prospective VS, it is information that one should keep in mind in a SBDD program, especially if the goal is to identify new scaffolds. In cases such as the B2AR BI-bound binding pockets (where all three binding pockets performed well in VS) the presence of additional polar and aromatic interactions in two of the structures relative to the best performer (4LDE) also hindered recovery of known ligands outside the chemotype of the co-crystallized ligand.

In a SBDD program, a prospective VS should include a step of thorough energy minimization on the ligand/receptor complex. Improving the model geometry using the same forcefield and scoring function as the ICM interactive score and docking would improve values of both. Additionally, a careful selection of binding pocket water molecules has been shown to have a positive influence on docking known ligands [50] and improving VS outcome [51]. Neither of these important factors were included in the current study, however, the use of tools that could include waters not observed in crystal structures due to low resolution may also aid in VS performance on crystal structures. To summarize, we have compared the VS performance of X-ray structures of the same GPCR bound to the same ligand and identified indications that small variations in structural features are responsible for their success in VS (Table 2). These results provide a framework to continue the development of computational tools aimed at the refinement of GPCR binding pocket conformation to improve their predictive power in VS.

Supporting information

S1 Fig. Comparison of VS performance with and without hydrogen bond optimization.

The known ligands vs. decoys and agonist vs. inhibitors (or vice versa) are compared respectively for (a,b) AA2AR-ZM 3EML, (c,d) AA2AR-ZM 4E1Y, (e,f) B1AR-DOB 2Y00-A, (g,h) B1AR-CYP 2VT4, (i,j) B1AR-CYP 2YCX, (k,l) B1AR-CYP 2YCY, (m,n) B1AR-CYP 4BVN, (o,p) B2AR-BI 3P0G, (q,r) B2AR-BI 4LDE, (s,t) B2AR-BI 3SN6, (u,v) B2AR-CAR 2RH1 and (w,x) DOR-NAL 4N6H.

(PDF)

S2 Fig. Ligand library original GLL/GDD vs racemic GLL/GDD NSQ_AUC comparisons.

Comparison of VS performance on groups of binding pockets bound by the same ligand depending on the ligand library used for screening: original GLL/GDD (hatched) or racemic GLL/GDD (plain). Values are NSQ_AUCs calculated on ROC curves comparing a) known ligands against decoys, and b) agonists against inhibitors (or vice-versa).

(PDF)

S3 Fig. Dendrogram of the ligand chemotypes for AA2AR. Known a) agonists and b) inhibitors. The number of ligands within each branch is noted. Clusters used in VS are circled and named, and the co-crystal X-ray ligand's position is identified. The asterisk denotes the location of the chemotype cluster center for its respective chemotype cluster, no cluster center is provided for the cluster 'other'.

(PDF)

S4 Fig. Dendrogram of the ligand chemotypes for B1AR. Known a) agonists and b) inhibitors. The number of ligands within each branch is noted. Clusters used in VS are circled and named, and the co-crystal X-ray ligand's position is identified. The asterisk denotes the location of the chemotype cluster center for its respective chemotype cluster, no cluster center is provided for the cluster 'other'.

(PDF)

S5 Fig. Dendrogram of the ligand chemotypes for B2AR. Known a) agonists and b) inhibitors. The number of ligands within each branch is noted. Clusters used in VS are circled and named, and the co-crystal X-ray ligand's position is identified. The asterisk denotes the location of the chemotype cluster center for its respective chemotype cluster, no cluster center is provided for the cluster 'other'.

(PDF)

S6 Fig. Dendrogram of the ligand chemotypes for DOR. The number of ligands within each branch is noted. Clusters used in VS are circled and named, and the co-crystal X-ray ligand's position is identified. The asterisk denotes the location of the chemotype cluster center for its respective chemotype cluster, no cluster center is provided for the cluster 'other'.

(PDF)

S7 Fig. Enrichment factors of AA2AR known agonist chemotypes for CGS-bound AA2AR binding pockets (4UG2-A, 4UG2-B, 4UHR). Enrichment factors at EF2, EF5 and EF10 using the 2D racemic ligand library.

(PDF)

S8 Fig. Cognate docking of the ZM ligand on all AA2AR ZM-bound binding pockets (3EML, 3PWH, 3VG9, 3VGA and 4EIY). All complexes were superimposed and only one representative receptor is displayed in grey, with TM6 and TM7 omitted for clarity. Carbon atoms of the ligands are colored as follows: 3EML (red), 3PWH (purple), 3VG9 (cyan), 3VGA (green), 4EIY (yellow).

(PDF)

S9 Fig. Enrichment factors of AA2AR known inhibitor chemotypes for ZM-bound AA2AR binding pockets (3EML, 3PWH, 3VG9, 3VGA, 4EIY). Enrichment factors at EF2, EF5 and EF10.

(PDF)

S10 Fig. Enrichment factors of B1AR known agonist chemotypes for DOB-bound B1AR binding pockets (2Y00-A, 2Y00-B, 2Y01-A, 2Y01-B). Enrichment factors at EF2, EF5 and EF10.

(PDF)

S11 Fig. Enrichment factors of B1AR known inhibitor chemotypes for CYP-bound B1AR binding pockets (2VT4, 2YCX, 2YCY, 4BVN). Enrichment factors at EF2, EF5 and EF10.

(PDF)

S12 Fig. Enrichment factors of B2AR known agonist chemotypes for BI-bound B2AR binding pockets (3P0G, 3SN6, 4LDE). Enrichment factors at EF2, EF5 and EF10.

(PDF)

S13 Fig. Enrichment factors of B2AR known inhibitor chemotypes for CAR-bound B2AR binding pockets (2RH1, 4GBR). Enrichment factors at EF2, EF5 and EF10.

(PDF)

S14 Fig. RSCC and B-factor plots for AA2AR CGS-bound binding pockets. Assessment of local model quality for: a) 4UG2-A, b) 4UG2-B and c) 4UHR. Real-space correlation coefficient (green) and B-factor values (red) are shown for all residues of the binding pocket and the bound ligand CGS. A green dotted line cutoff value of 0.8 highlights low RSCC values.

(PDF)

S15 Fig. RSCC and B-factor plots for AA2AR ZM-bound binding pockets. Assessment of local model quality for: a) 3EML, b) 3PWH, c) 3VG9, d) 3VGA and e) 4EIY. Real-space correlation coefficient (green) and B-factor values (red) are shown for all residues of the binding pocket and the bound ligand ZM. A green dotted line cutoff value of 0.8 highlights low RSCC values.

(PDF)

S16 Fig. RSCC and B-factor plots for B1AR DOB-bound binding pockets. Assessment of local model quality for: a) 2Y00-A, b) 2Y00-B, c) 2Y01-A and d) 2Y01-B. Real-space correlation coefficient (green) and B-factor values (red) are shown for all residues of the binding pocket and the bound ligand DOB. A green dotted line cutoff value of 0.8 highlights low RSCC values.

(PDF)

S17 Fig. RSCC and B-factor plots for B1AR CYP-bound binding pockets. Assessment of local model quality for: a) 2VT4, b) 2YCX, c) 2YCY and d) 4BVN. Real-space correlation coefficient (green) and B-factor values (red) are shown for all residues of the binding pocket and the bound ligand CYP. A green dotted line cutoff value of 0.8 highlights low RSCC values.

(PDF)

S18 Fig. RSCC and B-factor plots for B2AR BI-bound binding pockets. Assessment of local model quality for: a) 3P0G, b) 3SN6 and c) 4LDE. Real-space correlation coefficient (green) and B-factor values (red) are shown for all residues of the binding pocket and the bound ligand BI. A green dotted line cutoff value of 0.8 highlights low RSCC values.

(PDF)

S19 Fig. RSCC and B-factor plots for B2AR CAR-bound binding pockets. Assessment of local model quality for: a) 2RH1 and b) 4GBR. Real-space correlation coefficient (green) and B-factor values (red) are shown for all residues of the binding pocket and the bound ligand CAR. A green dotted line cutoff value of 0.8 highlights low RSCC values.

(PDF)

S20 Fig. RSCC and B-factor plots for DOR NAL-bound binding pockets. Assessment of local model quality for: a) 4EJ4 and b) 4N6H. Real-space correlation coefficient (green) and B-factor values (red) are shown for all residues of the binding pocket and the bound ligand NAL. A green dotted line cutoff value of 0.8 highlights low RSCC values.

(PDF)

S21 Fig. Analyzing the influence of the docking effort parameter on VS performance for DOR binding pockets (4EJ4 and 4N6H). VS results displayed as ROC curves of (a) DOR inhibitors against decoys and (b) DOR inhibitors against DOR agonists. The ROC curves are representations of the VS, picking the best scoring ligand after docking three independent times. A black line depicts the hypothetical random recovery of true positives. The rank of the docked co-crystal ligand relative to the percentage false positives is identified with a vertical dashed line. The inset values are NSQ_AUCs calculated on these representative curves. (PDF)

S1 Table. Known ligand library and decoys for each GPCR. Details about known ligand count, chiral center composition, as well as chemotype clusters names and counts. A chemical structure for the center of each chemotype cluster is represented, as well as each ligand from co-crystal X-ray structures. (PDF)

S2 Table. Statistical significance of VS performance between AA2AR CGS-bound binding pockets. One-way ANOVA was performed on mean NSQ_AUC \pm S.E.M. for each of the docking experiments, followed by a Tukey multiple comparison test for a) AA2AR agonists vs. decoys (Fig 1b) and b) AA2AR agonists vs. AA2AR inhibitors (Fig 1c). A one-way ANOVA was carried out, followed by a Tukey's multiple comparison test. Binding pocket performance was tested with P value noted as follows. *: $P \leq 0.05$, **: $P \leq 0.01$, ***: $P \leq 0.001$, ****: $P \leq 0.0001$, ns: not significantly different. Black asterisks signify the row structure is significantly better than the column structure, and vice-versa for red asterisks. (PDF)

S3 Table. Statistical significance of VS performance between AA2AR ZM-bound binding pockets. One-way ANOVA was performed on mean NSQ_AUC \pm S.E.M. for each of the docking experiments, followed by a Tukey multiple comparison test for a) AA2AR inhibitors vs. decoys (Fig 3b) and b) AA2AR inhibitors vs. AA2AR agonists (Fig 3c). A one-way ANOVA was carried out, followed by Tukey's multiple comparison test. Binding pocket performance is tested with P value noted as follows. *: $P \leq 0.05$, **: $P \leq 0.01$, ***: $P \leq 0.001$, ****: $P \leq 0.0001$, ns: not significantly different. Black asterisks signify the row structure is significantly better than the column structure, and vice-versa for red asterisks. (PDF)

S4 Table. Statistical significance of VS performance between B1AR DOB-bound binding pockets. One-way ANOVA was performed on mean NSQ_AUC \pm S.E.M. for each of the docking experiments, followed by a Tukey multiple comparison test for a) B1AR agonists vs. decoys (Fig 4b) and b) B1AR agonists vs. B1AR inhibitors (Fig 4c). A one-way ANOVA was carried out, followed by Tukey's multiple comparison test. Binding pocket performance is tested with P value noted as follows. *: $P \leq 0.05$, **: $P \leq 0.01$, ***: $P \leq 0.001$, ****: $P \leq 0.0001$, ns: not significantly different. Black asterisks signify the row structure is significantly better than the column structure, and vice-versa for red asterisks. (PDF)

S5 Table. Statistical significance of VS performance between B1AR CYP-bound binding pockets. One-way ANOVA was performed on mean NSQ_AUC \pm S.E.M. for each of the docking experiments, followed by a Tukey multiple comparison test for a) B1AR inhibitors vs. decoys (Fig 5b) and b) B1AR inhibitors vs. B1AR agonists (Fig 5c). A one-way ANOVA was carried out, followed by Tukey's multiple comparison test. Binding pocket performance is tested with P value noted as follows. *: $P \leq 0.05$, **: $P \leq 0.01$, ***: $P \leq 0.001$, ****: $P \leq 0.0001$,

ns: not significantly different. Black asterisks signify the row structure is significantly better than the column structure, and vice-versa for red asterisks.

(PDF)

S6 Table. Statistical significance of VS performance between B2AR BI-bound binding pockets. One-way ANOVA was performed on mean NSQ_AUC \pm S.E.M. for each of the docking experiments, followed by a Tukey multiple comparison test for a) B2AR agonists vs. decoys (Fig 6b) and b) B2AR agonists vs. B2AR inhibitors (Fig 6c). A one-way ANOVA was carried out, followed by Tukey's multiple comparison test. Binding pocket performance is tested with P value noted as follows. *: $P \leq 0.05$, **: $P \leq 0.01$, ***: $P \leq 0.001$, ****: $P \leq 0.0001$, ns: not significantly different. Black asterisks signify the row structure is significantly better than the column structure, and vice-versa for red asterisks.

(PDF)

S7 Table. Statistical significance of VS performance between B2AR CAR-bound binding pockets. One-way ANOVA was performed on mean NSQ_AUC \pm S.E.M. for each of the docking experiments, followed by a Tukey multiple comparison test for a) B2AR inhibitors vs. decoys (Fig 7b) and b) B2AR inhibitors vs. B2AR agonists (Fig 7c). A one-way ANOVA was carried out, followed by Tukey's multiple comparison test. Binding pocket performance is tested with P value noted as follows. *: $P \leq 0.05$, **: $P \leq 0.01$, ***: $P \leq 0.001$, ****: $P \leq 0.0001$, ns: not significantly different. Black asterisks signify the row structure is significantly better than the column structure, and vice-versa for red asterisks.

(PDF)

S8 Table. Statistical significance of VS performance between DOR NAL-bound binding pockets. One-way ANOVA was performed on mean NSQ_AUC \pm S.E.M. for each of the docking experiments, followed by a Tukey multiple comparison test for a) DOR inhibitors vs. decoys (Fig 8b) and b) DOR inhibitors vs. DOR agonists (Fig 8c). A one-way ANOVA was carried out, followed by Tukey's multiple comparison test. Binding pocket performance is tested with P value noted as follows. *: $P \leq 0.05$, **: $P \leq 0.01$, ***: $P \leq 0.001$, ****: $P \leq 0.0001$, ns: not significantly different. Black asterisks signify the row structure is significantly better than the column structure, and vice-versa for red asterisks.

(PDF)

Acknowledgments

The authors would like to thank Prof. Ruben Abagyan (UCSD) and Dr. Andrew Orry for helpful advice on the use of ICM. Thomas Coudrat acknowledges the Chemical Structure Association Trust for awarding him the 2016 CSA Trust Grant. This research was supported by the National Health and Medical Research Council of Australia (NHMRC), award numbers APP1055134 and APP106101044 to PMS and APP1089966 to DW, a NHMRC Career Development Fellow. This research was also supported by Melbourne Bioinformatics at the University of Melbourne, grant number VR0024 to PMS. PMS is a NHMRC Principal Research Fellow, and AC a NHMRC Senior Principal Research Fellow. The funders had no role in study design, data collection and analysis, decision to publish, or preparation of the manuscript.

Author Contributions

Conceptualization: TC AC PMS DW.

Data curation: TC PMS DW.

Formal analysis: TC PMS DW.

Funding acquisition: AC PMS DW.

Investigation: TC.

Methodology: TC.

Project administration: AC PMS DW.

Resources: PMS.

Software: TC.

Supervision: PMS DW.

Validation: TC AC PMS DW.

Visualization: TC PMS DW.

Writing ± original draft: TC.

Writing ± review & editing: AC PMS DW.

References

1. Lander ES, Linton LM, Birren B, Nusbaum C, Zody MC, Baldwin J, et al. Initial sequencing and analysis of the human genome. *Nature*. 2001; 409: 860±921. <https://doi.org/10.1038/35057062> PMID: 11237011
2. Venter JC, Adams MD, Myers EW, Li PW, Mural RJ, Sutton GG, et al. The sequence of the human genome. *Science*. 2001; 291: 1304±1351. <https://doi.org/10.1126/science.1058040> PMID: 11181995
3. Pierce KL, Premont RT, Lefkowitz RJ. Seven-transmembrane receptors. *Nat Rev Mol Cell Biol*. 2002; 3: 639±650. <https://doi.org/10.1038/nrm908> PMID: 12209124
4. Marinissen MJ, Gutkind JS. G-protein-coupled receptors and signaling networks: emerging paradigms. *Trends Pharmacol Sci*. 2001; 22: 368±376. PMID: 11431032
5. Overington JP, Al-Lazikani B, Hopkins AL. How many drug targets are there? *Nat Rev Drug Discov*. 2006; 5: 993±996. <https://doi.org/10.1038/nrd2199> PMID: 17139284
6. Heng BC, Aubel D, Fussenegger M. An overview of the diverse roles of G-protein coupled receptors (GPCRs) in the pathophysiology of various human diseases. *Biotechnol Adv*. 2013; 31: 1676±1694. <https://doi.org/10.1016/j.biotechadv.2013.08.017> PMID: 23999358
7. Shoichet BK. Virtual screening of chemical libraries. *Nature*. 2004; 432: 862±865. <https://doi.org/10.1038/nature03197> PMID: 15602552
8. Lawton G, Witty DR. *Progress in Medicinal Chemistry*. 1st ed. Elsevier Science Serials; 2014.
9. GPCRdb (<http://GPCRdb.org>) Accessed: 2016-10-17 [Internet]. <http://GPCRdb.org>
10. Costanzi S, Vilar S. In silico screening for agonists and blockers of the $\beta(2)$ adrenergic receptor: implications of inactive and activated state structures. *J Comput Chem*. 2012; 33: 561±572. <https://doi.org/10.1002/jcc.22893> PMID: 22170280
11. Kooistra AJ, Leurs R, de Esch IJP, de Graaf C. Structure-Based Prediction of G-Protein-Coupled Receptor Ligand Function: A β -Adrenoceptor Case Study. *J Chem Inf Model*. 2015; 55: 1045±1061. <https://doi.org/10.1021/acs.jcim.5b00066> PMID: 25848966
12. Ciancetta A, Cuzzolin A, Moro S. Alternative Quality Assessment Strategy to Compare Performances of GPCR-Ligand Docking Protocols: The Human Adenosine A2A Receptor as a Case Study. *J Chem Inf Model*. 2014; 54: 2243±2254. <https://doi.org/10.1021/ci5002857> PMID: 25046649
13. Doré AS, Robertson N, Errey JC, Ng I, Hollenstein K, Tehan B, et al. Structure of the adenosine A(2A) receptor in complex with ZM241385 and the xanthines XAC and caffeine. *Structure*. 2011; 19: 1283±1293. <https://doi.org/10.1016/j.str.2011.06.014> PMID: 21885291
14. Warne T, Moukhametzianov R, Baker JG, NehmÅR, Edwards PC, Leslie AGW, et al. The structural basis for agonist and partial agonist action on a $\beta(1)$ -adrenergic receptor. *Nature*. 2011; 469: 241±244. <https://doi.org/10.1038/nature09746> PMID: 21228877

15. Lebon G, Edwards PC, Leslie AGW, Tate CG. Molecular Determinants of CGS21680 Binding to the Human Adenosine A2A Receptor. *Mol Pharmacol*. 2015;
16. Jaakola V-P, Griffith MT, Hanson MA, Cherezov V, Chien EYT, Lane JR, et al. The 2.6 angstrom crystal structure of a human A2A adenosine receptor bound to an antagonist. *Science*. 2008; 322: 1211±1217. <https://doi.org/10.1126/science.1164772> PMID: 18832607
17. Hino T, Arakawa T, Iwanari H, Yurugi-Kobayashi T, Ikeda-Suno C, Nakada-Nakura Y, et al. G-protein-coupled receptor inactivation by an allosteric inverse-agonist antibody. *Nature*. 2012; 482: 237±240. <https://doi.org/10.1038/nature10750> PMID: 22286059
18. Liu W, Chun E, Thompson AA, Chubukov P, Xu F, Katritch V, et al. Structural basis for allosteric regulation of GPCRs by sodium ions. *Science*. 2012; 337: 232±236. <https://doi.org/10.1126/science.1219218> PMID: 22798613
19. Warne T, Serrano-Vega MJ, Baker JG, Moukhametziev R, Edwards PC, Henderson R, et al. Structure of a beta1-adrenergic G-protein-coupled receptor. *Nature*. 2008; 454: 486±491. <https://doi.org/10.1038/nature07101> PMID: 18594507
20. Moukhametziev R, Warne T, Edwards PC, Serrano-Vega MJ, Leslie AGW, Tate CG, et al. Two distinct conformations of helix 6 observed in antagonist-bound structures of a beta1-adrenergic receptor. *Proc Natl Acad Sci U A*. 2011; 108: 8228±8232.
21. Miller-Gallacher JL, Nehm  r, Warne T, Edwards PC, Schertler GFX, Leslie AGW, et al. The 2.1   resolution structure of cyanopindolol-bound  1-adrenoceptor identifies an intramembrane Na⁺ ion that stabilises the ligand-free receptor. *PLoS One*. 2014; 9: e92727. <https://doi.org/10.1371/journal.pone.0092727> PMID: 24663151
22. Rasmussen SGF, Choi H-J, Fung JJ, Pardon E, Casarosa P, Chae PS, et al. Structure of a nanobody-stabilized active state of the  (2) adrenoceptor. *Nature*. 2011; 469: 175±180. <https://doi.org/10.1038/nature09648> PMID: 21228869
23. Rasmussen SGF, DeVree BT, Zou Y, Kruse AC, Chung KY, Kobilka TS, et al. Crystal structure of the  2 adrenergic receptor-Gs protein complex. *Nature*. 2011; 477: 549±555. <https://doi.org/10.1038/nature10361> PMID: 21772288
24. Ring AM, Manglik A, Kruse AC, Enos MD, Weis WI, Garcia KC, et al. Adrenaline-activated structure of  2-adrenoceptor stabilized by an engineered nanobody. *Nature*. 2013; 502: 575±579. <https://doi.org/10.1038/nature12572> PMID: 24056936
25. Cherezov V, Rosenbaum DM, Hanson MA, Rasmussen SGF, Thian FS, Kobilka TS, et al. High-resolution crystal structure of an engineered human beta2-adrenergic G protein-coupled receptor. *Science*. 2007; 318: 1258±1265. <https://doi.org/10.1126/science.1150577> PMID: 17962520
26. Zou Y, Weis WI, Kobilka BK. N-terminal T4 lysozyme fusion facilitates crystallization of a G protein coupled receptor. *PLoS One*. 2012; 7: e46039. <https://doi.org/10.1371/journal.pone.0046039> PMID: 23056231
27. Granier S, Manglik A, Kruse AC, Kobilka TS, Thian FS, Weis WI, et al. Structure of the  -opioid receptor bound to naltrindole. *Nature*. 2012; 485: 400±404. <https://doi.org/10.1038/nature11111> PMID: 22596164
28. Fenalti G, Giguere PM, Katritch V, Huang X-P, Thompson AA, Cherezov V, et al. Molecular control of  -opioid receptor signalling. *Nature*. 2014; 506: 191±196. <https://doi.org/10.1038/nature12944> PMID: 24413399
29. Gaulton A, Bellis LJ, Bento AP, Chambers J, Davies M, Hersey A, et al. ChEMBL: a large-scale bioactivity database for drug discovery. *Nucleic Acids Res*. 2012; 40: D1100±7. <https://doi.org/10.1093/nar/gkr777> PMID: 21948594
30. Irwin JJ, Sterling T, Mysinger MM, Bolstad ES, Coleman RG. ZINC: a free tool to discover chemistry for biology. *J Chem Inf Model*. 2012; 52: 1757±1768. <https://doi.org/10.1021/ci3001277> PMID: 22587354
31. Bolton EE, Wang Y, Thiessen PA, Bryant SH. Chapter 12 PubC hem: Integrated Platform of Small Molecules and Biological Activities. In: Wheeler Ralph A. and Spellmeyer David C., editor. *Annual Reports in Computational Chemistry*. Elsevier; 2008. pp. 217±241.
32. Okuno Y, Tamon A, Yabuuchi H, Nijima S, Minowa Y, Tonomura K, et al. GLIDA: GPCR  ligand database for chemical genomics drug discovery   database and tools update. *Nucleic Acids Res*. 2008; 36: D907  D912. <https://doi.org/10.1093/nar/gkm948> PMID: 17986454
33. Pawson AJ, Sharman JL, Benson HE, Faccenda E, Alexander SPH, Buneman OP, et al. The IUPHAR/BPS Guide to PHARMACOLOGY: an expert-driven knowledgebase of drug targets and their ligands. *Nucleic Acids Res*. 2014; 42: D1098±106. <https://doi.org/10.1093/nar/gkt1143> PMID: 24234439
34. Gatica EA, Cavasotto CN. Ligand and decoy sets for docking to G protein-coupled receptors. *J Chem Inf Model*. 2012; 52: 1  6. <https://doi.org/10.1021/ci200412p> PMID: 22168315

35. Gentry PR, Kokubo M, Bridges TM, Kett NR, Harp JM, Cho HP, et al. Discovery of the First M5-Selective and CNS Penetrant Negative Allosteric Modulator (NAM) of a Muscarinic Acetylcholine Receptor: (S)-9b-(4-Chlorophenyl)-1-(3,4-difluorobenzoyl)-2,3-dihydro-1H-imidazo[2,1-a]isoindol-5(9bH)-one (ML375). *J Med Chem*. 2013; 56: 9351±9355. <https://doi.org/10.1021/jm4013246> PMID: 24164599
36. Woo AY-H, Wang T-B, Zeng X, Zhu W, Abernethy DR, Wainer IW, et al. Stereochemistry of an agonist determines coupling preference of beta2-adrenoceptor to different G proteins in cardiomyocytes. *Mol Pharmacol*. 2009; 75: 158±165. <https://doi.org/10.1124/mol.108.051078> PMID: 18838481
37. Abagyan R, Totrov M, Kuznetsov D. ICM Δ A new method for protein modeling and design: Applications to docking and structure prediction from the distorted native conformation. *J Comput Chem*. 1994; 15: 488±506.
38. OpenEye Scientific Software, Inc., Santa Fe, NM, USA, www.eyesopen.com. OEChem, version 1.7.4. 2010.
39. Abagyan R, Totrov M. Biased Probability Monte Carlo Conformational Searches and Electrostatic Calculations for Peptides and Proteins. *J Mol Biol*. 1994; 235: 983±1002. <https://doi.org/10.1006/jmbi.1994.1052> PMID: 8289329
40. Katritch V, Rueda M, Lam PC-H, Yeager M, Abagyan R. GPCR 3D homology models for ligand screening: lessons learned from blind predictions of adenosine A2a receptor complex. *Proteins*. 2010; 78: 197±211. <https://doi.org/10.1002/prot.22507> PMID: 20063437
41. Pearlman DA, Charifson PS. Improved scoring of ligand-protein interactions using OWFEG free energy grids. *J Med Chem*. 2001; 44: 502±511. PMID: 11170640
42. Hunter JD. Matplotlib: A 2D Graphics Environment. *Comput Sci Eng*. 2007; 9: 90±95.
43. van der Walt S, Colbert SC, Varoquaux G. The NumPy Array: A Structure for Efficient Numerical Computation. *Comput Sci Eng*. 2011; 13: 22±30.
44. Pedregosa F, Varoquaux G, Gramfort A, Michel V, Thirion B, Grisel O, et al. Scikit-learn: Machine Learning in Python. *J Mach Learn Res*. 2011; 12: 2825±2830.
45. Marcou G, Rognan D. Optimizing fragment and scaffold docking by use of molecular interaction fingerprints. *J Chem Inf Model*. 2007; 47: 195±207. <https://doi.org/10.1021/ci600342e> PMID: 17238265
46. Jones E, Oliphant T, Peterson P. {SciPy}: Open source scientific tools for {Python}. citeulike.org; 2001.
47. Brändén C-I, Alwyn Jones T. Between objectivity and subjectivity. *Nature*. 1990; 343: 687±689.
48. Burmeister WP. Structural changes in a cryo-cooled protein crystal owing to radiation damage. *Acta Crystallogr Biol Crystallogr*. 2000; 56: 328±341.
49. Adams PD, Afonine PV, Bunkóczi G, Chen VB, Davis IW, Echols N, et al. PHENIX: a comprehensive Python-based system for macromolecular structure solution. *Acta Crystallogr Biol Crystallogr*. 2010; 66: 213±221.
50. Goldfeld DA, Murphy R, Kim B, Wang L, Beuming T, Abel R, et al. Docking and free energy perturbation studies of ligand binding in the kappa opioid receptor. *J Phys Chem B*. 2015; 119: 824±835. <https://doi.org/10.1021/jp5053612> PMID: 25395044
51. Lenselink EB, Beuming T, Sherman W, van Vlijmen HWT, IJzerman AP. Selecting an optimal number of binding site waters to improve virtual screening enrichments against the adenosine A2A receptor. *J Chem Inf Model*. 2014; 54: 1737±1746. <https://doi.org/10.1021/ci5000455> PMID: 24835542



Published in final edited form as:

Biochem Pharmacol. 2017 July 15; 136: 99–108. doi:10.1016/j.bcp.2017.03.018.

Characterization of signal bias at the GLP-1 receptor induced by backbone modification of GLP-1

Marlies V. Hager^{1,†}, Lachlan Clydesdale^{2,†}, Samuel H. Gellman^{1,*}, Patrick M. Sexton^{2,*}, and Denise Wootten^{2,*}

¹Department of Chemistry, University of Wisconsin, Madison, Wisconsin

²Drug Discovery Biology, Monash Institute of Pharmaceutical Sciences and Department of Pharmacology, Monash University, Parkville, Australia

Abstract

The glucagon-like peptide-1 receptor (GLP-1R) is a class B G protein-coupled receptor that is a major therapeutic target for the treatment of type 2 diabetes. Activation of this receptor promotes insulin secretion and blood glucose regulation. The GLP-1R can initiate signaling through several intracellular pathways upon activation by GLP-1. GLP-1R ligands that preferentially stimulate subsets among the natural signaling pathways (“biased agonists”) could be useful as tools for elucidating the consequences of specific pathways and might engender therapeutic agents with tailored effects. Using HEK-293 cells recombinantly expressing human GLP-1R, we have previously reported that backbone modification of GLP-1, via replacement of selected α -amino acid residues with β -amino acid residues, generates GLP-1 analogues with distinctive preferences for promoting G protein activation versus β -arrestin recruitment. Here, we have explored the influence of cell background across these two parameters and expanded our analysis to include affinity and other key signaling pathways (intracellular calcium mobilization and ERK phosphorylation) using recombinant human GLP-1R expressed in a CHO cell background, which has been used extensively to demonstrate biased agonism of GLP-1R ligands. The new data indicate that α/β -peptide analogues of GLP-1 exhibit a range of distinct bias profiles relative to GLP-1 and that broad assessment of signaling endpoints is required to reveal the spectrum of behavior of modified peptides. These results support the view that backbone modification via $\alpha \rightarrow \beta$ amino acid replacement can enable rapid discovery of peptide hormone analogues that display substantial signal bias at a cognate GPCR.

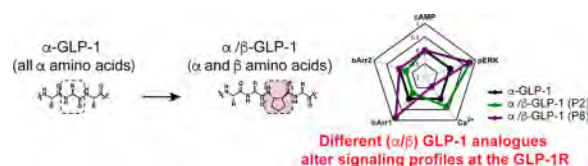
Graphical abstract

*To whom correspondence should be addressed.

†These authors contributed equally to this work

Conflict of interest statement

The authors declare the following competing financial interest(s): S.H.G. is an inventor on a patent application covering GLP-1 analogues described here; S.H.G. is a cofounder of Longevity Biotech, Inc., which is pursuing biomedical applications of α/β -peptides.



1. Introduction

Type 2 diabetes mellitus is a chronic metabolic disorder characterized by insulin resistance, decreased insulin production, and the gradual failure of pancreatic β cells.¹ These features result in consistently high glucose levels in patients,² a condition that can lead to severe complications and premature death.¹ Current diabetes treatments include insulin-sensitizing agents,³ exogenous insulin,⁴ and, more recently, agonists of the glucagon-like peptide 1 receptor (GLP-1R).⁵ This receptor has garnered interest because of its role not only in regulating blood glucose levels, but also in promoting other cellular and physiological outcomes that are impaired in diabetic patients; GLP-1R agonists increase satiety, decrease gastric emptying and enhance β cell health.⁶ The most potent native agonists of the GLP-1R are two closely related forms of the glucagon-like peptide-1, which are designated GLP-1(7–36)NH₂ and GLP-1(7–37). Both are generated via processing of a longer precursor. These two peptides are referred to collectively as “GLP-1” below.

Binding of GLP-1 to the extracellular surface of the GLP-1R promotes recruitment of several G proteins, including G α s, G α q, G α i and G α o,^{7–9} as well as β -arrestin 1 and β -arrestin 2, to the cytoplasmic surface of the receptor.^{9, 10} While Gs stimulation is principally linked to activation of adenylate cyclase and cAMP formation, the canonical driver of GLP-1-stimulated insulin secretion,⁶ Gs, Gq and Gi/o proteins can each lead to mobilization of intracellular calcium and/or ERK1/2 phosphorylation, in a ligand- and cell-type-specific manner.^{7–9} β -arrestins can modulate cell proliferation and apoptosis, at least in part through activation of MAPKs such as ERK1/2,^{11, 12} while also playing a role in β -cell-mediated insulin secretion.¹¹

The pleiotropy of signaling initiated by GPCRs allows for the potential of individual ligands of a specific receptor to generate distinct profiles of response, a phenomenon termed biased agonism.^{13–15} At a receptor level, bias is engendered by unique interactions between ligands and the receptor that, in turn, can stabilize distinct ensembles of conformations that promote differential engagement with effector proteins (e.g., a G protein or a β -arrestin).^{16, 17} Biased agonists have received substantial attention for their potential as tools for elucidating GPCR signaling mechanisms, and as therapeutic candidates that might exert focused physiological effects by minimizing activation of pathways other than those that offer therapeutic benefit.^{15, 18, 19}

Both peptidic and non-peptidic ligands of the GLP-1R can exhibit biased agonism.^{20–24} For example, oxyntomodulin, a natural ligand for the GLP-1R, and the clinically approved agonist exendin-4 exhibit bias in canonical signaling pathways and for arrestin recruitment, relative to GLP-1 in recombinant expression systems^{9, 25} and in insulinoma cells that natively express the GLP-1R.⁹ Moreover, an N-terminally modified form of exendin-4,

termed exendin P5, that exhibited bias away from arrestin recruitment (i.e., G protein-biased relative to exendin-4), had a distinct profile of response in rodent models of type 2 diabetes, providing evidence that biased agonists of the GLP-1R may provide novel opportunities for therapeutic intervention.²³

Recently, we have begun to explore a non-traditional approach to generate new GLP-1 analogues, involving replacement of selected α -amino acid residues with β -amino acid residues (Figure 1A).^{24, 26} This backbone-modification strategy has produced “ α/β -peptides” that function as β -arrestin-biased GLP-1R agonists in the context of HEK-293 cells recombinantly expressing the human GLP-1R.²⁴ Backbone modification has received relatively little attention as an approach to the design of peptide hormone analogues, but holds significant promise for generation of novel peptides.^{22, 24, 26–33}

Properly designed α/β -peptides can adopt a conformation that closely mimics the α -helix.³⁴ α -Helix-mimetic α/β -peptides can bind tightly to specific target proteins.³⁵ One advantage of α/β -peptides over their α -peptide counterparts is resistance to degradation by proteases;^{36, 37} proteolysis can limit the *in vivo* efficacy of α -peptides. The C-terminal portion of GLP-1 forms an α -helix in the GLP-1R-bound state,³⁸ and this structural insight encouraged us to examine α/β -peptide analogues of GLP-1.²⁶ Among previously described GLP-1 analogues **P1** - **P9** (Figure 1), the most highly substituted is α/β -peptide **P4**, which contains five $\alpha \rightarrow \beta$ substitutions in the C-terminal region and two Aib (α -aminoisobutyric acid) substitutions in the N-terminal region. The Aib replacements protect the N-terminus from degradation by dipeptidyl peptidase 4 (DPP4) and neprilysin. Peptides **P1** - **P3** and **P5** - **P9** each contain a subset of the seven substitutions in **P4**. The $\alpha \rightarrow \beta$ substitutions in **P4** occur in a repeating $\alpha\alpha\beta$ pattern (β residue at every fourth position), with the specific β residue sites based on positions at which GLP-1 tolerates side chain incorporation into a lactam bridge.^{39, 40} Previously, we found that **P1** - **P9** could activate the GLP-1R to stimulate cAMP production^{24, 26} and to recruit β -arrestins, and a subset of these α/β -peptides displayed biased signaling relative to GLP-1.²⁴

The ability to detect bias and indeed the observed direction of bias are dependent upon the breadth of endpoints studied and the cellular system used to explore this behavior. While the proximal driver for biased agonism may be at the level of receptor conformation, the expression of this bias (the observed bias) is critically dependent upon the expression, quantity and localization of effector and regulatory proteins within each cellular context.

The studies described below provide a new and deeper understanding of the signaling properties of **P1** - **P9** at the GLP-1R by analyzing these peptides in a different cellular context (recombinantly expressed human GLP-1R in CHO cells, in contrast to the HEK293 cells used in previous studies), measuring peptide affinities, and broadening the range of signaling endpoints to include ERK1/2 phosphorylation and intracellular calcium mobilization. These latter endpoints are both relevant to the physiological signaling of the GLP-1R and have been characterized in this cell background in response to other biased agonists of the GLP-1R. Thus, the new data allow direct comparison of biased profiles of the α/β -peptides with bias profiles of previously studied peptides.

2. Materials and Methods

2.1 Materials

Dulbecco's modified Eagle's medium (DMEM), hygromycin-B, and Fluo-4 acetoxymethyl ester were purchased from Invitrogen (Carlsbad, CA, USA). Fetal bovine serum (FBS) was purchased from Thermo Fisher Scientific (Melbourne, Victoria, Australia). AlphaScreen™ reagents, and LANCE HTRF cAMP kit were purchased from PerkinElmer Life Sciences (Waltham, MA, USA). SureFire™ ERK1/2 reagents were generously supplied by TGR Biosciences (Adelaide, South Australia, Australia). GLP-1 was purchased from Mimotopes (Victoria, Australia).

All other reagents were purchased from Sigma (St. Louis, MO, USA) or BDH Merck (Melbourne, Vic, Australia) and were of an analytical grade.

2.2 Peptide Synthesis

Peptides were synthesized in house as previously described.²⁴

2.3 Transfections and Cell Culture

Wildtype GLP-1R was isogenically integrated into FlpIn-Chinese hamster ovary (FlpInCHO) cells (Invitrogen), and selection of receptor-expressing cells was accomplished by treatment with 600 µg/mL hygromycin-B as previously reported.⁴¹ Transfected and parental FlpInCHO cells were maintained in Dulbecco's modified Eagle's medium supplemented with 5 % (v/v) FBS, 600 µg/mL hygromycin-B and incubated in a humidified environment at 37 °C in 5 % CO₂. FlpInCHO cells stably expressing the GLP-1R were used at passages 18–32. FlpInCHO cell lines stably expressing GLP-1 receptor-Rluc8 and β-arrestin-1-Venus were used at passages 16–35. FlpInCHO cell lines stably expressing GLP-1 receptor-Rluc8 and β-arrestin-2-Venus were used at passages 15–33.

2.4 Radioligand Binding Assays

GLP-1R FlpInCHO were seeded at a density of 3×10^4 cells/well into 96-well culture plates and incubated overnight at 37°C in 5% CO₂, and radioligand binding carried out as previously described using ¹²⁵I-GLP-1 as the radioligand.⁴² Briefly, binding assays were performed on whole cells incubated overnight at 4°C with 0.05 nM ¹²⁵I-GLP-1 tracer and increasing concentrations of unlabeled peptide. Cells were washed, solubilized in 0.1 M NaOH and radioactivity determined by γ-counting. For analysis, data were normalized to the specific binding for each individual experiment.

2.5 cAMP Accumulation

GLP-1R expressing FlpInCHO cells were seeded at a density of 3×10^4 cells/well into 96-well culture plates and incubated overnight at 37 °C in 5% CO₂. Growth media was replaced with stimulation buffer (phenol-free DMEM containing 0.1 % (w/v) BSA, 5 mM HEPES and 0.5 mM 3-isobutyl-1-methylxanthine) and incubated for 30 min at 37 °C in 5 % CO₂. Cells were stimulated with increasing concentrations of peptide ligand and incubated for 30 min at 37 °C in 5 % CO₂. The reaction was terminated by rapid removal of the ligand-containing buffer and addition of 50 µL of ice-cold 100 % ethanol. After ethanol

evaporation, 75 μ L of lysis buffer (0.1 % (w/v) BSA, 0.3 % (v/v) Tween 20, and 5 mM HEPES, pH 7.4) was added, and 5 μ L of lysate was transferred to a 384-well OptiPlate (PerkinElmer Life and Analytical Sciences).

The amount of cAMP present in each sample was determined using the Lance cAMP kit (PerkinElmer) with modifications to the manufacturer's instructions. Briefly, 5 μ L of the antibody solution (100-fold dilution of Alexa Fluor 647-anti cAMP antibody solution in detection buffer) was transferred into each well containing lysates/cAMP standard in reduced lighting conditions and incubated for 30 min at room temp. 10 μ L of detection mix (1:1:124 of solution 1 (2.5 % v/v Eu-W8044 labeled streptavidin (Eu-SA)), solution 2 (8.75 % v/v Biotin- cAMP) and detection buffer respectively) was added to each well in reduced lighting conditions, and the plate was incubated at room temperature for 1 h.

HTRF (Homogeneous Time Resolved Fluorescence) for each sample was detected using an EnVision™ plate reader with excitation at 320 nm and emission at 615 nm. cAMP was determined for all samples via conversion to concentration of cAMP using a cAMP standard curve that was detected in parallel. Data were normalized to the maximal response elicited by GLP-1. 100 μ M Forskolin was used as a positive control.

2.5 ERK1/2 Phosphorylation

GLP-1R expressing FlpInCHO cells were seeded at a density of 3×10^4 cells/well in DMEM with 5 % FBS into 96-well culture plates. The following day, the media was aspirated and the cells were washed twice with 100 μ L PBS. 90 μ L of serum free DMEM was then added and the cells were incubated overnight at 37 °C, 5 % CO₂. Ligand-mediated pERK1/2 was determined using the AlphaScreen™ ERK1/2 SureFire™ protocol as previously described.⁴³ Prior to generation of concentration response curves, initial pERK1/2 timecourse experiments were performed over 1 h using high concentrations of peptide ligand (1 μ M) to determine the time at which pERK1/2 was maximal after stimulation by agonists. Concentration response curves were then generated at this peak time point for each ligand. The kinetics of pERK1/2 response were similar for all ligands, peaking at 6 min. Data were normalized to the maximal response elicited by GLP-1. 10% FBS, determined at 6 min was used as a positive control.

2.7 Intracellular Calcium Mobilization

GLP-1R expressing FlpInCHO cells stably were seeded in clear 96-well plates, at a density of 3×10^4 cells/well, in growth media and allowed to adhere overnight. On the day of assay, cells were washed twice with 100 μ L modified Hanks buffered saline solution (HBSS containing; 150 mM NaCl, 2.6 mM KCl, 1.18 mM MgCl₂, 10 mM D-glucose, 10 mM HEPES, 2.2 mM CaCl₂, 2 mM probenecid, 0.5% (w/v) bovine serum albumin) and, in light diminished conditions, incubated for 1 h at 37°C with the cell permeant Ca²⁺ fluorophore, Fluo-4AM (final concentration of 10 μ M). After incubation, the assay plates were transferred to a Molecular Devices FlexStation (Molecular Devices, Palo Alto, CA, USA), and robotic addition of ligands was performed. Fluorescence was determined immediately after peptide addition, with an excitation wavelength set to 485 nm and an emission wavelength set to 525 nm, and readings were taken every 1.36 sec for 120 sec. Peak

magnitude was calculated using five-point smoothing, followed by correction against basal fluorescence. The peak value was used to create concentration-response curves. Data were normalized to the maximal response elicited by GLP-1. 100 μ M ATP was used as a positive control.

2.8 β -Arrestin Recruitment Assays

FlpInCHO cell lines stably expressing GLP-1 receptor-Rluc8 and either β -arrestin1- or β -arrestin2-Venus were generated using gateway technology. These cell lines were characterized and described previously.⁴⁴ Cells were seeded in 96-well white culture plates at a density of 4×10^4 cells/well and cultured for 24 h. Cells were rinsed once with HBSS to remove traces of phenol red and incubated in fresh HBSS for a further 15 min. The Rluc substrate coelenterazine-h was added to reach a final concentration of 5 μ M. After a 10 min incubation, the corresponding agonist was added, and bioluminescence resonance energy transfer (BRET) readings were collected using a LumiSTAR Omega instrument that allows sequential integration of signals detected in the 465–505 and 515–555 nm windows using filters with the appropriate band pass. The BRET signal was calculated by subtracting the ratio of 515–555 nm emission over 465–505 nm emission for a vehicle treated cell sample from the same ratio for the ligand treated cell sample. In this calculation, the vehicle treated cell sample represents background and results are expressed as ligand-induced BRET. This eliminates the requirement for measuring a donor only control sample. Initial time course experiments were performed over 20 min to determine the time at which β -arrestin1 and β -arrestin 2 recruitment was maximal for each ligand. Subsequent concentration response data were collected at this peak time. Data were normalized to the maximal response elicited by GLP-1.

2.9 Data Analysis

All data were analyzed using Prism 6 (GraphPad Software Inc., San Diego, CA, USA). For all analyses the data are unweighted, and each y value (mean of replicates for each individual experiment) is considered an individual point. To calculate IC_{50} , EC_{50} and E_{max} values, concentration response signaling data were analysed as previously described⁴¹ using a three-parameter logistic equation.

Signaling bias was also quantified as previously described by analysis of concentration-response curves with nonlinear regression using an operational model of agonism modified to directly estimate the ratio of τ/K_A .^{24, 25, 41}

$$Y = \frac{E_{max} \times (\tau_c/K_A)^n \times [A]^n}{[A]^n \times (\tau_c/K_A)^n + (1 + [A]/K_A)^n} \quad \text{Eq 1}$$

where E_m represents the maximal stimulation of the system, K_A is the agonist-receptor dissociation constant, in molar concentration, $[A]$ is the molar concentration of ligand and τ is the operational measure of efficacy in the system, which incorporates signaling efficacy and receptor density. All estimated τ/K_A ratios included propagation of error for both τ and K_A . Changes in τ/K_A ratios with respect to GLP-1 for each novel peptide was used to

quantitate bias between signalling pathways. Accordingly, bias factors included propagation of error from τ/K_A ratios of each pathway.

2.10 Statistics

Changes in peptide affinity, potency, efficacy or bias of each peptide in comparison to the GLP-1 control were statistically analysed with one-way analysis of variance and Dunnett's post test, and significance was accepted at $p < 0.05$.

3. Results

3.1 GLP-1R agonist affinities

We assessed the affinities of GLP-1 and peptides **P1** - **P9** for the GLP-1R expressed in FlpIn CHO cells via competition with a radiolabeled antagonist, ^{125}I -exendin(9–39) (Table 1, Figure 2A). The resulting IC_{50} values represent an averaged response arising from multiple receptor conformations that are present because individual GLP-1R molecules are presumably engaged by different intracellular partners; in this context the predominant signaling effector complex will have the most impact.

Incorporation of one (**P7**), three (**P1**, **P8**) or four (**P2**, **P9**) β amino acid residues, regardless of position, led to a ~10-fold reduction in affinity, relative to GLP-1, for the GLP-1R. Addition of a fifth β residue (**P3**, **P4**) further reduced affinity by 10-fold relative to other α/β -peptides in this set. α/β -Peptide **P4** contains two Aib substitutions, which seem to have little impact on affinity for the GLP-1R, because **P3** and **P4** are indistinguishable. This conclusion is supported by the observation that α -peptides **P5** and **P6**, which contain one or both of the Aib substitutions in **P4**, display only slightly reduced affinity for the GLP-1R relative to GLP-1.

3.2 Evaluation of cAMP production stimulated by **P1** - **P9**

We measured cAMP accumulation in response to **P1** - **P9** in FlpIn CHO cells stably expressing the human GLP-1R (Table 1, Figure 2B). We observed a modest decline in potency arising from $\alpha \rightarrow \beta$ replacement (**P1**→**P2**, **P3**), and a further decline upon Aib replacements (**P3**→**P4**). Peptides **P5** - **P7** were similar in potency to GLP-1, while **P8** and **P9** displayed substantially reduced potency relative to GLP-1. We previously assessed the activities of **P1** - **P9** in HEK293 cells transiently transfected with the human GLP-1R, using a kinetic GloSensor assay.^{24, 45} The cAMP potencies for **P1** - **P9** in the current study using an AlphaScreen assay are similar to those measured in HEK cells using the GloSensor assay.²⁴ The similarity between these two assays, involving different cell types, provides confidence that the trends are robust.

3.3 Evaluation of β -arrestin recruitment stimulated by **P1** - **P9**

We assessed β -arrestin-1 and β -arrestin-2 recruitment to the GLP-1R for **P1** - **P9** using β -arrestin-1 and β -arrestin-2 BRET assays in FlpInCHO cells stably expressing GLP-1R-Rluc8 and either β -arrestin-1 or β -arrestin-2-Venus (Table 1, Figure 2C,D). Among α/β -peptides **P1** - **P4**, we observed substantial declines in the recruitment of β -arrestins-1 and -2 upon introduction of β residues, relative to GLP-1, with little or no β -arrestin recruitment by

the maximally modified **P4**. α -Peptides **P5** and **P6** were similar to GLP-1 in terms of recruiting both β -arrestins-1 and -2 to the GLP-1R. α/β -Peptides **P7**, **P8** and **P9** exhibited substantial depressions in the maximum level of β -arrestin-1 and -2 recruited by the GLP-1R relative to GLP-1. The trends in β -arrestin recruitment are generally similar between the current set of assays and those reported previously,²⁴ and the inter-assay differences in peptide behavior are likely due to differences in cellular background (the original BRET assays involved transfected HEK293FT cells, while the new BRET assay were conducted in transfected FlpIn CHO cells) and differential expression of regulatory proteins between the two experiments. The previous BRET assays were conducted with cells that had been co-transfected with GRK5, which enhances the affinity of β -arrestins for GLP-1R by promoting receptor phosphorylation.^{10, 46} In contrast, GRK5 was not employed in the current BRET assays; thus, coupling between the receptor and each β -arrestin should be weakened in the new assays relative to the original assays. A second difference is specific to the β -arrestin-2 recruitment assay. The original BRET assay employed a mutated β -arrestin-2 plasmid (R393E, R395E), which is expected to enhance the BRET signal by preventing clathrin binding and subsequent receptor internalization.^{10, 46} In contrast, native β -arrestin-2 was used for the current assay.

3.4 Intracellular calcium mobilization stimulated by P1 - P9

To further explore how the different pathways activated by GLP-1 are affected by $\alpha \rightarrow \beta$ replacements, we measured the abilities of **P1 - P9** to promote intracellular calcium mobilization, which reports on $G\alpha_q$ and $G\alpha_s$ activation,^{9, 47-49} in FlpIn CHO cells stably expressing the human GLP-1R (Table 1, Figure 2E). Overall, $\alpha \rightarrow \beta$ replacements led to a reduction in calcium mobilization. Incorporation of three β -amino acid residues (**P1**) into the C-terminal region of GLP-1 had the smallest impact on activity, with the decrease in activity becoming more pronounced for analogues containing additional $\alpha \rightarrow \beta$ replacements extending toward the N-terminus of GLP-1 (**P2 - P4**). Incorporation of a single β residue at position 18 (**7**) led to a slight decrease in activity; further $\alpha \rightarrow \beta$ substitutions in the central region of GLP-1, to generate **P9**, essentially abolished calcium mobilization. Neither of the two Aib replacements (**P5** and **P6**) had a substantial effect on calcium mobilization in terms of potency or maximum response relative to GLP-1.

3.5 Stimulation of ERK1/2 phosphorylation stimulated by P1 - P9

As a complement to characterizing the activity of analogues **1-9** in activating various pathways directly mediated by interaction between the GLP-1R and intracellular effector proteins (i.e. G proteins $G\alpha_s$ and $G\alpha_q$, β -arrestin-1 or β -arrestin-2), we assessed the activity of **P1 - P9** in promoting ERK1/2 phosphorylation (Table 1, Figure 2F). GLP-1-mediated ERK1/2 phosphorylation is dependent on both G protein and β -arrestin activity,^{9, 11, 12, 49} which led us to explore how $\alpha \rightarrow \beta$ replacement would affect signaling in this composite pathway, particularly for the β -arrestin-biased α/β -peptides **P3**, **P8** and **P9**. Our data indicate that ERK1/2 phosphorylation was less strongly affected by $\alpha \rightarrow \beta$ replacements than was cAMP production, β -arrestin recruitment or calcium mobilization.

3.6 Stimulus bias induced by P1 - P9

To determine whether peptides among **P1 - P9** display signaling bias relative to GLP-1 in the expanded set of signaling pathways characterized, and to compare any bias between cAMP accumulation and β -arrestin recruitment in the CHO cell background to the β -arrestin bias we observed for α/β -peptides **P3**, **P8** and **P9** in the HEK293 cell, we analyzed the efficacy of each analogue in assays for cAMP accumulation, calcium mobilization, ERK1/2 phosphorylation, β -arrestin-1 recruitment or β -arrestin-2 recruitment using the operational model of agonism.^{50, 51} Transduction coefficients ($\log(\tau/K_A)$) for each analogue were extracted from concentration-response curves and compared with transduction coefficients for GLP-1 in each effector pathway. These comparisons allowed us to calculate a bias factor ($\log(\tau/K_A)$) for each peptide in terms of calcium mobilization, ERK1/2 phosphorylation, β -arrestin-1 recruitment or β -arrestin-2 recruitment relative to cAMP accumulation (Figure 3, Table 2). We also determined bias factors for each peptide in terms of β -arrestin-1 recruitment or β -arrestin-2 recruitment relative to either calcium mobilization or ERK1/2 phosphorylation (Figure 3, Table 2).

The bias factors summarized in Figure 3 and Table 2 reveal that α/β -peptides **P3**, **P4**, **P7**, **P8** and **P9** manifest significant bias in at least one pathway. For example, peptides **P3**, **P7** and **P8** are weakly biased toward cAMP accumulation relative to calcium mobilization (Figure 3A). Peptides **P3**, **P4** and **P9** are biased toward ERK1/2 phosphorylation relative to cAMP accumulation (Figure 3B). Peptides **P3**, **P8** and **P9** are biased toward β -arrestin-1 recruitment relative to cAMP production (Figure 3A). None among **P1 - P9** displayed bias toward or away from β -arrestin-2 recruitment relative to cAMP accumulation (Figure 3D); however, bias factors could not be calculated for **P4**, **P8** and **P9** due to weak β -arrestin-2 responses to these peptides (Figure 2, Table 1). For this reason, it was impossible to robustly compare β -arrestin-2 recruitment with other signaling pathways.

4. Discussion and Conclusions

The characterization of **P1 - P9** in the current study was performed in CHO cells, while our initial studies with these analogues were performed in HEK293 cells; thus, these two studies collectively allow one to assess the impact of cellular background on the manifestation of biased agonism.²⁴ Moreover, because the current studies evaluate bias for **P1 - P9** in terms of a more diverse set of signaling and regulatory endpoints relative to the previous study, the data reported here allow a more complete understanding of the activity profiles of these GLP-1 analogues, and these data can be used to compare the bias profiles of **P1 - P9** to the profiles of known agonists of the GLP-1R.

The bias factors for **P1 - P9** in terms of β -arrestin recruitment relative to cAMP production, shown in Figure 4 and Table 2, are reasonably consistent with those of our previous study,²⁴ particularly for β -arrestin-1. Small differences in bias factor are evident for analogues that do not display strong bias, but analogues that display strong bias, such as **P8** and **P9**, are biased toward β -arrestin-1 recruitment over cAMP (either accumulation or production) in both sets of experiments. Analogue **P3** is significantly biased in the CHO cell background, and trends towards bias in the HEK cells, although the latter effect is not statistically

significant. The consistency in bias factors for β -arrestin-1 recruitment relative to cAMP indicates that, for β -arrestin-1 recruitment, differences in cell background between the two sets of experiments do not significantly impact the identification of an analogue as either biased or not biased, even if changes in cellular background do slightly alter the relative efficacy for individual analogues between experiments. The β -arrestin-1 bias factors calculated for **P3**, **P8** and **P9** in CHO cells are consistently larger than those calculated for these peptides in HEK293 cells, suggesting more efficient coupling in the CHO cells, despite the overexpression of GRK5 in the HEK293 cells.²⁴ Thus, the current studies imply that GRKs other than GRK5 are the predominant sources of receptor phosphorylation in the CHO cell background.

In our previous study, **P3**, **P8** and **P9** exhibited bias toward β -arrestin-2 recruitment over cAMP production,²⁴ but in the new study activity was too low in the β -arrestin-2 recruitment assays to allow bias factor calculation for these α/β -peptides. The previous system was engineered to enhance β -arrestin-2 coupling through a combination of overexpression of GRK5 and mutation (R393E, R395E) of the arrestin that enhance the BRET signal by preventing clathrin binding and subsequent receptor internalization.^{10, 46} In the current assay, we examined recruitment of native β -arrestin-2, which was poorly recruited by lower-efficacy peptides. The lack of quantitative signal for these peptides makes interpretation of potential changes to signaling bias between the two cell types problematic. Overall, the pattern of bias changes in the enhanced β -arrestin-2 assay in HEK293 cells, along with the β -arrestin-1 profiles in both CHO and HEK cells, indicate fundamental differences in the properties of the **P3**, **P8** and **P9** α/β -peptides relative to the GLP-1 itself. Comparing the bias profiles of **P1** - **P9** between CHO and HEK293 cells highlights that the utility of using recombinant systems lies in probing bias and in fingerprinting the activity profiles of different agonists, but not in making specific claims about the relevance of observed bias to physiological effects manifested in native cells and whole organisms.

Expanding the diversity of pathways characterized in the current study, relative to the previous report, reveals more extensive bias within **P1** - **P9** beyond bias toward β -arrestin recruitment over cAMP (Table 2, Figure 3). Among **P3**, **P4**, **P7**, **P8** and **P9**, each α/β -peptide manifests significant bias in at least one pathway. **P3**, **P7** and **P8** are all weakly biased toward cAMP accumulation relative to calcium mobilization, though these analogues are only weakly active in both pathways. **P3**, **P4** and **P9** are biased toward ERK1/2 phosphorylation over cAMP accumulation; weak but statistically insignificant trends of this type are observed for other peptides, including **P2** and **P8**. Overall, backbone modification has only limited impact on ERK1/2 phosphorylation, leading to bias towards this pathway over those for which substantial changes in response are observed. The pathway that most closely parallels the trend in bias for ERK1/2 phosphorylation is β -arrestin-1 recruitment, toward which **P3**, **P8** and **P9** are biased over cAMP accumulation. The ERK1/2 phosphorylation signal in CHO cells is a composite of β -arrestin- and G protein-dependent signaling,^{9, 11, 12} and the correlation between ERK1/2 phosphorylation bias and β -arrestin-1 bias suggests that the β -arrestin pathway is predominant for **P3**, **P8** and **P9** for causing ERK1/2 phosphorylation. However, the proposed β -arrestin pathway dominance may not pertain to all α/β -peptides. Among the ERK1/2 phosphorylation-biased compounds, **P4** is

the most strongly biased toward ERK1/2 phosphorylation over cAMP production, but **P4** caused no measurable signal in the β -arrestin-recruitment assays, despite the robust pERK1/2 response. Understanding the relative bias of **P4** for ERK1/2 phosphorylation versus β -arrestin recruitment will require more sensitive assays of β -arrestin recruitment.

Some among **P1 - P9** display selective bias toward or away from either β -arrestin-1 recruitment or β -arrestin-2 recruitment when compared with various other pathways. **P6**, for example, is biased toward β -arrestin-1 recruitment over calcium mobilization, but not does not favor β -arrestin-2 recruitment over calcium mobilization. Moreover, **P7** favors ERK1/2 phosphorylation over β -arrestin-2 recruitment, while not favoring ERK1/2 phosphorylation over β -arrestin-1 recruitment or vice versa. Cases in which GLP-1 analogues selectively favor or disfavor either β -arrestin-1 or β -arrestin-2 recruitment suggest the intriguing possibility that these analogues could serve as starting points for more strongly biased GLP-1 agonists that could be used to parse the roles of β -arrestin-1 and β -arrestin-2 activity at the GLP-1R. However, this possibility would need to be carefully assessed in physiological target cells, because the efficiency of recruitment of each β -arrestin is likely to be influenced by the complement of GRKs that are expressed.

One interesting outlier in the comparison of ERK1/2 phosphorylation and β -arrestin-1 and -2 recruitment for our α/β -peptides is **P2**, which is significantly biased toward ERK1/2 phosphorylation over β -arrestin-2 recruitment (in addition, **P2** trends towards bias of ERK1/2 phosphorylation over β -arrestin-1 recruitment). **P2** is also biased towards calcium mobilization over β -arrestin-2 recruitment (with a trend in this direction for β -arrestin-1), suggesting that the **P2** α/β -peptide may have a novel G protein bias profile.

Several well-studied peptides, including exendin-4 and oxyntomodulin, have been identified as biased agonists of the GLP-1R.^{9, 25} Both exendin-4 and oxyntomodulin bias the GLP-1R toward β -arrestin-1 recruitment and β -arrestin-2 recruitment over cAMP accumulation in experiments performed in FlpIn CHO cells.^{9, 25} Oxyntomodulin also biases the GLP-1R toward ERK1/2 phosphorylation over cAMP accumulation, but exendin-4 does not exhibit bias toward ERK1/2 phosphorylation.^{9, 25} The observation that exendin-4 and oxyntomodulin are both biased toward β -arrestin recruitment but only oxyntomodulin is also biased toward ERK1/2 phosphorylation may be explained by different degrees of contribution from β -arrestin-1 and β -arrestin-2 activity in mediating downstream ERK1/2 phosphorylation.⁹ The distinct bias profiles for these two peptides indicate different modes of activation of the GLP-1R in response to either oxyntomodulin or exendin-4.

Because the bias factors calculated for **P1 - P9** in this work are derived from experiments performed in the same FlpIn CHO cells that were used in the experiments to determine bias for exendin-4 and oxyntomodulin, the bias for **P1 - P9** can be compared to that observed for exendin-4 and oxyntomodulin without concerns that either differences in cellular background or in assay format are the cause of distinct bias profiles between discrete agonists. Figure 5 provides a graphical summary of bias effects that allows ready comparison of **P1 - P9** (Figure 5A, B) or exendin-4⁹ and oxyntomodulin⁹ (Figure 5C) with GLP-1 in terms of all five of the GLP-1R signaling outcomes we monitored. Each “web of bias” is constructed to convey bias relative to the cAMP production pathway. **P4** is

illustrated in both Figure 5A, which highlights ERK1/2 phosphorylation-biased ligands, and 5B as a reference for the α/β peptides.

Comparing the bias profiles for oxyntomodulin and exendin-4 to those for **P3**, **P4**, **P8** and **P9**, which each display significant bias toward either β -arrestin-1 or ERK1/2 phosphorylation or both over cAMP,^{9, 24, 25} we can categorize each GLP-1 analogue as being either “oxyntomodulin-like” or “exendin-4-like” in terms of its bias profile. (This categorization is imperfect, because both oxyntomodulin and exendin-4 are also biased toward β -arrestin-2 over cAMP,^{9, 25} while no β -arrestin-2 bias factors could be calculated for any among **P3**, **P4**, **P8** or **P9**.) **P3** and **P9** are both biased toward β -arrestin-1 and ERK1/2 phosphorylation over cAMP, making them “oxyntomodulin-like” biased agonists of the GLP-1R. **P8** is biased toward β -arrestin-1 over cAMP but not toward ERK1/2 phosphorylation over cAMP, and is therefore an “exendin-4-like” biased agonist of the GLP-1R. The differences in bias profiles for **P8** compared to **P3** and **P9** indicate that these sets of analogues differ in how they activate the GLP-1R. **P4** is biased toward ERK1/2 phosphorylation over cAMP production, but no bias factor could be determined for **P4** in terms of β -arrestin-1 over cAMP; thus, the bias profile of **P4** is unique because it differs from the profile of either exendin-4 or oxyntomodulin.

We have previously shown that modifying the backbone of GLP-1 *via* incorporation of β -amino acid residues can generate agonists that engender significant bias toward β -arrestin-1 and/or β -arrestin-2 recruitment over cAMP production relative to GLP-1 itself.²⁴ Here, we expand the characterization of these biased peptides to include receptor-affinity measurements and additional signaling endpoint measurements. Our new data show that several among the α - and α/β -peptides we characterized are biased toward additional signaling outcomes beyond β -arrestin recruitment, thereby highlighting the importance of monitoring a diverse set of signaling and regulatory endpoints when characterizing novel agonists to identify biased agonists. These new results strengthen the conclusion that $\alpha \rightarrow \beta$ residue replacement can alter receptor signaling relative to the parent α -peptide. Thus, $\alpha \rightarrow \beta$ residue replacement may prove to be a general method by which receptor selectivity can be engineered into a peptide agonist that activates its cognate receptor to initiate different signaling pathways. The α/β -peptides characterized in this work may have utility as tools to probe the roles of β -arrestin recruitment and ERK1/2 phosphorylation in GLP-1R signaling. Moreover, these α/β -peptides could provide a platform to develop pathway-selective therapeutic agents targeting the GLP-1R.

Acknowledgments

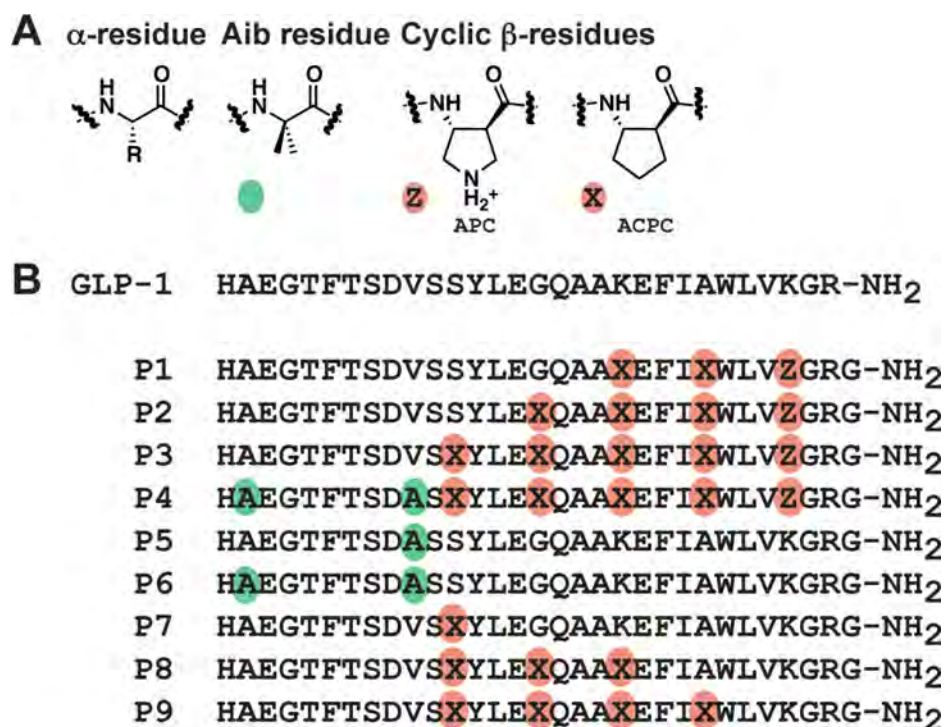
This work was supported by the National Institute of General Medical Sciences (NIGMS) (GM056414, to S.H.G.) and the National Health and Medical Research Council of Australia (NHMRC) (project grants [1061044] and [1065410], and NHMRC program grant [1055134] to P.M.S. and D.W.); P.M.S. is a NHMRC Principal Research Fellow. D.W. is a NHMRC Career Development Fellow. M.V.H. was supported in part by a Chemical Biology Interface Training Grant from NIGMS (T32 GM008505). Support for this research was provided by the University of Wisconsin–Madison, Office of the Vice Chancellor for Research and Graduate Education with funding from the Wisconsin Alumni Research Foundation.

References

1. Zaccardi F, Webb DR, Yates T, Davies MJ. Pathophysiology of type 1 and type 2 diabetes mellitus: a 90-year perspective. *Postgrad Med J*. 2016; 92:63–69. [PubMed: 26621825]
2. DeFronzo RA. Pathogenesis of Type 2 (non-insulin dependent) diabetes mellitus: a balanced overview. *Diabetologia*. 1992; 35:389–397. [PubMed: 1516769]
3. Hundal RS, Inzucchi SE. Metformin: new understandings, new uses. *Drugs*. 2003; 63:1879–1894. [PubMed: 12930161]
4. Swinnen SG, Hoekstra JB, DeVries JH. Insulin therapy for type 2 diabetes. *Diabetes Care*. 2009; 32(Suppl. 2):S253–259. [PubMed: 19875560]
5. Holst JJ, Knop FK, Vilsboll T, Krarup T, Madsbad S. Loss of incretin effect is a specific, important, and early characteristic of type 2 diabetes. *Diabetes Care*. 2011; 34(Suppl 2):S251–257. [PubMed: 21525464]
6. Baggio LL, Drucker DJ. (2007) Biology of incretins: GLP-1 and GIP. *Gastroenterology*. 2007; 132:2131–2157. [PubMed: 17498508]
7. Montrose-Rafizadeh C, Avdonin P, Garant MJ, Rodgers BD, Kole S, Yang H, et al. Pancreatic Glucagon-Like Peptide-1 Receptor Couples to Multiple G Proteins and Activates Mitogen-Activated Protein Kinase Pathways in Chinese Hamster Ovary Cells. *Endocrinology*. 1999; 140:132–1140.
8. Hallbrink M, Homqvist T, Olsson M, Ostenson CG, Efendic S, Langel U. Different domains in the third intracellular loop of the GLP-1 receptor are responsible for Gas Gai/Gao activation. *Biochim Biophys Acta*. 2001; 1546:79–86.
9. Wootten D, Reynolds CA, Smith KJ, Mobarec JC, Koole C, Savage EE, et al. The Extracellular Surface of the GLP-1 Receptor Is a Molecular Trigger for Biased Agonism. *Cell*. 2016; 165:1632–1643. [PubMed: 27315480]
10. Jorgensen R, Kubale V, Vrecl M, Schwartz TW, Elling CE. Oxyntomodulin differentially affects glucagon-like peptide-1 receptor beta-arrestin recruitment and signaling through Galpha(s). *J Pharmacol Exp Ther*. 2007; 322:148–154.
11. Sonoda N, Imamura T, Yoshizaki T, Babendure JL, Lu JC, Olefsky JM. Beta-Arrestin-1 mediates glucagon-like peptide-1 signaling to insulin secretion in cultured pancreatic beta cells. *Proc Natl Acad Sci USA*. 2008; 105:6614–6619. [PubMed: 18445652]
12. Quoyer J, Longuet C, Broca C, Linck N, Costes S, Varin E, et al. GLP-1 mediates antiapoptotic effect by phosphorylating Bad through a beta-arrestin 1-mediated ERK1/2 activation in pancreatic beta-cells. *J Biol Chem*. 2010; 285:1989–2002. [PubMed: 19915011]
13. Rajagopal S, Rajagopal K, Lefkowitz RJ. Teaching old receptors new tricks: biasing seven-transmembrane receptors. *Nat Rev Drug Discov*. 2010; 9:373–386. [PubMed: 20431569]
14. Reiter E, Ahn S, Shukla AK, Lefkowitz RJ. Molecular mechanism of beta-arrestin-biased agonism at seven-transmembrane receptors. *Annu Rev Pharmacol Toxicol*. 2002; 52:179–197.
15. Kenakin T, Christopoulos A. Signalling bias in new drug discovery: detection, quantification and therapeutic impact. *Nat Rev Drug Discov*. 2013; 12:205–216. [PubMed: 23411724]
16. Kobilka BK, Deupi X. Conformational complexity of G-protein-coupled receptors. *Trends Pharmacol Sci*. 2007; 28:397–406. [PubMed: 17629961]
17. Kenakin T. Ligand-selective receptor conformations revisited: the promise and the problem. *Trends Pharmacol Sci*. 2003; 24:346–354. [PubMed: 12871667]
18. Whalen EJ, Rajagopal S, Lefkowitz RJ. Therapeutic potential of beta-arrestin- and G protein-biased agonists. *Trends Mol Med*. 2011; 17:126–139. [PubMed: 21183406]
19. Appleton KM, Luttrell LM. Emergent biological properties of arrestin pathway-selective biased agonism. *J Recept Signal Transduct Res*. 2013; 33:153–161. [PubMed: 23448506]
20. Koole C, Wootten D, Simms J, Valant C, Sridhar R, Woodman OL, et al. Allosteric ligands of the glucagon-like peptide 1 receptor (GLP-1R) differentially modulate endogenous and exogenous peptide responses in a pathway-selective manner: implications for drug screening. *Mol Pharmacol*. 2010; 78:456–465. [PubMed: 20547734]

21. Wootten D, Savage EE, Willard FS, Bueno AB, Sloop KW, Christopoulos A, et al. Differential activation and modulation of the glucagon-like peptide-1 receptor by small molecule ligands. *Mol Pharmacol*. 2013; 83:822–834. [PubMed: 23348499]
22. Broichhagen J, Podewin T, Meyer-Berg H, von Ohlen Y, Johnston NR, Jones BJ, et al. Optical Control of Insulin Secretion Using an Incretin Switch. *Angew Chem Intl Ed Engl*. 2015; 54:15565–15569.
23. Zhang H, Sturchler E, Zhu J, Nieto A, Cistrone PA, Xie J, et al. Autocrine selection of a GLP-1R G-protein biased agonist with potent antidiabetic effects. *Nat Commun*. 2015; 6:8918. [PubMed: 26621478]
24. Hager MV, Johnson LM, Wootten D, Sexton PM, Gellman SH. beta-Arrestin-Biased Agonists of the GLP-1 Receptor from beta-Amino Acid Residue Incorporation into GLP-1 Analogues. *J Am Chem Soc*. 2016; 138:14970–14979. [PubMed: 27813409]
25. Wootten D, Simms J, Miller LJ, Christopoulos A, Sexton PM. Polar transmembrane interactions drive formation of ligand-specific and signal pathway-biased family B G protein-coupled receptor conformations. *Proc Natl Acad Sci USA*. 2013; 110:5211–5216. [PubMed: 23479653]
26. Johnson LM, Barrick S, Hager MV, McFedries A, Homan EA, Rabaglia ME, et al. A potent alpha/beta-peptide analogue of GLP-1 with prolonged action in vivo. *J Am Chem Soc*. 2014; 136:12848–12851. [PubMed: 25191938]
27. Denton EV, Craig CJ, Pongratz RL, Appelbaum JS, Doerner AE, Narayanan A, et al. A beta-Peptide Agonist of the GLP-1 Receptor, a Class B GPCR. *Org Lett*. 2013; 15:5318–5321. [PubMed: 24087900]
28. Bai X, Niu Y, Zhu J, Yang AQ, Wu YF, Ye XS. A new GLP-1 analogue with prolonged glucose-lowering activity in vivo via backbone-based modification at the N-terminus. *Bioorg Med Chem*. 2016; 24:1163–1170. [PubMed: 26895657]
29. Peggion E, Mammi S, Schievano E, Silvestri L, Schiebler L, Bisello A, et al. Structure-Function Studies of Analogues of Parathyroid Hormone (PTH)-1–34 Containing beta-Amino Acid Residues in Positions 11–13. *Biochemistry*. 2002; 41:8162–8175. [PubMed: 12069609]
30. Schievano E, Mammi S, Carretta E, Fiori N, Corich M, Bisello A, et al. Conformational and Biological Characterization of Human Parathyroid Hormone hPTH(1–34) Analogues Containing beta-Amino Acid Residues in Positions 17–19. *Biopolymers*. 2003; 70:534–547. [PubMed: 14648764]
31. Cheloha RW, Maeda A, Dean T, Gardella TJ, Gellman SH. Backbone modification of a polypeptide drug alters duration of action in vivo. *Nat Biotechnol*. 2014; 32:653–655. [PubMed: 24929976]
32. Olson KE, Kosloski-Bilek LM, Anderson KM, Diggs BJ, Clark BE, Gledhill JM Jr, et al. Selective VIP Receptor Agonists Facilitate Immune Transformation for Dopaminergic Neuroprotection in MPTP-Intoxicated Mice. *J Neurosci*. 2015; 35:16463–16478. [PubMed: 26674871]
33. Cheloha RW, Watanabe T, Dean T, Gellman SH, Gardella TJ. Backbone Modification of a Parathyroid Hormone Receptor-1 Antagonist/Inverse Agonist, *ACS Chem. Biol*. 2016; 11:2752–2762.
34. Horne WS, Johnson LM, Ketas TJ, Klasse PJ, Lu M, Moore JP, et al. Structural and biological mimicry of protein surface recognition by alpha/beta-peptide foldamers. *Proc Natl Acad Sci USA*. 2009; 106:14751–14756. [PubMed: 19706443]
35. Checco JW, Gellman SH. Targeting recognition surfaces on natural proteins with peptidic foldamers. *Curr Opin Struct Biol*. 2016; 39:96–105. [PubMed: 27390896]
36. Horne WS, Boersma MD, Windsor MA, Gellman SH. Sequence-based design of alpha/beta-peptide foldamers that mimic BH3 domains. *Angew Chem Intl Ed Engl*. 2008; 47:2853–2856.
37. Steer DS, Lew RA, Perlmutter P, Smith AI, Aguilar M-I. Beta-amino acids: versatile peptidomimetics. *Curr Med Chem*. 2002; 9:811–822. [PubMed: 11966446]
38. Underwood CR, Garibay P, Knudsen LB, Hastrup S, Peters GH, Rudolph R, et al. Crystal structure of glucagon-like peptide-1 in complex with the extracellular domain of the glucagon-like peptide-1 receptor. *J Biol Chem*. 2010; 285:723–730. [PubMed: 19861722]

39. Miranda LP, Winters KA, Gegg CV, Patel A, Aral J, Long J, et al. Design and Synthesis of Conformationally Constrained Glucagon-Like Peptide-1 Derivatives with Increased Plasma Stability and Prolonged in Vivo Activity. *J Med Chem*. 2008; 51:2758–2765. [PubMed: 18412318]
40. Murage EN, Schroeder JC, Beinborn M, Ahn JM. Search for alpha-helical propensity in the receptor-bound conformation of glucagon-like peptide-1. *Bioorg Med Chem*. 2008; 16:10106–10112. [PubMed: 18952440]
41. Koole C, Wootten D, Simms J, Miller LJ, Christopoulos A, Sexton PM. Second extracellular loop of human glucagon-like peptide-1 receptor (GLP-1R) has a critical role in GLP-1 peptide binding and receptor activation. *J Biol Chem*. 2012; 287:3642–3658. [PubMed: 22147710]
42. Koole C, Wootten D, Simms J, Valant C, Miller LJ, Christopoulos A, et al. Polymorphism and ligand dependent changes in human glucagon-like peptide-1 receptor (GLP-1R) function: allosteric rescue of loss of function mutation. *Mol Pharmacol*. 2011; 80:486–497. [PubMed: 21616920]
43. May LT, Avlani VA, Langmead CJ, Herdon HJ, Wood MD, Sexton PM, et al. Structure-function studies of allosteric agonism at M2 muscarinic acetylcholine receptors. *Mol Pharmacol*. 2007; 72:463–476. [PubMed: 17525129]
44. Savage EE, Wootten D, Christopoulos A, Sexton PM, Furness SG. A simple method to generate stable cell lines for the analysis of transient protein-protein interactions. *BioTechniques*. 2013; 54:217–221. [PubMed: 23581469]
45. Binkowski BF, Butler BL, Stecha PF, Eggers CT, Otto P, Zimmerman K, et al. A luminescent biosensor with increased dynamic range for intracellular cAMP. *ACS Chem Biol*. 2011; 6:1193–1197. [PubMed: 21932825]
46. Jorgensen R, Martini L, Schwartz TW, Elling CE. Characterization of glucagon-like peptide-1 receptor beta-arrestin 2 interaction: a high-affinity receptor phenotype. *Mol Endocrinol*. 2005; 19:812–823. [PubMed: 15528268]
47. Wheeler MB, Lu M, Dillon JS, Leng XH, Chen C, Boyd AE. Functional expression of the rat glucagon-like peptide-1 receptor, and evidence for coupling to both adenylyl cyclase and phospholipase-C. *Endocrinology*. 1993; 133:57–62. [PubMed: 8391428]
48. Holz GG. Epac: a new cAMP-binding protein in support of glucagon-like peptide-1 receptor-mediated signal transduction in the pancreatic beta-cell. *Diabetes*. 2004; 53:5–13. [PubMed: 14693691]
49. Thompson A, Kanamarlapudi V. Agonist-induced internalisation of the glucagon-like peptide-1 receptor is mediated by the Galphaq pathway. *Biochemical pharmacology*. 2015; 93:72–84. [PubMed: 25449603]
50. Black JW, Leff P. Operational models of pharmacological agonism. *Proc R Soc Lond B Biol Sci*. 1983; 220:141–162. [PubMed: 6141562]
51. Kenakin T, Watson C, Muniz-Medina V, Christopoulos A, Novick S. A simple method for quantifying functional selectivity and agonist bias. *ACS chemical neuroscience*. 2012; 3:193–203. [PubMed: 22860188]

**Figure 1.**

A. Amino acids used in this study. Colored circles indicate non-natural substitutions: green circles represent the non-proteinogenic α -residue Aib, and orange circles represent ring-constrained β -residues (X = ACPC, Z = APC). **B.** GLP-1(7–36)NH₂ and α/β -peptide analogues **1** - **9** (based on GLP-1(7–37)NH₂). Each peptide has a free N-terminus and a primary amide at the C-terminus.

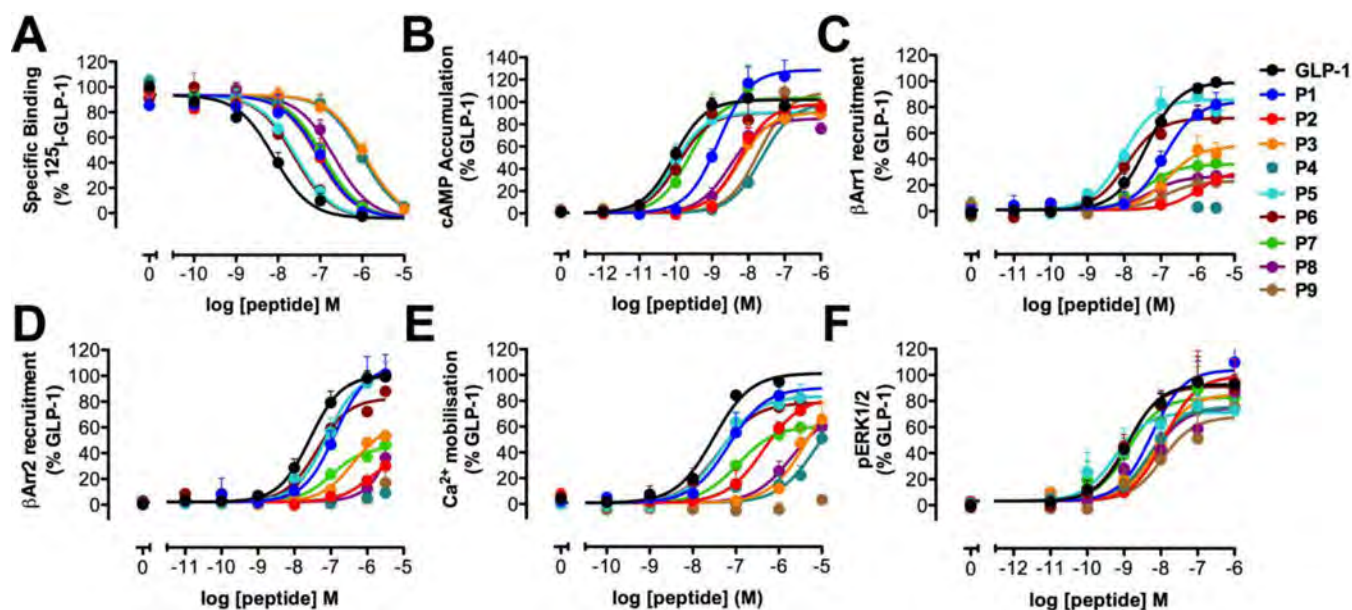


Figure 2.

Binding and signaling profiles of GLP-1 and α - and α/β -peptides **P1 – P9** in FlpInCHO cells stably expressing the human GLP-1R. Concentration-response curves for (A) GLP-1R binding, (B) cAMP accumulation, (C) Ca^{2+} mobilization, (D) ERK1/2 phosphorylation, (E) β -Arrestin-1 recruitment, and (F) β -Arrestin-2 recruitment. Data are normalized to the maximum response elicited by GLP-1 in each assay, and analyzed using a three-parameter logistic equation. Values are the mean + S.E.M. of three to four individual experiments, conducted in duplicate.

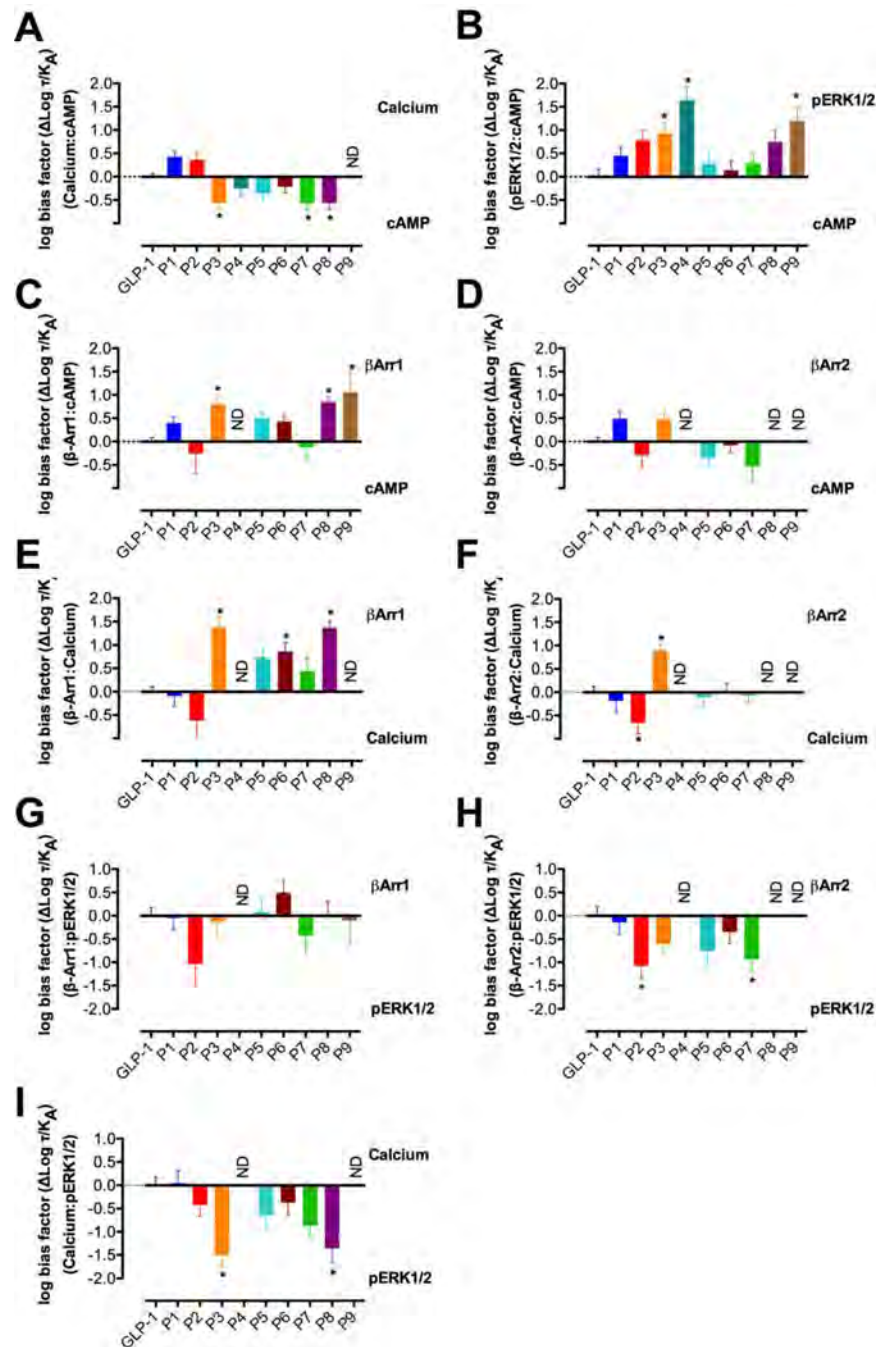


Figure 3.

Bias factors for α - and α/β -peptides **P1 – P9** relative to GLP-1 in Ca^{2+} mobilization relative to cAMP accumulation (A), ERK1/2 phosphorylation relative to cAMP accumulation (B), β -Arrestin-1 recruitment relative to cAMP accumulation (C), β -Arrestin-2 recruitment relative to cAMP accumulation (D), β -Arrestin-1 recruitment relative to Ca^{2+} mobilization (E), β -Arrestin-2 recruitment relative to Ca^{2+} mobilization (F), β -Arrestin-1 recruitment relative to ERK1/2 phosphorylation (G), and β -Arrestin-2 recruitment relative to ERK1/2 phosphorylation (H). Changes in $\log (\tau/K_A)$ were calculated to provide a measure of the

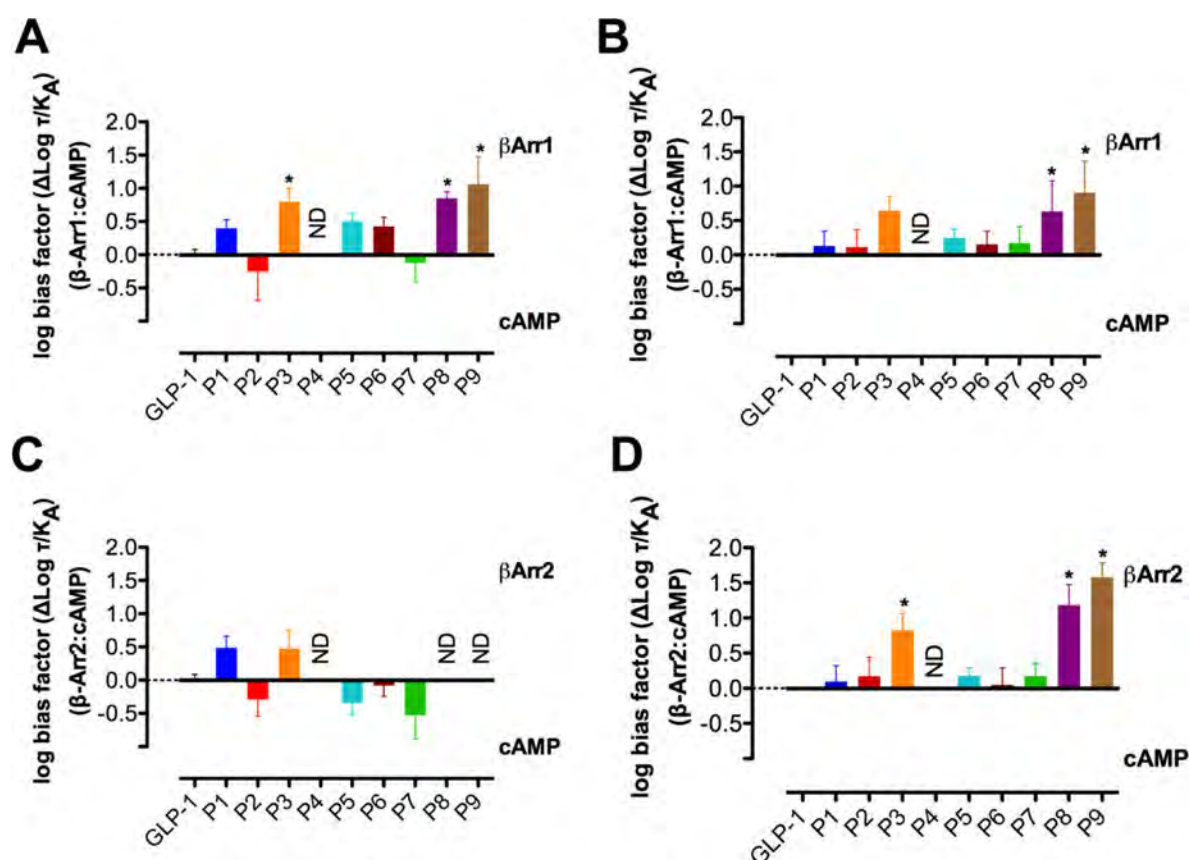
degree of stimulus bias exhibited between different signaling pathways relative to that of the reference agonist GLP-1. Values are the mean \pm SEM of three to four individual experiments, conducted in duplicate. * statistically significant difference from GLP-1 using one-way analysis of variance followed by Dunnett's test.

Author Manuscript

Author Manuscript

Author Manuscript

Author Manuscript

**Figure 4.**

Comparison of the bias factors for α- and α/β-peptides **P1 – P9** relative to GLP-1 for β-Arrestin-1 recruitment versus cAMP accumulation between FlnCHO cells (A) and HEK293 cells²⁴ (B) and for β-Arrestin-2 recruitment versus cAMP accumulation between FlnCHO cells (C) and HEK293 cells²⁴ (D). Changes in log (τ/K_A) were calculated to provide a measure of the degree of stimulus bias exhibited between different signaling pathways relative to that of the reference agonist GLP-1. * statistically significant difference from GLP-1 using one way analysis of variance followed by Dunnett's test (P<0.05).

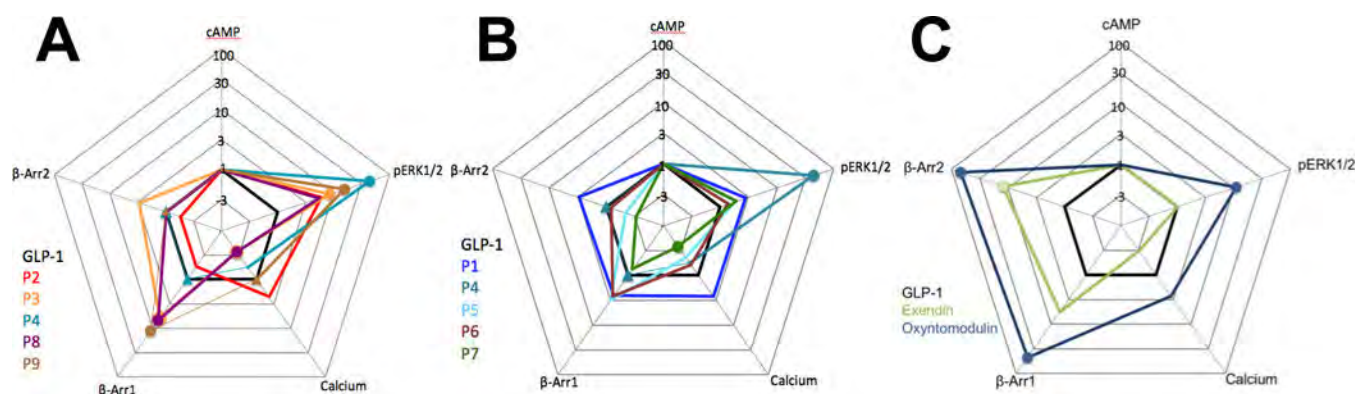


Figure 5.

Webs of bias for α - and α/β -peptides **P1 – P9** (A, B) and known biased agonists exendin-4 and oxyntomodulin⁹ (C) relative to GLP-1 in FlpInCHO cells stably expressing the human GLP-1R. Circles represent data that are significantly biased. Triangles represent data where no value could be defined. The τ/K_A ratio extracted from standard concentration-response data is used to calculate bias factors ((τ/K_A)) through normalization of the transduction coefficient (τ/K_A) to a reference ligand (GLP-1) and reference pathway (cAMP accumulation).

Table 1

Affinity and activity data for GLP-1 and α - and β -peptides **P1 – P9** in GLP-1R binding, cAMP accumulation, Ca^{2+} mobilization, ERK1/2 phosphorylation, β -Arrestin-1 recruitment, and β -Arrestin-2 recruitment.

	Affinity		cAMP		β -Arrestin-1		β -Arrestin-2		iCa^{2+}		pERK1/2	
	pIC ₅₀ (M)	pEC ₅₀ (M)	E _{max}	pEC ₅₀ (M)	E _{max}	pEC ₅₀ (M)	E _{max}	pEC ₅₀ (M)	E _{max}	pEC ₅₀ (M)	E _{max}	E _{max}
GLP-1	8.1 ± 0.1	10.0 ± 0.1	100	7.4 ± 0.1	100	7.6 ± 0.1	100	7.5 ± 0.1	100	8.9 ± 0.1	100	100
P1	7.0* ± 0.1	8.8* ± 0.1	130* ± 6	6.9 ± 0.2	85 ± 7	6.9 ± 0.1	108 ± 5	7.2 ± 0.3	89 ± 8	8.3 ± 0.2	112 ± 8	112 ± 8
P2	7.0* ± 0.1	8.2* ± 0.1	97 ± 6	6.0* ± 0.7	30* ± 20	5.9* ± 0.6	40* ± 20	6.4* ± 0.2	80 ± 10	7.9* ± 0.2	107 ± 9	107 ± 9
P3	5.9* ± 0.1	8.3* ± 0.2	89 ± 6	6.8 ± 0.3	50* ± 7	6.4* ± 0.3	61* ± 9	5.3* ± 0.3	100 ± 30	8.1 ± 0.2	92 ± 8	92 ± 8
P4	6.0* ± 0.1	7.6* ± 0.2	97 ± 7	N.D.	N.D.	N.D.	N.D.	5.2* ± 0.5	90 ± 40	8.3 ± 0.2	81 ± 8	81 ± 8
P5	7.6* ± 0.1	10.0 ± 0.1	102 ± 5	8.0 ± 0.1	87 ± 4	7.1 ± 0.1	102 ± 4	7.3 ± 0.2	82 ± 6	9.2 ± 0.3	89 ± 6	89 ± 6
P6	7.6* ± 0.1	9.9 ± 0.1	89 ± 5	7.9 ± 0.2	72 ± 4	7.4 ± 0.1	82 ± 5	7.4 ± 0.2	78 ± 5	8.9 ± 0.2	80 ± 7	80 ± 7
P7	6.9* ± 0.1	9.6 ± 0.1	89 ± 5	7.4 ± 0.4	36* ± 6	7.0 ± 0.2	45* ± 4	7.0 ± 0.2	60 ± 5	8.9 ± 0.2	89 ± 7	89 ± 7
P8	6.7* ± 0.1	8.5* ± 0.2	83 ± 5	7.3 ± 0.6	27* ± 9	N.D.	N.D.	5.7* ± 0.4	59* ± 7	8.2 ± 0.3	80 ± 8	80 ± 8
P9	7.0* ± 0.1	7.7* ± 0.1	107 ± 5	6.9 ± 0.5	23* ± 6	N.D.	N.D.	N.D.	N.D.	8.0* ± 0.3	73 ± 9	73 ± 9

All experiments were performed in FlpIn CHO cells stably expressing the human GLP-1R. Data are normalized to the maximum response elicited by GLP-1 in each assay, and analyzed using a three-parameter logistic equation. pEC₅₀ values are the logarithm of the concentration of agonist that produces half the maximal response. E_{max} represents the maximal response normalized to that of GLP-1. Values are the mean ± S.E.M. of three to four individual experiments, conducted in duplicate. Maximum response values for incomplete curves are the predicted maximum derived from curve fitting.

* statistically significant difference from GLP-1 using one way analysis of variance followed by Dunnett's test (P<0.05).

Table 2

Stimulus bias exhibited by α - and β -peptides **P1** – **P9** relative to the reference agonist GLP-1.

	log(τ/K_A)							
	Ca ²⁺ vs cAMP	pERK1/2 vs cAMP	β Arr1 vs cAMP	β Arr2 vs cAMP	β Arr1 vs Ca ²⁺	β Arr2 vs Ca ²⁺	β Arr1 vs pERK1/2	β Arr2 vs pERK1/2
GLP-1	0.0 \pm 0.1	0.0 \pm 0.2	0.0 \pm 0.1	0.0 \pm 0.1	0.0 \pm 0.1	0.0 \pm 0.1	0.0 \pm 0.2	0.0 \pm 0.2
P1	0.4 \pm 0.1	0.5 \pm 0.2	0.4 \pm 0.1	0.5 \pm 0.2	-0.1 \pm 0.2	-0.2 \pm 0.2	0.0 \pm 0.2	-0.1 \pm 0.3
P2	0.4 \pm 0.1	0.8 \pm 0.2	-0.3 \pm 0.4	-0.3 \pm 0.3	-0.7 \pm 0.5	-0.7 [*] \pm 0.2	-1.0 \pm 0.5	-1.0 [*] \pm 0.3
P3	-0.6 [*] \pm 0.1	0.9 [*] \pm 0.2	0.8 [*] \pm 0.2	0.5 \pm 0.3	1.4 [*] \pm 0.2	0.9 [*] \pm 0.1	-0.1 \pm 0.3	-0.6 \pm 0.2
P4	-0.2 \pm 0.2	1.6 [*] \pm 0.3	N.D.	N.D.	N.D.	N.D.	N.D.	N.D.
P5	-0.4 \pm 0.2	0.3 \pm 0.3	0.5 \pm 0.1	-0.3 \pm 0.2	0.7 \pm 0.2	-0.1 \pm 0.2	0.1 \pm 0.3	-0.8 \pm 0.3
P6	-0.1 \pm 0.2	0.1 \pm 0.2	0.4 \pm 0.1	-0.1 \pm 0.2	0.9 [*] \pm 0.2	0.0 \pm 0.2	0.5 \pm 0.3	-0.3 \pm 0.2
P7	-0.6 [*] \pm 0.1	0.3 \pm 0.2	-0.1 \pm 0.3	-0.5 \pm 0.4	0.4 \pm 0.3	-0.1 \pm 0.1	-0.4 \pm 0.4	-0.9 [*] \pm 0.3
P8	-0.6 [*] \pm 0.1	0.7 \pm 0.3	0.8 [*] \pm 0.1	N.D.	1.4 [*] \pm 0.1	N.D.	0.0 \pm 0.3	N.D.
P9	N.D.	1.2 [*] \pm 0.3	1.1 [*] \pm 0.4	N.D.	N.D.	N.D.	-0.1 \pm 0.5	N.D.

Stimulus bias exhibited by **P1** – **P9** relative to GLP-1 in Ca^{2+} mobilization relative to cAMP accumulation, ERK1/2 phosphorylation relative to cAMP accumulation, β -Arrestin-1 recruitment relative to cAMP accumulation, β -Arrestin-2 recruitment relative to cAMP accumulation, β -Arrestin-1 recruitment relative to Ca^{2+} mobilization, β -Arrestin-2 recruitment relative to Ca^{2+} mobilization, β -Arrestin-1 recruitment relative to ERK1/2 phosphorylation, and β -Arrestin-2 recruitment relative to ERK1/2 phosphorylation. Changes in $\log(\tau/K_A)$ were calculated to provide a measure of the degree of stimulus bias exhibited between different signaling pathways relative to that of the reference agonist GLP-1. Values are the mean \pm SEM of three to four individual experiments, conducted in duplicate.

* statistically significant difference from GLP-1 using one-way analysis of variance followed by Dunnett's test.

Phase-plate cryo-EM structure of a class B GPCR-G-protein complex

Yi-Lynn Liang^{1*}, Maryam Khoshouei^{2*}, Mazdak Radjainia^{3†*}, Yan Zhang^{4*}, Alisa Glukhova¹, Jeffrey Tarrasch⁴, David M. Thal¹, Sebastian G. B. Furness¹, George Christopoulos¹, Thomas Coudrat¹, Radostin Danev², Wolfgang Baumeister², Laurence J. Miller⁵, Arthur Christopoulos¹, Brian K. Kobilka⁶, Denise Wootten¹, Georgios Skiniotis⁴ & Patrick M. Sexton¹

Class B G-protein-coupled receptors are major targets for the treatment of chronic diseases, such as osteoporosis, diabetes and obesity. Here we report the structure of a full-length class B receptor, the calcitonin receptor, in complex with peptide ligand and heterotrimeric $G_{\alpha_s}\beta\gamma$ protein determined by Volta phase-plate single-particle cryo-electron microscopy. The peptide agonist engages the receptor by binding to an extended hydrophobic pocket facilitated by the large outward movement of the extracellular ends of transmembrane helices 6 and 7. This conformation is accompanied by a 60° kink in helix 6 and a large outward movement of the intracellular end of this helix, opening the bundle to accommodate interactions with the α_5 -helix of G_{α_s} . Also observed is an extended intracellular helix 8 that contributes to both receptor stability and functional G-protein coupling via an interaction with the $G\beta$ subunit. This structure provides a new framework for understanding G-protein-coupled receptor function.

G-protein-coupled receptors (GPCRs) are the most abundant cell-surface receptor proteins, important for virtually all physiological processes. As major targets for treatment of disease, understanding GPCR structure and how this relates to their function is critically important for optimal exploitation of their therapeutic potential¹. GPCRs allosterically transmit extracellular signals to the inside of cells by forming complexes with transducers, such as G proteins or arrestins². To date, crystal structures of around 40 inactive class A GPCRs (of more than 800 encoded in the human genome) have been solved, with most being engineered to improve stability in detergents and/or crystal packing³. Far fewer agonist-bound GPCR structures have been determined, and only one in complex with a full heterotrimeric $G_{\alpha\beta\gamma}$ protein⁴. Transmembrane domain structures of class B GPCRs have been especially refractory to crystallization and are currently limited to two inactive state structures^{5–7}, with no reported full-length class B GPCR structures, to our knowledge.

Class B GPCRs bind physiologically and clinically important peptide hormones and are attractive targets for treatment of major chronic diseases⁸. These receptors have a large extracellular N-terminal domain (ECD) that is important for peptide binding. Multiple structures of the ECD fragments bound to short peptides have been reported⁹, but these do not inform on how bound peptides bind the receptor core for activation. The calcitonin receptor (CTR), a class B GPCR, is a therapeutic target for the treatment of a range of bone diseases, with salmon calcitonin and human calcitonin approved for clinical use¹⁰.

Single-particle cryo-electron microscopy (cryo-EM) provides a method to obtain high-resolution protein structure information without the need for crystallization. Notwithstanding the recent advances in electron detectors and cryo-EM data analysis, successful application of this technology for proteins/complexes smaller than 200 kDa remains challenging owing to the inherent low contrast that limits accurate alignment of projections to derive high resolution^{11,12}. The recently introduced approach of using a Volta phase plate for data acquisition

with increased contrast sidesteps many trade-offs that hamper structure determination of small proteins by cryo-EM^{13–15}. In the current study, we used Volta phase plates to image particles of an approximately 150 kDa complex comprising an unmodified CTR bound to a peptide agonist in complex with a heterotrimeric G_s protein. This enabled us to obtain the first near-atomic-resolution structure of an activated GPCR using cryo-EM.

Structure determination

To enable efficient expression and purification, the CTR was modified to replace the native signal peptide with haemagglutinin (HA), followed by a Flag epitope for affinity purification and an HRV 3C cleavage site, while the C terminus was modified by the addition of an HRV 3C cleavage site and histidine affinity tag (Extended Data Fig. 1). These modifications had no effect on receptor pharmacology (Extended Data Fig. 2).

To form an active, G-protein-coupled complex, the CTR was co-expressed with G_{α_s} , His- $G\beta_1$, and $G\gamma_2$ in HighFive insect cells and stimulated with an excess of the high-affinity agonist, salmon calcitonin (sCT) that has a very slow off-rate^{16,17}. The complex was solubilized in MNG/cholesteryl hemisuccinate and purified using an anti-Flag antibody affinity column and size-exclusion chromatography (SEC) (Extended Data Fig. 3). Further complex stabilization was achieved with the addition of a camelid antibody, Nb35, which binds at the G_{α_s} - $G\beta$ interface and was used in the determination of the β_2 adrenergic receptor (β_2 AR)- G_s heterotrimer structure⁴. Addition of purified Nb35 to insect cell membranes expressing CTR, G_{α_s} and $\beta\gamma$ before purification produced a monodispersed complex by SEC that remained stable at 4 °C for at least 5 days; however, as noted for the β_2 AR- G_s complex, the G_s heterotrimer could no longer bind to GTP γ S (Extended Data Figs 2e and 3e).

We recorded images of frozen-hydrated sCT-CTR- G_s complex using Volta phase-plate cryo-EM, obtaining particle projections with high

¹Drug Discovery Biology and Department of Pharmacology, Monash Institute of Pharmaceutical Sciences, Monash University, Parkville, 3052 Victoria, Australia. ²Department of Molecular Structural Biology, Max Planck Institute of Biochemistry, 82152 Martinsried, Germany. ³Department of Biochemistry and Molecular Biology, Monash University, Clayton, 3800 Victoria, Australia.

⁴Life Sciences Institute and Department of Biological Chemistry, University of Michigan Medical School, Ann Arbor, Michigan 48109-2216, USA. ⁵Department of Molecular Pharmacology and Experimental Therapeutics, Mayo Clinic, Scottsdale, Arizona 85259, USA. ⁶Department of Molecular and Cellular Physiology, Stanford University School of Medicine, Stanford, California 94305, USA. [†]Present address: FEI, 5651 GG Eindhoven, The Netherlands.

*These authors contributed equally to this work.

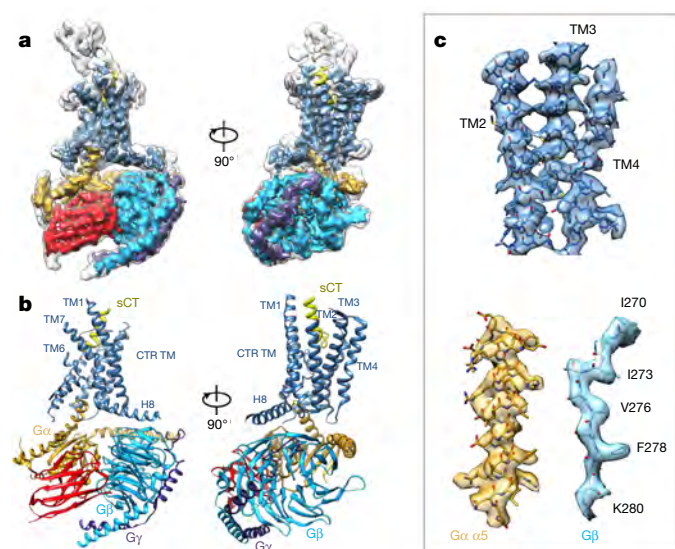


Figure 1 | The sCT-CTR- G_s cryo-EM structure. **a**, Orthogonal views of the cryo-EM map. The sharpened map with coloured densities (CTR transmembrane domain, blue; sCT, yellow; heterotrimeric G_s , copper, light blue and purple; Nb35, red) is overlaid with the non-sharpened map in transparency showing density for the ECD. **b**, Structure of the complex determined after refinement in the cryo-EM map. H8, helix 8. **c**, Snapshots of map versus model from transmembrane segments, Ras-like domain of $G\alpha$ α -helix 5 and $G\beta$.

contrast (Extended Data Fig. 4). 2D classification revealed averages with secondary structure features and sufficient distribution in orientation of particles to enable reconstructions. 3D classification with Relion¹⁸ facilitated the selection of about 106,000 particle projections, which were used to obtain a cryo-EM density map with a nominal global resolution of 4.1 Å, and 3.8 Å resolution at the interaction between the transmembrane region of CTR and G_s (Fig. 1, Extended Data Fig. 4).

The cryo-EM map allows for near-atomic interpretation of the regions of the complex corresponding to the G_s protein and nanobody and transmembrane helix bundle. An additional density, tightly inserted within an opening of the helical bundle and attributable to sCT is also resolved (Fig. 1a). The ECD is less well resolved owing to partial flexibility, while large variability in the $G\alpha_s$ α -helical domain (AHD) prevented reconstruction of this density (Extended Data Fig. 5). The AHD domain is discernible in low-resolution 3D maps, where it is observed to adopt variable conformations in respect to the Ras-like domain, consistent with previous studies on the β_2 AR- G_s heterotrimer complex¹⁹ and light-activated rhodopsin complexed with G_i ²⁰. This is interesting in the context of the CTR where two agonists, human and salmon calcitonin, promote ternary complexes with distinct G-protein conformations that exhibit different nucleotide affinities and have distinct efficacies¹⁷. The conformational heterogeneity of the sCT-CTR-complexed $G\alpha_s$ suggests that this may contribute to these observations.

We also observed multiple conformations of the receptor N-terminal ECD relative to the transmembrane core (Extended Data Fig. 5), indicating that, for the peptide-agonist-bound CTR, this domain remains flexible. This flexibility is likely to be important as modifications to sCT that extend secondary structure are detrimental to affinity and potency²¹. In the cryo-EM structure, the density corresponding to the ECD is lower in resolution than the rest of the complex (Extended Data Fig. 4d). Although this did not permit accurate modelling, there was strong agreement with the isolated ECD/sCT structure (Protein Data Bank (PDB) accession: 5II0)²² that could be fit to the density, contiguous with transmembrane domain 1 (TM1) (Extended Data Fig. 6a). There is also additional density in the ECD around residue 130, corresponding to predicted glycosylation in this region. As previously described²³, mutation of either Asn125 or Asn130 to Asp was

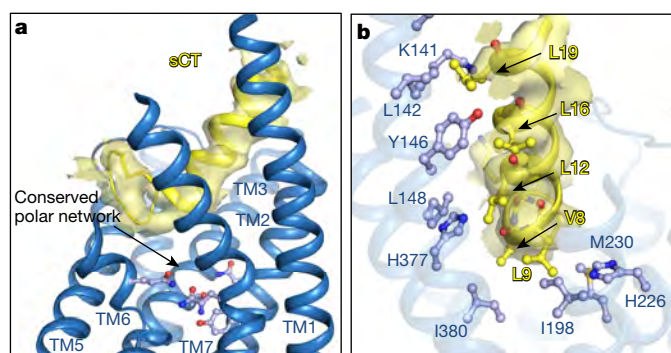


Figure 2 | The CTR transmembrane bundle orthosteric peptide-binding site. **a**, Cryo-EM density (yellow fill) for sCT in the CTR seven-transmembrane bundle (blue). The sCT N terminus sits one helical turn above a conserved polar network. Molecular models of the sCT backbone (yellow ribbon) align well with the density, side chain density, however, is not visible. **b**, Modelling suggests that the sCT hydrophobic face resides in a hydrophobic receptor environment formed by residues in TM1, TM2, TM3 and TM7.

detrimental to sCT affinity and function, suggesting that this glycosylation is required for normal agonist activity (Extended Data Fig. 6).

Structure of the activated CTR transmembrane bundle

The transmembrane bundle and the G-protein complex (minus the $G\alpha_s$ AHD) were resolved at a nominal resolution of 3.8 Å, with the quality of the cryo-EM density map highest within the G protein and at the $G\alpha_s$ -receptor interface. The local resolution varied within the CTR transmembrane bundle (Extended Data Fig. 4) with weaker density in the extracellular loops (ECLs), intracellular loops (ICLs), and the top of TM6. The limited resolution of the map in these regions suggests local flexibility that is probably required for receptor function. The CTR contains a very long extended helix 8, similar to that observed in the inactive state glucagon receptor (GCGR) structure⁷, implying that this may be a general feature for class B GPCRs. While the remaining CTR C terminus beyond helix 8 was present in the protein, it is not visible in the cryo-EM map, suggesting that this region remains mobile when the receptor is bound to a G protein.

sCT density indicates that the depth of the CTR orthosteric binding site (Figs 1 and 2a) is shallower than that predicted for some class B GPCRs^{7,24,25}, with the N terminus residing approximately one helical turn above a network of conserved class B polar residues. Limited density was observed for sCT side chains, making peptide modelling ambiguous. Although specific interactions could not be identified, sCT is likely to form extensive contacts with the tops of all transmembrane domains (with the exception of TM4), as well as ECL2. The N terminus of the calcitonin family of peptides is distinct from that of other orthosteric class B GPCR peptide ligands, with a cyclized N terminus formed by a disulfide bond between residues 1 and 7. The apparent outward movements of TM6 and TM7 (relative to inactive structures, as discussed below) appear crucial to accommodate the peptide N terminus (Fig. 2a).

Although there are multiple possible modelling solutions for sCT, we have reported the most parsimonious, taking into account the cryo-EM map and experimental data. This model predicts that sCT maintains helicity up to residue 6, forming an amphipathic helix with Val8, Leu12, Leu16 and Leu19 facing towards a hydrophobic receptor environment (Fig. 2b). This is in agreement with evidence that an amphipathic helix contributes to peptide activity²⁶ and consistent with that predicted from a solution NMR structure of sCT²⁷. Gln14 is predicted to form hydrogen bond interactions with the ECL2 backbone, yet is in an orientation with solvent accessibility (Extended Data Fig. 7a). This is an essential requirement as Gln14 can be directly labelled or replaced with a Lys to conjugate bulky substituents (radiolabels or fluorophores), while still maintaining peptide activity. In addition, two residues crucial for

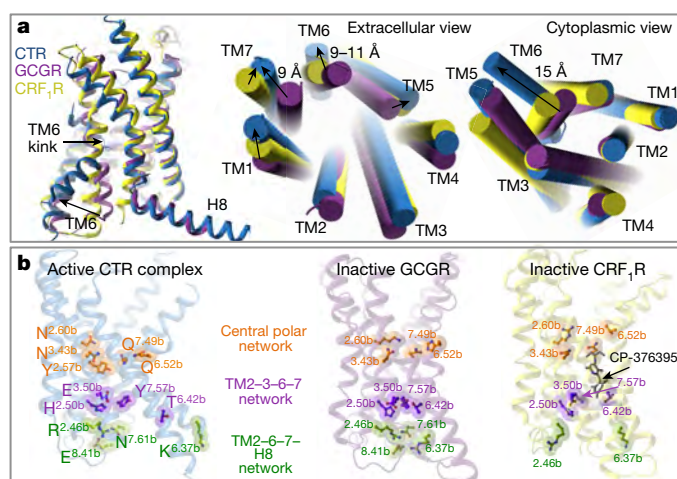


Figure 3 | Comparisons of inactive class B and the activated CTR structures. **a**, Side (left), extracellular (middle) and cytoplasmic (right) views of the sCT-CTR-G_s (blue) relative to inactive CRF₁R (PDB: 4Z9G, yellow) and GCGR (PDB: 5EE7, purple) structures. Differences in transmembrane domains at the extracellular and cytoplasmic faces are highlighted. **b**, The positions of class B conserved polar residues located within the activated CTR bundle (left), the inactive GCGR (middle) and the CP-376395-bound CRF₁R (right). The central polar network probably forms interactions in all structures, while the TM2-3-6-7 and TM2-6-7-H8 networks that stabilize class B inactive structures (as in the GCGR) are disrupted in the activated CTR. In the CRF₁R, CP-376395 binding also disrupts these interactions.

agonist activity, Ser5 and Thr6, are predicted to interact with TM5, potentially forming polar interactions with His302^{5.40b} (superscript indicates class B GPCR numbering²⁹) (Extended Data Fig. 7b). This model is supported by mutation of His302^{5.40b} to Ala that reduced sCT potency in cAMP production and ERK1/2 phosphorylation, consistent with reduced sCT affinity (Extended Data Fig. 7c). The first three residues in sCT make minimal receptor contacts in this model, consistent with experimental data showing that these residues can be removed without altering peptide activity²⁸.

Comparison of active CTR to inactive class B GPCR TMs

Comparison of the CTR complex with inactive class B GPCR structures (GCGR^{6,7} and corticotropin-releasing hormone receptor 1 (CRF₁R; ref. 5)) or inactive CTR homology models provides insight into transmembrane conformational transitions upon class B GPCR activation (Fig. 3a, Extended Data Fig. 8). The most striking observations relate to TM6 where there is a large outward movement at the cytoplasmic face in the activated CTR (approximately 15 Å) relative to the inactive structures when measured from the Cα at X^{6.35b}. An outward movement within TM6, as well as disordering and unwinding of this helix was observed at the extracellular face (9–11 Å when measured from the Cα of Phe^{5.56b}). This is correlated with an extremely sharp (around 60°) kink at the centre of TM6 formed around Pro^{6.47b}-X-X-Gly^{6.50b}. Importantly, residues within this motif influence agonist affinity, activation and function in both CTR and the related calcitonin receptor-like receptor^{30,31}. The very high conservation of the Pro^{6.47b}-X-X-Gly^{6.50b} motif in class B GPCRs (Supplementary Information Fig. 1) implies that these residues may be globally important for activation through the formation of a kink in TM6 that is much more pronounced than in any transmembrane helix in GPCR structures solved to date.

In comparison to both inactive structures, there is an inward movement at the top of TM1 in the CTR-G_s structure and a small outward movement at the top of TM5. TM7 movement differs when comparing individual inactive structures to the CTR-G_s complex (Fig. 3a). While the TM7 kink angle is similar in the inactive CRF₁R and the CTR, TM7

is shifted towards TM6 in the CTR. By contrast, there is a large, 9 Å outward movement in the top of TM7 in the CTR structure relative to the GCGR. While the differences observed in location of the top of transmembrane helices may represent physiologically relevant differences, we interpret them with caution because the inactive structures do not include the receptor ECDs. There is increasing evidence for a dynamic role of class B ECD-transmembrane-core interactions in receptor quiescence and activation^{32–35} and the large outward movement of helices 6 and 7 required for peptide binding support a model of class B GPCR quiescence where the tops of TM6 and TM7 are potentially constrained by ECL3 interactions with the far N-terminal ECD, a theory supported by experimental data on the glucagon receptor^{32–34}. Nonetheless, in all structures, the top of TM6/ECL3 has a large degree of structural flexibility, supported by its weak corresponding density in the cryo-EM map of the CTR-G_s complex (Extended Data Fig. 4d) and the high crystallographic temperature factors exhibited by inactive structures in these regions^{5,7}.

Interactions in conserved residues

Class B GPCRs contain highly conserved transmembrane domain polar residues that have crucial roles in receptor integrity, high-affinity agonist interaction and/or receptor activation and downstream signalling^{6,7,25,29,36–38}. A central polar network (Asn194^{2.60b}, Asn233^{3.43b}, Gln355^{6.52b} and Gln383^{7.49b} in the CTR) is present in all inactive structures^{5–7} and in our inactive CTR homology model. This network is preserved in the active CTR transmembrane bundle, although the exact interactions and their relative strengths probably vary in the different structures (Fig. 3b and Extended Data Fig. 8c), in a receptor- and peptide-specific manner^{25,29}. Not predicted from previous studies, Tyr191^{2.57b} is also involved in this network. This residue is unique to the CTR, being a hydrophobic Phe in all other class B receptors (Supplementary Fig. 1), suggesting receptor-specific differences in how the binding energy is translated through the protein to promote G-protein activation.

At the cytoplasmic face, an important interaction between His^{2.50b} and Glu^{3.50b}, considered to play an equivalent functional role in class B GPCRs to the DRY motif in class A GPCRs, is present in the inactive class B crystal structures^{5–7,29,36} and is maintained in the active CTR transmembrane bundle (Fig. 3b and Extended Data Fig. 8c). These residues form an extensive polar interaction network with Thr^{6.42b} and Tyr^{7.57b}, locking the base of the receptor in an inactive conformation in our inactive CTR homology model, consistent with that of the two published GCGR inactive structures^{6,7}. In the CRF₁R, these residues are further apart due to disruption by the thermostabilizing mutation Ala^{7.57b} and binding of the small-molecule antagonist⁵ (Fig. 3b). This network is broken in the CTR-G_s structure, with Tyr^{7.57b} forming new hydrogen bond interactions with the TM6 backbone (Fig. 3b and Extended Data Fig. 8c). This releases constraints on TM6 and probably assists in the large conformational transition of TM6 away from the core of the bundle. Consistent with this, mutation of these residues either results in constitutive activation³⁶ or reduced receptor expression^{29,36}.

At the cytoplasmic face, Arg^{2.46b}, Arg/Lys^{6.37b}, Asn^{7.61b} and Glu^{8.41b} (TM2-6-7-H8 network) form tight interactions in the GCGR inactive structure and our CTR homology model with two key salt bridges formed by Glu^{8.41b} with Arg^{2.46b} and Arg/Lys^{6.37b} (Fig. 3b). These interactions are not present in the inactive CRF₁R owing to the absence of helix 8, but have been predicted in other class B GPCRs^{36,38} and are likely conserved across the entire family. While the interaction between Glu^{8.41b} and Arg^{2.46b} is likely maintained in the active CTR-G_s structure, the salt bridge between Lys^{6.37b} and Glu^{8.41b} is broken with these residues residing 26 Å apart (Fig. 3b). The reordering of these side chains in the active structure releases ground state constraints on TM6.

The CTR-G_s interface

Extensive interactions formed between the CTR and Gα_s stabilize the active receptor conformation. The receptor-Gα_s interface is formed by

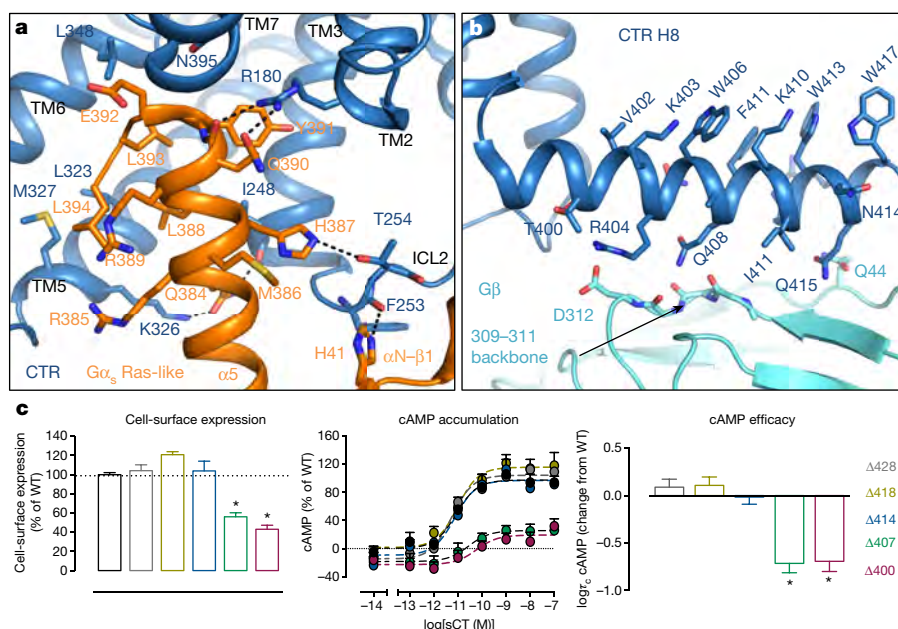


Figure 4 | CTR–G-protein interactions. **a**, $\alpha 5$ -helix of the Ras-like domain of $G\alpha_s$ (orange) docks into a CTR intracellular face cavity (blue) by the opening of TM6, forming polar and non-polar interactions. Histidine 41 at the $G\alpha_s$ αN – $\beta 1$ boundary interacts with the CTR ICL2 backbone. **b**, CTR helix 8 bulky aromatics heavily embed within the detergent micelle. Residues on the opposing face are in the vicinity of $G\beta_1$, where they probably form polar interactions. **c**, CTR pharmacological characterization in COS-7 cells following gradual deletion of the C terminus. Left, deletion after Trp406 ($\Delta 407$) results in markedly reduced cell-surface expression. Further truncation after Gln399 ($\Delta 400$) further reduced cell-surface expression, highlighting that bulky, detergent-buried residues within helix 8 are crucial for CTR cell-surface

localization. Middle, $\Delta 407$ and $\Delta 400$ had reduced maximal responses for cAMP production relative to wild type (WT). Right, calculation of cAMP efficacy via application of the Black–Leff operational model⁴³ to cAMP accumulation data, followed by correction for alterations in cell-surface expression, reveals that $\Delta 407$ has reduced cAMP efficacy ($\log_7 c$) that is not further reduced by additional truncation back to Gln399. This indicates that residues Thr400–Trp406 are crucial for cAMP efficacy that may be associated with their interaction with $G\beta_1$. Pharmacological data are given as mean + s.e.m. of five independent experiments performed in duplicate. * $P < 0.05$ compared to wild type using one-way analysis of variance followed by Dunnett's test.

residues located in TM2, 3, 5, 6, ICL2, ICL3 and helix 8 of the receptor with the $\alpha 4$ - and $\alpha 5$ -helices of the Ras-like domain of $G\alpha_s$, and the $G\alpha_s$ αN – $\beta 1$ junction of the G protein. The most extensive contacts consist of polar and hydrophobic van der Waals interactions between the receptor and the $\alpha 5$ -helix of the Ras-like domain of $G\alpha_s$ (Fig. 4a and Extended Data Fig. 9a). Class B GPCRs all predominantly couple to $G\alpha_s$ and several of the CTR residues that form interactions with the Ras-like domain of $G\alpha_s$ are highly conserved and have been previously implicated in G-protein coupling^{36,37}.

The buried interface between the receptor and the Ras-like domain of $G\alpha_s$ is 2,031 Å², while an interface of 663 Å² is also provided by the interaction of helix 8 of CTR with $G\beta_1$. Notably, helix 8 is heavily buried within the detergent micelle, facilitated by bulky aromatic residues and additional polar charged residues that can interact with lipid/detergent head groups (Fig. 4b and Extended Data Fig. 9b). Sequential deletions of the CTR C terminus support a role for helix 8 lipid interactions in receptor stability at the cell surface (Fig. 4c). While truncation after Trp413 ($\Delta 414$) had no effect on receptor function, truncation after Trp406 ($\Delta 407$) resulted in reduced cell-surface receptor expression. Further truncation ($\Delta 400$) resulted in a greater reduction in cell-surface expression, highlighting lipid interactions with receptor residues Thr400–Trp413 as essential for receptor stability. In addition, $\Delta 407$, but not $\Delta 414$ significantly reduced sCT-mediated cAMP efficacy, with no further reduction by $\Delta 400$, suggesting CTR– $G\beta$ interactions between residues 407 and 413 also contribute to the efficiency of G_s -mediated cAMP production (Fig. 4c). There is only limited density in this region of the map, however contacts would be predicted between the CTR Gln408 and $G\beta$ backbone. While side chain density is limited, the positioning of $C\alpha$ would orient Arg404 and Gln415 of the CTR towards Asp312 and Gln44 in $G\beta$, respectively. Nonetheless, these CTR residues have no effect on G_s -mediated cAMP

efficacy. $G\beta$ has additional roles in signalling, therefore it is possible that interactions in this region may contribute to other aspects of CTR function. A region of 12 amino acids within helix 8 that includes at least one important Trp residue is required for efficient cell-surface localization of the related calcitonin-like receptor³⁹. Owing to the presence of an extended α -helix in the inactive structure of the GCGR and the CTR, it is likely that this functional role of helix 8 in cell-surface stabilization and interactions with $G\beta$ is shared across the class B GPCR family.

The human CTR has a common, naturally occurring splice variant with an insertion of 16 amino acids between Arg174 and Ser175 that has attenuation of both G-protein-dependent signalling and receptor internalization⁴⁰. ICL1 is well resolved in the sCT–CTR– G_s structure, located above the first and seventh WD40 repeat (WD1 and WD7) domains of $G\beta$, and within close proximity to the N-terminal α -helical domain ($N\alpha$) of the α -subunit (Extended Data Fig. 9c). As such, the I1+ (CTb) isoform is likely to sterically interfere with receptor–G-protein interactions, leading to the attenuation in signalling.

Comparison of class A and class B GPCR– $G\alpha_s$ complex

An overlay of the G-protein heterotrimer in the sCT–CTR– G_s complex to that of the class A β_2 AR⁴ reveals only minor differences in the conformation of the G protein between the two structures (Fig. 5a). While the $G\alpha_s$ AHD was trapped in an open conformation in the β_2 AR– G_s crystal structure, it is not resolved at high resolution in the sCT–CTR– G_s complex owing to its inherent flexibility in the absence of nucleotide (Extended Data Fig. 5).

Comparing the two receptors reveals similar locations of the intracellular helical tips of TM1–3 and 5–7 (Fig. 5b). These transmembrane helices in class B inactive structures also overlay with class A inactive

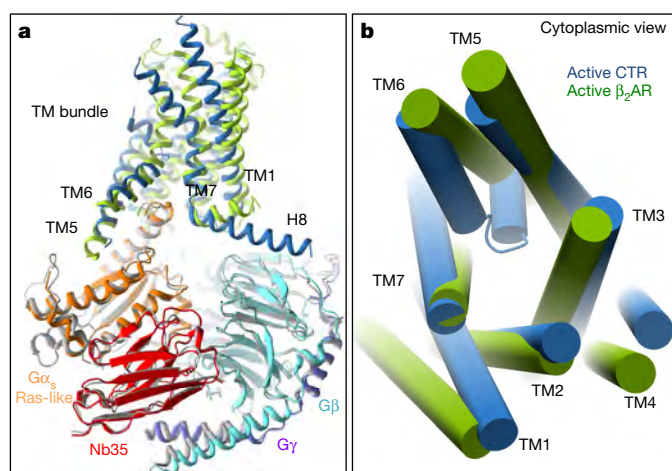


Figure 5 | Comparison of a class A and class B GPCR G_s ternary complex. **a**, Side view of the CTR– G_s complex (blue, CTR; orange, $G\alpha_s$; light blue, $G\beta$; purple, $G\gamma$; red, Nb35) aligned to the G-protein complex ($G\alpha\beta\gamma$) of the β_2 AR– G_s complex (grey, G protein; green, β_2 AR). The G protein closely aligns in the two structures. There are major differences between the receptor transmembrane domains at the extracellular surface. CTR has a more kinked TM6 and a longer helix 8; the cytoplasmic face of β_2 AR TM5 is extended. **b**, CTR (blue) and β_2 AR (green) transmembrane domains viewed from the cytoplasmic face. The intracellular transmembrane tips (with the exception of TM4) overlay, highlighting conserved movements within the intracellular face of class A and B GPCRs for G_s coupling.

receptors revealing conserved global cytoplasmic changes upon activation. Two notable differences include a helical extension of TM5 in the β_2 AR– G_s complex that was not evident for the CTR, and the long helix 8 that was not observed in the β_2 AR.

At the extracellular face there are major differences in the conformation of the two receptors, reflective of their distinct activating ligands, with the class B structure that is required to accommodate a peptide, being more open (Extended Data Fig. 10). There are remarkable differences in TM6 and TM7, which contain kinks in both receptors, but are more pronounced in the CTR. A large shift inwards and towards TM7 in extracellular side of TM1 is also evident in the class B structure relative to the β_2 AR, with this transmembrane domain also forming an extended helical structure (three additional turns), a feature reported previously for the inactive state structure of the GCGR⁷. A notable feature is the distinct location of TM4 in the CTR relative to the β_2 AR (Fig. 5 and Extended Data Fig. 10). This is particularly interesting as TM4 is the predominant interface for class B GPCR dimerization, with disruption of this interface leading to attenuated G-protein signalling for all receptors that have been assessed to date, including the CTR^{41,42}.

Conclusions

The cryo-EM structure of the sCT–CTR– G_s complex provides a near-atomic resolution view of a full-length class B GPCR and of an activated class B GPCR–G-protein ternary complex. Notably, the CTR is completely unmodified (with the exception of affinity tags) and is one of only a few structures of a wild-type GPCR, highlighting the potential of cryo-EM in solving structures of GPCR complexes. The structure also provides the first visualization of the binding site of the N terminus of a peptide agonist within the transmembrane bundle of a class B GPCR as well as some insight into the biological flexibility of the ternary complex. This study provides a framework to further investigate the mechanism of agonist interactions and activation of other class B GPCRs that may open up new avenues for rational design of novel therapeutics for this class of receptors.

Online Content Methods, along with any additional Extended Data display items and Source Data, are available in the online version of the paper; references unique to these sections appear only in the online paper.

Received 20 February; accepted 3 April 2017.

Published online 24 April 2017.

- Congreve, M. & Marshall, F. The impact of GPCR structures on pharmacology and structure-based drug design. *Br. J. Pharmacol.* **159**, 986–996 (2010).
- Kenakin, T. & Miller, L. J. Seven transmembrane receptors as shapeshifting proteins: the impact of allosteric modulation and functional selectivity on new drug discovery. *Pharmacol. Rev.* **62**, 265–304 (2010).
- Zhang, D., Zhao, Q. & Wu, B. Structural studies of G protein-coupled receptors. *Mol. Cells* **38**, 836–842 (2015).
- Rasmussen, S. G. *et al.* Crystal structure of the β_2 adrenergic receptor– G_s protein complex. *Nature* **477**, 549–555 (2011).
- Hollenstein, K. *et al.* Structure of class B GPCR corticotropin-releasing factor receptor 1. *Nature* **499**, 438–443 (2013).
- Jazayeri, A. *et al.* Extra-helical binding site of a glucagon receptor antagonist. *Nature* **533**, 274–277 (2016).
- Siu, F. Y. *et al.* Structure of the human glucagon class B G-protein-coupled receptor. *Nature* **499**, 444–449 (2013).
- Culhane, K. J., Liu, Y., Cai, Y. & Yan, E. C. Transmembrane signal transduction by peptide hormones via family B G protein-coupled receptors. *Front. Pharmacol.* **6**, 264 (2015).
- Pal, K., Melcher, K. & Xu, H. E. Structure and mechanism for recognition of peptide hormones by Class B G-protein-coupled receptors. *Acta Pharmacol. Sin.* **33**, 300–311 (2012).
- Poyner, D. R. *et al.* International Union of Pharmacology. XXXII. The mammalian calcitonin gene-related peptides, adrenomedullin, amylin, and calcitonin receptors. *Pharmacol. Rev.* **54**, 233–246 (2002).
- Bai, X. C., McMullan, G. & Scheres, S. H. How cryo-EM is revolutionizing structural biology. *Trends Biochem. Sci.* **40**, 49–57 (2015).
- De Zorzi, R., Mi, W., Liao, M. & Walz, T. Single-particle electron microscopy in the study of membrane protein structure. *Microscopy* **65**, 81–96 (2016).
- Danev, R., Tegunov, D. & Baumeister, W. Using the Volta phase plate with defocus for cryo-EM single particle analysis. *eLife* **6**, e23006 (2017).
- Khoshouei, M., Radjainia, M., Baumeister, W. & Danev, R. Cryo-EM structure of haemoglobin at 3.2 Å determined with the Volta phase plate. Preprint at <https://doi.org/10.1101/087841> (2016).
- Khoshouei, M. *et al.* Volta phase plate cryo-EM of the small protein complex Prx3. *Nat. Commun.* **7**, 10534 (2016).
- Hilton, J. M., Dowton, M., Houssami, S. & Sexton, P. M. Identification of key components in the irreversibility of salmon calcitonin binding to calcitonin receptors. *J. Endocrinol.* **166**, 213–226 (2000).
- Furness, S. G. *et al.* Ligand-dependent modulation of G protein conformation alters drug efficacy. *Cell* **167**, 739–749.e11 (2016).
- Scheres, S. H. RELION: implementation of a Bayesian approach to cryo-EM structure determination. *J. Struct. Biol.* **180**, 519–530 (2012).
- Westfield, G. H. *et al.* Structural flexibility of the $G\alpha_s$ α -helical domain in the β_2 -adrenoceptor G_s complex. *Proc. Natl Acad. Sci. USA* **108**, 16086–16091 (2011).
- Van Eps, N. *et al.* Interaction of a G protein with an activated receptor opens the interdomain interface in the alpha subunit. *Proc. Natl Acad. Sci. USA* **108**, 9420–9424 (2011).
- Andreotti, G. *et al.* Structural determinants of salmon calcitonin bioactivity: the role of the Leu-based amphipathic α -helix. *J. Biol. Chem.* **281**, 24193–24203 (2006).
- Johansson, E. *et al.* Type II turn of receptor-bound salmon calcitonin revealed by X-ray crystallography. *J. Biol. Chem.* **291**, 13689–13698 (2016).
- Ho, H. H., Gilbert, M. T., Nussenzveig, D. R. & Gershengorn, M. C. Glycosylation is important for binding to human calcitonin receptors. *Biochemistry* **38**, 1866–1872 (1999).
- Dods, R. L. & Donnelly, D. The peptide agonist-binding site of the glucagon-like peptide-1 (GLP-1) receptor based on site-directed mutagenesis and knowledge-based modelling. *Biosci. Rep.* **36**, e00285 (2015).
- Wootten, D. *et al.* The extracellular surface of the GLP-1 receptor is a molecular trigger for biased agonism. *Cell* **165**, 1632–1643 (2016).
- Houssami, S. *et al.* Divergent structural requirements exist for calcitonin receptor binding specificity and adenylate cyclase activation. *Mol. Pharmacol.* **47**, 798–809 (1995).
- Meadows, R. P., Nikonowicz, E. P., Jones, C. R., Bastian, J. W. & Gorenstein, D. G. Two-dimensional NMR and structure determination of salmon calcitonin in methanol. *Biochemistry* **30**, 1247–1254 (1991).
- Feyn, J. H. *et al.* N-terminal truncation of salmon calcitonin leads to calcitonin antagonists. Structure activity relationship of N-terminally truncated salmon calcitonin fragments *in vitro* and *in vivo*. *Biochem. Biophys. Res. Commun.* **187**, 8–13 (1992).
- Wootten, D., Simms, J., Miller, L. J., Christopoulos, A. & Sexton, P. M. Polar transmembrane interactions drive formation of ligand-specific and signal pathway-biased family B G protein-coupled receptor conformations. *Proc. Natl Acad. Sci. USA* **110**, 5211–5216 (2013).
- Bailey, R. J. & Hay, D. L. Agonist-dependent consequences of proline to alanine substitution in the transmembrane helices of the calcitonin receptor. *Br. J. Pharmacol.* **151**, 678–687 (2007).

31. Conner, A. C. *et al.* A key role for transmembrane prolines in calcitonin receptor-like receptor agonist binding and signalling: implications for family B G-protein-coupled receptors. *Mol. Pharmacol.* **67**, 20–31 (2005).
32. Koth, C. M. *et al.* Molecular basis for negative regulation of the glucagon receptor. *Proc. Natl Acad. Sci. USA* **109**, 14393–14398 (2012).
33. Mukund, S. *et al.* Inhibitory mechanism of an allosteric antibody targeting the glucagon receptor. *J. Biol. Chem.* **288**, 36168–36178 (2013).
34. Yin, Y. *et al.* An intrinsic agonist mechanism for activation of glucagon-like peptide-1 receptor by its extracellular domain. *Cell Discov.* **2**, 16042 (2016).
35. Zhao, L. H. *et al.* Differential requirement of the extracellular domain in activation of class B G protein-coupled receptors. *J. Biol. Chem.* **291**, 15119–15130 (2016).
36. Vohra, S. *et al.* Similarity between class A and class B G-protein-coupled receptors exemplified through calcitonin gene-related peptide receptor modelling and mutagenesis studies. *J. R. Soc. Interface* **10**, 20120846 (2012).
37. Wootten, D. *et al.* A hydrogen-bonded polar network in the core of the glucagon-like peptide-1 receptor is a fulcrum for biased agonism: lessons from class B crystal structures. *Mol. Pharmacol.* **89**, 335–347 (2016).
38. Wootten, D. *et al.* Key interactions by conserved polar amino acids located at the transmembrane helical boundaries in Class B GPCRs modulate activation, effector specificity and biased signalling in the glucagon-like peptide-1 receptor. *Biochem. Pharmacol.* **118**, 68–87 (2016).
39. Conner, M. *et al.* Functional and biophysical analysis of the C-terminus of the CGRP-receptor; a family B GPCR. *Biochemistry* **47**, 8434–8444 (2008).
40. Furness, S. G., Wootten, D., Christopoulos, A. & Sexton, P. M. Consequences of splice variation on Secretin family G protein-coupled receptor function. *Br. J. Pharmacol.* **166**, 98–109 (2012).
41. Harikumar, K. G., Ball, A. M., Sexton, P. M. & Miller, L. J. Importance of lipid-exposed residues in transmembrane segment four for family B calcitonin receptor homo-dimerization. *Regul. Pept.* **164**, 113–119 (2010).
42. Harikumar, K. G. *et al.* Glucagon-like peptide-1 receptor dimerization differentially regulates agonist signaling but does not affect small molecule allostery. *Proc. Natl Acad. Sci. USA* **109**, 18607–18612 (2012).
43. Black, J. W. & Leff, P. Operational models of pharmacological agonism. *Proc. R. Soc. Lond. B Biol. Sci.* **220**, 141–162 (1983).

Supplementary Information is available in the online version of the paper.

Acknowledgements This work was funded by the National Health and Medical Research Council of Australia (NHMRC) (grant numbers 1055134, 1061044 and 1120919) and NIH grants DK090165, NS092695. P.M.S. and A.C. are NHMRC Principal and Senior Principal Research Fellows, respectively. D.W. is a NHMRC Career Development Fellow. Computational studies were partially supported by Melbourne Bioinformatics at the University of Melbourne,

grant number VR0024. Negative-stain imaging and cryo-EM screening was performed at the Monash Ramaciotti Centre for Cryo-Electron Microscopy. The GPCRDdb (<http://gpcrddb.org>) was used for generation of initial alignments of human class B GPCR sequences. The authors thank the late M. Azria for 100 mg of sCT, used in initial work.

Author Contributions Y.-L.L. developed the expression and purification strategy (with D.M.T., S.G.B.F., B.K.K., D.W., G.S. and P.M.S.), performed virus production, insect cell expression, purification, complex stability, negative-stain EM, data acquisition/analysis, prepared samples for cryo-EM and assisted with manuscript preparation. M.K. performed phase-plate imaging, data collection, EM data processing and analysis and assisted with manuscript preparation. M.R. assisted with negative-stain analysis and conception of cryo-imaging by Volta phase plate, performed cryo-sample preparation, preliminary screening imaging and analysis and assisted with manuscript preparation. Y.Z. calculated the cryo-EM map, performed model building and refinement, and contributed to manuscript preparation. A.G. performed GTP γ S and radioligand binding, model building and refinement and contributed to manuscript preparation. J.T. assisted in negative-stain EM screening. D.M.T. contributed to purification strategy, model refinement and manuscript preparation. S.G.B.F. provided project strategy and protein purification advice, assisted data interpretation and manuscript preparation. G.C. performed cloning for baculovirus expression. T.C. performed homology modelling, assisted with model refinement and manuscript preparation. R.D. developed Volta phase-plate cryo-EM data acquisition strategy and wrote automation scripts. W.B. organized and managed the Volta phase plate development project. L.J.M. provided insights into class B GPCRs, assisted with data interpretation and reviewed the manuscript. A.C. assisted with data interpretation and manuscript preparation. B.K.K. provided advice on CTR-Gs complex formation and purification. D.W. was responsible for overall project strategy and management (along with P.M.S.) and performed pharmacological characterization, interpreted data and wrote the manuscript. G.S. provided feedback to guide cryo-EM, oversaw EM data processing, structure determination and refinement, data interpretation and manuscript writing. P.M.S. was responsible for overall project strategy and management, data interpretation and writing the manuscript.

Author Information Reprints and permissions information is available at www.nature.com/reprints. The authors declare no competing financial interests. Readers are welcome to comment on the online version of the paper. Publisher's note: Springer Nature remains neutral with regard to jurisdictional claims in published maps and institutional affiliations. Correspondence and requests for materials should be addressed to P.S. (patrick.sexton@monash.edu), D.W. (denise.wootten@monash.edu) or G.S. (skinioti@umich.edu).

Reviewer Information Nature thanks J. Standfuss and the other anonymous reviewer(s) for their contribution to the peer review of this work.

METHODS

No statistical methods were used to predetermine sample size. The experiments were not randomized and the investigators were not blinded to allocation during experiments and outcome assessment.

Constructs. Wild-type human calcitonin receptor (CTR) was modified to include an N-terminal Flag tag epitope and a C-terminal 8× histidine tag, both tags are removable by 3C protease cleavage (Extended Data Fig. 1). These constructs were generated in both mammalian and insect cell expression vectors.

Insect cell expression. CTR, human G_{α_s} short, His₆-tagged human $G\beta_1$ and $G\gamma_2$ were expressed in HighFive insect cells (Thermo Fisher Scientific) using baculovirus. Cell cultures were grown in ESF 921 serum-free media (Expression System) to a density of 4 million cells per ml and then infected with three separate baculovirus at a ratio of 1:2.2 for hCTR, G_{α_s} and $G\beta_1\gamma_2$. Cultures were grown at 27 °C and harvested by centrifugation 45 h post infection.

Complex purification. Cells were suspended in 20 mM HEPES pH 7.4, 50 mM NaCl, 2 mM $MgCl_2$ supplemented with cOmplete Protease Inhibitor Cocktail tablets (Roche). Complex formation was initiated by addition of 1 μ M salmon calcitonin, Nb35–His (10 μ g ml^{−1}) and Apyrase (25 mU ml^{−1}, NEB); the suspension was incubated for 1 h at room temperature. Membranes were collected by centrifugation at 30,000g for 30 min, and solubilized by 0.5% (w/v) lauryl maltose neopentyl glycol (LMNG, Anatrace) supplemented with 0.03% (w/v) cholesteryl hemisuccinate (CHS, Anatrace) for 2 h at 4 °C in the presence of 100 nM salmon calcitonin and Apyrase (25 mU ml^{−1}, NEB). Insoluble material was removed by centrifugation at 30,000g for 30 min and the solubilized complex was immobilised by batch binding to M1 anti-Flag affinity resin in the presence of 3 mM $CaCl_2$. The resin was packed into a glass column and washed with 20 column volumes of 20 mM HEPES pH 7.4, 100 mM NaCl, 2 mM $MgCl_2$, 3 mM $CaCl_2$, 100 nM sCT, 0.01% (w/v) MNNG and 0.006% (w/v) CHS before bound material was eluted in buffer containing 5 mM EGTA and 0.1 mg ml^{−1} Flag peptide. The complex was then concentrated using an Amicon Ultra Centrifugal Filter (MWCO 100 kDa) and subjected to size-exclusion chromatography on a Superdex 200 Increase 10/300 column (GE Healthcare) pre-equilibrated with 20 mM HEPES pH 7.4, 100 mM NaCl, 2 mM $MgCl_2$, 100 nM sCT, 0.01% (w/v) MNNG and 0.006% (w/v) CHS to separate complex from contaminants. Eluted fractions consisting of receptor and G-protein complex were pooled and concentrated. Final yield of purified complex was approximately 0.5 mg l^{−1} insect cell culture.

The stability of the CTR– G_s heterotrimer complex at 4 °C was monitored by analytical SEC. SEC-purified complex was incubated on ice and 50 μ g was applied onto Superose 6 Increase 10/300 GL column at 24 h interval for a total period of 5 days. Protein was detected by measuring absorbance at 280 nm with a fluorescence detector (RF-10AXL, Shimadzu).

SDS–PAGE and western blot analysis. Samples collected from each purification step were analysed by SDS–PAGE and western blot. For SDS–PAGE, precast gradient TGX gels (Bio-Rad) were used. Gels were either stained by Instant Blue (Expedeon) or immediately transferred to PVDF membrane (Bio-Rad) at 100 V for 1 h. The proteins on the PVDF membrane were probed with two primary antibodies, rabbit anti- G_s C-18 antibody (cat. no. sc-383, Santa Cruz) against G_{α_s} subunit and mouse penta-His antibody (cat. no. 34660, QIAGEN) against His tags. The membrane was washed and incubated with secondary antibodies, 680RD goat anti-mouse and 800CW goat anti-rabbit (LI-COR). Bands were imaged using an infrared imaging system (LI-COR Odyssey Imaging System).

Specimen preparation and data acquisition. Concentrated sample from Superdex 200 Increase 10/300 GL column was loaded onto a Superose 6 Increase 10/300 GL column (GE Healthcare). Eluted fractions were used to prepare specimens for EM imaging using conventional negative-staining protocol⁴⁴. Negative-stained samples were imaged at room temperature with a Tecnai T12 (FEI) electron microscope operated at 120 kV. Images were recorded at magnification of 57,000× and a defocus value of −1 μ m on a Gatan US4000 CCM camera. All images were binned to 2 × 2 pixels to obtain a pixel size of 4.16 Å.

For cryo-EM, purified CTR– G_s heterotrimer complex was diluted to 0.3 mg ml^{−1} with 20 mM HEPES pH 7.4, 100 mM NaCl, 2 mM $MgCl_2$, 100 nM sCT. Vitrified specimen was prepared by applying 5 μ l of protein complexes onto a glow-discharged 300 mesh copper Quantifoil R1.2/1.3 grid (Quantifoil Micro Tools), plunge-frozen in liquid ethane cooled by liquid nitrogen inside a Vitrobot Mark IV (FEI) with blotting time of 3 s and draining time of 0.5 s. Cryo-EM imaging was performed on a Titan Krios microscope operated at 300 kV (FEI) equipped with a Gatan Quantum energy filter, a Gatan K2 Summit direct electron camera (Gatan) and a Volta phase plate (FEI). A total of 2,780 recordings were taken in EFTEM nanoprobe mode, with 50 μ m C2 aperture, at a calibrated magnification of 47,170 corresponding to a magnified pixel size of 1.06 Å. Each movie comprises 50 sub frames with a total dose of 50 e[−] per Å², exposure time between 11 and 13.75 s and a dose rate between 4 and 5 e[−] per pixel per second on the detector.

Data acquisition was done using SerialEM software⁴⁵ and custom macros for automated single particle data acquisition with Volta phase plate at −500 nm defocus¹⁴. **Image processing and 3D reconstructions.** Image processing and three-dimensional reconstructions were performed as previously described⁴⁶. Dose fractionated image stacks were subjected to beam-induced motion correction, globally and locally, by MotionCor2⁴⁷. A sum of all frames, filtered according to exposure dose, in each image stack was used for further processing. CTF parameters for each micrograph were determined by CTFIND4⁴⁸.

Particle selection, two-dimensional classification and three-dimensional classification were performed on a binned data set with a pixel size of 2.12 Å using RELION2. Semi-automated selected 1,213,995 particle projections were subjected to reference-free two-dimensional classification to discard false-positive particles or particles categorized in poorly defined classes, resulting in 426,001 projections for further processing. An *ab initio* map generated by VIPER⁴⁹ was used as initial reference model for maximum-likelihood-based three-dimensional classification. One stable class with detailed features accounting for 106,838 particles was then subjected to focused refinement with a soft mask including receptor and G_s protein and excluding the α -helical domain, produced the final map with global nominal resolution of 4.1 Å, and nominal resolution of 3.8 Å in the seven-transmembrane and G-protein region.

Reported resolutions are based on the gold-standard Fourier shell correlation (FSC) using the 0.143 criterion. All density maps were corrected for the modulation transfer function (MTF) of the K2 summit direct detector and then sharpened by applying temperature factor that was estimated using post-processing in RELION¹⁸. Local resolution was determined using ResMap with half-reconstructions as input maps.

Model building. The initial template of hCTR was derived from a homology based predicted model calculated by I-TASSER⁵⁰. Models of sCT and G_s heterotrimer were adopted from the NMR structure (PDB: 2GLH) and β_2 AR– G_s crystal structure (PDB: 3SN6), respectively. All models were visualized and docked into the density in Chimera⁵¹, followed by manual adjustment and real-space refinement using COOT⁵². Sequence assignment was guided by bulky residues such as Phe, Tyr, Trp and Arg. The final model was subjected to global refinement and minimization in real space using the module phenix.real_space_refine in PHENIX⁵³. Owing to lower local resolution for the peptide, its model was omitted from the deposited structure. Model overfitting was evaluated through its refinement against one cryo-EM half map. FSC curves were calculated between the resulting model and the half map used for refinement as well as between the resulting model and the other half map for cross-validation (Extended Data Fig. 4). The final refinement statistics are provided in Supplementary Table 1.

Inactive homology model of hCTR. The glucagon receptor (GCGR) 4L6R X-ray structure⁷ was used as the template for the CTR homology model. A GCGR/CTR sequence alignment of the seven transmembrane domains and helix 8 was performed using the GPCRdb server⁵⁴. This alignment was modified by closing the gap at the extracellular end of TM5 and adding residues to CTR and GCGR from their respective gene sequences to complete the alignments at the cytoplasmic end of TM5 and TM6, respectively. We used ICM (Molsoft) to remove all atoms in the 4L6R template not present in this modified GCGR sequence, and generated a CTR homology model based on the modified sequence alignment. An ICM global optimization procedure was performed using Monte Carlo conformational space sampling of side chains with hydrogen bond optimization.

Insect cell membrane preparations for radioligand and [³⁵S]GTPγS binding. The CTR complex (CTR, G_{α_s} and $G\beta_1\gamma_2$) or CTR alone were expressed in insect HighFive cells (Expression Systems) with the same virus ratios used for the CTR complex preparation for cryo-EM. Cells were harvested approximately 42 h after the viral infection. For crude membrane preparations cells were resuspended in membrane buffer (20 mM HEPES 7.4, 50 mM NaCl, 2 mM $MgCl_2$, with protease inhibitors and benzonase), dounced 20 times followed by centrifugation (10 min, 350g, 4 °C). The pellet was again resuspended in membrane buffer, dounced and clarified by centrifugation at low g. Membranes were pelleted by centrifugation (1 h, 40,000g, 4 °C), resuspended in the membrane buffer and sonicated. The protein concentration was determined using Bradford reagent (Bio-Rad).

Radioligand competition binding experiments on CTR expressed in insect cells. Radioligand binding was performed in 20 mM HEPES pH 7.4; 100 mM NaCl; 10 mM $MgCl_2$; 0.1% BSA. First, membranes (1–2 μ g per sample) were incubated with different concentrations of sCT and Nb35 (7 μ g per sample, where applicable) for 1 h at 22 °C. Then [¹²⁵I]sCT(8–32) (truncated sCT antagonist) was added to a final concentration of approximately 50 pM [¹²⁵I]sCT(8–32) (precise concentrations in each experiment were determined by γ counting) followed by 1 h incubation at 30 °C. Membranes were harvested on UniFilter GF/C (Whatman) plates using Filtermate 196 harvester (Packard), extensively washed with ice-cold NaCl, dried and dissolved in 40 μ l of MicroScint-O scintillation cocktail (Packard) and counted

using a MicroBeta LumiJET counter (PerkinElmer). Non-specific binding was measured in the presence of 1 μ M of sCT(8–32). Curves were fitted to one- or two-site competition binding equations in Prism 6.0 (GraphPad). Data from each experiment were normalized to the response of membranes prepared from cells expressing all the components of the CTR complex (CTR, G α_s and G $\beta_1\gamma_2$) in the absence of sCT (100%).

[³⁵S]GTP γ S binding on CTR expressed in insect cells. Measurement of [³⁵S]GTP γ S incorporation was performed in 20 mM HEPES pH 7.4; 100 mM NaCl; 10 mM MgCl₂; 1 mM EDTA; 0.1% BSA; 30 μ g ml⁻¹ saponin. First, membranes (50 μ g per sample) were pre-incubated with 5 μ M GDP and increasing concentrations of sCT for 30 min at 22 °C. For experiments investigating the effects of Nb35, indicated amounts of Nb35 were also added at this step. Reactions were started by the addition of [³⁵S]GTP γ S and ATP to final concentrations of 300 pM and 50 μ M, respectively. After 1 h incubation at 30 °C, the reaction was terminated by harvesting the membranes on Whatman UniFilter GF/C plates using Filtermate 196 harvester (Packard). Membranes were extensively washed with ice-cold 50 mM Tris pH 7.6, 10 mM MgCl₂, 100 mM NaCl, dried, dissolved in 40 μ l of MicroScint-O scintillation cocktail (Packard) and counted using a MicroBeta LumiJET counter (PerkinElmer). Data from each experiment were normalized to the response of membranes prepared from cells expressing all the components of the CTR complex (CTR, G α_s and G $\beta_1\gamma_2$) in the presence of 1 μ M sCT (100%).

Generation of mutant receptors and C-terminal deletion constructs in mammalian cell vectors. Mutagenesis and C-terminal deletions were generated in a c-Myc epitope-tagged receptor that displays the same pharmacological properties as the wild-type receptor and the construct used for purification studies. The desired mutations were introduced into the CTR in the pEF5/FRT/V5-DEST destination vector (Invitrogen) using oligonucleotides for site-directed mutagenesis purchased from GeneWorks (Hindmarsh) and the QuikChange site-directed mutagenesis kit (Stratagene). C-terminal deletions were generated using primers designed to amplify the CTR from the N terminus to the various points within the C terminus via standard PCR methods. PCR products were purified using a Qiagen gel purification kit following the manufacturer's protocol. The primers for PCR contained sequences that incorporated sites into the PCR products for recombination into the destination vector pEF5/FRT/V5-DEST via Gateway technology. Sequences of receptor clones were confirmed by automated sequencing at the Australian Genome Research Facility.

Mammalian cell expression. COS-7 or 3T3 Fln cells (Invitrogen) were cultured in Dulbecco's Modified Eagle's Medium (DMEM) (Invitrogen) supplemented with 10% v/v fetal bovine serum (FBS) (Thermo Electron Corporation) at 37 °C and 95% O₂/5% CO₂ in a humidified incubator. Cells were routinely tested for mycoplasma contamination. Cells were transiently transfected, using polyethylenimine (PEI). DNA and PEI diluted in 150 mM NaCl were combined in a 1:6 ratio and incubated for 15 min, added to cell suspension and the cells plated.

Mammalian whole-cell binding experiments. Transfected COS-7 cells were seeded at a density of 3×10^4 cells per well into 96-well culture plates and incubated for 48 h at 37 °C in 5% CO₂, and radioligand binding carried out as previously described⁵⁵. For each cell line in all experiments, total binding was defined by 0.05 nM [¹²⁵I]sCT(8–32) alone, and non-specific binding was defined by co-incubation with 1 μ M sCT(8–32). For analysis, data are normalized to the specific binding for each individual experiment.

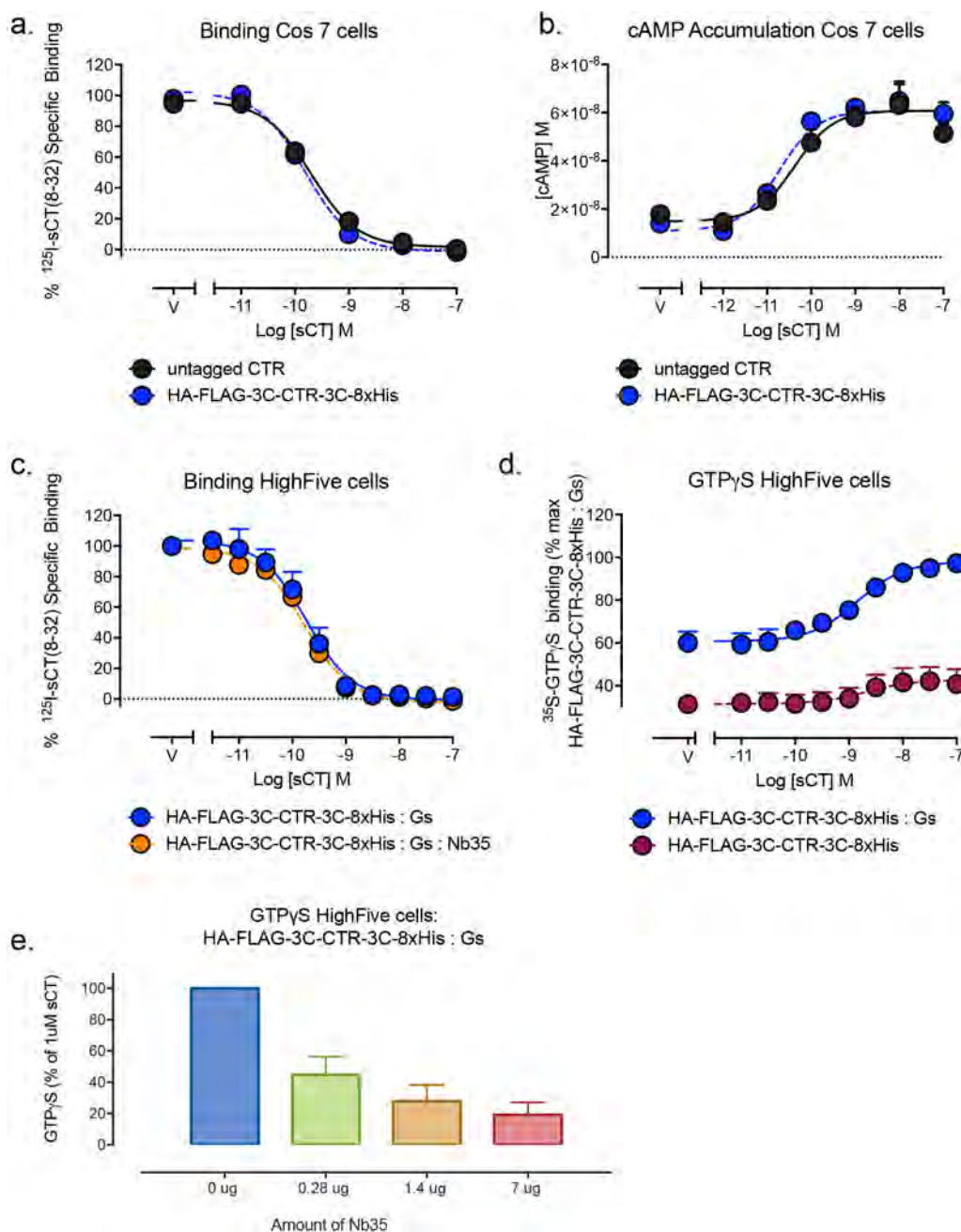
Mammalian cAMP assays. Transfected COS-7 or 3T3-Fln cells were seeded at a density of 3×10^4 cells per well into 96-well culture plates and incubated for 48 h at 37 °C in 5% CO₂, and cAMP detection carried out as previously described⁵⁶. All values were converted to concentration of cAMP using a cAMP standard curve performed in parallel, and data were subsequently normalized to the response of 100 μ M forskolin in each cell line.

Mammalian ERK1/2 phosphorylation assays. Transfected 3T3-Fln cells were seeded at a density of 3×10^4 cells per well into 96-well culture plates and incubated for 48 h at 37 °C in 5% CO₂, and pERK1/2 assays were carried out using Alphascreen technology as previously described^{55,56}. FBS was used as a positive control. Data were subsequently normalized to the response of 100 10% FBS in each cell line.

Statistics. Where required, statistics for mutational studies were performed using one-way analysis of variance followed by Dunnett's test using wild-type receptors as the control ($P < 0.05$). Sample sizes were based on those routinely used for mutational studies and determination of alterations in cell signalling.

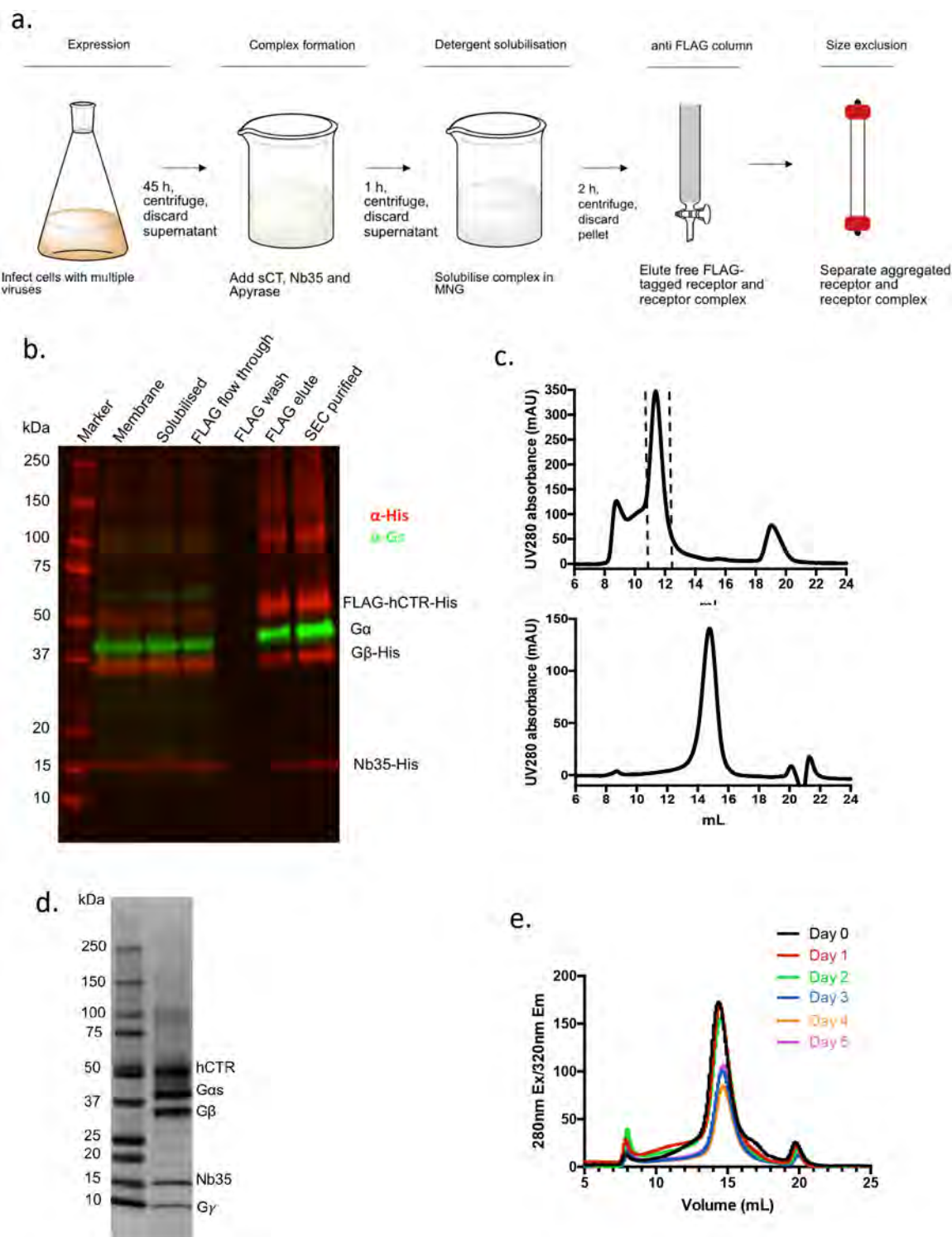
Data availability. All relevant data are available from the authors and/or are included with the manuscript or Supplementary Information. Atomic coordinates and the cryo-EM density map have been deposited in the Protein Data Bank under accession number 5UZ7 and the Electron Microscopy Data Bank under accession number EMD-8623.

44. Peisley, A. & Skiniotis, G. 2D projection analysis of GPCR complexes by negative stain electron microscopy. *Methods Mol. Biol.* **1335**, 29–38 (2015).
45. Mastronarde, D. N. Automated electron microscope tomography using robust prediction of specimen movements. *J. Struct. Biol.* **152**, 36–51 (2005).
46. Shalev-Benami, M. *et al.* 2.8-Å cryo-EM structure of the large ribosomal subunit from the eukaryotic parasite *Leishmania*. *Cell Reports* **16**, 288–294 (2016).
47. Zheng, S., Palovcak, E., Armache, J. P., Cheng, Y. & Agard, D. Anisotropic correction of beam-induced motion for improved single-particle electron cryo-microscopy. *Preprint at* <https://doi.org/10.1101/061960> (2016).
48. Rohou, A. & Grigorieff, N. CTFFIND4: Fast and accurate defocus estimation from electron micrographs. *J. Struct. Biol.* **192**, 216–221 (2015).
49. Penczek, P. A., Grassucci, R. A. & Frank, J. The ribosome at improved resolution: new techniques for merging and orientation refinement in 3D cryo-electron microscopy of biological particles. *Ultramicroscopy* **53**, 251–270 (1994).
50. Yang, J. & Zhang, Y. Protein structure and function prediction using I-TASSER. *Curr. Protoc. Bioinformatics* **52**, 1–15 (2015).
51. Pettersen, E. F. *et al.* UCSF Chimera—a visualization system for exploratory research and analysis. *J. Comput. Chem.* **25**, 1605–1612 (2004).
52. Emsley, P. & Cowtan, K. Coot: model-building tools for molecular graphics. *Acta Crystallogr. D Biol. Crystallogr.* **60**, 2126–2132 (2004).
53. Adams, P. D. *et al.* PHENIX: a comprehensive Python-based system for macromolecular structure solution. *Acta Crystallogr. D Biol. Crystallogr.* **66**, 213–221 (2010).
54. Munk, C. *et al.* GPCRdb: the G protein-coupled receptor database - an introduction. *Br. J. Pharmacol.* **173**, 2195–2207 (2016).
55. Koole, C. *et al.* Polymorphism and ligand dependent changes in human glucagon-like peptide-1 receptor (GLP-1R) function: allosteric rescue of loss of function mutation. *Mol. Pharmacol.* **80**, 486–497 (2011).
56. Koole, C. *et al.* Allosteric ligands of the glucagon-like peptide 1 receptor (GLP-1R) differentially modulate endogenous and exogenous peptide responses in a pathway-selective manner: implications for drug screening. *Mol. Pharmacol.* **78**, 456–465 (2010).



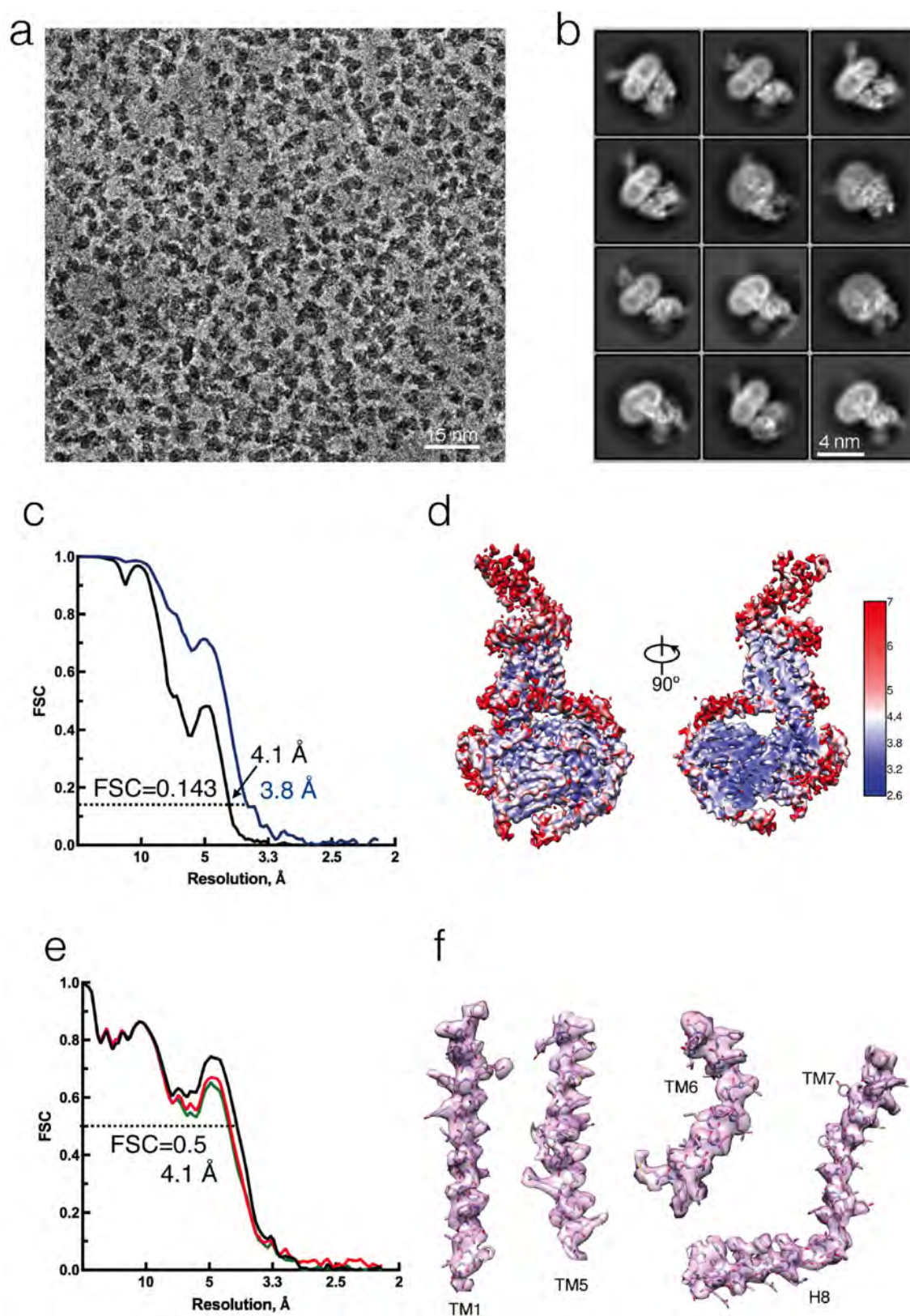
Extended Data Figure 2 | Pharmacology of the CTR construct used in this study. **a–d**, Pharmacological assessment in mammalian COS-7 cells (**a**, **b**) and HiveFive insect cells (**c**, **d**) of the untagged CTR and the construct shown in Extended Data Fig. 1 (HA-Flag-3C-CTR-3C-8 \times His). The presence of purification tags does not alter receptor pharmacology. **a**, Radioligand competition binding for sCT in competition with the radiolabelled ligand [^{125}I]sCT(8–32) in whole cells transiently expressing wild-type CTR or HA-Flag-3C-CTR-3C-8 \times His. Data are normalized to maximum [^{125}I]sCT(8–32) with nonspecific measured in the presence of 1 μM unlabelled sCT(8–32). **b**, Concentration response curves assessing G_s activation via measurement of cAMP accumulation at wild-type CTR and HA-Flag-3C-CTR-3C-8 \times His in the presence of sCT. **c**, Radioligand

competition binding for sCT or the radiolabelled ligand [^{125}I]sCT(8–32) performed with HA-Flag-3C-CTR-3C-8 \times His in the presence of G_s protein heterotrimer reveals similar affinities in insect cells versus mammalian cells. The presence of Nb35 does not alter ligand affinity. **d**, Concentration response curves to assess G-protein activation by HA-Flag-3C-CTR-3C-8 \times His via GTP γ S binding in the absence and presence of G_s protein heterotrimer reveals that the tagged CTR can robustly activate G_s in insect cells. **e**, GTP γ S binding to HA-Flag-3C-CTR-3C-8 \times His in the presence of 1 μM sCT is inhibited by increasing concentrations of Nb35. All data are mean \pm s.e.m. of four independent experiments, conducted in duplicate or triplicate.



Extended Data Figure 3 | Expression and purification of the sCT-CTR- G_s complex. **a**, Flow chart of the purification steps for the human CTR (hCTR)- G_s complex. **b**, SDS-PAGE/western blot of samples obtained at various stages of hCTR- G_s purification. hCTR and the G_s heterotrimer were co-expressed in insect cell membrane. Addition of the agonist salmon calcitonin initiates complex formation and was solubilized by detergent. Solubilized hCTR and the hCTR- G_s complex were immobilized on Flag antibody resin. Flag-eluted fractions were further purified by SEC. An anti-His antibody was used to detect Flag-CTR-His, $G\beta$ -His and Nb35-His (red) and an anti- G_s antibody was used to detect $G\alpha_s$ (green).

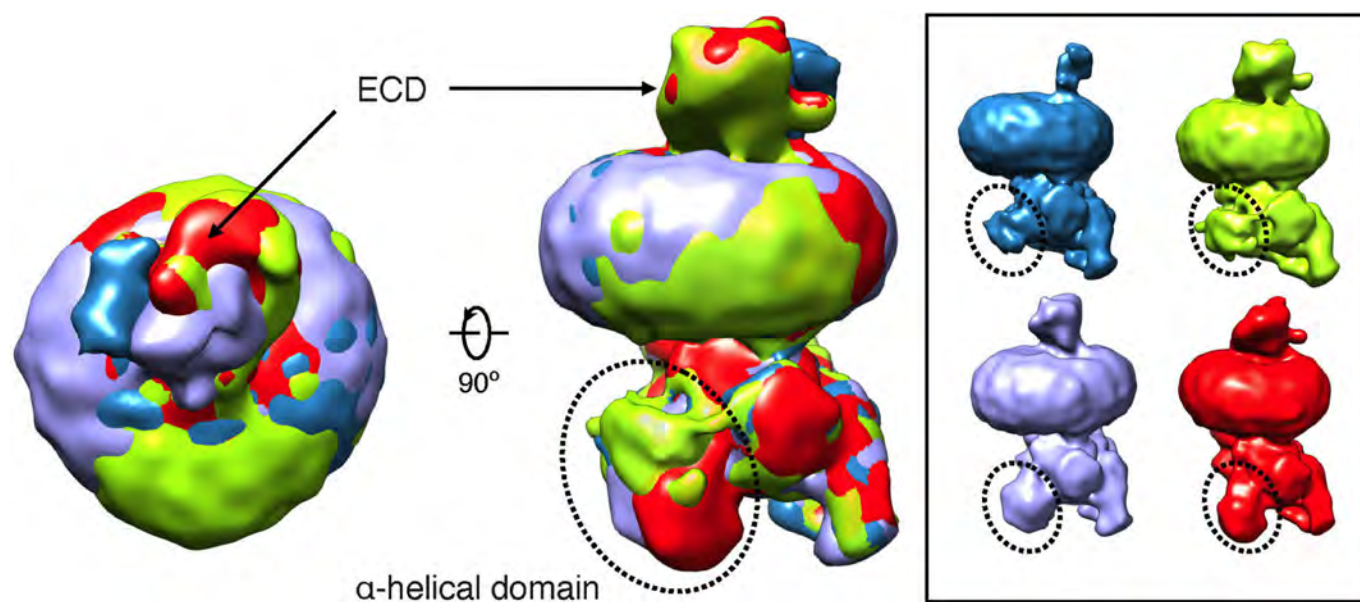
c, Representative elution profile of Flag-purified complex on Superdex 200 Increase 10/30 SEC (top). SEC fractions containing hCTR- G_s complex (within dashed lines) were pooled, concentrated and analysed by SEC on Superose 6 Increase 10/30 column (bottom). **d**, SDS-PAGE/Coomassie blue stain of the purified complex concentrated from the Superose 6 Increase 10/30 column. **e**, The stability of the purified hCTR- G_s was monitored by SEC following incubation at 4 °C for 5 days. All images and SEC profiles are representative of more than ten experiments, except for **e**, which was performed once.



Extended Data Figure 4 | Cryo-EM of the sCT-CTR-G_s complex.

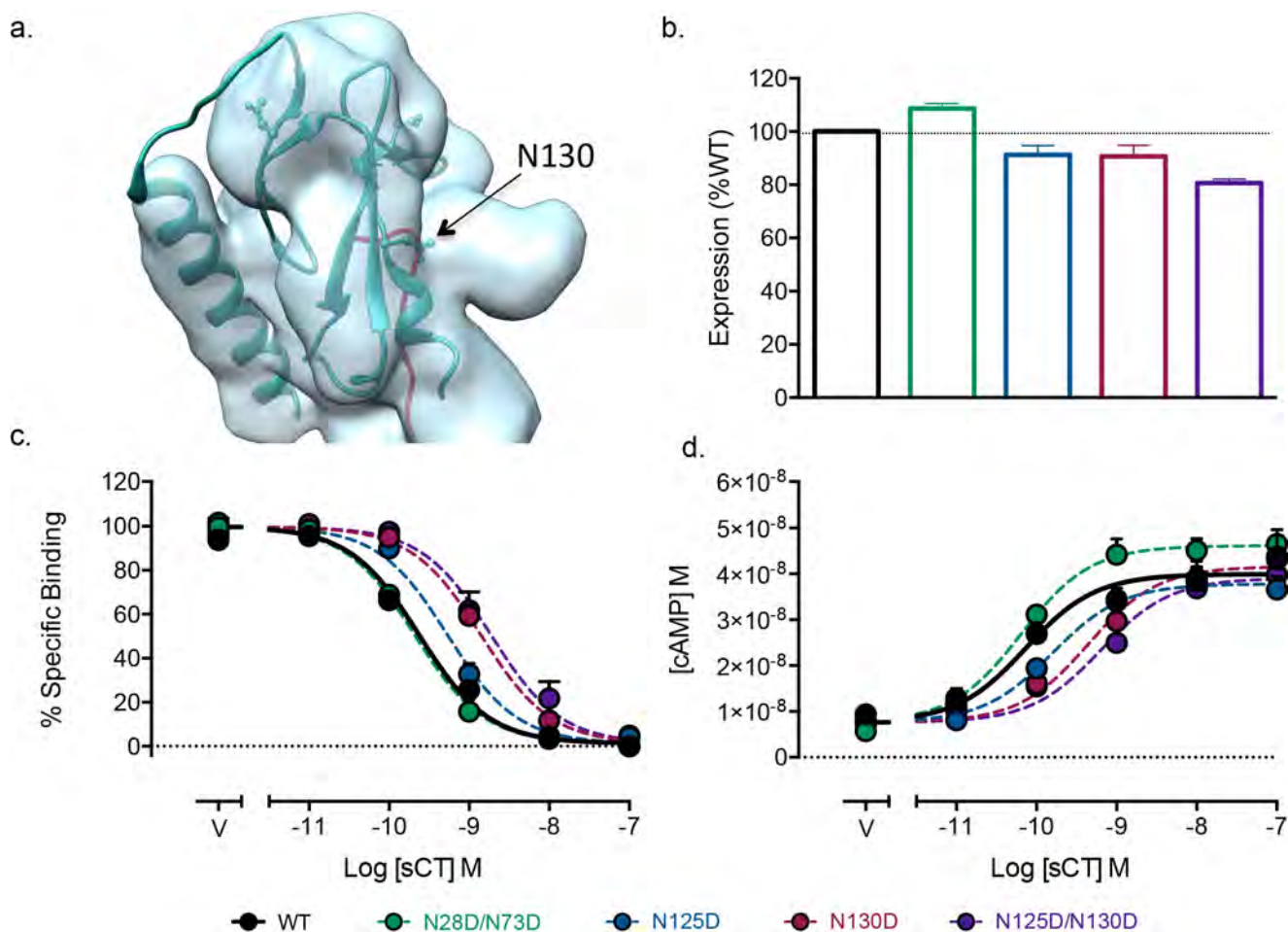
a, Representative Volta phase plate (of 2,780 recordings) cryo-EM micrograph of the sCT-CTR-G_s complex (scale bar, 15 nm). **b**, Reference-free two-dimensional averages of the complex in maltose-neopentyl glycol/cholesterol hemisuccinate micelle. **c**, Gold-standard Fourier shell correlation (FSC) curves, showing the overall nominal resolution at 4.1 Å and 3.8 Å on the stable region including the transmembrane domain and

G_s protein complex without AHD. **d**, Final three-dimensional density map coloured according to local resolution. **e**, FSC curves of the final refined model versus the final cryo-EM map (full dataset, black), of the outcome of model refinement with a half map versus the same map (red), and of the outcome of model refinement with a half map versus the other half map (green). At FSC = 0.5, the resolution is 4.1 Å. **f**, EM density of TM1, TM5, TM6, TM7 and helix 8.



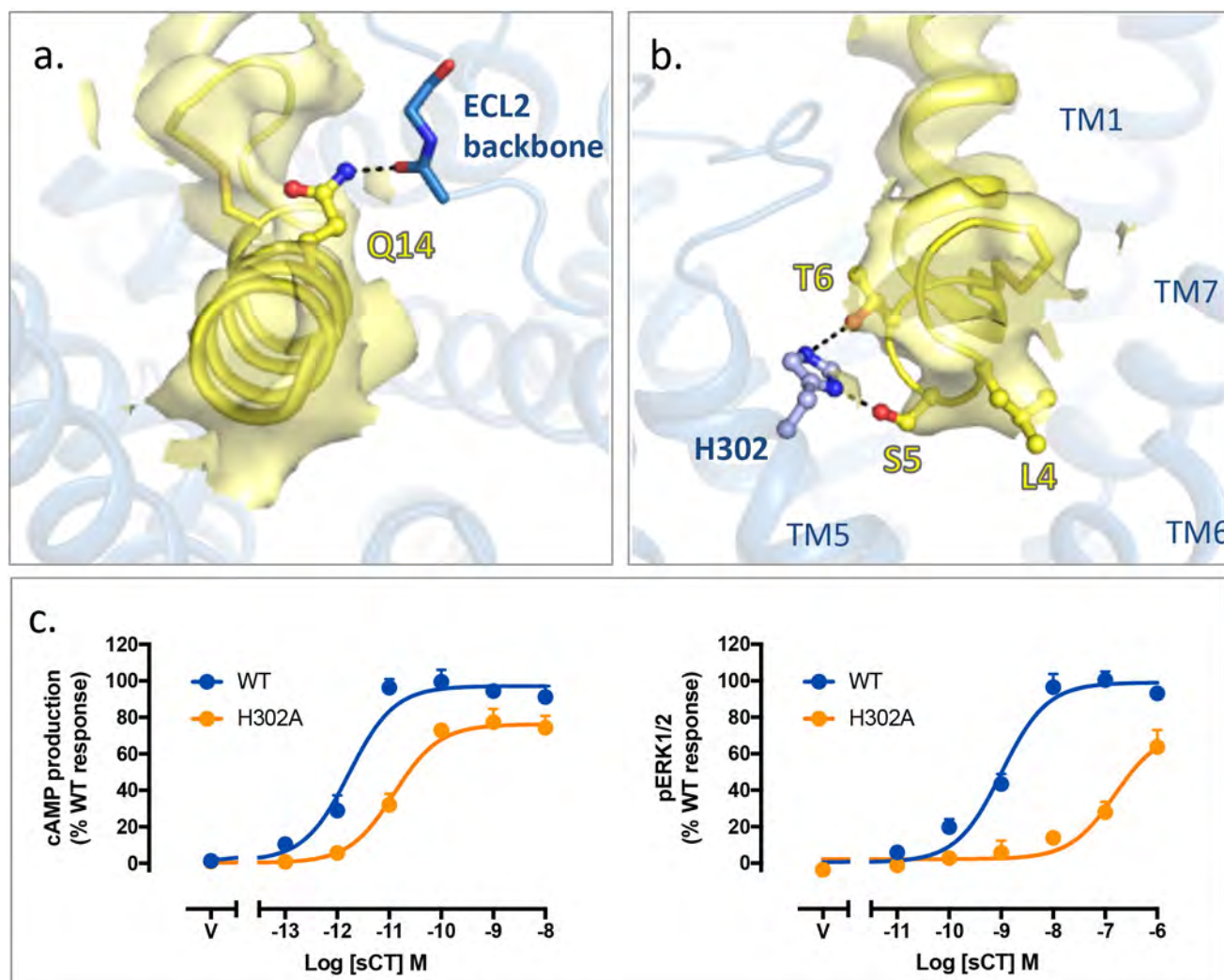
Extended Data Figure 5 | Flexibility of ECD and AHD in the sCT-CTR-G_s complex. Representative maps from three-dimensional classification showing the dynamics of the CTR ECD and G_{α_s} AHD. The overlaid maps are shown from top and side views. In the right panel the blue, green,

purple and red density maps show the four 3D classifications. These are overlaid on the left to demonstrate the observed flexibility of the G_{α_s} AHD and the CTR ECD.



Extended Data Figure 6 | The N-terminal ECD of the CTR. **a**, Rigid body fitting of the structure of CTR ECD bound to sCT (PDB: 5II0)²² into the corresponding regions of the cryo-EM map revealed additional density (close to residue 130) that may be attributed to glycosylation. **b–d**, Asp mutation of four consensus glycosylation residues (N28D, N73D, N125D and N130D) reveals the relative unimportance of glycosylation on cell-surface expression (**b**), determined via cell-surface ELISA for the N-terminal epitope tag. **c**, Competition radioligand binding studies for

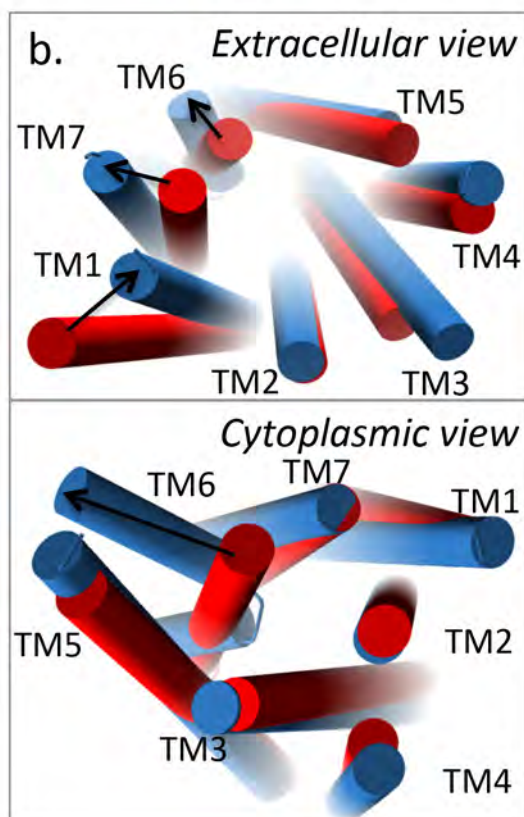
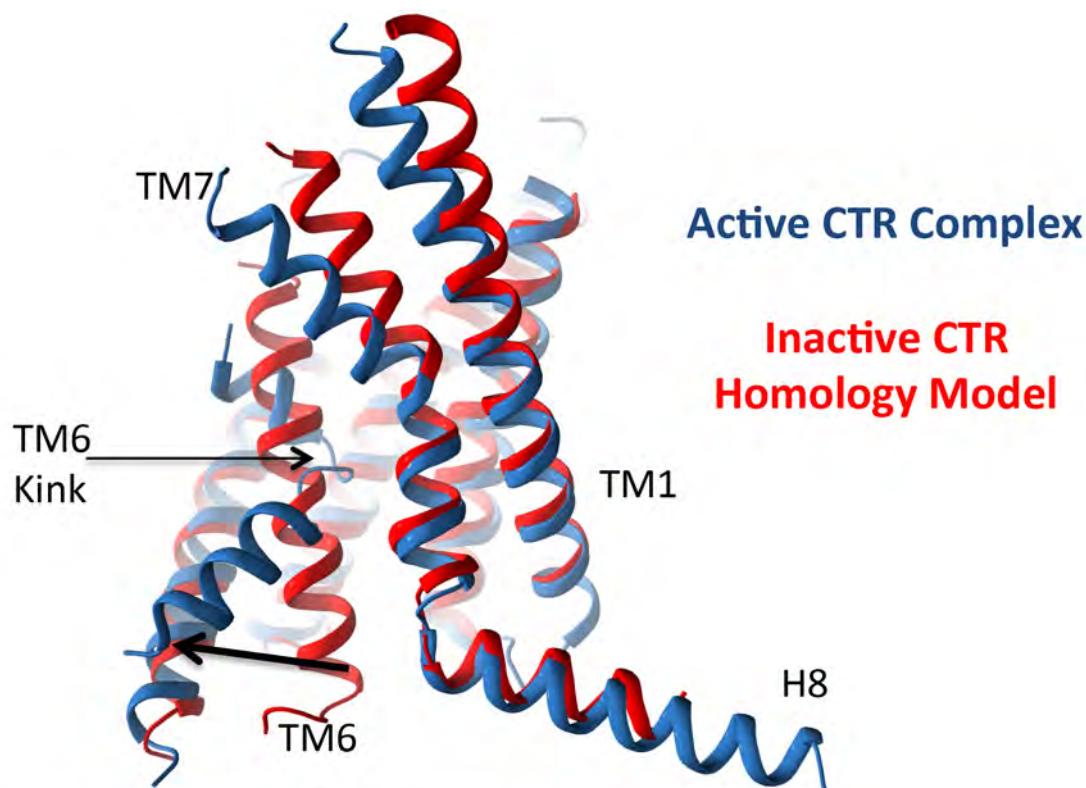
sCT in competition with the radiolabelled ligand [¹²⁵I]sCT(8–32) revealed reduced affinity for N130D, and to a lesser extent N125D, compared to the wild-type CTR. **d**, Concentration response curves for cAMP accumulation for mutant receptors relative to wild type show that N130D, and to a lesser extent N125D, reduce the potency of sCT in functional experiments. All data are mean + s.e.m. of five independent experiments, conducted in duplicate or triplicate.



Extended Data Figure 7 | Molecular modelling of sCT peptide reveals potential interactions between peptide and receptor. Cryo-EM density is shown in yellow fill, the sCT peptide model in yellow cartoon and the CTR in blue cartoon. **a**, Gln14 in sCT is predicted to form interactions with the backbone of ECL2. **b**, Ser5 and Thr6 are predicted to form hydrogen bonds with His302 in TM5 of the CTR, while Leu4 points down into

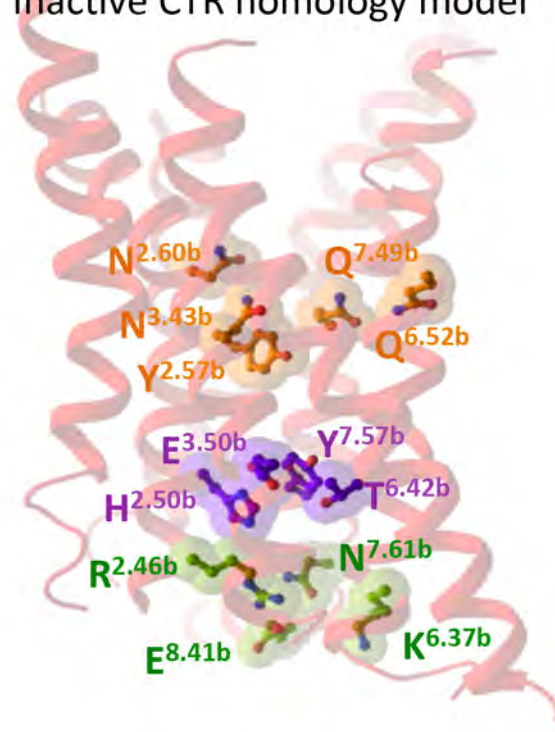
the bundle towards TM6. **c**, Mutation of H302 to Ala (H302A) results in reduced potency for sCT in cAMP production (left) and phosphorylation of ERK1/2 (right) when expressed in 3T3-FlpIn cells. This supports a role H302 in sCT affinity. Data are mean + s.e.m. of four independent experiments performed in duplicate

a.



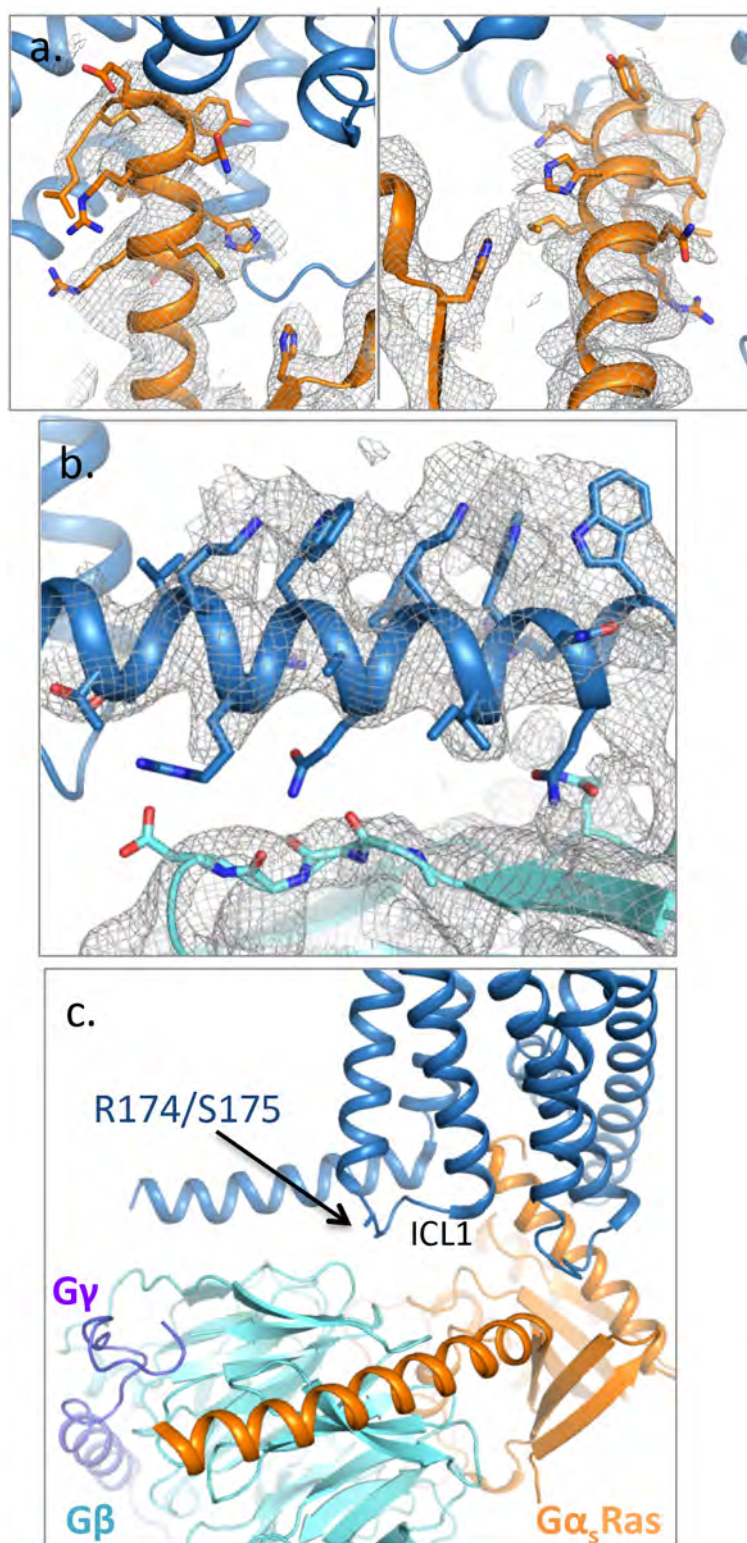
c.

Inactive CTR homology model



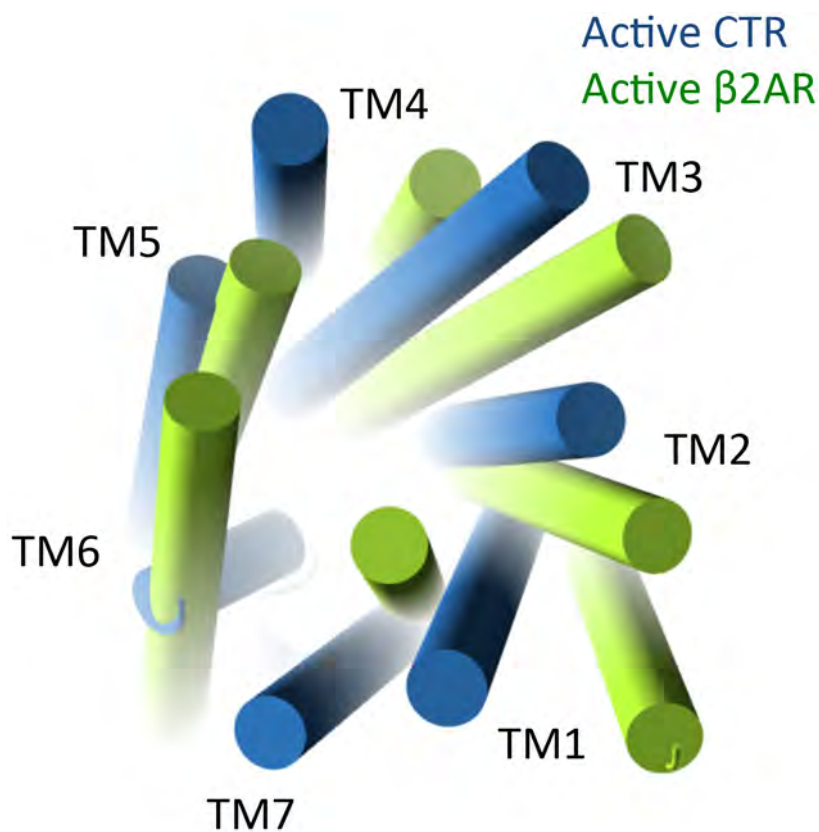
Extended Data Figure 8 | Comparisons of an inactive CTR homology model and the activate CTR structure. a, Side view of the activate sCT-CTR-G_s complex transmembrane structure (blue) relative to the inactive CTR homology model (red). b, Tube representation for transmembrane domains showing extracellular (top) and cytoplasmic (bottom) views of the activate sCT-CTR-G_s complex transmembrane structure (blue) relative to the inactive CTR homology model (red).

In a and b large differences are observed at the extracellular ends of TM6 and TM7, with additional differences within TM1 and TM5. In addition, a very large outward movement is observed within TM6 of the active structure relative to the inactive homology model at the intracellular face. c, The positions of class B conserved polar residues located within the inactive CTR homology model.



Extended Data Figure 9 | CTR-G α_s protein interactions. **a.** The $\alpha 5$ -helix of G α_s (orange) docks into a cavity formed on the intracellular side of the receptor (blue) by the opening of TM6. G-protein side chains within this cavity are supported by the cryo-EM map. **b.** Helix 8 of the CTR forms an amphipathic helix with multiple bulky aromatics heavily embedded within the detergent micelle that are evident in the map. Residues within the more

polar face of helix 8 are in the vicinity of G β , where they probably form polar interactions, although specific side chain density in this region is not evident. **c.** ICL1 is located in close proximity to the G protein. A common CTR splice variant contains a 16 amino acid insertion within this loop (between Arg174 and Ser175), an insertion that would sterically hinder G-protein interactions with the receptor.



Extracellular view

Extended Data Figure 10 | Comparison of the activated β_2 AR and CTR viewed from the extracellular face. Tube representation of the transmembrane domains of the CTR (blue) and β_2 AR (green) viewed from the cytoplasmic face (based on overlay of the G_s protein from each structure). Despite similarities in the position of transmembrane tips at

the intracellular face, there are substantial differences in the location of the extracellular transmembrane tips, highlighting marked differences in the ligand binding mode and initiation of receptor activation between class A and B GPCRs.

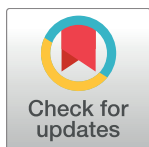
RESEARCH ARTICLE

Improving virtual screening of G protein-coupled receptors via ligand-directed modeling

Thomas Coudrat¹, John Simms², Arthur Christopoulos¹, Denise Wootten^{1*}, Patrick M. Sexton^{1*}

1 Drug Discovery Biology and Department of Pharmacology, Monash Institute of Pharmaceutical Sciences, Monash University, Parkville, Victoria, Australia, **2** School of Life and Health Sciences, Aston University, Birmingham, United Kingdom

* denise.wootten@monash.edu (DW); patrick.sexton@monash.edu (PMS)



OPEN ACCESS

Citation: Coudrat T, Simms J, Christopoulos A, Wootten D, Sexton PM (2017) Improving virtual screening of G protein-coupled receptors via ligand-directed modeling. *PLoS Comput Biol* 13 (11): e1005819. <https://doi.org/10.1371/journal.pcbi.1005819>

Editor: Avner Schlessinger, Icahn School of Medicine at Mount Sinai, UNITED STATES

Received: June 12, 2017

Accepted: October 12, 2017

Published: November 13, 2017

Copyright: © 2017 Coudrat et al. This is an open access article distributed under the terms of the [Creative Commons Attribution License](https://creativecommons.org/licenses/by/4.0/), which permits unrestricted use, distribution, and reproduction in any medium, provided the original author and source are credited.

Data Availability Statement: All relevant data are within the paper and its Supporting Information files.

Funding: This work was funded by the National Health and Medical Research Council of Australia (NHMRC) (Program grant # 1055134 to PMS and AC). PMS and AC are NHMRC Principal and Senior Principal Research Fellows, respectively. DW is a NHMRC Career Development Fellow. Computational studies were supported by Melbourne Bioinformatics at the University of

Abstract

G protein-coupled receptors (GPCRs) play crucial roles in cell physiology and pathophysiology. There is increasing interest in using structural information for virtual screening (VS) of libraries and for structure-based drug design to identify novel agonist or antagonist leads. However, the sparse availability of experimentally determined GPCR/ligand complex structures with diverse ligands impedes the application of structure-based drug design (SBDD) programs directed to identifying new molecules with a select pharmacology. In this study, we apply ligand-directed modeling (LDM) to available GPCR X-ray structures to improve VS performance and selectivity towards molecules of specific pharmacological profile. The described method refines a GPCR binding pocket conformation using a single known ligand for that GPCR. The LDM method is a computationally efficient, iterative workflow consisting of protein sampling and ligand docking. We developed an extensive benchmark comparing LDM-refined binding pockets to GPCR X-ray crystal structures across seven different GPCRs bound to a range of ligands of different chemotypes and pharmacological profiles. LDM-refined models showed improvement in VS performance over origin X-ray crystal structures in 21 out of 24 cases. In all cases, the LDM-refined models had superior performance in enriching for the chemotype of the refinement ligand. This likely contributes to the LDM success in all cases of inhibitor-bound to agonist-bound binding pocket refinement, a key task for GPCR SBDD programs. Indeed, agonist ligands are required for a plethora of GPCRs for therapeutic intervention, however GPCR X-ray structures are mostly restricted to their inactive inhibitor-bound state.

Author summary

G protein-coupled receptors (GPCRs) are a major target for drug discovery. These receptors are highly dynamic membrane proteins, and have had limited tractability using with biophysical screens that are widely adopted for globular protein targets. Thus, structure-based virtual screening (SBVS) holds great promise as a complement to physical screening

Melbourne, grant number VR0024 and a top up scholarship to TC. The funders had no role in study design, data collection and analysis, decision to publish, or preparation of the manuscript.

Competing interests: The authors have declared that no competing interests exist.

for rational design of novel drugs. Indeed, the increasing number of atomic-detail GPCR X-ray crystal structures has coincided with an increase in prospective SBVS studies that have identified novel compounds. However, experimentally solved GPCR structures do not meet the full demand for SBVS, as the GPCR structural landscape is incomplete, lacking both in coverage of available GPCRs, and diversity in both receptor conformations and the chemistry of co-crystallised ligands. Here we present a novel computational GPCR binding pocket refinement method that can generate predictive GPCR/ligand complexes with improved SBVS performance. This ligand-directed modeling workflow uses parallel processing and efficient algorithms to search the GPCR/ligand conformational space faster and more efficiently than the widely used protein refinement method molecular dynamics. In this study, the resulting models are evaluated both structurally, and in retrospective SBVS. We demonstrate improved performance of refined models over their starting structures in the majority of our test cases.

Introduction

G protein-coupled receptors (GPCRs) are the largest protein superfamily in mammalian genomes [1,2], encompassing close to 800 human genes that play key roles in modulating tissue and cell physiology and homeostasis [3]. Consequently, GPCRs are currently targeted by over 30% of all prescription pharmaceuticals on the market [4]. GPCRs all share a common transmembrane (TM) fold [5] and the superfamily is organised into four main classes according to the A-F classification system [6,7]. Their function is modulated by a wide variety of activity modulators, including peptide and non-peptide neurotransmitters and hormones, growth factors, ions, odorant and tastant molecules and even photons of light [8]. They are highly dynamic proteins that can adopt a range of conformations, some of which are sparsely populated in the ligand-free receptor. Binding of an agonist at the extracellular region of the TM domain of the GPCR induces a shift in the conformational equilibrium, pushing the receptor through a series of discrete conformational intermediates, ultimately leading to large rearrangements at the intracellular region that facilitate the interaction with intracellular effectors including heterotrimeric G proteins, arrestins, and G protein-coupled receptor kinases that lead to downstream signalling and regulation [9].

The past decade has seen an increase in structure determination of GPCRs in atomic detail, predominantly through the application of X-ray crystallography [10]. These studies have revealed the arrangement of the TM domain, location of ligand binding pockets, interaction patterns exhibited by agonists and inhibitors (antagonists and inverse agonists), and the structural rearrangements involved in conformational changes upon GPCR activation [11]. The GPCR structural coverage has now reached 192 structures of 44 different GPCRs, of which most belong to the Class A subfamily [12]. To date, most of these GPCR structures are in an inactive conformation, bound to an inhibitor, however more recently structures bound to agonists have been solved. These include intermediate conformations (e.g. beta-1 adrenergic receptor (B1AR) [13], beta-2 adrenergic receptor (B2AR) [14] and adenosine A2a receptor (AA2AR) [15,16]) that are solved without an intracellular effector and fully active receptors (e.g. bovine rhodopsin [17,18], B2AR [19+21], muscarinic acetylcholine receptor M2 (M2R) [22] and AA2AR [23]), solved with an agonist ligand and intracellular partner (either a G protein C-terminal fragment, heterotrimeric G protein, mini G alpha protein, G protein mimicking nanobody or an arrestin). Together these structures provide unprecedented insight into the structural and functional diversity of this protein family [24].

The wealth of structural information on Class A GPCRs (the GPCR superfamily targeted by the largest number of clinically used drugs [25]) is invaluable for structure-based drug discovery (SBDD) programs that complement traditional drug discovery efforts. These include using rational substitutions within ligand design that prioritise medicinal chemistry directions, and identification of new scaffolds or compounds using virtual screening (VS), which ranks libraries of small molecules based on the predicted interaction score between ligand and receptor binding pocket. VS has been extensively and successfully used on many soluble protein drug targets (e.g. enzymes) and more recently for GPCRs [26–31]. However, to fully harness VS for GPCR SBDD, greater structural coverage and diversity is required than has currently been experimentally derived, both in terms of the number of unique GPCRs and the variety of ligands that are bound to these receptors.

For GPCRs where structures are available, it is critical to increase the diversity of ligands bound in these structures to enhance their power in VS, as even small conformational differences are enough to distinguish agonist-bound from inhibitor-bound complexes. Indeed, principal component analysis (PCA) (see description in the [Methods](#) section) applied on B2AR and AA2AR X-ray structures that are used in this study identifies a separation between agonist-bound and inhibitor-bound binding pockets based on their conformation ([S1A and S1B Fig](#)). This has already been shown for rhodopsin X-ray structures [32]. Further, analysis of ligand-receptor interaction patterns with interaction fingerprint (IFP) clustering [33] (see description in the [Methods](#) section) reveals that agonist-bound and inhibitor-bound binding pockets have distinct fingerprints for individual receptors ([S1C and S1D Fig](#)). These small differences can influence a VS such that an inhibitor-bound structure will preferentially select for inhibitors in a VS and vice-versa for an agonist-bound structure [34]. While this information can be leveraged to bias VS of binding pockets towards the identification of ligands of a desired pharmacology, as shown in studies on adrenoceptors [35], it can also hinder the identification of novel ligands and ligands of a particular pharmacology in VS where limited structures are available. To attempt to overcome this, multiple GPCR binding pocket refinement methods have been applied to both X-ray crystal structures and GPCR homology models.

Molecular dynamics (MD) is a powerful computational tool that can be used for the refinement of a ligand-bound GPCR structure [36]. Classical MD has been used to understand GPCR activation mechanisms [37] and for GPCR model refinement [38,39]. Enhanced sampling methods, like accelerated MD, have also been used to explore receptor flexibility around a known ligand [40]. Two other methods that rely on MD are also gaining a lot of interest; (i) Markov state modeling, to identify ligand-induced binding pocket conformational changes [41] and (ii) free energy perturbations, to accurately recapitulate ligand binding affinities using X-ray structures [42] or a homology model [43] and the effect of mutations on agonist [44] and antagonist ligands [45]. MD however, remains a computationally expensive technique and efforts towards the development of computational methods that are more tractable for GPCR model refinement are being explored. One such set of methods, termed ligand-guided or ligand-steered modeling, relies on the optimization of residue conformations around a bound ligand to improve binding pocket VS performance using either manual [46] or automated protocols [47–49]. Another set of methods involves sampling of the whole receptor structure in the presence of a known ligand for the target receptor using protein sampling methods such as normal mode analysis [50–52] and Monte Carlo sampling [53]. Other methods focus on building de novo GPCR models, relying only on the protein sequence. These include threading [54,55] and helix packing [56–59] methods.

In this study, we present a novel computationally efficient ligand directed modeling (LDM) workflow that performs extensive sampling of a GPCR and ligand conformation to obtain a low energy minimum of the complex. The efficiency is achieved by running independent

conformational searches simultaneously on multiple compute cores and leveraging computationally efficient protein geometry-based sampling [60,61] and ligand molecular docking [62] methods. These methods also facilitate overcoming energy barriers. Furthermore, the LDM is an iterative process that integrates a combination of scoring functions used to prioritize complexes for further sampling, thus focusing the conformational search in the relevant space. Importantly, this method requires only a single known ligand for the GPCR to undergo its refinement, which is a sought-after feature for SBDD programs where only few ligands may be known. We evaluate the performance of this LDM protocol across a variety of refinement tasks of increasing difficulty, and identify advantages and shortcomings of using this LDM method for GPCR binding pocket refinement. The LDM generated models were evaluated using retrospective VS where we analysed the recovery of known ligands over decoys, the selectivity of agonists over inhibitors (or vice-versa) and the enrichment of specific ligand chemotypes. We demonstrate broad utility of this LDM approach for improving VS performance, particularly when searching for ligands of a defined pharmacology (for example agonists over inhibitors).

Methods

LDM workflow

The LDM method performs a GPCR binding pocket refinement around a small molecule ligand to establish a low energy minimum of the GPCR/ligand complex. The method requires an initial GPCR structure and a known small molecule ligand for the target GPCR. The LDM is optimised for refinement using ligands that bind to the canonical orthosteric binding pocket of Class A GPCRs, formed by the top of third of the TM bundle, using parameters defined in [S1 Table](#). The highly dynamic loops are deleted from the initial model, except for the distal portion of the extracellular loop 2 (ECL2). This portion consists of the segment of ECL2 downstream of the conserved ECL2 cysteine that forms a disulfide bridge with TM3. Although the ECL2 involvement in ligand recognition and kinetics has been extensively reviewed [63,64], ECL2 was shown not to be critical to VS outcome [65] and ECL2-distal specifically was shown to be involved in the orthosteric ligand final binding pose from many class A GPCR crystal structure analyses previously reviewed [5]. Ligand docking, which is a key component of the LDM workflow described below, does not apply any selective pressure on the conformation of other extracellular loops (ECLs) or intracellular loops (ICLs). The inclusion of ECLs and ICLs expands the conformational search space, thus for equal search time, reduces the conformational space explored within the more relevant canonical Class A GPCR binding pocket. Additionally, the highly flexible ECLs may occlude this binding pocket and prevent ligand docking on some generated conformations. Furthermore, two mutually exclusive regions are defined on the TM bundle, which are processed differently during the LDM workflow. The "extracellular region" corresponds to upper segments of TMs 2±7, while the "cytoplasmic region" corresponds to TM1 and the bottom of TMs 2±7 ([Fig 1B](#)). The cutoff point is a set of user defined residues that are located below the canonical orthosteric Class A binding pocket; these residues correspond to 1.48, 2.51, 3.38, 4.51, 5.50, 6.43, 7.45 defined using Ballesteros-Weinstein nomenclature [66]. This makes the extracellular region approximately 2/3 of the TM bundle and the rigid cytoplasmic region thus ensures that generated receptor structures retain their seven TM fold. The extracellular region, which contains the binding pocket, is also user defined before the start of the LDM but is updated during the workflow. The starting binding pocket was defined in this study by selecting residues within 1.5 Å of the binding pocket defined using the ICMPocketFinder tool. A box is created around these residues and used to calculate the docking grid.

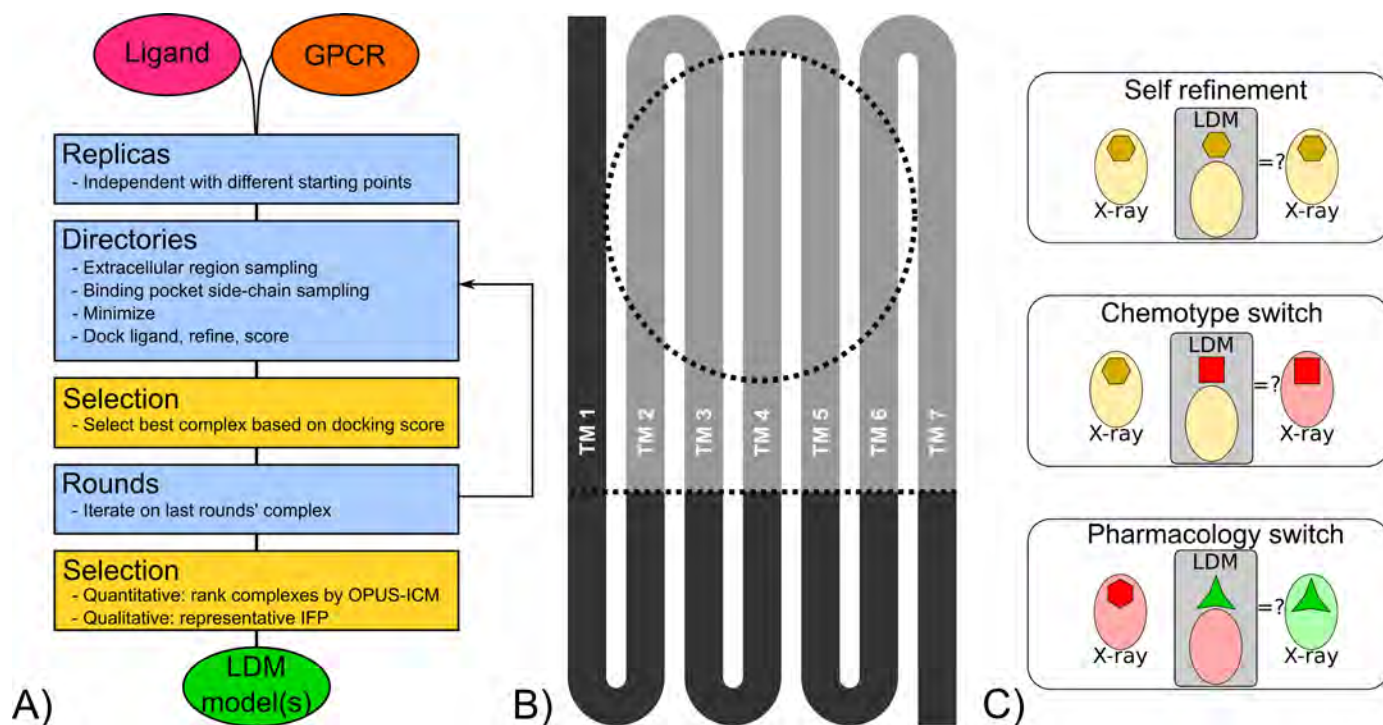


Fig 1. LDM workflow description. A) Schematic of the LDM workflow that takes a GPCR model and a ligand as input, and outputs LDM models. Sampling steps are represented in blue while selection steps are represented in yellow. B) GPCRs are separated in regions in the LDM workflow that have increasing degree of sampling. The TM1 and cytoplasmic region are kept static (dark grey), the rest of the GPCR is flexible (light grey). The binding pocket region defines the docking area and undergoes further sampling (dotted circle). C) The LDM was evaluated with a benchmark divided into three scenarios where an origin X-ray crystal structure binding pocket is refined by the LDM using the ligand found in a destination X-ray crystal structure, referred to here as origin and destination, respectively. In self refinement, the origin and destination are the same structure, in chemotype switch, the origin and destination are bound by ligands of the same pharmacology (agonist or inhibitor) but with different chemotypes and in pharmacology switch, origin and destination are bound by ligands of different pharmacology (agonist to inhibitor or vice-versa).

<https://doi.org/10.1371/journal.pcbi.1005819.g001>

The LDM workflow is provided as a set of scripts written in Bash designed to run on a computer cluster using either the SLURM or the PBS submission system (https://github.com/thomas-coudrat/lbm_scripts), with parameters that can be modified by the user. The parameters used in the following description (described in more detail in S1 Table) are the recommended parameters and those that were used in this study. The LDM workflow (Fig 1A) initiates several independent replicas where the input receptor structure is minimised with explicit waters using GROMACS [67] and undergoes minimal sampling with CONCOORD [60]. This ensures that each replica has a slightly different conformational starting point. In each replica, an iterative process is initiated and run over several rounds. Each round includes a series of sampling, selection and scoring steps with the first round processing the receptor alone and all subsequent rounds processing the receptor-ligand complex in the same manner. Both receptor and receptor-ligand complexes will be referred to as the system in the following description. During each round, a set of independent directories is created. In each of these, the system undergoes extracellular protein sampling with CONCOORD [60], followed by a selection of the resulting binding pockets that are within a cutoff distance from the starting system. The selected systems then undergo binding pocket side-chain sampling with tCONCOORD [61]. Pockets that conserved a fraction of binding pocket polar residues from the starting system are selected. Both these selection steps ensure that the resulting system does not deviate too greatly from the original and retains a suitable binding pocket. The LDM process therefore prioritizes incremental conformational changes. The system's side-chains, from

the cytoplasmic region of the system, are rebuilt using scomp [68], the whole system is then minimised in explicit waters with GROMACS readying it for the docking phase. ICM flexible ligand docking is performed with the single ligand onto the pre-calculated receptor docking grid. An area of 2 Å around the ligand is refined and ICM is used to score the ligand-receptor complex. This key step in the LDM workflow selects for binding pockets where the known ligand binds with a high score, thus providing a selective pressure on the binding pocket and the extra-cellular region of the receptor. The scoring phase within each replica then compares all complexes generated in individual directories based on their ICM score, with the best scoring complex extracted and assigned an OPUS score, using OPUS_PSP [69], which provides information on the overall quality of the protein fold. All other complexes are discarded. The extracted complex is then used as the starting point for a subsequent round of the iterative LDM workflow. After all rounds are completed, the LDM outputs a maximum number of models equal to the number of rounds times the number of replicas. This is a selection from a much larger total number of receptor-ligand complexes generated over the course of the workflow. These LDM output models are sorted with the quantitative ICM and OPUS score, where both methods are normalised and used in equal weights (OPUS-ICM score). In summary, the LDM workflow relies on the selection steps and scoring that prioritise binding pocket integrity and known ligand complementarity, the scoring that prioritises proteins with a correct fold and the static treatment of the cytoplasmic region of the receptor enable the LDM workflow. Together, these parameters optimise for GPCR binding pocket conformations that are compatible with a known ligand while not requiring an explicit lipid membrane for their computation. A description of the required software, preparation and parameters to run the LDM is provided in [S1 Text](#).

LDM assessment and benchmarks

X-ray structures used for this study (with abbreviations for GPCRs and their ligands) are listed in [S2 Table](#). These structures were selected based on the criteria that they were of human origin with binding pockets containing no or a limited number of mutations and unresolved side-chains. Benchmarking was designed so that the target result for each application of the method was available in the form of an X-ray structure. The LDM was applied on an origin X-ray structure refined using the ligand bound in a destination X-ray structure and the LDM results were compared to both the origin and destination X-ray crystal structures. All GPCRs that were considered for benchmarking also had libraries of known ligands and decoys available from the GPCR ligand library/GPCR decoy database (GLL/GDD) [70], described below.

Three different scenarios were assessed that evaluate different conformational distance between the origin and the destination X-ray structures representing varying levels of difficulty ([Fig 1C](#)). In the first scenario, various GPCRs were selected to perform self refinement of a ligand-bound X-ray structure, where a binding pocket is refined using its own bound ligand. The chemotype switch scenario evaluated the LDM at refining an agonist-bound (or inhibitor bound) binding pocket using an agonist (or inhibitor) of a different chemotype. The conformational rearrangement is more pronounced in this case relative to the self refinement. These experiments required the selection of X-ray structures where a single GPCR was bound by ligands of different chemotype. The final scenario assessed was pharmacology switch that refined an inhibitor-bound binding pocket using an agonist for LDM refinement (or vice-versa). This requires larger rearrangements of the binding pocket's protein backbone and represents the most difficult task. Pharmacology switch experiments were performed using examples of aminergic GPCRs (B2AR and M2R) that are available in inactive and fully active conformations. A nucleotide GPCR (AA2AR) with available agonist-bound and inhibitor-bound structures was also chosen to complete this benchmark.

In one pharmacology switch LDM experiment, the origin and destination X-ray structures contained different mutations (introduced for stabilisation and crystallisation). One of the mutations was within 4 Å of the bound ligand in the destination X-ray structure. For this LDM experiment, four mutations were introduced in the origin X-ray structure 3EML [71] to match the sequence of the destination X-ray structure 2YDV [15] (S2 Table). In all other cases, gene sequences were either identical between origin and destination X-ray structure, or mutations occurred far from the binding pocket.

Protein-ligand conformation analysis

As shown previously, the success of a GPCR binding pocket performance in VS is linked with the ICM interactive score and ligand/receptor interaction pattern [72]. The LDM workflow leverages the ICM interactive score during its iterative process, and combines this with the OPUS_PSP score for final ranking of LDM output models. To gain further insight into the outcome of the LDM workflow, LDM models were analysed using qualitative methods. For each LDM experiment described in this study, all LDM output models were superimposed onto the destination X-ray structure and the top 25 LDM models (models LDM 000 to LDM 024) along with the origin and destination X-ray structures were further analysed. Ligand/receptor interaction patterns were analysed using interaction fingerprints (IFPs) [73]. An IFP is a vector of booleans (True or False) that encode for the interaction type between each of the ordered list of residues lining the binding pocket and the bound ligand. Binding pocket conformational changes were also analysed using PCA, a dimensionality reduction algorithm. These analyses were performed using a set of Python [74] scripts developed in the laboratory: `toolbox_pdb` (https://github.com/thomas-coudrat/toolbox_pdb) [72]. These scripts use the open source libraries Matplotlib [75], Numpy [76], SciPy [77] and the PCA implementation uses scikit-learn [78] while the IFP implementation uses the OpenEye OEChem toolkit version 2014.10.2 [79].

Interaction fingerprints. IFPs were calculated for the top 25 LDM results and both origin and destination X-ray structures. IFPs were used as described by Marcou and Rognan [73] that include the presence or absence of hydrophobic, weak hydrogen bond (donor and acceptor), hydrogen bond (donor and acceptor), ionic (positive or negative) and aromatic interactions of each binding pocket residue with the ligand. Graphical outputs were generated for inspection of specific differences in interaction patterns, and IFPs were also clustered using the Jaccard distance with the result visualised as a dendrogram. The Jaccard distance is used as a measure of the dissimilarity between two boolean vectors of length n (IFPs), calculated using Eq 1 where the Jaccard index of co-occurrence C_{ij} is the number of occurrences of $u[k] = i$ and $v[k] = j$ for $k < n$. In these dendrograms, a distance of 0 corresponds to identical IFPs. A cutoff Jaccard distance defines the number of clusters at that distance. In this study, a distance of 0.6 or higher was routinely assigned to signify two sufficiently different IFPs. This cutoff was lowered to a less stringent value in a few cases, when the number of different clusters generated was large at 0.6. Grouping the LDM models and X-ray structures using IFP clustering aided prioritisation of LDM binding pockets for further assessment. Each LDM model was scored, ranked and named based on the OPUS-ICM metric, thus the highest scoring LDM model in each IFP cluster could be identified by its name and was thereafter defined as the representative for that cluster. These representative LDM models were assessed in VS and their ligand/receptor conformations were further analysed and compared to the origin and destination X-ray structures.

$$d_j = \frac{C_{TF} + C_{FT}}{C_{TT} + C_{TF} + C_{FT}}$$

Principal component analysis. The binding pocket conformation of the top 25 LDM models and X-ray structures were examined by comparing the positions of carbon alphas of the binding pocket residues using PCA that extracts the main variance of a dataset revealing its internal structure [80]. Principal components (PCs) are ordered based on their percentage of cumulative variance explained from the original dataset. The first two PCs were plotted onto a PCA score that provides information on the relationship between the binding pockets analysed, but also the importance of these relationships relative to the total amount of variance in the original dataset. The percentage of variation explained by each PC is shown in parenthesis (e.g. PC1 explains 50% of the variance in the data). Finally, a colour map was generated to display the IFP Jaccard distance between each of the complexes and the destination X-ray structure on the PCA plot.

Virtual screening

Retrospective VS performance was performed on the representative LDM binding pockets from each IFP cluster and compared to the VS performance of the origin and destination X-ray structures. The GLL/GDD small molecule libraries [70], which match known GPCR agonists and inhibitors with a respective sets of decoys of similar physical properties, was used for VS. The ligand libraries were optimised prior to use by deleting duplicates, adding X-ray co-crystal ligands from this study. The ligand library was then modified to a racemic library format, as described previously [72]. The activity profile of many ligands is experimentally determined on a racemic mix while only one enantiomer is active, thus considering all enantiomers in SBDD ensures the right active ligand is assessed. Finally, the ligand charge was set per the ICM pKa model and no additional tautomers were generated.

When screening the libraries, each ligand docking was repeated three times, and the best of the three scores was attributed to the ligand for ranking. Three metrics were established for evaluating VS performance [72]: recovery, selectivity and chemotype enrichment. Recovery and selectivity were visualised using receiver operating characteristic (ROC) curves that compare the recovery rate of known ligands against decoys (recovery) and inhibitors against agonists, or vice-versa (selectivity). Normalised square-root area under the curve (NSQ_AUC) [81] values were calculated for all ROC curves. In addition, the behaviour of all binding pockets with regards to specific chemotype recovery was also analysed. Dendrograms were developed for all known ligand chemotypes for GPCRs used in this study (S2 Fig). Enrichment factors (EFs) at 1, 5 and 10% of the total library were plotted for representative chemotype clusters when using a 0.5 pharmacophore cutoff. Representative clusters were selected on the following criteria; (i) if they contained a ligand that was present in an X-ray structure used in this study and (ii) if they contained a large number of the known ligands, thus offering a good coverage of the chemical diversity of the known ligand library (S2 Fig). The setup, management and analysis of VS experiments, including the plotting of ROC curves and EF bargraphs was performed using the open-source and available Python scripts toolbox_vs developed in the laboratory (https://github.com/thomas-coudrat/toolbox_vs) [72]. This package uses the following libraries: Matplotlib [75], Numpy [76] and scikit-learn [78].

Results

The influence of loops on X-ray structure VS performance

The influence of the loops on VS performance was assessed for all X-ray structures used in this study. All X-ray structures were processed by ICM by adding hydrogens and missing side-chains and flipping asparagine, glutamine and histidine side-chains to improve molecular interactions. No further refinement or energy minimisation was performed on these X-ray

structures. Two sets of binding pockets were generated; in the first set all X-ray structure ECLs were retained and in the second set all ECLs except for the distal part of ECL2 (ECL2-distal) were removed. The binding pocket pairs were compared using VS recovery and selectivity and plotted as ROC curves (S3 and S4 Figs) from which NSQ_AUC values were calculated (Fig 2). Overall, removing loops while leaving the ECL2-distal had little influence on VS recovery (Fig 2A) or selectivity (Fig 2B). However, a notable difference was identified with the M2R agonist-bound structure 4MQS-iperoxo (IXO), where the removal of loops with the exception of the ECL2-distal region resulted in a large improvement in VS performance, in both recovery and selectivity.

Self refinement

In this scenario, the ligand used for LDM refinement was the ligand found in the origin X-ray structure. The LDM models were thus compared to a single X-ray structure. The analysis of the results for this scenario was separated into two groups. The first group is represented by experiments where the LDM models showed improved or similar VS performance in overall recovery and/or selectivity relative to the X-ray structure, and also with a ligand pose similar to that of the X-ray structure. The second group consists of experiments where LDM models had lower overall VS performance, even if their binding pose was similar to that of the X-ray structure. Despite this, in all self refinement experiments, the LDM workflow performed its task of refinement around the ligand used, either "narrowing" the chemotypes that were enriched in the LDM models so that only the chemotypes similar to the refinement ligand were identified or displaying improved enrichment for the refinement ligand chemotype relative to the origin X-ray structure.

Group A. The first group is described in detail using the LDM experiment B2AR 4LDE-BI-167,107 (BI) (Fig 3). Seven other LDM experiments were performed that displayed a similar pattern, including B2AR 3P0G-BI (S5 Fig), AA2AR 4EIY-ZM-241,385 (ZM) (S6 Fig), 3PWH-ZM (S7 Fig), M2R 3UON-3-quinuclidinyl-benzilate (QNB) (S8 Fig), M2R 4MQS-IXO (S9 Fig), histamine H1 receptor (H1R) 3RZE-doxepin (DOX) (S10 Fig) and 5-hydroxytryptamine receptor 1B (5-HT1B) 4IAR-ergotamine (ERG) (S11 Fig). The B2AR BI-refined LDM models converged towards a similar binding pose to that of the X-ray structure, as the IFP of the top 25 LDM models are within 0.5 in Jaccard distance (Fig 3A) and form two clusters at a 0.45 cut-off, with representatives LDM 000 and LDM 021 for each cluster. Although LDM 021 was the closest to the X-ray structure in terms of interaction pattern, its binding pocket conformation was more distant to the X-ray structure than LDM 000 (Fig 3A and 3B). The binding poses overlaid very closely (Fig 3C), and both LDM models displayed the same polar and ionic interaction pattern as the X-ray structure at D113, S203 and N312 (Fig 3D). The two LDM models differed in their polar contacts, with LDM 000 displaying the same interaction with S204 and S207 as the X-ray structure, whereas LDM 021 had the same interaction pattern with N293 as the X-ray structure and an additional polar contact with T118.

Both LDM models outperformed the X-ray structure in overall VS recovery and selectivity (Fig 3E and 3F). In both cases, LDM 021 was the best performer, with NSQ_AUC values of 80.0 and 64.5 in recovery and selectivity, respectively. The chemotype enrichment analysis revealed an improved enrichment for the chemotype of the refinement ligand BI, for both LDM models compared to the X-ray structure at EF1 (Fig 3G). Interestingly, the highly populated chemotype cluster A was also enriched in both LDM models compared to the X-ray structure, while the under-populated chemotype cluster C was enriched to a lesser extent compared to the X-ray structure at EF1.

Key polar, ionic and aromatic interactions were recovered by LDM models in all seven experiments from this group, as illustrated for B2AR 4LDE-BI. However, notable ionic contacts were absent from LDM models in three experiments from this group (S8±S10 Figs).

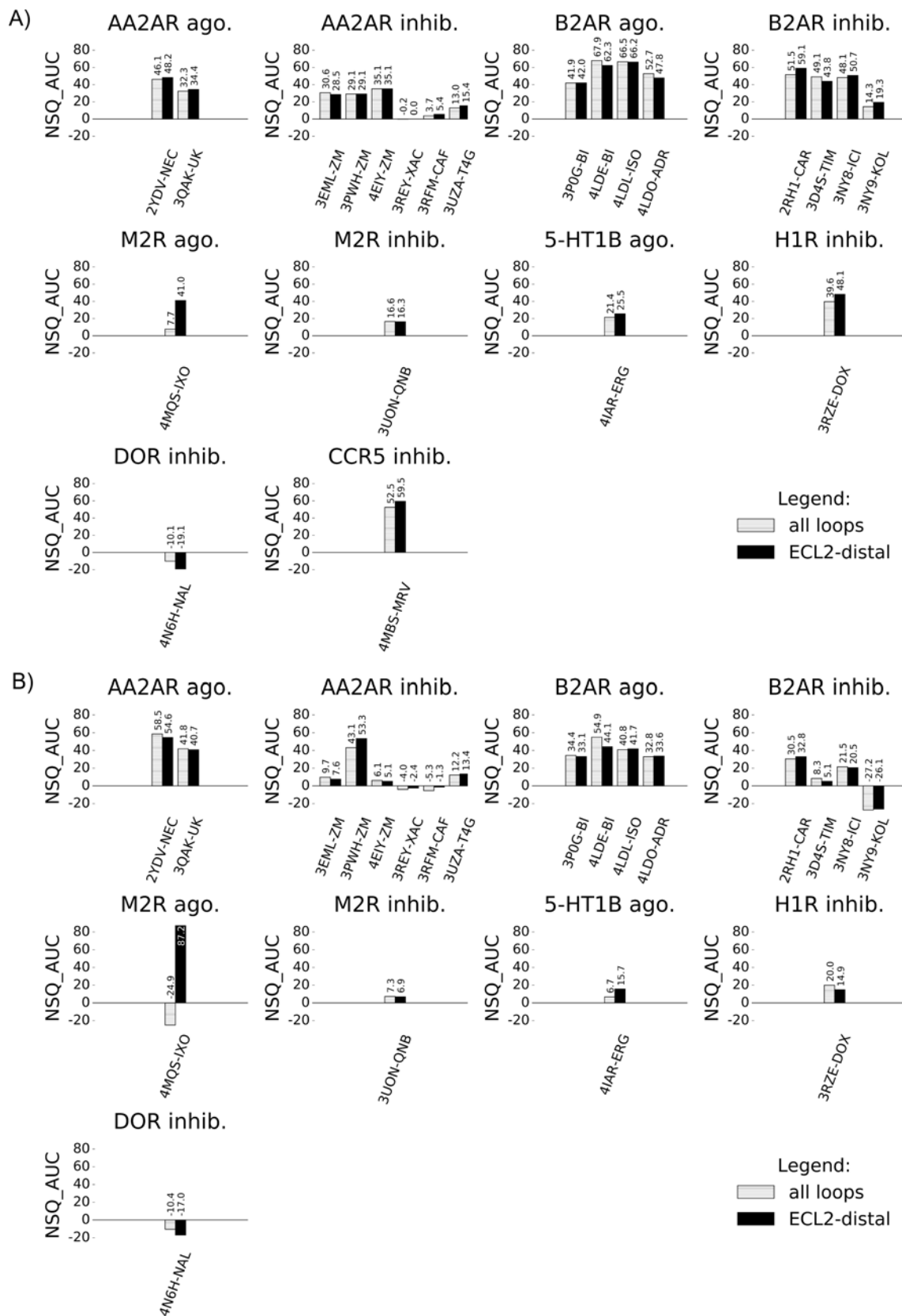


Fig 2. Comparison of VS performance for X-ray structures with all loops vs. ECL2-distal loop only. VS performance in NSQ_AUC values of X-ray structures measuring A) recovery of known ligands against decoys and B) selectivity of agonists vs. inhibitors (or vice-versa). X-ray structures with all loops are represented in dashed bars and X-ray structures with ECL2-distal only are represented in black bars.

<https://doi.org/10.1371/journal.pcbi.1005819.g002>

Despite this, as was the case for B2AR 4LDE-BI, LDM models showed improved enrichment for the refinement ligand chemotype and for other chemotypes in two other experiments (S5 and S10 Figs). However, in the five other experiments from this subgroup overall VS was similar to the X-ray structure, but with improvement and/or narrowed enrichment towards the refinement ligand chemotype (S6±S8 and S11 Figs).

Group B. The second group of self refinement LDM experiments is illustrated by B2AR 2RH1 refined by the ligand carazolol (CAR) (Fig 4). The three representative LDM models

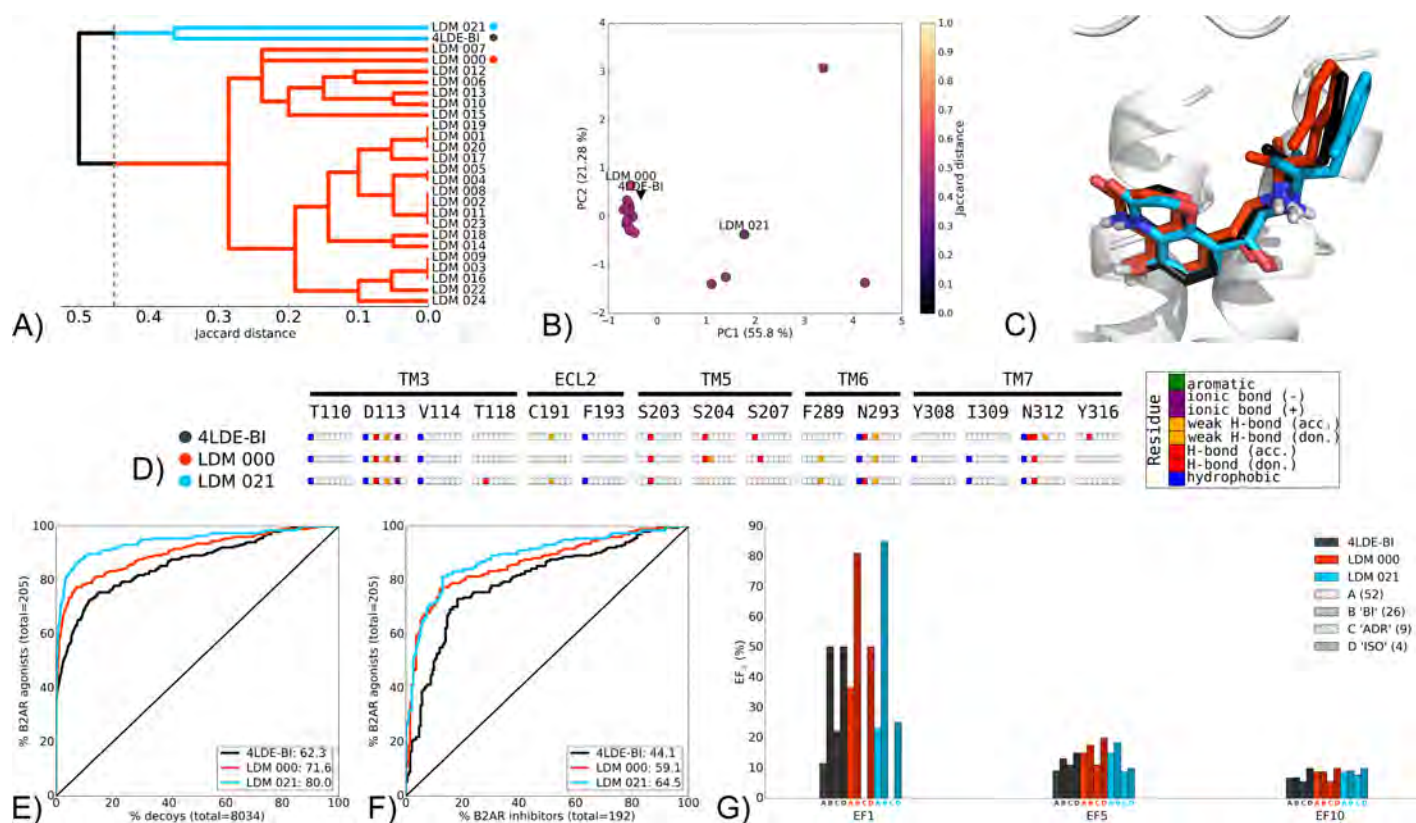


Fig 3. Self refinement LDM experiment on the B2AR 4LDE-BI, using BI as a refinement ligand. A) Dendrogram of the top 25 LDM models and the X-ray structures, a cut-off line identifies different LDM clusters and their representative LDM models are designated by a coloured dot. Representative LDM models are the highest scoring within the cluster based on the OPUS-ICM metric. B) PCA comparison of binding pocket conformation between the top 25 LDM models and the X-ray structures. LDM models are coloured based on their IFP Jaccard distance with the destination X-ray structure, 4LDE-BI. C) Binding poses of the representative LDM models and the destination X-ray structure with the X-ray ligand in black, LDM000 in red and LDM021 in blue. D) IFP of the representative LDM models and the X-ray structure. Interaction type is described for each residue of the binding pocket: hydrophobic interaction, hydrogen bond (H-bond) donor and acceptor, weak hydrogen bond (weak H-bond) donor and acceptor, ionic bond positive (+) and negative (-) and aromatic interaction. E, F, G) VS performance with the X-ray structure in black, LDM000 in red and LDM021 in blue. E) ROC curves visualising the recovery of B2AR agonists vs. decoys. F) ROC curves highlighting the selectivity of B2AR agonists over B2AR inhibitors. For E and F, the relative rank of the LDM refinement ligand is identified with a vertical dashed line. This vertical line is not visible as it overlays the axis indicating the refinement ligand is very highly ranked in all 3 cases. The ROC curve figure insets show NSQ_AUC values for each binding pocket. G) bar chart to visualise the EF for representative B2AR agonist chemotypes at EF1, EF5 and EF10. Chemotypes A, B 'BI'-like, C 'ADR'-like and D 'ISO'-like represent only a subset of B2AR agonist ligands (S2C Fig). The EF bar chart inset shows the number of ligands for each of these chemotype clusters between parenthesis. X-ray structure chemotype EF shown in black bars, with the LDM models coloured based on their relative clusters identified in A.

<https://doi.org/10.1371/journal.pcbi.1005819.g003>

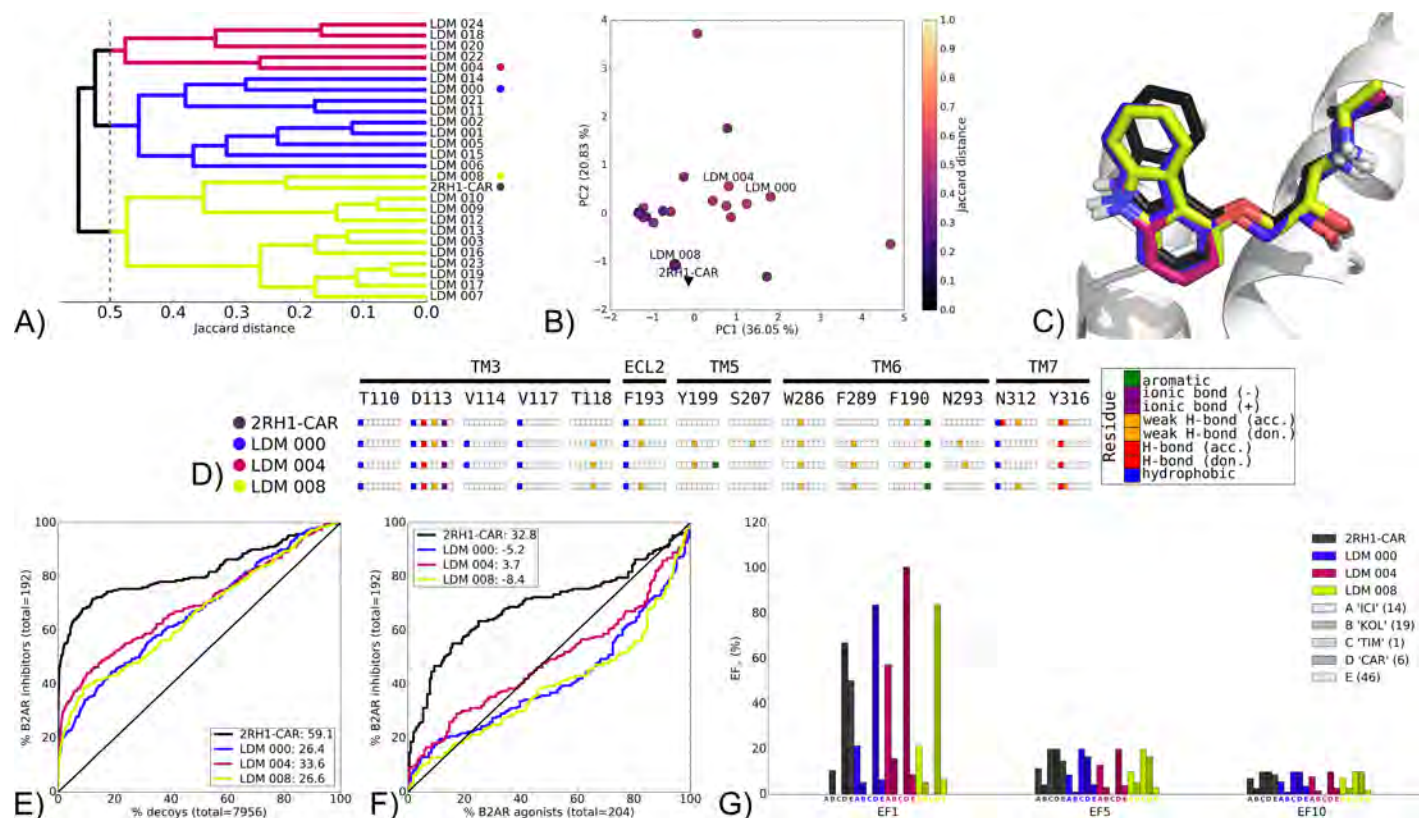


Fig 4. Self refinement LDM on the B2AR 2RH1-CAR, using CAR as the refinement ligand. A) Dendrogram of the top 25 LDM models and the X-ray structure, a cutoff line identifies different LDM clusters. Representative LDM models are the highest scoring within the cluster based on the OPUS-ICM metric and are designated by a coloured dot. B) Comparison of binding pocket conformation between the top 25 LDM models and the X-ray structure. LDM models are colored based on their IFP Jaccard distance with the destination X-ray structure, 2RH1-CAR. C) Binding poses of the representative LDM models and the destination X-ray structure with the X-ray ligand in black and the LDM models coloured based on their representative clusters defined in A. D) IFP of the representative LDM models and the X-ray structure. Interaction type is described for each residue of the binding pocket: hydrophobic interaction, hydrogen bond (H-bond) donor and acceptor, weak hydrogen bond (weak H-bond) donor and acceptor, ionic bond positive (+) and negative (-) and aromatic interaction. VS performance is described with ROC curves to visualise E) the recovery of B2AR inhibitors vs. decoys and F) the selectivity of B2AR inhibitors over B2AR agonists. X-ray structures are in black, with the LDM models coloured based on their relative clusters identified in A. The relative rank of the LDM refinement ligand is identified with a vertical dashed line. In all cases, this vertical line is masked by the axis indicating that the refinement ligand was very highly ranked. The ROC curve figure inset shows NSQ_AUC values for each binding pocket. G) bar chart is used to visualise the EF for representative B2AR inhibitor chemotypes at EF1, EF5 and EF10. Chemotypes A 'ICI'-like, B 'KOL'-like, C 'TIM'-like, D 'CAR'-like and E represent only a subset of B2AR inhibitor ligands (S2D Fig). The EF bar chart inset shows the number of ligands for each chemotype cluster between parenthesis. X-ray structure chemotype EF shown in black bars, with the LDM models coloured based on their relative clusters identified in A.

<https://doi.org/10.1371/journal.pcbi.1005819.g004>

selected from IFP clustering were very similar to the X-ray structure at 0.5 cutoff (Fig 4A, and 4C). Interestingly, LDM 008 was closest to the X-ray structure in both IFP (Fig 4A) and in binding pocket conformation (Fig 4B). The three LDM models had similar IFPs with LDM 004 uniquely displaying an aromatic interaction with Y199 (Fig 4D). However, none of the LDM models featured the polar interaction with N312 observed in the X-ray structure 2RH1-CAR.

All LDM models had a similar VS performance pattern, with LDM 004 slightly outperforming LDM 000 and LDM 008 in recovery (Fig 4E) and selectivity (Fig 4E). However, the X-ray structure (2RH1) binding pocket outperformed all LDM models in both overall recovery and selectivity (Fig 4E and 4F). Nonetheless, in all LDM models, the binding pockets were more selective for the CAR chemotype, as identified by their higher EF1 values. In addition, the best VS performer amongst LDM models, LDM 004, also had an improved chemotype enrichment

for ICI-like and KOL-like B2AR inhibitor chemotypes compared to the 2RH1-CAR (Fig 4G). In contrast, chemotype cluster E that represents a much larger number of known ligands was poorly enriched in all the LDM models relative to the X-ray structure.

The results of B2AR 2RH1-CAR were interesting as LDM models converged towards conformations that were very similar to the X-ray structure, yet overall VS performance was reduced for LDM models relative to the X-ray structure. However, chemotype enrichment for those related to the refinement ligand was higher. The same pattern was seen with AA2AR 2YDV-NEC (S12 Fig). While C-C chemokine receptor type 5 (CCR5) 4MBS-maraviroc (MRV) (S13 Fig) and δ -opioid receptor (DOR) 4N6H-naltrindole (NAL) (S14 Fig), did not converge to a unique binding pose, all experiments from this group had improved recovery for the refinement ligand chemotype (while also excluding other chemotypes, hence narrowing towards the refinement ligand chemotype) compared to their X-ray structure (Fig 4G and S12G, S13F and S14G Figs). In addition, similar to B2AR 2RH1-CAR, none of these LDM models outperformed the X-ray structures in overall VS performance.

Chemotype switch

We next evaluated the capacity of the LDM workflow to refine a GPCR binding pocket using a ligand of the same pharmacology (agonist or inhibitor) to that of the starting structure but belonging to a distinct ligand chemotype. This represents a larger conformational change relative to the self refinement. As with the self refinement studies, the LDM outcomes are presented in two separate groups with the first group describing LDM experiments where LDM models exhibited a better VS performance than the origin X-ray structures, with a similar binding pose to that of the destination X-ray structure. The second group comprised LDM experiments where LDM models improved VS performance over the origin X-ray structure, but had binding poses that differed from that of the destination X-ray structure.

Group A. This group is illustrated by the LDM experiment on the B2AR 4LDO X-ray structure bound by the agonist adrenaline (ADR), refined using the agonist hydroxybenzyl isoproterenol (ISO) found in the X-ray structure 4LDL (Fig 5). The group also includes the B2AR 3NY9 bound by the inhibitor described by Kolb et al. [82] (KOL), using CAR found in the X-ray structure 2RH1 (S15 Fig), AA2AR from 3QAK bound by UK-432,097 (UK) refined by NECA (NEC) found in the X-ray structure 2YDV (S16 Fig) and B2AR from 3D4S bound by timolol (TIM) refined by ICI-118,551 (ICI) found in the X-ray structure 3NY8 (S17 Fig).

The IFP clustering and visualization for B2AR 4LDO-ADR and 4LDL-ISO revealed the origin and destination X-ray structures shared a similar ligand/receptor interaction pattern (Fig 5A and 5D). Indeed, both complexes were characterised by polar contacts with D113, S203 and N312 and an ionic interaction with D113. Their conformational similarity was also illustrated by the relatively small distance in their PCA scores performed on binding pocket carbons alphas (Fig 5B). In this LDM experiment, the top 25 models mostly converged towards a large cluster represented by LDM 000, and three single leaf clusters containing LDM 006, LDM 015 and LDM 020 (Fig 5A). The binding poses for all these LDM models were close to that of the destination X-ray structure, with the exception of LDM 015 that was flipped around the anchor point formed by an ionic interaction between ISO's tertiary amine and D113 (Fig 5C and 5D). While several LDM models contained interactions present in one or both of the X-ray structures, they also contain several additional polar interactions with ECL2 (D192 and F193), TM5 (S204) and TM6 (K305).

Both the origin and destination X-ray structures performed well in recovery and agonist selectivity (Fig 5E and 5F), and they both obtained high EF1 values for chemotypes of their respective crystal ligands (Fig 5G). Overall the LDM models also performed well in both VS

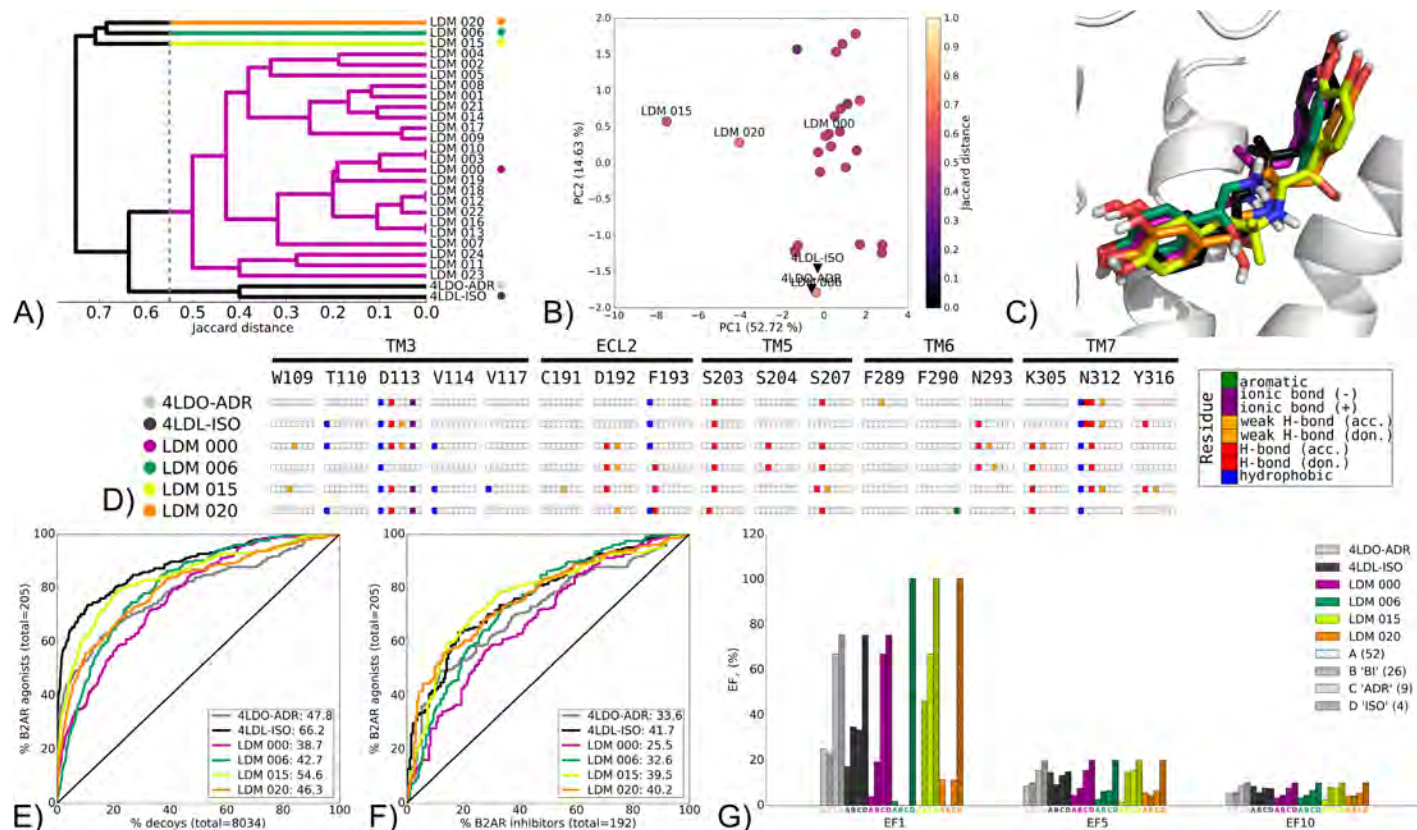


Fig 5. Chemotype switch LDM experiment on the B2AR from 4LDO-ADR to 4LDL-ISO, using ISO as a refinement ligand. A) Dendrogram of the top 25 LDM models and X-ray structures, a cutoff line identifies different LDM clusters and their representative LDM models are designated by a colored dot. Representative LDM models are the highest scoring within the cluster based on the OPUS-ICM metric. B) Comparison of binding pocket conformation between the top 25 LDM models and X-ray structures. LDM models are colored based on their IFP Jaccard distance with the destination X-ray structure, 4LDL-ISO. C) Binding poses of the representative LDM models and the destination X-ray structure with the X-ray ligand in black and the LDM models coloured based on their representative clusters defined in A. D) IFP of the representative LDM models and the X-ray structures. Interaction type is described for each residue of the binding pocket: hydrophobic interaction, hydrogen bond (H-bond) donor and acceptor, weak hydrogen bond (weak H-bond) donor and acceptor, ionic bond positive (+) and negative (-) and aromatic interaction. VS performance is described with ROC curves to visualise E) the recovery of B2AR agonists vs. decoys and F) the selectivity of B2AR agonists over B2AR inhibitors. X-ray structures are in black, with the LDM models coloured based on their relative clusters identified in A. The relative rank of the LDM refinement ligand is identified with a vertical dashed line. In all cases, this vertical line is masked by the axis indicating that the refinement ligand was very highly ranked. The ROC curve figure inset shows NSQ_AUC values for each binding pocket. G) bar chart is used to visualise the EF for representative B2AR agonist chemotypes at EF1, EF5 and EF10. Chemotypes A, B 'BI-like', C 'ADR-like' and D 'ISO-like' represent only a subset of B2AR agonist ligands (S2C Fig). The EF bar chart inset shows the number of ligands for each chemotype cluster between parenthesis.

<https://doi.org/10.1371/journal.pcbi.1005819.g005>

performance evaluations. Specifically, when compared to the origin X-ray structure, LDM 015 was superior in both recovery and selectivity while LDM 020 was also good at recovery and superior in selectivity. Interestingly, LDM 015 had a flipped binding pose while maintaining a similar ligand/receptor interaction pattern to the destination X-ray and other LDM models. In terms of chemotype recovery, all LDM models outperformed the destination X-ray structure 4LDL-ISO at EF1 for the D 'ISO-like' chemotype, except for LDM 000 that had the same EF1 score. The success of LDM 015 in overall VS performance can be linked to its superior EF1 score, relative to all other LDM models, for chemotype B 'BI-like', which is widely represented amongst B2AR agonists (26 ligands at 0.5 cutoff) (S2C Fig).

The other LDM experiments from this group exhibited a range of IFP distances between origin and destination X-ray structure (with Jaccard distances of ~0.6 for B2AR 3NY9-KOL to 2RH1-CAR, ~0.7 for AA2AR 3QAK-UK to 2YDV-NEC and ~0.3 for B2AR 3D4S-TIM to

3NY8-ICI, compared to ~ 0.4 for B2AR 4LDO-ADR to 4LDL-ISO (S15±S17A Figs and Fig 5A)). Two LDM experiments showed convergence towards the destination X-ray structure IFP (S15A and S16A Figs), while a third one (B2AR 3D4S-TIM to 3NY8-ICI) had its best performing LDM model appear in a small IFP cluster that was closest to the destination X-ray structure's interaction pattern (S17A Fig). This was similar to the B2AR 4LDO-ADR 4LDL-ISO example described above. For the B2AR 3D4S-TIM to 3NY8-ICI LDM experiment, we decided to evaluate all LDM models from this minor IFP cluster (S17A Fig) for VS performance (S18 Fig). The best VS performer in this cluster was the lower ranked LDM 020. Interestingly, this model did not exhibit the ionic interaction between the ligand and D113 that was found in all the X-ray structures (S18D Fig).

In the three cases outlined above, the analysis contained LDM models that outperformed their respective origin X-ray structures in VS recovery and selectivity (S15±S17E and S15±S17F Figs). In addition, in all these examples all LDM models improved enrichment of the LDM refinement ligand and its chemotype compared to the origin X-ray structure (S15±S17G Figs). LDM models from the B2AR 3NY9-KOL to 2RH1-CAR experiment even outperformed the destination X-ray structure 2RH1-CAR in CAR-like chemotype enrichment, and also displayed superior enrichment for chemotypes ICI-like and KOL-like compared to both origin and destination X-ray structures (S15G Fig).

Group B. The second group of observed chemotype switch experiments is illustrated using the LDM experiment on AA2AR 3PWH-ZM using caffeine (CAF) for refinement with comparison of these LDM models to 3RFM-CAF (Fig 6). This group also contained the LDM experiment on AA2AR 3UZA-1,2,4-triazine 4g (T4G) using the xanthine amine congener (XAC) for refinement, with LDM models compared to 3REY-XAC (S19 Fig). In these studies, a selected LDM model improved VS performance over the origin X-ray structure, however with a ligand/receptor interaction pattern that was different to that of the destination X-ray structure.

For the featured experiment of AA2AR 3PWH-ZM to 3RFM-CAF, the origin and destination X-ray structures displayed markedly different ligand/receptor interaction patterns at ~ 0.9 Jaccard distance (Fig 6A), however their binding pocket conformations did not differ greatly (Fig 6B and S1A and S1B Fig). The LDM model IFPs displayed two distinct positions inside the binding pocket. A shallow binding pose that was shared by the X-ray structure 3RFM-CAF, and a deeper binding pose (Fig 6A and 6C). The group of shallow LDM models included representative models LDM 000, LDM 001 and LDM 005. The former two LDM models shared an aromatic contact with F168 and a polar interaction with N253 (Fig 6D) and these interactions were also present in both origin and destination X-ray structures.

Interestingly, the origin X-ray structure in this case outperformed the destination X-ray structure in VS recovery and selectivity, even for recovery of the destination ligand (Fig 6E, and 6F). Compared to the destination X-ray structure, several LDM models, including LDM 000 and LDM 001, had a similar recovery and all three shallow binding pose LDM models had an improved overall inhibitor versus agonist selectivity relative to the destination structure (Fig 6E and 6F). In terms of CAF chemotype enrichment at EF1, the LDM models that showed a deeper binding pose outperformed the ones with a shallower pose (Fig 6G), despite a distinct ligand pose to the destination structure. All models improved the relative ranking of CAF compared to both X-ray structures.

This group of chemotype switch LDM experiments was also represented by the LDM experiment AA2AR 3UZA-T4G to 3REY-XAC (S19 Fig). Relative to AA2AR 3PWH-ZM 3RFM-CAF described above, AA2AR 3UZA-T4G and 3REY-XAC origin and destination X-ray structures are more closely clustered in IFP (Fig 6A and S19A Fig). Another notable difference in this experiment relative to the previous was the refinement ligand size. CAF was the smallest ligand used in this entire study and XAC is a large ligand with several rotational degrees of

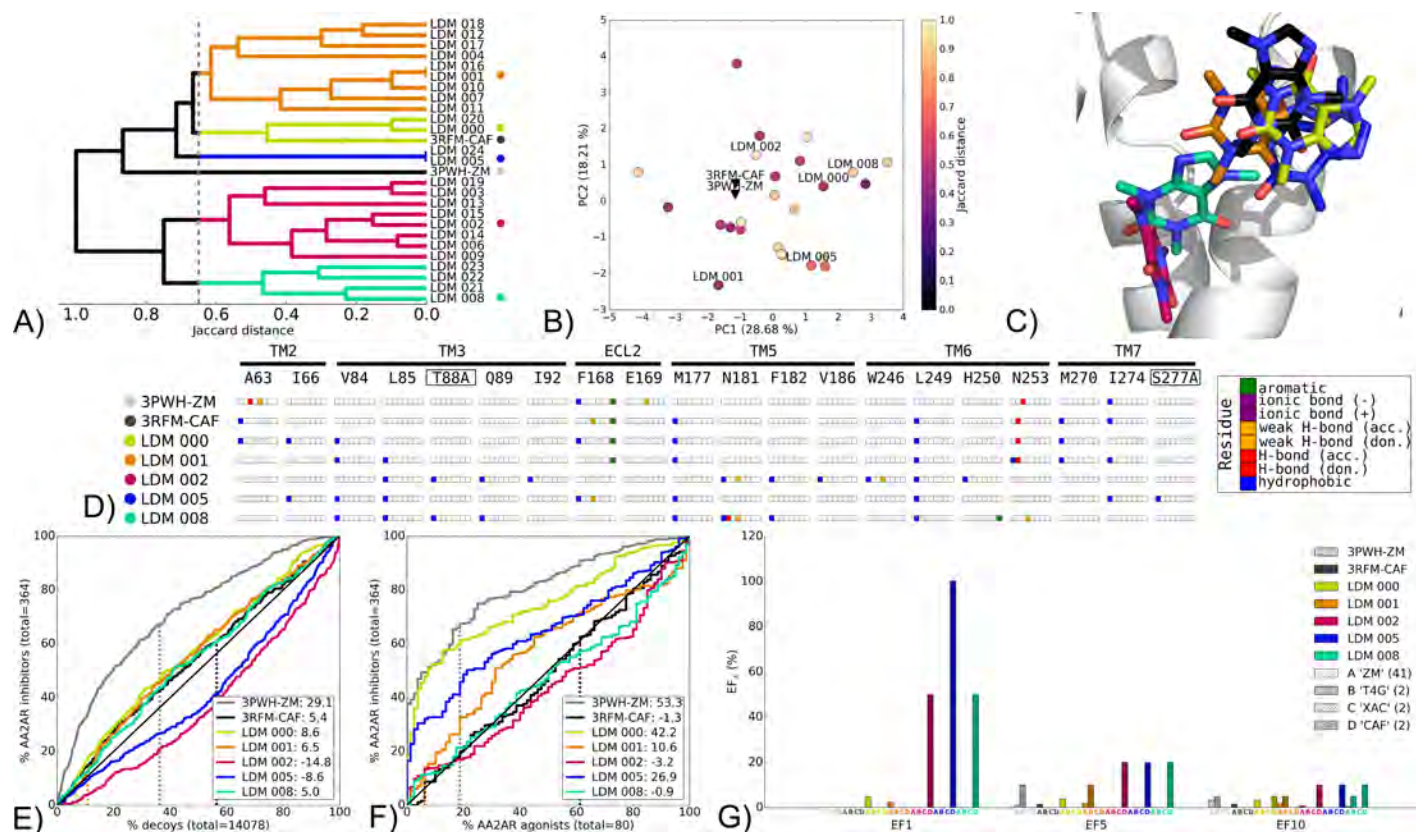


Fig 6. Chemotype switch LDM experiment on the AA2AR from 3PWH-ZM to 3RFM-CAF, using CAF as a refinement ligand. A) Dendrogram of the top 25 LDM models and X-ray structures, a cutoff line identifies different LDM clusters and their representative LDM models are designated by a colored dot. Representative LDM models are the highest scoring within the cluster based on the OPUS-ICM metric. B) Comparison of binding pocket conformation between the top 25 LDM models and X-ray structures. LDM models are colored based on their IFP Jaccard distance with the destination X-ray structure, 3RFM-CAF. C) Binding poses of the representative LDM models and the destination X-ray structure with the X-ray ligand in black and the LDM models coloured based on their representative clusters defined in A. D) IFP of the representative LDM models and the X-ray structures. Interaction type is described for each residue of the binding pocket: hydrophobic interaction, hydrogen bond (H-bond) donor and acceptor, weak hydrogen bond (weak H-bond) donor and acceptor, ionic bond positive (+) and negative (-) and aromatic interaction. VS performance is described with ROC curves to visualise E) the recovery of AA2AR inhibitors vs. decoys and F) the selectivity of AA2AR inhibitors over AA2AR agonists. X-ray structures are in black, with the LDM models coloured based on their relative clusters identified in A. The relative rank of the LDM refinement ligand is identified with a vertical dashed line. This vertical line for some models may be masked by others if the ligand is very highly ranked. The ROC curve figure inset shows NSQ_AUC values for each binding pocket. G) bar chart is used to visualise the EF for representative AA2AR inhibitor chemotypes at EF1, EF5 and EF10. Chemotypes A 'ZM'-like, B 'T4G'-like, C 'XAC'-like and D 'CAF'-like represent only a subset of AA2AR inhibitors ligands (S2B Fig). The EF bar chart inset shows the number of ligands for each chemotype cluster between parenthesis. Origin and destination X-ray structure chemotype EF shown in grey and black bars, respectively, with the LDM models coloured based on their relative clusters identified in A.

<https://doi.org/10.1371/journal.pcbi.1005819.g006>

freedom. Interestingly, as seen in the above example the origin X-ray structure outperformed the destination X-ray structure in VS recovery and selectivity (Fig 6E and 6F and S19E and S19F Fig). However, similar to the AA2AR 3PWH-ZM 3RFM-CAF experiment, LDM models in AA2AR 3UZA-T4G to 3REY-XAC LDM models outperformed the destination X-ray structure in VS recovery, selectivity and outperformed both the origin and destination structures in enrichment of the refinement ligand chemotype, XAC chemotype EF1 (S19E±S19G Fig).

Pharmacology switch

Pharmacology switch LDM experiments represent the most complex task as they involve the largest binding pocket conformation rearrangement, from inhibitor-bound to agonist-bound or vice-versa. This includes the reorientation of residues that can interact with the bound

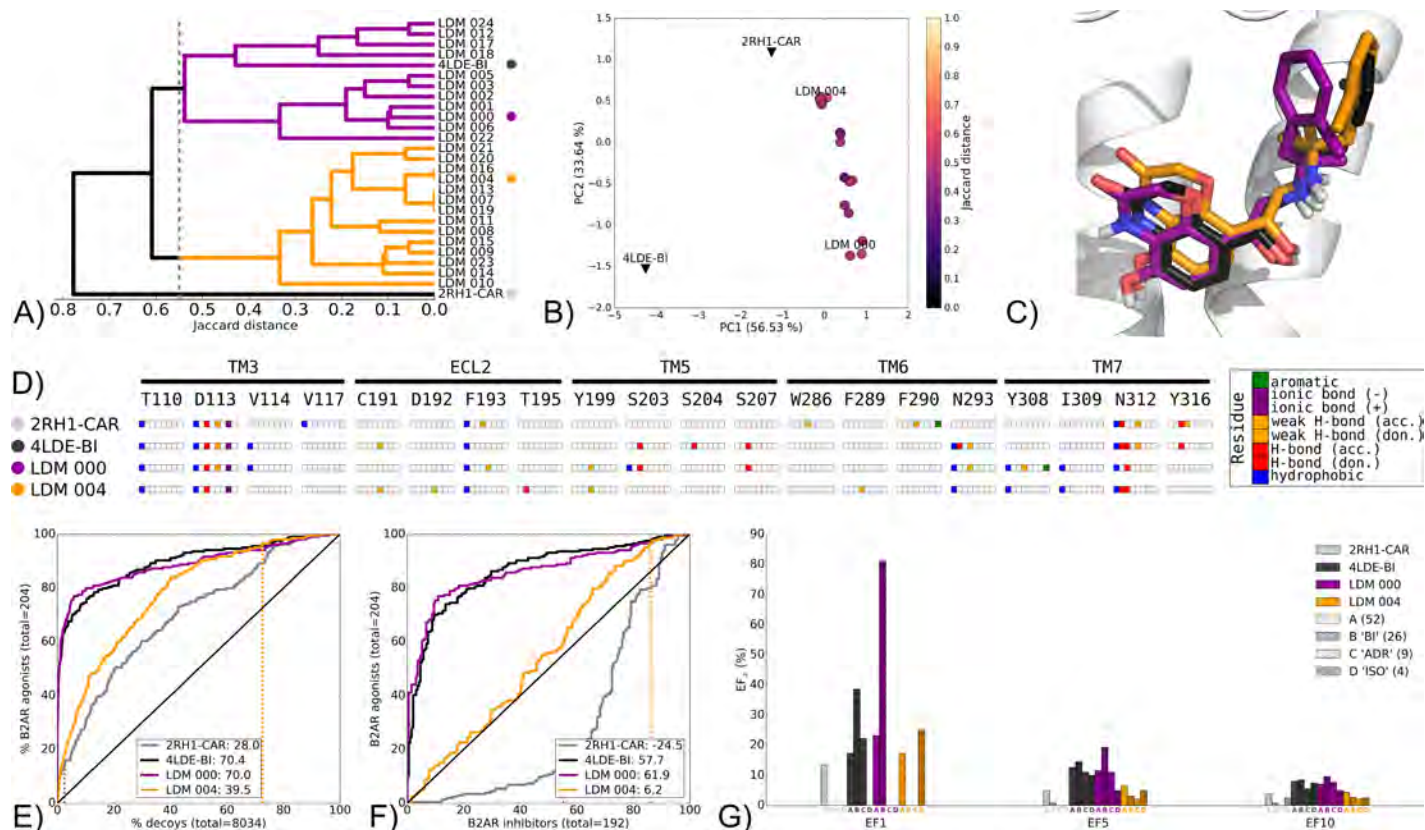


Fig 7. Pharmacology switch LDM experiment on the B2AR from 2RH1-CAR to 4LDE-BI, using BI as a refinement ligand. A) Dendrogram of the top 25 LDM models and X-ray structure(s), a cutoff line identifies different LDM clusters and their representative LDM models are designated by a colored dot. Representative LDM models are the highest scoring within the cluster based on the OPUS-ICM metric. B) Comparison of binding pocket conformation between the top 25 LDM models and X-ray structures. LDM models are colored based on their IFP Jaccard distance with the destination X-ray structure, 4LDE-BI. C) Binding poses of the representative LDM models and the destination X-ray structure with the X-ray ligand in black and the LDM models coloured based on their representative clusters defined in A. D) IFP of the representative LDM models and the X-ray structures. Interaction type is described for each residue of the binding pocket: hydrophobic interaction, hydrogen bond (H-bond) donor and acceptor, weak hydrogen bond (weak H-bond) donor and acceptor, ionic bond positive (+) and negative (-) and aromatic interaction. VS performance is described with ROC curves to visualise E) the recovery of B2AR agonists vs. decoys and F) the selectivity of B2AR agonists over B2AR inhibitors. The relative rank of the LDM refinement ligand is identified with a vertical dashed line. This vertical line may be masked by other curves if the ligand is very highly ranked. The ROC curve figure inset shows NSQ_AUC values for each binding pocket. Finally, a G) bar chart is used to visualise the EF for representative B2AR agonist chemotypes at EF1, EF5 and EF10. Chemotypes A, B 'BI-like', C 'ADR-like' and D 'ISO-like' represent only a subset of B2AR agonist ligands (S2C Fig). The EF bar chart inset shows the number of ligands for each chemotype cluster between parenthesis. Origin and destination X-ray structure chemotype EF shown in grey and black bars, respectively, with the LDM models coloured based on their relative clusters identified in A.

<https://doi.org/10.1371/journal.pcbi.1005819.g007>

ligand but also binding pocket backbone conformational changes. In all six pharmacology switch LDM experiments performed, a selected LDM model showed improved VS performance both in recovery and selectivity relative to the origin X-ray structure (Figs 7 and 8 and S20+S23 Figs). Additionally, these models had improved selectivity for the chemotype of the ligand used for refinement. Results of the pharmacology switch LDM scenario are divided into two groups that are explored in detail describing the two patterns identified.

Group A. This group includes LDM experiments for the B2AR and the M2R where pharmacology switch LDM experiments resulted in the LDM model sharing a similar binding pose to that of the destination X-ray structure. The experiments performed include the M2R from inhibitor-bound 3UON-QNB refined using the agonist ligand found in 4MQS-IXO (S20 Fig) and the reverse experiment on M2R where 4MQS-IXO was refined with the ligand QNB, that was present in the X-ray structure 3UON-QNB (S21 Fig). The experiment chosen to describe

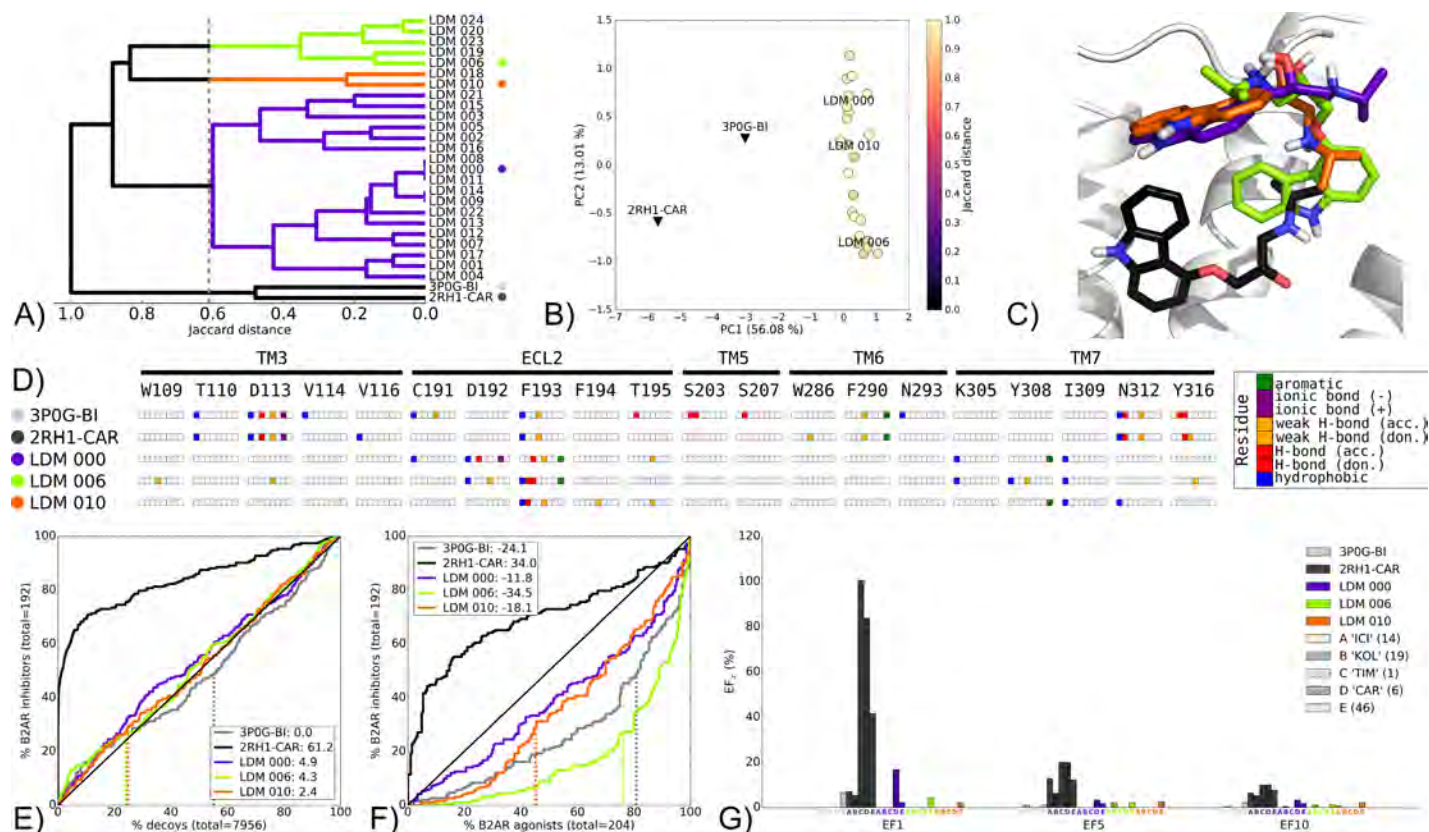


Fig 8. Pharmacology switch LDM experiment on the B2AR from 3P0G-BI to 2RH1-CAR, using CAR as a refinement ligand. A) Dendrogram of the top 25 LDM models and X-ray structures, a cutoff line identifies different LDM clusters and their representative LDM models are designated by a colored dot. Representative LDM models are the highest scoring within the cluster based on the OPUS-ICM metric. B) Comparison of binding pocket conformation between the top 25 LDM models and X-ray structures. LDM models are colored based on their IFP Jaccard distance with the destination X-ray structure, 2RH1-CAR. C) Binding poses of the representative LDM models and the destination X-ray structure with the X-ray ligand in black and the LDM models coloured based on their representative clusters defined in A. D) IFP of the representative LDM models and the X-ray structures. Interaction type is described for each residue of the binding pocket: hydrophobic interaction, hydrogen bond (H-bond) donor and acceptor, weak hydrogen bond (weak H-bond) donor and acceptor, ionic bond positive (+) and negative (-) and aromatic interaction. VS performance is described with ROC curves to visualise E) the recovery of B2AR inhibitors vs. decoys and F) the selectivity of B2AR inhibitors over B2AR agonists. The relative rank of the LDM refinement ligand is identified with a vertical dashed line. This vertical line may be masked by other curves if the ligand is very highly ranked. The ROC curve figure inset shows NSQ_AUC values for each binding pocket. Finally, a G) bar chart is used to visualise the EF for representative B2AR inhibitor chemotypes at EF1, EF5 and EF10. Chemotypes A 'ICI-like', B 'KOL-like', C 'TIM-like' and E represent only a subset of B2AR inhibitor ligands (S2B Fig). The EF bar chart inset shows the number of ligands for each chemotype cluster between parenthesis. Origin and destination X-ray structure chemotype EF shown in grey and black bars, respectively, with the LDM models coloured based on their relative clusters identified in A.

<https://doi.org/10.1371/journal.pcbi.1005819.g008>

this group is the B2AR LDM starting from the inhibitor CAR-bound X-ray structure 2RH1-CAR and using the refinement ligand BI167107 (BI) found in the destination X-ray structure 4LDE (Fig 7). The dendrogram of the ligand/receptor interaction patterns shows, as expected, separation of inhibitor-bound 2RH1-CAR and agonist-bound 4LDE-BI with each being located in two distinct clusters at a 0.55 Jaccard cutoff (Fig 7A). Two closely related groups of interaction patterns arose within the top 25 LDM models with the BI-bound X-ray structure (4LDE-BI) found in one of these clusters. The PCA plot provides a quantified representation of the collective binding pocket movement as a result of the LDM processing. The LDM models moved away from their origin X-ray structure 2RH1-CAR towards the destination X-ray structure 4LDE-BI, however, they did not reach the exact conformation of the destination X-ray structure due to insufficient sampling in PC1 (Fig 7B). The selected cluster representatives with the highest ranked scores within their respective IFP clusters (LDM 000 and LDM 004)

had a similar pose to the destination 4LDE-BI (Fig 7C). The origin X-ray structure, destination X-ray structure and the LDM models all share a conserved ionic interaction between BI and D113, and a polar interaction was also shared with BI and N312 (Fig 7D). LDM 000 uniquely exhibited a similar polar interaction pattern with 4LDE-BI through S203 and S207, and it was the only complex to present a weak hydrogen bond and aromatic interaction between BI and Y316.

VS on these binding pockets showed that, expectedly, the agonist-bound 4LDE-BI is superior in recovery of B2AR agonists over decoys (NSQ_AUC: 70.4) relative to the inhibitor-bound 2RH1-CAR (NSQ_AUC: 28.0) (Fig 7E). This pattern was even more pronounced when comparing the two X-ray structures at B2AR agonist over inhibitor selectivity, with 4LDE-BI and 2RH1-CAR obtaining NSQ_AUC scores of 57.7 and -24.5, respectively (Fig 7F). Both screened LDM pockets outperformed the origin X-ray 2RH1-CAR in recovery and selectivity. Furthermore, LDM 000 achieved a high recovery NSQ_AUC score of 70.0, outperforming 4LDE-BI in early recovery. LDM 000 also outperformed 4LDE-BI in selectivity with a NSQ_AUC of 61.9. This superior VS performance can be explained in part by taking a closer look at the pattern of chemotype early enrichment. Indeed, LDM 000 was superior to both X-ray structures at recovering the B "BI-like" chemotype, with 21/26 identified at EF1 (Fig 7D). While LDM 004 showed improved VS performance over the origin structure, it did not reach the same VS performance as the destination X-ray structure or LDM 000. In addition, LDM 004 recovered the refinement ligand, BI, late in both VS recovery and selectivity (Fig 7E and 7F). But interestingly, it showed a different chemotype recovery pattern compared to the other binding pockets. There was no BI chemotype recovery and similar recovery as the origin, destination and LDM 000 in chemotype A recovery, however LDM 004 also displayed ISO chemotype ligands recovery at EF1, a feature not observed with the other structures or models (Fig 7D).

The other two LDM experiments from this group of pharmacology switch experiments refined the IXO-bound (agonist) M2R to the QNB-bound (inhibitor) conformation (S21 Fig), and vice-versa (S20 Fig). The interaction pattern distance between IXO-bound and QNB-bound complexes (S20A and S21A Figs) is smaller than between CAR-bound and BI-bound X-ray structures (Fig 7A). This did not influence convergence of LDM complexes for refinement of IXO-bound with QNB as the top 25 QNB-refined models were closely related (S21A Fig). In contrast, QNB-bound structures refined by the small ligand IXO resulted in LDM models with three distinct ligand poses. In both cases however, there were representative LDM models that had a similar ligand pose to the destination X-ray structure (S20A, S20C, S20D, S21A, S21C and S21D Figs). Amongst these, LDM models outperformed the origin X-ray structure in VS recovery (S20E and S21E Figs), selectivity (S20F and S21F Figs) and refinement ligand enrichment (S20G and S21G Figs). However, they did not outperform the destination X-ray structure. In both cases, the best scoring LDM model (LDM 000) showed improved enrichment for the chemotype of the LDM refinement ligand relative to both the origin and destination X-ray structures.

Group B. In the second group of pharmacology switch experiments, each of the best performing LDM models had a distinct ligand pose to that of the destination X-ray structure, but exhibited superior performance in VS relative to the origin X-ray structure. Within this group are LDM experiments on the AA2AR inhibitor-bound 3EML-ZM refined with the ligand NEC in the agonist-bound X-ray structure AA2AR-NEC (S22 Fig) and the AA2AR agonist-bound 3QAK-UK refined with the ligand ZM found in the inhibitor-bound X-ray structure 3EML-ZM (S23 Fig). The third LDM experiment from this group described in more detail here was performed on the B2AR agonist-bound 3P0G-BI refined using the inhibitor CAR, which can be found in the X-ray structure 2RH1-CAR (Fig 8). Interestingly, the two X-ray structures in this example that are bound by ligands of different pharmacology, grouped

together in the interaction pattern dendrogram (Fig 8A). Indeed, the X-ray structures had a similar ligand interaction pattern with residues D113, F290, N312 and Y316 (Fig 8D). Notably, none of the representative LDM conformations exhibited this interaction pattern. Despite the absence of the ionic interaction with D113, an ionic interaction was identified in LDM 000 between the tertiary amine of CAR and D192.

The top 25 LDM models clustered into three groups with the largest convergence represented by LDM 000, followed by two smaller clusters each represented by LDM 006 and LDM 010 (Fig 8A). Interestingly, the collective conformational change in binding pockets induced by the LDM moves from 3P0G-BI away from 2RH1-CAR along PC1 (Fig 8B). However, in PC2, which explains an additional 13.01% of the ensemble's binding pocket conformation variation, a movement towards the destination X-ray structure 2RH1-CAR is observed. Viewing the representative LDM binding poses revealed alternative ligand and binding pocket conformations to that of the 2RH1-CAR (Fig 8C).

The destination X-ray structure 2RH1-CAR displayed high performance in B2AR inhibitor recovery over decoys with a NSQ_AUC of 61.2, while the origin agonist-bound X-ray structure 3P0G-BI performed the same as random at 0.0 NSQ_AUC. While the representative LDM models did improve on the performance of the origin X-ray structure, they performed only slightly better than random, but notably they all recovered CAR earlier than the origin X-ray structure (Fig 8E). In terms of B2AR inhibitor over agonist selectivity, each X-ray structure was selective for the pharmacology of their bound ligand. In this case both LDM 000 and LDM 010 improved on the inhibitor selectivity compared to the origin X-ray structure, although both were still more selective towards agonists (Fig 8F). Looking at the chemotype enrichment, LDM 000 recovered 1/6 ligands from the D 'CAR-like' chemotype at EF1. This corresponds to the CAR ligand itself that was highly ranked by LDM 000, however this was still an improvement compared to the origin X-ray structure 3P0G-BI that was unable to recover any CAR-like ligands, including CAR itself. The destination X-ray structure 2RH1-CAR, however, had a better EF1 value for the D 'CAR-like' chemotype with 5/6 and had overall a more versatile chemotype enrichment (Fig 8G).

The other two additional LDM experiments that made up this second pharmacology switch group were both performed on AA2AR. In each case, the interaction pattern distance between agonist-bound and inhibitor-bound complexes was greater than in the CAR-refinement experiment described above (S22A and S23A Figs). While the NEC-refined LDM models featured two distinct ligand poses (S22A, S22C and S22D Fig), the ZM-refined models converged towards a single one (S23A, S23C and S23D Fig). In both cases, these LDM complexes featured ligand poses that were different from their respective destination X-ray structures. Despite this, they displayed improved VS performance for recovery of known ligands over decoys (S22E and S23E Figs), selectivity (S22F and S23F Figs) and refinement ligand chemotype enrichment (S22G and S23G Figs) relative to their origin X-ray structures.

Discussion

The potential of *in silico* virtual screening for GPCRs is limited by poor representation of conformational sampling of these receptors in experimentally derived structures and homology models. Here we have developed an LDM method using a computational workflow that refines a GPCR binding pocket around a known ligand for that GPCR using iterative rounds of conformational sampling and scoring methods to identify low energy minimums of the system. Each LDM experiment in this study generated close to 1 million GPCR/ligand complexes and outputted up to 320 complexes as selected by its scoring method. In contrast with MD-based methods, the LDM readily overcomes energy barriers that hamper the transition between

conformational states as it relies on geometric sampling methods. Additionally, the workflow is highly parallelised running on multiple independent processes simultaneously that greatly accelerates the process of generating GPCR-ligand complexes compared to other available methods.

The performance of the LDM method was evaluated by designing LDM experiments where a GPCR X-ray binding pocket was refined using a ligand that was available in another GPCR X-ray co-crystal structure. Each LDM experiment thus consisted of a comparison between origin X-ray structure, LDM model(s) and destination X-ray structure in VS performance and GPCR/ligand conformation. For most LDM experiments performed in this study, the top 25 GPCR/ligand complexes of these LDM outputs contained a complex with a small heavy atom ligand root-mean-square deviation (RMSD) difference relative to the destination X-ray complex (S3 Table). Indeed, the LDM method successfully generated a ligand conformation that closely resembled the binding pose of the ligand in a solved X-ray structure in 18 out of 24 cases highlighting the overall success of the sampling performed by the LDM method. Interestingly, assessment of binding pocket conformation using PCA revealed that while agonist and inhibitor-bound X-ray binding pockets can be distinguished from one another (S1A and S1B Fig), the change in binding pocket conformation from origin to destination X-ray structure is not consistently indicative of improved VS performance and therefore additional metrics are required to evaluate LDM performance.

The scoring of LDM complexes uses both quantitative and qualitative scoring methods. During the LDM process, a quantitative scoring method is applied on GPCR/ligand complexes generated to iteratively select the most suitable candidate before it is used as the starting point for further sampling. The same quantitative ligand docking and protein geometry scores are combined in equal weights to generate a score that ranks the ~320 LDM results. As evidenced by the data in this study, the most highly scored LDM complex (LDM 000) was not consistently the best performer in retrospective VS. However, a complex was found within the top 25 ranked complexes in most LDM experiments that did outperform the origin X-ray structures, and even in some cases the destination X-ray structure, suggesting that the quantitative scoring method used is relevant for identification of a suitable binding pocket for VS. An additional qualitative IFP scoring method was employed for clustering based on GPCR/ligand interaction patterns. Although other more complex implementations of IFP were shown to perform better when used for scoring docked poses [83], we showed that the IFP implementation used in this study is useful for the identification of a GPCR binding pocket with good VS performance [72]. Furthermore, here we show that the IFP can capture differences between agonist-bound and inhibitor-bound X-ray structures (S1C and S1D Fig), as well as between structures and models that can distinguish between distinct ligand chemotypes. Using a combination of the quantitative scoring method and the qualitative IFP scoring was more effective at selecting LDM models for improved overall retrospective VS performance over the origin X-ray structure than the quantitative scoring alone with this method identifying improved binding pockets in 20/24 of the LDM experiments performed.

To evaluate the success of the LDM, LDM optimised GPCR binding pockets were screened with known ligands and decoys libraries developed by Cavasotto et al [70]. Known agonists or inhibitors for a given GPCR often share a common chemotype (S2 Fig). A key finding from this study was the ability of the refinement ligand used within the LDM method to influence the result of the LDM binding pocket's recovery or selectivity. In some cases, this resulted in the LDM models being superior to the origin X-ray structure and in some cases, also the destination structure, observations that were most evident in the pharmacology switch studies (S3 Table). However, there were also occurrences of LDM models that outperformed the destination, but not the origin X-ray structure, despite the refinement ligand being recovered earlier

in the VS with the LDM models. This scenario was observed in some of the chemotype switch LDM experiments. From these observations, it was apparent that when the refinement is performed with a ligand whose chemotype is highly represented amongst known ligands, a superior retrospective VS outcome is observed. In contrast, when the refinement ligand chemotype is poorly represented among known ligands, this often appears to result in an inferior retrospective VS outcome. The chemotype enrichment feature used in this study that evaluates the EF values for a representative set of chemotypes is an attractive tool to improve understanding of binding pocket ligand recognition in a VS setting. This revealed that in all cases, the LDM generates binding pockets that are either improved for identification of chemotypes related to the refinement ligand or narrowed in the identification towards the chemotype of the refinement ligand at the exclusion of other chemotypes, when compared to the origin X-ray structure (Table 1). Therefore, the LDM generates binding pockets that are more specific in their ligand recovery of particular chemotypes. This highlights the success of the LDM as the method is aimed at refining the binding pocket around a particular ligand, however this result also poses additional challenges and considerations around utilisation of LDM methods for prospective VS. Therefore, to maximise the chances of identifying new hits in a prospective VS, LDM refinement of GPCR X-ray structures using multiple known ligands with distinct chemotypes would generate a combination of LDM binding pockets, each biased to select for a complementary set of ligand chemotypes. This would likely result in improved VS outcomes, both in terms of numbers of compounds, but also with increased hit chemotype variety. In some cases, the chemotype preference of certain LDM models could even be leveraged in a SBDD program, for example using ligands exhibiting novel or underrepresented chemotypes, where the identification of novel scaffold is of paramount importance in the search of new lead compounds.

With the exception of a few receptors (for example B2AR, AA2A and M2R), the majority of GPCR X-ray structures are solved in inactive conformations, bound to inhibitor ligands. However, for many of these receptors, novel agonists are highly sought for drug development. As shown for the B2AR and AA2AR, GPCR binding pockets can be clustered based on their GPCR-ligand interaction pattern and their shapes that clearly separate agonist-bound from inhibitor-bound pockets (S1 Fig). The ability of the LDM to influence the types of ligand chemotype recovered in VS reveals a very powerful application of the LDM method for SBDD. Largely due to this feature, all pharmacology switch LDM experiments were successful in improving ligand selectivity (i.e. agonist vs inhibitor or vice-versa) relative to their origin X-ray structure, while also improving recovery of known ligands over decoys (Table 1). The pharmacology switch scenario represents the largest conformational change between origin and destination structures and the success of the method in terms of VS performance highlights the power and full potential of this LDM method for SBDD.

Within this study, there were some LDM experiments that were successful in terms of their VS performance, but where the LDM generated a binding pose different to that of the destination X-ray structure. The absence of convergence towards the putative global energy minimum represented by the destination X-ray structure could be due to several factors. While the LDM sampling and scoring scheme may have failed to converge towards the native binding pose, other factors may also be at play. During the docking stage of the LDM workflow, the ligand conformation search space is increased if the ligand is very small or if it contains many degrees of freedom. This may lead to an insufficient exploration of the ligand's native binding pose, which can result in poor convergence of the LDM workflow (Fig 6 and S13 Fig). Furthermore, two LDM experiments (B2AR refined with CAR (Fig 4) and B2AR refined with ICI (S17 Fig)) featured inhibitor binding poses that were located above the X-ray binding pose in a vestibule formed by ECL2 and the top of TM 5±7 (Fig 4C and S17C Fig). This corresponds to a vestibule

Table 1. Summary of the LDM benchmark outcomes. The results are organised by scenario: self refinement, chemotype switch and pharmacology switch. Each line describes an LDM experiment including the origin and destination X-ray structures as well as the overall VS performance outcome. The best LDM model is compared to the origin X-ray structure in recovery of known ligands vs. decoys, selectivity of agonists over inhibitors (or vice-versa) and chemotype enrichment. VS recovery and selectivity performance is improved ↑, similar → or worse ↓ using NSQ_AUC values. VS chemotype enrichment evaluates the LDM refinement ligand chemotype enrichment by comparing the EF1 values of LDM models with their origin X-ray structure. It is "improved" when an LDM model outperforms the origin X-ray structure, and it is "narrowed" when the same performance is observed and EF1 value for other chemotypes is worse for the LDM model. LDM experiments were assigned to two groups based on the similarity of their LDM model binding pose to that of the destination X-ray structure and their improvement in VS performance over the origin X-ray structure. Group A includes LDM models with similar binding poses and improved performance and group B includes LDM models with a different binding pose and improved performance or a similar binding pose and no performance improvement. CCR5 agonist ligands were not available from the GLL/GDD, hence VS selectivity for the self refinement CCR5-MRV experiment was not calculated and is marked N/A.

LDM benchmark scenarios	GPCR	Origin X-ray	Destination X-ray	Group	VS recovery	VS selectivity	VS chemotype enrichment	Figure
Self refinement	B2AR	4LDE-BI (ago.)	-	A	↑	↑	improved	Fig 3
	B2AR	3P0G-BI (ago.)	-	A	↑	↑	improved	S5 Fig
	AA2AR	4E1Y-ZM (inhib.)	-	A	→	↑	narrowed	S6 Fig
	AA2AR	3PWH-ZM (inhib.)	-	A	→	↓	narrowed	S7 Fig
	M2R	3UON-QNB (inhib.)	-	A	→	↑	narrowed	S8 Fig
	M2R	4MQS-IXO (ago.)	-	A	↑	↑	narrowed	S9 Fig
	H1R	3RZE-DOX (inhib.)	-	A	→	↑	improved	S10 Fig
	5-HT1B	4IAR-ERG (inhib.)	-	A	↓	↑	narrowed	S11 Fig
	B2AR	2RH1-CAR (inhib.)	-	B	↓	↓	improved	Fig 4
	AA2AR	2YDV-NEC (ago.)	-	B	↓	↓	narrowed	S12 Fig
	CCR5	4MBS-MRV (inhib.)	-	B	→	N/A	narrowed	S13 Fig
	DOR	4N6H-NAL (inhib.)	-	B	↑	↑	improved	S14 Fig
Chemotype switch	B2AR	4LDO-ADR (ago.)	4LDL-ISO (ago.)	A	↑	↑	improved	Fig 5
	B2AR	3NY9-KOL (inhib.)	2RH1-CAR (inhib.)	A	↑	↑	improved	S15 Fig
	AA2AR	3QAK-UK (ago.)	2YDV-NEC (ago.)	A	↑	↑	improved	S16 Fig
	B2AR	3D4S-TIM (inhib.)	3NY8-ICI (inhib.)	A	↓	↑	narrowed	S17 and S18 Figs
	AA2AR	3PWH-ZM (inhib.)	3RFM-CAF (inhib.)	B	↑	↑	improved	Fig 6
	AA2AR	3UZA-T4G (inhib.)	3REY-XAC (inhib.)	B	↑	↑	improved	S19 Fig
Pharmacology switch	B2AR	2RH1-CAR (inhib.)	4LDE-BI (ago.)	A	↑	↑	improved	Fig 7
	M2R	3UON-QNB (inhib.)	4MQS-IXO (ago.)	A	↑	↑	improved	S20 Fig
	M2R	4MQS-IXO (ago.)	3UON-QNB (inhib.)	A	↑	↑	improved	S21 Fig
	B2AR	3P0G-BI (ago.)	2RH1-CAR (inhib.)	B	↑	↑	improved	Fig 8
	AA2AR	3EML-ZM (inhib.)	2YDV-NEC (ago.)	B	↑	↑	narrowed	S22 Fig
	AA2AR	3QAK-UK (ago.)	3EML-ZM (inhib.)	B	↑	↑	improved	S23 Fig

<https://doi.org/10.1371/journal.pcbi.1005819.t001>

identified by Dror et al. in an unbiased molecular dynamics simulations performed with four different B2AR ligands [84]. Within these simulations each ligand associated with this vestibule, and exit from this pocket provided the largest energetic barrier for the ligand entry into the predominant binding pocket. These resulting LDM models may thus represent a valid but transient ligand pose. The identification of this transient ligand pose may have benefited from the inclusion of ECLs other than ECL2-distal, which are omitted in the LDM workflow to improve computational efficiency and focussed sampling of the binding pocket. However, this inclusion would not have contributed to LDM refinement goal, which is to identify the final ligand pose that initiates receptor activity and is observed in X-ray structures. Indeed, VS performance does not seem to be affected by the presence of ECLs other than ECL2-distal for X-ray structures used in this study, including B2AR (Fig 2). Although this may be true for most Class A GPCR orthosteric ligands, ECLs may be crucial for the binding of some ligands for example allosteric modulators of Class A GPCRs [22,85]. Thus, in some scenarios, loops should be built onto LDM models, for example if the end goal was to screen for allosteric ligands binding in the extracellular loop region. Finally, it should be noted that the LDM workflow does not take into account water molecules that can mediate and/or influence ligand/receptor interactions [86,87]. This may hinder the ability of the LDM workflow to identify a native ligand/receptor conformation that relies on such an interaction, as may be the case for opioid receptor bound by NAL (S14 Fig). Future improvements of our LDM method could take binding pocket waters into account, however this would be at a significant computational cost.

A range of different methods exist for the refinement of receptor models prior to prospective VS in GPCR SBDD. The conformational changes induced by ligand binding and receptor activation can be observed using unbiased MD [37,84]. However these microsecond timescale events require running these simulations over several days on special purpose hardware [88]. An alternative method uses multiple shorter MD runs stitched together using Markov state modeling and although this has been shown to be applicable to SBDD, large computing resources are still needed to develop such a statistical model [41]. And although progress has been made on enhanced sampling techniques such as accelerated MD which was applied to observe large GPCR conformational re-arrangements [89,90] and contributed to the preparation of receptor models for prospective VS [40], these methods still require several days of computing time to reach this result. In contrast, conventional MD has only been used to reach limited conformational changes for GPCR refinement [38,39], which have nonetheless seen applications in SBDD (e.g. [91,92]). A general issue that remains with MD simulations is the fact they are not designed to rapidly converge towards low energy minimums, which can lead to difficulties in identifying the receptor conformations that should be used for a subsequent VS. Other more computationally efficient methods such as the iterative use of the induced fit docking (IFD) protocol has also been successfully applied to refine GPCR binding pockets towards improved VS performance (e.g. [47,48]). However, these methods are not well suited to overcome the large energy barriers associated with the conformational rearrangements that occur during GPCR activation. Automated methods using alternative sampling strategies combined with molecular docking are better suited to such a task, such as that developed by Nguyen et al. [53]. This study generated models for a set of 14 available GPCRs X-ray structures, however it was validated only by structural comparisons to X-ray structures and no VS performance evaluation of the models was performed. Another such method is ALiBERO [50], which has been applied to generate neurotensin receptor 1 (NTSR1) models that outperformed the recently solved NTSR1 X-ray structure in a retrospective VS [51], and refine a homology model of the 5-hydroxytryptamine receptor 1A (5HT1A) that was used in a prospective VS to identify two new active compounds at the 5HT1A [52]. However, ALiBERO relies on the

availability of multiple known binders and non-binders or decoys for the GPCR to be refined. This data is unavailable for many GPCR targets of therapeutic relevance, highlighting the importance the current LDM approach as a GPCR refinement method that requires only a single ligand for binding pocket refinement. Lastly, ALiBERO relies on the refinement of a binding pocket ensemble and a similar approach can be undertaken with the current LDM. LDM models show enrichment for the chemotype of their refinement ligand and as described above, an ensemble of carefully selected LDM models that can enrich for a complementary set of ligand chemotypes may greatly improve VS outcome in identifying hits of diverse chemistries.

Conclusions

We present a new computational workflow that refines a GPCR binding pocket using a known ligand for that GPCR. This is achieved through an iterative process that relies on computationally inexpensive and highly parallelised methods including docking and geometric protein sampling. Thus, the LDM achieves relatively fast refinement of GPCR binding pockets and outputs LDM models that are ranked based on a quantitative docking and protein geometry score, and can be clustered based on a qualitative score, ligand/receptor interaction pattern. The LDM was evaluated with an extensive benchmark of 24 LDM experiments where in each experiment the binding pocket of an origin X-ray structure was refined using the ligand from a destination X-ray structure. These experiments were divided into three scenarios of increasing distance between the origin and destination X-ray structures, where the most complex task performs refinement from an inhibitor-bound to an agonist-bound binding pocket (or vice-versa). Overall an LDM model with ligand pose similar to that of the destination was reported in 18 out of 24 experiments, and an LDM model with improved VS performance over the origin X-ray structure was reported in 20 out of 24 experiments. One of the key findings of this study is that LDM models are found to be more selective for the chemotype of the ligand that was used for their binding pocket refinement. This may be a key factor in the LDM's success for all pharmacology switch experiments, a valued feature for SBDD programs that seek agonists on targets that only have inhibitor-bound experimentally determined structures. But this chemotype preference of LDM models could also be leveraged to influence the identification of specific scaffolds in a prospective VS setting.

Supporting information

S1 Table. Description of the LDM method and parameters. Description of the method used at each step of the LDM workflow. Parameters used in the current study for each of these methods. CONCOORD parameters that were common in both step where the software is used: secondary conformation detection: DSSP, forcefield: OPLS-UA (united atom), bond and angle parameters: CONCOORD default.
(PDF)

S2 Table. Information about X-ray structures used in the study. Details about ligand name and structure as well as mutations in the TM bundle and their proximity to the X-ray ligand.
(PDF)

S3 Table. LDM models and X-ray structure ligand RMSD and NSQ_AUC values. Selected LDM models and X-ray origin and destination structures are compared by ligand heavy atom RMSD to the destination X-ray structure and VS performance by recovery NSQ_AUC and selectivity NSQ_AUC values.
(PDF)

S1 Text. Executing the LDM scripts. Description of the required software, file preparation and parameters to run the LDM.
(PDF)

S1 Fig. Agonist and inhibitor-bound X-ray binding pocket comparisons for B2AR and AA2AR. Principal component analysis on the binding pocket residue coordinates of A) B2AR and B) AA2AR X-ray structures used in this study. Principal components (e.g. PC1 and PC2) are ordered based on their percentage of cumulative variance explained from the original dataset (e.g. PC1 explains 50% of the data variance). An arbitrary line drawn along the PC1 axis, which explains most of the variance in the dataset, separates agonist-bound and inhibitor-bound X-ray structures based on their binding pocket conformations. Dendrogram of the IFP clustering and IFP diagrams on the ligand/receptor interaction patterns for C) B2AR and D) AA2AR X-ray structures used in this study. The IFP dendrogram branches and the PCA labels representing agonist-bound and inhibitor-bound X-ray structures are colored green and red, respectively.
(TIF)

S2 Fig. Known agonist and inhibitor ligand library chemotypes. Ligand libraries were clustered based on pharmacophore properties and 0.5 cutoff was used to identify the different clusters. A limited number of representative chemotype clusters were identified by letters (A-E). Chemotype clusters that contain an X-ray ligand were chosen and additional populated clusters were added when increased chemotype coverage was necessary. The resulting chemotype clusters do not contain the entire ligand library but are used to represent its chemotype diversity. AA2AR agonists (A) and inhibitors (B), B2AR agonists (C) and inhibitors (D), M2R agonists (E) and inhibitors (F), CCR5 inhibitors (G), DOR inhibitors (H), H1R inhibitors (I), 5-HT1B inhibitors (J).
(PDF)

S3 Fig. ROC curves of VS performance for X-ray structures with all loops vs. ECL2-distal loop only. VS performance evaluated as recovery of known ligands against decoys and selectivity of agonists over inhibitors (or vice-versa). All loop structures are represented by black dotted lines and ECL2-distal only structures are represented by solid black lines. NSQ_AUC values for each curve is shown in the figure inset. AA2AR 2YDV-NEC recovery (A) and selectivity (B), AA2AR 3QAK-UK recovery (C) and selectivity (D), AA2AR 3EML-ZM recovery (E) and selectivity (F), AA2AR 3PWH-ZM recovery (G) and selectivity (H), AA2AR 4E1Y-ZM recovery (I) and selectivity (J), AA2AR 3REY-XAC recovery (K) and selectivity (L), AA2AR 3RFM-CAF recovery (M) and selectivity (N), AA2AR 3UZA-T4G recovery (O) and selectivity (P), B2AR 3P0G-BI recovery (Q) and selectivity (R), B2AR 4LDE-BI recovery (S) and selectivity (T), B2AR 4LDL-ISO recovery (U) and selectivity (V), B2AR 4LDO-ADR recovery (W) and selectivity (X).
(PDF)

S4 Fig. ROC curves of VS performance for X-ray structures with all loops vs. ECL2-distal loop only. VS performance evaluated as recovery of known ligands against decoys and selectivity of agonists over inhibitors (or vice-versa). All loop structures are represented by black dotted lines and ECL2-distal only structures are represented by solid black lines. NSQ_AUC values for each curve is shown in the figure inset. B2AR 2RH1-CAR recovery (A) and selectivity (B), B2AR 3D4S-TIM recovery (C) and selectivity (D), B2AR 3NY8-ICI recovery (E) and selectivity (F), B2AR 3NY9-KOL recovery (G) and selectivity (H), M2R 4MQS-IXO recovery (I) and selectivity (J), M2R 3UON-QNB recovery (K) and selectivity (L), 5-HT1B 4IAR-ERG recovery (M) and selectivity (N), DOR 4N6H-NAL (3D library) recovery (O) and selectivity

(P), H1R 3RZE-DOX recovery (Q) and selectivity (R), CCR5 4MBS-MRV recovery (S).
(PDF)

S5 Fig. Self refinement LDM experiment on the B2AR 3P0G-BI, using BI as a refinement ligand. A) Dendrogram of the top 25 LDM models and X-ray structure(s), a cutoff line identifies different LDM clusters and their representative LDM models are designated by a colored dot. Representative LDM models are the highest scoring within the cluster based on the OPU-S-ICM metric. B) Comparison of binding pocket conformation between the top 25 LDM models and X-ray structure(s). LDM models are colored based on their IFP Jaccard distance with the destination X-ray structure. C) Binding poses of the representative LDM model(s) and the destination X-ray structure. D) IFP of the representative LDM models and the X-ray structure. Interaction type is described for each residue of the binding pocket: hydrophobic interaction, hydrogen bond (H-bond) donor and acceptor, weak hydrogen bond (weak H-bond) donor and acceptor, ionic bond positive (+) and negative (-) and aromatic interaction. E) the recovery of known ligands vs. decoys and F) the selectivity of inhibitors over agonists (or vice-versa). The relative rank of the LDM refinement ligand is identified with a vertical dashed line. This vertical line may be masked by other curves if the ligand is very highly ranked. The ROC curve figure inset shows NSQ_AUC values for each binding pocket. Finally, a G) bar chart is used to visualise the EF for representative known ligand chemotypes at EF1, EF5 and EF10. Chemotypes A, B 'BI-like', C 'ADR-like' and D 'ISO-like' represent only a subset of B2AR agonist ligands (S2 Fig). The EF bar chart inset shows the number of ligands for each chemotype cluster between parenthesis. X-ray structure chemotype EF shown in black bars, with the LDM models coloured based on their relative clusters identified in A.
(TIF)

S6 Fig. Self refinement LDM experiment on the AA2AR 4E1Y-ZM, using ZM as a refinement ligand. A) Dendrogram of the top 25 LDM models and X-ray structure(s), a cutoff line identifies different LDM clusters and their representative LDM models are designated by a colored dot. Representative LDM models are the highest scoring within the cluster based on the OPUS-ICM metric. B) Comparison of binding pocket conformation between the top 25 LDM models and X-ray structure(s). LDM models are colored based on their IFP Jaccard distance with the destination X-ray structure. C) Binding poses of the representative LDM model(s) and the destination X-ray structure. D) IFP of the representative LDM models and the X-ray structure. Interaction type is described for each residue of the binding pocket: hydrophobic interaction, hydrogen bond (H-bond) donor and acceptor, weak hydrogen bond (weak H-bond) donor and acceptor, ionic bond positive (+) and negative (-) and aromatic interaction. VS performance is described with ROC curves to visualise E) the recovery of known ligands vs. decoys and F) the selectivity of inhibitors over agonists (or vice-versa). The relative rank of the LDM refinement ligand is identified with a vertical dashed line. This vertical line may be masked by other curves if the ligand is very highly ranked. The ROC curve figure inset shows NSQ_AUC values for each binding pocket. Finally, a G) bar chart is used to visualise the EF for representative known ligand chemotypes at EF1, EF5 and EF10. Chemotypes A 'ZM-like', B 'T4G-like', C 'XAC-like' and D 'CAF-like' represent only a subset of AA2AR inhibitors ligands (S2 Fig). The EF bar chart inset shows the number of ligands for each chemotype cluster between parenthesis. X-ray structure chemotype EF shown in black bars, with the LDM models coloured based on their relative clusters identified in A.
(TIF)

S7 Fig. Self refinement LDM experiment on the AA2AR 3PWH-ZM, using ZM as a refinement ligand. A) Dendrogram of the top 25 LDM models and X-ray structure(s), a cutoff line

identifies different LDM clusters and their representative LDM models are designated by a colored dot. Representative LDM models are the highest scoring within the cluster based on the OPUS-ICM metric. B) Comparison of binding pocket conformation between the top 25 LDM models and X-ray structure(s). LDM models are colored based on their IFP Jaccard distance with the destination X-ray structure. C) Binding poses of the representative LDM model(s) and the destination X-ray structure. D) IFP of the representative LDM models and the X-ray structure. Interaction type is described for each residue of the binding pocket: hydrophobic interaction, hydrogen bond (H-bond) donor and acceptor, weak hydrogen bond (weak H-bond) donor and acceptor, ionic bond positive (+) and negative (-) and aromatic interaction. VS performance is described with ROC curves to visualise E) the recovery of known ligands vs. decoys and F) the selectivity of inhibitors over agonists (or vice-versa). The relative rank of the LDM refinement ligand is identified with a vertical dashed line. This vertical line may be masked by other curves if the ligand is very highly ranked. The ROC curve figure inset shows NSQ_AUC values for each binding pocket. Finally, a G) bar chart is used to visualise the EF for representative known ligand chemotypes at EF1, EF5 and EF10. Chemotypes A 'ZM-like', B 'T4G-like', C 'XAC-like' and D 'CAF-like' represent only a subset of AA2AR inhibitors ligands (S2 Fig). The EF bar chart inset shows the number of ligands for each chemotype cluster between parenthesis. X-ray structure chemotype EF shown in black bars, with the LDM models coloured based on their relative clusters identified in A. (TIF)

S8 Fig. Self refinement LDM experiment on the M2R 3UON-QNB, using QNB as a refinement ligand. A) Dendrogram of the top 25 LDM models and X-ray structure(s), a cutoff line identifies different LDM clusters and their representative LDM models are designated by a colored dot. Representative LDM models are the highest scoring within the cluster based on the OPUS-ICM metric. B) Comparison of binding pocket conformation between the top 25 LDM models and X-ray structure(s). LDM models are colored based on their IFP Jaccard distance with the destination X-ray structure. C) Binding poses of the representative LDM model(s) and the destination X-ray structure. D) IFP of the representative LDM models and the X-ray structure. Interaction type is described for each residue of the binding pocket: hydrophobic interaction, hydrogen bond (H-bond) donor and acceptor, weak hydrogen bond (weak H-bond) donor and acceptor, ionic bond positive (+) and negative (-) and aromatic interaction. VS performance is described with ROC curves to visualise E) the recovery of known ligands vs. decoys and F) the selectivity of inhibitors over agonists (or vice-versa). The relative rank of the LDM refinement ligand is identified with a vertical dashed line. This vertical line may be masked by other curves if the ligand is very highly ranked. The ROC curve figure inset shows NSQ_AUC values for each binding pocket. Finally, a G) bar chart is used to visualise the EF for representative known ligand chemotypes at EF1, EF5 and EF10. Chemotypes A, B 'QNB-like' and C represent only a subset of M2R inhibitor ligands (S2 Fig). The EF bar chart inset shows the number of ligands for each chemotype cluster between parenthesis. X-ray structure chemotype EF shown in black bars, with the LDM models coloured based on their relative clusters identified in A. (TIF)

S9 Fig. Self refinement LDM experiment on the M2R 4MQS-IXO, using IXO as a refinement ligand. A) Dendrogram of the top 25 LDM models and X-ray structure(s), a cutoff line identifies different LDM clusters and their representative LDM models are designated by a colored dot. Representative LDM models are the highest scoring within the cluster based on the OPUS-ICM metric. B) Comparison of binding pocket conformation between the top 25 LDM models and X-ray structure(s). LDM models are colored based on their IFP Jaccard distance

with the destination X-ray structure. C) Binding poses of the representative LDM model(s) and the destination X-ray structure. D) IFP of the representative LDM models and the X-ray structure. Interaction type is described for each residue of the binding pocket: hydrophobic interaction, hydrogen bond (H-bond) donor and acceptor, weak hydrogen bond (weak H-bond) donor and acceptor, ionic bond positive (+) and negative (-) and aromatic interaction. VS performance is described with ROC curves to visualise E) the recovery of known ligands vs. decoys and F) the selectivity of inhibitors over agonists (or vice-versa). The relative rank of the LDM refinement ligand is identified with a vertical dashed line. This vertical line may be masked by other curves if the ligand is very highly ranked. The ROC curve figure inset shows NSQ_AUC values for each binding pocket. Finally, a G) bar chart is used to visualise the EF for representative known ligand chemotypes at EF1, EF5 and EF10. Chemotypes A, B and C 'IXO-like' represent only a subset of M2R agonist ligands (S2 Fig). The EF bar chart inset shows the number of ligands for each chemotype cluster between parenthesis. X-ray structure chemotype EF shown in black bars, with the LDM models coloured based on their relative clusters identified in A. (TIF)

S10 Fig. Self refinement LDM experiment on the H1R 3RZE-DOX, using DOX as a refinement ligand. A) Dendrogram of the top 25 LDM models and X-ray structure(s), a cutoff line identifies different LDM clusters and their representative LDM models are designated by a colored dot. Representative LDM models are the highest scoring within the cluster based on the OPUS-ICM metric. B) Comparison of binding pocket conformation between the top 25 LDM models and X-ray structure(s). LDM models are colored based on their IFP Jaccard distance with the destination X-ray structure. C) Binding poses of the representative LDM model(s) and the destination X-ray structure. D) IFP of the representative LDM models and the X-ray structure. Interaction type is described for each residue of the binding pocket: hydrophobic interaction, hydrogen bond (H-bond) donor and acceptor, weak hydrogen bond (weak H-bond) donor and acceptor, ionic bond positive (+) and negative (-) and aromatic interaction. VS performance is described with ROC curves to visualise E) the recovery of known ligands vs. decoys and F) the selectivity of inhibitors over agonists (or vice-versa). The relative rank of the LDM refinement ligand is identified with a vertical dashed line. This vertical line may be masked by other curves if the ligand is very highly ranked. The ROC curve figure inset shows NSQ_AUC values for each binding pocket. Finally, a G) bar chart is used to visualise the EF for representative known ligand chemotypes at EF1, EF5 and EF10. Chemotypes A 'DOX-like', B, C and D represent only a subset of H1R inhibitor ligands (S2 Fig). The EF bar chart inset shows the number of ligands for each chemotype cluster between parenthesis. X-ray structure chemotype EF shown in black bars, with the LDM models coloured based on their relative clusters identified in A. (TIF)

S11 Fig. Self refinement LDM experiment on the 5-HT1B 4IAR-ERG, using ERG as a refinement ligand. A) Dendrogram of the top 25 LDM models and X-ray structure(s), a cutoff line identifies different LDM clusters and their representative LDM models are designated by a colored dot. Representative LDM models are the highest scoring within the cluster based on the OPUS-ICM metric. B) Comparison of binding pocket conformation between the top 25 LDM models and X-ray structure(s). LDM models are colored based on their IFP Jaccard distance with the destination X-ray structure. C) Binding poses of the representative LDM model(s) and the destination X-ray structure. D) IFP of the representative LDM models and the X-ray structure. Interaction type is described for each residue of the binding pocket: hydrophobic interaction, hydrogen bond (H-bond) donor and acceptor, weak hydrogen bond (weak H-

bond) donor and acceptor, ionic bond positive (+) and negative (-) and aromatic interaction. VS performance is described with ROC curves to visualise E) the recovery of known ligands vs. decoys and F) the selectivity of inhibitors over agonists (or vice-versa). The relative rank of the LDM refinement ligand is identified with a vertical dashed line. This vertical line may be masked by other curves if the ligand is very highly ranked. The ROC curve figure inset shows NSQ_AUC values for each binding pocket. Finally, a G) bar chart is used to visualise the EF for representative known ligand chemotypes at EF1, EF5 and EF10. Chemotypes A 'ERG-like', B, C, D and E represent only a subset of 5-HT1B agonist ligands (S2 Fig). The EF bar chart inset shows the number of ligands for each chemotype cluster between parenthesis. X-ray structure chemotype EF shown in black bars, with the LDM models coloured based on their relative clusters identified in A.

(TIF)

S12 Fig. Self refinement LDM experiment on the AA2AR 2YDV-NEC, using NEC as a refinement ligand. A) Dendrogram of the top 25 LDM models and X-ray structure(s), a cutoff line identifies different LDM clusters and their representative LDM models are designated by a colored dot. Representative LDM models are the highest scoring within the cluster based on the OPUS-ICM metric. B) Comparison of binding pocket conformation between the top 25 LDM models and X-ray structure(s). LDM models are colored based on their IFP Jaccard distance with the destination X-ray structure. C) Binding poses of the representative LDM model (s) and the destination X-ray structure. D) IFP of the representative LDM models and the X-ray structure. Interaction type is described for each residue of the binding pocket: hydrophobic interaction, hydrogen bond (H-bond) donor and acceptor, weak hydrogen bond (weak H-bond) donor and acceptor, ionic bond positive (+) and negative (-) and aromatic interaction. VS performance is described with ROC curves to visualise E) the recovery of known ligands vs. decoys and F) the selectivity of inhibitors over agonists (or vice-versa). The relative rank of the LDM refinement ligand is identified with a vertical dashed line. This vertical line may be masked by other curves if the ligand is very highly ranked. The ROC curve figure inset shows NSQ_AUC values for each binding pocket. Finally, a G) bar chart is used to visualise the EF for representative known ligand chemotypes at EF1, EF5 and EF10. Chemotypes A 'UK-like', B 'ADE-like' and C 'NEC-like' represent only a subset of AA2AR agonist ligands (S2 Fig). The EF bar chart inset shows the number of ligands for each chemotype cluster between parenthesis. X-ray structure chemotype EF shown in black bars, with the LDM models coloured based on their relative clusters identified in A.

(TIF)

S13 Fig. Self refinement LDM experiment on the CCR5 4MBS-MRV, using MRV as a refinement ligand. A) Dendrogram of the top 25 LDM models and X-ray structure(s), a cutoff line identifies different LDM clusters and their representative LDM models are designated by a colored dot. Representative LDM models are the highest scoring within the cluster based on the OPUS-ICM metric. B) Comparison of binding pocket conformation between the top 25 LDM models and X-ray structure(s). LDM models are colored based on their IFP Jaccard distance with the destination X-ray structure. C) Binding poses of the representative LDM model (s) and the destination X-ray structure. D) IFP of the representative LDM models and the X-ray structure. Interaction type is described for each residue of the binding pocket: hydrophobic interaction, hydrogen bond (H-bond) donor and acceptor, weak hydrogen bond (weak H-bond) donor and acceptor, ionic bond positive (+) and negative (-) and aromatic interaction. VS performance is described with ROC curves to visualise E) the recovery of known ligands vs. decoys and F) the selectivity of inhibitors over agonists (or vice-versa). The relative rank of the LDM refinement ligand is identified with a vertical dashed line. This vertical line may be

masked by other curves if the ligand is very highly ranked. The ROC curve figure inset shows NSQ_AUC values for each binding pocket. Finally, a G) bar chart is used to visualise the EF for representative known ligand chemotypes at EF1, EF5 and EF10. Chemotypes A and B 'MRV-like' represent only a subset of CCR5 inhibitor ligands (S2 Fig). The EF bar chart inset shows the number of ligands for each chemotype cluster between parenthesis. X-ray structure chemotype EF shown in black bars, with the LDM models coloured based on their relative clusters identified in A. (TIF)

S14 Fig. Self refinement LDM experiment on the DOR 4N6H-NAL, using NAL as a refinement ligand, using the 3D ligand library. A) Dendrogram of the top 25 LDM models and X-ray structure(s), a cutoff line identifies different LDM clusters and their representative LDM models are designated by a colored dot. Representative LDM models are the highest scoring within the cluster based on the OPUS-ICM metric. B) Comparison of binding pocket conformation between the top 25 LDM models and X-ray structure(s). LDM models are colored based on their IFP Jaccard distance with the destination X-ray structure. C) Binding poses of the representative LDM model(s) and the destination X-ray structure. D) IFP of the representative LDM models and the X-ray structure. Interaction type is described for each residue of the binding pocket: hydrophobic interaction, hydrogen bond (H-bond) donor and acceptor, weak hydrogen bond (weak H-bond) donor and acceptor, ionic bond positive (+) and negative (-) and aromatic interaction. VS performance is described with ROC curves to visualise E) the recovery of known ligands vs. decoys and F) the selectivity of inhibitors over agonists (or vice-versa). The relative rank of the LDM refinement ligand is identified with a vertical dashed line. This vertical line may be masked by other curves if the ligand is very highly ranked. The ROC curve figure inset shows NSQ_AUC values for each binding pocket. Finally, a G) bar chart is used to visualise the EF for representative known ligand chemotypes at EF1, EF5 and EF10. Chemotypes A 'NAL-like' and B represent only a subset of DOR inhibitor ligands (S2 Fig). The EF bar chart inset shows the number of ligands for each chemotype cluster between parenthesis. X-ray structure chemotype EF shown in black bars, with the LDM models coloured based on their relative clusters identified in A. (TIF)

S15 Fig. Chemotype switch LDM experiment on the B2AR 3NY9-KOL to 2RH1-CAR, using CAR as a refinement ligand. A) Dendrogram of the top 25 LDM models and X-ray structure(s), a cutoff line identifies different LDM clusters and their representative LDM models are designated by a colored dot. Representative LDM models are the highest scoring within the cluster based on the OPUS-ICM metric. B) Comparison of binding pocket conformation between the top 25 LDM models and X-ray structure(s). LDM models are colored based on their IFP Jaccard distance with the destination X-ray structure. C) Binding poses of the representative LDM model(s) and the destination X-ray structure. D) IFP of the representative LDM models and the X-ray structures. Interaction type is described for each residue of the binding pocket: hydrophobic interaction, hydrogen bond (H-bond) donor and acceptor, weak hydrogen bond (weak H-bond) donor and acceptor, ionic bond positive (+) and negative (-) and aromatic interaction. VS performance is described with ROC curves to visualise E) the recovery of known ligands vs. decoys and F) the selectivity of inhibitors over agonists (or vice-versa). The relative rank of the LDM refinement ligand is identified with a vertical dashed line. This vertical line may be masked by other curves if the ligand is very highly ranked. The ROC curve figure inset shows NSQ_AUC values for each binding pocket. Finally, a G) bar chart is used to visualise the EF for representative known ligand chemotypes at EF1, EF5 and EF10. Chemotypes A 'ICI-like', B 'KOL-like', C 'TIM-like', D 'CAR-like' and E represent only a

subset of B2AR inhibitor ligands (S2 Fig). The EF bar chart inset shows the number of ligands for each chemotype cluster between parenthesis. Origin and destination X-ray structure chemotype EF shown in grey and black bars, respectively, with the LDM models coloured based on their relative clusters identified in A.

(TIF)

S16 Fig. Chemotype switch LDM experiment on the AA2AR 3QAK-UK to 2YDV-NEC, using NEC as a refinement ligand. A) Dendrogram of the top 25 LDM models and X-ray structure(s), a cutoff line identifies different LDM clusters and their representative LDM models are designated by a colored dot. Representative LDM models are the highest scoring within the cluster based on the OPUS-ICM metric. B) Comparison of binding pocket conformation between the top 25 LDM models and X-ray structure(s). LDM models are colored based on their IFP Jaccard distance with the destination X-ray structure. C) Binding poses of the representative LDM model(s) and the destination X-ray structure. D) IFP of the representative LDM models and the X-ray structures. Interaction type is described for each residue of the binding pocket: hydrophobic interaction, hydrogen bond (H-bond) donor and acceptor, weak hydrogen bond (weak H-bond) donor and acceptor, ionic bond positive (+) and negative (-) and aromatic interaction. VS performance is described with ROC curves to visualise E) the recovery of known ligands vs. decoys and F) the selectivity of inhibitors over agonists (or vice-versa). The relative rank of the LDM refinement ligand is identified with a vertical dashed line. This vertical line may be masked by other curves if the ligand is very highly ranked. The ROC curve figure inset shows NSQ_AUC values for each binding pocket. Finally, a G) bar chart is used to visualise the EF for representative known ligand chemotypes at EF1, EF5 and EF10. Chemotypes A 'UK-like', B 'ADE-like' and C 'NEC-like' represent only a subset of AA2AR agonist ligands (S2 Fig). The EF bar chart inset shows the number of ligands for each chemotype cluster between parenthesis. Origin and destination X-ray structure chemotype EF shown in grey and black bars, respectively, with the LDM models coloured based on their relative clusters identified in A.

(TIF)

S17 Fig. Chemotype switch LDM experiment on the B2AR 3D4S-TIM to 3NY8-ICI, using ICI as a refinement ligand. A) Dendrogram of the top 25 LDM models and X-ray structure (s), a cutoff line identifies different LDM clusters and their representative LDM models are designated by a colored dot. Representative LDM models are the highest scoring within the cluster based on the OPUS-ICM metric. B) Comparison of binding pocket conformation between the top 25 LDM models and X-ray structure(s). LDM models are colored based on their IFP Jaccard distance with the destination X-ray structure. C) Binding poses of the representative LDM model(s) and the destination X-ray structure. D) IFP of the representative LDM models and the X-ray structures. Interaction type is described for each residue of the binding pocket: hydrophobic interaction, hydrogen bond (H-bond) donor and acceptor, weak hydrogen bond (weak H-bond) donor and acceptor, ionic bond positive (+) and negative (-) and aromatic interaction. VS performance is described with ROC curves to visualise E) the recovery of known ligands vs. decoys and F) the selectivity of inhibitors over agonists (or vice-versa). The relative rank of the LDM refinement ligand is identified with a vertical dashed line. This vertical line may be masked by other curves if the ligand is very highly ranked. The ROC curve figure inset shows NSQ_AUC values for each binding pocket. Finally, a G) bar chart is used to visualise the EF for representative known ligand chemotypes at EF1, EF5 and EF10. Chemotypes A 'ICI-like', B 'KOL-like', C 'TIM-like', D 'CAR-like' and E represent only a subset of B2AR inhibitor ligands (S2 Fig). The EF bar chart inset shows the number of ligands for each chemotype cluster between parenthesis. Origin and destination X-ray structure

chemotype EF shown in grey and black bars, respectively, with the LDM models coloured based on their relative clusters identified in A.

(TIF)

S18 Fig. Chemotype switch LDM experiment on the B2AR 3D4S-TIM to 3NY8-ICI, using ICI as a refinement ligand, all LDM models from the best cluster. A) Dendrogram of the top 25 LDM models and X-ray structure(s), a cutoff line identifies different LDM clusters and their representative LDM models are designated by a colored dot. Representative LDM models are the highest scoring within the cluster based on the OPUS-ICM metric. B) Comparison of binding pocket conformation between the top 25 LDM models and X-ray structure(s). LDM models are colored based on their IFP Jaccard distance with the destination X-ray structure. C) Binding poses of the representative LDM model(s) and the destination X-ray structure. D) IFP of the representative LDM models and the X-ray structures. Interaction type is described for each residue of the binding pocket: hydrophobic interaction, hydrogen bond (H-bond) donor and acceptor, weak hydrogen bond (weak H-bond) donor and acceptor, ionic bond positive (+) and negative (-) and aromatic interaction. VS performance is described with ROC curves to visualise E) the recovery of known ligands vs. decoys and F) the selectivity of inhibitors over agonists (or vice-versa). The relative rank of the LDM refinement ligand is identified with a vertical dashed line. This vertical line may be masked by other curves if the ligand is very highly ranked. The ROC curve figure inset shows NSQ_AUC values for each binding pocket. Finally, a G) bar chart is used to visualise the EF for representative known ligand chemotypes at EF1, EF5 and EF10. Chemotypes A 'ICI-like', B 'KOL-like', C 'TIM-like', D 'CAR-like' and E represent only a subset of B2AR inhibitor ligands (S2 Fig). The EF bar chart inset shows the number of ligands for each chemotype cluster between parenthesis. Origin and destination X-ray structure chemotype EF shown in grey and black bars, respectively, with the LDM models coloured based on their relative clusters identified in A.

(TIF)

S19 Fig. Chemotype switch LDM experiment on the AA2AR 3UZA-T4G to 3REY-XAC, using XAC as a refinement ligand. A) Dendrogram of the top 25 LDM models and X-ray structure(s), a cutoff line identifies different LDM clusters and their representative LDM models are designated by a colored dot. Representative LDM models are the highest scoring within the cluster based on the OPUS-ICM metric. B) Comparison of binding pocket conformation between the top 25 LDM models and X-ray structure(s). LDM models are colored based on their IFP Jaccard distance with the destination X-ray structure. C) Binding poses of the representative LDM model(s) and the destination X-ray structure. D) IFP of the representative LDM models and the X-ray structures. Interaction type is described for each residue of the binding pocket: hydrophobic interaction, hydrogen bond (H-bond) donor and acceptor, weak hydrogen bond (weak H-bond) donor and acceptor, ionic bond positive (+) and negative (-) and aromatic interaction. VS performance is described with ROC curves to visualise E) the recovery of known ligands vs. decoys and F) the selectivity of inhibitors over agonists (or vice-versa). The relative rank of the LDM refinement ligand is identified with a vertical dashed line. This vertical line may be masked by other curves if the ligand is very highly ranked. The ROC curve figure inset shows NSQ_AUC values for each binding pocket. Finally, a G) bar chart is used to visualise the EF for representative known ligand chemotypes at EF1, EF5 and EF10. Chemotypes A 'ZM-like', B 'T4G-like', C 'XAC-like' and D 'CAF-like' represent only a subset of AA2AR inhibitors ligands (S2 Fig). The EF bar chart inset shows the number of ligands for each chemotype cluster between parenthesis. Origin and destination X-ray structure chemotype EF shown in grey and black bars, respectively, with the LDM models coloured based on

their relative clusters identified in A.
(TIF)

S20 Fig. Pharmacology switch LDM experiment on the M2R 3UON-QNB to 4MQS-IXO, using IXO as a refinement ligand. A) Dendrogram of the top 25 LDM models and X-ray structure(s), a cutoff line identifies different LDM clusters and their representative LDM models are designated by a colored dot. Representative LDM models are the highest scoring within the cluster based on the OPUS-ICM metric. B) Comparison of binding pocket conformation between the top 25 LDM models and X-ray structure(s). LDM models are colored based on their IFP Jaccard distance with the destination X-ray structure. C) Binding poses of the representative LDM model(s) and the destination X-ray structure. D) IFP of the representative LDM models and the X-ray structures. Interaction type is described for each residue of the binding pocket: hydrophobic interaction, hydrogen bond (H-bond) donor and acceptor, weak hydrogen bond (weak H-bond) donor and acceptor, ionic bond positive (+) and negative (-) and aromatic interaction. VS performance is described with ROC curves to visualise E) the recovery of known ligands vs. decoys and F) the selectivity of inhibitors over agonists (or vice-versa). The relative rank of the LDM refinement ligand is identified with a vertical dashed line. This vertical line may be masked by other curves if the ligand is very highly ranked. The ROC curve figure inset shows NSQ_AUC values for each binding pocket. Finally, a G) bar chart is used to visualise the EF for representative known ligand chemotypes at EF1, EF5 and EF10. Chemotypes A, B and C 'IXO-like' represent only a subset of M2R agonist ligands (S2 Fig). The EF bar chart inset shows the number of ligands for each chemotype cluster between parenthesis. Origin and destination X-ray structure chemotype EF shown in grey and black bars, respectively, with the LDM models coloured based on their relative clusters identified in A.
(TIF)

S21 Fig. Pharmacology switch LDM experiment on the M2R 4MQS-IXO to 3UON-QNB, using QNB as a refinement ligand. A) Dendrogram of the top 25 LDM models and X-ray structure(s), a cutoff line identifies different LDM clusters and their representative LDM models are designated by a colored dot. Representative LDM models are the highest scoring within the cluster based on the OPUS-ICM metric. B) Comparison of binding pocket conformation between the top 25 LDM models and X-ray structure(s). LDM models are colored based on their IFP Jaccard distance with the destination X-ray structure. C) Binding poses of the representative LDM model(s) and the destination X-ray structure. D) IFP of the representative LDM models and the X-ray structures. Interaction type is described for each residue of the binding pocket: hydrophobic interaction, hydrogen bond (H-bond) donor and acceptor, weak hydrogen bond (weak H-bond) donor and acceptor, ionic bond positive (+) and negative (-) and aromatic interaction. VS performance is described with ROC curves to visualise E) the recovery of known ligands vs. decoys and F) the selectivity of inhibitors over agonists (or vice-versa). The relative rank of the LDM refinement ligand is identified with a vertical dashed line. This vertical line may be masked by other curves if the ligand is very highly ranked. The ROC curve figure inset shows NSQ_AUC values for each binding pocket. Finally, a G) bar chart is used to visualise the EF for representative known ligand chemotypes at EF1, EF5 and EF10. Chemotypes A, B 'QNB-like' and C represent only a subset of M2R inhibitor ligands (S2 Fig). The EF bar chart inset shows the number of ligands for each chemotype cluster between parenthesis. Origin and destination X-ray structure chemotype EF shown in grey and black bars, respectively, with the LDM models coloured based on their relative clusters identified in A.
(TIF)

S22 Fig. Pharmacology switch LDM experiment on the AA2AR 3EML-ZM to 2YDV-NEC, using NEC as a refinement ligand. A) Dendrogram of the top 25 LDM models and X-ray structure(s), a cutoff line identifies different LDM clusters and their representative LDM models are designated by a colored dot. Representative LDM models are the highest scoring within the cluster based on the OPUS-ICM metric. B) Comparison of binding pocket conformation between the top 25 LDM models and X-ray structure(s). LDM models are colored based on their IFP Jaccard distance with the destination X-ray structure. C) Binding poses of the representative LDM model(s) and the destination X-ray structure. D) IFP of the representative LDM models and the X-ray structures. Interaction type is described for each residue of the binding pocket: hydrophobic interaction, hydrogen bond (H-bond) donor and acceptor, weak hydrogen bond (weak H-bond) donor and acceptor, ionic bond positive (+) and negative (-) and aromatic interaction. VS performance is described with ROC curves to visualise E) the recovery of known ligands vs. decoys and F) the selectivity of inhibitors over agonists (or vice-versa). The relative rank of the LDM refinement ligand is identified with a vertical dashed line. This vertical line may be masked by other curves if the ligand is very highly ranked. The ROC curve figure inset shows NSQ_AUC values for each binding pocket. Finally, a G) bar chart is used to visualise the EF for representative known ligand chemotypes at EF1, EF5 and EF10. Chemotypes A 'UK-like', B 'ADE-like' and C 'NEC-like' represent only a subset of AA2AR agonist ligands (S2 Fig). The EF bar chart inset shows the number of ligands for each chemotype cluster between parenthesis. Origin and destination X-ray structure chemotype EF shown in grey and black bars, respectively, with the LDM models coloured based on their relative clusters identified in A.

(TIF)

S23 Fig. Pharmacology switch LDM experiment on the AA2AR 3QAK-UK to 3EML-ZM, using ZM as a refinement ligand. A) Dendrogram of the top 25 LDM models and X-ray structure(s), a cutoff line identifies different LDM clusters and their representative LDM models are designated by a colored dot. Representative LDM models are the highest scoring within the cluster based on the OPUS-ICM metric. B) Comparison of binding pocket conformation between the top 25 LDM models and X-ray structure(s). LDM models are colored based on their IFP Jaccard distance with the destination X-ray structure. C) Binding poses of the representative LDM model(s) and the destination X-ray structure. D) IFP of the representative LDM models and the X-ray structures. Interaction type is described for each residue of the binding pocket: hydrophobic interaction, hydrogen bond (H-bond) donor and acceptor, weak hydrogen bond (weak H-bond) donor and acceptor, ionic bond positive (+) and negative (-) and aromatic interaction. VS performance is described with ROC curves to visualise E) the recovery of known ligands vs. decoys and F) the selectivity of inhibitors over agonists (or vice-versa). The relative rank of the LDM refinement ligand is identified with a vertical dashed line. This vertical line may be masked by other curves if the ligand is very highly ranked. The ROC curve figure inset shows NSQ_AUC values for each binding pocket. Finally, a G) bar chart is used to visualise the EF for representative known ligand chemotypes at EF1, EF5 and EF10. Chemotypes A 'ZM-like', B 'T4G-like', C 'XAC-like' and D 'CAF-like' represent only a subset of AA2AR inhibitors ligands (S2 Fig). The EF bar chart inset shows the number of ligands for each chemotype cluster between parenthesis. Origin and destination X-ray structure chemotype EF shown in grey and black bars, respectively, with the LDM models coloured based on their relative clusters identified in A.

(TIF)

Acknowledgments

Computational studies were supported by Melbourne Bioinformatics at the University of Melbourne. This research was supported in part by the Monash eResearch Centre and eSolutions-Research Support Services through the use of the Monash Campus HPC Cluster.

Author Contributions

Conceptualization: Thomas Coudrat, Arthur Christopoulos, Denise Wootten, Patrick M. Sexton.

Data curation: Thomas Coudrat.

Formal analysis: Thomas Coudrat, Denise Wootten.

Funding acquisition: Arthur Christopoulos, Patrick M. Sexton.

Investigation: Thomas Coudrat.

Methodology: Thomas Coudrat, John Simms.

Project administration: Denise Wootten, Patrick M. Sexton.

Resources: Thomas Coudrat.

Software: Thomas Coudrat, John Simms.

Supervision: Denise Wootten, Patrick M. Sexton.

Validation: Thomas Coudrat.

Writing ± original draft: Thomas Coudrat, Denise Wootten, Patrick M. Sexton.

Writing ± review & editing: Thomas Coudrat, John Simms, Arthur Christopoulos, Denise Wootten, Patrick M. Sexton.

References

1. Lander ES, Linton LM, Birren B, Nusbaum C, Zody MC, Baldwin J, et al. Initial sequencing and analysis of the human genome. *Nature*. 2001; 409: 860±921. <https://doi.org/10.1038/35057062> PMID: 11237011
2. Venter JC, Adams MD, Myers EW, Li PW, Mural RJ, Sutton GG, et al. The sequence of the human genome. *Science*. 2001; 291: 1304±1351. <https://doi.org/10.1126/science.1058040> PMID: 11181995
3. Heng BC, Aubel D, Fussenegger M. An overview of the diverse roles of G-protein coupled receptors (GPCRs) in the pathophysiology of various human diseases. *Biotechnol Adv*. 2013; 31: 1676±1694. <https://doi.org/10.1016/j.biotechadv.2013.08.017> PMID: 23999358
4. Rask-Andersen M, Almén MS, Schiöth HB. Trends in the exploitation of novel drug targets. *Nat Rev Drug Discov*. 2011; 10: 579±590. <https://doi.org/10.1038/nrd3478> PMID: 21804595
5. Venkatakrishnan AJ, Deupi X, Lebon G, Tate CG, Schertler GF, Babu MM. Molecular signatures of G-protein-coupled receptors. *Nature*. 2013; 494: 185±194. <https://doi.org/10.1038/nature11896> PMID: 23407534
6. Kolakowski LF Jr. GPCRdb: a G-protein-coupled receptor database. *Receptors Channels*. 1994; 2: 1±7. PMID: 8081729
7. Lagerström MC, Schiöth HB. Structural diversity of G protein-coupled receptors and significance for drug discovery. *Nat Rev Drug Discov*. 2008; 7: 339±357. <https://doi.org/10.1038/nrd2518> PMID: 18382464
8. Marinissen MJ, Gutkind JS. G-protein-coupled receptors and signaling networks: emerging paradigms. *Trends Pharmacol Sci*. 2001; 22: 368±376. PMID: 11431032
9. Kobilka BK, Deupi X. Conformational complexity of G-protein-coupled receptors. *Trends Pharmacol Sci*. 2007; 28: 397±406. <https://doi.org/10.1016/j.tips.2007.06.003> PMID: 17629961
10. Berman HM, Kleywegt GJ, Nakamura H, Markley JL. How community has shaped the Protein Data Bank. *Structure*. 2013; 21: 1485±1491. <https://doi.org/10.1016/j.str.2013.07.010> PMID: 24010707

11. Latorraca NR, Venkatakrishnan AJ, Dror RO. GPCR dynamics: structures in motion. *Chem Rev*. 2017; 117: 139±155. <https://doi.org/10.1021/acs.chemrev.6b00177> PMID: 27622975
12. Munk C, Isberg V, Mordalski S, Harpsøe K, Rataj K, Hauser AS, et al. GPCRdb: the G protein-coupled receptor database—An introduction. *Br J Pharmacol*. 2016; 173: 2195±2207. <https://doi.org/10.1111/bph.13509> PMID: 27155948
13. Warne T, Moukhametzianov R, Baker JG, Nehm  R, Edwards PC, Leslie AGW, et al. The structural basis for agonist and partial agonist action on a $\beta(1)$ -adrenergic receptor. *Nature*. 2011; 469: 241±244. <https://doi.org/10.1038/nature09746> PMID: 21228877
14. Rosenbaum DM, Zhang C, Lyons JA, Holl R, Aragao D, Arlow DH, et al. Structure and function of an irreversible agonist- $\beta(2)$ adrenoceptor complex. *Nature*. 2011; 469: 236±240. <https://doi.org/10.1038/nature09665> PMID: 21228876
15. Lebon G, Warne T, Edwards PC, Bennett K, Langmead CJ, Leslie AGW, et al. Agonist-bound adenosine A2A receptor structures reveal common features of GPCR activation. *Nature*. 2011; 474: 521±525. <https://doi.org/10.1038/nature10136> PMID: 21593763
16. Xu F, Wu H, Katritch V, Han GW, Jacobson KA, Gao Z-G, et al. Structure of an agonist-bound human A2A adenosine receptor. *Science*. 2011; 332: 322±327. <https://doi.org/10.1126/science.1202793> PMID: 21393508
17. Scheerer P, Park JH, Hildebrand PW, Kim YJ, Krauss N, Choe H-W, et al. Crystal structure of opsin in its G-protein-interacting conformation. *Nature*. 2008; 455: 497±502. <https://doi.org/10.1038/nature07330> PMID: 18818650
18. Kang Y, Zhou XE, Gao X, He Y, Liu W, Ishchenko A, et al. Crystal structure of rhodopsin bound to arrestin by femtosecond X-ray laser. *Nature*. 2015; 523: 561±567. <https://doi.org/10.1038/nature14656> PMID: 26200343
19. Steyaert J, Kobilka BK. Nanobody stabilization of G protein-coupled receptor conformational states. *Curr Opin Struct Biol*. 2011; 21: 567±572. <https://doi.org/10.1016/j.sbi.2011.06.011> PMID: 21782416
20. Ring AM, Manglik A, Kruse AC, Enos MD, Weis WI, Garcia KC, et al. Adrenaline-activated structure of $\beta2$ -adrenoceptor stabilized by an engineered nanobody. *Nature*. 2013; 502: 575±579. <https://doi.org/10.1038/nature12572> PMID: 24056936
21. Rasmussen SGF, DeVree BT, Zou Y, Kruse AC, Chung KY, Kobilka TS, et al. Crystal structure of the $\beta2$ adrenergic receptor-Gs protein complex. *Nature*. 2011; 477: 549±555. <https://doi.org/10.1038/nature10361> PMID: 21772288
22. Kruse AC, Ring AM, Manglik A, Hu J, Hu K, Eitel K, et al. Activation and allosteric modulation of a muscarinic acetylcholine receptor. *Nature*. 2013; 504: 101±106. <https://doi.org/10.1038/nature12735> PMID: 24256733
23. Carpenter B, Nehm  R, Warne T, Leslie AGW, Tate CG. Structure of the adenosine A(2A) receptor bound to an engineered G protein. *Nature*. 2016; 536: 104±107. <https://doi.org/10.1038/nature18966> PMID: 27462812
24. Katritch V, Cherezov V, Stevens RC. Structure-function of the G protein-coupled receptor superfamily. *Annu Rev Pharmacol Toxicol*. 2013; 53: 531±556. <https://doi.org/10.1146/annurev-pharmtox-032112-135923> PMID: 23140243
25. Tyndall JDA, Sandilya R. GPCR agonists and antagonists in the clinic. *Med Chem*. 2005; 1: 405±421. PMID: 16789897
26. Cooke RM, Brown AJH, Marshall FH, Mason JS. Structures of G protein-coupled receptors reveal new opportunities for drug discovery. *Drug Discov Today*. 2015; 20: 1355±1364. <https://doi.org/10.1016/j.drudis.2015.08.003> PMID: 26303408
27. Kaczor AA, Silva AG, Loza MI, Kolb P, Castro M, Poso A. Structure-based virtual screening for dopamine D₂ receptor ligands as potential antipsychotics. *ChemMedChem*. 2016; 11: 718±729. <https://doi.org/10.1002/cmdc.201500599> PMID: 26990027
28. Kelemen   A, Kiss R, Ferenczy GG, Kov  cs L, Flachner B, L  rincz Z, et al. Structure-based consensus scoring scheme for selecting Class A aminergic GPCR fragments. *J Chem Inf Model*. 2016; 56: 412±422. <https://doi.org/10.1021/acs.jcim.5b00598> PMID: 26760056
29. Kaserer T, Lantero A, Schmidhammer H, Spetea M, Schuster D. μ Opioid receptor: novel antagonists and structural modeling. *Sci Rep*. 2016; 6: 21548. <https://doi.org/10.1038/srep21548> PMID: 26888328
30. Rodr  guez D, Chakraborty S, Warnick E, Crane S, Gao Z-G, O'Connor R, et al. Structure-based screening of uncharted chemical space for atypical adenosine receptor agonists. *ACS Chem Biol*. 2016; 11: 2763±2772. <https://doi.org/10.1021/acschembio.6b00357> PMID: 27439119
31. Ranganathan A, Heine P, Rudling A, Pl  ckthun A, Kummer L, Carlsson J. Ligand discovery for a peptide-binding GPCR by structure-based screening of fragment- and lead-like chemical libraries. *ACS Chem Biol*. 2017; 12: 735±745. <https://doi.org/10.1021/acschembio.6b00646> PMID: 28032980

32. Bahar I. On the functional significance of soft modes predicted by coarse-grained models for membrane proteins. *J Gen Physiol*. 2010; 135: 563±573. <https://doi.org/10.1085/jgp.200910368> PMID: 20513758
33. Deng Z, Chuaqui C, Singh J. Structural interaction fingerprint (SIFT): a novel method for analyzing three-dimensional protein-ligand binding interactions. *J Med Chem*. 2004; 47: 337±344. <https://doi.org/10.1021/jm030331x> PMID: 14711306
34. Costanzi S, Vilar S. In silico screening for agonists and blockers of the $\beta(2)$ adrenergic receptor: implications of inactive and activated state structures. *J Comput Chem*. 2012; 33: 561±572. <https://doi.org/10.1002/jcc.22893> PMID: 22170280
35. Kooistra AJ, Leurs R, de Esch IJP, de Graaf C. Structure-Based Prediction of G-Protein-Coupled Receptor Ligand Function: A β -Adrenoceptor Case Study. *J Chem Inf Model*. 2015; 55: 1045±1061. <https://doi.org/10.1021/acs.jcim.5b00066> PMID: 25848966
36. McRobb FM, Negri A, Beuming T, Sherman W. Molecular dynamics techniques for modeling G protein-coupled receptors. *Curr Opin Pharmacol*. 2016; 30: 69±75. <https://doi.org/10.1016/j.coph.2016.07.001> PMID: 27490828
37. Dror RO, Arlow DH, Maragakis P, Mildorf TJ, Pan AC, Xu H, et al. Activation mechanism of the $\beta 2$ -adrenergic receptor. *Proc Natl Acad Sci*. 2011; 108: 18684±18689. <https://doi.org/10.1073/pnas.1110499108> PMID: 22031696
38. Zeng L, Guan M, Jin H, Liu Z, Zhang L. Integrating pharmacophore into membrane molecular dynamics simulations to improve homology modeling of G protein-coupled receptors with ligand selectivity: A_{2A} adenosine receptor as an example. *Chem Biol Drug Des*. 2015; 86: 1438±1450. <https://doi.org/10.1111/cbdd.12607> PMID: 26072970
39. Esguerra M, Siretskiy A, Bello X, Sallander J, Gutiérrez-de-Terán H. GPCR-ModSim: A comprehensive web based solution for modeling G-protein coupled receptors. *Nucleic Acids Res*. 2016; 44: W455±W462. <https://doi.org/10.1093/nar/gkw403> PMID: 27166369
40. Miao Y, Goldfeld DA, Moo EV, Sexton PM, Christopoulos A, McCammon JA, et al. Accelerated structure-based design of chemically diverse allosteric modulators of a muscarinic G protein-coupled receptor. *Proc Natl Acad Sci*. 2016; 113: E5675±E5684. <https://doi.org/10.1073/pnas.1612353113> PMID: 27601651
41. Kohlhoff KJ, Shukla D, Lawrenz M, Bowman GR, Konerding DE, Belov D, et al. Cloud-based simulations on Google Exacycle reveal ligand modulation of GPCR activation pathways. *Nat Chem*. 2014; 6: 15±21. <https://doi.org/10.1038/nchem.1821> PMID: 24345941
42. Lenselink EB, Louvel J, Forti AF, van Veldhoven JPD, de Vries H, Mulder-Krieger T, et al. Predicting binding affinities for GPCR ligands using free-energy perturbation. *ACS Omega*. 2016; 1: 293±304.
43. Cappel D, Hall ML, Lenselink EB, Beuming T, Qi J, Bradner J, et al. Relative binding free energy calculations applied to protein homology models. *J Chem Inf Model*. 2016; 56: 2388±2400. <https://doi.org/10.1021/acs.jcim.6b00362> PMID: 28024402
44. Keränen H, Åqvist J, Gutiérrez-de-Terán H. Free energy calculations of A_{2A} adenosine receptor mutation effects on agonist binding. *Chem Commun*. 2015; 51: 3522±3525.
45. Keränen H, Gutiérrez-de-Terán H, Åqvist J. Structural and Energetic Effects of A_{2A} Adenosine Receptor Mutations on Agonist and Antagonist Binding. Cavalli A, editor. *PLoS ONE*. 2014; 9: e108492. <https://doi.org/10.1371/journal.pone.0108492> PMID: 25285959
46. de Graaf C, Rognan D. Selective structure-based virtual screening for full and partial agonists of the $\beta 2$ adrenergic receptor. *J Med Chem*. 2008; 51: 4978±4985. <https://doi.org/10.1021/jm800710x> PMID: 18680279
47. Kořaczowski M, Bucki A, Feder M, Pawłowski M. Ligand-optimized homology models of D₁ and D₂ dopamine receptors: application for virtual screening. *J Chem Inf Model*. 2013; 53: 638±648. <https://doi.org/10.1021/ci300413h> PMID: 23398329
48. Thomas T, McLean KC, McRobb FM, Manallack DT, Chalmers DK, Yuriev E. Homology modeling of human muscarinic acetylcholine receptors. *J Chem Inf Model*. 2014; 54: 243±253. <https://doi.org/10.1021/ci400502u> PMID: 24328076
49. Rodríguez D, Ranganathan A, Carlsson J. Strategies for improved modeling of GPCR-drug complexes: blind predictions of serotonin receptors bound to ergotamine. *J Chem Inf Model*. 2014; 54: 2004±2021. <https://doi.org/10.1021/ci5002235> PMID: 25030302
50. Rueda M, Totrov M, Abagyan R. ALiBERO: evolving a team of complementary pocket conformations rather than a single leader. *J Chem Inf Model*. 2012; 52: 2705±2714. <https://doi.org/10.1021/ci3001088> PMID: 22947092
51. Lückmann M, Holst B, Schwartz TW, Frimurer TM. In silico investigation of the neurotensin receptor 1 binding site: overlapping binding modes for small molecule antagonists and the endogenous peptide agonist. *Mol Inf*. 2016; 35: 19±24.

52. Warszycki D, Rueda M, Mordalski S, Kristiansen K, SataøaG, Rataj K, et al. From homology models to a set of predictive binding pockets—a 5-HT_{1A} receptor case study. *J Chem Inf Model*. 2017; 57: 311±321. <https://doi.org/10.1021/acs.jcim.6b00263> PMID: 28055203
53. Nguyen ED, Norn C, Frimurer TM, Meiler J. Assessment and challenges of ligand docking into comparative models of G protein-coupled receptors. Seifert R, editor. *PLoS ONE*. 2013; 8: e67302. <https://doi.org/10.1371/journal.pone.0067302> PMID: 23844000
54. Zhang Y, Devries ME, Skolnick J. Structure modeling of all identified G protein-coupled receptors in the human genome. *PLoS Comput Biol*. 2006; 2: e13. <https://doi.org/10.1371/journal.pcbi.0020013> PMID: 16485037
55. Zhang J, Yang J, Jang R, Zhang Y. GPCR-I-TASSER: a hybrid approach to G protein-coupled receptor structure modeling and the application to the human genome. *Structure*. 2015; 23: 1538±1549. <https://doi.org/10.1016/j.str.2015.06.007> PMID: 26190572
56. Shacham S, Marantz Y, Bar-Haim S, Kalid O, Warshaviak D, Avisar N, et al. PREDICT modeling and in-silico screening for G-protein coupled receptors. *Proteins*. 2004; 57: 51±86. <https://doi.org/10.1002/prot.20195> PMID: 15326594
57. Abrol R, Bray JK, Goddard WA 3rd. Bihelix: Towards de novo structure prediction of an ensemble of G-protein coupled receptor conformations. *Proteins*. 2012; 80: 505±518. <https://doi.org/10.1002/prot.23216> PMID: 22173949
58. Bray JK, Abrol R, Goddard WA 3rd, Trzaskowski B, Scott CE. SuperBiHelix method for predicting the pleiotropic ensemble of G-protein-coupled receptor conformations. *Proc Natl Acad Sci U A*. 2014; 111: E72±8.
59. Bhattacharya S, Vaidehi N. LITiCon: a discrete conformational sampling computational method for mapping various functionally selective conformational states of transmembrane helical proteins. *Methods Mol Biol*. 2012; 914: 167±178. https://doi.org/10.1007/978-1-62703-023-6_10 PMID: 22976028
60. de Groot BL, van Aalten DM, Scheek RM, Amadei A, Vriend G, Berendsen HJ. Prediction of protein conformational freedom from distance constraints. *Proteins*. 1997; 29: 240±251. PMID: 9329088
61. Seeliger D, Haas J, de Groot BL. Geometry-based sampling of conformational transitions in proteins. *Structure*. 2007; 15: 1482±1492. <https://doi.org/10.1016/j.str.2007.09.017> PMID: 17997973
62. Abagyan R, Totrov M, Kuznetsov D. ICMØA new method for protein modeling and design: Applications to docking and structure prediction from the distorted native conformation. *J Comput Chem*. 1994; 15: 488±506.
63. Peeters MC, van Westen GJP, Li Q, IJzerman AP. Importance of the extracellular loops in G protein-coupled receptors for ligand recognition and receptor activation. *Trends Pharmacol Sci*. 2011; 32: 35±42. <https://doi.org/10.1016/j.tips.2010.10.001> PMID: 21075459
64. Woolley MJ, Conner AC. Understanding the common themes and diverse roles of the second extracellular loop (ECL2) of the GPCR super-family. *Mol Cell Endocrinol*. 2017; 449: 3±11. <https://doi.org/10.1016/j.mce.2016.11.023> PMID: 27899324
65. de Graaf C, Foata N, Engkvist O, Rognan D. Molecular modeling of the second extracellular loop of G-protein coupled receptors and its implication on structure-based virtual screening. *Proteins*. 2008; 71: 599±620. <https://doi.org/10.1002/prot.21724> PMID: 17972285
66. Ballesteros JA, Weinstein H. [19] Integrated methods for the construction of three-dimensional models and computational probing of structure-function relations in G protein-coupled receptors. *Methods in Neurosciences*. Elsevier; 1995. pp. 366±428.
67. Hess B, Kutzner C, van der Spoel D, Lindahl E. GROMACS 4: algorithms for highly efficient, load-balanced, and scalable molecular simulation. *J Chem Theory Comput*. 2008; 4: 435±447. <https://doi.org/10.1021/ct700301q> PMID: 26620784
68. Eyal E, Najmanovich R, McConkey BJ, Edelman M, Sobolev V. Importance of solvent accessibility and contact surfaces in modeling side-chain conformations in proteins. *J Comput Chem*. 2004; 25: 712±724. <https://doi.org/10.1002/jcc.10420> PMID: 14978714
69. Lu M, Dousis AD, Ma J. OPUS-PSP: an orientation-dependent statistical all-atom potential derived from side-chain packing. *J Mol Biol*. 2008; 376: 288±301. <https://doi.org/10.1016/j.jmb.2007.11.033> PMID: 18177896
70. Gatica EA, Cavasotto CN. Ligand and decoy sets for docking to G protein-coupled receptors. *J Chem Inf Model*. 2012; 52: 1±6. <https://doi.org/10.1021/ci200412p> PMID: 22168315
71. Jaakola V-P, Griffith MT, Hanson MA, Cherezov V, Chien EYT, Lane JR, et al. The 2.6 angstrom crystal structure of a human A2A adenosine receptor bound to an antagonist. *Science*. 2008; 322: 1211±1217. <https://doi.org/10.1126/science.1164772> PMID: 18832607

72. Coudrat T, Christopoulos A, Sexton PM, Wootten D. Structural features embedded in G protein-coupled receptor co-crystal structures are key to their success in virtual screening. *PLoS One*. 2017; 12: e0174719. <https://doi.org/10.1371/journal.pone.0174719> PMID: 28380046
73. Marcou G, Rognan D. Optimizing fragment and scaffold docking by use of molecular interaction fingerprints. *J Chem Inf Model*. 2007; 47: 195±207. <https://doi.org/10.1021/ci600342e> PMID: 17238265
74. Python Software Foundation, <https://www.python.org/>.
75. Hunter JD. Matplotlib: a 2D graphics environment. *Comput Sci Eng*. 2007; 9: 90±95.
76. der Walt S van, Colbert SC, Varoquaux G. The NumPy Array: A Structure for Efficient Numerical Computation. *Comput Sci Eng*. 2011; 13: 22±30.
77. Jones E, Oliphant T, Peterson P, others. SciPy: Open source scientific tools for Python [Internet]. 2001. Available: <http://www.scipy.org/>
78. Pedregosa F, Varoquaux G, Gramfort A, Michel V, Thirion B, Grisel O, et al. Scikit-learn: Machine Learning in Python. *J Mach Learn Res*. 2011; 12: 2825±2830.
79. OpenEye Scientific Software, Inc., Santa Fe, NM, USA, www.eyesopen.com. OEChem, version 1.7.4. 2010.
80. Wold S, Esbensen K, Geladi P. Principal component analysis. *Chemom Intellig Lab Syst*. 1987; 2: 37±52.
81. Katritch V, Rueda M, Lam PC-H, Yeager M, Abagyan R. GPCR 3D homology models for ligand screening: lessons learned from blind predictions of adenosine A2a receptor complex. *Proteins*. 2010; 78: 197±211. <https://doi.org/10.1002/prot.22507> PMID: 20063437
82. Kolb P, Rosenbaum DM, Irwin JJ, Fung JJ, Kobilka BK, Shoichet BK. Structure-based discovery of beta2-adrenergic receptor ligands. *Proc Natl Acad Sci U A*. 2009; 106: 6843±6848.
83. Lenselink EB, Jespers W, van Vlijmen HWT, IJzerman AP, van Westen GJP. Interacting with GPCRs: using interaction fingerprints for virtual screening. *J Chem Inf Model*. 2016; 56: 2053±2060. <https://doi.org/10.1021/acs.jcim.6b00314> PMID: 27626908
84. Dror RO, Pan AC, Arlow DH, Borhani DW, Maragakis P, Shan Y, et al. Pathway and mechanism of drug binding to G protein-coupled receptors. *Proc Natl Acad Sci*. 2011; 108: 13118±13123. <https://doi.org/10.1073/pnas.1104614108> PMID: 21778406
85. Christopoulos A. Advances in G Protein-Coupled Receptor Allostery: From Function to Structure. *Mol Pharmacol*. 2014; 86: 463±478. <https://doi.org/10.1124/mol.114.094342> PMID: 25061106
86. Goldfeld DA, Murphy R, Kim B, Wang L, Beuming T, Abel R, et al. Docking and free energy perturbation studies of ligand binding in the kappa opioid receptor. *J Phys Chem B*. 2015; 119: 824±835. <https://doi.org/10.1021/jp5053612> PMID: 25395044
87. Lenselink EB, Beuming T, Sherman W, van Vlijmen HWT, IJzerman AP. Selecting an optimal number of binding site waters to improve virtual screening enrichments against the adenosine A2A receptor. *J Chem Inf Model*. 2014; 54: 1737±1746. <https://doi.org/10.1021/ci5000455> PMID: 24835542
88. Shaw DE, Bowers KJ, Chow E, Eastwood MP, Ierardi DJ, Klepeis JL, et al. Millisecond-scale molecular dynamics simulations on Anton. *ACM Press*; 2009. p. 1. Available: <http://dl.acm.org/citation.cfm?doid=1654059.1654126>
89. Miao Y, Nichols SE, Gasper PM, Metzger VT, McCammon JA. Activation and dynamic network of the M2 muscarinic receptor. *Proc Natl Acad Sci*. 2013; 110: 10982±10987. <https://doi.org/10.1073/pnas.1309755110> PMID: 23781107
90. Tikhonova IG, Selvam B, Ivetac A, Wereszczynski J, McCammon JA. Simulations of biased agonists in the β_2 adrenergic receptor with accelerated molecular dynamics. *Biochemistry (Mosc)*. 2013; 52: 5593±5603.
91. Marti-Solano M, Iglesias A, de Fabritiis G, Sanz F, Brea J, Loza MI, et al. Detection of new biased agonists for the serotonin 5-HT2A receptor: modeling and experimental validation. *Mol Pharmacol*. 2015; 87: 740±746. <https://doi.org/10.1124/mol.114.097022> PMID: 25661038
92. Manglik A, Lin H, Aryal DK, McCorvy JD, Dengler D, Corder G, et al. Structure-based discovery of opioid analgesics with reduced side effects. *Nature*. 2016; 537: 185±190. <https://doi.org/10.1038/nature19112> PMID: 27533032

Phase-plate cryo-EM structure of a biased agonist-bound human GLP-1 receptor–Gs complex

Yi-Lynn Liang^{1*}, Maryam Khoshouei^{2*}, Alisa Glukhova^{1*}, Sebastian G. B. Furness¹, Peishen Zhao¹, Lachlan Clydesdale¹, Cassandra Koole¹, Tin T. Truong¹, David M. Thal¹, Saifei Lei^{3,4}, Mazdak Radjainia^{1,5}, Radostin Danev², Wolfgang Baumeister², Ming-Wei Wang^{3,4,6}, Laurence J. Miller^{1,7}, Arthur Christopoulos¹, Patrick M. Sexton^{1,6} & Denise Wootten¹

The class B glucagon-like peptide-1 (GLP-1) G protein-coupled receptor is a major target for the treatment of type 2 diabetes and obesity¹. Endogenous and mimetic GLP-1 peptides exhibit biased agonism—a difference in functional selectivity—that may provide improved therapeutic outcomes¹. Here we describe the structure of the human GLP-1 receptor in complex with the G protein-biased peptide exendin-P5 and a G α_s heterotrimer, determined at a global resolution of 3.3 Å. At the extracellular surface, the organization of extracellular loop 3 and proximal transmembrane segments differs between our exendin-P5-bound structure and previous GLP-1-bound GLP-1 receptor structure². At the intracellular face, there was a six-degree difference in the angle of the G α_s – $\alpha 5$ helix engagement between structures, which was propagated across the G protein heterotrimer. In addition, the structures differed in the rate and extent of conformational reorganization of the G α_s protein. Our structure provides insights into the molecular basis of biased agonism.

The GLP-1R, a class B G protein-coupled receptor (GPCR), is a key incretin hormone receptor and an important target for the development of therapies for the treatment of type 2 diabetes and obesity¹. Biased agonism is commonly observed at the GLP-1R^{3–5}, and exendin-P5 (ExP5) has been identified as a potent G protein-biased selective agonist of GLP-1R, with diminished coupling to β -arrestins⁶ and a unique *in vivo* profile in animal models of diabetes⁶. The prevalence of GLP-1R biased agonism and its therapeutic implications make understanding of the phenomenon at molecular and structural levels crucial for the rational design of novel ligands.

Like all class B GPCRs, the GLP-1R contains a large extracellular N-terminal domain (NTD) and a seven-transmembrane helix bundle, with peptide binding spanning both domains; the NTD interaction positions the peptide N terminus within the receptor core to facilitate receptor activation⁷. Clinically used therapeutic agents, including exendin-4, contain an N-terminal sequence that is relatively conserved with that of the native peptide, GLP-1⁸. Notably, ExP5 shares a common C terminus with exendin-4, but possesses a unique N-terminal domain (Extended Data Fig. 1a) that interacts with the GLP-1R transmembrane core to promote receptor activation.

Cryo-electron microscopy (cryo-EM) has enabled researchers to determine the structures of GPCR complexes without the need to extensively modify the receptor^{2,9}. A 4.1 Å full-length active structure of a wild-type rabbit GLP-1R was solved in complex with GLP-1 and heterotrimeric G s protein². In addition, the full-length active structure of the calcitonin receptor (CTR) was solved to a similar global resolution in complex with a peptide agonist and G s protein⁹ using phase contrast cryo-EM^{10–12}. Here, we used Volta phase plate cryo-EM to determine the structure of an active state, human GLP-1R bound

to ExP5 in complex with a heterotrimeric G s protein. The structure provides insights into the binding of ExP5 to the GLP-1R, with implications for receptor activation, G protein coupling and signalling for class B GPCRs.

To form an active, G protein-coupled complex, the GLP-1R was co-expressed with G α_s , His-G $\beta 1$, and G $\gamma 2$ in *Trichoplusia ni* (Tni) insect cells and stimulated with an excess of ExP5 in the presence of apyrase and the nanobody Nb35, which bridges the G protein α - and $\beta\gamma$ -subunits. A dominant-negative G α_s was used to enable the formation of a complex with improved stability. We characterized and purified the complex as described for the CTR⁹ (Extended Data Figs 1b, 2a).

Following imaging and initial 2D classification (Extended Data Fig. 2b, c), 3D classification revealed that the majority of the complex had stable features. The exception was the G α_s α -helical domain, the density of which was averaged out at higher resolution because it had substantial flexibility despite occupying a single predominant orientation (Fig. 1a). We used 184,672 particle projections to obtain a cryo-EM density map with nominal global resolution of 3.3 Å (Fig. 1a; Extended Data Fig. 2b).

An atomic resolution structure of the ExP5–GLP-1R–G α_s heterotrimeric G protein complex was built into the map and refined to reveal global features similar to those observed in other class B GPCR structures^{2,9,13–15}. Side chains of the majority of amino acid residues are clearly identifiable in the peptide, all of the transmembrane helices and the subunits of the G protein (Extended Data Fig. 3). Although linker region density between the NTD and the transmembrane core was visible in the cryo-EM map, it was less well-resolved than other receptor domains, suggesting substantial flexibility in the ExP5 bound state. Continuous density was observed for helix 8 (H8) and all intracellular and extracellular loops (ICLs and ECLs, respectively), with the exception of ICL3, which was not modelled. In addition, the cryo-EM map was poor for a region of four ECL3 residues (372–375) and therefore only the protein backbone was modelled in this region.

Within the NTD there was discontinuous density in the backbone for some regions. As such, the NTD structure bound to exendin(9–39)¹⁶ was used to perform a rigid body fit into the density. N-terminal residues 24–30 and residues beyond E423 at the receptor C terminus were not resolved. The G protein was well resolved, allowing modelling of all G protein components (with the exception of the G α_s α -helical domain).

The extracellular NTD conformation differs between the three agonist-bound G α_s heterotrimer class B GPCR structures (Extended Data Fig. 4a–c). Whereas multiple NTD conformations were evident for the CTR⁹, a single predominant conformation was stabilized in both GLP-1R structures². However, there were subtle differences in the relative positioning of the N terminus relative to the transmembrane

¹Drug Discovery Biology and Department of Pharmacology, Monash Institute of Pharmaceutical Sciences, Monash University, Parkville 3052, Victoria, Australia. ²Department of Molecular Structural Biology, Max Planck Institute of Biochemistry, 82152 Martinsried, Germany. ³University of Chinese Academy of Sciences, 19A Yuquan Road, Beijing 100049, China. ⁴The National Center for Drug Screening and CAS Key Laboratory of Receptor Research, Shanghai Institute of Materia Medica, Chinese Academy of Sciences, Shanghai 201203, China. ⁵FEI, 5651 GG Eindhoven, The Netherlands.

⁶School of Pharmacy, Fudan University, Shanghai 201203, China. ⁷Department of Molecular Pharmacology and Experimental Therapeutics, Mayo Clinic, Scottsdale, Arizona 85259, USA.

*These authors contributed equally to this work.

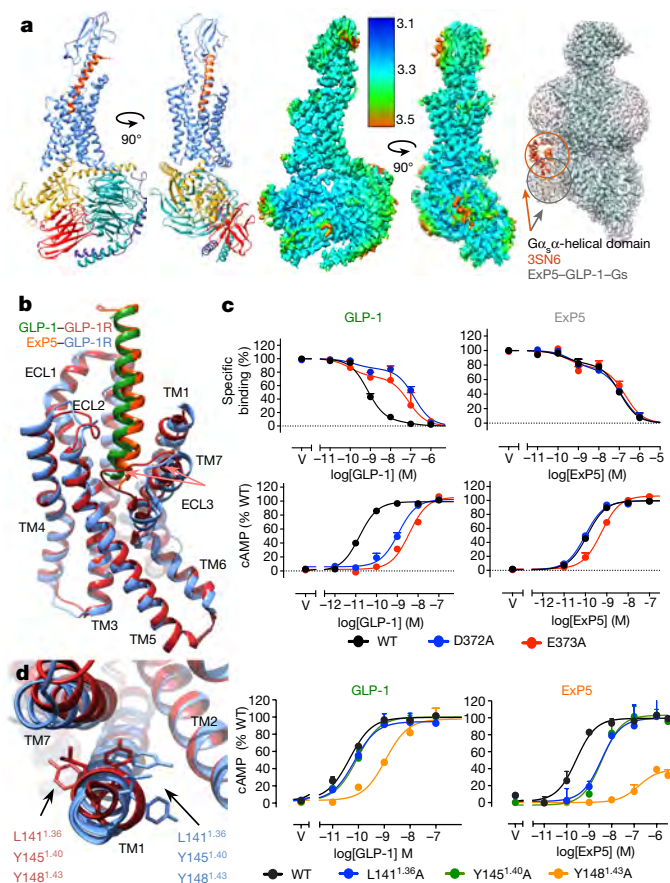


Figure 1 | The ExP5-GLP-1R-Gs cryo-EM structure reveals molecular details linked to GLP-1R biased agonism. **a**, Left, ExP5-GLP-1R-Gs structure after refinement in the cryo-EM map. Middle, cryo-EM density map coloured by local resolution (Å). Right, low-resolution cryo-EM map highlighting the predominant $G\alpha_s$ α -helical domain location in ExP5-GLP-1R-Gs (grey), compared to β_2 -AR-Gs (PDB:3SN6, orange). **b**, Transmembrane domain and peptide superimposition reveal backbone differences in ECL3, TM6, TM7 and TM1 when bound by GLP-1 relative to ExP5. ExP5 is located closer to TM1 than GLP-1. **c**, D372 and E373 in ECL3 are important for the pharmacology of GLP-1 and have a limited role in ExP5 affinity and signalling. WT, wild type; V, vehicle. **d**, Left, overlay of the GLP-1-GLP-1R deposited structure² (GLP-1R in red) and ExP5-GLP-1R (GLP-1R in blue) reveals a rotation in TM1 side chains. Right, L141^{1,36}, Y145^{1,40} and Y148^{1,43} mutations have a larger effect on ExP5-mediated than on GLP-1-mediated cAMP signalling. Whole-cell binding assays and cAMP signalling were assessed in CHOflpIn cells and data are means \pm s.e.m. of four (for TM1) and six (for ECL3) independent experiments, performed in duplicate.

bundle that contribute to the positioning of the N termini of GLP-1 and ExP5 (Extended Data Fig. 4b). Notably, the 11-mer agonist-bound GLP-1R structure solved without the $G\alpha_s$ heterotrimer¹⁵ displayed a unique NTD conformation relative to GLP-1 and ExP5 (Extended Data Fig. 4c). Collectively, these structures suggest that the binding of different peptide agonists alters the juxtaposition of the extracellular NTD and transmembrane bundle to regulate the ability of different peptides to activate class B GPCRs.

Compared to inactive class B GPCR transmembrane bundles, the GLP-1R in our structure undergoes similar macroscopic conformational transitions to those previously reported for the GLP-1-bound GLP-1R² and calcitonin-bound CTR⁹ (Extended Data Fig. 4d–h). These include considerable movements in the extracellular ends of transmembrane (TM) helices 1, 6 and 7, required to open the bundle to accommodate peptide binding, and a large 15–16 Å movement of TM6 away from the central transmembrane domain axis that opens up the cytoplasmic face to accommodate G protein interaction (Extended

Data Fig. 4d, f). These large conformational movements are coordinated around the highly conserved class B GPCR P^{6.47}XXG^{6.50} motif in TM6, and G^{7.50} in TM7 (Extended Data Fig. 4d). Nonetheless, there are notable differences in the extracellular face between the activated structures, particularly in the extent of movement of TM6, ECL3 and TM7, which probably reflect the distinct modes with which these ligands activate their respective receptors (Extended Data Fig. 4g, h).

ExP5 is a biased agonist relative to exendin-4⁶. Our pharmacological analysis revealed that ExP5 is also G protein-biased, with limited β -arrestin recruitment relative to GLP-1 (Extended Data Fig. 1d). Comparison of receptor occupancy with ligand potency and efficacy in cellular signalling assays showed that the bias of ExP5 arises primarily from enhanced efficacy in $G\alpha_s$ -mediated cAMP signalling, rather than a loss of β -arrestin coupling (Extended Data Fig. 1e). Ligand binding and GTP γ S studies performed in insect cells also support enhanced G protein efficacy of ExP5 relative to GLP-1 (Extended Data Fig. 1c). Thus, comparison of the GLP-1 and ExP5-bound GLP-1R- $G\alpha_s\beta\gamma$ structures provides insight into conformational differences that may be linked to biased agonism.

The largest distinctions between the GLP-1 and ExP5-bound GLP-1R transmembrane domains occur within TM1, the extracellular portions of TM6 and TM7, and the ECL3 conformation (Fig. 1b, Extended Data Fig. 5a), indicating that these domains may contribute to biased agonism. This is supported by earlier work identifying crucial roles for ECL3, and the extracellular helical boundaries of TM6 and TM7, within the GLP-1R for differential control of GLP-1R-mediated signalling¹⁷. Alanine scanning mutagenesis confirmed the importance of this domain for the differing pharmacological profiles of GLP-1 and ExP5 (Fig. 1c, Extended Data Table 1). Although some ECL3 residues (G377, K380) had similar roles in both GLP-1 and ExP5 function, the substitutions L379A, D372A and E373A substantially reduced GLP-1 affinity and signalling but had little effect on ExP5 function. Notably, the latter two residues lie within the region of ECL3 where the largest receptor backbone differences are observed between the two structures (Extended Data Fig. 5a), and alanine mutation converts the binding profile of GLP-1 to one that closely resembles the binding profile of ExP5 (Fig. 1c). Mutagenesis of these two residues also had a similar effect on the pharmacology of exendin-4, which has a bias profile similar to that of GLP-1 for these pathways (Extended Data Table 1). Moreover, mutation of L388^{7,43} within the top of TM7 had a greater effect on GLP-1 signalling than on ExP5 signalling (Extended Data Fig. 5b), further supporting the importance of this region in biased agonism of GLP-1R.

There are additional differences between the ExP5-bound structure and the deposited GLP-1-bound GLP-1R structure, in the reported positioning of the TM1 kink and orientation of side chains in the extracellular half of TM1 (Extended Data Fig. 5c, Fig. 1d). The location of the TM1 kink in the 11-mer-bound GLP-1R and the agonist-bound CTR structures is equivalent to that observed in the ExP5-bound structure and an overlay of the ExP5-bound and GLP-1-bound GLP-1R cryo-EM maps reveals that they have similar backbone densities (Extended Data Fig. 5c). Although the limited density in the GLP-1 bound structure precludes confidence, the TM1 backbone can also be modelled in this common conformation, suggesting that the gross positioning of TM1 may be conserved, although comparison of the density maps indicates that the side chain positioning differs between the ExP5- and GLP-1-bound structures, possibly contributing to the biased agonism of ExP5. Indeed, in the deposited GLP-1-bound model, L141^{1,36}, Y145^{1,40} and Y148^{1,43} face towards TM7, whereas in the ExP5 structure they reside closer to TM2 (Fig. 1d). Mutation of these residues to alanine had a stronger effect on ExP5-mediated cAMP signalling than on GLP-1 signalling, supporting a role for TM1 in the control of signalling and an interaction between TM1 and TM7–ECL3–TM6 that manifests as altered $G\alpha_s$ efficacy and biased agonism between GLP-1 and ExP5.

Strong density was observed for the entirety of ExP5 extending from the NTD into deep within the transmembrane core (Extended Data Fig. 3).

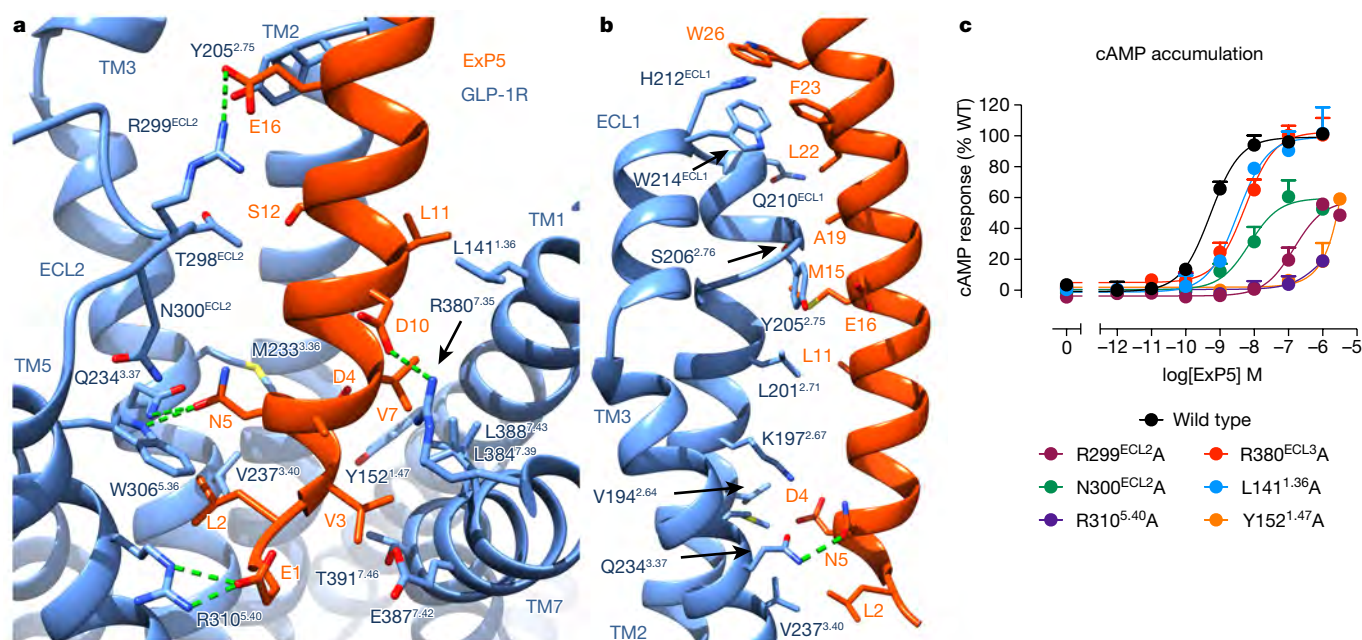


Figure 2 | The ExP5 binding site. **a**, Key interactions between ExP5 residues and TM1, TM3, TM5, TM7 and ECL2 of the GLP-1R transmembrane bundle (side chains located within 4 Å between the peptide (orange) and the GLP-1R (blue) are shown). ECL3 has been removed for clarity. **b**, Additional interactions formed by ExP5 with TM2, TM3 and ECL1. **c**, The functional effect on Gs-mediated cAMP

The peptide forms extensive interactions with residues in TMs 1, 2, 3, 5, 7 and all 3 ECLs (Fig. 2, Extended Data Table 2). Alanine mutagenesis confirmed the importance of key residues in the GLP-1R for ExP5 binding (Fig. 2c). Many of these residues lining the ExP5 binding site have previously been implicated as being important for binding of the cognate ligand, GLP-1^{7,17–23}.

E1 of ExP5 interacts with R310^{5.40} of GLP-1R and is crucial for the ability of ExP5 to promote signalling through G α_s , with R310^{5.40}A almost completely abolishing ExP5-mediated cAMP accumulation (Fig. 2a, c). Very clear density is evident for W306^{5.36}, which interacts directly with ExP5 through Van der Waal interactions with the aliphatic region of N5, as well as forming a direct hydrogen bond with N5 in the peptide. N5 also forms a hydrogen bond with Q234^{3.37}. N300^{ECL2} points down towards the receptor core within bonding distance of W306^{5.36} and may participate in stabilizing these interactions. A series of contacts occur between residues in TM2 and ExP5, mainly through hydrophobic Van der Waals interactions with either hydrophobic residues or aliphatic regions of polar side chains (Fig. 2b, Extended Data Table 2). Peptide interactions also occur within ECL1, a region that has been implicated in peptide binding of other GLP-1R agonists^{17,22} and ECL1 residues close to GLP-1 in the GLP-1-bound cryo-EM structure². Van der Waals interactions are also formed between ExP5 and residues in TM1 and TM7 (Fig. 2a, Extended Data Table 2). In addition, two key electrostatic interactions are formed by R299^{ECL2} in ECL2 and R380^{7.35} at the top of the TM7–ECL3 boundary with E16 and D10 of ExP5, respectively (Fig. 2a). These two residues also formed direct interactions with the 11-mer peptide agonist in the GLP-1R X-ray structure, interacting with a serine at position 8 (R299^{ECL2}) and an aspartic acid at position 9 (R380^{7.35})¹⁵. D9 in the 11-mer is the equivalent of D10 in ExP5 and D15 in native GLP-1. An interaction between GLP-1 D15 and R380^{7.35} has also been predicted by molecular dynamics simulations¹⁷ and mutagenesis²³, but was not reported in the GLP-1-bound GLP-1R structure². However, side chain densities were poorly resolved in this region of the deposited GLP-1–GLP-1R map; alternative modelling can preserve this interaction and therefore it is likely to be conserved across the three ligands for which structures are now available.

accumulation following mutagenesis of key ExP5 residues that form interactions (highlighted in **a**) in the refined model supports the role of these residues in ExP5 interactions. cAMP signalling was assessed in CHOFlpIn cells and data are means + s.e.m. of four independent experiments performed in duplicate.

The GLP-1-bound GLP-1R cryo-EM structure also reported that R299^{ECL2} dips into the receptor core to form a direct interaction with H7 of GLP-1². This modelling into the cryo-EM map is also ambiguous and contains an alternate positioning of W306^{5.36} (required for R299^{ECL2} to reach into the bundle) to the ExP5-bound and 11-mer-bound GLP-1R structures¹⁵. Because this positioning of W306^{5.36} is not supported by density, and the described interaction of R299^{ECL2} is highly energetically unfavourable, we hypothesize that W306^{5.36} is more likely to reside in a similar orientation to that observed in the ExP5- and 11-mer-bound structures, supported by good density in these maps. This orientation would promote interactions of R299^{ECL2} with GLP-1 higher up in the peptide.

Owing to the limited density available to define GLP-1 interactions in the GLP-1-bound GLP-1R cryo-EM map, it is difficult to assess direct differences in peptide interactions between the GLP-1- and ExP5-bound structures by relying on the structures alone. Nonetheless, alanine mutation of residues lining the ExP5-binding pocket (highlighted in Fig. 2c, Extended Data Table 1) confirmed a likely overlap of GLP-1R residues involved in interactions with GLP-1 and ExP5, with previous publications highlighting the importance of Y205^{2.75}, R299^{ECL2}, N300^{ECL2}, R380^{7.35} and R310^{5.40} in GLP-1 affinity and signalling^{1,17,20,21}, and our results confirming their importance for ExP5 binding (Fig. 2). The nature of these interactions is likely to differ, owing to the variations in peptide sequence and consequent receptor interactions, as highlighted by the TM1, TM7 and ECL3 mutagenesis in this study.

Class B GPCRs contain a number of highly conserved transmembrane polar residues that participate in key hydrogen bond interactions for receptor integrity and maintenance of the apo state. A central polar network formed by residues R^{2.60}, N^{3.43}, H^{6.52} and Q^{7.49} is located just below the peptide binding site in the ExP5-bound structure^{24,25} (Extended Data Fig. 6). Two highly conserved class B GPCR polar networks (TM2–TM3–TM6–TM7: H^{2.50}, E^{3.50}, T^{6.42}, Y^{7.57} and TM2–TM6–TM7–H8: R^{2.46}, R/K^{6.37}, N^{7.61}, E^{8.41}) at the cytoplasmic face lock the base of the receptor in an inactive conformation^{21,25}. Located between the central hydrogen bond network and the TM2–TM3–TM6–TM7 network is a cluster of conserved residues that form

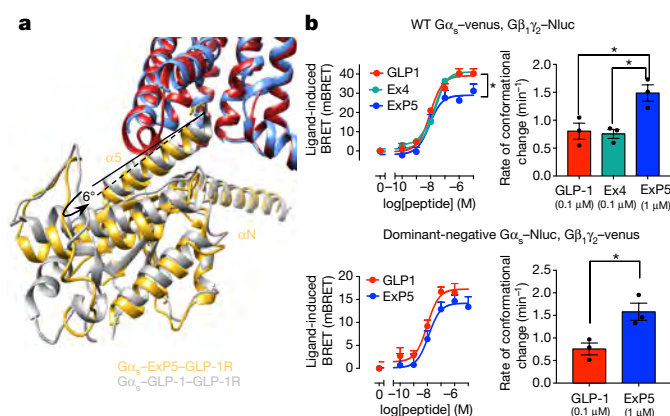


Figure 3 | Comparison of GLP-1R-mediated G protein conformation in GLP-1-bound and ExP5-bound receptors. **a**, Superimposition of the GLP-1R bundle bound by GLP-1 and by ExP5 reveals distinct angles of $G\alpha_s$ $\alpha 5$ engagement (6° measured using pisco). **b**, Top, BRET measurements show distinct conformational rearrangements between the $G\alpha_s$ α -helical domain and $G\gamma$ when the GLP-1R is activated by ExP5, relative to activation by GLP-1 or exendin-4. This is associated with a faster rate of rearrangement at equi-occupant ligand concentrations. Bottom, similar differences are observed with the dominant-negative $G\alpha_s$. Data are means \pm s.e.m. (left panels) or mean \pm s.e.m. (right panels) of three independent experiments performed in triplicate. * $P < 0.05$ by one-way analysis of variance followed by Tukey's multiple comparisons post-test.

hydrophobic packing interactions in the inactive state, stabilizing the TM6 P^{6.47}XXG^{6.50} motif in an inactive conformation (Extended Data Fig. 6). Upon peptide binding, a reorganization of the GLP-1R central hydrogen bond network is associated with destabilization within TM6 around the P^{6.47}XXG^{6.50} motif and a major rearrangement of the central hydrophobic network to form a new packing arrangement that stabilizes the active state (Extended Data Fig. 6, Supplementary Video 1). These major rearrangements break two hydrogen bond networks at the bottom of the receptor, facilitating movement of TM6 away from the transmembrane bundle to create a cavity for G protein binding (Extended Data Figs 6, 7b–d, Supplementary Video 1). Y^{7.57} and H^{2.50} are released from their ground state constraints and reorganize to form part of the hydrophobic network that stabilizes the active state. E^{3.50} maintains a hydrogen bond interaction with H^{2.50}, further stabilizing this active conformation.

The GLP-1R active conformation is stabilized by extensive interactions with the $G\alpha_s$ heterotrimeric protein (Extended Data Fig. 7). The receptor– $G\alpha_s$ heterotrimer interface is formed by residues located in TM2, TM3, TM5, TM6, TM7, ICL1, ICL2, ICL3 and H8 of the GLP-1R, and the $\alpha 5$ and αN regions of $G\alpha_s$ and $G\beta$ (Extended Data Table 3).

H8 in all active structures is amphipathic, with bulky aromatic residues on the membrane-proximal face heavily buried in the detergent micelle. Direct interactions of H8 and ICL1 with $G\beta$ are conserved across class B GPCR G protein structures^{2,9} (Extended Data Fig. 7e) and these are summarized in Extended Data Table 3. Though the importance of these interactions for the GLP-1R is unclear, truncation of H8 in the CTR reduced receptor expression and peptide-mediated cAMP efficacy, suggesting that receptor– $G\beta$ interactions are important for class B GPCR function⁹.

In all structures, the most extensive G protein contacts are formed by the $\alpha 5$ helix of the $G\alpha_s$ Ras-like domain, which inserts into the central GLP-1R transmembrane bundle cytoplasmic cavity formed by the 15 Å outward movement of TM6 (Extended Data Fig. 7). These contacts consist of both polar and hydrophobic Van der Waals interactions and there is, generally, a common interaction pattern between $G\alpha_s$ and the available active class B GPCRs (Extended Data Table 3).

Superimposition of the G proteins of the GLP-1- and ExP5-bound GLP-1R structures reveals only relatively small differences in the

receptor-complexed $G\alpha_s$ Ras and $G\beta\gamma$ domains (Extended Data Fig. 7f). The largest change was a 4 Å variance in the conformation of the $G\alpha_s$ αN domain at its N terminus, which may reflect a ligand-dependent difference in conformation.

Superimposition of the transmembrane domains of the GLP-1- and ExP5-bound structures reveals that, although there are limited differences in the overall $G\alpha_s$ Ras and $G\beta\gamma$ conformations, there is a six-degree variance in the angle at which the $G\alpha_s$ $\alpha 5$ helix engages in the GLP-1R cytoplasmic cavity. This results in an overall rotation of the G protein in the ExP5-bound structure relative to the GLP-1-bound structure (Fig. 3a, Extended Data Fig. 7f). Notably, when ExP5 is bound to the GLP-1R, the $\alpha 4$ helix and $\beta 3$ strand are located further from the receptor core, and no interactions are observed between the $\alpha 4$ helix and the GLP-1R intracellular face, whereas there are potential contacts for the GLP-1-bound structure². In addition, the αN – $\beta 3$ loop of $G\alpha_s$ is located further from ICL2 of the GLP-1R in the ExP5-bound structure; although these side chains are still within bonding distance, their interactions are likely to be weaker than those induced by GLP-1 binding. Notably, there was only very limited density within the backbone for residues in the bottom of TM5–ICL3 (residues 337–343) in the ExP5-bound structure, such that this region is not visible in high-resolution maps, whereas this backbone density was clearly visible for the GLP-1-bound structure (Extended Data Fig. 5d). This suggests that ICL3 of the GLP-1R is less flexible in the GLP-1- and G protein-bound state than in the ExP5- and G protein-bound state.

There are multiple lines of evidence that differences in ligand–receptor conformation propagate to G protein conformation^{26,27}. Direct assessment of conformational rearrangement between $G\alpha_s$ and $G\gamma$, using a bioluminescence resonance energy transfer (BRET) assay, revealed that ExP5 promotes a faster conformational change within $G\alpha_s$ than do GLP-1 or exendin-4 at equi-occupant concentrations, accompanied by a lower BRET maximal signal (E_{\max}) at saturating concentrations of peptide (Fig. 3b). Together with the structural data, these results are consistent with the distinct flexibilities of the bottom of TM5 and within ICL3 altering the conformational positioning of the $G\alpha_s$ α -helical domain and increasing the rate of G protein activation. Collectively, this may contribute to the enhanced $G\alpha_s$ protein-mediated efficacy of ExP5 that is a key element of its biased agonism.

In conclusion, the structure of the ExP5–GLP-1R– $G\alpha_s$ complex provides insights into the structural reorganization of class B GPCRs upon peptide activation, as well as the distinct engagement of GLP-1R agonists with differential signalling bias. Our results highlight that even when ligands share a common G protein transducer, differences in the mode of G protein binding can have consequences for conformational changes in the G protein that are linked to activation. The findings increase our understanding of biased agonism and may contribute to the rational design of novel therapeutics that target the GLP-1R.

Online Content Methods, along with any additional Extended Data display items and Source Data, are available in the online version of the paper; references unique to these sections appear only in the online paper.

Received 22 September 2017; accepted 17 January 2018.

Published online 21 February 2018.

- de Graaf, C. *et al.* Glucagon-like peptide-1 and its class B G protein-coupled receptors: a long march to therapeutic successes. *Pharmacol. Rev.* **68**, 954–1013 (2016).
- Zhang, Y. *et al.* Cryo-EM structure of the activated GLP-1 receptor in complex with a G protein. *Nature* **546**, 248–253 (2017).
- Hager, M. V., Clydesdale, L., Gellman, S. H., Sexton, P. M. & Wootten, D. Characterization of signal bias at the GLP-1 receptor induced by backbone modification of GLP-1. *Biochem. Pharmacol.* **136**, 99–108 (2017).
- Koole, C. *et al.* Allosteric ligands of the glucagon-like peptide 1 receptor (GLP-1R) differentially modulate endogenous and exogenous peptide responses in a pathway-selective manner: implications for drug screening. *Mol. Pharmacol.* **78**, 456–465 (2010).
- Wootten, D. *et al.* Differential activation and modulation of the glucagon-like peptide-1 receptor by small molecule ligands. *Mol. Pharmacol.* **83**, 822–834 (2013).
- Zhang, H. *et al.* Autocrine selection of a GLP-1R G-protein biased agonist with potent antidiabetic effects. *Nat. Commun.* **6**, 8918 (2015).

7. Mann, R. *et al.* Peptide binding at the GLP-1 receptor. *Biochem. Soc. Trans.* **35**, 713–716 (2007).
8. Manandhar, B. & Ahn, J. M. Glucagon-like peptide-1 (GLP-1) analogs: recent advances, new possibilities, and therapeutic implications. *J. Med. Chem.* **58**, 1020–1037 (2015).
9. Liang, Y. L. *et al.* Phase-plate cryo-EM structure of a class B GPCR–G-protein complex. *Nature* **546**, 118–123 (2017).
10. Danev, R., Buijsse, B., Khoshouei, M., Plitzko, J. M. & Baumeister, W. Volta potential phase plate for in-focus phase contrast transmission electron microscopy. *Proc. Natl Acad. Sci. USA* **111**, 15635–15640 (2014).
11. Khoshouei, M., Radjainia, M., Baumeister, W. & Danev, R. Cryo-EM structure of haemoglobin at 3.2 Å determined with the Volta phase plate. *Nat. Commun.* **8**, 16099 (2017).
12. Khoshouei, M. *et al.* Volta phase plate cryo-EM of the small protein complex Prx3. *Nat. Commun.* **7**, 10534 (2016).
13. Siu, F. Y. *et al.* Structure of the human glucagon class B G-protein-coupled receptor. *Nature* **499**, 444–449 (2013).
14. Hollenstein, K. *et al.* Structure of class B GPCR corticotropin-releasing factor receptor 1. *Nature* **499**, 438–443 (2013).
15. Jazayeri, A. *et al.* Crystal structure of the GLP-1 receptor bound to a peptide agonist. *Nature* **546**, 254–258 (2017).
16. Runge, S., Thøgersen, H., Madsen, K., Lau, J. & Rudolph, R. Crystal structure of the ligand-bound glucagon-like peptide-1 receptor extracellular domain. *J. Biol. Chem.* **283**, 11340–11347 (2008).
17. Wootten, D. *et al.* The extracellular surface of the GLP-1 receptor is a molecular trigger for biased agonism. *Cell* **165**, 1632–1643 (2016).
18. Coopman, K. *et al.* Residues within the transmembrane domain of the glucagon-like peptide-1 receptor involved in ligand binding and receptor activation: modelling the ligand-bound receptor. *Mol. Endocrinol.* **25**, 1804–1818 (2011).
19. Dods, R. L. & Donnelly, D. The peptide agonist-binding site of the glucagon-like peptide-1 (GLP-1) receptor based on site-directed mutagenesis and knowledge-based modelling. *Biosci. Rep.* **36**, e00285 (2015).
20. Koole, C. *et al.* Second extracellular loop of human glucagon-like peptide-1 receptor (GLP-1R) has a critical role in GLP-1 peptide binding and receptor activation. *J. Biol. Chem.* **287**, 3642–3658 (2012).
21. Wootten, D. *et al.* Key interactions by conserved polar amino acids located at the transmembrane helical boundaries in class B GPCRs modulate activation, effector specificity and biased signalling in the glucagon-like peptide-1 receptor. *Biochem. Pharmacol.* **118**, 68–87 (2016).
22. Yang, D. *et al.* Structural determinants of binding the seven-transmembrane domain of the glucagon-like peptide-1 receptor (GLP-1R). *J. Biol. Chem.* **291**, 12991–13004 (2016).
23. Moon, M. J. *et al.* Ligand binding pocket formed by evolutionarily conserved residues in the glucagon-like peptide-1 (GLP-1) receptor core domain. *J. Biol. Chem.* **290**, 5696–5706 (2015).
24. Wootten, D. *et al.* A hydrogen-bonded polar network in the core of the glucagon-like peptide-1 receptor is a fulcrum for biased agonism: lessons from class B crystal structures. *Mol. Pharmacol.* **89**, 335–347 (2016).
25. Wootten, D., Simms, J., Miller, L. J., Christopoulos, A. & Sexton, P. M. Polar transmembrane interactions drive formation of ligand-specific and signal pathway-biased family B G protein-coupled receptor conformations. *Proc. Natl Acad. Sci. USA* **110**, 5211–5216 (2013).
26. Furness, S. G. B. *et al.* Ligand-dependent modulation of G protein conformation alters drug efficacy. *Cell* **167**, 739–749.e11 (2016).
27. Gregorio, G. G. *et al.* Single-molecule analysis of ligand efficacy in β 2AR-G-protein activation. *Nature* **547**, 68–73 (2017).

Supplementary Information is available in the online version of the paper.

Acknowledgements The work was supported by the Monash University Ramaciotti Centre for Cryo-Electron Microscopy, the National Health and Medical Research Council of Australia (NHMRC) project grants (1061044, 1065410, 1120919 and 1126857), NHMRC program grant (1055134), Strategic Priority Research Program of the Chinese Academy of Sciences (XDA12020347) and Shanghai Science and Technology Development Fund (15DZ2291600). P.M.S., A.C., D.W. and C.K. are NHMRC Principal Research, Senior Principal Research, Career Development and CJ Martin Fellows, respectively. S.L. received the Postgraduate Overseas Study Fellowship from CAS. We thank J. Plitzko, G. Christopoulos, V. Julita, J. Michaelis, X. Zhang, P. Thompson and M. Liu for assay and technical support and B. Kobilka for technical advice and comments on the manuscript.

Author Contributions Y.-L.L. established the GLP-1R complex expression and purification strategy, expressed and purified the complex, and performed negative stain EM and data acquisition/analysis; Y.-L.L. and M.R. performed preliminary cryo-EM screening; M.K. performed cryo-sample preparation and phase plate imaging to acquire EM data and performed EM map calculations; A.G. built the model and performed refinement; A.G., C.K. and D.M.T. performed pharmacological assays; L.C., T.T.T. and S.L. performed the mutagenesis studies; S.G.B.F. and P.Z. designed and performed the G protein BRET assays; R.D. and W.B. organized and developed the Volta phase plate cryo-EM data acquisition strategy; Y.-L.L., M.K., A.G., S.G.B.F., P.Z., L.C., C.K., D.M.T., T.T.T., S.L., A.C., P.M.S. and D.W. performed data analysis; S.G.B.F., P.Z., C.K., A.C., L.J.M., M.-W.W. and A.C. assisted with data interpretation and preparation of the manuscript; Y.-L.L., M.K., A.G., P.M.S. and D.W. interpreted data and wrote the manuscript; P.M.S. and D.W. supervised the project.

Author Information Reprints and permissions information is available at www.nature.com/reprints. The authors declare no competing financial interests. Readers are welcome to comment on the online version of the paper. Publisher's note: Springer Nature remains neutral with regard to jurisdictional claims in published maps and institutional affiliations. Correspondence and requests for materials should be addressed to D.W. (denise.wootten@monash.edu) and P.M.S. (Patrick.sexton@monash.edu).

Reviewer Information *Nature* thanks R. Glaeser, F. Marshall and J. Mayer for their contribution to the peer review of this work.

METHODS

Constructs. The human GLP-1R was unmodified with the exception of replacing the native signal peptide with that of haemagglutinin (HA) to enhance receptor expression and the addition of affinity tags (an N-terminal Flag tag epitope and a C-terminal 8× His tag); both tags are removable by 3C protease cleavage. The construct was generated in both mammalian and insect cell expression vectors. These modifications did not alter receptor pharmacology (Extended Data Fig. 1b). A dominant-negative G_{α_s} (DNG α_s) construct was generated by site-directed mutagenesis to incorporate mutations that alter nucleotide handling (S54N²⁸ and G226A²⁹), stabilize the G_0 state (E268A³⁰) and substitute residues from $G_{\alpha_{i2}}$ (N271K, K274D, R280K, T284D and I285T^{31,32}) that are reported to improve the dominant-negative effect, presumably by stabilizing interactions with the $\beta\gamma$ subunits.

Insect cell expression. Human GLP-1R, human DNG α_s , and His₆-tagged human $G\beta_1$ and $G\gamma_2$ were expressed in Tni insect cells (Expression systems) using baculovirus. Cell cultures were grown in ESF 921 serum-free medium (Expression Systems) to a density of 4 million cells per ml and then infected with three separate baculoviruses at a ratio of 2:2:1 for GLP-1R, DNG α_s and $G\beta_1\gamma_2$. The culture was collected by centrifugation 60 h after infection and cell pellets were stored at -80°C .

Complex purification. Cell pellets were thawed in 20 mM HEPES pH 7.4, 50 mM NaCl, 2 mM MgCl₂ supplemented with cOmplete Protease Inhibitor Cocktail tablets (Roche). Complex formation was initiated by addition of 1 μM Exp5 (China Peptides), Nb35-His (10 $\mu\text{g}/\text{ml}$) and apyrase (25 mU/ml , NEB); the suspension was incubated for 1 h at room temperature. Membranes were collected by centrifugation at 30,000g for 30 min, and complex was solubilized from membrane using 0.5% (w/v) lauryl maltose neopentyl glycol (LMNG, Anatrace) supplemented with 0.03% (w/v) cholesteryl hemisuccinate (CHS, Anatrace) for 2 h at 4°C in the presence of 1 μM Exp5 and apyrase (25 mU/ml , NEB). Insoluble material was removed by centrifugation at 30,000g for 30 min and the solubilized complex was immobilized by batch binding to M1 anti-Flag affinity resin in the presence of 3 mM CaCl₂. The resin was packed into a glass column and washed with 20 column volumes of 20 mM HEPES pH 7.4, 100 mM NaCl, 2 mM MgCl₂, 3 mM CaCl₂, 1 μM Exp5, 0.01% (w/v) LMNG and 0.006% (w/v) CHS before bound material was eluted in buffer containing 5 mM EGTA and 0.1 mg/ml FLAG peptide. The complex was then concentrated using an Amicon Ultra Centrifugal Filter (MWCO, 100 kDa) and subjected to size-exclusion chromatography on a Superdex 200 Increase 10/300 column (GE Healthcare) that was pre-equilibrated with 20 mM HEPES pH 7.4, 100 mM NaCl, 2 mM MgCl₂, 1 μM Exp5, 0.01% (w/v) MNG and 0.006% (w/v) CHS to separate complex from contaminants. Eluted fractions consisting of receptor and G-protein complex were pooled and concentrated. The final yield of purified complex was approximately 0.2 mg per litre of insect cell culture.

SDS-PAGE and western blot analysis. Samples collected from size-exclusion chromatography were analysed by SDS-PAGE and western blot. For SDS-PAGE, precast gradient TGX gels (Bio-Rad) were used. Gels were either stained by Instant Blue (Expedeon) or immediately transferred to PVDF membrane (Bio-Rad) at 100 V for 1 h. The proteins on the PVDF membrane were probed with two primary antibodies, rabbit anti- G_{α_s} C-18 antibody (cat. no. sc-383, Santa Cruz) against the G_{α_s} subunit and mouse penta-His antibody (cat. no. 34660, QIAGEN) against His tags. The membrane was washed and incubated with secondary antibodies (680RD goat anti-mouse and 800CW goat anti-rabbit, LI-COR). Bands were imaged using an infrared imaging system (LI-COR Odyssey Imaging System).

Preparation of vitrified specimen. EM grids (Quantifoil, 200 mesh copper R1.2/1.3) were glow discharged for 30 s in high pressure air using Harrick plasma cleaner. Four microlitres of sample at 1.3 mg/ml was applied to the grid in the Vitrobot chamber (FEI Vitrobot Mark IV). The Vitrobot chamber was set to 100% humidity at 4°C . The sample was blotted for 5 s with a blot force of 20 and then plunged into propane-ethane mixture (37% ethane and 63% propane).

Data acquisition. Data were collected on a Titan Krios microscope operated at 300 kV (Thermo Fisher Scientific equipped with a Gatan Quantum energy filter, a Gatan K2 summit direct electron detector (Gatan) and a Volta phase plate (Thermo Fisher Scientific)). Videos were recorded in EFTEM nanoprobes mode, with 50- μm C2 aperture, at a calibrated magnification of 47,170 corresponding to a magnified pixel size of 1.06 Å. Each video comprised 50 frames with a total dose of $50\text{ e}^-/\text{Å}^2$ and exposure time was 8 s with a dose rate of 7 e^- per pixel per s on the detector. Data acquisition was done using SerialEM software at -500 nm defocus³³.

Data processing. We collected 2,793 movies and subjected them to motion correction using motioncor2³⁴. Contrast transfer function (CTF) estimation was done using Gctf software³⁵ on the non-dose-weighted micrographs. The particles were picked using gautomatch (developed by K. Zhang, MRC Laboratory of Molecular Biology, Cambridge, UK; <http://www.mrc-lmb.cam.ac.uk/kzhang/Gautomatch/>). An initial model was made using EMAN2³⁶ based on a few automatically picked micrographs and using the common-line approach. The particles were extracted in RELION 2.03³⁷ using a box size of 200 pixels. Picked particles (614,883) were

subjected to 3D classification with 5 classes. Particles (190,135) from the best-looking class were subjected to 3D auto-refinement in RELION 2.03. The refined particles were subjected to another run of 3D classification with 5 classes and without alignments, after which 184,672 particles were chosen for a final run of 3D auto-refinement in RELION 2.03. The final map was sharpened with a B -factor of -50 Å . Local resolution was determined using RELION³⁷ with half-reconstructions as input maps. The cryo-EM data collection, refinement and validation statistics are reported in Supplementary Table 1.

Modelling. The initial template for GLP-1R transmembrane regions, G protein and Nb35 was derived from rabbit GLP-1R in complex with G_{α_s} (PDB-5VAI)² followed by extensive remodelling using COOT³⁸. The ECL3 loop residues 372–376 were stubbed owing to insufficient density for unambiguous modelling, and no high-resolution density was present for ICL3 residues N338–T343, which were omitted from the deposited structure. Owing to discontinuous and/or variable density in the GLP-1R ECD region, we used the high-resolution X-ray crystal structure of the GLP-1R ECD–exendin(9–39) (PDB-3C5T)¹⁶ for a rigid body fit with limited manual adjustments. The Exp5 peptide was modelled manually. The final model was subjected to global refinement and minimization in real space using the module ‘phenix.real_space_refine’ in PHENIX³⁹. Validation was performed in MolProbity⁴⁰.

Insect cell membrane preparations. Crude membrane preparations were prepared from insect cells produced using the same expression conditions as used for cryo-EM samples. Cells were resuspended in buffer (20 mM HEPES 7.4, 50 mM NaCl, 2 mM MgCl₂, with protease inhibitors and benzonase) and dounced 20 times with the tight pestle, followed by centrifugation (10 min, 350g, 4°C). The pellet was resuspended in buffer, dounced and clarified by centrifugation at a low g . Membranes were pelleted by centrifugation (1 h, 40,000g, 4°C), resuspended in buffer and sonicated. Protein concentration was determined using Bradford reagent (Bio-Rad).

[³⁵S]GTP- γ S binding. Measurement of [³⁵S]GTP- γ S incorporation was performed in 20 mM HEPES pH 7.4; 100 mM NaCl; 10 mM MgCl₂; 1 mM EDTA; 0.1% (w/v) BSA; 30 $\mu\text{g}/\text{ml}$ saponin. Membranes (50 μg per sample) were pre-incubated with 1 μM GDP and increasing concentrations of ligand for 30 min at 22°C . Reactions were started by the addition of [³⁵S]GTP- γ S and ATP (final concentrations: 300 pM and 50 μM , respectively). After 1 h incubation at 30°C , the reaction was terminated by collecting the membranes on Whatman UniFilter GF/C plates using Filtermate 196 harvester (Packard). Membranes were extensively washed with ice-cold 50 mM Tris pH 7.6, 10 mM MgCl₂, 100 mM NaCl, dried, dissolved in 40 μl MicroScint-O scintillation cocktail (Packard) and counted using a MicroBeta LumijET counter (PerkinElmer). Data from each experiment were normalized to the response of GLP-1R-WTG α_s - $G\beta_1\gamma_2$ membranes at 1 μM GLP-1 (100%).

Radioligand competition binding experiments on insect cell membranes. Radioligand binding was performed in 20 mM HEPES, pH 7.4, 100 mM NaCl, 10 mM MgCl₂ and 0.1% (w/v) BSA. Competition binding assays with GLP-1 and Exp5 were performed in the presence of 50 pM [¹²⁵I]-exendin(9–39). Binding reactions were initiated with the addition of 4 μg of GLP-1R-expressing membranes (with or without G protein) followed by 1 h incubation at 30°C . Membranes were collected on UniFilter GF/C (Whatman) plates using a Filtermate 196 harvester (Packard), extensively washed with ice-cold NaCl, dried, dissolved in 40 μl of MicroScint-O scintillation cocktail (Packard), and counted using a MicroBeta LumijET counter (PerkinElmer). Data from each experiment were normalized to vehicle control and non-specific binding (1 μM exendin(9–39)). Curves were fit to a one- or two-site competition binding equation in Prism 6.0 (GraphPad).

Generation of mutant receptor constructs in mammalian cell lines. Mutant receptors were generated in a $2\times$ c-Myc epitope-tagged receptor in the pEF5/FRT/V5-DEST vector using QuikChange site-directed mutagenesis (Invitrogen) and sequences confirmed. Mutant receptors were stably expressed in CHOFlpIn cells using the FlpIn Gateway technology system (Invitrogen) and selected using 600 $\mu\text{g}/\text{ml}$ hygromycin B. All cells were tested and found to be free from mycoplasma contamination.

Mammalian whole-cell radioligand binding assays. Cells were seeded at a density of 30,000 cells per well into 96-well culture plates and incubated overnight in DMEM containing 5% FBS at 37°C in 5% CO₂. Growth medium was replaced with binding buffer (DMEM containing 25 mM HEPES and 0.1% (w/v) BSA) containing 0.1 nM [¹²⁵I]-exendin(9–39) and increasing concentrations of unlabelled peptide agonists. Cells were incubated overnight at 4°C , followed by three washes in ice cold $1\times$ PBS to remove unbound radioligand. Cells were then solubilized in 0.1 M NaOH, and radioactivity determined by gamma counting. For all experiments, nonspecific binding was defined by 1 μM exendin(9–39).

Mammalian cAMP assays. Cells were seeded at a density of 30,000 cells per well into 96-well culture plates and incubated overnight in DMEM containing 5% FBS at 37°C in 5% CO₂. cAMP detection was performed as previously described³. All values were converted to cAMP concentration using a cAMP standard curve

performed in parallel and data were subsequently normalized to the response of 100 μ M forskolin in each cell line.

β -Arrestin recruitment assay. Cells stably expressing GLP-1R–Rluc8 and β -arrestin1–venus were seeded at a density of 30,000 cells per well into 96-well culture plates and incubated overnight in DMEM containing 5% FBS at 37 °C in 5% CO₂. β -Arrestin recruitment was performed as previously described⁴¹.

Mammalian cell membrane preparations for G protein BRET assays. HEK293A Δ S–GLP-1R cells were transfected with G α_s –venus (inserted at position 72 of G α_s with a GSSSSG linker) or dominant-negative G α_s –nanoluc (inserted at position 72 of G α_s with a GSSSSG linker), G β_1 and G γ_2 –nanoluc or G γ_2 –venus (inserted at the N terminus of G γ_2 with a GSAGT linker) at a 1:1:1 ratio using PEI. Cell membranes were prepared as described previously²⁶ and stored at –80 °C. Twenty-four hours after transfection, cells were collected with membrane preparation buffer (20 mM BisTris, pH 7.4, 50 mM NaCl, 1 mM MgCl₂, 1 \times P8340 protease inhibitor cocktail (Sigma–Aldrich), 1 mM DTT and 0.1 mM PMSF). Cells were then homogenized, applied to a stepped sucrose gradient (60%, 40%, homogenate) and centrifuged at 22,500 r.p.m. for 2.5 h at 4 °C. The layers between 40% and homogenate were collected, diluted in membrane preparation buffer and centrifuged at 30,000 r.p.m. for 30 min at 4 °C. The final pellet was resuspended in membrane preparation buffer, and stored at –80 °C. Total protein concentration was determined using a NanoDrop.

G protein conformational determination using BRET. HEK293A Δ S cells stably expressing the GLP-1R (tested and confirmed to be free from mycoplasma) were transfected with a 1:1:1 ratio of G γ_2 :nanoluc–G α_s :72:venus–G β_1 or G γ_2 :venus–dominant-negative G α_s :72:nanoluc–G β_1 24 h before collection and preparation of cell plasma membranes (above). Five micrograms per well of cell membrane was incubated with furimazine (1:1,000 dilution from stock) in assay buffer (1 \times HBSS, 10 mM HEPES, 0.1% (w/v) BSA, 1 \times P8340 protease inhibitor cocktail, 1 mM DTT and 0.1 mM PMSF, pH 7.4). The GLP-1R-induced BRET signal between G α_s and G γ was measured at 30 °C using a PHERAstar (BMG LabTech). Baseline BRET measurements were taken for 2 min before addition of vehicle or ligand. BRET was measured at 15 s intervals for a further 7 min. All assays were performed in a final volume of 100 μ L.

Data analysis. Pharmacological data were analysed using Prism 7 (GraphPad). Concentration-dependent response signalling data were analysed as previously described²⁰ using a three-parameter logistic equation. Signalling bias was quantified by analysis of cAMP accumulation and β -arrestin1 recruitment concentration–response curves using an operational model of agonism modified to directly estimate the ratio of τ/K_A as described previously^{5,20,42}.

$$Y = \frac{E_{\max} \times (\tau_c/K_A)^n \times [A]^n}{[A]^n \times (\tau_c/K_A)^n + (1 + [A]/K_A)^n}$$

in which E_{\max} represents the maximal stimulation of the system, K_A is the agonist–receptor dissociation constant in molar concentration, $[A]$ is the molar concentration of ligand and τ is the operational measure of efficacy in the system, which incorporates signalling efficacy and receptor density. All estimated τ/K_A ratios included propagation of error for both τ and K_A . Changes in τ/K_A ratios with respect to GLP-1 for each novel peptide were used to quantify bias between signalling pathways. Accordingly, bias factors included propagation of error from the τ/K_A ratios of each pathway.

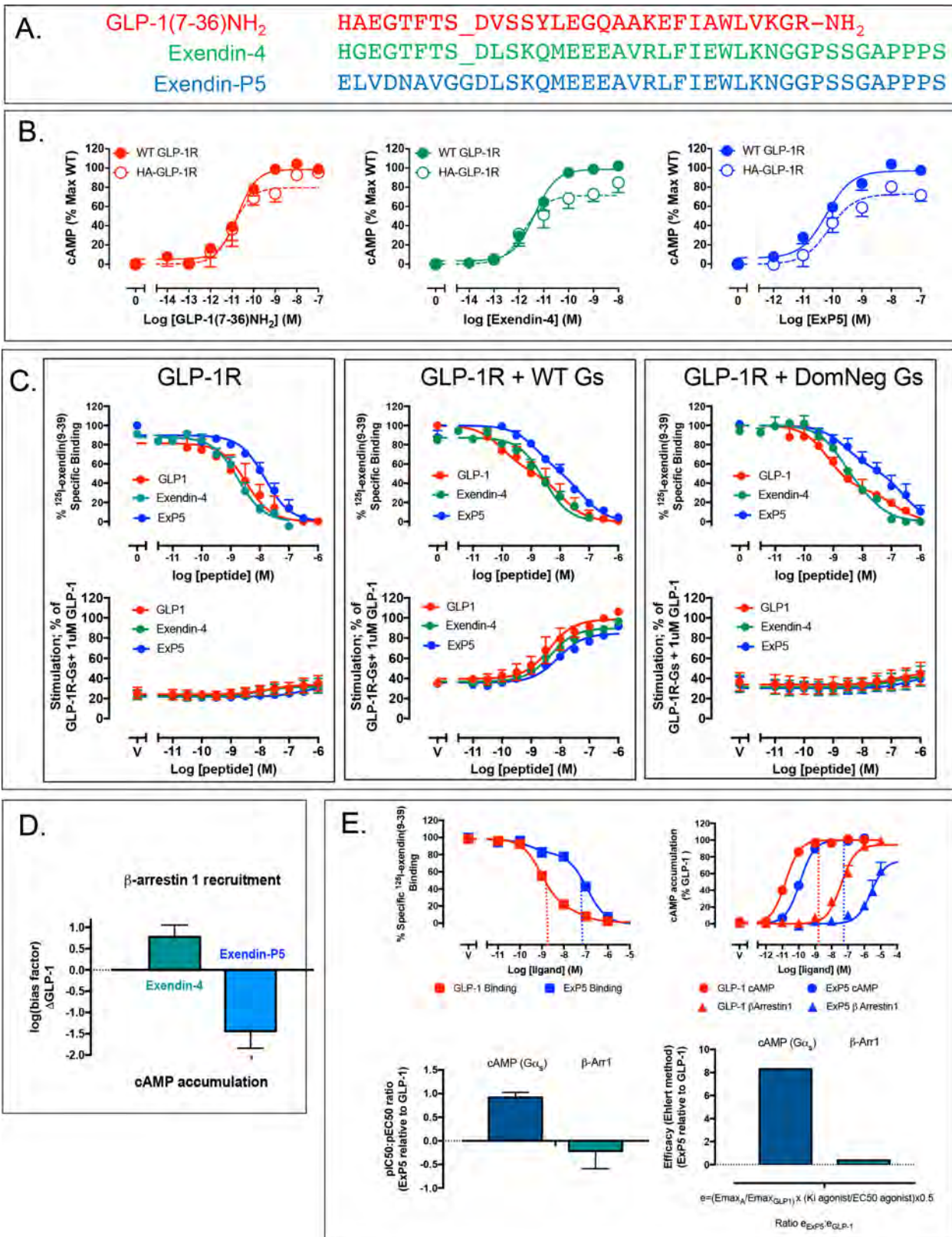
Changes in the rate of change in BRET signal were fitted to a one-phase association curve. Normalized AUC for the indicated ligand concentrations was plotted

as a concentration–response curve and fitted with a three-parameter logistic curve. Statistical analysis was performed with either one-way analysis of variance and a Tukey's post-test or a paired t -test, and significance accepted at $P < 0.05$.

Graphics. Molecular graphics images were produced using the UCSF Chimera package from the Computer Graphics Laboratory, University of California, San Francisco (supported by NIH P41 RR-01081)⁴³. Superposition of maps was performed in COOT using “transformation by LSQ model fit”³⁸. Measurements of GoRas α 5 movements between different structures was performed in Pymol using the psico python module.

Data availability. All relevant data are available from the authors and/or included in the manuscript or Supplementary Information. Atomic coordinates and the cryo-EM density map have been deposited in the Protein Data Bank (PDB) under accession number 6B3J and EMDB entry ID EMD-7039.

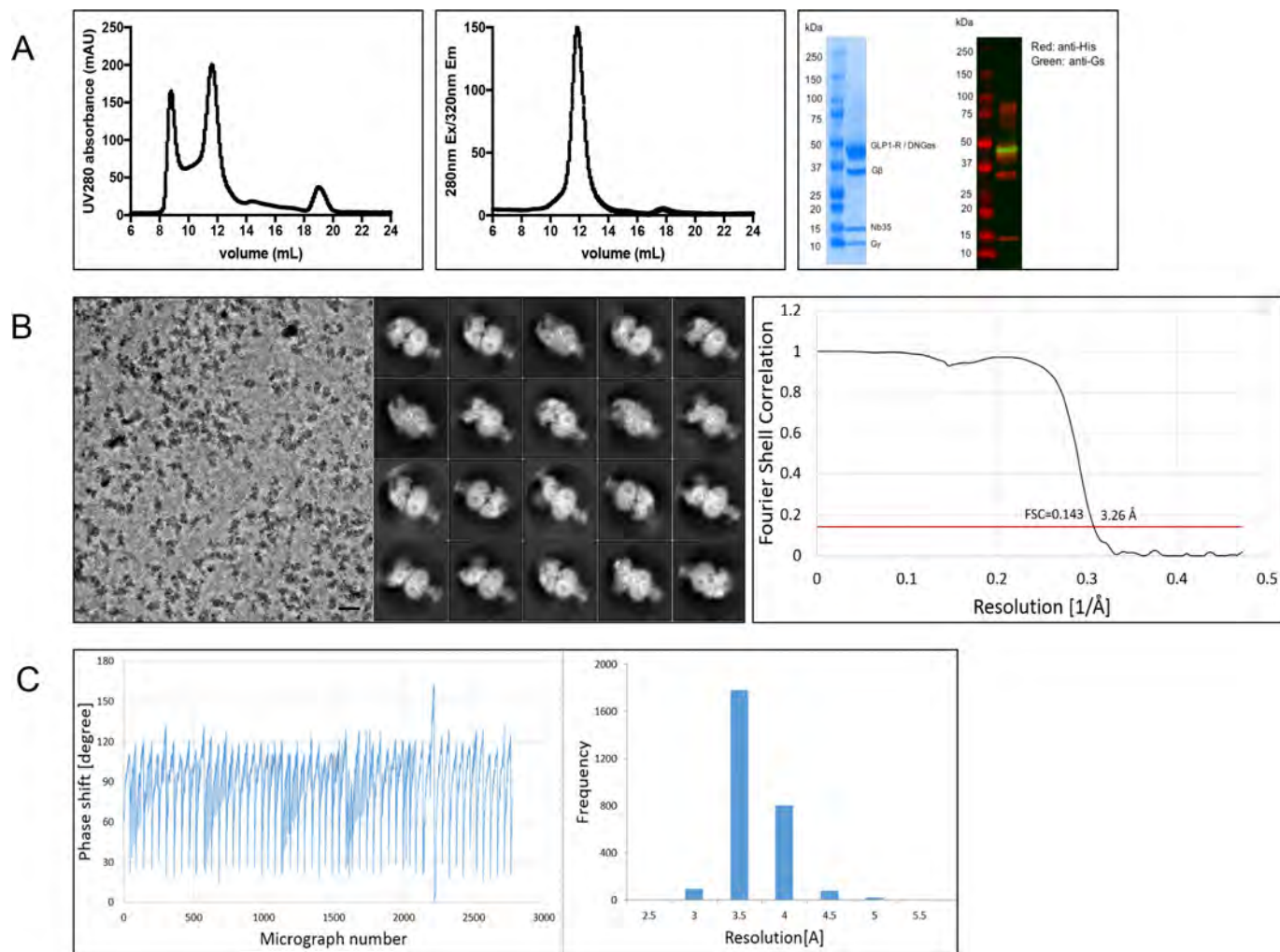
28. Cleator, J. H., Mehta, N. D., Kurtz, D. T. & Hildebrandt, J. D. The N54 mutant of G α_s has a conditional dominant negative phenotype which suppresses hormone-stimulated but not basal cAMP levels. *FEBS Lett.* **443**, 205–208 (1999).
29. Lee, E., Taussig, R. & Gilman, A. G. The G226A mutant of G α_s highlights the requirement for dissociation of G protein subunits. *J. Biol. Chem.* **267**, 1212–1218 (1992).
30. Iiri, T., Bell, S. M., Baranski, T. J., Fujita, T. & Bourne, H. R. A G α_s mutant designed to inhibit receptor signaling through Gs. *Proc. Natl Acad. Sci. USA* **96**, 499–504 (1999).
31. Berlot, C. H. A highly effective dominant negative α s construct containing mutations that affect distinct functions inhibits multiple Gs-coupled receptor signaling pathways. *J. Biol. Chem.* **277**, 21080–21085 (2002).
32. Berlot, C. H. & Bourne, H. R. Identification of effector-activating residues of G α_s . *Cell* **68**, 911–922 (1992).
33. Mastronarde, D. N. Automated electron microscope tomography using robust prediction of specimen movements. *J. Struct. Biol.* **152**, 36–51 (2005).
34. Zheng, S. Q. *et al.* MotionCor2: anisotropic correction of beam-induced motion for improved cryo-electron microscopy. *Nat. Methods* **14**, 331–332 (2017).
35. Zhang, K. Gctf: Real-time CTF determination and correction. *J. Struct. Biol.* **193**, 1–12 (2016).
36. Tang, G. *et al.* EMAN2: an extensible image processing suite for electron microscopy. *J. Struct. Biol.* **157**, 38–46 (2007).
37. Kimanius, D., Forsberg, B. O., Scheres, S. H. & Lindahl, E. Accelerated cryo-EM structure determination with parallelisation using GPUs in RELION-2. *eLife* **5**, e18722 (2016).
38. Emsley, P. & Cowtan, K. Coot: model-building tools for molecular graphics. *Acta Crystallogr. D* **60**, 2126–2132 (2004).
39. Adams, P. D. *et al.* PHENIX: a comprehensive Python-based system for macromolecular structure solution. *Acta Crystallogr. D* **66**, 213–221 (2010).
40. Chen, V. B. *et al.* MolProbity: all-atom structure validation for macromolecular crystallography. *Acta Crystallogr. D* **66**, 12–21 (2010).
41. Savage, E. E., Wooten, D., Christopoulos, A., Sexton, P. M. & Furness, S. G. A simple method to generate stable cell lines for the analysis of transient protein–protein interactions. *Biotechniques* **54**, 217–221 (2013).
42. Hager, M. V. J., Johnson, L. M., Wooten, D., Sexton, P. M. & Gellman, S. H. β -Arrestin-biased agonists of the GLP-1 receptor from β -amino acid residue incorporation into GLP-1 analogues. *J. Am. Chem. Soc.* **138**, 14970–14979 (2016).
43. Pettersen, E. F. *et al.* UCSF Chimera—a visualization system for exploratory research and analysis. *J. Comput. Chem.* **25**, 1605–1612 (2004).
44. Ehler, F. J. The relationship between muscarinic receptor occupancy and adenylate cyclase inhibition in the rabbit myocardium. *Mol. Pharmacol.* **28**, 410–421 (1985).



Extended Data Figure 1 | See next page for caption.

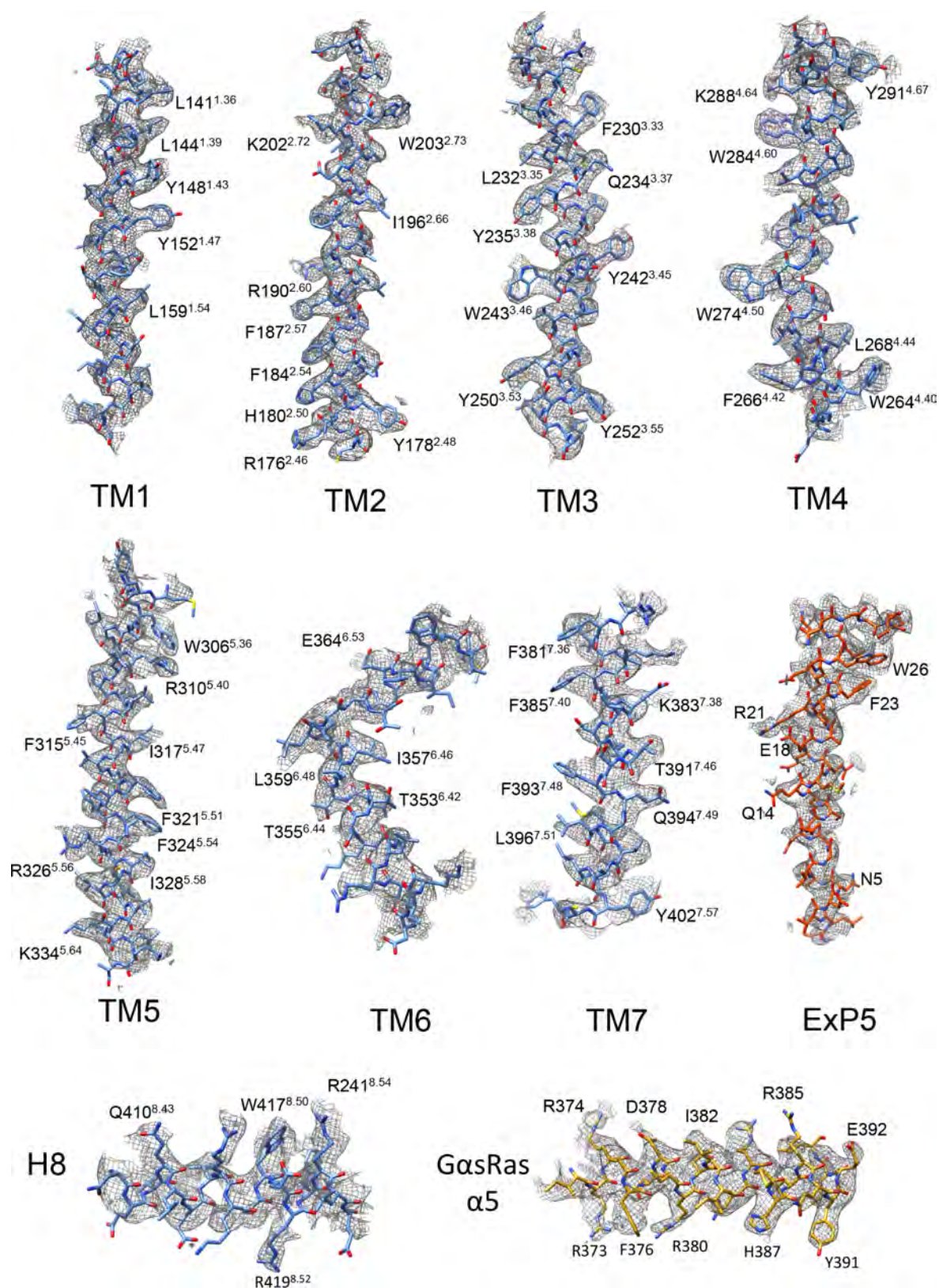
Extended Data Figure 1 | GLP-1R pharmacology. **a**, Peptide sequences. **b**, Pharmacology of untagged GLP-1R (WT GLP-1R) and the purification construct (HA-GLP-1R). **c**, Insect cell pharmacology of HA-GLP-1R. Top, radioligand competition binding. Bottom, GTP γ S binding. Left, no Gs protein. ExP5 has lower affinity than GLP-1 and exendin-4 and does not bind GTP γ S. Middle, wild-type Gs enhances peptide affinity and promotes GTP γ S binding. Right, dominant-negative Gs is similar to wild-type Gs in binding, but does not bind GTP γ S. **d**, Bias factors calculated from concentration–response curves using the Black and Leff operational model^{5,20,41} (see Methods) confirm that ExP5 is a biased agonist relative to GLP-1. **e**, Top left, pIC₅₀ of ExP5 is ~100-fold lower than of GLP-1 (CHOFlpIn whole cell). Top right, GLP-1 and ExP5 have β -arrestin1

coupling with pEC₅₀ ~30-fold to the right of their pIC₅₀ (dotted lines). ExP5 is more potent than GLP-1 in cAMP signalling (pEC₅₀ relative to pIC₅₀). Bottom left, pIC₅₀:pEC₅₀ ratios for G protein (cAMP) and β -arrestin1 of ExP5 relative to GLP-1 highlights ExP5 bias arises from enhanced Gs coupling, not reduced β -arrestin1 recruitment. Bottom right, ratio of ExP5 efficacy (calculated using the Ehlert method⁴⁴) relative to GLP-1 in cAMP and β -arrestin1 recruitment confirms that ExP5 bias arises from enhanced G α_s efficacy. Data in **b**, **c** are mean \pm s.e.m. of three (insect cells) or four (CHOFlpIn cells) independent experiments, conducted in duplicate or triplicate, respectively. Data in **d**, **e** are from 11 independent experiments performed in duplicate. * $P < 0.05$ by one-way analysis of variance and Dunnett's post-test.



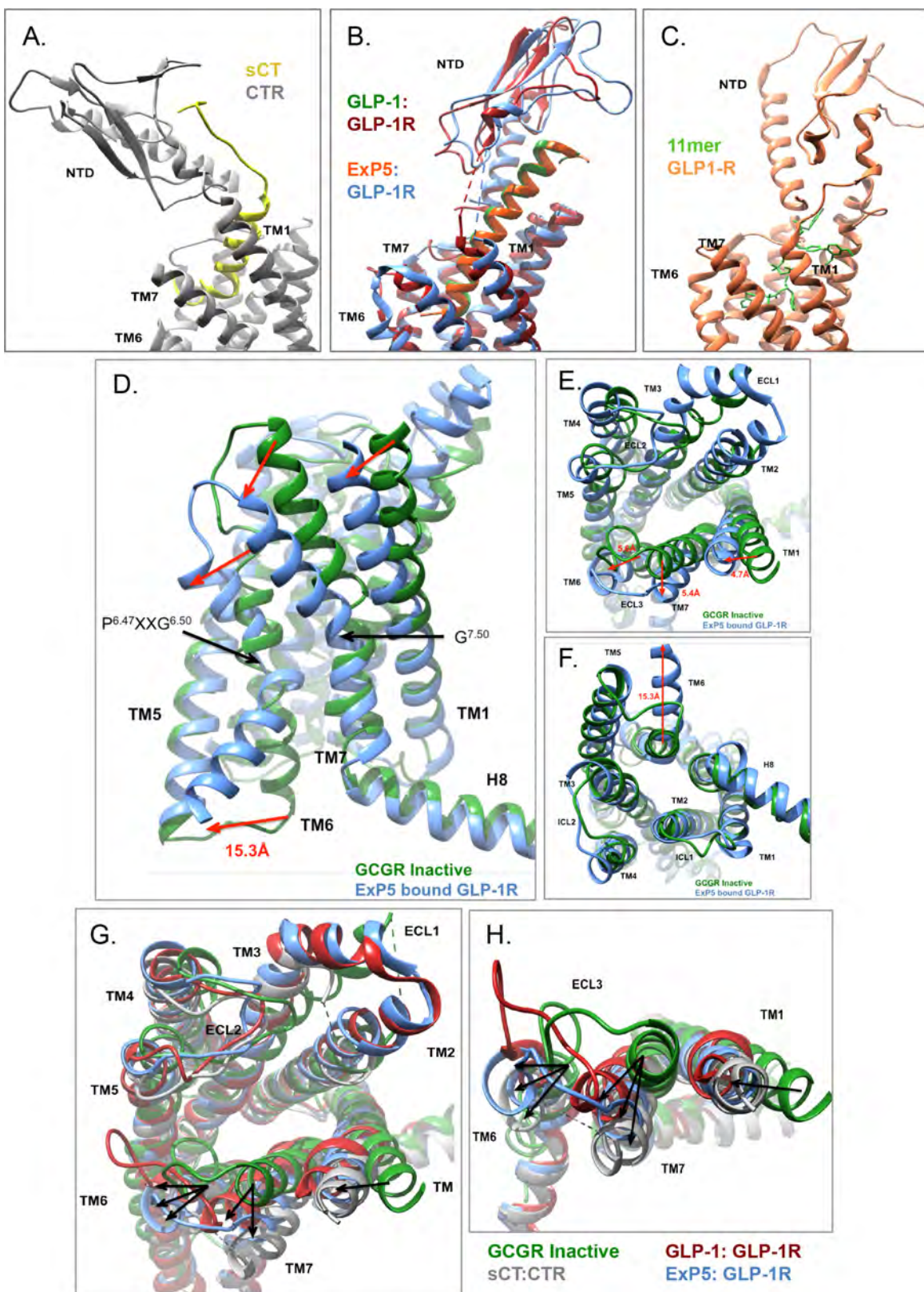
Extended Data Figure 2 | Purification and Volta phase plate imaging of the ExP5-GLP-1R-Gs complex. **a**, Left, elution profile of the purified complex. Middle, pooled complex fractions, concentrated and analysed by size exclusion chromatography (SEC). Right, SDS-PAGE/Coomassie blue stain and western blot of the complex showing all components. Anti-His antibody detects Flag-GLP-1R-His, G β -His and Nb35-His

(red) and anti-Gs antibody detects G α_s (green). **b**, Left, Volta phase plate micrograph of the complex (representative of 2,793). Middle, 2D class averages. Right, 'gold standard' Fourier shell correlation (FSC) curves; the overall nominal resolution is 3.26 Å. **c**, Left, Volta phase plate phase shift history throughout the dataset. Right, histogram of the estimated micrograph resolutions from the CTF.



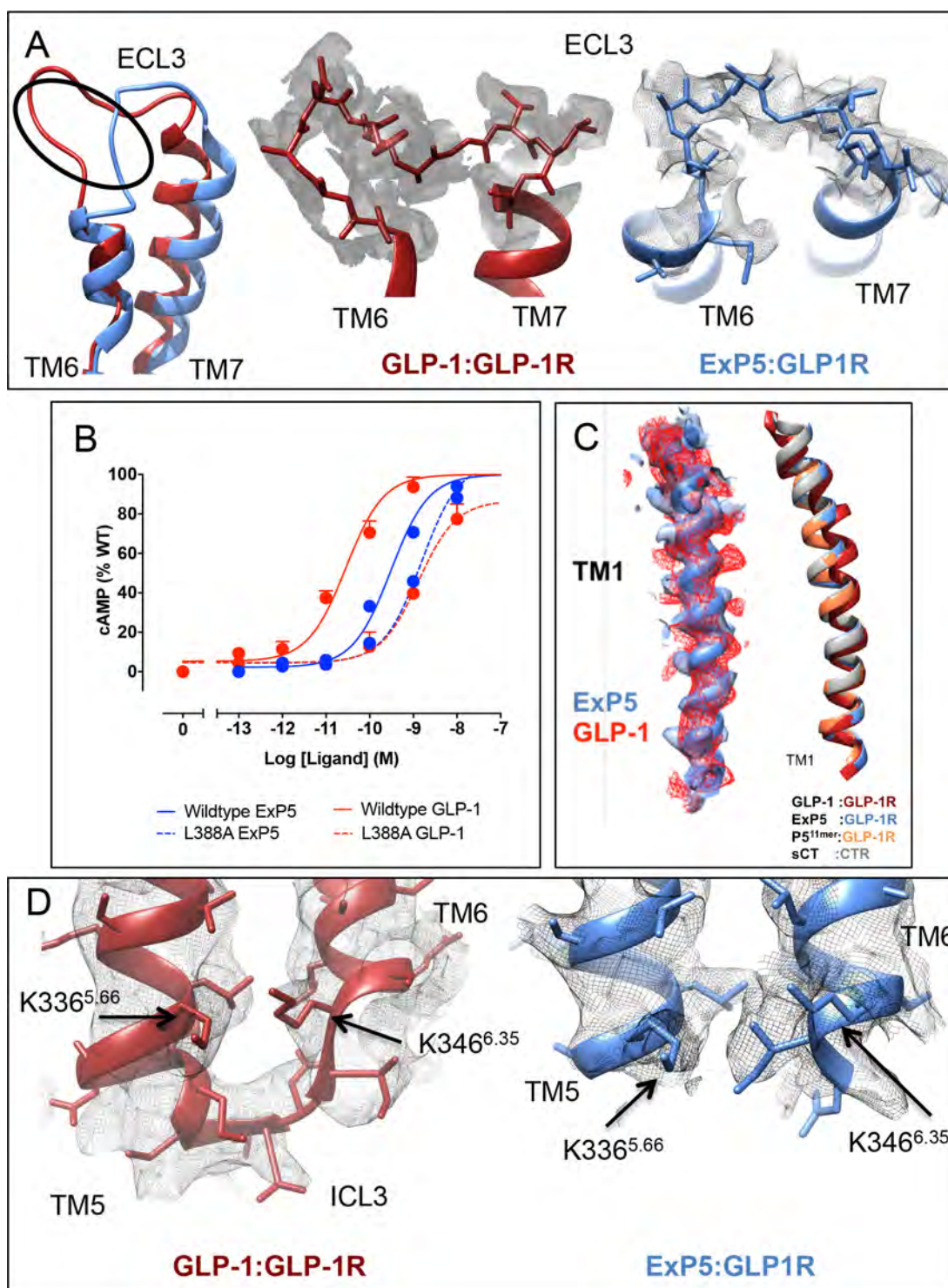
Extended Data Figure 3 | Atomic resolution model of the ExP5-GLP-1R-Gs heterotrimer in the cryo-EM density map. EM density map and model are shown for all seven transmembrane helices and H8

of the receptor, the ExP5 peptide and the $\alpha 5$ helix of the G α S α Ras-like domain. Bulky residues are highlighted. All transmembrane helices exhibit good density, with TM6—which is flexible—being the least well-resolved.



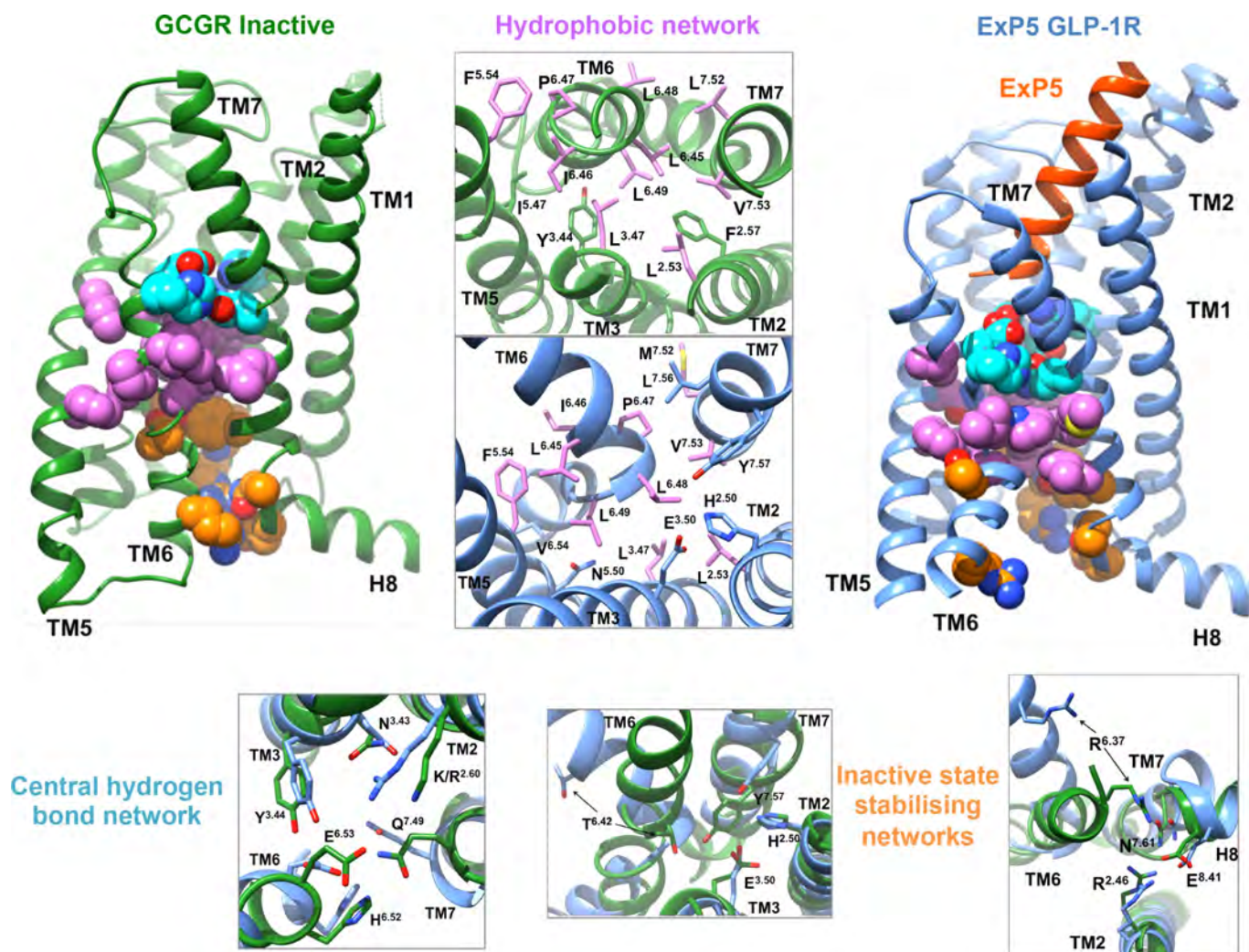
Extended Data Figure 4 | Comparison of class B GPCR structures. **a–c**, Agonist-bound full-length structures have distinct NTD orientations. **d–f**, Side view (**d**), extracellular view (**e**) and cytoplasmic view (**f**) of the conformational reorganization between inactive (GCGR, PDB 4L6R) and active structures (ExP5-bound GLP-1R). Distances are measured from Cα residues 1.33, 6.58, 7.35 and 6.35. Numbering uses the Wootten class B

system. **g–h**, Superimposition of transmembrane domains from sCT-CTR-Gs (grey, PDB 5U27), GLP-1-GLP-1R-Gs (red, PDB 5VA1) and ExP5-GLP-1R-Gs with the inactive GCGR (green, PDB 4L6R). The largest differences in active structures relative to the inactive GCGR occur in TM1, TM6, TM7 and ECL3 (**h**), but the nature and extent of conformational change varies.



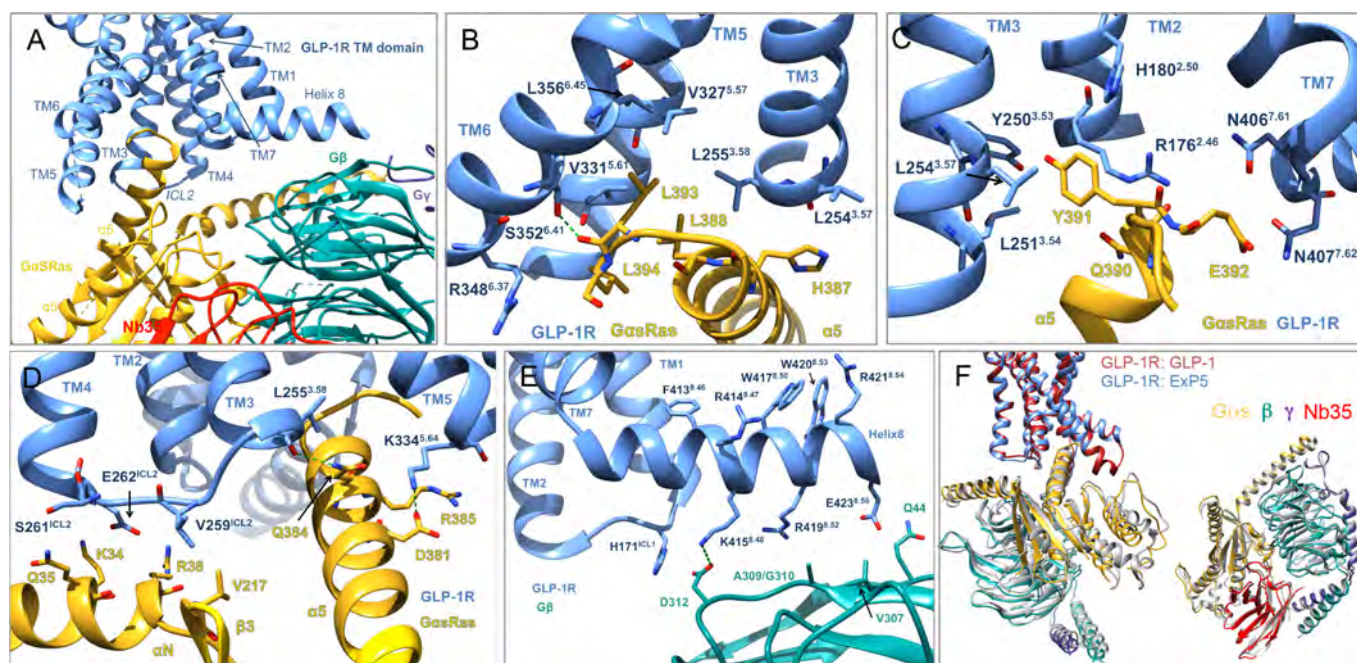
Extended Data Figure 5 | ECL3, TM7, TM1 and ICL3 may be associated with GLP-1R biased agonism. **a**, Conformational differences in GLP-1R ECL3 between ExP5-bound (blue) and GLP-1-bound (red) GLP-1R structures are supported by density in their respective cryo-EM maps. **b**, L388^{7.43}A affected the potency of GLP-1 mediated cAMP more than ExP5 (mean + s.e.m. of four independent experiments). **c**, Right, TM1 overlays from agonist-bound class B GPCR structures reveals a different

conformation for GLP-1–GLP-1R. Left, TM1 model overlays of ExP5–GLP-1R and GLP-1–GLP-1R with their associated cryo-EM maps (GLP-1, red ribbon/mesh; ExP5, blue ribbon/surface) reveals limited differences in the TM1 backbone, but potentially distinct side-chain orientations. **d**, Left, ICL3 backbone conformation in GLP-1–GLP-1R (PDB 5VA1) is supported by density (EMD-3653). Limited density is observed for ICL3 (337–343) in ExP5–GLP-1R.



Extended Data Figure 6 | Rearrangement of conserved networks upon GLP-1R binding to ExP5. Comparison of conserved networks in the inactive (green, GCGR) and activated (blue, ExP5-GLP-1R-Gs) states; central polar network (cyan), cytoplasmic polar networks (orange) and hydrophobic residues (pink). Inactive state interactions are incompatible with peptide binding and reorganize on activation. Upper middle, major rearrangements within the hydrophobic network (top, inactive; bottom,

activated); side chains involved in ground state stabilization in green, inactive and active state in pink and active state in blue. Lower left and lower right, reorganization of the central hydrogen bond network and cytoplasmic networks, respectively, where green is inactive and blue is active. Subscript, Wooten numbering. These conformational changes are detailed in Supplementary Video 1.



Extended Data Figure 7 | GLP-1R–G protein interactions. **a**, GLP-1R forms interactions with G α_s Ras and G β . **b–e**, Receptor side chains (blue) within 4.5 Å of G α_s side chains (gold) or G β side chains (cyan). **b–d**, G α_s α5 forms polar and non-polar interactions with the cytoplasmic cavity formed by TM6 opening. Potential interactions also occur between G α_s αN and ICL2 of GLP-1R. **e**, GLP-1R H8 aromatic residues embed

within the detergent micelle and polar residues form direct interactions with G β . **f**, Left, the distinct engagement angle of G α_s α5 with the receptor (Fig. 3) results in an overall rotation of the G α_s Ras,β,γ in ExP5–GLP-1R relative to GLP-1–GLP-1R. Right, overlaying G α_s from both structures reveals only minor differences in the G protein upon receptor engagement.

Extended Data Table 1 | Effects of extracellular loop 3 alanine mutants of human GLP-1R on agonist binding and cell surface expression

GLP-1R	Cell surface expression	Whole cell competition radioligand binding pK_i			cAMP Accumulation					
		GLP-1	Exendin-4	Exendin-P5	GLP-1		Exendin-4		Exendin-P5	
					pEC_{50}	E_{max}	pEC_{50}	E_{max}	pEC_{50}	E_{max}
Wild type	100 ± 3	8.81±0.04	8.97±0.07	9.61±0.45(0.18) 7.05±0.09	10.8±0.04	100±2	11.4±0.04	100±1	9.93±0.04	100±1
D372A	86 ± 4	9.62±0.47 (0.15)	9.29±0.56 (0.14) 7.40±0.21*	9.34±0.41 (0.24) 6.85±0.09	8.95±0.10*	103±4	10.1±0.09*	105±3	10.0±0.08	99±2
E373A	94 ± 7	9.80±0.39 (0.26)	9.67±0.42 (0.10) 7.41±0.15*	9.55±0.29 (0.22) 6.71±0.08	8.45±0.08*	104±4	9.3±0.09*	99±3	9.25±0.08*	106±3
H374A	82 ± 8	8.87±0.14	8.87±0.09	9.94±0.52 (0.10) 7.24±0.13	10.9±0.07	102±2	11.6±0.08	99±2	10.1±0.07	93±2
R376A	92 ± 7	8.53±0.10	8.92±0.10	9.61±0.48 (0.15) 7.05±0.09	10.3±0.09*	99±3	11.4±0.12	95±2	9.61±0.14	105±5
G377A	96 ± 3	8.27±0.06*	9.12±0.25 (0.68) 7.29±0.21*	- 7.03±0.10	9.9±0.08*	105±3	11.1±0.15	102±4	9.14±0.15*	106±5
T378A	173 ± 11*	8.87±0.06	8.71±0.11	- 6.75±0.08	10.7±0.10	93±2	11.5±0.17	85±7	10.0±0.10	95±3
L379A	90 ± 6	8.33±0.07*	8.15±0.15*	9.61±0.49 (0.15) 6.63±0.11*	9.74±0.13*	89±3	10.5±0.20*	92±5	10.2±0.10	96±3
R380A	73 ± 5	7.35±0.09*	7.65±0.05*	- 6.65±0.04*	7.74±0.07*	103±4	8.81±0.08*	103±3	8.21±0.11*	97±4
F381A	92 ± 5	8.97±0.06	8.94±0.05	9.22±0.51 (0.19) 6.32±0.15*	10.5±0.06	88±2	11.5±0.08	86±6	10.3±0.06	93±2
I382A	115 ± 6	8.92±0.06	8.91±0.06	9.71±0.51 (0.14) 6.79±0.12	10.9±0.12	99±3	11.3±0.09	95±2	10.2±0.12	102±4

Cell surface expression was determined through antibody detection of the N-terminal c-Myc epitope label and expressed as percentage of wild-type (WT) GLP-1R expression. Whole-cell competition radioligand binding data were analysed using either a one-site (a single pK_i) or a two-site binding curve (two pK_i values are reported with the fraction of receptors in the high affinity site reported in brackets) as determined by an *F*-test in Graphpad Prism. pK_i values represent the negative logarithm of the equilibrium dissociation constant (in molar) of agonist. Data were normalized to specific [125 I]-exendin(-9-39) binding. cAMP concentration response data were analysed using a three-parameter logistic curve to determine pEC_{50} and E_{max} values. pEC_{50} values represent the negative logarithm of agonist concentration that produces half maximal response. E_{max} values are maximal response as percentage of WT response. All values are expressed as mean ± s.e.m. of five independent experiments conducted in duplicate. Data were analysed using one-way analysis of variance and Dunnett's post-test. * $P < 0.05$ (in comparison with WT response).

Extended Data Table 2 | Interactions between the GLP-1R and ExP5

ExP5	Peptide side chain density at C β	Peptide side chain density at C γ	GLP-1R	Interaction
E1	yes	no	R310 ^{5.40} A368 ^{8.67}	Hydrogen bond
L2	yes	yes	V237 ^{3.40} I313 ^{5.43}	
V3	yes	N/A	L384 ^{7.38} E387 ^{7.42} L388 ^{7.43} T391 ^{7.68}	
D4	no	no	Y152 ^{1.47} V194 ^{2.64} M233 ^{3.36} K197 ^{3.69}	Potential H-bond Salt bridge
N5	yes	yes	Q234 ^{3.37} W306 ^{5.38}	Hydrogen bond Hydrogen bond
A6	yes	N/A		
V7	yes	N/A	L384 ^{7.38} L388 ^{7.43}	
G8	N/A	N/A		
G9	N/A	N/A		
D10	yes	no	R380 ^{7.35}	Salt bridge
L11	yes	no	L141 ^{1.36} Y145 ^{1.66} L201 ^{2.71}	
S12	yes	N/A	T298 ^{ECL2} L201 ^{2.71}	
K13	yes	yes	R299 ^{ECL2} backbone	potential H-bond to the backbone
Q14	yes	yes	E138 ^{1.33} L141 ^{1.36}	no side chain density for E138
M15	yes	yes	L201 ^{2.71} K202 ^{2.71} Y205 ^{2.75} S206 ^{2.76}	
E16	yes	yes	Y205 ^{2.75} R299 ^{ECL2} N32	Potential H-bond Salt bridge, Potential H-bond to the backbone
E17	yes	no	<i>Potentially TM1 stalk</i>	
E18	yes	yes	<i>Potentially TM1 stalk</i>	
A19	yes	N/A	Y205 ^{2.75}	
V20	yes	N/A	V30 ^{NTD} L32 ^{NTD} P90 ^{NTD}	
R21	yes	yes	<i>Potentially TM1 stalk</i>	
L22	yes	yes	Q210 ^{ECL1}	
F23	yes	yes	W214 ^{ECL1} L32 ^{NTD} L35 ^{NTD} Y26 ^{ITE} W39 ^{NTD}	
I24	yes	yes	V20 ^{NTD} Y69 ^{NTD} I89 ^{NTD} P90 ^{NTD} W91 ^{NTD}	
E25	yes	yes		
W26	yes	yes	H212 ^{ECL1} W214 ^{ECL1}	π -stack
L27-S33			N-terminal interactions	

Residues in black are within 4 Å of the bound peptide. Residues in grey italics are within 4.5 Å of the bound peptide, but out of bonding distance and may form transient interactions. Residues in blue italics are within 4 Å in our model but there is no side-chain density in the cryo-EM map.

Extended Data Table 3 | Interactions formed between class B receptor and Gs heterotrimeric Gs proteins

G protein subunit	G protein Residue no	GLP-1R (Exp5 bound)	GLP-1R (GLP-1 bound) PDB: 5VAI	CTR (sCT bound) PDB: 5UZ7
GαRas α5	R380	<i>F257^{ICL2}</i>	L256^{2.59}bb	K326^{6.54}
	D381	K334^{5.64}	K334^{5.64}	
	I383	<i>S258^{ICL2}</i>		V252^{ICL2}
	Q384	L255^{2.58}bb K334^{5.64}	L255^{2.58}bb K334^{5.64}	L248^{2.58}bb K326^{5.64}
	R385	K334^{5.64}bb	K334^{5.64}bb	K326^{5.64}
	H387	L254^{3.57} L255^{2.58}	L254^{3.57}	L247^{3.57}
	L388	L255^{2.58} V331^{5.61} K334^{5.64}	V331^{5.61}	L323^{5.61}
	Q390	R176^{2.46}	R176^{2.46} E408^{8.41}	R180^{2.46}
	Y391	<i>H180^{2.50}</i> Y250^{3.53} L251^{3.54} L254^{3.57}	<i>H180^{2.50}</i> L359^{6.48} L356^{6.45} L251^{3.54}	Y253^{ICL2} L244^{3.54}
	E392	N406^{7.61} N407^{7.62}	N406^{7.61} V405^{7.60}bb L401^{7.56}bb	C394^{7.60}bb N396^{7.62}
	L393	S352^{6.41}bb L356^{6.45} V327^{5.57} V331^{5.61}	S352^{6.41} L356^{6.45} T353^{6.42}	L348^{6.45}
	L394	V331^{5.61} R348^{6.37} (to L394 backbone)	L339^{5.59}	M327^{5.65}
GαRas αN	Q35	S261^{ICL2}	S261^{ICL2} E262^{ICL2}	
	R38	E262^{ICL2}		
	Q31	Q263^{ICL2} (not support density)	Q263^{ICL2}	
	K34	E262^{ICL2}	Q263^{ICL2}	
GαRas β3	V217	V259^{ICL2}		
GαRas α4	R385	<i>(N338 not resolved in cryo EM map but likely conserved)</i>	N338^{ICL3}	
Gβ	D312	H171^{ICL1} K415^{8.48}	H171^{ICL1} K415^{8.48}	R404^{8.48}
	A309/G310 (backbone)	R419^{8.52}	R419^{8.52}	Q408^{8.52}
	Q44	E423^{8.56}		Q415^{8.60}

All receptor residues within 4 Å (4.5 Å in non-bold italics) of G protein that were evident in the cryo-EM maps of the sCT-CTR-Gs, GLP-1-GLP-1R-Gs and Exp5-GLP-1R-Gs complexes are listed. Residues in red are conserved interactions between the three structures, those in blue are conserved between the two GLP-1R structures and those in black are unique in the different structures (bb indicates backbone interactions).

Life Sciences Reporting Summary

Nature Research wishes to improve the reproducibility of the work that we publish. This form is intended for publication with all accepted life science papers and provides structure for consistency and transparency in reporting. Every life science submission will use this form; some list items might not apply to an individual manuscript, but all fields must be completed for clarity.

For further information on the points included in this form, see [Reporting Life Sciences Research](#). For further information on Nature Research policies, including our [data availability policy](#), see [Authors & Referees](#) and the [Editorial Policy Checklist](#).

► Experimental design

1. Sample size

Describe how sample size was determined.

Sample size calculation was not required

2. Data exclusions

Describe any data exclusions.

No data were excluded

3. Replication

Describe whether the experimental findings were reliably reproduced.

Experimental findings were reliably reproduced

4. Randomization

Describe how samples/organisms/participants were allocated into experimental groups.

Randomization was not required

5. Blinding

Describe whether the investigators were blinded to group allocation during data collection and/or analysis.

Blinding was not required

Note: all studies involving animals and/or human research participants must disclose whether blinding and randomization were used.

6. Statistical parameters

For all figures and tables that use statistical methods, confirm that the following items are present in relevant figure legends (or in the Methods section if additional space is needed).

n/a Confirmed

- ☐ ☒ The exact sample size (n) for each experimental group/condition, given as a discrete number and unit of measurement (animals, litters, cultures, etc.)
- ☒ ☐ A description of how samples were collected, noting whether measurements were taken from distinct samples or whether the same sample was measured repeatedly
- ☐ ☒ A statement indicating how many times each experiment was replicated
- ☐ ☒ The statistical test(s) used and whether they are one- or two-sided (note: only common tests should be described solely by name; more complex techniques should be described in the Methods section)
- ☒ ☐ A description of any assumptions or corrections, such as an adjustment for multiple comparisons
- ☐ ☒ The test results (e.g. P values) given as exact values whenever possible and with confidence intervals noted
- ☐ ☒ A clear description of statistics including central tendency (e.g. median, mean) and variation (e.g. standard deviation, interquartile range)
- ☐ ☒ Clearly defined error bars

See the web collection on [statistics for biologists](#) for further resources and guidance.

► Software

Policy information about [availability of computer code](#)

7. Software

Describe the software used to analyze the data in this

GraphPad Prism, ImageJ, Motioncor2, Gctf, Gautomatch, EMAN2, Relion 2.03,

study.

PHENIX, MolProbity, COOT, Pymol, UCSF Chimera

For manuscripts utilizing custom algorithms or software that are central to the paper but not yet described in the published literature, software must be made available to editors and reviewers upon request. We strongly encourage code deposition in a community repository (e.g. GitHub). *Nature Methods* [guidance for providing algorithms and software for publication](#) provides further information on this topic.

► Materials and reagents

Policy information about [availability of materials](#)

8. Materials availability

Indicate whether there are restrictions on availability of unique materials or if these materials are only available for distribution by a for-profit company.

There are no restriction

9. Antibodies

Describe the antibodies used and how they were validated for use in the system under study (i.e. assay and species).

All antibodies were used for Western blot analysis and have been validated.
rabbit anti-Gs C-18 antibody (cat no sc-383), Santa Cruz
mouse Penta-His antibody (cat no 34660), QIAGEN
680RD goat anti-mouse antibody (LI-COR)
800CW goat anti-rabbit antibody (LICOR)

10. Eukaryotic cell lines

a. State the source of each eukaryotic cell line used.

Cells used in assays were obtained from ATCC

b. Describe the method of cell line authentication used.

No authentication required

c. Report whether the cell lines were tested for mycoplasma contamination.

Cell lines were tested and are free from mycoplasma contamination

d. If any of the cell lines used are listed in the database of commonly misidentified cell lines maintained by [ICLAC](#), provide a scientific rationale for their use.

Cells are not listed in the database

► Animals and human research participants

Policy information about [studies involving animals](#); when reporting animal research, follow the [ARRIVE guidelines](#)

11. Description of research animals

Provide details on animals and/or animal-derived materials used in the study.

Not applicable

Policy information about [studies involving human research participants](#)

12. Description of human research participants

Describe the covariate-relevant population characteristics of the human research participants.

Not applicable



Characterization of signalling and regulation of common calcitonin receptor splice variants and polymorphisms

Emma Dal Maso^a, Rasmus Just^b, Caroline Hick^a, Arthur Christopoulos^a, Patrick M. Sexton^{a,*}, Denise Wootten^{a,*}, Sebastian G.B. Furness^{a,*}

^a Drug Discovery Biology, Monash Institute of Pharmaceutical Sciences and Department of Pharmacology, Monash University, Parkville, Australia

^b ALK-Abello A/S, Bøge alle 3, 2970 Hørsholm, Denmark

ARTICLE INFO

Article history:

Received 16 November 2017

Accepted 19 December 2017

Available online 23 December 2017

Keywords:

Calcitonin

Calcitonin receptor

G protein-coupled receptor

Splice variant

Polymorphism

ABSTRACT

The calcitonin receptor (CTR) is a class B G protein-coupled receptor that is a therapeutic target for the treatment of hypercalcaemia of malignancy, Paget's disease and osteoporosis. In primates, the CTR is subject to alternative splicing, with a unique, primate-specific splice variant being preferentially expressed in reproductive organs, lung and kidney. In addition, humans possess a common non-synonymous single-nucleotide polymorphism (SNP) encoding a proline/leucine substitution in the C-terminal tail. In low power studies, the leucine polymorphism has been associated with increased risk of osteoporosis in East Asian populations and, independently, with increased risk of kidney stone disease in a central Asian population. The CTR is pleiotropically coupled, though the relative physiological importance of these pathways is poorly understood. Using both COS-7 and HEK293 cells recombinantly expressing human CTR, we have characterized both splice variant and polymorphism dependent response to CTRs from several species in key signalling pathways and competition binding assays. These data indicate that the naturally occurring changes to the intracellular face of CTR alter ligand affinity and signalling, in a pathway and agonist dependent manner. These results further support the potential for these primate-specific CTR variants to engender different physiological responses. In addition, we report that the CTR exhibits constitutive internalization, independent of splice variant and polymorphism and this profile is unaltered by peptide binding.

© 2017 Elsevier Inc. All rights reserved.

1. Introduction

The CTR (calcitonin receptor) was first described and cloned based on its role in acute regulation of elevated serum calcium concentration by the thyroid hormone, calcitonin [1,2]. Serum calcium is normally maintained within a very narrow range with both hypocalcaemia and hypercalcaemia being serious pathological conditions. In spite of this tight regulation of serum calcium, thyroidectomy and medullary thyroid tumours both result in gross changes in circulating calcitonin levels, and thus CTR activation. Yet these gross changes in calcitonin levels have little effect on adult plasma calcium concentration. In contrast, both human and salmon calcitonin are used clinically in cases of acute hypercalcaemia of malignancy [3], Paget's disease [4] and osteoporosis [5]. Thus, while CTRs can acutely regulate calcium homeostasis, it is more important under conditions of high bone turnover or calcium stress such as pregnancy, lactation, menopause and growth (reviewed in [6]). Beyond calcium homeostasis, the CTR has a cen-

tral role in food intake and is implicated in pain modulation, immune function, wound healing, reproductive physiology and several cancers. CTR expression also occurs in a subset of hematopoietic lineages (reviewed in [7]) and serum procalcitonin levels are strongly upregulated in bacterial sepsis (reviewed in [6]), implicating CTR in immune modulation. CTRs also occur in a variety of cancers and cancer cell lines [8–13], however its role in pathophysiology remains uncertain.

The CTR primarily couples to the adenylate cyclase stimulatory G protein isoform, $G_{\alpha s}$, promoting the formation of intracellular cAMP. However, the receptor is pleiotropically coupled, with evidence for activation of $G_{\alpha q}$ and $G_{\alpha i}$ G protein isoforms [14–16]. CTR activation promotes fast transient Ca^{2+} mobilization from intracellular stores and ERK1/2 (extracellular signal-regulated kinases 1 and 2) phosphorylation, and can induce CTR downregulation and cell remodelling via PKA (protein kinase A) (and perhaps PKC (protein kinase C)) [17], whereas secretion of HCl and other bone remodelling factors from osteoclasts is inhibited by PKC activation [18]. In hepatocytes and neurones, there is probably limited coupling to $G_{\alpha s}$, with other G protein coupling predominating (see [6,19–21]). The CTR is also reported to internalize following

* Corresponding authors.

E-mail address: sebastian.furness@monash.edu (S.G.B. Furness).

receptor activation [22,23]; however, to date, there is limited evidence for the recruitment of β -arrestins, which are key mediators of GPCR (G protein-coupled receptor) internalization [24], to the CTR [23].

In humans, the CTR is subject to alternative splicing of the 5' untranslated region as well as the coding region (reviewed in [25]), with the most common, coding splice variant arising from the inclusion of an additional 48-nucleotide exon that encodes an additional 16 amino acids in intracellular loop 1 (ICL1) of the receptor [2]. The current naming convention is CTR_a for the insert negative variant and CTR_b for the insert positive. Inspection of the current NCBI genome database suggests that the insert positive splice variant (CTR_b) is conserved in old-world monkeys (evident in Gorilla, Chimpanzee, Orangutan, Gibbon and Macaque) but appears to be absent in other mammals. The CTR_b variant shows more restricted expression compared with CTR_a but has high expression in the reproductive tract and lower expression in lung, kidney and bone marrow [26]. Interestingly, expression studies using peripheral blood mononuclear cells (PBMCs) of a cohort of 59 women show predominant (~60%) expression CTR_b mRNA (to the exclusion of CTR_a), ~20% with CTR_a only, 10% with both mRNA species and 10% with no detectable CTR message [27]. The presence of CTR_b in PBMCs was correlated with lower bone turnover. Previous comparisons of CTR_a and CTR_b showed no apparent difference in affinity for sCT (salmon calcitonin) or hCT (human calcitonin) but the CTR_b displays a reduction in potency for cAMP accumulation, a reduction in ERK1/2 phosphorylation in response to a single concentration of sCT and loss of coupling to intracellular calcium mobilization [17,28].

In 1994, Kuestner et al. [26] reported a polymorphism of the insert negative hCTR in which position 1340 (1377 for insert positive), with respect to the start codon, was either a C or T nucleotide encoding either a proline or leucine, respectively. Inspection of the NCBI genome database indicates other mammals are not polymorphic at this position with complete conservation of codons encoding proline at this position. This polymorphism is widespread [29–31] with prevalence of the specific polymorphic variant related to ethnic background; Caucasians, Hispanics and Afro-Americans predominantly have a genotype encoding the Leu variant or are heterozygous [32], while Asians, in particular the Japanese population, are predominantly homozygous for the Pro variant [29]. Some clinical studies have reported a potential correlation between a genotype encoding the Leu polymorphism and an increased incidence of osteoporosis [30,31,33–35] and kidney stone disease [36]; these have low power and other studies have failed to confirm these findings [37,38].

At a signalling level there has been rather limited analysis of any differences attributable to splice variants [17,26,39–41] or polymorphism [32]. This current study reports a robust, direct comparison of these human specific splice and polymorphic variants, for their ability to activate distinct signalling pathways in response to different CTR ligands. We have characterized the cellular responses triggered by a variety of agonists in two cellular backgrounds. These tools allow us to evaluate if ligands with distinct sequence can elicit biased agonism at the CTR and to assess if signalling profiles vary substantially between the different hCTR variants. Finally, we have assessed hCTR internalization and investigated the ability of the distinct peptides to recruit β -arrestin 1 or β -arrestin 2 to the hCTR variants.

2. Materials and methods

2.1. Materials

Dulbecco's modified Eagle's medium (DMEM), G418, Goat anti-mouse AF488 and AF647 secondaries, Sytox red, Sytox blue and

Fluo-4 acetoxymethyl ester were purchased from Invitrogen (Carlsbad, CA, USA). Puromycin was purchased from Invivogen (San Diego, CA, USA). Foetal bovine serum (FBS) was purchased from Thermo Fisher Scientific (Melbourne, Victoria, Australia). AlphaScreen™ reagents, and LANCE HTRF cAMP kit were purchased from PerkinElmer Life Sciences (Waltham, MA, USA). SureFire™ ERK1/2 reagents were generously supplied by TGR Biosciences (Adelaide, South Australia, Australia). Anti-CTR antibody (Mab4614) was purchased from R&D Systems (Minneapolis, MN, USA). Calcitonin peptides, including sCT-ROX, were purchased from Mimotopes (Victoria, Australia). Iodine-125 was purchased from Perkin-Elmer (Victoria, Australia). sCT(8–32)-AF568 was generated and validated as previously described [42]. 9E10-AF647 (anti-cMyc) was generated and validated as previously described [43].

All other reagents were purchased from Sigma (St. Louis, MO, USA) or BDH Merck (Melbourne, Vic, Australia) and were of an analytical grade.

2.2. Constructs and generation of cell lines

Both the insert negative and insert positive cDNA sequences of human CTR were modified to incorporate a cMyc epitope tag (EQKLISEEDL) immediately adjacent the predicted signal peptide cleavage site (Signal P 4.1), between amino acids 24 & 25 by overlap extension PCR. Proline variants of each construct were generated by site directed mutagenesis. To generate COS-7 cell lines, all variants were cloned into pEF-IRESpuro6 (modified from [44]) and for HEK293 cell lines variants were cloned into pcDNA3.1+ (Thermo scientific). For β -arrestin BRET assays the stop codon from each CTR variant was removed by site directed mutagenesis and variants were transferred to the dual vector BIVISTI in combination with either β -arrestin-1 or -2 [45]. The original GLP-1R BIVISTI vectors are described elsewhere [45,46]. Sanger sequencing confirmed the sequence of all inserts.

COS-7 cell lines were generated as follows: COS-7 cells (CRL-1651, ATCC) were transfected with each variant cloned in the pEF-IRESpuro6 backbone; a polyclonal population was selected (10 μ g/mL puromycin) and FACS sorted using 9E10 (anti-cMyc, produced in-house) and goat anti-mouse AF647 secondary (Thermo scientific) as previously described [23,42]. A corresponding control cell line was generated in parallel. HEK293 variants were tested functionally for lack of RAMP expression by transient transfection with CTR and comparison of hCT, sCT and amylin response in cAMP accumulation assays. HEKflp-IN-293 cells (Thermo scientific) that displayed similar potency for hCT and sCT dependent cAMP accumulation and low potency for amylin dependent cAMP accumulation were chosen for transfection (2 independent experiments). HEKflp-IN-293 cells were transfected with each variant cloned in the pcDNA3.1+ backbone; a polyclonal population was selected (1 mg/mL G418) and FACS sorted using 9E10 (anti-cMyc, produced in-house) and goat anti-mouse AF647 secondary (Thermo scientific).

2.3. Cell culture

COS-7 cell lines over-expressing the CTR variants and a vector control were maintained in DMEM with 5% FBS and 10 μ g/mL puromycin in a humidified 37 °C incubator with 5% CO₂ and passaged as required to maintain growth. HEK293 cell lines over-expressing the CTR variants and a vector control were maintained in DMEM with 5% FBS and 1 mg/mL G418 a humidified 37 °C incubator with 5% CO₂ and passaged as required to maintain growth.

2.4. Flow cytometry and fluorescence activated cell sorting

Cells were stained for flow cytometry and cell sorting. COS-7 or flpIN HEK293 stably expressing the human CTR variants or vector

control were seeded at 600,000 cells per well in a 6-well tray and grown overnight in standard media (above) in a humidified 37 °C incubator with 5% CO₂. The next day, cells were harvested with versene (PBS supplemented with 0.5 mM EDTA), centrifuged for 3 min at 350×g at 4 °C. Versene was aspirated and cells were resuspended in PBS containing 5% BSA & 2 mM EDTA (block buffer), transferred to wells of a 96-well v-bottom plate and incubated on ice for 40 min. Cells were centrifuged for 3 min at 350×g at 4 °C, blocking buffer removed, resuspended in 200 µl of 0.1% BSA & 2 mM EDTA in PBS containing 1 µg/mL anti-CTR primary antibody (R&D systems MAb4614) and incubated for 90 min at 4 °C. Cells were washed 3 times with 0.1% BSA & 2 mM EDTA in PBS by centrifugation for 3 min at 350×g at 4 °C followed by aspiration of supernatant. Cells were resuspended in 200 µl of 0.1% BSA & 2 mM EDTA in PBS containing 1 µg/mL anti-mouse secondary antibody (Thermo, either goat anti-mouse AF488 or goat anti-mouse AF647) and incubated on ice (in the dark) for 60 min. Cells were washed 3 times with 0.1% BSA & 2 mM EDTA in PBS by centrifugation for 3 min at 350×g at 4 °C followed by aspiration of supernatant. Cells were finally resuspended in 200 µl 0.1% BSA & 2 mM EDTA in PBS containing 1:2000 dilution of Sytox blue or Sytox red (as appropriate). All analytical flow cytometry was performed on a FACS Cantoll, while cells were sorted on the positive population (compared with stained vector control) on a MoFlo Astrios. All data analysis was performed using FlowJo.

2.5. Radioligand binding assays

sCT(8-32) was iodinated in-house to obtain mono-iodo-tyrosyl ¹²⁵I-sCT(8-32) as previously described [47]. In a 1.7 ml Eppendorf tube the following solutions were added in order: 5 µl of 1 mg/ml chloramine T (freshly prepared in PBS, pH 7.4) and 10 µl of ¹²⁵I (~350 mCi/ml, Perkin Elmer) were incubated at RT for 60 s. 20 µl of PBS and 5 µl of 0.1 mM sCT:8-32 were then added and iodination was left to proceed at room temperature for 10 s. Reaction was quenched by addition of 200 µl of KI (5 mg/ml prepared in PBS) and diluted with an additional 260 µl of PBS to the final volume of 500 µl. Excess, unincorporated ¹²⁵I was separated from peptide by reverse phase HPLC on a C-18 column using a gradient from 0.1% TFA in H₂O to 0.1% TFA in acetonitrile. BSA (final 0.1%) was added to fractions containing iodinated peptide and stored at –20 °C.

COS-7 cells expressing the CTR variants were seeded at 10,000 cells per well, overnight in DMEM, 5% FBS in a 96 well plate. On the day of the assay, cells were incubated with 80 µl of binding buffer (DMEM, 25 mM HEPES, 0.1% BSA, pH 7.4) and chilled at 4 °C for at least 1 h to limit receptor internalization. Approximately 50,000 cpm/well (corresponding to 100 pM) of ¹²⁵I-sCT(8-32) was added to each well (10 µl volume), followed immediately by 10 µl of relevant dilution of competing non-iodinated ligand. Plates were incubated overnight at 4 °C to reach equilibrium. Binding buffer was then removed and wells were washed 2× with ice cold PBS. Bound ligand was stripped with 50 µl of 0.1 M NaOH, transferred into scintillation tubes and γ radiation detected using a γ-counter (Wallac Wizard 1470 Gamma Counter, Perkin Elmer, 80% counter efficiency). Data were analysed in Prism and normalized to the total level of bound ¹²⁵I-sCT(8-32) ligand (100%) and non-specific binding; defined by a saturating concentration of sCT(8-32) (1 µM; 0%).

2.6. cAMP accumulation

Cells stably expressing CTR variants were seeded in 96 well trays; 10,000 cells/well for COS-7 or 25,000 cells/well for HEK293. Culture media was replaced with 135 µl of Stimulation Buffer (phenol red free DMEM, 0.1% BSA, 0.5 mM IBMX, 5 mM HEPES, pH 7.4) and incubated for 30 min at 37 °C, 5% CO₂. Cells were stimulated with either forskolin (10^{–4} M final), vehicle or

relevant concentrations of CTR agonists for 30 min at 37 °C, 5% CO₂, media was then removed and cells were lysed with 50 µl ice-cold 96% (v/v) ethanol. After ethanol was evaporated, 75 µl of lysis buffer, containing 0.3% Tween 20 (v/v), 5 mM HEPES and 0.1% BSA (w/v), pH 7.4 was added. Endogenously produced cAMP was measured using either a cAMP AlphaScreen or cAMP Lance ultra (PerkinElmer).

For the cAMP AlphaScreen 10 µl of lysate was transferred to a 384-well OptiPlate (PerkinElmer). 5 µl of acceptor bead mix (1.0% AlphaScreen cAMP acceptor beads diluted in lysis buffer) and 15 µl of donor bead mix (0.3% AlphaScreen cAMP donor beads, 0.025% AlphaScreen cAMP biotinylated cAMP (133 units/µl) diluted in lysis buffer, and preincubated for a minimum of 30 min) were added in reduced lighting conditions. Plates were incubated at room temperature overnight before measurement of the fluorescence using a Fusion-Alpha plate reader (PerkinElmer) with standard AlphaScreen settings. All values were converted to concentration of cAMP using a cAMP standard curve performed in parallel.

For Lance Ultra cAMP detection kit (PerkinElmer) 5 µl of cell lysate was transferred into a 384 well optiplate (PerkinElmer). 5 µl of anti-cAMP antibody mixture (Alexa fluor-647 anti-cAMP diluted in detection buffer supplied by the manufacturer) was added to each well of the optiplate and incubated for 30 min at RT in reduced lighting conditions. Subsequently, 10 µl of Eu-SA and biotinylated cAMP mix (EuW8044 labelled streptavidin (Eu-SA) and biotinylated cAMP diluted in kit detection buffer and pre-incubated for a minimum of 15 min) was added to each well and incubated at RT for 12–16 h before signal was measured using a top read on the Envision plate reader system. All values were converted to concentration of cAMP using a cAMP standard curve performed in parallel.

Data were normalized to the maximal response elicited by 100 µM forskolin, with 0% representing the concentration of cAMP in the presence of vehicle and 100% representing the concentration of cAMP in the presence of 100 µM forskolin.

2.7. ERK1/2 phosphorylation

Stably expressing cell lines were seeded at 10,000 cells/well for COS-7 or 25,000 cells/well for HEK293 in 96 well plates and incubated overnight at 37 °C with 5% CO₂ in DMEM, 5% FBS. Culture media was replaced with FBS-free DMEM incubated for a further 12–16 h. An initial time-course was performed for each ligand to assess the maximum peak of ERK1/2 phosphorylation, using relevant drugs at 1 µM (final concentration). Subsequently, concentration-response curves were performed for each drug at the time point of maximum ERK1/2 phosphorylation. In both cases, after stimulation, media was removed and cells were lysed in lysis buffer (TGR Bioscience). ERK1/2 phosphorylation was detected using an AlphaScreen kit (TGR Bioscience) as previously described [48]. All data were normalized to vehicle (0%) and 10% FBS (100%).

2.8. Intracellular calcium mobilization

Stably expressing cell lines were seeded at 10,000 cells/well for COS-7 or 25,000 cells/well for HEK293 in 96 well plates and incubated overnight at 37 °C, 5% CO₂ in DMEM, 5% FBS. Cells were washed twice with Ca²⁺ Buffer (150 mM NaCl, 10 mM HEPES, 10 mM D-glucose, 2.6 mM KCl, 1.18 mM MgCl₂, 2.2 mM CaCl₂, 0.5% BSA, 4 mM probenecid, pH 7.4) before addition of 1 µM Fluo4-AM diluted in Ca²⁺ buffer. Cells were incubated at 37 °C for 45–60 min (no CO₂) before stimulation and detection of Ca²⁺ mobilization in a FlexStation 1 or 3 (Molecular Devices) using following parameters: 37 °C, excitation 485 nm, emission 525 nm, baseline reads of 15 s before drug addition, fast drug dispense, and 120 s

reading. All data were extracted as the peak Ca^{2+} response correction against basal fluorescence (prior to agonist, vehicle or control addition). The peak value was used to create concentration-response curves. Data were normalized to the maximal response elicited by 100 μM ATP, with 0% representing the RFU measured in the presence of vehicle and 100% representing the RFU measured in the presence of 100 μM ATP.

2.9. β -arrestin recruitment assays

COS-7 or FlpInCHO cell lines were transiently transfected using PEI [48] with BIVISTI vectors containing CTR variants or GLP-1R C-terminally fused to an Rluc8 tag and either β -arrestin-1- or β -arrestin-2-Venus. 24 h post transfection cells were seeded in 96-well white culture plates at a density of 4×10^4 cells/well and cultured for 24 h in DMEM with 5% FBS. Cells were rinsed once with HBSS to remove traces of phenol red and incubated in fresh HBSS for a further 15 min. The Rluc substrate coelenterazine-h was added to reach a final concentration of 5 μM . After a 10 min incubation, the corresponding agonist was added and bioluminescence resonance energy transfer (BRET) readings were collected using a LumiSTAR Omega instrument that allows sequential integration of signals detected in the 465–505 and 515–555 nm windows using filters with the appropriate band pass. The BRET signal was calculated by subtracting the ratio of 515–555 nm emission over 465–505 nm emission for a vehicle treated cell sample from the same ratio for the ligand treated cell sample. In this calculation, the vehicle treated cell sample represents background and results are expressed as ligand-induced BRET. This eliminates the requirement for measuring a donor only control sample. Initial time course experiments were performed over 20 min in the presence of saturating concentration of ligand (1 or 10 μM) to determine the time at which β -arrestin-1 and β -arrestin-2 recruitment was maximal for each ligand. Subsequent concentration response data were collected at this peak time (2.5 min for all ligands). Data were normalized to the maximal response elicited by GLP-1, with 0% representing the RFU measured in the presence of vehicle and 100% representing the RFU measured in the presence of 100 nM GLP-1.

2.10. β -arrestin redistribution

To identify the redistribution of β -arrestins upon ligand stimulation, naive COS-7 or naive HEK-293 were transiently transfected with the 4 isoforms of CTR and either β -arrestin 1 or β -arrestin 2 labelled with a Venus-tag at the C-termini (each CTR variant was encoded in the dual vector pIRESpuo6 in combination with either β -arrestin 1 or 2). Cells plated at 30,000 cells/well in 96 well plates and incubated at 37 °C in 5% CO_2 in DMEM, 5% FBS for 48 h. On the day of the assay, cells were serum starved in DMEM for 2 h, 1 μM of relevant drugs were added at the various time-points and stimulation continued at 37 °C. Media was then removed and cells were fixed for 15 min in 4% PFA in PBS at 4 °C, followed by 3 \times PBS washes. Images were collected with Operetta (PerkinElmer), objectives: 20 \times /Olympus LUCPlanFLN, 0.45NA or 10 \times /Olympus U Plan FLN, 0.3NA.

2.11. Internalization of fluorescent ligand and tagged-receptor

To follow the internalization of the ligand, COS-7 stably expressing the 4 isoforms of the CTR were plated at 10,000 cells/well in a 96 well plate and stimulated with 1 or 0.1 μM of either sCT(8-32)-AF568 or sCT-ROX for 5, 10, 15, 30 or 60 min at 37 °C. Cells were subsequently fixed and imaged as described in Section 2.10 using the Operetta. Fluorophores were excited at 550–570 nm and emission was acquired at 570–620 nm.

2.12. Internalization of fluorescent antibody and tagged-receptor

To determine internalization of receptor, cMycCTR variants stably expressed in COS-7 were seeded overnight at 10,000 cells/well on μ -ibidi 8 well slide (DKSH Australia Pty Ltd.) and cultured overnight at 37 °C, 5% CO_2 . On the day of the assay, media was replaced with phenol red free DMEM, 0.1% BSA. Cells were chilled to 4 °C for 1 h and relevant compounds were added: anti-cMyc antibody 9E10-AF647 (1 $\mu\text{g}/\text{ml}$), sCT(8-32)-AF568 (1 μM) or sCT-ROX (100 nM) (fluorescently-conjugated ligands) or a combination of antibody and ligands. Cells were then incubated at 4 °C for 1 h to allow binding while limiting receptor internalization. Wells were washed 2 \times with ice cold PBS and 200 μl of cold media was added to each well. Slides were incubated in a 37 °C chamber built into a SP8 confocal microscope (Leica TCS SP8, LASX v2.1), using a 63 \times /U Plan APO CS2, 1.43NA and imaged every 1 min for 1 h (561 nm BP 570–610 and 633 nm BP 640–700).

2.13. Data analysis

All data were analysed using Prism 7 (GraphPad Software Inc., San Diego, CA, USA). For all analyses the data are unweighted and each y value (mean of replicates for each individual experiment) is considered an individual point. To calculate IC_{50} , EC_{50} and E_{max} values, concentration response signalling data were analysed as previously described [49] using either a biphasic or three-parameter logistic equation. The choice of fit was governed by an F-test. The equations used were:

Biphasic:

$$Y = \text{Bottom} + (\text{Top} - \text{Bottom}) \times \frac{\text{Frac}}{(1 + 10^{\log \text{EC}_{501} - X})} + (\text{Top} - \text{Bottom}) \times \frac{(1 - \text{Frac})}{(1 + 10^{\log \text{EC}_{502} - X})}$$

$$\text{three-parameter logistic: } Y = \text{Bottom} + (\text{Top} - \text{Bottom}) \frac{(\text{Top} - \text{Bottom})}{(1 + 10^{\log \text{EC}_{50} - X})}$$

2.14. Statistics

Changes in peptide affinity (pIC_{50}), potency (pEC_{50}) or E_{max} across all 4 receptor variants were statistically analysed with one-way analysis of variance (ANOVA) and either Bonferroni or Tukey's post-test (as indicated), and significance accepted at $p < .05$. Any statistical differences in unshared parameters determined by ANOVA were further tested against a common fit using an extra sum-of-squares F-test.

3. Results

3.1. hCT and sCT agonist affinities at the CTR

We assessed the affinities of the calcitonin antagonist sCT(8-32) as well as human (hCT) and salmon (sCT) calcitonin for the CTR, stably expressed in COS-7 cells via competition with a radiolabelled antagonist, ^{125}I -sCT(8-32) (Table 1, Fig. 1A). Consistent with previous literature the affinity of hCT was lower than that of either sCT(8-32) or sCT by 150–1000 fold (Fig. 1, Table 1)[26,32,41,42,50]. The aLeu variant had lower affinity for sCT(8-32) compared with all other forms ($p = .03$, against aPro, $p < .001$, against bLeu, and $p < .001$, against bPro; one-way ANOVA with Bonferroni post-test) and aPro had lower affinity than bPro for sCT8-32 ($p = .046$) in homologous competition binding (Fig. 1A and Table 1). No difference was measured for the affinity hCT at each of the variants (Fig. 1B and Table 1). On the other hand, the pIC_{50} of sCT

Table 1
Affinity data for human CTR variants.

	aLeu	aPro	bLeu	bPro
sCT(8-32) pIC ₅₀	9.33 ± 0.06 [†]	9.64 ± 0.07 [‡]	9.83 ± 0.07 ^{**}	9.94 ± 0.09 ^{**}
hCT pIC ₅₀	6.83 ± 0.19	7.20 ± 0.13	7.19 ± 0.12	7.12 ± 0.21
sCT pIC ₅₀	9.10 ± 0.11 [†]	9.70 ± 0.13 [†]	10.11 ± 0.09 ^{**}	10.11 ± 0.11 ^{**}

Experiments were performed in COS-7 cells stably expressing the human CTR. Whole cell radioligand binding was performed for each ligand and receptor variant using ¹²⁵I-sCT(8-32). All values are mean ± S.E.M. of 3–9 independent experiments conducted in duplicate. Differences in affinity are indicated: [†]different from all other forms, [‡]different from corresponding polymorph, ^{*}different from corresponding splice variant, ^{**}different from both polymorphs at alternatively spliced variant (p < .05, one-way ANOVA with a Tukey post test).

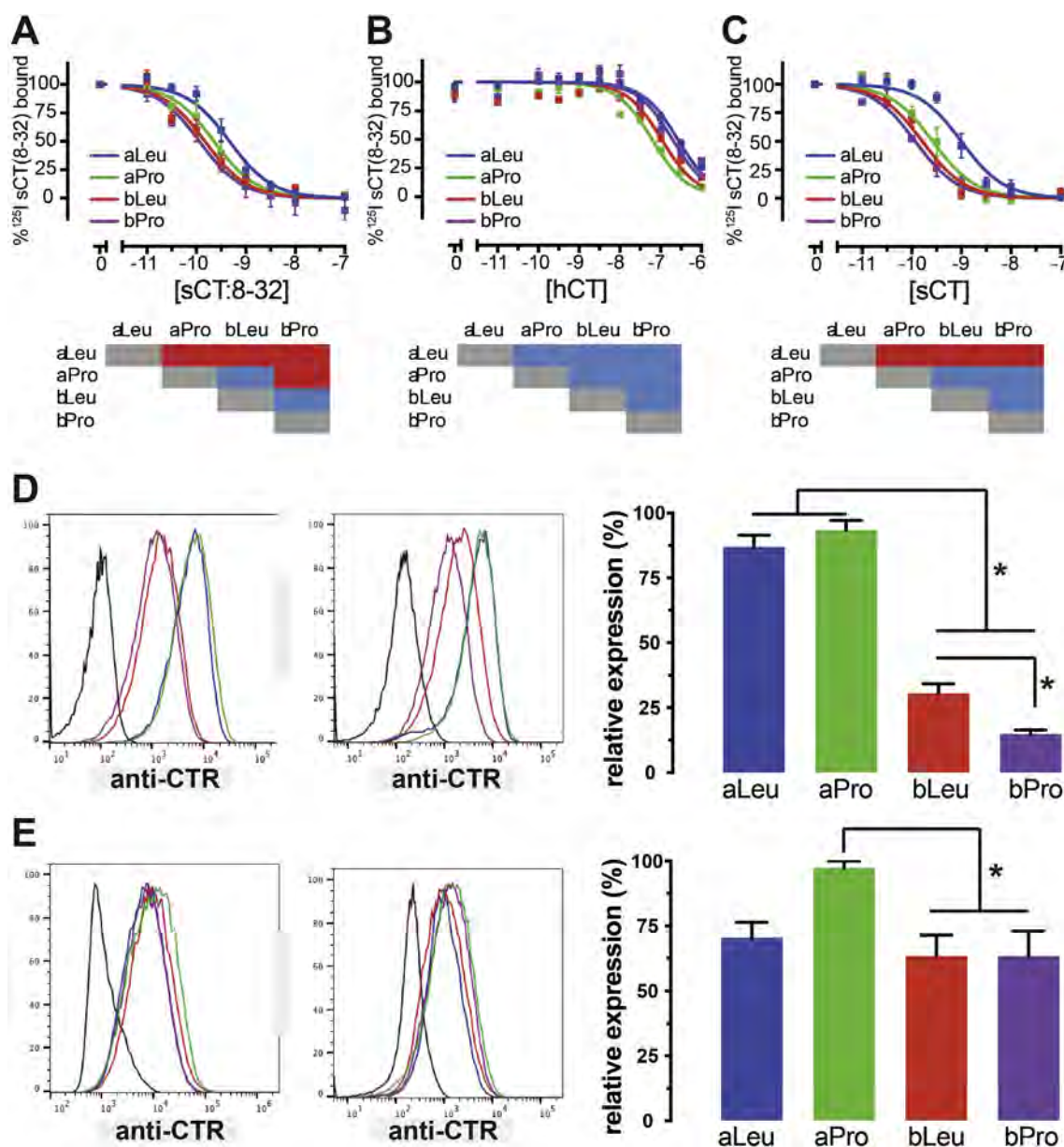


Fig. 1. Whole cell competition binding and cell surface expression by flow cytometry. A, B and C; Whole cell radioligand competition binding studies using the radio-ligand ¹²⁵I-sCT(8-32) at the 4 variants in the presence of cold competing sCT(8-32) (A), hCT (B) and sCT (C). In each graph the binding curve of hCT_aLeu is shown in blue, hCT_aPro in green, hCT_bLeu in red and hCT_bPro in purple with data from 3 to 9 independent experiments conducted in duplicate. Statistically significant differences in pIC₅₀ are indicated in red in the comparisons below the plots (P < .05). (D) The left 2 panels show representative flow cytometry histograms of CTR expression in the COS-7 stable cell line background, the colour scheme is the same as in A, B & C with the black histogram showing staining on vector transfected control cells. On the right is quantitated mean fluorescence intensity data + S.E.M. from 12 independent experiments normalized to staining on control cells (0%) and maximum fluorescent intensity for the particular experiment. The b variants display reduced expression compared with the a variants (p < .0001, one-way ANOVA with a Tukey post-test), while the bPro variant had lower expression compared with the aLeu variant (p = .028). (E) The left 2 panels show representative flow cytometry histograms of CTR expression in the HEK293 stable cell line background, the colour scheme is the same as in A, B & C with the black histogram showing staining on vector transfected control cells. On the right are quantitated mean fluorescence intensity data + S.E.M. from 8 independent experiments normalized to staining on control cells (0%) and maximum fluorescent intensity for the particular experiment. There was no statistical difference between polymorphs of the same variant but the aPro variant had higher expression than each of the b variants (p = .012, one-way ANOVA with a Tukey post-test). (For interpretation of the references to colour in this figure legend, the reader is referred to the web version of this article.)

at aLeu was statistically significantly lower than that measured at all other variants ($p = .001$, against aPro and $p < .001$, against “b” variants; one-way ANOVA with Bonferroni post-test, Fig. 1C and Table 1).

3.2. Cell surface expression of CTR variants

All cell lines were generated as polyclonal lines, selected for transgene integration using antibiotic resistance and positive expression by fluorescence activated cell sorting. On the COS-7 cell background the different splice variants were expressed at statistically significantly different levels ($p < .001$, for either CTR_a variant against either CTR_b variant; one-way ANOVA with Tukey's post-test) with the CTR_b variants expressed at approximately 15–30% of the CTR_a variants (Fig. 1D). There was no difference in expression of aLeu compared with aPro but expression of bPro was approximately 50% lower than bLeu (Fig. 1D, ($p = .028$; one-way ANOVA with Tukey's post-test). In comparison, expression of all variants was more similar to each other in the HEK293 background with the expression of aPro being higher than the other variants ($p = .011$ for bLeu and bPro; one-way ANOVA with Tukey's post-test) but not reaching significance for aLeu ($p = .057$) (Fig. 1E).

3.3. Evaluation of signalling of all variants in the COS-7 background

We measured cAMP accumulation, intracellular calcium mobilization and ERK1/2 phosphorylation at all 4 variants, stably expressed in COS-7 cells, in response to the 2 clinically used agonists, hCT and sCT. In cAMP accumulation, the data for the CTR_a variants were best fitted by a biphasic curve (F-test comparison with either 3 or 4 parameter curves, $p < .001$ for both ligands at both polymorphisms) where the two pEC_{50} values did not differ between polymorphisms or ligands (Fig. 2A and B and Table 2). For this splice variant there was also no statistical difference in the fraction of high potency and low potency response for the 2 polymorphisms with either agonist (Fig. 2A and B, Table 2), however there was a significant decrease in E_{max} for the aPro variant compared with aLeu for both ligands ($p < .001$; one-way ANOVA with Tukey's post-test; Fig. 2A and B and Table 2). At the CTR_b splice variant the cAMP accumulation data were best described by a 3-parameter curve fit with a pEC_{50} that was equivalent to the low potency pEC_{50} observed in the CTR_a variants (Fig. 2A and B and Table 2). Also, consistent with the CTR_a splice variant, we observed a significant reduction in E_{max} at the bPro variant for both agonists ($p < .001$; one-way ANOVA with Tukey's post-test, Fig. 2A and B

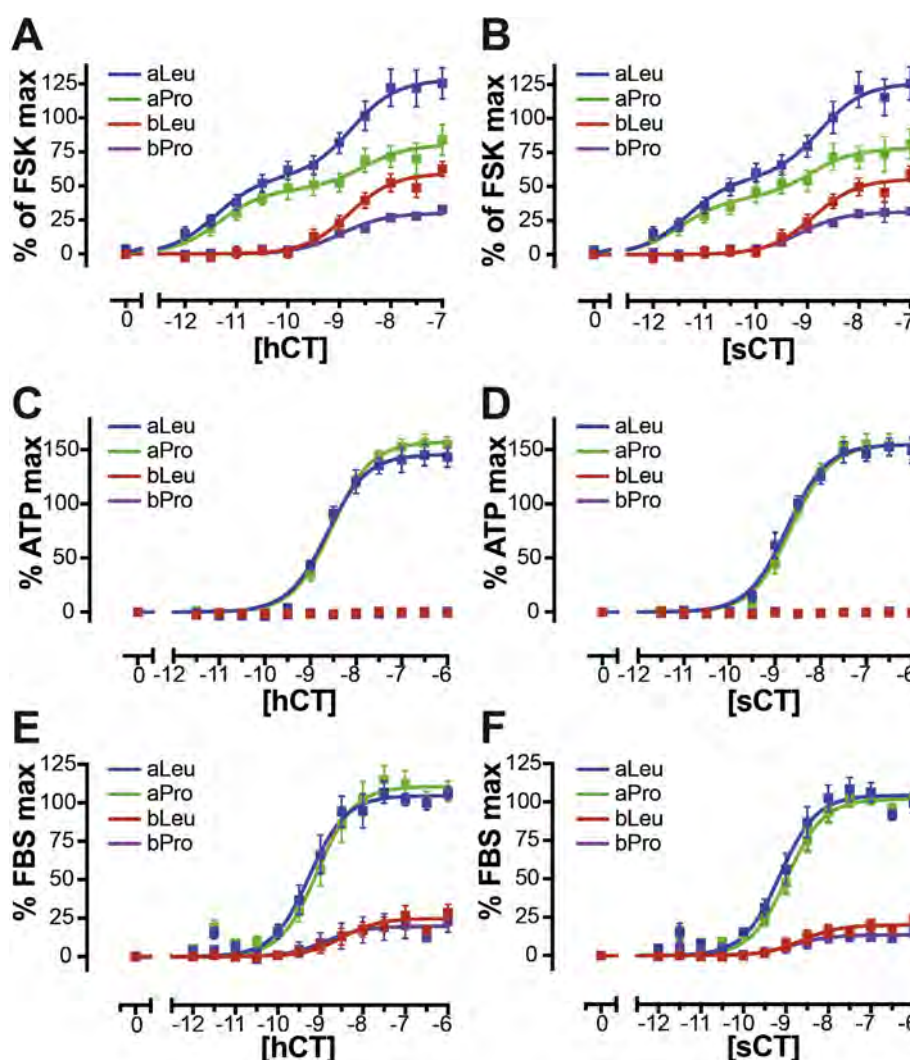


Fig. 2. Signalling profiles of CTR variants stably expressed on a COS-7 background. Concentration-response curves for hCT (A, C & E) and sCT (B, D & F) in cAMP accumulation, (A & B) Ca^{2+} mobilization, (C & D) and ERK1/2 phosphorylation, (E & F). Data are normalized to the maximum response elicited by forskolin (cAMP), ATP (Ca^{2+} mobilization) and 10% FBS (ERK1/2 phosphorylation) and analysed using either a biphasic fit or three-parameter logistic equation (as determined by an F-test to compare goodness of fits). Values are the mean \pm S.E.M. of 8–12 individual experiments, conducted in duplicate, triplicate or quadruplicate.

Table 2

Signalling data in all pathways for human CTR variants stably expressed in COS-7 cells.

		cAMP			pERK1/2		iCa ²⁺	
		pEC ₅₀ 1	pEC ₅₀ 2	E _{max}	pEC ₅₀	E _{max}	pEC ₅₀	E _{max}
hCT	aLeu	11.40 ± 0.23	8.76 ± 0.23	128.1 ± 6.3 [†]	9.26 ± 0.08	104.7 ± 1.3 [†]	8.63 ± 0.06	145.7 ± 3.5
	aPro	11.33 ± 0.23	8.55 ± 0.44	80.4 ± 6.2 [†]	9.10 ± 0.09	110.6 ± 3.6 [†]	8.53 ± 0.04	157.4 ± 2.7
	bLeu	–	8.80 ± 0.11	64.1 ± 2.9 [†]	8.49 ± 0.20	24.8 ± 2.1 [†]	–	–
	bPro	–	8.95 ± 0.10	38.0 ± 1.7 [†]	8.90 ± 0.38	19.6 ± 2.9 [†]	–	–
sCT	aLeu	11.35 ± 0.24	8.77 ± 0.24	126.1 ± 6.5 [†]	9.14 ± 0.08	104.4 ± 3.0 [†]	8.77 ± 0.06	151.6 ± 3.5
	aPro	11.46 ± 0.29	8.94 ± 0.41	78.2 ± 5.3 [†]	9.00 ± 0.06	101.9 ± 2.3 [†]	8.62 ± 0.06	158.2 ± 3.6
	bLeu	–	8.88 ± 0.12	60.4 ± 2.8 [†]	8.62 ± 0.16	19.9 ± 1.3 [†]	–	–
	bPro	–	9.15 ± 0.12	39.7 ± 1.9 [†]	8.90 ± 0.25	13.4 ± 1.3 [†]	–	–

Data in Fig. 2A and B were fitted with either a biphasic curve (CTR_a variants) or a three-parameter curve (CTR_b variants), based on an F-test to determine the best fit while constraining hill slopes for both sites to 1, the remainder of the data were fitted to a three-parameter curve (Fig. 2C through F). pEC₅₀ is the negative logarithm of the molar concentration of agonist that produces half the maximal response. (1) and (2) are the high and low potency pEC₅₀ values of the biphasic cAMP accumulation curve, respectively (CTR_a variants), or pEC₅₀ (2) calculated by the three-parameter logistic curve fit (CTR_b variants); the remaining signalling data are fit with a single pEC₅₀. E_{max} is the fitted maximum response to each agonist normalized to vehicle (0%) and the maximum response elicited by the internal control (forskolin for cAMP, FBS for pERK1/2, and ATP for iCa²⁺). All values are mean ± standard error from the curve fit of 8–12 independent experiments conducted in duplicate, triplicate or quadruplicate. Differences in pEC₅₀ or E_{max} are indicated: [†]different from all other forms, [‡]different from corresponding polymorph, ^{*}different from corresponding splice variant, ^{††}different from both polymorphs at alternatively spliced variant (p < .05, one-way ANOVA with a Tukey post-test).

and Table 2). Across all variants in cAMP, no statistical difference in the pEC₅₀ values for response to sCT and hCT was evident, which is consistent with our previous reports on the relatively high efficacy of hCT compared with sCT [42]. In intracellular calcium mobilization assays, there was no detectable response to either agonist at the CTR_b variants (Fig. 2C and D). In contrast, a robust response was observed to both agonists at the CTR_a variants with no differences in pEC₅₀ or E_{max} either across polymorphisms or between agonists (Fig. 2C and D and Table 2). In ERK1/2 phosphorylation assays a robust response was detected to both ligands at the insert negative splice variants with a lower response at the insert positive variants (Fig. 2E and F). There were no differences in pEC₅₀, both between agonists and across polymorphisms and splice variants (Fig. 2E and F and Table 2). However, the CTR_a variants showed a significant decrease in E_{max} compared with the CTR_b variants (p < .001, for all comparisons between CTR_a and CTR_b variants; one-way ANOVA with Tukey's post-test, Fig. 2E and F and Table 2). Overall, we observed a loss in signalling capacity at the CTR_b variants compared with CTR_a and at least some of this is explicable in terms of lower expression levels. The C-terminal tail polymorphism, on the other hand, only exhibited differences in coupling at cAMP, with the proline variant eliciting a lower E_{max} at both splice variants. The observation that this did not carry across to either calcium mobilization or ERK phosphorylation supports a model in which this polymorphism biases receptor signalling away from cAMP production relative to the leucine variant.

3.4. Evaluation of signalling of all variants in the HEK293 background

Parallel analysis of hCT and sCT response in cAMP accumulation, intracellular calcium mobilization and ERK1/2 phosphorylation at all 4 CTR variants, stably expressed in HEK293 cells, was also performed. In contrast to the cAMP data from the COS-7 stable cell lines, all cAMP data in the HEK293 cells were best fitted by a 3-parameter curve (Fig. 3A and B). The CTR_a variants displayed 300-fold higher potency for cAMP accumulation for both ligands compared with the CTR_b variants (p < .001, for all comparisons between CTR_a and CTR_b variants, Fig. 3A and B and Table 3). In contrast to the COS-7 background, although potency was greatly reduced at the CTR_b variants, their stimulation with either agonist elicited a similar E_{max} when compared to the CTR_a variants. Similar to cAMP in the COS-7 background, the aPro polymorph displayed a significantly lower E_{max} compared with the leucine variant

(Fig. 3A and B and Table 3), although this polymorph dependent difference did not hold at the CTR_b splice variant (p = .001, for all comparisons to aPro; one-way ANOVA with Tukey's post-test). Consistent with the results seen in the COS-7 background there was no statistical difference in the EC₅₀ values for response to sCT and hCT (Fig. 3A and B, Table 3). In intracellular calcium mobilization assays there was no detectable response to either agonist at the CTR_b variants (Fig. 3C and D), suggesting a loss in coupling efficiency for this splice variant at this pathway. In contrast, a robust signal was measured in response to both agonists at the CTR_a splice variants with no differences in pEC₅₀ (Fig. 3C and D and Table 3), but in contrast to the COS-7 background there was a statistically significant decrease in E_{max} for the aPro variant relative to the aLeu when stimulated with either ligand (p = .001 for hCT, and p = .006 for sCT). In ERK1/2 phosphorylation assays there was a robust response for both ligands at the CTR_a splice variants, while the CTR_b variants showed a significant decrease in E_{max} compared with the CTR_a variants (p < .001, Fig. 3E and F and Table 3). In addition, aPro showed a reduced E_{max} compared with aLeu for both hCT (p = .045) and sCT (p = .045). No difference in pEC₅₀ was detected across any variant with either ligand (Fig. 3E and F and Table 3). Overall, we observed a loss in signalling capacity at the CTR_b variants compared with CTR_a and, in contrast to the COS-7 background, this was not explicable in terms of lower expression levels, thus supporting a reduction in coupling efficiency for this splice variant to all pathways tested. On the other hand, at the CTR_a variant, the C-terminal tail Pro polymorphism exhibited significant reductions in E_{max} at cAMP, Ca²⁺ mobilization and ERK1/2 phosphorylation when compared with aLeu.

3.5. Signalling bias exhibited by distinct receptor variants

To better visualize the signalling data, we generated bias plots comparing all pathways with both agonists against all 4 variants in both cell backgrounds (Fig. 4A–F). In this analysis, the % of response for one pathway is plotted against a second pathway for each receptor variant at equipotent concentrations for each ligand (hCT shown solid and sCT shown dashed). While these derived plots are not quantitative, they enable a qualitative comparison of all signalling pathways across variants in both cell lines. Moreover, they allow the identification of potential biased signalling between receptor variants. Differences were observed between the different CTR polymorphs, however these effects are

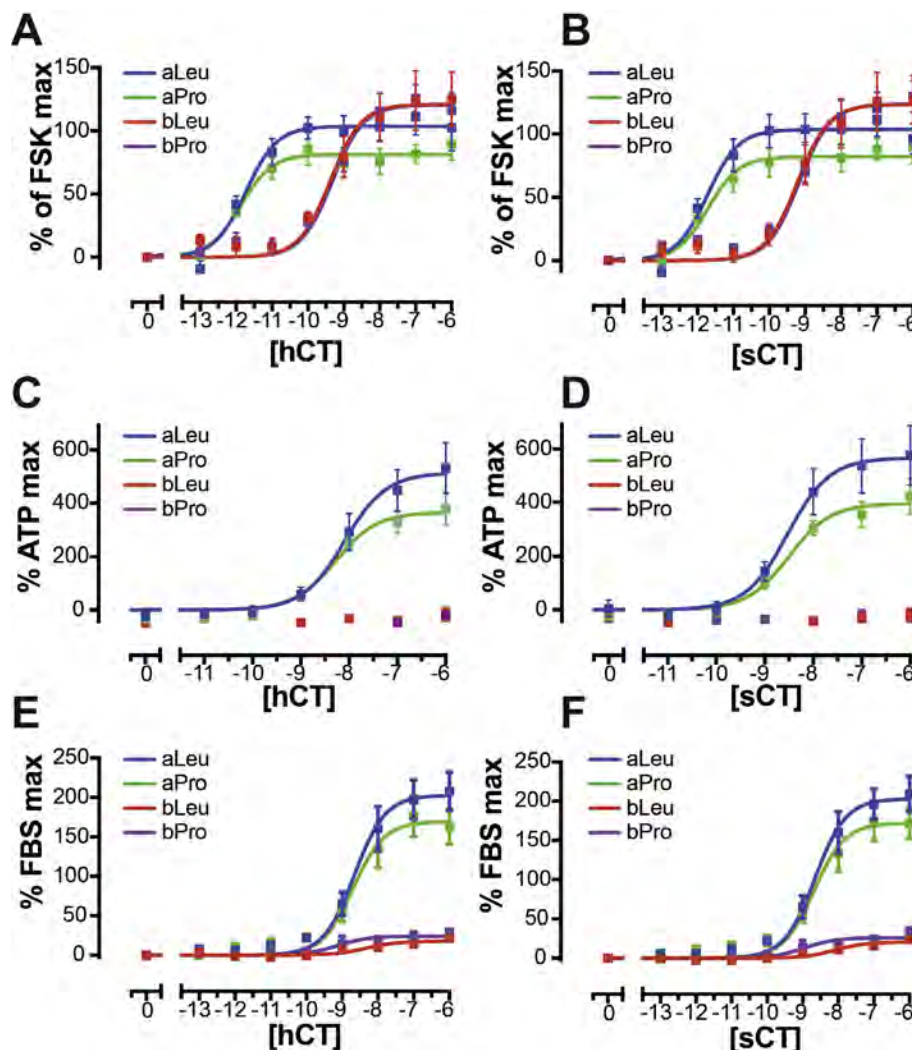


Fig. 3. Signalling profiles of CTR variants stably expressed on a HEK293 background. Concentration-response curves for hCT (A, C & E) and sCT (B, D & F) in cAMP accumulation, (A & B) Ca^{2+} mobilization, (C & D) and ERK1/2 phosphorylation, (E & F). Data are normalized to the maximum response elicited by forskolin (cAMP), ATP (Ca^{2+} mobilization) and 10% FBS (ERK1/2 phosphorylation) and analysed using either a biphasic fit or three-parameter logistic equation (as determined by an F-test to compare goodness of fits). Values are the mean \pm S.E.M. of four individual experiments, conducted in triplicate or quadruplicate.

Table 3

Signalling data in all pathways for human CTR variants stably expressed in HEK293 cells.

		cAMP		pERK1/2		Ca^{2+}	
		pEC ₅₀ 1 (M)	E _{max}	pEC ₅₀ (M)	E _{max}	pEC ₅₀ (M)	E _{max}
hCT	aLeu	11.73 \pm 0.17 [*]	103.7 \pm 4.6 [†]	8.66 \pm 0.14	202 \pm 10 [†]	8.09 \pm 0.17	514 \pm 38 [‡]
	aPro	11.87 \pm 0.17 [*]	81.4 \pm 3.6 [†]	8.69 \pm 0.16	169.3 \pm 9.7 [†]	8.23 \pm 0.17	366 \pm 21 [‡]
	bLeu	9.37 \pm 0.20 [*]	121.1 \pm 7.8 [*]	8.33 \pm 0.26	17.6 \pm 1.8 [*]	–	–
	bPro	9.32 \pm 0.13 [*]	120.5 \pm 5.1 [*]	9.13 \pm 0.36	24.1 \pm 3.1 [*]	–	–
sCT	aLeu	11.72 \pm 0.17 [*]	103.7 \pm 4.5 [†]	8.66 \pm 0.12	203 \pm 9.2 [†]	8.53 \pm 0.19	567 \pm 41 [‡]
	aPro	11.71 \pm 0.17 [*]	82.2 \pm 3.6 [†]	8.68 \pm 0.15	172.1 \pm 9.3 [†]	8.51 \pm 0.15	397 \pm 22 [‡]
	bLeu	9.22 \pm 0.18 [*]	123.4 \pm 7.8 [*]	8.09 \pm 0.20	20.5 \pm 1.8 [*]	–	–
	bPro	9.17 \pm 0.12 [*]	123.9 \pm 5.3 [*]	8.95 \pm 0.33	26.0 \pm 3.1 [*]	–	–

Data in Fig. 3A through F were fitted to a 3 parameter logistic equation. pEC₅₀ is the negative logarithm of the concentration of agonist that produces half the maximal response. E_{max} is the fitted maximum response to each agonist normalized to vehicle (0%) and the maximum response elicited by the internal control (forskolin). For cAMP, FBS for pERK1/2, and ATP for Ca^{2+} . All values are mean \pm standard error from the curve fit of 4 independent experiments conducted in triplicate. Differences in pEC₅₀ or E_{max} are indicated: [†]different from all other forms, [‡]different from corresponding polymorph, ^{*}different from corresponding splice variant, ^{††}different from both polymorphs at alternatively spliced variant ($p < .05$, one-way ANOVA with a Tukey post-test).

relatively subtle, whereas differences between splice variants were quite pronounced. In both cell backgrounds there was a similar pattern of signal bias for cAMP versus pERK1/2 with aPro being biased away from cAMP compared to aLeu (Fig. 4A and B), while

both CTR_b variants maintain bias towards cAMP over ERK1/2 phosphorylation at higher concentrations of ligand when compared with the CTR_a variants (Fig. 4A and B). When Ca^{2+} mobilization is plotted against cAMP accumulation, once again the aPro variant

is biased away from cAMP when compared with aLeu and this holds for both cell backgrounds (Fig. 4C and D). When plotting Ca^{2+} mobilization against ERK1/2 phosphorylation there is no evidence of altered signalling bias within the receptor variants (Fig. 4E and F). sCT and hCT exhibited very similar bias profiles across all receptor variants in both cell backgrounds with the possible exception of the aLeu variant comparing Ca^{2+} mobilization against ERK1/2 phosphorylation in the HEK293 cell background (Fig. 4F).

3.6. Evaluation of signalling with an extended ligand set in the COS-7 background

We have previously reported that although sCT and hCT have vastly different affinities for the human CTR, their potency in cAMP accumulation is not different at the aLeu variant [42]. This is due to enhanced efficacy of hCT, driven by a relatively higher G protein turnover rate compared with sCT [42]. To further probe the pharmacological behaviour of these CTR variants, and in particular to

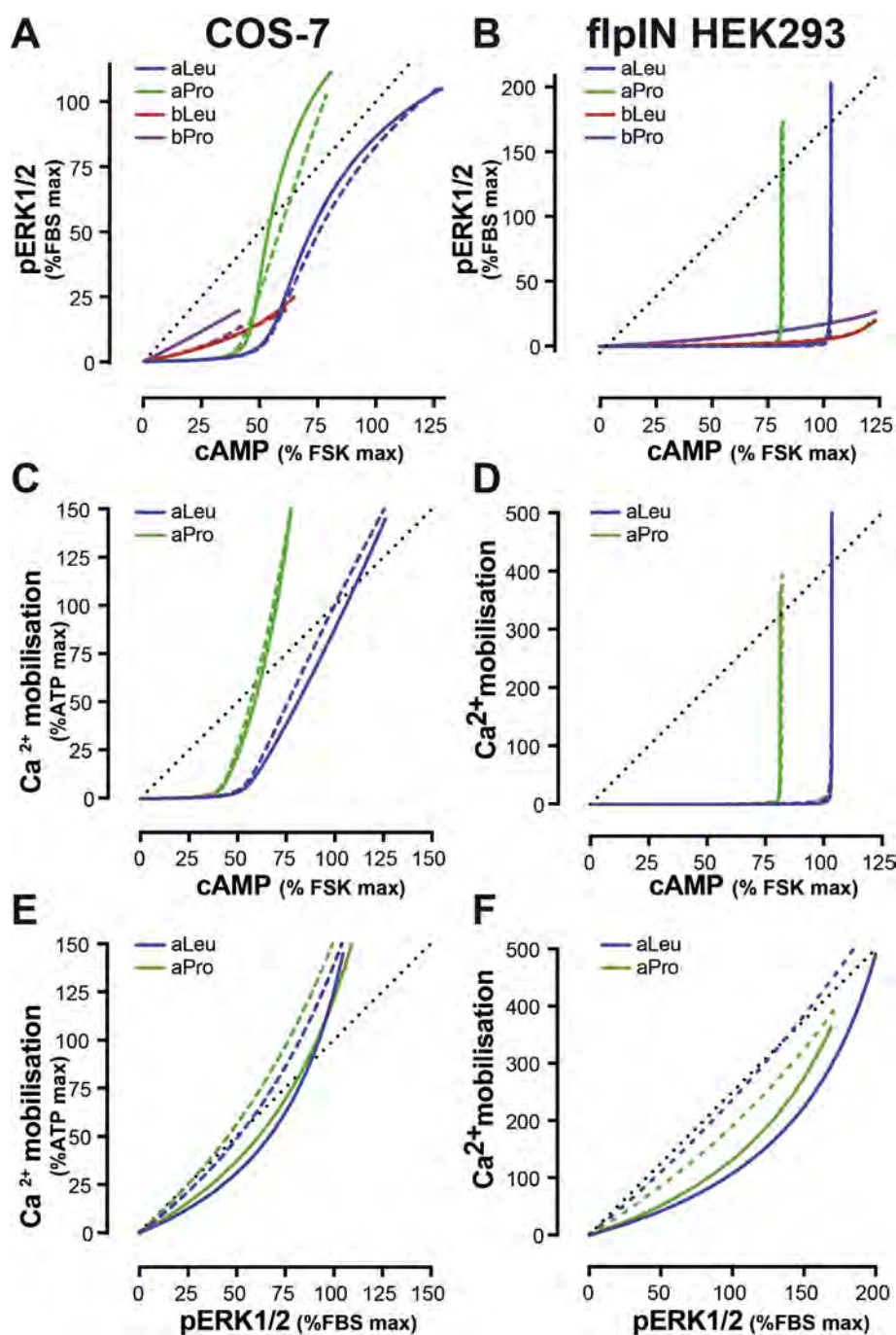


Fig. 4. Bias plots for hCT and sCT across all CTR variants. The plots display the proportion of response in each pathway to equi-occupant concentrations of each ligand. In A (COS-7) and B (HEK293) the response in cAMP is plotted against the response in ERK1/2 phosphorylation for each variant with the same colour code as Figs. 1–3 (aLeu = blue, aPro = green, bLeu = red, bPro = purple), hCT plots are solid lines and sCT are dashed, shown in black is an $\sim 45^\circ$ slope for reference only. In C (COS-7) and D (HEK293) the response to cAMP is plotted against Ca^{2+} mobilization with b variants omitted due to their lack of response in calcium, colours and dashes are the same as in A & B. In E (COS-7) and F (HEK293) the response to Ca^{2+} mobilization is plotted against ERK1/2 phosphorylation with b variants omitted due to their lack of response in calcium, colours and dashes are the same as in A & B. (For interpretation of the references to colour in this figure legend, the reader is referred to the web version of this article.)

try and reveal any further receptor variant-dependent differences, we performed competition-binding and signalling assays using porcine CT (pCT) and chicken CT (cCT). Although pigs are evolutionarily more closely related to humans than either to fish or birds, porcine CT is quite distantly related to human CT in sequence with 18 substitutions in this 32 amino acid peptide. Fig. 5A shows a sequence alignment of the 4 CT peptides used in this part of the study. In a parallel set of experiments we measured competition binding, cAMP accumulation, iCa^{2+} mobilization and ERK1/2 phosphorylation at all 4 variants, stably expressed in COS-7 cells, in response to all 4 peptides. In competition binding against ^{125}I -sCT(8–32) there was no difference in the pIC_{50} of pCT at any variant (Table 4 and Fig. 5B). On the other hand, cCT displayed a significantly lower affinity for aLeu compared with all other variants (Fig. 5C and Table 4, $p = .013$ against aPro, $p < .001$ against bLeu and bPro; one-way ANOVA with a Tukey post-test), which accords with the lower affinity observed at this variant with the related sCT peptide. Consistent with earlier experiments in cAMP accumulation, the data for the CTR_a variants with all ligands were best fitted by a biphasic curve (F-test comparison with either 3 or 4 parameter curves, $p < .05$), whereas the CTR_b variants were best described by a 3 parameter curve fit. At all variants the pEC_{50} values for cAMP accumulation trended lower with pCT (Table 5 and Fig. 5D) and higher with cCT (Table 5 and Fig. 5E) compared to both hCT and sCT. For cCT there was a reduction of E_{max} for the Pro polymorphism compared with Leu at either splice variant ($p = .008$ for aPro versus aLeu, $p = .014$ bPro versus bLeu; one-way ANOVA with a Tukey post-test, Fig. 5E and Table 5). As we saw for hCT and sCT, across all variants in cAMP, no statistical difference in the EC_{50} values for response to pCT and cCT was evident. In iCa^{2+} mobilization assays there was no detectable response to either cCT or pCT at the CTR_b variants (Fig. 5F and G). In contrast, a robust response was observed to both agonists at the CTR_a variant, with no differences in pEC_{50} or E_{max} either across polymorphisms or between agonists (Fig. 5F and G and Table 5). In pERK assays a robust response was detected for pCT and cCT at the CTR_a variants, with a lower response at the CTR_b variants (Fig. 5H and I). There were no differences in pEC_{50} , either between cCT and pCT, or across polymorphisms and splice variants (Fig. 5F, G and Table 5), however cCT did show a significant reduction in pEC_{50} when compared with both hCT and sCT at the aPro variant (Table 5, $p = .029$ against hCT, and $p = .019$ against sCT; one-way ANOVA with a Tukey post-test). As was observed for hCT and sCT, the CTR_b variants showed a significant decrease in E_{max} compared with the CTR_a variants ($p < .001$ for all comparisons between CTR_a and CTR_b variants; one-way ANOVA with Tukey's post-test, Fig. 5H, I and Table 5). Overall the CTR_b variant displayed decreased coupling at all pathways, so to explore whether the loss in calcium signalling at the CTR_b variant was explicable in terms of lower expression levels, or whether there might be a specific effect on Gq-effector coupling, iCa^{2+} mobilization at the CTR_a variants was assessed in the absence or presence of the specific Gq inhibitor UBO-QJC (FR900359) [51,52]. We tested two concentrations of all peptides at both aLeu (Fig. 5J) and aPro (Fig. 5K) in the presence or absence of 100 nM UBO-QJC and saw a statistically significant reduction in ligand-induced iCa^{2+} mobilization of more than 50%, indicating that most

of this response for CTR arises from activation of Gq. This suggests that the insert positive CTR_b variants may not be competent to activate Gq.

To better visualize signalling data for pCT and cCT at the different receptor variants, we generated bias plots comparing ligand-specific biased agonism at each receptor. This is directly illustrated in Fig. 6. At the aLeu variant (shown in Fig. 6A–C) the relative bias of pCT (teal) away from cAMP compared to other peptides can be seen, while the relative bias of cCT (olive) towards cAMP compared to other peptides is evident. In comparison, at aPro (Fig. 7D, E) there is little bias of pCT for cAMP against ERK1/2 phosphorylation and iCa^{2+} mobilization compared with hCT and sCT, although cCT maintains the bias towards cAMP relative to the other ligands seen at the aLeu variant. At the CTR_b variants these bias plots reveal that pCT is biased away from cAMP compared with other ligands at the bLeu variant (Fig. 6G, I), but that pCT and hCT demonstrate this relative bias at the bPro variant (Fig. 6H, I).

3.7. Evaluation of β -arrestin recruitment

Previous data at the porcine CTR [53] revealed the CTR C-terminus is required for receptor internalization, and the absolute conservation of proline at position 447 in other mammals suggests that this residue may be involved in regulation of receptor trafficking. The difference in relative expression of CTR_b and CTR_a splice variants in the COS-7 background may indicate differential trafficking in this cell background. The best characterized pathway for internalization of GPCRs is via ligand promoted receptor phosphorylation by GRKs (G protein-coupled receptor kinases) which is coupled to ligand promoted recruitment of β -arrestin and drives internalization (usually via clathrin mediated endocytosis) (see [24]). We therefore generated bicistronic constructs containing either β -arrestin-1 or β -arrestin-2 with a C-terminal Venus fusion and individual CTR variants with a C-terminal Rluc8 fusion to assess receptor variant and/or ligand dependent differences in β -arrestin recruitment. These CTR constructs retained signalling to cAMP when transiently transfected into COS-7 cells (Fig. 7A). We used BRET to assess ligand promoted β -arrestin-1 and β -arrestin-2 recruitment to the CTR, transiently transfected into COS-7 cell, for both hCT and sCT. In this assay no ligand promoted recruitment of arrestins was observed for either hCT or sCT (not shown). To ensure that the absence of observed β -arrestin recruitment was not due to low expression of GRKs in the cell system, GRK 2, 3, 5 and 6 were co-transfected with the bicistronic vector and the assay was repeated. Despite the overexpression of GRKs, no agonist-mediated change in arrestin BRET signal profile was observed for any of the tagged CTR variants (data not shown). This lack of ligand promoted β -arrestin recruitment was not due to a cell background effect; stimulation of COS-7 cells with GLP-1(7–36NH₂), when transiently transiently transfected with β -arrestin-1/GLP-1R or β -arrestin-2/GLP-1R, gave a similar magnitude of ligand promoted β -arrestin recruitment to that previously reported in other cell lines (Fig. 7B, C) [45,46]; indicating that the COS-7 cell background is competent to sponsor ligand promoted β -arrestin recruitment. Additional confirmation for the absence of a cell background effect was performed by transfecting the bicistronic CTR/arrestin

Fig. 5. Binding and signalling profiles of CTR variants stably expressed on a COS-7 background with pCT and cCT. A shows an alignment of mature calcitonin peptides from human (hCT), pig (pCT), salmon (sCT) and chicken (cCT), * – single, fully conserved residue, : – conservation of strong groups, . – conservation of weak groups, space – no consensus. B & C: Whole cell radioligand competition binding studies using the radio-ligand ^{125}I -sCT(8–32) at the 4 variants in the presence of cold competing pCT (B) and cCT (C). In each graph the binding curve of hCTR_aLeu is shown in blue, hCTR_aPro in green, hCTR_bLeu in red and hCTR_bPro in purple with data from 3 to 4 independent experiments conducted in duplicate. No difference in affinity of any variant for pCT, cCT showed a statistically significant decrease in affinity at aLeu compared with all other variants ($P < .05$ by one way ANOVA with Tukey post test.). Concentration-response curves for hCT (A, C & E) and sCT (B, D & F) in cAMP accumulation, (A & B) Ca^{2+} mobilization, (C & D) and ERK1/2 phosphorylation, (E & F). Data are normalized to the maximum response elicited by forskolin (cAMP), ATP (Ca^{2+} mobilization) and 10% FBS (ERK1/2 phosphorylation) and analysed using either a biphasic fit or three-parameter logistic equation (as determined by an F-test to compare goodness of fits). Values are the mean \pm S.E.M. of 8–12 individual experiments, conducted in duplicate, triplicate or quadruplicate.

A

hCT CGNLSTCMLGTYTQDFNKFHTFPQTAIGVGAP
sCT CSNLSTCVLGKLSQELHKLQTYPRNTGSGTP
cCT CASLSTCVLGKLSQELHKLQTYPRTDVGAGTP
pCT CSNLSTCVLSAYWRNLNNFHRFSGMGFGPETP
 * . . . * * * * : * . : : : : : : : : : : : * . *

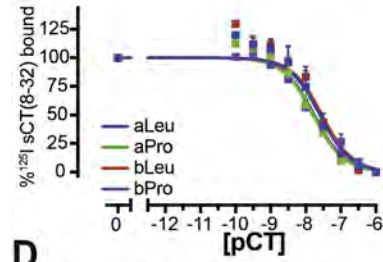
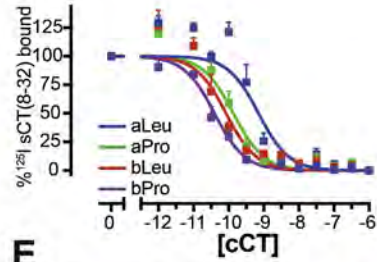
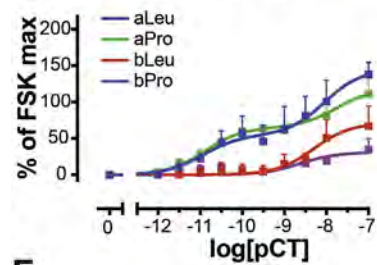
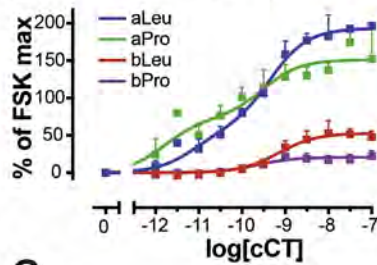
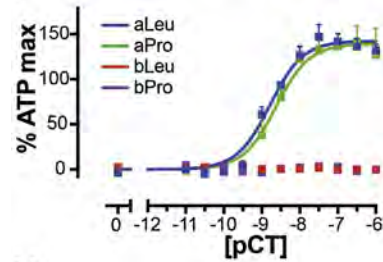
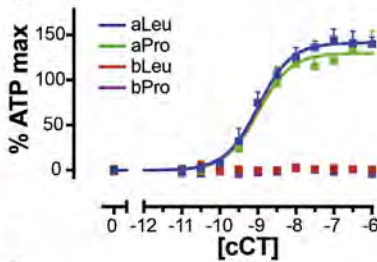
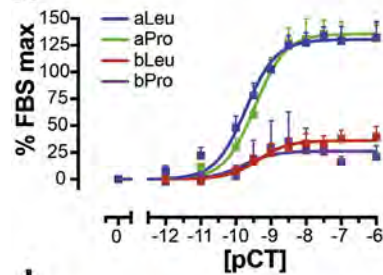
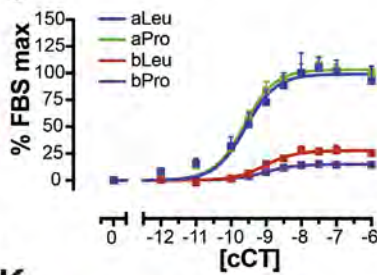
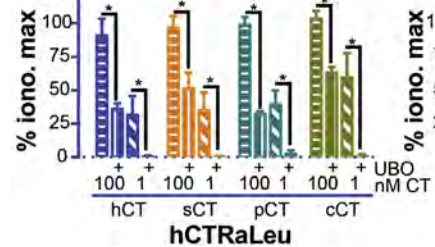
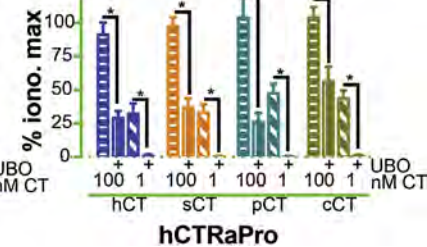
B**C****D****E****F****G****H****I****J****K**

Table 4
Affinity data for human CTR variants.

	aLeu	aPro	bLeu	bPro
pCT pIC ₅₀	7.77 ± 0.20	8.02 ± 0.16	7.95 ± 0.22	7.97 ± 0.16
cCT pIC ₅₀	9.37 ± 0.16 [†]	10.53 ± 0.12 [‡]	10.06 ± 0.14 [*]	10.61 ± 0.11 ^{**}

Experiments were performed in COS-7 cells stably expressing the human CTR. Whole cell radioligand binding was performed for each ligand and receptor variant using ¹²⁵I-sCT(8–32). All values are mean ± S.E.M. of 3–4 independent experiments conducted in duplicate. Differences in affinity are indicated: [†]different from all other forms, [‡]different from corresponding polymorph, ^{*}different from corresponding splice variant, ^{**}different from alternative polymorph at alternatively spliced variant (*p* < .05, one-way ANOVA with a Tukey post test).

Table 5
Signalling data in all pathways for human CTR variants stably expressed in COS-7 cells.

		cAMP			pERK1/2		iCa ²⁺	
		pEC ₅₀ 1 (M)	pEC ₅₀ 2 (M)	E _{max}	pEC ₅₀ (M)	E _{max}	pEC ₅₀ (M)	E _{max}
aLeu	hCT	11.40 ± 0.24	8.84 ± 0.32	142 ± 9	9.71 ± 0.10	117.9 ± 4.1	8.66 ± 0.15	148.9 ± 8.7
	sCT	11.39 ± 0.28	8.64 ± 0.37	159 ± 14	9.39 ± 0.12	120.7 ± 5.5 ^{**}	8.84 ± 0.10	159.6 ± 6.5
	pCT	10.93 ± 0.59	8.04 ± 0.51	145 ± 24	9.72 ± 0.09	130.3 ± 4.1 ^{**}	8.79 ± 0.08	142.3 ± 4.0
	cCT	11.58 ± 0.64	9.47 ± 0.18	192 ± 9	9.58 ± 0.13	99.1 ± 4.6 [†]	8.99 ± 0.07	141.3 ± 3.7
aPro	hCT	11.23 ± 0.17	8.21 ± 0.56	82 ± 8 ^{**}	9.17 ± 0.13 ^{**}	133.7 ± 6.7 ^{**}	8.76 ± 0.07	139.4 ± 3.9
	sCT	11.30 ± 0.37	8.36 ± 0.67	110 ± 17	9.14 ± 0.07 ^{**}	111.5 ± 3.2 [†]	8.81 ± 0.11	138.2 ± 6.0
	pCT	10.86 ± 0.23	7.70 ± 0.34	120 ± 15	9.46 ± 0.09	135.5 ± 4.6 ^{**}	8.62 ± 0.12	139.1 ± 6.6
	cCT	11.79 ± 0.48	9.52 ± 0.43	150 ± 10	9.62 ± 0.07 [†]	103.3 ± 2.7 [†]	8.99 ± 0.09	129.8 ± 4.4
bLeu	hCT	–	8.93 ± 0.22	78 ± 9	8.92 ± 0.27	39.8 ± 4.5 ^{**}	–	–
	sCT	–	8.94 ± 0.21	74 ± 8	9.17 ± 0.20	28.1 ± 2.2	–	–
	pCT	–	8.30 ± 0.26	71 ± 13	9.37 ± 0.22	36.0 ± 3.0	–	–
	cCT	–	9.15 ± 0.18	53 ± 4	9.04 ± 0.14	27.7 ± 1.6 [†]	–	–
bPro	hCT	–	9.27 ± 0.28	20 ± 2	9.21 ± 0.39	44.0 ± 6.6 ^{**}	–	–
	sCT	–	9.52 ± 0.17	28 ± 2	9.43 ± 0.30	20.2 ± 2.3 [†]	–	–
	pCT	–	8.62 ± 0.31	31 ± 6	9.79 ± 0.70	26.2 ± 6.0	–	–
	cCT	–	9.65 ± 0.29	21 ± 3	9.04 ± 0.13	15.0 ± 0.8 [†]	–	–

Data in Fig. 5B and B were fitted with either a biphasic curve (CTR_a variants) or a three-parameter curve (CTR_b variants), based on an F-test to determine the best fit while constraining hill slopes for both sites to 1, the remainder of the data were fitted to a three-parameter curve (Fig. 2C through F). pEC₅₀ is the negative logarithm of the concentration of agonist that produces half the maximal response. (1) and (2) are the high and low potency pEC₅₀ values of the biphasic curve, respectively (CTR_a variants), or calculated pEC₅₀(2) calculated by the three-parameter logistic curve fit (hCTR_b variants), the remaining signalling data are fit with a single pEC₅₀. E_{max} is the fitted maximum response to each agonist normalized to vehicle (0%) and the maximum response elicited by the internal control (forskolin. for cAMP, FBS for pERK1/2, and ATP for iCa²⁺). All values are mean ± standard error from the curve fit of 8–12 independent experiments conducted in duplicate, triplicate or quadruplicate. Differences in pEC₅₀ or E_{max} are indicated: [†]different from all other forms, [‡]different from corresponding polymorph, ^{*}different from corresponding splice variant, ^{**}different from both polymorphs at alternatively spliced variant (*p* < .05, one-way ANOVA with a Tukey post-test).

constructs into a CHO cell background, where GLP-1R β-arrestin recruitment was detected but CTR did not exhibit ligand-induced β-arrestin recruitment. To rule out the possibility that the Rluc8 tag on the C-terminus of CTR disrupts the ability of sCT and hCT to recruit β-arrestins to the receptor, we took an alternative approach that has been widely used. We assessed the ability of these ligands to promote redistribution of Venus tagged β-arrestins, in the presence of each CTR variant (with no C-terminal fusion) in response to agonist stimulation. The COS-7 cell lines, stably expressing hCTR variants, were transiently transfected with varying levels of the Venus tagged β-arrestins and stimulated with saturating concentrations of either sCT, sCT(8–32) or vehicle. No specific redistribution of either Venus tagged β-arrestin-1 or β-arrestin-2 could be observed in wide field images up to 60 min post stimulation, supporting the BRET data which showed that the CT peptides assessed are unable to promote recruitment of β-arrestin 1 or 2 to any of the variants of the hCTR (Fig. 8).

3.8. Receptor internalization

Although we could not measure any ligand promoted change in β-arrestin interaction with the CTR we sought to understand whether either the alternative splicing or the c-terminal tail polymorphism might alter receptor internalization. To assess CTR internalization, a confocal imaging approach was employed using the stable cell lines on the COS-7 background. sCT and the antagonist sCT(8–32) were modified by introducing the following substitutions: ^K11^R, ^K18^R and ^Q14^K. This yields a peptide that can be labelled

at position 14 using standard chemistry that is pharmacologically indistinguishable from the parental peptides [42,54]. These peptides were used to monitor receptor-mediated ligand internalization by confocal microscopy. At all variants, stably expressed in the COS-7 cells, rapid internalization of both fluorescently labelled peptides was observed (representative images in Fig. 9A, B) whereas no binding or internalization of either peptide was evident in the vector control transfected cells. One interpretation of this data could be that sCT(8–32) was an agonist with respect to receptor internalization; we therefore assessed agonist-independent receptor internalization by taking advantage of the cMyc epitope tag. Cells were labelled at 4 °C with an AF647 conjugated anti-cMyc antibody (9E10:AF647) that we have previously characterized [43]. Unbound antibody was removed by washing (at 4 °C) and cells were imaged by confocal microscopy at 37 °C (representative images in Fig. 10A). Rapid internalization, in the order of seconds to minutes, of the antibody was observed for all CTR variants that was not seen in vector control cells (Fig. 10A and Supplementary video 1), highlighting that the CTR undergoes ligand independent internalization. To understand whether this ligand independent internalization might be modified by an agonist or antagonist, cells were co-incubated with the antibody conjugate and fluorescent ligands at 4 °C, washed to remove unbound ligand and unbound antibody, and imaged at 37 °C. For all variants we observed the same pattern of internalization of the antibody conjugate as observed in the absence of ligand and both antagonist (representative images in Fig. 10B and Supplementary video 2) and agonist (representative Fig. 10C and Supplementary video 3) co-internalize with the antibody.

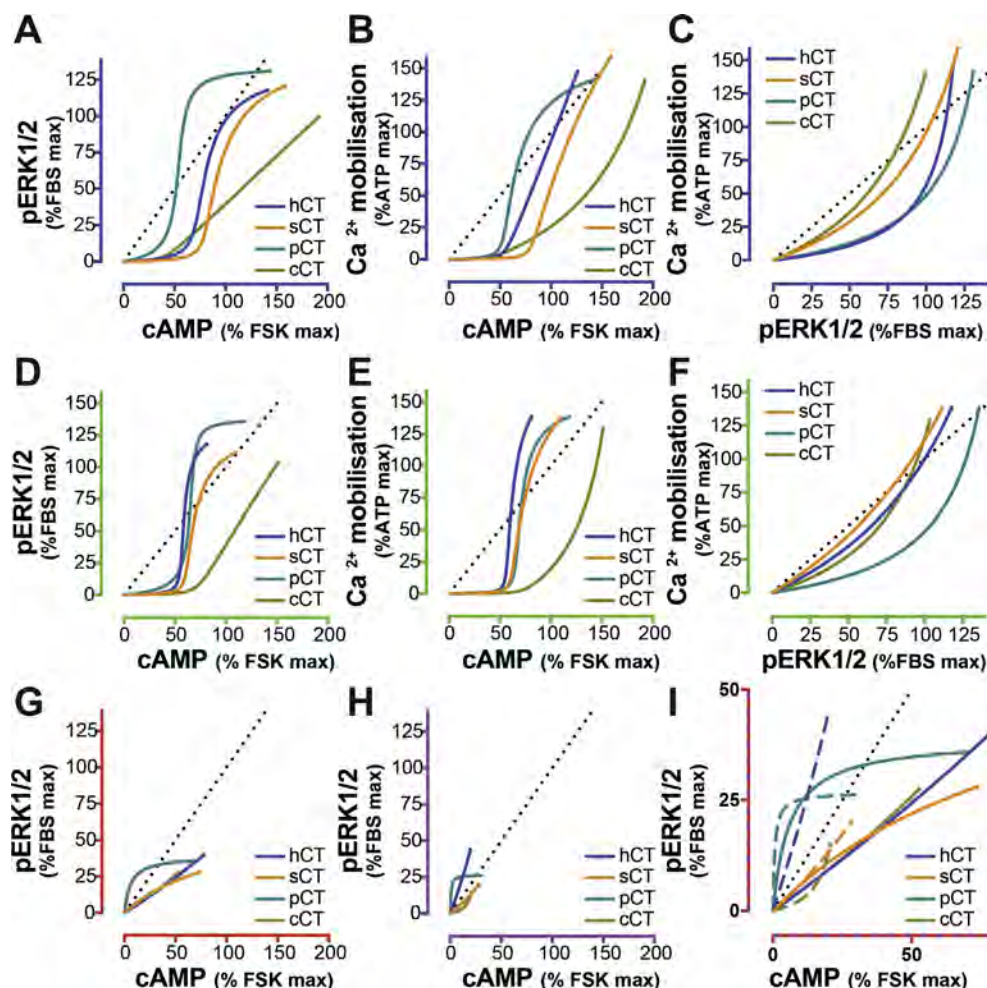
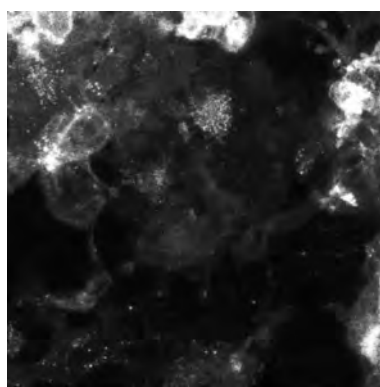
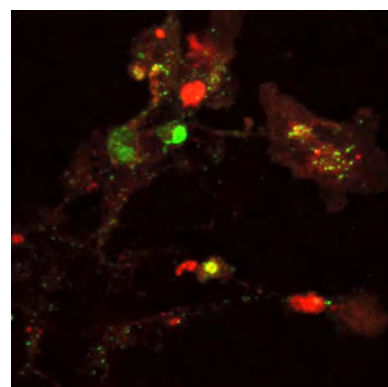


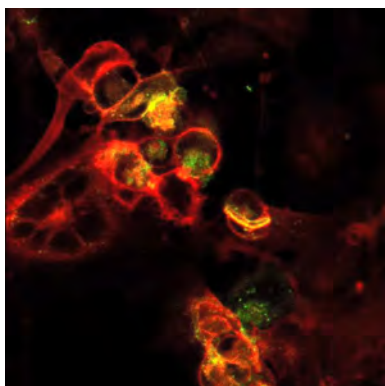
Fig. 6. Bias plots for all ligands at each CTR variants. The plots display the proportion of response in each pathway to equi-occupant concentrations of each ligand. In A, B and C the response to each ligand at the aLeu variant is plotted for (A) cAMP against ERK1/2 phosphorylation, (B) cAMP against Ca^{2+} mobilization and (C) ERK1/2 phosphorylation against Ca^{2+} mobilization for each ligand (hCT = blue, sCT = orange, pCT = teal, cCT = olive), and in black is an $\sim 45^\circ$ slope for reference only. In D, E and F the same comparisons are plotted for bPro using the same colour scheme. In G (pCT) and D (cCT) the response to cAMP is plotted against Ca^{2+} mobilization with b variants omitted due to their lack of response in calcium, colours and dashes are the same as in A & B. In E the response to each ligand at the bLeu variant is plotted for cAMP against ERK1/2 phosphorylation and in F the same plot for bPro. To allow comparison of bLeu with bPro I shows an expanded plot with bias curves of bLeu shown as solid lines and bPro as dashed.



Supplementary video 1. Internalization of 9E10-AF647 in COS-7 cells stably expressing the hCTRaLeu. Confocal field images of COS-7 stably expressing hCTRaLeu were incubated with 1 $\mu\text{g}/\text{ml}$ anti-cMyc antibody (9E10-AF647) on ice. Cells were extensively washed. Images were acquired every 1 min for 60 min at 37 $^\circ\text{C}$. Images are presented as maximum intensity projections for 9E10-AF647 emission. Representative images of 2 independent experiments.



Supplementary video 2. Internalization of sCT(8-32)-AF568 and 9E10-AF647 in COS-7 cells stably expressing the hCTRaLeu. Confocal field images of COS-7 stably expressing hCTRaLeu were incubated with 1 μM sCT(8-32)-AF568 and 1 $\mu\text{g}/\text{ml}$ anti-cMyc antibody (9E10-AF647) on ice. Cells were extensively washed. Images were acquired every 1 min for 60 min at 37 $^\circ\text{C}$. Images are presented as maximum intensity projections for 9E10-AF647 emission (green), sCT(8-32)-AF568 (red) emission. Representative images of 2 independent experiments.



Supplementary video 3. Internalization of sCT(1–32)-ROX and 9E10-AF647 in COS-7 cells stably expressing the hCTRLeu. Confocal field images of COS-7 stably expressing hCTRLeu were incubated with 1 μ M sCT-ROX and 1 μ g/ml anti-cMyc antibody (9E10-AF647) on ice. Cells were extensively washed. Images were acquired every 1 min for 60 min at 37 °C. Images are presented as maximum intensity projections for 9E10-AF647 emission (green), sCT-ROX (red) emission. Representative images of 2 independent experiments.

4. Discussion

Introduction of the additional 16 amino acids that result from *Cercopithecidae* specific alternative splicing has a major effect on CTR signalling and binding. In the previous publication by Moore et al. [41] they reported the affinity and signalling characteristics of the Leu polymorph on a BHK-1 (baby hamster kidney) cell background. They observed no impact of this intracellular loop insertion on affinity of the CTR for either hCT, pCT or sCT, whereas in our study both the sCT(8–32) antagonist and the 2 high affinity agonists, sCT and cCT displayed significantly lower affinity at CTR_a compared with CTR_b (at the Leu polymorph). Compared with hCT, which showed no difference in affinity between splice variants, sCT has a much higher propensity to form an alpha helix [55] and has high affinity driven primarily by very slow off-rate kinetics [50]. In the previous study, binding was performed for 1 h at 37 °C using an agonist probe ([¹²⁵I]sCT), whereas we performed binding for 16 h at 4 °C with an antagonist probe. While it is possible that the difference between studies may result from differences in cell background, the use of an agonist probe is very likely to alter the pool of receptors bound by the probe, favouring those in a high affinity state and thus providing a different estimate of affinity. It is also possible that our observed difference in affinity is driven by off rate kinetics that may be obscured by the short time-course of the previous study. By comparison, although sCT(8–32) and sCT also displayed higher affinity at the Pro polymorph of CTR_b, cCT affinity was not different, indicating complex ligand-dependent differences in the conformational connection between the extracellular and intracellular faces of the receptor. In contrast to the binding data, the CTR_b variant displayed a 10–100-fold decrease in the high potency cAMP response in both cell backgrounds assessed in this study, which is consistent with the 100–400 fold decrease reported previously at the Leu polymorph [41]. With respect to the high affinity agonist sCT, the cAMP response for the CTR_b variant lies close to, or even slightly right of, the measured equilibrium dissociation constant. While a large decrease in the maximum cellular cAMP response was observed in the COS-7 cell background, this was accompanied by a decrease in cell surface expression. In contrast, there was no difference in cell surface expression in the HEK293 background, yet the loss in potency of both ligands for eliciting a cAMP response at this variant remained, which is more similar to the pattern observed on the BHK background [41]. This supports a model in which the inclusion of this

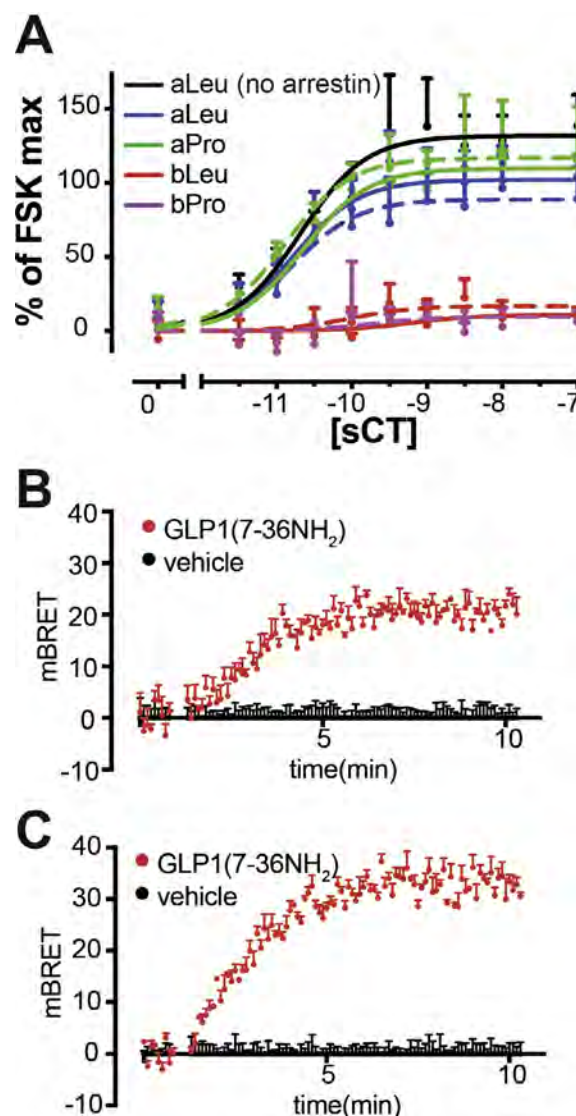


Fig. 7. Function of Rluc8 tagged CTR variants in bicistronic vector & β -arrestin recruitment at GLP-1R on the COS-7 cell background. **A**, COS-7 cells were transfected with unmodified CTR_aLeu (black) or bicistronic constructs containing CTR variants bearing a c-terminal Rluc8 tag and either β -arrestin-1 (solid lines) or β -arrestin-2 (dashed lines) fused to Venus and plated at 30,000 cells/well and stimulated with the indicated concentrations sCT. Data are analysed by non-linear regression with a three-parameter logistic curve. All values are mean + S.D. of 2 independent experiments conducted in duplicate. **B** & **C** COS-7 cells were transfected with unmodified bicistronic constructs containing GLP-1R bearing a c-terminal Rluc8 tag and either β -arrestin 1 (**C**) or β -arrestin 2 (**D**) fused to Venus and plated at 30,000 cells/well and stimulated with GLP-1(7–36NH₂). Time-courses (mean of 2 N + SD) of ligand-induced β -arrestin recruitment to the GLP-1 are shown.

extension to ICL1 reduces the functional affinity of the active receptor for $G\alpha_s$, which would be consistent with the apparent steric interference this extension would be predicted to have to the interaction of CTR with $G\alpha_s$ [56]. In both cell backgrounds CTR_b did not couple to the intracellular Ca^{2+} mobilization pathway. As our data indicated that the majority of the response to this pathway in the CTR_a variant is dependent on $G\alpha_q$, the lack of response for CTR_b likely reflects a complete lack of capacity for this splice variant to couple to $G\alpha_q$. In contrast to cAMP and intracellular Ca^{2+} mobilization, CTR_b exhibited no reduction in apparent EC₅₀ for ERK1/2 phosphorylation relative to CTR_a, but did show a marked reduction in the maximum response to all four agonists assessed. In the COS-7 background this was accompanied by a

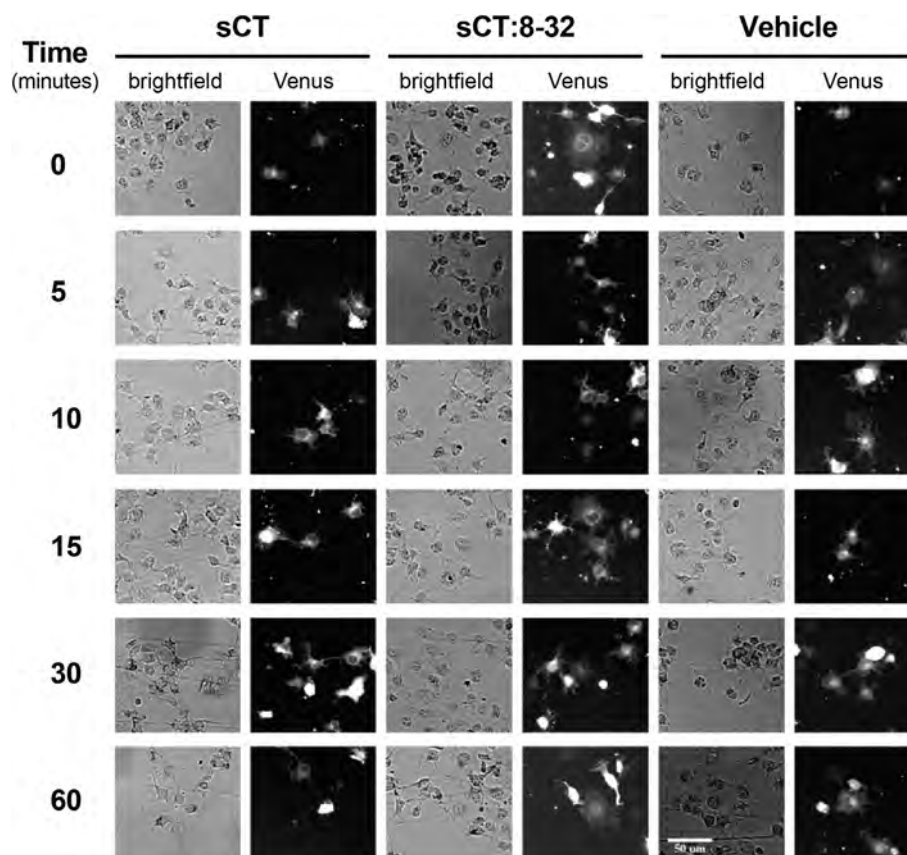


Fig. 8. Ligand dependent changes in cellular β -arrestin-1-Venus distribution. Wide-field representative images of COS-7 cells stably expressing hCTR_aLeu and transiently transfected with β -arrestin 1-Venus. Cells were stimulated with 1 μ M of sCT, sCT(8-32) or vehicle and imaged at 0, 5, 10, 30 and 60 min post ligand stimulation. Images were collected when the same cells were transfected with β -arrestin-2-Venus or with different splice variants of the receptor, with similar findings. Representative of at least 2 independent experiments.

reduction in cell surface expression but was unrelated to cell surface expression in the HEK293 background. This suggests that the insert positive CTR variant is less efficient at activating effectors linked to ERK1/2 phosphorylation compared with the insert negative variant. With only one study examining the sites of expression of the CTR_b variant it is difficult to provide a clear rationale for an old-world primate specific splice variant that exhibits preferential signalling to cAMP (as indicated via qualitative bias plots), albeit with lower efficacy. The CTR is widely expressed in the CNS [57] and mRNA for the CTR_b variant is present in the cerebellum; this may suggest that neurone-specific expression of this variant may provide a cognitive or behavioural adaptation for this family of mammals.

In all mammals, the amino acid position equivalent to 447 in humans is a conserved proline while in humans there is a widely distributed polymorphism, which replaces this with a leucine. In the context of the major role of CTR in bone homeostasis, a number of studies have attempted to correlate this polymorphism with changes in osteoporotic risk, with limited success [29,30,33,35,37]. While the transmembrane bundle proximal part of the c-terminal tail is required for G protein coupling [56] and the far distal tail has been implicated in regulation of tight junctions [58], no role has been ascribed to the region spanning amino acid 414–470 of the human receptor (amino acid numbers with respect to the insert negative splice variant). A small and statistically significant decrease in the whole-cell equilibrium binding affinity for sCT, sCT(8-32) and cCT was observed for the human specific leucine polymorphic variant compared with the conserved proline variant at the insert negative splice variant. This in contrast

to the previous report by Wolfe et al. [32] where no statistical difference in binding affinity was observed when the CTR_a Leu and Pro were compared. In contrast to our study, although COS-7 cells were also used for assay, their binding used the agonist [¹²⁵I]hCT on membranes prepared from transiently transfected cells and only incubated for 2 h at room temperature. GPCRs are thought to exhibit loose allosteric coupling between ligand and effector binding [59]. For some GPCRs, this results in the ability to detect multiple affinity sites in ligand binding studies. A high affinity, effector coupled state is not routinely observed in ligand binding for the CTR [42,56] and it was therefore surprising that a single amino acid change at the intracellular face of the receptor could alter affinity in a ligand specific manner. For the porcine CTR progressive truncation of the c-terminal tail increases the affinity of this receptor for sCT [53] that may suggest the c-terminal tail exerts a negative allosteric effect on ligand binding. The c-terminal tail of the porcine receptor is required for internalization [53] and this may translate to the human receptor whose c-terminal domain is also likely to be involved in coupling to cytoskeletal elements or internalization machinery. Differences in this type of coupling could easily influence coupling to signalling pathways by either altering the subcellular localization of the receptor or competing with effectors for receptor binding. Consistent with this, we observed a cell background independent bias away from the predominant cAMP and calcium -signalling pathways, relative to ERK1/2 phosphorylation, in the proline vs the leucine polymorph. This bias manifested itself as a decrease in the maximal cellular response and the fact that this effect was rather small in magnitude may be associated with the difficulty

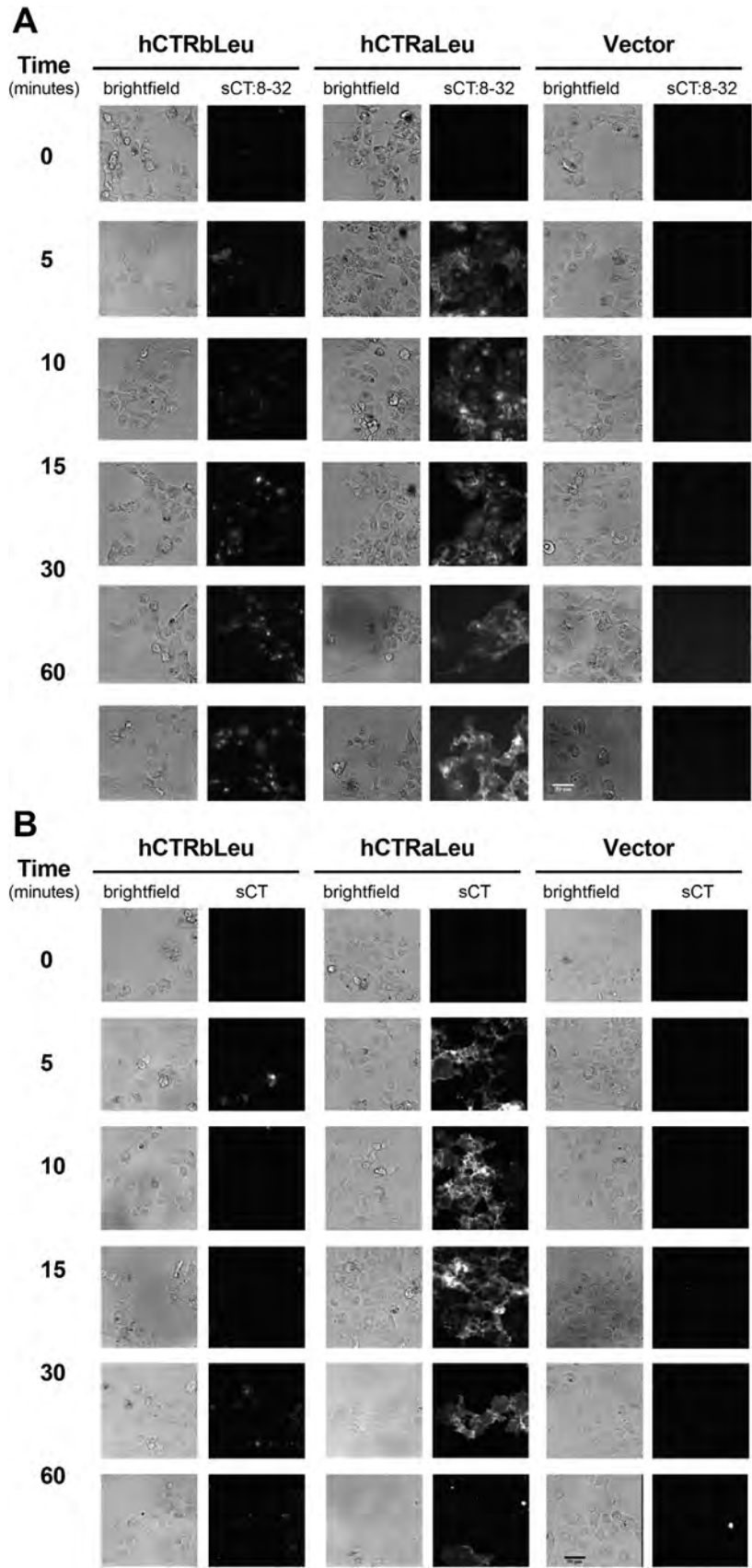


Fig. 9. Ligand internalization in COS-7 cells stably expressing the hCTR. Representative wide-field images of COS-7 stably expressing hCTR_aLeu, hCTR_bLeu or naïve COS-7. A, Cells were stimulated with 1 μ M sCT(8-32)-AF568 for 0, 5, 10, 15, 30 and 60 min, shown are bright field images and AF568 (labelled as sCT(8-32)) emission. B, Cells were stimulated with 100 nM sCT-ROX for 0, 5, 10, 15, 30 and 60 min, shown are bright field images and ROX (labelled as sCT) emission. Proline polymorphic variants showed similar results. Representative of at least 3 independent experiments (2 at the proline polymorphic variant).

researchers have had with correlating this polymorphism with changes in bone physiology.

In addition to these splice variant and polymorphism dependent differences in binding and signalling we saw ligand-dependent bias. At CTR_a variants the increase in cAMP E_{max}

invoked by cCT resulted in bias away from pERK1/2 phosphorylation and iCa^{2+} mobilization compared with the other ligands. In contrast, the CTR_aLeu specific reduction in cAMP E_{max} in response to pCT led to a variant specific bias away from this pathway compared to the other ligands. This pCT dependent bias away from cAMP compared to the other peptides extended to both polymorphs at the CTR_b variant. These differences in ligand bias suggest the possibility for patient dependent differences in response and indicate a need to assess any new clinical candidates for the CTR across all human variants.

Contrary to the splice variant and polymorphism dependent changes in signalling profiles we did not observe any gross changes in cell surface receptor localization, although the CTR_b variant was expressed at a significantly lower level on the COS-7 background. Early reports on both human [60] and pig [53] receptors tracked internalization of ^{125}I -sCT by measuring resistance to acid wash over time at 37 °C, which indicated that both receptors internalize in the presence of this ligand. In our previous report [23] the DiscoverX pathhunter U2OS cell line was used to assess β -arrestin recruitment. In this system, the CTR was modified by extension of its c-terminal tail with a complementation fragment of β -galactosidase, and β -arrestin recruitment was monitored by the irreversible formation of a reporter enzyme when the receptor and β -arrestin come in close proximity. Using this system, ligand promoted β -arrestin could be measured. Using the CTR with either its own, native, c-terminus or a tag to measure reversible protein proximity we were not able to demonstrate ligand-induced interaction with either β -arrestin-1 or -2 for any of the variants. Moreover, we did not see any ligand promoted relocalization of fluorescently tagged β -arrestin-1 or -2 using cell lines stably expressing CTR variants with unmodified c-termini, suggesting very limited interaction of CTRs with arrestins. Unexpectedly, CTR exhibited rapid constitutive internalization as measured by the ability of all receptor variants to induce internalization of a fluorescently labelled antibody directed against an N-terminal epitope tag. Taken together with our β -arrestin data this supports a model in which CTR internalization is not dependent on β -arrestin recruitment, but rather uses an alternative pathway. Our microscopy experiments were not able to distinguish either splice variant or polymorphism dependent differences in receptor internalization, although this does preclude the potential for subtle differences to occur. In addition, these experiments did not identify changes in this internalization profile induced by the agonist sCT, or the antagonist sCT(8-32). This ability for the receptor to constitutively internalize and co-localize with ligands inside the cell, suggests that this profile is important for CTR function and supports that this receptor may signal from intracellular compartments. Over the last ten years there has been an increasing body of evidence showing that GPCRs can signal from intracellular

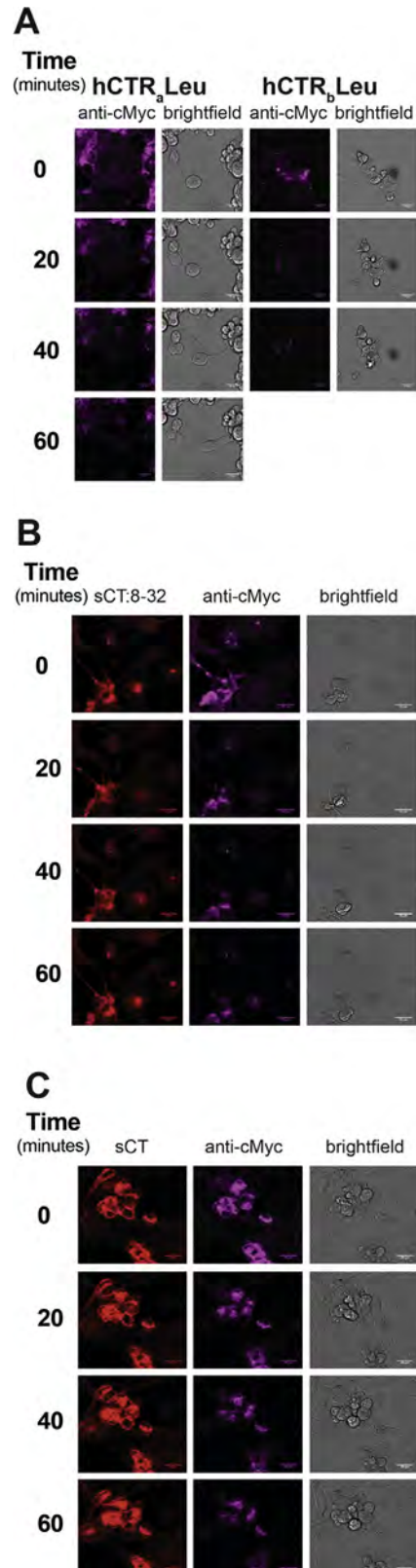


Fig. 10. Ligand-independent internalization of the CTR. A, Confocal images of COS-7 cells stably expressing hCTR_aLeu and pre-incubated with 1 μ g/ml anti-cMyc antibody (9E10-AF647) for 60–100 min on ice. Cells were extensively washed with cold PBS before imaging in a Leica SP-8 microscope for 60 min at 37 °C. Four focal planes were acquired every minute for 60 min. Representative images are maximum intensity projections of four planes processed in the Fiji distribution of ImageJ for 9E10-AF647 emission (labelled anti-cMyc) and bright field. Scale bar represents 30 μ m. B, Confocal images of COS-7 stably expressing hCTR_aLeu and pre-incubated with 1 μ M sCT(8-32)-AF568 and 1 μ g/ml anti-cMyc antibody (9E10-AF647) for 60–100 min on ice. Cells were extensively washed with cold PBS before imaging in the SP-8 for 60 min at 37 °C. Four focal planes were acquired every minute for 60 min and representative images are presented as maximum intensity projections of the four planes (processed in the Fiji distribution of ImageJ) for 9E10-AF647 emission (anti-cMyc), sCT(8-32)-AF568 emission (sCT(8-32)) and bright field. Scale bar represents 30 μ m. C, as for B but sCT-ROX agonist rather than sCT(8-32)-AF568 antagonist. All other variants showed similar results. Representative of at least 2 independent experiments.

compartments (reviewed in [61]), indeed the class B parathyroid hormone receptor, which mediates differential responses to parathyroid hormone and parathyroid hormone related-peptide, only signals from intracellular compartments in response to the former peptide whereas the latter induces signalling only from the cell surface [62]. Moreover, recent experiments on the closely related calcitonin receptor-like receptor (CLR) [63] have demonstrated that this receptor needs to signal from intracellular compartments to fulfil its role in pain transmission. Physiologically, constitutive receptor internalization would provide a means by which a sustained cellular response could be achieved after a transient exposure to ligand. Nonetheless, differences in persistent activation of CTRs by sCT and hCT in cAMP assays [23,64,65] suggest that additional levels of control must occur to regulate signalling.

Overall we observed ligand and CTR variant-dependent differences in receptor signalling that could also vary according to cell background. This highlights the potential complexity of CTR-dependent responses and understanding the physiological relevance of this altered pharmacology will require mapping of expression of these variants at a cellular level. Intriguingly, we observed a cell-background independent difference in the signalling capacity of the human polymorphic variants, underpinning the idea that there are, indeed, likely to be subtle physiological consequences for individuals bearing different genotypes and this has implications for the design of novel ligands targeting this receptor.

Conflict of interest statement

The authors declare no competing interests.

Acknowledgements

This work was supported by the National Health and Medical Research Council of Australia (NHMRC) (project grants [1061044] and [1120919], and NHMRC programme grant [1055134]); P.M.S. is a NHMRC Principal Research Fellow and A.C. is a NHMRC Senior Principal Research Fellow. D.W. is a NHMRC Career Development Fellow.

References

- [1] D.H. Copp, B. Cheney, Calcitonin—a hormone from the parathyroid which lowers the calcium-level of the blood, *Nature* 193 (1962) 381–382.
- [2] A.H. Gorn, H.Y. Lin, M. Yamin, P.E. Auron, M.R. Flannery, D.R. Tapp, et al., Cloning, characterization, and expression of a human calcitonin receptor from an ovarian carcinoma cell line, *J. Clin. Invest.* 90 (1992) 1726–1735.
- [3] A.F. Stewart, Clinical practice. Hypercalcemia associated with cancer, *N. Engl. J. Med.* 352 (2005) 373–379.
- [4] A.L. Langston, S.H. Ralston, Management of Paget's disease of bone, *Rheumatology (Oxford)* 43 (2004) 955–959.
- [5] F. Cosman, S.J. de Beur, M.S. LeBoff, E.M. Lewiecki, B. Tanner, S. Randall, et al., Clinician's guide to prevention and treatment of osteoporosis, *Osteoporos Int.* 25 (2014) 2359–2381.
- [6] A. Ostrovskaya, D.M. Findlay, P.M. Sexton, S.G.B. Furness, Calcitonin, Elsevier, 2017.
- [7] P. Wookey, A. Zulli, C. Lo, D. Hare, A. Schwarzer, I. Darby, et al., Calcitonin receptor expression in embryonic, foetal and adult tissues: developmental and pathophysiological implications, *Calcitonin Gene-Related Pept. Family* (2010) 199–233.
- [8] A. Venkatanarayan, P. Raulji, W. Norton, D. Chakravarti, C. Coarfa, X. Su, et al., IAPP-driven metabolic reprogramming induces regression of p53-deficient tumours in vivo, *Nature* (2014).
- [9] N. Segawa, M. Nakamura, Y. Nakamura, I. Mori, Y. Katsuoaka, K. Kakudo, Phosphorylation of mitogen-activated protein kinase is inhibited by calcitonin in DU145 prostate cancer cells, *Cancer Res.* 61 (2001) 6060–6063.
- [10] M. Nakamura, B. Han, T. Nishishita, Y. Bai, K. Kakudo, Calcitonin targets extracellular signal-regulated kinase signaling pathway in human cancers, *J. Mol. Endocrinol.* 39 (2007) 375.
- [11] P.J. Wookey, C.A. McLean, P. Hwang, S.G.B. Furness, S. Nguyen, A. Kourakis, et al., The expression of calcitonin receptor detected in malignant cells of the brain tumour glioblastoma multiforme and functional properties in the cell line A172, *Histopathology* 60 (2012) 895–910.
- [12] S. Thomas, G.M. Shah, Calcitonin induces apoptosis resistance in prostate cancer cell lines against cytotoxic drugs via the Akt/Survivin pathway - *Cancer Biology & Therapy - Volume 4, Issue 11, Cancer Biol. Ther.* (2005).
- [13] G.V. Shah, S. Thomas, A. Muralidharan, Y. Liu, P.L. Hermonat, J. Williams, et al., Calcitonin promotes in vivo metastasis of prostate cancer cells by altering cell signaling, adhesion, and inflammatory pathways, *Endocr. Relat. Cancer* 15 (2008) 953–964.
- [14] O. Chabre, B.R. Conklin, H.Y. Lin, H.F. Lodish, E. Wilson, H.E. Ives, et al., A recombinant calcitonin receptor independently stimulates 3',5'-cyclic adenosine monophosphate and Ca²⁺/inositol phosphate signaling pathways, *Mol. Endocrinol.* 6 (1992) 551–556.
- [15] Y. Chen, J.F. Shyu, A. Santhanagopal, D. Inoue, J.P. David, S.J. Dixon, et al., The calcitonin receptor stimulates Shc tyrosine phosphorylation and Erk1/2 activation Involvement of Gi, protein kinase C, and calcium, *J. Biol. Chem.* 273 (1998) 19809–19816.
- [16] M. Chakraborty, D. Chatterjee, S. Kellokumpu, H. Rasmussen, R. Baron, Cell cycle-dependent coupling of the calcitonin receptor to different G proteins, *Science* 251 (1991) 1078.
- [17] L.J. Raggatt, A. Evdokiou, D.M. Findlay, Sustained activation of Erk1/2 MAPK and cell growth suppression by the insert-negative, but not the insert-positive isoform of the human calcitonin receptor, *J. Endocrinol.* 167 (2000) 93–105.
- [18] M.G. Sørensen, M.A. Karsdal, M.H. Dziegiel, J.A. Boutin, O. Nojéan, K. Henriksen, Screening of protein kinase inhibitors identifies PKC inhibitors as inhibitors of osteoclastic acid secretion and bone resorption, *BMC Musculoskelet Disord.* 11 (2010) 250.
- [19] M. Yamaguchi, Stimulatory effect of calcitonin on Ca²⁺ inflow in isolated rat hepatocytes, *Mol. Cell. Endocrinol.* 75 (1991) 65–70.
- [20] C.S. Potes, C.N. Boyle, P.J. Wookey, T. Riediger, T.A. Lutz, Involvement of the extracellular signal-regulated kinase 1/2 signaling pathway in amylin's eating inhibitory effect, *Am. J. Physiol. Regul. Integr. Comp. Physiol.* 302 (2012) R340–51.
- [21] L. Bueno, F. Fioramonti, J.P. Ferre, Calcitonin—C.N.S. action to control the pattern of intestinal motility in rats, *Peptides* 4 (1983) 63–66.
- [22] T. Seck, R. Baron, W.C. Horne, Binding of filamin to the C-terminal tail of the calcitonin receptor controls recycling, *J. Biol. Chem.* 278 (2003) 10408–10416.
- [23] K.V. Andreassen, S.T. Hjuler, S.G. Furness, P.M. Sexton, A. Christopoulos, O. Nojéan, et al., Prolonged calcitonin receptor signaling by salmon, but not human calcitonin, reveals ligand bias, *PLoS ONE* 9 (2014) e92042.
- [24] M.J. Lohse, C. Hoffmann, Arrestin interactions with G protein-coupled receptors, *Handb. Exp. Pharmacol.* 219 (2014) 15–56.
- [25] S.G. Furness, D. Wootten, A. Christopoulos, P.M. Sexton, Consequences of splice variation on Secretin family G protein-coupled receptor function, *Br. J. Pharmacol.* 166 (2012) 98–109.
- [26] R.E. Kuestner, R.D. Elrod, F.J. Grant, F.S. Hagen, J.L. Kuijper, S.L. Mathewes, et al., Cloning and characterization of an abundant subtype of the human calcitonin receptor, *Mol. Pharmacol.* 46 (1994) 246–255.
- [27] J. Beaudreuil, J. Taboulet, P. Orcel, A.M. Graulet, M.A. Denne, C. Baudoin, et al., Calcitonin receptor mRNA in mononuclear leucocytes from postmenopausal women: decrease during osteoporosis and link to bone markers with specific isoform involvement, *Bone* 27 (2000) 161–168.
- [28] D.R. Nussenzweig, S. Mathew, M.C. Gershengorn, Alternative splicing of a 48-nucleotide exon generates two isoforms of the human calcitonin receptor, *Endocrinology* 136 (1995) 2047–2051.
- [29] M. Nakamura, Z.Q. Zhang, L. Shan, T. Hisa, M. Sasaki, R. Tsukino, et al., Allelic variants of human calcitonin receptor in the Japanese population, *Hum. Genet.* 99 (1997) 38–41.
- [30] L. Masi, L. Becherini, L. Gennari, E. Colli, R. Mansani, A. Falchetti, et al., Allelic variants of human calcitonin receptor: distribution and association with bone mass in postmenopausal Italian women, *Biochem. Biophys. Res. Commun.* 245 (1998) 622–626.
- [31] J. Taboulet, M. Frenkian, J.L. Frendo, N. Feingold, A. Jullienne, M.C. de Vernejoul, Calcitonin receptor polymorphism is associated with a decreased fracture risk in post-menopausal women, *Hum. Mol. Genet.* 7 (1998) 2129–2133.
- [32] L.A. Wolfe, M.E. Fling, Z. Xue, S. Armour, S.A. Kerner, J. Way, et al., In vitro characterization of a human calcitonin receptor gene polymorphism, *Mutat. Res.* 522 (2003) 93–105.
- [33] M. Nakamura, S. Morimoto, Z. Zhang, H. Utsunomiya, T. Inagami, T. Ogihara, et al., Calcitonin receptor gene polymorphism in Japanese women: correlation with body mass and bone mineral density, *Calcified Tissue Int.* 68 (2001) 211–215.
- [34] F.-J. Tsai, W.-C. Chen, H.-Y. Chen, C.-H. Tsai, The ALUI calcitonin receptor gene polymorphism (TT) is associated with low bone mineral density and susceptibility to osteoporosis in postmenopausal women, *Gynecol. Obstet. Invest.* 55 (2003) 82–87.
- [35] M. Musumeci, G. Vadalà, G. Tringali, E. Insirello, A.M. Roccazzello, J. Simporé, et al., Genetic and environmental factors in human osteoporosis from Sub-Saharan to Mediterranean areas, *J. Bone Miner Metab.* 27 (2009) 424–434.
- [36] P. Mitra, M. Guha, S. Ghosh, S. Mukherjee, B. Bankura, D.K. Pal, et al., Association of calcitonin receptor gene (CALCR) polymorphism with kidney stone disease in the population of West Bengal India, *Gene* 622 (2017) 23–28.
- [37] V. Braga, A. Sangalli, G. Malerba, M. Mottes, S. Mirandola, D. Gatti, et al., Relationship among VDR (BsmI and FokI), COL1A1, and CTR polymorphisms with bone mass, bone turnover markers, and sex hormones in men, *Calcified Tissue Int.* 70 (2002) 457–462.
- [38] M. Dehghan, R. Pourahmad-Jaktaji, Z. Farzaneh, Calcitonin receptor alui (rs1801197) and Taq1 calcitonin genes polymorphism in 45-and over 45-

- year-old women and their association with bone density, *Acta Inform. Med.* 24 (2016) 239–243.
- [39] K. Albrandt, E.M. Brady, C.X. Moore, E. Mull, M.E. Sierzege, K. Beaumont, Molecular cloning and functional expression of a third isoform of the human calcitonin receptor and partial characterization of the calcitonin receptor gene, *Endocrinology* 136 (1995) 5377–5384.
- [40] J. Beaudreuil, S. Balasubramanian, J. Chenais, J. Taboulet, M. Frenkian, P. Orcel, et al., Molecular characterization of two novel isoforms of the human calcitonin receptor, *Gene* 343 (2004) 143–151.
- [41] E.E. Moore, R.E. Kuestner, S.D. Stroop, F.J. Grant, S.L. Matthews, C.L. Brady, et al., Functionally different isoforms of the human calcitonin receptor result from alternative splicing of the gene transcript, *Mol. Endocrinol.* 9 (1995) 959–968.
- [42] S.G.B. Furness, Y.-L. Liang, C.J. Nowell, M.L. Halls, P.J. Wookey, E. Dal Maso, et al., Ligand-dependent modulation of G protein conformation alters drug efficacy, *Cell* 167 (2016). 739–749.e11.
- [43] A.E. Cook, S.N. Mistry, K.J. Gregory, S.G.B. Furness, P.M. Sexton, P.J. Scammells, et al., Biased allosteric modulation at the CaS receptor engendered by structurally diverse calcimimetics, *Br. J. Pharmacol.* 172 (2015) 185–200.
- [44] S. Hobbs, S. Jitrapakdee, J.C. Wallace, Development of a bicistronic vector driven by the human polypeptide chain elongation factor 1 α promoter for creation of stable mammalian cell lines that express very high levels of recombinant proteins, *Biochem. Biophys. Res. Commun.* 252 (1998) 368–372.
- [45] E.E. Savage, D. Wootten, A. Christopoulos, P.M. Sexton, S.G.B. Furness, A simple method to generate stable cell lines for the analysis of transient protein-protein interactions, *Biotech* 54 (2013) 217–221.
- [46] D. Wootten, E.E. Savage, F.S. Willard, A.B. Bueno, K.W. Sloop, A. Christopoulos, et al., Differential activation and modulation of the glucagon-like peptide-1 receptor by small molecule ligands, *Mol. Pharmacol.* 83 (2013) 822–834.
- [47] V. Pham, M. Dong, J.D. Wade, L.J. Miller, C.J. Morton, H.-L. Ng, et al., Insights into interactions between the α -helical region of the salmon calcitonin antagonists and the human calcitonin receptor using photoaffinity labeling, *J. Biol. Chem.* 280 (2005) 28610–28622.
- [48] L.T. May, V.A. Avlani, C.J. Langmead, H.J. Herdon, M.D. Wood, P.M. Sexton, et al., Structure-function studies of allosteric agonism at M2 muscarinic acetylcholine receptors, *Mol. Pharmacol.* 72 (2007) 463–476.
- [49] C. Koole, D. Wootten, J. Simms, L.J. Miller, A. Christopoulos, P.M. Sexton, Second extracellular loop of human glucagon-like peptide-1 receptor (GLP-1R) has a critical role in GLP-1 peptide binding and receptor activation, *J. Biol. Chem.* 287 (2012) 3642–3658.
- [50] J.M. Hilton, M. Dowton, S. Houssami, P.M. Sexton, Identification of key components in the irreversibility of salmon calcitonin binding to calcitonin receptors, *J. Endocrinol.* 166 (2000) 213–226.
- [51] D. Karpinsky-Semper, C.-H. Volmar, S.P. Brothers, V.Z. Slepak, Differential effects of the G β 5-RGS7 complex on muscarinic M3 receptor-induced Ca $^{2+}$ influx and release, *Mol. Pharmacol.* 85 (2014) 758–768.
- [52] V. Inamdar, A. Patel, B.K. Manne, C. Dangelmaier, S.P. Kunapuli, Characterization of UBO-QIC as a G α_q inhibitor in platelets, *Platelets* 26 (2015) 771–778.
- [53] D.M. Findlay, S. Houssami, H.Y. Lin, D.E. Myers, C.L. Brady, P.K. Darcy, et al., Truncation of the porcine calcitonin receptor cytoplasmic tail inhibits internalization and signal transduction but increases receptor affinity, *Mol. Endocrinol.* 8 (1994) 1691–1700.
- [54] C.S. D'Santos, G.C. Nicholson, J.M. Moseley, T. Evans, T.J. Martin, B.E. Kemp, Biologically active, derivatizable salmon calcitonin analog: design, synthesis, and applications, *Endocrinology* 123 (1988) 1483–1488.
- [55] T. Arvinte, A.F. Drake, Comparative study of human and salmon calcitonin secondary structure in solutions with low dielectric constants, *J. Biol. Chem.* 268 (1993) 6408–6414.
- [56] Y.-L. Liang, M. Khoshouei, M. Radjainia, Y. Zhang, A. Glukhova, J. Tarrasch, et al., Phase-plate cryo-EM structure of a class B GPCR-G-protein complex, *Nature* 546 (2017) 118–123.
- [57] R.L. Bower, S. Eftekhari, H.J. Waldvogel, R.L.M. Faull, J. Tajti, L. Edvinsson, et al., Mapping the calcitonin receptor in human brain stem, *Am. J. Physiol. Regul. Integr. Comp. Physiol.* 310 (2016) R788–93.
- [58] A. Aljameeli, A. Thakkar, S. Thomas, V. Lakshmikanthan, K.A. Iczkowski, G.V. Shah, calcitonin receptor-zonula occludens-1 interaction is critical for calcitonin-stimulated prostate cancer metastasis, *PLoS ONE* 11 (2016) e0150090.
- [59] A. Manglik, T.H. Kim, M. Masureel, C. Altenbach, Z. Yang, D. Hilger, et al., Structural insights into the dynamic process of β 2-Adrenergic receptor signaling, *Cell* 161 (2015) 1101–1111.
- [60] D.M. Findlay, T.J. Martin, Kinetics of calcitonin receptor internalization in lung cancer (BEN) and osteogenic sarcoma (UMR 106–06) cells, *J. Bone Miner. Res.* 1 (1986) 277–283.
- [61] R. Irannejad, M. von Zastrow, GPCR signaling along the endocytic pathway, *Curr. Opin. Cell Biol.* 27 (2014) 109–116.
- [62] S. Ferrandon, T.N. Feinstein, M. Castro, B. Wang, R. Bouley, J.T. Potts, et al., Sustained cyclic AMP production by parathyroid hormone receptor endocytosis, *Nat. Chem. Biol.* 5 (2009) 734–742.
- [63] R.E. Yarwood, W.L. Imlach, T. Lieu, N.A. Veldhuis, D.D. Jensen, C. Klein Herenbrink, et al., Endosomal signaling of the receptor for calcitonin gene-related peptide mediates pain transmission, *Proc. Natl. Acad. Sci. U.S.A.* (2017).
- [64] V.P. Michelangeli, D.M. Findlay, J.M. Moseley, T.J. Martin, Mechanisms of calcitonin induction of prolonged activation of adenylate cyclase in human cancer cells, *J. Cyclic Nucleotide Protein Phosphor. Res.* 9 (1983) 129–141.
- [65] G.C. Nicholson, J.M. Moseley, A.J. Yates, T.J. Martin, Control of cyclic adenosine 3',5'-monophosphate production in osteoclasts: calcitonin-induced persistent activation and homologous desensitization of adenylate cyclase, *Endocrinology* 120 (1987) 1902–1908.



Extracellular loops 2 and 3 of the calcitonin receptor selectively modify agonist binding and efficacy

Emma Dal Maso^{a,1}, Yue Zhu^{b,e,g,1}, Vi Pham^a, Christopher A. Reynolds^c, Giuseppe Deganutti^c, Caroline A. Hick^a, Dehua Yang^b, Arthur Christopoulos^a, Debbie L. Hay^d, Ming-Wei Wang^{b,e,f}, Patrick M. Sexton^{a,f,*}, Sebastian G.B. Furness^{a,*}, Denise Wootten^{a,*}

^a Drug Discovery Biology, Monash Institute of Pharmaceutical Sciences, Monash University, Parkville 3052, Victoria, Australia

^b The National Center for Drug Screening and CAS Key Laboratory of Receptor Research, Shanghai Institute of Materia Medica, Chinese Academy of Sciences, Shanghai 201203, China

^c School of Biological Sciences, University of Essex, Wivenhoe Park, Colchester CO4 3SQ, United Kingdom

^d The University of Auckland, School of Biological Sciences, 3 Symonds Street, Auckland 1142, New Zealand

^e University of Chinese Academy of Sciences, Beijing 100049, China

^f School of Pharmacy, Fudan University, Shanghai 201203, China

^g University of Chinese Academy of Sciences, 19A Yuquan Road, Beijing 100049, China

ARTICLE INFO

Keywords:

G protein-coupled receptor
Calcitonin receptor
GPCR structure-function
Biased agonism
Molecular modelling

ABSTRACT

Class B peptide hormone GPCRs are targets for the treatment of major chronic disease. Peptide ligands of these receptors display biased agonism and this may provide future therapeutic advantage. Recent active structures of the calcitonin (CT) and glucagon-like peptide-1 (GLP-1) receptors reveal distinct engagement of peptides with extracellular loops (ECLs) 2 and 3, and mutagenesis of the GLP-1R has implicated these loops in dynamics of receptor activation. In the current study, we have mutated ECLs 2 and 3 of the human CT receptor (CTR), to interrogate receptor expression, peptide affinity and efficacy. Integration of these data with insights from the CTR and GLP-1R active structures, revealed marked diversity in mechanisms of peptide engagement and receptor activation between the CTR and GLP-1R. While the CTR ECL2 played a key role in conformational propagation linked to Gs/cAMP signalling this was mechanistically distinct from that of GLP-1R ECL2. Moreover, ECL3 was a hotspot for distinct ligand- and pathway-specific effects, and this has implications for the future design of biased agonists of class B GPCRs.

1. Introduction

Class B1 G protein-coupled receptors (GPCRs) are the targets for peptide hormones that play major roles in the development and maintenance of lymphatic and cardiovascular function, bone homeostasis, metabolic regulation, migraine, stress and anxiety [1]. Consequently, these receptors are important therapeutic targets.

The calcitonin (CT), Class B1 GPCRs (CTRs), are highly expressed on osteoclasts and have been exploited therapeutically for treatment of bone disorders, including Paget's disease, hypercalcemia of malignancy and osteoporosis [2–5]. The receptors are also expressed in numerous other cells and tissues including leucocytes and their precursors, the central nervous system, kidney, lung, gastrointestinal tract and reproductive tissues [6], thereby influencing pain perception, feeding and reproduction, and ion secretion [2,7], though these actions are not well

understood. Furthermore, CTRs can interact with the receptor activity modifying protein (RAMP) family to form high affinity receptors for amylin (Amy) and calcitonin gene-related peptide (CGRP) [8].

CT peptides from different species have been identified and can be classified into 3 major subgroups based on evolution and sequence conservation: human/rodent, artiodactyl (e.g., porcine) and teleost (salmon/eel)/chicken. Both human and salmon CT have been approved for treatment of bone disorders including Paget's disease and osteoporosis, however, they have distinct binding kinetics, affinity and efficacy [9–11] that impact on G protein recruitment and activation [11], suggesting different modes of interaction with CTRs.

Orthosteric peptide ligands of Class B1 GPCRs are proposed to interact with their cognate receptors via a two-domain mechanism, with an initial engagement of the C-terminus of the peptide with the N-terminal extracellular domain (ECD) of the receptor that allows the

* Corresponding authors at: Monash Institute of Pharmaceutical Sciences, 381 Royal Parade, Parkville 3052, Victoria, Australia.

E-mail addresses: Patrick.sexton@monash.edu (P.M. Sexton), Sebastian.furness@monash.edu (S.G.B. Furness), denise.wootten@monash.edu (D. Wootten).

¹ These authors contributed equally to this work.

peptide N-terminus to bind to the transmembrane (TM) spanning receptor core comprising the 7 TM helices and 3 interconnecting extracellular loops (ECLs), leading to receptor activation [12]. This mode of binding is supported by recent full-length, active, Gs-complexed structures of the CTR [13] (bound to sCT) and glucagon-like peptide-1 (GLP-1) receptor (GLP-1R) (bound to GLP-1 [14], or exendin-P5 [15]). Nonetheless, there were marked differences in the orientation of the receptor ECD relative to the receptor core and correlative changes in presentation of the peptides to the receptor core, linked to differences in the degree of secondary structure of the peptides [13–15]. Moreover, the CT-family peptides have a cyclic, cysteine-disulfide linked N-terminus between amino acids 1 and 7 (2 and 7 for Amy and CGRP) that contrasts with the extended helix of GLP-1, and alters the relative interaction of the peptide N-termini with the ECLs and proximal TM helix segments.

Mutagenesis and crosslinking studies have shown that the ECLs of Class B1 GPCRs are critical for both peptide binding and propagation of conformational change associated with receptor activation [14–20]. For the GLP-1R, alanine-scanning mutagenesis revealed that the ECLs, particularly ECL2 and ECL3, were also important in the biased agonism of peptides, but had distinct contribution to pathway specific signalling [16,21]. For this receptor, both ECL2 and ECL3 played a critical role in cAMP formation, and intracellular calcium (Ca^{2+}) mobilisation, while effects on ERK phosphorylation (pERK) were principally confined to residues within ECL3.

In the current study, we have performed alanine-scanning mutagenesis of amino acids in ECLs 2 and 3 of the hCTR and interrogated mutant receptors for their effects on cell surface receptor expression, peptide affinity and efficacy for cAMP and IP1 accumulation, as well as pERK in response to calcitonin (sCT, hCT, pCT) and related family (Amy, CGRP) peptides. This work revealed both differences in how the receptor engages with and is activated by the different CT-family peptides, and in the role of ECLs 2 and 3 between the CTR and GLP-1R.

2. Materials and methods

2.1. Reagents

All peptides were purchased from Mimotopes. Dulbecco's Modified Eagle's Medium (DMEM) was purchased from Invitrogen. Foetal bovine serum (FBS) was purchased from Thermo Electron Corporation. AlphaScreen reagents, Lance cAMP kit, 384-well Optiplates were purchased from PerkinElmer. SureFire™ ERK1/2 reagents were obtained from TGR Biosciences and PerkinElmer. IP-One HTRF® assay kit was from CisBio. Antibodies were purchased from R&D systems and ThermoFisher. All other reagents were purchased from Sigma-Aldrich or BDH Merck and were of an analytical grade.

2.2. Mutagenesis

Desired mutations were introduced to N-terminally c-Myc tagged human CTR in pENTER11 (Invitrogen) via the Q5® High-Fidelity PCR Kit (New England Biolabs), then LR recombination reactions were conducted to transfer mutated and wild-type (WT) receptor into the pEF5/FRT/V5-DEST destination vector using Gateway Technology (Invitrogen). The oligonucleotides for mutagenesis were purchased from Gene-Works (Thebarton, SA, Australia) and mutants were confirmed by automated-sequencing.

2.3. Stable cell line generation and cell culture

The mutant or wild-type (WT) receptor genes were integrated into FlpIn-CV1 cells using Flp-In™ system (Invitrogen). Stable Flp-In expression cell lines were generated through polyclonal selection, screening and maintained in Dulbecco's modified Eagle's medium supplemented with 5% (v/v) FBS, 300 µg/ml hygromycin B

(Invitrogen) at 37 °C in 5% CO₂.

2.4. Homologous whole cell competition binding assay

Homologous radioligand competition was performed on 2.5×10^4 cells/well seeded into 96-well trays and cultured overnight. Cells were incubated overnight at 4 °C with two concentrations of ¹²⁵I-sCT(8-32) (between 25 and 100 pM; specific activity, 2000 Ci/mmol⁹) and serial dilutions of non-iodinated sCT(8-32). Non-bound ligand was removed and bound ligand activity was measured using a γ counter (Wallac Wizard 1470 Gamma Counter, Perkin Elmer, 80% counter efficiency). Values were normalized against non-specific binding (0%) defined by the presence of 1 µM of unlabelled sCT(8-32), and total ligand bound in absence of competing sCT(8-32) (100%).

2.5. Heterologous whole cell competition binding assay

Competition binding was performed as previously described [41] on whole cells in 96-well plates by using the antagonist radioligand ¹²⁵I-sCT(8-32) (~0.1 nM), and competing with increasing concentrations of unlabelled peptide. Non-specific binding was defined by co-incubation with 1 µM unlabelled sCT(8-32). Following overnight incubation non-bound ligand was removed and radioactivity was determined using a gamma counter.

2.6. Cell surface expression by FACS

Surface expression of c-Myc tagged CTR mutants stably expressed in CV-1 cells was quantified by flow cytometry using standard methods. Cells were plated into 6 well trays at approximately 5×10^5 cells per well the day before assay. Cells were harvested using versene. All staining steps were conducted in ice cold HBSS with 0.1% BSA and 20 mM HEPES (pH 7.4). Blocking was conducted in 5% BSA. Primary antibody staining was performed with a mixture of 5 µg/mL 9E10 (anti-c-Myc) and 1 µg/mL Mab4614 (anti-CTR, R&D Systems). The secondary antibody was 1 µg/mL goat anti-mouse AF647 (ThermoFisher). Sytox blue was used for live/dead discrimination. Data were collected on a FACS CantoII (BD Biosciences) with at least 20,000 live cells collected per sample, WT stained CTR sample and stained parental CV-1 cells were collected at the beginning and the end of each run. Data were analysed using FlowJo. The mean AF647 fluorescence intensity from each sample for a particular experiment was normalized against parental (0%) and CTR WT (100%) controls.

2.7. cAMP accumulation

Cells (2.5×10^4 cells/well) were seeded into 96-well plates and incubated overnight. Cells were stimulated with increasing concentrations of ligands for 30 min in the presence of IBMX. The liquid was discarded, changed to absolute ethanol and volatilized to dryness at room temperature. Samples were then lysed and intracellular cAMP was detected using PerkinElmer Lance kit as previously described [16]. Data were normalized to the response of 100 µM forskolin.

2.8. IP1 accumulation

Cells (2.5×10^4 cells/well) were plated into 96 well trays and cultured overnight. Cells were stimulated with increasing concentration of ligands for 60 min in the presence of LiCl. Samples were lysed and endogenous IP₁ was measured using an IP-One HTRF® assay kit (CisBio) as specified by the manufacturer. Data were normalized to the maximal response elicited by 100 µM of ATP.

2.9. ERK1/2 phosphorylation

Cells (2.5×10^4 cells/well) were seeded into 96-well culture plates

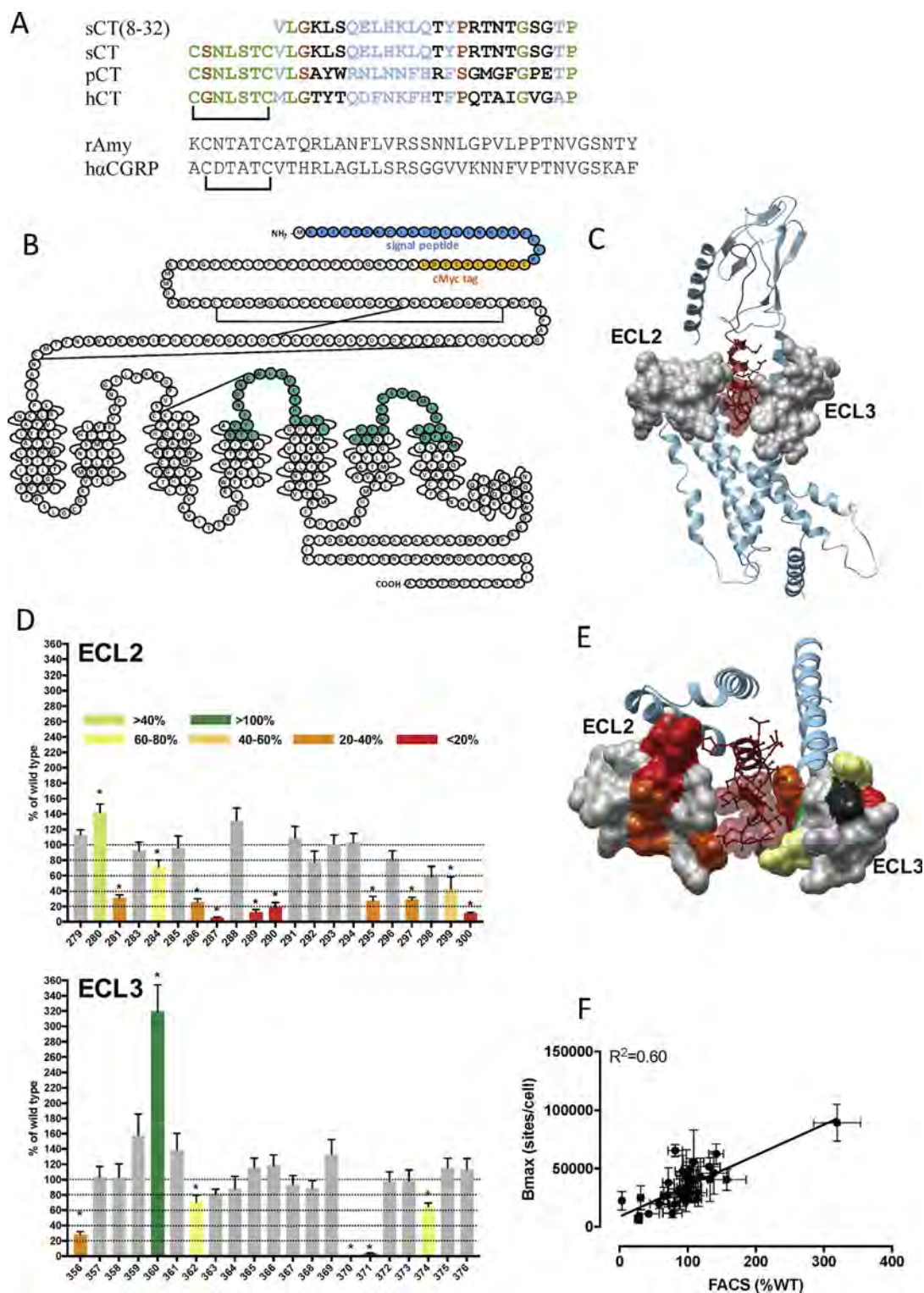


Fig. 1. Alanine mutation of ECL2 and ECL3 of the hCTR selectively alters expression of the receptor. (A) Alignment of CT and related peptide sequences was performed using Biology WorkBench (workbench.sdsc.edu). Identical residues are highlighted in green, conservative substitutions are coloured blue, and semi-conservative substitutions are in orange. Black text indicates the non-conserved. (B) Snake diagram of the hCTR: highlighted in blue are the residues that constitute the signal peptide of the receptor, in orange the c-Myc tag, and in green the residues that have been mutated to alanine. (C) Active state model of the hCTR (pale blue ribbon), with position of mutated residues displayed as grey surface map. sCT is shown as dark red, with side chains in proximity to the ECLs displayed in x-stick, and residues 1–7 that are critical for receptor activation displayed in transparent cpk. (D) Expression of mutant receptors determined by FACS analysis of antibody binding to the c-Myc epitope. (E) Top view of the ECLs with mutants that significantly altered receptor expression displayed in colour according to the magnitude of effect; grey indicates no significant effect and black mutants where expression could not be measured. The receptor ECD and C-terminal peptide residues are omitted for clarity (F). There was a strong correlation between cell surface receptor expression by FACS and homologous competition radioligand binding. * $P < 0.05$, one-way ANOVA with Dunn's post-test. Data are mean \pm S.E.M. (D) or \pm S.E.M. (F) of 3–6 (WT 10–12) independent experiments. (For interpretation of the references to colour in this figure legend, the reader is referred to the web version of this article.)

Table 1Effect of single alanine mutation in hCTR ECL2 or ECL3 on binding affinity (pK_i) of CT peptides, and receptor cell surface expression.

	hCT pK _i	sCT pK _i	pCT pK _i	sCT(8-32) pK _i	FACS (% of WT)	Bmax (sites/cell)
WT	6.72 ± 0.06 (16)	9.87 ± 0.03 (16)	8.27 ± 0.07 (17)	9.70 ± 0.05 (18)	100 (12)	22,900 ± 2500 (10)
I279A	6.16 ± 0.08 (3)	9.93 ± 0.18 (4)	7.83 ± 0.24 (4)	9.72 ± 0.08 (8)	113 ± 7 (4)	40,500 ± 11,300 (5)
T280A	6.71 ± 0.05 (4)	10.2 ± 0.03 (4)	8.20 ± 0.15 (4)	9.61 ± 0.08 (8)	142 ± 11 (4)	62,600 ± 8700* (4)
R281A	5.92 ± 0.28* (5)	9.10 ± 0.15* (6)	7.18 ± 0.23* (5)	9.07 ± 0.21* (10)	32 ± 4* (6)	24,900 ± 10,200 (3)
V283A	6.63 ± 0.11 (4)	9.78 ± 0.14 (4)	7.82 ± 0.08 (4)	9.67 ± 0.03 (8)	93 ± 11 (4)	47,600 ± 13,600 (4)
Y284A	6.61 ± 0.11 (5)	9.83 ± 0.07 (3)	7.84 ± 0.10 (4)	9.85 ± 0.10 (8)	72 ± 9* (4)	37,800 ± 12,800 (4)
F285A	6.60 ± 0.11 (4)	10.0 ± 0.12 (4)	7.92 ± 0.11 (4)	9.99 ± 0.05 (8)	96 ± 15 (4)	33,200 ± 11,000 (4)
N286A	N.D.	N.D.	N.D.	N.D.	26 ± 4* (4)	N.D.
D287A	N.D.	N.D.	N.D.	N.D.	5 ± 1* (4)	N.D.
N288A	6.35 ± 0.12 (4)	9.74 ± 0.13 (4)	8.03 ± 0.12 (5)	9.63 ± 0.04 (8)	132 ± 16 (4)	51,600 ± 2600* (4)
C289A	N.D.	N.D.	N.D.	N.D.	13 ± 3* (3)	N.D.
W290A	N.D.	N.D.	N.D.	N.D.	19 ± 6* (4)	N.D.
L291A	5.41 ± 0.10* (3)	9.75 ± 0.21 (5)	7.17 ± 0.12* (6)	8.76 ± 0.19* (9)	109 ± 15 (4)	55,700 ± 27,400 (3)
S292A	6.60 ± 0.05 (4)	10.4 ± 0.20* (4)	8.54 ± 0.22 (4)	10.2 ± 0.13 (8)	78 ± 14 (4)	11,600 ± 3600 (4)
V293A	6.22 ± 0.08 (4)	9.59 ± 0.05 (4)	7.85 ± 0.10 (4)	9.75 ± 0.08 (8)	101 ± 12 (4)	39,500 ± 13,000 (4)
E294A	6.73 ± 0.06 (5)	9.77 ± 0.08 (4)	7.93 ± 0.10 (4)	9.58 ± 0.07 (8)	103 ± 12 (4)	48,700 ± 10,100 (4)
T295A	5.90 ± 0.050* (4)	10.2 ± 0.16 (4)	7.49 ± 0.08* (4)	10.3 ± 0.09* (8)	27 ± 6* (4)	6600 ± 2300* (4)
H296A	6.95 ± 0.13 (4)	9.84 ± 0.09 (4)	8.07 ± 0.03 (4)	9.57 ± 0.07 (8)	82 ± 11 (4)	65,500 ± 5100* (4)
L297A	6.09 ± 0.05* (4)	10.1 ± 0.15 (4)	7.81 ± 0.19 (4)	10.2 ± 0.07 (8)	29 ± 3* (4)	9200 ± 2000* (4)
L298A	6.13 ± 0.08* (4)	9.76 ± 0.09 (4)	7.69 ± 0.10 (4)	9.83 ± 0.12 (8)	59 ± 14 (4)	19,600 ± 4000 (4)
Y299A	6.28 ± 0.02 (4)	9.41 ± 0.20 (4)	7.33 ± 0.20* (4)	9.97 ± 0.18 (8)	43 ± 16* (4)	11,100 ± 1900* (4)
I300A	N.D.	N.D.	N.D.	N.D.	11 ± 1* (4)	N.D.
F356A	6.58 ± 0.11 (5)	9.79 ± 0.34 (5)	7.92 ± 0.17 (4)	9.85 ± 0.25 (12)	28 ± 4* (6)	5900 ± 2200* (5)
V357A	6.13 ± 0.13* (5)	9.83 ± 0.18 (4)	7.89 ± 0.27 (4)	9.68 ± 0.10 (8)	104 ± 14 (4)	28,400 ± 7700 (4)
V358A	5.89 ± 0.15* (5)	9.62 ± 0.09 (4)	7.84 ± 0.13 (4)	9.81 ± 0.06 (8)	103 ± 18 (4)	34,100 ± 10,500 (4)
F359A	5.49 ± 0.12* (5)	9.50 ± 0.15 (4)	7.13 ± 0.19* (3)	9.66 ± 0.10 (10)	158 ± 28 (4)	40,400 ± 9200 (4)
P360A	5.65 ± 0.06* (5)	9.01 ± 0.13* (4)	7.30 ± 0.28* (4)	9.22 ± 0.10* (10)	320 ± 35* (5)	89,400 ± 15,800* (5)
W361A	5.99 ± 0.08* (5)	9.48 ± 0.08 (4)	7.47 ± 0.24* (4)	9.55 ± 0.11 (10)	139 ± 22 (4)	46,200 ± 18,200 (5)
R362A	5.96 ± 0.06* (4)	9.53 ± 0.13 (4)	7.33 ± 0.22* (4)	9.66 ± 0.14 (8)	71 ± 9* (4)	27,300 ± 1000 (4)
P363A	5.48 ± 0.26* (4)	9.44 ± 0.14 (4)	7.26 ± 0.13* (4)	9.45 ± 0.23 (8)	81 ± 7 (4)	19,400 ± 5800 (4)
S364A	6.61 ± 0.07 (4)	9.73 ± 0.06 (4)	8.27 ± 0.34 (4)	9.72 ± 0.08 (10)	88 ± 16 (4)	32,600 ± 11,200 (5)
N365A	6.68 ± 0.16 (4)	9.96 ± 0.06 (4)	8.68 ± 0.24 (4)	9.63 ± 0.10 (10)	116 ± 13 (4)	29,400 ± 11,900 (5)
K366A	6.47 ± 0.17 (4)	9.69 ± 0.05 (4)	7.96 ± 0.23 (4)	9.71 ± 0.12 (10)	119 ± 14 (4)	43,000 ± 16,000 (5)
M367A	6.24 ± 0.11 (4)	9.67 ± 0.09 (4)	7.67 ± 0.25 (4)	9.53 ± 0.14 (8)	94 ± 112 (4)	25,600 ± 7900 (4)
L368A	6.50 ± 0.13 (4)	9.81 ± 0.04 (4)	8.07 ± 0.19 (4)	9.68 ± 0.11 (8)	89 ± 9 (4)	28,200 ± 13,100 (4)
G369A	6.41 ± 0.10 (4)	9.89 ± 0.02 (4)	8.10 ± 0.19 (4)	9.64 ± 0.14 (10)	133 ± 20 (4)	40,600 ± 18,800 (5)
K370A	N.D.	N.D.	N.D.	N.D.	N.D.	N.D.
I371A	N.D.	N.D.	N.D.	N.D.	3 ± 1* (3)	N.D.
Y372A	6.09 ± 0.09* (4)	9.40 ± 0.06 (4)	7.55 ± 0.27* (4)	9.85 ± 0.19 (8)	98 ± 13 (4)	21,700 ± 8600 (4)
D373A	5.76 ± 0.22* (6)	9.36 ± 0.09* (4)	7.76 ± 0.28 (4)	9.28 ± 0.15 (8)	98 ± 14 (4)	43,500 ± 22,700 (5)
Y374A	6.64 ± 0.17 (4)	9.79 ± 0.13 (4)	8.23 ± 0.09 (4)	9.83 ± 0.13 (8)	65 ± 5* (4)	26,300 ± 7500 (4)
V375A	6.48 ± 0.19 (5)	9.83 ± 0.08 (4)	8.29 ± 0.25 (4)	9.72 ± 0.09 (8)	115 ± 13 (3)	22,500 ± 8000 (4)
M376A	6.06 ± 0.21* (6)	9.80 ± 0.15 (6)	8.11 ± 0.24 (4)	9.88 ± 0.10 (8)	113 ± 7 (4)	23,600 ± 3200 (4)

pK_i values were derived for each ligand and mutant receptor from analysis of either homologous (sCT(8-32)) or heterologous (sCT, hCT, pCT) competition of [¹²⁵I]-sCT(8-32) binding. The number of receptors per cell (Bmax) was estimated from homologous competition studies. All values are mean ± S.E.M. (independent “n” values are indicated within parentheses). Cell surface receptor expression was determined by FACS using an anti-c-myc antibody, and expression normalized to WT expression and expressed as %WT. Significance of changes in receptor expression, or pK_i of each ligand, was determined by comparison of mutant receptors to WT values by a one-way analysis of variance and Dunnett’s post-test for affinity data, and two-tailed *t*-test for expression data (*p* < 0.05 represented by *). (N.D.) affinity not determined as no radioligand binding was detected.

and incubated overnight. Initially, pERK1/2 time-course experiments were performed over 30 min to identify the time point when the pERK1/2 response is maximal (6–8 min). Subsequently, this time point was selected to generate concentration response for different agonists with ligand addition performed after overnight serum starvation. pERK1/2 was detected using an Alphascreen assay as previously described [22]. Data were normalized to the maximal response elicited by 10% FBS determined at 6 min.

2.10. Data analysis

IC₅₀ and Bmax values were estimated from competitive inhibition of [¹²⁵I]-sCT(8-32) binding using a 3-parameter logistic equation (log(inhibitor versus response)) in Prism (v7; Graphpad). Data were corrected for radioligand occupancy using the Cheng-Prusoff equation in Prism; as such data are reported as pK_i. Emax and EC₅₀ were estimated from concentration-response curves using with a 3-parameter logistic equation in Prism (v7). These values are a composite of functional affinity, efficacy and stimulus response coupling. The Black and Leff operational

model of agonism [23] was applied to separate effects on pathway-specific efficacy (τ) from those that modify ligand functional affinity (pK_A). Derived τ values were normalized to experimentally determined levels of cell surface expression to provide a measure of efficacy (τ_c) that is independent of affinity and altered cell surface receptor expression [16]. pK_i, pK_A and log τ_c values for mutant receptors were statistically compared to those of the WT receptor using a one-way analysis of variance (ANOVA) and Dunnett’s post-test. Significance was accepted at *P* < 0.05.

2.11. Molecular modelling and mapping of mutational effects

The structures of the CTR:CT complexes were generated from the cryo-electron microscopy structure of the calcitonin receptor [13] and the X-ray structure of the CTR ECD [24]. Missing loops were generated using Modeller [25] (1000 structures) and the final loop selected to ensure that the conserved residues faced inwards [26] by analysis of the correlation of the conservation, as measured using the Shannon entropy, and the extent to which a residue is buried [27].

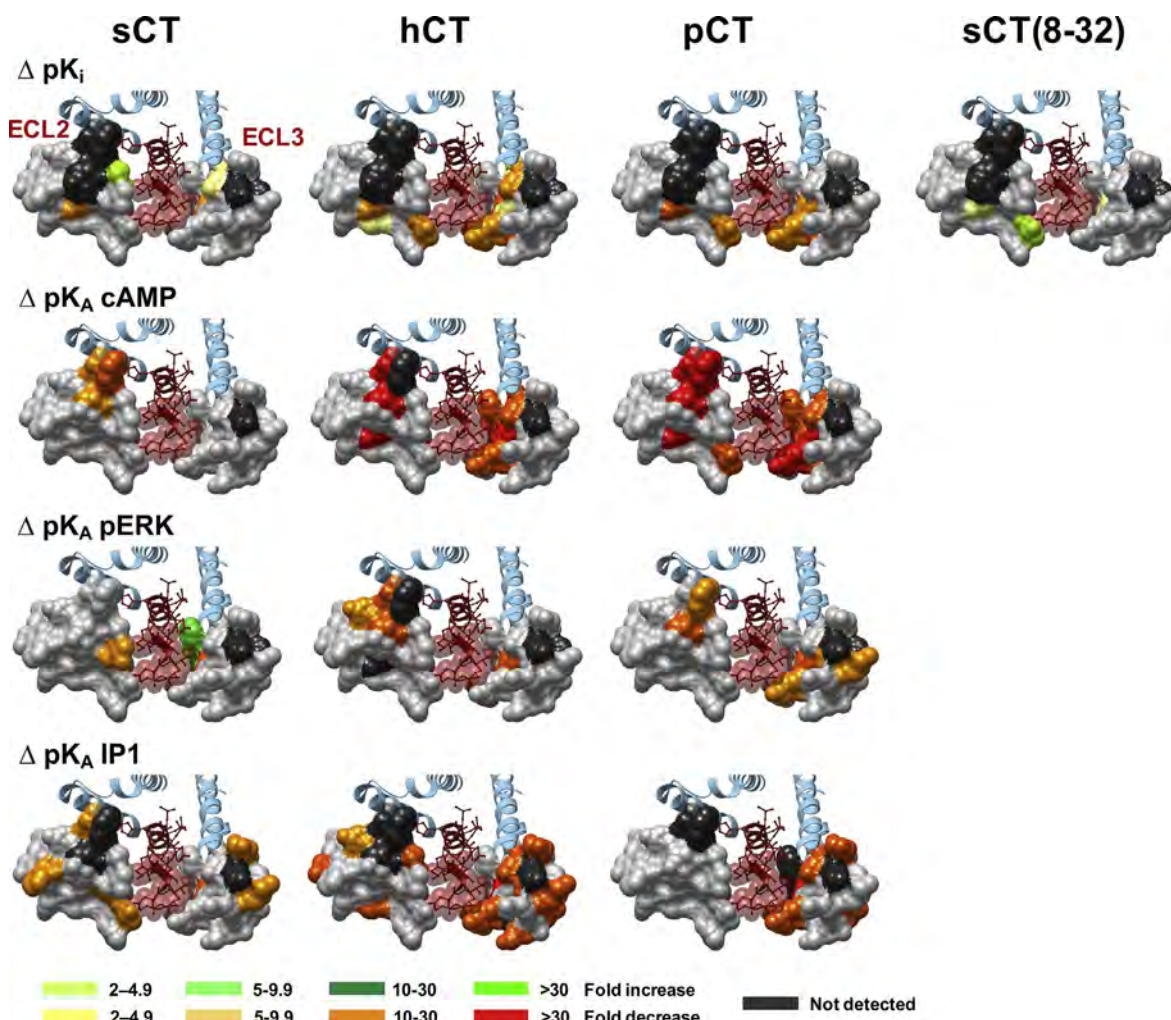


Fig. 2. Alanine mutation of ECL2 and ECL3 of the hCTR alters CT peptide binding pK_i and functional affinity (pK_A) in a peptide- and pathway-specific manner. The effect of mutation on peptide affinity in competition for the antagonist radioligand ^{125}I -sCT(8-32) is displayed as ΔpK_i in the upper panels, with functional affinities derived from operation fitting of concentration-response curves in cAMP accumulation, pERK and IP1 accumulation displayed as ΔpK_A in the mid and lower panels, respectively. Illustrated is a top view of the active, sCT-bound, hCTR model with ECL2 and ECL3 shown in surface representation. Mutations that significantly alter peptide affinity are coloured according to the magnitude of effect (from Tables 1 and 5), with mutated amino acids without significant alteration to affinity coloured grey. sCT is shown as dark red, with side chains in proximity to the ECLs displayed in x-stick, and residues 1–7 that are critical for receptor activation displayed in transparent cpk. (For interpretation of the references to colour in this figure legend, the reader is referred to the web version of this article.)

2.12. Molecular dynamics simulations

CTR:sCT and CTR:hCT complexes were prepared for molecular dynamics simulations by means of a multistep procedure that integrates both python htmD [28] and tcl (Tool Command Language) scripts. The pdb2pqr [29] and propka [30] software were used to check the protein's structural integrity and to add hydrogen atoms (configurations of titratable amino acid side chains were visually inspected) appropriate for a simulated pH of 7.0. The CTR was embedded in rectangular matrixes of a 1-palmitoyl-2-oleyl-sn-glycerol-3-phospho-choline (POPC) bilayer (previously built by using the VMD Membrane Builder plugin 1.1; <http://www.ks.uiuc.edu/Research/vmd/plugins/membrane>) through an insertion method [31]: receptors were first oriented according to the CTR coordinates from the OPM database [32], then lipids overlapping the protein were removed and TIP3P water molecules [33] were added to the simulation box by means of the VMD Solvate plugin 1.5 (<http://www.ks.uiuc.edu/Research/vmd/plugins/solvate>). Charge neutrality was finally reached by adding Na^+/Cl^- counter ions to a final concentration of 0.154 M, according to the VMD Autoionize plugin 1.3 (<http://www.ks.uiuc.edu/Research/vmd/plugins/autoionize>). The CHARMM36 force field [34] was used.

2.13. System equilibration and classic MD run settings

All the following MD simulation stages were performed by using Acemd [35]. Equilibration of the four systems was achieved in isothermal-isobaric conditions (NPT) using the Berendsen barostat [36] (target pressure 1 atm) and the Langevin thermostat [37] (target temperature 300 K) with a low damping of 1 ps^{-1} . A three-stage procedure with an integration time step of 2 fs was performed: in the first stage, 2000 conjugate-gradient minimization steps were applied to reduce the clashes between protein and lipids. Then, a 10 ns long MD simulation was performed in the NPT ensemble, with a positional constraint of $1 \text{ kcal mol}^{-1} \text{ \AA}^{-2}$ on protein and lipid phosphorus atoms. During the second stage, 30 ns of MD simulation in the NPT ensemble were performed, constraining all protein atoms but leaving the POPC residues free to diffuse in the bilayer. In the last equilibration stage, positional constraints were reduced by one half and applied only to the protein backbone alpha carbons for a further 10 ns of MD simulation.

For each intermolecular complex, a total of 2 μs of unbiased MD was performed, divided in one replica 1 μs long and two replicas 500 ns long. After equilibration, production MD trajectories were computed with an integration time step of 4 fs in the canonical ensemble (NVT) at 300 K, using a thermostat damping of 0.1 ps^{-1} and the M-SHAKE

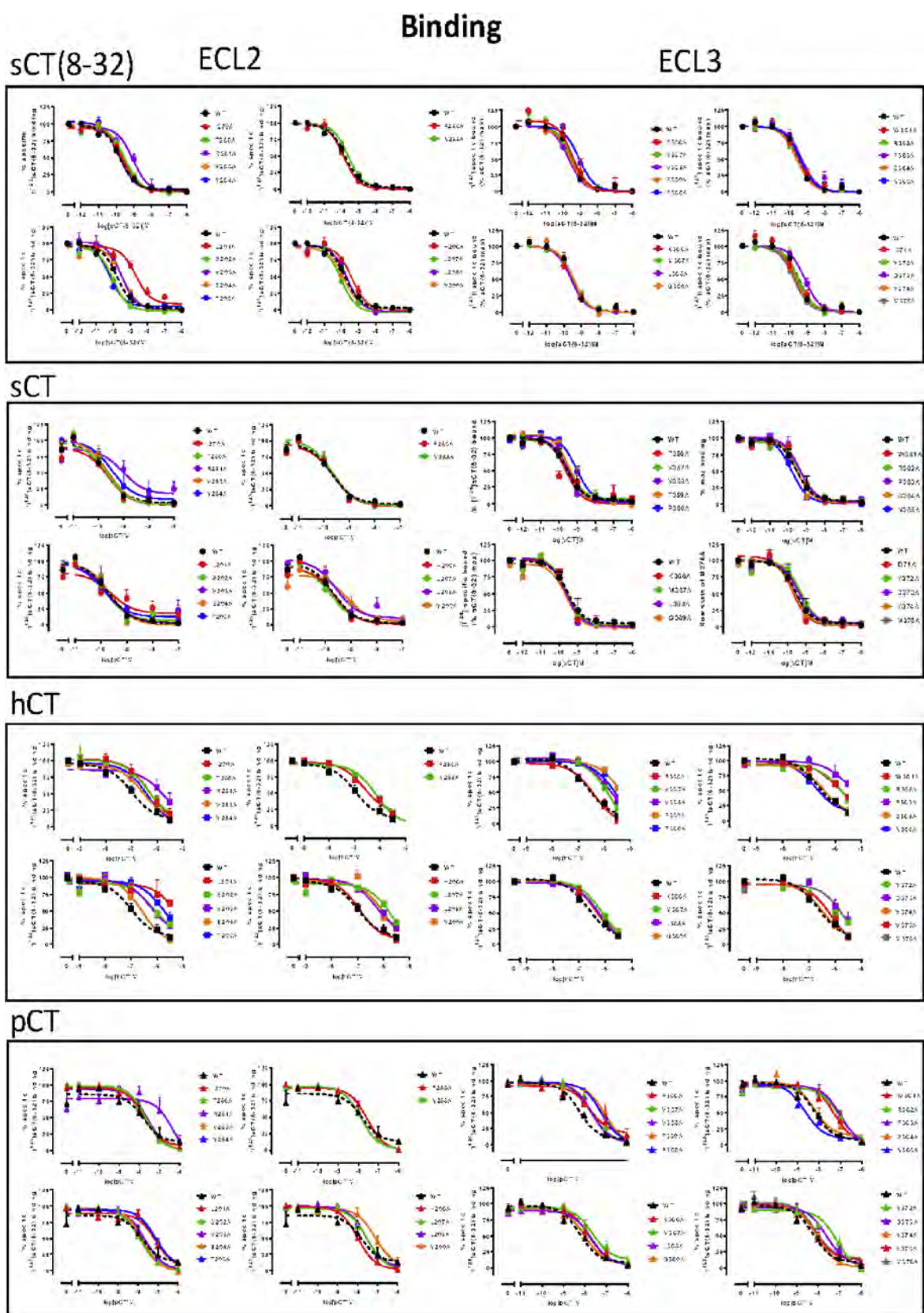


Fig. 3. Competition of ^{125}I -sCT(8-32) binding by CT peptides for wild-type (WT) and each of the hCTR mutants stably expressed in CV1- FlpIn cells. Whole cell radioligand binding was performed for each receptor mutant in presence of ^{125}I -sCT(8-32) and competing peptide ranging in concentration between 1 μM and 1 pM. Non-specific binding was determined in the presence of 1 μM of sCT(8-32) and was used to calculate % of specific binding. Data were fit with a three-parameter logistic equation. All values are mean \pm S.E.M. of 3–12 (WT 16–18) independent experiments, conducted in duplicate.

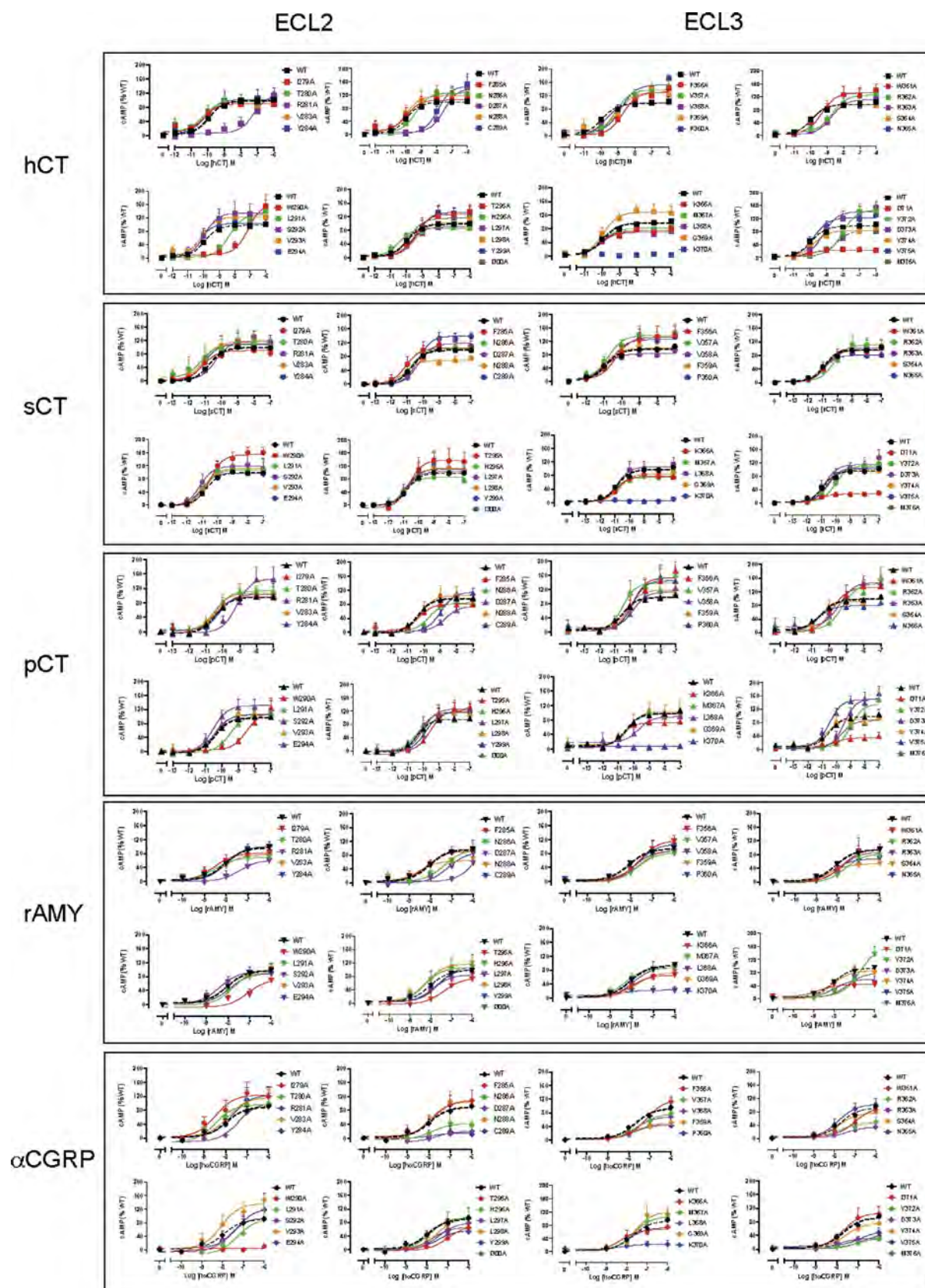


Fig. 4. cAMP accumulation profiles elicited by sCT, hCT, pCT, rat amylin (rAMY) or hCGRP in CV1-FlpIn cells stably expressing wild-type (WT) or single alanine mutations of ECL2 or ECL3. cAMP formation in the presence of agonist peptides was normalized to responses of the internal control (0.1 mM forskolin) and fit to a three-parameter logistic equation. Data was subsequently normalized to WT receptor response. All values are mean \pm S.E.M. of 4–11 (WT 25–36) independent experiments conducted in duplicate.

Table 2
Effect of single alanine mutation in hCTR ECL2 or ECL3 on cAMP signalling in response to CT-family peptides.

	hCT			sCT			pCT			rAmy			hαCGRP		
	pEC ₅₀	E _{max} (% WT)	N	pEC ₅₀	E _{max} (% WT)	N	pEC ₅₀	E _{max} (% WT)	N	pEC ₅₀	E _{max} (% WT)	N	pEC ₅₀	E _{max} (% WT)	N
WT	9.93 ± 0.06	100 ± 2	(36)	10.7 ± 0.05	100 ± 1	(36)	10.4 ± 0.10	100 ± 2	(31)	8.05 ± 0.11	100 ± 4	(31)	7.96 ± 0.21	100 ± 7	(25)
I279A	10.3 ± 0.18	91 ± 4	(4)	11.1 ± 0.25	90 ± 6	(5)	10.4 ± 0.15	97 ± 4	(6)	8.53 ± 0.35	81 ± 9	(5)	8.47 ± 0.41	139 ± 18	(5)
T280A	10.3 ± 0.28	97 ± 6	(4)	11.3 ± 0.56	107 ± 14	(4)	10.4 ± 0.17	113 ± 5	(5)	8.47 ± 0.38	69 ± 8	(4)	8.48 ± 0.49	107 ± 21	(5)
R281A	7.22 ± 0.26*	117 ± 15	(8)	10.4 ± 0.17	119 ± 5	(11)	9.19 ± 0.28*	147 ± 16*	(6)	7.36 ± 0.5	63 ± 14	(5)	7.41 ± 0.43	114 ± 25	(5)
V283A	10.4 ± 0.34	90 ± 7	(4)	11.1 ± 0.38	116 ± 12	(5)	10.5 ± 0.32	107 ± 9	(5)	8.17 ± 0.36	77 ± 10	(5)	7.89 ± 0.39	130 ± 19	(5)
Y284A	10.2 ± 0.35	103 ± 10	(5)	11.0 ± 0.35	111 ± 11	(5)	10.2 ± 0.29	104 ± 9	(6)	7.99 ± 0.25	101 ± 10	(5)	7.72 ± 0.39	139 ± 22	(5)
F285A	9.97 ± 0.42	105 ± 11	(5)	11.1 ± 0.29	105 ± 8	(5)	10.3 ± 0.45	81 ± 10	(6)	8.17 ± 0.28	92 ± 9	(5)	7.80 ± 0.39	122 ± 18	(5)
N286A	9.37 ± 0.17	126 ± 6	(5)	10.8 ± 0.22	103 ± 6	(5)	9.70 ± 0.22	84 ± 6	(5)	7.35 ± 0.35	97 ± 15	(5)	7.85 ± 0.75	46 ± 16	(5)
D287A	7.53 ± 0.30*	140 ± 18*	(6)	10.3 ± 0.22	119 ± 7	(10)	8.72 ± 0.34*	74 ± 9	(6)	N.D.	N.D.		N.D.	N.D.	
N288A	9.99 ± 0.32	117.0 ± 10	(5)	11.2 ± 0.28	69 ± 5*	(6)	10.2 ± 0.31	105 ± 10	(5)	8.52 ± 0.44	64 ± 8	(5)	7.99 ± 0.34	118 ± 17	(5)
C289A	7.92 ± 0.21*	148 ± 7*	(8)	10.3 ± 0.17	140 ± 7*	(10)	8.99 ± 0.16*	115 ± 7	(8)	7.17 ± 0.48	89 ± 23	(5)	N.D.	N.D.	
W290A	7.13 ± 0.24*	164 ± 20*	(10)	10.5 ± 0.16	154 ± 7*	(11)	8.48 ± 0.28*	113 ± 12	(5)	7.09 ± 0.55	72 ± 26	(5)	N.D.	N.D.	
L291A	8.36 ± 0.11*	131 ± 5*	(10)	10.9 ± 0.14	108 ± 4	(10)	9.50 ± 0.14*	105 ± 5	(6)	7.74 ± 0.31	101 ± 13	(5)	7.29 ± 0.64	101 ± 36	(5)
S292A	9.95 ± 0.35	135 ± 13	(6)	11.1 ± 0.38	119 ± 12	(6)	10.5 ± 0.26	131 ± 9*	(6)	8.39 ± 0.32	95 ± 10	(6)	7.65 ± 0.30	106 ± 14	(5)
V293A	10.1 ± 0.24	123 ± 8	(5)	10.9 ± 0.35	112 ± 11	(5)	10.3 ± 0.18	107 ± 5	(6)	8.13 ± 0.29	91 ± 10	(6)	8.06 ± 0.29	153 ± 17	(5)
E294A	10.3 ± 0.20	105 ± 5	(5)	11.1 ± 0.31	98 ± 9	(5)	10.4 ± 0.22	105 ± 6	(5)	7.92 ± 0.26	90 ± 9	(5)	7.31 ± 0.49	137 ± 31	(5)
T295A	9.44 ± 0.31	127 ± 11	(5)	10.5 ± 0.31	138 ± 13*	(5)	9.55 ± 0.21	123 ± 8	(5)	7.36 ± 0.48	74 ± 19	(5)	6.97 ± 0.42	79 ± 20	(5)
H296A	10.5 ± 0.19	87 ± 4	(10)	11.0 ± 0.18	86 ± 5	(10)	10.5 ± 0.29	96 ± 8	(5)	8.29 ± 0.48	107 ± 18	(5)	7.85 ± 0.41	106 ± 18	(6)
L297A	9.75 ± 0.25	91 ± 6	(4)	10.8 ± 0.4	103 ± 12	(4)	10.0 ± 0.20	127 ± 8	(6)	7.87 ± 0.30	85 ± 10	(5)	7.44 ± 0.34	88 ± 14	(5)
L298A	9.44 ± 0.20	103 ± 6	(5)	10.7 ± 0.3	112 ± 9	(5)	10.2 ± 0.20	118 ± 7	(5)	8.21 ± 0.30	117 ± 13	(5)	7.47 ± 0.36	109 ± 17	(5)
Y299A	9.33 ± 0.22	133 ± 9	(5)	10.9 ± 0.25	110 ± 7	(5)	9.87 ± 0.23	117 ± 9	(6)	7.71 ± 0.25	102 ± 1	(4)	7.48 ± 0.55	62 ± 16	(5)
I300A	9.83 ± 0.18	116 ± 6	(5)	10.7 ± 0.36	113 ± 11	(5)	10.3 ± 0.30	117 ± 11	(5)	7.61 ± 0.22	109 ± 10	(5)	7.71 ± 0.45	73 ± 14	(5)
F356A	8.71 ± 0.18*	131 ± 8*	(5)	10.9 ± 0.05	100 ± 1	(6)	10.5 ± 0.07	100 ± 2	(4)	7.62 ± 0.30	126 ± 15	(4)	7.18 ± 0.11	128 ± 10	(5)
V357A	9.15 ± 0.14*	137 ± 6*	(6)	10.3 ± 0.32	133 ± 12*	(6)	9.82 ± 0.35	154 ± 17*	(4)	7.69 ± 0.27	88 ± 10	(5)	7.53 ± 0.32	82 ± 10	(5)
V358A	9.72 ± 0.16	98 ± 4	(4)	10.8 ± 0.24	139 ± 9*	(4)	10.5 ± 0.38	140 ± 15*	(4)	7.86 ± 0.36	94 ± 13	(4)	7.68 ± 0.31	74 ± 9	(5)
F359A	8.95 ± 0.24*	130 ± 9*	(5)	11.0 ± 0.18	84 ± 4.0	(5)	9.79 ± 0.25	113 ± 8	(4)	7.63 ± 0.25	95 ± 9	(5)	7.73 ± 0.41	53 ± 8*	(5)
P360A	8.80 ± 0.17*	152 ± 8*	(5)	11.0 ± 0.18	100 ± 5	(5)	9.88 ± 0.27	146 ± 13	(4)	7.63 ± 0.30	115 ± 13	(5)	7.76 ± 0.28	48 ± 5*	(5)
W361A	9.32 ± 0.25	132 ± 9*	(5)	10.6 ± 0.19	126 ± 7*	(5)	9.83 ± 0.20	133 ± 9*	(4)	7.79 ± 0.31	102 ± 13	(5)	7.01 ± 0.30	102 ± 16	(5)
R362A	8.68 ± 0.24*	125 ± 9*	(4)	10.8 ± 0.14	95 ± 4	(4)	9.74 ± 0.21	138 ± 9*	(4)	7.61 ± 0.32	88 ± 12	(4)	7.75 ± 0.48	51 ± 9*	(5)
P363A	8.74 ± 0.13*	111 ± 5	(5)	10.3 ± 0.28	111 ± 9	(5)	9.41 ± 0.34*	148 ± 15*	(4)	7.82 ± 0.55	94 ± 20	(6)	7.41 ± 0.47	38 ± 7*	(5)
S364A	9.94 ± 0.36	97 ± 9	(5)	10.8 ± 0.26	102 ± 7	(5)	9.22 ± 0.29*	166 ± 16*	(4)	8.35 ± 0.38	56 ± 7*	(4)	7.78 ± 0.31	83 ± 10	(4)
N365A	9.91 ± 0.16	96 ± 4	(5)	10.8 ± 0.19	94 ± 5	(5)	10.5 ± 0.21	95 ± 5	(4)	8.18 ± 0.32	72 ± 8	(4)	7.81 ± 0.31	111 ± 13	(5)
K366A	10.1 ± 0.17	74 ± 3*	(5)	10.9 ± 0.23	81 ± 5*	(5)	10.7 ± 0.39	80 ± 8	(4)	8.02 ± 0.26	71 ± 7	(4)	8.27 ± 0.54	73 ± 13	(5)
M367A	10.0 ± 0.19	82 ± 4	(5)	10.9 ± 0.16	79 ± 3*	(5)	10.8 ± 0.34	73 ± 13	(4)	8.30 ± 0.26	93 ± 8	(4)	7.67 ± 0.31	114 ± 14	(5)
L368A	10.1 ± 0.23	70 ± 4*	(5)	11.1 ± 0.33	75 ± 7*	(5)	10.5 ± 0.26	96 ± 6	(4)	7.93 ± 0.34	95 ± 12	(5)	7.94 ± 0.4	78 ± 12	(5)
G369A	9.92 ± 0.27	129 ± 9*	(5)	10.8 ± 0.27	106 ± 8	(5)	9.69 ± 0.28	89 ± 7	(4)	7.83 ± 0.20	78 ± 6	(4)	7.61 ± 0.38	131 ± 20	(5)
K370A	N.D.	N.D.		N.D.	N.D.		N.D.	N.D.		N.D.	N.D.		N.D.	N.D.	
I371A	9.99 ± 0.47	24 ± 2.7*	(5)	11.2 ± 0.30	28 ± 2*	(5)	10.1 ± 0.21	35 ± 5*	(4)	8.73 ± 0.60	47 ± 7*	(5)	6.88 ± 0.54	58 ± 15*	(5)
Y372A	8.03 ± 0.20*	149 ± 12.*	(4)	10.0 ± 0.27	113 ± 10	(4)	8.94 ± 0.24*	137 ± 13*	(4)	6.73 ± 0.26	170 ± 26*	(5)	6.91 ± 0.45	36 ± 8*	(5)
D373A	9.20 ± 0.19	142 ± 8*	(4)	10.8 ± 0.25	116 ± 8	(4)	9.41 ± 0.16*	158 ± 9*	(4)	7.98 ± 0.70	64 ± 16	(5)	7.95 ± 0.41	34 ± 5*	(5)
Y374A	9.78 ± 0.23	83.2 ± 5	(5)	10.9 ± 0.18	96 ± 5	(5)	10.7 ± 0.39	90 ± 9	(4)	8.10 ± 0.24	92 ± 9	(4)	7.60 ± 0.36	82 ± 12	(5)
V375A	9.79 ± 0.22	122 ± 7*	(5)	10.6 ± 0.17	106 ± 5	(5)	10.5 ± 0.21	151 ± 8*	(4)	8.10 ± 0.27	92 ± 9	(5)	7.69 ± 0.38	114 ± 17	(5)
M376A	8.44 ± 0.37*	84.3 ± 10	(5)	10.6 ± 0.20	102 ± 6	(5)	9.63 ± 0.40	87 ± 11*	(4)	7.33 ± 0.34	85 ± 13	(5)	6.85 ± 0.26	47 ± 7*	(5)

For each receptor and ligand, data were fit to a three-parameter logistic equation to derive pEC₅₀ (negative logarithm of the concentration of ligand that produces half the maximal response) and E_{max} (maximal response, as % of WT). All values are mean ± S.E.M. (independent "n" values are indicated within parentheses). For each ligand, significance of changes in pEC₅₀ and E_{max} were determined by comparison of mutants to the WT receptor in a one-way analysis of variance followed by Dunnett's post-test (p < 0.05 represented by *). (N.D.) pEC₅₀ or E_{max} not determined.

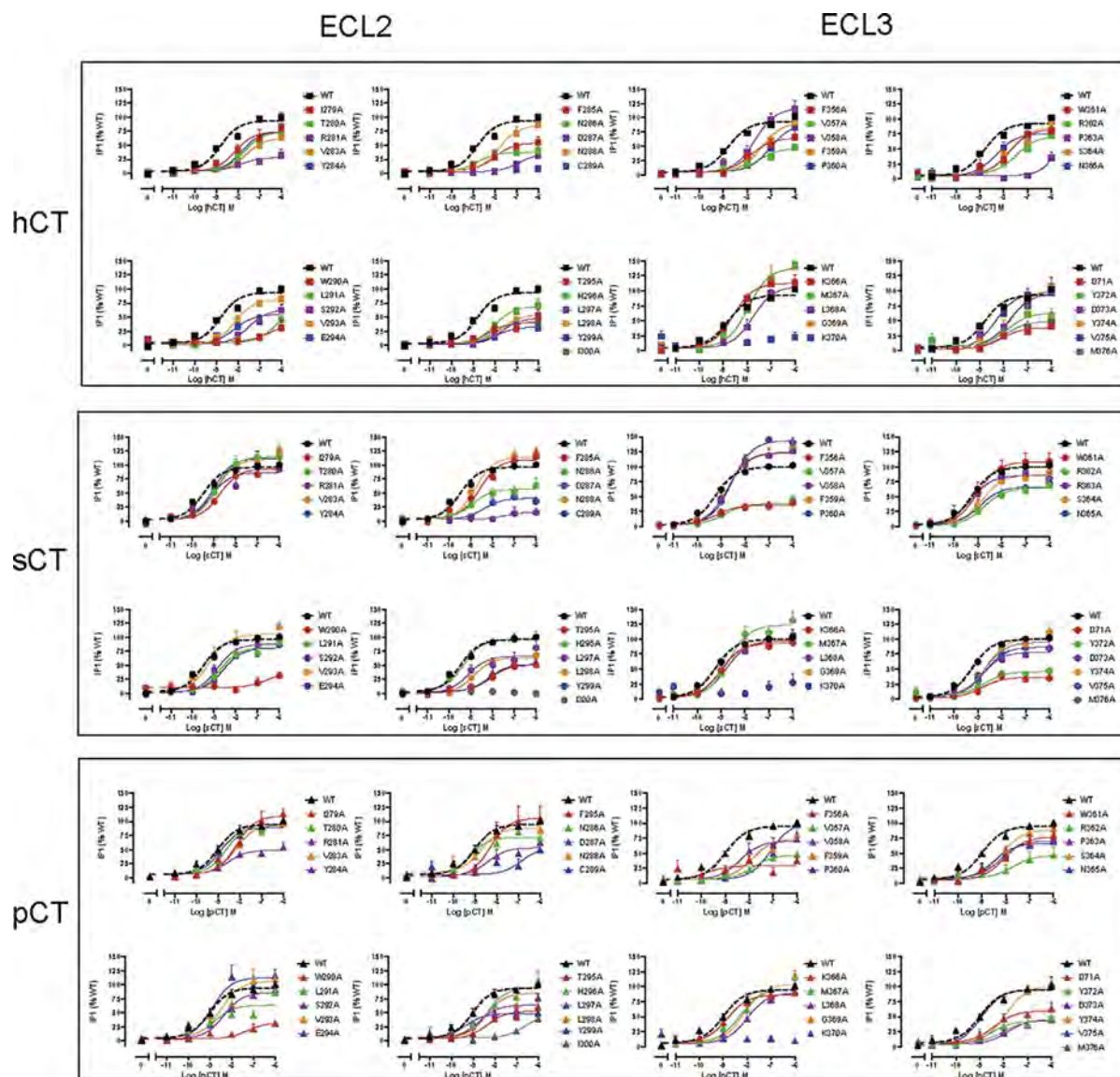


Fig. 5. IP1 accumulation profiles elicited by sCT, hCT, or pCT in CV1-FlpIn cells stably expressing wild-type (WT) or single alanine mutations of ECL2 or ECL3. IP1 accumulation in the presence of agonist peptides was normalized to responses of the internal control (0.1 mM ATP) and fit to a three-parameter logistic equation. Data was subsequently normalized to WT receptor response. All values are mean \pm S.E.M. of 4–7 (WT 37–47) independent experiments conducted in duplicate.

algorithm [38] to constrain the bond lengths involving hydrogen atoms. The cut off distance for electrostatic interactions was set at 9 Å, with a switching function applied beyond 7.5 Å. Long range Coulomb interactions were handled using the particle mesh Ewald summation method (PME) [39] by setting the mesh spacing to 1.0 Å

2.14. Analysis

Contacts and hydrogen bonds were quantified using VMD [40]. A contact between two residues was considered productive if at least two atoms were detected at distances less than 3.5 Å. A distance between acceptor and donor atoms of 3 Å and an angle value of 20° were set as the geometrical cut-off for hydrogen bonds. Equilibrated coordinates and parameters are available from the following doi: <https://doi.org/10.5526/ERDR-00000075>.

Data on the effect of ECL2 and ECL3 mutation on GLP-1R-mediated efficacy were mapped onto the high resolution 3.3 Å structure of exendin-P5 in complex with the hGLP-1R and dominant negative Gs heterotrimer (PDB = 6B3J [15]). Mapping and visualization of the effect of mutation on receptor structure was performed using ICM

(Molsoft).

3. Results

To assess the importance of ECL2 and ECL3 in CTR function, we performed alanine-scanning mutagenesis of residues within these loops as well as adjacent TMs, and assessed effects on cell surface receptor expression, competitive binding affinity and cAMP accumulation, IP1 accumulation and ERK1/2 phosphorylation (pERK). These pathways are important for physiological, CTR-mediated, signalling [2,7]. Responses were evaluated for representatives of the major structural/evolutionary clades of CT peptides, specifically, human CT (hCT) and salmon CT (sCT) that are both used clinically, as well as porcine CT (pCT) (Fig. 1A). We also assessed responses to the related peptides Amy and CGRP that bind to and activate the CTR with low affinity/potency, but are potent agonists of CTR/RAMP complexed receptors. Global affinity (pK_i) was determined from competition with the radiolabelled antagonist peptide 125 I-sCT(8–32), while functional affinity (pK_{eff}) and efficacy were determined by quantification of concentration-response data with the operational model of Black and Leff [23] that provides

Table 3
Effect of single alanine mutation in hCTR ECL2 or ECL3 on IP1 signalling in response to CT peptides.

	hCT			sCT			pCT		
	pEC ₅₀	E _{max} (% WT)	N	pEC ₅₀	E _{max} (% WT)	N	pEC ₅₀	E _{max} (% WT)	N
WT	8.80 ± 0.07	100 ± 3	(47)	9.24 ± 0.5	100 ± 3	(44)	8.86 ± 0.13	100 ± 3	(37)
I279A	8.08 ± 0.25	79 ± 7	(7)	8.72 ± 0.23	97 ± 7	(7)	8.18 ± 0.22	116 ± 10	(5)
T280A	7.68 ± 0.20*	79 ± 6	(6)	8.89 ± 0.12	119 ± 5	(7)	8.61 ± 0.21	100 ± 6	(7)
R281A	7.96 ± 0.37*	30 ± 4	(7)	9.03 ± 0.23	91 ± 6	(6)	8.65 ± 0.23	52 ± 4*	(6)
V283A	7.60 ± 0.21	67 ± 6*	(5)	8.87 ± 0.15	115 ± 6	(7)	8.21 ± 0.14	100 ± 5	(7)
Y284A	7.71 ± 0.37	81 ± 12	(7)	8.94 ± 0.20	118 ± 7	(6)	8.94 ± 0.20	94 ± 6	(7)
F285A	7.99 ± 0.27	58 ± 6*	(6)	8.59 ± 0.17	114 ± 6	(5)	8.30 ± 0.32	112 ± 13	(6)
N286A	8.82 ± 0.28	40 ± 3*	(6)	8.93 ± 0.26	59 ± 5*	(5)	9.25 ± 0.27	76 ± 6	(7)
D287A	N.D.	N.D.		N.D.	N.D.		8.43 ± 0.38	56 ± 7*	(6)
N288A	7.78 ± 0.22*	91 ± 8	(7)	8.80 ± 0.15	119 ± 6	(6)	8.72 ± 0.25	93 ± 7	(7)
C289A	N.D.	N.D.		8.52 ± 0.28	42 ± 4*	(6)	N.D.	N.D.	(7)
W290A	N.D.	N.D.		N.D.	N.D.		N.D.	N.D.	
L291A	6.28 ± 0.53*	71 ± 16*	(7)	8.73 ± 0.14	85 ± 4	(7)	8.79 ± 0.31	67 ± 6*	(7)
S292A	7.51 ± 0.20*	70 ± 6	(6)	8.86 ± 0.21	91 ± 6	(7)	8.37 ± 0.23	92 ± 7	(7)
V293A	8.12 ± 0.13	87 ± 4	(6)	9.21 ± 0.22	109 ± 7	(7)	8.49 ± 0.27	112 ± 10	(5)
E294A	8.21 ± 0.27	57 ± 6*	(6)	8.62 ± 0.18	84 ± 5	(6)	8.89 ± 0.22	119 ± 8	(6)
T295A	8.31 ± 0.27	43 ± 4*	(6)	8.11 ± 0.33*	53 ± 7*	(6)	8.34 ± 0.37	56 ± 7*	(6)
H296A	7.98 ± 0.19*	73 ± 6*	(7)	9.34 ± 0.19	101 ± 5	(7)	8.35 ± 0.21	101 ± 7	(6)
L297A	7.68 ± 0.25*	52 ± 5*	(7)	9.12 ± 0.32	69 ± 7*	(6)	8.70 ± 0.25	68 ± 5*	(7)
L298A	7.69 ± 1.10	58 ± 6*	(7)	8.88 ± 0.22	66 ± 5*	(7)	8.39 ± 0.25	91 ± 10	(5)
Y299A	7.94 ± 0.37	34 ± 5*	(6)	8.19 ± 0.27*	54 ± 5*	(6)	9.38 ± 0.25	52 ± 3*	(7)
I300A	8.12 ± 0.37	44 ± 4*	(6)	N.D.	N.D.		N.D.	N.D.	
F356A	7.95 ± 0.20*	69 ± 6*	(6)	9.23 ± 0.29	36 ± 3*	(6)	N.D.	N.D.	
V357A	7.61 ± 0.23*	50 ± 4*	(5)	8.90 ± 0.20	39 ± 3*	(5)	7.81 ± 0.20*	48 ± 4*	(5)
V358A	7.64 ± 0.18*	126 ± 9*	(6)	8.76 ± 0.15	123 ± 6*	(6)	8.48 ± 0.26	73 ± 6*	(5)
F359A	7.29 ± 0.20*	101 ± 9	(5)	8.72 ± 0.14	125 ± 6*	(5)	7.88 ± 0.18*	77 ± 6	(5)
P360A	7.06 ± 0.16*	95 ± 8	(5)	8.55 ± 0.11*	144 ± 5*	(6)	7.07 ± 0.23*	107 ± 12	(5)
W361A	7.77 ± 0.26	89 ± 9	(6)	9.01 ± 0.18	108 ± 6	(5)	8.08 ± 0.19*	80 ± 6	(6)
R362A	7.47 ± 0.34*	77 ± 11	(6)	8.74 ± 0.22	64 ± 5*	(5)	7.71 ± 0.50*	47 ± 9*	(6)
P363A	N.D.	N.D.		9.27 ± 0.35	86 ± 9	(5)	8.21 ± 0.38	73 ± 10*	(6)
S364A	7.77 ± 0.21*	93 ± 8	(5)	8.79 ± 0.21	87 ± 6	(5)	8.16 ± 0.29	93 ± 6	(5)
N365A	8.36 ± 0.21	81 ± 6	(5)	8.96 ± 0.18	66 ± 4*	(4)	8.65 ± 0.29	68 ± 6*	(5)
K366A	8.58 ± 0.16	121 ± 6	(5)	9.03 ± 0.15	93 ± 5	(5)	8.83 ± 0.23	91 ± 6	(5)
M367A	7.94 ± 0.14	149 ± 8*	(4)	8.71 ± 0.16	123 ± 6*	(6)	8.29 ± 0.23	101 ± 8	(5)
L368A	7.76 ± 0.14*	115 ± 7	(6)	8.79 ± 0.14	97 ± 4	(5)	8.00 ± 0.24*	94 ± 9	(5)
G369A	7.97 ± 0.17*	148 ± 10*	(5)	8.93 ± 0.22	97 ± 7	(5)	8.12 ± 0.14	110 ± 6	(5)
K370A	N.D.	N.D.		N.D.	N.D.		N.D.	N.D.	
I371A	8.09 ± 0.20	42 ± 3*	(7)	8.83 ± 0.21	31 ± 14*	(6)	8.38 ± 0.29	61 ± 6*	(5)
Y372A	7.83 ± 0.36	68 ± 9*	(5)	8.74 ± 0.29	46 ± 4*	(7)	8.54 ± 0.35	44 ± 5*	(5)
D373A	7.75 ± 0.26*	102 ± 10	(5)	8.79 ± 0.26	78 ± 6	(5)	7.83 ± 0.18*	46 ± 3*	(5)
Y374A	7.65 ± 0.20*	110 ± 9	(5)	8.67 ± 0.19*	102 ± 6	(6)	7.91 ± 0.15*	106 ± 6	(5)
V375A	8.34 ± 0.17	104 ± 6	(5)	8.72 ± 0.21	87 ± 5	(6)	8.93 ± 0.16	100 ± 5	(5)
M376A	8.08 ± 0.26	52 ± 5*	(4)	8.67 ± 0.13	95 ± 4	(4)	8.25 ± 0.27	47 ± 4*	(5)

For each receptor and ligand, data were fit to a three-parameter logistic equation to derive pEC₅₀ (negative logarithm of the concentration of ligand that produces half the maximal response) and E_{max} (maximal response, as % of WT). All values are mean ± S.E.M. (independent “n” values are indicated within parentheses). For each ligand, significance of changes in pEC₅₀ and E_{max} were determined by comparison of mutants to the WT receptor in a one-way analysis of variance followed by Dunnett’s post-test (*p* < 0.05 represented by *). (N.D.) pEC₅₀ or E_{max} not determined.

independent measures of pK_A and efficacy (τ). All experiments were performed in CV-1 FlpIn cells that lack functional CTR and RAMP expression, with receptors stably expressed following isogenic recombination. Data are mapped onto the active hCTR structure (5U27), following modelling of missing side chains and sampling by short time-scale MD.

3.1. Receptor expression

Residues for mutation were selected based on the recent structure of sCT/hCTR/Gs [13] and comprised amino acids I279–I300 (ECL2) and F356–M376 (ECL3) (Fig. 1B,C). Cell surface expression was determined by anti-c-Myc antibody binding to the c-Myc tag inserted after the receptor signal peptide in the N-terminal ECD (Fig. 1B), and quantified by FACS.

Most mutants demonstrated equivalent cell surface expression to that of the WT receptor (Fig. 1D; Table 1), however, a subset of mutants, particularly within ECL2, had altered expression. Only K370A in ECL3 had no detectable expression. D287A, C289A, W290A, and I300A

in ECL2, and I371 in ECL3, also had markedly diminished cell surface expression (< 20% of WT). R281A, N286A, T295A, L297A, Y299A in ECL2 and F356A in ECL3 were expressed at levels between 20% and ~40% of WT. A smaller but significant attenuation of expression was observed for Y284A, R362A and Y374A. In contrast, T280A significantly increased expression and P360A strongly augmented cell surface receptor expression (Fig. 1D; Table 1). Within ECL2, those residues with strongly attenuated expression formed a continuum within the central portion of the loop, suggesting that these residues participate in a network that helps to stabilize the apo receptor (Fig. 1E).

3.2. ECL2 and ECL3 mutants differentially modulate peptide-specific affinity

Global affinity was determined by competition of ¹²⁵I-sCT(8–32) binding in whole cells by each of the peptides. Homologous competition with sCT(8–32) revealed a pK_i for the WT receptor of 9.70 ± 0.05, and a B_{max} of 22,900 ± 2500 sites/cell (Table 1). Overall, there was a good correlation, for the mutant receptors relative to WT, between

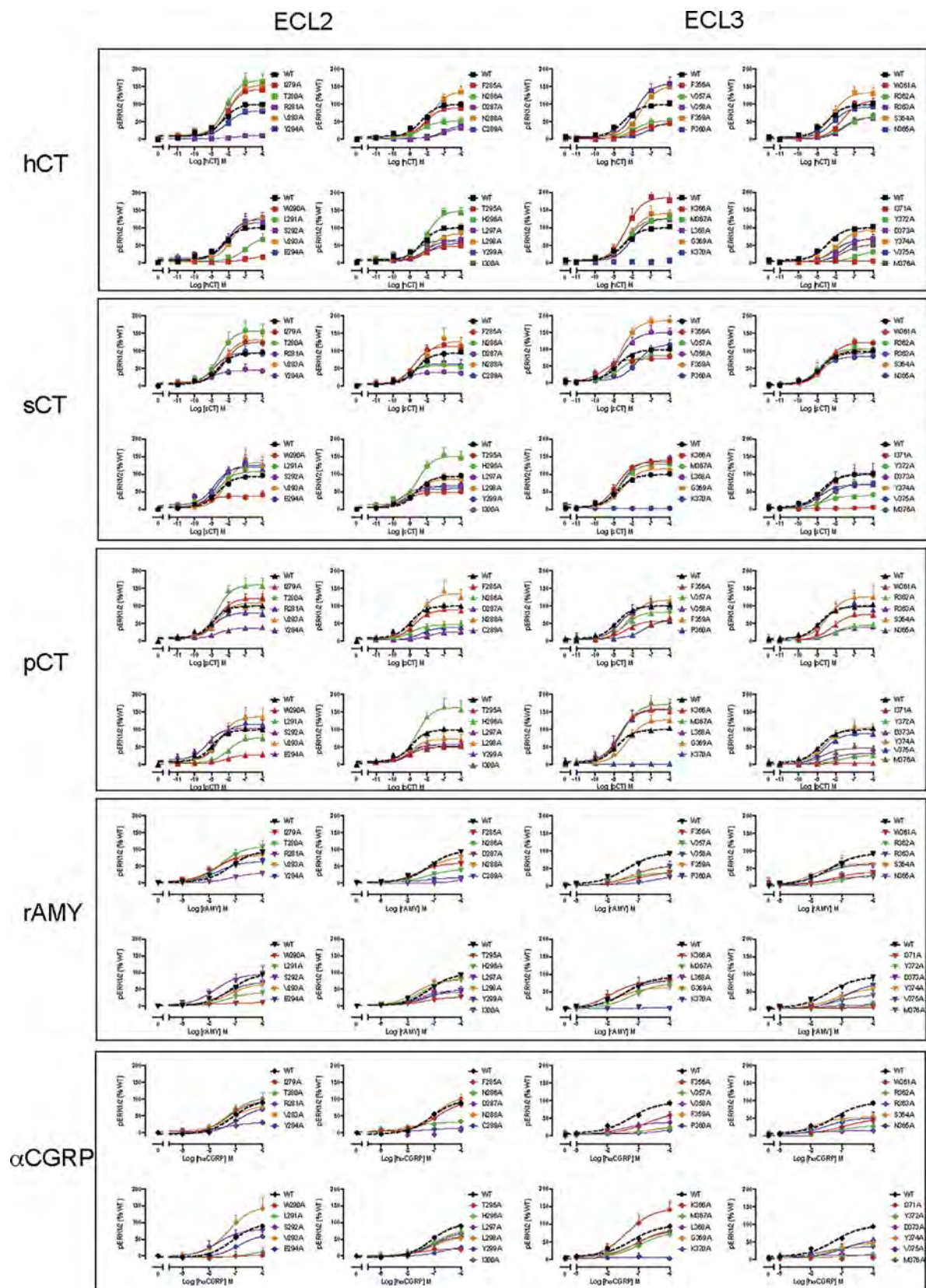


Fig. 6. Peak ERK1/2 phosphorylation (pERK) profiles elicited by sCT, hCT, pCT, rat amylin (rAMY) or hCGRP in CV1-FlpIn cells stably expressing wild-type (WT) or single alanine mutations of ECL2 or ECL3. pERK in the presence of agonist peptides was normalized to the WT receptor response and fit to a three-parameter logistic equation. All values are mean \pm S.E.M. of 4–6 (WT 30–35) independent experiments conducted in duplicate.

Table 4
Effect of single alanine mutation in hCTR ECL2 or ECL3 on pERK signalling in response to CT-family peptides.

	hCTR			sCTR			pCTR			rAmy			hcGRP		
	pEC ₅₀	E _{max} (% WT)	N	pEC ₅₀	E _{max} (% WT)	N	pEC ₅₀	E _{max} (% WT)	N	pEC ₅₀	E _{max} (% WT)	N	pEC ₅₀	E _{max} (% WT)	N
WT	8.32 ± 0.09	100.0 ± 3	(34)	8.62 ± 0.10	100 ± 3	(35)	8.95 ± 0.08	100 ± 3	(32)	7.19 ± 0.10	100 ± 5	(30)	7.11 ± 0.11	100 ± 6	(30)
I279A	8.09 ± 0.19	143 ± 10*	(5)	8.22 ± 0.11	126 ± 5*	(5)	8.66 ± 0.17	122 ± 7	(5)	7.74 ± 0.27	88 ± 9	(5)	7.30 ± 0.23	97 ± 11	(5)
T280A	8.17 ± 0.19	168 ± 12*	(6)	8.55 ± 0.25	158 ± 12*	(6)	8.69 ± 0.19	160 ± 10*	(5)	7.57 ± 0.23	110 ± 11	(6)	7.27 ± 0.23	106 ± 12	(6)
R281A	N.D.	N.D.		9.01 ± 0.43	45 ± 5*	(5)	8.64 ± 0.35	37 ± 4*	(5)	7.16 ± 0.27	31 ± 5*	(5)	7.46 ± 0.43	30 ± 5*	(5)
V283A	8.00 ± 0.24	155 ± 14*	(5)	8.30 ± 0.22	133 ± 10*	(6)	8.65 ± 0.34	109 ± 12	(5)	7.77 ± 0.27	83 ± 9	(5)	7.22 ± 0.18	81 ± 7	(4)
Y284A	8.08 ± 0.23	82 ± 7	(5)	8.83 ± 0.21	96 ± 6	(5)	8.92 ± 0.25	81 ± 6	(5)	7.69 ± 0.23	64 ± 6*	(5)	6.95 ± 0.31	79 ± 15	(5)
F285A	8.09 ± 0.33	91 ± 11	(5)	8.78 ± 0.16	114 ± 6	(5)	8.74 ± 0.20	88 ± 5	(5)	7.66 ± 0.28	60 ± 7*	(5)	6.90 ± 0.34	93 ± 18	(5)
N286A	8.37 ± 0.32	52 ± 5*	(5)	9.16 ± 0.28	59 ± 5*	(5)	8.92 ± 0.36	46 ± 5*	(5)	7.27 ± 0.32	41 ± 6*	(5)	7.89 ± 0.47	31 ± 5*	(5)
D287A	7.01 ± 0.25*	35 ± 5*	(5)	9.40 ± 0.23	39 ± 2*	(5)	7.9 ± 0.25*	27 ± 3*	(5)	N.D.	N.D.		N.D.	N.D.	
N288A	7.74 ± 0.15	137 ± 8*	(5)	8.36 ± 0.29	127 ± 13*	(5)	8.53 ± 0.26	135 ± 11*	(5)	7.28 ± 0.2	79 ± 7	(5)	7.01 ± 0.16	110 ± 10	(5)
C289A	7.10 ± 0.39*	40 ± 8*	(5)	9.07 ± 0.57	64 ± 11*	(5)	8.37 ± 0.28	38 ± 4*	(5)	N.D.	N.D.		N.D.	N.D.	
W290A	N.D.	N.D.		9.47 ± 0.41	38 ± 4*	(5)	8.13 ± 0.26	28 ± 3*	(5)	N.D.	N.D.		N.D.	N.D.	
L291A	7.05 ± 0.24*	72 ± 9	(5)	8.61 ± 0.15	107 ± 5	(5)	8.02 ± 0.18*	77 ± 5	(5)	7.35 ± 0.22	41 ± 4*	(5)	N.D.	N.D.	
S292A	8.02 ± 0.26	116 ± 11	(5)	8.84 ± 0.21	121 ± 7	(5)	9.26 ± 0.25	104 ± 7	(5)	7.76 ± 0.31	96 ± 12	(6)	7.68 ± 0.35	80 ± 12	(5)
V293A	7.78 ± 0.15	130 ± 8*	(5)	8.18 ± 0.24	135 ± 12*	(5)	8.50 ± 0.25	136 ± 11*	(5)	7.29 ± 0.26	67 ± 8*	(5)	7.28 ± 0.31	149 ± 22	(5)
E294A	8.07 ± 0.21	125 ± 10	(5)	8.67 ± 0.17	126 ± 7*	(5)	8.70 ± 0.24	115 ± 9	(5)	7.43 ± 0.22	72 ± 7	(5)	6.91 ± 0.36	66 ± 15	(5)
T295A	8.13 ± 0.34	48 ± 6*	(5)	9.27 ± 0.30	49 ± 4*	(5)	9.12 ± 0.32	50 ± 5*	(5)	7.35 ± 0.39	28 ± 5*	(5)	7.68 ± 0.38	22 ± 4*	(5)
H296A	8.02 ± 0.14	148 ± 8*	(5)	8.57 ± 0.20	152 ± 9*	(5)	8.63 ± 0.20	163 ± 10*	(5)	7.47 ± 0.22	82 ± 8	(5)	7.04 ± 0.27	77 ± 11	(5)
L297A	8.10 ± 0.22	63 ± 5*	(5)	9.05 ± 0.22	68 ± 4*	(5)	9.01 ± 0.26	59 ± 4*	(5)	7.55 ± 0.27	49 ± 6*	(5)	7.01 ± 0.29	73 ± 12	(5)
L298A	7.82 ± 0.29	84 ± 10	(5)	8.75 ± 0.21	85 ± 6	(5)	8.96 ± 0.28	73 ± 6*	(5)	7.69 ± 0.20	82 ± 7	(5)	7.12 ± 0.24	58 ± 8	(5)
Y299A	7.99 ± 0.28	56 ± 6*	(5)	9.23 ± 0.25	58 ± 4*	(5)	9.03 ± 0.19	51 ± 3*	(5)	7.22 ± 0.28	51 ± 7*	(5)	N.D.	N.D.	
I300A	8.71 ± 0.29	65 ± 6*	(5)	9.49 ± 0.21	63 ± 3*	(5)	9.55 ± 0.22	54 ± 3*	(5)	7.48 ± 0.25	44 ± 5*	(5)	7.17 ± 0.42	61 ± 13	(5)
F356A	7.77 ± 0.17*	43 ± 3*	(4)	9.52 ± 0.25*	72 ± 5*	(5)	8.35 ± 0.30	57 ± 6*	(4)	7.06 ± 0.23	41 ± 5*	(5)	6.74 ± 0.28	68 ± 11	(5)
V357A	7.92 ± 0.21	53 ± 5*	(4)	8.61 ± 0.27	82 ± 7*	(5)	8.43 ± 0.36	83 ± 10	(4)	7.46 ± 0.46	40 ± 8*	(5)	N.D.	N.D.	
V358A	7.83 ± 0.15*	160 ± 10*	(5)	8.68 ± 0.16	150 ± 8*	(4)	8.65 ± 0.26	101 ± 8	(4)	7.23 ± 0.35	59 ± 10*	(5)	7.49 ± 0.50	39 ± 8*	(5)
F359A	7.57 ± 0.12*	153 ± 8*	(5)	8.62 ± 0.12	186 ± 7*	(5)	8.20 ± 0.15	116 ± 6	(5)	7.22 ± 0.4	58 ± 11*	(5)	8.20 ± 0.15	116 ± 6	(5)
P360A	7.12 ± 0.24*	51 ± 6*	(5)	7.78 ± 0.19*	115 ± 9	(5)	7.40 ± 0.28*	59 ± 7*	(5)	N.D.	N.D.		N.D.	N.D.	
W361A	7.64 ± 0.12*	112 ± 6	(5)	8.52 ± 0.12	125 ± 5*	(4)	8.20 ± 0.22	76 ± 6*	(5)	7.24 ± 0.49	42 ± 9*	(4)	6.93 ± 0.31	49 ± 8*	(5)
R362A	7.68 ± 0.25*	64 ± 7*	(5)	8.81 ± 0.28	107 ± 10	(4)	8.12 ± 0.20	45 ± 4*	(5)	6.94 ± 0.36	36 ± 7*	(4)	6.95 ± 0.61	31 ± 8**	(5)
P363A	7.59 ± 0.23*	64 ± 6*	(5)	8.81 ± 0.15	95 ± 5*	(4)	8.24 ± 0.15	39 ± 2*	(5)	7.51 ± 0.81	28 ± 9*	(4)	N.D.	N.D.	
S364A	8.18 ± 0.20	135 ± 10*	(5)	8.56 ± 0.13	106 ± 4	(4)	8.44 ± 0.28	127 ± 12*	(4)	7.94 ± 0.36	66 ± 9*	(4)	7.97 ± 0.29	54 ± 6*	(4)
N365A	8.15 ± 0.16	93 ± 6	(5)	8.82 ± 0.12	84 ± 3	(4)	8.79 ± 0.32	98 ± 10*	(5)	7.73 ± 0.39	63 ± 10*	(5)	7.52 ± 0.39	52 ± 8*	(4)
K366A	8.33 ± 0.24	186 ± 16*	(5)	8.84 ± 0.11	136 ± 5*	(4)	8.72 ± 0.18	156 ± 9*	(5)	7.89 ± 0.33	84 ± 11	(5)	7.39 ± 0.27	146 ± 17*	(4)
M367A	8.26 ± 0.15	127 ± 7*	(5)	8.66 ± 0.10	130 ± 4*	(4)	8.56 ± 0.19	172 ± 10*	(5)	7.19 ± 0.15	77 ± 5	(5)	6.97 ± 0.27	78 ± 12	(4)
L368A	8.05 ± 0.14	126 ± 7*	(4)	8.62 ± 0.12	140 ± 6*	(4)	8.71 ± 0.23	159 ± 11*	(5)	7.56 ± 0.23	82 ± 8*	(4)	7.07 ± 0.37	84 ± 16	(4)
G369A	8.20 ± 0.18	141 ± 9*	(5)	8.53 ± 0.11	115 ± 4	(4)	8.28 ± 0.18	128 ± 8*	(5)	7.73 ± 0.34	63 ± 8*	(4)	7.09 ± 0.30	87 ± 14	(4)
K370A	N.D.	N.D.		N.D.	N.D.		N.D.	N.D.		N.D.	N.D.		N.D.	N.D.	
I371A	N.D.	N.D.		N.D.	N.D.		N.D.	N.D.		N.D.	N.D.		N.D.	N.D.	
Y372A	8.74 ± 0.29	46 ± 4*	(5)	8.64 ± 0.26	39 ± 3*	(4)	7.72 ± 0.41*	26 ± 4*	(4)	N.D.	N.D.		N.D.	N.D.	
D373A	7.63 ± 0.24*	71 ± 7*	(5)	8.62 ± 0.34	103 ± 11	(4)	8.31 ± 0.35	32 ± 4*	(5)	N.D.	N.D.		N.D.	N.D.	
Y374A	7.92 ± 0.09	94 ± 4	(5)	8.63 ± 0.14	99 ± 5	(4)	8.57 ± 0.24	105 ± 8	(4)	7.21 ± 0.17	61 ± 5*	(4)	7.21 ± 0.31	49 ± 8*	(5)
V375A	8.08 ± 0.13	67 ± 3*	(4)	8.83 ± 0.14	70 ± 3*	(5)	8.58 ± 0.14	89 ± 4*	(5)	6.91 ± 0.29	77 ± 13	(5)	6.96 ± 0.24	58 ± 7*	(5)
M376A	7.58 ± 0.21*	52 ± 4*	(4)	8.35 ± 0.2	72 ± 5*	(4)	8.71 ± 0.29	47 ± 4*	(5)	7.17 ± 0.32	43 ± 7*	(5)	7.74 ± 0.60	36 ± 8*	(5)

For each receptor and ligand, data were fit to a three-parameter logistic equation to derive pEC₅₀ (negative logarithm of the concentration of ligand that produces half the maximal response) and Emax (maximal response, as % of WT). All values are mean ± S.E.M. (independent “n” values are indicated within parentheses). For each ligand, significance of changes in pEC₅₀ and Emax were determined by comparison of mutants to the WT receptor in a one-way analysis of variance followed by Dunnett's post-test (p < 0.05 represented by *). (N.D.) pEC₅₀ or Emax not determined.

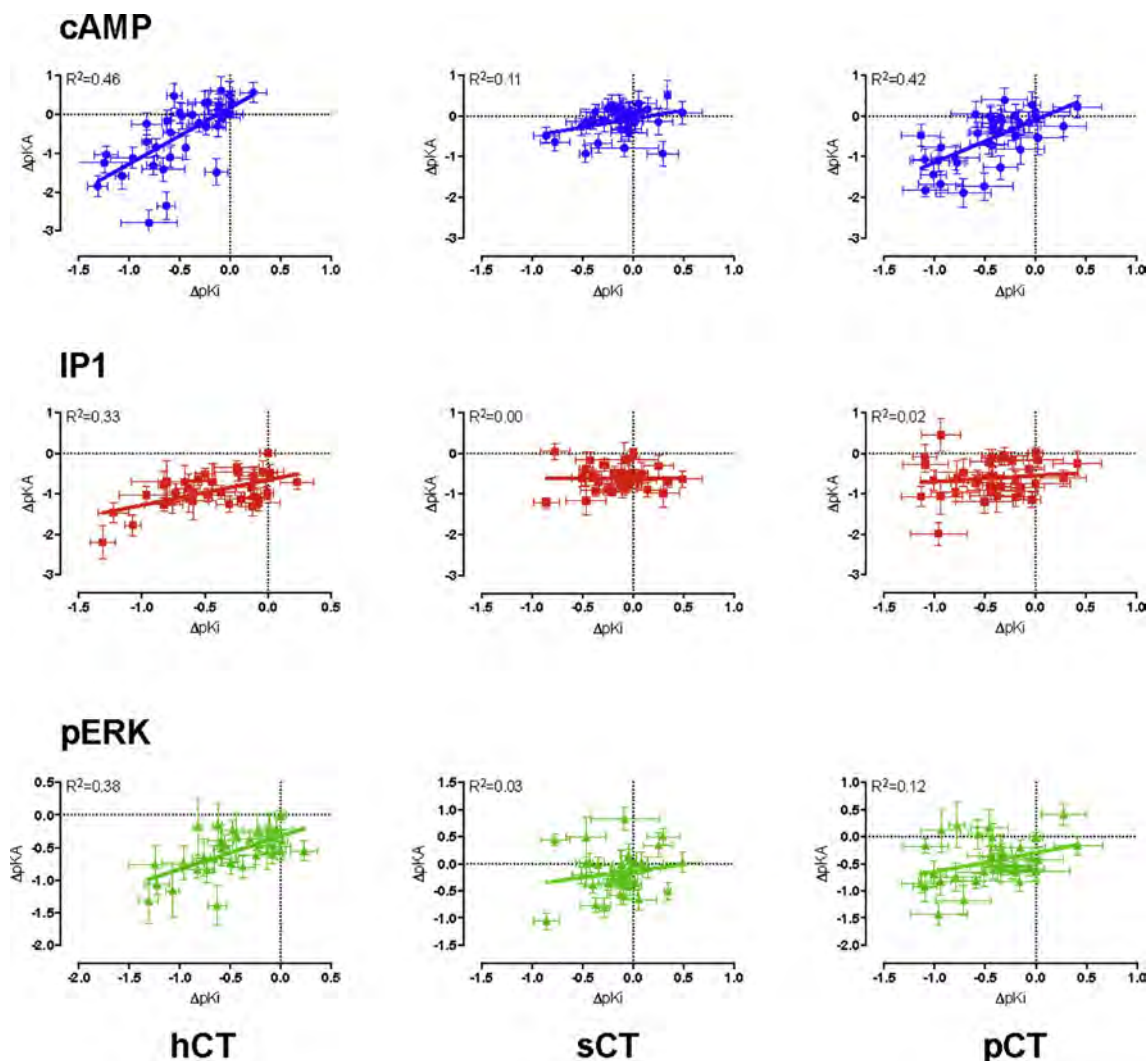


Fig. 7. Correlation between changes in global peptide affinity (pK_i) derived from heterologous competition binding assays, and functional pK_A for cAMP (upper panels), IP1 (middle panels) or pERK (bottom panels) signalling, for hCT (left hand panels), sCT (middle panels) or pCT (right hand panels). For all peptides, the highest correlation was seen between pK_i and pK_A derived from operational analysis of cAMP response data. Significant but weaker correlations were also observed between pK_i and functional affinities for IP1 and pERK signalling for hCT, and for pERK signalling alone for pCT. No correlation was observed for sCT pK_A values from IP1 or pERK assays or pCT IP1 assays.

measured B_{max} and cell surface expression data from antibody binding (Fig. 1F), although there was a high error in B_{max} estimates, consistent with expectations of cold saturation experiments with only two radioligand concentrations. sCT, hCT and pCT had pK_i values for the WT receptor of 9.87 ± 0.03 , 6.72 ± 0.06 and 8.27 ± 0.07 , respectively (Table 1), consistent with those reported in previous studies [9,10].

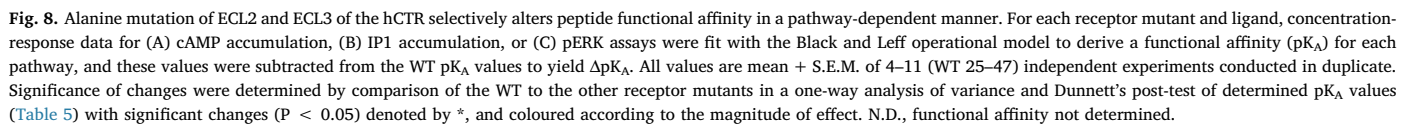
Mutants with very low expression, N286A, D287A, C289A, W290A, I300A, K370A and I371A, displayed little or no detectable ^{125}I -sCT(8-32) binding, thereby preventing assessment of global affinity, whereas all other mutant receptors exhibited a sufficient radioligand binding window to determine peptide affinity. Of these, only R281A, L291A and P360A reduced sCT(8-32) affinity, whereas T295A increased affinity of this peptide (Table 1, Fig. 2; Fig. 3). Similarly, there was only limited effect on sCT affinity, with reduced affinity for the R281A, P360A and D373A mutants, and increased affinity for S292A. Intriguingly, the L291A mutant that had reduced affinity for the antagonist and both hCT and pCT, did not alter sCT affinity. Both hCT and pCT were more broadly sensitive to mutation, with those affecting pCT common with hCT, including R281A, L291A, T295A, L298A, F359A-P363A and Y372A that principally resided either within 5 Å of sCT in the CTR model, or were involved in the network of amino acids in the core of ECL2 that was linked to receptor stability/expression (Table 1, Figs. 1 and 2). There was a significant reduction in pCT affinity for the Y299A

mutant that also trended lower for hCT. Moreover, there was selective, significant attenuation of hCT affinity for L297A, L298A, V357A, V358A, D373A and M376A (Table 1, Fig. 2).

CGRP and Amy displayed no detectable competition with the radioligand at the wildtype or mutant receptors within the concentration range assessed (up to 10 μM), confirming previous findings that these have low affinity for the CTR.

3.3. ECL2 and ECL3 mutants alter functional affinity in a ligand and pathway dependent manner

Concentration-response data, for cAMP accumulation, in response to each peptide was established for WT and mutant receptors (Fig. 4, Table 2), IP1 accumulation (Fig. 5; Table 3), and ERK1/2 phosphorylation (Fig. 6; Table 4). Functional affinity for each of the pathways was determined by operational fitting of the concentration response data. The effect of mutation on pK_A for cAMP formation was broadly similar to the derived pK_i values (Figs. 6 and 7), clustering to either residues in proximity to the peptide or in the central segment of ECL2 that was important for receptor stability and expression (Fig. 2, Fig. 8). Unlike the competition binding assay, estimates of pK_A could be derived for at least one of the peptides for all mutants, except K370A that was not expressed at the cell surface (Fig. 2, Fig. 8, Table 5). Of these,



There were distinct patterns in the effect of mutation on pK_A values both across pathways and between peptides. sCT functional affinities

The F359A and P360A mutants induced a global decrease in functional affinity for pERK and IP1 pathways, but had differential effect on cAMP responses. Neither affected sCT, while P360A attenuated pK_A values for both hCT and pCT, with a selective loss of affinity for hCT observed for the F359A mutant (Figs. 2, 8 and 9, Table 5).

For sCT, there was a selective decrease in pK_A values linked to pERK for the V293A mutant and a selective increase for the I300A and F356A mutants, while none of the other mutants altered pERK-derived pK_A

Table 5
Effect of single alanine mutation in hCTR ECL2 or ECL3 on functional affinities of CT-family peptides.

	hCT			sCT			pCT			rAmy			hcGRP	
	cAMP	IP1	pERK1/2	cAMP	IP1	pERK1/2	cAMP	IP1	pERK1/2	cAMP	pERK1/2	cA- MP	pERK1/2	cA- MP
WT	9.54 ± 0.09 (36)	8.54 ± 0.10 (47)	8.15 ± - 0.08 (34)	10.5 ± 0.09 (36)	9.2 ± 0.12 (44)	8.55 ± - 0.07 (35)	10.1 ± 0.10 (31)	8.75 ± 0.13 (37)	8.74 ± - 0.09 (32)	7.72 ± 0.11 (31)	7.23 ± 0.11 (30)	7.6-	9 ± 0.16 (25)	7.6-
7.10 ± 0.- 11 (30)														
I279A	10.0 ± 0.32 (4)	7.89 ± 0.16 (7)	7.68 ± - 0.16 (5)	10.8 ± 0.32 (5)	8.54 ± 0.19 (7)	7.89 ± - 0.19 (5)	10.1 ± 0.26 (6)	7.82 ± 0.2- 2* (5)	8.39 ± - 0.18 (5)	8.30 ± 0.25 (5)	7.58 ± 0.19 (5)	7.9-	9 ± 0.12 (5)	7.9-
7.03 ± 0.- 24 (5)														
T280A	10.0 ± 0.35 (4)	7.56 ± 0.1- 8* (6)	7.59 ± - 0.14 (6)	11.0 ± 0.35 (4)	8.49 ± 0.13 (7)	8.04 ± - 0.15 (6)	9.96 ± 0.26 (5)	8.35 ± 0.21 (7)	8.15 ± - 0.14 (6)	8.32 ± 0.25 (5)	7.27 ± 0.15 (6)	7.9-	2 ± 0.24 (5)	7.9-
6.95 ± 0.- 20 (6)														
R281A	6.74 ± 0.34* (8)	7.84 ± 0.50 (7)	N.D.	9.89 ± 0.21 (11)	9.24 ± 0.20 (6)	8.97 ± - 0.11 (5)	8.30 ± 0.15* (6)	8.47 ± 0.18 (6)	8.57 ± - 0.12 (5)	7.12 ± 0.12 (5)	7.01 ± 0.58 (5)	6.8-	9 ± 0.16 (5)	6.8-
7.71 ± 0.- 22 (5)														
V283A	10.2 ± 0.35 (4)	7.43 ± 0.2- 2* (5)	7.55 ± - 0.15 (5)	10.7 ± 0.28 (5)	8.63 ± 0.14 (7)	7.97 ± - 0.17 (6)	10.1 ± 0.27 (5)	7.94 ± 0.21 (7)	8.38 ± - 0.20 (5)	8.03 ± 0.17 (5)	7.59 ± 0.19 (5)	7.4-	9 ± 0.17 (5)	7.4-
7.18 ± 0.- 31 (4)														
Y284A	9.77 ± 0.29 (5)	7.92 ± 0.24 (7)	7.93 ± - 0.25 (5)	10.6 ± 0.28 (5)	8.51 ± 0.15 (6)	8.60 ± - 0.23 (5)	9.85 ± 0.25 (6)	8.64 ± 0.21 (7)	8.73 ± - 0.25 (5)	7.61 ± 0.30 (5)	7.55 ± 0.25 (5)	7.2-	0 ± 0.32 (5)	7.2-
6.69 ± 0.- 30 (5)														
F285A	9.65 ± 0.29 (5)	7.98 ± 0.24 (6)	7.93 ± - 0.23 (5)	10.7 ± 0.29 (5)	8.30 ± 0.1- 7* (5)	8.48 ± - 0.20 (5)	10.1 ± 0.30 (6)	7.93 ± 0.21 (6)	8.54 ± - 0.23 (5)	7.89 ± 0.31 (5)	7.47 ± 0.28 (5)	7.4-	6 ± 0.28 (5)	7.4-
6.76 ± 0.- 26 (5)														
N286A	8.81 ± 0.30 (5)	8.56 ± 0.32 (6)	8.16 ± - 0.41 (5)	10.4 ± 0.30 (5)	8.71 ± 0.27 (6)	8.99 ± - 0.37 (5)	9.43 ± 0.32 (5)	9.02 ± 0.26 (7)	8.75 ± - 0.26 (5)	7.05 ± 0.27 (5)	7.16 ± 0.44 (5)	7.6-	5 ± 0.23 (5)	7.6-
8.25 ± 0.- 29* (5)														
D287A	6.81 ± 0.32* (6)	N.D.	6.71 ± - 0.24* (5)	9.79 ± 0.22* (10)	N.D.	9.09 ± - 0.30 (5)	8.52 ± 0.42* (6)	8.33 ± 0.17 (6)	7.65 ± - 0.30* (5)	N.D.	N.D.	N.-	N.D.	N.-
N288A	9.52 ± 0.27 (5)	7.58 ± 0.1- 6* (7)	7.35 ± - 0.17* (6)	10.8 ± 0.29 (6)	8.45 ± 0.19 (6)	7.98 ± - 0.18 (5)	9.79 ± 0.27 (5)	8.56 ± 0.21 (7)	8.11 ± - 0.16 (6)	8.40 ± 0.23 (5)	-7.15 ± 0- .24 (5)	7.5-	5 ± 0.18 (5)	7.5-
6.74 ± 0.- 22 (5)														
C289A	7.02 ± 0.33* (8)	N.D.	6.84 ± - 0.36* (5)	9.57 ± 0.3* (10)	8.31 ± 0.3- 9* (6)	8.92 ± - 0.34 (5)	8.50 ± 0.35* (8)	N.D.	8.13 ± - 0.30 (5)	6.77 ± 0.1- 5* (5)	N.D.	N.-	N.D.	N.-
W290A	N.D.	N.D.	N.D.	9.45 ± 0.34* (11)	N.D.	9.03 ± - 0.43 (5)	8.08 ± 0.31* (5)	N.D.	7.84 ± - 0.35* (5)	6.55 ± 0.3- 2* (5)	N.D.	N.-	N.D.	N.-

(continued on next page)

Table 5 (continued)

	hCT			sCT			pCT			rAmy			hcCRP	
	cAMP	IP1	pERK1/2	cAMP	IP1	pERK1/2	cAMP	IP1	pERK1/2	cAMP	pERK1/2	cA-MP	cA-MP	pERK1/2
L291A	7.69 ± 0.27 [*] (10)	6.35 ± 0.4 [*] (7)	6.83 ± - 0.36 [*] (5)	10.4 ± 0.23 (10)	8.47 ± 0.21 (7)	8.36 ± - 0.21 (5)	9.05 ± 0.27 [*] (6)	8.67 ± 0.30 (7)	7.82 ± - 0.28 [*] (5)	7.29 ± 0.23 (5)	7.21 ± 0.43 (5)	6.6-	6.6-	7 ± 0.24 [*] (5)
N.D.														
S292A	9.24 ± 0.29 (6)	7.23 ± 0.2- 5 [*] (6)	7.82 ± - 0.18 (5)	10.6 ± 0.28 (6)	8.57 ± 0.19 (7)	8.58 ± - 0.18 (5)	9.87 ± 0.26 (6)	8.13 ± 0.20 (7)	9.15 ± - 0.20 (5)	8.05 ± 0.28 (6)	7.55 ± 0.16 (6)	7.2-	7.2-	0 ± 0.15 (5)
7.47 ± 0.- 25 (5)														
V293A	9.58 ± 0.28 (5)	8.01 ± 0.15 (7)	7.41 ± - 0.18 (5)	10.4 ± 0.28 (5)	8.92 ± 0.16 (7)	7.74 ± - 0.18 [*] (5)	9.95 ± 0.25 (6)	8.19 ± 0.22 (7)	8.13 ± - 0.17 (5)	7.84 ± 0.29 (6)	7.12 ± 0.28 (5)	7.4-	7.4-	1 ± 0.17 (5)
6.79 ± 0.- 19 (5)														
E294A	9.84 ± 0.29 (5)	8.05 ± 0.21 (6)	7.74 ± - 0.17 (5)	10.7 ± 0.30 (5)	8.36 ± 0.2- 4 [*] (6)	8.32 ± - 0.19 (5)	10.0 ± 0.27 (5)	8.62 ± 0.17 (6)	8.42 ± - 0.18 (5)	7.61 ± 0.32 (5)	7.24 ± 0.25 (5)	6.8-	6.8-	8 ± 0.35 (5)
6.64 ± 0.- 36 (5)														
T295A	8.83 ± 0.30 (5)	7.76 ± 0.32 (6)	7.97 ± - 0.44 (5)	9.60 ± 0.31 (5)	8.22 ± 0.3- 4 [*] (6)	9.05 ± - 0.15 (5)	8.98 ± 0.28 [*] (5)	8.15 ± 0.41 (6)	8.96 ± - 0.41 (5)	7.00 ± 0.17 (5)	N.D.	6.7-	6.7-	1 ± 0.21 [*] (5)
7.61 ± 0.- 24 (5)														
H296A	10.1 ± 0.25 (10)	7.83 ± 0.18 (7)	7.59 ± - 0.16 (5)	10.6 ± 0.24 (10)	9.08 ± 0.18 (7)	8.13 ± - 0.17 (5)	10.1 ± 0.29 (5)	8.07 ± 0.23 (6)	8.08 ± - 0.14 (6)	7.87 ± 0.29 (5)	7.30 ± 0.22 (5)	7.4-	7.4-	8 ± 0.16 (6)
6.91 ± 0.- 29 (5)														
L297A	9.37 ± 0.27 (4)	7.40 ± 0.3- 1 [*] (7)	7.99 ± - 0.33 (5)	10.4 ± 0.33 (4)	8.89 ± 0.27 (6)	8.90 ± - 0.22 (5)	9.44 ± 0.25 (6)	8.54 ± 0.30 (7)	8.91 ± - 0.35 (5)	7.59 ± 0.24 (5)	7.43 ± 0.35 (5)	7.1-	7.1-	4 ± 0.12 (5)
6.82 ± 0.- 31 (5)														
L298A	9.07 ± 0.31 (5)	7.58 ± 0.2- 5 [*] (7)	7.62 ± - 0.25 (6)	10.2 ± 0.29 (5)	8.72 ± 0.24 (7)	8.54 ± - 0.26 (5)	9.70 ± 0.26 (5)	8.09 ± 0.25 (5)	8.78 ± - 0.27 (5)	7.77 ± 0.28 (5)	7.49 ± 0.20 (5)	7.1-	7.1-	0 ± 0.30 (5)
6.95 ± 0.- 37 (5)														
Y299A	8.68 ± 0.32 (5)	7.97 ± 0.46 (6)	7.81 ± - 0.38 (5)	10.4 ± 0.31 (5)	8.04 ± 0.3- 6 [*] (6)	9.05 ± - 0.38 (5)	9.35 ± 0.24 (6)	9.20 ± 0.40 (7)	8.85 ± - 0.40 (5)	7.36 ± 0.10 (4)	-7.15 ± 0- .36 (5)	7.3-	7.3-	2 ± 0.19 (5)
N.D.														
I300A	9.31 ± 0.28 (5)	7.97 ± 0.32 (7)	8.55 ± - 0.31 (5)	10.2 ± 0.29 (5)	N.D.	9.29 ± - 0.36 [*] (5)	9.72 ± 0.26 (5)	N.D.	9.29 ± - 0.31 (5)	7.18 ± 0.33 (5)	7.38 ± 0.40 (5)	7.5-	7.5-	4 ± 0.24 (5)
7.03 ± 0.- 35 (5)														
F356A	8.05 ± 0.35 [*] (5)	7.70 ± 0.30 (6)	7.58 ± - 0.27 (4)	9.73 ± 0.21 (6)	9.05 ± 0.41 (6)	9.38 ± - 0.21 [*] (5)	8.85 ± 0.29 [*] (4)	N.D.	8.23 ± - 0.33 (4)	7.09 ± 0.32 (4)	6.95 ± 0.45 (5)	6.6-	6.6-	5 ± 0.21 [*] (5)
6.65 ± 0.- 34 (4)														

(continued on next page)

Table 5 (continued)

	hCT		sCT		pCT		rAmy		hcGRP	
	cAMP	IP1	pERK1/2	cAMP	IP1	pERK1/2	cAMP	IP1	pERK1/2	cA-MP
V357A	8.43 ± 0.25 [*] (6)	7.37 ± 0.4- 8 [*] (5)	7.74 ± - 0.26 (4)	10.1 ± 0.21 (6)	8.69 ± 0.42 (5)	8.44 ± - 0.19 (5)	9.73 ± 0.32 (4)	7.69 ± 0.4- 0 [*] (5)	8.19 ± - 0.25 (4)	7.36 ± 0.33 (5)
N.D.										
V358A	9.29 ± 0.28 (4)	7.28 ± 0.1- 7 [*] (6)	7.31 ± - 0.13 [*] (5)	10.7 ± 0.25 (4)	8.31 ± 0.1- 3 [*] (6)	8.19 ± - 0.13 (4)	9.40 ± 0.28 (4)	8.20 ± 0.26 (5)	8.38 ± - 0.20 (4)	7.50 ± 0.33 (4)
7.34 ± 0.- 50 (5)										
F359A	8.50 ± 0.21 [*] (5)	7.08 ± 0.2- 4 [*] (5)	7.07 ± - 0.15 [*] (5)	10.6 ± 0.20 (5)	8.29 ± 0.1- 4 [*] (5)	7.79 ± - 0.13 [*] (5)	9.65 ± 0.28 (4)	7.68 ± 0.2- 4 [*] (5)	7.87 ± - 0.18 [*] (5)	7.33 ± 0.31 (5)
6.64 ± 0.- 29 (5)										
P360A	7.96 ± 0.34 [*] (5)	6.77 ± 0.2- 6 [*] (5)	6.98 ± - 0.40 [*] (5)	10.0 ± 0.20 (5)	7.99 ± 0.1- 3 [*] (6)	7.50 ± - 0.15 [*] (5)	9.03 ± 0.27 [*] (4)	6.76 ± 0.2- 8 [*] (5)	7.31 ± - 0.22 [*] (5)	7.24 ± 0.28 (5)
N.D.										
W361A	8.69 ± 0.23 (5)	7.55 ± 0.2- 3 [*] (6)	7.30 ± - 0.20 [*] (5)	10.4 ± 0.21 (5)	8.66 ± 0.15 (5)	8.16 ± - 0.15 (4)	9.10 ± 0.31 (4)	7.80 ± 0.2- 5 [*] (6)	7.99 ± - 0.27 (5)	7.40 ± 0.28 (5)
6.90 ± 0.- 38 (5)										
R362A	8.22 ± 0.24 [*] (4)	7.34 ± 0.2- 7 [*] (6)	7.49 ± - 0.29 (5)	9.85 ± 0.23 (4)	8.51 ± 0.25 (5)	8.53 ± - 0.16 (4)	8.45 ± 0.32 [*] (4)	7.68 ± 0.4- 2 [*] (6)	7.91 ± - 0.25 [*] (5)	7.27 ± 0.38 (4)
7.01 ± 0.- 61 (5)										
P363A	8.29 ± 0.25- * (5)	N.D.	7.38 ± - 0.30 (5)	10.4 ± 0.20 (5)	9.04 ± 0.19 (5)	8.57 ± - 0.18 (4)	8.68 ± 0.30 [*] (4)	8.08 ± 0.25 (6)	8.05 ± - 0.25 (5)	7.48 ± 0.27 (6)
N.D.										
S364A	9.56 ± 0.21 (5)	7.47 ± 0.2- 2 [*] (5)	7.82 ± - 0.14 (5)	10.5 ± 0.21 (5)	8.56 ± 0.18 (5)	8.23 ± - 0.17 (4)	10.2 ± 0.35 (4)	-8.00 ± 0.- .20 (5)	8.11 ± - 0.17 (4)	8.18 ± 0.33 (4)
7.75 ± 0.- 30 (4)										
N365A	9.55 ± 0.22 (5)	8.08 ± 0.28 (5)	7.93 ± - 0.18 (5)	10.6 ± 0.24 (5)	8.71 ± 0.26 (4)	8.57 ± - 0.20 (4)	10.4 ± 0.27 (4)	8.49 ± 0.31 (5)	8.58 ± - 0.18 (5)	7.93 ± 0.30 (4)
7.30 ± 0.- 36 (4)										
K366A	9.84 ± 0.31 (5)	8.20 ± 0.17 (5)	7.52 ± - 0.14 (5)	10.6 ± 0.24 (5)	8.73 ± 0.17 (5)	8.41 ± - 0.13 (4)	10.5 ± 0.29 (4)	8.68 ± 0.21 (5)	8.17 ± - 0.13 (5)	7.83 ± 0.20 (4)
6.89 ± 0.- 16 (4)										
M367A	9.49 ± 0.34 (5)	7.50 ± 0.1- 7 [*] (5)	7.91 ± - 0.14 (5)	10.8 ± 0.25 (5)	8.27 ± 0.1- 3 [*] (6)	8.28 ± - 0.14 (4)	10.2 ± 0.31 (4)	8.02 ± 0.19 (5)	7.93 ± - 0.14 [*] (5)	8.09 ± 0.23 (4)
6.77 ± 0.- 27 (4)										
L368A	9.85 ± 0.32 (5)	7.41 ± 0.1- 7 [*] (6)	7.68 ± - 0.16 (4)	10.4 ± 0.20 (5)	8.51 ± 0.17 (5)	8.21 ± - 0.13 (4)	9.63 ± 0.33 (4)	7.66 ± 0.2- 2 [*] (5)	8.21 ± - 0.14 (5)	7.61 ± 0.28 (5)

(continued on next page)

Table 5 (continued)

	hCT		sCT		pCT		rAmy		hcGRP				
	cAMP	IP1	pERK1/2	cAMP	IP1	pERK1/2	cAMP	IP1	pERK1/2	cA-MP			
6.94 ± 0.-24 (4) G369A	9.31 ± 0.22 (5)	7.28 ± 0.2-1* (5)	7.78 ± -0.13 (5)	10.4 ± 0.24 (5)	8.61 ± 0.16 (5)	8.22 ± -0.16 (4)	9.97 ± 0.30 (4)	7.80 ± 0.19 (5)	7.90 ± -0.117* (5)	7.56 ± 0.28 (4)	7.55 ± 0.26 (4)	7.0- (5)	6 ± 0.25 (5)
6.84 ± 0.-23 (4) K370A	N.D.	N.D.	N.D.	N.D.	N.D.	N.D.	N.D.	N.D.	N.D.	N.D.	N.D.	N.-D.	N.D.
I371A	9.63 ± 0.33 (5)	8.07 ± 0.22 (5)	N.D.	10.8 ± 0.21 (5)	8.45 ± 0.19 (6)	N.D.	10 ± 0.30 (4)	8.58 ± 0.19 (5)	N.D.	8.29 ± 0.26 (5)	N.D.	7.0- (5)	2 ± 0.34 (5)
N.D. Y372A	7.18 ± 0.35* (4)	7.67 ± 0.35 (5)	6.76 ± -0.30* (5)	9.60 ± 0.22 (4)	8.81 ± 0.43 (5)	8.55 ± -0.42 (5)	8.23 ± 0.35* (4)	8.27 ± 0.34 (5)	7.57 ± -0.28* (4)	N.D.	N.D.	6.9- (5)	3 ± 0.25 (5)
N.D. D373A	8.41 ± 0.27* (4)	7.51 ± 0.2-0* (5)	7.41 ± -0.27 (5)	10.3 ± 0.21 (4)	8.60 ± 0.22 (5)	8.34 ± -0.15 (4)	8.39 ± 0.34* (4)	7.59 ± 0.2-8* (5)	8.09 ± -0.28 (4)	7.81 ± 0.29 (5)	N.D.	7.7- (5)	2 ± 0.24 (5)
N.D. Y374A	9.45 ± 0.28 (5)	7.32 ± 0.2-0* (5)	7.67 ± -0.18 (5)	10.5 ± 0.20 (5)	8.34 ± 0.1-5* (6)	8.36 ± -0.18 (4)	10.4 ± 0.32 (4)	7.60 ± 0.1-8* (5)	8.35 ± -0.20 (4)	7.75 ± 0.33 (4)	7.12 ± 0.3 (4)	7.3- (5)	5 ± 0.34 (5)
7.07 ± 0.-37 (5) V375A	9.21 ± 0.20 (5)	7.98 ± 0.28 (5)	7.88 ± -0.28 (4)	10.2 ± 0.20 (5)	8.32 ± 0.2-2* (6)	8.70 ± -0.23 (5)	9.59 ± 0.41 (4)	8.25 ± 0.31 (5)	8.32 ± -0.23 (5)	7.79 ± 0.29 (5)	6.70 ± 0.26 (4)	7.2- (5)	7 ± 0.26 (5)
6.78 ± 0.-40 (5) M376A	8.12 ± 0.31* (5)	7.83 ± 0.41 (4)	7.47 ± -0.21 (4)	10.2 ± 0.21 (5)	8.43 ± 0.19 (4)	8.17 ± -0.25 (4)	9.30 ± 0.36 (4)	7.90 ± 0.30 (5)	8.54 ± -0.14 (5)	7.09 ± 0.27 (5)	7.09 ± 0.43 (5)	6.6- (5)	3 ± 0.31* (6)
7.52 ± 0.-26 (5)													

For each receptor mutant and ligand, concentration-response data for each pathway were fit with the Black and Leff operational model to derive a functional affinity (pK_A) for each pathway. All values are mean ± S.E.M. (independent “n” values are indicated within parentheses). For each ligand, significance of changes was determined by comparison of mutant receptor pK_A to WT receptor pK_A in a one-way analysis of variance followed by Dunnett’s post-test (p < 0.05 represented by *). (N.D.) data were not able to be reliably determined. WT pK_A values for sCT were 10.52 ± 0.09, 9.20 ± 0.12, and 8.55 ± 0.07, for cAMP, IP1 and pERK signalling, respectively. The corresponding values for hCT were 9.54 ± 0.10, and 8.15 ± 0.08, and for pCT were 10.12 ± 0.10, 8.75 ± 0.13 and 8.74 ± 0.09, pK_A values for cAMP and pERK were, respectively, 7.50 ± 0.33 and 7.23 ± 0.11 for rAmy, and 7.69 ± 0.16 and 7.10 ± 0.11 for CGRP.

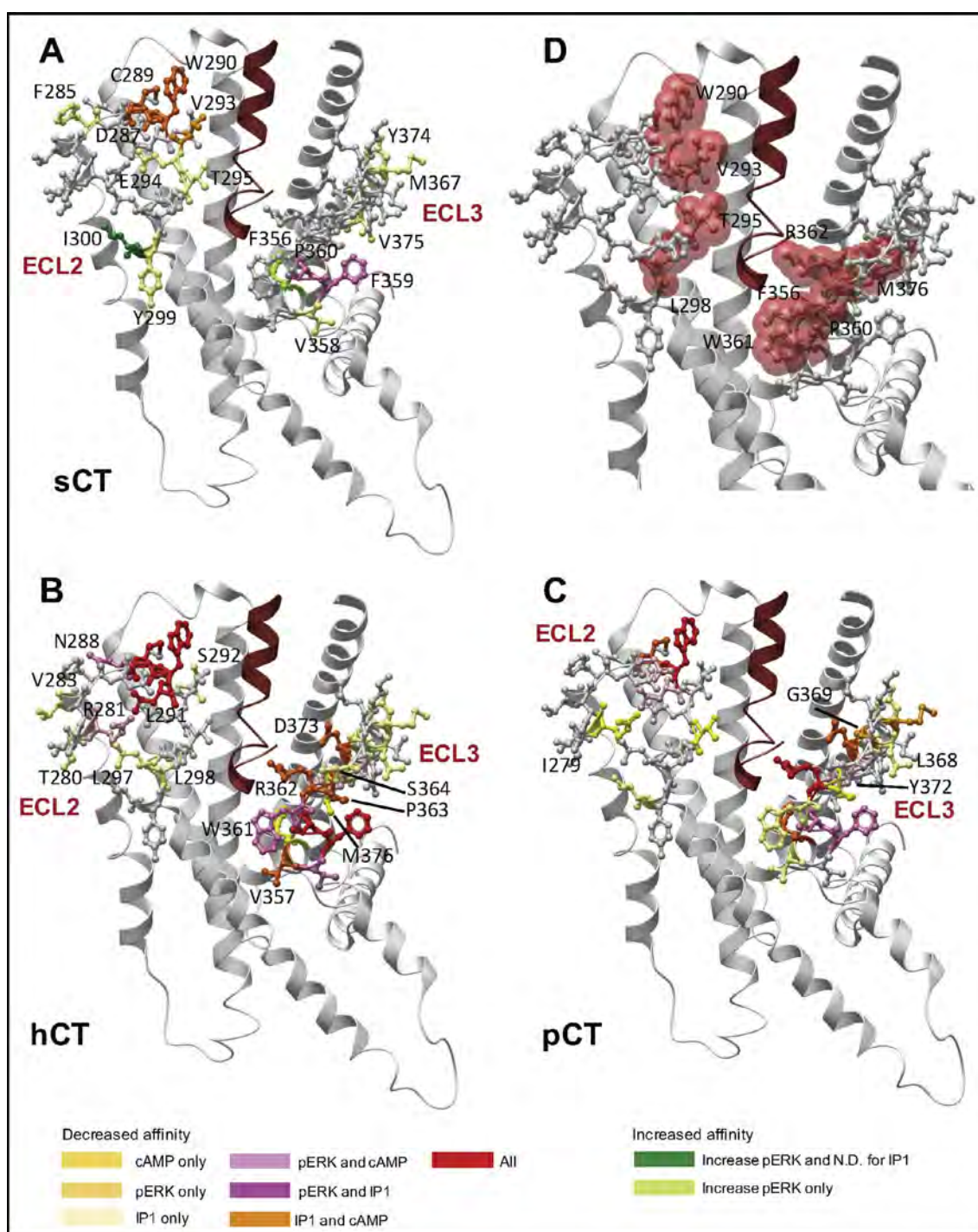


Fig. 9. Mutants that differentially alter peptide-dependent functional affinity cluster into subdomains in ECL2 and ECL3. (A–C) Mutants that alter functional affinity are displayed in x-stick representation, coloured according to effect on the different signalling pathways. (A) Effect of mutation on sCT, (B) hCT, or (C) pCT pK_A. Mutants that did not significantly affect functional affinity in any pathway are coloured grey. The full receptor TM domain is displayed as grey ribbon, and sCT in dark red ribbon, with the receptor ECD, and peptide C-terminal residues omitted for clarity. (D) ECL2 and ECL3 amino acids within 5 Å of sCT in the model are displayed in red transparent cpk representation. (For interpretation of the references to colour in this figure legend, the reader is referred to the web version of this article.)

values (Table 5). Analysis of IP1 signalling revealed an IP1 specific loss of affinity for all 3 peptides at the Y374A mutant, while there was preferential loss of affinity for sCT and hCT for the V358A and M367A mutants. For the latter mutant, while there was no significant effect on pCT functional affinity linked to IP1 signalling, there was a selective decrease in the pERK linked pK_A value. There was also a selective decrease in sCT IP1-derived functional affinity for the F285A, E294A, T295A, and Y299A mutants. No other mutants altered sCT functional

affinities for any of the pathways studied (Figs. 2, 8 and 9, Table 5).

hCT and pCT displayed intriguing differences in the pattern of mutational effect on pK_A values derived from analysis of IP1 and pERK responses. For hCT there was only limited effect of mutation in ECL3 on pERK-derived pK_A values and these were confined to the membrane proximal ECL3/TM6 boundary (V358A-R362A) and Y372A that packs up against this region in the WT receptor (Figs. 2, 8 and 9, Table 5). This segment was also important for pCT pERK-derived functional

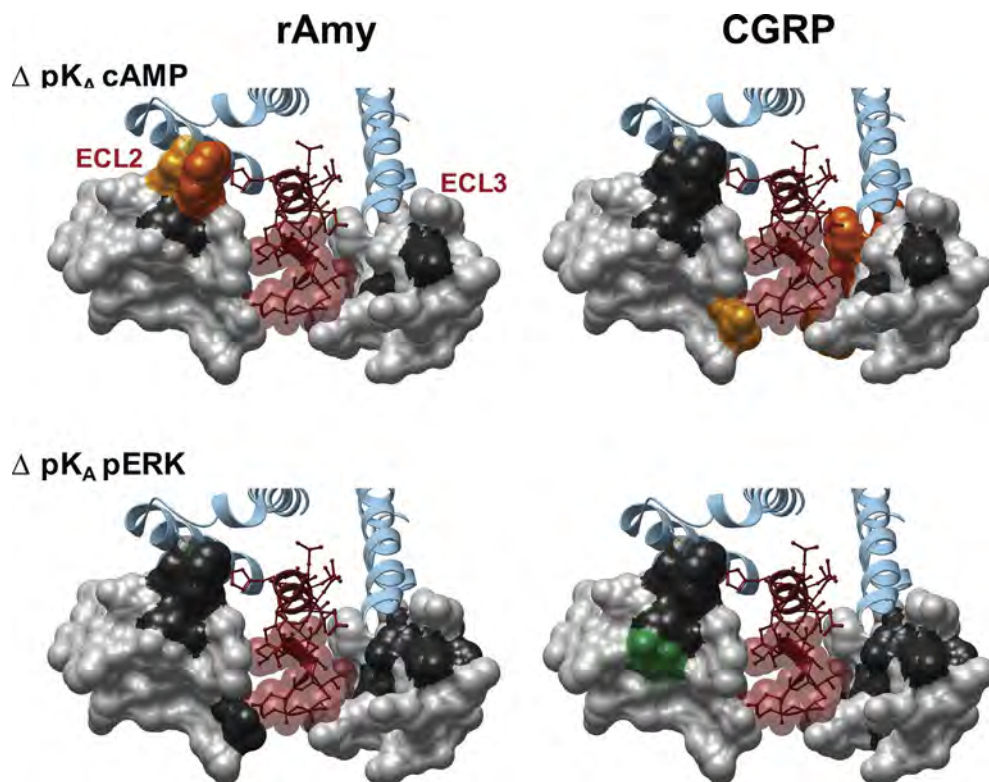


Fig. 10. Alanine mutation of ECL2 and ECL3 of the hCTR alters amylin and CGRP functional affinity (pK_A) in a peptide- and pathway-specific manner. Functional affinities derived from operation fitting of concentration-response curves in cAMP accumulation (upper panel) and pERK (lower panel) are displayed as ΔpK_A . Illustrated is a top view of the active, sCT-bound, hCTR model with ECL2 and ECL3 shown in surface representation. Mutations that significantly alter peptide affinity are coloured according to the magnitude of effect (from Table 5), with mutated amino acids without significant alteration to affinity coloured grey. sCT is shown as dark red, with side chains in proximity to the ECLs displayed in x-stick, and residues 1–7 that are critical for receptor activation displayed in transparent cpk. (For interpretation of the references to colour in this figure legend, the reader is referred to the web version of this article.)

affinity, but additional effect was seen with the M367A-G369A mutants that are involved with packing at the top of the extension of TM7, and which are important for IP1-derived functional affinity of hCT and pCT, albeit that not all effects reached significance for both peptides (Table 5). ECL3 was important for IP1-derived functional affinities for both hCT and pCT, with those mutations impacting on pCT also decreasing hCT pK_A values, including residues at the ECL3/TM6 boundary (F356A-R362A), residues in the distal part of ECL3 that are likely important for TM7/TM1 packing (D373A, Y374A) as well as residues located in the upper extension of TM7 (M368A-G369A) (Figs. 2, 8 and 9, Table 5). However, the network of residues important for hCT pK_A values was more extensive for both the TM6/ECL3 boundary (P363A, S364A), and the extension of TM7 (M367A). In contrast, ECL2 played only a limited role in pCT functional affinity derived from either IP1 or pERK signalling. Only the I279A mutant altered pCT IP1-derived pK_A values, although no quantifiable response was obtained for the poorly expressed C289A, W290A and I300A mutants (Table 5). For pERK functional affinity, only the D287A, W290A and L291A mutants attenuated pCT affinity. This central network was also important of hCT pERK-derived pK_A values, with N288A and C289A also reducing hCT functional affinity. It is likely that the R281A mutant additionally attenuates hCT affinity as no quantifiable response was detected, and there was a large decrease in cAMP-derived pK_A . For hCT functional affinity derived from IP1 signalling, there was a broader impact of mutation for ECL2 residues that included T280A-V283A, residues of the central core and boundary with ECL1 (D287A-S292A), and L297A and L298A (Figs. 2, 8 and 9, Table 5).

Due to the low affinity of amylin and CGRP for CTR, and poor coupling to IP1 signalling (data not shown), no competitive binding data or IP1-derived functional affinity data could be obtained for these peptides. pK_A values from operational analysis of the cAMP signalling could be derived for most mutants, revealing only limited impact on either amylin or CGRP functional affinity. This was particularly true for amylin that mirrored the observations for sCT, with ~10-fold loss of affinity for the C289A and W290A mutants. No quantifiable response for the D287A and Y372A mutants (that had weak reductions in sCT

functional affinity) was observed, while all other mutants failed to significantly alter affinity (Fig. 8; Table 5, Fig. 6). Although the magnitude of effect was also limited for CGRP in this pathway, there were broader effects of mutations, including loss of detectable response for D287A, C289A, and W290A, and reduced affinity for L291A, T295A, F356A, W361A and M376A. These residues were also important for hCT functional affinity at this pathway (Figs. 3 and 10; Table 5).

Both amylin and CGRP are only weakly coupled to pERK, and alanine mutation either had no effect or attenuated responses such that they there were not quantifiable. Nonetheless, interesting differences were observed between the effect on amylin and CGRP signalling. Residues with very low expression, including D287A, C289A, W290A and I371A had no detectable response for either peptide. Loss of response for both peptides was also seen for the P360A, Y372A and D373A mutants, despite similar or greater (P360A) cell surface expression of the receptor. The L291A, and Y299A mutants selectively attenuated, and the N286A mutant selectively enhanced, CGRP functional affinity. Functional CGRP affinity for T295A was not significantly altered, and not determined for amylin due to large error in parameter estimates, despite a measurable response (Figs. 8 and 10; Table 5).

3.4. ECL2 and ECL3 play distinct roles in pathway specific efficacy

3.4.1. Calcitonin peptides

Interestingly, despite detrimental effects on functional affinity, only enhancement of cAMP efficacy was observed for any of the CT peptides (Figs. 11A and 12A; Table 6). For sCT and hCT, the effect of mutation was similar, and confined to ECL2, with the exception of F356A that resides at the base of the peptide binding pocket. Enhanced efficacy was seen for both sCT and hCT for R281A, D287A, C289A, W290A, T295A and I300A (Fig. 11A and 12A; Table 6). These mutants also had reduced cell surface expression (Fig. 1), indicative of destabilization of the receptor in a manner that lowers the barrier to Gs coupling. N286A caused a selective enhancement of hCT efficacy, while pCT had both overlapping and distinct effects following receptor mutation. In ECL2, the effect of mutation was conserved with the other peptides except that

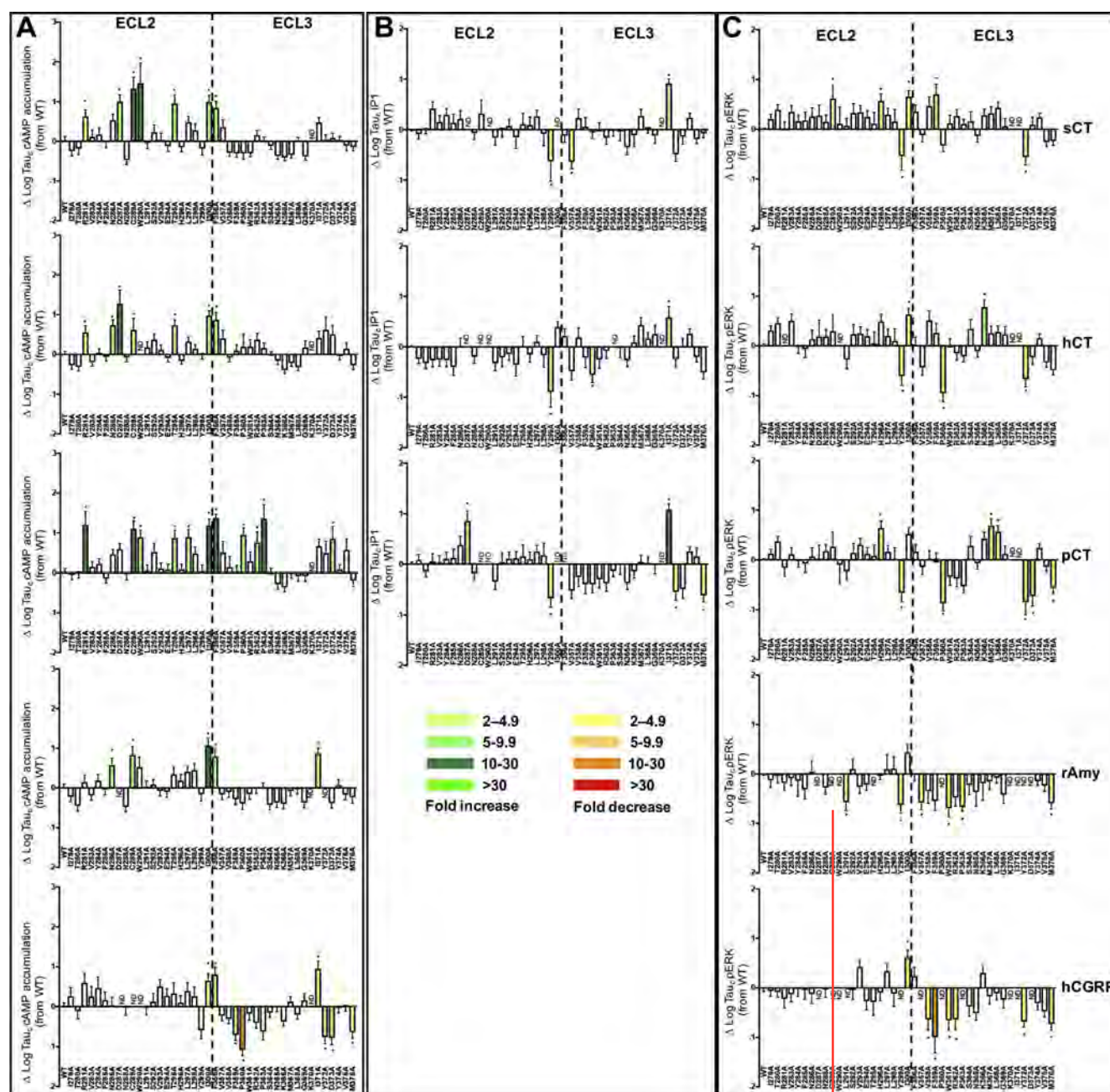


Fig. 11. Alanine mutation of ECL2 and ECL3 of the hCTR selectively alters peptide efficacy. Concentration-response data for each peptide in (A) cAMP accumulation, (B) IP1 accumulation, or (C) pERK assays were fit to the operational model of agonism to calculate the affinity-independent coupling efficacy $\log(\tau)$ of each receptor (mutant or WT) for each signalling pathway. The $\log(\tau)$ values of each receptor were then corrected for expression to obtain $\log(\tau_c)$. Graphs show the differences relative to WT. All values are mean \pm S.E.M. of 4–11 (WT 25–47) independent experiments conducted in duplicate. Significance of changes were determined by comparison of the WT to the other receptor mutants in a one-way analysis of variance and Dunnett's post-test of determined $\log(\tau_c)$ values (Table 2) with significant changes ($P < 0.05$) denoted by *, and coloured according to the magnitude of effect. N.D., efficacy not determined.

there was no change in pCT efficacy with the D287A mutant, and a selective enhancement of efficacy at the L297A mutant. Strikingly, ECL3 residues were also important for pCT cAMP efficacy, with P360A, R362A, P363A and D373A causing selective enhancement of efficacy (Fig. 11A and 12A; Table 6).

There was only limited impact of mutation on CT-mediated IP1 efficacy (Fig. 11B, Fig. 12B, Table 6). Within ECL2, no quantifiable response was seen with W290A for any of the peptides, with C289A for hCT and pCT (but no effect on sCT), and with D287A for sCT and hCT, but an enhanced efficacy for pCT with this mutation. The Y299A mutant attenuated efficacy for all peptides, while I300A abolished responses to sCT and pCT but not hCT (Table 6). Within ECL3, there was

no pCT response with the F356A mutant, but this did not alter efficacy for sCT or hCT. The I371A mutant significantly enhanced efficacy for all peptides. The P360A mutant selectively reduced hCT efficacy, while the Y372A and M376A mutants selectively attenuated efficacy for pCT. No other mutants altered peptide-mediated IP1 efficacy (Fig. 11B, Fig. 12B, Table 6).

Within ECL2, efficacy was attenuated for all peptides at the Y299A mutant and enhanced at the H296A and I300A mutants, albeit that the H296A and I300A mutants did not achieve significance for hCT or pCT, respectively (Fig. 11C, Fig. 12C, Table 6). The C289A mutant selectively enhanced sCT efficacy, while no quantifiable response was observed for hCT at the R281A and W290A mutants, which did not alter sCT or pCT

Table 6
Effect of single alanine mutation in hCTR ECL2 or ECL3 on efficacy of CT-family peptides.

	hCT			sCT			pCT			rAmy			haGGRP	
	cAMP	IP1	pERK1/2	cAMP	IP1	pERK1/2	cAMP	IP1	pERK1/2	cAMP	pERK1/2	cA-MP	cA-MP	MP
WT	0.18 ± 0.07 (36)	−0.07 ± 0- .02 (47)	−0.1- 1 ± 0.0- 4 (34)	0.25 ± 0.12 (36)	−0.04 ± 0- .02 (44)	−0.1- 5 ± 0.0- 2 (35)	0.12 ± 0.10 (31)	−0.07 ± 0- .04 (37)	−0.1- 1 ± 0.0- 3 (32)	0.12 ± 0.09 (31)	−0.10 ± 0- .03 (30)	0.1- 0.1- 0.1	1 ± 0.09 (25)	
−0.08 ± 0.08 (30)														
I279A	−0.09 ± 0- 10 (4)	−0.30 ± 0- .10 (7)	0.20 ± - 0.09 (5)	0.00 ± 0.13 (5)	−0.13 ± 0- .10 (7)	0.05 ± - 0.09 (5)	0.07 ± 0.12 (6)	0.01 ± 0.10 (5)	0.02 ± - 0.08 (5)	−0.11 ± 0- .12 (5)	−0.24 ± 0- .15 (5)	0.3- 0.3- 0.3	7 ± 0.22 (5)	
−0.14 ± 0.11 (5)														
T280A	−0.13 ± 0- 10 (4)	−0.39 ± 0- .11 (6)	0.35 ± - 0.11 (6)	0.06 ± 0.16 (4)	−0.01 ± 0- .11 (7)	0.24 ± - 0.10 (6)	0.14 ± 0.15 (5)	−0.22 ± 0- .10 (7)	0.27 ± - 0.10 (6)	−0.34 ± 0- .13 (4)	−0.15 ± 0- .14 (6)	0.3- 0.3- 0.3	−0.01 ± 0- .20 (5)	
−0.17 ± 0.11 (6)														
R281A	0.74 ± 0.17- * (8)	−0.33 ± 0- .14 (7)	N.D.	0.87 ± 0.17- * (11)	0.37 ± 0.14 (6)	−0.1- 6 ± 0.1- 6 (5)	1.31 ± 0.34- * (6)	−0.02 ± 0- .15 (6)	−0.2- 7 ± 0.1- 7 (5)	0.26 ± 0.18 (5)	−0.29 ± 0- .16 (5)	0.7- 0.7- 0.7	1 ± 0.24 (5)	
−0.30 ± 0.19 (5)														
V283A	−0.01 ± 0- 10 (4)	−0.32 ± 0- .13 (5)	0.40 ± - 0.14 (5)	0.36 ± 0.17 (5)	0.11 ± 0.13 (7)	0.20 ± - 0.13 (6)	0.26 ± 0.14 (5)	−0.04 ± 0- .13 (7)	0.00 ± - 0.13 (5)	−0.07 ± 0- .13 (5)	−0.19 ± 0- .15 (5)	0.3- 0.3- 0.3	6 ± 0.25 (5)	
−0.21 ± 0.15 (4)														
Y284A	0.22 ± 0.10 (5)	−0.33 ± 0- .13 (7)	−0.1- 2 ± 0.1- 4 (5)	0.42 ± 0.16 (5)	0.25 ± 0.13 (6)	0.01 ± - 0.13 (5)	0.33 ± 0.13 (6)	0.03 ± 0.13 (7)	−0.1- 2 ± 0.1- 3 (5)	0.30 ± 0.15 (5)	−0.24 ± 0- .32 (5)	0.5- 0.5- 0.5	7 ± 0.28 (5)	
−0.09 ± 0.16 (5)														
F285A	0.12 ± 0.10 (5)	−0.47 ± 0- .17 (6)	−0.1- 7 ± 0.1- 7 (5)	0.23 ± 0.15 (5)	0.09 ± 0.17 (5)	0.03 ± - 0.17 (5)	−0.02 ± 0- 11 (6)	0.05 ± 0.18 (6)	−0.1- 8 ± 0.1- 7 (5)	0.08 ± 0.14 (5)	−0.42 ± 0- .20 (5)	0.2- 0.2- 0.2	7 ± 0.21 (5)	
−0.12 ± 0.19 (5)														
N286A	0.92 ± 0.14- * (5)	−0.07 ± 0- .17 (6)	0.03 ± - 0.18 (5)	0.78 ± 0.15 (5)	0.17 ± 0.17 (5)	0.10 ± - 0.18 (5)	0.58 ± 0.12 (5)	0.30 ± 0.17 (7)	−0.0- 4 ± 0.1- 8 (5)	0.69 ± 0.1- 8* (5)	−0.07 ± 0- .24 (5)	0.1- 0.1- 0.1	3 ± 0.21 (5)	
−0.20 ± 0.20 (5)														
D287A	1.46 ± 0.34- * (6)	N.D.	0.08 ± - 0.33 (5)	1.25 ± 0.17- * (10)	N.D.	0.12 ± - 0.21 (5)	0.70 ± 0.14 (6)	0.78 ± 0.2- 0* (6)	−0.1- 0 ± 0.2- 9 (5)	N.D.	N.D.	N.- D.	N.D.	
N288A	0.11 ± 0.12 (5)	−0.26 ± 0- .13 (7)	0.08 ± - 0.15 (5)	−0.23 ± 0- 11 (6)	−0.11 ± 0- .13 (6)	0.00 ± - 0.14 (5)	0.09 ± 0.14 (5)	−0.25 ± 0- .14 (7)	0.07 ± - 0.14 (5)	−0.36 ± 0- .12 (5)	−0.38 ± 0- .14 (5)	0.1- 0.1- 0.1	0 ± 0.22 (5)	
−0.12 ± 0.16 (5)														
C289A	0.80 ± 0.28- * (8)	N.D.	0.19 ± - 0.34 (5)	1.57 ± 0.29- * (10)	0.27 ± 0.27 (6)	0.46 ± - 0.28* (5)	1.22 ± 0.20- * (8)	N.D.	0.16 ± - 0.29 (5)	0.95 ± 0.2- 1* (5)	N.D.	N.- D.	N.D.	
W290A	N.D.	N.D.	N.D.	1.71 ± 0.50- * (11)	N.D.	−0.0- 4 ± 0.3- 4 (5)	1.01 ± 0.18- * (5)	N.D.	−0.2- 0 ± 0.3- 7 (5)	0.64 ± 0.25 (5)	N.D.	N.- D.	N.D.	
L291A	0.36 ± 0.14 (10)	−0.39 ± 0- .15 (7)	−0.3- 8 ± 0.1- 9 (5)	0.20 ± 0.14 (10)	−0.21 ± 0- .15 (7)	−0.0- 8 ± 0.1- 5 (5)	0.17 ± 0.14 (6)	−0.41 ± 0- .15 (7)	−0.3- 4 ± 0.1- 6 (5)	0.13 ± 0.16 (5)	−0.68 ± 0- .16* (5)	0.0- 0.0- 0.0	9 ± 0.20 (5)	
N.D.														
S292A	0.56 ± 0.15 (6)	−0.28 ± 0- .19 (6)	0.13 ± - 0.19 (5)	0.48 ± 0.18 (6)	−0.01 ± 0- .19 (7)	0.17 ± - 0.19 (5)	0.64 ± 0.21 (6)	−0.04 ± 0- .19 (7)	0.03 ± - 0.19 (5)	0.20 ± 0.13 (6)	−0.01 ± 0- .19 (6)	0.2- 0.2- 0.2	3 ± 0.21 (5)	
−0.12 ± 0.20 (5)														
V293A	0.30 ± 0.12 (5)	−0.21 ± 0- .13 (6)	0.14 ± - 0.14 (5)	0.28 ± 0.17 (5)	0.03 ± 0.13 (7)	0.19 ± - 0.14 (5)	0.22 ± 0.14 (6)	0.03 ± 0.14 (5)	0.19 ± - 0.13 (5)	0.05 ± 0.13 (6)	−0.37 ± 0- .14 (5)	0.6- 0.6- 0.6	1 ± 0.17 (5)	
0.33 ± 0.15 (5)														

(continued on next page)

Table 6 (continued)

	hCT			sCT			pCT			rAmy			hαCGRP	
	cAMP	IP1	pERK1/2	cAMP	IP1	pERK1/2	cAMP	IP1	pERK1/2	cAMP	pERK1/2	cA-MP	cA-MP	pERK1/2
E294A	0.10 ± 0.10 (5)	−0.42 ± 0- .23 (6)	0.09 ± - 0.13 (5)	0.13 ± 0.14 (5)	−0.20 ± 0- .23 (6)	0.10 ± - 0.13 (5)	0.19 ± 0.14 (5)	0.04 ± 0.13 (6)	0.01 ± - 0.13 (5)	0.02 ± 0.14 (5)	−0.32 ± 0- .12 (5)	0.3-	0.3-	8 ± 0.18 (5)
−0.35 ± 0.18 (5)														
T295A	0.91 ± 0.14- * (5)	−0.08 ± 0- .21 (6)	−0.0- 5 ± 0.2- 3 (5)	1.20 ± 0.21- * (5)	0.06 ± 0.21 (6)	−0.0- 4 ± 0.2- 2 (5)	0.99 ± 0.19- * (5)	0.08 ± 0.23 (6)	−0.0- 3 ± 0.2- 2 (5)	0.46 ± 0.20 (5)	N.D.	0.4-	0.4-	4 ± 0.27 (5)
−0.37 ± 0.27 (5)														
H296A	0.02 ± 0.08 (10)	−0.21 ± 0- .16 (7)	0.39 ± - 0.15 (5)	0.10 ± 0.11 (10)	0.05 ± 0.16 (7)	0.42 ± - 0.15* (5)	0.20 ± 0.13 (5)	0.02 ± 0.14 (6)	0.53 ± - 0.14* (6)	0.30 ± 0.15 (5)	−0.14 ± 0- .08 (5)	0.2-	0.2-	1 ± 0.18 (6)
−0.18 ± 0.16 (5)														
L297A	0.51 ± 0.11 (4)	0.04 ± 0.12 (7)	0.09 ± - 0.13 (5)	0.72 ± 0.15 (4)	0.22 ± 0.12 (6)	0.14 ± - 0.13 (5)	1.01 ± 0.19- * (6)	0.17 ± 0.13 (7)	0.05 ± - 0.13 (5)	0.52 ± 0.14 (5)	−0.0- 1 ± 0.30 (5)	0.5-	0.5-	0 ± 0.21 (5)
0.25 ± 0.15 (5)														
L298A	0.33 ± 0.11 (5)	−0.23 ± 0- .24 (7)	−0.0- 1 ± 0.2- 4 (5)	0.52 ± 0.17 (5)	−0.13 ± 0- .24 (7)	0.00 ± - 0.24 (5)	0.59 ± 0.17 (5)	0.10 ± 0.24 (5)	−0.1- 0 ± 0.2- 4 (5)	0.56 ± 0.17 (5)	0.00 ± 0.25 (5)	0.3-	0.3-	7 ± 0.23 (5)
−0.20 ± 0.26 (5)														
Y299A	0.22 ± 0.15 (5)	−0.96 ± 0- .31* (6)	−0.7- 2 ± 0.1- 8* (5)	0.07 ± 0.16 (5)	−0.68 ± 0- .39* (6)	−0.6- 9 ± 0.2- 8* (5)	0.15 ± 0.16 (6)	−0.74 ± 0- .18* (7)	−0.7- 6 ± 0.1- 8* (5)	−0.04 ± 0- .17 (4)	−0.73 ± 0- .17* (5)	0-	0-	−0.49 ± 0- .21 (5)
N.D.														
I300A	1.16 ± 0.12- * (5)	0.33 ± 0.10 (7)	0.53 ± - 0.12* (5)	1.24 ± 0.17- * (5)	N.D.	0.50 ± - 0.12* (5)	1.3 ± 0.17* (5)	N.D.	0.41 ± - 0.13 (5)	1.19 ± 0.1- 8* (5)	0.33 ± 0.16 (5)	0.7-	0.7-	6 ± 0.19* (5)
0.54 ± 0.15* (5)														
F356A	1.05 ± 0.19- * (5)	0.15 ± 0.15 (6)	−0.1- 0 ± 0.1- 7 (4)	1.08 ± 0.17- * (6)	−0.16 ± 0- .14 (6)	0.20 ± - 0.12 (5)	1.49 ± 0.10- * (4)	N.D.	0.06 ± - 0.15 (4)	0.90 ± 0.1- 9* (4)	−0.12 ± 0- .14 (5)	0.9-	0.9-	1 ± 0.2* (5)
0.16 ± 0.18 (4)														
V357A	0.59 ± 0.21 (6)	−0.55 ± 0- .18 (5)	−0.5- 4 ± 0.1- 6 (4)	0.61 ± 0.18 (6)	−0.69 ± 0- .14* (5)	−0.2- 7 ± 0.1- 4 (5)	0.62 ± 0.28 (4)	−0.59 ± 0- .16 (5)	−0.2- 5 ± 0.1- 5 (4)	−0.05 ± 0- .13 (5)	−0.69 ± 0- .14* (5)	0-	0-	−0.12 ± 0- .13 (5)
N.D.														
V358A	0.10 ± 0.10 (4)	0.12 ± 0.19 (6)	0.41 ± - 0.19 (5)	−0.04 ± 0- 09 (4)	0.18 ± 0.18 (6)	0.31 ± - 0.18 (4)	0.25 ± 0.27 (4)	−0.32 ± 0- .19 (5)	−0.1- 0 ± 0.1- 9 (4)	0.02 ± 0.14 (4)	−0.45 ± 0- .24 (5)	0-	0-	−0.20 ± 0- .12 (5)
−0.72 ± 0.22* (5)														
F359A	0.28 ± 0.16 (5)	−0.28 ± 0- .20 (5)	0.15 ± - 0.19 (5)	−0.06 ± 0- 09 (5)	0.01 ± 0.19 (5)	0.55 ± - 0.20* (5)	0.14 ± 0.16 (4)	−0.46 ± 0- .19 (5)	−0.1- 6 ± 0.1- 9 (5)	−0.17 ± 0- .13 (5)	−0.66 ± 0- .19 (4)	0-	0-	−0.60 ± 0- .14* (5)
−1.08 ± 0.31* (5)														
P360A	0.38 ± 0.23 (5)	−0.62 ± 0- .15* (5)	−1.0- 6 ± 0.1- 6* (5)	−0.06 ± 0- 14 (5)	−0.10 ± 0- .12 (6)	−0.4- 8 ± 0.1- 2 (5)	1.07 ± 0.17- * (4)	−0.47 ± 0- .17 (5)	−0.9- 8 ± 0.1- 6* (5)	−0.28 ± 0- .15 (5)	N.D.	0-	0-	−0.98 ± 0- .14* (5)
N.D.														
W361A	0.38 ± 0.18 (5)	−0.32 ± 0- .17 (6)	−0.1- 4 ± 0.1- 7 (5)	−0.05 ± 0- 09 (5)	−0.08 ± 0- .17 (5)	−0.0- 3 ± 0.1- 7 (4)	0.4 ± 0.24 (4)	−0.36 ± 0- .17 (6)	−0.4- 4 ± 0.1- 7 (5)	−0.04 ± 0- .13 (5)	−0.80 ± 0- .18* (4)	0-	0-	−0.07 ± 0- .16 (5)
−0.74 ± 0.20* (5)														
R362A	0.56 ± 0.15 (4)	−0.15 ± 0- .15 (6)	−0.2- 6 ± 0.1- 5 (5)	0.40 ± 0.12 (4)	−0.20 ± 0- .14 (5)	0.11 ± - 0.13 (4)	0.87 ± 0.27- * (4)	−0.44 ± 0- .16 (6)	−0.4- 8 ± 0.1- 6 (5)	0.12 ± 0.15 (4)	−0.58 ± 0- .18 (4)	0-	0-	−0.30 ± 0- .14 (5)

(continued on next page)

Table 6 (continued)

	hCT			sCT			pCT			rAmy			haCGRP	
	cAMP	IP1	pERK1/2	cAMP	IP1	pERK1/2	cAMP	IP1	pERK1/2	cAMP	pERK1/2	cA-MP	cA-MP	pERK1/2
–0.71 ± 0.21* (5)														
P363A	0.34 ± 0.13 (5)	N.D.	–0.3-2 ± 0.1-2 (5)	0.26 ± 0.10 (5)	–0.05 ± 0.12 (5)	–0.0-5 ± 0.1 (4)	1.47 ± 0.35-*(4)	–0.21 ± 0-0.11 (6)	–0.6-3 ± 0.1-4 (5)	0.11 ± 0.12 (6)	–0.77 ± 0-0.08* (4)			–0.52 ± 0-0.21 (5)
N.D.														
S364A	0.16 ± 0.09 (5)	–0.08 ± 0-0.19 (5)	0.24 ± -0.19 (5)	0.13 ± 0.09 (5)	–0.08 ± 0-0.19 (5)	0.01 ± -0.19 (4)	0.09 ± 0.14 (4)	–0.08 ± 0-0.19 (5)	0.17 ± -0.19 (4)	–0.31 ± 0-0.12 (4)	–0.33 ± 0-0.20 (4)			–0.04 ± 0-0.12 (4)
–0.46 ± 0.20 (4)														
N365A	0.03 ± 0.10 (5)	–0.33 ± 0-0.13 (5)	–0.2-1 ± 0.1-2 (5)	–0.12 ± 0-0.08 (5)	–0.39 ± 0-0.15 (4)	–0.2-9 ± 0.1-2 (4)	–0.16 ± 0-0.13 (4)	–0.44 ± 0-0.13 (5)	–0.1-8 ± 0.1-2 (5)	–0.25 ± 0-0.13 (4)	–0.47 ± 0-0.29 (5)	0.1-0.1		1 ± 0.13 (5)
–0.59 ± 0.14 (4)														
K366A	–0.21 ± 0-0.09 (5)	0.02 ± 0.13 (5)	0.67 ± -0.15* (5)	–0.16 ± 0-0.08 (5)	–0.15 ± 0-0.23 (5)	0.13 ± -0.13 (4)	–0.24 ± 0-0.11 (4)	–0.22 ± 0-0.13 (5)	0.32 ± -0.13 (5)	–0.28 ± 0-0.13 (4)	–0.29 ± 0-0.35 (5)			–0.27 ± 0-0.11 (5)
0.22 ± 0.14 (4)														
M367A	–0.03 ± 0-0.09 (5)	0.36 ± 0.15 (4)	0.15 ± -0.13 (5)	–0.10 ± 0-0.08 (5)	0.22 ± 0.13 (6)	0.17 ± -0.13 (4)	0.11 ± 0.12 (4)	–0.03 ± 0-0.14 (5)	0.58 ± -0.14* (5)	0.04 ± 0.12 (4)	–0.26 ± 0-0.17 (5)	0.2-0.2		3 ± 0.13 (5)
–0.25 ± 0.16 (4)														
L368A	–0.13 ± 0-0.09 (5)	0.10 ± 0.12 (6)	0.17 ± -0.12 (4)	0.25 ± 0.10 (5)	0.00 ± 0.12 (5)	0.28 ± -0.12 (4)	0.04 ± 0.13 (4)	–0.06 ± 0-0.13 (5)	0.46 ± -0.12* (5)	0.09 ± 0.12 (5)	–0.18 ± 0-0.12 (4)			–0.09 ± 0-0.11 (5)
–0.19 ± 0.14 (4)														
G369A	0.36 ± 0.17 (5)	0.19 ± 0.18 (5)	0.12 ± -0.16 (5)	–0.13 ± 0-0.09 (5)	–0.16 ± 0-0.16 (5)	–0.0-9 ± 0.1-6 (4)	0.04 ± 0.13 (4)	–0.09 ± 0-0.16 (5)	0.01 ± -0.16 (5)	–0.25 ± 0-0.13 (4)	–0.53 ± 0-0.17 (4)	0.2-0.2		7 ± 0.17 (5)
–0.32 ± 0.17 (4)														
K370A	N.D.	N.D.	N.D.	N.D.	N.D.	N.D.	N.D.	N.D.	N.D.	N.D.	N.D.	N-		N.D.
I371A	0.60 ± 0.17 (5)	0.52 ± 0.2-1* (7)	N.D.	0.72 ± 0.13 (5)	0.87 ± 0.0-9* (6)	N.D.	0.78 ± 0.18 (4)	1.00 ± 0.1-2* (5)	N.D.	0.99 ± 0.1-3* (5)	N.D.	1.0-1.0		6 ± 0.19* (5)
N.D.														
Y372A	0.80 ± 0.33 (4)	–0.32 ± 0-0.16 (5)	–0.7-8 ± 0.1-5* (5)	0.29 ± 0.12 (4)	–0.53 ± 0-0.14 (5)	–0.7-2 ± 0.1-5* (4)	0.61 ± 0.29 (4)	–0.62 ± 0-0.16* (5)	–0.9-5 ± 0.2-5* (4)	N.D.	N.D.			–0.66 ± 0-0.16* (5)
N.D.														
D373A	0.69 ± 0.23 (4)	–0.06 ± 0-0.16 (5)	–0.3-4 ± 0.1-5 (5)	0.33 ± 0.12 (4)	–0.18 ± 0-0.16 (5)	–0.0-6 ± 0.1-5 (4)	0.96 ± 0.31-*(4)	–0.56 ± 0-0.19 (5)	–0.8-3 ± 0.2-* (5)	–0.27 ± 0-0.12 (5)	N.D.			–0.67 ± 0-0.18* (5)
N.D.														
Y374A	0.15 ± 0.09 (5)	0.19 ± 0.10 (5)	0.05 ± -0.09 (5)	0.28 ± 0.09 (5)	0.19 ± 0.09 (6)	0.09 ± -0.09 (4)	0.2 ± 0.12 (4)	0.18 ± 0.09 (5)	0.13 ± -0.09 (4)	0.19 ± 0.14 (4)	–0.25 ± 0-0.09 (4)	0.0-0.0		8 ± 0.13 (5)
–0.39 ± 0.14 (5)														
V375A	0.33 ± 0.15 (5)	–0.27 ± 0-0.10 (5)	–0.4-4 ± 0.1-0 (4)	0.14 ± 0.12 (5)	–0.23 ± 0-0.09 (6)	–0.4-1 ± 0.0-9 (5)	0.69 ± 0.28 (4)	0.08 ± 0.16 (5)	–0.2-5 ± 0.0-9 (5)	–0.05 ± 0-0.14 (5)	–0.34 ± 0-0.12 (5)			–0.15 ± 0-0.16 (5)
–0.56 ± 0.11 (5)														
M376A	–0.08 ± 0-0.11 (5)	–0.57 ± 0-0.13 (4)	–0.6-0 ± 0.0-9 (4)	0.10 ± 0.10 (5)	–0.12 ± 0-0.09 (4)	–0.3-9 ± 0.0-9 (4)	–0.07 ± 0-0.15 (4)	–0.69 ± 0-0.13* (5)	–0.6-6 ± 0.1-1* (5)	–0.12 ± 0-0.15 (5)	–0.70 ± 0-0.12* (5)			–0.53 ± 0-0.16* (5)
–0.81 ± 0.13* (5)														

For each receptor mutant and ligand, concentration-response data for each pathway were fit with the Black and Leff operational model to derive an affinity-independent measure of efficacy ($\log(\tau)$). These data were corrected for changes in cell surface expression from FACS to yield $\log(\tau)$. All values are mean \pm S.E.M. (independent “n” values are indicated within parentheses). For each ligand, significance of changes in $\log(\tau)$ was determined by comparison of mutants to the WT receptor in a one-way analysis of variance followed by Dunnett's post-test ($p < 0.05$ represented by *). (N.D.) data were not able to be reliably determined.

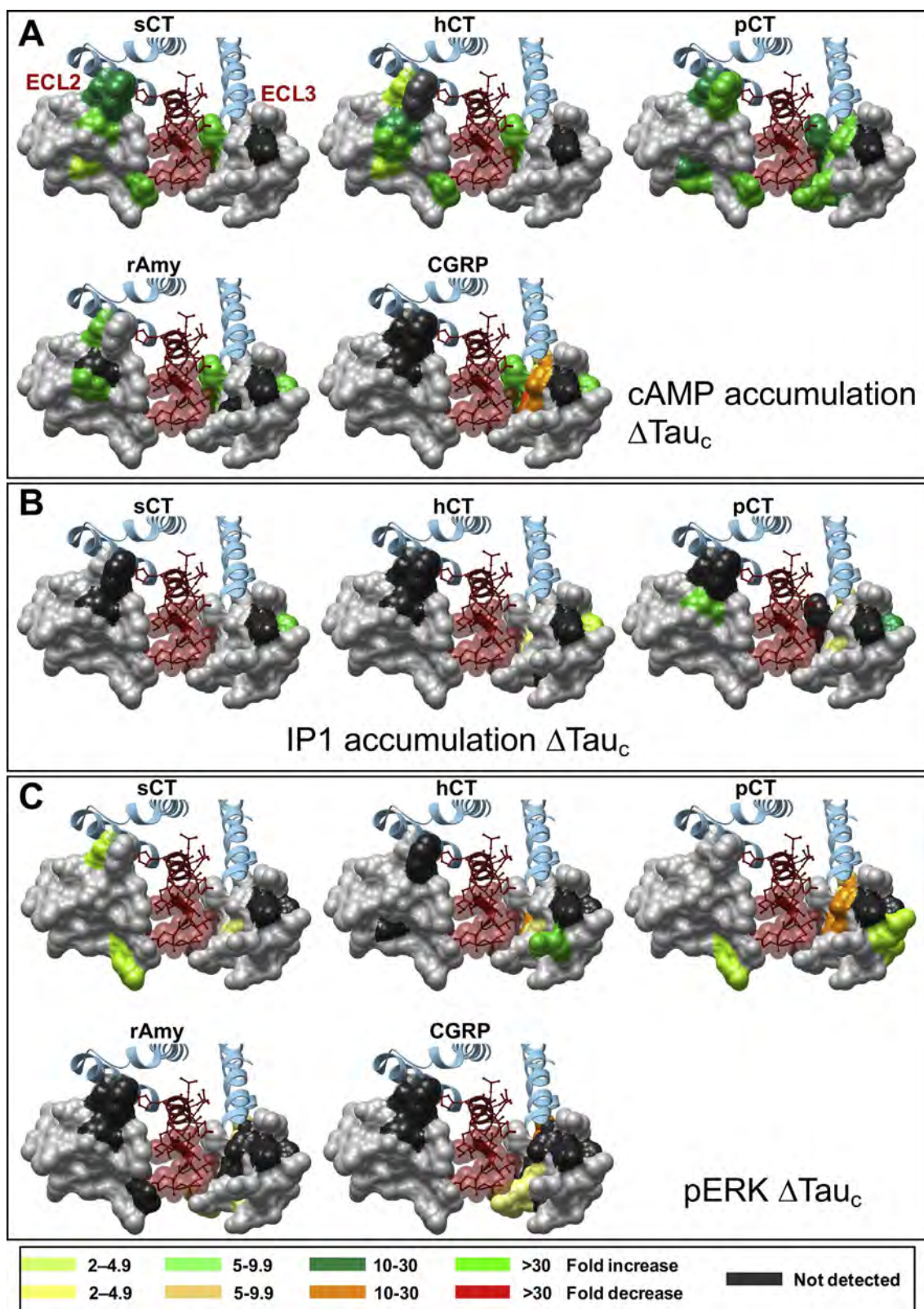


Fig. 12. Alanine mutation of ECL2 and ECL3 of the hCTR differentially modulates CT and related peptide efficacy in a pathway-dependent manner. Illustrated are top views of the active, sCT-bound, hCTR model with ECL2 and ECL3 shown in surface representation. Mutations that significantly alter peptide efficacy are coloured according to the magnitude of effect (from Table 6 and Fig. 11), with mutated amino acids without significant alteration to efficacy coloured grey. Salmon CT is shown as dark red, with side chains in proximity to the ECLs displayed in x-stick, and residues 1–7 that are critical for receptor activation display in transparent cpk. (A) Changes to cAMP efficacy. (B) Changes to IP1 efficacy. (C) Changes to pERK efficacy. (For interpretation of the references to colour in this figure legend, the reader is referred to the web version of this article.)

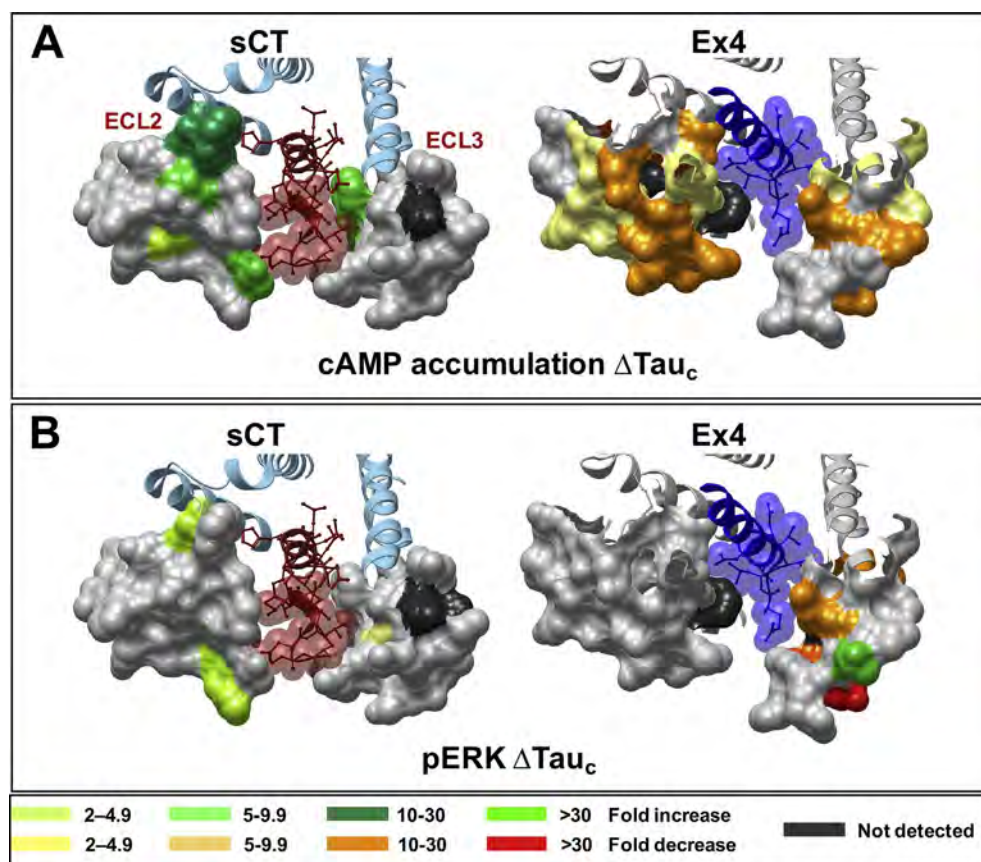


Fig. 13. Comparison of the effect of alanine-scanning mutagenesis of ECL2 and ECL3 on cAMP (A) and pERK (B) efficacy of sCT at the CTR or exendin-4 at the GLP-1R. Top views of active state structures of sCT/hCTR/Gs or Ex-P5/hGLP-1R/Gs, with the receptor ECD and peptide C-terminus omitted for clarity. Mutations that significantly alter peptide efficacy are coloured according the magnitude of effect, with mutated amino acids without significant alteration to efficacy coloured grey. Efficacy data for exendin-4 (Ex4) are from Wootten et al., 2016, and are mapped onto the structure of exendin-P5/hGLP-1R/Gs (PDB: 6B3J). sCT is shown as dark red, with side chains in proximity to the ECLs displayed in x-stick, and residues 1–7 that are critical for receptor activation displayed in transparent cpk. Exendin-P5 is shown as dark blue, with side chains in proximity to the ECLs displayed in x-stick, and residues 1–8 that are important for receptor activation displayed in transparent cpk. (For interpretation of the references to colour in this figure legend, the reader is referred to the web version of this article.)

efficacy. Within ECL3, the mutant effects tended to be relatively peptide specific, although no measurable response was observed for any peptide at the I371A mutant (Fig. 11C, Fig. 12C, Table 6). sCT efficacy was least impacted with loss of efficacy at the Y372A mutant (that was also seen with hCT and pCT), and selective enhancement of efficacy at the F359A, this latter effect contrasted with the enhanced efficacy seen for hCT and pCT. The P360A and M376A mutants attenuated pCT and hCT efficacy, albeit that the M376A mutant did not achieve significance for hCT. The K366A mutant selectively enhanced hCT efficacy, while there was a selective loss of pCT efficacy with the D373A mutant, and selective enhancement of efficacy for the M367A and L368A mutants with this peptide (Fig. 11C, Fig. 12C, Table 6).

3.4.2. Amylin and CGRP

Within ECL2 there was no quantifiable response for D287A for either amylin or CGRP, and no measurable response to CGRP at the C289A and W290A mutants, while the C289A mutant, along with N286A, had enhanced amylin efficacy (Fig. 11A, Fig. 12A, Table 6). Both amylin and CGRP efficacy were enhanced at the I300A mutant but there were no other significant effects for either peptide. Within ECL3, the F356A and I371A mutants enhanced efficacy for both peptides, while the Y372A mutant attenuated CGRP efficacy and abolished the response to amylin, but no other mutants impacted on amylin efficacy. For CGRP, loss of efficacy also occurred at the F359A, P360A, D373A and M376A mutants (Fig. 11A, Fig. 12A, Table 6).

Due to weak coupling of amylin and CGRP to IP1 signalling, effects of mutations on efficacy could not be determined.

As noted above for functional affinity data, as coupling of amylin and CGRP to pERK is relatively weak, many mutants had responses that could not be operationally quantified. Although some of these had selective effects on amylin or CGRP, in these cases the effects on affinity versus efficacy could not be separated.

Within ECL2, most mutants either had no quantifiable signalling or

did not affect peptide efficacy. Lack of signalling occurred for both peptides at the D287A, C289A and W290A mutants. Signalling was not quantifiable for L291A and Y299A for CGRP, and attenuated for amylin, while amylin signalling was not quantifiable at the T295A mutant, with no effect on CGRP (Fig. 11C, Fig. 12C, Table 6).

Within ECL3, no quantifiable signalling for either peptide was observed for the P360A, D373A and I371A mutants. At the Y372A mutant, efficacy was abolished for amylin and attenuated for CGRP. Efficacy of both peptides was reduced at the W361A and M376A mutants. It was reduced for amylin and abolished for CGRP at the P363A mutant. In general, mutations to the membrane proximal segment of TM6/ECL3 had greater impact on CGRP efficacy, with either loss (V357A) or attenuation (V358A, F359A, R362A) of efficacy for CGRP with less pronounced effects amylin efficacy (Fig. 11C, Fig. 12C, Table 6).

4. Discussion

Recent structural biology breakthroughs for the CTR and GLP-1R have provided new understanding of class B GPCR peptide binding and receptor activation that includes reorganisation of the packing of loop residues, and major, conserved, conformational changes in TM6/ECL3/TM7 at the extracellular face of the receptor that are linked to outward movement of the intracellular face of TM6 to accommodate G protein binding [13–15]. However, these studies also revealed peptide/receptor specific differences in presentation of the peptide N-terminus to the core and their engagement with the receptor surface, in particular for ECLs 2 and 3. For the GLP-1R, these loops play an important role in peptide binding, efficacy and biased agonism [15,16,21]. Intriguingly, the role of ECLs 2 and 3 of the CTR was generally distinct when compared to the GLP-1R. This could in part be attributed to distinct effector coupling profiles exhibited by the two different receptors with the GLP-1R capable of coupling to both G proteins and β -arrestins [16], whereas CTR is unable to recruit the latter when activated by CT peptides [41].

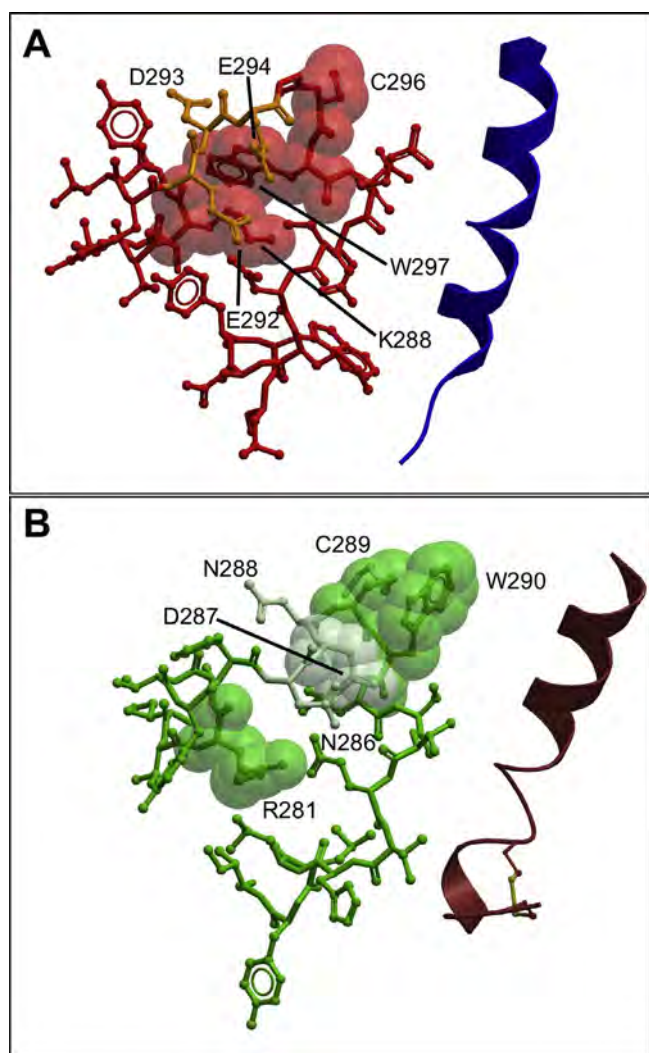


Fig. 14. CTR and GLP-1R have distinct conformations of ECL2 that are differentially stabilised by conserved residues in the core of the loop. (A) GLP-1R displaying loop residues in red x-stick and the highly conserved C296, W297 and K288 residues displayed in transparent cpk representation. Shown in orange are GLP-1R residues in the conserved polar network E292, D293, and E294. (B) CTR displaying loop residues in green x-stick and the highly conserved C289, W290 and R281 residues displayed in transparent cpk representation. Shown in light green are the CTR residues in the equivalent conserved polar network N286, D287, and N288. Ribbon representations of the proximal amino acids of exendin-P5 (blue) or sCT (dark red) are also displayed. (For interpretation of the references to colour in this figure legend, the reader is referred to the web version of this article.)

4.1. CTR ECL2 plays a key role in conformational propagation linked to Gs/cAMP signalling that is distinct from that of GLP-1R ECL2

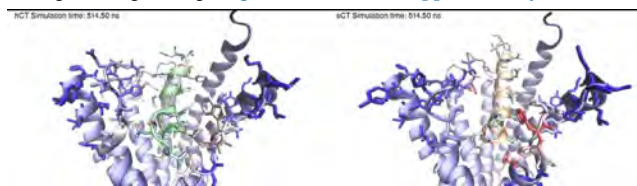
CTR stability, as indexed by cell surface expression, was highly sensitive to mutations in the core of ECL2 that formed an interconnected network but were located away from the principal binding site for sCT in the active structure. Moreover, mutation of this ECL2 network enhanced efficacy selectively for cAMP (all peptides) suggesting that the ECL2 destabilized state is linked to lowered barrier for Gs activation, despite decreased affinity of some mutations for peptides (lower pK_A). Indeed, some mutants demonstrated higher E_{max} than WT receptor, despite low cell surface expression. However, there was limited correlation of the loss of cell surface expression with efficacy in other pathways, indicating that this ECL2 conformation is poorly linked to activation of other pathways for this receptor.

This segment of ECL2 contains a number of residues that are very highly conserved across the CTR and GLP-1R (and indeed all class B

GPCRs), including R281/K288 (CTR/GLP-1R amino acids and residue number, respectively), C289/C296, W290/W297 and an polar/acidic motif between these residues N286,D287,N288 (CTR) and E292,D293,E294 (GLP-1R) [13–15]. Despite this, these residues are differentially important in receptor activation between those receptors. With minor exception, GLP-1R expression/stability was not markedly affected by mutation for any of the ECLs, including ECL2, however, ECL2 was broadly required for both Gs- (cAMP) and Gq- (iCa²⁺) mediated signalling with mutation decreasing peptide efficacy [16,21]. This contrasts with both the enhancement of cAMP efficacy for CT peptides, and the very limited importance of ECL2 in CT efficacy for IP1 signalling (Figs. 11, 12 and 13A). Comparison of the Gs complexed structures of the two receptors provides some potential insight into why these differences may occur, in particular, there are marked differences in positioning of W290/297 and the packing interactions of conserved residues around this residue. In the GLP-1R, W297 is completely flipped and buried within the core of the loop and this conformation is stabilized by K288, with the acidic/polar residues forming additional interactions that stabilize this conformation (Fig. 14). In contrast, the aromatic functional group of W290 in the CTR remains oriented towards the receptor core with extensive interactions observed with sCT and hCT that are stable in MD simulations (Fig. 15A, Table 7); D287 packs tightly with W290 and C289, while R281 forms alternate interactions to stabilize the loop conformation (Fig. 14B). The two receptors have very distinct preferred orientations of the N-terminal ECD and the peptide ligands enter the receptor core at different angles, with GLP-1/ExP5 closer to ECL2 such that their entry may require the major reorientation of W297 [15]. In this vein, it is interesting to note that while alanine mutations of C296 and W297 dramatically diminished GLP-1 and exendin-4 binding, they did not alter oxyntomodulin affinity [21], and it is possible that this peptide engages the receptor core in a manner more similar to that observed for sCT. For ECL2, CGRP and amylin were generally less affected by mutation and efficacy effects were either unmeasurable or only found in a subset of those with altered efficacy for CT peptides.

The CTR shares greatest homology with the calcitonin receptor-like receptor (CLR), including strong conservation of residues within ECL2. Unlike CTR, CLR requires RAMP interaction for functional cell surface expression and to form CGRP (CGRP₁, CLR/RAMP1) or adrenomedullin (AM₁, CLR/RAMP2; AM₂, CLR/RAMP3) receptors. In contrast to the CTR, CLR cell surface expression was not greatly impacted by alanine mutation of ECL2 residues [42,43]. However, there were similarities in the impact of mutation of conserved residues on cAMP pK_A (CTR) or cAMP potency (CLR/RAMP receptors). This included reductions in CGRP and adrenomedullin potency, for their respective receptors, for R274A (R281A, in CTR), D280A (D287A), C282A (C289A), W283A (W297A), and I284A (L291A) [42] that paralleled the losses in functional affinity seen with hCT and pCT, although this could be RAMP-dependent for the adrenomedullin receptors [43].

Within ECL2, amino acids proximal to the peptide in the sCT/CTR/Gs structure (W290-T295; L297,L298) tended to display peptide and/or pathway selective effects. These likely form dynamic and differential interactions with key polar residues of the peptides (S^{2,sCT/pCT}/G^{2,hCT}, N³, T⁶, Q^{14,sCT/hCT}, R^{14,pCT}, H^{17,sCT}/N^{17,hCT/pCT}) to influence peptide binding and signalling (Fig. 15A; Table 7; Supplementary Movie 1



Movie 1. Interactions between hCT (left hand panel) or sCT (right hand panel) with the CTR during 1 μ s MD simulation. Interactions between hCT and the CTR are less stable than those of sCT and the receptor. As a consequence, ECL2 in the hCT-bound CTR undergoes more dynamic conformational sampling. Of note, T288A, L290A, and

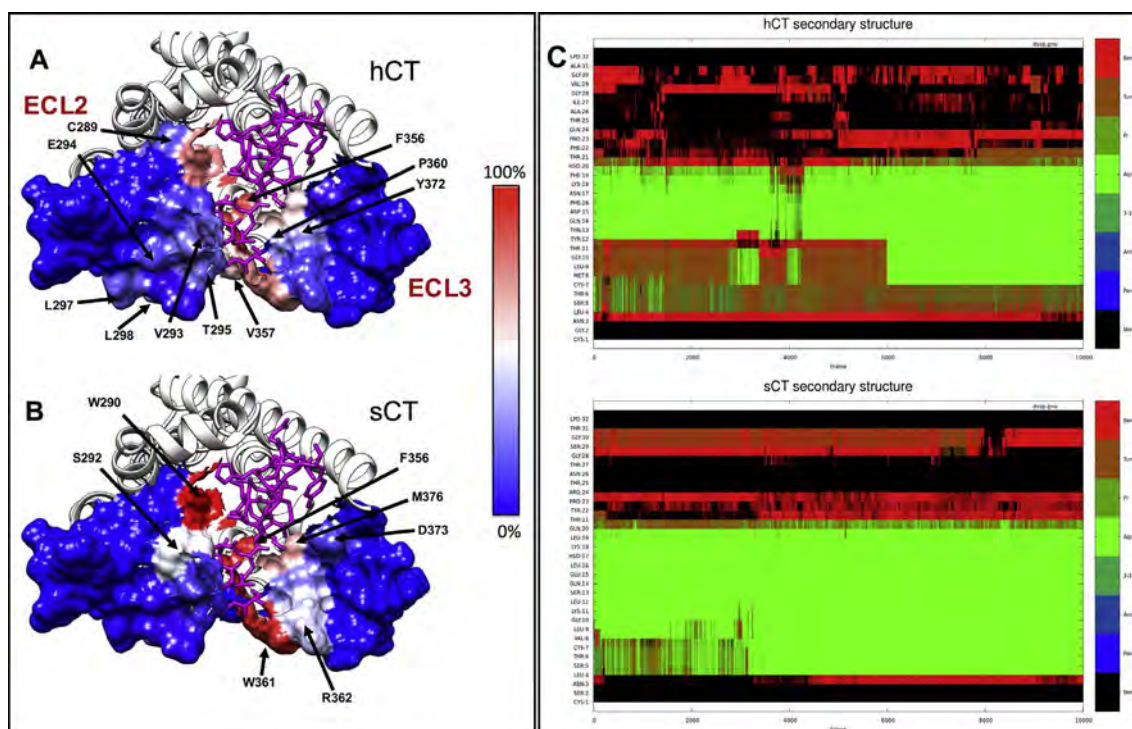


Fig. 15. Molecular dynamic simulations of sCT and hCT peptide-receptor interaction. CTR/CT contacts identified during 1 μ s MD simulations are plotted on the CTR molecular surface. The CT residues least engaged by the receptor (0% contact) are coloured blue, while residues most engaged by the receptor (100% contact) are coloured red. (A) hCT (magenta), (B) sCT (magenta). (C) Upper panel; secondary structure of hCT during the 1 μ s MD simulation of hCT bound to CTR, as determined using VMD. Lower panel; secondary structure of sCT during the 1 μ s MD simulation of sCT bound to CTR, as determined using VMD. (For interpretation of the references to colour in this figure legend, the reader is referred to the web version of this article.)

L291A of CLR, in a RAMP-dependent manner, also attenuated adrenomedullin (T288A) or CGRP (T288A,L290A,L291A) cAMP potency [42,43]. Intriguingly, comparison of 1 μ s MD simulations of hCT and sCT bound to the CTR indicated that ECL2 was more conformationally dynamic when the receptor was bound to hCT (Supplementary Movie 1), and this may also contribute to the differential effects of mutation between CT peptides.

4.2. ECL3 is a gateway for ligand, receptor and pathway specific modulation of class B GPCR function

Across the available active CTR and GLP-1R structures, the largest difference in the receptor core was the angle of tilt of TM6, and to a lesser extent TM7, and the interconnecting conformation of ECL3, with the CTR exhibiting the greatest outward movement of this domain [13–15]. Nonetheless, this was also the region of greatest divergence between the structures of GLP-1/GLP-1R/Gs and the G protein-biased analogue complex, ExP5/GLP-1R/Gs, indicating that peptide interactions with ECL3 play a critical role in differential modes of receptor activation [15]. Indeed, comparison of the effect of mutation in ECL3 across multiple peptides and pathways, and between the CTR and GLP-1Rs, revealed significant diversity in how ECL3 was engaged and contributed to peptide binding and propagation of conformational change linked to efficacy (Fig. 13). Interestingly, mutations that altered GLP-1R mediated Ca^{2+} (Gq) and pERK primarily clustered within ECL2 and ECL3 respectively, whereas CTR mutations that altered IP1 (Gq) and pERK displayed similar clustering, predominantly within ECL3 that distinct from those required for cAMP. pERK can be activated downstream of multiple effector proteins and is often a composite of many divergent signalling pathways [16,44]. While pERK1/2 mediated by the GLP-1R is a composite of both G protein and β -arrestin signalling [16], the CTR is unable to recruit β -arrestins, suggesting that the pERK response is likely to be predominantly G protein mediated [41]. While the

CTR can couple to multiple different G proteins, similar clustering in our of residues important for IP1 and pERK in our mutational analysis suggests that CTR mediated pERK, at least in part, may be downstream of Gq coupling, although further experimental data will be required to confirm this.

Despite the diversity in how CTR and GLP-1Rs engage ECL3 to promote signalling, there were clear patterns with respect to clustering of residues that were functionally important, particularly around the TM6 and TM7 proximal segments of ECL3 that were located with 5 Å of the sCT ligand, and the network of residues within the loop that stabilized these interactions. For hCT and pCT, the sequence of residues at the apex of the TM extension (K366-G369) was important, in a peptide specific manner, for IP1 or pERK signalling, indicating that secondary structure in this segment of ECL3 contributes to propagation of conformation linked to these pathways for the less well coupled peptides. Of particular note were the clear distinctions in the patterns of important residues for pCT versus other CT peptides, and CGRP across all peptides suggesting that these peptides have different modes of ligand engagement with the receptor relative to the other peptides.

Uniquely among class B GPCR peptide ligands, the CT-family peptides contain an N-terminal disulphide bridge between residues 1 and 7 (2 and 7 for CGRP and adrenomedullin), with a consequent bulky loop structure that contrasts to the linearly extended GLP-1R peptides observed in the active structures. This loop is oriented toward ECL3 and the larger outward movement of this domain is required to accommodate the peptide N-terminus. However, the peptides are predicted to make relatively weak (non-polar) and transient interactions with ECL3 (Fig. 15A; Table 7), and this is consistent with the high mobility of TM6/ECL3 in the sCT/CTR/Gs structure that could not be resolved at high resolution [13]. Linear analogues of sCT maintain high affinity and potency in cAMP signalling, whereas equivalent analogues of hCT have attenuated potency [9,45,46]. sCT has higher helical secondary structure propensity in the mid-region of the peptide, compared to hCT

Table 7

Interactions between either hCT or sCT and the CTR in MD simulations of bound peptide.

CTR Residue	Interaction	hCT	sCT
I279	CTR H bonds	/	/
	CTR Contacts	/	/
T280	CTR H bonds	/	/
	CTR Contacts	/	/
R281	CTR H bonds	/	/
	CTR Contacts	/	/
V283	CTR H bonds	/	/
	CTR Contacts	/	/
Y284	CTR H bonds	/	/
	CTR Contacts	/	/
F285	CTR H bonds	/	/
	CTR Contacts	/	/
N286	CTR H bonds	/	/
	CTR Contacts	/	/
D287	CTR H bonds	/	/
	CTR Contacts	/	/
N288	CTR H bonds	/	/
	CTR Contacts	/	/
C289	CTR H bonds	/	/
	CTR Contacts	Q14 34.4%	/
W290	CTR H bonds	/	H17 3.0% C1 2.5% (bb)
	CTR Contacts	Q14 57.0% N17 54.7% T13 30.9% K18 25.8%	S13 73.8% Q14 60.0% H17 59.0% G10 24.2%
L291	CTR H bonds	K18 2.3% (bs)	/
	CTR Contacts	Q14 54.9% T11 34.0%	/
S292	CTR H bonds	/	Q14 9.9%
	CTR Contacts	/	Q14 49.8% H17 28.0%
V293	CTR H bonds	/	/
	CTR Contacts	Q14 27.1%	Q14 21.8%
E294	CTR H bonds	C1 8.7% (sb)	/
	CTR Contacts	/	/
T295	CTR H bonds	/	/
	CTR Contacts	G2 22.5%	/
H296	CTR H bonds	/	/
	CTR Contacts	/	/
L297	CTR H bonds	/	/
	CTR Contacts	N3 26.2%	/
L298	CTR H bonds	N3 9.5% (bs)	/
	CTR Contacts	N3 62.5% T6 27.8%	N3 25.4%
Y299	CTR H bonds	/	/
	CTR Contacts	N3 47.8%	S2 29.5%
I300	CTR H bonds	/	/
	CTR Contacts	/	/
F356	CTR H bonds	/	S5 5.1% (bs)
	CTR Contacts	M8 74.1% S5 54.0% L4 37.1% L9 26.1%	L4 92.1% S5 77.4% V8 32.4%
V357	CTR H bonds	/	/
	CTR Contacts	L4 72.1% S5 41.7%	/
V358	CTR H bonds	/	/
	CTR Contacts	/	/
F359	CTR H bonds	/	/
	CTR Contacts	M8 42.8%	L4 60.6%
P360	CTR H bonds	/	/
	CTR Contacts	L4 67.2% M8 60.5% C7 41.8%	L4 89.6% C1 26.3%
W361	CTR H bonds	/	/
	CTR Contacts	C1 37.9% C7 34.3% L4 28.6% T11 25.9%	L4 58.4% C1 43.2% C7 34.9% V8 29.8% S2 26.8%
R362	CTR H bonds	/	/
	CTR Contacts	C1 20.3%	K11 60.2%

Table 7 (continued)

CTR Residue	Interaction	hCT	sCT
P363	CTR H bonds	/	/
	CTR Contacts	/	/
S364	CTR H bonds	/	/
	CTR Contacts	/	/
N365	CTR H bonds	/	/
	CTR Contacts	/	/
K366	CTR H bonds	/	/
	CTR Contacts	/	/
M367	CTR H bonds	/	/
	CTR Contacts	/	/
L368	CTR H bonds	/	/
	CTR Contacts	/	/
G369	CTR H bonds	/	/
	CTR Contacts	/	/
K370	CTR H bonds	/	/
	CTR Contacts	/	/
I371	CTR H bonds	/	/
	CTR Contacts	/	/
Y372	CTR H bonds	/	/
	CTR Contacts	M8 36.8%	L4 45.4%
D373	CTR H bonds	C1 6.8% (sb)	K11 13.0%
	CTR Contacts	/	K11 27.8%
Y374	CTR H bonds	/	/
	CTR Contacts	/	/
V375	CTR H bonds	/	/
	CTR Contacts	/	/
M376	CTR H bonds	/	/
	CTR Contacts	M8 77.2%	L4 82.2% V8 49.7%

Hydrogen bonds and generic contacts established between the CTR and both the human calcitonin (hCT) and salmon calcitonin (sCT), during 2 μ s of MD simulations (percentages are referred to the total number of frames). (sb): hydrogen bond involving a CTR side chain and the backbone of the hCT or sCT; (bs) hydrogen bond involving a CTR backbone atom and a hCT or sCT side chain. If not specified, the hydrogen bond refers to both the CTR and the hCT or sCT side chains. Only values higher than 2% for hydrogen bonds and 20% for generic contacts are reported.

[9,47] that likely constrains the location of the N-terminus to maintain interactions, whereas the additional constraints imposed by the disulphide bridge are required to facilitate interactions for hCT. Greater secondary structure of sCT versus hCT is seen in MD simulations of bound peptides (Fig. 15C) and this contributes to predicted differences in peptide-receptor interactions for these two peptides (Fig. 15B; Table 7, Supplementary Movie 1).

Intriguingly, comparison of the ExP5, and the GLP-1, receptor complexes, revealed distinct positioning of peptides (including minor difference in the relative orientation of the ECD) that likely contributes to engagement with ECL3/TM6 and TM7, and this had implications for ligand-dependent G protein conformations and cAMP signalling efficacy [14,15]. Amongst the cryo-EM structures, the GLP-1R complexes exhibited a single major conformation of the ECD relative to the receptor core, while the sCT/CTR/Gs complex contained multiple conformations of the ECD that were discernible at lower resolution [13]. CT family peptides have a relatively unstructured, and more flexible C-terminus than GLP-1 and related peptides [13,48], and it is likely that there would be greater potential for different CT peptides to have altered orientation within the receptor core, relative to sCT, as would be predicted from MD simulations (Fig. 15C). This would be consistent with the differential impact of ECL3 mutation on sCT versus hCT and pCT, and between hCT and pCT (eg. for pK_A in IP1 and pERK, and efficacy for cAMP and pERK).

Though it is difficult to draw direct comparisons, it is intriguing that select mutation of residues in ECL3 differentially affected potency/functional affinity of GLP-1 relative to ExP5 [15], and that this was also seen for sCT versus hCT. Like hCT and sCT that have altered Gs-mediated efficacy linked to different ligand-induced conformations of Gs [11], higher efficacy was observed for ExP5 (relative to affinity)

compared to GLP-1, and this was associated with lower population based assessment of max conformational change (hCT, Exp5 versus sCT, Ex4/GLP-1, respectively). This provides the first evidence of parallels in the mode of control of efficacy within relatively divergent class B subfamily members, albeit that there is still much to understand at a mechanistic level.

Amylin and CGRP are low affinity and potency agonists of CTR but are high potency ligands of CTR/RAMP complexes [8]. While this low potency limited analysis for poorly expressed CTR mutants, the impact of mutation on amylin was generally consistent with observations for CT peptides, especially sCT. In contrast, CGRP had a unique profile, particularly with respect to residues within ECL3 and proximal to TM6 (F356A-R362A), indicative of a non-canonical spectrum of interaction with this receptor segment. Of note, there were additional CGRP selective effects for mutations to CTR residues Y372 and D373 that could make direct peptide interactions, and M367 that packs between F356 and F359. Data from the related secretin receptor, has implicated TM6/TM7 as the principal membrane interface for RAMP interaction [49], and this is broadly consistent with the data for CLR [13], albeit that the authors of this latter work reached a different conclusion. While CTR and CLR interactions are more complex, with additional interaction between RAMP and receptor ECDs that contribute to altered peptide affinities [48–50], a TM6 interface would be consistent with the key role of ECL3 in biased signalling, and with the predicted impact of RAMP interactions on the conformation of ECL3 for adrenomedullin receptors [43]. RAMPs alter signalling profiles for multiple class B GPCRs, including glucagon, VPAC1 and CT receptors [50–55], even where altered binding phenotypes are not observed. The nature of the RAMP-induced enhancement of CGRP binding and potency at the CTR is particularly complex, with RAMP chimera and truncation studies indicative of a direct role of the short RAMP C-terminus in G protein engagement that is critical for CGRP potency [56,57], and this may also allosterically regulate CGRP engagement with ECL3. ECL3 was also important for cAMP signalling of CGRP or adrenomedullin at CLR/RAMP complexed receptors. Similar to observations for CT peptides at the CTR, both common and peptide specific effects were observed [58–60], confirming the dynamic role that ECL3 plays in this receptor subfamily. However, as the signalling data were not separated into the derivative effects on affinity and efficacy, it is difficult to make specific comparisons. Understanding the impact of RAMPs on CTR binding and activation by peptides will require additional structures and mutants of RAMP-complexed receptors.

Integration of alanine scanning analysis of the critically important ECLs 2 and 3, on peptide function, with new insights available from novel peptide-bound, active state, G protein complexed class B receptors, has revealed marked diversity in mechanisms of peptide engagement and receptor activation between the CTR and GLP-1R. A significant contributor appears to be the orientation of peptides within the receptor core, and this will be influenced by relative orientation of the ECD that engages the peptide C-terminus. While both domains play important functional roles, ECL3 appears to be a hotspot for distinct ligand and pathway specific effects, and this has implications for the future design of biased agonists of class B GPCRs.

Acknowledgements

This work was supported by National Health and Medical Research Council of Australia (NHMRC) project grants (1061044, 1065410 and 1126857), NHMRC program grant (1055134), Shanghai Science and Technology Development Fund (15DZ2291600), the Chinese Academy of Sciences (CAS)-Novo Nordisk Research Fund, and the United Kingdom Biotechnology Biological Sciences Research Council (BB/M006883/1). DW is a NHMRC Career Development Fellow, PMS is a NHMRC Principal Research Fellow and AC is a NHMRC Senior Principal Research Fellow. CAR is a Royal Society Industrial Fellow and DLH is a James Cook Research Fellow of the Royal Society of New

Zealand. Author contributions

P.M.S., D.W., E.D.M., Y.Z., S.G.B.F., D.Y., M.-W.W., D.L.H. study conception and design; E.D.M., Y.Z., V.P., C.A.H., G.D., S.G.B.F. performed experiments; P.M.S., D.W., E.D.M., Y.Z., S.G.B.F., G.D., C.A.R., A.C. analysed data; P.M.S., D.W., E.D.M., G.D., C.A.R. interpreted data; E.D.M., G.D., P.M.S., D.W. prepared figures; P.M.S., D.W., E.D.M. drafted manuscript; P.M.S., D.W., E.D.M., Y.Z., S.G.B.F., D.Y., M.-W.W., D.L.H., A.C., C.A.R., G.D. edited and revised manuscript.

Conflict of interest statement

The authors declare no competing interests.

References

- [1] D. Wootten, L.J. Miller, C. Koole, A. Christopoulos, P.M. Sexton, Allosteric and biased agonism at Class B G protein-coupled receptors, *Chem. Rev.* 117 (2017) 111–138.
- [2] D.M. Findlay, P.M. Sexton, T.J. Martin, Calcitonin, in: J.L. Jameson, L.J. De Groot, D.M. de Kretser, L.C. Giudice, A.B. Grossman, S. Melmed, J.T. Potts Jr., G.C. Weir (Eds.), *Endocrinology: Adult & Pediatric*, Vols 1 and 2, 7th ed. Philadelphia PA USA: Elsevier, pp. 1004–1017 14 p. (2015).
- [3] P.S. Minhas, J.K. Virdi, Hypercalcemia in inpatient setting: Diagnostic approach and management, *Curr. Emerg. Hosp. Med. Rep.* 5 (2017) 5–10.
- [4] A.L. Langston, S.H. Ralston, Management of Paget's disease of bone, *Rheumatology (Oxford)* 43 (2004) 955–959.
- [5] F. Cosman, S.J. de Beur, M.S. LeBoff, E.M. Lewiecki, B. Tanner, S. Randall, R. Lindsay/National Osteoporosis Foundation, Clinician's guide to prevention and treatment of osteoporosis, *Osteoporos. Int.* 25 (2014) 2359–2381.
- [6] R.E. Kuestner, R. Elrod, F.J. Grant, F.S. Hagen, J.L. Kuijper, S.L. Mathewes, P.O. Sheppard, S.D. Stroop, D.L. Thompson, T. Whitmore, D.M. Findlay, S. Houssami, P.M. Sexton, E.E. Moore, Cloning and characterization of an abundant subtype of the human calcitonin receptor, *Mol. Pharmacol.* 46 (1994) 246–255.
- [7] D.R. Poyner, P.M. Sexton, I. Marshall, R. Quirion, K. Kangawa, W. Born, J.A. Fischer, R. Muff, D.M. Smith, S.M. Foord, The mammalian CGRP, adrenomedullin, amylin and calcitonin receptors, *Pharmacol. Rev.* 54 (2002) 233–246.
- [8] D.L. Hay, A.A. Pioszak, Receptor activity-modifying proteins (RAMPs): new insights and roles, *Annu. Rev. Pharmacol. Toxicol.* 56 (2016) 469–487.
- [9] J.M. Hilton, M. Dowton, S. Houssami, P.M. Sexton, Identification of key components in the irreversibility of salmon calcitonin binding to calcitonin receptors, *J. Endocrinol.* 166 (2000) 213–226.
- [10] K.V. Andreassen, S.T. Hjuler, S.G. Furness, P.M. Sexton, A. Christopoulos, O. Nosjean, M.A. Karsdal, K. Henriksen, Prolonged calcitonin receptor signaling by salmon, but not human calcitonin, reveals ligand bias, *PLoS One* 9 (2014) e92042.
- [11] S.G.B. Furness, Y.L. Liang, C.J. Nowell, M.L. Halls, P.J. Wooley, E. Dal Maso, A. Inoue, A. Christopoulos, D. Wootten, P.M. Sexton, Ligand-dependent modulation of G protein conformation alters drug efficacy, *Cell* 167 (2016) 739–749.
- [12] C. de Graaf, G. Song, C. Cao, Q. Zhao, M.-W. Wang, B. Wu, R.C. Stevens, Extending the structural view of Class B GPCRs, *Trends Biochem. Sci.* (2017), <http://dx.doi.org/10.1016/j.tibs.2017.10.003>.
- [13] Y.L. Liang, M. Khoshouei, M. Radjainia, Y. Zhang, A. Glukhova, J. Tarrasch, D.M. Thal, S.G.B. Furness, G. Christopoulos, T. Coudrat, R. Danev, W. Baumeister, L.J. Miller.
- [14] A. Christopoulos, B.K. Kobilka, D. Wootten, G. Skiniotis, P.M. Sexton, Phase-plate cryo-EM structure of a class B GPCR-G-protein complex, *Nature* 546 (2017) 118–123.
- [15] Y. Zhang, B. Sun, D. Feng, H. Hu, M. Chu, Q. Qu, J.T. Tarrasch, S. Li, T.S. Kobilka, B.K. Kobilka, G. Skiniotis, Cryo-EM structure of the activated GLP-1 receptor in complex with a G protein, *Nature* 546 (2017) 248–253.
- [16] Y.L. Liang, M. Khoshouei, A. Glukhova, S.G.B. Furness, P. Zhao, L. Clydesdale, C. Koole, T.T. Truong, D.M. Thal, S. Lei, M. Radjainia, R. Danev, W. Baumeister, M.-W. Wang, L.J. Miller, A. Christopoulos, P.M. Sexton, D. Wootten, 3.3Å phase-plate cryo-EM structure of a biased agonist-bound human GLP-1 receptor-Gs complex, *Nature* 555 (2018) 121–125.
- [17] D. Wootten, C.A. Reynolds, K.J. Smith, J.C. Mobarec, C. Koole, E.E. Savage, K. Pabreja, J. Simms, R. Sridhar, S.G.B. Furness, M. Liu, P.E. Thompson, L.J. Miller, A. Christopoulos, P.M. Sexton, The extracellular surface of the GLP-1 receptor is a molecular trigger for biased agonism, *Cell* 165 (2016) 1632–1643.
- [18] M. Dong, P.C. Lam, A. Orry, P.M. Sexton, A. Christopoulos, R. Abagyan, L.J. Miller, Use of cysteine trapping to map spatial approximations between residues contributing to the helix N-capping motif of secretin and distinct residues within each of the extracellular loops of its receptor, *J. Biol. Chem.* 291 (2016) 5172–5184.
- [19] M. Dong, C. Koole, D. Wootten, P.M. Sexton, L.J. Miller, Structural and functional insights into the juxtamembranous amino-terminal tail and extracellular loop regions of class B GPCRs, *Br. J. Pharmacol.* 171 (2014) 1085–1101.
- [20] M.J. Woolley, A.C. Conner, Understanding the common themes and diverse roles of the second extracellular loop (ECL2) of the GPCR super-family, *Mol. Cell. Endocrinol.* 449 (2017) 3–11.
- [21] R.E. Weaver, J.C. Mobarec, M.J. Wigglesworth, C.A. Reynolds, D. Donnelly, High affinity binding of the peptide agonist TIP-39 to the parathyroid hormone 2 (PTH₂)

- receptor requires the hydroxyl group of Tyr-318 on transmembrane helix 5, *Biochem. Pharmacol.* 127 (2017) 71–81.
- [22] C. Koole, D. Wootten, J. Simms, C. Valant, R. Sridhar, O.L. Woodman, L.J. Miller, R.J. Summers, A. Christopoulos, P.M. Sexton, Allosteric ligands of the glucagon-like peptide 1 receptor (GLP-1R) differentially modulate endogenous and exogenous peptide responses in a pathway-selective manner: implications for drug screening, *Mol. Pharmacol.* 78 (2010) 456–465.
- [23] C. Koole, D. Wootten, J. Simms, L.J. Miller, A. Christopoulos, P.M. Sexton, Second extracellular loop of human glucagon-like peptide-1 receptor (GLP-1R) has a critical role in GLP-1 peptide binding and receptor activation, *J. Biol. Chem.* 287 (2012) 3642–3658.
- [24] E. Johansson, J.L. Hansen, A.M.K. Hansen, A.C. Shaw, P. Becker, L. Schaffer, S. Reetz-Runge, Type II Turn of receptor-bound salmon calcitonin revealed by X-ray crystallography, *J. Biol. Chem.* 291 (2016) 13689–13698.
- [25] N. Eswar, D. Eramian, B. Webb, M.Y. Shen, A. Sali, Protein structure modeling with MODELLER, *Methods Mol. Biol.* 426 (2008) 145–159.
- [26] J.M. Baldwin, G.F. Schertler, V.M. Unger, An alpha-carbon template for the transmembrane helices in the rhodopsin family of G-protein-coupled receptors, *J. Mol. Biol.* 272 (1997) 144–164.
- [27] T. Hamelryck, An amino acid has two sides: a new 2D measure provides a different view of solvent exposure, *Proteins* 59 (2005) 38–48.
- [28] S. Doerr, M.J. Harvey, F. Noé, G. De Fabritiis, HTMD: high-throughput molecular dynamics for molecular discovery, *J. Chem. Theory Comput.* 12 (2016) 1845–1852.
- [29] T.J. Dolinsky, J.E. Nielsen, J.A. McCammon, N.A. Baker, PDB2PQR: an automated pipeline for the setup of Poisson-Boltzmann electrostatics calculations, *Nucl. Acids Res.* 32 (2004) W665–W667.
- [30] H. Li, A.D. Robertson, J.H. Jensen, Very fast empirical prediction and rationalization of protein pKa values, *Proteins* 61 (2005) 704–721.
- [31] B. Sommer, Membrane packing problems: a short review on computational membrane modeling methods and tools, *Comput. Struct. Biotechnol. J.* 5 (2013) e201302014.
- [32] M.A. Lomize, A.L. Lomize, I.D. Pogozheva, H.I. Mosberg, OPM: orientations of proteins in membranes database, *Bioinformatics* 22 (2006) 623–625.
- [33] W.L. Jorgensen, J. Chandrasekhar, J.D. Madura, R.W. Impey, M.L. Klein, Comparison of simple potential functions for simulating liquid water, *J. Chem. Phys.* 79 (1983) 926.
- [34] J. Huang, A.D. MacKerell, CHARMM36 all-atom additive protein force field: validation based on comparison to NMR data, *J. Comput. Chem.* 34 (2013) 2135–2145.
- [35] M.J. Harvey, G. Giupponi, G.D. Fabritiis, ACEMD: accelerating biomolecular dynamics in the microsecond time scale, *J. Chem. Theory Comput.* 5 (2009) 1632–1639.
- [36] H.J.C. Berendsen, J.P.M. Postma, W.F. van Gunsteren, A. DiNola, J.R. Haak, Molecular dynamics with coupling to an external bath, *J. Chem. Phys.* 81 (1984) 3684.
- [37] R.J. Loncharich, B.R. Brooks, R.W. Pastor, Langevin dynamics of peptides: the frictional dependence of isomerization rates of N-acetylalanine-N'-methylamide, *Biopolymers* 32 (1992) 523–535.
- [38] V. Krautler, W.F. van Gunsteren, P.H. Hanenberger, A fast SHAKE algorithm to solve distance constraint equations for small molecules in molecular dynamics simulations, *J. Comput. Chem.* 22 (2001) 501–508.
- [39] U. Essmann, L. Perera, M.L. Berkowitz, T. Darden, H. Lee, L.G. Pedersen, A smooth particle mesh Ewald method, *J. Chem. Phys.* 103 (1995) 8577–8593.
- [40] W. Humphrey, A. Dalke, K. Schulten, VMD: visual molecular dynamics, *J. Mol. Graph* 14 (1996) 33–38.
- [41] E. Dal Maso, R. Just, C. Hick, A. Christopoulos, P.M. Sexton, D. Wootten, S.G.B. Furness, Characterisation and signalling and regulation of common calcitonin receptor splice variants and polymorphisms, *Biochem. Pharmacol.* 148 (2017) 111–129.
- [42] J.W. Black, P. Leff, Operational models of pharmacological agonism, *Proc. R. Soc. Lond. B Biol. Sci.* 220 (1983) 141–162.
- [43] M.J. Woolley, H.A. Watkins, B. Taddese, Z.G. Karakullukcu, J. Barwell, K.J. Smith, D.L. Hay, D.R. Poyner, C.A. Reynolds, A.C. Conner, The role of ECL2 in CGRP receptor activation: a combined modelling and experimental approach, *J. R. Soc. Interface* 10 (2013) 20130589.
- [44] M.M. Belcheva, C.J. Coscia, Diversity of G protein coupled receptor signalling pathways to ERK/MAP kinase, *Neurosignals* 11 (2002) 34–44.
- [45] H.A. Watkins, M. Chakravarthy, R.S. Abhayawardana, J.J. Gingell, M. Garelja, M. Pardamwar, J.M. McElhinney, A. Lathbridge, A. Constantine, P.W. Harris, T.Y. Yuen, M.A. Brimble, J. Barwell, D.R. Poyner, M.J. Woolley, A.C. Conner, A.A. Pioszak, C.A. Reynolds, D.L. Hay, Receptor activity-modifying proteins 2 and 3 generate adrenomedullin receptor subtypes with distinct molecular properties, *J. Biol. Chem.* 291 (2016) 11657–11675.
- [46] R.C. Orlowski, R.M. Epand, A.R. Stafford, Biologically potent analogues of salmon calcitonin which do not contain an N-terminal disulfide-bridged ring structure, *Eur. J. Biochem.* 162 (1987) 399–402.
- [47] J.H. Feyen, F. Cardinaux, R. Gamse, C. Bruns, M. Azria, U. Trechsel, N-terminal truncation of salmon calcitonin leads to calcitonin antagonists. Structure activity relationship of N-terminally truncated salmon calcitonin fragments in vitro and in vivo, *Biochem. Biophys. Res. Commun.* 187 (1992) 8–13.
- [48] R.M. Epand, R.F. Epand, R.C. Orlowski, Biologically active calcitonin analogs which have minimal interactions with phospholipids, *Biochem. Biophys. Res. Commun.* 152 (1988) 203–207.
- [49] J.M. Booe, C.S. Walker, J. Barwell, G. Kuteyi, J. Simms, M.A. Jamaluddin, M.L. Warner, R.M. Bill, P.W. Harris, M.A. Brimble, D.R. Poyner, D.L. Hay, A.A. Pioszak, Structural basis for receptor activity-modifying protein-dependent selective peptide recognition by a G protein-coupled receptor, *Mol. Cell* 58 (2015) 1040–1052.
- [50] K.G. Harikumar, J. Simms, G. Christopoulos, P.M. Sexton, L.J. Miller, Molecular basis of association of receptor activity-modifying protein 3 with the family B G protein-coupled secretin receptor, *Biochemistry* 48 (2009) 11773–11785.
- [51] K. Kuwasako, K. Kitamura, S. Nagata, J. Kato, Flow cytometric analysis of the calcitonin receptor-like receptor domains responsible for cell-surface translocation of receptor activity-modifying proteins, *Biochem. Biophys. Res. Commun.* 384 (2009) 249–254.
- [52] J. Gingell, J. Simms, J. Barwell, D.R. Poyner, H.A. Watkins, A.A. Pioszak, P.M. Sexton, D.L. Hay, An allosteric role for receptor activity-modifying proteins in defining GPCR pharmacology, *Cell Discov.* 2 (2016) 16012, <http://dx.doi.org/10.1038/celldisc.2016.12>.
- [53] A. Christopoulos, G. Christopoulos, M. Morfis, M. Udawela, M. Laburthe, A. Couvineau, K. Kuwasako, N. Tilakaratne, P.M. Sexton, Novel receptor partners and function of receptor activity-modifying proteins, *J. Biol. Chem.* 278 (2003) 3293–3297.
- [54] M. Morfis, N. Tilakaratne, S.G. Furness, G. Christopoulos, T.D. Werry, A. Christopoulos, P.M. Sexton, Receptor activity-modifying proteins differentially modulate the G protein-coupling efficiency of amylin receptors, *Endocrinology* 149 (2008) 5423–5431.
- [55] C. Weston, J. Lu, N. Li, K. Barkan, G.O. Richards, D.J. Roberts, T.M. Skerry, D. Poyner, M. Pardamwar, C.A. Reynolds, S.J. Dowell, G.B. Willars, G. Ladds, Modulation of glucagon receptor pharmacology by receptor activity-modifying protein-2 (RAMP2), *J. Biol. Chem.* 290 (2015) 23009–23022.
- [56] C. Weston, I. Winfield, M. Harris, R. Hodgson, A. Shah, S.J. Dowell, J.C. Mobarec, D.A. Woodlock, C.A. Reynolds, D.R. Poyner, H.A. Watkins, G. Ladds, Receptor activity-modifying protein-directed G protein signaling specificity for the calcitonin gene-related peptide family of receptors, *J. Biol. Chem.* 291 (2016) 21925–21944.
- [57] M. Udawela, G. Christopoulos, M. Morfis, A. Christopoulos, S. Ye, N. Tilakaratne, P.M. Sexton, A critical role for the short intracellular C terminus in receptor activity-modifying protein function, *Mol. Pharmacol.* 70 (2006) 1750–1760.
- [58] M. Udawela, G. Christopoulos, N. Tilakaratne, A. Christopoulos, A. Albiston, P.M. Sexton, Distinct receptor activity-modifying protein domains differentially modulate interaction with calcitonin receptors, *Mol. Pharmacol.* 69 (2006) 1984–1989.
- [59] J. Barwell, A. Conner, D.R. Poyner, Extracellular loops 1 and 3 and their associated transmembrane regions of the calcitonin receptor-like receptor are needed for CGRP receptor function, *Biochim. Biophys. Acta* 1813 (2011) 1906–1916.
- [60] K. Kuwasako, D.L. Hay, S. Nagata, T. Hikosaka, K. Kitamura, J. Kato, The third extracellular loop of the human calcitonin receptor-like receptor is crucial for the activation of adrenomedullin signalling, *Br. J. Pharmacol.* 166 (2012) 137–150.



Two distinct domains of the glucagon-like peptide-1 receptor control peptide-mediated biased agonism

Received for publication, April 2, 2018, and in revised form, April 20, 2018. Published, Papers in Press, May 1, 2018, DOI 10.1074/jbc.RA118.003278

Saifei Lei^{‡§1}, Lachlan Clydesdale[¶], Antao Dai[‡], Xiaoqing Cai[‡], Yang Feng[‡], Dehua Yang[‡], Yi-Lynn Liang[¶], Cassandra Koole^{¶12}, Peishen Zhao[¶], Thomas Coudrat[¶], Arthur Christopoulos^{¶13}, Ming-Wei Wang^{‡§||4}, Denise Wootten^{¶||5}, and Patrick M. Sexton^{¶||6}

From the [‡]National Center for Drug Screening and CAS Key Laboratory of Receptor Research, Shanghai Institute of Materia Medica, Chinese Academy of Sciences, Shanghai 201203, China, the [¶]Drug Discovery Biology, Monash Institute of Pharmaceutical Sciences, Monash University, Parkville, Victoria 3052, Australia, the [§]School of Pharmacy, University of Chinese Academy of Sciences, No. 19A Yuquan Road, Beijing 100049, China, and the ^{||}School of Pharmacy, Fudan University, Shanghai 201203, China

Edited by Henrik G. Dohlman

G protein-coupled receptors (GPCRs) can be differentially activated by ligands to generate multiple and distinct downstream signaling profiles, a phenomenon termed biased agonism. The glucagon-like peptide-1 receptor (GLP-1R) is a class B GPCR and a key drug target for managing metabolic disorders; however, its peptide agonists display biased signaling that affects their relative efficacies. In this study, we combined mutagenesis experiments and mapping of surface mutations onto recently described GLP-1R structures, which revealed two major domains in the GLP-1/GLP-1R/G_s protein active structure that are differentially important for both receptor quiescence and ligand-specific initiation and propagation of biased agonism. Changes to the conformation of transmembrane helix (TM) 5 and TM 6 and reordering of extracellular loop 2 were essential for the propagation of signaling linked to cAMP formation and intracellular calcium mobilization, whereas ordering and packing of residues in TMs 1 and 7 were critical for extracellular signal-regulated kinase 1/2 (pERK) activity. On the basis of these findings, we propose a model of distinct peptide-receptor interactions that selectively control how these different signaling pathways are engaged. This work provides important structural insight into class B GPCR activation and biased agonism.

This work was supported in part by National Health and Medical Research Council of Australia Project Grants 1061044, 1065410, and 1126857; National Health and Medical Research Council Program Grant 1055134; Shanghai Science and Technology Development Fund Grant 15DZ2291600; National Natural Science Foundation of China Grant 81573479; and Strategic Priority Research Program of the Chinese Academy of Sciences Grants XDA12020347 and XDA12040308. The authors declare that they have no conflicts of interest with the contents of this article.

¹ Recipient of the Postgraduate Overseas Study Fellowship from the Chinese Academy of Sciences.

² National Health and Medical Research Council C. J. Martin Fellow.

³ National Health and Medical Research Council of Australia Senior Principal Research Fellow.

⁴ To whom correspondence may be addressed. E-mail: mwwang@simmm.ac.cn.

⁵ National Health and Medical Research Council Career Development Fellow. To whom correspondence may be addressed. E-mail: denise.wootten@monash.edu.

⁶ National Health and Medical Research Council Principal Research Fellow. To whom correspondence may be addressed. Tel.: 61-3-9903-9069; E-mail: patrick.sexton@monash.edu.

GPCRs⁷ are ubiquitous integrators of extracellular signals for the control of cellular responses. As such, they are key drug targets, and ~40% of approved therapeutics act via this receptor class (1). Nonetheless, many potential drugs fail in late-stage clinical trials due to lack of predicted efficacy, indicating gaps in our understanding of drug action and/or the specific contributions of signaling events to the control of diseases.

It has become increasingly evident that GPCRs are highly dynamic proteins that can adopt numerous ligand-specific conformational ensembles with distinct impact on signaling and regulatory profiles, even with ligands acting via a common binding pocket, a phenomenon termed biased agonism (2, 3). This not only provides an unprecedented opportunity to sculpt biological responses for therapeutic benefit, but it also creates increased challenges for drug discovery and developmental programs to identify the spectra of ligand behavior and to elucidate structure-activity relationships linking observed behavior to physiology and disease processes.

Class B peptide hormone GPCRs bind important physiological peptides of about 30–40 amino acids, including calcitonin, amylin, adrenomedullin, calcitonin gene-related peptide, secretin, parathyroid hormones, vasoactive intestinal peptide, gastric inhibitory peptide, glucagon, and the glucagon-like peptides (4, 5). As such, these receptors are crucial targets for treatment of chronic diseases, notably osteoporosis, migraine, obesity, and type 2 diabetes. Class B GPCRs are pleiotropically coupled, and biased agonism is commonly observed when signaling is studied across multiple pathways, creating novel therapeutic opportunities. However, optimally exploiting this property requires detailed mechanistic understanding of the drivers of bias (4).

The glucagon-like peptide-1 (GLP-1) receptor (GLP-1R) is a class B GPCR that is both critical to the natural incretin response of the body and a major target for treatment of metabolic disorders. It is among the best studied for biased agonism, and such bias is readily observed for both naturally occurring

⁷ The abbreviations used are: GPCR, G protein-coupled receptor; GLP-1R, glucagon-like peptide-1 receptor; TM, transmembrane; ECL, extracellular loop; pERK, phosphorylation of extracellular signal-regulated kinase 1/2; ECD, extracellular domain; GPCR, glucagon receptor; NAM, negative allosteric modulator; PDB, Protein Data Bank; [Ca²⁺]_i, intracellular calcium; ANOVA, analysis of variance; hGLP-1R, human GLP-1R.

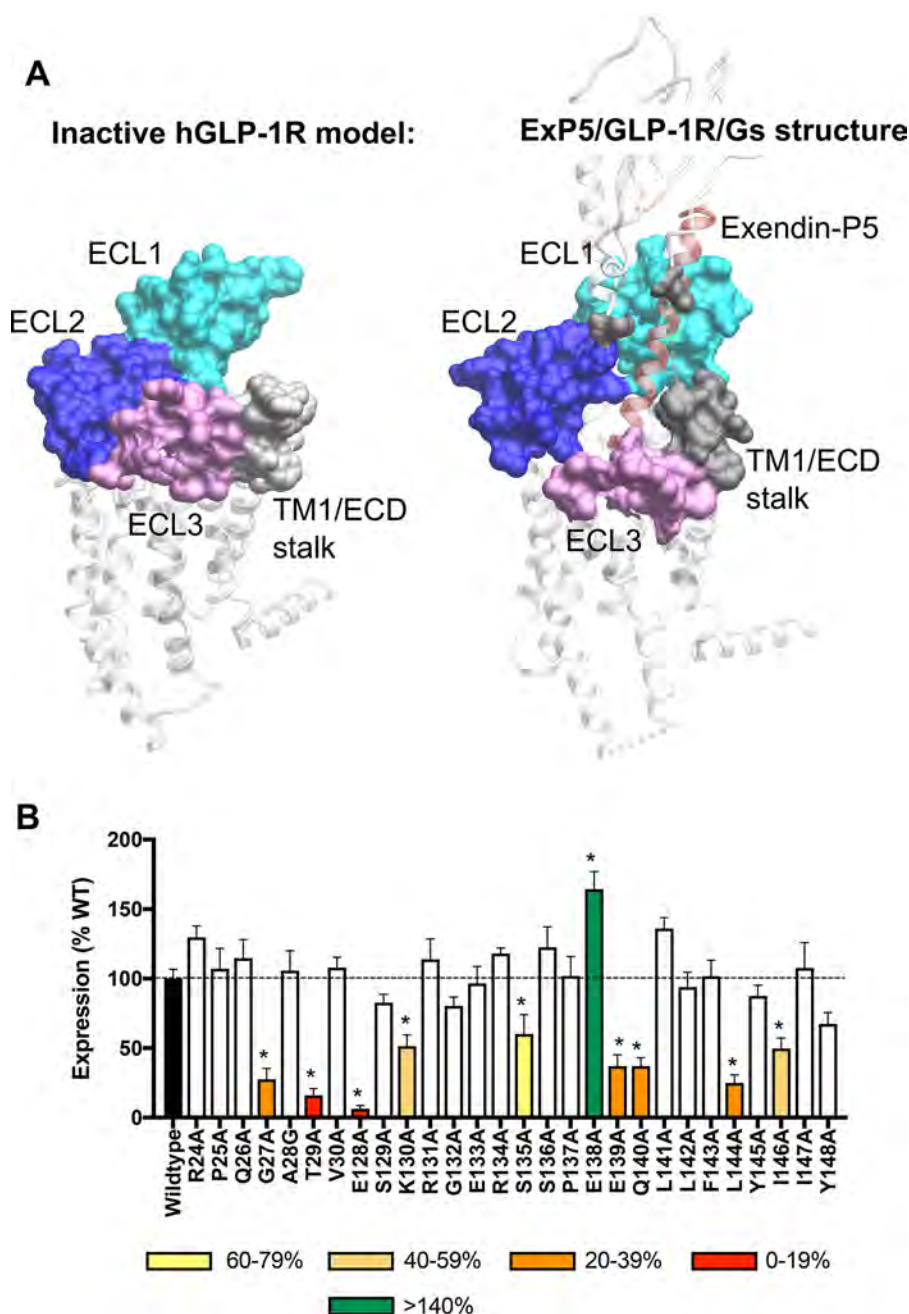


Figure 1. Location of the TM/N-terminal ECD interface in active and inactive models of the human GLP-1R and expression of GLP-1R constructs in stable cell lines. *A*, surface residues of the GLP-1R. *Left-hand panel*, inactive model of the hGLP-1R TM domain (residues 134–422) based on the inactive glucagon receptor (PDB code 4L6R). *Right-hand panel*, active full-length exendin-P5 (ExP5)–hGLP-1R–G_s complex (PDB code 6B3J). The far N-terminal ECD (residues 24–30) and the TM1/ECD stalk (residues 128–148) are illustrated in gray. ECL residues mutated in previous analyses (11) are colored by ECL. ECL1 (residues 201–223; cyan), ECL2 (residues 285–307; dark blue), ECL3 (residues 372–387; light purple) are shown. The position of exendin-P5 is shown as red ribbon representation. *B*, cell-surface expression was determined by ELISA to the N-terminal c-Myc epitope tag on the hGLP-1R and mutant hGLP-1R isogenically expressed in CHO–Flp-In cells. Data were normalized to the WT receptor. All values are mean \pm S.E. of four to six independent experiments, conducted in duplicate. One-way ANOVA and Dunnett's post-test were performed to determine statistical differences (*, $p < 0.05$).

and synthetic peptide mimetics (6–11). This biased agonism alters responses in pancreatic β -cells (11) and disease models *in vivo* (10). The prevailing view for class B GPCR peptide binding and receptor activation is a two-domain theory with initial binding of the peptide C terminus to the receptor extracellular domain (ECD) that positions the peptide N terminus relative to the receptor core to facilitate receptor activation (12). The prevalence of GLP-1R biased agonism and the therapeutic implications of this behavior make understanding of the trig-

gers for, and propagation of, bias important for rational drug design and development. We recently revealed that the extracellular loops (ECLs) of the GLP-1R play a crucial role in the biased agonism of exendin-4, oxyntomodulin, and GLP-1(7–36)-NH₂ (GLP-1): the first clinically approved GLP-1 mimetic, a biased endogenous GLP-1R peptide, and the most common circulating form of GLP-1, respectively (11, 13). Nonetheless, interpretation of the data was limited by lack of experimentally determined structure for the GLP-1R core and, indeed, any full-

Table 1**Effects of human GLP-1R TM1/N-terminal mutants on peptide ligand binding and cell-surface expression**

Binding data were analyzed using a three-parameter logistic equation and normalized to the maximal binding of the radiolabeled antagonist ^{125}I -exendin-4(9–39) and the nonspecific binding in the presence of $1\ \mu\text{M}$ exendin-4(9–39). pK_i is the negative logarithm of peptide affinity. All the values for binding are mean \pm S.E. of three independent experiments, conducted in triplicate. Cell-surface expression was accessed through ELISA detecting the N-terminal c-Myc epitope label on the receptor. Mutant data are compared with the wildtype human GLP-1R expression and shown as percentage. The data for cell-surface expression are mean \pm S.E. of four to six independent experiments, conducted in duplicate. One-way ANOVA and Dunnett's post-test were used to determine statistical differences (*, $p < 0.05$). ND, not determined.

	Whole-cell competition radioligand binding (pK_i)				Cell-surface expression (% wildtype)
	GLP-1(7–36)- NH_2	Exendin-4	Oxyntomodulin	Exendin(9–39)	
Wildtype	8.12 ± 0.06	9.31 ± 0.06	7.52 ± 0.08	7.85 ± 0.05	100 ± 7
R24A	8.10 ± 0.08	9.54 ± 0.13	7.69 ± 0.08	7.74 ± 0.06	130 ± 8
P25A	8.17 ± 0.09	9.56 ± 0.12	7.80 ± 0.08	7.71 ± 0.06	107 ± 15
Q26A	7.96 ± 0.09	9.23 ± 0.11	7.56 ± 0.10	7.72 ± 0.07	115 ± 13
G27A	ND	ND	ND	ND	$28 \pm 8^*$
A28G	$7.67 \pm 0.08^*$	$8.89 \pm 0.11^*$	$7.07 \pm 0.08^*$	7.61 ± 0.06	106 ± 15
T29A	ND	ND	ND	ND	$16 \pm 5^*$
V30A	8.16 ± 0.09	9.31 ± 0.11	7.72 ± 0.08	7.77 ± 0.08	108 ± 8
E128A	ND	ND	ND	ND	$6 \pm 2^*$
S129A	8.10 ± 0.11	9.94 ± 0.10	7.71 ± 0.15	7.79 ± 0.10	83 ± 6
K130A	8.12 ± 0.08	9.25 ± 0.07	7.52 ± 0.12	7.64 ± 0.09	$51 \pm 8^*$
R131A	8.28 ± 0.12	9.37 ± 0.09	7.72 ± 0.14	7.78 ± 0.09	114 ± 15
G132A	ND	ND	ND	ND	80 ± 6
E133A	8.16 ± 0.07	9.45 ± 0.10	7.70 ± 0.09	7.84 ± 0.10	97 ± 12
R134A	8.12 ± 0.09	9.14 ± 0.08	7.60 ± 0.12	7.65 ± 0.11	118 ± 4
S135A	8.35 ± 0.09	9.40 ± 0.10	7.79 ± 0.09	7.82 ± 0.09	$60 \pm 14^*$
S136A	7.84 ± 0.11	9.29 ± 0.07	7.39 ± 0.13	7.59 ± 0.15	123 ± 15
P137A	$7.18 \pm 0.13^*$	$8.54 \pm 0.09^*$	$6.94 \pm 0.12^*$	$6.98 \pm 0.18^*$	102 ± 14
E138A	8.22 ± 0.07	9.19 ± 0.10	7.21 ± 0.07	7.87 ± 0.07	$164 \pm 13^*$
E139A	ND	ND	ND	ND	$37 \pm 8^*$
Q140A	7.84 ± 0.15	$8.65 \pm 0.13^*$	7.68 ± 0.21	8.15 ± 0.16	$37 \pm 6^*$
L141A	7.50 ± 0.06	$8.53 \pm 0.06^*$	$6.17 \pm 0.28^*$	$7.17 \pm 0.06^*$	136 ± 8
L142A	7.89 ± 0.07	9.23 ± 0.07	$6.89 \pm 0.10^*$	7.84 ± 0.07	94 ± 11
F143A	8.19 ± 0.06	9.33 ± 0.09	7.35 ± 0.09	7.65 ± 0.06	102 ± 11
L144A	7.94 ± 0.15	9.41 ± 0.17	7.15 ± 0.19	8.03 ± 0.15	$25 \pm 6^*$
Y145A	8.25 ± 0.09	9.51 ± 0.09	7.38 ± 0.10	7.92 ± 0.07	88 ± 8
I146A	8.07 ± 0.09	9.32 ± 0.12	7.57 ± 0.14	7.91 ± 0.09	$50 \pm 8^*$
I147A	7.78 ± 0.05	9.00 ± 0.08	7.26 ± 0.08	7.67 ± 0.08	108 ± 18
Y148A	$6.79 \pm 0.15^*$	$8.06 \pm 0.06^*$	$6.26 \pm 0.25^*$	8.09 ± 0.08	67 ± 8

length and active class B GPCR structures. Recently, several near-atomic resolution structures of the GLP-1R have been published that include structures of a stabilized inhibitor-bound human receptor transmembrane (TM) domain (14), a stabilized full-length human receptor bound to a modified 11-mer peptide agonist (15), and GLP-1Rs in complex with heterotrimeric G_s protein and either GLP-1 (16) or a newly identified biased agonist, exendin-P5 (17). In the meantime, the structure of a full-length glucagon receptor (GCGR) in complex with a weak partial agonist (18) and the full-length active calcitonin receptor in complex with peptide agonist and heterotrimeric G_s were also solved (19). Collectively, this work has provided novel insights into gross conformational changes linked to the dynamics of class B GPCR activation, including marked kinking of transmembrane helix (TM) 6, outward movement of helices 6 and 7, and the interlinking ECL3, required for full activation, as well as manifest reorganization of other ECLs (16, 17, 19).

The ECD is structurally linked to the receptor core through extension of TM1, and there is accumulating evidence that the far N terminus of the ECD may have a dynamic role in class B GPCR function, both with respect to maintenance of an inactive state, as has been suggested for the glucagon receptor (GCGR) (20), and in ligand-dependent signaling (21, 22). Notably, the TM1 stalk domain is unstructured in complexes of class B receptors complexed to agonist and G protein, but it maintains an extended α -helix in GCGR bound to a partial agonist but without G protein (18). In this study, we performed alanine-scanning analysis of the GLP-1R surface of the far N-terminal 7 amino acids (residues 24–30, immediately after the receptor

signal peptide) and the 21 amino acids that link TM1 and the ECD (residues 128–148), and we assessed cell-surface expression, peptide affinity, and peptide efficacy for activation of pathways linked to cAMP accumulation, intracellular calcium ($[\text{Ca}^{2+}]_i$) mobilization and phosphorylation of extracellular signal-regulated kinase 1/2 (pERK). Each of these pathways is of physiological relevance for GLP-1R signaling (4, 23), and both these regions are dynamically involved in GLP-1R peptide affinity and signal transduction. The overlay of the new data and that from our prior mutagenic analysis of the ECLs (11) onto the recently solved GLP-1R structures revealed that changes to the conformation of TMs 5 and 6 and reordering of ECL2 were essential for propagation of cAMP formation and $[\text{Ca}^{2+}]_i$ mobilization signaling, whereas ordering and packing of residues in TMs 1 and 7 were critical for pERK that is principally driven by the G_i - $G\beta\gamma$ -arrestin interaction in the WT receptor.

Results

The far N-terminal ECD (Arg-24–Val-30) and TM1/ECD linker (Glu-128–Tyr-148) residues of GLP-1R were mutated to alanine by site-directed mutagenesis and stably expressed in CHO–Flp-In cells by isogenic recombination, with the exception of Ala-28 that was mutated to glycine. The location of these amino acids within the GLP-1R extracellular surface is illustrated on inactive (TM1/ECD linker only) and active hGLP-1R models in Fig. 1A.

Cell-surface expression levels for WT and mutant GLP-1Rs in the CHO–Flp-In stable cell lines were measured through ELISA of anti-c-Myc antibody binding to the N-terminal

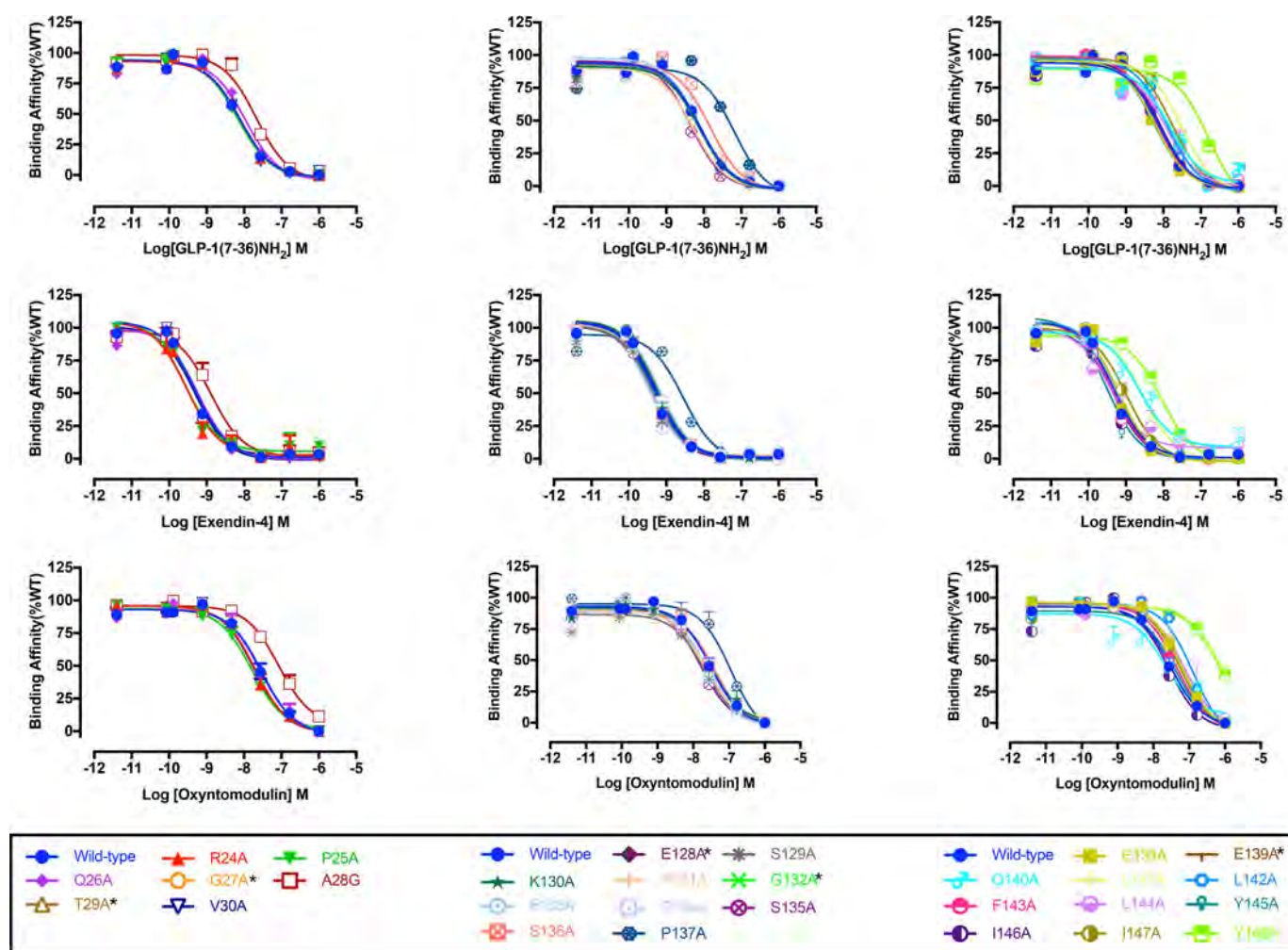


Figure 2. Competitive inhibition of ^{125}I -exendin(9–39) binding by peptide agonists for Ala mutants of the hGLP-1R N-terminal ECD and TM1 and linker region. Binding affinity data are expressed as a percentage of measured bound versus bound in the absence of peptide, each corrected for nonspecific binding (measured in the presence of $1\ \mu\text{M}$ unlabeled exendin(9–39)). Inhibition curves of WT and mutant receptors were stimulated by GLP-1(7–36) NH_2 (upper panels), exendin-4 (middle panels), or oxyntomodulin (lower panels) in CHO-Flp-In cells stably expressed WT or mutant receptors. Data were fitted with a three-parameter logistic equation. All values are means \pm S.E. of four to six independent experiments, conducted in duplicate.

c-Myc epitope. All receptors were expressed at the cell surface; however, the expression of G27A, T29A, E128A, K130A, S135A, E139A, Q140A, L144A, and I146A mutants was significantly lower and that of E138A was markedly higher than WT GLP-1R. All the other mutant receptors were not significantly different from the WT (Fig. 1B and Table 1).

Peptide agonist affinity

Heterologous whole-cell competition binding with ^{125}I -exendin-4(9–39) was performed to determine peptide agonist affinity for the WT and mutant GLP-1Rs. As reported previously (6), at the WT receptor exendin-4 had the highest affinity ($\text{pK}_i \approx 9.31$), followed by GLP-1 ($\text{pK}_i \approx 8.12$), whereas oxyntomodulin had the lowest affinity ($\text{pK}_i \approx 7.52$) (Table 1 and Fig. 2). No specific binding window could be established for the G132A mutant, despite good cell-surface expression by ELISA, or for the low-expressing mutants G27A, T29A, E128A, and E139A; for all others, competitive binding isotherms were established for each of the peptides. Of the far N-terminal ECD residues that exhibited specific binding, only the A28G mutation modified affinity (<5 -fold) for GLP-1 and exendin-4, with a similar

trend for oxyntomodulin (Figs. 2 and 3A and Table 1). Of the TM1/stalk residues, P137A, L141A, and Y148A mutations reduced affinity for each of the agonist peptides, whereas the P137A and L141A mutations also reduced affinity of the antagonist exendin-4(9–39). Ligand-specific reductions in affinity were seen for Q140A (exendin-4) and L142A (oxyntomodulin). All other mutations were without significant effect on peptide affinity (Figs. 2 and 3A and Table 1).

Agonist efficacy

Concentration-response curves for each of the peptides were established to determine agonist potency and maximal responses for canonical signaling endpoints, cAMP accumulation, $[\text{Ca}^{2+}]_i$ mobilization, and pERK1/2 (Figs. 3, B–D, and 4–6 and Tables 2–4). These data were subject to operational modeling (26) to determine affinity-independent measures of efficacy (τ for each pathway). The operational efficacy term “ τ ” is a measure of the number of receptors that need to be occupied to give a specified response. The τ values were normalized to receptor expression to derive a receptor expression-indepen-

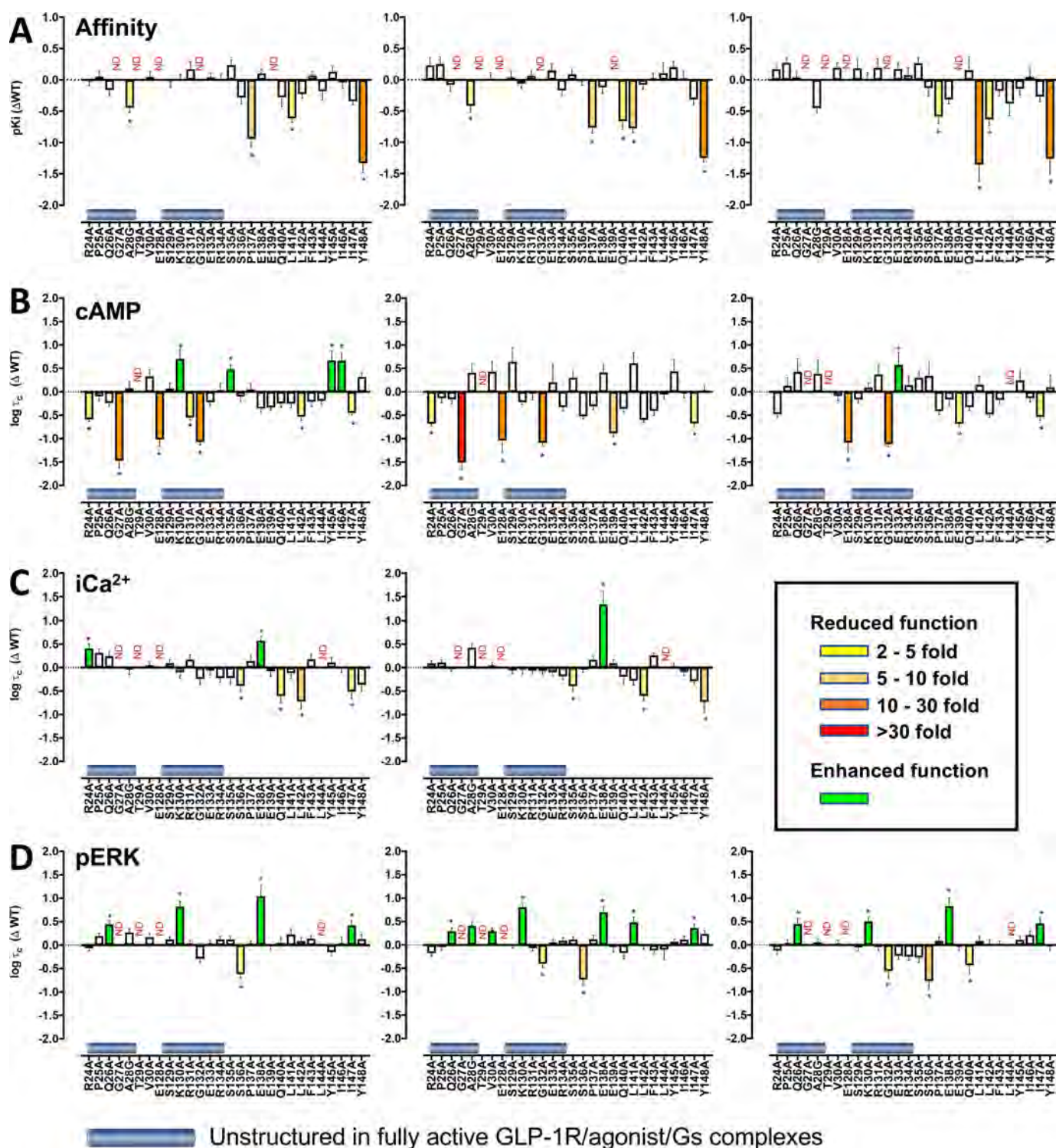


Figure 3. Changes in affinity (A) and efficacy (B–D) of the agonists GLP-1, exendin-4, and oxyntomodulin at mutant GLP-1Rs. A, pK_i values for the agonist peptides were derived from competition of [¹²⁵I]-exendin-4(9–39) binding. Data were plotted as differences in pIC_{50} of the alanine mutants compared with the wildtype (WT) hGLP-1R for GLP-1 (left panel), exendin-4 (middle panel), and oxyntomodulin (right panel). All pIC_{50} values were mean \pm S.E. of three independent experiments performed in triplicate. B–D, $\Delta \log \tau_c$ values are the difference in the coupling efficacy ($\log \tau_c$) for cAMP accumulation (B), [Ca^{2+}], mobilization (C), and ERK phosphorylation (pERK) (D) of the alanine mutant GLP-1Rs compared with the WT receptor for GLP-1 (left panels), exendin-4 (middle panels), and oxyntomodulin (right panels). All functional values are mean \pm S.E. of four to six independent experiments, conducted in duplicate. One-way ANOVA and Dunnett's post-test were performed to determined statistical differences (*, $p < 0.05$), and the bars are colored according to the fold-change between WT and mutant receptors (yellow, 2–5-fold decrease; light orange, 5–10-fold decrease; dark orange, 10–30-fold decrease; red, >30-fold decrease; green, increased affinity (A) or efficacy (B–D)). N.D., not defined.

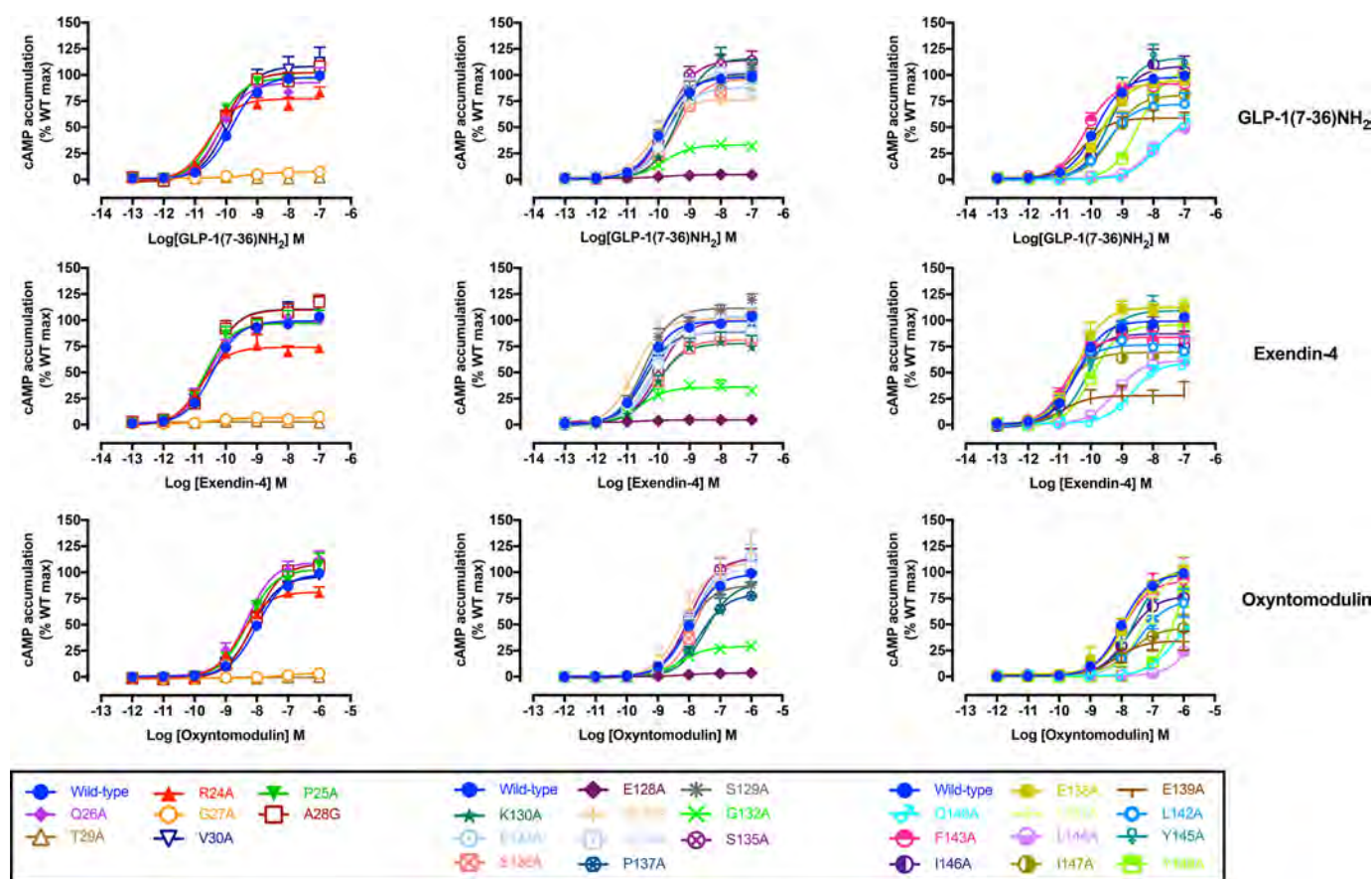


Figure 4. cAMP concentration-response curves for Ala mutants of the hGLP-1R N-terminal ECD and TM1 and linker region. Concentration-response curves for cAMP accumulation of WT and mutant receptors were stimulated by GLP-1(7–36)NH₂ (upper panels), exendin-4 (middle panels), or oxyntomodulin (lower panels) in CHO-Flp-In cells stably expressing WT or mutant receptors. Data were normalized to the response elicited by the WT and analyzed with an operational model of agonism. All values are means \pm S.E. of four to six independent experiments, conducted in duplicate.

dent and quantitative measure of pathway activation “ τ_c ” for individual peptides at each of the mutants (27, 28).

cAMP accumulation

Within the far N terminus of the ECD, mutants G27A and T29A that had poor expression displayed very weak to no measurable cAMP response. Unlike binding affinity, which was unaltered, the R24A mutant had reduced efficacy for GLP-1 and exendin-4 (Figs. 3B and 4 and Table 2). Within the TM1/ECD linker there was only limited correlation between effects on binding affinity and cAMP efficacy and on cAMP efficacy between peptides. E128A that was poorly expressed responded very weakly to all peptides. The I147A mutant induced modest loss of efficacy, and the G132A mutant exhibited 10–30-fold decreased efficacy for all peptides. The L142A mutant had a significantly attenuated efficacy for GLP-1, with similar fold decreases for exendin-4 and oxyntomodulin, although these latter effects did not achieve significance. The E139A mutant that had undetectable ¹²⁵I–exendin-4(9–39) binding had reduced efficacy with exendin-4 and to a lesser extent oxyntomodulin but not GLP-1. There were statistically significant increases in efficacy for oxyntomodulin at E133A, whereas K130A, S135A, Y145A, and I146A caused selective increases in GLP-1 efficacy, and R131A induced a weak and selective decrease in GLP-1 efficacy (Figs. 3B and 4 and Table 2).

iCa²⁺ mobilization

Because of relatively weak [Ca²⁺]_i mobilization by oxyntomodulin, only a single high concentration (~3 μ M) was assessed. For GLP-1 and exendin-4, no measurable response was seen at the poorly expressed G27A, T29A, and E128A mutants, whereas the E138A mutant exhibited increased efficacy for both peptides, even after correction for the higher cell-surface expression (Figs. 3C and 5 and Table 3). There was decreased efficacy for both peptides with the L142A mutant, whereas L144A abolished [Ca²⁺]_i mobilization, despite unaltered cAMP efficacy. There was selective loss of exendin-4 efficacy at the S135A and Y148A mutants and of GLP-1 efficacy at the S136A, Q140A, and I147A mutants, although these effects were relatively small (Figs. 3C and 5 and Table 3). There was also a weak and selective increase in GLP-1 efficacy at the R24A mutant, whereas the opposite effect was seen for GLP-1-dependent cAMP efficacy (Fig. 3, C versus B, and Tables 2 and 3). Of interest, although not quantitative, there was no measurable response for the single high concentration of oxyntomodulin at the P137A and Y148A mutants, despite approximately WT levels of cell-surface receptor expression and limited (for P137A) or no (Y148A) effect of the mutation on oxyntomodulin affinity (Fig. 3C and Table 1).

Table 2**Effects of human GLP-1R TM1/N-terminal mutants on agonist-mediated cAMP accumulation**

cAMP accumulation data were analyzed using a three-parameter logistic equation to determine pEC_{50} and E_{max} values. pEC_{50} is the negative logarithm of the molar concentration of agonist that induced half the maximal response. E_{max} for mutants is expressed as a percentage of wildtype. $Log \tau_c$ is the operational efficacy value (determined via the Black and Leff operational model (24)), corrected for cell-surface expression of GLP-1R. All values for cAMP accumulation are mean \pm S.E. of four to six independent experiments, conducted in duplicate. One-way ANOVA and Dunnett's post-test were used to determine statistical differences (*, $p < 0.05$). ND, not determined.

	Agonist-mediated cAMP accumulation								
	GLP-1(7–36)-NH ₂			Exendin-4			Oxyntomodulin		
	pEC_{50}	E_{max}	$Log \tau_c$	pEC_{50}	E_{max}	$Log \tau_c$	pEC_{50}	E_{max}	$Log \tau_c$
Wildtype	9.84 \pm 0.04	97.77 \pm 1.13	0.77 \pm 0.07	10.43 \pm 0.03	99.32 \pm 0.90	0.81 \pm 0.09	7.99 \pm 0.03	98.16 \pm 1.13	0.73 \pm 0.06
R24A	10.55 \pm 0.14*	77.09 \pm 2.92*	0.18 \pm 0.05*	10.83 \pm 0.16	74.16 \pm 3.10*	0.13 \pm 0.06*	8.52 \pm 0.11	81.17 \pm 2.99	0.25 \pm 0.06
P25A	10.33 \pm 0.08	97.02 \pm 2.21	0.67 \pm 0.10	10.67 \pm 0.18	97.12 \pm 4.65	0.67 \pm 0.10	8.29 \pm 0.11	102.90 \pm 4.26	0.86 \pm 0.18
Q26A	10.20 \pm 0.09	92.56 \pm 2.61	0.53 \pm 0.07	10.56 \pm 0.08	97.69 \pm 2.24	0.66 \pm 0.11	8.31 \pm 0.10	109.70 \pm 3.98	1.15 \pm 0.28
G27A	9.36 \pm 0.49	6.91 \pm 0.99*	−0.70 \pm 0.16*	10.39 \pm 0.57	6.62 \pm 0.94*	−0.70 \pm 0.16*	ND	ND	ND
A28G	10.14 \pm 0.10	102.20 \pm 3.14	0.84 \pm 0.15	10.51 \pm 0.12	110.00 \pm 3.61	1.22 \pm 0.19	8.10 \pm 0.07	108.20 \pm 3.07	1.13 \pm 0.30
T29A	ND	ND	ND	ND	ND	ND	ND	ND	ND
V30A	9.93 \pm 0.16	108.20 \pm 5.48	1.09 \pm 0.14	10.50 \pm 0.10	110.50 \pm 3.01	1.24 \pm 0.22	8.14 \pm 0.14	95.92 \pm 5.19	0.64 \pm 0.11
E128A	9.87 \pm 0.39	4.59 \pm 0.42*	−0.25 \pm 0.14*	10.62 \pm 0.72	4.63 \pm 0.48*	−0.22 \pm 0.25	8.08 \pm 0.53	4.15 \pm 0.83*	−0.35 \pm 0.20*
S129A	9.85 \pm 0.10	98.92 \pm 3.30	0.83 \pm 0.12	10.44 \pm 0.09	111.50 \pm 2.93	1.45 \pm 0.31*	8.10 \pm 0.11	87.57 \pm 3.84	0.57 \pm 0.07
K130A	9.35 \pm 0.09	116.20 \pm 3.83*	1.47 \pm 0.20*	10.05 \pm 0.18	77.74 \pm 4.44*	0.59 \pm 0.05	7.46 \pm 0.17	89.78 \pm 7.01	0.82 \pm 0.10
R131A	10.15 \pm 0.21	76.34 \pm 4.84*	0.22 \pm 0.05*	10.78 \pm 0.15	101.40 \pm 4.12	0.78 \pm 0.14	8.16 \pm 0.26	108.70 \pm 10.93	1.10 \pm 0.22
G132A	9.83 \pm 0.16	33.04 \pm 1.67*	−0.31 \pm 0.06*	10.58 \pm 0.25	35.90 \pm 2.36*	−0.28 \pm 0.06*	8.29 \pm 0.12	29.04 \pm 1.30*	−0.39 \pm 0.06*
E133A	9.74 \pm 0.17	87.76 \pm 4.92	0.55 \pm 0.07	10.09 \pm 0.16	103.40 \pm 5.28	1.01 \pm 0.38	7.90 \pm 0.11	110.50 \pm 5.20	1.30 \pm 0.26*
R134A	9.86 \pm 0.12	102.80 \pm 4.06	0.80 \pm 0.15	10.28 \pm 0.17	89.67 \pm 4.44	0.48 \pm 0.08	7.97 \pm 0.10	104.30 \pm 4.41	0.87 \pm 0.20
S135A	9.72 \pm 0.15	114.00 \pm 5.30*	1.24 \pm 0.11*	9.99 \pm 0.09	99.42 \pm 2.79	1.11 \pm 0.15	7.99 \pm 0.11	113.40 \pm 5.13	1.03 \pm 0.14
S136A	9.42 \pm 0.23	96.37 \pm 7.34	0.67 \pm 0.10	10.00 \pm 0.10	81.16 \pm 2.54*	0.29 \pm 0.05	7.70 \pm 0.10	116.20 \pm 5.12	1.07 \pm 0.33
P137A	9.64 \pm 0.12	101.30 \pm 3.90	0.82 \pm 0.13	10.45 \pm 0.29	88.74 \pm 7.37	0.50 \pm 0.07	7.65 \pm 0.20	79.11 \pm 6.64	0.32 \pm 0.07
E138A	9.63 \pm 0.15	94.25 \pm 4.49	0.41 \pm 0.08	10.46 \pm 0.14	112.30 \pm 4.24*	1.22 \pm 0.18	7.86 \pm 0.16	100.40 \pm 6.56	0.57 \pm 0.13
E139A	10.29 \pm 0.19	58.81 \pm 3.12*	0.43 \pm 0.06	10.90 \pm 0.51	28.03 \pm 3.75*	−0.08 \pm 0.07*	8.16 \pm 0.31	34.23 \pm 3.94*	0.04 \pm 0.06*
Q140A	7.91 \pm 0.15*	59.59 \pm 5.48*	0.52 \pm 0.08	8.68 \pm 0.14*	59.75 \pm 3.60*	0.45 \pm 0.07	6.32 \pm 0.18*	63.82 \pm 9.80	0.40 \pm 0.07
L141A	9.68 \pm 0.18	95.20 \pm 5.60	0.51 \pm 0.09	10.43 \pm 0.12	113.20 \pm 3.68*	1.42 \pm 0.23	7.22 \pm 0.18*	106.90 \pm 10.38	0.88 \pm 0.18
L142A	9.48 \pm 0.19	72.12 \pm 4.84*	0.24 \pm 0.08*	10.79 \pm 0.27	76.65 \pm 5.75*	0.21 \pm 0.05	7.41 \pm 0.18	72.94 \pm 5.98	0.25 \pm 0.08
F143A	10.18 \pm 0.13	91.47 \pm 3.55	0.56 \pm 0.11	10.78 \pm 0.21	84.00 \pm 4.91*	0.41 \pm 0.10	7.96 \pm 0.24	91.72 \pm 9.10	0.56 \pm 0.10
L144A	8.03 \pm 0.18*	53.89 \pm 5.51*	0.57 \pm 0.07	8.90 \pm 0.14*	68.52 \pm 3.71*	0.75 \pm 0.09	ND	ND	ND
Y145A	9.36 \pm 0.13	116.40 \pm 5.51*	1.44 \pm 0.21*	10.00 \pm 0.09	109.30 \pm 3.28	1.25 \pm 0.25	7.57 \pm 0.11	103.90 \pm 4.88	0.98 \pm 0.22
I146A	9.41 \pm 0.16	108.30 \pm 6.35	1.43 \pm 0.18*	10.55 \pm 0.21	87.23 \pm 5.09	0.78 \pm 0.10	7.79 \pm 0.27	77.14 \pm 8.62	0.59 \pm 0.07
I147A	9.34 \pm 0.20	80.68 \pm 5.54*	0.32 \pm 0.05*	10.83 \pm 0.39	69.46 \pm 7.47*	0.14 \pm 0.07*	7.74 \pm 0.36	46.61 \pm 6.97	0.19 \pm 0.07*
Y148A	8.45 \pm 0.12*	106.20 \pm 6.02	1.08 \pm 0.07	9.96 \pm 0.29	95.57 \pm 9.29	0.84 \pm 0.10	5.95 \pm 0.50*	173.10 \pm 106.70*	0.83 \pm 0.27

ERK1/2 phosphorylation

As seen with the other pathways, the poorly expressed mutants G27A, T29A, and E128A had no measurable pERK response to any of the peptides. For the far N-terminal ECD mutations, there was a slightly increased efficacy for all peptides with the Q26A mutant and a selective weak increase in efficacy for exendin-4 at the A28G and V30A mutants (Figs. 3D and 6 and Table 4). For the TM1/ECD linker, there was increased efficacy for all three peptides at the K130A, E138A and I147A mutants and decreased efficacy at the S136A mutant. A weak loss of efficacy for exendin-4 and oxyntomodulin, but not GLP-1, occurred with the G132A mutant, whereas the L144A mutant abolished pERK response to GLP-1 and oxyntomodulin but did not alter efficacy for exendin-4. Of the remaining mutants, only L141A (increased exendin-4 efficacy) and Q140A (weak loss of oxyntomodulin efficacy) had any significant effect (Figs. 3D and 6 and Table 4).

Discussion**Structural insights into GLP-1R biased agonism**

Our results indicate that the far N terminus and the linker region between TM1 and the ECD play discrete roles in receptor stability and expression and in peptide-specific signaling. Recent advances in structural determination for class B GPCRs and particularly the GLP-1R provide an unprecedented opportunity to map key surface residues in three-dimensional space relevant to both inactive and active structures. For the GLP-1R,

four new structures have recently been solved, which include a modified human GLP-1R TM domain structure bound to negative allosteric modulators (NAMs) (14), a thermostabilized full-length human GLP-1R bound to a modified 11-mer agonist peptide (15), a fully active rabbit GLP-1R in complex with GLP-1 and the heterotrimeric G_s protein (16), and human GLP-1R in complex with the biased agonist, exendin-P5, and the G_s protein (17). Details of structures, including differences from WT human GLP-1R, are described in Table 5. This work complements the previously published inactive structures of the related GCGR (29, 30). The NAM-bound GLP-1R contains structural alterations, including an introduced cysteine bridge between TM helices 5 and 6, that disrupt key networks of the native inactive receptor. As such, we have used the inactive GCGR (PDB code 4L6R) (29) as a template to model the inactive GLP-1R (Fig. 1A) (28). The active rabbit GLP-1R complex has a global resolution of 4.1 Å, with limited side-chain resolution and ambiguity in potential modeling of ECLs, whereas the exendin-P5–GLP-1R complex has a global resolution of 3.3 Å with good side-chain resolution for most of the receptor; we have used this structure as the principal template for comparative mapping of the effects of mutations between active and inactive states (Fig. 1A). All full-length structures lack density for residues 24–28 of the far N terminus, indicating that this segment is flexible upon ligand binding. However, the position of Val-30 that is resolved in the structures suggests that the far N-terminal residues likely make transient interactions with

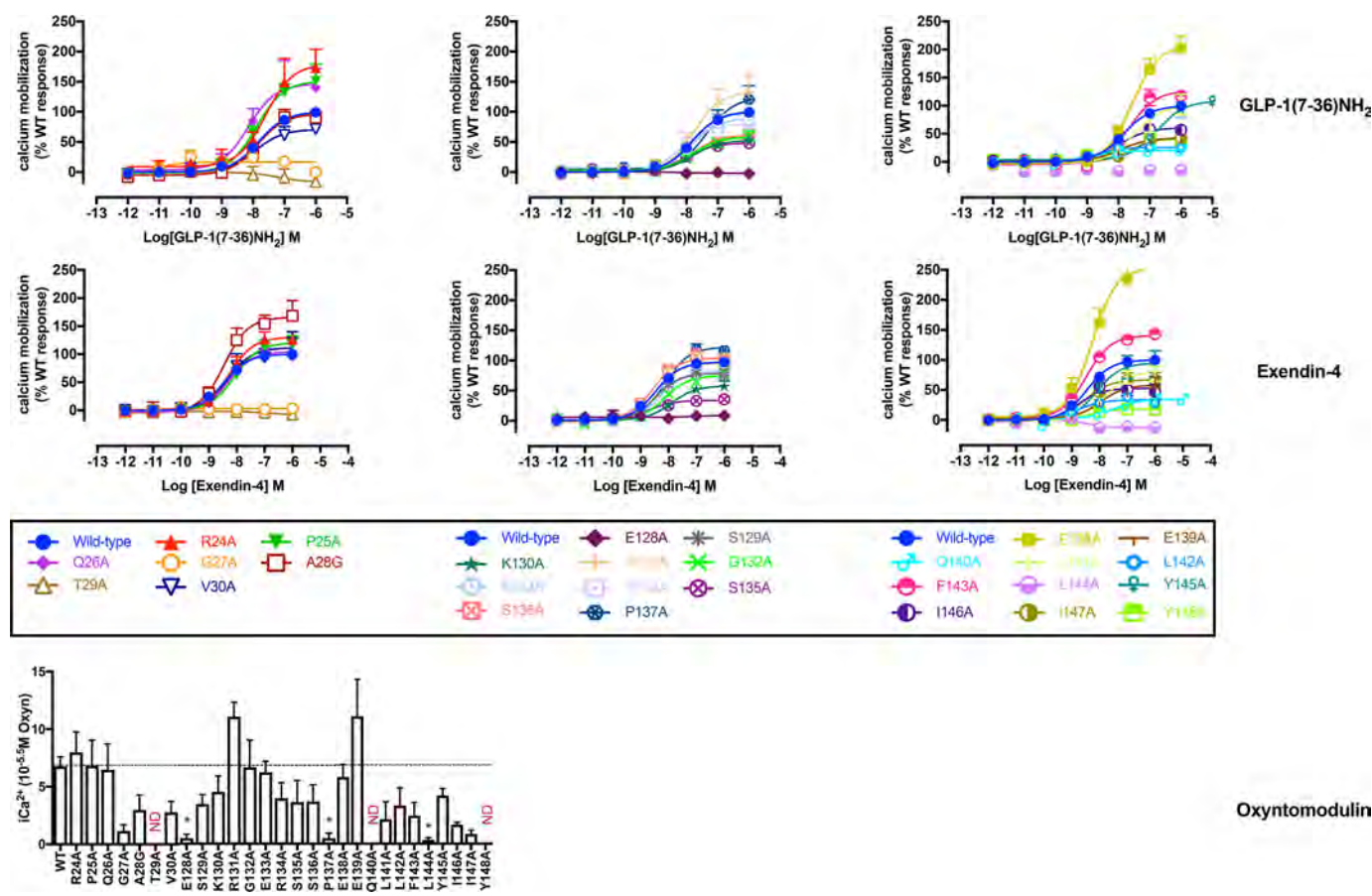


Figure 5. $[Ca^{2+}]_i$ mobilization concentration-response curves for Ala mutants of the hGLP-1R N-terminal ECD and TM1 and linker region. Concentration-response curves of $[Ca^{2+}]_i$ mobilization of WT and mutant receptors were stimulated by GLP-1(7–36)NH₂ (upper panels), exendin-4 (middle panels), or oxyntomodulin (lower panels) in CHO-Flp-In cells stably expressing WT or mutant receptors. Data were normalized to the response elicited by the WT and analyzed with an operational model of agonism. All values are means \pm S.E. of four to six independent experiments, conducted in duplicate.

ECLs 2 and 3 and/or the peptide agonist (Fig. 7). The new data are considered holistically consistent with previously published ECL alanine-scanning mutagenesis studies (11, 13) to yield a comprehensive structure-function analysis of signal propagation networks in the GLP-1R. Nonetheless, as with all such structure-function analyses, our observations are influenced by the recombinant cellular environment, including the relative expression of transducer and regulatory proteins that will differ from endogenous sites of receptor expression.

Structural reorganization upon receptor activation

ECD–receptor core interactions—There is accumulating evidence that interactions between the ECD and TM core of class B GPCRs contribute to receptor quiescence and peptide-mediated receptor activation (20, 21, 31). For the related GCGR, interactions of the far N terminus and the residues in ECL3 contribute to maintenance of a quiescent state (20), although ground state interactions at the intracellular face also play a key role (22, 32, 33). As noted above, the far N terminus is dynamic in peptide-bound states (15, 16), making interpretation of mutations in the context of available structures difficult. The dramatic loss of cell-surface expression for G27A and T29A is indicative of the important roles of these amino acids in receptor stability, potentially via loss of stabilizing interaction between Thr-29 and the receptor core that would be consistent

with a role of the far N terminus in maintaining receptor quiescence. Nevertheless, the GLP-1R is expressed at the cell surface when the full ECD is truncated (31), suggesting that loss of receptor expression is due to destabilizing interactions of the modified ECD. Glycines provide structural flexibility, and Gly-27 may be required for favorable positioning of Thr-29. In the active GLP-1- and exendin-P5–bound receptors, Thr-29 is proximal to the peptide ligand, although not within hydrogen-bonding distance. In the structure of the modified 11-mer bound receptor, the position of the ECD is not constrained by peptide binding, where Thr-29 interacts with the linker between TM1 and the ECD (Fig. 7B).

Class B GPCRs, including the GLP-1R, exhibit an extracellular-oriented V-shape cavity within the TM bundle that provides domain separation of the external facing segments of TMs 1, 7, and 6, and TMs 2–5 (Fig. 8A). Nonetheless, in the inactive model, there are key hydrogen-bonded interactions between Asp-198 of TM2 and Tyr-145, Tyr-148, and Thr-149 of TM1 that coordinate Tyr-145 and Tyr-148 away from TM7 (Fig. 9A), and this facilitates tight packing of TMs 1 and 7. Consistent with this, D198A mutation leads to marked loss of receptor expression and/or GLP-1-stimulated cAMP signaling (34–36). In the active, exendin-P5–bound structure, this hydrogen bond network is weakened, with loss of interactions between Asp-

Table 3**Effects of human GLP-1R TM1/N-terminal mutants on agonist-mediated $[Ca^{2+}]_i$ mobilization**

$[Ca^{2+}]_i$ mobilization data were analyzed using a three-parameter logistic equation to determine pEC_{50} and E_{max} values. pEC_{50} is the negative logarithm of the molar concentration of agonist that induced half the maximal response. E_{max} for mutants is expressed as a percentage of wildtype. $Log\tau_c$ is the operational efficacy value (determined via the Black and Leff operational model (24)), corrected for cell-surface expression of GLP-1R. All values for cAMP accumulation are mean \pm S.E. of four to six independent experiments, conducted in duplicate. One-way ANOVA and Dunnett's post-test were used to determine statistical differences (*, $p < 0.05$). ND, not determined.

	Agonist-mediated intracellular calcium mobilization					
	GLP-1(7–36)-NH ₂			Exendin-4		
	pEC_{50}	E_{max}	$Log\tau_c$	pEC_{50}	E_{max}	$Log\tau_c$
Wildtype	7.83 \pm 0.04	100.00 \pm 1.11	−0.22 \pm 0.03	8.45 \pm 0.04	100.00 \pm 1.35	−0.22 \pm 0.02
R24A	7.60 \pm 0.27	179.60 \pm 20.27*	0.19 \pm 0.10*	8.25 \pm 0.12	130.40 \pm 5.76*	−0.12 \pm 0.05
P25A	7.89 \pm 0.17	151.30 \pm 11.07*	0.09 \pm 0.09	8.07 \pm 0.14	120.50 \pm 6.80*	−0.11 \pm 0.05
Q26A	8.14 \pm 0.29	146.40 \pm 16.50*	0.02 \pm 0.09	8.31 \pm 0.12	104.50 \pm 4.87	−0.24 \pm 0.05
G27A	ND	16.77 \pm 4.36*	ND	ND	ND	ND
A28G	7.86 \pm 0.14	96.66 \pm 5.98	−0.27 \pm 0.10	8.45 \pm 0.19	165.90 \pm 11.23*	0.21 \pm 0.09
T29A	ND	ND	ND	ND	ND	ND
V30A	7.93 \pm 0.24	70.75 \pm 7.07*	0.17 \pm 0.07	8.31 \pm 0.24	111.50 \pm 9.64	−0.17 \pm 0.06
E128A	ND	ND	ND	ND	ND	ND
S129A	7.83 \pm 0.12	101.30 \pm 5.03	−0.13 \pm 0.07	8.47 \pm 0.19	80.73 \pm 5.52	−0.27 \pm 0.06
K130A	7.83 \pm 0.18	52.81 \pm 4.09*	−0.32 \pm 0.13	7.89 \pm 0.17	59.33 \pm 4.30*	−0.25 \pm 0.11
R131A	7.76 \pm 0.25	133.80 \pm 14.52*	−0.05 \pm 0.11	8.50 \pm 0.24	98.00 \pm 8.13	−0.28 \pm 0.07
G132A	7.79 \pm 0.20	58.45 \pm 4.75*	−0.47 \pm 0.13	8.14 \pm 0.23	76.96 \pm 7.21*	−0.29 \pm 0.07
E133A	7.84 \pm 0.18	89.51 \pm 6.77	−0.28 \pm 0.10	8.30 \pm 0.21	84.37 \pm 6.62	−0.31 \pm 0.06
R134A	8.15 \pm 0.32	79.99 \pm 9.90	−0.44 \pm 0.09	8.36 \pm 0.19	84.59 \pm 5.60	−0.40 \pm 0.06
S135A	7.99 \pm 0.20	48.35 \pm 3.85*	−0.44 \pm 0.15	8.71 \pm 0.22	34.19 \pm 2.48*	−0.61 \pm 0.11*
S136A	7.81 \pm 0.18	61.68 \pm 4.72*	−0.61 \pm 0.12*	8.56 \pm 0.16	106.70 \pm 5.75	−0.26 \pm 0.06
P137A	7.35 \pm 0.25	124.00 \pm 14.18	0.08 \pm 0.12	8.13 \pm 0.10	126.00 \pm 5.21	−0.04 \pm 0.08
E138A	7.56 \pm 0.13	209.20 \pm 11.92*	0.35 \pm 0.10*	8.27 \pm 0.20	253.40 \pm 18.09*	1.13 \pm 0.27*
E139A	7.94 \pm 0.20	42.50 \pm 3.51*	−0.30 \pm 0.11	7.94 \pm 0.21*	58.47 \pm 4.87*	−0.12 \pm 0.08
Q140A	8.89 \pm 0.30*	20.06 \pm 2.38*	−0.83 \pm 0.14*	7.49 \pm 0.42*	34.38 \pm 4.54*	−0.41 \pm 0.17
L141A	7.49 \pm 0.25	101.00 \pm 11.56	−0.34 \pm 0.11	7.79 \pm 0.18	80.46 \pm 6.34	−0.49 \pm 0.09
L142A	8.74 \pm 0.32*	25.97 \pm 2.71*	−0.95 \pm 0.17*	8.77 \pm 0.23	33.56 \pm 2.55*	−0.82 \pm 0.11*
F143A	7.65 \pm 0.12	127.20 \pm 7.06	−0.05 \pm 0.11	8.48 \pm 0.08	140.70 \pm 3.98*	0.05 \pm 0.05
L144A	ND	ND	ND	ND	ND	ND
Y145A	6.76 \pm 0.20*	108.50 \pm 10.35	−0.12 \pm 0.12	8.10 \pm 0.25	94.96 \pm 9.30	−0.19 \pm 0.09
I146A	7.97 \pm 0.19	60.52 \pm 4.60*	−0.23 \pm 0.10	8.80 \pm 0.28	52.91 \pm 5.09*	−0.30 \pm 0.07
I147A	7.60 \pm 0.22	44.28 \pm 4.42*	−0.73 \pm 0.15*	8.50 \pm 0.28	66.87 \pm 6.33*	−0.51 \pm 0.07
Y148A	7.99 \pm 0.25	40.42 \pm 3.79*	−0.59 \pm 0.14	8.30 \pm 0.21	18.91 \pm 1.50*	−0.95 \pm 0.22*

198 and both Tyr-148 and Thr-149, facilitating the movement of TM1 toward TM7, whereas the kink in TM1 is stabilized by hydrogen bonding of the side chain of Thr-149 with the backbone oxygen of Tyr-145 (Fig. 9B). A similar pattern of interaction is observed in the 11-mer bound structure (Fig. 9E). Although the position of the kink in TM1 of the GLP-1/GLP-1R structure is likely conserved (17) (although modeled differently in 5VAI), there is further loss of the interaction between Tyr-145 and Asp-198, and this leads to an anti-clockwise rotation of the upper end of TM1, with a parallel rotation of TM7 that is not seen in the exendin-P5 structure (Fig. 9, B and C). This likely contributes to the distinct conformation of ECL3 between the GLP-1- and exendin-P5-bound structures that has been linked to efficacy differences of the two peptides (17).

Both Tyr-148 and Thr-149 (37, 38) play important roles in peptide agonist affinity but do not make direct interactions with GLP-1 in the active structure, and the same is true for P137A and L141A in the TM1 stalk. Thus, these residues contribute to the reorganization of TM1 and packing with TM7. These changes are also likely to impact the position of Glu-139. Mutation of this amino acid causes loss of exendin-4(9–39) binding. In the GLP-1-bound active structure, the side chain of Glu-139 is directed toward the GLP-1 peptide, suggesting a direct interaction that may be more prevalent for the truncated exendin peptide (and indeed, this is observed in the exendin-P5/GLP-1R/G_s structure (17)). This would be consistent with the lack of effect of the E139A mutant on GLP-1 signaling, and only limited attenuation of oxyntomodulin and exendin-4-mediated

cAMP production (Fig. 3). Of the TM1 stalk residues, only mutations to Thr-149 also translate into a major impact on signaling (37, 38), implying that its role in structural reorganization is also critical for activation transition and effector binding. This loss can be recovered by allosteric modulator binding at the intracellular face of the receptor that is predicted to destabilize ground state interactions at the base of the receptor (14, 37, 38).

In the active and G_s protein-complexed receptor structures, the linker region between the ECD and the core is poorly resolved, suggesting a high degree of flexibility even when the peptide is bound. In the inactive GCGR (PDB 4L6R) (29), the TM1 stalk is present as an extended α -helix, and although this may be partially due to crystal-packing artifacts, an extended α -helix is also present in the structure of the full-length GCGR bound to a partial agonist peptide, NNC1702 (Fig. 7) (18). This suggests that order to disorder transition of the TM1 stalk may be required for full receptor activation. Indeed, this would be required to accommodate the movement of TM1 toward TM7, seen in the active and active-like structures. An important role for the TM1 stalk is supported by our current mutagenesis data (Fig. 3). Polar residues in this region, particularly Ser-136, Lys-130, and Glu-138, had effects on peptide signaling in a pathway- and peptide-specific manner, indicating that formation and disruption of interactions formed by these amino acids contribute to conformational transition for activation. Similar behavior was seen for the G132A mutant, suggesting that backbone flexibility plays a role in these effects. Somewhat surprisingly, E128A had a profound effect on receptor expression, presum-

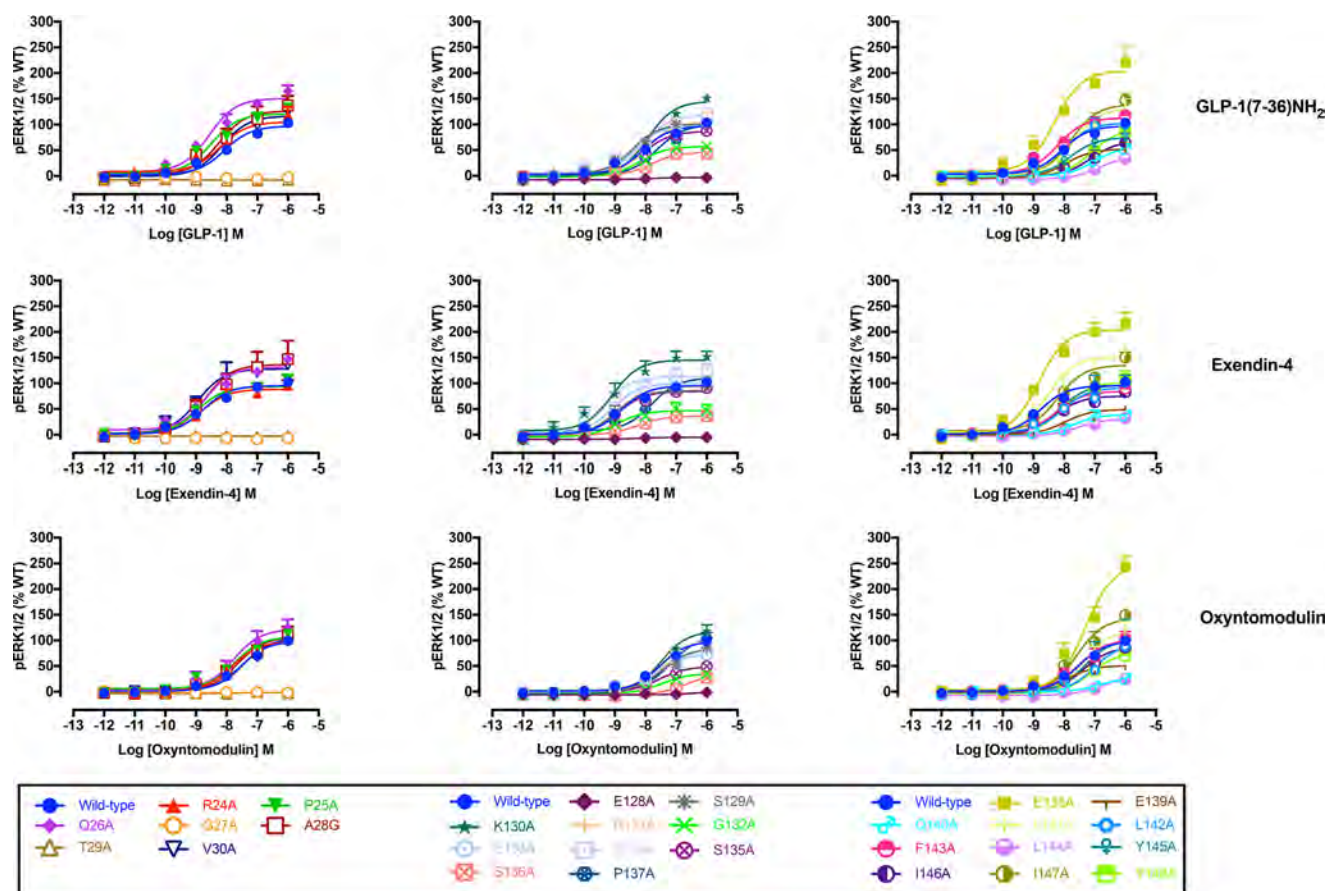


Figure 6. pERK1/2 concentration-response curves for Ala mutants of the hGLP-1R N-terminal ECD and TM1 and linker region. Concentration-response curves of pERK of WT and mutant receptors were stimulated by GLP-1(7–36)-NH₂ (upper panels), exendin-4 (middle panels), or oxyntomodulin (lower panels) in CHO-Flp-In cells stably expressing WT or mutant receptors. Data were normalized to the response elicited by the WT and analyzed with an operational model of agonism. All values are means \pm S.E. of four to six independent experiments, conducted in duplicate.

ably via destabilization of the receptor protein, in a similar manner to that observed for the T29A mutant. Although speculative, it is possible that these amino acids are in close proximity in the inactive receptor and form part of an important network that stabilizes this state. In studies where E128A is further over-expressed by transient expression, there is a <3 -fold loss of GLP-1 potency and an ~ 5 -fold loss of exendin-4 potency for cAMP production (39), consistent with a limited role of this residue for peptide binding.

In the inactive homology model, the deeper binding cavity occupied by agonist peptides is capped by a series of large aromatic residues, particularly Trp-297 and Tyr-305 (Fig. 8, *B* and *C* versus *D* and *E*), whose position is predicted to be stabilized by H-bonding. In the active structure, these amino acids undergo large-scale movements associated with reorganization of ECL2 that reorients Trp-297 away from the binding pocket, where it forms interactions with other ECL2 residues, accompanied by small outward movements of Arg-299 and Asn-300 that directly contact the peptide in the active structure. Release of ground state interactions in the inactive ECL2 loop structure enables unwinding of the top of TM6 with an $\sim 180^\circ$ rotation of Tyr-305 accompanied by an ~ 9 -Å displacement of the α carbon. Previous molecular dynamics simulations on the inactive GLP-1R model suggested that this aromatic cap provided a significant energy barrier to deeper entry of the GLP-1 N

terminus, with entry facilitated by Glu-9 of the peptide that forms a salt bridge with Arg-190 of the receptor (11). Intriguingly, mutation of Trp-297 and the adjacent Cys-296 (that is covalently linked to Cys-226 in TM3) markedly attenuated GLP-1 and exendin-4 affinity, but it did not impact oxyntomodulin affinity. Oxyntomodulin contains an uncharged Gln, positionally equivalent to GLP-1 Glu-9, and does not interact with Arg-190 in the receptor core (11). It is therefore possible that oxyntomodulin binds in a shallower orientation. A significant and selective decrease in oxyntomodulin affinity for F381A, L142A, and K202A mutants and lack of an effect for the R380A mutant are consistent with this hypothesis (Fig. 10).

Peptide-mediated signaling and bias—Comparison of the position of mutated residues that affect GLP-1-mediated cAMP formation between fully active and inactive models reveals two major networks involved in GLP-1R function (Figs. 10 and 11). The first includes residues of ECL2 and the membrane-proximal TM regions and the proximal segment of ECL3. K288A impacted ligand binding and was critical for propagation of cAMP signaling (13, 24, 40). It stabilizes the center of the ECL2 network and may coordinate interactions between the ECL2 residues. Both exendin-4 and oxyntomodulin were similarly affected by mutations to ECL2 indicating a general role in propagation of cAMP signaling (Figs. 10 and 11). Despite the lack of effect of W297A on oxyntomodulin binding,

Table 4**Effects of human GLP-1R TM1/N-terminal mutants on agonist-mediated pERK1/2**

pERK1/2 phosphorylation data were analyzed using a three-parameter logistic equation to determine pEC_{50} and E_{max} values. pEC_{50} is the negative logarithm of the molar concentration of agonist that induced half the maximal response. E_{max} for mutants is expressed as a percentage of wildtype. $Log\tau_c$ is the operational efficacy value (determined via the Black and Leff operational model (24)), corrected for cell-surface expression of GLP-1R. All values for cAMP accumulation are mean \pm S.E. of four to six independent experiments, conducted in duplicate. One-way ANOVA and Dunnett's post-test were used to determine statistical differences (*, $p < 0.05$). ND, not determined.

	Agonist-mediated ERK1/2 phosphorylation								
	GLP-1(7–36)-NH ₂			Exendin-4			Oxyntomodulin		
	pEC_{50}	E_{max}	$Log\tau_c$	pEC_{50}	E_{max}	$Log\tau_c$	pEC_{50}	E_{max}	$Log\tau_c$
Wildtype	8.07 \pm 0.05	100.00 \pm 1.87	0.03 \pm 0.02	8.77 \pm 0.05	98.37 \pm 1.56	0.02 \pm 0.02	7.53 \pm 0.04	101.40 \pm 1.64	0.05 \pm 0.03
R24A	8.21 \pm 0.19	108.50 \pm 7.64	−0.03 \pm 0.06	8.83 \pm 0.18	90.87 \pm 5.55	−0.16 \pm 0.07	7.82 \pm 0.11	100.40 \pm 4.85	−0.07 \pm 0.07
P25A	8.51 \pm 0.13	125.30 \pm 5.34	0.22 \pm 0.06	8.95 \pm 0.18	96.53 \pm 5.67	−0.03 \pm 0.06	7.73 \pm 0.14	110.80 \pm 6.22	0.09 \pm 0.07
Q26A	8.57 \pm 0.16	157.30 \pm 7.93*	0.47 \pm 0.08*	8.68 \pm 0.16	137.30 \pm 7.13*	0.31 \pm 0.08*	7.76 \pm 0.22	126.10 \pm 12.12	0.49 \pm 0.12*
G27A	ND	ND	ND	ND	ND	ND	ND	ND	ND
A28G	8.25 \pm 0.24	131.40 \pm 11.84*	0.30 \pm 0.08	8.71 \pm 0.29	142.10 \pm 13.91*	0.42 \pm 0.09*	7.66 \pm 0.20	110.20 \pm 9.56	0.11 \pm 0.08
T29A	ND	ND	ND	ND	ND	ND	ND	ND	ND
V30A	8.16 \pm 0.12	120.80 \pm 5.95	0.20 \pm 0.07	8.96 \pm 0.23	132.90 \pm 10.41*	0.31 \pm 0.07*	7.45 \pm 0.11	107.80 \pm 5.45	0.07 \pm 0.08
E128A	ND	ND	ND	ND	ND	ND	ND	ND	ND
S129A	8.42 \pm 0.12	104.10 \pm 4.55	0.15 \pm 0.06	9.00 \pm 0.17	87.98 \pm 5.16	0.01 \pm 0.06	7.45 \pm 0.15	86.48 \pm 5.89	−0.004 \pm 0.08
K130A	7.93 \pm 0.08	151.20 \pm 5.17*	0.85 \pm 0.11*	9.08 \pm 0.21	151.40 \pm 9.84*	0.83 \pm 0.09*	7.51 \pm 0.12	122.50 \pm 6.66	0.55 \pm 0.09*
R131A	7.93 \pm 0.16	109.70 \pm 7.47	0.06 \pm 0.07	8.88 \pm 0.13	96.88 \pm 4.49	−0.05 \pm 0.06	7.50 \pm 0.16	104.10 \pm 7.36	0.005 \pm 0.08
G132A	8.19 \pm 0.17	57.61 \pm 4.22*	−0.26 \pm 0.08	8.93 \pm 0.29	46.60 \pm 5.30*	−0.38 \pm 0.09*	7.45 \pm 0.24	35.06 \pm 4.55*	−0.51 \pm 0.15*
E133A	8.37 \pm 0.13	101.80 \pm 5.00	0.07 \pm 0.06	9.08 \pm 0.15	102.90 \pm 5.02	0.07 \pm 0.06	7.76 \pm 0.17	72.90 \pm 5.38	−0.19 \pm 0.08
R134A	8.09 \pm 0.13	122.30 \pm 6.33	0.15 \pm 0.07	9.36 \pm 0.21	116.90 \pm 7.21	0.11 \pm 0.06	7.63 \pm 0.16	79.86 \pm 5.78	−0.20 \pm 0.08
S135A	8.06 \pm 0.18	88.91 \pm 6.40	0.15 \pm 0.07	8.90 \pm 0.19	86.39 \pm 5.43	0.13 \pm 0.06	7.57 \pm 0.14	48.80 \pm 3.35*	−0.22 \pm 0.10
S136A	7.81 \pm 0.16	45.74 \pm 3.36*	−0.58 \pm 0.10*	8.26 \pm 0.16	35.37 \pm 2.32*	−0.72 \pm 0.13*	6.73 \pm 0.25*	32.54 \pm 6.85*	−0.73 \pm 0.16*
P137A	7.64 \pm 0.15	102.70 \pm 6.67	0.05 \pm 0.07	7.80 \pm 0.25*	114.50 \pm 11.67	0.14 \pm 0.08	7.17 \pm 0.16	112.30 \pm 9.51	0.13 \pm 0.09
E138A	8.29 \pm 0.21	214.30 \pm 16.04*	1.07 \pm 0.24*	8.82 \pm 0.13	214.00 \pm 9.04*	0.71 \pm 0.13*	7.30 \pm 0.16	258.30 \pm 20.51*	0.88 \pm 0.18*
E139A	7.95 \pm 0.20	52.17 \pm 4.96*	0.02 \pm 0.08	7.98 \pm 0.24*	48.99 \pm 5.12*	−0.02 \pm 0.11	7.90 \pm 0.18	51.16 \pm 4.23*	0.01 \pm 0.08
Q140A	7.02 \pm 0.21*	57.35 \pm 7.44*	0.08 \pm 0.11	7.70 \pm 0.31*	38.88 \pm 5.68*	−0.15 \pm 0.12	6.78 \pm 0.26*	27.40 \pm 5.10*	−0.39 \pm 0.19*
L141A	7.71 \pm 0.11	137.10 \pm 6.84*	0.26 \pm 0.09	8.52 \pm 0.13	158.10 \pm 6.82*	0.50 \pm 0.11*	7.30 \pm 0.18	126.10 \pm 11.22	0.13 \pm 0.10
L142A	8.00 \pm 0.16	106.40 \pm 6.71	0.12 \pm 0.06	8.05 \pm 0.17*	94.20 \pm 6.46	0.00 \pm 0.08	7.03 \pm 0.19	97.49 \pm 11.29	0.06 \pm 0.10
F143A	8.22 \pm 0.16	116.70 \pm 6.85	0.17 \pm 0.06	8.24 \pm 0.28	86.81 \pm 9.12	−0.10 \pm 0.07	7.50 \pm 0.22	104.80 \pm 10.36	0.06 \pm 0.08
L144A	ND	ND	ND	7.57 \pm 0.36*	29.28 \pm 5.54*	−0.08 \pm 0.21	ND	ND	ND
Y145A	7.78 \pm 0.41	76.36 \pm 13.92	−0.12 \pm 0.06	8.13 \pm 0.28*	99.84 \pm 11.07	0.08 \pm 0.06	7.32 \pm 0.46	106.00 \pm 24.78	0.15 \pm 0.09
I146A	7.14 \pm 0.34*	68.81 \pm 13.41*	0.07 \pm 0.13	8.30 \pm 0.22	76.61 \pm 6.48	0.13 \pm 0.08	7.38 \pm 0.18	89.57 \pm 8.13	0.26 \pm 0.08
I147A	7.77 \pm 0.16	144.90 \pm 9.75*	0.45 \pm 0.11*	8.21 \pm 0.12	140.80 \pm 6.46*	0.38 \pm 0.09*	7.58 \pm 0.17	149.10 \pm 11.18*	0.51 \pm 0.11*
Y148A	7.11 \pm 0.21*	93.43 \pm 11.28	0.16 \pm 0.11	8.01 \pm 0.20*	105.60 \pm 8.68	0.25 \pm 0.07	7.12 \pm 0.17	78.45 \pm 7.84	0.03 \pm 0.10

Table 5**Sequence variations in published structures**

PDB code	Description	Structure fragment	Mutations/differences from hGLP-1R	Missing residues in the structure
5VEW (Song <i>et al.</i> 14)	Crystal structure of human GLP-1R transmembrane domain in complex with negative allosteric modulator PF-06372222	Residues 128–431. Residues 258–260 at intracellular loop 2 were replaced with T4 lysozyme. Residues 205–214 from ECL1 were replaced by a GSG linker	S193C, I196F, Y205G, Δ Thr-207, Δ Ala-208, Δ Ala-209, Δ Gln-210, Δ Gln-211, Δ His-212, Δ Gln-213, W214G, S225A, M233X, S271A, I317C, G318I, K346A, C347F, G361C	Glu-128, Ser-129, Lys-130, Arg-131, Gly-132, Glu-133, Arg-134, Ser-135, Met-204, Asp-215, Glu-373, His-374, Ala-375, Arg-376, Gly-377, Thr-378, Leu-379, Glu-423, His-424, Leu-425, His-426, Ile-427, Gln-428, Arg-429, Asp-430, Ser-431
5NX2 (Jazayeri <i>et al.</i> 15)	Crystal structure of human GLP-1 receptor bound to the 11-mer agonist peptide 5	Residues 24–432	T207E, Q211A, D215R, L232F, L260F, G295A, T298A, C329A, P358A, G361A, H363V, V405A	Arg-24, Pro-25, Gln-26, Gly-27, Ala-28, Glu-418, Arg-419, Trp-420, Arg-421, Leu-422, Glu-423, His-424, Leu-425, His-426, Ile-427, Gln-428, Arg-429, Asp-430, Ser-431, Ser-432
5VAI (Zhang <i>et al.</i> 16)	Cryo-EM structure of active rabbit GLP-1 receptor in complex with GLP-1 and G _s protein	Residues 24–422	T106A, H112P, Q140R	Arg-24, Pro-25, Gln-26, Gly-27, Ala-28, Ser-129, Arg-130, Arg-131, Gly-132, Glu-133, Ser-134, Leu-422
6B3J (Liang <i>et al.</i> 17)	Cryo-EM structure of active human GLP-1 receptor in complex with exendin-P5 and G _s protein	Residues 23–466	None	Ala-23–Thr-29, Ser-129–Ser-136, Asn-338–Thr-342, His-424–Gly-466

it was crucial for signaling of all three peptides. In the active agonist-bound calcitonin receptor, there is a high degree of overlap in the structural organization of ECL2 despite considerable sequence variation; Arg-281 that is positionally equivalent to Lys-288 of the GLP-1R appears to play a similar coordinating role in maintenance of this structure (19, 25). The organization of the ECL2 network is also required for calcium

signaling, although it does not appear as important for peptide-mediated pERK (Figs. 10 and 11).

The second network involves residues in TM1 and the TM7 proximal residues of ECL3 (Figs. 10 and 11). This network exhibits a higher degree of peptide-specific effects that are likely related to both differences in the peptide sequences and orientation of the peptides in the active structures. As noted

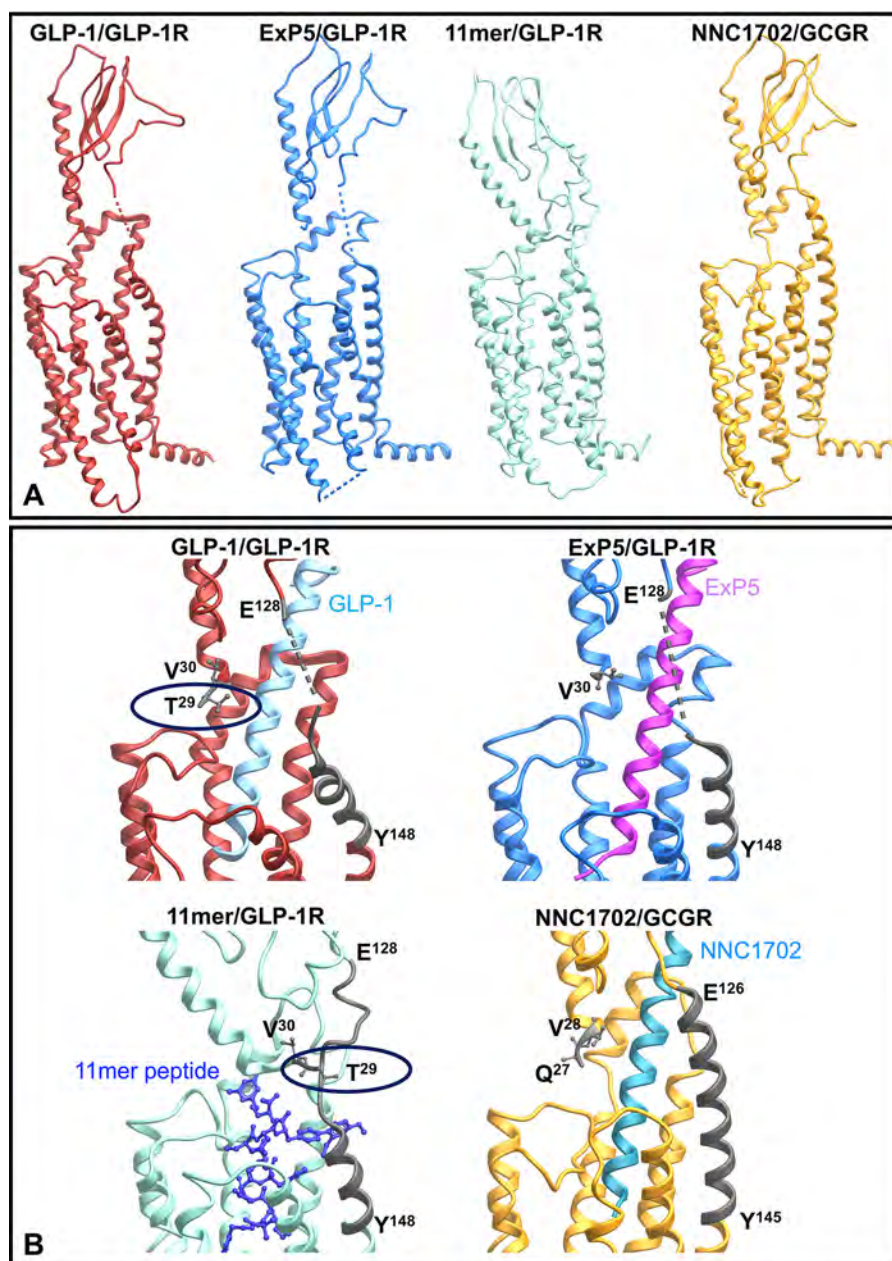


Figure 7. Peptide-bound full-length structures of GLP-1R and GCGR. *A*, full-length structures illustrating the relative position of the N-terminal ECD to the receptor core. *B*, zoom-in of the resolved far N-terminal residue(s) and TM1/ECD stalk (highlighted in dark gray). The backbones of the peptide agonists are illustrated in ribbon (GLP-1, exendin-P5 (*ExP5*), and NNC1702) or X-stick (11-mer).

above, this region of the receptor is involved in coordination of TM1 in the inactive structure and the reorganization and packing of TM1 with TM7 in the active structures (Fig. 9). Unlike GLP-1 and exendin-4, oxyntomodulin-mediated cAMP production is also weakly attenuated by mutation to amino acids in ECL1 that sit within the short α -helix formed in the active structure that extends to the ECL2 network. This is likely due to the predicted distinct positioning of oxyntomodulin when bound to the receptor (Fig. 10). The boundary of ECL1 at the top of TM3 is covalently linked to ECL2 by disulfide linkage of Cys-226 (TM3) and Cys-296 (ECL2), whereas Arg-227 in inactive/partially active structures may also stabilize ECL2. R227A mutation decreases affinity of all three peptides, but with minimal impact on signaling efficacy (32). As such, the extent to

which the oxyntomodulin-specific effects are due to unique direct interactions with ECL1 *versus* potential differences in Cys-296 and Trp-297 is not clear.

Overall, the pattern of effect of mutation was similar for calcium and cAMP signaling across GLP-1 and exendin-4 where efficacy effects could be quantified, although there was generally a greater magnitude of effect on calcium signaling (Figs. 10 and 11). Previous pharmacological inhibitor studies revealed that both these pathways were regulated by G protein interaction at the WT receptor in the CHO-Flp-In cell background, although G_i and G_q interactions had more prominent roles in calcium mobilization (11); this is indicative of broad similarities in changes required to enable G protein coupling. Exendin-4-mediated signaling is also gen-

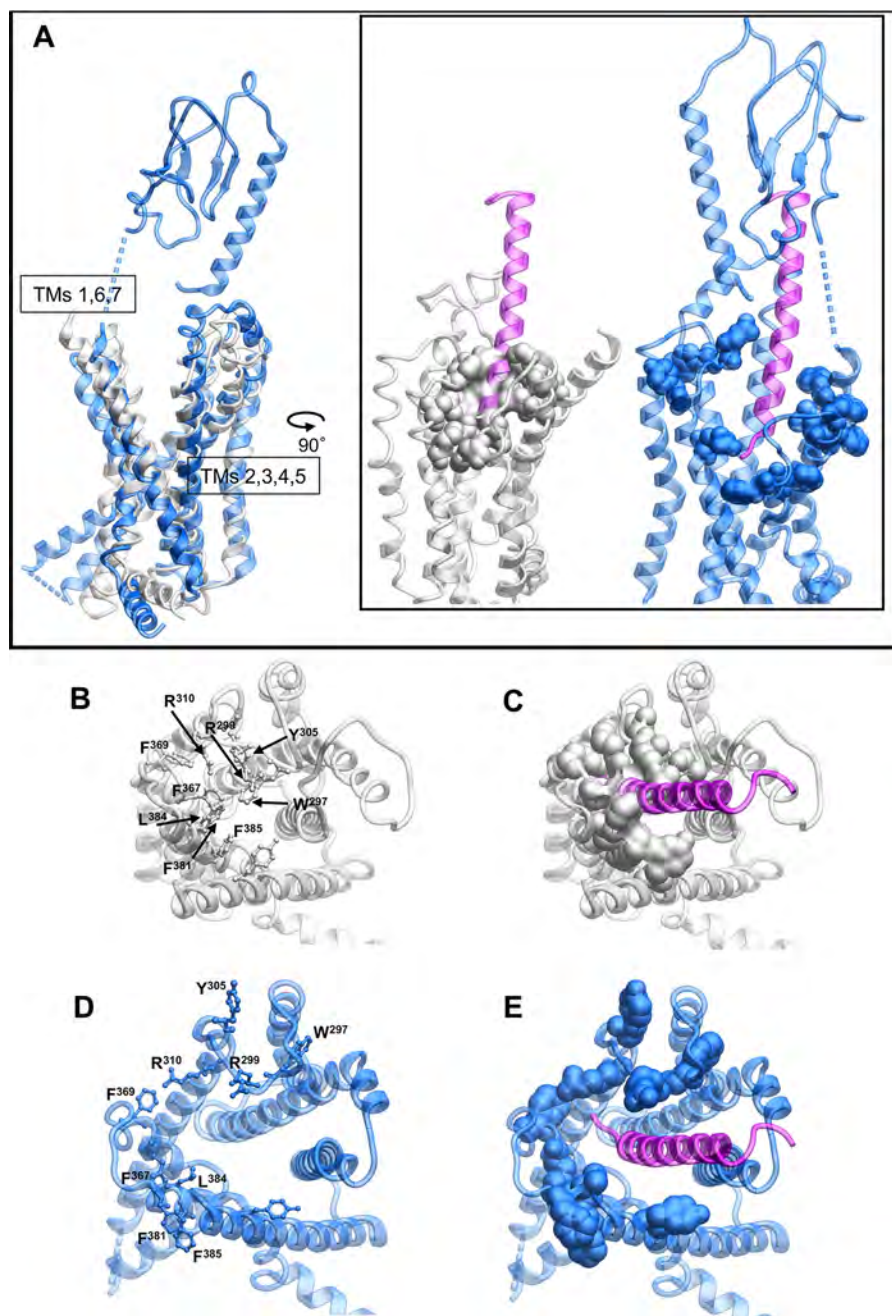


Figure 8. Peptide binding to the GLP-1R requires reorganization of aromatic/hydrophobic residues in the receptor core. A, side view of the inactive GLP-1R model (gray) or exendin-P5-bound GLP-1R structure (blue) with the exendin-P5 peptide illustrated in purple. Residues that occupy the core of the receptor in the inactive model are shown as space fill. B–E, top view of the structures where the ECD has been omitted for clarity. B and C, inactive GLP-1R model. D and E, exendin-P5-bound GLP-1R structure.

erally more sensitive to mutation than that mediated by GLP-1, and the required ECL2 network extends to the top of TM4 for this peptide (Fig. 10).

Peptide-mediated pERK was least sensitive to GLP-1R surface mutations, being principally confined to mutations of the distal ECL3/TM7 boundary, and residues of TM1 and the linker extension that provides physical connection to the ECD, which were revealed in this study (Figs. 10 and 11). This was particularly evident for exendin-4, which was least affected by mutation (Fig. 11). Intriguingly, there was effectively no involvement of the ECL2 residues that were absolutely required for cAMP and calcium signaling. Inhibitor studies at the WT receptor

indicated that G_s and G_q have limited contribution to exendin-4-mediated pERK, with signaling principally driven by G_i , $G\beta\gamma$, and arrestin interactions, although those are likely to be at least partly interdependent (11). For GLP-1, and more prominently oxyntomodulin, selective mutations in ECL2 also impacted pERK, and this could relate to greater contribution of G_q (GLP-1) and G_s (oxyntomodulin) in pERK at the WT receptor. Also of interest, for TM1 and ECL3/TM7, the effects of individual mutation were highly peptide-specific (Fig. 10). The data are consistent with a model whereby selective and peptide-specific interactions alter the TM1/TM7 interface linked to G_i / $G\beta\gamma$ /arrestin coupling to pERK. Moreover, our mutational

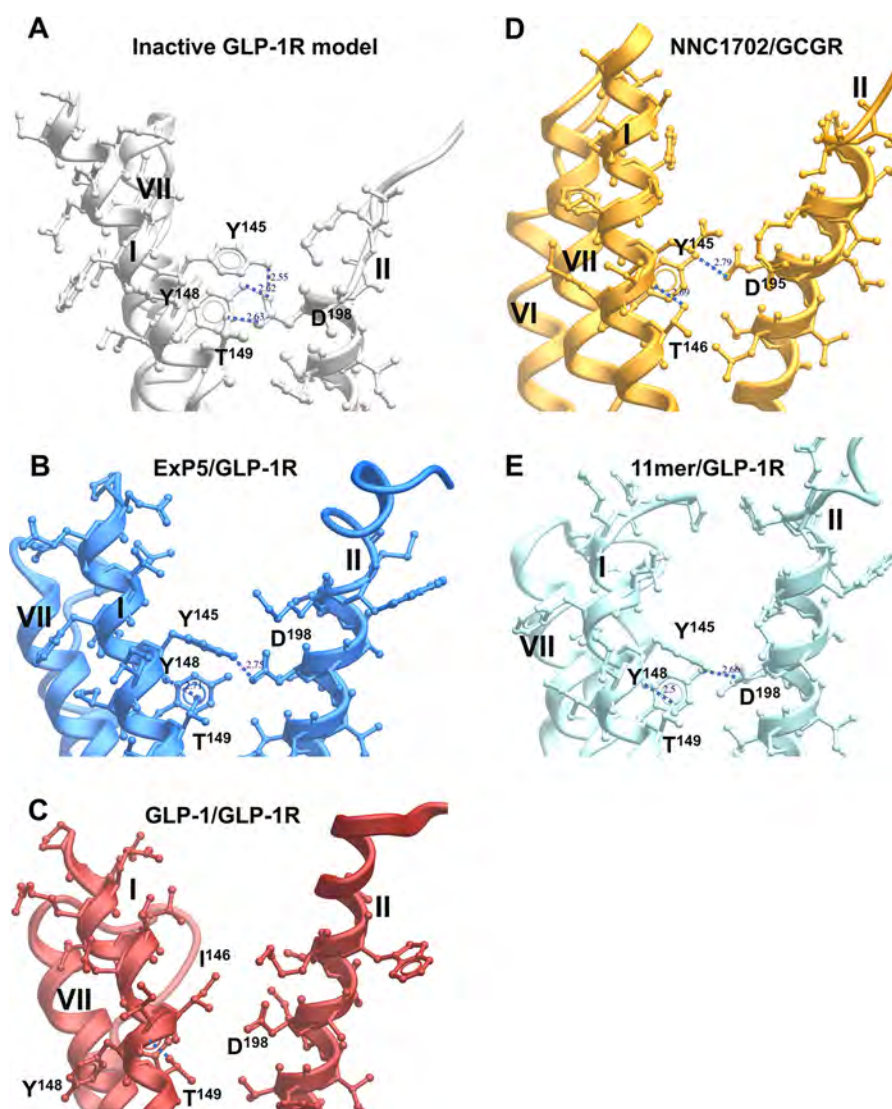


Figure 9. Polar residues in the GLP-1R TM1 are coordinated by Asp-198 (TM2) in the inactive model, orienting key side chains away from TM7 and facilitating tight packing of TM1/TM7. View facing the TM1/TM2 boundary is shown. Key TM1 side chains interacting with Asp-198 are depicted in X-stick representation and labeled. *A*, inactive GLP-1R model. *B*, exendin-P5 (ExP5)/GLP-1R structure. *C*, GLP-1/GLP-1R structure. *D*, NNC1702/GCGR structure. *E*, 11-mer agonist/GLP-1R structure. TM helices are labeled in roman numerals.

data suggest these changes can occur relatively independent of the reorganization of TMs 5 and 6 that are critical for cAMP formation and $[Ca^{2+}]_i$ mobilization, events that are G_s/G_q -dependent at the WT receptor. Exendin-P5 is a G protein-biased peptide agonist that exhibits bias toward cAMP relative to arrestin interaction, compared with the related exendin-4 peptide and GLP-1 (10, 17). It has distinct actions *in vivo* compared with exendin-4 (10). As noted above, comparison of the exendin-P5- and GLP-1-bound active GLP-1R structures reveals major differences in ECL3 and the upper TM boundaries of TMs 6 and 7 that are linked to distinct rotational differences in the upper region of TM1. Mutation in these domains has confirmed peptide-specific differences in the engagement of GLP-1 *versus* exendin-P5 with amino acids in TM1, as well as the TM6 proximal region of ECL3 (17), thereby providing additional structural evidence for distinctions in the role of these domains in propagation of signaling. An important caveat for extrapolation of our observations to more proximal measures of

signaling is that they are based on inferences from WT receptor signaling. Direct measurement of proximal transducer engagement for mutant receptors will be required to validate hypotheses.

The novel structures for the GLP-1R are enabling us to begin to unravel the complexities associated with receptor activation and biased agonism. Combining new data from this study with our previous work on GLP-1R ECLs in the context of inactive and active structures has advanced our understanding of receptor domains that control signaling. Importantly, the work provides evidence for two, at least partially independent, structural domains linked to signaling. The first involves the interface between TMs 5 and 6 and is linked to reorganization of ECL2 into a structured network that is required for propagation of signaling linked to G_s and G_q -dependent pathways at the WT receptor. The second is the interface between TMs 1 and 7 that, although important for at least G_s -dependent cAMP signaling, may be independently linked to $G_i/G\beta\gamma$ /arrestin-mediated signaling that is the key driver of pERK at the WT receptor. Our data support a model where dis-

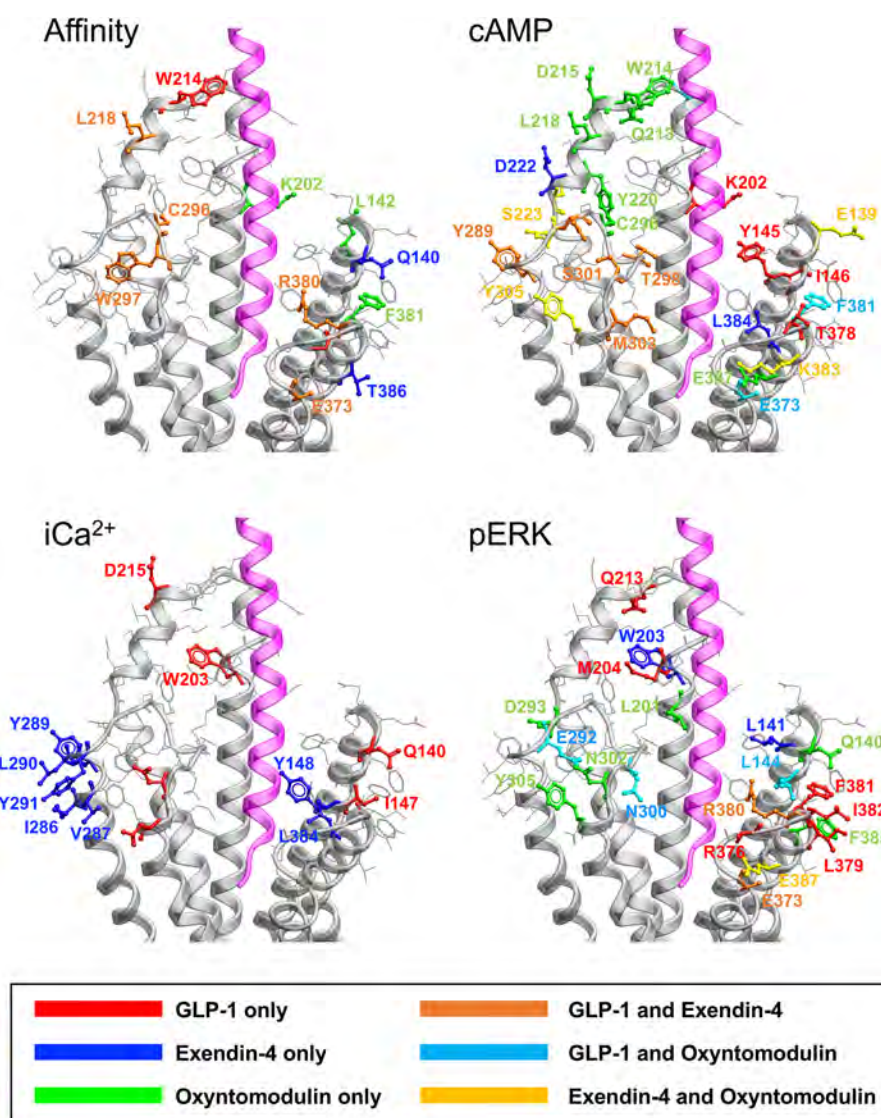


Figure 10. Peptide-selective effects on agonist affinity, cAMP accumulation, [Ca²⁺], mobilization, and pERK. Mutated amino acids with similar effects across peptides are not highlighted. Maps for affinity, cAMP, and pERK include all three peptides. The map for [Ca²⁺], includes only GLP-1 and exendin-4. The exendin-P5 peptide is displayed in magenta.

tinct peptide–receptor interactions can provide selective control of how these different networks are engaged.

Experimental procedures

Mutagenesis

Desired mutations were introduced to the N-terminal double c-Myc–labeled human *GLP-1R* gene in pDONR201 (Invitrogen) via the Muta-direct™ kit (Beijing SBS Genetech Co., Ltd., China), and then LR recombination reactions were conducted to transfer the N-terminal double c-Myc–labeled human *GLP-1R* gene into the pEF5/FRT/V5-DEST destination vector using Gateway Technology (Invitrogen). The oligonucleotides for mutagenesis were purchased from GeneWorks (Thebarton, SA, Australia), and mutants were confirmed by automated DNA sequencing.

Stable cell line generation and cell culture

The mutant or wildtype (WT) receptor genes were integrated into the Flp-In-Chinese hamster ovary (Flp-In-CHO)

cells, passage 4 (Invitrogen), using the Flp-In™ system. Stable Flp-In expression cell lines were generated through polyclonal selection, screened, and maintained in Dulbecco's modified Eagle's medium supplemented with 10% (v/v) FBS, 600 μg/ml hygromycin B at 37 °C in 5% CO₂. The WT receptor is expressed at ~170,000 receptors/cell. Cell lines were routinely tested for mycoplasma and were mycoplasma free. Stable cells were frozen at passage 14, and all assays were performed with cells between passage 14 and 25.

Heterologous whole-cell competitive binding assay

Competition of ¹²⁵I–exendin-4(9–39) binding to hGLP-1R was performed as described previously (13) on whole cells in 96-well plates using the radiolabeled antagonist ¹²⁵I–exendin-4(9–39) (~0.1 nM) and increasing concentrations of unlabeled peptide. Nonspecific binding was defined by co-incubation with 1 μM unlabeled exendin-4(9–39). Following overnight incubation, nonbound ligand was removed, and radioactivity was determined using a gamma counter.

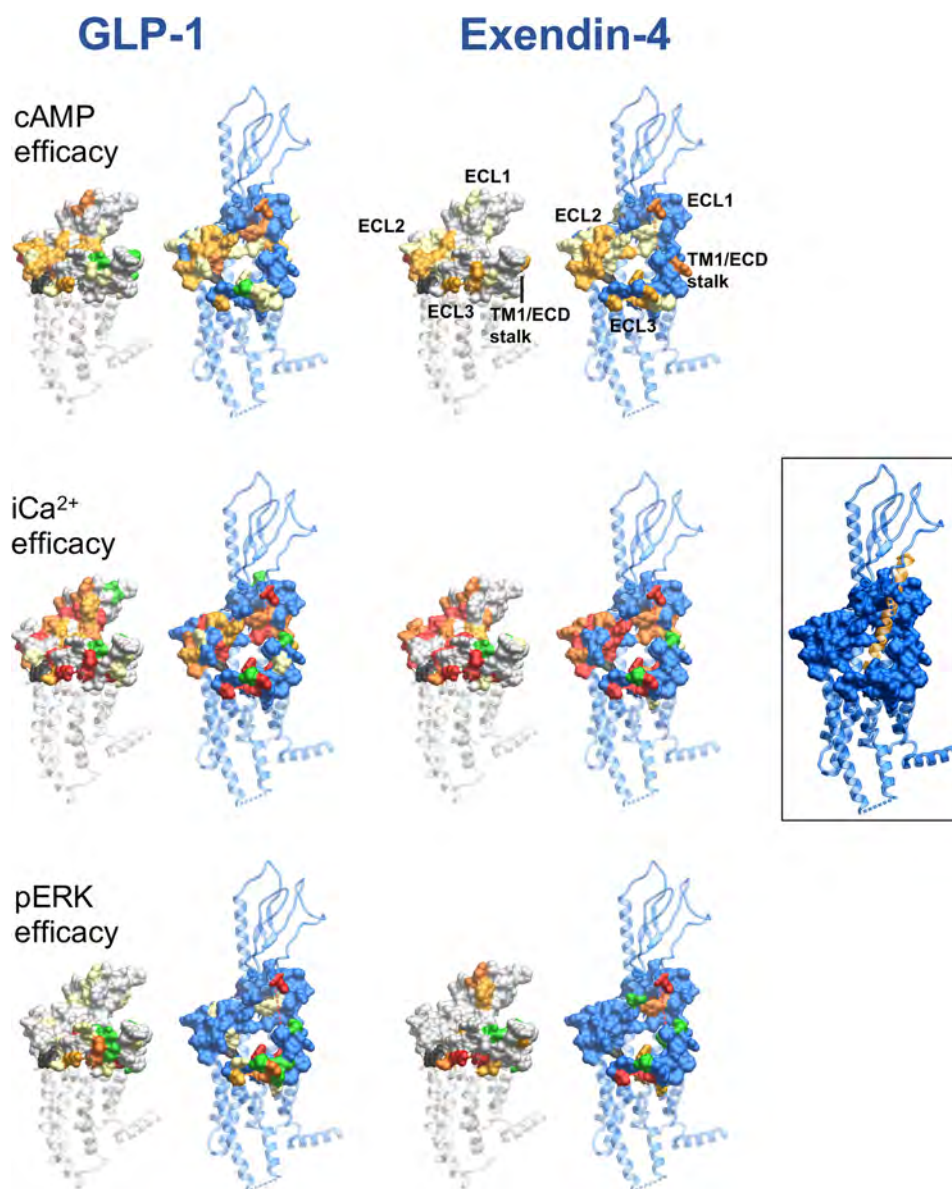


Figure 11. Reorganization of the extracellular surface of the GLP-1R is critical to propagation of signaling. Amino acids involved in efficacy across cAMP (upper panels), $[Ca^{2+}]_i$ (middle panels), and pERK (lower panels) for GLP-1 (left-hand panels) and exendin-4 (right-hand panels) were mapped onto the inactive GLP-1R model and the fully active exendin-P5 (ExP5)-bound GLP-1R structure. Displayed on surface representation are mutated amino acids that affect efficacy: yellow (2–5-fold reduction in affinity); light orange (5–10-fold reduction in affinity); red (>30-fold reduction in affinity); or green (increased affinity). Mutated residues not affected are displayed as gray (inactive receptor) or blue (active receptor).

Cell-surface expression by enzyme-linked immunosorbent assay

1.5×10^5 cells/well were seeded into 24-well culture plates and incubated overnight. Expression was determined through detection of N-terminal double c-Myc of GLP-1R by ELISA as described previously (13). Data were normalized to WT GLP-1R and Flp-In CHO parental cell lines.

Calcium mobilization

3×10^4 cells/well were seeded into 96-well culture plates and incubated overnight. Cells were incubated with Fluo4-AM for 45 min and stimulated with different concentrations of peptides, and fluorescence was determined in a FlexStation® plate reader every 1.36 s for 120 s after ligand addition as described previously (13).

Data were normalized to the maximal response elicited by $100 \mu\text{M}$ ATP.

cAMP accumulation

3×10^4 cells/well were seeded into 96-well culture plates and incubated overnight. Cells were stimulated with increasing concentrations of ligands for 30 min in the presence of isobutylmethylxanthine. The liquid was discarded, changed to absolute ethanol, and volatilized to dry in room temperature. cAMP was detected using a Lance kit (PerkinElmer Life Sciences), as described previously (11). Data were normalized to the response of $100 \mu\text{M}$ forskolin.

ERK1/2 phosphorylation

3×10^4 cells/well were seeded into 96-well culture plates and incubated overnight. Initially, pERK1/2 time-course experi-

ments were performed over 1 h to identify the time point when the pERK1/2 response is maximal. Subsequently, dose responses for different agonists were determined at this peak time point with stimulation performed after serum starvation overnight. pERK1/2 was detected using an AlphaScreen assay as described previously (13). Data were normalized to the maximal response elicited by 10% FBS determined at 6 min.

Data analysis

IC₅₀ values were estimated from competitive inhibition of [¹²⁵I]-exendin(9–39) binding using a three-parameter logistic equation (log(inhibitor *versus* response)) in Prism (version 7, Graphpad). In all cases, the concentration of the radioligand was ≤1% of the K_d values. Under these conditions, the IC₅₀ approximates K_i, and such data are reported as pK_i. E_{max} and EC₅₀ were estimated from concentration-response curves using with a three-parameter logistic equation in Prism (version 7). These values are a composite of affinity, efficacy, and stimulus response coupling. The Black and Leff operational model of agonism (26) was applied to separate effects on pathway-specific signaling from those that modify ligand affinity. Derived values (τ) were normalized to experimentally determined levels of cell-surface expression to provide a measure of efficacy (τ_c) that is independent of affinity and altered cell-surface receptor expression (11). Log τ_c values for mutant receptors were statistically compared with those of the WT receptor using a one-way analysis of variance (ANOVA) and Dunnett's post-test. Significance was accepted at *p* < 0.05.

Molecular modeling and mapping of mutational effects

A homology model of the inactive GLP-1R TM domain was built using the minimally modified GCGR (PDB code 4L6R) (29), as described previously (28); the first amino acid in this model is Arg-134. The thermostabilized and full-length human GLP-1R bound to modified 11-mer peptide agonist (PDB code 5NX2) (15); the full-length and GLP-1 bound to rabbit GLP-1R in complex with G_s (PDB code 5VAI) (16), and the full-length and exendin-P5 bound to human GLP-1R in complex with G_s (PDB code 6B3J) (16) were used as deposited; the first amino acids in these structures are Thr-29, Thr-29, and Val-30, respectively.

Author contributions—S. L., D. Y., M.-W. W., D. W., and P. M. S. conceptualization; S. L., L. C., D. Y., Y.-L. L., C. K., A. C., and D. W. formal analysis; S. L., L. C., A. D., X. C., Y. F., C. K., P. Z., and T. C. investigation; S. L. methodology; S. L., M.-W. W., D. W., and P. M. S. writing-original draft; S. L., C. K., P. Z., A. C., M.-W. W., D. W., and P. M. S. writing-review and editing; D. Y., M.-W. W., D. W., and P. M. S. supervision; C. K., A. C., M.-W. W., D. W., and P. M. S. funding acquisition; P. M. S. project administration.

References

- Santos, R., Ursu, O., Gaulton, A., Bento, A. P., Donadi, R. S., Bologa, C. G., Karlsson, A., Al-Lazikani, B., Hersey, A., Oprea, T. I., and Overington, J. P. (2017) A comprehensive map of molecular drug targets. *Nat. Rev. Drug Discov.* **16**, 19–34 [CrossRef Medline](#)
- Luttrell, L. M., Maudsley, S., and Bohn, L. M. (2015) Fulfilling the promise of "Biased" G protein-coupled receptor agonism. *Mol. Pharmacol.* **88**, 579–588 [CrossRef Medline](#)

- Costa-Neto, C. M., Parreiras-E-Silva, L. T., and Bouvier, M. (2016) A pluridimensional view of biased agonism. *Mol. Pharmacol.* **90**, 587–595 [CrossRef Medline](#)
- Wootten, D., Miller, L. J., Koole, C., Christopoulos, A., and Sexton, P. M. (2017) Allosteric and biased agonism at class B G protein-coupled receptors. *Chem. Rev.* **117**, 111–138 [CrossRef Medline](#)
- Hollenstein, K., de Graaf, C., Bortolato, A., Wang, M. W., Marshall, F. H., and Stevens, R. C. (2014) Insights into the structure of class B GPCRs. *Trends Pharmacol. Sci.* **35**, 12–22 [CrossRef Medline](#)
- Koole, C., Wootten, D., Simms, J., Valant, C., Sridhar, R., Woodman, O. L., Miller, L. J., Summers, R. J., Christopoulos, A., and Sexton, P. M. (2010) Allosteric ligands of the glucagon-like peptide 1 receptor (GLP-1R) differentially modulate endogenous and exogenous peptide responses in a pathway-selective manner: implications for drug screening. *Mol. Pharmacol.* **78**, 456–465 [CrossRef Medline](#)
- Hager, M. V., Johnson, L. M., Wootten, D., Sexton, P. M., and Gellman, S. H. (2016) β-Arrestin-biased agonists of the GLP-1 receptor from β-amino acid residue incorporation into GLP-1 analogues. *J. Am. Chem. Soc.* **138**, 14970–14979 [CrossRef Medline](#)
- Hager, M. V., Clydesdale, L., Gellman, S. H., Sexton, P. M., and Wootten, D. (2017) Characterization of signal bias at the GLP-1 receptor induced by backbone modification of GLP-1. *Biochem. Pharmacol.* **136**, 99–108 [CrossRef Medline](#)
- Weston, C., Poyner, D., Patel, V., Dowell, S., and Ladds, G. (2014) Investigating G protein signalling bias at the glucagon-like peptide-1 receptor in yeast. *Br. J. Pharmacol.* **171**, 3651–3665 [CrossRef Medline](#)
- Zhang, H., Sturchler, E., Zhu, J., Nieto, A., Cistrone, P. A., Xie, J., He, L., Yea, K., Jones, T., Turn, R., Di Stefano, P. S., Griffin, P. R., Dawson, P. E., McDonald, P. H., and Lerner, R. A. (2015) Autocrine selection of a GLP-1R G-protein biased agonist with potent antidiabetic effects. *Nat. Commun.* **6**, 8918 [CrossRef Medline](#)
- Wootten, D., Reynolds, C. A., Smith, K. J., Mobarec, J. C., Koole, C., Savage, E. E., Pabreja, K., Simms, J., Sridhar, R., Furness, S. G. B., Liu, M., Thompson, P. E., Miller, L. J., Christopoulos, A., and Sexton, P. M. (2016) The extracellular surface of the GLP-1 receptor is a molecular trigger for biased agonism. *Cell* **165**, 1632–1643 [CrossRef Medline](#)
- Hoare, S. R. (2005) Mechanisms of peptide and nonpeptide ligand binding to class B G-protein coupled receptors. *Drug Discov. Today* **10**, 417–427 [CrossRef Medline](#)
- Koole, C., Wootten, D., Simms, J., Miller, L. J., Christopoulos, A., and Sexton, P. M. (2012) Second extracellular loop of human glucagon-like peptide-1 receptor (GLP-1R) has a critical role in GLP-1 peptide binding and receptor activation. *J. Biol. Chem.* **287**, 3642–3658 [CrossRef Medline](#)
- Song, G., Yang, D., Wang, Y., de Graaf, C., Zhou, Q., Jiang, S., Liu, K., Cai, X., Dai, A., Lin, G., Liu, D., Wu, F., Wu, Y., Zhao, S., Ye, L., et al. (2017) Human GLP-1 receptor transmembrane domain structure in complex with allosteric modulators. *Nature* **546**, 312–315 [CrossRef Medline](#)
- Jazayeri, A., Rappas, M., Brown, A. J. H., Kean, J., Errey, J. C., Robertson, N. J., Fiez-Vandal, C., Andrews, S. P., Congreve, M., Bortolato, A., Mason, J. S., Baig, A. H., Teobald, I., Doré, A. S., Weir, M., et al. (2017) Crystal structure of the GLP-1 receptor bound to a peptide agonist. *Nature* **546**, 254–258 [CrossRef Medline](#)
- Zhang, Y., Sun, B., Feng, D., Hu, H., Chu, M., Qu, Q., Tarrasch, J. T., Li, S., Sun Kobilka, T., Kobilka, B. K., and Skiniotis, G. (2017) Cryo-EM structure of the activated GLP-1 receptor in complex with a G protein. *Nature* **546**, 248–253 [CrossRef Medline](#)
- Liang, Y. L., Khoshouei, M., Glukhova, A., Furness, S. G. B., Zhao, P., Clydesdale, L., Koole, C., Truong, T. T., Thal, D. M., Lei, S., Radjainia, M., Danev, R., Baumeister, W., Wang, M. W., Miller, L. J., et al. (2018) Phase-plate cryo-EM structure of a biased agonist-bound human GLP-1 receptor-Gs complex. *Nature* **555**, 121–125 [CrossRef Medline](#)
- Zhang, H., Qiao, A., Yang, L., Van Eps, N., Frederiksen, K. S., Yang, D., Dai, A., Cai, X., Zhang, H., Yi, C., Cao, C., He, L., Yang, H., Lau, J., Ernst, O. P., et al. (2018) Structure of the glucagon receptor in complex with a glucagon analogue. *Nature* **553**, 106–110 [CrossRef Medline](#)
- Liang, Y. L., Khoshouei, M., Radjainia, M., Zhang, Y., Glukhova, A., Tarrasch, J., Thal, D. M., Furness, S. G. B., Christopoulos, G., Coudrat, T., Danev, R., Baumeister, W., Miller, L. J., Christopoulos, A., Kobilka, B. K., et

- al. (2017) Phase-plate cryo-EM structure of a class B GPCR-G-protein complex. *Nature* **546**, 118–123 [CrossRef Medline](#)
20. Mukund, S., Shang, Y., Clarke, H. J., Madjidi, A., Corn, J. E., Kates, L., Kolumam, G., Chiang, V., Luis, E., Murray, J., Zhang, Y., Hötzel, I., Koth, C. M., and Allan, B. B. (2013) Inhibitory mechanism of an allosteric antibody targeting the glucagon receptor. *J. Biol. Chem.* **288**, 36168–36178 [CrossRef Medline](#)
 21. Zhao, L. H., Yin, Y., Yang, D., Liu, B., Hou, L., Wang, X., Pal, K., Jiang, Y., Feng, Y., Cai, X., Dai, A., Liu, M., Wang, M. W., Melcher, K., and Xu, H. E. (2016) Differential requirement of the extracellular domain in activation of class B G protein-coupled receptors. *J. Biol. Chem.* **291**, 15119–15130 [CrossRef Medline](#)
 22. Yin, Y., de Waal, P. W., He, Y., Zhao, L. H., Yang, D., Cai, X., Jiang, Y., Melcher, K., Wang, M. W., and Xu, H. E. (2017) Rearrangement of a polar core provides a conserved mechanism for constitutive activation of class B G protein-coupled receptors. *J. Biol. Chem.* **292**, 9865–9881 [CrossRef Medline](#)
 23. Graaf, C. d., Donnelly, D., Wootten, D., Lau, J., Sexton, P. M., Miller, L. J., Ahn, J. M., Liao, J., Fletcher, M. M., Yang, D., Brown, A. J., Zhou, C., Deng, J., and Wang, M. W. (2016) Glucagon-like peptide-1 and its class B G protein-coupled receptors: a long march to therapeutic successes. *Pharmacol. Rev.* **68**, 954–1013 [CrossRef Medline](#)
 24. Dods, R. L., and Donnelly, D. (2015) The peptide agonist-binding site of the glucagon-like peptide-1 (GLP-1) receptor based on site-directed mutagenesis and knowledge-based modelling. *Biosci. Rep.* **36**, e00285 [Medline](#)
 25. Dal Maso, E., Zhu, Y., Pham, V., Reynolds, C. A., Deganutti, G., Hick, C. A., Yang, D., Christopoulos, A., Hay, D. L., Wang, M. W., Sexton, P. M., Furness, S. G. B., and Wootten, D. (2018) Extracellular loops 2 and 3 of the calcitonin receptor selectively modify agonist binding and efficacy. *Biochem. Pharmacol.* **150**, 214–244 [CrossRef Medline](#)
 26. Black, J. W., and Leff, P. (1983) Operational models of pharmacological agonism. *Proc. R. Soc. Lond. B Biol. Sci.* **220**, 141–162 [CrossRef Medline](#)
 27. Kenakin, T., and Christopoulos, A. (2013) Signalling bias in new drug discovery: detection, quantification and therapeutic impact. *Nat. Rev. Drug Discov.* **12**, 205–216 [Medline](#)
 28. Wootten, D., Reynolds, C. A., Koole, C., Smith, K. J., Mobarec, J. C., Simms, J., Quon, T., Coudrat, T., Furness, S. G., Miller, L. J., Christopoulos, A., and Sexton, P. M. (2016) A hydrogen-bonded polar network in the core of the glucagon-like peptide-1 receptor is a fulcrum for biased agonism: lessons from class B crystal structures. *Mol. Pharmacol.* **89**, 335–347 [CrossRef Medline](#)
 29. Siu, F. Y., He, M., de Graaf, C., Han, G. W., Yang, D., Zhang, Z., Zhou, C., Xu, Q., Wacker, D., Joseph, J. S., Liu, W., Lau, J., Cherezov, V., Katritch, V., Wang, M. W., and Stevens, R. C. (2013) Structure of the human glucagon class B G-protein-coupled receptor. *Nature* **499**, 444–449 [CrossRef Medline](#)
 30. Jazayeri, A., Doré, A. S., Lamb, D., Krishnamurthy, H., Southall, S. M., Baig, A. H., Bortolato, A., Koglin, M., Robertson, N. J., Errey, J. C., Andrews, S. P., Teobald, I., Brown, A. J., Cooke, R. M., Weir, M., and Marshall, F. H. (2016) Extra-helical binding site of a glucagon receptor antagonist. *Nature* **533**, 274–277 [CrossRef Medline](#)
 31. Yin, Y., Zhou, X. E., Hou, L., Zhao, L. H., Liu, B., Wang, G., Jiang, Y., Melcher, K., and Xu, H. E. (2016) An intrinsic agonist mechanism for activation of glucagon-like peptide-1 receptor by its extracellular domain. *Cell Discov.* **2**, 16042 [CrossRef Medline](#)
 32. Wootten, D., Reynolds, C. A., Smith, K. J., Mobarec, J. C., Furness, S. G., Miller, L. J., Christopoulos, A., and Sexton, P. M. (2016) Key interactions by conserved polar amino acids located at the transmembrane helical boundaries in class B GPCRs modulate activation, effector specificity and biased signalling in the glucagon-like peptide-1 receptor. *Biochem. Pharmacol.* **118**, 68–87 [CrossRef Medline](#)
 33. Wootten, D., Simms, J., Miller, L. J., Christopoulos, A., and Sexton, P. M. (2013) Polar transmembrane interactions drive formation of ligand-specific and signal pathway-biased family B G protein-coupled receptor conformations. *Proc. Natl. Acad. Sci. U.S.A.* **110**, 5211–5216 [CrossRef Medline](#)
 34. Xiao, Q., Jeng, W., and Wheeler, M. B. (2000) Characterization of glucagon-like peptide-1 receptor-binding determinants. *J. Mol. Endocrinol.* **25**, 321–335 [CrossRef Medline](#)
 35. López de Maturana, R., and Donnelly, D. (2002) The glucagon-like peptide-1 receptor binding site for the N terminus of GLP-1 requires polarity at Asp198 rather than negative charge. *FEBS Lett.* **530**, 244–248 [CrossRef Medline](#)
 36. Coopman, K., Wallis, R., Robb, G., Brown, A. J., Wilkinson, G. F., Timms, D., and Willars, G. B. (2011) Residues within the transmembrane domain of the glucagon-like peptide-1 receptor involved in ligand binding and receptor activation: modelling the ligand-bound receptor. *Mol. Endocrinol.* **25**, 1804–1818 [CrossRef Medline](#)
 37. Koole, C., Wootten, D., Simms, J., Valant, C., Miller, L. J., Christopoulos, A., and Sexton, P. M. (2011) Polymorphism and ligand dependent changes in human glucagon-like peptide-1 receptor (GLP-1R) function: allosteric rescue of loss of function mutation. *Mol. Pharmacol.* **80**, 486–497 [CrossRef Medline](#)
 38. Koole, C., Wootten, D., Simms, J., Miller, L. J., Christopoulos, A., and Sexton, P. M. (2015) Differential impact of amino acid substitutions on critical residues of the human glucagon-like peptide-1 receptor involved in peptide activity and small-molecule allosteric. *J. Pharmacol. Exp. Ther.* **353**, 52–63 [CrossRef Medline](#)
 39. Underwood, C. R., Garibay, P., Knudsen, L. B., Hastrup, S., Peters, G. H., Rudolph, R., and Reedtz-Runge, S. (2010) Crystal structure of glucagon-like peptide-1 in complex with the extracellular domain of the glucagon-like peptide-1 receptor. *J. Biol. Chem.* **285**, 723–730 [CrossRef Medline](#)
 40. Al-Sabah, S., and Donnelly, D. (2003) The positive charge at Lys-288 of the glucagon-like peptide-1 (GLP-1) receptor is important for binding the N-terminus of peptide agonists. *FEBS Lett.* **553**, 342–346 [CrossRef Medline](#)

Two distinct domains of the glucagon-like peptide-1 receptor control peptide-mediated biased agonism

Saifei Lei, Lachlan Clydesdale, Antao Dai, Xiaoqing Cai, Yang Feng, Dehua Yang, Yi-Lynn Liang, Cassandra Koole, Peishen Zhao, Thomas Coudrat, Arthur Christopoulos, Ming-Wei Wang, Denise Wootten and Patrick M. Sexton

J. Biol. Chem. 2018, 293:9370-9387.

doi: 10.1074/jbc.RA118.003278 originally published online May 1, 2018

Access the most updated version of this article at doi: [10.1074/jbc.RA118.003278](https://doi.org/10.1074/jbc.RA118.003278)

Alerts:

- [When this article is cited](#)
- [When a correction for this article is posted](#)

[Click here](#) to choose from all of JBC's e-mail alerts

This article cites 40 references, 16 of which can be accessed free at <http://www.jbc.org/content/293/24/9370.full.html#ref-list-1>

Structure of the adenosine-bound human adenosine A₁ receptor–G_i complex

Christopher J. Draper-Joyce^{1,6}, Maryam Khoshouei^{2,3,6}, David M. Thal¹, Yi-Lynn Liang¹, Anh T. N. Nguyen¹, Sebastian G. B. Furness¹, Hariprasad Venugopal⁴, Jo-Anne Baltos¹, Jürgen M. Plitzko², Radostin Danev², Wolfgang Baumeister², Lauren T. May¹, Denise Wootten^{1,5}, Patrick M. Sexton^{1,5*}, Alisa Glukhova^{1*} & Arthur Christopoulos^{1*}

The class A adenosine A₁ receptor (A₁R) is a G-protein-coupled receptor that preferentially couples to inhibitory G_{i/o} heterotrimeric G proteins, has been implicated in numerous diseases, yet remains poorly targeted. Here we report the 3.6 Å structure of the human A₁R in complex with adenosine and heterotrimeric G_{i2} protein determined by Volta phase plate cryo-electron microscopy. Compared to inactive A₁R, there is contraction at the extracellular surface in the orthosteric binding site mediated via movement of transmembrane domains 1 and 2. At the intracellular surface, the G protein engages the A₁R primarily via amino acids in the C terminus of the Gα_i α5-helix, concomitant with a 10.5 Å outward movement of the A₁R transmembrane domain 6. Comparison with the agonist-bound β₂ adrenergic receptor–G_s–protein complex reveals distinct orientations for each G-protein subtype upon engagement with its receptor. This active A₁R structure provides molecular insights into receptor and G-protein selectivity.

Adenosine (ADO) receptors comprise four subtypes within the class A G-protein-coupled receptor (GPCR) superfamily that mediate the actions of the purine nucleoside, ADO¹. Activation of the A₁R is therapeutically desirable for ischaemia-reperfusion injury, atrial fibrillation, neuropathic pain and others¹. Although ADO is used clinically to treat supraventricular tachycardia, the development of A₁R-selective agonists for a broader range of disorders has thus far failed, primarily owing to dose-limiting on-target adverse effects². Alternative approaches are thus necessary for improved A₁R drug action, with studies focusing on the potential for greater A₁R selectivity through targeting allosteric sites, or via development of A₁R conformational state-selective biased agonists that can promote beneficial signalling while sparing pathways mediating on-target adverse effects^{3,4}.

One area for the development of selective A₁R-targeting drugs is the use of structure-based approaches that leverage advances in GPCR structural biology. Indeed, inactive-state, antagonist-bound, structures of the A₁R were solved using X-ray crystallography^{5,6}. However, these studies required modification of the A₁R via thermostabilizing mutations and/or fusion proteins, and cannot inform on mechanisms underlying agonist binding, A₁R activation and G-protein interaction. These features are necessary for the rational design of selective A₁R activators, biased agonists or positive allosteric modulators. An alternative approach to overcoming the current dearth of active-state, G-protein-bound, GPCRs is the use of single-particle cryo-electron microscopy (cryo-EM)^{7–9}. The promise of cryo-EM in yielding active-state GPCR complexes has recently been realized through the solution of several receptor structures bound to agonists and the heterotrimeric G_s protein, complementing the only crystal structure so far, to our knowledge, of an agonist-bound GPCR–G-protein complex, that of the β₂AR complexed to G_s protein^{7–10}. However, the A₁R preferentially couples to the G_{i/o} family of G-proteins¹. Indeed, of the more than 800 human GPCRs, most preferentially couple to G_{i/o} proteins. The G_{i/o} family has four members, which are the most abundantly expressed G proteins throughout the body¹¹. G_{i/o} protein activation is typically

associated with inhibition of adenylate cyclase, resulting in reduced cAMP accumulation, but they also regulate numerous effectors including enzymes, ion channels and small GTPases. Based predominantly on the high expression of both G_{i2} proteins and A₁Rs in brain and, albeit to a lesser degree, in cardiac tissues (both major organs for A₁R therapies), we chose to focus on G_{i2} as a transducer for the A₁R. Here we report the first, to our knowledge, structure of a GPCR coupled to a heterotrimeric G_i protein, specifically the A₁R–G_{i2} complex bound to its endogenous agonist, ADO, solved using Volta phase-plate (VPP) cryo-EM.

Solving the A₁R–G_{i2} complex

To facilitate complex formation, A₁R and G_{i2} were expressed separately in HighFive insect cells and combined after solubilizing in lauryl maltose-neopentyl glycol (LMNG) and cholesteryl hemisuccinate (CHS) with addition of apyrase and ADO (Extended Data Fig. 1). Stabilization of the A₁R–G_{i2} complex was achieved by introducing four Gα_{i2} subunit mutations that alter nucleotide binding and affinity for Gβγ⁸. This dominant-negative G_{i2} (DNG_{i2}) was sufficient to enable formation of a stable interaction with the receptor while insensitive to GTP (Extended Data Figs. 1 and 2c). The antagonist dipropylcyclopentylxanthine (DPCPX) displayed similar affinities for the A₁R whether alone or in the presence of wild-type Gα_{i2} or DNG_{i2} (Extended Data Fig. 2a), whereas ADO displayed biphasic binding curves with a similar dispersion of high and low affinity states in the presence, but not absence, of either wild-type Gα_{i2} or DNG_{i2} (Extended Data Fig. 2b); a characteristic feature of agonist binding to many GPCRs¹². By contrast, agonist-mediated [³⁵S]GTPγS binding to activated Gα subunits was only observed upon combination of the A₁R with wild-type Gα_{i2} (Extended Data Fig. 2c).

The A₁R–G_{i2} complex in LMNG detergent micelles was visualized using a Titan Krios microscope equipped with a VPP. After imaging and initial 2D classification (Extended Data Fig. 3a, b), 3D classification yielded a final map at a nominal resolution of 3.6 Å reconstructed from 263,321 particle projections (Fig. 1, Extended Data Fig. 3c, Extended

¹Drug Discovery Biology and Department of Pharmacology, Monash Institute of Pharmaceutical Sciences, Monash University, Parkville, Victoria, Australia. ²Department of Molecular Structural Biology, Max Planck Institute of Biochemistry, Martinsried, Germany. ³Novartis Institutes for Biomedical Research, Novartis Pharma AG, Basel, Switzerland. ⁴Department of Biochemistry and Molecular Biology, Monash University, Clayton, Victoria, Australia. ⁵School of Pharmacy, Fudan University, Shanghai, China. ⁶These authors contributed equally: Christopher J. Draper-Joyce, Maryam Khoshouei. *e-mail: patrick.sexton@monash.edu; alisa.glukhova@monash.edu; arthur.christopoulos@monash.edu

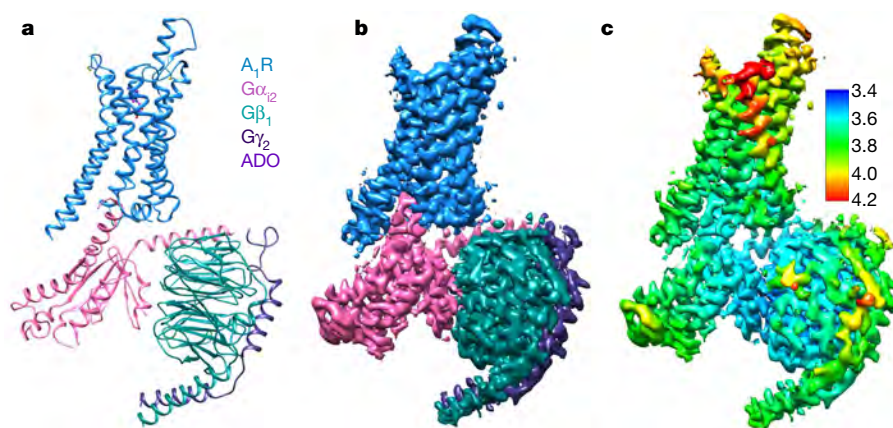


Fig. 1 | The ADO- A_1R - G_{12} cryo-EM structure. **a**, Structure determined after refinement in the cryo-EM map (A_1R , blue; ADO, purple; heterotrimeric G_{12} , pink, cyan and dark purple for α , β and γ , respectively).

Data Table 1). The cryo-EM density map exhibited well-resolved side chains, allowing confident rotamer placements for most amino acids (Extended Data Figs. 3d and 4). The A_1R transmembrane domain regions and extracellular and intracellular loops (ECL and ICL, respectively) are well defined, with the exception of 7 residues in ICL3 and the last 25 residues of helix 8. An ADO molecule is observed occupying the orthosteric site, and extra density at N159 indicates the presence of a glycosylation site that has a role in agonist binding; alanine substitution of this residue caused a significant reduction in the affinity of the ADO derivative NECA (1-(6-amino-9H-purin-9-yl)-1-deoxy-N-ethyl- β -D-ribofuranuronamide) (Extended Data Fig. 2d–g). The $G\beta$ and $G\gamma$ subunits are also well resolved, except for their flexible N and C termini. The α -helical domain of $G\alpha_{12}$ was averaged out in the 2D class averages owing to high flexibility and thus was masked out during map reconstruction, but the Ras-like domain is well ordered except for the flexible switch III region.

Structure of the active-state A_1R

Notably, despite the presence of a different class of G protein relative to all other active GPCR structures solved so far, there seems to be a general conservation in activation mechanisms. Comparison of the inactive A_1R bound to the covalent antagonist, DU172 (4-[3-(8-cyclohexyl-2,6-dioxo-1-propyl-7H-purin-3-yl)propylcarbamoyl]benzenesulfonyl fluoride; Protein Data Bank (PDB) accession 5UEN)⁶, and the active

b, 3D cryo-EM map, coloured according to protein chains. **c**, 3D cryo-EM map coloured according to local resolution (Å), defined from half-maps in Relion (v.2.1b1).

A_1R - G_{12} bound to ADO, reveals a global allosteric transition similar to that observed upon activation of the β_2AR bound to G_s , or multiple class A active state GPCRs stabilized with nanobodies or a 'mini- $G\alpha_s$ ' (mG_s) protein^{10,13–16} (Fig. 2a–c). A key characteristic of the A_1R activating transition is a large outward movement of the intracellular side of transmembrane helix 6 (TM6) by 10.5 Å to accommodate the $\alpha 5$ -helix of the $G\alpha_i$ protein (Fig. 2c). However, this is not as pronounced as in the G_s -bound β_2AR ¹⁰ (nor compared to the three class B G_s -bound structures^{7–9}), but similar to the change observed in the nanobody-stabilized β_2AR ¹⁶, M_2 muscarinic acetylcholine receptor (M_2R)¹⁵, μ -opioid receptor (μOR)¹⁴ and κ -opioid receptor (κOR)¹⁷ structures or the mG_s -stabilized A_{2AR} ¹³. Moreover, additional fundamental features of receptor activation previously observed in other (non- $G_{i/o}$ preferring) class A GPCRs are also preserved, including rearrangements in conserved class A activation 'microswitches', such as the PIF, NPXXY and DRY motifs¹⁸ (Fig. 2g), are very similar to the changes observed when comparing the active, agonist-bound, β_2AR - G_s complex and inactive carazolol-bound β_2AR ¹⁹. Small rearrangements at the conserved PIF motif (P192^{5,50}, I95^{3,40} and F243^{6,44} in the A_1R ; superscripts denote Ballesteros–Weinstein numbering) are associated with the movement of TM6. A 4 Å inward displacement of TM7 at the NPXXY motif (N284^{7,49}, P285^{7,50} and Y287^{7,52}) propagates to the base of helix 8, and is linked to an outward movement of ICL1. The partially formed 'ionic lock', important in maintaining the ground state of the

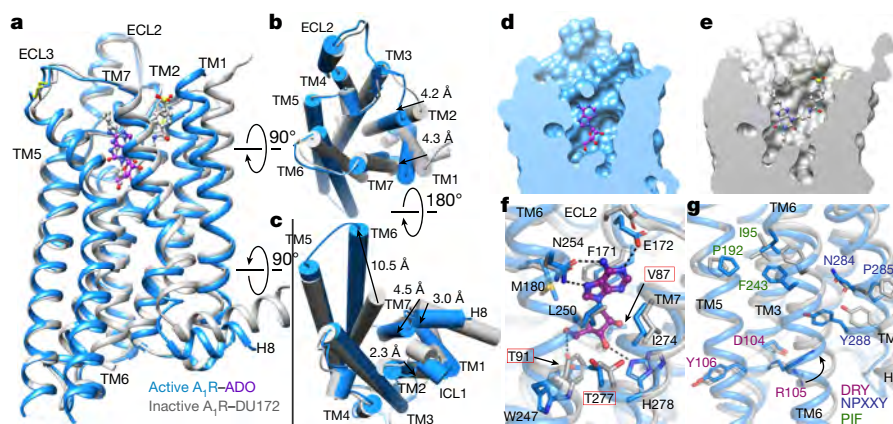


Fig. 2 | Comparison of active and inactive A_1R (PDB code 5UEN) structures. **a–c**, Side (**a**), extracellular (**b**) and cytoplasmic (**c**) views of the receptor (ADO- A_1R - G_{12} complex in blue; inactive DU172-bound A_1R in grey). **d, e**, Active ADO- A_1R (**d**) and inactive DU172- A_1R (**e**) surfaces sliced to show binding site cavity. **f**, Orthosteric binding site of the active A_1R - G_{12} complex with ADO (purple ball and sticks). Toggle

switch' W247^{6,48} and residues within 4 Å of ADO are labelled and shown as sticks. Red rectangles highlight rotamer changes upon activation. N, O and S atoms are coloured in blue, red and yellow, respectively. Dashed lines represent hydrogen bonds. **g**, Conserved class A GPCR motifs important for receptor activation (DRY motif, purple; NPXXY motif, blue; PIF motif, green). H8, helix 8.

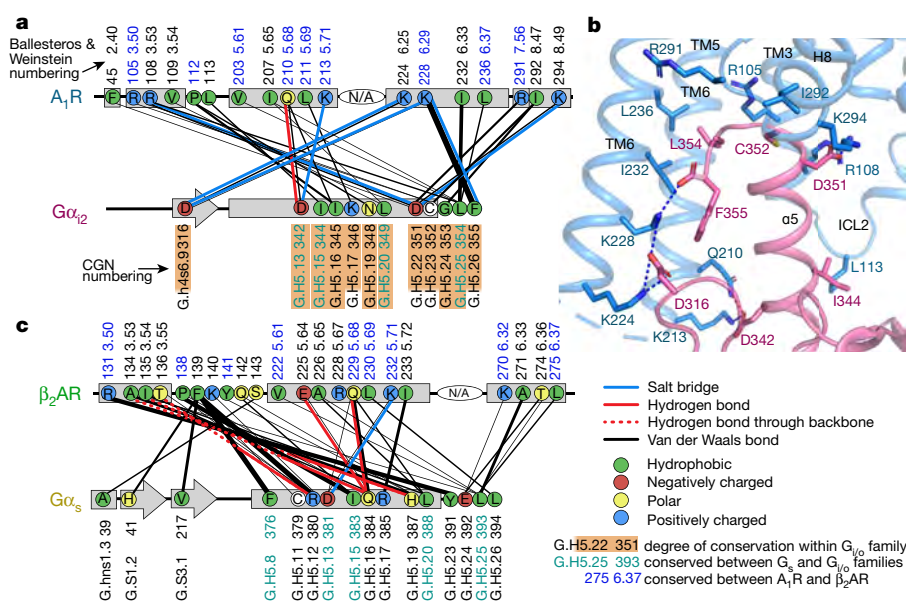


Fig. 3 | Comparison of $G\alpha_i$ and $G\alpha_s$ interactions. **a**, Diagram of the contacts between $G\alpha_{i2}$ and A_1R . Receptor residues are numbered according to Ballesteros and Weinstein numbering³⁴; G-protein residues are numbered according to the CGN scheme²⁹. Blue receptor residue numbers indicate conservation between A_1R and β_2AR . Length of orange

shading of $G\alpha_{i2}$ numbers illustrates degree of conservation within the $G\alpha_{i/o}$ family. **b**, View of key interactions between A_1R (blue) and $DNG\alpha_{i2}$ (pink). Hydrogen bonds and salt bridges are depicted as dashed lines coloured as in panel **a**. **c**, Diagram of the contacts between $G\alpha_s$ and β_2AR (based on PDB code 3SN6), coloured as in panel **a**.

receptor²⁰ and observed in the inactive A_1R ⁶, is broken, and R105^{3,50} of the DRY motif extends towards TM7 to form a lid over the $G\alpha_{i2}$ $\alpha 5$ -helix.

Another key feature of the inactive A_1R is the presence of a large binding cavity that accommodates the orthosteric site⁶. Upon activation, this wide cavity collapses owing to an approximately 4 Å inward movement of the extracellular ends of TM1 and TM2 (Fig. 2b, d, e). Of note, ECL2, which adopts a distinct orientation almost perpendicular to the plane of the membrane, and contributes to the binding of allosteric modulators³, remains essentially unaltered (Fig. 2a). The collapse of the extracellular cavity is less pronounced when compared to the inactive A_1R bound to the A_1 -selective xanthine-based antagonist PSB36 (1-butyl-8-(hexahydro-2,5-methanopentalen-3a(1H)-yl)-3,7-dihydro-3-(3-hydroxypropyl)-1H-purine-2,6-dione)⁵ (Extended Data Fig. 5), probably reflecting that the latter, reversibly binding, antagonist is smaller than the bulky DU172. Nonetheless, a shrinkage of the orthosteric site upon activation is also observed in A_2AR ^{13,21}, β_2AR ^{10,22}, M_2R ^{15,23} and μOR ^{14,24}. Interestingly, despite notable differences in the ligand-binding sites between the inactive A_1R and A_2AR , a comparison of the active states of the two subtypes reveals an almost perfect superimposition of their transmembrane domain regions (root mean squared deviation (r.m.s.d.) value of 1.03) (Extended Data Fig. 6a–c).

The side-chain conformations in the orthosteric site are very similar between the active and inactive A_1R s. Subtle upward movements of the TM3 backbone (approximately 1.5 Å), and TM7 towards TM6 (1 Å), side-chain movements of W247^{6,48} ('toggle switch') and H278^{7,43}, and a change in rotamer conformations of V87^{3,32}, T91^{3,36} and T277^{7,42} collectively serve to accommodate the ADO ribose moiety (Fig. 2f). A role for the two threonine residues is consistent with previous studies, whereas mutation of V87A was suggested to have no effect^{25,26}. We thus re-investigated the role of V87A and found that, in our hands, the mutation significantly reduced both the affinity and efficacy of NECA (Extended Data Fig. 2d–g). Interestingly, the related (but G_s -preferring) A_2AR has previously been solved not only in an active state, bound to NECA and a mG_s protein, but also an 'intermediate' state, bound to either NECA or ADO but in the absence of transducer^{13,21,27}. Further comparison of our active A_1R structure with either of the A_2AR active or intermediate agonist-bound states revealed similar shifts in TM3 and TM7, and similar changes in W246^{6,48}, H278^{7,43}, T88^{3,36} and V84^{3,32}

after agonist binding^{13,21,27} (Extended Data Fig. 6). These complementary rearrangements result in nearly identical orthosteric sites between agonist-bound A_1R and A_2AR , suggesting that the propagation and selection of coupling partner must involve conformational changes downstream of this binding site. Other notable interactions between orthosteric site residues and ADO in the A_1R include π -stacking with F171^{ECL2}, hydrogen bonding with N254^{6,55}, H278^{7,43} and E172^{ECL2}, and Van der Waals interactions with M180^{5,38} and L250^{6,51} (Fig. 2f, Extended Data Fig. 5f), which are all consistent with previous mutational and computational studies of agonist interactions with the A_1R ^{25,28}.

Structure, coupling and selectivity of the G_i heterotrimer

Despite the recent solution of a number of class A GPCR structures in 'active-like' states stabilized by nanobodies or mG_s , there still remains only a single class A GPCR structure bound to a heterotrimeric G protein—the β_2AR – G_s complex¹⁰. As also observed with that complex, interactions between G_i and the A_1R are extensive, with a total buried surface area of 1,964 Å² (958 Å² at the A_1R and 1,006 Å² at the $G\alpha_{i2}$). Another similarity between the two GPCR–G-protein complexes is that the G protein interacts primarily via the $G\alpha$ Ras-like domain. An alignment of both receptors (Extended Data Fig. 7a) and G proteins (Extended Data Fig. 7b), followed by a comparison of key interaction points between the $\alpha 5$ -helix of each $G\alpha$ subunit with its respective receptor, highlighted two distinct clusters (Fig. 3; Extended Data Fig. 4b, c). The first region is common to both $G\alpha_s$ and $G\alpha_i$, encompassing approximately residues 12–20 of each $\alpha 5$ -helix (H5.8–H5.20, common $G\alpha$ numbering (CGN) system²⁹), possibly highlighting the broad importance of this region in providing strong contacts for receptor binding. However, for the β_2AR – G_s complex, there are more interactions within this region of $\alpha 5$ with TM3 and TM5 of the receptor that consist of both polar and non-polar contacts. By contrast, there are fewer interactions for the A_1R – G_i complex and only D342 (G.H5.13) of the $G\alpha_i$ subunit forms a hydrogen bond with Q210^{5,68} and a salt bridge with K213^{5,71}, with the rest of the cluster making nonpolar interactions. The second key interaction region comprises the five C-terminal $\alpha 5$ -helix amino acid residues that provide more receptor interactions for the $G\alpha_i$ than the $G\alpha_s$ helix. These last five amino acids provide the strongest set of interactions for A_1R – G_{i2} (Fig. 3a, b), including inter-

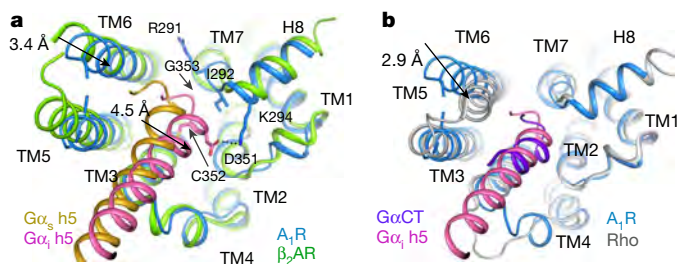


Fig. 4 | Orientation of $G\alpha$ subunits varies between GPCR-G-protein complexes. **a**, Cytoplasmic view shows $\alpha 5$ -helix orientation difference between G_i and G_s . Interacting residues of the $\alpha 5$ -helix (h5), TM7 and helix 8 are shown as sticks. The salt bridge is shown as a dashed line. **b**, Cytoplasmic view reveals a similar orientation of the $G\alpha_{i2}$ $\alpha 5$ -helix and a synthetic peptide derived from the $G\alpha$ subunit of transducin ($G\alpha_{CT}$, purple; PDB code 3PQR) relative to active A_1R and active Rho (in grey), respectively. The small inward movement of TM6 probably reflects a lack of additional contacts for Rho beyond the 11-mer $G\alpha_{CT}$ fragment, whereas the A_1R engages the entire G_{i2} heterotrimer.

actions with TM2, TM3, TM5–TM7 and helix 8. The carboxyl group of F355 (GH5.26) forms a salt bridge with K228^{6,29} (usually K/R in G_i -coupled receptors²⁹). L354 (GH5.25) extends from $G\alpha$ into a hydrophobic pocket lined with A_1R I232^{6,33}, L236^{6,37}, V203^{5,61} and I207^{5,65}. Residue D351 (GH5.22, D in $G\alpha_{i1/2}$ and E in $G\alpha_{i3}$) forms a salt bridge with R108^{3,53} and K294^{8,49}. Notably, studies of chimeric G proteins have suggested that these five C-terminal $\alpha 5$ -helix residues are generally sufficient for selective GPCR-G-protein coupling³⁰, although other residues are also involved³¹. Nonetheless, it is evident that this region makes a very different set of interactions with the A_1R compared to the same region in the β_2AR - G_s complex $\alpha 5$ -helix, the latter characterized by weaker Van der Waals interactions (Fig. 3c). In addition to the $\alpha 5$ -helical residues, D316 of the $\alpha 4$ – $\beta 6$ -loop of $G\alpha_{i2}$ stabilizes the interaction with the A_1R via a salt bridge with K224^{6,25} and K228^{6,29} (Fig. 3a, c).

Although both $G\alpha_i$ and $G\alpha_s$ interact with TM3, TM5, ICL1 and TM6 of their respective GPCRs (Extended Data Fig. 8), $G\alpha_i$ makes additional contacts with the cytoplasmic end of TM7 (R291^{7,56}) and helix 8 (I292^{8,47} and R294^{8,49}), which are absent in the β_2AR - G_s structure (Fig. 4a). In addition, extra density near the unmodelled flexible ICL3 of the A_1R suggests the potential for additional interactions between the receptor and the $G\alpha_i$ $\beta 6$ -sheet. Notably, A_1R L113^{ICL2} does not contribute substantially to $G\alpha_i$ binding, in contrast to the equivalent residue, F139^{ICL2}, in β_2AR - G_s . Indeed, L113^{ICL2} forms only a single Van der Waals bond with I344 (GH5.15), whereas β_2AR F139^{ICL2} binds in an extensive hydrophobic pocket formed by the $G\alpha_s$ $\alpha 5$ -helix, $\beta 2$ – $\beta 3$ -loop and $\beta 1$ -strands (Fig. 3a–c). As in the β_2AR - G_s complex, ICL1 and helix 8 of the A_1R are in close proximity to the $G\beta$ subunit (Extended Data Fig. 9a). The presence of multiple polar and charged amino acids at this interface suggests potential interactions; however, the side-chain density was insufficient for confident modelling.

There have been numerous studies identifying a role for the $G\alpha$ subunit $\alpha 5$ -helix C terminus in determining G-protein selectivity for GPCRs³¹, but less is known about receptor determinants that govern GPCR selectivity for G proteins²⁹. A receptor-based alignment of the A_1R - G_{i2} and β_2AR - G_s complexes revealed that each receptor engages its G protein in a different orientation (Fig. 4a; Extended Data Fig. 8); compared to β_2AR - G_s , G_i in the A_1R - G_{i2} complex is translated by approximately 4.5 Å relative to the receptor along the TM5–TM1 vector. This translation arises from a difference in the position of the $\alpha 5$ -helix relative to the receptor, leading to a movement of the rest of $G\alpha_i$ coupled with movements of $G\beta$ and $G\gamma$ subunits. There are two likely mechanisms contributing to the observed translation: conformational differences in the $G\alpha$ subunits and distinct receptor conformations. With respect to the first mechanism, a comparison of

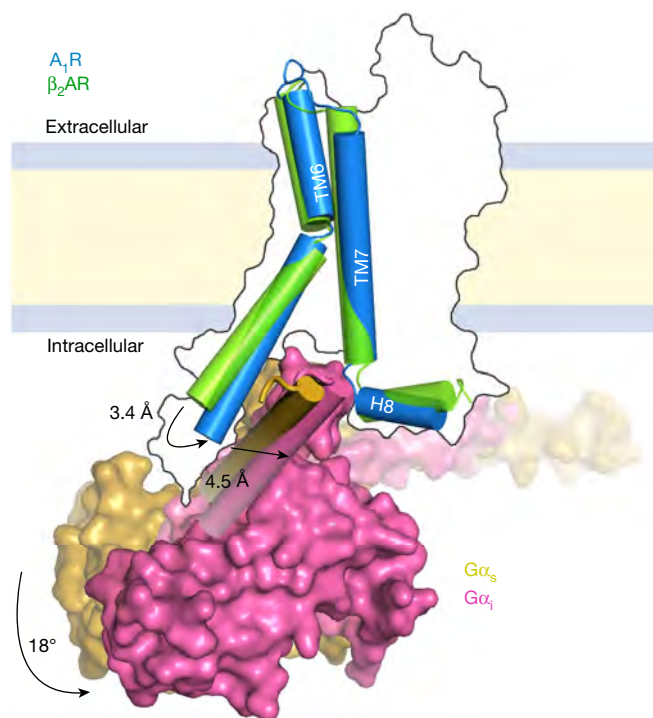


Fig. 5 | Schematic summarizing the key translational and rotational movements contributing to differences in G-protein coupling between A_1R - G_{i2} with β_2AR - G_s . The receptor outline is that of the A_1R as a reference. Key receptor transmembrane domains and the $G\alpha$ protein C-terminal $\alpha 5$ -helices are shown as cylindrical helices (β_2AR , green; A_1R , blue); the rest of the $G\alpha$ proteins are represented as contoured surfaces with $G\alpha_{i2}$ in pink and $G\alpha_s$ in gold.

the nucleotide-free, receptor-bound conformations of the G_i and G_s α -subunits revealed that while, overall, they adopt a similar backbone conformation (r.m.s.d. value of 1.34 Å), there are differences in the flexible loop regions and the $\alpha 5$ -helix conformation (Extended Data Fig. 9b), which arise as a consequence of the last two turns of the $G\alpha_s$ $\alpha 5$ -helix bending towards the $\alpha 4$ – $\beta 6$ -loop. This results in a 3.5 Å shift in positioning of the G.H5.23 C α residue (Extended Data Fig. 9c). However, the bend in the $G\alpha_s$ $\alpha 5$ -helix was not observed in cryo-EM structures^{7–9}. The second mechanism that may lead to distinct orientations of $G\alpha_{i2}$ relative to $G\alpha_s$ in complex with their receptors is related to conformational differences in the receptors themselves, particularly TM6. The A_1R structure displays a smaller outward movement of TM6 relative to β_2AR - G_s ¹⁰ (10.5 Å versus 14 Å, respectively), with the $\alpha 5$ -helix closer to TM7 and helix 8 that results in a difference in receptor interaction angle (approximately 18°) (Fig. 4a). This translation brings D351 (G.H5.22) within a salt-bridge distance of K294^{8,49}, and both C352 (G.H5.23) and G353 (G.H5.24) within Van der Waals radius of R291^{7,56} and I292^{8,47}. A comparison of A_1R - G_{i2} with metarhodopsin II (Rho), the active state of rhodopsin, bound to a C-terminal fragment of transducin ($G\alpha_{CT}$) reveals a similar location of the two domains for $G\alpha_i$ and transducin ($G\alpha_{CT}$) (Fig. 4b), consistent with the fact that $G\alpha_i$ is most closely related to G_i proteins³². The key global conformational differences between the β_2AR - G_s and A_1R - G_{i2} complexes are summarized in Fig. 5. Although it remains to be determined whether G-protein selectivity is mediated predominantly by specific receptor residue contacts as opposed to global conformational rearrangements shaping intracellular ‘pocket complementarity’^{29,33}, a key role for the degree of TM6 tilt is a possibility. However, this should be interpreted with caution because the distinct differences in the movement of TM6 between the β_2AR - G_s and A_1R - G_{i2} structures and translation of the G protein could actually manifest as a result of three different underlying mechanisms: (i) true differences in receptor activation independent of G-protein coupling; this is not readily apparent upon comparison of

the A₁R and A_{2A}R structures (Extended Data Fig. 6); (ii) the signalling state of the solved receptor–G-protein complex being influenced by the nanobody (Nb35) present in the β₂AR–G_s or the dominant-negative mutations present in the G_{α_{i2}} protein in our A₁R–G_{i2} structure; or (iii) a difference in the general activation mechanism for G_{i/o}-coupled compared to G_s-coupled GPCRs. This will ultimately require the solution of more GPCR–G-protein structures in a ‘native’ state as possible. Nonetheless, a role for the degree of TM6 tilt in G-protein selectivity is consistent with previous molecular dynamics studies on β₂AR complexes with C-terminal G_{α_s}- or G_{α_i}-derived peptides³³ and this is supported in the available G protein complexed GPCR structures.

In conclusion, this study presents the first, to our knowledge, active-state class A cryo-EM structure, highlighting the utility of this technique to determine new GPCR structural information. The structure of the ADO–A₁R–G_{i2} heterotrimer provides important insights into the activation mechanism of the A₁R in response to its endogenous agonist. It also allows the first comparison between different subtypes of heterotrimeric G proteins bound to activated GPCRs, which may be pivotal in understanding pleiotropic coupling of these receptors. Finally, the findings have broad implications for understanding the structural basis underlying GPCR–G-protein selectivity, and can facilitate rational, structure-based, approaches for the design of subtype-selective A₁R ligands as new therapeutic agents.

Online content

Any Methods, including any statements of data availability and Nature Research reporting summaries, along with any additional references and Source Data files, are available in the online version of the paper at <https://doi.org/10.1038/s41586-018-0236-6>.

Received: 6 February 2018; Accepted: 16 May 2018;

Published online 20 June 2018.

- Fredholm, B. B., Uzman, A. P., Jacobson, K. A., Linden, J. & Müller, C. E. International Union of Basic and Clinical Pharmacology. LXXXI. Nomenclature and classification of adenosine receptors—an update. *Pharmacol. Rev.* **63**, 1–34 (2011).
- Jacobson, K. A. & Gao, Z.-G. Adenosine receptors as therapeutic targets. *Nat. Rev. Drug Discov.* **5**, 247–264 (2006).
- Nguyen, A. T. N. et al. Role of the second extracellular loop of the adenosine A₁ receptor on allosteric modulator binding, signaling, and cooperativity. *Mol. Pharmacol.* **90**, 715–725 (2016).
- Valant, C. et al. Separation of on-target efficacy from adverse effects through rational design of a bitopic adenosine receptor agonist. *Proc. Natl Acad. Sci. USA* **111**, 4614–4619 (2014).
- Cheng, R. K. Y. et al. Structures of human A₁ and A_{2A} adenosine receptors with xanthines reveal determinants of selectivity. *Structure* **25**, 1275–1285.e4 (2017).
- Glukhova, A. et al. Structure of the adenosine A₁ receptor reveals the basis for subtype selectivity. *Cell* **168**, 867–877.e13 (2017).
- Liang, Y.-L. et al. Phase-plate cryo-EM structure of a class B GPCR–G-protein complex. *Nature* **546**, 118–123 (2017).
- Liang, Y.-L. et al. Phase-plate cryo-EM structure of a biased agonist-bound human GLP-1 receptor–G_s complex. *Nature* **555**, 121–125 (2018).
- Zhang, Y. et al. Cryo-EM structure of the activated GLP-1 receptor in complex with a G protein. *Nature* **546**, 248–253 (2017).
- Rasmussen, S. G. F. et al. Crystal structure of the β₂ adrenergic receptor–G_s protein complex. *Nature* **477**, 549–555 (2011).
- Alexander, S. P. et al. The Concise Guide To Pharmacology 2017/18: G protein-coupled receptors. *Br. J. Pharmacol.* **174** (Suppl. 1), S17–S129 (2017).
- De Lean, A., Stadel, J. M. & Lefkowitz, R. J. A ternary complex model explains the agonist-specific binding properties of the adenylate cyclase-coupled beta-adrenergic receptor. *J. Biol. Chem.* **255**, 7108–7117 (1980).
- Carpenter, B., Nehmé, R., Warne, T., Leslie, A. G. W. & Tate, C. G. Structure of the adenosine A_{2A} receptor bound to an engineered G protein. *Nature* **536**, 104–107 (2016).
- Huang, W. et al. Structural insights into μ-opioid receptor activation. *Nature* **524**, 315–321 (2015).
- Kruse, A. C. et al. Activation and allosteric modulation of a muscarinic acetylcholine receptor. *Nature* **504**, 101–106 (2013).
- Rasmussen, S. G. F. et al. Structure of a nanobody-stabilized active state of the β₂ adrenoceptor. *Nature* **469**, 175–180 (2011).
- Che, T. et al. Structure of the nanobody-stabilized active state of the kappa opioid receptor. *Cell* **172**, 55–67.e15 (2018).
- Erlandson, S. C., McMahon, C. & Kruse, A. C. Structural basis for G protein-coupled receptor signaling. *Annu. Rev. Biophys.* **47**, 1–18 (2018).
- Rosenbaum, D. M. et al. GPCR engineering yields high-resolution structural insights into β₂-adrenergic receptor function. *Science* **318**, 1266–1273 (2007).
- Savinainen, J. R., Saario, S. M., Niemi, R., Järvinen, T. & Laitinen, J. T. An optimized approach to study endocannabinoid signaling: evidence against constitutive activity of rat brain adenosine A₁ and cannabinoid CB₁ receptors. *Br. J. Pharmacol.* **140**, 1451–1459 (2003).
- Liu, W. et al. Structural basis for allosteric regulation of GPCRs by sodium ions. *Science* **337**, 232–236 (2012).
- Rasmussen, S. G. F. et al. Crystal structure of the human β₂ adrenergic G-protein-coupled receptor. *Nature* **450**, 383–387 (2007).
- Haga, K. et al. Structure of the human M2 muscarinic acetylcholine receptor bound to an antagonist. *Nature* **482**, 547–551 (2012).
- Manglik, A. et al. Crystal structure of the μ-opioid receptor bound to a morphinan antagonist. *Nature* **485**, 321–326 (2012).
- Rivkees, S. A., Barbhaiya, H. & Uzman, A. P. Identification of the adenine binding site of the human A₁ adenosine receptor. *J. Biol. Chem.* **274**, 3617–3621 (1999).
- Townsend-Nicholson, A. & Schofield, P. R. A threonine residue in the seventh transmembrane domain of the human A₁ adenosine receptor mediates specific agonist binding. *J. Biol. Chem.* **269**, 2373–2376 (1994).
- Lebon, G. et al. Agonist-bound adenosine A_{2A} receptor structures reveal common features of GPCR activation. *Nature* **474**, 521–525 (2011).
- Nguyen, A. T. N. et al. Extracellular loop 2 of the adenosine A₁ receptor has a key role in orthosteric ligand affinity and agonist efficacy. *Mol. Pharmacol.* **90**, 703–714 (2016).
- Flock, T. et al. Universal allosteric mechanism for G_α activation by GPCRs. *Nature* **524**, 173–179 (2015).
- Stewart, G. D. et al. Determination of adenosine A₁ receptor agonist and antagonist pharmacology using *Saccharomyces cerevisiae*: implications for ligand screening and functional selectivity. *J. Pharmacol. Exp. Ther.* **331**, 277–286 (2009).
- Oldham, W. M. & Hamm, H. E. Heterotrimeric G protein activation by G-protein-coupled receptors. *Nat. Rev. Mol. Cell Biol.* **9**, 60–71 (2008).
- Choe, H.-W. et al. Crystal structure of metarhodopsin II. *Nature* **471**, 651–655 (2011).
- Rose, A. S. et al. Position of transmembrane helix 6 determines receptor G protein coupling specificity. *J. Am. Chem. Soc.* **136**, 11244–11247 (2014).
- Ballesteros, J. A. & Weinstein, H. Integrated methods for the construction of three-dimensional models and computational probing of structure-function relations in G protein-coupled receptors. *Methods Neurosci.* **25**, 366–428 (1995).

Acknowledgements This work was supported by the Monash University Ramaciotti Centre for Cryo-Electron Microscopy, National Health and Medical Research Council of Australia (NHMRC) project grant APP1145420 and NHMRC program grant APP1055134. A.C., P.M.S. and D.W. are NHMRC Senior Principal Research, Principal Research and Career Development Fellows, respectively. A.G. and D.M.T. are Australian Research Council Discovery Early Career Research Fellows. L.T.M. is an Australian Heart Foundation Future Leaders Fellow.

Reviewer information Nature thanks D. Wacker and the other anonymous reviewer(s) for their contribution to the peer review of this work.

Author contributions C.J.D.-J. developed the expression and purification strategy, performed virus production, insect cell expression, purification, and membrane-based pharmacological assays, negative-stain electron microscopy data acquisition/analysis and prepared samples for cryo-EM; M.K. performed sample plunging for cryo-EM, phase-plate imaging and data collection, electron microscopy data processing and analysis; D.M.T. developed the expression and purification strategy, assisted with biochemistry, structure refinement and validation and model interpretation; Y.-L.L. and S.G.B.F. developed the strategy to generate the dominant-negative G_{α_{i2}}; R.D. and W.B. organized and developed the Volta phase-plate cryo-EM data acquisition strategy; H.V. organized microscopy time and provided oversight of image acquisition within the Monash EM facility; J.M.P. provided advice on microscope setup for phase-plate imaging and EM facility access within the Max Planck Institute; A.T.N.N. and J.A.B. performed whole-cell pharmacological assays; L.T.M. supervised whole-cell pharmacological assays; C.J.D.-J., A.T.N.N., J.A.B. and L.T.M. performed data analysis; M.K., D.M.T., Y.-L.L., S.G.B.F., L.T.M., D.W. and P.M.S. assisted with data interpretation and preparation of the manuscript; A.G. developed the expression and purification strategy, performed negative-stain electron microscopy, cryo-EM sample preparation, model building, refinement and validation; C.J.D.-J., A.G. and A.C. wrote the manuscript; P.M.S., A.G. and A.C. supervised the project.

Competing interests The authors declare no competing interests.

Additional information

Extended data is available for this paper at <https://doi.org/10.1038/s41586-018-0236-6>.

Supplementary information is available for this paper at <https://doi.org/10.1038/s41586-018-0236-6>.

Reprints and permissions information is available at <http://www.nature.com/reprints>.

Correspondence and requests for materials should be addressed to P.M.S., A.G. or A.C.

Publisher's note: Springer Nature remains neutral with regard to jurisdictional claims in published maps and institutional affiliations.

METHODS

No statistical methods were used to predetermine sample size. The experiments were not randomized and investigators were not blinded to allocation during experiments and outcome assessment.

Constructs. Wild-type human A₁R was modified to include an N-terminal Flag tag epitope and a C-terminal 8 × histidine tag; both tags are removable by 3C protease cleavage (Extended Data Fig. 1a). A DNGG₁₂ construct was generated by site-directed mutagenesis to incorporate mutations that alter nucleotide binding (S47N, G204A and A327S) and a mutation (E246A) that improves the dominant-negative effect by weakening a salt bridge that helps to stabilize the nucleotide-bound conformation^{8,35–38}. These constructs were generated in insect cell expression vectors.

Insect cell expression. A₁R, human DNGG₁₂, His₆-tagged human Gβ₁ and Gγ₁₂ were expressed in HighFive insect cells (Expression Systems) using baculovirus. Cell cultures were grown in ESF 921 serum-free media (Expression System) to a density of 4 million cells per ml and then infected with either A₁R baculovirus or both G₁₂ and Gβ₁γ₁₂ baculovirus, at a ratio of 1:1. Cultures were grown at 27 °C and collected by centrifugation 60 h after infection. Cells were snap frozen and stored at –80 °C for later use.

Complex purification. Cells from either A₁R or heterotrimeric G_i expression were solubilized separately in 20 mM HEPES pH 7.4, 100 mM NaCl, 5 mM MgCl₂, 5 mM CaCl₂, 0.5% (w/v) lauryl maltose neopentyl glycol (LMNG, Anatrace), 0.01% (w/v) cholesteryl hemisuccinate (CHS, Anatrace) supplemented with Complete Protease Inhibitor Cocktail tablets (Roche). Complex formation was initiated combining solubilized A₁R and heterotrimeric G_i and by addition of 1 mM ADO (Sigma) and apyrase (25 mU ml^{–1}, NEB); followed by 2 h incubation at 4 °C. Insoluble material was removed by centrifugation at 30,000g for 30 min and the solubilized complex was immobilized by batch binding to M1 anti-Flag affinity resin in the presence of 5 mM CaCl₂. The resin was packed into a glass column and washed with 20 column volumes of 20 mM HEPES pH 7.4, 100 mM NaCl, 5 mM MgCl₂, 5 mM CaCl₂, 1 mM ADO, 0.01% (w/v) LMNG and 0.001% (w/v) CHS before bound material was eluted in buffer containing 10 mM EGTA and 0.1 mg ml^{–1} Flag peptide. The complex was concentrated using an Amicon Ultra Centrifugal Filter (MWCO 100 kDa) and subjected to size-exclusion chromatography on a Superdex 200 Increase 10/300 column (GE Healthcare) pre-equilibrated with 20 mM HEPES pH 7.4, 100 mM NaCl, 5 mM MgCl₂, 1 mM ADO, 0.01% (w/v) and 0.001% (w/v) CHS to separate complex from contaminants. Eluted fractions consisting of receptor and G-protein complex were pooled and concentrated. Final yield of purified complex was approximately 0.2 mg l^{–1} insect cell culture.

SDS–PAGE and western blot analysis. Samples collected from each purification step were analysed by SDS–PAGE and western blot. For SDS–PAGE, precast gradient TGX gels (Bio-Rad) were used. Gels were either stained by Instant Blue (Expedeon) or immediately transferred to PVDF membrane (Bio-Rad) at 100 V for 1 h. The proteins on the PVDF membrane were probed first with the primary mouse anti-His antibody (34660, QIAGEN), followed by washing and incubation with secondary anti-mouse antibody (680RD). The membranes were again washed and incubated with an AlexaFluor488 conjugated G₁₂ mouse monoclonal antibody (sc13534, Santa Cruz) against G₁₂. Bands were imaged using a Typhoon multimode imager (GE Healthcare Life Sciences).

Preparation of vitrified specimen. For cryo-EM, purified A₁R–G₁₂ complex was diluted to 1.3 mg ml^{–1} with 20 mM HEPES 7.4, 100 mM NaCl, 5 mM MgCl₂, 1 mM ADO. EM grids (Quantifoil, 200 mesh copper R1.2/1.3) were glow discharged for 30 s using Harrick plasma cleaner (Harrick). 4 µl sample was applied on the grid in the Vitrobot chamber (FEI Vitrobot Mark IV). The chamber of Vitrobot was set to 100% humidity at 4 °C. The sample was blotted for 4.5 s with blot force of 20 and then plunged into propane-ethane mixture (37% ethane and 63% propane).

Data acquisition. Datasets were collected on an FEI Titan Krios microscope operated at 300 kV (FEI) equipped with a Gatan Quantum energy filter, a Gatan K2 summit direct electron camera (Gatan) and a Volta phase-plate^{39–42} (FEI). Movies were taken in EFTEM nanoprobe mode, with 50 µm C2 aperture, at a calibrated magnification of 47,170 corresponding to a magnified pixel size of 1.06 Å. Each movie comprises 50 sub frames with a total dose of 50 e[–] Å^{–2}, exposure time was 12.5 s with the dose rate of 4.5 e[–] pixels^{–1} s^{–1} on the detector. Data acquisition was done using SerialEM software at –500 nm defocus⁴³.

Data processing. A total of 3,220 movies were collected and subjected for motion correction using motioncor2⁴⁴. The movies were collected after installation of a new VPP. Each position on the VPP was used for 24 h. CTF estimation was done using Gctf software⁴⁵ on non-dose-weighted micrographs. The particles were picked using gautomatch (developed by K. Zhang, MRC Laboratory of Molecular Biology, Cambridge, UK, <http://www.mrc-lmb.cam.ac.uk/kzhang/Gautomatch/>). An initial model was made using EMAN2⁴⁶ based on automatically picked few micrographs and using the common-line approach. The particles were extracted in RELION 2.01b1⁴⁷ using a box size of 180 pixels. Next, 831,602 picked particles were subjected to two rounds of 3D classification with three classes. After selecting the best-looking class with 263,321 particles, 3D auto-refinement was done in

RELION 2.01b1. The final map was sharpened with a B-factor of –196 Å². Local resolution was determined using the internal local resolution procedure in Relion, using half-reconstruction as input maps.

Model building. The initial receptor model for A₁R–G₁₂ complex refinement was a chimera between an active state A₁R homology model, made using the SWISS-MODEL server⁴⁸, based on the A_{2A}–mG_s structure (PDB code 5G53) and the inactive A₁R structure (PDB code 5UEN). The initial model for the receptor-bound G₁₂ subunit was a chimera between a G₁₂ homology model, based on the β₂AR-bound heterotrimeric G_s structure (PDB code 3SN6), and a homology model based on the GDP-bound dominant-negative G_{i1} heterotrimer structure (PDB code 5TDH). Gβ and Gγ models were taken from the β₂AR–G_s structure. Refinement, using the phenix.real_space_refine module in PHENIX⁴⁹, was iterated with manual model adjustment and rebuilding in COOT⁵⁰. Restraints for the agonist ADO were generated using the GRADE server, <https://www.globalphasing.com> (v.12.13). Model validation was performed in MolProbity⁵¹. For validation of model overfitting to the cryo-EM maps we displaced the model atoms (the same model used for the final refinement step) up to 0.5 Å using ‘Shake’ in the CCPEM suite⁵². Subsequently, refinement was performed against the sharpened half-map 1 (HM1) (sharpened in Refmac using the full map as the reference⁵³) using phenix.real_space_refine module in PHENIX⁴⁹ with the same parameters used in the final refinement step. Fourier shell correlation (FSC) curves were generated in the MTRIAGE module⁵⁴ in Phenix for: 1) shaken pdb refined against HM1 versus HM1; 2) shaken pdb refined against HM1 versus HM2 (also sharpened in Refmac using the full map as the reference); 3) the final pdb versus the full sharpened map (also sharpened in Refmac using the full map as the reference). Figures were prepared in UCSF Chimera⁵⁵ or PyMOL Molecular Graphics System, Version 2.0 (Schrödinger, LLC).

Insect cell membrane preparations for [³H]DPCPX and [³⁵S]GTPγS binding. The A₁R complex with wild-type heterotrimeric G₁₂ (A₁R, wild-type G₁₂, Gβ₁γ₁₂), DNG₁₂ (A₁R, DNG₁₂, Gβ₁γ₁₂) or A₁R alone were expressed in HighFive insect cells (Expression systems). Cells were collected approximately 48 h after the viral infection. For crude membrane preparations, cells were resuspended in membrane buffer (20 mM HEPES 7.4, 100 mM NaCl, 5 mM MgCl₂, 1 mM EDTA, with protease inhibitors and benzonase), dounced 20 times, followed by centrifugation (5 min, 350g, 4 °C). The pellet was again resuspended in membrane buffer, dounced and clarified by centrifugation at low g. Membranes were pelleted by centrifugation (1 h, 30,000g, 4 °C), resuspended in the membrane buffer and sonicated. The protein concentration was determined using Bradford reagent (Bio-Rad).

Radioligand competition binding experiments in membranes from insect cells expressing the A₁R. [³H]DPCPX binding was performed in 20 mM HEPES pH 7.4, 100 mM NaCl, 5 mM MgCl₂, 0.1% BSA. Membranes were incubated for 1 h at 37 °C with 1 nM of [³H]DPCPX and increasing concentrations of either ADO or cold DPCPX. Membranes were collected on UniFilter GF/C (Whatman) plates using Filtermate 196 harvester (Packard), extensively washed with ice-cold NaCl, dried and dissolved in 50 µl MicroScint-O scintillation cocktail (Packard) and counted using a MicroBeta LumijET counter (PerkinElmer). Non-specific binding was determined in the presence of 10 µM SLV320. Competition binding curves between [³H]DPCPX and either unlabelled DPCPX or ADO were fitted to one- or two-site competition binding equations in Prism 6.0 (GraphPad).

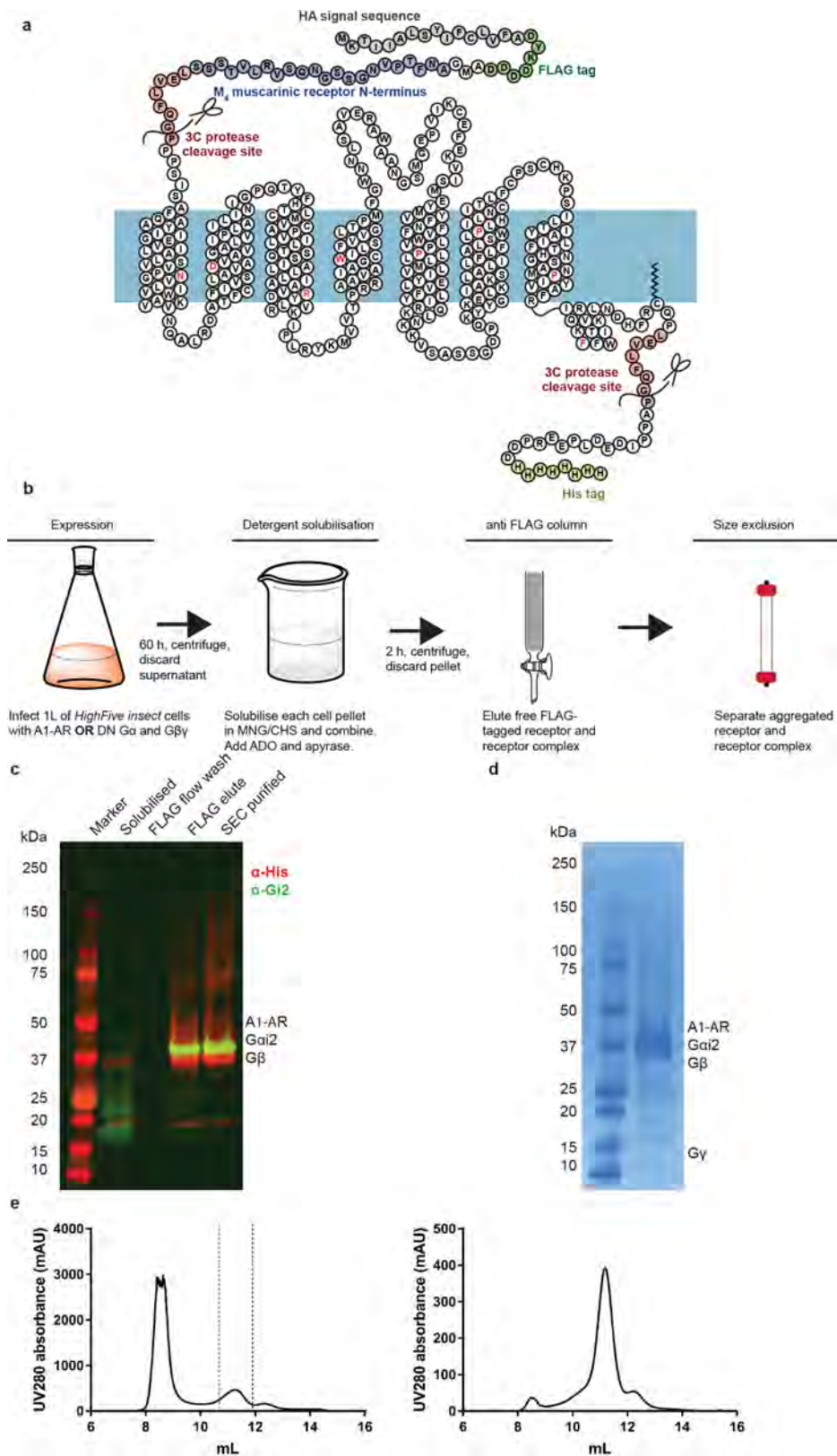
[³⁵S]GTPγS binding in membranes from insect cells expressing the A₁R. Measurement of [³⁵S]GTPγS incorporation to activated G proteins was performed in 20 mM HEPES pH 7.4, 100 mM NaCl, 10 mM MgCl₂, 1 mM EDTA, 0.1% BSA, 30 µg ml^{–1} saponin. First, membranes (10 µg per sample) were pre-incubated with 1 µM GDP and increasing concentrations of ADO for 45 min at 22 °C. Reactions were then started by the addition of [³⁵S]GTPγS and ATP to final concentrations of 300 pM and 50 µM, respectively. After 1 h incubation at 30 °C, the reaction was terminated by harvesting the membranes on Whatman UniFilter GF/C plates using Filtermate 196 harvester (Packard). Membranes were extensively washed with ice-cold 50 mM Tris pH 7.6, 10 mM MgCl₂, 100 mM NaCl, dried, dissolve in 50 µl MicroScint-O scintillation cocktail (Packard) and counted using a MicroBeta LumijET counter (PerkinElmer).

Radioligand competition binding and cAMP accumulation assays in whole cells expressing the wild-type or mutant A₁R. Generation of Chinese hamster ovary (CHO) FlpIN cell lines, stably expressing a 3 × haemagglutinin (HA)-tagged wild-type human A₁R or alanine substitution mutations (V87A; N159A), [³H]DPCPX competition binding, and inhibition of forskolin-stimulated cAMP accumulation by the agonist, NECA, were all performed as described previously²⁸. Generation of the N159A mutation has also been previously described²⁸. For V87A, the following oligonucleotides were used to introduce the valine to alanine substitution at position 87; forward: CATGGTTCCTGTCCGGCCCTCATCTCATCCAG, reverse: CTGGGTGAGGATGAGGGCCGAGCAGGCAACCATG. All other details were as previously described²⁸. Cells were routinely tested and confirmed to be free from mycoplasma contamination.

Reporting summary. Further information on experimental design is available in the Nature Research Reporting Summary linked to this paper.

Data availability. All relevant data are available from the corresponding authors and/or included in the manuscript or Supplementary Information. Atomic coordinates and the cryo-EM density map have been deposited in the Protein Data Bank (PDB) under accession number 6D9H and Electron Microscopy Data Bank (EMDB) entry EMD-7835.

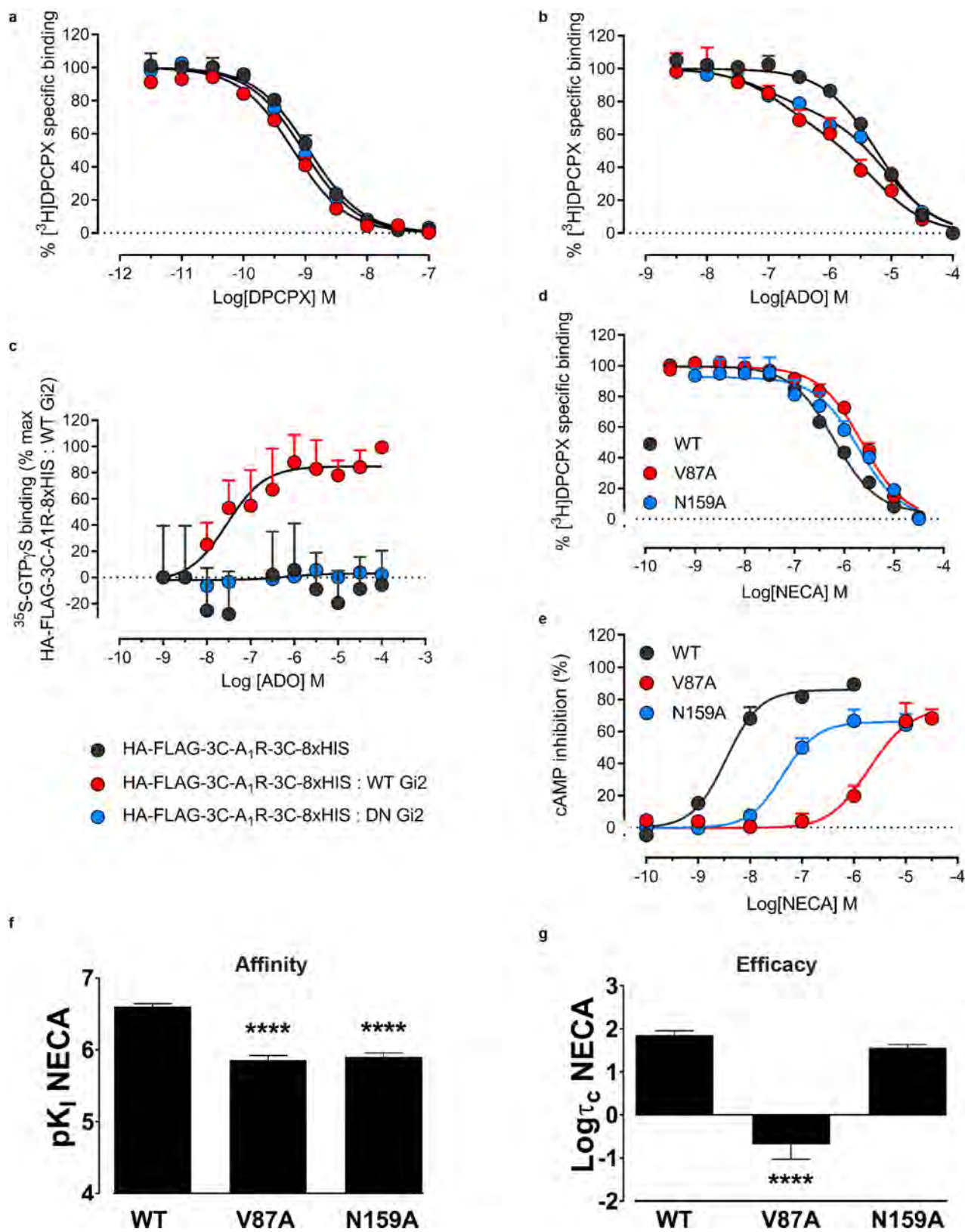
35. Cleator, J. H., Mehta, N. D., Kurtz, D. T. & Hildebrandt, J. D. The N54 mutant of G_{α_s} has a conditional dominant negative phenotype which suppresses hormone-stimulated but not basal cAMP levels. *FEBS Lett.* **443**, 205–208 (1999).
36. Iiri, T., Bell, S. M., Baranski, T. J., Fujita, T. & Bourne, H. R. A G_{α_o} mutant designed to inhibit receptor signaling through G_s . *Proc. Natl Acad. Sci. USA* **96**, 499–504 (1999).
37. Lee, E., Taussig, R. & Gilman, A. G. The G226A mutant of G_{α_o} highlights the requirement for dissociation of G protein subunits. *J. Biol. Chem.* **267**, 1212–1218 (1992).
38. Posner, B. A., Mixon, M. B., Wall, M. A., Sprang, S. R. & Gilman, A. G. The A326S mutant of $G_{\alpha_{i1}}$ as an approximation of the receptor-bound state. *J. Biol. Chem.* **273**, 21752–21758 (1998).
39. Danev, R., Buijsse, B., Khoshouei, M., Plitzko, J. M. & Baumeister, W. Volta potential phase plate for in-focus phase contrast transmission electron microscopy. *Proc. Natl Acad. Sci. USA* **111**, 15635–15640 (2014).
40. Khoshouei, M., Danev, R., Plitzko, J. M. & Baumeister, W. Revisiting the structure of hemoglobin and myoglobin with cryo-electron microscopy. *J. Mol. Biol.* **429**, 2611–2618 (2017).
41. Khoshouei, M. et al. Volta phase plate cryo-EM of the small protein complex Prx3. *Nat. Commun.* **7**, 10534 (2016).
42. Khoshouei, M., Radjainia, M., Baumeister, W. & Danev, R. Cryo-EM structure of haemoglobin at 3.2 Å determined with the Volta phase plate. *Nat. Commun.* **8**, 16099 (2017).
43. Mastronarde, D. N. Automated electron microscope tomography using robust prediction of specimen movements. *J. Struct. Biol.* **152**, 36–51 (2005).
44. Zheng, S. Q. et al. MotionCor2: anisotropic correction of beam-induced motion for improved cryo-electron microscopy. *Nat. Methods* **14**, 331–332 (2017).
45. Zhang, K. Gctf: Real-time CTF determination and correction. *J. Struct. Biol.* **193**, 1–12 (2016).
46. Tang, G. et al. EMAN2: an extensible image processing suite for electron microscopy. *J. Struct. Biol.* **157**, 38–46 (2007).
47. Kimanius, D., Forsberg, B. O., Scheres, S. H. & Lindahl, E. Accelerated cryo-EM structure determination with parallelisation using GPUs in RELION-2. *eLife* **5**, 19 (2016).
48. Arnold, K., Bordoli, L., Kopp, J. & Schwede, T. The SWISS-MODEL workspace: a web-based environment for protein structure homology modelling. *Bioinformatics* **22**, 195–201 (2006).
49. Adams, P. D. et al. PHENIX: a comprehensive Python-based system for macromolecular structure solution. *Acta Crystallogr. D* **66**, 213–221 (2010).
50. Emsley, P., Lohkamp, B., Scott, W. G. & Cowtan, K. Features and development of Coot. *Acta Crystallogr. D* **66**, 486–501 (2010).
51. Chen, V. B. et al. MolProbity: all-atom structure validation for macromolecular crystallography. *Acta Crystallogr. D* **66**, 12–21 (2010).
52. Burnley, T., Palmer, C. M. & Winn, M. Recent developments in the CCP-EM software suite. *Acta Crystallogr. D* **73**, 469–477 (2017).
53. Brown, A. et al. Tools for macromolecular model building and refinement into electron cryo-microscopy reconstructions. *Acta Crystallogr. D* **71**, 136–153 (2015).
54. Afonine, P. V. et al. New tools for the analysis and validation of Cryo-EM maps and atomic models. *bioRxiv* <https://doi.org/10.1101/279844> (2018).
55. Pettersen, E. F. et al. UCSF Chimera—a visualization system for exploratory research and analysis. *J. Comput. Chem.* **25**, 1605–1612 (2004).



Extended Data Fig. 1 | See next page for caption.

Extended Data Fig. 1 | Expression and purification of the ADO–A₁R–G_{i2} complex. **a**, Schematic of the haemagglutinin (HA) and Flag-tagged M4R-3C-A1R-3C-8×His construct. The most conserved residue for class A GPCRs (X.50 class A numbering³⁴) are highlighted for each transmembrane domain in red. **b**, Purification step flowchart for the A₁R–G_{i2} complex. **c**, SDS–PAGE/western blot of samples obtained at various stages of A₁R–G_{i2} purification. A₁R and the G_{i2} heterotrimer were expressed separately in insect cell membranes. Addition of ADO initiated complex formation, which was solubilized by detergent. Solubilized A₁R and A₁R–G_{i2} complex were immobilized on Flag antibody resin.

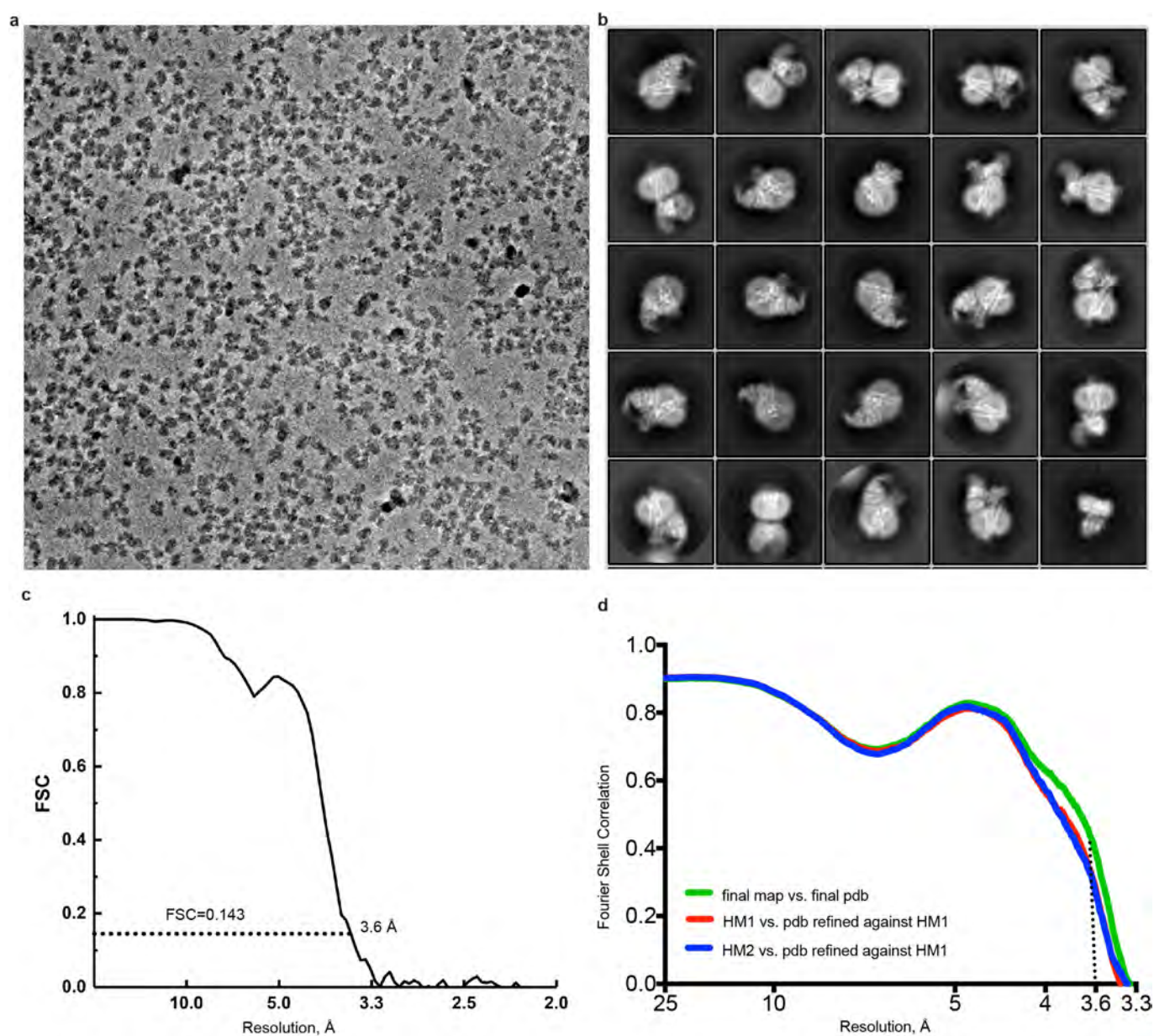
Flag-eluted fractions were purified by size-exclusion chromatography (SEC). An anti-His antibody was used to detect Flag–A₁R–His and Gβ–His (red) and an anti-G_{i2} antibody was used to detect Gα_{i2} (green). **d**, SDS–PAGE/Coomassie blue stain of the purified complex concentrated from the Superdex 200 Increase 10/30 column. **e**, Left, representative elution profile of Flag-purified complex on Superdex 200 Increase 10/30 SEC. Right, SEC fractions containing A₁R–G_{i2} complex (within dashed lines) were pooled, concentrated and analysed by re-running on Superdex 200 Increase 10/30 column. All images and SEC profiles are representative of more than three independent experiments.



Extended Data Fig. 2 | See next page for caption.

Extended Data Fig. 2 | Pharmacology of the A₁R construct and rationally chosen mutations. **a, b,** Competition between the antagonist [³H]DPCPX and either unlabelled DPCPX (**a**) or ADO (**b**), in membranes expressing HA-Flag-3C-A1R-3C-8×His construct in the absence or presence of wild-type (WT) G_{i2} heterotrimer or dominant-negative (DN) G_{i2} heterotrimer. Data are normalized to [³H]DPCPX binding in the absence of unlabelled competitor, with nonspecific binding determined in the presence of 1 μM of the antagonist, SLV320. **c,** ADO-mediated binding of [³⁵S]GTPγS as a measure of G-protein activation by the HA-Flag-3C-A1R-3C-8×His construct in High Five cells expressing receptor alone, or together with either wild-type or dominant-negative G_{i2} heterotrimer.

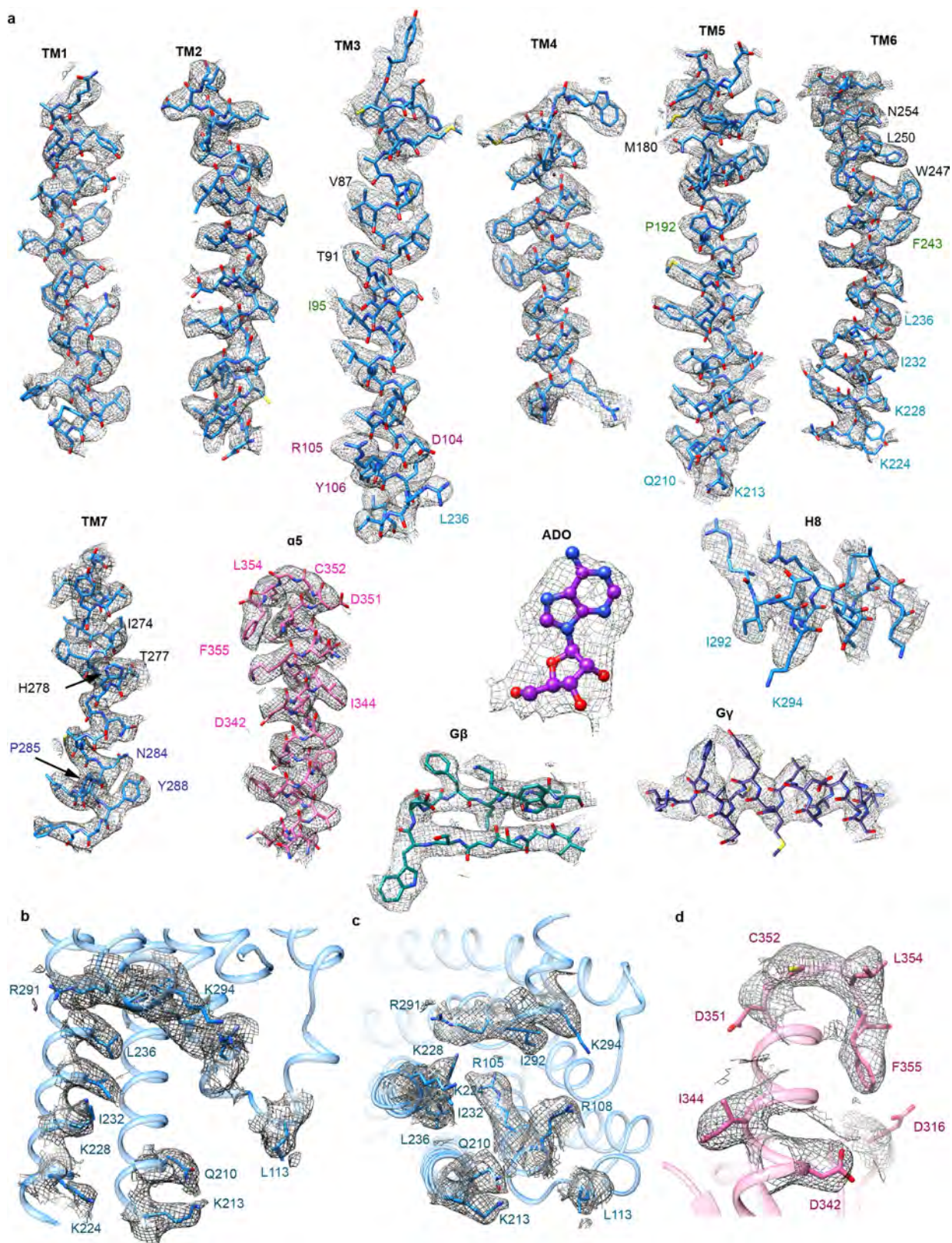
d, e, [³H]DPCPX competition assays (**d**) or inhibition of forskolin-stimulated cAMP accumulation (**e**), at the wild-type human A₁R or two key alanine substitution mutations stably expressed in CHOFlpIn cells. **f,** Changes in agonist (NECA) affinity (K_i) from the experiments shown in **d, g,** Changes in NECA signalling efficacy corrected for receptor expression (τ_c), determined from the experiments shown in **e**. Parameter estimates are the mean ± s.e.m. determined from 3 (**a–c**) or 6–48 (**d–g**) independent experiments performed in duplicate. **** $P < 0.0001$ (compared with wild type; one-way analysis of variance (ANOVA), Dunnett's post hoc test). Data for wild-type and N159A are replotted from Nguyen et al²⁸.



Extended Data Fig. 3 | Cryo-EM of the ADO-A₁R-G_{i2} complex.

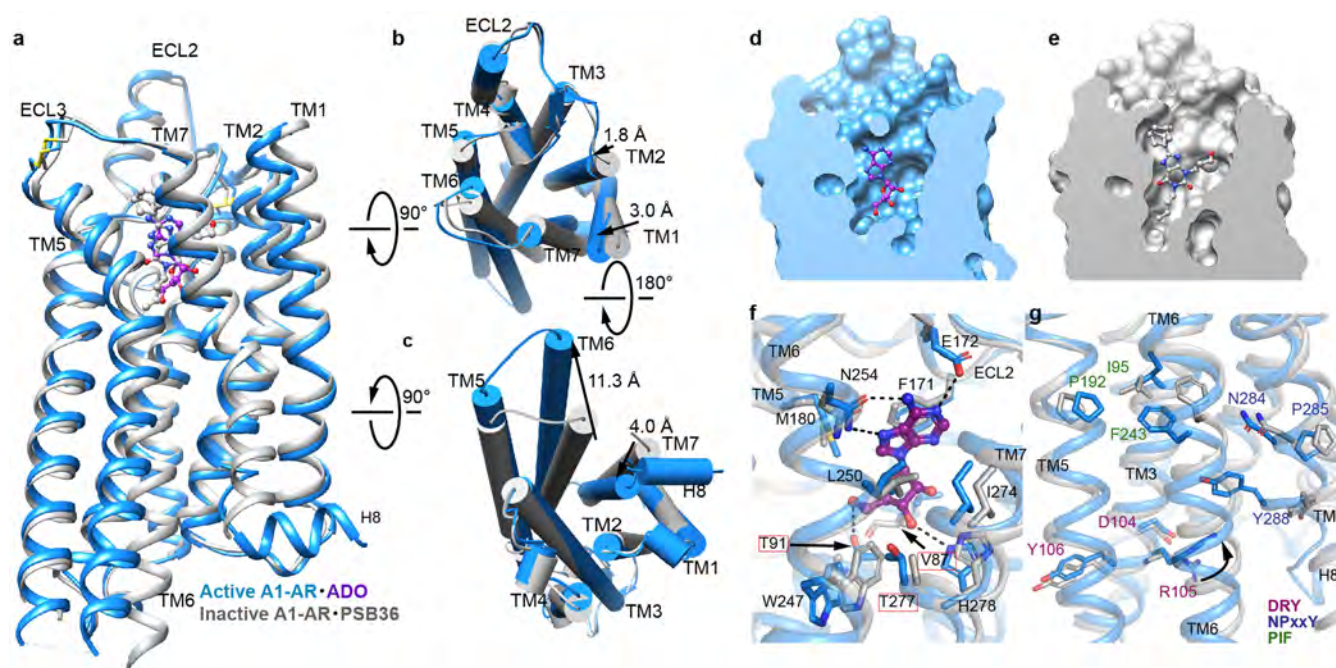
a, Representative VPP cryo-EM micrograph (of 3,220 recordings) of the ADO-A₁R-G_{i2} complex. **b**, Reference-free 2D class averages of the complex in LMNG and CHS detergent micelles. **c**, Gold-standard Fourier

shell correlation (FSC) curves, showing the overall nominal resolution at 3.6 Å. **d**, FSC curves for the final model versus the final map and the half maps for overfitting validation (see Methods).



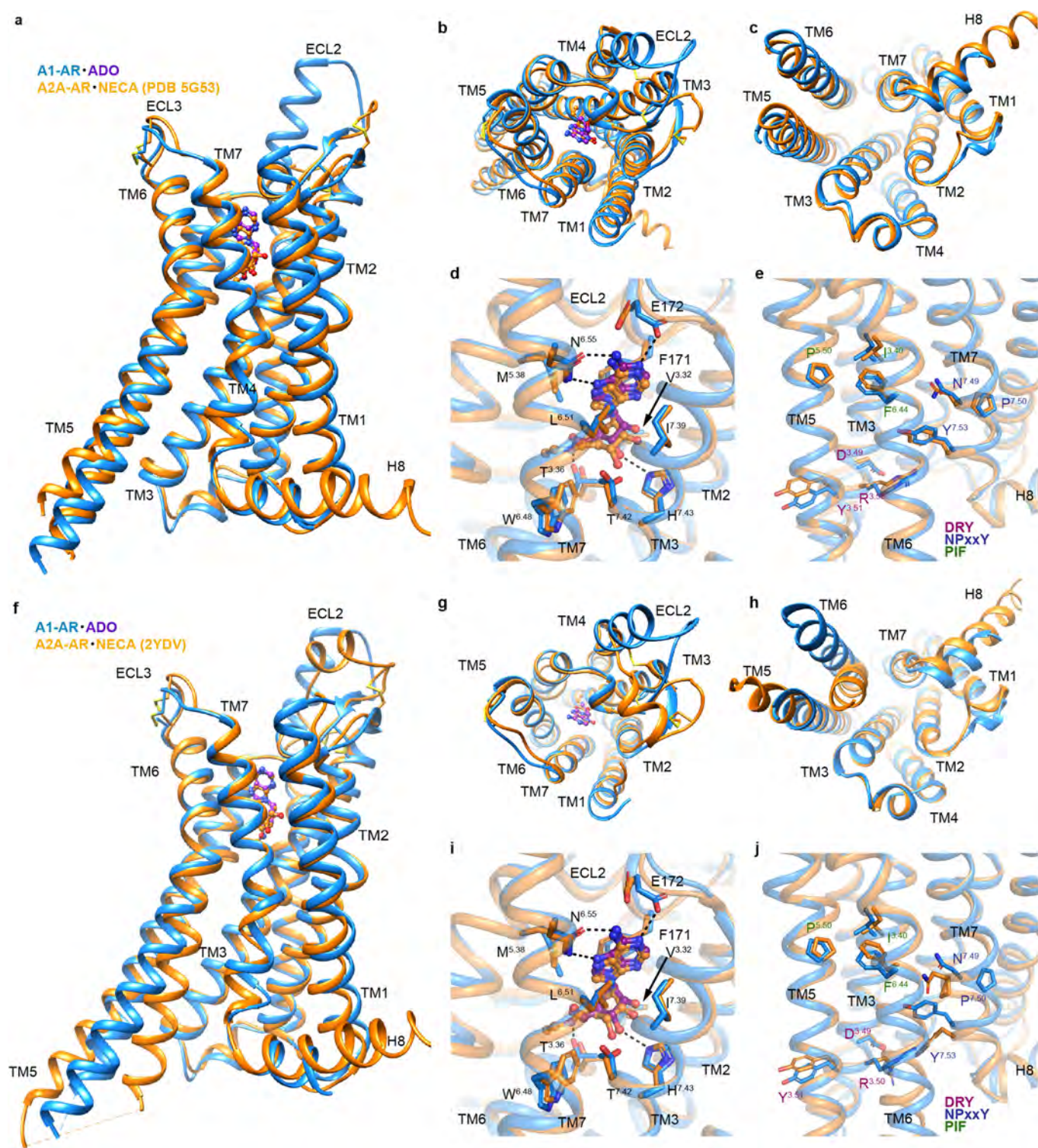
Extended Data Fig. 4 | Atomic resolution model of A₁R transmembrane domains, the G α protein α 5-helix, ADO, and representative regions of G β and G γ in the cryo-EM density map. a, The molecular model is shown in stick representation and the cryo-EM map in mesh contoured

at 0.06. **b–d**, A1R residues (**b**, **c**) and G α_{i2} α 5-helix residues (**d**). The molecular model is shown in stick representation and the cryo-EM map in mesh contoured at 0.06.



Extended Data Fig. 5 | Comparison of active and alternative inactive A₁R (PDB code 5NS2) structure. **a–c**, Side (a), extracellular (b) and cytoplasmic (c) view of the ADN-A₁R-G₁₂ structure (blue) compared to the inactive PSB36-bound A₁R (grey). **d, e**, Active ADO-A₁R (d) and inactive PSB36-A₁R (e) receptor surfaces sliced to show binding site cavity. **f**, Orthosteric binding site of the active A₁R-G₁₂ complex with ADO

(purple ball and sticks). 'Toggle switch' W247^{6,48} and residues within 4 Å of ADO are labelled and shown as sticks. Red rectangles highlight rotamer changes upon receptor activation. N, O and S atoms are coloured in blue, red and yellow, respectively. Dashed lines represent hydrogen bonds. **g**, GPCR motifs important for receptor activation (DRY motif, purple; NPXXY motif, blue; PIF motif, green).



Extended Data Fig. 6 | Comparison of active A₁R with active A_{2A}R (PDB code 5G53) or agonist-bound ‘intermediate’ state A_{2A}R (PDB code 2YDV). **a–j**, Side views (**a**, **f**), extracellular views (**b**, **g**) and cytoplasmic views (**c**, **h**) of the active ADO–A₁R–G₁₂ structure (blue) compared to the active NECA–A_{2A}R–mini-G_s structure (**a–e**) or ‘intermediate’ NECA–A_{2A}R structure (orange) (**f–j**). **d**, **i**, Orthosteric binding site of the active

A₁R–G₁₂ complex with ADO (purple ball and sticks) or A_{2A}R with NECA (orange ball and sticks). ‘Toggle switch’ residue W^{6.48} and residues within 4 Å of ADO are labelled and shown as sticks. N, O and S atoms are coloured in blue, red and yellow, respectively. Dashed lines represent hydrogen bonds. **e**, **j**, Conserved class A GPCR motifs important for receptor activation (DRY motif, purple; NPXXY motif, blue; PIF motif, green).

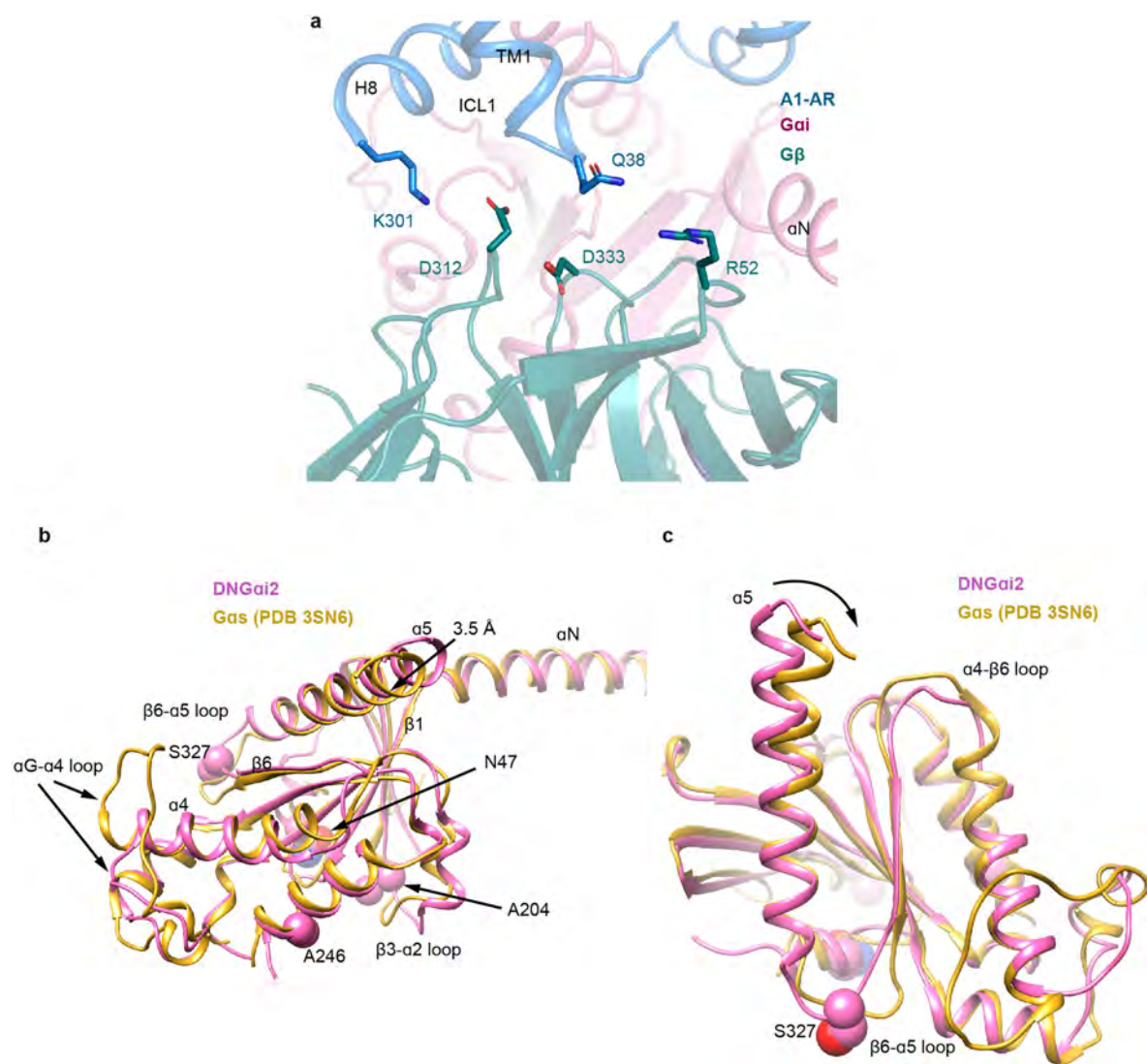


Extended Data Fig. 7 | Alignments of A₁R with β_2 AR or dominant-negative G α_{i2} with G α_s . a, A₁R alignment with β_2 AR. b, G α_s alignment with dominant-negative G α_{i2} . Key Ballesteros–Weinstein numbers are shown in red. Grey bars indicate the positions of the α -helices in the

A₁R–G α_{i2} structure, whereas red bars indicate these regions in the β_2 AR–G α_s structure. Dominant-negative G α_{i2} point mutations are highlighted in yellow.



Extended Data Fig. 8 | Comparison of the A_1R - G_{i2} with β_2AR - G_s structures. Overlay of A_1R - G_{i2} with β_2AR - G_s (PDB code 3SN6) complexes. (A_1R - G_{i2} is coloured as in Fig. 1; β_2AR is in green, G_{α_s} is in gold, G_{β} is in light cyan, G_{γ} is in light purple).



Extended Data Fig. 9 | View of key residues at the interface of A₁R and G β , and G α conformations. a, A₁R is in blue and G β is in dark cyan. **b, c**, Different views comparing DNG α _{i2} and G α _s from A₁R and β ₂AR (PDB code 3SN6) receptor-bound structures (DNG α _{i2}, pink; G α _s, gold).

Spheres indicate the positions of the dominant-negative mutations on the DNG α _{i2} with N, O and C atoms coloured in blue, red and pink, respectively. The α 5-helix bend and loops that are the most different between G α _{i2} and G α _s are indicated.

Extended Data Table 1 | Cryo-EM data collection, refinement and validation statistics

A1-AR·G _{i2} (EMDB- EMD-7835) (PDB 6D9H)	
Data collection and processing	
Magnification	47170
Voltage (kV)	300
Electron exposure (e ⁻ /Å ²)	50e/A ²
Defocus range (nm)	-500
Pixel size (Å)	1.06
Symmetry imposed	C1
Initial particle images (no.)	831,602
Final particle images (no.)	263,321
Map resolution (Å)	3.6
FSC threshold	0.143
Map resolution range (Å)	3.4 - 4.2
Refinement	
Initial model used (PDB code)	5UEN, 5G53, 3SN6, 5TDH
Model resolution (Å)	
FSC threshold	0.143
Model resolution range (Å)	3.6
Map sharpening <i>B</i> factor (Å ²)	-196
Model composition	
Protein residues	893
Ligand (ADO)	1
<i>B</i> factors (Å ²)	
Protein residues	21-125 (avr. 54)
Ligand (ADO)	44.5
R.m.s. deviations	
Bond lengths (Å)	0.007
Bond angles (°)	1.2
Validation	
MolProbity score	1.42
Clashscore	4.18
Poor rotamers (%)	0
Ramachandran plot	
Favored (%)	96.6
Allowed (%)	3.4
Disallowed (%)	0

Reporting Summary

Nature Research wishes to improve the reproducibility of the work that we publish. This form provides structure for consistency and transparency in reporting. For further information on Nature Research policies, see [Authors & Referees](#) and the [Editorial Policy Checklist](#).

Statistical parameters

When statistical analyses are reported, confirm that the following items are present in the relevant location (e.g. figure legend, table legend, main text, or Methods section).

n/a Confirmed

- ☐ ☒ The exact sample size (n) for each experimental group/condition, given as a discrete number and unit of measurement
- ☐ ☒ An indication of whether measurements were taken from distinct samples or whether the same sample was measured repeatedly
- ☐ ☒ The statistical test(s) used AND whether they are one- or two-sided
Only common tests should be described solely by name; describe more complex techniques in the Methods section.
- ☒ ☐ A description of all covariates tested
- ☐ ☒ A description of any assumptions or corrections, such as tests of normality and adjustment for multiple comparisons
- ☐ ☒ A full description of the statistics including central tendency (e.g. means) or other basic estimates (e.g. regression coefficient) AND variation (e.g. standard deviation) or associated estimates of uncertainty (e.g. confidence intervals)
- ☐ ☒ For null hypothesis testing, the test statistic (e.g. F , t , r) with confidence intervals, effect sizes, degrees of freedom and P value noted
Give P values as exact values whenever suitable.
- ☒ ☐ For Bayesian analysis, information on the choice of priors and Markov chain Monte Carlo settings
- ☒ ☐ For hierarchical and complex designs, identification of the appropriate level for tests and full reporting of outcomes
- ☒ ☐ Estimates of effect sizes (e.g. Cohen's d , Pearson's r), indicating how they were calculated
- ☐ ☒ Clearly defined error bars
State explicitly what error bars represent (e.g. SD, SE, CI)

Our web collection on [statistics for biologists](#) may be useful.

Software and code

Policy information about [availability of computer code](#)

Data collection

Serial EM

Data analysis

GraphPad Prism 6.0, Gctf software, RELION 2.01b1, USCF Chimera, PyMOL Molecular Graphics System, PHENIX, COOT, Motioncor2, MolProbity, Gautomatch, EMAN2, CCPEM, Refmac

For manuscripts utilizing custom algorithms or software that are central to the research but not yet described in published literature, software must be made available to editors/reviewers upon request. We strongly encourage code deposition in a community repository (e.g. GitHub). See the Nature Research [guidelines for submitting code & software](#) for further information.

Data

Policy information about [availability of data](#)

All manuscripts must include a [data availability statement](#). This statement should provide the following information, where applicable:

- Accession codes, unique identifiers, or web links for publicly available datasets
- A list of figures that have associated raw data
- A description of any restrictions on data availability

All relevant data are available from the authors and/or included in the manuscript or Supplementary Information. Atomic coordinates and the cryo-EM density map have been deposited in the Protein Data Bank (PDB) under accession number 6D9H and EMDB entry ID EMD-7835.

Field-specific reporting

Please select the best fit for your research. If you are not sure, read the appropriate sections before making your selection.

☒ Life sciences ☐ Behavioural & social sciences ☐ Ecological, evolutionary & environmental sciences

For a reference copy of the document with all sections, see [nature.com/authors/policies/ReportingSummary-flat.pdf](https://www.nature.com/authors/policies/ReportingSummary-flat.pdf)

Life sciences study design

All studies must disclose on these points even when the disclosure is negative.

Sample size	Number of technical replicates and biological replicates are reported in the figure legends. Sample size was determined based on variability of the response deviating from the mean as indicated by the standard error of the mean (SEM), which is also represented in the figures
Data exclusions	No data were excluded from analysis
Replication	All data was replicable, with the number of replicates provided in text and/ or figure legends.
Randomization	Randomization was not required
Blinding	Blinding was not required

Reporting for specific materials, systems and methods

Materials & experimental systems

n/a	Involved in the study
<input checked="" type="checkbox"/>	<input type="checkbox"/> Unique biological materials
<input type="checkbox"/>	<input checked="" type="checkbox"/> Antibodies
<input type="checkbox"/>	<input checked="" type="checkbox"/> Eukaryotic cell lines
<input checked="" type="checkbox"/>	<input type="checkbox"/> Palaeontology
<input checked="" type="checkbox"/>	<input type="checkbox"/> Animals and other organisms
<input checked="" type="checkbox"/>	<input type="checkbox"/> Human research participants

Methods

n/a	Involved in the study
<input checked="" type="checkbox"/>	<input type="checkbox"/> ChIP-seq
<input checked="" type="checkbox"/>	<input type="checkbox"/> Flow cytometry
<input checked="" type="checkbox"/>	<input type="checkbox"/> MRI-based neuroimaging

Antibodies

Antibodies used	Anti-His antibody (cat. no. 564 34660, QIAGEN) 1:5000 Goat anti-mouse Alex647 (cat. no. A-21235, ThermoScientific) 1:1000 AlexaFluor®488 conjugated Gai2 mouse monoclonal antibody (cat. no. sc13534, Santa 567 Cruz) 1:1000
Validation	All antibodies have been commercially obtained and are described as required in Methods.

Eukaryotic cell lines

Policy information about [cell lines](#)

Cell line source(s)	All cell lines were originally obtained from ATCC or Expression Systems
Authentication	None of the cell lines have been authenticated
Mycoplasma contamination	"All cell lines tested negative for mycoplasma contamination" has been declared in Methods.
Commonly misidentified lines (See ICLAC register)	No commonly misidentified cell lines were used.

Cryo-EM structure of the active, G_s-protein complexed, human CGRP receptor

Yi-Lynn Liang^{1,11}, Maryam Khoshouei^{2,10,11}, Giuseppe Deganutti³, Alisa Glukhova¹, Cassandra Koole¹, Thomas S. Peat⁴, Mazdak Radjainia^{1,5}, Jürgen M. Plitzko², Wolfgang Baumeister², Laurence J. Miller^{1,6}, Deborah L. Hay^{7,8}, Arthur Christopoulos¹, Christopher A. Reynolds³, Denise Wootten^{1,9*} & Patrick M. Sexton^{1,9*}

Calcitonin gene-related peptide (CGRP) is a widely expressed neuropeptide that has a major role in sensory neurotransmission. The CGRP receptor is a heterodimer of the calcitonin receptor-like receptor (CLR) class B G-protein-coupled receptor and a type 1 transmembrane domain protein, receptor activity-modifying protein 1 (RAMP1). Here we report the structure of the human CGRP receptor in complex with CGRP and the G_s-protein heterotrimer at 3.3 Å global resolution, determined by Volta phase-plate cryo-electron microscopy. The receptor activity-modifying protein transmembrane domain sits at the interface between transmembrane domains 3, 4 and 5 of CLR, and stabilizes CLR extracellular loop 2. RAMP1 makes only limited direct contact with CGRP, consistent with its function in allosteric modulation of CLR. Molecular dynamics simulations indicate that RAMP1 provides stability to the receptor complex, particularly in the positioning of the extracellular domain of CLR. This work provides insights into the control of G-protein-coupled receptor function.

CGRP is a physiologically important sensory neuropeptide with roles that include modulation of metabolism, inflammatory response and blood pressure, as well as auditory nerve development and function^{1–4}. It is a potent vasodilator that is released during neurogenic inflammation and contributes to the pathology of migraine. A first-in-class drug targeting the CGRP receptor was recently approved for treatment of this condition, and many other therapeutic agents aimed at reducing CGRP activity are under development⁵. By contrast, CGRP is protective in models of inflammatory bowel disease and hypertension, and is a critical neuropeptide for development and modulation of auditory responses^{1–4}.

Receptor activity-modifying proteins (RAMPs) are essential accessory proteins for presentation of the class B CLR to the cell surface. They are integral components of the phenotypically ascribed CGRP and adrenomedullin receptors, through which CLR–RAMP1 mediates a selective response to CGRP, and CLR–RAMP2 or CLR–RAMP3 mediate selective responses to adrenomedullin⁶. RAMPs are also partners for the calcitonin receptor (CTR), but are not required for cell surface trafficking; they generate distinct amylin receptor phenotypes¹. There is considerable crosstalk between calcitonin-family peptides and receptors; however, research has largely focused on how RAMPs influence cAMP signalling¹. The three RAMPs each contain a structured, N-terminal extracellular domain (ECD) of about 100 amino acids, a single transmembrane domain and a short intracellular C terminus. There is evidence that RAMPs co-evolved with GPCRs⁷; supporting this, we and others have shown that they can partner with numerous GPCRs from all major subclasses, and are not exclusively partners for CLR and CTR^{8–11}.

Structures of heteromeric complexes of the isolated extracellular domains (ECDs) of RAMPs and CLR bound to C-terminal peptide fragments have been solved^{12,13}, and provide important but limited data

on how RAMPs and CLR interact; however, they are unable to explain peptide selectivity. Therefore, structures of full-length, active CGRP and adrenomedullin receptor complexes are required.

Recent advances in cryo-electron microscopy (cryo-EM) have enabled elucidation of structures of full-length, class B GPCRs bound to peptide agonists, in complex with their canonical G_s-protein heterotrimers^{14–16}. These studies revealed class-specific, conserved, global conformational changes linked to receptor activation, and unexpected divergence in the modes of peptide binding, even within the same receptor^{14–18}. In the current work, we have used Volta phase-plate cryo-EM to determine the structure—at a global resolution of 3.3 Å—of the human CGRP receptor complex bound to its endogenous peptide agonist and canonical transducer. This structure provides insights into how RAMPs interact with GPCRs and modulate their activity.

Structure determination

We modified the CLR to replace the native signal peptide with that of haemagglutinin and affinity tags bracketed by 3C cleavage sites were introduced at the N and C terminus (Flag and His, respectively) (Extended Data Fig. 1). RAMP1 was modified with a haemagglutinin signal peptide followed by a Flag epitope (Extended Data Fig. 1). These modifications did not alter the receptor pharmacology (Extended Data Fig. 2a).

To form an active, G-protein-coupled complex, CLR and RAMP1 were co-expressed with G_{αs}, His-Gβ₁ and Gγ₂ in *Trichoplusia ni* insect cells, and stimulated with 10 μM CGRP. A stabilized G_{αs}¹⁵ was used together with the camelid antibody-derived nanobody Nb35^{14–16}, enabling formation of a complex with improved stability¹⁹. The complex was treated with 3C enzyme to remove tags from CLR, solubilized in lauryl maltose neopentyl glycol (LMNG) and cholesteryl hemisuccinate and then purified by sequential nickel-affinity and

¹Drug Discovery Biology and Department of Pharmacology, Monash Institute of Pharmaceutical Sciences, Monash University, Parkville, Victoria, Australia. ²Department of Molecular Structural Biology, Max Planck Institute of Biochemistry, Martinsried, Germany. ³School of Biological Sciences, University of Essex, Colchester, UK. ⁴CSIRO Biomedical Manufacturing, Melbourne, Victoria, Australia. ⁵Thermo Fisher Scientific, Eindhoven, The Netherlands. ⁶Department of Molecular Pharmacology and Experimental Therapeutics, Mayo Clinic, Scottsdale, AZ, USA. ⁷School of Biological Sciences, University of Auckland, Auckland, New Zealand. ⁸Maurice Wilkins Centre for Molecular Biodiscovery, University of Auckland, Auckland, New Zealand. ⁹School of Pharmacy, Fudan University, Shanghai, China. ¹⁰Present address: Novartis Institutes for Biomedical Research, Novartis Pharma, Basel, Switzerland. ¹¹These authors contributed equally: Yi-Lynn Liang, Maryam Khoshouei. *e-mail: denise.wootten@monash.edu; patrick.sexton@monash.edu

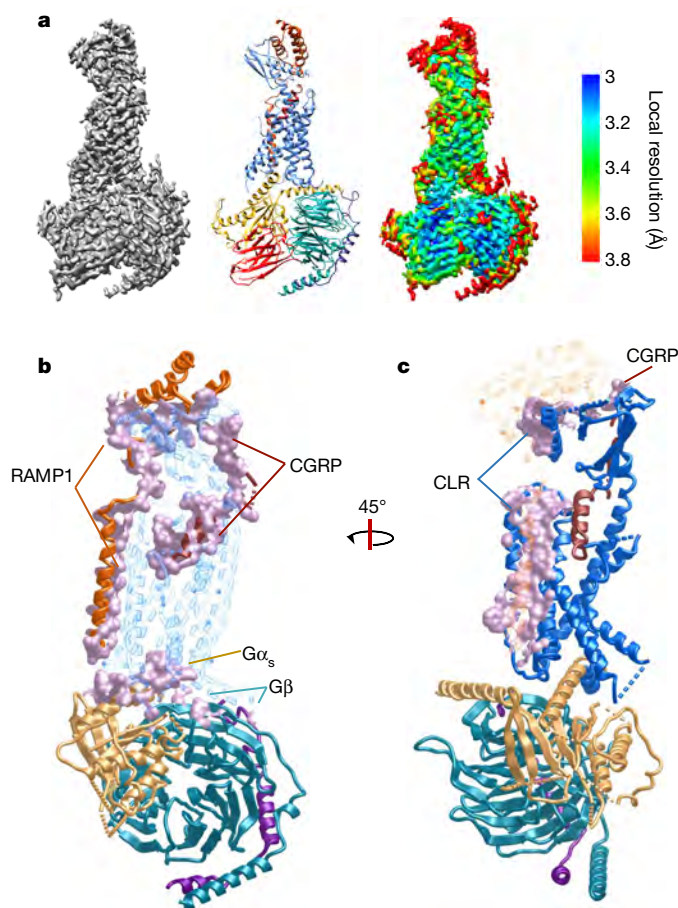


Fig. 1 | The cryo-EM structure of CGRP-CLR-RAMP1-Gs reveals molecular details of the RAMP-receptor interface. **a**, Left, 3.3 Å-resolution cryo-EM density map of the CGRP-CLR-RAMP1-Gs complex; the detergent micelle has been masked out for clarity. Middle, the structure in ribbon representation after refinement in the cryo-EM map. CGRP, dark red; CLR, blue; RAMP1, dark orange; G α_s -Ras domain, gold; G β -subunit, cyan; G γ -subunit, purple; Nb35, red. Right, the cryo-EM density map coloured by local resolution. **b**, **c**, CGRP receptor complex (ribbon representation coloured as in **a**), illustrating the extent of CLR interactions with other proteins in the complex (**b**), or the extent of RAMP1 interactions with other proteins in the complex (**c**), shown in mauve coloured surface representation. CGRP and RAMP1 form extensive contacts with CLR, with 61.5% and 23% of their surface being buried, respectively.

Flag-antibody columns, to ensure that only RAMP1-bound complexes were present, and then further purified by size-exclusion chromatography to yield a monodisperse complex that contained all the components (Extended Data Fig. 2b, c).

Vitrified complexes were imaged using a Titan Krios microscope equipped with a Volta phase plate^{20,21}. Following imaging (Extended Data Fig. 3a) and initial 2D classification (Extended Data Fig. 3b), 3D classification yielded a final map at a resolution of 3.3 Å reconstructed from 407,000 particle projections (Fig. 1a, Extended Data Fig. 3c–e, Supplementary Table 1). The cryo-EM density map exhibited well-resolved side chains, allowing confident rotamer placements for most amino acids within the peptide, receptor and RAMP transmembrane domains, and the G protein (Extended Data Fig. 4). The RAMP and CLR ECDs had lower overall resolution, with discontinuous density for CLR ECD loop 1 and loop 5 (Fig. 1a, Extended Data Figs. 1, 5). Nonetheless, there was a strong correlation between the cryo-EM density of the ECD and those of the individual ECDs of either CLR or RAMP1 in a deposited X-ray structure (RCSB Protein Data Bank code (PDB): 4RWG¹²). These were rigid-body fitted into the ECD density, with side-chain adjustment where this was supported by density in the

cryo-EM map. Whereas individual ECDs from the X-ray structures exhibited close approximation to the cryo-EM map, there were differences between the two structures in the relative positioning of the CLR and RAMP1 ECDs (Extended Data Fig. 5) that are likely to have arisen from anchoring constraints of the transmembrane domains in the full-length structure. Continuous density was observed for the RAMP1 ECD and transmembrane domain, including the unstructured linker domain, but not for the short C-terminal tail of RAMP (Thr144-Glu-Gly-Ile-Val148), indicating that it is mobile in the active receptor complex (Fig. 1). There was robust density for most of the transmembrane core and loops of CLR, but not for segments of extracellular loop 3 (ECL3) and intracellular loop 3 (ICL3) (Fig. 1, Extended Data Fig. 4). Additional density was observed adjacent to the base of transmembrane domain 2 (TM2) and TM4, which may represent lipid interactions with CLR (Extended Data Fig. 3g). There was a relatively short helix 8 (H8), with no density for the C terminus of CLR beyond Y402^{8,53} (receptor residues in superscript are defined using the class B numbering system^{14,22}) or for the far N terminus of the ECD (Fig. 1, Extended Data Fig. 1), indicating that these regions are also mobile. The N terminus of CGRP (A1–V23), which binds within the receptor core, was well-defined in the map, and the majority of side chains in the CGRP C terminus (F27–F37) that interact exclusively with receptor ECDs, were also supported by good density (Extended Data Fig. 4). Similar to salmon calcitonin (sCT) in the G $_s$ -coupled CTR¹⁴, there is a large kink in the peptide that enables interaction across the two receptor domains, with the CGRP linker (K24–N26) being poorly resolved in the map. Within the receptor core, side chains that had limited density were stubbed in the model (Extended Data Fig. 1). There was well-resolved density for the G $_s$ heterotrimer across the receptor interface and between subunits. The α -helical domain of the α -subunit was present only in a small number of the 2D class averages and was masked out during map refinement. In general, the regions of lower resolution or those lacking density were segments of the complex that exhibited higher mobility in molecular dynamics simulations of the full complex (Extended Data Fig. 6, Supplementary Videos 1, 2).

The CLR-RAMP1 interface

The 2D class averages reveal that there is a single predominant orientation of the ECDs of the complex relative to the CLR-RAMP1 core (Extended Data Fig. 3b). This is in contrast to the variability in ECD orientation observed for the CTR¹⁴. RAMP1 makes extensive contacts with CLR, with around 23% of its surface being buried within this interface (Fig. 1b, c). The extensive interface across the ECDs has been reported in X-ray crystal structures^{12,23}. In contrast to predictions in published models of RAMPs in complex with CLR or CTR^{24–27}, the RAMP1 transmembrane domain sits at an interface formed by TM3, TM4 and TM5 of CLR, with interactions of the upper half occurring principally with TM5 (T288^{5.33/ECL2}, H289^{5.34/ECL2}, I293^{5.38}) (Fig. 2a, b) and at the base with TM3 (L231^{3.48}, I235^{3.52}, T239^{3.56}, V243^{ICL2}) and TM4 (W254^{4.44}, Y255^{4.45}, L258^{4.48}, F262^{4.52}) (Fig. 2a, c). These interactions were primarily van der Waals interactions, although there was potential for hydrogen-bond formation between Y255^{4.45} and RAMP1 S141. D113 in the membrane-proximal segment of RAMP1 formed hydrogen bonds with residues in ECL2 proximal to CLR TM4 (Y278^{ECL2}) and TM5 (T288^{5.33}, H289^{5.34}) (Fig. 2b). Alanine mutagenesis studies of CLR residues^{28–33} revealed decreased CGRP potency for the Y278^{ECL2}, T288^{5.33/ECL2} and W254^{4.44} mutants, with no effect from H289^{5.34/ECL2}, I293^{5.38}, T239^{3.56}, V243^{ICL2} or Y255^{4.45} mutants^{32,33}, consistent with important but weak interactions between RAMP1 and CLR. Likewise, there was a small decrease in CGRP potency with the RAMP1(D113A) mutant, indicating an indirect effect on CGRP binding³⁴. To understand the dynamics of the RAMP1-CLR interface, we performed molecular dynamics simulations, following modelling of missing amino acids and side chains into the full protein complex (Extended Data Fig. 7a, b, Supplementary Table 2, Supplementary Video 1); these simulations confirmed the importance of interactions between RAMP1 D113 and CLR ECL2 (Extended Data Fig. 7a).

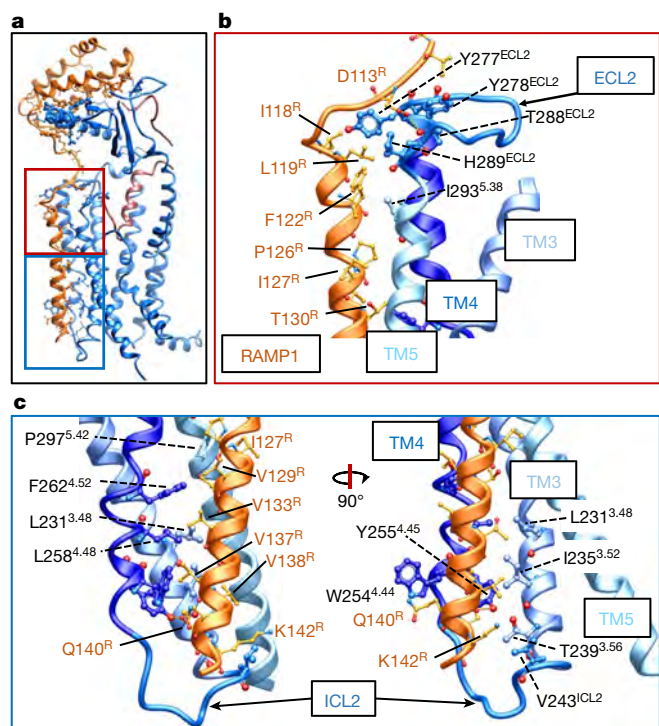


Fig. 2 | RAMP1 forms stable interactions with the CLR core and ECD.

a, The CGRP–CLR–RAMP1 complex, with the interacting residues depicted in x-stick representation, and the backbone shown in ribbon representation. CGRP, dark red; CLR, blue; RAMP1, dark orange. Boxes indicate regions that are expanded in **b** (red) and **c** (blue). **b**, RAMP1 interacts with ECL2 and the top of TM5 towards the extracellular face of the receptor. **c**, RAMP1 interacts with TM3 and TM4 towards the intracellular face of the receptor; interacting side chains are depicted in x-stick representation and the backbone is depicted in ribbon representation. Superscript R indicates residues of RAMP1.

The simulations also predicted that E47^{ECD} formed persistent hydrogen-bond interactions with RAMP1 R112, in addition to hydrogen bonds to the RAMP1 backbone (G108 and A110) in the linker region. RAMP1 R112 was also predicted to form less frequent hydrogen bonds with D90^{ECD}, but may maintain more persistent ionic interactions. Collectively, these interactions are likely to contribute to the limited mobility of the RAMP1 linker and stable positioning of the ECDs relative to the receptor core (Extended Data Fig. 7a, Supplementary Table 2, Supplementary Videos 2, 3). From the cryo-EM map, there were no resolved interactions between the RAMP and G protein; however, there was no density for the C-terminal tail of RAMP1. Molecular dynamics simulations in which the C terminus of RAMP1 was modelled predicted transient interactions with ICL2 and the α N helix of the G α protein, with potential interactions that could extend to ICL1 (Supplementary Table 2); nevertheless, this segment was highly mobile in the simulations.

The CGRP-binding site

CGRP forms extensive interactions with the CLR–RAMP1 complex, with 61.5% of its surface buried. Notably, the only direct contact between the peptide and RAMP1 occurs at the far C terminus of the peptide, principally with the cluster of RAMP residues (F83–P85) that have been observed in isolated ECD structures¹² (Fig. 3a). The N-terminal peptide loop that is constrained within CGRP (C2–C7) is deeply buried and extends into an amphipathic α -helix, up to CGRP V23, which forms extensive van der Waals interactions with CLR (Fig. 3d). There are only a small number of hydrogen bonds formed in the static structure between the N terminus of the peptide and the core of CLR; these include interactions between Y292^{5.37} and the backbone of CGRP D3, between H295^{5.40} and CGRP T6, and between S286^{ECL2}

and the backbone of CGRP H10 (Fig. 3c, d). Of these, only the interaction between H295^{5.40} and CGRP T6 is functionally important; the H295^{5.40} A mutation cause a loss of about 30-fold in CGRP potency on cAMP accumulation²⁸. The equivalent residue in CTR is H302^{5.40}, which is predicted to form a hydrogen bond with T6 of sCT¹⁴. Alanine substitution of CGRP T6 leads to a loss of about 80-fold in peptide potency²⁹, confirming the importance of this bond and other interactions. There are extensive interactions between the peptide and TM3, TM5 and ECL2 of CLR. Below H295^{5.40}, a series of amino acids that includes I298^{5.43}, L302^{5.47}, M223^{3.40} and Y227^{3.44} forms the bottom of the peptide-binding pocket (Fig. 3c, d, Extended Data Fig. 8b). Alanine substitution of CGRP T4 leads to a more than 20-fold reduction in CGRP potency²⁹. However, this residue forms only limited interactions with the receptor; side-chain-to-backbone interactions within the peptide that contribute to the loop fold and initiation of the peptide helix may underlie its functional importance. CGRP T9 and H10 pack within an extended cluster of residues that includes T191^{2.64}, L195^{2.68}, H219^{3.36}, S286^{ECL2} and I284^{ECL2} (Fig. 3c, Extended Data Fig. 8b). With the exception of S286^{ECL2}, alanine mutation of these residues caused marked impairment in CGRP signalling^{28,30–32} (Extended Data Fig. 8b), with I284^{ECL2} and L195^{2.68} forming a hydrophobic barrier that coincides with the exit of the peptide from the receptor core (Extended Data Fig. 8b); molecular dynamics simulations predict transient hydrogen-bond formation between CGRP T9 and H219^{3.36} (Extended Data Fig. 9e, Supplementary Table 3). Alanine substitution of CGRP T9 causes a 15-fold loss of CGRP potency²⁹, consistent with the importance of interactions with this side chain. Whereas mutations to amino acids in the distal segment of ECL2 (S286^{ECL2}, D287^{ECL2}, H289^{ECL2}, L291^{5.36}) had relatively limited effects on CGRP potency²⁸ (Extended Data Fig. 8b), ECL2 conformation is critical to CGRP activation of its receptor, with R274^{4.64} A and, in particular, W283^{ECL2} A mutations being highly detrimental to CGRP signalling³² (Extended Data Fig. 8b). These residues are critical for the stable packing of ECL2 in the active structure, similar to those observed in other active, class B GPCR structures^{14–16}. There are only limited contacts between ECL1 and the peptide, the most prevalent being from CGRP L16 and S17 to A199^{ECL1}, N200^{ECL1}, Q202^{ECL1} and V205^{ECL1} (Fig. 3b, Extended Data Fig. 8b). Q202^{ECL1} is within weak hydrogen-bond distance of the backbone oxygen of CGRP S17 (Extended Data Fig. 8b); however, alanine mutation of Q202^{ECL1}, N200^{ECL1} or V205^{ECL1} had no effect on CGRP potency, indicating the limited importance of this domain for CGRP activity³⁰. CLR and CTR have shorter ECL1 loops compared to the related glucagon receptor³⁵, or glucagon-like peptide-1 receptor (GLP-1R)^{15,16}. These receptors have longer TM2 and TM3 helices (Extended Data Fig. 10a, b) that interact with the extended helix of peptide agonists of these receptors^{15,16,35}. In the cryo-EM map, there was no high-resolution density for ECL3, consistent with only limited interaction between CGRP and this receptor segment. This high mobility and lack of persistent interactions was also observed in our molecular dynamics simulations (Extended Data Fig. 9a–f, Supplementary Table 3, Supplementary Video 2), whereas previous alanine mutagenesis studies also support a limited role of this domain in CGRP-mediated cAMP production^{28,30} (Extended Data Fig. 8b).

CGRP V8, L12 and L16 are on the same face of the peptide α -helix and sit deep within a groove formed by TM1 and TM7, where they pack among multiple residues on the receptor. Alanine mutations of individual receptor amino acids within this groove have very little effect on CGRP-mediated cAMP production (Extended Data Fig. 8b), consistent with only weak contacts being made by individual receptor amino acids. Nevertheless, alanine substitution of either CGRP L12 or L16 markedly impaired CGRP potency³⁶, indicating that the packing of the hydrophobic face of the peptide helix is critical for receptor activation.

In the cryo-EM structure, CGRP R11 forms polar interactions with the backbone of CGRP T4 and C2, with potential salt-bridge interactions with CGRP D3 and D366^{7.39} on the receptor, and may contribute to stability of the CGRP loop conformation (Fig. 3C).

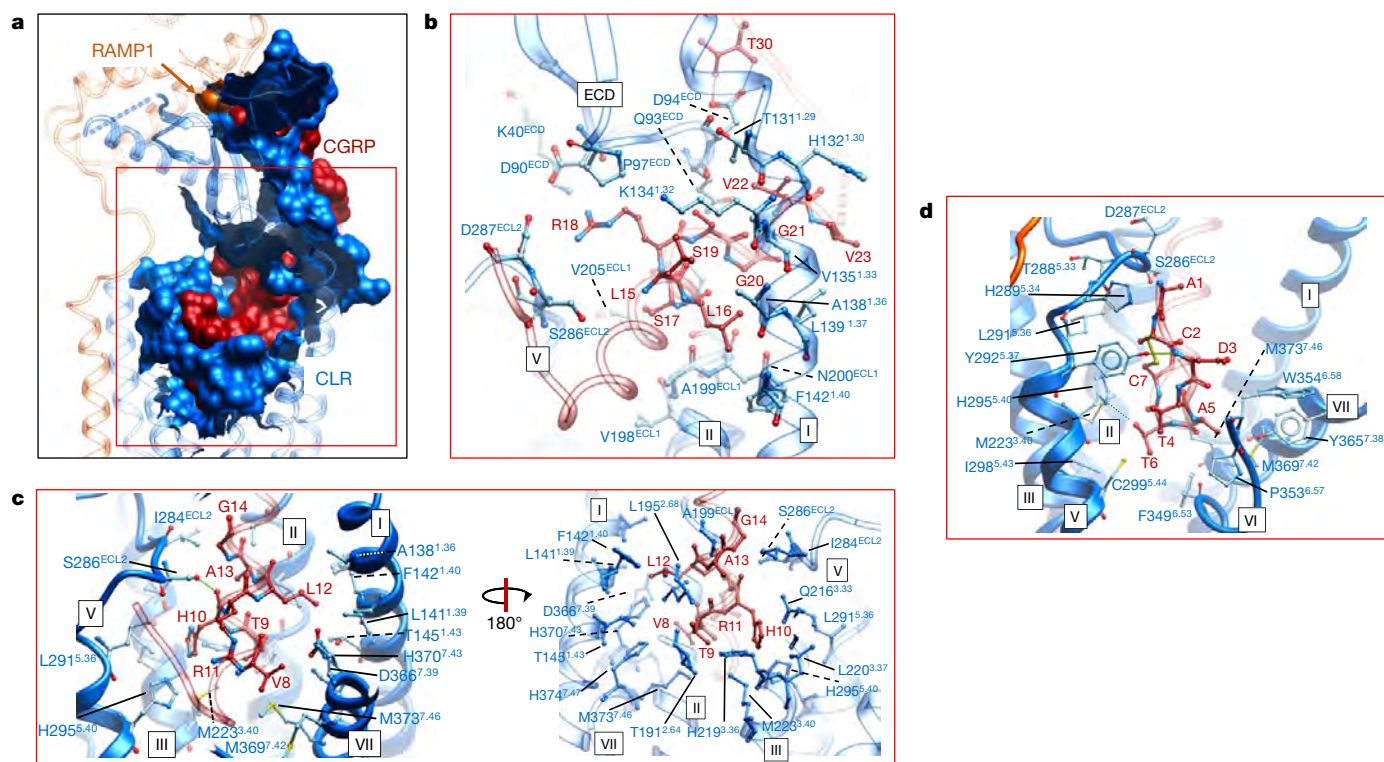


Fig. 3 | The CGRP-binding site. a, The CGRP-interaction surfaces (amino acids within 5 Å) of CLR (blue) or RAMP1 (dark orange), illustrating how the peptide N terminus is buried within CLR. CGRP is shown in dark red surface representation. **b–d**, Amino acid side chains of CLR proximal to CGRP residues; amino acids are shown in x-stick representation with carbons in blue (CLR) or dark red (CGRP), and other atoms are coloured

by type. Receptor transmembrane helices are numbered using roman numerals. **b**, Contact residues in CGRP, L15–V23; T30, which forms two hydrogen bonds with CLR D94^{ECD} is also shown. **c**, CGRP contact residues V8–G14. **d**, CGRP contact residues A1–C7. There are very few hydrogen bonds between the peptide N terminus and CLR in the static structure.

In molecular dynamics simulations, CGRP R11 formed persistent hydrogen bonds with D366^{7.39}, although these interactions are not observed in the cryo-EM map. CGRP R18 is within salt-bridge distance of D287^{ECL2} and D90^{ECD}, and forms a hydrogen bond with D287^{ECL2} in nearly 25% of frames in the simulation (Fig. 3b, Extended Data Fig. 9d, e).

The resolutions of the peptide C terminus and receptor ECDs are lower than the resolution in the receptor core, and they were primarily modelled by rigid-body fitting of the available X-ray structure (PDB: 4RWG¹²). To test the stability of interactions in the fully active structure, we ran 6.4-μs molecular dynamics simulations. Our data are consistent with the interactions previously reported in the isolated ECD structure¹², and are summarized in Extended Data Fig. 9a–f and Supplementary Table 3. The main intermolecular interactions were between CGRP T30 and D94^{ECD} (Fig. 3b, Extended Data Fig. 9e), and between the amide of CGRP F37 and backbone atoms of T122^{ECD} (Extended Data Fig. 9e). There were no persistent hydrogen bonds between CGRP and RAMP1. The critical importance of interactions between the C terminus of CGRP (F27–F37) and the ECDs of CLR and RAMP1 for CGRP signalling has been highlighted by previous mutagenesis studies^{12,23,34,37,38}, and are illustrated in Extended Data Fig. 8a. The extent to which this is dependent upon the stability of the relative positioning of the ECD to the receptor core is unclear, but RAMP1 is a major contributor to the limited conformational flexibility of the ECD domain of CLR (Supplementary Video 3).

Comparisons with the CTR structure

CTR is most closely related to CLR, and can also interact with RAMP1 to form a high-affinity CGRP receptor¹. Therefore, we compared the structure of the sCT–CTR–G_s complex to the CGRP–receptor complex. Owing to the relatively limited resolution in the peptide-binding domain and N terminus of the CTR, comparisons were limited to the backbone structures in these regions. Overall, there was a high degree

of similarity between the CLR and CTR structures, with both exhibiting an extended TM1 α-helical stalk that interconnects the receptor core and ECD, and a similar organization of the upper segments of TM6 and TM7 to accommodate the bulk of the cysteine-bridged loops of the peptides (Fig. 4a).

The largest difference between the CTR and CLR structures was in the orientation of the ECD relative to the receptor core (Fig. 4a, b). This located the C terminus of the peptides at nearly equivalent positions, with the N-terminal activation domain of the peptides also occupying a similar binding cavity (Fig. 4b). Within the receptor core, there was an inward shift of approximately 2 Å of the CLR relative to CTR at the apex of TM5, which is likely to be a result of the interaction of RAMP1 with this domain (Fig. 4c). There is a high degree of sequence conservation between CLR and CTR among the residues that contacted the RAMP (Fig. 4d), which may explain the similar broad specificity for RAMP interaction of these receptors. In previous simulations of the CTR bound to human CT versus sCT, there was destabilization of ECL2 for human CT relative to the sCT-bound receptor that was indicative of a role for conformational dynamics of this receptor domain in ligand interaction and efficacy¹⁸. The interactions of RAMP1 with ECL2 may therefore contribute to peptide selectivity and/or efficacy.

At the base of the receptor, the structured H8 of CLR was much shorter than that of CTR (Fig. 4a), and consequently exhibited more-limited interaction with the Gβ-subunit. Nevertheless, truncation studies of the CTR C terminus indicated that only the segment that is also present in the CGRP receptor structure is functionally important for G_s-mediated signalling¹⁴. Perhaps more relevant, although the α-helix 5 of the Ras-like domain of Gα_s (Gα_s–Ras) is aligned between the two structures, there are differences within the G protein, particularly with respect to the positioning of the αN helix of Gα_s–Ras; these differences are propagated across the β- and γ-subunits (Fig. 4e).

Broader comparison of protein interactions of G_s to include the structures of GLP-1R bound to either exendin-P5¹⁵ or GLP-1¹⁶

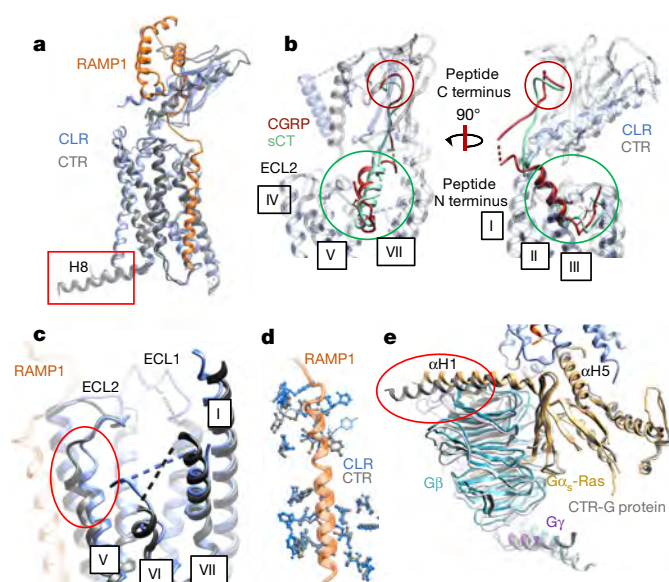


Fig. 4 | The CTR and CGRP receptor complexes display similar backbone conformations but have distinct conformations of the $G\alpha_s$ -Ras domain. **a**, Alignment of the CLR–RAMP1–CTR (blue, dark orange and grey ribbon, respectively) structures; for the CTR the ECD is from the X-ray structure of the sCT–CTR X-ray structure (PDB: 5II0³⁹), following rigid-body fitting to the CTR cryo-EM map¹⁴. Receptor transmembrane helices are numbered using roman numerals. **b**, Magnified view of the peptide-binding sites. CGRP (dark red) and sCT (green) are shown as ribbon, CLR (blue) and CTR (grey) are shown as transparent ribbon. The circles highlight the similarities in position of the peptide N- (green) and C- (red) termini. RAMP1 has been omitted for clarity. **c**, Magnified view highlighting differences in the upper segment of TM5 (red circle). **d**, Overlap in RAMP1-contact residues between CLR (blue x-stick) and CTR (grey x-stick). **e**, The $G\alpha_s$ -Ras–H5 is superimposed in the two structures, but the α -H1 helix is in a different orientation (red circle) and leads to distinct positioning of the $G\beta$ - and $G\gamma$ -subunits. The CTR G protein is shown as grey ribbon, the CGRP receptor G protein as coloured ribbon. $G\alpha_s$ -Ras, gold; $G\beta$, cyan; $G\gamma$, dark purple. Regions of the receptor structures that are missing in the PDB files are shown as dashed lines.

(Extended Data Fig. 10a, b) also revealed differences in the relative positioning of G_s . However, this was principally due to translational differences in the engagement of the receptors and α -helix 5 (Extended Data Fig. 10c), with strong overlap in the backbone of the $G\alpha$ -subunit when these are aligned (Extended Data Fig. 10d). ICL2 of CLR and of CTR are longer than that of GLP-1R, and there is an increase of about 2 Å in the outward movement of the base of TM6 of CLR and CTR compared to GLP-1R (Extended Data Fig. 10a); these differences are likely to account for the translational differences in engagement of the G_s protein by GLP-1R.

Stability of the complex in the absence of RAMP1

In molecular dynamics simulations of the complex in the presence and absence of RAMP1, the orientation of the ECD of CLR remains relatively stable in CLR–CGRP–RAMP1– $G\alpha\beta\gamma$ -Nb35 (6.4- μ s simulation) and CLR–CGRP–RAMP1–mini- $G\alpha$ (2- μ s simulation), but not in CLR–CGRP–mini- $G\alpha$ (2- μ s simulation) (Supplementary Videos 1–3). In the absence of RAMP1, only CGRP and TM1—with its extension—hold the ECD in place relative to the transmembrane domain. The N-terminal region (A1–R18) of CGRP is stable (Supplementary Video 2) even in the absence of RAMP1, but the C-terminal region is affected by the mobility of the CLR ECD and is much more mobile in the absence of RAMP1 (Extended Data Fig. 6, Supplementary Video 3). A consequence of this C-terminal mobility in the absence of RAMP1 is reduced persistence of hydrogen bonds formed by CGRP in this region (Supplementary Table 4).

RAMP1 provides additional stability to ECL2, a major contact point for CGRP—though this loop is relatively stable even in the absence of RAMP1. In the simulation in the absence of RAMP1, there is a marked reduction in the persistence of hydrogen bonds between R274^{4.64} and D280^{ECL2} (Supplementary Table 5). In the cryo-EM structure, these two residues form a salt-bridge interaction, and this interaction in the presence of RAMP1 is likely to affect signal propagation. Indeed, mutagenesis of either of these residues greatly affects CGRP-mediated cAMP signalling^{28,32}. RAMP1 interaction does not affect the mobility of the distally located ECL1 and ICL3. The least mobile points of each transmembrane domain generally correspond to points of helix intersection; for TM3 this is in the vicinity of Y227^{3.44}, which provides a deep stable contact point for CGRP.

Whereas these simulations provide insight into the contribution of RAMP1 to the preformed active complex, this complex does not form in the absence of RAMP1, even where CLR is present at the cell surface⁶, indicating that the CLR–RAMP1 interaction is also critical for initial peptide binding and presentation to the receptor core.

In conclusion, the structure of the CGRP–CLR–RAMP1– G_s complex provides insight into the organization of functionally important heteromeric GPCR complexes. RAMP1 causes marked stabilization of the ECD of CLR, and therefore has a critical role in ligand presentation to the receptor core. It further enhances stability of the transmembrane domain interface and ECL2, which are important for propagation of peptide-induced signalling. This study provides a framework for the development of novel therapeutics that target the CGRP system.

Online content

Any methods, additional references, Nature Research reporting summaries, source data, statements of data availability and associated accession codes are available at <https://doi.org/10.1038/s41586-018-0535-y>.

Received: 1 June 2018; Accepted: 26 June 2018;

Published online 12 September 2018.

- Hay, D. L., Garelja, M. L., Poyner, D. R. & Walker, C. S. Update on the pharmacology of calcitonin/CGRP family of peptides: IUPHAR Review 25. *Br. J. Pharmacol.* **175**, 3–17 (2018).
- Russell, F. A., King, R., Smillie, S. J., Kodji, X. & Brain, S. D. Calcitonin gene-related peptide: physiology and pathophysiology. *Physiol. Rev.* **94**, 1099–1142 (2014).
- Dickerson, I. M., Bussey-Gaborski, R., Holt, J. C., Jordan, P. M. & Luebke, A. E. Maturation of suprathreshold auditory nerve activity involves cochlear CGRP-receptor complex formation. *Physiol. Rep.* **4**, e12869 (2016).
- Walker, C. S. et al. Mice lacking the neuropeptide α -calcitonin gene-related peptide are protected against diet-induced obesity. *Endocrinology* **151**, 4257–4269 (2010).
- Karsan, N. & Goadsby, P. J. Calcitonin gene-related peptide and migraine. *Curr. Opin. Neurol.* **28**, 250–254 (2015).
- McLachlie, L. M. et al. RAMPs regulate the transport and ligand specificity of the calcitonin-receptor-like receptor. *Nature* **393**, 333–339 (1998).
- Barbash, S., Lorenzen, E., Persson, T., Huber, T. & Sakmar, T. P. GPCRs coevolved with receptor activity-modifying proteins, RAMPs. *Proc. Natl Acad. Sci. USA* **114**, 12015–12020 (2017).
- Hay, D. L. & Pioszak, A. A. Receptor activity-modifying proteins (RAMPs): new insights and roles. *Annu. Rev. Pharmacol. Toxicol.* **56**, 469–487 (2016).
- Routledge, S. J., Ladds, G. & Poyner, D. R. The effects of RAMPs upon cell signalling. *Mol. Cell. Endocrinol.* **449**, 12–20 (2017).
- Wootton, D. et al. Receptor activity modifying proteins (RAMPs) interact with the VPAC2 receptor and CRF1 receptors and modulate their function. *Br. J. Pharmacol.* **168**, 822–834 (2013).
- Christopoulos, A. et al. Novel receptor partners and function of receptor activity-modifying proteins. *J. Biol. Chem.* **278**, 3293–3297 (2003).
- Booe, J. M., Warner, M. L., Roehrkasse, A. M. & Pioszak, A. A. Structural basis for receptor activity-modifying protein-dependent selective peptide recognition by a G protein-coupled receptor. *Mol. Cell* **58**, 1040–1052 (2015).
- Booe, J. M. et al. Probing the mechanism of receptor activity-modifying protein modulation of GPCR ligand selectivity through rational design of potent adrenomedullin and calcitonin gene-related peptide antagonists. *Mol. Pharmacol.* **93**, 355–367 (2018).
- Liang, Y. L. et al. Phase-plate cryo-EM structure of a class B GPCR-G-protein complex. *Nature* **546**, 118–123 (2017).
- Liang, Y. L. et al. Phase-plate cryo-EM structure of a biased agonist-bound human GLP-1 receptor-G α complex. *Nature* **555**, 121–125 (2018).
- Zhang, Y. et al. Cryo-EM structure of the activated GLP-1 receptor in complex with a G protein. *Nature* **546**, 248–253 (2017).

17. Wootten, D. et al. The extracellular surface of the GLP-1 receptor is a molecular trigger for biased agonism. *Cell* **165**, 1632–1643 (2016).
18. Dal Maso, E. et al. Extracellular loops 2 and 3 of the calcitonin receptor selectively modify agonist binding and efficacy. *Biochem. Pharmacol.* **150**, 214–244 (2018).
19. Liang, Y.-L. et al. Dominant negative G proteins enhance formation and purification of agonist-GPCR–G protein complexes for structure determination. *ACS Pharmacol. Transl. Sci.* <https://doi.org/10.1021/acspsci.8b00017> (2018).
20. Khoshouei, M. et al. Volta phase plate cryo-EM of the small protein complex Prx3. *Nat. Commun.* **7**, 10534 (2016).
21. Khoshouei, M., Radjainia, M., Baumeister, W. & Danev, R. Cryo-EM structure of haemoglobin at 3.2 Å determined with the Volta phase plate. *Nat. Commun.* **8**, 16099 (2017).
22. Wootten, D., Simms, J., Miller, L. J., Christopoulos, A. & Sexton, P. M. Polar transmembrane interactions drive formation of ligand-specific and signal pathway-biased family B G protein-coupled receptor conformations. *Proc. Natl. Acad. Sci. USA* **110**, 5211–5216 (2013).
23. Ter Haar, E. et al. Crystal structure of the ectodomain complex of the CGRP receptor, a class-B GPCR, reveals the site of drug antagonism. *Structure* **18**, 1083–1093 (2010).
24. Watkins, H. A. et al. Receptor activity-modifying proteins 2 and 3 generate adrenomedullin receptor subtypes with distinct molecular properties. *J. Biol. Chem.* **291**, 11657–11675 (2016).
25. Woolley, M. J. et al. Receptor activity-modifying protein dependent and independent activation mechanisms in the coupling of calcitonin gene-related peptide and adrenomedullin receptors to Gs. *Biochem. Pharmacol.* **142**, 96–110 (2017).
26. Weston, C. et al. Receptor activity-modifying protein-directed G protein signaling specificity for the calcitonin gene-related peptide family of receptors. *J. Biol. Chem.* **291**, 21925–21944 (2016).
27. Bower, R. L. et al. Molecular signature for receptor engagement in the metabolic peptide hormone amylin. *ACS Pharmacol. Transl. Sci.* <https://doi.org/10.1021/acspsci.8b00002> (2018).
28. Woolley, M. J. et al. Understanding the molecular functions of the second extracellular loop (ECL2) of the calcitonin gene-related peptide (CGRP) receptor using a comprehensive mutagenesis approach. *Mol. Cell. Endocrinol.* **454**, 39–49 (2017).
29. Hay, D. L. et al. Structure-activity relationships of the N-terminus of calcitonin gene-related peptide: key roles of alanine-5 and threonine-6 in receptor activation. *Br. J. Pharmacol.* **171**, 415–426 (2014).
30. Barwell, J., Conner, A. & Poyner, D. R. Extracellular loops 1 and 3 and their associated transmembrane regions of the calcitonin receptor-like receptor are needed for CGRP receptor function. *Biochim. Biophys. Acta* **1813**, 1906–1916 (2011).
31. Vohra, S. et al. Similarity between class A and class B G-protein-coupled receptors exemplified through calcitonin gene-related peptide receptor modelling and mutagenesis studies. *J. R. Soc. Interface* **10**, 20120846 (2012).
32. Woolley, M. J. et al. The role of ECL2 in CGRP receptor activation: a combined modelling and experimental approach. *J. R. Soc. Interface* **10**, 20130589 (2013).
33. Conner, A. C., Simms, J., Howitt, S. G., Wheatley, M. & Poyner, D. R. The second intracellular loop of the calcitonin gene-related peptide receptor provides molecular determinants for signal transduction and cell surface expression. *J. Biol. Chem.* **281**, 1644–1651 (2006).
34. Simms, J. et al. Structure-function analysis of RAMP1 by alanine mutagenesis. *Biochemistry* **48**, 198–205 (2009).
35. Zhang, H. et al. Structure of the glucagon receptor in complex with a glucagon analogue. *Nature* **553**, 106–110 (2018).
36. Simms, J. et al. Photoaffinity cross-linking and unnatural amino acid mutagenesis reveal insights into calcitonin gene-related peptide binding to the calcitonin receptor-like receptor/receptor activity-modifying protein 1 (CLR/RAMP1) complex. *Biochemistry* **57**, 4915–4922 (2018).
37. Garelja, M. L. et al. Receptor activity modifying proteins have limited effects on the Class B G protein-coupled receptor calcitonin receptor-like receptor stalk. *Biochemistry* **57**, 1410–1422 (2018).
38. Hay, D. L., Christopoulos, G., Christopoulos, A. & Sexton, P. M. Determinants of 1-piperidinecarboxamide, *N*-[2-[[[5-amino-1-[[4-(4-pyridinyl)-1-piperazinyl]carbonyl]pentyl]amino]-1-[(3,5-dibromo-4-hydroxyphenyl)methyl]-2-oxoethyl]-4-(1,4-dihydro-2-oxo-3(2H)-quinazolinyl)] (BIBN4096BS) affinity for calcitonin gene-related peptide and amylin receptors—the role of receptor activity modifying protein 1. *Mol. Pharmacol.* **70**, 1984–1991 (2006).
39. Johansson, E. et al. Type II turn of receptor-bound salmon calcitonin revealed by X-ray crystallography. *J. Biol. Chem.* **291**, 13689–13698 (2016).

Acknowledgements The work was supported by the Monash University Ramaciotti Centre for Cryo-Electron Microscopy, National Health and Medical Research Council of Australia (NHMRC) project grant (1120919), and NHMRC program grant (1055134). P.M.S. and A.C. are NHMRC Principal and Senior Principal Research Fellows, respectively. D.W. is a NHMRC Career Development Fellow, and C.K. is a NHMRC CJ Martin Fellow. A.G. is an Australian Research Council DECRA Fellow. D.L.H. is a James Cook Research Fellow and is supported by the Marsden Fund (both Royal Society of New Zealand). C.A.R. is a Royal Society Industry Fellow and acknowledges support from the BBSRC (BB/M006883/1). We are grateful to G. Christopoulos and V. Julita for assay and technical support, T. Coudrat for initial homology modelling of CLR from the active CTR, and to S. Furness, P. Zhao and D. Thal for useful discussion.

Reviewer information *Nature* thanks K. Caron, S. Dang, B. Wu and the other anonymous reviewer(s) for their contribution to the peer review of this work.

Author contributions Y.-L.L. performed virus production, insect cell expression, purification, negative stain electron microscopy, data acquisition and analysis, and prepared samples for cryo-EM, was responsible for model building and refinement, and assisted with manuscript preparation. M.K. performed cryo-sample preparation, phase-plate imaging, data collection, electron microscopy data processing and analysis, calculated the cryo-EM map and assisted with manuscript preparation. G.D. performed molecular dynamics simulations and assisted in manuscript preparation. A.G. assisted with model building and refinement and contributed to manuscript preparation. T.S.P. assisted with model building and refinement and reviewed the manuscript. C.K. performed cell-based assays and data analysis and reviewed the manuscript. M.R. performed preliminary cryo-EM screening and reviewed the manuscript. J.M.P. and W.B. organized and managed the Volta phase-plate development project. D.L.H. provided insights into the CGRP receptor, assisted with data interpretation, and reviewed the manuscript. L.J.M. provided insights into class B GPCRs, assisted with data interpretation and reviewed the manuscript. A.C. assisted with data interpretation and manuscript preparation. C.A.R. designed molecular dynamics simulations, assisted in data interpretation and contributed to writing of the manuscript. D.W. was responsible for overall project strategy and management, data analysis and interpretation and contributed to writing of the manuscript. P.M.S. was responsible for overall project strategy and management, data interpretation and wrote the manuscript.

Competing interests The authors declare no competing interests.

Additional information

Extended data is available for this paper at <https://doi.org/10.1038/s41586-018-0535-y>.

Supplementary information is available for this paper at <https://doi.org/10.1038/s41586-018-0535-y>.

Reprints and permissions information is available at <http://www.nature.com/reprints>.

Correspondence and requests for materials should be addressed to D.W. or P.M.S.

Publisher's note: Springer Nature remains neutral with regard to jurisdictional claims in published maps and institutional affiliations.

METHODS

No statistical methods were used to predetermine sample size. The experiments were not randomized. The investigators were not blinded to allocation during experiments and outcome assessment.

Constructs. CLR was modified to include an N-terminal Flag-tag epitope and a C-terminal $8 \times$ His tag; both tags are removable by 3C protease cleavage. The construct was generated in both mammalian and insect cell expression vectors. RAMP1 was modified to include an N-terminal Flag-tag epitope. For both constructs, the natural signal peptide was replaced with that of haemagglutinin to improve expression (Extended Data Fig. 1).

Expression in insect cells. CLR, RAMP1, DNG α_s ¹⁵, His₆-tagged human G β 1 and G γ 2 were expressed in *Trichoplusia ni* insect cells (Expression Systems) using baculovirus. Cell cultures were grown in ESF 921 serum-free medium (Expression Systems) to a density of 4×10^6 cells per ml and then infected with the three baculoviruses CLR, RAMP1, DNG α_s and G β 1 γ 2 at a ratio of 1:5:2:1. Culture was collected by centrifugation 48 h after infection and cell pellet was stored at -80°C . **Complex purification.** Cell pellet was thawed in 20 mM HEPES pH 7.4, 50 mM NaCl, 2 mM MgCl₂ supplemented with cOmplete Protease Inhibitor Cocktail tablets (Roche). Complex formation was initiated by addition of 10 μM human αCGRP (Chinapeptide), Nb35–His (10 $\mu\text{g}/\text{ml}$), 3C protease (10 $\mu\text{g}/\text{ml}$) and apyrase (25 mU/ml, NEB); the suspension was incubated for 1 h at room temperature. Membranes were collected by centrifugation at 30,000g for 30 min. Complexes from membranes were solubilized by 0.5% (w/v) lauryl maltose neopentyl glycol (LMNG, Anatrace) supplemented with 0.03% (w/v) cholesteryl hemisuccinate (CHS, Anatrace) for 2 h at 4°C in the presence of 1 μM CGRP and apyrase (25 mU/ml, NEB). Insoluble material was removed by centrifugation at 30,000g for 30 min and the solubilized complex was immobilized by batch binding to Ni-NTA resin. The resin was packed into a glass column and washed with 20 column volumes of 20 mM HEPES pH 7.4, 100 mM NaCl, 2 mM MgCl₂, 0.01% (w/v) LMNG and 0.006% (w/v) CHS, 1 μM CGRP, before bound material was eluted in buffer containing 250 mM imidazole. The Ni-NTA-purified fraction was immobilized by batch binding to M1 anti-Flag affinity resin in the presence of 3 mM CaCl₂. The resin was packed into a glass column and washed with 20 column volumes of 20 mM HEPES pH 7.4, 100 mM NaCl, 2 mM MgCl₂, 3 mM CaCl₂, 1 μM CGRP, 0.01% (w/v) LMNG and 0.006% (w/v) CHS before bound material was eluted in buffer containing 5 mM EGTA and 0.1 mg/ml Flag peptide. The complex was then concentrated using an Amicon Ultra Centrifugal Filter (MWCO 100 kDa) and subjected to size-exclusion chromatography on a Superose 6 Increase 10/300 column (GE Healthcare) that was pre-equilibrated with 20 mM HEPES pH 7.4, 100 mM NaCl, 2 mM MgCl₂, 1 μM CGRP, 0.01% (w/v) LMNG and 0.006% (w/v) CHS. Eluted fractions consisting of receptor and G-protein complex were pooled and concentrated. Final yield of purified complex was approximately 0.3 mg per litre of insect cell culture.

SDS–PAGE and western blot analysis. Sample collected from size-exclusion chromatography was analysed by SDS–PAGE and western blot as previously described¹⁵. For SDS–PAGE, precast gradient TGX gels (Bio-Rad) were used. The final elution peak from size-exclusion chromatography was stained using Instant Blue (Expedeon).

Modelling into cryo-EM density. An initial template for CLR was generated by homology modelling using the cryo-EM structure of human CTR (PDB: 5UZ7)¹⁴, performed with the Molsoft ICM modelling software⁴⁰. Manual adjustment and rebuilding was performed in Coot⁴¹. Owing to limited density in CLR and RAMP1 ECD regions, we used the high-resolution X-ray crystal structure (PDB: 4RWG)¹² for modelling. ECDs of CLR and RAMP1 were, separately, rigid-body fitted into density before the final iteration of global refinement. DNG α_s , G β 1, G γ 2 and Nb35 models were taken from the GLP1–R–G α_s –ExP5 structure (PDB: 6B3J)¹⁵. The CGRP peptide and RAMP1 transmembrane domain were modelled manually. The final model was subjected to global refinement and minimization in real space using the module 'phenix.real_space_refine' in PHENIX⁴². Validation was performed in MolProbity⁴³.

Preparation of vitrified specimen. Electron microscopy grids (Quantifoil, 200-mesh copper R1.2/1.3) were glow-discharged for 30 s using Harrick plasma cleaner (Harrick). Four microlitres of sample was applied on the grid in the Vitrobot Mark IV chamber (Thermo Fisher Scientific). The chamber of the Vitrobot was set to 100% humidity at 4°C . The sample was blotted for 4.5 s with a blot force of 20 and then plunged into propane–ethane mixture (37% ethane and 63% propane).

Data acquisition. Datasets were collected on a Thermo Fisher Scientific Titan Krios microscope operated at 300 kV (FEI) equipped with a Gatan Quantum energy filter, a Gatan K2 summit direct electron camera (Gatan) and a Volta phase plate (Thermo Fisher Scientific). Movies were taken in EFTEM nanoprobe mode, with 50- μm C2 aperture, at a calibrated magnification of 47170 corresponding to a magnified pixel size of 1.06 Å. Each movie comprises 50 subframes with a total dose of 50 e[−] per Å², exposure time was 13 s with a dose rate of 4.8 e[−] pixel^{−1} s^{−1}

on the detector. Data acquisition was done using SerialEM software at -600-nm defocus⁴⁴.

Data processing. A total of 3,180 movies were collected and subjected to motion correction using MotionCor2⁴⁵. CTF estimation was done using Gctf software⁴⁶ on non-dose-weighted micrographs. The particles were picked using Gautamatch (<http://www.mrc-lmb.cam.ac.uk/kzhang/Gautamatch/>). An initial model was made using the common-line approach in EMAN2⁴⁷, based on a few automatically picked micrographs and using the common-line approach. The particles were extracted in RELION v.2.01b1⁴⁸ using a box size of 200 pixels. A total of 1,205,000 picked particles were subjected to 2D classification with 100 classes, followed by 3D classification. After selecting the best-looking class, with 407,000 particles, 3D auto-refinement was performed in RELION v.2.01b1. The final map was sharpened with a B-factor of -50 Å^2 . The processing workflow is outlined in Extended Data Fig. 3c. Model overfitting was evaluated by randomly displacing all atoms by 0.5 Å and refined against one cryo-EM half map. Fourier shell correlation curves were calculated between the resulting model and the half map used for refinement, the resulting model and the other half map for cross validation, and the final refined model and the full map (Extended Data Fig. 3f).

Mammalian cell cAMP assays. COS-7 cells, which were confirmed to be free from mycoplasma, were transfected in suspension in 96-well plates (10,000 cells per well) with 50 ng CLR + 50 ng human RAMP1 using 600 ng polyethylenimine (PEI). The transfection was performed in DMEM with 5% FBS, 200 μl total volume per well, and cells were incubated for 48 h at 37°C , 5% CO₂. cAMP detection was performed as described⁴⁹. All values were converted to cAMP concentration using a cAMP standard curve performed in parallel and data were subsequently normalized to the response to 100 μM forskolin.

Conformational clustering of CGRP ECL3 and RAMP1. The missing loops throughout CLR were generated using PLOOP⁵⁰, which has been shown to be effective in generating GPCR loop conformations⁵¹. The missing side chains were iteratively optimized to convergence using PLOOP. In addition, to enhance the conformational sampling of ECL3, which is likely to interact with the CGRP peptide, a preliminary clustering of 4,000 different loop models generated using Modeller 9.16⁵² was performed by means of the Clustering VMD plugin (available at <http://physiology.med.cornell.edu/faculty/hweinstein/vmdplugins/clustering/>). Conformational clustering was based on the coordinates of side chains belonging to residues W354^{6,58}, R355^{6,59}, P356^{ECL3}, E357^{ECL3}, K359^{ECL3}, I360^{ECL3}, A361^{ECL3} and E362^{ECL3}. A total of 10 clusters was generated with a root mean standard deviation cut-off value of 3 Å and a representative structure with a low distributed optimized potential energy score from the four most-populated ensembles was extracted and prepared for molecular dynamics simulations.

A similar approach was employed for clustering the modelled RAMP1 C terminus (residues T144–V148): the original PLOOP-generated conformation was combined with each of the 4 initially selected ECL3 conformations, whereas a highly distinct RAMP1 C-terminus orientation was arbitrarily combined with ECL3 conformation number 1.

Molecular dynamics simulations. A total of seven systems was prepared for molecular dynamics simulations with the CHARMM36 force field⁵³ (Supplementary Table 6) using a multistep procedure that combines Python HTMD⁵⁴ and tool command language scripts. Hydrogen atoms were first added by means of pdb2pqr⁵⁵ and propka⁵⁶ software (considering a simulated pH of 7.0); the protonation of titratable side chains was checked by visual inspection. CLR and RAMP1 were embedded in a square $116 \text{ Å} \times 116 \text{ Å}$ 1-palmitoyl-2-oleyl-*sn*-glycerol-3-phospho-choline (POPC) bilayer (previously built using the VMD Membrane Builder plugin 1.1: <http://www.ks.uiuc.edu/Research/vmd/plugins/membrane/>) through an insertion method⁵⁷. More precisely, the opportune receptor orientation was obtained by superposing CLR coordinates on the CTR structure retrieved from the OPM database⁵⁸. Lipids overlapping the receptor transmembrane-domain bundle and RAMP1 were removed and TIP3P water molecules⁵⁹ were added to the simulation box ($116 \text{ Å} \times 116 \text{ Å} \times 185 \text{ Å}$) by means of the VMD Solvate plugin v.1.5 (<http://www.ks.uiuc.edu/Research/vmd/plugins/solvate/>). Overall charge neutrality was finally reached by adding Na⁺/Cl[−] counter ions (final ionic strength of 0.150 M), using the VMD Autoionize plugin 1.3 (<http://www.ks.uiuc.edu/Research/vmd/plugins/autoionize/>).

To evaluate the influence exerted by RAMP1 on the CGRP–CLR complex, two simplified systems were embedded in $96 \text{ Å} \times 96 \text{ Å}$ POPC bilayers and solvated as described above: one was composed of CLR–CGRP–RAMP1 and the C terminus (residues N371^G–L394^G) of the G-protein α -subunit (CLR–CGRP–RAMP1–G α (371–394)); the other was formed by CLR–CGRP and the C terminus of the G α -subunit (CLR–CGRP–G α (371–394)). The original PLOOP-generated conformations of CLR and RAMP1 were used.

Systems equilibration and molecular dynamics settings. The molecular dynamics engine ACEMD⁶⁰ was used for both the equilibration and productive simulations. Equilibration was achieved in isothermal-isobaric conditions (NPT) using the Berendsen barostat⁶¹ (target pressure 1 atm) and the Langevin thermostat⁶²

(target temperature 300 K) with a low damping of 1 ps^{-1} . A three-stage procedure was performed (integration time-step of 2 fs): first, clashes between protein and lipid atoms were reduced through 2,500 conjugate-gradient minimization steps, then a 2-ns-long molecular dynamics simulation was run with a positional constraint of $1 \text{ kcal mol}^{-1} \text{ \AA}^{-2}$ on protein and lipid phosphorus atoms. During the second stage, 40 ns of simulation was performed, constraining only the protein atoms, whereas in the last equilibration stage, positional constraints were applied only to the protein backbone alpha carbons, for a further 5 ns.

Supplementary Table 6 summarizes all the simulations performed. Trajectories were computed with an integration time-step of 4 fs in the canonical ensemble (NVT) at 300 K, using a thermostat damping of 0.1 ps^{-1} and the M-SHAKE algorithm⁶³ to constrain the bond lengths involving hydrogen atoms. The cut-off distance for electrostatic interactions was set at 9 Å, with a switching function applied beyond 7.5 Å. Long-range Coulomb interactions were handled using the particle mesh Ewald summation method (PME)⁶⁴ by setting the mesh spacing to 1.0 Å.

Molecular dynamics analysis. Atomic contacts, hydrogen bonds and root mean square fluctuation (RMSF) were computed using VMD⁶⁵. A contact was considered productive if the distance between two atoms was smaller than 3.5 Å. For hydrogen-bond detection, a donor-acceptor distance of 3 Å and an angle value of 160° were set as geometrical cut-offs. The hydrogen-bond persistence is defined as the number of frames in which the hydrogen bond is formed, divided by the total number of frames $\times 100$. The RAMP1 influence on van der Waals contacts and hydrogen bonds was evaluated by computing the numerical difference between the total numbers of contacts or hydrogen bonds between each CLR and CGRP side chain during the simulations in the presence and absence of RAMP1.

Reporting Summary. Further information on research design is available in the Nature Research Reporting Summary linked to this paper.

Data availability. All relevant data are available from the authors and/or included in the manuscript or Supplementary Information. Atomic coordinates and the cryo-EM density map have been deposited in the Protein Data Bank under accession number 6E3Y and the Electron Microscopy Data Bank, entry EMD-8978.

40. Abagyan, R. & Totrov, M. Biased probability Monte Carlo conformational searches and electrostatic calculations for peptides and proteins. *J. Mol. Biol.* **235**, 983–1002 (1994).
41. Emsley, P. & Cowtan, K. Coot: model-building tools for molecular graphics. *Acta Crystallogr. D* **60**, 2126–2132 (2004).
42. Adams, P. D. et al. PHENIX: a comprehensive Python-based system for macromolecular structure solution. *Acta Crystallogr. D* **66**, 213–221 (2010).
43. Chen, V. B. et al. MolProbity: all-atom structure validation for macromolecular crystallography. *Acta Crystallogr. D* **66**, 12–21 (2010).
44. Mastrorade, D. N. Automated electron microscope tomography using robust prediction of specimen movements. *J. Struct. Biol.* **152**, 3651 (2005).
45. Zheng, S. Q. et al. MotionCor2: anisotropic correction of beam-induced motion for improved cryo-electron microscopy. *Nat. Methods* **14**, 331–332 (2017).
46. Zheng, K. Gctf: Real-time CTF determination and correction. *J. Struct. Biol.* **193**, 1–12 (2016).
47. Tang, G. et al. EMAN2: an extensible image processing suite for electron microscopy. *J. Struct. Biol.* **157**, 38–46 (2007).
48. Kimanius, D., Forsberg, B. O., Scheres, S. H. & Lindahl, E. Accelerated cryo-EM structure determination with parallelisation using GPUs in RELION-2. *eLife* **5**, e18722 (2016).
49. Hager, M. V., Clydesdale, L., Gellman, S. H., Sexton, P. M. & Wootten, D. Characterization of signal bias at the GLP-1 receptor induced by backbone modification of GLP-1. *Biochem. Pharmacol.* **136**, 99–108 (2017).
50. Jacobson, M. P. et al. A hierarchical approach to all-atom protein loop prediction. *Proteins* **55**, 351–367 (2004).
51. Goldfeld, D. A., Zhu, K., Beuming, T. & Friesner, R. A. Successful prediction of the intra- and extracellular loops of four G-protein-coupled receptors. *Proc. Natl Acad. Sci. USA* **108**, 8275–8280 (2011).
52. Eswar, N. et al. Comparative protein structure modeling using Modeller. *Curr. Protoc. Bioinformatics* **15**, 5.6.1–5.6.30 (2006).
53. Huang, J. & MacKerell, A. D. CHARMM36 all-atom additive protein force field: validation based on comparison to NMR data. *J. Comput. Chem.* **34**, 2135–2145 (2013).
54. Doerr, S., Harvey, M. J., Noé, F. & De Fabritiis, G. HTMD: high-throughput molecular dynamics for molecular discovery. *J. Chem. Theory Comput.* **12**, 1845–1852 (2016).
55. Dolinsky, T. J., Nielsen, J. E., McCammon, J. A. & Baker, N. A. PDB2PQR: an automated pipeline for the setup of Poisson–Boltzmann electrostatics calculations. *Nucleic Acids Res.* **32**, W665–667 (2004).
56. Olsson, M. H. M., Søndergaard, C. R., Rostkowski, M. & Jensen, J. H. PROPKA3: consistent treatment of internal and surface residues in empirical pK predictions. *J. Chem. Theory Comput.* **7**, 525–537 (2011).
57. Sommer, B. Membrane packing problems: a short review on computational membrane modeling methods and tools. *Comput. Struct. Biotechnol. J.* **5**, e201302014 (2013).
58. Lomize, M. A., Lomize, A. L., Pogozheva, I. D. & Mosberg, H. I. OPM: orientations of proteins in membranes database. *Bioinformatics* **22**, 623–625 (2006).
59. Jorgensen, W. L., Chandrasekhar, J., Madura, J. D., Impey, R. W. & Klein, M. L. Comparison of simple potential functions for simulating liquid water. *J. Chem. Phys.* **79**, 926 (1983).
60. Harvey, M. J., Giupponi, G. & Fabritiis, G. D. ACEMD: accelerating biomolecular dynamics in the microsecond time scale. *J. Chem. Theory Comput.* **5**, 1632–1639 (2009).
61. Berendsen, H. J. C., Postma, J. P. M., van Gunsteren, W. F., DiNola, A. & Haak, J. R. Molecular dynamics with coupling to an external bath. *J. Chem. Phys.* **81**, 3684 (1984).
62. Loncharich, R. J., Brooks, B. R. & Pastor, R. W. Langevin dynamics of peptides: the frictional dependence of isomerization rates of *N*-acetylalanine-*N'*-methylamide. *Biopolymers* **32**, 523–535 (1992).
63. Kräutler, V., van Gunsteren, W. F. & Hünenberger, P. H. A fast SHAKE algorithm to solve distance constraint equations for small molecules in molecular dynamics simulations. *J. Comput. Chem.* **22**, 501–508 (2001).
64. Essmann, U. et al. A smooth particle mesh Ewald method. *J. Chem. Phys.* **103**, 8577 (1995).
65. Humphrey, W., Dalke, A. & Schulten, K. VMD: visual molecular dynamics. *J. Mol. Graph.* **14**, 33–38 (1996).

Native protein sequence

HA signal peptide

FLAG epitope

3C cleavage site

His tag

TMs

Omitted residues due to lack of EM density

Stubbed residues

CLR – Expression construct

```

1  MEKKCTLYFL VLLPFFMILV T
1  MKTIIALSYI FCLVFADYKD DDDLEVLFFQ PAELEESPED SIQLGVTRNK
51  IMTAQYECYQ KIMQDPIQQA EGVYCNRTWD GWLCWNDVAA GTESMQLCPD
101 YFQDFDPSEK VTKICDQDGN WFRHPASNRT WTNYTQCNVN THEKVKTALN
      stalk, TM1                      TM2
151 LFYLTIIHGHSIASLLISL GIFFYFKSLS CQRITLHKNL PFSFVCNSVV
      TM3
201 TIIHLTAIVAN NQALVATNPV SCKVSQFIHL YLMGCNYFWM LCEGIYLHTI
      TM4
251 IVVAVFAEKQ HLMWYYFLGW GFPLIPACIH AIARSLYYND NCWISSDTHL
      TM5                      TM6
301 LYIIHGPICA ALLVNLFFLL NIVRVLITKI KVTHQAESNL YMKAVRATLI
      TM7
351 LVPLLGIIEFV LIPWRPEGKI AEEVYDYIMH ILMHFQGLLV STIFCFFNGE
      H8
401 VQAILRRNWN QYKIQFGNSF SNSEALRSAS YTVSTISDGP GYSHDCPSEH
451 LNGKSIHDIE NVLLKPENLY NPAGLEVLFQ GPHHHHHHHH

```

RAMP1- Expression construct

```

1  MARALCRLPR RGLWLLLAHH LFMTTA
1  MKTIIALSYI FCLVFADYKD DDDKHGSCQE ANYGALLREL CLTQFQVDME
51  AVGETLWCDW GRTIRSYREL ADCTWHMAEK LGCFWPNAEV DRFFLAVHGR
101 YFRSCPISGR AVRDPGSI LYPFIVVPITV TLLVTALVVW QSKRTGIV

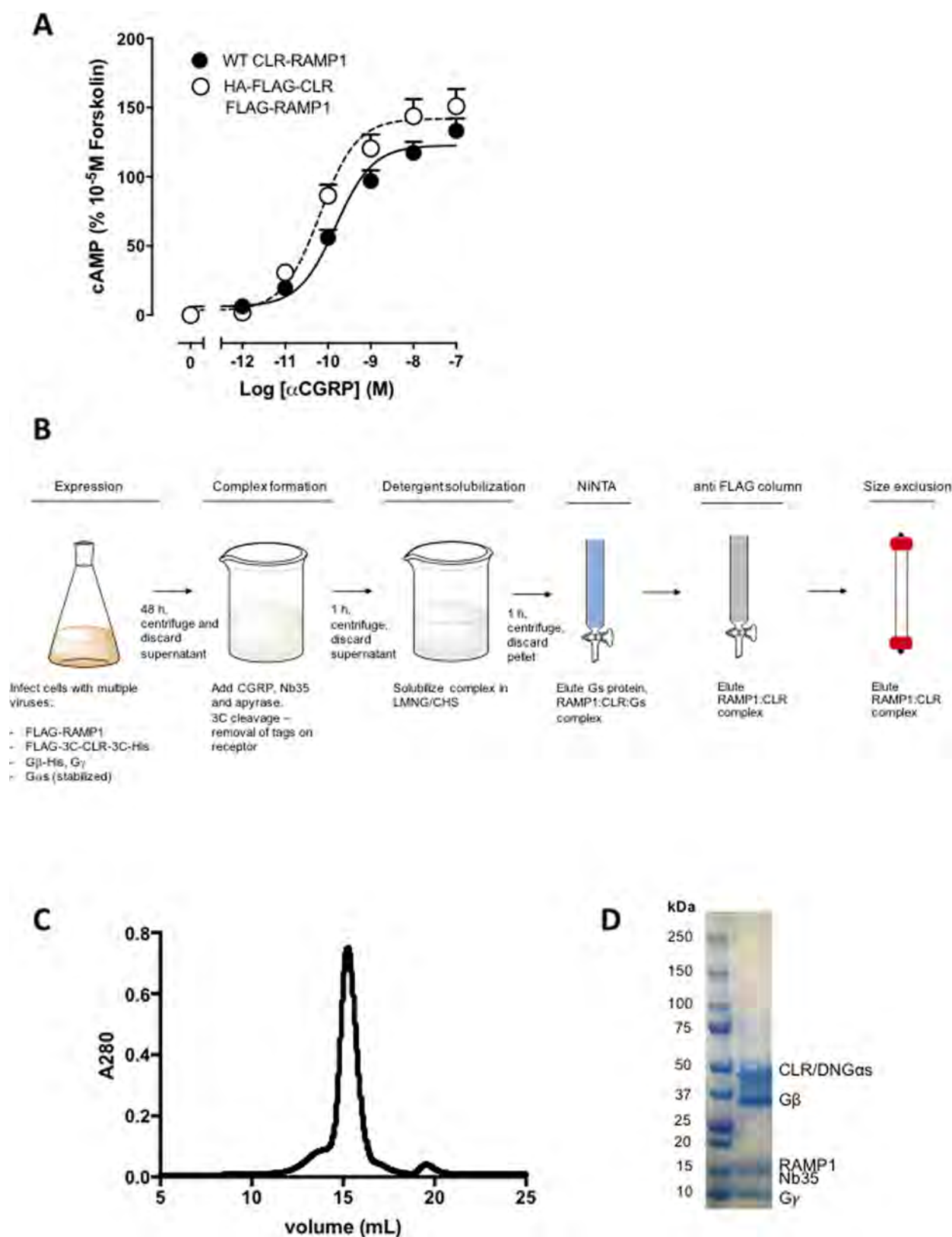
```

CGRP

ACDTATCVTH RLAGLLSRSG GVVKNNFVPT NVGSKAF-NH₂

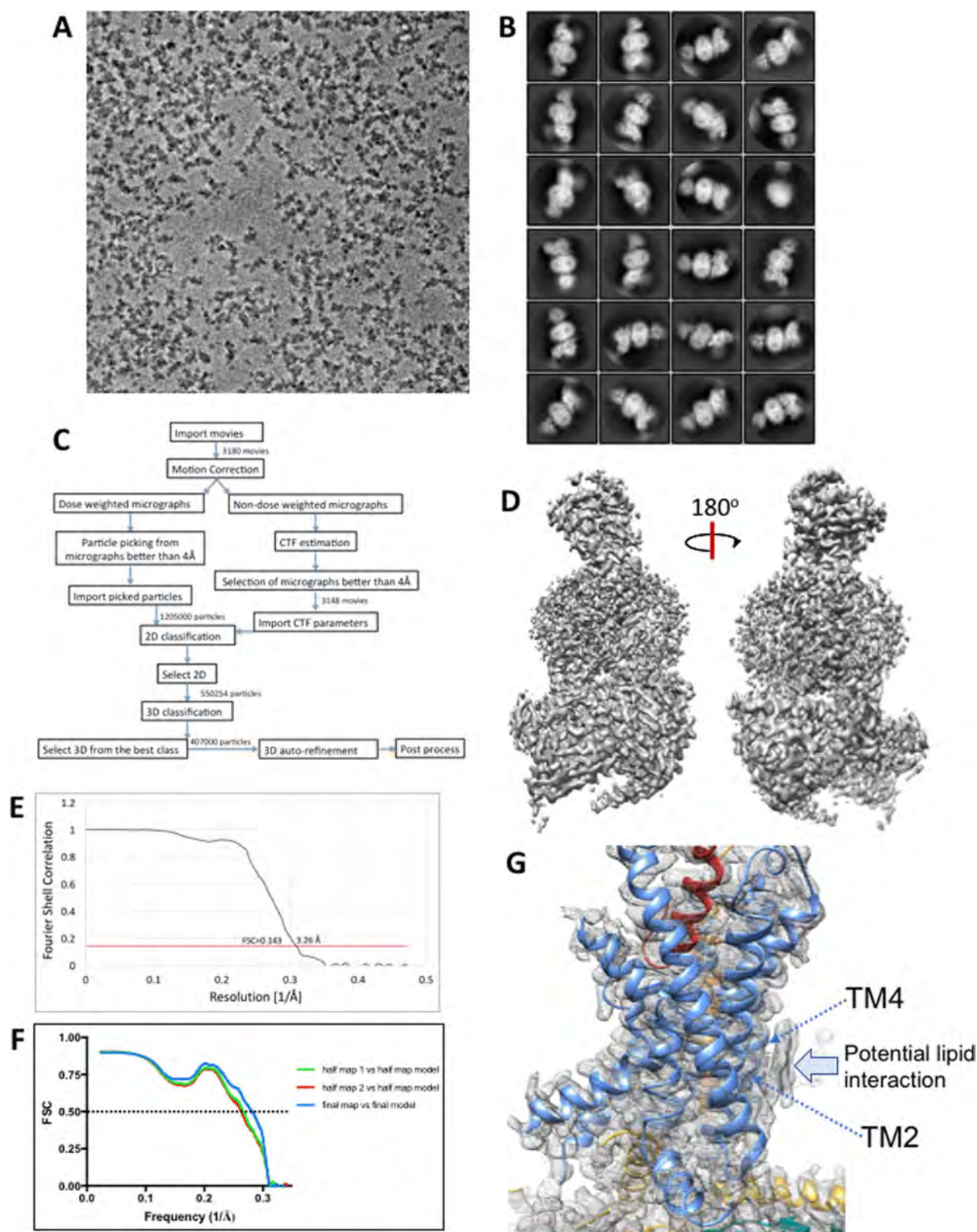
Extended Data Fig. 1 | Amino acid sequences of the CGRP peptide, CLR and RAMP1 constructs used for determination of structure. The sequences are annotated to denote the location of the haemagglutinin (HA) signal sequence (red highlight), 3C cleavage sites (grey highlight), Flag (dark olive-green highlight) and His tags (purple highlight). The substituted sequences of the native proteins are listed above the construct

sequences and highlighted in blue. Transmembrane helical domains in CLR and RAMP1 are boxed and highlighted in green. Segments of the proteins that were not resolved in the cryo-EM map are highlighted in yellow. Amino acids for which backbone density was present but there was limited side-chain density were stubbed in the model; these are shown in bold red in the sequences.



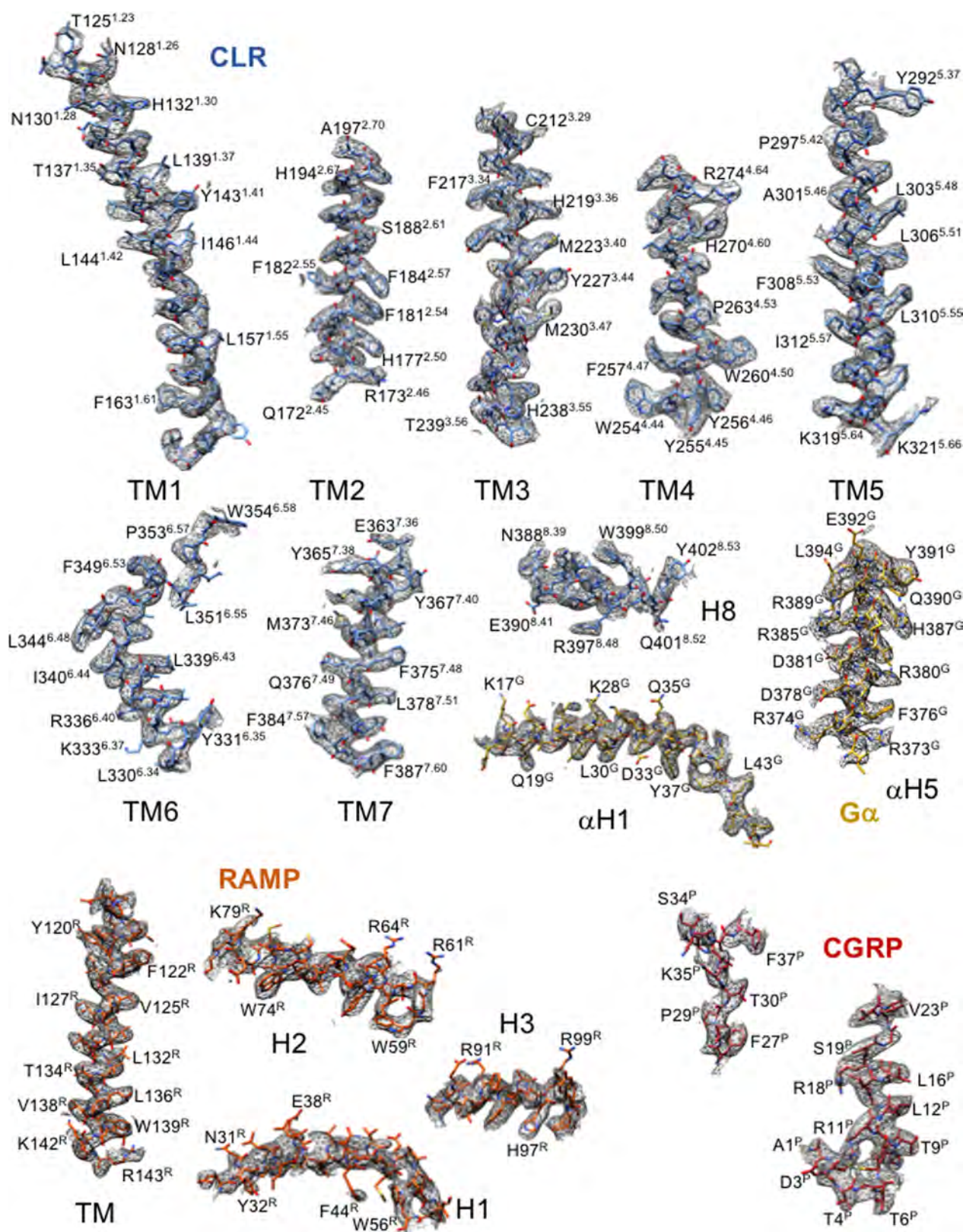
Extended Data Fig. 2 | CGRP receptor pharmacology and purification of the CGRP-CLR-RAMP1-G_s complex. **a**, Pharmacology of untagged CLR-RAMP1 (wild-type (WT) CLR-RAMP1) and the purification construct (HA-Flag-CLR and Flag-RAMP1), in CGRP-mediated cAMP accumulation assays performed in transiently transfected COS-7

cells. $n = 5$ independent experiments with triplicate repeats; data are mean \pm s.e.m. **b**, Expression and purification strategy. **c**, Final size-exclusion chromatography elution profile of the complex. **d**, SDS-PAGE and Coomassie blue staining of the size-exclusion chromatography peak, demonstrating the presence of each of the components of the complex.



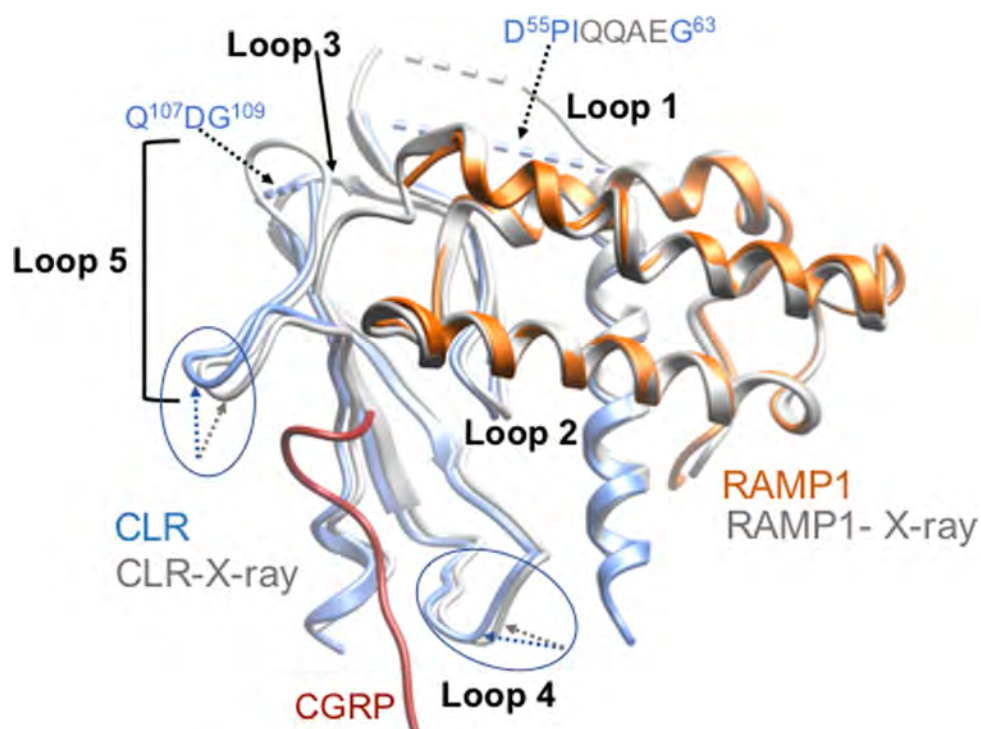
Extended Data Fig. 3 | Volta phase-plate imaging of the CGRP-CLR-RAMP1-G_s complex. **a**, Volta phase-plate micrograph of the complex (representative of 3,180 movies). High-contrast phase-plate imaging facilitates robust particle selection despite low defocus and tight packing of particles. **b**, RELION 2D class averages. **c**, Workflow for map refinement. **d**, Final 3D cryo-EM map calculated in RELION after auto-refinement and map sharpening. **e**, Gold standard Fourier shell correlation curve; the

overall nominal resolution is 3.26 Å. **f**, Model overfitting was evaluated by randomly displacing all atoms by 0.5 Å and refined against one cryo-EM half map. Fourier shell correlation curves were calculated between the resulting model and the half map used for refinement (green); the resulting model and the other half map for cross validation (red), and the final refined model and the full map (blue). **g**, Potential lipid interaction with the base of TM4 and TM2 of CLR.



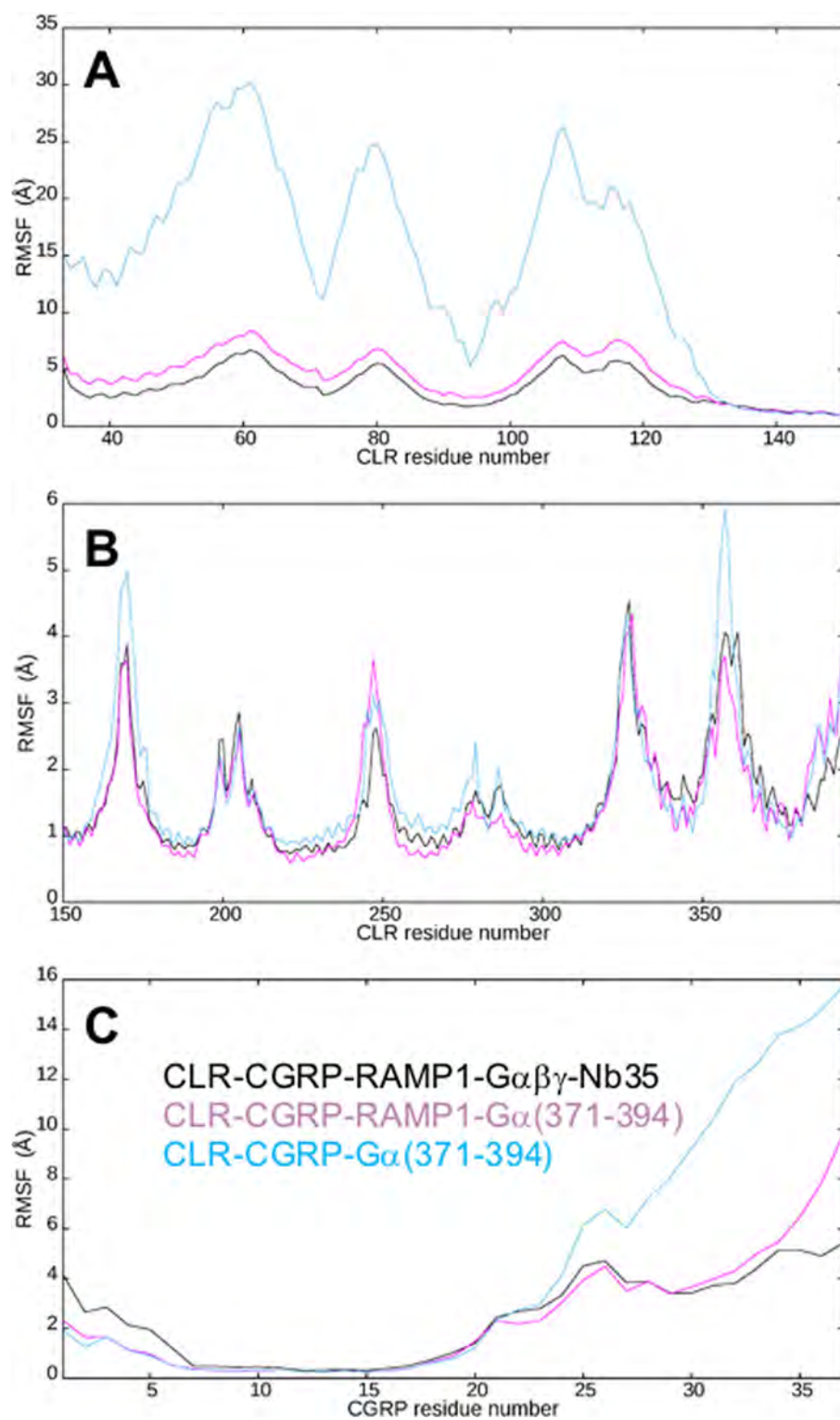
Extended Data Fig. 4 | Atomic-resolution model of the CGRP-CLR-RAMP1-G_s complex in the cryo-EM density map. Cryo-EM density map and model are shown for all seven transmembrane helices and H8 of the receptor, the CGRP peptide (excluding the Lys24-Asn25-Asn26 sequence that was not resolved in the map), the RAMP transmembrane domain and

each of the RAMP ECD helices. There was only limited side-chain density for RAMP1 H1, with side chains modelled from rigid-body fitting of the RAMP1 ECD in PDB: 4RWG¹². The N-terminal (α H1) and C-terminal (α H5) α -helices of the G α_s -Ras domain are also shown. Superscript P indicates residues of CGRP.



Extended Data Fig. 5 | Alignment of modelled active complex and X-ray structure. Backbone of the ECD of CLR (blue ribbon) and RAMP1 (orange ribbon) from the modelled, active complex, and the structure of the isolated CLR–RAMP1 ECD complex solved by X-ray crystallography¹² (light grey ribbon). The structures were aligned on the RAMP1 ECD. The CLR loops (loops 1–5) are annotated. The CLR loop 1 and loop 5

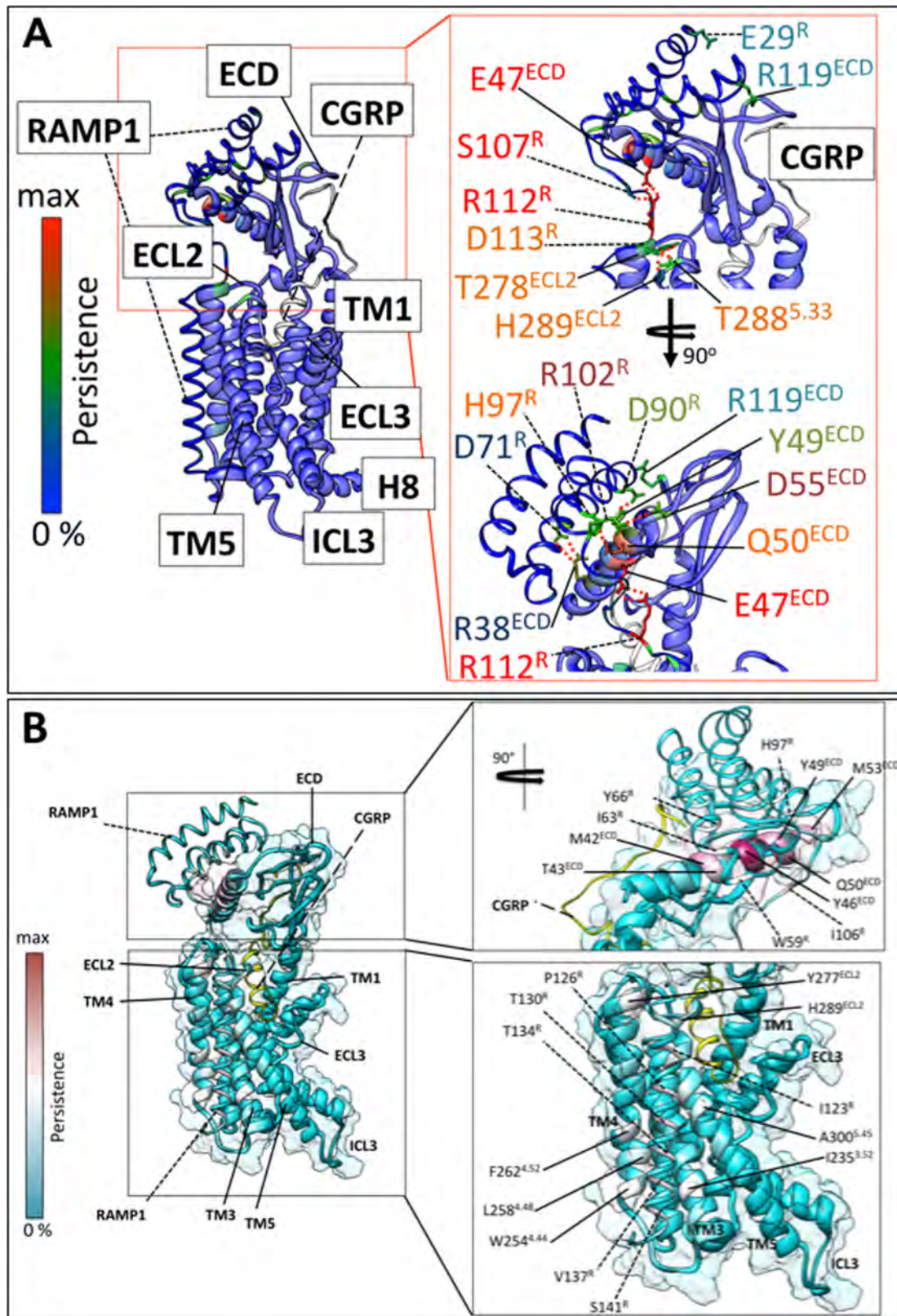
sequences that were not resolved in the cryo-EM map are indicated by dotted black arrows. Differences in the backbone position of CLR loops 4 and 5 are indicated in blue (active complex) and grey (isolated ECD complex) dotted arrows. The location of the CGRP peptide is shown in dark red.



Extended Data Fig. 6 | See next page for caption.

Extended Data Fig. 6 | RMSF for CGRP and CLR taken from the three simulations. Simulations of CLR-CGRP-RAMP1-G $\alpha\beta\gamma$ -Nb35 (black, 2.4 μ s), CLR-CGRP-RAMP1-G α (371–394) (purple, 2 μ s) and CLR-CGRP-G α (371–394) (blue, 2 μ s). **a**, The CLR ECD region. **b**, The CLR transmembrane region. **c**, CGRP (superposed on T6–S17, and therefore valid for the N-terminal half). In general, the missing segments in the cryo-EM density map correspond to regions of high RMSF, and indeed the difficulty of fitting the ECD as a whole is linked to its high RMSF (**a**; Supplementary Videos 2, 3). The segments missing from the ECD (D55^{ECD}–V63^{ECD}) and (Q107^{ECD}–G109^{ECD}) correspond to external loop regions furthest removed from the transmembrane domain. Despite their polar nature they displayed no persistent interactions during the molecular dynamics simulations; D55^{ECD}–V63^{ECD} displayed the largest backbone RMSF of 8 Å, whereas Q107^{ECD}–G109^{ECD} displayed a similarly high RMSF of 7.5 Å. The next-highest RMSF peaks around A79^{ECD}–G81^{ECD} and P115^{ECD}–S117^{ECD} are just a little lower, but are nonetheless resolved (**a**).

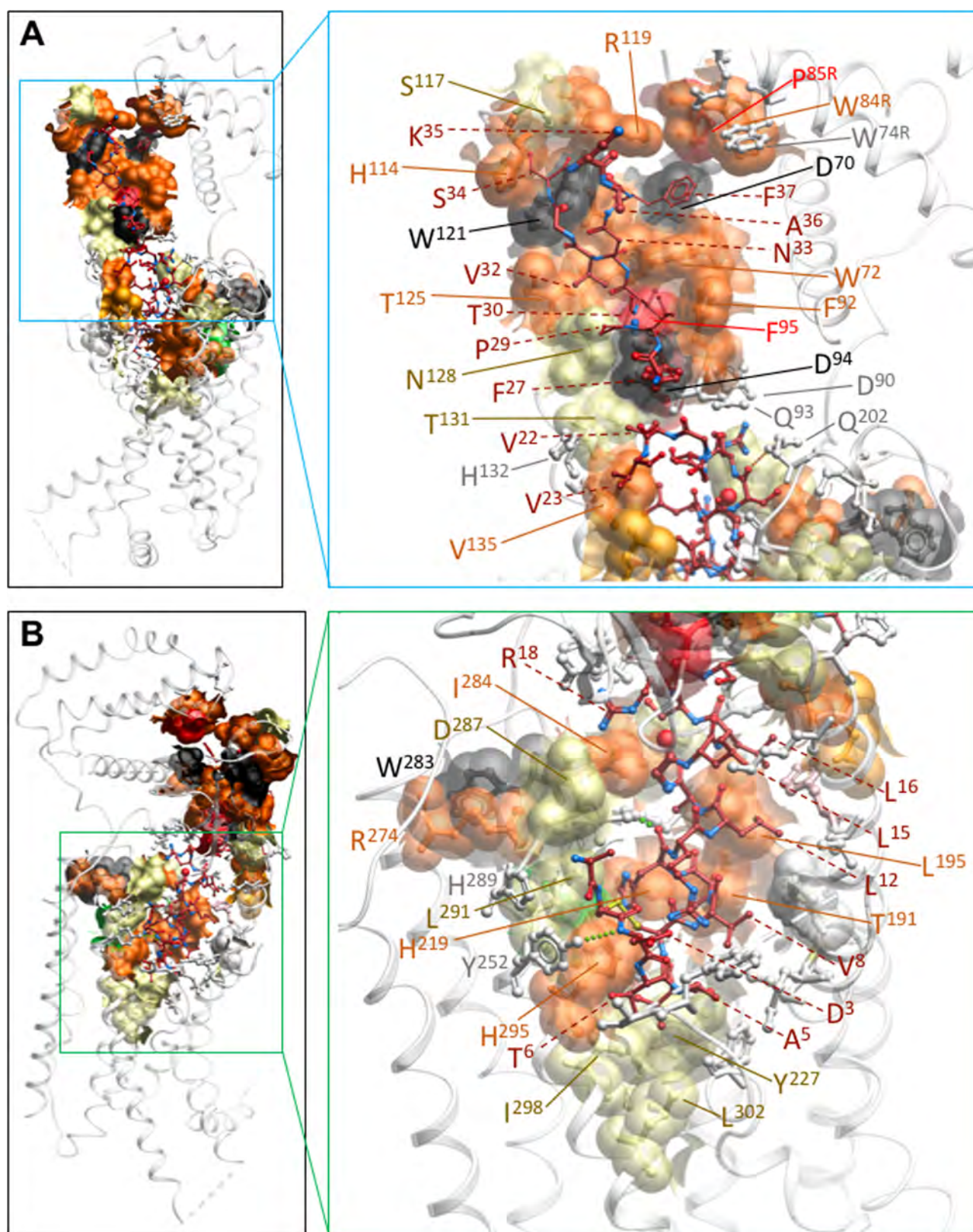
Within the transmembrane domain, ICL3 (H324^{ICL3}–S328^{ICL3}) and ECL3 (P356^{ECL3}–E362^{ECL3}) both contain missing residues and have a high RMSF above 4.5 Å (**b**). This region displays no persistent interactions during the molecular dynamics simulations, although CGRP does interact with the proximal (non-missing) region of ECL3. The high RMSF values for ICL1 (3.6 Å) and ICL2 (3.6 Å) give rise to stubbed residues (K167^{ICL1}) and E248^{ICL2}–Q250^{ICL2}) but the backbone is resolved. For CGRP, the peak in the RMSF around residue 26 (**c**) corresponds to the three highly mobile external residues (Lys24–Asn25–Asn26) in the outward-facing loop that do not interact with CLR (Extended Data Fig. 8); these residues could not be placed from the electron density. These three CGRP residues form a hinge, enabling changes in the orientation of the CLR ECD, especially in the absence of RAMP1; the higher RMSF values C-terminal to this are an artefact of the superposition strategy and the two-domain nature of CLR, but their relative values still hold. The high mobility of some of the extracellular loops is visible in videos (Supplementary Videos 1–3).



Extended Data Fig. 7 | See next page for caption.

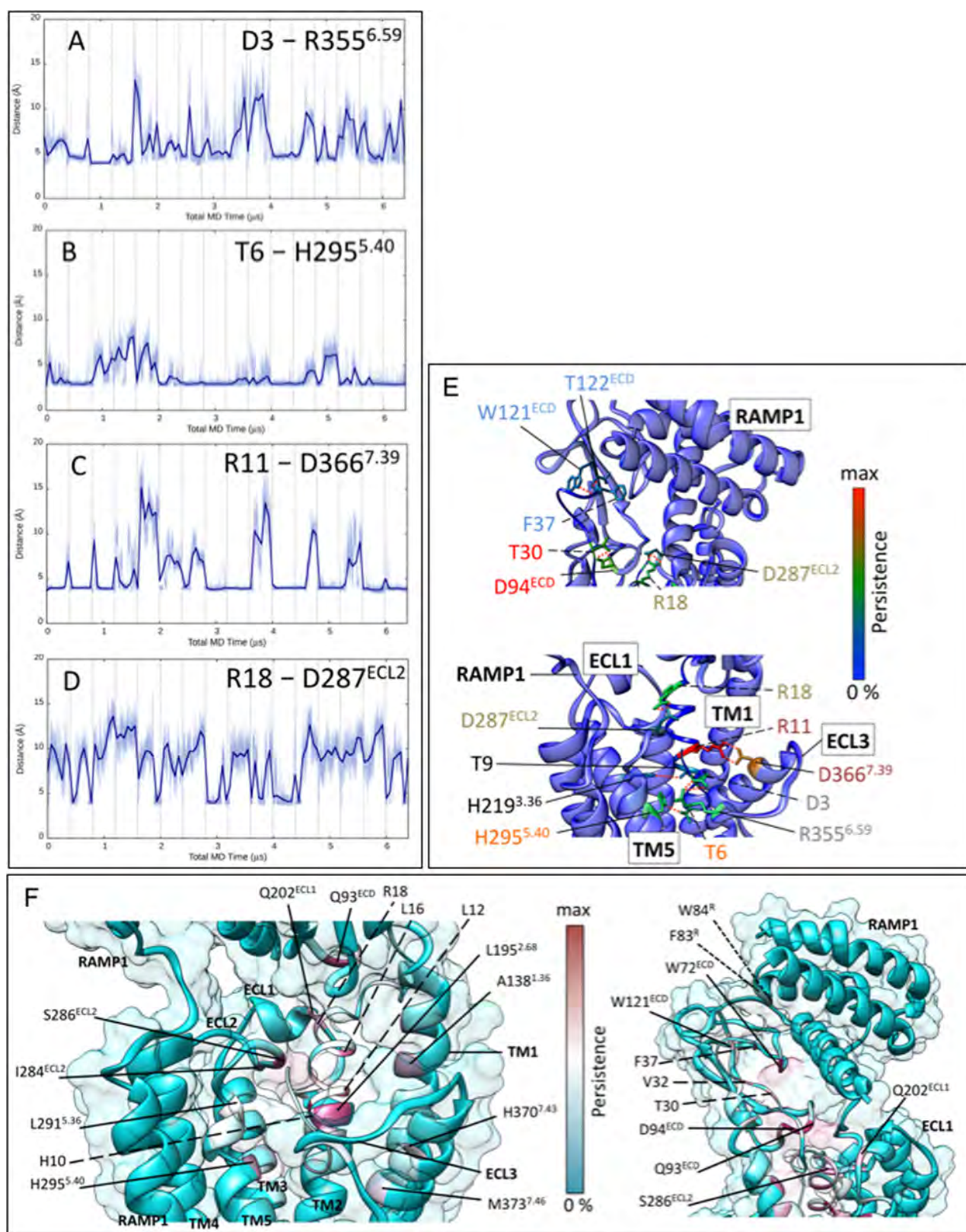
Extended Data Fig. 7 | RAMP1 makes extensive stable interactions with CLR. **a**, Hydrogen bonds between RAMP1 and CLR during molecular dynamics simulations (6.4 μ s). The total persistence is plotted onto the experimental structure according to a rainbow colour scale, with residues that are never involved in dark blue and residues that are highly involved in red. The receptor is shown as a bulky ribbon, RAMP1 as a thin coloured ribbon and the peptide as a thin white ribbon. Key side chains are shown, but for intermittent hydrogen bonds the rotameric state has been modified to show an interaction. Residues forming an interaction network are labelled with the same colour. Left, overall topology of the system. Right top, magnified view of the upper portion of the CLR transmembrane domain and ECD; right bottom, view rotated by 90° on the z axis. Hydrogen bonds involved in the RAMP1–CLR interaction, R112^R–E47^{ECD} and D113^R–T288^{ECL2}/H289^{ECL2} are notable because they link the transmembrane domain to the ECD, and for stabilizing ECL2. Other hydrogen bonds implicated in stabilizing the CLR and RAMP1 ECD interaction include S107^R–E47^{ECD}, R102^R–D55^{ECD}, H97^R–Q50^{ECD}, D90^R–Y49^{ECD}, D71^R–R38^{ECD} and E29^R–R119^{ECD}. Quantitative data on

the persistence of hydrogen bonds during the simulations are reported in Supplementary Table 2. **b**, Contacts between RAMP1 and CLR during simulations (6.4 μ s). The total persistence of a residue side chain is plotted onto the experimental structure according to a cyan–maroon colour scale, with residues that are never involved in cyan and residues that are highly involved in maroon. The peptide (*italics*, dashed line) is depicted as a thin ribbon, whereas the receptor (solid line) is shown as a bulky ribbon and transparent surface. Left, overall topology of the system. Top right, the most-persistent interactions involving RAMP residues and the CLR ECD, W59^R, I63^R, Y66^R, H97^R and I106^R help to anchor α H3 and the C-terminal RAMP1 regions of α H2 to (residues M42^{ECD}, T43^{ECD}, Y46^{ECD}, Y49^{ECD}, Q50^{ECD} and M53^{ECD} of the CLR ECD). Bottom right, the most-persistent hydrophobic interactions between the transmembrane domains of RAMP1 and CLR, namely I123^R, P126^R, T130^R, T134^R and V137^R (plus S141^R) help to anchor the RAMP transmembrane helix to CLR (TM3–TM5; CLR residues Y277^{ECL2}, H289^{ECL2}, A300^{5,45}, I235^{3,52}, F262^{4,52}, L258^{4,48} and W254^{4,44}).



Extended Data Fig. 8 | Effect of alanine mutagenesis of CLR or RAMP1 on CGRP potency in cAMP accumulation assays. a, ECD alanine mutations. b, CLR core alanine mutations. Residues that have been mutated are displayed in x-stick format. Mutated residues with no effect on signalling are coloured off-white. Residues that have significantly altered CGRP signalling^{12,23,28,30–32,34,37,38} are also highlighted in transparent

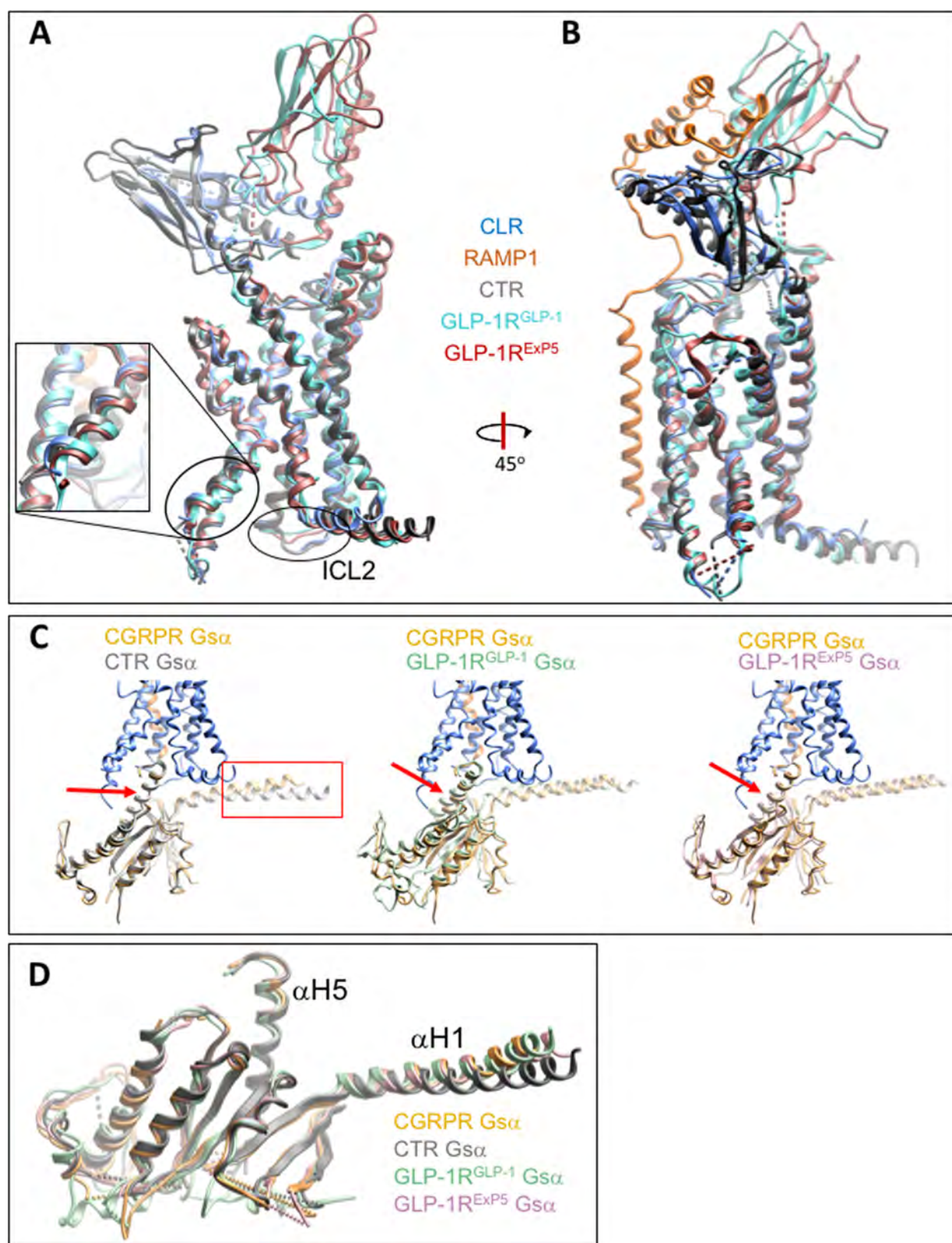
CPK representation, coloured according to magnitude of effect. Yellow, <10 fold; dark orange, 10–100 fold; red, 100–1,000 fold; black, >1,000 fold. The backbones of CLR and RAMP (solid lines) are displayed in transparent, off-white coloured ribbon. The CGRP peptide (dashed lines) is represented in x-stick format with carbon atoms in dark red and polar atoms coloured in red or blue.



Extended Data Fig. 9 | See next page for caption.

Extended Data Fig. 9 | CGRP makes extensive stable interactions with CLR. **a–d**, Distances between CGRP and CLR residues relevant to key hydrogen bonds. The *x* axis denotes sampling time for the 16 merged molecular dynamics replicas of the whole system (each replica is separated by a vertical dashed line). **a**, Distance between the peptide Asp3 carboxylic carbon and receptor R355^{6,59} guanidinium carbon. **b**, Distance between the peptide Thr6 side-chain oxygen atom and the receptor H295^{5,40} side-chain nitrogen atoms (for each frame, the closest nitrogen to Thr6 was considered). **c**, Distance between the peptide Arg11 guanidinium carbon and the receptor D366^{7,39} carboxylic carbon. **d**, Distance between peptide Arg18 guanidinium carbon and receptor D287^{ECL2} carboxylic carbon. In most cases, the distances corresponding to hydrogen-bond formation are slightly longer than the standard 2.8 Å. **e**, Hydrogen bonds between CGRP and CLR during molecular dynamics simulations (6.4 μs). The total persistence of a residue side chain is plotted onto the experimental structure according to a rainbow colour scale, with residues that are never involved in blue and residues that are highly involved in red. The peptide (italics, dashed line) is depicted as thin ribbon, whereas the receptor (solid line) is shown as bulky ribbon. Key side chains are shown, but for intermittent hydrogen bonds, the rotameric state has been modified to

show an interaction. Residues forming an interaction network are labelled with the same colour. Bottom, hydrogen bonds between the CGRP N terminus and the transmembrane bundle of CLR. Top, hydrogen bonds between the CGRP C terminus and the ECD of CLR; quantitative data on the persistence of hydrogen bonds during the simulations are reported in Supplementary Table 3. **f**, Contacts between CGRP and CLR–RAMP1 during molecular dynamics simulations (6.4 μs). The total persistence of a residue side chain is plotted onto the experimental structure according to a cyan–maroon colour scale, with residues that are never involved in cyan and residues that are highly involved in maroon. The peptide (italics, dashed line) is depicted as a thin ribbon, while the receptor (solid line) is shown as a bulky ribbon and transparent surface. Left, contacts between the N terminus of CGRP and the transmembrane bundle of the CLR: highly persistent hydrophobic interactions characterize peptide residues Leu12, Leu16, His10 and receptor residues L195^{2,68}, A138^{1,36} and H295^{5,40}. Right, contacts between the C terminus of CGRP and the ECD of CLR; highly persistent contacts characterize peptide residues Val32, Thr30, Phe37 and receptor residues Q93^{ECD} and W72^{ECD}. RAMP1 residues F83^R, W84^R are mainly engaged by CGRP residue Phe37.



Extended Data Fig. 10 | Class B GPCRs display similar active state conformations. **a, b,** Alignment of the CGRP-CLR-RAMP1, sCT-CTR, ExP5-GLP-1R and GLP-1-GLP-1R structures (aligned on the transmembrane domains). Regions of divergence between CLR/CTR and GLP-1R are circled. In **a**, RAMP1 has been omitted for clarity. **c,** Position

of the G α_s -Ras domain in the CTR (left), GLP-1R (GLP-1 bound; middle) and GLP-1R (ExP5 bound; right). The receptor transmembrane domains were aligned. Only the CLR (blue) and RAMP1 (orange) are displayed for clarity. **d,** The G α_s -Ras domain from each of the four structures, aligned to the G α_s -Ras of the CGRP receptor (CGRPR) complex.

Reporting Summary

Nature Research wishes to improve the reproducibility of the work that we publish. This form provides structure for consistency and transparency in reporting. For further information on Nature Research policies, see [Authors & Referees](#) and the [Editorial Policy Checklist](#).

Statistical parameters

When statistical analyses are reported, confirm that the following items are present in the relevant location (e.g. figure legend, table legend, main text, or Methods section).

n/a Confirmed

- ☐ ☒ The exact sample size (n) for each experimental group/condition, given as a discrete number and unit of measurement
- ☐ ☒ An indication of whether measurements were taken from distinct samples or whether the same sample was measured repeatedly
- ☒ ☐ The statistical test(s) used AND whether they are one- or two-sided
Only common tests should be described solely by name; describe more complex techniques in the Methods section.
- ☒ ☐ A description of all covariates tested
- ☒ ☐ A description of any assumptions or corrections, such as tests of normality and adjustment for multiple comparisons
- ☒ ☐ A full description of the statistics including central tendency (e.g. means) or other basic estimates (e.g. regression coefficient) AND variation (e.g. standard deviation) or associated estimates of uncertainty (e.g. confidence intervals)
- ☒ ☐ For null hypothesis testing, the test statistic (e.g. F , t , r) with confidence intervals, effect sizes, degrees of freedom and P value noted
Give P values as exact values whenever suitable.
- ☒ ☐ For Bayesian analysis, information on the choice of priors and Markov chain Monte Carlo settings
- ☒ ☐ For hierarchical and complex designs, identification of the appropriate level for tests and full reporting of outcomes
- ☒ ☐ Estimates of effect sizes (e.g. Cohen's d , Pearson's r), indicating how they were calculated
- ☐ ☒ Clearly defined error bars
State explicitly what error bars represent (e.g. SD, SE, CI)

Our web collection on [statistics for biologists](#) may be useful.

Software and code

Policy information about [availability of computer code](#)

Data collection

SerialEM

Data analysis

GraphPad Prism (v7), Motioncor2 (v1.1), Gctf (v1.18), Gautomatch (0.56), EMAN2 (2.02), RELION 2.01b1, PHENIX (1.13), MolProbity (4.4), COOT (0.8.9.1), Pymol (2.1), UCSF Chimera (1.11.2), Modeller (9.16), pdb2pqr (2.0), propka (3.0), VMD (1.9.3), VMD Membrane Builder Plugin (1.1), VMD Solvate Plugin (1.5), VMD Autoionize Plugin (1.3), ACEMD (1.13), Molsoft ICM (3.8-7)

For manuscripts utilizing custom algorithms or software that are central to the research but not yet described in published literature, software must be made available to editors/reviewers upon request. We strongly encourage code deposition in a community repository (e.g. GitHub). See the Nature Research [guidelines for submitting code & software](#) for further information.

Data

Policy information about [availability of data](#)

All manuscripts must include a [data availability statement](#). This statement should provide the following information, where applicable:

- Accession codes, unique identifiers, or web links for publicly available datasets
- A list of figures that have associated raw data
- A description of any restrictions on data availability

PDB and EMDB files have been created and will be available on publication. Modeling files will be available from a freely accessible doi hosted by the University of Essex.

Field-specific reporting

Please select the best fit for your research. If you are not sure, read the appropriate sections before making your selection.

☒ Life sciences ☐ Behavioural & social sciences ☐ Ecological, evolutionary & environmental sciences

For a reference copy of the document with all sections, see [nature.com/authors/policies/ReportingSummary-flat.pdf](https://www.nature.com/authors/policies/ReportingSummary-flat.pdf)

Life sciences study design

All studies must disclose on these points even when the disclosure is negative.

Sample size	Sample size calculation was not required
Data exclusions	No data were excluded.
Replication	All experimental findings were reliably reproduced.
Randomization	Randomization was not required.
Blinding	Blinding was not required.

Reporting for specific materials, systems and methods

Materials & experimental systems

n/a	Involvement in the study
<input checked="" type="checkbox"/>	<input type="checkbox"/> Unique biological materials
<input type="checkbox"/>	<input checked="" type="checkbox"/> Antibodies
<input type="checkbox"/>	<input checked="" type="checkbox"/> Eukaryotic cell lines
<input checked="" type="checkbox"/>	<input type="checkbox"/> Palaeontology
<input checked="" type="checkbox"/>	<input type="checkbox"/> Animals and other organisms
<input checked="" type="checkbox"/>	<input type="checkbox"/> Human research participants

Methods

n/a	Involvement in the study
<input checked="" type="checkbox"/>	<input type="checkbox"/> ChIP-seq
<input checked="" type="checkbox"/>	<input type="checkbox"/> Flow cytometry
<input checked="" type="checkbox"/>	<input type="checkbox"/> MRI-based neuroimaging

Antibodies

Antibodies used	rabbit anti-Gs C-18 antibody (cat no sc-383), Santa Cruz mouse Penta-His antibody (cat no 34660), QIAGEN 680RD goat anti-mouse antibody (LI-COR), 800CW goat anti-rabbit antibody (LICOR) The primary Abs anti-Gs and Penta-His are used at 1ug/mL The secondary Abs are used at 0.2ug/mL
Validation	All antibodies were used for Western blot analysis and have been validated. Liang et al., Nature 2018.

Eukaryotic cell lines

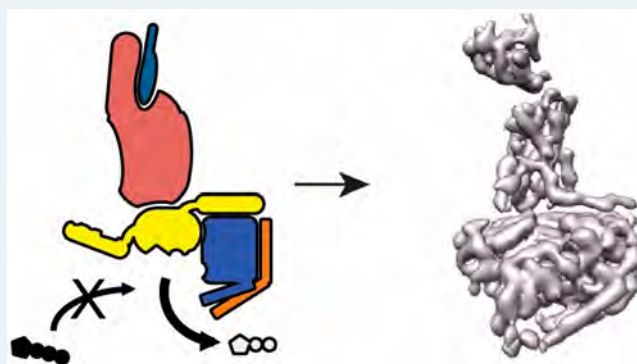
Policy information about [cell lines](#)

Cell line source(s)	Cos7 cells used in assays were obtained from ATCC; Tni cells were from Expression Systems.
Authentication	None of the cells used was authenticated
Mycoplasma contamination	Cell lines were tested and are free from mycoplasma contamination
Commonly misidentified lines (See ICLAC register)	The cells are not listed in the database

Dominant Negative G Proteins Enhance Formation and Purification of Agonist-GPCR-G Protein Complexes for Structure Determination

Yi-Lynn Liang,^{†,‡} Peishen Zhao,^{†,‡} Christopher Draper-Joyce,^{†,‡} Jo-Anne Baltos,[†] Alisa Glukhova,[†] Tin T. Truong,[†] Lauren T. May,[†] Arthur Christopoulos,[†] Denise Wootten,^{*,†,‡} Patrick M. Sexton,^{*,†,‡} and Sebastian G. B. Furness^{*,†}[†]Drug Discovery Biology, Monash Institute of Pharmaceutical Sciences, Monash University, Parkville, 3052, Australia[‡]School of Pharmacy, Fudan University, Shanghai 201203, China

ABSTRACT: Advances in structural biology have yielded exponential growth in G protein-coupled receptor (GPCR) structure solution. Nonetheless, the instability of fully active GPCR complexes with cognate heterotrimeric G proteins has made them elusive. Existing structures have been limited to nanobody-stabilized GPCR:Gs complexes. Here we present methods for enhanced GPCR:G protein complex stabilization via engineering G proteins with reduced nucleotide affinity, limiting $G\alpha:G\beta\gamma$ dissociation. We illustrate the application of dominant negative G proteins of $G\alpha s$ and $G\alpha i2$ to the purification of stable complexes where this was not possible with wild-type G protein. Active state complexes of adenosine:A1 receptor: $G\alpha i2\beta\gamma$ and calcitonin gene-related peptide (CGRP):CLR:RAMP1: $G\alpha s\beta\gamma$:Nb35 were purified to homogeneity and were stable in negative stain electron microscopy. These were suitable for structure determination by cryo-electron microscopy at 3.6 and 3.3 Å resolution, respectively. The dominant negative $G\alpha$ -proteins are thus high value tools for structure determination of agonist:GPCR:G protein complexes that are critical for informed translational drug discovery.



GPCRs are premier drug targets and there is substantial interest in structural understanding of these proteins to determine mechanisms of drug interaction and activation. Recent methodological developments in GPCR engineering, including introduction of thermo-stabilizing mutations, replacement of flexible loops with small stable fusion proteins, and specialized binding partners, have enabled the determination of structures of 53 unique receptors.¹ Of these structures only five receptors are in a fully active, transducer-complexed, state. This state is only achieved when both agonist and trimeric G protein (or other transducer) are present, commonly referred to as the ternary complex.² Thus, understanding the structural basis of this state is critical to understanding mechanisms of GPCR signal transduction and for utilizing this information for structure-based drug design. G protein bound active state receptor structures have been achieved using several approaches; of the five published $G\alpha s$ containing structures, four (three unique receptors) utilized a camelid nanobody, Nb35, to stabilize the $G\alpha$ – $G\beta\gamma$ interface,^{3–6} while the structure of Adenosine A2A receptor utilized a highly engineered mini-Gs partner.⁷ The active state of opsin was determined using a c-terminal peptide fragment of G_r .⁸

The agonist-bound GPCR acts as a guanine–nucleotide exchange factor (GEF) for the $G\alpha$ subunit, promoting GDP release and subsequent GTP binding. This occurs while the $G\alpha$ subunit is bound to the $G\beta\gamma$ heterodimer. Physiologically, where

GDP and GTP concentrations are relatively high, the ternary complex is unstable, the G protein heterotrimer dissociates from the receptor, and into its component parts, $G\alpha$ and $G\beta\gamma$, that engage downstream signaling effectors.⁹ This inherent instability makes it extremely challenging to trap and purify complexes of GPCRs bound to heterotrimeric G proteins for structural studies.

Using the extensive literature on G protein mutagenesis, mutations within $G\alpha i2$ and $G\alpha s$ (highlighted in Figure 1) predicted to stabilize the ternary complex state were selected. These reduce nucleotide-binding affinities and enhance the stability of agonist:GPCR:G protein heterotrimer complexes; achieving the latter is critical for structural studies. Mutations included four residues conserved across all G protein subclasses. Ser^{H1.02} (CGN numbering system¹⁰), involved in coordinating Mg^{2+} and contacting GTP's β -phosphate, whose mutation to Asn in $G\alpha s$ ¹¹ and Cys in $G\alpha i2$,¹² $G\alpha o$,¹² and $G\alpha t$ ¹³ generates a dominant negative G protein. This inhibits signaling by formation of a stabilized (nondissociating) ternary complex. Gly^{S3H2.02} of $G\alpha$ forms a backbone amide hydrogen bond with the γ -phosphate of GTP¹⁴ with Ala substitution increasing the GDP dissociation rate and blocking GTP induced dissociation from the β_2 receptor.¹⁵ A combination of Gly^{S3H2.02}Ala with

Received: June 12, 2018

Published: July 26, 2018



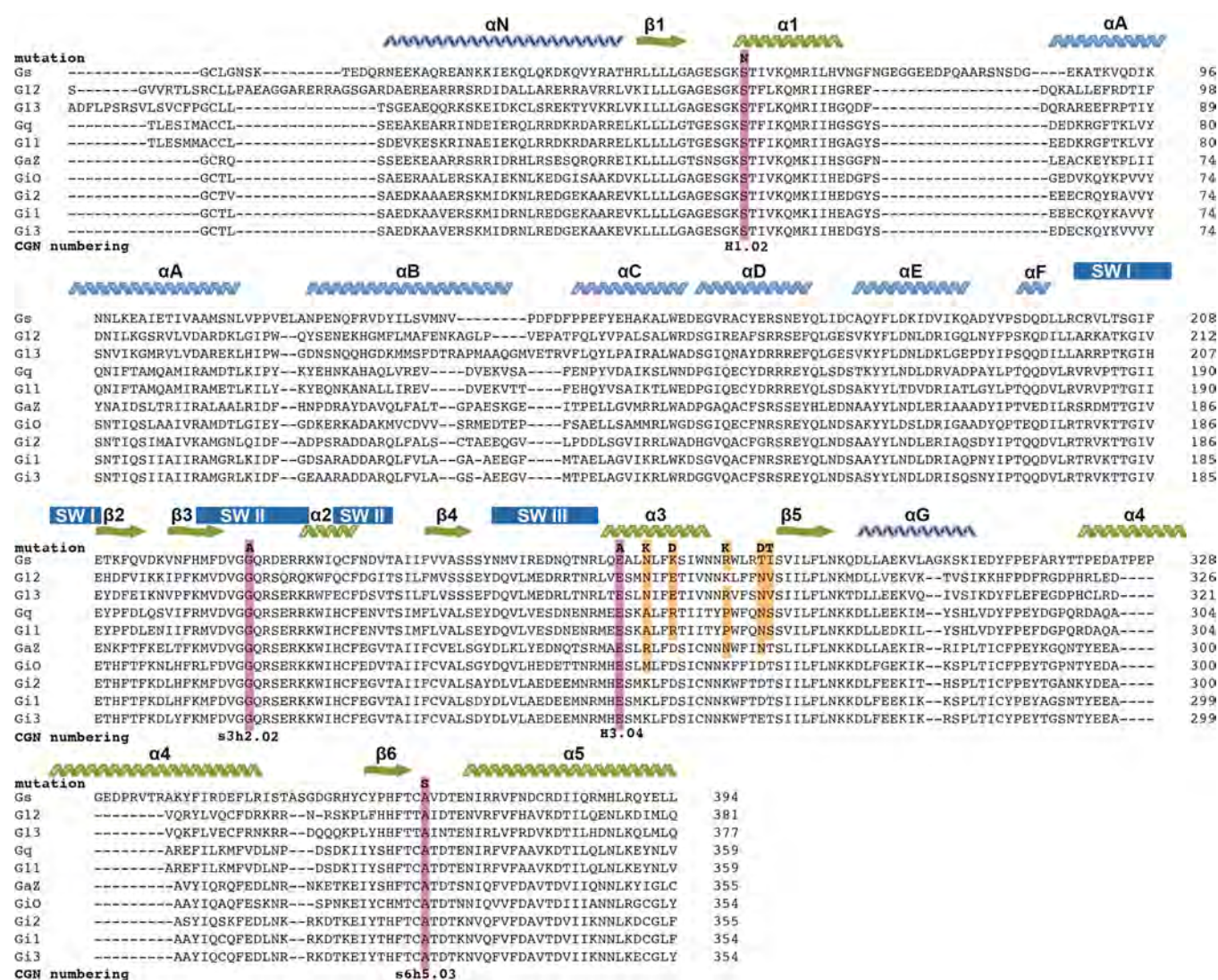


Figure 1. Alignment of human $G\alpha$ isoforms. Clustalw omega alignment of reference sequences for human $G\alpha$ isoforms manually adjusted to take into account secondary elements from deposited PDB structures: 1SVK, 3FFB, 1ZCA, 1ZCB, 2BCJ, 1AZT, and 3SN6. α -Helices (zig-zags) from the α -helical domain are indicated in light blue, in dark blue are those outside either core domain and in green are those from the Ras-like domain. β -Strands are indicated in the same color scheme with wavy arrows. Secondary structure elements from the α -helical domain are indicated with letters and the Ras-like domain with numbers. The position and substitution for common DN-substitutions are highlighted in purple with the CGN numbering¹⁰ shown below. Highlighted in yellow are Gai residues that are substituted into Gs, which improve the dominant negative effect.

Glu^{H3.04}Ala generates a dominant negative¹⁶ presumably through disruption of the conserved salt-bridge between residues at s3h2.04 and H3.04,¹⁴ which is also seen during the conformational rearrangement in the nucleotide free state.³ Ala^{s6h5.03} to Ser substitution increases GDP dissociation rate. Although, with these mutations, the free $G\alpha\beta\gamma$ heterotrimer is thermolabile on its own; in combination with Gly^{s3h2.02}Ala, Glu^{H3.04}Ala, and Ala^{s6h5.03}Ser, it appears more stable, presumably because of constitutive interactions with GPCRs.¹⁷ For the G_{as} mutant, five additional mutations substituting residues of Gai2 into G_{as} within the $\alpha3$ helix or $\alpha3$ helix– $\beta5$ strand linker were introduced, improving the dominant negative effect of G_{as} .¹⁷

Here we present data showing the utility of these engineered dominant negative (DN) $G\alpha$ subunits to enhance formation of stable complexes for structural studies by cryo-electron microscopy (cryo-EM). These G_{as} and Gai2 constructs have enabled solution of fully active structures of glucagon-like peptide 1 receptor (GLP-1R),⁶ adenosine A1 receptor (A1-

AR),¹⁸ and calcitonin gene-related peptide receptor (CGRP-R)¹⁹ at resolutions that allow reliable placement of side-chain rotomers for most amino acids in the receptor core, supporting their broad applicability for purification of stable GPCR:heterotrimeric G protein complexes.

In the case of GLP-1R, purification of GLP-1R:Gs complexes were attempted using exendin-P5 (ExP5), a biased agonist with lower cAMP efficacy than the native GLP-1 that had been used by others to determine a 4.1 Å structure in complex with wild type (WT) Gs.⁵ The ExP5 complexes were initially formed with ExP5:GLP-1R:WT- G_{as} : $\beta\gamma$ in the absence of Nb35. These were benchmarked against the same complex containing the DN- G_{as} as well as against sCT:CTR containing either WT or DN- G_{as} as shown in Figure 2a. The ExP5:GLP-1R:WT- G_{as} : $\beta\gamma$ could not be purified to homogeneity; however, the inclusion of the DN- G_{as} allowed both GLP-1R and CTR containing complexes to be purified to homogeneity (Figure 2a), yielding around 200 $\mu\text{g L}^{-1}$. These Nb35 free complexes were subjected to negative

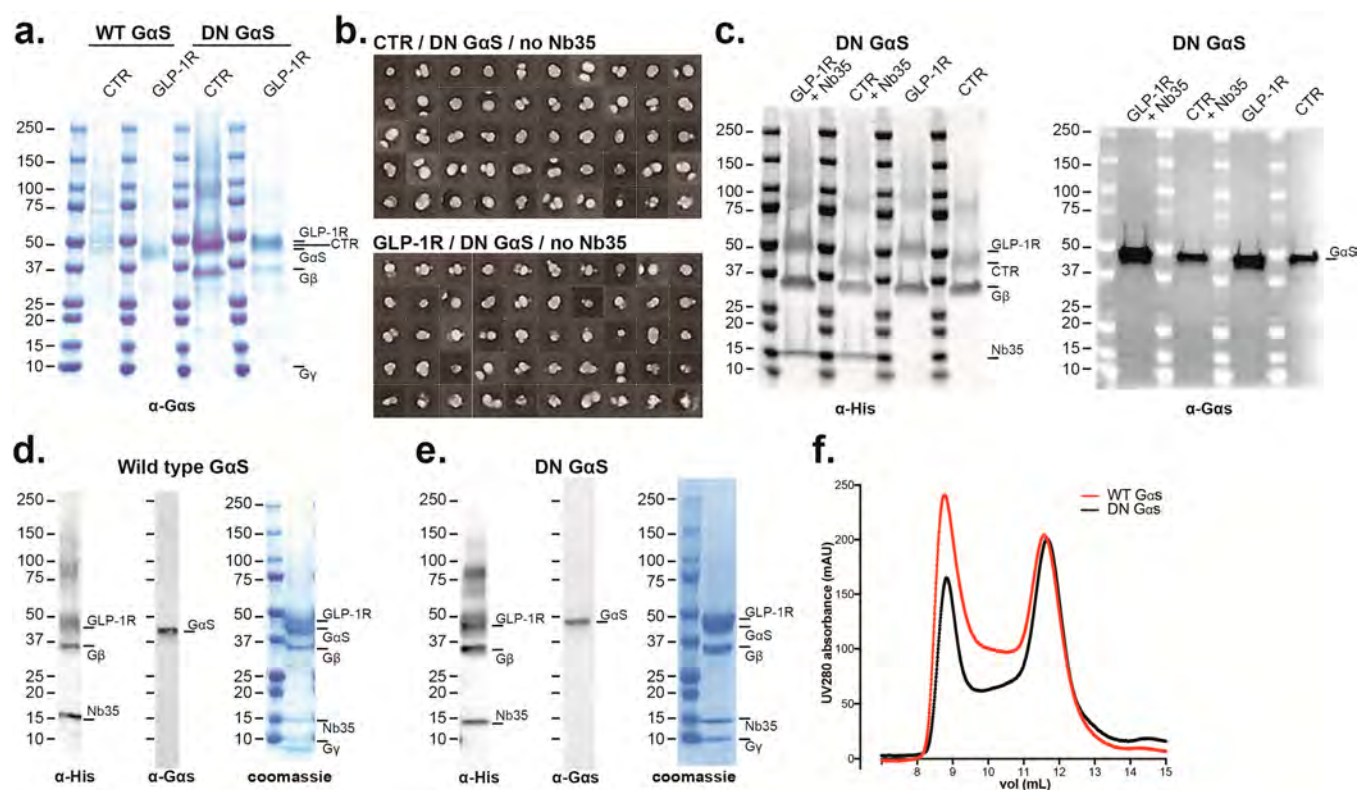


Figure 2. Comparison of purification of WT-Gs and DN-Gs containing heterotrimers with CTR and GLP-1R. (a) Coomassie stained gel showing relative abundance of various components of CTR (with salmon calcitonin) and GLP-1R (with exendin-P5)-G protein complexes following FLAG purification in the presence of either WT or DN-Gs but not Nb35. (b) 2D class averages from negative stained EM micrographs of the CTR:DN Gs and GLP-1R:DN Gs complexes in the absence of Nb35. (c) Western blot against His-tag ($G\beta$, Nb35, and CTR:GLP-1R) and Gas from purified active complex with DN-Gs in the presence or absence of Nb35. (d,e), Western blot and coomassie stained gel of WT- (d) and DN- (e) containing GLP-1R:Gs complexes in the presence of Nb35 and corresponding SEC traces (f), illustrating that both complexes can be purified but that the proportion of complex in the void/aggregate is slightly higher with the WT-Gas (c).

stain EM and yielded $\sim 28\%$ full complex out of the total unfiltered particles (Figure 2b). Inclusion of Nb35 with either WT or DN-Gas generated a complex with similar yield and stoichiometry to Nb35 free complexes as assessed by Western blot (Figure 2c), slightly improved purity as assessed by coomassie stain (compare Figure 2a with 2d, 2e), and a monodisperse peak by size exclusion chromatography (SEC). When either was subjected to negative stain EM, the full complex represented $\sim 70\%$ of total unfiltered particles (data not shown) and we chose to image the DN complex. This allowed solution of the structure at 3.3 \AA .⁶ We further assessed the utility of DN Gs for formation and purification of complexes with low efficacy agonists, using the endogenous GLP-1R agonist, oxyntomodulin, that has 100-fold lower cAMP potency than GLP-1. All preparations included Nb35 to maximize complex stability and yields. The initial formation of complexes was attempted using $1 \mu\text{M}$ peptide, as per previous studies. Complexes were weakly formed with both WT (Figure 3a) and DN Gs (Figure 3b), with the latter providing higher yields. Increasing the agonist concentration to $50 \mu\text{M}$ during initial formation of the complex substantially improved yields with the DN Gs preparation (Figure 3c), enabling recovery of a monodisperse peak following a second round of purification by SEC (Figure 3d). This peak exhibited apparent stoichiometric levels of component proteins by coomassie stain (Figure 3e) and large numbers of 2D classes of the full complex by negative stain EM (Figure 3f).

Subsequently, we applied this methodology to structure determination of the CGRP receptor. This receptor is a heterodimeric complex containing the calcitonin receptor-like receptor (CLR) and the single pass transmembrane protein, receptor activity-modifying protein 1 (RAMP1), requiring a more complex purification protocol (see Methods). Formation of this complex using the agonist αCGRP , WT-Gas, $G\beta\gamma$, and Nb35 enabled its purification, as shown in Figure 4a; however, the yield was extremely poor ($<25 \mu\text{g L}^{-1}$) such that insufficient material was available for SEC. In contrast, the use of the DN-Gas enabled complex purification with a yield similar to that of our GLP-1R complex ($\sim 200 \mu\text{g L}^{-1}$) that ran as a monodisperse peak by SEC and contained apparent stoichiometric amounts of all components (CGRP:CLR:RAMP1:DN-Gas: $\beta\gamma$:Nb35; Figure 4b,c). This was confirmed when complexes were subjected to negative stain EM and 2D class averaging, for which particles were homogeneous and stable (Figure 4d,e). Single particle cryo-EM imaging enabled solution of the fully active CGRP receptor to a resolution of 3.3 \AA ¹⁹ (Figure 4f). Our data, using GLP-1R and CGRP-R as examples, indicate that, while the use of WT Gas and Nb35 may be sufficient for purification of some GPCR:Gas complexes, the use of a DN Gas provides additional advantages for solving active structures by single particle cryo-EM, particularly for agonist:GPCR:Gs protein combinations that may be less stable.

To assess the applicability of using DN G proteins for structural studies on GPCRs with non-Gas partners, we selected the A1-AR as an exemplar. The A1-AR preferentially couples to

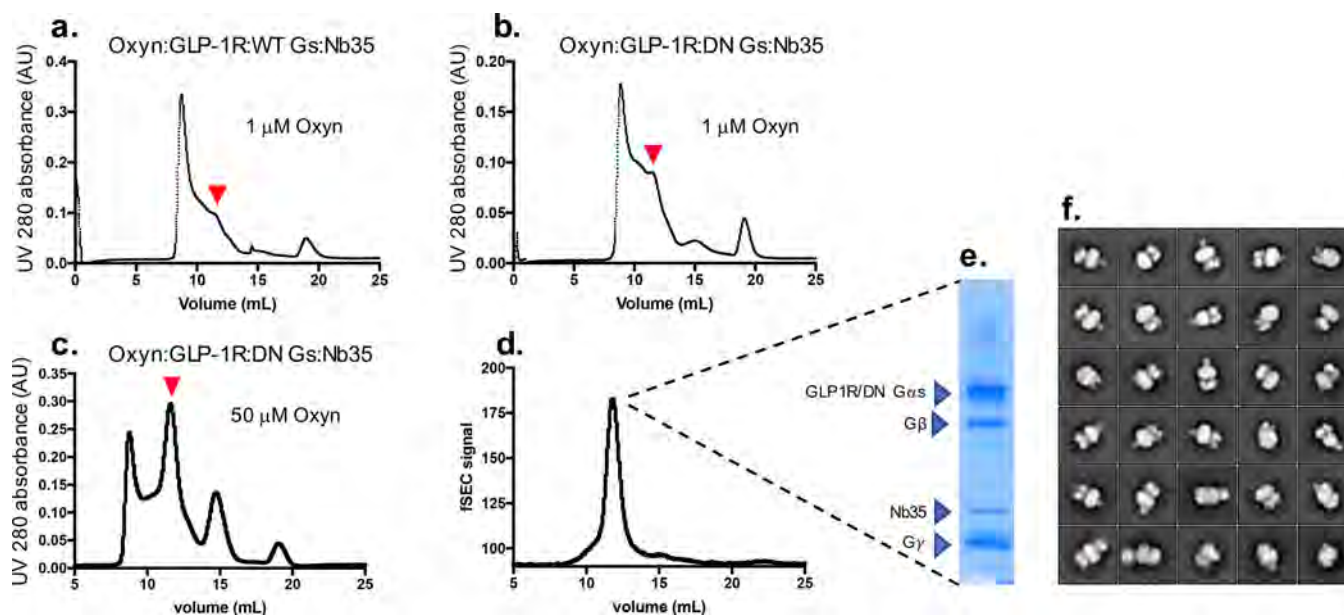


Figure 3. Formation and purification of WT-Gs and DN-Gs containing heterotrimers by oxyntomodulin with GLP-1R. (a,b) Size exclusion chromatography of complexes initiated with 1 μ M oxyntomodulin revealed higher yield of complexes with the DN-Gs (b) relative to that seen with WT-Gs (a), although both had relatively low yields for complex formation (the elution position of the complexes is illustrated by the red arrow). (b) Increasing the concentration of oxyntomodulin to 50 μ M in the Oxy:GLP-1R:DN-Gs:Nb35 preparation during the initiation step markedly improved the yield of complexes, which could be purified to homogeneity by an additional size exclusion chromatography step (d). (e) Coomassie stained gel from the peak in panel d, illustrating high purity and recovery of each of the component proteins. (f) 2D class averages from negative stain EM demonstrate the presence of complexes suitable for single-particle cryo-EM structure determination.

Gai/o proteins. We selected *Gai2* as the G protein partner, because of high expression in both brain and heart; both major organs for therapeutic targeting of the A1-AR.²⁰ Unlike with ExP5:GLP-1R:WT-Gs, we could form an active ADO:A1-AR:WT-*Gai2*: $\beta\gamma$ complex using the endogenous agonist adenosine (ADO) that could be purified with a yield of approximately 150 μ g L⁻¹. When this complex was subjected to SEC it gave a very broad peak, characteristic of a low affinity complex with rapid exchange kinetics (Figure 5a). Consistent with this, the SEC fraction collected from the 11 mL peak contained substoichiometric quantities of G protein components relative to receptor. In contrast, complex formation and purification in the presence of DN-*Gai2* yielded a monodispersed peak by SEC (Figure 5a) and apparent stoichiometric amounts of receptor and G protein when assessed by Western blot (Figure 5b), with a marginally improved yield of 200 μ g L⁻¹. Negative stain EM data and 2D class averaging revealed uniformity and stable complex particles (Figure 5c,d) suitable for cryo-EM. This led to the solution of a high resolution map (3.6 Å) of this small (~120 kDa) complex (Figure 5e).¹⁸ Although the A1-AR exhibits physiologically important coupling to *Gi2* proteins, it can couple to other members of the *Gi/o* subfamily. Stable complexes could also be formed and purified using adenosine:A1-AR:DN-*Gi3* (Figure 5f–h), yielding a monodisperse SEC peak (Figure 5f), well behaved particles in negative stain EM (Figure 5g), and a similar distribution of 2D class averages (Figure 5h), to that seen with DN-*Gi2* complexes.

Our data reveal that DN $G\alpha$ subunits are invaluable structure determination tools. We wanted to confirm that the agonist:GPCR mediated conformational transitions induced within the DN $G\alpha$: $\beta\gamma$ heterotrimers were similar to those of the WT $G\alpha$: $\beta\gamma$. The ability of either DN-*Gas* or DN-*Gai2* to promote the high-affinity state of the A1-AR was not different to that of the equivalent WT- $G\alpha$ subunits.¹⁸ Moreover, in

membrane-based bioluminescence resonance energy transfer (BRET) assays with CTR (Figure 6a) or GLP-1R (Figure 6b), there was no difference in the rate (Figure 6a,b) or extent of conformational rearrangement of WT- and DN-*Gas* (Figure 6a,b) in response to agonist. Similarly, the rate and extent of ligand-induced conformational change mediated by GLP-1R activation at WT- and DN-*Gai2* was not different (Figure 6c). For DN-*Gas*, there was reduced sensitivity, whereas *Gai* was completely resistant to GTP induced conformational change, supporting the designed reduction in affinity/sensitivity of the G protein to GTP from the introduced mutations (Figure 6a–c).

In conclusion, we show that incorporation of DN mutations in *Gai* and *Gas* subunits enhances the stability of the G proteins in complex with an agonist-bound receptor. Four of these are absolutely conserved residues across G proteins, and mutation of these would be predicted to have similar effects. Additional substitutions from the *Gai/o* family members into *Gas* provides further stability to the GPCR:G protein ternary complex, facilitating structural studies. Despite decreased nucleotide affinity, modified $G\alpha$ -proteins maintain similar allosteric and conformational function to WT. These DN $G\alpha$ -proteins are extremely valuable tools for high-resolution structure determination of agonist:GPCR:G protein complexes and provide an important advance for translational drug discovery.

METHODS

Constructs. The human CTR,⁴ GLP-1R,⁶ CLR,¹⁹ and A1-AR¹⁸ were all modified at the N-terminus with replacement of the signal peptide with that of hemagglutinin (HA) to enhance expression, followed by an N-terminal FLAG epitope and 3C protease cleavage site. At the C-terminus all receptors were appended with a 3C protease site followed by an 8 \times histidine tag. Human RAMP1 was modified at the N-terminus with a HA signal peptide and N-terminal FLAG tag.

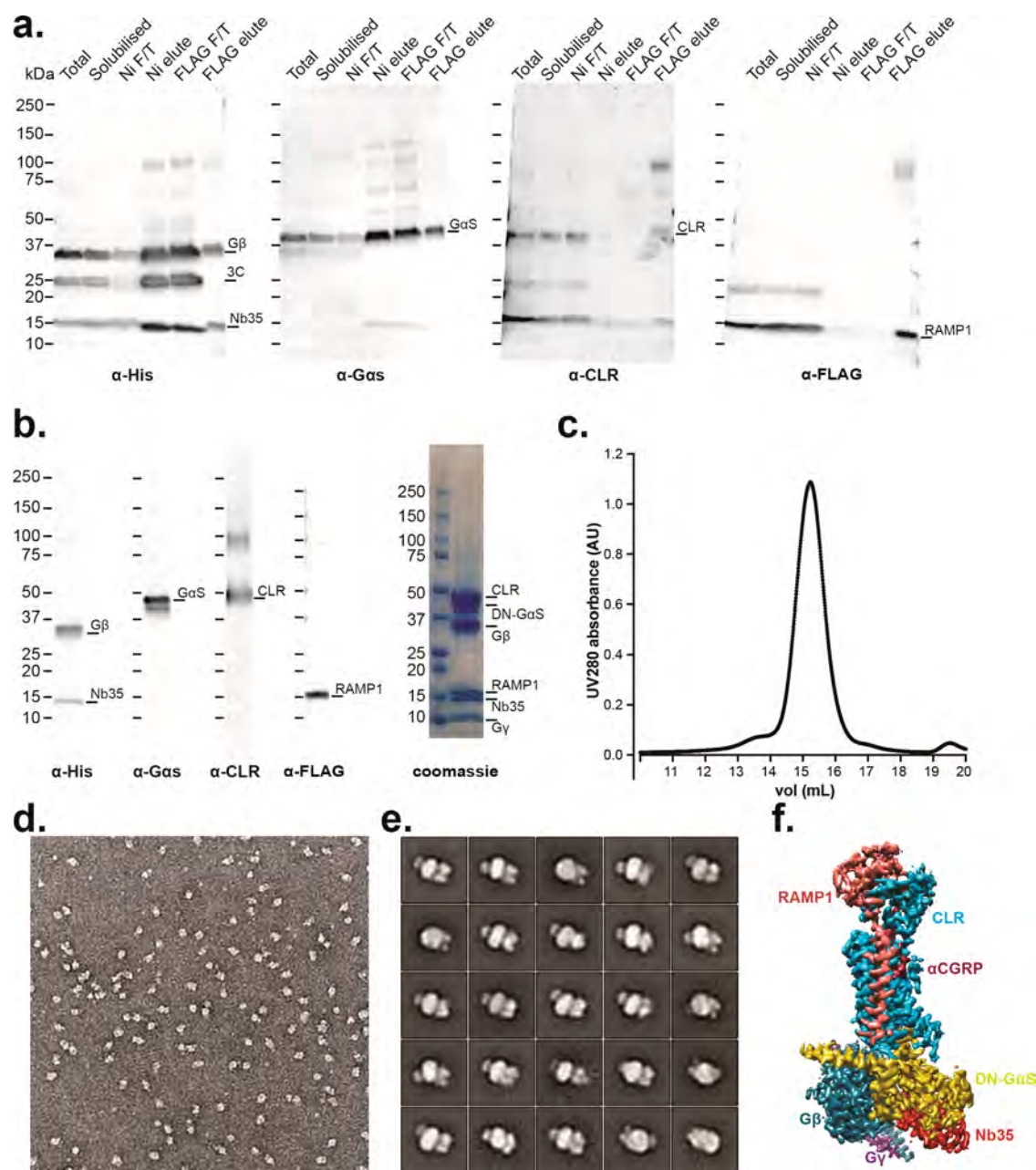


Figure 4. DN-Gas allows purification and structure determination of the fully active heteromeric CGRP receptor. (a) Western blots of purification fractions of the CGRP active complex using WT-Gas showing purification is possible but yield is poor (see text): (left) anti-His antibody against His tags on $G\beta_1$ and Nb35; (middle left) anti-Gas antibody for Gas detection; (middle right) anti-CLR antibody for CLR detection; (right) anti-FLAG antibody against the FLAG tag on RAMP1. (b) (Left) Western blot of the final purified fraction of the CGPR complex formed using DN-Gas showing that all components are present; (right) coomassie stained gel showing stoichiometric recovery of proteins. (c) Monodisperse peak of the purified complex following size exclusion chromatography. (d) Negative stain EM micrograph. (e) 2D class averages from the negative stain EM data. (f) 3D cryo-EM map from single particle cryo-EM determination of structure, colored according to each protein subunit (the 3D map was adapted from Liang et al.¹⁹).

The DN-Gas construct was generated, as previously described,⁶ by site-directed mutagenesis to incorporate the following mutations: S(H1.02)N (S54N), G(s3h2.02)A (G226A), E(H3.04)A (E268A), N(H3.07)K (N271K), K(H3.10)D (K274D), R(H3.16)K (R280K), T(h3s5.01)D (T284D), I(h3s5.02)T (I285T), and A(s6h5.03)S (A366S). The format for these mutations is natural residue (CGN number¹⁰) mutated residue (natural residue reference sequence number mutated residue).

The DN-Gai₂ construct was generated, as previously described,¹⁸ by site directed mutagenesis to incorporate the following mutations: S(H1.02)N (S47N), G(s3h2.02)A (G204A), E(H3.04)A (E246A), and A(s6h5.03)S (A327S). The format for these mutations is natural residue (CGN number) mutated residue (natural residue reference sequence number mutated residue).

The N-terminally tagged Venus-G γ 2 has been previously described.²¹ The nanoluc tagged Gas and Gai₂ had the engineered version of the shrimp luciferase from *Oplophorus*

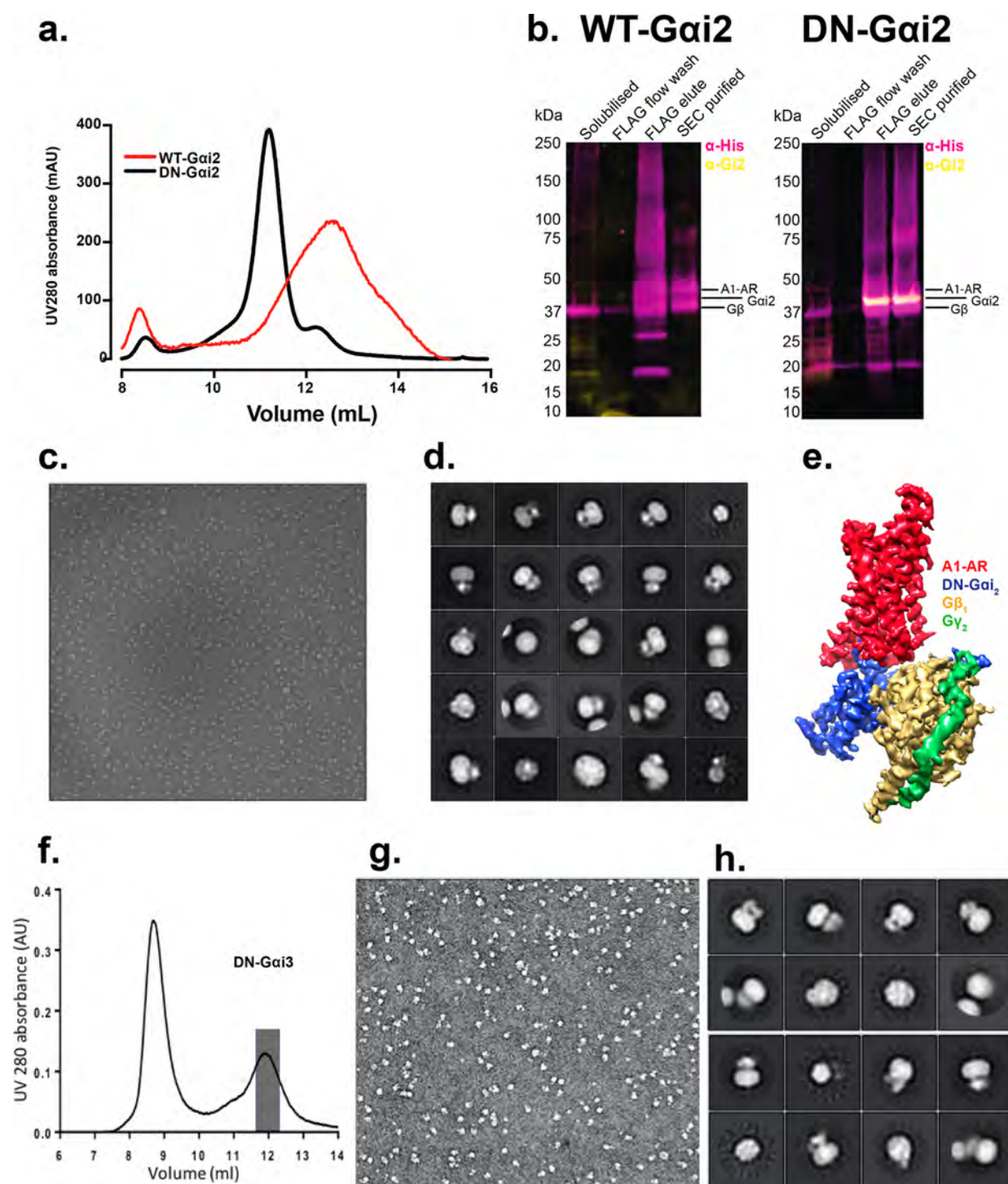


Figure 5. DN-*Gai*₂ allows purification and structure determination of the fully active A1-AR. (a) Size exclusion chromatography trace showing a broad peak for ADO:A1-AR:G protein complex in the presence of WT *Gi*₂, and a monodisperse peak in the presence of DN *Gi*₂. (b) Western blot of final purified fraction showing (left) limited *Gai*₂ recovery in the ADO:A1-AR:WT G protein complex and (right) stoichiometric recovery of G protein in the ADO:A1-AR:DN G protein complex (modified from Ext. Data Figure 1c¹⁸). (c) Negative stain EM micrograph of the ADO:A1-AR:DN *Gi*₂ protein complex. (d) 2D class averages from the negative stain EM micrographs; (e) 3D cryo-EM map, A1-AR is in red, heterotrimeric DN-*Gi*₂ is in blue, gold, and green for α , β , and γ , respectively. The DN-*Gi*₂ data were adapted from Draper-Joyce et al. 2018.¹⁸ (f) Size exclusion chromatography illustrating purification of the ADO:A1-AR:DN-*Gi*₃ complex; the peak fractions (gray box) were pooled and assessed by negative stain EM (g), with 2D class averages shown in panel h.

gracilirostris flanked by SGGGS linkers and was inserted after G(h1ha10) in *G α s* or E(HA.03) in *Gai*₂.

Insect Cell Expression. For CTR, GLP-1R, and CLR:RAMP1, the receptors, together with human WT- or

DN-*G α s*, His6-tagged human G β 1 and G γ 2, were coexpressed in *Tni* insect cells (Expression Systems) using baculovirus. Cell cultures were grown in ESF 921 serum-free media (Expression Systems) to a density of 4 million cells mL⁻¹ and then infected

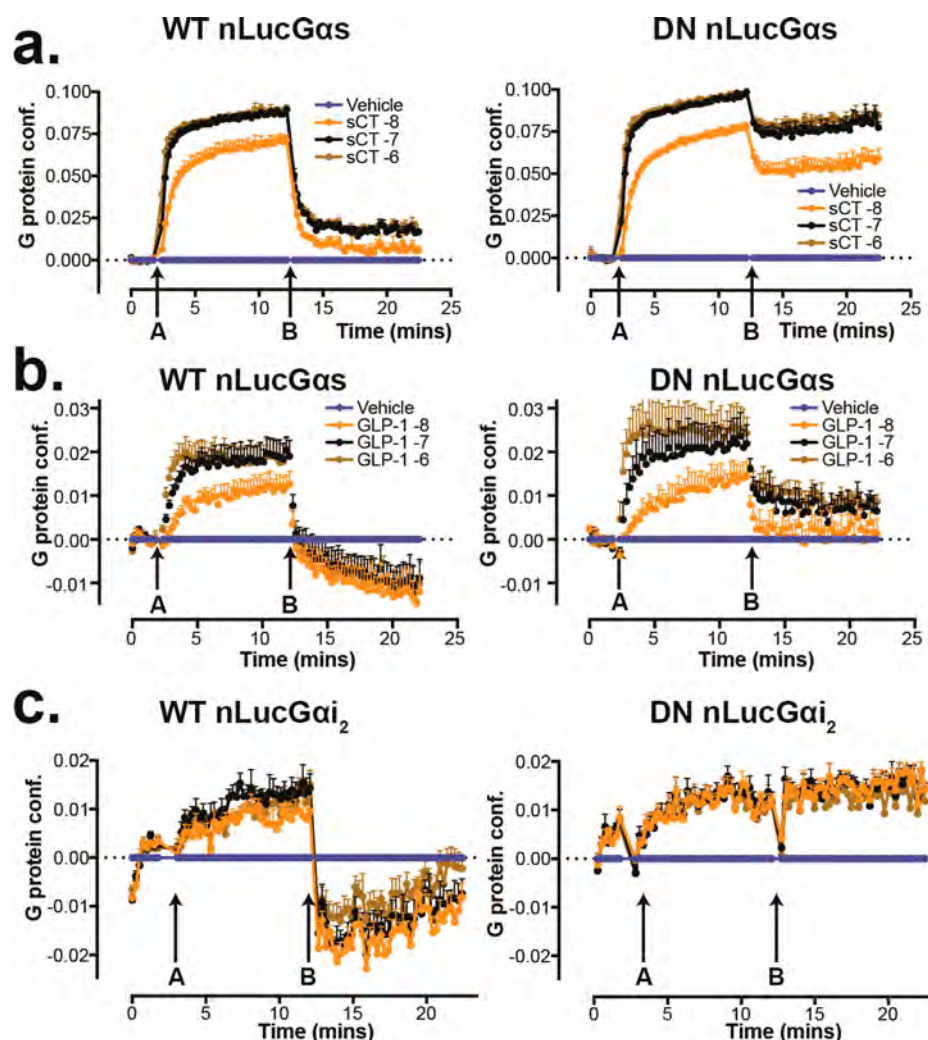


Figure 6. Functional analysis of DN-G proteins. (a) Time-course for ligand-induced changes in BRET of WT-Gas or DN-Gas (nanoLuc tagged) and $G\gamma$ (Venus) at increasing concentrations of salmon calcitonin (sCT) (arrow, A) followed by the addition of 30 μ M GTP (arrow, B) on membranes from HEK293 cells that lack endogenous Gas and were stably transfected with the human CTR; the rate and magnitude of agonist-induced structural rearrangement are similar, but the DN-Gas is resistant to GTP-induced conformational rearrangement. (b) Comparison of time-courses for agonist-induced changes in BRET of WT-Gas/ $G\gamma$ and DN-Gas/ $G\gamma$ are shown for GLP-1(7–36) NH_2 activated GLP-1R; both WT- and DN-Gas report the same difference in rate and extent of ligand-induced G protein conformational change (A); however, after the addition of 30 μ M GTP (B), the DN-Gas is less susceptible to conformational change. (c) time-course for GLP-1(7–36) NH_2 -induced changes in BRET of WT-Gai₂ or DN-Gai₂ (nanoLuc tagged) and $G\gamma$ (Venus) (A), followed by the addition of 30 μ M GTP (B), on membranes from HEK293 cells that lack endogenous Gas/Gaq/11/Gai2/13 and were stably transfected with the human GLP-1 receptor. The rate and magnitude of structural rearrangement are similar but the DN-Gai₂ is resistant to GTP-induced conformational rearrangement. All data are $N = 3 + \text{SEM}$.

with three separate baculoviruses at a ratio of 1:2:2 for CTR, WT or DN-Gas, and $G\beta 1\gamma 2$; 2:2:1 for GLP-1R, WT or DN-Gas, and $G\beta 1\gamma 2$; and 5:1:2:1 for RAMP1, CLR, WT or DN-Gas, and $G\beta 1\gamma 2$. Cultures were harvested by centrifugation 60 h postinfection and the cell pellet was stored at -80°C . For the A1-AR, the receptor was expressed separately to the G proteins. The A1-AR was expressed in *Tni* insect cells using baculovirus. The human WT or DN-Gai₂/Gai₁₃, His₆-tagged human $G\beta 1$ and $\gamma 2$ were coexpressed in *Tni* insect cells using baculovirus at a 1:1 ratio. Cell cultures were grown in ESF 921 serum-free media (Expression System) to a density of 4 million cells mL^{-1} and then infected with baculovirus, at the ratios detailed above. Cultures were grown at 27°C and harvested by centrifugation 60 h postinfection. Cells were snap frozen and stored at -80°C for later use.

Complex Purification. All cell pellets, except for A1-AR and heterotrimeric G_i protein, were thawed in 20 mM HEPES pH

7.4, 50 mM NaCl, and 2 mM MgCl_2 supplemented with cComplete Protease Inhibitor Cocktail tablets (Roche). GLP-1R and CLR/RAMP1 were coexpressed with heterotrimeric G_s protein, whereas A1-AR and heterotrimeric G_i protein were expressed separately. Complex formation for GLP-1R and CLR/RAMP1 were initiated by addition of either 1 μ M exendin-P5, 50 μ M oxyntomodulin (Chinapeptide), or 10 μ M α CGRP, Nb35–His (10 $\mu\text{g mL}^{-1}$), apyrase (25 mU mL^{-1} , NEB) and, in the case of CLR:RAMP1, 3C protease (10 $\mu\text{g mL}^{-1}$); the suspension was incubated for 1 h at room temperature. Membranes were collected by centrifugation at 30 000g for 30 min. The complex from the membrane fraction was solubilized with 0.5% (w/v) lauryl maltose neopentyl glycol (LMNG, Anatrace) supplemented with 0.03% (w/v) cholesteryl hemisuccinate (CHS, Anatrace) for 2 h at 4°C in the presence of 1 μ M exendin-P5, oxyntomodulin, or α CGRP and apyrase (25 mU mL^{-1} , NEB). For A1-AR, cells from either A1-AR or

heterotrimeric G_i protein expression were solubilized separately in 20 mM HEPES pH 7.4, 100 mM NaCl, 5 mM $MgCl_2$, 5 mM $CaCl_2$, 0.5% (w/v) LMNG, 0.01% (w/v) CHS, supplemented with cOmplete Protease Inhibitor Cocktail tablets (Roche). Complex formation was initiated by combining solubilized A1-AR and heterotrimeric G_i and by addition of 1 mM adenosine (ADO) (Sigma) and apyrase (25 mU ml^{-1} , NEB), followed by 2 h incubation at 4 °C. Insoluble material was removed by centrifugation at 30 000g for 30 min. For the CLR:RAMP1 complex only the solubilized complex was immobilized by batch binding to NiNTA resin. The resin was packed into a glass column and washed with 20 column volumes of 20 mM HEPES pH 7.4, 100 mM NaCl, 2 mM $MgCl_2$, 0.01% (w/v) LMNG, and 0.006% (w/v) CHS, 1 μ M CGRP, before bound material was eluted in buffer containing 250 mM imidazole. The solubilized GLP-1R or A1-AR complex, or NiNTA purified CLR:RAMP1 complex was immobilized by batch binding to M1 anti-FLAG affinity resin in the presence of 3 mM $CaCl_2$. The resin was packed into a glass column and washed with 20 column volumes of 20 mM HEPES pH 7.4, 100 mM NaCl, 2 mM $MgCl_2$, 3 mM $CaCl_2$, 1 μ M exendin-P5, 0.01% (w/v) LMNG and 0.006% (w/v) CHS before bound material was eluted in buffer containing 5 mM EGTA and 0.1 mg/mL FLAG peptide. The complex was then concentrated using an Amicon Ultra Centrifugal Filter (MWCO 100 kDa) and subjected to size-exclusion chromatography on a Superdex 200 Increase 10/300 column (GE Healthcare) that was pre-equilibrated with 20 mM HEPES pH 7.4, 100 mM NaCl, 2 mM $MgCl_2$, 1 μ M exendin-P5 or 1 μ M oxyntomodulin, 0.01% (w/v) LMNG and 0.006% (w/v) CHS to separate complex from contaminants. Eluted fractions consisting of receptor and G protein complex were pooled and concentrated.

SDS-PAGE and Western Blot Analysis. Samples collected from each purification step were analyzed by SDS-PAGE and Western blot. For SDS-PAGE, precast gradient TGX gels (Bio-Rad) were used. Gels were either stained by Instant Blue (Expedeon) or immediately transferred to PVDF membrane (Bio-Rad) at 100 V for 1 h. The proteins on the PVDF membrane were probed first with the primary mouse anti-His antibody (cat. no. 34660, QIAGEN), and, for membranes with $G_{\alpha s}$ coincubated, with rabbit anti-Gs C-18 antibody (cat. no. sc-383, Santa Cruz), followed by washing and incubation with secondary antimouse antibody (680RD). For blots with $G_{\alpha s}$ 800CW, a goat anti-rabbit antibody (Li-Cor) was used. For blots with $G_{\alpha i2}$, membranes were again washed and then incubated with an AlexaFluor488 conjugated anti- $G_{\alpha i2}$ mouse monoclonal antibody (cat. no. sc13534, Santa Cruz). Bands were imaged using a Typhoon multimode imager (GE Healthcare life sciences) or Li-Cor Odyssey.

Mammalian Cell Membrane Preparations for G Protein BRET Assays. HEK293AΔ $G_{\alpha s}$ -GLP-1R, HEK293AΔ $G_{\alpha s}$ /Gaq11/Gα12/13-GLP-1R or HEK293AΔ $G_{\alpha s}$ -CTR cells were transfected WT or DN $G_{\alpha s}$ -Nanoluc, WT or DN $G_{\alpha i2}$ -Nanoluc, and $G_{\alpha i2}$ -Venus at 1:1:1 ratio using PEI. Cell membranes were prepared as described previously and stored at −80 °C.¹⁹ At 24 h after transfection, cells were harvested with membrane preparation buffer (20 mM BisTris [pH7.4], 50 mM NaCl, 1 mM $MgCl_2$, 1 × P8340 (protease inhibitor cocktail, Sigma), 1 mM DTT and 0.1 mM PMSF). For $G_{\alpha i2}$ membrane preparation, 50 μ M GDP was included in the buffer to improve protein stability. Cells were then homogenized, applied to a stepped sucrose gradient (60%, 40%, homogenate) and centrifuged at 100 000g for 2.5 h at 4 °C.

The layers between 40% and homogenate were collected, diluted in membrane preparation buffer, and centrifuged at 160 000g for 30 min at 4 °C. The final pellet was resuspended in membrane preparation buffer and stored at −80 °C.

Agonist-Induced G Protein Conformational Changes.

Receptor mediated BRET signals between $G_{\alpha s}$ and G_{γ} were measured at 30 °C using a PHERAstar (BMG LabTech, Offenburg, Germany). 5 μ g/well cell of membrane was incubated with 1 × Furimazine in assay buffer (1 × HBSS, 10 mM HEPES, 0.1% BSA, 1 × P8340, 1 mM DTT, and 0.1 mM PMSF, pH 7.4) for 5 min in a white 96-well plate before initiation of the assay BRET was measured at 15 s intervals before and after ligand and nucleotide addition at the indicated concentrations.

Negative Stain TEM. SEC eluted fractions were used to prepare specimens for negative stain EM using a conventional negative staining protocol.²² Negative-stained samples were imaged at room temperature with a Tecnai T12 (FEI) electron microscope. Images were collected at a magnification of 52 000× and a defocus value of −1 μ m on a FEI Eagle 4K camera with a pixel size of 2.06 Å.

AUTHOR INFORMATION

Corresponding Authors

*E-mail: Sebastian.furness@monash.edu.

*E-mail: Patrick.sexton@monash.edu.

*E-mail: denise.wootten@monash.edu.

ORCID

Patrick M. Sexton: 0000-0001-8902-2473

Author Contributions

#These authors contributed equally.

Notes

The authors declare no competing financial interest.

ACKNOWLEDGMENTS

This work was supported by the Monash University Ramaciotti Centre for Cryo-Electron Microscopy, National Health and Medical Research Council of Australia (NHMRC) project Grants APP1145420, APP1120919, and NHMRC program Grant (APP1055134). A.C., P.M.S., and D.W. are NHMRC Senior Principal Research, Principal Research, and Career Development Fellows, respectively. AG is an Australian Research Council Discovery Early Career Research Fellows. L.T.M. is an Australian Heart Foundation Future Leaders Fellow. The work was supported by the Monash University Ramaciotti Centre for Cryo-Electron Microscopy.

REFERENCES

- (1) Thal, D. M., Vuckovic, Z., Draper-Joyce, C. J., Liang, Y. L., Glukhova, A., Christopoulos, A., and Sexton, P. M. (2018) Recent advances in the determination of G protein-coupled receptor structures. *Curr. Opin. Struct. Biol.* 51, 28–34.
- (2) Kenakin, T. (2017) Theoretical aspects of GPCR-ligand complex pharmacology. *Chem. Rev.* 117, 4–20.
- (3) Rasmussen, S. G., DeVree, B. T., Zou, Y., Kruse, A. C., Chung, K. Y., Kobilka, T. S., Thian, F. S., Chae, P. S., Pardon, E., Calinski, D., Mathiesen, J. M., Shah, S. T., Lyons, J. A., Caffrey, M., Gellman, S. H., Steyaert, J., Skiniotis, G., Weis, W. I., Sunahara, R. K., and Kobilka, B. K. (2011) Crystal structure of the β_2 adrenergic receptor-Gs protein complex. *Nature* 477, 549–555.
- (4) Liang, Y. L., Khoshouei, M., Radjainia, M., Zhang, Y., Glukhova, A., Tarrasch, J., Thal, D. M., Furness, S. G. B., Christopoulos, G., Coudrat, T., Danev, R., Baumeister, W., Miller, L. J., Christopoulos, A.,

Kobilka, B. K., Wootten, D., Skiniotis, G., and Sexton, P. M. (2017) Phase-plate cryo-EM structure of a class B GPCR-G-protein complex. *Nature* 546, 118–123.

(5) Zhang, Y., Sun, B., Feng, D., Hu, H., Chu, M., Qu, Q., Tarrasch, J. T., Li, S., Kobilka, T. S., Kobilka, B. K., and Skiniotis, G. (2017) Cryo-EM structure of the activated GLP-1 receptor in complex with a G protein. *Nature* 546, 248–253.

(6) Liang, Y. L., Khoshouei, M., Glukhova, A., Furness, S. G. B., Zhao, P., Clydesdale, L., Koole, C., Truong, T. T., Thal, D. M., Lei, S., Radjainia, M., Danev, R., Baumeister, W., Wang, M. W., Miller, L. J., Christopoulos, A., Sexton, P. M., and Wootten, D. (2018) Phase-plate cryo-EM structure of a biased agonist-bound human GLP-1 receptor-Gs complex. *Nature* 555, 121–125.

(7) Carpenter, B., Nehmé, R., Warne, T., Leslie, A. G. W., and Tate, C. G. (2016) Structure of the adenosine A(2A) receptor bound to an engineered G protein. *Nature* 536, 104–107.

(8) Scheerer, P., Park, J. H., Hildebrand, P. W., Kim, Y. J., Krauss, N., Choe, H. W., Hofmann, K. P., and Ernst, O. P. (2008) Crystal structure of opsin in its G-protein-interacting conformation. *Nature* 455, 497–502.

(9) Clapham, D. E., and Neer, E. J. (1997) G protein beta gamma subunits. *Annu. Rev. Pharmacol. Toxicol.* 37, 167–203.

(10) Flock, T., Ravarani, C. N. J., Sun, D., Venkatakrishnan, A. J., Kayikci, M., Tate, C. G., Veprintsev, D. B., and Babu, M. M. (2015) Universal allosteric mechanism for G_{α} activation by GPCRs. *Nature* 524, 173–179.

(11) Cleator, J. H., Mehta, N. D., Kurtz, D. T., and Hildebrandt, J. D. (1999) The N54 mutant of G_{α} has a conditional dominant negative phenotype which suppresses hormone-stimulated but not basal cAMP levels. *FEBS Lett.* 443, 205–208.

(12) Slepak, V. Z., Katz, A., and Simon, M. I. (1995) Functional analysis of a dominant negative mutant of $G_{\alpha}i2$. *J. Biol. Chem.* 270, 4037–4041.

(13) Ramachandran, S., and Cerione, R. A. (2011) A dominant-negative G_{α} mutant that traps a stable rhodopsin- G_{α} -GTP- $\beta\gamma$ complex. *J. Biol. Chem.* 286, 12702–12711.

(14) Sunahara, R. K., Tesmer, J. J., Gilman, A. G., and Sprang, S. R. (1997) Crystal structure of the adenylyl cyclase activator G_{α} . *Science* 278, 1943–1947.

(15) Lee, E., Taussig, R., and Gilman, A. G. (1992) The G226A mutant of G_{α} highlights the requirement for dissociation of G protein subunits. *J. Biol. Chem.* 267, 1212–1218.

(16) Iiri, T., Bell, S. M., Baranski, T. J., Fujita, T., and Bourne, H. R. A. (1999) G_{α} mutant designed to inhibit receptor signaling through G_{α} . *Proc. Natl. Acad. Sci. U. S. A.* 96, 499–504.

(17) Berlot, C. H. (2002) A highly effective dominant negative α s construct containing mutations that affect distinct functions inhibits multiple Gs-coupled receptor signaling pathways. *J. Biol. Chem.* 277, 21080–21085.

(18) Draper-Joyce, C. J., Khoshouei, M., Thal, D. M., Liang, Y. L., Nguyen, A. T. A., Furness, S. G. B., Venugopal, H., Baltos, J. A., Plitzko, J. M., Danev, R., Baumeister, W., May, L. T., Wootten, D., Sexton, P. M., Glukhova, A., and Christopoulos, A. (2018) Structure of the adenosine-bound human adenosine A1 receptor-Gi complex. *Nature* 558, 559–563.

(19) Liang, Y. L., Khoshouei, M., Deganutti, G., Glukhova, A., Koole, C., Peat, T. S., Radjainia, M., Plitzko, J. M., Baumeister, W., Miller, L. J., Hay, D. L., Christopoulos, A., Reynolds, C. A., Wootten, D., and Sexton, P. M. Cryo-EM structure of the active, Gs-protein complexed, human CGRP receptor. *Nature* (In Press).

(20) Jacobson, K. A., and Gao, Z.-G. (2006) Adenosine receptors as therapeutic targets. *Nat. Rev. Drug Discovery* 5, 247–264.

(21) Furness, S. G. B., Liang, Y. L., Nowell, C. J., Halls, M. L., Wookey, P. J., Dal Maso, E., Inoue, A., Christopoulos, A., Wootten, D., and Sexton, P. M. (2016) Ligand-dependent modulation of G protein conformation alters drug efficacy. *Cell* 167, 739–749.

(22) Peisley, A., and Skiniotis, G. (2015) 2D Projection Analysis of GPCR complexes by negative stain electron microscopy. *Methods Mol. Biol.* 1335, 29–38.



Glucagon-like peptide-1 receptor internalisation controls spatiotemporal signalling mediated by biased agonists

Madeleine M. Fletcher^a, Michelle L. Halls^a, Peishen Zhao^a, Lachlan Clydesdale^a,
Arthur Christopoulos^a, Patrick M. Sexton^{a,b,*}, Denise Wootten^{a,b,*}

^a Drug Discovery Biology, Monash Institute of Pharmaceutical Sciences, Faculty of Pharmacy and Pharmaceutical Sciences, Monash University, Parkville, Melbourne, Victoria 3052, Australia

^b School of Pharmacy, Fudan University, Shanghai 201203, China

ARTICLE INFO

Keywords:

Glucagon-like peptide 1 receptor
Biased agonism
Receptor trafficking
Internalisation
Spatiotemporal signalling

ABSTRACT

The glucagon-like peptide-1 receptor (GLP-1R) is a major therapeutic target in the treatment of type 2 diabetes due to its roles in regulating blood glucose and in promoting weight loss. Like many GPCRs, it is pleiotropically coupled, can be activated by multiple ligands and is subject to biased agonism. The GLP-1R undergoes agonist mediated receptor internalisation that may be associated with spatiotemporal control of signalling and biased agonism, although to date, this has not been extensively explored. Here, we investigate GLP-1R trafficking and its importance with regard to signalling, including the localisation of key signalling molecules, mediated by biased peptide agonists that are either endogenous GLP-1R ligands or are used clinically. Each of the agonists promoted receptor internalisation through a dynamin and caveolae dependent mechanism and traffic the receptor to both degradative and recycling pathways. This internalisation is important for signalling, with cAMP and ERK1/2 phosphorylation (pERK1/2) generated by both plasma membrane localised and internalised receptors. Further assessment of pERK1/2 revealed that all peptides induced nuclear ERK activity, but ligands, liraglutide and oxyntomodulin that are biased towards pERK1/2 relative to cAMP (when compared to GLP-1 and exendin-4), also stimulated pERK1/2 activity in the cytosol. This compartmentalisation of ERK1/2 signalling was reliant on receptor internalisation, with restriction of receptor localisation to the plasma membrane limiting ERK1/2 signalling to the cytosol. Thus, this study implicates a role of receptor internalisation in spatiotemporal control of ERK1/2 signalling that may contribute to GLP-1R biased agonism.

1. Introduction

The glucagon-like peptide-1 receptor (GLP-1R) has been extensively studied due to its physiological importance in mediating the effects of the incretin hormone GLP-1 in regulation of blood glucose levels. It is a major, validated, therapeutic target for the treatment of type 2 diabetes [1]. The GLP-1R is expressed in pancreatic β -cells where it mediates direct glucoregulatory effects by increasing insulin, and decreasing glucagon, secretion [2]. In addition, GLP-1 increases the mass of pancreatic β -cells by increasing β -cell neogenesis and proliferation, while decreasing apoptosis [3]. Independent of insulin, GLP-1R activation also reduces plasma glucose concentrations through the inhibition of gastric emptying and reduces appetite and body weight, which can assist with controlling obesity, a condition that is often associated with diabetes [4].

The GLP-1R is a class B G protein-coupled receptor (GPCR) that has

multiple endogenous agonists, including GLP-1 and oxyntomodulin. It is targeted clinically to treat type 2 diabetes and obesity, with exendin-4 and liraglutide being the two most commonly prescribed of the 6 FDA approved GLP-1R drugs. Upon activation, the receptor predominantly activates G α s proteins to promote the production of cAMP. However, it is pleiotropically coupled and signals via other G protein-dependent and independent mechanisms, activating downstream pathways including intracellular calcium (iCa^{2+}) mobilisation and phosphorylation of mitogen activated kinases, such as extracellular regulated kinases 1 and 2 (ERK1/2) [5–7]. Due to this pleiotropic coupling, the GLP-1R is subject to biased agonism, where different GLP-1R agonists can induce distinct patterns of receptor signalling and regulation. Relative to GLP-1, oxyntomodulin exhibits bias towards ERK1/2 phosphorylation over cAMP production and iCa^{2+} mobilisation, and both oxyntomodulin and exendin-4 are biased towards β -arrestin recruitment [7,8].

A growing body of evidence suggests that the location (spatial) and

* Corresponding authors at: 381 Royal Parade, Parkville, VIC 3052, Australia.

E-mail addresses: patrick.sexton@monash.edu (P.M. Sexton), denise.wootten@monash.edu (D. Wootten).

<https://doi.org/10.1016/j.bcp.2018.09.003>

Received 10 July 2018; Accepted 5 September 2018

Available online 07 September 2018

0006-2952/ © 2018 Elsevier Inc. All rights reserved.

duration (temporal) of signalling within a cell play an important role in the diverse cellular outputs that are mediated by GPCRs and in the generation of differential ligand responses at the same GPCR [9–11]. Spatiotemporal compartmentalisation of signalling can arise through multiple mechanisms that include (but are not restricted to) regulatory mechanisms that control the location and duration of receptor activation, such as desensitisation and internalisation [12]. Upon activation, the GLP-1R internalises rapidly and enters pathways that either recycle the receptor back to the plasma membrane or that sort the receptor to lysosomal and recycling pathways [13–15]. GLP-1 and exendin-4 are reported to be 10-fold more potent at inducing internalisation than liraglutide, but GLP-1 causes the receptor to recycle two–three times faster than when stimulated with exendin-4 or liraglutide [13]. The mechanism underlying this internalisation is unclear, with both clathrin- and caveolae-dependent mechanisms being identified that vary with cell type [16–19]. Sustained signalling by internalised GLP-1Rs and colocalisation of intracellular GLP-1R with GLP-1, adenylate cyclase and Gas has also been reported, with inhibition of receptor internalisation decreasing GLP-1 mediated cAMP formation, ERK1/2 phosphorylation, Ca^{2+} mobilisation and insulin secretion [14,20,21].

To date, the influence of compartmentalised signalling on GLP-1R biased agonism and the role of GLP-1R internalisation in this process has not been extensively explored. In this study, we test the hypothesis that GLP-1R internalisation is important for the spatiotemporal control of signalling and that this in turn may be linked to biased agonism. Here, we characterise signalling, regulatory protein interactions, internalisation and trafficking of the GLP-1R and identify distinct profiles of compartmentalised signalling that are influenced by receptor internalisation for different biased agonists.

2. Materials and methods

2.1. Peptides

GLP-1, exendin-4 and oxyntomodulin were purchased from Mimotopes (Melbourne, VIC, Australia). Liraglutide was purchased from Bachem (Bubendorf, Switzerland). Dulbecco's modified Eagle's medium (DMEM) was purchased from Invitrogen (Carlsbad, CA, USA). AlphaScreen™ reagents, Bolton-Hunter reagent [^{125}I] and 384-well ProxiPlates were purchased from PerkinElmer Life and Analytical Sciences (Waltham, MA, USA). Fetal bovine serum (FBS) was purchased from Thermo Fisher Scientific (Melbourne, VIC, Australia). SureFire™ ERK1/2 reagents were generously supplied by TGR Biosciences (Adelaide, SA, Australia). Unless specifically listed below, all other reagents were purchased from Sigma-Aldrich (St. Louis, MO, USA) or BDH Merck (Melbourne, VIC, Australia) and were of an analytical grade.

2.2. Plasmids and constructs

Human c-myc-GLP1R was generated in the laboratory as previously described [7]. The c-myc-GLP-1R-Rluc8 was generated by removal of the GLP-1R stop-codon and sub-cloning it into a gateway cassette (Invitrogen, Carlsbad, CA) containing a Rluc8 insert. The c-myc and Rluc8 tags have no effect on GLP-1R pharmacology [22]. Caveolin-1 (cav-1) and cav-1 P132L were generated via site-directed mutagenesis to introduce a stop codon in the Cav-1 P132L-mEGFP plasmid (prior to the mEGFP) from Addgene (Cambridge, MA, USA) with the QuikChange mutagenesis kit (Agilent Technologies, Santa-Clara, USA). The BRET sensors Rab5a, Rab7a, Rab11 and KRas-Venus were provided by Nevin Lambert (Augusta University, Georgia) and have been described previously [23,24]. The cAMP FRET sensors were provided by Martin Lohse (cytoEpac2 [25]) and Dermot Cooper (pmEpac2 [26]), the ERK FRET sensors were obtained from Addgene (nucEKAR plasmid 18,681 and cytoEKAR plasmid 18,679 [27]). HA-dynamin I K44E (dyn-K44E) and HA-dynamin I (dyn) constructs were provided by Nigel Bunnett

(Columbia University) and have been previously described [28].

2.3. Cell culture and transfection

FlpIn-Chinese hamster ovary (FlpIn-CHO) cells (Invitrogen) were used due to their lack of endogenous GLP-1R expression. GLP-1R signalling has been well-characterised in this cell background [22]. Cells were cultured in Dulbecco's Modified Eagle's Medium (DMEM) (Invitrogen) supplemented with 5% v/v heat-inactivated fetal bovine serum (FBS) (Thermo Electron Corporation, Melbourne, VIC, Australia) at 37°C and 95% O_2 /5% CO_2 in a humidified incubator. FlpIn-CHO cells were either stably transfected with either human c-myc-GLP-1R, or c-myc-GLP-1R-Rluc8 with either β -arrestin1- or β -arrestin2-Venus using gateway technology. These cell lines were characterised and described previously [22,29]. Parental FlpIn-CHO cells were also transiently transfected, using polyethylenimine (PEI) (Polysciences, Warrington, PA), and plated simultaneously. DNA and PEI diluted in 150 mM NaCl were combined in a 1:6 ratio and incubated for 15 min, before the mixture was added to the cell suspension and the cells plated.

2.4. cAMP accumulation

FlpIn-CHO cells stably transfected with human c-myc-GLP-1R cells were seeded at a density of 30,000 cells/well into clear 96-well culture plates and incubated overnight at 37 °C in 5% CO_2 . For cAMP accumulation assays in conditions where GLP-1R internalisation was inhibited, parental FlpIn-CHO cells were transiently transfected with 42 ng/well of human c-myc-GLP-1R and 107 ng/well of dyn-K44E or pcDNA3.1 and 15,000 cells/well were seeded into clear 96-well plates and incubated at 37 °C in 5% CO_2 for 48 h.

On the day of assay, growth media was replaced with stimulation buffer [phenol-free DMEM containing 0.1% (w/v) BSA, 1 M HEPES and 0.5 mM 3-isobutyl-1-methylxanthine, pH 7.4] and incubated for 30 min at 37 °C in 5% CO_2 before cells were stimulated with the indicated concentrations of peptide. After 30 min the reaction was terminated by aspiration of the buffer and addition of 50 μl of ice-cold 100% (v/v) ethanol. Upon evaporation of ethanol, 75 μl of lysis buffer [5 mM HEPES, 0.1% (w/v) BSA, 0.3% (w/v) Tween20, pH 7.4] was added. Five μl of lysate was transferred to a 384-well OptiPlate (PerkinElmer). The cAMP detection was performed using a LANCE TR FRET kit (Perkin Elmer). 5 μl of anti-cAMP antibody (0.5% v/v diluted in the detection buffer) was added in reduced lighting conditions and the plate incubated for 30 min at room temperature. 10 μl of detection mix was added [0.02% v/v Eu-W8044 labelled streptavidin, 0.07% v/v biotin-cAMP diluted in the detection buffer] in reduced-lighting. The plate was incubated for 60 min at RT before measurement on the EnVision multi-label plate reader (PerkinElmer) using the LANCE protocol settings. All values were converted to an absolute concentration of cAMP using a cAMP standard curve performed in parallel. Data were analysed and curve fitting performed using a three-parameter logistic equation using GraphPad Prism version 6.0 (Graphpad Software Inc.).

2.5. ERK1/2 phosphorylation

FlpIn-CHO cells stably transfected with human c-myc-GLP-1R cells were seeded at a density of 30,000 cells/well into clear 96-well culture plates and incubated overnight for 30 min at 37 °C in 5% CO_2 , and serum-starved in FBS-free DMEM for 6 h prior to being assayed. For pERK1/2 assays in conditions where GLP-1R internalisation was inhibited, parental FlpIn-CHO cells were transiently transfected with 75 ng/well of human c-myc-GLP-1R and 75 ng/well of dyn-K44E or pcDNA3.1 and seeded into clear 96-well plates at 30,000 cells/well and assayed 48 h later. Cells were serum-starved overnight before the assay.

On the day of assay, cells were stimulated with ligand for the indicated time periods at 37 °C before stimulation was terminated by removal of media, then the addition of 40 μl of SureFire lysis buffer

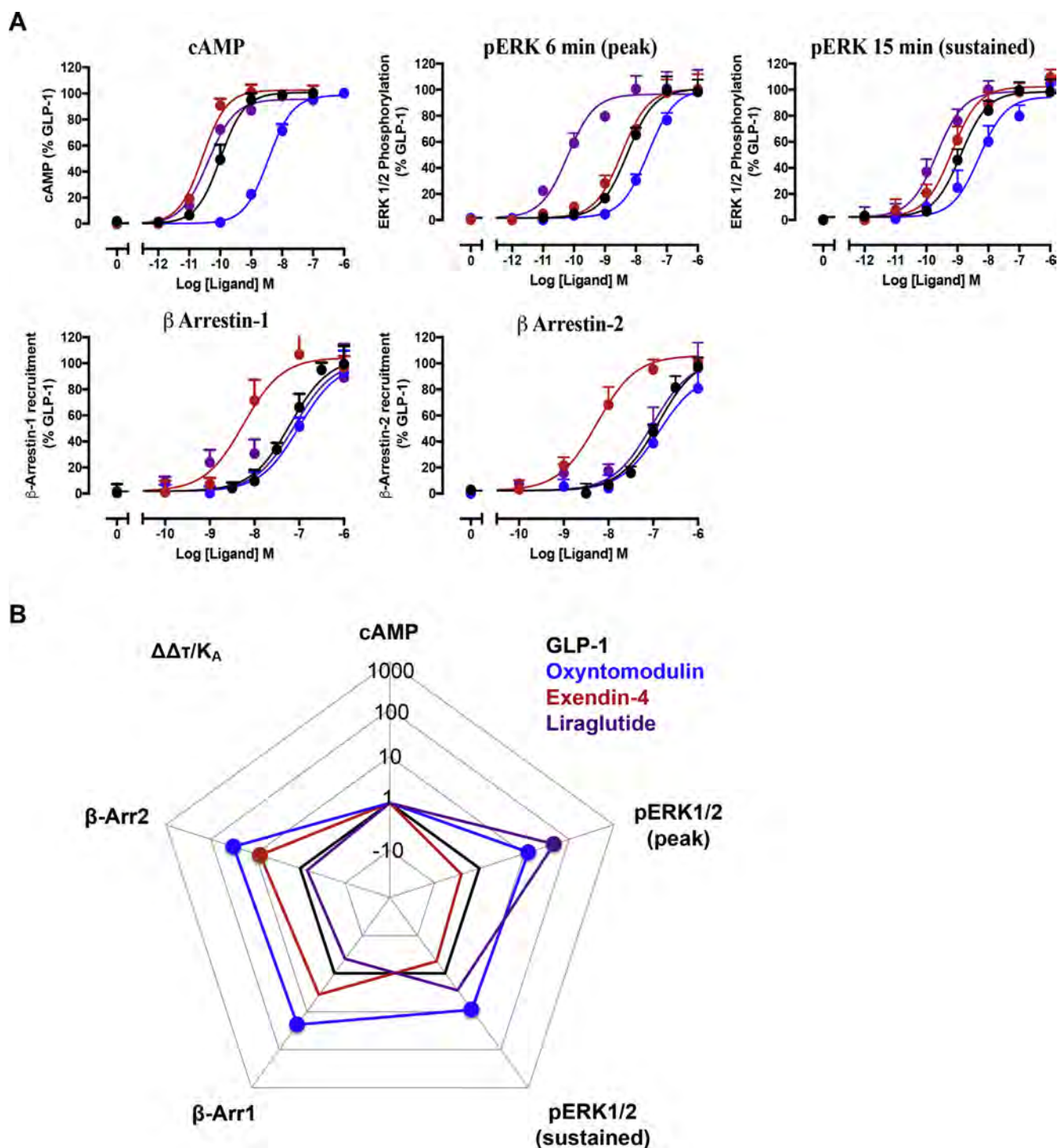


Fig. 1. Signalling bias exhibited by GLP-1R ligands in FlpIn-CHO cells stably expressing the GLP-1R. (A) Concentration-response data for GLP-1 (black), exendin-4 (red), oxyntomodulin (blue) and liraglutide (purple) for cAMP signalling, pERK1/2 signalling at two time points and β -Arrestin (β -Arr) 1 and 2 recruitment. (B) Web of bias illustrating peptide bias relative to GLP-1 and cAMP signalling. Concentration-response data were analysed using the operational model to determine bias factors (τ/K_A). These were normalized to GLP-1 and cAMP accumulation ($\Delta\Delta\tau/K_A$) and plotted on a logarithmic scale on the web. Circles represent data significantly different from GLP-1 as assessed using a one-way ANOVA followed by Dunnett's post test ($P < 0.05$). Data are mean + SEM from four to five experiments performed in duplicate. (For interpretation of the references to colour in this figure legend, the reader is referred to the web version of this article.)

(TGR Biosciences) and the plate agitated for two min. 5 μ l of lysate was added to a 384-well ProxiPlate (PerkinElmer), and 8.5 μ l of detection buffer [10 parts Activation buffer, 60 parts Reaction buffer, 0.3 parts AlphaScreen acceptor beads, 0.3 parts AlphaScreen donor beads] was added in reduced lighting conditions. The plate was incubated at 37 $^{\circ}$ C for 1 h, the plate cooled to RT for 30 min, before reading on the EnVision multilabel plate reader (PerkinElmer) (excitation

wavelength = 680 nm; emission wavelength = 520–620 nm). All data were expressed as a percentage of the ERK1/2 phosphorylation mediated after 6 or 15 min of exposure to 10% v/v FBS (as stated). Data were analysed and curve fitting performed using a three-parameter logistic equation using GraphPad Prism version 6.0.

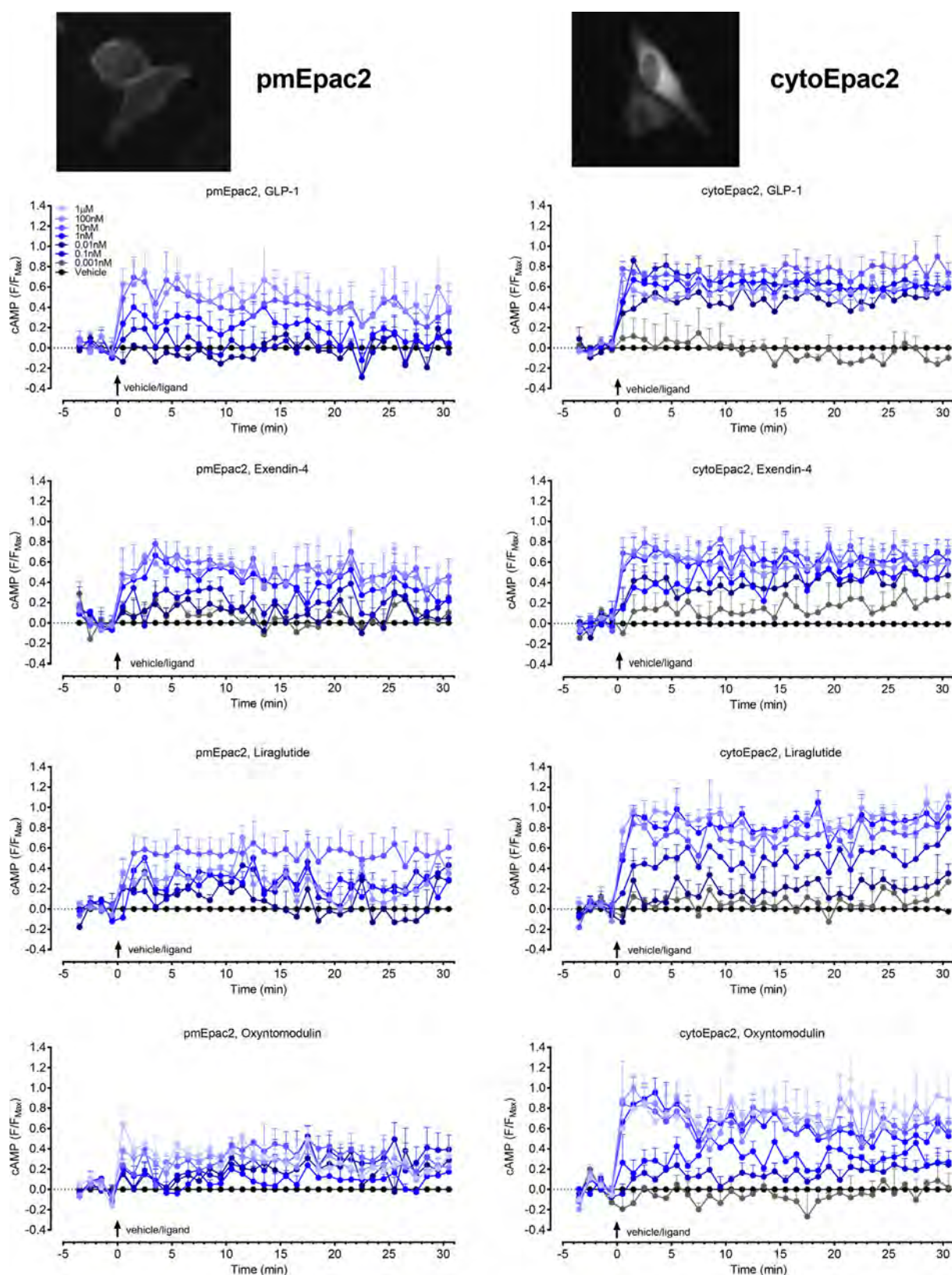


Fig. 2. Compartmentalised cAMP signalling. Time course of cAMP signalling upon stimulation of GLP-1R, by GLP-1, exendin-4, liraglutide and oxyntomodulin as measured by the FRET sensors pmEpac2 and cytoEpac2 in FlpIn-CHO cells following transient transfection of the GLP-1R and the relevant FRET sensor. Cell images for each sensor are shown, confirming the localization of the two sensors to the plasma membrane (pmEpac2) or the cytosol (cytoEpac2). Data are plotted as change in CFP/YFP ratio relative to the maximum response (F_{\max}) for each cell and baseline corrected to the vehicle response. Data points are mean + SEM, of 3–6 individual experiments (n), with 48–211 individual cells per condition in each individual n.

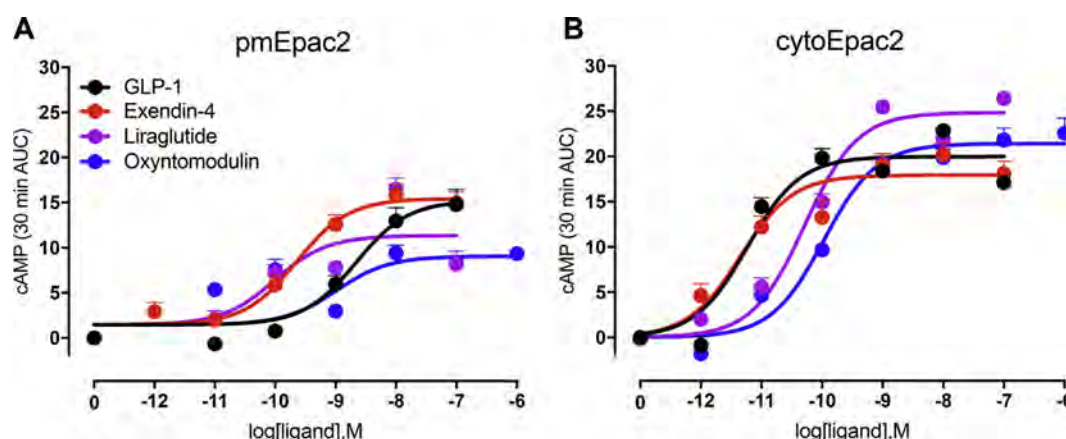


Fig. 3. Concentration-response curves of cAMP signalling upon stimulation of GLP-1R, by GLP-1, exendin-4, liraglutide and oxyntomodulin measured using FRET sensors pmEpac2 and cytoEpac2 in FlpIn-CHO cells following transient transfection of the GLP-1R and the relevant FRET sensor. Data are the AUC of F/F_{\max} over 30 min as in Fig. 2. Data points are mean \pm SEM, of 3–6 individual experiments (n), with 48–211 individual cells per condition in each individual n.

Table 1

Summary of the pEC_{50} and E_{\max} values of AUC concentration–response curves of cAMP detected by the pmEpac2 and cytoEpac2 sensors upon stimulation of GLP-1R with peptide ligands. pEC_{50} is the negative logarithm of the concentration that produces 50% of the maximal response. E_{\max} is the maximal response, as indicated by the maximum of the concentration–response curve. Values are mean \pm SEM calculated from a three-parameter curve fit. Statistical tests are one-way ANOVA, followed by Tukey's post-test, # compared to GLP-1 for each sensor, # $p < 0.01$.

	pEC_{50} (M)			
	GLP-1	Exendin-4	Liraglutide	Oxyntomodulin
pmEpac2	8.66 ± 0.40 (3)	9.64 ± 0.36 (3)	10.01 ± 0.47 (3)	8.98 ± 0.61 (3)
cytoEpac2	11.23 ± 0.20 (3)	11.35 ± 0.23 (5)	10.28 ± 0.17 (3)	9.97 ± 0.18 (3)#
E_{\max} (relative units AUC)				
	GLP-1	Exendin-4	Liraglutide	Oxyntomodulin
pmEpac2	15.23 ± 0.28 (3)	15.44 ± 0.77 (3)	11.31 ± 2.44 (3)	9.06 ± 2.24 (3)
cytoEpac2	19.99 ± 1.16 (3)	17.93 ± 1.14 (5)	24.84 ± 1.35 (3)	21.42 ± 1.19 (3)

2.6. Bioluminescence resonance energy transfer (BRET) assays to assess β -arrestin recruitment

FlpIn-CHO cells stably expressing the human c-myc-GLP-1R-Rluc8 and either β -arrestin1- or β -arrestin2-Venus were seeded in 96-well white-walled CulturPlates (PerkinElmer) at a density of 30,000 cells/well and cultured for 24 h. Cells were washed once with HBSS with 0.1% w/v BSA, to remove traces of phenol red and incubated in this solution for a further 15 min. Cells were challenged with drug or vehicle at indicated time points, and the Rluc substrate coelenterazine-h (Nanolight) added to reach a final concentration of 5 μ M 10 min before BRET reads. BRET readings were collected using a LumiSTAR Omega (BMG LabTech) that allows sequential integration of signals detected in the 465–505 nm and 515–555 nm windows using filters with the appropriate band pass. The BRET ratio for each sample (515–555 nm emission over 465–505 nm emission) was vehicle subtracted to express results as ligand-induced BRET. This eliminates the requirement for measuring a donor only control sample. Initial time course experiments were performed over 20 min to determine the time at which β -arrestin1 and β -arrestin2 recruitment was maximal for each ligand. Subsequent concentration response data were collected at this peak time. Data were normalized to the maximal response elicited by GLP-1. Data were analysed and curve fitting performed using a three-parameter logistic equation using GraphPad Prism version 6.0.

2.7. BRET assays to assess receptor trafficking

FlpIn-CHO were transiently transfected with 20 ng/well human c-myc-GLP-1R-Rluc8, 80 ng/well BRET biosensor (either Rab5a-, Rab7a-, Rab11- or KRas- Venus) and 50 ng/well of either dyn-K44E, dyn, cav-1,

cav-1 P132L or pcDNA3.1. The cells were plated at 15,000 cells/well, into 96-well white-walled CulturPlates (PerkinElmer) and assays performed 48 h later. Cells were washed once with HBSS containing 0.1% w/v BSA and 10 μ g/ μ l cycloheximide (Sigma Aldrich), then incubated in this solution for another 30 min. Cycloheximide was added to prevent *de novo* protein synthesis.

In Pitstop2 studies, 30 μ M of Pitstop2 was added to the buffer for the 30 min incubation. Cells were challenged with the drug or vehicle at indicated time-points and washed 30 min after addition. Ten min before reading the plate, coelenterazine h was added to give a final concentration of 5 μ M. The plate was read on a LumiStar Omega using 465–505/515–555 nm filters. The BRET ratio for each sample (515–555 nm emission over 465–505 nm emission) was vehicle subtracted to express results as ligand-induced BRET, and corrected to baseline values at time 0.

2.8. Forster resonance energy transfer assays to assess signalling

FlpIn-CHO cells were transiently transfected with 55 ng/well human c-myc-GLP-1R and 45 ng/well of FRET sensor (cytoEpac2, pmEpac, nucEKA or cytoEKA) or for studies assessing the impact of internalisation, 42 ng/well receptor, 45 ng/well biosensor (cytoEpac2, pmEpac, nucEKA or cytoEKA) and 63 ng/well of dyn-K44E or pcDNA3.1. Cells were seeded at 15,000 cells/well into 96-well clear-bottomed, black-walled ViewPlates (PerkinElmer). Assays were performed 48 h after transfection and cells were serum-starved overnight before assay. The assay method is adapted from that previously described [30]. On the day of assay cells were equilibrated in HBSS at 37°C for 30 min. Fluorescence was measured on the GE Healthcare high-content INCell 2000 Analyzer, with CFP and YFP filters and a

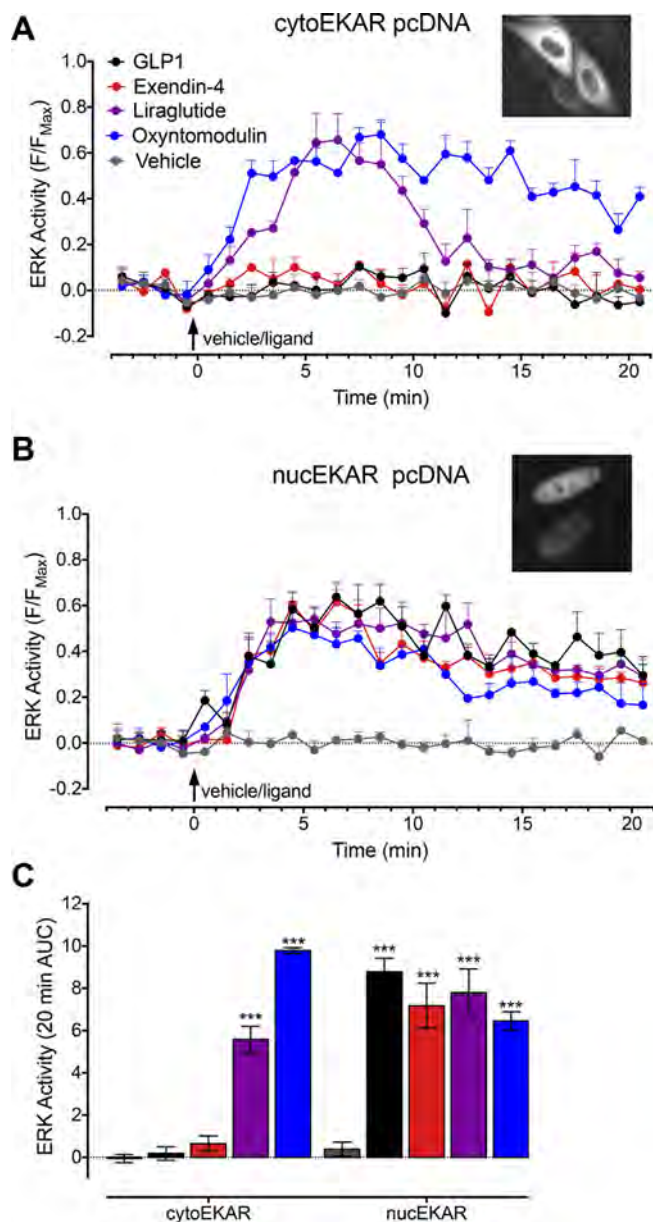


Fig. 4. Time course of ERK activity upon stimulation of GLP-1R, by GLP-1, exendin-4, liraglutide (100 nM) and oxyntomodulin (1 μ M) as measured by cytoE KAR (A) and nucE KAR (B) in FlpIn-CHO cells following transient transfection of the human GLP-1R and the relevant FRET sensor. Cell images are shown in A and B to confirm the localization of the sensors to the cytosol (cytoE KAR) or the nucleus (nucE KAR). Data are plotted as change in cerulean/venus ratio relative to the maximum response to FBS (F_{max}) for each cell. Data points are mean \pm SEM, of three individual experiments (n), with 68–176 total cells per condition. Statistical tests are two-way ANOVA, followed by Dunnett's test compared to vehicle, *** $p < 0.001$.

polychroic optimised for the CFP/YFP filter pair (Quad3). Images of up to 14 wells were collected at one min intervals. Baseline emission ratio images were captured for four min. Cells were challenged with the drug or vehicle and the images captured for 30 min, before the cells were stimulated with the positive control [10 μ M forskolin and 100 μ M 3-isobutyl-1-methylxanthine (IBMX) for cAMP or 200 nM phorbol-12,13-dibutyrate for ERK] for 10 min to generate maximal FRET, and positive images collected for four min. Data were analysed with three macros that run in the FIJI distribution of Image J, as previously described [30]. Briefly, the baseline, stimulated and positive image stacks were collated and aligned with the StackCreator script. The cells and

background were selected, the fluorescence intensity measured across the stack, and the background fluorescence subtracted. The FRET response was graphed as the FRET ratio relative to the positive control (F/F_{max}) for each cell at each time-point. Only cells with $> 5\%$ increase in the background corrected FRET ratio (F/F_0) to the positive control were selected for analysis. To generate the concentration–response curves, the area under the curve was plotted against the log concentration of peptide, and the curves were fit in GraphPrism version 6 using a three-parameter logistic equation.

2.9. Bias calculations

To quantify biased agonism, which may be manifested as selective functional affinity (K_A) and/or efficacy (τ) of an agonist for a given pathway, concentration response data were analysed with an operational model of agonism directly modified to estimate the ratio of τ/K_A for each pathway as described previously [7]. All estimated parameters are expressed as logarithms (mean \pm S.E.M.).

2.10. Statistics

Comparisons of multiple different groups were assessed using a one-way or two-way analysis of variance (ANOVA) followed by either Sidak's, Dunnett's or Tukey's post-test. Paired or unpaired t-tests were performed to compare the effects of dyn-K44E and pcDNA and differences between the pmEpac2 and cytoEpac2 sensors with regard to potency and maximal responses calculated from concentration response curves. Significance was accepted at $p < 0.05$.

3. Results

3.1. Exendin-4, liraglutide and oxyntomodulin are biased peptides relative to GLP-1

Agonist concentration–response data were generated to assess biased agonism in multiple pathways; cAMP accumulation, ERK1/2 phosphorylation and β -arrestin recruitment (Fig. 1A). cAMP assays were performed as an accumulation assay over 30 min. For β -arrestin recruitment, concentration–response data were generated at the time-point of the peak response (3 min). For ERK1/2 phosphorylation, concentration–response curves were generated at two time points, chosen to reflect peak response (6 min) and the sustained response (15 min), as determined from kinetic time course experiments. Calculation of transduction ratios (τ/K_A) determined from operational fitting to concentration–response data [31], revealed both oxyntomodulin and liraglutide are biased agonists relative to GLP-1, generating greater ERK1/2 phosphorylation relative to the same amount of cAMP (Fig. 1B). This bias was greater for liraglutide than oxyntomodulin at the peak (6 min) response, but oxyntomodulin was greater when measuring the sustained response (15 min time point). When assessing β -arrestin 1 or 2 recruitment, liraglutide displayed no bias relative to cAMP when compared with GLP-1. This was in contrast to oxyntomodulin and exendin-4 that were both biased towards recruitment of β -arrestin 2, similar to previous observations (Fig. 1B), [32]. Oxyntomodulin was also significantly biased towards β -arrestin 1.

3.2. Ligand-dependent spatiotemporal signalling of the GLP-1R

To gain temporal and spatial resolution of GLP-1R signalling, we utilised a cytosolically located (cytoEpac2) and a plasma membrane targeted (pmEpac2) cAMP Epac2 biosensor. cAMP was detected with both sensors, immediately upon stimulation with all peptides (Fig. 2). cAMP signals at lower concentrations of ligand were more transient at the plasma membrane, decreasing back towards baseline over the 30 min after stimulation. Cytosolically localised responses were sustained over this time scale. Taking the area under the curve (AUC) of

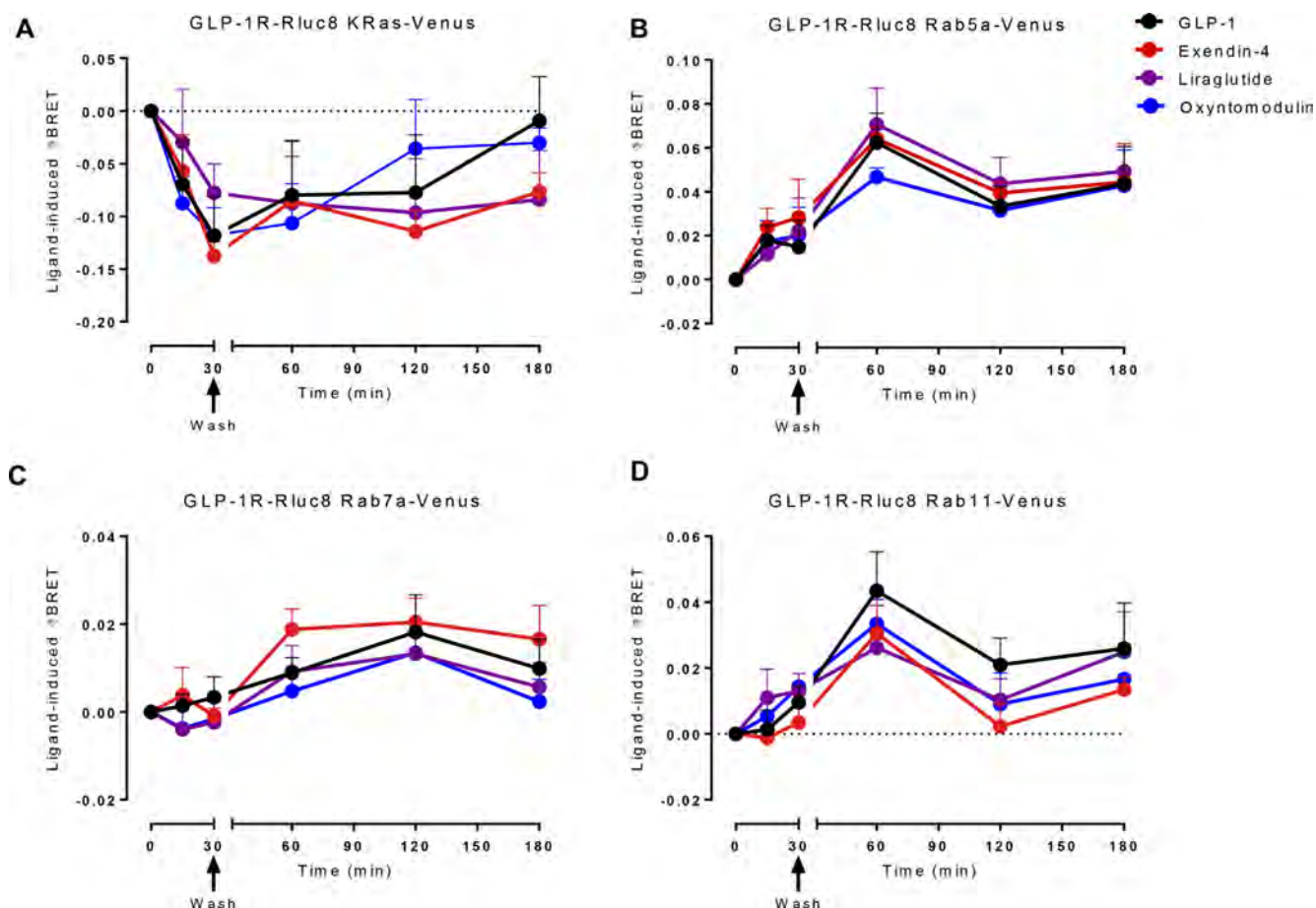


Fig. 5. The trafficking of GLP-1R-Rluc8 in FlpIn-CHO cells upon stimulation with GLP-1 (100 nM), exendin-4 (100 nM), liraglutide (100 nM) and oxyntomodulin (1 μ M). Cells were transiently transfected with human GLP-1R-Rluc8 and the relevant BRET sensor targeted to the various subcellular compartments. Cells were challenged with ligand for 30 min before they were washed and BRET measured between GLP-1R-Rluc8 and subcellular markers (A) KRas (plasma membrane), (B) Rab5a (early endosome), (C) Rab7a (late endosome) and (D) Rab11 (recycling endosome). Data are mean + SEM from four to five experiments performed in triplicate.

each of these graphs, concentration–response curves were plotted (Fig. 3, Table 1). Consistent with population-based global assays of cellular cAMP, oxyntomodulin had the weakest response in both cellular compartments with statistically lower potency relative to GLP-1 at the cytoplasmic localised sensor and a lower maximal response than GLP-1 in generating plasma membrane-localised cAMP (Table 1). Interestingly, equipotent responses were measured for liraglutide in both compartments, whereas GLP-1, exendin-4 and oxyntomodulin were 372-, 51- and 10- fold more potent, respectively, in detecting cAMP using the cytosolically localised sensor relative to the plasma membrane localised sensor. Consequently, GLP-1 and exendin-4 were significantly more potent in the generation of cytosolic cAMP than liraglutide. In contrast, GLP-1 was 10-fold less potent than exendin-4 and liraglutide, which were equipotent, in the generation of cAMP at the plasma membrane (albeit these differences did not reach statistical significance for this sensor). These data suggest that individual peptides differentially generate localised pools of cAMP.

Compartmentalised ERK activation was detected in time-course assays using a single saturating concentration of ligand, by ERK activity sensors localised to the cell cytosol (cytoEKAR; Fig. 4A) or nucleus (nucEKAR; Fig. 4B). Nuclear ERK activity was detected upon stimulation with all four peptides, although the oxyntomodulin response was more transient than the other three ligands (Fig. 4B, 4C). In contrast, within the cytosol, a different profile of ERK activity was observed where the biased agonists liraglutide and oxyntomodulin generated cytosolic ERK activity but GLP-1 and exendin-4 did not elicit a response

(Fig. 4A and C). Interestingly, the response to oxyntomodulin was sustained over the 20 min time-course, whereas the response to liraglutide was transient, decreasing back to baseline by 15 min.

3.3. GLP-1R internalises into early, recycling and late endosomes upon activation by all peptide ligands

To assess the role of receptor internalisation in GLP-1R signalling, we first assessed the internalisation and trafficking of the GLP-1R using bioluminescence resonance energy transfer (BRET) to measure the co-localisation of a Rluc8 tagged receptor (GLP-1R-Rluc8) with Venus-tagged markers that are targeted to defined subcellular locations (KRas-Venus, Rab5a-Venus, Rab7a-Venus, Rab11-Venus). Upon stimulation with all four peptide ligands, the GLP-1R rapidly internalised as detected by a decrease in co-localisation of the GLP-1R and the plasma membrane marker KRas (decrease in BRET signal) that reached a maximum at 30 min post ligand stimulation (Fig. 5A). Accordingly, this was correlated with increased co-localisation between the GLP-1R and the early endosomal marker Rab5a (increased BRET signal), which peaked at 60 min (Fig. 5B). These data exemplify the GLP-1R leaving the plasma membrane, via internalisation, and entering early endosomes. An increase in BRET was also observed with GLP-1R and the markers Rab11 and Rab7a, peaking at 60 and 120 min, respectively (Fig. 5C and D). This indicates that receptor trafficking diverges into both recycling and late endosomes, from which the receptor is likely trafficked either back to the plasma membrane or to lysosomes. No

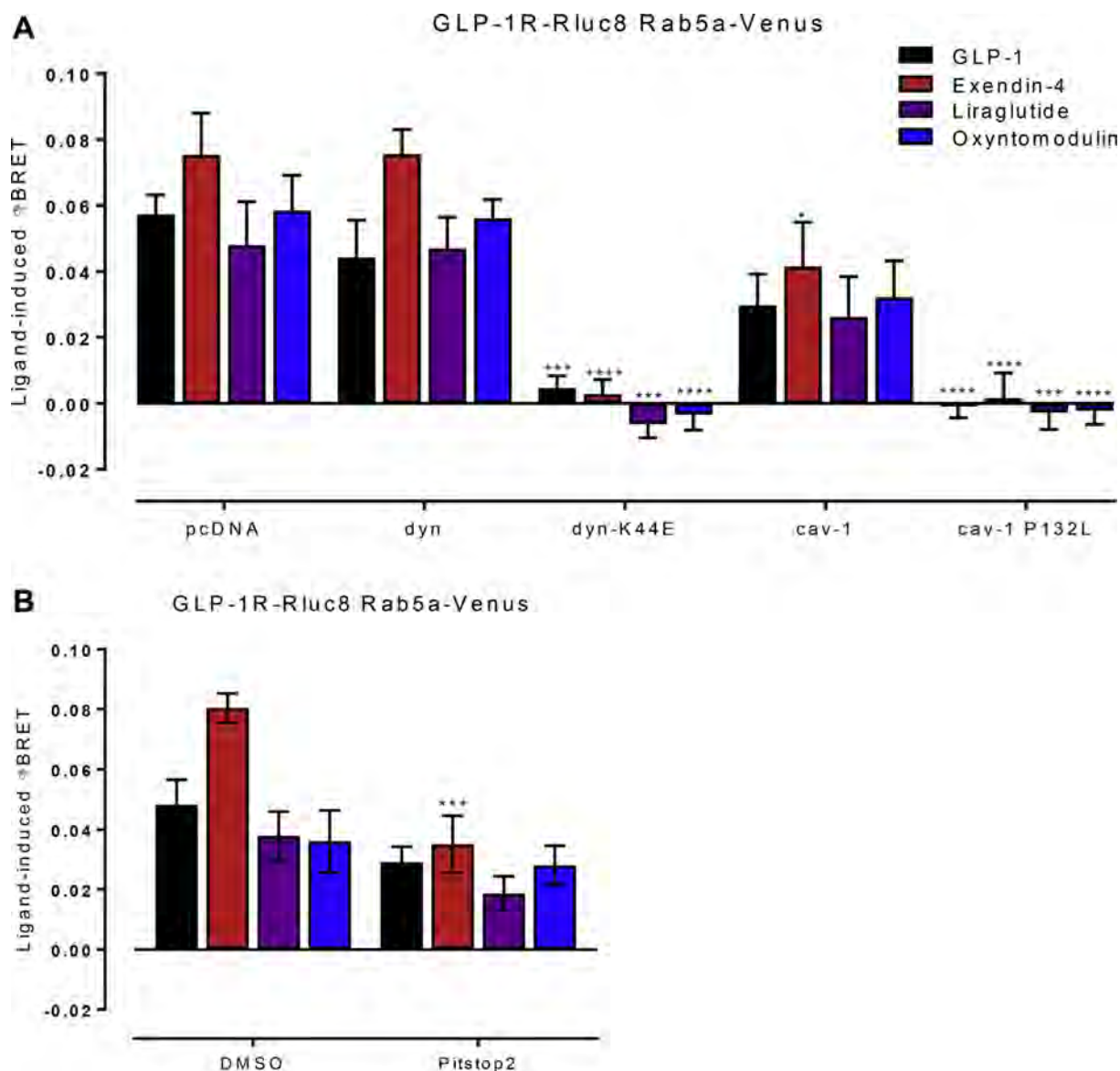


Fig. 6. The co-localisation of GLP-1R-Rluc8 with the early endosome was assessed in Fln-CHO cells transiently transfected with GLP-1R-Rluc8, Rab5a-Venus and either dyn, cav-1 or their dominant-negative forms, dyn-K44E and cav-1-P132L (A) or treated with clathrin inhibitor Pitstop2 (B). Cells were treated with peptide agonists GLP-1 (100 nM), exendin-4 (100 nM), liraglutide (100 nM) and oxyntomodulin (1 μ M), the ligand was washed out at 30 min and the BRET between GLP-1R-Rluc8 and Rab5a-Venus (early endosome) measured at 60 min. Data points are vehicle-corrected and are mean \pm SEM from five experiments, performed in triplicate. Statistical tests are two-way ANOVA, (with variables pcDNA3 and each inhibitor) followed by Dunnett's post-test, compared to pcDNA3 control for each ligand (A) or two-way ANOVA, (variables DMSO control and Pitstop2), followed by Sidak's post-test, compared to DMSO control for each ligand (* p < 0.05, ** p < 0.001, **** p < 0.0001) (B).

statistical difference was observed in the kinetics or magnitude of ligand-induced trafficking between the different peptide agonists at any time point assessed.

3.4. GLP-1R internalises via caveolin-1, clathrin and dynamin-dependent mechanisms in Fln-CHO cells

Previous literature has provided evidence for clathrin and/or caveolae-mediated GLP-1R internalisation across a range of cellular backgrounds. A partial role of clathrin-coated pits has been implicated in CHO and CHL cells [16,17], whereas a caveolin-1 dependent mechanism has been observed in HEK293 cells, with GLP-1R and caveolin-1 co-localising inside the cell [18,19]. Both clathrin and caveolae-mediated mechanisms are dynamin-dependent. To determine the mechanism by which GLP-1R internalises in the Fln-CHO cells used in the current study, we measured BRET between the early endosomal

marker, Rab5a-Venus, and the GLP-1R-Rluc8 60 min after ligand stimulation, in the presence or absence of various inhibitors of GPCR internalisation. Consistent with previous reports, overexpression of dyn-K44E, a dominant negative form of dynamin with no GTPase activity [33], abolished all ligand-mediated GLP-1R internalisation when compared to the wild type dynamin and the pcDNA3.1 transfection control (Fig. 6A). Also consistent with published literature, the clathrin-dependent inhibitor, Pitstop2, partially inhibited internalisation for exendin-4 (Fig. B). Caveolin-1 (cav-1) is a key protein in the formation of caveolae, and cav1-P132L, is dominant negative mutant of the protein that is intracellularly retained [34]. Transfection of cav1-P132L also abolished internalisation of GLP-1R compared to wildtype and pcDNA3.1 for all peptides (Fig. 6A).

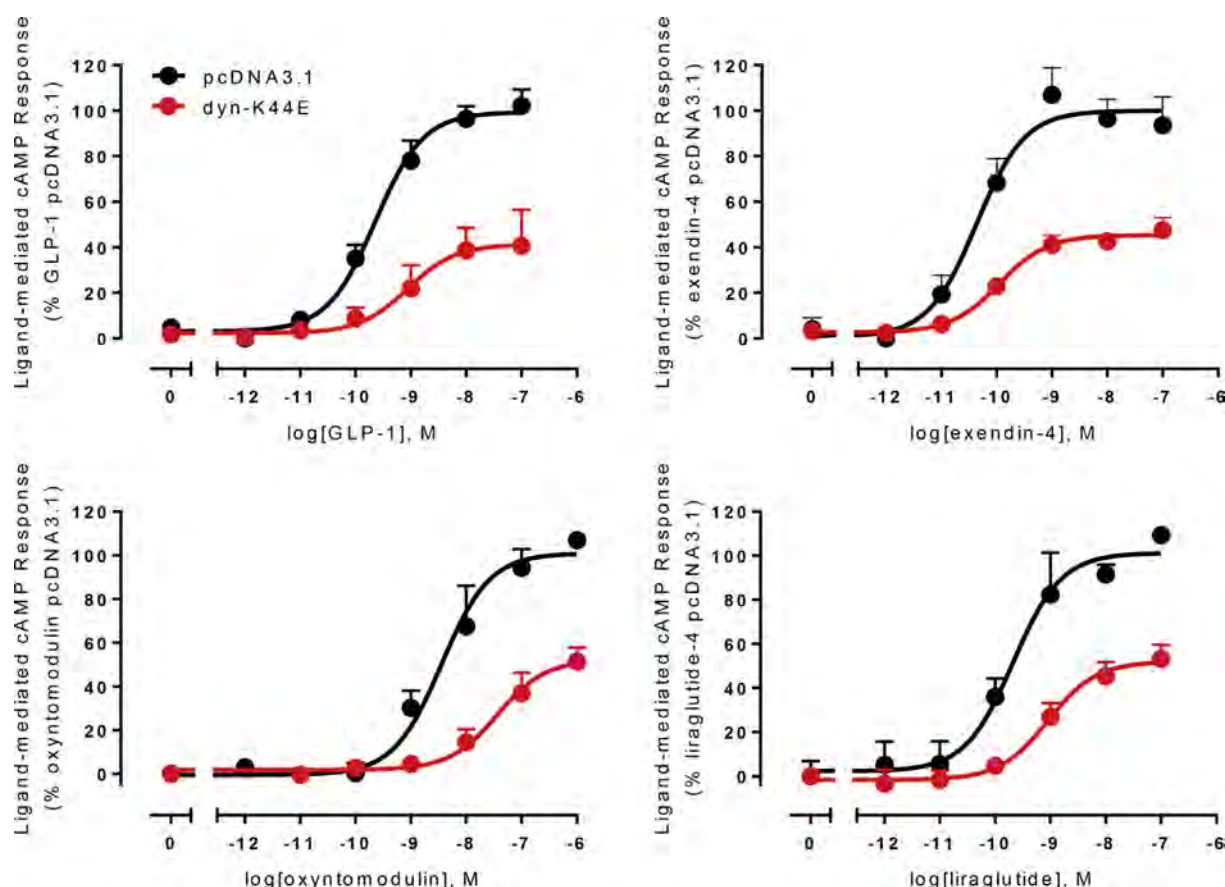


Fig. 7. Concentration-response curves for 30 min cAMP accumulation upon stimulation of the GLP-1R with GLP-1, liraglutide, oxyntomodulin, exendin-4, in FlpIn-CHO cells transiently transfected with GLP1R and either dyn-K44E or pcDNA. Data points are vehicle corrected and represent the mean + SEM from four to five individual experiments performed in triplicate.

Table 2

pEC₅₀ and E_{max} values calculated from concentration-response data performed in FlpIn CHO cells transfected with either dyn-K44E or pcDNA3.1. E_{max} is the maximal response expressed as a percentage of the pcDNA3.1 control. Values represent the mean ± SEM from 3 to 5 individual experiments performed in triplicate. Individual number of experiments are shown in brackets. Statistical tests are unpaired students t-tests comparing dyn-K44E to the pcDNA3.1 control for each ligand *p < 0.05.

		GLP-1		Exendin-4		Liraglutide		Oxyntomodulin	
		pEC ₅₀	E _{max}	pEC ₅₀	E _{max}	pEC ₅₀	E _{max}	pEC ₅₀	E _{max}
cAMP	pcDNA3.1	9.65 ± 0.12 (5)	100 ± 4	10.4 ± 0.19 (5)	100 ± 5	9.76 ± 0.22 (5)	100 ± 7	8.45 ± 0.17 (4)	100 ± 6
	dyn-K44E	8.97 ± 0.29 (4)	47 ± 6*	9.95 ± 0.15 (5)	45 ± 2*	8.98 ± 0.19 (5)	51 ± 4*	7.43 ± 0.23 (4)*	51 ± 5*
pERK1/2	pcDNA3.1	8.93 ± 0.11 (3)	100 ± 4	9.18 ± 0.17 (5)	100 ± 6	9.63 ± 0.15 (5)	100 ± 5	8.23 ± 0.19 (4)	100 ± 7
	dyn-K44E	7.98 ± 0.43 (3)	65 ± 12*	8.88 ± 0.41 (5)	60 ± 7*	8.72 ± 0.22 (5)*	73 ± 7*	7.03 ± 0.35* (4)	64 ± 12*

3.5. Inhibition of GLP-1R internalisation decreases global cAMP formation and ERK1/2 phosphorylation

To determine the influence of GLP-1R internalisation on cAMP mediated signalling, cAMP production was assessed in a population-based accumulation assay in the presence of dyn-K44E to completely abolish ligand-mediated receptor internalisation (Fig. 7). Overexpression of dyn-K44E reduced the maximal cAMP response for all peptides by approximately 50% (Fig. 7, Table 2). In contrast, there was only limited attenuation of GLP-1, exendin-4 or liraglutide potency for cAMP signalling, while a significant reduction of potency was observed for oxyntomodulin (Fig. 7, Table 2).

To assess the influence of receptor internalisation on ERK1/2 phosphorylation, an initial kinetic assay was performed in a population-based cell assay with GLP-1 in the absence or presence of dyn-K44E

(Fig. 8A). A decrease in pERK1/2 response in the presence of dyn-K44E was evident across the entire time-course with the greatest reduction occurring at 15 min. As such, concentration response curves for ERK1/2 phosphorylation were performed at 15 min. Treatment of cells with dyn-K44E attenuated responses of all four ligands (Fig. 8B). For liraglutide and oxyntomodulin, both potency and maximal responses, relative to the control, were statistically reduced upon inhibition of internalisation (Fig. 8B, Table 2). For GLP-1 and exendin-4, there was little effect on potency, however a similar reduction in maximal response (Fig. 8B, Table 2).

3.6. GLP-1R internalisation plays a role in the control of spatiotemporal signalling

To observe if the reduced cAMP production and pERK1/2 observed

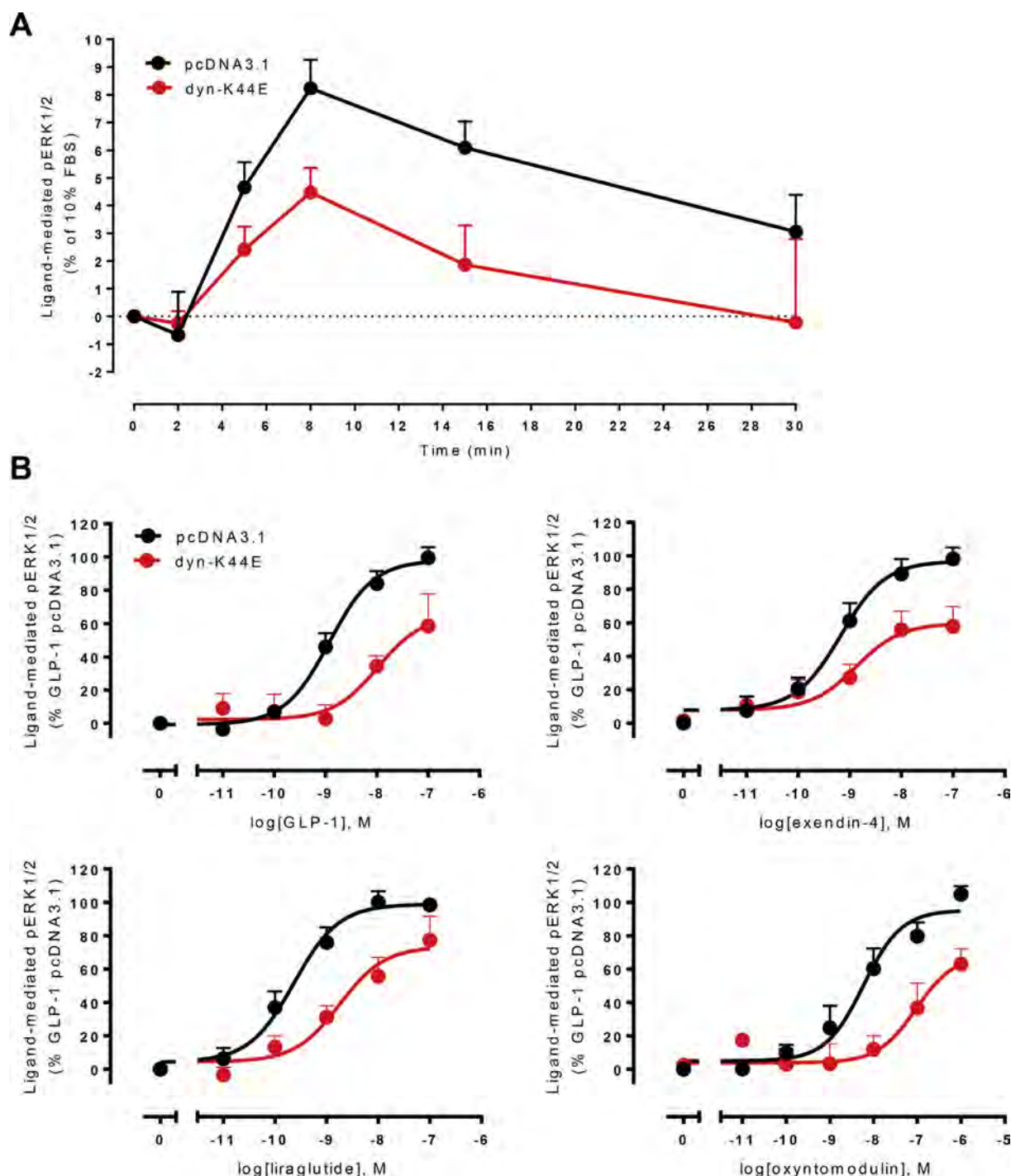


Fig. 8. pERK1/2 in FlpIn-CHO cells transiently transfected with the GLP-1R and either pcDNA or dyn-K44E. **A)** Time course of ERK1/2 phosphorylation over 30 min after stimulation with GLP-1 (100 nM) normalised to FBS response at 6 min. dyn-K44E reduced pERK1/2 relative the control (pcDNA3). **B)** Concentration-response curves for pERK1/2 after 15 min stimulation with GLP-1, liraglutide, exendin-4 and oxyntomodulin. Data are vehicle-corrected and mean + SEM from three (A) or three-five (B) experiments performed in triplicate.

upon inhibition of GLP-1R internalisation in global assays is correlated to alterations in spatiotemporal profiles of cAMP production or ERK1/2 activity, a single saturating concentration of peptide was used to assess the role of receptor internalisation in the generation of compartmentalised cAMP and pERK1/2 activity. Inhibition of GLP-1R internalisation using dyn-K44E attenuated cAMP signaling in both compartments, although the magnitude of the effect was both peptide- and compartment-dependent. Using the plasma membrane-localised sensor, there was a reduction in AUC response for exendin-4 and liraglutide in the

presence of dyn-K44E, but no effect on oxyntomodulin (Fig. 9A and C). In contrast, cAMP production measured with the cytosolically-localised sensor was attenuated for GLP-1, exendin-4 and oxyntomodulin, but not liraglutide, following inhibition of GLP-1R internalisation (Fig. 9B and C).

Intriguingly, inhibition of GLP-1R internalisation using dyn-K44E eliminated all nuclear ERK activity. In contrast, inhibition of GLP-1R internalisation revealed cytoERKAR responses to GLP-1 and exendin-4 that did not produce cytosolic signalling under control conditions

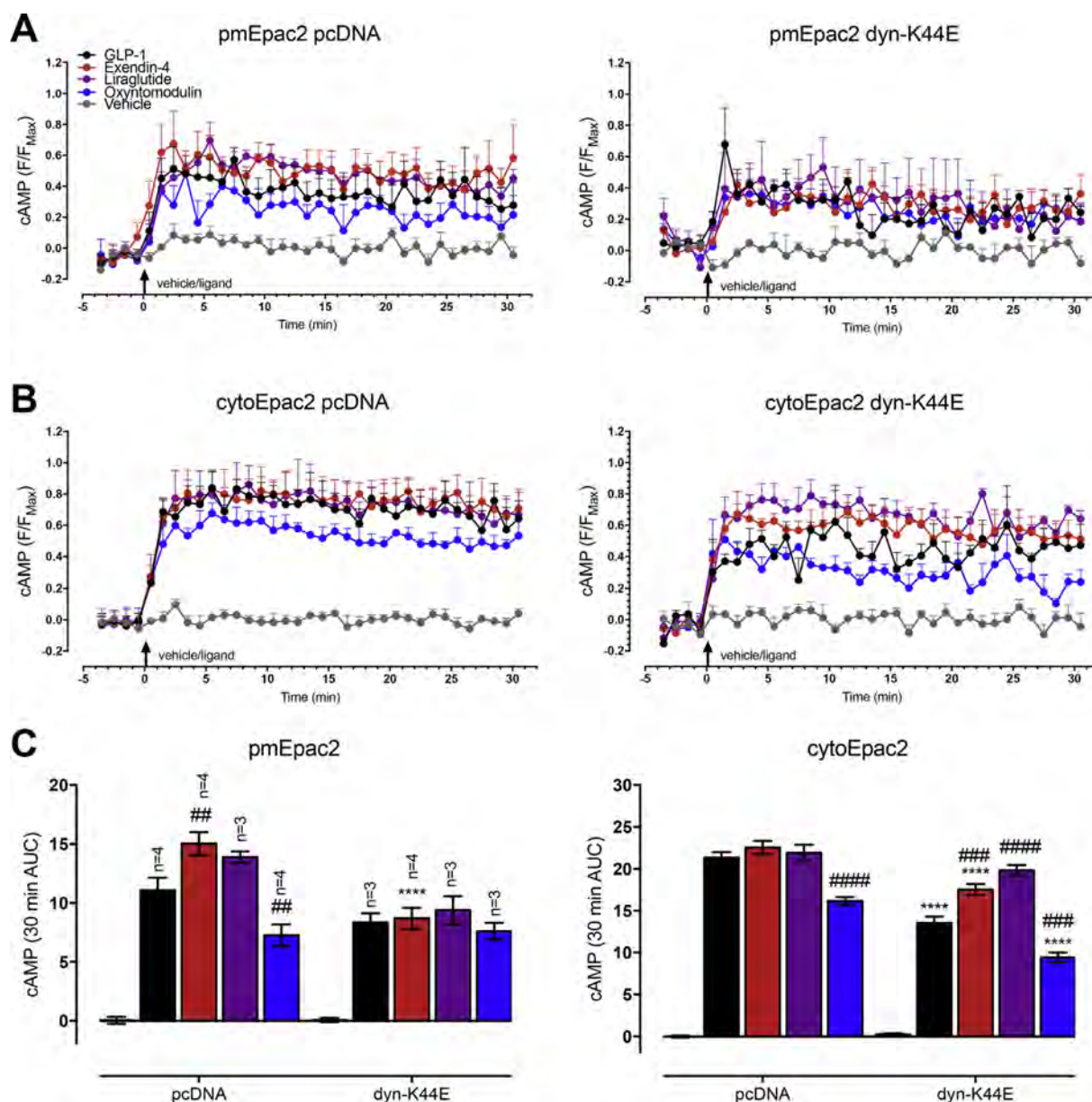


Fig. 9. Time course of cAMP signalling upon stimulation of GLP-1R, in FlpIn-CHO cells transiently transfected with the GLP-1R, the relevant FRET sensor and either pcDNA or dyn-K44E, by equi-occupant concentrations of GLP-1, exendin-4, liraglutide (1 nM) and oxyntomodulin (10 nM) as measured by FRET sensors pmEpac2 and cytoEpac2. Data are plotted as change in CFP/YFP ratio relative to the maximum response for forskolin and IBMX (F_{max}) for each cell. Data points are mean \pm SEM, of three-four individual experiments for pmEpac2 and three individual experiments for cytoEpac2, with 141–324 total cells per condition. Statistical tests are two-way ANOVA, (variables pcDNA and dyn-K44E), followed by Sidak's post test to compare each ligand in the different treatments, (**** $p < 0.0001$) or Dunnett's post test, to compare each ligand to GLP-1 within each treatment (## $p < 0.01$, ### $p < 0.001$, #### $p < 0.0001$).

(Fig. 10A–C). In addition, the temporal profile of liraglutide ERK activity within the cytosol switches from a transient response to a sustained profile, consistent with retention of the receptor at the plasma membrane. Consequently, a similar degree of sustained cytosolic ERK activity was observed for all four peptides following inhibition of internalisation (Fig. 10A and C).

4. Discussion

Biased agonism is well established at the GLP-1R and multiple recent studies have implicated a role for receptor internalisation in the control of GLP-1R signalling that may have clinical implications for development of novel therapeutics. Here, we reveal important and unappreciated roles of internalisation and trafficking in the control of differential GLP-1R activation that leads to distinct spatiotemporal

signalling profiles by GLP-1R biased agonists.

Consistent with previous publications [32], this study confirmed oxyntomodulin as a biased GLP-1R agonist favouring pERK1/2 and β -arrestin recruitment relative to cAMP when compared with GLP-1. The clinically used ligands exendin-4 and liraglutide are also biased agonists; for liraglutide this manifests as bias towards pERK1/2 in the absence of β -arrestin bias relative to cAMP, whereas exendin-4 displayed a modest degree of bias towards β -arrestin recruitment with no change in pERK1/2 relative to cAMP. pERK1/2 is predicted to be downstream of β -arrestin recruitment, however the lack of direct correlation between pERK1/2 and β -arrestin bias relative to cAMP for some ligands suggest multiple signalling and regulatory pathways link GLP-1R activation and signalling to downstream mediators, such as pERK1/2. This is consistent with our earlier work that demonstrates both β -arrestin and G protein mediated pathways play a role in

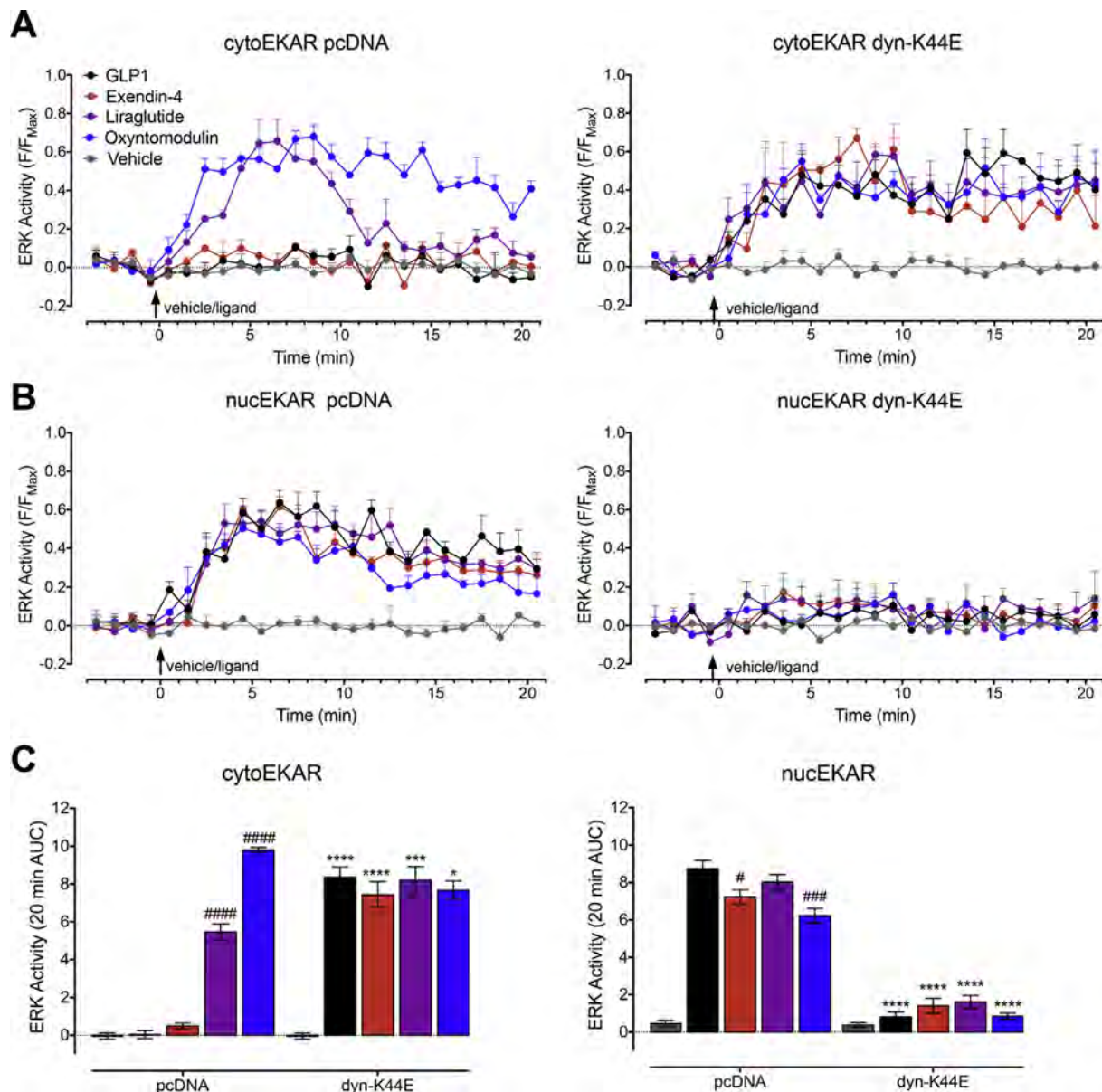


Fig. 10. Time course of ERK activity upon stimulation of GLP-1R in FlpIn-CHO cells transiently transfected with the GLP-1R, the relevant FRET sensor and either pcDNA or dyn-K44E, by GLP-1 (100 nM), exendin-4 (100 nM), liraglutide (100 nM) and oxyntomodulin (1 μ M) as measured by cytoERK (A) and nucERK (B). Data are plotted as change in cerulean/venus ratio relative to the maximum response to FBS (F_{max}) for each cell. Data points are mean \pm SEM, of 3 individual experiments, with 75–253 cells per condition. Statistical tests are two-way ANOVA (variables pcDNA and dyn-K44E), followed by Sidak's post test to compare each ligand in the different treatments, (* p < 0.05, ** p < 0.001, *** p < 0.0001) or followed by Dunnett's post test, to compare each ligand to GLP-1 within each treatment (# p < 0.05, ### p < 0.001, #### p < 0.0001).

activating this pathway [32].

Using biophysical approaches to assess GLP-1R signalling in real time revealed differential activation of the GLP-1R leads to distinct spatiotemporal profiles of signalling, particularly for ERK1/2 activity that may, in part, account for some of the observed GLP-1R biased agonism. Strikingly, while GLP-1, exendin-4, liraglutide and oxyntomodulin all promoted nuclear localised ERK1/2 activity (albeit with slightly different temporal properties), only the pERK1/2 biased agonists liraglutide and oxyntomodulin were able to generate cytosolic pERK1/2. Interestingly, oxyntomodulin produced a more sustained response than liraglutide, a kinetic profile consistent with the observed bias relative to cAMP observed from global ERK assays, whereby oxyntomodulin was biased when assessed at two distinct time points (6 and 15 mins), but liraglutide was only biased at the 6 min time point. This highlights the importance that spatiotemporal profiles of signalling can

play in engendering biased agonist profiles, as has been noted for other receptor systems [35]. Interestingly, these two ligands each have a different profile for β -arrestin recruitment, with oxyntomodulin being a biased agonist favouring recruitment, while liraglutide displayed similar recruitment relative to GLP-1. β -arrestins are scaffolding proteins that can regulate GPCR signalling. Speculatively, this β -arrestin bias may in part lead to the differences in the cytosolic ERK1/2 kinetic profile. Indeed, β -arrestin 1-dependent GLP-1R ERK1/2 activation is reported to be sustained and cytosolically restricted, at least in β -cells [36].

Differences in temporal cAMP signalling were less striking than those for ERK activity, nonetheless some important observations were revealed in our study. Whereas all ligands displayed sustained signalling that was detected within the cytosol, responses detected by the plasma membrane localised sensor for GLP-1 and exendin-4 had greater

E_{\max} values immediately following ligand stimulation, but they were also more transient in nature than those generated by liraglutide and oxyntomodulin. Of particular interest was the relative rank order of potencies where GLP-1 and exendin-4 were more potent at production of cAMP within the cytosol than liraglutide, but GLP-1 had weaker potency than exendin-4 and liraglutide detectable by the plasma membrane localised sensor. This reveals that different ligands may display distinct spatiotemporal profiles of signalling that may differentially influence physiological functions.

Assessment of GLP-1R internalisation in our system revealed that the receptor internalises rapidly when activated by GLP-1, exendin-4, liraglutide and oxyntomodulin, where it traffics into early endosomes, before moving through either recycling or degradative pathways, illustrated by co-localisation with both Rab7a and Rab11 biosensor reporters. This is consistent with previous observations in HEK293 cells and the insulinoma cell line, BRIN-BD11 [13,14]. In our study no significant differences between the ligands could be established, in the route or in kinetics of trafficking, however these studies were performed with saturating concentrations of ligand and it is possible that distinction in recycling versus degradative trafficking may occur with lower ligand concentrations. Unfortunately, limitations in the sensitivity of this assay for Rab7a and Rab11 markers precluded establishment of concentration responses. Nonetheless, it has been reported that liraglutide induces greater receptor internalisation than GLP-1 and exendin-4 [15] and that exendin-4 and liraglutide stimulated receptors recycle slower than those activated with GLP-1 [13]. These data suggest that the differences in spatiotemporal profiles of signalling that we observed using our localised FRET sensors may be linked to the internalisation and localisation of the receptor following ligand stimulation.

Dynamin, clathrin and caveolin are important for GLP-1R internalisation in the cells assessed within this study with inhibition of dynamin and caveolin completely ablating receptor internalisation and clathrin inhibition resulting in a partial reduction. Consistent with previous studies [14,21], inhibition of GLP-1R internalisation markedly decreased global cAMP accumulation and pERK1/2 mediated by GLP-1 and exendin-4. This was also true for the pERK1/2 biased ligands oxyntomodulin and liraglutide suggesting that, for all four ligands, internalised receptors contribute to the overall signalling response. Intriguingly, inhibition of internalisation had differential effects on the integrated cAMP signaling from equi-occupant concentrations of individual peptides when localised signaling was examined (Fig. 9). This may be related to the subtle differences in ligand-dependent receptor trafficking noted above [13,15]. Perhaps not surprisingly, cAMP responses were still measurable with the cytosolic Epac2 sensor despite inhibition of internalisation, indicating that plasma membrane generated cAMP is likely to rapidly diffuse into the cytosol (and maybe vice versa), contributing to the measured response. Thus, while our data illustrates that compartmentalisation of cAMP signaling is a likely component of observed biased agonism, more discriminative tools will be required to fully understand these behaviours. In contrast to the limitations with the cAMP biosensors, there was clear separation of signaling with the cytosolic and nuclear localized ERK sensors that revealed important, localisation-dependent, distinctions in peptide-mediated ERK activity. Maintaining the GLP-1R at the plasma membrane eliminated all nuclear ERK signaling, while either preserving (liraglutide, oxyntomodulin) or engendering (GLP-1, exendin-4) cytosolic ERK activity. This indicates that GLP-1R-mediated nuclear ERK activity is generated from internalised receptors while cytosolic ERK is generated by plasma membrane localised receptors. These different localised signals are likely to produce distinct cellular outcomes. Indeed, cytosolic and nuclear ERK activity have been implicated in different physiological roles with nuclear translocation involved in transcriptional control [36] and cytosolically restricted ERK mediating anti-apoptotic effects in β cells [36].

Mechanistic insight into GLP-1R biased agonism at the cellular level is of importance due to the broad therapeutic relevance of the receptor

to diseases ranging from diabetes and obesity through to neurodegenerative diseases including Parkinson's and Alzheimer's. Our study further highlights the role of receptor internalisation in control of spatiotemporal GLP-1R signalling that contributes to biased agonism. Promising recent studies in rodent models of diabetes suggest that biased GLP-1R agonists with a reduced ability to internalise may offer a therapeutic advantage as they produce greater long-term insulin release, faster agonist dissociation rates and elicit glycemic benefits without signs of nausea in animal models, which is a common side effect of GLP-1R therapies [15]. Our work, combined with this recent study, thus emphasises the need to fully understand the interplay between GLP-1R internalisation, spatiotemporally organised signalling and biased agonism and how these ligand behaviours can be utilised to develop novel, optimised disease-specific therapeutics.

5. Conflict of interest statement

The authors declare no competing interests.

Acknowledgements

This work was supported by the National Health and Medical Research Council of Australia (NHMRC) (project grants [1061044], [1065410] and [1126857], and NHMRC program grant [1055134]); P.M.S. is a NHMRC Principal Research Fellow and A.C. is a NHMRC Senior Principal Research Fellow. M.L.H. and D.W. are NHMRC RD Wright Career Development Fellows (1061687 (M.L.H.), 1089966 (D.W.)).

References

- [1] C. Orskov, A. Wettergren, J.J. Holst, Biological effects and metabolic rates of glucagon-like peptide-1 7–36 amide and glucagon-like peptide-1 7–37 in healthy subjects are indistinguishable, *Diabetes* 42 (5) (1993) 658–661.
- [2] D.J. Drucker, J. Philippe, S. Mojsov, W.L. Chick, J.F. Habener, Glucagon-like peptide I stimulates insulin gene expression and increases cyclic AMP levels in a rat islet cell line, *Proc. Natl. Acad. Sci. U.S.A.* 84 (10) (1987) 3434–3438.
- [3] L. Farilla, A. Bulotta, B. Hirshberg, S. Li Calzi, N. Khoury, H. Noshmehr, et al., Glucagon-like peptide 1 inhibits cell apoptosis and improves glucose responsiveness of freshly isolated human islets, *Endocrinology* 144 (12) (2003) 5149–5158.
- [4] J.D. Roth, M.R. Erickson, S. Chen, D.G. Parkes, GLP-1R and amylin agonism in metabolic disease: complementary mechanisms and future opportunities, *Br. J. Pharmacol.* 166 (1) (2012) 121–136.
- [5] C. Montrose-Rafizadeh, P. Avdonin, M.J. Garant, B.D. Rodgers, S. Kole, H. Yang, et al., Pancreatic glucagon-like peptide-1 receptor couples to multiple G proteins and activates mitogen-activated protein kinase pathways in Chinese hamster ovary cells, *Endocrinology* 140 (3) (1999) 1132–1140.
- [6] N. Sonoda, T. Imamura, T. Yoshizaki, J.L. Babendure, J.C. Lu, J.M. Olefsky, Beta-Arrestin-1 mediates glucagon-like peptide-1 signaling to insulin secretion in cultured pancreatic beta cells, *Proc. Natl. Acad. Sci. U.S.A.* 105 (18) (2008) 6614–6619.
- [7] C. Koole, D. Wootten, J. Simms, C. Valant, R. Sridhar, O.L. Woodman, et al., Allosteric ligands of the glucagon-like peptide 1 receptor (GLP-1R) differentially modulate endogenous and exogenous peptide responses in a pathway-selective manner: implications for drug screening, *Mol. Pharmacol.* 78 (3) (2010) 456–465.
- [8] R. Jorgensen, V. Kubale, M. Vrecl, T.W. Schwartz, C.E. Elling, Oxyntomodulin differentially affects glucagon-like peptide-1 receptor beta-arrestin recruitment and signaling through G α (s), *J. Pharmacol. Exp. Ther.* 322 (1) (2007) 148–154.
- [9] S. Ferrandon, T.N. Feinstein, M. Castro, B. Wang, R. Bouley, J.T. Potts, et al., Sustained cyclic AMP production by parathyroid hormone receptor endocytosis, *Nat. Chem. Biol.* 5 (10) (2009) 734–742.
- [10] D. Calebiro, V.O. Nikolaev, M.C. Gagliani, T. de Filippis, C. Dees, C. Tacchetti, et al., Persistent cAMP-signals triggered by internalized G-protein-coupled receptors, *PLoS Biol.* 7 (8) (2009) e1000172.
- [11] R. Irannejad, V. Pessino, D. Mika, B. Huang, P.B. Wedegaertner, M. Conti, et al., Functional selectivity of GPCR-directed drug action through location bias, *Nat Chem Biol* 13 (7) (2017) 799–806.
- [12] K. Eichel, D. Jullie, M. von Zastrow, beta-Arrestin drives MAP kinase signalling from clathrin-coated structures after GPCR dissociation, *Nat Cell Biol* 18 (3) (2016) 303–310.
- [13] S.N. Roed, P. Wismann, C.R. Underwood, N. Kulahin, H. Iversen, K.A. Cappelen, et al., Real-time trafficking and signaling of the glucagon-like peptide-1 receptor, *Mol Cell Endocrinol* 382 (2) (2014) 938–949.
- [14] R.S. Kuna, S.B. Girada, S. Asalla, J. Vallentyne, S. Maddika, J.T. Patterson, et al., Glucagon-like peptide-1 receptor-mediated endosomal cAMP generation promotes glucose-stimulated insulin secretion in pancreatic beta-cells, *Am J Physiol*

- Endocrinol Metab 305 (2) (2013) E161–70.
- [15] B. Jones, T. Buenaventura, N. Kanda, P. Chabosseau, B.M. Owen, R. Scott, et al., Targeting GLP-1 receptor trafficking to improve agonist efficacy, *Nat Commun* 9 (1) (2018) pp. 1602–018-03941-2.
- [16] C. Widmann, W. Dolci, B. Thorens, Agonist-induced internalization and recycling of the glucagon-like peptide-1 receptor in transfected fibroblasts and in insulinomas, *Biochem. J.* 310 (Pt 1) (1995) 203–214.
- [17] P. Vazquez, I. Roncero, E. Blazquez, E. Alvarez, The cytoplasmic domain close to the transmembrane region of the glucagon-like peptide-1 receptor contains sequence elements that regulate agonist-dependent internalisation, *J. Endocrinol.* 186 (1) (2005) 221–231.
- [18] C.A. Syme, L. Zhang, A. Bisello, Caveolin-1 regulates cellular trafficking and function of the glucagon-like peptide 1 receptor, *Mol. Endocrinol.* 20 (12) (2006) 3400–3411.
- [19] A. Thompson, V. Kanamarlapudi, Agonist-induced internalisation of the glucagon-like peptide-1 receptor is mediated by the Galphq pathway, *Biochem Pharmacol* 93 (1) (2015) 72–84.
- [20] S.B. Girada, R.S. Kuna, S. Bele, Z. Zhu, N.R. Chakravarthi, R.D. DiMarchi, et al., Galphas regulates Glucagon-Like Peptide 1 Receptor-mediated cyclic AMP generation at Rab5 endosomal compartment, *Mol Metab* 6 (10) (2017) 1173–1185.
- [21] S.N. Roed, A.C. Nøhr, P. Wismann, H. Iversen, H. Bräuner-Osborne, S.M. Knudsen, et al., Functional consequences of glucagon-like peptide-1 receptor cross-talk and trafficking, *J. Biol. Chem.* 290 (2) (2015) 1233–1243.
- [22] D. Wootten, E.E. Savage, F.S. Willard, A.B. Bueno, K.W. Sloop, A. Christopoulos, et al., Differential activation and modulation of the glucagon-like peptide-1 receptor by small molecule ligands, *Mol. Pharmacol.* 83 (4) (2013) 822–834.
- [23] T.H. Lan, Q. Liu, C. Li, G. Wu, N.A. Lambert, Sensitive and high resolution localization and tracking of membrane proteins in live cells with BRET, *Traffic* 13 (11) (2012) 1450–1456.
- [24] H.R. Yeatman, J.R. Lane, K.H.C. Choy, N.A. Lambert, P.M. Sexton, A. Christopoulos, et al., Allosteric modulation of M1 muscarinic acetylcholine receptor internalization and subcellular trafficking, *J. Biol. Chem.* 289 (22) (2014 May 30) 15856–15866.
- [25] V.O. Nikolaev, M. Bunemann, L. Hein, A. Hannawacker, M.J. Lohse, Novel single chain cAMP sensors for receptor-induced signal propagation, *J. Biol. Chem.* 279 (36) (2004) 37215–37218.
- [26] S. Wachten, N. Masada, L.J. Ayling, A. Ciruela, V.O. Nikolaev, M.J. Lohse, et al., Distinct pools of cAMP centre on different isoforms of adenylyl cyclase in pituitary-derived GH3B6 cells, *J. Cell Sci.* 123 (Pt 1) (2010) 95–106.
- [27] C.D. Harvey, A.G. Ehrhardt, C. Cellurale, H. Zhong, R. Yasuda, R.J. Davis, et al., A genetically encoded fluorescent sensor of ERK activity, *Proc. Natl. Acad. Sci. U.S.A.* 105 (49) (2008) 19264–19269.
- [28] F. Schmidlin, O. Dery, K.O. DeFea, L. Slice, S. Patierno, C. Sternini, et al., Dynamin and Rab5a-dependent trafficking and signaling of the neurokinin 1 receptor, *J Biol Chem* 276 (27) (2001) 25427–25437.
- [29] E.E. Savage, D. Wootten, A. Christopoulos, P.M. Sexton, S.G. Furness, A simple method to generate stable cell lines for the analysis of transient protein-protein interactions, *BioTechniques* 54 (4) (2013) 217–221.
- [30] M.L. Halls, D.P. Poole, A.M. Ellisdon, C.J. Nowell, M. Canals, Detection and quantification of intracellular signaling Using FRET-based biosensors and high content imaging, *Methods Mol. Biol.* 1335 (2015) 131–161.
- [31] T. Kenakin, C. Watson, V. Muniz-Medina, A. Christopoulos, S. Novick, A simple method for quantifying functional selectivity and agonist bias, *ACS Chem. Neurosci.* 3 (3) (2011) 193–203.
- [32] D. Wootten C.A. Reynolds K.J. Smith J.C. Mobarec C. Koole E.E. Savage et al. The extracellular surface of the GLP-1 receptor Is a molecular trigger for biased agonism *Cell* 2016 165 7 1632 1643.
- [33] J.S. Herskovits, C.C. Burgess, R.A. Obar, R.B. Vallee, Effects of mutant rat dynamin on endocytosis, *J. Cell Biol.* 122 (3) (1993 Aug) 565–578.
- [34] H. Lee, D.S. Park, B. Razani, R.G. Russell, R.G. Pestell, M.P. Lisanti, Caveolin-1 mutations (P132L and null) and the pathogenesis of breast cancer: caveolin-1 (P132L) behaves in a dominant-negative manner and caveolin-1 (-/-) null mice show mammary epithelial cell hyperplasia, *Am. J. Pathol.* 161 (4) (2002 Oct) 1357–1369.
- [35] C. Klein Herenbrink, D.A. Sykes, P. Donthamsetti, M. Canals, T. Coudrat, J. Shonberg, et al., The role of kinetic context in apparent biased agonism at GPCRs, *Nat. Commun.* 24 (7) (2016 Feb) 10842.
- [36] J. Quoyer, C. Longuet, C. Broca, N. Linck, S. Costes, E. Varin, et al., GLP-1 mediates antiapoptotic effect by phosphorylating Bad through a beta-arrestin 1-mediated ERK1/2 activation in pancreatic beta-cells, *J. Biol. Chem.* 285 (3) (2010) 1989–2002.

The Molecular Control of Calcitonin Receptor Signaling

Emma dal Maso,^{†,‡} Alisa Glukhova,^{†,‡} Yue Zhu,^{‡,§} Javier Garcia-Nafria,^{||} Christopher G. Tate,^{||} Silvia Atanasio,[⊥] Christopher A. Reynolds,[⊥] Erney Ramírez-Aportela,[▲] Jose-Maria Carazo,[▲] Caroline A. Hick,[†] Sebastian G. B. Furness,^{†,¶} Debbie L. Hay,^{∇,¶} Yi-Lynn Liang,[†] Laurence J. Miller,^{||} Arthur Christopoulos,[†] Ming-Wei Wang,^{‡,§,●} Denise Wooten,^{*,†,●} and Patrick M. Sexton^{*,†,●,¶}

[†]Drug Discovery Biology, Monash Institute of Pharmaceutical Sciences, Monash University, Parkville 3052, Victoria Australia

[‡]The National Center for Drug Screening and CAS Key Laboratory of Receptor Research, Shanghai Institute of Materia Medica, Chinese Academy of Sciences, Shanghai 201203, China

[§]University of Chinese Academy of Sciences, 19A Yuquan Road, Beijing 100049, China

^{||}MRC Laboratory of Molecular Biology, Francis Crick Avenue, Cambridge, CB2 0QH, U.K.

[⊥]School of Biological Sciences, University of Essex, Wivenhoe Park, Colchester CO4 3SQ, U.K.

[▲]Biocomputing Unit, National Center for Biotechnology (CNB-CSIC), C/Darwin, 3, Campus Universidad Autónoma, 28049 Cantoblanco, Madrid Spain

[∇]The University of Auckland, School of Biological Sciences, 3 Symonds Street, Auckland 1142, New Zealand

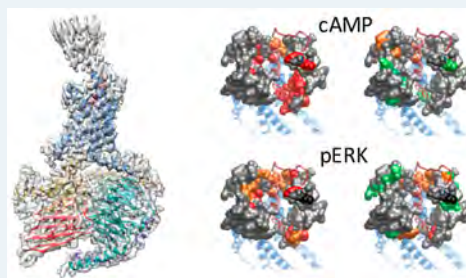
^{||}Department of Molecular Pharmacology and Experimental Therapeutics, Mayo Clinic, Scottsdale, Arizona 85259, United States

[●]School of Pharmacy, Fudan University, Shanghai 201203, China

Supporting Information

ABSTRACT: The calcitonin receptor (CTR) is a class B G protein-coupled receptor (GPCR) that responds to the peptide hormone calcitonin (CT). CTs are clinically approved for the treatment of bone diseases. We previously reported a 4.1 Å structure of the activated CTR bound to salmon CT (sCT) and heterotrimeric Gs protein by cryo-electron microscopy (Liang, Y.-L., *et al.* Phase-plate cryo-EM structure of a class B GPCR-G protein complex. *Nature* 2017, 546, 118–123). In the current study, we have reprocessed the electron micrographs to yield a 3.3 Å map of the complex. This has allowed us to model extracellular loops (ECLs) 2 and 3, and the peptide N-terminus that previously could not be resolved. We have also performed alanine scanning mutagenesis of ECL1 and the upper segment of transmembrane helix 1 (TM1) and its extension into the receptor extracellular domain (TM1 stalk), with effects on peptide binding and function assessed by cAMP accumulation and ERK1/2 phosphorylation. These data were combined with previously published alanine scanning mutagenesis of ECL2 and ECL3 and the new structural information to provide a comprehensive 3D map of the molecular surface of the CTR that controls binding and signaling of distinct CT and related peptides. The work highlights distinctions in how different, related, class B receptors may be activated. The new mutational data on the TM1 stalk and ECL1 have also provided critical insights into the divergent control of cAMP versus pERK signaling and, collectively with previous mutagenesis data, offer evidence that the conformations linked to these different signaling pathways are, in many ways, mutually exclusive. This study furthers our understanding of the complex nature of signaling elicited by GPCRs and, in particular, that of the therapeutically important class B subfamily.

KEYWORDS: cryo-electron microscopy, calcitonin receptor, G protein-coupled receptor, receptor structure–function, cell signaling



INTRODUCTION

Class B1 G protein-coupled receptors (GPCRs) respond to peptide hormones that regulate important physiological functions including bone and glucose homeostasis, energy expenditure, maintenance of vascular tone and immune function.^{2–4} These receptors are also validated targets for diseases including osteoporosis, Paget's disease, diabetes, obesity, and migraine,^{3–6} making understanding of their structure–function important for the development of novel therapeutics.

The calcitonin (CT) receptor (CTR) is a class B1 GPCR that is broadly expressed in tissues and cells including leucocytes, the brain, kidney, gastrointestinal tract, lung, and reproductive organs.³ However, it is best recognized for its expression in bone where it is highly expressed on osteoclasts. As a consequence, CTR has been exploited clinically to treat

Received: December 14, 2018

Published: January 11, 2019

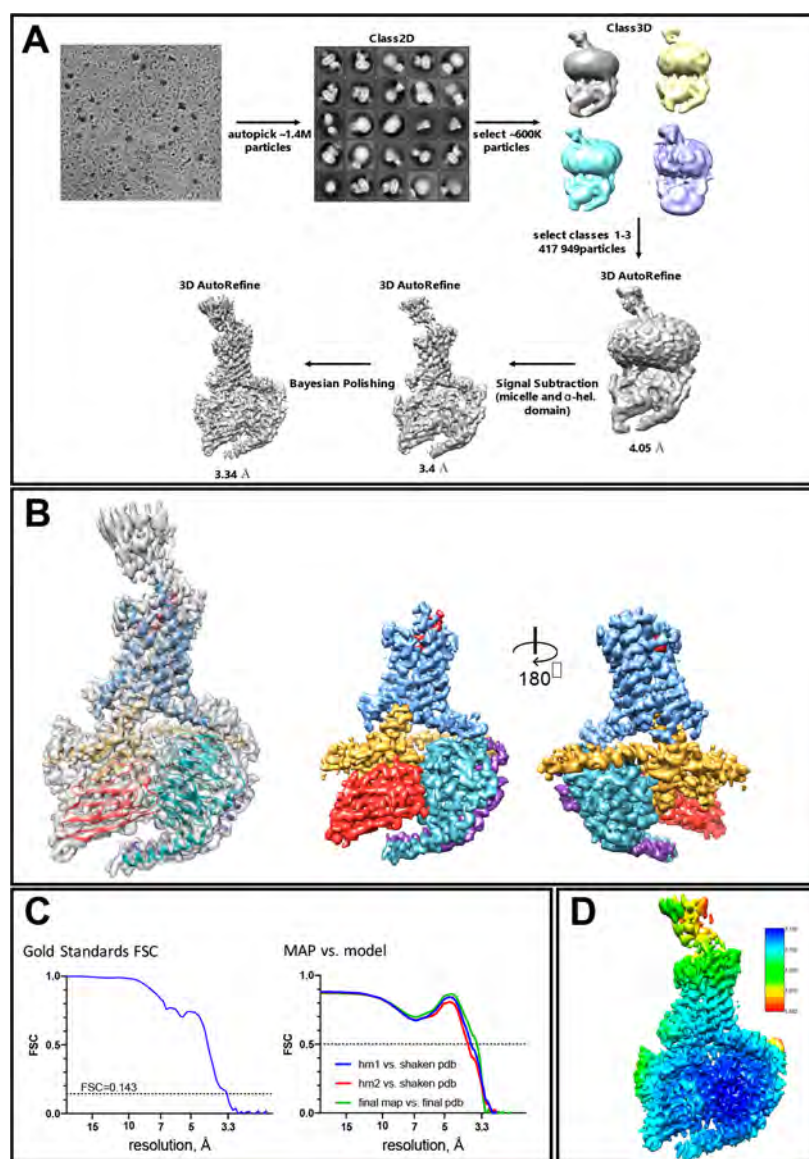


Figure 1. Refined EM map of the sCT:CTR:Gs:Nb35 complex. (A) Workflow for the EM map refinement. (B) Full map (LH panel) sharpened using LocalDeblur, and views of the density for the CTR core (blue), peptide N-terminus (dark red-orange), G protein α -subunit (gold), β -subunit (cyan), γ -subunit (dark purple), and Nb35 (red) (middle and RH panel). (C) FSC curve for the final map (LH panel) and map validation from half maps (RH panel). (D) LocalResolution-filtered EM map displaying local resolution (Å) colored from highest resolution (dark blue) to lowest resolution (red).

bone disorders including hypercalcemia of malignancy, osteoporosis, and Paget's disease.^{3,7}

CT peptides have been identified from multiple species and subclassified according to sequence conservation and activity into three major classes, human/rodent, artiodactyl (e.g., porcine CT) and teleost/avian (including salmon, eel, and chicken).⁷ Human and fish/eel CTs have been used clinically, although they have distinct properties for engagement and activation of CTRs.^{8–10}

The CTR can also interact with the receptor activity-modifying protein (RAMP) family to form distinct amylin and CGRP receptor phenotypes.⁴ In a recent study, we used alanine scanning mutagenesis of extracellular loops (ECL) 2 and 3 to reveal peptide and pathway specific differences in the role of these two loops.¹¹

To provide additional insights into CTR structure and function, we solved a 4.1 Å structure of the activated CTR in

complex with heterotrimeric G protein and salmon CT (sCT) that was the first GPCR structure solved by cryo-electron microscopy (cryo-EM).¹ While this revealed key features of active state class B1 GPCRs, it had limited resolution, particularly for the ECLs and for the peptide. In the current study, we have taken advantage of recent advances in cryo-EM software to reanalyse our original cryo-EM images enabling improvement in the global resolution of CTR map to ~3.3 Å. This provides enhanced resolution of receptor side chains, including ECL2 and ECL3, and in the N-terminus of the peptide that binds to the receptor core. We have combined this with new data comprising alanine mutagenesis of ECL1 of the receptor and upper segment of transmembrane domain (TM) 1 and its extension that links TM1 to the extracellular domain (ECD) (herein referred to as the TM1 stalk), and reassessment of alanine mutants of ECL2 and ECL3, in light of the new structural data. This gives enhanced details of the

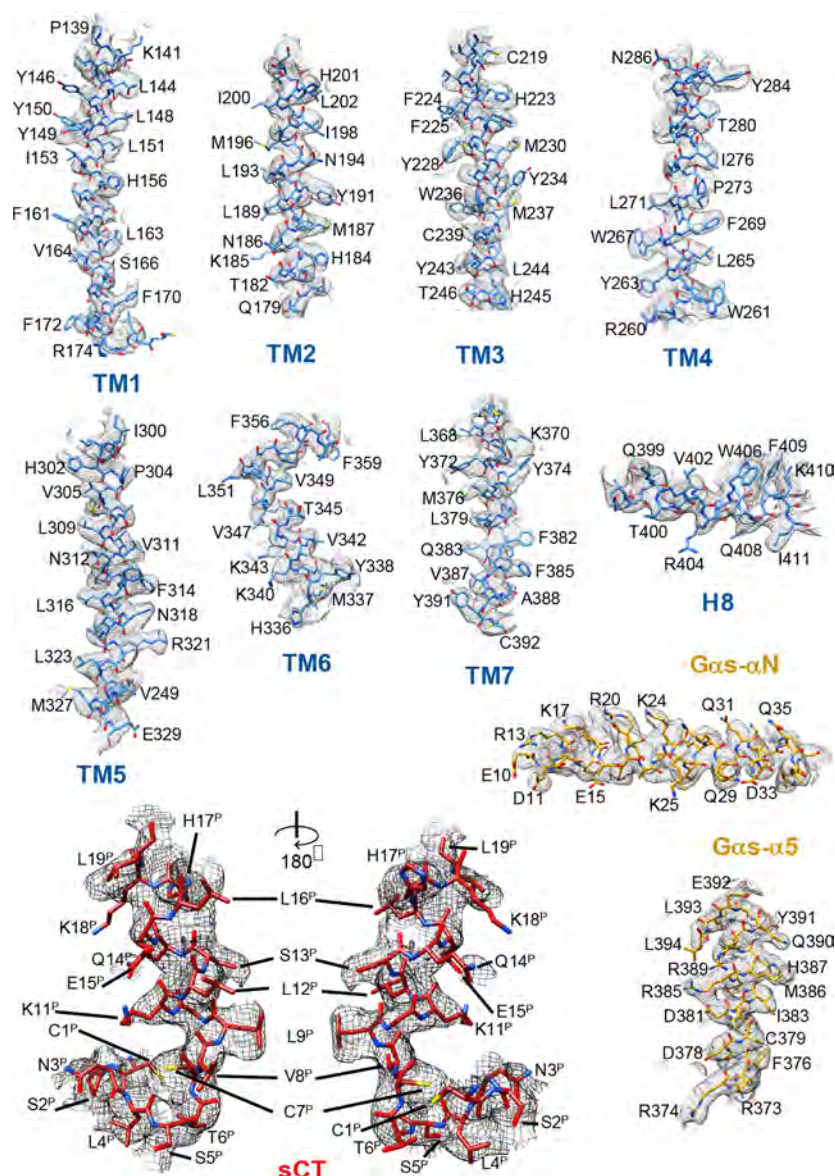


Figure 2. Atomic coordinates of the sCT:CTR:Gs complex in the cryo-EM density map. Cryo-EM density map and model are shown for all seven transmembrane helices and H8 of the receptor; the sCT peptide (amino acids 1–19), the N-terminal (α N), and C-terminal (α 5) α -helices of the Gas-Ras domain are also shown. Superscript P indicates residues of sCT. The EM map was zoned at 2.5 Å around the protein segments.

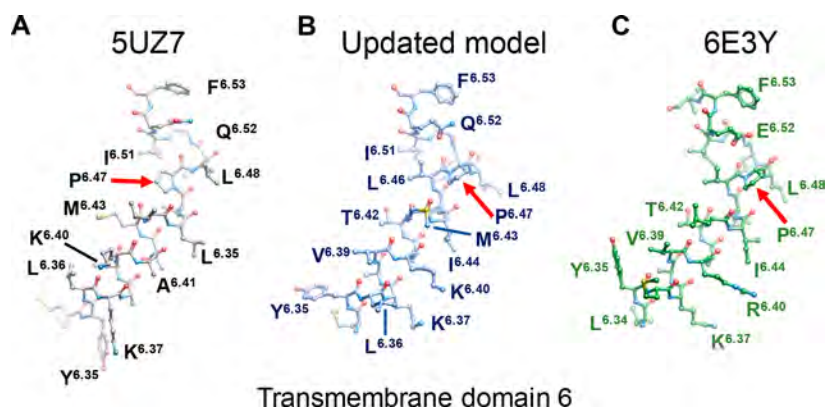


Figure 3. Improved modeling of transmembrane domain 6. (A) Model of TM6 from PDB 5UZ7, derived from the 4.1 Å EM map of the active CTR complex. (B) Model of TM6 from the current map, illustrating changed registry of amino acids below Pro.^{6.47} (C) Model of TM6 from the related CLR of the CGRP receptor (PDB 6E3Y) illustrating conservation in the position of side-chains between CTR and CLR.

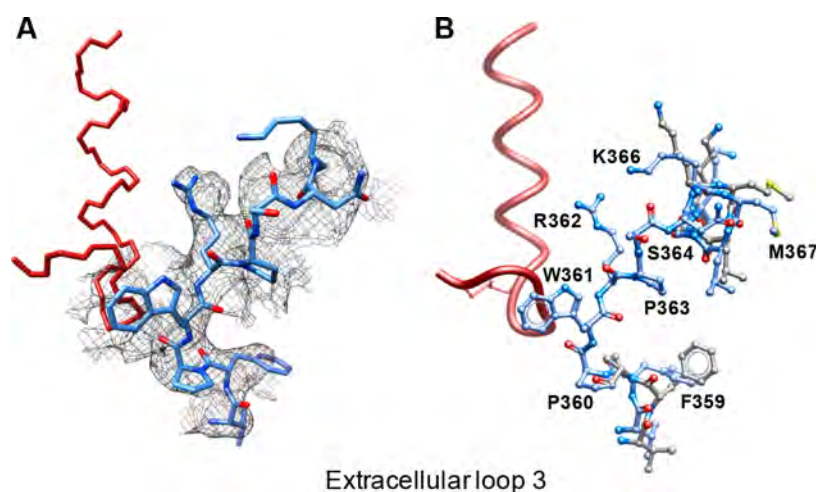


Figure 4. Modeling of CTR ECL3 in the active state complex. (A) Cryo-EM density map and model of ECL3. (B) Model of ECL3 illustrating the position of loop side-chains.

molecular control of CTR activation by CT and related peptides.

RESULTS AND DISCUSSION

A 3.3 Å Cryo-EM Map of the sCT:CTR:Gs:Nb35 Complex. We have utilized advances in cryo-EM data refinement to reprocess the original micrographs used to report the 4.1 Å structure of the complex.¹ Approximately 1.4 million particles were autopicked and subject to initial 2D classification, from which ~600,000 particles were selected for 3D classification (Figure 1A). This yielded 4 classes, with classes 1–3 containing 417 949 particles, then subject to autorefinement to yield an initial map at 4.1 Å. Signal subtraction of the micelle and mobile α -helical domain of the Gs α subunit, following by further refinement provided a map at 3.4 Å global resolution. Subsequent use of Bayesian polishing in RELION 3 provided a small additional increase in resolution but further increased the map quality to yield the final 3.34 Å map (Figure 1A–C). As previously noted for the lower resolution map,¹ the highest local resolution was seen for the G protein and receptor core with lower resolution for the more mobile ECLs and receptor ECD (Figure 1B,D). The map provided good side-chain resolution for most of the CTR TM helices, as well as the G protein (Figure 2). We used this map to remodel the protein complex, including the peptide N-terminus and ECL2 and ECL3, regions that were not previously modeled due to lack of robust density.

In general, there was good agreement with the deposited model (PDB SUZ7) across the receptor TM, with the exception of TM6 (Supplementary Figure 1, Figure 3). Owing to the weak density in the original map, the kink around the conserved P^{6.47}-X-X-G^{6.50} (superscript numbers refer to the Wootten numbering scheme for class B GPCRs¹²) motif was incorrectly modeled leading to residues below P^{6.47} being out of register by one amino acid (Figure 3A and 3B). As the first ever active class B GPCR solved there was no equivalent structure available for comparison. Subsequently, active structures of the glucagon-like peptide-1 receptor (GLP-1R),^{13,14} and the closely related calcitonin gene related peptide receptor (CGRPR)¹⁵ were solved. Structural alignment between the remodeled CTR and CT-receptor-like receptor (CLR) in the CGRPR (PDB 6E3Y) revealed that they exhibited very close location of TM6 side chains (Figure

3B,C), and the positionally equivalent residues in the GLP-1R have similar orientation,^{13,14} confirming that class B GPCRs have similar organization of key TM6 side chains that are likely important for G protein engagement.¹⁶

In the new map, there was a well resolved density for most residues in ECL3 (Figure 4A) enabling this to be modeled for the first time (Figure 4B). The side-chains of P360^{ECL3}, W361^{ECL3}, R362^{ECL3}, P363^{ECL3}, and S364^{ECL3} displayed clear density with W361^{ECL3}, R362^{ECL3} oriented toward the agonist peptide, sCT (Figure 4A,B), while the backbone of P360^{ECL3} formed a hydrogen-bond with Ser5^P of the peptide (Figure 4C,D). These interactions are consistent with our previously reported alanine mutagenesis of ECL3 where, with the exception of S364^{ECL3}, alanine mutation had peptide and pathway specific effects on receptor function.¹¹ K366^{ECL3} had only limited side-chain density, indicating that it forms only weak interactions with sCT. The remainder of ECL3 was not in proximity to the peptide.

In the originally published map, there was only limited density for ECL2 and only the backbone was modeled¹ (Figure 5A,B). In the current map, resolved density was observed for all of ECL2, enabling more accurate placement of the backbone, as well as modeling of the amino acid side-chains (Figure 5C, Supplementary Figure 2). The CTR has the closest homology to CLR, including ECL2 (Figure 6). There was strong conservation in both the backbone position and packing of residues between CTR and CLR (Figure 5A,C,D), with R281^{ECL2} and W290^{ECL2} packed within the core of the loop. The structure of the loop was supported by polar interactions between, in particular, R281^{ECL2}, D287^{ECL2}, and S292^{ECL2}, as well as predicted H-bonding between backbone atoms, including N288^{ECL2}-L291^{ECL2} and R281^{ECL2}-N286^{ECL2}.

In the current map, there was also improved density for most of the N-terminal residues of sCT (between residues 1 and 19) that enabled this to be formally modeled into density for the first time (Figure 2, Figure 6). The peptide N-terminus forms extensive, primarily hydrophobic, interactions with the receptor core. The far N-terminus exhibits a loop between Cys1^P and Cys7^P that is critically important for agonist activity: deletion of this segment yielded the high affinity antagonist/very weak partial agonist sCT_(8–32).¹⁷ The current model identified H-bond interactions between Ser5^P and the backbone of P360^{ECL3} and F359^{ECL3}, and the hydroxyl of

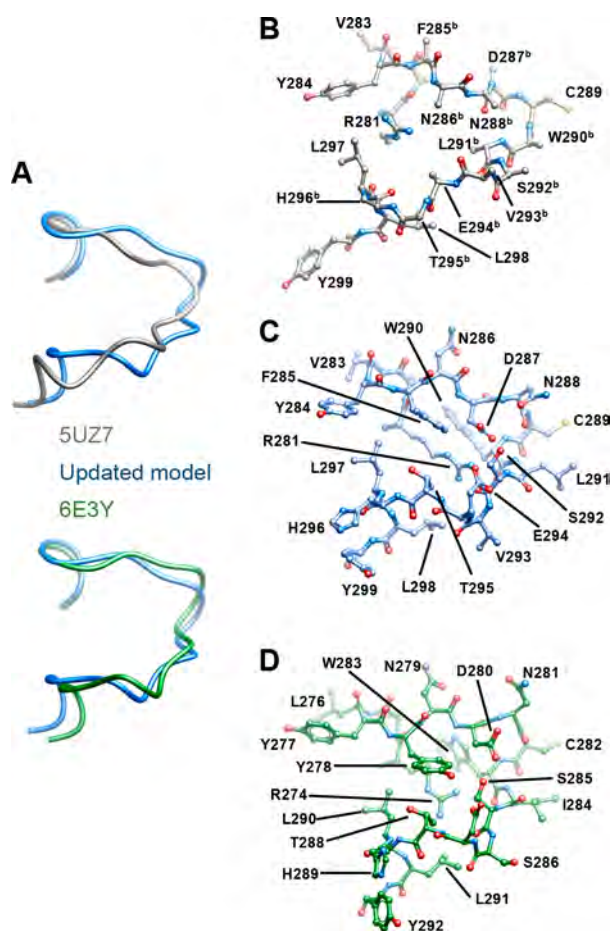


Figure 5. Modeling of CTR ECL2 in the active state complex. (A) Comparison of the backbone of CTR and CLR ECL2 in the original model (PDB SUZ7, gray), the current CTR model (blue) and CLR of the CGRP receptor (PDB 6E3Y, green). (B) CTR ECL2 from PDB SUZ7. (C) New model of CTR ECL2 from the reprocessed map. (D) CLR from ECL2 (PDB 6E3Y). The EM density for ECL2 is shown in Supplementary Figure 2.

Y372^{7,38} at the boundary of ECL3, while Thr6^P forms a H-bond with H302^{5,40} (Figure 6C,D); the latter is consistent with previously predicted interaction between these residues,¹ and is also conserved between CGRP Thr6^P and H^{5,40} of CLR in the CGRP receptor.¹⁵ Ser2^P forms a H-bond with the hydroxyl of Y299^{5,37}, while the backbone nitrogen of Cys1^P is within H-bond distance of backbone atoms of T295^{ECL2} and V293^{ECL2}. The peptide N-terminal loop formed only limited interaction with ECL2, including hydrophobic interactions with L298^{ECL2} and V293^{ECL2}. This is in agreement with the limited effect of mutations within ECL2 on the binding affinity of CT peptides.¹¹ As previously predicted from the available density, sCT displays an amphipathic α -helix from Val8^P–Leu19^P, and the hydrophobic face forms an extended interface, principally with hydrophobic residues of TM1 and TM7 (Figure 6A,B,D). In the current model Gln14^P is within H-bond distance of E294^{ECL2}; however, there was little density for the peptide side-chain, indicating that it is mobile and is likely to form only weak, transient interactions. Within the peptide, there was very little interaction with ECL1 residues and this was limited to weak hydrophobic interaction with H201^{ECL1} (Ser13^P) and V205 (His17^P) (Figure 6D). There were additional interactions between the C-terminal extension of the peptide helix

that bind within the receptor core and the TM1 stalk; however, there was only limited density for the receptor in this region of the map, likely due to averaging of the signal from the large number of particles, suggesting that this is likely to an area of mobility in the agonist-receptor complex.

Importance of the CTR Extracellular Surface on Receptor Function. In addition to the TM1 stalk, ECL1 was still poorly resolved in the new map and could not be directly modeled. To gain further insight into the importance of the extracellular surface of the receptor in the binding and activation of the receptor by different CT and related peptide agonists, we performed alanine scanning of ECL1 (H201–C219) and the TM1 stalk (S129–L151), and analyzed each of the mutants for cell surface expression (Figure 7, Table 1), binding affinity in competitive radioligand binding assays (Figure 8, Supplementary Figures 3–6, Table 1), and functional response (cAMP formation and ERK1/2 phosphorylation) for each peptide (Figures 10, 11, 13, and 14, Supplementary Figures 7–16, Tables 2 and 3). The results of these experiments were combined with our previously published mutagenesis of ECL2 and ECL3¹¹ and mapped onto the revised structure of the sCT:CTR:Gs complex (Figures 9, 12 and 15). In this revised structure, residues and side-chains with no visible density in the cryo-EM map were independently modeled into the available structure, and the receptor ECD and the far peptide C-terminus rigid body fit into the map. This full-length structure was subjected to a short MD simulation (200 ns) to resolve energetically unfavorable interactions and yield the model used to visualize the data (Figures 9, 12, and 15).

Receptor Expression. Cell surface expression was assessed by antibody binding to the c-Myc tag incorporated at the far N-terminus of the receptor and analyzed by FACS. Only C134^{ECD}A in the TM1 stalk, and C219^{3,29}A in ECL1 had marked negative impact on receptor expression (<20% of WT) at the cell surface. Increased expression was seen with alanine mutants of S129^{ECD}, Y131^{ECD}, F137^{1,28}, E140^{1,31}, K141^{1,32}, L142^{1,33}, N144^{1,35}, Y146^{1,37}, V147^{1,38}, Y149^{1,40}, and Y150^{1,41}, in the TM1 stalk (Figure 7 upper panel, Table 1). There was a more limited effect on ECL1 with a small decrease in expression of the H201^{2,67}A mutant and increased expression of the L202^{2,68}, P207^{ECL1}, E209^{ECL1}, V212^{ECL1}, P216^{3,26}, and S218^{3,28} to alanine mutants (Figure 7 lower panel, Table 1, Figure 9B).

Peptide Affinity (Competition Binding). The impact on peptide affinity was assessed by competition with ¹²⁵I-sCT_(8–32) binding. In this assay, amylin and CGRP were not evaluated due to limited competition for binding over the concentrations used (up to 1 μ M). Within the TM1 stalk, affinity for the poorly expressed C134^{ECD}A mutant could not be assessed. There was also insufficient robustness to determine pK_i values for the N135^{ECD}A mutant for sCT_(8–32) and hCT, and the Y131^{ECD}A mutant for hCT and sCT_(8–32) (Figure 8, Table 1). Of the mutants where a robust inhibition curve could be derived, none significantly altered sCT pK_i (Figure 8B, Table 1, Supplementary Figure 4A–D). There was reduced pK_i of sCT_(8–32) for alanine mutants of S129^{ECD}, Y131^{ECD}, L142^{1,33}, Y146^{1,37}, L148^{1,39}, Y150^{1,41}, and L151^{1,42} (Figure 8A, Table 1, Supplementary Figure 3A–D). Reduced hCT pK_i was observed for all mutants that affect sCT_(8–32), but reduced affinity was also seen with the M133^{ECD}, T138^{1,29}, K141^{1,32}, K143^{1,34}, and Y149^{1,40} to alanine mutants (Figure 8C, Table 1,

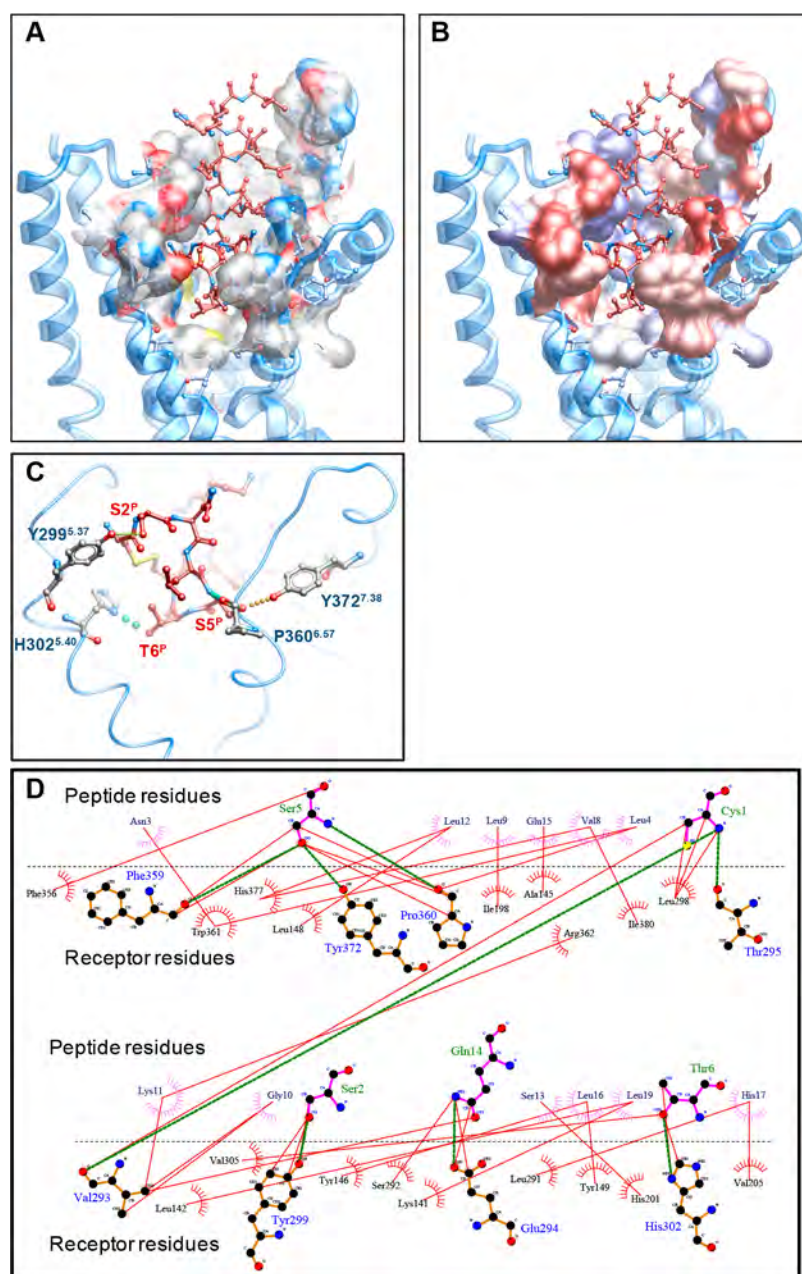


Figure 6. Modeling of sCT binding to the CTR core. Panels A and B illustrate the CTR binding surface colored according to atom type (A) or hydrophobicity (B) in ICM. The receptor ECD has been omitted for clarity. (C) Key hydrogen-bond interactions between the sCT N-terminus and CTR (H-bonds are differentially colored and sized in ICM according to bond strength). (D) Summary of the peptide-receptor interface calculated and displayed by LigPlot+. Green lines illustrate H-bonds. Red lines illustrate hydrophobic interactions. The extension of hydrophobic interaction from each residue is also displayed (sCT, pink; CTR, red).

Supplementary Figure 5A–D). There was greater impact of mutations to ECD proximal residues on pCT pK_i with reductions in affinity observed for all residues from 129^{ECD}–138^{1,29}. Of the remaining mutants, only alanine mutants of K141^{1,32}, L142^{1,33}, L148^{1,39}, and Y149^{1,40} reduced pCT affinity (Figure 8D, Table 1, Supplementary Figure 6A–D). Within ECL1, there was very little impact on peptide pK_i , with the exceptions being V20S^{ECL1A} for sCT_(8–32) and pCT, and L202^{2,68A} for hCT (Figure 8E–H, Supplementary Figures 3E–H to 6E–H). The poorly expressed C219^{3,29A} was not assessed due to insufficient response in the concentration range assessed.

While there was only limited effect on binding pK_i for sCT and sCT_(8–32), mapping of the mutational data for effect on peptide pK_i for both the current study and previous work on ECL2 and ECL3¹¹ revealed that the loss of affinity for hCT and pCT was principally associated with amino acids that formed the interface between the peptide and receptor in the model. This was particularly true for amino acids along the hydrophobic interface of TM1 and TM7, and proximal residues of ECL3 (Figure 9E,F). Of note, the extension of the TM1 stalk (S129^{ECD}–N135^{ECD}) resides within receptor ECD, with C134^{ECD} forming a disulfide bond to C95^{ECD}, and this is one of three conserved ECD disulfide bonds seen in class B GPCRs³. Moreover, S129^{ECD}–Y131^{ECD} forms back-

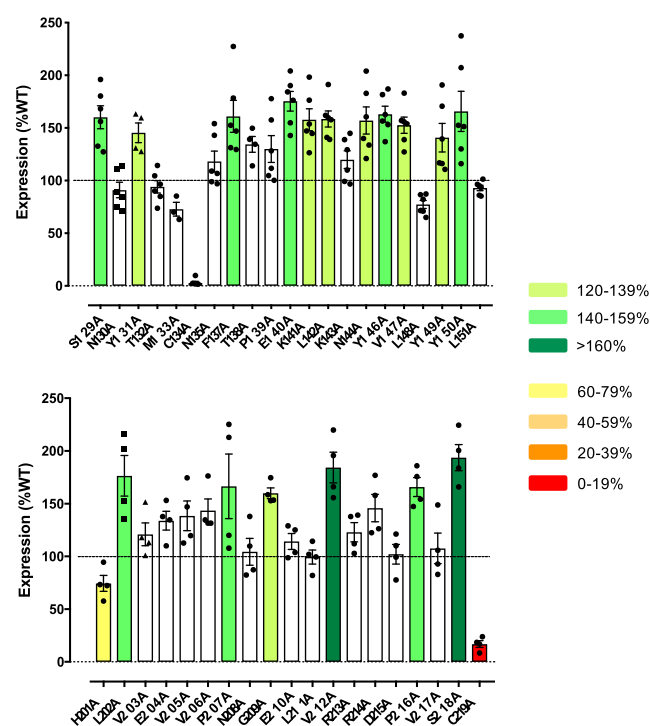


Figure 7. Effect of alanine mutation on the cell surface expression of the CTR. (Upper panel) Effect of alanine mutation of the TM1 stalk on CTR expression monitored by FACS of anti-c-Myc antibody binding to the N-terminal c-Myc epitope on the receptor. (Lower panel) Effect of alanine mutation of ECL1. Data are normalized to the expression of the wild-type (WT) receptor (100%). Significant differences in the level of cell surface expression were determined by one-way ANOVA followed by Dunnett's post-test comparison to the WT. $P < 0.05$ was used to denote significance (marked by an asterisk), and colored according to the magnitude of change. Individual experimental "n" are shown within the bars.

bone H-bond interactions with the C-terminal Pro-NH₂ of sCT¹⁸ and, presumptively, related CT peptides likely underlie the importance of the integrity of this region of the receptor. Interestingly, in contrast to other class B GPCRs such as the glucagon-like peptide-1 receptor (GLP-1R), there was a lesser impact of alanine mutation of residues of ECL2 that likely reflects the limited role of ECL2 side-chains in the peptide binding interface. Intriguingly, the mutations had only limited impact on the pK_i of sCT (Figure 9D) or sCT_(8–32) (Figure 9C), and this likely reflects the tighter binding of the teleost peptide^{8,10,19} such that the individual receptor mutation has limited effect on the overall affinity.

Functional Affinity. Concentration response curves were established for each of the peptides in functional assays of cAMP accumulation and ERK1/2 phosphorylation (Supplementary Figures 7–16), and data were analyzed using the operational model for agonism to derive pathway specific estimates of functional affinity (pK_A) and efficacy (tau) (Figures 10, 11, 13, and 14, Tables 2 and 3). The latter was corrected for differences in cell surface expression.

The alanine mutation had only limited significant effect on pK_A estimates from cAMP accumulation experiments across the TM1 stalk and ECL1 (Figure 10, Table 2). While there were trends toward significant effects for a number of mutants, only the following achieved statistical significance. For sCT there was reduced pK_A for N130^{ECD}A, while for hCT significant reductions were seen for N130^{ECD}A, Y131^{ECD}A,

M133^{ECD}A, and Y149^{1.40}A in the TM1 stalk and L202^{2.68}A and V205^{ECL1}A for ECL1. For pCT, reductions in pK_A were seen for the N130^{ECD}A and M133^{ECD}A mutants in the TM1 stalk and V205^{ECL1}A in ECL1. The data for amylin and CGRP had higher variance. Of these, the only statistically significant effect was for amylin with the M133^{ECD}A mutant in the TM1 stalk.

Because of the weak response of amylin and CGRP in stimulation of pERK, only limited data sets could be fitted with the operational model (Table 3). For the CT peptides, a significant decrease in pK_A was observed for sCT for the N130^{ECD}A mutant, although there were trends toward an effect for other mutants in the TM1 stalk (Figure 11, Table 3), with no effect of ECL1 mutants. For hCT, there was insufficient robustness in response to determine pK_A for the N130^{ECD}A mutant, with significant loss of pK_A for Y131^{ECD}A, L142^{1.33}A, Y146^{1.37}A, and Y149^{1.40}A in the TM1 stalk, and L202^{2.68}A, V205^{ECL1}A, P207^{ECL1}A, G209^{ECL1}A, and V212^{ECL1}A in ECL1. There was greater variance in the data for pCT where many alanine mutants trended toward reduced pK_A, of which only E140^{1.31}A and L142^{1.33}A achieved statistical significance. Only the P207^{ECL1}A mutation within ECL1 significantly reduced pK_A (Figure 11, Table 3).

Mapping of the data onto the 3D receptor model demonstrated parallels between the observed effect of mutation on cAMP pK_A and pK_i from binding assays for each of the CT peptides (Figures 9 and 12), which is consistent with Gs coupling being the primary signaling pathway for these peptides and the allosteric influence of Gs on binding of hCT and sCT¹⁰. Of note, sCT binding is effectively insensitive to the effects of excess guanine nucleotide,^{8,19} and this is reflected in the limited effect of mutation on pK_i and functional pK_A. Interestingly, the pattern of effect of mutation on pERK pK_A was distinct including a lesser effect of mutation within ECL3, and this was most evident for hCT where ECL1 appeared to have an extended role in the functional affinity for this pathway (Figure 12). This likely reflects differences in the coupling pathways downstream of receptor activation by different CT peptides, as has been previously observed.^{9,10,20}

The Molecular Control of Efficacy. The efficacy parameter tau from the operational model provides a measure for pathway coupling efficiency relating the number of receptors occupied to response.²¹ Within the TM1 stalk, the effect of alanine mutation on cAMP accumulation efficacy was similar across the CT peptides with an enhancement of efficacy (or trend toward this) seen with residues proximal to the interaction site of Pro³²-NH₂ of sCT in the structure (Figure 13, Table 2). However, mutation of most other residues had no effect. The exception to this was a significant loss of efficacy for hCT with the Y150^{1.41}A mutant, and a small enhancement of pCT efficacy with the L151^{1.42}A mutant. The pattern of effect was similar for amylin, but with V147^{1.38}A and Y149^{1.40}A exhibiting reduced efficacy within the distal (TM1) residues. The effect on CGRP cAMP efficacy was distinct with most mutations either decreasing efficacy or trending toward lower efficacy. The exception to this was the N130^{ECD}A mutant that, like the other peptides, led to increased efficacy (Figure 13, Table 2). Loss of interaction of the peptide C-terminus with the ECD would be predicted to increase mobility of the ECD and peptide suggesting that receptor–ligand dynamics contribute to the control of cAMP efficacy (presumably affecting Gs coupling). Interestingly, whereas alanine mutagenesis was generally less impactful on sCT binding and function, ECL1 alanine mutation had the greatest impact on

Table 1. Effect of Single Alanine Mutation in the CTR TM1 Stalk or ECL1 on Binding Affinity (pK_i) of CT Peptides Derived from Competition Binding Isotherms, And Receptor Cell Surface Expression^a

	sCT pK_i	hCT pK_i	pCT pK_i	sCT(8–32) pK_i	FACS (% of WT)
WT	9.57 ± 0.13 (7)	6.97 ± 0.13 (7)	8.08 ± 0.13 (8)	9.20 ± 0.06 (9)	100.0 ± 3.3 (8)
S129A	9.15 ± 0.19 (6)	5.72 ± 0.10* (5)	7.06 ± 0.12* (6)	8.44 ± 0.04* (5)	160.1 ± 26.9* (6)
N130A	8.98 ± 0.20 (6)	N.D.	7.32 ± 0.28* (6)	N.D.	91.0 ± 18.0 (6)
Y131A	N.D.	N.D.	7.08 ± 0.42* (5)	N.D.	145.4 ± 18.7* (4)
T132A	9.67 ± 0.06 (4)	6.66 ± 0.21 (5)	7.09 ± 0.18* (5)	8.86 ± 0.08* (4)	94.0 ± 14.4 (6)
M133A	9.73 ± 0.11 (4)	6.14 ± 0.07* (5)	6.95 ± 0.19* (5)	8.99 ± 0.07 (4)	72.7 ± 11.3 (3)
C134A	N.D.	N.D.	N.D.	N.D.	2.6 ± 4.0* (6)
N135A	N.D.	N.D.	N.D.	N.D.	118.1 ± 24.2 (6)
F137A	9.24 ± 0.21 (6)	6.52 ± 0.13 (5)	6.74 ± 0.13* (5)	9.06 ± 0.07 (4)	161.0 ± 37.0* (6)
T138A	9.21 ± 0.25 (5)	6.21 ± 0.14* (4)	6.94 ± 0.16* (5)	9.46 ± 0.10 (4)	134.3 ± 15.0 (4)
P139A	9.57 ± 0.13 (5)	6.50 ± 0.10 (4)	7.76 ± 0.06 (4)	9.26 ± 0.07 (4)	130.0 ± 31.3 (6)
E140A	9.64 ± 0.10 (4)	6.60 ± 0.07 (5)	7.89 ± 0.10 (5)	8.84 ± 0.10* (4)	175.4 ± 22.9* (6)
K141A	9.38 ± 0.12 (5)	6.22 ± 0.13* (4)	7.25 ± 0.10* (4)	8.85 ± 0.10* (4)	157.8 ± 25.5* (6)
L142A	9.41 ± 0.05 (4)	6.19 ± 0.04* (4)	7.24 ± 0.06* (4)	8.39 ± 0.07* (4)	158.4 ± 18.8* (6)
K143A	9.60 ± 0.11 (5)	6.41 ± 0.10* (5)	7.75 ± 0.18 (5)	8.93 ± 0.10 (4)	119.8 ± 20.7 (6)
N144A	9.47 ± 0.10 (4)	6.46 ± 0.06 (4)	7.84 ± 0.04 (4)	9.05 ± 0.11 (4)	157.0 ± 31.7* (6)
Y146A	8.98 ± 0.32 (5)	5.78 ± 0.14* (5)	7.43 ± 0.14 (4)	7.96 ± 0.13* (4)	162.9 ± 18.6* (6)
V147A	9.66 ± 0.04 (4)	6.58 ± 0.10 (5)	7.94 ± 0.15 (5)	9.13 ± 0.05 (4)	152.6 ± 18.9* (6)
L148A	9.41 ± 0.27 (5)	5.75 ± 0.22* (5)	7.16 ± 0.13* (5)	8.67 ± 0.14* (5)	77.2 ± 9.3 (6)
Y149A	9.60 ± 0.07 (4)	5.18 ± 0.21* (5)	7.32 ± 0.07* (4)	8.72 ± 0.09* (4)	140.7 ± 33.1* (6)
Y150A	9.60 ± 0.06 (4)	5.99 ± 0.06* (4)	7.55 ± 0.06 (4)	8.48 ± 0.04* (4)	165.7 ± 46.9* (6)
L151A	9.59 ± 0.06 (4)	6.27 ± 0.04* (5)	7.92 ± 0.08 (5)	8.73 ± 0.05* (4)	92.9 ± 6.3 (6)
WT	9.73 ± 0.07 (5)	6.78 ± 0.21 (5)	7.83 ± 0.18 (5)	9.20 ± 0.12 (5)	100 ± 2.0 (6)
H201A	9.41 ± 0.22 (4)	6.53 ± 0.09 (4)	8.20 ± 0.12 (4)	9.27 ± 0.22 (4)	74.5 ± 15.2* (4)
L202A	9.45 ± 0.06 (4)	5.75 ± 0.36* (5)	7.50 ± 0.16 (4)	8.87 ± 0.10 (4)	176.4 ± 38.5* (4)
V203A	9.60 ± 0.07 (4)	6.46 ± 0.19 (4)	7.55 ± 0.17 (4)	8.99 ± 0.12 (4)	120.9 ± 21.6 (4)
E204A	9.55 ± 0.17 (4)	6.69 ± 0.18 (5)	7.79 ± 0.11 (4)	9.26 ± 0.09 (4)	133.9 ± 17.8 (4)
V205A	9.62 ± 0.16 (4)	6.14 ± 0.38 (3)	6.66 ± 0.17* (5)	8.27 ± 0.22* (5)	138.5 ± 28.2 (4)
V206A	9.59 ± 0.07 (4)	7.24 ± 0.31 (4)	7.54 ± 0.14 (4)	8.78 ± 0.10 (4)	143.5 ± 21.9* (4)
P207A	9.61 ± 0.11 (4)	6.71 ± 0.13 (5)	7.37 ± 0.18 (4)	8.97 ± 0.22 (4)	166.5 ± 61.1* (4)
N208A	9.52 ± 0.09 (5)	6.44 ± 0.15 (5)	7.02 ± 0.13 (4)	8.81 ± 0.22 (4)	104.4 ± 25.4 (4)
G209A	9.60 ± 0.11 (4)	6.46 ± 0.22 (5)	7.79 ± 0.16 (4)	9.01 ± 0.17 (4)	159.9 ± 10.2* (4)
E210A	9.39 ± 0.19 (4)	6.89 ± 0.08 (4)	7.69 ± 0.12 (4)	8.89 ± 0.26 (4)	114.2 ± 15.1 (4)
L211A	9.66 ± 0.09 (4)	5.92 ± 0.16 (3)	6.94 ± 0.04 (4)	8.78 ± 0.19 (4)	99.5 ± 13.4 (4)
V212A	9.70 ± 0.06 (4)	6.32 ± 0.17 (4)	7.89 ± 0.10 (4)	9.25 ± 0.20 (4)	184.3 ± 29.1* (4)
R213A	9.74 ± 0.18 (4)	6.41 ± 0.29 (5)	7.52 ± 0.30 (5)	8.98 ± 0.11 (4)	123.0 ± 18.3 (4)
R214A	9.65 ± 0.09 (4)	7.15 ± 0.18 (4)	7.76 ± 0.16 (4)	9.28 ± 0.12 (4)	145.9 ± 26.1 (4)
D215A	9.51 ± 0.08 (4)	6.12 ± 0.10 (5)	7.39 ± 0.17 (4)	8.73 ± 0.07 (4)	102.1 ± 18.6 (4)
P216A	9.58 ± 0.05 (4)	6.14 ± 0.11 (4)	7.43 ± 0.12 (4)	8.88 ± 0.14 (4)	165.8 ± 18.0* (4)
V217A	9.54 ± 0.05 (4)	6.81 ± 0.19 (5)	7.85 ± 0.11 (4)	9.32 ± 0.21 (4)	107.6 ± 29.0 (4)
S218A	9.44 ± 0.05 (4)	6.28 ± 0.23 (5)	7.55 ± 0.11 (4)	9.06 ± 0.13 (4)	193.6 ± 24.9* (4)
C219A	N.D.	N.D.	N.D.	N.D.	16.9 ± 6.4* (4)

^a pK_i values were derived for each ligand and mutant receptor from analysis of either homologous (sCT(8–32)) or heterologous (sCT, hCT, pCT) competition of [¹²⁵I]-sCT(8–32) binding. Cell surface receptor expression was determined by FACS using an anti-c-myc antibody, and normalized to WT expression and expressed as %WT. All values are mean ± S.E.M. (independent “*n*” values are indicated within parentheses). Significance of changes in receptor expression, or pK_i of each ligand, was determined by comparison of mutant receptors to WT values by a one-way ANOVA and Dunnett’s post-test ($p < 0.05$ represented by an asterisk (*)). N.D. denotes affinity not determined as robust radioligand binding was not detected.

sCT-mediated cAMP efficacy with significantly decreased efficacy seen for E204^{2,70}A, V206^{ECL1}A, P207^{ECL1}A, G209^{ECL1}A, V212^{ECL1}A, R214^{ECL1}A, P216^{3,26}A, and S218^{3,28}A. Of note, within ECL1 only H201^{2,67} and V205^{ECL1} are in direct contact with sCT (Figure 6D), implying that ECL1 is likely to be important for propagation of conformational change linked to cAMP (Gs) efficacy for this peptide. For hCT, the distal V212^{ECL1}A, R214^{ECL1}A, and S218^{3,28}A also impacted cAMP efficacy, as well as L202^{2,68}A. Both V212^{ECL1}A and R214^{ECL1}A were also important for pCT efficacy, with only P207^{ECL1}A achieving significance for reduced efficacy (Figure 13, Table

2). ECL1 alanine mutations had lesser overall impact on amylin and CGRP efficacy with only L202^{2,68}A (both peptides), V212^{ECL1}A (amylin) and P216^{3,26}A/Ser218^{3,28}A (CGRP) causing significant reductions in efficacy (Figure 13, Table 2).

As described above, the weak pERK response meant that only a limited subset of mutants could be robustly fitted with the operational model for amylin and CGRP (Table 3). For the CT peptides, the pattern of effect of alanine mutation on pERK efficacy was generally distinct from that observed for cAMP efficacy (Figures 13–15, Table 3). Loss of efficacy was

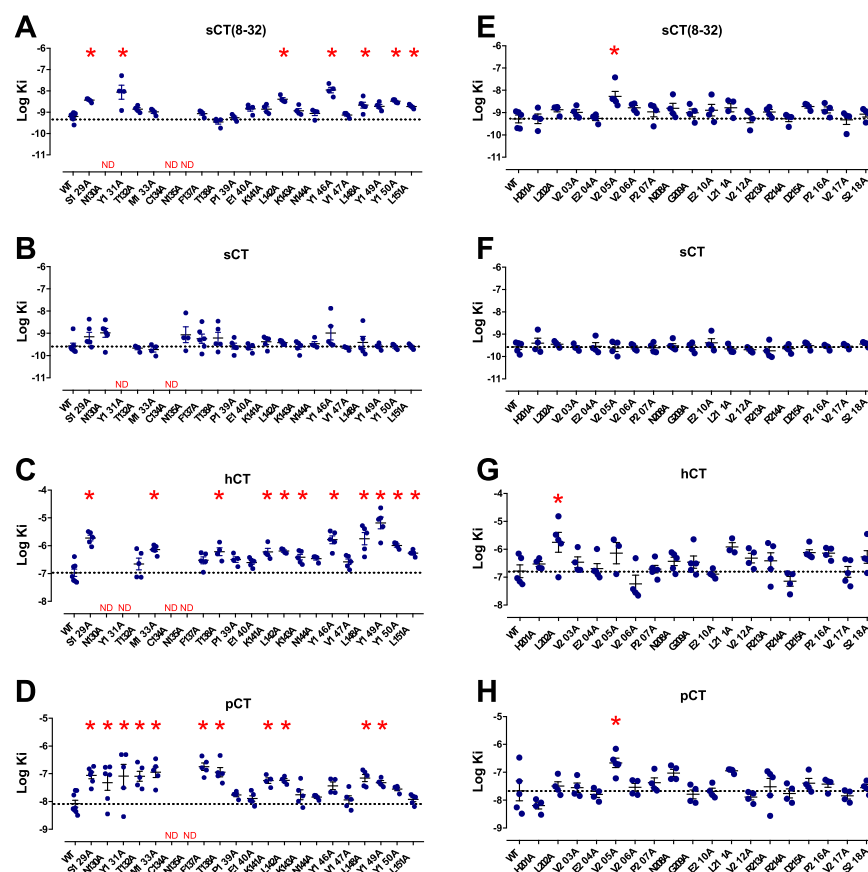


Figure 8. Alanine mutation of the TM1 stalk and ECL1 of the CTR selectively alters peptide affinity. For each receptor mutant and ligand, competition binding curves were established and $\log K_i$ determined: (A) effect of TM1 stalk mutants on sCT_(8–32) $\log K_i$; (B) effect of TM1 stalk mutants on sCT $\log K_i$; (C) effect of TM1 stalk mutants on hCT $\log K_i$; (D) effect of TM1 stalk mutants on pCT $\log K_i$; (E) effect of ECL1 mutants on sCT_(8–32) $\log K_i$; (F) effect of ECL1 mutants on sCT $\log K_i$; (G) effect of ECL1 mutants on hCT $\log K_i$; (H) effect of ECL1 mutants on pCT $\log K_i$. Significance of changes was established by comparison of the WT to the other receptor mutants in a one-way ANOVA and Dunnett's post-test to determine $\log K_i$ values with significant changes ($P < 0.05$) denoted by an asterisk (*). N.D., functional affinity not determined. Individual “n” values are shown. The dotted line is the WT mean.

observed for N130^{ECD}A for all peptides and Y131^{ECD}A for sCT and pCT. There was loss of efficacy of the T138^{1.29}A mutant for sCT and hCT but not pCT, and of E140^{1.31}A for sCT and pCT, whereas there was increased hCT efficacy of this mutant, together with selective enhancement of hCT efficacy with P139^{1.30}A. Similarly, there was enhanced efficacy for K141^{1.32}A and L142^{1.33}A for sCT and pCT, with no effect on hCT efficacy. In the distal segment, peptide-specific effects were observed although the trend for pCT followed that of sCT with enhanced efficacy for Y146^{1.37}A (trend for pCT) and V147^{1.38}A and decreased efficacy for L151^{1.42}A (trend for pCT). The effect of mutation was distinct for hCT with decreased efficacy for Y146^{1.37}A (and a trend toward a decrease for V147^{1.38}A). There was also selective increased efficacy of L148^{1.39}A and decreased efficacy of Y149^{1.40}A for hCT (Figure 14, Table 3). Within ECL1, there was increased efficacy of E204^{2.70}A and R213^{ECL1}A for all peptides, with selectively increased efficacy of D215^{3.25}A and V217^{3.27}A for hCT, and H201^{2.67}A and E210^{ECL1}A for pCT. For all three peptides, there was a trend toward decreased efficacy of the V205^{ECL1}A mutant, but this was only significant for hCT (Figure 14, Table 3).

Mapping of all alanine mutants of the extracellular surface of the CTR on peptide efficacy revealed both commonalities and distinctions in how peptides engage with the receptor and

propagate efficacy (Figure 15). As reported previously,¹¹ mutations of residues in the core of ECL2 that contribute to packing of this loop have a general effect to enhance cAMP efficacy, likewise for the CT peptides and amylin, there is a common effect to increase efficacy of mutants within the ECD proximal to sCT Pro32-NH₂ in the structure, and also in the proximal end of ECL3 deep within TM6. In distinction to the other peptides, pCT exhibited increased efficacy with mutations that lined the TM1/TM7 interface and contrasted to the loss of functional affinity observed for this pathway for most of these mutants (Figures 12 and 15). Interestingly, mutation of ECL1 led to decreased cAMP efficacy, with greatest impact on sCT. Overall, with the exception of ECL1, the surface residues of the CTR act to constrain the activation of receptor for “Gs” coupling. Of note, a significant portion of ECL1 could not be modeled into the EM map due to lack of robust density, indicating that it has greater mobility than the rest of the receptor, potentially caused by lack of significant direct interactions with the peptide. For the purpose of mutation mapping, this segment of the receptor was modeled based on ECL1 of the CGRP receptor that forms a short α -helix¹⁵ and disruption of secondary structure of this loop could potentially contribute to the negative effects on cAMP efficacy observed for the CT peptides. Intriguingly, deletion of V205^{ECL1} within ECL1 of CLR causes marked loss of function

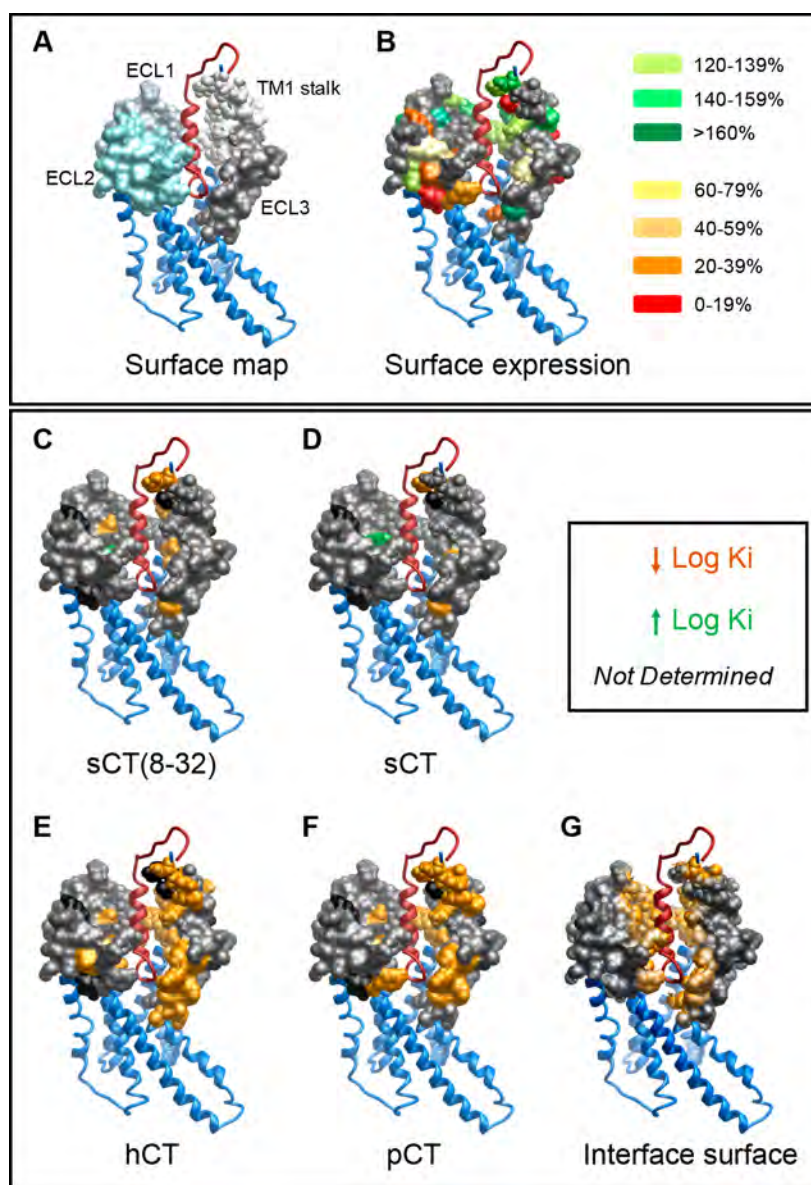


Figure 9. Identification of key amino acids of the CTR extracellular surface for peptide binding affinity ($\log K_i$): (A) top view of the active, sCT-bound, CTR model with the extracellular surface subject to alanine scanning depicted in gray (combined surface/cpk representation); (B) effect of mutation on cell surface receptor expression; (C–D,F) effect of mutation on CT peptide affinity ($\log K_i$); (C) sCT_(8–32); (D) sCT; (E) hCT; (F) pCT. Mutations that significantly alter peptide affinity are colored dark orange for decreased $\log K_i$, and green for increased $\log K_i$, with mutated amino acids without significant alteration to $\log K_i$ colored gray. sCT is shown as dark red, in ribbon representation. Amino acid mutations where there was an insufficiently robust functional effect to quantify by radioligand competition binding are depicted in black. (G) Illustration of the interaction surface for sCT (dark orange). The receptor ECD is not shown for clarity.

for the adrenomedullin (CLR:RAMP2) receptor,²² and this would be consistent with the importance of maintenance of secondary structure within ECL1.

In general, there were parallels between the effect of alanine mutation on CT peptide cAMP efficacy and that observed for amylin, albeit that there was more limited impact for the latter. In contrast, the effect on CGRP-dependent cAMP efficacy was generally distinct and this was evident for the mutations to the TM1 stalk (Figures 13 and 15) and previously published data on ECL3¹¹. In the recently solved CGRP receptor structure, the CLR ECD has a different orientation to that of the CTR, but the CGRP peptide C-terminal Phe37-NH₂ is located in a spatially equivalent position to the sCT C-terminus,¹⁵ where it interacts with residues at the RAMP1:CLR ECD interface

rather than the extension of the TM1 stalk that is observed for sCT. This may account for at least some of the differences in the impact of mutation to the CTR TM1 stalk on CGRP versus other peptide binding.

Remarkably, with minor exception, the effect of mutation of pPERK efficacy was “globally” in the opposite direction when compared to cAMP (Figure 15), albeit that the specific residues contributing enhanced or diminished efficacy were not necessarily equivalent. This is clearly seen for the effect of ECL1 mutation, and in the distinct patterns of effect on pPERK and cAMP efficacy for pCT and hCT (Figure 15). This suggests that the drivers of cAMP formation (presumptively Gs) and pPERK are quite distinct and appear to be associated with mutually exclusive conformations/conformational dynam-

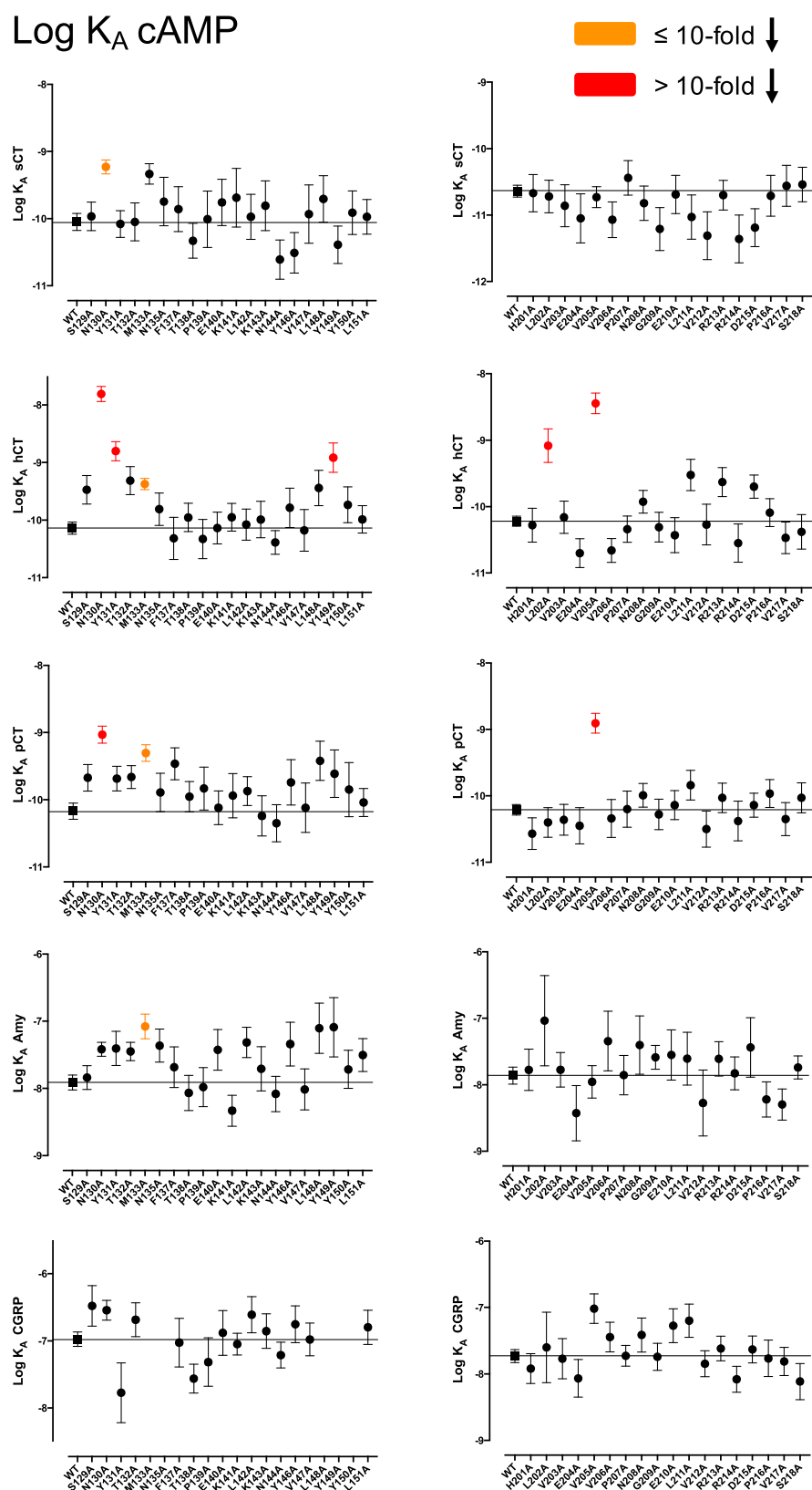


Figure 10. Alanine mutation of the TM1 stalk and ECL1 of the CTR alters cAMP functional affinity ($\log K_A$) in a peptide- and pathway-specific manner. Functional affinities derived from operational fitting of concentration–response curves in cAMP accumulation for alanine mutation of the TM1 stalk (LHS) and ECL1 (RHS) are displayed as Log K_A . Significance of changes was established by comparison of the WT to the other receptor mutants following one-way ANOVA and Dunnett's post-test with $P < 0.05$ accepted as significant. Mutants that gave significant reductions between 3- and 10-fold are colored orange, and those with reductions greater than 10-fold colored red. Where data were insufficiently robust to derive a reliable value for log K_A no symbol is shown.

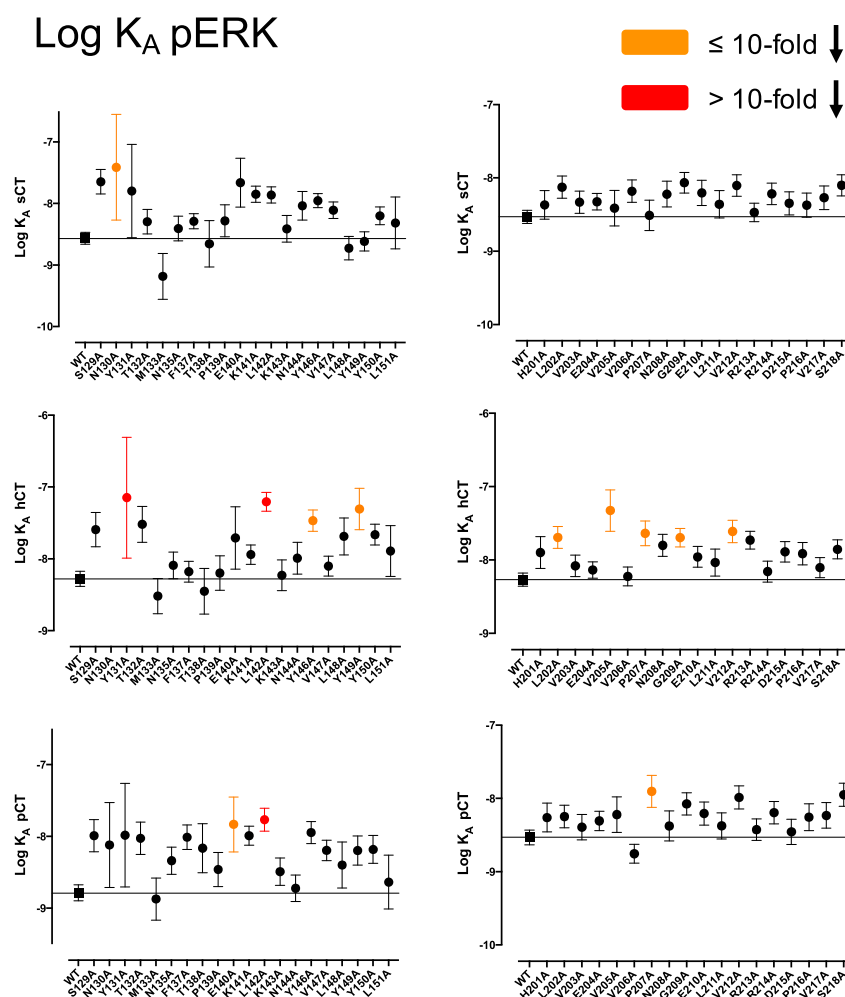


Figure 11. Alanine mutation of the TM1 stalk and ECL1 of the CTR alters pERK functional affinity ($\log K_A$) in a peptide- and pathway-specific manner. Functional affinities derived from operational fitting of concentration–response curves in pERK for alanine mutation of the TM1 stalk (LHS) and ECL1 (RHS) are displayed as Log K_A . Significance of changes was established by comparison of the WT to the other receptor mutants following one-way ANOVA and Dunnett's post-test with $P < 0.05$ accepted as significant. Mutants that gave significant reductions between 3- and 10-fold are colored orange, and those with reductions greater than 10-fold are colored red. Where data were insufficiently robust to derive a reliable value for log K_A no symbol is shown.

ics. Previous analysis of pathways linked to pERK for hCT provides support for this hypothesis, whereby pERK was independent of protein kinase A and $G_{i/o}$ pertussis toxin sensitive G proteins, but could be diminished by inhibition of phospholipase C and protein kinase C.²⁰ Unlike the GLP-1R, where β -arrestins are a significant contributor to pERK,²⁴ the native hCTR does not recruit arrestin,⁹ and as such the distinct pattern of effects on pERK are independent of β -arrestins.

Another striking feature of the pattern of effect of mutation on CT peptide efficacy is the major differences between the CTR and the related class B GPCR GLP-1R for which equivalent alanine scanning mutagenesis and operational analysis have been completed.²³ For this receptor, ECL2 is a major determinant of cAMP (Gs) signaling and mutation markedly attenuates peptide efficacy.^{23,24} Although this distinction has been noted previously,¹¹ the CTR ECL2 was modeled with distinct packing and W290^{ECL2} was modeled toward the peptide.^{1,11} The improved resolution obtained in the current study has enabled this loop to be accurately modeled for the first time, and it exhibits similar packing of the W290^{ECL2} and R281^{4.64} residues to that observed in the GLP-1R structure. The closest homologue of the CTR is the CLR

and there is very similar packing observed for ECL2 of both these receptors (Figure 6). While equivalent analysis to separate functional affinity and efficacy has not been performed on the CLR, alanine mutation of CLR in the context of the complex with RAMP1 to form the CGRP receptor is clearly associated with a loss of potency and/or E_{max} in cAMP signaling,¹⁵ even where expression is not changed. This suggests that ECL2 of CLR may have a more similar role to that of the GLP-1R than the more closely related CTR. Nonetheless, like CLR, the CTR can interact with each of the 3 RAMPs to form different amylin receptors.⁴ It is unclear if this would alter the role of ECL2 in propagation of conformational change linked to Gs coupling; however, in the CGRP:CLR:RAMP1:Gs structure, ECL2 of the CLR is partially stabilized by interactions of RAMP1.¹⁵ Mutations within ECL2 of CLR have distinct effects on cAMP production in the presence of different RAMPs, supporting the idea that ECL2 is capable of influencing Gs coupling²⁵ and that the importance of this domain for the CTR family of receptors may be dependent on the receptor/RAMP combination.

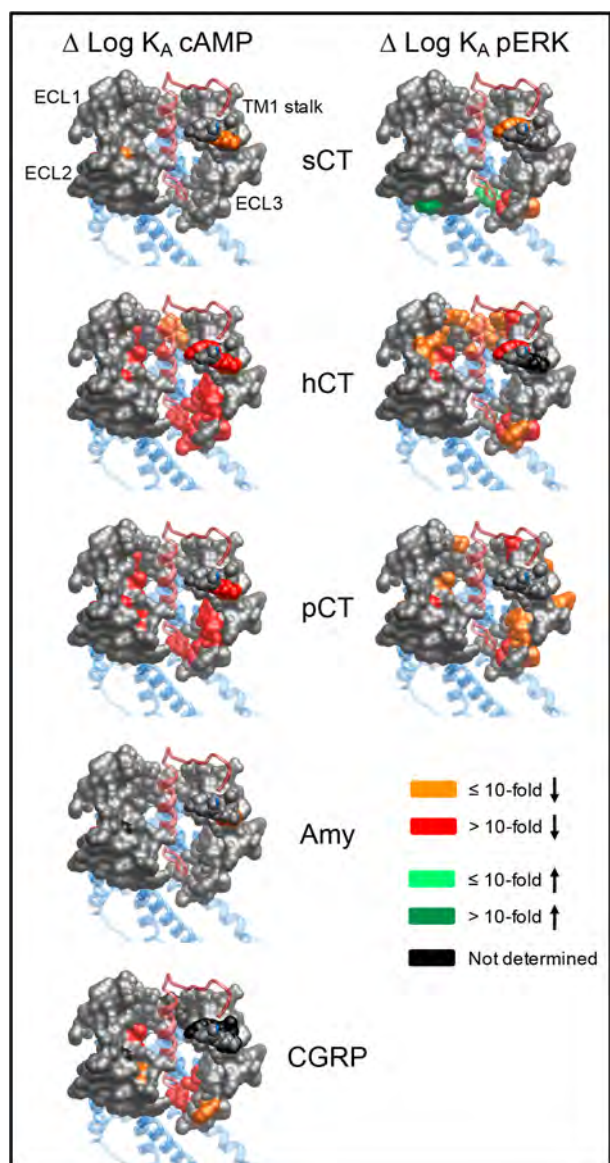


Figure 12. Alanine mutation of the extracellular surface of the CTR alters functional affinity ($\log K_A$) in a peptide- and pathway-specific manner. Functional affinities derived from operational fitting of concentration–response curves in cAMP accumulation (LHS) and pERK (RHS) are displayed as $\Delta \log K_A$ from wild-type. Illustrated is a top view of the active, sCT-bound, CTR model with the extracellular surface subject to alanine scanning depicted (combined surface/cpk representation). Mutations that significantly alter peptide functional $\log K_A$ are colored according to the magnitude of effect, with mutated amino acids without significant alteration to $\log K_A$ colored gray. sCT is shown as dark red, in ribbon representation. Amino acid mutations where there was an insufficiently robust functional effect to quantify by operational modeling are depicted in black. The receptor ECD is not shown for clarity.

CONCLUSION

In this study the enhanced resolution of the sCT:CTR:Gs structure has provided novel insights into the importance of the extracellular surface of the CTR in peptide-mediated binding and pathway-specific efficacy. It has confirmed the conservation of secondary structural elements of the ECL2 and highlighted distinctions in how different, related class B GPCRs may be activated. New mutational data on the TM1

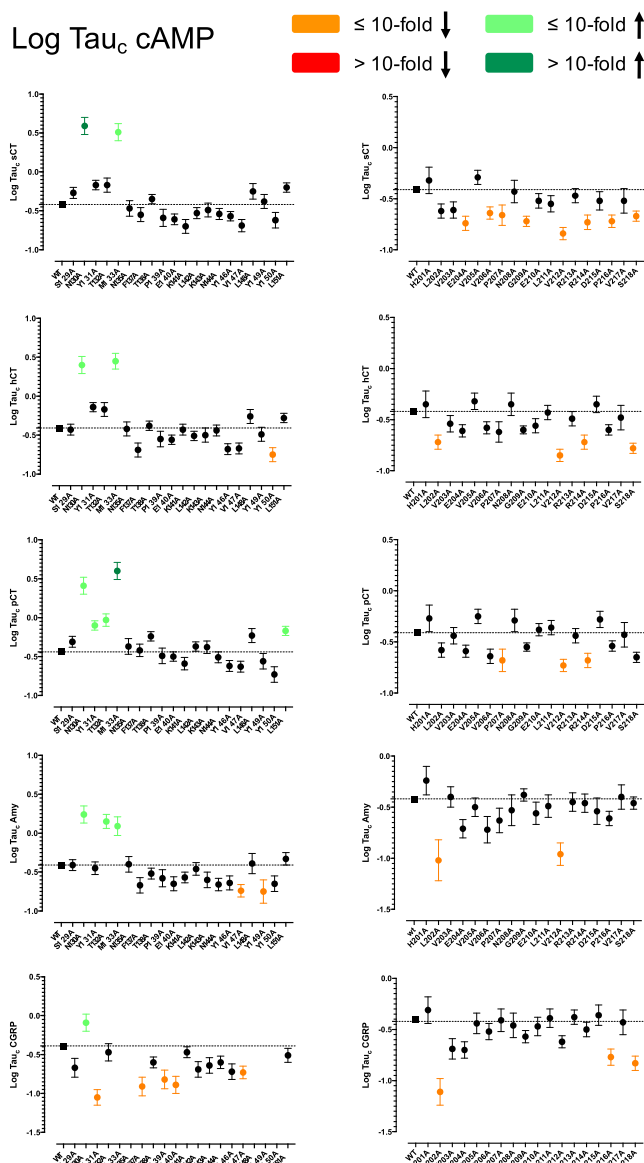


Figure 13. Alanine mutation of the TM1 stalk and ECL1 of the CTR alters peptide efficacy in cAMP accumulation assays. Efficacy (log tau) was derived from operational fitting of concentration–response curves in cAMP accumulation for alanine mutation of the TM1 stalk (LHS) and ECL1 (RHS) and are displayed as Log Tau_o, where calculated log tau values were corrected for changes to receptor cell surface expression to give log tau_c. Significance of changes to peptide efficacy was established by comparison of the WT to the other receptor mutants following one-way ANOVA and Dunnett’s post-test with $P < 0.05$ accepted as significant. Mutants that gave significant reductions between 3- and 10-fold are colored orange, and those with reductions greater than 10-fold colored red. Mutants that gave significant enhancements to efficacy between 3- and 10-fold are colored light green and those that enhanced efficacy >10-fold in dark green. Where data were insufficiently robust to derive a reliable value for log tau no symbol is shown.

stalk and ECL1 have also offered new knowledge of the distinct control of cAMP versus pERK signaling. Collectively, these data in conjunction with previous mutagenesis data have presented evidence that the conformations linked to the different signaling pathways are, in many ways, mutually exclusive. This work furthers our understanding of the complex

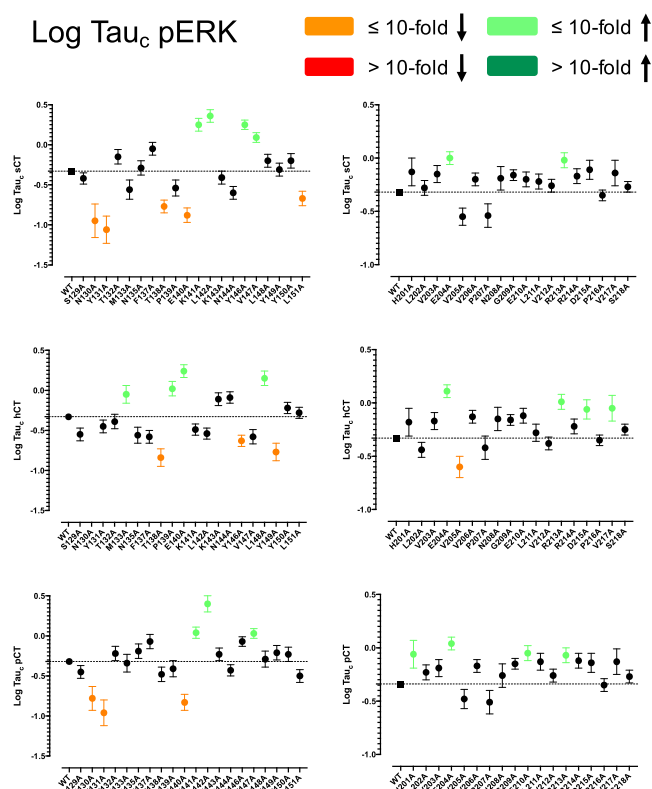


Figure 14. Alanine mutation of the TM1 stalk and ECL1 of the CTR alters peptide efficacy in pERK assays. Efficacy (log tau) was derived from operational fitting of concentration–response curves in pERK assays for alanine mutation of the TM1 stalk (LHS) and ECL1 (RHS), and are displayed as Log Tau_c, where calculated log tau values were corrected for changes to receptor cell surface expression to give log tau_c. Significance of changes to peptide efficacy was established by comparison of the WT to the other receptor mutants following one-way ANOVA and Dunnett's post-test with $P < 0.05$ accepted as significant. Mutants that gave significant reductions between 3- and 10-fold are colored orange. Mutants that gave significant enhancements to efficacy between 3- and 10-fold are colored light green. Where data were insufficiently robust to derive a reliable value for log tau no symbol is shown.

nature of signaling elicited by GPCRs and, in particular, that of the therapeutically important class B1 GPCR subfamily.

METHODS

Reagents. All peptides were purchased from Mimotopes. Dulbecco's Modified Eagle's Medium (DMEM) was purchased from Invitrogen. Foetal bovine serum (FBS) was purchased from Thermo Fisher Scientific. AlphaScreen reagents, Lance cAMP kit, and 384-well Optiplates were purchased from PerkinElmer. SureFire ERK1/2 reagents were obtained from TGR Biosciences and PerkinElmer. IP-One HTRF assay kit was from CisBio. Antibodies were purchased from R&D Systems and ThermoFisher. All other reagents were purchased from Sigma-Aldrich or BDH Merck and were of an analytical grade.

Mutagenesis. Desired mutations were introduced to N-terminally c-Myc tagged human CTR in pENTER11 (Invitrogen) via the Q5 High-Fidelity PCR Kit (New England Biolabs), then LR recombination reactions were conducted to transfer mutated and wild-type (WT) receptors into the pEF5/FRT/V5-DEST destination vector using Gateway Technology

(Invitrogen). The oligonucleotides for mutagenesis were purchased from Bioneer Pacific, and mutants were confirmed by automated-sequencing.

Stable Cell Line Generation and Cell Culture. The mutant or wild-type (WT) receptor genes were integrated into FlpIn-CV1 cells using Flp-In system (Invitrogen). Stable Flp-In expression cell lines were generated through polyclonal selection, screening and maintained in DMEM supplemented with 5% (v/v) FBS, 300 $\mu\text{g/mL}$ hygromycin B (Invitrogen) at 37 °C in 5% CO₂. Independent WT controls were established in parallel for the TM1 stalk and ECL1 mutants.

Whole Cell Competition Binding Assays. Radioligand competition binding was performed as previously described^{10,11} on whole cells seeded into 96-well plates and cultured overnight. For homologous competition binding experiments, cells were incubated overnight at 4 °C with ~ 100 pM ¹²⁵I-sCT_(8–32) (specific activity, 2000 Ci/mmol) and serial dilutions of noniodinated sCT_(8–32). For heterologous competition binding assays, cells were incubated overnight with the antagonist radioligand ¹²⁵I-sCT_(8–32), and serial dilutions of competing unlabeled peptide. Nonbound ligand was removed and bound ligand activity was measured using a γ counter (Wallac Wizard 1470 Gamma Counter, PerkinElmer, 78% counter efficiency). Values were normalized against nonspecific binding, defined by the presence of 1 μM of unlabeled sCT_(8–32), and total ligand bound radioligand.

Cell Surface Expression by FACS. Surface expression of c-Myc tagged CTR mutants stably expressed in CV-1 cells was quantified by flow cytometry using standard methods. Cells were grown in 6-well plates at $\sim 5 \times 10^5$ cells per well the day before assay. Cells were harvested in the presence of versene. All staining steps were conducted in ice cold Hank's Balanced Salt Solution (HBSS) with 0.1% bovine serum albumin (BSA) and 20 mM HEPES (4-(2-hydroxyethyl)-1-piperazineethanesulfonic acid, pH 7.4). Blocking was conducted in 5% BSA. Primary antibody staining was performed with 5 $\mu\text{g/mL}$ 9E10 (anti-c-Myc) antibody. The secondary antibody was 1 $\mu\text{g/mL}$ goat antimouse AF647 (ThermoFisher). Sytox blue was used for live/dead discrimination. Data were collected on a FACS CantosII (BD Biosciences) with at least 20 000 live cells collected per sample. WT stained CTR sample and stained parental CV-1 cells were collected at the beginning and the end of each run. Data were analyzed using FlowJo. The mean AF647 fluorescence intensity from each sample for a particular experiment was normalized against parental (0%) and WT CTR (100%) controls.

cAMP Accumulation Assay. Cells (2.5×10^4 cells/well) were seeded into 96-well plates and incubated overnight. Cells were stimulated with increasing concentrations of ligands for 30 min in the presence of 0.5 mM 3-isobutyl-1-methylxanthine (IBMX). The liquid was discarded, changed to absolute ethanol and volatilized to dryness at room temperature. Samples were then lysed and intracellular cAMP was detected using the PerkinElmer Lance kit as previously described.¹⁴ Data were normalized to the response of 100 μM forskolin.

ERK1/2 Phosphorylation. Cells (2.5×10^4 cells/well) were seeded into 96-well culture plates and incubated overnight. Initially, pERK1/2 time-course experiments were performed over 30 min to identify the time point when the pERK1/2 response is maximal (6–8 min). Subsequently, this time point was selected to generate concentration response for different agonists with ligand addition performed after overnight serum starvation. pERK1/2 was detected using an

Table 2. Effect of Single Alanine Mutation in CTR TM1 or ECL1 on cAMP Signalling Efficacy and Functional Affinity of CT-Family Peptides^a

	log(<i>τ</i>) sCT	hCT	pCT	rAmy	hαCGRP	pK _A sCT	hCT	pCT	rAmy	hαCGRP
WT	-0.33 ± 0.03 (23)	-0.33 ± 0.03 (23)	-0.32 ± 0.03 (21)	-0.42 ± 0.03 (25)	-0.23 ± 0.07 (25)	8.57 ± 0.10	8.28 ± 0.11	8.79 ± 0.11	7.57 ± 0.10	6.95 ± 0.19
S129A	-0.42 ± 0.07 (5)	-0.55 ± 0.08 (5)	-0.45 ± 0.08 (5)	-0.72 ± 0.09 (5)	N.D.	7.65 ± 0.20	7.59 ± 0.24	7.99 ± 0.22	7.33 ± 0.28	N.D.
N130A	-0.95 ± 0.21* (5)	N.D.	-0.78 ± 0.15* (5)	N.D.	-0.41 ± 0.19 (7)	7.41 ± 0.86*	N.D.	8.12 ± 0.59	N.D.	6.79 ± 0.50
Y131A	-1.06 ± 0.17* (3)	-0.45 ± 0.08 (3)	-0.96 ± 0.16* (3)	-0.77 ± 0.12 (3)	N.D.	7.80 ± 0.76	7.15 ± 0.84*	7.98 ± 0.72	7.21 ± 0.44	N.D.
T132A	-0.15 ± 0.09 (4)	-0.39 ± 0.09 (4)	-0.22 ± 0.09 (5)	N.D.	-0.61 ± 0.30 (5)	8.30 ± 0.20	7.52 ± 0.25	8.03 ± 0.23	N.D.	6.70 ± 0.88
M133A	-0.56 ± 0.12 (5)	-0.05 ± 0.11* (5)	-0.34 ± 0.11 (5)	-0.37 ± 0.12 (5)	-0.06 ± 0.15 (8)	9.19 ± 0.37	8.52 ± 0.25	8.87 ± 0.29	7.25 ± 0.28	6.89 ± 0.32
C134A	N.D.	N.D.	N.D.	N.D.	N.D.	N.D.	N.D.	N.D.	N.D.	N.D.
N135A	-0.29 ± 0.09 (4)	-0.56 ± 0.10 (5)	-0.19 ± 0.09 (5)	-0.69 ± 0.11 (5)	N.D.	8.41 ± 0.20	8.09 ± 0.19	8.34 ± 0.19	7.56 ± 0.31	N.D.
F137A	-0.05 ± 0.08 (5)	-0.58 ± 0.08 (5)	-0.07 ± 0.09 (4)	-0.60 ± 0.09 (5)	-0.86 ± 0.25 (4)	8.29 ± 0.12	8.18 ± 0.14	8.01 ± 0.17	7.49 ± 0.22	7.11 ± 0.89
T138A	-0.77 ± 0.08* (4)	-0.84 ± 0.11* (4)	-0.48 ± 0.09 (3)	-0.67 ± 0.08 (4)	-0.87 ± 0.27 (4)	8.66 ± 0.38	8.45 ± 0.32	8.16 ± 0.34	7.66 ± 0.29	7.18 ± 1.05
P139A	-0.54 ± 0.10 (5)	0.02 ± 0.09* (5)	-0.41 ± 0.10 (5)	-0.53 ± 0.10 (5)	-0.39 ± 0.26 (5)	8.28 ± 0.26	8.20 ± 0.24	8.46 ± 0.24	7.44 ± 0.23	6.43 ± 0.62
E140A	-0.88 ± 0.09* (5)	0.24 ± 0.08* (5)	-0.83 ± 0.10* (5)	N.D.	N.D.	7.66 ± 0.40	7.71 ± 0.43	7.83 ± 0.38*	N.D.	N.D.
K141A	0.25 ± 0.08* (4)	-0.49 ± 0.07 (5)	0.04 ± 0.07* (6)	N.D.	-0.20 ± 0.12 (6)	7.85 ± 0.13	7.94 ± 0.13	7.99 ± 0.13	N.D.	7.00 ± 0.30
L142A	0.36 ± 0.08* (4)	-0.54 ± 0.07 (5)	0.40 ± 0.10* (4)	-1.24 ± 0.22* (5)	N.D.	7.86 ± 0.13	7.21 ± 0.13*	7.77 ± 0.16*	7.01 ± 0.79	N.D.
K143A	-0.41 ± 0.08 (5)	-0.11 ± 0.08 (5)	-0.23 ± 0.08 (5)	-0.54 ± 0.09 (5)	-0.42 ± 0.19 (5)	8.41 ± 0.22	8.23 ± 0.21	8.49 ± 0.18	7.64 ± 0.23	6.80 ± 0.50
N144A	-0.60 ± 0.08 (5)	-0.09 ± 0.07 (5)	-0.43 ± 0.07 (6)	-0.72 ± 0.09 (5)	-0.87 ± 0.20 (5)	8.04 ± 0.23	7.99 ± 0.22	8.72 ± 0.18	7.44 ± 0.28	7.44 ± 0.79
Y146A	0.25 ± 0.06* (5)	-0.63 ± 0.07* (6)	-0.07 ± 0.06* (5)	-0.93 ± 0.11* (5)	N.D.	7.96 ± 0.11	7.47 ± 0.15*	7.95 ± 0.15	7.22 ± 0.41	N.D.
V147A	0.09 ± 0.06* (4)	-0.58 ± 0.09 (5)	0.03 ± 0.06* (5)	-0.63 ± 0.10 (5)	-0.47 ± 0.15 (6)	8.11 ± 0.13	8.10 ± 0.14	8.19 ± 0.14	6.85 ± 0.27*	6.83 ± 0.42
L148A	-0.20 ± 0.08 (5)	0.15 ± 0.09* (5)	-0.29 ± 0.10 (4)	-0.67 ± 0.11 (6)	-0.28 ± 0.16 (6)	8.73 ± 0.19	7.69 ± 0.26	8.40 ± 0.32	7.62 ± 0.38	7.02 ± 0.48
Y149A	-0.31 ± 0.08 (5)	-0.77 ± 0.11* (5)	-0.21 ± 0.09 (4)	-0.93 ± 0.12* (6)	N.D.	8.62 ± 0.16	7.31 ± 0.29*	8.20 ± 0.20	7.45 ± 0.41	N.D.
Y150A	-0.20 ± 0.09 (5)	-0.22 ± 0.07 (5)	-0.23 ± 0.09 (4)	-0.64 ± 0.10 (5)	-0.69 ± 0.16 (6)	8.20 ± 0.14	7.66 ± 0.14	8.18 ± 0.19	7.48 ± 0.23	7.27 ± 0.53
L151A	-0.67 ± 0.09* (5)	-0.28 ± 0.07 (5)	-0.50 ± 0.08 (4)	-0.88 ± 0.12* (5)	N.D.	8.32 ± 0.42	7.89 ± 0.35	8.64 ± 0.38	7.85 ± 0.51	N.D.
WT	-0.32 ± 0.02 (17)	-0.33 ± 0.02 (17)	-0.34 ± 0.03 (17)	-0.36 ± 0.04 (16)	-0.39 ± 0.08 (16)	8.53 ± 0.08	8.27 ± 0.09	8.53 ± 0.10	6.96 ± 0.11	6.91 ± 0.21
H201A	-0.13 ± 0.13 (4)	-0.18 ± 0.13 (3)	-0.06 ± 0.13* (4)	N.D.	N.D.	8.37 ± 0.17	7.90 ± 0.21	8.26 ± 0.19	N.D.	N.D.
L202A	-0.28 ± 0.07 (4)	-0.44 ± 0.07 (5)	-0.23 ± 0.07 (4)	N.D.	N.D.	8.13 ± 0.13	7.70 ± 0.14*	8.25 ± 0.15	N.D.	N.D.
V203A	-0.15 ± 0.08 (4)	-0.17 ± 0.08 (4)	-0.19 ± 0.08 (4)	N.D.	-0.64 ± 0.17 (4)	8.33 ± 0.13	8.08 ± 0.14	8.39 ± 0.17	N.D.	7.35 ± 0.56
E204A	0.00 ± 0.06* (5)	0.11 ± 0.06* (4)	0.04 ± 0.06* (4)	0.25 ± 0.09* (5)	-0.23 ± 0.11 (6)	8.33 ± 0.10	8.14 ± 0.11	8.31 ± 0.13	6.54 ± 0.13	7.06 ± 0.25
V205A	-0.55 ± 0.08 (4)	-0.60 ± 0.10* (4)	-0.48 ± 0.09 (4)	N.D.	N.D.	8.41 ± 0.21	7.34 ± 0.28*	8.22 ± 0.24	N.D.	N.D.
V206A	-0.20 ± 0.06 (4)	-0.13 ± 0.06 (4)	-0.17 ± 0.06 (5)	N.D.	N.D.	8.18 ± 0.13	8.23 ± 0.13	8.76 ± 0.13	N.D.	N.D.
P207A	-0.54 ± 0.11 (4)	-0.42 ± 0.11 (4)	-0.51 ± 0.11 (4)	N.D.	N.D.	8.51 ± 0.18	7.64 ± 0.16*	7.90 ± 0.21*	N.D.	N.D.
N208A	-0.19 ± 0.11 (4)	-0.15 ± 0.11 (4)	-0.26 ± 0.11 (4)	N.D.	-0.69 ± 0.19 (5)	8.22 ± 0.15	7.80 ± 0.15	8.38 ± 0.20	N.D.	7.53 ± 0.59
G209A	-0.16 ± 0.05 (4)	-0.16 ± 0.05 (4)	-0.15 ± 0.05 (4)	N.D.	N.D.	8.07 ± 0.12	7.70 ± 0.12*	8.08 ± 0.15	N.D.	N.D.
E210A	-0.20 ± 0.07 (4)	-0.12 ± 0.07 (4)	-0.05 ± 0.07* (4)	N.D.	N.D.	8.20 ± 0.15	7.96 ± 0.14	8.21 ± 0.15	N.D.	N.D.
L211A	-0.22 ± 0.07 (4)	-0.28 ± 0.08 (4)	-0.13 ± 0.08 (4)	N.D.	N.D.	8.36 ± 0.16	8.04 ± 0.18	8.38 ± 0.17	N.D.	N.D.
V212A	-0.26 ± 0.06 (4)	-0.38 ± 0.06 (4)	-0.26 ± 0.06 (4)	N.D.	-0.64 ± 0.15 (4)	8.10 ± 0.13	7.61 ± 0.15*	7.99 ± 0.15	N.D.	7.08 ± 0.44
R213A	-0.02 ± 0.07* (4)	0.01 ± 0.07* (4)	-0.07 ± 0.07* (4)	N.D.	-0.38 ± 0.10 (6)	8.47 ± 0.11	7.73 ± 0.12	8.43 ± 0.14	N.D.	7.43 ± 0.29
R214A	-0.17 ± 0.07 (4)	-0.22 ± 0.07 (4)	-0.12 ± 0.07 (4)	N.D.	-0.47 ± 0.16 (4)	8.22 ± 0.13	8.16 ± 0.14	8.20 ± 0.15	N.D.	6.97 ± 0.40
D215A	-0.11 ± 0.09 (4)	-0.06 ± 0.09* (4)	-0.14 ± 0.09 (4)	N.D.	-0.47 ± 0.17 (5)	8.35 ± 0.14	7.89 ± 0.14	8.46 ± 0.17	N.D.	7.02 ± 0.45
P216A	-0.35 ± 0.05 (4)	-0.35 ± 0.05 (4)	-0.35 ± 0.06 (4)	N.D.	-0.42 ± 0.10 (6)	8.37 ± 0.14	7.92 ± 0.15	8.26 ± 0.18	N.D.	7.26 ± 0.27
V217A	-0.14 ± 0.12 (4)	-0.05 ± 0.12* (4)	-0.13 ± 0.12 (4)	N.D.	-0.54 ± 0.22 (4)	8.27 ± 0.14	8.11 ± 0.13	8.23 ± 0.17	N.D.	6.91 ± 0.54
S218A	-0.27 ± 0.05 (4)	-0.25 ± 0.05 (4)	-0.27 ± 0.06 (4)	N.D.	-0.49 ± 0.13 (5)	8.10 ± 0.13	7.86 ± 0.13	7.95 ± 0.15	N.D.	6.83 ± 0.32
C219A	N.D.	N.D.	N.D.	N.D.	N.D.	N.D.	N.D.	N.D.	N.D.	N.D.

Table 2. continued

^aFor each receptor mutant and ligand, concentration-response data for each pathway were fit with the Black and Leff operational model to derive an affinity-independent measure of efficacy ($\log(\tau)$) and functional affinity (pK_A). These data were corrected for changes in cell surface expression from FACS to yield $\log(\tau c)$. All values are mean \pm S.E.M. (independent “*n*” values are indicated within parentheses). For each ligand, significance of changes in $\log(\tau c)$ or pK_A was determined by comparison of mutants to the WT receptor in a one-way ANOVA followed by Dunnett’s post-test ($p < 0.05$ represented by an asterisk (*)). N.D. denotes that data were not able to be reliably determined.

AlphaScreen assay as previously described.²⁶ Data were normalized to the maximal response elicited by 10% FBS determined at 6 min.

Pharmacological Data Analysis. IC_{50} and B_{max} values were estimated from competitive inhibition of ^{125}I -sCT_(8–32) binding using a three-parameter logistic equation [\log -(inhibitor versus response)] in Prism (v7 or v8; GraphPad). Data were corrected for radioligand occupancy using the Cheng–Prusoff equation in Prism, as such data are reported as pK_i . E_{max} and EC_{50} were estimated from concentration–response curves using a 3-parameter logistic equation in Prism. These values are a composite of functional affinity, efficacy, and stimulus response coupling. The Black and Leff operational model of agonism^{21,27} was applied to separate effects on pathway-specific efficacy (defined by the value τ , τ) from those that modify ligand functional affinity (pK_A). Derived τ values were normalized to experimentally determined levels of cell surface expression to provide a measure of efficacy (τc) that is independent of affinity and altered cell surface receptor expression.²⁷ pK_i , pK_A , and $\log \tau c$ values for mutant receptors were statistically compared to those of the respective WT receptor using a one-way analysis of variance (ANOVA) and Dunnett’s post-test. Significance was accepted at $P < 0.05$.

3D Cryo-EM Map Reconstruction. Data Processing. Complex purification and data collection were described in the original publication.¹ We reprocessed the raw movies using RELION 2.1²⁸ and RELION 3.0²⁹ to gain a map at a significantly higher resolution of the ECLs and the peptide ligand. Raw movies were corrected for stage drift and beam-induced motion using MotionCorr2.1.³⁰ Contrast transfer function (CTF) estimation was done using Gctf software³¹ using the nondose-weighted micrographs. All subsequent steps were performed in RELION. Autopicked particles (~ 1.4 M particles) were extracted using a 180 pixel box size (1.06 Å/pix) and subjected to 2D classification in Relion 2.1, followed by 3D classification using the denovo generated initial model. The combination of the three best classes (417 949 particles) yielded a 4.05 Å map, similar to the one we deposited previously¹, albeit with $\sim 3\times$ more particles). These particles were used for further data processing. First, the highly mobile Gas α -helical domain and the detergent micelle were removed using signal subtraction protocols in RELION. Specifically, we created a mask encompassing only the protein component of the complex (and without the α -helical domain), subtracted it from the refined map of the entire complex and used the resulting mask for signal-subtraction. 3D-autorefinement of the signal-subtracted particles yielded a 3.4 Å map. Signal subtraction of the N-terminal ECD did not yield further improvements in map quality. After the release of RELION 3.0, we applied Bayesian Polishing, and this yielded a final map at 3.34 Å resolution. While the Bayesian Polishing did not improve the resolution numerically, the map quality was improved significantly. During refinement, a regularization parameter was used to relax the low-pass filter effect of the Wiener filter ($T = 3$) as performed as previously described,^{32,33} while keeping half-maps completely separate and basing the resolution on the standard Fourier shell correlation (FSC) at the postprocessing stage in RELION. The final map was sharpened in RELION with a *B*-factor of -40 Å (RELION sharpening) or alternatively using LocalDeblur (LocalDeblur map³⁴). Local resolution was determined using RELION 3.0.

Modeling. The previously deposited CTR complex model (PDB-SUZ7) served as an initial model. Manual remodeling

Table 3. Effect of Single Alanine Mutation in CTR TM1 or ECL1 on pERK Efficacy and Functional Affinity of CT-Family Peptides^a

	log(<i>τ</i>)					pK _A				
	sCT	hCT	pCT	rAmy	hαCGRP	sCT	hCT	pCT	rAmy	hαCGRP
WT	-0.33 ± 0.03 (23)	-0.33 ± 0.03 (23)	-0.32 ± 0.03 (21)	-0.42 ± 0.03 (25)	-0.23 ± 0.07 (25)	8.57 ± 0.10	8.28 ± 0.11	8.79 ± 0.11	7.57 ± 0.10	6.95 ± 0.19
S129A	-0.42 ± 0.07 (5)	-0.55 ± 0.08 (5)	-0.45 ± 0.08 (5)	-0.72 ± 0.09 (5)	N.D.	7.65 ± 0.20	7.59 ± 0.24	7.99 ± 0.22	7.33 ± 0.28	N.D.
N130A	-0.95 ± 0.21* (5)	N.D.	-0.78 ± 0.15* (5)	N.D.	-0.41 ± 0.19 (7)	7.41 ± 0.86*	N.D.	8.12 ± 0.59	N.D.	6.79 ± 0.50
Y131A	-1.06 ± 0.17* (3)	-0.45 ± 0.08 (3)	-0.96 ± 0.16* (3)	-0.77 ± 0.12 (3)	N.D.	7.80 ± 0.76	7.15 ± 0.84*	7.98 ± 0.72	7.21 ± 0.44	N.D.
T132A	-0.15 ± 0.09 (4)	-0.39 ± 0.09 (4)	-0.22 ± 0.09 (5)	N.D.	-0.61 ± 0.30 (5)	8.30 ± 0.20	7.52 ± 0.25	8.03 ± 0.23	N.D.	6.70 ± 0.88
M133A	-0.56 ± 0.12 (5)	-0.05 ± 0.11* (5)	-0.34 ± 0.11 (5)	-0.37 ± 0.12 (5)	-0.06 ± 0.15 (8)	9.19 ± 0.37	8.52 ± 0.25	8.87 ± 0.29	7.25 ± 0.28	6.89 ± 0.32
C134A	N.D.	N.D.	N.D.	N.D.	N.D.	N.D.	N.D.	N.D.	N.D.	N.D.
N135A	-0.29 ± 0.09 (4)	-0.56 ± 0.10 (5)	-0.19 ± 0.09 (5)	-0.69 ± 0.11 (5)	N.D.	8.41 ± 0.20	8.09 ± 0.19	8.34 ± 0.19	7.56 ± 0.31	N.D.
F137A	-0.05 ± 0.08 (5)	-0.58 ± 0.08 (5)	-0.07 ± 0.09 (4)	-0.60 ± 0.09 (5)	-0.86 ± 0.25 (4)	8.29 ± 0.12	8.18 ± 0.14	8.01 ± 0.17	7.49 ± 0.22	7.11 ± 0.89
T138A	-0.77 ± 0.08* (4)	-0.84 ± 0.11* (4)	-0.48 ± 0.09 (3)	-0.67 ± 0.08 (4)	-0.87 ± 0.27 (4)	8.66 ± 0.38	8.45 ± 0.32	8.16 ± 0.34	7.66 ± 0.29	7.18 ± 1.05
P139A	-0.54 ± 0.10 (5)	0.02 ± 0.09* (5)	-0.41 ± 0.10 (5)	-0.53 ± 0.10 (5)	-0.39 ± 0.26 (5)	8.28 ± 0.26	8.20 ± 0.24	8.46 ± 0.24	7.44 ± 0.23	6.43 ± 0.62
E140A	-0.88 ± 0.09* (5)	0.24 ± 0.08* (5)	-0.83 ± 0.10* (5)	N.D.	N.D.	7.66 ± 0.40	7.71 ± 0.43	7.83 ± 0.38*	N.D.	N.D.
K141A	0.25 ± 0.08* (4)	-0.49 ± 0.07 (5)	0.04 ± 0.07* (6)	N.D.	-0.20 ± 0.12 (6)	7.85 ± 0.13	7.94 ± 0.13	7.99 ± 0.13	N.D.	7.00 ± 0.30
L142A	0.36 ± 0.08* (4)	-0.54 ± 0.07 (5)	0.40 ± 0.10* (4)	-1.24 ± 0.22* (5)	N.D.	7.86 ± 0.13	7.21 ± 0.13*	7.77 ± 0.16*	7.01 ± 0.79	N.D.
K143A	-0.41 ± 0.08 (5)	-0.11 ± 0.08 (5)	-0.23 ± 0.08 (5)	-0.54 ± 0.09 (5)	-0.42 ± 0.19 (5)	8.41 ± 0.22	8.23 ± 0.21	8.49 ± 0.19	7.64 ± 0.23	6.80 ± 0.50
N144A	-0.60 ± 0.08 (5)	-0.09 ± 0.07 (5)	-0.43 ± 0.07 (6)	-0.72 ± 0.09 (5)	-0.87 ± 0.20 (5)	8.04 ± 0.23	7.99 ± 0.22	8.72 ± 0.18	7.44 ± 0.28	7.44 ± 0.79
Y146A	0.25 ± 0.06* (5)	-0.63 ± 0.07* (6)	-0.07 ± 0.06* (5)	-0.93 ± 0.11* (5)	N.D.	7.96 ± 0.11	7.47 ± 0.15*	7.95 ± 0.15	7.22 ± 0.41	N.D.
V147A	0.09 ± 0.06* (4)	-0.58 ± 0.09 (5)	0.03 ± 0.06* (5)	-0.63 ± 0.10 (5)	-0.47 ± 0.15 (6)	8.11 ± 0.13	8.10 ± 0.14	8.19 ± 0.14	6.85 ± 0.27*	6.83 ± 0.42
L148A	-0.20 ± 0.08 (5)	0.15 ± 0.09* (5)	-0.29 ± 0.10 (4)	-0.67 ± 0.11 (6)	-0.28 ± 0.16 (6)	8.73 ± 0.19	7.69 ± 0.26	8.40 ± 0.32	7.62 ± 0.38	7.02 ± 0.48
Y149A	-0.31 ± 0.08 (5)	-0.77 ± 0.11* (5)	-0.21 ± 0.09 (4)	-0.93 ± 0.12* (6)	N.D.	8.62 ± 0.16	7.31 ± 0.29*	8.20 ± 0.20	7.45 ± 0.41	N.D.
Y150A	-0.20 ± 0.09 (5)	-0.22 ± 0.07 (5)	-0.23 ± 0.09 (4)	-0.64 ± 0.10 (5)	-0.69 ± 0.16 (6)	8.20 ± 0.14	7.66 ± 0.14	8.18 ± 0.19	7.48 ± 0.23	7.27 ± 0.53
L151A	-0.67 ± 0.09* (5)	-0.28 ± 0.07 (5)	-0.50 ± 0.08 (4)	-0.88 ± 0.12* (5)	N.D.	8.32 ± 0.42	7.89 ± 0.35	8.64 ± 0.38	7.85 ± 0.51	N.D.
WT	-0.32 ± 0.02 (17)	-0.33 ± 0.02 (17)	-0.34 ± 0.03 (17)	-0.36 ± 0.04 (16)	-0.39 ± 0.08 (16)	8.53 ± 0.08	8.27 ± 0.09	8.53 ± 0.10	6.96 ± 0.11	6.91 ± 0.21
H201A	-0.13 ± 0.13 (4)	-0.18 ± 0.13 (3)	-0.06 ± 0.13* (4)	N.D.	N.D.	8.37 ± 0.17	7.90 ± 0.21	8.26 ± 0.19	N.D.	N.D.
L202A	-0.28 ± 0.07 (4)	-0.44 ± 0.07 (5)	-0.23 ± 0.07 (4)	N.D.	N.D.	8.13 ± 0.13	7.70 ± 0.14*	8.25 ± 0.15	N.D.	N.D.
V203A	-0.15 ± 0.08 (4)	-0.17 ± 0.08 (4)	-0.19 ± 0.08 (4)	N.D.	-0.64 ± 0.17 (4)	8.33 ± 0.13	8.08 ± 0.14	8.39 ± 0.17	N.D.	7.35 ± 0.56
E204A	0.00 ± 0.06* (5)	0.11 ± 0.06* (4)	0.04 ± 0.06* (4)	0.25 ± 0.09* (5)	-0.23 ± 0.11 (6)	8.33 ± 0.10	8.14 ± 0.11	8.31 ± 0.13	6.54 ± 0.13	7.06 ± 0.25
V205A	-0.55 ± 0.08 (4)	-0.60 ± 0.10* (4)	-0.48 ± 0.09 (4)	N.D.	N.D.	8.41 ± 0.21	7.34 ± 0.28*	8.22 ± 0.24	N.D.	N.D.
V206A	-0.20 ± 0.06 (4)	-0.13 ± 0.06 (4)	-0.17 ± 0.06 (5)	N.D.	N.D.	8.18 ± 0.13	8.23 ± 0.13	8.76 ± 0.13	N.D.	N.D.
P207A	-0.54 ± 0.11 (4)	-0.42 ± 0.11 (4)	-0.51 ± 0.11 (4)	N.D.	N.D.	8.51 ± 0.18	7.64 ± 0.16*	7.90 ± 0.21*	N.D.	N.D.
N208A	-0.19 ± 0.11 (4)	-0.15 ± 0.11 (4)	-0.26 ± 0.11 (4)	N.D.	-0.69 ± 0.19 (5)	8.22 ± 0.15	7.80 ± 0.15	8.38 ± 0.20	N.D.	7.53 ± 0.59
G209A	-0.16 ± 0.05 (4)	-0.16 ± 0.05 (4)	-0.15 ± 0.05 (4)	N.D.	N.D.	8.07 ± 0.12	7.70 ± 0.12*	8.08 ± 0.15	N.D.	N.D.
E210A	-0.20 ± 0.07 (4)	-0.12 ± 0.07 (4)	-0.05 ± 0.07* (4)	N.D.	N.D.	8.20 ± 0.15	7.96 ± 0.14	8.21 ± 0.15	N.D.	N.D.
L211A	-0.22 ± 0.07 (4)	-0.28 ± 0.08 (4)	-0.13 ± 0.08 (4)	N.D.	N.D.	8.36 ± 0.16	8.04 ± 0.18	8.38 ± 0.17	N.D.	N.D.
V212A	-0.26 ± 0.06 (4)	-0.38 ± 0.06 (4)	-0.26 ± 0.06 (4)	N.D.	-0.64 ± 0.15 (4)	8.10 ± 0.13	7.61 ± 0.15*	7.99 ± 0.15	N.D.	7.08 ± 0.44
R213A	-0.02 ± 0.07* (4)	0.01 ± 0.07* (4)	-0.07 ± 0.07* (4)	N.D.	-0.38 ± 0.10 (6)	8.47 ± 0.11	7.73 ± 0.12	8.43 ± 0.14	N.D.	7.43 ± 0.29
R214A	-0.17 ± 0.07 (4)	-0.22 ± 0.07 (4)	-0.12 ± 0.07 (4)	N.D.	-0.47 ± 0.16 (4)	8.22 ± 0.13	8.16 ± 0.14	8.20 ± 0.15	N.D.	6.97 ± 0.40
D215A	-0.11 ± 0.09 (4)	-0.06 ± 0.09* (4)	-0.14 ± 0.09 (4)	N.D.	-0.47 ± 0.17 (5)	8.35 ± 0.14	7.89 ± 0.14	8.46 ± 0.17	N.D.	7.02 ± 0.45
P216A	-0.35 ± 0.05 (4)	-0.35 ± 0.05 (4)	-0.35 ± 0.06 (4)	N.D.	-0.42 ± 0.10 (6)	8.37 ± 0.14	7.92 ± 0.15	8.26 ± 0.18	N.D.	7.26 ± 0.27
V217A	-0.14 ± 0.12 (4)	-0.05 ± 0.12* (4)	-0.13 ± 0.12 (4)	N.D.	-0.54 ± 0.22 (4)	8.27 ± 0.14	8.11 ± 0.13	8.23 ± 0.17	N.D.	6.91 ± 0.54
S218A	-0.27 ± 0.05 (4)	-0.25 ± 0.05 (4)	-0.27 ± 0.06 (4)	N.D.	-0.49 ± 0.13 (5)	8.10 ± 0.13	7.86 ± 0.13	7.95 ± 0.15	N.D.	6.83 ± 0.32
C219A	N.D.	N.D.	N.D.	N.D.	N.D.	N.D.	N.D.	N.D.	N.D.	N.D.

Table 3. continued

^aFor each receptor mutant and ligand, concentration-response data for each pathway were fit with the Black and Leff operational model to derive an affinity-independent measure of efficacy ($\log(\tau)$) and functional affinity (pK_A). These data were corrected for changes in cell surface expression from FACS to yield $\log(\tau_c)$. All values are mean \pm S.E.M. (independent “*n*” values are indicated within parentheses). For each ligand, significance of changes in $\log(\tau_c)$ or pK_A was determined by comparison of mutants to the WT receptor in a one-way ANOVA followed by Dunnett’s post-test ($p < 0.05$ represented by an asterisk (*)). N.D. denotes that data were not able to be reliably determined.

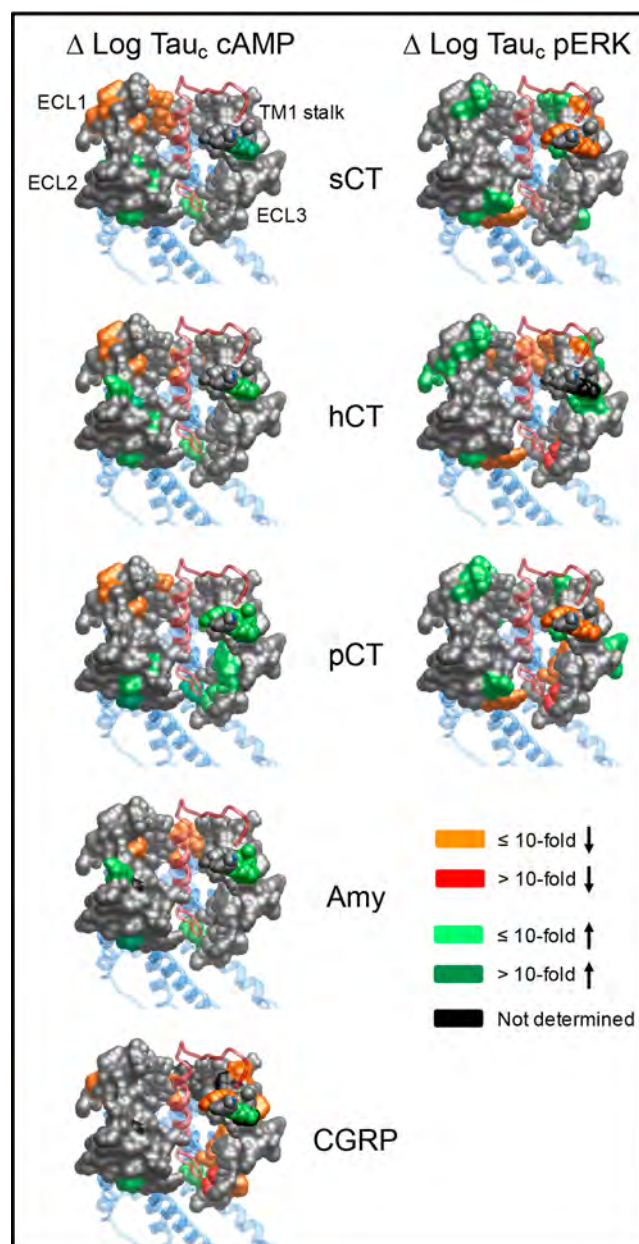


Figure 15. Alanine mutation of the extracellular surface of the CTR reveals markedly different mechanisms for efficacy propagation for cAMP accumulation and pERK. Efficacy values ($\log \tau_c$) derived from operational fitting of concentration–response curves in cAMP accumulation (LHS) and pERK (RHS) are displayed as $\Delta \log \tau_c$ from the WT. Illustrated is a top view of the active, sCT-bound, CTR model with the extracellular surface subject to alanine scanning depicted (combined surface/cpk representation). Mutations that significantly alter peptide efficacy are colored according to the magnitude of effect, with mutated amino acids without significant alteration to $\log K_A$ colored gray. sCT is shown as dark red, in ribbon representation. Amino acid mutations where there was an insufficiently robust functional effect to quantify by operational modeling are depicted in black. The receptor ECD is not shown for clarity.

was done in COOT,³⁵ followed by real space refinement using “phenix.real_space_refine” in PHENIX.³⁶ Model validation was performed using MolProbity.³⁷ Validation of model overfitting to the cryo-EM maps was performed as described previously.³⁸ Figures were prepared in USCF Chimera³⁹ or

Molsoft ICM. Ligand–receptor interactions were also assessed and illustrated using LigPlot⁺ (v2.01).⁴⁰

The CTR complex mode is deposited as PDB 6NIY and the unprocessed, RELION postprocessed, and LocalDeblur postprocessed maps are deposited in the EMDB, EMD-9382.

Completing the CTR Structure. A hybrid CTR/CGRPR structure was built in which the bulk of the amino acid sequence was taken from CTR, but with ECL1 initially taken from the CGRPR sequence, as this structure is present in the active CGRPR complex PDB (PDB 6E3Y);¹⁵ this was used to replace the missing residues by the process of molecular superposition using ccp4 mg.⁴¹ The homology modeling module of PLOP⁴² was then used to mutate the hybrid structure completely to CTR while adding the missing residues. The structure was preprocessed using the Schrödinger Protein Preparation Wizard (Maestro version 9.8, Schrödinger LLC, NY), which flagged molecular clashes. As a result, Lys18^P of sCT was rebuilt using PLOP, while the remaining steric clashes were removed through minimization using PLOP.

Molecular Dynamics (MD) Simulations. CTR in complex with sCT and the C-terminus of the G protein α subunit ($\alpha_{370-394}$) was prepared for MD simulations with the CHARMM36 force field⁴³ using a multistep procedure that combines python htm⁴⁴ and tcl (Tool Command Language) scripts. Hydrogen atoms were first added by means of the pdb 2pqr⁴⁵ and propka⁴⁶ software (considering a simulated pH of 7.0); the protonation of titratable side chains was checked by visual inspection. The system CTR:sCT:G $\alpha_{370-394}$ was embedded in a square 106 Å × 106 Å 1-palmitoyl-2-oleyl-*sn*-glycerol-3-phospho-choline (POPC) bilayer (previously built by using the VMD Membrane Builder plugin 1.1, Membrane Plugin, version 1.1. at <http://www.ks.uiuc.edu/Research/vmd/plugins/membrane/>) through an insertion method.⁴⁷ The receptor orientation was obtained by superposing CTR coordinates on the CTR-Gs complex (PDB 5UZ7) structure retrieved from the OPM database.⁴⁸ Lipids overlapping the receptor TM bundle were removed and TIP3P water molecules⁴⁹ were added to the simulation box (106 Å × 106 Å × 136 Å) by means of the VMD Solvate plugin 1.5 (Solvate Plugin, version 1.5. at <http://www.ks.uiuc.edu/Research/vmd/plugins/solvate/>). Overall charge neutrality was finally reached by adding Na⁺/Cl[−] counterions (final ionic strength of 0.150 M), using the VMD Autoionize plugin 1.3 (Autoionize Plugin, version 1.3, <http://www.ks.uiuc.edu/Research/vmd/plugins/autoionize/>).

Systems Equilibration and MD Settings. The MD engine ACEMD⁵⁰ was employed for both the equilibration and productive simulations. Equilibration was achieved in isothermal–isobaric conditions (NPT) using the Berendsen barostat⁵¹ (target pressure 1 atm) and the Langevin thermostat⁵² (target temperature 300 K) with a low damping of 1 ps^{−1}. A three-stage procedure was performed (integration time step of 2 fs). In the *first stage*, clashes between protein and lipid atoms were reduced through 2500 conjugate-gradient minimization steps, then a 2 ns long MD simulation was run with a positional constraint of 1 kcal mol^{−1} Å^{−2} on protein and lipid phosphorus atoms. In the *second stage*, 33 ns of MD simulation were performed constraining only the protein atoms. Finally, in the *third stage*, positional constraints were applied only to the protein backbone alpha carbons, for a further 2 ns.

Three replicas of 200 ns long each were computed with an integration time step of 4 fs in the canonical ensemble (NVT)

at 300 K, using a thermostat damping of 0.1 ps^{−1} and the M-SHAKE algorithm⁵³ to constrain the bond lengths involving hydrogen atoms. The cutoff distance for electrostatic interactions was set at 9 Å, with a switching function applied beyond 7.5 Å. Long range Coulomb interactions were handled using the particle mesh Ewald summation method (PME)⁵⁴ by setting the mesh spacing to 1.0 Å.

■ ASSOCIATED CONTENT

● Supporting Information

The Supporting Information is available free of charge on the ACS Publications website at DOI: 10.1021/acspsci.8b00056.

Atomic resolution models; concentration-response curves; competition binding isotherms (PDF)

■ AUTHOR INFORMATION

Corresponding Authors

*E-mail: Patrick.sexton@monash.edu.

*E-mail: denise.wootten@monash.edu.

ORCID

Sebastian G. B. Furness: 0000-0001-8655-8221

Debbie L. Hay: 0000-0002-9558-5122

Patrick M. Sexton: 0000-0001-8902-2473

Author Contributions

*E.d.M. and A.G. contributed equally to this work. The following contributions were made: contributed to experimental design (E.d.M., D.L.H., M.-W.W., D.W., P.M.S.); performed experiments (E.d.M., Y.Z., C.A.H., Y.-L.L.); contributed to conceptual development of the project (S.G.B.F., D.L.H., A.C., L.J.M., M.-W.W., D.W., P.M.S.); performed data EM analysis (A.G., J.G.-N., C.G.T., E.R., J.-M.C.); performed modeling of the protein into the E.M. map (A.G.); performed molecular modeling (S.A., C.A.R.); performed pharmacological data analysis (E.d.M., D.W., P.M.S.); contributed to production of figures (E.d.M., A.G., D.W., P.M.S.); provided oversight of the project (D.W., P.M.S.); edited the manuscript (all authors); drafted the manuscript (P.M.S.).

Notes

The authors declare no competing financial interest.

■ ACKNOWLEDGMENTS

This work was supported by the National Health and Medical Research Council of Australia (NHMRC) program Grant 1055134 and project Grants 1061044, 1159006, Shanghai Science and Technology Development Fund (15DZ2291600), the Chinese Academy of Sciences (CAS)-Novo Nordisk Research Fund, and the Biotechnology and Biological Sciences Research Council (BBSRC; BB/M006883/1). A.G. is an Australian Research Council (ARC) Discovery Early Career Research Award Fellow. S.F. is an ARC Future Fellow. D.W. is a Senior Research Fellow, and A.C. and P.M.S. are Senior Principal Research Fellows, of the NHMRC. D.L.H. is a James Cook Research Fellow of the Royal Society of New Zealand. C.A.R. is a Royal Society Industrial Fellow. S.A. is supported by the Peter Nicholls bequest. Data processing for map reconstruction was performed on the Monash University MASSIVE M3 high performance computing cluster.

REFERENCES

- (1) Liang, Y.-L., Khoshouei, M., Radjainia, M., Zhang, Y., Glukhova, A., Tarrasch, J., Thal, D. M., Furness, S. G. B., Christopoulos, G., Coudrat, T., Danev, R., Baumeister, W., Miller, L. J., Christopoulos, A., Kobilka, B. K., Wootten, D., Skiniotis, G., and Sexton, P. M. (2017) Phase-plate cryo-EM structure of a class B GPCR-G protein complex. *Nature* 546, 118–123.
- (2) Wootten, D., Miller, L. J., Koole, C., Christopoulos, A., and Sexton, P. M. (2017) Allostery and Biased Agonism at Class B G Protein-Coupled Receptors. *Chem. Rev.* 117, 111–138.
- (3) Ostrovskaya, A., Findlay, D. M., Sexton, P. M., and Furness, S. G. B. (2017). Calcitonin. *Reference Module in Neuroscience and Biobehavioral Psychology*, 1–12. DOI: 10.1016/B978-0-12-809324-5.03223-5, Elsevier.
- (4) Hay, D. L., Garelja, M. L., Poyner, D. R., and Walker, C. S. (2018) Update on the pharmacology of calcitonin/ CGRP family of peptides: IUPHAR Review 25. *Br. J. Pharmacol.* 175, 3–17.
- (5) Graaf, C. D., Donnelly, D., Wootten, D., Lau, J., Sexton, P. M., Miller, L. J., Ahn, J. M., Liao, J., Fletcher, M. M., Yang, D., Brown, A. J., Zhou, C., Deng, J., and Wang, M. W. (2016) Glucagon-Like Peptide-1 and Its Class B G Protein-Coupled Receptors: A Long March to Therapeutic Successes. *Pharmacol. Rev.* 68, 954–1013.
- (6) Russo, A. F. (2018) CGRP-Based Migraine Therapeutics: How Might They Work, Why So Safe, and What Next? *ACS Pharmacol Transl Sci.*, 1 in press DOI: 10.1021/acspstci.8b00036.
- (7) Findlay, D. M., Sexton, P. M., and Martin, T. J. (2015) Calcitonin. *Endocrinology: Adult & Pediatric*, (Jameson, J. L., De Groot, L. J., de Kretser, D. M., Giudice, L. C., Grossman, A. B., Melmed, S., Potts, J. T., Jr, and Weir, G. C. Eds.) 7th ed., Vols 1 and 2, pp 1004–101714, Elsevier, Philadelphia, PA USA.
- (8) Furness, S. G. B., Liang, Y.-L., Nowell, C. J., Halls, M. L., Wookey, P. J., Dal Maso, E., Inoue, A., Christopoulos, A., Wootten, D., and Sexton, P. M. (2016) Ligand-dependent modulation of G protein conformation alters drug efficacy. *Cell* 167, 739–749.
- (9) Dal Maso, E., Just, R., Hick, C., Christopoulos, A., Sexton, P. M., Wootten, D., and Furness, S. G. B. (2018) Characterisation of signaling and regulation of common calcitonin receptor splice variants and polymorphisms. *Biochem. Pharmacol.* 148, 111–129.
- (10) Andreassen, K. V., Hjuler, S. T., Furness, S. G., Sexton, P. M., Christopoulos, A., Nosjean, O., Karsdal, M. A., and Henriksen, K. (2014) Prolonged calcitonin receptor signaling by salmon, but not human calcitonin, reveals ligand bias. *PLoS One* 9, No. e92042.
- (11) Dal Maso, E., Zhu, Y., Pham, V., Reynolds, C. A., Deganutti, G., Hick, C. A., Yang, D., Christopoulos, A., Hay, D. L., Wang, M.-W., Sexton, P. M., Furness, S. G. B., and Wootten, D. (2018) Extracellular loops 2 and 3 of the calcitonin receptor selectively modify agonist binding and efficacy. *Biochem. Pharmacol.* 150, 214–244.
- (12) Wootten, D., Simms, J., Miller, L. J., Christopoulos, A., and Sexton, P. M. (2013) Polar transmembrane interactions drive formation of ligand-specific and signal pathway-biased Family B GPCR conformations. *Proc. Natl. Acad. Sci. U. S. A.* 110, 5211–5216.
- (13) Zhang, Y., Sun, B., Feng, D., Hu, H., Chu, M., Qu, Q., Tarrasch, J. T., Li, S., Kobilka, T. S., Kobilka, B. K., and Skiniotis, G. (2017) Cryo-EM structure of the activated GLP-1 receptor in complex with a G protein. *Nature* 546, 248–253.
- (14) Liang, Y.-L., Khoshouei, M., Glukhova, A., Furness, S. G. B., Zhao, P., Clydesdale, L., Koole, C., Troung, T. T., Thal, D. M., Lei, S., Radjainia, M., Danev, R., Baumeister, W., Wang, M.-W., Miller, L. J., Christopoulos, A., Sexton, P. M., and Wootten, D. (2018) Phase-plate cryo-EM structure of a biased agonist-bound human GLP-1 receptor-Gs complex. *Nature* 555, 121–125.
- (15) Liang, Y.-L., Khoshouei, M., Deganutti, G., Glukhova, A., Koole, C., Peat, T. S., Radjainia, M., Plitzko, J. M., Baumeister, W., Miller, L. J., Hay, D. L., Christopoulos, A., Reynolds, C. A., Wootten, D., and Sexton, P. M. (2018) Cryo-EM structure of the active, Gs-protein complexed, human CGRP receptor. *Nature* 561, 492–497.
- (16) Glukhova, A., Draper-Joyce, C. J., Sunahara, R. K., Christopoulos, A., Wootten, D., and Sexton, P. M. (2018) Rules of engagement: GPCRs and G proteins. *ACS Pharmacol. Transl. Sci.* 1, 73–83.
- (17) Houssami, S., Findlay, D. M., Brady, C. L., Martin, T. J., Epanand, R. M., Moore, E. E., Murayama, E., Tamura, T., Orlowski, R. C., and Sexton, P. M. (1995) Divergent structural requirements exist for calcitonin receptor binding specificity and adenylate cyclase activation. *Mol. Pharmacol.* 47, 798–809.
- (18) Johansson, E., Hansen, J. L., Hansen, A. M., Shaw, A. C., Becker, P., Schäffer, L., and Reedtz-Runge, S. (2016) Type II Turn of Receptor-bound Salmon Calcitonin Revealed by X-ray Crystallography. *J. Biol. Chem.* 291, 13689–13698.
- (19) Hilton, J. M., Dowton, M., Houssami, S., and Sexton, P. M. (2000) Identification of key components in the irreversibility of salmon calcitonin binding to calcitonin receptors. *J. Endocrinol.* 166, 213–226.
- (20) Morfis, M., Tilakaratne, N., Furness, S. G. B., Christopoulos, G., Werry, T. D., Christopoulos, A., and Sexton, P. M. (2008) Receptor activity modifying proteins differentially modulate the G protein-coupling efficiency of amylin receptors. *Endocrinology* 149, 5423–5431.
- (21) Black, J. W., and Leff, P. (1983) Operational models of pharmacological agonism. *Proc. R Soc. Lond B Biol. Sci.* 220, 141–162.
- (22) Mackie, D. I., Al Mutairi, F., Davis, R. B., Kechele, D. O., Nielsen, N. R., Snyder, J. C., Caron, M. G., Kliman, H. J., Berg, J. S., Simms, J., Poyner, D. R., and Caron, K. M. (2018) hCALCRL mutation causes autosomal recessive nonimmune hydrops fetalis with lymphatic dysplasia. *J. Exp. Med.* 215, 2339–2353.
- (23) Lei, S., Clydesdale, L., Dai, A., Cai, X., Feng, Y., Yang, D., Liang, Y.-L., Koole, C., Zhao, P., Coudrat, T., Christopoulos, A., Wang, M.-W., Wootten, D., and Sexton, P. M. (2018) Two distinct domains of the glucagon-like peptide-1 receptor control peptide-mediated biased agonism. *J. Biol. Chem.* 293, 9370–9387.
- (24) Wootten, D., Reynolds, C. A., Smith, K. J., Mobarec, J. C., Koole, C., Savage, E. E., Pabreja, K., Simms, J., Sridhar, R., Furness, S. G. B., Liu, M., Thompson, P. E., Miller, L. J., Christopoulos, A., and Sexton, P. M. (2016) The GLP-1 receptor extracellular surface is a molecular trigger for biased agonism. *Cell* 165, 1632–1643.
- (25) Watkins, H. A., Chakravarthy, M., Abhayawardana, R. S., Gingell, J. J., Garelja, M., Pardamwar, M., McElhinney, J. M., Lathbridge, A., Constantine, A., Harris, P. W., Yuen, T. Y., Brimble, M. A., Barwell, J., Poyner, D. R., Woolley, M. J., Conner, A. C., Pioszak, A. A., Reynolds, C. A., and Hay, D. L. (2016) Receptor activity-modifying proteins 2 and 3 generate adrenomedullin receptor subtypes with distinct molecular properties. *J. Biol. Chem.* 291, 11657–11675.
- (26) Koole, C., Wootten, D., Simms, J., Valant, C., Sridhar, R., Woodman, O. L., Miller, L. J., Summers, R. J., Christopoulos, A., and Sexton, P. M. (2010) Allosteric ligands of the glucagon-like peptide 1 receptor (GLP-1R) differentially modulate endogenous and exogenous peptide responses in a pathway-selective manner; implications for drug screening. *Mol. Pharmacol.* 78, 456–465.
- (27) Koole, C., Wootten, D., Simms, J., Miller, L. J., Christopoulos, A., and Sexton, P. M. (2012) The second extracellular loop of the human glucagon-like peptide-1 receptor (GLP-1R) has a critical role in GLP-1 peptide binding and receptor activation. *J. Biol. Chem.* 287, 3642–3648.
- (28) Kimanius, D., Forsberg, B. O., Scheres, S. H., and Lindahl, E. (2016) Accelerated cryo-EM structure determination with parallelisation using GPUs in RELION-2. *eLife* 5, 19.
- (29) Zivanov, J., Nakane, T., Forsberg, B. O., Kimanius, D., et al. (2018) New tools for automated high-resolution cryo-EM structure determination in RELION-3. *eLife* 7, 163.
- (30) Zheng, S. Q., et al. (2017) MotionCor2: anisotropic correction of beam-induced motion for improved cryo-electron microscopy. *Nat. Methods* 14, 331–332.
- (31) Zhang, K. (2016) Gctf: Real-time CTF determination and correction. *J. Struct. Biol.* 193, 1–12.

- (32) García-Nafria, J., Lee, Y., Bai, X., Carpenter, B., and Tate, C. G. (2018) Cryo-EM structure of the adenosine A2A receptor coupled to an engineered heterotrimeric G protein. *eLife* 7, No. e35946.
- (33) García-Nafria, J., Nehmé, R., Edwards, P. C., and Tate, C. G. (2018) Cryo-EM structure of the serotonin 5-HT1B receptor coupled to heterotrimeric Go. *Nature* 558, 620–623.
- (34) Ramirez-Aportela, E., Vilas, J. L., Melero, R., Conesa, P., Martinez, M., Maluenda, D., Mota, J., Jimenez, A., Vargas, J., Marabini, R., Carazo, J. M., and Sorzano, C. O. S. (2018) Automatic local resolution-based sharpening of cryo-EM maps. *bioRxiv* DOI: 10.1101/433284.
- (35) Emsley, P., Lohkamp, B., Scott, W. G., and Cowtan, K. (2010) Features and development of Coot. *Acta Crystallogr., Sect. D: Biol. Crystallogr.* 66, 486–501.
- (36) Adams, P. D., et al. (2010) PHENIX: a comprehensive Python-based system for macromolecular structure solution. *Acta Crystallogr., Sect. D: Biol. Crystallogr.* 66, 213–221.
- (37) Chen, V. B., et al. (2010) MolProbity: all-atom structure validation for macromolecular crystallography. *Acta Crystallogr., Sect. D: Biol. Crystallogr.* 66, 12–21.
- (38) Draper-Joyce, C. J., Khoshouei, M., Thal, D., Liang, Y.-L., Nguyen, A. T. N., Furness, S. G. B., Venugopal, H., Baltos, J., Plitzko, J. M., Danev, R., Baumeister, W., May, L. T., Wootten, D., Sexton, P. M., Glukhova, A., and Christopoulos, A. (2018) Structure of the adenosine-bound human adenosine A1 receptor-Gi complex. *Nature* 558, 559–563.
- (39) Pettersen, E. F., et al. (2004) UCSF Chimera—a visualization system for exploratory research and analysis. *J. Comput. Chem.* 25, 1605–1612.
- (40) Laskowski, R. A., and Swindells, M. B. (2011) LigPlot+: multiple ligand-protein interaction diagrams for drug discovery. *J. Chem. Inf. Model.* 51, 2778–2786.
- (41) McNicholas, S., Potterton, E., Wilson, K. S., and Noble, M. E. (2011) Presenting your structures: the CCP4mg molecular-graphics software. *Acta Crystallogr., Sect. D: Biol. Crystallogr.* 67, 386–394.
- (42) Goldfeld, D. A., Zhu, K., Beuming, T., and Friesner, R. A. (2011) Successful prediction of the intra- and extracellular loops of four G-protein-coupled receptors. *Proc. Natl. Acad. Sci. U. S. A.* 108, 8275–8280.
- (43) Huang, J., and MacKerell, A. D. (2013) CHARMM36 all-atom additive protein force field: validation based on comparison to NMR data. *J. Comput. Chem.* 34, 2135–2145.
- (44) Doerr, S., Harvey, M. J., Noé, F., and De Fabritiis, G. (2016) HTMD: High-Throughput Molecular Dynamics for Molecular Discovery. *J. Chem. Theory Comput.* 12, 1845–1852.
- (45) Dolinsky, T. J., Nielsen, J. E., McCammon, J. A., and Baker, N. A. (2004) PDB2PQR: an automated pipeline for the setup of Poisson-Boltzmann electrostatics calculations. *Nucleic Acids Res.* 32, W665–W667.
- (46) Olsson, M. H. M., Søndergaard, C. R., Rostkowski, M., and Jensen, J. H. (2011) PROPKA3: Consistent Treatment of Internal and Surface Residues in Empirical pKa Predictions. *J. Chem. Theory Comput.* 7, 525–537.
- (47) Sommer, B. (2013) Membrane Packing Problems: A short Review on computational Membrane Modeling Methods and Tools. *Comput. Struct. Biotechnol. J.* 5, No. e201302014.
- (48) Lomize, M. A., Lomize, A. L., Pogozheva, I. D., and Mosberg, H. I. (2006) OPM: orientations of proteins in membranes database. *Bioinformatics* 22, 623–625.
- (49) Jorgensen, W. L., Chandrasekhar, J., Madura, J. D., Impey, R. W., and Klein, M. L. (1983) Comparison of simple potential functions for simulating liquid water. *J. Chem. Phys.* 79, 926–935.
- (50) Harvey, M. J., Giupponi, G., and De Fabritiis, G. (2009) ACEMD: Accelerating Biomolecular Dynamics in the Microsecond Time Scale. *J. Chem. Theory Comput.* 5, 1632–1639.
- (51) Berendsen, H. J. C., Postma, J. P. M., van Gunsteren, W. F., DiNola, A., and Haak, J. R. (1984) Molecular dynamics with coupling to an external bath. *J. Chem. Phys.* 81, 3684–3690.
- (52) Loncharich, R. J., Brooks, B. R., and Pastor, R. W. (1992) Langevin dynamics of peptides: the frictional dependence of isomerization rates of N-acetylalanine-N'-methylamide. *Biopolymers* 32, 523–535.
- (53) Kräutler, V., Van Gunsteren, W. F., and Hünenberger, P. H. (2001) A fast SHAKE algorithm to solve distance constraint equations for small molecules in molecular dynamics simulations. *J. Comput. Chem.* 22, 501–508.
- (54) Essmann, U., et al. (1995) A smooth particle mesh Ewald method. *J. Chem. Phys.* 103, 8577–8593.

Deconvoluting the Molecular Control of Binding and Signaling at the Amylin 3 Receptor: RAMP3 Alters Signal Propagation through Extracellular Loops of the Calcitonin Receptor

Vi Pham,^{†,‡} Yue Zhu,^{‡,§,‡} Emma Dal Maso,^{†,‡} Christopher A. Reynolds,^{||} Giuseppe Deganutti,^{||} Silvia Atanasio,^{||} Caroline A. Hick,[†] Dehua Yang,[‡] Arthur Christopoulos,[†] Debbie L. Hay,[⊥] Sebastian G. B. Furness,[†] Ming-Wei Wang,^{*,‡,§} Denise Wootten,^{*,†} and Patrick M. Sexton^{*,†}

[†]Drug Discovery Biology, Monash Institute of Pharmaceutical Sciences, Monash University, Parkville 3052, Victoria, Australia

[‡]The National Center for Drug Screening and CAS Key Laboratory of Receptor Research, Shanghai Institute of Materia Medica, Chinese Academy of Sciences, Shanghai 201203, China

[§]University of Chinese Academy of Sciences, 19A Yuquan Road, Beijing 100049, China

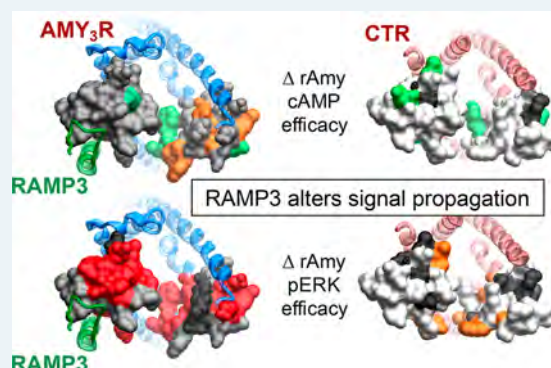
^{||}School of Biological Sciences, University of Essex, Wivenhoe Park, Colchester CO4 3SQ, U.K.

[⊥]The University of Auckland, School of Biological Sciences, 3 Symonds Street, Auckland 1142, New Zealand

Supporting Information

ABSTRACT: Amylin is coexpressed with insulin in pancreatic islet β -cells and has potent effects on gastric emptying and food intake. The effect of amylin on satiation has been postulated to involve AMY_3 receptors (AMY_3R) that are heteromers of the calcitonin receptor (CTR) and receptor activity-modifying protein 3 (RAMP3). Understanding the molecular control of signaling through the AMY_3R is thus important for peptide drug targeting of this receptor. We have previously used alanine scanning mutagenesis to study the contribution of the extracellular surface of the CTR to binding and signaling initiated by calcitonin (CT) and related peptides (Dal Maso, E., *et al.* (2019) The molecular control of calcitonin receptor signaling. *ACS Pharmacol. Transl. Sci.* 2, 31–51). That work revealed ligand- and pathway-specific effects of mutation, with extracellular loops (ECLs) 2 and 3 particularly important in the distinct propagation of signaling mediated by individual peptides. In the current study, we have used equivalent alanine scanning of ECL2 and ECL3 of the CTR in the context of coexpression with RAMP3 to form AMY_3Rs , to examine functional affinity and efficacy of peptides in cAMP accumulation and extracellular signal-regulated kinase (ERK) phosphorylation (pERK). The effect of mutation was determined on representatives of the three major distinct classes of CT peptide, salmon CT (sCT), human CT (hCT), and porcine CT (pCT), as well as rat amylin (rAmy) or human α -CGRP (calcitonin gene-related peptide, hCGRP) whose potency is enhanced by RAMP interaction. We demonstrate that the dynamic nature of CTR ECL2 and ECL3 in propagation of signaling is fundamentally altered when complexed with RAMP3 to form the AMY_3R , despite only having predicted direct interactions with ECL2. Moreover, the work shows that the role of these loops in receptor signaling is highly peptide dependent, illustrating that even subtle changes to peptide sequence may change signaling output downstream of the receptor.

KEYWORDS: amylin receptor, calcitonin receptor, receptor activity-modifying protein, G protein-coupled receptor, receptor structure–function, cell signaling



INTRODUCTION

G protein-coupled receptors (GPCRs) are the largest superfamily of cell surface protein conduits of extracellular chemical information to the inside of cells.¹ As such, understanding the molecular basis of how these extracellular signals are conformationally propagated through the GPCR to recruit and activate signal transducers is critically important to development of novel therapeutics that regulate this process. Moreover, GPCRs can recruit multiple different transducers and other regulatory proteins and this can be altered in a

ligand-specific manner, leading to biased agonists that hold promise as precision medicines to treat various diseases.²

Class B1 GPCRs are an important subfamily for key physiological peptides that regulate diverse functions including energy homeostasis, bone metabolism, immune function, lymph and vascular formation, and the control of vascular tone.³ The calcitonin receptor (CTR) is a broadly expressed

Received: February 7, 2019

Published: March 18, 2019

class B1 GPCR that is most recognized for its expression in bone resorbing osteoclasts, and its role in bone metabolism.⁴ However, CTRs also interact with a family of 3 receptor activity-modifying proteins (RAMPs) to yield high affinity receptors for amylin and calcitonin gene-related peptide (CGRP).⁵ These are termed AMY₁, AMY₂, and AMY₃ receptors according to the interacting RAMP, i.e., RAMP1, RAMP2, and RAMP3, respectively. In addition to modifying the binding specificity of the CT family of receptors, a major consequence of GPCR-RAMP interaction is alteration to the signaling profile of the receptor,⁶ and this has been observed for the AMY receptors relative to CTR alone.⁷

Amylin is coexpressed with insulin in pancreatic islet β -cells and has potent effects on gastric emptying and food intake.⁸ Pramlintide, a nonamyloidogenic analogue of human amylin is approved for the treatment of type 1 diabetes in combination with insulin.⁸ However, amylin analogues also promote satiation and can lead to significant weight loss in overweight patients, and cause marked weight loss in animal models of obesity when coadministered with other agents that promote weight loss, such as glucagon-like peptide-1 (GLP-1) receptor agonists or leptin.^{9,10} Accordingly, there is significant interest in the development of new amylin analogues to better treat obesity.⁸

The amylin effect on satiation has been localized to amylin receptors in the area postrema and has been proposed to involve the AMY₃R subtype (CTR:RAMP3 heteromer),¹¹ although all three RAMPs are present in the area postrema.⁸ Understanding the molecular control of signaling through the AMY₃R is thus crucial for peptide drug targeting of this receptor.

Recent advances in cryo-electron microscopy have allowed determination of the structures of active state class B GPCRs in complex with peptide agonists and the canonical Gs protein,^{12–15} including complexes of the CTR^{12,16} and the CGRP receptor.¹⁵ The latter is a heteromer of the related calcitonin receptor-like receptor (CLR) and RAMP1. These structures have allowed identification of the peptide binding domain within the receptor core and serve as a template for 3-dimensional (3D) mapping of the effect of mutation on receptor function. Importantly, the solution of the CGRP receptor (CGRPR) complex revealed a novel interface for RAMP interaction with transmembrane helices 4 and 5 that extended to parts of extracellular loop (ECL) 2,¹⁵ and allows for the first-time structure-based modeling of related RAMP-class B GPCR complexes.

We have previously used alanine scanning mutagenesis to study the contribution of the extracellular surface of the CTR to binding and signaling initiated by CT and related peptides.^{16,17} This work revealed ligand- and pathway-specific effects of mutation, with ECLs 2 and 3 particularly important in the distinct propagation of signaling mediated by individual peptides.¹⁷ In the current study, we have used equivalent alanine scanning of ECL2 and ECL3 of the CTR in the context of coexpression with RAMP3 to form AMY₃Rs, in order to examine functional affinity and efficacy of peptides in cAMP accumulation and extracellular signal-regulated kinase (ERK) phosphorylation (pERK). The effect of mutation was determined on representatives of the three major distinct classes of CT peptide, salmon CT (sCT), human CT (hCT), and porcine CT (pCT), as well as rat amylin (rAmy) or human α -CGRP (hCGRP) whose potency is enhanced by RAMP interaction. The work illustrates that interaction with RAMP3

dynamically alters how ECL2 and ECL3 contribute to propagation of signaling through the CTR.

RESULTS AND DISCUSSION

Importance of ECL2 and ECL3 in the Control of AMY₃R Function. To gain insight into the role of RAMP3 in the AMY₃R phenotype we performed alanine scanning mutagenesis on CTR ECL2 (I279-I300) and ECL3 (F356-M376) that play important roles in peptide binding and propagation of signaling at the CTR in the absence of RAMPs.¹⁷ Each of these mutants was analyzed for their effect on cell surface expression (Figure 1), binding affinity in

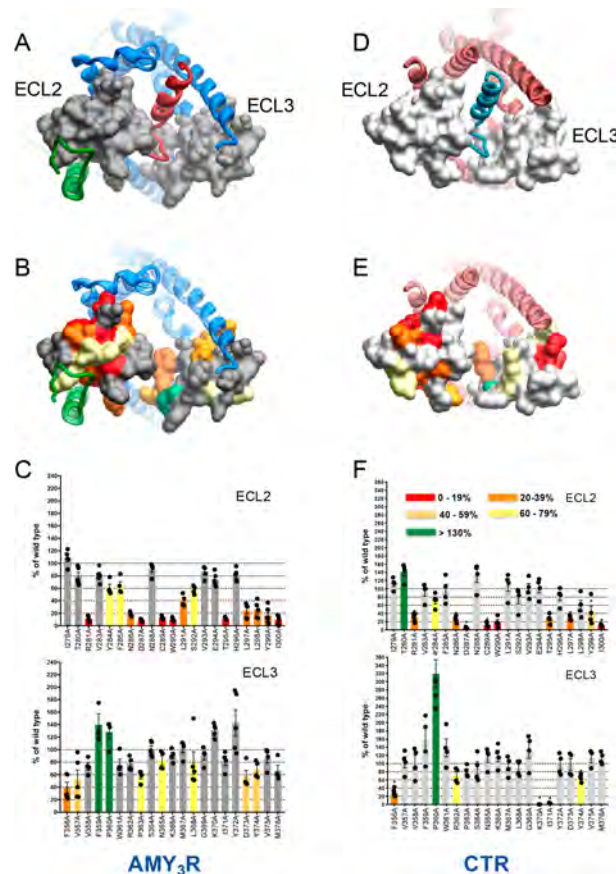


Figure 1. Effect of alanine mutation on the cell surface expression of the AMY₃R and CTR. (A–C) AMY₃R; (D–F) CTR (extracted from Dal Maso et al, 2018¹⁷). (A, D) Top view of the active, sCT-bound, AMY₃R (A) or CTR (6NIY) (D) model with the extracellular surface subject to alanine scanning depicted in gray (A) or off-white (D) (combined surface/cpk representation). The rest of the protein complex is shown in ribbon representation. CTR (blue, AMY₃R; dark red, CTR), sCT peptide (dark red, AMY₃R; aquamarine, CTR), RAMP3 (green). The receptor ECD is omitted for clarity. (B, E) Map of the effect of mutation on cell surface receptor expression colored according to the legend in panel F. (C, F) Effect of alanine mutation of ECL2 and ECL3 on CTR expression monitored by FACS of anti-c-Myc antibody binding to the N-terminal c-Myc epitope on the receptor. Data are normalized to the expression of the wild-type (WT) receptor (100%). Significant differences in the level of cell surface expression were determined by one-way ANOVA followed by Dunnett's post-test comparison to the WT. $P < 0.05$ was used to denote significance, and colored according to the magnitude of change. Individual values (separate experiments) are shown within the bars.

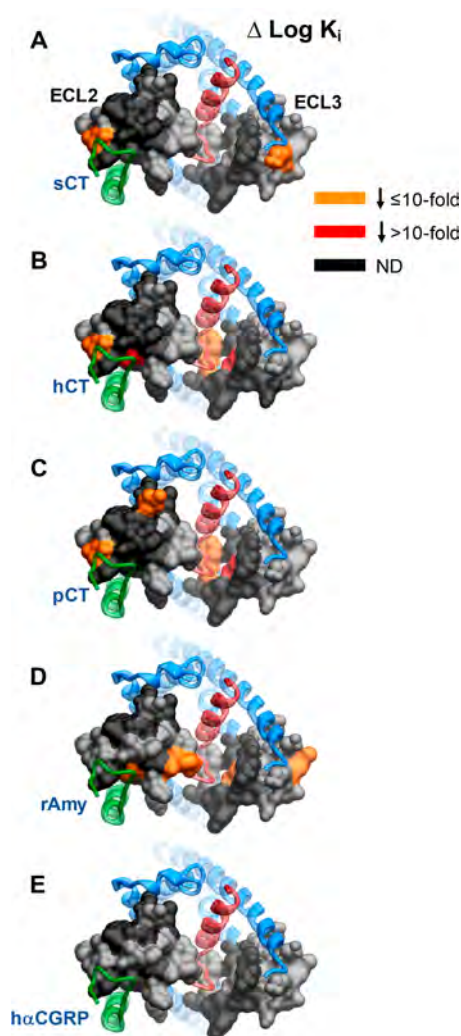


Figure 2. Identification of key amino acids of AMY₃R ECL2 and ECL3 for peptide binding affinity ($\log K_i$). (A) sCT; (B) hCT; (C) pCT; (D) rAmy; (E) hCGRP. Mutations that significantly decreased peptide affinity in radioligand competition assay are colored dark orange (≤ 10 -fold effect) or red (> 10 -fold effect), with mutated amino acids without significant alteration to $\log K_i$ colored gray. Amino acid mutations where there was an insufficiently robust functional effect to quantify by radioligand competition binding are depicted in black. The receptor ECD is not shown for clarity, with the CTR TM bundle in blue ribbon and RAMP3 in green ribbon. Quantitative data are reported in Table 1.

competitive radioligand binding assays (Figure 2, Table 1, Figures S1–S6), and functional response (pERK and cAMP accumulation) for each peptide (Figures 3–8, Figures S7–S16, Tables 2–5). A homology model of the AMY₃R complex was built from deposited structures of the CTR (6NIY¹⁶) and CGRPR (6E3Y;¹⁵ for initial positioning of RAMP3) active complexes and subjected to a short molecular dynamics (MD) simulation (200 ns) to resolve energetically unfavorable interactions. This model was used to map effects of mutation on the AMY₃R and to enable comparison to the effects of previously published equivalent mutations on the CTR,^{16,17} mapped onto the recently published 3.3 Å structure (6NIY) that included ECL2 and ECL3 side chains¹⁶ (Figures 9–12).

Receptor Expression. AMY₃Rs were expressed using a Flp-In bicistronic vector of N-terminally tagged cMyc-CTR and RAMP3, where the RAMP is overexpressed relative to the CTR, and stable cell lines of each mutant receptor generated by isogenic integration into Flp-In CV-1 cells. Anti-cMyc antibody binding to the CTR was measured by FACS as a marker of the cell surface expression of the AMY₃R (Figure 1).

There was a marked decrease in surface expression of CTR in the AMY₃R for the R281A, N286A, D287A, C289A, W290A, T295A, L297A, L298A, Y299A, and I300A mutants within ECL2, with decreased expression to a lesser extent also seen with Y284A, F285A, L291A, and S292A mutants within this loop (Figure 1B,C). In general, the pattern of effect was similar to that seen with the CTR expressed alone¹⁷ (Figure 1E,F) although greater loss of expression was seen for the L291A and S292A mutants when the receptor was coexpressed with RAMP3. Alanine mutation within ECL3 had less overall impact relative to ECL2, with moderate, significant, decreases in expression for F356A, V357A, P363A, N365A, L286A, D373A, and Y374A, and increases for F359A and P360A (Figure 1B,C). The lack of effect of K370A and I371A mutation of the AMY₃R was in marked contrast to the effect of these mutants in the absence of RAMP3, where there was almost undetectable levels of CTR expression, and very high levels of expression observed for the P360A mutation (Figure 1E,F), although overall there was only limited impact of mutation in ECL3. Although RAMP3 is overexpressed relative to CTR in the bicistronic vector, it is likely that both AMY₃R and CTR alone forms of the receptor are formed. Nonetheless, the marked difference in surface expression of the K370A and I371A mutants (100% versus $< 5\%$ for AMY₃R and CTR, respectively) supports that the cocomplex with RAMP3 accounts for the majority of receptors in the CV-1 cells.

Peptide Affinity (Competition Binding). To specifically examine the impact of mutation on the affinity of peptide ligands for the AMY₃R, radioligand competition binding studies were performed with ¹²⁵I-rAmylin. We have previously demonstrated that there is no measurable specific binding to CTR alone at the concentrations of radioligand used.¹⁸ No specific binding was detected for the R281A, Y284A, N286A, D287A, C289A, W290A, L291A, T295A and I300A mutants in ECL2, or for the V357A, P360A, W361A R362A, P363A, L368A, D373A, and M376A mutants in ECL3 (Table 1, Figure 2). Many of these within ECL2 also had low cell surface expression (Figure 1C). In contrast, there was moderate to strong cell surface expression of most ECL3 mutants indicating that the loss of binding was likely due to alterations to binding affinity of the radioligand. Of those mutants with a robust specific binding window, there was a subset that exhibited loss of affinity, in a peptide specific manner (Table 1, Figure 2, Figures S1–S6). hCGRP was least impacted, with no significant change in observed affinity (Figure S1E). There was a selective loss of rAmy affinity for the E294A and G369A mutants (Figure S1D), of hCT for the T280A, L298A, and S364A mutants (Figure S1B), of sCT for the K366A mutant, and pCT for the N288A mutant (Figures S1A and S1C, respectively). F285A and Y299A displayed a selective loss of affinity for CT peptides with no significant effect on rAmy or hCGRP. Similarly, there was loss of affinity for all CT peptides for the V358A and F359A mutants; rAmy affinity was also decreased at V358A (Table 1, Figures S1A–D). There was selective loss of affinity for sCT and pCT at the V283A mutant, hCT, pCT, and rAmy at the L297A and Y372A mutants, and

Table 1. Effect of Single Alanine Mutation in AMY₃R ECL2 or ECL3 on Binding Affinity (log K_i) of Peptides Derived from Competition Binding Isotherms^a

	sCT			hCT			pCT			rAmy			hCGRP		
	Mean	S.E.M.	N	Mean	S.E.M.	N	Mean	S.E.M.	N	Mean	S.E.M.	N	Mean	S.E.M.	N
WT	-9.70	0.07	16	-7.01	0.08	17	-7.83	0.06	17	-8.75	0.06	19	-6.88	0.07	17
I279A	-9.26	0.17	5	-7.17	0.16	5	-8.02	0.10	5	-8.83	0.09	5	-6.92	0.12	5
T280A	-9.13	0.22	3	-6.13	0.35	3	-7.73	0.22	3	-8.52	0.17	4	-6.63	0.26	4
R281A															
V283A	-9.14	0.14	5	-6.92	0.17	5	-7.15	0.17	5	-8.40	0.13	5	-7.00	0.10	5
Y284A															
F285A	ND			ND			ND			-8.68	0.20	3	-6.87	0.15	3
N286A															
D287A															
N288A	-9.45	0.25	5	-6.46	0.24	5	-7.28	0.12	5	-8.51	0.11	5	-6.90	0.16	5
C289A															
W290A															
L291															
S292A	-9.74	0.15	4	-6.65	0.12	3	-8.08	0.13	5	-8.37	0.11	5	-6.59	0.12	5
V293A	-9.34	0.17	5	-6.94	0.14	5	-7.40	0.24	4	-8.82	0.08	5	-7.39	0.17	5
E294A	-9.74	0.12	5	-6.88	0.22	5	-7.78	0.17	5	-8.20	0.11	5	-6.80	0.16	4
T295A															
H296A	-9.59	0.14	4	-6.91	0.13	4	-7.45	0.13	5	-8.78	0.13	4	-6.70	0.13	5
L297A	-9.58	0.27	3	<-6		3	ND			-8.09	0.19	4	-6.82	0.21	4
L298A	-9.51	0.14	5	-6.11	0.19	5	-7.48	0.10	5	-8.94	0.10	5	-6.64	0.16	5
Y299A	ND			ND			ND			-8.26	0.24	4	-6.75	0.27	3
I300A															
F356A	-9.63	0.11	5	-6.34	0.11	5	-7.35	0.10	5	-8.82	0.06	5	-7.16	0.08	5
V357A															
V358A	ND			ND			-7.11	0.20	3	-8.01	0.17	5	-6.83	0.21	4
F359A	ND			ND			-6.84	0.26	3	-8.36	0.21	5	-6.93	0.16	3
P360A															
W361A															
R362A															
P363A															
S364A	-9.37	0.17	3	ND			-7.46	0.11	4	-8.80	0.15	4	-6.91	0.15	4
N365A	-9.38	0.11	3	-7.07	0.21	3	-7.99	0.18	4	-8.94	0.12	4	-7.04	0.17	5
K366A	-8.79	0.18	5	-6.93	0.13	4	-7.57	0.12	5	-8.85	0.20	5	-7.00	0.14	5
M367A	-9.46	0.25	3	ND			-7.05	0.14	5	-8.25	0.21	4	-6.94	0.14	4
L368A															
G369A	-9.95	0.20	4	-6.87	0.16	4	-7.60	0.10	4	-8.02	0.14	4	-7.07	0.18	4
K370A	-9.66	0.12	5	-7.05	0.14	5	-7.61	0.10	5	-8.93	0.12	5	-6.99	0.12	5
I371A	-9.64	0.13	4	-7.06	0.19	4	-7.80	0.13	4	-8.47	0.12	4	-6.83	0.16	4
Y372A	-9.14	0.16	4	<-6		4	-6.74	0.15	5	-7.92	0.10	5	-7.21	0.16	4
D373A															
Y374A	-9.63	0.18	3	-6.87	0.21	4	-7.54	0.12	4	-8.69	0.11	5	-6.98	0.15	5
V375A	-9.49	0.15	5	-7.03	0.10	5	-7.54	0.08	5	-8.92	0.11	5	-6.99	0.12	5
M376A															

^aLog K_i values were derived for each ligand and mutant receptor from analysis of either homologous (rAmy) or heterologous (sCT, hCT, pCT, hCGRP) competition of ¹²⁵I-rAmy binding. Mean, S.E.M. and the individual experimental “n” values are reported. Significance of changes in log K_i of each ligand was determined by comparison of mutant receptors to WT values by a one-way ANOVA and Dunnett’s post-test ($p < 0.05$ denoted by bold coloured entries. Orange, significant decrease ≤ 10 -fold; red, significant decrease > 10 -fold). Gray shading indicates mutants where robust radioligand binding was not detected. N.D. indicates that no value could be derived due to lack of robust competition and high data variance.

of hCT and pCT at the F356A and M367A mutants (Table 1, Figures S1A–D). The effect of mutations within ECL2 appeared to coincide with residues known to contribute to packing of ECL2 in CTR¹⁶ or were in close proximity to the predicted RAMP3 interface (Figure 2). In contrast, the effect of most mutations within ECL3 were consistent with potential peptide binding interfaces and differential strength of interaction for individual peptides (Figure 2).

Peptide Functional Affinity. For each peptide, concentration–response isotherms were established in assays of cAMP accumulation and pERK1/2 (Figures S7–S16), and data were analyzed by operational modeling to derive estimates of functional affinity (log K_A) (Figures 3 and 4, Tables 2 and 3) and efficacy (log τ) for each pathway; the latter were corrected for differences in cell surface expression (Figures 6 and 7, Tables 4 and 5).

There was a marked peptide dependence in the effect of mutation on cAMP functional affinity, with the greatest impact on hCT and pCT across both ECL2 and ECL3 (Figure 3, Table 2). hCGRP functional affinity was minimally affected by mutation with significant loss of affinity for L368A, but no

detectable response (ND) for C289A, P363A, and D373A (Figures 3A,B; and 5E). Similarly, there was only limited effect on rAmy functional affinity, with loss of affinity for W290A and L291A in ECL2 and F359A, P363A, L368A, and D373A in ECL3 (Figures 3D,I; 5D). For sCT, only V357A in ECL3 altered affinity, with greater impact in ECL2 with decreased functional affinity for D287A, W290A, S292A and I300A (Figures 3A,B; 5A). In distinction to the limited effects of mutations on responses to these peptides, there was very marked, extended impact on hCT and pCT (Figures 3B,C,G,H; 5B,C). Within ECL2 and the TMS proximal segment of ECL3, there was very similar impact on cAMP functional affinity for both peptides with attenuated affinity for R281A (ND for hCT), N286A, D297A, C289A, W290A (ND for hCT), L291A, S292A, T295A, and L297A–I300A within ECL2, and F359A–P363A in ECL3, with the exception of L297A, L298A, and V358A that had no significant effect on pCT affinity. Similarly, there was parallel loss of affinity for Y372A, D373A, and M376A for both peptides. Nonetheless, divergent effects were seen for K366A, M367A, and V375A (selective increased affinity for pCT), and L368A (selective

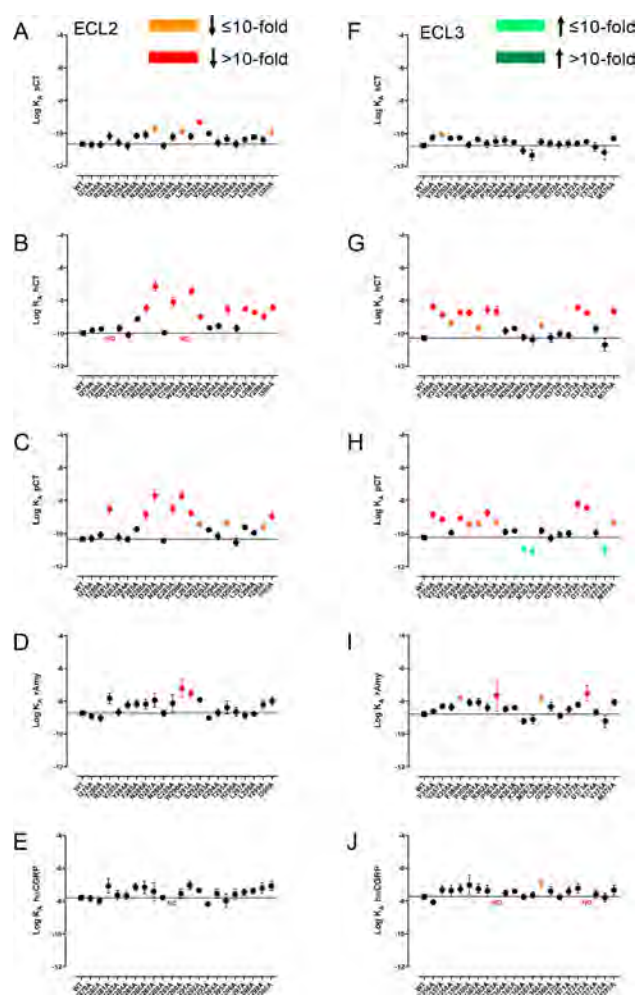


Figure 3. Alanine mutation of ECL2 and ECL3 of AMY_3R alters cAMP functional affinity ($\log K_A$) in a peptide-specific manner. Functional affinities derived from operational fitting of concentration–response curves in cAMP accumulation for alanine mutation of ECL2 (A–E) and ECL3 (F–J) are displayed as $\log K_A$. Significance of changes was established by comparison of the WT to the other receptor mutants following one-way ANOVA and Dunnett's post-test with $P < 0.05$ accepted as significant. Mutants that gave significant reductions between 3- and 10-fold are colored orange, and those with reductions greater than 10-fold are colored red. Mutants giving significant increases in $\log K_A$ are colored green. Where data were insufficiently robust to derive a reliable value for $\log K_A$ no symbol is shown (ND). Quantitative data are reported in Table 2.

decreased affinity for hCT) (Figures 3B,C,G,H; 5B,C; Table 2).

In contrast to the dramatic effect on cAMP functional affinity, there was no significant effect on measured pERK functional affinity for any of the peptides (Figures 4 and 5, Table 3). However, robust responses were not seen for the following mutants and peptides; R281A (hCT), D287A (hCT, pCT, hCGRP), C289A (hCT, rAmy), W290A (hCGRP), L291A (hCT, hCGRP), L298A, I300A, P360A (hCGRP), R362A, P363A (rAmy, hCGRP), K370A (rAmy), I371A (hCT, rAmy, hCGRP), D373A, V375A, and M376A (hCGRP) and thus the nature of the loss of response could not be determined.

These data revealed marked differences in how ECL2 and ECL3 contribute to functional affinity across the two pathways at the AMY_3R (Figure 5). The most notable differences were

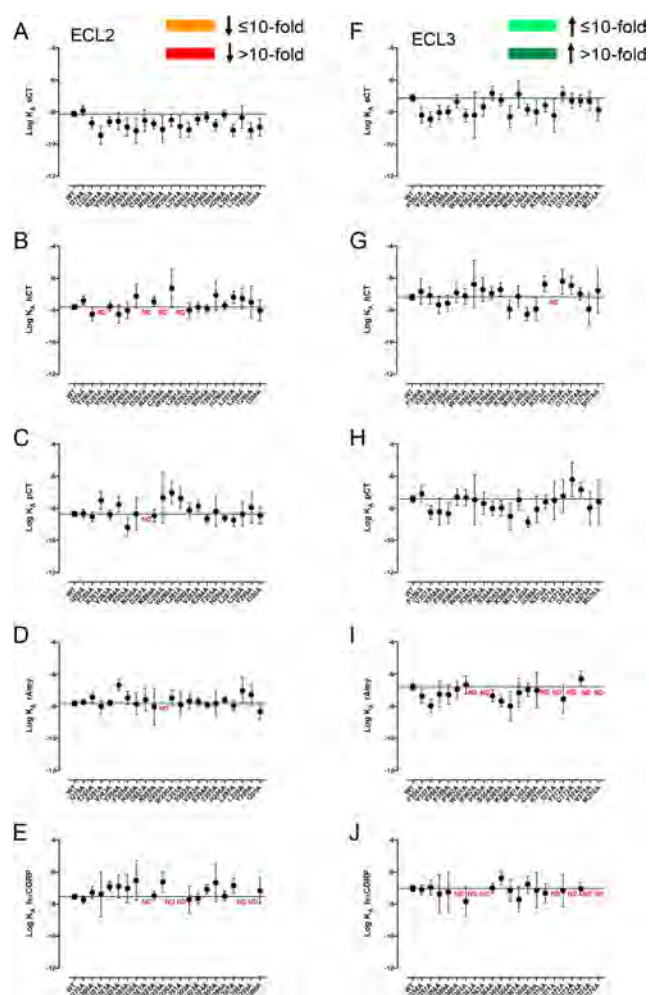


Figure 4. Alanine mutation of ECL2 and ECL3 of AMY_3R has limited effect on pERK functional affinity ($\log K_A$). Functional affinities derived from operational fitting of concentration–response curves in ERK phosphorylation for alanine mutation of ECL2 (A–E) and ECL3 (F–J) are displayed as $\log K_A$. No significant changes in $\log K_A$ from WT were seen for receptor mutants following one-way ANOVA and Dunnett's post-test with $P < 0.05$ accepted as significant. Where data were insufficiently robust to derive a reliable value for $\log K_A$ no symbol is shown (ND). Quantitative data are reported in Table 3.

seen for hCT and pCT for which there was broad importance of the amino acids in the core of ECL2, and peptide proximal residues of ECL3, in cAMP but not pERK functional affinity (Figure 5B,C versus Figure 5G,H). Alanine mutants that selectively increased cAMP functional affinity for pCT clustered away from the peptide binding site and were located on the periphery of the receptor transmembrane domain. This region would be predicted to interact with the membrane bilayer, suggesting that these candidate receptor–membrane interactions constrain the receptor in a way that limits pCT functional affinity when RAMP3 is present, as the effect of mutation was not seen with mutants of CTR alone¹⁷ (Figure 6C versus Figure 6H). For the other peptides, there was limited effect of loop mutation on functional affinity for either pathway, with the quantifiable effects primarily occurring within residues involved in packing of the ECL2 in the active structures (Figure 5). While no quantifiable effect was seen on pERK functional affinity, there was a cluster of residues at the apex of ECL3 that adversely affected rAmy and hCGRP

Table 2. Effect of Single Alanine Mutation in AMY₃R ECL2 or ECL3 on cAMP Functional Affinity (log K_A) of Peptides^a

	sCT			hCT			pCT			rAmy			hCGRP		
	Mean	S.E.M.	N	Mean	S.E.M.	N	Mean	S.E.M.	N	Mean	S.E.M.	N	Mean	S.E.M.	N
WT (ECL2)	-10.66	0.07	26	-9.99	0.06	23	-10.32	0.06	26	-8.73	0.06	26	-7.79	0.05	34
I279A	-10.70	0.20	4	-9.81	0.17	4	-10.29	0.18	4	-8.91	0.18	4	-7.83	0.18	4
T280A	-10.70	0.20	4	-9.75	0.09	11	-10.07	0.18	4	-9.04	0.20	4	-7.98	0.20	4
R281A	-10.17	0.24	4	ND		4	-8.56	0.24	4	-7.83	0.34	4	-7.06	0.45	7
V283A	-10.57	0.22	4	-9.68	0.18	4	-10.20	0.22	4	-8.68	0.24	4	-7.63	0.27	4
Y284A	-10.76	0.22	4	-10.10	0.17	4	-10.34	0.19	4	-8.24	0.24	4	-7.67	0.21	4
F285A	-10.15	0.16	4	-9.12	0.15	5	-9.71	0.15	4	-8.16	0.23	4	-7.15	0.22	4
N286A	-10.09	0.23	4	-8.46	0.23	5	-8.87	0.23	4	-8.19	0.31	4	-7.16	0.38	4
D287A	-9.76	0.21	4	-7.12	0.31	5	-7.70	0.36	4	-7.95	0.41	7	-7.42	0.55	6
N288A	-10.76	0.19	4	-9.97	0.14	4	-10.43	0.15	4	-8.75	0.19	4	-7.79	0.13	4
C289A	-10.21	0.24	5	-8.08	0.28	5	-8.51	0.27	5	-8.13	0.52	9	ND		
W290A	-9.89	0.19	4	ND		4	-7.76	0.27	4	-7.22	0.55	4	-7.54	0.30	4
L291A	-10.20	0.20	4	-7.42	0.20	4	-8.80	0.18	4	-7.52	0.24	4	-7.03	0.26	7
S292A	-9.31	0.14	4	-8.98	0.10	5	-9.45	0.09	4	-7.92	0.12	4	-7.33	0.12	4
V293A	-10.01	0.12	4	-9.66	0.11	5	-9.76	0.12	4	-9.03	0.13	4	-8.17	0.15	4
E294A	-10.58	0.22	4	-9.55	0.17	4	-10.15	0.21	4	-8.71	0.23	4	-7.54	0.28	4
T295A	-10.36	0.26	4	-8.54	0.25	4	-9.36	0.24	4	-8.39	0.40	4	-7.97	0.41	8
H296A	-10.66	0.23	4	-9.70	0.19	4	-10.52	0.24	4	-8.65	0.26	4	-7.57	0.32	4
L297A	-10.39	0.17	7	-8.52	0.16	7	-9.60	0.15	7	-8.86	0.21	7	-7.45	0.19	7
L298A	-10.23	0.14	7	-8.73	0.11	7	-9.95	0.13	7	-8.77	0.14	7	-7.38	0.18	7
Y299A	-10.41	0.22	5	-8.96	0.20	5	-9.57	0.22	5	-8.20	0.27	5	-7.21	0.33	8
I300A	-9.91	0.22	7	-8.41	0.17	6	-8.98	0.20	6	-7.98	0.27	7	-7.08	0.27	7
WT (ECL3)	-10.73	0.08	26	-10.28	0.07	29	-10.22	0.07	25	-8.79	0.06	25	-7.73	0.06	27
F356A	-10.24	0.19	5	-8.36	0.19	5	-8.85	0.18	5	-8.61	0.15	5	-8.07	0.14	5
V357A	-10.07	0.15	5	-8.88	0.14	5	-9.16	0.15	5	-8.30	0.16	5	-7.32	0.23	5
V358A	-10.28	0.15	5	-9.35	0.18	4	-9.92	0.16	4	-8.35	0.21	4	-7.37	0.36	4
F359A	-10.26	0.12	5	-8.72	0.13	4	-9.09	0.12	4	-7.81	0.15	4	-7.26	0.27	4
P360A	-10.68	0.20	4	-8.74	0.18	4	-9.46	0.16	4	-8.08	0.22	4	-7.02	0.59	5
W361A	-10.36	0.15	5	-9.65	0.17	5	-9.41	0.16	6	-8.07	0.25	5	-7.25	0.27	5
R362A	-10.61	0.23	4	-8.55	0.23	4	-8.77	0.22	4	-8.39	0.23	4	-7.37	0.34	4
P363A	-10.48	0.30	4	-8.65	0.28	4	-9.30	0.31	4	-7.65	0.96	4	ND		
S364A	-10.41	0.25	5	-9.85	0.21	5	-9.88	0.19	5	-8.48	0.18	5	-7.51	0.18	5
N365A	-10.52	0.15	5	-9.70	0.13	5	-9.80	0.13	5	-8.39	0.11	5	-7.40	0.12	5
K366A	-11.03	0.22	4	-10.23	0.20	4	-10.90	0.18	4	-9.21	0.18	4	-7.74	0.16	4
M367A	-11.32	0.33	3	-10.38	0.26	3	-11.08	0.24	3	-9.11	0.27	3	-7.63	0.19	3
L368A	-10.52	0.22	5	-9.52	0.19	5	-9.79	0.19	5	-7.84	0.21	5	-6.94	0.29	5
G369A	-10.59	0.22	4	-10.25	0.27	4	-10.26	0.22	4	-8.32	0.26	4	-7.38	0.26	4
K370A	-10.67	0.22	5	-10.04	0.22	5	-10.04	0.19	5	-8.88	0.16	5	-7.76	0.16	5
I371A	-10.60	0.23	4	-10.11	0.20	4	-9.98	0.19	4	-8.49	0.20	4	-7.39	0.24	3
Y372A	-10.61	0.17	5	-8.41	0.18	5	-8.22	0.22	5	-8.20	0.16	5	-7.22	0.30	5
D373A	-10.49	0.12	5	-8.75	0.11	5	-8.46	0.15	5	-7.52	0.46	5	ND		
Y374A	-10.82	0.27	5	-9.72	0.24	5	-9.93	0.24	5	-8.66	0.20	5	-7.58	0.25	4
V375A	-11.15	0.43	3	-10.70	0.38	3	-10.98	0.35	3	-9.20	0.39	3	-7.79	0.26	3
M376A	-10.30	0.14	5	-8.66	0.18	4	-9.29	0.19	4	-8.08	0.20	4	-7.33	0.31	4

^aFor each receptor mutant and ligand, concentration–response data for each pathway were fit with the Black and Leff operational model to derive an affinity-independent measure of efficacy and functional affinity (log K_A). Mean, S.E.M., and the individual experimental “n” values are reported. Significance of changes in log K_A of each ligand was determined by comparison of mutant receptors to WT values by a one-way ANOVA and Dunnett’s post-test ($p < 0.05$ denoted by bold coloured entries. Orange, significant decrease ≤ 10 -fold; red, significant decrease > 10 -fold; Light green, significant increase ≤ 10 -fold; Dark green, significant increase > 10 -fold). ND, data were not able to be reliably determined.

responses, but not those of CT peptides, suggesting that they are important for initiation or propagation of pERK signaling (Figure 5I,J, see red arrows).

The equivalent amino acids in CTR did not impact on pERK functional affinity of these peptides (Figure 7D,E versus Figure 7I,J), consistent with RAMP3 allosterically altering interaction of rAmy and hCGRP with this segment of the receptor, potentially through effects on engagement of the receptor with the midregion of the agonist peptide α -helix.

In general, the effect of ECL2 and ECL3 mutation was similar for AMY₃R and CTR for cAMP functional affinity (Figure 6), for most peptides, although RAMP3 appeared to impart increased sensitivity to mutation for hCT and pCT. The exception to this was hCGRP in which a greater effect of mutation was seen for CTR relative to AMY₃R (Figure 6E versus Figure 6J), and this might reflect increased strength of interaction of this peptide at the AMY₃R such that individual mutation of amino acids had lesser effect.

Intriguingly, while overall there was relatively limited impact of ECL2 or ECL3 mutation on pERK functional affinity for either AMY₃R or CTR, there was a greater effect of mutation on CTR, particularly for CT peptides and within ECL3 (Figure

7A–C versus 7F–H). This greater effect on CTR mutation occurred for select amino acids deep in the peptide binding pocket, with additional effects on pCT for residues that extended, in 3D space, from the peptide proximal residues.

Peptide Efficacy. The operationally derived efficacy parameter, τ , is a measure of pathway-specific coupling efficiency that relates the number of receptors occupied to response.¹⁹ Peptide efficacy for cAMP accumulation was largely unaffected by mutation to ECL2 residues (Figure 8A–E, Table 4), albeit that the relatively high variance may have limited those effects that achieved statistical significance.

Overall, ECL2 mutation tended to lead to increased measures of peptide efficacy for CT peptides (Figure 8A–C), with effects achieving significance for S292A mutation (sCT, pCT), L298A (sCT) and I300A (hCT). Increased efficacy of rAmy was also observed with the S292A mutant (Figure 8D). In contrast, both increased and decreased efficacy was observed following mutation of amino acids in ECL3, in a peptide-dependent manner (Figure 8F–J). Greater numbers of mutations had significant effects within ECL3; however, this was partially attributable to more robust expression of ECL3

Table 3. Effect of Single Alanine Mutation in AMY₃R ECL2 or ECL3 on pERK Functional Affinity (log K_A) of Peptides^a

	sCT			hCT			pCT			rAmy			hCGRP		
	Mean	S.E.M.	N	Mean	S.E.M.	N	Mean	S.E.M.	N	Mean	S.E.M.	N	Mean	S.E.M.	N
WT (ECL2)	-8.13	0.17	27	-7.81	0.15	33	-8.36	0.16	31	-7.83	0.10	33	-7.54	0.16	25
I279A	-7.91	0.31	5	-7.41	0.27	7	-8.35	0.27	6	-7.74	0.15	7	-7.73	0.22	5
T280A	-8.69	0.31	5	-8.26	0.42	8	-8.53	0.31	6	-7.46	0.31	7	-7.28	0.38	7
R281A	-9.45	0.55	6	ND			-7.52	0.55	6	-8.02	0.38	8	-7.39	1.40	6
V283A	-8.61	0.28	5	-7.77	0.25	7	-8.39	0.26	7	-7.79	0.18	8	-6.91	0.26	6
Y284A	-8.59	0.54	7	-8.25	0.57	6	-7.77	0.46	5	-6.69	0.35	5	-6.90	0.70	5
F285A	-8.94	0.57	6	-8.02	0.50	7	-9.19	0.61	5	-7.49	0.43	6	-7.02	0.90	5
N286A	-9.18	0.77	6	-7.12	0.77	6	-8.36	1.02	5	-7.85	0.66	6	-6.54	1.24	5
D287A	-8.54	0.67	6	ND		ND				-7.59	0.70	7	ND		
N288A	-8.73	0.29	6	-7.48	0.29	6	-8.47	0.39	5	-8.03	1.14	3	-7.47	0.26	6
C289A	-9.09	0.84	6	ND			7.35	1.59	5	ND			-6.62	0.63	6
W290A	-8.51	0.38	6	-6.63	1.22	7	-7.04	0.71	5	-7.49	0.49	6	-7.49	1.62	5
L291A	-8.90	0.69	5	ND			-7.39	0.63	6	-7.92	0.78	5	ND		
S292A	-9.12	0.45	6	-8.02	0.46	7	-8.13	0.46	5	-7.65	0.46	6	-7.72	0.83	6
V293A	-8.46	0.30	6	-7.83	0.30	7	-7.86	0.32	5	-7.72	0.27	6	-7.65	0.31	6
E294A	-8.32	0.31	4	-7.90	0.25	7	-8.67	0.25	7	-7.92	0.17	9	-7.09	0.26	6
T295A	-8.81	0.35	6	-7.07	0.93	8	-8.19	0.95	4	-7.84	0.79	7	-6.66	1.16	7
H296A	-8.16	0.27	5	-7.71	0.25	7	-8.60	0.24	7	-7.60	0.17	8	-7.51	0.29	6
L297A	-9.15	0.39	5	-7.19	0.37	6	-8.74	0.39	5	-7.97	0.33	4	-6.83	0.46	4
L298A	-8.33	0.71	3	-7.28	0.65	3	-8.38	0.77	3	-7.02	0.83	3	ND		
Y299A	-9.15	0.48	6	-7.51	1.01	5	-7.95	0.98	5	-7.29	0.67	5	ND		
I300A	-8.94	0.55	5	-8.04	0.63	6	-8.46	0.52	6	-8.35	0.44	6	-7.16	0.80	4
WT (ECL3)	-7.13	0.23	28	-7.19	0.20	24	-7.43	0.23	21	-6.79	0.24	23	-7.03	0.19	24
F356A	-8.20	0.48	6	-6.85	0.80	6	-7.11	0.52	6	-7.37	0.43	6	-7.12	0.31	6
V357A	-8.45	0.48	6	-7.09	0.53	6	-8.26	0.43	6	-7.98	0.43	6	-6.96	0.46	6
V358A	-8.04	0.43	6	-7.67	0.54	4	-8.23	0.84	4	-7.25	0.80	4	-7.37	1.21	4
F359A	-8.00	0.36	6	-7.58	0.50	4	-8.33	0.63	4	-7.29	0.61	4	-7.25	1.27	4
P360A	-7.34	0.41	6	-6.92	0.62	5	-7.31	0.53	5	-6.96	0.48	6	ND		5
W361A	-8.22	0.41	4	-7.13	0.48	3	-7.34	0.49	3	-6.66	0.57	3	-7.84	0.94	3
R362A	8.20	1.43	3	6.40	1.48	3	-7.49	1.56	3	ND			ND		
P363A	-7.68	0.58	5	-6.72	0.75	5	-7.72	0.71	5	ND			ND		
S364A	-6.84	0.44	6	-6.95	0.41	5	-8.02	0.46	3	-7.35	0.37	4	-7.00	0.30	5
N365A	-7.26	0.38	6	-6.72	0.42	5	-7.99	0.46	3	-7.69	0.34	4	-6.38	0.40	5
K366A	-8.29	0.69	3	-7.95	0.57	3	-8.51	0.82	3	-7.99	0.90	3	-7.15	0.68	3
M367A	-6.90	0.83	3	-7.13	0.66	3	-7.48	0.67	3	-7.16	0.89	3	-7.70	0.80	3
L368A	-7.84	0.35	6	-8.25	0.42	4	-8.87	0.34	5	-6.97	0.41	5	-6.76	0.53	5
G369A	-8.00	0.76	3	-7.92	0.71	3	-8.07	0.83	3	-7.01	1.11	3	-7.14	1.11	3
K370A	-7.59	0.41	6	-6.38	0.49	5	-7.61	0.43	4	-6.05	1.07	3	-7.32	0.58	3
I371A	-8.22	1.03	3	ND			-7.52	1.17	3	-8.02	1.71	3	ND		
Y372A	-6.88	0.44	6	-6.21	0.79	6	-7.24	1.04	5	-7.55	0.92	5	-7.15	1.01	5
D373A	-7.30	0.48	6	-6.47	0.56	6	-6.22	1.05	5	ND			-6.43	1.02	5
Y374A	-7.31	0.38	6	-6.99	0.37	5	-6.85	0.46	4	-6.29	0.49	5	-7.05	0.38	5
V375A	-7.32	0.55	6	-7.93	0.98	5	-7.99	1.01	4	-6.56	1.52	4	ND		
M376A	-7.87	0.72	6	-6.78	1.42	4	-7.60	1.40	4	-6.56	1.89	4	ND		

^aFor each receptor mutant and ligand, concentration–response data for each pathway were fit with the Black and Leff operational model to derive an affinity-independent measure of efficacy and functional affinity (log K_A). Mean, S.E.M. and the individual experimental “n” values are reported. ND, data were not able to be reliably determined. Where quantitative data could be derived, no significant differences from WT values were observed, as assessed by a one-way ANOVA and Dunnett’s post-test (significance set at $p < 0.05$).

mutants (Figure 1, Table 1) and greater precision in the calculation of log τ (Table 4).

The pattern of effect was similar for CT peptides, with increased efficacy for each peptide observed with the F356A, V358A, N365A, and D373A mutants and loss of efficacy for the V375A mutant (Figure 8F–H). Nonetheless, peptide specific effects were also observed with increased efficacy at the V358A (sCT), F359A (sCT, pCT), W361A (sCT), and M376A (sCT) mutants. Selective attenuation of efficacy was seen at the G369A and K370A (hCT) and Y372A (pCT) mutants (Figure 8F–H). While there were parallels in the effect of the F356A and N365A mutation for rAmy and hCGRP, the pattern of effect was generally distinct (Figure 8I,J), and more similar for these two peptides than between them and the CT peptides (Figure 8F–J). Of all the ECL3 mutants, only the F356A and N365A mutants had equivalent effect (increased efficacy) on rAmy, hCGRP, and CT peptides, while the effects of increased efficacy (V357A) and decreased efficacy (V375A) were also observed for rAmy but not hCGRP. Similar effects, distinct from those for CT peptides, were observed for both rAmy and hCGRP for P360A, W361A, P363A, and D373A (decreased efficacy or ND), with the nature of effect of the D373A mutant opposite to that seen for

all CT peptides (Figure 8F–J). Peptide-specific loss of efficacy was seen for V358A, F359A, R362A, Y372A (hCGRP), M367A, and G369A (rAmy) (Figure 8I,J).

Remarkably, there was a dramatic loss of peptide efficacy for pERK for most individual mutants within both ECL2 and ECL3 (Figure 9, Table 5), although there was a lesser effect of ECL2 mutation on hCGRP efficacy (Figure 9E). Within ECL2, only I279A did not have any negative effect on CT or Amy peptide efficacy, albeit that the loss of efficacy did not achieve significance for V283A (hCT, pCT, rAmy), Y284A (rAmy), N288A (hCT), V293A (pCT), E294A, H296A (sCT, hCT, pCT, rAmy), L297A (hCT, pCT, rAmy), and L298A (hCT) (Figure 9A–D, Table 5). As noted above, for hCGRP, no robust response was observed for D287A, L291A, L298A, and Y299A (Tables 3, 5). Of the other ECL2 mutants, only the S292A mutant produced a significant loss of hCGRP efficacy (Figure 9E). Like ECL2, alanine mutation of ECL3 broadly led to loss of peptide efficacy (Figure 9F–J). For this loop, the pattern of effect was also mirrored for hCGRP (Figure 9J). Of the ECL3 residues, only S364A, N365A, and Y284A did not significantly reduce efficacy of any of the peptides (Table 5). For W361A and L368A, while loss of efficacy occurred for all peptides, this was not statistically significant for some of the

Table 4. Effect of Single Alanine Mutation in AMY₃R ECL2 or ECL3 on cAMP Signaling Efficacy (log τ_c) of Peptides^a

	sCT				hCT				pCT				rAmy				hCGRP		
	Mean	S.E.M.	N		Mean	S.E.M.	N		Mean	S.E.M.	N		Mean	S.E.M.	N		Mean	S.E.M.	N
WT (ECL2)	-0.18	0.02	26		-0.19	0.02	23		-0.18	0.02	26		-0.18	0.02	26		-0.20	0.02	34
I279A	-0.37	0.06	4		-0.40	0.06	4		-0.38	0.06	4		-0.36	0.06	4		-0.43	0.07	4
T280A	-0.19	0.09	4		-0.12	0.09	11		-0.22	0.09	4		-0.24	0.10	4		-0.29	0.10	4
R281A	0.39	0.31	4	ND			4		0.32	0.31	4		0.15	0.32	4		-0.22	0.33	7
V283A	-0.30	0.06	4		-0.33	0.05	4		-0.37	0.05	4		-0.39	0.06	4		-0.51	0.08	4
Y284A	-0.20	0.09	4		-0.14	0.09	4		-0.15	0.09	4		-0.22	0.10	4		-0.24	0.10	4
F285A	0.08	0.13	4		-0.11	0.13	5		-0.04	0.13	4		-0.18	0.14	4		-0.15	0.14	4
N286A	0.20	0.10	4		0.04	0.10	5		0.09	0.10	4		0.00	0.11	4		-0.12	0.14	4
D287A	0.46	0.20	4		0.19	0.22	5		0.12	0.22	4		-0.11	0.22	7		-0.29	0.23	6
N288A	-0.26	0.05	4		-0.16	0.04	4		-0.16	0.04	4		-0.31	0.05	4		-0.08	0.05	4
C289A	0.27	0.26	5		0.08	0.26	5		0.15	0.26	5		-0.34	0.27	9	ND			
W290A	0.49	0.27	4	ND			8		0.23	0.27	4		-0.04	0.30	4		0.15	0.27	4
L291A	0.13	0.08	4		0.12	0.09	4		0.08	0.08	4		0.03	0.10	4		-0.34	0.10	7
S292A	1.10	0.10	4		0.42	0.05	5		0.61	0.05	4		0.96	0.09	4		0.27	0.05	4
V293A	0.24	0.05	4		-0.14	0.04	5		-0.05	0.04	4		-0.03	0.05	4		-0.19	0.05	4
E294A	-0.27	0.05	4		-0.24	0.05	4		-0.32	0.05	4		-0.34	0.06	4		-0.46	0.08	4
T295A	0.31	0.26	4		0.25	0.26	4		0.29	0.26	4		0.06	0.27	4		-0.26	0.27	8
H296A	-0.35	0.06	4		-0.36	0.05	4		-0.43	0.05	4		-0.44	0.07	4		-0.58	0.09	4
L297A	0.24	0.21	7		0.19	0.21	7		0.22	0.21	7		0.04	0.21	7		0.12	0.21	7
L298A	0.39	0.15	7		0.39	0.15	7		0.28	0.15	7		0.29	0.15	7		0.17	0.15	7
Y299A	0.12	0.27	5		0.04	0.27	5		0.04	0.27	5		-0.03	0.28	5		-0.36	0.28	8
I300A	0.35	0.43	7		0.48	0.43	6		0.37	0.43	6		0.22	0.43	7		0.24	0.43	7
WT (ECL3)	-0.19	0.02	26		-0.18	0.02	29		-0.19	0.02	25		-0.19	0.02	25		-0.20	0.02	27
F356A	0.25	0.07	5		0.19	0.07	5		0.12	0.07	5		0.19	0.06	5		0.21	0.07	5
V357A	0.32	0.10	5		0.28	0.10	5		0.19	0.10	5		0.07	0.10	5		-0.10	0.11	5
V358A	0.09	0.04	5		-0.09	0.05	4		-0.07	0.04	4		-0.31	0.05	4		-0.58	0.09	4
F359A	0.06	0.05	5		-0.04	0.05	4		0.11	0.05	4		-0.30	0.05	4		-0.66	0.08	4
P360A	-0.31	0.05	4		-0.31	0.05	4		-0.23	0.05	4		-0.54	0.06	4		-1.19	0.15	5
W361A	0.01	0.06	5		-0.18	0.06	5		-0.20	0.06	6		-0.50	0.08	5		-0.49	0.09	5
R362A	-0.22	0.06	4		-0.24	0.07	4		-0.29	0.06	4		-0.36	0.06	4		-0.53	0.09	4
P363A	-0.24	0.08	4		-0.26	0.09	4		-0.34	0.08	4		-0.94	0.21	4	ND			
S364A	-0.30	0.06	5		-0.29	0.06	5		-0.27	0.06	5		-0.25	0.06	5		-0.26	0.07	5
N365A	0.12	0.07	5		0.11	0.07	5		0.06	0.06	5		0.19	0.07	5		0.12	0.07	5
K366A	-0.22	0.04	4		-0.21	0.04	4		-0.25	0.04	4		-0.28	0.04	4		-0.20	0.05	4
M367A	-0.43	0.06	3		-0.37	0.06	3		-0.38	0.05	3		-0.51	0.06	3		-0.28	0.07	3
L368A	-0.14	0.08	5		-0.13	0.08	5		-0.21	0.07	5		-0.28	0.08	5		-0.39	0.11	5
G369A	-0.23	0.05	4		-0.42	0.06	4		-0.32	0.05	4		-0.48	0.06	4		-0.43	0.08	4
K370A	-0.36	0.05	5		-0.42	0.05	5		-0.38	0.05	5		-0.35	0.05	5		-0.32	0.05	5
I371A	-0.24	0.07	4		-0.19	0.07	4		-0.23	0.07	4		-0.29	0.07	4		-0.27	0.09	3
Y372A	-0.26	0.05	5		-0.27	0.06	5		-0.46	0.06	5		-0.36	0.06	5		-0.69	0.09	5
D373A	0.43	0.06	5		0.50	0.06	5		0.12	0.06	5		-0.58	0.12	5	ND			
Y374A	-0.25	0.08	5		-0.24	0.08	5		-0.27	0.08	5		-0.22	0.08	5		-0.27	0.09	4
V375A	-0.54	0.08	3		-0.55	0.08	3		-0.55	0.07	3		-0.66	0.09	3		-0.42	0.08	3
M376A	0.14	0.07	5		-0.07	0.07	4		-0.11	0.07	4		-0.24	0.07	4		-0.46	0.10	4

^aFor each receptor mutant and ligand, concentration–response data for each pathway were fit with the Black and Leff operational model to derive an affinity-independent measure of efficacy (log τ) and functional affinity. These data were corrected for changes in cell surface expression from FACS to yield Log τ_c . Mean, S.E.M., and the individual experimental “n” values are reported. Significance of changes in log τ_c of each ligand was determined by comparison of mutant receptors to WT values by a one-way ANOVA and Dunnett’s post-test ($p < 0.05$ denoted by bold coloured entries. Orange, significant decrease ≤ 10 -fold; red, significant decrease > 10 -fold; light green, significant increase ≤ 10 -fold; dark green, significant increase > 10 -fold). ND, data were not able to be reliably determined.

peptides. Of the other mutants only K370A (hCT), F357A, and D373A (hCGRP) did not have significant effects on pERK peptide efficacy (Figure 9F–J).

Mapping the effects of ECL2 and ECL3 mutation onto the 3D AMY₃R model revealed major differences in the effect of alanine mutation on the two signaling pathways (Figure 10). Mutations through the core of ECL2 dramatically reduced CT peptide and rAmy efficacy for pERK but had very limited impact on the efficacy in cAMP assays (Figure 10).

Within ECL2, the most notable effect on cAMP efficacy was increased efficacy with the S292A mutation. This contrasts to the decreased functional affinity of the CT peptides for this pathway. S292 is capable of forming polar interactions and, in the CTR, contributes to packing of ECL2 in the active state.¹⁶ Nonetheless, in CTR the S292A mutation does not alter either affinity or efficacy of peptides for this pathway.¹⁷ This suggests that RAMP3 allosterically alters CTR ECL2 conformation, potentially allowing this residue to interact with rAmy and CT peptides when coupled to Gs.

Within ECL3, the mutation of residues at the proximal end of TM6 that are located deep in the peptide binding pocket led

to enhanced cAMP efficacy for all peptides (Figure 10A–E). Interestingly, N365, whose alanine mutation also enhanced cAMP efficacy for all peptides, is located at the external face of the receptor (Figure 10A–E), and thus may make polar interactions with lipid head groups that constrain conformational propagation for Gs engagement in the context of the AMY₃R. This amino acid was one of very few that did not adversely affect pERK efficacy (Figure 10A–E versus Figure 10F–J), suggesting that such a constraint does not affect non-Gs pathways. We have previously shown that pERK is independent of cAMP-dependent PKA activity, and PTX-sensitive Gi/o proteins for the AMY₃R⁷ indicating that, like CTR, the effect of mutations on the two measured pathways reveal distinct conformational propagation pathways. Comparison of the effect of mutation on AMY₃R and CTR pointed to peptide-specific influence on cAMP efficacy (Figure 11).

Intriguingly, while the pattern of effect was similar, alanine mutation in ECL3 had greater impact on sCT efficacy at AMY₃R compared to CTR, with mutation of the deeper, peptide-proximal residues within ECL3 enhancing cAMP efficacy (Figure 11A versus Figure 11F), implying a role for

Table 5. Effect of Single Alanine Mutation in AMY₃R ECL2 or ECL3 on pERK Signaling Efficacy (log τ_c) of Peptides^a

	sCT				hCT				pCT				rAmy				hCGRP		
	Mean	S.E.M.	N		Mean	S.E.M.	N		Mean	S.E.M.	N		Mean	S.E.M.	N		Mean	S.E.M.	N
WT (ECL2)	0.86	0.11	27		0.88	0.10	33		0.84	0.10	31		0.04	0.04	33		-0.50	0.07	25
I279A	1.05	0.24	5		1.09	0.21	7		0.94	0.18	6		0.31	0.09	7		-0.43	0.10	5
T280A	-0.36	0.17	5		-1.29	0.20	8		-0.30	0.16	6		-1.13	0.16	7		-1.03	0.20	7
R281A	-0.93	0.37	6	ND					-0.53	0.40	6		-0.91	0.35	8		-1.45	0.60	6
V283A	-0.15	0.14	5		0.11	0.14	7		0.09	0.13	7		-0.48	0.09	8		-0.42	0.12	6
Y284A	-1.52	0.26	7		-1.48	0.25	6		-0.75	0.23	5		-0.72	0.20	5		-1.34	0.33	5
F285A	-1.52	0.27	6		-1.37	0.25	7		-1.36	0.26	5		-1.40	0.22	6		-1.57	0.41	5
N286A	-1.56	0.31	6		-1.28	0.38	6		-1.63	0.40	5		-1.57	0.27	6		-1.27	0.58	5
D287A	-1.10	0.35	6	ND				ND					-1.47	0.34	7	ND			
N288A	-0.52	0.14	6		-0.04	0.16	6		-0.71	0.17	5		-2.33	0.39	3		-0.69	0.12	6
C289A	-1.51	0.41	6	ND					-1.87	0.72	5	ND					-0.68	0.40	6
W290A	-0.26	0.32	6		-1.63	0.69	7		-0.63	0.44	5		-0.99	0.34	6		-1.55	0.63	5
L291A	-1.45	0.29	5	ND					-1.08	0.30	6		-1.81	0.30	5	ND			
S292A	-1.24	0.19	6		-1.29	0.20	7		-0.85	0.20	5		-1.56	0.20	6		-1.74	0.34	6
V293A	-0.55	0.15	6		-0.55	0.14	7		-0.02	0.16	5		-1.03	0.12	6		-1.00	0.16	6
E294A	0.09	0.17	4		0.19	0.13	7		0.15	0.12	7		-0.49	0.08	9		-0.47	0.12	6
T295A	-0.18	0.30	6		-1.54	0.51	8		-1.17	0.45	4		-1.63	0.39	7		-1.23	0.59	7
H296A	0.53	0.17	5		0.30	0.14	7		0.47	0.13	7		-0.38	0.08	8		-0.81	0.14	6
L297A	-0.43	0.26	5		0.01	0.28	6		-0.17	0.26	5		-0.48	0.25	4		-0.42	0.30	4
L298A	-0.82	0.35	3		-0.52	0.35	3		-0.86	0.33	3		-1.23	0.39	3	ND			
Y299A	-0.98	0.34	6		-1.72	0.51	5		-1.57	0.48	5		-1.40	0.39	5	ND			
I300A	-0.68	0.48	5		-0.92	0.50	6		-0.53	0.48	6		-0.86	0.46	6		-0.72	0.54	4
WT (ECL3)	1.21	0.17	28		1.16	0.15	24		1.07	0.16	21		1.13	0.18	23		0.68	0.12	24
F356A	-0.75	0.24	6		-1.66	0.45	6		-0.79	0.29	6		-0.55	0.22	6		0.19	0.16	6
V357A	-0.95	0.23	6		-1.06	0.31	6		-0.84	0.22	6		-0.82	0.22	6		-0.51	0.23	6
V358A	-0.77	0.22	6		-1.22	0.27	4		-2.09	0.38	4		-1.62	0.39	4		-1.79	0.46	4
F359A	-0.34	0.20	6		-1.26	0.26	4		-1.79	0.29	4		-1.42	0.31	4		-2.05	0.50	4
P360A	-0.42	0.24	6		-1.56	0.35	5		-1.29	0.28	5		-1.09	0.26	6	ND			
W361A	0.09	0.23	4		-0.09	0.30	3		-0.14	0.29	3		-0.24	0.36	3		-1.48	0.35	3
R362A	-2.59	0.61	3		-2.09	0.91	3		-2.71	0.73	3	ND			3	ND			
P363A	-1.11	0.30	5		-1.49	0.44	5		-1.73	0.35	5	ND			5	ND			
S364A	0.38	0.30	6		1.62	0.34	5		-0.27	0.24	3		0.22	0.22	4		0.39	0.18	5
N365A	0.51	0.25	6		1.20	0.33	5		0.03	0.26	3		0.45	0.20	4		1.04	0.31	5
K366A	-1.26	0.32	3		-1.15	0.28	3		-1.86	0.35	3		-1.80	0.38	3		-0.96	0.30	3
M367A	-1.12	0.49	3		-1.17	0.37	3		-1.26	0.35	3		-1.61	0.44	3		-1.37	0.31	3
L368A	0.30	0.21	6		-0.60	0.21	4		-0.23	0.17	5		-0.18	0.24	5		-0.65	0.26	5
G369A	-1.39	0.36	3		-1.62	0.34	3		-1.81	0.38	3		-1.85	0.55	3		-1.53	0.46	3
K370A	-0.55	0.23	6		0.59	0.37	5		-0.43	0.23	4		-0.65	0.75	3		-0.87	0.25	3
I371A	-2.03	0.46	3	ND					-2.27	0.56	3		-2.69	0.67	3	ND			
Y372A	-0.03	0.29	6		-1.33	0.54	6		-2.53	0.53	5		-2.26	0.42	5		-0.55	0.18	5
D373A	-0.58	0.27	6		-0.65	0.37	6		-1.30	0.70	5	ND					0.25	0.05	5
Y374A	0.36	0.25	6		0.54	0.26	5		0.96	0.33	4		0.88	0.38	5		0.23	0.07	5
V375A	-1.20	0.30	6		-2.64	0.46	5		-2.38	0.46	4		-2.26	0.83	4	ND			
M376A	-1.90	0.35	6		-2.62	0.78	4		-2.78	0.65	4		-2.50	1.02	4	ND			

^aFor each receptor mutant and ligand, concentration–response data for each pathway were fit with the Black and Leff operational model to derive an affinity-independent measure of efficacy (log τ) and functional affinity. These data were corrected for changes in cell surface expression from FACS to yield log τ_c . Mean, S.E.M., and the individual experimental “n” values are reported. Significance of changes in log τ_c of each ligand was determined by comparison of mutant receptors to WT values by a one-way ANOVA and Dunnett’s post-test ($p < 0.05$ denoted by bold coloured entries. Red, significant decrease > 10 -fold). ND, data were not able to be reliably determined.

RAMP3 in directing the conformation change required for activation of the Gs pathway for this peptide. For hCT, RAMP3 in AMY₃R appeared to shift the path of change from ECL2 to ECL3, based on the shift in mutational sensitivity between the two receptors (Figure 11B,G), while, in 3D representation, the effect of mutation of pCT cAMP response was similar across AMY₃R and CTR (Figure 11C,H).

The largest divergence between the effect of mutation for AMY₃R and CTR, on peptide-mediated cAMP efficacy, occurred for rAmy, in which, outside of deep pocket residues described above, mutation in ECL3 was generically associated with loss of efficacy for AMY₃R but had limited effect on CTR (Figure 11D,I). This is consistent with the selective enhancement of rAmy affinity and potency seen at the AMY₃R. While hCGRP potency is also enhanced at the AMY₃R, this effect is less prominent than that induced by RAMP1.²⁰ As such, it is perhaps unsurprising that the effect of mutation on hCGRP cAMP efficacy at the AMY₃R was generally similar to that observed for CTR (Figure 11E,J).

Among the most profound differences in the effect of mutation on AMY₃R versus CTR was the effect on pERK efficacy (Figure 12). For the CTR, there was minimal observed effect of ECL2 and ECL3 mutation on CTR-mediated pERK

(Figure 12F–J). In contrast, there was broad loss of pERK efficacy for mutation of AMY₃R across both ECL2 and ECL3 (Figure 12A–E), supporting a model in which RAMP3 causes a switch in the intracellular transducers engaged by CTR that are linked to the pERK pathway. While there has not been much investigation into the pathways linked to pERK downstream of AMY₃R and CTR, the use of pathway inhibitors has implicated PKC, PI3K, and PLC in the phosphorylation of ERK.⁷ While those studies suggested subtle differences in the effect of inhibitors between AMY₃R and CTR,⁷ the mechanistic basis for the major changes to sensitivity of mutants for AMY₃R versus CTR remains to be elucidated. Nonetheless, they suggest that RAMP3 alters conformational propagation at least through ECL2 and ECL3. The exception to this was hCGRP that exhibited a similar pattern of mutational effect for both receptor phenotypes (Figure 12E,J). This lack of effect may reflect the limited induction of hCGRP binding and signaling that occurs with RAMP3, relative to CTR alone, when compared to the phenotypic induction by RAMP1.²⁰

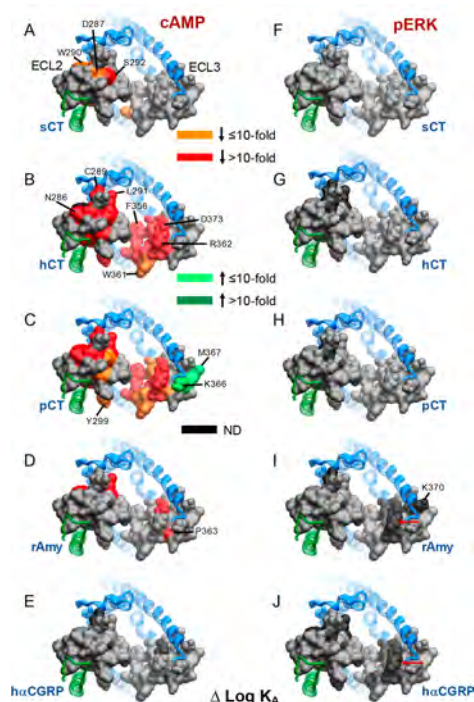


Figure 5. Alanine mutation of ECL2 and ECL3 of AMY_3R alters functional affinity ($\log K_A$) in a peptide- and pathway-specific manner. Functional affinities derived from operational fitting of concentration–response curves in cAMP accumulation (A–E) and pERK (F–J) are displayed as $\Delta \log K_A$ from wild-type. Illustrated is a top view of the AMY_3R model with the extracellular surface subject to alanine scanning depicted (combined surface/cpk representation). Mutations that significantly alter peptide functional $\log K_A$ are colored according to the magnitude of effect, with mutated amino acids without significant alteration to $\log K_A$ colored gray. Amino acid mutations for which there was an insufficiently robust functional effect to quantify by operational modeling are depicted in black. The receptor ECD and peptide are not shown for clarity, with the CTR TM bundle in blue ribbon and RAMP3 in green ribbon. Red arrows in panels I and J indicate residues at the apex of ECL3 that are affected for Amy and CGRP but not CT peptides.

CONCLUSION

Biased agonism is a key pharmacological behavior of both endogenous GPCR ligands and drugs that target these receptors. Class B GPCRs are important physiological targets that display biased signaling in response to both endogenous and exogenous agonists, although the mechanistic basis for these differential effects is unclear. In this study, we demonstrate that the dynamic nature of CTR ECL2 and ECL3 in propagation of signaling is fundamentally altered when complexed with RAMP3 to form the AMY_3R , despite only having predicted direct interactions with ECL2. Moreover, the work shows that the role of these loops in receptor signaling is highly peptide dependent, illustrating that even subtle changes to peptide sequence may change signaling output downstream of the receptor. The work further supports the allosteric role proposed for RAMPs in altering GPCR function^{21–25} with these changes, as assessed in the current study, extending well beyond the RAMP-CTR interface. While full understanding of these findings will likely require solution of structures of CTR:RAMP3 along with individual agonist peptides and transducer proteins, the current work advances our understanding of peptide control of class B GPCR

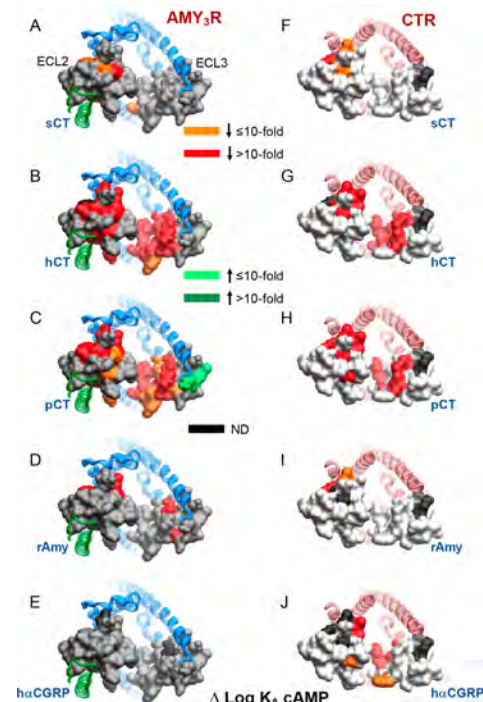


Figure 6. Alanine mutation of ECL2 and ECL3 has distinct effects on AMY_3R and CTR cAMP functional affinity ($\log K_A$). Functional affinities derived from operational fitting of concentration–response curves in cAMP accumulation are displayed as $\Delta \log K_A$ from wild-type for AMY_3R (A–E) and CTR (F–J). Illustrated are top views of the receptors with the extracellular surface subject to alanine scanning depicted (combined surface/cpk representation). Mutations that significantly alter peptide functional $\log K_A$ are colored according to the magnitude of effect, with mutated amino acids without significant alteration to $\log K_A$ colored gray. Amino acid mutations where there was an insufficiently robust functional effect to quantify by operational modeling are depicted in black. The receptor ECD and peptide are not shown for clarity, with the CTR TM bundle in blue ribbon and RAMP3 in green ribbon in panels A–E, and CTR TM bundling in red ribbon in panels F–J. Data for CTR functional affinity are from Dal Maso et al., 2018.¹⁷

signaling and the molecular basis for RAMP modulation of receptor function.

METHODS

Reagents. All peptides were purchased from Mimotopes. Dulbecco's Modified Eagle's Medium (DMEM) was purchased from Invitrogen. Fetal bovine serum (FBS) was purchased from ThermoFisher Scientific. AlphaScreen reagents, Lance cAMP kit, and 384-well Optiplates were purchased from PerkinElmer. SureFire ERK1/2 reagents were obtained from TGR Biosciences and PerkinElmer. Antibodies were purchased from R&D Systems and ThermoFisher. All other reagents were purchased from Sigma-Aldrich or BDH Merck and were of an analytical grade.

Mutagenesis. Desired mutations were introduced to N-terminally c-Myc tagged human CTR in pENTER11 (Invitrogen) as previously described,¹⁷ then LR recombination reactions were conducted to transfer mutated and wild-type (WT) receptor into the pEF5/FRT/Rluc-8/IRES/RAMP3/Venus destination vector using Gateway Technology (Invitrogen), similar to our previously reported design of

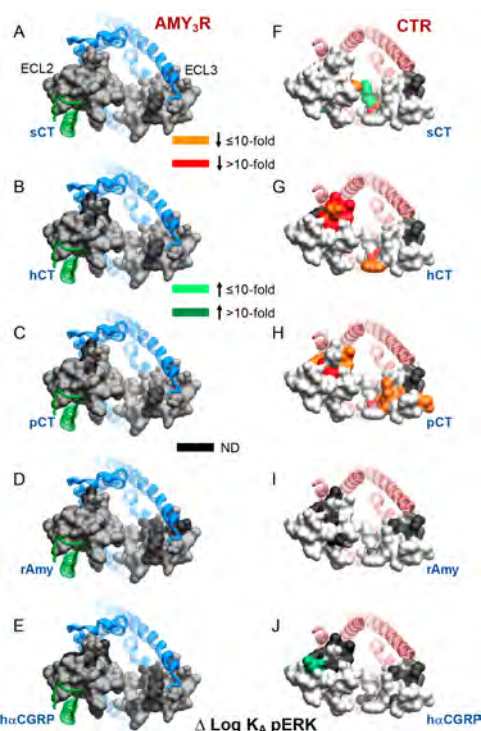


Figure 7. Alanine mutation of ECL2 and ECL3 has distinct effects on AMY_3R and CTR pERK functional affinity ($\log K_A$). Functional affinities derived from operational fitting of concentration–response curves in pERK are displayed as $\Delta \log K_A$ from wild-type for AMY_3R (A–E) and CTR (F–J). Illustrated are top views of the receptors with the extracellular surface subject to alanine scanning depicted (combined surface/cpk representation). Mutations that significantly alter peptide functional $\log K_A$ are colored according to the magnitude of effect, with mutated amino acids without significant alteration to $\log K_A$ colored gray. Amino acid mutations where there was an insufficiently robust functional effect to quantify by operational modeling are depicted in black. The receptor ECD and peptide are not shown for clarity, with the CTR TM bundle in blue ribbon and RAMP3 in green ribbon in A–E, and CTR TM bundling in red ribbon in F–J. Data for CTR functional affinity are from Dal Maso et al., 2018.¹⁷

bicistronic constructs.²⁶ Mutants were confirmed by automated-sequencing.

Stable Cell Line Generation and Cell Culture. The mutant or WT receptor genes were integrated into Flp-In-CV1 cells using Flp-In system (Invitrogen). Stable Flp-In expression cell lines were generated through polyclonal selection and screening and maintained in DMEM supplemented with 5% (v/v) FBS, 300 $\mu\text{g/mL}$ hygromycin B (Invitrogen) at 37 °C in 5% CO_2 . Independent WT controls were established for each of the ECL2 and ECL3 mutants, as these were created at different times.

Whole Cell Competition Binding Assay. Radioligand competition binding was performed as previously described¹⁷ on whole cells seeded into 96-well plates and cultured overnight, except that ^{125}I -rAmy was used as the radioligand. For homologous competition binding experiments, cells were incubated overnight at 4 °C with ~ 100 pM ^{125}I -rAmy (specific activity, 2000 Ci/mmol) and serial dilutions of non-iodinated rAmy, while heterologous competition was in the presence of increasing concentrations of unlabeled peptide. Non-bound ligand was removed and bound ligand activity was measured using a γ counter (Wallac Wizard 1470 Gamma Counter,

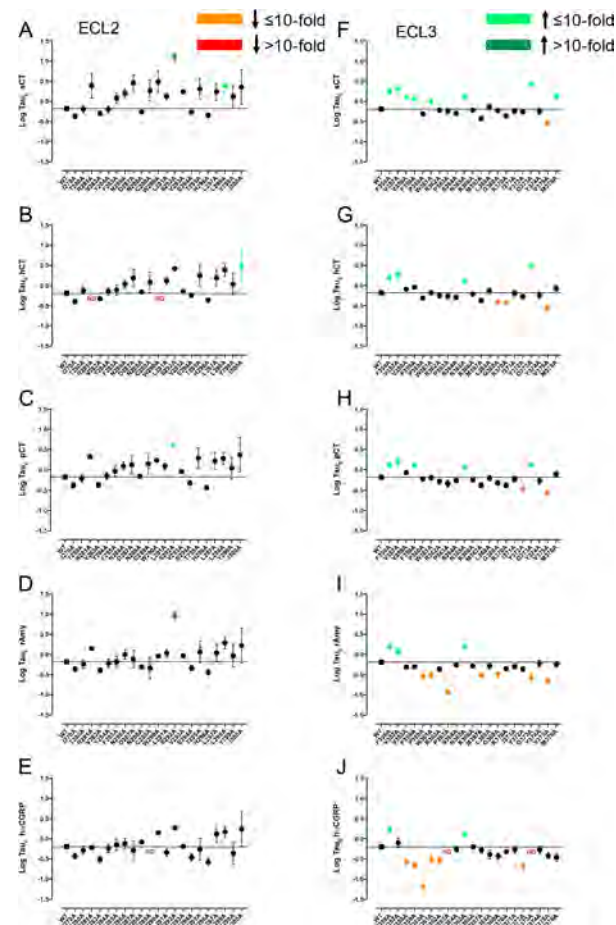


Figure 8. Alanine mutation of ECL2 and ECL3 of AMY_3R alters cAMP efficacy ($\log \tau_c$) in a peptide-specific manner. Peptide efficacy ($\log \tau$) was derived from operational fitting of concentration–response curves in cAMP accumulation for alanine mutation of ECL2 (A–E) and ECL3 (F–J), and corrected for cell surface receptor expression to yield $\log \tau_c$. Significance of mutation effect was established by comparison of the WT to the other receptor mutants following one-way ANOVA and Dunnett's post-test with $P < 0.05$ accepted as significant. Mutants that significantly reduced $\log \tau_c$ are colored orange (≤ 10 -fold change), or red (> 10 -fold change). Mutants that significantly increased $\log \tau_c$ are colored green (≤ 10 -fold change, light green; > 10 -fold, dark green). Where data were insufficiently robust to derive a reliable value for $\log \tau_c$ no symbol is shown (ND). Quantitative data are reported in Table 4.

PerkinElmer, 78% counter efficiency). Values were normalized against nonspecific binding, defined by the presence of 1 μM of unlabeled rAmy, and total ligand bound radioligand.

Cell Surface Expression Assessment by FACS. Surface expression of AMY_3R mutants stably expressed in CV-1 cells was quantified by flow cytometry of antibody binding to the c-Myc tagged CTR subunit of the receptor using standard methods. Cells were grown in 6-well plates at $\sim 5 \times 10^5$ cells per well the day before assay. Cells were harvested in the presence of versene. All staining steps were conducted in ice cold Hank's Balanced Salt Solution (HBSS) with 0.1% bovine serum albumin (BSA) and 20 mM HEPES (4-(2-hydroxyethyl)-1-piperazineethanesulfonic acid, pH 7.4). Blocking was conducted in 5% BSA. Primary antibody staining was performed with 5 $\mu\text{g/mL}$ 9E10 (anti-c-Myc) antibody. The secondary antibody was 1 $\mu\text{g/mL}$ goat antimouse AF647 (ThermoFisher). Sytox blue was used for live/dead discrim-

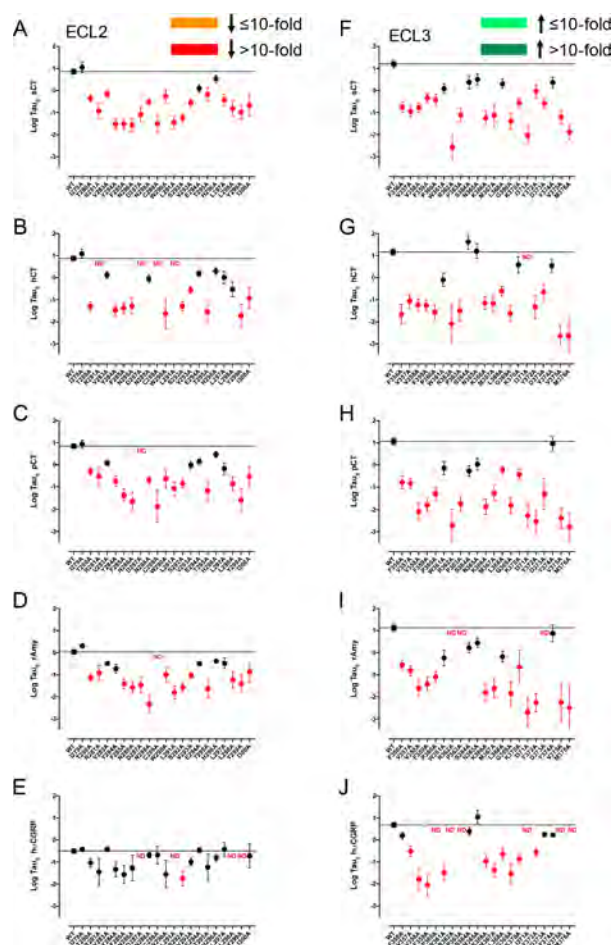


Figure 9. Alanine mutation of ECL2 and ECL3 of AMY_3R alters pERK efficacy ($\log \tau_c$) in a peptide-specific manner. Peptide efficacy ($\log \tau$) was derived from operational fitting of concentration–response curves in pERK for alanine mutation of ECL2 (A–E) and ECL3 (F–J), and corrected for cell surface receptor expression to yield $\log \tau_c$. Significance of mutation effect was established by comparison of the wild-type to the other receptor mutants following one-way ANOVA and Dunnett's post-test with $P < 0.05$ accepted as significant. Mutants that significantly reduced $\log \tau_c$ are colored orange (≤ 10 -fold change), or red (> 10 -fold change). Where data were insufficiently robust to derive a reliable value for $\log \tau_c$ no symbol is shown (ND). Quantitative data are reported in Table 5.

ination. Data were collected on a FACS CantosII (BD Biosciences) with at least 20 000 live cells collected per sample. WT stained CTR sample and stained parental CV-1 cells were collected at the beginning and the end of each run. Data were analyzed using FlowJo. The mean AF647 fluorescence intensity from each sample for a particular experiment was normalized against parental (0%) and WT CTR (100%) controls.

cAMP Accumulation Assay. Cells (2.5×10^4 cells/well) were seeded into 96-well plates and incubated overnight. Complete media was replaced with phenol red-free DMEM containing 0.5 mM 3-isobutyl-1-methylxanthine (IBMX) and 0.1% BSA and preincubated for 30 min. Cells were stimulated with increasing concentrations of ligands for 30 min in the presence of 0.5 mM 3-isobutyl-1-methylxanthine (IBMX). The media was discarded, changed to absolute ethanol and volatilized to dryness at room temperature. Samples were then lysed and intracellular cAMP was detected using the

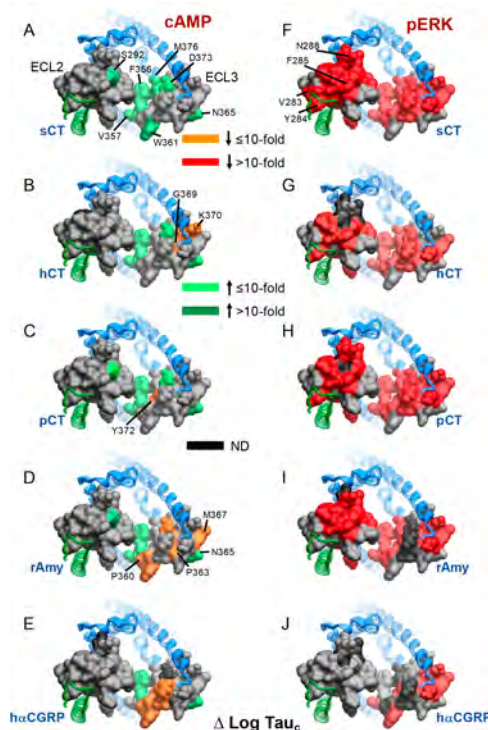


Figure 10. Alanine mutation of ECL2 and ECL3 of AMY_3R alters peptide efficacy ($\log \tau_c$) in a pathway-specific manner. Efficacy values derived from operational fitting of concentration–response curves in cAMP accumulation (A–E) and pERK (F–J) are displayed as $\Delta \log \tau_c$ from wild-type. Illustrated is a top view of the AMY_3R model with the extracellular surface subject to alanine scanning depicted (combined surface/cpk representation). Mutations that significantly alter peptide $\log \tau_c$ are colored according to the magnitude of effect, with mutated amino acids without significant alteration to $\log \tau_c$ colored gray. Amino acid mutations for which there was an insufficiently robust functional effect to quantify by operational modeling are depicted in black. The receptor ECD and peptide are not shown for clarity, with the CTR TM bundle in blue ribbon and RAMP3 in green ribbon.

PerkinElmer Lance kit as previously described.¹⁴ Data were normalized to the maximal response of each peptide.

ERK1/2 Phosphorylation. Cells (2.5×10^4 cells/well) were seeded into 96-well culture plates and incubated overnight. Initially, pERK1/2 time-course experiments were performed over 30 min to identify the time point when the pERK1/2 response is maximal (6–8 min). Subsequently, this time point was selected to generate concentration response curves for different agonists with ligand addition performed after overnight serum starvation with DMEM. FBS was used as a positive control. pERK1/2 was detected using an AlphaScreen assay as previously described.²⁷ Data were normalized to the maximal response elicited by each peptide.

Pharmacological Data Analysis. IC_{50} and B_{max} values were estimated from competitive inhibition of ^{125}I -rAmy binding using a three-parameter logistic equation [Log-(inhibitor versus response)] in Prism (v7 or v8; GraphPad). The concentration of the radioligand was $\leq 5\%$ of the K_D values. Under these conditions, the IC_{50} approximates K_i and such data are reported as $\log K_i$. The Black and Leff operational model of partial agonism^{19,27} was applied to separate effects on pathway-specific efficacy (defined by the value τ) from those that modify ligand functional affinity ($\log K_A$). Derived τ values were normalized to experimentally

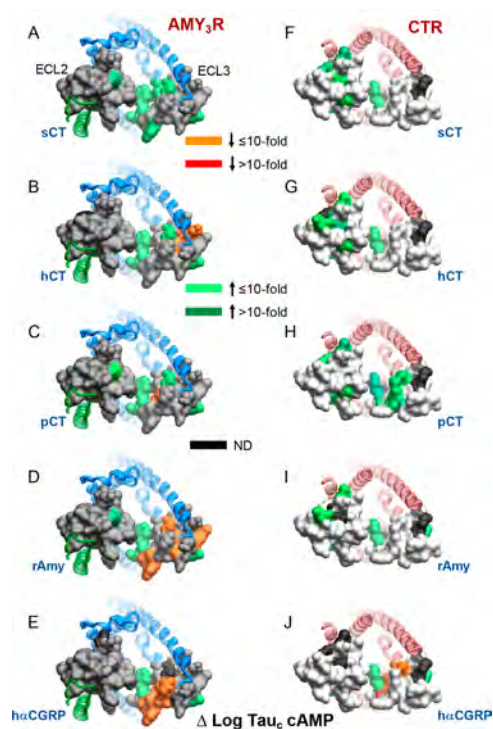


Figure 11. Alanine mutation of ECL2 and ECL3 has distinct effects on cAMP peptide efficacy for AMY₃R and CTR. Peptide efficacy, derived from operational fitting of concentration–response curves in cAMP accumulation, are displayed as $\Delta \log \tau_c$ from wild-type for AMY₃R (A–E) and CTR (F–J). Illustrated are top views of the receptors with the extracellular surface subject to alanine scanning depicted (combined surface/cpk representation). Mutations that significantly alter peptide functional $\log \tau_c$ are colored according to the magnitude of effect, with mutated amino acids without significant alteration to $\log \tau_c$ colored gray. Amino acid mutations for which there was an insufficiently robust functional effect to quantify by operational modeling are depicted in black. The receptor ECD and peptide are not shown for clarity, with the CTR TM bundle in blue ribbon and RAMP3 in green ribbon in A–E, and CTR TM bundling in red ribbon in F–J. Data for CTR peptide efficacy are from Dal Maso et al., 2018.¹⁷

determined levels of cell surface expression to provide a measure of efficacy (τ_c) that is independent of affinity and altered cell surface receptor expression.²⁸ pK_i , pK_A , and $\log \tau_c$ values for mutant receptors were statistically compared to those of the respective WT receptor using a one-way analysis of variance (ANOVA) and Dunnett's post-test. Significance was accepted at $P < 0.05$.

Computational Methods. System Preparation. The CTR:RAMP3 complex was built using the Modeler comparative modeling program from the full CGRPR¹⁵ and CTR¹⁶ 3.3 Å cryo-EM receptor structures, which included the missing loops, and the 1.76 Å CLR:RAMP2 X-ray crystal structure of the extracellular domain of the adrenomedullin receptor²⁹ (PDB codes 6E3Y, 6NIY, and 4RWF, respectively). The disulfide bond between RAMP3 residues Cys 28 and Cys 72 was included. The structure with the best discrete optimized protein energy (DOPE) score³⁰ out of 1000 generated models was prepared for molecular dynamics simulation using a combination of python htmd³¹ and tcl (Tool Command Language) scripts. Hydrogen atoms were added using pdb 2pqr;³² the protonation state of titratable side chains was determined using propka³³ (run at pH 7) coupled with visual

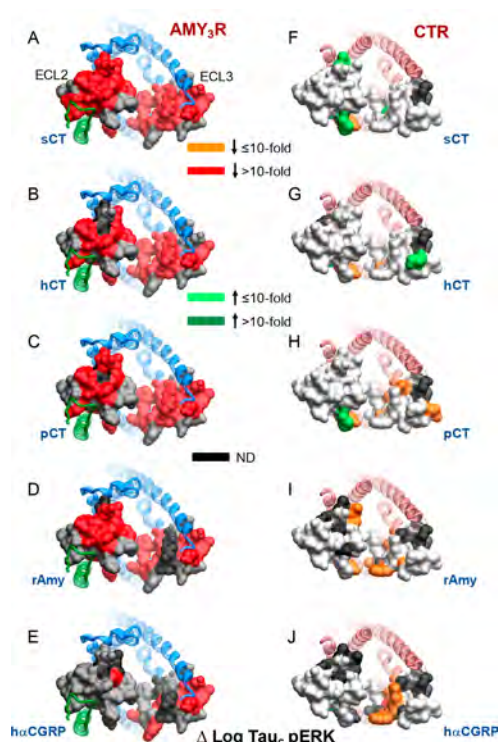


Figure 12. Alanine mutation of ECL2 and ECL3 has distinct effects on pERK peptide efficacy for AMY₃R and CTR. Peptide efficacy, derived from operational fitting of concentration–response curves in pERK, are displayed as $\Delta \log \tau_c$ from wild-type for AMY₃R (A–E) and CTR (F–J). Illustrated are top views of the receptors with the extracellular surface subject to alanine scanning depicted (combined surface/cpk representation). Mutations that significantly alter peptide functional $\log \tau_c$ are colored according to the magnitude of effect, with mutated amino acids without significant alteration to $\log \tau_c$ colored gray. Amino acid mutations for which there was an insufficiently robust functional effect to quantify by operational modeling are depicted in black. The receptor ECD and peptide are not shown for clarity, with the CTR TM bundle in blue ribbon and RAMP3 in green ribbon in A–E, and CTR TM bundling in red ribbon in F–J. Data for CTR peptide efficacy are from Dal Maso et al., 2018.¹⁷

inspection. The systems were embedded in a pre-existing 1-palmitoyl-2-oleyl-*sn*-glycerol-3-phospho-choline (POPC) bi-layer using an insertion method,³⁴ with overlapping lipids removed. The receptor orientation was determined from the Calcitonin receptor-Gs complex (PDB ID: 5UZ7) entry in the OPM database.³⁵ TIP3P water molecules³⁶ were added to the 106 Å × 106 Å × 141 Å simulation box using the VMD Solvate plugin version 1.5 (<http://www.ks.uiuc.edu/Research/vmd/plugins/solvate/>). Sodium and chloride ions were added to mimic an ionic strength of 0.150 M and to obtain overall charge neutrality, using the VMD Autoionize plugin 1.3 (Autoionize Plugin, Version 1.3, at < <http://www.ks.uiuc.edu/Research/vmd/plugins/autoionize/>).

Systems Equilibration and MD Settings. The MD engine ACEDMD³⁷ was employed for both the equilibration and productive simulations, which employed the CHARMM36 force field.³⁸ Equilibration was achieved in isothermal–isobaric conditions (NPT) using the Langevin thermostat³⁹ (target: 300 K) with a low damping of 1 ps^{−1} and the Berendsen barostat⁴⁰ (target: 1 atm) over a three-stage procedure using an integration time step of 2 fs. First, clashes between protein and lipid atoms were reduced through 2500 conjugate-gradient

minimization steps followed by a 2 ns long MD simulation with a positional constraint of 1 kcal mol⁻¹ Å⁻² on protein and lipid phosphorus atoms. Second, 33 ns of MD simulation was performed with only the protein atoms constrained. Third, positional constraints were applied only to the protein backbone alpha carbons for a further 35 ns.

A 1 μ s simulation was run in the canonical ensemble (NVT) at 300 K, using a thermostat damping of 0.1 ps⁻¹. The M-SHAKE algorithm⁴¹ was used to constrain the covalent bonds involving hydrogen atoms, enabling a time step of 4 fs. A 9 Å cutoff distance was used for the electrostatic interactions, with a switching function applied beyond 7.5 Å; long-range Coulomb interactions were handled using the particle mesh Ewald summation method (PME)⁴² with a mesh spacing to 1.0 Å. The mutagenesis results were plotted on the 200 ns structure, since this was deemed sufficient to remove any strain within the initial structure.

■ ASSOCIATED CONTENT

● Supporting Information

The Supporting Information is available free of charge on the ACS Publications website at DOI: 10.1021/acsptsci.9b00010.

Effect of alanine mutation of ECL2 and ECL3 of AMY₃R on peptide affinity; competition binding isotherms at WT and mutant AMY₃R; concentration response curves in cAMP accumulation assays and in ERK1/2 phosphorylation assays at WT and mutant AMY₃R (PDF)

■ AUTHOR INFORMATION

Corresponding Authors

*E-mail: Patrick.sexton@monash.edu.

*E-mail: denise.wootten@monash.edu.

*E-mail: mwwang@sim.ac.cn.

ORCID

Debbie L. Hay: 0000-0002-9558-5122

Sebastian G. B. Furness: 0000-0001-8655-8221

Patrick M. Sexton: 0000-0001-8902-2473

Author Contributions

Contributed to experimental design (E.d.M., D.L.H., D.Y., M.-W.W., D.W., P.M.S.); performed experiments (V.P., E.d.M., Y.Z., C.A.H.); contributed to conceptual development of the project (S.G.B.F., D.L.H., A.C., D.Y., M.-W.W., D.W., P.M.S.); performed molecular modeling (G.D., S.A., C.A.R.); performed pharmacological data analysis (V.P., Y.Z., E.d.M., D.W., P.M.S.); contributed to production of figures (Y.Z., E.d.M., D.W., P.M.S.); provided oversight of the project (M.-W.W., D.W., P.M.S.); drafted the manuscript (Y.Z., P.M.S.).

Author Contributions

[#]These authors contributed equally to this work.

Notes

The authors declare no competing financial interest.

■ ACKNOWLEDGMENTS

This work was supported by the National Health and Medical Research Council of Australia (NHMRC) program grant (1055134) and project grants (1061044, 1159006), the National Key R&D Program of China grant (2018YFA0507000), the National Mega R&D Program for Drug Discovery grants (2018ZX09711002-002-005 and 2018ZX09735-001), the National Natural Science Foundation

of China grants (81573479 and 81773792), Shanghai Science and Technology Development Fund grant (15DZ2291600 and 16ZR1407100), Novo Nordisk-CAS Research Fund grant (NNCAS-2017-1-CC), and the Biotechnology and Biological Sciences Research Council (BBSRC; BB/M006883/1). S.G.B.F. is an ARC Future Fellow. D.W. is a Senior Research Fellow, and A.C. and P.M.S. are Senior Principal Research Fellows, of the NHMRC. D.L.H. is a James Cook Research Fellow of the Royal Society of New Zealand. C.A.R. is a Royal Society Industrial Fellow. S.A. is supported by the Peter Nicholls bequest.

■ REFERENCES

- (1) Alexander, S. P., Christopoulos, A., Davenport, A. P., Kelly, E., Marrion, N. V., Peters, J. A., Faccenda, E., Harding, S. D., Pawson, A. J., Sharman, J. L., Southan, C., and Davies, J. A. (2017) CGTP Collaborators. The concise guide to pharmacology 2017/18: G protein-coupled receptors. *Br. J. Pharmacol.* 174 (Suppl. 1), S17–S129.
- (2) Wootten, D., Christopoulos, A., Marti-Solano, M., Babu, M. M., and Sexton, P. M. (2018) Mechanisms of signalling and biased agonism in G-protein-coupled receptors. *Nat. Rev. Mol. Cell Biol.* 19, 638–653.
- (3) Wootten, D., Miller, L. J., Koole, C., Christopoulos, A., and Sexton, P. M. (2017) Allostery and Biased Agonism at Class B G Protein-Coupled Receptors. *Chem. Rev.* 117, 111–138.
- (4) Ostrovskaya, A., Findlay, D. M., Sexton, P. M., and Furness, S. G. B. (2017) Calcitonin. *Reference Module in Neuroscience and Biobehavioral Psychology*, 1–12.
- (5) Hay, D. L., Garejia, M. L., Poyner, D. R., and Walker, C. S. (2018) Update on the pharmacology of calcitonin/ CGRP family of peptides: IUPHAR Review 25. *Br. J. Pharmacol.* 175, 3–17.
- (6) Routledge, S. J., Ladds, G., and Poyner, D. R. (2017) The effects of RAMPs upon cell signalling. *Mol. Cell. Endocrinol.* 449, 12–20.
- (7) Morfis, M., Tilakaratne, N., Furness, S. G. B., Christopoulos, G., Werry, T. D., Christopoulos, A., and Sexton, P. M. (2008) Receptor activity modifying proteins differentially modulate the G protein-coupling efficiency of amylin receptors. *Endocrinology* 149, 5423–5431.
- (8) Hay, D. L., Chen, S., Lutz, T. A., Parkes, D. G., and Roth, J. D. (2015) Amylin: pharmacology, physiology and clinical potential. *Pharmacol. Rev.* 67, 564–600.
- (9) Gydesen, S., Andreassen, K. V., Hjuler, S. T., Hellgren, L. I., Karsdal, M. A., and Henriksen, K. (2017) Optimization of tolerability and efficacy of the novel dual amylin and calcitonin receptor agonist KBP-089 through dose escalation and combination with a GLP-1 analog. *Am. J. Physiol. Endocrinol. Metab.* 313, E598–E607.
- (10) Levin, B. E., and Lutz, T. A. (2017) Amylin and Leptin: Co-Regulators of Energy Homeostasis and Neuronal Development. *Trends Endocrinol. Metab.* 28, 153–164.
- (11) Liberini, C. G., Boyle, C. N., Cifani, C., Venniro, M., Hope, B. T., and Lutz, T. A. (2016) Amylin receptor components and the leptin receptor are co-expressed in single rat area postrema neurons. *Eur. J. Neurosci.* 43, 653–661.
- (12) Liang, Y.-L., Khoshouei, M., Radjainia, M., Zhang, Y., Glukhova, A., Tarrasch, J., Thal, D. M., Furness, S. G. B., Christopoulos, G., Coudrat, T., Danev, R., Baumeister, W., Miller, L. J., Christopoulos, A., Kobilka, B. K., Wootten, D., Skiniotis, G., and Sexton, P. M. (2017) Phase-plate cryo-EM structure of a class B GPCR-G protein complex. *Nature* 546, 118–123.
- (13) Zhang, Y., Sun, B., Feng, D., Hu, H., Chu, M., Qu, Q., Tarrasch, J. T., Li, S., Kobilka, T. S., Kobilka, B. K., and Skiniotis, G. (2017) Cryo-EM structure of the activated GLP-1 receptor in complex with a G protein. *Nature* 546, 248–253.
- (14) Liang, Y.-L., Khoshouei, M., Glukhova, A., Furness, S. G. B., Zhao, P., Clydesdale, L., Koole, C., Truong, T. T., Thal, D. M., Lei, S., Radjainia, M., Danev, R., Baumeister, W., Wang, M.-W., Miller, L. J., Christopoulos, A., Sexton, P. M., and Wootten, D. (2018) Phase-plate

cryo-EM structure of a biased agonist-bound human GLP-1 receptor-Gs complex. *Nature* 555, 121–125.

(15) Liang, Y.-L., Khoshouei, M., Deganutti, G., Glukhova, A., Koole, C., Peat, T. S., Radjainia, M., Plitzko, J. M., Baumeister, W., Miller, L. J., Hay, D. L., Christopoulos, A., Reynolds, C. A., Wootten, D., and Sexton, P. M. (2018) Cryo-EM structure of the active, Gs-protein complexed, human CGRP receptor. *Nature* 561, 492–497.

(16) Dal Maso, E., Glukhova, A., Zhu, Y., Garcia-Nafria, J., Tate, C. G., Atanasio, S., Reynolds, C. A., Ramirez-Aportela, E., Carazo, J.-M., Hick, C. A., Furness, S. G. B., Hay, D. L., Liang, Y.-L., Miller, L. J., Christopoulos, A., Wang, M.-W., Wootten, D., and Sexton, P. M. (2019) The molecular control of calcitonin receptor (CTR) signaling. *ACS Pharmacol Transl Sci.* 2, 31–51.

(17) Dal Maso, E., Zhu, Y., Pham, V., Reynolds, C. A., Deganutti, G., Hick, C. A., Yang, D., Christopoulos, A., Hay, D. L., Wang, M.-W., Sexton, P. M., Furness, S. G. B., and Wootten, D. (2018) Extracellular loops 2 and 3 of the calcitonin receptor selectively modify agonist binding and efficacy. *Biochem. Pharmacol.* 150, 214–244.

(18) Christopoulos, G., Perry, K. J., Morfis, M., Tilakaratne, N., Gao, Y., Fraser, N. J., Main, M. J., Foord, S. M., and Sexton, P. M. (1999) Multiple amylin receptors arise from receptor-activity modifying protein interaction with the calcitonin receptor gene product. *Mol. Pharmacol.* 56, 235–242.

(19) Black, J. W., and Leff, P. (1983) Operational models of pharmacological agonism. *Proc. R Soc. Lond B Biol. Sci.* 220, 141–162.

(20) Hay, D. L., Christopoulos, G., Christopoulos, A., Poyner, D. R., and Sexton, P. M. (2005) Pharmacological discrimination of calcitonin receptor:receptor activity-modifying protein complexes. *Mol. Pharmacol.* 67, 1655–1665.

(21) Woolley, M. J., Reynolds, C. A., Simms, J., Walker, C. S., Mobarec, J. C., Garelja, M. L., Conner, A. C., Poyner, D. R., and Hay, D. L. (2017) Receptor activity-modifying protein dependent and independent activation mechanisms in the coupling of calcitonin gene-related peptide and adrenomedullin receptors to Gs. *Biochem. Pharmacol.* 142, 96–110.

(22) Gingell, J. J., Simms, J., Barwell, J., Poyner, D. R., Watkins, H. A., Pioszak, A. A., Sexton, P. M., and Hay, D. L. (2016) An allosteric role for receptor activity-modifying proteins in defining GPCR pharmacology. *Cell Discov.* 2, 16012.

(23) Watkins, H. A., Chakravarthy, M., Abhayawardana, R. S., Gingell, J. J., Garelja, M., Pardamwar, M., McElhinney, J. M., Lathbridge, A., Constantine, A., Harris, P. W., Yuen, T. Y., Brimble, M. A., Barwell, J., Poyner, D. R., Woolley, M. J., Conner, A. C., Pioszak, A. A., Reynolds, C. A., and Hay, D. L. (2016) Receptor activity-modifying proteins 2 and 3 generate adrenomedullin receptor subtypes with distinct molecular properties. *J. Biol. Chem.* 291, 11657–11675.

(24) Lee, S. M., Hay, D. L., and Pioszak, A. A. (2016) Calcitonin and amylin receptor peptide interaction mechanisms: Insights into peptide-binding modes and allosteric modulation of the calcitonin receptor by receptor activity-modifying proteins. *J. Biol. Chem.* 291, 8686–8700.

(25) Booe, J. M., Warner, M. L., Roehrke, A. M., Hay, D. L., and Pioszak, A. A. (2018) Probing the Mechanism of receptor activity-modifying protein modulation of GPCR ligand selectivity through rational design of potent adrenomedullin and calcitonin gene-related peptide antagonists. *Mol. Pharmacol.* 93, 355–367.

(26) Savage, E. E., Wootten, D., Christopoulos, A., Sexton, P. M., and Furness, S. G. (2013) A simple method to generate stable cell lines for the analysis of transient protein-protein interactions. *BioTechniques* 54, 217–221.

(27) Koole, C., Wootten, D., Simms, J., Valant, C., Sridhar, R., Woodman, O. L., Miller, L. J., Summers, R. J., Christopoulos, A., and Sexton, P. M. (2010) Allosteric ligands of the glucagon-like peptide 1 receptor (GLP-1R) differentially modulate endogenous and exogenous peptide responses in a pathway-selective manner; implications for drug screening. *Mol. Pharmacol.* 78, 456–465.

(28) Koole, C., Wootten, D., Simms, J., Miller, L. J., Christopoulos, A., and Sexton, P. M. (2012) The second extracellular loop of the

human glucagon-like peptide-1 receptor (GLP-1R) has a critical role in GLP-1 peptide binding and receptor activation. *J. Biol. Chem.* 287, 3642–3648.

(29) Booe, J. M., Walker, C. S., Barwell, J., Kuteyi, G., Simms, J., Jamaluddin, M. A., Warner, M. L., Bill, R. M., Harris, P. W., Brimble, M. A., Poyner, D. R., Hay, D. L., and Pioszak, A. A. (2015) Structural basis for receptor activity-modifying protein-dependent selective peptide recognition by a G protein-coupled receptor. *Mol. Cell* 58, 1040–1052.

(30) Shen, M., and Sali, A. (2006) Statistical potential for assessment and prediction of protein structures. *Protein Sci.* 15, 2507–2524.

(31) Doerr, S., Harvey, M. J., Noé, F., and De Fabritiis, G. (2016) HTMD: High-Throughput Molecular Dynamics for Molecular Discovery. *J. Chem. Theory Comput.* 12, 1845–1852.

(32) Dolinsky, T. J., Nielsen, J. E., McCammon, J. A., and Baker, N. A. (2004) PDB2PQR: an automated pipeline for the setup of Poisson-Boltzmann electrostatics calculations. *Nucleic Acids Res.* 32, W665–W667.

(33) Olsson, M. H. M., Søndergaard, C. R., Rostkowski, M., and Jensen, J. H. (2011) PROPKA3: Consistent treatment of internal and surface residues in empirical pKa predictions. *J. Chem. Theory Comput.* 7, 525–537.

(34) Sommer, B. (2013) Membrane packing problems: A short review on computational membrane modeling methods and tools. *Comput. Struct. Biotechnol. J.* 5, No. e201302014.

(35) Lomize, M. A., Lomize, A. L., Pogozheva, I. D., and Mosberg, H. I. (2006) OPM: orientations of proteins in membranes database. *Bioinformatics* 22, 623–625.

(36) Jorgensen, W. L., Chandrasekhar, J., Madura, J. D., Impey, R. W., and Klein, M. L. (1983) Comparison of simple potential functions for simulating liquid water. *J. Chem. Phys.* 79, 926–935.

(37) Harvey, M. J., Giupponi, G., and De Fabritiis, G. (2009) ACEMD: Accelerating biomolecular dynamics in the microsecond time scale. *J. Chem. Theory Comput.* 5, 1632–1639.

(38) Huang, J., and MacKerell, A. D. (2013) CHARMM36 all-atom additive protein force field: validation based on comparison to NMR data. *J. Comput. Chem.* 34, 2135–2145.

(39) Loncharich, R. J., Brooks, B. R., and Pastor, R. W. (1992) Langevin dynamics of peptides: the frictional dependence of isomerization rates of N-acetylalanine-N'-methylamide. *Biopolymers* 32, 523–535.

(40) Berendsen, H. J. C., Postma, J. P. M., van Gunsteren, W. F., DiNola, A., and Haak, J. R. (1984) Molecular dynamics with coupling to an external bath. *J. Chem. Phys.* 81, 3684–3690.

(41) Kräutler, V., Van Gunsteren, W. F., and Hünenberger, P. H. (2001) A fast SHAKE algorithm to solve distance constraint equations for small molecules in molecular dynamics simulations. *J. Comput. Chem.* 22, 501–508.

(42) Essmann, U., Perera, L., Berkowitz, M. L., Darden, T., Lee, H., and Pedersen, L. G. (1995) A smooth particle mesh Ewald method. *J. Chem. Phys.* 103, 8577–8593.

Cryo-electron microscopy structure of the glucagon receptor with a dual-agonist peptide

Received for publication, April 9, 2020, and in revised form, April 30, 2020. Published, Papers in Press, May 5, 2020, DOI 10.1074/jbc.RA120.013793

Rulue Chang^{1,†}, Xin Zhang^{2,†}, Anna Qiao^{3,4}, Antao Dai^{3,5}, Matthew J. Belousoff², Qiuxiang Tan^{3,4}, Lijun Shao^{3,4,6}, Li Zhong^{3,4}, Guangyao Lin^{3,4,6}, Yi-Lynn Liang², Limin Ma³, Shuo Han³, Dehua Yang^{3,5}, Radostin Danev⁷, Ming-Wei Wang^{1,3,4,5,6,*}, Denise Wootten^{2,*}, Beili Wu^{3,4,6,*}, and Patrick M. Sexton^{2,*}

¹School of Pharmacy, Shanghai Medical College, Fudan University, Shanghai, China, ²Monash Institute of Pharmaceutical Sciences, Drug Discovery Biology, Monash University, Parkville, Victoria, Australia, ³The CAS Key Laboratory of Receptor Research, Shanghai Institute of Materia Medica, Chinese Academy of Sciences, Shanghai, China, ⁴University of Chinese Academy of Sciences, Beijing, China, ⁵The National Center for Drug Screening, Shanghai, China, ⁶School of Life Science and Technology, ShanghaiTech University, Shanghai, China, and ⁷Graduate School of Medicine, University of Tokyo, Tokyo, Japan

Edited by Henrik G. Dohlman.

Unimolecular dual agonists of the glucagon (GCG) receptor (GCGR) and glucagon-like peptide-1 receptor (GLP-1R) are a new class of drugs that are potentially superior to GLP-1R-specific agonists for the management of metabolic disease. The dual-agonist, peptide 15 (P15), is a glutamic acid 16 analog of GCG with GLP-1 peptide substitutions between amino acids 17 and 24 that has potency equivalent to those of the cognate peptide agonists at the GCGR and GLP-1R. Here, we have used cryo-EM to solve the structure of an active P15-GCGR-G_s complex and compared this structure to our recently published structure of the GCGR-G_s complex bound to GCG. This comparison revealed that P15 has a reduced interaction with the first extracellular loop (ECL1) and the top of transmembrane segment 1 (TM1) such that there is increased mobility of the GCGR extracellular domain and at the C terminus of the peptide compared with the GCG-bound receptor. We also observed a distinct conformation of ECL3 and could infer increased mobility of the far N-terminal His-1 residue in the P15-bound structure. These regions of conformational variance in the two peptide-bound GCGR structures were also regions that were distinct between GCGR structures and previously published peptide-bound structures of the GLP-1R, suggesting that greater conformational dynamics may contribute to the increased efficacy of P15 in activation of the GLP-1R compared with GCG. The variable domains in this receptor have previously been implicated in biased agonism at the GLP-1R and could result in altered signaling of P15 at the GCGR compared with GCG.

The G protein-coupled receptor (GPCR) superfamily is one of the largest membrane protein families, and GPCRs are widely distributed in the human body, where they are involved in most physiological activities (1). GPCRs can be divided into subclasses based on sequence homology and evolution, and among these the B1 class encompasses receptors for many important peptide hormones (1, 2). There are 15 class B1 GPCRs, including the glucagon receptor subfamily that comprises

receptors for glucagon (GCG), glucagon-like peptide-1 (GLP-1), glucagon-like peptide-2 (GLP-2), and gastric inhibitory peptide (GIP). GCG, GLP-1, and GIP are key metabolic hormones that are essential for glucose homeostasis and caloric intake and disposal, with the peptides having both complementary and opposing actions (3).

There has been much interest in receptors for these metabolic hormones as potential therapeutic targets, with GLP-1 receptor (GLP-1R) agonists now established as highly effective drugs for treatment of type 2 diabetes and obesity (4). In a drug-specific manner, the GLP-1R agonists may also have cardiovascular and weight loss benefits in overweight and obese patients (5). To date, there are no drugs that target the GCG receptor (GCGR) and this is primarily because of the complexity of glucagon-regulated physiological effects. Glucagon is a key regulator of carbohydrate, lipid, and amino acid metabolism that is recognized for its counter-regulatory role to the actions of insulin, and is responsible for glycogen and glycolipid decomposition resulting in elevation of blood glucose (6). However, glucagon also increases energy expenditure and can attenuate food intake leading to interest in combinatory effects with GLP-1R agonists for treatment of obese and diabetic patients. Recently, novel unimolecular agonists that target multiple receptors of the GCGR family have been developed and have shown high efficacy and promising safety profiles in clinical trials (7). Among them, dual agonists of GLP-1R and GCGR have attracted much attention as they were more effective than single drug or multi-drug combination (8–10). Here, we report the cryo-EM structure of GCGR in complex with heterotrimeric G_s protein and a dual agonist, peptide 15 (P15) (11), at a global resolution of 3.4 Å. This structure, combined with mutagenesis and pharmacological studies, reveals molecular details of ligand binding and activation of the GCGR. The results provide valuable information for the design and development of future drugs.

Results

P15 is a modified form of the GCG peptide containing the following residues from GLP-1 (numbered from the GCG sequence), Gln-17, Ala-18, Lys-20, Glu-21, Ile-23, and Ala-24,

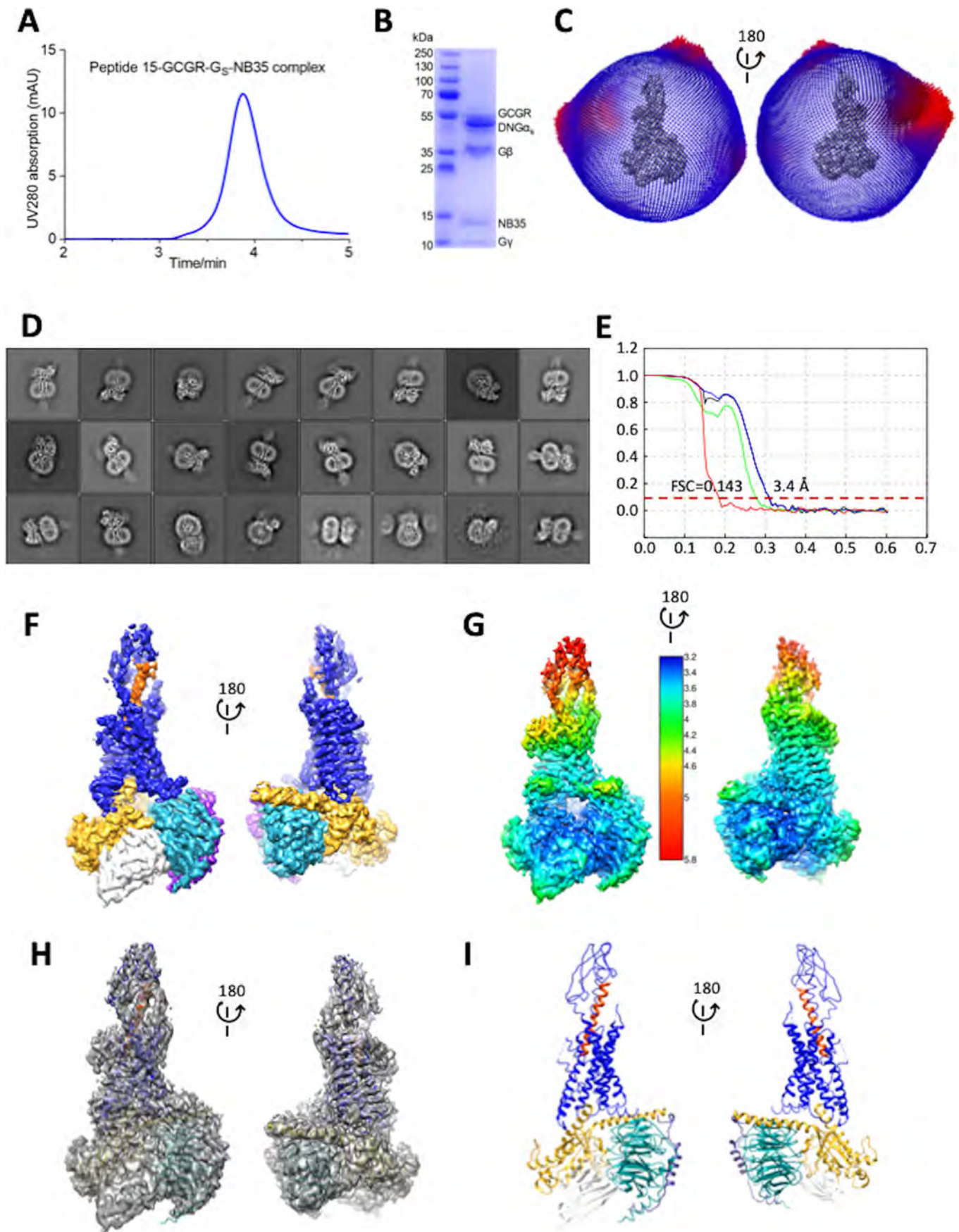
This article contains supporting information.

[†]These authors contributed equally to this work.

*For correspondence: Patrick M. Sexton, Patrick.sexton@monash.edu; Ming-Wei Wang, mwwang@simmm.ac.cn; Denise Wootten, denise.wootten@monash.edu; Beili Wu, beiliwu@simmm.ac.cn.

This is an Open Access article under the CC BY license.

Active GCGR structure with a dual peptide agonist



with an additional Ser to Glu substitution at position 16 (Fig. S1A) (11). The peptide had approximately equal potency to GLP-1(7-36)NH₂ in CHO-K1 cells expressing the WT human GLP-1R (Fig. S1B and Table S1), and to GCG in CHO-K1 cells expressing WT human GCGR (Fig. S1C and Table S1). However, it had ~10-fold lower affinity than the cognate peptides for each receptor in competition binding assays in these cells (Fig. S1, D and E and Table S2).

Structure determination

To understand molecular details of P15 binding to GCGR, we determined a cryo-EM structure of the active P15-GCGR-G_s complex. To achieve this, we utilized the GCGR expression construct (HA-GCGR-HPC4) previously used for determination of the active GCG-GCGR structure (12), with the complex stabilized by use of a dominant negative form of Gα_s (13, 14), and nanobody 35 (Nb35) that binds across the Gα_s-Gβ interface (15). Although the HA-GCGR-HPC4 construct had lower expression than the WT GCGR in CHO-K1 cells, the relative pharmacology of P15 and GCG was equivalent for both receptors (Fig. S1, C and E and Tables S1 and S2). Purified complex was resolved as a monodisperse peak on size exclusion chromatography (SEC) (Fig. 1A), with all components of the complex identified in Coomassie Blue-stained SDS-PAGE of the SEC peak (Fig. 1B). Although there was significant orientation preference of particles (Fig. 1C), cryo-EM imaging of the sample yielded 2D class averages with well-resolved secondary structure (Fig. 1D) that was reconstructed into a consensus 3D density map with a global resolution at gold standard FSC 0.143 of 3.4 Å, with local resolution ranging from 3.2 to 5.8 Å (Fig. 1, E–H). Highest resolution was observed in the G protein and at the interface between the G protein and receptor, with lower resolution at the extracellular face of the receptor and only limited resolution for the receptor ECD (Fig. 1G), indicative of higher mobility of this domain. The α-helical domain of the Gα_s subunit was poorly resolved and masked out during the final refinement. The map resolution enabled modeling of side chains of most amino acids in the receptor core and G protein, albeit that assignment of rotamers was often ambiguous (Fig. S2). Density for parts of ECL1 (Gln-204–Ser-213), ICL3 (His-340–Asp-342), and ECL3 (Val-368–Gly-375) was ambiguous and these segments were not modeled. There was no density for Ala-26^{ECD} or C-terminal residues beyond Trp-418^{8.53} and these were not modeled. Where there was insufficient density to model the α-carbon of side chains, these residues were stubbed, including many residues in the ECD, along with Leu-354^{6.45} (superscript numbers refer to the Wootten *et al.* (16) class B GPCR numbering scheme), Thr-376^{7.33}, and Leu-377^{7.34} (Fig. S3). The N terminus of P15 was reasonably resolved, but there was more limited density for the C-terminal half of the pep-

tide (Fig. S2), consistent with the notion of reduced stability of interactions between the receptor ECD and peptide C terminus.

Peptide–receptor interactions

P15 formed an extended α-helix, exiting the receptor core with an ~30-degree angle from perpendicular (Fig. 1I) and displayed polar and hydrophobic interactions with both the ECD and the receptor core (Fig. 2). The deepest residue was His-1^{P15} that was located above the conserved central polar network of class B GPCRs but that interacted principally with residues in TM5, Trp-304^{5.36}, Arg-308^{5.40}, and Val-311^{5.43} (Fig. 2B and Fig. 3A). However, there was alternative density for His-1^{P15} in lower contoured maps that extended toward the central polar network (Fig. 3A) that was not observed in equivalent low contour maps of the GCG-bound GCGR (Fig. 3B), suggesting that this residue in P15 is more dynamic. Gln-3^{P15} was within H-bonding distance of the hydroxyl of Tyr-149^{1.47} that may stabilize the peptide N terminus in the receptor core (Fig. 2, A–C). Additional polar interactions were predicted between Ser-8^{P15} and the backbone of Asn-298^{ECL2}, Ser-11^{P15}, and both Thr-296^{ECL2} and Ser-297^{ECL2}, whereas Asp-15^{P15} interacted with both Gln-293^{ECL2} and residues of the far N terminus, Gln-27^{ECD} and Met-29^{ECD} (Fig. 2). These interactions were supported by density in the EM map (Fig. 2C). An extended network of hydrophobic interactions also occurred between the peptide and TM1 (Val-134^{1.32}, Ala-135^{1.33}, Tyr-138^{1.36}, and Tyr-145^{1.43}), and TM7 (Asp-385^{7.42}, Leu-386^{7.43}), as well as with parts of TM2/ECL1 (Leu-198^{2.71}, Tyr-202^{2.75}). Alanine mutation of residues within the binding pocket provided support for many of the key interactions identified in the active structure (Tables 1 and 2 and Figs. S4 and S5), including Tyr-145^{1.43}, Tyr-149^{1.47}, Tyr-202^{2.75}, Arg-308^{5.40}, Asp-385^{7.42}, and Leu-386^{7.43}. There was also a range of effects observed that likely relates to impact of alanine mutation on the secondary structure or dynamics of the receptor. For example, whereas the H-bond between Ser-8^{P15} and Asn-298^{ECL2} was with the amino acid backbone, the N298A mutation likely disrupts the potential polar interaction of the side chain of Asn-298^{ECL2} and the backbone of Asn-300^{ECL2} that helps maintain the fold of ECL2. Likewise, the large impact of the T295^{ECL2}A mutant is likely because of disruption to the active ECL2 conformation. In the map, the tops of TM6/TM7/ECL3 were poorly defined, suggesting that this segment has higher mobility. The mutational analysis also revealed >10-fold loss of potency for residues at the top of TM7/ECL3 (R378^{7.35}A, L382^{7.39}A), suggesting that they may play a role via either transient interactions with the peptide or in influencing the mobility of ECL3. Not surprisingly, we also observed marked loss of potency with mutation of key residues of the central polar network, Lys-187^{2.60} and Glu-362^{6.53}, consistent with the key role of this network in signal propagation of many class B GPCRs (17–19).

Figure 1. Cryo-EM structure of the P15-GCGR-GsDN-Nb35 complex. A, analytical SEC trace of the purified complex. B, Coomassie blue-stained SDS-PAGE of the purified complex. C, 3D histogram representation of the Euler angle distribution of all the particles used in the reconstruction overlaid on the density map drawn on the same coordinate axis. D, 2D class averages of cryo-EM projections of the receptor complex. E, gold standard Fourier shell correlation (FSC) curves for the final map and map validation from half maps, showing the overall nominal resolution of 3.4 Å. F, surface representation of the final map colored by protein segment. G, local resolution-filtered EM map displaying local resolution (Å) colored from highest resolution (dark blue) to lowest resolution (red). H, full map containing the backbone model of the complex in ribbon format. I, backbone model of the receptor complex in ribbon format. Blue, GCGR; orange, P15; gold, Gα_s; cyan, Gβ1; purple, Gγ2; white, Nb35.



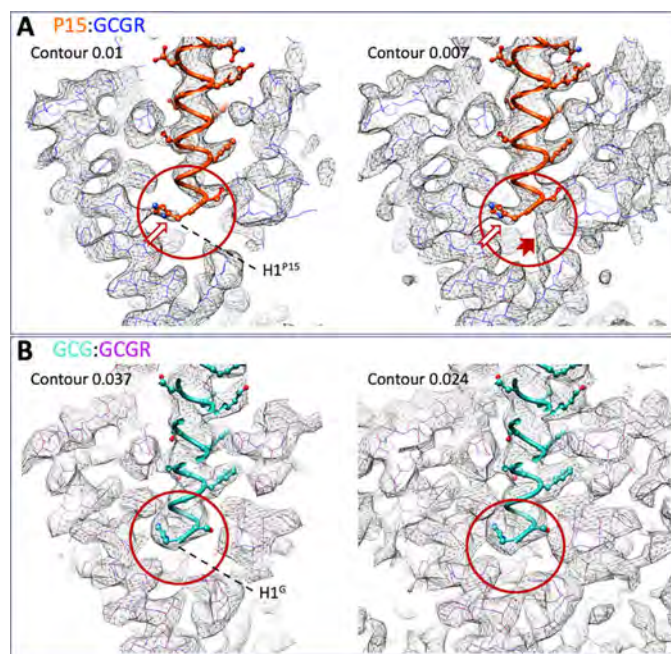


Figure 3. A and B, map to model figures for the P15-GCGR-GsDN-Nb35 (A) and GCG-GCGR-GsDN-Nb35 (PDB:6LMK; EMD-0917) (B) structures at different levels of contour. In the higher contour map for the P15 complex, there is incomplete density for His-1^{P15} (A, left panel, white arrow); however, density for the full side chain is present at lower contour, along with density that would support an alternate location for this residue (A, right panel; solid red arrow). In contrast, a single continuous density is observed for His-1^{GCG} in both higher contour and lower contour maps (B, red circles). GCGR residues in the P15 complex are displayed in blue wire format, and purple wire format for the GCG complex. P15 is displayed in orange, protein worm, and x-stick format. GCG is displayed in light blue, protein worm and x-stick format.

G protein interactions

The P15-bound GCGR formed a series of polar and nonpolar interactions with the $G\alpha_s$ subunit, particularly with the α H5 helix and the proximal segment of the α N helix (Fig. 4, A–C). Polar interactions occurred between Arg-38 ^{α N} and Thr-257^{ICL2} and also the backbone of Pro-259^{ICL2}, together with side chain to receptor backbone interactions for His-41 ^{α N} and Ala-256^{ICL2}, Gln-384 ^{α H5} and Leu-253^{3.58}, Arg-385 ^{α H5} and Lys-332^{5.64}, His-387 ^{α H5} and Leu-252^{3.57}, and between Glu-392 ^{α H5} and Lys-405^{H8.40} (Fig. 4, B and C). ICL2 of GCGR formed additional hydrophobic interactions with both $G\alpha$ N and $G\alpha$ H5, while the $G\alpha$ H5 had extended interactions with TM2, TM3, TM5, TM6, and TM7 (Fig. 4). There were also limited interactions between the $G\beta$ subunit (Phe-335 ^{β} , Arg-52 ^{β}) and ICL1 (Ser-167^{ICL1}, Leu-169^{ICL1}, His-170^{ICL1}) and between $G\beta$ (Ala-309 ^{β} , Asp-312 ^{β}) and helix 8 of the receptor (Arg-417^{8.52}, Arg-413^{8.48}), with the potential for an H-bond or salt bridge to be formed with Asp-312 ^{β} ; however, there was limited density in the EM map, indicating that this was likely to be transient if it were formed.

Table 1

Quantitative analysis of peptide competition for ¹²⁵I-glucagon binding and cell surface expression of WT and mutant GCGRs

Mutant	Glucagon pIC ₅₀ ± S.E. ^a	Peptide 15 pIC ₅₀ ± S.E. ^a	Expression (% of WT) ^b
WT-GCGR	7.47 ± 0.03	6.52 ± 0.03	100 ± 0
Q142 ^{1.40b} A	7.03 ± 0.07 ^{**}	6.29 ± 0.07	80 ± 5
Y145 ^{1.43b} A	Nb ^d	Nb	38 ± 4 ^{***}
Y149 ^{1.47b} A	Nb	Nb	103 ± 3
K187 ^{2.60b} A	7.98 ± 0.09 ^{***}	7.11 ± 0.05 ^{***}	78 ± 8
V191 ^{2.64b} A	Nb	Nb	119 ± 11
I194 ^{2.67b} A	7.57 ± 0.05	6.78 ± 0.06 [*]	94 ± 8
Y202 ^{2.75b} A	Nb	Nb	74 ± 4
M231 ^{3.36b} A	7.60 ± 0.05	6.58 ± 0.06	95 ± 5
Q232 ^{3.37b} A	7.02 ± 0.09 ^{***}	6.20 ± 0.11 [*]	83 ± 4
I235 ^{3.40b} A	7.34 ± 0.09	6.34 ± 0.10	71 ± 6 [*]
N238 ^{3.43b} A	7.22 ± 0.09	6.42 ± 0.09	41 ± 2 ^{***}
W295 ^{ECL2} A	Nb	Nb	68 ± 6 [*]
S297 ^{ECL2} A	7.59 ± 0.06	6.65 ± 0.06	62 ± 6 [*]
N298 ^{ECL2} A	6.90 ± 0.13 ^{***}	Nb	68 ± 14 [*]
R308 ^{5.40b} A	Nb	Nb	71 ± 7 [*]
N318 ^{5.50b} A	Nb	Nb	80 ± 3
H361 ^{6.52b} A	7.11 ± 0.08 [*]	6.60 ± 0.07	85 ± 3
E362 ^{6.53b} A	6.98 ± 0.15 ^{***}	Nb	67 ± 8 [*]
R378 ^{7.35b} A	7.17 ± 0.08 [*]	6.79 ± 0.07 [*]	115 ± 5
L382 ^{7.39b} A	Nb	Nb	84 ± 5
D385 ^{7.42b} A	7.65 ± 0.06	6.76 ± 0.06	65 ± 4 [*]
L386 ^{7.43b} A	Nb	Nb	86 ± 16
S389 ^{7.46b} A	7.28 ± 0.08	6.38 ± 0.09	90 ± 8
Q392 ^{7.49b} A	7.01 ± 0.07 ^{***}	6.25 ± 0.13 [*]	70 ± 8 [*]

^a pIC₅₀ values are shown as means ± S.E. of at least three independent experiments.

^b Cell surface expression was detected by flow cytometry and is reported as percentage of WT-GCGR.

^c Data from Fig. S5 were fitted to a three-parameter logistic equation. Statistical evaluation was performed using one-way analysis of variance and Dunnett's post test, *, $p < 0.05$; **, $p < 0.001$; ***, $p < 0.0001$ compared with WT control.

^d Nb, insufficiently robust binding to enable a curve to be fitted.

Comparison of P15-bound and GCG-bound GCGR and GLP-1-bound GLP-1R structures

Overall, there was a high degree of conservation in the structure of the GCGR bound to GCG (12) versus P15, including the location of the ECD; most TM helices; and in the conformation of ECL2, ICL2, and ICL3 (Fig. 5A). However, key distinctions were observed, most notably in the resolution and secondary structure of ECL1, ECL3, the upper segment of TM1 on the extracellular face of the receptor, and ICL1 on the intracellular face (Fig. 5A), with these differences clearly observed in comparisons of the cryo-EM maps for the two structures (Fig. 6, A–D). P15 differs from GCG across residues 16–24 where 6/8 amino acids are distinct (Fig. S1A). These differences alter the interaction of the peptides with ECL1 and the top of the TM1 helix where GCG makes more extensive interactions (Fig. 7, A and B) that in turn stabilize the secondary structure of the receptor in these regions (Fig. 7B). In the EM density map, there is limited density for the P15 substituted residues, indicative of weak or transient interactions and greater mobility of the peptide C terminus that likely also contributes to the limited resolution of the ECD (Fig. 6, A and B). Despite the conservation in the N terminus of P15 and GCG, there was marked difference

Figure 2. The peptide 15-binding interface with GCGR. A, GCGR (blue) residues within 5 Å of P15 are displayed in wire format with the GCGR protein backbone in ribbon format. Blue dashed lines represent segments of GCGR that could not be modeled because of ambiguous density. P15 is colored orange with amino acid side chains in x-stick format and backbone shown as ribbon display. H-bonds are displayed as dashed green lines. The insets include surface display of interacting GCGR residues with the dark blue-colored surface illustrating the proportion of the side chain within 5 Å. B, interactions were determined using LigPlot+. GCGR residues are located above the dashed black line, and P15 residues below the line. Hydrophobic interactions are illustrated by red (P15) or pink (GCGR) arcs, and interacting residues are joined by a red line. Amino acids involved in H-bonds are shown in atomic detail with H-bonds shown as dashed green lines. C, map to model densities for side chains involved in H-bond (green dashed lines) formation.

Table 2**Quantitative analysis of peptide-mediated cAMP accumulation in cells stably expressing WT or mutant GCGRs**

Mutants	Glucagon		Peptide 15	
	pEC ₅₀ ± S.E.M. ^a	E _{max} ^b (% of WT)	pEC ₅₀ ± S.E.M	E _{max} ^b (% of WT)
WT-GCGR	10.99 ± 0.03	100 ± 1.3	10.65 ± 0.04	100 ± 1.5
Q142 ^{1.40b} A	10.44 ± 0.06 ^{c***}	100 ± 2.2	9.84 ± 0.06 ^{***}	100 ± 2.4
Y145 ^{1.43b} A	8.93 ± 0.05 ^{***}	97 ± 2.2	8.27 ± 0.04 ^{***}	95 ± 1.7
Y149 ^{1.47b} A	9.20 ± 0.06 ^{***}	92 ± 2.5	8.57 ± 0.04 ^{***}	93 ± 1.7
K187 ^{2.60b} A	9.34 ± 0.08 ^{***}	99 ± 3.4	8.81 ± 0.03 ^{***}	97 ± 1.1
V191 ^{2.64b} A	8.69 ± 0.04 ^{***}	100 ± 2.0	7.93 ± 0.05 ^{***}	100 ± 2.7
I194 ^{2.67b} A	10.52 ± 0.05 ^{***}	95 ± 1.7	10.39 ± 0.06 [*]	94 ± 2.5
Y202 ^{2.75b} A	9.65 ± 0.05 ^{***}	102 ± 2.0	9.21 ± 0.05 ^{***}	103 ± 2.2
M231 ^{3.36b} A	10.74 ± 0.04 [*]	100 ± 1.8	10.22 ± 0.05 ^{***}	102 ± 2.2
Q232 ^{3.37b} A	10.49 ± 0.04 ^{***}	101 ± 1.7	9.62 ± 0.05 ^{***}	103 ± 2.0
I235 ^{3.40b} A	10.97 ± 0.04	99 ± 1.8	10.37 ± 0.05 [*]	100 ± 2.1
N238 ^{3.43b} A	10.67 ± 0.08 ^{***}	97 ± 2.9	9.93 ± 0.05 ^{***}	99 ± 2.1
W295 ^{ECL2} A	7.30 ± 0.05 ^{***}	101 ± 3.0	6.33 ± 0.04 ^{***}	105 ± 2.6
S297 ^{ECL2} A	10.83 ± 0.05	96 ± 1.9	10.66 ± 0.05	98 ± 2.0
N298 ^{ECL2} A	9.26 ± 0.04 ^{***}	101 ± 1.9	8.23 ± 0.06 ^{***}	100 ± 2.7
R308 ^{5.40b} A	8.14 ± 0.04 ^{***}	104 ± 2.4	7.21 ± 0.05 ^{***}	93 ± 2.3
N318 ^{5.50b} A	9.33 ± 0.14 ^{***}	56 ± 3.4 ^{***}	8.45 ± 0.16 ^{***}	56 ± 3.7 ^{***}
H361 ^{6.52b} A	10.57 ± 0.06 ^{***}	98 ± 2.2	9.74 ± 0.09 ^{***}	98 ± 3.6
E362 ^{6.53b} A	9.34 ± 0.04 ^{***}	100 ± 1.7	8.49 ± 0.05 ^{***}	99 ± 2.1
R378 ^{7.35b} A	7.72 ± 0.02 ^{***}	106 ± 1.3	6.90 ± 0.06 ^{***}	94 ± 3.1
L382 ^{7.39b} A	9.62 ± 0.05 ^{***}	97 ± 2.1	8.78 ± 0.05 ^{***}	96 ± 2.1
D385 ^{7.42b} A	9.31 ± 0.05 ^{***}	100 ± 2.1	8.60 ± 0.08 ^{***}	98 ± 3.0
L386 ^{7.43b} A	8.86 ± 0.03 ^{***}	103 ± 1.5	7.93 ± 0.06 ^{***}	101 ± 2.9
S389 ^{7.46b} A	10.94 ± 0.05	100 ± 2.2	10.25 ± 0.08 ^{***}	99 ± 3.4
Q392 ^{7.49b} A	10.85 ± 0.05	101 ± 2.2	10.00 ± 0.07 ^{***}	101 ± 3.1

^a pEC₅₀ values are shown as means ± S.E. of at least three independent experiments.^b E_{max} means the maximal response measured relative to that of WT GCGR. Data from Fig. S4 were fit to a three-parameter logistic equation.^c Statistical evaluation was performed using one-way analysis of variance and Dunnett's post test, *, *p* < 0.05; **, *p* < 0.001; ***, *p* < 0.0001 compared with WT control.

in the conformation of ECL3 in the consensus map with substantially reduced interaction between the top of TM6/TM7/ECL3 for P15 (Fig. 6, C and D). Although the GCGR-G_s heterotrimer interface was very similar for the P15 and GCG-bound structures, there were distinct conformations of ICL1 that altered the interface with the Gβ subunit (Fig. 8, A–C). This was correlated with a small local shift in the orientation of the G protein (Fig. 8A).

Intriguingly, the areas of distinction in structure of the peptide-binding domain of GCGR bound to P15 *versus* GCG were also the major sites of difference in conformation between the active GLP-1-bound GLP-1R (20) and the GCGR structures (Fig. 5, B *versus* A). A notable difference to the GCGR structures, in the GLP-1–GLP-1R structure, and also the published Exp5-bound GLP-1R structure (13), is disordering of the top of the TM1 helix and the stalk connecting TM1 to the ECD (Figs. 5–7). The ECD orientation between the related receptors is remarkably similar, and this is likely driven by the overlap in the angle that the peptides exit the receptor (Fig. 5), with the minor differences related to the extent of interaction between the L2 loop of the ECD and the C termini of the peptides (Fig. 5B).

Discussion

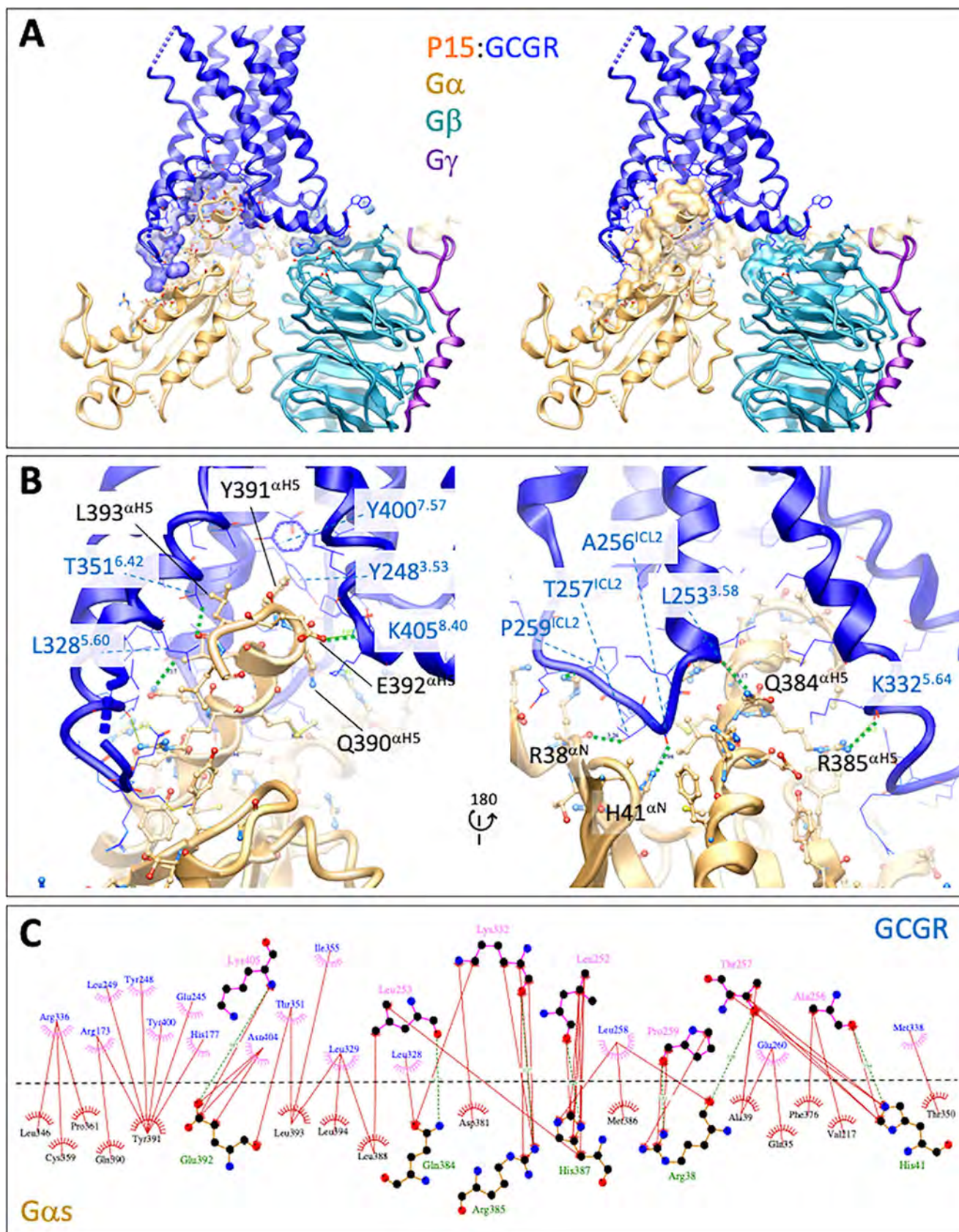
Diabetes and obesity are major health burdens, and there has been much interest in harnessing physiological systems that regulate metabolism for treatment of these diseases. Among the key glucoregulatory hormones are GLP-1 and GCG that have opposing actions on regulation of plasma glucose but complementary actions in regulation of food intake, energy ex-

penditure, and other metabolic events (3, 6). Oxyntomodulin is a related peptide that, like GLP-1, is secreted from the intestine following meal ingestion that is a dual agonist of GLP-1R and GCGR but with lower potency in canonical cAMP signaling assays than the “cognate” agonists of these receptors (21). Pre-clinical studies provided early evidence that chronic oxyntomodulin administration could induce greater weight loss than GLP-1 selective agonists with equivalent glycemic control (22–24), suggesting that dual agonists of GLP-1R and GCGR could provide additional benefits above that of GLP-1R agonists in treatment of metabolic disease. This has driven interest in development of stable, high-potency unimolecular dual agonists of GCGR and GLP-1R, and also tri-agonists that also target GIP receptor (7, 8, 11, 25–28), and several of these have now entered clinical trials (9, 10, 26, 27).

The principal approach to engendering GCGR/GLP-1R dual agonism with high potency has been substitution of nonconserved residues in the mid and C-terminal segments of the peptides. An exemplar is the dual agonist P15, first described by Day and colleagues (11). It is a substituted analog of GCG that retains equivalent potency to the parental peptide at the GCGR but has equal potency in cAMP assay to GLP-1 at the GLP-1R. We recently published the first active structure of the GCGR bound to GCG (12) and in the current study sought to understand the impact of the P15 modifications on the engagement of this peptide with the receptor.

Multiple structures have now been solved for active-state, G protein-coupled class B GPCRs, including the calcitonin receptor (29, 30), calcitonin gene-related peptide (31) and adrenomedullin receptors (32), parathyroid hormone-1 receptor (33), corticotrophin releasing factor-1 and -2 receptors (34, 35), pituitary adenylate cyclase-activating peptide receptor (35–37), as well as the GCG-bound GCGR (12) and multiple GLP-1R complexes (13, 20, 38). Comparison of the P15-bound GCGR to other class B GPCR active structures reveals that it most closely resembles the peptide-bound structures of the GCGR receptor subfamily (Fig. 5) (12, 13, 20), particularly with respect to the consensus orientation of the ECD that is a major area of divergence within this broader receptor class (discussed in detail in Ref. 35). However, the P15-GCGR-G_s structure exhibits the classic hallmarks of activated class B GPCRs compared with inactive class B GPCR structures exemplified by the GCGR (39, 40) that include the pronounced kink in TM6 around the conserved Pro^{6.47}-X-X-Gly^{6.50} motif, and the intracellular reorganization of TMs 5 and 6 that allows engagement with the G protein; class-dependent details of the global changes that occur in activated receptors are described in detail elsewhere (12, 34, 35). Although there are receptor-specific differences in interactions with G_s protein, there is general conservation in the receptor regions involved in binding, which have been discussed previously (41, 42), that are also conserved for the P15-bound GCGR. As such, we have concentrated the following discussion on the distinctions between GCG and P15-bound GCGR that may give insight into the nature of dual agonism that is a property of P15.

The N-terminal 15 residues of GCG and P15 are identical and, unsurprisingly, the two active GCGR structures had a high degree of overlap in the transmembrane domain bundle and in



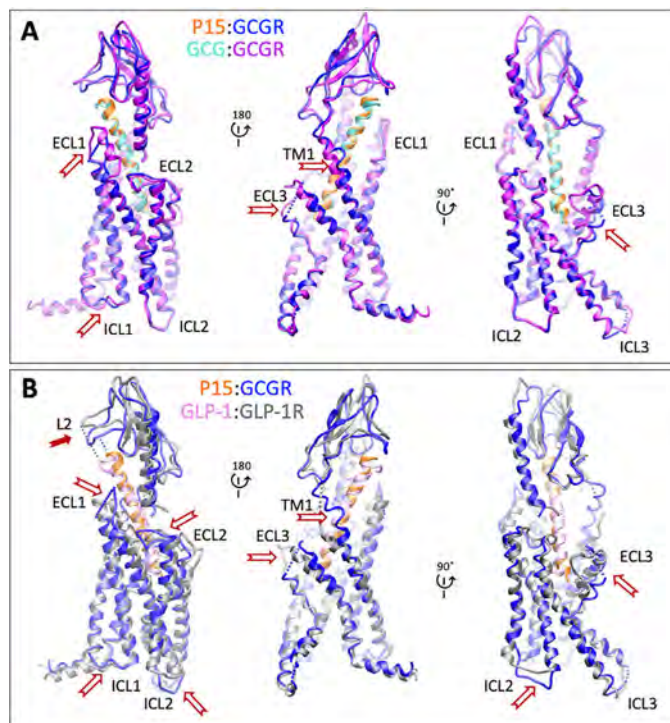


Figure 5. A and B, comparison of the active P15-GCGR-GsDN-Nb35 complex with GCG-GCGR-GsDN-Nb35 (A, PDB: 6LMK) and GLP-1-GLP1R-GsDN-Nb35 (B, PDB: 5VAI) complexes. Protein backbone is shown in ribbon format. Only the receptor and peptides are displayed for clarity. GCGR is blue and P15 orange in the P15-GCGR complex. GCGR is purple and GCG light blue in the GCG-GCGR complex. GLP-1R is gray and GLP-1 pink in the GLP-1-GLP1R complex. White arrows depict areas of conformational divergence between the complexes. The solid red arrow highlights the differential positioning of the L2 loop of the GCGR and GLP-1R ECDs relative to the C terminus of peptides.

the receptor-G protein interface, with mutations in the TM-binding pocket having similar impact on both P15- and GCG-induced cAMP production (Table 2). Nonetheless, interesting differences in the structures were observed, even in proximity to the conserved sequence of the peptides. Of particular note, there was marked difference in the conformation of ECL3, with this loop folded toward and forming additional interactions with GCG compared with P15 (Fig. 7). In contrast, in the P15-bound structure, ECL3 is poorly resolved and oriented away from the peptide. Within the deep binding pocket, the density for His-1^{P15} is less well resolved, although it best supports modeling of the side chain in an equivalent orientation to that observed for GCG (12) (Fig. 3). At lower contour of the EM maps, as noted above, there is additional density that could support alternate modeling of His-1^{P15} whereas no equivalent density is observed in lower contoured maps of the GCG-bound GCGR, and this may relate to the more extended interactions of this peptide with ECL3 that could limit conformational dynamics within the core. In the GLP-1-GLP1R active complex, ECL3 is folded in toward the peptide, similar to GCG-GCGR

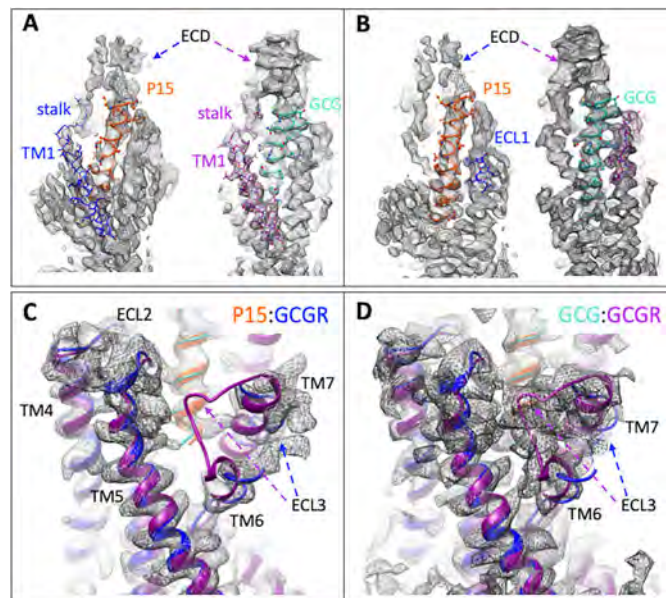


Figure 6. EM density maps for divergent regions of GCGR in the P15-versus GCG-bound active structures. A, highlights differences in peptide interactions with the upper segment of TM1 that extends and connects the receptor ECD and transmembrane domain bundle. Left panel, the P15 (orange)-GCGR (blue) active complex. Right panel, the GCG (light blue)-GCGR (purple) active structure. GCGR is in wire format. Peptides are shown in protein worm and x-stick format. B, highlights differences in peptide interactions with GCGR ECL1. Left panel, the P15 (orange)-GCGR (blue) active complex. Right panel, the GCG (light blue)-GCGR (purple) active structure. GCGR is in wire format. Peptides are shown in protein worm and x-stick format. C and D, differences in the conformation of ECL3 between the P15 complex (C) and GCG complex (D). Proteins are displayed in ribbon format with colors as in A and B.

(Fig. 4), however, ECL3 is among the least conserved, conformationally, across different structures of active GLP-1R complexes (13, 20, 38). Moreover, mutational analysis of GLP-1R ECL3/TM7 has revealed that this domain is critically important in the biased agonism of GLP-1R agonists, including the dual agonist oxyntomodulin (43), and ExP5 (13). Later work suggested that TM6/ECL3/TM7 is functionally linked to TM1 in controlling GLP-1R signaling (44). This is notable as the top of TM1 was also structurally different in GCGR bound to P15 versus GCG. In the GCG-bound structure, TM1 forms an extended α -helix that is stabilized by direct interaction with GCG residues that are distinct in P15 (Fig. 5). In the native GCG sequence, residue 18 is Arg but Ala in P15 (and GLP-1). Arg-18^{GCG} extends toward and is tightly packed with residues in ECL1 and this loop is highly structured in the GCG-GCGR complex (12). In contrast, there is much more limited interaction between P15 and ECL1 and the loop is disordered and less well resolved. Thus, there is reduced interaction between P15 and the receptor as the peptide exits the GCGR core and this in turn leads to greater mobility of the peptide and receptor ECD that is reflected in the reduced resolution of this domain in the

Figure 4. The GCGR-Gs protein interface of the active P15-bound complex. A, overview of the interface with protein backbones displayed in ribbon format and side chains within 5 Å displayed in either x-stick (G protein) or wire (GCGR) format. Left panel includes surface representation of the interacting GCGR residues. Right panel includes surface representation of the interacting G protein residues. GCGR, blue; $G\alpha_s$, gold; $G\beta_1$, cyan; $G\gamma_2$, purple. B, close up of the $G\alpha_s$ -GCGR interface. Predicted H-bonds are displayed as green dashed lines. C, GCGR- $G\alpha_s$ interface. Interactions were determined using LigPlot+. GCGR residues are located above the dashed black line, and $G\alpha_s$ residues below the line. Hydrophobic interactions are illustrated by red ($G\alpha_s$) or pink (GCGR) arcs, and interacting residues are joined by a red line. Amino acids involved in H-bonds are shown in atomic detail with H-bonds shown as dashed green lines.

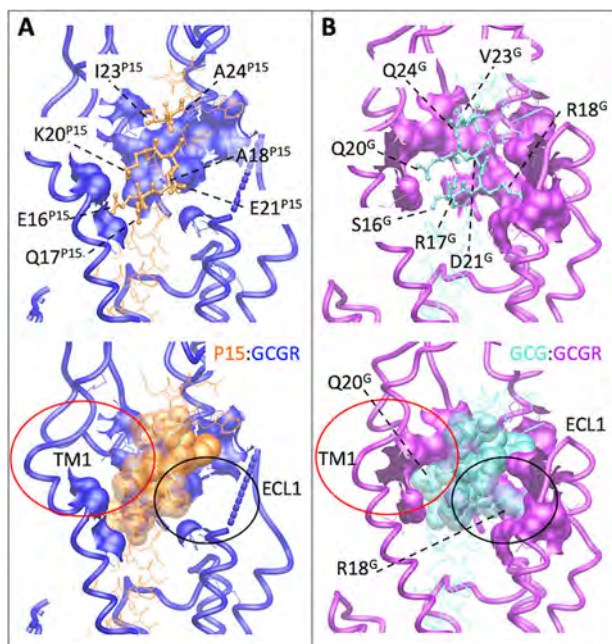


Figure 7. Peptide 15 and glucagon make distinct interactions with GCGR. A, P15–GCGR interface with the divergent peptide amino acids from GCG displayed in x-stick format and conserved residues in wire format. GCGR residues that interact with the nonconserved peptide amino acids are displayed in wire and surface representation. GCGR is blue and P15 orange. The receptor backbone is shown in protein worm representation. B, GCG–GCGR interface with the divergent peptide amino acids from P15 displayed in x-stick format and conserved residues in wire format. GCGR residues that interact with the nonconserved peptide amino acids are displayed in wire and surface representation. GCGR is purple and GCG light blue. The receptor backbone is shown in protein worm representation. Lower panels include cpk representation of the nonconserved peptide residues. The red circle highlights the distinction in interaction surfaces between the top of TM1 and the two peptides. The black circle highlights the distinction in interaction surfaces between ECL1 and the two peptides.

EM density map, compared with GCG–GCGR. This likely also contributes to the stability of interaction of the peptide and ECL3 and the resolution of this domain.

With the exception of ECL3, the areas of difference between the P15- and GCG-bound GCGR are the major areas of structural distinction observed between peptide-bound structures of GLP-1R and GCGR, and indeed areas that are less well resolved in GLP-1R *versus* the GCG–GCGR EM density maps. While highly speculative, flexibility of the receptor ECD and interaction of this domain with peptide agonists may be a requirement for efficacious engagement. As such, one of the mechanisms underlying increased potency of P15 at the GLP-1R may be related to enhanced conformational dynamics of this peptide *versus* GCG when binding to GLP-1R. In support of this hypothesis, ECL1 plays a more important role in the cAMP response to oxyntomodulin at the GLP-1R compared with selective GLP-1R agonists (43), consistent with greater interaction of oxyntomodulin with this domain than the selective agonists.

As noted above, at the GLP-1R, mutagenesis studies have provided evidence that residues in TM1 and ECL3/TM7 give rise to divergent signaling profiles in a peptide-specific manner (43, 44). These regions were among the most distinct in conformation between the P15- *versus* GCG-bound GCGR and, by analogy, would suggest that these two peptides would have

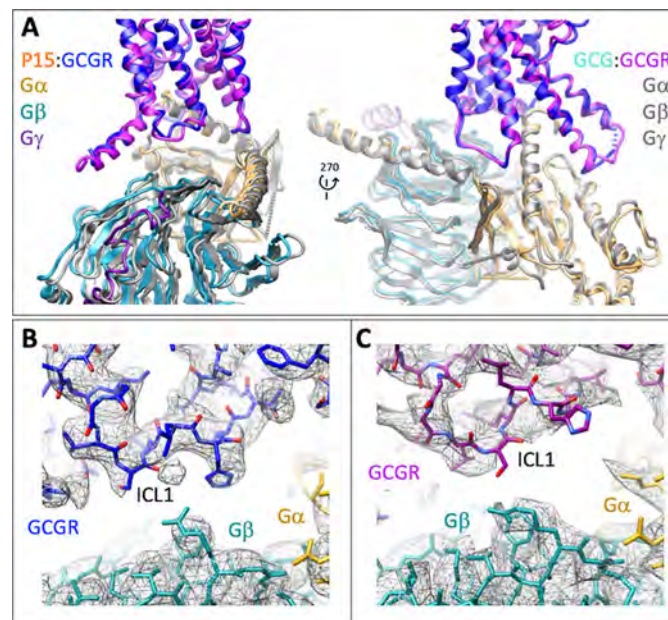


Figure 8. Distinctions in the conformation of ICL1 between the P15-bound and GCG-bound GCGR structures alter the orientation of the G_s protein interface. A, ribbon representation of the protein backbone of GCGR and G protein subunits. GCGR in the P15 bound complex is blue and in the GCG bound complex, purple. In the P15 complex structure, $G\alpha_s$ is gold; $G\beta_1$, cyan; $G\gamma_2$, dark purple. All subunits are colored gray in the GCG-bound complex. B, EM density map (contour 0.01) to model for GCGR ICL1 in the P15-bound complex. GCGR, blue; $G\alpha_s$, gold; $G\beta_1$, cyan. C, EM density map (contour 0.037) to model for GCGR ICL1 in the GCG bound complex. GCGR, purple; $G\alpha_s$, gold; $G\beta_1$, cyan.

altered signaling profiles and that P15 could be a biased agonist of the GCGR.

In conclusion, our data reveal conformational differences in the active, G_s -complexed structure of GCGR when bound to the dual agonist, P15 *versus* GCG. The distinct residues in the mid/C-terminal region of the peptide reduce engagement of the peptide with receptor as it exits the receptor core, leading to loss of GCGR secondary structure in these regions and overall increased mobility of the peptide and ECD. These alterations in GCGR structure occur in regions that are also different between GCGR and known structures of GLP-1R and likely contribute to the increased efficacy of P15 at the GLP-1R, but may also alter the signaling profile of P15 relative to the native peptides at both receptors.

Experimental Procedures

The human GCGR gene was cloned into pFastBac1 vector with GP64 promoter to enhance the protein yield. Forty-five residues (His-433–Phe-477) were truncated at the C terminus to improve the thermostability, and the affinity tag hpc4 was added at the C terminus (GP64-HA-GCGR-GSGS linker-HPC4).

The modified GCGR had decreased expression and subsequent peptide-induced cAMP accumulation when expressed in CHO-K1 cells (Fig. S1 and Table S1) but equivalent pharmacology to the WT receptor in HEK-293 cells (12). $G\alpha_s$ was modified to become dominant negative (DN) with eight mutations (S54N, G226A, E268A, N271K, K274D, R280K, T284D, and

I285T) thereby stabilizing the interaction with $\beta\gamma$ subunits (13, 14). Nb35 was expressed and purified as described previously (12).

Insect cell expression

Human GCGR construct, DNG α_s , His₆-tagged G β_1 and G γ_2 were co-expressed in HighFive insect cells (Invitrogen), which were infected with three separate baculoviruses at a ratio of 4:1:1. Cells were grown to a density of 3 million cells/ml and cultured for 48 h thereafter before collection by centrifugation (1500 rpm, 15 min). The pellets were stored at -80°C for subsequent protein purification.

Complex purification

Cell pellets were resuspended in 20 mM HEPES, pH 7.4, 50 mM NaCl, 2 mM MgCl₂ with protease inhibitor cOmplete mixture tablets (Roche), 5 μM P15 (GL Biochem), 10 $\mu\text{g/ml}$ Nb35 and 25 milliunits/milliliter apyrase (New England Biolabs). The suspension was incubated for 1 h at room temperature to promote the formation of complexes. Membranes were collected by centrifugation at 30,000 rpm for 30 min and solubilized in 0.5% (w/v) lauryl maltose neopentyl glycol (LMNG) (Anatrace), 0.03% (w/v) cholesteryl hemisuccinate (CHS) (Anatrace), 5 μM P15, and 25 milliunits/milliliter apyrase (New England Biolabs) for 2 h at 4°C . Supernatant was collected by centrifugation at 30,000 rpm for 30 min. GCGR complex was immobilized by anti-hpc4 affinity resin in the presence of 2 mM CaCl₂ overnight, washed with 20 column volumes of 20 mM HEPES, pH 7.4, 100 mM NaCl, 2 mM MgCl₂, 2 mM CaCl₂, 5 μM P15, 0.01% (w/v) LMNG, and 0.006% (w/v) CHS, and eluted with 5 column volumes of buffer by adding 6 mM EDTA and 5 μM P15. The complexes were concentrated using a 100-kDa molecular weight cutoff concentrator (Millipore) and then further separated by SEC on a Superdex 200 Increase 10/300 column (GE Healthcare) pre-equilibrated with 20 mM HEPES, pH 7.4, 100 mM NaCl, 2 mM MgCl₂, 0.01% (w/v) LMNG, 0.006% (w/v) CHS, and 5 μM P15 was employed to yield the final product. The purified complex was subsequently concentrated to 3–5 mg/ml with a 100-kDa molecular weight cutoff concentrator, and analyzed by SDS-PAGE and analytical SEC. Negative stain transmission EM was performed on the final purified complex as previously described (29).

Cryo-EM

Cryo-EM samples were prepared by plunge vitrification in liquid ethane on a Vitrobot Mark IV (Thermo Fisher Scientific) with blotting chamber set to 4°C and 100% humidity. A 3- μl sample solution was applied on Quantifoil R1.2/1.3 Cu 200 mesh (Quantifoil) glow-discharged grids and blotted for 10 s before plunging. Data were collected on a Titan Krios G3i (Thermo Fisher Scientific) 300 kV electron microscope equipped with a Gatan BioQuantum energy filter and K3 direct electron detector (Gatan). The microscope was set to zero-loss EFTEM NanoProbe mode at $\times 105,000$ indicated magnification with 25 eV energy selection slit, 50 μm condenser aperture, 100 μm objective aperture, spot 4, beam diameter 1.85 μm . The equivalent pixel size on the detector was 0.83 $\text{\AA}/\text{pixel}$ in non-superresolution

counting mode. The exposure parameters were as follows: exposure rate 9.9 $\text{e}^-/\text{pixel/s}$ = 14.4 $\text{e}^-/\text{\AA}^2/\text{s}$, exposure time 4.015 s, total exposure 57.8 $\text{e}^-/\text{\AA}^2$, number of frames 67. Multiframe movies were automatically acquired with SerialEM software (45) in non-gain-normalized compressed TIFF format with a 9-position beam-image shift data acquisition scheme and target defocus range of 0.8 to 1.5 μm . In total, 5571 movies were acquired in 22.5 h with an average throughput of 255 movies/h.

Data processing

Movies were motion-corrected, dose-weighted, and integrated using UCSF MotionCor2 (46, 47). This was followed by CTF estimation using the GCTF (48) software package. Particles were picked from the micrographs using the automated procedure in the cryOLO software package (49). Particle extraction and reference-free 2D classification was carried out in RELION (version 3.0.7) (50). CryoSPARC (version 2.7) (51) was used to generate an *ab initio* model of the GCGR complex, which was used in RELION for 3D classification. A homogeneous subset of particles was then subjected to cycles of Bayesian particle polishing and CTF refinement as implemented in RELION. This homogeneous subset of polished particles was used for a 3D refinement in RELION and was further classified into 3D classes with a fine grain angular sampling only allowing for local Euler angle searches. Particles belonging to the 3D class were further refined in RELION (version 3.1), where their higher order CTF parameters were re-refined, taking into account particles belonging to each image shift group. Further 3D refinements where the α -helical domain of the G α_s protein and the detergent micelle were masked and a final 3D refinement was carried out in RELION (version 3.1), yielding consensus maps of the complex at a global resolution (FSC = 0.143) of 3.4 \AA .

Atomic model refinement

The model of GCGR-G_s complex bound to GCG (PDB: 6LMK) (12) was used as the initial template and was fitted in the cryo-EM density map in Chimera (UCSF), followed by molecular dynamics flexible fitting simulation with nanoscale molecular dynamics (52). The initial model was then subjected to real-space refinement, as implemented in the PHENIX (53). GCGR transmembrane domain, G_s protein and Nb35 were further refined by manual model building in COOT (54). After iterative refinement and manual adjustments, comprehensive validation implemented in PHENIX was performed to assess the model quality as presented in Table S3. No electron density was observed for N-terminal residues before Ala-26^{ECD} or C-terminal residues beyond Trp-418^{8.53} of the GCGR, N terminus of G β (Arg-8) and G γ (Leu-15). The extracellular domain (ECD) was less resolved and was modeled at a backbone level beyond Leu-50^{ECD}. Density of ECL1 (Gln-204^{ECL1}–Ser-213^{ECL1}), ICL3 (His-340^{ICL3}–Asp-342^{ICL3}), and ECL3 (Val-368^{ECL3}–Gly-375^{ECL3}) was discontinuous and these sequences were deleted from the final model. Side chains of Leu-354^{6.45}, Thr-376^{7.33}, and Leu-377^{7.34} were omitted because of limited density. Structure statistics are detailed in Table S3.

Receptor mutagenesis and mammalian cell culture

WT GCGR was subcloned into pDONR201 plasmids. Alanine mutagenesis was achieved using the Muta-direct Site-Directed Mutagenesis Kit according to the manufacturer's instructions (SBS Genetech). The target gene was transferred to pEF5/FRT/V5-DEST destination vector by LR recombination reaction and FlpIn-Chinese hamster ovary (CHO) cells stably expressing WT or mutant GCGR were established using Gateway technology (Invitrogen). The cells were selected and maintained in F12 medium supplemented with 10% FBS, 600 $\mu\text{g}/\text{ml}$ hygromycin B and incubated in a humidified atmosphere at 37°C in 5% CO_2 . Cells were routinely tested for mycoplasma contamination.

cAMP accumulation assay

cAMP accumulation was measured using a TR-FRET cAMP kit (PerkinElmer) according to manufacturer's instructions. Briefly, cells were seeded into 384-well culture plates (1.2×10^4 cells/well) and incubated overnight at 37°C in 5% CO_2 . Upon removal of the culture medium, stimulating solution (5 $\mu\text{l}/\text{well}$ containing 0.5 mM IBMX) and 5 $\mu\text{l}/\text{well}$ ligands of different concentrations were added and incubated for 40 min at room temperature. Eu-cAMP tracer (5 μl) and 5 μl ULight-anti-cAMP were introduced followed by 1 h incubation at room temperature. Signal was detected thereafter with an Envision Multilabel Plate Reader (PerkinElmer). Data were converted to absolute concentration of cAMP using a cAMP standard curve generated in parallel. For analysis, data were normalized to the response of WT receptor and analyzed using a three-parameter logistic equation in GraphPad Prism (v8.0; GraphPad Software Inc.).

Whole cell radioligand binding assay

Cells were seeded into 96-well culture plates (5×10^4 cells/well) and incubated for 24 h at 37°C in 5% CO_2 . They were then washed twice using F12 with 0.1% BSA and 33 mM HEPES and incubated for 2 h at 37°C. The medium was removed and ^{125}I -GLP-1 or ^{125}I -glucagon (40 picomolar) (PerkinElmer) as well as increasing concentrations of unlabeled ligand were added. After overnight incubation at 4°C, cells were washed three times with ice-cold PBS and lysed in PBS with 1% Triton X-100 and 20 mM Tris-HCl. After addition of scintillation mixture (PerkinElmer), radioactivity (counts per minute) was counted on a MicroBeta² microplate counter (PerkinElmer). Data were normalized to the response of WT and analyzed using a three-parameter logistic equation.

Receptor expression

The cell surface expression level of GCGR was determined by flow cytometry with an anti-GCGR antibody (Abcam). Cells were seeded at a density of 2×10^4 cells/well into 6-well culture plates and incubated overnight at 37°C in 5% CO_2 . They were washed three times in PBS and Hanks' Balanced Salt Solution with 0.02% EDTA was added until cells were dispersed. They were then washed three times in PBS, counted, and resuspended in 1% BSA at a density of 4×10^6 cells/tube. Cell sus-

pension (50 μL) was transferred to a new centrifuge tube and blocked by 5% BSA for 15 min at room temperature. The primary antibody (1:100) was then introduced followed by 1 h incubation at room temperature. After three washes with 1% BSA, anti-rabbit Alexa Fluor 488-conjugated secondary antibody (1:1000, Cell Signaling Technology) was added for 1 h at 4°C in the dark. Cells were resuspended in 200 μl PBS containing 1% BSA after three washes and fluorescence signals were detected by NovoCyte flow cytometer (ACEA Biosciences) using laser excitation and emission wavelengths of 488 nm and 519 nm, respectively. For each data point, ~20,000 cellular events were collected, and the total fluorescence intensity of positive expression cell population was calculated. Data were normalized to the WT GCGR.

Statistical analysis

Data were analyzed using GraphPad Prism (v8.0). Statistic evaluation was performed using one-way analysis of variance and Dunnett's post test. Significance was accepted at $p < 0.05$.

Data availability

Cryo-EM maps and atomic models are deposited in the PDB and EMDB databases with the following codes: [6WHC](#), [EMD-21671](#).

Acknowledgments—We thank the cryo-EM facility at Shanghai Institute of Materia Medica, Chinese Academy of Sciences, the Monash University Ramaciotti Center for cryo-electron microscopy, and the Monash University MASSIVE high-performance computing facility.

Author contributions—R. C., X. Z., M. J. B., S. H., D. Y., R. D., M.-W. W., D. W., B. W., and P. M. S. formal analysis; R. C., X. Z., A. Q., A. D., M. J. B., Q. T., L. S., L. Z., G. L., Y.-L. L., L. M., and R. D. investigation; R. C., S. H., D. Y., D. W., and P. M. S. visualization; R. C., D. Y., M.-W. W., D. W., B. W., and P. M. S. writing-original draft; R. C., X. Z., A. Q., A. D., M. J. B., Q. T., L. S., L. Z., G. L., Y.-L. L., L. M., S. H., D. Y., R. D., M.-W. W., D. W., B. W., and P. M. S. writing-review and editing; X. Z. and M. J. B. data curation; X. Z. and D. Y. validation; X. Z., M. J. B., and R. D. methodology; Y.-L. L., D. Y., M.-W. W., D. W., B. W., and P. M. S. supervision; D. Y., R. D., M.-W. W., D. W., B. W., and P. M. S. funding acquisition; M.-W. W., D. W., B. W., and P. M. S. conceptualization; M.-W. W., D. W., B. W., and P. M. S. project administration.

Funding and additional information—This work was supported by the National Natural Science Foundation of China Grants 81872915 (to M.-W. W.), 31825010 (to B. W.), 81973373 (to D. Y.), and 81773792 (to D. Y.); the National Science & Technology Major Project "Key New Drug Creation and Manufacturing Program," China, Grants 2018ZX09735-001 (to M.-W. W.), 2018ZX09711002-002-005 (to D. Y.), and 2018ZX09711002-001 (to L. M.); the National Key R&D Program of China Grant 2018YFA0507000 (to M.-W. W. and B. W.); Novo Nordisk-CAS Research Fund NNCAS-2017-1-CC (to D. Y.); the National Health and Medical Research Council of Australia (NHMRC) Project Grants 1184726 and 1126857 (to D. W.) and Program

Grant 1150083 (to P. M. S.); Takeda Science Foundation 2019 Medical Research Grant (to R. D.); and Japan Science and Technology Agency (JST) PRESTO 18069571 (to R. D.). P. M. S. is a Senior Principal Research Fellow and D. W. a Senior Research Fellow of the NHMRC.

Conflict of interest—The authors declare that they have no conflicts of interest with the contents of this article.

Abbreviations—The abbreviations used are: GPCR, G protein-coupled receptor; GCG, glucagon; GIP, gastric inhibitory peptide; Nb, nanobody; SEC, exclusion chromatography; FSC, Fourier shell correlation; ECD, extracellular domain; LMNG, lauryl maltose neopentyl glycol; CHS, cholesteryl hemisuccinate; CTF, contrast transfer function; CHO, Chinese hamster ovary.

References

- Alexander, S. P. H., Christopoulos, A., Davenport, A. P., Kelly, E., Mathie, A., Peters, J. A., Veale, E. L., Armstrong, J. F., Faccenda, E., Harding, S. D., Pawson, A. J., Sharman, J. L., Southan, C., and Davies, J. A. CGTP Collaborators (2019) The concise guide to pharmacology 2019/20: G protein-coupled receptors. *Br. J. Pharmacol.* **176**, Suppl. 1, S21–S141 [CrossRef Medline](#)
- Wootten, D., Miller, L. J., Koole, C., Christopoulos, A., and Sexton, P. M. (2017) Allosteric and biased agonism at class B G protein-coupled receptors. *Chem. Rev.* **117**, 111–138 [CrossRef Medline](#)
- Sekar, R., Singh, K., Arokiaaraj, A. W., and Chow, B. K. (2016) Pharmacological actions of glucagon-like peptide-1, gastric inhibitory polypeptide, and glucagon. *Int. Rev. Cell. Mol. Biol.* **326**, 279–341 [CrossRef Medline](#)
- Aroda, V. R. (2018) A review of GLP-1 receptor agonists: Evolution and advancement, through the lens of randomised controlled trials. *Diabetes Obes. Metab.* **20**, Suppl. 1, 22–33 [CrossRef Medline](#)
- Chudleigh, R. A., Platts, J., and Bain, S. C. (2020) Comparative effectiveness of long-acting GLP-1 receptor agonists in Type 2 diabetes: A short review on the emerging data. *Diabetes Metab. Syndr. Obes.* **13**, 433–438 [CrossRef Medline](#)
- Campbell, J. E., and Drucker, D. J. (2015) Islet α -cells and glucagon-critical regulators of energy homeostasis. *Nat. Rev. Endocrinol.* **11**, 329–338 [CrossRef Medline](#)
- Knerr, P. J., Mowery, S. A., Finan, B., Perez-Tilve, D., Tschöp, M. H., and DiMarchi, R. D. (2020) Selection and progression of unimolecular agonists at the GIP, GLP-1, and glucagon receptors as drug candidates. *Peptides* **125**, 170225 [CrossRef Medline](#)
- Sánchez-Garrido, M. A., Brandt, S. J., Clemmensen, C., Müller, T. D., DiMarchi, R. D., and Tschöp, M. H. (2017) GLP-1/glucagon receptor co-agonism for treatment of obesity. *Diabetologia* **60**, 1851–1861 [CrossRef Medline](#)
- Ambery, P., Parker, V. E., Stumvoll, M., Posch, M. G., Heise, T., Plum-Moerschel, L., Tsai, L. F., Robertson, D., Jain, M., Petrone, M., Rondinone, C., Hirshberg, B., and Jeremut, L. (2018) MEDI0382, a GLP-1 and glucagon receptor dual agonist, in obese or overweight patients with type 2 diabetes: A randomised, controlled, double-blind, ascending dose and phase 2a study. *Lancet* **391**, 2607–2618 [CrossRef Medline](#)
- Tillner, J., Posch, M. G., Wagner, F., Teichert, L., Hijazi, Y., Einig, C., Keil, S., Haack, T., Wagner, M., Bossart, M., and Larsen, P. J. (2019) A novel dual glucagon-like peptide and glucagon receptor agonist SAR425899: Results of randomized, placebo-controlled first-in-human and first-in-patient trials. *Diabetes Obes. Metab.* **21**, 120–128 [CrossRef Medline](#)
- Day, J. W., Ottaway, N., Patterson, J. T., Gelfanov, V., Smiley, D., Gidda, J., Findeisen, H., Bruemmer, D., Drucker, D. J., Chaudhary, N., Holland, J., Hembree, J., Abplanalp, W., Grant, E., Ruehl, J., et al. (2009) A new glucagon and GLP-1 co-agonist eliminates obesity in rodents. *Nat. Chem. Biol.* **5**, 749–757 [CrossRef Medline](#)
- Qiao, A., Han, S., Li, X., Li, Z., Zhao, P., Dai, A., Chang, R., Tai, L., Tan, Q., Chu, X., Ma, L., Thorsen, T. S., Reedtz-Runge, S., Yang, D., Wang, M. W., et al. (2020) Structural basis of Gs and Gi recognition by the human glucagon receptor. *Science* **367**, 1346–1352 [CrossRef Medline](#)
- Liang, Y. L., Khoshouei, M., Glukhova, A., Furness, S. G. B., Zhao, P., Clydesdale, L., Koole, C., Truong, T. T., Thal, D. M., Lei, S., Radjainia, M., Danev, R., Baumeister, W., Wang, M. W., Miller, L. J., et al. (2018) Phase-plate cryo-EM structure of a biased agonist-bound human GLP-1 receptor-Gs complex. *Nature* **555**, 121–125 [CrossRef Medline](#)
- Liang, Y. L., Zhao, P., Draper-Joyce, C., Baltos, J. A., Glukhova, A., Truong, T. T., May, L. T., Christopoulos, A., Wootten, D., Sexton, P. M., and Furness, S. G. B. (2018) Dominant negative G proteins enhance formation and purification of agonist-GPCR-G protein complexes for structure determination. *ACS Pharmacol. Transl. Sci.* **1**, 12–20 [CrossRef Medline](#)
- Rasmussen, S. G., DeVree, B. T., Zou, Y., Kruse, A. C., Chung, K. Y., Kobilka, T. S., Thian, F. S., Chae, P. S., Pardon, E., Calinski, D., Mathiesen, J. M., Shah, S. T., Lyons, J. A., Caffrey, M., Gellman, S. H., et al. (2011) Crystal structure of the β_2 adrenergic receptor-Gs protein complex. *Nature* **477**, 549–555 [CrossRef Medline](#)
- Wootten, D., Simms, J., Miller, L. J., Christopoulos, A., and Sexton, P. M. (2013) Polar transmembrane interactions drive formation of ligand-specific and signal pathway-biased family B G protein-coupled receptor conformations. *Proc. Natl. Acad. Sci. U. S. A.* **110**, 5211–5216 [CrossRef Medline](#)
- Wootten, D., Reynolds, C. A., Koole, C., Smith, K. J., Mobarec, J. C., Simms, J., Quon, T., Coudrat, T., Furness, S. G., Miller, L. J., Christopoulos, A., and Sexton, P. M. (2016) A hydrogen-bonded polar network in the core of the glucagon-like peptide-1 receptor is a fulcrum for biased agonism: Lessons from class B crystal structures. *Mol. Pharmacol.* **89**, 335–347 [CrossRef Medline](#)
- Chugunov, A. O., Simms, J., Poyner, D. R., Dehouck, Y., Rooman, M., Gilis, D., and Langer, I. (2010) Evidence that interaction between conserved residues in transmembrane helices 2, 3, and 7 are crucial for human VPAC1 receptor activation. *Mol. Pharmacol.* **78**, 394–401 [CrossRef Medline](#)
- Vertongen, P., Solano, R. M., Perret, J., Langer, I., Robberecht, P., and Waelbroeck, M. (2001) Mutational analysis of the human vasoactive intestinal peptide receptor subtype VPAC(2): Role of basic residues in the second transmembrane helix. *Br. J. Pharmacol.* **133**, 1249–1254 [CrossRef Medline](#)
- Zhang, Y., Sun, B., Feng, D., Hu, H., Chu, M., Qu, Q., Tarrasch, J. T., Li, S., Kobilka, T. S., Kobilka, B. K., and Skiniotis, G. (2017) Cryo-EM structure of the activated GLP-1 receptor in complex with a G protein. *Nature* **546**, 248–253 [CrossRef Medline](#)
- Pocai, A. (2014) Action and therapeutic potential of oxyntomodulin. *Mol. Metab.* **3**, 241–251 [CrossRef Medline](#)
- Du, X., Kosinski, J. R., Lao, J., Shen, X., Petrov, A., Chicchi, G. G., Eiermann, G. J., and Pocai, A. (2012) Differential effects of oxyntomodulin and GLP-1 on glucose metabolism. *Am. J. Physiol. Endocrinol. Metab.* **303**, E265–E271 [CrossRef Medline](#)
- Kosinski, J. R., Hubert, J., Carrington, P. E., Chicchi, G. G., Mu, J., Miller, C., Cao, J., Bianchi, E., Pessi, A., Sinharoy, R., Marsh, D. J., and Pocai, A. (2012) The glucagon receptor is involved in mediating the body weight lowering effects of oxyntomodulin. *Obesity* **20**, 1566–1571 [CrossRef Medline](#)
- Santoprete, A., Capitò, E., Carrington, P. E., Pocai, A., Finotto, M., Langella, A., Ingallinella, P., Zytka, K., Bufali, S., Cianetti, S., Veneziano, M., Bonelli, F., Zhu, L., Monteagudo, E., Marsh, D. J., et al. (2011) DPP-IV-resistant, long-acting oxyntomodulin derivatives. *J. Pept. Sci.* **17**, 270–280 [CrossRef Medline](#)
- Finan, B., Yang, B., Ottaway, N., Smiley, D. L., Ma, T., Clemmensen, C., Chabenne, J., Zhang, L., Habegger, K. M., Fischer, K., Campbell, J. E., Sandoval, D., Seeley, R. J., Bleicher, K., Uhles, S., et al. (2015) A rationally designed monomeric peptide triagonist corrects obesity and diabetes in rodents. *Nat. Med.* **21**, 27–36 [CrossRef Medline](#)
- Visentin, R., Schiavon, M., Göbel, B., Riz, M., Cobelli, C., Klabunde, T., and Dalla Man, C. (2020) Dual glucagon-like peptide-1 receptor/glucagon receptor agonist SAR425899 improves beta-cell function in type 2 diabetes. *Diabetes Obes. Metab.* **22**, 640–647 [CrossRef Medline](#)
- Parker, V. E. R., Robertson, D., Wang, T., Hornigold, D. C., Petrone, M., Cooper, A. T., Posch, M. G., Heise, T., Plum-Moerschel, L., Schlichthaar, H., Klaus, B., Ambery, P. D., Meier, J. J., and Hirshberg, B. (2020) Efficacy, safety, and mechanistic insights of cotadutide, a dual receptor glucagon-

- like peptide-1 and glucagon agonist. *J. Clin. Endocrinol. Metab.* **105**, dgz047 [CrossRef Medline](#)
28. Capozzi, M. E., DiMarchi, R. D., Tschöp, M. H., Finan, B., and Campbell, J. E. (2018) Targeting the incretin/glucagon system with triagonists to treat diabetes. *Endocr. Rev.* **39**, 719–738 [CrossRef Medline](#)
 29. Liang, Y. L., Khoshouei, M., Radjainia, M., Zhang, Y., Glukhova, A., Tarasch, J., Thal, D. M., Furness, S. G. B., Christopoulos, G., Coudrat, T., Danev, R., Baumeister, W., Miller, L. J., Christopoulos, A., Kobilka, B. K., *et al.* (2017) Phase-plate cryo-EM structure of a class B GPCR-G-protein complex. *Nature* **546**, 118–123 [CrossRef Medline](#)
 30. Dal Maso, E., Glukhova, A., Zhu, Y., Garcia-Nafria, J., Tate, C. G., Atanasio, S., Reynolds, C. A., Ramirez-Aportela, E., Carazo, J. M., Hick, C. A., Furness, S. G. B., Hay, D. L., Liang, Y. L., Miller, L. J., Christopoulos, A., *et al.* (2019) The molecular control of calcitonin receptor signaling. *ACS Pharmacol. Transl. Sci.* **2**, 31–51 [CrossRef Medline](#)
 31. Liang, Y. L., Khoshouei, M., Deganutti, G., Glukhova, A., Koole, C., Peat, T. S., Radjainia, M., Plitzko, J. M., Baumeister, W., Miller, L. J., Hay, D. L., Christopoulos, A., Reynolds, C. A., Wootten, D., and Sexton, P. M. (2018) Cryo-EM structure of the active, Gs-protein complexed, human CGRP receptor. *Nature* **561**, 492–497 [CrossRef Medline](#)
 32. Liang, Y. L., Belousoff, M. J., Fletcher, M. M., Zhang, X., Khoshouei, M., Deganutti, G., Koole, C., Furness, S. G. B., Miller, L. J., Hay, D. L., Christopoulos, A., Reynolds, C. A., Danev, R., Wootten, D., and Sexton, P. M. (2020) Structure and dynamics of adrenomedullin receptors AM₁ and AM₂ reveal key mechanisms in the control of receptor phenotype by receptor activity-modifying proteins. *ACS Pharmacol. Transl. Sci.* **3**, 263–284 [CrossRef Medline](#)
 33. Zhao, L. H., Ma, S., Sutkeviciute, I., Shen, D. D., Zhou, X. E., de Waal, P. W., Li, C. Y., Kang, Y., Clark, L. J., Jean-Alphonse, F. G., White, A. D., Yang, D., Dai, A., Cai, X., Chen, J., *et al.* (2019) Structure and dynamics of the active human parathyroid hormone receptor-1. *Science* **364**, 148–153 [CrossRef Medline](#)
 34. Ma, S., Shen, Q., Zhao, L. H., Mao, C., Zhou, X. E., Shen, D. D., de Waal, P. W., Bi, P., Li, C., Jiang, Y., Wang, M. W., Sexton, P. M., Wootten, D., Melcher, K., Zhang, Y., *et al.* (2020) Molecular basis for hormone recognition and activation of corticotropin-releasing factor receptors. *Mol. Cell.* **77**, 669–680.e4 [CrossRef Medline](#)
 35. Liang, Y. L., Belousoff, M. J., Zhao, P., Koole, C., Fletcher, M. M., Truong, T. T., Julita, V., Christopoulos, G., Xu, H. E., Zhang, Y., Khoshouei, M., Christopoulos, A., Danev, R., Sexton, P. M., and Wootten, D. (2020) Toward a structural understanding of class B GPCR peptide binding and activation. *Mol. Cell.* **77**, 656–668.e5 [CrossRef Medline](#)
 36. Kobayashi, K., Shihoya, W., Nishizawa, T., Kadji, F. M. N., Aoki, J., Inoue, A., and Nureki, O. (2020) Cryo-EM structure of the human PAC1 receptor coupled to an engineered heterotrimeric G protein. *Nat. Struct. Mol. Biol.* **27**, 274–280 [CrossRef Medline](#)
 37. Wang, J., Song, X., Zhang, D., Chen, X., Li, X., Sun, Y., Li, C., Song, Y., Ding, Y., Ren, R., Harrington, E. H., Hu, L. A., Zhong, W., Xu, C., Huang, X., *et al.* (2020) Cryo-EM structures of PAC1 receptor reveal ligand binding mechanism. *Cell Res.* **30**, 436–445 [CrossRef Medline](#)
 38. Zhao, P., Liang, Y. L., Belousoff, M. J., Deganutti, G., Fletcher, M. M., Willard, F. S., Bell, M. G., Christe, M. E., Sloop, K. W., Inoue, A., Truong, T. T., Clydesdale, L., Furness, S. G. B., Christopoulos, A., Wang, M. W., *et al.* (2020) Activation of the GLP-1 receptor by a non-peptidic agonist. *Nature* **577**, 432–436 [CrossRef Medline](#)
 39. Siu, F. Y., He, M., de Graaf, C., Han, G. W., Yang, D., Zhang, Z., Zhou, C., Xu, Q., Wacker, D., Joseph, J. S., Liu, W., Lau, J., Cherezov, V., Katritch, V., Wang, M. W., *et al.* (2013) Structure of the human glucagon class B G-protein-coupled receptor. *Nature* **499**, 444–449 [CrossRef Medline](#)
 40. Zhang, H., Qiao, A., Yang, D., Yang, L., Dai, A., de Graaf, C., Reedtz-Runge, S., Dharmarajan, V., Zhang, H., Han, G. W., Grant, T. D., Sierra, R. G., Weierstall, U., Nelson, G., Liu, W., *et al.* (2017) Structure of the full-length glucagon class B G-protein-coupled receptor. *Nature* **546**, 259–264 [CrossRef Medline](#)
 41. Glukhova, A., Draper-Joyce, C. J., Sunahara, R. K., Christopoulos, A., Wootten, D., and Sexton, P. M. (2018) Rules of engagement: GPCRs and G proteins. *ACS Pharmacol. Transl. Sci.* **1**, 73–83 [CrossRef Medline](#)
 42. García-Nafria, J., and Tate, C. G. (2019) Cryo-EM structures of GPCRs coupled to Gs, Gi and Go. *Mol. Cell. Endocrinol.* **488**, 1–13 [CrossRef Medline](#)
 43. Wootten, D., Reynolds, C. A., Smith, K. J., Mobarec, J. C., Koole, C., Savage, E. E., Pabreja, K., Simms, J., Sridhar, R., Furness, S. G. B., Liu, M., Thompson, P. E., Miller, L. J., Christopoulos, A., and Sexton, P. M. (2016) The extracellular surface of the GLP-1 receptor is a molecular trigger for biased agonism. *Cell* **165**, 1632–1643 [CrossRef Medline](#)
 44. Lei, S., Clydesdale, L., Dai, A., Cai, X., Feng, Y., Yang, D., Liang, Y. L., Koole, C., Zhao, P., Coudrat, T., Christopoulos, A., Wang, M. W., Wootten, D., and Sexton, P. M. (2018) Two distinct domains of the glucagon-like peptide-1 receptor control peptide-mediated biased agonism. *J. Biol. Chem.* **293**, 9370–9387 [CrossRef Medline](#)
 45. Schorb, M., Haberbosch, I., Hagen, W. J. H., Schwab, Y., and Mastronarde, D. N. (2019) Software tools for automated transmission electron microscopy. *Nat. Methods* **16**, 471–477 [CrossRef Medline](#)
 46. Li, X., Mooney, P., Zheng, S., Booth, C. R., Braumfeld, M. B., Gubbens, S., Agard, D. A., and Cheng, Y. (2013) Electron counting and beam-induced motion correction enable near-atomic-resolution single-particle cryo-EM. *Nat. Methods* **10**, 584–590 [CrossRef Medline](#)
 47. Zheng, S. Q., Palovcak, E., Armache, J. P., Verba, K. A., Cheng, Y., and Agard, D. A. (2017) MotionCor2: Anisotropic correction of beam-induced motion for improved cryo-electron microscopy. *Nat. Methods* **14**, 331–332 [CrossRef Medline](#)
 48. Zhang, K. (2016) Gctf: Real-time CTF determination and correction. *J. Struct. Biol.* **193**, 1–12 [CrossRef Medline](#)
 49. Wagner, T., Merino, F., Stabrin, M., Moriya, T., Antoni, C., Apelbaum, A., Hagel, P., Sitsel, O., Raisch, T., Prumbaum, D., Quentin, D., Roderer, D., Tacke, S., Siebolds, B., Schubert, E., *et al.* (2019) SPHIRE-crYOLO is a fast and accurate fully automated particle picker for cryo-EM. *Commun. Biol.* **2**, 21810 [CrossRef Medline](#)
 50. Zivanov, J., Nakane, T., Forsberg, B. O., Kimanius, D., Hagen, W. J., Lindahl, E., and Scheres, S. H. (2018) New tools for automated high-resolution cryo-EM structure determination in RELION-3. *eLife* **7**, e42166 [CrossRef Medline](#)
 51. Punjani, A., Rubinstein, J. L., Fleet, D. J., and Brubaker, M. A. (2017) cryo-SPARC: Algorithms for rapid unsupervised cryo-EM structure determination. *Nat. Methods* **14**, 290–296 [CrossRef Medline](#)
 52. Phillips, J. C., Braun, R., Wang, W., Gumbart, J., Tajkhorshid, E., Villa, E., Chipot, C., Skeel, R. D., Kale, L., and Schulten, K. (2005) Scalable molecular dynamics with NAMD. *J. Comp. Chem.* **26**, 1781–1802 [CrossRef Medline](#)
 53. Liebschner, D., Afonine, P. V., Baker, M. L., Bunkóczi, G., Chen, V. B., Croll, T. I., Hintze, B., Hung, L.-W., Jain, S., McCoy, A. J., Moriarty, N. W., Oeffner, R. D., Poon, B. K., Prisant, M. G., Read, R. J., *et al.* (2019) Macromolecular structure determination using X-rays, neutrons and electrons: Recent developments in PHENIX. *Acta Crystallogr. D Struct. Biol.* **75**, 861–877 [CrossRef Medline](#)
 54. Emsley, P., Lohkamp, B., Scott, W. G., and Cowtan, K. (2010) Features and development of Coot. *Acta Crystallogr. D Biol. Crystallogr.* **66**, 486–501 [CrossRef Medline](#)

Supporting Information

Cryo-electron microscopy structure of the glucagon receptor with a dual-agonist peptide

Rulue Chang^{1^}, Xin Zhang^{2^}, Anna Qiao^{3,4}, Antao Dai^{3,5}, Matthew J. Belousoff², Qiuxiang Tan^{3,4}, Lijun Shao^{3,4,6}, Li Zhong^{3,4}, Guangyao Lin^{3,4,6}, Yi-Lynn Liang², Limin Ma³, Shuo Han³, Dehua Yang^{3,5}, Radostin Danev⁷, Ming-Wei Wang^{1,3,4,5,6*}, Denise Wootten^{2*}, Beili Wu^{3,4,6*}, Patrick M. Sexton^{2*}

¹School of Pharmacy, Shanghai Medical College, Fudan University, Shanghai 201203, China

²Drug Discovery Biology theme, Monash Institute of Pharmaceutical Sciences, Monash University, Parkville 3052, Victoria, Australia

³The CAS Key Laboratory of Receptor Research, Shanghai Institute of Materia Medica, Chinese Academy of Sciences, Shanghai 201203, China

⁴University of Chinese Academy of Sciences, Beijing 100049, China

⁵The National Center for Drug Screening, Shanghai 201203, China

⁶School of Life Science and Technology, ShanghaiTech University, Shanghai 201210, China

⁷Graduate School of Medicine, University of Tokyo, 113-0033 Tokyo, Japan

Table S1	page S2
Table S2	page S2
Table S3	page S3

Supplementary Figure 1	page S4
Supplementary Figure 2	page S5
Supplementary Figure 3	page S6
Supplementary Figure 4	page S7
Supplementary Figure 5	page S8

Table S1. Quantitative parameters for peptide-mediated cAMP accumulation in CHO cells expressing wild-type or expression constructs of GCGR and GLP-1R.

Construct ^a	GLP1(7-36)NH ₂	Peptide 15		Glucagon	
	pEC ₅₀ ± SEM ^b	pEC ₅₀ ± SEM ^b	E _{max} ^c (% of WT)	pEC ₅₀ ± SEM ^b	E _{max} ^c (% of WT)
WT-GLP-1R	10.68 ± 0.15	10.67 ± 0.10		8.82 ± 0.08	
WT-GCGR		10.47 ± 0.10	100 ± 4	10.88 ± 0.11	100 ± 5
HA-GCGR-HPC4		8.70 ± 0.08	64 ± 2	9.45 ± 0.08	63 ± 2

^aConstructs were cloned into pcDNA3.1 plasmid and transiently transfected into CHO-K1 cells to assess agonist-mediated cAMP accumulation.

^bData shown are means ± SEM of at least four experiments.

^cE_{max} is shown as percent of the span compared with wild-type (WT).

Data were derived from fitting concentration-response data (Suppl. Figure 1) to a 3-parameter logistic equation.

Table S2. Quantitative analysis of peptide competition for radiolabeled ligand binding to wild-type or expression constructs of GCGR and GLP-1R.

Construct ^a	GLP1(7-36)NH ₂	Peptide 15	Glucagon	Expression ^c (% of WT)
	pIC ₅₀ ± SEM ^b	pIC ₅₀ ± SEM ^b	pIC ₅₀ ± SEM ^b	
WT-GLP-1R	8.18 ± 0.07	7.69 ± 0.07		
WT-GCGR		6.25 ± 0.04	7.32 ± 0.06	100 ± 0
HA-GCGR-HPC4		6.45 ± 0.17	7.31 ± 0.17	77 ± 4

^aConstructs are as described in Table S1.

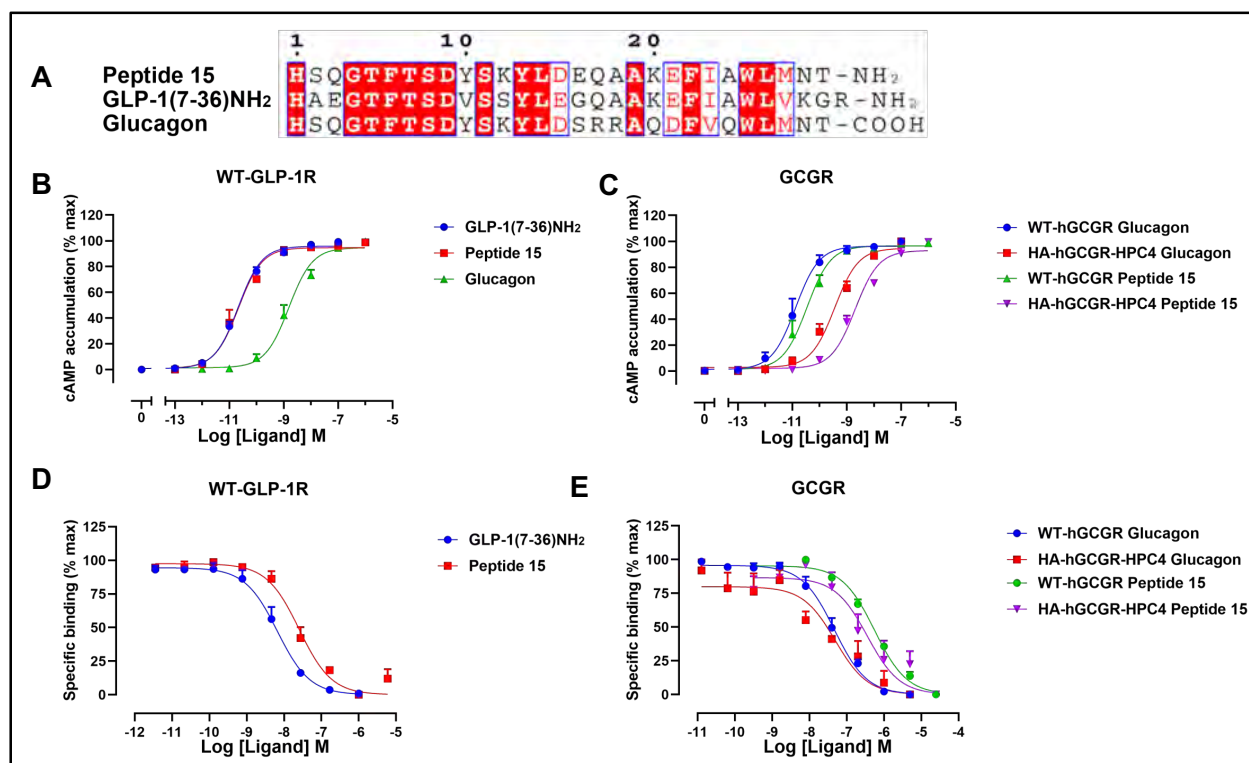
^bData shown are means ± SEM of at least three independent experiments.

^cCell surface expression was detected by flow cytometry with anti-GLP-1R antibody for GLP-1R and anti-GCGR antibody for GCGR (representing at least four independent experiments). Data are reported as percentage of wild-type (WT).

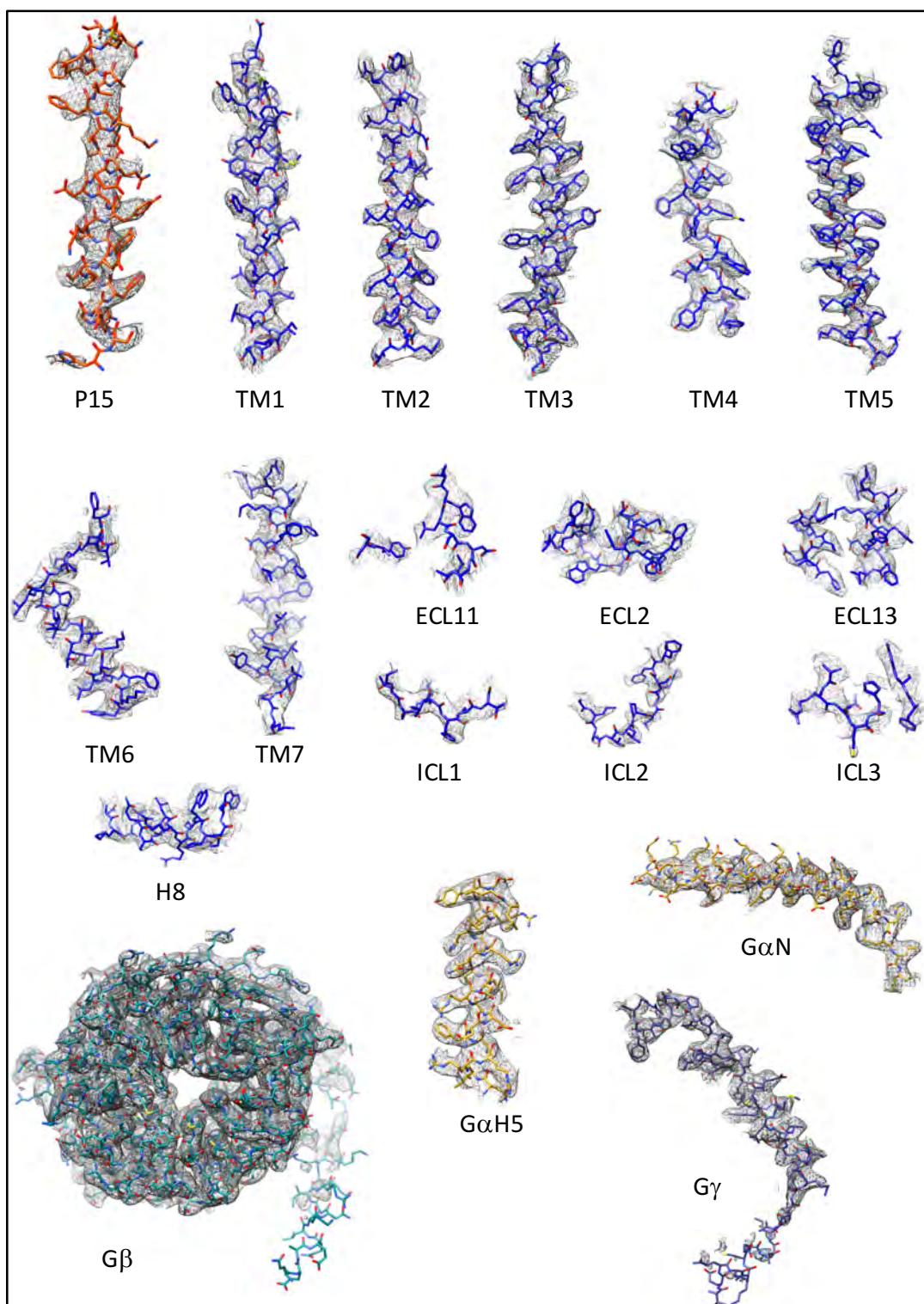
Data were derived from fitting concentration-response data (Suppl. Figure 1) to a 3-parameter logistic equation.

Table S3. Structure statistics.

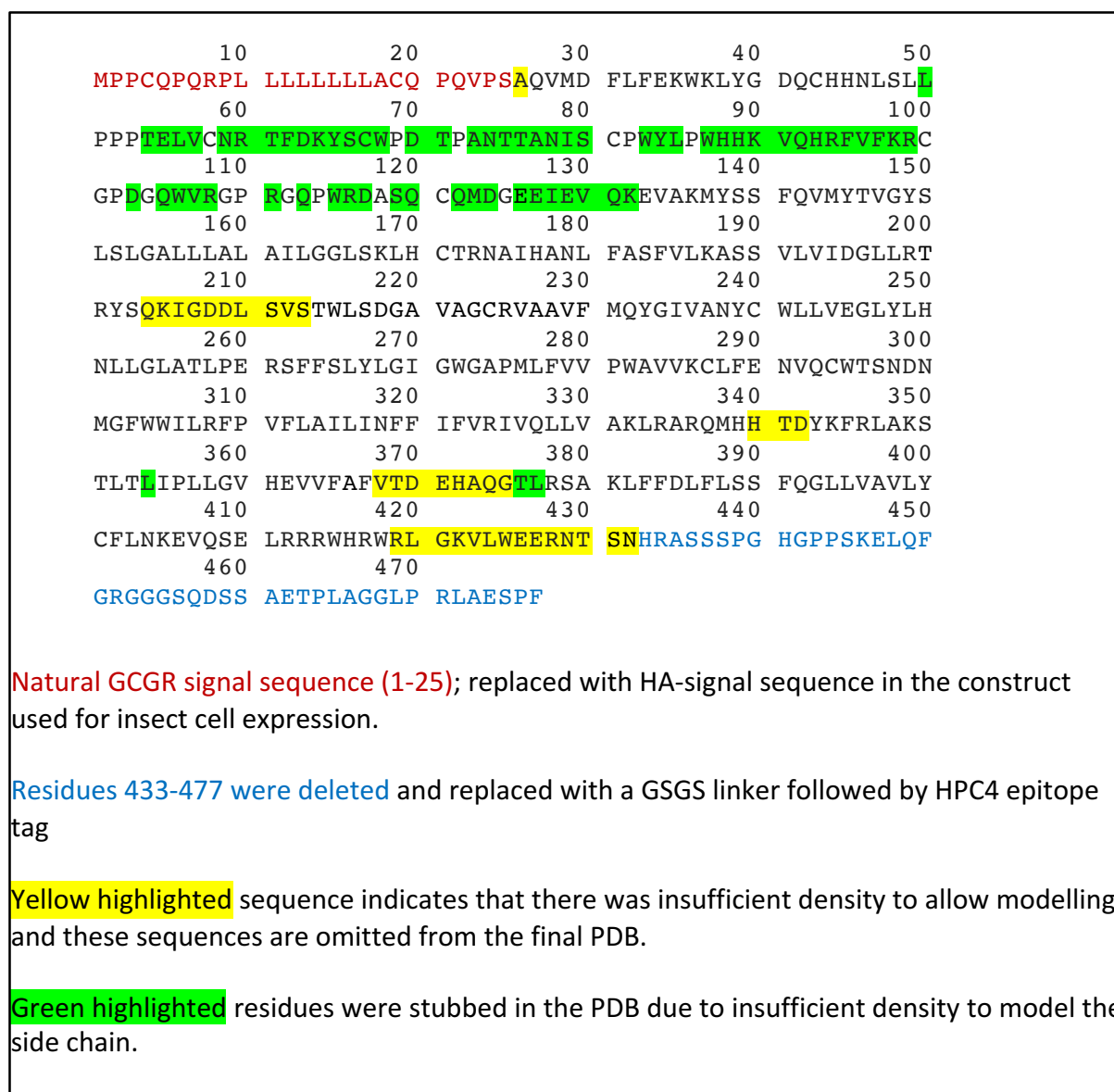
Data Collection	GCGR-Peptide15 Complex
Micrographs	5571
Particles (Final map)	175k
Pixel size (Å)	0.83
Defocus range (µm)	0.5-1.5
Voltage (kV)	300
Electron dose (e/Å ²)	58
Resolution (0.143 FSC) (Å)	3.4
Refinement	
CC _{map-model}	0.83
Model Quality	
<i>RMSD</i>	
Bond length (Å) / Bond angles (°)	0.004/0.777
<i>Ramachandran</i>	
Favoured (%)	96.01
Outliers (%)	0
<i>Rotamer outliers</i> (%)	0.11
<i>C-Beta deviations</i> (%)	0
<i>Clashscore</i>	6.20
<i>MolProbity Score</i>	1.61



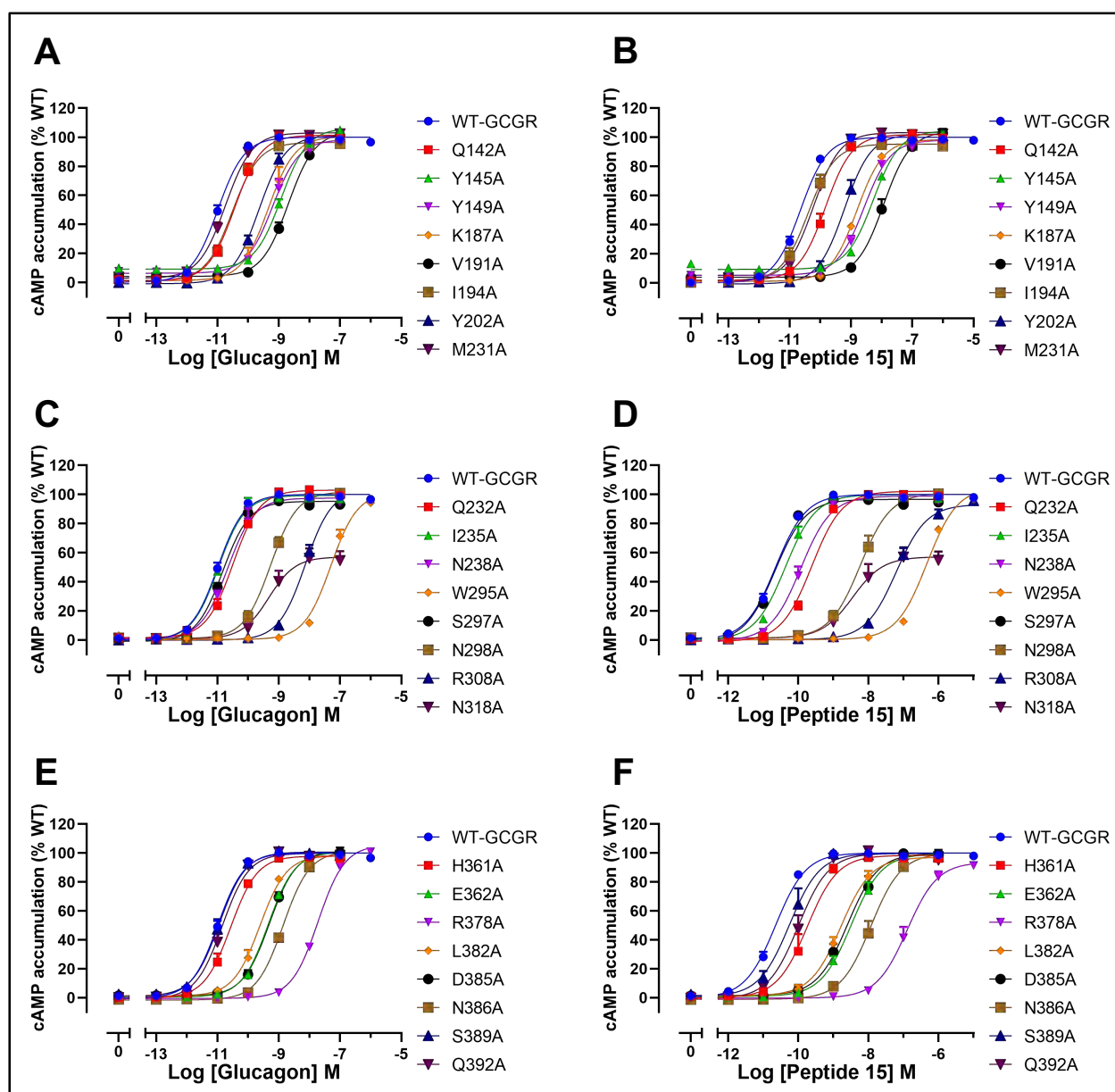
Supplementary Figure 1. Pharmacological characterisation of peptides and receptor constructs. **A**, Sequence alignment of the dual agonist peptide 15, GLP-1(7-36)NH₂ and glucagon. Conserved amino acids are shown as white text with red shading, similar residues are shown in red text. Non-conserved amino acids are in black text. **B**, Agonist-mediated cAMP accumulation in CHO-K1 cells expressing wild-type (WT) GLP-1R, **(C)** Agonist-mediated cAMP accumulation in CHO-K1 cells for GCGR constructs, or GCGR constructs modified with HA signal peptide and hpc4 tag for expression and purification of receptors for cryo-EM. **D**, Competition of ¹²⁵I-GLP-1 radio-ligand binding to the GLP-1R by peptide 15 or GLP-1(7-36)NH₂. **E**, Competition of ¹²⁵I-glucagon radio-ligand binding to WT or expression construct of GCGR by peptide 15 or GCG. Data were fit with a 3-parameter logistic equation.



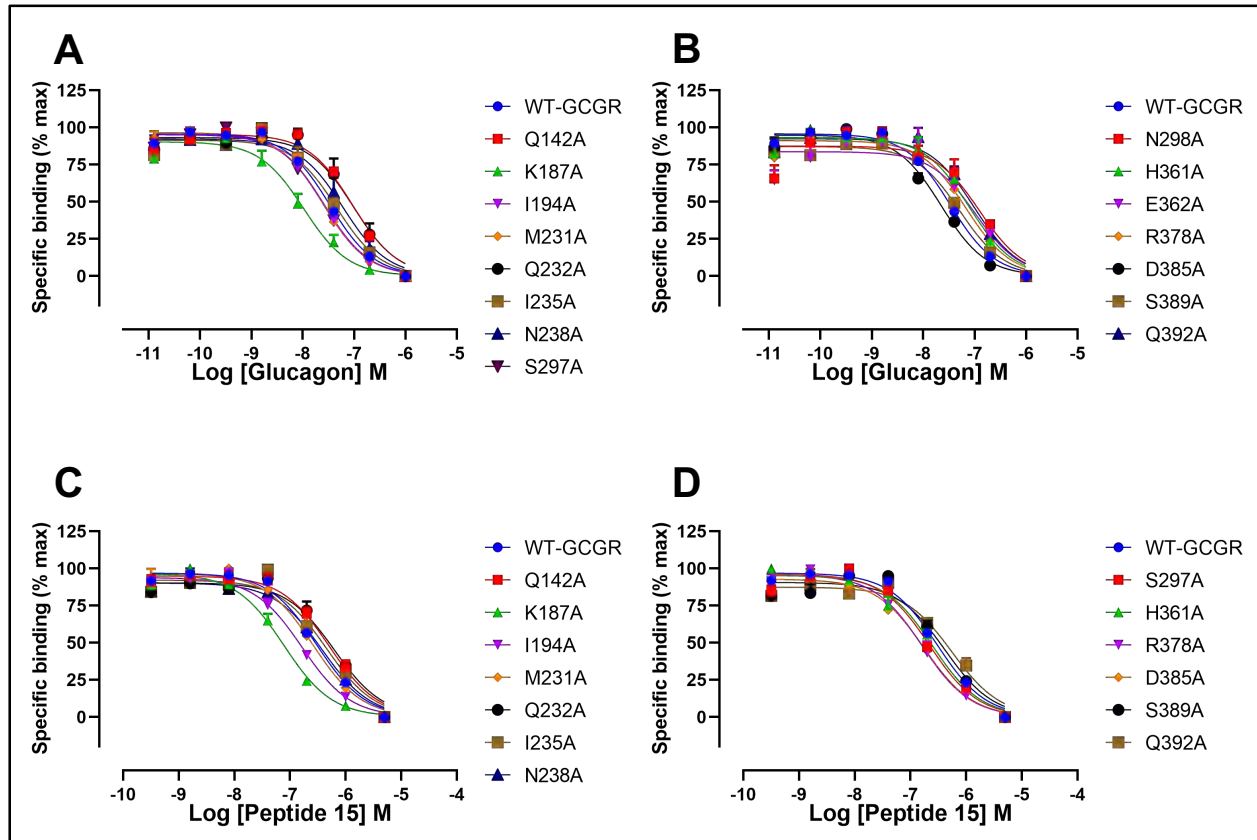
Supplementary Figure 2. Atomic coordinates of the P15:GCGR:GsDN:Nb35 complex in the cryo-EM density map. Cryo-EM density map and model are shown for all seven transmembrane helices, ECLs, ICLs and H8 of GCGR; peptide 15 (P15); the N-terminal (α N), and C-terminal (α H5) α -helices of the Gas-Ras domain, G β 1 and Gy2 are also shown. The EM map was zoned at 2.0 Å around the protein segments with the contour set at 0.01.



Supplementary Figure 3. GCGR sequence illustrating modelled residues, and highlighting sequences that were either fully omitted from the atomic model, or where the side chains were stubbed due lack of, or ambiguity in the EM density map.



Supplementary Figure 4. Impact of alanine mutation of GCGR amino acids in proximity to the activation domain of P15 and GCG peptides on peptide induced cAMP accumulation in CHO-FlpIn cells stably expressing each of the receptors. A, C, E, mutational effects on GCG response. B, D, F, mutational effects on P15 responses. Data are normalised to the maximal response of the WT receptor for each of the peptides.



Supplementary Figure 5. Impact of alanine mutation of GCGR amino acids in proximity to the activation domain of P15 and GCG peptides on affinity of peptides in competition for ^{125}I -glucagon in CHO-FlpIn cells stably expressing each of the receptors. **A, B, mutational effects on GCG affinity. **C, D**, mutational effects on P15 affinity. Data are displayed as specific binding, normalised to binding of the radio-ligand to the WT receptor.**

ARTICLE


<https://doi.org/10.1038/s41467-020-17791-4>

OPEN

Structure and dynamics of the active Gs-coupled human secretin receptor

Maoqing Dong^{1,8}, Giuseppe Deganutti^{2,6,8}, Sarah J. Piper^{3,8}, Yi-Lynn Liang^{3,8}, Maryam Khoshouei^{4,7,8}, Matthew J. Belousoff³, Kaleeckal G. Harikumar¹, Christopher A. Reynolds², Alisa Glukhova³, Sebastian G. B. Furness³, Arthur Christopoulos³, Radostin Danev⁵, Denise Wootten³, Patrick M. Sexton³ & Laurence J. Miller¹

The class B secretin GPCR (SecR) has broad physiological effects, with target potential for treatment of metabolic and cardiovascular disease. Molecular understanding of SecR binding and activation is important for its therapeutic exploitation. We combined cryo-electron microscopy, molecular dynamics, and biochemical cross-linking to determine a 2.3 Å structure, and interrogate dynamics, of secretin bound to the SecR:Gs complex. SecR exhibited a unique organization of its extracellular domain (ECD) relative to its 7-transmembrane (TM) core, forming more extended interactions than other family members. Numerous polar interactions formed between secretin and the receptor extracellular loops (ECLs) and TM helices. Cysteine-cross-linking, cryo-electron microscopy multivariate analysis and molecular dynamics simulations revealed that interactions between peptide and receptor were dynamic, and suggested a model for initial peptide engagement where early interactions between the far N-terminus of the peptide and SecR ECL2 likely occur following initial binding of the peptide C-terminus to the ECD.

¹Department of Molecular Pharmacology and Experimental Therapeutics, Mayo Clinic, Scottsdale, AZ 85259, USA. ²School of Biological Sciences, University of Essex, Colchester CO4 3SQ, UK. ³Drug Discovery Biology Theme, Monash Institute of Pharmaceutical Sciences, Monash University, Parkville, VIC 3052, Australia. ⁴Department of Molecular Structural Biology, Max Planck Institute of Biochemistry, 82152 Martinsried, Germany. ⁵Graduate School of Medicine, University of Tokyo, N415, 7-3-1 Hongo, Bunkyo-ku 113-0033 Tokyo, Japan. ⁶Present address: Centre for Sport, Exercise and Life Sciences, Faculty of Health and Life Sciences, Alison Gingell Building, Coventry University, CV1 2DS Coventry, UK. ⁷Present address: Novartis Institutes for Biomedical Research, Novartis Pharma AG, 4002 Basel, Switzerland. ⁸These authors contributed equally: Maoqing Dong, Giuseppe Deganutti, Sarah J. Piper, Yi-Lynn Liang, Maryam Khoshouei. ✉email: denise.wootten@monash.edu; patrick.sexton@monash.edu; miller@mayo.edu

G protein-coupled receptors (GPCRs) are the largest family of cell surface receptors and pre-eminent drug targets. There are four major subclasses of GPCRs: A, B, C, and F. Peptide hormone class B GPCRs are a subfamily of GPCRs that are particularly important in physiology and disease, since their endogenous ligands play major roles in homeostatic control of bone and energy metabolism, cardiovascular, and immune responses¹. Consequently, these receptors are important targets for treatment of disorders of these functions. Class B GPCRs encompass targets for approved drugs that treat diabetes, obesity, osteoporosis, hypercalcemia, and Paget's disease, all of which are major global health burdens¹. However, targeting these receptors for therapeutic benefit is suboptimal¹. Class B receptors are also pleiotropically coupled and we currently lack a complete understanding of the breadth of signaling that is required for specific clinical efficacy and how this can be optimally achieved.

The class B secretin GPCR (SecR) is renowned for its physiological role as a regulator of pancreatic and biliary ductular epithelial secretion². Subsequent studies, including phenotypic analysis of mice genetically engineered to have no secretin peptide (Sec^{-/-})³ or receptor (SecR^{-/-})⁴, have revealed a much broader profile of action and the potential for secretin receptor agonists to fill key unmet clinical need across a range of diseases including obesity and diabetes, as well as heart failure⁵, among the most prevalent, costly, and debilitating public health problems. For example, secretin produces satiety to reduce body weight⁶, has direct thermogenic effects on adipocytes⁷ and elicits a glucose-sensitive incretin effect to help normalize glucose⁸. Further, secretin increases cardiac output and stroke volume and reduces systemic vascular resistance, while increasing coronary, renal, mesenteric, and carotid flow, providing benefits for heart failure⁵. Understanding the molecular basis for secretin receptor binding and activation is therefore important for therapeutic exploitation of this receptor.

In this study, we have combined single-particle cryo-electron microscopy, molecular dynamics (MD), and biochemical cross-linking to determine the structure and dynamics of secretin bound to the human SecR:Gs protein complex. While there are parallels to other active class B peptide hormone receptor structures, the SecR demonstrates a unique organization of the receptor extracellular domain (ECD) to the 7-transmembrane (TM) domain core, forming more extended interactions than other class B GPCRs. Secretin formed numerous polar interactions between the N-terminal half of the peptide and receptor extracellular loops (ECLs) and TM helices, with the importance of these interactions supported by mutagenesis data. Cysteine-cross-linking analysis and MD simulations revealed that the interactions between SecR and secretin were dynamic, and suggested a model for initial peptide engagement where early interactions between the far N-terminus of the peptide and the SecR ECL2 likely occur following initial binding of the peptide C-terminus to the receptor ECD.

Results

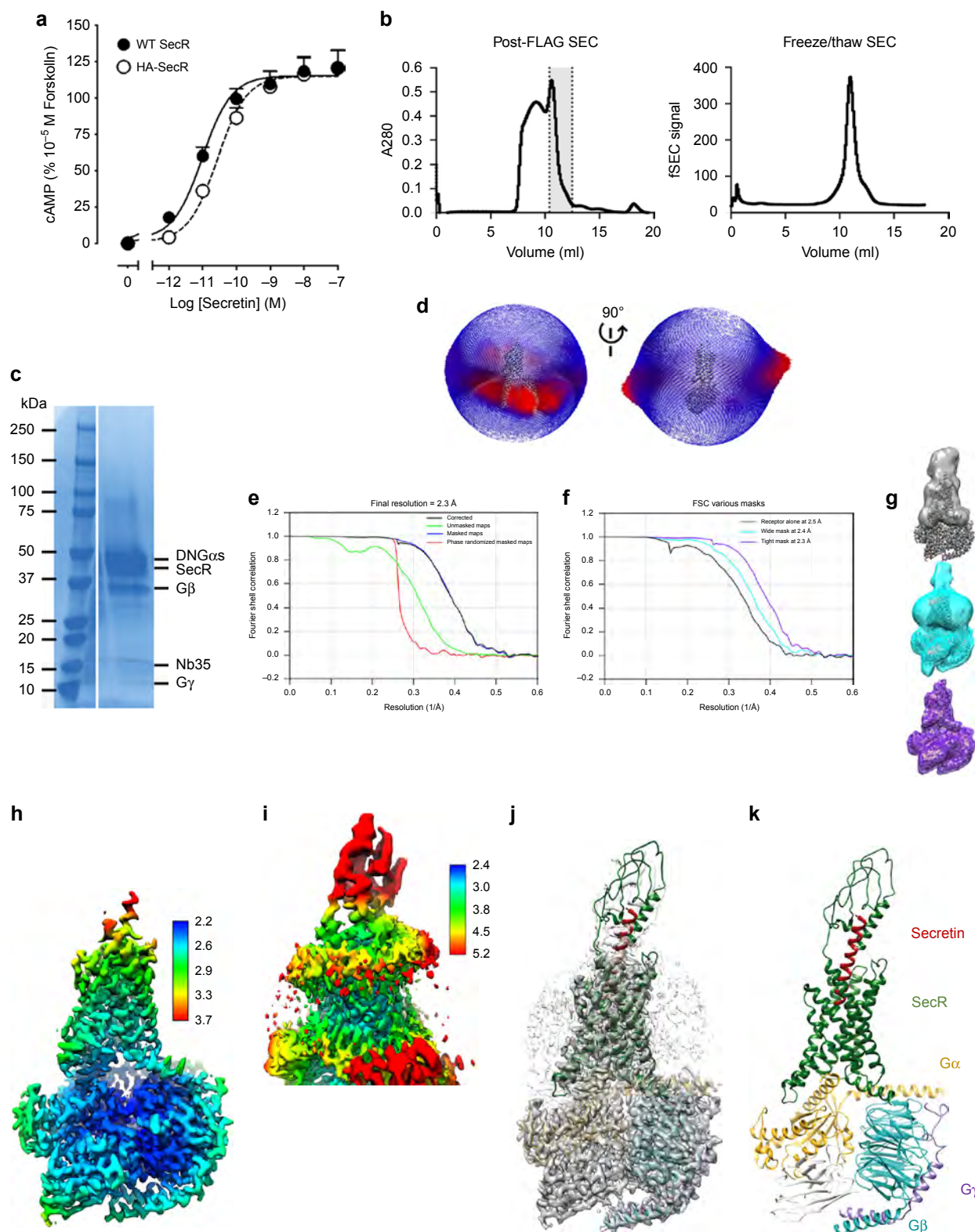
Cryo-EM determination of the secretin:SecR:Gs complex. The human SecR was modified to replace the native signal sequence with that of hemagglutinin (HA), followed by a Flag epitope, and inclusion of a C-terminal His tag, both flanked by 3C cleavage sites, as previously described for other class B GPCRs⁹. The expression construct maintained an equivalent ability to wild-type receptor to signal to Gs-mediated cAMP production (Fig. 1a). Complexes of the receptor with dominant negative Gα_s: Gβ₁γ₂^{9,10} were formed by the addition of 1 μM secretin. Two distinct datasets were collected >12 months apart, however, the biochemistry for formation of the two complexes was equivalent,

except that the Gα_s protein contained an additional A366S mutation (DN Gα_sv2) for the latter complex^{10,11}. The complexes exhibited a monodisperse peak on size-exclusion chromatography (SEC) (Fig. 1b, Supplementary Fig. 1a, right panels), following purification by anti-Flag antibody chromatography and an initial SEC separation (Fig. 1b, Supplementary Fig. 1a, left panels), containing each of the component proteins (Fig. 1c, Supplementary Fig. 1b). The complexes were imaged by single-particle cryo-EM. The first data set yielded a map of FSC 0.143, 4.3 Å global resolution, and this was used to build the initial model used for MD simulations (Supplementary Fig. 1d–f). A second data set was collected using improved vitrification and imaging protocols established subsequently in the Danev laboratory¹¹. Only the high-resolution structure is described below; however, the original model derived from the lower resolution map exhibited high overall concordance with the model constructed into the high-resolution map (Supplementary Fig. 1g–i).

Although there was preferred orientation of the particles (Fig. 1d), these data were processed to yield final maps with global resolutions, by gold standard FSC 0.143, of 2.3–2.5 Å (Fig. 1e, f). The highest local resolution was present for the receptor transmembrane domain, G protein, and for the peptide N-terminus that binds deep into the receptor core, and this was reflected in the 2.3 Å (tight mask excluding micelle and Gs α-helical domain (AHD)) and 2.4 Å (wide mask) maps (Fig. 1h, i). An atomic model of the complex was built into the electron density map using MD-guided fitting and manually inspected and adjusted using geometric constraints (Supplementary Fig. 2). Both the high-resolution map with the tight mask (Fig. 1g, h) and the receptor-focused map (Fig. 1g, i) were used in modeling, since the latter had better resolution for the loops and peptide C-terminus (Supplementary Fig. 2). Overall, the maps allowed accurate placement of side-chain rotamers for most of the receptor transmembrane domain, all ECLs, ICL1 and ICL2, and G protein, as well as the N-terminus of the peptide (Supplementary Fig. 2); however, the ECD resolution did not allow unambiguous placement of side chains, and only the backbone was modeled between R30^{ECD} (the first modeled amino acid) and S130^{ECD}. Similarly, residues 254–263 of Gα_s were only modeled as a backbone trace, while the AHD of Gα_s (62–204) was omitted from the model. We also performed extensive MD simulations (3 × ~1 μs) to derive further insight into binding dynamics of the secretin peptide to the receptor and engagement of the receptor with the Gs protein.

General features of the secretin:SecR:Gs complex. The active SecR complex exhibits the key features of active class B GPCRs with outward movement of the tops of TM6/TM7/ECL3, lateral movement of TM1 and reordering of ECL2 into a common fold (Fig. 1j, k, Supplementary Fig. 3)¹², paralleled by a large outward movement of TM6 at the base of the receptor to accommodate G protein binding (Supplementary Fig. 3c). The secretin peptide forms an extended α-helix that exits the receptor almost perpendicular to the membrane, extending out of the transmembrane domain core (Figs. 1j, k and 2, Supplementary Fig. 4). The N-terminus terminates above the conserved class B receptor central polar network, similar to the related GCG family of peptides at their cognate receptors^{9,12,13} and forms extensive interactions with TM1, TM2, TM5, TM6, and TM7 (Supplementary Fig. 3D, Supplementary Tables 1–4).

SecR ECD. The ECD orientation of class B GPCRs is one of the most variable features observed in active structures¹², and we have speculated that this may be important in the activity of the individual receptors. The N-terminal helix of the ECD in the SecR



extends deep towards the ECL regions of the receptor core where it makes interactions with ECL1, ECL2, and the secretin peptide that likely stabilize the overall dynamics of the ECD (Figs. 1k and 2, Supplementary Fig. 5b–d). Fine angular sampling using the receptor-focused mask identified two distinct classes with altered positioning of the ECD, and this likely contributes to the lower overall resolution in the consensus maps (Supplementary Fig. 5). Dynamic motions of the receptor are discussed further below.

The most closely related orientation of the ECD is seen with the GCG receptor family that are the most evolutionarily conserved with SecR, and the far N-terminal helix of these receptors also extends to the top of the ECLs, though not to the extent of the SecR (Fig. 2a). While the PAC1 and PTH1 receptor ECDs exhibit partial overlap in orientation to the SecR, the far N-terminus is oriented further away from the receptor core (Fig. 2b). Interestingly, the location of the ECD for the CRF receptor family

Fig. 1 Cryo-EM structure of the secretin:SecR:DN α v2:Nb35 complex. **a** Pharmacology of the expression construct for HA-SecR versus WT-SecR (WT-SecR, pEC50 11.0 ± 0.1 ; HA-SecR, pEC50 10.6 ± 0.2 ; $n = 4$). **b** SEC trace of post FLAG-affinity column elution (left panel), the complex peak (gray, dotted lines) was isolated and used for cryo-EM imaging, with the right panel illustrating stability of the complex following one cycle of freeze-thawing. **c** Coomassie stain of the purified complex separated by PAGE (right panel). **d** 3-D histogram representation of the Euler angle distribution of all the particles used in the reconstruction overlaid on the density map drawn on the same coordinate axis (shown from the front and 90° rotated). **e** Gold standard Fourier shell correlation (FSC) curves for the global, postprocessed map using a tight mask showing the overall nominal resolution of 2.3 Å. **f** Corrected FSC curves of maps using different masking: consensus refinement, postprocessed using a tight mask (excluding ECD and micelle, 2.3 Å, in purple), consensus refinement, postprocessed using a wide mask (2.4 Å, in cyan), and local refinement with using a receptor-only mask (2.5 Å, in gray). **g** Masks used for calculating FSC curves in **f**, displayed onto the global refinement map (colored according to **f**). **h** Local resolution-filtered EM map displaying local resolution (in Å) colored from highest resolution (blue) to lowest resolution (red) of the global map. **i** Local resolution-filtered EM map displaying local resolution (in Å) of the receptor-only refinement. **j** Global map (dark gray) overlaid with receptor-only map (gray transparent) containing the backbone model of the complex in ribbon format; SecR (dark green), secretin (dark red), G protein α -subunit (gold), β -subunit (cyan), γ -subunit (dark purple), and Nb35 (white). **k** Ribbon representation of the secretin:SecR:DN α v2:Nb35 complex colored according to **j**.

overlaps closely with that of the SecR, but they do not have an equivalent N-terminal α -helix and thus lack equivalent interactions with the receptor core (Fig. 2c), and this likely accounts for the lower relative resolution of the ECD in structures of these receptors^{12,14}. The calcitonin family receptors have a markedly distinct ECD orientation from other class B GPCRs that is enabled by an unstructured peptide C-terminus (Fig. 2d)¹⁵. These receptors form prominent interactions with the receptor activity-modifying protein (RAMP) family to yield unique receptor phenotypes for binding of CGRP, adrenomedullin (AM), amylin, and related peptides¹⁶. Interestingly, the location of the RAMP ECD overlaps the position of the SecR ECD (Fig. 2d, Supplementary Fig. 4). Although the SecR can also interact with RAMP3¹⁷, the structural data indicates that it is unlikely to engage via an equivalent (TM3, TM4, TM5, and ECD) interface to that of the CT family receptors¹⁵. This is consistent with our previous work illustrating that it is the transmembrane domain, and not ECD, which is most critical for RAMP3 and SecR dimerization, and that TM6 and TM7 of SecR may form the site of interaction with the RAMP3 TM domain¹⁷. As all class B GPCR peptides, except those of the CT receptor subgroup, have C-terminal extended α -helices, and thus a principally vertical ECD orientation, similar to SecR (Fig. 2, Supplementary Fig. 4), it is likely that the RAMP engagement that is seen with most other class B GPCRs would follow an interaction model similar to SecR.

Secretin binding site. Dynamics of the SecR complex was examined by 3D multivariate analysis of the cryo-EM data and in the long time-scale MD simulations. Separation of the conformational variance in the cryo-EM data into the three main principal components revealed that receptor exhibits twisting and rocking motions that are apparent relative to the G protein. These motions are similar to but less dynamic than those previously observed for the TM core of AM receptors¹¹. Across each of the principal components, the receptor ECD exhibited higher relative motion than the rest of the receptor but was nonetheless restricted by interactions with the peptide and receptor core, where the far N-terminus made dynamic interactions with the ECLs; however, no substantial translational motions were evident (Video 1). This contrasted to the much broader motions that were previously observed for the ECD of AM receptors using equivalent analyses¹¹. Importantly, the cryo-EM conformational variance data were consistent with the MD simulations where, overall, the receptor TM domain core and the secretin peptide exhibited limited dynamic motion of the peptide backbone, whereas the ECD exhibited higher mobility that was independent of motions of the rest of the receptor and peptide (Fig. 3a, Video 2). Within the ECD, those regions that maintained stable contacts with the secretin peptide had substantially less motion

than the rest of the ECD that lacked these constraints (Supplementary Tables 2–4, Fig. 3b, Video 2).

Atomic modeling into the static consensus high-resolution maps revealed specific details on the interactions between secretin and SecR and these are reported in (Supplementary Table 1, Supplementary Fig. 6a, b). To better understand these interactions, we interrogated their stability in a simulated POPC lipid environment over microseconds of MD. The secretin peptide forms an amphipathic α -helix and contains many polar and charged amino acids, and perhaps not surprisingly forms extensive stable and transient H-bond interactions over the course of the microsecond simulations, particularly with the receptor core and ECLs. The first three amino acids of secretin are among the most critical for receptor activation^{18,19}, and each of these residues forms critical H-bond interactions with the receptor (Supplementary Table 1, Supplementary Fig. 6a, b). In the simulations, His^{1P} and Ser^{2P} (peptide residues are recorded using the three-letter amino acid code, with sequence numbers superscripted) are predicted to form stable backbone and/or side-chain interactions with E373^{7.42} (superscript numbers refer to the Wootten et al. class B numbering system²⁰) deep within the receptor core, with His^{1P} forming additional transient interactions with R299^{5.40}, Y230^{3.44}, Q223^{3.37}, and potential weak interactions with the backbone of ECL3 residues E363 and M366 (Fig. 4a, Supplementary Tables 2, 3). Asp^{3P} is predicted to form relatively stable interactions with R188^{2.60} of the central polar network, as well as with R299^{5.40} and Y146^{1.43} (Fig. 4a, Supplementary Table 2); the latter are distinct from the interactions observed in the static consensus structure and highlight the likely importance of conformational dynamics in the action of peptide agonists. The identified class B receptor residues form conserved interactions with most cognate class B peptides¹², and prior mutagenesis has also demonstrated importance of at least Y146^{1.43}, R188^{2.60}, and Q223^{3.37} for peptide function in the SecR^{21–23}. Gly^{4P}, Thr^{5P}, Thr^{7P}, and Ser^{8P} are predicted to form potential weak H-bonds with residues within ECL2 of the SecR, with the most persistent interactions occurring between Ser^{8P} and N289^{ECL2} (Fig. 4a, Supplementary Tables 2, 3). Glu^{9P} is predicted to form a stable interaction with R135^{1.32}, while the cluster of basic residues, Arg^{14P}, Arg^{18P}, and Arg^{21P} that reside on one face of the secretin peptide form extensive electrostatic and H-bond interactions with a cluster of acidic Asp residues within or adjacent to ECL1, D196^{2.68}, D203^{ECL1}, D204^{ECL1}, and D209^{ECL1} (Fig. 4a, Supplementary Tables 2, 3). In contrast to the extensive polar interactions with the receptor core, only relatively few H-bond interactions were predicted between the secretin peptide and SecR ECD; these were between Glu^{15P} and R30^{ECD}, Gln^{24P} and N120^{ECD}, and the backbone of Leu^{26P}, and to a lesser extent Val^{27P} and N72^{ECD} (Fig. 4a, Supplementary Tables 2, 3), although these interactions

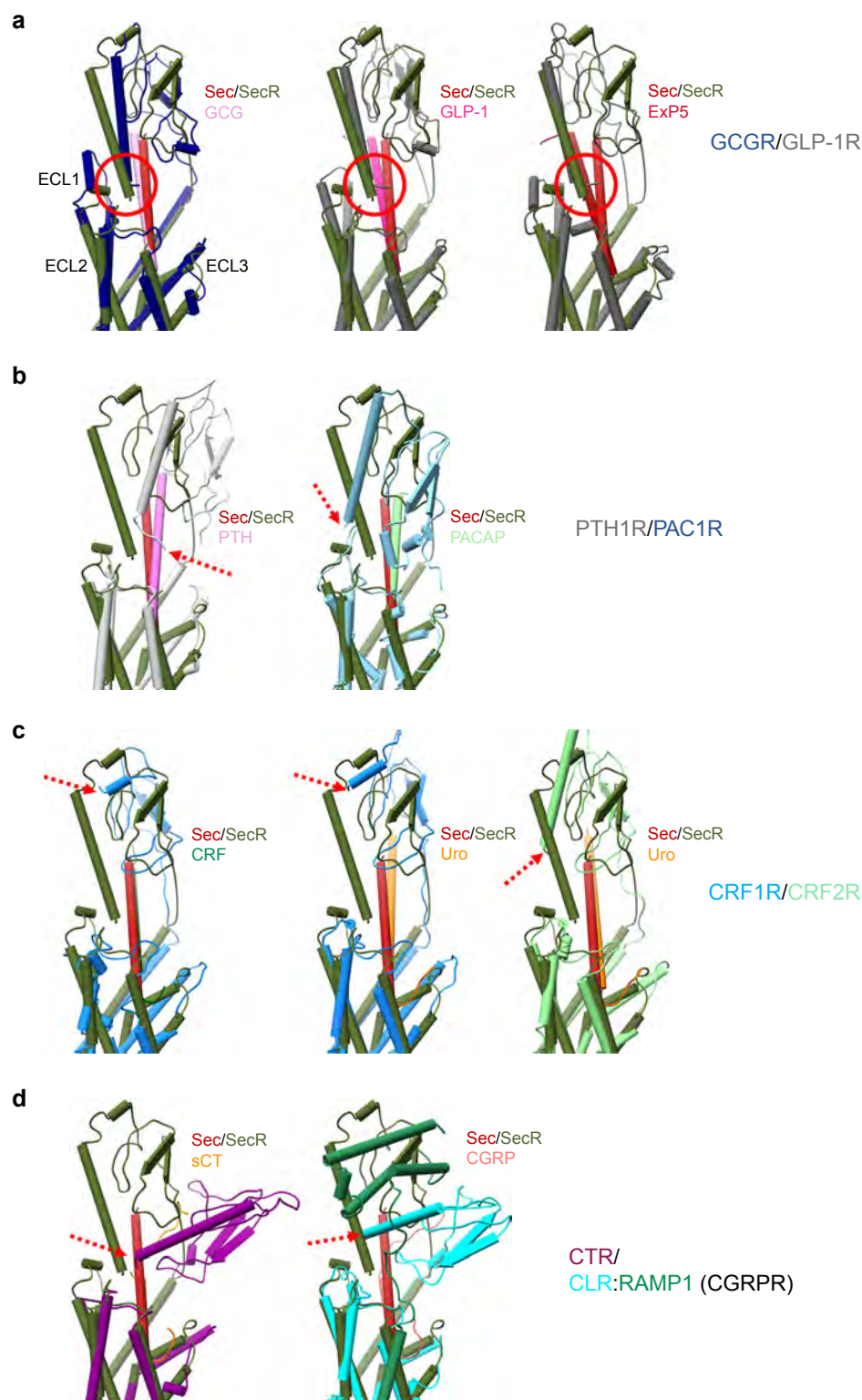


Fig. 2 Comparison of SecR and other class B GPCR Gs-coupled active structures. Overlay of secretin (dark red) and SecR (dark green) and different class B GPCR subfamilies emphasizing the position of the receptor ECD and location of the far N-terminus of the receptor (highlighted by red circle (**a**) or red arrows (**b-d**)). **a** Glucagon (GCG, pink; GCGR dark blue) and GLP-1 receptors (GLP-1, dark pink; ExP5, red; GLP-1R, dark gray). **b** PTH1 (PTH, pink; PTH1R, light gray) and PAC1 receptors (PACAP38, pale green; PAC1R, light blue). **c** CRF1 (CRF, dark green; Urocortin (Uro), orange; CRF1R, blue) and CRF2 receptors (Uro, orange; CRF2R, green). **d** Calcitonin (sCT, orange; CTR, purple) and CGRP (CGRP, coral; CLR, cyan; RAMP1, green) receptors. Helical secondary structure is shown as cylinders; beta sheets are displayed as flattened arrows.

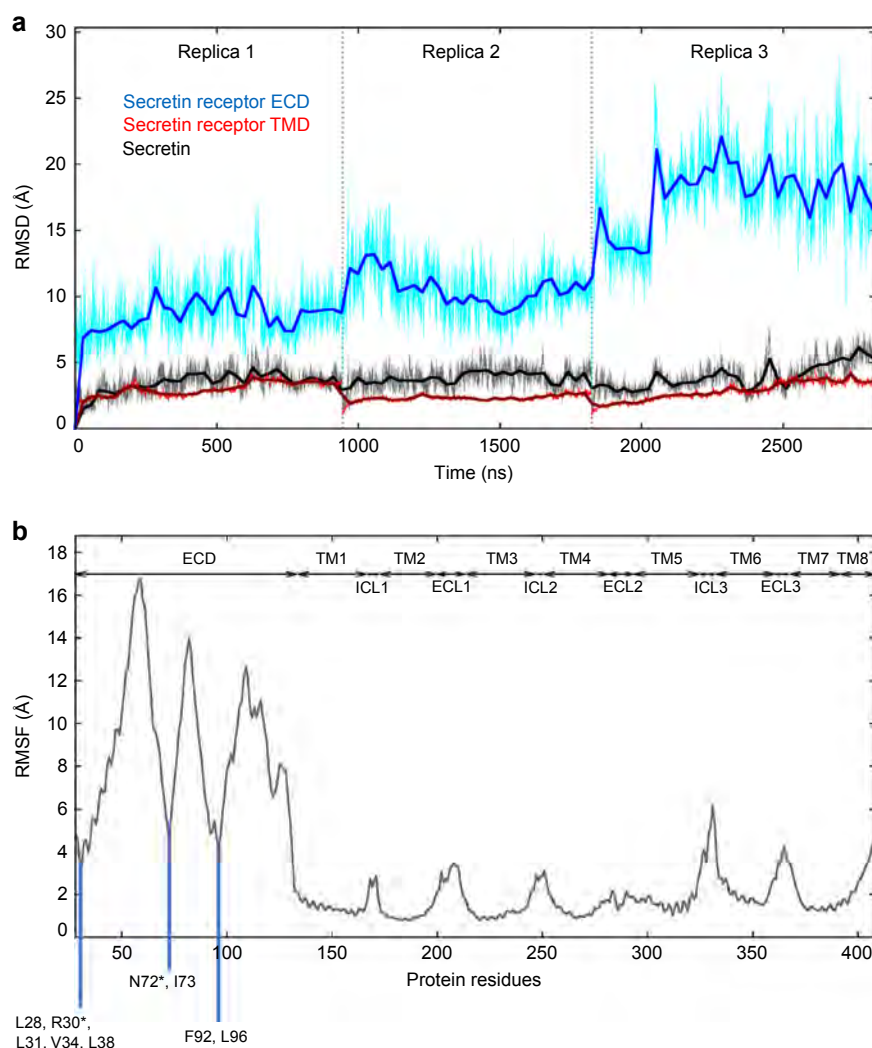
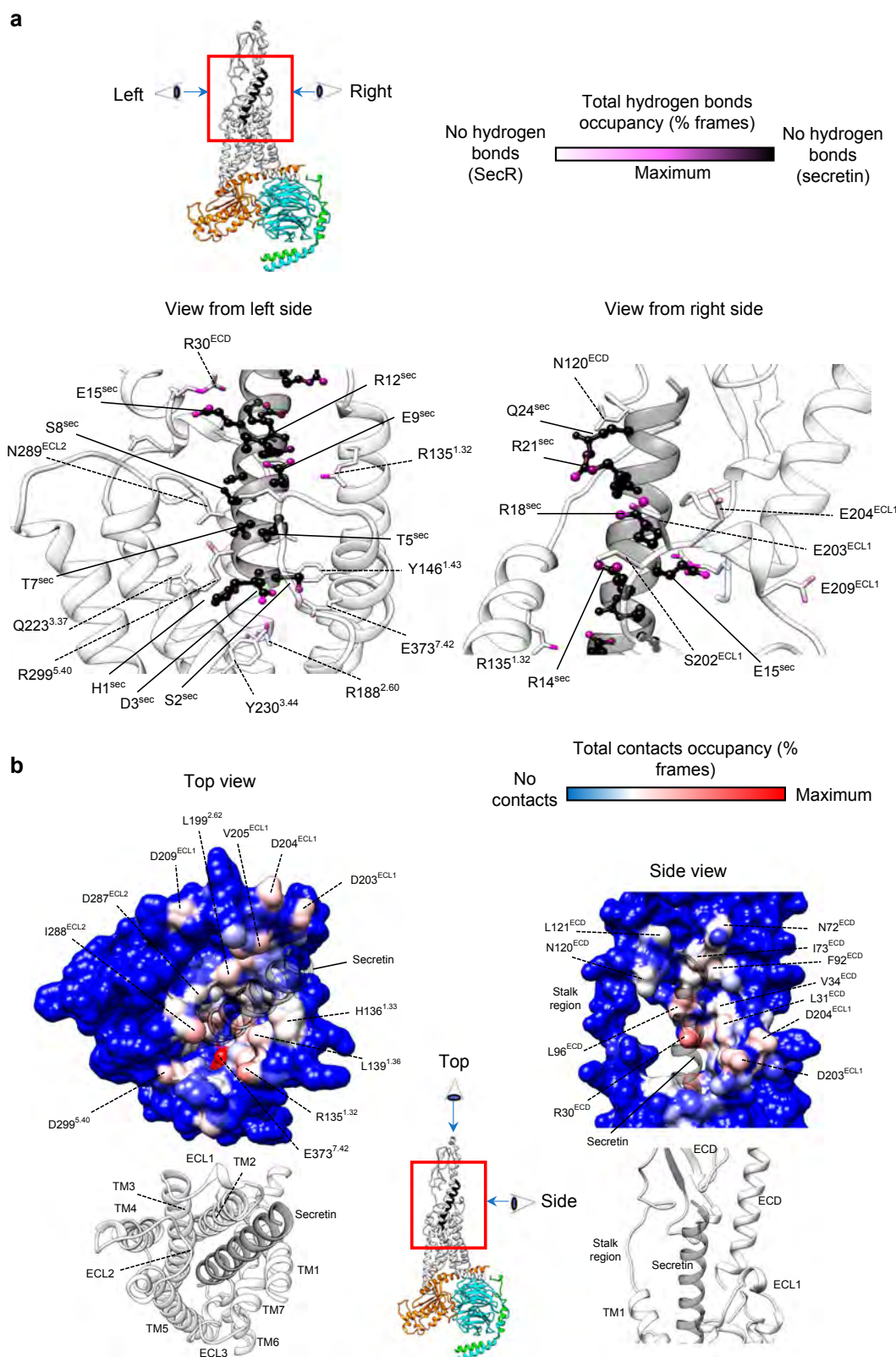


Fig. 3 The SecR TM domain and the secretin were stable during MD simulations. **a** The RMSD (starting structure set as reference) of alpha carbon atoms of the secretin, the SecR TMD (residues from K134^{1.31} to L391^{7.60}), and the SecR ECD (residues from L28^{ECD} to E133^{ECD}) was plotted over the total simulation time (single MD replicas are separated by the dotted lines). The ECD high degree of flexibility did not involve the peptide, and the SecR TMD backbone showed low mobility over the simulations (RMSD usually lower than 3.0 Å). **b** SecR alpha carbons RMSF values during MD simulations. TM helices, intracellular loops (ICLs), and extracellular loops (ECLs) positions are indicated at the top. Areas of lower RMSF in the ECD correspond to regions of stable interaction with secretin peptide during MD simulations with specific interacting residues highlighted. Those with asterisks (*) are predicted to form stable H-bonds (see Supplementary Tables 2, 3).

were predicted to limit mobility within the ECD as noted above (Fig. 3b).

In addition to the polar interactions described above, there were extensive predicted hydrophobic interactions between the peptide and receptor, particularly from the lipophilic face of the peptide (Phe^{6P}, Leu^{10P}, and Leu^{13P}) that made broad interactions with aliphatic side chains of residues in TM7 and TM1 (L374^{7.43}, H136^{1.33}, L139^{1.36}, L142^{1.39}, and K143^{1.40}) (Fig. 4b, Supplementary Table 4). Within the ECD there was a hydrophobic surface comprised of the aliphatic side chains of L28^{ECD}, R30^{ECD}, L31^{ECD}, V34^{ECD}, and L38^{ECD} of the N-terminal α -helix, and loop residues N72^{ECD}, I73^{ECD}, F92^{ECD}, and L96^{ECD} that provide the principal ECD binding groove for the peptide and interacted with Leu^{19P}, Gln^{20P}, Leu^{22P}, Leu^{23P}, Leu^{26P}, and Val^{27P} (Fig. 4b, Supplementary Table 4). Moreover, the simulations predicted that Arg^{18P} and Leu^{22P} could form interactions with both ECL1 and the ECD (Supplementary Table 4) potentially contributing to stability of the location and dynamics of ECD-core interactions.

We have previously performed cysteine scanning mutagenesis of ECLs 1, 2, and 3 and analyzed these for effect on cell surface receptor expression, secretin affinity and secretin efficacy in cAMP production^{23,24} (Supplementary Table 5). In the current study this analysis was extended to include residues at the top of TM1 (Supplementary Table 6). Strikingly, mutation of residues in ECL1 and its proximal extension to TM2 had the greatest impact on both secretin affinity and potency (Supplementary Fig. 7a, b), consistent with the key role of this receptor region in interactions with both the secretin peptide and the far N-terminus of the ECD. Similarly, receptor residues in ECL2 and ECL3 that formed side-chain interactions with the peptide impacted on either peptide affinity or potency (Supplementary Fig. 7a, b). Interestingly, although mutations to residues in TM1 had relatively limited impact on secretin potency (Supplementary Fig. 7a), there was increased apparent affinity of secretin with mutation of residues towards the apex of TM1 but which were mostly oriented away from the peptide interaction interface (Supplementary Fig. 7b). It is possible that substitution with the small amino acid cysteine



may have increased flexibility of this region to allow more favorable peptide interactions.

Cysteine cross-linking of Cys-substituted secretin peptides. Disulfide cross-linking between cysteines requires both spatial proximity and appropriate geometry to occur²⁵. As such, it has become a useful tool to study trajectories of protein-protein

interaction that can include intermediate states involved in peptide binding. We have previously determined the efficiency of the cross-linking of N-terminally Cys-substituted secretin peptide analogs at positions 2, 5, 6, and 7 to SecR with individual Cys mutation throughout the ECLs^{23,24} (Supplementary Table 7), and these can now be mapped onto the active SecR structure. In the current study, we have extended our analysis to include amino

Fig. 4 Interactions between SecR and secretin during MD simulations. **a** Hydrogen bonds between SecR and secretin. The total occupancy (% frames) of each atom is plotted onto the equilibrated complex according to a color scale, with SecR atoms never involved in white, secretin atoms never involved in black and atoms highly involved in magenta. The peptide (ball and stick residues indicated with solid lines) is depicted as black, partially transparent ribbon, while the receptor (stick residues indicated with dashed lines) is shown as white, partially transparent ribbon. The central image specifies the relative perspectives from the right and left sides. Right side view) Hydrogen bonds between the N-terminus of secretin and the TM bundle of the SecR; the main interactions involved S2^{sec}—E373^{7.42}, D3^{sec}—R188^{2.60}, and E9^{sec}—R135^{1.32}. Left side view) Hydrogen bonds between the C-terminus of secretin and the ECL1 of the SecR; main intermolecular interactions involved R14^{sec}, R18^{sec}, R21^{sec} on the peptide, and D203^{ECL1}, D204^{ECL1}, and D209^{ECL1} on the receptor. **b** Contacts between SecR and secretin. The total occupancy (% frames) of each atom is plotted onto the surface of the equilibrated SecR according to a color scale, with SecR atoms never involved in blue, and atoms highly involved in red. The peptide is shown as transparent gray ribbon. The central image specifies the relative perspectives from the top and side. Top view) Contacts between secretin and the TM bundle of the SecR (residues from L28^{ECD} to E133^{ECD} have been removed for clarity); the bottom figure shows the ribbon representation as reference. Main interactions involved TM1 (R135^{1.32}, H136^{1.33}, and L139^{1.36}), TM2 (L199^{2.71}), ECL2 (D287^{ECL2} and I288^{ECL2}), TM5 (D299^{5.40}), and TM7 (E373^{7.42}). Side view) Contacts between secretin C-terminal and SecR; the bottom figure shows the ribbon representation as reference. Main interactions involved ECL1 (D203^{ECL1}, D204^{ECL1}, and D209^{ECL1}), and ECD (R30^{ECD}, L31^{ECD}, V34^{ECD}, F92^{ECD}, I73^{ECD}, and L96^{ECD}).

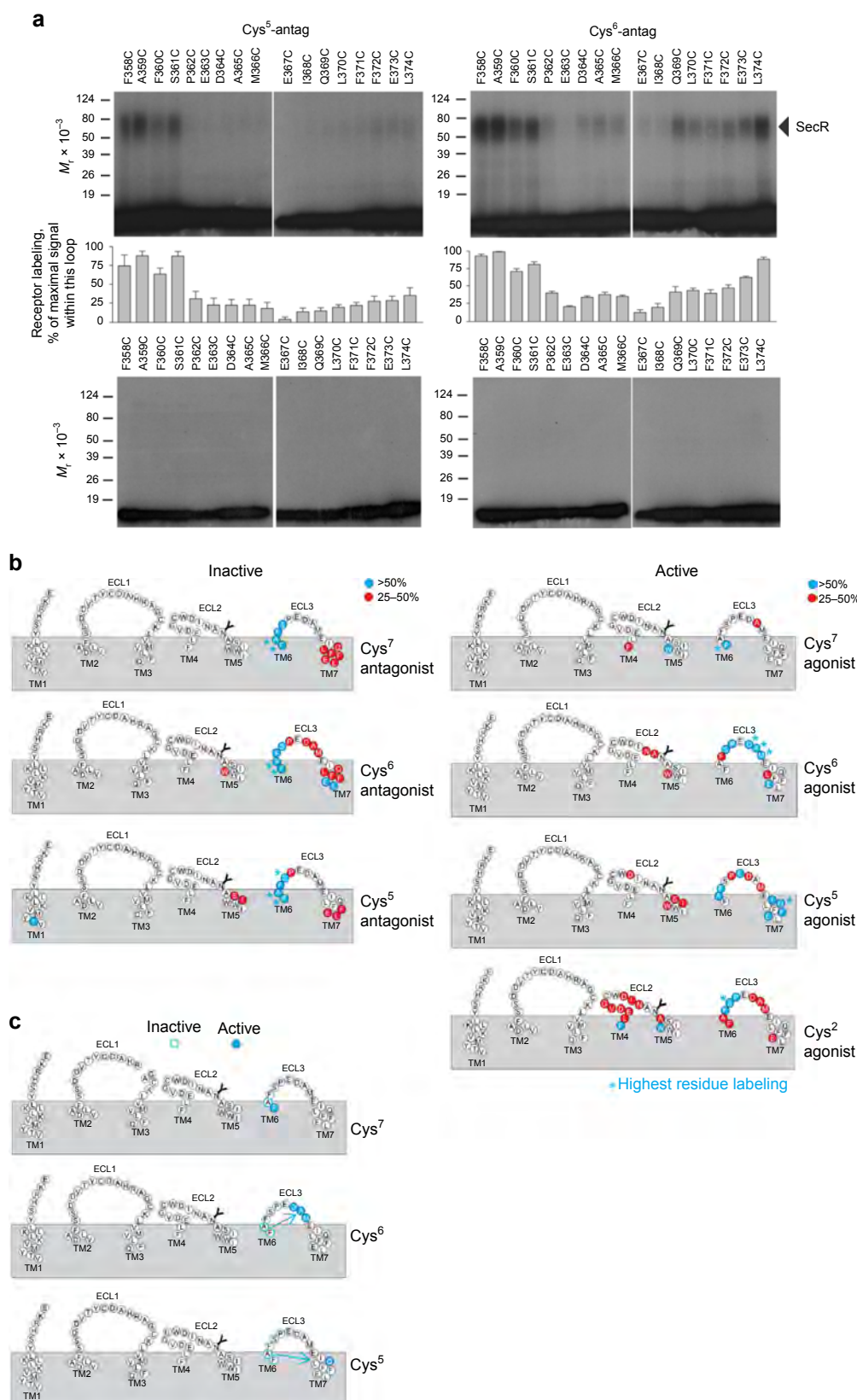
acids in the upper segment of TM1, as well as comparison of cross-linking patterns to radiolabelled analogs of the antagonist peptide secretin (c[E¹⁶, K²⁰, I¹⁷, Cha²², R²⁵]_{sec}(5–27), cysteine-substituted at positions 5, 6, and 7 (Figs. 5 and 6, Supplementary Tables 8, 9, Supplementary Figs 8–13). No cross-linking was observed within TM1 for any of the agonist analogs (Supplementary Fig. 13). In contrast, cross-linking to Y146^{1.43} was observed for both the Cys^{5P} and Cys^{7P} antagonist peptides (Supplementary Table 9, Supplementary Fig. 13). No cross-linking of antagonist peptides was observed within ECL1 (Supplementary Table 8), consistent with observations for the agonist analogs^{23,24} (Fig. 5). In contrast, extensive cross-linking was observed within ECL2 (Supplementary Fig. 10) and, in particular, ECL3 (Fig. 5A). For the Cys^{5P} analog, efficient cross-linking (>25% cross-linking efficiency relative to the highest signal for any of the peptides) was observed for SecR residues Y146^{1.43}, F358^{6.56/ECL3}, A359^{ECL3}, F360^{ECL3}, and S361^{ECL3}. The Cys^{6P} and Cys^{7P} also exhibited efficient cross-linking to F358^{ECL3}–S361^{ECL3}, with the Cys^{6P} also cross-linking efficiently to F372^{7.41} and E373^{7.42}. Perhaps unsurprisingly, there was considerable overlap in the location of cross-linking identified for cysteine substitution at equivalent positions in the agonist and antagonist peptides. Nonetheless, important differences occurred in the sites of highest cross-linking efficiency and indeed in the extent of SecR residues that were cross-linked for the two peptides^{23,24} (Supplementary Tables 7–9, Figs. 5, 6). In general, more cross-linking was observed for the agonist substituted peptides that may reflect higher mobility of the receptor bound to the agonist and/or additional conformational sampling due to transducer engagement. In addition, the most efficient site(s) of cross-linking within ECL3 tended to move from the membrane proximal segment of TM6, for the antagonist, to mid-ECL3 or the TM7 proximal segment for the agonist peptides^{23,24} (Fig. 5c), and this is also consistent with ECL3 being the most conformationally divergent among the solved class B GPCR structures¹².

While cross-linking occurred between the peptide cysteine and receptor residues that were proximal in the active, G protein-bound, structure, in all cases, additional sites of efficient cross-linking were observed, both for agonist and antagonist peptides (Fig. 6). MD simulations to probe partial unbinding and rebinding provided heatmaps for residue proximity that were consistent with most sites of cross-linking identified in the biochemical analysis (Fig. 7a, b, Video 3). However, they did not explain interactions observed for some of the SecR residues in ECL2 (e.g. W295^{ECL2}), although this could potentially be accounted for by a binding interaction model where, early in engagement, the peptide C-terminus engaged with the receptor ECD while the peptide was almost horizontal with the membrane (Fig. 7c); this would site the peptide N-terminus in proximity to

ECL2 during early phases of binding. Alternatively, the peptide may have a more disordered structure during initial binding allowing simultaneous engagement of the peptide N-terminus and ECL2, and peptide C-terminus and receptor ECD. While speculative, others have previously proposed models of peptide-membrane interaction that could promote peptide secondary structure²⁶, potentially providing a mechanistic reason for why this might occur. In this model, the initial peptide engagement would disrupt constraining interactions of the ECD and membrane core to provide the ECD flexibility required to allow key interactions between the peptide N-terminus and the receptor core to form.

The SecR-G protein interface. In the static consensus map, SecR forms extensive polar and nonpolar interactions with the G protein, predominantly with the α5-helix of Gas (Supplementary Table 1, Supplementary Fig 6c, d). As for the secretin:SecR interface, we have used the MD simulations in POPC to interrogate interaction dynamics between SecR and Gs. Not surprisingly, the interactions between the SecR and Gs heterotrimer were similar to those previously reported for other class B GPCRs¹², with both polar and hydrophobic interactions between the Gas protein and TMs 2, 3, 5, and 6 (Supplementary Tables 10–12, Fig. 8, Video 4). However, while most other class B GPCRs exhibit contacts between Gas and the base of TM7 and junction with helix 8 (H8), there were few stable interactions between this domain of the SecR and the G protein. This was most similar to the PTH1R that also lacked substantive interactions with the TM7/H8 junction^{12,27}. For the SecR, stable H-bond or salt-bridge interactions were predicted to occur principally between ICL3, and bottoms of TM5 and TM6 and the Ga subunit, with more limited interactions between Q35, R38, Q384 and R380, and ICL2 or the backbone of the nearby L244^{3.58} (Supplementary Tables 10, 11, Fig. 8). The polar interactions with TM5/ICL3/TM6 were predominantly to the α5-helix of Gas, with more limited interactions predicted to occur with R342 and D323 in the Ga protein. Similar to other class B GPCRs, there were also predicted interactions between the Gβ subunit and the receptor, with the most prominent interactions being between D312^β and K401^{8.48} in H8 and R169 in ICL1, which were also observed in the cryo-EM consensus map (Supplementary Table 1, Supplementary Tables 10–12, Fig. 8).

In the SecR EM map, there is clear density for F248^{1CL2} that is located in the junction between the Gs αN helix and α5-helix (Supplementary Fig. 14a). A positionally equivalent aromatic (Phe or Tyr) is seen in most active, G protein-complexed, class B GPCR structures solved to date¹², as well as the class A Gs-coupled EP2 and β2-adrenergic receptors^{28,29}, although select class B GPCRs have a lipophilic Leu, and the GIPR has a distinct



sequence¹². It is hypothesized that interactions between ICL2 and the G protein may contribute to G protein activation, contributing to conformational changes in the G protein linked to GDP release²⁸. Interestingly, during the course of the simulations, F248^{ICL2} rapidly exits the α N/ α 5 junction (Supplementary

Fig. 14b, c, Video 4) suggesting that the ICL2-G protein interface is dynamic, and it is possible that the observed orientation of the ICL2 in the consensus map may be partially constrained by the tools used to stabilize the $G\alpha$ - $G\beta\gamma$ interface (Nb35, DNGas), although Nb35 was also present in the simulation.

Fig. 5 Overview of cysteine-cross-linking by analogous cysteine-substituted agonist and antagonist secretin peptides. **a** Cysteine trapping of secretin receptor ECL3 cysteine replacement mutants with ^{125}I -labeled Cys⁵- or Cys⁶-containing secretin antagonist analogs. Shown are typical autoradiographs of 10% SDS-PAGE gels used to separate the products of cysteine trapping of the indicated ECL3 SecR cysteine replacement mutants transiently expressed in COS-1 cells for each of the noted cysteine-containing secretin antagonist probes, under nonreducing (top panel) and reducing (bottom panel) conditions. Autoradiographs are representative of a minimum of three independent experiments. Densitometric analysis of data from three similar experiments for each probe is shown (middle panel), with intensities representing the percentages of the signal for the maximal labeling of a residue within ECL3 by that probe. **b** Illustration of the difference of labeling within the extracellular loops of the cysteine-substituted secretin receptor mutants by cysteine-containing antagonist (left hand panels) and agonist (right hand panels) probes. Blue colored residues are those with most efficient labeling (>50% of the highest efficiency label), with the highest labeled residue denoted with a blue asterisk. Red colored residues denote those that cross-linked with intermediate efficiency (25–50% of the highest efficiency label). **c** Schematic illustration of the major shifts in residue labeling between equivalent agonist and antagonist probes.

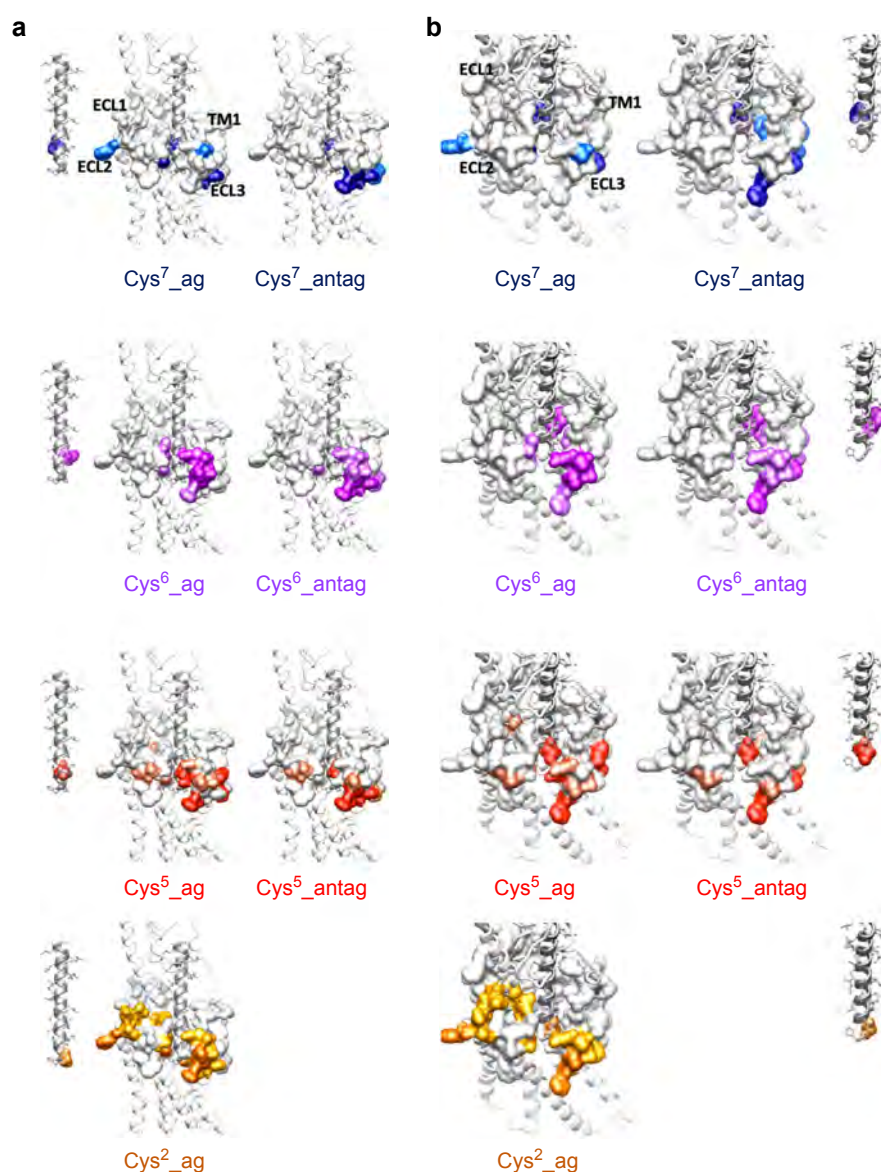


Fig. 6 Mapping of cysteine cross-linking data onto the active SecR structure. **a** Side view. Left panel, secretin peptide analog; Middle panel, agonist cross-linking pattern; Right panel, antagonist cross-linking pattern. **b** Magnified view looking into the SecR TM core. Left panel, agonist cross-linking pattern; Middle panel, antagonist cross-linking pattern; Right panel, secretin peptide analog. Peptides are displayed in ribbon format with x-stick representation of side chains, colored gray. The position of cysteine substitution is shown in colored cpk format (Cys⁷, dark blue; Cys⁶, purple; Cys⁵, red; Cys², orange). The SecR is shown in ribbon format with the location of the cysteine mutants displayed in combination cpk and surface representation. Sites of cross-linking are colored according to the site of peptide substitution with dark shading for those with highest efficiency (>50% of the highest efficiency label) and those with intermediate efficiency (25–50% of the highest efficiency label) having light shading.

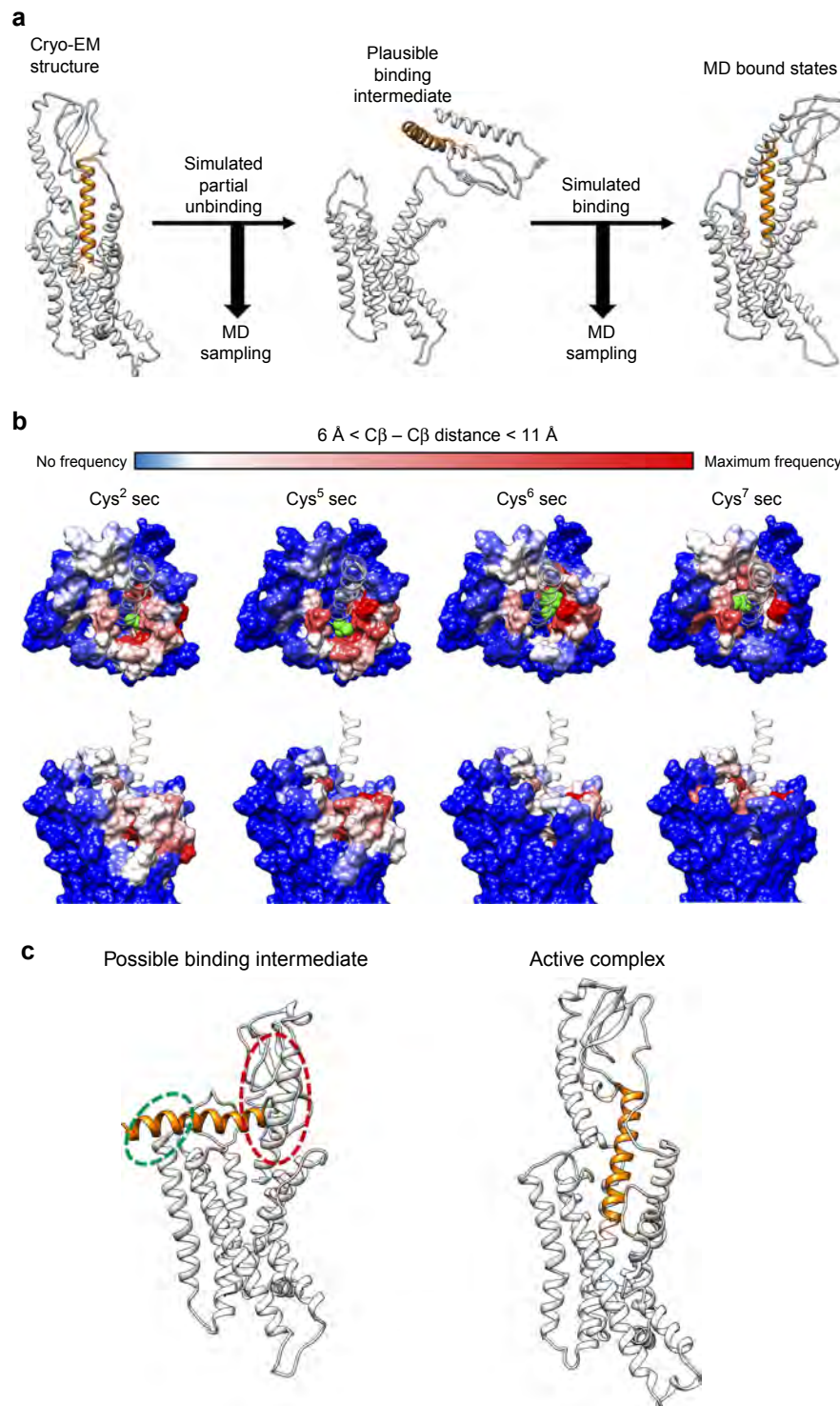
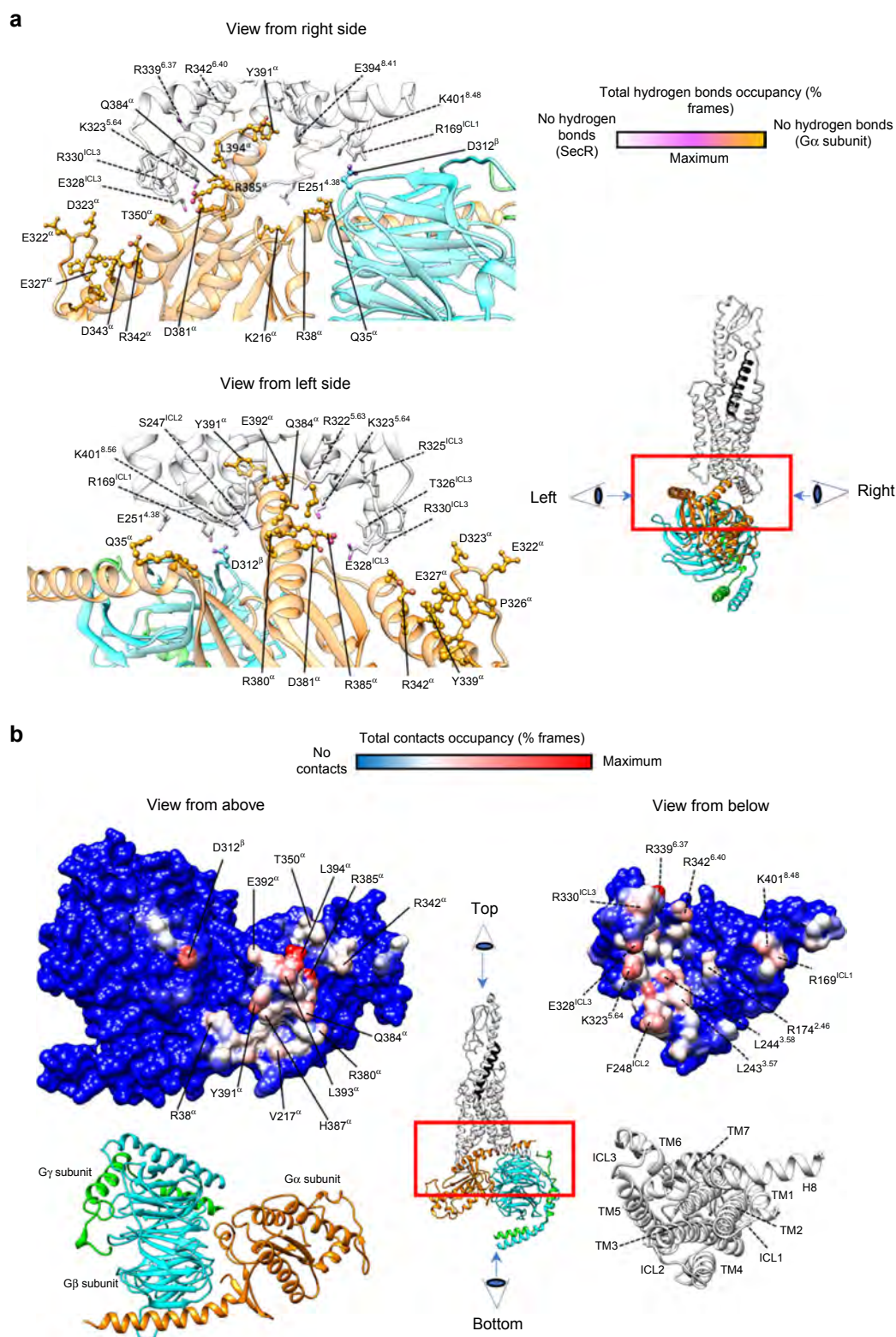


Fig. 7 Simulated partial unbinding and binding of secretin using well-tempered metadynamics simulations. **a** Overview of the simulation displayed in Video 3. **b** Heat map of the interaction of secretin residues 2 (left panel), 5 (left middle panel), 6 (right middle panel), and 7 (right panel), equivalent to the positions of cysteine substitution in cross-linking studies, with the SecR core during simulations. The position of the secretin residue in the cryo-EM structure is displayed in green cpk representation, with the rest of the peptide displayed in transparent light gray ribbon format. The receptor core is shown in surface representation colored according to frequency of interactions during the simulation. **c** Speculative schematic illustrating a potential binding intermediate that could account for observed cysteine-cross-linking data prior to the peptide reaching its metastable position observed in the active, G protein-coupled receptor structure.

Discussion

In conclusion, the structure of the SecR provides new insight into peptide binding and activation of class B GPCRs, and the dynamic nature of these interactions. The SecR exhibited the strongest

interaction between the receptor ECD and the transmembrane core of the receptor of all class B GPCRs structures solved to date, and this likely contributed to higher relative stability of the ECD relative to the rest of the receptor. This was reflected in the relative



robustness of EM density for the ECD, compared to the rest of the receptor, which is less well resolved in other class B GPCR structures. Combining structural data, MD simulations and biochemical cross-linking data advanced understanding of the dynamics of the interaction between secretin and its receptor and models for potential initial engagement of peptide and receptor.

Methods

Constructs. Human SecR was modified to include an N-terminal HA tag and FLAG epitope and a C-terminal 8×HIS tag; both of these are removable by 3C protease cleavage. The construct was generated in both mammalian and insect cell expression vectors. Previously described constructs for dominant negative human Gα_s (DNGα_sv1)⁹, (DNGα_sv2)^{10,11} human His₆-tagged Gβ₁, and Gγ₂⁹ in baculovirus expression vectors were used for complex generation.

Fig. 8 Interactions between SecR and Gs protein during MD simulations. **a** Hydrogen bonds between SecR and Gs protein. The total occupancy (% frames) of each atom is plotted onto the equilibrated complex according to a color scale, with SecR atoms never involved in white, G protein (G α subunit) never involved in orange, and G protein (G β subunit) never involved in cyan; atoms highly involved are magenta. The G γ subunit is shown as green ribbon, the G α subunit (ball and stick residues indicated with solid lines) is depicted in orange, partially transparent ribbon, the G β subunit (ball and stick residues indicated with solid lines) is shown as cyan, partially transparent ribbon; the SecR (stick residues indicated with dashed lines) is shown as white partially transparent ribbon. The image on the right specifies the relative perspectives from the left and right sides. View from the TM6/TM7/TM8 side; View from right side) View from the TM1/TM2/TM3 side. Main hydrogen bonds involved SecR ICL1 (R169^{ICL1}), TM5 (K323^{5.64}) ICL3 (E328^{ICL3}, R330^{ICL3}, T326^{ICL3}, and R325^{ICL3}), TM6 (R339^{6.37} and R342^{6.40}), and H8 (K401^{8.56}). On the G protein, the α subunit residues L394, Y391, R385, Q384, D381, R342, D343, and Q35 were highly involved; the only β subunit side-chain engaged was D312. **b** Contacts between SecR and Gs protein. The total occupancy (% frames) of each atom is plotted onto the surface of the equilibrated complex according to a color scale, with atoms never involved in blue, and atoms highly involved in red. The central image specifies the relative perspectives from above and below. View from above) Contacts plotted on the G protein surface (the bottom figure shows the ribbon representation as reference). Main interactions involved D312 (G β subunit), L394, E392, L393, Y391, H387, R385, Q384, R380, R342, R38 (G α subunit). View from below) Contacts plotted on the SecR surface (the bottom figure shows the ribbon representation as reference). Main interactions involved ICL1 (R169^{ICL1}), TM2 (R174^{2.46}), ICL2 (F248^{ICL2}), TM3 (L243^{3.57} and L244^{3.58}), TM5 (K323^{5.64}), ICL3 (E328^{ICL3} and R330^{ICL3}), TM6 (R339^{6.37} and R342^{6.40}), and H8 (K401^{8.56}).

Insect cell expression. The SecR, DNG α v1 or DNG α v2 (the latter containing an additional A366S mutation)¹⁰, G β 1, and G γ 2 were expressed in *Tni* insect cells (Expression Systems) using baculovirus. For the first preparation, cell cultures were grown in ESF 921 serum-free media (Expression Systems) to a density of 4 million cells/mL, and then infected with three separate baculoviruses at a ratio of 4:2:1 for SecR, DNG α v1, and G β 1 γ 2, respectively. In the second preparation, cell cultures were grown to a density of 3.3 million cells/mL, and then infected with the baculoviruses at a ratio of 3:2:1 for SecR, DNG α v2, and G β 1 γ 2, respectively. Culture was harvested by centrifugation ~48 h post infection and cell pellet was stored at -80°C .

Complex purification. Cell pellet was thawed in 20 mM HEPES pH 7.4, 50 mM NaCl, 2 mM MgCl₂ supplemented with complete Protease Inhibitor Cocktail tablets (Roche) and benzonase nuclease (Merck Millipore). Complex formation was initiated by addition of 1 μM human secretin (China Peptides), Nb35-His (10 $\mu\text{g}/\text{mL}$) and apyrase (25 mU/mL, NEB); the suspension was incubated for 1 h at room temperature. Membranes were collected by centrifugation at 30,000 $\times g$ for 30 min, and the complex from the membrane was solubilized by 0.5% (w/v) lauryl maltose neopentyl glycol (LMNG, Anatrace) supplemented with 0.03% (w/v) cholesteryl hemisuccinate (CHS, Anatrace) for 2 h at 4°C in the presence of 1 μM secretin and apyrase (25 mU/mL, NEB). Insoluble material was removed by centrifugation at 30,000 $\times g$ for 30 min and the solubilized complex was immobilized by batch binding to M1 anti-FLAG-affinity resin in the presence of 3 mM CaCl₂. The resin was packed into a glass column and washed with 20 column volumes of 20 mM HEPES pH 7.4, 100 mM NaCl, 2 mM MgCl₂, 3 mM CaCl₂, 1 μM secretin, 0.01% (w/v) LMNG, and 0.0006% (w/v) CHS before bound material was eluted in buffer containing 5 mM EGTA and 0.1 mg/mL FLAG peptide. The complex was then concentrated using an Amicon Ultra Centrifugal Filter (MWCO 100 kDa) and subjected to SEC on a Superdex 200 Increase 10/300 column (GE Healthcare) that was pre-equilibrated with 20 mM HEPES pH 7.4, 100 mM NaCl, 2 mM MgCl₂, 1 μM secretin, 0.01% (w/v) LMNG, and 0.0006% (w/v) CHS to separate complex from contaminants. Eluted fractions consisting of receptor and G protein complex were pooled and concentrated and stored at -80°C . Purity and stability of the complex following thawing was confirmed by fSEC. Final yield of purified complex was approximately 0.125 mg/L of insect cell culture.

SDS-PAGE and western blot analysis. Sample collected from SEC was analyzed by SDS-PAGE and western blot. For SDS-PAGE, precast gradient TGX gels (Bio-Rad) were used. Gels were stained by Instant Blue (Expedeon). Antisera included rabbit anti-Gs C-18 antibody (cat no. sc-383, Santa Cruz), goat anti-rabbit antibody (800CW, LI-COR), mouse Penta-His antibody (cat no. 34660, QIAGEN), and goat anti-mouse antibody (680RD, LI-COR).

Preparation of vitrified specimen. For the initial preparation, electron microscopy grids (Quantifoil, 200-mesh copper R1.2/1.3) were glow-discharged for 90 s using PELCO easiGlow. Four microliters of sample was applied on the grid in Vitrobot Mark IV chamber (Thermo Fisher Scientific). The chamber of Vitrobot was set to 100% humidity at 4°C . The sample was blotted for 5.5 s with a blot force of 25, and then plunged into ethane. For the second preparation, acetone pre-washed electron microscopy grids (Ultrafoil R1.2/1.3 Au 300 mesh) were glow-discharged and 3 μL of sample was applied to the grid in a Vitrobot Mark IV chamber (Thermo Fisher Scientific), set to 100% humidity at 4°C . The sample was blotted for 10 s with a blot force of 19, and then flash frozen in liquid ethane.

Data acquisition. Initial datasets were collected on a Thermo Fisher Scientific Titan Krios microscope operated at 300 kV equipped with a Gatan Quantum energy filter, a Gatan K2 summit direct electron camera (Gatan). Movies were

taken in EFTEM nanoprobe mode, with 50- μm C2 aperture and pixel size of 0.86 Å. Each movie comprises 40 subframes with a total dose of 46 e⁻ per Å, with exposure time of 10 s with a dose rate of 3.42 e⁻ pixel⁻¹ s⁻¹ on the detector. Data acquisition was done using EPU software (Thermo Fisher Scientific) at -500 nm to -1.9 μm defocus (200 nm step). Data from the second sample were collected on a Titan Krios microscope operated at an accelerating voltage of 300 kV with a 50 μm C2 aperture at an indicated magnification of 105,000 $\times g$ in EFTEM nanoprobe mode and a spot size of 5. A Gatan K3 direct electron detector, positioned post a Gatan Quantum energy filter (Gatan, Pleasanton, CA, USA) with a slit width of 25 eV, was used to collect movies in CDS mode. Movies were recorded as compressed TIFFs in normal-resolution mode yielding a physical pixel size of 0.83 Å/pixel with an exposure time of 5.011 s amounting to a total exposure of 52.9 e⁻/Å² for an exposure rate of 7.27 e⁻/pixel/second that was fractionated into 71 subframes. Defocus was varied in the range between -0.7 and -1.5 μm . Beam-image shift, with beam-tilt compensation, was used to acquire data from nine surrounding holes after which the stage was moved to the next collection area using a custom SerialEM script^{30,31}.

Data processing. For the initial sample, a total of 6500 movies were collected and subjected to motion correction using MotionCor2 implemented in RELION v3.0.7³². CTF estimation was done using Gctf software³³ on nondose-weighted micrographs. The particles were picked using cisTEM³⁴. An initial model was made using the common-line approach in EMAN2³⁵. Picked particles from cisTEM were imported in RELION v3.0.7. The particles were extracted using a box size of 240 pixels. A total of 1,200,000 picked particles were subjected to two rounds of 2D classification, followed by 3D classification. After selecting the best-looking class, with 159k particles, 3D auto-refinement was done followed by another round of 3D classification without alignment. Lastly, 77,754 particles from the best-looking class were subjected to 3D auto-refinement.

For the second sample, a total of 5600 movies were collected and subjected to motion correction using MotionCor2³² and CTF estimation was done using the Gctf³³ software on nondose-weighted micrographs, implemented in Relion v3.1-beta³⁶. The particles were picked using the automated procedure in crYOLO³⁷ and coordinates were imported into Relion. Subsequent data processing steps were carried out using Relion v3.1-beta³⁶. Particles were extracted initially using a box of 64 pixels, and after curation of particles in 2D and 3D classifications, re-extracted using a final box size of 288. As an initial 3D reference, a previous GPCR complex map was used and 60 Å low-pass filtered to prevent model bias. 3D references in subsequent steps derived from the data itself. Subsequent rounds of 3D classifications, 3D refinements, and 3D classification without angular and translational alignment were used to create a homogenous set of ~350,000 particles and was further subjected to Bayesian particle polishing and CTF refinements (as implemented in Relion v3.1-beta). A final global 3D refinement using a wide mask (including the entire complex and micelle) was carried out, resulting in a global resolution (FSC = 0.143) of 2.4 Å. In postprocessing, different masks were applied on the global refinement map, resulting in global resolutions (FSC = 0.143) of 2.4 Å using the wide mask and 2.3 Å using a tight mask (excluding the ECD of the receptor, AHD of the G α protein and micelle) (Fig. 1e–g). To better resolve features of the receptor loops and ECD, the global refinement map was subjected to 3D classification and 3D refinement with fine angular sampling using a mask including only the receptor and peptide (referred to as “receptor-only” refinement). The receptor-only map resulted in a global resolution (FSC = 0.143) of 2.5 Å (Fig. 1f, g). Local resolution estimates and maps were produced in Relion. All masks were created with a custom script using e2proc3D.py from EMAN2³⁵.

Atomic model refinement. Initial models into the 4.3 Å map for SecR complex were made with the Rosetta software package using the structure threading/comparative modeling and model relaxation protocols³⁸. Fitting the Rosetta-generated

models in the cryo-EM density maps was performed with the MDFF routine in namd2³⁹. The fitted models were further refined by rounds of manual model building in coot⁴⁰ and real-space refinement, as implemented in the Phenix software package⁴¹. The density around the N-terminal ECDs was poorly resolved, and this domain was modeled by further rounds of focused MDFF. As the maps in this region were locally resolved to ~7 Å, only the backbone trace of the protein was kept for deposition. Map and model statistics are detailed in Supplementary Table 13. In the final model (PDB 6W19), the first modeled residue is R30^{ECD} and the last modeled residue is L408^{H8}. Residues R30^{ECD}–S130^{ECD} have only been modeled as backbone trace, and amino acids S201^{ECL1}–H211^{ECL1} have been omitted from the model.

Based on the initial SecR model (PDB 6W19), atomic coordinates were refined into the new cryo-EM maps. The majority of the model (Ga, Gβ, Gy, TMs, and peptide N-terminus) was refined into the global postprocessed map using Phenix⁴¹ and manually inspected using Coot⁴⁰. Lower resolution areas (in particular ECD, ECL1, and ICL1-3) were furthermore refined using the receptor-only map, initially by flexible fitting and refinement using Isolve⁴², Namdinator⁴³ and namd2³⁹ and finally by real-space refinement in Phenix and manual inspection in Coot. The density of the ECD remained poorly resolved and therefore only the backbone of the residues R30^{ECD}–S130^{ECD} was deposited. The final receptor model (PDB 6WZG) starts with residue R30^{ECD} and ends with residue L408^{H8} (with residues 30–130^{ECD} of the receptor and 254–263 of the Ga protein modeled as backbone trace). Amino acids from the AHD of the Ga protein (62–204) have been omitted from the model.

Model residue interaction analysis. Interactions in the PDB (6WZG), between the chains of the peptide and receptor (P:R) or receptor and G proteins (R:A and R:B), were analyzed using the “Dimplot” module within the Ligplot+ program (v2.2)⁴⁴. Hydrogen bonds were additionally analyzed using the UCSF ChimeraX package, with relaxed distance and angle criteria (0.4 Å and 20° tolerance, respectively). Additional analyses and production of images were performed using the UCSF Chimera package (v1.14) from the Computer Graphics Laboratory, University of California, San Francisco (supported by NIH P41 RR-01081) and ChimeraX⁴⁵ (support from National Institutes of Health R01-GM129325).

3D variability analysis in Cryosparc. Particle stacks from the Relion global consensus refinement as well as the refinement map were imported into the Cryosparc v2 pipeline⁴⁶. A consensus refinement in Cryosparc using the Homogeneous refinement tool and the imported Relion map as a reference volume was produced, which was used as an input for the 3D variability analysis¹¹. For the variability analysis, the wide mask created automatically during refinement in Cryosparc (including micelle) and a 2.8 Å filter was applied. The frames of the three components generated in the 3D variability analysis were visualized in the ChimeraX volume series, and movements were recorded as movies (see also: Supplementary Fig. 15).

Mammalian cAMP assays. HA-secretin receptor-bearing COS-1 cells (CRL-1650, American Type Culture Collection) were seeded at a density of 30,000 cells/well into 96-well culture plates and incubated over-night in DMEM containing 5% FBS at 37 °C in 5%CO₂. cAMP detection was performed as previously described⁹. All values were converted to cAMP concentration using a cAMP standard curve performed in parallel and data were subsequently normalized to the response of 100 μM forskolin in each cell line. Data were analyzed by a 3-parameter logistic fit in Prism v7 (GraphPad).

Peptides. Four cysteine-containing peptides were designed to incorporate a cysteine for disulfide trapping in positions 5, 6, 7, and 10 of the secretin antagonist, (c[E16, K20], Y10, I17, Cha22, R25)sec(5–27) (identified as Cys⁵, Cys⁶-, Cys⁷-, and Cys¹⁰-antag) that we reported previously⁴⁷. The Cys⁵-antag, Cys⁶-antag, and Cys⁷-antag incorporated a tyrosine to replace the leucine in position 10 for radioiodination⁴⁸, while a tyrosine was incorporated in position 26 of the Cys¹⁰-antag²⁴ (Supplementary Fig. 8a). In addition, five cysteine-containing full-length secretin agonist analogs we synthesized previously^{23,24} were also used in this study for cysteine trapping of the 14 new cysteine mutants of the juxtamembranous region of the amino-terminal domain of the secretin receptor (Supplementary Fig. 8a). All peptides were synthesized and purified by China Peptides (Shanghai, China), with their identities verified by electrospray ionization mass spectrometry.

Radioiodination. The secretin-like radioligand [Y10]secretin(1–27) used in competition ligand binding assays, the newly synthesized Cys⁵-antag, Cys⁶-antag, Cys⁷-antag, and Cys¹⁰-antag, as well as the five cysteine-containing full-length secretin agonist analogs we synthesized previously^{23,24} were radioiodinated oxidatively using procedures previously described⁴⁹. This was done by incubating ~10 μg of each peptide with 1 mCi Na¹²⁵I in 0.1 M borate buffer (pH 9.0) and exposure for 15 s to the solid phase oxidant, *N*-chlorobenzenesulfonamide (Iodination bead) (Pierce, Rockford, IL). The radioiodinated peptides were purified by reversed-phase HPLC to yield specific radioactivities of ~2000 Ci/mmol using procedures we previously described⁴⁹.

Receptor constructs. The wild-type human secretin receptor (CHO-SecR) stably expressed in Chinese Hamster Ovary (CHO-K1) cells (CCL-61, American Type Culture Collection) that was established previously⁵⁰ was used for characterizing binding affinities and biological activities of Cys⁵-antag, Cys⁶-antag, Cys⁷-antag, and Cys¹⁰-antag. This cell line was cultured at 37 °C in an environment containing 5% CO₂ on tissue culture plasticware in Ham's F-12 medium supplemented with 5% fetal clone II, and was passaged approximately twice a week.

For cysteine trapping studies with the Cys⁵-antag, Cys⁶-antag, Cys⁷-antag, and Cys¹⁰-antag probes, wild type and a total of 61 previously characterized secretin receptor constructs incorporating cysteine replacements for natural residues in each of the positions of the three ECLs except for positions with a naturally occurring cysteine were used. They were transiently expressed on COS-1 cells (American Type Culture Collection, Manassas, VA) after transfection using the polyethylenimine method as we have previously described²³. Cells were maintained in Dulbecco's modified Eagle's medium (Invitrogen, Carlsbad, CA) supplemented with 5% fetal clone II and studied 48 h after transfection.

In addition, 14 new constructs incorporating cysteine replacements for natural residues in each of the positions of the juxtamembranous region of the amino-terminal domain of the secretin receptor ranging from residue Lys¹¹³ to Thr¹²⁶ were generated. These cysteine mutants were prepared using an oligonucleotide-directed approach with the QuikChange site-directed mutagenesis kit from Stratagene (La Jolla, CA) (primers listed in Supplementary Table 14), with the products verified by direct DNA sequencing. They were expressed transiently on COS-1 cells (CRL-1650, American Type Culture Collection) after transfection using a modification of the DEAE-dextran method for binding and biological activity characterization⁵¹ or using the polyethylenimine method as we have previously described for cysteine trapping experiments²³. These constructs were used in cysteine trapping studies using both agonist and antagonist cysteine secretin probes.

Immunostaining. To determine levels of cell surface expression of the 14 new constructs incorporating cysteine replacements for natural residues in each of the positions of the juxtamembranous region of the amino-terminal domain of the secretin receptor, immunostaining using an amino-terminal region secretin receptor antibody was performed in COS-1 cells (CRL-1650, American Type Culture Collection) transiently transfected with these constructs. This polyclonal antibody⁵² was raised by GenScript (Piscataway, NJ) using the peptide antigen representing amino acids 51–65 of the human secretin receptor (anti-hSecR(51–65) that was synthesized and purified in-house.

Transfected cells grown on polylysine-coated glass coverslips in six-well plates for 24 h were washed once with PBS followed by two washes with PBS containing 1% normal goat serum. Coverslips were then incubated for 1 h at room temperature with the anti-hSecR(51–65) polyclonal antibody⁵² (1:500 in PBS with 1% normal goat serum) followed by one PBS wash before being fixed with 2% paraformaldehyde (Electron Microscopy Sciences, Hatfield, PA) in PBS for 15 min. Coverslips were then washed three times with PBS containing 1% normal goat serum and incubated for 1 h with 1:200 Alexa Fluor 488-conjugated anti-rabbit IgG secondary antibody (Molecular Probes, Eugene, OR). Coverslips were washed three times with PBS and mounted on microscope slides with Vectashield mounting medium (Vector Laboratories, Burlingame, CA). All above procedures were performed at room temperature. Cells were visualized with a ×40 objective on a Zeiss inverted microscope controlled by QED In Vivo software (Media Cybernetics, Bethesda, MD). Quantification of receptor cell surface expression as fluorescence percentage of wild-type secretin receptor was done by analyzing 6–8 cells for each of the mutants using the ImageJ software (National Institutes of Health, Bethesda, MD).

Receptor binding assay. The ability of the Cys⁵-antag, Cys⁶-antag, Cys⁷-antag, and Cys¹⁰-antag probes to bind to the secretin receptor was assessed by a radioligand competition-binding assay with intact receptor-expressing CHO-SecR cells in 24-well tissue culture plates. In brief, CHO-SecR cells were grown to ~90% confluence and were washed twice with Krebs–Ringers/HEPES (KRH) medium (25 mM HEPES, pH 7.4, 104 mM NaCl, 5 mM KCl, 2 mM CaCl₂, 1 mM KH₂PO₄, 1.2 mM MgSO₄) containing 0.01% soybean trypsin inhibitor and 0.2% bovine serum albumin. Cells were then incubated with a constant amount of radioligand, [¹²⁵I]-[Y10]sec(1–27) (~5 pM, ~10,000 cpm) in the absence and presence of increasing concentrations (ranging from 0 to 1 μM) of each of the cysteine-containing secretin antagonist probes for 1 h at room temperature (reaction volume, 250 μL). Cells were then washed twice with ice-cold KRH medium containing 0.01% soybean trypsin inhibitor and 0.2% bovine serum albumin to separate bound from free radioligand before being lysed with 0.5 M NaOH and quantified using a γ-spectrometer. Nonspecific binding was determined in the presence of 0.1 μM unlabeled secretin and represented <15% of total radioligand bound. Binding data were analyzed and plotted using the nonlinear regression analysis program in the Prism software suite version 7.0 (GraphPad Software, San Diego, CA) (Supplementary Fig. 8b). The same assay was also used to characterize the binding activity of COS-1 cells transiently expressing the 14 new receptor cysteine mutant constructs described above.

Intracellular cAMP assay. The biological activity of the Cys⁵-antag, Cys⁶-antag, Cys⁷-antag, and Cys¹⁰-antag probes was assessed by examining their ability to stimulate cAMP responses in CHO-SecR cells⁵⁰ using a time-resolved fluorescence-based cAMP assay. In brief, ~8000 cells per well were grown in 96-well plates for 48 h prior to the assay. Cells were washed with PBS and stimulated with increasing concentrations (ranging from 0 to 1 μ M) of secretin or each of the cysteine-containing secretin antagonist probes in KRH medium containing 0.01% soybean trypsin inhibitor, 0.2% bovine serum albumin, 0.1% bacitracin, and 1 mM 3-isobutyl-1-methylxanthine for 30 min at 37 °C. After incubation, the reaction solution was aspirated and cells were lysed with 6% ice-cold perchloric acid for 15 min with vigorous shaking. The cell lysates were adjusted to pH 6 with 30% NaHCO₃ and assayed for cAMP levels in a 384-well white Optiplate using a LANCE cAMP kit from PerkinElmer (Boston, MA) (Supplementary Fig. 8c). Antagonism of secretin-induced cAMP accumulation was also assessed by co-incubation of increasing concentrations of each of the antagonists with 0.1 nM secretin (Supplementary Fig. 8d). The cAMP concentration-response curves were analyzed and plotted using the nonlinear regression analysis routine in Prism Software Suite (GraphPad, San Diego, CA). The same assay was also used to characterize the biological activity of COS-1 cells transiently expressing the 14 new receptor cysteine mutant constructs described above.

Cysteine trapping. Four days prior to the cysteine trapping experiments, 5×10^4 COS-1 cells per well were plated in 24-well tissue culture plates. On the following day, cells were transfected in batches with wild type, all the 61 cysteine secretin receptor mutants that we previously used and 14 new receptor cysteine mutant constructs described above using the polyethylenimine method as we have previously described²³. On the day of assay, medium was removed by aspiration and cells were washed once with DMEM containing 5% fetal clone II before being incubated for 1.5 h at room temperature with 200 μ L DMEM containing 5% fetal clone II and ¹²⁵I-Cys⁵-antag, or ¹²⁵I-Cys⁶-antag or ¹²⁵I-Cys⁷-antag or ¹²⁵I-Cys¹⁰-antag or the five secretin agonist probes we used previously^{23,24} (~100,000 cpm per well) in the absence or presence of 0.1 μ M secretin. After the medium was removed, cells were washed once with ice-cold PBS and incubated with 80 μ L SDS Laemmli sample buffer with or without 0.1 M dithiothreitol on a shaker for 45 min. Cells were then scraped and the lysates were transferred to 1.5 mL microcentrifuge tubes using wide-bore tips. Samples were briefly sonicated to break the sticky DNA and resolved in 10% SDS-polyacrylamide gels. Gels were dried, and bands of interest were visualized by autoradiography with band densitometry analyzed by the ImageJ software. The apparent molecular weights of the radioactive bands were determined by interpolation on a plot of the mobility of the appropriate ProSieve protein markers (Cambrex, Rockland, ME, USA) vs. the log values of their apparent masses.

Modeling methods. The MD was based on the initial PDB model (6WI9) that was available at the time. The missing stalk region was generated using Modeller⁵³ and refined using the loop modeling feature; the loop with the lowest DOPE score⁵⁴ (out of 2000 generated loops) was selected. The missing loops in the G protein (L296-K307, C365-E370) were generated from the corresponding loops in the β_2 -adrenergic receptor-G protein complex, PDB code 3SN6⁵⁵ by fitting them with VMD⁵⁶ to the flanking residues. The 3SN6 G protein X-ray structure is 99% identical to the G protein used in this study; it generally gave a lower root mean squared deviation value on molecular superposition than the alternatives (e.g., PDB code 6b3j). The joining point was taken as the closest atom pairs (usually separated by ~0.2 Å) that maintained an appropriate Ca-Ca distance (3.8 ± 2 Å) across the join; selected residues spanning the join were minimized using PLOP⁵⁷ where additional refinement was desirable. The S250-T263 loop was completed using the shorter loop from the adenosine A2A receptor-G-protein complex, PDB code 5G53⁵⁸. The helical domain (residues A48-V204) was not visible in the cryo-EM structure and was omitted as in earlier work¹².

Systems preparation. The full-length model of the secretin:SecR:G protein:Nb35 complex was prepared for simulation with the CHARMM36 force field⁵⁹, through use of in-house python htm⁶⁰ and TCL (Tool Command Language) scripts. The pdb2pqr⁶¹ and propka⁶² software were used to add hydrogen atoms appropriate for a simulated pH of 7.0; the protonation of titratable side chains was checked by visual inspection. The obtained structure was superimposed on the GLP-1R (PDB ID 5VAI) from the OPM database⁶³ so as to orient the receptor prior to insertion in a rectangular prebuilt $125 \times 116 \times 1$ -palmitoyl-2-oleyl-sn-glycerol-3-phosphocholine (POPC) bilayer; lipid molecules overlapping the receptor were removed. TIP3P water molecules were added to the $125 \times 116 \times 178$ Å simulation box using the VMD Solvate plugin 1.5 (Solvate Plugin, Version 1.5. at <http://www.ks.uiuc.edu/Research/vmd/plugins/solvate/>). Overall charge neutrality was maintained by adding Na⁺ and Cl⁻ counter ions to a final ionic concentration of 150 mM using the VMD Autoionize plugin 1.3 (Autoionize Plugin, Version 1.3. at <http://www.ks.uiuc.edu/Research/vmd/plugins/autoionize/>).

Systems equilibration and MD settings. ACEMD⁶⁴ was used for both equilibration and MD productive simulations. Isothermal-isobaric conditions (Langevin

thermostat⁶⁵ with a target temperature of 300 K and damping of 1 ps⁻¹ and Berendsen barostat⁶⁶ with a target pressure 1 atm) were employed to equilibrate the systems through a multistage procedure (integration time step of 2 fs). Initial steric clashes between lipid atoms were reduced through 2500 conjugate-gradient minimization steps, then a 2 ns MD simulation was run with a positional constraint of 1 kcal mol⁻¹ Å⁻² on protein atoms and lipid phosphorus atoms. Subsequently, 20 ns of MD were performed constraining only the protein atoms. In the final equilibration stage, only the protein backbone alpha carbons were constrained, to a total simulation time of 100 ns.

Productive trajectories in the canonical ensemble (NVT) at 300 K (three replicas of 0.94 μ s, 0.88 μ s, and 1.00 μ s, respectively) were computed using a thermostat damping of 0.1 ps⁻¹ with an integration time step of 4 fs and the M-SHAKE algorithm⁶⁷ to constrain the bond lengths involving hydrogen atoms. The cut-off distance for electrostatic interactions was set at 9 Å, with a switching function applied beyond 7.5 Å. Long range Coulomb interactions were handled using the particle mesh Ewald summation method⁶³ (PME) by setting the mesh spacing to 1.0 Å. Trajectory frames were written every 100 ps of simulations.

Secretin partial unbinding and binding protocol. The secretin:SecR complex (obtained removing both the G protein and Nb35) was prepared and equilibrated as reported above. The secretin partial unbinding was then simulated in two different well-tempered metadynamics replicas⁶⁸, biasing the distance between the residues H1-R14 (secretin) and K135^{1,31}L391^{7,60} (SecR) centroids. Plumed2.3⁶⁹ was used to seed a Gaussian energy function every 1 ps (height = 0.1 kcal/mol, width = 0.1 Å, with a biasfactor = 20), at a simulated temperature of 300 K, until the distance reached 30 Å.

Starting from the final state of one of the two unbinding trajectories, the secretin partial binding was simulated in six replicas supervising⁷⁰ the same centroids distance considered for the partial unbinding, during successive time windows of 2 ns.

To increase the overall MD sampling, each unbinding/binding replica was grouped into 1 Å width bins according to the root mean square fluctuation (RMSF) of the secretin Ca carbon to the initial positions. One frame was extracted from each cluster and used as seed for a 30 ns long classic MD simulation, for a resulting total MD time sampling of 6.4 μ s.

MD analysis. Atomic contacts were computed using the GetContacts analysis tool (at <https://getcontacts.github.io/>), with the donor-acceptor threshold distance set to 3.5 Å and the angle set to 120°. Videos were generated using VMD⁵⁶ and avconv (at <https://libav.org/avconv.html>). Root mean square deviation and RMSF values were computed using VMD⁵⁶ after superposition of the MD trajectories frames on the alpha carbon of the TM domain (residues K134^{1,31} to L391^{7,60}). VMD was also employed to compute the C β -C β carbon distances on the 6.4 μ s nonequilibrium MD (secretin partial unbinding/binding), selecting the C β carbon of secretin residues S2, T5, F6, and T7 and all the SecR C β atoms.

Reporting summary. Further information on research design is available in the Nature Research Reporting Summary linked to this article.

Data availability

Data supporting the findings of this manuscript are available from the corresponding authors upon reasonable request. A reporting summary for this article is available as a Supplementary Information file.

Atomic coordinates and the cryo-EM density map have been deposited in the Protein Data Bank (PDB) under accession numbers

PDB 6WI9 (low resolution model) and PDB 6WZG (high-resolution model), and Electron Microscopy Data Bank (EMDB) accession numbers EMD-21683 (4.3 Å maps) and EMD-21972 (high-resolution maps). Source data are provided with this paper.

Received: 13 March 2020; Accepted: 15 July 2020;

Published online: 18 August 2020

References

- Wootten, D., Miller, L. J., Koole, C., Christopoulos, A. & Sexton, P. M. Allosteric and biased agonism at class B G protein-coupled receptors. *Chem. Rev.* **117**, 111–138 (2017).
- Afroze, S. et al. The physiological roles of secretin and its receptor. *Ann. Transl. Med.* **1**, 29 (2013).
- Lee, V. H. et al. An indispensable role of secretin in mediating the osmoregulatory functions of angiotensin II. *FASEB J.* **24**, 5024–5032 (2010).
- Chu, J. Y. et al. Phenotypes developed in secretin receptor-null mice indicated a role for secretin in regulating renal water reabsorption. *Mol. Cell Biol.* **27**, 2499–2511 (2007).

5. Gunnes, P. & Rasmussen, K. Haemodynamic effects of pharmacological doses of secretin in patients with impaired left ventricular function. *Eur. Heart J.* **7**, 146–149 (1986).
6. Cheng, C. Y., Chu, J. Y. & Chow, B. K. Central and peripheral administration of secretin inhibits food intake in mice through the activation of the melanocortin system. *Neuropsychopharmacology* **36**, 459–471 (2011).
7. Li, Y. et al. Secretin-activated brown fat mediates prandial thermogenesis to induce satiation. *Cell* **175**, 1561–1574 e1512 (2018).
8. Boyns, D. R., Jarrett, R. J. & Keen, H. Intestinal hormones and plasma insulin: an insulinotropic action of secretin. *Br. Med. J.* **2**, 676–678 (1967).
9. Liang, Y. L. et al. Phase-plate cryo-EM structure of a biased agonist-bound human GLP-1 receptor-Gs complex. *Nature* **555**, 121–125 (2018).
10. Liang, Y. L. et al. Dominant negative G proteins enhance formation and purification of agonist-GPCR-G protein complexes for structure determination. *ACS Pharm. Transl. Sci.* **1**, 12–20 (2018).
11. Liang, Y. L. et al. Structure and dynamics of adrenomedullin receptors AM1 and AM2 reveal key mechanisms in the control of receptor phenotype by receptor activity-modifying proteins. *ACS Pharm. Transl. Sci.* **3**, 263–284 (2020).
12. Liang, Y. L. et al. Toward a structural understanding of class B GPCR peptide binding and activation. *Mol. Cell* **77**, 656–668 e655 (2020).
13. Qiao, A. et al. Structural basis of Gs and Gi recognition by the human glucagon receptor. *Science* **367**, 1346–1352 (2020).
14. Ma, S. et al. Molecular basis for hormone recognition and activation of corticotropin-releasing factor receptors. *Mol. Cell* **77**, 669–680 e664 (2020).
15. Dal Maso, E. et al. The molecular control of calcitonin receptor signaling. *ACS Pharm. Transl. Sci.* **2**, 31–51 (2019).
16. Hay, D. L., Garelja, M. L., Poyner, D. R. & Walker, C. S. Update on the pharmacology of calcitonin/CGRP family of peptides: IUPHAR Review 25. *Br. J. Pharm.* **175**, 3–17 (2018).
17. Harikumar, K. G., Simms, J., Christopoulos, G., Sexton, P. M. & Miller, L. J. Molecular basis of association of receptor activity-modifying protein 3 with the family B G protein-coupled secretin receptor. *Biochemistry* **48**, 11773–11785 (2009).
18. Dong, M. et al. Importance of each residue within secretin for receptor binding and biological activity. *Biochemistry* **50**, 2983–2993 (2011).
19. Dong, M. et al. Lactam constraints provide insights into the receptor-bound conformation of secretin and stabilize a receptor antagonist. *Biochemistry* **50**, 8181–8192 (2011).
20. Wootten, D., Simms, J., Miller, L. J., Christopoulos, A. & Sexton, P. M. Polar transmembrane interactions drive formation of ligand-specific and signal pathway-biased family B G protein-coupled receptor conformations. *Proc. Natl Acad. Sci. USA* **110**, 5211–5216 (2013).
21. Di Paolo, E. et al. Contribution of the second transmembrane helix of the secretin receptor to the positioning of secretin. *FEBS Lett.* **424**, 207–210 (1998).
22. Di Paolo, E. et al. Mutations of aromatic residues in the first transmembrane helix impair signalling by the secretin receptor. *Receptors Channels* **6**, 309–315 (1999).
23. Dong, M. et al. Mapping spatial approximations between the amino terminus of secretin and each of the extracellular loops of its receptor using cysteine trapping. *FASEB J.* **26**, 5092–5105 (2012).
24. Dong, M. et al. Use of cysteine trapping to map spatial approximations between residues contributing to the helix N-capping motif of secretin and distinct residues within each of the extracellular loops of its receptor. *J. Biol. Chem.* **291**, 5172–5184 (2016).
25. Pellequer, J. L. & Chen, S. W. Multi-template approach to modeling engineered disulfide bonds. *Proteins* **65**, 192–202 (2006).
26. Piserchio, A., Bisello, A., Rosenblatt, M., Chorev, M. & Mierke, D. F. Characterization of parathyroid hormone/receptor interactions: structure of the first extracellular loop. *Biochemistry* **39**, 8153–8160 (2000).
27. Zhao, L. H. et al. Structure and dynamics of the active human parathyroid hormone receptor-1. *Science* **364**, 148–153 (2019).
28. Du, Y. et al. Assembly of a GPCR-G protein complex. *Cell* **177**, 1232–1242 e1211 (2019).
29. Yano, A. et al. An aromatic amino acid within intracellular loop 2 of the prostaglandin EP2 receptor is a prerequisite for selective association and activation of Galphas. *Biochim Biophys. Acta Mol. Cell Biol. Lipids* **1862**, 615–622 (2017).
30. Schorb, M., Haberbosch, I., Hagen, W. J. H., Schwab, Y. & Mastronarde, D. N. Software tools for automated transmission electron microscopy. *Nat. Methods* **16**, 471–477 (2019).
31. Danev, R., Yanagisawa, H. & Kikkawa, M. Cryo-electron microscopy methodology: current aspects and future directions. *Trends Biochem. Sci.* **44**, 837–848 (2019).
32. Zheng, S. Q. et al. MotionCor2: anisotropic correction of beam-induced motion for improved cryo-electron microscopy. *Nat. Methods* **14**, 331–332 (2017).
33. Zhang, K., Gctf & Real-time, C. T. F. determination and correction. *J. Struct. Biol.* **193**, 1–12 (2016).
34. Grant, T., Rohou, A. & Grigorieff, N. cisTEM, user-friendly software for single-particle image processing. *Elife* **7**, <https://doi.org/10.7554/eLife.35383> (2018).
35. Tang, G. et al. EMAN2: an extensible image processing suite for electron microscopy. *J. Struct. Biol.* **157**, 38–46 (2007).
36. Zivanov, J. et al. New tools for automated high-resolution cryo-EM structure determination in RELION-3. *Elife* **7**, <https://doi.org/10.7554/eLife.42166> (2018).
37. Wagner, T. et al. SPHIRE-crYOLO is a fast and accurate fully automated particle picker for cryo-EM. *Commun. Biol.* **2**, 218 (2019).
38. Leaver-Fay, A. et al. ROSETTA3: an object-oriented software suite for the simulation and design of macromolecules. *Methods Enzymol.* **487**, 545–574 (2011).
39. Chan, K. Y., Trabuco, L. G., Schreiner, E. & Schulten, K. Cryo-electron microscopy modeling by the molecular dynamics flexible fitting method. *Biopolymers* **97**, 678–686 (2012).
40. Emsley, P., Lohkamp, B., Scott, W. G. & Cowtan, K. Features and development of Coot. *Acta Crystallogr. D. Biol. Crystallogr.* **66**, 486–501 (2010).
41. Adams, P. D. et al. PHENIX: a comprehensive Python-based system for macromolecular structure solution. *Acta Crystallogr. D. Biol. Crystallogr.* **66**, 213–221 (2010).
42. Croll, T. I. ISOLDE: a physically realistic environment for model building into low-resolution electron-density maps. *Acta Crystallogr. D. Struct. Biol.* **74**, 519–530 (2018).
43. Kidmose, R. T. et al. Namdinator—automatic molecular dynamics flexible fitting of structural models into cryo-EM and crystallography experimental maps. *IUCr* **6**, 526–531 (2019).
44. Laskowski, R. A. & Swindells, M. B. LigPlot+: multiple ligand-protein interaction diagrams for drug discovery. *J. Chem. Inf. Model* **51**, 2778–2786 (2011).
45. Goddard, T. D. et al. UCSF ChimeraX: meeting modern challenges in visualization and analysis. *Protein Sci.* **27**, 14–25 (2018).
46. Punjani, A., Rubinstein, J. L., Fleet, D. J. & Brubaker, M. A. cryoSPARC: algorithms for rapid unsupervised cryo-EM structure determination. *Nat. Methods* **14**, 290–296 (2017).
47. Dong, M. et al. Rational development of a high-affinity secretin receptor antagonist. *Biochem. Pharm.* **177**, 113929 (2020).
48. Gardner, J. D., Conlon, T. P., Beyerman, H. C. & Van Zon, A. Interaction of synthetic 10-tyrosyl analogues of secretin with hormone receptors on pancreatic acinar cells. *Gastroenterology* **73**, 52–56 (1977).
49. Powers, S. P., Pinon, D. I. & Miller, L. J. Use of N,O-bis-Fmoc-D-Tyr-ONSu for introduction of an oxidative iodination site into cholecystokinin family peptides. *Int. J. Pept. Protein Res.* **31**, 429–434 (1988).
50. Harikumar, K. G., Pinon, D. I. & Miller, L. J. Transmembrane segment IV contributes a functionally important interface for oligomerization of the Class II G protein-coupled secretin receptor. *J. Biol. Chem.* **282**, 30363–30372 (2007).
51. Lopata, M. A., Cleveland, D. W. & Sollner-Webb, B. High level transient expression of a chloramphenicol acetyl transferase gene by DEAE-dextran mediated DNA transfection coupled with a dimethyl sulfoxide or glycerol shock treatment. *Nucleic Acids Res.* **12**, 5707–5717 (1984).
52. Garcia, G. L., Dong, M. & Miller, L. J. Differential determinants for coupling of distinct G proteins with the class B secretin receptor. *Am. J. Physiol. Cell Physiol.* **302**, C1202–C1212 (2012).
53. Eswar, N. et al. Comparative protein structure modeling using MODELLER. *Curr. Protoc. Protein Sci.* **2**, 9 (2007).
54. Shen, M. Y. & Salí, A. Statistical potential for assessment and prediction of protein structures. *Protein Sci.* **15**, 2507–2524 (2006).
55. Rasmussen, S. G. et al. Crystal structure of the beta2 adrenergic receptor-Gs protein complex. *Nature* **477**, 549–555 (2011).
56. Humphrey, W., Dalke, A. & Schulten, K. VMD: visual molecular dynamics. *J. Mol. Graph.* **14**, 33–38 (1996).
57. Jacobson, M. P. et al. A hierarchical approach to all-atom protein loop prediction. *Proteins* **55**, 351–367 (2004).
58. Carpenter, B., Nehme, R., Warne, T., Leslie, A. G. & Tate, C. G. Structure of the adenosine A(2A) receptor bound to an engineered G protein. *Nature* **536**, 104–107 (2016).
59. Huang, J. & MacKerell, A. D. Jr. CHARMM36 all-atom additive protein force field: validation based on comparison to NMR data. *J. Comput. Chem.* **34**, 2135–2145 (2013).
60. Doerr, S., Harvey, M. J., Noe, F. & De Fabritiis, G. HTMD: high-throughput molecular dynamics for molecular discovery. *J. Chem. Theory Comput.* **12**, 1845–1852 (2016).
61. Dolinsky, T. J., Nielsen, J. E., McCammon, J. A. & Baker, N. A. PDB2PQR: an automated pipeline for the setup of Poisson-Boltzmann electrostatics calculations. *Nucleic Acids Res.* **32**, W665–W667 (2004).

62. Olsson, M. H., Sondergaard, C. R., Rostkowski, M. & Jensen, J. H. PROPKA3: consistent treatment of internal and surface residues in empirical pKa predictions. *J. Chem. Theory Comput.* **7**, 525–537 (2011).
63. Lomize, M. A., Lomize, A. L., Pogozheva, I. D. & Mosberg, H. I. OPM: orientations of proteins in membranes database. *Bioinformatics* **22**, 623–625 (2006).
64. Harvey, M. J., Giupponi, G. & Fabritiis, G. D. ACEMD: accelerating biomolecular dynamics in the microsecond time scale. *J. Chem. Theory Comput.* **5**, 1632–1639 (2009).
65. Loncharich, R. J., Brooks, B. R. & Pastor, R. W. Langevin dynamics of peptides: the frictional dependence of isomerization rates of N-acetylalanine-N'-methylamide. *Biopolymers* **32**, 523–535 (1992).
66. Berendsen, H. J. C. P., Postma, J. P. M., van Gunsteren, W. F., DiNola, A. & Haak, J. R. Molecular dynamics with coupling to an external bath. *J. Chem. Phys.* **81**, 3684 (1984).
67. Kräutler, V., van Wilfred F., G. & Philippe H., H. A fast SHAKE algorithm to solve distance constraint equations for small molecules in molecular dynamics simulations. *J. Comput. Chem.* **22**, 501–508 (2001).
68. Barducci, A., Bussi, G. & Parrinello, M. Well-tempered metadynamics: a smoothly converging and tunable free-energy method. *Phys. Rev. Lett.* **100**, 020603 (2008).
69. Tribello, G. A., Bonomi, M., Branduardi, D., Camilloni, C. & Bussi, G. PLUMED 2: new feathers for an old bird. *Comp. Phys. Commun.* **185**, 604–613 (2014).
70. Cuzzolin, A. et al. Deciphering the complexity of ligand-protein recognition pathways using supervised molecular dynamics (SuMD) simulations. *J. Chem. Inf. Model* **56**, 687–705 (2016).

Acknowledgements

The work was supported by a grant from the National Institutes of Health, GM-132095 (L.J.M. and P.M.S.), the Monash University Ramaciotti Centre for Cryo-Electron Microscopy, the Monash MASSIVE high-performance computing facility, the National Health and Medical Research Council of Australia (NHMRC) project grant (1120919), and NHMRC program grant (1150083). P.M.S. and A.C. are NHMRC Senior Principal Research Fellows and D.W. is an NHMRC Senior Research Fellow. C.A.R. holds a Royal Society Industry Fellowship and acknowledges a grant from the United Kingdom Biotechnology and Biological Sciences Research Council (BB/M006883/1). R.D. was supported by Takeda Science Foundation 2019 Medical Research Grant and Japan Science and Technology Agency PRESTO (18069571).

Author contributions

M.D. and K.G.H. performed the cysteine-cross-linking analysis and pharmacological characterization of mutant receptors. S.J.P. and Y.-L.L. expressed, purified the complex

and cross-checked the atomic models. A.G. and S.G.B.F. helped develop biochemical approaches for generation and or purification of protein complexes. S.J.P., M.K., and R.D. performed cryo-sample preparation and imaging to acquire EM data, processed the EM data and performed EM map calculations. S.J.P. and M.J.B. built the model and performed refinement. S.J.P. performed the 3D multivariate analysis. G.D. and C.A.R. designed, implemented and analyzed the MD simulations. S.J.P., M.K., and G.D. assisted with data interpretation, figure and manuscript preparation. All authors reviewed and edited the manuscript; A.C., P.M.S., D.W., and L.J.M. designed the project and interpreted data. P.M.S., D.W., and L.J.M. supervised the project, generated figures, and wrote the manuscript.

Competing interests

The authors declare no competing interests.

Additional information

Supplementary information is available for this paper at <https://doi.org/10.1038/s41467-020-17791-4>.

Correspondence and requests for materials should be addressed to D.W., P.M.S. or L.J.M.

Peer review information *Nature Communications* thanks Osamu Nureki and other, anonymous, reviewers for their contributions to the peer review of this work.

Reprints and permission information is available at <http://www.nature.com/reprints>

Publisher's note Springer Nature remains neutral with regard to jurisdictional claims in published maps and institutional affiliations.



Open Access This article is licensed under a Creative Commons Attribution 4.0 International License, which permits use, sharing, adaptation, distribution and reproduction in any medium or format, as long as you give appropriate credit to the original author(s) and the source, provide a link to the Creative Commons license, and indicate if changes were made. The images or other third party material in this article are included in the article's Creative Commons license, unless indicated otherwise in a credit line to the material. If material is not included in the article's Creative Commons license and your intended use is not permitted by statutory regulation or exceeds the permitted use, you will need to obtain permission directly from the copyright holder. To view a copy of this license, visit <http://creativecommons.org/licenses/by/4.0/>.

© The Author(s) 2020

Structure and dynamics of the active, Gs-coupled, human secretin receptor

Maoqing Dong^{1*}, Giuseppe Deganutti^{2*}, Sarah J. Piper^{3*}, Yi-Lynn Liang^{3*}, Maryam Khoshouei^{4^}, Matthew J. Belousoff³, Kaleeckal G. Harikumar¹, Christopher A Reynolds², Alisa Glukhova³, Sebastian G. B. Furness³, Arthur Christopoulos³, Radostin Danev⁵, Denise Wootten^{3#}, Patrick M. Sexton^{3#}, Laurence J. Miller^{1#}

Supplementary Information

Supplementary Tables 1–14. Pages 1 – 12.

Supplementary Figures 1–15. Pages 13 - 27

Supplementary Table 1. SecR interaction with secretin peptide and G protein subunits derived from PDB 6WZG. LigPlot+ was used to identify interacting residues. Only secretin residues 1-23 were used to calculate interactions due to the limited resolution in the receptor ECD. Both side-chain and backbone H-bond interactions are included, and displayed in bold type.

<u>Secretin</u>	<u>SecR</u>	<u>Interaction</u>	<u>Gas</u>	<u>SecR</u>	<u>Interaction</u>
H1	Q223^{3.37}	H-bond	H41	F248 ^{ICL2}	hydrophobic
H1	I226 ^{3.40}	hydrophobic	V217	F248 ^{ICL2}	hydrophobic
H1	I298 ^{5.44}	hydrophobic	F219	F248 ^{ICL2}	hydrophobic
H1	Y230 ^{3.44}	hydrophobic	Y358	Q327 ^{ICL3}	hydrophobic
H1	W295 ^{5.36}	hydrophobic	F376	F248 ^{ICL2}	hydrophobic
S2	E373^{7.42}	H-bond	C379	F248 ^{ICL2}	hydrophobic
S2	L370 ^{7.39}	hydrophobic	R380	A245^{ICL2}	H-bond
S2	Q369 ^{ECL3}	hydrophobic	R380	S247^{ICL2}	H-bond
D3	Y150^{1.47}	H-bond	R380	F248 ^{ICL2}	hydrophobic
D3	R188^{2.60}	H-bond	D381	K323^{5.64}	H-bond
D3	N192^{2.64}	H-bond	Q384	K323^{5.64}	H-bond
D3	L374 ^{7.43}	hydrophobic	Q384	L244^{ICL2}	H-bond
D3	F222 ^{3.36}	hydrophobic	R385	T326^{ICL3}	H-bond
F6	L374 ^{7.43}	hydrophobic	R385	K323 ^{5.64}	hydrophobic
F6	L139 ^{1.36}	hydrophobic	H387	L243 ^{3.57}	hydrophobic
F6	K143 ^{1.40}	hydrophobic	H387	S250 ^{ICL2}	hydrophobic
F6	Y146 ^{1.43}	hydrophobic	L388	L244 ^{ICL2}	hydrophobic
T7	K195^{2.67}	H-bond	Q390	R174 ^{2.46}	hydrophobic
T7	F222 ^{3.36}	hydrophobic	Y391	Y239 ^{3.53}	hydrophobic
T7	F200 ^{ECL1}	hydrophobic	Y391	R174 ^{2.46}	hydrophobic
S8	N289^{ECL2}	H-bond	Y391	L240 ^{3.54}	hydrophobic
S8	I288 ^{ECL2}	hydrophobic	E392	G393^{8.40}	H-bond
S8	D287 ^{ECL2}	hydrophobic	E392	R342^{6.40}	H-bond
E9	R135^{1.32}	H-bond	L393	S343^{6.41}	H-bond
E9	M366 ^{7.35}	hydrophobic	E392	N392 ^{7.61}	hydrophobic
L10	K143 ^{1.40}	hydrophobic	L393	R339 ^{6.37}	hydrophobic
L10	L139 ^{1.36}	hydrophobic	L394	R339 ^{6.37}	hydrophobic

S11	D287^{ECL2}	H-bond	L394	L320 ^{5.61}	hydrophobic
S11	F200 ^{ECL1}	hydrophobic			
S11	I288 ^{ECL2}	hydrophobic	Gβ	SecR	Interaction
R12	I288 ^{ECL2}	hydrophobic	D312	K401^{8.48}	H-bond
L13	H136 ^{1.33}	hydrophobic	D312	R169 ^{ICL1}	hydrophobic
L13	L139 ^{1.36}	hydrophobic	R52	R168 ^{ICL1}	hydrophobic
R14	S202^{ECL1}	H-bond			
R14	H136 ^{1.33}	hydrophobic			
R14	F200 ^{ECL1}	hydrophobic			
E15	L31^{ECD}	H-bond			
E15	R30 ^{ECD}	hydrophobic			
R18	D203^{ECL1}	H-bond			
R18	V205 ^{ECL1}	hydrophobic			
R21	D203^{ECL1}	H-bond			
L23	V125 ^{1.22}	hydrophobic			

Supplementary Table 2. Main SecR:secretin hydrogen bonds (side chain-side chain) during MD simulations. Data are expressed as the occupancy (% of frames) in which the interactions were present.

Secretin receptor residue	Secretin residue	Occupancy (%frames)
R135^{1.32}	E9	83.7
R30^{ECD}	E15	73.9
E373^{7.42}	S2	68.7
R188^{2.60}	D3	51.5
R299^{5.40}	D3	31.1
D204^{ECL1}	R21	31.0
D203^{ECL1}	R18	30.9
D204^{ECL1}	R21	30.5
D203^{ECL1}	R18	27.8
Y146^{1.43}	D3	26.8
D209^{ECL1}	R18	25.6
D209^{ECL1}	R18	22.3
D203^{ECL1}	R14	17.6
D203^{ECL1}	R14	16.5
D203^{ECL1}	R21	14.8
D204^{ECL1}	R18	14.0
R299^{5.40}	H1	13.9
D203^{ECL1}	R21	13.6
D196^{2.68}	R14	13.4
D196^{2.68}	R14	12.9
D204^{ECL1}	R18	12.4
Y230^{3.44}	H1	10.4
N289^{ECL2}	T5	10.1
D209^{ECL1}	R14	9.4

D209 ^{ECL1}	R14	8.1
N120 ^{ECD}	Q24	7.2
Q223 ^{3.37}	H1	6.7

Supplementary Table 3. Main SecR:secretin hydrogen bonds (side chain-backbone) during MD simulations. Data are expressed as the occupancy (% of frames) in which the interactions were present. (bb) indicates residue involved at the backbone atoms level (if both of the two residues are indicated with bb, then alternated side chain-backbone interactions occurred during MD).

Secretin receptor residue	Secretin residue	Occupancy (%frames)
E373 ^{7.42}	H1(bb)	89.7
E373 ^{7.42}	S2(bb)	58.9
N289 ^{ECL2} (bb)	S8	50.6
N72 ^{ECD}	L26(bb)	41.1
R30 ^{ECD} (bb)	E15	28.0
D203 ^{ECL1} (bb)	R18	21.9
R299 ^{5.40}	H1(bb)	14.6
S201 ^{ECD} (bb)	R14	14.1
A365 ^{ECL3} (bb)	T5	13.7
N289 ^{ECL2}	G4(bb)	11.6
D203 ^{ECL1} (bb)	R21	11.3
L199 ^{2.71} (bb)	R14	9.8
E363 ^{ECL3} (bb)	H1(bb)	8.2
L199 ^{2.71} (bb)	R18	8.2
N72 ^{ECD}	V27(bb)	6.0
D204 ^{ECL1} (bb)	R18	6.0
D287 ^{ECL2} (bb)	T7	5.6
M366 ^{7.35} (bb)	H1	5.6

Supplementary Table 4. SecR:secretin generic contacts during MD simulations. Contacts are determined as the occupancy (% of frames) in which at least two atoms were in contact.

Secretin receptor residue	Secretin residue	Occupancy (%frames)
E373 ^{7.42}	H1	94.0
E373 ^{7.42}	S2	86.5
H136 ^{1.33}	L13	86.3
R135 ^{1.32}	E9	84.3
R30 ^{ECD}	E15	82.6
L374 ^{7.43}	F6	74.5
N72 ^{ECD}	L26	72.9
V205 ^{ECL1}	R18	61.0
L96 ^{ECD}	L19	60.8

I288 ^{ECL2}	S8	60.2
L199 ^{2.71}	R14	60.1
N289 ^{ECL2}	S8	59.6
L370 ^{7.39}	S2	59.1
L139 ^{1.36}	E9	54.8
D203 ^{ECL1}	R18	54.8
R188 ^{2.60}	D3	52.3
L142 ^{1.39}	F6	50.2
L28 ^{ECD}	E15	50.1
L31 ^{ECD}	L19	49.4
L38 ^{ECD}	L26	45.6
K143 ^{1.40}	L10	45.2
D287 ^{ECL2}	S11	43.2
L31 ^{ECD}	R18	43.0
K143 ^{1.40}	F6	42.5
I288 ^{ECL2}	S11	41.9
Y146 ^{1.43}	F6	41.6
L96 ^{ECD}	L23	41.0
I288 ^{ECL2}	R12	41.0
D287 ^{ECL2}	S8	39.5
V34 ^{ECD}	L19	39.1
R299 ^{5.40}	H1	37.7
F92 ^{ECD}	L23	37.5
V205 ^{ECL1}	L22	37.4
N289 ^{ECL2}	G4	36.7
L139 ^{1.36}	F6	35.9
I73 ^{ECD}	L26	34.3
F200 ^{ECL1}	R14	33.5
I73 ^{ECD}	L23	33.3
V205 ^{ECL1}	R21	32.9
F92 ^{ECD}	L26	32.8
L139 ^{1.36}	L13	32.2
D204 ^{ECL1}	R21	32.2
R30 ^{ECD}	R12	32.1
R299 ^{5.40}	D3	32.1
L96 ^{ECD}	Q20	32.0
I73 ^{ECD}	V27	31.9
V34 ^{ECD}	L22	31.6
F358 ^{6.56}	H1	31.3
W295 ^{5.36}	H1	30.3

Supplementary Table 5[#]. Secretin binding affinity and cAMP response for wild type and extracellular loop cysteine mutant secretin receptors expressed in COS-1 cells.

Receptor constructs	Secretin binding		Intracellular cAMP response	
	K_i nM	B_{max} binding sites/cell $\times 10^3$	EC_{50} nM	E_{max} pmol/ 10^6 cells
WT	1.2 \pm 0.1	111.7 \pm 4.9	0.02 \pm 0.01	189 \pm 46
ECL1				
D196C	N.D.	N.D.	566 \pm 58**	156 \pm 44
A197C	8.3 \pm 1.2**	101.3 \pm 46.6	0.04 \pm 0.01	167 \pm 56
V198C	2.7 \pm 0.2**	4.3 \pm 1.0**	0.4 \pm 0.1*	166 \pm 39
L199C	N.D.	N.D.	33.2 \pm 5.6**	159 \pm 50
F200C	N.D.	N.D.	16.2 \pm 4.2*	178 \pm 40
S201C	N.D.	N.D.	1.5 \pm 0.5*	158 \pm 58
S202C	N.D.	N.D.	6.3 \pm 1.9*	176 \pm 45
D203C	N.D.	N.D.	3.9 \pm 0.5**	156 \pm 54
D204C	N.D.	N.D.	2.1 \pm 0.5*	189 \pm 47
V205C	N.D.	N.D.	2.1 \pm 0.4**	176 \pm 38
T206C	1.9 \pm 0.4	9.8 \pm 3.9**	0.3 \pm 0.1*	167 \pm 36
Y207C	N.D.	N.D.	0.3 \pm 0.05**	156 \pm 48
D209C	2.7 \pm 0.2**	6.9 \pm 3.4**	0.2 \pm 0.07	190 \pm 46
A210C	3.9 \pm 0.7*	4.8 \pm 1.4**	2.2 \pm 0.7*	178 \pm 34
H211C	N.D.	N.D.	2.1 \pm 0.4**	176 \pm 55
R212C	N.D.	N.D.	4.1 \pm 1.2*	165 \pm 34
A213C	5.4 \pm 0.7**	19.2 \pm 5.3*	0.1 \pm 0.04	202 \pm 59
G214C	4.8 \pm 0.8*	22.1 \pm 6.8**	0.08 \pm 0.03	201 \pm 38
K216C	5.4 \pm 0.4**	7.9 \pm 1.3**	0.3 \pm 0.1*	198 \pm 49
L217C	7.1 \pm 0.5**	62.0 \pm 11.7*	0.02 \pm 0.01	200 \pm 25
V218C	6.6 \pm 0.3**	53.5 \pm 4.7**	0.04 \pm 0.01	166 \pm 36
M219C	3.5 \pm 0.6*	4.1 \pm 0.5**	0.3 \pm 0.1*	159 \pm 34
V220C	8.5 \pm 1.4**	67 \pm 0.6**	0.04 \pm 0.02	169 \pm 45
L221C	6.9 \pm 0.5**	57.7 \pm 21.4	0.02 \pm 0.004	168 \pm 48
F222C	19.7 \pm 2.3**	55.9 \pm 12.6*	1.5 \pm 0.6	166 \pm 48
Q223C	8.2 \pm 1.5**	22.4 \pm 9.1**	1.2 \pm 0.4*	191 \pm 23
ECL2				
F279C	9 \pm 1.8*	89.7 \pm 15.0	0.04 \pm 0.01	209 \pm 65
L280C	6.8 \pm 1.2**	69.7 \pm 19.7	0.06 \pm 0.01*	187 \pm 54
E281C	3.3 \pm 0.4**	2.6 \pm 0.1**	4.4 \pm 1.2*	157 \pm 43
D282C	N.D.	N.D.	0.3 \pm 0.1*	199 \pm 50
V283C	2.7 \pm 0.7	6.9 \pm 0.9**	0.2 \pm 0.04*	167 \pm 39
G284C	N.D.	N.D.	3.4 \pm 1.1*	155 \pm 55
W286C	N.D.	N.D.	N.D.	N.D.
D287C	2.5 \pm 0.2**	2.8 \pm 0.4**	0.8 \pm 0.2*	177 \pm 40
I288C	7.9 \pm 1.9*	23.3 \pm 7.1**	0.5 \pm 0.2	197 \pm 42
N289C	5.9 \pm 1.3*	23.1 \pm 2.3**	0.3 \pm 0.1*	178 \pm 37
A290C	3.4 \pm 0.2**	10.6 \pm 1.1**	0.1 \pm 0.04	177 \pm 36
N291C	6.5 \pm 0.3**	45.8 \pm 7.4**	0.03 \pm 0.01	197 \pm 29
A292C	5.5 \pm 0.7**	43.3 \pm 6.1**	0.07 \pm 0.03	170 \pm 57
S293C	9.3 \pm 1.7**	52.5 \pm 17.9*	0.1 \pm 0.03	176 \pm 43
I294C	9.2 \pm 0.7**	40.9 \pm 17.5*	0.2 \pm 0.05*	188 \pm 35
W295C	28.9 \pm 3.8**	46.3 \pm 12.8**	3.4 \pm 0.8*	187 \pm 41
W296C	6.4 \pm 0.8**	33.0 \pm 13.4**	0.05 \pm 0.02	205 \pm 33
I297C	5.5 \pm 0.7**	35.9 \pm 16.3*	0.04 \pm 0.02	196 \pm 36
ECL3				
F358C	23.1 \pm 3.0**	88.6 \pm 26.3	3.2 \pm 0.9*	156 \pm 46
A359C	7.6 \pm 0.6**	53.4 \pm 17.8	0.07 \pm 0.03	175 \pm 55
F360C	10.0 \pm 1.3**	44.8 \pm 20.5*	0.1 \pm 0.02*	185 \pm 45
S361C	12.3 \pm 1.0**	63.8 \pm 21.3	0.05 \pm 0.02	187 \pm 49
P362C	5.1 \pm 0.8**	24.1 \pm 8.7**	0.4 \pm 0.1*	199 \pm 40
E363C	4.0 \pm 0.6*	12.5 \pm 5.0**	0.1 \pm 0.03	212 \pm 52
D364C	5.2 \pm 0.6**	21.87 \pm 7.1**	0.06 \pm 0.02	200 \pm 56
A365C	9.2 \pm 1.9*	35.51 \pm 12.0**	0.06 \pm 0.03	181 \pm 41
M366C	7.2 \pm 0.9**	18.1 \pm 5.6**	0.3 \pm 0.1*	182 \pm 36
E367C	5.3 \pm 1.0*	12.6 \pm 5.1**	0.3 \pm 0.04**	197 \pm 47
I368C	5.0 \pm 0.6**	27.7 \pm 7.3**	0.1 \pm 0.04	202 \pm 42
Q369C	5.0 \pm 0.7**	37.4 \pm 15.1**	0.05 \pm 0.01	204 \pm 52
L370C	6.2 \pm 0.9**	11.9 \pm 2.8**	0.2 \pm 0.04*	179 \pm 46
F371C	3.7 \pm 0.5	26.5 \pm 13.4**	0.03 \pm 0.01	170 \pm 39
F372C	11.0 \pm 0.9**	36.8 \pm 19.4*	0.2 \pm 0.03**	169 \pm 50
E373C	6.8 \pm 1.5*	27.5 \pm 7.8**	0.5 \pm 0.2	194 \pm 44
L374C	4.9 \pm 0.3**	87.0 \pm 23.9	1.0 \pm 0.2**	210 \pm 42

#Data are from reference #23, and re-tabled with SecR residues number from the initiator methionine as residue 1 to assist in data comparisons within the current manuscript.

Supplementary Table 6. Secretin binding affinity and cAMP response for wild type and TM1/juxtamembranous region cysteine mutant secretin receptors expressed in COS-1 cells.

Receptor constructs	Secretin binding		Intracellular cAMP response to secretin
	pK_i	B_{max} $\times 10^5 \text{ sites/cell}$	pEC_{50}
WT	8.7 ± 0.1	0.8 ± 0.1	10.8 ± 0.2
K134C	9.4 ± 0.1	0.6 ± 0.1	11.2 ± 0.3
R135C	8.9 ± 0.2	0.6 ± 0.1	9.9 ± 0.3
H136C	9.3 ± 0.3	0.6 ± 0.05	10.1 ± 0.4
S137C	$9.6 \pm 0.2^*$	0.6 ± 0.1	10.4 ± 0.2
Y138C	9.4 ± 0.2	0.6 ± 0.1	10.7 ± 0.2
L139C	<i>N.D.</i>	<i>N.D.</i>	$8.8 \pm 0.06^*$
L140C	8.6 ± 0.1	0.7 ± 0.1	10.3 ± 0.3
K141C	<i>N.D.</i>	<i>N.D.</i>	$9.5 \pm 0.2^*$
L142C	8.8 ± 0.3	0.8 ± 0.1	10.9 ± 0.1
K143C	<i>N.D.</i>	<i>N.D.</i>	9.6 ± 0.1
V144C	8.9 ± 0.1	0.8 ± 0.1	10.9 ± 0.6
M145C	8.6 ± 0.3	0.7 ± 0.1	10.5 ± 0.2
Y146C	$8.1 \pm 0.1^*$	0.7 ± 0.1	$9.3 \pm 0.4^*$
T147C	8.6 ± 0.3	0.7 ± 0.1	9.9 ± 0.4

Shown are pK_i and B_{max} values of secretin binding to COS-1 cells expressing each of the noted secretin receptor constructs. Shown also are EC_{50} values of secretin-stimulated intracellular cAMP accumulation in these cells. All values represent means \pm SEM of data from a minimum three independent experiments performed in duplicate. Asterisk denotes that the value is significantly different from that of wild type (WT) secretin receptor determined using ANOVA with Dunnett's post-test ($p < 0.05$). *N.D.*, binding not detectable.

Supplementary Table 7. Summary of the highest efficiency cysteine trapping constraints (human SecR sequence) by cysteine secretin agonist probes.

Secretin peptide residue	Secretin receptor residues	References
Cys ²	Phe ²⁷⁹ , Trp ²⁹⁵ , Phe ³⁶⁰ , Ser ³⁶¹ , Pro ³⁶²	(Dong et al., 2012) ²³
Cys ⁵	Ala ³⁵⁹ , Phe ³⁶⁰ , Glu ³⁶³ , Ile ³⁶⁸ , Gln ³⁶⁹ , Phe ³⁷² , Glu ³⁷³	(Dong et al., 2012) ²³
Cys ⁶	Ser ³⁶¹ , Pro ³⁶² , Asp ³⁶⁴ , Ala ³⁶⁵ , Met ³⁶⁶ , Glu ³⁷³	(Dong et al., 2016) ²⁴
Cys ⁷	Trp ²⁹⁵ , Phe ³⁵⁸	(Dong et al, 2016) ²⁴

Supplementary Table 8. Identification of receptor residues in the three extracellular loops of SecR important for spatial approximation using antagonist Cys-trapping probes.

Receptor constructs	Cys ⁵⁻ (c[E ¹⁶ ,K ²⁰],I ¹⁷ ,Cha ²² ,R ²⁵)sec(5-27)		Cys ⁶⁻ (c[E ¹⁶ ,K ²⁰],I ¹⁷ ,Cha ²² ,R ²⁵)sec(5-27)		Cys ⁷⁻ (c[E ¹⁶ ,K ²⁰],I ¹⁷ ,Cha ²² ,R ²⁵)sec(5-27)	
	Intraloop labeling efficiency (% of max)	Overall labeling efficiency (% of max)	Intraloop labeling efficiency (% of max)	Overall labeling efficiency (% of max)	Intraloop labeling efficiency (% of max)	Overall labeling efficiency (% of max)
WT	<i>N.D.</i>	<i>N.D.</i>	<i>N.D.</i>	<i>N.D.</i>	<i>N.D.</i>	<i>N.D.</i>
ECL1						
D196C	<i>N.D.</i>	< 1	<i>N.D.</i>	< 1	<i>N.D.</i>	< 1
A197C	<i>N.D.</i>	< 1	<i>N.D.</i>	< 1	<i>N.D.</i>	< 1
V198C	<i>N.D.</i>	< 1	<i>N.D.</i>	< 1	<i>N.D.</i>	< 1
L199C	<i>N.D.</i>	< 1	<i>N.D.</i>	< 1	<i>N.D.</i>	< 1
F200C	<i>N.D.</i>	< 1	<i>N.D.</i>	< 1	<i>N.D.</i>	< 1
S201C	<i>N.D.</i>	< 1	<i>N.D.</i>	< 1	<i>N.D.</i>	< 1
S202C	<i>N.D.</i>	< 1	<i>N.D.</i>	< 1	<i>N.D.</i>	< 1
D203C	<i>N.D.</i>	< 1	<i>N.D.</i>	< 1	<i>N.D.</i>	< 1
D204C	<i>N.D.</i>	< 1	<i>N.D.</i>	< 1	<i>N.D.</i>	< 1
V205C	<i>N.D.</i>	< 1	<i>N.D.</i>	< 1	<i>N.D.</i>	< 1
T206C	<i>N.D.</i>	< 1	<i>N.D.</i>	< 1	<i>N.D.</i>	< 1
Y207C	<i>N.D.</i>	< 1	<i>N.D.</i>	< 1	<i>N.D.</i>	< 1
D209C	<i>N.D.</i>	< 1	<i>N.D.</i>	< 1	<i>N.D.</i>	< 1
A210C	<i>N.D.</i>	< 1	<i>N.D.</i>	< 1	<i>N.D.</i>	< 1
H211C	<i>N.D.</i>	< 1	<i>N.D.</i>	< 1	<i>N.D.</i>	< 1
R212C	<i>N.D.</i>	< 1	<i>N.D.</i>	< 1	<i>N.D.</i>	< 1
A213C	<i>N.D.</i>	< 1	<i>N.D.</i>	< 1	<i>N.D.</i>	< 1
G214C	<i>N.D.</i>	< 1	<i>N.D.</i>	< 1	<i>N.D.</i>	< 1
K216C	<i>N.D.</i>	< 1	<i>N.D.</i>	< 1	<i>N.D.</i>	< 1
L217C	<i>N.D.</i>	< 1	<i>N.D.</i>	< 1	<i>N.D.</i>	< 1
V218C	<i>N.D.</i>	< 1	<i>N.D.</i>	< 1	<i>N.D.</i>	< 1
M219C	<i>N.D.</i>	< 1	<i>N.D.</i>	< 1	<i>N.D.</i>	< 1
V220C	<i>N.D.</i>	< 1	<i>N.D.</i>	< 1	<i>N.D.</i>	< 1
L221C	<i>N.D.</i>	< 1	<i>N.D.</i>	< 1	<i>N.D.</i>	< 1
F222C	<i>N.D.</i>	< 1	<i>N.D.</i>	< 1	<i>N.D.</i>	< 1
Q223C	<i>N.D.</i>	< 1	<i>N.D.</i>	< 1	<i>N.D.</i>	< 1
ECL2						
F279C	18.3 ± 3.7	5.6 ± 1.7	32.1 ± 11.6	12.6 ± 5.7	17.6 ± 7.2	6.6 ± 2.9
L280C	23.0 ± 3.1	7.4 ± 2.3	39.4 ± 11.5	14.3 ± 4.6	58.0 ± 11.2	16.4 ± 4.1
E281C	11.7 ± 6.6	4.4 ± 3.2	20.8 ± 7.1	7.4 ± 2.8	39.8 ± 16.1	12.0 ± 5.1
D282C	9.0 ± 9.0	3.9 ± 3.9	12.5 ± 4.1	4.7 ± 1.5	26.0 ± 14.5	8.2 ± 4.7
V283C	15.3 ± 6.5	5.5 ± 3.3	16.2 ± 5.7	5.8 ± 2.4	26.3 ± 13.9	8.9 ± 5.4
G284C	12.9 ± 6.6	4.8 ± 3.1	14.2 ± 5.4	4.8 ± 1.6	27.8 ± 12.5	8.4 ± 5.8
W286C	14.0 ± 8.7	5.5 ± 4.0	12.3 ± 4.9	4.2 ± 1.3	22.3 ± 12.5	9.1 ± 5.5
D287C	18.6 ± 4.8	6.3 ± 2.9	14.7 ± 5.8	5.0 ± 1.9	33.7 ± 11.0	11.0 ± 5.5
I288C	22.2 ± 1.7	6.9 ± 1.8	30.1 ± 5.4	11.7 ± 2.4	59.3 ± 17.5	17.3 ± 8.1
N289C	44.6 ± 16.4	16.4 ± 4.6	28.0 ± 4.4	5.8 ± 2.0	30.3 ± 12.1	9.7 ± 5.9
A290C	52.2 ± 9.8	21.6 ± 3.2	21.3 ± 9.1	6.9 ± 2.5	59.5 ± 12.0	16.3 ± 4.8
N291C	59.0 ± 11.0	24.5 ± 5.5	30.7 ± 14.1	9.7 ± 3.9	76.2 ± 10.8	21.6 ± 6.4
A292C	78.2 ± 6.4	23.4 ± 2.9	41.7 ± 11.4	14.7 ± 2.1	72.3 ± 9.5	22.3 ± 6.7
S293C	89.1 ± 5.5	<u>27.0 ± 4.4</u>	23.9 ± 9.2	8.0 ± 2.3	73.4 ± 7.9	23.5 ± 5.5
I294C	84.6 ± 12.7	<u>26.8 ± 8.3</u>	43.6 ± 14.3	14.9 ± 3.0	81.2 ± 5.8	23.5 ± 5.6
W295C	76.5 ± 13.5	23.8 ± 6.8	100.0 ± 0.0	<u>40.8 ± 7.0</u>	77.9 ± 9.6	22.9 ± 5.8
W296C	45.9 ± 18.7	23.9 ± 8.5	34.9 ± 2.8	13.7 ± 1.5	62.6 ± 5.8	17.3 ± 3.6
I297C	42.9 ± 7.4	16.9 ± 5.4	24.4 ± 7.7	8.4 ± 1.9	47.5 ± 7.5	14.3 ± 4.9
ECL3						
F358C	74.4 ± 14.5	74.4 ± 14.5*	93.1 ± 2.8	93.1 ± 2.8*	95.0 ± 4.1	95.0 ± 4.1*
A359C	87.8 ± 6.3	87.8 ± 6.3*	99.3 ± 0.7	99.3 ± 0.7*	84.2 ± 13.0	84.2 ± 13.0*
F360C	63.3 ± 8.1	63.3 ± 8.1*	70.7 ± 4.0	70.7 ± 4.0*	70.5 ± 12.8	70.5 ± 12.8*
S361C	87.5 ± 6.3	87.5 ± 6.3*	81.0 ± 3.6	81.0 ± 3.6*	79.8 ± 5.7	79.8 ± 5.7*
P362C	30.6 ± 9.7	<u>30.6 ± 9.7</u>	40.0 ± 2.5	<u>40.0 ± 2.5</u>	23.8 ± 2.7	23.8 ± 2.7
E363C	22.3 ± 9.1	22.3 ± 9.1	20.2 ± 1.2	20.2 ± 1.2	13.7 ± 4.2	13.7 ± 4.2
D364C	22.0 ± 7.7	22.0 ± 7.7	33.7 ± 2.0	<u>33.7 ± 2.0</u>	18.7 ± 4.2	18.7 ± 4.2
A365C	22.0 ± 8.1	22.0 ± 8.1	37.7 ± 3.2	<u>37.7 ± 3.2</u>	21.5 ± 1.9	21.5 ± 1.9
M366C	17.7 ± 7.9	17.7 ± 7.9	34.9 ± 1.8	<u>34.9 ± 1.8</u>	17.5 ± 3.0	17.5 ± 3.0
E367C	4.2 ± 3.0	4.2 ± 3.0	11.7 ± 4.1	11.7 ± 4.1	4.9 ± 2.1	4.9 ± 2.1
I368C	13.2 ± 4.9	13.2 ± 4.9	19.3 ± 5.6	19.3 ± 5.6	12.2 ± 3.1	12.2 ± 3.1
Q369C	14.2 ± 4.5	14.2 ± 4.5	41.0 ± 8.0	<u>41.0 ± 8.0</u>	25.6 ± 6.0	<u>25.6 ± 6.0</u>
L370C	19.2 ± 3.5	19.2 ± 3.5	43.5 ± 3.4	<u>43.5 ± 3.4</u>	27.4 ± 4.2	<u>27.4 ± 4.2</u>
F371C	21.8 ± 3.9	21.8 ± 3.9	39.6 ± 4.9	<u>39.6 ± 4.9</u>	43.7 ± 9.5	<u>43.7 ± 9.5</u>
F372C	27.3 ± 6.8	<u>27.3 ± 6.8</u>	46.9 ± 4.7	<u>46.9 ± 4.7</u>	39.4 ± 6.1	<u>39.4 ± 6.1</u>
E373C	28.2 ± 5.8	<u>28.2 ± 5.8</u>	62.4 ± 1.4	62.4 ± 1.4*	38.9 ± 4.4	<u>38.9 ± 4.4</u>
L374C	35.0 ± 10.3	<u>35.0 ± 10.3</u>	88.6 ± 2.8	88.6 ± 2.8*	45.5 ± 12.5	<u>45.5 ± 12.5</u>

Intraloop labeling efficiency represents intensity of labeling of each band as a percentage of the intensity of the band with the highest labeling intensity within each loop, while overall labeling efficiency represents intensity of labeling of each band as a percentage of the intensity of the band with the highest labeling intensity using that probe in all three loops. Values with underlines and asterisks represent constructs with overall intensities above 25% and 50%, respectively. Values represent means ± SEM of data from a minimum of three independent experiments. *N.D.*, not detectable.

Supplementary Table 9. Identification of receptor residues in the juxtamembranous region of the amino-terminal domain important for spatial approximation using antagonist Cys-trapping probes.

Receptor constructs	Cys ⁵ - (c[E ¹⁶ ,K ²⁰],I ¹⁷ ,Cha ²² ,R ²⁵)sec(5-27)		Cys ⁶ - (c[E ¹⁶ ,K ²⁰],I ¹⁷ ,Cha ²² ,R ²⁵)sec(5-27)		Cys ⁷ - (c[E ¹⁶ ,K ²⁰],I ¹⁷ ,Cha ²² ,R ²⁵)sec(5-27)	
	Intrasegment labeling efficiency (% of max)	Overall labeling efficiency (% of max)	Intrasegment labeling efficiency (% of max)	Overall labeling efficiency (% of max)	Intrasegment labeling efficiency (% of max)	Overall labeling efficiency (% of max)
WT	<i>N.D.</i>	<i>N.D.</i>	<i>N.D.</i>	<i>N.D.</i>	<i>N.D.</i>	<i>N.D.</i>
TM1						
K134C	<i>N.D.</i>	< 1	<i>N.D.</i>	< 1	<i>N.D.</i>	< 1
R135C	<i>N.D.</i>	< 1	<i>N.D.</i>	< 1	<i>N.D.</i>	< 1
H136C	<i>N.D.</i>	< 1	<i>N.D.</i>	< 1	<i>N.D.</i>	< 1
S137C	<i>N.D.</i>	< 1	<i>N.D.</i>	< 1	<i>N.D.</i>	< 1
Y138C	<i>N.D.</i>	< 1	<i>N.D.</i>	< 1	<i>N.D.</i>	< 1
L139C	<i>N.D.</i>	< 1	<i>N.D.</i>	< 1	<i>N.D.</i>	< 1
L140C	<i>N.D.</i>	< 1	<i>N.D.</i>	< 1	<i>N.D.</i>	< 1
K141C	<i>N.D.</i>	< 1	<i>N.D.</i>	< 1	<i>N.D.</i>	< 1
L142C	<i>N.D.</i>	< 1	<i>N.D.</i>	< 1	<i>N.D.</i>	< 1
K143C	<i>N.D.</i>	< 1	<i>N.D.</i>	< 1	<i>N.D.</i>	< 1
V144C	<i>N.D.</i>	< 1	<i>N.D.</i>	< 1	<i>N.D.</i>	< 1
M145C	<i>N.D.</i>	< 1	<i>N.D.</i>	< 1	<i>N.D.</i>	< 1
Y146C	100 ± 0	61 ± 12.2*	<i>N.D.</i>	< 1	100 ± 0	23 ± 5.5
T147C	<i>N.D.</i>	< 1	<i>N.D.</i>	< 1	<i>N.D.</i>	< 1

Intrasegment labeling efficiency represents intensity of labeling of each band as a percentage of the intensity of the band with the highest labeling intensity within the TM1, while overall labeling efficiency represents intensity of labeling of each band as a percentage of the intensity of the band with the highest labeling intensity using that probe in all three ECLs (see Supplementary Table 8). Value with asterisks represents construct with overall intensity above 50%. Values represent means ± SEM of data from a minimum of three independent experiments. *N.D.*, not detectable.

Supplementary Table 10. Main SecR:G protein hydrogen bonds (side chain-side chain) during MD simulations. Data are expressed as the occupancy (% of frames) in which the interactions were present. ^B indicates residues located at the Gβ subunit.

G protein residue	Secretin receptor residue	Occupancy (%frames)
D381	K323 ^{5.64}	79.2
D312^B	K401 ^{8.48}	62.2
R385	E328 ^{ICL3}	54.7
R385	E328 ^{ICL3}	54.1
E392	R342 ^{6.40}	53.5
D312^B	R169 ^{ICL1}	44.2
R342	E328 ^{ICL3}	32.3
R342	E328 ^{ICL3}	32.2
Q384	K323 ^{5.64}	30.6
R38	E251 ^{ICL2}	28.4
R38	E251 ^{ICL2}	27.6

D343	R330 ^{ICL3}	26.5
R385	T326 ^{ICL3}	19.4
R385	Q327 ^{ICL3}	13.0
T350	E333 ^{6.31}	11.8
R380	S247 ^{ICL2}	11.6
E322	R330 ^{ICL3}	11.2
E392	R339 ^{6.37}	10.9
Q384	S247 ^{ICL2}	8.0
D381	R322 ^{5.63}	7.1
D323	R325 ^{ICL3}	6.5
Y391	E236 ^{3.50}	5.9
Q35	E251 ^{ICL2}	5.6

Supplementary Table 11. Main SecR:G protein hydrogen bonds (side chain-backbone) during MD simulations. Data are expressed as the occupancy (% of frames) in which the interactions were present. (bb) indicates residues involved at the backbone atoms level (if both of the two residues are indicated with bb, then alternated side chain-backbone interactions occurred during MD); (Ct) indicates residues involved at the C terminus. ^B indicates residues located in the G β subunit. All other interactions are to the G α subunit.

G protein Residue	SecR Residue	Occupancy (%frames)
L394(Ct)	R339 ^{6.37}	92.9
Q384	L244 ^{3.58} (bb)	53.4
L393(bb)	S343 ^{6.41}	44.9
E392(bb)	R342 ^{6.40}	33.5
R380	L244 ^{3.58} (bb)	22.3
G310^B(bb)	Q405 ^{8.52}	15.8
R385	K323 ^{5.64} (bb)	15.8
H387	L243 ^{3.57} (bb)	14.3
T350(bb)	R330 ^{ICL3} (bb)	13.8
K216(bb)	S250 ^{ICL2}	12.2
R380	A245 ^{3.59} (bb)	10.8
R380	I246 ^{3.60} (bb)	8.6
Q35	E251 ^{4.38} (bb)	7.0
L394(Ct)	N322 ^{6.30}	6.5

Supplementary Table 12. SecR:G protein generic contacts during MD simulations. Contacts are determined as the occupancy (% of frames) in which at least two atoms were in contact.

^B indicates residues located at the G β subunit.

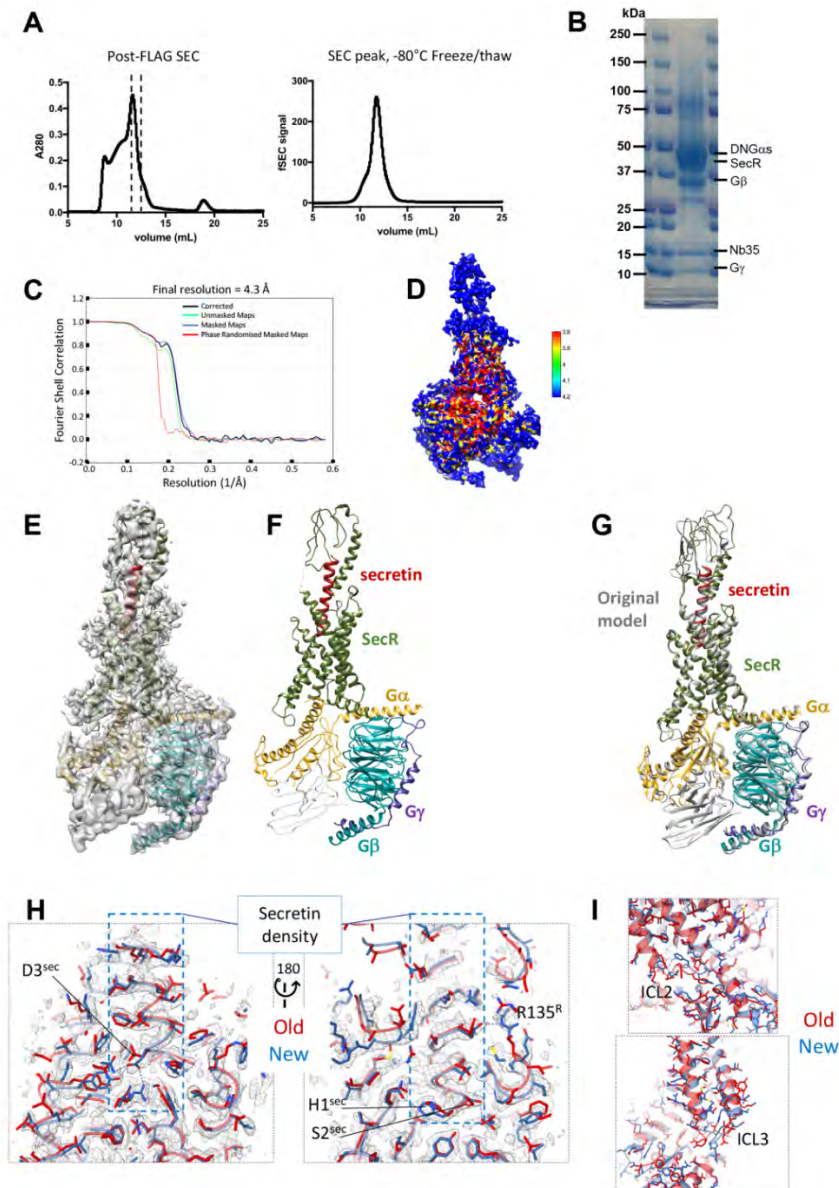
G protein Residue	Secretin receptor Residue	Occupancy (%frames)
L394	R339 ^{6.37}	93.2
L393	S343 ^{6.41}	89.5
Q384	L244 ^{3.58}	84.5
H387	L243 ^{3.57}	81.6
D381	K323 ^{5.64}	79.5
Y391	R174 ^{2.46}	72.2
L393	L320 ^{5.61}	66.2
Y391	L240 ^{3.54}	64.4
E392	R342 ^{6.40}	63.9
D312^B	K401 ^{8.48}	63.2
R385	E328 ^{ICL3}	54.4
R385	K323 ^{5.64}	54.0
E392	L346 ^{6.44}	53.3
Q384	K323 ^{5.64}	51.8
T350	R330 ^{ICL3}	50.4
R380	S247 ^{ICL2}	49.1
Y391	L243 ^{3.57}	48.7
D312^B	R169 ^{ICL1}	47.7
H387	L244 ^{3.58}	45.1
F376	F248 ^{ICL2}	44.4
R38	L244 ^{3.58}	40.0
V217	F248 ^{ICL2}	39.4
I383	S247 ^{ICL2}	39.1
L393	L347 ^{6.45}	37.1
H41	F248 ^{ICL2}	36.1
R380	L244 ^{3.58}	34.4
Y391	Y239 ^{3.53}	34.1
R342	E328 ^{ICL3}	32.2
R38	E251 ^{4.38}	32.1
L393	L346 ^{6.44}	31.8
R380	F248 ^{ICL2}	30.8

Supplementary Table 13. CryoEM collection parameters and refined structure statistics.

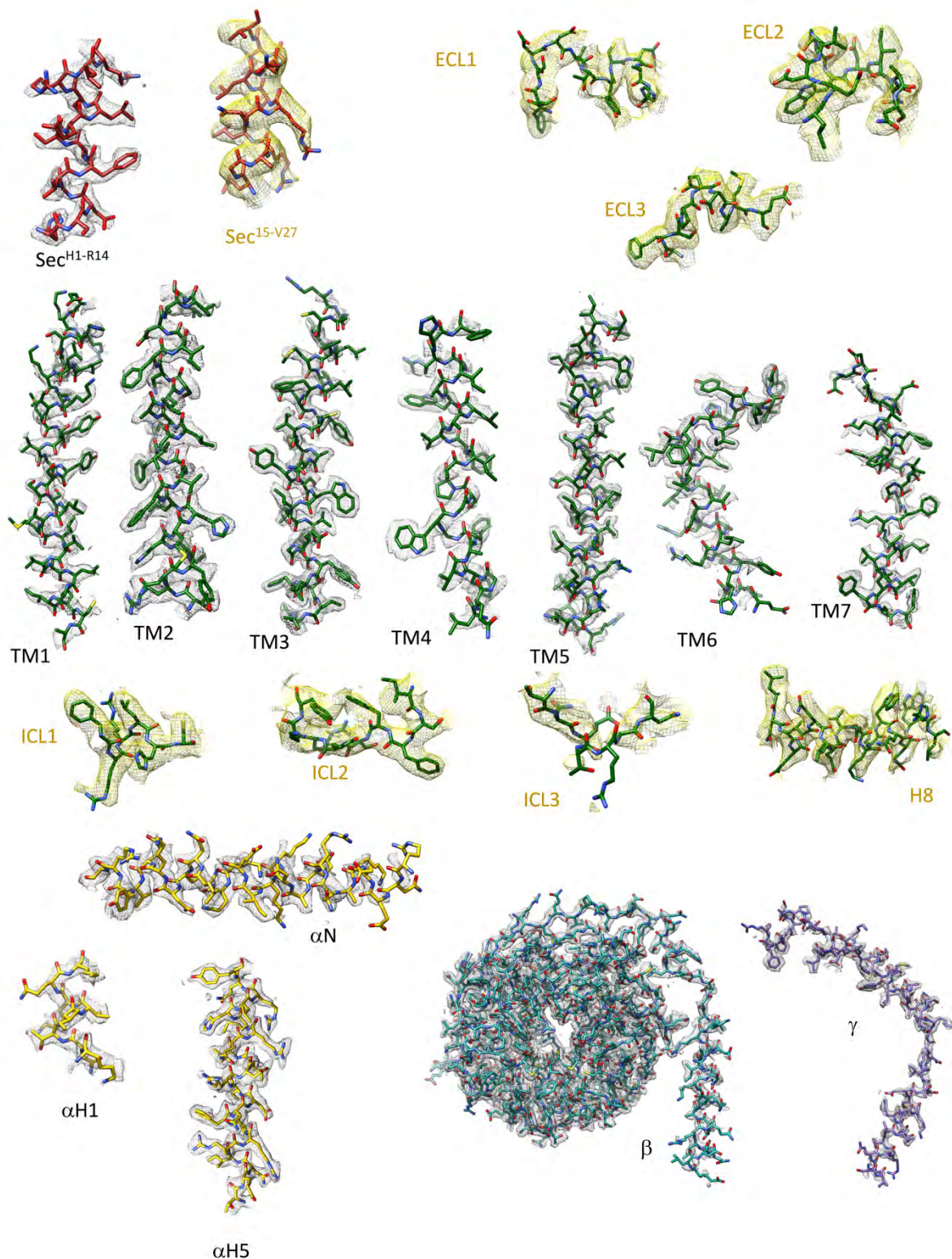
	EMD-21683; PDB 6WI9	EMD-21972; PDB 6WZG
Data Collection	SecR:sec:DNG α_s v1:Nb35	SecR:sec:DNG α_s v2:Nb35
Micrographs	6500	5600
Particles (Final map)	78k	350k
Pixel size (Å)	0.86	0.83
Defocus range (μm)	0.5-1.9	0.7-1.5
Voltage (kV)	300	300
Electron dose (e/Å ²)	46	52.9
Resolution (0.143 FSC) (Å)	4.3	2.3 (tight), 2.4 (wide)
Refinement		
CC _{map_model}	0.78	0.71
Model Quality		
<i>RMSD</i>		
Bond length (Å) / Bond angles (°)	0.001/0.396	0.012/1.586
<i>Ramachandran</i>		
Favoured (%)	95.72	98
Outliers (%)	0	0
<i>Rotamer outliers</i> (%)	0	1.65
<i>C-Beta deviations</i> (%)	0	1.65
<i>Clashscore</i>	5.29	4.8
<i>MolProbity Score</i>	1.58	1.41

Supplementary Table 14. List of primers used to prepare secretin receptor constructs with mutations in the TM1 stalk region. Shown are the forward and reverse primer sequences.

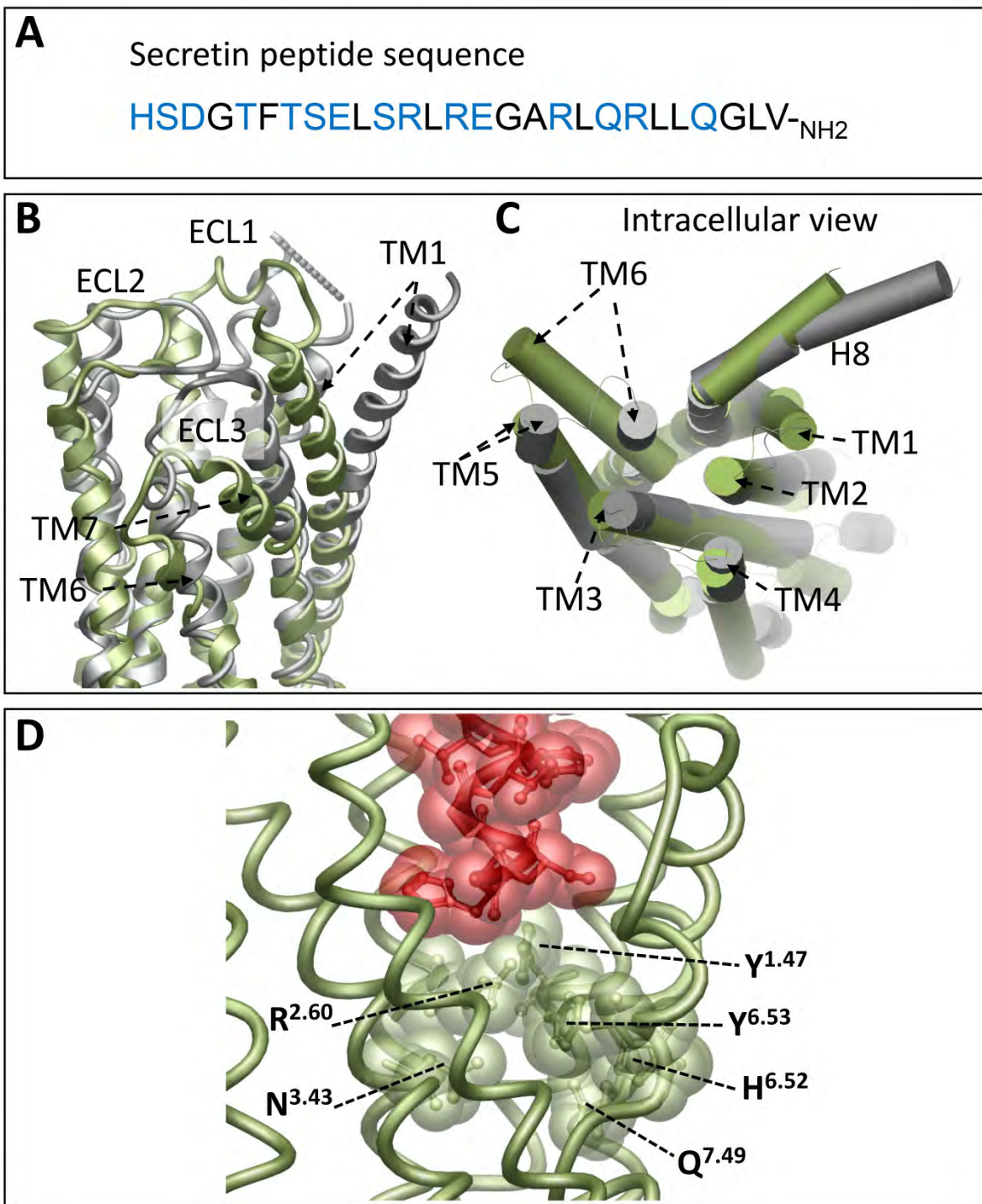
Constructs	Forward primer sequence	Reverse primer sequence
SecR (K134C)	CTTCCAACGAGTGCCGGCACTCCTAC	GTAGGAGTGCCGGCACTCGTTGGAAG
SecR (R135C)	CAACGAGAAGTGTCACCTAC	GTAGGAGTGACACTTCTCGTTG
SecR (H136C)	CAACGAGAAGCGGTGCTCCTACCTG	CAGGTAGGAGCACCGCTTCTCGTTG
SecR (S137C)	GAGAAGCGGCACTGCTACCTGCTGAAG	CTTCAGCAGGTAGCAGTGCCGCTTCTC
SecR (Y138C)	CACTCCTGCCTGCTGAAGCTGAAAG	CTTTCAGCTTCAGCAGGCAGGAGTG
SecR (L139C)	CTCCTACTGTCTGAAGCTGAAAG	CTTTCAGCTTCAGACAGTAGGAG
SecR (L140C)	CTCCTACCTGTGTAAGCTGAAAG	CTTTCAGCTTACACAGGTAGGAG
SecR (K141C)	CTACCTGCTGTGTCTGAAAGTC	GACTTTCAGACACAGCAGGTAG
SecR (L142C)	CTGCTGAAGTGTAAGTCATGTAC	GTACATGACTTTACACTTCAGCAG
SecR (K143C)	CTGAAGCTGTGTGTCATGTACAC	GTGTACATGACACACAGCTTCAG
SecR (V144C)	CTGAAGCTGAAATGCATGTACAC	GTGTACATGCATTTTCAGCTTCAG
SecR (M145C)	GAAGCTGAAAGTCTGTTACACCGTG	CACGGTGTAACAGACTTTTCAGCTTC
SecR (Y146C)	CTGAAAGTCATGTGCACCGTGG	CCACGGTGACATGACTTTTCAG
SecR (T147C)	GAAAGTCATGTACTGCGTGGGCTACAG	CTGTAGCCACGCAGTACATGACTTTC



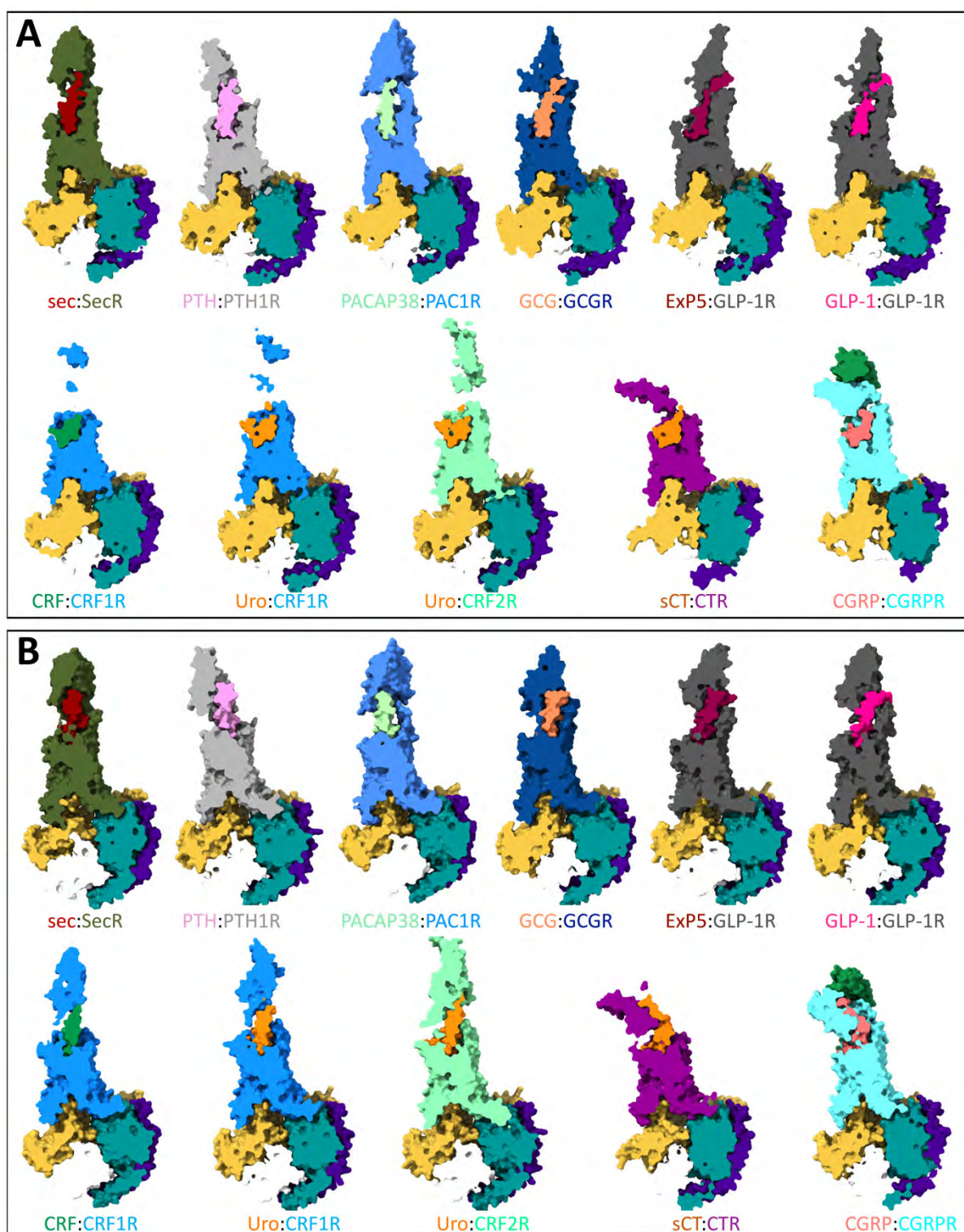
Supplementary Figure 1. Initial cryo-EM structure of the secretin:SecR:GsDNv1:Nb35 complex. **A.** SEC trace of post FLAG-affinity column elution (Left panel), the complex peak (dashed lines) was isolated and used for cryo-EM imaging, with the Right panel illustrating stability of the complex following one cycle of freeze-thawing. **B.** Coomassie stain of the purified complex separated by PAGE (Right panel). **C.** Gold standard Fourier shell correlation (FSC) curves for the final map and map validation from half maps, showing the overall nominal resolution of 4.3 Å. **D.** LocalResolution-filtered EM map displaying local resolution (Å) colored from highest resolution (red) to lowest resolution (dark blue). **E.** Full map containing the backbone model of the complex in ribbon format; SecR (olive green), secretin (dark red), G protein α-subunit (gold), β-subunit (cyan), γ-subunit (dark purple), and Nb35 (white). **F.** Ribbon representation of the secretin:SecR:GsDN:Nb35 complex colored according to (E). **G.** Overlay of the initial model from the 4.3 Å map (grey) and final pdb model built from the high-resolution maps (Figure 1). **H, I.** Detailed overlay of the initial (red) and final (blue) models together with the high-resolution cryo-EM map density (grey mesh) depicting the secretin peptide-SecR interaction (**H**) and intracellular loops/G protein (**I**), illustrating high concordance between the models.



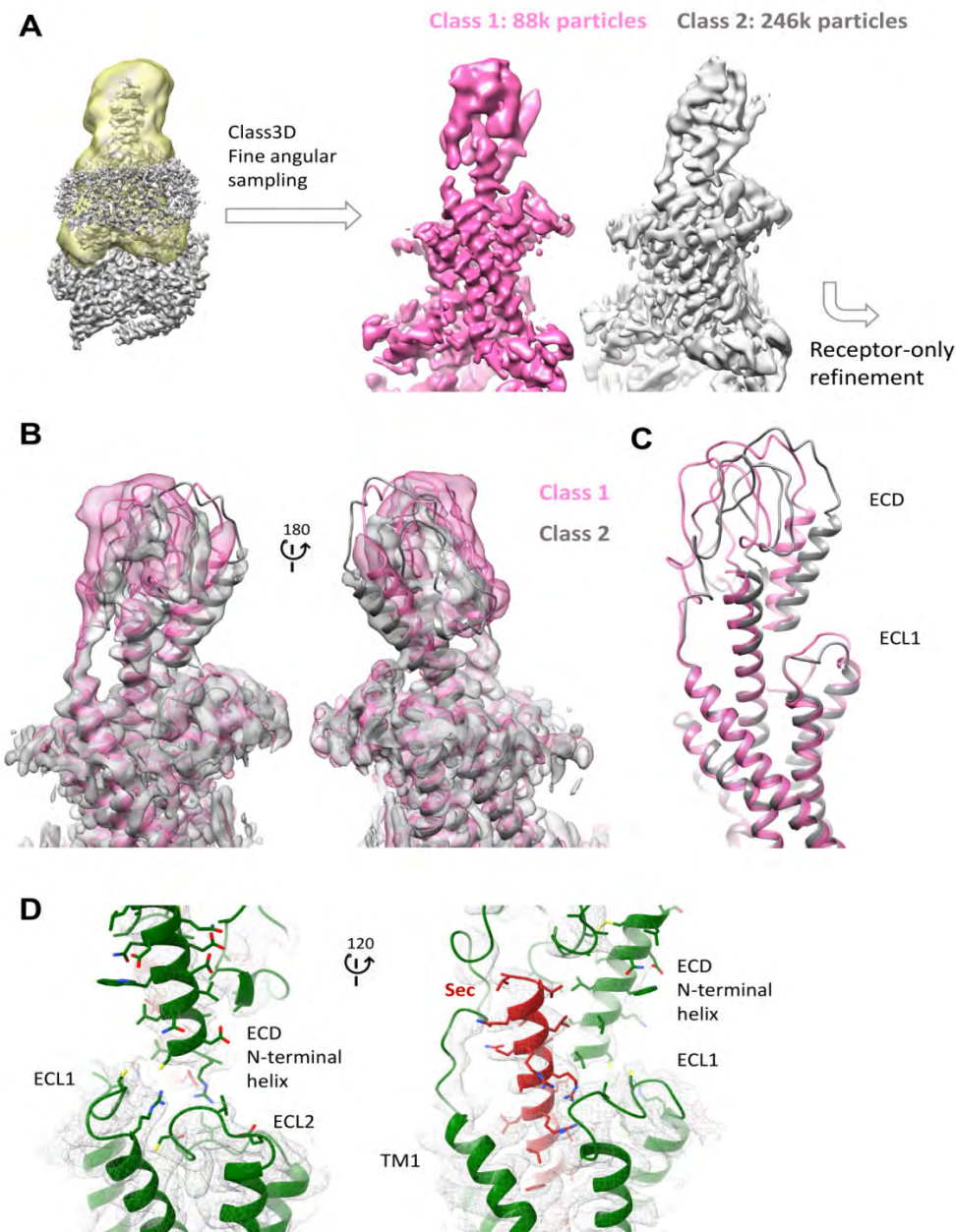
Supplementary Figure 2. Atomic modelling of the secretin:SecR:GsDN:Nb35 complex in the cryo-EM density maps. Grey represents the 2.3 Å global map and yellow represents the 2.5 Å receptor-only map (loops). Density maps and models are shown for all seven transmembrane helices, ECL1-3, ICL1-3 and H8 of SecR; the secretin peptide; the N-terminal (α N), α H1, and C-terminal (α H5) α -helices of the G α s-Ras domain, G β ₁ and G γ ₂ are also shown. The EM map was zoned at 2.0 Å around the protein segments. Images were generated in ChimeraX with a contour setting of 0.032 for the 2.3 Å consensus map, and 0.02 for the 2.5 Å receptor-alone map.



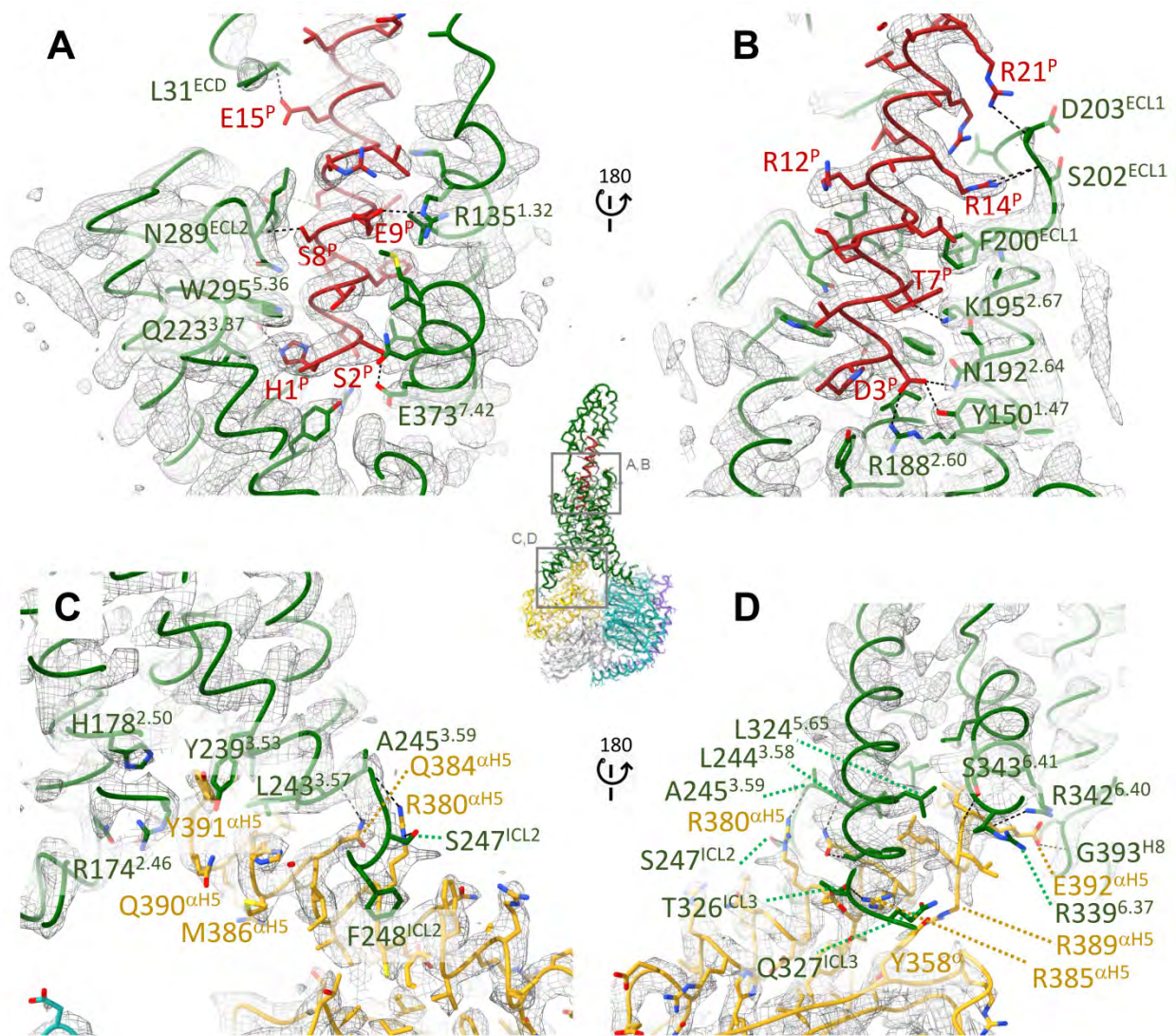
Supplementary Figure 3. A. Secretin peptide sequence with polar amino acids highlighted in blue. **B, C.** Comparison of the transmembrane core of the active SecR structure (olive green) and the inactive structure of the related glucagon receptor (dark grey; PDB: 4L6R) highlighting major differences in the location of each of the ECLs and TM1 (**B**, secondary structure displayed in ribbon format) and in the position of the base of TMs 5 and 6 (**C**, helices displayed as cylinders). **D.** The secretin N-terminus is located above the conserved class B central polar network and forms extensive interactions with this network across TM1, TM2, TM5, TM6 and TM7 (see also Supplementary Tables 2-4). Displayed is the consensus cryo-EM derived structural model (PDB 6WZG).



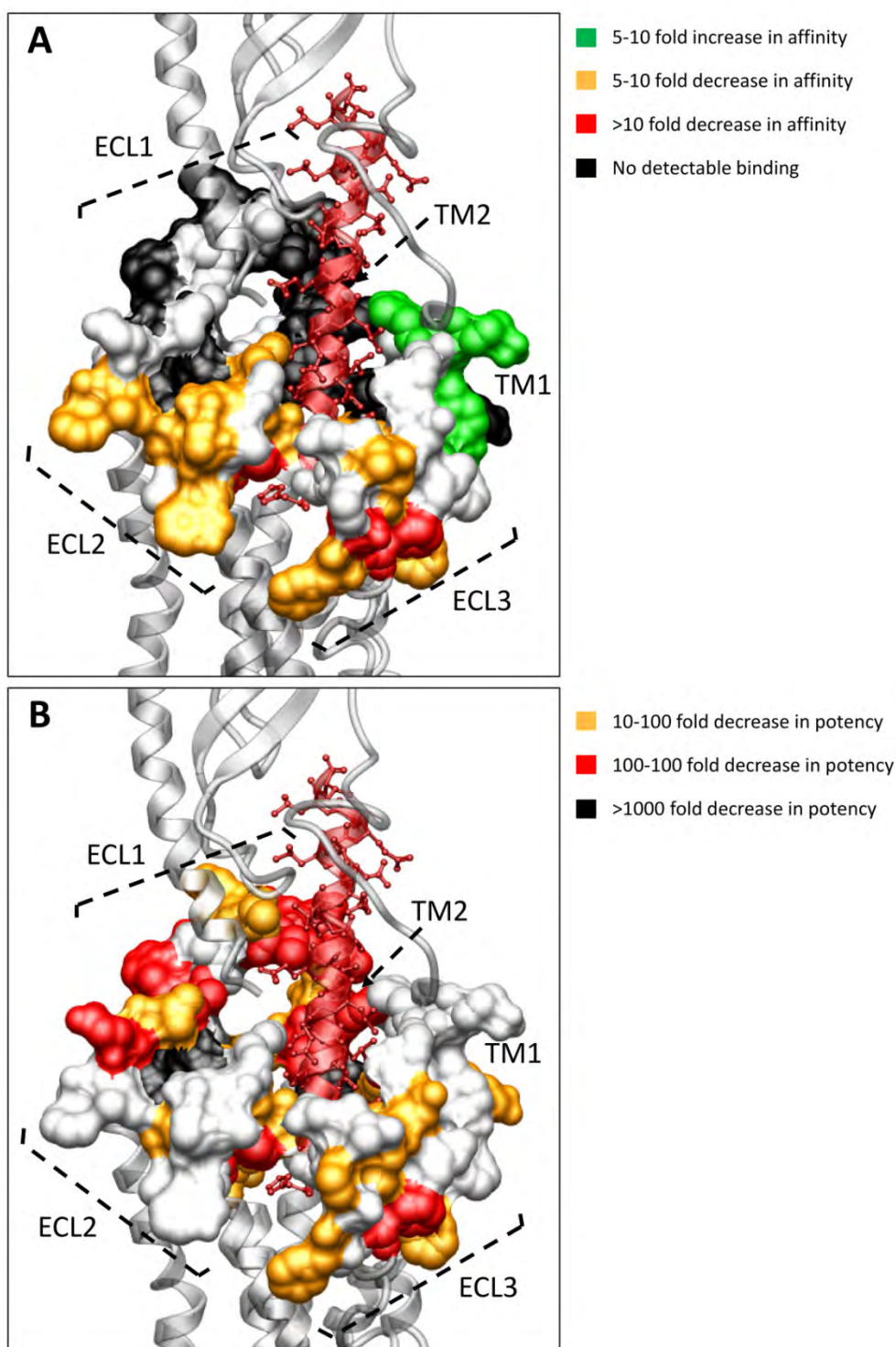
Supplementary Figure 4. Comparison of pdb models from cryo-EM maps of available class B active, Gs coupled, receptors. Peptides and receptors are colored according to the legend beneath each figure. G α s, gold; G β ₁, dark cyan; G γ ₂, dark slate blue; Nb35, white. **A** and **B** illustrate slices through the models at different levels to highlight either the depth of binding of peptides within the receptor core (**A**) or relative orientation of peptides to ECDs of the receptors (**B**).



Supplementary Figure 5. Variability in receptor-only classification. **(A)** Focused 3D classification using a mask including only the SecR and peptide (yellow) on global refinement particles. 3D classification reveals two predominant classes with variability in the ECD and ECL1 (Class 1 in pink and Class 2 in grey). Particles from Class 2 were further used for the receptor-only refinement. **(B, C)** Backbone models fitted into the two 3D classes (transparent surface representation): the final consensus PDB model is shown in grey. For the Class 1 model, the final PDB model was subjected to a crude flexible fitting of the backbone into the Class 1 map using Namdinator and Isolde (pink). **(D)** Modelling of receptor side chains (x-stick representation) into the SecR electron density map (grey mesh) that are within 6 Å of the far N-terminal helix, illustrating zones of potential interaction. SecR is coloured green, secretin peptide is dark red; the protein backbone is shown in ribbon format. Maps and models are displayed using Chimera **(A-C)** or ChimeraX **(D)**.



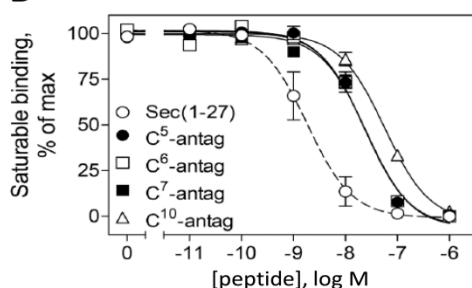
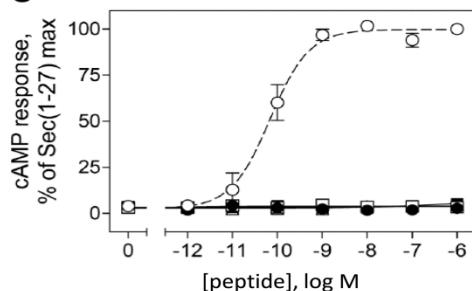
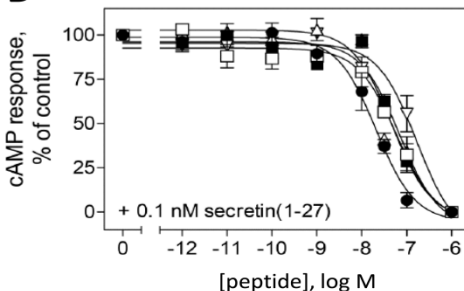
Supplementary Figure 6. Interaction of SecR with the secretin peptide and G α protein. **(A, B)** Cut-away views of the secretin receptor (green) and peptide (red), together with the receptor-only cryo-EM density map (grey mesh). Peptide residues as well as receptor residues within a 4 Å zone around the peptide are shown as stick model. **(C, D):** Cut-away views of SecR (green) and G α (yellow), together with the cryo-EM density from the global map (grey mesh). G α C-terminal residues as well as receptor residues within a 4 Å zone around the G α C-terminus (α H5) are shown as stick model. ChimeraX predicted hydrogen bonds (relaxed distance and angles) between receptor and other chains are shown as black dotted lines.



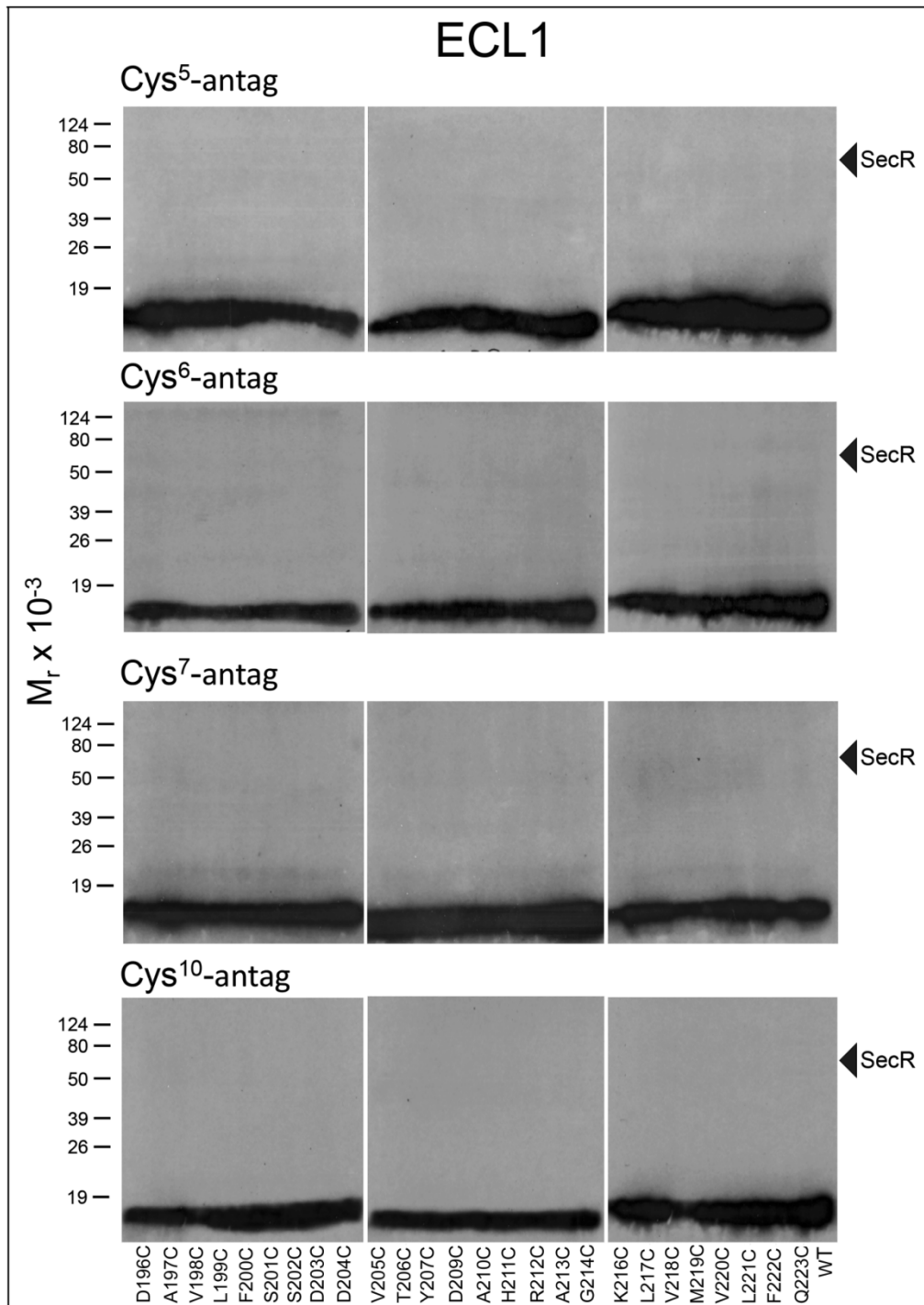
Supplementary Figure 7. Effect of cysteine substitution on secretin affinity in competition for ^{125}I -[Y¹⁰]secretin(1-27) binding to hSecR **(A)** or secretin-induced cAMP accumulation **(B)**. Mutated residues are depicted in grey surface and cpk representation. Colored residues in **(A)** depict 5-10 fold increase (green), 5-10 fold decrease (light orange), >10-fold decrease (red) in affinity, or no detectable binding (black). Colored residues in **(B)** depict >10-fold decrease in potency (light orange), >100-fold decrease in potency (red) or >1000-fold decrease in potency (black). Data are from references^{23,24} and Supplementary Tables 5, 6.

A

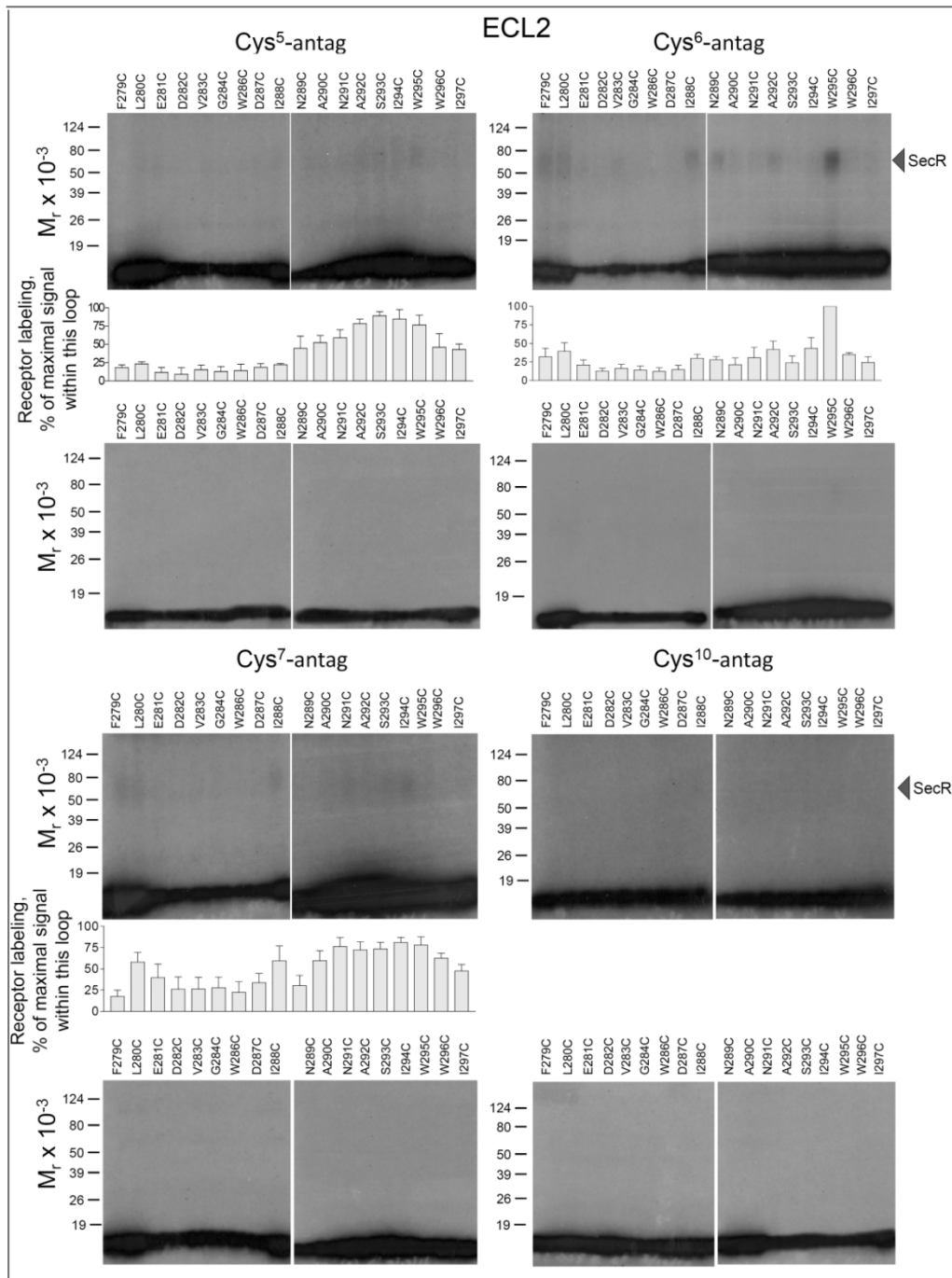
Agonist	1	5	10	15	20	25
Sec(1-27)	H	S	D	G	T	F
C ² -(Y ¹⁰)Sec(1-27) (C ² -Sec)	H	C	D	G	T	F
C ⁵ -(Y ¹⁰)Sec(1-27) (C ⁵ -Sec)	H	S	D	G	C	F
C ⁶ -(Y ¹⁰)Sec(1-27) (C ⁶ -Sec)	H	S	D	G	T	C
C ⁷ -(Y ¹⁰)Sec(1-27) (C ⁷ -sec)	H	S	D	G	T	C
C ¹⁰ -(Y ¹⁰)sec(1-27) (C ¹⁰ -sec)	H	S	D	G	T	C
Antagonist						
C ⁵ -(c[E ¹⁶ ,K ²⁰],Y ¹⁰ ,I ¹⁷ ,Cha ²² ,R ²⁵)sec(5-27) (C ⁵ -antag)	C	F	T	S	E	Y
C ⁶ -(c[E ¹⁶ ,K ²⁰],Y ¹⁰ ,I ¹⁷ ,Cha ²² ,R ²⁵)sec(5-27) (C ⁶ -antag)	T	C	T	S	E	Y
C ⁷ -(c[E ¹⁶ ,K ²⁰],Y ¹⁰ ,I ¹⁷ ,Cha ²² ,R ²⁵)sec(5-27) (C ⁷ -antag)	T	F	C	S	E	Y
C ¹⁰ -(c[E ¹⁶ ,K ²⁰],I ¹⁷ ,Cha ²² ,R ²⁵ ,Y ²⁶)sec(5-27) (C ¹⁰ -antag)	T	F	T	S	E	C

B**C****D**

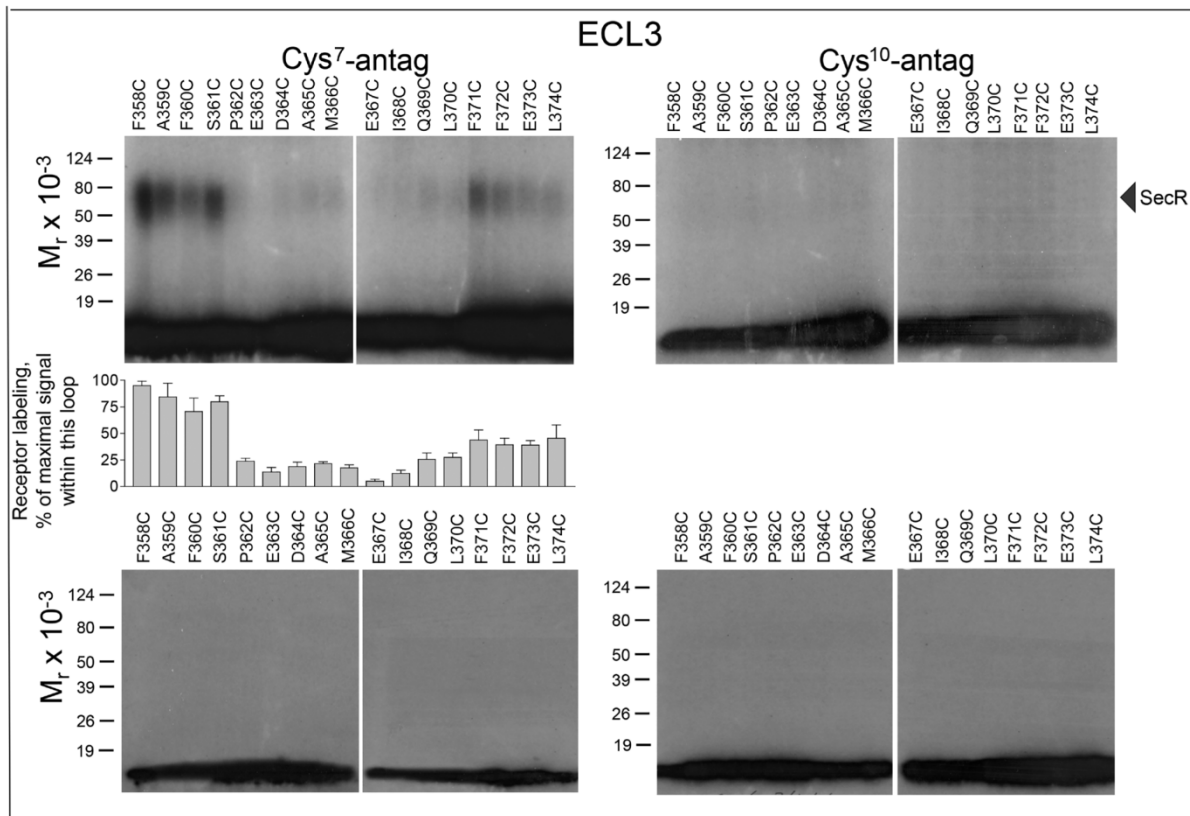
Supplementary Figure 8. A. Primary structures of cysteine-containing secretin agonist and antagonist analogues used in this study. Shown are the amino acid sequences of full length secretin(1-27), cysteine containing agonist (Cys²-, Cys⁵-, Cys⁶-, Cys⁷- and Cys¹⁰-sec) that we used previously^{31,32} and antagonist (Cys⁵-, Cys⁶-, Cys⁷- and Cys¹⁰-antag) (developed in this study) probes. Natural residues are colored gray, while modified residues are colored black. Lactam bridges linking the side chains of residues Glu¹⁶ and Lys²⁰ are illustrated with brackets. **B.** Inhibition curves of increasing concentrations of secretin, Cys⁵-, Cys⁶-, Cys⁷- and Cys¹⁰-antag probes to compete for binding of the secretin radioligand, ¹²⁵I-[Tyr¹⁰]sec(1-27), to secretin receptor-bearing CHO-SecR cells. Values represent the percentages of saturable binding, expressed as the means \pm S.E.M. of duplicate values from a minimum of three independent experiments. **C.** Intracellular cAMP accumulation in CHO-SecR cells stimulated with increasing concentrations of each of the antagonist analogues or secretin peptide. Data points represent the means \pm S.E.M. of data from three independent experiments performed in duplicate. **D.** Inhibition of 0.1 nM secretin mediated cAMP accumulation by increasing concentration of antagonist analogues. Data points represent the means \pm S.E.M. of data from three independent experiments performed in duplicate.



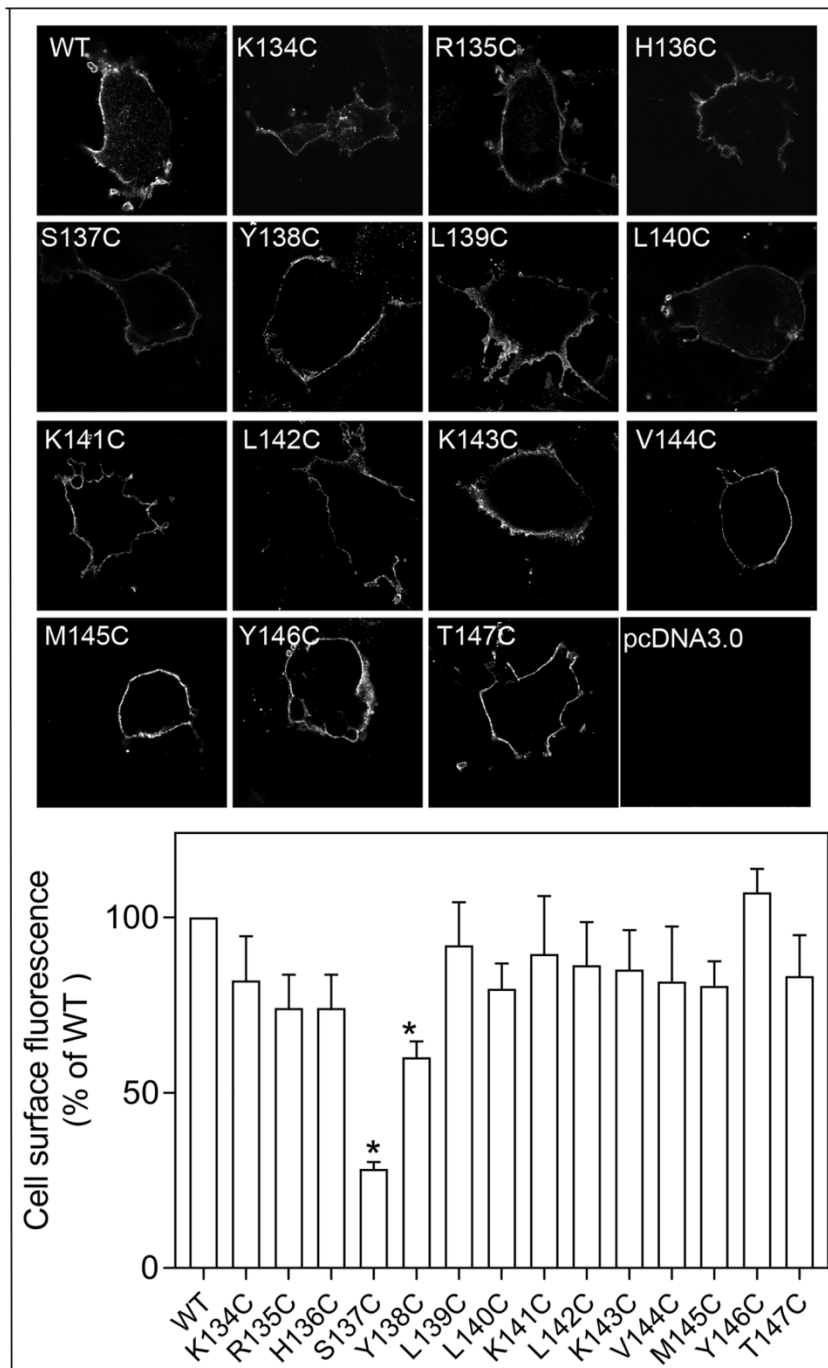
Supplementary Figure 9. Cysteine trapping of secretin receptor ECL1 cysteine replacement mutants with ^{125}I -labelled cysteine-containing secretin antagonist analogues. Shown are typical autoradiographs of 10% SDS-PAGE gels used to separate the products of cysteine trapping of the indicated ECL1 SecR cysteine mutants transiently expressed in COS-1 cells for each of the noted cysteine-containing secretin antagonist probes. Autoradiographs are representative of a minimum of three independent experiments. Since no significant receptor labeling was observed under non-reducing conditions, autoradiographs of reducing gels that also did not show significant labeling are not shown.



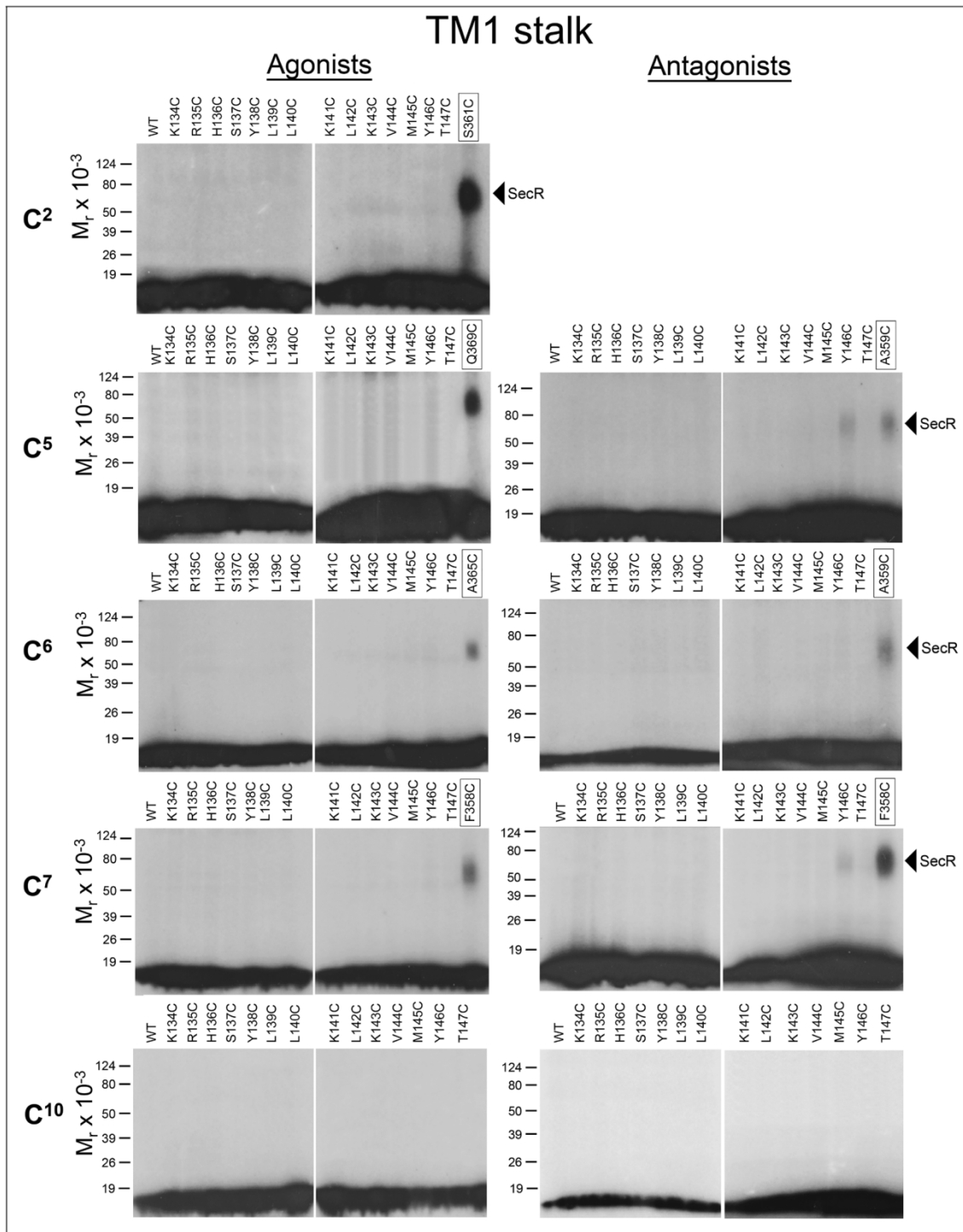
Supplementary Figure 10. Cysteine trapping of secretin receptor ECL2 cysteine replacement mutants with ¹²⁵I-labelled cysteine-containing secretin antagonist analogues. Shown are typical autoradiographs of 10% SDS-PAGE gels used to separate the products of cysteine trapping of the indicated ECL2 SecR cysteine replacement mutants transiently expressed in COS-1 cells for each of the noted cysteine-containing secretin antagonist probes, under non-reducing (top panel) and reducing (bottom panel) conditions. Autoradiographs are representative of a minimum of three independent experiments. Densitometric analysis of data from three similar experiments with the Cys⁵-, Cys⁶-, and Cys⁷-antagonist probes is shown (middle panel), with intensities representing the percentages of the signal for the maximal labeling of a residue within ECL2 by that probe. Quantification of labeling is not shown for experiments with the Cys¹⁰-antagonist probe because no significant labeling was observed with any of the receptor cysteine replacement mutants.



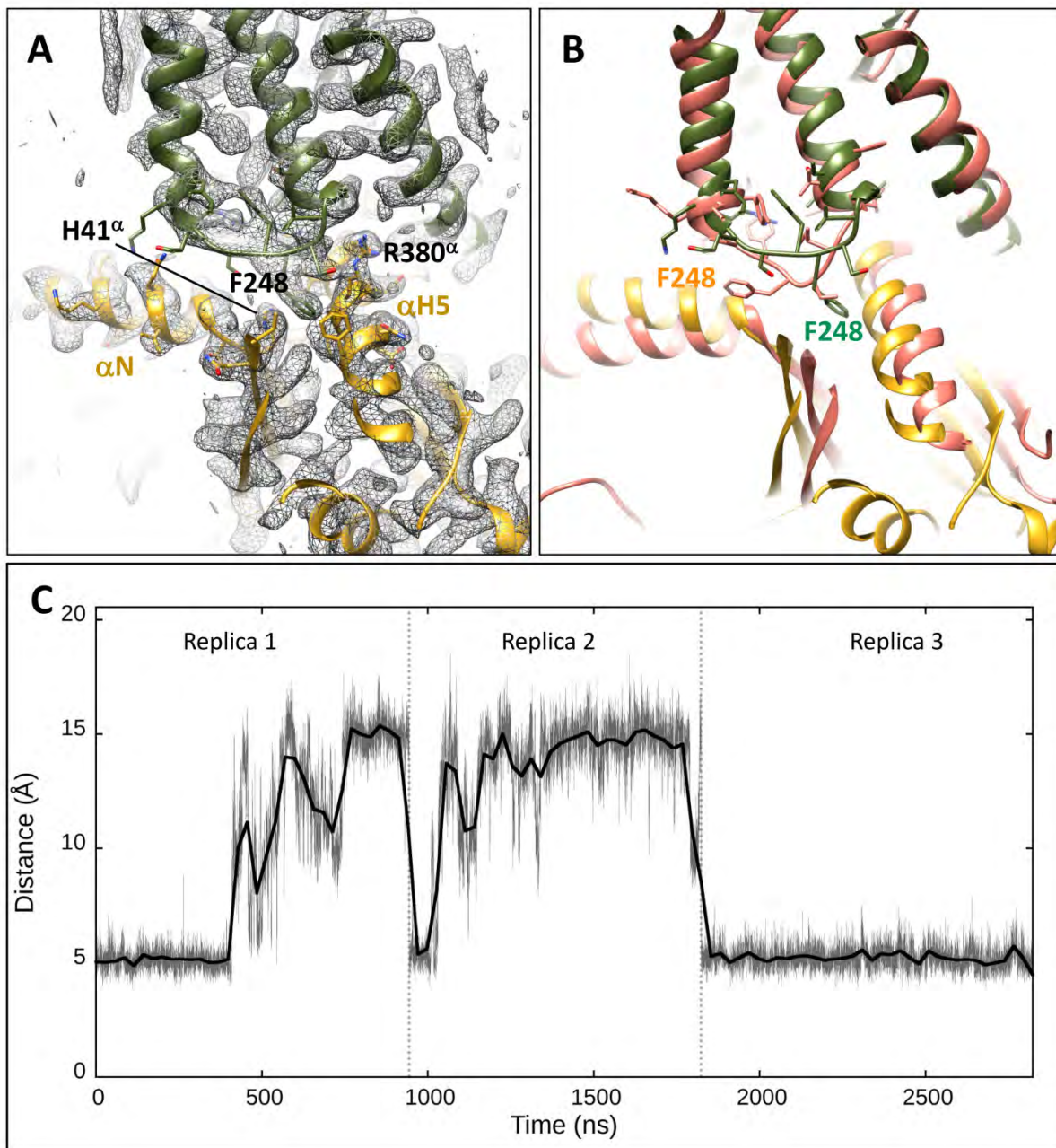
Supplementary Figure 11. Cysteine trapping of secretin receptor ECL3 cysteine replacement mutants with ¹²⁵I-labelled Cys⁷- or Cys¹⁰- containing secretin antagonist analogues. Shown are typical autoradiographs of 10% SDS-PAGE gels used to separate the products of cysteine trapping of the indicated ECL3 SecR cysteine replacement mutants transiently expressed in COS-1 cells for each of the noted cysteine-containing secretin antagonist probes, under non-reducing (top panel) and reducing (bottom panel) conditions. Autoradiographs are representative of a minimum of three independent experiments. Densitometric analysis of data from three similar experiments with the Cys⁷-antagonist probe is shown (middle panel), with intensities representing the percentages of the signal for the maximal labeling of a residue within ECL3 by that probe. Quantification of labeling is not shown for experiments with the Cys¹⁰-antagonist probe because no significant labeling was observed with any of the receptor cysteine replacement mutants.



Supplementary Figure 12. Morphological evidence of normal surface expression of the cysteine replacement receptor mutants incorporated in each of the positions of the juxtamembranous region of the amino-terminal domain of the secretin receptor. The upper panel shows representative microscopic images of immunostaining of COS-1 cells transiently transfected with wild-type secretin receptor (WT) or noted receptor cysteine replacement constructs, as well as the empty pcDNA3.0 eukaryotic expression vector. Images are representative of three independent experiments. The lower panel shows quantification of receptor cell surface expression as fluorescence percentage of wild type secretin receptor by analyzing 6-8 cells for each of the mutant receptors. The asterisks denote values that are significantly different from that of wild type ($p < 0.05$), determined using ANOVA with Dunnett's post-test to analyze the raw data.



Supplementary Figure 13. Cysteine trapping of the cysteine replacement receptor mutants incorporated in each of the positions of the juxtamembranous region of the amino-terminal domain of the secretin receptor with ^{125}I -labelled cysteine-containing secretin agonist and antagonist analogues. Shown are typical autoradiographs of 10% SDS-PAGE gels used to separate the products of cysteine trapping of indicated SecR cysteine replacement mutants transiently expressed in COS-1 cells with each of the noted cysteine-containing secretin agonist (left panel) and antagonist (right panel) probes. Autoradiographs are representative of a minimum of three independent experiments.

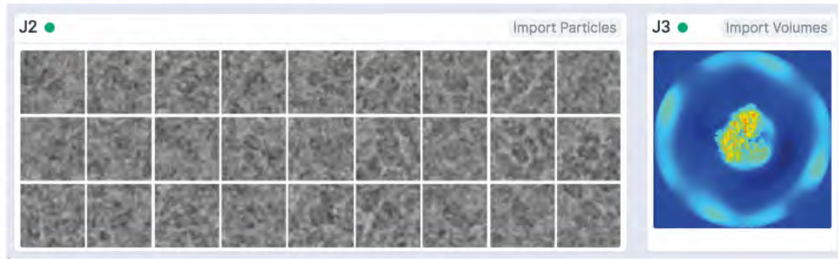


Supplementary Figure 14. Conformational variance in the conformation of ICL2 and the G α s interface observed in long timescale MD simulations. **A.** EM density and model of the SecR ICL2 – G α s interface, illustrating the location of F248^{ICL2} at the junction between the α N and α 5 helices. SecR (green), G α s (gold), G β ₁ (cyan) are shown in ribbon format with select residues displayed in x-stick. **B.** Comparison of the ICL2 conformation, and position of F248^{ICL2} relative to G α s between the starting conformation from the consensus EM map and at the end of the replica 1 MD simulation (pink colored model) (**Video 4**). **C.** Distance between F248^{ICL2} (SecR) and F387^{G α} benzene rings during MD simulations. Distances close to 5 Å correspond to F248^{ICL2} inserted in the junction between the Gs α N helix and α 5 helix.

Cryosparc 3D Variability pipeline

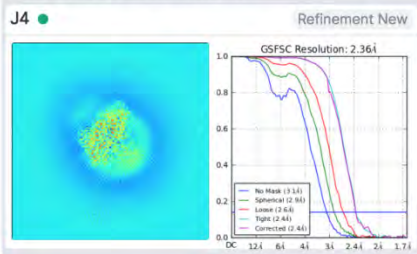
Imported particles from
Relion consensus refinement

Imported volume from
Relion consensus refinement



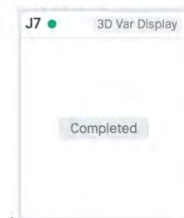
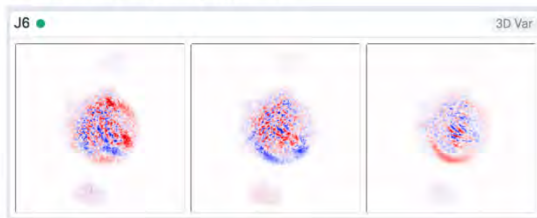
Homogenous refinement

Refinement map and mask

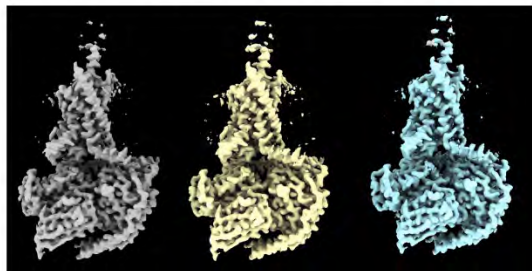


3D Variability
2.8 Å filter, 3 Components

3D Variability Display
2.8 Å filter



ChimeraX display
Component 1, Component 2, Component 3



Supplementary Figure 15. Cryosparc 3D variability analysis pipeline. Particle stacks and 3D volume from the Relion consensus refinement imported into Cryosparc to generate a homogenous refinement, prior to 3D variability analysis using Cryosparc v2. Outputs were visualized using ChimeraX.

Structure and Dynamics of Adrenomedullin Receptors AM₁ and AM₂ Reveal Key Mechanisms in the Control of Receptor Phenotype by Receptor Activity-Modifying Proteins

Yi-Lynn Liang,[○] Matthew J. Belousoff,[○] Madeleine M. Fletcher,[○] Xin Zhang, Maryam Khoshouei, Giuseppe Deganutti, Cassandra Koole, Sebastian G. B. Furness, Laurence J. Miller, Debbie L. Hay, Arthur Christopoulos, Christopher A. Reynolds, Radostin Danev, Denise Wootten,^{*} and Patrick M. Sexton^{*}

Cite This: <https://dx.doi.org/10.1021/acsptsci.9b00080>

Read Online

ACCESS |



Metrics & More



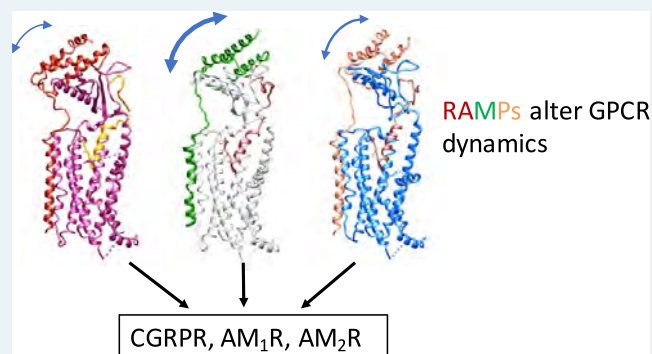
Article Recommendations



Supporting Information

ABSTRACT: Adrenomedullin (AM) and calcitonin gene-related peptide (CGRP) receptors are critically important for metabolism, vascular tone, and inflammatory response. AM receptors are also required for normal lymphatic and blood vascular development and angiogenesis. They play a pivotal role in embryo implantation and fertility and can provide protection against hypoxic and oxidative stress. CGRP and AM receptors are heterodimers of the calcitonin receptor-like receptor (CLR) and receptor activity-modifying protein 1 (RAMP1) (CGRPR), as well as RAMP2 or RAMP3 (AM₁R and AM₂R, respectively). However, the mechanistic basis for RAMP modulation of CLR phenotype is unclear. In this study, we report the cryo-EM structure of the AM₁R in complex with AM and Gs at a global resolution of 3.0 Å, and structures of the AM₂R in complex with either AM or intermedin/adrenomedullin 2 (AM2) and Gs at 2.4 and 2.3 Å, respectively. The structures reveal distinctions in the primary orientation of the extracellular domains (ECDs) relative to the receptor core and distinct positioning of extracellular loop 3 (ECL3) that are receptor-dependent. Analysis of dynamic data present in the cryo-EM micrographs revealed additional distinctions in the extent of mobility of the ECDs. Chimeric exchange of the linker region of the RAMPs connecting the TM helix and the ECD supports a role for this segment in controlling receptor phenotype. Moreover, a subset of the motions of the ECD appeared coordinated with motions of the G protein relative to the receptor core, suggesting that receptor ECD dynamics could influence G protein interactions. This work provides fundamental advances in our understanding of GPCR function and how this can be allosterically modulated by accessory proteins.

KEYWORDS: cryo-electron microscopy, adrenomedullin, calcitonin gene-related peptide, G protein-coupled receptor, receptor activity-modifying protein, allosteric modulation, receptor structure–function



G protein-coupled receptors (GPCRs) comprise the largest superfamily of cell surface receptors, and they are ubiquitously important for normal physiology, as well as key mediators of disease and disease resolution.^{1,2} The complexity of GPCR function is further increased through interaction with accessory proteins that can modulate receptor phenotype. Prototypical of these accessory proteins is the receptor activity-modifying protein (RAMP) family of 3 single transmembrane spanning proteins, RAMP1–3, respectively.³ There is increasing evidence that RAMPs can interact broadly with GPCRs,^{3,4} but they are best studied for their interaction with the calcitonin (CT) family Class B GPCRs, the CT receptor (CTR), and CT receptor-like receptor (CLR), where they are responsible for formation of amylin receptors with CTR and the CT gene-related peptide (CGRP) and

adrenomedullin (AM) receptors with CLR.^{3,5} The CGRP receptor (CGRPR) is a heterodimer of CLR and RAMP1, while AM₁ and AM₂ receptors are heterodimers of CLR and RAMP2 or RAMP3, respectively.^{3,5}

CGRP is a commonly expressed neuropeptide that performs a key role in sensory neurotransmission. It has wide-ranging physiological functions that include roles in metabolism, blood

Special Issue: Advances in GPCR Signal Transduction

Received: October 8, 2019

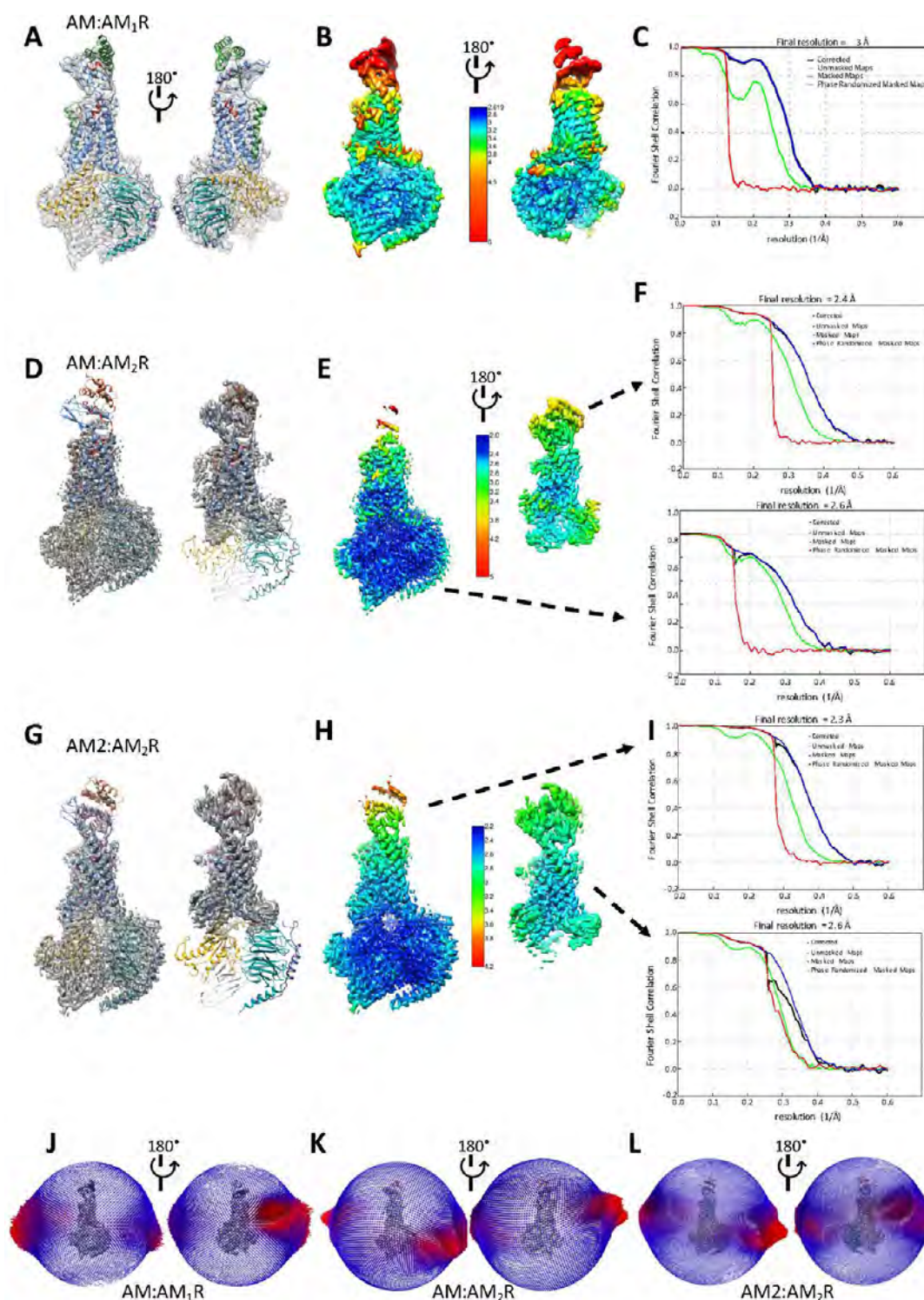


Figure 1. Refined EM maps of the AM receptor complexes. (A–C) AM:CLR:RAMP2:GsDN:Nb35 complex. (D–F) AM:CLR:RAMP3:GsDN:Nb35 complex. (G–I) AM2:CLR:RAMP3:GsDN:Nb35 complex. (A, D, G) Full maps and receptor only maps (D, G) containing the backbone model of the complexes in ribbon format; CLR (blue), RAMP2 (green), RAMP3 (coral), AM (red), AM2 (dark pink), G protein α -subunit (gold), β -subunit (cyan), γ -subunit (dark purple), and Nb35 (white). (B, E, H) Local-resolution-filtered EM maps displaying local resolution (Å) colored from highest (dark blue) to lowest resolution (red). (C, F, I) Gold standard Fourier shell correlation (FSC) curves for the final maps and map validation from half maps, showing overall nominal resolutions of 3.0, 2.4, and 2.3 Å for the AM:AM₁R (C), AM:AM₂R (F), and AM2:AM₂R (I), respectively, and 2.6 Å for the receptor only maps (F, I). (J–L) 3D histogram representations of the Euler angle distribution of all the particles used in the reconstruction overlaid on the density map drawn on the same coordinate axis for complexes of the AM:AM₁R (J), AM:AM₂R (K), and AM2:AM₂R (L), respectively.

pressure regulation, inflammatory response, and auditory nerve development and function.^{6–8} It is a potent vasodilator

released during neurogenic inflammation. CGRP contributes to the pathology of migraine, with multiple antibody

therapeutics approved that either reduce levels of the peptide or inhibit its target receptor.⁹ In contrast, CGRP is protective in experimental models of inflammatory bowel disease and hypertension, and it is a critical neuropeptide for development and modulation of auditory responses. Moreover, CGRP is reported to protect against HIV infection.^{10,11}

AM, a potent vasodilator peptide hormone, is essential for normal physiology and development, with transgenic knock-out of the peptide causing embryologic lethality.¹² It is required for normal lymphatic and blood vascular development and angiogenesis.¹³ It plays a pivotal role in embryo implantation and fertility^{14,15} and provides protection against hypoxic and oxidative stress.¹⁶ Experimental manipulation of AM levels or AM receptor activity is indicative of protective roles in hypertension, myocardial infarction, and inflammatory disease, while AM peptides can also promote cancer growth and metastasis. A related peptide, intermedin/adrenomedullin 2 (AM2), also has a number of important regulatory functions and binds to the AM receptors.^{5,17} Modulation of AM peptide signaling has significant therapeutic potential,^{17–19} and an understanding of the structural basis for AM and AM2 binding to AM₁ and AM₂ receptors is required for rational exploitation of these targets.

We recently reported the structure of the CGRPR, and this revealed an unexpected interface for RAMP1 interaction with CLR and that the only direct interaction of RAMP1 with CGRP is limited to the peptide C-terminal residue,²⁰ first reported in isolated extracellular domains (ECDs) of CLR:RAMP1.²¹ As such, the effect of RAMP1 on CLR pharmacology is predominantly allosteric. Mechanistic understanding of the allosteric control of CLR phenotype by different RAMPs requires structures of CLR with RAMP2 and RAMP3.

In this study, we report the cryo-EM structure of the AM₁R in complex with AM and Gs and structures of the AM₂R in complex with either AM or intermedin/adrenomedullin 2 (AM2) and Gs. The structures reveal distinctions in the primary orientation of the ECDs relative to the receptor core and distinctions in the position of extracellular loop 3 (ECL3) that are receptor-dependent. Analysis of dynamic data present in the micrographs revealed additional distinctions in the extent of mobility of the ECDs, and chimeric exchange of the linker region of the RAMPs connecting the transmembrane (TM) helix and the ECD supports a role for this segment in controlling receptor phenotype. Moreover, a subset of the motions of the ECD appeared coordinated with motions of the G protein relative to the receptor core, suggesting that receptor ECD dynamics could influence G protein interactions (and thus efficacy), which has been previously postulated but as-yet not demonstrated.^{22,23}

■ RESULTS AND DISCUSSION

Structure Determination. The CLR expression construct previously used for determination of the CGRPR structure²⁰ was used to form complexes with RAMP2 (AM₁R) or RAMP3 (AM₂R). This construct had the native signal peptide substituted with that of hemagglutinin (HA) and affinity tags bracketed by 3C cleavage sites at the N- and C-terminus (FLAG and His, respectively). RAMP2 and RAMP3 were modified to include a HA signal sequence, followed by a FLAG epitope without a 3C cleavage site (Figure S1). These modifications did not alter receptor pharmacology (Figure S2A,B).

Active complexes of AM₁R or AM₂R with heterotrimeric Gs were formed following coexpression of CLR and RAMP2, or of CLR and RAMP3, with a stabilized form of G α s, His-G β 1, and G γ 2 in *Trt* insect cells.^{20,24,25} Complex formation was initiated by addition of excess AM(13–52) (AM₁R and AM₂R) or AM2 (47 amino acid peptide) (AM₂R) and stabilized by removal of nucleotide with apyrase and addition of nanobody 35 (Nb35) that binds across the G α s–G β 1 interface.^{26,27} The CLR affinity tags were cleaved with 3C enzyme, and the complex was solubilized in lauryl maltose neopentyl glycol (LMNG)/cholesteryl and then purified by nickel and anti-FLAG chromatography, followed by size-exclusion chromatography (SEC) to yield monodisperse peaks that contained each of the components of the complex with each of the peptide ligands (Figure S2C–H), with good 2D classes in negative stain transmission electron microscopy (TEM). Vitrified samples for each receptor complex were imaged by conventional cryo-TEM on a Titan Krios to yield consensus maps at gold standard FSC 0.143 of 3.0, 2.4, and 2.3 Å for the AM₁R, AM₂R, and AM2₂R complexes, respectively (Figures 1A–I and S3A–C), despite varying levels of preferred orientation within the vitrified samples (Figure 1J–L). Focused refinement of the AM₂Rs using a mask around the receptor generated maps of 2.6 Å global resolution, with improved local resolution of the receptor ECD that allowed this domain to be directly modeled (Figures 1D–I and S3B,C).

High-resolution features were observed for each of the maps with local resolution ranging from 2.6 Å to >6 Å (AM₁R), 2.0 Å to >4 Å (AM₂R), and 2.2 Å to >4 Å (AM2₂R) (Figures 1B,E,H and S4–S6), with highest resolution in the G protein, the G protein–CLR interface, and TM core for each of the receptors. Lower resolution was observed for the RAMP:CLR ECDs and associated peptide C-termini, with low resolution for the RAMP TM-ECD linker region and parts of ICL3 and ECL3 for each of the receptors (Figures S4–S6). No density was observed for most of the C-terminus of CLR, with limited density for C-terminal residues of the RAMPs (summarized in Figure S7). No clear density was observed for the N-terminal AM residue (S13) or for the N-terminal AM2 residues (T1–V8). The C-terminus of AM in the AM₁R ECD was poorly resolved. For this receptor, the backbone structure of the peptide in the ECD X-ray crystal structure (4RWF)²¹ was used to assist in assigning the peptide density. In the case of the AM₂Rs, the maps from focused refinement allowed *ab initio* modeling of most of the ECD and peptide C-terminus. The C-terminal peptide backbones of AM and AM2 in the AM₂Rs were similar to those observed in related ECD X-ray crystal structures (4RWF²¹ and 6D1U).²⁸ There was very limited density for the G α s α -helical domain, and this was masked out in final refinements. Density for the C-terminal ends of G β 1 and G γ 2 were variable across the receptors (Figures S4–S6). For the rest of the receptor and G protein the map density allowed robust assignment of side-chain rotamers using either the full map, or receptor focused maps (Figures S4–S6).

Global Structural Features of AM Receptors. While the ECDs of the complexes exhibited lower resolution in the consensus maps, the resolution did allow fitting of backbone models of the ECD of CLR and each of the RAMPs into the density to identify the primary metastable positions of these domains (Figure 2A,B). The AM and AM2 co-complexes of

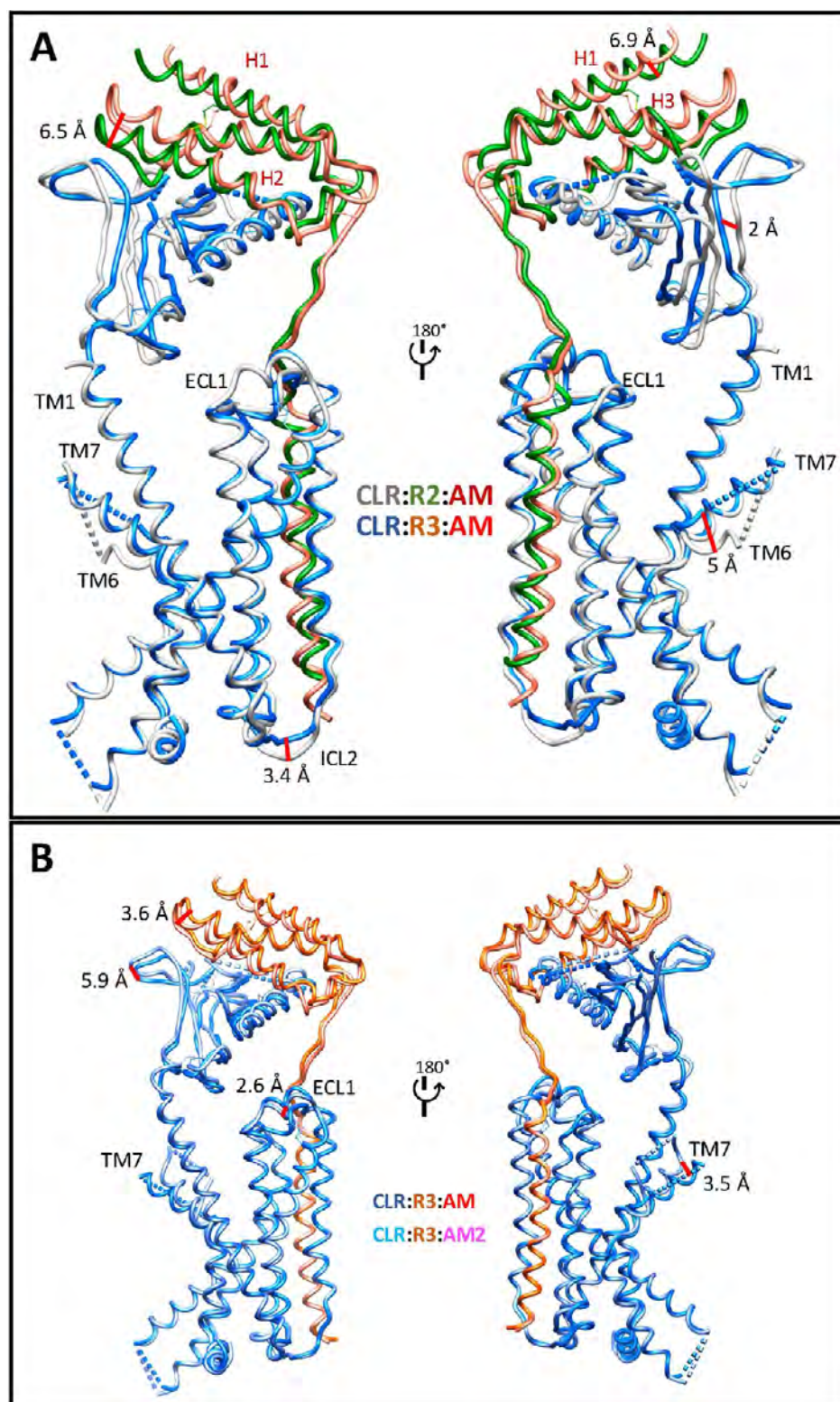


Figure 2. Overlay of the backbone structures in protein worm format of (A) the AM:AM₁R (CLR:R2:AM) and AM:AM₂R (CLR:R3:AM) complexes and (B) the AM:AM₂R and AM₂:AM₂R (CLR:R3:AM₂) complexes. The peptide and G proteins have been omitted for clarity. (A) RAMP2 and RAMP3 ECDs have different orientations relative to the CLR ECD, whereas (B) the difference in positioning of the ECD between the two AM₂Rs is due to a rigid body lateral movement. Distances in the TM domain in (A) are between the C α of TM6 L351^{6,55} (~5 Å) and ICL2 F246^{ICL2} (~3 Å) and in (B) are ECL1 V205^{ECL1} (2.6 Å) and TM7 V364^{7,37} (2.6 Å). The CLR in the RAMP3 (R3) complexes is colored blue, and it is gray in the RAMP2 complex. RAMP2 is green, and RAMP3 is coral.

the AM₂R exhibited very similar backbone conformation for the transmembrane core of both CLR and RAMP3, with an ~3.5–6 Å lateral rigid body displacement of the CLR:RAMP3

ECD that propagated from a minor difference in the position of the extended TM1 helix (Figure 2B). Within the receptor core, there was a 2.6 Å shift in the position of ECL1

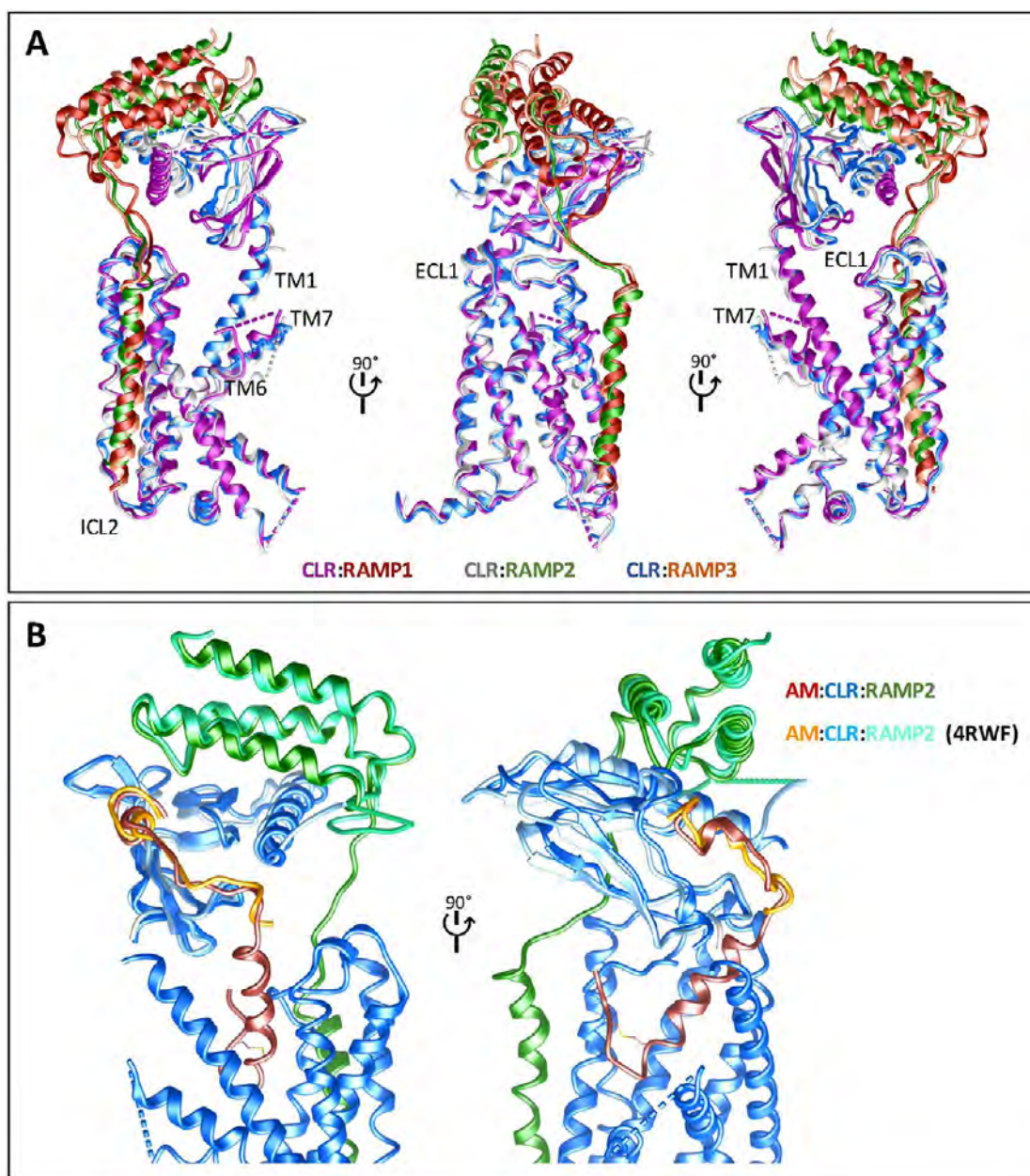


Figure 3. (A) Overlay of the backbone structures in ribbon format of the CGRP bound CGRPR (CLR:R1:CGRP), AM-bound AM₁R (CLR:R2:AM), and AM-bound AM₂R (CLR:R3:AM) complexes. CLR is colored as follows: in the CGRPR, dark pink, in the AM₁R, gray, and in the AM₂R, blue. RAMP1 is colored dark red, and RAMP2 is shown as green. RAMP3 is shown as coral. (B) Backbone (ribbon format) overlay of the AM:CLR:RAMP2 structure with the X-ray crystal structure of the ECDs of AM:CLR:RAMP2 (4RWF). Colors are as follows: cryo-EM structure: AM (red), CLR (blue), RAMP2 (green); 4RWF: AM (orange), CLR (light blue), RAMP2 (aquamarine).

(measured from the $C\alpha$ of V205^{ECL1}), and distinctions in the location of the tops of TM6 and TM7, and by implication to the conformation of ECL3, although this was not resolved in the maps (Figure 2B). In contrast, there were greater differences in the receptor conformations of AM bound to the AM₁ and AM₂ receptors, respectively (Figure 2A). The most striking of these was in the orientation of the CLR ECD relative to either RAMP2 or RAMP3. In addition, there was a marked difference in the conformation of TM6 that was more kinked in the AM₁R (outwardly displaced by ~ 5 Å, measured from the $C\alpha$ of L351^{6.51}; superscript corresponds to receptor amino acids are the conserved class B GPCR numbers; Figure 2A).²⁹ Prior mutagenesis studies have shown that there are

differential impacts of several residues in this region on AM activity between the two receptors.³⁰

At the intracellular face of the receptor, the largest difference observed was for ICL2 with a 3.4 Å displacement measured at the $C\alpha$ of F246^{ECL2} (Figure 2A). The conformation of the transmembrane bundle of CLR in the CGRPR²⁰ most closely resembles that seen in the AM₁R, including the conformation of ICL2 and the angle of TM6 and TM7 at the extracellular face (Figure 3); however, the CLR:RAMP1 ECDs are more dramatically rotated compared to both AM receptors (Figure 3). This may contribute to the distinct peptide binding specificity of the CGRP receptor, although it is evident that the dynamic motion of the RAMPs and CLR play a key role in the allosteric modulation of

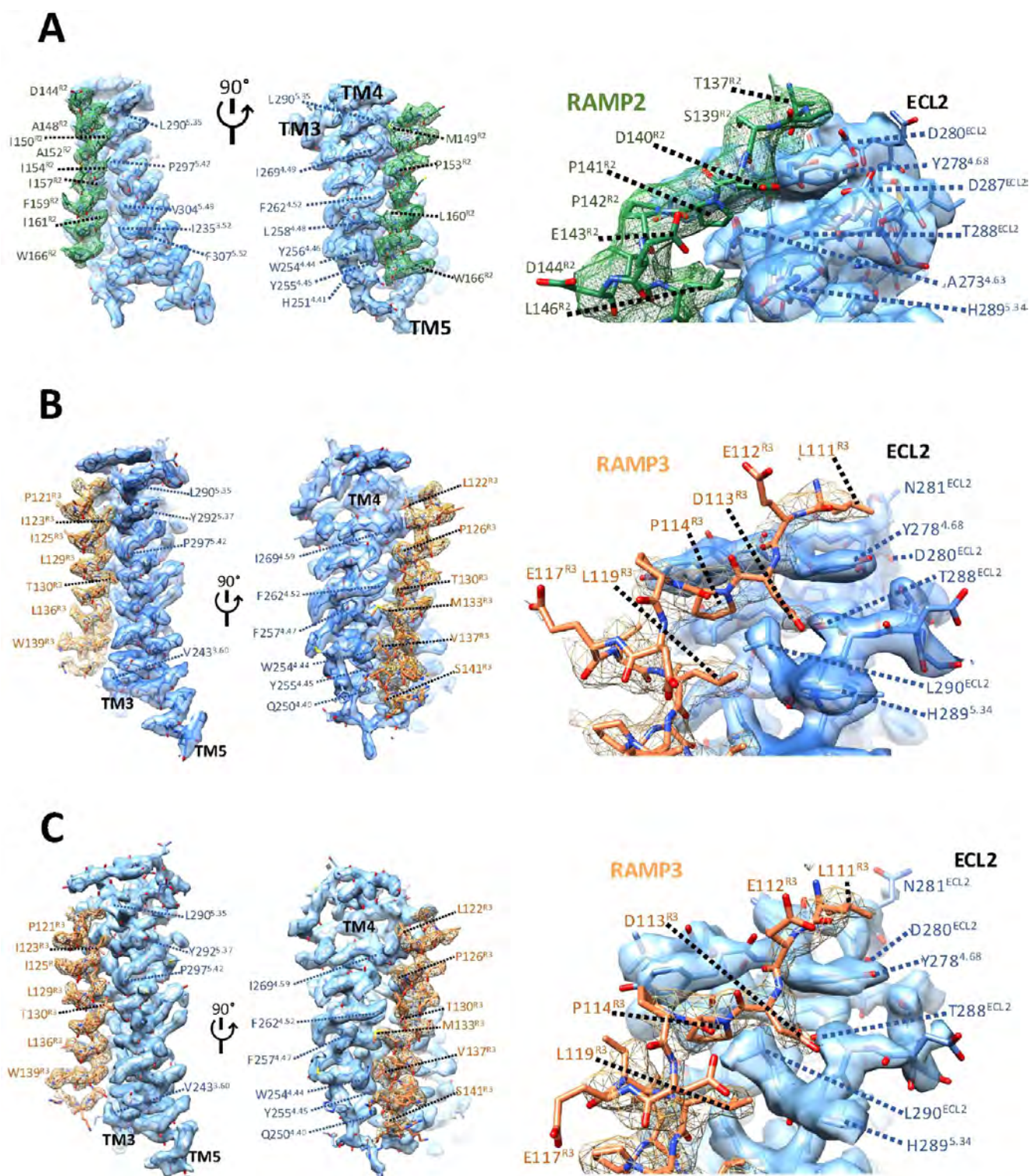


Figure 4. CLR-RAMP interface for the AM₁R (A), AM₂R (B), and AM₂R (C). Map to model figures illustrating tightness of TM packing (left panels), and extent of engagement of the proximal RAMP linker with ECL2 (right panel). Map density for the RAMP is shown as mesh. Map density for CLR is shown as a transparent surface. RAMP2 (green), RAMP3 (coral), and CLR (blue).

receptor phenotype by RAMPs (see below). We also compared the ECD of the AM-bound AM₁R to that of the equivalent structure of the isolated ECD domain solved by X-ray crystallography²¹ (Figure 3B). While there was high similarity in the overall backbone conformation, when aligned to the CLR ECD, the RAMP2 ECD occupied a distinct position in the two structures. This is similar to the

observation made for the CGRPR²⁰ and may reflect distinctions associated with the additional interactions that occur in the full-length, active receptor. Nonetheless, as noted below, the ECD is a highly dynamic domain in the cryo-EM structures.

RAMP–CLR Interface in AM Receptors. The surface charge of RAMP2 was predicted to be more acidic than that

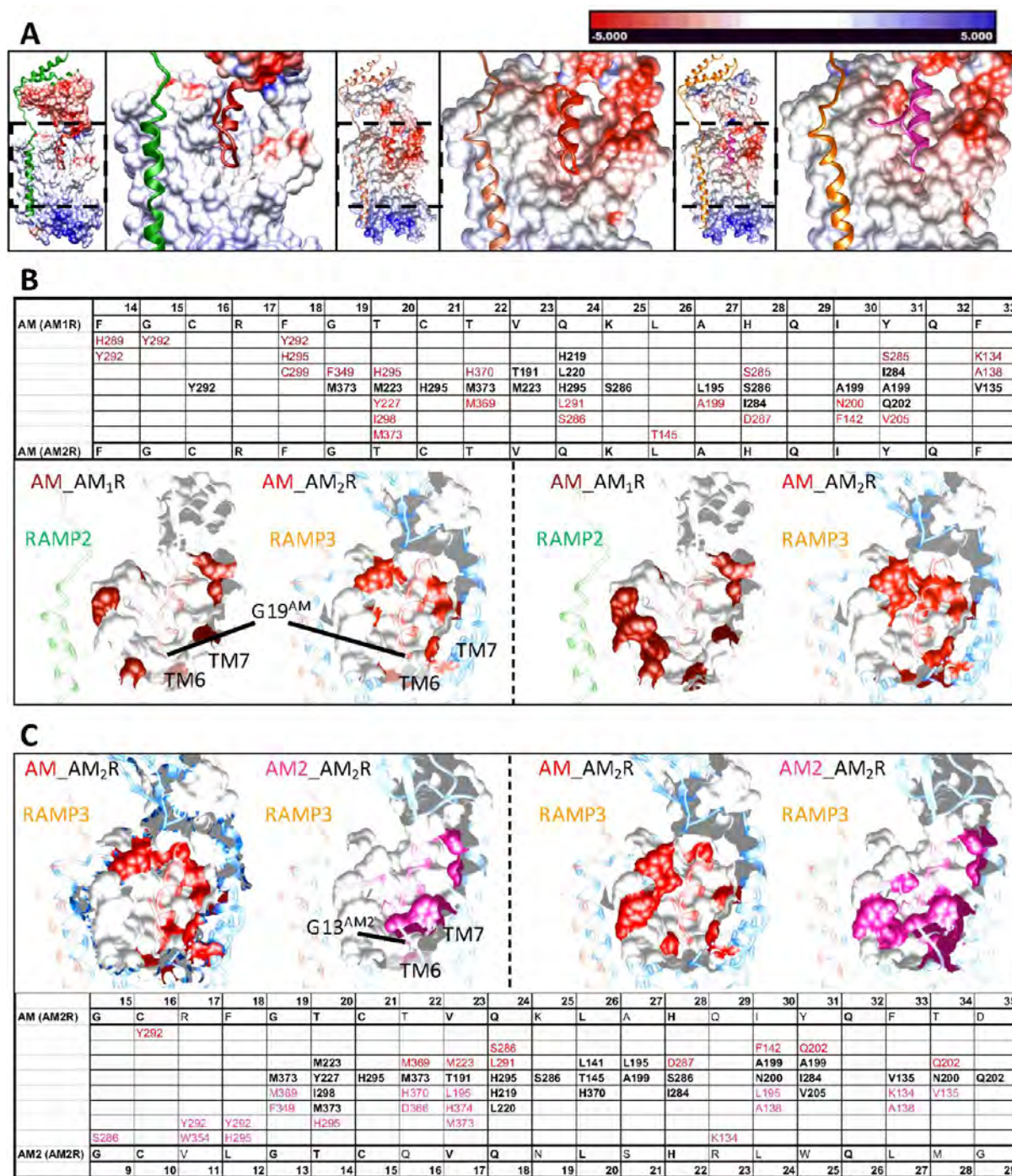


Figure 5. AM and AM2 peptide binding to AM receptors. (A) Electrostatic surface potential for CLR for each of the receptor complexes (AM₁R ECD is from PDB: 4WRF), with the peptides and RAMPs shown as ribbon representation. Colors are as follows: in the AM₁R: AM (red) and RAMP2 (green); in the AM₂R: AM (dark red) and RAMP3 (light pink). The electrostatic potential ranges from -5 (red) to $+5$ (blue) kT e^{-1} . (B) CLR residues selectively engaged (left panels) or differentially engaged (right panels) by equivalent amino acids of AM with the AM₁R and AM₂R, with common residues shown as gray surface representation and distinct interactions mapped in red (AM_AM₂R) or dark red (AM_AM₁R); specific interacting residues are detailed below. (C) CLR residues selectively engaged (left panels) or differentially engaged by (right panels) positionally equivalent amino acids of AM or AM2 with the AM₂R, with common residues shown as gray surface representation and distinct interactions mapped in red (AM_AM₂R) or dark pink (AM2_AM₂R); specific interacting residues are detailed below. The location of the deepest peptide residue in the binding pocket is highlighted (G19^{AM}, G13^{AM2}). For clarity in (B) and (C), CLR is colored differently; other colors are as follows: light gray, AM_AM₁R; blue, AM_AM₂R; light blue, AM2_AM₂R.

of RAMP3 (Figure S8A versus 8B,C), and the RAMPs formed extensive interactions with CLR between both the ECDs and TM domains. The former has previously been described for

X-ray crystallography structures of the isolated ECDs of CLR and RAMPs.^{21,28,31} Moreover, as observed in the full-length CGRPR,²⁰ interactions between RAMP and the peptide

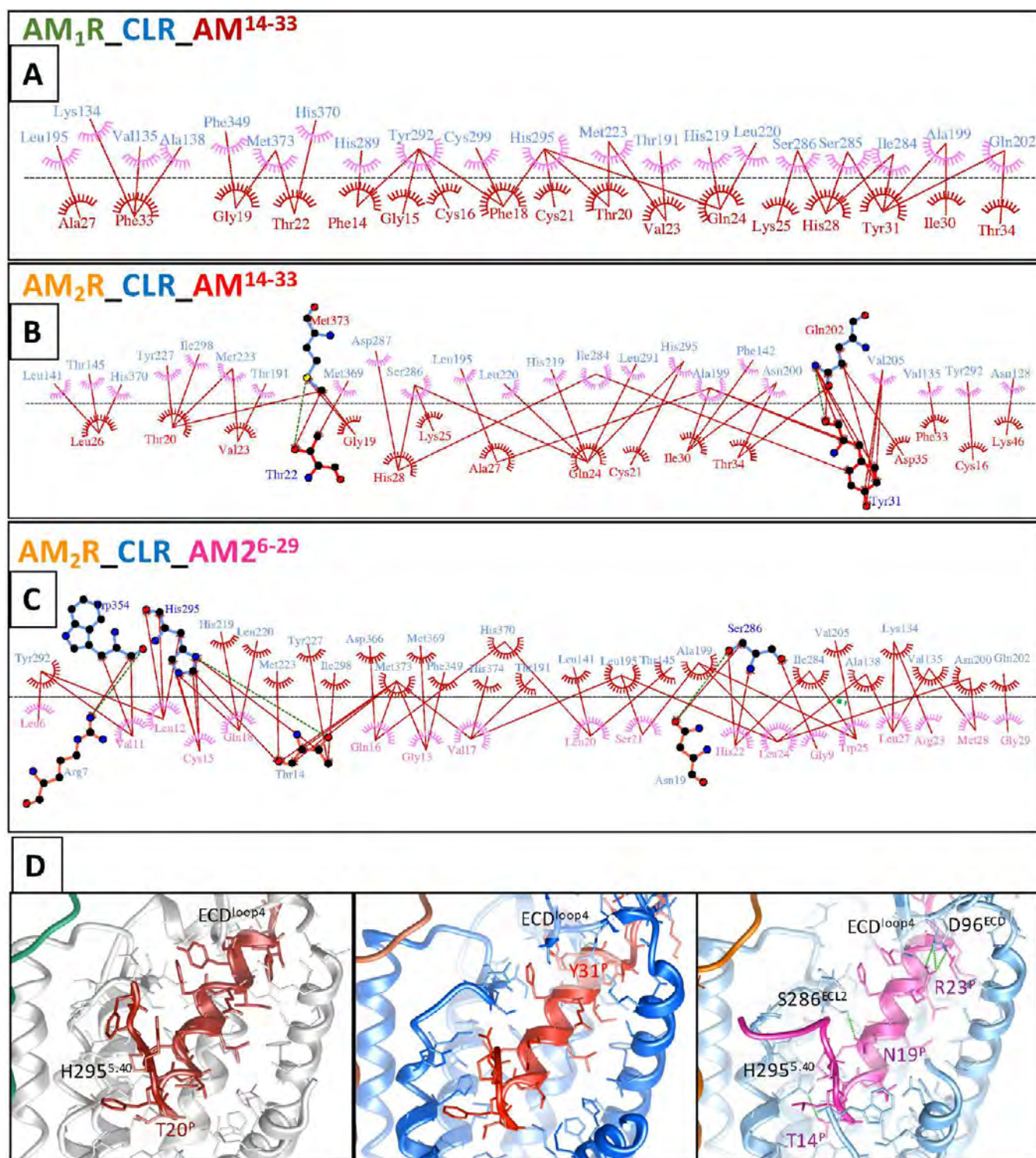


Figure 6. N-terminal peptide interactions with the TM core of CLR for the AM-bound AM₁R (A), AM-bound AM₂R (B), and AM2-bound AM₂R (C) calculated with using LigPlot+. Peptide residues are colored dark red (AM at AM₁R), red (AM at AM₂R), and dark pink (AM2 at AM₂R), and receptor residues are colored blue. Hydrophobic interactions are illustrated by red (AM) or pink (AM2) arcs with CLR in the reverse color, and interacting residues are joined by a red line. Amino acids involved in H-bonds are shown in atomic detail and H-bonds are shown as dashed green lines. (D) Structure models of N-terminal peptide binding to the AM₁R (left panel; AM, dark red; RAMP2, green; CLR, gray) or the AM₂R (middle panel: AM, red; RAMP3, coral; CLR, blue; right panel: AM2, dark pink; RAMP3, coral; CLR, light blue). The protein backbone is shown in a ribbon format, and side chains are shown in the x-stick format.

agonists were restricted to the far C-terminus of the peptides (Figure S8A–C).

Unsurprisingly, RAMP2 and RAMP3 interact with the equivalent transmembrane segments of CLR as observed for

RAMP1,²⁰ forming an interface with TM3–5 (Figures 4A–C and S8A–F) and looping over ECL2 of CLR before forming a relatively disordered linker that connects the TMD to the RAMP ECD. Overall, RAMP3 exhibited tighter packing with

the CLR TMD compared with RAMP2 (Figure 4B,C versus 4A). While both RAMP2 and RAMP3 formed interactions with ECL2, the organization of the membrane proximal RAMP linker was distinct between the two RAMPs. In both AM and AM2 occupied structures, RAMP3 formed a H-bond between D113^{R3} and both T288^{ECL2} and H289^{ECL2} (Figures 4B,C and S8E,F). The interaction with T288^{ECL2} is also observed for RAMP1 and CLR in the CGRPR,²⁰ however, this was absent from RAMP2 despite conservation of the Asp residue, with no interaction of the positionally equivalent D140^{R2} with ECL2 of CLR (Figures 4A and S8D). However, a potential H-bond occurring between S139^{R2} and T288^{ECL2} may also limit productive engagement with ECL2 (Figures 4A and S8D).

Peptide Binding to AM Receptors. Density for AM peptide and receptor in the ECD in AM₁R, and the overall density of both RAMP2 and RAMP3 ECD in all structures was limited. As such, we concentrated our analysis on the engagement of the peptide N-terminus with the receptor core that drives receptor activation. AM and AM2 have extended N-termini, relative to CGRP, but these residues are not required for functional activity of the peptides.^{29,32,33}

Similar to the CGRPR,²⁰ there were no direct interactions between the peptide N-termini and the RAMPs (Figures 5 and 6). All peptides adopted a similar conformation consisting of an N-terminal loop formed by a conserved disulfide bridge (C16^{AM}–C21^{AM}; C10^{AM2}–C15^{AM2}) followed by a short amphipathic α -helix that terminated where the peptides exited the TM core of the receptors (C21^{AM}–F33^{AM}; C15^{AM2}–Q26^{AM2}) (Figures 5B,C and 6D). The structure of the loop was further reinforced by likely H-bonds between backbone of C10^{AM2}/C16^{AM} and the side chain of N19^{AM2} or K25^{AM}. Substitution of K25^{AM} with Ala results in modest effects on signaling.³³ The far N-terminus of the peptides exited away from the surface of the receptor, providing a structural explanation for the lack of functional importance of the extended N-termini of AM and AM2.

The deepest residue in the receptor core was the conserved Gly, G13^{AM2}/G19^{AM} (Figure 5B,C). Substitution of G19^{AM} with Ala has profound effects on activity in a pathway-specific manner,³³ while substitution of G13^{AM2} with Ala has marked effects on peptide potency.³² In all cases, the peptides bind into an open cavity that is enabled by the splayed outward movement of TM6/TM7/ECL3, and there are limited interactions between the peptides and this segment of the receptors (Figure 5A). Despite all interactions between the peptide and receptors in the receptor core occurring with the common CLR subunit, the binding pocket for the AM₂R presented a more acidic environment than that of the AM₁R, albeit that this was partially influenced by the bound peptide (Figure 5A).

Unsurprisingly, the overall pattern of peptide interaction for the two AM receptors was similar, with interactions principally with TM3, TM5, and ECL2, with additional interactions toward the top of TM2 and TM1 (Figures 5B,C and 6). These included key conserved interactions observed across other class B GPCRs,²³ such as with positions 1.33, 1.36, 2.64, 2.68, 3.36, 3.37, 3.44, and 5.40. For the latter, H29S^{5,40} in CLR, this formed a H-bond with T14^{AM2} in the AM₂ receptor, while it likely forms transient H-bonds with T20^{AM} at AM₁R and AM₂R. CLR mutagenesis studies support this role of H29S^{5,40}, and substitution of T20^{AM} with Ala substantially reduces peptide activity.³³ Similarly, a loss of peptide potency

has been observed in prior investigation³² of T14^{AM2}. As previously noted,²³ mutation of 5.40 in class B GPCRs leads to attenuation of signaling, indicative of a key role in driving G protein coupling.^{26,33–37} Interestingly, for AM binding to the AM₁R there are more selective interaction or distinct types of interactions with the distal segment of ECL2 compared with AM₂R interactions, where there were more selective interactions with the middle region of ECL2 and adjacent residues that line the binding site as the peptide exits the TM core (Figure 5B). Comparison of the interactions between AM and AM2 with the AM₂R revealed that AM2 made more extensive interactions than AM, with positionally equivalent amino acids, perhaps not surprisingly, forming distinct interaction patterns with residues in TM1, TM7, and ECL2 (Figures 5C, right panels, and 6B,C), although there were more selective residue interactions observed for AM (Figure 5C, left panels). N19^{AM2} forms a H-bond with S286^{ECL2} and this may increase stability of AM2 binding in the AM₂R, despite generally greater specific interactions between AM and ECL2 in this receptor (Figures 5C and 6B,C). Interestingly, the interactions of AM, AM2, and CGRP²⁰ with ECL2 occur principally at the mid-distal (TM5) end of the helix, similar to what is also observed for the related CTR but distinct from other class B GPCRs that bind peptides with extended helices. In those receptors, the interactions are greater with more proximal ECL2 residues, and this distinction may, in part, explain the large differences in the effect of Ala mutations of ECL2 on peptide efficacy seen between GLP-1R and CTR,^{38–40} which can be further modified by RAMP interaction.⁴¹

The lateral displacement of TM1 and the ECD in the AM2:AM₂R leads to the fourth loop of the CLR ECD being located closer to the AM2 peptide as it exits the receptor, compared with AM at either the AM₁R or AM₂R (Figure 6D). In the AM2:AM₂R complex, there is extensive H-bonding between R23^{AM2} and D96^{ECD} and the potential for additional transient H-bonds with S98^{ECD} (Figure 6D), and this may influence the relative positioning of the ECDs relative to the receptor core.

In general, there were more differential interactions between AM binding to the AM₂R rather than at the AM₁R and for AM2 compared with AM binding to the AM₂R (Figure 5B,C). The latter differences are likely due to the divergence in more C-terminal residues of the peptide helices between AM and AM2, leading to distinct interactions of AM2 with TM1 and the ECD as the peptide exits the receptor core (Figures 5B,C and 6). This may, in part, contribute to the greater potency of AM2 at the AM₂R relative to AM₁R.⁵ Collectively, the observed interactions in the structures are generally consistent with the known structure–function relationships for AM peptides binding to AM receptors,^{30,32,33,37,42} with exceptions likely related to dynamics of binding to the receptor, including entry to and egress from the receptor core.

Unlike other active-class B GPCR structures, including the CGRPR,^{20,23} there is very limited interaction between the peptides and TM7 of the AM receptors. In other class B GPCRs, it has been postulated that peptide-specific interactions with TM7/ECL3/TM6 may be involved in biased agonism that has been described at these receptors.⁴³ The functional significance of the current observations is unclear; however, little biased agonism is seen at the AM receptors,³³ consistent with interactions with TM7/ECL3/

TM6 being drivers for biased agonism, at least for class B GPCRs.

Receptor–G Protein Interface. The conformation of the receptor at the interface with the G protein was very similar for all three structures, with the exception of ICL2 that adopted a distinct conformation in a RAMP-dependent manner (Figure 7A–C). Not surprisingly, the overall interface

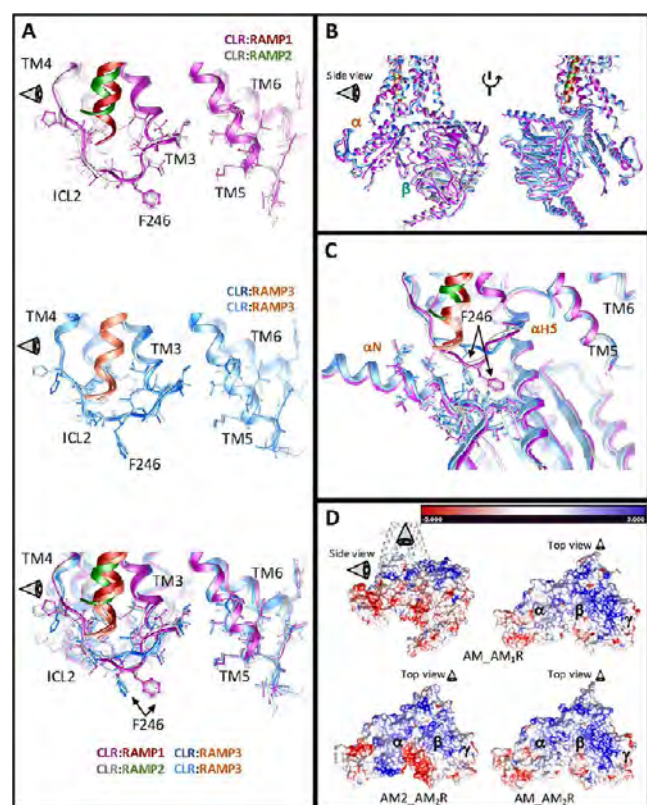


Figure 7. Comparison of the receptor:G protein interface across CLR:RAMP receptor heterodimers. (A) Overlay of the intracellular face of the CGRP and AM₁ receptors, highlighting the common positioning of most side chains. The largest exception was in the position of F246 in ICL2 that occupied a common position between the CGRPR and AM₁R (upper panel), as well as between the different peptide-bound AM₂R (middle panel), but was distinct between AM₂R and the other receptors (lower panel). (B) The G protein occupies a common global interaction position that is highly similar in conformation across receptors. (C) Close up of panel B, boxed area, focusing on the interaction with ICL2. (D) The bound Gs heterotrimer has a similar surface electrostatic potential when binding to AM receptors. The protein backbone is shown in a ribbon format, and side chains are shown in the x-stick format. RAMP1 is colored dark red, RAMP2, green, RAMP3, coral. CLR in the CGRPR is colored dark pink, in the AM-bound AM₁R, gray, in the AM-bound AM₂R, blue, in the AM₂-bound AM₂R, light blue. G proteins are colored equivalent to CLR for each receptor.

of the G protein with the receptor was nearly identical (Figure 7D), with the G proteins virtually overlaid across both the AM receptors and the previously published CGRPR²⁰ (Figure 7B). Within ICL2, the largest difference was in the location of F246^{ICL2} that was deeper in the groove between the GαN and αH5 helices for the AM₁R, compared to the AM₂R, regardless of bound peptide. Interestingly, the position of F246^{ICL2} in the CGRPR was equivalent to that of the AM₁R (Figure 7A,C). The specific interactions of the C-terminal end

of the Gs αH5 that extends into the receptor cavity were highly conserved across the three structures, particularly for the last 5 amino acids (Figures 7C and 8C). However, there were differences in engagement of the Gs αN arising from the distinct ICL2 conformation (Figures 7 and 8). In the complexes, the G protein–receptor interaction is stabilized by mutations to the α-subunit^{20,24,25} and Nb35, a prerequisite to stable complex formation and structure determination. Nonetheless, this may contribute to the similarity in observed interactions in the current structures. The CLR-based receptors also interact with an additional, intracellular accessory protein, CGRP Receptor Component Protein (RCP), and this interaction is important for efficiency of Gs signaling by CGRP and AM receptors.⁴⁴ The site of RCP interaction with CLR is reported to be ICL2.⁴⁵ As such, RAMP-dependent differences in the conformation of CLR ICL2 could influence RCP engagement and Gs signaling.

RAMPs Allosterically Alter CLR Conformational Dynamics to Engender CGRP and AM Receptor Phenotype.

One of the most fundamental questions for RAMP-complexed GPCRs is what is the mechanistic basis for RAMP modulation of receptor phenotype? This has been particularly puzzling as the RAMPs form only very limited direct interaction with the far C-terminus of the peptides, and substitution of the C-terminal peptide residues does not lead to substantially altered receptor specificity.²¹ Likewise, structural and biochemical studies of the isolated ECDs of CGRP and AM₁ and AM₂ receptors have not provided clues as to the major determinant(s) for the altered receptor phenotypes, despite identification of important ECD residues for peptide interactions.^{21,28,31,42,46} The current AM receptor structures, together with our previously published structure of the CGRPR, has enabled consideration of the differences that occur across the three RAMP modulated receptors in their peptide-bound activated states. Somewhat surprisingly, with the exception of TM7/ECL3/TM6 that do not directly contact the peptides, the packing of the transmembrane core and the interactions made by the peptide N-terminal domain with the core were remarkably similar in the consensus structures. This suggests that conformational dynamics of the RAMP–CLR complexes, rather than the consensus metastable interactions, may be the principal drivers of distinct receptor phenotypes. The largest difference in the structures was in the location of the ECDs, relative to the receptor core (Figures 2 and 3), with the location of the ECDs in the CGRPR more distinct from the AM receptors than the differential location of the ECDs between AM₁R and AM₂R. Previous molecular dynamics (MD) simulations of the CGRPR in the presence and absence of RAMP1 indicated that the presence of the RAMP limits the dynamic motion of the CLR ECD,²⁰ consistent with the notion that the RAMP influence on receptor dynamics could underpin differences in observed functional phenotype.

Unlike X-ray crystallography, a potential advantage of cryo-EM is the ability to observe dynamics of the protein complexes as distinct conformations captured during sample vitrification.^{47,48} The lower resolution of the ECDs in the consensus maps suggested that such dynamic information was present in the current cryo-EM data, and the large number of particles and high relative resolution of the data provided a potential opportunity to understand relative motions of the different AM receptor complexes. 3D multivariate analysis in cryoSPARC was applied to the AM receptor data, as outlined

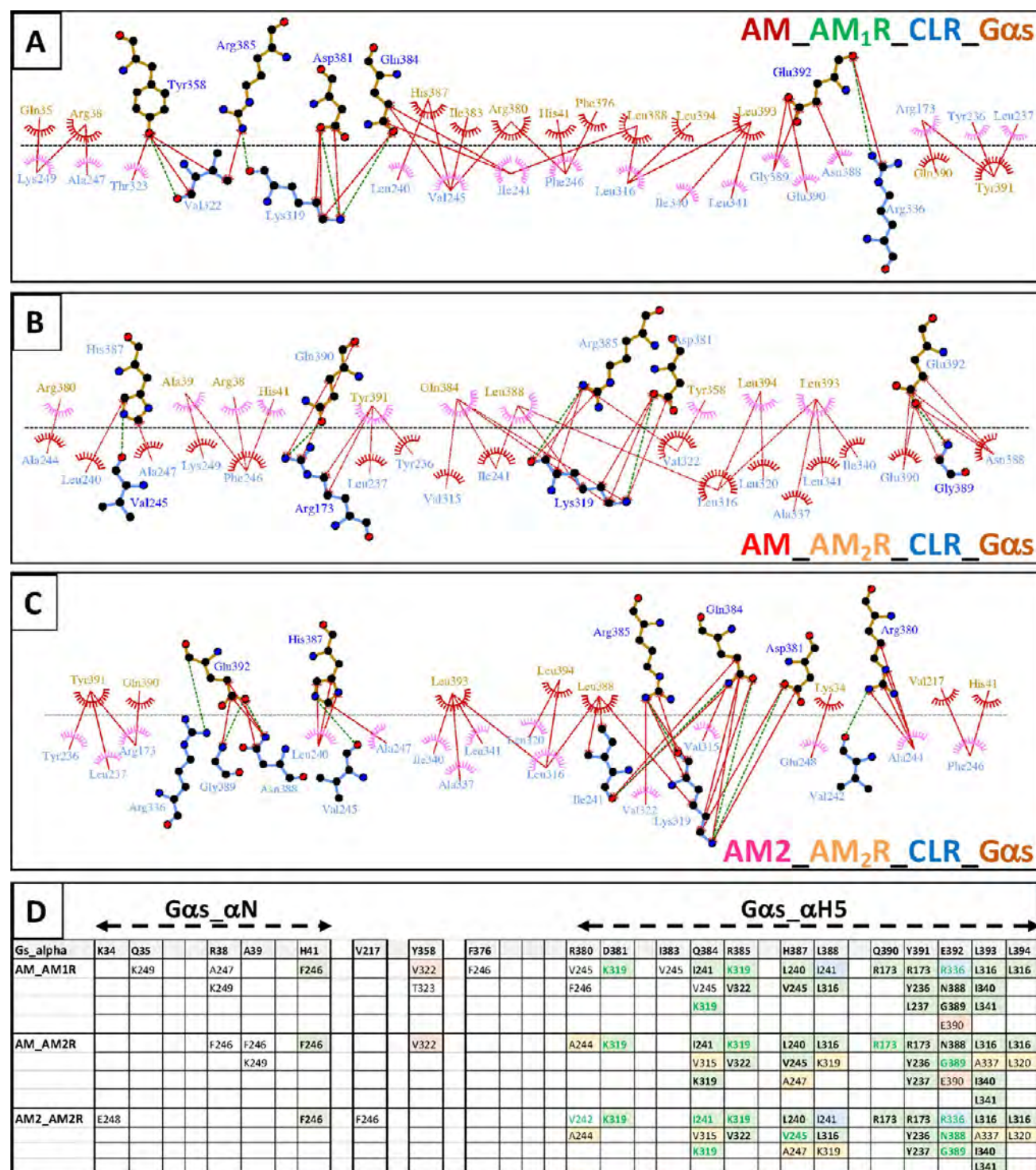


Figure 8. CLR–Gαs interface for AM_AM₁R (A), AM_AM₂R (B), and AM₂_AM₂R (C). Interactions were determined using LigPlot+. Gαs residues are gold, and receptor residues are blue. Hydrophobic interactions are illustrated by red or pink arcs adjacent to residue labels, and interacting residues are joined by a red line. Amino acids involved in H-bonds are shown in atomic detail with H-bonds shown as dashed green lines. (D) Summary of the specific interactions. Interactions common to all 3 receptor complexes are shown in bold and are shaded light green. Residues involved in H-bond interactions are shown in green type. Interactions common to AM bound to AM₁R and AM₂R only are shaded light orange. Interactions common to complexes of the AM₂R only are shaded yellow. Interactions common to AM bound to AM₁R and AM₂R only are shaded blue.

in Figure S9. This analysis has the potential to separate global motions that can be grouped via principal components. As such, this can provide insight into the coordinated motion of the complexes. For all receptors data was partitioned into 3 normal modes (Movies S1–S3, S6–S8, and S11–S13), and

this analysis indicated that a component of the motions of the ECDs and G protein occur in a coordinated manner, suggesting that the breadth of ECD motion may be partially linked to conformational dynamics of the receptor–G protein interface (and vice versa). While the quality of the data for the

AM₁R complex with AM created additional noise relative to the AM₂R complexes, the analysis revealed that the AM₁R had greater overall motion (Movies S1–S3) than the corresponding AM₂Rs (Movies S6–S8 and S11–S13), and this was particularly reflected in the dynamics of the ECD, and is consistent with the lower resolution of this domain for AM₁R in the consensus map (Figure 1B). As noted above for the consensus map, the RAMP3 TM has tighter packing interactions with the receptor TM and stronger interactions between the proximal linker domain and the receptor ECL2. This limits the motion of the RAMP3 and maintains interactions with ECL2 across the observed sub conformations (Figure 9B,C; Movies S9 and S14). In contrast, the

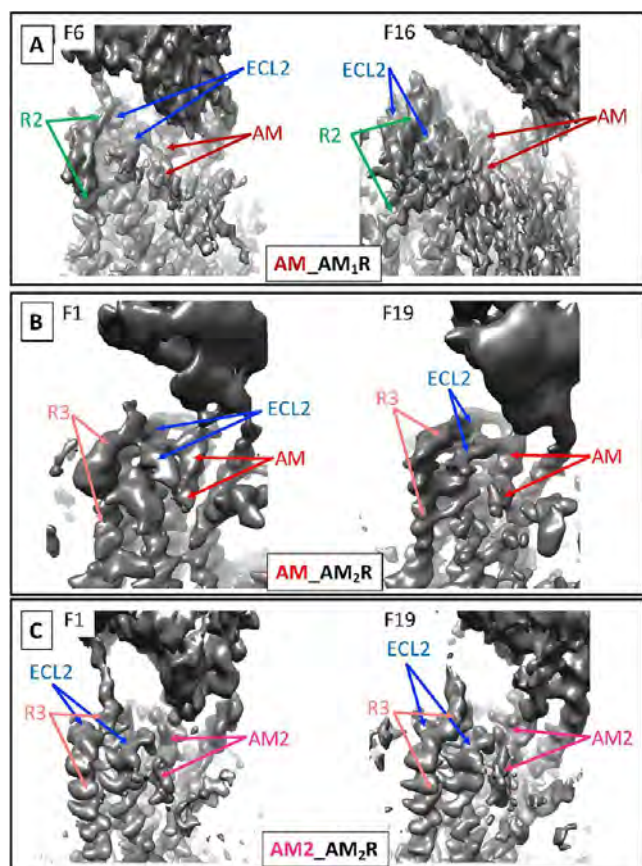


Figure 9. cryoSPARC multivariate analysis of the AM-bound AM₁R (A), AM-bound AM₂R (B), and AM₂-bound AM₂R (C) focusing on the interface of the RAMP and ECL2. Three normal modes were captured as 20 map files for each receptor complex and snapshots of the first and last frame (F1 and F19, respectively) are displayed for the AM₂R complexes (B, C). For AM₁R, due to the greater noise in the data, the early and late frames primarily reflected loss of signal; as such, F6 and F16, which represent the ends of the motion, are displayed (A). Map density is displayed as a gray surface.

weaker interactions of RAMP2 appear to lead to almost complete disengagement of the proximal linker with ECL2 and the much broader motions of the ECD noted above (Figure 9A; Movie S4), with the AM peptide also appearing to make more transient interactions with the receptor core than either of the peptides with the AM₂R, although the resolution of the AM₁R complex does not allow for this to be analyzed at a molecular level.

A second interesting observation from the dynamic conformational analysis was revelation that the RAMP3 C-terminus made transient interactions with the G protein α N helix for both AM₂ and AM-bound complexes (Figure 10B,C;

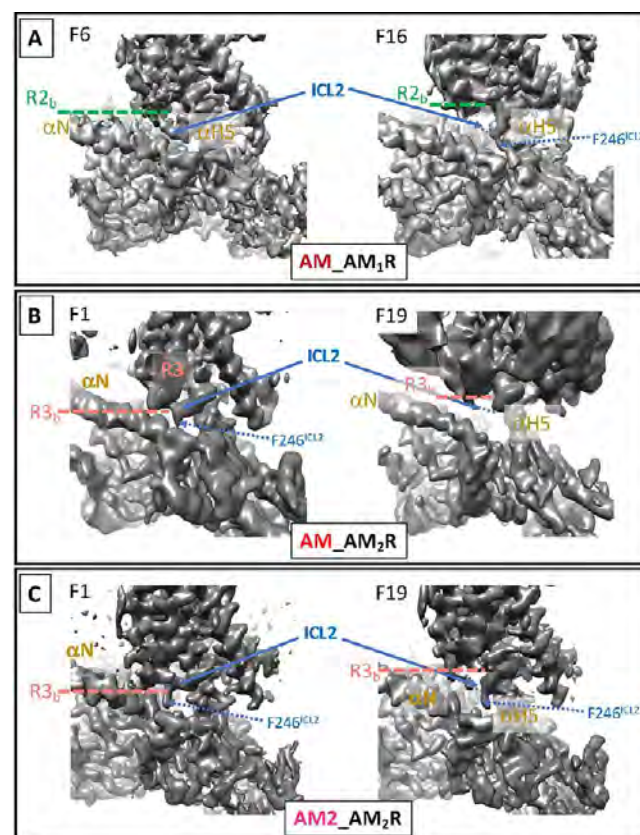


Figure 10. cryoSPARC multivariate analysis of the AM-bound AM₁R (A), AM-bound AM₂R (B), and AM₂-bound AM₂R (C) focusing on the interface of Gas and the receptors, particularly the RAMP C-terminus and ICL2. Three normal modes were captured as 20 map files for each receptor complex and snapshots of the first and last frame (F1 and F19, respectively) are displayed for the AM₂R complexes (B, C). For the AM₁R, due to the greater noise in the data, the early and late frames primarily reflected loss of signal; as such, F6 and F16, which represent the ends of the motion, are displayed (A). Map density is displayed as a gray surface. Color key: CLR, blue; RAMP2, green; RAMP3, coral; Gas, gold. The end of the resolved density for each of the RAMPs is illustrated with a dashed line labeled with R2b (RAMP2) or R3b (RAMP3).

Movies S10 and S15), although this was more evident in the AM₂:AM₂R data. However, this was not observed for the RAMP2 complex (Figure 10A; Movie S5) and may contribute to the differences in the metastable ICL2 conformation noted in the consensus structures, although the functional importance of this is currently unclear. This may be linked to the conformational sampling of ICL2 as the extension to the base of RAMP3 appeared to be correlated with strength of the density for F246^{ICL2} in the consensus map position for the AM₂R structures (Figure 10B,C; Movies S10 and S15).

As the multivariate analysis could not be applied to the CGRPR (RAMP1) data, we performed MD simulations on the CGRPR complex in comparison to equivalent simulations on the AM₁R complex (Movie S16). Consistent with the observations in analysis of the cryo-EM data, in the simulations RAMP2 formed transient interactions with

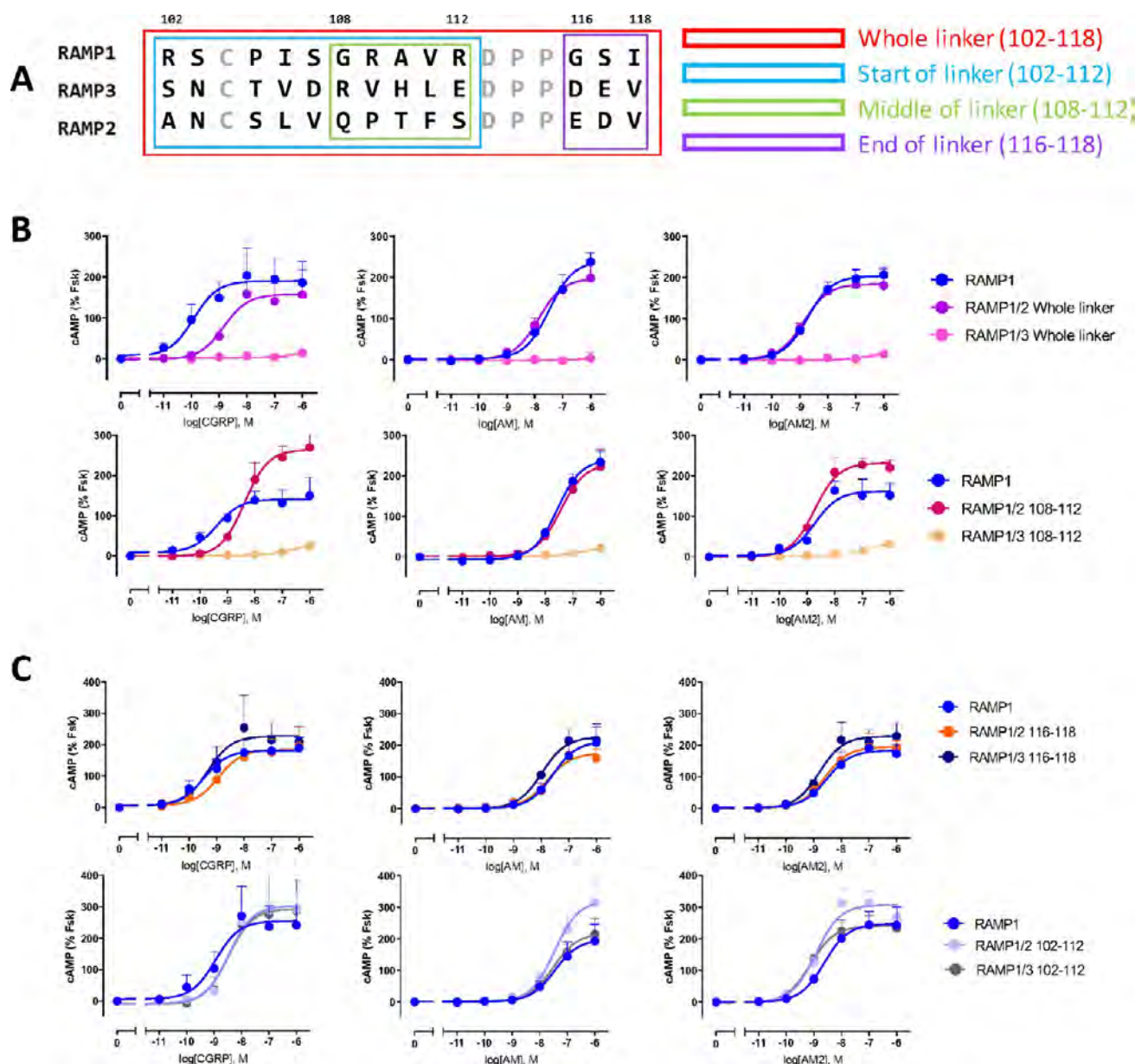


Figure 11. Pharmacological analysis of RAMP1 linker chimeras with RAMP2 or RAMP3. (A) Amino acid sequence of the linker regions (numbered using the RAMP1 sequence for simplicity), with the different length chimeras denoted by colored boxes: red, whole linker (102–118); blue, N-terminal linker region (102–112); green, mid-linker region (108–112); purple, C-terminal linker region (116–118). Conserved residues are in gray, and divergent residues are in black. (B, C) Peptide concentration–response was measured in cAMP accumulation assay, following transient expression of constructs into COS-7 cells, for full linker exchange (B, upper panel) or exchange of the 108–112 segment (B, lower panel), the 116–118 segment (C, upper panel), or the 102–112 segment (C, lower panel).

ECL2, and this was paralleled by relatively transient interactions of the more distal segment of the linker with the CLR ECD, giving rise to broad motions of the ECD relative to the receptor core. In contrast, the proximal RAMP1 linker formed much more stable interaction with ECL2, and this was also true of the distal linker with the CLR ECD, giving rise to both the distinct orientation seen in the cryo-EM structure and much more limited mobility of the ECD domain. We also extended the analysis of the AM₁R using principal component analysis (Movies S17 and S18–S22), and this revealed similar patterns of coordinated motions between the receptor and G protein to those observed in the different normal modes of the 3D multivariate analysis of the cryo-EM data, providing additional support for the notion of

coordinated motion between the receptor ECD and G protein (Movies S17 and S20–S22).

Membrane-Proximal RAMP Linker Region Is Critical in AM Receptor Dynamics and Functional Phenotype.

The multivariate analysis described above revealed greater dynamic motion of the AM₁R relative to the AM₂Rs, including movement of the membrane proximal RAMP2 linker away from ECL2 and destabilization of the AM binding pose that is likely associated with the weaker interactions observed in the static structure. As such, we postulated that this domain may be a key contributor to the allosteric regulation of CLR phenotype by RAMPs and consequently generated a series of chimeras between the three RAMPs, exchanging different segments of the linkers (summarized in Figure 11A; Table 1).

Table 1. Summary of pEC_{50} and E_{max} Values for cAMP Production at CLR + RAMPs or RAMP Chimera Constructs in Cos7 Cells Stimulated with CGRP, AM, or AM2^a

	CGRP		AM		AM2	
	pEC_{50}	E_{max}	pEC_{50}	E_{max}	pEC_{50}	E_{max}
RAMP1 Whole Linker						
RAMP1	9.96 ± 0.42 (3)	190 ± 21	7.48 ± 0.11 (5)	239 ± 12	8.72 ± 0.13 (5)	203 ± 6
RAMP1/2	8.84 ± 0.37 (3) ^c	157 ± 20	7.86 ± 0.20 (5)	197 ± 18	8.86 ± 0.24 (5)	184 ± 14
RAMP1/3	N.D.	N.D.	N.D.	N.D.	N.D.	N.D.
RAMP1 102–112						
RAMP1	8.95 ± 0.40 (3)	256 ± 33	7.45 ± 0.30 (4)	199 ± 28	8.62 ± 0.28 (4)	248 ± 23
RAMP1/2	8.47 ± 0.17 (3)	304 ± 18	7.46 ± 0.23 (4)	321 ± 34 ^b	8.92 ± 0.17 (4)	308 ± 17
RAMP1/3	8.49 ± 0.48 (3)	294 ± 51	7.50 ± 0.21 (4)	217 ± 21	9.13 ± 0.14 (4)	241 ± 11
RAMP1 108–112						
RAMP1	9.40 ± 0.35 (5)	141 ± 13	7.57 ± 0.12 (5)	241 ± 13	8.72 ± 0.27 (5)	162 ± 14
RAMP1/2	8.38 ± 0.19 (4) ^c	265 ± 18 ^b	7.45 ± 0.16 (4)	230 ± 17	8.73 ± 0.14 (4)	232 ± 11 ^b
RAMP1/3	N.D.	N.D.	N.D.	N.D.	N.D.	N.D.
RAMP1 116–118						
RAMP1	9.46 ± 0.31 (4)	181 ± 15	7.58 ± 0.31 (4)	213 ± 29	8.52 ± 0.23 (4)	183 ± 14
RAMP1/2	8.94 ± 0.38 (4)	185 ± 22	7.78 ± 0.22 (4)	175 ± 16	8.60 ± 0.22 (4)	195 ± 15
RAMP1/3	9.32 ± 0.45 (4)	228 ± 30	7.97 ± 0.17 (4)	227 ± 16	8.79 ± 0.25 (4)	229 ± 19
RAMP2 Whole Linker						
RAMP2	7.06 ± 0.13 (3)	101 ± 7	9.59 ± 0.36 (5)	78 ± 8	8.50 ± 0.20 (5)	97 ± 7
RAMP2/1	6.93 ± 0.25 (3)	205 ± 31 ^b	9.77 ± 0.49 (5)	162 ± 20 ^b	8.16 ± 0.30 (5)	163 ± 20 ^b
RAMP2/3	7.20 ± 0.07 (3)	142 ± 5	9.12 ± 0.35 (5)	202 ± 23 ^b	9.05 ± 0.23 (5)	162 ± 12 ^b
RAMP2 Shorter Chimera						
RAMP2	N.D.	N.D.	9.51 ± 0.18 (8)	97 ± 5	8.73 ± 0.17 (8)	99 ± 6
RAMP2/3 102–112	N.D.	N.D.	9.81 ± 0.28 (4)	75 ± 6	9.00 ± 0.31 (4)	83 ± 8
RAMP2/3 108–112	N.D.	N.D.	9.77 ± 0.54 (3)	82 ± 12	8.20 ± 0.30 (3)	92 ± 11
RAMP2/3 116–118	N.D.	N.D.	9.70 ± 0.28 (4)	92 ± 7	8.82 ± 0.30 (4)	109 ± 11
RAMP3 Whole Linker						
RAMP3	6.96 ± 0.20 (4)	159 ± 19	9.38 ± 0.37 (5)	107 ± 12	9.34 ± 0.16 (5)	120 ± 6
RAMP3/1	7.08 ± 0.19 (4)	177 ± 18	9.17 ± 0.18 (5)	160 ± 9 ^c	9.33 ± 0.16 (5)	159 ± 8 ^b
RAMP3/2	7.16 ± 0.31 (4)	93 ± 15	10.46 ± 0.74 (5)	98 ± 17	8.96 ± 0.32 (5)	101 ± 11
RAMP3 Shorter Chimera						
RAMP3	N.D.	N.D.	9.61 ± 0.38 (8)	138 ± 13	9.59 ± 0.30 (8)	149 ± 12
RAMP3/2 102–112	N.D.	N.D.	9.10 ± 0.26 (4)	138 ± 10	9.00 ± 0.44 (4)	128 ± 18
RAMP3/2 108–112	N.D.	N.D.	9.36 ± 0.17 (4)	146 ± 7	9.41 ± 0.13 (4)	165 ± 6
RAMP3/2 116–118	N.D.	N.D.	9.60 ± 0.27 (4)	136 ± 10	9.50 ± 0.35 (4)	115 ± 11

^aValues are mean ± SEM from 3 to 8 individual experiments performed in triplicate. Numbers of individual experiments are in brackets. E_{max} values are normalized to the response with 100 μ M forskolin. N.D. is used when no curve could be fit to the data. Separate control (wild-type) RAMPs were used for each batch of chimeric RAMPs. ^bSignificantly different from parental construct at 95% confidence intervals. ^cSignificantly different from parental construct by *F*-test of fitted value at *P* < 0.05.

These were studied in assays of receptor expression and cAMP accumulation (Figures 11, 12, and S10). Most of the chimeras retained the ability to traffic with CLR to the cell surface, with the exceptions being exchange of RAMP1 for the full linker (102–118) or mid-linker region (108–112) of RAMP3 that were poorly expressed and could not be characterized (Figure S10). For simplicity, the numbering for all exchanges is that of the linker in the RAMP1 peptide (Figure 11A).

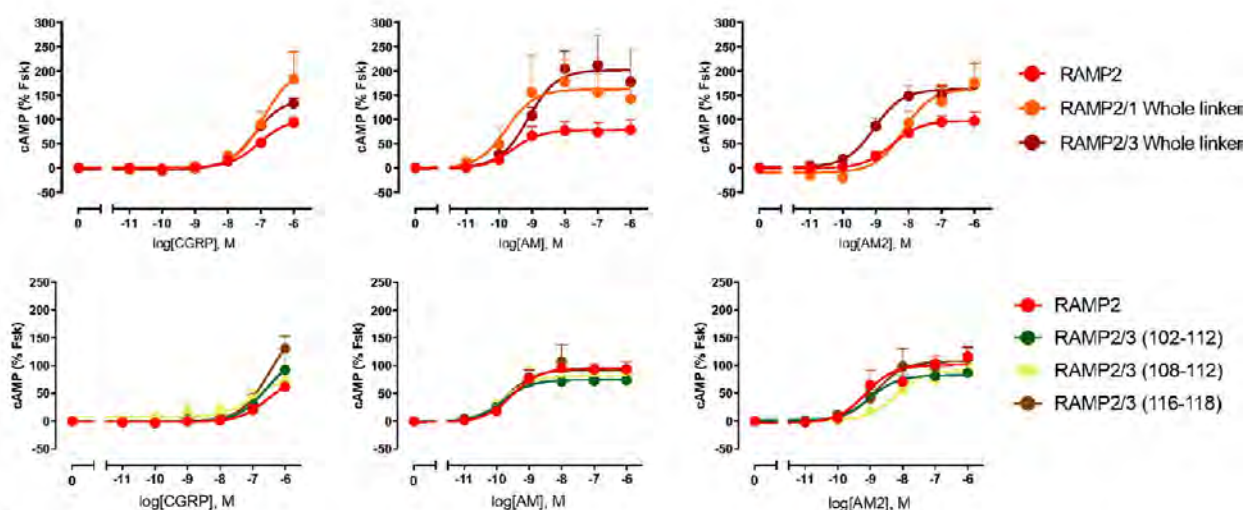
RAMP1 Linker Exchange. Exchange of the RAMP1 linker with the whole RAMP2 linker, or the shorter 108–112 in each case led to loss of CGRP potency, while there was a smaller attenuation of potency for the 116–118 fragment that did not achieve significance (Figures 11B,C, Table 1). Intriguingly, for the 108–112 chimera, this was also accompanied by enhanced E_{max} . This latter observation may be consistent with the correlated dynamics of the ECDs and G protein observed in the analysis of conformational dynamics described above whereby changes to mobility of the RAMP1

ECD with the chimeras may also alter efficiency of G protein turnover, which is linked to ligand efficacy.⁴⁹ There was only relatively limited impact of the exchanges on AM potency but enhanced E_{max} of AM2 was observed for the 108–112 RAMP1/2 chimera (Figure 11B, Table 1).

RAMP2 Linker Exchange. Full RAMP2 linker exchange with either that of either RAMP1 or RAMP3 had substantive effects on AM and AM2 responses. For AM or AM2, the response E_{max} was increased with either exchange (Figure 12A; Table 1), and potency was also increased for AM2 with the RAMP3 exchange, albeit that this did not achieve statistical significance (Figure 12A; Table 1). For CGRP, an increased response was observed with both chimeras but the potency was too low to robustly quantify (Figure 12A). Shorter chimeras with RAMP3 had minimal effect on AM or AM2 responses (Figure 12A; Table 1).

RAMP3 Linker Exchange. Full linker exchange with RAMP1 induced only small increases in both AM and AM2 peptide E_{max} . The exchange with RAMP2 also led to an

A



B

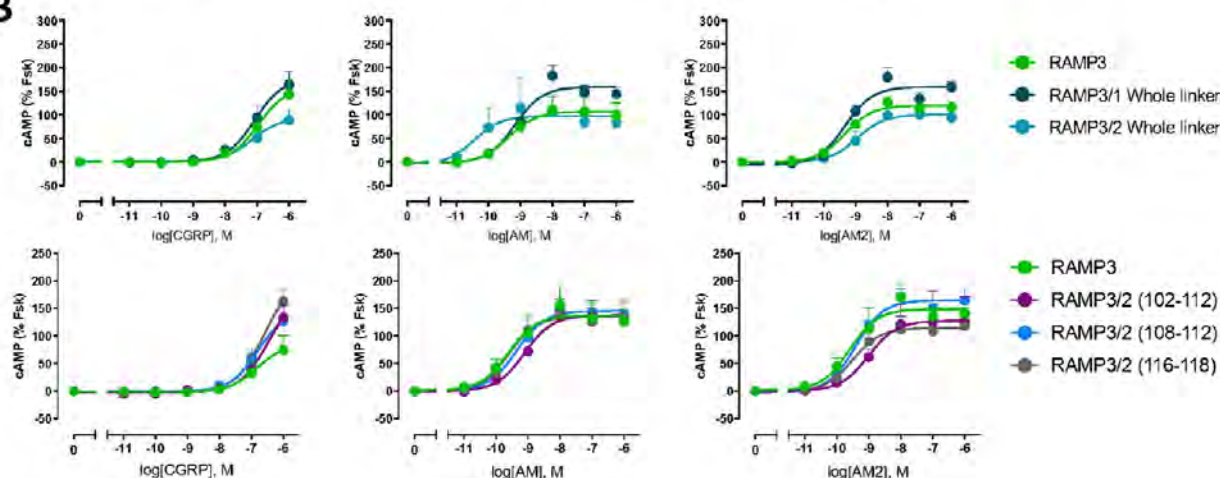


Figure 12. Pharmacological analysis of RAMP2 linker chimeras with RAMP1 or RAMP3 (A) or RAMP3 chimeras with RAMP1 or RAMP2 (B). Peptide concentration–response was measured in cAMP accumulation assay, following transient expression of constructs into COS-7 cells, for full linker exchange (A, B, upper panels) or exchange of the RAMP2 108–112 segment, the 116–118 segment, or the 102–112 segment with that of RAMP3 (A, lower panel), or exchange of the RAMP3 108–112 segment, the 116–118 segment, or the 102–112 segment with that of RAMP2 (B, lower panel).

increase in AM potency, with an apparent small decrease in AM2 potency; however, neither of these was statistically significant. Shorter exchanges of RAMP2 did not modify AM responses and had relatively minor effects on AM2 potency or E_{\max} (Figure 12B; Table 1).

Overall, the pharmacological analysis of the RAMP linker chimeras provides strong evidence of involvement of this domain in the allosteric modulation of CLR phenotype, most likely due to changes to the dynamics of the RAMP–CLR interaction and subsequently the dynamics of the receptor ECDs. This is consistent with the observed distinctions in the dynamics of each of the CGRP and AM₁ and AM₂ receptors. The coordinated motions of the ECD and G protein are also indicative of a role of the ECD dynamics in G protein coupling efficiency and of an allosteric link between G protein coupling, ECD dynamics, and receptor phenotype. While this has not been studied for CLR, overexpression of different G proteins can influence binding of amylin to CTR–RAMP heterodimers.⁵⁰ As such, the current observations could provide a mechanism for how chimeric exchange of the C-

terminus of RAMP1 and RAMP2 alters selective responsiveness to CGRP.⁵¹ Moreover, biased agonism has been observed at the CLR:RAMP family of receptors, with relative potency of the peptides varying in a receptor- and pathway-dependent manner⁵² suggesting that the dynamics found for Gs coupled receptors could also influence the spectrum of signaling response. Our observations are also consistent with known behavior of enzymes that exhibit dynamic allostery, whereby long-range binding information is transmitted to control catalysis.⁵³

CONCLUSION

In this study, we have generated novel structures of AM receptor complexes that have provided details of the consensus modes of peptide interaction at AM₁ and AM₂ receptors. This is supported by an Ala scan of AM in our companion paper.³³ Moreover, we have used the power of cryo-EM to derive information on the dynamics of RAMP–CLR complexes demonstrating that cryo-EM can resolve aspects of the motions of highly dynamic proteins, including

GPCRs. Importantly, it was this dynamic conformational information that provided key insight into the molecular mechanism for RAMP modulation of CLR phenotypes that was subsequently experimentally verified. Thus, this work provides fundamental advances in our understanding of GPCR function and of allosteric regulation of GPCRs by large accessory proteins.

METHODS

Constructs. *Expression Constructs.* CLR was modified as previously described,²⁰ with replacement of the native signal peptide with that of hemagglutinin to improve expression, and inclusion of an N-terminal FLAG tag epitope and a C-terminal 8× histidine tag, each flanked by 3C protease cleavage sites (Figure S1). RAMP2 and RAMP3 were modified to replace the native signal peptide and inclusion of an N-terminal FLAG tag epitope (Figure S1). The constructs were generated in both mammalian and insect cell expression vectors as previously described.^{20,23}

Constructs for Pharmacological Analyses. C-myc-tagged CLR was a gift from Dr. Steve Foord.⁵⁴ Chimeras of the RAMPs were generated by substituting different segments of the linker, between the RAMP transmembrane domain and ECD, into CD33-FLAG-tagged RAMPs in pcDNA 3.1. Short chimeras (less than 5 amino acids) were generated using single oligo mutagenesis by Q5 DNA polymerase. PCR was performed using a sense mutant oligo coding the chimeric amino acids flanked by 15 homologous nucleotides on either side. According to the protocol, 2× Q5 High Fidelity master mix (New England Biolabs) was used with 0.5 μ L of 10 mM dNTPs. Reactions were treated overnight with DpnI to digest the parental WT DNA template. The long chimeras (10–16 amino acids) were generated using a nonoverlap double oligo mutagenesis method to insert the chimeric amino acids. Sense and antisense oligos were created and 5′ phosphorylated at synthesis. The sense oligos had the second half of the chimeric amino acids coded at the 5′ end, followed by the homologous sequence, and the antisense oligos had the first half of the chimeric amino acids coded at the 3′ end preceded by homologous sequence. Both oligos were added into a PCR reaction using Phusion High-Fidelity DNA polymerase and Phusion High Fidelity buffer (New England Biolabs), with the following PCR cycling protocol: 1 cycle: 2 min at 98 °C; 35 cycles: 98 °C 10 s, 55 °C 30 s, 72 °C 4 min; 1 cycle: 72 °C 5 min. The PCR reaction was treated with DpnI for 3 h to digest the parental template DNA. The blunt ends were annealed together in a 10 μ L of ligation reaction (1 μ L of T4 DNA ligase buffer, 1 μ L of PCR reaction, 8 μ L of water, 1 μ L of T4 DNA ligase) for 1 h at room temperature and then at 4 °C overnight. Samples (3 μ L) of all reactions were transformed in DH5 α cells, and DNA was isolated from colonies through the Qiagen Miniprep kit (Venlo, Netherlands). Constructs confirmed by sequencing.

Protein Expression and Purification. CLR, RAMP2 or RAMP3, human DNG_{as},^{24,25} His6-tagged human G β 1 and G γ 2 were expressed in *Tni* insect cells (Expression systems) using baculovirus. For the AM₂R complexes, the DNGs contained an additional mutation, Gas A366S. Cell cultures were grown in ESF 921 serum-free media (Expression Systems) to a density of 4 million cells per mL and then infected with four separate baculoviruses for 48 h. Cell pellets were frozen at −80 °C until use. The cell pellet was thawed in 20 mM 4-(2-hydroxyethyl)-1-piperazineethanesulfonic acid

(HEPES) pH 7.4, 50 mM NaCl, and 2 mM MgCl₂, supplemented with cComplete Protease Inhibitor Cocktail tablets (Roche). Complex formation was initiated by addition of 10 μ M AM or AM2 peptide (Chinapeptides), Nb35-His (10 μ g/mL), 3C protease (10 μ g/mL; to cleave tags from CLR), and Apyrase (25 mU/mL, NEB); the suspension was incubated for 1 h at room temperature. Membranes were collected by centrifugation at 30 000g for 30 min; complex from the membrane was solubilized using 0.5% (w/v) lauryl maltose neopentyl glycol (LMNG, Anatrace) supplemented with 0.03% (w/v) cholesteryl hemisuccinate (CHS, Anatrace) for 2 h at 4 °C in the presence of 1 μ M of AM or AM2 peptide and Apyrase (25 mU/mL, NEB). Insoluble material was removed by centrifugation at 30 000g for 30 min, and the solubilized complex was immobilized by batch binding to NiNTA resin. The resin was packed into a glass column and washed with 20 column volumes of 20 mM HEPES pH 7.4, 100 mM NaCl, 2 mM MgCl₂, 0.01% (w/v) MNG, 0.0006% (w/v) CHS, and 1 μ M AM or AM2 peptide before bound material was eluted in buffer containing 250 mM imidazole. The NiNTA purified fraction was immobilized by batch binding to M1 anti-FLAG affinity resin in the presence of 3 mM CaCl₂. The resin was packed into a glass column and washed with 20 column volumes of 20 mM HEPES pH 7.4, 100 mM NaCl, 2 mM MgCl₂, 3 mM CaCl₂, 1 μ M AM or AM2 peptide, 0.01% (w/v) MNG, and 0.0006% (w/v) CHS before bound material was eluted in buffer containing 5 mM EGTA and 0.1 mg/mL FLAG peptide. The complex was then concentrated using an Amicon Ultra Centrifugal Filter (MWCO 100 kDa) and subjected to SEC on either a Superose 6 Increase 10/300 column (GE Healthcare) (AM:AM₁R, AM2:AM₂R), or a Superdex 200 Increase 10/300 column (GE Healthcare) (AM:AM₂R) that was pre-equilibrated with 20 mM HEPES pH 7.4, 100 mM NaCl, 2 mM MgCl₂, 1 μ M AM or AM2 peptide, 0.01% (w/v) MNG, and 0.0006% (w/v) CHS. Eluted fractions consisting of receptor and G protein complex were pooled and concentrated.

SDS–PAGE and Western Blot Analysis. Samples collected from SEC were analyzed by SDS–PAGE and Western blot as previously described.²⁶ For SDS–PAGE, precast gradient TGX gels (Bio-Rad) were used. The final SEC elution peak was stained by Instant Blue (Expedeon).

Electron Microscopy. Samples (3 μ L) were applied to acetone-prewashed, glow-discharged Quantifoil R1.2/1.3 CuRh 200 mesh holey carbon grids (Quantifoil GmbH, Großlobbichau, Germany) for AM:CLR:RAMP2:–GasDN:G β 1:G γ 2:Nb35 and Ultrafoil R1.2/1.3 Au 300 mesh for AM2:CLR:RAMP3:GasDN:G β 1:G γ 2:Nb35) and AM:CLR:RAMP3:GasDN:G β 1:G γ 2:Nb35. Samples were flash frozen in liquid ethane using a Vitrobot Mark IV (Thermo Fisher Scientific, Waltham, MA, USA). Data were collected on a Titan Krios microscope (Thermo Fisher Scientific, Waltham, MA, USA) operated at an accelerating voltage of 300 kV with a 50 μ m C2 aperture at an indicated magnification of 105 000× in nanoprobe EFTEM mode and a spot size of 4. A Gatan K3 direct electron detector positioned post a Gatan Quantum energy filter (Gatan, Pleasanton, CA, USA), operated in a zero-energy-loss mode with a slit width of 25 eV was used to acquire dose-fractionated images of the AM₁R and AM₂R samples. Movies were recorded as compressed TIFFs in normal-resolution mode yielding a physical pixel size of 0.83 Å/pixel with an exposure time of 3.5

s amounting to a total exposure of 60–68 $e^-/\text{\AA}^2$ for at an exposure rate of 13.5–20.0 $e^-/\text{pixel}/\text{second}$ that was fractionated into 70 subframes. Defocus was varied in the range between -0.7 to $-1.5 \mu\text{m}$. Beam-image shift was used to acquire data from 9 surrounding holes after which the stage was moved to the next collection area using a custom script for the SerialEM software package.^{55,56} This allowed for a higher throughput data collection, corresponding to an acquisition rate of more than 200 micrographs/hour.⁵⁷

Data Processing. Movies were motion-corrected, dose-weighted, and integrated using UCSF MotionCor2.^{58,59} This was followed by CTF estimation using the GCTF⁶⁰ software package. Particles were picked from the micrographs using the automated procedure in the crYOLO software package.⁶¹ Particle extraction and reference-free 2D classification was carried out in RELION (version 3.0.7 for RAMP2:AM and version 3.1 for RAMP3:AM and RAMP3:AM2).^{62–65} CryoSPARC (version 2.7) was used to generate an *ab initio* model of the AM:CLR:RAMP2:GasDN:G β 1:G γ 2:Nb35,⁶⁶ which was used in RELION for 3D classification, as well as the other two GPCR complexes. A homogeneous subset of particles was then subjected to cycles of Bayesian particle polishing and CTF refinement as implemented in RELION (See Figure S3 for cryoEM workflow on each complex). This homogeneous subset of polished particles was used for a 3D refinement in RELION and was further classified into 3D classes without angular and translational alignments, or with a fine grain angular sampling only allowing for local Euler angle searches. Particles belonging to the 3D class that yielded the best resolved map were then subjected to further 3D refinements where the α -helical domain of the Gas protein and the detergent micelle were masked and a final 3D refinement was carried out in RELION with a mask that included the detergent micelle but not the poorly resolved α -helical domain of the G- α subunit, yielding consensus maps of the complexes with global resolutions (FSC = 0.143) of 3.0 \AA (AM:CLR:RAMP2:GasDN:G β 1:G γ 2:Nb35), 2.3 \AA (AM2:CLR:RAMP3:GasDN:G β 1:G γ 2:Nb35), and 2.4 \AA (AM:CLR:RAMP3:GasDN:G β 1:G γ 2:Nb35), respectively. Local resolution estimations were performed using RELION. Additional focused refinements of the AM₂R complexes were performed through separate masking of the receptor domain using RELION⁶⁵ to yield “receptor-only” maps with global resolution of 2.6 \AA for both AM₂Rs that had markedly improved local resolution of the receptor ECD.

Atomic Model Refinement. Initial models for each of the AM receptor complexes were made with the Rosetta software package using the structure threading/comparative modeling and model relaxation protocols.⁶⁸ Fitting the Rosetta generated models in the cryo-EM density maps was performed with the MDFF routine in namd2.⁶⁹ The fitted models were further refined by rounds of manual model building in coot⁷⁰ and real-space refinement, as implemented in the Phenix software package.⁷¹ The crystal structure of the CLR:RAMP1 extracellular domain heterodimer in complex with adrenomedullin 2 (PDB: 6D1U)²⁸ was used as a guide for the C-terminal portion of the AM and AM2 peptides for the AM₂R models. The density around the N-terminal extracellular domains was poorly resolved for the AM₁R and was only modeled at a backbone level. Map and model statistics are detailed in Table S1.

CryoEM Dynamics Analysis. cryoSPARC 3D Variability. The final Polished and CTFRefined particle stacks from

RELION consensus refinements were imported into the cryoSPARC environment. To ensure only highly resolved particles were analyzed, 2D classification and selection as well as a multiple volume 3D refinements were carried out. Only particles that contributed to a high-resolution refinement were further analyzed. These particles then underwent a consensus high-resolution 3D refinement, using a low-pass-filtered RELION consensus model as a starting model. A generous mask that included the detergent micelle, which had a 5 pixel map expansion and 10 pixel soft edge, was built in RELION, so any possible motions could be accounted for during the 3D variability analysis. 3D variability was then calculated as implemented in cryoSPARC (v2.9). During the variability analysis, data was considered to a resolution of 3.2 \AA . The volume frame data was then generated in cryoSPARC and examined in UCSF Chimera. Output files were visualized in Chimera using the Volume Series command and captured as movies.

Interaction surfaces between peptide ligands and receptors, or those between receptors and G protein, were analyzed using the “Dimplot” module within the Ligplot+ program (v2.1).⁷² Additional analyses and production of images were performed using either Molsoft ICM (v3.8–7) or the UCSF Chimera package (v1.14) from the Computer Graphics Laboratory, University of California, San Francisco (supported by NIH P41 RR-01081). Electrostatic potential calculations were performed separately on the individual proteins. Calculations were performed using the EP function, calculated by the REBEL boundary element solution of the Poisson equation, in ICMPPro using default settings.⁷³ The scale is -5 to $+5 \text{ kT } e^{-1}$.

Modeling. The CLR ICL3 loop was generated using PLOOP⁷⁴ and minimized in the presence of G α to eliminate steric clashes. The G α loop between A249–N264 was modeled using the shorter loop from the adenosine A_{2A} receptor:G protein complex (PDB code 5G53).⁷⁵ Other missing loops in the G protein were added by molecular superposition from the β_2 -adrenergic receptor:G protein complex (PDB code 3SN6).²⁷ The joining point was taken as the closest atom pairs (usually $\sim 0.2 \text{\AA}$) that maintained an appropriate Ca–Ca distance (3.7–3.9 \AA) across the join; selected residues spanning the join were minimized using PLOOP as necessary. The helical domain between G α residues G47 and G207, not visible in the cryo-EM structure, was omitted.

Molecular Dynamics (MD) Simulations. The CLR:RAMP1:CGRP:Gs complex MD trajectories were produced for our previous work.²⁰ The CLR:RAMP2:AM:Gs complex was prepared with the CHARMM36 force field⁷⁶ using in-house scripts that combine python HTMD⁷⁷ and tcl (Tool Command Language) languages. Briefly, the PDB 2pqr⁷⁸ and propka⁷⁹ software were employed to add hydrogen atoms (considering a simulated pH of 7.0); the protonation of titratable side chains was checked by visual inspection. The resulting system was first opportunely oriented according to the CGRPR structure retrieved from the OPM database⁸⁰ and then embedded in a square 120 $\text{\AA} \times 120 \text{\AA}$ 1-palmitoyl-2-oleyl-*sn*-glycerol-3-phosphocholine (POPC) bilayer (previously built by using the VMD Membrane Builder plugin 1.1, Membrane Plugin, version 1.1. at <http://www.ks.uiuc.edu/Research/vmd/plugins/membrane/>) through an insertion method. Lipids overlapping the receptor TM bundle and the RAMP were removed and TIP3P water molecules⁸¹ were added to the simulation box (120 $\text{\AA} \times 120 \text{\AA} \times 175 \text{\AA}$)

utilizing the VMD Solvate plugin 1.5 (Solvate Plugin, Version 1.5. at <http://www.ks.uiuc.edu/Research/vmd/plugins/solvate/>). Finally, the system charge neutrality was reached by adding Na^+/Cl^- counterions (final ionic strength of 0.150 M), using the VMD Autoionize plugin 1.3 (Autoionize Plugin, Version 1.3. at <http://www.ks.uiuc.edu/Research/vmd/plugins/autoionize/>).

Systems Equilibration and MD Settings. ACEMD⁸² was employed for both the equilibration and productive MD simulations. The equilibration steps were performed in isothermal–isobaric conditions (NPT) using the Berendsen barostat⁸³ (target pressure 1 atm) and the Langevin thermostat⁸⁴ (target temperature 300 K) with low damping of 1 ps^{-1} , using an integration time step of 2 fs. Clashes between protein and lipid atoms were first reduced through 2500 conjugate–gradient minimization steps, then a 2 ns long MD simulation was run with a positional restraint of $1 \text{ kcal mol}^{-1} \text{ \AA}^{-2}$ on protein and lipid phosphorus atoms. During a further 20 ns of MD simulation, restraints were applied only to the protein atoms, while in the last equilibration stage, positional restraints were applied only to the protein backbone alpha carbons, for a further 80 ns. Productive trajectories (12 replicas of 500 ns each, for a total simulation time of 6 μs) were computed with an integration time step of 4 fs (through hydrogen mass repartitioning)⁸⁵ in the canonical ensemble (NVT) at 300 K, using a thermostat damping of 0.1 ps^{-1} and the M-SHAKE algorithm⁸⁶ to constrain the bond lengths involving hydrogen atoms. The cutoff distance for electrostatic interactions was set at 9 \AA , with a switching function applied beyond 7.5 \AA . Long-range Coulomb interactions were handled using the particle mesh Ewald summation method (PME)⁸⁷ by setting the mesh spacing to 1.0 \AA .

Mammalian Cell cAMP Assays. Cos7 cells, confirmed to be mycoplasma-free, were transfected in suspension in 96-well plates. The transfection was performed in 5% FBS DMEM (200 μL total volume per well) and cells were incubated for 48 h at 37°C and 5% CO_2 . For expression constructs, 10 000 cells/well were transfected with 50 ng of CLR + 50 ng of human RAMP2 or RAMP3 using 600 ng of PEI. For analysis of chimeric RAMP constructs, 15 000 cells/well were transfected with 32.5 ng of CLR + 32.5 ng of RAMP construct using 390 ng of PEI. Different chimeras were assessed as distinct batches, with a separate control wild-type RAMP included for each, due to the expression variance inherent in transient transfection. cAMP detection was performed as previously described.⁸⁸ Peptides for concentration response curves were from China Peptides. All values were converted to cAMP concentration using a cAMP standard curve performed in parallel, and data were subsequently normalized to the response of 100 μM forskolin. Data were analyzed using a 3-parameter logistic fit in Prism v8.2 (GraphPad) and assessed for differences in fitted parameters from the parental construct at 95% confidence intervals. Differences in globally fitted curves were also assessed using an extra sum of squares *F*-test at $P < 0.05$, with posthoc assessment of individual fitted parameters where curves were statistically different. All statistical analysis was performed in Prism v8.2.

Cell Surface Expression of Proteins: Assessment by FACS. Surface expression of c-Myc CLR or RAMP/RAMP chimeric constructs was quantified by flow cytometry analysis of antibody binding to the cMyc-tagged CLR or FLAG-tagged RAMP, respectively, using standard methods. Cos7 cells,

confirmed to be mycoplasma-free, were transfected in suspension in 6-well plates. Into 450,000 cells/well was transfected 975 ng of CLR + 975 ng of RAMP construct using 11.7 mg of PEI. The transfection was performed in 5% FBS DMEM, and cells were incubated for 48 h at 37°C and 5% CO_2 . All staining steps were conducted in ice-cold Hank's Balanced Salt Solution (HBSS) with 0.1% bovine serum albumin (BSA) and 20 mM HEPES pH 7.4. Blocking was conducted in 5% BSA. Primary antibody staining was performed with 3 $\mu\text{g/mL}$ 9E10 (anti-c-Myc) antibody or 1 $\mu\text{g/mL}$ M2 (anti-FLAG) antibody. The secondary antibody was 1 $\mu\text{g/mL}$ goat anti-mouse AF647 (ThermoFisher). Sytox blue was used for live/dead discrimination. Data were collected on a FACS CantosII (BD Biosciences). Data were analyzed using FlowJo. The mean AF647 fluorescence intensity is of live cells, and the percentage of live cells gated as positive for AF647 was against the pcDNA control.

■ ASSOCIATED CONTENT

● Supporting Information

The Supporting Information is available free of charge at <https://pubs.acs.org/doi/10.1021/acspsci.9b00080>.

Table S1: structure statistics; Figures S1–S10: sequences, pharmacology of the expression constructs, workflow for the consensus EM map refinements, atomic coordinates in the cryo-EM density maps, summary of atomic modelling, CLR–RAMP interface model and electrostatic surface diagrams, overview of the receptor conformation dynamic analysis, and cell surface expression of constructs (PDF)

Movies S1–S15: CryoSPARC 3D multivariate analyses S1–S3 (AM_AM₁R, full complex, normal modes 1–3), S4 (AM_AM₁R, ECL2 zoom, normal mode 1), S5 (AM_AM₁R, ICL2 zoom, normal mode 1). S6–S8 (AM_AM₂R, full complex, normal modes 1–3), S9 (AM_AM₂R, ECL2 zoom, normal mode 2), S10 (AM_AM₂R, ICL2 zoom, normal mode 3). S11–S13 (AM₂_AM₂R, full complex, normal modes 1–3), S14 (AM₂_AM₂R, ECL2 zoom, normal mode 1), S15 (AM₂_AM₂R, ICL2 zoom, normal mode 1) (ZIP)

Movie S16: Comparative MD simulations of the CGRPR complex²⁰ (left panel) and the AM-bound AM₁R complex (right panel). The AM_AM₁R has greater relative motion of the ECD and the RAMP2 linker forms more transient interactions with both the receptor ECL2 and ECD than the corresponding CGRPR complex. Movie S17: Long time-scale simulation of the AM-bound AM₁R complex illustrating mobility of the full complex at 2 angles (ZIP)

Movies S18–S22: Principal component analysis of the MD simulation of the AM-bound AM₁R complex shown in Movie S17, showing the 5 main principal components in each of Movies S18–S22. The arrows track the motions in each principal component and illustrate coordinated motions between the receptor and G protein (ZIP)

■ AUTHOR INFORMATION

Corresponding Authors

Patrick M. Sexton – Drug Discovery Biology, Monash Institute of Pharmaceutical Sciences, Monash University, Parkville 3052, Victoria, Australia; School of Pharmacy, Fudan University,

Shanghai 201203, China; orcid.org/0000-0001-8902-2473; Email: Patrick.sexton@monash.edu

Denise Wootten – Drug Discovery Biology, Monash Institute of Pharmaceutical Sciences, Monash University, Parkville 3052, Victoria, Australia; School of Pharmacy, Fudan University, Shanghai 201203, China; Email: denise.wootten@monash.edu

Authors

Yi-Lynn Liang – Drug Discovery Biology, Monash Institute of Pharmaceutical Sciences, Monash University, Parkville 3052, Victoria, Australia

Matthew J. Belousoff – Drug Discovery Biology, Monash Institute of Pharmaceutical Sciences, Monash University, Parkville 3052, Victoria, Australia

Madeleine M. Fletcher – Drug Discovery Biology, Monash Institute of Pharmaceutical Sciences, Monash University, Parkville 3052, Victoria, Australia

Xin Zhang – Drug Discovery Biology, Monash Institute of Pharmaceutical Sciences, Monash University, Parkville 3052, Victoria, Australia

Maryam Khoshouei – Department of Molecular Structural Biology, Max Planck Institute of Biochemistry, 82152 Martinsried, Germany

Giuseppe Degnutt – School of Biological Sciences, University of Essex, Colchester CO4 3SQ, United Kingdom; orcid.org/0000-0001-8780-2986

Cassandra Koole – Drug Discovery Biology, Monash Institute of Pharmaceutical Sciences, Monash University, Parkville 3052, Victoria, Australia

Sebastian G. B. Furness – Drug Discovery Biology, Monash Institute of Pharmaceutical Sciences, Monash University, Parkville 3052, Victoria, Australia; orcid.org/0000-0001-8655-8221

Laurence J. Miller – Drug Discovery Biology, Monash Institute of Pharmaceutical Sciences, Monash University, Parkville 3052, Victoria, Australia; Department of Molecular Pharmacology and Experimental Therapeutics, Mayo Clinic, Scottsdale, Arizona 85259, United States

Debbie L. Hay – School of Biological Sciences, and Maurice Wilkins Centre for Molecular Biodiscovery, University of Auckland, Auckland 1142, New Zealand; orcid.org/0000-0002-9558-5122

Arthur Christopoulos – Drug Discovery Biology, Monash Institute of Pharmaceutical Sciences, Monash University, Parkville 3052, Victoria, Australia

Christopher A. Reynolds – School of Biological Sciences, University of Essex, Colchester CO4 3SQ, United Kingdom

Radostin Danev – Graduate School of Medicine, University of Tokyo, 113-0033 Tokyo, Japan; orcid.org/0000-0001-6406-8993

Complete contact information is available at:
<https://pubs.acs.org/10.1021/acspsci.9b00080>

Author Contributions

[○]Y.-L.L., M.J.B., and M.M.F. contributed equally to this work. Y.-L.L. developed the biochemistry for complex formation, generated purified stable complex, characterized the protein by negative stain TEM, and contributed to writing of the manuscript. M.J.B. analyzed the micrographs, generated the refined maps, generated the atomic models, completed conformational analysis on the AM receptor maps, prepared figures, and contributed to writing of the manuscript. M.M.F.

completed pharmacological characterization of chimeric RAMPs, generated figures, and contributed to writing of the manuscript. X.Z. completed conformational analyses on the CGRP receptor maps and contributed to editing of the manuscript. M.K. completed initial cryo-EM imaging and analysis of the AM₁ receptor complex. G.D. and C.A.R. completed the MD simulations, contributed to analysis and interpretation of the data, and contributed to editing of the manuscript. C.K. completed pharmacological characterization of constructs and contributed to editing of the manuscript. L.J.M., S.G.B.F., D.L.H., and A.C. contributed to project development, interpretation of the data, and editing of the manuscript. R.D. developed the vitrification strategy, collected the cryo-EM data for all of the structures, contributed to analysis and interpretation of the data, and contributed to writing of the manuscript. D.W. and P.M.S. oversaw the project (including analysis and interpretation of the data), generated figures, and wrote the manuscript.

Notes

The authors declare no competing financial interest.

Cryo-EM maps are deposited in the PDB and EMDB databases with the following codes: AM:AM₁R:Gs (6UUN, EMD-20883), AM:AM₂R:Gs (6UUS, EMD-20901), and AM2:AM₂R:Gs (6UVA, EMD-20906).

ACKNOWLEDGMENTS

This work was supported by the Monash University Ramaciotti Centre for Cryo-Electron Microscopy, the Monash MASSIVE high-performance computing facility, the National Health and Medical Research Council of Australia (NHMRC) (project grants 1120919 and 1159006) and NHMRC program grant (1150083), the Japan Society for the Promotion of Science (JSPS, KAKENHI no. 18H06043) and Japan Science and Technology Agency (JST, PRESTO no. 18069571, and Biotechnology and Biological Sciences Research Council, UK (BBSRC, grant BB/M006883). P.M.S. and A.C. are NHMRC Senior Principal Research Fellows. D.W. is an NHMRC Senior Research Fellow. C.K. is a NHMRC CJ Martin Fellow. S.G.B.F. is an Australian Research Council Future Fellow. C.A.R. is a Royal Society Industry Fellow. The authors thank George Christopoulos and Villy Julita for technical support.

REFERENCES

- (1) Hauser, A. S., Chavali, S., Masuho, I., Jahn, L. J., Martemyanov, K. A., Gloriam, D. E., and Babu, M. M. (2018) Pharmacogenomics of GPCR Drug Targets. *Cell* 172, 41–54.
- (2) Alexander, S. P., Christopoulos, A., Davenport, A. P., Kelly, E., Marrion, N. V., Peters, J. A., Faccenda, E., Harding, S. D., Pawson, A. J., Sharman, J. L., Southan, C., and Davies, J. A. (2017) The concise guide to pharmacology 2017/18: G 697 protein-coupled receptors. *Br. J. Pharmacol.* 174, S17–S129.
- (3) Hay, D. L., and Pioszak, A. A. (2016) Receptor Activity-Modifying Proteins (RAMPs): New Insights and Roles. *Annu. Rev. Pharmacol. Toxicol.* 56, 469–487.
- (4) Lorenzen, E., Dodig-Crnković, T., Kotliar, I. B., Pin, E., Ceraudo, E., Vaughan, R. D., Uhlén, M., Huber, T., Schwenk, J. M., and Sakmar, T. P. (2019) Multiplexed analysis of the secretin-like GPCR-RAMP interactome. *Sci. Adv.* 5 (9), No. eaaw2778.
- (5) Hay, D. L., Garelja, M. L., Poyner, D. R., and Walker, C. S. (2018) Update on the pharmacology of calcitonin/CGRP family of peptides: IUPHAR Review 25. *Br. J. Pharmacol.* 175, 3–17.
- (6) Dickerson, I. M., Bussey-Gaborski, R., Holt, J. C., Jordan, P. M., and Luebke, A. E. (2016) Maturation of suprathreshold auditory

nerve activity involves cochlear CGRP-receptor complex formation. *Physiol. Rep.* 4, No. e12869.

(7) Russell, F. A., King, R., Smillie, S. J., Kodji, X., and Brain, S. D. (2014) Calcitonin gene-related peptide: physiology and pathophysiology. *Physiol. Rev.* 94, 1099–1142.

(8) Walker, C. S., Li, X., Whiting, L., Glyn-Jones, S., Zhang, S., Hickey, A. J., Sewell, M. A., Ruggiero, K., Phillips, A. R., Kraegen, E. W., Hay, D. L., Cooper, G. J., and Loomes, K. M. (2010) Mice lacking the neuropeptide alpha-calcitonin gene-related peptide are protected against diet-induced obesity. *Endocrinology* 151, 4257–4269.

(9) Russo, A. F. (2019) CGRP-Based Migraine Therapeutics: How Might They Work, Why So Safe, and What Next? *ACS Pharmacol. Transl. Sci.* 2, 2–8.

(10) Ganor, Y., Drillet-Dangeard, A. S., and Bomsel, M. (2015) Calcitonin gene-related peptide inhibits human immunodeficiency type 1 transmission by Langerhans cells via an autocrine/paracrine feedback mechanism. *Acta Physiol.* 213, 432–441.

(11) Bomsel, M., and Ganor, Y. (2017) Calcitonin Gene-Related Peptide Induces HIV-1 Proteasomal Degradation in Mucosal Langerhans Cells. *J. Virol.* 91, No. e01205.

(12) Caron, K. M., and Smithies, O. (2001) Extreme hydrops fetalis and cardiovascular abnormalities in mice lacking a functional adrenomedullin gene. *Proc. Natl. Acad. Sci. U. S. A.* 98, 615–619.

(13) Klein, K. R., and Caron, K. M. (2015) Adrenomedullin in lymphangiogenesis: from development to disease. *Cell. Mol. Life Sci.* 72, 3115–3126.

(14) Matson, B. C., Pierce, S. L., Espenschied, S. T., Holle, E., Sweatt, I. H., Davis, E. S., Tarran, R., Young, S. L., Kohout, T. A., van Duin, M., and Caron, K. M. (2017) Adrenomedullin improves fertility and promotes pinopodes and cell junctions in the peri-implantation endometrium. *Biol. Reprod.* 97, 466–477.

(15) Li, M., Schwerbrock, N. M., Lenhart, P. M., Fritz-Six, K. L., Kadmiel, M., Christine, K. S., Kraus, D. M., Espenschied, S. T., Willcockson, H. H., Mack, C. P., and Caron, K. M. (2013) Fetal-derived adrenomedullin mediates the innate immune milieu of the placenta. *J. Clin. Invest.* 123, 2408–2420.

(16) Xian, X., Sakurai, T., Kamiyoshi, A., Ichikawa-Shindo, Y., Tanaka, M., Koyama, T., Kawate, H., Yang, L., Liu, T., Imai, A., Zhai, L., Hirabayashi, K., Dai, K., Tanimura, K., Liu, T., Cui, N., Igarashi, K., Yamauchi, A., and Shindo, T. (2017) Vasoprotective Activities of the Adrenomedullin-RAMP2 System in Endothelial Cells. *Endocrinology* 158, 1359–1372.

(17) Zhang, S.-Y., Xu, M.-J., and Wang, X. (2018) Adrenomedullin 2/intermedin: a putative drug candidate for treatment of cardiometabolic disease. *Br. J. Pharmacol.* 175, 1230–1240.

(18) Cheung, B. M., and Tang, F. (2012) Adrenomedullin: exciting new horizons. *Recent Pat. Endocr., Metab. Immune Drug Discovery* 6, 4–17.

(19) Ashizuka, S., Inatsu, H., Inagaki-Ohara, K., Kita, T., and Kitamura, K. (2013) Adrenomedullin as a potential therapeutic agent for inflammatory bowel disease. *Curr. Protein Pept. Sci.* 14, 246–255.

(20) Liang, Y.-L., Khoshouei, M., Deganutti, G., Glukhova, A., Koole, C., Peat, T. S., Radjainia, M., Plitzko, J. M., Baumeister, W., Miller, L. J., et al. (2018) Cryo-EM structure of the active, Gs-protein complexed, human CGRP receptor. *Nature* 561, 492–497.

(21) Booe, J. M., Walker, C. S., Barwell, J., Kuteyi, G., Simms, J., Jamaluddin, M. A., Warner, M. L., Bill, R. M., Harris, P. W., Brimble, M. A., Poyner, D. R., Hay, D. L., and Pioszak, A. A. (2015) Structural Basis for Receptor Activity-Modifying Protein-Dependent Selective Peptide Recognition by a G Protein-Coupled Receptor. *Mol. Cell* 58, 1040–1052.

(22) Draper-Joyce, C., and Furness, S. G. B. (2019) Conformational Transitions and the Activation of Heterotrimeric G Proteins by G Protein-Coupled Receptors. *ACS Pharmacol. Transl. Sci.* 2, 285–290.

(23) Liang, Y. L., Belousoff, M. J., Zhao, P., Koole, C., Fletcher, M. M., Truong, T. T., Julita, V., Christopoulos, G., Xu, H. E., Zhang, Y., Khoshouei, M., Christopoulos, A., Danev, R., Sexton, P. M., and

Wootten, D. (2020) Towards a structural understanding of class B GPCR peptide binding and activation. *Mol. Cell* 77, 656.

(24) Liang, Y.-L., Khoshouei, M., Glukhova, A., Furness, S. G. B., Zhao, P., Clydesdale, L., Koole, C., Truong, T. T., Thal, D. M., Lei, S., et al. (2018) Phase-plate cryo-EM structure of a biased agonist-bound human GLP-1 receptor-Gs complex. *Nature* 555, 121–125.

(25) Liang, Y.-L., Zhao, P., Draper-Joyce, C., Baltos, J., Glukhova, A., Truong, T. T., May, L. T., Christopoulos, A., Wootten, D., Sexton, P. M., and Furness, S. G. B. (2018) Dominant negative G proteins enhance formation and purification of agonist-GPCR-G protein complexes for structure determination. *ACS Pharmacol. Transl. Sci.* 1, 12–20.

(26) Liang, Y. L., Khoshouei, M., Radjainia, M., Zhang, Y., Glukhova, A., Tarrasch, J., Thal, D. M., Furness, S. G. B., Christopoulos, G., Coudrat, T., et al. (2017) Phase-plate cryo-EM structure of a class B GPCR-G-protein complex. *Nature* 546, 118–123.

(27) Rasmussen, S. G., DeVree, B. T., Zou, Y., Kruse, A. C., Chung, K. Y., Kobilka, T. S., Thian, F. S., Chae, P. S., et al. (2011) Crystal structure of the β 2 adrenergic receptor-Gs protein complex. *Nature* 477, 549–555.

(28) Roehrkasse, A. M., Booe, J. M., Lee, S. M., Warner, M. L., and Pioszak, A. A. (2018) Structure-function analyses reveal a triple β -turn receptor-bound conformation of adrenomedullin 2/intermedin and enable peptide antagonist design. *J. Biol. Chem.* 293, 15840–15854.

(29) Wootten, D., Simms, J., Miller, L. J., Christopoulos, A., and Sexton, P. M. (2013) Polar transmembrane interactions drive formation of ligand-specific and signal pathway-biased family B G protein-coupled receptor conformations. *Proc. Natl. Acad. Sci. U. S. A.* 110, 5211–5216.

(30) Watkins, H. A., Chakravarthy, M., Abhayawardana, R. S., Gingell, J. J., Garejla, M., Pardamwar, M., McElhinney, J. M. W. R., Lathbridge, A., Constantine, A., Harris, P. W. R., Yuen, T.-Y., Brimble, M. A., Barwell, J., Poyner, D. R., Woolley, M. J., Conner, A. C., Pioszak, A. A., Reynolds, C. A., and Hay, D. L. (2016) Receptor activity-modifying proteins 2 and 3 generate adrenomedullin receptor subtypes with distinct molecular properties. *J. Biol. Chem.* 291, 11657–11675.

(31) Booe, J. M., Warner, M. L., Roehrkasse, A. M., Hay, D. L., and Pioszak, A. A. (2018) Probing the Mechanism of Receptor Activity-Modifying Protein Modulation of GPCR Ligand Selectivity through Rational Design of Potent Adrenomedullin and Calcitonin Gene-Related Peptide Antagonists. *Mol. Pharmacol.* 93, 355–367.

(32) Musa, H., Hendrikse, E. R., Brimble, M. A., Garejla, M. L., Watkins, H. A., Harris, P. W. R., and Hay, D. L. (2019) Pharmacological characterization and investigation of N terminal loop amino acids of adrenomedullin 2 that are important for receptor activation. *Biochemistry* 58, 3468–3474.

(33) Garejla, M., Au, M., Brimble, M. A., Gingell, J. J., Hendrikse, E. R., Lovell, A., Poyner, D. R., Prodan, N., Siow, A., and Sexton, P. M. et al. (2020) Molecular mechanisms of class B GPCR activation: insights from adrenomedullin receptors. *ACS Pharmacol. Transl. Sci.* DOI: 10.1021/acspsci.9b00083.

(34) Wootten, D., Reynolds, C. A., Smith, K. J., Mobarec, J. C., Furness, S. G., Miller, L. J., Christopoulos, A., and Sexton, P. M. (2016) Key interactions by conserved polar amino acids located at the transmembrane helical boundaries in Class B GPCRs modulate activation, effector specificity and biased signalling in the glucagon-like peptide-1 receptor. *Biochem. Pharmacol.* 118, 68–87.

(35) Siu, F. Y., He, M., de Graaf, C., Han, G. W., Yang, D., Zhang, Z., Zhou, C., Xu, Q., Wacker, D., Joseph, J. S., et al. (2013) Structure of the human glucagon class B G-protein-coupled receptor. *Nature* 499, 444–449.

(36) Vohra, S., Taddese, B., Conner, A. C., Poyner, D. R., Hay, D. L., Barwell, J., Reeves, P. J., Upton, G. J., and Reynolds, C. A. (2013) Similarity between class A and class B G-protein-coupled receptors exemplified through calcitonin gene-related peptide receptor modelling and mutagenesis studies. *J. R. Soc., Interface* 10, 20120846.

- (37) Woolley, M. J., Reynolds, C. A., Simms, J., Walker, C. S., Mobarec, J. C., Garelja, M. L., Conner, A. C., Poyner, D. R., and Hay, D. L. (2017) Receptor activity-modifying protein dependent and independent activation mechanisms in the coupling of calcitonin gene-related peptide and adrenomedullin receptors to Gs. *Biochem. Pharmacol.* 142, 96–110.
- (38) Dal Maso, E., Zhu, Y., Pham, V., Reynolds, C. A., Deganutti, G., Hick, C. A., Yang, D., Christopoulos, A., Hay, D. L., Wang, M. W., Sexton, P. M., Furness, S. G. B., and Wootten, D. (2018) Extracellular loops 2 and 3 of the calcitonin receptor selectively modify agonist binding and efficacy. *Biochem. Pharmacol.* 150, 214–244.
- (39) Dal Maso, E., Glukhova, A., Zhu, Y., Garcia-Nafria, J., Tate, C. G., Atanasio, S., Reynolds, C. A., Ramirez-Aportela, E., Carazo, J.-M., Hick, C. A., et al. (2019) The molecular control of calcitonin receptor (CTR) signaling. *ACS Pharmacol. Transl. Sci.* 2, 31–51.
- (40) Wootten, D., Reynolds, C. A., Smith, K. J., Mobarec, J. C., Koole, C., Savage, E. E., Pabreja, K., Simms, J., Sridhar, R., Furness, S. G. B., et al. (2016) The GLP-1 receptor extracellular surface is a molecular trigger for biased agonism. *Cell* 165, 1632–1643.
- (41) Pham, V., Zhu, Y., Dal Maso, E., Reynolds, C. A., Deganutti, G., Atanasio, S., Hick, C. A., Yang, D., Christopoulos, A., Hay, D. L., Furness, S. G. B., Wang, M. W., Wootten, D., and Sexton, P. M. (2019) Deconvoluting the Molecular Control of Binding and Signaling at the Amylin 3 Receptor: RAMP3 Alters Signal Propagation through Extracellular Loops of the Calcitonin Receptor. *ACS Pharmacol. Transl. Sci.* 2, 183–187.
- (42) Watkins, H. A., Walker, C. S., Ly, K. N., Bailey, R. J., Barwell, J., Poyner, D. R., and Hay, D. L. (2014) Receptor activity-modifying protein-dependent effects of mutations in the calcitonin receptor-like receptor: implications for adrenomedullin and calcitonin gene-related peptide pharmacology. *Br. J. Pharmacol.* 171, 772–788.
- (43) Lei, S., Clydesdale, L., Dai, A., Cai, X., Feng, Y., Yang, D., Liang, Y. L., Koole, C., Zhao, P., Coudrat, T., et al. (2018) Two distinct domains of the glucagon-like peptide-1 receptor control peptide-mediated biased agonism. *J. Biol. Chem.* 293, 9370–9387.
- (44) Dickerson, I. M. (2013) Role of CGRP-receptor component protein (RCP) in CLR/RAMP function. *Curr. Protein Pept. Sci.* 14, 407–415.
- (45) Egea, S. C., and Dickerson, I. M. (2012) Direct interactions between calcitonin-like receptor (CLR) and CGRP-receptor component protein (RCP) regulate CGRP receptor signaling. *Endocrinology* 153, 1850–1860.
- (46) Barwell, J., Miller, P. S., Donnelly, D., and Poyner, D. R. (2010) Mapping interaction sites within the N-terminus of the calcitonin gene-related peptide receptor; the role of residues 23–60 of the calcitonin receptor-like receptor. *Peptides* 31, 170–176.
- (47) Lau, C., Hunter, M. J., Stewart, A., Perozo, E., and Vandenberg, J. I. (2018) Never at rest: insights into the conformational dynamics of ion channels from cryo-electron microscopy. *J. Physiol.* 596, 1107–1119.
- (48) Murata, K., and Wolf, M. (2018) Cryo-electron microscopy for structural analysis of dynamic biological macromolecules. *Biochim. Biophys. Acta, Gen. Subj.* 1862, 324–334.
- (49) Furness, S. G. B., Liang, Y. L., Nowell, C. J., Halls, M. L., Wooley, P. J., Dal Maso, E., Inoue, A., Christopoulos, A., Wootten, D., and Sexton, P. M. (2016) Ligand-Dependent Modulation of G Protein Conformation Alters Drug Efficacy. *Cell* 167, 739–749.
- (50) Morfis, M., Tilakaratne, N., Furness, S. G., Christopoulos, G., Werry, T. D., Christopoulos, A., and Sexton, P. M. (2008) Receptor activity-modifying proteins differentially modulate the G protein-coupling efficiency of amylin receptors. *Endocrinology* 149, 5423–5431.
- (51) Udawela, M., Christopoulos, G., Tilakaratne, N., Christopoulos, A., Albiston, A., and Sexton, P. M. (2006) Distinct receptor activity-modifying protein domains differentially modulate interaction with calcitonin receptors. *Mol. Pharmacol.* 69, 1984–1849.
- (52) Weston, C., Winfield, I., Harris, M., Hodgson, R., Shah, A., Dowell, S. J., Mobarec, J. C., Woodlock, D. A., Reynolds, C. A., Poyner, D. R., Watkins, H. A., and Ladds, G. (2016) Receptor Activity-modifying Protein-directed G protein Signaling Specificity for the Calcitonin Gene-related Peptide Family of Receptors. *J. Biol. Chem.* 291, 21925–21944.
- (53) Lisi, G. P., and Loria, J. P. (2017) Allostery in enzyme catalysis. *Curr. Opin. Struct. Biol.* 47, 123–130.
- (54) McLatchie, L. M., Fraser, N. J., Main, M. J., Wise, A., Brown, J., Thompson, N., Solari, R., Lee, M. G., and Foord, S. M. (1998) RAMPs regulate the transport and ligand specificity of the calcitonin-receptor-like receptor. *Nature* 393, 333–339.
- (55) Mastronarde, D. N. (2018) Advanced data acquisition from electron microscopes with SerialEM. *Microsc. Microanal.* 24, 864–865.
- (56) Schorb, M., Haberbosch, I., Hagen, W. J. H., Schwab, Y., and Mastronarde, D. N. (2019) Software tools for automated transmission electron microscopy. *Nat. Methods* 16, 471–477.
- (57) Danev, R., Yanagisawa, H., and Kikkawa, M. (2019) Cryo-electron microscopy methodology: Current aspects and future directions. *Trends Biochem. Sci.* 44, 837–848.
- (58) Li, X., Mooney, P., Zheng, S., Booth, C. R., Braunfeld, M. B., Gubbens, S., Agard, D. A., and Cheng, Y. (2013) Electron counting and beam-induced motion correction enable near-atomic-resolution single-particle cryo-EM. *Nat. Methods* 10, 584–590.
- (59) Zheng, S. Q., Palovcak, E., Armache, J. P., Verba, K. A., Cheng, Y., and Agard, D. A. (2017) MotionCor2: anisotropic correction of beam-induced motion for improved cryo-electron microscopy. *Nat. Methods* 14, 331–332.
- (60) Zhang, K. (2016) Gctf: Real-time CTF determination and correction. *J. Struct. Biol.* 193, 1–12.
- (61) Wagner, T., Merino, F., Stabrin, M., Moriya, T., Antoni, C., Apelbaum, A., Hagel, P., Sitsel, O., Rausch, T., Prumbaum, D., et al. (2019) SPHIRE-crYOLO is a fast and accurate fully automated particle picker for cryo-EM. *Commun. Biol.* 2, 218.
- (62) Scheres, S. H. W. (2015) Semi-automated selection of cryo-EM particles in RELION-1.3. *J. Struct. Biol.* 189, 114–122.
- (63) Kimanius, D., Forsberg, B. O., Scheres, S. H. W., and Lindahl, E. (2016) Accelerated cryo-EM structure determination with parallelisation using GPUs in RELION-2. *eLife* 5, No. e18722.
- (64) Fernandez-Leiro, R., and Scheres, S. H. W. (2017) A pipeline approach to single-particle processing in RELION. *Acta Crystallogr. D Struct. Biol.* 73, 496–502.
- (65) Zivanov, J., Nakane, T., Forsberg, B. O., Kimanius, D., Hagen, W. J., Lindahl, E., and Scheres, S. H. (2018) New tools for automated high-resolution cryo-EM structure determination in RELION-3. *eLife* 7, No. e42166.
- (66) Punjani, A., Rubinstein, J. L., Fleet, D. J., and Brubaker, M. A. (2017) cryoSPARC: algorithms for rapid unsupervised cryo-EM structure determination. *Nat. Methods* 14, 290–296.
- (67) Nakane, T., Kimanius, D., Lindahl, E., and Scheres, S. H. W. (2018) Characterisation of molecular motions in cryo-EM single particle data by multi-body refinement in RELION. *eLife* 7, No. e36861.
- (68) Leaver-Fay, A., Tyka, M., Lewis, S. M., Lange, O. F., Thompson, J., Jacak, R., Kaufman, K., Renfrew, P. D., Smith, C. A., Sheffler, W., et al. (2011) ROSETTA3: an object-oriented software suite for the simulation and design of macromolecules. *Methods Enzymol.* 487, 545–574.
- (69) Chan, K. Y., Trabuco, L. G., Schreiner, E., and Schulten, K. (2012) Cryo-electron microscopy modeling by the molecular dynamics flexible fitting method. *Biopolymers* 97, 678–686.
- (70) Emsley, P., Lohkamp, B., Scott, W. G., and Cowtan, K. (2010) Features and development of Coot. *Acta Crystallogr., Sect. D: Biol. Crystallogr.* 66, 486–501.
- (71) Adams, P. D., Afonine, P. V., Bunkoczi, G., Chen, V. B., Davis, I. W., Echols, N., Headd, J. J., Hung, L. W., Kapral, G. J., Grosse-Kunstleve, R. W., et al. (2010) PHENIX: a comprehensive Python-

based system for macromolecular structure solution. *Acta Crystallogr. Sect. D: Biol. Crystallogr.* 66, 213–221.

(72) Laskowski, R. A., and Swindells, M. B. (2011) LigPlot+: multiple ligand-protein interaction diagrams for drug discovery. *J. Chem. Inf. Model.* 51, 2778–2786.

(73) Totrov, M., and Abagyan, R. (2001) Rapid boundary element solvation electrostatics calculations in folding simulations: successful folding of a 23-residue peptide. *Biopolymers* 60, 124–133.

(74) Jacobson, M. P., Pincus, D. L., Rapp, C. S., Day, T. J., Honig, B., Shaw, D. E., and Friesner, R. A. (2004) A hierarchical approach to all-atom protein loop prediction. *Proteins: Struct., Funct., Genet.* 55, 351–367.

(75) Carpenter, B., Nehmé, R., Warne, T., Leslie, A. G. W., and Tate, C. G. (2016) Structure of the adenosine A(2A) receptor bound to an engineered G protein. *Nature* 536, 104–107.

(76) Huang, J., and MacKerell, A. D. (2013) CHARMM36 all-atom additive protein force field: validation based on comparison to NMR data. *J. Comput. Chem.* 34, 2135–2145.

(77) Doerr, S., Harvey, M. J., Noé, F., and De Fabritiis, G. (2016) HTMD: High-Throughput Molecular Dynamics for Molecular Discovery. *J. Chem. Theory Comput.* 12, 1845–1852.

(78) Dolinsky, T. J., Nielsen, J. E., McCammon, J. A., and Baker, N. A. (2004) PDB2PQR: an automated pipeline for the setup of Poisson-Boltzmann electrostatics calculations. *Nucleic Acids Res.* 32, W665–W667.

(79) Olsson, M. H. M., Søndergaard, C. R., Rostkowski, M., and Jensen, J. H. (2011) PROPKA3: Consistent Treatment of Internal and Surface Residues in Empirical pK Predictions. *J. Chem. Theory Comput.* 7, 525–537.

(80) Lomize, M. A., Lomize, A. L., Pogozheva, I. D., and Mosberg, H. I. (2006) OPM: orientations of proteins in membranes database. *Bioinformatics* 22, 623–625.

(81) Jorgensen, W. L., Chandrasekhar, J., Madura, J. D., Impey, R. W., and Klein, M. L. (1983) Comparison of simple potential functions for simulating liquid water. *J. Chem. Phys.* 79, 926.

(82) Harvey, M. J., Giupponi, G., and Fabritiis, G. D. (2009) ACEMD: Accelerating Biomolecular Dynamics in the Microsecond Time Scale. *J. Chem. Theory Comput.* 5, 1632–1639.

(83) Berendsen, H. J. C., Postma, J. P. M., van Gunsteren, W. F., DiNola, A., and Haak, J. R. (1984) Molecular dynamics with coupling to an external bath. *J. Chem. Phys.* 81, 3684.

(84) Loncharich, R. J., Brooks, B. R., and Pastor, R. W. (1992) Langevin dynamics of peptides: the frictional dependence of isomerization rates of N-acetylalanyl-N'-methylamide. *Biopolymers* 32, 523–535.

(85) Hopkins, C. W., Le Grand, S., Walker, R. C., and Roitberg, A. E. (2015) Long-Time-Step Molecular Dynamics through Hydrogen Mass Repartitioning. *J. Chem. Theory Comput.* 11, 1864–1874.

(86) Forester, T. R., and Smith, W. (1998) SHAKE, rattle, and roll: Efficient constraint algorithms for linked rigid bodies. *J. Comput. Chem.* 19, 102–111.

(87) Essmann, U. P. L., Perera, L., Berkowitz, M. L., Darden, T., Lee, H., and Pedersen, L. G. (1995) A smooth particle mesh Ewald method. *J. Chem. Phys.* 103, 8577–8593.

(88) Hager, M. V., Clydesdale, L., Gellman, S. H., Sexton, P. M., and Wootten, D. (2017) Characterization of signal bias at the GLP-1 receptor induced by backbone modification of GLP-1. *Biochem. Pharmacol.* 136, 99–108.

Supporting information:

Structure and Dynamics of the Adrenomedullin (AM) Receptors, AM₁ and AM₂, Reveals Key Mechanisms in the Control of Receptor Phenotype by RAMPs

Yi-Lynn Liang^{1¶}, Matthew J. Belousoff^{1¶}, Madeleine M Fletcher^{1¶}, Xin Zhang¹, Maryam Khoshouei^{2#}, Giuseppe Deganutti³, Cassandra Koole¹, Sebastian G. B. Furness¹, Laurence J. Miller^{1,4}, Debbie L. Hay⁵, Arthur Christopoulos¹, Christopher A Reynolds³, Radostin Danev⁶, Denise Wootten^{1,7*}, Patrick M. Sexton^{1,7*}

1. Drug Discovery Biology, Monash Institute of Pharmaceutical Sciences, Monash University, Parkville 3052, Victoria, Australia.
2. Department of Molecular Structural Biology, Max Planck Institute of Biochemistry, 82152 Martinsried, Germany.
3. School of Biological Sciences, University of Essex, Colchester CO4 3SQ, U.K.
4. Department of Molecular Pharmacology and Experimental Therapeutics, Mayo Clinic, Scottsdale, Arizona 85259, U.S.A.
5. School of Biological Sciences, and Maurice Wilkins Centre for Molecular Biodiscovery, University of Auckland, Auckland, New Zealand.
6. Graduate School of Medicine, University of Tokyo, S402, 7-3-1 Hongo, Bunkyo-ku, 113-0033 Tokyo, Japan
7. School of Pharmacy, Fudan University, Shanghai 201203, China.

Table of contents

Supplementary Table 1	p2
Supplementary Figure 1	p3
Supplementary Figure 2	p4
Supplementary Figure 3	p5-6
Supplementary Figure 4	p7
Supplementary Figure 5	p8
Supplementary Figure 6	p9
Supplementary Figure 7	p10
Supplementary Figure 8	p11
Supplementary Figure 9	p12
Supplementary Figure 10	p13-14

Table S1
Structure statistics

Data Collection	AM:CLR:RAMP2:G α s DN:G β 1:G γ 2:Nb35	AM2:CLR:RAMP3:G α s DN:G β 1:G γ 2:Nb35	AM:CLR:RAMP3:G α s DN:G β 1:G γ 2:Nb35
Micrographs	7164	5706	5058
Particles (Final map)	111k	656k	521k
Pixel size (Å)	0.83	0.83	0.83
Defocus range (μm)	0.5-1.5	0.5-1.5	0.5-1.5
Voltage (kV)	300	300	300
Electron dose (e/Å ²)	67.7	60.6	59.5
Resolution (0.143 FSC) (Å)	3.0	2.3	2.4
Refinement			
CC _{map_model}	0.82	0.72	0.79
Model Quality			
<i>RMSD</i>			
Bond length (Å) / Bond angles (°)	0.003/0.474	0.002/0.534	0.002/0.489
<i>Ramachandran</i>			
Favoured (%)	96.76	96.83	97.24
Outliers (%)	0	0	0
<i>Rotamer outliers (%)</i>	0	3.36	3.27
<i>C-Beta deviations (%)</i>	0	0	0
<i>Clashscore</i>	6.56	6.6	7.39
<i>MolProbity Score</i>	1.56	1.96	1.94

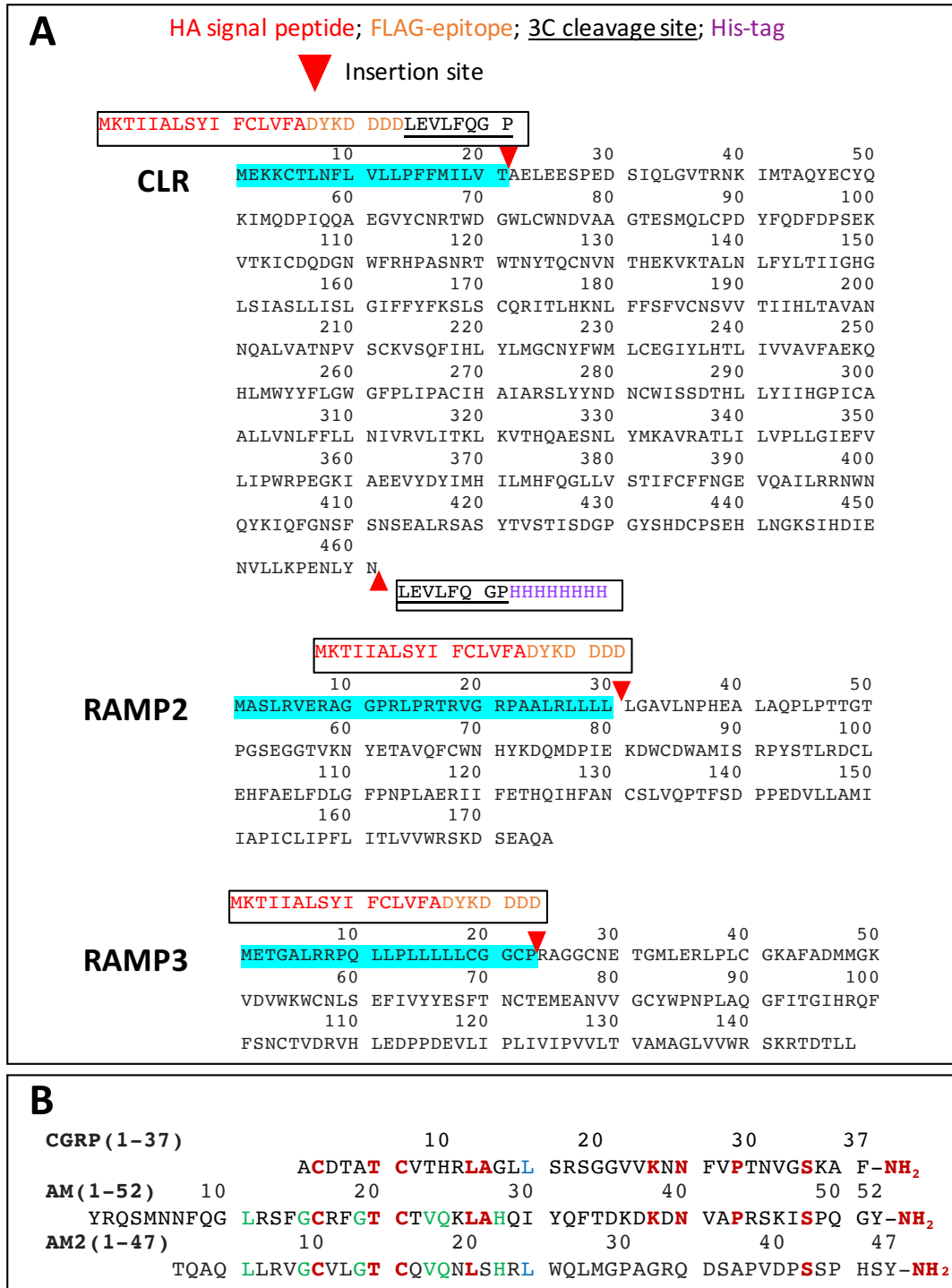


Figure S1. A. Sequences of expression constructs used in determination of structure in the current study. **B.** Sequence of peptides used in the current study. The AM (13-52) sequence was used as this is equipotent to AM (1-52); the 1-12 sequence of the full-length peptide is shaded in grey. Amino acids common to all peptides are shown in bold red, those common to AM and AM2 in green, and those common to AM2 and CGRP in blue.

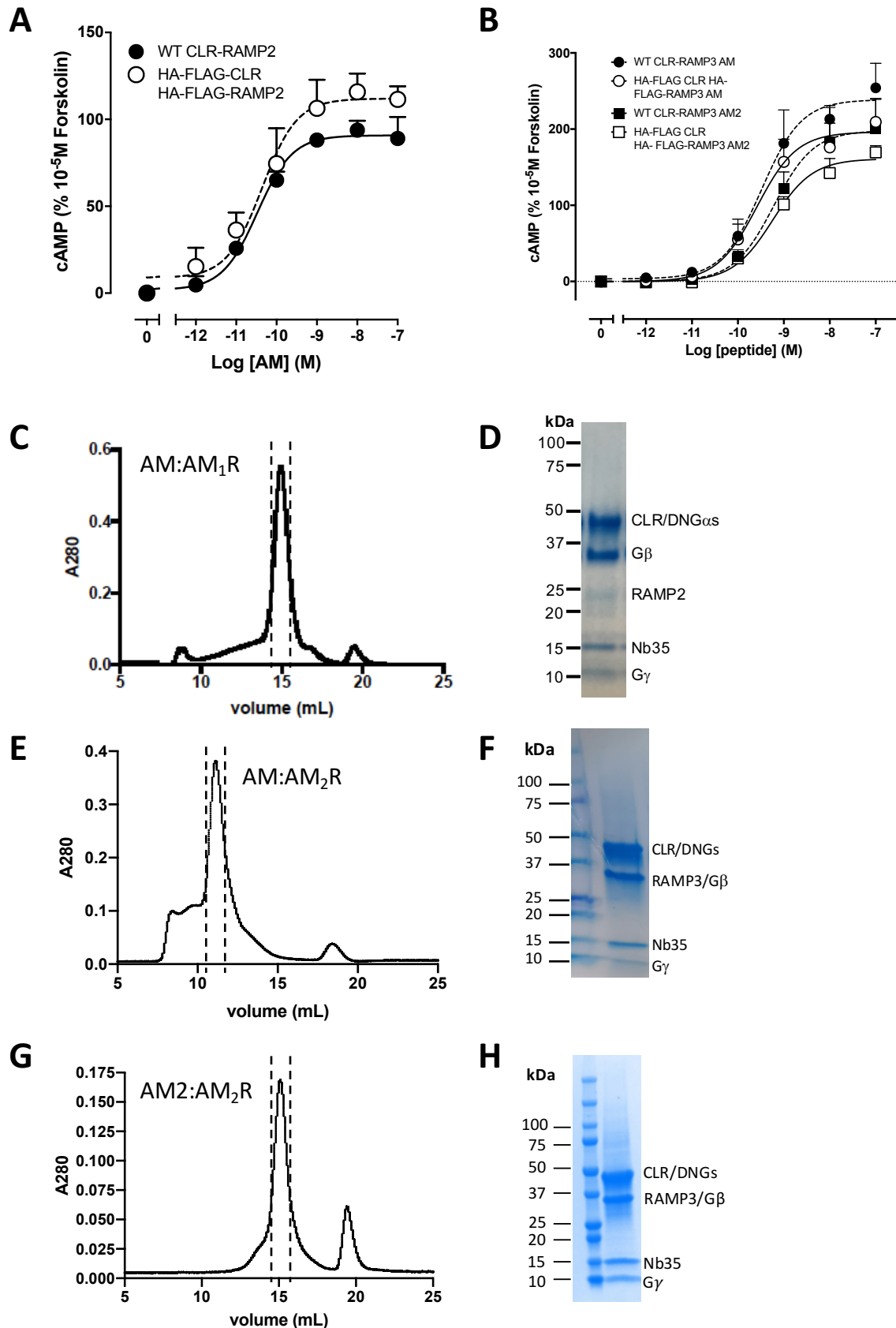
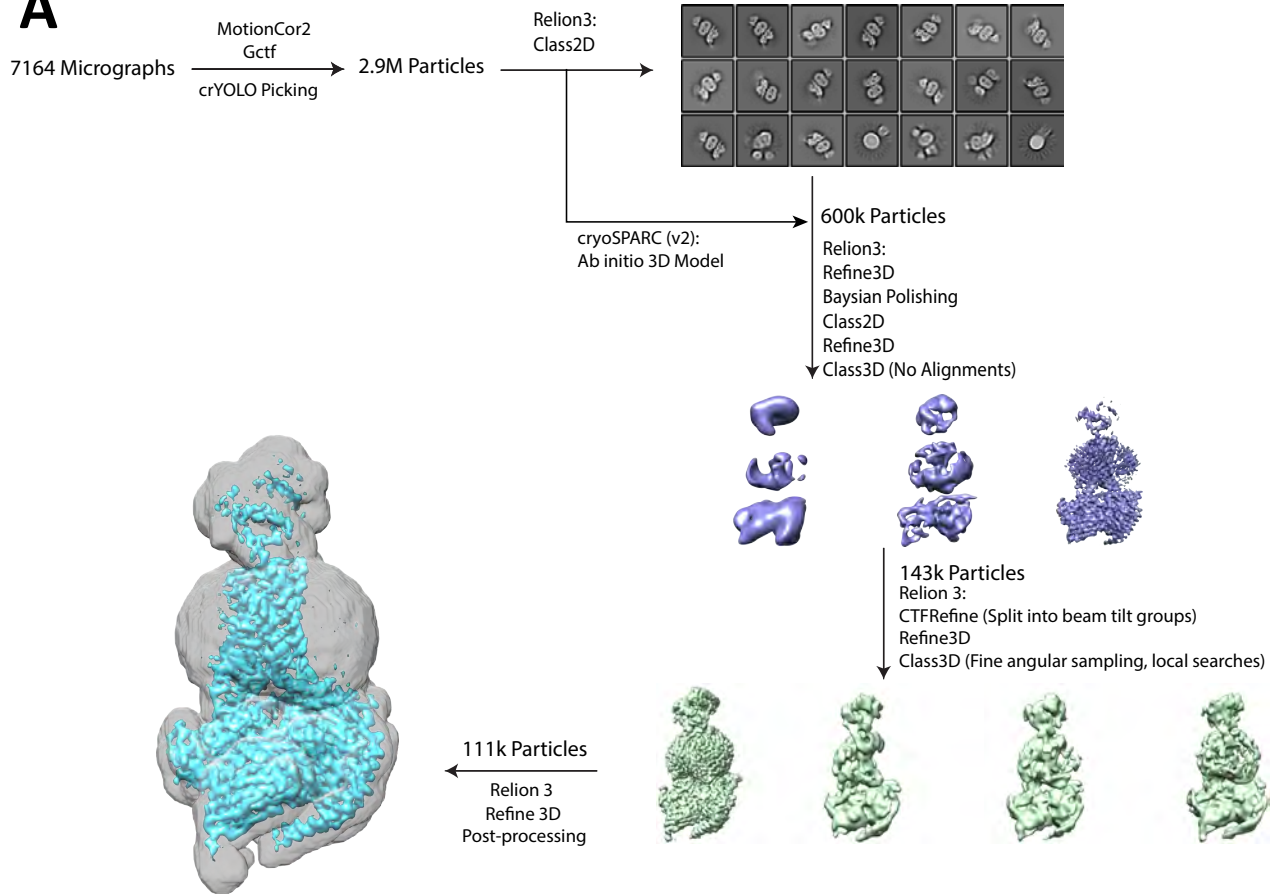
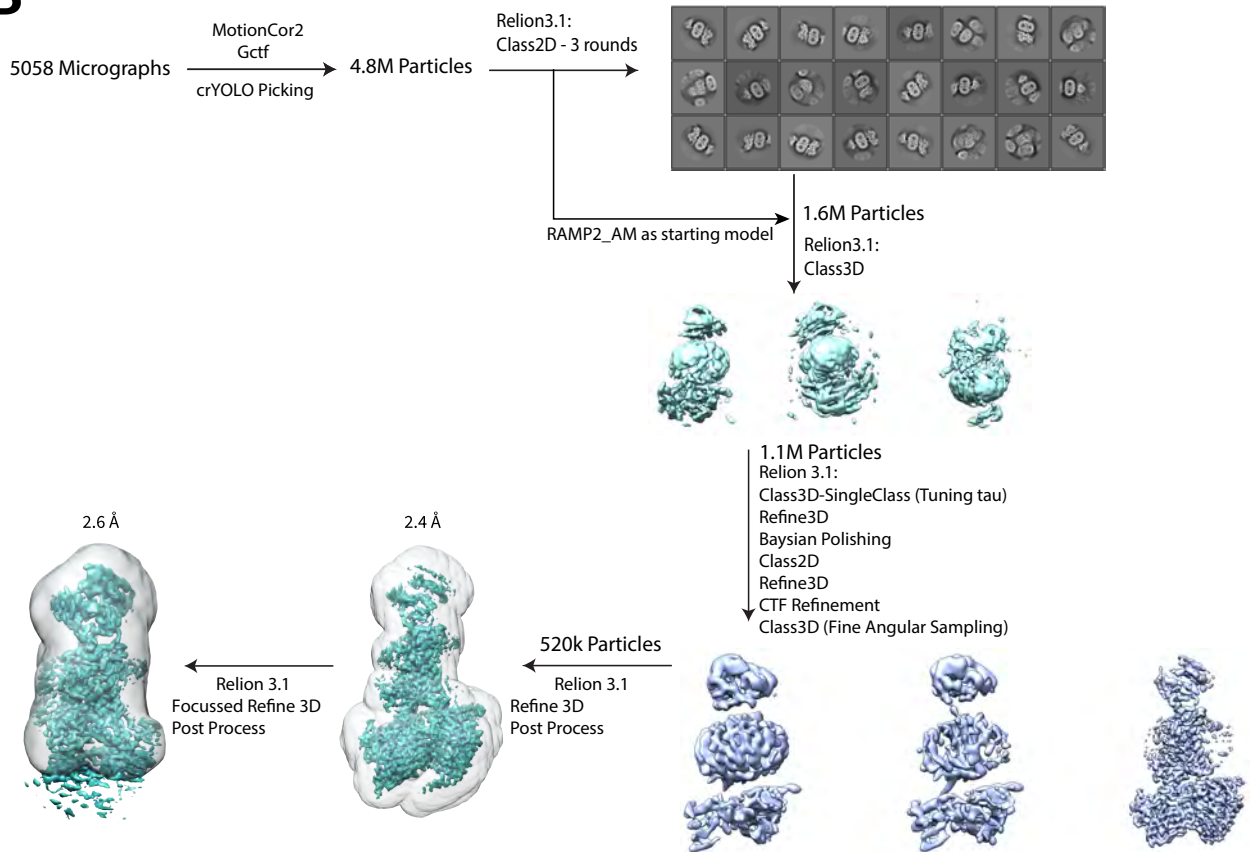


Figure S2. **A, B**, Pharmacology of the expression constructs for the AM₁R (**A**) and AM₂R (**B**). **C, D**, Final SEC trace (**C**) with dotted lines indicating the fractions used for cryo-EM, and coomassie blue stained PAGE gel (**D**) of purified AM:CLR:RAMP2:GsDN:Nb35 construct, demonstrating presence of each of the components of the complex. **E, F**, Final SEC trace (**E**) and coomassie blue stained PAGE gel (**F**) of purified AM:CLR:RAMP3:GsDN:Nb35 construct. **G, H**, Final SEC trace (**G**) and coomassie blue stained PAGE gel (**H**) of purified AM2:CLR:RAMP3:GsDN:Nb35 construct.

A**B**

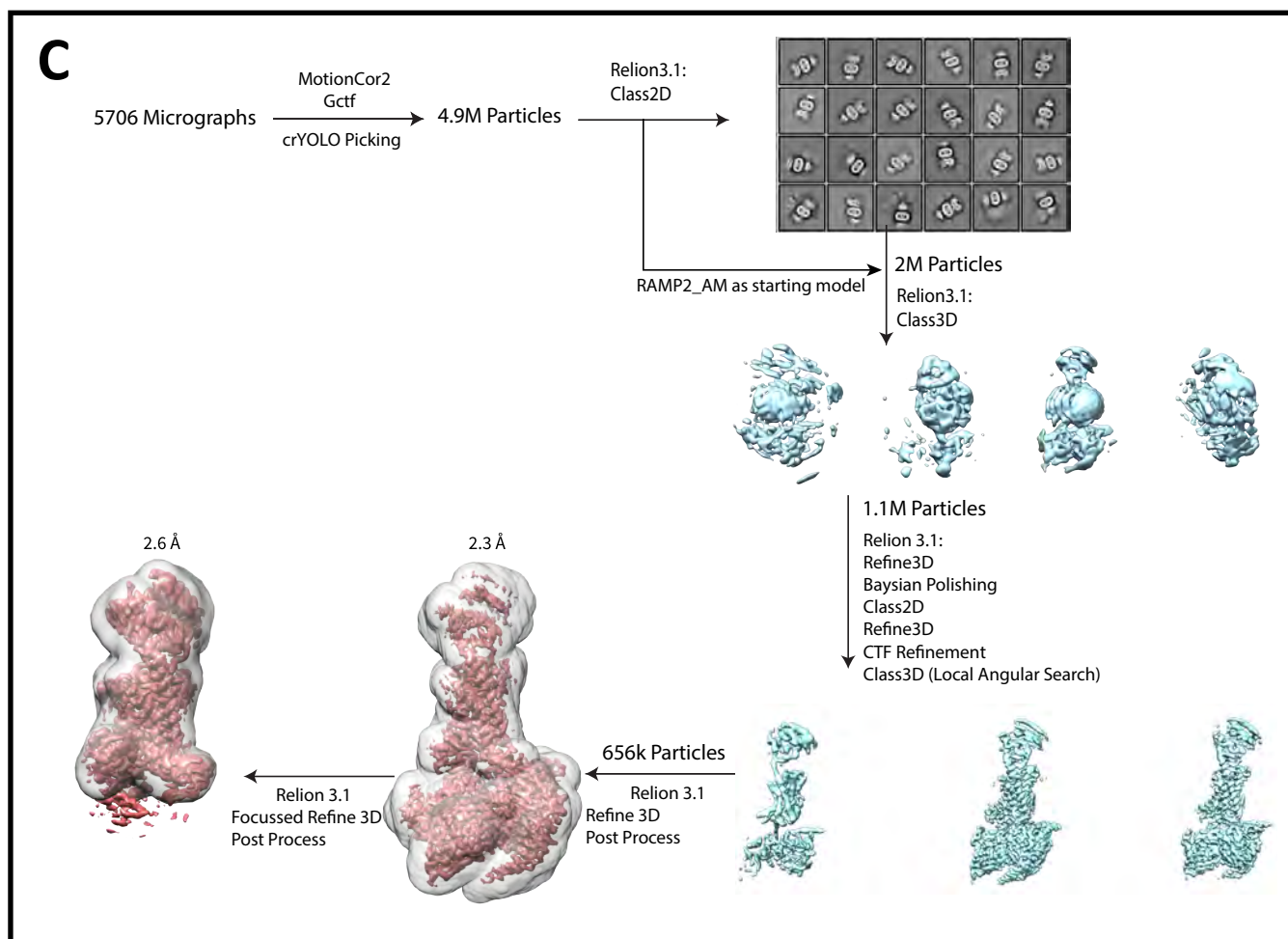


Figure S3. Workflow for the consensus EM map refinements for each of the AM receptor complexes. **(A)** AM:CLR:RAMP2:GsDN:Nb35 complex, **(B)** AM:CLR:RAMP3:GsDN:Nb35 complex and **(C)** AM2:CLR:RAMP3:GsDN:Nb35 complex .

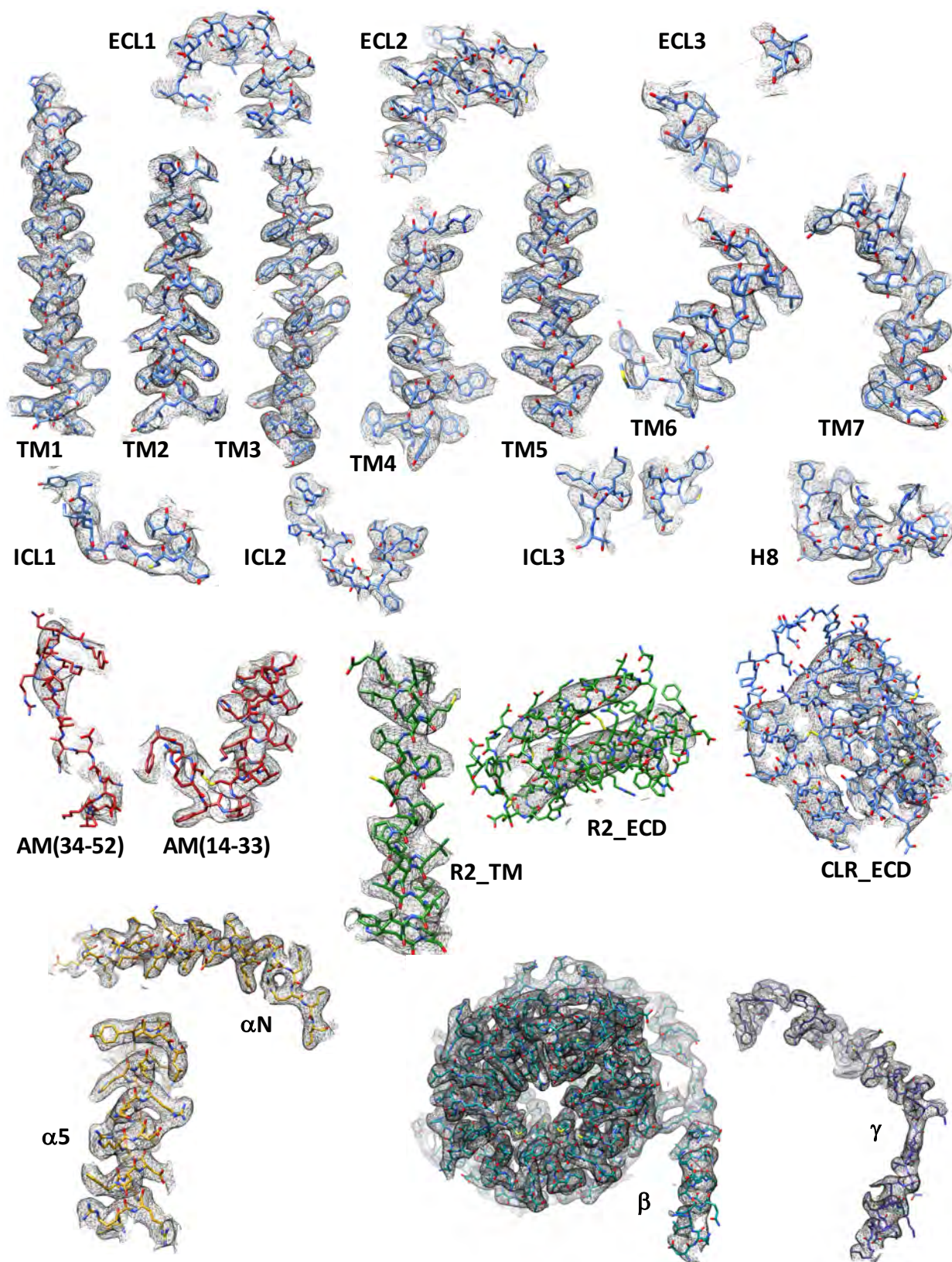


Figure S4. Atomic coordinates of the AM:CLR:RAMP2:GsDN:Nb35 complex in the cryo-EM density map. Cryo-EM density map and model are shown for all seven transmembrane helices, ECLs, ICLs and H8 of CLR; the RAMP2 transmembrane helix; the AM peptide; the N-terminal (α N), and C-terminal (α H5) α -helices of the G α s-Ras domain, G β 1 and G γ 2 are also shown. The low resolution density for the CLR and RAMP2 ECDs is also illustrated for comparison. The EM map was zoned at 2.0 Å around the protein segments.

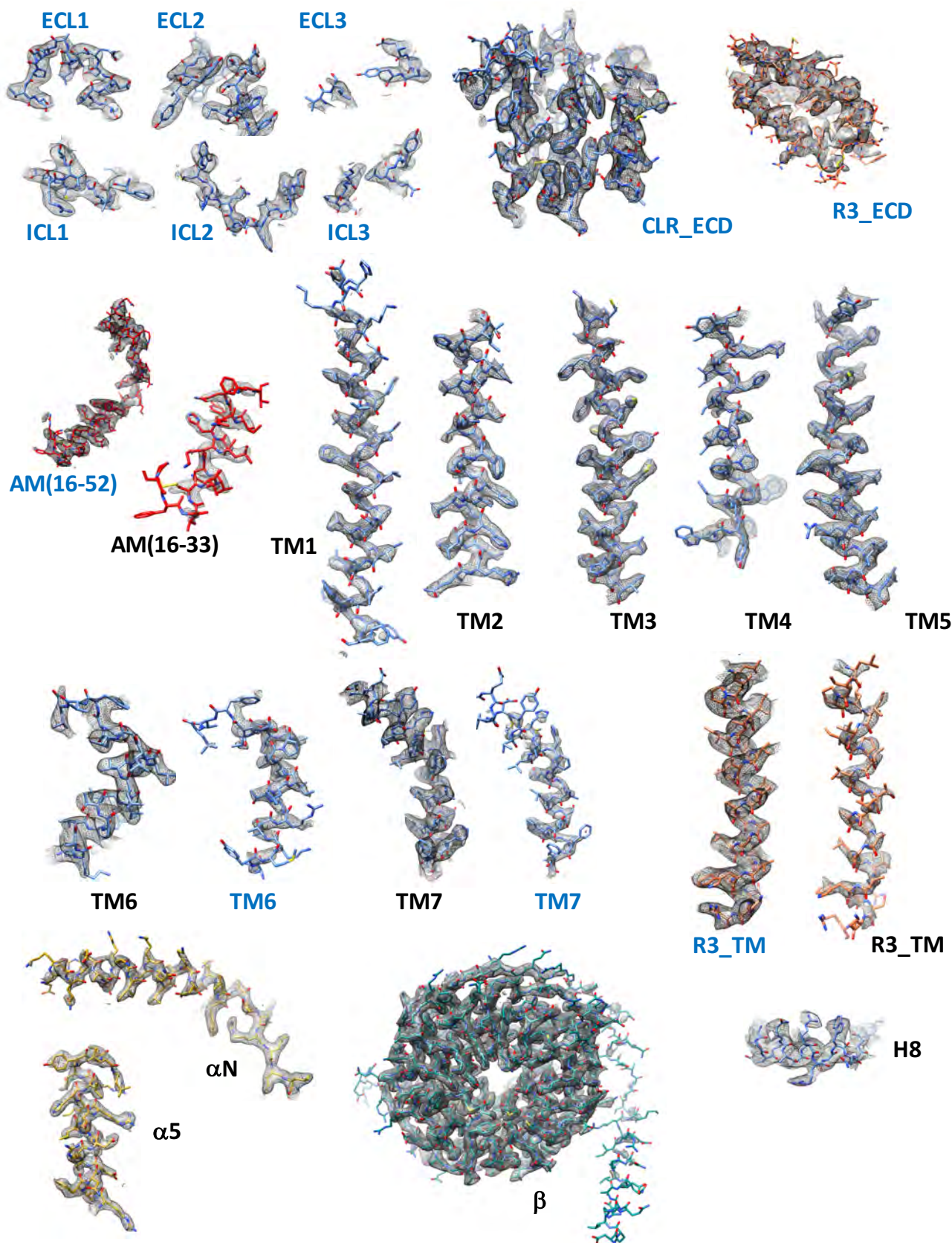


Figure S5. Atomic coordinates of the AM:CLR:RAMP3:GsDN:Nb35 complex in the cryo-EM density map. Cryo-EM density map and model are shown for all seven transmembrane helices, ECD, ECLs, ICLs and H8 of CLR; the RAMP3 (R3) transmembrane helix and ECD; the AM peptide; the N-terminal (α N), and C-terminal (α H5) α -helices of the G α s-Ras domain, G β 1 is also shown. The EM map was zoned at 2.0 Å around the protein segments. Black text indicates use of the 2.4 Å global map. The blue text indicates use of the 2.6 Å map with focused refinement of the receptor.

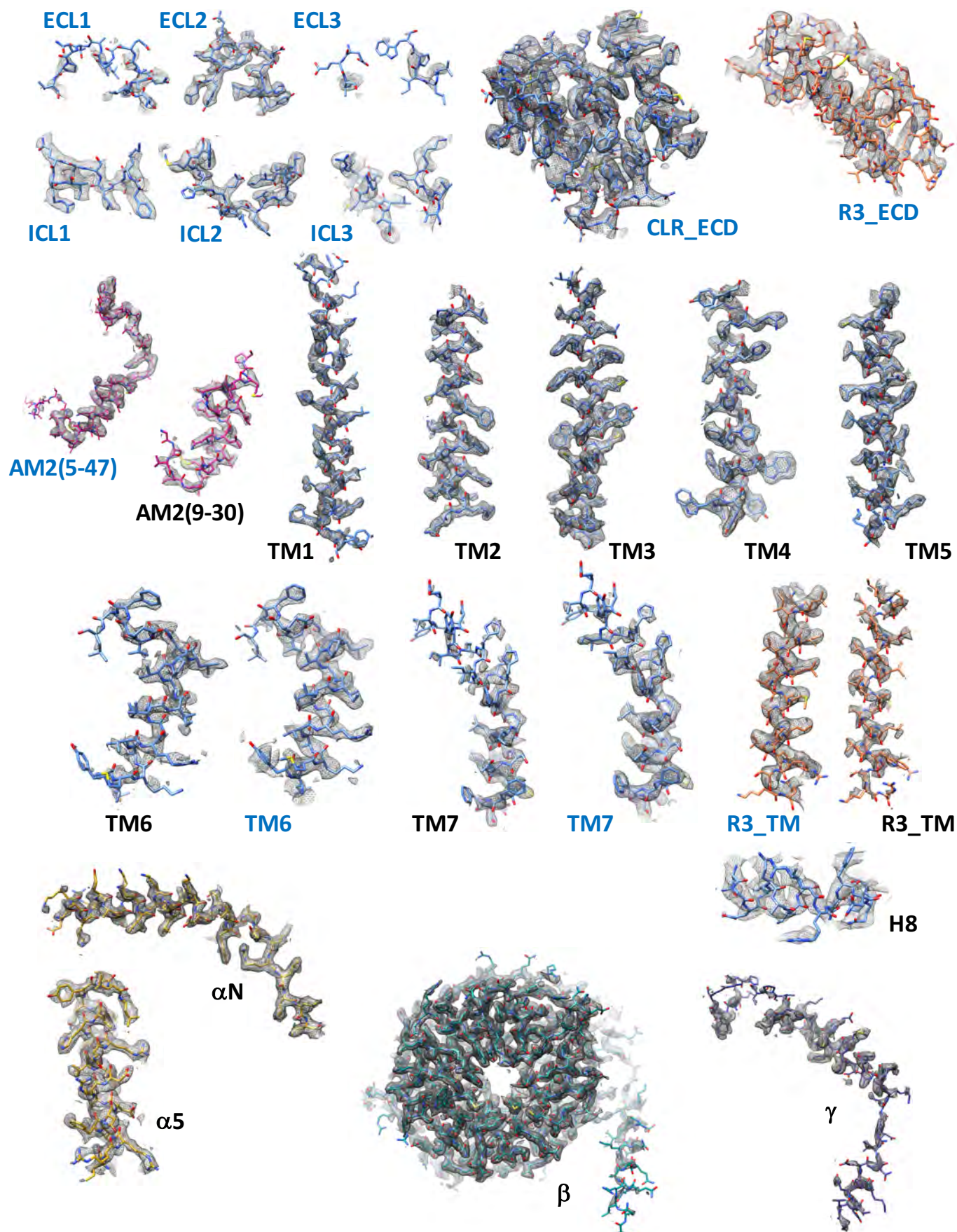


Figure S6. Atomic coordinates of the AM2:CLR:RAMP3:GsDN:Nb35 complex in the cryo-EM density map. Cryo-EM density map and model are shown for all seven transmembrane helices, ECD, ECLs, ICLs and H8 of CLR; the RAMP3 (R3) transmembrane helix and ECD; the AM peptide; the N-terminal (α N), and C-terminal (α H5) α -helices of the G α s-Ras domain, G β 1 and G γ 2 are also shown. The EM map was zoned at 2.0 Å around the protein segments. Black text indicates use of the 2.3 Å global map. The blue text indicates use of the 2.6 Å map with focused refinement of the receptor.

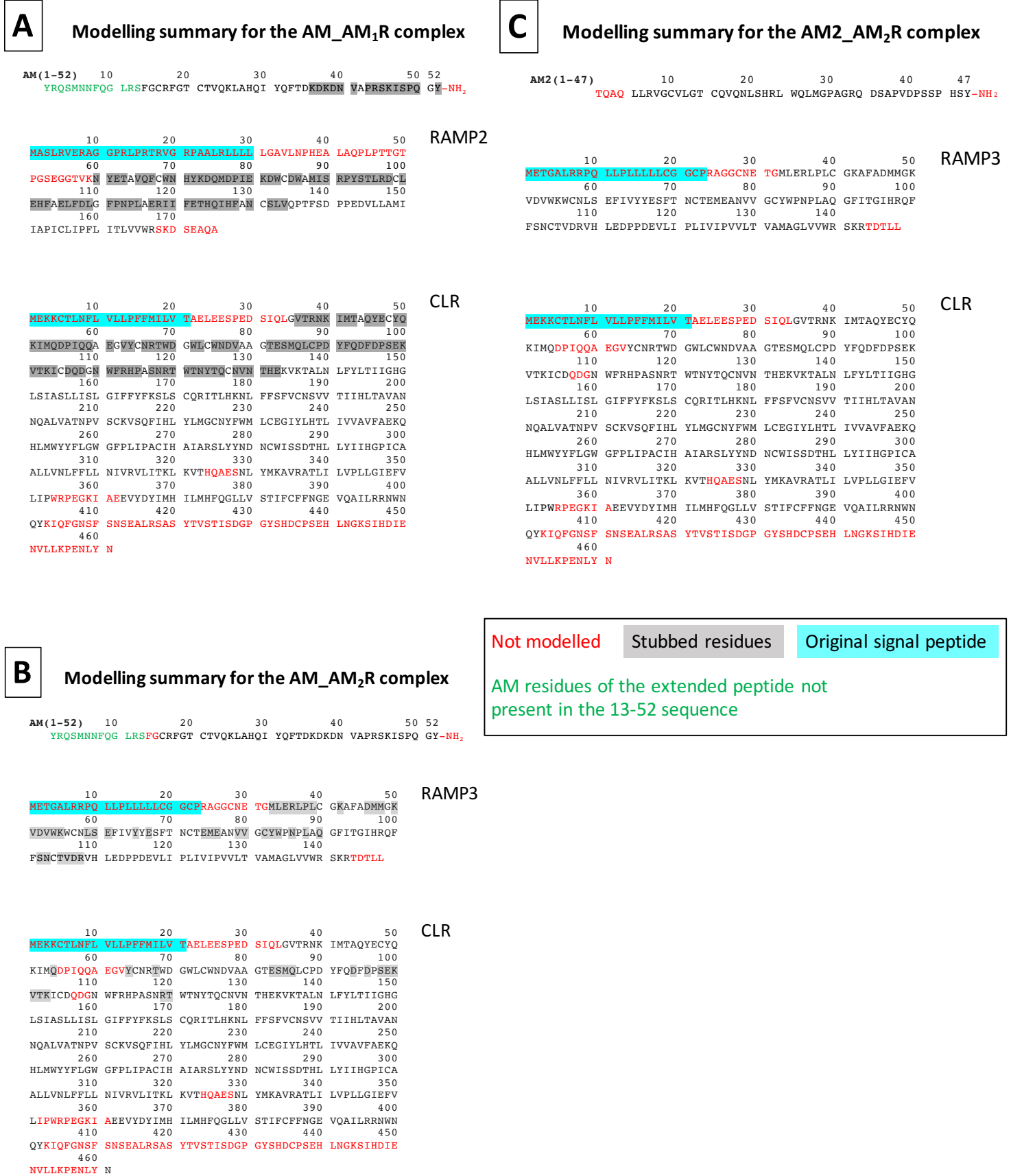


Figure S7. Summary of atomic modelling into the receptor maps. (A) AM₁AM₁R, (B) AM₁AM₂R, (C) AM₂AM₂R.

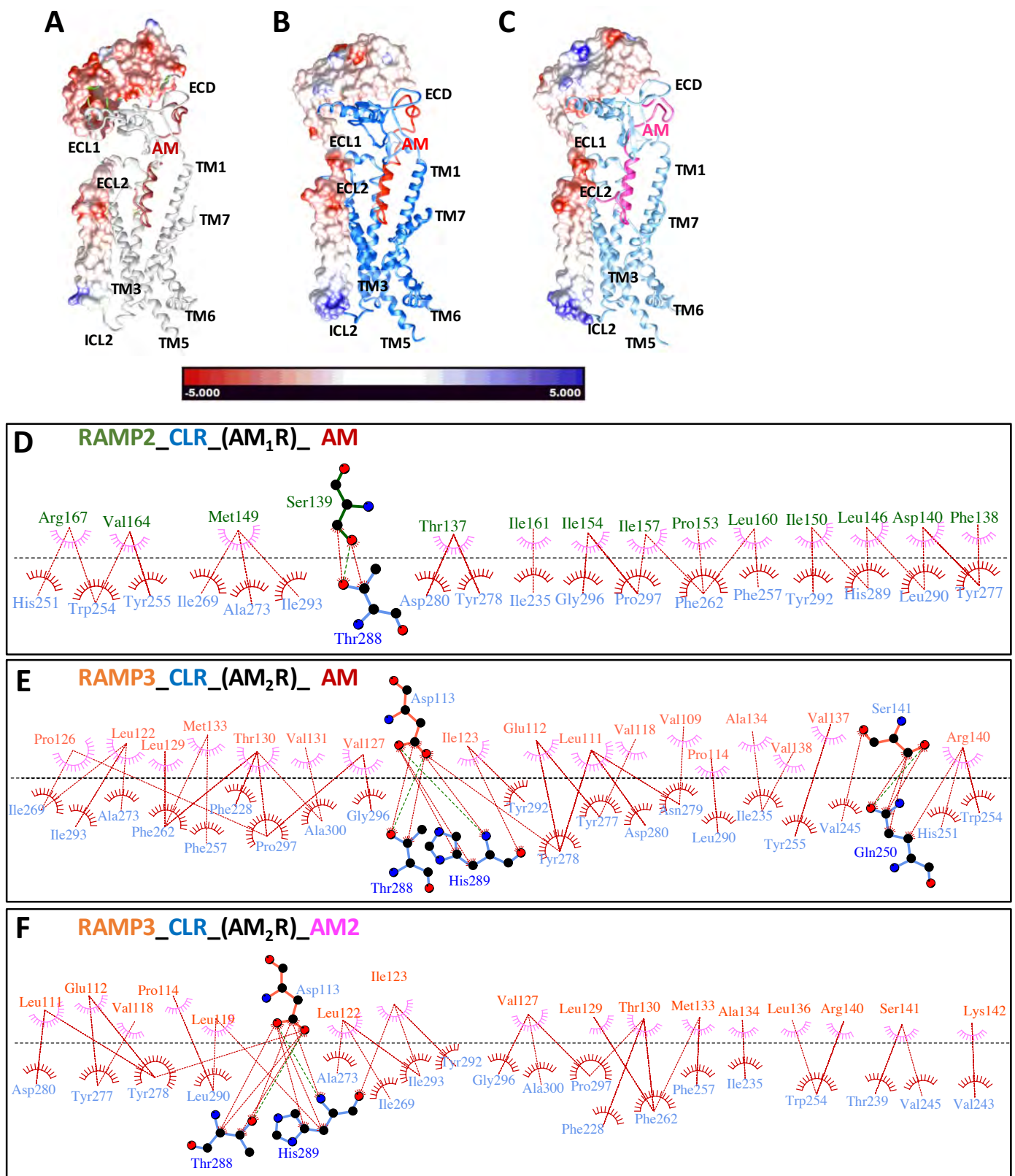


Figure S8. The CLR-RAMP interface for the AM₁R (A, D), AM₂R (B, E) and AM₂AM₂R (C, F). **A-C.** Electrostatic surface of the RAMP; (A) RAMP2 in the AM₁R complex, (B) RAMP3 in the AM₂R complex, (C) RAMP3 in the AM₂AM₂R complex. The electrostatic potential ranges from -5 (red) to +5 (blue) kT e⁻¹. The electrostatic potential for the ECD of RAMP2 in (A) is from PDB:4RWF. **D-E.** Schematics of the interactions between RAMP2 (D) or RAMP3 (E, F) and CLR resolved in the cryo-EM map. Interactions were determined using LigPlot+. RAMP residues are colored green (RAMP2) or coral (RAMP3) and receptor residues blue. Hydrophobic interactions are illustrated by pink (RAMP) or red (receptor) arcs, and interacting residues are joined by a red line. Amino acids involved in H-bonds are labeled in blue with H-bonds shown as dashed green lines.

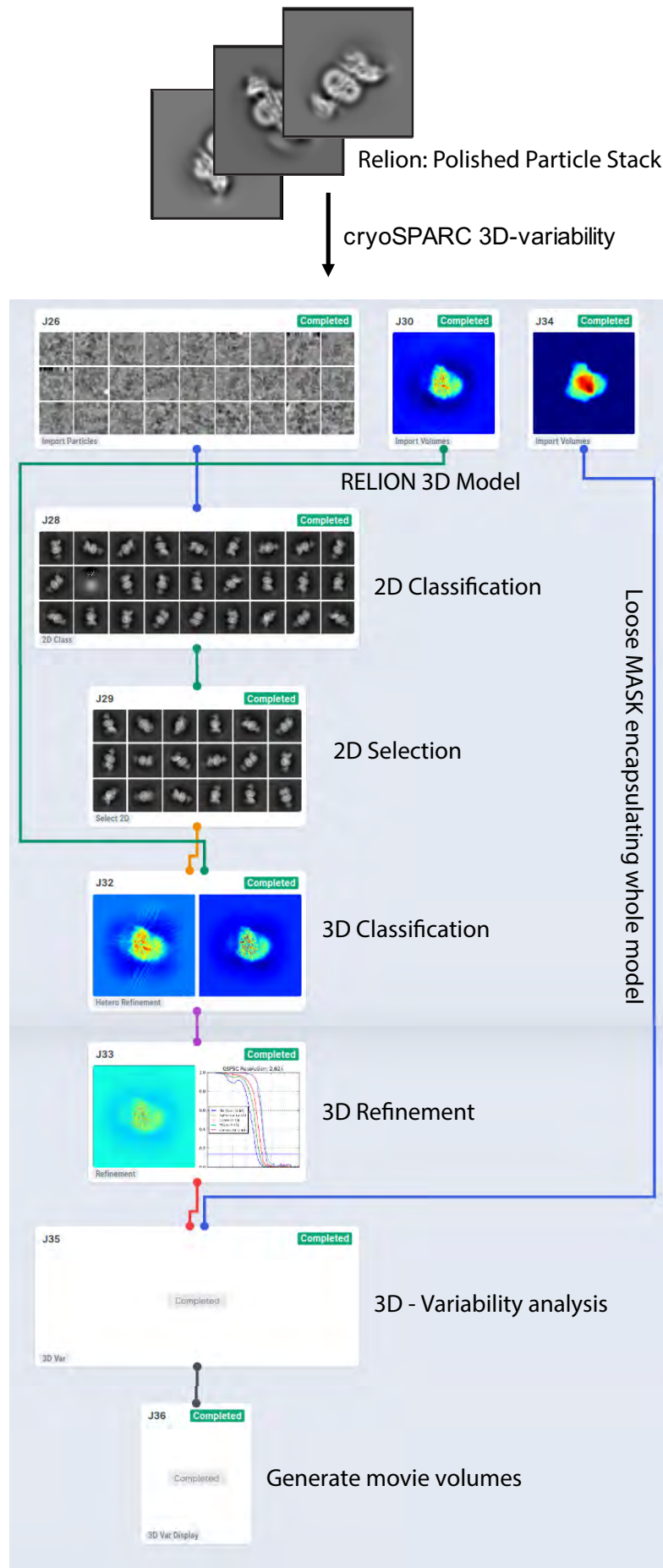
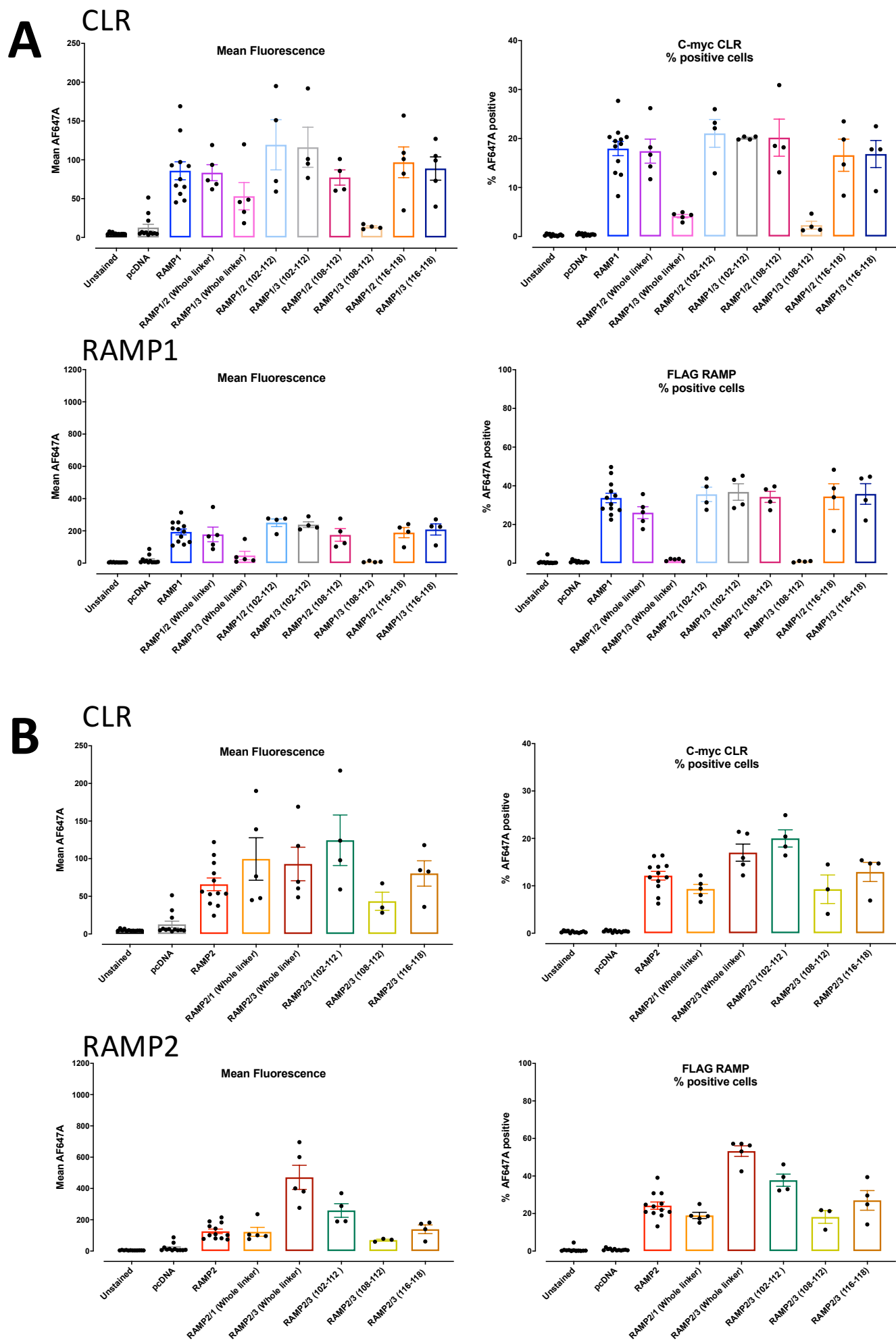


Figure S9. Overview of the receptor conformation dynamic analysis using the cryoSPARC 3D-variability algorithm.



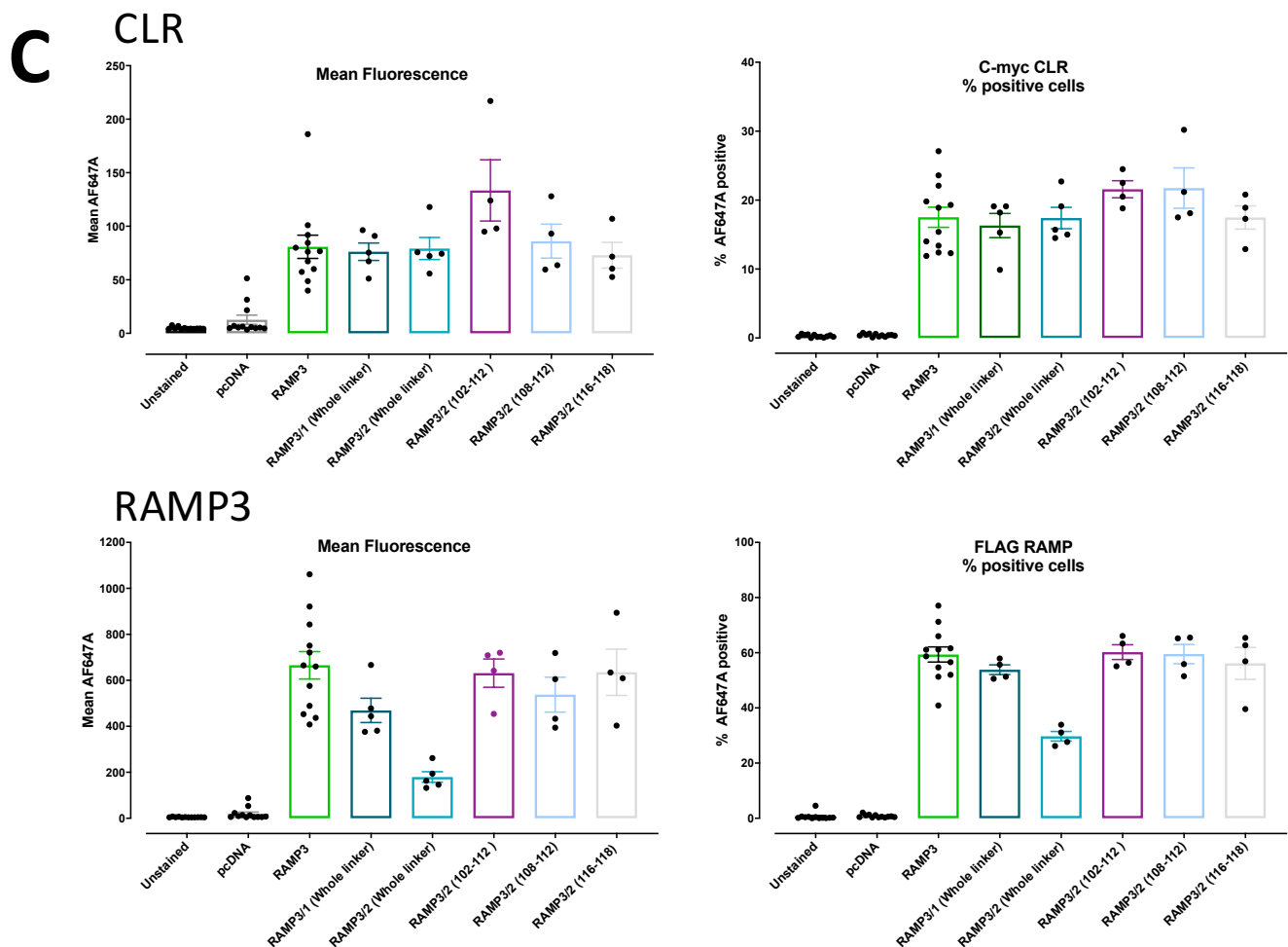


Figure S10. Cell surface expression of CLR and RAMP constructs. **A**, Cell surface expression of the CGRP receptor (CLR:RAMP1) constructs, **B**, AM_1 receptor (CLR:RAMP2) constructs, or **C**, AM_2 receptor (CLR:RAMP3) constructs, assessed by FACS using antibodies to the N-terminal c-myc tag of CLR (upper panels) or N-terminal FLAG tag of each of the RAMPs (lower panels), expressed as mean fluorescence (left panels) or as % positive cells (right panels).

REVIEWS

The Best of Both Worlds? Bitopic Orthosteric/Allosteric Ligands of G Protein–Coupled Receptors

Celine Valant,* J. Robert Lane,* Patrick M. Sexton,**
and Arthur Christopoulos**

Drug Discovery Biology, Monash Institute of Pharmaceutical Sciences, and Department of Pharmacology, Monash University, Parkville, Victoria 3052, Australia;
email: celine.valant@monash.edu, rob.lane@monash.edu, patrick.sexton@monash.edu,
arthur.christopoulos@monash.edu

Annu. Rev. Pharmacol. Toxicol. 2012. 52:153–78

First published online as a Review in Advance on
September 9, 2011

The *Annual Review of Pharmacology and Toxicology*
is online at pharmtox.annualreviews.org

This article's doi:
10.1146/annurev-pharmtox-010611-134514

Copyright © 2012 by Annual Reviews.
All rights reserved

0362-1642/12/0210-0153\$20.00

*These authors contributed equally to the work.

**Corresponding authors.

Keywords

allosteric modulation, biased agonism, bivalent ligand, drug discovery,
functional selectivity, receptor theory

Abstract

It is now acknowledged that G protein–coupled receptors, the largest class of drug targets, adopt multiple active states that can be preferentially stabilized by orthosteric ligands or allosteric modulators, thus giving rise to the phenomenon of pathway-biased signaling. In the past few years, researchers have begun to explore the potential of linking orthosteric and allosteric pharmacophores to yield bitopic hybrid ligands. This approach is an extension of the more traditional bivalent ligand concept and shares some of the same challenges, including the choice and role of the linker between the two pharmacophores and the validation of mechanism of action. Nonetheless, the promise of bitopic ligands is the generation of novel chemical tools that have improved affinity and/or selectivity profiles. Previously identified functionally selective compounds (and medicines) also may act via a bitopic mechanism, suggesting that the phenomenon is more widespread than currently appreciated.

GPCR: G protein–coupled receptor

TM: transmembrane-spanning

Bitopic ligand: a single chemical entity composed of an orthosteric pharmacophore covalently linked to an allosteric pharmacophore

Orthosteric site: the endogenous agonist-binding site on a receptor

Allosteric site: a binding site on the receptor that is topographically distinct from the endogenous agonist-binding (orthosteric) site

INTRODUCTION

G protein–coupled receptors (GPCRs) are the largest family of cell surface receptors in living organisms, constituting ~2% of the human genome (1). Structurally, all GPCRs share a characteristic architecture that consists of an extracellular N-terminal domain, an intracellular C-terminal domain, and seven transmembrane-spanning (TM) domains (TM1–TM7) connected by three extracellular and three intracellular loops. Despite this common architecture, GPCRs can be activated by a diverse array of stimuli such as photons, ions, odorants, biogenic amines, lipids, and complex polypeptides to transduce extracellular signals into intracellular responses. Although the best-characterized intracellular GPCR coupling partners are the family of heterotrimeric G proteins, GPCRs also interact with other intracellular and membrane-associated signaling and scaffolding proteins. This remarkable flexibility allows GPCRs to modulate virtually any physiological process. Not surprisingly, GPCRs are highly tractable drug targets; approximately one-third of all medicines on the market target this protein family (2, 3). However, despite this proven success, only a small proportion of these receptors is currently targeted by therapeutics (3, 4), a fact that likely arises from a variety of reasons. For instance, not all GPCRs are necessarily of immediate relevance to the pharmaceutical industry; most olfactory GPCRs have not been traditionally targeted in this regard. Furthermore, some GPCR classes (e.g., biogenic amines) have been relatively easier to target than others (e.g., peptide receptors) and have simply benefited from more time spent on research into their properties. Orphan GPCRs present a challenge because of the lack of identified endogenous agonists. In all instances, however, additional issues are involved in the failure to appreciate novel paradigms of drug action at these receptors because this area is constantly in flux and rapidly expanding. Specific challenges in this regard include the fact that a single GPCR may couple promiscuously to more than one type of G protein in a cell- and tissue-dependent manner; signal through G protein–independent pathways; undergo complex regulatory processes; be allosterically modulated by small molecules and other proteins, including other GPCRs (5, 6); and adopt ligand-specific conformations that may be signal complex–biased or pathway-biased (5, 7, 8). Although these phenomena present novel avenues for achieving selectivity in drug action, the same functional versatility makes the identification and validation of effective therapeutics increasingly multidimensional. In recent years, this picture has become even more interesting owing to the discovery of bitopic ligands, i.e., molecules that can engender selectivity through concomitant engagement with orthosteric and allosteric sites on GPCRs. This review focuses on the key developments in the field that have led to the current interest in bitopic GPCR ligands.

GPCRs POSSESS MULTIPLE MODES FOR BINDING AND ACTIVATION

Although all mammalian members of the GPCR family possess a similar structural architecture, they are characterized by a relatively low sequence identity and can be distributed into families and subfamilies that have distinctive structural elements and themes for ligand binding, activation, and regulation (2, 9, 10). Family A (also termed Class I; 690 members) GPCRs constitute the rhodopsin-like group and include important drug targets such as the biogenic amine receptors and opioid receptors. Family B (Class II; 48 members) receptors constitute the secretin-like and adhesion GPCRs and include several current candidates for the development of potentially important drugs, such as the glucagon-like peptide 1 receptor. Family C GPCRs constitute the glutamate-like group (Class III; 22 members); they have a large amino-terminal domain that adopts a Venus flytrap–like structure containing the endogenous agonist-binding (orthosteric) site. The diverse

ligands for these receptors include very small molecules such as glutamate, γ -aminobutyric acid (GABA), or calcium. Although implicated in the action of many GPCRs, receptor dimerization is a particularly fundamental theme for Family C GPCRs (11).

At the turn of this millennium, structural studies of GPCRs utilized the high-resolution crystal structure of rhodopsin (12) as the prototypical template. Since 2007, more structures of Family A GPCRs have been determined, including the β_1 and β_2 adrenergic receptors, the adenosine A_{2A} receptor, the dopamine D_3 receptor, and the chemokine CXCR4 receptor (13–20). All these structures have highly similar helical bundles but reveal substantial divergence in the loop and tail regions (**Figure 1**). The structures not only highlight an intrahelical ligand-binding cavity but also indicate an important role of the extracellular loops for ligand binding and/or ligand entry. Until recently, most high-resolution GPCR structures were of antagonist- or inverse agonist-bound inactive states, but they nonetheless served to highlight the fact that different GPCR-targeting ligands can adopt strikingly different poses depending on the receptor type. The first minimally active conformation of a Family A GPCR was directly appreciated when the crystal structure was solved for opsin associated with a C-terminal peptide fragment of its G subunit, transducin (21). This structure suggested the presence of a substantial change in the arrangement of the helical bundle, with prominent movement of TM6. More recent studies have now provided insight into the mechanism of activation of other GPCRs, specifically the β adrenergic and adenosine A_{2A} receptors (22–25). Using a camellid antibody that stabilized the active state of the receptor (analogous to the action of a G_s protein), Rasmussen et al. (22) found that significant changes occur at the cytoplasmic face of the receptor, including the outward displacement of TM6 and TM5 and an inward movement of TM7 and TM3. In the recently published agonist-bound adenosine A_{2A} structure, significant movements of the cytoplasmic ends of TM3, TM6, and TM7 were observed, similar to those seen in both the opsin and the β_2 adrenergic receptor. In both cases, these changes are coupled to relatively subtle changes in the agonist-binding pocket when compared with the antagonist-binding pocket. This leads to the question: Which agonist-receptor interactions are essential to receptor activation? Although similar conformational changes occur at the intracellular sides of the agonist-bound β_2 adrenergic receptor and the agonist-bound A_{2A} adenosine receptor, these changes appear to be mediated by distinct agonist-binding interactions. In the β_1 adrenergic receptor, Warne et al. (24) observed that full agonists were able to form a hydrogen bond with a conserved serine from TM5. This interaction may reduce the energy barrier to allow the residue repacking and helix rotation that are observed in the β_2 adrenergic receptor–agonist-antibody complex. Conversely, binding of the A_{2A} adenosine receptor agonist does not directly affect TM5; instead, the most pronounced ligand-induced changes involve TM3, TM6, and TM7, as well as a significant movement of extracellular loop 3.

Collectively, the recently solved GPCR structures highlight how a common architecture can nonetheless accommodate a structurally diverse set of ligands to mediate conformational changes that lead to signal transduction. However, crystal structures only provide snapshots of discrete states and cannot directly interrogate the dynamic equilibria between conformational transitions. In this regard, alternative approaches are warranted to allow visualization of receptor structural changes not currently amenable to X-ray crystallography. For example, a recent study by Bokoch et al. (26) used nuclear magnetic resonance spectroscopy to investigate dynamic, ligand-specific changes around a salt bridge linking extracellular loops 2 and 3 of the β_2 adrenergic receptor. An important finding from this study was the identification of conformational coupling between the extracellular domain and the orthosteric binding site. This finding adds weight to the growing body of data indicating that the extracellular surface of a GPCR is remarkably diverse and therefore also represents another target region for the discovery of subtype-selective drugs.

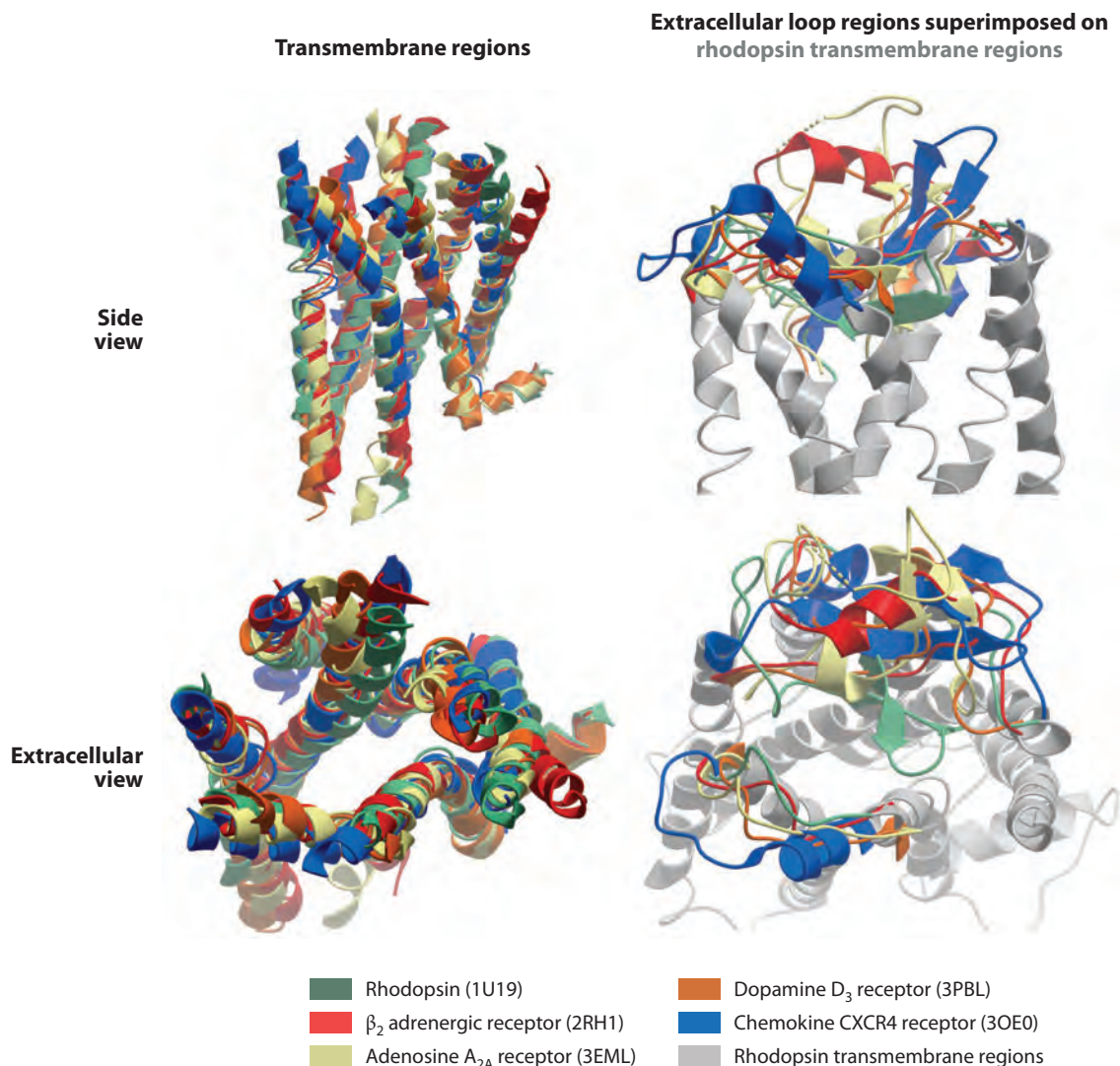


Figure 1

Overlay of high-resolution, inactive-state, crystal structures of G protein-coupled receptors reveals similar transmembrane helical arrangements but divergent extracellular loop regions. Left panels show alpha helical regions only from the side (*top panel*) or from an extracellular view (*bottom panel*). Right panels highlight equivalent views of the extracellular loops superimposed on the transmembrane regions of rhodopsin.

STIMULUS BIAS AND ALLOSTERIC MODULATION AS KEY PARADIGMS FOR GPCR SELECTIVITY

Given the increase in biochemical and biophysical data showing that GPCRs are highly dynamic proteins and that functionally distinct ligands can stabilize specific receptor conformations (5, 8, 26–35), it stands to reason that the vast array of behaviors that a GPCR can exhibit, e.g., from G protein activation to desensitization and internalization, need not be sequentially linked. Accordingly, different ligands acting at the same receptor and in the same cellular environment

cannot be assumed to promote similar repertoires of receptor behaviors. Numerous examples now exist to support the concept of a single ligand promoting distinct functional outcomes at a given receptor, depending on the pathway with which the receptor is engaged (5, 7, 8, 28, 30). A striking example of the lack of concordance between ligand efficacies has been observed with compounds traditionally classed as β -blockers at the β_2 adrenoceptor. Propranolol and ICI118551 are inverse agonists for G_s protein-mediated stimulation of adenylate cyclase but produce partial agonist responses for β arrestin-dependent activation of extracellular signal-regulated kinases 1 and 2 (ERK1/2) (28); i.e., they display opposite efficacies depending on the signal pathway being recruited. The ability of different ligands to engender discrete signaling activities at a given GPCR has been termed stimulus bias, stimulus trafficking, collateral efficacy, biased agonism, or functional selectivity (5, 7, 8). A common indicator of stimulus bias is the reversal of potency order or maximal effects for different agonists at a given receptor when they are examined across alternative signaling pathways, although such findings usually represent the extremes of the phenomenon; stimulus bias is also likely to be operative if the potency or efficacy preferences of a test agonist do not track with those of the endogenous agonist across different pathways (36–39).

The overall promise of stimulus bias is the ability to design ligands that selectively engage therapeutically relevant signaling pathways while sparing those that contribute to undesirable side effects; drug discovery emphasis is shifted from a traditional receptor subtype-centric view toward a receptor active-state-centric or pathway-selective view. The key challenges in this regard are twofold. First, it is usually not known which signaling pathway is most predictive of the desired therapeutic outcome. Second, it is necessary for functional screening of potential drug candidates to be performed across multiple assay formats. Nonetheless, recent provocative findings suggest that such functional selectivity may indeed be therapeutically advantageous. For instance, the GPR109A receptor agonist, nicotinic acid, is an effective antilipolytic, but its use is limited by serious cutaneous flushing (40). This flushing effect is mediated by a β arrestin-dependent pathway, whereas the beneficial lipolytic effect is believed to be mediated by a G_i protein-dependent reduction of cyclic adenosine monophosphate (41). Consequently, an agonist that selectively activates the G_i pathway but not the β arrestin pathway could prove to be a superior treatment for dyslipidemia. Interestingly, this pharmacological profile was recently identified in a novel series of pyrazole GPR109 receptor agonists (41, 42), providing proof of concept for such a pathway-targeted approach.

The phenomenon of stimulus bias effectively highlights the natural allosteric nature of GPCRs as signaling machines; the binding of an extracellular ligand promotes a conformational change that is transmitted to topographically distinct intracellular sites, which then selectively engage signaling proteins. There is no *a priori* reason why such allosteric effects cannot also be propagated between distinct binding domains on the extracellular surfaces of GPCRs. Indeed, the vectorial nature of information transfer across GPCRs (43) suggests that this should be the case (**Figure 2**). As discussed above, the diverse modes of ligand engagement within the various subfamilies of GPCRs indicate that a common structural topography is nonetheless flexible enough to provide different types of pockets for different types of ligands. Thus, the orthosteric-binding domain for one type of GPCR may represent an allosteric-binding motif in another type of GPCR that recognizes substantially different endogenous ligands. This clearly represents an exciting opportunity for novel drug discovery, especially with regard to synthetic small molecules, which remain a priority for the pharmaceutical industry.

The exploitation of allosteric sites on GPCRs provides a means by which numerous important issues associated with the difficulty in discovering small-molecule orthosteric ligands of certain GPCRs can be overcome, in particular for GPCRs in which the orthosteric site is highly conserved between subtypes (5, 6, 44, 45). Allosteric modulators are defined as ligands that (*a*) bind to GPCRs

ERK1/2: extracellular signal-regulated kinases 1 and 2

Stimulus bias (functional selectivity):

a ligand-mediated stabilization of distinct receptor active states to the relative exclusion of others, leading to selective signaling via a subset of the signaling repertoire normally available to a receptor in a given cell type

Allosteric modulator:

a ligand that binds to an allosteric site and modifies the binding and/or signaling of another cobound ligand

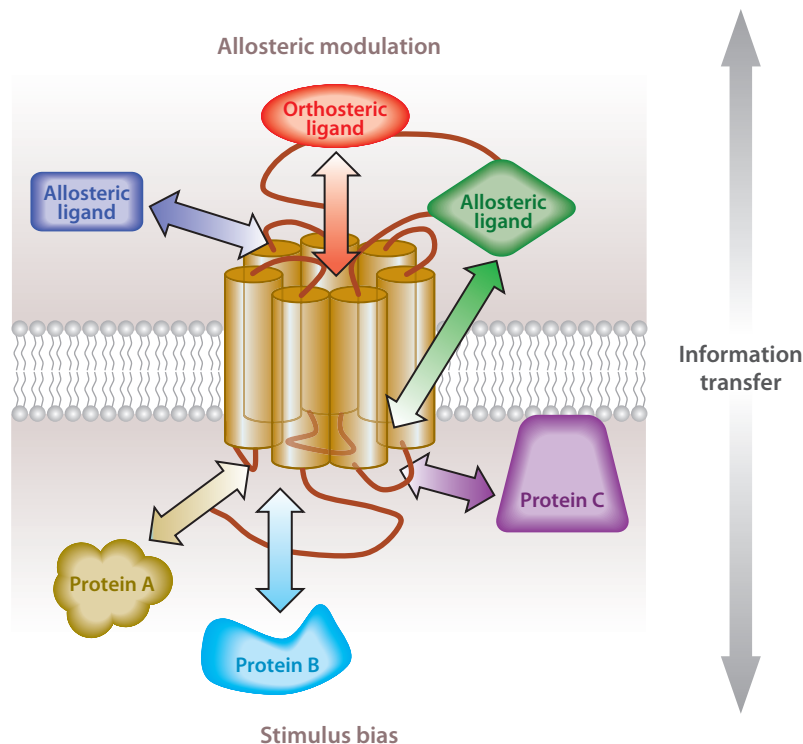


Figure 2

Bidirectional information transfer in G protein-coupled receptors (GPCRs) gives rise to the phenomena of allosteric modulation and stimulus bias. In both instances, the binding of a ligand to a GPCR promotes a conformational change that alters the interactive properties of other proteins or ligands at a topographically distinct region of the receptor.

at sites that are topographically distinct from the orthosteric site and (*b*) promote a conformational change that modulates orthosteric ligand affinity and/or efficacy. Some allosteric ligands can also act as (allosteric) agonists or inverse agonists in the absence of an orthosteric ligand (5, 6, 44, 45). In all instances, a receptor occupied by an allosteric ligand should be viewed as a novel receptor type with its own unique repertoire of behaviors.

Compounds that possess an allosteric mode of action can display numerous theoretical therapeutic advantages over orthosteric ligands. The most obvious advantage is the potential for greater selectivity across receptor subtypes because an allosteric site may have greater divergence in sequence between subtypes compared with the orthosteric domain. If the allosteric modulator displays minimal agonism in its own right, then it exerts its effect only in the presence of the orthosteric agonist, potentially maintaining both temporal and spatial aspects of endogenous physiological signaling. Because the magnitude of an allosteric effect is governed by the degree of cooperativity manifested between allosteric and orthosteric sites, the effects of allosteric modulators with limited positive or negative cooperativity have a ceiling level above which no further target-based modulation occurs, irrespective of modulator concentration. This means that large doses of allosteric modulators can be administered with a lower propensity toward target-based toxicity than that seen with orthosteric agonists or antagonists. Finally, given that allosteric modulators themselves promote a conformational change in GPCR structure, these compounds may

engender functional selectivity, either by themselves or by modulating the actions of the orthosteric ligand in a pathway-biased manner. Such pathway-selective modulation has already been observed in the actions of synthetic small molecules (46–49).

Interestingly, the recent focus on allosteric modulators of GPCRs has unmasked small molecules that can also bind to intracellular GPCR regions. For example, a combination of homology modeling, chimeric receptors, and mutagenesis studies implicated a potential intracellular binding pocket for a small-molecule inhibitor of the CXCR2 chemokine receptor (50). A similar intracellular site of interaction was suggested for small-molecule inhibitors of the chemokine CCR4 receptor (51). These studies suggest that such an intracellular site may exist across this receptor family and be exploited for drug discovery. This hypothesis is corroborated by the development of pepducins, which are created through the attachment of a lipidated group, such as an acyl chain, to a peptide that corresponds to a portion of one of the intracellular loops of a GPCR of interest (52). Mechanistic studies have revealed that the action of pepducins requires an intact receptor, and studies on a protease-activated receptor 1–directed pepducin highlighted the C-terminal tail of the receptor as a potential interaction site (53). Thus, pepducins can be regarded as novel allosteric modulators of GPCR function. Both agonistic and antagonistic pepducins have been developed against a variety of GPCRs, including protease-activated receptors, chemokine receptors, and the sphingosine-1-phosphate receptor 3 (52–63).

Irrespective of the location of the allosteric site, one of the key challenges associated with allosteric modulator drug discovery is the need to quantify allosteric effects in a manner that can, ideally, also be used to guide structure-activity and compound optimization studies. At the molecular level, allosteric modulation can be described thermodynamically in terms of the affinities that the orthosteric and allosteric ligands have for different receptor states in both the absence and the presence of the cobinding of one another as well as the cobinding of interacting cellular proteins that initiate signal transduction (5, 43). This is routinely presented in mass-action form as a variety of allosteric ternary complex models of different degrees of complexity, depending on the number of receptor states being represented (6, 64–67). A common feature of these models is the incorporation of one or more cooperativity factors that accounts for the effect(s) that each of the two ligands brings to bear upon the interaction of the other with the receptor. Unfortunately, these thermodynamic parameters are not easily attainable from routine experimental data except in the simplest cases of allosteric modulation. As a consequence, researchers have developed various operational models of allostery that can be applied to experimental data in a manner that facilitates determination of the affinity of the modulator for the allosteric site on the receptor, as well as operational measures of the modulator's cooperativity and any signaling efficacy (68–71).

THE MESSAGE-ADDRESS CONCEPT IN THE DESIGN OF GPCR-TARGETING LIGANDS

Stimulus bias and allosteric modulation promise new modes of selectivity at GPCRs. A more historical approach to designing ligands is encompassed in the message-address concept, a term coined by Schwyzer (72) in the late 1970s and first applied to GPCRs by Portoghesi and colleagues (73, 74). This concept posits that each ligand exhibits two components: the message, which is composed of the main receptor recognition motif and therefore promotes the transduction of the signal from the receptor to the effector, and the address, which is located near the message component and provides additional ligand-receptor interactions (**Figure 3**). This address component can be either on a region proximal to the message component (i.e., within the same binding site) or on a more distal region, such as a different binding site, within the same receptor or even on a different receptor. Incorporation of the address component proximal to the

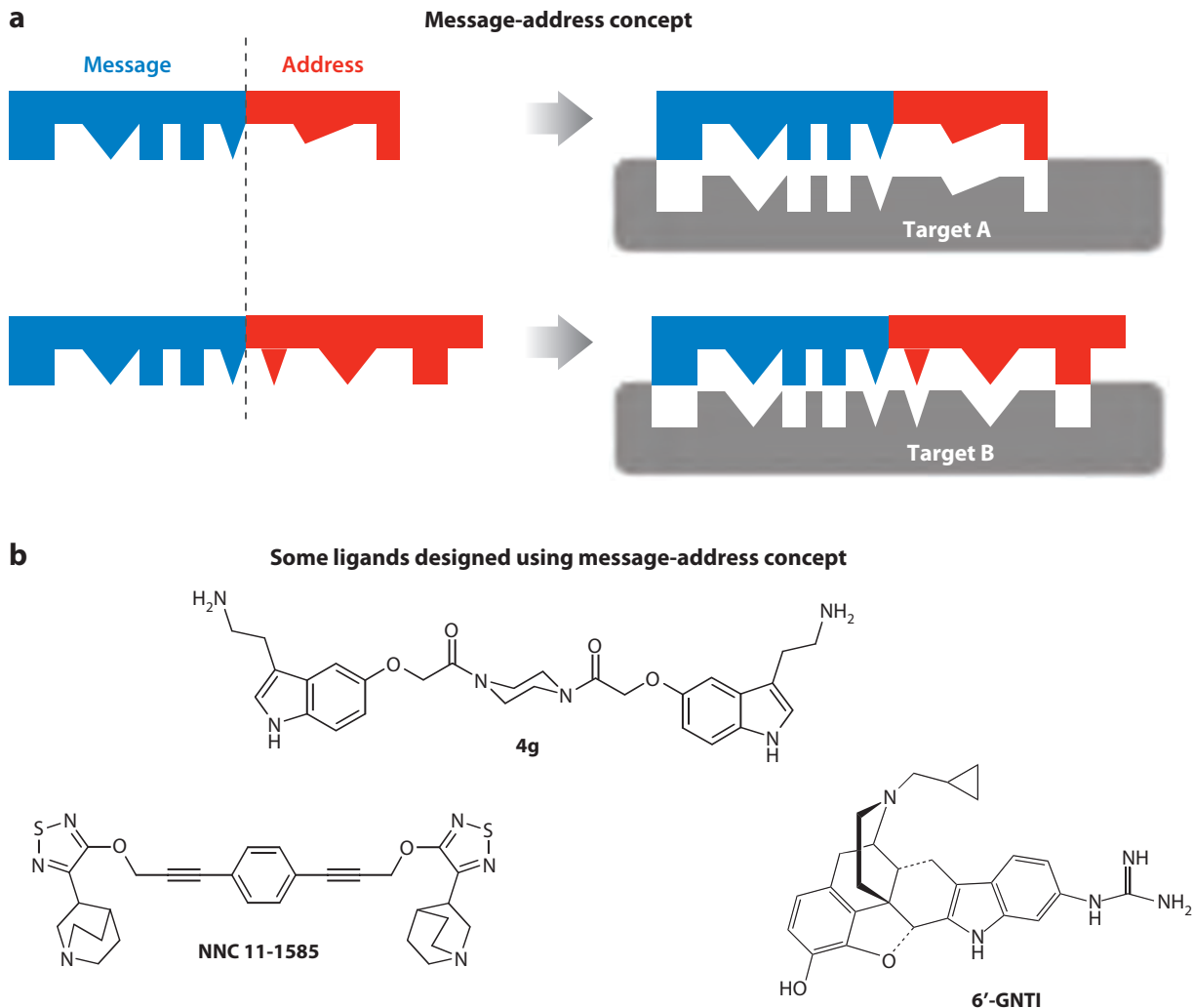


Figure 3

(a) The message-address concept defines selective drug design in terms of pharmacophore elements (message) that engage a conserved region of the target protein, responsible for signal transduction/termination, and additional moieties (address) that target less conserved regions associated with the target. (b) Some examples of ligands that have been designed using this principle are also illustrated: 4g (5HT_{1B/D} receptors); NNC 11-1585 (mAChRs); and 6'-guanidinonaltrindole, also known as 6'-GNTI (δ - κ opioid dimers).

Bivalent ligand: a single chemical entity composed of two covalently linked pharmacophores

message component has been the most thoroughly utilized approach, as reflected by the plethora of endogenous orthosteric ligand analogs available for many GPCR families. Subsequent studies have focused on extending the distance between message and address components in ligands to exploit regions of the target receptor that are more distal to the main binding pocket. Furthermore, novel compounds have been synthesized by the linking of two distinct pharmacophores via an appropriately sized spacer to create bivalent ligands. The past three decades have witnessed the development of highly selective bivalent ligands for GPCRs (75), such as for the opioid receptors (76–78), muscarinic acetylcholine receptors (mAChRs) (79–81), serotonin receptors (82–84), cannabinoid receptors (85), and gonadotropin-releasing hormone receptors (86). Some examples

of such ligands are illustrated in **Figure 3**. This concept has even been extended to other proteins, such as acetylcholinesterases (87) and the tyrosine kinase receptors TrkA (88) and TrkC (85).

6'-GNTI: 6'-guanidinonaltrindole

HOMO- AND HETEROBIVALENT LIGANDS

A bivalent ligand is, by definition, a single chemical entity composed of two covalently linked pharmacophores. If the pharmacophores are identical, then the ligand is defined as a homobivalent ligand, whereas the linking of two different pharmacophores yields a heterobivalent ligand. Both homo- and heterobivalent ligands have been developed for GPCRs as pharmacological tools to achieve receptor subtype selectivity and/or, increasingly, as a means to study receptor dimerization. However, the earliest studies on GPCR bivalent ligands did not necessarily aim to target dimeric complexes, and many such ligands have relatively short linking groups between the pharmacophores (89). This suggests that these bivalent compounds may be interacting with neighboring binding sites on a single receptor rather than bridging two binding sites across a receptor dimer. One such example is the development of norbinaltorphimine, which is a homobivalent ligand selective for the κ opioid receptor (89). This compound consists of two naltrexone (opioid receptor antagonist) pharmacophores joined by a pyrrole spacer, but only part of the second pharmacophore was found to be necessary for κ opioid receptor selectivity (89). A similar finding relates to 6'-guanidinonaltrindole (6'-GNTI) (**Figure 3**), which was originally designed to be a κ opioid receptor agonist on the basis of the message-address concept but was subsequently revealed to be a more potent and selective agonist of the δ - κ opioid receptor heterodimer (90) (**Figure 4a**). It is unlikely, however, that this heterodimer selectivity is achieved by simultaneous interaction of one molecule of 6'-GNTI with the two orthosteric sites from each of the δ and κ opioid receptors, given the molecule's size. However, other ligands selective for δ - κ opioid

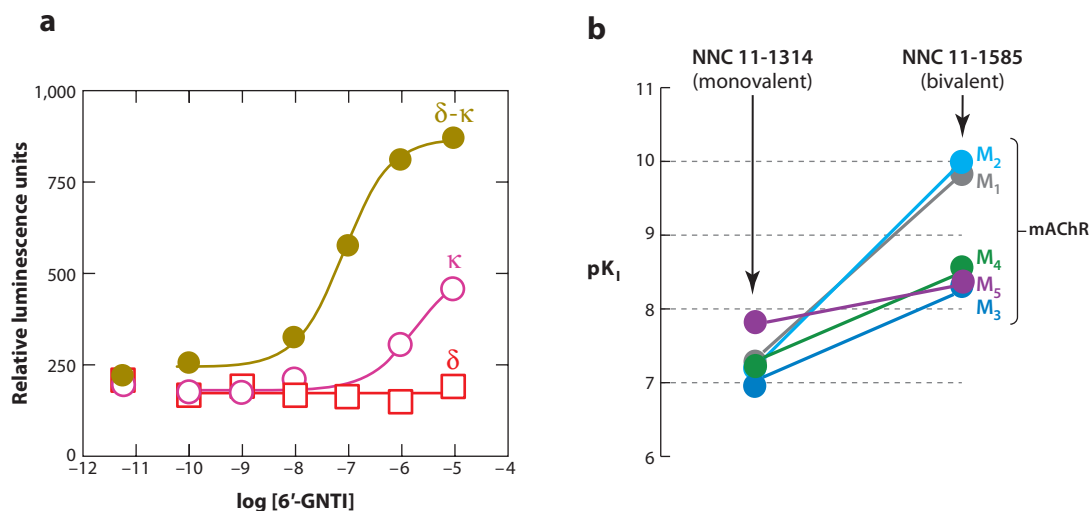


Figure 4

Bivalent ligands can lead to improvements in selectivity and/or affinity. (a) 6'-guanidinonaltrindole (6'-GNTI) has higher efficacy for promoting intracellular calcium mobilization in human embryonic kidney cells containing the δ - κ opioid heterodimer compared with cells individually expressing either δ or κ opioid receptors. Data replotted from Reference 90. (b) The homobivalent muscarinic acetylcholine receptor (mAChR) agonist NNC 11-1585 displays markedly higher affinity and selectivity for M₁ and M₂ mAChRs compared with its monovalent pharmacophore, NNC 11-1314. Data taken from Reference 79. The pK₁ is the negative logarithm of the ligand equilibrium dissociation constant.

receptor heterodimers have been developed; these have substantially longer linker lengths that are more compatible with two distinct pharmacophores bridging a dimeric receptor complex. For example, the tethering of the κ -selective antagonist pharmacophore 5'-guanidinonaltrindole to the δ -selective antagonist pharmacophore naltrindole yielded optimal *in vitro* and *in vivo* potency when a linker region of 20–21 atoms was used (91, 92). Interestingly, all studies of μ - δ and μ - μ opioid receptor bivalent ligands have found similar optimal spacer lengths of 18–21 atoms (93, 94). Owing to the therapeutic potential of targeting GPCR homo- or heterodimers, numerous studies have utilized such a bivalent ligand approach. In other cases, heterobivalent ligands have been designed simply with the desire to combine pharmacophores that result in a common therapeutic endpoint. For instance, the conjugation of the β_2 adrenergic receptor agonist isoproterenol to the adenosine A₁ receptor agonist adenosine had been attempted in an effort to derive novel tools for modulating cardiac arrhythmias (95).

THE WORLD BETWEEN PHARMACOPHORES: THE CRITICAL ROLE OF THE LINKER

Because all bivalent ligands exhibit two pharmacophores joined by a linker, the nature, length, and flexibility of this latter structural feature itself can significantly influence the activity of the designed bivalent ligand. For instance, if the linker is too short, the ligand cannot bridge both binding sites simultaneously and shows little to no enhancement of activity compared with the monovalent ligand. Common types of linkers include polyethylene glycol, polyamide, or even polymethylene linkers, and each has its own chemical properties that also play a role in the final observed interactions. Another important consideration is the rigidity or flexibility of the structure of the linker because this contributes to the degrees of freedom available to the bivalent ligand. In the case of a rigid linker structure, if the orientation of the pharmacophores is not optimal, a reduction of activity may be anticipated. However, linker rigidity can also prove advantageous. For example, one way to elucidate the nature of GPCR homo- or heterodimers is to use bivalent ligands as pharmacological tools to facilitate the precise determination of the distance between each binding site from each monomer. However, simple linear linkers can be problematic because they can adopt variable secondary structures; at best, they can provide an estimate of the maximum distance between vicinal recognition sites. In contrast, a recent study has demonstrated that it is possible to target two different sites across GPCRs using a highly rigid bivalent ligand (96). Poly(L-proline) is a highly structured chain, which forms a helix that maintains a length of 0.9 nm per turn (**Figure 5a**). Owing to the distinctive cyclic structure of proline's side chain, this amino acid provides exceptional conformational rigidity compared with that of others. Therefore, for a given number of prolines per linker, a precise linker length can be determined, rendering rigid bivalent ligands utilizing this linker extremely useful for providing topographical information. Within a range of linker lengths between 2 and 8 nm, followed by coupling with the appropriate pharmacophores, investigators found bivalent ligands of the CXCR4 receptor that exhibited the highest affinity when the linker length was approximately 6 nm (96). This result provides new insight for the design of bivalent ligands for this receptor as well as knowledge about the possible topography of the associated binding sites.

In the case of flexible linkers, one possible advantage is that they can allow the address component of the bivalent ligand to more freely move around and bind to its own binding site, which may result in a higher likelihood of increased affinity (but see the next section for caveats). Often, the introduction of a linker into a pharmacophore occurs on a phenyl ring, which raises the possibility of ortho-, meta- or parasubstitution; each of these influences the specific orientation of the linker relative to the pharmacophore. Although investigating all possibilities is certainly

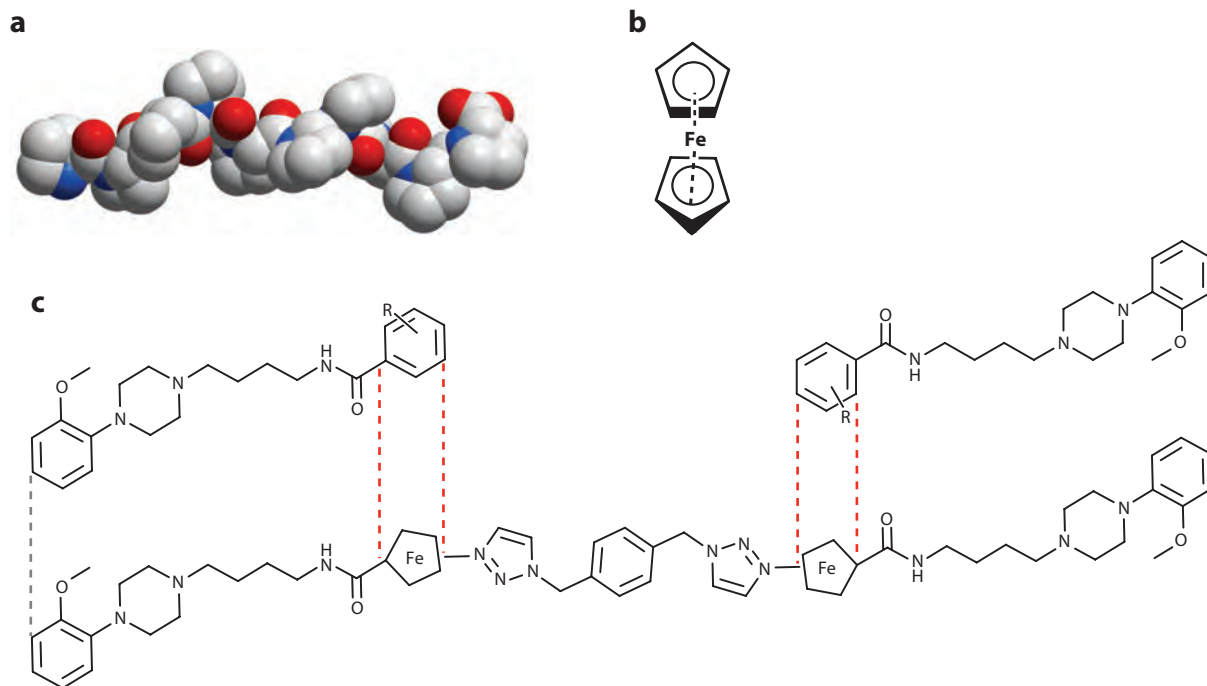


Figure 5

Rigid or flexible linkers can be used in bivalent ligand design. (a) The rigid helical structure adopted by a poly(L-proline) linker can be used as a “molecular tape measure.” (b) The structure of ferrocene, which can be used in bioisosteric replacement of phenyl rings in bivalent compound linker regions. (c) An example of bioisosteric replacement of phenyl rings in a dopamine D₃ receptor-selective pharmacophore to yield a dopamine D₂-selective homobivalent ligand (see Reference 97).

possible, time and cost considerations have prompted the exploration of alternative approaches, such as the use of flexible analogs of the phenyl ring. One interesting study recently investigated the effect of highly flexible linkers by means of bioisosteric replacement using metallocene-based subunits (97). Specifically, owing to their similar physical and chemical properties, a phenyl may be interchangeable with a ferrocenyl that consists of two cyclopentadienyl rings bound on opposite sides of a central iron atom. A particular useful feature of the ferrocenyl is that the two cyclopentadienyl rings are able to rotate freely around each other; the absence of an individual bond between the rings and the iron metal causes this configuration to act like a hinge, which confers flexibility to the ferrocenyl (**Figure 5b**). Following this principle, researchers designed a highly flexible homobivalent ligand that exhibited agonism at the dopamine D₂ receptor and antagonism at the dopamine D₃ and D₄ receptor subtypes (**Figure 5c**). This type of profile may be associated with putative atypical antipsychotic activity (97).

IMPROVING AFFINITY AND SELECTIVITY WITH BIVALENT LIGANDS

Most bivalent ligands have been developed with a dual aim: (a) to improve affinity, by providing additional interactions, and (b) to improve selectivity, if these additional interactions involve less conserved regions across a family of receptors (**Figure 4**). Regardless of the pharmacophore (homobivalent or heterobivalent), there are generally two types of bivalent ligands: those with

relatively short linkers and those with long linkers. As indicated above, bivalent ligands with short linking groups may interact with a neighboring site on a single GPCR, via amino acid residues that are potentially less conserved, such as residues in the extracellular loops. Such additional interactions may be sufficient for an improvement of affinity, in addition to better selectivity; the previously mentioned example of the κ -selective opioid receptor antagonist, norbinaltorphimine, represents one such instance. In contrast, bivalent ligands with longer linking groups may utilize a neighboring site on a different receptor (or associated protein) to increase affinity and/or selectivity. The effect on affinity is predominantly due to a reduction of the overall energy required for the second pharmacophore to bind to its site. Simplistically, the binding of the first pharmacophore induces an increase in the proximity of the second pharmacophore to its binding site, therefore reducing the energy cost of the second pharmacophore to bind to its site compared with the energy required by two separate monovalent ligands. In theory, the affinity increase for appropriately designed bivalent ligands that meet this criterion should be equal to the product of the binding contributions of the individual pharmacophores (98), which can equate to a dramatic increase in ligand potency. Furthermore, if the two pharmacophores are identical, the “effective” concentration of the active pharmacophore within the immediate region of the protein binding site is elevated, which increases the probability of binding. This alone can also lead to an increase in the observed potency of the compound.

In addition to improving affinity, the linking of two pharmacophores may also increase the degree of these ligands’ selectivity for a receptor target. The most obvious example of this scenario is the targeting of heterodimeric receptors, which can exhibit both tissue- and drug-specific properties. Using a bivalent ligand that can target such an entity exhibits a higher degree of selectivity than using the monovalent ligands separately and may even result in functionally selective signaling as well. For example, the bivalent opioid μ agonist/ δ antagonist MDAN-21 exhibits reduced tolerance and physical dependency compared with its individual constituent opioid ligand pharmacophores (94). Furthermore, MDAN-21 is 50-fold more potent than morphine and therefore provides proof of principle for the concept of bivalent ligands as tools for the development of analgesics that do not induce tolerance and dependency in patients.

Intriguingly, some examples of bivalent ligands do not show the expected enhancement of affinity (86, 99). In this case, it is necessary to consider both the enthalpic and entropic components of the free-energy change associated with ligand binding, encompassed by the classic equation $\Delta G = \Delta H - T\Delta S$ (where G is the Gibbs free energy, H is the enthalpy, T is a constant temperature, and S is the entropy). Perhaps the most intuitive reason for nonsynergistic affinity would be the bivalent ligand having a linker of insufficient length to allow simultaneous occupation of both binding sites (98). In addition, the linker itself may participate in an undesirable interaction that blunts the potential affinity gain (76). Although a relatively flexible linker increases the likelihood that all ligand-receptor interactions can occur without energetic strain, this can result in unexpected entropic costs (98). Specifically, if the binding of a bivalent ligand is a two-step process, then binding of the second pharmacophore will be unfavorable for conformational entropy because the number of conformations available to the bivalent ligand before complexation will be greater than that following complexation. Ultimately, enthalpy and entropy can have partly compensating effects; if so, then the affinity gain expected from linking pharmacophores is not straightforward to predict. A final issue to consider is the cooperative interaction between the two binding sites of the linked pharmacophores. If the binding of one of the pharmacophores of a bivalent ligand induces a conformation of the remaining binding site that impairs the binding of the second pharmacophore, then the gain in enthalpy of the bivalent ligand will be smaller than the sum of enthalpy gains of the two separate monovalent components.

FROM BIVALENT TO BITOPIC LIGANDS

The growing interest in allosteric modulators of GPCRs has culminated in recent studies seeking to exploit this paradigm within the context of the bivalent ligand approach, that is, to create molecules that explicitly combine defined orthosteric and allosteric pharmacophores in one ligand. Such bivalent compounds have been termed bitopic or dualsteric (100, 101) to explicitly acknowledge the hybrid orthosteric/allosteric nature of the molecule, as opposed to the more general umbrella term bivalent. One may choose to pursue a bitopic ligand approach for numerous reasons. First, the use of a standard allosteric modulator relies on the presence of appropriate endogenous agonist tone, which may not always be the case, e.g., as with neurodegenerative disorders such as Parkinson's and Alzheimer's diseases that involve a loss of neurotransmitter-releasing nerves but not their postsynaptic GPCR targets. Second, the design of a bitopic ligand possessing appropriately paired orthosteric and allosteric fragments can theoretically achieve improvements in affinity, owing to the utilization of two binding sites, and selectivity, owing to the targeting of an allosteric site and/or the promotion of stimulus bias. Importantly, these advantages can be attained through use of a single biologically active molecule.

The first example of a rationally engineered bitopic ligand came from the work of De Amici, Holzgrabe, and colleagues (102), who synthesized hybrid ligands targeting the mAChRs with an orthosteric pharmacophore based on the agonist oxotremorine, which was linked to hexamethonium-derived allosteric modulators. These hybrid molecules did not display improved affinity compared with their individual constituents but did gain subtype selectivity as compared with the parent orthosteric agonist. One reason that the mAChRs represent the best-studied exemplar model of bitopic GPCR ligands is that they have a rich allosteric pharmacology and substantial structural evidence that supports a relatively close apposition of the TM-domain-located orthosteric site with at least one allosteric site comprising more extracellular-facing residues, including some of the extracellular loops (44, 103–105). Accordingly, Steinfeld and colleagues (106) also synthesized a bitopic ligand targeting these regions of the M₂ subtype of mAChR. In this instance, a substantial increase in affinity was noted for the bitopic ligand THRX-160209 (**Figure 6**), compared with either of its orthosteric (3-benzhydryl pyrrolidine) or allosteric (4-aminobenzylpiperidine) moieties (106), as predicted for classic bivalent ligands. Another important outcome from that study was the demonstration that the seven-chain pharmacophore linker itself also promoted an increase in compound affinity, highlighting the importance of including incremental fragments of novel bitopic ligands in control experiments. Most recently, these same researchers have extended this approach to the design of bitopic ligands that appear to target two classes of GPCRs, namely the mAChRs and the β_2 adrenergic receptor (106). In this latter instance, the two pharmacophores that were chosen were an orthosteric antagonist of the mAChRs and an orthosteric agonist of the β_2 receptor, but these were subsequently shown to be allosteric modulators at their nonpreferred receptor (i.e., the mAChR antagonist was an allosteric modulator of the β_2 receptor, and vice versa). Thus, when these pharmacophores were conjugated to form the bivalent ligand THRX-198321 (**Figure 6**), they also yielded, by definition, a bitopic ligand for each receptor.

Observations such as those described above clearly point to the complexities associated with the design of bitopic and bivalent ligands. Empirical approaches to combining pharmacophores with appropriately chosen linkers remain an important part of the process but can also be guided by the application of theoretical models that can describe potential bitopic ligand behaviors. One such model (6, 101, 107) appears in **Figure 7**, which shows that the simplest mass-action description of a bitopic ligand interacting with a receptor in the presence or absence of an orthosteric ligand is an amalgam of the classic orthosteric competitive model and the allosteric ternary complex model. Theoretically, the bitopic ligand can be distributed across a given receptor population in

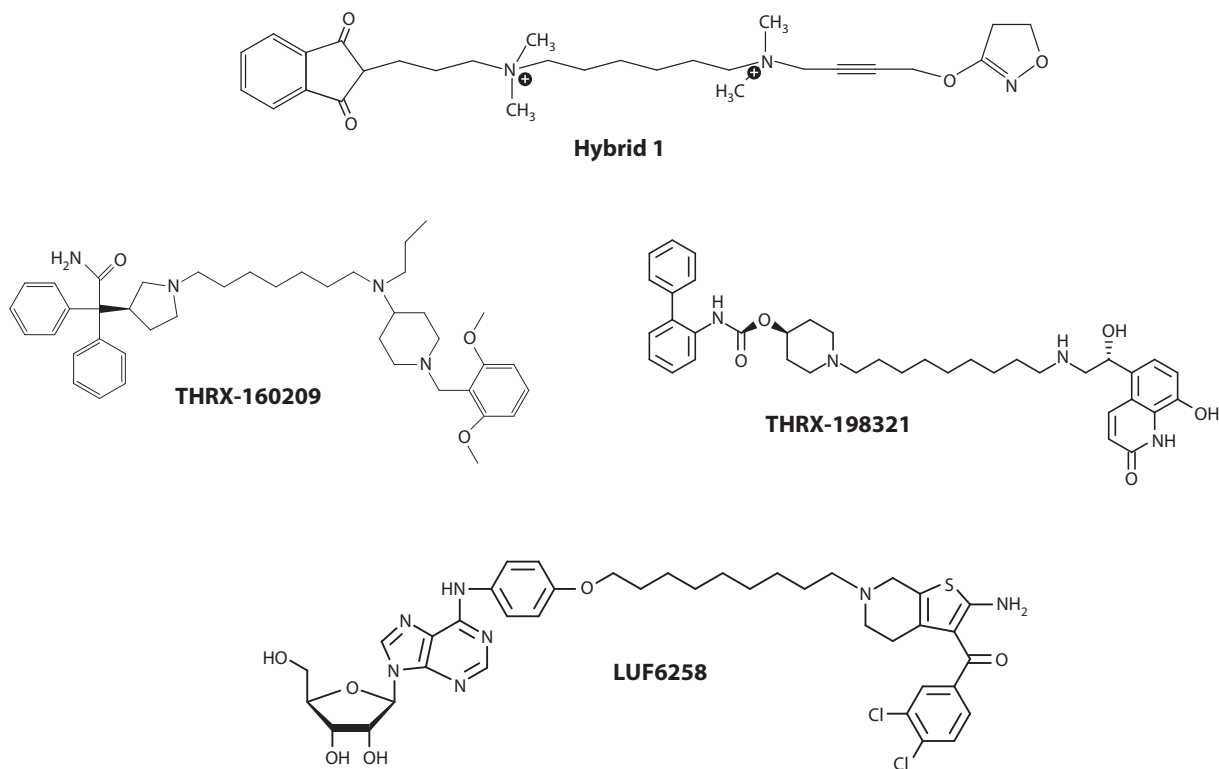


Figure 6

Examples of engineered bitopic ligands of GPCRs. Hybrid 1 and THRX-160209 preferentially target the M_2 mAChR; THRX-198321 targets M_2/M_3 mAChRs and the β_2 adrenergic receptor; LUF6258 targets the adenosine A_1 receptor.

more than one orientation: It can engage both orthosteric and allosteric sites in a bitopic mode, which is indistinguishable from a classic orthosteric binding event, or it can adopt a different pose that recognizes the allosteric site exclusively while allowing the orthosteric site to be exposed for interaction with an orthosteric ligand. The bitopic mode is determined by the strength of the equilibrium dissociation constant $K_{B-ortho}$, whereas the allosteric mode is determined by the equilibrium constant K_{B-allo} and by the cooperativity factor α for the interaction with a classic orthosteric ligand. From this model, the fractional occupancy of orthosteric ligand A in the presence of bitopic ligand B is given by the following equation:

$$\rho_A = \frac{[A]}{[A] + K_A \frac{1 + [B] \left(\frac{1}{K_{B-ortho}} + \frac{1}{K_{B-allo}} \right)}{1 + \frac{\alpha[B]}{K_{B-allo}}}} \quad 1.$$

This model was utilized in an elegant study by Mohr and colleagues (108) to inform the selection of allosteric and orthosteric building blocks that yielded theoretically predicted profiles of behavior and that, when combined to create hybrid ligands for the M_2 mAChR (e.g., Hybrid 1, **Figure 6**; Hybrid 2, **Figure 8**), also behaved as predicted by the model (**Figure 8**). The study thus provided additional validation that the mode of action of these hybrids was bitopic. An important property of these compounds was the achievement of subtype-selective and stimulus-biased agonism (108, 109).

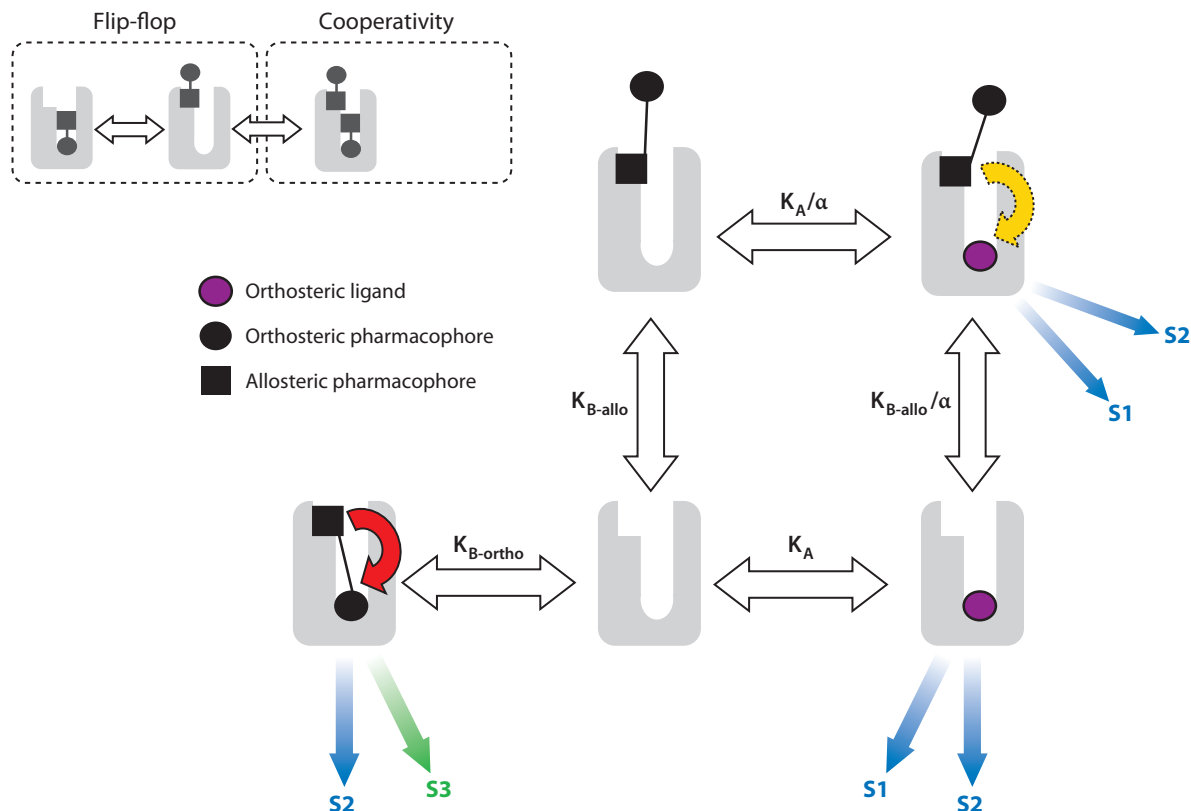


Figure 7

Bitopic mechanisms may display features associated with both competitive and allosteric mass-action schemes. In the main figure, the purple circle denotes the orthosteric ligand, whereas the black circle and square denote the orthosteric and allosteric pharmacophores, respectively. The scheme also illustrates the potential for differential signaling (pathways denoted by the letter S) that may arise between an orthosteric and a bitopic ligand because of the ability of the allosteric moiety in the latter to direct the efficacy of the orthosteric moiety encoded in the same molecule. The inset illustrates variations of the bitopic theme, whereby the molecule cannot bind concomitantly to both sites but distributes between orthosteric or allosteric orientations (flip-flop mechanism) or displays cooperative binding to interact with both sites simultaneously.

Most recently, IJzerman and colleagues (110) extended the bitopic ligand approach to another GPCR, the adenosine A_1 receptor. In that study, an orthosteric adenosine-derived agonist was combined with the allosteric modulator (2-amino-4,5-dimethyl-3-thienyl)-[3-(trifluoromethyl)phenyl]methanone via a flexible 9-carbon linker to yield the bitopic ligand LUF6258 (**Figure 6**). Because the allosteric pharmacophore was an enhancer of the orthosteric agonist pharmacophore, researchers anticipated a substantial increase in potency given that both ligands preferred an active receptor state. Surprisingly, however, the expected gain in affinity was not observed; indeed, the potency of the bitopic ligand was an order of magnitude lower than that of the parent orthosteric agonist (110). It is possible that the flexible carbon linker contributed to a high entropic cost that offset any possible enthalpic gains that may have been achieved by the positive cooperativity between orthosteric and allosteric moieties. Nonetheless, the bitopic ligands demonstrated a reversal of potencies for A_1 receptor-mediated ERK1/2 phosphorylation as compared with those observed in a [35 S]GTP γ S assay (110), indicating that stimulus bias was engendered by the hybrid molecules.

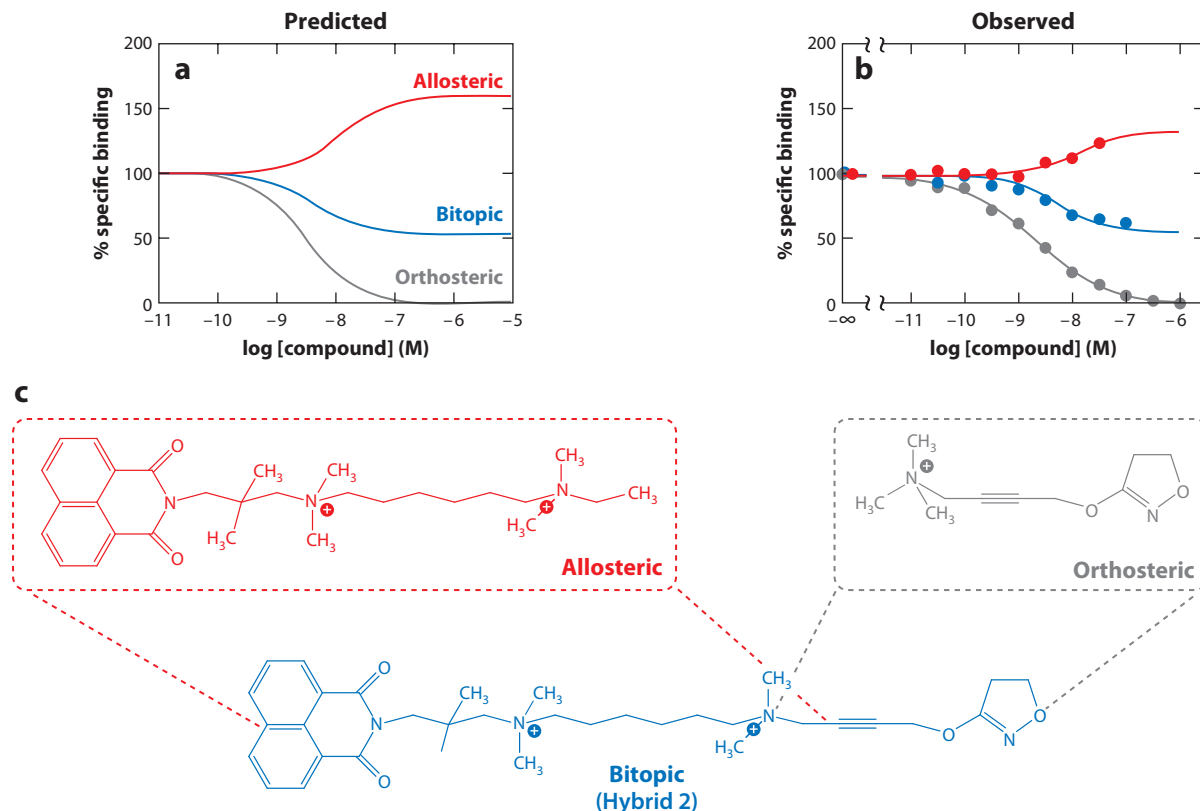


Figure 8

A bitopic model can be used to predict the pharmacology of engineered ligands. To predict the profiles of behavior shown in panel *a*, simulations based on the bitopic model were performed using the following parameters: $[A] = K_A = 1$ nM; $K_{B\text{-ortho}} = 3$ nM; $K_{B\text{-allo}} = 30$ nM; $\alpha = 4$. Orthosteric and allosteric compounds (panel *c*) approximating this profile of behaviors were used to construct the indicated bitopic ligand. Panel *b* illustrates the observed experimental effects of each of the compounds against the orthosteric antagonist, $[^3\text{H}]\text{N-methylscopolamine}$, at the M_2 mAChR. Data replotted from Reference 108.

Of course, variations of the scheme shown in **Figure 7** can also be envisaged, for instance, in which the attachment occurs only via the orthosteric site or the allosteric site (perhaps due to a nonoptimal linker length; **Figure 7** inset). This type of flip-flop mechanism (111) would be virtually indistinguishable experimentally from one in which both orthosteric and allosteric sites were concomitantly engaged in the one receptor by the one molecule. An additional possibility is that the bitopic ligand adopts two poses simultaneously in the one receptor, i.e., engaging both orthosteric and allosteric sites (**Figure 7** inset). However, if this were the case, one could expect to see evidence of cooperative binding in the bitopic molecule under appropriate experimental conditions. These types of considerations highlight the need to validate bitopic mechanisms by a variety of experimental approaches. One example, described above, is to use a theoretical model to predict and accommodate the behavior of both the individual pharmacophores and the bitopic ligand. Another method is to use mutagenesis to selectively perturb the orthosteric or allosteric pockets in a GPCR and thus “unmask” predominantly orthosteric or allosteric effects of the bitopic ligand at the mutant receptor. For example, the previously mentioned study by Mohr and

colleagues (108) created M_2 mAChRs with loss-of-function mutations in either the orthosteric site or an extracellular allosteric pocket and found that the bitopic ligand exhibited predominantly allosteric or orthosteric behavior at each mutant, respectively, which is expected if both sites need to be engaged simultaneously at the wild-type receptor. This latter approach, however, requires knowledge of key residues contributing to an allosteric site on the target GPCR. For many GPCRs, including the adenosine A_1 receptor, such knowledge is largely lacking, and alternative approaches to validation of mechanism of action are required. Thus, the study of A_1 bitopic ligands by Narlawar et al. (110) utilized an alternative strategy that assessed the sensitivity of putative bitopic ligand to the coaddition of an excess of monomeric allosteric pharmacophore. An insensitivity to the addition of excess monovalent modulator was observed for bitopic ligands with a linker length greater than 7 carbon atoms long, and this value was thus presumed to represent the minimum length needed for simultaneous occupation of both the orthosteric and allosteric binding sites. In turn, this finding led the authors to suggest a potential role of residues within extracellular loop 2 for the interaction with the allosteric pharmacophore (110).

BITOPIC AGONISM AS AN UNAPPRECIATED PARADIGM UNDERLYING FUNCTIONAL SELECTIVITY

The discovery of bitopic modes of ligand action raises the question of whether other previously described, functionally selective GPCR ligands attain such selectivity (at least in part) through a bitopic mechanism. This was shown to be the case with McN-A-343, a well-known partial agonist of the M_2 mAChR that also displays biased signaling at this receptor type (107, 112, 113). Specifically, by constructing a series of progressively truncated derivatives of this molecule, Valant et al. (107) identified two fragments, tetramethylammonium (TMA) and 3-chlorophenylcarbamate (DBBL-4), that, when combined, recapitulated the pharmacology of the parent molecule (**Figure 9**). On its own, TMA behaved as a high-efficacy orthosteric agonist, whereas DBBL-4 acted as a negative allosteric modulator of TMA signaling efficacy, resulting in a weak partial agonist profile upon coaddition of the two fragments that appeared similar to the profile of the intact McN-A-343 molecule itself. Additionally, mutation of a key residue in the second extracellular loop of the M_2 mAChR to alanine ($Y^{177}A$), which plays a major role in the potency of prototypical allosteric ligands, resulted in a significant reduction of the negative allosteric effect promoted by DBBL-4; the same mutation caused a substantial increase in the signaling efficacy of McN-A-343, presumably because the DBBL-4 component of the molecule could no longer mediate the negative allosteric effect on the TMA component. A molecular model was also proposed for the binding of McN-A-343 at the M_2 mAChR; this model was consistent with a bitopic pose for the molecule (**Figure 10**).

The finding that a previously validated, functionally selective agonist possesses a bitopic mode of action begs the question of whether this applies to other selective agonists. The past few years have witnessed the discovery of novel mAChR agonists that share two common characteristics—namely, that each appears functionally selective for the M_1 mAChR and that each has been suggested to possess an allosteric mode of interaction at this receptor. This list of novel selective agonists includes 4-n-butyl-1-[4-(2-methylphenyl)-4-oxo-1-butyl] piperidine hydrogen chloride (AC-42), 1-[3-(butyl-1-piperidinyl)propyl]-3,4-dihydro-2(1H)quinolinone (77-LH-28-1), *N*-desmethyloclozapine (NDMC), and 1-[1'-(2-methylbenzyl)-1,4'bipiperidin-4-yl]-1,3-dihydro-2H-benzimidazol-2-one (TBPB) (114–117). However, unambiguous evidence that the agonistic properties of these molecules arise from a purely allosteric mode of interaction is lacking. Although they possess some structural features distinct from those of prototypical orthosteric mAChR-targeting ligands, they also share some similarities. The key experimental

TMA: tetramethylammonium

AC-42: 4-n-butyl-1-[4-(2-methylphenyl)-4-oxo-1-butyl] piperidine hydrogen chloride

DBBL-4: 3-chlorophenylcarbamate

77-LH-28-1: 1-[3-(butyl-1-piperidinyl)propyl]-3,4-dihydro-2(1H)quinolinone

NDMC: *N*-desmethyloclozapine

TBPB: 1-[1'-(2-methylbenzyl)-1,4'bipiperidin-4-yl]-1,3-dihydro-2H-benzimidazol-2-one

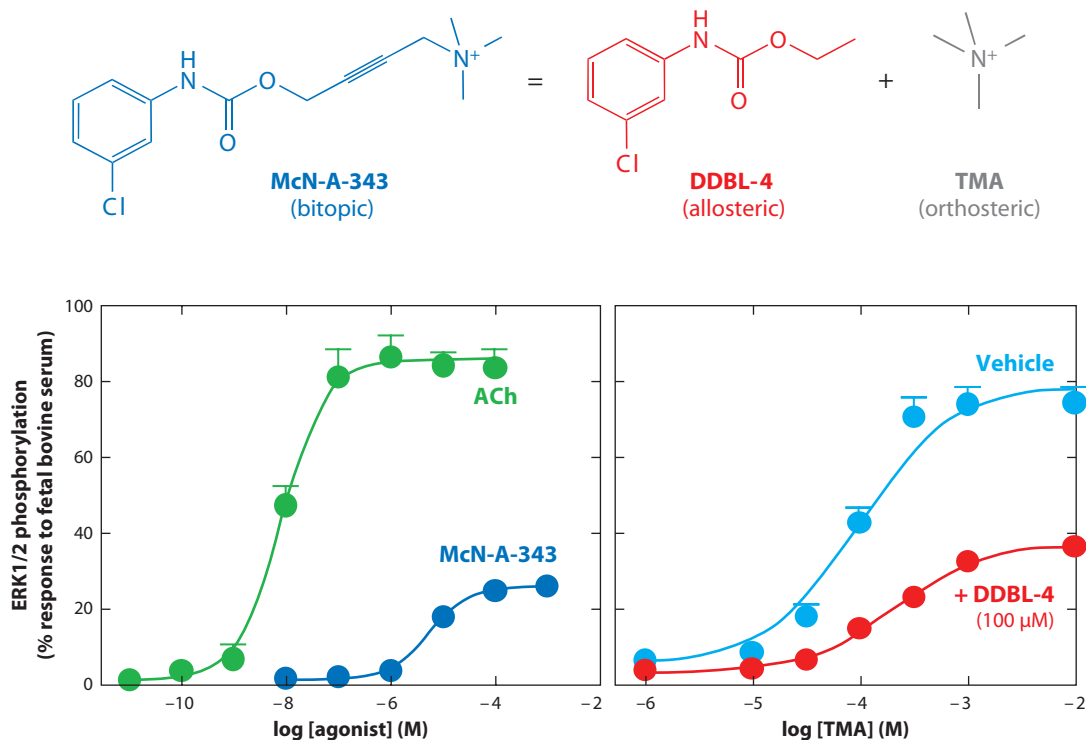


Figure 9

McN-A-343 is a bitopic agonist at the M₂ mAChR. Combination of the orthosteric agonist TMA with the negative allosteric modulator DDBL-4 recapitulates the pharmacology of the parent molecule, McN-A-343, in an assay of M₂ mAChR-mediated ERK1/2 phosphorylation, suggesting a bitopic mechanism as the basis for McN-A-343 partial agonism at this receptor subtype. Data replotted from Reference 108. Abbreviations: ACh, acetylcholine; DDBL-4, 3-chlorophenylcarbamate; ERK1/2, extracellular signal-regulated kinases 1 and 2; mAChR, muscarinic acetylcholine receptor; TMA, tetramethylammonium.

evidence that these compounds can interact allosterically at the mAChRs comes from their ability to retard the dissociation rate of the orthosteric antagonist [³H]*N*-methylscopolamine (118–120), and/or from different patterns of response of the agonists to mutations of the orthosteric site, when compared with ACh-like agonists (36, 117, 120, 121). However, both of these approaches have their own limitations when it comes to confirming a purely allosteric mode of action. Radioligand dissociation rate studies monitor interactions on a receptor that has been preequilibrated with orthosteric ligand; these experiments can reveal that a ligand may adopt a (secondary) allosteric binding mode if the orthosteric site is already occupied, but they cannot be used alone to conclude that an agonist will adopt an allosteric binding mode at the unoccupied receptor. The ligands may adopt a bitopic mode instead in this latter instance, hence activating the receptor via the orthosteric site. In terms of mutagenesis studies, differential agonist sensitivity to specific mutations can certainly be indicative of a different mode of binding but may not necessarily be proof of interaction with an entirely topographically distinct region from the orthosteric site owing to the difficulty in interpreting direct versus indirect effects of receptor mutation.

As shown in **Figure 10**, a recent study of the binding mode of 77-LH-28-1 at the M₁ mAChR suggested an “extended” binding pose that not only encompasses key TM regions implicated in orthosteric binding but also reaches up toward the extracellular domains (119). This is reminiscent

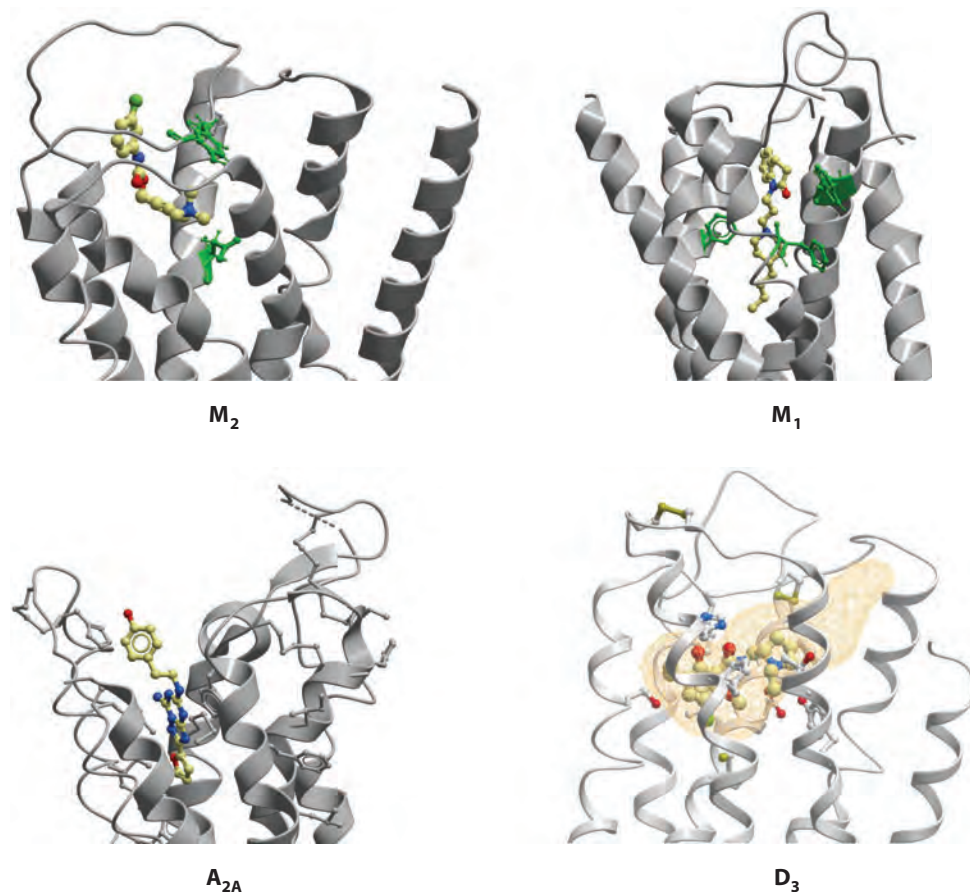


Figure 10

Bitopic binding modes may be more common than currently appreciated. Extended binding poses have been predicted for the functionally selective agonists McN-A-343 (107) and 1-[3-(butyl-1-piperidinyl)propyl]-3,4-dihydro-2(1H)quinolinone (77-LH-28-1) (119); residues highlighted in green have been implicated in the pharmacology of the indicated ligands through mutagenesis. Solution of the crystal structure of the inactive state of the adenosine A_{2A} receptor also identified an extended binding pose for the inverse agonist ZM241385 (16). Finally, the recent determination of the crystal structure of the dopamine D_3 receptor bound to the inverse agonist eticlopride also identified an extended binding cavity (*orange mesh*) that may provide space for the binding of bitopic ligands (14).

of the proposed binding mode of McN-A-343 at the M_2 mAChR. Interestingly, the publication of high-resolution GPCR crystal structures also reveals novel structural features that may be indicative of the potential for bitopic ligand binding modes. For instance, the pose adopted by the inverse agonist ZM241385 in the inactive state of the adenosine A_{2A} receptor extends perpendicular to the plane of the membrane (**Figure 10**) and makes key contact with regions in the extracellular loops as well as in the TM domains (16). In addition, the recent solution of the structure of the dopamine D_3 receptor bound to the inverse agonist eticlopride revealed a “second” binding pocket extending out from the classic orthosteric domain (**Figure 10**) that may provide additional points of contact for extended ligands, which may prove to be bitopic (14).

CONCLUSIONS

The concept of bitopic orthosteric/allosteric ligands is a new one, having emerged only in the past few years. However, the principles behind the design of such ligands are the same as those applied to the generation of more traditional bivalent ligands. In both instances, the promise lies in the generation of chemical biological tools that can display novel modes of selectivity and/or improved affinity for a target receptor and, thus, allow for new insights to be gained into the biology of GPCRs. Ideally, some bitopic ligands may also prove to be useful drug leads, although the increase in the size of such molecules may pose “druggability” challenges. Clearly, there is much more work ahead for the field in this regard, but the promise of sculpting target selectivity and pathway selectivity by exploiting the best of both (orthosteric and allosteric) worlds is an exciting one.

SUMMARY POINTS

1. GPCRs are the largest class of drug targets in the genome. Despite a common structural architecture, these receptors display a remarkable diversity in the nature of ligands that they can recognize and intracellular effectors with which they interact, indicating a substantial degree of conformational flexibility.
2. The dynamic nature of GPCR conformational changes is being increasingly exploited through the discovery of allosteric modulators, which bind to sites that are topographically distinct from the endogenous agonist (orthosteric) binding site, and biased agonists, which promote unique signaling profiles via a given receptor to the relative exclusion of other pathways. These two phenomena reflect a common underlying mechanism, and it is now acknowledged that allosteric ligands can engender biased signaling in the actions of coadministered orthosteric ligands.
3. Numerous previous studies aimed at designing more potent and/or more selective ligands targeting GPCRs and their associated pathways exploited the message-address concept. This concept views drug design in terms of the synthesis of moieties that target a conserved region of the target responsible for signal transduction (message) and moieties that target less conserved regions (address), with the latter leading to enhanced selectivity. An important outcome of this approach was the joining of two distinct pharmacophores via an appropriately spaced linker to yield what are termed bivalent GPCR ligands. Such ligands have proven useful in achieving higher affinity for target GPCRs or better selectivity—in some instances owing to the fact that they can target dimeric receptor complexes.
4. The most recent modification of the bivalent ligand approach has been the linking of defined orthosteric ligands and allosteric modulators to yield what are known as bitopic ligands. These ligands offer the potential of achieving selectivity by virtue of targeting less conserved allosteric regions on GPCRs while ensuring activation via concomitant interaction with the orthosteric site. Furthermore, bitopic engagement of a GPCR can yield biased signaling via the selection of unique receptor conformation(s).
5. Important challenges to the design of bitopic ligands are the need to validate the mechanism of action using complementary experimental approaches and the need to control for possible effects of the linker moiety that is used to join the orthosteric and allosteric pharmacophores.

6. It is possible that previously identified biased agonists of GPCRs may also act via a bitopic mechanism; studies using fragments of functionally selective ligands, receptor mutagenesis, or X-ray crystallography provide support for bitopic GPCR ligand binding poses. This suggests that the phenomenon of bitopic ligands may be more widespread than currently appreciated.

FUTURE ISSUES

1. Why do some rationally designed bitopic ligands not show the expected gains in affinity at their target GPCRs?
2. How can a bitopic mechanism of action be unambiguously demonstrated?
3. Do other functionally selective compounds achieve their selectivity through a bitopic mechanism?
4. How many GPCRs can be targeted using a bitopic approach?
5. What is the practical limit in the design of bitopic molecules with regard to retaining drug-like characteristics?

DISCLOSURE STATEMENT

The following is a list of factors over the past three years that might be viewed as biasing this review: consultancies for Johnson & Johnson, Kai Pharmaceuticals, and Alchemia by A.C.; receipt of a Program Grant from the National Health and Medical Research Council (NHMRC) of Australia by A.C. and P.M.S. to study allosteric modulation and stimulus bias; receipt of two NHMRC Project Grants, one by A.C. and one by P.M.S., to study GPCR modulation; receipt of an Australian Research Council Discovery Project Grant by A.C. to study bitopic ligands.

ACKNOWLEDGMENTS

Work cited from the authors' laboratory is funded by the NHMRC of Australia. A.C. and P.M.S. are senior and principal research fellows, respectively, of the NHMRC. The authors thank Dr. Denise Wootten for generating **Figure 1**.

LITERATURE CITED

1. Lagerström MC, Schiöth HB. 2008. Structural diversity of G protein-coupled receptors and significance for drug discovery. *Nat. Rev. Drug Discov.* 7:339–57
2. Overington JP, Al-Lazikani B, Hopkins AL. 2006. How many drug targets are there? *Nat. Rev. Drug Discov.* 5:993–96
3. Jacoby E, Bouhelal R, Gerspacher M, Seuwen K. 2006. The 7 TM G-protein-coupled receptor target family. *ChemMedChem* 1:761–82
4. Lin SH, Civelli O. 2004. Orphan G protein-coupled receptors: targets for new therapeutic interventions. *Ann. Med.* 36:204–14
5. Kenakin T, Miller LJ. 2010. Seven transmembrane receptors as shapeshifting proteins: the impact of allosteric modulation and functional selectivity on new drug discovery. *Pharmacol. Rev.* 62:265–304
6. May LT, Leach K, Sexton PM, Christopoulos A. 2007. Allosteric modulation of G protein-coupled receptors. *Annu. Rev. Pharmacol. Toxicol.* 47:1–51

7. Leach K, Sexton PM, Christopoulos A. 2007. Allosteric GPCR modulators: taking advantage of permissive receptor pharmacology. *Trends Pharmacol. Sci.* 28:382–89
8. Mailman RB. 2007. GPCR functional selectivity has therapeutic impact. *Trends Pharmacol. Sci.* 28:390–96
9. Foord SM. 2002. Receptor classification: post genome. *Curr. Opin. Pharmacol.* 2:561–66
10. Fredriksson R, Lagerström MC, Lundin LG, Schiöth HB. 2003. The G-protein-coupled receptors in the human genome form five main families. Phylogenetic analysis, paralogon groups, and fingerprints. *Mol. Pharmacol.* 63:1256–72
11. White JH, Wise A, Main MJ, Green A, Fraser NJ, et al. 1998. Heterodimerization is required for the formation of a functional GABA_B receptor. *Nature* 396:679–82
12. Palczewski K, Kumasaka T, Hori T, Behnke CA, Motoshima H, et al. 2000. Crystal structure of rhodopsin: a G protein-coupled receptor. *Science* 289:739–45
13. Cherezov V, Rosenbaum DM, Hanson MA, Rasmussen SGF, Thian FS, et al. 2007. High-resolution crystal structure of an engineered human β_2 -adrenergic G protein-coupled receptor. *Science* 318:1258–65
14. Chien EYT, Liu W, Zhao Q, Katritch V, Han GW, et al. 2010. Structure of the human dopamine D3 receptor in complex with a D2/D3 selective antagonist. *Science* 330:1091–95
15. Hanson MA, Cherezov V, Griffith MT, Roth CB, Jaakola VP, et al. 2008. A specific cholesterol binding site is established by the 2.8 Å structure of the human β_2 -adrenergic receptor. *Structure* 16:897–905
16. Jaakola V, Griffith M, Hanson M, Cherezov V, Chien E, et al. 2008. The 2.6 angstrom crystal structure of a human A_{2A} adenosine receptor bound to an antagonist. *Science* 322:1211–17
17. Rasmussen SGF, Choi H-J, Rosenbaum DM, Kobilka TS, Thian FS, et al. 2007. Crystal structure of the human β_2 adrenergic G-protein-coupled receptor. *Nature* 450:383–87
18. Rosenbaum DM, Cherezov V, Hanson MA, Rasmussen SGF, Thian FS, et al. 2007. GPCR engineering yields high-resolution structural insights into β_2 -adrenergic receptor function. *Science* 318:1266–73
19. Warne T, Serrano-Vega M, Baker J, Moukhametzianov R, Edwards P, et al. 2008. Structure of a β_1 -adrenergic G-protein-coupled receptor. *Nature* 454:486–91
20. Wu B, Chien EYT, Mol CD, Fenalti G, Liu W, et al. 2010. Structures of the CXCR4 chemokine GPCR with small-molecule and cyclic peptide antagonists. *Science* 330:1066–71
21. Scheerer P, Park J, Hildebrand P, Kim Y, Krauss N, et al. 2008. Crystal structure of opsin in its G-protein-interacting conformation. *Nature* 455:497–502
22. Rasmussen SGF, Choi H-J, Fung JJ, Pardon E, Casarosa P, et al. 2011. Structure of a nanobody-stabilized active state of the β_2 adrenoceptor. *Nature* 469:175–80
23. Rosenbaum DM, Zhang C, Lyons JA, Holl R, Aragao D, et al. 2011. Structure and function of an irreversible agonist- β_2 adrenoceptor complex. *Nature* 469:236–40
24. Warne T, Moukhametzianov R, Baker JG, Nehme R, Edwards PC, et al. 2011. The structural basis for agonist and partial agonist action on a β_1 -adrenergic receptor. *Nature* 469:241–44
25. Xu F, Wu H, Katritch V, Han GW, Jacobson KA, et al. 2011. Structure of an agonist-bound human A_{2A} adenosine receptor. *Science* 332(6027):322–27
26. Bokoch MP, Zou Y, Rasmussen SGF, Liu CW, Nygaard R, et al. 2010. Ligand-specific regulation of the extracellular surface of a G-protein-coupled receptor. *Nature* 463:108–12
27. Kobilka BK, Deupi X. 2007. Conformational complexity of G-protein-coupled receptors. *Trends Pharmacol. Sci.* 28:397–406
28. Galandrin S, Bouvier M. 2006. Distinct signaling profiles of β_1 and β_2 adrenergic receptor ligands toward adenylyl cyclase and mitogen-activated protein kinase reveals the pluridimensionality of efficacy. *Mol. Pharmacol.* 70:1575–84
29. Galés C, Van Durm JJ, Schaak S, Pontier S, Percherancier Y, et al. 2006. Probing the activation-promoted structural rearrangements in preassembled receptor–G protein complexes. *Nat. Struct. Mol. Biol.* 13:778–86
30. Ghanouni P, Gryczynski Z, Steenhuis J, Lee T, Farrens D, et al. 2001. Functionally different agonists induce distinct conformations in the G protein coupling domain of the β_2 adrenergic receptor. *J. Biol. Chem.* 276:24433–36
31. Hoffmann C, Zürn A, Bünnemann M, Lohse MJ. 2008. Conformational changes in G-protein-coupled receptors—the quest for functionally selective conformations is open. *Br. J. Pharmacol.* 153(Suppl. 1):S358–66

32. Kim J, Ahn S, Ren XR, Whalen EJ, Reiter E, et al. 2005. Functional antagonism of different G protein-coupled receptor kinases for β -arrestin-mediated angiotensin II receptor signaling. *Proc. Natl. Acad. Sci. USA* 102:1442–47
33. Vaidehi N, Kenakin T. 2010. The role of conformational ensembles of seven transmembrane receptors in functional selectivity. *Curr. Opin. Pharmacol.* 10:775–81
34. Yao XJ, Vélez Ruiz G, Whorton MR, Rasmussen SGF, DeVree BT, et al. 2009. The effect of ligand and efficacy on the formation and stability of a GPCR-G protein complex. *Proc. Natl. Acad. Sci. USA* 106:9501–6
35. Ye S, Zaitseva E, Caltabiano G, Schertler GFX, Sakmar TP, et al. 2010. Tracking G-protein-coupled receptor activation using genetically encoded infrared probes. *Nature* 464:1386–89
36. Gregory KJ, Hall NE, Tobin AB, Sexton PM, Christopoulos A. 2010. Identification of orthosteric and allosteric site mutations in M₂ muscarinic acetylcholine receptors that contribute to ligand-selective signaling bias. *J. Biol. Chem.* 285:7459–74
37. Koole C, Wootten D, Simms J, Valant C, Sridhar R, et al. 2010. Allosteric ligands of the glucagon-like peptide 1 receptor (GLP-1R) differentially modulate endogenous and exogenous peptide responses in a pathway-selective manner: implications for drug screening. *Mol. Pharmacol.* 78:456–65
38. Valant C, Aurelio L, Urmaliya VB, White P, Scammells PJ, et al. 2010. Delineating the mode of action of adenosine A₁ receptor allosteric modulators. *Mol. Pharmacol.* 78:444–55
39. Evans BA, Broxton N, Merlin J, Sato M, Hutchinson DS, et al. 2011. Quantification of functional selectivity at the human α_{1A} -adrenoceptor. *Mol. Pharmacol.* 79:298–307
40. Pike NB. 2005. Flushing out the role of GPR109A (HM74A) in the clinical efficacy of nicotinic acid. *J. Clin. Investig.* 115:3400–3
41. Walters RW, Shukla AK, Kovacs JJ, Violin JD, DeWire SM, et al. 2009. β -Arrestin1 mediates nicotinic acid-induced flushing, but not its antilipolytic effect, in mice. *J. Clin. Investig.* 119:1312–21
42. Jung JK, Johnson BR, Duong T, Decaire M, Uy J, et al. 2007. Analogues of acifran: agonists of the high and low affinity niacin receptors, GPR109a and GPR109b. *J. Med. Chem.* 50:1445–48
43. Kenakin TP. 2009. 7TM receptor allostery: putting numbers to shapeshifting proteins. *Trends Pharmacol. Sci.* 30:460–69
44. Conn PJ, Christopoulos A, Lindsley CW. 2009. Allosteric modulators of GPCRs: a novel approach for the treatment of CNS disorders. *Nat. Rev. Drug Discov.* 8:41–54
45. Langmead CJ, Christopoulos A. 2006. Allosteric agonists of 7TM receptors: expanding the pharmacological toolbox. *Trends Pharmacol. Sci.* 27:475–81
46. Leach K, Loiacono RE, Felder CC, McKinzie DL, Mogg A, et al. 2010. Molecular mechanisms of action and in vivo validation of an M₄ muscarinic acetylcholine receptor allosteric modulator with potential antipsychotic properties. *Neuropsychopharmacology* 35:855–69
47. Mathiesen JM, Ulven T, Martini L, Gerlach LO, Heinemann A, Kostenis E. 2005. Identification of indole derivatives exclusively interfering with a G protein-independent signaling pathway of the prostaglandin D₂ receptor CRTH2. *Mol. Pharmacol.* 68:393–402
48. Maillet EL, Pellegrini N, Valant C, Bucher B, Hibert M, et al. 2007. A novel, conformation-specific allosteric inhibitor of the tachykinin NK₂ receptor (NK₂R) with functionally selective properties. *FASEB J.* 21:2124–34
49. Stewart GD, Sexton PM, Christopoulos A. 2010. Prediction of functionally selective allosteric interactions at an M₃ muscarinic acetylcholine receptor mutant using *Saccharomyces cerevisiae*. *Mol. Pharmacol.* 78:205–14
50. Nicholls DJ, Tomkinson NP, Wiley KE, Brammall A, Bowers L, et al. 2008. Identification of a putative intracellular allosteric antagonist binding-site in the CXC chemokine receptors 1 and 2. *Mol. Pharmacol.* 74:1193–202
51. Andrews G, Jones C, Wreggett KA. 2008. An intracellular allosteric site for a specific class of antagonists of the CC chemokine G protein-coupled receptors CCR4 and CCR5. *Mol. Pharmacol.* 73:855–67
52. Tressel SL, Koukos G, Tchernychev B, Jacques SL, Covic L, Kuliopulos A. 2011. Pharmacology, biodistribution, and efficacy of GPCR-based peptidins in disease models. *Methods Mol. Biol.* 683:259–75
53. Covic L, Gresser AL, Talavera J, Swift S, Kuliopulos A. 2002. Activation and inhibition of G protein-coupled receptors by cell-penetrating membrane-tethered peptides. *Proc. Natl. Acad. Sci. USA* 99:643–48

54. Agarwal A, Covic L, Seigny LM, Kaneider NC, Lazarides K, et al. 2008. Targeting a metalloprotease-PAR1 signaling system with cell-penetrating pepducins inhibits angiogenesis, ascites, and progression of ovarian cancer. *Mol. Cancer Ther.* 7:2746-57
55. Covic L, Misra M, Badar J, Singh C, Kuliopulos A. 2002. Pepducin-based intervention of thrombin-receptor signaling and systemic platelet activation. *Nat. Med.* 8:1161-65
56. Kaneider NC, Agarwal A, Leger AJ, Kuliopulos A. 2005. Reversing systemic inflammatory response syndrome with chemokine receptor pepducins. *Nat. Med.* 11:661-65
57. Kubo S, Ishiki T, Doe I, Sekiguchi F, Nishikawa H, et al. 2006. Distinct activity of peptide mimetic intracellular ligands (pepducins) for proteinase-activated receptor-1 in multiple cells/tissues. *Ann. N. Y. Acad. Sci.* 1091:445-59
58. Kuliopulos A, Covic L. 2003. Blocking receptors on the inside: pepducin-based intervention of PAR signaling and thrombosis. *Life Sci.* 74:255-62
59. Lee HY, Kim SD, Shim JW, Kim HJ, Kwon JY, et al. 2010. Activation of human monocytes by a formyl peptide receptor 2-derived pepducin. *FEBS Lett.* 584:4102-8
60. Lomas-Neira J, Ayala A. 2005. Pepducins: an effective means to inhibit GPCR signaling by neutrophils. *Trends Immunol.* 26:619-21
61. Tchernychev B, Ren Y, Sachdev P, Janz JM, Haggis L, et al. 2010. Discovery of a CXCR4 agonist pepducin that mobilizes bone marrow hematopoietic cells. *Proc. Natl. Acad. Sci. USA* 107:22255-59
62. Wielders SJ, Bennaghmouch A, Reutelingsperger CP, Bevers EM, Lindhout T. 2007. Anticoagulant and antithrombotic properties of intracellular protease-activated receptor antagonists. *J. Thromb. Haemost.* 5:571-76
63. Yang E, Boire A, Agarwal A, Nguyen N, O'Callaghan K, et al. 2009. Blockade of PAR1 signaling with cell-penetrating pepducins inhibits Akt survival pathways in breast cancer cells and suppresses tumor survival and metastasis. *Cancer Res.* 69:6223-31
64. Christopoulos A, Kenakin T. 2002. G protein-coupled receptor allostery and complexing. *Pharmacol. Rev.* 54:323-74
65. Ehlert FJ. 1988. Estimation of the affinities of allosteric ligands using radioligand binding and pharmacological null methods. *Mol. Pharmacol.* 33:187-94
66. Ehlert FJ, Griffin MT. 2008. Two-state models and the analysis of the allosteric effect of gallamine at the M₂ muscarinic receptor. *J. Pharmacol. Exp. Ther.* 325:1039-60
67. Hall DA. 2000. Modeling the functional effects of allosteric modulators at pharmacological receptors: an extension of the two-state model of receptor activation. *Mol. Pharmacol.* 58:1412-23
68. Price MR, Baillie GL, Thomas A, Stevenson LA, Easson M, et al. 2005. Allosteric modulation of the cannabinoid CB₁ receptor. *Mol. Pharmacol.* 68:1484-95
69. Ehlert FJ. 2005. Analysis of allostery in functional assays. *J. Pharmacol. Exp. Ther.* 315:740-54
70. Kenakin T. 2005. New concepts in drug discovery: collateral efficacy and permissive antagonism. *Nat. Rev. Drug Discov.* 4:919-27
71. Keov P, Sexton PM, Christopoulos A. 2011. Allosteric modulation of G protein-coupled receptors: a pharmacological perspective. *Neuropharmacology* 60:24-35
72. Schwyzler R. 1977. ACTH: a short introductory review. *Ann. N. Y. Acad. Sci.* 297:3-26
73. Portoghese PS, Nagase H, Lipkowski AW, Larson DL, Takemori AE. 1988. Binaltorphimine-related bivalent ligands and their κ opioid receptor antagonist selectivity. *J. Med. Chem.* 31:836-41
74. Portoghese PS. 1989. Bivalent ligands and the message-address concept in the design of selective opioid receptor antagonists. *Trends Pharmacol. Sci.* 10:230-35
75. Messer WS Jr. 2004. Bivalent ligands for G protein-coupled receptors. *Curr. Pharm. Des.* 10:2015-20
76. Berque-Bestel I, Lezoualc'h F, Jockers R. 2008. Bivalent ligands as specific pharmacological tools for G protein-coupled receptor dimers. *Curr. Drug Discov. Technol.* 5:312-8
77. Peng X, Neumeyer JL. 2007. κ receptor bivalent ligands. *Curr. Top. Med. Chem.* 7:363-73
78. Portoghese PS. 1990. The bivalent ligand approach in the design of highly selective opioid receptor antagonists. *NIDA Res. Monogr.* 96:3-20
79. Christopoulos A, Grant MK, Ayoubzadeh N, Kim ON, Sauerberg P, et al. 2001. Synthesis and pharmacological evaluation of dimeric muscarinic acetylcholine receptor agonists. *J. Pharmacol. Exp. Ther.* 298:1260-68

80. Rajeswaran WG, Cao Y, Huang XP, Wroblewski ME, Colclough T, et al. 2001. Design, synthesis, and biological characterization of bivalent 1-methyl-1,2,5,6-tetrahydropyridyl-1,2,5-thiadiazole derivatives as selective muscarinic agonists. *J. Med. Chem.* 44:4563–76
81. Piergentili A, Quaglia W, Tayebati SK, Paparelli F, Malmusi L, Brasili L. 1994. Synthesis and muscarinic receptors affinity of a series of antagonist bivalent ligands. *Farmaco* 49:83–87
82. Soulier JL, Russo O, Giner M, Rivail L, Berthouze M, et al. 2005. Design and synthesis of specific probes for human 5-HT₄ receptor dimerization studies. *J. Med. Chem.* 48:6220–28
83. Lezoualc'h F, Jockers R, Berque-Bestel I. 2009. Multivalent-based drug design applied to serotonin 5-HT₄ receptor oligomers. *Curr. Pharm. Des.* 15:719–29
84. Russo O, Berthouze M, Giner M, Soulier JL, Rivail L, et al. 2007. Synthesis of specific bivalent probes that functionally interact with 5-HT₄ receptor dimers. *J. Med. Chem.* 50:4482–92
85. Liu J, Brahimi F, Saragovi HU, Burgess K. 2010. Bivalent diketopiperazine-based tropomyosin receptor kinase C (TrkC) antagonists. *J. Med. Chem.* 53:5044–48
86. Bongers KM, van den Berg RJBH, Heitman LH, IJzerman AP, Oosterom J, et al. 2007. Synthesis and evaluation of homo-bivalent GnRHR ligands. *Bioorg. Med. Chem.* 15:4841–56
87. Ma HJ, Xie RL, Zhao QF, Mei XD, Ning J. 2010. Synthesis and insecticidal activity of novel carbamate derivatives as potential dual-binding site acetylcholinesterase inhibitors. *J. Agric. Food Chem.* 58:12817–21
88. Brahimi F, Liu J, Malakhov A, Chowdhury S, Purisima EO, et al. 2010. A monovalent agonist of TrkA tyrosine kinase receptors can be converted into a bivalent antagonist. *Biochim. Biophys. Acta* 1800:1018–26
89. Portoghese PS. 2001. From models to molecules: opioid receptor dimers, bivalent ligands, and selective opioid receptor probes. *J. Med. Chem.* 44:2259–69
90. Waldhoer M, Fong J, Jones RM, Lunzer MM, Sharma SK, et al. 2005. A heterodimer-selective agonist shows in vivo relevance of G protein-coupled receptor dimers. *Proc. Natl. Acad. Sci. USA* 102:9050–55
91. Bhushan RG, Sharma SK, Xie Z, Daniels DJ, Portoghese PS. 2004. A bivalent ligand (KDN-21) reveals spinal δ and κ opioid receptors are organized as heterodimers that give rise to δ_1 and κ_2 phenotypes. Selective targeting of δ - κ heterodimers. *J. Med. Chem.* 47:2969–72
92. Xie Z, Bhushan RG, Daniels DJ, Portoghese PS. 2005. Interaction of bivalent ligand KDN21 with heterodimeric δ - κ opioid receptors in human embryonic kidney 293 cells. *Mol. Pharmacol.* 68:1079–86
93. Daniels DJ, Kulkarni A, Xie Z, Bhushan RG, Portoghese PS. 2005. A bivalent ligand (KDAN-18) containing δ -antagonist and κ -agonist pharmacophores bridges δ_2 and κ_1 opioid receptor phenotypes. *J. Med. Chem.* 48:1713–16
94. Daniels DJ, Lenard NR, Etienne CL, Law P-Y, Roerig SC, Portoghese PS. 2005. Opioid-induced tolerance and dependence in mice is modulated by the distance between pharmacophores in a bivalent ligand series. *Proc. Natl. Acad. Sci. USA* 102:19208–13
95. Karellas P, McNaughton M, Baker SP, Scammells PJ. 2008. Synthesis of bivalent β_2 -adrenergic and adenosine A₁ receptor ligands. *J. Med. Chem.* 51:6128–37
96. Tanaka T, Nomura W, Narumi T, Masuda A, Tamamura H. 2010. Bivalent ligands of CXCR4 with rigid linkers for elucidation of the dimerization state in cells. *J. Am. Chem. Soc.* 132:15899–901
97. Huber D, Hübner H, Gmeiner P. 2009. 1,1'-Disubstituted ferrocenes as molecular hinges in mono- and bivalent dopamine receptor ligands. *J. Med. Chem.* 52:6860–70
98. Mammen M, Choi S-K, Whitesides GM. 1998. Polyvalent interactions in biological systems: implications for design and use of multivalent ligands and inhibitors. *Angew. Chem. Int. Ed.* 37(20):2754–94
99. Mathew SC, Ghosh N, By Y, Berthault A, Virolleaud MA, et al. 2009. Design, synthesis and biological evaluation of a bivalent μ opiate and adenosine A₁ receptor antagonist. *Bioorg. Med. Chem. Lett.* 19:6736–39
100. Mohr K, Tränkle C, Kostenis E, Barocelli E, De Amici M, Holzgrabe U. 2010. Rational design of dualsteric GPCR ligands: quests and promise. *Br. J. Pharmacol.* 159:997–1008
101. Valant C, Sexton PM, Christopoulos A. 2009. Orthosteric/allosteric bitopic ligands: going hybrid at GPCRs. *Mol. Interv.* 9:125–35
102. Disingrini T, Muth M, Dallanocce C, Barocelli E, Bertoni S, et al. 2006. Design, synthesis, and action of oxotremorine-related hybrid-type allosteric modulators of muscarinic acetylcholine receptors. *J. Med. Chem.* 49:366–72

103. Christopoulos A, Lanzafame A, Mitchelson F. 1998. Allosteric interactions at muscarinic cholinceptors. *Clin. Exp. Pharmacol. Physiol.* 25:185–94
104. Gregory KJ, Sexton PM, Christopoulos A. 2007. Allosteric modulation of muscarinic acetylcholine receptors. *Curr. Neuropharmacol.* 5:157–67
105. Lazareno S, Popham A, Birdsall NJ. 2003. Progress toward a high-affinity allosteric enhancer at muscarinic M₁ receptors. *J. Mol. Neurosci.* 20:363–67
106. Steinfeld T, Mammen M, Smith JAM, Wilson RD, Jasper JR. 2007. A novel multivalent ligand that bridges the allosteric and orthosteric binding sites of the M₂ muscarinic receptor. *Mol. Pharmacol.* 72:291–302
107. Valant C, Gregory K, Hall N, Scammells P, Lew M, et al. 2008. A novel mechanism of G protein-coupled receptor functional selectivity: muscarinic partial agonist McN-A-343 as a bitopic orthosteric/allosteric ligand. *J. Biol. Chem.* 283:29312–21
108. Antony J, Kellershohn K, Mohr-Andrä M, Kebig A, Prilla S, et al. 2009. Dualsteric GPCR targeting: a novel route to binding and signaling pathway selectivity. *FASEB J.* 23:442–50
109. Kebig A, Kostenis E, Mohr K, Mohr-Andrä M. 2009. An optical dynamic mass redistribution assay reveals biased signaling of dualsteric GPCR activators. *J. Recept. Signal Transduct. Res.* 29:140–45
110. Narlawar R, Lane J, Doddareddy M, Lin J, Brussee J, IJzerman A. 2010. Hybrid ortho/allosteric ligands for the adenosine A₁ receptor. *J. Med. Chem.* 53:3028–37
111. Schwartz TW, Holst B. 2007. Allosteric enhancers, allosteric agonists and ago-allosteric modulators: Where do they bind and how do they act? *Trends Pharmacol. Sci.* 28:366–73
112. Roszkowski AP. 1961. An unusual type of sympathetic ganglionic stimulant. *J. Pharmacol. Exp. Ther.* 132:156–70
113. Caulfield MP, Birdsall NJ. 1998. International Union of Pharmacology. XVII. Classification of muscarinic acetylcholine receptors. *Pharmacol. Rev.* 50:279–90
114. Spalding TA, Trotter C, Skjaerbaek N, Messier TL, Currier EA, et al. 2002. Discovery of an ectopic activation site on the M₁ muscarinic receptor. *Mol. Pharmacol.* 61:1297–302
115. Langmead CJ, Austin NE, Branch CL, Brown JT, Buchanan KA, et al. 2008. Characterization of a CNS penetrant, selective M₁ muscarinic receptor agonist, 77-LH-28-1. *Br. J. Pharmacol.* 154:1104–15
116. Sur C, Mallorga PJ, Wittmann M, Jacobson MA, Pascarella D, et al. 2003. *N*-desmethylozapine, an allosteric agonist at muscarinic 1 receptor, potentiates *N*-methyl-D-aspartate receptor activity. *Proc. Natl. Acad. Sci. USA* 100:13674–79
117. Jones CK, Brady AE, Davis AA, Xiang Z, Bubser M, et al. 2008. Novel selective allosteric activator of the M₁ muscarinic acetylcholine receptor regulates amyloid processing and produces antipsychotic-like activity in rats. *J. Neurosci.* 28:10422–33
118. Langmead CJ, Fry VA, Forbes IT, Branch CL, Christopoulos A, et al. 2006. Probing the molecular mechanism of interaction between 4-*n*-butyl-1-[4-(2-methylphenyl)-4-oxo-1-butyl]-piperidine (AC-42) and the muscarinic M₁ receptor: direct pharmacological evidence that AC-42 is an allosteric agonist. *Mol. Pharmacol.* 69:236–46
119. Avlani VA, Langmead CJ, Guida E, Wood MD, Tehan BG, et al. 2010. Orthosteric and allosteric modes of interaction of novel selective agonists of the M₁ muscarinic acetylcholine receptor. *Mol. Pharmacol.* 78:94–104
120. Jacobson MA, Kreatsoulas C, Pascarella DM, O'Brien JA, Sur C. 2010. The M₁ muscarinic receptor allosteric agonists AC-42 and 1-[1'-(2-methylbenzyl)-1,4'-bipiperidin-4-yl]-1,3-dihydro-2*H*-benzimidazol-2-one bind to a unique site distinct from the acetylcholine orthosteric site. *Mol. Pharmacol.* 78:648–57
121. Lebon G, Langmead CJ, Tehan BG, Hulme EC. 2009. Mutagenic mapping suggests a novel binding mode for selective agonists of M₁ muscarinic acetylcholine receptors. *Mol. Pharmacol.* 75:331–41

Recent advances in understanding GLP-1R (glucagon-like peptide-1 receptor) function

Cassandra Koole*, Kavita Pabreja*, Emilia E. Savage*, Denise Wootten*, Sebastian G.B. Furness*, Laurence J. Miller†, Arthur Christopoulos* and Patrick M. Sexton*¹

*Monash Institute of Pharmaceutical Sciences and Department of Pharmacology, Monash University, 381 Royal Parade, Parkville 3052, Victoria, Australia, and

†Department of Molecular Pharmacology and Experimental Therapeutics, 13400 E. Shea Blvd., Scottsdale, AZ 85259, U.S.A.

Abstract

Type 2 diabetes is a major global health problem and there is ongoing research for new treatments to manage the disease. The GLP-1R (glucagon-like peptide-1 receptor) controls the physiological response to the incretin peptide, GLP-1, and is currently a major target for the development of therapeutics owing to the broad range of potential beneficial effects in Type 2 diabetes. These include promotion of glucose-dependent insulin secretion, increased insulin biosynthesis, preservation of β -cell mass, improved peripheral insulin sensitivity and promotion of weight loss. Despite this, our understanding of GLP-1R function is still limited, with the desired spectrum of GLP-1R-mediated signalling yet to be determined. We review the current understanding of GLP-1R function, in particular, highlighting recent contributions in the field on allosteric modulation, probe-dependence and ligand-directed signal bias and how these behaviours may influence future drug development.

Introduction

Type 2 DM (diabetes mellitus) is a global epidemic, with worldwide prevalence increasing exponentially and future projections estimating that almost 10% of the adult population will suffer from the condition by the year 2030 [1]. A complex disease, arising from multiple aetiological factors including genetic predisposition and modern lifestyle, Type 2 DM is typically diagnosed by chronic hyperglycaemia; however, the two distinct features allowing disease progression are impaired β -cell function and a target organ reduction in sensitivity to insulin. In the later stages of the condition, the continual demand for elevated insulin to compensate for insulin insensitivity results in β -cell exhaustion and glucose toxicity [2]. Aside from these characteristic traits of Type 2 DM, there are also many other associated pathophysiologies including vascular dysfunction, the consequences of which include retinopathy, nephropathy, neuropathy and atherosclerosis, the latter increasing the risk of heart attack and stroke in addition to significantly increasing the risk of cardiovascular mortality [2]. The evolution of understanding into both the physiology of glucose homeostasis as well as the pathophysiology of Type 2 DM has highlighted the importance of endogenously produced incretin hormones in facilitating nutrient-induced insulin biosynthesis and secretion, as well as preserving β -cell function, decreasing β -cell apoptosis, slowing gastric emptying, and enhancing insulin sensitivity at peripheral

tissues (reviewed in [3]). This article provides a brief overview of the GLP-1R (glucagon-like peptide-1 receptor), the major target of incretin mimetic therapies, and highlights some of the previous work on this receptor.

Physiology of the incretin system

Accounting for as much as 70% of insulin secreted from pancreatic β -cells following nutrient consumption, incretin hormones are key mediators in communicating nutrient content of the gastrointestinal tract to insulin producing pancreatic β -cells [3]. The principal incretin hormones include GLP-1, primarily expressed in L cells of the ileum and colon, and gastric inhibitory polypeptide/glucose-dependent insulinotropic polypeptide, primarily expressed in K cells of the duodenum and jejunum. Although secreted levels of both incretin hormones are reduced in Type 2 DM subjects, only GLP-1 has been observed to retain its potent insulinotropic activity, and has therefore attracted significant interest in the development of Type 2 DM therapeutics [4].

The principal stimuli for GLP-1 secretion is nutrient content of the gastrointestinal tract [5]; however, the mechanisms behind GLP-1 secretion are complex and largely unclear, with multiple factors thought to impact on its release, including neural and endocrine factors (reviewed in [6]). GLP-1 is rapidly secreted postprandially, peaking at 10–15 min followed by a sustained peak at 30–60 min [5]. The insulinotropic effects induced by secreted GLP-1 are mediated through interaction with its transmembrane expressed GPCR (G-protein-coupled receptor), the GLP-1R, promoting intracellular signalling mechanisms to aid in increasing the expression, biosynthesis and secretion of insulin from pancreatic β -cells in a glucose-dependent manner [7]. Highlighting the importance of GLP-1-mediated

Key words: allosteric modulation, biased signalling, G-protein-coupled receptor, glucagon-like peptide-1 receptor, glucagon-like peptide-1, probe-dependence.

Abbreviations used: BETP, 4-(3-(benzyloxy)phenyl)-2-(ethylsulfinyl)-6-(trifluoromethyl)pyrimidine; DM, diabetes mellitus; DPPIV, dipeptidyl peptidase IV; EGFR, epidermal growth factor receptor; ERK1/2, extracellular-signal-regulated kinase 1 and 2; GLP-1R, glucagon-like peptide-1 receptor; GPCR, G-protein-coupled receptor; GRK, G-protein-coupled receptor kinase; PAM, positive allosteric modulator; PI3K, phosphoinositide 3-kinase; PK, protein kinase.

¹To whom correspondence should be addressed (email patrick.sexton@monash.edu).

signalling in the endocrine pancreas, all studies of *GLP-1R*^{-/-} mice observe at least a modest reduction in glucose tolerance and impaired glucose-stimulated insulin secretion [8]. In addition to glucoregulation, GLP-1 has a fundamental role in increasing neogenesis, proliferation and decreasing apoptosis of pancreatic β -cells in animal models, leading to an increase in β -cell mass and subsequently aiding the glucose-dependent augmentation of insulin secretion [9].

Aside from the pancreatic effects, there is significant evidence illustrating biological actions of GLP-1 via its receptor in other tissues (extensively reviewed in [3]). Briefly, GLP-1 activity suppresses appetite and inhibits gastric emptying, in turn influencing ingestive behaviour. Other roles include inhibition of glucagon release and augmenting glycogen synthase activity in muscle, adipose and hepatic cells, favouring incorporation of glucose into glycogen. Furthermore, GLP-1 and GLP-1-related peptides enhance peripheral insulin sensitivity and reduce steatosis. In the nervous system, GLP-1 augments neogenesis, proliferation and anti-apoptotic behaviour of neuronal cells, enhancing memory, and spatial and associative learning. Other documented roles include contribution to normal cardiovascular, respiratory and renal function. The diverse and beneficial actions of GLP-1 have consequently attracted significant attention in the development of therapeutics that mimic the endogenous GLP-1 system, particularly for the management of Type 2 DM.

GLP-1 receptor

The GLP-1R is a 463-amino-acid transmembrane-spanning protein belonging to the family B/secretin GPCRs, mediating the effects of both endogenous GLP-1 peptides [four forms: GLP-1(1–36)NH₂, GLP-1(7–36)NH₂, GLP-1(1–37) and GLP-1(7–37)], as well as the endogenous peptide oxyntomodulin and exogenous peptide exendin-4 (Figure 1A). Characteristic of family B GPCRs, the GLP-1R possesses a long extracellular N-terminus with an α -helical region, five β -strands forming two antiparallel β -sheets and six conserved cysteine residues that form disulfide interactions [10–12]. Together, these features allow the receptor to adopt the classic ‘Sushi domain’ or ‘short consensus repeat’, which aids N-terminal stability and confers a high level of structural homology within the N-terminal regions of family B GPCRs. The large extracellular N-terminus has a significant role in peptide binding, supported by GLP-1 binding the isolated N-terminus of the GLP-1R [13] and crystal structures of the isolated GLP-1R N-terminus in complex with GLP-1 and exendin peptides [11,12]. Specifically, the C-terminus of the peptide interacts with the N-terminus of the receptor, which is proposed to be responsible for ligand recognition and specificity, while the N-terminus of the peptide is proposed to associate with the core of the receptor, and is suggested to have a major influence in signalling specificity and transmission [14,15]. This widely accepted two-domain model of ligand binding is also experimentally supported by chimaeric receptors [16,17], photolabile peptide cross-

linking [18–20], and to some extent, mutagenesis analysis [21–25]. However, despite the seemingly abundant data, there is still a wide knowledge gap with respect to the complete structure of any receptor in this family, as well as whether a definitive binding crevice exists that is common across all receptors of the family. Furthermore, the orientation of the receptor N-terminus in relation to the transmembrane bundle is uncertain, and has been inherently difficult to establish either experimentally or using molecular modelling [15,20].

GLP-1R signalling and regulation

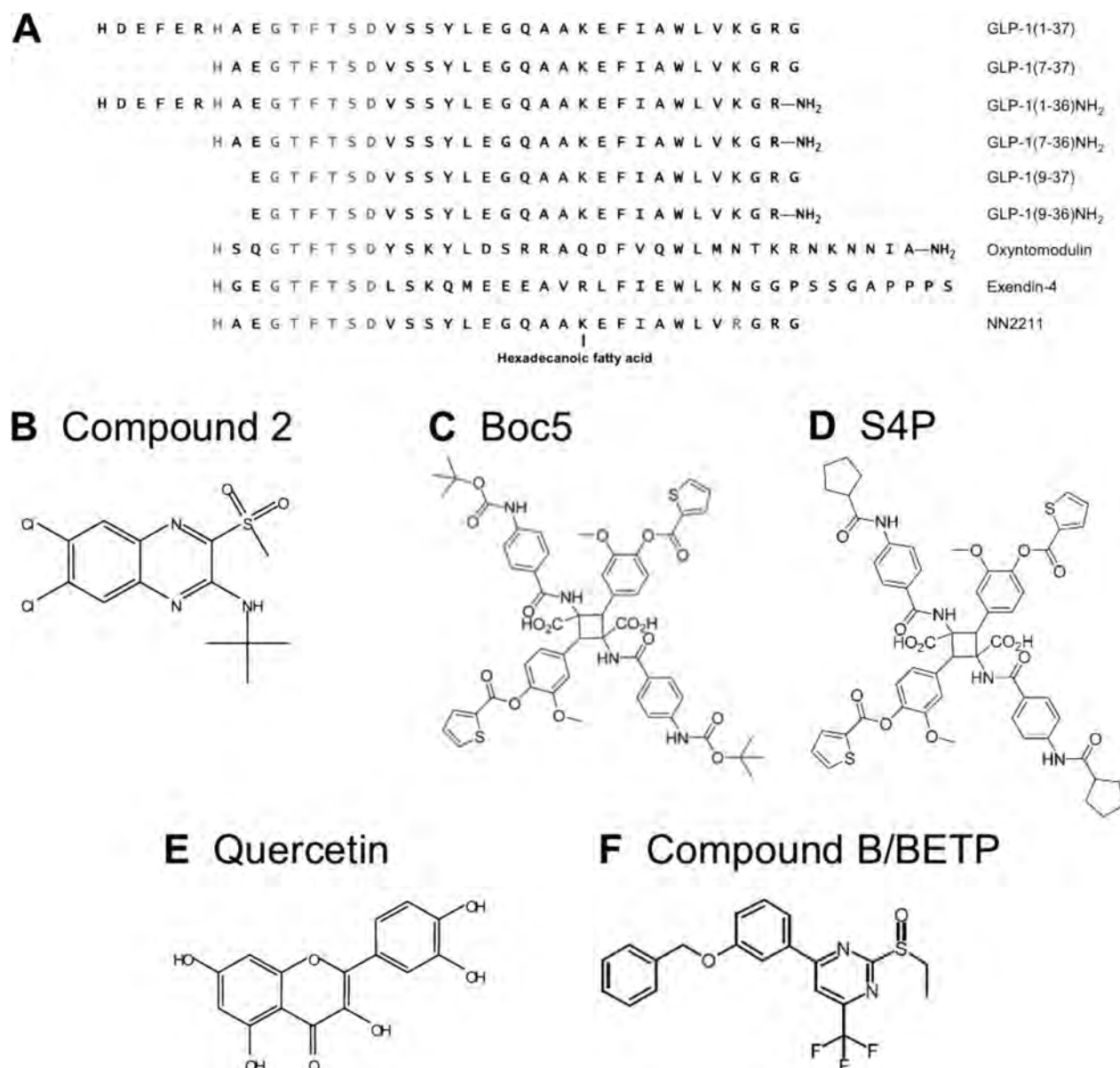
The physiological changes observed with increases in GLP-1, including increases in insulin secretion and β -cell mass, rely on signalling via GLP-1R-mediated intracellular pathways (Figure 2). The GLP-1R is a pleiotropically coupled receptor, with evidence for signalling via multiple G-protein-coupled pathways including $G_{\alpha s}$, $G_{\alpha i}$, $G_{\alpha o}$ and $G_{\alpha q/11}$ [26,27]. However, the GLP-1R is most well documented for its role in $G_{\alpha s}$ coupling, favouring production of cAMP through increasing enzymatic activity of adenylate cyclase [7]. This subsequently promotes increases in both PKA (protein kinase A) and Epac2 (exchange protein activated by cAMP-2), which is directly involved in enhancing proinsulin gene transcription [28]. Furthermore, GLP-1R activation induces membrane depolarization of β -cells through inhibition of K⁺ channels, allowing VDCCs (voltage-dependent Ca²⁺ channels) to open and acceleration of Ca²⁺ influx to occur, resulting in the exocytosis of insulin from β -cells. Therefore the production of cAMP and influx of Ca²⁺ are vital components in the biosynthesis and secretion of insulin. GLP-1R activity also promotes EGFR (epidermal growth factor receptor) transactivation, PI3K (phosphoinositide 3-kinase) activity, IRS-2 (insulin receptor substrate-2) signalling, and subsequently, ERK1/2 (extracellular-signal-regulated kinase 1 and 2) activity, as well as nuclear translocation of PKC ζ to mediate β -cell proliferation and differentiation as well as promote insulin gene transcription (reviewed in [3]). Aside from G-protein-coupled pathways, there are recently emerging studies suggesting that GRK (GPCR kinase) and β -arrestin recruitment are involved in optimal GLP-1R function [29–32]. Clear evidence for this is seen in β -cell knockdown of β -arrestin-1, that results in attenuated cAMP and consequently diminished insulin secretion [29]. There is also evidence supporting β -arrestin-1-mediated ERK1/2 activation as a mechanism for β -cell preservation [32]. Although GRKs and β -arrestins are well documented for their role in regulating cell-surface receptor function and expression through receptor desensitization and internalization, it is unclear how these scaffolding proteins regulate this process at the GLP-1R.

GLP-1 mimetics in the treatment of Type II DM

With the ability to address almost all manifestations of Type 2 DM, the GLP-1R system has become one of the

Figure 1 | Peptide and small molecule ligands of the GLP-1R

(A) Peptide ligands of the GLP-1R, including four endogenous forms of GLP-1, two of which have glycine residues extended at the C-terminus [GLP-1(1–37) and GLP-1(7–37)] and two of which have undergone C-terminal amidation (GLP-1(1–36)NH₂ and GLP-1(7–36)NH₂). DPPIV degradation yields N-terminally truncated metabolites GLP-1(9–37) and GLP-1(9–36)NH₂. The endogenous agonist oxyntomodulin and the exogenous agonist exendin-4 share high homology in the N-terminal region of the peptide. The clinically used GLP-1 analogue, liraglutide (NN2211), shares the same amino acid sequence as GLP-1(7–37), but with modifications as indicated. (B) Compound 2 (6,7-dichloro-2-methylsulfonyl-3-t-butylaminoquinoline), synthetic allosteric agonist and positive modulator of cAMP formation. (C) Boc5, synthetic allosteric agonist in cAMP formation. (D) S4P, synthetic allosteric agonist in cAMP formation. (E) Quercetin (3,3',4,5,7-pentahydroxyflavone), naturally occurring PAM (positive allosteric modulator) of intracellular Ca²⁺ mobilization. (F) Compound B/BETP, 4-(3-(benzyloxy)phenyl)-2-(ethylsulfinyl)-6-(trifluoromethyl)pyrimidine, synthetic allosteric agonist in cAMP formation.

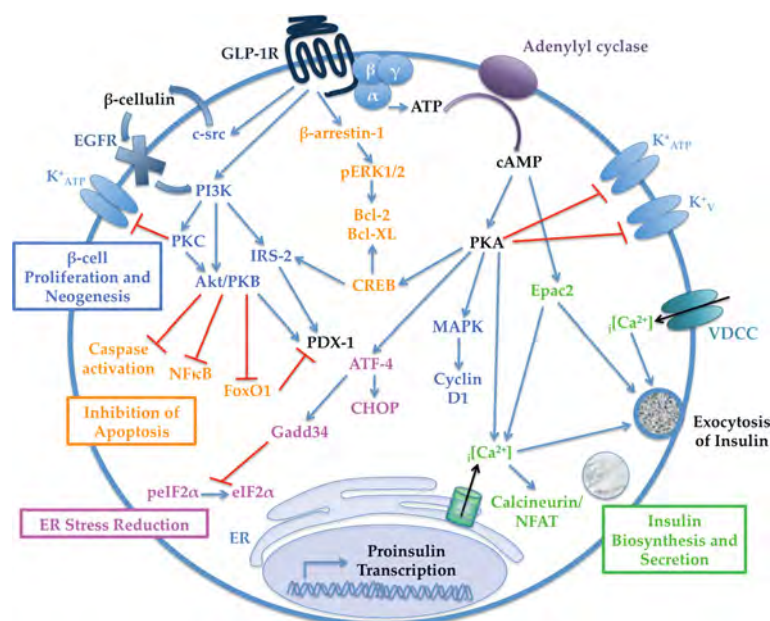


most appealing targets in the development of therapies for management of the condition. However, the leading problem in enhancing this system with GLP-1 administration directly is the rapid breakdown of the peptides by the enzyme DPPIV (dipeptidyl peptidase IV) into low activity metabolites. As

such, the most prominent avenue of drug development aims to imitate endogenous peptide activity but limit peptide breakdown (GLP-1 mimetics). The most well-known GLP-1 mimetic prescribed for the management of Type 2 DM is exenatide (Byetta®), a synthetically produced equivalent

Figure 2 | GLP-1R-mediated signalling in pancreatic β -cells

Signalling in pancreatic β -cells via the classical GLP-1R-coupled $G_{\alpha s}$ pathway mediates increases in cAMP to up-regulate PKA and Epac2 (exchange protein activated by cAMP 2), enhancing $[Ca^{2+}]$ (intracellular Ca^{2+}) mobilization and calcineurin/NFAT (nuclear factor of activated T cells). In association with increases in $[Ca^{2+}]$ through inhibition of K^+ channels and acceleration of Ca^{2+} influx through VDCCs (voltage-dependent Ca^{2+} channels), these pathways lead to increases in insulin biosynthesis and secretion (green). Activation of proto-oncogene tyrosine kinase src (c-src), increases in β -cellulin and subsequent transactivation of EGFR aid in increasing PI3K, IRS-2 and PKB (Akt) to enhance β -cell neogenesis and proliferation (blue). This is also facilitated in part by PKA-mediated increases in MAPKs (mitogen-activated protein kinases) and cyclin-D1. Inhibition of caspases, FoxO1 (forkhead box protein O1) and NF- κ B (nuclear factor κ B), in addition to regulation of CREB (cAMP-response-element-binding protein) and protein survival factors Bcl-2 and Bcl-XL, aid in the inhibition of apoptosis (orange), a process also mediated by β -arrestin-1 and the pERK1/2 (phosphorylation of ERK1/2). ER (endoplasmic reticulum) stress reduction (pink) involves the up-regulation of multiple transcription factors, including ATF-4 (activating transcription factor-4), CHOP [C/EBP (CCAAT/enhancer-binding protein)-homologous protein], and Gadd34 (growth arrest and DNA damage-inducible protein), which inhibits the dephosphorylation of eIF2 α (eukaryote initiation factor 2 α). Cross-talk exists between most pathways, including the regulation of the important promotor of insulin gene transcription, synthesis and secretion, Pdx-1 (pancreas duodenum homeobox-1) via both cAMP-dependent and IRS-dependent mechanisms.



of the venom-derived peptide exendin-4 (Figure 1A). Similar to GLP-1, exendin-4 decreases plasma glucose levels immediately following nutrient ingestion in both healthy and diabetic subjects, promotes β -cell proliferation, and augments the synthesis and secretion of insulin [33]. However, unlike GLP-1, exendin-4 is resistant to the proteolytic activity of DPPIV, prolonging its activity *in vivo*.

Unlike exendin-4, all other GLP-1 mimetics are synthetically developed, modified GLP-1 peptides that are designed to take advantage of the peptide's specificity for the receptor, but have alterations to enhance stability and/or function *in vivo*. These modifications typically involve the substitution of Ala⁸ of the GLP-1 peptide, such that the peptide becomes resistant to enzymatic degradation by DPPIV. Examples of this include (Val⁸)GLP-1, (Thr⁸)GLP-1, (Ser⁸)GLP-1 and (Gly⁸)GLP-1, each of which display insulinotropic activity and enhanced metabolic stability [34].

Peptide modifications through fatty acid derivatization have also been pursued in order to extend biological half-life in plasma. A well-recognized example of this is liraglutide (NN2211, Victoza[®]), which covalently couples a hexadecanoic fatty acid at the Lys²⁶ residue of the GLP-1 peptide, as well as containing an arginine substitution at residue 34 [35] (Figure 1A). Similar to GLP-1 and exendin-4, liraglutide significantly improves glycaemic control, enhances β -cell function and promotes weight loss, and, similar to exendin-4, has a significantly improved plasma half-life due to DPPIV resistance [33].

There are many other synthetically engineered peptide analogues for the GLP-1R that have been shown to have insulinotropic activity and enhanced metabolic stability, including the GLP-1 analogues LY315902 and CJC-1131 and the albumin-conjugated dimeric GLP-1 analogue, albiglutide [34,36], and exendin-4 analogues AC3174 and CJC-1134-PC

[36,37]. In another previous study, modification through biotin and polyethylene glycol labelling of GLP-1 and exendin-4 peptides have been explored as a means to aid oral delivery of antidiabetic treatments through enhancing intestinal absorption [38].

Collectively, synthetically produced GLP-1 and exendin-4 analogues illustrate that biological activity can be mimicked and in some cases favourably enhanced. However, generation and application of peptides remains a difficult and complex task, with peptide stability and administration route a major challenge, as well as controversy over the long-term consequences of use, including reports of pancreatitis and C-cell hyperplasia, a precursor for thyroid cancer [39,40]. In addition, all analogous peptides are coupled to some extent with adverse side effects, the most prominent being nausea. For this reason, there is significant interest in novel treatments that have similar physiological effects to GLP-1, but which can be administered orally and eliminate, or at least minimize, side effects.

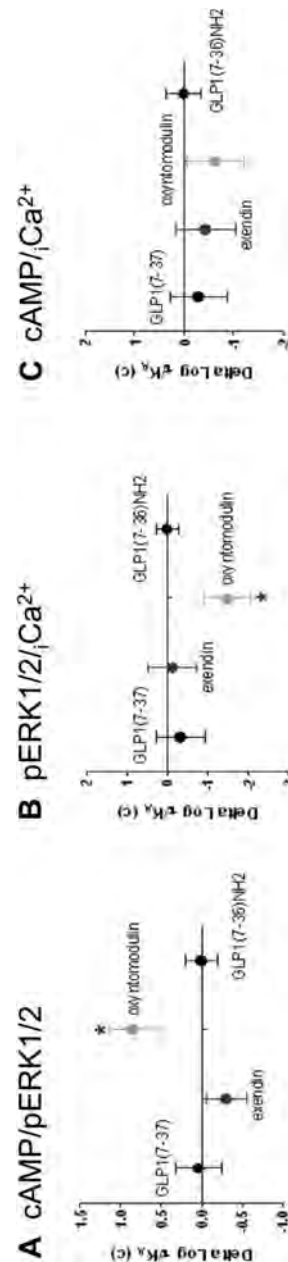
Biased signalling

GPCRs are widely accepted to be promiscuous, signalling via multiple G-protein-dependent and -independent mechanisms on receptor activation. It has become increasingly evident that in such pleiotropically coupled receptor systems, receptor activation can engender differential effects via multiple pathways depending on the ligand present in the system. This phenomenon is termed 'biased signalling', but may also be referred to as ligand-directed signalling, ligand-directed stimulus bias, functional selectivity or stimulus trafficking, and is a result of different ligands stabilizing distinct receptor conformations, which subsequently influence the nature and strength of pathway coupling that may include alterations to G-protein coupling profiles, but also to non-G-protein signalling pathways such as those mediated by β -arrestins [41]. Biased signalling has been observed at many receptors including the pituitary adenylate cyclase-activating polypeptide receptor, 5-hydroxytryptamine 2c receptor, μ -opioid receptor, dopamine receptors, V_2 vasopressin receptor, β_2 -adrenergic receptor and recently at the GLP-1R [41,42].

Recent analytical advances in the field have demonstrated that bias in a system can be quantified through estimating τ/K_A ratios, where τ equates to the efficacy in the system [24,25]. This is a novel method to determine signalling bias in a system where profound reversal of potencies is not observed. At the GLP-1R, all peptide agonists preferentially activate cAMP over ERK1/2 and Ca^{2+} *in vitro*. However, the relative degree of bias is variable between ligands, with truncated GLP-1 peptides and exendin-4 having greater bias towards cAMP than full-length GLP-1 peptides and oxyntomodulin (Figure 3) [24,25,42]. This is particularly important to consider in pharmacological characterization of any receptor, and may have the potential to be exploited in the rational design of therapeutics that target pathways associated with beneficial effects over pathways that are associated with detrimental effects.

Figure 3 | Biased signalling at the GLP-1R

Degree of bias of GLP-1R peptide agonists for (A) cAMP/pERK1/2, (B) pERK1/2/ iCa^{2+} and (C), cAMP/ iCa^{2+} relative to the values for GLP-1(7–36)NH₂ (control agonist), where τ is coupling efficacy, corrected for cell-surface expression (c), and K_A is the affinity of the agonist. Statistical significance of changes in coupling efficacy in comparison with GLP-1 (7–36)NH₂ is indicated with an asterisk (* $P < 0.05$). Data taken from [42].



Allosteric modulation

Aside from both the endogenous and exogenous peptide agonists, there have been several synthetic and naturally occurring ligands of the GLP-1R that have been proposed to act allosterically, that is, at sites distinct to the endogenous ligand (Figures 1B–1F). From a therapeutic perspective, ligands acting allosterically have several major advantages,

including enhanced receptor subtype selectivity, the ability to simultaneously bind to the receptor with the endogenous ligand (restoring physiologically relevant temporal control), inducing a new repertoire of receptor conformations and therefore influencing receptor activity, and in particular for peptide-activated receptors, the potential for oral administration. With respect to the GLP-1R, allosteric ligands that enhance the insulinotropic effects of the system are desired [PAMs (positive allosteric modulators)].

At present, very few allosterically acting ligands have been identified for the GLP-1R. The Novo Nordisk compounds 2-(2'-methyl)thiadiazolylsulfanyl-3-trifluoromethyl-6,7-dichloroquinoxaline (compound 1) and 6,7-dichloro-2-methylsulfonyl-3-t-butylaminoquinoxaline (compound 2) [43] were the first non-peptide agonists identified for the GLP-1R, the latter of which demonstrates glucose-dependent insulin release via the GLP-1R [44,45]. Similarly, the cyclobutanes Boc5 and S4P stimulate GLP-1R activity, whereas the inability to fully inhibit ^{125}I -GLP-1(7–36) NH_2 binding suggests an allosteric mechanism of action [43,46]. Although S4P is only a partial agonist in GLP-1R-expressing immortal cell lines, Boc5 is a fully efficacious agonist with maximal responses for decreasing plasma glucose and reducing nutrient intake in obese mice, comparable with the native GLP-1 peptide [47]. Unlike the compounds detailed above, quercetin (3,3',4,5,7-pentahydroxyflavone) is a naturally occurring compound belonging to the flavonoid family, and has been observed to allosterically enhance GLP-1 efficacy and potency in intracellular Ca^{2+} mobilization *in vitro* [42,48]. The most recently identified allosterically acting synthetic ligand of the GLP-1R, 4-(3-(benzyloxy)phenyl)-2-(ethylsulfinyl)-6-(trifluoromethyl)pyrimidine (BETP or compound B), increases glucose-dependent insulin release from normal and diabetic human islet cells [49]. Support for an allosteric mode of action is seen in the removal of the GLP-1R N-terminus, which does not influence the activity of the compound [49].

Although several additional synthetic small molecule ligands have been reported to increase GLP-1R-mediated cAMP production, increase plasma GLP-1 levels or decrease acute nutrient intake (reviewed in [50]), they have not been fully characterized pharmacologically, and thus it remains to be determined whether they are true GLP-1R ligands. Although allosteric modulation is fast gaining traction as a desired therapeutic approach to many disorders and conditions, there are many challenges in the identification and application of allosteric modulators. One most prominent complexity is that of probe-dependence, which describes the extent and direction of allosteric modulation on an orthosteric ligand (the probe), and is correlated with the co-operativity between the allosteric and orthosteric ligand in the system (reviewed in [51]). Indeed, this has already been observed at the GLP-1R *in vitro* and *in vivo*, with differential effects observed between orthosterically acting peptide ligands and the allosteric ligands BETP or compound 2, with preferential enhancement of signalling via oxyntomodulin relative to GLP-1 or exendin-4 [42,52].

Intriguingly, these allosteric compounds also markedly enhance the activity of the inactive metabolite of GLP-1 (GLP-1(9–36) NH_2), suggesting that therapies directed to altering metabolite activity may be possible [53]. Although the physiological importance of probe-dependence is yet to be determined, it illustrates an important consideration when pharmacologically characterizing allosteric ligands at receptors possessing multiple orthosteric ligands.

Conclusions

The rapidly increasing incidence of Type 2 DM and significant impact on quality-of-life demands the development of superior therapeutics for the management of the condition. Despite the GLP-1R having a pivotal role in glucose homeostasis and currently being a highly valued therapeutic target, there are still significant knowledge gaps that limit understanding of this complex receptor system, particularly with respect to receptor structure and the nature of allosterism. In addition, the physiological importance of biased signalling and probe-dependence remains largely unexplored. Further research into these aspects of receptor function will have an impact on the future design and development of therapeutics for the management of Type 2 DM.

Funding

This work was supported by the National Health and Medical Research Council of Australia (NHMRC) [grant numbers 519461 and 1002180], with Senior Research Fellowship awarded to A.C. and Principal Research Fellowship awarded to P.M.S.

References

- Shaw, J.E., Sicree, R.A. and Zimmet, P.Z. (2010) Global estimates of the prevalence of diabetes for 2010 and 2030. *Diabetes Res. Clin. Pract.* **87**, 4–14
- Ross, S.A., Gulve, E.A. and Wang, M. (2004) Chemistry and biochemistry of Type 2 diabetes. *Chem. Rev.* **104**, 1255–1282
- Baggio, L.L. and Drucker, D.J. (2007) Biology of incretins: GLP-1 and GIP. *Gastroenterology* **132**, 2131–2157
- Nauck, M.A., Heimesaat, M.M., Orskov, C., Holst, J.J., Ebert, R. and Creutzfeldt, W. (1993) Preserved incretin activity of glucagon-like peptide 1 [7–36 amide] but not of synthetic human gastric inhibitory polypeptide in patients with Type-2 diabetes mellitus. *J. Clin. Invest.* **91**, 301–307
- Herrmann, C., Goke, R., Richter, G., Fehmann, H.C., Arnold, R. and Goke, B. (1995) Glucagon-like peptide-1 and glucose-dependent insulin-releasing polypeptide plasma levels in response to nutrients. *Digestion* **56**, 117–126
- Reimann, F. (2010) Molecular mechanisms underlying nutrient detection by incretin-secreting cells. *Int. Dairy J.* **20**, 236–242
- Drucker, D.J., Philippe, J., Mojsov, S., Chick, W.L. and Habener, J.F. (1987) Glucagon-like peptide I stimulates insulin gene expression and increases cyclic AMP levels in a rat islet cell line. *Proc. Natl. Acad. Sci. U.S.A.* **84**, 3434–3438
- Scrocchi, L.A., Brown, T.J., MaClusky, N., Brubaker, P.L., Auerbach, A.B., Joyner, A.L. and Drucker, D.J. (1996) Glucose intolerance but normal satiety in mice with a null mutation in the glucagon-like peptide 1 receptor gene. *Nat. Med.* **2**, 1254–1258
- Farilla, L., Bulotta, A., Hirshberg, B., Li Calzi, S., Khoury, N., Noushmehr, H., Bertolotto, C., Di Mario, U., Harlan, D.M. and Perfetti, R. (2003) Glucagon-like peptide 1 inhibits cell apoptosis and improves glucose responsiveness of freshly isolated human islets. *Endocrinology* **144**, 5149–5158

- 10 Bazarsuren, A., Grauschopf, U., Wozny, M., Reusch, D., Hoffmann, E., Schaefer, W., Panzner, S. and Rudolph, R. (2002) *In vitro* folding, functional characterization, and disulfide pattern of the extracellular domain of human GLP-1 receptor. *Biophys. Chem.* **96**, 305–318
- 11 Runge, S., Thogersen, H., Madsen, K., Lau, J. and Rudolph, R. (2008) Crystal structure of the ligand-bound glucagon-like peptide-1 receptor extracellular domain. *J. Biol. Chem.* **283**, 11340–11347
- 12 Underwood, C.R., Garibay, P., Knudsen, L.B., Hastrup, S., Peters, G.H., Rudolph, R. and Reedt-Runge, S. (2010) Crystal structure of glucagon-like peptide-1 in complex with the extracellular domain of the glucagon-like peptide-1 receptor. *J. Biol. Chem.* **285**, 723–730
- 13 Wilmen, A., Goke, B. and Goke, R. (1996) The isolated N-terminal extracellular domain of the glucagon-like peptide-1 (GLP)-1 receptor has intrinsic binding activity. *FEBS Lett.* **398**, 43–47
- 14 Al-Sabah, S. and Donnelly, D. (2003) A model for receptor-peptide binding at the glucagon-like peptide-1 (GLP-1) receptor through the analysis of truncated ligands and receptors. *Br. J. Pharmacol.* **140**, 339–346
- 15 Coopman, K., Wallis, R., Robb, G., Brown, A., Wilkinson, G.F., Timms, D. and Willars, G.B. (2011) Residues within the transmembrane domain of the glucagon-like peptide-1 receptor involved in ligand binding and receptor activation. *Mol. Endocrinol.* **25**, 1804–1818
- 16 Runge, S., Wulff, B.S., Madsen, K., Brauner-Osborne, H. and Knudsen, L.B. (2003) Different domains of the glucagon and glucagon-like peptide-1 receptors provide the critical determinants of ligand selectivity. *Br. J. Pharmacol.* **138**, 787–794
- 17 Graziano, M.P., Hey, P.J. and Strader, C.D. (1996) The amino terminal domain of the glucagon-like peptide-1 receptor is a critical determinant of subtype specificity. *Recept. Channels* **4**, 9–17
- 18 Chen, Q., Pinon, D.I., Miller, L.J. and Dong, M. (2009) Molecular basis of glucagon-like peptide 1 docking to its intact receptor studied with carboxyl-terminal photolabile probes. *J. Biol. Chem.* **284**, 34135–34144
- 19 Chen, Q., Pinon, D.I., Miller, L.J. and Dong, M. (2010) Spatial approximations between residues 6 and 12 in the amino-terminal region of glucagon-like peptide 1 and its receptor: a region critical for biological activity. *J. Biol. Chem.* **285**, 24508–24518
- 20 Miller, L.J., Chen, Q., Lam, P.C., Pinon, D.I., Sexton, P.M., Abagyan, R. and Dong, M. (2011) Refinement of glucagon-like peptide 1 docking to its intact receptor using mid-region photolabile probes and molecular modeling. *J. Biol. Chem.* **286**, 15895–15907
- 21 Lopez de Maturana, R., Treece-Birch, J., Abidi, F., Findlay, J.B. and Donnelly, D. (2004) Met-204 and Tyr-205 are together important for binding GLP-1 receptor agonists but not their N-terminally truncated analogues. *Protein Pept. Lett.* **11**, 15–22
- 22 Lopez de Maturana, R. and Donnelly, D. (2002) The glucagon-like peptide-1 receptor binding site for the N-terminus of GLP-1 requires polarity at Asp198 rather than negative charge. *FEBS Lett.* **530**, 244–248
- 23 Xiao, Q., Jeng, W. and Wheeler, M.B. (2000) Characterization of glucagon-like peptide-1 receptor-binding determinants. *J. Mol. Endocrinol.* **25**, 321–335
- 24 Koole, C., Wootten, D., Simms, J., Miller, L.J., Christopoulos, A. and Sexton, P.M. (2012) Second extracellular loop of human glucagon-like peptide-1 receptor (GLP-1R) has a critical role in GLP-1 peptide binding and receptor activation. *J. Biol. Chem.* **287**, 3642–3658
- 25 Koole, C., Wootten, D., Simms, J., Savage, E.E., Miller, L.J., Christopoulos, A. and Sexton, P.M. (2012) Second extracellular loop of human glucagon-like peptide-1 receptor (GLP-1R) differentially regulates orthosteric but not allosteric agonist binding and function. *J. Biol. Chem.* **287**, 3659–3673
- 26 Hallbrink, M., Holmqvist, T., Olsson, M., Ostenson, C.G., Efendic, S. and Langel, U. (2001) Different domains in the third intracellular loop of the GLP-1 receptor are responsible for $G_{\alpha s}$ and $G_{\alpha i}/G_{\alpha o}$ activation. *Biochim. Biophys. Acta* **1546**, 79–86
- 27 Montrose-Rafizadeh, C., Avdonin, P., Garant, M.J., Rodgers, B.D., Kole, S., Yang, H., Levine, M.A., Schwindinger, W. and Bernier, M. (1999) Pancreatic glucagon-like peptide-1 receptor couples to multiple G proteins and activates mitogen-activated protein kinase pathways in Chinese hamster ovary cells. *Endocrinology* **140**, 1132–1140
- 28 Holz, G.G. (2004) Epac: a new cAMP-binding protein in support of glucagon-like peptide-1 receptor-mediated signal transduction in the pancreatic β -cell. *Diabetes* **53**, 5–13
- 29 Sonoda, N., Imamura, T., Yoshizaki, T., Babendure, J.L., Lu, J.C. and Olefsky, J.M. (2008) β -arrestin-1 mediates glucagon-like peptide-1 signaling to insulin secretion in cultured pancreatic beta cells. *Proc. Natl. Acad. Sci. U.S.A.* **105**, 6614–6619
- 30 Jorgensen, R., Kubale, V., Vrecl, M., Schwartz, T.W. and Elling, C.E. (2007) Oxyntomodulin differentially affects glucagon-like peptide-1 receptor β -arrestin recruitment and signaling through $G_{\alpha s}$. *J. Pharmacol. Exp. Ther.* **322**, 148–154
- 31 Jorgensen, R., Martini, L., Schwartz, T.W. and Elling, C.E. (2005) Characterization of glucagon-like peptide-1 receptor β -arrestin 2 interaction: a high-affinity receptor phenotype. *Mol. Endocrinol.* **19**, 812–823
- 32 Quoyer, J., Longuet, C., Broca, C., Linck, N., Costes, S., Varin, E., Bockaert, J., Bertrand, G. and Dalle, S. (2010) GLP-1 mediates anti-apoptotic effect by phosphorylating Bad through a β -arrestin 1-mediated ERK1/2 activation in pancreatic β -cells. *J. Biol. Chem.* **285**, 1989–2002
- 33 Barnett, A.H. (2009) New treatments in Type 2 diabetes: a focus on the incretin-based therapies. *Clin. Endocrinol. (Oxford, U.K.)* **70**, 343–353
- 34 Green, B.D. and Flatt, P.R. (2007) Incretin hormone mimetics and analogues in diabetes therapeutics. *Best Pract. Res. Clin. Endocrinol. Metab.* **21**, 497–516
- 35 Knudsen, L.B., Nielsen, P.F., Huusfeldt, P.O., Johansen, N.L., Madsen, K., Pedersen, F.Z., Thogersen, H., Wilken, M. and Agerso, H. (2000) Potent derivatives of glucagon-like peptide-1 with pharmacokinetic properties suitable for once daily administration. *J. Med. Chem.* **43**, 1664–1669
- 36 Christensen, M. and Knop, F.K. (2010) Once-weekly GLP-1 agonists: how do they differ from exenatide and liraglutide? *Curr. Diab. Rep.* **10**, 124–132
- 37 Hargrove, D.M., Kendall, E.S., Reynolds, J.M., Lwin, A.N., Herich, J.P., Smith, P.A., Gedulin, B.R., Flanagan, S.D., Jodka, C.M., Hoyt, J.A. et al. (2007) Biological activity of AC3174, a peptide analog of exendin-4. *Regul. Pept.* **141**, 113–119
- 38 Chae, S.Y., Jin, C.H., Shin, H.J., Youn, Y.S., Lee, S. and Lee, K.C. (2008) Preparation, characterization, and application of biotinylated and biotin-PEGylated glucagon-like peptide-1 analogues for enhanced oral delivery. *Bioconjugate Chem.* **19**, 334–341
- 39 Parks, M. and Rosebraugh, C. (2010) Weighing risks and benefits of liraglutide: the FDA's review of a new antidiabetic therapy. *N. Engl. J. Med.* **362**, 774–777
- 40 Olansky, L. (2010) Do incretin drugs for Type 2 diabetes increase the risk of acute pancreatitis? *Cleveland Clin. J. Med.* **77**, 503–505
- 41 Kenakin, T. (1995) Agonist-receptor efficacy. II. Agonist trafficking of receptor signals. *Trends Pharmacol. Sci.* **16**, 232–238
- 42 Koole, C., Wootten, D., Simms, J., Valant, C., Sridhar, R., Woodman, O.L., Miller, L.J., Summers, R.J., Christopoulos, A. and Sexton, P.M. (2010) Allosteric ligands of the glucagon-like peptide 1 receptor (GLP-1R) differentially modulate endogenous and exogenous peptide responses in a pathway-selective manner: implications for drug screening. *Mol. Pharmacol.* **78**, 456–465
- 43 Teng, M., Johnson, M.D., Thomas, C., Kiel, D., Lakis, J.N., Kercher, T., Aytes, S., Kostrowicki, J., Bhuralkar, D., Truesdale, L. et al. (2007) Small molecule ago-allosteric modulators of the human glucagon-like peptide-1 (hGLP-1) receptor. *Bioorg. Med. Chem. Lett.* **17**, 5472–5478
- 44 Knudsen, L.B., Kiel, D., Teng, M., Behrens, C., Bhuralkar, D., Kodra, J.T., Holst, J.J., Jeppesen, C.B., Johnson, M.D., de Jong, J.C. et al. (2007) Small-molecule agonists for the glucagon-like peptide 1 receptor. *Proc. Natl. Acad. Sci. U.S.A.* **104**, 937–942
- 45 Irwin, N., Flatt, P.R., Patterson, S. and Green, B.D. (2010) Insulin-releasing and metabolic effects of small molecule GLP-1 receptor agonist 6,7-dichloro-2-methylsulfonyl-3-N-tert-butylaminoquinoline. *Eur. J. Pharmacol.* **628**, 268–273
- 46 Chen, D., Liao, J., Li, N., Zhou, C., Liu, Q., Wang, G., Zhang, R., Zhang, S., Lin, L., Chen, K. et al. (2007) A nonpeptidic agonist of glucagon-like peptide 1 receptors with efficacy in diabetic db/db mice. *Proc. Natl. Acad. Sci. U.S.A.* **104**, 943–948
- 47 Su, H., He, M., Li, H., Liu, Q., Wang, J., Wang, Y., Gao, W., Zhou, L., Liao, J., Young, A.A. and Wang, M.W. (2008) Boc5, a non-peptidic glucagon-like peptide-1 receptor agonist, invokes sustained glycemic control and weight loss in diabetic mice. *PLoS ONE* **3**, e2892
- 48 Wootten, D., Simms, J., Koole, C., Woodman, O.L., Summers, R.J., Christopoulos, A. and Sexton, P.M. (2011) Modulation of the glucagon-like peptide-1 receptor signaling by naturally occurring and synthetic flavonoids. *J. Pharmacol. Exp. Ther.* **336**, 540–550
- 49 Sloop, K.W., Willard, F.S., Brenner, M.B., Ficorilli, J., Valasek, K., Showalter, A.D., Farb, T.B., Cao, J.X., Cox, A.L., Michael, M.D. et al. (2010) Novel small molecule glucagon-like peptide-1 receptor agonist stimulates insulin secretion in rodents and from human islets. *Diabetes* **59**, 3099–3107
- 50 Wang, M.W., Liu, Q. and Zhou, C.H. (2010) Non-peptidic glucose-like peptide-1 receptor agonists: aftermath of a serendipitous discovery. *Acta Pharmacol. Sin.* **31**, 1026–1030

-
- 51 Keov, P., Sexton, P.M. and Christopoulos, A. (2011) Allosteric modulation of G protein-coupled receptors: a pharmacological perspective. *Neuropharmacology* **60**, 24–35
- 52 Willard, F.S., Wootten, D., Showalter, A.D., Savage, E.E., Ficorilli, J., Farb, T.B., Bokvist, K., Alsina-Fernandez, J., Furness, S.G., Christopoulos, A. et al. (2012) Small molecule allosteric modulation of the glucagon-like peptide-1 receptor enhances the insulinotropic effect of oxyntomodulin. *Mol. Pharmacol.* **82**, 1066–1073
- 53 Wootten, D., Savage, E.E., Valant, C., May, L.T., Sloop, K.W., Ficorilli, J., Showalter, A.D., Willard, F.S., Christopoulos, A. and Sexton, P. (2012) Allosteric modulation of endogenous metabolites as an avenue for drug discovery. *Mol. Pharmacol.* **82**, 281–290
-

Received 24 September 2012
doi:10.1042/BST20120236

Emerging paradigms in GPCR allostery: implications for drug discovery

Denise Wootten, Arthur Christopoulos and Patrick M. Sexton

Abstract | Allosteric ligands bind to G protein-coupled receptors (GPCRs; also known as seven-transmembrane receptors) at sites that are distinct from the sites to which endogenous ligands bind. The existence of allosteric ligands has enriched the ways in which the functions of GPCRs can be manipulated for potential therapeutic benefit, yet the complexity of their actions provides both challenges and opportunities for drug screening and development. Converging avenues of research in areas such as biased signalling by allosteric ligands and the mechanisms by which allosteric ligands modulate the effects of diverse endogenous ligands have provided new insights into how interactions between allosteric ligands and GPCRs could be exploited for drug discovery. These new findings have the potential to alter how screening for allosteric drugs is performed and may increase the chances of success in the development of allosteric modulators as clinical lead compounds.

Lead compounds

Chemical compounds that have the desired pharmacological properties and structures to be used as starting points for chemical modifications to improve their pharmacological and/or pharmacokinetic profile.

Orthosteric binding sites

Ligand binding sites on a G protein-coupled receptor for the endogenous ligand. These binding sites are also recognized by classical competitive antagonists and inverse agonists.

*Drug Discovery Biology,
Monash Institute of
Pharmaceutical Sciences
and Department of
Pharmacology, Monash
University, Melbourne,
Victoria 3052, Australia.
Correspondence to P.M.S.
e-mail:
patrick.sexton@monash.edu
doi:10.1038/nrd4052*

Despite the tractability of G protein-coupled receptors (GPCRs; also known as seven-transmembrane receptors) as drug targets, there are substantial challenges in understanding the mechanisms of drug action at these receptors and in the translation of this knowledge into the discovery and development of more selective and effective medicines. GPCRs are encoded by approximately 1,000 genes, yet synthetic ligands have only been identified for a small number of receptors. In addition, for many GPCRs, efforts to develop highly selective lead compounds have failed¹.

Emerging knowledge of the structure and physiological functions of GPCRs has begun to alter the approaches to GPCR drug discovery. Traditional efforts have focused on targeting the orthosteric binding sites of GPCRs where the endogenous ligands bind to elicit signal transduction. This approach yields compounds that either directly activate the target GPCR (agonists) or block the actions of the endogenous ligand (antagonists or inverse agonists). The past decade has witnessed a pronounced increase in the pursuit of allosteric ligands that influence receptor activity by binding to sites that are topographically distinct from the orthosteric binding site². Allosteric ligands mediate their effects by inducing conformational changes in the GPCR protein that are transmitted from the allosteric binding pocket to the orthosteric site and/or directly to effector protein coupling sites³.

Allosteric ligands have a diverse range of activities; these include intrinsic agonism and/or the ability to act as positive allosteric modulators, inverse agonism and/or the ability to act as negative allosteric modulators or the ability to act as neutral allosteric ligands (NALs), which were previously termed silent allosteric modulators but this terminology was misleading as they do not modulate orthosteric ligand activity (FIG. 1). As such, allosteric ligands provide novel opportunities to modulate GPCR function that cannot be achieved by ligands that bind to the orthosteric site, as discussed below. Moreover, several properties of allosteric ligands can present therapeutic advantages over orthosteric ligands (reviewed in REF. 3).

In this Review we discuss the potential advantages of allosteric ligands from a drug discovery perspective, highlight key advances in the field of GPCR allostery and the opportunities arising from these advances. These developments include the finding that the nature of an allosteric interaction between an allosteric ligand and a GPCR is dependent on the orthosteric ligand (probe), the implications of probe dependence in signalling systems with multiple endogenous ligands, the influence of the metabolism of orthosteric and allosteric ligands on their allosteric interaction, and the ability of allosteric ligands to induce biased signalling by the orthosteric ligand. We also highlight key challenges in the identification of

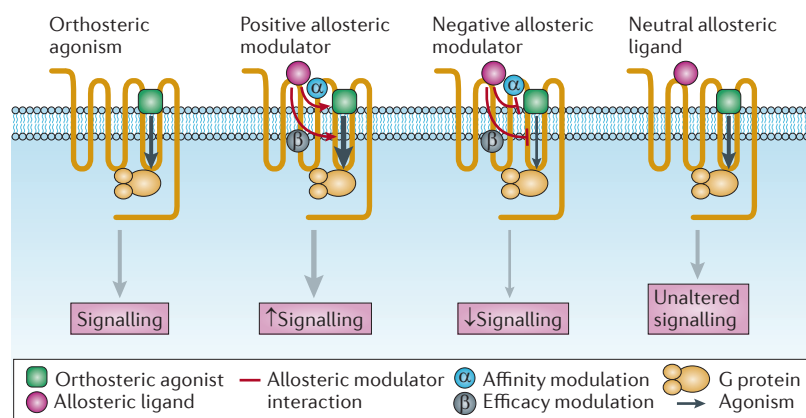


Figure 1 | How allosteric ligands influence orthosteric ligand function.

Orthosteric agonists bind to the G protein-coupled receptor (GPCR), which induces a conformational change that results in the activation of downstream signalling. Positive allosteric modulators are allosteric ligands that bind to a topographically distinct site to the orthosteric agonist and enhance the affinity (cooperativity factor- α) and/or efficacy (modulation factor- β) of the orthosteric agonist. Negative allosteric modulators are allosteric ligands that decrease the affinity (cooperativity factor- α) and/or efficacy (modulation factor- β) of the orthosteric agonist. Allosteric ligands that have no effect on the affinity and/or efficacy mediated by the orthosteric agonist are termed neutral allosteric ligands. The red arrows denote the allosteric interaction of the modulator with the orthosteric ligand, and the black arrows denote the allosteric interaction between the ligand binding sites and the effector binding site within the GPCR, resulting in downstream activation of signalling pathways (this is known as orthosteric agonism).

Inverse agonists

Ligands that bind to a receptor and decrease its basal signalling activity.

Positive allosteric modulators

Allosteric modulators that enhance the affinity and/or responsiveness of the orthosteric ligand.

Negative allosteric modulators

Allosteric modulators that decrease the affinity and/or responsiveness of the orthosteric ligand.

Neutral allosteric ligands

(Previously referred to as silent allosteric modulators). Allosteric ligands that bind to a G protein-coupled receptor but do not alter the affinity or efficacy of the orthosteric ligand.

Allosteric interaction

An interaction between two topographically distinct binding sites on the same receptor complex. These interactions can be between two ligand binding sites or between a ligand binding site and an effector binding site.

allosteric drug-like compounds that target GPCRs. Finally, we discuss how key information gained from the recently solved GPCR structures could influence the drug discovery process and screening for allosteric ligands in the future.

Advantages of allosteric modulators

Allosteric modulators that lack intrinsic efficacy will only exert their effects in the presence of a released endogenous agonist. Thus, they can selectively tune cellular responses in tissues where the endogenous agonist exerts its physiological effects, therefore maintaining both temporal and spatial aspects of endogenous physiological signalling. In addition, the complete occupancy of the allosteric site produces a saturation of effect, which, in turn, limits the effect of the allosteric modulator on the function of the orthosteric ligand. This action protects against potential overdosing of a drug³.

Another advantage of allosteric modulators is that they have the potential to achieve greater selectivity at subtypes of GPCRs³. This could be due to greater variance in the amino acid sequence in the allosteric binding pockets compared to the orthosteric binding pocket or via selective cooperativity between the allosteric and orthosteric site (and/or effector coupling sites) at a given GPCR subtype. In addition, on GPCRs for which the orthosteric binding site is diffuse and poorly druggable, the allosteric binding site might be amenable to targeting with small molecules; this has been observed for receptors with large peptidic ligands and is commonly found

with the class B subfamily of GPCRs. Generally, these advantages of allosteric modulators apply regardless of the particular therapeutic area or the location of the receptor being targeted.

Bitopic ligands

Although allosteric ligands could provide greater selectivity for a given GPCR target, many have a lower affinity than ligands targeted to the orthosteric binding site of the same GPCR⁴. This finding formed the basis for recent studies that exploited the properties of both orthosteric and allosteric ligands by creating molecules that combine both pharmacophores in one ligand^{5–7}. These bivalent ligands (termed bitopic, multivalent or dual steric ligands) may offer several advantages over an allosteric ligand. First, a ligand that is designed to have suitably paired orthosteric and allosteric fragments can theoretically have improved affinity over pure allosteric ligands owing to a greater number of ligand–GPCR contacts (by simultaneously binding to both sites), and it may also engender selectivity by targeting an allosteric site. Achieving these effects through the use of a single biologically active molecule may be particularly relevant in diseases in which endogenous agonist tone is lost — for example, neurodegenerative disorders such as Alzheimer's disease and Parkinson's disease — as a pure allosteric modulator cannot exert its effect when endogenous tone is absent⁴.

One example of a bitopic ligand is the M_2 muscarinic acetylcholine receptor (mAChR) ligand McN-A-343. This compound was one of the earliest examples of a mAChR partial agonist but, depending on the experimental paradigm, it was predicted to act at either an allosteric binding site or the orthosteric binding site of the M_2 mAChR^{8,9}. By reverse-engineering this molecule, two constituent fragments with discrete pharmacology were identified: tetramethylammonium (TMA), which is an orthosteric agonist, and 3'-chlorophenylcarbamate (DDBL-4), which is a negative allosteric modulator of TMA activity. When they interacted in the same assay, these two fragments behaved in a similar manner to the parent molecule (McN-A-343)⁷. The DDBL-4 pharmacophore of the ligand thus produced the partial agonist activity of McN-A-343, as it reduced the efficacy of the TMA moiety.

It has been suggested that several other selective agonists (such as AC-42, 77-LH-28-1, *N*-desmethylozapine and TBPB) and antagonists (such as methoctramine and AF-DX) of mAChRs act at an allosteric binding site (although the evidence for this is conflicting) and these ligands could have a bitopic mode of action^{10–13}. However, there is no definitive proof that each of these ligands is composed of distinct orthosteric and allosteric moieties. There is also evidence that selective ligands of other GPCRs (for example, dopamine receptors) have a bitopic mode of binding¹⁴. Moreover, bitopic ligands have been rationally designed by joining orthosteric and allosteric ligands with a linker^{6,15,16}. Thus, the pursuit of bitopic ligands may offer additional potential for selectively targeting GPCRs, and/or sculpting the signalling response, and may provide new therapeutic

lead compounds. However, the increase in size of such molecules may pose challenges to designing compounds that have drug-like properties.

Detection and quantification of allosteric ligands

Interactions between allosteric ligands and GPCRs can be complex. Various pharmacological approaches can be used, either individually or in tandem, to detect and successfully quantify allosteric interactions at GPCRs.

Binding assays are important tools for studying GPCR allostery as they can often directly validate whether a ligand has an allosteric mode of action. Classic equilibrium binding assays can be useful for detecting and quantifying the actions of allosteric modulators; depending on the cooperativity factor- α , allosteric antagonists can be identified by their inability to fully inhibit the specific binding of a radiolabelled orthosteric probe. However, this effect may not always be readily apparent, as modulators that have a high degree of negative cooperativity can be mistaken as competitive ligands if low levels of radioligand occupancy are investigated.

Studying the effects of a potential allosteric modulator on the rate of association or, in particular, on the rate of dissociation of an orthosteric ligand from the GPCR is another useful application of binding assays for the detection and quantification of allosteric interactions. This method exploits the fact that the dissociation rate of a pre-equilibrated radiolabelled orthosteric radioligand-GPCR complex can be perturbed by ligands that modulate the affinity of the orthosteric ligand, as such ligands induce a conformational change in the GPCR that alters the kinetic rate constants that govern the binding of the orthosteric ligand¹⁷. The dissociation rate can be increased or decreased by allosteric ligands that exploit this mechanism. A major advantage of kinetic binding assays is that they can detect allosteric effects and directly validate allosteric modulators that may be missed in equilibrium binding studies.

Owing to the introduction of new and improved high-throughput technologies for detecting intracellular signalling responses, functional assays are now the assays of choice for GPCR-based drug discovery¹⁸. The logical advantages of using these types of assays for primary screening are that the desired functional end point can be directly determined. As the ability of an allosteric ligand to modulate the affinity of an orthosteric ligand does not always correlate with the effects of the allosteric ligand on orthosteric ligand efficacy (and vice versa), it is possible to use functional assays to detect small-molecule modulators of receptor function that would not be identified in binding assays. Therefore, functional assays offer an additional advantage when used for screening. The easiest approach for detecting as well as quantifying allosteric effects in a functional assay is to perform interaction assays that investigate the effects of increasing concentrations of an allosteric ligand on the EC_{50} value and/or E_{max} value of the orthosteric agonist.

One of the key challenges associated with the discovery of allosteric modulators is the need to quantify allosteric effects in a way that can be used to guide structure-activity relationship and compound optimization studies.

Currently, structure-activity relationship studies are predominantly guided by the affinity and the efficacy (that is, agonism) of the modulator. We advocate that two additional properties should be taken into account during structure-activity relationship studies of allosteric modulators: the magnitude by which the allosteric ligand modulates the affinity of the orthosteric ligand (and vice versa) when both ligands are co-bound; and the magnitude by which the allosteric ligand modulates the efficacy of the orthosteric ligand. The efficacy and the magnitude by which the allosteric ligand modulates the efficacy of the orthosteric ligand should be determined independently for each signalling pathway that is being investigated (see below for a discussion on biased signalling induced by allosteric modulators).

Thermodynamic models can be used to describe the interactions among orthosteric ligands, allosteric ligands, receptors and effector proteins. However, such models are mechanistic, highly parameterized and deriving all of these values from routine experimental data is difficult (for example, these experiments are not readily amenable to high-throughput formats, and they are also costly and time consuming)³.

The simplest model for quantifying the minimal number of parameters required to understand the behaviour of allosteric ligands and to inform drug optimization is an amalgam of the Ehlert model of allosteric receptor effect and the Black-Leff operational model of receptor function^{19,20}. This amalgamated model can be used to quantify how allosteric ligands modulate the response of orthosteric ligands in functional assays. The cooperative effect between the two ligands is estimated as a composite of their cooperative effects on affinity (cooperativity factor- α) and efficacy (modulation factor- β). However, a direct estimation of the cooperative effect on affinity can be derived via equilibrium and dissociation binding experiments¹⁸ (BOX 1).

Probe dependence and its implications

Both binding and functional assays have specific advantages when they are used to screen for allosteric modulators of GPCRs. However, the extent and direction (that is, positive, negative or neutral) of the interaction between the allosteric and orthosteric ligand depends on which orthosteric ligand is bound to the GPCR; this phenomenon is termed probe dependence (FIG. 2). Probe dependence can lead to problems in detecting and validating the receptor specificity of allosteric ligands. For example, the CC-chemokine receptor 5 (CCR5) allosteric modulator aplaviroc produced very little effect on the binding of the chemokine ligand CCL5 to the receptor but completely blocked the binding of the chemokine ligand CCL3 (REF. 21).

Probe dependence could affect both the therapeutic application and the mode of discovery of allosteric modulators. Ideally, the physiological orthosteric ligand should be used as a probe in the screening process of drug discovery programmes. However, in many cases the natural agonist may be chemically unsuitable for screening and subsequent *in vivo* experiments. Therefore, surrogate agonists are often used. In such instances, the

Probe dependence

The ability of an allosteric ligand to display different cooperativities with individual orthosteric ligands acting at the same G protein-coupled receptor.

Biased signalling

The ability of a ligand to preferentially stabilize specific G protein-coupled receptor conformations at the exclusion of others, with each conformational state associated with its own repertoire of signalling behaviours.

Allosteric modulators

Ligands that bind to an allosteric site on a receptor and modulate the binding and/or signalling efficacy of orthosteric ligands.

Intrinsic efficacy

The ability of a molecule to induce a physiological or pharmacological response when bound to a receptor.

Allosteric binding site

A ligand binding site on a G protein-coupled receptor that is topographically distinct from the orthosteric site.

Partial agonist

An agonist that produces a signalling response that is lower than the maximum response achievable for the given signalling system. Partial agonists can antagonize the effects of full agonists.

Binding assays

Assays that are used to assess ligand affinities and/or the kinetics of ligand binding.

Cooperativity factor- α

A parameter that is used to describe and quantify the intensity of the effect of allosteric ligand binding on the affinity of the orthosteric ligand (and vice versa).

Allosteric antagonists

Ligands that bind to the allosteric site but do not have efficacy, yet their binding disrupts or inhibits the binding of other allosteric ligands.

Box 1 | Quantification of allosteric ligand behaviour

Ideally, approaches that are used for guiding preclinical allosteric drug discovery should aim to enrich structure–activity relationships by quantifying key properties of allosteric ligands that go beyond simple measures of affinity or potency. Operational models of allostery have been developed for this purpose, with the model formulated by Leach *et al.*³⁴, shown below:

$$E = \frac{E_m(\tau_A[A](K_B + \alpha\beta[B]) + \tau_B[B]K_A)^n}{([A]K_B + K_AK_B + [B]K_A + \alpha[A][B])^n + (\tau_A[A](K_B + \alpha\beta[B]) + \tau_B[B]K_A)^n}$$

In the above model, *E* is response (efficacy); K_A and K_B denote the equilibrium dissociation constants of an orthosteric ligand (A) and an allosteric ligand (B), respectively; α denotes the cooperativity that each ligand exerts on the binding affinity of the other ligand; β denotes the allosteric effect of the modulator on orthosteric ligand efficacy; and τ_A and τ_B denote the capacity of orthosteric and allosteric ligands, respectively, to exhibit agonism — a parameter that is influenced by the intrinsic efficacy of the ligand itself, in addition to receptor density and system responsiveness. The remaining parameters, E_m and n , denote the maximum possible system response and the slope of the transducer function that links receptor occupancy to response, respectively.

Operational models provide a powerful tool that can be used to assign quantitative parameters to allosteric ligands and are thus useful in helping to quantify and understand the effects of allosteric modulators. These models can be applied to functional data where concentration–response curves for the orthosteric ligands are performed in the presence of increasing concentrations of allosteric ligands. The values K_A , K_B , τ_A , τ_B , α and β can be calculated from these data. A direct estimation of the cooperative effect (α) exerted by each ligand on the binding affinity of the other ligand can also be derived from equilibrium and dissociation-binding experiments¹⁸.

Negative cooperativity

The ability of a negative allosteric modulator to decrease the affinity or efficacy of an orthosteric ligand. This is defined by a cooperativity factor- α or modulation factor- β that is between 0 and 1.

Competitive ligands

Two or more ligands that bind to (and therefore compete for) the same ligand binding site. This term is typically used to describe orthosteric ligands.

Rate constants

Values that quantify the rate of association and dissociation for the binding of a ligand or an effector to a receptor.

Functional assays

Assays that are used to assess ligand efficacy in defined signalling response pathways.

EC₅₀ value

The concentration of an agonist that produces 50% of the maximal response to the given agonist for a defined signalling response pathway.

E_{max} value

The maximal response of an agonist for a defined signalling response pathway.

allosteric modulator should be tested with the natural ligand as early on in the discovery process as possible to determine whether the effects that are achieved are equivalent to those seen with the surrogate ligand.

For example, a positive allosteric modulator may be useful in augmenting deteriorating cholinergic neuronal transmission in Alzheimer's disease²², but the natural agonist acetylcholine is chemically unsuitable in screening for such compounds as it is highly unstable. Cholinergic surrogate ligands such as carbachol or pilocarpine are used for screening, and stable analogues such as oxotremorine are used to validate the effects of mAChR allosteric modulators *in vivo*²³. However, the effects of positive allosteric modulators such as LY2033298 are dependent on which orthosteric agonist (carbachol or pilocarpine) is used^{24,25} — an effect that could lead to unexpected profiles of the allosteric ligand in later stages of the drug discovery process.

The ability of allosteric ligands to have differential probe dependence across multiple receptor subtypes (even if these receptor subtypes bind to the same allosteric and orthosteric ligand pairs) is an additional consideration that can have major implications on the screening process. For example, LY2033298 was reported to be a selective positive allosteric modulator of the M4 mAChR based on experimental data revealing that LY2033298 strongly potentiated acetylcholine-mediated calcium responses at the M₄ mAChR but not at the other four receptor subtypes²⁶ (this effect was driven by the cooperative interaction between the orthosteric and allosteric ligand rather than the differential affinity of the

modulator for the receptor subtypes). This modulator has recently been shown to have high positive cooperativity with the surrogate orthosteric ligands oxotremorine and TMA at the M₂ mAChR²⁵; this positive cooperative effect is similar to that observed with LY2033298 and oxotremorine at the M₄ mAChR. As such, the probe-dependent interaction of oxotremorine at both the M₂ and M₄ receptor subtypes can confound experimental interpretation of the effect of the allosteric ligand *in vivo* (where oxotremorine is often used as a surrogate for acetylcholine to provide endogenous tone)²³. This highlights the need to understand the probe dependence of allosteric ligands at related receptors to ensure robust target validation is achieved.

Moreover, the potential combination of an allosteric ligand with an existing therapeutic that is an orthosteric ligand for a given GPCR must also take into account the possibility of probe-dependent off-target effects at related GPCRs.

Probe dependence may be irrelevant in many physiological systems that have only one endogenous ligand for the receptor. However, many individual receptors respond to multiple endogenous ligands, either physiologically or pathophysiologically. Examples include the chemokine receptors²⁷, the melanocortin receptors²⁸, parathyroid hormone receptor 1 (REF. 29), relaxin receptors³⁰, the calcium-sensing receptor³¹, calcitonin and calcitonin-like receptors³², as well as glucagon and glucagon-like peptide 1 (GLP1) receptors³³. For receptors such as these, probe dependence is a major consideration for the identification, development and use of allosteric modulators as therapeutics.

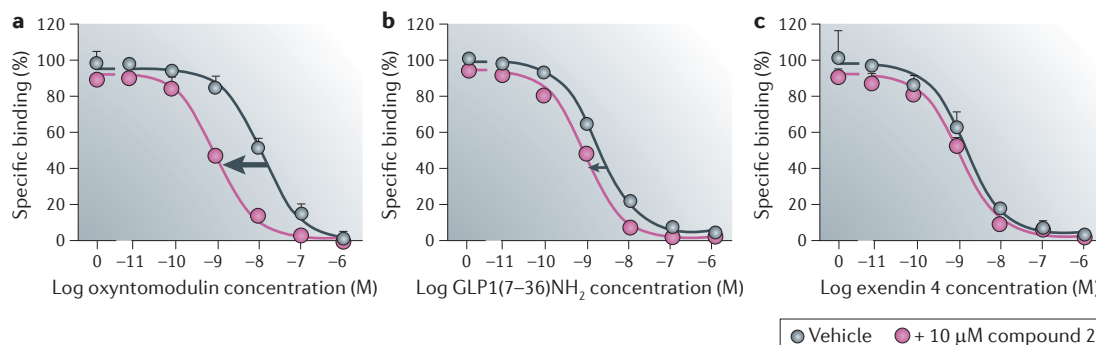
Allosteric modulation and signal bias

Distinct ligands can have a varying capacity to activate different signalling pathways linked to a given GPCR^{3,34} — an effect that is termed biased signalling (also known as stimulus bias, functional selectivity, ligand-directed stimulus trafficking or biased agonism; see FIG. 2). Examples of ligands that produce biased signalling include classical orthosteric β -adrenergic receptor antagonists and inverse agonists (clinically known as beta blockers) that antagonize receptor-mediated cyclic AMP production but promote cAMP response element-mediated gene transcription³⁵.

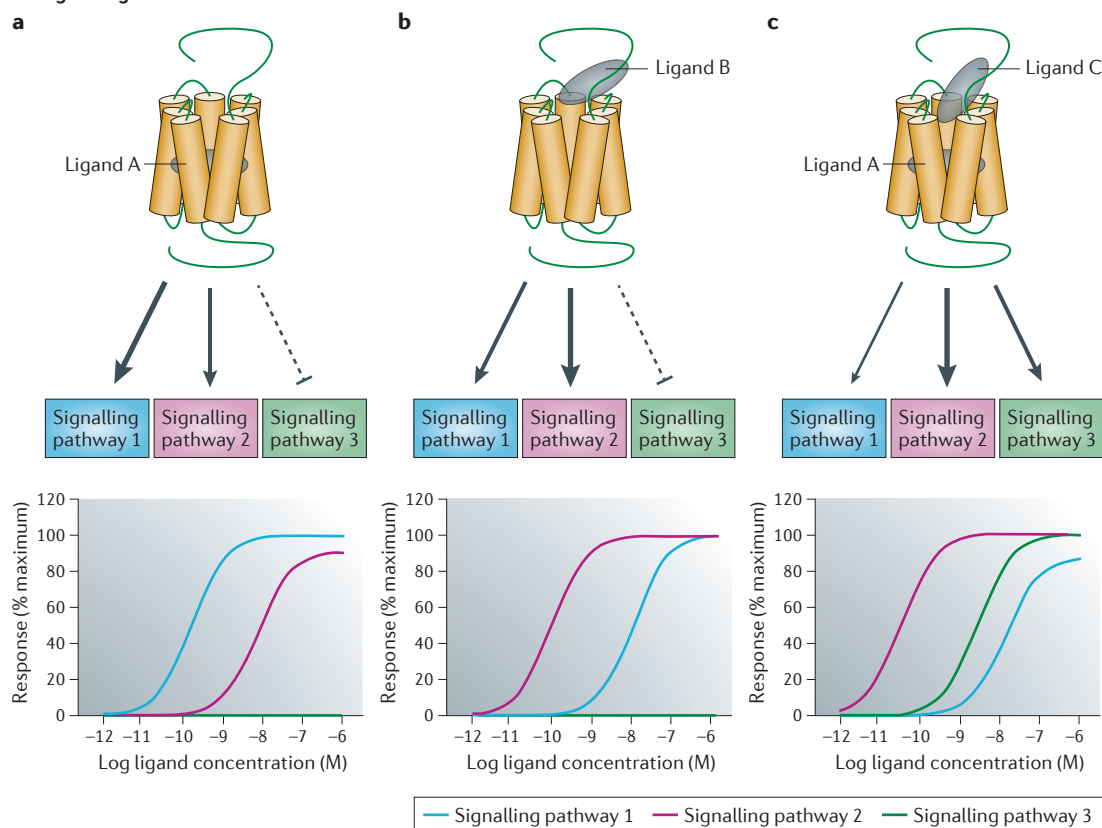
Investigation of carvedilol, a beta blocker that has higher efficacy than other beta blockers for the treatment of heart failure, revealed that although the compound was an inverse agonist for cAMP production, it had partial agonism for β -arrestin-mediated extracellular signal-regulated kinase 1 (ERK1) and ERK2 phosphorylation³⁶. These types of observations have led to speculation that the optimal combination of efficacies for different pathways will determine the ultimate clinical efficacy of GPCR ligands. Although biased signalling has been better documented for orthosteric agonists of GPCRs, it is probable that many — if not all — allosteric ligands will also have biased properties.

Classically, biased signalling and allosteric modulation of GPCRs by ligands are described as separate phenomena, but both are due to ligand-specific conformational

A Probe dependence



B Signalling bias



Ehler model

An allosteric ternary complex model that is used to estimate affinities of allosteric ligands and to quantify the effect of an allosteric ligand on the binding affinity of an orthosteric ligand.

Black–Leff operational model

A model that is used to describe and quantify the ability of an agonist to activate a cellular stimulus response upon binding to a receptor.

Modulation factor-β

A parameter that is used to describe and quantify the allosteric effect of an allosteric ligand on the efficacy of the orthosteric ligand.

Positive cooperativity

The ability of a positive allosteric modulator to enhance the affinity or efficacy of an orthosteric ligand. This is defined by a cooperativity factor-α or modulation factor-β that is greater than 1.

Figure 2 | Probe dependence and biased signalling. **A** | Probe dependence of the allosteric ligand compound 2 is shown with various agonists. **Aa** | The allosteric ligand compound 2 potentiates the ability of oxyntomodulin to inhibit the binding of the antagonist [¹²⁵I]exendin(9–39) at the human glucagon-like peptide 1 (GLP1) receptor. **Ab** | Compound 2 has very weak or almost neutral cooperativity with GLP1(7–36)NH₂. **Ac** | Compound 2 has neutral cooperativity with exendin 4. **B** | Signalling bias describes the ability of different ligands acting at the same receptor to activate unique combinations of various signalling pathways. A common indicator of signalling bias is the reversal in the rank order of potency or efficacy (that is, the maximal agonist effect) of distinct agonists when they are examined across different signalling pathways. **Ba** | Ligand A has high potency and full agonist activity at signalling pathway 1, a lower potency and weaker agonist effects at signalling pathway 2, and no signalling at signalling pathway 3. **Bb** | Allosteric ligand B has a reverse profile whereby it has a higher potency for signalling pathway 1 than for signalling pathway 2. **Bc** | Although an orthosteric ligand bound to a receptor on its own may preferentially signal to a particular subset of pathways, the co-binding of an allosteric modulator can differentially alter the signalling bias of the receptor. When ligand C is co-bound with ligand A, it potentiates a stimulus through signalling pathway 2 and signalling pathway 3, but negatively affects signalling pathway 1, as evidenced by a switch in the potency and maximal response between signalling pathway 2 and signalling pathway 3 compared with signalling pathway 1.

changes in the GPCR that involve a change in the 'shape' of the receptor. Therefore, the signalling profile imparted by either the modulator or the orthosteric ligand can be altered when both ligands are co-bound. As a consequence, some pathways may be selectively modulated (either positively or negatively) at the expense of others.

For example, the allosteric inhibitor of parturition (PDC113.824) induces biased signalling when an orthosteric ligand is co-bound to the prostaglandin F2 α receptor. In mouse models, this compound acts as a negative allosteric modulator of prostaglandin F2 α receptor-mediated cytosolic and myometrial contraction by uncoupling the receptor from the G α_{12} -RHO-ROCK (RHO-associated protein kinase) signalling pathway, yet it significantly augments the activation of ERK1 and/or ERK2 via the G α_q protein³⁷. A calcium-sensing receptor autoantibody causes acquired hypocalcaemic hypercalcaemia by selectively potentiating G α_q -mediated inositol phosphate turnover while inhibiting G α_i -dependent activation of mitogen-activated protein kinase (MAPK)³⁸; this is an example where biased signalling induced by an allosteric modulator results in disease.

These examples illustrate the need to understand the effect of allosteric modulation at several different signalling and/or regulatory pathways, as potentiation or inhibition of all pathways that are linked to a given GPCR will not necessarily give the desired therapeutic outcome.

In operational modelling terms, biased signalling that is mediated by an allosteric modulator will manifest as a pathway-dependent change in the signalling capacity of the orthosteric ligand in a manner that cannot be correlated with the intrinsic signalling efficacy of orthosteric or allosteric ligands³⁹. Experimentally, the most extreme situation of biased signalling induced by allosteric modulators is when the allosteric ligand positively modulates one pathway but negatively modulates another pathway, as in the examples outlined above.

However there are more subtle exemplars of this. For example, potentiation of M $_4$ mAChR signalling by the allosteric ligand LY2033298 engendered substantial differences in the magnitude of positive cooperativity across several signalling pathways⁴⁰. In addition, allosteric modulators of the GLP1 receptor can substantially enhance cAMP production while having a smaller or no effect on β -arrestin recruitment, calcium signalling or ERK1 and/or ERK2 phosphorylation^{41,42}.

To date, most allosteric modulators have been identified following screening assays, such as those carried out to identify agonists or antagonists, or through a screen that was specific for allosteric modulators, rather than through rational design. The design of allosteric ligands that alter orthosteric signal bias offers the potential of augmenting physiologically beneficial signalling pathways while excluding detrimental pathways and providing a novel mechanism to further reduce unwanted side effect profiles. However, for most GPCRs there is only a limited understanding of which signalling pathways or combination of pathways are most predictive of the desired therapeutic outcome, which poses a key challenge. Before it can be possible to rationally design biased ligands, a greater understanding will be

required of the molecular determinants and conformational dynamics that contribute to biased signalling upon GPCR activation.

Signalling bias and probe dependence

For GPCRs that have more than one endogenous ligand and for which allosteric ligands display probe dependence, it is possible to observe differential effects on signalling for each allosteric-orthosteric ligand combination. For example, at the GLP1 receptor, two positive allosteric modulators (compound 2 and BETP (4-(3-benzyloxyphenyl)-2-ethylsulfanyl-6-(trifluoromethyl)pyrimidine)) showed probe dependence; they produced an 18- to 25-fold potentiation in the affinity of the endogenous agonist oxyntomodulin but had little effect on four endogenous variants of GLP1 (REFS 41,43). Moreover, these allosteric ligands engendered biased signalling in the responses induced by oxyntomodulin. They potentiated cAMP production, β -arrestin recruitment and insulin secretion, but did not potentiate intracellular calcium mobilization or ERK1 and/or ERK2 phosphorylation. The ability of an allosteric ligand to modulate all or only some endogenous ligands in a pathway-dependent or -independent manner could affect both the discovery of allosteric modulators and the therapeutic application of these ligands.

Opportunities for therapeutic targeting and implications in drug screening. Although GPCRs that have multiple endogenous ligands and pleiotropic coupling pose challenges to the discovery of allosteric ligands, these factors can also provide advantages. When all endogenous ligands for a given GPCR exert similar physiological profiles, probe dependence provides several opportunities for the identification of novel therapeutics. For example, both of the endogenous agonists of the GLP1 receptor — GLP1(7–36)NH $_2$ and oxyntomodulin — have insulinotropic properties and can act as satiety agents; these properties are attractive for therapeutics that may be used to treat patients with type 2 diabetes⁴⁴. Modulation of oxyntomodulin by the allosteric ligand BETP *in vivo* is sufficient to provide an improved physiological outcome (enhanced insulin secretion) without having any synergistic effect on the GLP1(7–36)NH $_2$ response^{43,45}.

Current allosteric screening programmes routinely seek compounds that modulate the actions of the primary endogenous ligand. However, screening against alternative endogenous ligands, even if they have lower affinity or efficacy (for example, screening for allosteric modulators of the GLP1 receptor using oxyntomodulin instead of GLP1(7–36)NH $_2$), may yield novel chemical leads that might not be identified if screening for cooperative effects is only performed using the primary endogenous ligand.

The possibility that a given allosteric modulator will block or potentiate the effects of an endogenous agonist without affecting other endogenous agonists could provide a therapeutic advantage if the agonists exert different physiological effects. For example, a study has shown that several allosteric antagonists of CCR5 block the binding of HIV-1 to CCR5, thereby inhibiting

infection, but have varying relative activities for HIV-1 blockade versus chemokine-induced blockade of CCR5 internalization⁴⁶. It is not completely clear, therefore, whether sparing the natural chemokine function of CCR5 would be therapeutically beneficial or detrimental. However, the ability of allosteric ligands to block HIV-1 entry but not CCR5 internalization by chemokines may be advantageous in AIDS therapy, as CCR5 mediates favourable protection in the progression to AIDs after HIV-1 infection⁴⁷.

In general, both probe-dependent effects and the ability of allosteric ligands to induce biased signalling could be exploited to modulate GPCR function so that the signalling pathways that lead to favourable physiological outputs are preferentially targeted.

Importance of interspecies variation

Species differences among receptors can cause variability in the cooperativity of the response between an orthosteric ligand and an allosteric ligand, or it can cause variability in the signal bias induced by the allosteric-orthosteric ligand combination. Although target-based species differences need to be taken into account in any screening programme, the additional complexities of allosteric interactions (positive or negative modulation, probe dependence, alterations in signal bias, and so on) mean that interspecies variation is an underappreciated phenomenon in the screening of allosteric compounds at GPCRs. Although not well documented, it is possible that compounds that are identified as promising based on screens using a human GPCR cell line do not produce the desired effects when they are tested in an appropriate animal model. This may not be due to a true lack of efficacy but instead due to a lack of cooperativity with the endogenous agonist of the equivalent GPCR in the animal model relative to the human GPCR. This is exemplified by the allosteric ligand LY2033298 at the M₄ mAChR²³.

Metabolism and allosteric drug discovery

Metabolism of endogenous ligands and allosteric targeting. Allosteric modulators can influence the signalling of metabolites of endogenous ligands^{42,48,49} (FIG. 3). The most extensively investigated system is the GLP1 receptor: its parental agonist GLP1(7–36)NH₂ is rapidly degraded upon its release by dipeptidase IV to yield GLP1(9–36)NH₂ (REF. 50). This metabolite, which has a lower affinity for the GLP1 receptor than the parental agonist, was only able to induce cAMP production or insulin release in GLP1 receptor-expressing cells in the presence of either compound 2 or BETP, which are two structurally distinct allosteric ligands^{42,48}. This allosteric enhancement of GLP1(9–36)NH₂-mediated insulin secretion and lowering of blood glucose levels was confirmed in rats, providing proof of concept that allosteric modulation of metabolite signalling is physiologically possible.

The effects of metabolites of other endogenous GPCR ligands can also be modulated by allosteric ligands. The actions of choline (the metabolite of acetylcholine) can be potentiated by the allosteric ligand LY2033298 at the M₂ mAChR⁴², and the functional responses of inosine (the metabolite of adenosine) can be potentiated at A₁

adenosine receptors⁴² and A₃ adenosine receptors⁴⁹ by respective subtype-selective allosteric ligands. These studies suggest that allosteric modulation of inert metabolites may be a viable option for drug discovery at several GPCR targets.

Many GPCR ligands are rapidly degraded (for example, GLP1 is degraded within 1–2 minutes of release, and acetylcholine and adenosine are degraded within seconds)^{50–52}, so the metabolites are often present in higher concentrations than the parental ligand^{53–55}. In these situations, screening programmes aimed at discovering ligands to potentiate the actions of these metabolites could present a new opportunity for developing therapeutics. In addition, owing to the ability of allosteric ligands to induce signal bias, it may also be possible to develop allosteric ligands that selectively modulate certain signalling pathways in response to the metabolite. For example, allosterically modulating the effects of GLP1(9–36)NH₂ at the GLP1 receptor selectively potentiates cAMP signalling without affecting phosphorylated ERK1 and/or ERK2 and intracellular calcium mobilization⁴². Furthermore, primary metabolites are often further metabolized, offering additional scope for drug discovery.

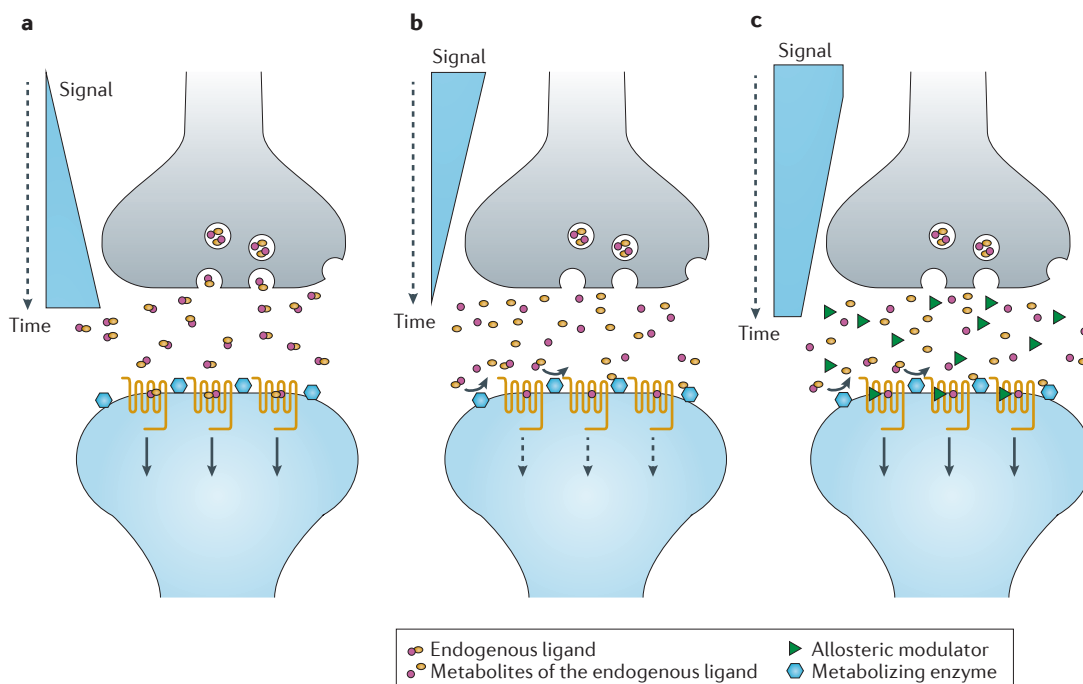
To date, compounds that allosterically modulate the effects of metabolites have been identified by screening against natural potent ligands rather than by undertaking a targeted search for potent modulators of metabolite activity. As such, it is not surprising that current compounds may lack the level of modulation that is required for therapeutic viability. Nonetheless, it is possible to identify allosteric ligands that greatly potentiate the response of the targeted ligand. For example, screening programmes have identified allosteric ligands of the M₄ and M₁ mAChRs that potentiated the actions of acetylcholine by 780-fold^{26,40} and 10,000-fold⁵⁶, respectively; these levels of potentiation could shift metabolite activity into a physiological range.

Allosteric modulation of metabolite activity could also contribute to unwanted or unanticipated side effects of drugs. Therefore, it is necessary to understand the effects of allosteric ligands on all physiological ligands, including those metabolites that are normally considered to be inactive.

Metabolism of allosteric drugs. The pharmacology of the circulating metabolites that are formed from the breakdown of allosteric ligands also needs to be understood before ligands are advanced into clinical trials. Although this also applies to orthosteric ligands, the effects of metabolites of allosteric ligands at the target GPCR and, to some extent, related GPCRs, need to be understood to a greater degree because of the wider range of properties exerted by allosteric ligands.

For example, subtle structural changes to multiple allosteric ligands of metabotropic glutamate receptors (mGluRs) and mAChRs result in unexpected changes in their pharmacology, changing positive allosteric modulators into negative allosteric modulators or neutral allosteric ligands (and vice versa), many of which would be impossible to predict based on pre-existing empirical

A Physiological signalling of postsynaptic GPCRs



B Modulation of metabolites by allosteric ligands

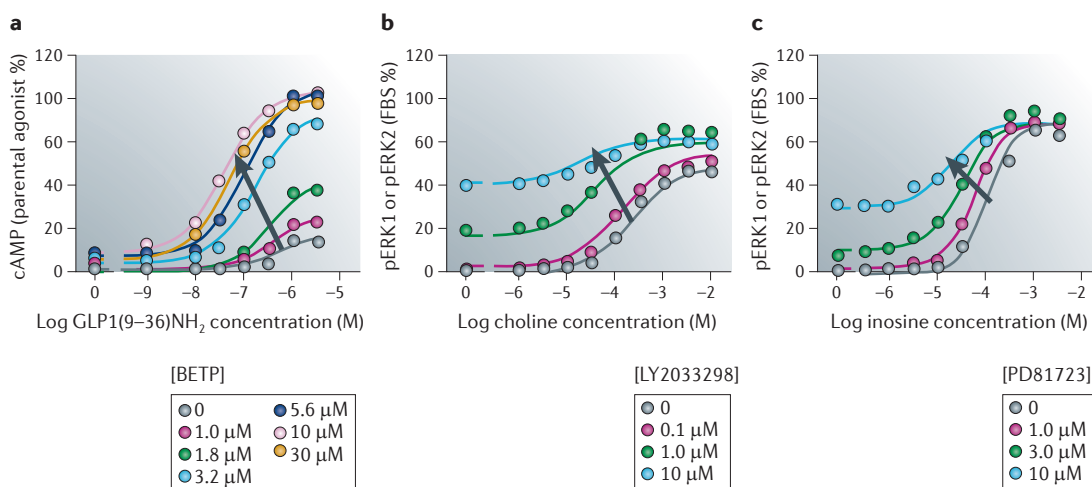


Figure 3 | Allosteric modulation of metabolites. **A** | A schematic illustration of physiological signalling that is followed by the activation of postsynaptic G protein-coupled receptors (GPCRs). **Aa** | The neurotransmitter is released into the synaptic cleft and then binds to postsynaptic GPCRs to elicit physiological signalling. **Ab** | The neurotransmitter is rapidly degraded by metabolizing enzymes, which leads to a decay of physiological signalling. **Ac** | A positive allosteric modulator co-binds to the GPCR with the metabolite, which extends the duration of receptor activation and the timescale of physiological signalling. A similar process can be predicted for rapidly metabolized hormones. **B** | Examples of metabolites that can be modulated by allosteric ligands. **Ba** | Increasing concentrations of BETP positively potentiate GLP1(9–36)NH₂-mediated cyclic AMP signalling at the glucagon-like peptide 1 (GLP1) receptor. **Bb** | LY2033298 is a positive modulator of choline-mediated extracellular signal-regulated kinase 1 (ERK1) or ERK2 activation at the M₂ muscarinic acetylcholine receptor. **Bc** | Responses to phosphorylated ERK1 (pERK1) or pERK2, mediated by inosine at the adenosine A₁ receptor, are enhanced by the allosteric ligand PD81723. The bold black arrows indicate the level of modulation by the allosteric ligand as observed by a leftwards shift (and/or an increase in the E_{max} value) in the concentration–response curves produced by the metabolite. This figure is modified, with permission, from REF. 42 © (2012) The American Society for Pharmacology and Experimental Therapeutics. FBS, fetal bovine serum.

data^{57–60}. One such example was derived from the exploration of the structure–activity relationship of a weak negative allosteric modulator of mGluR5 (that induced only partial blockade of receptor signalling); a 3-methyl substituent to the distal phenyl ring produced a full negative allosteric modulator, whereas a 4-methyl substituent produced a positive allosteric modulator (FIG. 4). In addition, small structural alterations in allosteric ligands of mGluRs^{57,58} and mAChRs^{59,60} can alter receptor subtype selectivity. Although these structural changes may not necessarily be induced by metabolism, they provide evidence that very small changes in chemical structure (that would be consistent with metabolic effects) can have very substantial effects on the activity of allosteric ligands.

GPCR structure and allosteric modulation

Drug discovery at GPCRs relies on high-throughput screening using compound libraries. This process has a low efficiency rate and many of the molecules that are identified as hits often have low affinity and/or efficacy and poor drug-like properties. Structure-enabled drug discovery has been used to identify modulators of soluble proteins (such as enzymes and kinases), and this has led to a lower failure rate in preclinical studies and clinical trials compared to drug development at GPCRs⁶¹.

A greater knowledge of GPCR structure is required, as well as an understanding of how ligands interact with them and mechanistic information on how ligand binding alters their function. This could contribute to the development of allosteric and orthosteric drugs in two ways: first, by guiding the optimization of lead candidates; and second, by using molecular docking and related techniques to enable the discovery of novel compound scaffolds.

Although GPCRs share a common architecture, they can interact with an array of endogenous ligands. This is partly achieved by the different modes of orthosteric ligand binding to GPCRs⁶².

Over the past 5 years, there have been tremendous advances in the application of structural biology techniques to GPCRs, and these have led to numerous high-resolution structures of class A GPCRs. These include high-resolution structures of rhodopsin⁶³, β -adrenergic receptors^{64,65}, mAChRs^{66,67}, the dopamine D3 receptor¹⁴, opioid receptors^{68,69}, adenosine receptors^{70,71}, proteinase-activated receptor 1 (PAR1)⁷², the CXCR4 chemokine receptor⁷³ and the histamine H₁ receptor⁷⁴. All of these receptors are complexed with orthosteric agonists or antagonists. These structures share a similar helical bundle but have considerable divergence in their intracellular and extracellular loops. Collectively, the high-resolution structures highlight how the common transmembrane domain architecture can accommodate a structurally diverse set of ligands. Although there are no full-length crystal structures available of class B^{75,76} and class C^{77,78} GPCRs, structures of the isolated amino-terminal domains highlight how these receptors bind to their respective orthosteric ligands within these domains. However, for receptors outside the class A family of GPCRs, it is less clear how binding to the extracellular domain induces the conformational changes that are required to initiate intracellular signalling.

Structural basis of allosteric ligand interactions. Despite the advances in structural biology, there are as yet no high-resolution structures of a GPCR in complex with an allosteric ligand. However, because of the diversity in orthosteric binding modes of these receptors, the orthosteric binding pocket on one GPCR may be structurally similar to the allosteric binding site of another GPCR. For example, extensive studies on the mAChRs have identified at least one allosteric site that is composed of epitopes in the extracellular loops and the top of the transmembrane bundle^{24,25,79–82} in addition to the intramembranous orthosteric site.

By contrast, studies on peptide GPCRs, such as those of chemokines (class A GPCRs)^{83–87} or corticotropin releasing factor receptor 1 (a class B GPCR)⁸⁸, have shown that these receptors use extracellular domains and the top of the transmembrane bundle to bind to their orthosteric ligands, but they have allosteric sites that are localized to the transmembrane bundle or intracellular regions. In addition, investigations of class C GPCRs have identified more than one potential allosteric pocket for small-molecule modulators within the transmembrane bundle^{89–94}. Furthermore, pepducins (lipidated peptides that target a portion of intracellular regions of the GPCR of interest) are potential allosteric modulators of some GPCRs that — in the case of PAR1, for instance — are proposed to bind to the carboxy-terminal tail^{95,96}.

Despite the lack of available structures bound to allosteric ligands, the available crystal and NMR structures are nonetheless useful for predicting the location of allosteric binding pockets and the mechanisms of allosteric modulation. Moreover, molecular dynamics simulations on the structures of M₂ and M₃ mAChRs suggest that as the orthosteric ligand binds to or dissociates from the receptor, it pauses at an alternative binding site in an extracellular vestibule⁶⁶. This is the site that has been experimentally validated as an allosteric site for the mAChRs and, intriguingly, the predicted pose adopted by the ligand in the extracellular vestibule differs between the two receptor structures. These simulations may therefore represent the first ‘structural’ view of a ligand (albeit an orthosteric one) bound to an allosteric site.

Moreover, the binding of allosteric ligands to this extracellular binding pocket would be expected to influence the association and dissociation rates of orthosteric ligands. In addition, one residue — Trp422^{7,35} — that is implicated in the binding of allosteric ligands to the M₂ mAChR, forms an ‘edge to face’ aromatic interaction with the Tyr403^{6,51} residue that forms part of the aromatic cage surrounding the charged amine of the bound orthosteric ligand in the solved crystal structure (FIG. 5a). Therefore, these two aromatic residues may have a crucial role in driving allosteric cooperativity between the orthosteric and allosteric sites for the M₂ mAChR. So, it may be possible to rationally design ligands that bind to these two sites.

Structural insights into receptor allostery. In the future, structure-based drug discovery efforts may be guided by a detailed understanding of the transitions in GPCR

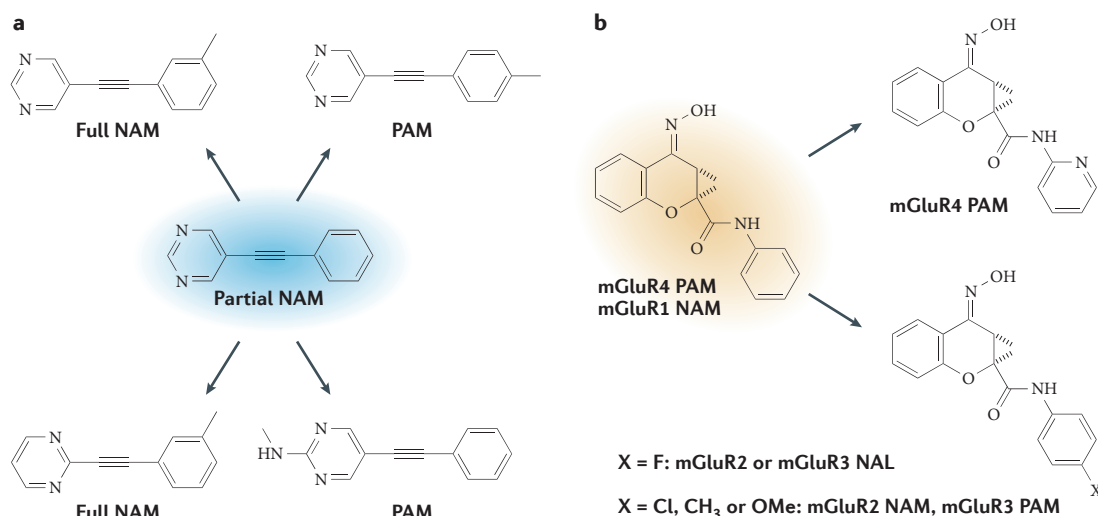


Figure 4 | Metabolism of allosteric ligands. Examples are shown of subtle structural modifications to allosteric ligands of the metabotropic glutamate receptor (mGluR) subfamily that can either drastically change their allosteric profile (panel **a**) or alter their subtype selectivity (panel **b**). NAM, negative allosteric modulator; PAM, positive allosteric modulator; NAL, negative allosteric ligand (also known as silent allosteric modulator).

conformation that are required for a ligand to allosterically promote the coupling of intracellular proteins to the cytoplasmic face. Aided by molecular dynamics simulations, the recently solved structure of the β_2 -adrenergic receptor in complex with an agonist and a G protein allowed the visualization of the structural basis for the natural allosteric effect induced by the G protein on the receptor to promote a high-affinity agonist binding epitope^{64,97,98}. These studies revealed an allosteric network that was composed of three regions in the β_2 -adrenergic receptor, each of which can switch individually between multiple distinct conformations and link small perturbations at the orthosteric agonist binding site to large conformational changes at the intracellular face.

The residues in and directly below the ligand binding site of the receptor transition from an active to inactive conformation as the G protein dissociates, and they can be divided into two spatial clusters with residues in each cluster moving in concert (FIG. 5b). These simulations also suggest that a metastable intermediate conformation between the inactive and active crystallographic structures exists that may represent a receptor conformation to which the G protein binds during the activation process. These findings also suggest that the first structural changes often occur at the intracellular face of the β_2 -adrenergic receptor, away from the ligand binding sites.

These findings provide further evidence for the reciprocal allosteric effect between the agonist binding pocket and the binding site for the effector protein on the intracellular face of the GPCR. These types of structures and molecular dynamics simulations may aid in the rational design of allosteric ligands (agonists or positive allosteric modulators) targeting individual GPCRs.

There is emerging evidence from *in silico* docking screens that the conformational state of the receptor strongly influences ligand efficacy, which is probably

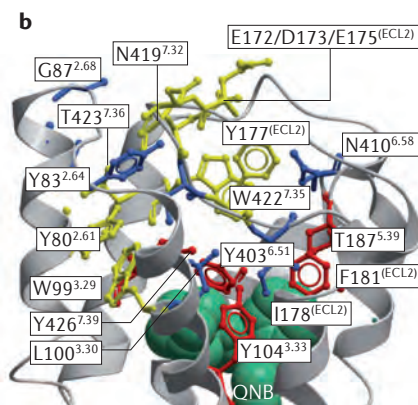
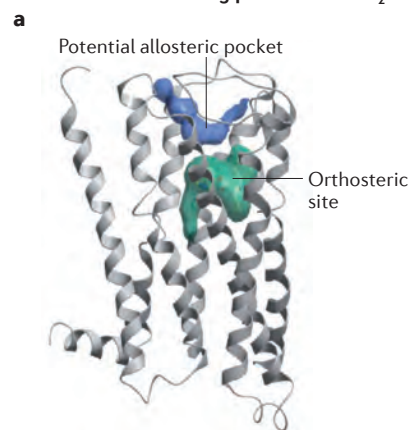
due to the reciprocal allosteric effect between effector binding sites and ligand binding sites. Therefore, virtual screens attempting to identify allosteric agonists or positive allosteric modulators would need to be performed on activated receptors and engage a similar allosteric network within the receptor to induce the activation of signalling proteins.

Negative allosteric modulation of many GPCRs by the sodium ion has been documented: for example, it has been observed for the α_{2A} -adrenergic receptor, the A_{2A} -adenosine receptor, μ - and δ -opioid receptors as well as the dopamine D2 receptor^{99–102}. Mutagenesis data suggest that this effect is linked to residues surrounding and including the highly conserved Asp^{2.50} residue^{102–105}. Recently, two high-resolution GPCR structures revealed the precise location of the sodium ion and resolved the complete network of water molecules surrounding this ion, in addition to the conformation of all residues that are involved in direct or water-mediated hydrogen bond coordination (FIG. 5c).

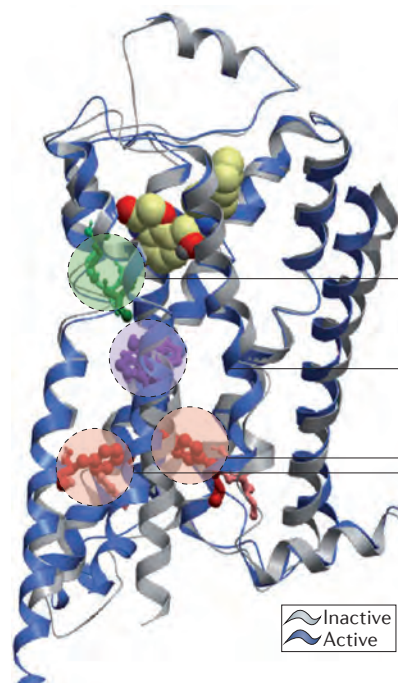
In both the 1.8 Å adenosine A_{2A} receptor structure¹⁰⁶ and the PAR1 structure⁷², the central water cluster where the sodium ion resides is engaged in hydrogen bonding with several highly conserved class A GPCR residues, including Asn^{1.50}, Asp^{2.50}, Ser^{3.39}, Trp^{6.48}, Asn^{7.45}, Asn/Asp^{7.49} and Tyr^{7.53}. This conserved central water-mediated hydrogen bond network is thought to have a crucial role in the activation of class A GPCRs^{64,107}. The comparison of inactive versus activated receptor conformations suggests that upon activation the inward movement of the seventh transmembrane domain in this region collapses the pocket, which results in a smaller binding pocket that, in an active-like state, contains a maximum of three water molecules. This would not provide sufficient coordination for a sodium ion, which indicates that high-affinity agonist binding and the presence of the

Allosteric agonists
Ligand that bind to an allosteric site and cause G protein-coupled receptor activation in the absence of an orthosteric ligand.

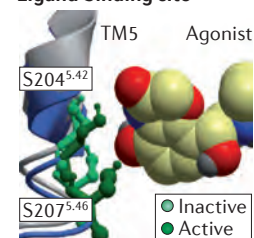
A An allosteric binding pocket in the M_2 mAChR



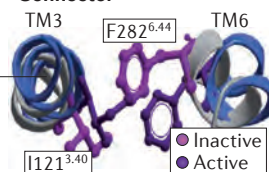
B Allosteric network between the orthosteric ligand binding site and G protein binding site



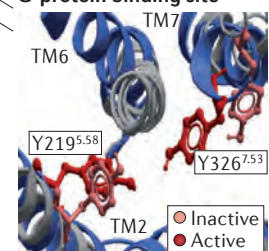
Ligand binding site



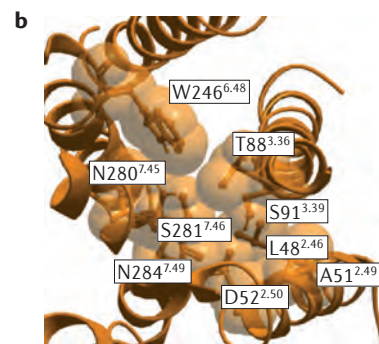
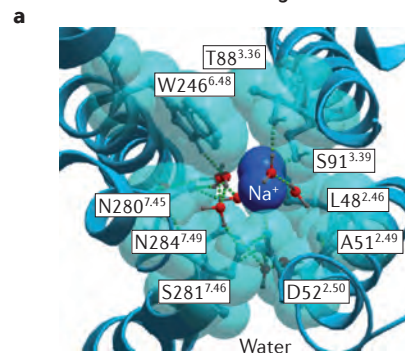
Connector



G-protein binding site



C Structural basis for the negative modulation of GPCRs by Na^+



◀ **Figure 5 | Emerging structural insights into allostery.** **Aa** | An allosteric binding pocket (shown in blue) is located in the extracellular vestibule of the crystal structure of the M_2 muscarinic acetylcholine receptor (mAChR) (Protein Data Bank (PDB) code: 3UON); the location of the orthosteric site where the orthosteric ligand quinuclidinyl benzilate (QNB) was co-crystallized is shown in turquoise. **Ab** | Residues surrounding the extracellular pocket are shown in blue or yellow. Residues highlighted in yellow have been shown via mutagenesis studies to be involved in interactions with allosteric ligands. These residues show variability among different subtypes of mAChRs, whereas residues contacting the orthosteric ligand QNB (represented by the green space) are highly conserved among different mAChR subtypes. Residues shown in red bridge the allosteric and orthosteric sites and may be important for allosteric cooperativity. **B** | The allosteric network linking the agonist and G protein binding sites in the β_2 -adrenergic receptor. The first cluster consists of residues in the fifth transmembrane domain of the ligand binding site, and the second cluster is composed primarily of two highly conserved hydrophobic residues (at positions 3.40 and 6.44). The first cluster connects ligand interaction to the second cluster, and this second cluster is linked to the G protein-coupling site, forming an allosteric interaction network between the ligand binding pocket and the G protein binding site. **C** | The structural basis for the negative modulation of G protein-coupled receptor (GPCR) activation by Na^+ . **Ca** | The Na^+ ion in the middle of the inactive A_{2A} adenosine receptor bundle (PDB code: 4EIY) is coordinated by the highly conserved Asp2.50 residue (D52^{2.50}), the Ser3.39 residue (S91^{3.39}) and water molecules. The residues involved in interactions are represented by turquoise sticks and spheres, water molecules in the cluster are represented by grey sticks and red spheres, and the green dotted lines indicate hydrogen bonds and the salt bridge formed between Na^+ and the Asp2.50 residue. **Cb** | In the active-like state of the A_{2A} receptor structure (PDB code: 3QAK), the pocket collapses upon activation, precluding the Na^+ binding site.

sodium ion in this site are mutually exclusive. Therefore, the availability of these high-resolution structures can explain the observed negative allosteric effects of sodium ions on the binding of agonists.

The information obtained from these structures provides some insight into the conformations that are induced by the negative allosteric modulation of these receptors. Therefore, receptors that are crystallized in the presence of sodium coordination may be useful templates for homology modelling and docking for *in silico* screens of negative allosteric modulators (if this is the desired phenotype for a particular drug target).

At present, it is too early to evaluate the impact of these new GPCR structures on pharmaceutical drug discovery; however, given the remarkable progress in GPCR structural biology over the past several years, this will probably become an integral part of many new drug discovery efforts.

GPCR dimerization and allostery

Increasing evidence suggests that GPCR dimerization may be common to all three classes of GPCRs. It is possible for a modulator (either endogenous or exogenous) binding to the orthosteric binding site of one monomer of a dimer to modulate the binding and/or function of the orthosteric ligand in the other monomer. In this way, the orthosteric ligand of one GPCR can allosterically modulate the second GPCR. There are examples in the literature showing that GPCR oligomerization affects the affinity and specificity of ligand binding, the pattern of signalling and internalization^{108,109,110}.

For class A GPCRs there are no obvious rules regarding which subsets of receptors form dimers or have a particular functional effect. Class B GPCRs form stable

homodimers through interactions that involve the lipid-exposed face of the fourth transmembrane domain^{111–115}. It has been postulated that these complexes are important for the stabilization of a high-affinity complex between the GPCR and G protein. Interestingly, a recent study revealed that the homodimeric form of the GLP1 receptor was required for high-affinity peptide agonist binding, and disruption of the dimer resulted in a shift in G protein-mediated signalling to that of the low-affinity state (that is, there was a ten-fold difference in orthosteric agonist potency between the monomeric and dimeric forms of this GPCR). However, the dimer was essential for formation of cAMP induced by an allosteric agonist, as this response was almost completely abrogated with the monomeric receptor¹¹¹.

Although orthosteric ligands of class C GPCRs require the association of dimers to mediate their effects, a positive allosteric modulator of mGluRs was recently shown to exhibit strong agonism at the monomeric form of the receptor despite having no agonism at the dimeric form of the receptor¹¹⁶. Allosteric modulators that bind to one monomer of a GPCR dimer can also modulate the binding and/or function of the orthosteric ligand in the other monomer. In addition, the effects of allosteric ligands have been studied on both monomeric and dimeric forms of the GLP1 receptor. In this case, although the dimeric form of the receptor is required for the allosteric ligand to directly activate G protein-mediated signalling, modulation of orthosteric ligand function by two different classes of allosteric ligands occurs in *cis* within a single receptor protomer¹¹¹.

Further studies on individual GPCRs will be required to identify the mechanism of action and to determine whether monomeric or oligomeric forms of these GPCRs are required for the actions of allosteric ligands. However, as the lateral allosteric effect of dimerization on orthosteric ligand function varies at different GPCRs, it is probable that the mechanistic basis for allosteric modulation will also vary among different GPCR–allosteric ligand–orthosteric ligand complexes.

Considerations for allosteric drug development

The potential therapeutic advantages of allosteric ligands are well understood, but the clinical translation of this is still in its infancy. To date, only two allosteric ligands have been approved as therapeutics: cinacalcet (Sensipar; Amgen), which is a positive allosteric modulator of the calcium-sensing receptor^{117,118}; and maraviroc (Selzentry/Celsentri; Pfizer), which is a negative allosteric modulator of CCR5 (REFS 119,120). The complex properties of allosteric ligands, which include probe dependence and biased signalling, can present both challenges and opportunities for preclinical drug discovery. Allosteric modulators can open up new avenues for receptor-selective as well as signalling pathway-selective therapies. However, there are substantial challenges in the design and identification of allosteric ligands that fulfil their desired effects *in vitro*, and their subsequent application *in vivo*.

The principal approach that is currently used to identify allosteric modulators is high-throughput functional screening, which generally involves one

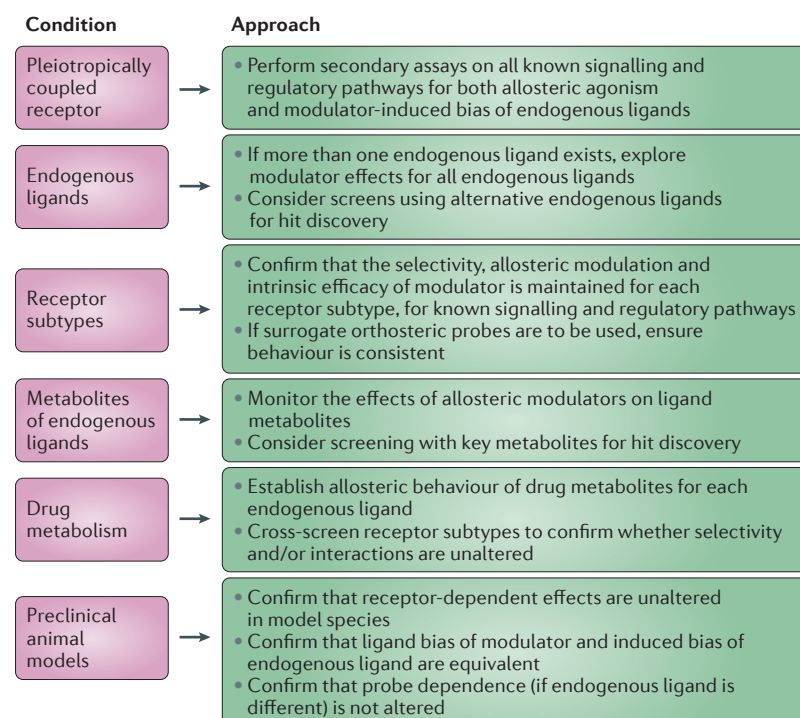


Figure 6 | Strategies for enhancing the translational outcomes of allosteric modulators. The boxes on the left highlight potential issues that arise during drug screening or development, and the boxes on the right describe approaches that could be considered to overcome these problems.

particularly important for receptor systems that have multiple endogenous ligands) or ligands that are rapidly metabolized. Ideally, all of these concepts should be taken into account when screening for novel compounds (FIG. 6).

Although the practicalities of screening programmes are likely to limit initial hit discovery to a single pathway, it is important that there is a clear link between the chosen signalling pathway and at least one of the main therapeutic goals. Likewise, it is important that a parallel assessment of alternative signalling pathways is undertaken at a relatively early stage of candidate selection. Due consideration should also be given to investigating whether alternative endogenous ligands or metabolic products can be targeted to ensure that there is maximum potential for exploring the chemical space and identifying alternative candidates and/or chemotypes that could underpin a drug discovery and development programme (FIG. 6).

For many GPCR targets, the required spectrum of signalling needed to attain optimal therapeutic benefit is currently unknown, which limits the rational selection of both allosteric and orthosteric drug candidates. Therefore, drug discovery at these tractable targets is considerably challenging. As the field acquires greater knowledge on these concepts, it will be increasingly important to perform an extensive pharmacological profile of ligands to enable the exploration of biased signalling and probe dependence. These types of studies will facilitate the effective translation of *in vitro* findings into preclinical models and eventually into clinical trials.

The increasing number of GPCR crystal structures will also yield information that may aid in the rational design of allosteric ligands. The pursuit of crystal structures in the presence of different agonists (both orthosteric and allosteric) and different effector proteins, if successful, may allow the rational design not only of ligands that target allosteric sites but also of potentially probe-dependent biased allosteric modulators.

signalling output and assesses effects in the presence of one orthosteric ligand (usually the most physiologically relevant endogenous ligand). Although this approach has proven to be successful in the past (for example, for identifying ligands of the calcium-sensing receptor and of CCR5), such programmes have limitations as they do not account for the promiscuity of pleiotropically coupled GPCRs, the potential for biased signalling, the possibility of probe-dependent effects (which is

- Jacoby, E., Bouhelal, R., Gerspacher, M. & Seuwen, K. The 7 TM G-protein-coupled receptor target family. *ChemMedChem* **1**, 761–782 (2006).
- Melancon, B. J. *et al.* Allosteric modulation of seven transmembrane spanning receptors: theory, practice, and opportunities for central nervous system drug discovery. *J. Biol. Chem.* **287**, 1445–1464 (2012).
- Kenakin, T. & Miller, L. J. Seven transmembrane receptors as shapeshifting proteins: the impact of allosteric modulation and functional selectivity on new drug discovery. *Pharmacol. Rev.* **62**, 265–304 (2010).
- Valant, C., Lane, J. R., Saxon, P. M. & Christopoulos, A. The best of both worlds? Biotopic orthosteric/allosteric ligands of G protein-coupled receptors. *Annu. Rev. Pharmacol. Toxicol.* **52**, 153–178 (2012). This is a detailed review on the advantages of ligands that have a biotopic mode of action.
- Antony, J. *et al.* Dualistic GPCR targeting: a novel route to binding and signaling pathway selectivity. *FASEB J.* **23**, 442–450 (2009).
- Steinfeld, T., Mammen, M., Smith, J. A., Wilson, R. D. & Jasper, J. R. A novel multivalent ligand that bridges the allosteric and orthosteric binding sites of the M2 muscarinic receptor. *Mol. Pharmacol.* **72**, 291–302 (2007).
- Valant, C. *et al.* A novel mechanism of G protein-coupled receptor functional selectivity. Muscarinic partial agonist McN-A-343 as a biotopic orthosteric/allosteric ligand. *J. Biol. Chem.* **283**, 29312–29321 (2008).
- Waelbroeck, M. Identification of drugs competing with α -tubocurarine for an allosteric site on cardiac muscarinic receptors. *Mol. Pharmacol.* **46**, 685–692 (1994).
- Christopoulos, A. & Mitchelson, F. Pharmacological analysis of the mode of interaction of McN-A-343 at atrial muscarinic M2 receptors. *Eur. J. Pharmacol.* **339**, 153–156 (1997).
- Gregory, K. J., Hall, N. E., Tobin, A. B., Sexton, P. M. & Christopoulos, A. Identification of orthosteric and allosteric site mutations in the M₁ muscarinic acetylcholine receptors that contribute to ligand-selective signalling bias. *J. Biol. Chem.* **285**, 7459–7474 (2010).
- Langmead, C. J. *et al.* Probing the molecular mechanism of interaction between 4-*n*-butyl-1-[4-(2-methylphenyl)-4-oxo-1-butyl]-piperidine (AC-42) and the muscarinic M₁ receptor: direct pharmacological evidence that AC-42 is an allosteric agonist. *Mol. Pharmacol.* **69**, 236–246 (2006).
- Avlani, V. A. *et al.* Orthosteric and allosteric modes of interaction of novel selective agonists of the M₁ muscarinic acetylcholine receptor. *Mol. Pharmacol.* **78**, 94–104 (2010).
- Lebon, G., Langmead, C. J., Tehan, B. G. & Hulme, E. C. Mutagenic mapping suggests a novel binding mode for selective agonists of M₁ muscarinic acetylcholine receptors. *Mol. Pharmacol.* **75**, 331–341 (2009).
- Chien, E. Y. *et al.* Structure of the human dopamine D3 receptor in complex with a D2/D3 selective antagonist. *Science* **330**, 1091–1095 (2010).
- Disingrini, T. *et al.* Design, synthesis, and action of oxotremorine-related hybrid-type allosteric modulators of muscarinic acetylcholine receptors. *J. Med. Chem.* **49**, 366–372 (2006).
- Narlawar, R. *et al.* Hybrid ortho/allosteric ligands for the adenosine A₁ receptor. *J. Med. Chem.* **53**, 3028–3037 (2010).
- Kostenis, E. & Mohr, K. Two-point kinetic experiments to quantify allosteric effects on radioligand dissociation. *Trends Pharmacol. Sci.* **17**, 280–283 (1996).
- May, L. T., Leach, K., Sexton, P. M. & Christopoulos, A. Allosteric modulation of G protein-coupled receptors. *Annu. Rev. Pharmacol. Toxicol.* **47**, 1–51 (2007).

19. Ehrlert, F. J. Estimation of the affinities of allosteric ligands using radioligand binding and pharmacological null methods. *Mol. Pharmacol.* **33**, 187–194 (1988). **This paper provides an introduction to the theory that underlies the ternary complex model for allosteric interactions.**
20. Black, J. W. & Leff, P. Operational models of pharmacological agonism. *Proc. R. Soc. B Biol. Sci.* **220**, 141–162 (1983).
21. Watson, C., Jenkinson, S., Kazmierski, W. & Kenakin, T. The CCR5 receptor-based mechanism of action of 873140, a potent allosteric noncompetitive HIV entry inhibitor. *Mol. Pharmacol.* **67**, 1268–1282 (2005).
22. Krause, R. M. *et al.* Ivermectin: a positive allosteric effector of the $\alpha 7$ neuronal nicotinic acetylcholine receptor. *Mol. Pharmacol.* **53**, 283–294 (1998).
23. Suratman, S. *et al.* Impact of species variability and 'probe-dependence' on the detection and *in vivo* validation of allosteric modulation at the M4 muscarinic acetylcholine receptor. *Br. J. Pharmacol.* **162**, 1659–1670 (2011).
24. Nawaratne, V., Leach, K., Felder, C. C., Sexton, P. M. & Christopoulos, A. Structural determinants of allosteric agonism and modulation at the M4 muscarinic acetylcholine receptor: identification of ligand-specific and global activation mechanisms. *J. Biol. Chem.* **285**, 19012–19021 (2010).
25. Valant, C., Felder, C. C., Sexton, P. M. & Christopoulos, A. Probe dependence in the allosteric modulation of a G protein-coupled receptor: implications for detection and validation of allosteric ligand effects. *Mol. Pharmacol.* **81**, 41–52 (2012).
26. Chan, W. Y. *et al.* Allosteric modulation of the muscarinic M4 receptor as an approach to treating schizophrenia. *Proc. Natl Acad. Sci. USA* **105**, 10978–10983 (2008). **This paper describes the discovery of the mAChR allosteric ligand LY2033298, which has activity in animal models that are predictive of clinical antipsychotic drug efficacy.**
27. Charo, I. F. & Ransohoff, R. M. The many roles of chemokines and chemokine receptors in inflammation. *N. Engl. J. Med.* **354**, 610–621 (2006).
28. Tao, Y. X. The melanocortin-4 receptor: physiology, pharmacology, and pathophysiology. *Endocr. Rev.* **31**, 506–543 (2010).
29. Gardella, T. J. & Juppner, H. Interaction of PTH and PTHrP with their receptors. *Rev. Endocr. Metab. Disord.* **1**, 317–329 (2000).
30. Halls, M. L., van der Westhuizen, E. T., Bathgate, R. A. & Summers, R. J. Relaxin family peptide receptors — former orphans reunite with their parent ligands to activate multiple signalling pathways. *Br. J. Pharmacol.* **150**, 677–691 (2007).
31. Conigrave, A. D., Quinn, S. J. & Brown, E. M. L-amino acid sensing by the extracellular Ca^{2+} -sensing receptor. *Br. J. Pharmacol.* **97**, 4814–4819 (2000).
32. Poyner, D. R. *et al.* International Union of Pharmacology. XXXII. The mammalian calcitonin gene-related peptides, adrenomedullin, amylin, and calcitonin receptors. *Pharmacol. Rev.* **54**, 233–246 (2002).
33. Estall, J. L. & Drucker, D. J. Glucagon and glucagon-like peptide receptors as drug targets. *Curr. Pharm. Des.* **12**, 1731–1750 (2006).
34. Leach, K., Sexton, P. M. & Christopoulos, A. Allosteric GPCR modulators: taking advantage of permissive receptor pharmacology. *Trends. Pharmacol. Sci.* **28**, 382–389 (2007). **This is the first description of the most simple model (that is, an amalgam of the Ehlert model of allosteric effects and the Black–Leff operational model) to describe the functional effects of allosteric modulators.**
35. Baker, J. G., Hall, I. P. & Hill, S. J. Agonist and inverse agonist actions of β -blockers at the human $\beta 2$ -adrenoceptor provide evidence for agonist-directed signalling. *Mol. Pharmacol.* **64**, 1357–1369 (2003).
36. Wisler, J. W. *et al.* A unique mechanism of β -blocker action: carvedilol stimulates β -arrestin signaling. *Proc. Natl Acad. Sci. USA* **104**, 16657–16662 (2007). **This paper describes the first demonstration of biased signalling by clinically relevant beta blockers, which may provide an explanation for the differential efficacies of these therapeutics in the treatment of heart failure.**
37. Goupil, E. *et al.* A novel biased allosteric compound inhibitor of parturition selectively impedes the prostaglandin $\text{F}_{2\alpha}$ -mediated Rho/ROCK signaling pathway. *J. Biol. Chem.* **285**, 25624–25636 (2010).
38. Makita, N. *et al.* An acquired hypocalciuric hypercalcemia autoantibody induces allosteric transition among active human Ca-sensing receptor conformations. *Proc. Natl Acad. Sci. USA* **104**, 5443–5448 (2007).
39. Canals, M., Sexton, P. M. & Christopoulos, A. Allostery in GPCRs: 'MWC' revisited. *Trends. Biochem. Sci.* **36**, 663–672 (2011).
40. Leach, K. *et al.* Molecular mechanisms of action and *in vivo* validation of an M4 muscarinic acetylcholine receptor allosteric modulator with potential antipsychotic properties. *Neuropsychopharmacology* **35**, 855–869 (2010).
41. Koole, C. *et al.* Allosteric ligands of the glucagon-like peptide 1 receptor (GLP-1R) differentially modulate endogenous and exogenous peptide responses in a pathway-selective manner: implications for drug screening. *Mol. Pharmacol.* **78**, 456–465 (2010).
42. Wootton, D. *et al.* Allosteric modulation of endogenous metabolites as an avenue for drug discovery. *Mol. Pharmacol.* **82**, 281–290 (2012). **This study provided *in vivo* validation that metabolites of endogenous ligands can be physiologically modulated by allosteric ligands.**
43. Willard, F. S. *et al.* Small molecule allosteric modulation of the glucagon-like peptide-1 receptor enhances the insulinotropic effect of oxyntomodulin. *Mol. Pharmacol.* **82**, 1066–1073 (2012).
44. Stanley, S., Wynne, K. & Bloom, S. Gastrointestinal satiety signals III. Glucagon-like peptide 1, oxyntomodulin, peptide YY, and pancreatic polypeptide. *Am. J. Physiol. Gastrointest. Liver Physiol.* **286**, G693–G697 (2004).
45. Sloop, K. W. *et al.* Novel small molecule glucagon-like peptide-1 receptor agonist stimulates insulin secretion in rodents and from human islets. *Diabetes* **59**, 3099–3107 (2010).
46. Muniz-Medina, V. M. *et al.* The relative activity of "function sparing" HIV-1 entry inhibitors on viral entry and CCR5 internalization: is allosteric functional selectivity a valuable therapeutic property? *Mol. Pharmacol.* **75**, 490–501 (2009).
47. Gonzalez, E. *et al.* The influence of CCL3L1 gene-containing segmental duplications on HIV-1/AIDS susceptibility. *Science* **307**, 1434–1440 (2005).
48. Willard, F. S. *et al.* Small molecule allosteric modulation of the glucagon-like peptide-1 receptor enhances the insulinotropic effect of oxyntomodulin. *Mol. Pharmacol.* **82**, 1066–1073 (2012).
49. Gao, Z. G. *et al.* Functionally biased modulation of A_3 adenosine receptor agonist efficacy and potency by imidazoquinolinamine allosteric enhancers. *Biochem. Pharmacol.* **82**, 658–668 (2011).
50. Deacon, C. F., Johnsen, A. H. & Holst, J. J. Degradation of glucagon-like peptide-1 by human plasma *in vitro* yields an N-terminally truncated peptide that is a major endogenous metabolite *in vivo*. *J. Clin. Endocrinol. Metab.* **80**, 952–957 (1995).
51. Birks, R. I. & Macintosh, F. C. Acetylcholine metabolism at nerve endings. *Br. Med. Bull.* **13**, 157–161 (1957).
52. Plagemann, P. G., Wohlhueter, R. M. & Kraupp, M. Adenosine uptake, transport, and metabolism in human erythrocytes. *J. Cell. Physiol.* **125**, 330–336 (1985).
53. Tucek, S. *et al.* The concentration of choline and the activities of cholinesterases, creatine kinase and lactate dehydrogenase in the blood plasma of piglets with the syndrome of splayleg (congenital myofibrillar hypoplasia). *Zentralbl. Veterinarmed.* **A 32**, 1–10 (1985).
54. Backstrom, T., Gojny, M., Lockowandt, U., Liska, J. & Franco-Cereceda, A. Cardiac outflow of amino acids and purines during myocardial ischemia and reperfusion. *J. Appl. Physiol.* **94**, 1122–1128 (2003).
55. Tomas, E., Stanojevic, V. & Habener, J. F. GLP-1 (9–36) amide metabolite suppression of glucose production in isolated mouse hepatocytes. *Horm. Metab. Res.* **42**, 657–662 (2010).
56. Canals, M. *et al.* A Monod-Wyman-Changeux mechanism can explain G protein-coupled receptor (GPCR) allosteric modulation. *J. Biol. Chem.* **287**, 650–659 (2012).
57. Williams, R. *et al.* Re-exploration of the PHCC scaffold: discovery of improved positive allosteric modulators of mGluR4. *ACS Chem. Neurosci.* **1**, 411–419 (2010).
58. Schann, S. *et al.* Chemical switch of a metabotropic glutamate receptor 2 silent allosteric modulator into dual metabotropic glutamate receptor 2/3 negative/positive allosteric modulators. *J. Med. Chem.* **53**, 8775–8779 (2010).
59. Bridges, T. M. *et al.* Chemical lead optimization of a pan G_i mAChR M_1 , M_2 , M_3 positive allosteric modulator (PAM) lead. Part I: development of the first highly selective M_2 PAM. *Bioorg. Med. Chem. Lett.* **20**, 558–562 (2010).
60. Bridges, T. M. *et al.* Discovery and development of a second highly selective M_1 positive allosteric modulator (PAM). *Probe Reports from the NIH Molecular Libraries Program* [online], <http://www.ncbi.nlm.nih.gov/books/NBK50704/> (National Center for Biotechnology Information, 2010).
61. Borshell, N., Papp, T. & Congreve, M. Deal watch: Valuation benefits of structure-enabled drug discovery. *Nature Rev. Drug Discov.* **10**, 166 (2011).
62. Lagerstrom, M. C. & Schioth, H. B. Structural diversity of G protein-coupled receptors and significance for drug discovery. *Nature Rev. Drug Discov.* **7**, 339–357 (2008).
63. Palczewski, K. *et al.* Crystal structure of rhodopsin: a G protein-coupled receptor. *Science* **289**, 739–745 (2000).
64. Rasmussen, S. G. *et al.* Crystal structure of the $\beta 2$ adrenergic receptor-Gs protein complex. *Nature* **477**, 549–555 (2011). **This paper describes the first crystal structure of an agonist-GPCR-G protein ternary complex.**
65. Warne, T., Edwards, P. C., Leslie, A. G. & Tate, C. G. Crystal structures of a stabilized $\beta 1$ -adrenoceptor bound to the biased agonists bucindolol and carvedilol. *Structure* **20**, 841–849 (2012).
66. Kruse, A. C. *et al.* Structure and dynamics of the M3 muscarinic acetylcholine receptor. *Nature* **482**, 552–556 (2012).
67. Haga, K. *et al.* Structure of the human M2 muscarinic acetylcholine receptor bound to an antagonist. *Nature* **482**, 547–551 (2012).
68. Granier, S. *et al.* Structure of the δ -opioid receptor bound to naltrindole. *Nature* **485**, 400–404 (2012).
69. Wu, H. *et al.* Structure of the human κ -opioid receptor in complex with JDTic. *Nature* **485**, 327–332 (2012).
70. Xu, F. *et al.* Structure of an agonist-bound human $\text{A}_{2\text{A}}$ adenosine receptor. *Science* **332**, 322–327 (2011).
71. Lebon, G. *et al.* Agonist-bound adenosine $\text{A}_{2\text{A}}$ receptor structures reveal common features of GPCR activation. *Nature* **474**, 521–525 (2011).
72. Zhang, C. *et al.* High-resolution crystal structure of human protease-activated receptor 1. *Nature* **492**, 387–392 (2012).
73. Wu, B. *et al.* Structures of the CXCR4 chemokine GPCR with small-molecule and cyclic peptide antagonists. *Science* **330**, 1066–1071 (2010).
74. Shimamura, T. *et al.* Structure of the human histamine H1 receptor complex with doxepin. *Nature* **475**, 65–70 (2011).
75. Runge, S., Thogersen, H., Madsen, K., Lau, J. & Rudolph, R. Crystal structure of the ligand-bound glucagon-like peptide-1 receptor extracellular domain. *J. Biol. Chem.* **283**, 11340–11347 (2008).
76. Pioszak, A. A., Parker, N. R., Suino-Powell, K. & Xu, H. E. Molecular recognition of corticotropin-releasing factor by its G-protein-coupled receptor CRFR1. *J. Biol. Chem.* **283**, 32900–32912 (2008).
77. Tsuchiya, D., Kunishima, N., Kamiya, N., Jingami, H. & Morikawa, K. Structural views of the ligand-binding cores of a metabotropic glutamate receptor complexed with an antagonist and both glutamate and Gd^{3+} . *Proc. Natl Acad. Sci. USA* **99**, 2660–2665 (2002).
78. Muto, T., Tsuchiya, D., Morikawa, K. & Jingami, H. Structures of the extracellular regions of the group II/III metabotropic glutamate receptors. *Proc. Natl Acad. Sci. USA* **104**, 3759–3764 (2007).
79. Matsui, H., Lazareno, S. & Birdsall, N. J. Probing of the location of the allosteric site on M1 muscarinic receptors by site-directed mutagenesis. *Mol. Pharmacol.* **47**, 88–98 (1995).
80. Trankle, C. *et al.* Interactions of orthosteric and allosteric ligands with [^3H]dimethyl-W84 at the common allosteric site of muscarinic M2 receptors. *Mol. Pharmacol.* **64**, 180–190 (2003).
81. Prilla, S., Schrobang, J., Ellis, J., Holtje, H. D. & Mohr, K. Allosteric interactions with muscarinic acetylcholine receptors: complex role of the conserved tryptophan M242Trp in a critical cluster of amino acids for baseline affinity, subtype selectivity, and cooperativity. *Mol. Pharmacol.* **70**, 181–193 (2006).
82. Avlani, V. A. *et al.* Critical role for the second extracellular loop in the binding of both orthosteric and allosteric G protein-coupled receptor ligands. *J. Biol. Chem.* **282**, 25677–25686 (2007).

83. Dragic, T. *et al.* A binding pocket for a small molecule inhibitor of HIV-1 entry within the transmembrane helices of CCR5. *Proc. Natl Acad. Sci. USA* **97**, 5639–5644 (2000).
84. Gerlach, L. O., Skerlj, R. T., Bridger, G. J. & Schwartz, T. W. Molecular interactions of cyclam and bicyclam non-peptide antagonists with the CXCR4 chemokine receptor. *J. Biol. Chem.* **276**, 14153–14160 (2001).
85. Maeda, K. *et al.* Structural and molecular interactions of CCR5 inhibitors with CCR5. *J. Biol. Chem.* **281**, 12688–12698 (2006).
86. Nicholls, D. J. *et al.* Identification of a putative intracellular allosteric antagonist binding-site in the CXCR4 chemokine receptors 1 and 2. *Mol. Pharmacol.* **74**, 1193–1202 (2008).
87. Andrews, G., Jones, C. & Wreggett, K. A. An intracellular allosteric site for a specific class of antagonists of the CC chemokine G protein-coupled receptors CCR4 and CCR5. *Mol. Pharmacol.* **73**, 855–867 (2008).
88. Liaw, C. W., Grigoriadis, D. E., Lorang, M. T., De Souza, E. B. & Maki, R. A. Localization of agonist- and antagonist-binding domains of human corticotropin-releasing factor receptors. *Mol. Endocrinol.* **11**, 2048–2053 (1997).
89. Dupuis, D. S., Relkovic, D., Lhuillier, L., Mosbacher, J. & Kaupmann, K. Point mutations in the transmembrane region of GABA_A facilitate activation by the positive modulator N,N'-dicyclopentyl-2-methylsulfanyl-5-nitro-pyrimidine-4,6-diamine (GS39783) in the absence of the GABA_A subunit. *Mol. Pharmacol.* **70**, 2027–2036 (2006).
90. Pagano, A. *et al.* The non-competitive antagonists 2-methyl-6-(phenylethynyl)pyridine and 7-hydroxyiminocyclopropan[b]chromen-1a-carboxylic acid ethyl ester interact with overlapping binding pockets in the transmembrane region of group I metabotropic glutamate receptors. *J. Biol. Chem.* **275**, 33750–33758 (2000).
91. Knoflach, F. *et al.* Positive allosteric modulators of metabotropic glutamate 1 receptor: characterization, mechanism of action, and binding site. *Proc. Natl Acad. Sci. USA* **98**, 13402–13407 (2001).
92. Petrel, C. *et al.* Modeling and mutagenesis of the binding site of Calhex 231, a novel negative allosteric modulator of the extracellular Ca²⁺-sensing receptor. *J. Biol. Chem.* **278**, 49487–49494 (2003).
93. Malherbe, P. *et al.* Mutational analysis and molecular modeling of the allosteric binding site of a novel, selective, noncompetitive antagonist of the metabotropic glutamate 1 receptor. *J. Biol. Chem.* **278**, 8340–8347 (2003).
94. Miedlich, S. U., Gama, L., Seuwen, K., Wolf, R. M. & Breitwieser, G. E. Homology modeling of the transmembrane domain of the human calcium sensing receptor and localization of an allosteric binding site. *J. Biol. Chem.* **279**, 7254–7263 (2004).
95. Cisowski, J. *et al.* Targeting protease-activated receptor-1 with cell-penetrating peptidins in lung cancer. *Am. J. Pathol.* **179**, 513–523 (2011).
96. Tressell, S. L. *et al.* Pharmacology, biodistribution, and efficacy of GPCR-based peptidins in disease models. *Methods Mol. Biol.* **683**, 259–275 (2011).
97. Rosenbaum, D. M. *et al.* Structure and function of an irreversible agonist-β₂ adrenoceptor complex. *Nature* **469**, 236–240 (2011).
98. Rasmussen, S. G. *et al.* Structure of a nanobody-stabilized active state of the β₂ adrenoceptor. *Nature* **469**, 175–180 (2011).
99. Horstman, D. A. *et al.* An aspartate conserved among G-protein receptors confers allosteric regulation of alpha 2-adrenergic receptors by sodium. *J. Biol. Chem.* **265**, 21590–21595 (1990).
100. Costa, T., Lang, J., Gless, C. & Herz, A. Spontaneous association between opioid receptors and GTP-binding regulatory proteins in native membranes: specific regulation by antagonists and sodium ions. *Mol. Pharmacol.* **37**, 383–394 (1990).
101. Gao, Z. G. & Ijzerman, A. P. Allosteric modulation of A_{2A} adenosine receptors by amiloride analogues and sodium ions. *Biochem. Pharmacol.* **60**, 669–676 (2000).
102. Selent, J., Sanz, F., Pastor, M. & De Fabritiis, G. Induced effects of sodium ions on dopaminergic G-protein coupled receptors. *PLoS Comput. Biol.* **6**, e1000884 (2010).
103. Neve, K. A. *et al.* Modeling and mutational analysis of a putative sodium-binding pocket on the dopamine D2 receptor. *Mol. Pharmacol.* **60**, 373–381 (2001).
104. Parker, M. S., Wong, Y. Y. & Parker, S. L. An ion-responsive motif in the second transmembrane segment of rhodopsin-like receptors. *Amino Acids* **35**, 1–15 (2008).
105. Vrolijk, B. *et al.* GPCRDB: information system for G protein-coupled receptors. *Nucleic Acids Res.* **39**, D309–D319 (2011).
106. Liu, W. *et al.* Structural basis for allosteric regulation of GPCRs by sodium ions. *Science* **337**, 232–236 (2012).
- This paper shows the structural basis for the observed negative allosteric effect of sodium ions on GPCR activity.**
107. Standfuss, J. *et al.* The structural basis of agonist-induced activation in constitutively active rhodopsin. *Nature* **471**, 656–660 (2011).
108. Rocheville, M. *et al.* Receptors for dopamine and somatostatin: formation of hetero-oligomers with enhanced functional activity. *Science* **288**, 154–157 (2000).
109. El-Asmar, L. *et al.* Evidence for negative binding cooperativity within CCR5–CCR2b heterodimers. *Mol. Pharmacol.* **67**, 460–469 (2005).
110. Ellis, J., Pediani, J. D., Canals, M., Milasta, S. & Milligan, G. Orexin-1 receptor-cannabinoid CB1 receptor heterodimerization results in both ligand-dependent and -independent coordinated alterations of receptor localization and function. *J. Biol. Chem.* **281**, 38812–38824 (2006).
111. Harikumar, K. G. *et al.* Glucagon-like peptide-1 receptor dimerization differentially regulates agonist signaling but does not affect small molecule allosteric. *Proc. Natl Acad. Sci. USA* **109**, 18607–18612 (2012).

This study demonstrated that dimerization of a class B GPCR is important for the efficacy of orthosteric ligands but is not important for allosteric modulation, which occurs within a single receptor protomer.

112. Harikumar, K. G., Ball, A. M., Sexton, P. M. & Miller, L. J. Importance of lipid-exposed residues in transmembrane segment four for family B calcitonin receptor homo-dimerization. *Regul. Pept.* **164**, 113–119 (2010).
113. Harikumar, K. G., Happs, R. M. & Miller, L. J. Dimerization in the absence of higher-order oligomerization of the G protein-coupled secretin receptor. *Biochim. Biophys. Acta* **1778**, 2555–2563 (2008).
114. Harikumar, K. G., Pinon, D. I. & Miller, L. J. Transmembrane segment IV contributes a functionally important interface for oligomerization of the class II G protein-coupled secretin receptor. *J. Biol. Chem.* **282**, 30363–30372 (2007).
115. Gao, F. *et al.* Functional importance of a structurally distinct homodimeric complex of the family B G protein-coupled secretin receptor. *Mol. Pharmacol.* **76**, 264–274 (2009).
116. El Moustaine, D. *et al.* Distinct roles of metabotropic glutamate receptor dimerization in agonist activation and G-protein coupling. *Proc. Natl Acad. Sci. USA* **109**, 16342–16347 (2012).
117. Block, G. *et al.* Cinacalcet for secondary hyperparathyroidism in patients receiving hemodialysis. *N. Engl. J. Med.* **350**, 1516–1525 (2004).
- This is the first demonstration of an allosteric modulator that has clinical efficacy.**
118. Brown, E. M. Clinical lessons from the calcium sensing receptor. *Nature Clin. Pract. Endocrinol. Metab.* **3**, 122–133 (2007).
119. Fatkenheuer, G. *et al.* Efficacy of short-term monotherapy with maraviroc, a new CCR5 antagonist, in patients infected with HIV-1. *Nature Med.* **11**, 1170–1172 (2005).
120. Wood, A. & Armour, D. The discovery of the CCR5 receptor antagonist, UK-427,857, a new agent for the treatment of HIV infection and AIDS. *Prog. Med. Chem.* **43**, 239–271 (2005).

Acknowledgements

P.M.S. and A.C. are principal research fellows of the National Health and Medical Research Council (NHMRC) of Australia, and their work is funded by an NHMRC program grant (number 519461).

Competing interests statement

The authors declare [competing financial interests](#): see Web version for details.

FURTHER INFORMATION

Protein Data Bank: <http://www.rcsb.org>

ALL LINKS ARE ACTIVE IN THE ONLINE PDF

Minireview: Signal Bias, Allosterism, and Polymorphic Variation at the GLP-1R: Implications for Drug Discovery

Cassandra Koole, Emilia E. Savage, Arthur Christopoulos, Laurence J. Miller, Patrick M. Sexton, and Denise Wootten

Department of Drug Discovery Biology (C.K., E.E.S., A.C., P.M.S., D.W.), Monash Institute of Pharmaceutical Sciences, and Department of Pharmacology, Monash University, Parkville 3052, Victoria, Australia; and Department of Molecular Pharmacology and Experimental Therapeutics (L.J.M.), Mayo Clinic, Scottsdale, Arizona 85259

The glucagon-like peptide-1 receptor (GLP-1R) controls the physiological responses to the incretin hormone glucagon-like peptide-1 and is a major therapeutic target for the treatment of type 2 diabetes, owing to the broad range of effects that are mediated upon its activation. These include the promotion of glucose-dependent insulin secretion, increased insulin biosynthesis, preservation of β -cell mass, improved peripheral insulin action, and promotion of weight loss. Regulation of GLP-1R function is complex, with multiple endogenous and exogenous peptides that interact with the receptor that result in the activation of numerous downstream signaling cascades. The current understanding of GLP-1R signaling and regulation is limited, with the desired spectrum of signaling required for the ideal therapeutic outcome still to be determined. In addition, there are several single-nucleotide polymorphisms (used in this review as defining a natural change of single nucleotide in the receptor sequence; clinically, this is viewed as a single-nucleotide polymorphism only if the frequency of the mutation occurs in 1% or more of the population) distributed within the coding sequence of the receptor protein that have the potential to produce differential responses for distinct ligands. In this review, we discuss the current understanding of GLP-1R function, in particular highlighting recent advances in the field on ligand-directed signal bias, allosteric modulation, and probe dependence and the implications of these behaviors for drug discovery and development. (*Molecular Endocrinology* 27: 1234–1244, 2013)

Glucagon-like peptide-1 (GLP-1) is one of the key incretin hormones that regulate insulin secretion in response to meal ingestion, and thus, the principal stimulus for GLP-1 secretion is the nutrient content of the gastrointestinal (GI) tract. However, the mechanism underlying GLP-1 secretion is complex with multiple factors thought to impact on its release, including neural and endocrine factors such as gastrin-releasing peptide, leptin, and acetylcholine (reviewed in References 1 and 2). After ingestion of a glucose-rich meal, GLP-1 is rapidly secreted from intestinal L cells of the distal small intestine, leading to a

biphasic response peaking at 10–15 minutes and then a sustained peak again at 30–60 minutes after nutrient ingestion (3).

GLP-1 has a diverse range of physiological functions that rely on its association with the GLP-1 receptor (GLP-1R), which belongs to the family B subclass of G protein-coupled receptors (GPCRs), and subsequent regulation of intracellular signaling components to induce biological effects. The principal physiological effect that arises from GLP-1R activation is the amplification of intracellular signaling components that drive the expression, biosyn-

ISSN Print 0888-8809 ISSN Online 1944-9917
Printed in U.S.A.
Copyright © 2013 by The Endocrine Society
Received April 26, 2013. Accepted July 5, 2013.
First Published Online July 17, 2013

Abbreviations: BETP, 4-(3-benzyloxyphenyl)-2-ethylsulfinyl-6-(trifluoromethyl)pyrimidine; Boc5, 1,3-bis [[4-(tert-butoxycarbonylamino)benzoyl]amino]-2,4-bis[3-methoxy-4-(thiophene-2-carboxyloxy)-phenyl]cyclobutane-1,3-dicarboxylic acid; CaSR, Ca^{2+} -sensing receptor; GI, gastrointestinal; GLP-1, glucagon-like peptide-1; GLP-1R, GLP-1 receptor; GPCR, G protein-coupled receptor; Ca^{2+} , intracellular calcium; NK2, neurokinin 2; pERK1/2, ERK1/2 phosphorylation; PKA, protein kinase A; SNP, single-nucleotide polymorphism; TM, transmembrane.

thesis, and secretion of insulin from pancreatic β -cells in a glucose-dependent manner (4). While promoting insulin secretion, GLP-1 also inhibits glucagon secretion from pancreatic α -cells (5). Other physiological processes in the endocrine pancreas that are mediated by GLP-1 include increasing neogenesis, proliferation, and decreasing apoptosis of pancreatic β -cells; this leads to an increase in β -cell mass and subsequently aids the glucose-dependent augmentation of insulin secretion (6, 7). This has been confirmed in GLP-1R^{-/-} mice, which exhibit normal β -cell mass but have altered islet cell topography and defective β -cell regeneration in addition to reduced glucose tolerance, indicative that GLP-1 function is important in islet cell maintenance and development (8). Extra-pancreatic effects of GLP-1 occur in the central and peripheral nervous systems, GI system, cardiovascular system, muscle, adipose tissue, liver, hypothalamus, respiratory system, pulmonary arteries, and kidney, each of which express the GLP-1R (9).

In the nervous system, the GLP-1 peptide influences control of ingestive behavior and appetite regulation, possibly through crossing the blood-brain barrier into the hypothalamus and modulating the secretion of appetite regulatory hormones (10). In addition, GLP-1 augments neogenesis, proliferation, and antiapoptotic behavior of neuronal cells and also enhances memory and associative and spatial learning in rodents (11).

GLP-1 can also improve endothelial function in the human cardiovascular system (12), and decreases infarct size and increases ventricular activity in rodents (13). Furthermore, GLP-1R^{-/-} mice have abnormal cardiac wall thickness, ventricular contractility, and diastolic function (14), consistent with a role for GLP-1 in normal cardiovascular function.

In the GI system, GLP-1 inhibits gastric emptying. This is particularly important because it regulates nutrient content in the small intestine and consequently levels of GLP-1 and insulin secretion (15). This is also mediated in part by the nervous system, whereby sensory information in the GI tract is relayed to the brain and hypothalamus and hormones are released to aid in the control of gastric emptying (10).

In muscle and adipose and hepatic cells, GLP-1 augments glycogen synthase activity and therefore favors incorporation of glucose into glycogen (2), whereas GLP-1 and GLP-1-related agonists may also enhance peripheral insulin sensitivity and reduce steatosis (16). In addition, GLP-1 can reduce hepatic glucose production, which combined with the effects observed in muscle and adipose tissue aids in the reduction of plasma glucose (17).

In the respiratory system, GLP-1 is involved in the production of mucus in the lungs and trachea as well as

inducing pulmonary relaxation (18), and in the kidney, GLP-1 increases the rate of glomerular filtration and Na⁺ excretion (19). Consequently, this inhibits the development of hypertension and improves endothelial integrity, supporting a role for GLP-1 in renal protection.

Signaling via GLP-1Rs

The physiological changes observed with GLP-1 administration, including increases in insulin secretion and β -cell mass, are dependent on signaling via GLP-1R-mediated intracellular pathways. The GLP-1R is pleiotropically coupled to G α_s -, G α_i -, G α_o -, and G $\alpha_{q/11}$ -mediated pathways (20) as well as G protein-independent (β -arrestin mediated) pathways (21, 22). However, the GLP-1R preferentially couples to G α_s -regulated pathways, favoring production of cAMP through increasing adenylate cyclase activity (4). This subsequently promotes increases in both protein kinase A (PKA) and exchange protein activated by cAMP-2, the latter of which is directly involved in enhancing proinsulin gene transcription and subsequent insulin biosynthesis and secretion (23). In addition, GLP-1R activation induces membrane depolarization of β -cells through the inhibition of K⁺ channels, most likely through a cAMP/PKA-dependent mechanism, enabling voltage-dependent Ca²⁺ channels to open and acceleration of Ca²⁺ influx, resulting in the exocytosis of insulin from β -cells (24). Therefore, the combination of both cAMP production and influx of Ca²⁺ are vital components in the biosynthesis and secretion of insulin. Furthermore, signaling via these intracellular messengers is important in up-regulating intestinal and pancreatic expression of the proglucagon gene, the precursor for GLP-1 (25, 26). Elevated insulin levels and hypoglycemia as a result of enhanced GLP-1 activity subsequently prompts the down-regulation of proglucagon gene transcription, ensuring tight regulation of glucose homeostasis (2).

In addition to elevating cAMP and Ca²⁺ influx, GLP-1R activity also promotes insulin receptor substrate-2 signaling, phosphoinositide-3-kinase, and ERK1/2 activity, which mediate β -cell proliferation and differentiation (22, 27–29) and contribute to insulin gene transcription (30). Moreover, epidermal growth factor receptor transactivation via GLP-1R enhancement of c-src and subsequently β -cellulin production also promotes phosphoinositide-3-kinase activity and nuclear translocation of protein kinase C- ζ as well as several other transcription factors to contribute to β -cell proliferation (2, 31). Additional support for the involvement of GLP-1 in β -cell proliferation is seen in GLP-1R^{-/-} mice, in which abnormal islet topography and increases in glucagon-producing α -cells are observed (8). In accord, continuous

GLP-1 administration into diabetic rodent models shows an increase in islet size and β -cell mass and a substantial decrease in apoptotic β -cells (32) while also enhancing glucose sensitivity in β -cells (33).

Emerging evidence also reveals a role for β -arrestins in GLP-1-mediated biological effects (21, 22). In particular, β -arrestin-1 knockdown using small interfering RNA in pancreatic β -cells resulted in a decrease in ERK1/2/cAMP-response element binding protein activation, insulin receptor substrate-2 expression, cAMP production, and insulin secretion after GLP-1R activation, suggesting an important role in the regulation of $G\alpha_s$ -mediated activities (21). A separate study revealed that GLP-1R activation induces 2 distinct ERK1/2 phosphorylation (pERK1/2) responses. The first is a PKA-dependent pathway that mediates rapid and transient pERK1/2 leading to nuclear translocation of the activated kinase and the second, is a late pERK1/2 response mediated by β -arrestin-1 that is restricted to the β -cell cytoplasm. Furthermore, this study found β -arrestin-1-dependent ERK1/2 signaling engaged by GLP-1 stimulates p90RSK activity, mediating the phosphorylation of Bcl-2 antagonist of cell death that leads to an antiapoptotic effect (22).

After activation, GPCRs are often internalized, resulting in the loss of signaling, and are then either resensitized by being recycled back to the membrane or they are down-regulated via the degradation of the receptor. For the GLP-1R, these processes are poorly understood, but there is limited evidence that GLP-1R desensitization/internalization is independent of β -arrestin-mediated events (21) and is dependent on caveolin-1 (34). The role that β -arrestins and G protein-coupled receptor kinases play in this process (if any) is still unclear, but existing studies on regulation and arrestin recruitment/signaling have predominantly focused on GLP-1(7–36)NH₂ as an agonist, despite there being multiple endogenous ligands (at least 6) and exogenous ligands that are used clinically for this receptor.

The GLP-1R and type 2 diabetes

Type 2 diabetes mellitus and associated obesity is a major disease of the Western world and is a substantial burden to the health care system. Activation of the GLP-1R elicits a broad range of complementary effects including increased insulin production and secretion, preservation of β -cell mass, inhibition of gastric emptying, and glucagon release and suppression of food intake, all of which are of therapeutic benefit in type 2 diabetic patients (35). Currently Food and Drug Administration-approved drugs for this disease include 2 peptides that act via the GLP-1R [exendin-4 (Byetta) and liraglutide (Victoza)] (36, 37), but despite their clinical success, their use

has been limited to injection and associated with significant adverse side effects in some patients, including nausea, pancreatitis, and pancreatic cancer (36, 38, 39), the mechanistic basis of which is not known. Currently there is major pharmaceutical interest in the development of small-molecule orally active drugs that augment GLP-1R signaling.

The GLP-1R is a family B GPCR that physiologically responds to at least 6 endogenous agonists [GLP-1(7–36)NH₂, GLP-1(1–36)NH₂, GLP-1(7–37), GLP-1(1–37), GLP-1(9–36)NH₂, and oxyntomodulin] and can also be pharmacologically targeted by exogenous peptides (exendin-4, liraglutide, Bristol-Myers Squibb Company peptide 21) and small molecule ligands, some of which act at allosteric sites (BETP [4-(3-benzyloxyphenyl)-2-ethylsulfenyl-6-(trifluoromethyl)pyrimidine], compound 2, TT15 [(2S-3-(49-cyanobiphenyl-4-yl)-2-(((8S)-3-{4-[(3,4-dichlorobenzyl)oxy]phenyl}-2-oxo-7-(phenylcarbonyl)-2,3,6,7,8,9-nexahydro-1H-[1,4]oxazino[3,2-G]isoquinolin-8-yl)carbonyl)amino)propanoic acid], Boc5 [1,3-bis [[4-(tert-butoxycarbonylamino)benzoyl]amino]-2,4-bis[3-methoxy-4-(thiophene-2-carbonyloxy)-phenyl]cyclobutane-1,3-dicarboxylic acid]) (40–42), providing opportunities for novel drug discovery. However, the identification of suitable orally active small molecules as potential drug candidates remains elusive.

Ligand-directed signal bias and allosterism in GPCR drug discovery

GPCRs are the largest class of targets for clinically used drugs (43), however, some drugs yield better therapeutic outcomes than others, despite showing similar activity at their target receptors in common screening assays. This situation reflects a lack of mechanistic understanding of the consequences of new and emerging paradigms in GPCR biology (ligand directed signal bias and allosterism). Distinct ligands acting at the same GPCR (within the same cellular background) can engender unique ensembles of receptor conformations that can give rise to discrete signaling profiles (44). This behavior can be observed through differences in the activation of second messengers but also through changes to how receptors are desensitized and down-regulated. Stimulus bias is further complicated when allosteric drugs are considered because conformational preferences of the receptor when allosteric and orthosteric (endogenous ligand) binding sites are co-occupied may be different from when either site is individually occupied. Furthermore, the effect of a particular allosteric drug may be specific to the individual endogenous ligand (an effect termed probe dependence), as has been observed for the modulation of the GLP-1R (discussed below). These paradigms are particularly rele-

vant to receptor systems like the GLP-1R that have multiple endogenous ligands, in which exogenous mimetics are used in the clinical treatment of patients, and for allosteric drug action and development. In terms of drug discovery for the GLP-1R, targeting of allosteric sites by small-molecule compounds that are pure modulators can allow maintenance of spatial-temporal signaling patterns as well as the opportunity for attaining pathway selectivity through stimulus bias as a means of maximizing beneficial physiological effects and limiting pathways associated with detrimental effects.

Ligand-directed signaling at the GLP-1R

The peptide ligands of the GLP-1R are generally expected to activate the receptor by similar mechanisms, albeit with different potency driven by differing ligand affinity for the receptor. It is only recently, through parallel studies of multiple peptide ligands and their ability to activate a spectrum of signaling pathways, that clear evidence for ligand-directed signal bias has emerged (45–47). A key factor in the detection of ligand-directed signal bias has been the development of quantitative analytical methods that can distinguish between unbiased effects on strength of signaling from selective or preferential activation of distinct signaling pathways (48). The most robust measures to date are derived from the ratio of ligand binding affinity to efficacy (for each pathway) as defined by the tau term in the operational model (49).

Application of these methods to the GLP-1R for individual peptides in activation of 3 key signaling pathways (cAMP formation, pERK1/2, or $i\text{Ca}^{2+}$ [intracellular calcium] levels) has allowed clear distinction in the signaling profile of peptide ligands of the receptor (45). Relative to GLP-1(7–36) NH_2 , both full-length GLP-1 peptides [GLP-1(1–36) NH_2 and GLP-1(1–37)] and oxyntomodulin exhibit bias for cAMP over pERK1/2, with oxyntomodulin also relatively biased for $i\text{Ca}^{2+}$ over pERK1/2. Exendin-4 and GLP-1(7–37) were not significantly biased [relative to the signaling profile of GLP-1(7–36) NH_2] for any of these 3 pathways. Nonetheless, mutational data for conserved polar residues (across family B GPCRs) revealed divergence in the impact of alanine mutation of specific residues (for example, R¹⁹⁰, N²⁴⁰, H³⁶³, Q³⁹⁴) for GLP-1(7–36) NH_2 and exendin-4, demonstrating that even these pharmacologically similar peptides engender unique receptor conformations that drive receptor function (50). Additional support for the distinct effect of GLP-1R interaction with exendin-4 vs GLP-1 is seen in studies of heterodimers between the GLP-1R and the gastric inhibitory polypeptide receptor (51).

The search for small-molecule agonists/modulators of the GLP-1R has led to the identification of multiple com-

pounds that can bind to and modulate GLP-1R function. Many of these also have intrinsic efficacy at the GLP-1R, at least for the generation of cAMP, and can augment insulin secretion either alone or in combination with peptide agonists of the GLP-1R (40–42, 46, 52, 53). Detailed analysis of the signaling profile of BETP, compound 2, TT15, Boc5, and a small peptide, Bristol-Myers Squibb Company peptide 21, for both the regulation of classic signaling pathways (cAMP, pERK1/2, and $i\text{Ca}^{2+}$) and their ability to recruit β -arrestin-1 or β -arrestin-2 revealed that each of these compounds have a unique signaling fingerprint (47), and this can be visualized in a web of signaling bias plot, relative to the reference ligand GLP-1(7–36) NH_2 and reference pathway, cAMP (Figure 1). Understanding how these unique signaling profiles affects function of physiologically relevant systems (eg, the synthesis and release of insulin or modulation of proliferation and apoptosis) is yet to be elucidated.

Allosteric ligands alter the signal bias of peptidic ligands of the GLP-1R

Most, if not all, small-molecule ligands bind to an allosteric site(s) on the GLP-1R and consequently have the ability to simultaneously bind with orthosteric peptides and to modulate their binding and/or function. One of the first GLP-1R allosteric ligands identified was the Novo-Nordisk molecule, compound 2 (40). This compound exhibited classic probe-dependent interactions with orthosteric peptide agonists, displaying preferential positive

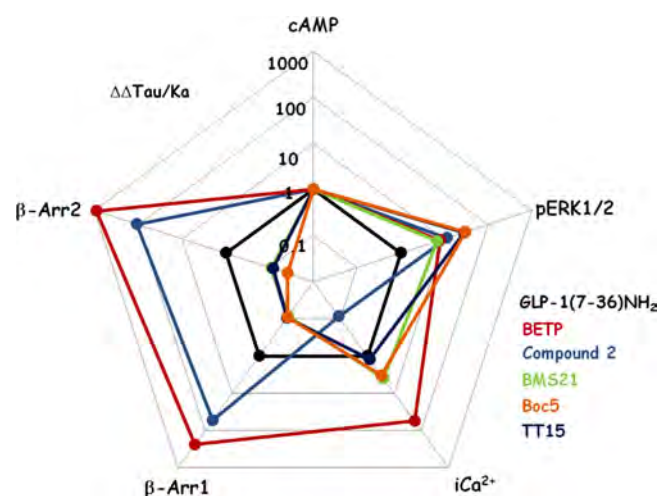


Figure 1. Web of bias for GLP-1R small synthetic ligands relative to GLP-1(7–36) NH_2 . Quantification of signal bias using experimental measures of agonist affinity (K_a) and efficacy (τ) for 5 signaling pathways. The τ to K_a ratio extracted from standard concentration-response data is used to calculate bias factors or $\Delta\Delta(\tau/K_a)$ values through normalization of the transduction coefficient (τ/K_a) to a reference ligand and a reference pathway (89). All small synthetic ligands display signaling bias relative to the reference agonist [GLP-1(7–36) NH_2 (black)] and the reference pathway (cAMP). Note: log scale.

allosteric modulation of oxyntomodulin over GLP-1(7–36)NH₂ and GLP-1(7–37) (weak positive cooperativity) but exhibiting neutral cooperativity with GLP-1(1–36)NH₂, GLP-1(1–37), and exendin-4 (45, 54). In addition to these probe-dependent effects, compound 2 altered signaling bias of the modulated peptide, with positive cooperativity limited to binding affinity and cAMP accumulation and no modulation of pERK1/2 or Ca^{2+} mobilization. Compound 2 also behaved as an agonist in the absence of orthosteric ligand binding at the GLP-1R but only in the activation of cAMP and to a lesser extent ERK1/2 signaling and not for Ca^{2+} mobilization. Interestingly, compound 2 only enhanced orthosteric peptide signaling in the pathway for which it was most efficacious as an agonist, providing support for a linkage between efficacy modulation and agonism of allosteric ligands, consistent with currently proposed allosteric theory (55–58). The higher efficacy of compound 2 in cAMP formation suggests that the energy barrier to achieve active receptor conformation(s) associated with cAMP is lower than the energy barrier to achieve conformations associated with pERK1/2 and Ca^{2+} mobilization. Although this may be an artifact of the experimental system, high receptor expression and the sensitivity of the assay detection methods used suggest this is not likely to be the case, instead being a property of the molecule itself (57).

Unlike compound 2, BETP, an allosteric ligand identified by Eli Lilly, exhibited weak agonism for activation of cAMP, pERK1/2, and Ca^{2+} . However, similar to compound 2, BETP also displayed probe-dependent, signal-biased interactions with orthosteric ligands. This compound also exhibited positive cooperativity with oxyntomodulin in binding and cAMP, but not in pERK1/2 or Ca^{2+} , and neutral cooperativity with GLP-1(7–36)NH₂, GLP-1(1–36)NH₂, and exendin-4 in these pathways (47).

Probe dependence and altered signaling bias are also seen with the flavonoid quercetin (45). Quercetin lacked intrinsic efficacy in all GLP-1R-mediated signaling pathways assessed, but selectively augmented the efficacy, in Ca^{2+} mobilization, of the high-affinity agonists GLP-1(7–36)NH₂, GLP-1(7–37), and exendin-4, and not that of the lower-affinity ligands GLP-1(1–36)NH₂, GLP-1(1–37), and oxyntomodulin. The same trend was also evident for 4'-hydroxyflavonol and 3'4'-dihydroxyflavonol, suggesting hydroxyl groups in these positions are an important chemical feature engendering cooperativity. Conversely, the flavanoid catechin negatively modulated GLP-1(7–36)NH₂, GLP-1(7–37), GLP-1(1–36)NH₂, and to a lesser extent exendin-4 and GLP-1(1–37), but not oxyntomodulin in cAMP accumulation assays (59). In both cases, the absence of modulation in agonist binding

affinity suggests an efficacy-driven mechanism of action. Furthermore, the differential cooperativity in binding and signaling assays for quercetin, 4'-hydroxyflavonol, 3'4'-dihydroxyflavonol, and catechin, and indeed also compound 2 and BETP (59), are clear examples that the action of allosteric modulators cannot be classified solely through measurement of one pathway. This has also been exemplified at other receptors, including the cannabinoid CB₁ receptor, whereby allosteric Organon Research compounds positively modulate agonist binding affinity but negatively modulate agonist-mediated luciferase signaling (60). In addition, the allosteric ligand LPI805 negatively modulates cAMP activity of the tachykinin neurokinin 2 (NK2) receptor but shows weak positive modulation of Ca^{2+} mobilization (61).

From these studies, it is clear that biased signaling exists across multiple GPCR systems, and this is further complicated with the addition of an allosteric modulator. Exploiting these pharmacological characteristics presents both a challenging yet potentially advantageous avenue for the design and development of superior therapeutics. However, with limited knowledge into whether activation of all GLP-1R-coupled pathways or whether a combination of collateral efficacies would be most effective in the management of type 2 diabetes, it remains to be elucidated how biased signaling could be used clinically to enhance therapies targeting this receptor. Although it has been demonstrated that compound 2, BETP, and Boc5 have the ability to potentiate GLP-1-mediated insulin secretion (40, 62), there is no literature examining the effects of these compounds on β -cell mass and gastric emptying. These may be important considerations in the design of type 2 diabetic therapies because a reduction in β -cell mass and increased gastric emptying are key symptoms associated with the condition (63).

Metabolism of GLP-1 and allosteric drugs

All forms of secreted GLP-1 (truncated and full length, amidated and nonamidated) are very rapidly degraded by dipeptidyl peptidase IV to GLP-1(9–36)NH₂ or GLP-1(9–37) within 1–2 minutes after release, resulting in less than 10% of this released GLP-1 reaching the systemic circulation. These metabolites are therefore the major circulating forms of GLP-1, but they do not stimulate cAMP or insulin secretion (52). As noted above, the allosteric ligands BETP and compound 2 are unable to strongly potentiate cAMP production mediated by GLP-1(7–36)NH₂ or GLP-1(1–36)NH₂; however, both compounds robustly potentiate cAMP production mediated by the metabolite GLP-1(9–36)NH₂ (52, 64). A key finding from these studies was that one of these compounds, BETP, could also strongly potentiate the ability of the

metabolite to induce insulin secretion in both in vivo and ex vivo (β -islets) rat models (52). This probe-dependent nature of GLP-1 allosteric ligands has multiple implications in GLP-1R drug discovery, and the ability to modulate the actions of the normally inert metabolite could be exploited to develop novel therapeutics for the treatment of type 2 diabetes.

The role of dimerization in GLP-1R signaling

Although long viewed as monomeric signal transducers, there is now overwhelming evidence that most GPCRs can form dimers or higher-order oligomers. Family C GPCRs, such as metabotropic glutamate receptors, the Ca^{2+} -sensing receptor (CaSR), and taste receptors, act as obligate dimers in which one partner binds ligand while the other couples to the intracellular effector(s) (65). In the case of family A GPCRs, the evidence is more equivocal. There is accumulating evidence, particularly via resonance energy transfer (bioluminescence resonance energy transfer and fluorescence resonance energy transfer), that family B GPCRs undergo both homo- and heterodimerization, which is also supported by functional effects of dominant-negative receptors (66), and heterodimerization (51, 67, 68). Where investigated, there appears to be a common theme for family B GPCR dimerization, with the lipid-exposed face of transmembrane (TM) IV the site of receptor-receptor interaction; disruption of this interface via mutation or coinubation with TMIV peptides decreases high-affinity agonist binding and peptide-mediated cAMP responses (69–71). Although the same is true for the GLP-1R, broader functional characterization revealed a greater loss of Ca^{2+} signaling relative to the effects of disruption of dimerization on cAMP or pERK1/2 signaling, suggesting that dimerization contributes to signal preference of the receptor (69). Moreover, the impact of dimerization was distinct for the small-molecule agonists compound 2 and BETP relative to the peptide agonists with a complete abrogation of cAMP signaling for the small-molecule li-

gands compared with an approximately 10-fold attenuation of peptide signaling. Nonetheless, pERK1/2 signaling for both peptides and compound 2 was similarly affected with less than 10-fold loss of potency [(69); Figure 2]. Intriguingly, the allosteric modulation of peptide signaling was not altered by disruption to receptor dimerization, indicating that the allosteric effect occurs in cis (69).

In addition to forming homodimers, the GLP-1R can form heterodimers with other family B GPCRs. The heterologous coexpression of the GLP-1R and gastric inhibitory polypeptide receptor results in alterations to both Ca^{2+} mobilization and β -arrestin recruitment (51). Because these receptors are physiologically coexpressed in the pancreatic β -cells, heterodimerization may provide an additional mechanism for ligand-induced signal bias.

Single-nucleotide polymorphisms (SNPs) and polymorphic variants of the GLP-1R

SNPs occur widely in the genes encoding receptor proteins; many of these are silent and thus maintain wild-type receptor phenotype. However, the presence of SNPs has in some cases been linked to the development of disease or the effectiveness of treatments targeted to that receptor. Examples of this include the human CaSR, whose primary role is the regulation of extracellular Ca^{2+} by inhibition of PTH secretion (72), which has SNPs that engender both the loss and gain of function of the encoded receptor and subsequently influence the development of hyper- and hypocalcemia, respectively (reviewed in Reference 73). These conditions are treatable with calcimimetics or calcilytics (74).

Jensen's metaphyseal chondrodysplasia, a rare form of short-limbed dwarfism typically coupled with increased bone resorption and low serum PTH levels, has been associated with the presence of at least 1 of 3 SNPs that lead to single-amino acid change in the PTH1 receptor (H^{223}R , T^{410}P , or I^{458}R) (75, 76). In vitro, receptor proteins with the R^{233} , P^{410} , or R^{458} variant are constitutively active when assessed in cAMP formation (76, 77). The

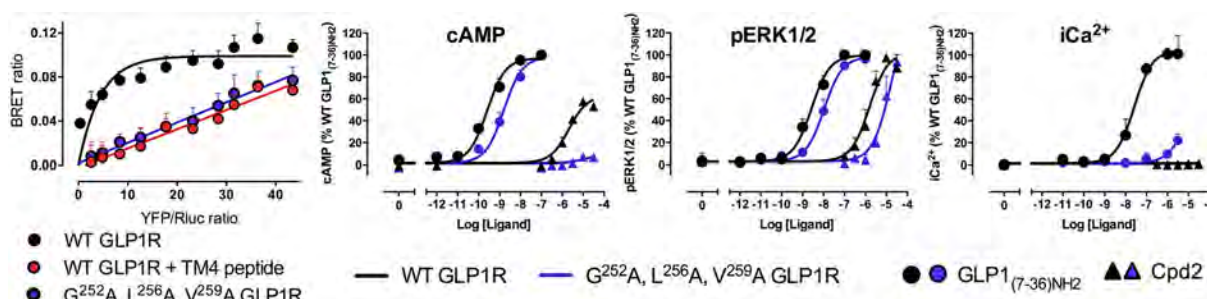


Figure 2. Dimerization of the GLP-1R modulates signaling preference of peptide and nonpeptide agonists. Left, Bioluminescence resonance energy transfer (BRET) between Rluc- and yellow fluorescent protein-tagged GLP-1Rs show that the GLP-1R forms homodimers that can be disrupted by mutations in TMIV (G²⁵²A/L²⁵⁶A/V²⁵⁹A) or by a TMIV peptide. Right, G²⁵²A/L²⁵⁶A/V²⁵⁹A causes a marked loss of Ca^{2+} signaling, limited attenuation of cAMP and pERK1/2 by peptides, but attenuated cAMP with only limited effect on pERK1/2 by compound 2 (Cpd2).

glucagon receptor possesses a SNP (G⁴⁰S) that significantly reduces glucagon binding affinity in vitro (78). In addition, in a population study, an increase in late-onset type 2 diabetes incidence was observed in subjects possessing this SNP (78), whereas an independent study showed an increase in central adipose tissue in the presence of this receptor variant (79). Thus, it is becoming increasingly evident that there are multitudes of receptor variations associated with the onset of disease and/or effectiveness of drug treatments. It is therefore important to address genetic differences underlying receptor variations in the design and development of therapeutics. This concept of pharmacogenomics creates an exciting yet complicated avenue for drug design. Population analysis has revealed several GLP-1R SNPs, one of which leads to attenuated function in vitro and has been reported to have an association with the onset of type 2 diabetes (80, 81). Ten GLP-1R polymorphic variants are identifiable in the SNP database (Table 1 and Figure 3). Initial studies that examined cAMP signaling and GLP-1 binding revealed limited change to receptor function except for the M¹⁴⁹ variant, which displayed reduced GLP-1 binding and cAMP signaling (80, 82).

Comparative analysis of the effect of different ligands across multiple signaling pathways (cAMP, pERK1/2, and iCa^{2+}) revealed additional insights into the effect of the GLP-1R polymorphisms. Although a similar trend in peptide responses was seen for receptor variants in cAMP

and pERK1/2, peptide efficacy in iCa^{2+} mobilization was varied for each SNP (83). Although the effect on iCa^{2+} signaling was often mirrored by changes in cell surface expression of the receptor variants, it also suggested that coupling to this pathway is much more sensitive to changes in the receptor protein. This is also evident from studies on dimerization of the GLP-1R, in which iCa^{2+} responses were much more strongly attenuated than cAMP or pERK1/2 signaling (69). In accord with previous work (80), a significant reduction in GLP-1R function was seen at the M¹⁴⁹ variant; however, the extent of reduction of functional response was dependent on the ligand used to elicit signaling, and the reduction in oxynotomodulin-mediated cAMP was much greater than that of other peptide agonists relative to the wild-type receptor response (83). Perhaps more importantly, the reduction in exendin-4-mediated cAMP was greater than that of the endogenous peptide, GLP-1(7–36)NH₂, these 2 peptides generally being considered functionally equivalent (83). This is consistent with each of these peptides engendering different conformational states of the receptor and is important in demonstrating that seemingly functionally equivalent ligands do not necessarily stabilize identical receptor-active states. Distinct mechanisms of receptor activation by exendin-4 and GLP-1(7–36)NH₂ are also supported by mutational studies of the GLP-1R that differentially impact on signaling by these 2 peptides (47, 84).

Table 1. Human GLP-1R SNPs

Position of Residue in the GLP-1R	Nucleotide Substitution	Amino Acid	Frequency of Occurrence		NCBI Identification Number
			Homozygous	Heterozygous	
7	CCG	Pro	0.60	0.29	rs10305420
	CTG	Leu	0.11		
20	AGG	Arg	0.99	0.01	rs10305421
	AAG	Lys	Unknown		
44	CGC	Arg	0.99	0.01	rs2295006
	CAC	His	Unknown		
131	CGA	Arg	0.92	0.08	rs3765467
	CAA	Gln	Unknown		
149	ACG	Thr	Unknown	Unknown	112198
	ATG	Met	Unknown		
168	GGC	Gly	0.76	0.2	rs6923761
	AGC	Ser	0.04		
260	TTC or TTT	Phe	0.31	0.56	rs1042044
	TTA	Leu	0.13		
316	GCC	Ala	0.98	0.02	rs10305492
	ACC	Thr	Unknown		
333	TCC	Ser	0.99	0.01	rs10305493
	TGC	Cys	Unknown		
421	CGG	Arg	0.99	0.01	rs10305510
	CAG	Gln	Unknown		

Abbreviation: NCBI, National Center for Biotechnology Information. SNPs are identified in the Swissprot database (www.uniprot.org/uniprot/P43220) in association with those identified to exist in a cohort of normal and diabetic subjects as reported elsewhere (81). Frequency data are reported from the Swissprot database. The table is modified from a previously published report (83).

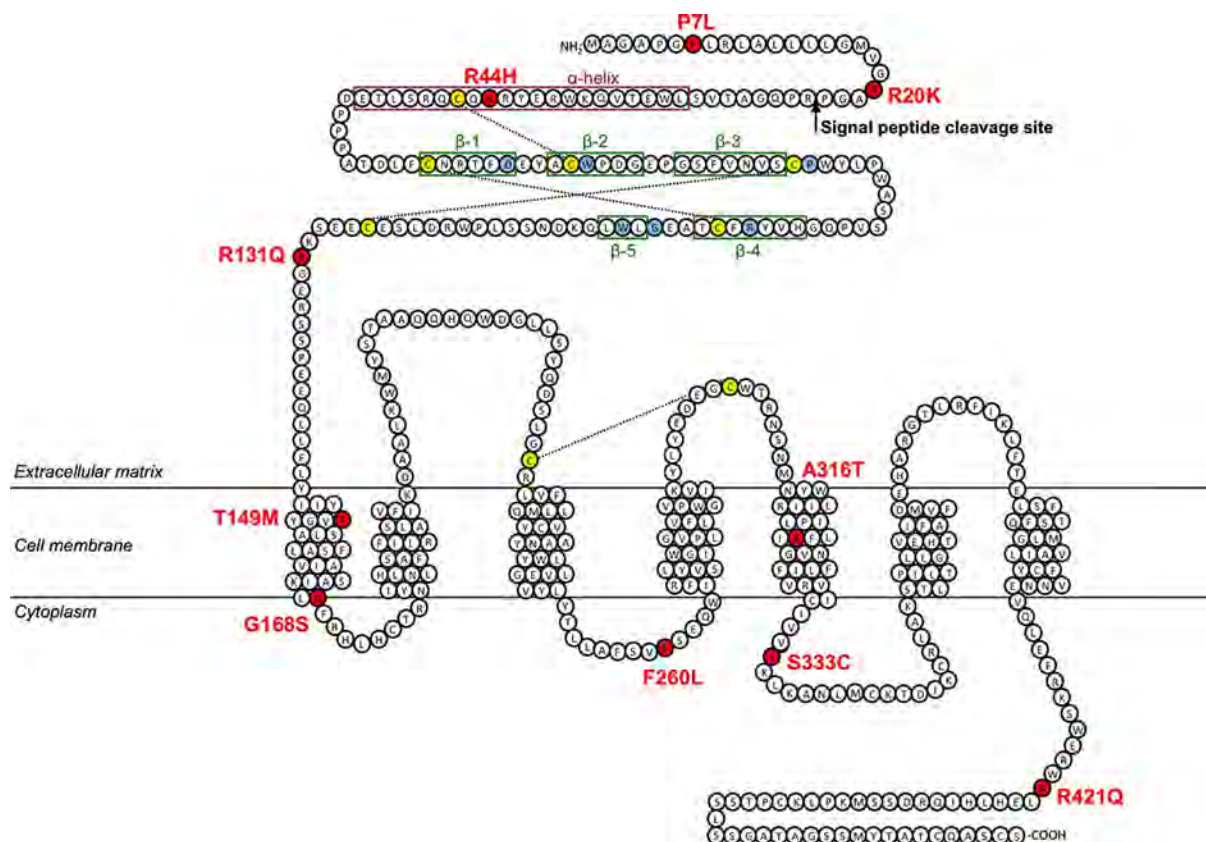


Figure 3. Snake diagram of the amino acid residues that comprise the human GLP-1R. Cysteine residues highlighted in yellow are involved in disulfide interactions, denoted by the dashed lines. Conserved N-terminal residues are highlighted in blue, and N-terminal secondary structure is indicated in purple boxes (α -helix) and green boxes (β -sheets). Residues subject to SNPs are highlighted in red with the residue number and documented polymorphic variations of amino acids indicated. Putative signal peptide cleavage site is depicted with a black arrow.

In contrast to the loss of peptide binding and agonism, the allosteric agonism of compound 2 was retained at the M¹⁴⁹ receptor variant in both cAMP and pERK1/2 signaling. Conversely, a significant reduction in compound 2 agonism was noted at the C³³³ receptor variant in cAMP but not pERK1/2 signaling, despite no significant deviation in peptide responses from that of wild type (83). These data provide further evidence for a distinct mechanism of receptor activation by small-molecule allosteric agonists from that used by orthosteric peptide agonists, which is supported by mutational studies of TM domain and loop regions of the GLP-1R (50, 84).

Polymorphic variation and small-molecule modulation of peptide responses

Peptide agonists of the GLP-1R and other family B GPCRs have diffuse pharmacophores that span the N terminal and TM domains as well as the extracellular loops (85). Not surprisingly, small-molecule ligands do not mimic this mode of interaction with the receptor and indeed principally act at allosteric sites. In addition to intrinsic efficacy, these compounds can modulate the activity of endogenous peptide ligands. This cooperative

interaction can be modified independently of effects on the intrinsic efficacy or affinity of ligands binding to the free receptor, and as such polymorphic variation is relevant to allosteric drug behavior and development. Examination of the ability of compound 2 to modulate cAMP responses of peptide agonists revealed that polymorphic receptor variants with wild-type peptide behavior in cAMP signaling were not necessarily modulated to the same extent by compound 2 compared with the wild-type receptor. In fact, modulation of oxyntomodulin-mediated cAMP accumulation by compound 2 was attenuated at many receptor variants relative to that observed at the wild-type GLP-1R, with no significant modulation evident at the C³³³ variant receptor (83).

Perhaps one of the most exciting findings of that study was the allosteric rescue of the loss of binding affinity and cAMP functional response of all peptide agonists at the M¹⁴⁹ receptor variant in the presence of compound 2. This is distinct from the pattern of modulation seen at the wild-type receptor, in which cooperativity was highly probe dependent [weakly positive for GLP-1(7–36)NH₂, GLP-1(7–37), strongly positive for oxyntomodulin and

neutral for exendin-4 (45)]. This suggests that compound 2 can lower the barrier to achieve peptide-induced active conformations more readily at the M¹⁴⁹ receptor variant. However, the ability of compound 2 to positively modulate receptor activity was restricted only to peptide binding and cAMP signaling, with no modulation observed in ERK1/2 signaling or Ca^{2+} mobilization, suggesting that pathway specificity of cooperativity is maintained in a manner similar to the wild-type receptor.

The potential to rescue nonfunctional receptor variants through allosteric modulation or pharmacochaperoning has also recently been described at other receptors. Two naturally occurring polymorphic variants of the LH receptor, A⁵⁹³P and S⁶¹⁶Y, result in the onset of Leydig cell hyperplasia as a consequence of intracellular retention and subsequently no or little biological activity, respectively (86). In an in vitro cell system, incubation of each of these mutated receptors with the low molecular weight compound ORG42599 increased cell surface expression and subsequently receptor function (86). A similar observation is also evident at the CaSR, in which many loss-of-function mutations that lead to intracellular retention of the receptor can be rescued to the cell membrane through the use of the calcimimetic chaperone NPS R-568 (87, 88). These studies indicate that allosteric ligands have the potential to be of great clinical value, through the ability to address a broad spectrum of pathophysiological conditions associated with receptor misfolding or improper function.

Summary and conclusion

Type 2 diabetes is a major health burden, with significant impact on quality of life that requires the development of new and improved therapeutics for the management of this disease. The pivotal role of the GLP-1R in glucose homeostasis makes this receptor a very attractive therapeutic target. In recent years, there have been major advances in understanding GLP-1R function; however, despite this, there are still significant challenges in understanding the mechanisms of drug action at this receptor that allow translation into improved therapeutics. Although biased signaling and allosteric modulation (particularly their probe dependent nature for modulation of different endogenous ligands) are now recognized at the GLP-1R, the physiological importance of these phenomenon still remains largely unexplored. Future research, particularly into these areas of GLP-1R function, will address challenges associated with discovery, validation and development of novel, selective drugs with an improved therapeutic profile for the management of type 2 diabetes.

Acknowledgments

Address all correspondence and requests for reprints to: Professor Patrick M. Sexton or Dr Denise Wootten, Monash Institute of Pharmaceutical Sciences, 381 Royal Parade, Parkville, Victoria 3052, Australia. E-mail: patrick.sexton@monash.edu; or E-mail: denise.wootten@monash.edu.

This work was supported by the National Health and Medical Research Council (NHMRC) Program Grant 519461 and NHMRC Project Grant 1002180. P.M.S. and A.C. are principal research fellows of the NHMRC. L.J.M. was partially supported by the National Institutes of Health Grant DK046577.

Disclosure summary: P.M.S., A.C., and D.W. have an academic collaboration on GLP-1Rs with scientists at Eli Lilly. The authors receive no funding from Eli Lilly to support this work.

References

1. Reimann F. Molecular mechanisms underlying nutrient detection by incretin-secreting cells. *Int Dairy J.* 2010;20:236–242.
2. Baggio LL, Drucker DJ. Biology of incretins: GLP-1 and GIP. *Gastroenterology.* 2007;132:2131–2157.
3. Herrmann C, Goke R, Richter G, Fehmann HC, Arnold R, Goke B. Glucagon-like peptide-1 and glucose-dependent insulin-releasing polypeptide plasma levels in response to nutrients. *Digestion.* 1995; 56:117–126.
4. Drucker DJ, Philippe J, Mojsos S, Chick WL, Habener JF. Glucagon-like peptide I stimulates insulin gene expression and increases cyclic AMP levels in a rat islet cell line. *Proc Natl Acad Sci U S A.* 1987;84:3434–3438.
5. Orskov C, Holst JJ, Nielsen OV. Effect of truncated glucagon-like peptide-1 [proglucagon-(78–107) amide] on endocrine secretion from pig pancreas, antrum, and nonantral stomach. *Endocrinology.* 1988;123:2009–2013.
6. Li Y, Hansotia T, Yusta B, Ris F, Halban PA, Drucker DJ. Glucagon-like peptide-1 receptor signaling modulates β cell apoptosis. *J Biol Chem.* 2003;278:471–478.
7. Farilla L, Bulotta A, Hirshberg B, et al. Glucagon-like peptide 1 inhibits cell apoptosis and improves glucose responsiveness of freshly isolated human islets. *Endocrinology.* 2003;144:5149–5158.
8. Ling Z, Wu D, Zambre Y, et al. Glucagon-like peptide 1 receptor signaling influences topography of islet cells in mice. *Virchows Arch.* 2001;438:382–387.
9. Dunphy JL, Taylor RG, Fuller PJ. Tissue distribution of rat glucagon receptor and GLP-1 receptor gene expression. *Mol Cell Endocrinol.* 1998;141:179–186.
10. Larsen PJ, Tang-Christensen M, Jessop DS. Central administration of glucagon-like peptide-1 activates hypothalamic neuroendocrine neurons in the rat. *Endocrinology.* 1997;138:4445–4455.
11. During MJ, Cao L, Zuzga DS, et al. Glucagon-like peptide-1 receptor is involved in learning and neuroprotection. *Nat Med.* 2003;9: 1173–1179.
12. Nystrom T. The potential beneficial role of glucagon-like peptide-1 in endothelial dysfunction and heart failure associated with insulin resistance. *Horm Metab Res.* 2008;40:593–606.
13. Bose AK, Mocanu MM, Carr RD, Yellon DM. Myocardial ischaemia-reperfusion injury is attenuated by intact glucagon like peptide-1 (GLP-1) in the in vitro rat heart and may involve the p70s6K pathway. *Cardiovasc Drugs Ther.* 2007;21:253–256.
14. Gros R, You X, Baggio LL, et al. Cardiac function in mice lacking

- the glucagon-like peptide-1 receptor. *Endocrinology*. 2003;144:2242–2252.
15. Wettergren A, Schjoldager B, Mortensen PE, Myhre J, Christiansen J, Holst JJ. Truncated GLP-1 (proglucagon 78–107-amide) inhibits gastric and pancreatic functions in man. *Dig Dis Sci*. 1993;38:665–673.
 16. Young AA, Gedulin BR, Bhavsar S, et al. Glucose-lowering and insulin-sensitizing actions of exendin-4: studies in obese diabetic (ob/ob, db/db) mice, diabetic fatty Zucker rats, and diabetic rhesus monkeys (*Macaca mulatta*). *Diabetes*. 1999;48:1026–1034.
 17. Prigeon RL, Quddusi S, Paty B, D'Alessio DA. Suppression of glucose production by GLP-1 independent of islet hormones: a novel extrapancreatic effect. *Am J Physiol Endocrinol Metab*. 2003;285:E701–E707.
 18. Richter G, Feddersen O, Wagner U, Barth P, Goke R, Goke B. GLP-1 stimulates secretion of macromolecules from airways and relaxes pulmonary artery. *Am J Physiol*. 1993;265:L374–L381.
 19. Gutzwiller JP, Hruz P, Huber AR, et al. Glucagon-like peptide-1 is involved in sodium and water homeostasis in humans. *Digestion*. 2006;73:142–150.
 20. Montrose-Rafizadeh C, Avdonin P, Garant MJ, et al. Pancreatic glucagon-like peptide-1 receptor couples to multiple G proteins and activates mitogen-activated protein kinase pathways in Chinese hamster ovary cells. *Endocrinology*. 1999;140:1132–1140.
 21. Sonoda N, Imamura T, Yoshizaki T, Babendure JL, Lu JC, Olefsky JM. β -Arrestin-1 mediates glucagon-like peptide-1 signaling to insulin secretion in cultured pancreatic β cells. *Proc Natl Acad Sci USA*. 2008;105:6614–6619.
 22. Quoyer J, Longuet C, Broca C, et al. GLP-1 mediates antiapoptotic effect by phosphorylating Bad through a β -arrestin 1-mediated ERK1/2 activation in pancreatic β -cells. *J Biol Chem*. 2010;285:1989–2002.
 23. Holz GG. Epac: a new cAMP-binding protein in support of glucagon-like peptide-1 receptor-mediated signal transduction in the pancreatic β -cell. *Diabetes*. 2004;53:5–13.
 24. MacDonald PE, El-Kholy W, Riedel MJ, Salapatek AM, Light PE, Wheeler MB. The multiple actions of GLP-1 on the process of glucose-stimulated insulin secretion. *Diabetes*. 2002;51:S434–S442.
 25. Drucker DJ, Jin T, Asa SL, Young TA, Brubaker PL. Activation of proglucagon gene transcription by protein kinase-A in a novel mouse enteroendocrine cell line. *Mol Endocrinol*. 1994;8:1646–1655.
 26. Drucker DJ, Brubaker PL. Proglucagon gene expression is regulated by a cyclic AMP-dependent pathway in rat intestine. *Proc Natl Acad Sci USA*. 1989;86:3953–3957.
 27. Arnette D, Gibson TB, Lawrence MC, et al. Regulation of ERK1 and ERK2 by glucose and peptide hormones in pancreatic β cells. *J Biol Chem*. 2003;278:32517–32525.
 28. Buteau J, Foisy S, Rhodes CJ, Carpenter L, Biden TJ, Prentki M. Protein kinase C ζ activation mediates glucagon-like peptide-1-induced pancreatic β -cell proliferation. *Diabetes*. 2001;50:2237–2243.
 29. Park S, Dong X, Fisher TL, et al. Exendin-4 uses Irs2 signaling to mediate pancreatic β cell growth and function. *J Biol Chem*. 2006;281:1159–1168.
 30. Khoo S, Griffen SC, Xia Y, Baer RJ, German MS, Cobb MH. Regulation of insulin gene transcription by ERK1 and ERK2 in pancreatic β cells. *J Biol Chem*. 2003;278:32969–32977.
 31. Buteau J, Foisy S, Joly E, Prentki M. Glucagon-like peptide 1 induces pancreatic β -cell proliferation via transactivation of the epidermal growth factor receptor. *Diabetes*. 2003;52:124–132.
 32. Farilla L, Hui H, Bertolotto C, et al. Glucagon-like peptide-1 promotes islet cell growth and inhibits apoptosis in Zucker diabetic rats. *Endocrinology*. 2002;143:4397–4408.
 33. Holz GG, Kuhlreiter WM, Habener JF. Pancreatic β -cells are rendered glucose-competent by the insulinotropic hormone glucagon-like peptide-1(7–37). *Nature*. 1993;361:362–365.
 34. Syme CA, Zhang L, Bisello A. Caveolin-1 regulates cellular trafficking and function of the glucagon-like peptide 1 receptor. *Mol Endocrinol*. 2006;20:3400–3411.
 35. Drucker DJ, Nauck MA. The incretin system: glucagon-like peptide-1 receptor agonists and dipeptidyl peptidase-4 inhibitors in type 2 diabetes. *Lancet*. 2006;368:1696–1705.
 36. Nauck M, Frid A, Hermansen K, Shah NS, et al. Efficacy and safety comparison of liraglutide, glimepiride, and placebo, all in combination with metformin, in type 2 diabetes: the LEAD (liraglutide effect and action in diabetes)-2 study. *Diabetes Care*. 2009;32:84–90.
 37. Robles GI, Singh-Franco D. A review of exenatide as adjunctive therapy in patients with type 2 diabetes. *Drug Des Dev Ther*. 2009;3:219–240.
 38. Cure P, Pileggi A, Alejandro R. Exenatide and rare adverse events. *N Engl J Med*. 2008;358:1969–1970; discussion 1971–1962.
 39. Singh S, Chang HY, Richards TM, Weiner JP, Clark JM, Segal JB. Glucagonlike peptide 1-based therapies and risk of hospitalization for acute pancreatitis in type 2 diabetes mellitus: a population-based matched case-control study. *JAMA Intern Med*. 2013;173:534–539.
 40. Knudsen LB, Kiel D, Teng M, et al. Small-molecule agonists for the glucagon-like peptide 1 receptor. *Proc Natl Acad Sci USA*. 2007;104:937–942.
 41. Sloop KW, Willard FS, Brenner MB, et al. Novel small molecule glucagon-like peptide-1 receptor agonist stimulates insulin secretion in rodents and from human islets. *Diabetes*. 2010;59:3099–3107.
 42. Chen D, Liao J, Li N, et al. A nonpeptidic agonist of glucagon-like peptide 1 receptors with efficacy in diabetic db/db mice. *Proc Natl Acad Sci USA*. 2007;104:943–948.
 43. Overington JP, Al-Lazikani B, Hopkins AL. How many drug targets are there? *Nat Rev Drug Discov*. 2006;5:993–996.
 44. Kenakin T. Functional selectivity and biased receptor signaling. *J Pharmacol Exp Ther*. 2011;336:296–302.
 45. Koole C, Wootten D, Simms J, et al. Allosteric ligands of the glucagon-like peptide 1 receptor (GLP-1R) differentially modulate endogenous and exogenous peptide responses in a pathway-selective manner: Implications for drug screening. *Mol Pharmacol*. 2010;78:456–465.
 46. Willard FS, Wootten D, Showalter AD, et al. Small molecule allosteric modulation of the glucagon-like peptide-1 receptor enhances the insulinotropic effect of oxyntomodulin. *Mol Pharmacol*. 2012;82:1066–1073.
 47. Wootten D, Savage EE, Willard FS, et al. Differential activation and modulation of the glucagon-like peptide-1 receptor by small molecule ligands. *Mol Pharmacol*. 2013;83:822–834.
 48. Kenakin T, Watson C, Muniz-Medina V, Christopoulos A, Novick S. A simple method for quantifying functional selectivity and agonist bias. *ACS Chem Neurosci*. 2012;3:193–203.
 49. Black JW, Leff P. Operational models of pharmacological agonism. *Proc R Soc Lond B Biol Sci*. 1983;220:141–162.
 50. Wootten D, Simms J, Miller LJ, Christopoulos A, Sexton PM. Polar transmembrane interactions drive formation of ligand-specific and signal pathway-biased family B G protein-coupled receptor conformations. *Proc Natl Acad Sci USA*. 2013;110:5211–5216.
 51. Schelshorn D, Joly F, Mutel S, et al. Lateral allostereism in the glucagon receptor family: glucagon-like peptide 1 induces G-protein-coupled receptor heteromer formation. *Mol Pharmacol*. 2012;81:309–318.
 52. Wootten D, Savage EE, Valant C, May LT, et al. Allosteric modulation of endogenous metabolites as an avenue for drug discovery. *Mol Pharmacol*. 2012;82:281–290.
 53. Mapelli C, Natarajan SI, Meyer JP, et al. Eleven amino acid glucagon-like peptide-1(7–37) analogs with varying degrees of insulinotropic activity.

- gon-like peptide-1 receptor agonists with antidiabetic activity. *J Med Chem*. 2009;52:7788–7799.
54. Coopman K, Huang Y, Johnston N, Bradley SJ, Wilkinson GF, Willars GB. Comparative effects of the endogenous agonist glucagon-like peptide-1 (GLP-1)-(7–36) amide and the small-molecule ago-allosteric agent “compound 2” at the GLP-1 receptor. *J Pharmacol Exp Ther*. 2010;334:795–808.
55. Monod J, Changeux JP, Jacob F. Allosteric proteins and cellular control systems. *J Mol Biol*. 1963;6:306–329.
56. Monod J, Wyman J, Changeux JP. On the nature of allosteric transitions: a plausible model. *J Mol Biol*. 1965;12:88–118.
57. Canals M, Sexton PM, Christopoulos A. Allosterism in GPCRs: ‘MWC’ revisited. *Trends Biochem Sci*. 2011;36(12):663–672.
58. Keov P, Sexton PM, Christopoulos A. Allosteric modulation of G protein-coupled receptors: a pharmacological perspective. *Neuropharmacology*. 2011;60:24–35.
59. Wootten D, Simms J, Koole C, et al. Modulation of the glucagon-like peptide-1 receptor signaling by naturally occurring and synthetic flavonoids. *J Pharmacol Exp Ther*. 2011;336:540–550.
60. Price MR, Baillie GL, Thomas A, et al. Allosteric modulation of the cannabinoid CB1 receptor. *Mol Pharmacol*. 2005;68:1484–1495.
61. Maillet EL, Pellegrini N, Valant C, et al. A novel, conformation-specific allosteric inhibitor of the tachykinin NK2 receptor (NK2R) with functionally selective properties. *FASEB J*. 2007;21:2124–2134.
62. Irwin N, Flatt PR, Patterson S, Green BD. Insulin-releasing and metabolic effects of small molecule GLP-1 receptor agonist 6,7-dichloro-2-methylsulfonyl-3-N-tert-butylaminoquinoxaline. *Eur J Pharmacol*. 2010;628:268–273.
63. DeFronzo RA. Pathogenesis of type 2 (non-insulin dependent) diabetes mellitus: a balanced overview. *Diabetologia*. 1992;35:389–397.
64. Li N, Lu J, Willars GB. Allosteric modulation of the activity of the glucagon-like peptide-1 (GLP-1) metabolite GLP-1 9–36 amide at the GLP-1 receptor. *PLoS ONE*. 2012;7:e47936.
65. Rondard P, Goudet C, Kniazeff J, Pin JP, Prezeau L. The complexity of their activation mechanism opens new possibilities for the modulation of mGlu and GABAB class C G protein-coupled receptors. *Neuropharmacology*. 2011;60:82–92.
66. Ding WQ, Cheng ZJ, McElhiney J, Kuntz SM, Miller LJ. Silencing of secretin receptor function by dimerization with a misspliced variant secretin receptor in ductal pancreatic adenocarcinoma. *Cancer Res*. 2002;62:5223–5229.
67. Whitaker GM, Lynn FC, McIntosh CH, Accili EA. Regulation of GIP and GLP1 receptor cell surface expression by N-glycosylation and receptor heteromerization. *PLoS ONE*. 2012;7:e32675.
68. Harikumar KG, Morfis MM, Lisenbee CS, Sexton PM, Miller LJ. Constitutive formation of oligomeric complexes between family B G protein-coupled vasoactive intestinal polypeptide and secretin receptors. *Mol Pharmacol*. 2006;69:363–373.
69. Harikumar KG, Wootten D, Pinon DI, et al. Glucagon-like peptide-1 receptor dimerization differentially regulates agonist signaling but does not affect small molecule allosterism. *Proc Natl Acad Sci USA*. 2012;109:18607–18612.
70. Harikumar KG, Ball AM, Sexton PM, Miller LJ. Importance of lipid-exposed residues in transmembrane segment four for family B calcitonin receptor homo-dimerization. *Regul Pept*. 2010;164:113–119.
71. Harikumar KG, Pinon DI, Miller LJ. Transmembrane segment IV contributes a functionally important interface for oligomerization of the class II G protein-coupled secretin receptor. *J Biol Chem*. 2007;282:30363–30372.
72. Brown EM, Gamba G, Riccardi D, et al. Cloning and characterization of an extracellular Ca(2+)-sensing receptor from bovine parathyroid. *Nature*. 1993;366:575–580.
73. Brown EM. The calcium-sensing receptor (CaR) and its disorders. *Hormones (Athens)*. 2002;1:10–21.
74. Brown EM. The calcium-sensing receptor: physiology, pathophysiology and CaR-based therapeutics. *Subcell Biochem*. 2007;45:139–167.
75. Schipani E, Kruse K, Juppner H. A constitutively active mutant PTH-PTHrP receptor in Jansen-type metaphyseal chondrodysplasia. *Science*. 1995;268:98–100.
76. Schipani E, Langman CB, et al. Constitutively activated receptors for parathyroid hormone and parathyroid hormone-related peptide in Jansen’s metaphyseal chondrodysplasia. *N Engl J Med*. 1996;335:708–714.
77. Schipani E, Jensen GS, Pincus J, Nissenson RA, Gardella TJ, Juppner H. Constitutive activation of the cyclic adenosine 3’,5’-monophosphate signaling pathway by parathyroid hormone (PTH)/PTH-related peptide receptors mutated at the two loci for Jansen’s metaphyseal chondrodysplasia. *Mol Endocrinol*. 1997;11:851–858.
78. Hager J, Hansen L, Vaisse C, et al. A missense mutation in the glucagon receptor gene is associated with non-insulin-dependent diabetes mellitus. *Nat Genet*. 1995;9:299–304.
79. Siani A, Iacone R, Russo O, et al. Gly40Ser polymorphism of the glucagon receptor gene is associated with central adiposity in men. *Obes Res*. 2001;9:722–726.
80. Beinborn M, Worrall CL, McBride EW, Kopin AS. A human glucagon-like peptide-1 receptor polymorphism results in reduced agonist responsiveness. *Regul Pept*. 2005;130:1–6.
81. Tokuyama Y, Matsui K, Egashira T, Nozaki O, Ishizuka T, Kanatsuka A. Five missense mutations in glucagon-like peptide 1 receptor gene in Japanese population. *Diabetes Res Clin Pract*. 2004;66:63–69.
82. Fortin JP, Schroeder JC, Zhu Y, Beinborn M, Kopin AS. Pharmacological characterization of human incretin receptor missense variants. *J Pharmacol Exp Ther*. 2010;332:274–280.
83. Koole C, Wootten D, Simms J, et al. Polymorphism and ligand dependent changes in human glucagon-like peptide-1 receptor (GLP-1R) function: allosteric rescue of loss of function mutation. *Mol Pharmacol*. 2011;80:486–497.
84. Koole C, Wootten D, Simms J, et al. Second extracellular loop of human glucagon-like peptide-1 receptor (GLP-1R) differentially regulates orthosteric but not allosteric agonist binding and function. *J Biol Chem*. 2012;287:3659–3673.
85. Hoare SR. Mechanisms of peptide and nonpeptide ligand binding to class B G-protein-coupled receptors. *Drug Discov Today*. 2005;10:417–427.
86. Newton CL, Whay AM, McArdle CA, et al. Rescue of expression and signaling of human luteinizing hormone G protein-coupled receptor mutants with an allosterically binding small-molecule agonist. *Proc Natl Acad Sci USA*. 2011;108:7172–7176.
87. White E, McKenna J, Cavanaugh A, Breitwieser GE. Pharmacochaperone-mediated rescue of calcium-sensing receptor loss-of-function mutants. *Mol Endocrinol*. 2009;23:1115–1123.
88. Huang Y, Breitwieser GE. Rescue of calcium-sensing receptor mutants by allosteric modulators reveals a conformational checkpoint in receptor biogenesis. *J Biol Chem*. 2007;282:9517–9525.
89. Kenakin T, Christopoulos A. Signalling bias in new drug discovery: detection, quantification and therapeutic impact. *Nat Rev Drug Discov*. 2012;12:205–216.

STRUCTURAL BIOLOGY

Meet the B family

The first crystal structures of class B G-protein-coupled receptors have been solved. They reveal features that might inform drug-development strategies for diseases ranging from osteoporosis to diabetes.

PATRICK M. SEXTON & DENISE WOOTTEN

G-protein-coupled receptors (GPCRs) are the largest group of cell-surface receptors and are major targets for drug development^{1,2}. These proteins are characterized by a common architecture of seven transmembrane-spanning helical domains, and can be subdivided into three main groups: classes A, B and C. High-resolution structures of the membrane-spanning domain of GPCRs — the conduit for transmission of extracellular signals to the inside of a cell — provide snapshots that indicate how activating and inactivating ligands modify the receptor structure. Until now, however, such studies have been principally restricted to class A receptors. In papers published on *Nature's* website today, Hollenstein *et al.*³ and Siu *et al.*⁴ present the structures of the transmembrane domains of two class B members: corticotrophin-releasing factor-1 receptor and

the glucagon receptor, respectively.

Class B GPCRs include receptors for several peptide hormones, which are involved in a host of physiological functions from bone maintenance and glucose regulation to immune function and pain transmission. As a result, these receptors are targets for existing drugs that treat several disorders, including osteoporosis and type 2 diabetes, and are being actively pursued as targets for treating many more, from obesity and migraine to depression and chronic obstructive pulmonary disease.

Hollenstein and colleagues present a 3.0-ångström-resolution structure of the corticotrophin-releasing factor-1 receptor (CRF₁R) in complex with a small-molecule inhibitor. They arrived at this structure by introducing 12 thermostabilizing mutations into this GPCR and inserting the protein T4 lysozyme into its second intracellular loop. Siu and co-workers produced their 3.4-Å-resolution structure of the glucagon receptor (GCGR)

using a version of the protein that was largely unmodified, except that its amino-terminal domain had been replaced with a thermally stabilized protein. The native N-terminal domain of class B GPCRs is crucial for peptide binding, but both teams removed this region to aid crystallization of the proteins.

As predicted, the core of both structures features seven transmembrane helices (TM1–TM7). However, although the relative positions of these helices at the intracellular face of the proteins overlap with those in class A GPCRs, there is substantial deviation between the two classes at the extracellular face. In both class B proteins, there are differences in the positioning of TM6 and TM7 that result in TM6 being shifted away from TM5, with TM1 seeming to move in parallel with TM7. This results in a wider and deeper extracellular cavity in the receptor core of the class B proteins that presumably forms part of the peptide-binding site. In addition, there are differences between the CRF₁R and GCGR structures themselves, in the upper segments of TM6 and TM7 (Fig. 1). Although it is unclear whether these differences were influenced by the crystallization process, they indicate that the solution of transmembrane-core structures for other class B receptors will be required to help us understand how ligands bind and activate these proteins.

A major obstacle for the therapeutic targeting of class B receptors has been their notorious intractability for the identification of small-molecule ligands, in particular, small-molecule activators. The new structures shed light on why this is so: the openness of the receptors' binding pocket makes it difficult for a small ligand to engage sufficient key amino-acid residues to initiate activation of the receptor. Nonetheless, the solved structures show distinct subpockets that could represent sites for structure-based drug design.

Intriguingly, Hollenstein and colleagues' structure shows that the small-molecule inhibitor binds to a very deep pocket in the intracellular half of the CRF₁R core. This ligand forms extensive contacts with residues in TM3, TM5 and TM6, and presumably inhibits receptor activation by tethering the cytoplasmic half of TM6 to TM3 and TM5, thereby restricting conformational rearrangement of the intracellular face. This represents a new target for the design of small-molecule ligands. However, the amino-acid side chains in the equivalent region in the GCGR structure are more compact and would require reorganization to allow similarly sized ligands to bind.

The evolutionarily conserved amino-acid motifs in class A receptors have an important role in maintaining the receptors in an inactive (or weakly active) state. Although the

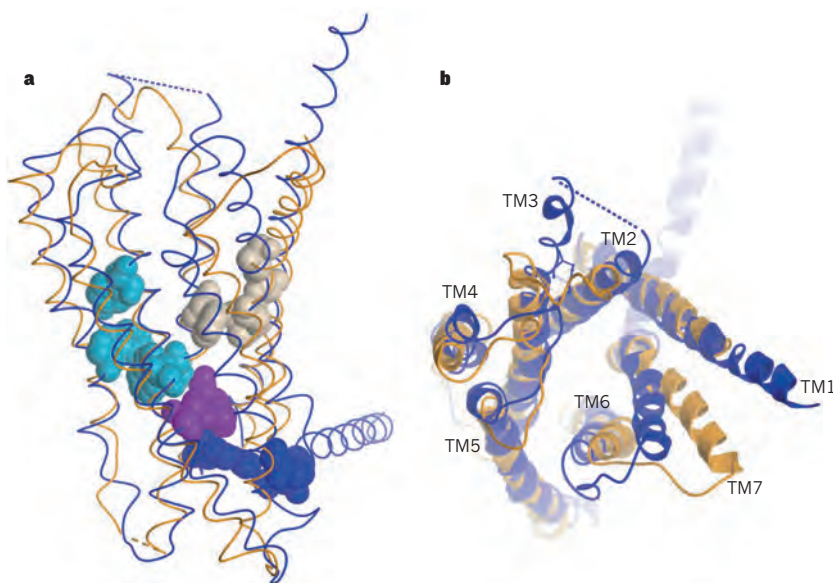


Figure 1 | Structural features of class B GPCRs. Hollenstein *et al.*³ and Siu *et al.*⁴ present the crystal structures of two class B G-protein-coupled receptors: CRF₁R (orange ribbons) and GCGR (blue ribbons), respectively. **a**, The structures reveal the locations of conserved amino-acid residues that form similar interactions in the two receptors, including between the transmembrane helices TM2, TM3 and TM4 (cyan), TM2 and TM3 (purple), TM1, TM2 and TM7 (beige), and TM2 and TM6 with the intracellular helix 8 (blue). **b**, The view of the proteins from outside the cell highlights the differences between the two structures at their extracellular faces, particularly in TM6 and TM7.

intracellular face of the class B receptors is similar to that seen for class A proteins (with the exception of an inward shift of TM7), some of the interactions that maintain the inactive class A conformations (including the ionic lock that tethers the cytoplasmic half of TM3 to TM6, the CWXP motif in TM6 and the NPXXY motif in TM7) are not present in the two class B receptors studied.

Class B receptors also have a distinct pattern of conserved amino-acid motifs that are important for maintenance of the inactive conformation and/or for conformational transitions required for activation. The CRF₁R and GCGR structures suggest conserved interactions between some of these key residues (Fig. 1). In addition, similar regions of contact are present between TM1 and TM2, TM1 and TM7, TM3

and TM4, and TM3 and TM6 in structures of both class A and B, although these interactions are mediated by different patterns of residues in each class. Thus, the new structures suggest that the two classes of proteins use distinct mechanisms for conformational control.

Although these reports represent a tremendous breakthrough in GPCR biology, as with all crystal structures, the intramembranous class B structures provide only a snapshot of the receptors, which in reality are known (from cysteine-trapping studies⁵) to be highly dynamic proteins. Important questions remain about the final orientations of the N-terminal domains and transmembrane helices of the receptors, and about how natural activator molecules engage with both domains to activate the receptors. Answering these questions

will require both crystallization of an intact ligand–receptor–G-protein complex and studies of receptor dynamics. ■

Patrick M. Sexton and Denise Wootten are at the Monash Institute of Pharmaceutical Sciences, Monash University, Parkville 3052, Victoria, Australia.

e-mails: patrick.sexton@monash.edu; denise.wootten@monash.edu

1. Fredriksson, R., Lagerström, M. C., Lundin, L. G. & Schiöth, H. B. *Mol. Pharmacol.* **63**, 1256–1272 (2003).
2. Overington, J. P., Al-Lazikani, B. & Hopkins, A. L. *Nature Rev. Drug Discov.* **5**, 993–996 (2006).
3. Hollenstein, K. *et al. Nature* <http://dx.doi.org/10.1038/nature12357> (2013).
4. Siu, F. Y. *et al. Nature* <http://dx.doi.org/10.1038/nature12393> (2013).
5. Dong, M. *et al. FASEB J.* **26**, 5092–5105 (2012).

Allostery and Biased Agonism at Class B G Protein-Coupled Receptors

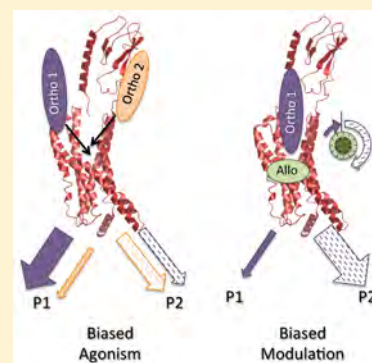
Denise Wootten,^{*,†} Laurence J. Miller,^{*,‡} Cassandra Koole,^{†,§} Arthur Christopoulos,[†] and Patrick M. Sexton^{*,†}

[†]Drug Discovery Biology and Department of Pharmacology, Monash Institute of Pharmaceutical Sciences, Monash University, Parkville 3052, Victoria, Australia

[‡]Department of Molecular Pharmacology and Experimental Therapeutics, Mayo Clinic, Scottsdale, Arizona 85259, United States

[§]Laboratory of Chemical Biology and Signal Transduction, The Rockefeller University, New York, New York 10065, United States

ABSTRACT: Class B G protein-coupled receptors (GPCRs) respond to paracrine or endocrine peptide hormones involved in control of bone homeostasis, glucose regulation, satiety, and gastro-intestinal function, as well as pain transmission. These receptors are targets for existing drugs that treat osteoporosis, hypercalcaemia, Paget's disease, type II diabetes, and obesity and are being actively pursued as targets for numerous other diseases. Exploitation of class B receptors has been limited by difficulties with small molecule drug discovery and development and an under appreciation of factors governing optimal therapeutic efficacy. Recently, there has been increasing awareness of novel attributes of GPCR function that offer new opportunity for drug development. These include the presence of allosteric binding sites on the receptor that can be exploited as drug binding pockets and the ability of individual drugs to enrich subpopulations of receptor conformations to selectively control signaling, a phenomenon termed biased agonism. In this review, current knowledge of biased signaling and small molecule allostery within class B GPCRs is discussed, highlighting areas that have progressed significantly over the past decade, in addition to those that remain largely unexplored with respect to these phenomena.



CONTENTS

1. Introduction	111
2. Allostery and Biased Agonism	112
2.1. Allostery	112
2.2. Biased Agonism	114
2.3. Intersection between Bias and Allostery	114
2.4. Quantification of Allostery and Bias	115
3. Class B GPCRs	115
3.1. Structural Classification	115
3.2. Signaling Pleiotropy	115
3.3. Receptor Dimerization	116
4. Class B GPCR Biased Agonism	117
4.1. Secretin Receptor	117
4.2. Receptors for PTH	117
4.3. Receptors for PACAP and VIP	118
4.4. Receptors for CT, amylin, CGRP, and adrenomedullin	119
4.5. Receptors for Glucagon, GLP-1, GLP-2, and GIP	120
4.5.1. GLP-1 Receptor	120
4.5.2. Nonpeptidic-Biased Agonism at the GLP-1 Receptor	121
4.5.3. GLP-2 Receptor	122
4.5.4. GIP Receptor	122
4.5.5. Glucagon Receptor	122
4.6. GHRH Receptor	123

4.7. CRF Receptors	124
5. Mechanistic Studies of Biased Agonism	124
6. Allosteric Modulation of Class B GPCRs	126
7. Summary/Conclusion/Future Directions	128
Author Information	128
Corresponding Authors	128
Notes	129
Biographies	129
Acknowledgments	129
References	129

1. INTRODUCTION

Class B G protein-coupled receptors (GPCRs) respond to paracrine or endocrine peptide hormones involved in the physiology or pathophysiology of bone homeostasis, glucose regulation, satiety and gastro-intestinal function, as well as pain transmission. As a result, these receptors are targets for existing drugs that treat osteoporosis, hypercalcaemia, Paget's disease, type II diabetes, and obesity and are being actively pursued as targets for migraine, depression and anxiety, irritable bowel syndrome/Crohn's disease, cancer and pancreatic cancer

Special Issue: G-Protein Coupled Receptors

Received: January 19, 2016

Published: April 4, 2016

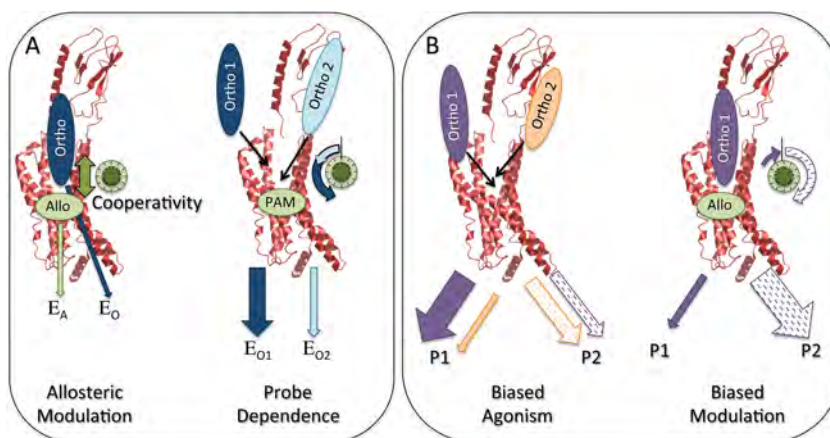


Figure 1. Overview of allosteric modulation and biased signaling. (A) Allosteric interactions. (Left-hand panel) Orthosteric (Ortho) and allosteric (Allo) ligands can bind to the free receptor and each may have its own intrinsic efficacy (E_O and E_A , respectively). However, as these bind to topographically distinct sites, they can also bind concomitantly to yield cooperative effects (depicted by the rheostat). Allosteric interactions can be positive (positive allosteric modulator, PAM), negative (negative allosteric modulator, NAM), or neutral (neutral allosteric ligand, NAL). (A, right-hand panel) The concept of probe dependence. As individual ligands bind with different chemical contacts (even if they share an overlapping binding site), there is the potential for the same allosteric modulator to have an orthosteric-ligand specific effect (and vice versa). Depicted are 2 orthosteric ligands (Ortho 1, Ortho 2) with probe-dependent effects of a positive modulator (PAM). In this example, the PAM increases the efficacy of Ortho 1 (E_{O1}) to a greater extent than it does for Ortho 2 (E_{O2}); the potential for opposite effects on orthosteric ligand efficacy (i.e., PAM vs NAM) also exists. (B) Biased agonism. (Left-hand panel) Two chemically distinct orthosteric agonists, Ortho 1 and Ortho 2, can bind to the receptor in a competitive manner. A comparison of two signaling pathways, P1 and P2, reveals that Ortho 1 has greater efficacy in stimulating P1, relative to P2, whereas Ortho 2 displays the opposite pattern of effect. The differential stimulation of the two pathways can result in distinct cellular function. (Right-hand panel) An example of biased allosteric modulation, with interaction between the allosteric modulator and Ortho 1 changing the quality of the signal, increasing signaling from P2, while decreasing signaling from P1.

diagnostics.^{1–7} These diseases represent major global health burdens; however, the exploitation of class B receptors has been limited by difficulties with small molecule drug discovery and development and an under appreciation of factors governing optimal therapeutic efficacy. Recently, there has been increasing awareness of novel attributes of GPCR function that offer new opportunity for drug development. These include the presence of allosteric (topographically distinct) binding sites on the receptor, in addition to the classic orthosteric (endogenous ligand) binding site, which can be exploited as drug binding pockets, and the ability of individual drugs to enrich subpopulations of receptor conformations to selectively control signaling, a phenomenon termed biased agonism.^{8–11} These two phenomena, summarized in Figure 1, are particularly relevant to peptide hormone class B GPCR drug discovery as these receptors are pleiotropically coupled (Table 1) and have broad, diffuse pharmacophores that are not readily mimicked by small molecule drugs. In this review, the present knowledge of biased signaling and small molecule allostery within class B GPCRs is discussed, highlighting areas that have progressed significantly over the past decade, in addition to those that remain largely unexplored with respect to these phenomena.

2. ALLOSTERY AND BIASED AGONISM

2.1. Allostery

GPCRs are natural allosteric proteins that translate extracellular binding events to activation of intracellular effectors via conformational rearrangements, enabling the engagement of effectors, classically G proteins. As such, modulation of the conformational landscape, be it via additional protein–protein interactions or via interaction with drugs, can alter the way the receptor responds to its endogenous ligand(s).

The orthosteric binding site of a protein is defined as the canonical binding site of the recognized natural ligand of the

receptor.¹² For many class A GPCRs, including those for the biogenic amines, this site is located within the transmembrane (TM) core of the receptor, however, the location of the orthosteric site can vary greatly between different subclasses of GPCRs and has been localized to different positions within the TM bundle, within the extracellular domain of the receptor or in the interface between these domains. Indeed, the nature of the access and egress from the orthosteric site can vary; while some pockets are accessible via free diffusion, others are located deeper within the receptor core and entry to these may be via the lipid bilayer or via an extracellular vestibule that forms an intermediate binding site.

Allosteric binding sites are spatially distinct from the orthosteric ligand-binding site, such that the potential exists for orthosteric and allosteric ligands to bind simultaneously. Each of these ligands can interact with the free receptor and will have characteristic properties when bound, including an affinity for the receptor and varying degrees of efficacy for activation of effector proteins or recruitment of regulatory proteins (Figure 1A). However, the ability of an orthosteric and an allosteric ligand to cobind allows each of the ligands to influence the behavior of the other, and this effect is termed cooperativity.^{8,10,13} This cooperative effect can be on the affinity of the ligand or on the efficacy of the ligand to alter signaling of the receptor. Moreover, effects on binding are reciprocal between the orthosteric and allosteric ligands. In effect, the binding of an allosteric ligand changes the conformational landscape of the receptor such that it can be considered a unique receptor. Positive allosteric modulators (PAMs) produce a net enhanced effect on the receptor function, while PAMs with intrinsic activity are termed PAM-agos; negative allosteric modulators (NAMs) reduce receptor function, while neutral allosteric ligands (NALs) bind the allosteric site on the receptor but do not alter receptor function.¹³

Table 1. Summary of Class B GPCRs. Adapted from Bortolato et al.,¹ Culhane et al.,⁷ Hoare et al.,⁹⁶ and Archbold et al.²⁸³

Receptor	Functional Composition	Receptor Interactions (non-essential)	Receptor Variants	Splice	Endogenous Ligands	Major Signaling Pathways	Main Function	Physiological	Main Relevance	Pathological	Examples of Exogenous Ligands/Small Molecule Ligands
Secretin receptor	SecR	RAMP3			Secretin	cAMP, Ca^{2+} , β -arrestins	Pancreatic secretion	Duodenal Gastrinoma	ulcers		RG-1068 (synthetic secretin)
Parathyroid Hormone 1 receptor	PTH1R	RAMP2			PTH PTH-related protein (PTHrP)	cAMP, Ca^{2+} , β -catenin, CREB, PLC, ERK1/2, Activation of voltage gated Ca^{2+} channels	Phosphate excretion Calcium homeostasis Cytokine secretion Development	Osteoporosis Hyperparathyroidism			Teriparatide, Procs. AH-3960, SW106 (D-Trp ²⁵), Tyr ²⁵ PTH(7-34), PTH(1-84), PTHrP(1-34), PTHrP(1-34), PTHrP(1-36), PTHrP(1-74), PTHrP(1-84), PTHrP(107-111), PTH(1-34)
Parathyroid Hormone 2 receptor	PTH2R	RAMP3			PTH Tuberoinsular residues (TIP39)		Hypothalamic secretion Nociception		Nociception		
Vasoactive Intestinal Polypeptide receptor 1	VPAC1	RAMP1 RAMP2 RAMP3			VIP PACAP-27 PACAP-38		Vasodilation Neurotransmission Neuroendocrine regulation Smooth muscle relaxation	Inflammation Neurodegeneration			VIP(Aia ¹ , Ala ²⁷ , Ala ²⁸) analogs Ro25-1553, cyclic analogs of VIP, Bay55-9837
Vasoactive Intestinal Polypeptide receptor 2	VPAC2					cAMP, IP, Ca^{2+}					
Pituitary Adenylate Cyclase-Activating Polypeptide type 1 receptor	PAC1		Short variant "Hip" variant "Hap" variant Sequence changes in TM2/TM4		PACAP-27 PACAP-38 VIP		Neurotransmission Neuroendocrine regulation	Neurodegeneration Nociception			Maxadilan
Calcitonin receptor	CTR				Calcitonin Amylin α -CGRP β -CGRP Adrenomedullin-2 Adrenomedullin Calcitonin α -CGRP β -CGRP Adrenomedullin-2 Adrenomedullin		Calcium homeostasis	Osteoporosis			Miacalcin, Fortical, SUN B8155, pyrazolopyridine-based CTR agonists
Amylin receptor 1 (AMY1)	CTR + RAMP1										
Amylin receptor 2 (AMY2)	CTR + RAMP2			CTRa (insert -ve) CTRb (insert +ve)		cAMP, Ca^{2+} , PKA, PKC					Pramlintide (synthetic amylin)
Amylin receptor 3 (AMY3)	CTR + RAMP3				Amylin Calcitonin Calcitonin β -Amyloid α -CGRP β -CGRP Adrenomedullin Adrenomedullin-2		Energy homeostasis	Diabetes Obesity			
Calcitonin Receptor-Like receptor	CLR	N/A	N/A		N/A	N/A	N/A	N/A	N/A		N/A
Calcitonin Receptor-Related Peptide	CLR+RAMP1	RCP			α -CGRP β -CGRP Adrenomedullin Adrenomedullin-2 amylin calcitonin	cAMP, Ca^{2+} , MAPK	Vasodilation	Migraine			Telcagepant, olcegepant, MK-2918, MK-3207
Adrenomedullin receptor 1 (AM1)	CLR+RAMP2										adrenomedullin(13-52), adrenomedullin PEGylated
Adrenomedullin receptor 2 (AM2)	CLR+RAMP3									Cardiovascular disease	adrenomedullin(13-52)
Glucagon receptor	GCGR	RAMP2			glucagon oxyntomodulin	cAMP, Ca^{2+} , PLC, PKA, ERK1/2, Wnt, β -catenin	Energy homeostasis Insulin and glucagon regulation	Diabetes Obesity			TH-glucagon, NNC0640
Glucagon-Like Peptide-1 receptor	GLP-1R				GLP-1 oxyntomodulin	cAMP, Ca^{2+} , PLC, PKA, ERK1/2, GRKs, β -arrestins					GLP-1 analogs, exendin-4, liraglutide, 11-mer peptides (e.g. BMS21), TT15, Boc5, BETP/compound B, NN compound 2, P5, (S)-9b, flavonols
Glucagon-Like Peptide-2 receptor	GLP-2R				GLP-2	cAMP, Ca^{2+} , cfos, cjun, junB, zif248, p70S6 kinase, inhibition of ERK1/2	Gut mucosal growth Epithelial cell proliferation	Bowel diseases			Teduglutide, ZP1848, 2-[(2Z)-2-(2,3-dichloroheptan-3-yl)-2-(hydroxymino)ethyl]sulfanybenzoate
Gastric Inhibitory Polypeptide receptor	GIPR				GIP	cAMP, Ca^{2+} , PI3K, PKA, Akt, p38 MAPK, phospholipase A2, GRK2, β -arrestin-1	Energy homeostasis Insulin regulation	Diabetes Obesity			GIP analogs (e.g. D-Ala ² -GIP (1-30)), N-acGIP(Lys ² MYR), N-AcGIP(Lys ² MYR) and N-AcGIP(LysPAL ²), [Pro ²]-GIP
Growth-Releasing Hormone receptor	GHRHR				GHRH	cAMP, Ca^{2+} , PLC, PKA, phosphorylation of CREB, ERK1/2, Akt	Regulation of growth Metabolism of carbohydrates, protein, and lipids	Dwarfism			GHRH analogs, [Dat1, Gln8, Orn12,21, Abu15, Nle27, Asp28, Arg29]hGHRH(1-29)
Corticotropin-Releasing Receptor 1	Factor CRF1R	RAMP2		CRF1a CRF1b CRF1c CRF1d CRF1e CRF1f CRF1g CRF1h	CRF Urocortin-1	cAMP, Ca^{2+} , PLC, PKC, β -arrestin-2	Stress response	Stress inflammation			Corticotropin, Pexacerfont, Bpa pr, Nal urocortin analogs, CP-376395
Corticotropin-Releasing Receptor 2	Factor CRF2R			CRF2a CRF2b CRF2c	CRF Urocortin-1 Urocortin-2 Urocortin-3		Stress response Cardiac contractility	Heart failure hypertension			

In the context of drug discovery, allosteric ligands offer both opportunities and challenges. These have been reviewed in detail elsewhere,^{8,13–17} so they are only briefly summarized below. As allosteric sites are generally less conserved than orthosteric sites, there is the potential for these to present novel pockets for drug development, often with greater subtype selectivity than drugs targeting the conserved orthosteric binding site. Allosteric drugs can also provide mechanism-based safety in overdose, as the magnitude of the on-target drug effect is limited by the cooperativity, regardless of drug concentration. However, the effect of an allosteric drug will be specific to the orthosteric ligand present, a phenomenon termed “probe dependence”.¹⁶ This is of particular importance for class B GPCRs, where many receptors respond to multiple endogenous ligands, including, glucagon-like peptide-1 (GLP-1), oxyntomodulin, and glucagon for the GLP-1 receptor, and

parathyroid hormone (PTH) and PTH-related protein (PTHrP) for the PTH1 receptor, as examples. As such, the response of an allosteric drug will depend not only on the intrinsic affinity and efficacy of the drug but also on the nature of cooperativity of the drug with each of the endogenous ligands and the concentrations of ligands at the site of action. Furthermore, the quality of the orthosteric drug response can change with the cooperative effects often varying across different effector and regulatory pathways, with the exception of the simplest cases where cooperativity follows the “two-state” characteristics of the classic Monod, Wyman, and Changeux model.¹⁴ These latter properties create significant challenges for allosteric drug discovery but nonetheless provide an unprecedented opportunity to sculpt cellular response for therapeutic benefit.

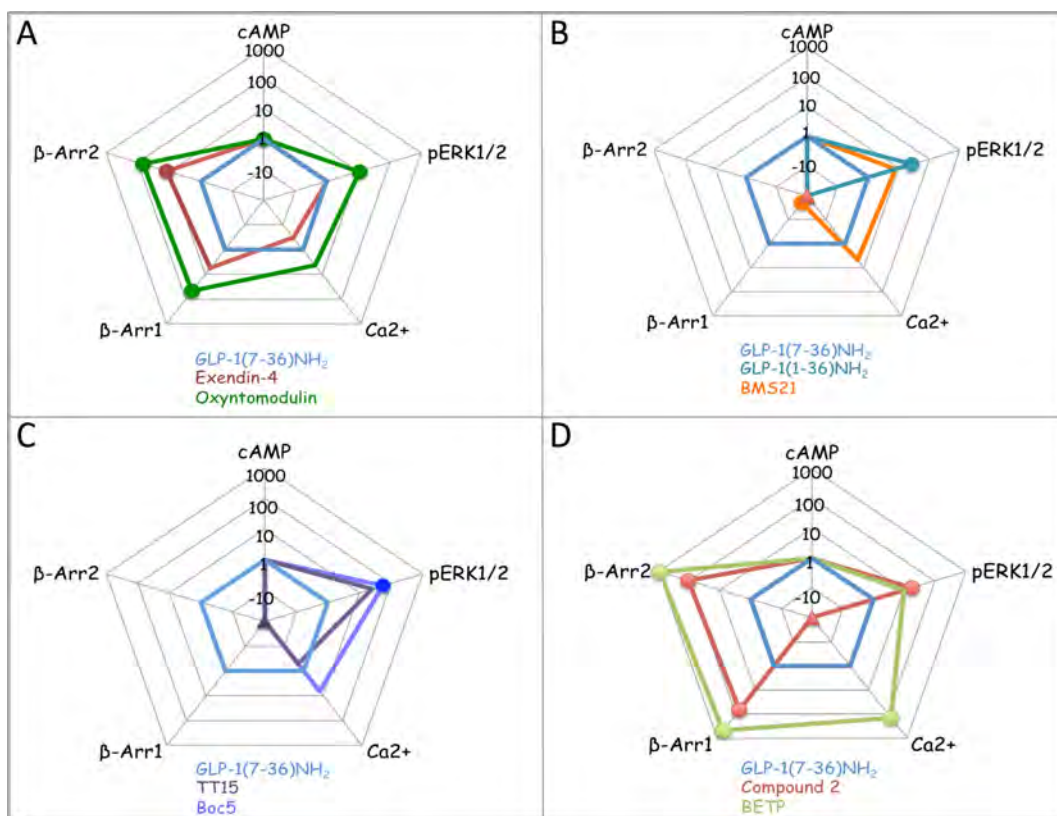


Figure 2. Web of bias illustrating distinctions in the pattern of signaling of GLP-1 receptor agonists. (A) High affinity peptide agonists, (B) low-affinity peptide agonists, (C) nonpeptidic agonists interacting with the extracellular face of the receptor, and (D) nonpeptidic agonists interacting with the intracellular face of the receptor. The “web of bias” plots $\Delta\Delta\tau/K_A$ values on a logarithmic scale for each ligand and for each signaling pathway tested. Determination of these values requires normalization to a reference ligand (GLP-1_{7–36} amide in this example) and a reference pathway (cAMP accumulation). The plots do not provide information on absolute potency but on relative efficacy for signaling of individual pathways in comparison with that for cAMP. Data are from refs 83, 159, and 170. Data points plotted as ● indicate statistically significant bias relative to GLP-1 and cAMP, whereas data plotted as ▲ (at a value of -100) indicate that no significant signal could be detected for a particular pathway.

2.2. Biased Agonism

It is increasingly recognized that the binding of individual ligands to a GPCR can elicit a distinct spectra of responses, even when acting via a common binding pocket (Figure 1B). As each ligand is chemically distinct, they can form unique contacts or combinations of contacts with the receptor, and this is true for peptide ligands with differing amino acid sequences or small molecule drugs. These distinctive ligand interaction patterns govern both the kinetics of binding and how binding events are propagated through the GPCR and the conformational ensembles available to interact with signaling and regulatory proteins.^{9,18,19} Differences in ligand responses may occur via differential recruitment of signaling proteins, including G proteins, or they may alter the interaction with regulatory or scaffolding proteins. The latter events can change receptor trafficking and compartmentalization that may in turn alter the nature of cellular signaling. Similarly, individual ligands can drive differential phosphorylation of the receptor via GPCR kinases (GRKs) or second messenger kinases to engender specific interactions with arrestins and other proteins.^{9,20–23} This phenomenon of biased agonism (also known as ligand-directed signaling bias or functional selectivity) is believed to underlie differences in therapeutic efficacy of existing drugs, including β -adrenoceptor antagonists that inhibit canonical G_{α_s} -mediated cAMP formation but induce selective effects on mitogen-activated protein (MAP) kinases, including extrac-

ellular-signal regulated kinase 1/2 (ERK1/2).²⁴ Biased agonism is currently a major paradigm in GPCR drug discovery, with multiple companies seeking to separate on-target therapeutic efficacy from on-target side effects. Examples of this include biased angiotensin peptides, biased opioids, and biased adenosine receptor compounds.^{20,25} The increasing evidence for biased agonism has arisen as investigators have realized that most, if not all, GPCRs can couple to multiple effectors, including multiple G proteins, arrestins, as well as other scaffolding and regulatory proteins. This has led to concurrent investigation of multiple signaling end points, the most widely studied end point being recruitment of arrestin proteins, in addition to the canonical signaling pathways, revealing distinct ligand responses.^{20,26,27}

2.3. Intersection between Bias and Allostery

Both biased agonism and allosteric modulation of a receptor are mediated by changes to the conformational ensemble sampled by the receptor in the presence of individual agonists or by allosteric drugs or proteins. As allosteric agonists bind to topographically distinct sites, it is not surprising that these types of ligands are often observed to display distinct signaling/regulatory bias relative to the natural, orthosteric ligand. Similarly, as allosteric drugs alter the conformational landscape of the receptor, they can change the signaling profile of the endogenous ligand(s), and this is true for both pure modulators

and “PAM-Agos” (Figure 1B). The exceptions to this are PAMs that only alter the affinity of the orthosteric ligand but do not alter efficacy.

2.4. Quantification of Allostery and Bias

The exploitation of both biased agonism and allostery for therapeutic development requires quantitative frameworks to define key parameters of drug action. In the case of biased agonism, this needs to be distinguished from system-dependent parameters, including partial agonism. Similarly, although gross changes in signal bias can be recognized as a reversal of efficacy or potency,^{9,15,28} more subtle effects require a quantitative framework to identify true differences in ligand response. While a range of quantitative models exist,^{11,29–32} the most robust method to quantify efficacy is the operational model;¹¹ here the transduction ratio of τ/K_a is used to define strength of signaling of an individual ligand for a specific pathway, and this ratio can be determined from classic concentration–response experiments.³¹ τ is the operational term for efficacy, relating receptor occupancy to response, while K_a is the functional affinity (expressed as an equilibrium dissociation constant) for the receptor-effector complex driving signaling. Normalizing responses to a reference ligand (normally the main endogenous agonist) enables differences in signaling profiles between agonists to be calculated. Further normalization to a reference pathway enables broad signaling profiles to be readily displayed for multiple ligands (Figure 2). Although mechanistic models describing allosteric interactions can be developed, these are often too complex to derive meaningful information on key parameters for drug development from routine experiments.³³ As such, we have adopted an operational model of allostery that can parsimoniously describe the key parameters of drug action. These are K_b , the affinity (dissociation constant) of the allosteric ligand for the free receptor, α , the cooperative effect on affinity, β , the modulatory effect on efficacy (that needs to be independently derived for each signaling pathway), and intrinsic efficacy (τ) for each pathway.

3. CLASS B GPCRS

3.1. Structural Classification

Class B receptors are a small subfamily of 15 GPCRs (20 recognized phenotypes with multiple novel phenotypes arising from GPCR/receptor activity modifying protein (RAMP) heterodimerization) that bind physiologically important peptides (Table 1). Structurally, class B receptors range in length from approximately 450 to 600 amino acids in humans. They have a relatively large N-terminal extracellular domain (ECD) of 120 to 200 amino acids that include six conserved disulfide-bonded cysteines. While amino acid homology between receptors is relatively limited within this domain, all the ECDs display similar tertiary structure with a conserved internal fold, termed a “sushi domain” that is supported by the disulfide-bonded cysteines. The structure of the ECD has been solved at high resolution for the glucagon receptor,^{34,35} GLP-1 receptor,^{36,37} gastric inhibitory polypeptide (GIP) receptor,^{38,39} PTH-1 receptor,^{40–42} corticotropin releasing factor (CRF)-1 and CRF-2 receptors,^{43–47} pituitary adenylate cyclase (PAC)-1 receptor,^{48,49} and the calcitonin receptor-like receptor (CLR), the latter in complex with RAMP1 or RAMP2 to yield the ECD of the calcitonin gene-related peptide (CGRP) and adrenomedullin (AM)-1 receptors, respectively.^{50–52} Most of these structures have been cocrystallized with C-terminal fragments of the cognate peptides for the

receptor. The 7 transmembrane (TM) domain core shares < 10% homology with class A or class C GPCRs and ~30% conservation within the class B subfamily. Two X-ray crystal structures have been solved for the TM domain of class B receptors, the glucagon receptor⁵³ and the CRF-1 receptor.⁵⁴ Consistent with the differences in amino acid sequence between class B GPCRs and other receptor classes, the TM domain has a distinct structural organization with a wide-open extracellular face, at least in the apo/inactive form that presumably favors interaction of the receptor core with the N-terminal domain of peptide agonists. Similarities and differences between the TM domains between different GPCR subclasses have been reviewed extensively elsewhere.^{1,7,55,56} To enable direct comparison of amino acids within the TM core of class B receptors, a numbering scheme has been developed⁵⁷ based on that utilized by Ballesteros and Weinstein⁵⁸ for class A receptors. In this scheme, the most conserved residue within each TM helix is designated the number “50” with numbering of other TM residues sequentially from this residue. Thus, the most conserved residue in TM2 will be numbered “2.50”, those preceding it 2.49, 2.48 etc., and those following it 2.51, 2.52, etc. This numbering convention allows direct comparison of functional importance of individual residues across the class B subfamily. Throughout this review, superscripted Wootten numbering⁵⁷ for residues within the TM domain will follow receptor amino acid numbers.

3.2. Signaling Pleiotropy

The canonical signaling pathway for class B GPCRs is $G\alpha_s$ -mediated production of cAMP. However, all receptors couple promiscuously to other effectors, including other G proteins, scaffolding proteins, including arrestins, and various regulatory and trafficking proteins,^{3–7} leading to activation of a diverse array of downstream effectors including multiple second messenger kinases [e.g., protein kinase (PK) A, PKC, PKB], MAP kinases (e.g., ERK1/2, p38), transactivation of tyrosine kinase receptors, opening of ion channels, as well as other effectors controlling gene transcription. This leads to a great diversity in cellular responses that are often context/tissue dependent and may include distinct signaling from different cellular compartments (e.g., lipid rafts or endosomal compartments).^{59,60} It is the cumulative sum of all these pathways that controls specific cellular responses. Clear roles for individual signaling pathways have been described for specific cell types, including requirement for cAMP for GLP-1-mediated insulin secretion, PTH-mediated Ca^{2+} and phosphate mobilization, and vasoactive intestinal peptide (VIP)-mediated smooth muscle relaxation. The great diversity in cellular response provides fertile ground for potential drug development for the selective control of cellular function. However, in many/most cases the link between signaling and physiological effect is still poorly or only partially resolved and requires better understanding for effective exploitation of biased ligands. Nonetheless, the realization that biased agonism is likely to be commonplace has led to a redesign of experimental approaches to drug development such that measurement of multiple end points is now routinely incorporated into many drug discovery programs, leading to an increase in the number of tools (potential biased ligands, genetically and chemogenetically modified animals) to probe how different signaling profiles are linked to cellular function. This is discussed below in the context of specific class B receptors.

3.3. Receptor Dimerization

The association of GPCRs to form oligomeric complexes within the plasma membrane is now well-recognized and accepted, although the structural basis, stability, and functional implications of such complexes are quite varied across this superfamily.⁶¹ Dimerization of class C GPCRs is pervasive and most stable, often required for ligand recognition, selectivity, and signaling, with some complexes even defined by covalent disulfide bonds through amino-terminal domains of involved receptor protomers.⁶² Currently, there are no recognized rules for the association of class A GPCRs, with all combinations of occurrence, functional impact, and stability having been described for different family members, and with these complexes often oligomeric rather than dimeric, and involving multiple potential interfaces.⁶¹ The theme for class B GPCR association seems to be intermediate between the other more dominant classes of GPCRs. All members of the class B family have been described to form homodimeric complexes, with many also capable of forming heterodimeric complexes.^{63–66} Of note, the complexes that have been structurally defined dimerize along the lipid face of TM4⁶⁷ and, as expected from a single defined interface, these do not form higher-order oligomeric complexes.⁶⁸ While ligand binding does not appear to affect the formation or stability of these complexes,^{65,67} they seem to be more stable than the often transient complexes that may be formed for class A GPCRs and appear to be less stable than the dimeric complexes of class C GPCRs. The stability of these complexes varies among the members studied, and the functional impact has also varied quantitatively. Where it has been studied, via disruption of the dimer interface by either mutation of key residues in TM4 or via competition for the dimeric interface with TM4 peptides, homodimeric complexes of class B GPCRs are required to facilitate high affinity binding and potency of natural agonists.⁶⁷ This has been particularly well-studied for the secretin receptor, where disruption of the dimeric interface causes nearly a 100-fold decrease in secretin potency for cAMP formation.⁶⁷ Cysteine substitution and cross-linking of external facing TM4 amino acids revealed key residues that are involved in high affinity secretin binding, although functional studies could not be performed.⁶⁹ Nonetheless, dimerization is also observed to be important for G_{α_s} -mediated cAMP formation via the calcitonin receptor (CTR)⁷⁰ and GLP-1 receptor,⁷¹ albeit that the magnitude of effect was less (~10-fold) than that seen for the secretin receptor.⁶⁷ As such, dimerization of class B receptors appears to have an important contribution to efficacy of G_{α_s} -mediated signaling.

There has been no systematic evaluation of the impact of class B GPCR dimerization on the association with specific G proteins, although as a family, G_{α_s} association is typically most stable and dominant after agonist occupation. G_{α_i} and G_{α_q} association is also characteristic of this family, although typically much higher concentrations of the natural agonist are necessary to stabilize such complexes. There has only been a single report of the impact of the dimerization of members of this family on the function of orthosteric and allosteric agonist ligands across different signaling end points.⁷¹ In this study, following mutational disruption of the dimeric TM4 interface, there was preferential loss of intracellular Ca^{2+} (iCa^{2+}) mobilization in response to peptide agonists of the GLP-1 receptor, including GLP-1(7–36)NH₂, exendin-4, and oxyntomodulin, over that for cAMP formation,⁷¹ albeit that the latter was also decreased, as noted above. This suggests dimerization may also contribute to differential coupling of the receptor and thus to

biased agonism where the latter is observed. The impact of class B GPCR homodimerization on recruitment of scaffolding and regulatory proteins has yet to be studied. Interestingly, disruption of the GLP-1 receptor dimer interface abolishes cAMP responses of the allosteric agonists, Novo Nordisk's 6,7-dichloro-2-methylsulfonyl-3-*tert*-butylaminoquinoxaline (NN compound 2) and 4-(3-benzyloxyphenyl)-2-ethylsulfinyl-6-(trifluoromethyl) pyrimidine (BETP/compound B), while ERK1/2 phosphorylation is relatively preserved. These small molecule ligands act via the intracellular face of the receptor, forming a covalent attachment to Cys347 (intracellular loop (ICL) 3)⁷² and thus are mechanistically distinct in their mode of receptor activation, requiring the homodimeric form of the receptor for efficient G_{α_s} coupling. Nonetheless, despite abolition of their intrinsic activity under monomeric conditions, the allosteric modulation of peptide-mediated cAMP formation is preserved,⁷¹ indicating that the allosteric effect is likely occurring in *cis* and that potentiation of cAMP signaling can occur under conditions of diminished homodimerization. This may be an important consideration for future studies, as the absolute stoichiometry of receptor protomers to G proteins and the structural basis underpinning their interaction has not yet been experimentally defined.

In addition to forming homodimeric complexes, heteroreceptor complexes involving more than one member of the class B receptor family have also been reported.^{64–66,73–75} Use of resonance transfer techniques and coimmunoprecipitation has provided evidence that most class B receptors can coassociate with each other. In one study, the secretin receptor demonstrated associations with VIP receptor (VPAC)-1, VPAC2, growth hormone releasing hormone (GHRH) receptor, GLP-1 receptor, GLP-2 receptor, CLR, PTH1 receptor, and PTH2 receptor, but not the CTR.⁶⁴ On the basis of our understanding of the lipid-exposed face of TM4 of several of the class B GPCRs being the predominant determinant of homodimerization, it is likely that the same interface is active for class B GPCR heterodimerization events, although this has not been directly established. Inconsistencies with respect to the ligand binding on these complexes impacts data interpretation; it is likely that ligand-induced changes in conformation of the component receptors have produced at least some of these observations.

The impact of heteroreceptor association within this family on signaling is unclear, as no major changes have been reported for agonist-stimulated signaling events. With all class B GPCRs known to signal via similar pathways, where G_{α_s} coupling and cAMP generation is most prominent, this is perhaps not surprising. The most obvious functional impact of receptor heteroassociation has been related to receptor trafficking, exemplified by an intracellularly trapped GIP receptor mutant lacking glycosylation sites that can be functionally restored by coexpression with the GLP-1 receptor.⁷⁵ While agonist occupation typically stimulates internalization of class B GPCRs, the impact of occupation of one receptor in a heterocomplex with another has been inconsistent, sometimes resulting in cross-receptor internalization and other times in the absence of effect. This may, in part, reflect the stoichiometry of coexpression and the presence of heterogeneity in the system (a conglomerate of monomers, homo-, and heterodimers). Nonetheless, despite the importance of homodimerization observed for class B receptor signaling, heterodimer formation should not be overlooked, as it has the propensity to significantly impact receptor function.

GPCR oligomeric complexes are not limited to the involvement of structurally related protomers but have also been documented across classes.^{76,77} The association of the class B secretin receptor with the class A angiotensin receptor has been shown to have physiological significance for drinking behavior. In this context, angiotensin appears to predominantly signal via cAMP, rather than stimulating Ca^{2+} mobilization, suggesting that heterodimerization with the secretin receptor could introduce bias into the system.⁷⁷

In addition to receptor–receptor interactions, many class B receptors can heterodimerize with RAMPs. This family of three single transmembrane spanning proteins was originally identified as requisite partners of the CLR to form receptors for CGRP (CLR/RAMP1) and adrenomedullin (AM1, CLR/RAMP2; AM2, CLR/RAMP3).⁷⁸ They have subsequently been shown to interact with the CTR to generate three forms of amylin receptor (AMY1, CT/RAMP1; AMY2, CT/RAMP2; and AMY3, CT/RAMP3).^{79,80} Currently, at least nine class B receptors are reported to interact with at least one of the RAMPs, as determined by the ability of receptors to translocate RAMPs to the cell surface: CLR, CTR, CRF-1, VPAC1, VPAC2, secretin, PTH1, PTH2, and the glucagon receptor (Table 1).⁸¹ With the exception of CLR and CTR, in the majority of cases, the functional importance of RAMP/class B GPCR heterodimers is unclear, although there is accumulating evidence for a role in signaling initiated by peptides (see below) and as such could contribute to observed bias in some systems.

4. CLASS B GPCR BIASED AGONISM

As noted above (Table 1), many class B receptors can respond to multiple endogenous ligands and thus there is significant potential for signaling bias between these different ligands to contribute to control of physiological responses. One of the first published cases of biased agonism was on the class B, PAC1 receptor, where differential responses to PACAP-27 and PACAP-38 were observed.⁸² More recently, biased agonism of endogenous orthosteric ligands has also been observed for the GLP-1 receptor.⁸³ These are discussed in more detail below.

4.1. Secretin Receptor

To date, only a single form of the secretin receptor⁸⁴ and a single endogenous ligand for this receptor⁸⁵ have been recognized and described. The secretin receptor was the first member of this family identified and is prototypic of the family. The secretin receptor signals principally through G_{α_s} coupling, while high concentrations of natural agonist also mediate G_{α_q} coupling. The most potent signaling responses involve cAMP and its recognized impact on other cellular signaling components, while the iCa^{2+} response occurs with approximately 100-fold lower potency. Systematic evaluation of G protein-coupling through receptor mutation found determinants in the cytosolic face that differentially affect coupling with G_{α_s} and G_{α_q} .⁸⁶ In addition, secretin receptor agonists are known to stimulate receptor phosphorylation, β -arrestin translocation, and subsequent receptor internalization.^{87,88} To date, no small molecule ligands acting allosterically have been described for this receptor. As noted above, the complex of secretin and angiotensin receptors can have a disproportionate impact on cAMP over Ca^{2+} signaling.⁷⁷

4.2. Receptors for PTH

There are two structurally related class B GPCRs that bind and are activated by parathyroid PTH and related peptides.⁸⁹ The PTH1 receptor responds similarly to PTH and PTHrP, while

the PTH2 receptor is activated by a precursor-derived PTH peptide (TIP39) and PTH but poorly activated by PTHrP. Of note, TIP39 is a weak antagonist of the PTH1 receptor. All of these naturally occurring peptides couple most strongly to cAMP responses (acting through G_{α_s}) and are much less potent agonists of iCa^{2+} (G_{α_q}). G_{α_s} association results in increased cAMP and activation of PKA that is known to activate MAP kinases, β -catenin, and cAMP response element-binding protein (CREB). This pathway is believed to be responsible for both anabolic and catabolic actions on bone, regulation of phosphate excretion in renal proximal tubules, and regulation of cytokine secretion at both of the most prominent target organs, bone, and kidney.^{6,90–92} G_{α_q} association results in phospholipase (PL) C activation and increased iCa^{2+} , that also results in activation of MAP kinases and ERK1/2. The G_{α_q} -coupled pathway is also believed to be responsible for activation of L-type voltage-gated Ca^{2+} channels. A direct interaction of low-density lipoprotein-related protein-6 (LRP-6)⁹³ and disheveled⁹⁴ has been observed with the PTH receptor, the latter providing another regulatory input into the Wnt pathway affecting β -catenin. Agonists of these receptors also stimulate β -arrestin translocation⁹⁵ to mediate both receptor desensitization and regulate independent signaling events.

The naturally occurring PTH peptides are thought to signal similarly to each other and, therefore, by definition, are not biased, although this may be due to limited examination of signaling end points to date. However, many analogues have been studied to examine structure–activity relationships. Like most natural peptide ligands of receptors in this family, the critical determinants of biological activity are predominantly located in the amino terminus of the ligands, a region believed to interact with the receptor core helical bundle.⁹⁶ The midregion and carboxy-terminal portions of the ligands tend to form alpha helices with a hydrophobic face that docks within a cleft in the receptor amino terminus, providing much of the binding energy and binding affinity. Like most natural ligands for receptors in this family, progressive truncation of the amino terminus of PTH peptides gradually decreases and ultimately eliminates biological activity.⁹⁷ Modifications of the amino terminus are described to preferentially activate (bias) signaling through G_{α_s} over signaling through G_{α_q} , but this may also reflect the loss in potency of the ligands and sensitivity of the assays.

A particularly interesting analogue of PTH has been reported as the best current candidate for therapeutically relevant bias.⁹⁸ This peptide, [(D-Trp¹², Tyr³⁴)bPTH(7–34)], is reported to act as an inverse agonist of PTH-stimulated cAMP responses, while stimulating the translocation of β -arrestin and stimulating ERK1/2 in osteoblasts. In mice, this peptide increases lumbar spine bone mineral density, trabecular volume, thickness, and number but does not initiate osteoclast recruitment.⁹⁸ These effects were absent in β -arrestin-2-null mice, consistent with a biased mode of action. However, this apparent biased response may be limited to a particular cellular environment, with no activation of the pathways attributed to β -arrestin observed in transfected HEK-293 or CHO cells or in the human osteoblastic cell line, U2OS.^{91,99} Nonetheless, the pattern of β -arrestin bias observed at this receptor in a physiological setting has a theoretical advantage in osteoporosis, since this has been suggested to mediate the anabolic bone effect of PTH, while reducing bone resorption associated with a PTH-like full agonist.¹⁰⁰

Differences in spatial and temporal aspects of signaling have recently been recognized as another explanation for apparent differences in functional profiles stimulated by a given agonist. The PTH receptor is one in which endosomal signaling has been postulated to exist.^{101,102} It is not clear whether the responses from an intracellular compartment might differ from those originating at the plasma membrane, but this could provide another mechanism for apparent signaling bias. This might be particularly relevant to the long-acting PTH analogues developed in efforts to improve therapeutic efficacy.

Currently, two forms of PTH are approved for clinical use, recombinant human PTH(1–84) and the amino-terminal fragment PTH(1–34). While no particular bias has been reported between these two forms of this hormone, it is possible that future allosteric modulators could have differential impact on biological effects of these two forms of PTH. Additionally, a number of PTH receptor agonists are in the drug development pipeline and may reach clinical use,¹⁰³ including PTH analogues that can be administered orally, transdermally, or via inhalation. Examples of such analogs include the PTH(1–31) fragment that has been studied for both oral and subcutaneous administration.¹⁰⁴ Additionally, a PTH(1–31) analogue with Leu²⁷ and cyclo(Glu²²-Lys²⁶) modification is also being studied for inhalation-based therapy. Other injectable forms include Pro-Pro[Arg¹¹]PTH(1–34)-Pro-Pro-Asp, a PTH(1–34) analogue with Leu⁸, Asp¹⁰, Lys¹¹, Ala¹⁶, Gln¹⁸, Thr³³, and Ala³⁴ modifications, and a cyclic analogue of PTH(1–17) with AcC¹, Aib³, Leu⁸, Gln¹⁰, Har¹¹, Ala¹², Trp¹⁴, and Asp¹⁷ modifications.^{105–107} Although already used therapeutically, PTH(1–34) continues to be studied, with recent progress using a transdermal patch showing promise,¹⁰⁸ while the β -arrestin-biased analogue described above, [(D-Trp¹², Tyr³⁴)bPTH(7–34)], is being evaluated in preclinical studies.

In addition to PTH analogues, fragments of PTHrP, are also undergoing preclinical studies and clinical trials. These include amino-terminal fragments, PTHrP(1–34), PTHrP(1–36), PTHrP(1–74), and PTHrP(1–84),^{109,110} as well as RS-66271, an analogue of PTHrP(1–34) in which a model amphipathic α -helical decapeptide is inserted in place of residues 22–31, reducing affinity and traditional activity (presumably by reducing G protein coupling), while enhancing anabolic activity.^{111,112} Furthermore, a carboxyl-terminal fragment, PTHrP(107–111), is also being studied.¹⁰⁴

4.3. Receptors for PACAP and VIP

The endogenous peptide ligands for this group of receptors include PACAP-38 and PACAP-27 encoded by the AD-CYAP1R1 gene, and VIP, peptide His Ile/Met (PHI/PHM), and peptide His Val (PHV) encoded by the VIP gene.^{4,113} Three receptors bind and respond to PACAP, the PAC1, VPAC1, and VPAC2 receptors, with the latter two also responding to VIP.^{4,113} Several splice variants of PAC1 have been described in different species, leading to variation in sequence of the ICL3, with a short (S) variant and hip or hop variants that include cassettes of 27 or 28 residues. One short variant has been reported to respond to both PACAP-38 and PACAP-27, with strong cAMP responses, yet only PACAP-38 stimulates IP₃ responses at this form of the receptor.^{82,114,115} The inclusion of the hip cassette has been reported to be associated with reduced cAMP responses and absent Ca²⁺ responses, likely mediated by affecting G protein-coupling.¹¹⁶ A shortened amino-terminal tail variant has also been described,

changing the selectivity for PACAP-27 and PACAP-38 and their ability to stimulate a Ca²⁺ response.^{117,118} Another variant involves sequence changes in TM2 and TM4, described as having no effect on cAMP or Ca²⁺ responses to PACAP but resulting in influx of Ca²⁺ through L-type voltage-sensitive Ca²⁺ channels not normally observed.¹¹⁹

Of the naturally occurring peptide ligands for these receptors, there are differences in binding affinities and potencies to stimulate signaling. The PAC1 receptor responds much better to PACAP peptides than to VIP. pK_i values range from 8.8 to 9.0 for PACAP-38, 8.5 for PACAP-27 and 6.0–6.3 for VIP. Of note, the short form of PAC1 recognizes VIP much better than PACAP peptides, evident by a pK_i of 8.4 for VIP. VPAC1 recognizes all of these peptides quite well, with pK_i values of 8.5–9.8 for VIP, 8.9 for PACAP-27, and 8.2 for PACAP-38. PHI, PHM, and PHV also recognize this receptor with pK_i in the 6 range. VPAC2 recognizes VIP better than PACAP peptides, with pK_i values of 7.8–8.8 for VIP, 7.7–9.3 for PACAP-38, and 7.6–8.0 for PACAP-27. PHI and PHV recognize this receptor better than the other receptors, with pK_i values of 7.5 and 8.8, respectively. Modification of these natural peptide ligands, as well as other unrelated peptides, yields more selective agonists of this group of receptors. Of the analogues widely studied, the most selective peptide ligand for the PAC1 receptor is maxadilan, isolated from sand fly salivary gland with no sequence homology to either PACAP or VIP, yet with a pEC₅₀ value of 9.2.¹²⁰ A VIP analogue with Ala in positions 11, 22, and 28 is currently the most selective agonist for the VPAC1 receptor,¹²¹ while Ro 25–1553, a cyclic analogue of VIP,¹²² and Bay 55–9837 [(Lys¹⁵, Arg¹⁶, Leu²⁷)VIP(1–7)/GRF(8–27)]¹²³ are the most selective ligands reported for the VPAC2 receptor. The relative abilities of these agonists to stimulate the various signaling pathways as a measure of possible signaling bias have not yet been explored. Recently, an extensive systematic structure–activity series including 46 conformationally restrained analogues was reported, with each peptide evaluated for binding, cAMP, and inositol phosphate responses.¹²⁴ Fifteen of these analogues had increased selectivity for the PAC1 receptor over the VPAC1 receptor, improving binding up to 778-fold and 13 of these were agonists. The most selective agonist analogue was a PACAP(1–38) variant with Iac¹ (4-imidazole acrylic acid), Ala¹⁶, Ala¹⁷, and D-Lys³⁸ modifications. Some analogues also markedly reduced the inositol phosphate responses relative to the cAMP responses by up to 103-fold. Twenty-nine of these analogues had increased selectivity for the PAC1 receptor over the VPAC2 receptor, the most selective increasing 806-fold [Ala²²(PACAP(1–38))]. This provides highly useful new insight into the determinants for selectivity and biological activity among these peptides.

In addition to differences in signaling arising from individual peptides activating the receptor, for at least one of these receptors, VPAC1, an additional level of control can occur via the interaction of this receptor with select members of the RAMP family. VPAC1 receptors interact with all three RAMPs,¹²⁵ and while the significance of the interaction with RAMP1 and RAMP3 has yet to be identified, coexpression of RAMP2 and VPAC1, at least in recombinant systems, selectively augments VIP-mediated phosphoinositide hydrolysis, without altering cAMP signaling, suggesting that RAMPs can alter the bias of the receptor.

4.4. Receptors for CT, amylin, CGRP, and adrenomedullin

The calcitonin (CT) family of peptides bind to two class B GPCRs, alone (CTR) or in combination with one of the RAMPs (CTR and CLR) (Table 1).^{81,126} Each of these receptors can bind other members of the peptide family to varying extents. CTR alone responds with high affinity to CT but lower affinity to amylin and CGRP, with limited affinity for adrenomedullin or adrenomedullin-2 (also known as intermedin). The human CTR has two major splice variants that differ by 16 amino acids in ICL1 (CTRa, insert negative; CTRb, insert positive), altering signaling and regulatory responses of the receptor.^{127,128} In addition, the receptor is subject to a major single nucleotide polymorphism encoding either a Leu or Pro at amino acid 447 in the insert negative form of the receptor.^{129,130} The vast majority of studies have been conducted with the CTRa. Expressed alone, the CTR has high affinity for CT but lower affinity for related peptides.^{79,126} The CTR can activate a broad array of pathways across a wide variety of cell types,^{131–133} although the direct link to proximal effectors is not well-resolved in most cases. In osteoclasts, both G_{α_s} /PKA and G_{α_q} /PKC pathways have been implicated in inhibition of cellular function, in a species-dependent manner,¹³⁴ but it is likely that other signaling effectors are also involved. There has been very limited assessment on whether biased agonism occurs at the CTR. In an intriguing study, Watson and colleagues¹³⁵ examined the impact of overexpression of different G protein α -subunits on responses of different species of CT, CGRP, or amylin peptides. In that study, overexpression of G_{α_s} led to host cell-dependent shifts in iCa^{2+} potency ratios, between different peptides (e.g., rat CT and rat amylin or porcine CT and rat amylin), indicative of agonist selective arrays of conformational states that differentially interact with G proteins. In a recent study, Andreassen et al.¹³⁶ demonstrated distinct responses to human CT (hCT) and the clinically used salmon CT (sCT). sCT undergoes a slow transition to a pseudo irreversible state¹³⁷ and thus has a distinct kinetic profile of interaction with the CTR to that of hCT. In short-term assays of cAMP signaling or β -arrestin recruitment, hCT and sCT had similar responses, but while hCT responses were lost relatively rapidly, sCT responses persisted for up to 72 h.¹³⁶ While some of the persistent response was related to maintenance of receptor occupancy at the cell surface, acid washing did not fully abrogate sCT responses, indicating that some signaling arose from intracellular compartments. These data support agonist-specific differences in signaling that are at least partially related to differences in the binding kinetics of the ligands, and to differences in agonist-induced receptor trafficking and signaling over time. The importance of time in the measurement and quantification of biased agonism has recently been addressed in the context of dopamine receptor signaling.¹⁹

In the presence of RAMPs, the CTR forms amylin receptors. AMY1 (CT/RAMP1) has high affinity for amylin and CGRP and lower affinity for hCT, while AMY2 (CT/RAMP2) and AMY3 (CT/RAMP3) have the highest affinity for amylin but lower affinity for CGRP and hCT.^{79,126} While biased agonism at AMY receptors has not been widely investigated, earlier experiments suggest that RAMPs, in addition to altering ligand specificity, change the signaling preference of the receptors. Comparison of the signaling between different pathways indicates that RAMP interaction with CTRa engenders selective modulation of signaling pathways activated by the receptor complex. A 20- to 30-fold increase in amylin potency at AMY1

and AMY3 receptors, compared with CTRa alone, for formation of cAMP is paralleled by a similar increase in amylin binding affinity.¹³⁸ In contrast, only a 2- to 5-fold induction of amylin potency was seen for iCa^{2+} mobilization or activation of ERK1/2. Additionally, in COS-7 cells, the increase in amylin potency for Ca^{2+} mobilization was 2-fold greater for AMY3 receptors over that induced at AMY1 receptors and this paralleled the relative capacity of overexpression of G_{α_q} proteins to augment induction of high affinity ¹²⁵I-amylin binding. Collectively, these data are consistent with RAMP-complexed receptors having a different signaling profile to CTR expressed in the absence of RAMPs, and this is likely due to effects of the RAMP on G protein-coupling efficiency. A direct involvement of RAMPs in G protein-coupling efficiency of CT-complexed receptors is supported by RAMP C-terminal deletion or exchange chimera experiments. Deletion of the short RAMP C-terminus reduces induction of AMY phenotype and CTR-mediated translocation to the cell surface;¹³⁹ these effects could be partially reversed by overexpression of G_{α_s} , suggesting the RAMP C-terminus directly contributes to G protein-coupling efficiency of AMY receptors. Interestingly, exchange of the C-terminus between RAMP1 and RAMP2 altered ligand specificity, with CGRP potency linked to the presence of the RAMP1 C-terminus, providing evidence of long-range allosteric interactions between the intracellular face of the CTR/RAMP complex and the peptide-binding site that involve interaction with intracellular effectors.¹⁴⁰

Unlike the CTR, CLR cannot function independently of RAMPs, forming receptors for CGRP and adrenomedullin only when coexpressed with RAMP1 and RAMP2 or RAMP3, respectively.^{78,81,126} These receptor heteromers also interact with an additional protein, receptor component protein (RCP), critical for efficient coupling of the receptor to G_{α_s} .^{141,142} As such, the expression of RCP is likely to affect signaling via this subfamily of receptors. Both CGRP and AM receptors exhibit pleiotropic coupling that can arise from both G protein-dependent and -independent effector coupling, in turn contributing to a diverse range of physiological functions, including regulation of pain and vascular tone (CGRP), lymphogenesis, cardiac, and neuroprotection (adrenomedullin).^{143–146} However, the link between specific proximal effector coupling events and physiological signaling is not fully resolved. The CGRP receptor has high affinity for α -CGRP (also known as CGRP1) and β -CGRP (CGRP2) peptides but lower affinity for adrenomedullin, adrenomedullin-2, and weak affinity/potency for other peptides. To date, a detailed, multipathway comparison of signaling has not been performed for different endogenous ligands of the CGRP or AM receptors, and as such, no data on potential for biased agonism for natural ligands is available. Considerable work has been performed analyzing structure–function relationships of CGRP peptide analogues;¹⁴⁷ however, these have been mostly described in the context of the canonical cAMP pathway, with limited work examining effects across different pathways. An intriguing study that looked at amino acid substitutions within the N-terminus of CGRP provided evidence for differential effects on cAMP formation versus β -arrestin translocation, with disparate effects on potency and/or E_{max} responses for the two pathways, which appeared greatest for amino acids 5 or 6.¹⁴⁸ However, these responses were measured in different cell types (SK-N-MC for cAMP formation; CHO-K1 for β -arrestin translocation), making clear conclusions about introduction of bias difficult. Nonetheless, the data support the potential for

engineering of peptides to alter the signaling bias at the CGRP receptor.

To date, very limited studies have been performed with modified adrenomedullin peptides. Full-length human adrenomedullin is 52 amino acids; however, many studies utilize the 13–52 fragment, as this has similar affinity and potency for generation of cAMP. Adrenomedullin-2 is a 53 amino acid peptide that can undergo further, N-terminal processing to yield 47 and 40 amino acid peptides. Adrenomedullin has high affinity for both the AM1 (CLR/RAMP2) and AM2 (CLR/RAMP3) receptors, while adrenomedullin-2 is reported to have higher affinity/potency at AM2 receptors.^{144–146} Both AM1 and AM2 have low affinity/cAMP potency for other related CT family peptides.¹⁴⁴ The actions of adrenomedullin-2 generally resemble those of adrenomedullin, although in some systems it is reportedly more potent, or appears to have unique actions.^{149,150} Whether these reported differences could be due to biased signaling or to activation of distinct populations of receptors has not been investigated. As adrenomedullin has only a short plasma half-life, the peptide has been modified by N-terminal conjugation to polyethylene glycol, leading to a 7- to 8-fold increase in half-life.¹⁵¹ This peptide has lower potency than parental adrenomedullin in cAMP assays, but no multipathway analysis has been performed to date, so it is unclear if this changes the signaling/regulatory profile of the peptide/receptor complex.

4.5. Receptors for Glucagon, GLP-1, GLP-2, and GIP

4.5.1. GLP-1 Receptor. The best-studied class B receptor with respect to biased agonism is the GLP-1 receptor. The GLP-1 receptor is a key incretin receptor with a wide range of physiologically beneficial actions, including glucose-dependent insulin secretion, promotion of insulin synthesis, inhibition of glucagon release, inhibition of gastric acid emptying, reduced feeding, and cardio and neuroprotection.^{5,152–154} Multiple endogenous peptides interact with and activate the GLP-1 receptor that include the fully processed GLP-1(7–37) and GLP-1(7–36)NH₂ peptides, extended GLP-1(1–37) and GLP-1(1–36)NH₂ forms as well as oxyntomodulin, and to a lesser extent glucagon. The search for more stable forms of GLP-1 for therapeutic use in type II diabetes and obesity has also led to synthesis of mimetic peptides, including exendin-4 and modified forms of GLP-1.^{155–157} Early characterization of the pharmacology of ligands for the GLP-1 receptor was mostly limited to measurement of the canonically coupled cAMP, critical for the incretin effect in pancreatic β -cells. Thus, it is only relatively recently, following the adoption of multipathway analysis of peptide signaling, that evidence for ligand-directed signaling has emerged.

A study by Koole et al.⁸³ utilized heterologously expressed GLP-1 receptor to more broadly examine and quantify ligand-mediated signaling, focusing on three important signaling pathways linked to physiological function in β -cells, explicitly, cAMP accumulation, phosphorylation of ERK1/2, and iCa²⁺ mobilization. Even with this relatively limited assessment of signaling, the first quantitative evidence for peptide-mediated biased agonism was observed. Oxyntomodulin, an endogenous ligand for the GLP-1 receptor, demonstrated a relative bias toward ERK1/2 phosphorylation over cAMP and iCa²⁺ signaling compared to either GLP-1(7–36)NH₂ or exendin-4,⁸³ and this supported earlier observations of differences between oxyntomodulin and GLP-1(7–36)NH₂ in cAMP signaling versus β -arrestin recruitment.¹⁵⁸ In the Koole et al.

study,⁸³ GLP-1(1–36)NH₂ was also biased, with a relative bias toward ERK1/2 but a loss of iCa²⁺ signaling compared to the N-terminally processed form of the peptide. Thus, this work revealed that the GLP-1 receptor exhibits peptide-mediated biased agonism, though no significant bias was observed between nonamidated and amidated forms of the processed peptide or between GLP-1(7–36)NH₂ and exendin-4 for the three signaling pathways studied.⁸³ Broader analysis of receptor function, including recruitment of arrestins, identified further evidence of biased signaling, with both exendin-4 and oxyntomodulin displaying stronger recruitment of β -arrestin-1 and β -arrestin-2, relative to GLP-1(7–36)NH₂, while GLP-1(1–36)NH₂ did not recruit arrestins even at micromolar concentrations (Figure 2).¹⁵⁹ In contrast, BMS21, a synthetic 11mer peptide, while much less potent than GLP-1(7–36)NH₂, displayed a similar profile of activation for ERK1/2 phosphorylation, cAMP production, and iCa²⁺ mobilization, but did not recruit arrestins.¹⁵⁹ Of note, the main metabolite of GLP-1, GLP-1(9–36)NH₂, exhibits a relative preservation of ERK1/2 signaling,^{160,161} despite abrogation of cAMP production and the ability to promote insulin secretion.¹⁶⁰ This indicates that the metabolite is heavily biased toward ERK1/2 and could promote physiologically relevant signaling via this pathway. Further evidence for peptide-mediated biased agonism has been observed using a yeast assay of chimeric G protein activation.¹⁶² In this system, exendin-4, oxyntomodulin and glucagon, when compared to signaling by GLP-1(7–36)NH₂, displayed relative bias toward the GPA1/G α_i chimera over the GPA1/G α_s chimera. In contrast, liraglutide was not biased away from GLP-1(7–36)NH₂ across these two pathways.¹⁶² Thus, biased agonism is observed even at the most proximal measures of receptor activation and is consistent with the stabilization of distinct ensembles of receptor conformations by individual peptides.

There has been widespread interest in the development of novel peptides as therapeutic agonists of the GLP-1 receptor. This investigation has concentrated on modifications to the peptides to improve plasma half-life, through resistance to protease degradation (exendin-4, dulaglutide, GLP-1 amino acid substitutions),^{155–157,163} increased binding to plasma proteins (e.g., liraglutide),^{155,156} or to enhance bioavailability (stabilized 11-mer peptides).^{164,165} Others have been designed to interact with both GLP-1 and glucagon, or GLP-1 and GIP receptors.^{166–168} To date, there has been only limited investigation into whether these modifications alter signaling bias of the ligands. As noted above, broad analysis of signaling/regulatory protein interaction has revealed bias for the clinically approved exendin-4,¹⁵⁹ and there is also preliminary evidence of potential biased agonism of liraglutide in driving GLP-1 receptor internalization, although this has not been directly quantified. The potency for liraglutide-mediated receptor internalization was 10-fold lower than the potencies for internalization of exendin-4 and GLP-1(7–36)NH₂, despite similar kinetics of internalization for all three peptides.¹⁶⁹ While biased agonism by other peptides has not been directly assessed, the BMS21 11-mer peptide displays marked bias compared to GLP-1(7–36)NH₂,¹⁵⁹ suggesting that distinct patterns of signaling response are also likely with other 11-mer peptides. Similarly, given the strong bias of oxyntomodulin,^{83,159,170} which is a dual agonist of the GLP-1 and glucagon receptors, it seems probable that other designed dual agonists or mixed agonist/antagonists will also have altered interactions with the GLP-1 receptor.

but reduced ERK1/2 phosphorylation, whereas NN compound 2 has the reverse profile (compared to the signaling profile of GLP-1 and the reference cAMP pathway).^{159,170} Other differences in the pharmacological behavior of BETP and/or NN compound 2 have also been noted by other investigators;^{175–177} however, the lack of a quantitative framework for these analyses has limited the extent to which these differences can be attributed to true biased agonism. That nonpeptidic ligands have distinct signaling profiles from peptide agonists, and other nonpeptidic compounds is unsurprising as their chemical diversity will engender quite distinct interactions with the receptor. Indeed, BETP and NN compound 2 interact, via covalent modification, with Cys347 in the ICL3 of the GLP-1 receptor.⁷²

4.5.3. GLP-2 Receptor. GLP-2 receptor expression is restricted predominantly to the gastrointestinal tract and CNS, primarily regulating nutrient absorption and energy homeostasis.¹⁷⁸ There are very few ligands identified to date that activate this receptor. GLP-2 is found endogenously and promotes signaling via interaction with the GLP-2 receptor coupling it to G_{α_s} and formation of cAMP.^{179,180} Profiling of additional signaling pathways has only been conducted in limited cell lines including BHK fibroblasts that overexpress the GLP-2 receptor¹⁸¹ and in murine subepithelial myofibroblasts.¹⁸² These revealed pleiotropic signaling from activation of the GLP-2 receptor, including increases in levels of iCa^{2+} , early gene expression of *c-fos*, *c-jun*, *junB*, and *zif268*, transient increases in p70 S6 kinase, inhibition of ERK1/2 and coupling to AP-1-dependent transcriptional activity that was dependent on PKA.^{180,181,183}

One of the principal actions of GLP-2 is to stimulate epithelial cell proliferation and inhibition of enterocyte apoptosis.¹⁷⁸ While cell proliferation was enhanced by GLP-2 in BHK fibroblasts, this was not dependent on cAMP.¹⁸¹ Studies in the subepithelial myofibroblasts revealed these effects may be dependent on the PI-3 kinase/Akt pathway, with no cAMP, ERK1/2 or iCa^{2+} signaling observed at low concentrations of GLP-2.¹⁸²

There are also a number of identified GLP-2 receptor agonists and partial agonists, some of which have been developed for clinical/preclinical trials for various gastrointestinal diseases. However, to date there has been no detailed multipathway analysis of these ligands; therefore, there are no reported biased ligands of this receptor. Like most natural ligands of class B GPCRs, truncated metabolites of GLP-2 [GLP-2(2–33), GLP-2(3–33)] are low-affinity partial agonists for GLP-2 receptor-mediated cAMP,^{180,184} however, as the GLP-2 receptor is pleiotropically coupled, there is the potential that these metabolites are biased ligands similar to studies that imply biased agonism from metabolites that activate the related GLP-1 receptor.¹⁸⁵ Teduglutide is a modified form of GLP-2 that differs by just a single amino acid to GLP-2 and has an improved half-life through resistance to protease cleavage.¹⁸⁶ This is reported to be a full agonist and is used clinically to treat short bowel syndrome; however, whether it exerts any biased agonism in relation to GLP-2 is not known.

A series of analogues derived from the compound methyl 2-[[[(2Z)-2-(2,5-dichlorothiophen-3-yl)-2-(hydroxyimino)ethyl]-sulfanyl]benzoate (compound 1) are the only GLP-2 receptor small molecule agonists reported to date.¹⁸⁷ These compounds are positive allosteric modulators of GLP-2 signaling but also act as agonists for cAMP production. Further profiling of these compounds in other signaling pathways has not been

performed; however, given the extremely biased profile of small molecule agonists at the GLP-1 receptor, it may be expected that these compounds would also be biased agonists of the GLP-2 receptor.

4.5.4. GIP Receptor. GIP, the endogenous agonist for the GIP receptor, is an incretin hormone with a principal role in promoting glucose-dependent insulin secretion, as well as pancreatic β -cell proliferation and survival. The receptor has also been implicated in control of body weight and appetite. Activation of the GIP receptor is coupled to increases in cAMP and iCa^{2+} levels, in addition to activation of PI3-kinase, PKA, Akt, p38 MAP kinases, and phospholipase A2. GIP receptor agonists also induce rapid internalization and reversible desensitization that involves regulator of G protein signaling 2 (RGS-2), G protein-coupled receptor kinase (GRK) 2, and β -arrestin-1.

Like other incretins, GIP is subject to proteolytic cleavage that has driven the development of novel degradation-resistant C-terminally truncated analogues of GIP. One such analogue, D-Ala²-GIP (1–30), robustly improved glucose homeostasis in rats, reduced β -cell apoptosis in isolated islets, and preserved β -cell mass in rodents.¹⁸⁸ However, it is not as potent as full length GIP at inducing lipoprotein lipase in 3T3L1 cells, suggestive that there may be some biased agonism with this analogue, although direct comparisons across multiple end points will need to be performed to conclude this.

GIP receptor antagonists have also been developed, by either truncation of both the N- and C-terminal region of the peptides [GIP(6–30) and GIP(7–30)] or a Pro³ substitution in native GIP.^{189,190} These analogues are not reported to promote intracellular signaling (cAMP or insulin secretion), and antagonize the actions of GIP in vitro and in vivo.^{189,191} However, sustained chronic administration of [Pro³]-GIP into obese diabetic mice engendered improvements in glucose levels, glycated hemoglobin, and pancreatic insulin,¹⁹² effects that are also reported with GIP. Interestingly, this analogue also reduces body weight, although GIP does not have any significant effects on food intake or body weight, despite significantly improving metabolic profiles.¹⁹³ Long-acting GIP analogues GIP(Lys³⁷MYR), N-AcGIP(Lys³⁷MYR), and N-AcGIP(Lys³⁷PAL) also have no effect on body weight or food intake.^{194,195} This suggests that either [Pro³]-GIP is a partial agonist of the GIP receptor, has altered interaction with related receptors, or potentially displays biased agonism compared to GIP, but direct comparative studies profiling related receptors across multiple signaling and physiological end points will be required to confirm this.

4.5.5. Glucagon Receptor. The glucagon receptor plays an essential role in regulating blood glucose levels through controlling the rate of hepatic glucose production, promoting glycogen hydrolysis and gluconeogenesis, and regulating pathways controlling hepatic lipid oxidation and lipid secretion.¹⁹⁶ The glucagon receptor is activated by glucagon, thus glucagon has a counter regulatory role to insulin in controlling glucose homeostasis. The glucagon receptor is also expressed in extrahepatic tissues including the central and peripheral nervous system, blood vessels and heart, pancreas, adipose tissue, kidney, and smooth muscle cells in the gastrointestinal tract where it has multiple physiological roles.¹⁹⁷

Activation of the glucagon receptor promotes cAMP formation via G_{α_s} coupling in multiple cell types and backgrounds. Glucagon also activates iCa^{2+} mobilization via

the inositol phosphate/PLC pathway that have been linked to cell type-dependent G_{α_s} , G_{α_q} , and/or G_{α_i} signaling. These pathways are believed to be responsible for the majority of the physiological and pharmacological effects of glucagon. Glucagon-mediated production of cAMP stimulates glucose output in the liver,^{198,199} lipolysis in adipose tissue,²⁰⁰ insulin secretion in pancreatic islets, and inotropy and chronotropy in the heart.^{201–203} In recombinant cells lines, glucagon receptor stimulation enhances ERK1/2 phosphorylation via cAMP-mediated PKA; however, iCa^{2+} mobilization is required for PKA to maximally activate this pathway.²⁰⁴ PKA-mediated ERK1/2 phosphorylation is responsible for activation of K-type ATP channels in the CNS that are stimulated through the dorsal vagal complex to lower hepatic glucose production.²⁰⁵

Increased cAMP and activation of PKA also activates Wnt/ β -catenin signaling, consistent with reports linking activation of this pathway by cAMP/PKA in the PTH-1 receptor.^{94,206} A direct interaction of the glucagon receptor with low-density lipoprotein-5 Lrp5 enhances glucagon receptor-mediated β -catenin signaling that is believed to contribute to the metabolic phenotypes of Lrp5 mutations associated with metabolic syndrome.²⁰⁷ However, despite glucagon promoting cAMP production, there are multiple lines of evidence to support cAMP-independent actions of glucagon on adipose tissue, liver, and heart.²⁰⁸ In the liver, glucagon can promote glycogenolysis, gluconeogenesis, and glucose output at very low concentrations without activating adenylate cyclase.²⁰⁹ This occurs through rapid inhibition of pyruvate kinase mediated by inositol phosphate- Ca^{2+} -dependent signaling. In the heart, activation of PI3-kinase/Akt at concentrations of glucagon that do not activate cAMP promotes myocardial glycolysis,²¹⁰ while activation of p38 MAP kinase promotes cardiomyocyte apoptosis, reducing survival in mouse models of post myocardial infarction remodeling and heart failure.²¹¹

In addition to glucagon, there are further endogenous ligands for this receptor, although their importance and role is less well-understood. Oxyntomodulin is a low-affinity agonist with dual actions at both the glucagon receptor and the GLP-1 receptor. Mini-glucagon, the C-terminal 19–29 fragment processed from glucagon, is present in pancreatic cells and is a potent inhibitor of glucagon- and GLP-1-mediated insulin secretion; however, these effects may be independent of the glucagon receptor itself.^{212,213} The GLP-1 receptor agonists, GLP-1 and liraglutide are also agonists at the glucagon receptor, albeit with lower efficacy than at the GLP-1 receptor.²¹⁴

To date, there is limited information around biased agonism at the glucagon receptor, as most efforts in ligand development have focused on development of antagonists that are normally profiled in inhibition of either glucagon binding or glucagon-mediated cAMP. Detailed multipathway profiling for agonists at this receptor has not been performed. However, early studies by Houslay and colleagues^{209,215} reported an interesting analogue (1-*N*- α -trinitrophenylhistidine,12-homoarginine)-glucagon (TH-glucagon) that may be a biased glucagon receptor agonist. These studies showed that TH-glucagon did not exert any increase in cAMP in hepatocytes, yet could stimulate production of inositol phosphates and could fully stimulate glycogenolysis, gluconeogenesis, and urea synthesis in vivo, further supporting the hypothesis that these physiological functions occur independent of cAMP. These effects at the time of publication were hypothesized to arise due to two different glucagon receptors, but the most likely explanation for these data is biased agonism. Although not quantified, this study

implies that TH-glucagon may be a biased glucagon receptor agonist when compared to glucagon.

The glucagon receptor can also be regulated by interaction with RAMP2, resulting in changes in both ligand selectivity and G protein-coupling preference that can bias the signaling profile of the receptor.^{123,214} In recombinant cells, coexpression of RAMP2 with the glucagon receptor potentiated both glucagon- and oxyntomodulin-mediated cAMP production; however, the mechanism by which this occurred was different for the two ligands. Use of a yeast assay of chimeric G protein activation revealed that RAMP2 decreased glucagon-mediated activation of G_{α_i} proteins while enhancing G_{α_s} , whereas modulation of oxyntomodulin responses occurred solely through enhanced G_{α_s} . In addition, RAMP2 also abolished the partial activity observed by GLP-1 and liraglutide at the glucagon receptor.²¹⁴ RAMP expression levels vary in different tissues and in disease and therefore may contribute to distinct signaling profiles that lead to discrete physiological functions of glucagon receptor activation.

4.6. GHRH Receptor

When activated by GHRH, the GHRH receptor stimulates growth hormone production and release that is required for normal postnatal growth with roles in bone growth and regulatory effects on protein, carbohydrate, and lipid metabolism.²¹⁶ The receptor is primarily located in the anterior pituitary and when activated promotes both cAMP-dependent signaling by coupling to G_{α_s} and inositol phosphate/DAG/PLC-mediated iCa^{2+} release. Growth hormone production is stimulated via cAMP/PKA-mediated phosphorylation of CREB, whereas both GHRH-mediated cAMP-dependent and -independent pathways are required for influx of extracellular Ca^{2+} , leading to the release of growth hormone secretory granules that result in the rapid rise in circulating growth hormone. Recent work has also identified a role for the GHRH receptor in proliferation of cardiac stem cells with agonists of this receptor promoting survival through mechanisms involving ERK1/2 and Akt.²¹⁷

Interestingly, while GHRH receptor expression is predominantly limited to the pituitary, a number of splice variants for the receptor have been identified in various nonpituitary tissues and in human tumor cell lines.^{218–221} The most common of these splice variants, SV1, lacks only a portion of the extracellular domain of the full length receptor but is still activated by GHRH to promote cAMP signaling and stimulate cell proliferation.²²² However, SV1 also promotes ligand-independent constitutive proliferative effects on cells. In addition, GHRH antagonists produce antiproliferative effects in tumor cell lines expressing GHRH receptor splice variants.^{219–222} These studies suggest that these splice variants are biased receptors relative to full length GHRH, with different basal receptor conformational landscapes that promote ligand-independent signaling and may have roles in development of malignancies. In addition to splice variants, there are also a number of confirmed GHRH receptor polymorphic variants that can alter the signaling capacity of the receptor, some of which have been linked to disease.^{223–225}

Consistent with glucagon/GLP-1/GLP-2 receptor ligands, substitution of D-Ala at position 2 of the GHRH peptide ligand provides resistance to proteolytic degradation. Interestingly, this analogue has significantly enhanced potency for growth hormone release compared to GHRH.²²⁶ Another series of GHRH analogues generated around the scaffold [Dat¹,Gln⁸,

Orn^{12,21}, Abu¹⁵, Nle²⁷, Asp²⁸, Arg²⁹]hGHRH(1–29), also display higher potency than GHRH for growth hormone release in vivo.²²⁷ However, to date, no detailed multipathway profiling of any of these peptides has been performed, and therefore, it is unknown if any of these compounds display biased agonism or whether these effects are due to increased affinity/stability of the modified peptides for the receptor.

4.7. CRF Receptors

The related receptors CRF1 and CRF2 bind the endogenous peptide CRF and the urocortin family of peptides.²²⁸ These receptors have approximately 70% similarity at the amino acid level but differ principally in their N-terminal domains, which is responsible for their distinct pharmacological properties and agonist selectivity. CRF1 receptors bind both CRF and urocortin-1 with equal affinity but do not bind the related peptides urocortin-2 and urocortin-3. In contrast, CRF2 receptors bind CRF and all three urocortin peptides; however, the urocortin peptides display higher affinity than CRF.^{229–231} Both receptors also bind the related peptide agonists from fish (urotensin-1) and amphibians (sauvagine).

CRF and urocortins acting at CRF receptors are important for mediating central and peripheral stress responses.²³² Studies in native tissues, recombinant cell lines, and in yeast expressing different $G\alpha$ chimeric proteins demonstrate that CRF receptors are highly promiscuous in their G protein-coupling, with evidence for coupling to $G\alpha_s$, $G\alpha_{q/11}$, $G\alpha_o$, and $G\alpha_{i1/2}$.^{233–236} CRF1 and 2 receptors predominantly activate cAMP via $G\alpha_s$ coupling and transient Ca^{2+} mobilization by activation of PLC and PKC through a combination of $G\alpha_s$, $G\alpha_q$, and $G\alpha_i$ coupling.^{237–239} CRF receptors are internalized following agonist binding in a process that is dependent on β -arrestin-2.

There are nine CRF1 variants, with CRF1_a the main functional receptor and the one most characterized. The CRF1_b isoform has a 29 amino acid insertion in ICL1, impairing agonist activity.²⁴⁰ Most other isoforms (CRF1_{c-h}) have exon 6 spliced out and cannot signal but may play a modulatory role in CRF1_a function as expression of e and h isoforms in COS7 cells either decreased or amplified urocortin-1-mediated cAMP at the CRF1_a receptor, respectively.^{241,242} CRF1_i is characterized by a deletion of exon 4 but is functional in promoting ERK1/2 phosphorylation in transfected HEK-293 cells, although no further assessment of signaling has been performed.²⁴³ For CRF2 receptors, there are three reported biologically important splice variants (CRF2_{a-c}) that differ predominantly in their N-terminal domain. The predominately expressed and most well-characterized of these is CRF2_a, and while differential pharmacological or biological properties of these splice variants have not been reported, there are apparent effects with respect to tissue distribution.²⁴⁴

Most of the physiological functions of CRF receptors in the CNS and periphery have been linked to $G\alpha_s$ coupling. However, in the placenta, these receptors are unable to activate $G\alpha_s$ proteins, while still activating MAP kinases and iCa^{2+} pathways.²⁴⁵ In contrast, in SK-N-MC neuroblastoma cells, CRF receptor activation induces robust $G\alpha_s$ -mediated cAMP with no iCa^{2+} mobilization.²³⁸ This reveals distinct signaling profiles by the same ligands acting at the same receptors in discrete tissues, although the physiological basis for this signaling specificity is not clear.

Ligand selective signaling is also evident at CRF receptors. Ten analogues of urocortin-1 involving single amino acids substitutions with either a Bpa group or a Nal group (Bpa-6, -7,

-8, -9, -10, -13; Nal-6, -9, -13, -15) were identified that promoted $G\alpha_s$ activation similar to the native peptide but were inactive at coupling to $G\alpha_i$ activation in HEK-293 cells overexpressing the CRF1 receptor.²⁴⁶ This reveals the potential for different agonists to alter receptor conformation resulting in differential effector coupling at these receptors; however, to date, no comprehensive multipathway comparisons have been performed between endogenous agonists of CRF receptors.

Interestingly, gender differences in CRF receptor signaling have been reported, with CRF being a more potent electrophysiological activator of rat LC neurons (the primary target of CRF during stress) in females compared with males. Furthermore, this activation is almost completely prevented by a PKA antagonist in females, but only 50% inhibition was observed in males.²⁴⁷ CRF1 receptors isolated from the cortex of unstressed female mice were associated with similar levels of $G\alpha_s$ to stressed males and significantly more $G\alpha_s$ than unstressed males. In addition, CRF1 receptors in LC neurons of female animals do not recruit β -arrestin-2 following stress; however, after exposure of male animals to stress, there was enhanced association of CRF1 receptors with β -arrestin-2. These differences in receptor association with signaling/regulatory effectors observed between the two genders indicate differences in the way the receptor signals. Additionally, these differences were also coupled with distinctive localization of receptors, both before and after exposure to stress.²⁴⁷ CRF1 receptors were located at the plasma membrane and cytosolically in unstressed males with an increase in cytoplasmic localization, indicative of internalization, following stress. In contrast, in unstressed female LC neurons, the receptor was predominantly localized intracellularly, with stress shifting the distribution to the plasma membrane. Differences in spatial and temporal aspects of signaling are now well-recognized for influencing bias profiles of agonist ligands. Females are more vulnerable to certain stress-related disease and this could be attributed in part to differential signaling/trafficking profiles of CRF receptors in males and females due to their ability to adapt to the excessive CRF that is predicted to be present in diseases related to severe or chronic stress. This may have therapeutic implications for biased CRF1 receptor agonists that can shift the bias of signaling toward β -arrestin-2 in female LC neurons.

An additional level of signal regulation has been reported for the CRF1 receptor via the interaction of this receptor with RAMP2.²⁴⁸ This results in selective augmentation of Ca^{2+} signaling but occurs in a ligand-dependent manner, with augmentation of CRF and urocortin-1 responses, yet no effect on sauvagine-induced Ca^{2+} mobilization. Of note, in RAMP2 \pm mice, CRF responses are diminished, suggesting that these RAMP2-mediated effects are physiologically important.²⁴⁸ Intriguingly, RAMP2 also interacts with the VPAC1 receptor to selectively augment inositol phosphate signaling.¹²⁵ Inositol triphosphate is a key initiator of iCa^{2+} mobilization, suggesting that the effect of RAMP2 on CRF1 and VPAC1 receptor signaling may be mechanistically similar. To date, there are no reports assessing the influence of RAMPs on CRF2 receptor function.

5. MECHANISTIC STUDIES OF BIASED AGONISM

There have been relatively limited studies addressing the mechanism underlying differential signaling of peptides from individual class B receptors. Conformational changes promoting activation transition involve reorganization of polar, hydrogen bond networks, and intrahelical packing that drive

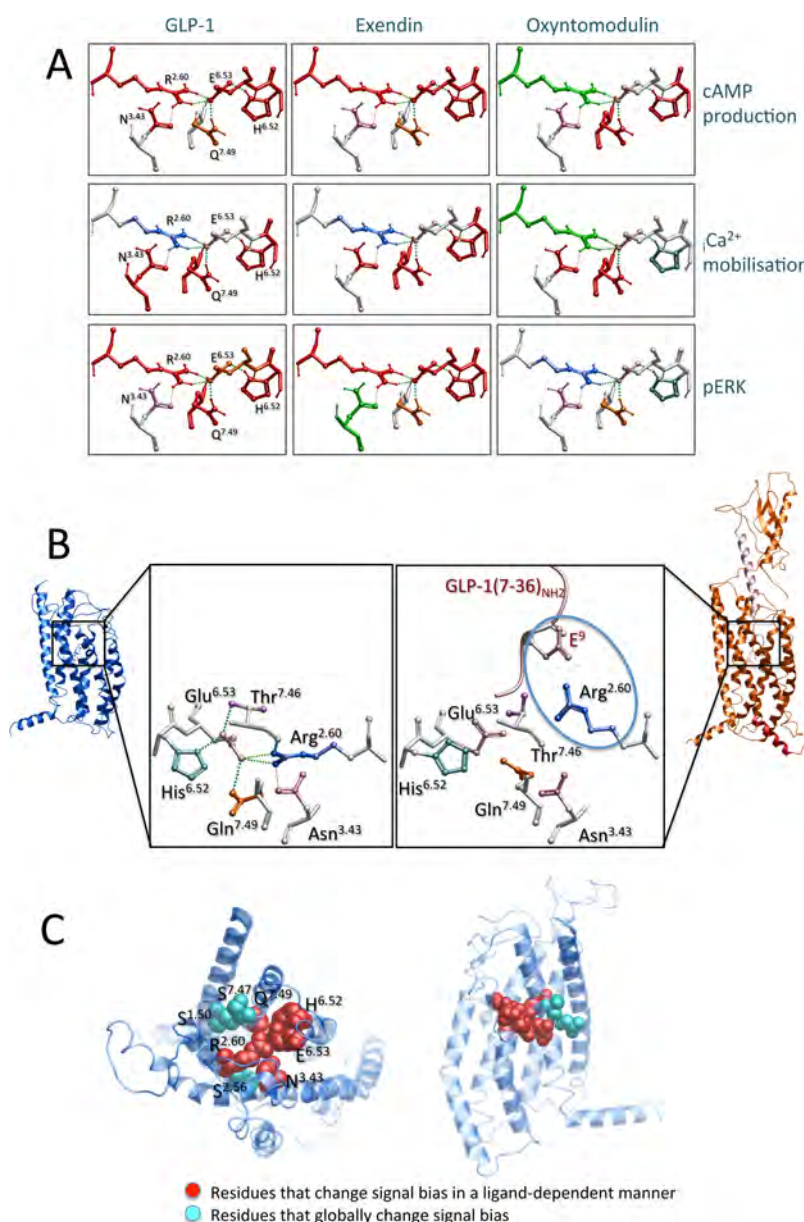


Figure 4. A central, polar, hydrogen-bonded network controls biased agonism at the GLP-1 receptor. Homology modeling of the inactive GLP-1 receptor predicts a stable interaction network comprising R2.60, N3.43, H6.52, E6.53 and Q7.49. (A) Mutational analysis reveals differential usage of the amino acids within this network by individual peptides, in a pathway-specific manner; amino acids are depicted in x-stick, with unaffected amino acids colored by side chain; red, mutation decreases efficacy; green, mutation increases efficacy. (B) Apo (blue) and GLP-1-bound (orange) models of the GLP-1 receptor. The expanded region illustrates the network in each of the models with amino acids in x-stick format, colored by side chain. The network is predicted to be disrupted in the peptide-bound model, with a predicted key interaction between R2.60 and the glutamic acid at position 9 in the GLP-1(7–36)NH₂ sequence when this peptide is present. (C) Inactive model with top down (left-hand panel) and side (right-hand panel) views illustrating the position of the central network residues (red space fill) and also small amino acids (blue) that are globally important (all ligands) for signaling through individual pathways. Individual panels reproduced with permission from ref 254. Copyright 2016 ASPET.

reordering of the intracellular surface of GPCRs to engender interaction with effector proteins.^{249–252} Although best studied for class A receptors, these polar networks are conserved within GPCR subfamilies, suggesting evolutionary preservation of the molecular mechanisms controlling activation transition.²⁵³ It is anticipated that such conserved polar residues within class B GPCRs play an equally important structural role and contribute to the mechanism of biased agonism.

A major fulcrum for activation transition in the class B GLP-1 receptor is located in the core of the TM domain bundle at the point of convergence of the splayed extracellular TM helices.

Mutagenesis of polar residues conserved across class B receptors revealed a cluster of residues, comprising Arg190^{2.60}, Asn240^{3.43}, His363^{6.52}, and Gln394^{7.49} that alter the pattern of peptide-mediated signaling for cAMP formation, pERK1/2, and iCa^{2+} mobilization in a peptide and amino acid specific manner.^{57,254} Molecular modeling, based on the recently solved inactive crystal structure of the glucagon receptor,⁵³ predict that these residues form a hydrogen-bonded network inclusive of Glu364^{6.53}, a less conserved amino acid within the B subclass.²⁵⁴ Differences in the profile of responses were particularly notable between GLP-1(7–36)NH₂ and

oxyntomodulin, with the predicted interaction between Arg190^{2,60} and Glu364^{6,53} important for GLP-1 action but not oxyntomodulin signaling.²⁵⁴ However, selective differences between GLP-1(7–36)NH₂ and exendin-4, in the effect of mutation, were also observed. Collectively, this provides molecular evidence for mechanistic differences in receptor activation between the three peptides through the central polar network (Figure 4). Analysis of the equivalent central network residues in the glucagon⁵³ and CRF1⁵⁴ receptor structures revealed conservation in relative orientation of side chains,²⁵⁴ despite TM6 of the CRF1 receptor having distinct amino acids, namely Thr at 6.52 and Tyr at 6.53. In the glucagon receptor, maintenance of the central network was predicted to be partially coordinated by water-mediated H-bonding and likely to exist in a highly constrained state in the inactive form of the receptor.²⁵⁴ The structural consistency in side chain position in the solved class B crystal structures, combined with conservation of key residues in the network and its fulcrum position in the crystal structures, is consistent with a critical role of the network in signaling for this subfamily. There are supporting data from other class B GPCRs of a key role of this network in receptor activation, with interaction of Arg188^{2,60}, Asn229^{3,43}, and Gln380^{7,49} predicted from mutagenesis and modeling studies of the VPAC1 receptor.^{255–257} Interestingly, Arg188^{2,60} is predicted to engage, via a salt-bridge, with Asp³ of VIP, with this interaction contributing to receptor activation;²⁵⁶ in GLP-1(7–36)NH₂ and exendin-4, the equivalent amino acid is Glu, whereas in oxyntomodulin it is a Gln. Molecular modeling of GLP-1(7–36)NH₂ docking to the full-length receptor²⁵⁴ has predicted a direct, salt-bridge interaction between peptide Glu⁹ and Arg190^{2,60} (Figure 4), and it is speculated that the lack of an acidic residue at the third amino acid of oxyntomodulin may underlie the lack of engagement of the Arg190^{2,60}/Glu364^{6,53} interaction in receptor activation, thus contributing to the biased agonism observed for this peptide. The extent to which the central network contributes to biased agonism of other class B peptides has yet to be investigated.

In addition to the fulcrum amino acids that exhibit ligand-specific effects, a series of Ser residues (Ser155^{1,50}, Ser186^{2,56}, and Ser392^{7,47}) in the GLP-1 receptor have been identified to contribute to control of receptor-dependent signal bias, where mutation of these amino acids globally affects GLP-1, exendin-4, and oxyntomodulin signaling.⁵⁷ These amino acids are situated at the interface between either TM1 and TM7 (Ser155^{1,50} and Ser392^{7,47}) or between TM2 and TM3 (Ser186^{2,56}), and likely contribute to tight packing of these TM helices. There is an additional polar Thr149^{1,44} in TM1 that is the site of a naturally occurring Thr/Met polymorphism, although the Thr is not broadly conserved in class B receptors.²⁵⁸ Met at this position leads to a marked attenuation of peptide-mediated cAMP production^{258,259} and iCa²⁺ mobilization, while ERK1/2 phosphorylation is relatively preserved,²⁵⁹ and like the Ser residues in TM1, this was a global effect for peptide agonists.²⁵⁹ In homology-based molecular models of the GLP-1 receptor TM domain, the smaller polar residues that are globally important for signaling are located external to the central polar network that is involved in ligand-dependent signaling (Figure 4).

While there is an emerging appreciation of how peptides can selectively alter key hydrogen bonding networks to control signaling, there is relatively limited information on how amino acids in the extracellular loops (ECLs) contribute to ligand-

mediated bias. Nonetheless, this has been investigated for canonical signaling of the amidated GLP-1 peptides, exendin-4 and oxyntomodulin via Ala scanning mutagenesis of ECL2.^{260,261} Lys288, Cys296, Trp297, and Asn300 had important roles in controlling signal bias of the receptor but were also globally significant for peptide signaling. Nonetheless, peptide-selective effects on relative efficacy and signal bias were most frequently seen for residues 301–305, although the mutation of Arg299Ala also led to distinct effects for individual peptides. Met303 played a greater role for exendin-4 and oxyntomodulin action than those of GLP-1 peptides. Interestingly, ECL2 mutation was overall more disadvantageous to exendin-4-mediated iCa²⁺ mobilization than GLP-1(7–36)NH₂, providing further support for subtle variances in receptor activation by these peptides. Collectively, this provides initial insight into the early engagement of peptides with the receptor and how conformational propagation is differentially controlled.

6. ALLOSTERIC MODULATION OF CLASS B GPCRS

Allosteric modulation of GPCRs is now a well-established paradigm that provides both challenges and advantages for drug discovery over classic orthosteric ligands.⁸ As noted above, peptide ligands engage class B receptors via a diffuse pharmacophore including critical interactions for affinity with the N-terminal extracellular domain and less well-defined interactions with the ECLs and TM domain core that initiate and propagate receptor activation. Nonpeptidic ligands have an alternate mode of binding, often involving topographically distinct, allosteric sites from those of the native peptides, allowing cooperative interactions on binding or efficacy to occur.^{8,10,16,33,262} Nonetheless, nonpeptidic ligands for class B GPCRs have been notoriously difficult to discover and to develop, and for those that have been identified, full molecular and pharmacological characterization of their mode of binding and action is often absent.

Small molecule ligands fall principally into two categories: those whose binding is topographically distinct and those that have at least partial overlap with the binding site of orthosteric peptides. As peptide binding to class B receptors is multimodal with both a receptor N-terminal (N-domain) and juxtamembrane/TM core interaction (J-domain),^{96,263} it is possible for the latter class of ligands to exhibit allosteric inhibitor properties (concomitant binding, changes to ligand kinetics), while inhibiting receptor function by competitive interaction with the peptide N-terminus that binds to the receptor core. As discussed by Hoare,²⁶³ the explicit description of this phenomenon is the “Charniere” effect,²⁶⁴ and a key expectation of this type of interaction is that peptide interaction with small molecule (where this is the reporter) should appear fully competitive, without any effect on small molecule ligand dissociation.²⁶³ The paucity of high affinity, labeled small molecule ligands limits testing for this type of interaction. Nonetheless, other approaches can provide insight into potential mechanism of action. One example is small molecule ligands of the PTH1 receptor, AH-3960 and SW106, initially described as agonist and antagonist, respectively,^{265–267} though the latter may be a very weak partial agonist.²⁶⁸ ECD truncation receptor studies support binding of these ligands to the TM core of the PTH1 receptor. Both small molecules alter the dissociation kinetics of PTH(1–34) that binds according to the classic two domain model; however, they do not alter the kinetics of a modified PTH(1–11) peptide agonist that binds

only within the TM core.²⁶⁸ Nonetheless, SW106 displays competitive inhibition of the PTH(1–11)-mediated cAMP production elicited from both full-length and the N-terminally deleted PTH1 receptor.²⁶⁸ Similar behavior has been observed for small molecule inhibitors of the CGRP receptor that partially overlap the binding of peptides to the N-terminal complex of CLR/RAMP1.^{50,52} Likewise, Boc5, an agonist of the GLP-1 receptor, is reported to interact via the N-terminal ECD with apparent competitive interaction with peptide ligands.¹⁷²

In contrast, at least one class of CRF1 inhibitor acts via classic allosteric inhibition. This is exemplified by the crystal structure of the CRF1 receptor in complex with CP-376395.⁵⁴ The cocrystallized small molecule inhibitor binds deep within the TM core toward the intracellular face of the receptor;⁵⁴ comparative mapping of the location of drug binding sites in current published crystal structures indicates this is the deepest structurally characterized binding pocket identified to date¹ and is located away from the peptide binding pocket, which is predicted to reside within the extracellular face of the receptor. Although structural detail on the site of interaction is not yet available, the low-affinity small molecule inhibitors of the VPAC2 receptor (termed “compound 1” and “compound 2”) bind in the TM core of the receptor and demonstrate noncompetitive inhibition of VIP signaling,²⁶⁹ consistent with an allosteric mode of action. T-0632, an inhibitor of GLP-1 receptor signaling, is reported to bind to the receptor ECD in a manner that is dependent upon the presence of Trp33, as substitution of this residue with Ser (the equivalent amino acid in the rat receptor) led to a 100-fold loss in affinity.²⁷⁰ Further investigation is required to determine whether this could lead to partial occlusion of peptide binding or whether the ligand acts in a fully allosteric manner. Beyond CRF1 receptors, the most active inhibitor drug discovery programs have targeted the glucagon receptor, as a potential antidiabetic therapy.²⁷¹ These are predicted to bind within the TM bundle of the glucagon receptor, and indeed one of these inhibitors, NNC0640, was required for the successful crystallization of the TM domain of the glucagon receptor.⁵³ Unfortunately, there was insufficient electron density resolved within the solved crystal structure to localize the site of small molecule binding.

In addition to small molecule allosteric antagonists, antibodies that recognize the extracellular domain of the glucagon receptor can allosterically regulate its activity. The antibody mAb7 behaves as a negative allosteric modulator by binding to two regions within the N-terminal domain distinct to that of the glucagon binding cleft, inhibiting glucagon binding via an allosteric mechanism.³⁵ In contrast, the antibody mAb23 blocks glucagon binding by directly occluding the hormone binding cleft. However, this antibody is an inverse agonist, inhibiting basal activity of the receptor by removing interactions of the N-terminal domain with ECL3, interactions that are required to allosterically regulate ligand-independent receptor activity.³⁴

While small molecule drug discovery for all class B receptors has been difficult, this is particularly true for agonists or positive allosteric modulators. The best-studied examples of PAMs are modulators of the GLP-1 receptor. GLP-1 receptor PAMs were first identified by Novo Nordisk and are exemplified by NN compound 2, an allosteric agonist of the receptor for cAMP production. In addition to its intrinsic efficacy, this series of compounds augmented the binding of radiolabeled GLP-1, indicating that it could act as a PAM.¹⁷³ Nonetheless, there was only limited impact on the efficacy of GLP-1(7–36)NH₂ for cAMP signaling.⁸³ As described above, a hallmark of allosteric

interactions is “probe-dependence” that describes the differential effects occurring dependent upon the orthosteric and allosteric ligand combination (Figure 1). This is clearly observed for ligands of the GLP-1 receptor. While NN compound 2 has very little effect on GLP-1(7–36)NH₂-induced cAMP production, it engenders a ~30-fold enhancement of oxyntomodulin signaling via this pathway.^{83,159,170} Probe-dependence is also observed for effects on the extended GLP-1 peptides and exendin-4, where very limited effect on cAMP production is observed. A similar profile of effect is seen for the Eli Lilly compound BETP (“compound B”) in that BETP enhances oxyntomodulin-mediated cAMP production but has minimal effect on GLP-1(7–36)NH₂, exendin-4, or GLP-1(1–36)NH₂-mediated signaling via this pathway.^{159,170} Limited augmentation of NN compound 2-mediated cAMP accumulation (or surrogate measures of cAMP such as CRE-luciferase) has also been noted for interaction of this ligand with truncated forms of exendin-4, including exendin-4(5–39), exendin-4(7–39), and exendin-4(9–39), even where no intrinsic activity was measurable.^{175,176}

Remarkably, NN compound 2 and BETP dramatically augment cAMP production elicited by the principal GLP-1 metabolite, GLP-1(9–36)NH₂; ~400-fold for NN compound 2.^{160,161} Parallel enhancement of insulin secretion was observed in isolated rat islets and in vivo when rats were stimulated with pharmacological levels of the metabolite together with subthreshold levels of BETP.¹⁶⁰ The increase in signaling was principally limited to cAMP production, although weak potentiation of ERK1/2 phosphorylation and iCa²⁺ mobilization has been observed in INS1E cells and HEK-293 cells recombinantly expressing the GLP-1 receptor,¹⁶¹ but not in CHO cells expressing the receptor,¹⁶⁰ providing additional evidence that allosteric modulators have the ability to change the signal bias of the receptor. Nonetheless, a lack of effect on the extended, amidated GLP-1 peptide suggests that the magnitude of cooperativity of NN compound 2 and BETP is not manifested solely by the intrinsic efficacy of the activating ligand.

NN compound 2 and BETP are highly electrophilic and are capable of forming adducts with free cysteine residues,²⁷² and indeed covalent interaction of the compounds with Cys347 in ICL3 is critical for both the intrinsic efficacy and the allosteric cooperative effect.⁷² Nonetheless, this covalent interaction is insufficient to fully explain the activity of these compounds, as NN compound 2 and BETP have distinct profiles of intrinsic efficacy (see above; Figure 2) and display differences in their cooperative effect.¹⁵⁹ Intriguingly, the naturally occurring human GLP-1 receptor polymorphism Ser/Cys333 selectively attenuates NN compound 2-mediated cAMP formation and the positive cooperativity between NN compound 2 and oxyntomodulin for this pathway, without altering orthosteric peptide agonist response.^{259,273} These data are consistent with the environment surrounding Cys347 contributing to the selective actions of NN compound 2. In contrast to the effect of position 333 polymorphism, the Met149^{1.44} polymorphic variant does not impact on the intrinsic efficacy of NN compound 2; however, as discussed above, it engenders a strong abrogation of peptide-mediated cAMP production with >100-fold loss of exendin-4 and GLP-1(7–36)NH₂ potency. At this mutant, NN compound 2 led to recovery of the potency of both GLP-1(7–36)NH₂ and exendin-4 to that of the T149^{1.44} polymorphic variant of the receptor.²⁵⁹ Thus, allosteric

modulators can alleviate loss of function of the GLP-1 receptor arising from disease of genetic origin.

While electrophilic compounds such as NN compound 2 and BETP are the most widely studied allosteric modulators of the GLP-1 receptor, other modulators of peptide response have been reported. One example is the flavonol, 3,3',4',5,7-pentahydroxyflavone (quercetin) that has no inherent intrinsic activity but specifically enhances iCa^{2+} mobilization elicited by efficacious peptides such as GLP-1(7–36)NH₂, GLP-1(7–37), and exendin-4, albeit with a bell-shaped effect, inhibiting responses observed at high concentrations of the flavonol.^{83,274} This amplification of iCa^{2+} mobilization required the presence of a 3-hydroxyl group on the flavone backbone and was greater if a 3'4'-dihydroxyl was present.²⁷⁴ Other compounds that selectively increased iCa^{2+} signaling were recently reported following identification by high-throughput screening.²⁷⁵ In contrast to the flavonols, this compound series had significant intrinsic efficacy for iCa^{2+} mobilization. A prototypical ligand from this series, termed (S)-9b, was reported to also augment exendin-4-mediated insulin secretion in primary mouse islets as well as liraglutide-mediated GLP-1 receptor internalization in recombinant cells.²⁷⁵ However, the insulin secretagogue effect occurred in both high and low glucose conditions, which would be therapeutically problematic but may also indicate a requirement for further investigation to determine if this is truly a GLP-1 receptor-mediated event. In addition to the insulinotropic effects, (S)-9b was also reported to reduce haloperidol-induced catalepsy in rats,²⁷⁵ but again, confirmation that this is mediated via the GLP-1 receptor is required. In other work using virtual screening against a molecular model of the glucagon receptor, de Graaf and colleagues²⁷⁶ identified compounds with both glucagon and GLP-1 receptor activity. This included weak inhibitors of both receptors but also one compound that displayed weak positive modulation of GLP-1-mediated cAMP production via the GLP-1 receptor, but was an inhibitor of glucagon-mediated cAMP signaling via the glucagon receptor.²⁷⁶

Outside of the GLP-1 receptor, and the single example from the PTH1 receptor (described above), there are very few reports of small molecule agonists/PAMs for class B receptors. Yamazaki and colleagues¹⁸⁷ identified a series of 2-([(2Z)-2-(2,5-dichlorothiophen-3-yl)-2-(hydroxyimino)ethyl]sulfanyl)-benzoate-based compounds as PAM-agos of the GLP-2 receptor that potentiated the placental alkaline phosphatase activity of various GLP-2 peptides in recombinant HEK-293 cells expressing the GLP-2 receptor. It is unclear whether the sulfanyl group could also be reactive in a similar manner to the covalent GLP-1 receptor PAM-agos described. The only other receptor for which small molecule agonists have been described is the CTR. SUN B8155, a small molecule agonist of the CTR identified by Katayama and colleagues²⁷⁷ induced cAMP production in a manner that was inhibited by the peptide antagonist sCT(8–32). However, this compound did not compete for ¹²⁵I-hCT binding. The mode of binding of this compound has not been investigated further. More recently, a series of pyrazolopyridine-based CTR agonists were described.²⁷⁸ Chimeric and mutagenesis studies indicate that these compounds bind to the CTR at the TM1/ECD interface and that amino acids 150/151 are critical for their activity.²⁷⁹ The compounds exhibit incomplete inhibition of ¹²⁵I-hCT binding and weakly potentiate cAMP production by hCT,²⁷⁹ suggesting a pure allosteric mode of interaction.

As discussed above, the physiological and/or therapeutic implications of biased signaling are largely unknown, and this is particularly true for allosteric small molecule agonists/PAMs. Despite the distinct signaling/regulatory profiles of ligands such as Boc5 or TT15, these compounds (or related analogues) modulate both *ex vivo* and *in vivo* insulin secretion.^{172,280} Allosteric compounds such as NN compound 2 or BETP can also augment insulin secretion, albeit that mechanistic interpretation of such responses is complicated by endogenous circulating peptides. Pharmacologically, both NN compound 2 and BETP enhance select responses of oxyntomodulin and the GLP-1 metabolite, GLP-1(9–36)NH₂, and this is linked to higher *in vivo* insulin secretion, at least in the context of threshold doses of the orthosteric and allosteric ligands.^{160,170} Broader, *in vitro* investigation of the effect of the modulators on the signaling profile of oxyntomodulin or GLP-1(9–36)NH₂ revealed that the most prominent modulatory effect was augmentation of cAMP production, implying that, at least in the context of the baseline signaling of the peptides/modulators, this alone may be sufficient to improve insulin secretion. The significance of allosterically driven bias for GLP-1 receptor function outside of insulin secretion is even more ambiguous, due to lack of investigation of the impact of modulation on these other functions, and none controlled for the influence of biased signaling. Unfortunately, most non-peptidic compounds have low potency, nonfavorable pharmacokinetic profiles, or unknown interactions with other targets, limiting their utility.

7. SUMMARY/CONCLUSION/FUTURE DIRECTIONS

Class B GPCRs are physiologically important receptors that are potential high value targets for the treatment of both acute and chronic disease. These receptors are pleiotropically coupled and can regulate signaling from distinct compartments in a cell specific manner, making them ideal candidates for exploitation by biased and/or allosteric drugs. Peptide-based therapies are well-advanced for many of these receptors; however, the current lack of detailed understanding of both the signaling properties of these peptides and the relationship between select signaling pathways and cellular response may limit optimal therapeutic development as these parameters are critical for successful application of superior, biased drug therapies. This is an area that requires urgent investigation. Small molecule and allosteric drug development have been difficult areas for class B GPCRs. One novel approach to drug development that is being actively pursued for other (nonclass B) peptide GPCRs is that of pepducins. These lipid-modified peptides, based on ICL or helix 8 sequences of receptors, allosterically modulate target receptors.^{281,282} Positive, negative, and biased pepducin modulators have been described for other classes of GPCRs, and these could likely also be developed for class B receptors. Nonetheless, recent advances in structural understanding of this family of receptors offers new insight for directed drug design, both for structure-based design of biased peptides and for the identification and development of small molecule compounds.

AUTHOR INFORMATION

Corresponding Authors

*E-mail: denise.wootten@monash.edu.

*E-mail: ljm@mayo.edu.

*E-mail: patrick.sexton@monash.edu.

Notes

The authors declare no competing financial interest.

Biographies

Dr. Denise Wootten is a Career Development Fellow of National Health and Medical Research Council of Australia and Research Fellow working at the Monash Institute of Pharmaceutical Sciences in Melbourne, Australia. Her expertise is in the study of G protein-coupled receptors (GPCRs), particularly the Class B subfamily. The principal interest of her research is directed toward understanding the modes of their signaling and regulation in an effort to identify novel approaches for drug discovery. Her research efforts encompass differential signaling, interaction of receptors with regulatory accessory proteins, allosterism, and the structure and mechanism by which these GPCRs are activated. More recently her work has focused on addressing the link between in vitro pharmacology and signal transduction with the physiological effects elicited in vivo following activation of these receptors.

Laurence J. Miller is Professor of Medicine, Biochemistry & Molecular Biology, and Pharmacology at Mayo Clinic College of Medicine, located at Mayo Clinic in Scottsdale, Arizona. He trained as a physician at Jefferson Medical College and Mayo Clinic and received his scientific training in the Cell Biology Department at Yale University School of Medicine. His scientific interests focus on the molecular basis of drug action at G protein-coupled receptors.

Cassandra Koole received her Bachelor of Biomedical Science with Honors from Deakin University, Melbourne, in 2007. She then completed her Ph.D. in Molecular Pharmacology at Monash University, Melbourne, in 2012, under the supervision of Prof Patrick Sexton, with pharmacological and structure function analysis of the human glucagon-like peptide-1 receptor a major focus of her research throughout her candidature. In 2013, she was awarded a CJ Martin Postdoctoral Fellowship by the National Health and Medical Research Council of Australia to continue and broaden this research in the laboratory of Dr. Thomas Sakmar at the Rockefeller University, New York.

Arthur Christopoulos is a Professor of Pharmacology and Senior Principal Research Fellow of the National Health and Medical Research Council of Australia. His research focuses on the detection and quantification of allosteric drugs and biased agonists at G protein-coupled receptors. His studies cross academic and industry boundaries and incorporate computational and mathematical modeling, medicinal chemistry, structural and chemical biology, cellular biochemistry and signal transduction, and in vivo animal models of behavior. He is an author of over 240 scientific articles, is the recipient of numerous prizes and awards for his research, serves/has served on the Editorial Board of eight international journals and is/has been a Principal Investigator on numerous grant/contracts from various sources. He is a Consultant for a number of large pharma and biotechnology companies and is Deputy Chair of the Nomenclature Committee of the International Union of Basic and Clinical Pharmacology (NC-IUPHAR). In 2014 and 2015, he was named a Highly Cited Researcher (Pharmacology and Toxicology) by Thomson Reuters.

Patrick Sexton is currently the Head of the Drug Discovery Biology theme at the Monash Institute of Pharmaceutical Sciences, a Professor of Pharmacology, and an Australian National Health and Medical Research Council Principal Research Fellow. His research focuses on understanding G protein-coupled receptors (GPCRs), and in particular with respect to allosteric modulation of receptors, biased agonism and in the structure/function of Class B GPCRs and accessory proteins. His research crosses industry and academic

boundaries through elucidation of fundamental biology and the intersection of this with drug-receptor interactions. He has authored over 230 publications, is a 2014 Thomson Reuters highly cited researcher in Pharmacology and Toxicology, and the recipient of a 2015 Thomson Reuters Citation Award (Biology and Biochemistry). He is an elected Fellow of the British Pharmacological Society, an Associate Editor for Pharmacological Reviews, and is on the scientific advisory board of the Chinese National Centre for Drug Screening.

ACKNOWLEDGMENTS

This work was supported by National Health and Medical Research Council of Australia (NHMRC) project Grants [1061044] and [1065410], and NHMRC program Grant [1055134]. P.M.S. is a NHMRC Principal Research Fellow. A.C. is a NHMRC Senior Principal Research Fellow. D.W. is a NHMRC Career Development Fellow. C.K. is a NHMRC CJ Martin Postdoctoral Fellow.

REFERENCES

- (1) Bortolato, A.; Dore, A. S.; Hollenstein, K.; Tehan, B. G.; Mason, J. S.; Marshall, F. H. Structure of Class B GPCRs: New Horizons for Drug Discovery. *Br. J. Pharmacol.* **2014**, *171*, 3132–3145.
- (2) Dong, M.; Koole, C.; Wootten, D.; Sexton, P. M.; Miller, L. J. Structural and Functional Insights into the Juxtamembranous Amino-Terminal Tail and Extracellular Loop Regions of Class B GPCRs. *Br. J. Pharmacol.* **2014**, *171*, 1085–1101.
- (3) Couvineau, A.; Laburthe, M. VPAC Receptors: Structure, Molecular Pharmacology and Interaction with Accessory Proteins. *Br. J. Pharmacol.* **2012**, *166*, 42–50.
- (4) Haimar, A. J.; Fahrenkrug, J.; Gozes, I.; Laburthe, M.; May, V.; Pisegna, J. R.; Vaudry, D.; Vaudry, H.; Waschek, J. A.; Said, S. I. Pharmacology and Functions of Receptors for Vasoactive Intestinal Peptide and Pituitary Adenylate Cyclase-Activating Polypeptide: IUPHAR Review 1. *Br. J. Pharmacol.* **2012**, *166*, 4–17.
- (5) Mayo, K. E.; Miller, L. J.; Bataille, D.; Dalle, S.; Goke, B.; Thorens, B.; Drucker, D. J. International Union of Pharmacology. XXXV. The Glucagon Receptor Family. *Pharmacol. Rev.* **2003**, *55*, 167–194.
- (6) Gardella, T. J.; Vilardaga, J. P. International Union of Basic and Clinical Pharmacology. XCIII. The Parathyroid Hormone Receptors - Family B G Protein-Coupled Receptors. *Pharmacol. Rev.* **2015**, *67*, 310–337.
- (7) Culhane, K. J.; Liu, Y.; Cai, Y.; Yan, E. C. Transmembrane Signal Transduction by Peptide Hormones Via Family B G Protein-Coupled Receptors. *Front. Pharmacol.* **2015**, *6*, 264.
- (8) Wootten, D.; Christopoulos, A.; Sexton, P. M. Emerging Paradigms in GPCR Allosterism: Implications for Drug Discovery. *Nat. Rev. Drug Discovery* **2013**, *12*, 630–644.
- (9) Shonberg, J.; Lopez, L.; Scammells, P. J.; Christopoulos, A.; Capuano, B.; Lane, J. R. Biased Agonism at G Protein-Coupled Receptors: The Promise and the Challenges - A Medicinal Chemistry Perspective. *Med. Res. Rev.* **2014**, *34*, 1286–1330.
- (10) Gentry, P. R.; Sexton, P. M.; Christopoulos, A. Novel Allosteric Modulators of G Protein-Coupled Receptors. *J. Biol. Chem.* **2015**, *290*, 19478–19488.
- (11) Kenakin, T.; Christopoulos, A. Signalling Bias in New Drug Discovery: Detection, Quantification and Therapeutic Impact. *Nat. Rev. Drug Discovery* **2012**, *12*, 205–216.
- (12) Neubig, R. R.; Spedding, M.; Kenakin, T.; Christopoulos, A. International Union of Pharmacology Committee on Receptor Nomenclature and Drug Classification. XXXVIII. Update on Terms and Symbols in Quantitative Pharmacology. *Pharmacol. Rev.* **2003**, *55*, 597–606.
- (13) Christopoulos, A.; Changeux, J. P.; Catterall, W. A.; Fabbro, D.; Burris, T. P.; Cidlowski, J. A.; Olsen, R. W.; Peters, J. A.; Neubig, R. R.; Pin, J. P.; et al. International Union of Basic and Clinical Pharmacology. XC. Multisite Pharmacology: Recommendations for

the Nomenclature of Receptor Allostery and Allosteric Ligands. *Pharmacol. Rev.* **2014**, *66*, 918–947.

(14) Canals, M.; Sexton, P. M.; Christopoulos, A. Allostery in GPCRs: 'MWC' Revisited. *Trends Biochem. Sci.* **2011**, *36*, 663–672.

(15) Kenakin, T.; Miller, L. J. Seven Transmembrane Receptors as Shapeshifting Proteins: The Impact of Allosteric Modulation and Functional Selectivity on New Drug Discovery. *Pharmacol. Rev.* **2010**, *62*, 265–304.

(16) May, L. T.; Leach, K.; Sexton, P. M.; Christopoulos, A. Allosteric Modulation of G Protein-Coupled Receptors. *Annu. Rev. Pharmacol. Toxicol.* **2007**, *47*, 1–51.

(17) Christopoulos, A. Advances in GPCR Allostery: From Function to Structure. *Mol. Pharmacol.* **2014**, *86*, 463–478.

(18) Kenakin, T. P. Biased Signalling and Allosteric Machines: New Vistas and Challenges for Drug Discovery. *Br. J. Pharmacol.* **2012**, *165*, 1659–1669.

(19) Klein-Henrichsen, C.; Sykes, D. A.; Donthamsetti, P.; Canals, M.; Coudrat, T.; Shonberg, J.; Scammells, P. J.; Capuano, B.; Sexton, P. M.; Charlton, S. J.; et al. The Vital Role of Kinetic Context in Biased Agonism at GPCRs. *Nat. Commun.* **2016**, *7*, 10842.

(20) Rankovic, Z.; Brust, T. F.; Bohn, L. M. Biased Agonism: An Emerging Paradigm in GPCR Drug Discovery. *Bioorg. Med. Chem. Lett.* **2016**, *26*, 241–250.

(21) Tobin, A. B.; Butcher, A. J.; Kong, K. C. Location, Location, Location...Site-Specific GPCR Phosphorylation Offers a Mechanism for Cell-Type-Specific Signalling. *Trends Pharmacol. Sci.* **2008**, *29*, 413–420.

(22) Bradley, S. J.; Riaz, S. A.; Tobin, A. B. Employing Novel Animal Models in the Design of Clinically Efficacious GPCR Ligands. *Curr. Opin. Cell Biol.* **2014**, *27*, 117–125.

(23) Nobles, K. N.; Xiao, K.; Ahn, S.; Shukla, A. K.; Lam, C. M.; Rajagopal, S.; Strachan, R. T.; Huang, T. Y.; Bressler, E. A.; Hara, M. R.; et al. Distinct Phosphorylation Sites on the Beta(2)-Adrenergic Receptor Establish a Barcode that Encodes Differential Functions of Beta-Arrestin. *Sci. Signaling* **2011**, *4*, ra51.

(24) Thanawala, V. J.; Forkuo, G. S.; Stallaert, W.; Leff, P.; Bouvier, M.; Bond, R. Ligand Bias Prevents Class Equality Among Beta-Blockers. *Curr. Opin. Pharmacol.* **2014**, *16*, 50–57.

(25) Valant, C.; May, L. T.; Aurelio, L.; Chuo, C. H.; White, P. J.; Baltos, J. A.; Sexton, P. M.; Scammells, P. J.; Christopoulos, A. Separation of On-Target Efficacy from Adverse Effects through Rational Design of a Bitopic Adenosine Receptor Agonist. *Proc. Natl. Acad. Sci. U. S. A.* **2014**, *111*, 4614–4619.

(26) Luttrell, L. M.; Maudsley, S.; Bohn, L. M. Fulfilling the Promise of "Biased" G Protein-Coupled Receptor Agonism. *Mol. Pharmacol.* **2015**, *88*, 579–588.

(27) Liu, Y.; Yang, Y.; Ward, R.; An, S.; Guo, X. X.; Li, W.; Xu, T. R. Biased Signalling: The Instinctive Skill of the Cell in the Selection of Appropriate Signalling Pathways. *Biochem. J.* **2015**, *470*, 155–167.

(28) Koole, C.; Savage, E. E.; Christopoulos, A.; Miller, L. J.; Sexton, P. M.; Wootten, D. Minireview: Signal Bias, Allostery, and Polymorphic Variation at the GLP-1R: Implications for Drug Discovery. *Mol. Endocrinol.* **2013**, *27*, 1234–1244.

(29) Ehlert, F. J. On the Analysis of Ligand-Directed Signaling at G Protein-Coupled Receptors. *Naunyn-Schmiedeberg's Arch. Pharmacol.* **2008**, *377*, 549–577.

(30) Stahl, E. L.; Zhou, L.; Ehlert, F. J.; Bohn, L. M. A Novel Method for Analyzing Extremely Biased Agonism at G Protein-Coupled Receptors. *Mol. Pharmacol.* **2015**, *87*, 866–877.

(31) Kenakin, T.; Watson, C.; Muniz-Medina, V.; Christopoulos, A.; Novick, S. A Simple Method for Quantifying Functional Selectivity and Agonist Bias. *ACS Chem. Neurosci.* **2012**, *3*, 193–203.

(32) Rajagopal, S.; Ahn, S.; Rominger, D. H.; Gowen-Macdonald, W.; Lam, C. M.; Dewire, S. M.; Violin, J. D.; Lefkowitz, R. J. Quantifying Ligand Bias at Seven-Transmembrane Receptors. *Mol. Pharmacol.* **2011**, *80*, 367–377.

(33) Keov, P.; Sexton, P. M.; Christopoulos, A. Allosteric Modulation of G Protein-Coupled Receptors: A Pharmacological Perspective. *Neuropharmacology* **2011**, *60*, 24–35.

(34) Koth, C. M.; Murray, J. M.; Mukund, S.; Madjid, A.; Minn, A.; Clarke, H. J.; Wong, T.; Chiang, V.; Luis, E.; Estevez, A.; et al. Molecular Basis for Negative Regulation of the Glucagon Receptor. *Proc. Natl. Acad. Sci. U. S. A.* **2012**, *109*, 14393–14398.

(35) Mukund, S.; Shang, Y.; Clarke, H. J.; Madjid, A.; Corn, J. E.; Kates, L.; Kolumam, G.; Chiang, V.; Luis, E.; Murray, J.; et al. Inhibitory Mechanism of an Allosteric Antibody Targeting the Glucagon Receptor. *J. Biol. Chem.* **2013**, *288*, 36168–36178.

(36) Runge, S.; Thogersen, H.; Madsen, K.; Lau, J.; Rudolph, R. Crystal Structure of the Ligand-Bound Glucagon-Like Peptide-1 Receptor Extracellular Domain. *J. Biol. Chem.* **2008**, *283*, 11340–11347.

(37) Underwood, C. R.; Garibay, P.; Knudsen, L. B.; Hastrup, S.; Peters, G. H.; Rudolph, R.; Reedtz-Runge, S. Crystal Structure of Glucagon-Like Peptide-1 in Complex with the Extracellular Domain of the Glucagon-Like Peptide-1 Receptor. *J. Biol. Chem.* **2010**, *285*, 723–730.

(38) Ravn, P.; Madhurantakam, C.; Kunze, S.; Matthews, E.; Priest, C.; O'Brien, S.; Collinson, A.; Papworth, M.; Fritsch-Fredin, M.; Jermutus, L.; et al. Structural and Pharmacological Characterization of Novel Potent and Selective Monoclonal Antibody Antagonists of Glucose-Dependent Insulinotropic Polypeptide Receptor. *J. Biol. Chem.* **2013**, *288*, 19760–19772.

(39) Parthier, C.; Kleinschmidt, M.; Neumann, P.; Rudolph, R.; Manhart, S.; Schlenzig, D.; Fanghanel, J.; Rahfeld, J. U.; Demuth, H. U.; Stubbs, M. T. Crystal Structure of the Incretin-Bound Extracellular Domain of a G Protein-Coupled Receptor. *Proc. Natl. Acad. Sci. U. S. A.* **2007**, *104*, 13942–13947.

(40) Pioszak, A. A.; Harikumar, K. G.; Parker, N. R.; Miller, L. J.; Xu, H. E. Dimeric Arrangement of the Parathyroid Hormone Receptor and a Structural Mechanism for Ligand-Induced Dissociation. *J. Biol. Chem.* **2010**, *285*, 12435–12444.

(41) Pioszak, A. A.; Parker, N. R.; Gardella, T. J.; Xu, H. E. Structural Basis for Parathyroid Hormone-Related Protein Binding to the Parathyroid Hormone Receptor and Design of Conformation-Selective Peptides. *J. Biol. Chem.* **2009**, *284*, 28382–28391.

(42) Pioszak, A. A.; Xu, H. E. Molecular Recognition of Parathyroid Hormone by Its G Protein-Coupled Receptor. *Proc. Natl. Acad. Sci. U. S. A.* **2008**, *105*, 5034–5039.

(43) Pioszak, A. A.; Parker, N. R.; Suino-Powell, K.; Xu, H. E. Molecular Recognition of Corticotropin-Releasing Factor by Its G Protein-Coupled Receptor CRFR1. *J. Biol. Chem.* **2008**, *283*, 32900–32912.

(44) Pal, K.; Swaminathan, K.; Xu, H. E.; Pioszak, A. A. Structural Basis for Hormone Recognition by the Human CRFR2(alpha) G Protein-Coupled Receptor. *J. Biol. Chem.* **2010**, *285*, 40351–40361.

(45) Grace, C. R.; Perrin, M. H.; DiGruccio, M. R.; Miller, C. L.; Rivier, J. E.; Vale, W. W.; Riek, R. NMR Structure and Peptide Hormone Binding Site of the First Extracellular Domain of a Type B1 G Protein-Coupled Receptor. *Proc. Natl. Acad. Sci. U. S. A.* **2004**, *101*, 12836–12841.

(46) Grace, C. R.; Perrin, M. H.; Gulyas, J.; Digruccio, M. R.; Cantele, J. P.; Rivier, J. E.; Vale, W. W.; Riek, R. Structure of the N-Terminal Domain of a Type B1 G Protein-Coupled Receptor in Complex with a Peptide Ligand. *Proc. Natl. Acad. Sci. U. S. A.* **2007**, *104*, 4858–4863.

(47) Grace, C. R.; Perrin, M. H.; Gulyas, J.; Rivier, J. E.; Vale, W. W.; Riek, R. NMR Structure of the First Extracellular Domain of Corticotropin-Releasing Factor Receptor 1 (ECD1-CRF-R1) Complexed with a High Affinity Agonist. *J. Biol. Chem.* **2010**, *285*, 38580–38589.

(48) Sun, C.; Song, D.; Davis-Taber, R. A.; Barrett, L. W.; Scott, V. E.; Richardson, P. L.; Pereda-Lopez, A.; Uchic, M. E.; Solomon, L. R.; Lake, M. R.; et al. Solution Structure and Mutational Analysis of Pituitary Adenylate Cyclase-Activating Polypeptide Binding to the Extracellular Domain of PAC1-RS. *Proc. Natl. Acad. Sci. U. S. A.* **2007**, *104*, 7875–7880.

(49) Kumar, S.; Pioszak, A.; Zhang, C.; Swaminathan, K.; Xu, H. E. Crystal Structure of the PAC1R Extracellular Domain Unifies a

Consensus Fold for Hormone Recognition by Class B G Protein-Coupled Receptors. *PLoS One* **2011**, *6*, e19682.

(50) ter Haar, E.; Koth, C. M.; Abdul-Manan, N.; Swenson, L.; Coll, J. T.; Lippke, J. A.; Lepre, C. A.; Garcia-Guzman, M.; Moore, J. M. Crystal Structure of the Ectodomain Complex of the CGRP Receptor, a Class-B GPCR, Reveals the Site of Drug Antagonism. *Structure* **2010**, *18*, 1083–1093.

(51) Kusano, S.; Kukimoto-Niino, M.; Hino, N.; Ohsawa, N.; Okuda, K.; Sakamoto, K.; Shirouzu, M.; Shindo, T.; Yokoyama, S. Structural Basis for Extracellular Interactions Between Calcitonin Receptor-Like Receptor and Receptor Activity-Modifying Protein 2 for Adrenomedullin-Specific Binding. *Protein Sci.* **2012**, *21*, 199–210.

(52) Booe, J. M.; Walker, C. S.; Barwell, J.; Kuteyi, G.; Simms, J.; Jamaluddin, M. A.; Warner, M. L.; Bill, R. M.; Harris, P. W.; Brimble, M. A.; et al. Structural Basis for Receptor Activity-Modifying Protein-Dependent Selective Peptide Recognition by a G Protein-Coupled Receptor. *Mol. Cell* **2015**, *58*, 1040–1052.

(53) Siu, F. Y.; He, M.; de Graaf, C.; Han, G. W.; Yang, D.; Zhang, Z.; Zhou, C.; Xu, Q.; Wacker, D.; Joseph, J. S.; et al. Structure of the Human Glucagon Class B G Protein-Coupled Receptor. *Nature* **2013**, *499*, 444–449.

(54) Hollenstein, K.; Kean, J.; Bortolato, A.; Cheng, R. K.; Dore, A. S.; Jazayeri, A.; Cooke, R. M.; Weir, M.; Marshall, F. H. Structure of Class B GPCR Corticotropin-Releasing Factor Receptor 1. *Nature* **2013**, *499*, 438–443.

(55) Hollenstein, K.; de Graaf, C.; Bortolato, A.; Wang, M. W.; Marshall, F. H.; Stevens, R. C. Insights into the Structure of Class B GPCRs. *Trends Pharmacol. Sci.* **2014**, *35*, 12–22.

(56) Lee, S. M.; Booe, J. M.; Pioszak, A. A. Structural Insights into Ligand Recognition and Selectivity for Classes A, B, and C GPCRs. *Eur. J. Pharmacol.* **2015**, *763*, 196–205.

(57) Wootten, D.; Simms, J.; Miller, L. J.; Christopoulos, A.; Sexton, P. M. Polar Transmembrane Interactions Drive Formation of Ligand-Specific and Signal Pathway-Biased Family B G Protein-Coupled Receptor Conformations. *Proc. Natl. Acad. Sci. U. S. A.* **2013**, *110*, 5211–5216.

(58) Ballesteros, J. A.; Weinstein, H. Integrated Methods for the Construction of Three-Dimensional Models and Computational Probing of Structure-Function Relations in G Protein-Coupled Receptors. *Methods Neurosci.* **1995**, *25*, 366–428.

(59) Gidon, A.; Al-Bataineh, M. M.; Jean-Alphonse, F. G.; Stevenson, H. P.; Watanabe, T.; Louet, C.; Khatri, A.; Calero, G.; Pastor-Soler, N. M.; Gardella, T. J.; et al. Endosomal GPCR Signaling Turned Off by Negative Feedback Actions of PKA and v-ATPase. *Nat. Chem. Biol.* **2014**, *10*, 707–709.

(60) Kuna, R. S.; Girada, S. B.; Asalla, S.; Vallentyne, J.; Maddika, S.; Patterson, J. T.; Smiley, D. L.; DiMarchi, R. D.; Mitra, P. Glucagon-Like Peptide-1 Receptor-Mediated Endosomal cAMP Generation Promotes Glucose-Stimulated Insulin Secretion in Pancreatic Beta-Cells. *Am. J. Physiol. Endocrinol. Metab.* **2013**, *305*, E161–170.

(61) Ferre, S.; Casado, V.; Devi, L. A.; Filizola, M.; Jockers, R.; Lohse, M. J.; Milligan, G.; Pin, J. P.; Guitart, X. G Protein-Coupled Receptor Oligomerization Revisited: Functional and Pharmacological Perspectives. *Pharmacol. Rev.* **2014**, *66*, 413–434.

(62) Kunishima, N.; Shimada, Y.; Tsuji, Y.; Sato, T.; Yamamoto, M.; Kumasaka, T.; Nakanishi, S.; Jingami, H.; Morikawa, K. Structural Basis of Glutamate Recognition by a Dimeric Metabotropic Glutamate Receptor. *Nature* **2000**, *407*, 971–977.

(63) Miller, L. J.; Dong, M.; Harikumar, K. G. Ligand Binding and Activation of the Secretin Receptor, a Prototypic Family B G Protein-Coupled Receptor. *Br. J. Pharmacol.* **2012**, *166*, 18–26.

(64) Harikumar, K. G.; Morfis, M. M.; Sexton, P. M.; Miller, L. J. Pattern of Intra-Family Hetero-Oligomerization Involving the G Protein-Coupled Secretin Receptor. *J. Mol. Neurosci.* **2008**, *36*, 279–285.

(65) Roed, S. N.; Orgaard, A.; Jorgensen, R.; De Meyts, P. Receptor Oligomerization in Family B1 of G Protein-Coupled Receptors: Focus on BRET Investigations and the Link Between GPCR Oligomerization

and Binding Cooperativity. *Front. Endocrinol. (Lausanne, Switz.)* **2012**, *3*, 62.

(66) Schelshorn, D.; Joly, F.; Mutel, S.; Hampe, C.; Breton, B.; Mutel, V.; Lutjens, R. Lateral Allosterism in the Glucagon Receptor Family: Glucagon-Like Peptide-1 Induces G Protein-Coupled Receptor Heteromer Formation. *Mol. Pharmacol.* **2012**, *81*, 309–318.

(67) Harikumar, K. G.; Pinon, D. I.; Miller, L. J. Transmembrane Segment IV Contributes a Functionally Important Interface for Oligomerization of the Class II G Protein-Coupled Secretin Receptor. *J. Biol. Chem.* **2007**, *282*, 30363–30372.

(68) Harikumar, K. G.; Happs, R. M.; Miller, L. J. Dimerization in the Absence of Higher-Order Oligomerization of the G Protein-Coupled Secretin Receptor. *Biochim. Biophys. Acta, Biomembr.* **2008**, *1778*, 2555–2563.

(69) Dong, M.; Xu, X.; Ball, A. M.; Makhoul, J. A.; Lam, P. C.; Pinon, D. I.; Orry, A.; Sexton, P. M.; Abagyan, R.; Miller, L. J. Mapping Spatial Approximations Between the Amino Terminus of Secretin and Each of the Extracellular Loops of Its Receptor Using Cysteine Trapping. *FASEB J.* **2012**, *26*, 5092–5105.

(70) Harikumar, K. G.; Ball, A. M.; Sexton, P. M.; Miller, L. J. Importance of Lipid-Exposed Residues in Transmembrane Segment Four for Family B Calcitonin Receptor Homo-Dimerization. *Regul. Pept.* **2010**, *164*, 113–119.

(71) Harikumar, K. G.; Wootten, D.; Pinon, D. I.; Koole, C.; Ball, A. M.; Furness, S. G.; Graham, B.; Dong, M.; Christopoulos, A.; Miller, L. J.; et al. Glucagon-Like Peptide-1 Receptor Dimerization Differentially Regulates Agonist Signaling but Does Not Affect Small Molecule Allosterism. *Proc. Natl. Acad. Sci. U. S. A.* **2012**, *109*, 18607–18612.

(72) Nolte, W. M.; Fortin, J. P.; Stevens, B. D.; Aspnes, G. E.; Griffith, D. A.; Hoth, L. R.; Ruggeri, R. B.; Mathiowetz, A. M.; Limberakis, C.; Hepworth, D.; et al. A Potentiator of Orthosteric Ligand Activity at GLP-1R Acts Via Covalent Modification. *Nat. Chem. Biol.* **2014**, *10*, 629–631.

(73) Harikumar, K. G.; Morfis, M. M.; Lisenbee, C. S.; Sexton, P. M.; Miller, L. J. Constitutive Formation of Oligomeric Complexes Between Family B G Protein-Coupled Vasoactive Intestinal Polypeptide and Secretin Receptors. *Mol. Pharmacol.* **2005**, *69*, 363–373.

(74) Langer, I.; Gaspard, N.; Robberecht, P. Pharmacological Properties of Chinese Hamster Ovary Cells Coexpressing Two Vasoactive Intestinal Peptide Receptors (hVPAC1 and hVPAC2). *Br. J. Pharmacol.* **2006**, *148*, 1051–1059.

(75) Whitaker, G. M.; Lynn, F. C.; McIntosh, C. H.; Accili, E. A. Regulation of GIP and GLP1 Receptor Cell Surface Expression by N-Glycosylation and Receptor Heteromerization. *PLoS One* **2012**, *7*, e32675.

(76) Navarro, G.; Quiroz, C.; Moreno-Delgado, D.; Sierakowiak, A.; McDowell, K.; Moreno, E.; Rea, W.; Cai, N. S.; Aguinaga, D.; Howell, L. A.; et al. Orexin-Corticotropin-Releasing Factor Receptor Heteromers in the Ventral Tegmental Area as Targets for Cocaine. *J. Neurosci.* **2015**, *35*, 6639–6653.

(77) Lee, L. T.; Ng, S. Y.; Chu, J. Y.; Sekar, R.; Harikumar, K. G.; Miller, L. J.; Chow, B. K. Transmembrane Peptides as Unique Tools to Demonstrate the In Vivo Action of a Cross-Class GPCR Heterocomplex. *FASEB J.* **2014**, *28*, 2632–2644.

(78) McLatchie, L. M.; Fraser, N. J.; Main, M. J.; Wise, A.; Brown, J.; Thompson, N.; Solari, R.; Lee, M. G.; Foord, S. M. RAMPs Regulate the Transport and Ligand Specificity of the Calcitonin-Receptor-Like Receptor. *Nature* **1998**, *393*, 333–339.

(79) Christopoulos, G.; Perry, K. J.; Morfis, M.; Tilakaratne, N.; Gao, Y.; Fraser, N. J.; Main, M. J.; Foord, S. M.; Sexton, P. M. Multiple Amylin Receptors Arise from Receptor Activity-Modifying Protein Interaction with the Calcitonin Receptor Gene Product. *Mol. Pharmacol.* **1999**, *56*, 235–242.

(80) Sexton, P. M.; Poyner, D. R.; Simms, J.; Christopoulos, A.; Hay, D. L. Modulating Receptor Function Through RAMPs: Can They Represent Drug Targets in Themselves? *Drug Discovery Today* **2009**, *14*, 413–419.

- (81) Hay, D. L.; Pioszak, A. A. Receptor Activity-Modifying Proteins (RAMPs): New Insights and Roles. *Annu. Rev. Pharmacol. Toxicol.* **2016**, *56*, 469–487.
- (82) Spengler, D.; Waeber, C.; Pantaloni, C.; Holsboer, F.; Bockaert, J.; Seeburg, P. H.; Journot, L. Differential Signal Transduction by Five Splice Variants of the PACAP Receptor. *Nature* **1993**, *365*, 170–175.
- (83) Koole, C.; Wootten, D.; Simms, J.; Valant, C.; Sridhar, R.; Woodman, O. L.; Miller, L. J.; Summers, R. J.; Christopoulos, A.; Sexton, P. M. Allosteric Ligands of the Glucagon-Like Peptide-1 Receptor (GLP-1R) Differentially Modulate Endogenous and Exogenous Peptide Responses in a Pathway-Selective Manner: Implications for Drug Screening. *Mol. Pharmacol.* **2010**, *78*, 456–465.
- (84) Ishihara, T.; Nakamura, S.; Kaziro, Y.; Takahashi, T.; Takahashi, K.; Nagata, S. Molecular Cloning and Expression of a cDNA Encoding the Secretin Receptor. *EMBO J.* **1991**, *10*, 1635–1641.
- (85) Kopin, A. S.; Wheeler, M. B.; Leiter, A. B. Secretin: Structure of the Precursor and Tissue Distribution of the mRNA. *Proc. Natl. Acad. Sci. U. S. A.* **1990**, *87*, 2299–2303.
- (86) Garcia, G. L.; Dong, M.; Miller, L. J. Differential Determinants for Coupling of Distinct G Proteins with the Class B Secretin Receptor. *Am. J. Physiol. Cell Physiol.* **2012**, *302*, C1202–1212.
- (87) Holtmann, M. H.; Roettger, B. F.; Pinon, D. I.; Miller, L. J. Role of Receptor Phosphorylation in Desensitization and Internalization of the Secretin Receptor. *J. Biol. Chem.* **1996**, *271*, 23566–23571.
- (88) Shetzline, M. A.; Premont, R. T.; Walker, J. K.; Vigna, S. R.; Caron, M. G. A Role for Receptor Kinases in the Regulation of Class II G Protein-Coupled Receptors: Phosphorylation and Desensitization of the Secretin Receptor. *J. Biol. Chem.* **1998**, *273*, 6756–6762.
- (89) Gardella, T. J.; Vilardaga, J. P. International Union of Basic and Clinical Pharmacology. XCIII. The Parathyroid Hormone Receptors - Family B G Protein-Coupled Receptors. *Pharmacol. Rev.* **2015**, *67*, 310–337.
- (90) Gesty-Palmer, D.; Chen, M.; Reiter, E.; Ahn, S.; Nelson, C. D.; Wang, S.; Eckhardt, A. E.; Cowan, C. L.; Spurney, R. F.; Luttrell, L. M.; et al. Distinct Beta-Arrestin- and G Protein-Dependent Pathways for Parathyroid Hormone Receptor-Stimulated ERK1/2 Activation. *J. Biol. Chem.* **2006**, *281*, 10856–10864.
- (91) Cupp, M. E.; Nayak, S. K.; Adem, A. S.; Thomsen, W. J. Parathyroid Hormone (PTH) and PTH-Related Peptide Domains Contributing to Activation of Different PTH Receptor-Mediated Signaling Pathways. *J. Pharmacol. Exp. Ther.* **2013**, *345*, 404–418.
- (92) Gardella, T. J.; Juppner, H. Interaction of PTH and PTHrP with Their Receptors. *Rev. Endocr. Metab. Disord.* **2000**, *1*, 317–329.
- (93) Wan, M.; Yang, C.; Li, J.; Wu, X.; Yuan, H.; Ma, H.; He, X.; Nie, S.; Chang, C.; Cao, X. Parathyroid Hormone Signaling through Low-Density Lipoprotein-Related Protein 6. *Genes Dev.* **2008**, *22*, 2968–2979.
- (94) Romero, G.; Sneddon, W. B.; Yang, Y.; Wheeler, D.; Blair, H. C.; Friedman, P. A. Parathyroid Hormone Receptor Directly Interacts with Dishevelled to Regulate Beta-Catenin Signaling and Osteoclastogenesis. *J. Biol. Chem.* **2010**, *285*, 14756–14763.
- (95) Bianchi, E. N.; Ferrari, S. L. Beta-Arrestin2 Regulates Parathyroid Hormone Effects on a p38 MAPK and NFκB Gene Expression Network in Osteoblasts. *Bone*. **2009**, *45*, 716–725.
- (96) Hoare, S. R. Mechanisms of Peptide and Nonpeptide Ligand Binding to Class B G Protein-Coupled Receptors. *Drug Discovery Today* **2005**, *10*, 417–427.
- (97) Goltzman, D.; Peytremann, A.; Callahan, E.; Tregear, G. W.; Potts, J. T., Jr. Analysis of the Requirements for Parathyroid Hormone Action in Renal Membranes with the Use of Inhibiting Analogues. *J. Biol. Chem.* **1975**, *250*, 3199–3203.
- (98) Gesty-Palmer, D.; Flannery, P.; Yuan, L.; Corsino, L.; Spurney, R.; Lefkowitz, R. J.; Luttrell, L. M. A Beta-Arrestin-Biased Agonist of the Parathyroid Hormone Receptor (PTH1R) Promotes Bone Formation Independent of G Protein Activation. *Sci. Transl. Med.* **2009**, *1*, 1ra1.
- (99) van der Lee, M. M.; Verkaar, F.; Wat, J. W.; van Offenbeek, J.; Timmerman, M.; Voorneveld, L.; van Lith, L. H.; Zaman, G. J. Beta-Arrestin-Biased Signaling of PTH Analogs of the Type 1 Parathyroid Hormone Receptor. *Cell. Signalling* **2013**, *25*, 527–538.
- (100) Cheloha, R. W.; Gellman, S. H.; Vilardaga, J. P.; Gardella, T. J. PTH Receptor-1 Signalling-Mechanistic Insights and Therapeutic Prospects. *Nat. Rev. Endocrinol.* **2015**, *11*, 712–724.
- (101) Okazaki, M.; Ferrandon, S.; Vilardaga, J. P.; Bouxsein, M. L.; Potts, J. T., Jr.; Gardella, T. J. Prolonged Signaling at the Parathyroid Hormone Receptor by Peptide Ligands Targeted to a Specific Receptor Conformation. *Proc. Natl. Acad. Sci. U. S. A.* **2008**, *105*, 16525–16530.
- (102) Ferrandon, S.; Feinstein, T. N.; Castro, M.; Wang, B.; Bouley, R.; Potts, J. T.; Gardella, T. J.; Vilardaga, J. P. Sustained Cyclic AMP Production by Parathyroid Hormone Receptor Endocytosis. *Nat. Chem. Biol.* **2009**, *5*, 734–742.
- (103) Polyzos, S. A.; Makras, P.; Efstathiadou, Z.; Anastasilakis, A. D. Investigational Parathyroid Hormone Receptor Analogs for the Treatment of Osteoporosis. *Expert Opin. Invest. Drugs* **2015**, *24*, 145–157.
- (104) Whitfield, J. F.; Isaacs, R. J.; Jouishomme, H.; MacLean, S.; Chakravarthy, B. R.; Morley, P.; Barisoni, D.; Regalia, E.; Armato, U. C-Terminal Fragment of Parathyroid Hormone-Related Protein, PTHrP-(107–111), Stimulates Membrane-Associated Protein Kinase C Activity and Modulates the Proliferation of Human and Murine Skin Keratinocytes. *J. Cell. Physiol.* **1996**, *166*, 1–11.
- (105) Neerup, T. S.; Stahlhut, M.; Petersen, J. S.; Dagaard, J. R.; Jensen, J. E.; Peng, Z.; Morko, J.; Thorkildsen, C. ZP2307, a Novel, Cyclic PTH(1–17) Analog that Augments Bone Mass in Ovariectomized Rats. *Bone*. **2011**, *48*, 1319–1327.
- (106) Lin, K.; Len, Y.; Feng, J.; Gao, H.; You, Q.; Lin, D.; Liu, J. Structure of a Novel PTH-Related Peptide hPTH' and Its Interaction with the PTH Receptor. *J. Pept. Sci.* **2012**, *18*, 413–417.
- (107) Whitfield, J. F.; Morley, P.; Willick, G.; Langille, R.; Ross, V.; MacLean, S.; Barbier, J. R. Cyclization by a Specific Lactam Increases the Ability of Human Parathyroid Hormone (hPTH)-(1–31)NH₂ to Stimulate Bone Growth in Ovariectomized Rats. *J. Bone Miner. Res.* **1997**, *12*, 1246–1252.
- (108) Cosman, F.; Lane, N. E.; Bolognese, M. A.; Zanchetta, J. R.; Garcia-Hernandez, P. A.; Sees, K.; Matriano, J. A.; Gaumer, K.; Daddona, P. E. Effect of Transdermal Teriparatide Administration on Bone Mineral Density in Postmenopausal Women. *J. Clin. Endocrinol. Metab.* **2010**, *95*, 151–158.
- (109) Horwitz, M. J.; Tedesco, M. B.; Sereika, S. M.; Hollis, B. W.; Garcia-Ocana, A.; Stewart, A. F. Direct Comparison of Sustained Infusion of Human Parathyroid Hormone-Related Protein-(1–36) [hPTHrP-(1–36)] Versus hPTH-(1–34) on Serum Calcium, Plasma 1,25-dihydroxyvitamin D Concentrations, and Fractional Calcium Excretion in Healthy Human Volunteers. *J. Clin. Endocrinol. Metab.* **2003**, *88*, 1603–1609.
- (110) Horwitz, M. J.; Tedesco, M. B.; Sereika, S. M.; Garcia-Ocana, A.; Bisello, A.; Hollis, B. W.; Gundberg, C.; Stewart, A. F. Safety and Tolerability of Subcutaneous PTHrP(1–36) in Healthy Human Volunteers: A Dose Escalation Study. *Osteoporosis Int.* **2006**, *17*, 225–230.
- (111) Pellegrini, M.; Bisello, A.; Rosenblatt, M.; Chorev, M.; Mierke, D. F. Conformational Studies of RS-66271, an Analog of Parathyroid Hormone-Related Protein with Pronounced Bone Anabolic Activity. *J. Med. Chem.* **1997**, *40*, 3025–3031.
- (112) Vickery, B. H.; Avnur, Z.; Cheng, Y.; Chiou, S. S.; Leaffer, D.; Caulfield, J. P.; Kimmel, D. B.; Ho, T.; Krstenansky, J. L. RS-66271, a C-Terminally Substituted Analog of Human Parathyroid Hormone-Related Protein (1–34), Increases Trabecular and Cortical Bone in Ovariectomized, Osteopenic Rats. *J. Bone Miner. Res.* **1996**, *11*, 1943–1951.
- (113) Vaudry, D.; Falluel-Morel, A.; Bourgault, S.; Basille, M.; Burel, D.; Wurtz, O.; Fournier, A.; Chow, B. K.; Hashimoto, H.; Galas, L.; et al. Pituitary Adenylate Cyclase-Activating Polypeptide and Its Receptors: 20 Years After the Discovery. *Pharmacol. Rev.* **2009**, *61*, 283–357.

- (114) Blechman, J.; Levkowitz, G. Alternative Splicing of the Pituitary Adenylate Cyclase-Activating Polypeptide Receptor PAC1: Mechanisms of Fine Tuning of Brain Activity. *Front. Endocrinol. (Lausanne, Switz.)* **2013**, *4*, 55.
- (115) Walker, C. S.; Sundrum, T.; Hay, D. L. PACAP Receptor Pharmacology and Agonist Bias: Analysis in Primary Neurons and Glia from the Trigeminal Ganglia and Transfected Cells. *Br. J. Pharmacol.* **2014**, *171*, 1521–1533.
- (116) Pisegna, J. R.; Wank, S. A. Cloning and Characterization of the Signal Transduction of Four Splice Variants of the Human Pituitary Adenylate Cyclase Activating Polypeptide Receptor. Evidence for Dual Coupling to Adenylate Cyclase and Phospholipase C. *J. Biol. Chem.* **1996**, *271*, 17267–17274.
- (117) Pantaloni, C.; Brabet, P.; Bilanges, B.; Dumuis, A.; Houssami, S.; Spengler, D.; Bockaert, J.; Journot, L. Alternative Splicing in the N-Terminal Extracellular Domain of the Pituitary Adenylate Cyclase-Activating Polypeptide (PACAP) Receptor Modulates Receptor Selectivity and Relative Potencies of PACAP-27 and PACAP-38 in Phospholipase C Activation. *J. Biol. Chem.* **1996**, *271*, 22146–22151.
- (118) Lutz, E. M.; Ronaldson, E.; Shaw, P.; Johnson, M. S.; Holland, P. J.; Mitchell, R. Characterization of Novel Splice Variants of the PAC1 Receptor in Human Neuroblastoma Cells: Consequences for Signaling by VIP and PACAP. *Mol. Cell. Neurosci.* **2006**, *31*, 193–209.
- (119) Chatterjee, T. K.; Liu, X.; Davisson, R. L.; Fisher, R. A. Genomic Organization of the Rat Pituitary Adenylate Cyclase-Activating Polypeptide Receptor Gene. Alternative Splicing within the 5'-Untranslated Region. *J. Biol. Chem.* **1997**, *272*, 12122–12131.
- (120) Moro, O.; Lerner, E. A. Maxadilan, the Vasodilator from Sand Flies, is a Specific Pituitary Adenylate Cyclase Activating Peptide Type I Receptor Agonist. *J. Biol. Chem.* **1997**, *272*, 966–970.
- (121) Nicole, P.; Lins, L.; Rouyer-Fessard, C.; Drouot, C.; Fulcrand, P.; Thomas, A.; Couvineau, A.; Martinez, J.; Brasseur, R.; Laburthe, M. Identification of Key Residues for Interaction of Vasoactive Intestinal Peptide with Human VPAC1 and VPAC2 Receptors and Development of a Highly Selective VPAC1 Receptor Agonist. Alanine Scanning and Molecular Modeling of the Peptide. *J. Biol. Chem.* **2000**, *275*, 24003–24012.
- (122) Gourlet, P.; Vertongen, P.; Vandermeers, A.; Vandermeers-Piret, M. C.; Rathe, J.; De Neef, P.; Waelbroeck, M.; Robberecht, P. The Long-Acting Vasoactive Intestinal Polypeptide Agonist RO 25–1553 is Highly Selective of the VIP2 Receptor Subclass. *Peptides* **1997**, *18*, 403–408.
- (123) Tsutsumi, M.; Claus, T. H.; Liang, Y.; Li, Y.; Yang, L.; Zhu, J.; Dela Cruz, F.; Peng, X.; Chen, H.; Yung, S. L.; et al. A Potent and Highly Selective VPAC2 Agonist Enhances Glucose-Induced Insulin Release and Glucose Disposal: A Potential Therapy for Type 2 Diabetes. *Diabetes* **2002**, *51*, 1453–1460.
- (124) Ramos-Alvarez, I.; Mantey, S. A.; Nakamura, T.; Nuche-Berenguer, B.; Moreno, P.; Moody, T. W.; Maderdrut, J. L.; Coy, D. H.; Jensen, R. T. A Structure-Function Study of PACAP Using Conformationally Restricted Analogs: Identification of PAC1 Receptor-Selective PACAP Agonists. *Peptides* **2015**, *66*, 26–42.
- (125) Christopoulos, A.; Christopoulos, G.; Morfis, M.; Udawela, M.; Laburthe, M.; Couvineau, A.; Kuwasako, K.; Tilakaratne, N.; Sexton, P. M. Novel Receptor Partners and Function of Receptor Activity-Modifying Proteins. *J. Biol. Chem.* **2003**, *278*, 3293–3297.
- (126) Hay, D. L.; Poyner, D. R.; Sexton, P. M. GPCR Modulation by RAMPs. *Pharmacol. Ther.* **2006**, *109*, 173–197.
- (127) Gorn, A. H.; Lin, H. Y.; Yamin, M.; Auron, P. E.; Flannery, M. R.; Tapp, D. R.; Manning, C. A.; Lodish, H. F.; Krane, S. M.; Goldring, S. R. Cloning, Characterization, and Expression of a Human Calcitonin Receptor from an Ovarian Carcinoma Cell Line. *J. Clin. Invest.* **1992**, *90*, 1726–1735.
- (128) Kuestner, R. E.; Elrod, R. D.; Grant, F. J.; Hagen, F. S.; Kuijper, J. L.; Matthewes, S. L.; O'Hara, P. J.; Sheppard, P. O.; Stroop, S. D.; Thompson, D. L.; et al. Cloning and Characterization of an Abundant Subtype of the Human Calcitonin Receptor. *Mol. Pharmacol.* **1994**, *46*, 246–255.
- (129) Taboulet, J.; Frenkian, M.; Frendo, J. L.; Feingold, N.; Jullienne, A.; de Vernejoul, M. C. Calcitonin Receptor Polymorphism is Associated with a Decreased Fracture Risk in Post-Menopausal Women. *Hum. Mol. Genet.* **1998**, *7*, 2129–2133.
- (130) Wolfe, L. A., 3rd; Fling, M. E.; Xue, Z.; Armour, S.; Kerner, S. A.; Way, J.; Rimele, T.; Cox, R. F. In Vitro Characterization of a Human Calcitonin Receptor Gene Polymorphism. *Mutat. Res., Fundam. Mol. Mech. Mutagen.* **2003**, *522*, 93–105.
- (131) Sexton, P. M.; Findlay, D. M.; Martin, T. J. Calcitonin. *Curr. Med. Chem.* **1999**, *6*, 1067–1093.
- (132) Poyner, D. R.; Sexton, P. M.; Marshall, I.; Smith, D. M.; Quirion, R.; Born, W.; Muff, R.; Fischer, J. A.; Foord, S. M. International Union of Pharmacology. XXXII. The Mammalian Calcitonin Gene-Related Peptides, Adrenomedullin, Amylin, and Calcitonin Receptors. *Pharmacol. Rev.* **2002**, *54*, 233–246.
- (133) Purdue, B. W.; Tilakaratne, N.; Sexton, P. M. Molecular Pharmacology of the Calcitonin Receptor. *Recept. Channels* **2002**, *8*, 243–255.
- (134) Yamamoto, Y.; Yamamoto, Y.; Udagawa, N.; Okumura, S.; Mizoguchi, T.; Take, I.; Yamauchi, H.; Yamauchi, H.; Noguchi, T.; Takahashi, N. Effects of Calcitonin on the Function of Human Osteoclast-Like Cells Formed From CD14-Positive Monocytes. *Cell Mol. Biol. (Noisy-le-grand)* **2006**, *52*, 25–31.
- (135) Watson, C.; Chen, G.; Irving, P.; Way, J.; Chen, W. J.; Kenakin, T. The Use of Stimulus-Biased Assay Systems to Detect Agonist-Specific Receptor Active States: Implications for the Trafficking of Receptor Stimulus by Agonists. *Mol. Pharmacol.* **2000**, *58*, 1230–1238.
- (136) Andreassen, K. V.; Hjuler, S. T.; Furness, S. G.; Sexton, P. M.; Christopoulos, A.; Nosjean, O.; Karsdal, M. A.; Henriksen, K. Prolonged Calcitonin Receptor Signaling by Salmon, but Not Human Calcitonin, Reveals Ligand Bias. *PLoS One* **2014**, *9*, e92042.
- (137) Hilton, J. M.; Dowton, M.; Houssami, S.; Sexton, P. M. Identification of Key Components in the Irreversibility of Salmon Calcitonin Binding to Calcitonin Receptors. *J. Endocrinol.* **2000**, *166*, 213–226.
- (138) Morfis, M.; Tilakaratne, N.; Furness, S. G.; Christopoulos, G.; Werry, T. D.; Christopoulos, A.; Sexton, P. M. Receptor Activity-Modifying Proteins Differentially Modulate the G Protein-Coupling Efficiency of Amylin Receptors. *Endocrinology* **2008**, *149*, 5423–5431.
- (139) Udawela, M.; Christopoulos, G.; Morfis, M.; Christopoulos, A.; Ye, S.; Tilakaratne, N.; Sexton, P. M. A Critical Role for the Short Intracellular C-Terminus in Receptor Activity-Modifying Protein Function. *Mol. Pharmacol.* **2006**, *70*, 1750–1760.
- (140) Udawela, M.; Christopoulos, G.; Tilakaratne, N.; Christopoulos, A.; Albiston, A.; Sexton, P. M. Distinct Receptor Activity-Modifying Protein Domains Differentially Modulate Interaction with Calcitonin Receptors. *Mol. Pharmacol.* **2006**, *69*, 1984–1989.
- (141) Dickerson, I. M. Role of CGRP-Receptor Component Protein (RCP) in CLR/RAMP Function. *Curr. Protein Pept. Sci.* **2013**, *14*, 407–415.
- (142) Evans, B. N.; Rosenblatt, M. I.; Mnayer, L. O.; Oliver, K. R.; Dickerson, I. M. CGRP-RCP, a Novel Protein Required for Signal Transduction at Calcitonin Gene-Related Peptide and Adrenomedullin Receptors. *J. Biol. Chem.* **2000**, *275*, 31438–31443.
- (143) Walker, C. S.; Conner, A. C.; Poyner, D. R.; Hay, D. L. Regulation of Signal Transduction by Calcitonin Gene-Related Peptide Receptors. *Trends Pharmacol. Sci.* **2010**, *31*, 476–483.
- (144) Hong, Y.; Hay, D. L.; Quirion, R.; Poyner, D. R. The Pharmacology of Adrenomedullin 2/Intermedin. *Br. J. Pharmacol.* **2012**, *166*, 110–120.
- (145) Kato, J.; Kitamura, K. Bench-to-Bedside Pharmacology of Adrenomedullin. *Eur. J. Pharmacol.* **2015**, *764*, 140–148.
- (146) Cheung, B. M. Y.; Tang, F. Adrenomedullin: Exciting New Horizons. *Recent Pat. Endocr., Metab. Immune Drug Discovery* **2012**, *6*, 4–17.
- (147) Watkins, H. A.; Rathbone, D. L.; Barwell, J.; Hay, D. L.; Poyner, D. R. Structure-Activity Relationships for Alpha-Calcitonin Gene-Related Peptide. *Br. J. Pharmacol.* **2013**, *170*, 1308–1322.

- (148) Hay, D. L.; Harris, P. W.; Kowalczyk, R.; Brimble, M. A.; Rathbone, D. L.; Barwell, J.; Conner, A. C.; Poyner, D. R. Structure-Activity Relationships of the N-Terminus of Calcitonin Gene-Related Peptide: Key Roles of Alanine-5 and Threonine-6 in Receptor Activation. *Br. J. Pharmacol.* **2014**, *171*, 415–426.
- (149) Taylor, M. M.; Samson, W. K. Stress Hormone Secretion is Altered by Central Administration of Intermedin/Adrenomedullin-2. *Brain Res.* **2005**, *1045*, 199–205.
- (150) Hashimoto, H.; Hyodo, S.; Kawasaki, M.; Shibata, M.; Saito, T.; Suzuki, H.; Otsubo, H.; Yokoyama, T.; Fujihara, H.; Higuchi, T.; et al. Adrenomedullin 2 (AM2)/Intermedin is a More Potent Activator of Hypothalamic Oxytocin-Secreting Neurons than AM Possibly Through an Unidentified Receptor in Rats. *Peptides* **2007**, *28*, 1104–1112.
- (151) Kubo, K.; Tokashiki, M.; Kuwasako, K.; Tamura, M.; Tsuda, S.; Kubo, S.; Yoshizawa-Kumagaye, K.; Kato, J.; Kitamura, K. Biological Properties of Adrenomedullin Conjugated with Polyethylene Glycol. *Peptides* **2014**, *57*, 118–121.
- (152) Koole, C.; Pabreja, K.; Savage, E. E.; Wootten, D.; Furness, S. G.; Miller, L. J.; Christopoulos, A.; Sexton, P. M. Recent Advances in Understanding GLP-1R (Glucagon-Like Peptide-1 Receptor) Function. *Biochem. Soc. Trans.* **2013**, *41*, 172–179.
- (153) Baggio, L. L.; Drucker, D. J. Biology of Incretins: GLP-1 and GIP. *Gastroenterology* **2007**, *132*, 2131–2157.
- (154) Pabreja, K.; Mohd, M. A.; Koole, C.; Wootten, D.; Furness, S. G. Molecular Mechanisms Underlying Physiological and Receptor Pleiotropic Effects Mediated by GLP-1R Activation. *Br. J. Pharmacol.* **2014**, *171*, 1114–1128.
- (155) Drab, S. R. Glucagon-Like Peptide-1 Receptor Agonists for Type 2 Diabetes: A Clinical Update of Safety and Efficacy. *Curr. Diabetes Rev.* **2016**, *12*, 1–11.
- (156) Tomlinson, B.; Hu, M.; Zhang, Y.; Chan, P.; Liu, Z. M. An Overview of New GLP-1 Receptor Agonists for Type 2 Diabetes. *Expert Opin. Invest. Drugs* **2016**, *25*, 145–158.
- (157) Johnson, L. M.; Barrick, S.; Hager, M. V.; McFedries, A.; Homan, E. A.; Rabaglia, M. E.; Keller, M. P.; Attie, A. D.; Saghatelian, A.; Bisello, A.; et al. A Potent Alpha/Beta-Peptide Analogue of GLP-1 with Prolonged Action In Vivo. *J. Am. Chem. Soc.* **2014**, *136*, 12848–12851.
- (158) Jorgensen, R.; Kubale, V.; Vrecl, M.; Schwartz, T. W.; Elling, C. E. Oxyntomodulin Differentially Affects Glucagon-Like Peptide-1 Receptor Beta-Arrestin Recruitment and Signaling through Galpha(s). *J. Pharmacol. Exp. Ther.* **2007**, *322*, 148–154.
- (159) Wootten, D.; Savage, E. E.; Willard, F. S.; Bueno, A. B.; Sloop, K. W.; Christopoulos, A.; Sexton, P. M. Differential Activation and Modulation of the Glucagon-Like Peptide-1 Receptor by Small Molecule Ligands. *Mol. Pharmacol.* **2013**, *83*, 822–834.
- (160) Wootten, D.; Savage, E. E.; Valant, C.; May, L. T.; Sloop, K. W.; Ficorilli, J.; Showalter, A. D.; Willard, F. S.; Christopoulos, A.; Sexton, P. Allosteric Modulation of Endogenous Metabolites as an Avenue for Drug Discovery. *Mol. Pharmacol.* **2012**, *82*, 281–290.
- (161) Li, N.; Lu, J.; Willars, G. B. Allosteric Modulation of the Activity of the Glucagon-Like Peptide-1 (GLP-1) Metabolite GLP-1 9–36 Amide at the GLP-1 Receptor. *PLoS One* **2012**, *7*, e47936.
- (162) Weston, C.; Poyner, D.; Patel, V.; Dowell, S.; Ladds, G. Investigating G Protein Signaling Bias at the Glucagon-Like Peptide-1 Receptor in Yeast. *Br. J. Pharmacol.* **2014**, *171*, 3651–3665.
- (163) Guo, X. H. The Value of Short- and Long-Acting Glucagon-Like Peptide-1 Agonists in the Management of Type 2 Diabetes Mellitus: Experience with Exenatide. *Curr. Med. Res. Opin.* **2016**, *32*, 61–76.
- (164) Mapelli, C.; Natarajan, S. I.; Meyer, J. P.; Bastos, M. M.; Bernatowicz, M. S.; Lee, V. G.; Pluscec, J.; Riexinger, D. J.; Sieber-McMaster, E. S.; Constantine, K. L.; et al. Eleven Amino Acid Glucagon-Like Peptide-1 Receptor Agonists with Antidiabetic Activity. *J. Med. Chem.* **2009**, *52*, 7788–7799.
- (165) Hoang, H. N.; Song, K.; Hill, T. A.; Derksen, D. R.; Edmonds, D. J.; Kok, W. M.; Limberakis, C.; Liras, S.; Loria, P. M.; Mascitti, V.; et al. Short Hydrophobic Peptides with Cyclic Constraints Are Potent Glucagon-Like Peptide-1 Receptor (GLP-1R) Agonists. *J. Med. Chem.* **2015**, *58*, 4080–4085.
- (166) Finan, B.; Ma, T.; Ottaway, N.; Muller, T. D.; Habegger, K. M.; Heppner, K. M.; Kirchner, H.; Holland, J.; Hembree, J.; Raver, C.; et al. Unimolecular Dual Incretins Maximize Metabolic Benefits in Rodents, Monkeys, and Humans. *Sci. Transl. Med.* **2013**, *5*, 209ra151.
- (167) Finan, B.; Yang, B.; Ottaway, N.; Smiley, D. L.; Ma, T.; Clemmensen, C.; Chabenne, J.; Zhang, L.; Habegger, K. M.; Fischer, K.; et al. A Rationally Designed Monomeric Peptide Triagonist Corrects Obesity and Diabetes in Rodents. *Nat. Med.* **2014**, *21*, 27–36.
- (168) Axelsen, L.; Keung, W.; Pedersen, H.; Meier, E.; Riber, D.; Kjolbye, A.; Petersen, J.; Proctor, S.; Holstein-Rathlou, N. H.; Lopaschuk, G. Glucagon and a Glucagon-GLP-1 Dual-Agonist Increases Cardiac Performance with Different Metabolic Effects in Insulin-Resistant Hearts. *Br. J. Pharmacol.* **2012**, *165*, 2736–2748.
- (169) Roed, S. N.; Wismann, P.; Underwood, C. R.; Kulahin, N.; Iversen, H.; Cappelen, K. A.; Schaffer, L.; Lehtonen, J.; Hecksher-Soerensen, J.; Secher, A.; et al. Real-Time Trafficking and Signaling of the Glucagon-Like Peptide-1 Receptor. *Mol. Cell. Endocrinol.* **2014**, *382*, 938–949.
- (170) Willard, F. S.; Wootten, D.; Showalter, A. D.; Savage, E. E.; Ficorilli, J.; Farb, T. B.; Bokvist, K.; Alsina-Fernandez, J.; Furness, S. G.; Christopoulos, A.; et al. Small Molecule Allosteric Modulation of the Glucagon-Like Peptide-1 Receptor Enhances the Insulinotropic Effect of Oxyntomodulin. *Mol. Pharmacol.* **2012**, *82*, 1066–1073.
- (171) Zhang, H.; Sturchler, E.; Zhu, J.; Nieto, A.; Cistrone, P. A.; Xie, J.; He, L.; Yea, K.; Jones, T.; Turn, R.; et al. Autocrine Selection of a GLP-1R G Protein Biased Agonist with Potent Antidiabetic Effects. *Nat. Commun.* **2015**, *6*, 8918.
- (172) Chen, D.; Liao, J.; Li, N.; Zhou, C.; Liu, Q.; Wang, G.; Zhang, R.; Zhang, S.; Lin, L.; Chen, K.; et al. A Nonpeptidic Agonist of Glucagon-Like Peptide-1 Receptors with Efficacy in Diabetic db/db Mice. *Proc. Natl. Acad. Sci. U. S. A.* **2007**, *104*, 943–948.
- (173) Knudsen, L. B.; Kiel, D.; Teng, M.; Behrens, C.; Bhumralkar, D.; Kodra, J. T.; Holst, J. J.; Jeppesen, C. B.; Johnson, M. D.; de Jong, J. C.; et al. Small-Molecule Agonists for the Glucagon-Like Peptide 1 Receptor. *Proc. Natl. Acad. Sci. U. S. A.* **2007**, *104*, 937–942.
- (174) Willard, F. S.; Bueno, A. B.; Sloop, K. W. Small Molecule Drug Discovery at the Glucagon-Like Peptide-1 Receptor. *Exp. Diabetes Res.* **2012**, *2012*, 1–9.
- (175) Coopman, K.; Huang, Y.; Johnston, N.; Bradley, S. J.; Wilkinson, G. F.; Willars, G. B. Comparative Effects of the Endogenous Agonist Glucagon-Like Peptide-1 (GLP-1)-(7–36) Amide and the Small-Molecule Ago-Allosteric Agent "Compound 2" at the GLP-1 Receptor. *J. Pharmacol. Exp. Ther.* **2010**, *334*, 795–808.
- (176) Cheong, Y. H.; Kim, M. K.; Son, M. H.; Kaang, B. K. Two Small Molecule Agonists of Glucagon-Like Peptide-1 Receptor Modulate the Receptor Activation Response Differently. *Biochem. Biophys. Res. Commun.* **2012**, *417*, 558–563.
- (177) Thompson, A.; Kanamarlapudi, V. Agonist-Induced Internalisation of the Glucagon-Like Peptide-1 Receptor is Mediated by the Galphaq Pathway. *Biochem. Pharmacol.* **2015**, *93*, 72–84.
- (178) Janssen, P.; Rotondo, A.; Mule, F.; Tack, J. Review Article: A Comparison of Glucagon-Like Peptides 1 and 2. *Aliment. Pharmacol. Ther.* **2013**, *37*, 18–36.
- (179) Yusta, B.; Boushey, R. P.; Drucker, D. J. The Glucagon-Like Peptide-2 Receptor Mediates Direct Inhibition of Cellular Apoptosis Aia a cAMP-Dependent Protein Kinase-Independent Pathway. *J. Biol. Chem.* **2000**, *275*, 35345–35352.
- (180) Munroe, D. G.; Gupta, A. K.; Kooshesh, F.; Vyas, T. B.; Rizkalla, G.; Wang, H.; Demchyshyn, L.; Yang, Z. J.; Kamboj, R. K.; Chen, H.; et al. Prototypic G Protein-Coupled Receptor for the Intestiniotropic Factor Glucagon-Like Peptide 2. *Proc. Natl. Acad. Sci. U. S. A.* **1999**, *96*, 1569–1573.
- (181) Yusta, B.; Somwar, R.; Wang, F.; Munroe, D.; Grinstein, S.; Klip, A.; Drucker, D. J. Identification of Glucagon-Like Peptide-2 (GLP-2)-Activated Signaling Pathways in Baby Hamster Kidney Fibroblasts Expressing the Rat GLP-2 Receptor. *J. Biol. Chem.* **1999**, *274*, 30459–30467.

- (182) Leen, J. L.; Izzo, A.; Upadhyay, C.; Rowland, K. J.; Dube, P. E.; Gu, S.; Heximer, S. P.; Rhodes, C. J.; Storm, D. R.; Lund, P. K.; et al. Mechanism of Action of Glucagon-Like Peptide-2 to Increase IGF-I mRNA in Intestinal Subepithelial Fibroblasts. *Endocrinology* **2011**, *152*, 436–446.
- (183) Yusta, B.; Estall, J.; Drucker, D. J. Glucagon-Like Peptide-2 Receptor Activation Engages Bad and Glycogen Synthase Kinase-3 in a Protein Kinase A-Dependent Manner and Prevents Apoptosis Following Inhibition of Phosphatidylinositol 3-Kinase. *J. Biol. Chem.* **2002**, *277*, 24896–24906.
- (184) Thulesen, J.; Knudsen, L. B.; Hartmann, B.; Hastrup, S.; Kissow, H.; Jeppesen, P. B.; Orskov, C.; Holst, J. J.; Poulsen, S. S. The Truncated Metabolite GLP-2 (3–33) Interacts with the GLP-2 Receptor as a Partial Agonist. *Regul. Pept.* **2002**, *103*, 9–15.
- (185) Wootten, D.; Savage, E. E.; Valant, C.; May, L. T.; Sloop, K. W.; Ficorilli, J.; Showalter, A. D.; Willard, F. S.; Christopoulos, A.; Sexton, P. M. Allosteric Modulation of Endogenous Metabolites as an Avenue for Drug Discovery. *Mol. Pharmacol.* **2012**, *82*, 281–290.
- (186) Jeppesen, P. B.; Sanguinetti, E. L.; Buchman, A.; Howard, L.; Scolapio, J. S.; Ziegler, T. R.; Gregory, J.; Tappenden, K. A.; Holst, J.; Mortensen, P. B. Teduglutide (ALX-0600), a Dipeptidyl Peptidase IV Resistant Glucagon-Like Peptide 2 Analogue, Improves Intestinal Function in Short Bowel Syndrome Patients. *Gut* **2005**, *54*, 1224–1231.
- (187) Yamazaki, K.; Terauchi, H.; Iida, D.; Fukumoto, H.; Suzuki, S.; Kagaya, T.; Aoki, M.; Koyama, K.; Seiki, T.; Takase, K.; et al. Allosteric Modulators of Human Glucagon-Like Peptide-2 Receptor. *Bioorg. Med. Chem. Lett.* **2012**, *22*, 6126–6135.
- (188) Widenmaier, S. B.; Kim, S. J.; Yang, G. K.; De Los Reyes, T.; Nian, C.; Asadi, A.; Seino, Y.; Kieffer, T. J.; Kwok, Y. N.; McIntosh, C. H. A GIP Receptor Agonist Exhibits Beta-Cell Anti-Apoptotic Actions in Rat Models of Diabetes Resulting in Improved Beta-Cell Function and Glycemic Control. *PLoS One* **2010**, *5*, e9590.
- (189) Gault, V. A.; O'Harte, F. P.; Harriott, P.; Mooney, M. H.; Green, B. D.; Flatt, P. R. Effects of the Novel (Pro3)GIP Antagonist and Exendin(9–39)Amide on GIP- and GLP-1-Induced Cyclic AMP Generation, Insulin Secretion and Postprandial Insulin Release in Obese Diabetic (ob/ob) Mice: Evidence that GIP is the Major Physiological Incretin. *Diabetologia* **2003**, *46*, 222–230.
- (190) Gelling, R. W.; Coy, D. H.; Pederson, R. A.; Wheeler, M. B.; Hinke, S.; Kwan, T.; McIntosh, C. H. GIP(6–30amide) Contains the High Affinity Binding Region of GIP and is a Potent Inhibitor of GIP1–42 Action In Vitro. *Regul. Pept.* **1997**, *69*, 151–154.
- (191) Gault, V. A.; O'Harte, F. P.; Harriott, P.; Flatt, P. R. Characterization of the Cellular and Metabolic Effects of a Novel Enzyme-Resistant Antagonist of Glucose-Dependent Insulinotropic Polypeptide. *Biochem. Biophys. Res. Commun.* **2002**, *290*, 1420–1426.
- (192) McClean, P. L.; Irwin, N.; Cassidy, R. S.; Holst, J. J.; Gault, V. A.; Flatt, P. R. GIP Receptor Antagonism Reverses Obesity, Insulin Resistance, and Associated Metabolic Disturbances Induced in Mice by Prolonged Consumption of High-Fat Diet. *Am. J. Physiol. Endocrinol. Metab.* **2007**, *293*, E1746–E1755.
- (193) Gault, V. A.; Porter, D. W.; Irwin, N.; Flatt, P. R. Comparison of Sub-Chronic Metabolic Effects of Stable Forms of Naturally Occurring GIP(1–30) and GIP(1–42) in High-Fat Fed Mice. *J. Endocrinol.* **2011**, *208*, 265–271.
- (194) Irwin, N.; Green, B. D.; Gault, V. A.; Cassidy, R. S.; O'Harte, F. P.; Harriott, P.; Flatt, P. R. Effects on Glucose Homeostasis and Insulin Secretion of Long Term Activation of the Glucose-Dependent Insulinotropic Polypeptide (GIP) Receptor by N-AcGIP(LysPAL37) in Normal Mice. *Peptides* **2006**, *27*, 893–900.
- (195) Kerr, B. D.; Irwin, N.; O'Harte, F. P.; Bailey, C. J.; Flatt, P. R.; Gault, V. A. Fatty Acid Derivatised Analogues of Glucose-Dependent Insulinotropic Polypeptide with Improved Antihyperglycaemic and Insulinotropic Properties. *Biochem. Pharmacol.* **2009**, *78*, 1008–1016.
- (196) Habegger, K. M.; Heppner, K. M.; Geary, N.; Bartness, T. J.; DiMarchi, R.; Tschoop, M. H. The Metabolic Actions of Glucagon Revisited. *Nat. Rev. Endocrinol.* **2010**, *6*, 689–697.
- (197) Campbell, J. E.; Drucker, D. J. Islet Alpha Cells and Glucagon - Critical Regulators of Energy Homeostasis. *Nat. Rev. Endocrinol.* **2015**, *11*, 329–338.
- (198) Exton, J. H.; Hardman, J. G.; Williams, T. F.; Sutherland, E. W.; Park, C. R. Effects of Guanosine 3',5'-Monophosphate on the Perfused Rat Liver. *J. Biol. Chem.* **1971**, *246*, 2658–2664.
- (199) Laville, M.; Khalfallah, Y.; Vidai, H.; Beylot, M.; Comte, B.; Riou, J. P. Hormonal Control of Glucose Production and Pyruvate Kinase Activity in Isolated Rat Liver Cells: Influence of Hypothyroidism. *Mol. Cell. Endocrinol.* **1987**, *50*, 247–253.
- (200) Sonne, O.; Gliemann, J. Receptor Binding of Glucagon and Adenosine 3',5'-Monophosphate Accumulation in Isolated Rat Fat Cells. *Biochim. Biophys. Acta, Gen. Subj.* **1977**, *499*, 259–272.
- (201) Epstein, S. E.; Skelton, C. L.; Levey, G. S.; Entman, M. Adenyl Cyclase and Myocardial Contractility. *Ann. Intern. Med.* **1970**, *72*, 561–578.
- (202) Mery, P. F.; Brechler, V.; Pavoine, C.; Pecker, F.; Fischmeister, R. Glucagon Stimulates the Cardiac Ca²⁺ Current by Activation of Adenyl Cyclase and Inhibition of Phosphodiesterase. *Nature* **1990**, *345*, 158–161.
- (203) Rodgers, R. L.; MacLeod, K. M.; McNeill, J. H. Responses of Rat and Guinea Pig Hearts to Glucagon. Lack of Evidence for a Dissociation Between Changes in Myocardial Cyclic 3',5'-Adenosine Monophosphate and Contractility. *Circ. Res.* **1981**, *49*, 216–225.
- (204) Jiang, Y.; Cypess, A. M.; Muse, E. D.; Wu, C. R.; Unson, C. G.; Merrifield, R. B.; Sakmar, T. P. Glucagon Receptor Activates Extracellular Signal-Regulated Protein Kinase 1/2 Via cAMP-Dependent Protein Kinase. *Proc. Natl. Acad. Sci. U. S. A.* **2001**, *98*, 10102–10107.
- (205) LaPierre, M. P.; Abraham, M. A.; Yue, J. T.; Filippi, B. M.; Lam, T. K. Glucagon Signalling in the Dorsal Vagal Complex is Sufficient and Necessary for High-Protein Feeding to Regulate Glucose Homeostasis In Vivo. *EMBO Rep.* **2015**, *16*, 1299–1307.
- (206) Ke, J.; Zhang, C.; Harikumar, K. G.; Zylstra-Diegel, C. R.; Wang, L.; Mowry, L. E.; Miller, L. J.; Williams, B. O.; Xu, H. E. Modulation of Beta-Catenin Signaling by Glucagon Receptor Activation. *PLoS One* **2012**, *7*, e33676.
- (207) Fujino, T.; Asaba, H.; Kang, M. J.; Ikeda, Y.; Sone, H.; Takada, S.; Kim, D. H.; Ioka, R. X.; Ono, M.; Tomoyori, H.; et al. Low-Density Lipoprotein Receptor-Related Protein 5 (LRP5) is Essential for Normal Cholesterol Metabolism and Glucose-Induced Insulin Secretion. *Proc. Natl. Acad. Sci. U. S. A.* **2003**, *100*, 229–234.
- (208) Rodgers, R. L. Glucagon and Cyclic AMP: Time to Turn the Page? *Curr. Diabetes Rev.* **2012**, *8*, 362–381.
- (209) Wakelam, M. J.; Murphy, G. J.; Hruby, V. J.; Houslay, M. D. Activation of Two Signal-Transduction Systems in Hepatocytes by Glucagon. *Nature* **1986**, *323*, 68–71.
- (210) Harney, J. A.; Rodgers, R. L. Insulin-Like Stimulation of Cardiac Fuel Metabolism by Physiological Levels of Glucagon: Involvement of PI3K but Not cAMP. *Am. J. Physiol. Endocrinol. Metab.* **2008**, *295*, E155–E161.
- (211) Ali, S.; Ussher, J. R.; Baggio, L. L.; Kabir, M. G.; Charron, M. J.; Ilkayeva, O.; Newgard, C. B.; Drucker, D. J. Cardiomyocyte Glucagon Receptor Signaling Modulates Outcomes in Mice with Experimental Myocardial Infarction. *Mol. Metab.* **2015**, *4*, 132–143.
- (212) Dalle, S.; Fontes, G.; Lajoix, A. D.; LeBrigand, L.; Gross, R.; Ribes, G.; Dufour, M.; Barry, L.; LeNguyen, D.; Bataille, D. Miniglucagon (Glucagon 19–29): A Novel Regulator of the Pancreatic Islet Physiology. *Diabetes* **2002**, *51*, 406–412.
- (213) Dalle, S.; Smith, P.; Blache, P.; LeNguyen, D.; LeBrigand, L.; Bergeron, F.; Ashcroft, F. M.; Bataille, D. Miniglucagon (Glucagon 19–29), A Potent and Efficient Inhibitor of Secretagogue-Induced Insulin Release Through a Ca²⁺ Pathway. *J. Biol. Chem.* **1999**, *274*, 10869–10876.
- (214) Weston, C.; Lu, J.; Li, N.; Barkan, K.; Richards, G. O.; Roberts, D. J.; Skerry, T. M.; Poyner, D.; Pardamwar, M.; Reynolds, C. A.; et al. Modulation of Glucagon Receptor Pharmacology by Receptor Activity-Modifying Protein-2 (RAMP2). *J. Biol. Chem.* **2015**, *290*, 23009–23022.

- (215) Houslay, M. D.; Wakelam, M. J.; Murphy, G. J.; Gawler, D. J.; Pyne, N. J. Glucagon Stimulates Adenylate Cyclase Through GR2 Glucagon Receptors: A Process which Can be Attenuated by Glucagon Stimulating Inositol Phospholipid Metabolism Through GR1 Glucagon Receptors. *Biochem. Soc. Trans.* **1987**, *15*, 21–24.
- (216) Frohman, L. A.; Kineman, R. D. Growth Hormone-Releasing Hormone and Pituitary Somatotrope Proliferation. *Minerva Endocrinol.* **2002**, *27*, 277–285.
- (217) Florea, V.; Majid, S. S.; Kanashiro-Takeuchi, R. M.; Cai, R. Z.; Block, N. L.; Schally, A. V.; Hare, J. M.; Rodrigues, C. O. Agonists of Growth Hormone-Releasing Hormone Stimulate Self-Renewal of Cardiac Stem Cells and Promote Their Survival. *Proc. Natl. Acad. Sci. U. S. A.* **2014**, *111*, 17260–17265.
- (218) Busto, R.; Schally, A. V.; Varga, J. L.; Garcia-Fernandez, M. O.; Groot, K.; Armatis, P.; Szepeshazi, K. The Expression of Growth Hormone-Releasing Hormone (GHRH) and Splice Variants of Its Receptor in Human Gastroenteropancreatic Carcinomas. *Proc. Natl. Acad. Sci. U. S. A.* **2002**, *99*, 11866–11871.
- (219) Chatzistamou, I.; Schally, A. V.; Varga, J. L.; Groot, K.; Busto, R.; Armatis, P.; Halmos, G. Inhibition of Growth and Metastases of MDA-MB-435 Human Estrogen-Independent Breast Cancers by an Antagonist of Growth Hormone-Releasing Hormone. *Anti-Cancer Drugs* **2001**, *12*, 761–768.
- (220) Kahan, Z.; Varga, J. L.; Schally, A. V.; Rekasi, Z.; Armatis, P.; Chatzistamou, I.; Czompoly, T.; Halmos, G. Antagonists of Growth Hormone-Releasing Hormone Arrest the Growth of MDA-MB-468 Estrogen-Independent Human Breast Cancers in Nude Mice. *Breast Cancer Res. Treat.* **2000**, *60*, 71–79.
- (221) Rekasi, Z.; Varga, J. L.; Schally, A. V.; Halmos, G.; Armatis, P.; Groot, K.; Czompoly, T. Antagonists of Growth Hormone-Releasing Hormone and Vasoactive Intestinal Peptide Inhibit Tumor Proliferation by Different Mechanisms: Evidence from In Vitro Studies on Human Prostatic and Pancreatic Cancers. *Endocrinology* **2000**, *141*, 2120–2128.
- (222) Kiaris, H.; Chatzistamou, I.; Schally, A. V.; Halmos, G.; Varga, J. L.; Koutselini, H.; Kalofoutis, A. Ligand-Dependent and -Independent Effects of Splice Variant 1 of Growth Hormone-Releasing Hormone Receptor. *Proc. Natl. Acad. Sci. U. S. A.* **2003**, *100*, 9512–9517.
- (223) Carakushansky, M.; Whatmore, A. J.; Clayton, P. E.; Shalet, S. M.; Gleeson, H. K.; Price, D. A.; Levine, M. A.; Salvatori, R. A New Missense Mutation in the Growth Hormone-Releasing Hormone Receptor Gene in Familial Isolated GH Deficiency. *Eur. J. Endocrinol.* **2003**, *148*, 25–30.
- (224) Salvatori, R.; Fan, X.; Phillips, J. A., 3rd; Espigares-Martin, R.; Martin De Lara, I.; Freeman, K. L.; Plotnick, L.; Al-Ashwal, A.; Levine, M. A. Three New Mutations in the Gene for the Growth Hormone (GH)-Releasing Hormone Receptor in Familial Isolated GH Deficiency Type Ib. *J. Clin. Endocrinol. Metab.* **2001**, *86*, 273–279.
- (225) Salvatori, R.; Hayashida, C. Y.; Aguiar-Oliveira, M. H.; Phillips, J. A., 3rd; Souza, A. H.; Gondo, R. G.; Toledo, S. P.; Conceicao, M. M.; Prince, M.; Maheshwari, H. G.; et al. Familial Dwarfism Due to a Novel Mutation of the Growth Hormone-Releasing Hormone Receptor Gene. *J. Clin. Endocrinol. Metab.* **1999**, *84*, 917–923.
- (226) Coy, D. H.; Jiang, N. Y.; Fuselier, J.; Murphy, W. A. Structural Simplification of Potent Growth Hormone-Releasing Hormone Analogs: Implications for Other Members of the VIP/GHRH/PACAP Family. *Ann. N. Y. Acad. Sci.* **1996**, *805*, 149–158.
- (227) Cai, R.; Schally, A. V.; Cui, T.; Szalontay, L.; Halmos, G.; Sha, W.; Kovacs, M.; Jaszberenyi, M.; He, J.; Rick, F. G.; et al. Synthesis of New Potent Agonistic Analogs of Growth Hormone-Releasing Hormone (GHRH) and Evaluation of Their Endocrine and Cardiac Activities. *Peptides* **2014**, *52*, 104–112.
- (228) Lovenberg, T. W.; Liaw, C. W.; Grigoriadis, D. E.; Clevenger, W.; Chalmers, D. T.; De Souza, E. B.; Oltersdorf, T. Cloning and Characterization of a Functionally Distinct Corticotropin-Releasing Factor Receptor Subtype from Rat Brain. *Proc. Natl. Acad. Sci. U. S. A.* **1995**, *92*, 836–840.
- (229) Vaughan, J.; Donaldson, C.; Bittencourt, J.; Perrin, M. H.; Lewis, K.; Sutton, S.; Chan, R.; Turnbull, A. V.; Lovejoy, D.; Rivier, C.; et al. Urocortin, a Mammalian Neuropeptide Related to Fish Urotensin I and to Corticotropin-Releasing Factor. *Nature* **1995**, *378*, 287–292.
- (230) Hsu, S. Y.; Hsueh, A. J. Human Stresscopin and Stresscopin-Related Peptide are Selective Ligands for the Type 2 Corticotropin-Releasing Hormone Receptor. *Nat. Med.* **2001**, *7*, 605–611.
- (231) Lewis, K.; Li, C.; Perrin, M. H.; Blount, A.; Kunitake, K.; Donaldson, C.; Vaughan, J.; Reyes, T. M.; Gulyas, J.; Fischer, W.; et al. Identification of Urocortin III, an Additional Member of the Corticotropin-Releasing Factor (CRF) Family with High Affinity for the CRF2 Receptor. *Proc. Natl. Acad. Sci. U. S. A.* **2001**, *98*, 7570–7575.
- (232) Bale, T. L.; Vale, W. W. CRF and CRF Receptors: Role in Stress Responsivity and Other Behaviors. *Annu. Rev. Pharmacol. Toxicol.* **2004**, *44*, 525–557.
- (233) Grammatopoulos, D. K.; Dai, Y.; Randeva, H. S.; Levine, M. A.; Karteris, E.; Easton, A. J.; Hillhouse, E. W. A Novel Spliced Variant of the Type 1 Corticotropin-Releasing Hormone Receptor with a Deletion in the Seventh Transmembrane Domain Present in the Human Pregnant Term Myometrium and Fetal Membranes. *Mol. Endocrinol.* **1999**, *13*, 2189–2202.
- (234) Ladds, G.; Davis, K.; Hillhouse, E. W.; Davey, J. Modified Yeast Cells to Investigate the Coupling of G Protein-Coupled Receptors to Specific G Proteins. *Mol. Microbiol.* **2003**, *47*, 781–792.
- (235) Papadopolou, N.; Chen, J.; Randeva, H. S.; Levine, M. A.; Hillhouse, E. W.; Grammatopoulos, D. K. Protein Kinase A-Induced Negative Regulation of the Corticotropin-Releasing Hormone R1alpha Receptor-Extracellularly Regulated Kinase Signal Transduction Pathway: The Critical Role of Ser301 for Signaling Switch and Selectivity. *Mol. Endocrinol.* **2004**, *18*, 624–639.
- (236) Wietfeld, D.; Heinrich, N.; Furkert, J.; Fechner, K.; Beyermann, M.; Bienert, M.; Berger, H. Regulation of the Coupling to Different G Proteins of Rat Corticotropin-Releasing Factor Receptor Type 1 in Human Embryonic Kidney 293 Cells. *J. Biol. Chem.* **2004**, *279*, 38386–38394.
- (237) Blank, S.; Arnoldi, M.; Khoshnavaz, S.; Treccani, L.; Kuntz, M.; Mann, K.; Grathwohl, G.; Fritz, M. The Nacre Protein Perlucin Nucleates Growth of Calcium Carbonate Crystals. *J. Microsc.* **2003**, *212*, 280–291.
- (238) Dautzenberg, F. M.; Gutknecht, E.; Van der Linden, I.; Olivares-Reyes, J. A.; Durrenberger, F.; Hauger, R. L. Cell-Type Specific Calcium Signaling by Corticotropin-Releasing Factor Type 1 (CRF1) and 2a (CRF2(a)) Receptors: Phospholipase C-Mediated Responses in Human Embryonic Kidney 293 but Not SK-N-MC Neuroblastoma Cells. *Biochem. Pharmacol.* **2004**, *68*, 1833–1844.
- (239) Gutknecht, E.; Van der Linden, I.; Van Kolen, K.; Verhoeven, K. F.; Vauquelin, G.; Dautzenberg, F. M. Molecular Mechanisms of Corticotropin-Releasing Factor Receptor-Induced Calcium Signaling. *Mol. Pharmacol.* **2009**, *75*, 648–657.
- (240) Markovic, D.; Grammatopoulos, D. K. Characterization of Structural Determinants of Type 1 Corticotropin Releasing Hormone (CRH) Receptor Signalling Properties. *Methods Mol. Biol.* **2010**, *634*, 285–307.
- (241) Slominski, A.; Pisarchik, A.; Tobin, D. J.; Mazurkiewicz, J. E.; Wortsman, J. Differential Expression of a Cutaneous Corticotropin-Releasing Hormone System. *Endocrinology* **2004**, *145*, 941–950.
- (242) Slominski, A.; Wortsman, J.; Pisarchik, A.; Zbytek, B.; Linton, E. A.; Mazurkiewicz, J. E.; Wei, E. T. Cutaneous Expression of Corticotropin-Releasing Hormone (CRH), Urocortin, and CRH Receptors. *FASEB J.* **2001**, *15*, 1678–1693.
- (243) Wu, S. V.; Yuan, P. Q.; Lai, J.; Wong, K.; Chen, M. C.; Ohning, G. V.; Tache, Y. Activation of Type 1 CRH Receptor Isoforms Induces Serotonin Release from Human Carcinoid BON-1N Cells: An Enterochromaffin Cell Model. *Endocrinology* **2011**, *152*, 126–137.
- (244) Valdenaire, O.; Giller, T.; Breu, V.; Gottowik, J.; Kilpatrick, G. A New Functional Isoform of the Human CRF2 Receptor for

Corticotropin-Releasing Factor. *Biochim. Biophys. Acta, Gene Struct. Expression* **1997**, *1352*, 129–132.

(245) Karteris, E.; Grammatopoulos, D.; Randeva, H.; Hillhouse, E. W. Signal Transduction Characteristics of the Corticotropin-Releasing Hormone Receptors in the Feto-Placental Unit. *J. Clin. Endocrinol. Metab.* **2000**, *85*, 1989–1996.

(246) Beyermann, M.; Heinrich, N.; Fechner, K.; Furkert, J.; Zhang, W.; Kraetke, O.; Bienert, M.; Berger, H. Achieving Signalling Selectivity of Ligands for the Corticotropin-Releasing Factor Type 1 Receptor by Modifying the Agonist's Signalling Domain. *Br. J. Pharmacol.* **2007**, *151*, 851–859.

(247) Bangasser, D. A.; Curtis, A.; Reyes, B. A.; Bethea, T. T.; Parastatidis, I.; Ischiropoulos, H.; Van Bockstaele, E. J.; Valentino, R. J. Sex Differences in Corticotropin-Releasing Factor Receptor Signaling and Trafficking: Potential Role in Female Vulnerability to Stress-Related Psychopathology. *Mol. Psychiatry* **2010**, *15* (877), 896–904.

(248) Wootten, D.; Lindmark, H.; Kadmiel, M.; Willcockson, H.; Caron, K. M.; Barwell, J.; Drmot, T.; Poyner, D. R. Receptor Activity Modifying Proteins (RAMPs) Interact with the VPAC2 Receptor and CRF1 Receptors and Modulate their Function. *Br. J. Pharmacol.* **2013**, *168*, 822–834.

(249) Illergard, K.; Kauko, A.; Elofsson, A. Why Are Polar Residues within the Membrane Core Evolutionary Conserved? *Proteins: Struct., Funct., Genet.* **2011**, *79*, 79–91.

(250) Zhou, F. X.; Cocco, M. J.; Russ, W. P.; Brunger, A. T.; Engelman, D. M. Interhelical Hydrogen Bonding Drives Strong Interactions in Membrane Proteins. *Nat. Struct. Biol.* **2000**, *7*, 154–160.

(251) Curran, A. R.; Engelman, D. M. Sequence Motifs, Polar Interactions and Conformational Changes in Helical Membrane Proteins. *Curr. Opin. Struct. Biol.* **2003**, *13*, 412–417.

(252) Angel, T. E.; Chance, M. R.; Palczewski, K. Conserved Waters Mediate Structural and Functional Activation of Family A (Rhodopsin-Like) G Protein-Coupled Receptors. *Proc. Natl. Acad. Sci. U. S. A.* **2009**, *106*, 8555–8560.

(253) Venkatakrishnan, A. J.; Deupi, X.; Lebon, G.; Tate, C. G.; Schertler, G. F.; Babu, M. M. Molecular Signatures of G Protein-Coupled Receptors. *Nature* **2013**, *494*, 185–194.

(254) Wootten, D.; Reynolds, C. A.; Koole, C.; Smith, K. J.; Mobarec, J. C.; Simms, J.; Quon, T.; Coudrat, T.; Furness, S. G.; Miller, L. J.; et al. A Hydrogen-Bonded Polar Network in the Core of the Glucagon-Like Peptide-1 Receptor Is a Fulcrum for Biased Agonism: Lessons from Class B Crystal Structures. *Mol. Pharmacol.* **2016**, *89*, 335–347.

(255) Chugunov, A. O.; Simms, J.; Poyner, D. R.; Dehouck, Y.; Rooman, M.; Gilis, D.; Langer, I. Evidence that Interaction Between Conserved Residues in Transmembrane Helices 2, 3, and 7 are Crucial for Human VPAC1 Receptor Activation. *Mol. Pharmacol.* **2010**, *78*, 394–401.

(256) Langer, I. Conformational Switches in the VPAC(1) Receptor. *Br. J. Pharmacol.* **2012**, *166*, 79–84.

(257) Solano, R. M.; Langer, I.; Perret, J.; Vertongen, P.; Juarranz, M. G.; Robberecht, P.; Waelbroeck, M. Two Basic Residues of the h-VPAC1 Receptor Second Transmembrane Helix Are Essential for Ligand Binding and Signal Transduction. *J. Biol. Chem.* **2001**, *276*, 1084–1088.

(258) Beinborn, M.; Worrall, C. I.; McBride, E. W.; Kopin, A. S. A Human Glucagon-Like Peptide-1 Receptor Polymorphism Results in Reduced Agonist Responsiveness. *Regul. Pept.* **2005**, *130*, 1–6.

(259) Koole, C.; Wootten, D.; Simms, J.; Valant, C.; Miller, L. J.; Christopoulos, A.; Sexton, P. M. Polymorphism and Ligand Dependent Changes in Human Glucagon-Like Peptide-1 Receptor (GLP-1R) Function: Allosteric Rescue of Loss of Function Mutation. *Mol. Pharmacol.* **2011**, *80*, 486–497.

(260) Koole, C.; Wootten, D.; Simms, J.; Miller, L. J.; Christopoulos, A.; Sexton, P. M. Second Extracellular Loop of Human Glucagon-like Peptide-1 Receptor (GLP-1R) Has a Critical Role in GLP-1 Peptide Binding and Receptor Activation. *J. Biol. Chem.* **2012**, *287*, 3642–3658.

(261) Koole, C.; Wootten, D.; Simms, J.; Savage, E. E.; Miller, L. J.; Christopoulos, A.; Sexton, P. M. Second Extracellular Loop of Human Glucagon-like Peptide-1 Receptor (GLP-1R) Differentially Regulates Orthosteric but Not Allosteric Agonist Binding and Function. *J. Biol. Chem.* **2012**, *287*, 3659–3673.

(262) Leach, K.; Sexton, P. M.; Christopoulos, A. Allosteric GPCR Modulators: Taking Advantage of Permissive Receptor Pharmacology. *Trends Pharmacol. Sci.* **2007**, *28*, 382–389.

(263) Hoare, S. R. Allosteric Modulators of Class B G Protein-Coupled Receptors. *Curr. Neuropharmacol.* **2007**, *5*, 168–179.

(264) Rocha E Silva, M. A Thermodynamic Approach to Problems of Drug Antagonism I. The "Charniere Theory". *Eur. J. Pharmacol.* **1969**, *6*, 294–302.

(265) Rickard, D. J.; Wang, F. L.; Rodriguez-Rojas, A. M.; Wu, Z.; Trice, W. J.; Hoffman, S. J.; Votta, B.; Stroup, G. B.; Kumar, S.; Nuttall, M. E. Intermittent Treatment with Parathyroid Hormone (PTH) as well as a Non-Peptide Small Molecule Agonist of the PTH1 Receptor Inhibits Adipocyte Differentiation in Human Bone Marrow Stromal Cells. *Bone* **2006**, *39*, 1361–1372.

(266) McDonald, I. M.; Austin, C.; Buck, I. M.; Dunstone, D. J.; Gaffen, J.; Griffin, E.; Harper, E. A.; Hull, R. A.; Kalindjian, S. B.; Linney, I. D.; et al. Discovery and Characterization of Novel, Potent, Non-Peptide Parathyroid Hormone-1 Receptor Antagonists. *J. Med. Chem.* **2007**, *50*, 4789–4792.

(267) Carter, P. H.; Liu, R. Q.; Foster, W. R.; Tamasi, J. A.; Tebben, A. J.; Favata, M.; Staal, A.; Cvijic, M. E.; French, M. H.; Dell, V.; et al. Discovery of a Small Molecule Antagonist of the Parathyroid Hormone Receptor by Using an N-Terminal Parathyroid Hormone Peptide Probe. *Proc. Natl. Acad. Sci. U. S. A.* **2007**, *104*, 6846–6851.

(268) Carter, P. H.; Dean, T.; Bhayana, B.; Khatri, A.; Rajur, R.; Gardella, T. J. Actions of the Small Molecule Ligands SW106 and AH-3960 on the Type-1 Parathyroid Hormone Receptor. *Mol. Endocrinol.* **2015**, *29*, 307–321.

(269) Chu, A.; Caldwell, J. S.; Chen, Y. A. Identification and Characterization of a Small Molecule Antagonist of Human VPAC(2) Receptor. *Mol. Pharmacol.* **2010**, *77*, 95–101.

(270) Tibaduiza, E. C.; Chen, C.; Beinborn, M. A Small Molecule Ligand of the Glucagon-Like Peptide-1 Receptor Targets Its Amino-Terminal Hormone Binding Domain. *J. Biol. Chem.* **2001**, *276*, 37787–37793.

(271) Sammons, M. F.; Lee, E. C. Recent Progress in the Development of Small-Molecule Glucagon Receptor Antagonists. *Bioorg. Med. Chem. Lett.* **2015**, *25*, 4057–4064.

(272) Eng, H.; Sharma, R.; McDonald, T. S.; Edmonds, D. J.; Fortin, J. P.; Li, X.; Stevens, B. D.; Griffith, D. A.; Limberakis, C.; Nolte, W. M.; et al. Demonstration of the Innate Electrophilicity of 4-(3-(benzyloxy)phenyl)-2-(ethylsulfinyl)-6-(trifluoromethyl)pyrimidine (BETP), a Small-Molecule Positive Allosteric Modulator of the Glucagon-Like Peptide-1 Receptor. *Drug Metab. Dispos.* **2013**, *41*, 1470–1479.

(273) Koole, C.; Wootten, D.; Simms, J.; Miller, L. J.; Christopoulos, A.; Sexton, P. M. Differential Impact of Amino Acid Substitutions on Critical Residues of the Human Glucagon-Like Peptide-1 Receptor Involved in Peptide Activity and Small-Molecule Allosteric. *J. Pharmacol. Exp. Ther.* **2015**, *353*, 52–63.

(274) Wootten, D.; Simms, J.; Koole, C.; Woodman, O. L.; Summers, R. J.; Christopoulos, A.; Sexton, P. M. Modulation of the Glucagon-Like Peptide-1 Receptor Signaling by Naturally Occurring and Synthetic Flavonoids. *J. Pharmacol. Exp. Ther.* **2011**, *336*, 540–550.

(275) Morris, L. C.; Nance, K. D.; Gentry, P. R.; Days, E. L.; Weaver, C. D.; Niswender, C. M.; Thompson, A. D.; Jones, C. K.; Locuson, C. W.; Morrison, R. D.; et al. Discovery of (S)-2-Cyclopentyl-N-((1-isopropylpyrrolidin-2-yl)-9-methyl-1-oxo-2,9-dihydro-1H-pyrido[3,4-b]indole-4-carboxamide (VU0453379): A Novel, CNS Penetrant Glucagon-Like Peptide 1 Receptor (GLP-1R) Positive Allosteric Modulator (PAM). *J. Med. Chem.* **2014**, *57*, 10192–10197.

(276) de Graaf, C.; Rein, C.; Piwnicka, D.; Giordanetto, F.; Rognan, D. Structure-Based Discovery of Allosteric Modulators of Two Related

Class B G Protein-Coupled Receptors. *ChemMedChem* **2011**, *6*, 2159–2169.

(277) Katayama, T.; Furuya, M.; Yamaichi, K.; Konishi, K.; Sugiura, N.; Murafuji, H.; Magota, K.; Saito, M.; Tanaka, S.; Oikawa, S. Discovery of a Non-Peptide Small Molecule that Selectively Mimics the Biological Actions of Calcitonin. *Biochim. Biophys. Acta, Gen. Subj.* **2001**, *1526*, 183–190.

(278) Boros, E. E.; Cowan, D. J.; Cox, R. F.; Mebrahtu, M. M.; Rabinowitz, M. H.; Thompson, J. B.; Wolfe, L. A., 3rd. Hantzsch Synthesis of Pyrazolo[1',2':1,2]pyrazolo[3,4-b]pyridines: Partial Agonists of the Calcitonin Receptor. *J. Org. Chem.* **2005**, *70*, 5331–5334.

(279) Dong, M.; Cox, R. F.; Miller, L. J. Juxtamembranous Region of the Amino Terminus of the Family B G Protein-Coupled Calcitonin Receptor Plays a Critical Role in Small-Molecule Agonist Action. *J. Biol. Chem.* **2009**, *284*, 21839–21847.

(280) He, M.; Guan, N.; Gao, W. W.; Liu, Q.; Wu, X. Y.; Ma, D. W.; Zhong, D. F.; Ge, G. B.; Li, C.; Chen, X. Y.; et al. A Continued Saga of Boc5, the First Non-Peptidic Glucagon-Like Peptide-1 Receptor Agonist with In Vivo Activities. *Acta Pharmacol. Sin.* **2012**, *33*, 148–154.

(281) Zhang, P.; Covic, L.; Kuliopulos, A. Pepducins and Other Lipidated Peptides as Mechanistic Probes and Therapeutics. *Methods Mol. Biol.* **2015**, *1324*, 191–203.

(282) O'Callaghan, K.; Kuliopulos, A.; Covic, L. Turning Receptors On and Off with Intracellular Pepducins: New Insights into G Protein-Coupled Receptor Drug Development. *J. Biol. Chem.* **2012**, *287*, 12787–12796.

(283) Archbold, J. K.; Flanagan, J. U.; Watkins, H. A.; Gingell, J. J.; Hay, D. L. Structural Insights Into RAMP Modification of Secretin Family G Protein-Coupled Receptors: Implications for Drug Development. *Trends Pharmacol. Sci.* **2011**, *32*, 591–600.



Recent advances in the determination of G protein-coupled receptor structures

David M Thal, Ziva Vuckovic, Christopher J Draper-Joyce, Yi-Lynn Liang, Alisa Glukhova, Arthur Christopoulos and Patrick M Sexton

G protein-coupled receptors (GPCRs) are the largest superfamily of cell surface receptor proteins and are important drug targets for many human diseases. In the last decade, remarkable progress has been made in the determination of atomic structures of GPCRs with over 200 structures from 53 unique receptors having been solved. Technological advances in protein engineering and X-ray crystallography have driven much of the progress to date. However, recent advances in cryo-electron microscopy have facilitated the structural determination of three new structures of active-state GPCRs in complex with heterotrimeric G protein. These advances have led to significant breakthroughs in our understanding of GPCR biology including not only how signal transducers such as G proteins or arrestins interact with receptors, but also pave the way for future structure-based drug design.

Address

Drug Discovery Biology, Monash Institute of Pharmaceutical Sciences, Monash University, 381 Royal Parade, Parkville 3052, Victoria, Australia

Corresponding authors: Thal, David M (david.thal@monash.edu), Sexton, Patrick M (patrick.sexton@monash.edu)

Current Opinion in Structural Biology 2018, 51:28–34

This review comes from a themed issue on **Membranes**

Edited by **Susan Buchanan** and **Nicholas Noinaj**

<https://doi.org/10.1016/j.sbi.2018.03.002>

0959-440/© 2018 Elsevier Ltd. All rights reserved.

Introduction

Since the first structures of rhodopsin in 2000 [1] and the β_2 adrenergic receptor in 2007 [2,3], the number of G protein-coupled receptor (GPCR) structures has increased almost exponentially, ushering in a GPCR structural revolution that has brought new insight into GPCR biology and renewed interest in GPCR drug discovery. The driving force behind the revolution was new techniques to aid GPCR expression, purification, and crystallization coinciding with advancements in

synchrotron technology [4]. At the beginning of the revolution, most GPCR structures were of inactive states as these conformations were more readily accessible to the developments at the time. There are now over 200 GPCR structures from more than 50 unique receptors spanning a range of conformational states from multiple inactive states, active-intermediate states, and active states in complex with G proteins or arrestin (Table 1). This review will focus on recent advances in protein engineering, synchrotron technology, and cryo-electron microscopy (cryo-EM) that have enabled new GPCR structures and brought new biological insight.

Engineering GPCRs for crystallization

While there are many obstacles to overcome when determining GPCRs structures, the main hurdles are purifying sufficient amounts of homogenous correctly folded protein and producing well-ordered diffracting crystals. Several innovative approaches were developed to overcome these challenges such as the use point mutations to add thermostability [5], fusion proteins to replace flexible loop regions with readily crystallizable proteins [2,6], binding partners to stabilize specific conformational states [7], and various combinations of these approaches. We will use the adenosine A_1 receptor (A_1 -AR) as exemplar of protein engineering to enable structure determination. Recently, two structures of the A_1 -AR were solved using different methods [8^{**},9^{*}]. In work from our laboratory, we initially tried to determine the structure of the A_1 -AR by designing constructs similar to a previously determined high-resolution structure of the related A_{2A} -AR [10]. These early constructs expressed poorly, and comparison of expression levels suggested that most of the receptor was internalized. Trafficking of GPCRs to the plasma membrane requires post-translational modifications [11], and the majority of GPCRs contain at least one N-glycosylation site. These sites are typically removed by either point mutation or enzymatic de-glycosylation as they introduce heterogeneity that can prevent crystallization. The A_1 -AR has no N-glycosylation sites on the N-terminus of the receptor, and, therefore, the first 22 amino acids from the human M_4 muscarinic acetylcholine receptor, which contains three N-glycosylation sites, were added to the A_1 -AR N-terminus to try and improve receptor expression and trafficking (Figure 1a). The addition of the M4 N-terminus resulted in a ~ 10 -fold increase

Table 1**GPCR structures by method^a**

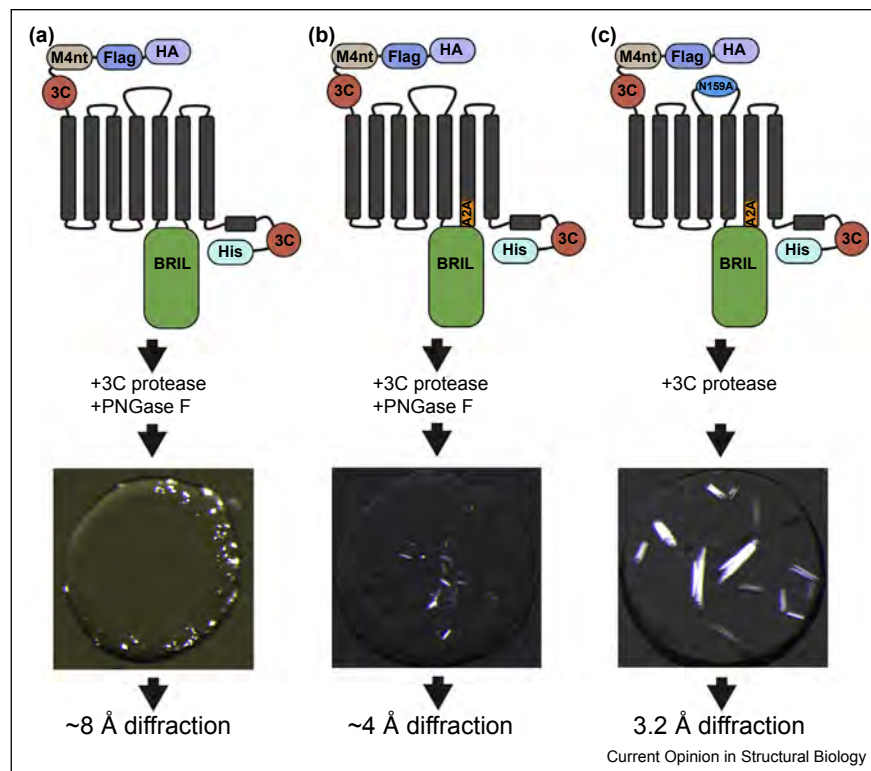
Method	PDB entries
X-ray crystallography	
LCP ^b	149
Vapor diffusion ^b	68
XFEL	17
Cryo-EM	3
Solid-state NMR	1
Solution NMR	2
Rerefinement	3
Total PDB entries	243
Unique GPCRs	53

^a PDB entries as of February 28th, 2018.^b Determined by synchrotron radiation.

in receptor expression and provided sufficient quantities to begin crystallization trials [8^{••}].

The first A₁-AR construct to go into crystallization trials had truncated N-termini and C-termini to remove labile ends and the insertion of a thermostable apocytochrome

b₅₆₂RIL (BRIL) between transmembrane (TM) 5 and TM6 to improve crystallization. This construct produced small crystals in numerous conditions; however, diffraction was limited to ~8 Å in resolution (Figure 1a). We next focused on altering the location of the BRIL fusion, as shifting the fusion site by a single residue can impact expression and crystallization [12,13,14[•]]. In the case of the A₁-AR, there is high sequence identity with the A_{2A}-AR around the BRIL insertion site. Therefore, a chimera was designed that replaced the first eight residues of TM6 (post-BRIL) in the A₁-AR with corresponding residues in the high-resolution A_{2A}-AR structure [10] (Figure 1b). The new A₁-AR chimera construct yielded crystals that were significantly improved in diffraction power ~4 Å. A similar fusion protein chimera strategy was used in the determination of the CC chemokine 2 receptor (CCR2) structure in which residues of TM5 and TM6 surrounding the T4L fusion were replaced by residues from the M2 muscarinic acetylcholine receptor [15[•],16]. Thus, creating receptor-fusion protein chimeras may be a viable approach to reducing some of the guesswork involved in placing fusion proteins.

Figure 1

Examples of engineered constructs for determination of the A₁-AR structure (PDB 5UEN). **(a)** The initial crystallization construct contained a hemagglutinin signal sequence (HA), a FLAG epitope (Flag), the N-terminus of the M4 receptor (M4nt), 3C protease cleavage sites (3C), a BRIL fusion between TM5 and TM6, and an 8x-histidine tag (His). The purified receptor was treated with 3C protease and PNGase F. Crystals in LCP were less than 10 μm in size and diffracted poorly. **(b)** A subsequent construct based on (a) was designed that replaced the first 8 residues of TM6, post-BRIL, with the corresponding residues of a high-resolution A_{2A}-AR structure (PDB 4EIY) highlighted in orange. These crystals were 10–20 μm in size with considerable improvement in resolution. **(c)** The final crystallization construct was based on (b), but incorporated mutation N159A to remove an N-glycosylation site. These crystals were 20–50 μm in size and diffracted to a resolution of 3.2 Å.

It was noted that the A₁-AR has an N-glycosylation site in the second extracellular loop (ECL2). In previous constructs, this site was removed by enzymatic treatment with the de-glycosylase PNGase F (Figure 1). Removal of N-glycosylation sites by enzymatic treatment is not always complete, so to further reduce sample heterogeneity the site was removed by mutation to alanine. The resulting construct produced crystals in lipid cubic phase (LCP) that were significantly larger and improved in diffraction power, allowing determination of the structure to a resolution of 3.2 Å (Figure 1c). A second A₁-AR structure was recently solved that was similar in design but included six mutations to improve receptor stability [9[•]]. In contrast, our A₁-AR study used a high-affinity irreversible antagonist to increase stability [8^{••}]. Together, these studies highlight the various strategies in protein engineering that are used to successfully determine GPCR structures, with the resultant structures providing novel insight into the mechanism of drug selectivity at adenosine receptors.

Advances in data collection

One of the main difficulties in determining GPCR structures by X-ray crystallography is producing well-diffracting crystals of sufficient size. Most non-rhodopsin GPCR structures were determined using LCP crystallization (Table 1), a technique that incorporates membrane proteins into a bi-continuous lipid bilayer to provide a more native-like environment that promotes crystallization [17]. Crystals grown in LCP vary in size but are typically 10–50 µm in the longest direction. Isolation of single crystals is nearly impossible due to their small size and the high viscosity of the surrounding LCP. Therefore, an entire bolus of LCP is harvested, which may contain as little as one to over a hundred crystals. Under these

conditions, data collection is challenging; however, developments in micro-focus X-ray sources at synchrotrons and X-ray free electron lasers (XFELs) have substantially improved data collection contributing to the rise in GPCR structures.

Data for most GPCR structures has been collected using micro-focus X-ray sources with beamlines at the Advanced Photon Source (APS), Diamond, SPring-8, and the European Synchrotron Radiation Facility (ESRF) being particularly successful [18]. New advances in data collection have combined the use of automatic rastering, data collection, and processing allowing users to collect and merge data from hundreds of crystals quickly. For example, a recent structure of the lysophosphatidic acid receptor 6 (LPA6) was determined at SPring-8 (BL32XU) with 241 crystals using automated collection and processing software [19[•],20].

Structures of the same GPCR determined by XFEL and synchrotron sources have allowed direct comparison between techniques (Table 2) [21,22^{••},23,24[•],25^{••},26–28,29^{••},30,31]. Both methods are suitable for small and fragile crystals, though synchrotron methods rely on cryo-cooled samples, while XFEL experiments are at room temperature [32]. Room temperature data collection can overcome problems that arise from cryo-cooling, and are more likely to accurately represent receptor structure and dynamics in native environments [33–36]. Structures of the 5-HT_{2B} receptor in complex with ergotamine were solved by synchrotron radiation to 2.7 Å [21] and by XFEL to 2.8 Å [22^{••}]. Overall, both structures are quite similar, though the XFEL structure has higher B-factors around the loop regions, which is consistent with the larger thermal motions that occur at higher temperature.

Table 2

GPCR structures determined by XFEL and comparative synchrotron radiation

GPCR	Structures by XFEL			Structures by synchrotron ^a		
	Resolution (Å)	PDB code	Refs.	Resolution (Å)	PDB code	Refs.
5-HT _{2B}	2.8	4NC3	[22 ^{••}]	2.7	4IB4	[21]
	3.0	5TUD	[54]			
A _{2A} -AR	2.5	5K2A	[23]	1.95	5NM2	[24 [•]]
	2.5	5K2B	[23]			
	1.9	5K2C	[23]			
	1.9	5K2D	[23]			
	1.7	5NM4	[24 [•]]			
Angiotensin II Type 2	2.8	5UNF	[25 ^{••}]	2.9	5UNH	[25 ^{••}]
	2.8	5UNG	[25 ^{••}]			
Angiotensin II Type 1	2.9	4YAY	[26]	2.8	4ZUD	[27]
Delta opioid	2.7	4RWD	[28]	3.28	4RWA	[28]
Glucagon	3.0	5XEZ	[29 ^{••}]	3.19	5XF1	[29 ^{••}]
Orexin 2	2.3	5WS3	[55]	1.96	5WQC	[55]
Smoothed	3.2	4O9R	[30]	3.0	5V57	[31]
	2.9	5V56	[31]			
Rhodopsin-arrestin	3.3	4ZWJ	[37 ^{••}]			
	3.0	5W0P	[38 [•]]			

^a Structure was chosen by publication of similar resolution to corresponding XFEL structure(s).

Since then, structures of eight more GPCRs have been determined by XFEL (Table 2), however the only uniquely solved structure is of rhodopsin in complex with arrestin [37^{••},38[•]].

One of the main developments enabling GPCR structure determination by XFEL is the use of a serial femtosecond crystallography (SFX) approach [39]. This method combines the high pulse rates of XFEL radiation with a high-viscosity LCP injector [30] and a high frame-rate detector, which can generate millions of detector images in a short time frame [32]. While there are drawbacks to using XFEL, including limited user access and challenges in detector development [40], these issues will resolve with time as new facilities and next-generation XFEL detectors come online [23]. Taking into account that half of solved XFEL structures were determined in the last year, this suggests that we can expect more XFEL structures in the near future.

Excitingly, technological advancements from XFEL are now being carried over to synchrotron sources allowing for room temperature data collection in an approach similar to SFX, but on a millisecond (SMX) rather than femtosecond timescale [24[•],41]. Recently, SMX was used to determine a high-resolution structure of the A_{2A}-AR that was of similar quality to a conventional cryo-cooled structure [24[•]]. The authors also demonstrate that SMX can produce high-quality data that is required for native-SAD phasing. In comparison to data collected on an XFEL, the SMX structures were of slightly lower resolution but needed less data for *de novo* phasing [24[•]]. Other new advances have aimed at making GPCR structure determination more high-throughput and include the use of LCP ligand soaking [42] and plate based (*in situ*) X-ray screening [43].

GPCR structures determined by single particle cryo-EM

In recent years, cryo-electron microscopy (cryo-EM) has emerged as a novel method for the determination of membrane protein structures [44]. Unlike X-ray crystallography, which requires proteins samples to be homogeneous in conformation, proteins with different conformations can be more readily separated using cryo-EM, thus allowing for a certain degree of sample heterogeneity. Cryo-EM requires only microgram quantities of protein, providing a significant advantage over X-ray crystallography. For these reasons, cryo-EM has been the long-time choice for determining structures of large and flexible macromolecules [45]. Recent technological advances in cryo-EM, including development of direct electron detectors, improvements in vitrification and image processing technology have enabled this method to be successfully applied to proteins smaller than 200 kDa [46]. Furthermore, a striking improvement in data collection quality for small particles has been accomplished with the

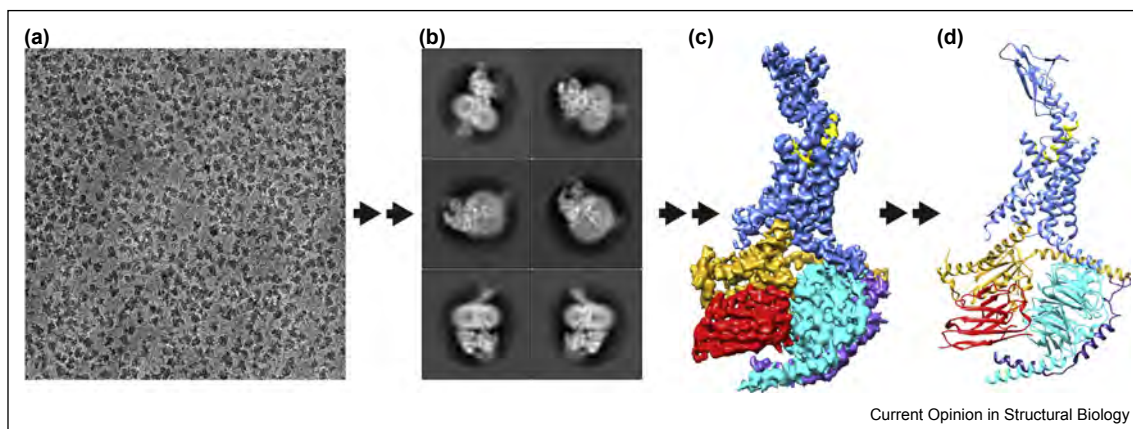
Volta phase plate, which dramatically increases the image contrast, allowing the structure of a small protein like hemoglobin (64 kDa) to be determined at 3.2 Å [47]. Overall, single particle cryo-EM provides an alternative method to obtain high-resolution protein structures, while avoiding the need for crystals.

Most structures of GPCRs have been determined by X-ray crystallography and in inactive or partially active conformations (Table 1). Structures of active GPCRs in complex with G proteins were limited to the β_2 -adrenergic receptor (β_2 AR) [48] and A_{2A}-AR [49[•]]. Challenges in GPCR complex crystallography include producing enough high-quality protein and the inherent conformational flexibility that hinders the formation of well-ordered crystals. Three recent publications addressed this problem by using single-particle cryo-EM as the method of structure determination [50^{••},51^{••},52], demonstrating that near-atomic resolution structures of GPCR complexes can be obtained using this technique. The cryo-EM structures of the calcitonin receptor (CTR) and the glucagon-like peptide-1 receptor in complex with heterotrimeric G protein (G_s) have provided valuable insight into understanding class B GPCR structure and function (Figure 2) [50^{••},51^{••}]. Using cryo-EM, multiple orientations of the receptor extracellular domain were observed in the CTR structure, which is a critical domain involved in the activation of all class B GPCRs [50^{••}]. Activation of both receptors drives a conformational rearrangement in the intracellular face of the TM bundle similar to class A GPCRs, formed by a sharp kink in the middle of TM6 around a highly conserved PXXG motif that is unique to class B GPCRs. This kink results in an outward movement of TM6 creating a binding pocket to accommodate the α 5-helix of the G α_s subunit (Figure 2). As observed previously in negative stain EM of the β_2 AR-G_s structure, both cryo-EM structures displayed a high degree of flexibility in the α -helical domain of G α_s . A notably different observation in both class B active structures is an extended helix-8 at the C-terminal tail of the receptor, which was absent in the β_2 AR-G_s structure. In the cryo-EM structures, helix-8 is near the G β subunit, suggesting that the C-terminal helix-8 of the receptor may be involved in direct interaction with heterotrimeric G proteins [50^{••}] (Figure 2). These recent breakthrough cryo-EM GPCR structures are examples of how the resolution obtained by this method can facilitate an understanding in the mechanisms of GPCR activation. Furthermore, ongoing advancements in detectors and data processing promise to increase both the utility and resolution of this method for GPCR structure determination.

Summary and outlook

There is no magic bullet when it comes to determining GPCR structures, as even the determination of closely related subfamily members can be challenging [8^{••},9[•]].

Figure 2



Determination of the CTR-Gs structure using single particle cryo-EM. **(a)** Representative Volta phase cryo-EM micrograph. **(b)** Reference-free two-dimensional averages of the CTR-Gs complex. **(c)** Final three-dimensional electron density map and **(d)** protein model (PDB 5UZ7) colored according to protein: CTR (blue), salmon-calcitonin (yellow), Gas (gold), Gb (cyan), Gg (purple), and nanobody-35 (Nb35, red).

This is perhaps to be expected given the extreme diversity of ligands that bind to GPCRs, coupled with their dynamic nature and the numerous proteins that interact with them. While, there are now structures for 53 unique GPCRs from over 200 PDB entries, these have presented many unexpected findings in regard to both the mode of ligand binding and the diversity of the structure required to enable ligand binding. Each new structure evolves our understanding of the complexity of this receptor superfamily, and there is still much to be learned about the ‘control’ of receptor activation as most GPCR structures are of inactive conformations. Encouragingly, researchers are continuously developing novel tools to aid GPCR structure determination. For instance, the re-engineering of G proteins to be more amenable to crystallography [49*,53] should facilitate future GPCR-G protein complexes. Further advances in technology at micro-focus beamlines and XFELs will continue to push the boundaries on data collection and improvements in the quality of datasets will be of direct use for structure-based drug design approaches. Furthermore, with the 2017 Nobel Prize in Chemistry awarded to the pioneers of cryo-EM, it is welcoming to see the first GPCR structures determined by this breakthrough technique. Altogether, the future is bright for GPCR structural biology as the rapid development of parallel techniques will undoubtedly bring forth many new biological insights and continue to accelerate structure-based drug design.

Acknowledgements

This work was funded by the National Health and Medical Research Council of Australia (NHMRC) (grant numbers 1055134, 1061044 and 1084246). D.M.T. and A.G. are Australian Research Council Discovery Early Career Research Fellows, P.M.S. is a NHMRC Principal Research Fellow and A.C. a NHMRC Senior Principal Research Fellow.

References and recommended reading

Papers of particular interest, published within the period of review, have been highlighted as:

- of special interest
 - of outstanding interest
1. Palczewski K, Kumasaka T, Hori T, Behnke CA, Motoshima H, Fox BA, Le Trong I, Teller DC, Okada T, Stenkamp RE *et al.*: **Crystal structure of rhodopsin: a G protein-coupled receptor.** *Science* 2000, **289**:739-745.
 2. Cherezov V, Rosenbaum DM, Hanson MA, Rasmussen SG, Thian FS, Kobilka TS, Choi HJ, Kuhn P, Weis WI, Kobilka BK *et al.*: **High-resolution crystal structure of an engineered human beta2-adrenergic G protein-coupled receptor.** *Science* 2007, **318**:1258-1265.
 3. Rasmussen SG, Choi HJ, Rosenbaum DM, Kobilka TS, Thian FS, Edwards PC, Burghammer M, Ratnala VR, Sanishvili R, Fischetti RF *et al.*: **Crystal structure of the human beta2 adrenergic G-protein-coupled receptor.** *Nature* 2007, **450**:383-387.
 4. Ghosh E, Kumari P, Jaiman D, Shukla AK: **Methodological advances: the unsung heroes of the GPCR structural revolution.** *Nat Rev Mol Cell Biol* 2015, **16**:69-81.
 5. Serrano-Vega MJ, Magnani F, Shibata Y, Tate CG: **Conformational thermostabilization of the beta1-adrenergic receptor in a detergent-resistant form.** *Proc Natl Acad Sci U S A* 2008, **105**:877-882.
 6. Chun E, Thompson AA, Liu W, Roth CB, Griffith MT, Katritch V, Kunken J, Xu F, Cherezov V, Hanson MA *et al.*: **Fusion partner toolchest for the stabilization and crystallization of G protein-coupled receptors.** *Structure* 2012, **20**:967-976.
 7. Manglik A, Kobilka BK, Steyaert J: **Nanobodies to study G protein-coupled receptor structure and function.** *Annu Rev Pharmacol Toxicol* 2017, **57**:19-37.
 8. Glukhova A, Thal DM, Nguyen AT, Vecchio EA, Jörg M, Scammells PJ, May LT, Sexton PM, Christopoulos A: **Structure of the adenosine A₁ receptor reveals the basis for subtype selectivity.** *Cell* 2017, **168**:867-877.e813.
 9. Cheng RKY, Segala E, Robertson N, Defflorian F, Dore AS, Errey JC, Fiez-Vandal C, Marshall FH, Cooke RM: **Structures of**
- The 3.2 Å resolution structure of the adenosine A₁-AR in complex with an irreversible antagonist. This structure provides insight into the ways selectivity among adenosine subtypes is achieved and identifies a secondary binding pocket as a possible allosteric site.

human A1 and A2A adenosine receptors with xanthines reveal determinants of selectivity. *Structure* 2017, **25**:1275–1285. e1274.

This subsequent 3.3 Å resolution structure of the adenosine A₁ structure in complex with an A₁-AR recapitulates important determinants for binding selectivity between the A₁ and A_{2A} adenosine receptors (see also Ref. [8••]).

10. Liu W, Chun E, Thompson AA, Chubukov P, Xu F, Katritch V, Han GW, Roth CB, Heitman LH, AP IJ et al.: **Structural basis for allosteric regulation of GPCRs by sodium ions.** *Science* 2012, **337**:232–236.
 11. Rands E, Candelore MR, Cheung AH, Hill WS, Strader CD, Dixon RA: **Mutational analysis of beta-adrenergic receptor glycosylation.** *J Biol Chem* 1990, **265**:10759–10764.
 12. Zou Y, Weis WI, Kobilka BK: **N-terminal T4 lysozyme fusion facilitates crystallization of a G protein coupled receptor.** *PLOS ONE* 2012, **7**:e46039.
 13. Granier S, Manglik A, Kruse AC, Kobilka TS, Thian FS, Weis WI, Kobilka BK: **Structure of the delta-opioid receptor bound to naltrindole.** *Nature* 2012, **485**:400–404.
 14. Lv X, Liu J, Shi Q, Tan Q, Wu D, Skinner JJ, Walker AL, Zhao L, Gu X, Chen N et al.: **In vitro expression and analysis of the 826 human G protein-coupled receptors.** *Protein Cell* 2016, **7**:325–337.
- An impressive study comparing expression of all 826 human GPCRs in insect cells with a BRIL fusion at either the N-terminus or between the third intracellular loop.
15. Zheng Y, Qin L, Zacarias NV, de Vries H, Han GW, Gustavsson M, Dabros M, Zhao C, Cherney RJ, Carter P et al.: **Structure of CC chemokine receptor 2 with orthosteric and allosteric antagonists.** *Nature* 2016, **540**:458–461.
- A 2.81 Å resolution structure of the CC chemokine receptor 2 in a ternary complex with an orthosteric and allosteric antagonist. Surprisingly, the allosteric modulator bound to a druggable pocket located near the intracellular surface. Determination of this structure involved the use of an M2 muscarinic acetylcholine receptor chimera at the T4L fusion site.
16. Haga K, Kruse AC, Asada H, Yurugi-Kobayashi T, Shiroishi M, Zhang C, Weis WI, Okada T, Kobilka BK, Haga T et al.: **Structure of the human M2 muscarinic acetylcholine receptor bound to an antagonist.** *Nature* 2012, **482**:547–551.
 17. Caffrey M: **A comprehensive review of the lipid cubic phase or in meso method for crystallizing membrane and soluble proteins and complexes.** *Acta Crystallogr F Struct Biol Commun* 2015, **71**:3–18.
 18. Tesmer JJ: **Hitchhiking on the heptahelical highway: structure and function of 7TM receptor complexes.** *Nat Rev Mol Cell Biol* 2016, **17**:439–450.
 19. Taniguchi R, Inoue A, Sayama M, Uwamizu A, Yamashita K, Hirata K, Yoshida M, Tanaka Y, Kato HE, Nakada-Nakura Y et al.: **Structural insights into ligand recognition by the lysophosphatidic acid receptor LPA6.** *Nature* 2017, **548**:356–360.
- The structure of the lysophosphatidic acid receptor LPA₆ was determined using automatic data collection and processing to determine a 3.20 Å resolution structure from an impressive 241 crystals.
20. Ueno G, Hikima T, Yamashita K, Hirata K, Hasegawa K, Murakami H, Furukawa Y, Mizuno N, Kumasaka T, Yamamoto M: **Remote access and automation of SPring-8 MX beamlines.** *AIP Conf Proc* 2016, **1741**:050021.
 21. Wacker D, Wang C, Katritch V, Han GW, Huang XP, Vardy E, McCorvy JD, Jiang Y, Chu M, Siu FY et al.: **Structural features for functional selectivity at serotonin receptors.** *Science* 2013, **340**:615–619.
 22. Liu W, Wacker D, Gati C, Han GW, James D, Wang D, Nelson G, Weierstall U, Katritch V, Barty A et al.: **Serial femtosecond crystallography of G protein-coupled receptors.** *Science* 2013, **342**:1521–1524.
- The first crystal structure of a GPCR determined by XFEL. Comparison of this 5-HT_{2B} structure with a traditional cryo-cooled structure revealed differences in the thermal motions and conformations of residues around the loop regions, which may better reflect receptor structure and dynamics in a cellular environment.
23. Batyuk A, Galli L, Ishchenko A, Han GW, Gati C, Popov PA, Lee MY, Stauch B, White TA, Barty A et al.: **Native phasing of X-ray free-electron laser data for a G protein-coupled receptor.** *Sci Adv* 2016, **2**:e1600292.
 24. Weinert T, Olieric N, Cheng R, Brunle S, James D, Ozerov D, Gashi D, Vera L, Marsh M, Jaeger K et al.: **Serial millisecond crystallography for routine room-temperature structure determination at synchrotrons.** *Nat Commun* 2017, **8**:542.
- An interesting study that used a high-viscosity LCP injector, typically used for XFEL experiments, to determine several room-temperature structures using synchrotron radiation. This includes multiple A_{2A}-AR structures that were determined in rapid time, and included comparison of structures determined by XFEL, SMX, and traditional methods.
25. Zhang H, Han GW, Batyuk A, Ishchenko A, White KL, Patel N, Sadybekov A, Zamylny B, Rudd MT, Hollenstein K et al.: **Structural basis for selectivity and diversity in angiotensin II receptors.** *Nature* 2017, **544**:327–332.
- The first structures of the angiotensin II type 2 receptor (AT₂R) bound to two different compounds. Interestingly, crystals of AT₂R in complex with compound 1 formed crystals more suitable for structure determination by XFEL, while crystals with compound 2 were more suitable for synchrotron radiation. Unexpectedly, helix-8 of AT₂R is in an unusual position stabilizing an active-like state, presumably blocking G protein and β-arrestin recruitment.
26. Zhang H, Unal H, Gati C, Han GW, Liu W, Zatzepin NA, James D, Wang D, Nelson G, Weierstall U et al.: **Structure of the angiotensin receptor revealed by serial femtosecond crystallography.** *Cell* 2015, **161**:833–844.
 27. Zhang H, Unal H, Desnoyer R, Han GW, Patel N, Katritch V, Karnik SS, Cherezov V, Stevens RC: **Structural basis for ligand recognition and functional selectivity at angiotensin receptor.** *J Biol Chem* 2015, **290**:29127–29139.
 28. Fenalti G, Zatzepin NA, Betti C, Giguere P, Han GW, Ishchenko A, Liu W, Guillemin K, Zhang H, James D et al.: **Structural basis for bifunctional peptide recognition at human delta-opioid receptor.** *Nat Struct Mol Biol* 2015, **22**:265–268.
 29. Zhang H, Qiao A, Yang D, Yang L, Dai A, de Graaf C, Reedtz-Runge S, Dharmarajan V, Zhang H, Han GW et al.: **Structure of the full-length glucagon class B G-protein-coupled receptor.** *Nature* 2017, **546**:259–264.
- The first structure of a full-length glucagon receptor (GCGR) determined at a resolution of 3.20 Å by synchrotron radiation and 3.0 Å by XFEL. Insight into the different conformational states of GCGR was provided by coupling data from molecular dynamic simulations with data from cross-linking experiments and hydrogen-deuterium exchange.
30. Weierstall U, James D, Wang C, White TA, Wang D, Liu W, Spence JC, Bruce Doak R, Nelson G, Fromme P et al.: **Lipidic cubic phase injector facilitates membrane protein serial femtosecond crystallography.** *Nat Commun* 2014, **5**:3309.
 31. Zhang X, Zhao F, Wu Y, Yang J, Han GW, Zhao S, Ishchenko A, Ye L, Lin X, Ding K et al.: **Crystal structure of a multi-domain human smoothened receptor in complex with a super stabilizing ligand.** *Nat Commun* 2017, **8**:15383.
 32. Johansson LC, Stauch B, Ishchenko A, Cherezov V: **A bright future for serial femtosecond crystallography with XFELs.** *Trends Biochem Sci* 2017, **42**:749–762.
 33. Moraes I, Evans G, Sanchez-Weatherby J, Newstead S, Stewart PD: **Membrane protein structure determination – the next generation.** *Biochim Biophys Acta* 2014, **1838**:78–87.
 34. Bill RM, Henderson PJ, Iwata S, Kunji ER, Michel H, Neutze R, Newstead S, Poolman B, Tate CG, Vogel H: **Overcoming barriers to membrane protein structure determination.** *Nat Biotechnol* 2011, **29**:335–340.
 35. Venkatakrishnan AJ, Deupi X, Lebon G, Tate CG, Schertler GF, Babu MM: **Molecular signatures of G-protein-coupled receptors.** *Nature* 2013, **494**:185–194.
 36. Kobilka B, Schertler GF: **New G-protein-coupled receptor crystal structures: insights and limitations.** *Trends Pharmacol Sci* 2008, **29**:79–83.
 37. Kang Y, Zhou XE, Gao X, He Y, Liu W, Ishchenko A, Barty A, White TA, Yefanov O, Han GW et al.: **Crystal structure of**

rhodopsin bound to arrestin by femtosecond X-ray laser.

Nature 2015, **523**:561-567.

The first structure of GPCR-arrestin complex. Synchrotron radiation resulted in a low-resolution dataset at 7.7 Å. Therefore, the structure was determined by XFEL to a resolution of 3.3–3.8 Å (anisotropic) highlighting the usefulness of this technique for determining the structures of challenging proteins.

38. Zhou XE, He Y, de Waal PW, Gao X, Kang Y, Van Eps N, Yin Y, Pal K, Goswami D, White TA *et al.*: **Identification of phosphorylation codes for arrestin recruitment by G protein-coupled receptors.** *Cell* 2017, **170**:457–469.e413.

Reprocessing of previous XFEL data using new software has led to a higher resolution structure (0.2–0.3 Å difference in resolution) of rhodopsin in complex with arrestin. The improvement in resolution allows the detection of phosphorylated residues in the C-terminus of the structure, and provides a basis for determining a common phosphorylation code among GPCRs.

39. Chapman HN, Fromme P, Barty A, White TA, Kirian RA, Aquila A, Hunter MS, Schulz J, DePonte DP, Weierstall U *et al.*: **Femtosecond X-ray protein nanocrystallography.** *Nature* 2011, **470**:73–77.
40. Fromme P: **XFELs open a new era in structural chemical biology.** *Nat Chem Biol* 2015, **11**:895–899.
41. Martin-Garcia JM, Conrad CE, Nelson G, Stander N, Zatspein NA, Zook J, Zhu L, Geiger J, Chun E, Kissick D *et al.*: **Serial millisecond crystallography of membrane and soluble protein microcrystals using synchrotron radiation.** *IUCrJ* 2017, **4**:439–454.
42. Rucktooa P, Cheng RKY, Segala E, Geng T, Errey JC, Brown GA, Cooke RM, Marshall FH, Dore AS: **Towards high throughput GPCR crystallography: in meso soaking of adenosine A2A receptor crystals.** *Sci Rep* 2018, **8**:41.
43. Broecker J, Morizumi T, Ou WL, Klingel V, Kuo A, Kissick DJ, Ishchenko A, Lee MY, Xu S, Makarov O *et al.*: **High-throughput in situ X-ray screening of and data collection from protein crystals at room temperature and under cryogenic conditions.** *Nat Protoc* 2018, **13**:260–292.
44. Fernandez-Leiro R, Scheres SH: **Unravelling biological macromolecules with cryo-electron microscopy.** *Nature* 2016, **537**:339–346.
45. Jonić S: **Cryo-electron microscopy analysis of structurally heterogeneous macromolecular complexes.** *Comput Struct Biotechnol J* 2016, **14**:385–390.
46. Danev R, Baumeister W: **Expanding the boundaries of cryo-EM with phase plates.** *Curr Opin Struct Biol* 2017, **46**:87–94.
47. Khoshouei M, Radjainia M, Baumeister W, Danev R: **Cryo-EM structure of haemoglobin at 3.2 Å determined with the Volta phase plate.** *Nat Commun* 2017, **8**:16099.

48. Rasmussen SG, DeVree BT, Zou Y, Kruse AC, Chung KY, Kobilka TS, Thian FS, Chae PS, Pardon E, Calinski D *et al.*: **Crystal structure of the beta2 adrenergic receptor-Gs protein complex.** *Nature* 2011, **477**:549–555.

49. Carpenter B, Nehme R, Warne T, Leslie AG, Tate CG: **Structure of the adenosine A(2A) receptor bound to an engineered G protein.** *Nature* 2016, **536**:104–107.

A 3.4 Å resolution structure of an active-state A_{2A}-R in complex with a mini-G_s protein. This structure revealed a common mechanism for the coupling of G_s to different GPCRs. The resultant work also provides new avenues for determining GPCR-G protein complexes (also see Ref. [53]).

50. Liang YL, Khoshouei M, Radjainia M, Zhang Y, Glukhova A, Tarrasch J, Thal DM, Furness SGB, Christopoulos G, Coudrat T *et al.*: **Phase-plate cryo-EM structure of a class B GPCR-G protein complex.** *Nature* 2017, **546**:118–123.

This first structure of a GPCR determined by cryo-EM is also the first structure of a full-length class B GPCR in complex with G_s. Notably, the only modification to the receptor was replacement of the native signal peptide, and insertion of tags at the N-termini and C-termini for purification. Overall, this structure revealed important similarities and differences between class A and class B GPCR-G_s complexes, and marks the transformation of GPCR structural biology into the era of cryo-EM.

51. Zhang Y, Sun B, Feng D, Hu H, Chu M, Qu Q, Tarrasch JT, Li S, Sun Kobilka T, Kobilka BK *et al.*: **Cryo-EM structure of the activated GLP-1 receptor in complex with a G protein.** *Nature* 2017, **546**:248–252.

Cryo-EM structure of the glucagon-like peptide 1 receptor (GLP-1R) in complex with G_s at a resolution of 4.1 Å. This structure highlights commonalities in class B receptor activation, and further demonstrates the power of cryo-EM.

52. Liang YL, Khoshouei M, Glukhova A, Furness SGB, Zhao P, Clydesdale L, Koole C, Truong TT, Thal DM, Lei S *et al.*: **Phase-plate cryo-EM structure of a biased agonist-bound human GLP-1 receptor-Gs complex.** *Nature* 2018 <http://dx.doi.org/10.1038/nature25773>.
53. Nehme R, Carpenter B, Singhal A, Stregre A, Edwards PC, White CF, Du H, Grishammer R, Tate CG: **Mini-G proteins: novel tools for studying GPCRs in their active conformation.** *PLOS ONE* 2017, **12**:e0175642.
54. Ishchenko A, Wacker D, Kapoor M, Zhang A, Han GW, Basu S, Patel N, Messerschmidt M, Weierstall U, Liu W *et al.*: **Structural insights into the extracellular recognition of the human serotonin 2B receptor by an antibody.** *Proc Natl Acad Sci U S A* 2017, **114**:8223–8228.
55. Suno R, Kimura KT, Nakane T, Yamashita K, Wang J, Fujiwara T, Yamanaka Y, Im D, Horita S, Tsujimoto H *et al.*: **Crystal structures of human orexin 2 receptor bound to the subtype-selective antagonist EMPA.** *Structure* 2018, **26**:7–19.e15.

Mechanisms of signalling and biased agonism in G protein-coupled receptors

Denise Wootten^{1,2*}, Arthur Christopoulos¹, Maria Marti-Solano³, M. Madan Babu^{1,2*} and Patrick M. Sexton^{1,2*}

Abstract | G protein-coupled receptors (GPCRs) are the largest group of cell surface receptors in humans that signal in response to diverse inputs and regulate a plethora of cellular processes. Hence, they constitute one of the primary drug target classes. Progress in our understanding of GPCR dynamics, activation and signalling has opened new possibilities for selective drug development. A key advancement has been provided by the concept of biased agonism, which describes the ability of ligands acting at the same GPCR to elicit distinct cellular signalling profiles by preferentially stabilizing different active conformational states of the receptor. Application of this concept raises the prospect of 'designer' biased agonists as optimized therapeutics with improved efficacy and/or reduced side-effect profiles. However, this application will require a detailed understanding of the spectrum of drug actions and a structural understanding of the drug–receptor interactions that drive distinct pharmacologies. The recent revolution in GPCR structural biology provides unprecedented insights into ligand binding, conformational dynamics and the control of signalling outcomes. These insights, together with new approaches to multi-dimensional analysis of drug action, are allowing refined classification of drugs according to their pharmacodynamic profiles, which can be linked to receptor structure and predictions of preclinical drug efficacy.

Rhodopsin

A light-sensitive G protein-coupled receptor involved in visual phototransduction.

¹Drug Discovery Biology, Monash Institute of Pharmaceutical Sciences, Monash University, Parkville, Victoria, Australia.

²School of Pharmacy, Fudan University, Shanghai, China.

³MRC Laboratory of Molecular Biology, Francis Crick Avenue, Cambridge Biomedical Campus, Cambridge, UK.

*e-mail: denise.wootten@monash.edu; patrick.sexton@monash.edu

<https://doi.org/10.1038/s41580-018-0049-3>

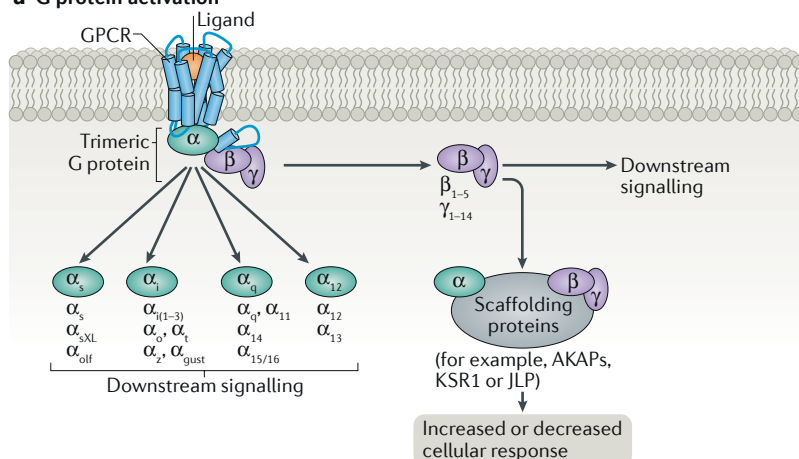
G protein-coupled receptors (GPCRs) are the largest family of cell surface receptor proteins in eukaryotes. In humans, they are encoded by over 800 individual genes and are widely expressed in various tissues, where they control a broad range of physiological processes. The pervasive role of GPCRs in human physiology arises from evolutionary diversity in the sequence encoding the seven transmembrane domains (TMDs), which form the core of the receptor common to all GPCRs. On the basis of sequence and evolutionary conservation, these receptors are divided into subfamilies that include class A (rhodopsin-like), class B1 (secretin receptor-like), class B2 (adhesion receptors), class C (metabotropic glutamate receptor-like) and class F (frizzled-like) subfamilies as well as the taste 2 sensory receptor subfamily (GPCR Database). GPCR diversity is further elaborated by numerous mechanisms including alternative splicing, RNA editing, post-translational modifications and protein–protein interactions that alter both the repertoire of ligand interaction and the functional consequences of receptor activation¹. This diversity allows these receptors to recognize and respond to an enormous variety of

ligands that range from photons, odorants, ions, small neurotransmitters and small neuromodulatory peptides to large peptide hormones, glycoprotein hormones and other large protein domains, including those involved in direct cell–cell communication and viral entry². Another key component of the versatility of GPCR signalling is the breadth of intracellular proteins that they can engage with (see next paragraph). These intracellular partners include numerous heterotrimeric G proteins, which serve as canonical transducer proteins, as well as regulatory and scaffolding proteins such as arrestins, PDZ-domain-containing scaffolds and non-PDZ scaffolds, such as A kinase anchor proteins (AKAPs) that initiate or control distinct patterns of signalling^{3–7} (FIG. 1).

To elicit signalling, GPCRs need to couple with intracellular transducers such as heterotrimeric G proteins, which are formed by G α , G β and G γ subunits. In humans, there are 16 G α , 5 G β and 13 G γ subunits that can combine to form a wide range of heterotrimeric G proteins. Each G α subunit can signal independently, whereas the G β subunits and G γ subunits are obligate heterodimers that function as a single unit (G $\beta\gamma$).

The 16 Ga subunits can be classified into 4 major Ga families (G_s , $G_{i/o}$, $G_{q/11}$ and $G_{12/13}$) that regulate key effectors (for example, adenylyl cyclase, phospholipase C, etc.) and the generation of secondary messengers (for example,

a G protein activation



b Scaffolding proteins regulating GPCR signalling

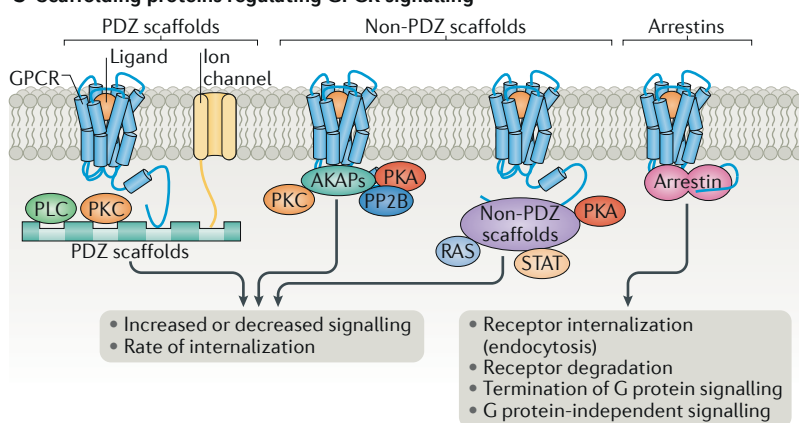


Fig. 1 | Schematic illustration of GPCR signalling. a | Canonical G protein-coupled receptor (GPCR) signalling occurs via coupling to heterotrimeric G proteins ($G\alpha$, $G\beta$ and $G\gamma$). Upon activation by a GPCR, the $G\alpha$ and $G\beta\gamma$ subunits dissociate and can each activate downstream signalling. $G\alpha$ proteins can be subdivided into four main families with different signalling properties. There are also multiple $G\beta$ and $G\gamma$ subunits, which further diversifies signalling responses. $G\alpha$ and $G\beta\gamma$ subunits can also associate with scaffolding proteins that regulate their signalling profiles. **b |** A schematic of GPCR scaffolding proteins that have key roles in the regulation of GPCR signalling and are also involved in forming higher order, tightly regulated signalling complexes, termed signalosomes. These scaffolds can be divided into three broad categories: PDZ scaffolds, which associate with the distal portions of GPCR carboxyl termini and can couple the GPCR to various signalling proteins such as kinases (for example, protein kinase C (PKC)), phospholipases (for example, phospholipase C (PLC)) and ion channels; non-PDZ scaffolds, such as A kinase anchor proteins (AKAPs), which bind to the cytoplasmic face of GPCRs and also associate with multiple signalling partners including kinases (for example, PKA and PKC), phosphatases (for example, serine/threonine-protein phosphatase 2B (PP2B)) and intracellularly localized receptors (such as inositol 1,4,5-triphosphate receptors ($InsP_3Rs$) in the endoplasmic reticulum; not shown); and arrestins, which associate with many GPCRs, disrupting G protein–GPCR interactions and driving GPCR internalization via endocytosis, and act as scaffolds to facilitate multiple interactions between GPCRs and cytoplasmic signalling proteins in a G protein-independent manner. Of note, GPCRs themselves can serve as scaffolding proteins for other membrane proteins, including other GPCRs and receptor modifying proteins, as exemplified by receptor activity-modifying proteins (RAMPs) (not shown). JLP, JNK-associated leucine-zipper protein (also known as SPAG9); KSR1, kinase suppressor of RAS1; STAT, signal transducer and activator of transcription.

cAMP, Ca^{2+} , inositol 1,4,5-triphosphate (Ins(1,4,5) P_3), etc.), which in turn trigger distinct signalling cascades. It is now well established that numerous distinct receptors can couple to the same G α protein and that the same receptor can also couple to more than one G α protein. G $\beta\gamma$ subunits have both regulatory and signalling functions, including, for example, serving as scaffolds for receptor kinases and as modulators of ion channels⁸. More recently, our understanding of G protein activation has progressed to include ligand-dependent effects on G protein conformation that are linked to signalling efficacy^{9,10}. Advances in cloning and sequencing and global approaches to identification of other GPCR–protein interactions^{11,12} have further expanded the repertoire and/or complexity of potential consequences of GPCR activation. The most abundantly studied of these GPCR interacting partners are arrestins, which serve as negative regulatory proteins for signalling through G proteins (by blocking the activated receptors from binding to heterotrimeric G proteins (signalling desensitization) and by targeting ligand-occupied GPCRs for endocytosis). However, they can also function as scaffolds for initiation of additional signalling, prominently including activation of various MAPKs, such as ERK¹³. The latter is often termed ‘arrestin-dependent, G protein-independent’ signalling¹⁴, although the extent to which such signalling may require initial G protein recruitment, or can be modulated by G protein-dependent signalling, is still under study¹⁵. For example, a thought-provoking recent study on the requirement for G protein for arrestin-mediated signalling has revealed that signalling (ERK phosphorylation), mediated by arrestin may require G protein, but that arrestin-dependent receptor internalization can be achieved in the absence of functional G protein¹⁵. Indeed, arrestin engagement by GPCRs may occur in the absence of receptor activation owing to heterologous phosphorylation by second messenger kinases¹⁶, and these behaviours need to be understood when developing novel GPCR ligands.

Given the near universal importance of GPCRs in normal development and physiology, it is not surprising that perturbations in GPCRs and/or their transducers can have major roles in the initiation and progression of disease. Currently, ~30% of approved drugs target GPCRs, but these drugs act at only a small subset of the GPCR repertoire^{17,18}, and there is intense interest in further pharmaceutical exploitation of these proteins¹⁸. Nonetheless, lack of expected clinical efficacy remains a major cause of GPCR drug failure that is indicative of important gaps in our understanding of GPCR signalling and, in particular, their response to specific ligands. The current obstacles to successful pharmacological targeting of GPCRs include the disease-specific variability in drug efficacy that occurs in a signalling pathway-dependent manner, disease heterogeneity, the state of disease progression and the variation in receptor behaviour associated with polymorphisms in receptor sequences within the human population^{18,19}. In the past decade, and particularly in recent years, there has been a leap in our understanding of the complexity of the mechanisms and dynamics of GPCR function that promises to provide new paths to both identification

and development of novel GPCR drugs and translational understanding of how these can be optimally used for therapeutic intervention. Among the foremost of these developments is recognition that GPCR ligands can

exhibit biased agonism, the ability of individual ligands acting at the same receptor to initiate diverse cellular outcomes. In this Review, we outline recent advances in our understanding of the mechanistic basis for receptor activation and biased agonism.

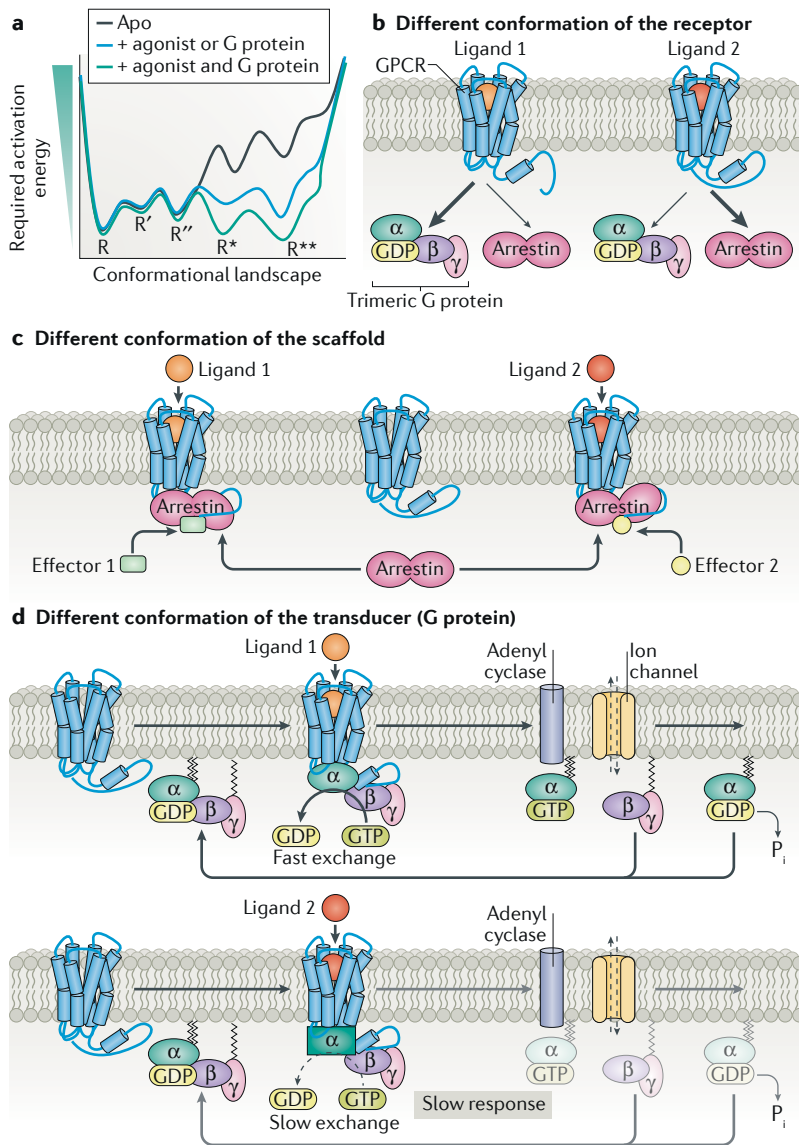


Fig. 2 | Mechanisms of ligand-induced biased agonism. **a** | A schematic illustrating conformational dynamics occurring in G protein-coupled receptors (GPCRs). GPCRs can move between various inactive-like (R , R' and R'') and active-like (R^* and R^{**}) states. This can occur in the absence of ligand (Apo, black line); however, the energy barrier to achieving these states makes their occurrence a low probability. Addition of agonist or G protein (blue line) can decrease the energy required to reach active states, but full conformational change is favoured by the addition of both agonist and G protein (green line). **b–d** | Biased agonism can arise via multiple mechanisms. Distinct ligands induce different conformations within the receptor, resulting in different recruitment profiles for effector proteins such as G proteins and arrestins (part **b**). Ligand-induced receptor conformations can promote different conformational changes within scaffolding proteins such as arrestins, which in turn promotes activation of different downstream signalling pathways (for example, different MAPKs) (part **c**). Different ligands can induce distinct conformational rearrangements within G proteins that result in differences in the rate of GTP–GDP exchange. Ligands that induce a faster rate of GTP association (and hydrolysis) (top panel) allow quantitatively more G protein and downstream signalling events per unit of time than ligands that induce a slow rate of exchange (bottom panel) (part **d**). P_i , inorganic phosphate.

Complexity of GPCR signalling

Historically, GPCRs were viewed as quiescent proteins that require activation by an agonist, which allows them to act as selective conduits between a physiological (or pharmacological) ligand and a specific G protein transducer pathway. Consequently, GPCR subtypes are still often classified according to both their activating ligand and their preferentially recognized subfamily of G proteins. Nonetheless, most, if not all, GPCRs can couple to multiple transducer and modulatory proteins as a consequence of the conformational dynamics intrinsic to all these proteins^{5,20,21} (FIG. 2).

Conformational dynamics of GPCRs and diversity in GPCR signalling. GPCRs are allosteric proteins that allow communication from the outside to the inside of cells. To achieve this, they sample multiple conformations, even in the absence of activating ligands (the apo state) (FIG. 2a). Endogenous ligands and drugs alter these receptor conformational dynamics, affecting the temporal and spatial profile of transducer and regulatory protein engagement. There is now evidence that this conformational plasticity can profoundly influence responses that are elicited by a given ligand^{14,5,22–24}. Ligand behaviour can be described by two key parameters: affinity (the ability to bind) and efficacy (the functional consequence of binding) (BOX 1). Our understanding of the complexity of GPCR responses has evolved from a simplistic, linear model of agonist efficacy — where all signalling is proportional — to a model that encompasses the pluridimensionality of receptor–transducer coupling and transducer activation as well as the concept of biased agonism — the ability of individual interacting ligands to differentially alter the pattern of the downstream cellular response^{13,25} (BOX 2).

Furthermore, for some receptors, including viral chemokine receptor GPCR homologue US28 (REF.²⁶), dopamine receptors²⁷, and 5-hydroxytryptamine receptor 2C (5HT_{2C})²⁸, ligand-independent signalling (constitutive activity) that can often be unmasked by overexpression or mutation of the GPCR can also be observed. This implies that GPCRs have been selected to exhibit a broad spectrum of intrinsic quiescence versus constitutive activity according to functional need. Biophysical and biochemical studies have confirmed that the level of constitutive activity exhibited by individual receptors is linked to their conformational dynamics and is modulated by the strength of interactions between amino acids within the transmembrane core of the receptor, particularly between the conserved polar amino acids that form interaction networks at the base of the receptor^{5,21,29}. Constitutive activity of GPCRs can be modulated both physiologically, through changes to expression of receptor or transducer, RNA splicing or RNA editing (as noted for 5HT_{2C})²⁷, or through post-translational modifications, and in disease, when

Box 1 | Understanding drug behaviour for clinical translation

To contextualize new advances in understanding structure–function relationships in G protein-coupled receptors (GPCRs), we must first consider how we describe and classify drug behaviour and define those components that are intrinsic to the bi-molecular interaction between ligand and receptor relative to those that may be cell-type-specific, organ-specific or even disease-specific (so-called system-dependent parameters).

Modelling signalling output

In its simplest form, the action of a drug can be separated into two key parameters: the ability of a drug to bind to the receptor (affinity) and its ability to trigger a cellular response upon binding (efficacy). A common pharmacological model for describing drug action at the receptor and cellular level is the operational model of agonism¹⁷⁸, which ascribes a functional affinity and efficacy value to an observed response. This was originally applied to quantification of physiological measures, such as changes in whole organ responses, with the functional affinity value (K_A) representing a macroscopic composite of all true microscopic affinities for each physical ligand–receptor–transducer complex making up the conformational ensemble. The efficacy parameter (τ) in the operational model is a composite measure subsuming: the strength of interaction between each ligand–receptor complex that determines receptor coupling to a transducer protein to initiate a cellular signalling stimulus; the efficiency with which the stimulus is processed by cellular signalling pathways; and the total number of receptors mediating the observed response. By contrast, clinical efficacy is the observed, whole body outcome of integrated cellular responses across all target tissues upon administration of any pharmacological agent. At the most fundamental level, differences in drug behaviour are driven by the distinct chemical interactions between ligand and receptor, which determine the conformational sampling of the ligand–receptor complex to influence both transducer and regulatory protein interaction and transducer activation. This behaviour is independent of cellular context, and quantification of individual pathway efficacies in a chosen cell type can allow phenotypic clustering of drug chemotypes (see also below). Nonetheless, such surrogate measures of drug behaviour will be distinct from those displayed in native context, as each cell type will exhibit a unique level of expression, repertoire of receptors and composition of transducer, scaffolding and regulatory proteins that combine to determine cellular and tissue response. Moreover, this response can be further diversified by disease-specific changes to the proteins and the cellular environment. Successful drug discovery and development requires both an understanding of the full spectrum of drug behaviour and the ability to predict those properties in a manner that can bridge preclinical and clinical efficacy.

Overcoming translational barriers

Knowing that we have an incomplete understanding of the cellular consequence of GPCR drug action, how can we overcome the barrier of their pharmacological diversity? Observed bias can, and does, change with time, and it varies according to the breadth of end points used to analyse drug action. An increasingly popular approach is broad assaying of drug behaviour to cluster compounds into functional chemotypes^{66,151,179–182}. The most advanced of these types of approach can interrogate over 30 end points of GPCR function, including kinetic measurement of effects on G protein recruitment and activation, signalling via second messengers and regulatory kinases and alterations to receptor trafficking. The functional chemotypes determined with these methods^{180,183} can now be linked to clinical drug behaviour (M. Bouvier, personal communication). Incorporating a minimum panel of diverse measures that can define a meaningful functional chemotype during compound validation, hit-to-lead and candidate nomination pathways that occur within a drug discovery pipeline may improve preclinical to clinical translation through greater pharmacological understanding of the drug leads entering into trials. Most importantly, though, insights from structural studies are now leading to the design of compounds with specific efficacies⁷², and solution of new structures of these designer ligands in complex with target receptors, combined with broad cellular assessment of receptor function, will provide increasing insight into the interactions that selectively alter receptor dynamics, leading to desired signalling profiles.

alterations to these mechanisms, such as by mutation of active-conformation-stabilizing amino acid networks or via alterations to the cellular environment (changes to membrane environment, pH, etc.), can occur^{30,31}. Activity of GPCRs may also be intrinsically regulated, with examples of receptors that require induced expression (or chaperones)^{32–34} to reach the cell surface, and receptors that undergo very rapid turnover, being dynamically endocytosed and recycled from and to the membrane³⁵. Pathological constitutive activity can be disease causing, as observed for the role of the constitutively active mutant of the parathyroid hormone/parathyroid hormone-related peptide receptor (PTH1R) in the pathology of Jansen's metaphyseal chondrodysplasia³⁶ or by the impact of constitutively active mutants of the extracellular Ca^{2+} -sensing receptor CASR on the loss of Ca^{2+} homeostasis³⁷. Aberrant constitutive activity can also modify disease, as illustrated by the role of constitutively active metabotropic glutamate receptor 5 (mGluR5) in brain alterations observed in autism spectrum disorder³⁸.

It is now clear that GPCRs exist in multiple inactive and active conformations, even in the apo state (FIG. 2a). Studies on rhodopsin have provided clear delineation of multiple meta-stable conformational states of varying half-life that are altered during photon-driven isomerization of retinal and receptor activation³⁹. Multiple ligand-independent and ligand-specific states have also been observed for other GPCRs^{5,21}.

An evolving view of ligand pharmacology. The goal of the vast majority of pharmaceutical discovery and development programmes is to identify drugs that either block or promote receptor activation. For a given readout of activation, an individual ligand can be typically classified as a full agonist, partial agonist, neutral antagonist or inverse (full or partial) agonist (BOX 2). Differences in both the type and the strength of chemical interactions between distinct ligands and an individual GPCR can affect ligand residence times, drive changes in receptor conformation and determine

Arrestins

A family of intracellular transducers that can act as G protein-coupled receptor modulators by blocking G protein-mediated signalling, promoting receptor internalization and activating G protein-independent signalling pathways.

Agonist

A molecule that binds to and stabilizes the receptor in an active conformation, thereby resulting in an intracellular response.

Box 2 | Ligand classification, pluridimensionality of signalling and biased agonism

Ligands can be classified according to their binding site on the receptor, with the binding site of the canonical endogenous agonist termed the orthosteric site and binding sites that are topographically distinct from the orthosteric site termed allosteric sites. In some cases, orthosteric binding sites and allosteric binding sites can reside in close proximity, with ligands that can concomitantly bridge these two sites termed bitopic ligands¹⁸⁴. Major outcomes from the increasing number of G protein-coupled receptor (GPCR) structures is recognition of the diversity of location of orthosteric and allosteric binding sites (with the location of these sites interchangeable across some receptor classes) and the observation that most, if not all, GPCRs possess at least one allosteric site¹⁸⁵. Furthermore, allosteric ligands can be highly diverse, including Na⁺, which is a negative allosteric modulator of many class A GPCRs, classic small molecule compounds, antibodies, lipids and lipidated peptides (for example, pepducins)^{185,186}. When used as drugs, allosteric ligands can possess the same spectrum of pharmacological activity as orthosteric ligands, but they establish distinct chemical interactions with the receptor. As allosteric ligands can bind simultaneously with orthosteric ligands, they can also alter the pharmacology of the latter, providing novel therapeutic opportunities (reviewed extensively elsewhere^{184–186}). In effect, when bound to an allosteric ligand, the receptor–ligand complex can be viewed as a novel receptor with respect to how an orthosteric agonist propagates activation-associated conformational changes, and not surprisingly, alteration to the profile of transducer engagement is a common feature of many allosteric modulators.

An individual ligand can be typically classified as a full agonist, partial agonist, neutral antagonist or inverse (full or partial) agonist. The changes in receptor function arise from the specific chemical interactions that each ligand establishes with its target receptor, which impact the conformational ensemble of the GPCR, shifting the states sampled and the rate of interchange between conformational states. The efficiency with which the resulting conformational ensemble subsequently engages with or disengages from transducer–effector pathways thus leads to the aforementioned traditional phenotypic drug classifications. However, hitherto unappreciated differences in both the nature and the strength of chemical interaction between distinct ligands and an individual receptor can also drive changes in ligand residency and in transducer and/or regulator engagement that can vary for every downstream pathway. This is often referred to as ‘pluridimensional signalling’ and has led to the discovery of biased agonists as drugs that differentially promote this phenomenon. Although such differences in receptor–ligand complex conformations can be biophysically measured, these measurements are technically difficult and are often restricted to measurement of distance changes between a single pair of residues within the receptor.

In practice, the identification of biased agonism occurs via functional measures in cells but can be determined only when multiple (at least two) signalling end points are measured. Moreover, changes to signalling profiles can be subtle, requiring both depth of cellular interrogation and quantitative methods for measurement of relative agonist efficacy across all pathways. Because assessment of signalling bias is based on phenomenological readouts, the result can vary greatly according to cellular background and the nature of the response. Furthermore, biased agonism is always a relative term that is meaningful only when described relative to any differences from a reference agonist that has been assessed in parallel in the same assay and cell type. Terms such as unbiased ligand or balanced ligand, when used to describe a ligand with equivalent potency and/or efficacy in two different assays, can be problematic when system-dependent end points are measured (for example, cAMP accumulation versus arrestin recruitment), as alterations to the system background can change such relative potencies (for example, increased expression of G protein or altered expression of a GPCR kinase, which is linked to efficiency of arrestin recruitment). Thus, while biased agonism can be demonstrated from only two measures of cellular response, for example, G protein-mediated signalling versus arrestin-mediated signalling, this can provide only a very limited understanding of the potential pharmacologies of studied drugs. Consequently, if the two end points, even if different, are not the only (or worse, are not directly related to) therapeutically relevant signalling outputs, clinical translation will remain problematic.

transducer and/or regulator engagement, resulting in biased agonism.

While there has been general agreement that the fundamental basis for biased agonism is ligand-specific changes to GPCR conformation^{40–42}, until recently, the classical view has been that differential signalling by a particular ligand (and alterations to drug efficacy) arises from the differences in efficiency of recruitment of the different transducers to the specific ligand–receptor complex conformation (FIG. 2). New studies that used bioluminescence resonance energy transfer (BRET)-based and fluorescence resonance energy transfer (FRET)-based conformational biosensors embedded within subdomains of specific G proteins^{9,10,43} or arrestins^{44,45} have now revealed that the conformational differences in ligand–receptor complexes are also propagated to the transducers. For arrestins, such conformational changes influence the interaction with potential scaffolded partners. For G proteins, these changes influence the rate of GTP binding as well as G protein residence times in

GPCR-bound complexes and, thus, G protein turnover, thereby modulating the activation of their downstream signalling targets (FIG. 2). Furthermore, the nature of the GPCR–arrestin interaction is at least partially dependent upon phosphorylation of conserved motifs on the receptor by either GPCR kinases (GRKs) or second messenger kinases⁴⁶. There is accumulating evidence that individual ligands can induce specific patterns of receptor phosphorylation (termed phosphorylation barcodes⁴⁷) linked to specific GRK recruitment^{13,48} that control both the strength of arrestin interaction with the GPCR and the subsequent recruitment of downstream effectors^{13,46–52}.

Structural basis of GPCR signalling

Advances in GPCR structure determination and biophysical measures of GPCR dynamics are now providing key insights into how GPCRs are activated by both cognate ligands and pharmacological agents. While details vary between GPCR classes and even between closely related receptors, the propagation of conformational

Bioluminescence resonance energy transfer

(BRET). A biophysical technique combining a photon-emitting bioluminescent luciferase and an acceptor fluorescent protein, which is used to monitor changes in intramolecular and intermolecular proximity.

Fluorescence resonance energy transfer

(FRET). A biophysical technique combining a donor chromophore and an acceptor chromophore, which is used to monitor changes in intramolecular and intermolecular proximity.

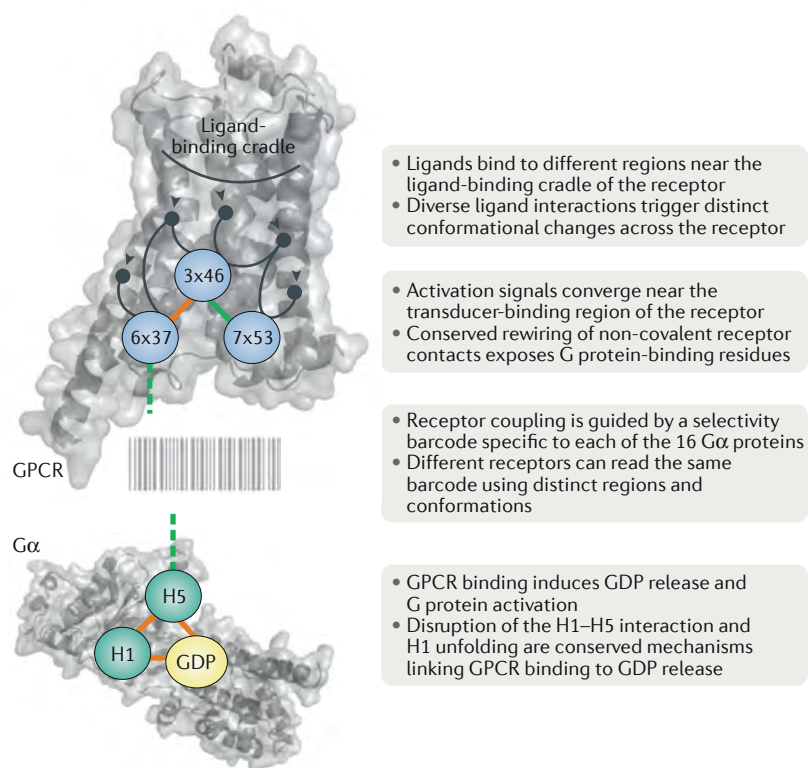


Fig. 3 | Conserved residue contact networks between class A GPCRs and G proteins. The G protein-coupled receptor (GPCR) and the G protein have been depicted in grey in cartoon and surface representations. Binding of ligands near the ligand-binding cradle in the receptor triggers distinct conformational changes in different receptor regions (schematically represented as black circles). These changes converge near the effector-binding region of the receptor through a conserved rewiring of non-covalent contacts among key receptor residues (represented as circles and labelled according to [GPCR Database](#) nomenclature). Engagement of these residues exposes receptor regions capable of recognizing a conserved G protein selectivity barcode (a pattern of amino acids specific to a given G protein; shown as a barcode logo). Binding to the receptor triggers a universal G protein allosteric mechanism that uncouples interactions between the $\alpha 1$ helix (H1), the $\alpha 5$ helix (H5) and the GDP-binding site of the G α subunit and leads to GDP release. This allows GDP exchange for GTP and activation of the G protein. Connections between residues reflect inactivating (orange lines) and activating (green lines) contacts between them. Green dashed lines indicate that activation signals do not occur through direct contact.

GPCR kinases

(GRKs). G protein-coupled receptor (GPCR)-regulating protein kinases that phosphorylate intracellular receptor sites and modulate the ability of GPCRs to interact with G proteins and other intracellular transducers.

Transducer mimetic

A non-functional protein such as a camelid nanobody that binds within the transducer-binding cleft of an activated receptor to induce structural reorganization of the receptor similar to that induced by functional transducers (for example, G proteins).

changes arising from agonist engagement converges at the intracellular face of the receptor and leads to a conserved outward movement of transmembrane helix 6 (TM6) that allows transducer recruitment and activation. Nevertheless, despite conserved mechanisms of transducer engagement, downstream signalling from GPCRs can vary considerably depending on the context. Here, we analyse the three best studied classes of GPCR, focusing on structural details that determine their signalling and contribute to biased agonism.

Class A GPCRs. Class A GPCRs are the most abundant GPCR subfamily, and this is reflected in the number of unique receptor structures solved for the members of this class. Despite the vast diversity in their size and architecture⁵³, a detailed analysis of several GPCR structures has revealed common, conserved, non-covalent contacts between equivalent receptor residues in the TMD, termed molecular signatures, which are linked

to receptor quiescence and transition to activation (FIG. 3). The existence of a ligand-binding cradle has also been determined⁵⁴. Although the structures of numerous receptors have been solved, there are very few receptors for which structures of both the agonist–receptor–transducer (or transducer mimetic) complex and the inactive, antagonist-bound or inverse agonist-bound state are available. Receptors solved in these two states include rhodopsin, $\beta 2$ -adrenergic receptor ($\beta 2$ -AR), muscarinic acetylcholine receptor M2 (mAChR), adenosine receptor A2A, μ -type opioid receptor (μ -OR) and κ -type opioid receptor (κ -OR)⁵. There are common general features that can be drawn from these structures. For example, the extracellular face of the receptor undergoes contraction upon agonist binding, and this contraction is allosterically linked to the opening of the transducer-binding site. Moreover, this allosteric mechanism is reciprocal, also working in the opposite direction, whereby the binding of the intracellular transducer fosters ligand-binding site closure⁵⁵.

An analysis of non-covalent contacts between equivalent residues of the available structures in the active and inactive conformations has also revealed that, despite the diversity in the conformational changes near the ligand-binding region between receptors, the changes converge near the G protein-coupling region (FIG. 3). This convergence is mediated by a highly conserved structural rearrangement of residue contacts between TM3, TM6 and TM7 that exposes G protein-contacting residues⁵⁶. This permits interaction with subdomains of the G α subunit, including the carboxy-terminal $\alpha 5$ helix that is inserted deep within the receptor, as seen in the solved active state structures. These interactions promote nucleotide exchange and enable G protein activation. This convergence may possibly explain how the conformational changes initiated by ligands that are very structurally diverse enable GPCRs to bind a common repertoire of transducers.

It is clear that reorganization of receptors to a fully active state is not related to agonist binding alone but rather reflects changes to receptor dynamics that are driven by both the agonist and the transducer^{5,21}. This reorganization is sometimes referred to as a ‘loose allosteric coupling’ and is based on the concept that the receptor can explore multiple inactive, intermediate and active-like states in the absence of a bound ligand (FIG. 2a). This loose allosteric coupling can be visualized in molecular dynamic simulations that examine the stability of the active receptor–agonist complex following G protein removal, as illustrated for the $\beta 2$ -AR–G α structure. These simulations revealed that the receptor could revert to an inactive-like conformation, even in the presence of agonist⁵⁷. Nonetheless, multiple potential meta-stable conformations were sampled during the simulation, in particular, conformations associated with changes to TM7, where TM6 was still retained in an active-like conformation. This is consistent with NMR studies implicating relative differences in the positioning of TM5 and TM7, but not necessarily TM6, in states of the $\beta 2$ -AR favoured by agonists^{58,59} and with the idea that interactions with the transducers are required for the receptor to acquire a fully active state^{58,59}. Recent data suggest that G proteins can also form non-functional

interactions with receptors that can prime the receptor for activation^{60,61}. Such data also provide evidence that, besides the conserved deep binding of the $\alpha 5$ helix of the $G\alpha$ subunit into the receptor core, other important interactions between the receptor and the G protein can be established. Nonetheless, this conserved, deep interaction between the GPCR and the G protein is likely required for G protein activation, as it contributes to the allosteric conformational changes required for full nucleotide exchange^{62,63}.

The expanding availability of solved receptor structures and their complexes with signal transducers has also allowed a more systematic analysis of receptor–transducer coupling and of how downstream G proteins are activated. Analysis of receptor-bound and unbound G proteins, together with a detailed investigation of sequence conservation among $G\alpha$ subunits, has helped elucidate a universal allosteric mechanism for $G\alpha$ activation by GPCRs⁶² (FIG. 3). This was further facilitated by the development of a **common $G\alpha$ subunit numbering (CGN)** system that allows identification of equivalent residues across the different G proteins⁶². $G\alpha$ proteins contain a RAS domain (named for its homology to the small G protein RAS). Short segments within this domain undergo disorder-to-order transitions as part of the G protein activation mechanism (initially described for the activation of RAS), and these changes could provide a mechanism that is compatible with conserved allosteric activation pathways and the selective binding of the G protein to specific receptor types. In more detail, following recruitment to the receptor, the carboxy-terminal part of the $\alpha 5$ helix in the $G\alpha$ subunit adopts a more ordered helical structure, which is required to expose residues responsible for the tight and specific binding of different $G\alpha$ subtypes to the GPCR. Molecular dynamics simulations indicate that removal of GDP from $G\alpha$ subunits is sufficient to allow this helical ordering of the $\alpha 5$ helix⁶³ and suggest that nucleotide release precedes full engagement of the G protein by the receptor. Indeed, in the inactive G protein, GDP is in direct contact with the $\alpha 5$ helix and also with the $\alpha 1$ helix. The $\alpha 1$ helix is allosterically linked to nucleotide release via an increase in flexibility resulting from the disorder-to-order transition of the $\alpha 5$ helix described above. Thus, recruitment of the G protein to the GPCR could drive GDP release mediated by allosteric effects from the receptor, and this in turn could allow subsequent full engagement of receptor and G protein through the rearrangement of $\alpha 5$ helix. This might potentially explain how the GPCR– $G\alpha$ system can be so diverse while conserving a common allosteric activation mechanism across the different G proteins⁶². Recent studies have also sought a structural explanation for why particular receptors have the ability to couple to some G protein types and not others, a question that until recently had remained elusive. A detailed sequence and structural analysis of human GPCRs and G proteins revealed the existence of patterns of amino acids, termed G protein selectivity barcodes, on each of the 16 human $G\alpha$ proteins that can be recognized by distinct regions on the approximately 800 human receptors. Importantly, some of the positions in the barcode are highly

conserved, whereas others are unique to the individual G proteins. While the highly conserved positions in the selectivity barcode allow the receptors to bind and activate G proteins in a similar manner, the unique positions are recognized by specific receptors through distinct residues, and only some barcodes can be recognized by any given receptor. This situation could be compared with a scenario of having multiple keys (receptors) opening the same lock (G protein) using non-identical patterns. Furthermore, it was shown that studying the evolutionary history of GPCRs allows the identification of these selectivity-determining residues on the receptor²⁰.

Beyond G protein engagement, there is increasing evidence, at least for class A GPCRs, that the conformation of TM7 and, in particular, that of its conserved NPXXY (in single letter amino acid code, where X is any amino acid) motif can contribute to the efficiency of arrestin coupling and activation and consequently to the observed signalling bias between agonists^{21,64–66}. This is supported by spectroscopy studies of $\beta 2$ -AR in complex with agonists with divergent pharmacology, particularly those that activate both G protein and arrestin signalling and those biased towards arrestin recruitment⁶⁷. In that study, in the absence of transducer, G protein-competent and arrestin-competent ligands altered conformations of both TM6 and TM7, whereas those that exhibited limited G protein engagement and favoured arrestin-mediated signalling primarily altered only the TM7 conformation. Similarly, the differential recruitment of arrestin to κ -OR versus μ -OR by the ligand 3-iodobenzoyl naltrexamine (IBNtxA) could be altered by mutation of a key residue in TM7 (Y/W7.35; single amino acid code numbered according to the Ballesteros and Weinstein class A numbering scheme⁶⁸). This mutation induced subtle changes in ligand orientation across the two receptors, suggesting that this difference in ligand-binding pose, and in the strength of chemical bonds between ligand and receptor, is sufficient to alter key components of the intramolecular allosteric networks within the receptor that govern selective signalling⁶⁹. A role for TM7 conformational changes has also been proposed for the differential engagement of transducers by 5HT1B and 5HT2B stimulated by a promiscuous agonist ergotamine. This ligand activated both G protein and arrestin pathways downstream from 5HT1B and primarily activated arrestin-mediated signalling downstream from 5HT2B. In this case, a key difference was the extent of conformational change to TM7 (REF.⁶⁵). Additional insights into mechanisms governing arrestin recruitment arise from the crystal structure of 5HT2B bound to lysergic acid diethylamide (LSD), whereby a single point mutation in extracellular loop 2 (ECL2; connecting TM4 and TM5) that reduced interaction with LSD and increased ligand off-rate markedly attenuated arrestin recruitment^{70,71}. Interestingly, combining this knowledge with previous information on biased agonism at dopaminergic receptors allowed the identification of a set of polypharmacological compounds exhibiting β -arrestin bias⁷².

It is known that differentially phosphorylated carboxy-terminal peptides that mimic phosphorylated receptor carboxy-terminal tails can induce distinct arrestin conformations in regions responsible for protein scaffolding^{73,74}. Thus, an additional mechanism

Inhibitory antibody

An antibody directed against a G protein-coupled receptor that inhibits receptor activation.

for bias may be related to ligand-specific differences in coupling of the receptor–ligand complex with different kinases, which in turn alter patterns of receptor carboxy-terminal phosphorylation (phosphorylation barcode). Very recent work has shed additional light on the complex relationship between phosphorylation of the receptor carboxy-terminal tail and arrestin recruitment, with evidence for allosteric modulation of the receptor core by the phospho-carboxy-terminal tail, which regulated arrestin binding to the core of $\beta 2$ -AR⁵². Many GRKs require interaction with the $\beta\gamma$ subunit of the G protein, providing a potential explanation as to why arrestin signalling requires G protein binding to the receptor. Notably, ligating the same phosphopeptide to different class A GPCRs has been shown to elicit distinct effects on arrestin engagement with the receptor⁷⁵. These differences in arrestin engagement by phosphorylated receptors could be explained by the fact that at least two major conformations exist for arrestin–GPCR interactions: a tail conformation and a core conformation, which differ for different arrestin–GPCR pairs. The tail conformation arises from interaction of arrestin with the phosphorylated carboxy-terminal tail of the GPCR⁷⁶ and is compatible with concomitant GPCR–G protein interaction⁷⁷. In the core conformation, in addition to the interaction with the tail, arrestin establishes interactions with the receptor core through a finger–loop domain, as illustrated by the rhodopsin–arrestin crystal structure⁷⁶. These two conformations have been linked to specific functions of arrestins (arrestin in tail conformation was shown to be functional in GPCR internalization and some forms of signalling, whereas receptor desensitization was attributed to the core conformation)⁴⁹. It will be important to understand the extent to which the receptor carboxyl tail (or intracellular loops) undergoes structural reorganization upon phosphorylation to influence both receptor and transducer conformations. Currently, these regions are often excluded from structural analyses to limit receptor flexibility, although recent work with minimally modified class B GPCRs^{43,78,79} indicates that the receptor carboxyl tail is conformationally dynamic, at least in a G protein-bound state.

Most studies that link protein structure to biased agonism have been limited to the primary G protein transducer of the target receptor and arrestin recruitment, and this limits our understanding of the spectrum of ligand-mediated conformational switching that contributes to biased signalling. As a consequence, there has recently been substantial interest in developing multiplexed approaches to interrogate changes to GPCR function (BOX 1). The power of using a broader range of measures of GPCR function is illustrated by a recent study that combined evolutionary trace analysis to predict, and subsequently mutate, 28 amino acids in the $\beta 2$ -AR that may be involved in the distinct conformational networks that govern biased signalling⁶⁶. Through assessment of constitutive and agonist-induced G protein recruitment, G protein activation, arrestin recruitment and receptor endocytosis, this work provided additional evidence for the predominant importance of conserved motifs in TM7 in the differential ability of $\beta 2$ -AR to engage different transducers.

Class B GPCRs. Class A GPCRs display considerable diversity in the size and architecture of their amino-terminal extracellular domains (ECDs). By contrast, class B1 peptide hormone GPCRs share ECDs that are approximately 100–150 amino acids in length and form a conserved 3D fold that binds the carboxy-terminal segment of activating peptide ligands⁸⁰. Recent structural studies have provided major advances in our understanding of the activation of class B1 GPCRs and first insights into the mechanisms that can contribute to biased agonism. These receptors are maintained in inactive states by a series of conserved, polar, hydrogen-bonded amino acid networks at the base of the receptor, which are observed in inactive state structures of the isolated TMD^{81–84} (FIG. 4a). Additionally, there is evidence that domain–domain interaction between the amino-terminal ECD and the transmembrane receptor core may support receptor quiescence^{85,86}.

In the past year, multiple structures containing both the ECD and the transmembrane core have been solved, including receptor complexes with an inhibitory antibody⁸⁷ and partial agonists^{88,89} as well as three structures of full-length receptors in complex with both peptide agonists and the heterotrimeric G_s protein^{43,78,79}, making this the richest receptor class for fully active, G protein-bound structures. Comparison of TMDs of the inactive state structures with the agonist–receptor–G protein-bound structures of the calcitonin receptor (CTR)⁷⁸ and glucagon-like peptide 1 (GLP-1) receptor (GLP-1R)^{43,79} revealed common large-scale changes in the transmembrane core architecture upon binding of peptide agonists. These included marked kinking and an outward movement of the extracellular ends of TM6 and TM7 and an inward movement of the extracellular top of TM1. These changes are unique to class B GPCRs, but as observed for class A GPCRs, they are translated into the outward movement of TM6 at the base of the receptor. This event is conserved across all GPCR classes and allows accommodation of the $\alpha 5$ helix of G_a . These large-scale changes occur around conserved class B1 motifs, including the Pro^{6.47b}–X–X–Gly^{6.50b} (superscript numbers refer to the class B GPCR transmembrane core numbering system⁹⁰) in TM6, Gly^{7.50b} in TM7 and Gly^{1.46b} in TM1.

Comparison of fully active, G protein-bound GLP-1R with the recent structure of the related glucagon receptor (GCGR) bound to a partial agonist, in the absence of G protein⁸⁸, may provide clues to the sequence of conformational changes that are required for G protein engagement for class B GPCRs. In the partial agonist–GCGR structure, the receptor displays only a subset of the transmembrane core changes observed in the G protein-bound structures. Specifically, while there is a reorganization of ECL1 and ECL2 and an outward movement of TM6 to accommodate peptide binding, TM1 and TM7 are not kinked, and the base of the receptor overlaps with the structure observed for inactive receptors. While we do not yet understand the sequence of events that drive full receptor activation, structures of GLP-1R bound to an 11-mer peptide agonist⁸⁹ and an allosteric inhibitor⁸⁴ provide additional clues as to the minimal conformational changes that may allow adoption of a

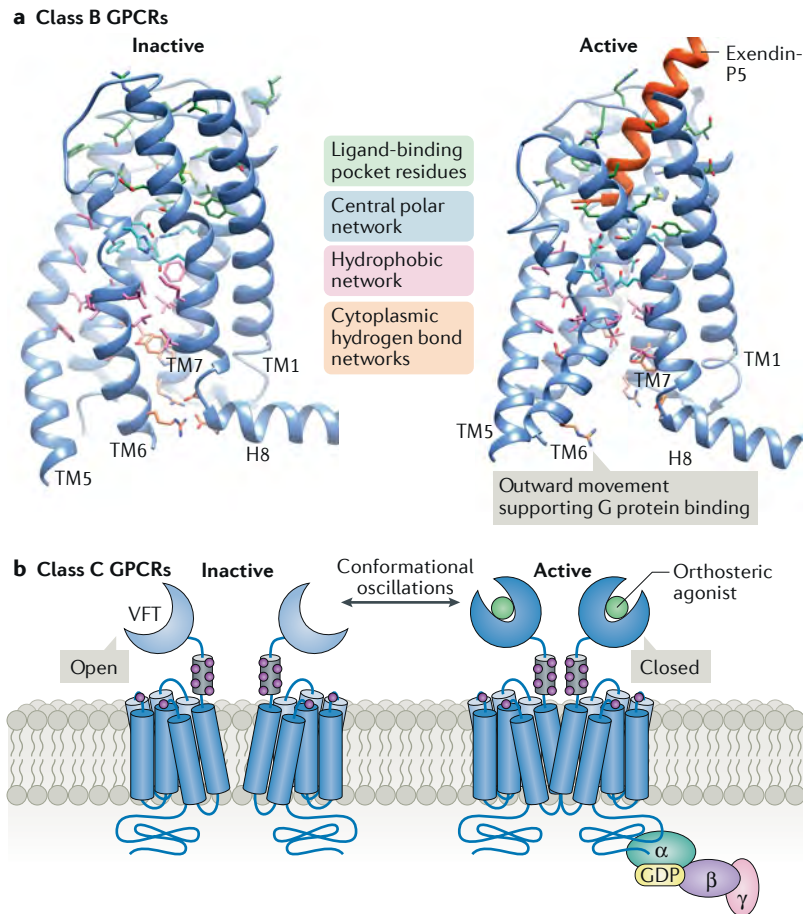


Fig. 4 | Conformational changes in class B and class C GPCRs required for G protein coupling. **a** | The inactive homology model of glucagon-like peptide 1 receptor (GLP-1R), based on the inactive structure of the related glucagon receptor (left) and active, exendin-P5-bound GLP-1R structure⁴⁰ (right), highlighting key amino acid side chains that undergo reorganization during activation transition. These are grouped according to their function and displayed in distinct colours. Prominently, polar, hydrogen-bonded interactions at the base of the receptor are broken or reorganized in the active state. Clear differences in the organization of the hydrophobic network can also be observed between the inactive and active receptor structure. Class B G protein-coupled receptor (GPCR) activation is also associated with conserved changes in the orientation of transmembrane (TM) helices, an outward movement of the extracellular ends of TM6 and TM7 and an inward movement of the extracellular end of TM1. These changes culminate in an outward movement of TM6 at the cytosolic side, which supports accommodation of the transducer. **b** | A schematic of class C GPCR activation. These receptors are functionally dimeric (homodimer form shown) and bind ligand (green circle) via the large extracellular 'venus fly trap' (VFT) domain. Notably, the VFT domain spontaneously oscillates between open and closed conformations. Agonist binding leads to conformational changes in the VFT domain that support the closed conformation of the VFT, and these alterations are linked to repositioning of the TM domain bundles from the two receptor subunits towards each other. As a result, these transitions induce an asymmetric conformational change in one protomer that enables G protein binding. The structural details behind these transitions are not known. The purple circles indicate cysteines in the TM bundle or cysteine-rich linker domain. H8, helix 8.

fully active state. Each of these latter structures exhibits key features of the fully active state in the organization of the extracellular segment of the receptor core, including reorganization of ECL2, outward movement of TM6 and TM7 and inward movement of TM1. Both structures were modified in key transmembrane segments to allow receptor stabilization and crystallization. In the GLP-1R inhibitor-bound structure, a disulfide bond

was introduced between TM6 and TM5, which resulted in the breaking of interactions that stabilize the inactive state, implying that this breakage may be sufficient to drive structural change in the absence of other constraints. In the 11-mer-agonist-bound structure, the Pro-X-X-Gly motif in TM6 had been mutated, and this may also contribute to mimicry of the fully active state of the upper half of the receptor core. It is likely that there is a coordinated series of interactions between the peptide and receptor and between the receptor and the G protein (or other transducer) that are allosterically transmitted between the intracellular and extracellular domains and allow adoption of the fully active state. These transitions are consistent with the loose allosteric coupling described above for class A GPCRs and correspond well with biophysical observations of conformational changes associated with agonist-receptor, receptor-G protein and full agonist-receptor-G protein complexes in class A GPCRs^{5,21}.

The current general model for class B GPCR activation can be summarized as follows: after initial binding of peptide agonists, there is reorganization of receptor ECLs, which accommodates peptide binding to the receptor core and contributes to propagation of conformational change that is linked to both receptor activation and biased agonism^{43,91,92}. Within the core of the receptor, there is reorganization of a conserved central network of polar amino acids, and mutational data support a subtle role for this network in peptide-specific signal bias⁹³. Below this network, towards the intracellular face of the receptor, are hydrophobic residues that stabilize both the inactive and the active (G protein-complexed) states, although these processes occur via distinct interactions. Receptor activation is associated with breakage of key polar networks at the base of the receptor; this is required for TM6 movement and G protein interaction^{43,78,79,94,95} (FIG. 4a). The dynamics underlying these conformational changes are not currently understood. However, mutational data support a role for redistribution of conserved, polar or tightly packed small amino acids in this transition⁹⁰. The recent structures of the GLP-1R bound to its primary physiological ligand, GLP-1 (REF.⁷⁹), or the biased agonist exendin-P5 (REF.⁴³) have also provided new insight into the structural basis of efficacy and biased signalling at this receptor, revealing key differences in the conformation of ECL3 and the top of TM1 of the receptor, when bound by the different ligands.

Intriguingly, all G protein-complexed structures solved to date exist in monomeric forms. However, there is robust evidence that class B1 GPCRs undergo both homodimerization and heterodimerization and that this is functionally important, as disruption of dimerization is associated with reduced agonist potency for canonical G_s coupling with the receptor⁸⁰. Dimerization may also contribute to the biased profiles of agonists⁹⁶ and to alteration of cellular response to agonists in select class B receptor heterodimers^{97,98}, though this has not yet been extensively investigated. The limited data suggest that the receptors are dimeric upon initial interaction with the ligand, which contributes to high-affinity binding, but that these dimers are destabilized upon activation and G protein interaction, which may favour preferential

isolation of the monomeric receptor–G protein complex in structural studies^{9,80,99}.

Class C GPCRs. Unlike many other GPCR families, class C GPCRs are obligate dimers, and this is critically linked to their activation^{100–102}. For example, the GABA type B receptor is an obligate heterodimer with one subunit providing the agonist-binding site and the other providing the G protein-binding domain¹⁰³. Class C receptors contain very large extracellular domains that comprise a structurally conserved ‘venus fly trap’ (VFT) module, which acts as the endogenous ligand-binding site, and an interconnecting domain that is contiguous with the TMD. VFT modules exhibit varying complexity depending on receptor subtype. Orthosteric agonist binding to the VFT domain engenders a conformational shift of the VFT module from an open to closed state, which in turn provides marked alteration to the position and orientation of the TMDs within the receptor dimer that trigger transducer binding¹⁰⁴ (FIG. 4b). FRET studies of conformational dynamics within mGluRs have indicated that the VFT domains can spontaneously oscillate between the resting (open) and active (closed) orientations and that agonists of different efficacies distinctly alter this equilibrium¹⁰⁴, which serves as a mechanism driving receptor activation. To date, no structures of full-length receptors are available, and the nature of the interaction between TMDs of the dimer that contribute to receptor activation is still unclear. However, for mGluR2, cysteine disulfide bridging of the TM4–TM5 interface of the dimer subunits prevents agonist-mediated activation, while TM6–TM6 crosslinking engenders a constitutively active receptor¹⁰¹, which is consistent with reorganization of the dimeric interface as part of the activation mechanism. Of note, both positive and negative modulators that bind in the TMD have been identified for most class C receptors¹⁰⁵. In the full-length receptor, most positive modulators lack intrinsic efficacy, though they can activate amino-terminally truncated receptors lacking the ECD, implying that the ECD contributes to maintenance of an inactive state. Nonetheless, such modulators can modify the profile of orthosteric agonist signalling, as has been observed for CASR¹⁰⁶. This observation indicates that, in class C receptors, similar to other classes of GPCR, the allosteric modulators alter conformational sampling of the receptor during activation transition^{80,107}.

Local control of GPCR signalling

Our understanding of GPCR signalling has also benefited from an evolution in appreciation of the importance of the receptor location within the cell and the role of the environmental context within each location (FIG. 5). This local control can include ‘lateral’ allostery via interaction with membrane lipids and changes to lipid composition^{108–113} and recruitment of the receptor into protein signalosome complexes that restrict or alter effector and regulator interactions with the receptor and thereby the signalling effect^{4,114}. Moreover, receptor location can also influence the functional selectivity of agonists of differing physicochemical properties, whereby hydrophilic compounds require cell surface expression

of receptors to act but lipophilic compounds may access spatially restricted receptors located within the cell, as has been demonstrated for $\beta 1$ -AR²³.

Membrane composition. While we commonly refer to the receptor environment as a lipid bilayer and have presumed that the plasma membrane is the key signalling domain, physiological membranes can be very complex, containing up to 1,000 different types of lipid^{115,116} that can interact directly with receptors and can also be assembled into microdomains through interactions with membrane proteins (the most common being caveolins to form caveolae). Such microdomains can be enriched with specific transducers, including G protein subtypes¹¹⁷. Differences in lipid composition also alter membrane curvature, which in turn may influence GPCR conformational dynamics¹¹⁸. Notably, GPCRs can dynamically partition between such microdomains, leading to alterations in signalling, and this can contribute to observed differences in drug behaviour. An important example is the μ -OR, as compartmentalization of this receptor within distinct plasma membrane subdomains has a key role in the distinct pharmacological response of drugs²⁴.

Receptor trafficking. GPCRs undergo cycles of dynamic trafficking through different cellular compartments. This aspect is also regulated by ligand-dependent interactions as part of desensitization of specific signalling transducers and adoption of alternative signalling engagement, as well as downregulation of receptor response, which is accomplished by targeting receptors to degradative pathways. The rates of spontaneous and ligand-dependent trafficking of receptors between different membrane compartments are coordinated by the selective interaction of receptors with the repertoire of sorting and transporting machineries. Notably, receptor trafficking rates show great variability among GPCRs and can be differentially altered with distinct ligands^{119–123}. These trafficking events are controlled by conformational sampling of receptor states (and subsequent events including post-translational modifications such as phosphorylation, palmitoylation and ubiquitylation) and have been shown to be specific to ligand concentration, chemotype and residency time^{119–123}. Not surprisingly, even in the absence of intracellular signalling, agonist-selective differences in the rate and extent of receptor trafficking can alter the pattern of cellular response and constitute a component of the pharmacological profile of drugs that contributes to observed cellular efficacy.

Assembly of signalosomes. Although we have understood for many years that GPCRs and other proteins can assemble into multi-protein complexes and that this can alter observed receptor function and cellular response (explicitly exemplified by the signalling at the neuronal synapse), our appreciation of the importance of these events for concepts such as biased agonism is only recently being realized⁴. The simplest assembly unit comprises receptor dimers or oligomers, and this has been discussed extensively elsewhere^{124,125}. It is

Protein signalosome

A spatially restricted group of transducers and/or regulatory proteins that jointly produce a specific signalling output.

Chemotype

A chemical description of a molecule that allows identification of the similarities and differences in chemical structure compared with other molecules.

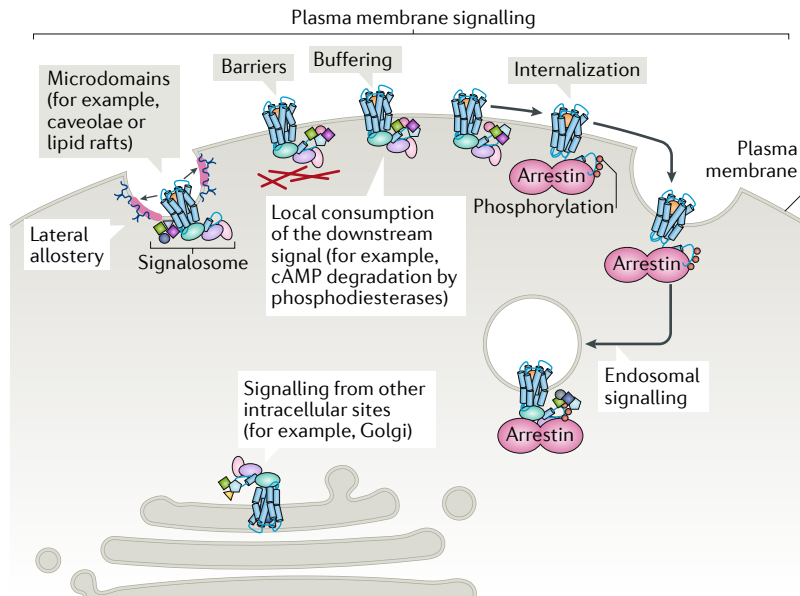


Fig. 5 | Compartmentalization of signalling by GPCRs. Signalling by G protein-coupled receptors (GPCRs) can be spatially (and temporally) compartmentalized to encode unique responses at the cellular level. This is facilitated by the formation of higher order protein complexes (signalosomes) around GPCRs and through the signalling of GPCRs at multiple locations within the cell — apart from the canonical signalling initiated at the plasma membrane, GPCRs can signal from endosomes after receptor internalization. They can also be activated by membrane-permeable ligands from intracellular organelles (including endosomes and the Golgi apparatus). The composition of the lipid bilayer can also influence GPCR signalling. For example, localization of receptors and their signalling partners into microdomains (such as caveolae or lipid rafts) can physically influence their conformation and signalling output through interactions with lipids and membrane proteins that are enriched in these domains (lateral allostery). Spatial and temporal dynamics can also be regulated by physical barriers, such as the cytoskeleton, and by biochemical buffering. An example of this latter process is the buffering of GPCR-dependent G_s -mediated cAMP production, whereby discretely positioned phosphodiesterases degrade cAMP, acting as local cAMP sinks. This buffering can occur at various sites within the cell, including at the plasma membrane and the endosomes, to control cAMP diffusion and to create discrete cAMP gradients within a cell.

worth noting that heteromeric assembly of receptors can alter transducer engagement or receptor trafficking in response to physiological ligands^{125,126} and that dynamic changes of one of the receptor partners could contribute to either disease or disease treatment. GPCRs can also interact with non-GPCR partners to alter ligand recognition, transducer engagement and activation, or receptor trafficking. This includes the interaction of GPCRs with scaffolding proteins such as AKAPs and other proteins^{3–5,7,103}, which are recognized scaffolds for multi-protein assembly that provide fine control of signalling (see below). GPCRs can also interact with membrane proteins such as receptor activity-modifying proteins (RAMPs)³³, melanocortin receptor-accessory proteins (MRAPs)³⁴ and low-density lipoprotein (LDL) receptor-related proteins (LRP)¹²⁷. RAMPs, a family of three single-pass transmembrane proteins, exemplify the spectrum of effects that can be engendered by such interacting proteins. RAMPs were originally recognized for their prerequisite role in trafficking of functional calcitonin receptor-like receptor (CALCRL)–RAMP1 heterodimers (CGRP) or adrenomedullin receptors (CALCRL–RAMP2 or

CALCRL–RAMP3 heterodimers) to the cell surface, contributing to both escape of CALCRL from the Golgi apparatus and/or endoplasmic reticulum and the formation of the ligand-binding pocket of these receptors¹²⁸. RAMPs are now recognized as broad partners of GPCRs, including those from all major subfamilies^{32,33}. While not widely required for cell surface expression of GPCRs, RAMPs can alter receptor regulation, ligand specificity and the pattern of transducer engagement³³. As RAMPs, and other interacting proteins, are dynamically regulated in normal physiology and in disease, the impact of these GPCR partners on receptor function must be considered in drug screening and development strategies.

Overall, assembly of GPCRs into signalosomes can provide the cell with very fine control of signalling events and has been correlated with spatially restricted signalling^{114,129–132}, very high sensitivity of response¹³³ and control of specificity of transducer coupling^{103,134,135} (FIG. 5). This latter property in particular should be considered in the translation of biased agonist profiles measured in receptors expressed via recombinant protein expression systems versus those exhibited in target cells in whole organs (healthy and diseased). Moreover, the assembly of GPCRs into signalosome complexes is likely to alter their conformational sampling, with the potential for such interactions to allosterically regulate ligand binding, downstream signalling and other regulatory mechanisms, as has been observed with RAMP–GPCR interactions³³.

Physiological consequences of compartmentalized signalling. The potential for GPCRs to signal from intracellular compartments has been traditionally associated with arrestin-dependent receptor internalization and recruitment of G protein-independent transducers to endocytosed receptors. However, phenomena such as persistent activation of G protein-dependent pathways have alluded to a role for G protein signalling from sites beyond the plasma membrane¹³⁶. Advances in tools to localize components of signalling complexes have led to the detection of transducer activation within different cellular subdomains, and there is evidence of signalling, apart from endosomes after endocytosis, also from sites including secretory compartments (the endoplasmic reticulum and the Golgi apparatus), the nucleus and mitochondria^{137–142}. Moreover, experiments to selectively intervene with signalling from intracellular compartments have demonstrated that this signalling is physiologically important and can be potentially targeted therapeutically, with prominent examples for the β_2 -AR¹⁴¹, NK-1 receptor (NK-1R; also known as TACR1)¹⁴³, CGRP¹⁴⁴ and PTH1R^{136,142}. Intriguingly, crosstalk between receptors can drive changes in compartmentalized signalling, with a recent example of transient activation of β_2 -AR, via $G\beta\gamma$ subunits, modulating prolonged endosomal PTH1R signalling¹⁴⁵.

Alterations to physiologically important compartmentalization of signalling are likely to be disease causing or disease modifying, as has been demonstrated for β -ARs in heart failure^{129,130,146} and melanocortin receptor 4 (MC4-R) in some genetic forms of obesity¹³⁴. For example, the spatial restriction of β_2 -AR (and consequent

Chemogenetically modified receptors

Genetically engineered receptors that can be chemically modified to be able to alter receptor signalling properties. These include receptors selected for their capacity to interact with previously unrecognized ligands.

Optogenetics

A biophysical technique that uses modified, light-activated G protein-coupled receptors or channels to control cells in living tissue.

cAMP signalling) to the deep transverse tubules of healthy cardiomyocytes is disrupted in a rat model of chronic heart failure, leading to diffuse pathological cAMP signalling¹³. Moreover, the selective ability of individual ligands of a receptor to regulate receptor transitions between compartments (for example, between different cellular compartments or between plasma membrane microdomains) may contribute to the observed biased agonist profiles^{24,147}.

Translational considerations

Taken together, the aforementioned advances in GPCR structural biology have contributed to a more nuanced picture of the influence of ligand, receptor and signal transducer structural determinants on signalling and ligand efficacy. Importantly, these structural insights have pointed to novel ways to modulate GPCRs in a more refined manner, thus paving the way for the development of new chemical biology tools to interrogate receptor function and, most importantly, for the development of a new generation of drug candidates.

Understanding the impact of ligand–receptor kinetics on receptor signalling. Although not explicitly elaborated in this Review, many of the receptor–transducer interaction and transducer activation properties described above are a consequence of the kinetics of ligand–receptor interaction, ligand residency and the consequent probability of transducer or regulatory protein engagement. This is a component of the selective, bi-molecular interaction between individual ligands and target receptors and has become an increasing focus of some therapeutic drug development programmes. Not surprisingly, the classification of observed biased agonism can change depending on the temporal resolution of the functional readout of signalling, and this also provides potential rationalization for discrepancy in ligand classification between different laboratories²². Ligand residency, in particular, has become an area of focus in understanding pharmacological differentiation of compounds, and kinetics of ligand–receptor interaction have been linked to signalling efficacy, pleiotropy (including arrestin recruitment) and clinical efficacy of compounds^{22,71,148–150}.

Identification and progression of biased agonists in drug pipelines. A key lesson from the increasingly detailed molecular insights into GPCR behaviour and consequences of their interaction with drugs is that GPCR signalling is complex and that, consequently, drug discovery and development for these receptors is challenging. Biased agonism can be detected with, at a minimum, two measures of cellular function (that is, by monitoring the activity of two independent signalling outputs), but understanding the nature of the signalling bias of a drug and its contribution to disease modulation requires an understanding of the pathways linked to both the desired therapeutic efficacy and potential side effects¹⁵¹. At best, we currently have only partial understanding of therapeutic signalling. So how do we progress? The answer is multi-pronged.

There are increasingly sophisticated studies using mice with chemogenetically modified receptors or light-modulated receptors (optogenetics) to specifically alter receptor signalling and to try to dissect key physiological and pathophysiological responses to such altered signalling^{142–155}. These types of study can determine key signalling components that may be selectively targeted (either activated or deactivated) and they can be further adopted to models of disease progression. In fact, in vivo studies using different disease models have already started to shed light on the relative contribution of selected receptor pathways to therapeutic effects. Some efforts in this direction include the characterization of β -arrestin 2-biased ligands for type 1 angiotensin II receptor in mouse models of cardiomyopathy^{156,157} and the in vivo analysis of analgesic and side-effect profiles of G protein biased compounds in κ -OR¹⁵⁸ and μ -OR^{159,160}. Importantly, a study systematically analysing a collection of differentially biased ligands of μ -OR recently demonstrated a positive correlation between their degree of G protein-mediated signalling over arrestin recruitment (G protein bias) and the width of their therapeutic window (the balance between therapeutic efficacy and side effects), providing a framework for the development of therapeutics with improved clinical effect for this class of drugs¹⁶¹. At the level of drug discovery, we can now use our knowledge of receptor structure and dynamics, the capacity to chemically modify the type of biased signalling and the diversity of drug response to incorporate multiplexed and kinetic measurements of cellular function to improve pharmacological clustering of chemotypes (BOX 1). Distinct pharmacological chemotypes can then be empirically linked to desired in vivo effects. Such studies can be incorporated into decision points for drug candidate selection.

Understanding the impact of disease context on drug action. Pathological states can modify cellular function, including through alterations to the local environment of receptors. One example is changes in membrane composition, which can be observed in metabolic diseases such as hyperlipidaemia, obesity and diabetes¹⁶² and in disorders of the central nervous system including Alzheimer disease and schizophrenia¹⁶³. Events such as hypoxia, pH changes and redox alterations and generalized inflammatory responses can all change the local cellular environment and thus a potential drug response^{164–168}. One example where such changes occur is the tumour microenvironment, which is frequently acidic. Notably, GPCRs contain networks of residues that can be protonated and are sensitive to altered pH, with alteration to these networks being consequential for receptor activation. In particular, select GPCRs are believed to function as proton sensors via alteration of the protonation state of conserved negatively charged residues (such as D3.32 and D2.50 (using the class A GPCR numbering scheme⁶⁸)) as well as the charge of buried histidines^{168,169} that could lead to altered receptor signalling in low pH environments. Alterations to the levels of other ions should also be considered when assessing GPCR signalling. Importantly, cations, such as Na⁺, are among the most ubiquitous allosteric

modulators of GPCR function and contribute to receptor activity (quiescence versus constitutive activation) and to the nature of biased signalling^{69,170,171}. As such, the nature of GPCR responses to drugs could be altered dramatically in diverse disease contexts, resulting, for example, in differences in transducer and regulatory protein engagement (that is, changing the observed bias profile of ligands). Moreover, most diseases are heterogeneous and evolve as they progress. Therefore, using drug interventions optimized for disease stage is an important component for translational success. More complex model systems that mimic the disease context are thus important for understanding efficacy translation and for establishing the extent to which clustering of drug behaviour in routine recombinant cell studies remains predictive of their behaviour under conditions of altered cellular environment.

Considering the impact of natural receptor variation on GPCR–drug interaction.

Other key considerations that can influence drug discovery, development and eventually translational success include the genetic variation of receptor sequences (polymorphisms) and the variability in receptor expression between individuals in the human population. Several independent studies have characterized the functional impact, including differential drug response, of a number of polymorphisms in a collection of receptor types^{172–174}. Importantly, a recent study that comprehensively analysed genome sequence data from 68,496 individuals showed that currently drugged GPCRs present extensive genetic variation within functional regions such as drug-binding and transducer-binding sites¹⁹. Experimental follow-up of μ -OR revealed that individuals with certain polymorphisms had unexpected response to agonists, partial agonists and antagonists. For instance, polymorphisms at positions near the drug-binding pocket rendered a gain of function effect, whereby an antagonist or partial agonist could elicit a full agonist response. Studies on cholecystokinin receptor type A further revealed that certain polymorphisms near the G protein-binding region of this receptor completely altered the selectivity profile of transducer coupling¹⁹. Similarly, genetic variation can alter receptor engagement with arrestins to impact receptor regulation and/or downstream signalling as noted for CXCR4-chemokine receptor 4 (REF.¹⁷⁵) and vasopressin receptors¹⁷⁶. Such altered or gain of function effects can result in severe side effects of drugs and

possibly life-threatening consequences. These findings highlight the need to understand and characterize receptor variants that are prevalent in the human population and consider them in the drug discovery pipeline. Such consideration should help limit failure of drugs during clinical trials, which can be both very expensive and time consuming and may put patients at unnecessary risk. Characterizing variants of the current GPCR drug targets also has the potential to improve the precision of drug prescription by patient stratification into defined genotypic groups with predicted drug responses. Such stratification would increase drug safety and efficacy and in consequence would improve the quality of life of patients and relieve the economic and societal burden resulting from non-optimal and/or ineffective drug action.

Conclusions and perspectives

Biased agonism is a fundamental property of GPCR ligands that can be used — serendipitously or constructively — for improved therapeutic targeting of these receptors. Consideration of this aspect of GPCR pharmacology will be key to achieving clinical drug efficacy and safety. Our understanding of drug action is limited to what we measure as a drug response, and high-resolution structural insights into the control of GPCR conformation are still at an early stage, providing limitations to conscious application of the principle of biased agonism in drug design. Advances in structural approaches to understand drug–receptor interaction and the increasing ability of researchers to analyse multiple signalling end points and to measure these events in real-time are progressively enabling integration of a breadth of cellular signalling outcomes, and of the kinetic and spatial elements of GPCR signalling, into structure-based drug discovery. This progress is expected to improve drug candidate selection. Nonetheless, applying the biased agonist properties of ligands for improvement of the therapeutic effect of new drugs will require an understanding of the expression of receptors and components of their signalling pathways in different tissues and of the tissue-specific and context-specific, integrated signalling that differentiates beneficial from detrimental effects. Given this complexity, rational application of biased agonism is expected to have the greatest impact on the treatment of diseases for which pathological mechanisms are well characterized¹⁷⁷.

Published online 13 August 2018

- Venkatakrishnan, A. J. et al. Structured and disordered facets of the GPCR fold. *Curr. Opin. Struct. Biol.* **27**, 129–137 (2014).
- Alexander, S. P. et al. The concise guide to pharmacology 2017/18: G protein-coupled receptors. *Br. J. Pharmacol.* **174**, S17–S129 (2017).
- Dunn, H. A. & Ferguson, S. S. G. PDZ protein regulation of G protein-coupled receptor trafficking and signaling pathways. *Mol. Pharmacol.* **88**, 624–639 (2015).
- Ellisdon, A. M. & Halls, M. L. Compartmentalization of GPCR signalling controls unique cellular responses. *Biochem. Soc. Trans.* **44**, 562–567 (2016).
- Hilger, D., Masureel, M. & Kobilka, B. K. Structure and dynamics of GPCR signaling complexes. *Nat. Struct. Mol. Biol.* **25**, 1–34 (2017).
- Komolov, K. E. & Benovic, J. L. G protein-coupled receptor kinases: past, present and future. *Cell. Signal.* **41**, 17–24 (2018).
- Peterson, Y. K. & Luttrell, L. M. The diverse roles of arrestin scaffolds in G protein-coupled receptor signaling. *Pharmacol. Rev.* **69**, 256–297 (2017).
- Khan, S. M., Sung, J. Y. & Hébert, T. E. G $\beta\gamma$ subunits — different spaces, different faces. *Pharmacol. Res.* **111**, 434–441 (2016).
- Furness, S. G. B. et al. Ligand-dependent modulation of G protein conformation alters drug efficacy. *Cell* **167**, 739–749 (2016). **This study demonstrates that differential ligand–receptor conformations propagate to G proteins to control efficacy and that this propagation could contribute to biased agonism.**
- Gregorio, G. G. et al. Single-molecule analysis of ligand efficacy in β 2AR–G-protein activation. *Nature* **547**, 68–73 (2017).
- Paek, J. et al. Multidimensional tracking of GPCR signaling via peroxidase-catalyzed proximity labeling. *Cell* **169**, 338–349 (2017).
- Sokolina, K. et al. Systematic protein–protein interaction mapping for clinically relevant human GPCRs. *Mol. Syst. Biol.* **13**, 918 (2017).
- Smith, J. S., Lefkowitz, R. J. & Rajagopal, S. Biased signalling: from simple switches to allosteric microprocessors. *Nat. Rev. Drug Discov.* **17**, 243–260 (2018).
- Ranjan, R., Dwivedi, H., Baidya, M., Kumar, M. & Shukla, A. K. Novel structural insights into GPCR– β -arrestin interaction and signaling. *Trends Cell Biol.* **27**, 851–862 (2017).
- Grundmann, M. et al. Lack of beta-arrestin signaling in the absence of active G proteins. *Nat. Commun.* **9**, 341 (2018).

16. Tóth, A. D. et al. Heterologous phosphorylation-induced formation of a stability lock permits regulation of inactive receptors by β -arrestins. *J. Biol. Chem.* **293**, 876–892 (2018).
17. Sriram, K. & Insel, P. A. GPCRs as targets for approved drugs: how many targets and how many drugs? *Mol. Pharmacol.* **93**, 251–258 (2018).
18. Hauser, A. S., Attwood, M. M., Rask-Andersen, M., Schiöth, H. B. & Gloriam, D. E. Trends in GPCR drug discovery: new agents, targets and indications. *Nat. Rev. Drug Discov.* **16**, 829–842 (2017).
19. Hauser, A. S. et al. Pharmacogenomics of GPCR drug targets. *Cell* **172**, 41–54 (2018).
This comprehensive study reveals that several GPCRs that are targeted by common drugs show extensive genetic variation in the human population, suggesting that taking GPCR variants into account when prescribing drugs would minimize ineffective treatments, adverse reactions and health-care expenses.
20. Flock, T. et al. Selectivity determinants of GPCR-G protein binding. *Nature* **545**, 1–33 (2017).
This study reveals the existence of selectivity barcodes on G proteins that are recognized by GPCRs and lays the foundation for understanding the molecular basis of G protein-coupling specificity.
21. Latorraca, N. R., Venkatakrishnan, A. J. & Dror, R. O. GPCR dynamics: structures in motion. *Chem. Rev.* **117**, 139–155 (2017).
22. Klein Herenbrink, C. et al. The role of kinetic context in apparent biased agonism at GPCRs. *Nat. Commun.* **7**, 1–14 (2016).
This is the first detailed study on the role of kinetics in GPCR biased agonism that highlights the importance of considering kinetic context in the design and interpretation of biased agonism.
23. Irannejad, R. et al. Functional selectivity of GPCR-directed drug action through location bias. *Nat. Chem. Biol.* **13**, 799–806 (2017).
24. Halls, M. L. et al. Plasma membrane localization of the μ -opioid receptor controls spatiotemporal signaling. *Sci. Signal.* **9**, ra16 (2016).
25. Kenakin, T. Theoretical aspects of GPCR–ligand complex pharmacology. *Chem. Rev.* **117**, 4–20 (2017).
26. Burg, J. S. et al. Structural basis for chemokine recognition and activation of a viral G protein-coupled receptor. *Science* **347**, 1113–1117 (2015).
27. Zhang, B., Albaker, A., Plouffe, B., Lefebvre, C. & Tiberi, M. Constitutive activities and inverse agonism in dopamine receptors. *Adv. Pharmacol.* **70**, 175–214 (2014).
28. Stamm, S., Gruber, S. B., Rabchevsky, A. G. & Emeson, R. B. The activity of the serotonin receptor 2C is regulated by alternative splicing. *Hum. Genet.* **136**, 1079–1091 (2017).
29. Lebon, G., Warne, T. & Tate, C. G. Agonist-bound structures of G protein-coupled receptors. *Curr. Opin. Struct. Biol.* **22**, 482–490 (2012).
30. Jacobsen, S. E. et al. The GPRC6A receptor displays constitutive internalization and sorting to the slow recycling pathway. *J. Biol. Chem.* **292**, 6910–6926 (2017).
31. Cooney, K. A., Molden, B. M., Kowalczyk, N. S., Russell, S. & Baldini, G. Lipid stress inhibits endocytosis of melanocortin-4 receptor from modified clathrin-enriched sites and impairs receptor desensitization. *J. Biol. Chem.* **292**, 17731–17745 (2017).
32. Barbash, S., Lorenzen, E., Persson, T., Huber, T. & Sakmar, T. P. GPCRs globally coevolved with receptor activity-modifying proteins, RAMPs. *Proc. Natl Acad. Sci. USA* **114**, 12015–12020 (2017).
33. Hay, D. L. & Pioszak, A. A. Receptor activity-modifying proteins (RAMPs): new insights and roles. *Annu. Rev. Pharmacol. Toxicol.* **56**, 469–487 (2016).
34. Rouault, A. A. J., Srinivasan, D. K., Yin, T. C., Lee, A. A. & Sebag, J. A. Melanocortin receptor accessory proteins (MRAPs): functions in the melanocortin system and beyond. *Biochim. Biophys. Acta* **1863**, 2462–2467 (2017).
35. Molleskov-Jensen, A. S., Oliveira, M. T., Farrell, H. E. & Davis-Poynter, N. Virus-encoded 7 transmembrane receptors. *Prog. Mol. Biol. Transl. Sci.* **129**, 353–393 (2015).
36. Cheloha, R. W., Gellman, S. H., Vilardaga, J.-P. & Gardella, T. J. PTH receptor-1 signalling — mechanistic insights and therapeutic prospects. *Nat. Rev. Endocrinol.* **11**, 712–724 (2015).
37. Hannan, F. M., Olesen, M. K. & Thakker, R. V. Calcimimetic and calcilytic therapies for inherited disorders of the calcium-sensing receptor signalling pathway. *Br. J. Pharmacol.* <https://doi.org/10.1111/bph.14086> (2017).
38. Zantomio, D. et al. Convergent evidence for mGluR5 in synaptic and neuroinflammatory pathways implicated in ASD. *Neurosci. Biobehav. Rev.* **52**, 172–177 (2015).
39. Brown, L. S. & Ernst, O. P. Recent advances in biophysical studies of rhodopsins — oligomerization, folding, and structure. *Biochim. Biophys. Acta* **1865**, 1512–1521 (2017).
40. Zürn, A. et al. Fluorescence resonance energy transfer analysis of alpha 2a-adrenergic receptor activation reveals distinct agonist-specific conformational changes. *Mol. Pharmacol.* **75**, 534–541 (2009).
41. Maier-Peuschel, M. et al. A fluorescence resonance energy transfer-based M2 muscarinic receptor sensor reveals rapid kinetics of allosteric modulation. *J. Biol. Chem.* **285**, 8793–8800 (2010).
42. Devost, D. et al. Conformational profiling of the AT1 angiotensin II receptor reflects biased agonism, G protein coupling, and cellular context. *J. Biol. Chem.* **292**, 5443–5456 (2017).
43. Liang, Y.-L. et al. Phase-plate cryo-EM structure of a biased agonist-bound human GLP-1 receptor-Gs complex. *Nature* **555**, 121–125 (2018).
This study provides the highest resolution cryo-electron microscopy (cryo-EM) structure of a GPCR to date and the first structure of a GPCR bound by a biased peptide ligand.
44. Lee, M.-H. et al. The conformational signature of β -arrestin2 predicts its trafficking and signalling functions. *Nature* **531**, 665–668 (2016).
This study identifies distinct β -arrestin 2 conformational signatures that reflect the diverse functional roles of β -arrestins.
45. Nuber, S. et al. β -Arrestin biosensors reveal a rapid, receptor-dependent activation/deactivation cycle. *Nature* **531**, 661–664 (2016).
46. Busillo, J. M. et al. Site-specific phosphorylation of CXCR4 is dynamically regulated by multiple kinases and results in differential modulation of CXCR4 signaling. *J. Biol. Chem.* **285**, 7805–7817 (2010).
47. Kim, J. et al. Functional antagonism of different G protein-coupled receptor kinases for beta-arrestin-mediated angiotensin II receptor signaling. *Proc. Natl Acad. Sci. USA* **102**, 1442–1447 (2005).
48. Zidar, D. A., Violin, J. D., Whalen, E. J. & Lefkowitz, R. J. Selective engagement of G protein coupled receptor kinases (GRKs) encodes distinct functions of biased ligands. *Proc. Natl Acad. Sci. USA* **106**, 9649–9654 (2009).
49. Cahill, T. J. et al. Distinct conformations of GPCR– β -arrestin complexes mediate desensitization, signaling, and endocytosis. *Proc. Natl Acad. Sci. USA* **114**, 2562–2567 (2017).
50. Butcher, A. J. et al. Differential G-protein-coupled receptor phosphorylation provides evidence for a signaling bar code. *J. Biol. Chem.* **286**, 11506–11518 (2011).
51. Nobles, K. N. et al. Distinct phosphorylation sites on the β 2-adrenergic receptor establish a barcode that encodes differential functions of β -arrestin. *Sci. Signal.* **4**, ra51 (2011).
52. Shiraiishi, Y. et al. Phosphorylation-induced conformation of β 2-adrenoceptor related to arrestin recruitment revealed by NMR. *Nat. Commun.* **9**, 194 (2018).
53. Katritch, V., Cherezov, V. & Stevens, R. C. Diversity and modularity of G protein-coupled receptor structures. *Trends Pharmacol. Sci.* **33**, 17–27 (2012).
54. Venkatakrishnan, A. J. et al. Molecular signatures of G-protein-coupled receptors. *Nature* **494**, 185–194 (2013).
This work shows that, despite the very large diversity in the structure of class A GPCRs, there are common sets of non-covalent contacts between structurally equivalent residues that constitute the molecular signature of this GPCR class.
55. DeVree, B. T. et al. Allosteric coupling from G protein to the agonist-binding pocket in GPCRs. *Nature* **535**, 182–186 (2016).
56. Venkatakrishnan, A. J. et al. Diverse activation pathways in class A GPCRs converge near the G-protein-coupling region. *Nature* **40**, 383–388 (2016).
This is a systematic analysis of GPCR structures that reveals conserved interaction networks and characteristic features of GPCR binding and conformational changes upon activation.
57. Dror, R. O. et al. Activation mechanism of the β 2-adrenergic receptor. *Proc. Natl Acad. Sci. USA* **108**, 18684–18689 (2011).
58. Nygaard, R. et al. The dynamic process of β 2-adrenergic receptor activation. *Cell* **152**, 532–542 (2013).
59. Manglik, A. et al. Structural insights into the dynamic process of β 2-adrenergic receptor signaling. *Cell* **161**, 1101–1111 (2015).
60. Malik, R. U., Dysthe, M., Ritt, M., Sunahara, R. K. & Sivaramakrishnan, S. ERK linked GPCR-G protein fusions systematically modulate second messenger response in cells. *Sci. Rep.* **7**, 7749 (2017).
61. Gupte, T. M., Malik, R. U., Sommes, R. F., Ritt, M. & Sivaramakrishnan, S. Priming GPCR signaling through the synergistic effect of two G proteins. *Proc. Natl Acad. Sci. USA* **114**, 3756–3761 (2017).
62. Flock, T. et al. Universal allosteric mechanism for Ga activation by GPCRs. *Nature* **524**, 173–179 (2015).
63. Dror, R. O. et al. Structural basis for nucleotide exchange in heteromeric G proteins. *Science* **348**, 1361–1365 (2015).
This study used atomic-level simulations to elucidate the nucleotide release mechanism, which is critical for G protein activation.
64. Wacker, D., Wang, C., Katritch, V. & Han, G. Structural features for functional selectivity at serotonin receptors. *Science* **469**, 175–180 (2013).
65. Peng, Y. et al. 5-HT 2C receptor structures reveal the structural basis of GPCR polypharmacology. *Cell* **172**, 719–730 (2018).
66. Schönege, A. M. et al. Evolutionary action and structural basis of the allosteric switch controlling β 2AR functional selectivity. *Nat. Commun.* **8**, 2169 (2017).
67. Liu, J. J., Horst, R., Katritch, V., Stevens, R. C. & Wüthrich, K. Biased signaling pathways in β 2-adrenergic receptor characterized by 19F-NMR. *Science* **335**, 1106–1110 (2012).
This study uses NMR techniques to observe conformational differences induced in a GPCR by biased ligands.
68. Ballesteros, J. A. & Weinstein, H. Integrated methods for the construction of three-dimensional models and computational probing of structure-function relations in G protein-coupled receptors. *Methods Neurosciences* **25**, 366–428 (1995).
69. Che, T. et al. Structure of the nanobody-stabilized active state of the kappa opioid receptor. *Cell* **172**, 55–61 (2018).
70. Wacker, D. et al. Crystal structure of an LSD-bound human serotonin receptor. *Cell* **168**, 377–389 (2017).
71. Wacker, D., Stevens, R. C. & Roth, B. L. How ligands illuminate GPCR molecular pharmacology. *Cell* **170**, 414–427 (2017).
72. McCorvy, J. D. et al. Structure-inspired design of β -arrestin-biased ligands for aminergic GPCRs. *Nat. Chem. Biol.* **14**, 126–134 (2017).
73. Shukla, A. K. et al. Visualisation of arrestin recruitment by a G-protein-coupled receptor. *Nature* **512**, 218–222 (2014).
74. Yang, F. et al. Phospho-selective mechanisms of arrestin conformations and functions revealed by unnatural amino acid incorporation and (19)F-NMR. *Nat. Commun.* **6**, 8202 (2015).
75. Staus, D. P. et al. Sortase ligation enables homogeneous GPCR phosphorylation to reveal diversity in β -arrestin coupling. *Proc. Natl Acad. Sci. USA* **115**, 3834–3839 (2018).
76. Zhou, X. E. et al. Identification of phosphorylation codes for arrestin recruitment by G protein-coupled receptors. *Cell* **170**, 457–459 (2017).
77. Thomsen, A. R. B. et al. GPCR-g-protein-beta-arrestin super-complex mediates sustained G protein signaling. *Cell* **166**, 907–919 (2016).
78. Liang, Y. L. et al. Phase-plate cryo-EM structure of a class B GPCR-G-protein complex. *Nature* **546**, 118–123 (2017).
This study presents the first cryo-EM structure of a GPCR and the first structure of a class B GPCR in an active state bound by a peptide agonist and a heterotrimeric G protein.
79. Zhang, Y. et al. Cryo-EM structure of the activated GLP-1 receptor in complex with a G protein. *Nature* **546**, 248–253 (2017).
80. Wooten, D., Miller, L. J., Koole, C., Christopoulos, A. & Sexton, P. M. Allostery and biased agonism at class B G protein-coupled receptors. *Chem. Rev.* **117**, 111–138 (2017).

81. Siu, F. Y. et al. Structure of the human glucagon class B G-protein-coupled receptor. *Nature* **499**, 444–449 (2013).
82. Hollenstein, K. et al. Structure of class B GPCR corticotropin-releasing factor receptor 1. *Nature* **499**, 438–443 (2013).
Together with reference 80, this study describes the first TMD structures of a class B GPCR and reveals a unique binding mode for an allosteric antagonist, which occurs deep in the transmembrane bundle.
83. Jazayeri, A. et al. Extra-helical binding site of a glucagon receptor antagonist. *Nature* **533**, 274–277 (2016).
84. Song, G. et al. Human GLP-1 receptor transmembrane domain structure in complex with allosteric modulators. *Nature* **546**, 312–315 (2017).
85. Koth, C. M. et al. Molecular basis for negative regulation of the glucagon receptor. *Proc. Natl Acad. Sci. USA* **109**, 14393–14398 (2012).
86. Mukund, S. et al. Inhibitory mechanism of an allosteric antibody targeting the glucagon receptor. *J. Biol. Chem.* **288**, 36168–36178 (2013).
87. Zhang, H. et al. Structure of the full-length glucagon class B G-protein-coupled receptor. *Nature* **546**, 259–264 (2017).
88. Zhang, H. et al. Structure of the glucagon receptor in complex with a glucagon analogue. *Nature* **553**, 106–110 (2018).
89. Jazayeri, A. et al. Crystal structure of the GLP-1 receptor bound to a peptide agonist. *Nature* **546**, 254–258 (2017).
90. Wootten, D., Simms, J., Miller, L. J., Christopoulos, A. & Sexton, P. M. Polar transmembrane interactions drive formation of ligand-specific and signal pathway-biased family B G protein-coupled receptor conformations. *Proc. Natl Acad. Sci. USA* **110**, 5211–5216 (2013).
91. Wootten, D. et al. The extracellular surface of the GLP-1 receptor is a molecular trigger for biased agonism. *Cell* **165**, 1632–1643 (2016).
This study provides some of the first molecular and mechanistic insights into the initiation and activation of biased agonism for a GPCR.
92. Dal Maso, E. et al. Extracellular loops 2 and 3 of the calcitonin receptor selectively modify agonist binding and efficacy. *Biochem. Pharmacol.* **150**, 214–244 (2018).
93. Wootten, D. et al. A hydrogen-bonded polar network in the core of the glucagon-like peptide-1 receptor is a fulcrum for biased agonism: lessons from class B crystal structures. *Mol. Pharmacol.* **89**, 335–347 (2016).
94. Wootten, D. et al. Key interactions by conserved polar amino acids located at the transmembrane helical boundaries in Class B GPCRs modulate activation, effector specificity and biased signalling in the glucagon-like peptide-1 receptor. *Biochem. Pharmacol.* **118**, 68–87 (2016).
95. de Graaf, C. et al. Extending the structural view of class B GPCRs. *Trends Biochem. Sci.* **42**, 946–960 (2017).
96. Hari Kumar, K. G. et al. Glucagon-like peptide-1 receptor dimerization differentially regulates agonist signaling but does not affect small molecule allostery. *Proc. Natl Acad. Sci. USA* **109**, 18607–18612 (2012).
97. Hari Kumar, K. G., Lau, S., Sexton, P. M., Wootten, D. & Miller, L. J. Coexpressed class B G protein-coupled secretin and GLP-1 receptors self- and cross-associate: impact on pancreatic islets. *Endocrinology* **158**, 1685–1700 (2017).
98. Schelshorn, D. et al. Lateral allostery in the glucagon receptor family: glucagon-like peptide 1 induces G-protein-coupled receptor heteromer formation. *Mol. Pharmacol.* **81**, 309–318 (2012).
99. Pediani, J. D., Ward, R. J., Marsango, S. & Milligan, G. Spatial intensity distribution analysis: studies of G protein-coupled receptor oligomerisation. *Trends Pharmacol. Sci.* **39**, 175–186 (2018).
100. Møller, T. C., Moreno-Delgado, D., Pin, J.-P. & Kniazeff, J. Class C G protein-coupled receptors: reviving old couples with new partners. *Biophys. Rep.* **3**, 57–63 (2017).
101. Geng, Y. et al. Structural mechanism of ligand activation in human calcium-sensing receptor. *eLife* **5**, e13662 (2016).
102. Geng, Y., Bush, M., Mosyak, L., Wang, F. & Fan, Q. R. Structural mechanism of ligand activation in human GABAB receptor. *Nature* **504**, 254–259 (2013).
103. Frangaj, A. & Fan, Q. R. Structural biology of GABA B receptor. *Neuropharmacology* **136**, 68–79 (2017).
104. Xue, L. et al. Major ligand-induced rearrangement of the heptahelical domain interface in a GPCR dimer. *Nat. Chem. Biol.* **11**, 134–140 (2015).
105. Leach, K. & Gregory, K. J. Molecular insights into allosteric modulation of Class C G protein-coupled receptors. *Pharmacol. Res.* **116**, 105–118 (2017).
106. Cook, A. E. et al. Biased allosteric modulation at the CaS receptor engendered by structurally diverse calcimimetics. *Br. J. Pharmacol.* **172**, 185–200 (2015).
107. Foster, D. J. & Conn, P. J. Allosteric modulation of GPCRs: new insights and potential utility for treatment of schizophrenia and other CNS disorders. *Neuron* **94**, 431–446 (2017).
108. Dijkman, P. M. & Watts, A. Lipid modulation of early G protein-coupled receptor signalling events. *Biochim. Biophys. Acta* **1848**, 2889–2897 (2015).
109. Desai, A. J., Dong, M., Langlais, B. T., Dueck, A. C. & Miller, L. J. Cholecystokinin responsiveness varies across the population dependent on metabolic phenotype. *Am. J. Clin. Nutr.* **106**, 447–456 (2017).
110. Desai, A. J., Dong, M. & Miller, L. J. Beneficial effects of β -sitosterol on type 1 cholecystokinin receptor dysfunction induced by elevated membrane cholesterol. *Clin. Nutr.* **35**, 1374–1379 (2016).
111. Zocher, M., Zhang, C., Rasmussen, S. G. F., Kobilka, B. K. & Müller, D. J. Cholesterol increases kinetic, energetic, and mechanical stability of the human β 2-adrenergic receptor. *Proc. Natl Acad. Sci. USA* **109**, E3463–E3472 (2012).
112. Inagaki, S. et al. Modulation of the interaction between neurotensin receptor NTS1 and Gq protein by lipid. *J. Mol. Biol.* **417**, 95–111 (2012).
113. Dawaliby, R. et al. Allosteric regulation of G protein-coupled receptor activity by phospholipids. *Nat. Chem. Biol.* **3**, 35–39 (2015).
114. Guinzeberg, R. et al. Newly synthesized cAMP is integrated at a membrane protein complex signalosome to ensure receptor response specificity. *FEBS J.* **284**, 258–276 (2017).
115. Stillwell, W. *An Introduction to Biological Membranes: Composition, Structure and Function* (Elsevier Science, 2016).
116. Harayama, T. & Riezman, H. Understanding the diversity of membrane lipid composition. *Nat. Rev. Mol. Cell Biol.* **19**, 281–296 (2018).
117. Parton, R. G. & del Pozo, M. A. Caveolae as plasma membrane sensors, protectors and organizers. *Nat. Rev. Mol. Cell Biol.* **14**, 98–112 (2013).
118. Rosholm, K. R. et al. Membrane curvature regulates ligand-specific membrane sorting of GPCRs in living cells. *Nat. Chem. Biol.* **13**, 724–729 (2017).
This study highlights the importance of membrane curvature in regulation of GPCR function.
119. Shukla, A. K. *G Protein-Coupled Receptors: Signaling, Trafficking and Regulation* Vol. 132 (Academic Press, 2016).
120. Wu, G. *Trafficking of GPCRs* Vol. 132 (Academic Press, 2015).
121. Bahouth, S. W. & Nooh, M. M. Barcoding of GPCR trafficking and signaling through the various trafficking roadmaps by compartmentalized signaling networks. *Cell. Signal.* **36**, 42–55 (2017).
122. Wang, G., Wei, Z. & Wu, G. Role of Rab GTPases in the export trafficking of G protein-coupled receptors. *Small GTPases* **26**, 130–135 (2017).
123. Irannejad, R., Tsvetanova, N. G., Lobingier, B. T. & von Zastrow, M. Effects of endocytosis on receptor-mediated signaling. *Curr. Opin. Cell Biol.* **35**, 137–143 (2015).
124. Farran, B. An update on the physiological and therapeutic relevance of GPCR oligomers. *Pharmacol. Res.* **117**, 303–327 (2017).
125. Franco, R., Martínez-Pinilla, E., Lanciego, J. L. & Navarro, G. Basic pharmacological and structural evidence for class A G-protein-coupled receptor heteromerization. *Front. Pharmacol.* **7**, 76 (2016).
126. Gomes, I. et al. G protein-coupled receptor heteromers. *Annu. Rev. Pharmacol. Toxicol.* **56**, 403–425 (2016).
127. DeBruine, Z. J., Xu, H. E. & Melcher, K. Assembly and architecture of the Wnt/ β -catenin signalosome at the membrane. *Br. J. Pharmacol.* **174**, 4564–4574 (2017).
128. McLatchie, L. M. et al. RAMPs regulate the transport and ligand specificity of the calcitonin-receptor-like receptor. *Nature* **393**, 333–339 (1998).
129. Nikolaev, V. O. et al. Beta2-adrenergic receptor redistribution in heart failure changes cAMP compartmentation. *Science* **327**, 1653–1657 (2010).
130. Lyon, A. R. et al. Plasticity of surface structures and beta2-adrenergic receptor localization in failing ventricular cardiomyocytes during recovery from heart failure. *Circ. Heart Fail.* **5**, 357–365 (2012).
131. Jensen, D. D. et al. Endothelin-converting enzyme 1 and β -arrestins exert spatiotemporal control of substance P-induced inflammatory signals. *J. Biol. Chem.* **289**, 20283–20294 (2014).
132. Ayling, L. J. et al. Adenylyl cyclase AC8 directly controls its micro-environment by recruiting the actin cytoskeleton in a cholesterol-rich milieu. *J. Cell Sci.* **125**, 869–886 (2012).
133. Halls, M. L. & Cooper, D. M. F. Sub-picomolar relaxin signalling by a pre-assembled RXFP1, AKAP79, AC2, β -arrestin 2, PDE4D3 complex. *EMBO J.* **29**, 2772–2787 (2010).
This study identifies pre-assembled, ligand-independent GPCR signalosomes that allow a GPCR to respond to extremely low concentrations of circulating ligands.
134. Siljee, J. E. et al. Subcellular localization of MC4R with ADCY3 at neuronal primary cilia underlies a common pathway for genetic predisposition to obesity. *Nat. Genet.* **50**, 180–185 (2018).
135. Navarro, G. et al. Evidence for functional pre-coupled complexes of receptor heteromers and adenylyl cyclase. *Nat. Commun.* **9**, 1242 (2018).
136. Webbi, V. L. et al. Noncanonical GPCR signaling arising from a PTH receptor–arrestin–G β complex. *Proc. Natl Acad. Sci. USA* **110**, 1530–1535 (2013).
This study is one of the first to report a GPCR that promotes persistent G protein signalling from intracellular endosomal compartments, which is mediated by β -arrestins.
137. Suofu, Y. et al. Dual role of mitochondria in producing melatonin and driving GPCR signaling to block cytochrome c release. *Proc. Natl Acad. Sci. USA* **114**, E7997–E8006 (2017).
138. Tadevosyan, A. et al. Intracellular angiotensin-II interacts with nuclear angiotensin receptors in cardiac fibroblasts and regulates RNA synthesis, cell proliferation, and collagen secretion. *J. Am. Heart Assoc.* **6**, e004965 (2017).
139. Vaniotis, G. et al. Regulation of cardiac nitric oxide signaling by nuclear β -adrenergic and endothelin receptors. *J. Mol. Cell. Cardiol.* **62**, 58–68 (2013).
140. Tsvetanova, N. G., Irannejad, R. & von Zastrow, M. G. Protein-coupled receptor (GPCR) signaling via heterotrimeric G proteins from endosomes. *J. Biol. Chem.* **290**, 6689–6696 (2015).
141. Tsvetanova, N. G. & von Zastrow, M. Spatial encoding of cyclic AMP signaling specificity by GPCR endocytosis. *Nat. Chem. Biol.* **10**, 1061–1065 (2014).
142. Vilardaga, J.-P., Jean-Alphonse, F. G. & Gardella, T. J. Endosomal generation of cAMP in GPCR signaling. *Nat. Chem. Biol.* **10**, 700–706 (2014).
143. Jensen, D. D. et al. Neurokinin 1 receptor signaling in endosomes mediates sustained nociception and is a viable therapeutic target for prolonged pain relief. *Sci. Transl. Med.* **9**, eaa13447 (2017).
This study reveals a critical role for endosomal signalling of a GPCR in pain perception and demonstrates the potential therapeutic use of endosomally targeted GPCR antagonists.
144. Yarwood, R. E. et al. Endosomal signaling of the receptor for calcitonin gene-related peptide mediates pain transmission. *Proc. Natl Acad. Sci. USA* **114**, 12309–12314 (2017).
145. Jean-Alphonse, F. G. et al. β 2-adrenergic receptor control of endosomal PTH receptor signaling via G β . *Nat. Chem. Biol.* **13**, 259–261 (2017).
146. Wright, P. T. et al. Caveolin-3 regulates compartmentation of cardiomyocyte beta2-adrenergic receptor-mediated cAMP signaling. *J. Mol. Cell. Cardiol.* **67**, 38–48 (2014).
147. Beaurtrait, A. et al. A new inhibitor of the β -arrestin/AP2 endocytic complex reveals interplay between GPCR internalization and signalling. *Nat. Commun.* **8**, 15054 (2017).
148. Sykes, D. A. et al. Extrapyramidal side effects of antipsychotics are linked to their association kinetics at dopamine D2 receptors. *Nat. Commun.* **8**, 763 (2017).
149. Wacker, D. et al. Crystal structure of an LSD-bound human serotonin receptor. *Cell* **168**, 377–389 (2017).
150. Lane, J. R., May, L. T., Parton, R. G., Sexton, P. M. & Christopoulos, A. A kinetic view of GPCR allostery and biased agonism. *Nat. Chem. Biol.* **13**, 929–937 (2017).
151. Benredjem, B., Dallaire, P. & Pineyro, G. Analyzing biased responses of GPCR ligands. *Curr. Opin. Pharmacol.* **32**, 71–76 (2017).

152. Bradley, S. J., Tobin, A. B. & Prihandoko, R. The use of chemogenetic approaches to study the physiological roles of muscarinic acetylcholine receptors in the central nervous system. *Neuropharmacology* **136**, 421–426 (2018).
153. Roth, B. L. DREADDs for neuroscientists. *Neuron* **89**, 683–694 (2016).
154. Bruchas, M. R. & Roth, B. L. New technologies for elucidating opioid receptor function. *Trends Pharmacol. Sci.* **37**, 279–289 (2016).
155. Spangler, S. M. & Bruchas, M. R. Optogenetic approaches for dissecting neuromodulation and GPCR signaling in neural circuits. *Curr. Opin. Pharmacol.* **32**, 56–70 (2017).
156. Boerrigter, G., Soergel, D. G., Violin, J. D., Lark, M. W. & Burnett, J. C. TRV120027, a novel beta-arrestin biased ligand at the angiotensin II type I receptor, unloads the heart and maintains renal function when added to furosemide in experimental heart failure. *Circ. Heart Fail.* **5**, 627–634 (2012).
157. Tarigopula, M. et al. Cardiac myosin light chain phosphorylation and inotropic effects of a biased ligand, TRV120023, in a dilated cardiomyopathy model. *Cardiovasc. Res.* **107**, 226–234 (2015).
158. Brust, T. F. et al. Biased agonists of the kappa opioid receptor suppress pain and itch without causing sedation or dysphoria. *Sci. Signal.* **9**, ra117 (2016).
159. DeWire, S. M. et al. A G protein-biased ligand at the mu-opioid receptor is potentially analgesic with reduced gastrointestinal and respiratory dysfunction compared with morphine. *J. Pharmacol. Exp. Ther.* **344**, 708–717 (2013).
160. Manglik, A. et al. Structure-based discovery of opioid analgesics with reduced side effects. *Nature* **537**, 185–190 (2016).
161. Schmid, C. L. et al. Bias factor and therapeutic window correlate to predict safer opioid analgesics. *Cell* **171**, 1165–1175 (2017).
- This is an important study that examines the correlation between measures of biased agonism and in vivo therapeutic index (the ratio of beneficial to detrimental effects).**
162. Desai, A. J. & Miller, L. J. Changes in the plasma membrane in metabolic disease: impact of the membrane environment on G protein-coupled receptor structure and function. *Br. J. Pharmacol.* <https://doi.org/10.1111/bph.13943> (2018).
163. Vijayakumar, N. et al. White matter integrity in individuals at ultra-high risk for psychosis: a systematic review and discussion of the role of polyunsaturated fatty acids. *BMC Psychiatry* **16**, 287 (2016).
164. Cheong, H. I. et al. Hypoxia sensing through β -adrenergic receptors. *JCI Insight* **1**, e90240 (2016).
165. Shellhammer, J. P. et al. Amino acid metabolites that regulate G protein signaling during osmotic stress. *PLoS Genet.* **13**, e1006829 (2017).
166. Ardura, J. A., Alonso, V., Esbrit, P. & Friedman, P. A. Oxidation inhibits PTH receptor signaling and trafficking. *Biochem. Biophys. Res. Commun.* **482**, 1019–1024 (2017).
167. Ghanouni, P. et al. The effect of pH on beta(2) adrenoceptor function. Evidence for protonation-dependent activation. *J. Biol. Chem.* **275**, 3121–3127 (2000).
168. Vickery, O. N., Machtens, J. P. & Zachariae, U. Membrane potentials regulating GPCRs: insights from experiments and molecular dynamics simulations. *Curr. Opin. Pharmacol.* **30**, 44–50 (2016).
169. Isom, D. G. & Dohlman, H. G. Buried ionizable networks are an ancient hallmark of G protein-coupled receptor activation. *Proc. Natl Acad. Sci. USA* **112**, 5702–5707 (2015).
170. Katritch, V. et al. Allosteric sodium in class A GPCR signaling. *Trends Pharmacol. Sci.* **39**, 233–244 (2014).
171. Massink, A. et al. Sodium ion binding pocket mutations and adenosine A2A receptor function. *Mol. Pharmacol.* **82**, 305–313 (2015).
172. Thompson, M. D. et al. Pharmacogenetics of the G protein-coupled receptors. *Methods Mol. Biol.* **1175**, 189–242 (2014).
173. Perez, J. M. et al. β 1-adrenergic receptor polymorphisms confer differential function and predisposition to heart failure. *Nat. Med.* **9**, 1300–1305 (2003).
174. Liggett, S. B. et al. A polymorphism within a conserved beta(1)-adrenergic receptor motif alters cardiac function and beta-blocker response in human heart failure. *Proc. Natl Acad. Sci. USA* **103**, 11288–11293 (2006).
175. Freitas, C. et al. Lymphoid differentiation of hematopoietic stem cells requires efficient Cxcr4 desensitization. *J. Exp. Med.* **214**, 2023–2040 (2017).
176. Barak, L. S., Oakley, R. H., Laporte, S. A. & Caron, M. G. Constitutive arrestin-mediated desensitization of a human vasopressin receptor mutant associated with nephrogenic diabetes insipidus. *Proc. Natl Acad. Sci. USA* **98**, 93–98 (2001).
177. Michel, M. C. & Charlton, S. J. Biased agonism in drug discovery — is it too soon to choose a path? *Mol. Pharmacol.* **93**, 259–265 (2018).
178. Black, J. & Leff, P. Operational models of pharmacological agonism. *Proc. R. Soc. Zool.* **220**, 141–162 (1983).
179. Hager, M. V., Clydesdale, L., Gellman, S. H., Sexton, P. M. & Wootton, D. Characterization of signal bias at the GLP-1 receptor induced by backbone modification of GLP-1. *Biochem. Pharmacol.* **136**, 99–108 (2017).
180. Thompson, G. L. et al. Systematic analysis of factors influencing observations of biased agonism at the mu-opioid receptor. *Biochem. Pharmacol.* **113**, 70–87 (2016).
181. Karamitri, A. et al. Melatonin MT2 receptor variants associated with type 2 diabetes affect specific subsets of the receptor signaling modalities. *Sci. Signal.* (in the press) (2018).
182. Qin, C. X. et al. Small-molecule-biased formyl peptide receptor agonist compound 17b protects against myocardial ischaemia-reperfusion injury in mice. *Nat. Commun.* **8**, 14232 (2017).
183. van der Westhuizen, E. T., Breton, B., Christopoulos, A. & Bouvier, M. Quantification of ligand bias for clinically relevant β 2-adrenergic receptor ligands: implications for drug taxonomy. *Mol. Pharmacol.* **85**, 492–509 (2014).
184. Valant, C., Robert Lane, J., Sexton, P. M. & Christopoulos, A. The best of both worlds? Bitopic orthosteric/allosteric ligands of G protein-coupled receptors. *Annu. Rev. Pharmacol. Toxicol.* **52**, 153–178 (2012).
185. Thal, D., Glukhova, A., Sexton, P. M. & Christopoulos, A. Structural insights into G-protein-coupled receptor allostery. *Nature* **559**, 45–53 (2018).
186. Christopoulos, A. et al. International Union of Basic and Clinical Pharmacology. XC. Multisite pharmacology: Recommendations for the nomenclature of receptor allostery and allosteric ligands. *Pharmacol. Rev.* **66**, 918–947 (2014).

Acknowledgements

P.M.S., A.C. and D.W. are Principal, Senior Principal and Career Development Fellows of the National Health and Medical Research Council of Australia, respectively. M.M.B. and M.M.-S. acknowledge the UK Medical Research Council (MC_U105185859) for support. M.M.-S. is supported by a Federation of European Biochemical Societies Long-Term Fellowship, and M.M.B. is a Lister Institute Fellow and is also supported by the European Research Council (ERC-COG-2015-682414).

Author contributions

D.W., A.C., M.M.-S., M.M.B. and P.M.S. researched data for the article. D.W., A.C., M.M.B. and P.M.S. substantially contributed to discussion of content. D.W., M.M.B., M.M.-S. and P.M.S. wrote the article. D.W., A.C., M.M.-S., M.M.B. and P.M.S. reviewed and edited the manuscript before submission.

Competing interests

The authors declare no competing interests.

Publisher's note

Springer Nature remains neutral with regard to jurisdictional claims in published maps and institutional affiliations.

Reviewer information

Nature Reviews Molecular Cell Biology thanks T. Hebert, V. Katritch, S. Rajagopal and the other anonymous reviewer(s) for their contribution to the peer review of this work.

RELATED LINKS

Common Gα Subunit Numbering (CGN): <https://www.mrc-lmb.cam.ac.uk/CGN/>
 GPCR Drug Browser: <http://gpcrdb.org/drugs/drugbrowser>
 GPCR Database: www.gpcrdb.org
 Natural variation of GPCRs in the human population: http://www.gpcrdb.org/mutational_landscape/statistics
 Protein Contacts Atlas: <https://www.mrc-lmb.cam.ac.uk/pca>
 Selectivity determinants of GPCR-G protein signalling: <http://www.gpcrdb.org/signprot/statistics>

Rules of Engagement: GPCRs and G Proteins

Alisa Glukhova,^{*,†} Christopher J. Draper-Joyce,[†] Roger K. Sunahara,[‡] Arthur Christopoulos,[†] Denise Wootten,^{†,§} and Patrick M. Sexton^{*,†,§}[†]Drug Discovery Biology and Department of Pharmacology, Monash Institute of Pharmaceutical Sciences, Monash University, Parkville, Victoria 3052, Australia[‡]Department of Pharmacology, University of California San Diego School of Medicine, La Jolla, California 92093, United States[§]School of Pharmacy, Fudan University, Shanghai, 201203, China

ABSTRACT: G protein-coupled receptors (GPCRs) are a key drug target class. They account for over one-third of current pharmaceuticals, and both drugs that inhibit and promote receptor function are important therapeutically; in some cases, the same GPCR can be targeted with agonists and inhibitors, depending upon disease context. There have been major breakthroughs in understanding GPCR structure and drug binding through advances in X-ray crystallography, and membrane protein stabilization. Nonetheless, these structures have predominately been of inactive receptors bound to inhibitors. Efforts to capture structures of fully active GPCRs, in particular those in complex with the canonical, physiological transducer G protein, have been limited via this approach. Very recently, advances in cryo-electron microscopy have provided access to agonist:GPCR:G protein complex structures. These promise to revolutionize our understanding of GPCR:G protein engagement and provide insight into mechanisms of efficacy and coupling selectivity and how these might be controlled by biased agonists. Here we review what we have currently learned from the new GPCR:Gs and GPCR:Gi/o complex structures.

KEYWORDS: G protein-coupled receptor, G protein, cryo-electron microscopy, receptor-G protein coupling



■ INTRODUCTION

G protein-coupled receptors (GPCRs) are transmembrane proteins that respond to a variety of stimuli including hormones, neurotransmitters, peptides, and small molecules. Signal transmission inside the cell occurs through GPCR interaction with their downstream partners, such as G proteins,¹ G protein-coupled receptor kinases (GRKs),² and arrestins.³

G proteins, the canonical coupling partner whose interaction has defined the naming of GPCRs, are heterotrimers consisting of α , β , and γ subunits. Each subunit is present in the human genome as multiple genes encoding distinct subunit subtypes, resulting in many variations in heterotrimer assembly. G proteins are primarily distinguished based on their $G\alpha$ subunits, which are grouped into 4 families based on sequence similarities and functional output: G_s ($G\alpha_s$ and $G\alpha_{olf}$), $G_{i/o}$ ($G\alpha_{i1-3}$, $G\alpha_{oA}$, $G\alpha_{oB}$, $G\alpha_v$, $G\alpha_{g1}$, $G\alpha_z$), G_q ($G\alpha_q$, $G\alpha_{11}$, $G\alpha_{14}$, $G\alpha_{15/16}$) and G_{12} ($G\alpha_{12}$ and $G\alpha_{13}$).⁴ Both G_s and $G_{i/o}$ family members regulate activity of adenylate cyclases, either stimulating ATP to cAMP conversion (G_s) or inhibiting it, leading to a decrease in cAMP levels ($G_{i/o}$).

Despite extensive biochemical characterization, structural information on receptor complexes with G proteins remained elusive for many years until the first structure of the β_2 -adrenergic receptor (β_2 AR) complex with heterotrimeric G_s protein was solved in 2011 by Kobilka, Sunahara, and colleagues using X-ray crystallography.⁵ Nonetheless, other GPCR-G protein complexes have remained refractive to crystallization and/or high-resolution diffraction that have

limited additional structure determination by this methodology. Very recently, the “resolution revolution” in cryo-electron microscopy (cryo-EM)⁶ has enabled application of this technique to structure determination of other GPCR- G_s complexes, namely of A_{2A} adenosine receptor (A_{2A} AR),⁷ calcitonin receptor (CTR),⁸ calcitonin-like receptor-RAMP complex (CLR-RAMP, CGRP receptor),⁹ and multiples of glucagon-like peptide 1 receptor (GLP1R).^{10,11} Nonetheless, GPCR complexes with other G proteins remained elusive until June 2018 when four groups, utilizing distinct approaches, independently determined structures of GPCRs with members of the $G_{i/o}$ family: A_1 adenosine receptor (A_1 AR)- G_{i2} ,¹² μ opioid receptor (μ OR)- G_{i1} ,¹³ rhodopsin (Rho)- G_{i1} ,¹⁴ and serotonin 5-HT_{1B}-mG_o.¹⁵ Comparison of these structures, together with previously solved structures of G_s complexes, gives us the first glimpse at molecular mechanisms responsible for signal transmission from GPCRs to G proteins, and structural evaluation of selectivity determinants for both interaction partners. This review will focus on all the structures of active state GPCR-heterotrimeric G protein complexes determined to date in the context of GPCR and G protein activation, complex formation, and mechanisms of discrimination between G_s and $G_{i/o}$ families.

Received: August 14, 2018

Published: September 7, 2018

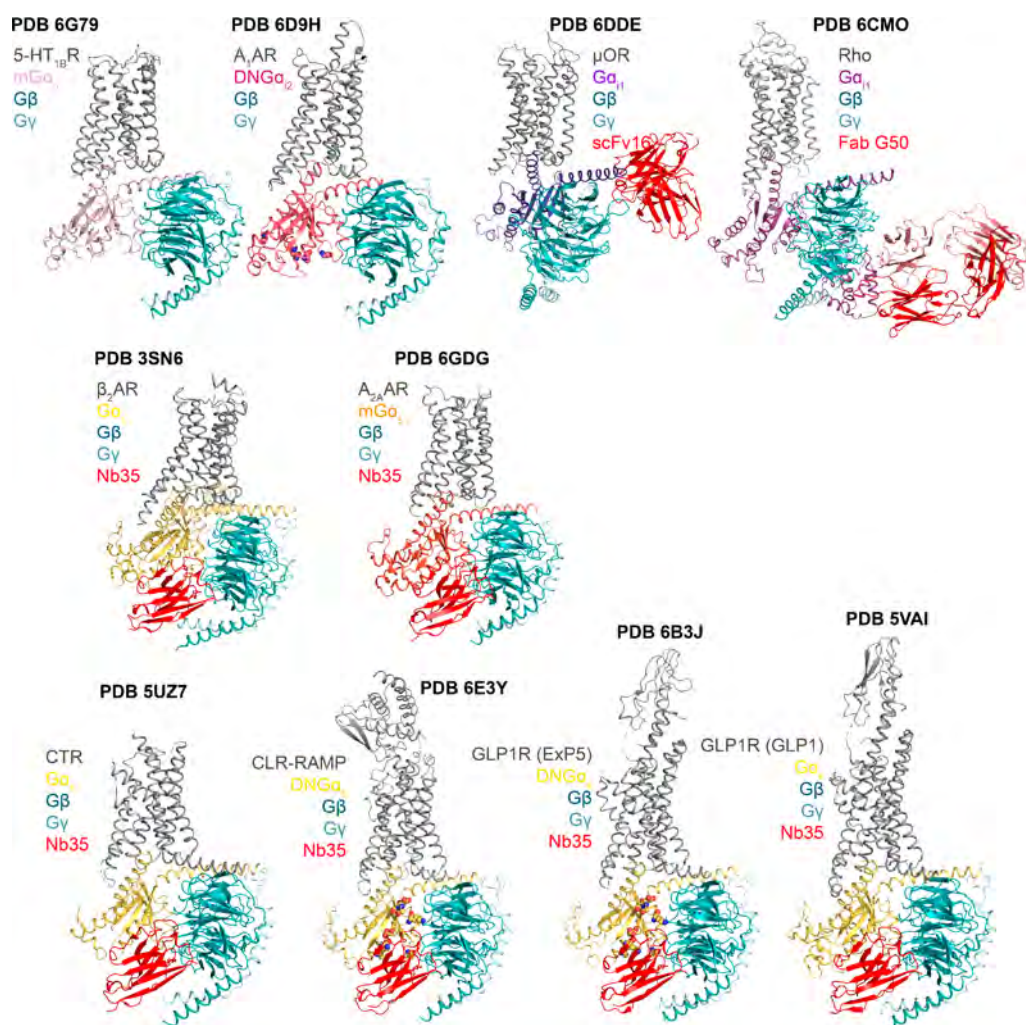


Figure 1. Methods for GPCR-G protein complex stabilization. Complexes are shown as cartoon, with receptors shown in gray, $G\alpha_s$ and $G\alpha_{i/o}$ in yellow and shades of pink, $G\beta$ in cyan, and $G\gamma$ in pale cyan. Proteins used for complex stabilization are shown in red. Stabilizing mutations in DN G proteins are shown as spheres.

■ APPROACHES TO GPCR-G PROTEIN COMPLEX STABILIZATION

One of the main difficulties in structure determination of GPCR-G protein complexes is the transient nature of the interaction. Capture of the very first β_2 AR- G_s complex was made possible through the combined application of apyrase and nanobody 35 (Nb35).⁵ Apyrase, a nonselective nucleotide lyase, is capable of sequentially hydrolyzing GTP and GDP to GMP, trapping the receptor-G protein complex in a nucleotide-free state. All GPCR-G protein structures solved to date required apyrase treatment for complex formation. Selectively for $G\alpha_s G\beta\gamma$ heterotrimers, the nanobody (Nb35) binds and stabilizes the interface between $G\beta\gamma$ subunit and Ras Homology Domain (RHD) of $G\alpha_s$, rendering the complex insensitive to GTP γ S.¹⁶ Nb35 proved to be an invaluable tool for G_s complex stabilization leading to the first full-length structure of a class B GPCR, the CTR,⁸ and subsequent structures of the GLP-1R^{10,11} and CGRP receptor.⁹ While the availability of Nb35 for stabilization of G_s complexes was important for other structures, more tools were developed to strengthen the interaction between receptor and G protein and reduce complex flexibility (Figure 1).

The Tate group developed minimal G proteins or mini-G (mG), a rationally designed RHD containing only the GTPase region of $G\alpha$ proteins with additional mutations that increased thermostability and reduced nucleotide affinity.^{17,18} The mG_s on its own was used for crystallization and X-ray structure determination of the A_{2A} AR.¹⁹ Another version of mG_s protein, with an extended N-terminal helix, capable of binding the $G\beta\gamma$ subunit, was used to solve the structure of A_{2A} AR: $mG\alpha_s\beta\gamma$:Nb35 complex by cryo-EM.⁷ Development of the mini-G versions of other $G\alpha$ family members yielded mG_o and made possible the determination of the serotonin 5-HT_{1B}: $mG\alpha_s\beta\gamma$ structure (but no additional stabilizing protein partner was required).¹⁵

Another approach for complex stabilization, exploited by the Sexton and Wooten laboratories, is targeted mutagenesis of the $G\alpha$ subunit.²⁰ Following previous literature that described mutational effects on G proteins, mutations of residues involved in coordination of Mg^{2+} , and GTP's β - and γ -phosphates, plus additional residues that improved overall complex stability, led to the creation of dominant negative (DN) G proteins with reduced nucleotide affinity and enhanced interaction between $G\alpha$ and $G\beta\gamma$.^{21–25} This strategy was applied to $G\alpha_s$, yielding the structures of GLP1R:DNG $\alpha_s\beta\gamma$:Nb35 with the biased agonist exendin-

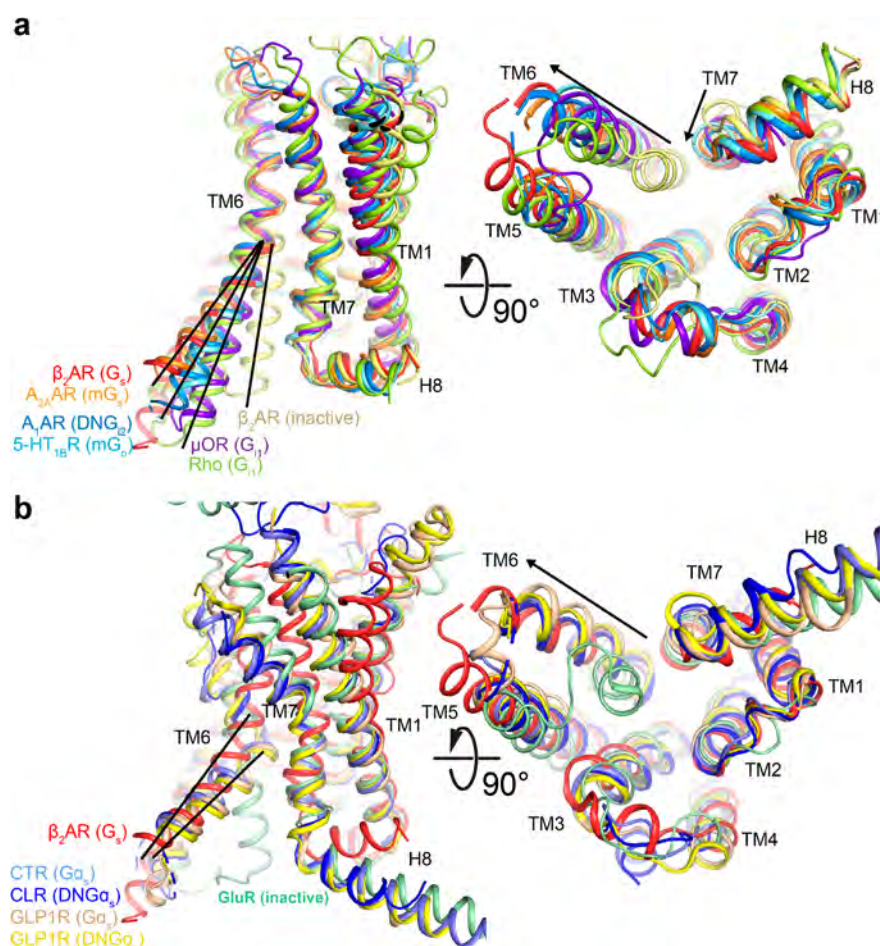


Figure 2. Receptor conformations in G_s and G_{i/o} complexes. Aligned receptors are shown as cartoons and the black line depicts average TM6 displacement for Class A G_s, G_{i11}, and G_{i2/mGo} complexes (a) or Class B G_s complexes with β₂AR shown for comparison (b). Arrows show the direction of TM6 and TM7 movement upon receptor activation.

P5¹⁰ and the heteromeric CGRP receptor, CLR:RAMP1:DN- α β γ :Nb35 complexes,⁹ and may be important for complex stabilization for lower efficacy agonists, in which the use of Nb35 alone is insufficient.²⁰ The DN G protein approach was also successfully applied to G α_{i2} , resulting in the A₁AR:DN α_{i2} β γ structure (without additional stabilizing protein partner).¹²

More targeted approaches for complex stabilization were also developed. In one study, an antibody single-chain variable fragment (scFv16) against a complex of Rho-G_{i1} was generated, targeting the interface of the α N helix of G α_{i1} and the β -propeller of G β ; this prevented GTP γ S-dependent complex dissociation.¹³ Consequently, this Fab was used for structure determination of the μOR:G α_{i1} β γ :scFv16 complex. In a separate study, a phage display library was used to screen for G_{i1} heterotrimer-binding Fabs, followed by negative stain EM-guided selection of Fab_{G50} that bound at the interface of the α -Helical Domain (AHD) of G α_{i1} and the G β γ subunit and stabilized a Rho:G α_{i1} β γ :Fab_{G50} complex.¹⁴

■ RECEPTOR CONFORMATIONS IN GPCR-G PROTEIN COMPLEXES

In total, there are 10 structures of active-state GPCRs in complex with heterotrimeric G proteins. The class A rhodopsin subfamily is represented by β₂AR and A_{2A}AR complexes with G_s and A₁AR, μOR, Rho, and 5-HT_{1B}-complexes with G_{i/o},

while class B GPCRs are represented by CTR, CLR-RAMP1, and GLP1R complexes with G_s heterotrimers. A comparison of active state receptors with corresponding inactive state structures reveals a common mechanism of activation for both G_s and G_i-coupled receptors.

In the class A GPCRs solved to date, agonist binding in itself stabilizes a small conformational rearrangement around the ligand binding site of the receptor. Closure of the orthosteric site appears to be receptor-specific and independent of the G protein binding partner. A small shift of the top of TM1 for μOR, was observed in both G_{i1}-coupled and G protein-mimetic, Nb39-bound structures.^{13,26} Similarly, movements of the top of TM1 and TM2 of A_{2A}AR are initiated by agonist binding even in the absence of an intracellular binding partner.²⁷ These conformational changes are required to effectively accommodate agonists in the binding site. In accordance with this, only small changes in rotamer orientations were observed upon agonist binding in intermediate-active A_{2A}AR and 5-HT_{1B} structures in the absence of G proteins.^{27,28}

On the other hand, reorganization of D^{3.49}R^{3.50}Y^{3.51}, P^{3.40}I^{5.50}F^{6.44}, and N^{7.49}P^{7.50}xxY^{7.53} motifs in class A GPCRs is the hallmark of receptor activation and is only observed upon receptor stabilization in the active state with either a G protein or a G protein-mimicking nanobody,²⁹ or at least partially, in receptors with high constitutive activity.³⁰ Similar rotameric

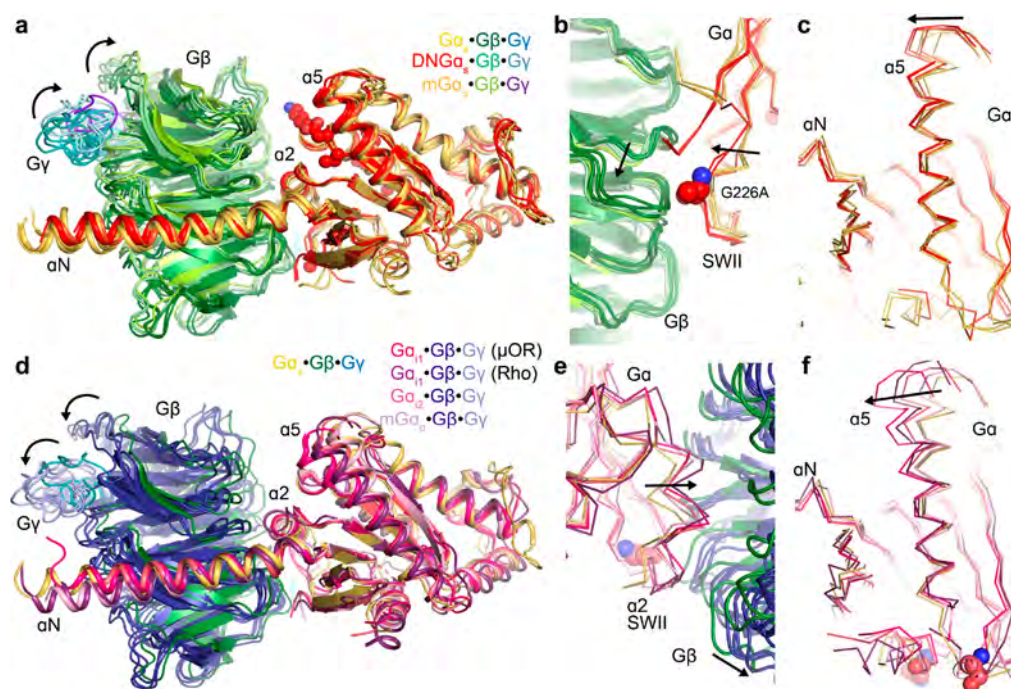


Figure 3. Heterotrimer conformations in GPCR-G protein complexes. (a–c) G_s and (d–f) $G_{i/o}$ heterotrimer conformations in receptor-G protein complexes aligned using the core of $G\alpha$ subunit. (a and c) $G\beta$ and $G\gamma$ rotate around SWII region in complexes formed with different $G_{i/o}$ family members or differently stabilized G_s complexes (wt G_s , DNG s , or m G_s); (b and e) conformation of SWII region affects $G\beta$ position relative to $G\alpha$ subunit; (c and f) flexibility of the $\alpha 5$ helix. Dominant negative mutations in GLP1R(ExP5) are shown in spheres.

changes are observed in both G_s - and $G_{i/o}$ -coupled receptor structures and are consistent with TM6 and TM7 movements that allow accommodation of the $\alpha 5$ helix of the $G\alpha$ subunit.

The most pronounced movements during receptor activation are observed for TM6 and TM7 (Figure 2). The ~ 2 Å inward shift of TM7 and H8 is similar between G_s and G_i coupled complex structures. However, the extent of displacement of TM6 appears to be, at least partially, dependent on the G protein subtype. For the class A GPCRs, the largest movement is observed in G_s -coupled β_2 AR and A_{2A} AR with 31.4° and 30.7° bends in TM6, relative to their inactive-state structures (PDBs 2RH1³¹ and 4E1Y,³² respectively) (Figure 2a). An even larger displacement is observed for G_s -coupled class B receptor structures with 63 – 73° angles for CTR, CLR, and GLP1R (all measured relative to the TM6 of the inactive-state glucagon receptor, PDB 4L6R³³) (Figure 2b). The $G_{i/o}$ coupling stabilizes conformations that exhibit smaller movements, the extent of which might also depend on the identity of the $G_{i/o}$ family member. The G_{i1} coupling leads to a 19.3° bend and an 18.3° bend in TM6 for μ OR and Rho, respectively (relative to PDBs 4DKL³⁴ and 1U19³⁵), G_{i2} to a 21° bend for A_1 AR (compare to SUEN³⁶) and G_o to a 24.4° bend for 5-HT_{1B} (compare to the “intermediate-active” 4IAR²⁸). Interestingly, both receptors with the smallest TM6 angle, μ OR and Rho, have ordered ICL3s that make interaction with the $\beta 1$ - $\alpha 1$ interface of the $G\alpha$ Ras domain. It is unclear whether the flexibility of ICL3 in other complexes is due to their longer length or increased distance from the G protein, as a consequence of the larger TM6 kink. Molecular dynamics simulations of Rho, μ OR, β_2 AR, and A_{2A} AR testing TM6 movement relative to the TM bundle revealed that the extent of TM6 displacement might be an intrinsic property of a particular receptor, with β_2 AR and A_{2A} AR undergoing larger TM6 swings, compared to Rho and μ OR.¹⁴

ICL1 differences are very subtle between GPCR-G protein complexes and inactive-state structures: it tends to move outward for most active-state structures, with the exception of A_{2A} AR and 5-HT_{1B}. ICL2 loops for A_1 AR, 5-HT_{1B}, β_2 AR, and A_{2A} AR adopt similar helical conformation. In contrast, Rho and μ OR ICL2 are shifted outward. This could contribute to the very different angle of engagement that $G\alpha$ adopts relative to Rho when compared to other structures (discussed below).

■ G PROTEIN ACTIVATION MECHANISMS

To understand conformational differences between GPCR-G protein complexes, it is important to compare structures of G proteins in the absence of receptors in an effort to distinguish changes arising from binding to different GPCRs from variations between G protein family members or complex stabilization techniques.

Previous structural studies and molecular dynamics simulations revealed that GPCR binding causes similar global conformational changes in both G_s and $G_{i/o}$ heterotrimers.^{37–39} Rotation and extension of the $\alpha 5$ helix into the receptor core is associated with disorder in the nucleotide binding site at the interface of the RHD and AHD of the $G\alpha$ subunit (P-loop and $\beta 6$ - $\alpha 5$ loop), nucleotide release and the opening of the interface between the RHD and AHD. Without stabilization by crystal contacts (β_2 AR- G_s) or Fab (Rho- G_{i1}), AHDs remain very flexible, as seen in class 2D averages in negative stain and cryo-EM.^{8,11–13,16} While this domain is generally masked out to maximize the resolution of EM maps, the available data indicate that there can be a preferred orientation (as seen with the ExP5 bound GLP-1R complex¹⁰), or multiple identifiable orientations (as seen with the sCT bound CTR⁸). The extent to which the relative mobility of the AHD of $G\alpha$ -subunits is a property of the specific receptor with which it is engaged or is a component of the specific agonist-

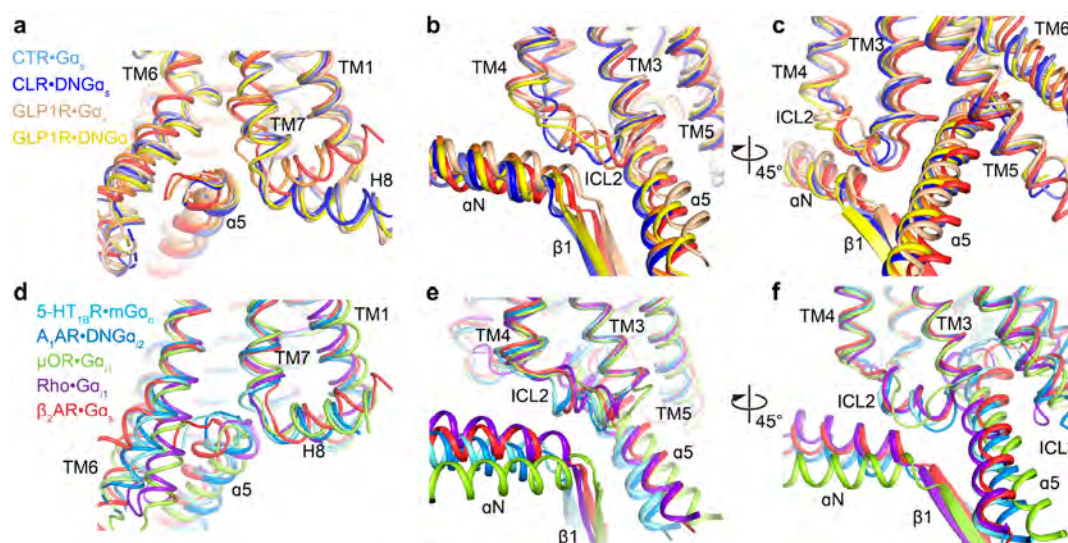


Figure 4. Receptor- $G\alpha$ orientations are influenced by TM6 movement and ICL2 conformation. (a–c) $G\alpha_s$ and (d–f) $G\alpha_{i/o}$ shifts relative to the receptor in different structures. GPCR-G protein complexes were aligned using TM bundles. $G\beta$, $G\gamma$, and the majority of $G\alpha$ (with the exception of αN , $\alpha 5$ helices and the $\beta 1$ sheet) are not shown for clarity. Structures a and d show $\alpha 5$ helix displacement; structures b, c, e, and f show αN and $\alpha 5$ helix displacement caused by ICL2 and TM5/ICL3 of the receptor. Receptors are displayed in thinner cartoon, compare to $G\alpha$.

GPCR complex, is unclear. However, biophysical studies using bioluminescence energy transfer have demonstrated that conformational sampling of the G protein, linked to the position of the α -helical domain, can be influenced by individual agonists and may contribute to observed efficacy.^{10,40}

Superposition of G_s complexes, on the core of the RHD of $G\alpha_s$ (excluding $\alpha 5$ and αN helices), revealed that stabilizing mutations have subtle effects on heterotrimer conformation leading to reduced flexibility of DN- G_s heterotrimers compared to WT- G_s (Figure 3). Notably, $G\beta$ and $G\gamma$ subunits of WT- G_s heterotrimers appear to adopt multiple positions relative to $G\alpha$, which is not observed for complexes formed with DN- G_s . This is likely the effect of G226A mutation in DNG α_s that causes a different backbone conformation of the $\beta 3$ - $\alpha 2$ loop in the switch II (SWII) region of $G\alpha$, leading to SWII stabilization and reduced affinity for GTP.²⁴ The stabilized SWII region makes stronger interactions with $G\beta$ leading to reduced flexibility of the $G\alpha$ - $G\beta$ subunit orientations in DN- G_s . In contrast, in complexes formed with WT- G_s , $G\beta$ rotates around SWII leading to an ~ 4 Å displacement; measured at T34 C α of $G\beta$ (β_2 AR and GLP1R/GLP1 complexes). Because of the extensive interactions of the $G\beta$, their displacement, in turn, affects the orientation of the αN helix relative to the core of the $G\alpha$ subunit, leading to different degrees of αN rotation away from the $\alpha 4$ helix of $G\alpha$ in different WT- G_s complexes. Increased flexibility of WT- G_s heterotrimers extends to the $\alpha 5$ helix, resulting in maximal differences of 3.2 Å at E390 C α for WT- G_s (β_2 AR and CTR complexes) compared to only 1.3 Å for DN- G_s (GLP1R(ExP5) and CLR-RAMP complexes). The flexibility in the $\alpha 5$ helix could potentially be the result of other DN mutations, crystallographic artifacts for the β_2 AR complex, or a strain induced by interactions with individual agonist:GPCR complexes. While these data are intriguing, we still have only a very limited number of solved structures, and no direct comparisons of the same agonist:GPCR in complex with WT-G versus DN-G, which will be required to more

definitively classify the distinct effects of stabilizing technologies.

A comparison of activated $G_{i/o}$ and G_s heterotrimers reveals G protein family specific variations. Different amino acid sequences and, thus, the conformation of the SWII region lead to a rotation of the $G\beta$ subunit relative to $G\alpha$ for $G_{i/o}$ versus G_s proteins, though in an opposite direction to that seen with DN- G_s . The $G\beta$ rotation is followed by an αN tilt away from the $\alpha 4$ helix of $G\alpha$ with the largest displacement observed for 5-HT_{1B}R. The $\alpha 5$ helix also adopts multiple conformations, with variations of tilt angles relative to the $G\alpha$ core. The degree of $G\beta$, αN , and $\alpha 5$ displacement is different between different $G_{i/o}$ complexes and it is unclear whether it is the result of the specific $G\alpha$ subunit, complex stabilization method, or bound receptor. Other G protein-specific variations include much longer αG - $\alpha 4$ loops in $G\alpha_s$ that extend toward ICL3 of the receptor, however, no interactions with ICL3 are apparent. Interestingly, the αG and $\alpha 1$ loops are displaced in Rho- $G_{i/o}$ complex structure, compared to other $G_{i/o}$ complexes, this could be a result of Fab G50 binding to both the $G\beta$ and AHD of $G\alpha$ and stabilization of a particular lower energy conformation.

■ G PROTEIN ENGAGEMENT OF ACTIVATED GPCRS

Comparison of all 10 available GPCR-G protein heterotrimer complex structures allowed us, for the first time, to propose general rules for G protein engagement and to identify distinct aspects in the mode of engagement for different G protein families. Class A and class B GPCRs share low sequence identity and are quite different in their tertiary structure. Subsequently, we only aligned receptors within each receptor family for detailed G protein binding comparison, with the exception of a general analysis of G_s engagement with class A and class B GPCRs where we aligned the lower halves of the β_2 AR and A_{2A}AR TM bundles with the GLP-1R (ExP5) structure.

The most extensive interactions between GPCRs and G proteins occur via the $\alpha 5$ helix of the RHDs: this extends into the receptor core and principally interacts with the bottom

halves of TM3, TM5, TM6, along with ICL2 and ICL3. However, different complexes have other, less pronounced, interfaces that may be receptor and/or G protein-specific.

Comparison of G_s complexes reveals that the $G\alpha$ C-terminal loop ("wavy hook") adopts a similar overall conformation within the receptor core of Class B GPCRs (Figure 4a). When compared to the position in class A receptors, the C-terminal loop exhibits lateral displacement of 3.7 Å (measured between Q390 C α), which is likely due to the distinct TM6 conformations between the major subclasses (Figure 2b). Interestingly, the $\alpha 5$ angle is fixed relative to TM3 of the receptor in all G_s structures (147–149°). However, the $G\alpha$ subunits (and thus, $G\beta\gamma$) in different G_s complexes rotate in the plane parallel to the membrane relative to the receptor (up to 12° rotation in GLP-1R(GLP-1)) using the β_2 AR structure as the reference. This is likely a consequence of either a difference in ICL2, H8, or both between class A and class B receptors; however, the lack of lipid environment in a detergent micelle could also play a role. It is possible that the ICL2 size and conformation could determine $G\alpha_s$ orientation relative to the receptor, with longer ICL2s creating steric hindrance with the middle part of the $\alpha 5$ helix, potentially leading to $\alpha 5$ tilting away from ICL2, followed by a rotation in the entire $G\alpha$ subunit, and consequently also $G\beta\gamma$. In particular, β_2 AR and A_{2A} AR display a small two-turn helix in ICL2 that packs against the interface of the αN - $\beta 1$ junction, $\beta 2$ - $\beta 3$ turn and $\alpha 5$ helix (Figure 4b,c) "pushing" the $\alpha 5$ helix toward TM5. The hydrophobic amino acid, F139 in ICL2, is important for a G_s -mediated response from β_2 AR and for G_q -mediated responses for M1 and M3 muscarinic acetylcholine receptors (mAChRs),⁴¹ indicating that ICL2 is important for G protein interaction for at least some of class A GPCRs. In contrast, $\alpha 5$ interactions with ICL2 of class B GPCRs that lack an equivalent helical structure and are shorter in length (5 residues in GLP-1R and 8 residues in CTR and CLR), likely lead to its rotation away from TM5. Alternatively, the different angle of heterotrimer interaction between class A and class B receptors could result from differences in the orientation of helix 8 (H8). Compared to solved class A complexes, the longer H8 in class B GPCRs is tilted away from the plane of the membrane (~20° tilt compared to class A GPCRs) that might, through distinct interactions with the $G\beta$ subunit, lead to the repositioning of the entire heterotrimer.

Comparison of the class B CLR:RAMP1- and CTR- G_s complexes, solved using DN or WT $G\alpha_s$ subunit, respectively, revealed that the DN mutations had little effect on $G\alpha$ orientation relative to the receptor when compared to the effect caused by amino acid divergence across the receptors and local conformational changes between the GPCR structures. The GLP-1R has a shorter ICL2 compared to either CTR or CLR and this likely causes the ~5° difference in angle in the engagement of $G\alpha_s$ between these receptors. There is evidence that the C-terminus of RAMP can potentially influence G protein binding;^{42,43} however, it was unresolved in CLR:RAMP1: G_s density,⁹ and it is likely that this interaction is either transient or requires additional accessory proteins, such as RCP.⁴⁴

Compared to G_s complexes, the "wavy hook" at the extreme end of the $\alpha 5$ helix in $G_{i/o}$ subunits is translated toward ICL1 and the TM7–H8 junction (Figure 4c). The degree of this shift is directly proportional to the extent that TM6 kinks upon receptor activation, with the largest movement observed for

G_{i1} -bound Rho and μ OR, followed by G_{i2} -bound A_1 AR, mG $_o$ -bound 5-HT $_{1B}$ R, and G_s complexes of β_2 AR and A_{2A} AR.

Similar to class B GPCRs, the angle of the $\alpha 5$ helix insertion (and, thus, αN position and the tilt of the entire G protein) appears to depend on ICL2 and TM5 interactions with the $G\alpha$ subunit. More extensive interactions with the middle part of the $G\alpha$ protein $\alpha 5$ helix rigidify its position in G_s complexes (via conserved H-bonds with Q384^{G.H5.16} and R385^{G.H5.17} or a salt bridge with D381^{G.H5.13}). In contrast, the receptor- $G_{i/o}$ subunit interactions primarily depend on weak van der Waals interactions, with the exception of a salt bridge through D342^{G.H5.13} in G_{i2} and mG $_o$ complexes, and H-bonds (K345^{G.H5.17} for G_{i1} -Rho and N347^{G.H5.19} for G_{i1} - μ OR) leading to an increased $\alpha 5$ helix-TM3 angle (152–162°) and larger spreads in $G\alpha$ rotation angles relative to the receptor (8–22°) (Figure 4d,e). Most notably, the ICL2 of Rho lacks any secondary structure and adopts a unique conformation by extending away from the receptor. As a result, the G_{i1} rotates, relative to the receptor, preserving potential contacts between ICL2 and the αN helix, leading to a substantially different receptor-G protein organization compared to other complexes.¹⁴

Interactions with ICL3 of receptors might also influence G protein orientation relative to the receptor. Unfortunately, ICL3s are not well resolved in all available structures though this likely reflects the extent of conformational dynamics for individual GPCR:G protein complexes. For example, the density of the A_1 AR- G_{i2} complex map suggests likely interactions between ICL3 and the $G\alpha$ subunit; however, the map quality was insufficient for modeling, indicative of conformational fluidity of this receptor segment in the active structure. Note that this loop is better resolved for Rho and μ OR suggesting that receptors with smaller TM6 kinks possibly have less flexibility due to proximity to interacting $G\alpha$. The length of ICL3 also varies dramatically between receptors. Thus, the unresolved ICL3 in A_1 AR, 5-HT $_{1B}$ R β_2 AR, and A_{2A} AR might simply reflect flexibility and/or lack of secondary structure elements. Nonetheless, for the class B GLP-1R, for which structures have been solved with multiple peptide agonists, it has been speculated that stability of the interactions between ICL3 and G_s , reflected in the ICL3 map density, may be linked to G protein turnover and thus agonist efficacy.⁵

Taking all available structures into consideration, it appears that the TM6 movement and the G protein $\alpha 5$ C-terminal loop position might depend on the G protein family member in complex with the receptor, while interactions of ICL2 with the $\alpha 5$ helix might be receptor specific.

■ BASIS OF SELECTIVITY BETWEEN G_s AND $G_{i/o}$ COMPLEXES

GPCRs frequently couple to multiple G protein families. This includes the β_2 AR and A_1 AR that couple to G_s and $G_{i/o}$, making it very difficult to identify receptor residues responsible for the selective engagement of a particular binding partner. Even the $G_{i/o}$ exclusive coupler μ OR can activate multiple $G\alpha$ subunits from that family. Multiple investigators have attempted to identify consensus motifs for G protein binding, with limited success. This is likely due to a large divergence in the amino acid sequences of GPCRs that can couple to particular G proteins. As such, the determinants of G protein binding are likely formed by a three-dimensional epitope during receptor activation; this could differ from one receptor

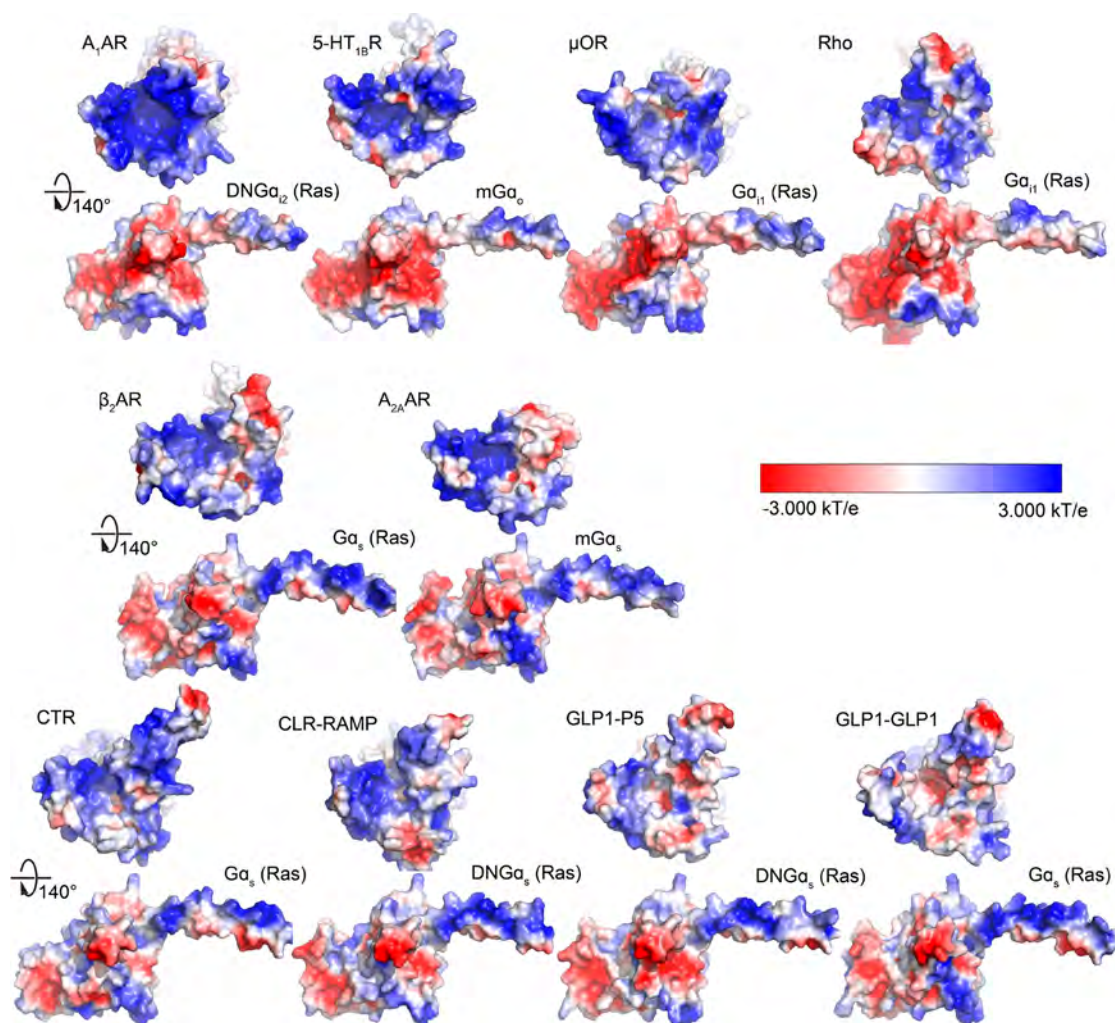


Figure 5. Electrostatic charge distribution in G protein complexes. Surface representation of receptors and $G\alpha$ subunits colored according to their electrostatic charge. Charge distribution was calculated using APBS plugin in Pymol⁵⁹ following reinstatement of full side-chains where these had been stubbed in the deposited structures.

to another and, at least in part, depend on the extent of TM6 movement.⁴⁵ Nevertheless, some generalizations can be made from the comparison of the available active-state structures.

A concentration of positive charge on the intracellular side of GPCRs has been noted previously and is proposed to be important for interactions with arrestins.⁴⁶ Indeed, there is a concentration of positively charged amino acids at the G protein-binding interface that is more prominent for the class A receptors solved to date (relative to class B GPCRs); nonetheless, the charge distribution appears to vary between receptors (Figure 5). In most class A and class B receptors, the TM6–TM7 surface that faces the G protein binding site appears to be positively charged; however, the μ OR and GLP-1R appear to be exceptions. While the end of the G protein $\alpha 5$ helix is negatively charged in all $G\alpha$ subunits, $G\alpha_{11}$, $G\alpha_{12}$, and $mG\alpha_o$ have a complementary large negative charged surface formed by the $\alpha 5$, $\alpha 4$, and $\beta 6$ interface. It is tempting to speculate that this charge–charge interaction could be important for receptors engaging with $G_{i/o}$ proteins. In addition, flexibility in ICL3 that is enriched in positively charged amino acids for most class A receptors could contribute to dynamic interactions between the receptor and G protein. Though speculative, changes in ICL3 conformations induced by different biased agonists could alter the strength of

G protein coupling and alter relative signaling efficacy. ICL3 is poorly resolved in the class A A_1 AR, 5-HT_{1B}R, β_2 AR, and A_{2A} AR consistent with the potential for agonist-dependent changes to conformational sampling to contribute to the strength and specificity of G protein binding via with this interface. It is important to note that, physiologically, GPCR:G protein interactions occur within a lipid bilayer enriched in polar lipid headgroups, and interactions between both G proteins and lipids and between receptor and lipids are functionally relevant. These play an important role in GPCR stability, GPCR:G protein interactions, and G protein activation,^{47–50} and are likely to provide limitations on orientations of G protein engagement with receptors that do not occur in detergents. To date, only the β_2 -AR:Gs and A_{2A} AR:miniGs solved by lipidic cubic phase crystallography are in a lipidic environment,^{5,19} though it is encouraging that the orientation of miniGs alone and miniGs-G $\beta\gamma$ are equivalent in complexes with agonist-bound A_{2A} AR, solved by crystallography and cryoEM, respectively.^{7,19}

Most fully active GPCR complexes solved to date have been determined at a resolution sufficient for reasonably confident side chain placement (<4 Å), particularly for the GPCR:G protein interface, and thus informative comparisons between structures can be made. While there is no obvious consensus

G proteins

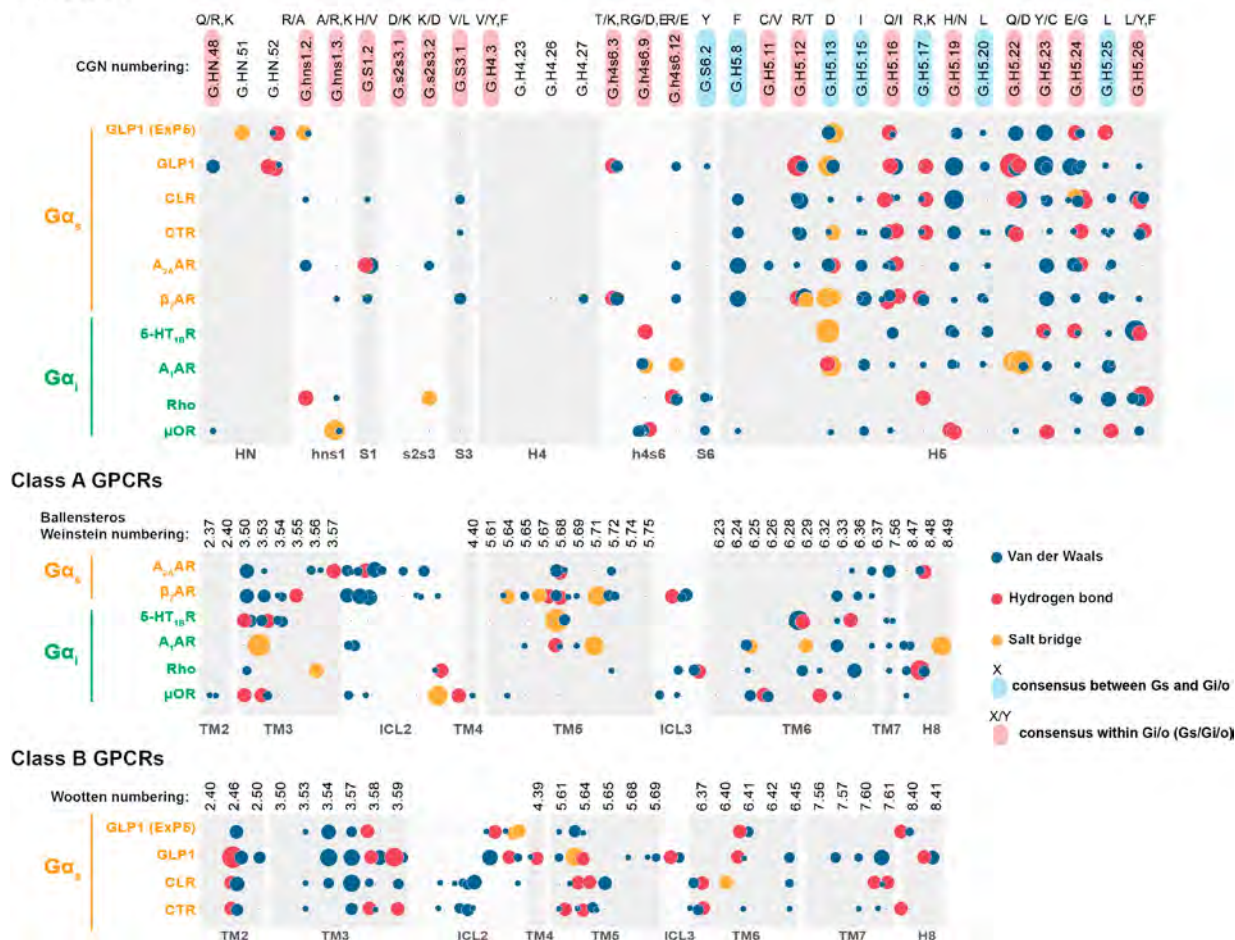


Figure 6. Receptor- $G\alpha$ subunit interaction map in determined complex structures. Panels represent van der Waals (blue), H-bonds (red), and salt bridge (yellow) interactions observed in X-ray or cryo-EM structures, as calculated by 2P2I Inspector⁶⁰ using 3.5 Å, 4 Å, and 4.5 Å cut-offs for H-bond, van der Waals, and salt bridge interactions, respectively. The relative size of the depicted interaction is proportional to bond energy (proportional to the number of formed interactions for van der Waals bonds).

sequence(s) that discriminate between G_i and G_s binding, there are some receptor regions that seem to be selectively engaged: receptors in G_s complexes appear to have more interactions through their ICL2 and TMS, while TM6 and H8 are more engaged in $G_{i/o}$ complexes; this is in good correlation with the overall difference in G protein orientation relative to receptors (see above) (Figure 6). The importance of binding domains, rather than amino acid sequence for G protein selectivity have been proposed previously⁵¹ and is an attractive hypothesis considering the plethora of GPCRs that couple to relatively few $G\alpha$ subunits.

Specific for G_s binding, residue 5.64 (Wootten numbering is used for class B GPCRs) and the equivalent class A residue 5.68 (Ballesteros–Weinstein numbering) make strong interactions with the $G\alpha$ protein $\alpha 5$ helix either via H-bond to Q384^{G.H5.16} (CGN numbering,⁵² Ile in $G_{i/o}$ family) or a salt bridge with D381^{G.H5.13} (conserved in both G protein families). Other class B-specific interactions include a H-bond between Q384^{G.H5.16} and the backbone of residue 3.58, and a H-bond between D380^{G.H5.22} and the absolutely conserved class B GPCR residue, R^{2.46}.

In addition, receptor-specific interactions also contribute to G protein binding. Thus, ICL2 of μ OR makes strong interactions with the αN - $\beta 1$ junction, via a D177^{34.55}.

R32^{G.hns1.3} salt bridge, and the G protein $\alpha 5$ helix, via R179^{34.57}-D350^{G.H5.22} H-bond. In GLP-1R, ICL2 also contributes to G protein binding via a S261-Q35^{HN.51} H-bond, and E262^{4.38}-K34^{G.HN.51} and R38^{G.hns1.2} salt bridges.

G protein residues responsible for receptor discrimination are also more likely to follow general trends as opposed to hard rules, given the different angle of $\alpha 5$ insertion into the receptor core. $G_{i/o}$ subunits primarily engage the receptor via the C-terminal part of the $\alpha 5$ helix and the “wavy hook” residues, in the same way as $G_{\alpha s}$. This is consistent with prior studies that identified the last five amino acid residues of the $\alpha 5$ helix as sufficient for switching G protein selectivity.^{53,54} Interestingly, the last three amino acids of $G_{\alpha 12}$ are all that is required for gaining coupling of a $G_{\alpha i}$ chimera to the A_1 AR and D_2 dopamine receptor⁵⁵ that preferentially couples to $G_{i/o}$ proteins. This is likely explained by steric hindrance between the TM7-H8 junction and larger side chains at the −3 positions of the $\alpha 5$ C-terminus in G_s (Glu) and G_q (Asn) families compared to the absolutely conserved Gly in the $G_{i/o}$ family. The larger TM6 movements observed in G_s complexes positions the $\alpha 5$ helix further away from TM7, allowing for accommodation of bulkier side chains.

While the C-terminus of $\alpha 5$ is also important for G_s binding, the middle of $\alpha 5$ appears to contribute strong interactions for

receptor engagement. In particular, residue Q384^{GHS.16} makes a H-bond in all G_s complexes. In contrast, G_{i/o} complexes compensate for fewer $\alpha 5$ contacts with additional $\alpha 4$ - $\beta 6$ loop interactions, and this may possibly be linked to a smaller TM6 movement. In agreement with this, interactions with the $\alpha 4$ helix and/or $\alpha 4$ - $\beta 6$ loop were found to be important for G_{i/o} coupling for a number of receptors (5-HT_{1A}R, 5-HT_{1B}R and M₂mACHR,⁵¹ Rho⁵⁶) and could also be involved as determinants of selectivity within the G_{i/o} family, for example, for discrimination between G α_t and G α_{i1} subunits.⁵¹ In contrast, the $\alpha 4$ - $\beta 6$ loop is not essential for G_s coupling to the β_2 AR,⁵⁷ consistent with the hypothesis that, in different G protein families, distinct domains of the G α subunit could be responsible for receptor selectivity.

It is expected that with the wide adaptation of cryo-EM the number of GPCR-G protein structures will continue to rise rapidly, providing many more GPCR-G protein complexes that will advance our understanding of molecular mechanisms of cellular signaling. An important caveat to the interpretation of available (and likely future) structural data is that they are determined in non-native environments. All cryo-EM structures to date have been solved in detergent micelles, and it is well-known that G proteins form subtype-, and subunit-, specific interactions with lipids (reviewed in ref 58) that may spatially restrict the relative orientations that G proteins can adopt when bound to activated receptor. Crystal structures require distinct stabilization strategies and very specific conditions to allow productive crystal packing. Comparisons of individual agonist:GPCR complexes, solved by alternate stabilization technologies, and solved in both detergent and more native lipid environments, will be required for a more nuanced understanding of what the new structures can tell us about G protein selectivity and activation; behaviors that are critical to mechanistic understanding of efficacy and biased agonism. For example, contact differences occur between the GLP-1 receptor and Gs protein in structures solved with agonists of different efficacy (Figure 6, lower panel),^{10,11} indicating that the nature of the ligand will contribute to the transducer interface. Nonetheless, we have entered into an exciting new era of GPCR structural biology that promises to answer many long-held questions on how GPCRs work.

AUTHOR INFORMATION

Corresponding Authors

*E-mail: alisa.glukhova@monash.edu.

*E-mail: patrick.sexton@monash.edu.

ORCID

Patrick M. Sexton: 0000-0001-8902-2473

Notes

The authors declare no competing financial interest.

ACKNOWLEDGMENTS

P.M.S. is a Principal Research Fellow of the National Health and Medical Research Council of Australia (NHMRC). A.C. is a Senior Principal Research Fellow of the NHMRC. D.W. is a Career Development Fellow of the NHMRC. A.G. is an Australian Research Council (ARC) Discovery Early Career Researcher Award recipient.

REFERENCES

- (1) Mahoney, J. P., and Sunahara, R. K. (2016) Mechanistic insights into GPCR-G protein interactions. *Curr. Opin. Struct. Biol.* 41, 247–254.
- (2) Gurevich, E. V., Tesmer, J. J. G., Mushegian, A., and Gurevich, V. V. (2012) G protein-coupled receptor kinases: More than just kinases and not only for GPCRs. *Pharmacol. Ther.* 133, 40–69.
- (3) Luttrell, L. M., and Lefkowitz, R. J. (2002) The role of beta-arrestins in the termination and transduction of G-protein-coupled receptor signals. *J. Cell. Sci.* 115, 455–465.
- (4) Syrovatkina, V., Alegre, K. O., Dey, R., and Huang, X.-Y. (2016) Regulation, signaling, and physiological functions of G-proteins. *J. Mol. Biol.* 428, 3850–3868.
- (5) Rasmussen, S. G. F., DeVree, B. T., Zou, Y., Kruse, A. C., Chung, K. Y., Kobilka, T. S., Thian, F. S., Chae, P. S., Pardon, E., Calinski, D., Mathiesen, J. M., Shah, S. T. A., Lyons, J. A., Caffrey, M., Gellman, S. H., Steyaert, J., Skiniotis, G., Weiss, W. I., Sunahara, R. K., and Kobilka, B. K. (2011) Crystal structure of the β_2 adrenergic receptor-Gs protein complex. *Nature* 477, 549–555.
- (6) Kuhlbrandt, W. (2014) The Resolution Revolution. *Science* 343, 1443–1444.
- (7) García-Nafria, J., Lee, Y., Bai, X., Carpenter, B., and Tate, C. G. (2018) Cryo-EM structure of the adenosine A2A receptor coupled to an engineered heterotrimeric G protein. *eLife* 7, 213.
- (8) Liang, Y.-L., Khoshouei, M., Radjainia, M., Zhang, Y., Glukhova, A., Tarrasch, J., Thal, D. M., Furness, S. G. B., Christopoulos, G., Coudrat, T., Danev, R., Baumeister, W., Miller, L. J., Christopoulos, A., Kobilka, B. K., Wootten, D., Skiniotis, G., and Sexton, P. M. (2017) Phase-plate cryo-EM structure of a class B GPCR-G-protein complex. *Nature* 546, 118–123.
- (9) Liang, Y.-L., Khoshouei, M., Deganutti, G., Glukhova, A., Koole, C., Peat, T. S., Radjainia, M., Plitzko, J. M., Baumeister, W., Miller, L. J., Hay, D. L., Christopoulos, A., Reynolds, C. A., Wootten, D., and Sexton, P. M. (2018) Cryo-EM structure of the active, Gs-protein complexed, human CGRP receptor. *Nature*, DOI: 10.1038/s41586-018-0535-y.
- (10) Liang, Y.-L., Khoshouei, M., Glukhova, A., Furness, S. G. B., Zhao, P., Clydesdale, L., Koole, C., Truong, T. T., Thal, D. M., Lei, S., Radjainia, M., Danev, R., Baumeister, W., Wang, M.-W., Miller, L. J., Christopoulos, A., Sexton, P. M., and Wootten, D. (2018) Phase-plate cryo-EM structure of a biased agonist-bound human GLP-1 receptor-Gs complex. *Nature* 555, 121–125.
- (11) Zhang, Y., Sun, B., Feng, D., Hu, H., Chu, M., Qu, Q., Tarrasch, J. T., Li, S., Sun Kobilka, T., Kobilka, B. K., and Skiniotis, G. (2017) Cryo-EM structure of the activated GLP-1 receptor in complex with a G protein. *Nature* 546, 248–253.
- (12) Draper-Joyce, C. J., Khoshouei, M., Thal, D. M., Liang, Y.-L., Nguyen, A. T. N., Furness, S. G. B., Venugopal, H., Baltos, J.-A., Plitzko, J. X. R. M., Danev, R., Baumeister, W., May, L. T., Wootten, D., Sexton, P. M., Glukhova, A., and Christopoulos, A. (2018) Structure of the adenosine-bound human adenosine A₁ receptor-Gi complex. *Nature* 558, 559–563.
- (13) Koehl, A., Hu, H., Maeda, S., Zhang, Y., Qu, Q., Paggi, J. M., Latorraca, N. R., Hilger, D., Dawson, R., Matile, H., Schertler, G. F. X., Granier, S., Weiss, W. I., Dror, R. O., Manglik, A., Skiniotis, G., and Kobilka, B. K. (2018) Structure of the μ -opioid receptor-Gi protein complex. *Nature* 558, 547–552.
- (14) Kang, Y., Kuybeda, O., de Waal, P. W., Mukherjee, S., Van Eps, N., Dutka, P., Zhou, X. E., Bartsaghi, A., Erramilli, S., Morizumi, T., Gu, X., Yin, Y., Liu, P., Jiang, Y., Meng, X., Zhao, G., Melcher, K., Ernst, O. P., Kossiakoff, A. A., Subramaniam, S., and Xu, H. E. (2018) Cryo-EM structure of human rhodopsin bound to an inhibitory G protein. *Nature* 558, 553–558.
- (15) García-Nafria, J., Némé, R., Edwards, P. C., and Tate, C. G. (2018) Cryo-EM structure of the serotonin 5-HT_{1B} receptor coupled to heterotrimeric Go. *Nature* 558, 620–623.
- (16) Westfield, G. H., Rasmussen, S. G. F., Su, M., Dutta, S., DeVree, B. T., Chung, K. Y., Calinski, D., Velez-Ruiz, G., Oleskie, A. N., Pardon, E., Chae, P. S., Liu, T., Li, S., Woods, V. L., Steyaert, J.,

- Kobilka, B. K., Sunahara, R. K., and Skiniotis, G. (2011) Structural flexibility of the G α s α -helical domain in the β 2-adrenoceptor Gs complex. *Proc. Natl. Acad. Sci. U. S. A.* 108, 16086–16091.
- (17) Carpenter, B., and Tate, C. G. (2016) Engineering a minimal G protein to facilitate crystallisation of G protein-coupled receptors in their active conformation. *Protein Eng. Des. Sel.* 29, 583–594.
- (18) Nehmé, R., Carpenter, B., Singhal, A., Strege, A., Edwards, P. C., White, C. F., Du, H., Grisshammer, R., Garcia-Nafria, J., and Shukla, A. (2017) Mini-G proteins: Novel tools for studying GPCRs in their active conformation. *PLoS ONE* 12, e0175642.
- (19) Carpenter, B., Nehmé, R., Warne, T., Leslie, A. G. W., and Tate, C. G. (2016) Structure of the adenosine A_{2A} receptor bound to an engineered G protein. *Nature* 536, 104–107.
- (20) Liang, Y.-L., Zhao, P., Draper-Joyce, C., Baltos, J.-A., Glukhova, A., Truong, T. T., May, L. T., Christopoulos, A., Wootten, D., Sexton, P. M., and Furness, S. G. B. (2018) Dominant negative G proteins enhance formation and purification of agonist-GPCR-G protein complexes for structure determination. *ACS Pharmacol. Transl. Sci.* 1, 12–20.
- (21) Berlot, C. H., and Bourne, H. R. (1992) Identification of effector-activating residues of Gs α . *Cell* 68, 911–922.
- (22) Berlot, C. H. (2002) A highly effective dominant negative Gs construct containing mutations that affect distinct functions inhibits multiple Gs-coupled receptor signaling pathways. *J. Biol. Chem.* 277, 21080–21085.
- (23) Cleator, J. H., Mehta, N. D., Kurtz, D. T., and Hildebrandt, J. D. (1999) The N54 mutant of G α has a conditional dominant negative phenotype which suppresses hormone-stimulated but not basal cAMP levels. *FEBS Lett.* 443, 205–208.
- (24) Iiri, T., Bell, S. M., Baranski, T. J., Fujita, T., and Bourne, H. R. (1999) A Gs α mutant designed to inhibit receptor signaling through Gs. *Proc. Natl. Acad. Sci. U. S. A.* 96, 499–504.
- (25) Lee, E., Taussig, R., and Gilman, A. G. (1992) The G226A mutant of Gs α highlights the requirement for dissociation of G protein subunits. *J. Biol. Chem.* 267, 1212–1218.
- (26) Huang, W., Manglik, A., Venkatakrishnan, A. J., Laeremans, T., Feinberg, E. N., Sanborn, A. L., Kato, H. E., Livingston, K. E., Thorsen, T. S., Kling, R. C., Granier, S., Gmeiner, P., Husbands, S. M., Traynor, J. R., Weis, W. I., Steyaert, J., Dror, R. O., and Kobilka, B. K. (2015) Structural insights into μ -opioid receptor activation. *Nature* 524, 315–321.
- (27) Lebon, G., Warne, T., Edwards, P. C., Bennett, K., Langmead, C. J., Leslie, A. G. W., and Tate, C. G. (2011) Agonist-bound adenosine A_{2A} receptor structures reveal common features of GPCR activation. *Nature* 474, 521–525.
- (28) Wang, C., Jiang, Y., Ma, J., Wu, H., Wacker, D., Katritch, V., Han, G. W., Liu, W., Huang, X.-P., Vardy, E., McCorvy, J. D., Gao, X., Zhou, X. E., Melcher, K., Zhang, C., Bai, F., Yang, H., Yang, L., Jiang, H., Roth, B. L., Cherezov, V., Stevens, R. C., and Xu, H. E. (2013) Structural basis for molecular recognition at serotonin receptors. *Science* 340, 610–614.
- (29) Erlandson, S. C., McMahon, C., and Kruse, A. C. (2018) Structural basis for G protein-coupled receptor signaling. *Annu. Rev. Biophys.* 47, 1–18.
- (30) Burg, J. S., Ingram, J. R., Venkatakrishnan, A. J., Jude, K. M., Dukkupati, A., Feinberg, E. N., Angelini, A., Waghay, D., Dror, R. O., Ploegh, H. L., and Garcia, K. C. (2015) Structural biology. *Science* 347, 1113–1117.
- (31) Rosenbaum, D. M., Cherezov, V., Hanson, M. A., Rasmussen, S. G. F., Thian, F. S., Kobilka, T. S., Choi, H.-J., Yao, X.-J., Weis, W. I., Stevens, R. C., and Kobilka, B. K. (2007) GPCR engineering yields high-resolution structural insights into β 2-adrenergic receptor function. *Science* 318, 1266–1273.
- (32) Liu, W., Chun, E., Thompson, A. A., Chubukov, P., Xu, F., Katritch, V., Han, G. W., Roth, C. B., Heitman, L. H., IJzerman, A. P., Cherezov, V., and Stevens, R. C. (2012) Structural basis for allosteric regulation of GPCRs by sodium ions. *Science* 337, 232–236.
- (33) Siu, F. Y., He, M., de Graaf, C., Han, G. W., Yang, D., Zhang, Z., Zhou, C., Xu, Q., Wacker, D., Joseph, J. S., Liu, W., Lau, J., Cherezov, V., Katritch, V., Wang, M.-W., and Stevens, R. C. (2013) Structure of the human glucagon class B G-protein-coupled receptor. *Nature* 499, 444–449.
- (34) Manglik, A., Kruse, A. C., Kobilka, T. S., Thian, F. S., Mathiesen, J. M., Sunahara, R. K., Pardo, L., Weis, W. I., Kobilka, B. K., and Granier, S. (2012) Crystal structure of the μ -opioid receptor bound to a morphinan antagonist. *Nature* 485, 321–326.
- (35) Okada, T., Sugihara, M., Bondar, A.-N., Elstner, M., Entel, P., and Buss, V. (2004) The retinal conformation and its environment in rhodopsin in light of a new 2.2 Å crystal structure. *J. Mol. Biol.* 342, 571–583.
- (36) Glukhova, A., Thal, D. M., Nguyen, A. T., Vecchio, E. A., Jörg, M., Scammells, P. J., May, L. T., Sexton, P. M., and Christopoulos, A. (2017) Structure of the adenosine A₁ receptor reveals the basis for subtype selectivity. *Cell* 168, 867–877 e13.
- (37) Chung, K. Y., Rasmussen, S. G. F., Liu, T., Li, S., DeVree, B. T., Chae, P. S., Calinski, D., Kobilka, B. K., Woods, V. L., and Sunahara, R. K. (2011) Conformational changes in the G protein Gs induced by the β 2 adrenergic receptor. *Nature* 477, 611–615.
- (38) Dror, R. O., Mildorf, T. J., Hilger, D., Manglik, A., Borhani, D. W., Arlow, D. H., Philippesen, A., Villanueva, N., Yang, Z., Lerch, M. T., Hubbell, W. L., Kobilka, B. K., Sunahara, R. K., and Shaw, D. E. (2015) Structural basis for nucleotide exchange in heterotrimeric G proteins. *Science* 348, 1361–1365.
- (39) Kaya, A. I., Lokits, A. D., Gilbert, J. A., Iverson, T. M., Meiler, J., and Hamm, H. E. (2014) A conserved phenylalanine as a relay between the α 5 helix and the GDP binding region of heterotrimeric Gi protein α subunit. *J. Biol. Chem.* 289, 24475–24487.
- (40) Furness, S. G. B., Liang, Y.-L., Nowell, C. J., Halls, M. L., Wookey, P. J., Dal Maso, E., Inoue, A., Christopoulos, A., Wootten, D., and Sexton, P. M. (2016) Ligand-dependent modulation of G protein conformation alters drug efficacy. *Cell* 167, 739–744 e11.
- (41) Moro, O., Lameh, J., Högger, P., and Sadée, W. (1993) Hydrophobic amino acid in the i2 loop plays a key role in receptor-G protein coupling. *J. Biol. Chem.* 268, 22273–22276.
- (42) Udawela, M., Christopoulos, G., Morfis, M., Christopoulos, A., Ye, S., Tilakaratne, N., and Sexton, P. M. (2006) A critical role for the short intracellular C terminus in receptor activity-modifying protein function. *Mol. Pharmacol.* 70, 1750–1760.
- (43) Udawela, M., Christopoulos, G., Tilakaratne, N., Christopoulos, A., Albiston, A., and Sexton, P. M. (2006) Distinct receptor activity-modifying protein domains differentially modulate interaction with calcitonin receptors. *Mol. Pharmacol.* 69, 1984–1989.
- (44) Dickerson, I. M. (2013) Role of CGRP-receptor component protein (RCP) in CLR/RAMP function. *Curr. Protein Pept. Sci.* 14, 407–415.
- (45) Rose, A. S., Elgeti, M., Zachariae, U., Grubmüller, H., Hofmann, K. P., Scheerer, P., and Hildebrand, P. W. (2014) Position of transmembrane helix 6 determines receptor G protein coupling specificity. *J. Am. Chem. Soc.* 136, 11244–11247.
- (46) Kang, Y., Zhou, X. E., Gao, X., He, Y., Liu, W., Ishchenko, A., Barty, A., White, T. A., Yefanov, O., Han, G. W., Xu, Q., de Waal, P. W., Ke, J., Tan, M. H. E., Zhang, C., Moeller, A., West, G. M., Pascal, B. D., Van Eps, N., Caro, L. N., Vishnivetskiy, S. A., Lee, R. J., Suino-Powell, K. M., Gu, X., Pal, K., Ma, J., Zhi, X., Boutet, S., Williams, G. J., Messerschmidt, M., Gati, C., Zatspein, N. A., Wang, D., James, D., Basu, S., Roy-Chowdhury, S., Conrad, C. E., Coe, J., Liu, H., Lisova, S., Kupitz, C., Grotjohann, I., Fromme, R., Jiang, Y., Tan, M., Yang, H., Li, J., Wang, M., Zheng, Z., Li, D., Howe, N., Zhao, Y., Standfuss, J., Diederichs, K., Dong, Y., Potter, C. S., Carragher, B., Caffrey, M., Jiang, H., Chapman, H. N., Spence, J. C. H., Fromme, P., Weierstall, U., Ernst, O. P., Katritch, V., Gurevich, V. V., Griffin, P. R., Hubbell, W. L., Stevens, R. C., Cherezov, V., Melcher, K., and Xu, H. E. (2015) Crystal structure of rhodopsin bound to arrestin by femtosecond X-ray laser. *Nature* 523, 561–567.
- (47) Dawaliby, R., Trubbia, C., Delporte, C., Masureel, M., Van Antwerpen, P., Kobilka, B. K., and Govaerts, C. (2016) Allosteric

regulation of G protein-coupled receptor activity by phospholipids. *Nat. Chem. Biol.* 12, 35–39.

(48) Jastrzebska, B., Goc, A., Golczak, M., and Palczewski, K. (2009) Phospholipids are needed for the proper formation, stability, and function of the photoactivated rhodopsin–transducin complex. *Biochemistry* 48, 5159–5170.

(49) Inagaki, S., Ghirlando, R., White, J. F., Gvozdenovic-Jeremic, J., Northup, J. K., and Grisshammer, R. (2012) Modulation of the Interaction between Neurotensin Receptor NTS1 and Gq Protein by Lipid. *J. Mol. Biol.* 417, 95–111.

(50) Gibson, N. J., and Brown, M. F. (1993) Lipid headgroup and acyl chain composition modulate the MI-MII equilibrium of rhodopsin in recombinant membranes. *Biochemistry* 32, 2438–2454.

(51) Slessareva, J. E., Ma, H., Depree, K. M., Flood, L. A., Bae, H., Cabrera-Vera, T. M., Hamm, H. E., and Graber, S. G. (2003) Closely related G-protein-coupled receptors use multiple and distinct domains on G-protein α -subunits for selective coupling. *J. Biol. Chem.* 278, 50530–50536.

(52) Flock, T., Ravarani, C. N. J., Sun, D., Venkatakrishnan, A. J., Kayikci, M., Tate, C. G., Veprintsev, D. B., and Babu, M. M. (2015) Universal allosteric mechanism for $G\alpha$ activation by GPCRs. *Nature* 524, 173–179.

(53) Brown, A. J., Dyos, S. L., Whiteway, M. S., White, J. H., Watson, M. A., Marzioch, M., Clare, J. J., Cousens, D. J., Paddon, C., Plumpton, C., Romanos, M. A., and Dowell, S. J. (2000) Functional coupling of mammalian receptors to the yeast mating pathway using novel yeast/mammalian G protein α -subunit chimeras. *Yeast* 16, 11–22.

(54) Stewart, G. D., Valant, C., Dowell, S. J., Mijaljica, D., Devenish, R. J., Scammells, P. J., Sexton, P. M., and Christopoulos, A. (2009) Determination of adenosine A1 receptor agonist and antagonist pharmacology using *Saccharomyces cerevisiae*: implications for ligand screening and functional selectivity. *J. Pharmacol. Exp. Ther.* 331, 277–286.

(55) Conklin, B. R., Farfel, Z., Lustig, K. D., Julius, D., and Bourne, H. R. (1993) Substitution of three amino acids switches receptor specificity of Gq α to that of Gi α . *Nature* 363, 274–276.

(56) Natochin, M., Granovsky, A. E., Muradov, K. G., and Artemyev, N. O. (1999) Roles of the transducin α -subunit α 4-helix/ α 4- β 6 loop in the receptor and effector interactions. *J. Biol. Chem.* 274, 7865–7869.

(57) Grishina, G., and Berlot, C. H. (2000) A surface-exposed region of G(salpa) in which substitutions decrease receptor-mediated activation and increase receptor affinity. *Mol. Pharmacol.* 57, 1081–1092.

(58) Vögler, O., Barceló, J. M., Ribas, C., and Escribá, P. V. (2008) Membrane interactions of G proteins and other related proteins. *Biochim. Biophys. Acta, Biomembr.* 1778, 1640–1652.

(59) Jurrus, E., Engel, D., Star, K., Monson, K., Brandi, J., Felberg, L. E., Brookes, D. H., Wilson, L., Chen, J., Liles, K., Chun, M., Li, P., Gohara, D. W., Dolinsky, T., Konecny, R., Koes, D. R., Nielsen, J. E., Head-Gordon, T., Geng, W., Krasny, R., Wei, G.-W., Holst, M. J., McCammon, J. A., and Baker, N. A. (2018) Improvements to the APBS biomolecular solvation software suite. *Protein Sci.* 27, 112–128.

(60) Basse, M. J., Betzi, S., Bourgeas, R., Bouzidi, S., Chetrit, B., Hamon, V., Morelli, X., and Roche, P. (2012) 2P2ldb: a structural database dedicated to orthosteric modulation of protein–protein interactions. *Nucleic Acids Res.* 41, D824–D827.